UNIVERSITY OF ILORIN
FACULTY OF ENGINEERING AND TECHNOLOGY

1st FACULTY OF ENGINEERING AND TECHNOLOGY International Conference (FETiCON 2023)

Conference Proceedings

THEME:

ADVANCES AND TECHNOLOGICAL INNOVATIONS IN NATION BUILDING AND ATTAINMENT OF SUSTAINABLE DEVELOPMENT GOALS

5th-7th June, 2023

NLNG Building, Faculty of Engineering & Technology,
University of Ilorin, Ilorin, Nigeria.

SPONSORS

TotalEnergies

FEMTECH

...technology concern

IHS
Towers of strength

MARIMICH
NIGERIA LIMITED

item7go

7UP

YOLAS CONSULTANTS
Consulting with Experience and Integrity

KW-IRS
KWARA STATE INTERNAL REVENUE SERVICE

ARAFIMS
Hostels

SELLYFAK
ENERGY

PARTICIPANT COUNTRIES

FETiCON 2023 ORGANISING COMMITTEE

Prof. Omodele A. A. Eletta, Department of Chemical Engineering, University of Ilorin – General Chair
Prof. J. K. Odusote, Department of Materials and Metallurgical Engineering, University of Ilorin, Ilorin, Nigeria.
Dr. M. O. Sunmonu, Department of Food Engineering, University of Ilorin
Dr. Olubunmi A. Mokuolu, Department of Water Resources and Environmental Engineering, University of Ilorin
Dr. S. I. Talabi, Department of Materials & Metallurgical Engineering, University of Ilorin
Dr. Nasmat T. Surajudeen-Bankinde, Department of Electrical & Electronics Engineering, University of Ilorin
Dr. A. O. Otuoze, Department of Electrical & Electronics Engineering, University of Ilorin
Dr. T. D. Akpenpuun, Department of Agricultural & Biosystems Engineering, University of Ilorin
Dr. S. I. Mustapha, Department of Chemical Engineering, University of Ilorin
Dr. H.U. Hambali, Department of Chemical Engineering, University of Ilorin
Dr. O. O. Mohammed, Department of Electrical & Electronics Engineering, University of Ilorin
Dr. S. A. Yahaya, Department of Biomedical Engineering, University of Ilorin – General Secretary

PUBLICATIONS COMMITTEE

Dr. H. U. Hambali, Department of Chemical Engineering, University of Ilorin - Chair
Dr. A. B. Ehinmowo, Department of Chemical and Petroleum Engineering, University of Lagos, Nigeria
Dr. E. O. Ige, Afe Babalola University, Ado-Ekiti, Nigeria
Dr. T. D. Akpenpuun, Department of Agricultural & Biosystems Engineering, University of Ilorin, Ilorin.
Dr. S. A. Yahaya, Department of Biomedical Engineering, University of Ilorin – Secretary

EDITORS

Prof. Omodele A. A. Eletta
Prof. O. A. Lasode
Prof. J. K. Odusote

LOCAL ADVISORY COMMITTEE

Prof. O. A. Lasode, Dean, Faculty of Engineering and Technology, University of Ilorin, Ilorin.
Prof. B. F. Sule, Department of Water Resources and Environmental Engineering, University of Ilorin, Ilorin.
Prof. J. A. Olorunmaiye, Department of Mechanical Engineering, University of Ilorin, Ilorin.
Prof. D. S. Ogunniyi, Department of Chemical Engineering, University of Ilorin, Ilorin.
Prof. J. O. Olaoye, Department of Agricultural and Biosystems Engineering, University of Ilorin, Ilorin.

INTERNATIONAL ADVISORY COMMITTEE

Prof J. O. Ojo, Tennessee Technological University, Cookeville, USA
Prof. C. J. Hogan JR, Department of Mechanical Engineering, University of Minnesota, USA
Prof. W. Northrop, Department of Mechanical Engineering, University of Minnesota, USA
Prof. James Katende, Namibia University of Science and Technology
Prof. Yusuf Isa Makarfi, University of the Witwatersrand, Johannesburg, South Africa
Prof. Pandolfelli Victor Carlos, Federal University of São Carlos, Brazil.
Prof. Adnan Rasheed, Kyungpook National University Daegu, South Korea
Prof. Esther T. Ososanya, University of the District of Columbia, Washington DC
Prof. Sadhan K. Ghosh, Department of Mechanical Engineering and Coordinator, Centre for QMS, Jadavpur University, India.
Prof. A. M. Zungeru, Botswana University of Science and Technology, Botswana

www.feticon.com.ng
feticonchair@unilorin.edu.ng

PREFACE

It is with immense pleasure and a profound sense of accomplishment that we present the Book of Proceedings for the University of Ilorin 1st Faculty of Engineering International Conference (FETiCON 2023). This collection represents the culmination of a remarkable event that took place between 5th and 7th June 2023, bringing together brilliant minds from diverse disciplines within the realm of engineering and technological development.

FETiCON 2023 was envisioned as a platform to foster collaboration, share cutting-edge research, and inspire innovation that could drive sustainable technological development and nation-building. The conference was meticulously designed to encourage meaningful interactions among scientists, scholars, engineers, and industry leaders, creating an environment conducive to intellectual exploration and discovery.

Within these pages, we present a compilation of research papers, presentations, and insights that encapsulate the rich tapestry of ideas and advancements shared during the conference. The contributions come from a diverse array of professionals and scholars who have dedicated their expertise to addressing some of the most pressing challenges facing our world today.

The thematic areas covered in this book encompass a wide spectrum of engineering disciplines, including Aeronautic Engineering, Agricultural and Biosystems Engineering, Biomedical Engineering, Chemical Engineering, Civil Engineering, Computer Engineering, Electrical and Electronics Engineering, Food Engineering, Materials and Metallurgical Engineering, Mechanical Engineering, and Water Resources and Environmental Engineering. Each contribution reflects the dedication and passion of its respective authors, whose commitment to their fields of study is commendable.

This Book of Proceedings also serves as a testament to the invaluable support we have received from numerous individuals and organizations. We extend our deepest gratitude to our sponsors, whose generous contributions made this conference possible. Their commitment to promoting knowledge exchange and technological advancement is truly commendable.

We are equally indebted to our keynote speaker, plenary presenters, and all the presenters who enriched the conference with their insightful contributions. Their expertise and thought-provoking ideas have set new benchmarks for future research endeavors.

Our heartfelt appreciation also goes to our Vice Chancellor, Professor Wahab Olasupo Egbewole and all principal officers, our Dean, Professor Olumuyiwa Ajani Lasode, the faculty members, students, and dedicated conference planning committee who worked tirelessly to ensure the smooth organization and seamless execution of FETiCON 2023. Your efforts have left an indelible mark on the success of this conference. We also remember the good effort of Late Professor M.F. Akorede, with whom this journey was started. May the good Lord continue to rest his soul in peace.

Lastly, we express our gratitude to the University of Ilorin and all supporting institutions for their unwavering support and encouragement. Their commitment to promoting excellence in engineering and technology education has been the bedrock of our endeavors.

In conclusion, we hope that this Book of Proceedings will serve as a source of inspiration, knowledge, and collaboration for researchers, students, policymakers, and industry leaders alike. We are confident that the research and ideas presented here will contribute significantly to the advancement of engineering knowledge and the attainment of sustainable development goals.

Thank you for being a part of FETiCON 2023, and we look forward to future collaborations and endeavors that will continue to shape the landscape of engineering and technological development.

Prof. Omodele A. A. Eletta
General Chair
FETiCON 2023

TABLE OF CONTENTS

PAPER 13 – Application of Smoothing Techniques in Stream Flow Prediction of Semi-Arid Region: A Case of Hadejia River, Nigeria

N.I. Abdullahi*, S.J. Ijimdia, A.D. Adamu, and M.M. Muhammad

Department of Water Resources and Environmental Engineering; Ahmadu Bello University Zaria, Nigeria
*Email: nurafbg@gmail.com

ABSTRACT

This paper assessed the prediction capability of time series smoothing techniques in predicting the stream flow of Hadejia River. Four smoothing techniques were employed for the analysis of 36 years monthly stream flow data (1965 – 2000). The techniques are Moving Average (MAS), Holt and Winters (HWS), Simple Exponential (SES), and Fourier (FS) methods. The performance evaluation parameters used in assessing the suitability of the techniques were mean squared error (MSE), root mean squared error (RMSE), mean absolute percentage error (MAPE), coefficient of determination (R^2), and Nash-Sutcliff Coefficient of Efficiency (NSE). The predicting capability of stream flow using MAS, HWS, and SES was found to be inadequate (MSE, RMSE, MAPE, R^2, and NSE values are out of range) whereas the FS technique was found to be suitable. Aside the month of June where R^2 and NSE were 0.43, all other model's parameters of FS were adequate. The MSE was found to vary between 3.92 and 247.10, RMSE between 1.98 and 15.72, MAPE between 13.51 and 546.06, R^2 between 0.434 and 0.923, and NSE between 0.430 and 0.923. The study concludes that Fourier smoothing technique is the most suitable for predicting the stream flow of the study area among all the techniques assessed.

KEYWORDS: Nash-Sutcliff, River, Smoothing, Stream flow, and Root Mean Squared Error.

1 INTRODUCTION

Stream flow, or discharge, is the volume of water that moves over a designated point over a fixed period of time which is directly correlated to the amount of water moving off the watershed into the stream channel (EPA, 2012). Precise prediction of stream flow is of great importance for the effective management of water resources systems (Karran *et al.*, 2014; Adhikary *et al.,* 2018; and Güneş *et al.,* 2021). Among other benefits, stream flow prediction can influence important decisions such as water allocation, cropping strategies, water market planning, environmental watering, operating multi-storage water supply schemes, and drought management.
Many techniques have been applied in predicting stream flow values. Examples can be found in Post and Jakeman (1999) and Chiew *et al.* (2018) where they applied the Rainfall-Runoff model; Patel *et, al.* (2016) and Mehraein *et. al.,* (2022) applied different regression techniques; Adnan *et al.* (2017a); Liu *et al.* (2020) applied Artificial Neural Network; Parisouj *et al.,* (2022) applied coupled model by combining model-driven models and machine learning. Further examples could be found in Adnan *et al.,* (2017b); Machekposhti *et al.,* (2018) where they applied time series Autoregressive Integrated Moving Average (ARIMA) and Autoregressive Moving Average Model (ARMA) models. Time series smoothing models were also applied at various times. Examples can be found in Lukman and Tanan (2020), Papacharalampous and Tyralis (2020) and Brito et al. (2021). This paper is therefore set to assess the prediction capability of time series smoothing techniques in predicting the stream flow of Hadejia River, Nigeria.

2 THEORETICAL ANALYSIS

The smoothing technique is defined by an expression Y_t where t = 1,2,..n and the time series of concern defined by P_tY_{t+h} where the predictor Y_{t+h} is that which returns minimum mean square error and ε_t that follows N(0,1) a white noise. Four smoothing methods are deployed in predicting the stream flow of the study area. The methods are; moving average, Holt and winters, simple exponential, and Fourier. The smoothing models are observed to be non-stationary that do not assume homoscedasticity (Rosenblad, 2021); the techniques chosen were thus all applied to the untransformed (raw) data.

2.1 Moving Average Method

The moving average model takes into account past (and optionally future) observations to predict values and it works as a filter that removes white noise. An observation influences all future predictions and it is defined by Equation (2.1). The analysis utilized the equal weights method at 95% confidence level with q=2

$$\begin{cases} Y_t = \mu_t + \varepsilon_t \\ \mu_t = \dfrac{\sum_{i=q}^{ql} \omega_i Y_{t+i}}{\sum_{i=q}^{ql} \omega_i} \end{cases} \quad 2.1$$

2.2 Holt's and winters (Linear Holt)

The linear Holt's model (sometimes referred to as Holt's-Winters non-seasonal algorithm) takes into account a trend and a permanent component that varies with time. The model is defined by Equation (2.2). The analysis was performed at 95% confidence level and α and β =0.2.

$$\begin{cases} Y_t = \mu_t + \beta_t t + \varepsilon_t & \\ P_t Y_{t+h} = \mu_t + \beta_t t & h = 1,2,.. \\ S_t = \propto Y_t + (1-\propto)(S_{t-1} + T_{t-1}) & 0 < \propto < 2 \\ T_t = \beta(S_t - S_{t-1}) + (1-\beta)T_{t-1} & 0 < \beta < \dfrac{4}{\alpha - 2} \\ Y_{t+h} = P_t Y_{t+h} = S_t + hT_t, & h = 1,2,.. \end{cases} \quad 2.2$$

2.3 Simple Exponential

The exponential smoothing model takes into account past observations to predict values. The weight of the past observations decreases exponentially. The simple exponential model is defined by Equation (2.3). This study is performed at 95% confidence level with α=0.2.

$$\begin{cases} Y_t = \mu_t + \varepsilon_t & \\ P_t Y_{t+h} = \mu_t & h = 1,2,\ldots \\ S_t Y_{t+h} = \propto Y_t + (1-\propto) S_{t-1} & 0 < \propto < 2 \\ Y_{t+h} = P_t Y_{t+h} = S_t, & h = 1,2,\ldots \end{cases} \quad 2.3$$

2.4 The Fourier Smoothing

The concept of the Fourier smoothing is to transform a time series into its Fourier coordinates, then remove part of the higher frequencies, and then transform the coordinates back to a signal. This new signal is a smoothed series.

3 MATERIALS AND METHODS

The paper utilized xlstat (an Excel extension) for the analysis. Four smoothing techniques were employed for the analysis of 36 years monthly stream flow data (1965 – 2000) of the Hadejia River to ascertain their suitability in predicting the flow of the river. The techniques are Moving Average (MAS), Holt and Winters (HWS), Simple Exponential (SES), and Fourier (FS) methods. The fitness of each method is ascertained by sets of performance evaluation parameters. The parameters were mean squared error (MSE), root mean squared error (RMSE), mean absolute percentage error (MAPE), coefficient of determination (R^2), and Nash-Sutcliff Coefficient of Efficiency (NSE).

i. The MSE measures the amount of error in statistical models. It assesses the average squared difference between the observed and predicted values. When a model has no error, the MSE equals zero. As model error increases, its value increases. Values closer to zero represent a relatively fit model.
ii. The RMSE is commonly used in model performance evaluation that computes and reported in the same unit as the model output of concern. It works well for continuous long-term simulations. The values of RMSE range between zero and infinity (0 - ∞) with 0 as the optimal value (Moriasi *et al.,* 2015). Values closer to zero represent a relatively fitter model.
iii. The MAPE measures the accuracy of a forecast system. It measures this accuracy as a percentage and can be calculated as the average absolute per cent error for each time period minus actual values divided by actual values. MAPE values range from zero to infinity (0 - ∞), where the lower the value the more accurate the prediction is.
iv. R^2 is widely used in hydrological modelling studies, thus serving as a benchmark for performance evaluation. The values of R^2 range between zero and one (0 – 1). For a monthly flow simulation, R^2 >

0.85 shows a very good model, $0.75 < R^2 <= 0.85$ a good model, $0.60 < R^2 <= 0.75$ a satisfactory model, and $R^2 <= 0.60$ shows not satisfactory model (Moriasi *et al.,* 2015).

v. The NSE is used to evaluate model performance for several output responses (including stream flow) and can also be used to determine how well a model simulates trends for output responses of concern. The values of NSE range between minus infinity and one (-∞ - 1.0) with an optimal value of 1.0. For a monthly flow simulation, NSE > 0.8 shows a very good model, 0.70 < NSE <= 0.8 shows a good model, 0.50 < NSE <= 0.70 a satisfactory model, and NSE <= 0.5 shows not satisfactory model (Moriasi *et al.,* 2015).

4 RESULTS AND DISCUSSION

The stream flow of the Hadejia River (1965 – 2000) at Hadejia Bridge Station is predicted using four time series smoothing modelling techniques; MAS, SES, HWS, and FS. The Mean Squared Error (MSE), Root Mean Squared Error (RMSE), Mean Absolute Percentage Error (MAPE), Coefficient of Determination, and Nash-Sutcliff Coefficient of Efficiency (NSE) were the parameters used to assess the performance of the models.

4.1 Moving Average (MAS)

The stream flow prediction using MAS returns a result that can best be described as an unfit model. As presented in Table 4.1, the model initially shows some glimpse of fitness with R^2 values in the first three months (January, February, and March) and returns a good fit model with values of 0.831, 0.813, and 0.759 respectively and the last two months (November and December) with values of 0.880 and 0.847 respectively. The MSE, RMSE, and NSE in the first month also return promising values at 9, 2.93, 87.93 and 0.827 respectively. Only January has a satisfactory NSE value. The MSE, RMSE, and MAPE values also return values that are not close to zero. It could be seen from the performance evaluation parameters that the model was only able to predict the flow in January, a period of low flow. The poor performance of the model could be as a result of the disadvantage of the technique in applying it to a data series that have trend and seasonality components and its suitability for relatively short-term forecasting as reported by Lukman and Tanan (2020).

4.2 Holt's and Winters (HWS)

The HWS shows a relatively better prediction capability than MAS. As presented in Table 4.1, aside R^2 which varies between 0.030 and 0.481 all other performance evaluation parameters return relatively better results than that of MAS. The MSE results vary between 28.75 and 687, RMSE between 4.564 and 26.223, MAPE between 32.024 and 355.772, and NSE between -0.451 and 0.481. The HWS model also predicts better during the period of low flows as results of R^2, NSE, RMSE, and MSE are better from January to April (even though the R^2 and NSE were not adequate) which corresponds to the period of low flow. The result agrees with the work of Toro *et, al.,* (2008) where HWS performed relatively better than MAS and lower than SES (as is also the case here which can be understood better after reading the next paragraph).

4.3 Simple Exponential Smoothing (SES)

The SES shows a relatively better prediction capability than HWS. As presented in Table 4.2, the MSE varies between 17.853 and 721.072, RMSE between 4.225 and 26.853, MAPE between 32.365 and 333.473, R^2 between 0.005 and 0.621, and NSE between -0.064 and 0.415. The model also predicts better during a period of low flow as the performance evaluation parameters return a better result between January and April. The result is in agreement with the work of Lukman and Tanan (2020) where SES was observed to be weak in predicting monthly stream flow by returning the same average discharge value for each month (January – December). In the work, the model accuracy was found to be -0.08 while the MAPE value was found to be 142.55 which are all within the range of the values found by this study. The result is also in agreement with Toro *et al.,* (2023) where SES predicts stream flow relatively better than HWS. Overall, the model performance is also inadequate in predicting the stream flow of the study area. For this limitation, Dullah *et al.,* (2023) proposed the integration of a nonlinear autoregressive neural network with HWS and SES which improves the precision of the prediction beyond applying the HWS or SES alone. Overall, the predicting capability of stream flow of the study area using HWS is inadequate.

4.4 Fourier (FS)

The FS technique returns a much better predicting capability in the study area than the previous three models (MAS, HWS, and SES). Aside the month of June where R^2 and NSE were 0.43, all other model parameters are

good. The MSE was found to vary between 3.92 and 247.10, RMSE between 1.98 and 15.72, MAPE between 13.51 and 546.06, R^2 between 0.434 and 0.923, and NSE between 0.430 and 0.923. The model also shows greater prediction capabilities in the period of low flow even though its predicting capabilities for the remaining months (except June) are adequate. The model's performance evaluation parameters are presented in Table 4.2 while Fig. 4.1 presents the results showing the observed versus simulated stream flow across all months. This result can be supported by the work of Bayazit et al., (2001) where they found Fourier analysis to be able to simulate monthly stream flow relatively well with reasonably small variations within the simulations.

5 CONCLUSIONS

This paper assessed the prediction capability of four time series smoothing techniques (moving average, Holt and winters (linear), simple exponential, and Fourier) in predicting a monthly stream flow of Hadejia River, Nigeria. The predicting capabilities of moving average, Holt and winters, and simple exponential were found to be inadequate. The Fourier method returns a relatively better technique for predicting the stream flow of the river. The Fourier performance evaluation parameters return RMSE value in the range of 1.98 and 13.51, R^2 and NSE values in the range of 0.4 and 0.9. This paper, therefore, recommends the application of Fourier in predicting of monthly stream flow of the Hadejia River

Table 4.1: Performance Evaluation Parameters of MAS and HWS

	Moving Average (Equal Weight Method)					**Holt and winters (Linear Holt)**				
	MSE	**RMSE**	**MAPE**	**R²**	**NSE**	**MSE**	**RMSE**	**MAPE**	**R²**	**NSE**
Jan	9	2.93	87.25	0.8310	0.827	28.754	5.362	95.254	0.544	0.481
Feb	98	9.88	197.35	0.8130	-1.661	24.096	4.909	78.273	0.433	0.406
Mar	453	21.29	485.61	0.7590	-9.134	30.413	5.515	84.124	0.418	0.397
Apr	1529	39.11	1033.31	0.4570	-54.176	20.834	4.564	129.466	0.354	0.332
May	4091	63.96	753.90	0.3820	-107.96	35.882	5.990	244.330	0.176	0.151
Jun	11612	107.76	568.83	0.0002	-113.525	150.934	12.286	355.772	0.030	-0.387
July	32130	179.25	303.59	0.0170	-0.217	150.849	12.282	36.356	0.050	-0.301
Aug	91420	302.36	266.30	0.0003	-308.587	291.167	17.064	32.024	0.222	-0.399
Sep	262559	512.40	295.91	0.2390	-359.085	681.905	26.113	36.995	0.268	-0.415
Oct	779165	882.70	1220.54	0.4590	-1011.316	687.656	26.223	74.955	0.235	0.038
Nov	2196079	1481.92	5455.70	0.8800	-7891.579	253.197	15.912	88.477	0.388	0.181
Dec	6099860	2469.79	21138.40	0.8470	-49721.141	105.049	10.249	186.070	0.366	0.236

Table 4.2: Performance Evaluation Parameters of SES and FS

	Simple Exponential					**FOURIER**				
	MSE	**RMSE**	**MAPE**	**R²**	**NSE**	**MSE**	**RMSE**	**MAPE**	**R²**	**NSE**
Jan	29.950	5.473	96.510	0.621	0.415	3.92	1.98	70.50	0.923	0.923
Feb	23.137	4.810	62.855	0.532	0.387	3.63	1.90	176.59	0.904	0.904
Mar	29.857	5.464	58.847	0.491	0.351	11.53	3.40	546.06	0.749	0.749
Apr	17.853	4.225	90.635	0.454	0.374	4.99	2.23	176.01	0.825	0.825
May	31.426	5.606	182.739	0.260	0.186	13.99	3.74	105.25	0.638	0.638
Jun	119.122	10.914	333.473	0.005	-0.201	59.07	7.69	170.68	0.434	0.430
July	150.195	12.255	37.736	0.014	-0.221	48.81	6.99	21.01	0.677	0.674
Aug	250.000	15.811	32.365	0.058	-0.345	57.83	7.60	13.51	0.810	0.810
Sep	644.468	25.386	40.994	0.054	-0.227	247.10	15.72	25.22	0.671	0.671
Oct	721.072	26.853	111.252	0.052	-0.064	218.71	14.79	64.09	0.724	0.724
Nov	250.598	15.830	91.057	0.335	0.115	90.84	9.53	84.10	0.683	0.683
Dec	103.778	10.187	183.425	0.404	0.175	46.11	6.79	148.04	0.635	0.635

.

Fig 4.1: Observed Versus Simulated Stream Flow Across All Months.

REFERENCES

Adhikary, S. K., Muttil, N., & Yilmaz, A. G. (2018). Improving streamflow forecast using optimal rain gauge network-based input to artificial neural network models. *Hydrology Research*, *49*(5), 1559–1577. https://doi.org/10.2166/nh.2017.108

Adnan, R. M., Yuan, X., Kisi, O., & Yuan, Y. (2017a). Streamflow Forecasting Using Artificial Neural Network and Support Vector Machine Models. *American Scientific Research Journal for Engineering*. http://asrjetsjournal.org/

Adnan, R. M., Yuan, X., Kisi, O., & Curtef, V. (2017b). Application of Time Series Models for Streamflow Forecasting. *Civil and Environmental Research*, *9*(3), 56–63. www.iiste.org

Alonso Brito, G. R., Rivero Villaverde, A., Lau Quan, A., & Ruíz Pérez, M. E. (2021). Comparison between SARIMA and Holt–Winters models for forecasting monthly streamflow in the western region of Cuba. *SN Applied Sciences*, *3*(6). https://doi.org/10.1007/s42452-021-04667-5

Bayazit, M., ÖNÖZ, B., & Aksoy, H. (2001). Nonparametric stream flow simulation by wavelet or Fourier analysis. *Hydrological Sciences Journal*, *46*(4), 623–634. https://doi.org/10.1080/02626660109492855

Chiew, F. H. S., Zheng, H., & Potter, N. J. (2018). Rainfall-Runoff modelling considerations to predict streamflow characteristics in ungauged catchments and under climate change. *Water (Switzerland)*, *10*(10). https://doi.org/10.3390/w10101319

Dullah, H., Ahmed, A.N., Kumar, P. *et al.* (2023). Integrated nonlinear autoregressive neural network and Holt winters exponential smoothing for river streaming flow forecasting at Aswan High. *Earth Sci Inform* **16**, 773–786. https://doi.org/10.1007/s12145-022-00913-5

EPA (2012). *Stream Flow: Monitoring & Assessment*. United State Environmental Protection Agency. https://archive.epa.gov/water/archive/web/html/vms51.html

Güneş, M. Ş., Parim, C., Yıldız, D., & Büyüklü, A. H. (2021). Predicting monthly streamflow using a hybrid wavelet neural network: Case study of the Çoruh river basin. *Polish Journal of Environmental Studies*, *30*(4), 3065–3075. https://doi.org/10.15244/pjoes/130767

Karran, D. J., Morin, E., & Adamowski, J. (2014). Multi-step streamflow forecasting using data-driven non-linear methods in contrasting climate regimes. *Journal of Hydroinformatics*, *16*(3), 671–689. https://doi.org/10.2166/hydro.2013.042

Kumar, M., Jawaharlal, H., Krishi Vishwavidyalaya, N., Seetpal, M., Patel, S., Hardaha, M. K., Seetpal, M. K., & Madankar, K. K. (2016). Multiple Linear Regression Model for Stream Flow Estimation of Wainganga River. *American Journal of Water Science and Engineering*, *2*(1), 1–5. https://doi.org/10.11648/j.ajwse.20160201.11

Liu, D., Jiang, W., Mu, L., & Wang, S. (2020). Streamflow Prediction Using Deep Learning Neural Network: Case Study of Yangtze River. *IEEE Access*, *8*, 90069–90086. https://doi.org/10.1109/ACCESS.2020.2993874

Lukman, M., & Tanan, B. (2021). Time Series Modeling by using Exponential Smoothing Technique For River Flow Discharge Forecasting : A Case Study of Cabenge, Walanae, and Cenranae rivers system. *IOP Conference Series: Materials Science and Engineering*, *1088*(1), 012100. https://doi.org/10.1088/1757-899x/1088/1/012100

Machekposhti, K. M., Sedghi, H., Telvari, A., & Babazadeh, H. (2018). Flood Predicting in Karkheh River Basin Using Stochastic ARIMA Model. *International Journal of Agricultural and Biosystems Engineering*, *12*(3), 84–91.

Mehraein, M., Mohanavelu, A., Naganna, S. R., Kulls, C., & Kisi, O. (2022). Monthly Streamflow Prediction by Metaheuristic Regression Approaches Considering Satellite Precipitation Data. *Water (Switzerland)*, *14*(22). https://doi.org/10.3390/w14223636

Moriasi, D. N., Gitau, M. W., Pai, N., & Daggupati, P. (2015). Hydrologic and water quality models: Performance measures and evaluation criteria. *Transactions of the ASABE*, *58*(6), 1763–1785. https://doi.org/10.13031/trans.58.10715

Papacharalampous, G., & Tyralis, H. (2020). Hydrological time series forecasting using simple combinations: Big data testing and investigations on one-year ahead river flow predictability. *Journal of Hydrology*, *590*. https://doi.org/10.1016/j.jhydrol.2020.125205

Parisouj, P., Mokari, E., Mohebzadeh, H., Goharnejad, H., Jun, C., Oh, J., & Bateni, S. M. (2022). Physics-Informed Data-Driven Model for Predicting Streamflow: A Case Study of the Voshmgir Basin, Iran. *Applied Sciences (Switzerland)*, *12*(15). https://doi.org/10.3390/app12157464

Post, D. A., & Jakeman, A. J. (1999). Predicting the daily streamflow of ungauged catchments in S.E. Australia by regionalising the parameters of a lumped conceptual rainfall-runoff model. *Ecological Modelling*, *123*, 91–104. www.elsevier.com/locate/ecolmodel

Rosenblad, A.K. (2021): Accuracy of automatic forecasting methods for univariate time series data: A case study predicting the results of the 2018 Swedish general election using decades-long data series. Communications in Statistics: Case Studies, Data Analysis and Applications, 7:3, 475-493, DOI: 10.1080/23737484.2021.1964407

Toro, F. C. H., González, D., Benedicto, P., González, S., Fernández, F., & Riverola. (2008). Water flows modeling and forecasting using a RBF neural network. *Julio*, *6*(12), 13–31.

PAPER 15 – REVIEW of Geothermal Electricity Generation and its Environmental ImpaCts in nigeria

F.U Ilo

Department of Electrical and Electronic Engineering, Enugu State University of Science and Technology
Email: ude.ilo@esut.edu.ng

ABSTRACT

This paper discusses the technologies involved in generating electricity through geothermal energy and its environmental impacts. The inability of the federal government of Nigeria to maintain steady power supply for the populace has necessitated the need to research into alternative sources of power supply. The focus of this work is on geothermal energy as one of the renewable energy source. In this work, the technology of geothermal was analyzed. The details of how electricity can be generated from geothermal technology were explained. A review of recent previous works by others researchers and the major components of geothermal energy system were discussed. Effort was made in this report to discuss the classifications of geothermal energy and the merits of using geothermal energy as source for electricity generation. The environmental impacts of using geothermal technology to generate electricity were also highlighted. The geological features and subsurface temperature data of oil and shallow water wells from both Northern and Southern part of this country shows the possible presence of geothermal energy due to the thermal gradient. If tapped, this will serve as alternative energy, as being utilized by several other countries since it can produce base load electricity which is reliable and sustainable unlike many other renewable energy sources that are affected by weather and seasonal variations.

KEYWORDS: geothermal energy, renewable energy, electricity generation, alternative energy and environmental impacts

1. INTRODUCTION

This study focuses on technologies of geothermal electricity generation and its environmental impacts in Nigeria. Geothermal energy refers to the production of energy using the internal heat of the earth's crust. This heat comes from the radioactive decay of minerals and continual heat loss from the earth's original formation. Nigeria is blessed with many abundant natural mineral resources such as gypsum, iron core, gold, bitumen, coal, among others. All the natural minerals resources are as a result of the decayed plants and animal residues. The epileptic electricity power supply has become a fundamental issue affecting the economic development of Nigeria. Geothermal energy, which results from the radioactive decay of minerals within the Earth's core and solar energy systems have been discovered and utilized by several countries. Nigeria is still far behind in tapping the abundance of geothermal energy resources (Dorcas, etal. 2016). Figure 1 show the geological setting and location of the major structural units in Nigeria where geothermal energy can be utilized. Classification systems used for classifying geothermal resources are based mainly on their temperatures, geologic settings and intrinsic properties of reservoirs. This work treats geothermal energy resources as renewable, alternative and sustainable energy resources with capabilities of generating electricity and heat for direct use applications and commercial purposes. The earth possesses vast underground stores of energy supply in form of heat, whose potentials are yet to be fully realized. The earth is divided into shells; the crust, the mantle and the core. Its interiors where this heat energy occurs, reach temperatures greater than $4{,}000^0$C. The heat generated and stored in the earth is known as geothermal energy. Geothermal energy is generated from the earth's core, almost 6,400km beneath the earth's surface. The double-layered core is made up of hot melted rock (magma) surrounding a solid iron center. Very high temperatures are continuously produced inside the earth by the slow decay of radioactive materials, a natural process in all rocks. Surrounding the outer core is the mantle, which is about 2,900km thick and made up of magma and rock (Colin, etal. 2011). The outermost layer of the earth, the land forming the continents and ocean floors, is called the crust. The crust is not a solid plate; it is divided or broken into pieces called plates. Magma from deep within the earth gets to the earth's surface through openings at the edges of these plates and volcanic processes are very common at these edges. Deep underground, rocks and water trapped in the earth absorb heat from this magma.

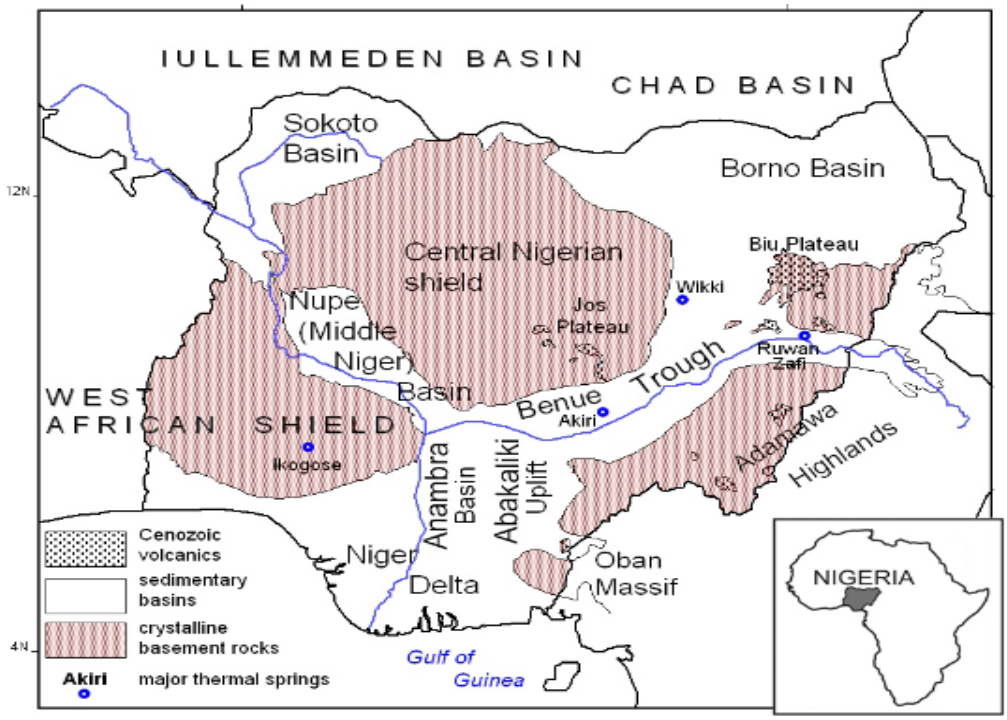

Figure 1: Geological setting and location of the major structural units in Nigeria. Source: (Kurowska, E, and Schoeneich, K , 2010)

2. REVIEW OF PREVIOUS WORKS

Geothermal resources are created and put away in the earth (Garba, etal., 2022). This review focuses on the geothermal energy investigations in Nigeria with focus on researches that have been conducted so far, their outcome, challenges and the future through the geo-scientific oculus. The author made effort to cover notable geo-scientific researches' from geological, geophysical and geochemical perspective, which also focused on geothermal electricity generation. This review is made to stimulate interest in geothermal energy in Nigeria and also invigorate the geo-scientific community toward extensive research in the field. This review should eventually lead to understanding of the technologies involved during conversion of geothermal energy into electricity. A warm spring location in Nigeria that has received geophysical examination is the Wikki Warm Spring (WWS) located in Bauchi State, northeastern Nigeria. Preliminary geophysical investigation of the source of heat of the WWS was conducted by Omanga, (1998). He used the electrical resistivity, radiometric methods and gamma ray spectrometry around the WWS area. The ultimate aim was to investigate the source of heat at the WWS region. Within the WWS, fourteen (14) sounding were conducted using vertical electrical sounding (VES) method and measurements of the concentrations of radioactive elements such as uranium (U), thorium (Th) and an isotope of potassium (K) in the area were estimated. The resistivity results showed that low resistivity values exist around the WWS area while the radiometric survey measurements revealed high gamma activity in that region. This high radioactivity in the area is an indication of the importance of radiogenic heat activities within the WWS area and a pointer to the heat source probably due to radioactivity. So far, there is probably the only one (direct) geothermal energy utilization site in Nigeria, a swimming pool where water from Ikogosi warm spring (37°C) is used. It is located in south-western part of the country, in Ekiti State. Other possible sources of geothermal energy in Nigeria are Kerang Springs in Plateau State, Rafin Rewa Warm Spring in Jos Plateau, Nike Lake in Enugu state and Wikki Warm Springs in Abuja Nigeria.

Steps needed to generate electricity from geothermal energy

If you dig a big hole straight down into the Earth, you would notice that temperature increases as the dept increases. That is because the inside of the Earth is full of heat (Kurowska and Schoeneich, 2017). That heat is called geothermal energy. Below are steps of generating electricity from the geothermal energy

a) Hot water is pumped from deep underground through a well under high pressure,
b) when the water reaches the surface, the pressure is dropped, which causes the water to turn into steam,

c) the steam spins a turbine, which is connected to a generator that produces electricity,
d) the steam cools off in a cooling tower and condenses back to water and
e) the cooled water is pumped back into the Earth to begin the process again.

Component of Geothermal Energy System

The major components of geothermal energy system are the:

a) Heat source
b) Reservoir and
c) Carrier (fluid)

3. MATERIALS AND METHODS

Materials and Devices used:

Methods Adopted:

The methods adopted for the realization of this work are descriptive and analytical techniques. The technique enables the author to give a clear description of the technology of geothermal and also do analysis on environmental impacts in Nigeria.

Technologies of Geothermal Electricity Generation

Geothermal power plants draw fluids from underground reservoirs to the surface to produce steam. This steam then drives turbines that generate electricity. There are three main types of geothermal power plant technologies namely: dry steam, flash steam, and binary cycle.

Dry Steam Power Plant

This type of power plants uses hydrothermal fluids that are mostly steam and which is relatively natural occurrence. The steam is drawn directly to a turbine, which drives a generator that produces electricity. After the steam condenses, it is frequently re-injected into the reservoir. Figure 2 is a diagram showing the processes involved in dry steam power plant.

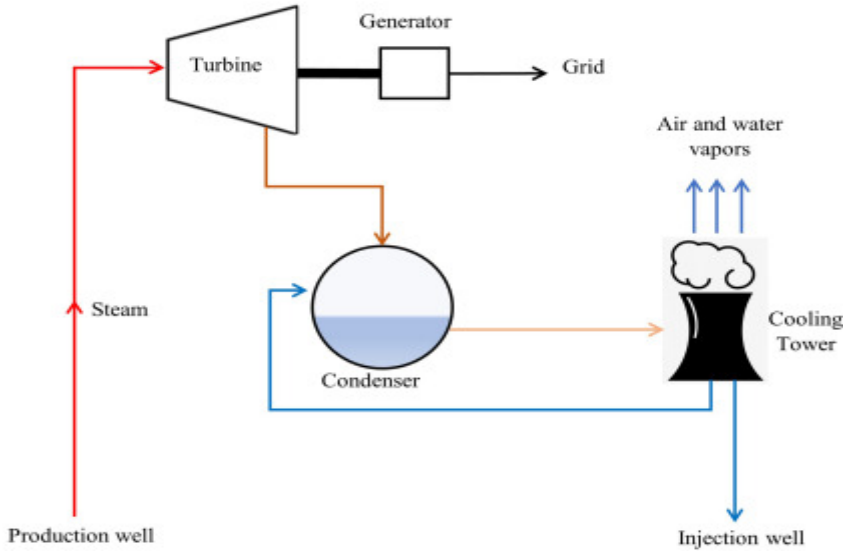

Figure 2: dry steam power plant. (Kurowska, and Schoeneich, 2017)

Since steam is directly used to run a steam turbine, it eliminates the need for burning of coal or other fossil fuels to generate electricity. Figure 2 shows a schematic diagram of a dry steam power plant. When the steam cools, it condenses to water and is injected back into the ground to be used again.

Flash Steam Power Plant

Flash steam plants take high-pressure hot water from deep inside the earth and convert it to steam that drives generator turbines. When the steam cools, it condenses to water and is injected back into the ground to be used again. Single flash power plants are usually considered as the most economical alternative for available geothermal resources temperature above 190 °C**.** Higher temperature resources will produce more liquid and steam for natural pressure conditions. Figure 3 is a typical example of flash steam power plant. It illustrates the stages of flash steam power plant from production well to Load.

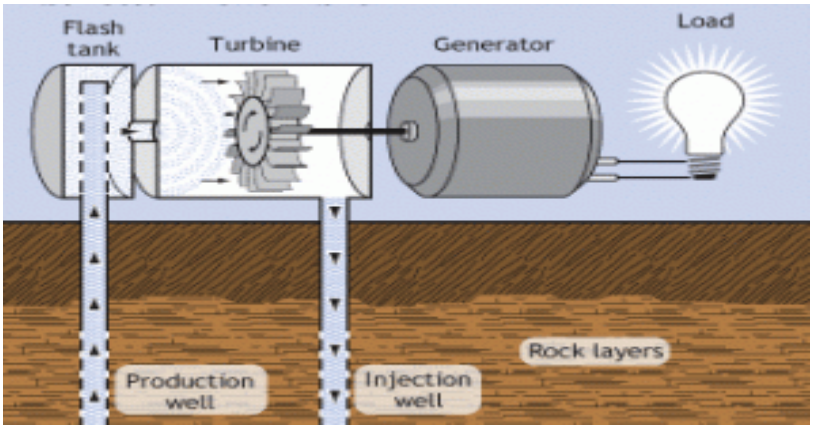

Figure 3: flash steam power plant. (Kurowska, and Schoeneich, 2017).

Binary-Cycle Power Plant

Binary cycle plants use the heat from the hot water to boil a working fluid, usually an organic compound with a low boiling point. The working fluid is vaporized in a heat exchanger and used to turn a turbine. The water is then injected back into the ground to be reheated. In this first unit, the organic Rankine cycle was used to generate electricity using Iso-pentane as a working fluid. Figure 4 is a sketch showing step by step processes involved in binary cycle power plant.

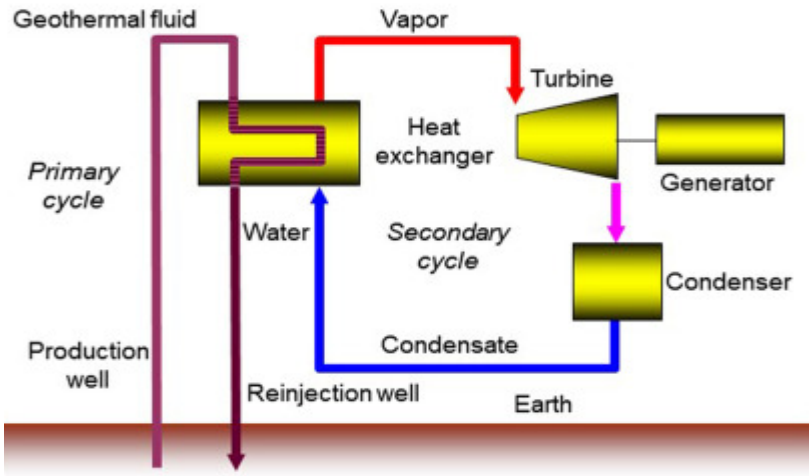

Figure 4: binary cycle power plant. (Kagel, 2007)

Environmental impacts of using geothermal technology to generate electricity in Nigeria

The environmental impacts of electricity generation using geothermal as it affect Nigeria were discussed. The three major affected areas are water quality, air pollution and land use. The environmental effects of geothermal energy depend on how geothermal energy is used or how it is converted to useful energy. There are positive and negative effects of using geothermal technology in generating electricity.

Positive effects

1. Reduced energy costs: Geothermal energy systems provide consistent and stable energy at lower costs, leading to significant savings for consumers.
2. Job creation: Geothermal energy installation and maintenance requires skilled labor, creating job opportunities for locals and boosting the economy.
3. Increased tax revenue: Geothermal energy projects generate tax revenue for the government, leading to an increase in funds available for public services and infrastructure development.
4. Improved energy security: Geothermal energy is a local and indigenous source of energy, reducing reliance on foreign sources and promoting energy security.
5. Reduced greenhouse gas emissions: Geothermal energy produces almost no emissions, leading to a reduction in air pollution and greenhouse gas emissions.
6. Increased electricity reliability: Geothermal energy systems are highly reliable, providing consistent and stable electricity supply with minimal disruptions.
7. Potential for export: Nigeria has significant geothermal energy potential, providing opportunities for exporting excess electricity to neighboring countries.
8. Increased tourism: Geothermal energy installations can attract tourists and visitors to the region, boosting the local economy and creating additional job opportunities.
9. Improved public health: Reduced air pollution from geothermal energy can lead to improved public health outcomes, including reduced respiratory illnesses and related healthcare costs.
10. Increased property values: Properties with geothermal energy systems have higher resale values, leading to increased property tax revenue for local governments.

Negative Effect

Water quality and use

Geothermal power plants have impacts on both water quality and consumption. Hot water pumped from underground reservoirs often contain high levels of sulfur, salt, and other minerals. So it is not the best for consumption.

Air emissions

The distinction between open- and closed-loop systems is important with respect to air emissions. In closed-loop systems, gases removed from the well are not exposed to the atmosphere and are injected back into the ground after giving up their heat, so air emissions are minimal. In contrast, open-loop systems emit hydrogen sulfide, carbon dioxide, ammonia, methane, and boron. Hydrogen sulfide, which has a distinctive “rotten egg” smell, is the most common emission (Kagel, 2007).

Land use

The amount of land required by a geothermal plant varies depending on the properties of the resource reservoir, the amount of power capacity, the type of energy conversion system, the type of cooling system, the arrangement of wells and piping systems, and the substation and auxiliary building needs (Kagel, 2008).

Merits of Geothermal Energy

The merits of geothermal energy are:

1. They are natural source.
2. Due to the near limitless ability of the earth to produce magma, and the continuous transfer of heat between subsurface rock and water, geothermal energy is considered a renewable resource (Rybach, 2007).

3. Geothermal energy produces base load electricity as it is available 24 hours a day, 365 days a year, unlike many other renewable energy resources that are affected by weather and seasonal variations.
4. They are cost effective
5. The energy source is reliable, sustainable, and environmentally friendly
6. Geothermal power has the potential to help mitigate global warming if widely deployed in place of fossil fuels.

1. CONCLUSION

The technologies of geothermal electricity generation were discussed. From the discussion, it is clear that, federal government of Nigeria should focus attention on geothermal electricity generation as an alternative power source. This is because of the benefits it has over the currently used conventional power sources. The environmental impact of geothermal electricity generation is almost zero. There is need to encourage Nigerian`s to invest on geothermal electricity generation as alternative source for power generation

REFERENCES

Dorcas S. Eyinla, Michael A. Oladunjoye, Thompson H.T. Ogunribido and Olumuyiwa A. Odundun (2016). An Overview of Geothermal Energy Resources in Nigeria. *Environtropica – An International Journal of the Tropical Environment. Pages61-71,* ISSN 1597-815X

Colin, F.W, Reed, J.R and Anderson A.F.,(2011). Updating the Classification of Geothermal

Resources. U.S Geological Survey (USGS), Menlo Park, CA 94025, Department ofEnergy, Geothermal Technologies Program Washington, DC.

Garba M . L, Kurowska E, Schoeneich K and Abdullahi I (2022) Rafin rewa warm spring, a new geothermal discovery. American International Journal of Contemporary Research 2: 231-236.

Omanga USA, (1998) Preliminary geophysical investigation of the source of heat of the wikki warm spring, Bauchi, Nigeria. A Thesis Submitted to the Department of Physics, Ahmadu Bello University, Zaria, in Partial Fulfilment for the Award of the Degree of Master of Science in Applied Geophysics, 1-93.

Kurowska E and Schoeneich K, (2017) Geothermal exploration in Nigeria. Proceedings of World Geothermal Congress, Indonesia, 25-29.

Kagel, A, (2007). A Guide to Geothermal Energy and the Environment. Washington, DC: Geothermal Energy Association.

Kagel, A. (2008). The State of Geothermal Technology. Part II: Surface Technology. Washington, DC: Geothermal Energy Association.

Rybach, L. (2007). "Geothermal Sustainability". *Proceedings European Geothermal Congress,*Unterhaching, Germany, 5 p.

Kurowska E. and Schoeneich K. (2010). *Proceedings World Geothermal Congress 2010 Bali,Indonesia*, 25-29 April 2010.

PAPER 17 – Modelling Internet of Things Architecture for Accident Detection and Reporting for Emergency Medical Assistance

E. E. C. Igbonoba, A. Obayuwana

Department of Computer Engineering, University of Benin, Benin City, Edo State, Nigeria.
Email: igbonoba2000@live.com

ABSTRACT

This research work focused on accident detection system for emergency medical aid; the study identifies the society's slow response to medical emergencies as a major problem. In order to enhance and maximize the anticipated reaction time, this system aims to provide an early detection of accidents and transmit the information promptly to the emergency unit. The study was carried out in Benin city, Nigeria utilizing a test bed methodology that included a wireless embedded system, a cloud platform, and several electronic sensors and modules, including a Global system for mobile communications (GSM) module (SIM800l), a Global positioning system (GPS) module (NEO-6M), an accelerometer (ADX335), a shock sensor, an Atmega328p microcontroller, etc. The developed device was connected to the cloud platform via GSM module, which also served as the device's GPS receiver and shock sensor. The accelerometer and shock sensor were utilized to identify crashes. The detection rate provided by the created accident detection algorithm served as the metric for the system's accuracy. The response time ranges between 9 and 12 seconds was obtained as time taken to identify the accident and alert the closest hospital. This verifies the systems' degree of accuracy when used in real-time.Keywords: Cloud Platform, database, internet of things, web application, wireless system.

1. INTRODUCTION

The internet of things (IoT) is a term used to describe physical objects that can be connected to a network and exchange data with other objects and systems via the internet or other communication networks. Its main focus is on information that is gathered in real time and decision-making based on this information (Mouha, 2021). The emergence of IoT holds potential for the creation of intelligent systems and applications, such as smart farming, smart homes, among others. Its use in transportation management or systems is receiving a lot of attention from academia and business, and, it is considered as a way to improve road safety in smart cities (Gomathy et al., 2022). Vehicles equipped with a variety of sensors make it possible to not only keep an eye on the surroundings and the vehicle itself in real time, but, it also makes incident detection easier. The current trend in the death rate from road accidents made the use of this technique necessary. Despite the significant efforts made by international road safety organisations to reduce the number of deaths related to road accidents by organising awareness campaigns, discouraged drinking and driving, promoting the use of seat belts and airbags, and other innovative traffic solutions, accident crashes still remain high.

The problem of false alarms emerges because the majority of these works primarily focus on the accidents detection with little or no technique for accident reporting (alert system). The majority of these road fatalities occur as a result of emergency management authorities' and medical personnel's poor reaction times (Devi and Anila, 2018; Adelabu, 2017). If emergency medical care is offered at the scene of an accident, an accident victim's odds of survival may rise dramatically (Aloul et al., 2014). Getting to collisions faster is one of the most efficient strategies to reduce road traffic deaths. Several tools, like e-Notify, are available to aid in the detection and reporting of road traffic accidents (Aloul et al., 2014 and Bhatti el al., 2019). Each vehicle must have an on-board unit (OBU) to use the e-Notify system. Even though this might be a good option, it is pricey and not all vehicles might have on-board devices. The eCall system was created by the European Commission, who also mandated its installation in every vehicle created after 2015. The emergency number 112, 999 in the UK, and some other countries are alerted when the eCall system discovers an accident (Zhao, 2000; Ali and Alwan, 2015).

The goal of this project is to combine low-cost devices, several sensors, a database of hospital profiles, an effective detection algorithm, and IoT infrastructure to increase the accuracy of accident detection and emergency response times for traffic incidents in Benin City, Nigeria. According to a recent World Health Organization (WHO) report, Africa has the highest annual death and injury rates at 1.35 million and 50 million, respectively (WHO, 2018).

Furthermore, Nigeria recorded over thirty nine thousand (39,000) fatalities from these statistics. Road accidents are the eighth leading cause of fatalities globally, according to the Association for Safe International Road Travel (ASIRT), and it is projected to be the fifth leading cause of fatalities in the near future unless significant changes are made with the aid of technology and increased public awareness (ASIRT, 2020).

According to ASIRT, managing road accidents and the resulting social harm costs every country a significant amount of money—about two percent (2%) of its annual budget (ASIRT, 2020). In response to the depressing figures listed above, researchers have developed strategies to address the issues of accident collisions and fatalities, including drivers monitoring systems, smart traffic systems, establishing road management agencies, emergency management devices etc.

The objective of the study is to: - enhance and maximize the anticipated reaction time to road crashes thereby reducing mortality rates associated with road crashes in the society. A test bed methodology that included a wireless embedded system, a cloud platform, and several electronic sensors and modules were adopted.

The existing assistance system in the event of a car accident focuses mostly on one sensor (Amin et al., 2012). Researchers Vinod et al. (2019); Rajkiran and Anusha (2014) and Vinod et al. (2019) presented a system that uses GPS to automatically detect accidents and alerts all nearby hospitals and law enforcement agencies. This hardware-based system only uses one sensor to identify accidents; if this sensor malfunctions, the entire system fails. Some technologies detect accidents and alert rescue crews using the gravitational pitch. These systems, like those described in Bhatti et al. (2019), suffer from the same issue of using just one sensor. Relying on a single sensor increases the possibility of false positives, or the reporting of an accident when none actually occurred. Some systems, described in Suo et al. (2012), employ accelerometer data as a trigger to alert emergency services of a collision.

The result obtained showed that the system was able to react quickly to accident crashes. Finally, the results show that the emergency response time - the time it takes to locate the accident and notify the closest hospital is between 9 to 12 seconds. This demonstrates the accuracy level of the technologies when utilized in real-time.

2. THEORETICAL ANALYSIS

In this research, four layers model design namely: perception or sensory layer, network layer, intermediate layer, and application layer was adopted in order to achieve the intended goal (Bhatti et al., 2019; Pathik et al., 2022). The IoT architecture used is graphically depicted in Figure 1.

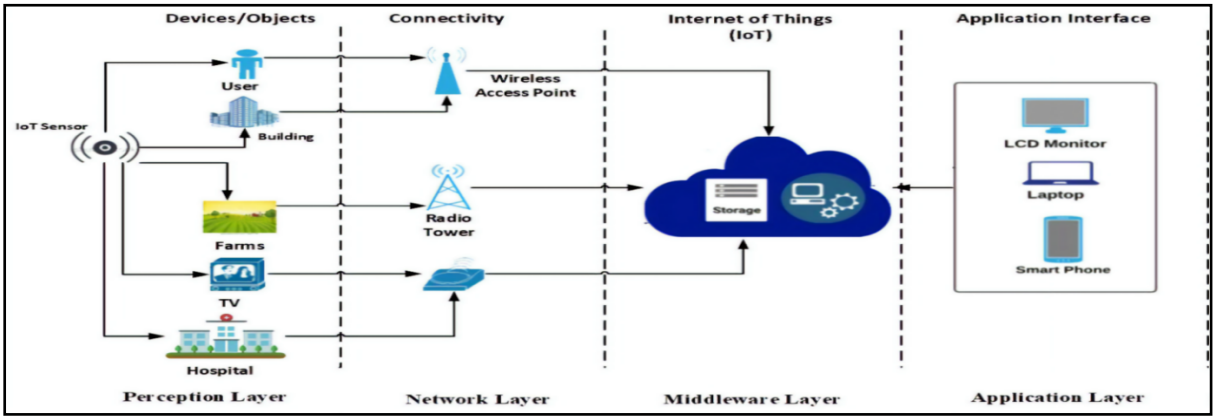

Figure 1: Internet of Things Architecture Adopted

3. MATERIAL AND METHODS

3.1 Methods

In order to decrease the reaction time for rescue operations, a novel IoT technology was created to identify accident crashes and notify the required personnel. The cloud system and the wireless embedded device were linked to function as one unified entity from the designed methodology. Figure 2 depicts the system's architecture modeled from (Ali and Alwan, 2015).

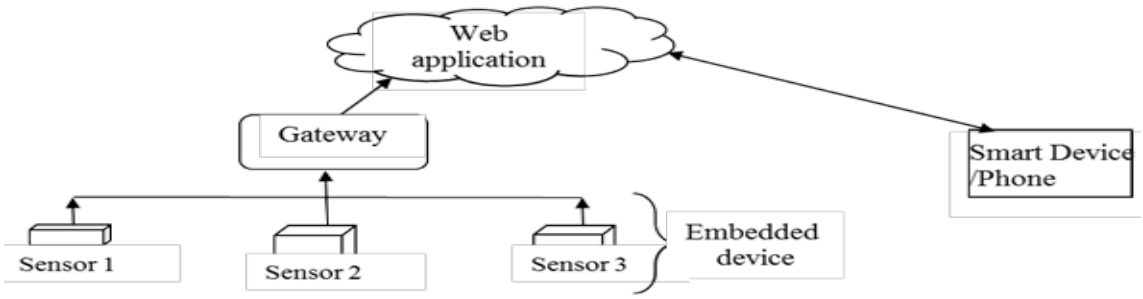

Figure 2: IoT Architecture for Intelligent Accident Detection System

3.2 Development of the wireless embedded device

The GSM module, GPS module, accelerometer, shock sensor, and other types of modules and sensors were used to create the wireless embedded device. To create the working system, these components were interfaced with a microcontroller as illustrated in the block diagram of Figure 3.

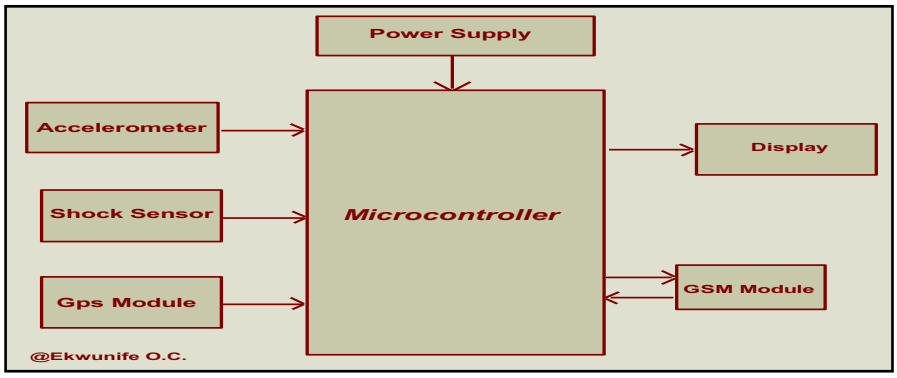

Figure 3: Wireless embedded device

The various wireless embedded device modules were created to carry out their specific tasks in order to accomplish the predetermined objectives as shown in the system circuit diagram in appendix A.

3.3 Development of web application for accident detection

An approach for identifying, outlining, and organizing system requirements is called a use case. The web application that is being created to complement the device is referred to in this context as the "system." Unified Modeling Language (UML), a common notation for modeling actual objects and systems is realized by adopting use case diagram in Figure 4 which depicts steps needed by an accident detection device, commencing with driver registration and ending with emergency or crash notification.

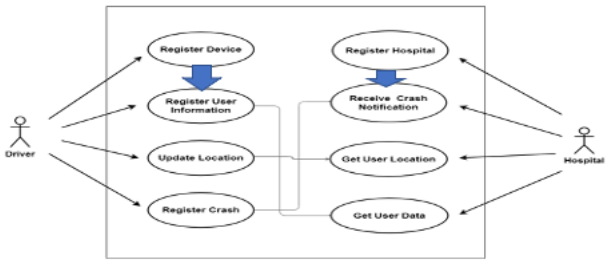

Figure 4: Use Case Diagram

3.4 Software development methodology

The Waterfall Model was the software development approach employed. The waterfall model divides a project's operations into a series of linear phases, each of which is composed of specialized tasks and is dependent on the previous phase's deliverables. The method is common in some branches of engineering design. Although progress moves mostly in one direction ("downwards" like a waterfall) through the phases of conception, initiation, analysis, design, construction, testing, deployment, and maintenance, it tends to be among the less iterative and adaptable approaches in software development. Given that the software system needs to connect with the hardware sensing device and other software systems, it is employed here to enable optimize the architecture of the development process. The process' most frequent steps are shown in Figure 5.

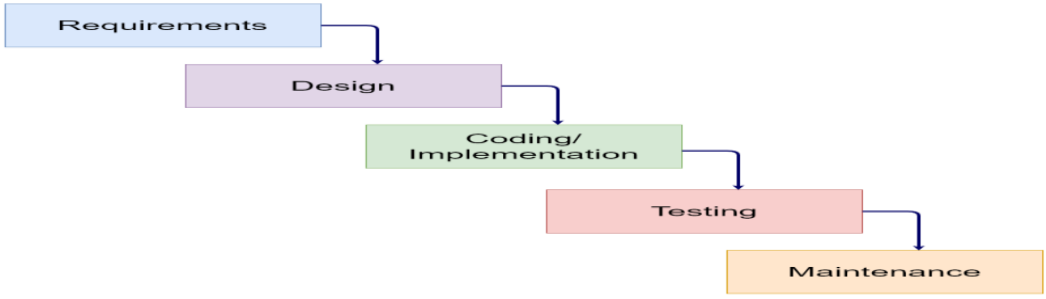

Figure 5: System architecture

The connections between the various system components are shown in Figure 6. The GPRS gateway transmits data from the embedded device to the web application. Figure 6 depicts the data movement diagram that explains how data moves throughout the cloud system, from the wireless electronic device to the backend, database, webpages (frontend), and google map. Static Maps API and Locations API were used to create the web application. Google offers a consumer application and web mapping platform called Google Maps. It provides route planning for walking, driving, flying (in beta), and taking public transportation, as well as satellite imagery, aerial photography, street maps, 360-degree interactive panorama views of streets (Street View), and real-time traffic conditions.

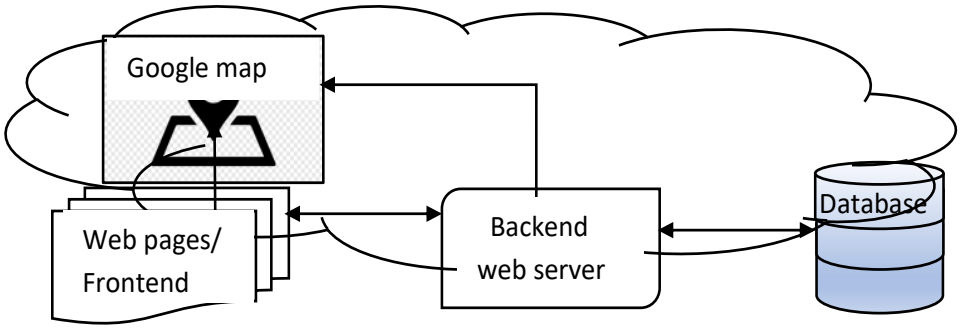

Figure 6: Cloud structure showing data flow (Ali and Alwan, 2015)

3.5 Database development

In this work, the database system was implemented using MongoDB. Instead of using tables and rows like standard relational databases, it employs collections and documents. The system's database was modeled using the embedded data model, which MongoDB offers in addition to the normalized model. With this method of data modeling, the designer has the option of including all relevant data in a single document. The MongoDB collections for the hospitals providing ambulance services near Benin City were carried out showing its: - hospital name, address, location, phone numbers and number of ambulances and other data available.

3.6 Working principle of the system

The system is designed to function in a manner that the device's end-user sensor values are communicated to the backend web server using an HTTP POST request (every 10 seconds). These readings include the device's latitude and longitude as determined by the GPS receiver, the shock sensor, and the accelerometer. This device data is supplied into the body of the request in the JavaScript Object Notation (JSON) format. When the web server receives this data, it analyses it to determine whether an automobile crash has been detected or not. In the event of an unplanned system reboot, it is also possible to quickly access the last device location by storing the received data in a database system. In order to compute the route between the location of the device at the moment and the closest hospital, the backend additionally connects to the Google Maps API platform (all hospital locations are to be stored on the database). The affected person's information is then transmitted by SMS to the closest hospital providing ambulance services. Figure 7 shows the working principle of the system.

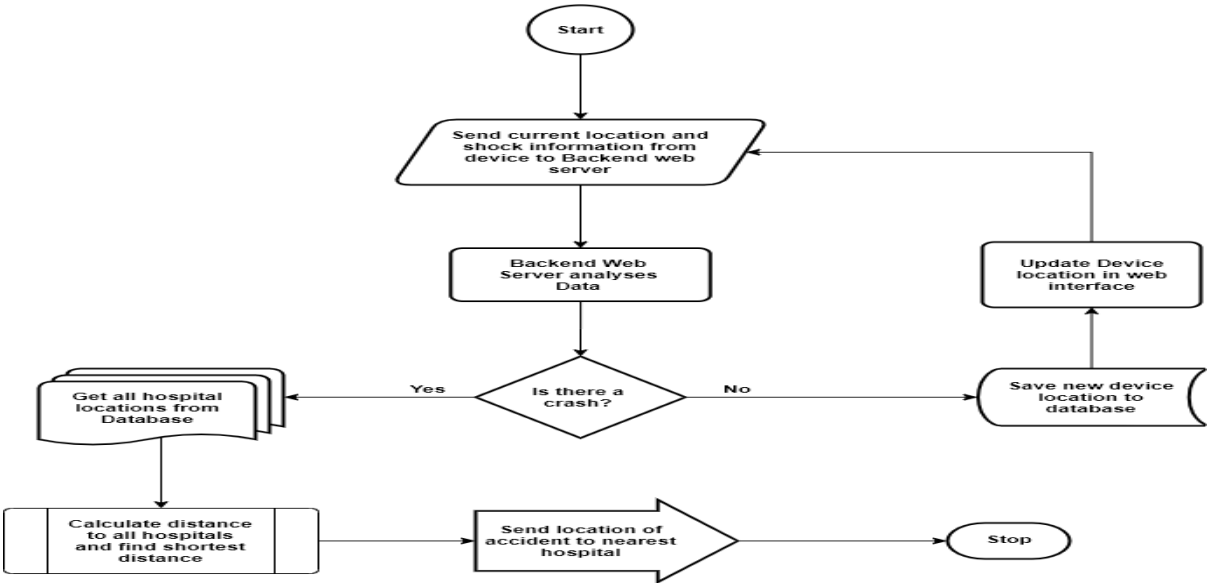

Figure 7 Functional Flow Chart of the System

4. RESULT AND DISCUSSION

The hardware device's circuit prototype was created using the proteus simulation software, implemented on a breadboard, and then transferred to a Veroboard, Figure 8. The code was written using the Arduino IDE, and the Atmega328p microcontroller was programmed using the TL866 universal programmer.

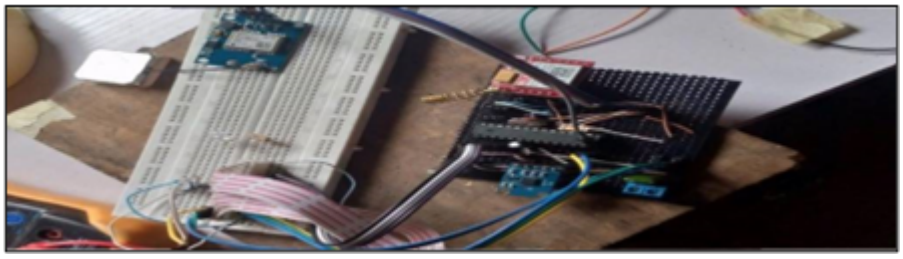

Figure 8: Circuit prototyping

On the platform, a few hospitals in Benin City were registered, together with the integrated wireless gadget. Figure 9 displays screenshots of the registration page from the web application's graphical user interface.

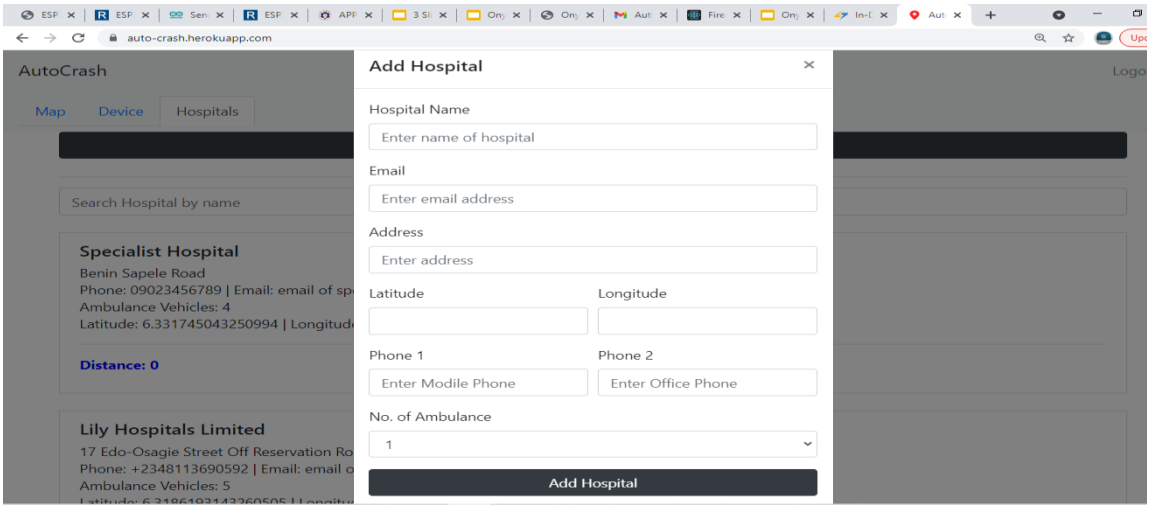

Figure 9: Hospital registration page

The platform for registering the hospitals offering ambulance services is presented in the screenshot above with information relating to the hospitals, such as name, email, latitude, and longitude. These were collected and utilized to find the closest hospital and, call in case of an accident crash.

In an open area, the device was turned on and moved around. The first screenshot, Figure 10, depicts the device's movement on a map, and the second screenshot, Figure 11, depicts the distance between the device and the registered hospitals. The screenshot information in Figure 11 indicates that the University of Benin teaching hospital was the closest hospital location to the device at the time the test was conducted.

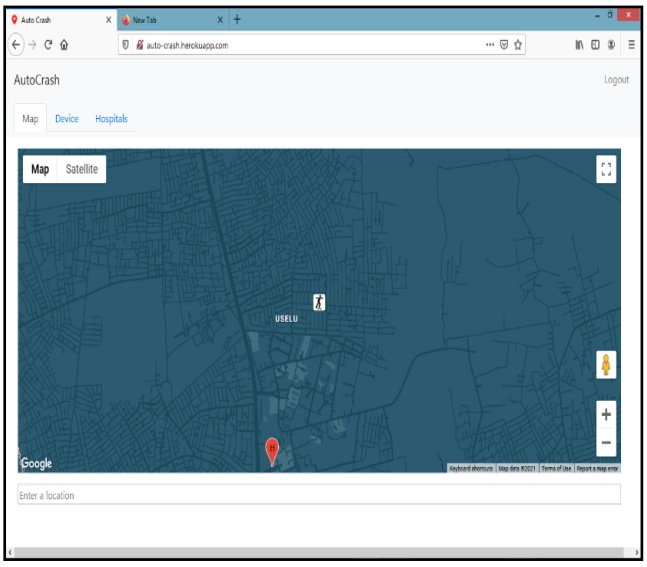

Figure 10: movement of the device on Google map

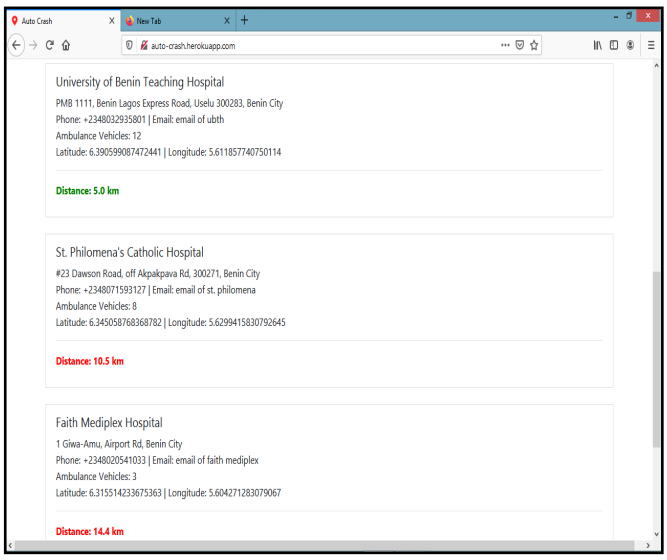

Figure11: Distances of the registered hospitals from the device

Finally, after the apparatus smashed against a wall while being supported by ball-shaped desk legs, the following observations were noticed on the platform: the shock state that was initially FALSE became TRUE (which showed device has detected an accident). With the information saved on the device, an SMS was sent to the closest hospital. The movement on the map then came to an end. The system was tested for accuracy and the result tabulated as shown in Table 2

Table 2: Accuracy and Response time result

S/N	Accident Time	System Response	System Response Time	Calculated Response Time
1	11:19:09 am	Accident Detected	11:19:19 am	10 seconds
2	11:19:30 am	Accident Detected	11:19:39 am	09 seconds
3	11:19:42 am	Accident Detected	11:19:52 am	10 seconds
4	12:01:00 pm	Accident Detected	12:01:12 pm	12 seconds

Four tests were run on the system to ascertain its reaction and response time based on the results shown in table 2. As an experiment, the system was able to react quickly to an accident crash. The data that were displayed indicate that the response time ranges between 9 and 12 seconds. This is the amount of time it took the system to identify the accident and alert the closest hospital with an ambulance service. Furthermore, the complete circuit diagram for hardware implementation of the wireless embedded device for the delivery of the internet of things architecture for accident detection and reporting for emergency medical assistance is presented in appendix A.

5. CONCLUSION

Finally, the internet of things accident detection and alert system for emergency medical aid was developed employing a variety of current technologies. A profile and database of hospitals providing ambulance services, the development of a web-based platform for accident detection and alert system with integrated emergency alert system, and IOT-based embedded device for the detection and transmission of location and status of vehicular accidents' crashes were all successfully accomplished by the new system. Finally, the results show that the emergency response time - the time it takes to locate the accident and notify the closest hospital is between -9 to 12 seconds. This demonstrates the accuracy level of the technologies when utilized in real-time. The research was successfully implemented and evaluated, and because the design is relatively adaptable, further enhancements in the coverage area can be achieved.

REFERENCES

Mouha, R. A. (2021). Internet of Things. Journal of data analysis and information processing, Vol. 09. No.2, pp. 77-101. https://doi.org/10.4236/jdaip.2021.92006

Gomathy, C. K., Rohan, K., Reddy, B. M. K. & Geetha, V. (2022). Accident detection and alert system. Journal of engineering, computing and architecture, ISSN NO:1934-7197, Vol. 12, Issue 3, pp. 32-43. http://www.journaleca.com/ Page No: 32

Devi, P. & Anila, S. (2018). Accident Detection and Reporting System using Internet of Things. International Journal of Current Engineering and Scientific Research (IJCESR), ISSN: 2393-8374, Vol.5 (12), pp.57- 61

Adelabu, W. O. (2017). Design and Construction of a Vehicle Tracking and Accident Alert System Using GPS and GSM Module. Afribary. http://www.afribary.com/works/design-and-construction-of-a-vehicle-tracking-and-accident-alert-system-using-gps-and-gsm-module

Aloul, F., Zualkernan, I., Abu-Salma, R., Al-Ali, H., & Al-Merri, M. (2014). iBump: Smartphone application to detect car accidents. International Conference on Industrial Automation, Information and Communications Technology, ISBN: 978-1-4799-4909-0, pp.52-56.http://doi:10.1109/IAICT.2014.6922107

Zhao, Y. (2000). Mobile Phone Location Determination and its Impact on Intelligent Transportation Systems. IEEE Transactions on Intelligent Transportation Systems, Vol. 1. No.1, pp. 55-64. https://doi.org/10.1109/6979.869021

Ali, H. M. & Alwan, Z. S. (2015). Car Accident Detection and Notification System Using Smartphone. International Journal of Computer Science and Mobile Computing, Vol. 4(4), pp. 620–635.

World Health Organization. (2018). Global Status Report on Road Safety. World Health Organization: Geneva, Switzerland.

Association for Safe International Road Travel. (2020). Road Crash Statistics. Available Online: https://www.asirt.org/safe-travel/road-safety-facts.

Amin, M. S., Jalil, J. and Reaz, M. B. I. (2012). Accident Detection and Reporting System Using GPS, GPRS and GSM Technology. *2012 International Conference on Informatics, Electronics & Vision (ICIEV)*, pp. 640-643. https://doi: 10.1109/ICIEV.2012.6317382.

Vinod, S. Kumar, P. S. &Vimal, V. R. (2019). IOT Based Automatic Accident Vehicle Location Sharing Systema Smart Emergency System, international journal of scientific & technology research, ISSN: 2277-8616,Vol. 8, Issue 10, pp.1249-1252,

Rajkiran, A. & Anusha, M. (2014). Intelligent Automatic Vehicle Accident Detection System Using Wireless Communication. Int. J. Res. Stud. Sci. Eng. Technology, Vol. 1, pp. 98–101.

Bhatti, F., Shah, M. A., Maple, C., & Islam, S. U. (2019). A Novel Internet of Things-Enabled Accident Detection and Reporting System for Smart City Environments. Sensors, Vol. 19(9). https://doi.org/10.3390/s19092071

Suo, H., Wan, J., Zou C. & Liu, J. (2012). Security in the Internet of Things: A Review. International Conference on Computer Science and Electronics Engineering (ICCSEE), pp. 648-651.

Pathik, N., Gupta, R.K., Sahu, Y., Sharma, A., Masud, M., & Baz, M. (2022). AI Enabled Accident Detection and Alert System Using IoT and Deep Learning for Smart Cities. Sustainability MDPI 2022, Vol. 14, Issue 13, pp. 1-24. https://doi.org/10.3390/su14137701

Appendix A

The appendix A is the complete circuit diagram for hardware implementation of the wireless embedded device for the delivery of the internet of things architecture for accident detection and reporting for emergency medical assistance.

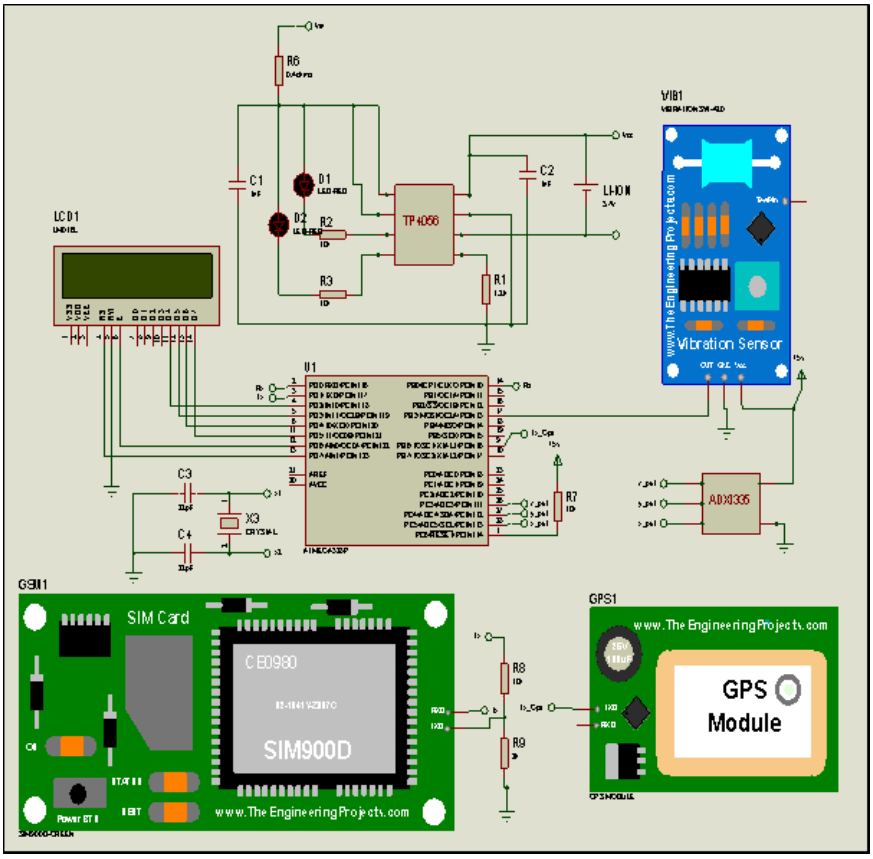

Complete circuit diagram for IOT wireless embedded device

PAPER 19 – EVALUATION OF THE THERMAL ENVIRONMENTS OF TWO SINGLE-SPAN TRIPLE-LAYERED GREENHOUSES EQUIPPED WITH CIRCULAR AND HORIZONTAL AIRFLOW FANS

T. D. Akpenpuun[1,3], Q. O. Ogunlowo[2,5], Wook-Ho Na[3], A. Rabiu[2], M. A. Adesanya[2], P. Dutta[4], E. Zakir[4], O. S. Tomomewo[6], M. O. Sunmonu[7], Hyeon-Tae Kim[8], Hyun-Woo Lee[2,3*]

[1]Department of Agricultural, and Biosystems Engineering, University of Ilorin, Ilorin 240003, Nigeria;
[2]Department of Agricultural Civil Engineering, College of Agricultural and Life Sciences, Kyungpook National University, Daegu 41566, Korea;
[3]Smart Agriculture Innovation Centre, Kyungpook National University, Daegu 41566, Korea;
[4]Department of Food Security and Agriculture Development
[5]Department of Agricultural, and Bioenvironmental Engineering, Federal College of Agriculture, Moor Plantation, PMB 5029, Ibadan, Nigeria
[6]Institute for Energy Studies, University of North Dakota, USA.
[7]Department of Food Engineering, University of Ilorin, PMB 1515, Ilorin 240003, Nigeria
[8]Department of Bio-Industrial Machinery, Gyeongsang National University, Jinju 52828, Korea
*Email: whlee@knu.ac.kr, akpenpuun.td@unilorin.edu.ng

ABSTRACT
The microclimate of indoor production systems is highly dependent on the macroclimate of the ambient. As a result, the microclimate fluctuates with time with respect to the macroclimate and eventually making it have higher measurable climate parameters than the macroclimate. This study was carried out at Sangju Smart Farm Innovation Valley, Sangju-si to compare and analyse changes in the thermal environment in two adjacent single-span tunnel greenhouses covered with two layers of polyethylene films (200 μm thick) and a layer of thermal curtain (3.5 mm thick). While one greenhouse was equipped with five circular airflow fans (HUMITEM-GH), the other had five horizontal airflow fans (Conv-GH). The *Seolhyang* variety of strawberries was used as the test crop. The greenhouse temperature (T_a), relative humidity (RH), vapour pressure difference (VPD), solar radiation (SR), and carbon dioxide (CO_2) data were collected using standard methods and data was analysed using MINITAB software. The statistical tools used for data analysis were descriptive statistics, analysis of variance (ANOVA), and t-Test. The total yield and marketable yield in the HUMITEM-GH was higher than the Conv-GH by 116.33 kg and 97.69 kg, respectively. There were significant differences between the two greenhouses microclimate both in the daytime and night-time with the HUMITEM-GH having higher and near-optimal climate parameters. This result has shown that the newly developed HUMITEM air circulation fan has a superior air circulation and flow capability than the conventional air circulation fans. This information may be of interest to farmers, horticulturists, and researchers who are involved in protected vegetable production.
KEYWORDS: CAF; HAF; HUMITEM; air-circulation; distribution; airflow

1. INTRODUCTION

A greenhouse is an indoor cropping system that allows the manipulation and control of environmental, nutrition, and biological variables. Additionally, it makes it possible to implement management techniques for successful crop production. Regardless of the unfavourable external conditions that may exist at the location, a variety of ornamental, food and cash crops can be cultivated steadily indoors. Throughout the growing season, the ideal indoor microclimate necessary for crop growth and development must be maintained (Iddio *et al.*, 2020; Ogunlowo *et al.*, 2022). Indoor cultivation is a widely accepted technique that has been adopted by small-, medium- and large-scale farmers with an estimated 5,630,000 hectares of protected agriculture all over the world as of 2019 (Hickman, 2019). Averagely, more than two countries per continent are engaged in greenhouse crop production and more than 60 countries where greenhouse commercial production is practised. Indoor cultivation has numerous advantages namely the ability to control the indoor thermal environment, protect against pest infestation and disease attack, multiple cropping, Off-season cropping, increased crop productivity per unit land area and labour, vertical cropping technology, guarantee food security, maximize high-quality products while minimizing production cost and increased water and chemical use efficiency (Katsoulas and Stanghellini, 2019). Despite the numerous benefits of indoor agriculture, there are some drawbacks namely: high initial investment, and a shortage of greenhouse-specific tools and machinery (Reddy, 2016).

The internal microclimate of a greenhouse is primarily influenced by the climatic conditions of the surrounding environment. As a result, to achieve optimal crop production within the greenhouse, the microclimate in terms of light level (SR), air temperature (T_a), soil temperature (T_s), relative humidity (RH), and carbon dioxide (CO_2) must be manipulated to the recommended ranges for specific crops (Akpenpuun and Mijinyawa, 2020). Adequate

control strategies are required to keep the environmental variables within the optimum limits because these variables directly influence the efficiency of the cultivation system in terms of yield and expended energy either for cooling or heating (Yang *et al.*, 2022). Several studies have been conducted to investigate the impact of greenhouse microclimate parameters such as temperature, vapour pressure deficit, relative humidity, carbon dioxide concentration soil temperature, and solar radiation level and have shown that ranges of these parameters outside the optimum harm crop growth, development, and yield (Sim *et al.*, 2020; Kim *et al.*, 2022). Multiple cooling strategies can be used in greenhouses to provide an appropriate microenvironment including (i) shading methods such as applying whitewash or plastic nets or thermal screens, (ii) fans-pads evaporative cooling systems, fogging and evaporative roof cooling, and (iii) ventilation systems such as forced ventilation, using air circulation fans in combination with natural ventilation through sidewalls and roof vents as ventilation aids even distribution of climatic variables (Shamshiri *et al.*, 2018).

In the greenhouse, airflow is restricted by the structural members, plants, and equipment, resulting in a sharp increase in indoor temperature. Therefore, knowing the behaviour of meteorological elements, such as temperature, RH, VPD, SR, and CO_2 in a greenhouse, is essential to exploiting the benefits of protected cultivation. To achieve the optimal comfort level indoors in terms of T_a, RH, VPD, SR, and CO_2 appropriate climate control pieces of equipment are needed. Even though, there are several fans (different sizes and power ratings) for the greenhouse industry the choice of a particular circulation fan depends on the greenhouse's size, design, and desired environmental condition. As the air moves inside the greenhouse environment, gradients of these meteorological elements are formed throughout the structure and can result in a heterogeneous microclimate, which may be undesirable for plants (Cesar *et al.*, 2021). In addition to these parameters, it is also important to monitor and control pests and diseases, as well as maintain proper soil moisture and nutrient levels. Regular monitoring and adjustments to the greenhouse environment would help ensure the optimal growth and productivity of plants. The objectives of this study were to compare and analyze changes in the thermal environment of two tunnel greenhouses equipped with newly manufactured HUMITEM air-circulation fans (a circular airflow fan) and Conventional air-circulation fans (a horizontal airflow fan) and to determine the resultant effect of the air-circulation fans on the microclimate using statistical analysis.

2. MATERIALS AND METHODS

2.1 Study area

Sangju Smart Farm Innovation Valley, Sangju-si, Gyeongsangbuk-do (also known as in the North Gyeongsang Province), South Korea, was the experimental site location. Sangju is situated in the south-eastern part of the province, about 20 km southwest of the city of Gumi and about 50 km southeast of the city of Daegu. The city is surrounded by mountains and is situated on the banks of the Nakdong River. Gyeongsangbuk-do is located between the latitudes of 35.4°N and 37.4°N and the longitudes of 128.3°E and 131.4°E and is approximately 60 m above the mean sea level (Park *et al.*, 2011). Gyeongsangbuk-do has a humid subtropical climate with annual mean relative humidity, rainfall, length of day (photoperiod), minimum temperature, and maximum temperature of 73%, 1050 mm, 6.2 hours, -3 °C, and 26°C, respectively. Gyeongsangbuk-do has four seasons: spring (March-May), summer (June-August), fall (September-November), and winter (December-March) (Korea Meteorological Administration, http://www.kma.go.kr, accessed on 07 December 2022). Rice, barley, beans, cabbage, strawberries, sesame seeds, garlic, plums, potatoes, tomatoes, apples, cucumber, chestnuts, radish, agaric, and sweet potatoes are among the food crops grown in Gyeongsangbuk-do.

2.2 Experimental setup

This experiment was performed in two tunnel greenhouses and the duration of the experiment was from December 29 2022 to March 30, 2023. The rule of thumb recommends that a single-span greenhouse on a latitude above 40°N should have its ridge running east to west to allow low-angle solar rays into the greenhouse from the long sides rather than the ends, while below 40°N latitude the ridge of a single-span greenhouse should be oriented towards north to south since the angle of the sun is higher, was applied. As a result, the orientation of the greenhouses was in the east-west direction, which is the most suitable orientation for SR reception in the study area (Reddy, 2016). The arch-shaped greenhouses were covered with polyolefin and a layer of thermal screen, had the same dimensions of 52.8 m * 6.8 m * 2.5 m (length × breadth × height) and the same structural configuration (eaves and ridges height of 1.5 m and 2.8 m, respectively Each had a floor area of 18 m^2 (3 m × 6 m). The thickness and transmittance of the polyethylene film were 200 µm and 91%, correspondingly, while the thickness, conductivity, transmittance, reflectance, and emittances of the thermal screen were 3.5 mm, 0.037 Wm^{-1} K^{-1}, 0.001, 0.10, and 0.90, correspondingly. Five HUMITEM air-circulation fans (voltage: 220 V; frequency: 60 HZ; allowable fan capacity: 1.16 A; fan maximum speed: 2290 m^3/h; power rating: 4.43 hp (3300 W); window-size: 30 cm; wing diameter: 28 cm) were installed in the HUMITEM greenhouse, whereas in the conventional greenhouse (Conv-GH), five conventional air-circulation fans (voltage: 220 V; frequency: 60 HZ; allowable fan capacity: 0.2 A; fan maximum speed: 1500 m^3/h; power rating: 0.54 hp (400 W); window-size: 25 cm; wing

diameter: 23 cm) were installed to aid ventilation and distribution of climate variables. The fans in both greenhouses were installed at a distance of 13.2 m from each other. The side vents opened automatically when the greenhouse air temperature was above the set temperature point of 20 ℃, correspondingly. The optimum air temperature range to enable strawberry development and growth occurs between 18℃ to 24℃. Since the experiments were conducted in the winter, a boiler was installed to keep the greenhouses' air space temperature range within the optimum range. The boilers' heating range was 15,000 kcal/h to 62,802 kcal/h, while the heating and continuous hot water supply efficiency were both 90% each. The boilers were set to switch on and start the heating process when the greenhouse air temperature was 9 ℃ and switched off as soon as the greenhouse air temperature rose to 10 ℃.

The *Seolhyang* variety of strawberries was the model crop in the experiments and was transplanted on five 51.2 m long greenhouse benches, that were spaced 1.3 m centre-centre. The strawberry plants were planted in two rows per bed with a centre-centre row spacing of 25 cm apart, resulting in a plant density of 410 per bed and 2050 plants per greenhouse. The same open-loop drip-fertigation system supplied both greenhouses with water and nutrient solution five times daily at an interval of 1 h 30 min, beginning at 08:30, and the duration of each fertigation period was 3 minutes. Standard cultivation practices adopted by Akpenpuun *et al.* (2021) were followed. Figure 1 shows the sensors' location.

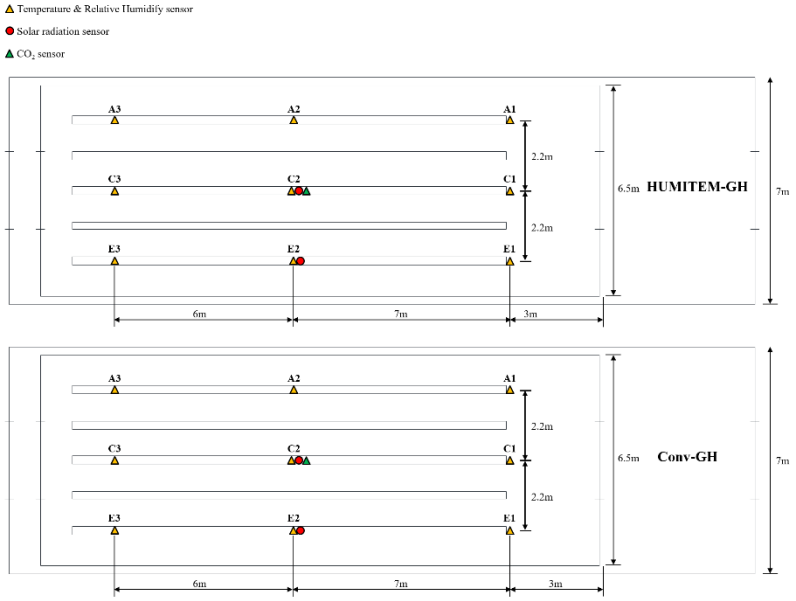

Figure 1. Sensors' location in both GH

2.3 Data collection

The air temperature and relative humidity sensors (temperature: measurement range: -20 °C to 80 °C; accuracy: ±0.25 °C; humidity: measurement range: 0% to 100% accuracy: ±2%, HOBO PRO v2 U23 Pro v2, ONSET, USA) were installed (three per row) at 1.54 m from the floor and placed in protective plastic cases to shield them from direct solar radiation, which could result to inaccuracies in the data. The solar radiation sensors (measurement range: 0 to 1280 W/m^2; accuracy: ±10 W/m^2 operating temperature range: −40 °C to 70 °C, HOBO RX3000, ONSET, USA) and CO_2 data loggers (Range: 0 to 5,000 ppm; Accuracy: ±50 ppm ±5% of reading at 25°C (77°F), less than 90% RH; Non-linearity: <1% of FS; Operating Pressure Range: 950 to 1,050 mbar; Sensing Method: Non-dispersive infrared (NDIR) absorption, HOBO MX1102, ONSET, USA) were installed just above the crop canopy. All data loggers recorded readings at ten-minute intervals. The daytime and nighttime data were between the hours of 09:00-16:40 and 16:50-08:50. Total marketable berry fruits were measured (Undeformed fruits and fruits that were 25-30 g and 40-60 mm in diameter). Vapour pressure deficit (VPD) was computed using the method adopted by Abd-El Baky *et al.*(2004)**.**

2.4 Research hypotheses

The hypotheses of a study comparing the climate of two greenhouses might be:

I. Null Hypothesis (H0): The null hypothesis (H0) suggests that there is no significant difference in the climate of the two greenhouses.
II. Alternative Hypothesis (H1): The alternative hypothesis (H1) suggests that there is a significant difference in the climate of the two greenhouses.

2.5 Statistical analysis

To analyze the data collected in the study, descriptive statistics were used to describe the basic features of the data, while the independent samples t-test at p = 0.01 or 0.05 levels was used to compare the means of the thermal environments of the two greenhouses. These analyses were carried out using Minitab Statistical software, version 17 (Minitab, LLC, State College, Pennsylvania, USA).

3. RESULTS

The HUMITEM-GH and Conv-GH indoor climate data were recorded for 92 days (29 December 2022-30 March 2023). The daytime climate indices minimum values were 6.24 ^{o}C, 39.22%, 0.04 kPa, 0.37 W/m^2, and 318 ppm for HUMITEM-GH and 5.57 ^{o}C, 19.73%, 0.04 kPa, 0.69 W/m^2, and 355 ppm for Conv-GH. Table 1 presents the comprehensive descriptive statistics of the of the daytime and night-time climate data.

Table 1. Descriptive statistics of both greenhouses' daytime and night-time microclimate indices

Microclimate indices		Temperature (^{o}C)	RH (%)	VPD (kPa)	SR (W/m^2)	CO_2 (ppm)
Daytime						
HUMITEM-GH	**Mean (±sd)**	20.41±4.04	75.63±12.09	0.68±0.42	110.58±84.79	636.9±204.32
	Variance	16.34	146.05	0.18	7189.13	41745.91
	Standard error	0.07	0.22	0.01	1.53	3.69
Conv-GH	**Mean (±sd)**	17.06±3.95	63.64±19.22	0.78±0.50	157.94±102.76	616.48±139.02
	Variance	15.62	369.58	0.25	10559.55	19327.89
	Standard error	0.07	0.35	0.01	1.86	2.51
Night-time						
HUMITEM-GH	**Mean (±sd)**	11.10±2.47	90.66±4.00	0.13±0.09		936.26±224.97
	Variance	6.08	16.01	0.01		50609.73
	Standard error	0.03	0.05	0.00		2.97
Conv-GH	**Mean (±sd)**	10.06±1.74	84.43±6.40	0.19±0.11		730.78±117.81
	Variance	3.03	40.99	0.01		13880.23
	Standard error	0.02	0.08	0.00		1.56

RH = relative humidity; VPD = Vapour pressure deficit; PAR = Photosynthetically active radiation; CO_2 = Carbon dioxide; GH = greenhouse

The T_a distribution ranges of 6 ^{o}C-10 ^{o}C, 11 ^{o}C-15 ^{o}C, 16 ^{o}C-20 ^{o}C, 21 ^{o}C-25 ^{o}C and 26 ^{o}C -30 ^{o}C had a frequency of 36, 401, 609, 1786, and 233, respectively, in the HUMITEM-GH, while in the Conv-GH the frequencies were 208, 645, 1433, 768 and 1, respectively. The frequency of the RH distribution ranges of 41%-55%, 56%-70%,71-85% and 86%-98% in the HUMITEM-GHwas 3, 129, 939 and 1994, respectively, and 50, 371, 650, 639 and 1355, respectively, in the Cov._GH. The frequency VPD distribution was 92, 3064 and 1in the HUMITEM-GHand 119, 3040 and 25 in the Conv-GH for VPD ranges of 0.09 kPa-0.29 kPa, 0.30 kPa-2.00 kPa and >2.00 kPa, respectively.

The analysis of variance (ANOVA) test performed on the daytime data with degrees of freedom of 1 and 6128 gave $F_{statistics}$, $F_{critical}$ and P_{value} values of 1075.39, 6.64 and <0.01, 854.55, 6.64 and <0.01, 81.47, 6.64 and <0.01, 387.29, 6.64 and <0.01 and 20.93, 6.64 and <0.01, respectively, for Ta, RH, VPD, SR and CO_2. The ANOVA on the night-time data with the degree of freedom of 1 and 11450 gave $F_{statistics}$, $F_{critical,}$ and P-value of 678.17, 6.64 and <0.01, 3896.91, 6.64, <0.01, 1187.87, 6.64 and <0.01 and 3748.96, 6.64 and <0.01, respectively, for T_a, RH, VPD and CO_2. The daytime and night-time comparisons were significantly different at 1% and 5% confidence levels.

The t-test two-sample assuming equal variances result also shows the comparison of the T_a, RH, VPD, SR, and CO_2 were significantly different at P-value less than 1% and 5%, $t_{critical}$ value of 1.96 for daytime data and 2.58 for the night-time data. The t-test result further shows that the comparison between the HUMITEM and conventional greenhouses satisfied the alternative hypothesis that there is a significant difference in the climate of the two greenhouses. This further suggests that the microclimate variables being compared were affected by the type of fan used.

The highest daytime temperature recorded in the HUMITEM-GH and Conv-GH was 25.39 °C and 26.20 °C on 21/02/2023, while the least daytime temperature in the HUMITEM-GH and Conv-GH was 6.24 °C and 5.57 °C, respectively, recorded on the 24/01/2023. Finally, HUMITEM-GH and Conv-GH T_a were 24.91 °C and 24.69 °C, respectively, on 30/03/2023 the last day of the experiment. The daytime and night-time T_a in the HUMITEM-GH was considerably higher than the T_a in the Conv-GH by 3.35 °C and 1.04 °C.

Likewise, the highest daytime and night-time RH values were 96.27% and 97.20%, and 97.86% and 97.71%, respectively, for HUMITEM-GH and Conv-GH, while the least daytime and night-time RH values were 39.22% and 19.73%, and 46.28% and 20.76%, respectively, for HUMITEM-GH and Conv-GH. Most of the time during the day, RH in the HUMITEM-GH was higher than RH in the Conv-GH because the HUMITEM circulation fans were able to move a greater volume of air around the greenhouse and outside than the conventional air circulation fans. The difference between the least RH in the HUMITEM-GH and Conv-GH was 19.49% in the daytime and 25.52% in the night-time. Even though HUMITEM-GH and Conv GH both had slightly higher RH levels, the differences between the two were not particularly noteworthy.

The HUMITEM-GH and Conv-GH had respective mean daytime VPD of 0.68±0.42 kPa and 0.78±0.50. In the HUMITEM-GH and Conv GH, respectively, the maximum values of VPD during the daytime were 2.07 kPa and 2.25 kPa. The HUMITEM-GH mean daytime VPD was slightly lower than Conv-GH VPD. The night-time VPD mean was 0.13±0.09 kPa and 0.19±0.11 kPa in the HUMITEM-GH and Conv-GH, respectively. VPD in the Conv-GH was higher than HUMITEM-GH most of the time during the day and followed the same trend as RH. Although slightly higher VPD was observed in the Conv-GH than in the HUMITEM-GH, the overall difference was statistically insignificant. However, both greenhouses had roughly the same mean night-time VPD and a similar pattern of variation.

The daytime CO_2 range in the HUMITEM-GH, Conv GH, and outdoor was 318.0-2083 ppm and 355.0-*1514* ppm, respectively. The night-time CO_2 range in the HUMITEM-GH and Conv GH was 344-2669 ppm and 356-1081 ppm. According to the descriptive statistics, the mean daytime CO_2 in the HUMITEM-GH and Conv-GH were, respectively, 636.90±204.32 ppm and 616.48±139.02 ppm. The night-time CO_2 mean was also 936.26±224.97 ppm and 730.78±117.81 ppm, respectively, in the HUMITEM-GH, Conv GH, and outdoor. The result of the analysis of variance showed that the CO_2 levels in both greenhouses were statistically significant at a 99% level of confidence (df1 = 1, df2 = 6128). Also, the t-Test showed that the CO_2 levels were statistically significant.

Since both greenhouses had the same orientation, structural layout, covering material, and dimensions from the start, the SR of the HUMITEM-GH and the Conv-GH had the same pattern, but the differences were statistically insignificant.

The total yield in the HUMITEM-GH and Conv-GH was 444.51 kg and 328.18 kg, respectively, making the yield in the HUMITEM-GH higher than the Conv-GH by 116.33 kg. The marketable yield was 388.05 kg and 290.36 kg, respectively, for the HUMITEM-GH and Conv-GH. The mean marketable yield was 6.93±4.28 kg and 5.19±3.72 kg in the HUMITEM-GH and Conv-GH, in that order. The total and marketable yields in the HUMITEM-GH were statistically significant from the Conv-GH at the confidence level of 95%.

4. DISCUSSION

The daytime T_a recorded in the HUMITEM-GH and Conv-GH was in the range of 6.24 °C-26.81 °C and 5.57 °C-26.20 °C, correspondingly, while the night-time T_a was 6.07 °C-23.77 °C and 5.57 °C-20.84 °C, respectively for the HUMITEM-GH and Conv-GH. Pearce *et al.* (1993) reported that temperatures between 10 °C and 30 °C positively impact the growth rates of fruit in a closed environment. Balendonck *et al.* (2010) experimented with measuring the extent of climate unevenness and determining the number of sensing points for precise estimation of the spatial and temporal climate variable distribution in four commercial greenhouses observed averaged spatial differences of 1.0 °C - 3.4 °C for temperature, whereas in this experiment average spatial differences were 0.26 °C-5.24 °C and 0.65 °C-5.69 °C in the HUMITEM-GH and Conv-GH. During this research, the maximum daytime and night-time temperature difference between HUMITEM-GH and Conv-GH were found to be 0.60 °C and 2.94 °C with the HUMITEM-GH having higher temperatures than the Conv-GH. Sim *et al.* (2020) reported day- and night-time temperatures in the range of 15°C-25°C and 5°C-10°C, correspondingly, in an air-inflated and conventional double-layer greenhouse. It was observed that just as spring began in March, the mean temperatures in both greenhouses increased by 0.55 °C and 1.46 °C, respectively, in the HUMITEM-GH and Conv-GH. This increase in greenhouse air temperature could be explained by a greater number of sunny days and photoperiod per day as a result of higher solar radiation intensity compared to winter.

The RH recorded in the HUMITEM-GH and Conv-GH was in the range of 40.22%-97.20% and 19.73%-97.79%, and 46.28%-97.86% and 20.76%-97.75%, correspondingly, for daytime and night-time. Jayasekara *et al.* (2018) reported 85% in a double-layer greenhouse that was heavily saturated at night, however, during the daytime, RH was as low as 40%. Kroggel and Kubota (2017) recommended a maximum night-time RH of 95% and an optimum daytime humidity in the range of 40%–60% to avoid tip burn. Only the HUMITEM-GH had its RH within the recommended ranges. The change in weather from winter to spring which caused an increase in temperature

resulted in increased plant growth and physiological activity including evaporation and consequent increase in the RH by 6.22% and 8.04% in the HUMITEM-GH and Conv-GH, respectively.

The VPD recorded in the HUMITEM-GH and Conv-GH was in the range of 0.04 kPa to 2.07 kPa and 0.03 kPa to 2.25 kPa, and 0.03 kPa -1.57 kPa and 0.03 kPa -1.73 kPa, correspondingly, in the day and night. The difference between the outdoor VPD and that inside the HUMITEM-GH was 0.18 kPa. Amani *et al.* (2020) and recommended ranges of 0.3 to 1.3 kPa and 0.8 to 1.0 kPa, correspondingly. Although the lower limit of VPD recorded in both greenhouses was lower than the recommended 0.5 kPa, the frequency of the VPD values that were within the recommended range of 0.3 to 2.0 kPa was 2921 and 2972 for the HUMITEM-GH and Conv-GH, respectively. The VPD in both greenhouses was significantly different with the HUMITEM-GH having higher VPD values that are within the recommended range that the Conv-GH.

The CO_2 recorded in the HUMITEM-GH and Conv-GH greenhouse was in the range of 318 $\mu mol \cdot mol^{-1}$-2083 $\mu mol \cdot mol^{-1}$ and 355 $\mu mol \cdot mol^{-1}$ 1514 v $\mu mol \cdot mol^{-1}$, correspondingly. There is evidence that CO_2 concentrations in the range of 800 $\mu mol \cdot mol^{-1}$ and 1500 $\mu mol \cdot mol^{-1}$ can considerably improve growth, while exposure to a CO_2 concentration of less than 350 ppm, the outdoor CO_2 concentration indoors, could be detrimental to growth (Kim *et al.*, 2022). The mean daytime and night-time CO_2 concentration in the HUMITEM-GH was higher than the concentration in the Conv-GH and there was a significant difference between the two greenhouses. However, the CO_2 concentration in the HUMITEM-GH was still in the ranges of 340-1000 $\mu mol \cdot mol^{-1}$, 800-1000 $\mu mol \cdot mol^{-1}$, 1000 -1500 $\mu mol \cdot mol^{-1}$ and 900-1000 ppm recommended by Garcia and Kubota (2017), and Durkin (1992), correspondingly. The lower CO_2 concentration recorded in HUMITEM-GH can be attributed to the operation of the HUMITEM fans which had a higher capacity for circulation and increased ventilation rates.

The SR recorded in the HUMITEM-GH and Conv-GH was in the range of 0.37 W/m^2-520.74 W/m^2 and 0.69 W/m^2-448.68 W/m^2, respectively. These SR ranges are similar to the SR range of 8.7 W/m^2 -549.8 W/m^2 and 3.2 W/m^2-631.6 W/m^2 recorded by Akpenpuun et al. (2021) in single-layer and double-layer greenhouses. The SR in both greenhouses was nearly the same as there was no significant difference between the amount of radiation received by each greenhouse. This might be because both greenhouses were side by side and structurally the same and the fans had no interference with SR reception. The HUMITEM-GH and Conv-GH receive more solar irradiance (20 W/m^2 over 10 hours) in March when the sun was more southerly compared to November to February (9 W/m^2 over 8 hours) when the sun was more easterly.

5. CONCLUSIONS

The finding from the research highlights the importance of selecting the appropriate air-circulating fan to improve the microclimate of a naturally ventilated greenhouse. The study found that by using HUMITEM air-circulating fans, the distribution of climate variables was significantly improved, resulting in a near-optimal growing condition. The significant difference between the Conv-GH and HUMITEM-GH yield can be attributed to the significant difference between the Conv-GH and HUMITEM-GH microclimates. The use of HUMITEM air-circulating fans could have a significant impact on the commercial production of plants, providing farmers and horticulturists with a tool to optimize the growing conditions of their crops. The improved distribution of climate variables can increase the efficiency of the greenhouse environment, thereby, resulting in higher yield, reduced energy consumption, and consequently resulting in cost savings for growers.

Funding: This study was supported by the Korea Institute of Planning, and Evaluation for Technology in Food, Agriculture, Forestry, and Fisheries (IPET) through the Agriculture, Food, and Rural Affairs Convergence Technologies Program for Educating Creative Global Leaders, funded by the Ministry of Agriculture, Food, and Rural Affairs (MAFRA) (717001-7). This research was supported by the Basic Science Research Program through the National Research Foundation of Korea (NRF) funded by the Ministry of Education (NRF-2019R1I1A3A01051739).

REFERENCES

Abd-El Baky, H. M., Ali, S. A., El Haddad, Z. A., and El Ansary, M. Y. (2004). Some Environmental Parameters Affecting Sweet Pepper Growth and Productivity Under Different Greenhouse Forms in Hot and Humid Climatic Conditions. Mansoura University Journal of Soil Sciences and Agricultural Engineering, 1(3), 225-247.

Akpenpuun, T. D., and Mijinyawa, Y. (2020). Impact of a split-gable greenhouse microclimate on the yield of irish potato (solanum tuberosum l.) under tropical conditions. Journal of Agricultural Engineering and Technology, 25(1), 54-78.

Akpenpuun, T. D., Na, W. H., Ogunlowo, Q. O., Rabiu, A., Adesanya, M. A., Addae, K. S., Kim, H. T., and Lee, H.-W. (2021). Effect of glazing configuration as an energy-saving strategy in naturally ventilated greenhouses for strawberry (Seolhyang sp.) cultivation. Journal of Agricultural Engineering, 52(2), 1-8.

Akpenpuun, T. D., Ogunlowo, Q. O., Afolabi, D. T., Ogundele, O. M., Hassan, M. B., Ajayi, T. A., Oparemi, I. O., Oyeniyi, L. J., and Olaniyan, J. O. (2022, September 20Th – 24Th 2022). Development of a building energy model for selected greenhouse designs cladded with polyolefin under tropical conditions. Paper presented at the Proceedings of the 22nd international conference and 42nd annual general meetings of the Nigerian Institution of Agricultural Engineers (A division of the Nigerian Society of Engineers), Asaba, Delta State, Nigeria.

Amani, M., Foroushani, S., Sultan, M., and Bahrami, M. (2020). Comprehensive review on dehumidification strategies for agricultural greenhouse applications. Applied Thermal Engineering, 181, 115979.

ASABE. (2015). Heating, Ventilating and Cooling Greenhouses ANSI/ASAE Standard EP406.4. St. Joseph, MI, USA: American Society of Agricultural and Biological Engineers.

Balendonck, J., Van Os, E. A., Van Der Schoor, R., Van Tuijl, B. A. J., and Keizer, L. C. P. (2010). Monitoring Spatial and Temporal Distribution of Temperature and Relative Humidity in Greenhouses based on Wireless Sensor Technology. Paper presented at the International Conference on Agricultural Engineering - AgEng 2010: towards environmental technologies, Clermont-Ferrand, France.

Cesar, T. Q. Z., Leal, P. A. M., Branquinho, O. C., and Miranda, F. A. M. (2021). Wireless sensor network to identify the reduction of meteorological gradients in greenhouse in subtropical conditions. Journal Agricultural Engineering, 52(1), 1–8.

Durkin, D. J. (1992). Roses. In R. A. Larson (Ed.), Introduction to Floriculture (Vol. Second Edition, pp. 67-92). San Diego, California 92101-4495: Academic Press.

Garcia, K., and Kubota, C. (2017). Physiology of strawberry plants under controlled environment: Diurnal change in leaf net photosynthetic rate. Acta Horticulturae, 1156, 445-452. DOI: https://www.doi.org/10.17660/ActaHortic.2017.1156.66

Hickman, G. W. (2019). World Greenhouse Vegetable Statistics updated for 2019. Retrieved 23/02/2023, from Fresh Publishers https://tinyurl.com/fn3deske

Iddio, E., Wang, L., Thomas, Y., McMorrow, G., and Denzer, A. (2020). Energy efficient operation and modelling for greenhouses: A literature review. Renewable and Sustainable Energy Reviews, 117, 109480.

Jayasekara, S. N., Na, W. H., Owolabi, A. B., Lee, J. W., Rasheed, A., Kin, H. T., and Lee, H. W. (2018). Comparison of environmental conditions and insulation effect between air inflated and conventional double layer greenhouse. Protected horticulture & plant factory, 27(1), 46 – 53.

Katsoulas, N., and Stanghellini, C. (2019). Modelling Crop Transpiration in Greenhouses: Different Models for Different Applications. Agronomy, 9(392), 2 – 17.

Kim, H.-K., Lee, S.-Y., Kwon, J.-K., and Kim, Y.-H. (2022). Evaluating the Effect of Cover Materials on Greenhouse Microclimates and Thermal Performance. Agronomy, 12(1), 143.

Kläring, H. -P., Hauschild, C., Heißner, A., and Bar-Yosef, B. (2007). Model-based control of carbon dioxide concentration in greenhouses at ambient levels increases cucumber yield. Agricultural and Forest Meteorology, 143(3 - 4), 208 – 216.

Kroggel, M., and Kubota, C. (2017). Controlled environment strategies for tipburn management in greenhouse strawberry production. Acta Hort, 1156, 529-536.

Ogunlowo, Q. O., Na, W. H., Rabiu, A., Adesanya, M. A., Akpenpuun, T. D., Kim, H. T., and Lee, H. W. (2022). Effect of envelope characteristics on the accuracy of discretized TRNSYS building energy simulation model. Journal of Agricultural Engineering, 53(3), 1420.

Park, S., Oh, C., Jeon, S., Jung, H., and Choi, C. (2011). Soil erosion risk in Korean watersheds, assessed using the revised universal soil loss equation. Journal of Hydrology, 399(3-4), 263-273.

Pearce, B. D., Grange, R. I., and Hardwick, K. (1993). The growth of young tomato fruit. I. Effects of temperature and irradiance on fruit grown in controlled environments. Journal of Horticultural Science, 68(1), 1 - 11.

Reddy, P. P. (2016). Protected Cultivation. In P. P. Reddy (Ed.), Sustainable Crop Protection under Protected Cultivation (pp. 1 - 11). Singapore: Springer.

Shamshiri, R. R., Jones, J. W., Thorp, K. R., Ahmad, D., Che Man, H., and Taheri, S. (2018). Review of optimum temperature, humidity, and vapour pressure deficit for microclimate evaluation and control in greenhouse cultivation of tomato. International agrophysics, 32(2), 287 - 302.

Sim, H. S., Kim, D. S., Ahn, M. G., Ahn, S. R., and Kim, S. K. (2020). Prediction of strawberry growth and fruit yield based on environmental and growth data in a greenhouse for soil cultivation with applied autonomous facilities. Horticultural science & technology, 38(6), 840 - 849.

Yang, L., Liu, H., Cohen, S., and Gao, Z. (2022). Microclimate and Plant Transpiration of Tomato (Solanum lycopersicum L.) in a Sunken Solar Greenhouse in North China. Agriculture, 12(2), 260.

PAPER 23 – MODIFICATION OF SOME QUALITY ATTRIBUTES OF BROWN RICE-BAMBARA NUTS-PINEAPPLE PEELS EXTRUDED SNACKS THROUGH EXTRUSION CONDITIONS

M. S. Sanusi*, M. O. Sunmonu, S. O. Alasi, A. A. Adebowale, I. T. Esho, A. A. Tajudeen

Department of Food Engineering, Faculty of Engineering and Technology, University of Ilorin, Nigeria.
*Email: Sanusi.ms@unilorin.edu.ng

ABSTRACT
This study aimed to create ready-to-eat extruded snacks using underutilized broken brown rice flour, Bambara nuts flour, and pineapple peel powder as primary ingredients in a 50:45:5 ratio. The effects of extrusion exit temperature, feed moisture content, and barrel screw speed on protein, total phenolic content, 2,2-diphenyl-1-picrylhydrazyl (DPPH) radical scavenging activity, and vitamin C were assessed and modelled using polynomial regression. The Pareto chart showed that protein and vitamin C were significantly influenced by the quadratic effect of barrel screw speed, while total phenolic content was significantly influenced by barrel screw speed, and DPPH radical scavenging activity was significantly influenced by extrusion exit temperature. The extruded snacks had protein content ranging from 12.87 to 16.36%, total phenolic content ranging from 14.17 to 18.02 mg GAE/g, DPPH radical scavenging ranging from 14.57 to 16.25%, and vitamin C ranging from 12.05 to 14.25 mg/100g. The developed regression model predicted the quality attributes well, with a coefficient of determination ranging between 0.99 and 1. The optimum extrusion conditions for maximizing quality attributes differed, and the development of extruded snacks from brown rice, pineapple peels, and Bambara nuts would promote sustainable food production and reduce food waste.

KEYWORDS: Bambara nuts, Pineapple peels, Brown rice, Extrusion, Ready-to-eat extruded snacks

1. INTRODUCTION

There is a constant increase in the consumption of ready-to-eat extruded snacks by many individuals, especially children, which form a significant part of the daily diet (Ziena and Ziena, 2022). Children and adults are often captivated by numerous ready-to-eat products such as extruded snacks and noodles, credited for their pleasing smell, taste, texture, appearance, and ease of consumption. However, the raw materials commonly used in extrudates are cereals and grains, which are low in certain essential nutrients such as protein, antioxidants, and vitamins, consequently leading to malnutrition thus, there is a growing demand for healthier snacks.

Bambara nuts (*Vigna subterranean*) is a legume crop that has substantial socio-economic significance in emerging markets and is considered a "crop for the future," but is currently underutilized (Diedericks *et al.,* 2020; Muhammad *et al.,* 2020). The nuts consist of a high proportion of protein, ranging from 17 to 27%. They also contain a reasonable amount of carbohydrate and fat (Muhammad *et al.,* 2020). Fruit waste, such as pineapple peel, is an excellent source of low-cost proteins and antioxidants, such as polyphenol compounds and DPPH radical scavenging activity (Roda and Lambri, 2019). They are also rich in vitamins C, vitamin A, and vitamin B_6 (Franklyn *et al.,* 2018). Rice flour from brown rice has become a suitable and established material for numerous ready-to-eat extruded snacks due to its suitability, hypo-allergenicity, pleasing flavour, and good digestibility (Dalbhagat *et al.,* 2019; Sanusi and Akinoso, 2021). It is a good source of dietary fibre and antioxidants. Brown rice contains a higher protein content than hulled rice due to the presence of bran but is relatively low in vitamin C. Thus, it is necessary to enhance the protein, vitamin C, and antioxidant properties of products produced from rice. The chemical composition and antioxidant properties of extruded snacks could significantly influence the acceptability of the final product. The inclusion of Bambara nuts and pineapple peel into rice-based snacks could increase the quality attributes of the extruded snacks and provide a promising technique to improve product quality. However, there is a scarcity of information on the utilization of broken brown rice, Bambara nuts, and pineapple peel to develop extruded snacks.

Extrusion technology has revolutionized numerous traditional techniques for manufacturing snacks due to its high suitability, flexibility for different raw materials, and ability to modify the quality characteristics of raw materials through transformations such as starch gelatinization, protein denaturation, pigment degradation, and amylose formation (Offiah *et al.,* 2019; Dey *et al.,* 2021). Extrusion conditions significantly influence the overall compositions and quality of extruded products when they experience shear forces, extreme temperatures, and extreme pressure treatment, which have been widely studied in the literature (Sukumar and Athmaselvi, 2019;

Choton *et al.,* 2020; Sahu *et al.,* 2022; Sanusi *et al.,* 2023). However, a few research works focused on the effect of extrusion conditions on the quality attributes (protein, total phenolic content, DPPH radical scavenging activity, and vitamin C content) of brown rice-Bambara nuts-pineapple peel extruded snacks. Therefore, this study aims to examine the effect of extrusion conditions on the quality attributes of brown rice-Bambara nuts-pineapple peel extruded snacks.

2. MATERIALS AND METHODS

2.1 Materials

Broken brown rice and Bambara nuts were purchased from a local market in Ilorin, Nigeria, while pineapple peels were obtained from a fruit store in Ilorin, Nigeria. The broken brown rice was weighed and milled into flour using a hammer mill (Nukor, Model: SG 30, South Africa). Bambara nuts were soaked in lukewarm water (40°C) for 12 h, the hull removed, and dried using a fabricated forced-air dryer at 60ºC for 12 h. The dried Bambara nuts were then milled into flour using a hammer mill. The pineapple peels were washed and blanched at 55°C for 30 min to reduce microbial contamination. The blanched pineapple peels were drained, dried at 45ºC in a fabricated forced-air dryer, and then milled into a fine powder using an electric grinder (Grinder GR708HA, China).

2.2 Blends Preparation

A preliminary assessment was conducted using the mixture design feature in Minitab Statistical Software version 20.3 to determine the optimal combination of brown rice flour, Bambara nuts flour, and pineapple peel powder that can provide the highest protein content. Based on the results of the preliminary experiment, the mixture consisting of 50% brown rice flour, 45% bambara nut flour, and 5% pineapple peel powder was selected due to maximum protein content of 13%.

2.3. Experimental design

The study utilized an integration of Taguchi and response surface methodology (RSM) to investigate how extrusion conditions; extrusion exit temperature (120°C, 130°C, and 140°C), barrel screw speed (300 rpm, 360 rpm and 420 rpm) and feed moisture content (16%, 17% and 18%) affect the protein, total phenolic content, DPPH radical scavenging activity, and vitamin C content of the brown rice-bambara nut-pineapple peels extruded snacks. The Taguchi design results were analyzed by the second-order polynomial model of RSM, where the linear, quadratic, and interaction relationships of EET, BSS, and FMC were related to the protein, total phenolic content, DPPH radical scavenging activity, and vitamin C contents, as shown in Equation 1:

$$Y = C + \beta_1 x_1 + \beta_2 x_2 + \beta_3 x_3 + \beta_1 x_1^2 + \beta_2 x_2^2 + \beta_3 x_3^2 + \beta_{12} x_{12} + \beta_{13} x_{13} \quad (1)$$

Here, C represents the model constant coefficients, $\beta_1 x_1$, $\beta_2 x_2$, and $\beta_3 x_3$ are the linear terms, $\beta_1 x_1^2$, $\beta_2 x_2^2$, and $\beta_3 x_3^2$ are the quadratic terms, and $\beta_{12} x_{12}$ and $\beta_{13} x_{13}$ are the interaction terms. The responses (protein, total phenolic content, DPPH radical scavenging activity, and vitamin C) are represented by Y, while x_1, x_2, and x_3 denote the extrusion exit temperature (EET), barrel screw speed (BSS), and feed moisture content (FMC), respectively. The models' fitness for the quality attributes was evaluated using the coefficient of determinations (R^2, R^2_{adj}, and R^2_{pred}). The study also employed analysis of variance (ANOVA) to determine the p-values at a 95% confidence level and Fischer values (F-value) of the quality attributes. The significant extrusion parameter based on their linear, quadratic and interaction effects were determined using the Pareto chart in Minitab software version 20.3, with a reference line indicating the p=0.05 threshold for statistically significant effects.

2.4 Brown rice-Bambara nuts-pineapple peels extruded snacks production

A twin-screw extruder (Model: HN-65, Zhouheng Product, Jinan City, China) was used for producing the brown rice-bambara nuts-pineapple peel extruded snacks. The flour blends were fed into a co-rotating twin-screw extruder that contains a barrel, three electric band heaters, and a standard co-rotating screw. Water of 16%, 17%, and 18% of the entire mass (3 kg) blends were added and mixed using a mixer (Sokany Stand Mixer, Model: Cx-6612, China). The set temperature of the first and second heating bands of the extruder was 80°C and 100°C, respectively while the last heating band was varied between 120°C, 130°C and 140°C. A constant feed speed of 120 rpm was used to feed the samples into the barrel through the hopper, where proper cooking took place. The fed blends passed through the three heating barrel zones at different barrel screw speeds of 300, 360, and 420 rpm during the extrusion cooking. The cooked samples passed through a die orifice with a diameter of 4 mm in the

barrel. The extruded products were cut at a speed of 1500 rpm. The final extruded products were collected, dried using a forced-air dryer at 80 ± 5°C and packed in a zip-lock nylon at room temperature for storage.

e. Quality attributes

The protein content was evaluated using the standard method of Association of Analytical Chemists (AOAC) (2010). The total phenolic content and 2,2 -Diphenyl-1- Picrylhydrazyl (DPPH) radical scavenging activity were evaluated based on the procedures described by Sanusi *et al.* (2023). The method described by Gumul *et al.* (2013) was used to determine the Vitamin C.

2.6 Statistical analysis

The experiments were replicated, and the data were analyzed using the SPSS package (SPSS 20.0, SPSS Inc., Chicago, IL, USA) through one-way analysis of variance (ANOVA). Significant differences between means were determined using Duncan's multiple tests with a confidence interval of 95%.

3. RESULTS AND DISCUSSION

3.1 Influence of extrusion conditions on protein content

The protein content of the extruded snacks under the influence of extrusion conditions ranged between 12.87 and 16.36%. The highest crude protein content (16.36%) was attained at 130°C EET, 16% FMC, and 420 rpm BSS. According to Gbenyi *et al.* (2016), a food product with 15% crude protein content is recommended as the basic protein requirement to arrest protein malnutrition and to also supplement low-protein foods. The protein content obtained in the extruded snacks is higher than the 13% protein content from the blends of 50% brown rice flour, 45% Bambara nuts flour, and 5% pineapple peel powder. This could be attributed to the high temperature and high-pressure processing that occurs during extrusion. This process denatures the protein in the flour blend, making it more available for digestion and increasing its concentration in the final product. Sanusi *et al.* (2023) reported similar findings in the production of brown rice-watermelon seeds extruded snacks. The quadratic effect of BSS showed the most significant influence on the protein content as shown in Figure 1a of the Pareto chart. The BSS significantly affects the residence time of the products, which consequently influences the disruption and denaturation of the proteins of extruded products. Alam *et al.* (2016) reported similar findings. The quadric effect of EET also had a significant effect on the protein content as shown in the Pareto chart. The protein content of the extruded snacks can increase at high BSS and low EET or at higher EET and lower BSS (Figure 1b). From Figure 1c, the protein content increased with an increase in FMC at a lower EET. The linear, quadratic, interaction effect of EET, BSS, and FMC were significant at $p<0.05$ on the protein content of the extruded snacks with an F-value of 21624.77. Equation 2 shows the polynomial regression model developed for predicting the protein content. The R^2, R^2_{pred} and R^2_{adj} of the model measure the degree of fitness and had high values of 1.0. This shows that the model is perfectly sufficient to predict the protein content. A model fitness with R^2 close to unity (1) is the best (Sukumar and Athmaselvi, 2019; Sanusi and Akinoso, 2021).

$$Y_{protein} = -133.82 - 1.28x_1 - 0.15x_2 + 30.59x_3 + 0.0087x_1^2 + 0.00048x_2^2 - 0.795x_3^2 + 0.0014x_1x_2 + 0.028x_1x_3 \quad 2$$

Table 1. Effects of extrusion conditions on quality attributes of rice-bambara nuts-pineapple peel extruded snacks

Sample	FMC (%)	EET (°C)	BSS (rpm)	CP (%)	TPC mg GAE/g	DPPH (%)	Vitamin C (mg/100g)
A	16	120	300	16.23±.00^{b}	16.28±.00^{c}	14.57±.00^{g}	12.08±.01^{f}
B	17	120	360	14.24±.01^{e}	16.21±.00^{d}	14.86±.00^{f}	12.28±.01^{e}
C	18	120	420	14.08±.01^{d}	14.17±.00^{g}	15.21±.00^{c}	14.25±.01^{a}
D	17	130	300	15.35±.01^{d}	18.02±.01^{a}	16.25±.00^{a}	14.03±.00^{c}
E	18	130	360	14.04±.01^{g}	15.74±.00^{e}	15.25±.00^{b}	12.05±.01^{g}
F	16	130	420	16.36±.01^{a}	16.21±.00^{d}	16.25±.00^{a}	12.07±.01^{fg}
G	18	140	300	14.26±.01^{e}	18.02±.00^{a}	16.24±.00^{a}	14.02±.01^{c}
H	16	140	360	12.87±.00^{h}	16.58±.00^{b}	15.02±.00^{e}	12.66±.01^{d}
I	17	140	420	15.43±.01^{c}	15.27±.00^{f}	15.11±.00^{d}	14.21±.01^{b}

Mean values and superscripts with dissimilar letters along the same column are significantly different at $p<0.05$. CP- Crude Protein, TPC- Total Phenol Content, 2,2-diphenyl-1-picrylhydrazyl (DPPH) radical scavenging activity

3.2 Influence of extrusion conditions on vitamin C content

The vitamin C content of the extruded snacks ranged between 12.05 and 14.25 mg/100g (Table 1). All values are significantly different at $p< 0.05$. The highest vitamin C content was attained at 18% FMC, 420 rpm BSS, and 120°C EET whereas the least vitamin C content was attained at 18% FMC, 360 rpm BSS, and 130°C EET. The linear, quadratic, interaction effect of EET, BSS, and FMC were significant at $p<0.05$ on the vitamin C content of the extruded snacks. The quadratic effect of BSS and EET was observed to have a significant effect on the vitamin C content (Figure 1d). The vitamin C content of the extruded snacks increased with an increase in BSS at higher temperature or lower EET at lower BSS (Figure 1e). Also, high FMC and moderate EET increased vitamin C content (Figure 1f). This result corroborates with the findings of Choton *et al.* (2020) that lower feed moisture and higher extrusion temperature could lead to loss of vitamin C and that short barrel screw speed has a higher retention rate of water-soluble vitamins such as vitamin C compared to long barrel screw extruders which will take longer for the extruded products to leave the barrel chamber. The regression model generated for predicting the vitamin C content in Equation 3 showed that the F-value, R^2, R^2_{adj} and R^2_{pre} were 3334.61, 1.0, 0.99, and 0.99 respectively, which demonstrated its high accuracy for predicting the model relationship.

$$Y_{vitamin\ c} = -88.19 + 1.66x_1 - 0.14x_2 + 7.56x_3 + 0.0084x_1^2 + 0.00031x_2^2 - 0.22x_3^2 + 0.0014x_1x_2 + 0.0008x_1x_3 \quad 3$$

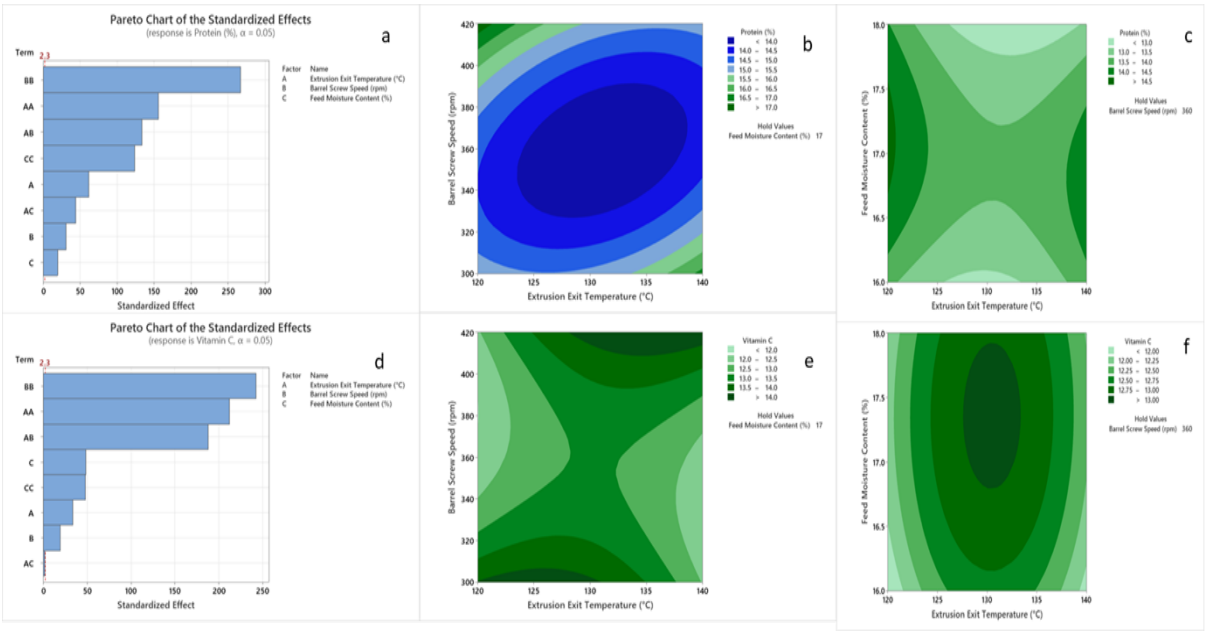

Figure 1. Pareto chats and Contour plots of protein content and vitamin C content of rice-bambara nut-pineapple peels based extrudates snacks. (a) Pareto chat of protein content, (b) Contour plot of BSS and EET of protein content, (c) Contour plot of FMC and EET of protein content, (d) Pareto chat of vitamin C content, (e) Contour plot of BSS and EET of vitamin C content (f) Contour plot of FMC and EET of vitamin C content.

3.3 Influence of extrusion conditions on total phenolic content

The measurement of total phenolic content in food products is important because it can help to determine the potential health benefits of consuming that food. Foods with higher total phenolic content are generally considered to be healthier options. The total phenolic content of the extruded snacks under the effect of extrusion conditions ranged from 14.17 - 18.02 mg GAE/g (Table 1). The highest TPC was found at 17% FMC, 130°C EET, 300 rpm BSS and 18% FMC, 140°C EET, 300 rpm BSS while the lowest was found at 18% FMC, 120°C EET, and 420 rpm BSS. The linear effect of barrel screw speed had the most impactful effect on the total phenolic content (Figure 2a) and this could be attributed to the high shear forces generated by the screw which can break down cell walls and release phenolic compounds from the food matrix, thereby increasing their availability. The total phenolic content of the extruded snack increased at higher EET and lower BSS (Figure 2b). At lower FMC, the total phenolic content of the extruded snacks increased significantly (Figure 2c). This result also supports the findings of Samyor *et al.* (2018) in the production of red rice and passion fruit powder-based extrudates. The linear, quadratic, interaction effect of EET, BSS, and FMC were significant at $p<0.05$ on the total phenolic content of the extruded snacks. Equation 4 shows the polynomial regression model developed for predicting the total

phenolic content. Furthermore, the high F-value (272390.7), and the R^2, R^2 adj. and R^2 pred of the model are 1 thus affirming its high precision for the prediction of total phenolic content.

$$Y_{TPC} = -56.68 - 0.15x_1 + 0.17x_2 + 7.25x_3 - 0.0051x_1^2 - 0.00010x_2^2 - 0.61x_3^2 - 0.00092x_1x_2 + 0.0108x_1x_3 \quad 4$$

3.4 Influence of extrusion conditions on DPPH radical scavenging activity

The influence of extrusion conditions on the DPPH radical scavenging activity of the extruded snacks ranged from 14.57 - 16.25% (Table 1). The rice-bambara nut-pineapple peels extruded snacks attained an optimum DPPH radical scavenging activity in sample D and sample F with extrusion conditions of 17% FMC, 130°C EET, and 300 rpm BSS, and 16% FMC, 130°C EET, and 420 rpm BSS respectively. The least DPPH radical scavenging activity was attained at 17% FMC, 120°C EET, and 360 rpm BSS. There is a non-significant difference at $p > 0.05$ in the DPPH radical scavenging activity of sample D and sample F. The DPPH radical scavenging activity of a food sample depends directly on the food's total phenolic content (Samyor *et al.,* 2018). The linear effect of EET had the most significant influence on the DPPH radical scavenging activity of the extruded snacks (Figure 2d). Lower BSS and moderate EET increases the DPPH radical scavenging activity of the extruded snacks (Figure 2e) while lower FMC and EET increase the DPPH radical scavenging activity (Figure 2f). These results corroborate the findings of Samyor *et al.* (2018) that the DPPH radical scavenging activity of the rice-passion fruit powder blend extrudates decreased with an increase in barrel speed and extrusion temperature. The high DPPH radical scavenging activity observed in this study might be a result of the linear relationship between TPC and DPPH radical scavenging activity, while the decrease in DPPH radical scavenging activity could also be credited to the reduction in TPC during high extrusion temperature. Basilio-Atencio *et al.* (2020) also reported similar observations in the DPPH radical scavenging activity of kiwicha extrudates. Equation 5 shows the polynomial regression model developed for predicting the DPPH radical scavenging activity with a high F-value of 272390.7, and the R^2, R^2 adj and R^2 pred of the model is 1 thus affirming its high precision for the prediction of DPPH radical scavenging activity.

$$Y_{DPPH} = 134.67 - 1.10x_1 + 0.024x_2 - 5.86x_3 - 0.000591x_1^2 + 0.00004x_2^2 - 0.13x_3^2 - 0.00042x_1x_2 + 0.081x_1x_3 \quad 5$$

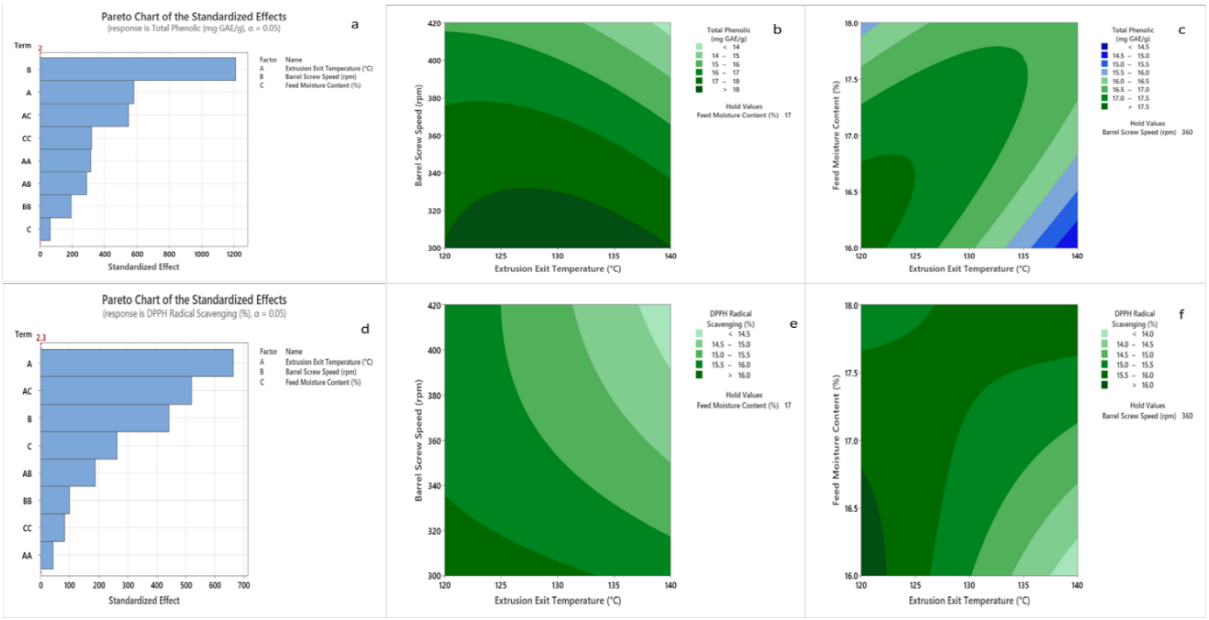

Figure 2. Pareto chats and Contour plots of total phenolic content and DPPH content of rice-bambara nut-pineapple peels based extrudates snacks. (a) Pareto chat of total phenolic content, (b) Contour plot of BSS and EET of total phenolic content, (c) Contour plot of FMC and EET of total phenolic content, (d) Pareto chat of DPPH radical scavenging activity, (e) Contour plot of BSS and EET of DPPH radical scavenging activity (f) Contour plot of FMC and EET of DPPH radical scavenging activity.

4. CONCLUSIONS

Blends of broken brown rice flour, Bambara nut flour, and pineapple peel powder were used to produce ready-to-eat extruded snacks at a ratio of 50:45:5. The extrusion exit temperature, feed moisture content, and barrel screw speed significantly affected the protein, total phenolic content, DPPH radical scavenging activity, and vitamin C

contents of the snacks. Polynomial regression models were developed to predict the influence of extrusion conditions on quality attributes, with R^2, R^2_{adj}, and R^2_{pred} ranging between 0.99 and 1.0, indicating high adequacy. Optimum extrusion conditions for maximizing quality attributes differed, and the developed models could aid in optimizing the quality attributes of extruded snacks, leading to improved product development. Furthermore, the development of extruded snacks from brown rice, pineapple peels, and Bambara nuts would promote sustainable food production and reduce food waste.

ACKNOWLEDGEMENT

The authors appreciate the Department of Food Engineering, University of Ilorin for supporting this study with facilities.

REFERENCES

Alam, M. S., Jasmeen, K., Harjot, K., & Kalika, G. (2016). Extrusion and extruded products: Changes in quality attributes as affected by extrusion process parameters: A review, *Critical Reviews in Food Science and Nutrition*, 56(3), 445-473.

Association of Official Analytical Chemists AOAC. (2010). Official methods of analysis (18th ed.). *Washington DC: Association of Official*

Basilio-Atencio, J., Condezo-Hoyos, L., & Repo-Carrasco-Valencia, R. (2020). Effect of extrusion cooking on the physical-chemical properties of whole kiwicha (*Amaranthus caudatu*s L) flour variety centenario: Process optimization. *LWT*, 128, 109426.

Choton, S., Gupta, N., Bandral, J. D., Anjum, N., & Choudary, A. (2020). Extrusion technology and its application in food processing: A review. *The Pharma Innovation Journal*, 9(2), 162-168.

Dalbhagat, C. G., Mahato, D. K., & Mishra, H. N. (2019). Effect of extrusion processing on physicochemical, functional and nutritional characteristics of rice and rice-based products: A review. *Trends in Food Science & Technology*, 85, 226-240.

Dey, D., Richter, J. K., Ek, P., Gu, B. J., & Ganjyal, G. M. (2021). Utilization of food processing by-products in extrusion processing: A review. *Frontiers in Sustainable Food Systems*, 4, 603751.

Diedericks, C. F., Venema, P., Mubaiwa, J., Jideani, V. A., & van der Linden, E. (2020). Effect of processing on the microstructure and composition of Bambara groundnut (*Vigna subterranea* (L.) Verdc.) seeds, flour and protein isolates. *Food Hydrocolloids*, 108, 106031.

Franklyn da Cruz, L. I. M. A., Simões, A. J. A., Vieira, I. M. M., Silva, D. P., & Ruzene, D. S. (2018). An overview of applications in pineapple agroindustrial residues. *Acta Agriculturae Slovenica*, 111(2), 445-462.

Gbenyi, D., Nkama, I., Badau, M., & Idakwo, P. (2016). Effect of extrusion conditions on nutrient status of ready-to-eat breakfast cereals from sorghum-cowpea extrudates. *Journal Food Processing & Beverages*, 4(2), 8.

Gumul, D., Ziobro, R., Zięba, T., & Rój, E. (2013). Physicochemical characteristics of cereal extrudates with different levels of defatted blackcurrant seeds. *Journal of Food Quality*, *36*(6), 385-393.

Muhammad, I., Rafii, M. Y., Ramlee, S. I., Nazli, M. H., Harun, A. R., Oladosu, Y., & Arolu, I. W. (2020). Exploration of bambara groundnut (Vigna subterranea (L.) Verdc.), an underutilized crop, to aid global food security: Varietal improvement, genetic diversity and processing. *Agronomy*, 10(6), 766.

Offiah, V., Kontogiorgos, V., & Falade, K. O. (2019). Extrusion processing of raw food materials and by-products: A review. *Critical reviews in Food Science and Nutrition*, 59(18), 2979-2998.

Roda, A., & Lambri, M. (2019). Food uses of pineapple waste and by-products: a review. *International Journal of Food Science & Technology*, 54(4), 1009-1017.

Sahu, C., Patel, S., & Tripathi, A. K. (2022). Effect of extrusion parameters on physical and functional quality of soy protein enriched maize based extruded snack. *Applied Food Research*, 2(1), 100072.

Samyor, D., Deka, S. C., & Das, A. B. (2018). Effect of extrusion conditions on the physicochemical and phytochemical properties of red rice and passion fruit powder based extrudates. *Journal of Food Science and Technology*, 55(12), 5003-5013.

Sanusi, M. S., & Akinoso, R. (2021). Modelling and optimising the impact of process variables on brown rice quality and overall energy consumption. *International Journal of Postharvest Technology and Innovation*, *8*(1), 70-88.

Sanusi, M. S., Sunmonu, M. O., Alasi, S. O., Adebiyi, A. A., & Tajudeen, A. A. (2023). Composition, Bioactive Constituents and Glycemic index of Brown Rice-Watermelon Seeds Extruded Snacks as Stimulated by Extrusion Conditions. *Applied Food Research*, 100287.

Sukumar, A., & Athmaselvi, K. A. (2019). Optimization of process parameters for the development of finger millet based multigrain extruded snack food fortified with banana powder using RSM. *Journal of Food Science and Technology*, 56, 705-712.

Ziena, H. M., & Ziena, A. H. M. (2022). Nutritious novel snacks from some of cereals, legumes and skimmed milk powder. *Applied Food Research*, 2(1), 100092.

PAPER 24 – APPLICATION OF MODIFIED HOLLOW PVDF-MEMBRANE SYSTEM FOR REMEDIATING PALM OIL MILL EFFLUENT

M. Abdulsalam*, I. B. Dalha, S. U. Yunusa

Department of Agricultural and Bio-resources Engineering, Faculty of Engineering, Ahmadu Bello University, Zaria.
*Email: m.abdulsalamim@gmail.com

ABSTRACT
The objective of this work was to introduce an advanced wastewater treatment technology; co-polymerized polyvinyl difluoride (PVDF)-polyethylene glycol (PEG) membrane system for anaerobically-pretreated palm oil mill effluent (POME) treatment. The co-polymerized hollow fibre membranes were fabricated using a wet spinning technique and then used to remediate POME as the feedstock. The physicochemical properties of the POME were analyzed before and after treatment with the hollow fibre. The analyzed parameters included chemical oxygen demand (COD), colour, total suspended solids (TSS), turbidity (TDS), and total nitrogen (TN). A preliminary test was carried out using distilled water before continuing with POME as a feed solution. The average permeate flux obtained by the PVDF-PEG membrane was 70 L/m^2.hr with a slight flux decline that is probably due to the attachment of foulants compounds on the membrane surface and pores. The synthesized modified membrane reduced the COD, colour, TSS, TDS and TN by 92.1, 86, 97.89, 99.98 and 80.26 %, respectively. In conclusion, it can be said that the modified PVDF-PEG membrane demonstrated excellent performance in treating the POME to produce a permeate with better qualities.

KEYWORDS: Nano-MgO, PVDF-PEG Membrane, POME, Filtration, Contaminants Removal

1 INTRODUCTION

The commonly applied nanoparticles to modified polymeric membranes includes ZnO, TiO_2, Ag_2O_3, Al_2O_3, graphene oxide, SiO_2 and CuO (Jhaveri & Murthy, 2016). Tan et al., (2017) enhanced the permeation and antifouling properties of a bared PVDF membrane by incorporating synthesized Zn-Fe oxide (ZIO) into the matrix structure. The nanocomposite membrane with 0.5 wt % ZIO loading demonstrated a significant increase in permeate flux to the magnitude of 25% raise compared to the bared PVDF membrane. Also, Shen et al., (2012) modified the matrix structure of polymeric membrane using ZnO nano-additive. The result showed that the additive had significant influence on the pores structure as well as the hydrophilicity of the membrane. Over 254% improvement in permeability flux was reported at the loading of 0.3 g ZnO nano-additive. Furthermore, the authors validated that the porosity of the modified composite membrane increased with the presence of the nano-additive, which ultimately justified the reported high flux. The Nano-ZnO has large surface area that expedite the formation of hydroxyl (–OH) functional group on the surface. The presence of –OH enhanced hydrophilicity of the PVDF polymeric membrane, thus mitigating fouling rate. Analogously, TiO_2 Ag_2O_3 and Al_2O_3 also exhibit similar features when incorporated into the matrix structure of polymeric membrane. (Subramaniam et al., 2017) synthesized titanate nanotubes using nano-TiO_2 as a precursor to modify the PVDF membrane. The results substantiated that under photo-catalytic condition, the involvement of TiO_2 in the dope formulation improved the permeation consistency (35.8 L/m^{2}h) of the resultant nanocomposite membrane. Negligible fouling was observed at 0.5 wt % TNT loading throughout the 4 h continuous filtration. Another report has shown strong agreement with this observation, and the results indicated that the antifouling performance of TiO_2 was due to generated –OH under UV spectrum and its aptitude to exhibit self-cleaning. Also, attention has long drifted to the use of nano-Ag_2O_3 to modify polymeric membrane (Biswas & Bandyopadhyaya, 2017). The nano-additive released Ag ions to inhibit the metabolism of the microbial-foulants, thereby preventing the generation of the extracellular polymeric substance (EPS). Thus, this ultimately curtailed the organic and bio-fouling. Maximous et al., (2010) investigated the antifouling impact of Al_2O_3 and the results showed that at optimum 0.05 wt % loading, the modified composite polymeric membrane was less prone to fouling. Besides, the presence of Al_2O_3 in the matrix structure of a polymeric membrane not only reduces the fouling but also improves the flux consistency.

Most of the widely used nanoparticles, particularly as mentioned above, are photo-catalytic driven to address the fouling issue. This implies that the presence of ultraviolent radiation is a prerequisite to precede the antifouling performance. More so, the issue continues releasing antifouling radicals and superoxide could seriously jeopardize the stability of the composite matrix structure. In line with this, Tan et al. (2017) reported that the structural instability of the modified nanocomposite PVDF-ZIO membrane was discernible after four filtration cycles due

to the collapse of the incorporated nanoparticles. This could significantly undermine the overall antifouling performance and also re-expose the modified membrane to inconsistencies in permeation flux along with frequent fouling challenges. Moreover, the nano- ZnO, TiO_2, Ag_2O_3, Al_2O_3 and CuO are relatively expensive and the running cost could be unsustainable for industrial applications (Jhaveri & Murthy, 2016).

Meanwhile, nano-MgO has remained one of the antimicrobial and super hydrophilic nanomaterials yet to be fully explored in improving filtration and antifouling performance of polymeric membrane (Parvizian et al., 2017). The nano-MgO has the ability to release reactive oxygen species (ROS) which directly extract lipid from the cells of the microbial-foulants. This ultimately disrupted the metabolic activities and hindered biofilm formation. More interestingly, the nano-MgO not only averts bio-fouling formation but, it is also capable of evincing self-cleaning mechanism. The nano-MgO precursor is readily available and comparably cheaper than other nanomaterials (such as TiO_2, Ag_2O_3, Al_2O_3, and ZnO). Therefore, MgO-nanoparticles intimate a promising additive capable of enhancing antifouling properties and permeation performance of polymeric membranes for industrial filtration purposes. Currently, application of a modified Nano-MgO (MGO) composite PVDF-PEG membrane for separation of color pigment from POME has not been reported.

In view of these, the present study focuses on modifying the structure of an in-house fabricated PVDF-PEG ultrafiltration membrane at various loadings of MGO. The impacts of the incorporated MGO were examined based on the morphological changes, hydrophilicity, the permeability flux and fouling resistance of the resultant membrane. Furthermore, the rejection and color separation efficiency were studied, and also the used membranes were characterized using Fourier transform infrared spectroscopy. The outcome of the study demonstrated that the involvement of the MGO in the dope formulation significantly improved the antifouling properties and the permeation performance, alongside with color separation from palm oil mill effluent (POME) via the synergy of surface deprotonation and pore size screening mechanism.

2 MATERIALS AND METHODS/METHODOLOGY/EXPERIMENTAL PROCEDURE

2.1. Materials

Nano-MgO (MGO: particles size (BET) < 50 nm; MW = 40.30 g/Mol; purification 99.9%), Pellets PVDF (Kynar 740) and polyethylene glycol (PEG: 12,000 g/mol) were procured from Sigma Aldrich (M) Sdn Bhd, Selangor, Malaysia. The PVDF was applied as the major membrane matric polymer, while the PEG as co-polymer to enhance pore formation. The N,N-dimethylformamide (DMF), ethanol and glycerol were also obtained from Sigma Aldrich (M) Sdn Bhd, Selangor, Malaysia, and respectively used as doping and post-treatment solvents without any further purification. LiCl2.H2O was purchased from Acros Organic Industry, Chemicals and Reagents, Semenyih, Selangor, Malaysia Also, POME sample was collected from an Oil Palm Milling industryin Malaysia.

2.2. Synthesis of Nanocomposite PVDF/PEG-MGO

2.2. Dope Formulation

The dope formulation was preceded by adding nano-MgO into DMF and then subjected to sonication using digital ultrasonic water bath (VWR 142-0300) at 75 ^oC for a period of 20 min. Subsequently, $LiCl_2\_H_2O$ was added into the mixture with steady agitation of 350 rpm and 75 ^oC for a period of 24 h. Essentially, this procedure assists in dispersion of the MgO as well as ensuring good blending of the mixtures. The mixture was followed by adding the dehydrated PVDF pellets and the co-polymer, PEG. The combination was stirred continuously at 350 rpm and 100 ^oC for another 24 h using a hot-plate stirrer (Monotaro; C-MAG HS7, Malaysia) to achieve a homogenous solution. The amount of the MgO contained in the dope solutions were varied as contained in Table 1.

Table 1: dope formulation

Description	**PVDF:PEG g**	**Nano-MgO**	**$LiCl.H_2O$**	**DMF**
Neat Sample	30:10	0.0	2	158
Modified Sample	30:10	0.5	2	158

2.3. Spinning of Nano-Hybrid PVDF/PEG-MGO Hollow Membrane

It is important to note that same spinning parameters were applied for all of the samples. The dopes were spun through dry-jet wet swirling technique employing an annular spinneret. The inner and outside diameter of annular spinneret was 0.55 and 1.15 mm, respectively. During the fabrication of the membrane, tap water and distilled water was used as the external and internal coagulant. In addition, the pick speed control, collecting drum speed, extrusion rate, air gap, external coagulant temperature, room temperature and room humidity remains constant at 7 rpm, 11 rpm, 5 mL/min, 10 cm, 25 °C, 29.5 °C and 72.7%, respectively. The spun fibers were drench in a continues flow water-bath at least for a period of 24 h to dislodged solvent remnants. In order to minimize shrinkage, post-treatments were applied on the fibers by immersing in ethanol for 12 h, then followed by drenching in glycerol for 5 h, respectively. The post-treated fibers were air-dried for at least 24 h to ensure complete dehydration.

2.4. Morphology Characterization

The cross section and surface morphology of the synthesized Nano-hybrid fiber were examined using scanning-electron-microscope, (SEM: S-3400N). The composite fibers were immersed into liquid nitrogen for f 5 minto ensure sharp breaking of the fiber to reveal the cross-sectional structure. Then, the fractured samples were sputtered coated with gold thin layer, and the voltage acceleration was maintained constant at 20 kV during the image capturing.

2.5. Flux analysis

The filtration performance was examined using a fabricated dead-end permeation system, equipped with membrane module cell and a peristaltic pump to provide the required suction pressure. Each of the modules comprises of 10 units of the membrane with equal length of 20 cm. initially, the membrane was compacted at a pressure of 0.4 MPa for a period of 30 min to ensure steady flux, while the subsequent filtration operations were performed at lower pressure of 0.3 MPa. The DI water (Jw) and permeate flux (Jp) were determined using Equation (1):

$$J = \frac{V_p}{A_s \Delta t} \quad (1)$$

where J denotes the flux in L/m^2_h, V is the volume of permeate (L), A_s is membrane surface area (m^2) and Δt is filtration time in h.

2.6. POME Remediation

The membrane fibers were subjected to filtration of diluted POME with 4285 ADMI color concentration using same set-up as applied when pure water was used as feed. Initially, the membranes fibers were submerged in the POME solution for 90 min to initiate adhesion of thin layer color pigments on the fibers. This procedure assists in achieving accurate color rejection performances of the fibers (Subramanium et al. 2017). The apparent color content of the feed POME and permeate were analyzed in ADMI using UV-spectrophotometer (DR4000U, HACH) at an absorbance wavelength of 400 nm. The POME decolorization efficiency was determined using Equation (2):

$$\%C_{removal} = \left(1 - \frac{C_p}{C_{POME}}\right) \times 100 \quad (2)$$

2.7. Analytical Methods

The chemical oxygen demand (COD), ammonia nitrogen (AN), total suspended solids (TSS), turbidity (TDS), and colour removal were analyzed using recommended standard procedures (APHA, 2005).

3. RESULTS AND DISCUSSION

3.1. Membrane Morphology

Figure 1a presents the scanning electron microscope (SEM) images of cross-sectional view of the neat and modified hybrid nano-MgO (MGO) PVDF-PEG membranes. It is obvious that the neat fiber had 3 layers. The middle layer constitutes majorly of sandwich-like morphology containing short finger-like pores at both sides toward the ultra-thin layers. However, different scenarios were observed with the modified nanocomposite membranes. A finger-like pore became longer and the number of the micro-pores structure increased considerably

Figure 1b (Shen et al. 2012) . In addition, some spongy macro-voids were also noticed towards the inner ultra-thin layer. This observation is in agreement with previous studies reported (Shen et al. 2012). From Figure 1b, it can be deduced that the 0.5g MgO loading was successfully and homogenously dispersed within the matrix structure. This also show good compartment at this loading.

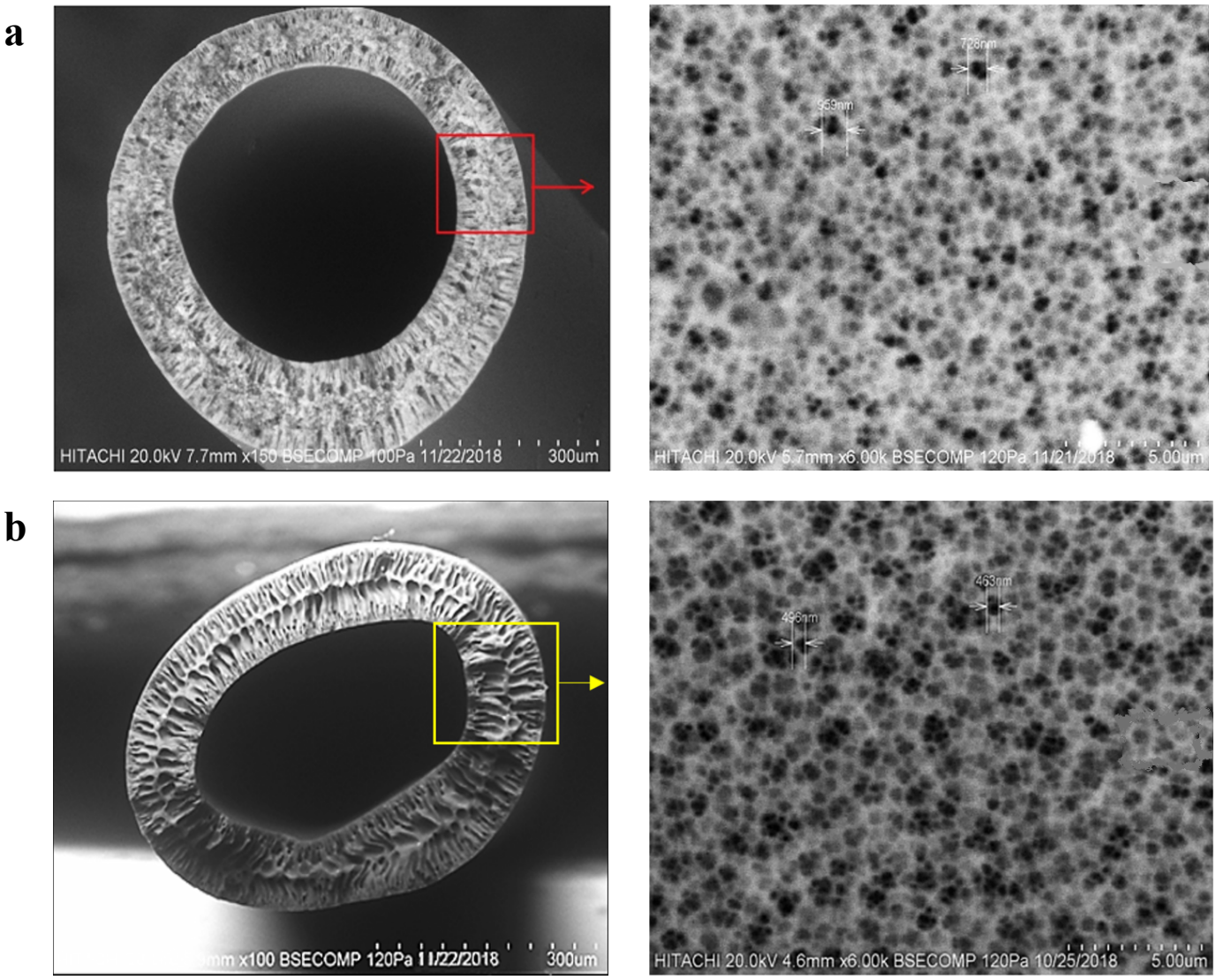

Figure **1:** Cross-section and surface view of the SEM analysis of the (a) neat and (b) modified membrane with MgO

3.2. Flux performance

The modified membranes presents higher flux of 70 L/m2·h, as against 48.59 L/m^2h for the neat membrane. Collectively, the magnitude of the fluxes in POME filtration were noticeably lower compared to the pure water filtration. This could be due to the presencecontaminants, such as suspended solids, color pigments, organic and inorganic substances) in the POME, which apparently restrict the free flow of permeate through the membranes. Basically, the selectivity and rejection of the contaminants is based on size differences in the pores as well as the surface zeta potential of the membrane (Tan et al. 2017).

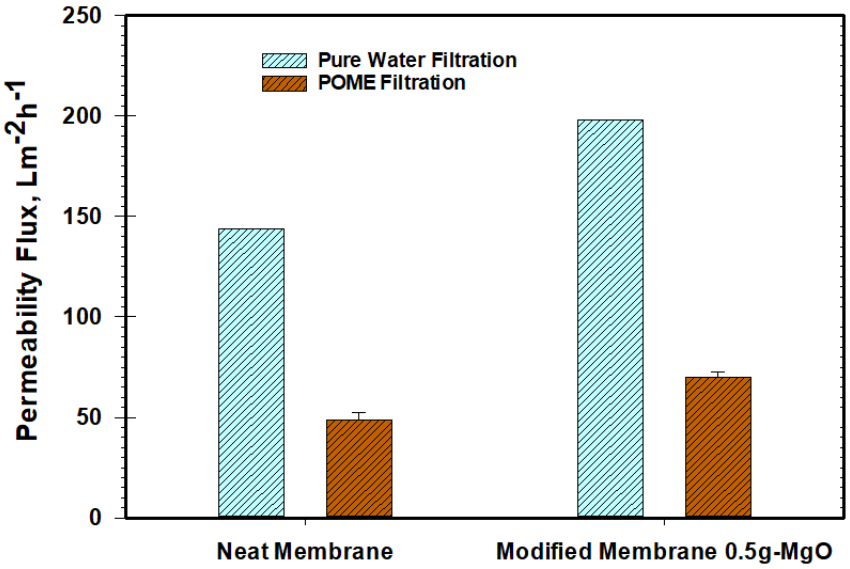

Figure 2: Pure water and POME Permeability flux for the Neat and Modified Membrane

3.3. POME Remediation Performance

Figure 3 present the remediation performance of both the neat and modified membrane. The neat membrane successfully reduced the COD, colour, TDS, TSS and TN concentration in the POME by 80.15, 67.5, 83.6, 87.01 and 70 %, respectively. However, under same conditions of operations, the modified membrane presented a superior performance with an upturn of 92.1, 86, 97.89, 99.98 and 80.26%, respectively. The better separation performance of the modified membrane may be due to the incorporated nano-MgO. The blended nanoparticles serve as filler which is capable of reducing the pore sizes and thus improve the selectivity (Nunes-Pereira et al., 2017). More so, nano-MgO introduces hydroxyl functional group (OH^{-}) into the matrix structure, and this enhances waterlike characteristic of the polymeric membrane, thus the permeability flux (Khamkongkaeo et al., 2017).

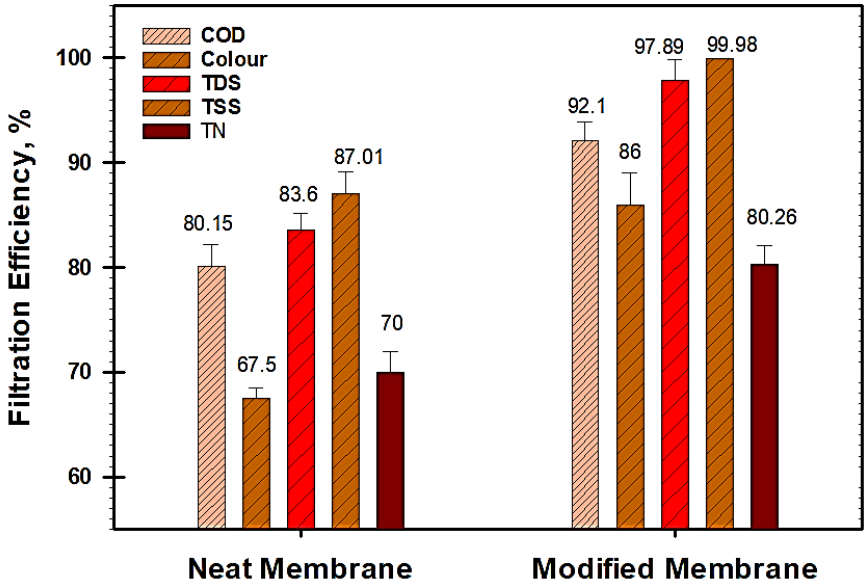

Figure 3: Filtration Efficacy: COD, Colour, TDS, TSS and TN Separation

4. CONCLUSION

Hybrid PVDF-PEG hollow fibers blended with nano-MgO was fabricated using phase inversion technique. The loading at 0.50 g-MGO presented auspicious performance with 198.35 and 70 L/m^{2}h of pure water and POME

filtration flux, respectively. Also, the synthesized modified membrane reduced the COD, colour, TSS, TDS and TN by 92.1, 86, 97.89, 99.98 and 80.26 %, respectively. As against 80.15, 67.5, 83.6, 87.01 and 70 %, respectively for the neat membrane. Therefore, it can be deduced that nano MgO-hybrid PVDF-PEG membrane with 0.50 g-MgO loading presents a better permeate flux and separation performance compared to the neat membrane.

ACKNOWLEDGEMENT

The Authors wish to acknowledged the support of Universiti Putra Malaysia

REFERENCES

Biswas, P., & Bandyopadhyaya, R. (2017). Biofouling prevention using silver nanoparticle impregnated polyethersulfone (PES) membrane: E. coli cell-killing in a continuous cross-flow membrane module. *Journal of Colloid and Interface Science*, *491*, 13–26. https://doi.org/10.1016/j.jcis.2016.11.060

Jhaveri, J. H., & Murthy, Z. V. P. (2016). A comprehensive review on anti-fouling nanocomposite membranes for pressure driven membrane separation processes. *Desalination*, *379*, 137–154. https://doi.org/10.1016/j.desal.2015.11.009

Khamkongkaeo, A., Mothaneeyachart, N., Sriwattana, P., Boonchuduang, T., Phetrattanarangsi, T., Thongchai, C., Sakkomolsri, B., Pimsawat, A., Daengsakul, S., Phumying, S., Chanlek, N., Kidkhunthod, P., & Lohwongwatana, B. (2017). Ferromagnetism and diamagnetism behaviors of MgO synthesized via thermal decomposition method. *Journal of Alloys and Compounds*, *705*, 668–674. https://doi.org/10.1016/j.jallcom.2017.02.170

Maximous, N., Nakhla, G., Wong, K., & Wan, W. (2010). Optimization of Al2O3/PES membranes for wastewater filtration. *Separation and Purification Technology*, *73*(2), 294–301. https://doi.org/10.1016/j.seppur.2010.04.016

Nunes-Pereira, J., Silva, A. R., Ribeiro, C., Carabineiro, S. A. C., Buijnsters, J. G., & Lanceros-Méndez, S. (2017). Nanodiamonds/poly(vinylidene fluoride) composites for tissue engineering applications. *Composites Part B: Engineering*, *111*, 37–44. https://doi.org/10.1016/j.compositesb.2016.12.014

Parvizian, F., Sadeghi, Z., & Hosseini, S. M. (2017). PVC Based Ion-Exchange Membrane Blended with Magnesium Oxide Nanoparticles for Desalination: Fabrication, Characterization and Performance. *Journal of Applied Membrane Science & Technology*, *21*(1), 11–24. https://doi.org/10.11113/amst.v21i1.105

Shen, L., Bian, X., Lu, X., Shi, L., Liu, Z., Chen, L., Hou, Z., & Fan, K. (2012). Preparation and characterization of ZnO/polyethersulfone (PES) hybrid membranes. *Desalination*, *293*(2012), 21–29. https://doi.org/10.1016/j.desal.2012.02.019

Subramaniam, M. N., Goh, P. S., Lau, W. J., Tan, Y. H., Ng, B. C., & Ismail, A. F. (2017). Hydrophilic hollow fiber PVDF ultrafiltration membrane incorporated with titanate nanotubes for decolourization of aerobically-treated palm oil mill effluent. *Chemical Engineering Journal*, *316*, 101–110. https://doi.org/10.1016/j.cej.2017.01.088

Tan, Y. H., Goh, P. S., Ismail, A. F., Ng, B. C., & Lai, G. S. (2017). Decolourization of aerobically treated palm oil mill effluent (AT-POME) using polyvinylidene fluoride (PVDF) ultrafiltration membrane incorporated with coupled zinc-iron oxide nanoparticles. *Chemical Engineering Journal*, *308*, 359–369. https://doi.org/10.1016/j.cej.2016.09.092

PAPER 25 – LEACHATE AS A POWERFUL PRECURSOR FOR HYDROGEN SYNTHESIS: PROCESS OPTIMIZATION

M. Abdulsalam* and Dalha I. B.

Department of Agricultural and Bio-resources, Ahmadu Bello University, 810107, Zaria, Nigeria
*Email: m.abdulsalamim@gmail.com

ABSTRACT
Renewable energy is getting more attention due to the depleting of non-renewable fossil fuels and its effects on global warming issues thus trigger the intense research in finding better alternative energy with low emission. The present work aims to study the potential of hydrogen gas production (for renewable energy) by electrocoagulation process from landfill leachate. The central composite design from response surface methodology (RSM) software was implemented to investigate the process variables in the hydrogen production system. The effects of three independent variables; namely pH (4-8) and voltage (3-9V), using different types of electrodes (Al, Fe, and Ni) were studied. At optimal condition of voltage 9V and initial pH 6 at 20 minutes, the Al electrode recorded an upturn maximum H_2 yield of 697 ppm, while 554 and 551 ppm were obtained with Ni and Fe electrode, respectively. More so, a good correlation between the actual and the predicted data was observed as elucidated by the coefficient of determination (R^2).

KEYWORDS: H_2 Production, Electrocoagulation, CCD Response Surface Methodology, Electrodes

1. INTRODUCTION

Since hydrogen gas burns quickly, emits no greenhouse gases, has a higher energy density, requires little ignition energy, and has a very high research octane number, it is commonly regarded as a fuel of the future (Nanthagopal et al., 2011). It is important to clarify that the octane number is a measurement of a fuel's resistance to knocking in spark-ignition internal combustion engines, and it is typically used to rate gasoline. Hydrogen's high RON indicates that it has a high resistance to knocking, similar to premium gasoline. However, 95% of the hydrogen produced worldwide now comes from fossil fuels, mostly from the steam reforming of natural gas (Ogden, 1999). Numerous other processes, including electrolysis, thermolysis of water, and the thermocatalytic reformation of hydrocarbons, are also referred to as industrial hydrogen production processes (Demirbas et al., 2010). However, the scope of large-scale hydrogen production using these techniques is undesirable because of the concurrent synthesis mixture with the oxygen (Smolinka et al., 2009). This is especially true for the electrolysis of water.

But electrocoagulation (EC) technology is a method of treatment that uses electrical current to treat pollutants by including coagulant. According to Shammas et al. (2010), in addition to lowering residue for waste production, coagulation has the ability to remove small particles inside pollutants and set them into motion with the applied current. EC can be used to de-fluoridate water and is capable of removing a wide range of contaminants under a variety of circumstances, including suspended particles, metals, petroleum products, colour from dye solutions, and aquatic humus (Holt et al., 1999). This demonstrates that the treatment conditions—such as pH, voltage, electrode types, etc.—have a significant impact on how well the EC process works.

For instance, Shivayogimath et al. (2014) explored the impact of pH values (4, 5.8 and 8) on the elimination of COD throughout the course of a batch run lasting 40 minutes at a 3V applied cell voltage. It was shown that the COD removals increased with a longer reaction time for all three pH values. However, a pH value of 5.8 resulted in the best COD elimination. With 35 minutes of the reaction period and this pH, COD was reduced from 4820 mg/L to 2250 mg/L, yielding a COD removal efficiency of 53.3%. Similar to this, Abdallah et al. (2013) confirmed that pH might considerably affect the generation of both hydrogen and oxygen.

According to the results of the experiments, the synthesis of hydrogen and oxygen is improved the further away from pH 7 there is in the range of pH from 3 to 13. Furthermore, according to Song et al. (2008), it was discovered that an ozone electro-coagulator with an optimal pH of 10, dye concentration of 100 mg/L, a current density of 10 mA/cm^2, salt concentration of 3,000 mg/L, the temperature of 30 ℃, ozone flow rate of 20 mg/L, and electrode distance of 3 cm effectively removed 96% of colour and 80% TOC. Sengil et al. (2009) reported the results of the second investigation, which used electrocoagulation with iron electrodes to remove 98% of Reactive Black 5 from synthetic wastewater.

A dye concentration of 100 mg/L, a pH of 5, a current density of 4.575 mA/cm^2, a salt concentration of 3,000 mg/L, a temperature of 20 ℃, and an inter-electrode spacing of 2.5 cm are the ideal treatment conditions. Additionally, it has been noted that electrocoagulation using Al electrodes has a greater removal effectiveness than electrocoagulation using Fe electrodes (Wang, 2009). According to Ilhan (2008), under the identical treatment settings, Al electrodes provide greater COD and NH_3N elimination of 56% as opposed to 35% for the Fe electrode. According to Shivayogimath et al. (2013), the pH of 6 and a voltage of 9V guarantee the best hydrogen yield when utilising Al electrodes.

It is noteworthy that leachate has the capacity to electrocoagulate hydrogen gas at yields that are close to the theoretical maximum of 4 mol H_2/mol of hexose consumed (Pawar et al., 2013). The EC method for using leachate to produce hydrogen is still only being widely adopted by a small number of companies. Due to the large quantity of garbage that is being accumulated today and how negatively it will damage the environment for decades, there have been few research on the production of hydrogen gas from leachate, despite the fact that it is essential to fixing the leachate problem. The major goal of this work is to investigate the potential for producing hydrogen gas by the EC process utilizing several electrode types (Al, Ni, and Fe), and then to use response surface methodology (RSM) to optimize the operating conditions (pH and voltage).

3 MATERIALS AND METHODS/METHODOLOGY/EXPERIMENTAL PROCEDURE (10 point)

a. Materials Source

Leachate samples of about 75 litres were taken from one of the Malaysian treatment facilities in Selangor for the electrocoagulation process. The samples were initially kept in a refrigerator at 4 degrees Celsius. Aluminium, Nickel, and Iron electrodes of three different types, a DC-voltage rectifier with a variable device (BK PRECISION - DC regulated power supply model 1621A), a gas bag and delivery tube (TEDLAR 0.6 LITRES), and acidic buffer solutions (prepared sulphuric solution) were sourced and used in the subsequent experiments.

b. Physicochemical Characteristics of leachate

The gathered leachate was sent for laboratory analysis utilising a variety of methodologies, including APHA 2007 and direct measurement with YSI probe (QWI-CH/17-33) to ascertain its properties for comparison with the findings from experiments conducted. According to the ALS Technichem, characteristics like temperature, pH, total suspended solids (TSS), copper, aluminium, and zinc content, as well as biochemical and chemical oxygen demands (BOD and COD), were examined. Using a gas detector (Crowcon), the composition of the biogas that the leachate from each experiment produced was identified.

c. Experimental Set-up

The electro-coagulation experimental setup for this study is presented in Figure 1. The experimental set was applied distinctly for the three types of electrodes (Al, Ni and Fe) considered in this study. This shows that electrodes were continuously changed. Initially, 800 ml of the leachate sample was filled into the glass container of 1.3L. The glass container was placed on the hot plate magnetic stirrer (E) while the instalment of electrodes plates (A and B) was connected to the power supply for adjusting different voltage (F) throughout the experiment. After each experiment, the gas collected in the gas bag (D) through the delivery tube (C) was transferred out using a syringe into the Crowcon gas analyser. The volume of gas in ppm was detected and shown in the device for comparing and recording.

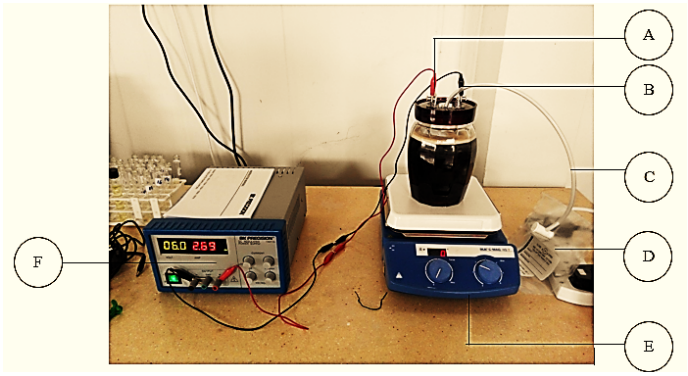

Figure 1. Experiment set-up for the electrocoagulation process for H_2 production from leachate (A-anode wiring, B-cathode wiring, C-tubing of gas flow, D-gas bag 0.6L, E-hot plate magnetic stirrer, F-DC regulated power supply)

d. Experimental layout and Performance Optimisation

Design-Expert version 7.0 was used to develop the experimental layout based on the considered two independent factors (voltage and pH). The developed experimental layout was applied independently using the selected electrodes (Al, Ni and Fe). The summary of the experimental layout is presented in Table 1. The experimental factors were varied to different levels which ranged from 4-8 and 3-9V for the pH and voltage, respectively.

Table 1. Summary of the CCD experimental layout for the combined pH-X1 and voltage-X2 factors

Variable	**Parameters**	**Level**		
		+1	**0**	**-1**
X_1	pH-A	4	6	8
X_2	Voltage (V)- B	3	6	9

The central composite design (CCD) component of the response surface methodology (Design-Expert version 10.0) was employed in the optimization of hydrogen gas production from the electrocoagulation process through leachate as a substrate. Based on the experimental layout, a total of 13 runs of experiments were required to perform with 4 replications of the centre point. The regression model was calculated by analysing the analysis of variance (ANOVA), p-and F-value. The adequacy of the model was expressed by the coefficient of determination, R^2 followed by the predicted- R^2 and adjusted R^2 value. The model describes the interaction among the parameters influencing the response by varying them concurrently by 3D surface graph and ANOVA. The value of R^2 was compared to visualized the modelling abilities towards the experimental data. Hence, readings of predicted values against the experimental values were plotted and investigated for its suitability for optimal conditions. These procedures were applied distinctly for the three types of the electrodes considered in this study, and then the H_2 yield under the varying conditions was compared.

e. Analytical Methods

At the end of each experiment using a particular type of the electrode, the collected hydrogen gas in the gas-bag was retrieved with a syringe, H (Model: TERUMO-60ml) and then analysed using Crowcon gas analyser, G (as depicted in Figure 2). Also, the physicochemical characteristics of the leachate were analysed using calorimetric methods in accordance with (APHA Standard Method, 2007).

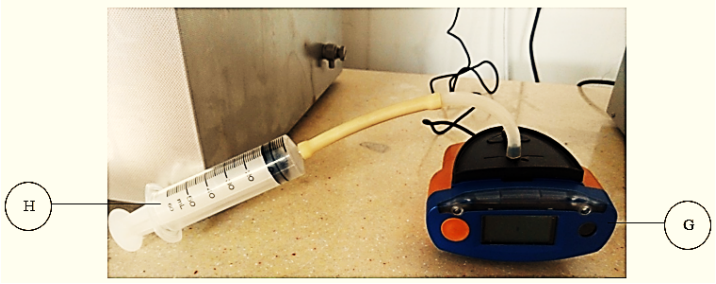

Figure 2. Setup for gas analysis using the Crowcon Analyser

4 RESULTS AND DISCUSSION

a. Physicochemical characteristics

Table 2 presents the physicochemical properties of the leachate sample alongside the Malaysian discharge limit. Virtually all the examined parameters exceed the standard limits, and this further confirms that releasing of such waste without proper remediation is unhealthy for the environment. It was only the pH that can be considered within the acceptable limit, but as for the other parameters they were far above the Department of Environment Malaysia (DOE) limit (Table 2). It is important to note that the level of contaminants concentrations in leachates depends on several factors such as deposition durations, method of depositions, environmental factors as well as the types of waste (Kabuk *et al*., 2013; Shivayogimath *et al*., 2013). Thus, it is crucial to determine the initial physiochemical characteristics of the leachate before treatment to establish the basis for comparison with the DOE standard and level remediation.

Table 2. Physiochemical characteristics of the leachate sample

Parameters	**Unit**	**Leachate**	**DOE Standards**
pH	--	9.7	6-9
Temperature	^{o}C	20.8	20
Total Suspended Solid (TSS)	mg/L	870	50
Biochemical Oxygen Demand (BOD)	mg/L	1610	20
Chemical Oxygen Demand (COD)	mg/L	4340	120
Ammonia-N	mg/L	2440	50
Free Chlorine	mg/L	<0.5	

b. Experimental results

Based on the CCD experimental layout, the treatments were applied and the corresponding hydrogen gas produced using Al; Ni and Fe electrode were recorded into the experimental matrix, as presented in Table 3. Essentially, the three electrodes were subjected to similar treatment conditions.

Table 3. Experimental matrix for treatment factors with respective H_2 values for the electrodes

	Factor 1	**Factor 2**	**Hydrogen Gas (ppm)**		
Run	A: pH	B: Voltage	**Al-** Electrode	**Ni-** Electrode	**Fe-** Electrode
1	9	6	510	332	422
2	8	9	696	538	551
3	4	6	463	450	262
4	6	6	697	683	550
5	4	3	153	77	101
6	6	6	697	690	546
7	4	9	697	809	554
8	6	6	697	554	551
9	6	2	151	89	109
10	8	3	156	108	103
11	6	2	173	77	109
12	6	6	695	550	551
13	6	6	600	457	552

The highest volume of 809 ppm of the hydrogen gas was obtained at 9V voltage and pH of 4 with Ni electrodewhile, 697 and 554 ppm were recorded with Al and Fe electrodes, respectively. At this same voltage magnitude of 9V but pH of 8, the H_2 yield with Ni reduced to 538 ppm, while for AL and Fe electrode remains approximately stable at 696 and 551 ppm, respectively. As the voltage reduced to 2-3V, the H_2 yield using Ni electrode dramatically reduced to 77 ppm and this recorded the least hydrogen gas production in this study. At treatment condition of 6 V and pH of 6, an upturn performance of 697 ppm was obtained with the Al electrode as

against 554 and 551 ppm for the Ni and Fe electrodes, respectively. It can be noticed that higher voltage favours more hydrogen gas production. This remark is in strong agreement with previous studies (Shivayogimath *et al*., 2013; Bazrafshan. *et a*l., 2007 and Yao Hua Ch. *et al*., 2008).

c. Analysis of variance (ANOVA) and regression model

The results of the analysis of variance for the H_2 yield data obtained for the three electrodes are as shown in Table 4. The Model F-value of 64.90, 21.42 and 24.34 for the Al, Ni and Fe imply the model is significant at $P<0.05$ and there is only 0.01-0.04% chance of disturbance due to noise (Table 4). In this analysis, a "Prob > F" value less than 0.0500 indicate model terms are significant. Thus, it is obvious that the regression analysis of the experimental design for the Al-electrode shows that the linear model terms B(Voltage) and the two quadratic model term (A^2 and B^2) are significant at this confidence level ($P<0.05$) with respective F-values of 146.37, 39.00 and 26.48. It can be noticed that the only significant terms when the Ni electrode was used were B and the quadratic term of A^2, and the corresponding F-values were 56.24 and 8.75, respectively. The Fe electrodes show a similar response to that of Al. The significant terms were B, A^2 and B^2, with corresponding F-values of 57.99, 16.68 and 7.68, respectively. It can be noticed that in all the three regression analysis B-linear term (voltage) is highly significant but its quadratic term only shows some effect with Al and Fe electrode. However, the linear term A (pH) was not significant irrespective of the type electrode. Thus, the regression model for the H_2 production based on the significant terms using Al, Ni and Fe electrodes were as expressed in Eq. 1, 2 and 3, respectively.

$$H_{2-\mathbf{Al}\ Electrode} = 691.32 + 257.69 \times B - 131.57 \times A^2 - 115.92 \times B^2 \quad (1)$$

$$H_{2-\mathbf{Ni}\ Electrode} = 581.11 + 281.65 \times B - 109.89 \times A^2 \quad (2)$$

$$H_{2-\mathbf{Fe}\ Electrode} = 538.06 + 218.35 \times B - 115.82 \times A^2 - 84.04 \times B^2 \quad (3)$$

Table 4. Analysis of variance (ANOVA) of the model for H2 production using Al, Ni and Fe electrode

Source	**Al-Electrode**		**Ni-Electrode**		**Fe-Electrode**	
	F - Value	**Prob > F**	**F Value**	**Prob > F**	**F Value**	**Prob > F**
Model	64.90	< 0.0001	21.42	0.0004	24.34	0.0003
A-pH	*3.84*	*0.0843*	*0.86*	*0.3837*	*3.34*	*0.0758*
B-Voltage	*146.37*	*< 0.0001*	*56.24*	*0.0001*	*57.99*	*0.0001*
AB	*1.005E-003*	*0.9756*	*3.28*	*0.1132*	*2.465E-004*	*0.9879*
A^2	*39.00*	*0.0004*	*8.75*	*0.0211*	*16.68*	*0.0047*
B^2	*26.48*	*0.0013*	*3.70*	*0.0957*	*7.68*	*0.0276*
R^2	0.9789		0.9387		*0.9251*	
Adj-R^2	0.9638		0.8948		0.8165	
Pred-R^2	0.5123		0.6374		0.6021	

The fit of the regression models for the three electrodes was also expressed by the coefficients of determinations R^2, which were found to be 0.9789, 0.9387 and 0.9251 for Al, Ni and Fe electrodes, respectively. The data were further diagnosed by plotting a linear graph between the actual and predicted values, as presented in Figure 3a, b and c, respectively. It can be observed that the data points were all around the diagonal line, and this implies insignificant deviations. More so, the respective adjustable and predicted R^2 values were (0.9638; 0.5123), (0.8948; 0.6374) and (0.8165, 0.6021). Thus, the excellent correlation values of R^2 shows that the regression models are adequate to navigate the design space, and as such, they are suitable for predicting the H_2 yield.

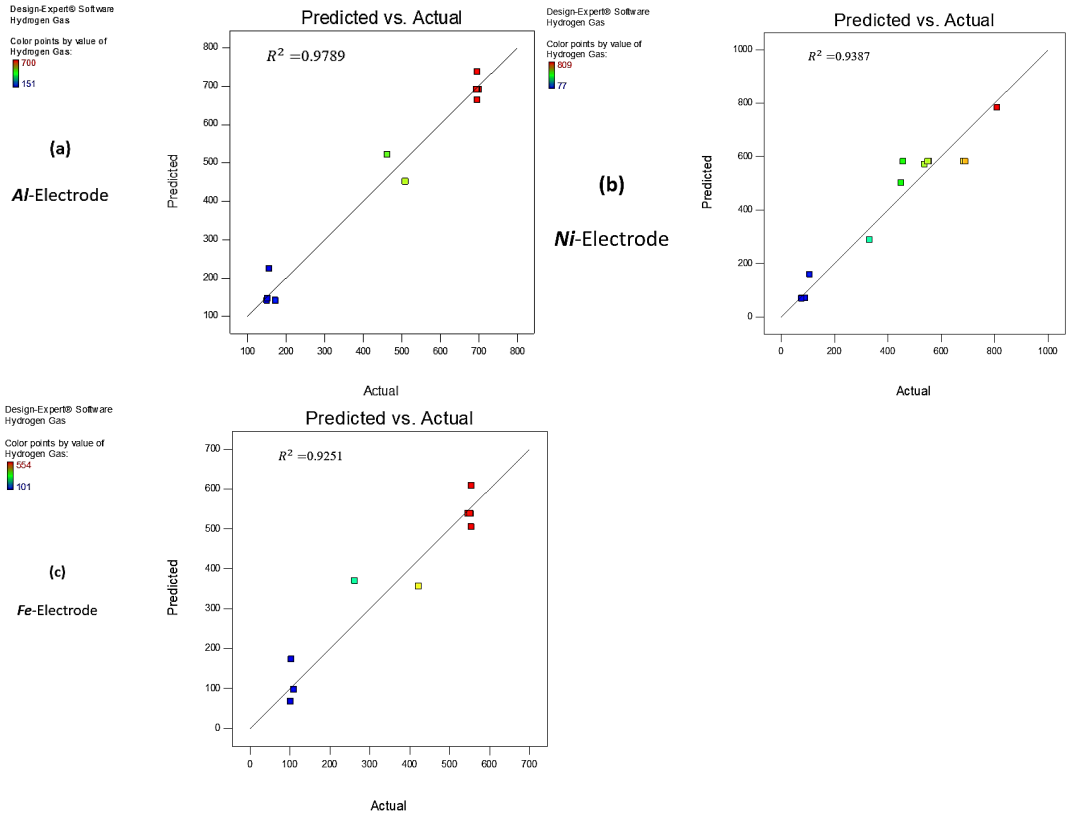

Figure 3. Linear correlation between the actual and predicted H_2 yield using **(a)** Al-electrode, **(b)** Ni-electrode, and **(c)** Fe- electrode

d. Response Surface of the synergistic effect of treatment factors on the optimal hydrogen gas production

As shown in Figure 4a, b and c, hydrogen gas production increases with the voltage but decreases gradually as the voltage decreases to lower ranges. The surface response alongside with contour of Figure 4a, based on the optimization criterion, the optimal hydrogen yield (697 ppm) was obtained at the voltage 9V and pH of 6 with Al electrode, though the corresponding predicted value was 833.091 ppm. Figure 4(b) illustrated the optimized condition for H_2 production using the Ni electrode. Similarly, higher voltage (9V) favours H_2 production with an optimal yield of 554 ppm and the predicted values of 617.391 ppm, but this is considerably lower compared to that of the Al-electrode. This observation is in good agreement with the report of Shivayogimath *et al*., (2013). Furthermore, Figure 4(c) depicts the surface response of the combined effect of voltage and pH on the optimal hydrogen production using the Fe. An optimal value of 551 ppm with a corresponding predicted value of 672.372 ppm was obtained. Generally, it can be noticed from these figures that the impact of the pH on the H_2 yield was not significant. Bazrafshan. *et a*l., 2007 and Yao Hua Ch. *et al*., 2008 reported that the increase in pH may be as a result of hydrogen evolution at the cathodes electrode. Chafi *et al*. (2011) contested that the surge in pH was only due to the release of CO_2 from the wastewater, though H_2 bubble were generated as disturbance during the process. They further explained that, at lower pH, the CO_2 is over-saturated in wastewater and as such H_2 is released leading to an increase in the pH value. In this study, the pH did not affect the treatment processes significantly despite the wide range of the variation.

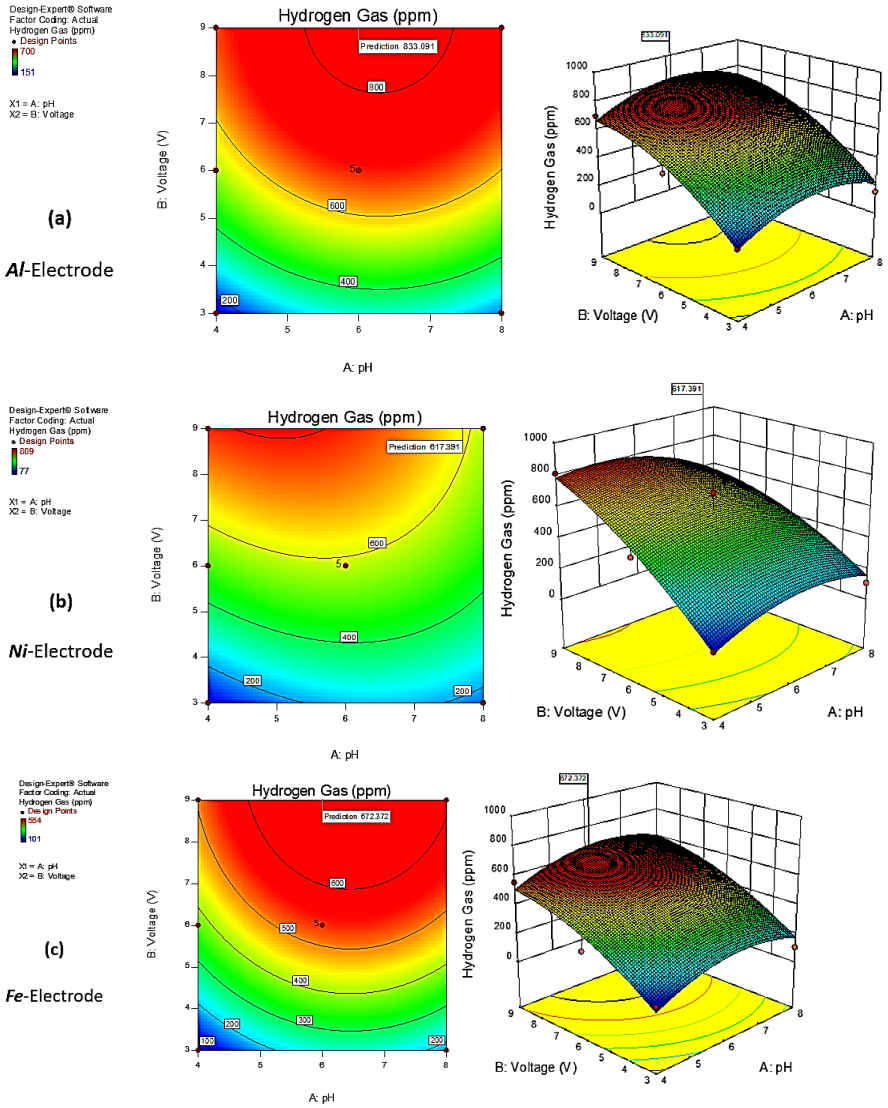

Figure 4. contour plots and response surface of the synergistic effect of combined pH and voltage on optimal hydrogen gas production using **(a)** Al-electrode, **(b)** Ni-electrode, and **(c)** Fe- electrode

4.0. CONCLUSION

The electrocoagulation process based on varying voltage and pH, using different types of electrodes (Al, Ni, Fe) for hydrogen production from leachate was successfully optimized using response surface methodology (RSM). CCD optimization component of RSM was applied in this study and the results show that the Al electrodes give an upturn optimum H_2 yield of 697 ppm at the most suitable treatment parameters of pH 6 with the voltage of 9V for 20 min treatment durations. While, the H_2 yield under these same conditions using Ni and Fe electrodes were 554 and 551 ppm, respectively. The respective model coefficient of correlation (R^2) for the experimental and predicted H_2 value were 0.9789, 0.9387 and 0.9251. This shows the precision of the regression model is adequate to navigate the design space, and as such, it can be efficiently used for the prediction of hydrogen production from leachate under the electrocoagulation process conditions.

5.0. ACKNOWLEDGEMENT

The authors would like to acknowledge the general support provided by Universiti Putra Malaysia.

REFERENCES

Abdallah, S., Yousef, E., Katab, M., Abdullah, I. (2013). The Effect of pH on the Hydrogen and Oxygen Production Using Photovoltaic Power Generator. Photovoltaic Power Generation, Volume 5, No. 1 (2013) 7-12

Ali, E., & Yaakob, Z. (2012). Electrocoagulation for Treatment of Industrial Effluents and Hydrogen Production. Electrolysis. doi:10.5772/48633

APHA Standard Method. (2007). *Standard Operating Procedure for: Total Suspended Solids*. 11. https://beta-static.fishersci.com/content/dam/fishersci/en_US/documents/programs/scientific/technical-documents/white-papers/apha-total-suspended-solids-procedure-white-paper.pdf

Bazrafshan E, Mahvi A H, Nasseri S & Shaighi M, Iran. J. (2007). Environ. Health. Sci. Eng, 2(4), 127.

Chafi, M.; Gourich, B.; Essadki, A.H.; Vial, C.; Fabregat, A. (2011). Comparison of electrocoagulation using iron and aluminium electrodes with chemical coagulation for the removal of a highly soluble acid dye. Vol 281, 285–292.

Demirbas, A. (2010). Fuels from Biomass.Biorefineries, Springer London, 33-73.

Holt, P., Barton, G., Mitchell, C. (1999). Electrocoagulation as Wastewater Treatment, The Third Annual Australian Environmental Engineering Research Event, Castlemaine, Victoria.

Ilhan, F., Kurt, U., Apaydin, O., & Gonullu, M. T. (2008). Treatment of leachate by electrocoagulation using aluminum and iron electrodes. Journal of Hazardous Materials,154(1-3), 381-389. doi:10.1016/j.jhazmat.2007.10.035

Kabuk, H., Ilhan, F., Avsar, Y., Kurt, U., Apaydin, O., & Gonullu, M. (2013). Investigation of Leachate Treatment with Electrocoagulation and Optimization by Response Surface Methodology. Clean Soil Air Water CLEAN - Soil, Air, Water, 571-577.

Nanthagopal, K., Subbarao, R., Elango, T., Baskar, P., & Annamalai, K. (2011). Hydrogen enriched compressed natural gas (HCNG): A futuristic fuel for internal combustion engines. THERM SCI Therm Sci THERMAL SCI Thermal Science, 15(4), 1145-1154. doi:10.2298/tsci100730044n

Ogden, J.M. (1999). "Prospects for building a hydrogen energy infrastructure". Annual Review of Energy and the Environment 24: 227–279. doi:10.1146/annurev.energy.24.1.227

Pawar, S., Nkemka, V., Zeidan, A., Murto, M., & Niel, E. (2013). Biohydrogen production from wheat straw hydrolysate using Caldicellulosiruptor saccharolyticus followed by biogas production in a two-step uncoupled process. International Journal of Hydrogen Energy, Volume 38 (Issue 22), 9121-9130.

Shammas, N.K.; Pouet, M.; Grasmick, A. (2010). Wastewater Treatment by Electrocoagulation–Flotation. In Flotation Technology; Wang, L., Eds.; Springer: New York, NY, USA; pp. 99-124.

Shivayogimath, C. (2013). Treatment of Solid Waste Leachate By Electrocoagulation Technology. International Journal of Research in Engineering and Technology IJRET, 266-269.

Shivayogimath, C., Watawati, C. (2014). Landfill leachate treatment by electrocoagulation process using iron sacrificial electrodes. International Journal of Research in Engineering and Technology ISSN 2348 0157, Vol. 02, No. 03,

Şengil, İ.A.; Kulaç, S.; Özacar, M. (2009). Treatment of tannery liming drum wastewater by electrocoagulation. J. Hazard. Mater., 167, 940-946.

Smolinka, T. (2009). Fuels-Hydrogen Production, Water Electrolysis. Encycl Electro-chem Power Sources: 394–413.

Song, S.; Yao, J.; He, Z.; Qiu, J.; Chen, J.(2008). Effect of operational parameters on the decolorization of C.I. Reactive Blue 19 in aqueous solution by ozone-enhanced electrocoagulation. J. Hazard. Mater., 152, 204-210.

Wang C.T., Chou W.L., Kuo Y.M. (2009). Removal of COD from laundry wastewater by electrocoagulation/ electroflotation. J. Hazard. Mater. 164, 81.

Yao Hua, Ch., Lien Loa, Sh., Kuan, W.H and Lee, Y.D, (2008). Sep. Purif. Technol, 60, 1.

PAPER 26 – PHYTOREMEDIATION OF LEAD-POLLUTED DUMPSITE SOILS USING A NOVEL HYPER-ACCUMULANT IN COMBINATION WITH A BIODEGRADABLE CHELATING AGENT

R. T. Iwar*, G. O. Ogbeh

Department of Agricultural and Environmental Engineering, Joseph Sarwuan Tarka University, Makurdi, Nigeria.
*Email: iwar.raphael@uam.edu.ng

ABSTRACT
The effects of toxic substances including heavy metals (HMs) in the human environment have become a significant source of worry for the wellbeing of man and his dwellings**.** This work focused on the containment of HMs pollution in dumpsite soils through phytoremediation using Stinging Nettle (*Urtica dioica)* as macrophyte. The effects of macrophyte density (1 – 3 plants/m^2) and bio-degradable chelating agent (Citric acid) concentration (3 – 9 mmol/kg) on the phyto-extraction efficiency of Pb was considered in this study. Soil trials were taken from a municipal dumpsite (depth 0 – 20 cm) in Makurdi, North-Central Nigeria which was already found to contain elevated Pb concentrations (106.20 mg/kg) for the phytoremediation experiments. Control pots that received same treatment without the addition of citric acid were also set up and monitored for comparisons. The bio-concentration factor for Pb was less than unity (BCF < 1), while the translocation factor was greater than one (TF > 1) at all macrophyte densities with the maximum occurring at macrophyte density of 3 plants/m^2. Overall, uptake of Pb by *Urtica dioica* increased with increment in the macrophyte density and at moderate lime concentration (6 mmol/kg).
Thus, *Urtica dioica* is an efficient natural hyper-accumulant for Pb pollution control in tropical soils.

KEYWORDS: Chelating agent, Dumpsites, Heavy metals, Soil, Phytoremediation, Stinging Nettle.

1. INTRODUCTION

The persistence and toxicity of heavy metals in the environment has been a global ecological and human wellbeing concern in recent times. Both natural and human-induced practices contribute to the accumulation of heavy metals in various environmental matrices including soils, water, food and air. The most common anthropogenic causes emerge through improper solid and liquid waste management practices. These result in the creation of huge quantities of non-useful substances that prompt the discharge of harmful features to the environment including heavy metals (Abdu *,Yusuf,* 2013; Nuhu *et al.,* 2014; Ma *et al*., 2015). Additionally, the quantum of heavy metal occurrence in soils is influenced by the geological composition of the soils (Sivarajasekar *et al.,* 2018).

Food security, green revolution and agricultural endowment are greatly related to the quality and quantity of soil available. However, as a result of rapid urbanization and spring-up of industries, the quantity and quality of soils available for agricultural production have been greatly retarded (Sivarajasekar *et al.,* 2018). Heavy metals are among the most worrisome group of soil pollutants due to their toxicity to humans and the ecosystem. When present in soils , heavy metals solubilize in the soil-water-nutrient interaction and are taken up by plant/crop roots and translocated to the whole parts of the plants where they are persistently stored in stems and leaves of the plants. When such crops are consumed by man and his animals, they are exposed to the toxic and carcinogenic effects of heavy metals (Ayoub *et al.,* 2010; Ihedioha *et al.,* 2017).

Research efforts in the past have been focused on ascertaining the status of heavy metal (Pb, Zn, Cd, Ni, Cu etc.) contamination in and around dumpsites with little efforts given towards its removal for the safety of the ecosystem (Wang *et al.,* 2016; Gabarron *et al.,* 2017). Unfortunately, active or non-active municipal solid waste dumpsite soils which are associated with alarming heavy metal pollution status are frequently utilized for urban agriculture; a situation that subjects the end consumers of such food to the deleterious consequences of the toxic heavy metals due to bio-accumulation and food chain contamination problems (Wu *et al.,* 2018).

The most common methods for remediating heavy metal contamination in soils include; electro-chemistry, biochar addition, bioremediation and phytoremediation. Among these methods, phytoremediation which is the application of growing ornamental plants for the removal of toxic pollutants including heavy metals in soils is mostly considered. Phytoremediation is favoured for soil remediation because of its low cost, efficiency and low energy inputs when compared with the other methods. Several researchers have reported the deployment of phytoremediation as a treatment for reducing heavy metals in polluted soils. These researches cut across various continent of the world and have utilized different plants/macrophyte for phytoremediation trials. For instance, in

Asia, Massadeh snd Massadeh (2019), used citrus lemon (Rutaceae), Ceratonia siliqua L., Olea europaea (Oleaceae), Washingtonia filifera, and Myoporum (Myoporaceae) to examine the removal of copper (Cu) and zinc (Zn) ions from aqueous solutions, while in Africa, Ameh *et al.,* (2020), used groundnut (*Arachis hypogaea*) and beans (*Phaseolus vulgaris*) plants to examine the removal of cadmium, chromium, copper and lead from soil.

Phytoremediation as a sole strategy is conventionally limited for large scale uses targeting non- bioavailable heavy metals in soils. This is largely due to the long durations associated with the process (Wang *et al.,* 2019). Thus the use of improved techniques such as induced phytoremediation, chelate-assisted phytoremediation and genetic manipulation of the macrophyte prior to its use for phytoremediation has been recently advocated.

The choice of phytoremediation and its successful implementation for heavy metal control in soils is dependent on the availability of plant species that are hyper-accumulants of heavy metals. To this end, it is pertinent to study the suitability of local plants for their efficacy in phytoremediation with respect to heavy metals decontamination of soil of which several tropical ornamental and food crops are yet to be tested in this regard. The macrophyte of choice in the current work: Stinging nettle (*Urtica dioica)* was previously tested for its heavy metal uptake in soils without much success due to the non-bioavailability of heavy metals in the polluted soils (Shams *et al.,* 2009; Murtic *et al.,* 2021: Sharifi *et al.,* 2023). Recently, researchers have advocated the use of improved techniques for enhanced phytoremediation of heavy metals by *Urtica dioica*. For instance Viktorova *et al.* (2016) asserted that the phytoremediation ability of *Urtica dioica* can be greatly enhanced by genetic manipulation of the macrophyte using constitutive CaMV 35S promoter. Another improved technique is the use of biodegradable and non-biodegradable chelating agents to improve the bioavailability of heavy metals towards its effective phyto-extraction by the chosen macrophyte. These techniques have been explored by some researchers for enhanced phytoremediation of heavy metals using macrophyte such as *Amaranthus caudatus L. and Tagetes patula L.* (Aghelan *et al.,* 2021), *Sasa argenteostriata* (Yang *et al.,* 2022), and *Pfaffia glomerata* (Huang *et al.,* 2021) among others. The use of biodegradable chelating agents for improved phyto-extraction of heavy metals from contaminated soils is promoted ahead of the use of the non-biodegradable types due to its environmental friendliness and non-secondary pollution disposition. The most commonly tested biodegradable chelating agents and plant species have been chronicled by Shinta *et al.* (2021).

Despite the huge potentials of improved phytoremediation and environmental safety of biodegradable chelating agents towards heavy metal extraction from polluted sites, these techniques have not been tested using *Urtica dioica;* A macrophyte that has already shown significant prospects as a hyper-accumulant of heavy metals should the technique be improved. Therefore, this study was set out to fill this knowledge gap with the following specific objectives: (1) to comparatively study the phytoremediation of Pb by *Urtica dioica* under the application of citric acid (a biodegradable chelating agent) and non-application scenario in a controlled environment pot experiments using actual contaminated dumpsite soils, (2) to test the effects of macrophyte density and chelating agent concentration on the phytoremediation of Pb using *Urtica dioica*.

2. MATERIALS AND METHODS

The materials for this study were laboratory auger, aluminium foil, and polyethylene bags, lead contaminated soils, a screen house, standard analytical reagents and laboratory wares, stinging nettle plants, distilled water, concentrated citric acid and perforated cylindrical plastic pots. The experiments were carried out at the Research Farm of the Department of Agricultural and Environmental Engineering, Joseph Sarwuan Tarka University, Makurdi using standard pot cultures in a controlled environment devoid of external environmental influences. Soil samples from a municipal dumpsite that were already established to contain elevated levels of Pb in our previous study were used for the phytoremediation experiments. The Pb uptake ability of a locally available plant: Stinging nettle (*Urtica dioica*) was tested at varying plant/macrophyte densities and chelating agent (citric acid) concentrations using distilled water for irrigation. Control pots that did not receive chelating agent and/or not planted with *Urtica dioica* but received irrigation or planted in non-polluted soils were also set-up for comparisons.

Inferential indices considered in the evaluation of the system were the translocation factor, bio-concentration factor, and overall Pb uptake in the roots and aerial parts of the plants as well as the plant height over the growing period. These parameters were determined following the method of Das *et al.* (2014).

2.1 Soil Sample Collection and Determination of Initial Pb Concentration

Soil samples were collected in the month of September, 2022 from an identified dumpsite with elevated concentration of lead in an urban settlement in Makurdi, North-central, Nigeria. The soils were randomly collected in sufficient quantities at a depth of 0 -20 cm using a laboratory auger in order to prevent the interference of wastes

and degrading materials in the samples. The soils were initially homogenized by thorough mixing before putting same in polyethylene bags, enclosed with aluminium foils and transported to the laboratory and experimental site for further analysis and use respectively (Ihedioha *et al.,* 2017).

In the laboratory, the soil were homogenized again and characterized for the physico-chemical properties (details not reported here) and then stored at room temperature before analysis for heavy metal content. For the determination of Pb concentration in the soil sample, the method of Hedge *et al.* (2009) was followed for sample digestion, while the concentration of Pb (mg/kg) in the sample was determined using a flame atomic adsorption spectrophotometer (Shimadzu model AA 700) equipped with a deuterium lamp and air/acetylene head burner as carrier gas system in accordance with the method of Wamalwa *et al.* (2018) at a wave length of 283.3 nm. Quality assurance was done by determining the concentration of Pb in spiked and unspiked control soil samples and the computing the percentage recovery following the procedure of Naz *et al.* (2018).

2.2 Experimental Set-up

The experiments were set-up in perforated cylindrical plastic pots of 250 mm^2 top areas and depth of 200 mm. the experiments were conducted for a total duration of 60 days with an additional initial seven day acclimatization period. The pots were filled with homogenized samples of contaminated soils (3 kg) with an inherent Pb concentration of 106.20 mg/kg. A drainage water collection vessel was placed underneath each experimental pot to collect and recycle water/nutrients in the system. The pots were initially treated with deionized water at 60 % of field capacity and left for one week. After that, the already established *Urtica dioica* plants grown in a nursery were transplanted into the experimental pots at the desired plant densities and following standard agronomic practices. Edge effects were minimized by routine randomization of the experiment pots in the screen house. The planting densities adopted were 1, 2 and 3 plants/m^2. Initially, the pots were planted with 6, 10 and 14 plants and later tinned to 4, 8 and 12 plants to give planting densities of 1, 2 and 3 plants/m^2 respectively as desired. The chelator treatments using citric acid were started on day 30 after transplanting at dosages of 3.0, 6.0 and 9.0 mmol/kg and planting density of 3 plants/m^2. Similar control pots that received only deionized water without the additions of citric acid (chelating agent) were also set up and monitored for comparison. Each experimental treatment was replicated thrice and arranged in a completely randomized design form.

In order to maintain the cleanliness of the experimental environment, weeding was done manually without the use of herbicides and insect infestation were prevented by the screen house, thus no insecticides were used. Photo and dark periods of 14 and 10 hours/day respectively were maintained throughout the experimental period in the screen house. Similarly, room temperatures of 30 ± 2 °C and 23 ± 2 °C were maintained during the day and night times respectively. Fig. S1 in appendix shows the schematic of the experimental set-up. The average height (ft) of the macrophyte was monitored using a flexible tape over the growing period at an interval of 5 days with emphasis on the experimental pots with three plants/m^2 and varying citric acid concentrations (0 -9 mmol/kg).

2.3 Determination of Pb Concentration in Harvested Plant (*Urtica dioica*) Parts and Data Analysis

At the end of the 60 days experimental period, the experiments were terminated and the *Urtica dioica* plants were separately harvested from the experimental pots and prepared for further analysis. The roots and shoots of each plant category were carefully separated using a disinfected knife. The separated parts of the plants were separately and carefully washed with deionized water; air dried and weighed using a digital weighing balance (Adam model PW 184). Each weighed sample was labelled and placed in dry plastic pots for further determination of the inherent Pb concentrations (mg/kg). Again the concentration of Pb in the component parts of the plants for each experimental treatments and control were determined after ashing in a muffle furnace set at 800 °C (Carbolite model GPC 12/81 + 103, Sheffield, England) and digestion using a flame atomic adsorption spectrophotometer in accordance with the methods of Rashid *et al.* (2016). Then the phytoremediation potentials of *Urtica dioica* for Pb under the various experimental treatments and control were determined as the Bio-concentration Factor (BCF), Translocation Factor (TF) and Enrichment Factor (EC_r) using equations 1, 2 and 3 respectively (Das *et al.,* 2014; Madanan *et al.,* 2021). The percentage reduction in Pb concentration in the soil was measured to indicate the chelating efficiency using equation 4, ANOVA was used to analyse the data sets (P = 0.05). The growth (height) profile of *Urtica dioica* was also measured at an interval of 5 days for the 60 day experimental period using a flexible meter rule.

$$BCF = \frac{s}{q} \quad (1)$$

Where s = the combined concentration (mg/kg) of Pb in the plant aerial parts and roots
q = the initial concentration of Pb (mg/kg) in the soil.

$$TF = \frac{z}{r} \quad (2)$$

Where, z = Pb concentration in aerial parts of the plant

r = Pb concentration in the plant roots

$$EC_r = \frac{z}{q} \quad (3a)$$

Or $$EC_r = \frac{r}{q} \quad (3b)$$

Where z, r and q are as defined above.

$$\%\ Reduction = \frac{initial\ \ concentration\ of Pb - final\ concentration\ of\ Pb\ in\ soil}{initial\ concentration\ of\ Pb\ in\ soil} \times 100 \quad (4)$$

3. RESULTS AND DISCUSSION

The results of these experiments are presented in the following sections with discussion of findings and implications. These have been sub-dived into; The effects of plant density on the uptake of Pb in soils, The effect of planting density on the Pb phytoremediation potentials of *Urtica dioica,* effects of chelating agent concentration and plant density on percentage reduction of Pb in soils and the growth characteristics of *Urtica dioica* under Pb contaminated soils and control.

3.1 Effects of Plant Density on Phytoremediation of Pb by *Urtica dioica*

The influence of plant density (1 – 3 plants.m^2) on the total uptake of Pb (mg/kg) from contaminated soil by *Urtica dioica* is shown in Table 1 for both the aerial parts and roots of the macrophyte. In the aerial parts, Pb uptake ranged from 0.00 ± 0.00 to 11.10 ± 0.23 mg/kg. The uptake of Pb from the dumpsite soils increased with increase in the plant density and was significant at P = 0.05 (Table 2). Similarly, the uptake of Pb in the roots of *Urtica dioica* increased with increase in planting density (0.00 ± 0.00 – 19.80 ± 0.14 mg/kg) and was significant at P ≤ 0.05 (Tables S1 – S2a-e in appendix). The control showed no uptake since the soils were not contaminated with Pb. The BCF was 0.00 ± 0.00 – 0.29 ± 0.20 (Table 1) and was significantly higher in experimental pots having 3 plants/m^2 (P ≤ 0.05).

The BCF is an indicator of the macrophyte ability to accumulate pollutants including heavy metals depending on its initial concentration in the polluted media (Madanan *et al.,* 2021). Increase in the BCF as the plant density was increased indicate that more Pb was accumulated when the extracting macrophyte were increased thus signifying a liner relationship. Macrophyte with BCF values between 1 and 2 are considered as suitable for phyto-extraction (Das *et al.,* 2014). The BCF values in phytoremediation are not enough to elucidate on the absolute suitability of a macrophyte as a hyper-accumulant, thus to unravel this, a more suitable index known as the TF is used. In this study, the TF ranged from 0.00 ± 0.00 in the control to 1.89 ± 0.06 in the 1 plant/m^2 experimental pots. It was further observed that an increase in the plant density lead to a decrease in the TF. This trend was ascribed to competition among the macrophyte to phyto-extraction of Pb in the polluted soil. Macrophyte that extract heavy metals and largely store it in the roots have TF < 1, while TF >1 indicate the transfer of the extracted metals to the aerial parts of the plant. In this vein, *Urtica dioica* was found to phytoextract Pb in the soil and efficiently transfer same to its shoots for all plant densities considered in this work (Table 1). This shows that *Urtica dioica* is a good accumulator of Pb ions from polluted soils.

Similar to the BCF and as shown in Table 1, the EF was also found to increase with an increase in the plant density (0.00 ± 0.00 – 0.17 ± 0.006). The EF shows the relationship between the concentrations of the extracted pollutant in the aerial parts of the macrophyte to the remaining concentration in the soil. Thus values > 1 show hyper-accumulation, while those lower than 1 indicate moderate to good accumulation of the pollutant (Madanan *et al.,* 2021).

Table 1: Effects of Plant Density on Phytoremediation of Pb

S/No	Phytoremediation Parameter	Plant Density (Plants/m^2)			
		1	2	3	Control
1.	Bio-concentration Factor	0.28 ± 0.006^b	0.28 ± 0.006^b	0.29 ± 0.20^c	0.00 ± 0.00^a
2.	Translocation Factor	1.89 ± 0.06^c	1.85 ± 0.01^c	1.74 ± 0.00^b	0.00 ± 0.00^a
3.	Enrichment Factor	0.15 ± 0.006^b	0.15 ± 0.02^b	0.17 ± 0.006^c	0.00 ± 0.00^a
4.	Aerial Pb Uptake (mg/kg)	10.00 ± 0.66^b	10.54 ± 0.96^b	11.10 ± 0.23^b	0.00 ± 0.00^a
5.	Root Pb Uptake (mg/kg)	19.20 ± 0.42^b	19.20 ± 0.11^b	19.80 ± 0.14^c	0.00 ± 0.00^a

Values are means and standard deviations of triplicate experiment. Values with same superscript across rows are not significantly different at P = 0.05.

3.2 Effects of Chelating Agent Concentration on Pb Removal by *Urtica dioica*

The effect of citric agent concentration as a chelating agent to aid bioavailability of Pb in polluted soils was tested in the range of 3.0 – 9.0 mmol/kg. A control that received 0.0 mmol/kg of citric acid was also monitored for comparison. One way ANOVA and Duncan Multiple Range Test (DMRT) indicated a significant difference in

the levels of citric acid considered (P = 0.05) as shown in Table S3 and S4 in the Appendix respectively. Pb removal efficiency ranged from 68.90 ±6.12 – 88.35±2.08 % (Table S5 in appendix) with the lowest and highest values observed in the control and pots with citric acid concentration of 9.0 mmol/kg respectively (Fig. 1). ANOVA also showed that there was no significant difference in the Pb uptake efficiency of the 6.0 and the 9.0 mmol/kg set set-ups. Thus it was recommended that the moderate citric acid concentration of 6.0 mmol/kg is optimal for bioavailability and subsequent uptake of Pb from polluted soils by *Urtica dioica* macrophyte. Thus in this study it was found that a planting density of 3 plants/m^2 and citric acid concentration of 6 mmol/kg are ideal for efficient removal and translocation of Pb by ornamental *Urtica dioica* macrophyte.

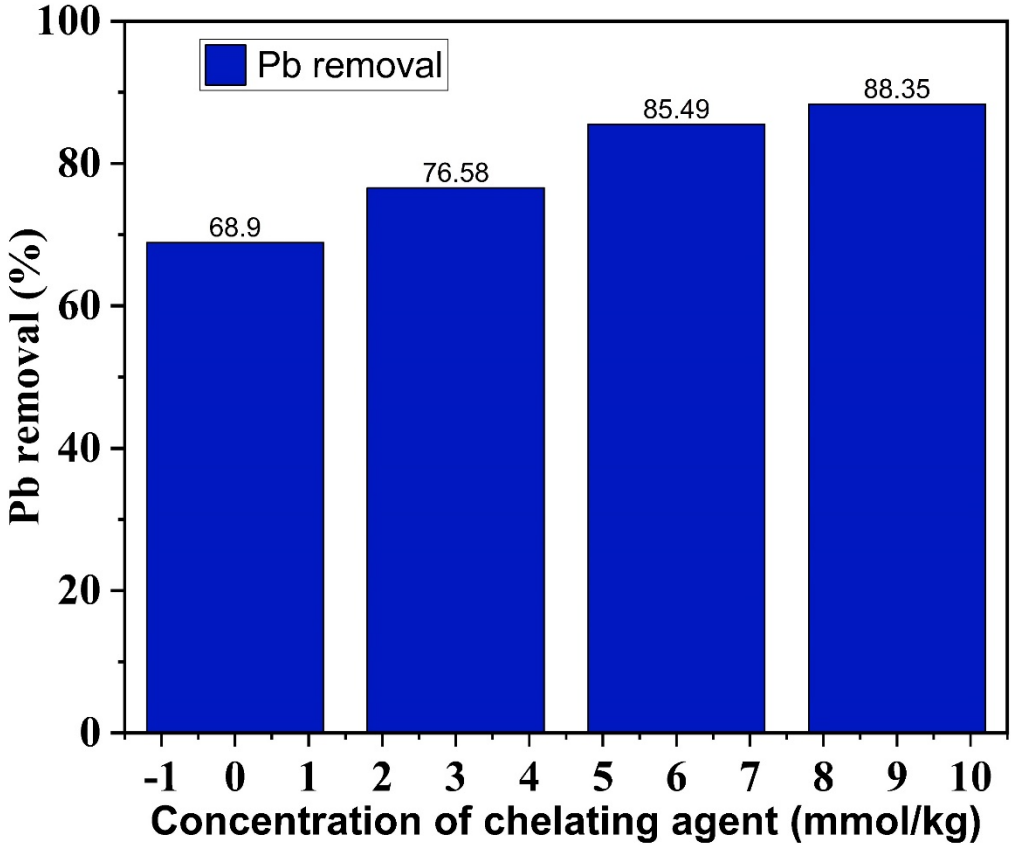

Figure 1: Pb Removal Efficiency as Influenced by Citric Acid Concentration

3.3 Growth of *Urtica dioica* at varying Chelating Agent Concentration in Polluted Soils.

The average height of *Urtica dioica* as a phytoremediation plant was monitored for 60 days in the pots containing 3 plants/m^2 and at the various chelating agent concentrations. The control pots which had 0.0 mmol/kg of citric acid were found to exhibit higher growth as compared with the pots that received various citric acid concentrations. Initially, before the introduction of the chelating agent to the experimental pots (0 -30 days), the plant height were not different, however, when the chelating agent was introduced (30 – 60 days), the growth of the macrophyte began to decline with increase in the concentration of the citric acid (Fig. 2). This was ascribed to the toxicity of Pb, which hindered its optimal growth. As stated earlier, when the concentration of citric acid was increased, the bioavailability of of Pb in the soils for phytoextraction by *Urtica dioica* was also enhanced. This situation encouraged Pb toxicity to the plants, leading to a diminished growth pattern as evidenced in Fig 1. Similar toxicities were documented by other researchers (Zair *et al.,* 2014).

4. CONCLUSION

In this work a novel macrophyte: *Urtica dioica* (Stinging nettle) was used for the first time towards the phytoremediation of Pb in polluted dumpsite soils. The influence of macrophyte density and biodegradable chelating agent concentration on the phytoremediation ability of the macrophyte was carefully studied in macrocosm pot experiments conducted under a controlled environment (screen house). The bio-concentration factor and enrichment factor were lower than unity at all planting densities and were significantly higher at higher plant density (3 plants/m^2), while the translocation factor indicated the excellent phyto-extraction capability of

Urtica dioica as values were > 1 for all planting densities and significantly reduced with increase in the plant density. The Pb removal efficiency was found to depend on the chelating agent (citric acid concentration) and significantly increased with an increase in the chelating agent concentration up to a moderate value of 6.0 mmol/kg. The growth of *Urtica dioica* in the polluted soil media was inhibited by an increase in the chelating agent concentrations which promoted the bioavailability of Pb, its subsequent phyto-extraction and translocation which increased Pb toxicities in the plants morphological physiological functions.

It was therefore concluded that *Urtica dioica* is a good candidate for phytoremediation of Pb polluted soils at higher planting densities and moderate chelating agent concentrations.

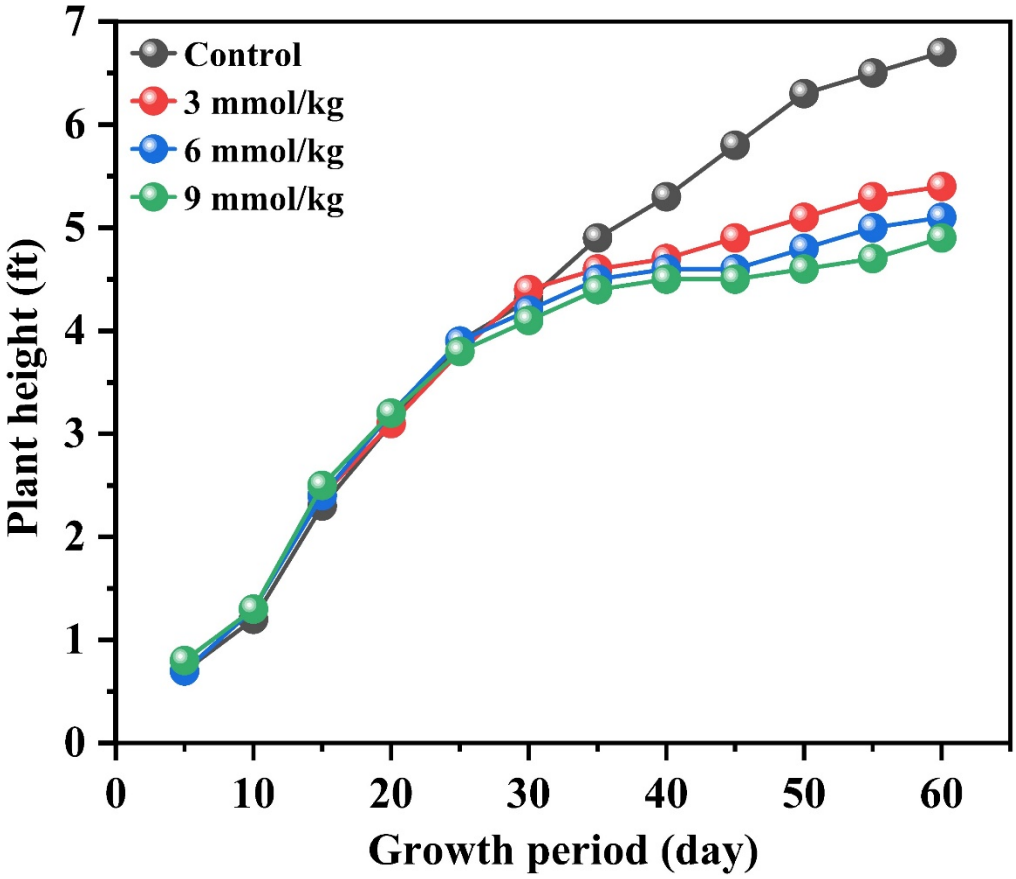

Figure2: Effects of Citric Acid concentration on the Growth of *Urtica dioica* in Pb Contaminated soils

ACKNOWLEDGEMENT

The authors acknowledge the Laboratory space provided by the Department of Soil Science, Joseph Sarwuan Tarka University, Makurdi for the conduct of laboratory tests. The Department of Agricultural and Environmental Engineering, Joseph Sarwuan Tarka University, Makurdi is also acknowledged for providing the screen house where the experiments were set-up.

REFERENCES

Abdu, N., Yusuf, A. (2013). Human health risk characterization of lead pollution in contaminated farmlands of Abare village, Zamfara State, Nigeria. *Afr. J. Environ Sci. Technol.* 7(9):911–916.

Aghelan, N., Sobhanardakani S., Cheraghi M., Lorestani B., Mernkhpour H. (2021). Evaluation of some chelating agents on phytoremediation efficiency of *Amaranthus caudatus* L. *and Tagetes patula* L. in soils contaminated with lead. *J. Environ. Health Sci. Eng.* 19(1): 503 – 514.

Ameh, G. I., Nwamba, O. H., Njam,V, S., Ofordile, E, C.(2020).Phytoremediation of heavy metals using some selected leguminous crops. *Afr. J. Agric. Res.* ISSN: 1991-637X. https://doi.org/10.5897/AJAR.

Ayoub K., van Hullebusch E. D., Cassir M., Bermond A. (2010). Application of advanced oxidation processes for TNT removal: a review. *J. Hazard. Mater,* 178:10–28. https ://doi.org/10.1016/j.jhazmat.2010.02.042.

Das S., Goswami S., Talukdar A. D. (2014). A Study on Cadmium Phytoremediation Potential of Water Lettuce, Pistia stratiotes L.. *Bull Environ. Contam. Toxicol. 92,* 169–174.

Gabarrón M., Faz A., Martínez-Martínez S., Zornoza R., Acosta J. A. (2017). Assessment of metals behaviour in industrial soil using sequential extraction, multivariable analysis and a geostatistical approach. *J. Geochem. Explor.* 172, 174–183.

Hegde A. G., Verma P. C., and Rajan M. P. (2009). "Standard protocol for conducting pre-operational environmental surveillance around nuclear facilities". A Publication of the Government of India, Atomic Energy Group, Bhabha Atomic Research Centre, Mumbai, India, BARC/2009/E/004, 144 pp.

Huang R., Cui X., Luo X., Mao P., Zhuang P., Li Y. *et al.* (2021). Effects of plant growth regulator and chelating agent on the phytoextraction of heavy metals by *Pfaffia glomerata* and on the soil microbial community. *Environmental Pollution,* 283: 117159.

Ihedioha J., Ukoha P., Ekere N. (2017). Ecological and human health risk assessment of heavy metal contamination in soil of a municipal solid waste dump in Uyo. Nigeria. *Environ. Geochemist. Health* 39(3):497–515.

Ma L., Sun J., Yang Z., Wang L. (2015). Heavy metal contamination of agricultural soils affected by minig activities around the Ganxi River in Chenzhou. Southern China. *Environ. Monit. Assess,* 187(12):731.

Madanan T. M., Shah G. K., Varghese G. K. (2021). Application of Aztec Marigold (*Tagete erecta* L.) for phytoremediation of heavy metal polluted lateritic soil. *Environ. Chem. Ecotoxicol.,* 3: 17 - 22.

Massadeh M. A., Massadeh S. A. (2019). Removal of Cu and Zn from aqueous solutions by selected tree leaves with phytoremediation potential. *Water Air Soil pollution,* 230: 264.

Murtic S., Zahirovic C., Civic H., Sijahovic E., Jurkovic J., Avdic J. *et al.* (2021). Phytoaccumulation of heavy metals in native plants growing on soils in the Spreca river valley, Bosnia and Herzegovina. *Plant, Soil and Environment,* 67(9): 533 – 540.

Naz A., Chowdhury A., Mishra B. K. (2018). Distribution of heavy metals and associated human health risk in mine, agricultural and roadside soils at the largest chromite mine of India. *Environ Geochem Health,* 40: 2155–2175.

Nuhu A. A., Sallau M., Majiya M. (2014). Heavy metal pollution: the environmental impact of artisanal gold mining on Bagega village of Zamfara State, Nigeria. *Res. J. Pharm. Biol .Chem. Sci.* 5(6):306–313.

Rashid M. H., Fardous Z., Chowdhury M. A. Z. (2016). Determination of heavy metals in the soils of tea plantations and in fresh and processed tea leaves: an evaluation of six digestion methods. *Chemistry Central Journal 10(7):* https://doi.org/10.1186/s13065-016-0154-3.

Shams K. M., Tichy G., Fischer A., Sagar, M., Peer T., Bashar A. Fllip K. (2009). Aspects of phytoremediation for chromium contaminated sites using common plants *Urtica dioica, Brassica napus and Zea mays*. *Plant and Soil,* 328(1): 175 – 189.

Sharifi K., Rahnavard A., Saeb K., Fahimi F. D., Tavana A. (2023). Ability of Urtica dioica L. to adsorb heavy metals from (Pb, Cd, As and Ni) from contaminated soils. *Soil and Sediment Contamination: An International Journal*, 32(1): 51 – 84.

Shinta Y. C., Zaman B., Sumiyati I. (2021). Citric acid and EDTA as chelating agents in phytoremediation of heavy metals in polluted soils: A review. *IOP conf. ser.: Earth Environ Sci.,* 896: 012023.

Sivarajasekar N., Nainamalai M., Sivamani S., Ganesh M. I., Ram Kothandan, M. S. (2018). Comparative modeling of fluoride biosorption onto waste Gossypium hirsutum seed microwave-bichar using response surface methodology and artificial neural networks*, IEEE Xplore.* 1631–1635.

Viktorova, J., Jandova Z., Madlenakova M., Prouzova P., Bartunek V., Vichotova B. *et al.* (2016). Native phytoremediation potentials of *Urtica dioica* for removal of PCBs and heavy metals can be improved by genetic manipulations using constitutive CaMV 35S promoter. *PLOS ONE,* 11(12): e0167927.

Wang J.Z., Peng S.C., Chen T.H., Zhang L. (2016). Occurrence, source identification and ecological risk evaluation of metal elements in surface sediment: Toward a comprehensive understanding of heavy metal pollution in Chaohu Lake, Eastern China*. Environ. Sci. Pollut. Res.* 23: 307–314.

Wamalwa K., Lusweti J., Lutta S., Anditi B. C., Imbila O. M., Muthoka T. M. (2018). Variation of Pollutant Levels in Vegetables: A Case Study of Kitale Municipality, Trans-Nzoia County, Kenya*. Afri. J. Edu. Sci. Technol.,* 2(2): 146-160.

Wu W., Wu P., Yang F., Sun D.L., Zhang D. X., Zhou Y.K. (2018). Assessment of heavy metal pollution and human health risks in urban soils around an electronics manufacturing facility. *Sci. Total Environ.* 630: 53–61.

Yang Y., Liao J., Chen Y., Tian Y., Chen Q., Gao S. et al. (2022). Efficiency of heterogeneous chelating agents on the phytoremediation potential and growth of *Sasa argenteostriata* (Regel) E.G. Camus on Pb-contaminated soil. *Ecotoxicol. Environ. Safety,* 238: 113603.

Zaier H., Ghnaya T., Ghabriche R. (2014). EDTA - enhancedphytoremediation of lead-cotaminated soil by the halophyte *Sesuvium portulacastrum. Environ. Sci. Pollut.* 21: 7607 - 7615.

PAPER 27 – COMPARATIVE STUDY OF BIOLOGICAL DEGRADATION OF CRYSTAL VIOLET BY MICROBIAL MIXED CULTURES FROM COW DUNG AND SOIL

A. A. Rasheed*, U. R. Abdullahi, M. O. Umar

Department of Chemical and Petroleum Engineering, Bayero University Kano, Kano, Nigeria
*Email: aarasheed.cpe@buk.edu.ng

ABSTRACT
The removal of dyes such as crystal violet (CV) from effluents is a major concern worldwide due to their toxic and carcinogenic nature. Recently, biodegradation through microorganisms has emerged as a potential method for eliminating these pollutants. This study was carried out to investigate the extent and the kinetic parameters of biological degradation of crystal violet by mixed-microbial cultures from cow dung and soil. A solution containing 100 mg/l of CV was prepared and added to a reactor inoculated with cow dung and another with soil. The reactors were stirred continuously for 300 mins with concentration of CV measured every 15 mins. For 1 g/l initial inoculum size, 92% and 75 % of CV degradation was achieved with cow dung and soil respectively. Adsorption test showed both cow dung and soil have negligible adsorption capacities. Kinetic parameters like maximum growth rate (m_{max}) and half-saturation constant (K_S) were estimated to be 2.65 day^{-1} and 0.45 g/l for cow dung. However, 0.82 $day^{-1}$and 1.33 g/l as m_{max} and K_S for soil were estimated respectively. These results showed mixed microbial cultures from cow dung and soil can effectively degrade CV. It also suggests that cow dung is a more efficient inoculum than soil in degrading CV.

KEYWORDS: Crystal Violet, biodegradation, kinetic parameters, microorganisms, cow dung, soil

5. INTRODUCTION

The presence of dyes in effluents of various industries like textile, cosmetics, pharmaceuticals, rubber and plastic poses a serious threat to the environment when they are discharged without sufficient level of treatment (Hussain et al., 2020; Singha et al., 2021). Dye-coloured effluent directly discharged into rivers and lakes does not only introduce aesthetic problems but, also obstruct penetration of light, as a result hindering aquatic plant photosynthesis, reducing dissolved oxygen concentration and creating toxic conditions to aquatic flora and fauna (Dutta & Bhattacharjee, 2022). The environmental issues surrounding the presence of colour in effluent is a continuing problem for dyestuff manufactures, dyers, finishers and water companies, because increasingly stringent colour consent standards are being enforced by regulatory bodies to reduce the quality of colour in effluent and water courses (Kannan & Sundaram, 2001; Al-Tohamy et al., 2022). Crystal violet (CV) is one of the most used dyes in textile and pharmaceutical industries. It is very notorious due to its structural stability and resistance to heat and light. Crystal violet is toxic, mutagenic and carcinogenic (Mudhoo et al., 2020; Patil et al., 2022). This detrimental effect means eliminating crystal violet from effluents cannot be over emphasized.

There are various physicochemical techniques for the treatment of effluents containing dyes such as adsorption, precipitation, reverse osmosis, chemical oxidation, photodegradation, advanced oxidation, coagulation, membrane filtration, electrochemical processes, and ultrasonic irradiation (Abdi et al., 2020; Samsami et al., 2020). However, most of these methods of decolorizing and treating dye-containing effluents are not widely used due to high investment cost, formation of sludge, formation of hazardous by-products and intensive energy requirements (Abdi et al., 2020; Al-Tohamy et al., 2022). Physiochemical methods of dye removal are effective only if the effluent volume is small and still generates toxic sludge. This has therefore resulted in considerable interest in the use of biological techniques for the treatment of these effluents. Biodegradation and bioremediation, especially through bacteria, is becoming an emerging and important sector in effluent treatment. Recently, microbial degradation of textile effluent has been reported as eco-friendly and more economical than physiochemical methods (Shah, 2013).

Biodegradation utilizes microorganisms such as bacteria, fungi and protozoa to breakdown the organic wastes or contaminants into smaller less harmful substances. Such biological processes are cheaper, produce less sludge, cost effective processes and have the potential to remove or decolorize the dye completely (Kalyani et al., 2009; Hussain et al., 2020). Microorganisms from different sources such as animal waste, food waste, sewage, sludge, cow dung, soil, etc. have the potential to achieve a higher degree of dye-degradation and can process a complete

mineralization of dyes under optimal conditions (Asad et al., 2007). Although the ability of isolated bacteria to metabolize CV dye has been investigated by a number of researchers (Chen et al., 2007; Mondal et al., 2010; Parshetti et al., 2011), biodegradation of crystal violet and other dyes can be less effective because of the inherent characteristics of dyes like anti-septic and anti-fungal nature, complex chemical structure, toxicity, high weight, and strong molecular bonds (Mani & Bharagava, 2016). To date, there is little information, if any, on the extent of crystal violet degradation using mixed microbial cultures (unacclimated) and the biokinetic parameters.

Thus, this present study work was carried out to investigate the comparative effectiveness of crystal violet degradation using mixed microbial cultures from cow dung and soil. The study also aimed to estimate and compare the main kinetic parameters of biodegradation for both cow dung and soil.

6. METHODOLOGY

2.1 Materials and apparatus

The materials and main apparatus used include: analytical grade crystal violet (Sigma Aldrich, Germany), analytical grade ammonium chloride (99.5% Sigma Aldrich, Germany), magnetic stirrer (TOP-SH2, China), UV-vis spectrophotometer (Zuzi 4201/20, France) and weighing balance (Ohaus SP202, Scoutt Pro, USA). Distilled water was produced using water distiller (SZ-96 Mon Scientific, Nigeria). Other apparatus used were stopwatch and glassware.

2.2 Collection and preparation of inoculum

Cow dung and soil are the inoculum used in this study. They were collected from a farm used by the Center for Dryland Agriculture at Bayero University Kano. The cow dung and soil were collected and separately sieved to minimize stones and dirt and also to obtain uniform particle size of < 250 mm. The samples were then stored in airtight plastic containers prior to usage.

2.3 Preparation of dye solution and calibration

A 1000 mg/l stock solution of dye was prepared by dissolving crystal violet powder in distilled water. NH_4Cl was also added in trace amount (100 mg) to the solution. Afterwards, six (6) samples of 0, 2, 4, 6, 8 and 10 ppm of CV were prepared by diluting the stock solution with appropriate volumes of distilled water. The absorbance of each of the six samples was measured using a UV spectrophotometer at a 565 nm wavelength.

2.4 Biodegradation experiment

2.4.1 Adsorption studies

Two parallel batch reactors with 500 ml working volume were set up and operated at room temperature (25°C) to allow the treatment of the 100 mg/l CV dye solution with cow dung and soil simultaneously. Mixing was carried out using a magnetic stirrer. Adsorption capacity was calculated for cow dung and soil by mixing 100 mg/l of CV solution in 500 ml reactors with 0.5 g of cow dung in the first reactor and 0.5 g of soil in the second reactor. The reactors were allowed to mix continuously for 30 minutes and the concentration of CV in the reactor was measured afterwards. The adsorption capacity (q_{ad}) and adsorption coefficient (K_d) for both cow dung and soil were calculated using equations 1 and 2 below (Habib et al., 2004):

$$q_{ads} = (C_0 - C_{eq})\frac{V}{m} \quad \text{.....(1)}$$

$$K_d = q_{ads} / C_{eq} \quad \text{.....(2)}$$

where C_o and C_{eq} are the initial and equilibrium CV concentration (ppm), V is the volume of the reactor (0.5 l), m is the mass of inoculum (g) and K_d is the adsorption coefficient (l/g).

2.4.2 Biodegradation studies

The biodegradation studies began by mixing 100 mg/l of CV in 500 ml reactors with 0.5 g of inoculum in separate reactors. The reactors ran continuously for 5 hrs. In each reactor, 5 ml of well-mixed solution was withdrawn every 15 minutes to determine the concentration of CV. The same experiment was repeated with a higher inoculum size of 1.5 g for both cow dung and soil.

2.5 Calculation of kinetic parameters

The half saturation constant (K_s) and maximum growth rate (m_{max}) on crystal violet for the microorganisms in cow dung and soil in the reactor were calculated using the Monod model:

$$r_X = \frac{\mu_{MAX} S}{K_S + S} X \quad \text{.....(3)}$$

$$-r_S = \frac{\mu_{MAX} S}{K_S + S} \frac{X}{Y} \quad \text{.....(4)}$$

where r_x indicates the cell growth rate (mg biomass/l/h), r_s is the substrate utilisation rate (mg CV/l/h), X the cell concentration (mg /l), S the CV concentration, m_{max} the maximum growth rate (h^{-1}), K_S the half-saturation constant (mg CV/l) and Y the biomass growth yield on CV (mg biomass/mg CV). The m_{max} and K_s were calibrated on the basis of the time profiles of CV Concentration during the biodegradation experiment. The values of m_{max} and K_s calculated using non-linear regression of the Monod equations. Y was assumed to be equal to 0.47 mg biomass/mg substrate, on the basis of the biomass yield reported in many textile effluent studies (Insel et al., 2002; Henze et al., 2008).

3 RESULTS AND DISCUSSION

3.1 Adsorption studies

The aim of the adsorption experiments was to quantify the contributions of CV removal due to adsorption during operation of the bioreactors. A contact time of 30 minutes was chosen because adsorption is generally considered to be a fast process (Zhao et al., 2008). The results of adsorption studies for cow dung and soil are shown in Table 1. The amount of CV adsorbed on cow dung is lower than 2 mg CV/g and the adsorption coefficient was less than 0.02 l/g. The CV adsorbed on soil was much lower than that of cow dung as 0.47 mg CV/g soil. The adsorption coefficient of soil was also about seven times lower than that of cow dung. This is a clear indication that CV adsorption on the inoculum used in this study is very low and therefore can be considered negligible. Hence, it can be said that any reduction in CV concentration in the biodegradation experiments is solely due to microbial action.

Table 1: Adsorption of crystal violet on the cow dung and soil used in this study

Inoculum	Inoculum Concentration (g/l)	CV adsorbed (mg CV/g inoculum)	K_d (l/g)
Cow Dung	1	1.465	0.014
Soil	1	0.473	0.0019

The adsorption coefficient (K_d) between CV and the inoculum obtained in this study is in agreement with the values reported by Fent et al. (2003) in a different study, which observed K_d values (units converted for consistency) between 0.0055 and 0.074 l/g. The results in Table 1 also shows that cow dung has better adsorption potential as compared to soil.

3.2 Biodegradation experiment

Figures 1 and 2 show the concentration profiles of CV in the reactors with 1 g/l and 3 g/l initial inoculum size respectively.

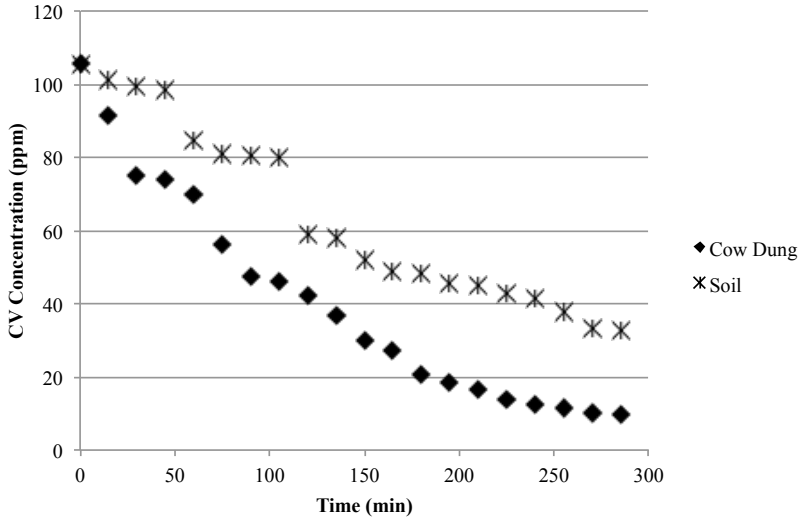

Figure 1: CV concentration profile in the reactors inoculated with 1 g/l Cow dung and 1 g/l Soil

Figure 1 shows that CV degradation was faster with cow dung as compared to soil when the initial inoculation size was 1 g/l. It further shows that about 92 % of CV was degraded within 300 minutes. However, only about 75% degradation of CV was achieved with soil. It was also observed that the CV concentration dropped by about 30 % and 20 % within the first 60 minutes for cow dung and soil respectively. On the other hand, as observed in Figure 2, increasing the inoculation size from 1 g/l to 3 g/l significantly improved the degradation rate of CV in the reactor with soil, achieving almost 93% degradation within 200 minutes. It can also be observed that increasing the inoculum size of both cow dung and soil virtually doubled the rate of CV degradation where 65% and 42% of the CV removal was achieved within 60 minutes respectively. It is important to observe that most studies reported in the literature were carried out using isolated bacteria (pure culture). Roy et al. (2018) reported 81.25 % degradation of CV after 72 hours using isolated bacteria. Ayed et al. (2009) also achieved up to 92% decolorization of CV within 3 hours using isolated bacteria. In another study, Parshetti et al. (2011) achieved 100 % decolorization of CV within 5 hours using isolated radiobacter. Indeed, this study has shown that mixed microbial cultures (not isolated) can achieve high CV degradation similar to the ones achieved with pure cultures.

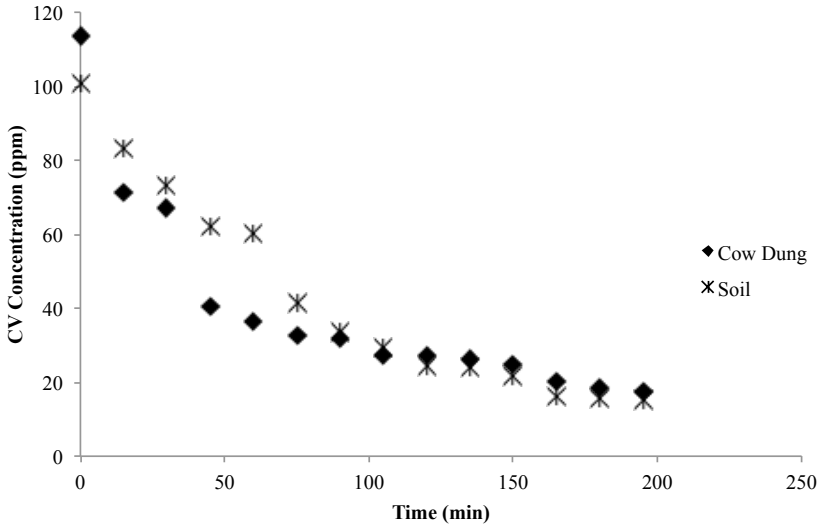

Figure 2: CV concentration profile over in the reactors inoculated with 3 g/l Cow dung and 3 g/l Soil.

3.3 Kinetic parameters of growth

The data generated from the batch operation of the reactors and the time profiles collected were used to estimate the maximum growth rate of the microorganisms growing on CV. Figures 3 and 4 show the estimated m_{max} and K_s values for cow dung and soil respectively. The m_{max} for cow dung was estimated to be 2.65 day^{-1}, which is about three times higher, compared to soil with 0.82 day^{-1}. In terms of K_s, soil was estimated to have higher value than cow dung (1.33 vs 0.45 g/l respectively). This is expected because higher degradation rate corresponds to higher m_{max} and lower K_s (Henze et al., 2008). Typical values of m_{max} reported in literature ranges from 0.22 – 13.2 day^{-1} and K_s vary from 0.005 – 2.93 g/l (Sollfrank & Gujer, 1991; Pala & Tokat, 2002; Al-Malack, 2006; Rajagopalu & Kanmani, 2008). In general, the values of m_{max} and K_s obtained in this study are within the range of the reported values for these parameters in the literature.

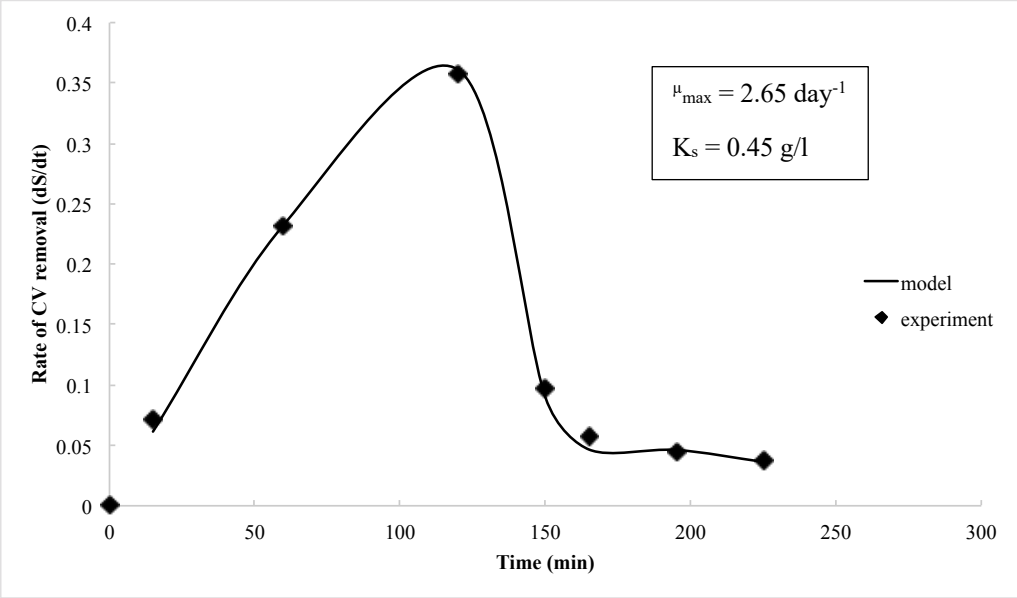

Figure 3: Rate of CV degradation over time. Comparison of experimental and model data for batch experiment with cow dung. The estimated m_{max} and K_s are reported on the graph

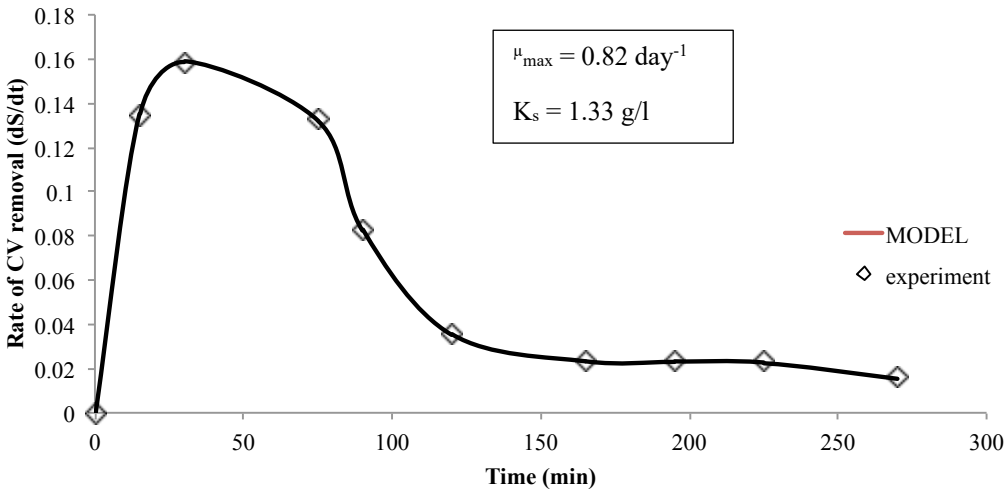

Figure 4: Rate of CV degradation over time. Comparison of experimental and model data for batch experiment with soil. The estimated m_{max} and K_s are reported on the graph

4 CONCLUSION

This study has shown that crystal violet can be degraded by mixed microbial cultures inoculated from cow dung and unacclimated soil in a batch reactor. The observed extent of CV degradation with cow dung was 90 – 92 % for cow dung and 75 – 93 % with soil. CV adsorption on cow dung and soil used as inoculum was measured and was found that adsorption was a negligible for CV removal in this case. This study shows that increasing the initial inoculum size increases the rate of degradation for both cow dung and soil. Kinetic parameters like maximum growth rate and half saturation constant were estimated to be 2.65 day^{-1} and 0.45 g/l for cow dung. The values for soil were found to be 0.82 day^{-1} and 1.33 g/l, and these are in agreement with the literature. The results obtained suggest that cow dung is a more efficient inoculum than soil in degrading CV.

ACKNOWLEDGEMENT

We acknowledge the Department of Chemical and Petroleum Engineering, Bayero University Kano for making this work possible by providing the lab space and technical support.

REFERENCES

Abdi, M., Balagabri, M., Karimi, H., Hossini, H., & Rastegar, S. O. (2020). Degradation of crystal violet (CV) from aqueous solutions using ozone, peroxone, electroperoxone, and electrolysis processes: a comparison study. *Applied Water Science*, *10*(7), 1-10.

Al-Malack, M. H. (2006). Determination of biokinetic coefficients of an immersed membrane bioreactor. *Journal of Membrane Science*, *271*(1-2), 47-58.

Al-Tohamy, R., Ali, S. S., Li, F., Okasha, K. M., Mahmoud, Y. A. G., Elsamahy, T., ... & Sun, J. (2022). A critical review on the treatment of dye-containing wastewater: Ecotoxicological and health concerns of textile dyes and possible remediation approaches for environmental safety. *Ecotoxicology and Environmental Safety*, *231*, 113160.

Asad, S., Amoozegar, M. A., Pourbabaee, A., Sarbolouki, M. N., & Dastgheib, S. M. M. (2007). Decolorization of textile azo dyes by newly isolated halophilic and halotolerant bacteria. *Bioresource technology*, *98*(11), 2082-2088.

Ayed, L., Cheriaa, J., Laadhari, N., Cheref, A., & Bakhrouf, A. (2009). Biodegradation of crystal violet by an isolated Bacillus sp. *Annals of microbiology*, *59*, 267-272.

Chen, C. C., Liao, H. J., Cheng, C. Y., Yen, C. Y., & Chung, Y. C. (2007). Biodegradation of crystal violet by Pseudomonas putida. *Biotechnology letters*, *29*, 391-396.

Dutta, S., & Bhattacharjee, J. (2022). A comparative study between physicochemical and biological methods for effective removal of textile dye from wastewater. In *Development in Wastewater Treatment Research and Processes* (pp. 1-21). Elsevier.

Fent, G., Hein, W. J., Moendel, M. J., & Kubiak, R. (2003). Fate of 14C-bisphenol A in soils. *Chemosphere*, *51*(8), 735-746.

Habeeb, O. A., Ramesh, K., Ali, G. A., Yunus, R. M., & Olalere, O. A. (2017). Kinetic, isotherm and equilibrium study of adsorption capacity of hydrogen sulfide-wastewater system using modified eggshells. *IIUM Engineering Journal*, *18*(1), 13-25.

Henze, M., van Loosdrecht, M. C., Ekama, G. A., & Brdjanovic, D. (Eds.). (2008). *Biological wastewater treatment*. IWA publishing.

Hussain, S., Khan, N., Gul, S., Khan, S., & Khan, H. (2020). Contamination of water resources by food dyes and its removal technologies. *Water Chemistry*, 1-14.

Insel, G., Karahan Gül, Ö., Orhon, D. E. R. I. N., Vanrolleghem, P. A., & Henze, M. (2002). Important limitations in the modeling of activated sludge: biased calibration of the hydrolysis process. *Water Science and Technology*, *45*(12), 23-36.

Kalyani, D. C., Telke, A. A., Dhanve, R. S., & Jadhav, J. P. (2009). Ecofriendly biodegradation and detoxification of Reactive Red 2 textile dye by newly isolated Pseudomonas sp. SUK1. *Journal of hazardous materials*, *163*(2-3), 735-742.

Kannan, N., & Sundaram, M. M. (2001). Kinetics and mechanism of removal of methylene blue by adsorption on various carbons—a comparative study. *Dyes and pigments*, *51*(1), 25-40.

Mani, S., & Bharagava, R. N. (2016). Exposure to crystal violet, its toxic, genotoxic and carcinogenic effects on environment and its degradation and detoxification for environmental safety. *Reviews of Environmental Contamination and Toxicology Volume 237*, 71-104.

Mondal, P. K., Ahmad, R., & Usmani, S. Q. (2010). Anaerobic biodegradation of triphenylmethane dyes in a hybrid UASFB reactor for wastewater remediation. *Biodegradation*, *21*, 1041-1047.

Mudhoo, A., Ramasamy, D. L., Bhatnagar, A., Usman, M., & Sillanpää, M. (2020). An analysis of the versatility and effectiveness of composts for sequestering heavy metal ions, dyes and xenobiotics from soils and aqueous milieus. *Ecotoxicology and Environmental Safety*, *197*, 110587.

Pala, A., & Tokat, E. (2002). Color removal from cotton textile industry wastewater in an activated sludge system with various additives. *Water research*, *36*(11), 2920-2925.

Parshetti, G. K., Parshetti, S. G., Telke, A. A., Kalyani, D. C., Doong, R. A., & Govindwar, S. P. (2011). Biodegradation of crystal violet by Agrobacterium radiobacter. *Journal of environmental sciences*, *23*(8), 1384-1393.

Patil, R., Zahid, M., Govindwar, S., Khandare, R., Vyavahare, G., Gurav, R., ... & Jadhav, J. (2022). Constructed wetland: a promising technology for the treatment of hazardous textile dyes and effluent. In *Development in Wastewater Treatment Research and Processes* (pp. 173-198). Elsevier.

Rajagopalu, V., & Kanmani, S. (2008). Activated sludge process treatability studies on combined tannery and domestic wastewaters. *Journal of Indian Water Works Association*, *40*, 143-149.

Roy, D. C., Biswas, S. K., Saha, A. K., Sikdar, B., Rahman, M., Roy, A. K., ... & Tang, S. S. (2018). Biodegradation of Crystal Violet dye by bacteria isolated from textile industry effluents. *PeerJ*, *6*, e5015.

Samsami, S., Mohamadizaniani, M., Sarrafzadeh, M. H., Rene, E. R., & Firoozbahr, M. (2020). Recent advances in the treatment of dye-containing wastewater from textile industries: Overview and perspectives. *Process safety and environmental protection*, *143*, 138-163.

Shah, M. P. (2013). Microbial degradation of textile dye (Remazol Black B) by Bacillus spp. ETL-2012. *Journal of Applied & Environmental Microbiology*, *1*(1), 6-11.

Singha, K., Pandit, P., Maity, S., & Sharma, S. R. (2021). Harmful environmental effects for textile chemical dyeing practice. In *Green Chemistry for Sustainable Textiles* (pp. 153-164). Woodhead Publishing.

Sollfrank, U., & Gujer, W. (1991). Characterisation of domestic wastewater for mathematical modelling of the activated sludge process. *Water Science and Technology*, *23*(4-6), 1057-1066.

Zhao J, Li Y, Zhang C, Zeng Q, Zhou Q. (2008). Sorption and degradation of bisphenol A by aerobic activated sludge. *J Hazard Mater* 155(1):305-11.

PAPER 28 – Mathematical Model for the Prediction of the Transport and Fate of Oil Spill

O. A. Aworanti[1], O. O. Agbede[1]*, S. O. Alagbe[1], S. E. Agarry[1], K. K. Salam[1], A. O. Popoola[3], D. A. Ogunsola[4], A. O. Alade[2], A. O. Ajani[1], A. O. Alabi[2], A. O. Adedapo[1]*, R. A. Adeniji[1]

[1]Biochemical and Bioenvironmental Engineering Research Group, (BBERG), Department of Chemical Engineering, Ladoke Akintola University of Technology, P. M. B. 4000, Ogbomoso, Nigeria.

[2]Bioenvironmental, Water and Engineering Research Group, (BWERG), Ladoke Akintola University of Technology, Ogbomoso, Nigeria

[3] Environmental Engineering Research Group, (EERG) Department of Chemical Engineering, Ladoke Akintola University of Technology, P. M. B. 4000, Ogbomoso, Nigeria.

[4]Department of Mechanical Engineering, Ladoke Akintola University of Technology, P. M. B. 4000, Ogbomoso, Nigeria

*Email: ooagbede@lautech.edu.ng; waledapo12@gmail.com

ABSTRACT

The mathematical model (MT) was used to identify and predict oil spill (OS) movement. The MT was developed based on the solution governing the partial differential equations of flow to simulate the processes of spreading and advection of oil slick on the surface and the oil droplet concentration distribution in the H_2O column, respectively. The oil movement (OM) was estimated by the vector sum of the wind drift, the surface current, spreading and diffusion. The transport of the oil phases in the water (H_2O) column was computed using the advection–diffusion equation. The variables determined were: oil spread rate on the H_2O surface, concentration of oil per area of spread in the H_2O column, concentration of oil per time in the H_2O column and spreading area per time. The kinetic models were developed to determine the rate of OM on the H_2O surface and column. The result obtained indicated that the concentration of the OS on H_2O surface per surface area of spread decreases as the surface area increases while the concentration of the OS decreases with time. The concentration of the OS per unit area at an area of 100m^2 reduced from 0.06432 to 0.01114 kg/ m^3 at 200 m^2.

KEYWORDS: Oil spill, Wind speed, Oil slick, Time, Water column

1. INTRODUCTION

Rapid economic growth has caused a significant increase in fossil fuel consumption in recent decades. World oil production increased to about 74 million barrels per day by January 2005, and was fairly constant until 2011 when it started to increase to 77.8 mb/d in 2014 (Murray, 2015). The world production of crude oil is about 3 billion tons per year and half of it is transported by sea (Goldemberg, 2006; Ibeawuchi, 2016). Oil is often spilled during its transportation through the sea in accidental discharge or through accident during road transportation with the aid of tankers. Most oil has a density less than water, which makes it to float in water. Oil tends to spread into a thin layer on the surface of water as sheen (Claireaux and Davoodi, 2010).

The discharged oil is of different varieties such as crude oil, refined petroleum products (such as gasoline or diesel fuel) or by-products and can be further categorized into light, medium and heavy oils. Very light oils such as jet fuel, and gasoline is highly volatile and evaporate quickly. Very light oils are one of the most acutely toxic oils and generally affect aquatic life (fish, invertebrates, and plants) that live in the upper water column. Light oils (diesel, light crude, heating oils) are moderately volatile and can leave a residue of up to one-third of the amount spilled after several days. Light oils leave a film on intertidal resources and have the potential to cause long-term contamination. Medium oils (most crude oils) and heavy oil can cause severe and long-term contamination to intertidal areas but medium oils are less likely to mix with water, while heavy oils (heavy crude, No. 6 fuel oil and Bunker C) do not readily mix with water and have far less evaporation and dilution potential (Okoye and Okunrobo, 2014). Heavy oils have severe impacts on waterfowl and fur-bearing marine mammals. These oils tend to weather slowly. Clean-up of heavy oil is difficult and usually a long-term process. Very heavy oils can float, mix, sink, or hang in the water. These oils can become oil drops and mix in the water, accumulate at the bottom,

mix with sediment and then sink. (Anderson et al., 1993). When liquid oil is spilled on the sea surface, it spreads over the surface of the water and forms a thin film called, oil slick (Okoye and Okunrobo, 2014). The movement of the slick is governed by the advection and turbulent diffusion due to current and wind action (Koch and Bavumiragira, 2019).

When an oil spill occurs on water, the three (3) major step of controlling and managing it is as follows; mechanical containment, recovery and clean up. When an oil spill happens on water, it is critical to contain the spill as quickly as possible to minimize danger and potential damage to persons, property, and natural resources. Containment equipment is used to restrict the spread of oil and to allow for its recovery, removal, or dispersal. The most common types of equipment used to control the spread of oil and recover oil from the surface are floating barriers, called booms, skimmers sorbents, netting systems, sorbent booms, improvised booms and barriers, bubble barriers and chemical barriers, while the clean-up techniques are bioremediation and dispersants. Bioremediation involves the use of microorganisms or biological agents to break down or remove oil. Selection of the most appropriate for a specific oil spill situation will depend on the particular conditions. Once an oil spill has been contained, efforts to remove the oil from the water can begin. After a large oil spill, the oil slick is sometimes treated with a dispersant. Dispersants emulsify petroleum by reducing the interfacial tension between petroleum and water. The small droplets that are formed are dispersed into a water column to a depth of several meters, preventing wind-induced drift of the oil slick. It is claimed that treatment by a dispersant enhances the biodegradation of petroleum. Oil spillage affects both animals and human staying close to the shore or those whose livelihood depends on the surrounding water and ultimately trigger health-associated problems. For effective management of oil spread on the surface of the water, laboratory investigations have been conducted to study the variables that affect the spread of oil with some submissions that makes it possible to manage it. Extending laboratory work by using them as a basis for the prediction of oil spills will assist in monitoring and taking proactive decisions to minimize the effect of spillage in the environment.

2. METHODOLOGY

2.1 Model Development for Spreading and Advection of oil spills

In the majority of cases, a mathematical model is the only available tool for rapid computation of the spilled oil fate, and for simulation of the various clean-up operations. Two major processes transport oil spilled on water: spreading and advection. For small spills (<100 barrels), the spreading process is complete within the first hour of the release. Winds, currents, and large-scale turbulence (mixing) are advection mechanisms that can transport oil at great distances.

In general, the oil movement can be estimated as the vector sum of the wind drift (using 3% of the wind speed), the surface current, spreading and larger-scale turbulence (diffusion).

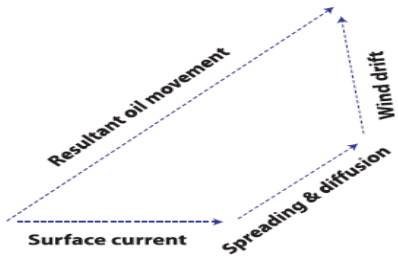

Fig 2: Oil Movement

The governing equation for oil spread on the water in radial coordinate (r), is derived by taking an elemental volume of oil.

(Rate of mass input) – (Rate of mass Output) + (Rate of production from Source) = (Rate of production from source)

2.1.1 Convective Movement

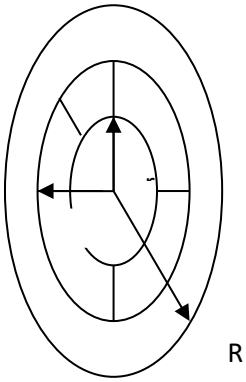

Fig 3: Convective Radial Movement

Rate of Mass Input of oil spill $= velocity \times area \times concentration$

The velocity of water current in the radial direction $= U_{A0}$; Area of circle (at r) $= 4\pi r^2 \mid_r$; Concentration (at r) $= C_{A0} \mid_r$

$\therefore$ Rate of Mass Input $= U_{A0}.4\pi r^2 C_{A0} \mid_r$ (1)

Rate of mass output of the spill $= velocity \times area \times concentration$; Velocity of water current in radial direction $= U_{A1}$; Area of circle (at r+dr) $= 4\pi r^2 \mid_{r+dr}$; Concentration (at r+dr) $= C_{A1} \mid_{r+dr}$;

$\therefore$ Rate of Mass Output $= U_{A1}.4\pi r^2 C_{A1} \mid_{r+dr}$ (2)

2.1.2 Diffusive Movement

Rate of Mass Input = area x flux; Area or circle $= 4\pi r^2$; Flux $= N_A = -D\frac{\partial c}{\partial r}$

Rate of mass input $= -D\frac{\partial c}{\partial r}\mid_r \; 4\pi r^2 \mid_r = -4\pi r^2 D\frac{\partial c}{\partial r}\mid_r$ (3)

Rate of mass output $= -D\frac{\partial c}{\partial r}\mid_{r+dr} .4\pi r^2 \mid_{r+dr} = -4\pi r^2 D\frac{\partial c}{\partial r}\mid_{r+dr}$ (4)

Rate of Mass Input for Convection and Diffusion

Rate of mass input $= U_{A0}.4\pi r^2 C_{A0} \mid_r \; -4\pi r^2 D\frac{\partial c}{\partial r}\mid_r$ (5)

Rate of Mass Output for Convection and Diffusion

Rate of mass output $= U_{A1}.4\pi r^2 C_{A1} \mid_{r+dr} - 4\pi r^2 D\frac{\partial c}{\partial r}\mid_{r+dr}$ (6)

Rate of Production from source

Rate of production $= R_A \times 4\pi r^2 dr$; Source term $= R_A$ (7)

Rate of Accumulation

Rate of Accumulation = Volume x rate of concentration $= 4\pi r^2 dr \times \frac{\partial c}{\partial t}$ (8)

Combining equations 5, 6, 7, 8

$$\left[U_{A0}.4\pi r^2 C_{A0}\mid_r -4\pi r^2 D\frac{\partial c}{\partial r}\mid_r\right]-\left[U_{A1}.4\pi r^2 C_{A1}\mid_{r+dr} -4\pi r^2 D\frac{\partial c}{\partial r}\mid_{r+dr}\right]$$

$$+R_A\times 4\pi r^2 dr = 4\pi r^2 dr\times\frac{\partial c}{\partial t} \quad (9)$$

$$\frac{\left[U_{A0}C_{A0}\mid_r -D\frac{\partial c}{\partial r}\mid_r\right]}{\partial r}-\frac{\left[U_{A1}C_{A1}\mid_{r+dr} -D\frac{\partial c}{\partial r}\mid_{r+dr}\right]}{\partial r}+R_A=\frac{\partial c}{\partial t} \quad (10)$$

$\lim dr \to 0$

$$\frac{\partial c}{\partial t}=\frac{d}{dr}\left[U_A C_A - D\frac{\partial c}{\partial r}\right]+R_A \quad (11)$$

Similarly;

$$\frac{\partial h}{\partial t}=\frac{d}{dr}\left[Uh_A - D_A\frac{\partial h}{\partial r}\right]+R \quad (12)$$

$$D_A = gh^2(\rho-\rho_0)\frac{\rho_0}{\rho f} \quad (13)$$

Boundary Conditions

$\frac{\partial C_A}{\partial r}=0$ at $r=0$ at the centre ; $\frac{\partial C_A}{\partial r}=0$ at $r=R$

2.2 Numerical Solution

2.2.1 Computational Techniques

Using the Governing Equation 11

$$\frac{\partial c}{\partial t}=\frac{d}{dr}\left[U_A C_A - D\frac{\partial c}{\partial r}\right]+R_A \quad ; \quad \frac{\partial c}{\partial t}=U_A\frac{\partial C_A}{\partial r}-D\frac{\partial^2 c}{\partial r^2}+R_A \quad (14)$$

In the presence of strong currents, the mass transport phenomenon becomes advection-dominant, which increases the requirement for the accuracy of a numerical scheme to be applied for the integration of the transports Equation 14. To decrease the numerical diffusion (approximation error) below the physical one, the accuracy of approximation of the advection terms. Development of a high-order numerical scheme for advection terms can be illustrated as follows:

Assuming the diffusion term is Zero

$R_A = 0$ (Since the source is instantaneous)

$$\frac{\partial c}{\partial t} = U_A \frac{\partial C_A}{\partial r} \tag{15}$$

2.2.2 Explicit Method of Finite Difference

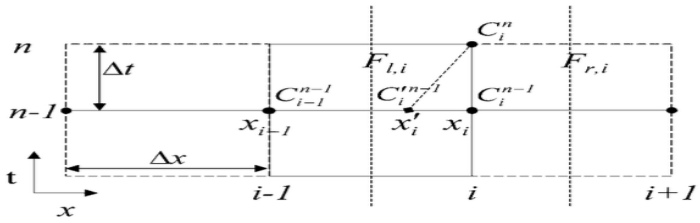

Fig 4: Subdivision of the r-t domain into intervals of Δr and Δt for finite–difference representation of the one-dimensional, time-dependent fluid advection equation.

Then, the concentration C[r, t] at a location r and a time t is denoted by the symbol C_i^n

$$C[r,t] = C\left[i\Delta r, n\Delta t\right] = C_i^n \tag{16}$$

Various derivatives appearing in the above fluid convection equation are approximated as above.

The first derivative of concentration with respect to the time variable (t) at a position (iΔr) and at a time (nΔt) is represented by;

$$\frac{\partial c}{\partial t}\Big|_{i,n} = \frac{C_i^{n+1} - C_i^n}{\Delta t} \tag{17}$$

The first derivative of concentration with respect to the radius (r) at a position (nΔx) and at a time (iΔt) is represented by;

$$\frac{\partial c_A}{\partial r}\Big|_{i,n} = \frac{C_n^{i+1} - C_n^i}{\Delta r} \tag{18}$$

Substituting equations 3.18 and 3.17 into equation 3.15

The finite difference form of the time-dependent fluid-convection equations becomes:

$$\frac{C_i^{n+1} - C_i^n}{\Delta t} = U_A \frac{C_n^{i+1} - C_n^i}{\Delta r} \tag{19}$$

$$C_i^{n+1} - C_i^n = U_A \frac{\Delta t}{\Delta r} C_n^{i+1} - C_n^i \quad ; \quad \therefore \alpha = U_A \frac{\Delta t}{\Delta r} = \text{Courant Number} \tag{20}$$

$$C_i^{n+1} - C_i^n = \alpha\left[C_n^{i+1} - C_n^i\right] \quad ; \quad C_i^{n+1} = C_i^n + \alpha\left[C_n^{i+1} - C_n^i\right] \tag{21}$$

2.3 Computational Technique

2.3.1 The oil spreading Law

Gravity, inertia, viscosity and surface tension forces cause the horizontal expansion of an oil slick (i.e. spreading).

Oil spreading Radius (OSR) = Gravity inertia + Viscosity + Surface tension force. Using experimental evidence, Lehr *et al*.(2003) suggested that an oil slick spreads as an ellipse according to the following:

$$A_e = \frac{\pi}{4} \times R_{\max} \times R\min \tag{22}$$

$$R_{\min} = 1.7\left[\frac{\rho - \rho_0}{\rho}\right]^{1/3} V^{1/3} t^{1/4} \tag{23}$$

$$R_{\max} = R_{\min} + 0.03U^{4/3} t^{3/4} \tag{24}$$

Using the modified Fay-type spreading equation considering the influence of wind

$$A = 2290\left[\frac{\Delta\rho}{\rho_0}\right]^{2/3} V^{2/3} + 40\left[\frac{\Delta\rho}{\rho_0} VU_W\right]^{2/3} t \quad ; \Delta\rho = \rho - \rho_0 \tag{25}$$

Simulation Data (Lehr *et al.*, 2003)

The following data were used to simulate the model: $V = 600m^3$, $U_w = 10m/s, 20m/s$, $\rho = 1000kg/m^3$, $\rho_0 = 840kg/m^3$, $E = 2m/s^2$, $u = 0.02m/s$, $Z_m = 1.5m$, $f = 0.02kg/m^3 s$ and $C_{\min} = 1\times10^{-8}$

3. RESULTS AND DISCUSSION

3.1 Simulation of area of spreading with time using Matlab

It was observed from the graph (Figure 5&6) that rate of spread of the oil spill increases with time covering more areas. The rate of spreading was greatly influenced by the meteorological condition of the water body. At a wind speed of 10 m/s, the oil spread to an area of 40 m^2 within 300 seconds. At a wind speed of 20 m/s, the rate of spreading is almost double.

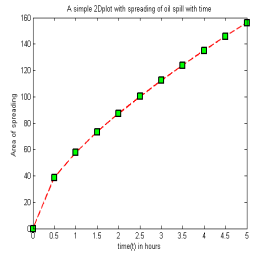

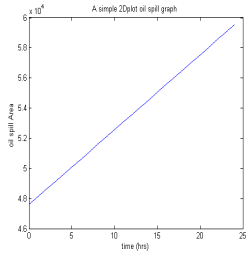

Fig 5: Plot of Area of spill against time **Fig 6: 2D Plot of oil spill Area against Time**

3.2 Simulation of volumetric concentration of oil per area of spread

The graph (Figure 7) shows the volumetric concentration of oil per area of spread. it can be deduced that the concentration of the oil spill on the water surface per surface area of spread decreases as the area increases. The concentration of the spilled oil per unit area at an area of 100m^2 reduced from 0.06432 to 0.01114 kg/ m^3 at 200 m^2. This is due to the effect of other weathering processes like evaporation, emulsification, dispersion and other oil fate processes that occur when the oil enters the water column.

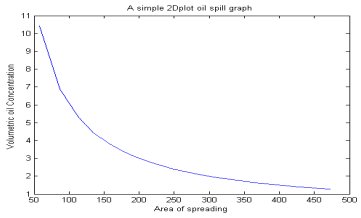

Fig 7: 2D Plot of Volumetric oil concentration against the Area of Spreading

3.3 Simulation of volumetric concentration of oil spill with time

From Figures 8a and b, it was observed that the concentration of oil spills decreases with time. This is due to the fact that as the oil spread with time, the surface area of the oil increases thus leading to faster evaporation of the light oil fraction and the entrainment of the rest component into the water column. Comparing the result of the simulated data of the oil spill, it was observed that the modified oil spreading model gave a better simulation of the spill situation with the inclusion of the wind speed.

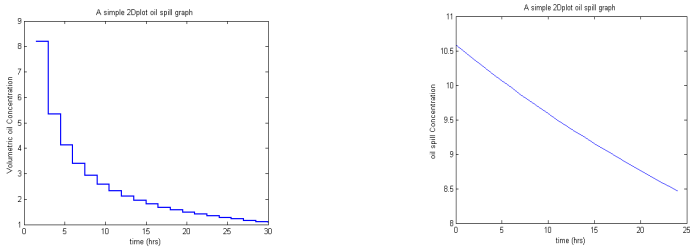

(a) **(b)**

Fig 8: 2D Plot of Volumetric oil (a) and oil spill concentration (b) against time

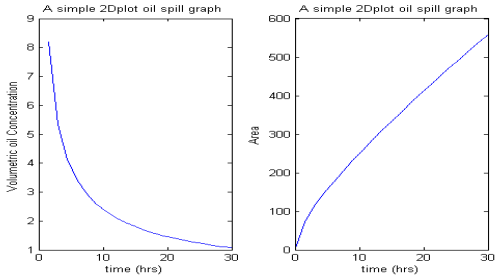

Fig 9: 2D Plot of Volumetric oil concentration and Area of Spreading with time

4. CONCLUSION

An oil spreading model has been developed to predict the movement of surface oil slicks on water bodies. Using this model, the area of spreading and concentration of the oil spill at different time intervals can be solved. With the required simulation data input into the model, the simulation results show the process of oil slick movement on the water surface**.** This model would help to develop proper contingency plans as well as assist in deciding the best containment and recovery approach in case of a spill. Though the model can predict the concentration of oil spill and the area of spread at different time intervals, the followings are recommended:

- The meteorological data of water bodies should be readily available for immediate simulation in case of an oil spill
- Different oil spill models should be tested to discover the best that would simulate the accurate condition of the oil spill

- Environmental consequences of the combating techniques application have to be carefully calculated before the actual usage.

REFERENCES

Anderson, E.L., E. Howlett, K. Jayko, V. Kolluru, M. Reed, and Spaulding, M. (1993). The worldwide oil spill model (WOSM): an overview in Proceedings of the 16th Arctic and Marine Oil Spill Program, Technical Seminar. Ottawa, Ontario: Environment Canada. 627–646.

Bird, R. B., Stewart, E. W. Warren, Lightfoot, N. E. (2006). Transport Phenomena, Wiley, India. p.78

Kuch, G.S. and Bavumiragira, J.P. (2019). Impacts of crude oil exploration and production on environment and its implications on human health: South Sudan Review. International Journal of Scientific and Research Publications, 9 (4), 247-256.

Lehr and Smith (2003). The spread of oil slicks on a calm sea, in oil on the sea. New York: McGraw-Hill, p.110-120.

NOAA (2002). Environmental Sensitivity Index Guidelines, version 3.0. NOAA Technical Memorandum NOS OR&R 11. Seattle: Hazardous Response and Assessment Division, National Oceanic and Atmospheric Administration, 129p.

Nwilo and Badejo (2005). Causes of oil spills in Nigeria, African News 13: 14.

Okoye, C.O. and Okunrobo, L.A. (2014). Impact of oil spill on land and water and its health implications in Odugboro community, Sagamu, Ogun State, Nigeria. Available at http://www.scenrp.com/World%20Journal%20of%20Environmental%20Sciences%20&%20Engineering/WJESE_Vol.%201,%20No.%201,%20January%202014/IMPACT%20OF%20OIL.pdf> assessed on 17th June, 2016.

Prince R., (1993).Petroleum Spill Bioremediation in Marine Environments. Critical Rev. Micobiol. 19(4): 217-242.

Rossouw, M., (1998). Oil Spill Simulation: Reducing the Impact. START/IOC/LOICZ Workshop on Climate Change and Coastal Process in Cotonou, Benin, West

Wikipedia, (2008). Oil spill incidents. http://www.wikipedia.com.

PAPER 29 – ACHIEVING QUALITY OF EXPERIENCE IN TELECOMMUNICATION SERVICE

Abdulrasheed Umar[1] , C. O. Alenoghena[2], S. Zubair[2]

Telecommunication Engineering Department, Federal University of Technology Minna, Nigeria
umar.pg915182@st.futminna.edu.ng
carol@futminna.edu.ng
zubairman@futminna.edu.ng

ABSTRACT

This paper presents a perspective view into network performance achievement via quality of experience (QoE) improvement of telecommunication service in Nigeria. Monitoring the quality of experience undergone by mobile network operators (MNO) has become paramount for policy makers who need to ensure high quality levels to limit customer annoyance due to quality dissatisfaction. The components of QoE and mechanisms of analyzing and evaluating them are discussed. The paper also identifies the important key performance indicators (KPIs) for QoE achievement. Telecom operators have recently faced the need for a crucial change from technical quality requirements to user experience guarantees. An abstract framework for achieving end-to-end QoE provisioning is proposed and described in detail in terms of its design, its constituents and their interactions, as well as the key implementation challenges. An evaluation study serves as a proof of concept for this framework, and demonstrates the potential benefits of implementing such a quality management scheme on top of current or future generations of mobile cellular networks. The paper is concluded with recommendations on how to achieve and improve the QoE in telecommunication service of the Nigeria.

Keywords *– Quality of Experience (QoE), key performance indicator (KPI), Mobile network operator (MNO).*

1.0 INTRODUCTION

Over 75% of all mobile network traffic will be exhausted and generated by smartphones by 2019(Cisco online, 2020). As such there is an ever-growing interest from mobile network operators to better understand and assess the performance of their networks as viewed by end-users directly. The wide usage of internet based services has been traced down to the emergence of high-speed mobile network situated on Universal Mobile Telecommunication Systems (UMTS), Long Term Evolution (LTE) and other telecommunications standards. Equally, the availability of higher data transmission speed (throughput) enables mobile internet users to go beyond internet surfing, by enabling services such as file transfer, file download, video streaming and voice over internet protocol (VOIP). However, the Mobile network operators (MNOs) tend to limit the existing data-rate achievable by the users because of the high cost involved in acquiring spectrum (Tsiaras, et al, 2011). At the same time, the increase in the rate of subscribers have enhanced competitive advantage and provision of affordable services, thereby imposing additional challenge on the MNOs in providing a satisfactory level of service performance to the mobile internet users (Ibarrola et al, 2011), (Shaikh et al, 2010). Specifically, mobile networks are vulnerable to channel availability (such as decreased channel availability) that dynamically changes overtime because of the local congestion, which often result into compromising the user session (Goleva et al, 2012). The stated instances, increase in limited data rate and local congestion can seriously have impact on network telecommunication service experienced by users. Quality of experience is used in achieving evaluation of telecommunication service because it gives customers and service providers a comprehensive understanding of how users experience the service. Quality of experience metrics allow service providers to identify areas that require improvement and take action to ensure the highest levels of customer satisfaction. Quality of experience metrics also provides valuable insights into customer trends, behaviors, and preferences that can be used to optimize services and improve the customer experience. Quality of service (QoS) focuses on technical performance metrics such as network latency and packet loss, while quality of experience (QoE) focuses on the subjective experience of customers such as how satisfied they are with the service and how easy it was to use. QoS measures the technical performance of the service, while QoE measures the customer experience of the service. QoS is typically measured by service providers, while QoE is usually measured by customers. Both customers and service providers benefit from QoE evaluation of telecommunication service. Customers benefit from improved service experiences, as service providers use QoE data to identify areas for improvement and optimize services. Service providers benefit from greater customer satisfaction, as well as insights into customer trends and behaviors that can be used to target campaigns and services more effectively. In this paper we look at ways to achieve QoE in telecommunication networks.

1.1 QoE Measurement for Analysis on Telecommunications Network

Barakovic et al, (2013) defined QoE "as the degree of delight or annoyance of the user of an application or service. It results from the fulfillment of his or her expectations with respect to the utility and / or enjoyment of the application or service in the light of the user's personality and current state." QoE definition connects user perception, expectations, experience of the service application and network operators. User perceived QoE is often affected by varieties of influence factors. QoE influence factors are the characteristics of the service provided by the MNOs such as system (throughput, delay, jitter, loss, and security), human (gender, age, background, and education) and context (location, movement, time of the day costs and subscription type) influence factors (LeCallet et al, 2012). Quantified QoE influence factors allow the estimations of QoE as perceived by the users (Barakovic et al, 2013). The most studied QoE influence factor is the system factors constituting the Quality of service (QoS) parameters (throughput, loss, bandwidth, delay, and jitter). Because some parameters like bandwidth can be adjusted to increase the end user's satisfaction (Alreshoodi et al, 2013). While there exist many studies that examined throughput measurement for wireless applications for web traffic (Rugedj et al, 2014), (Singh et al, 2013), few studies used user experience measurements obtained from the mobile network traffic, as most studies focus on collecting basic network information and performance data in a laboratory experiments through the desktop applications. Measurements obtained from the desktop in laboratory experiment are less useful because of the fixed contextual factor. Therefore, it is imperative to examine specific service-related throughput in mobile network traffic in relation to expectations, mobility (location and time), and different services like file transfer protocol (FTP) and Hypertext Transfer Protocol (HTTP). It is therefore imperative to take QoE measurement from the mobile network traffic to understand the experience of the user from both the network and user's perspectives. Although crowd sourced data could also be used in measuring the extent of a user's experience as to services provided by MNOs. The data gotten from the users are then collated, analyzed and interpreted in order to get a better first-hand comparative report as to MNPs service and how well to suggest improvement to services rendered.

There are mainly two types of perceived QoE measurements, - subjective and objective measurements. The subjective measurements are based on customer perception of the services delivered to the customers, while objective measurement is the means of estimating subjective quality solely from the measurement obtained from the network traffic (Barakovic et al, 2013). The subjective measurement is the standard and most reliable way of assessing the QoE. Subjective measurement has been used in several studies to analyze the mean opinion score (MOS) in the form of numeric value ranging from 1 to 5 (from poor to excellent) (Singh et al, 2013). The limitation of subjective measurement is time consuming, expensive, lacks repeatability and not effective in real-time (Alreshoodi et al, 2013). In contrast to the subjective measurement like a survey measurement, mostly conducted in a laboratory experiment, objective measurement aims at predicting the subjective assessment methods based on the estimated MOS. Objective measurement requires a meaningful mapping function into the predicted subjective measurement (Shaikh et al, 2010). Objective measurement is a preferred measurement tool for analyzing network service because of its ability to be implemented and be embedded into the network using software applications and the capability to allow researchers model the relationship between the expectation and perceived influence factors to determine the MOS (i.e. perceived QoE) (Apajalahti et al, 2018).

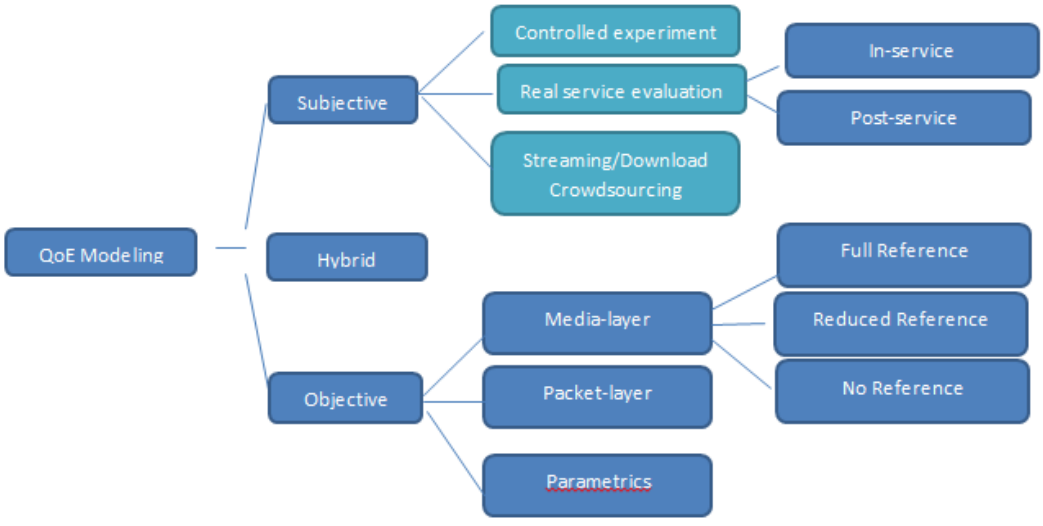

FIGURE 1: Classification of QoE modeling approaches (Dimitris *et al,* 2017)

1.2 KPI/QoE Metrics in Telecommunication Network

An increasing number of new network based application are entering the market and each application causes difference in performance objective. Application often evaluates the success of their objectives using KPI and QoE metrics. KPI and QoE metrics help application in telecommunications network to determine how effectively the application is achieving its performance objectives. The network as a driving force of such application plays a vital role in the end-to-end performance of application. Therefore, the performance of application highly depends on how well the network understands and serves the application requirement. The table below shows the performance metrics of the select KPI for QoE as against other methods of QoS. Some characteristic parameters were taken into account to better narrow down the test and also evaluate results.

A possible framework for achieving end-to-end QoE provisioning in telecommunication service would include the following elements:

1. Quality of Service (QoS): to ensure that the data is delivered with the required quality, the network needs to have adequate capacity and be able to manage traffic in an efficient manner. This would include ensuring adequate bandwidth and latency, as well as ensuring that traffic is properly routed and prioritized.
2. End-to-end Monitoring: to ensure that QoE is met, the network needs to be monitored for any performance issues or disruptions. This could be done through the use of monitoring tools such as packet sniffers, network probes, and application performance monitors.
3. Service Level Agreements (SLAs): to ensure that the QoE is maintained, SLAs should be established between the service provider and its customers. These SLAs should specify the expected performance levels, as well as any penalties or rewards that will be imposed if these performance levels are not met.
4. Automated Fault Detection and Resolution: to ensure that any performance issues are identified and addressed quickly, the network should have automated tools for fault detection and resolution. These tools should be able to detect any performance issues, alert the service provider, and then automatically take corrective action to resolve the problem.
5. Customer Feedback: finally, customer feedback is essential for ensuring that the QoE is being maintained. This can be done through surveys, feedback forms, and other customer feedback mechanisms. This feedback can then be used to further refine and improve the service.

Table 1: QoE KPI evaluation matrices as against others

Performance Characteristics	**Drive Test**	**Using Data Centers**	**Crowdsourced Applications**
Required equipment	Special test phones, RF scanners	Special hardware and additional server	Smart phones
Cost availability	Expensive and hardware are not readily available	Very expensive and requires permission	App is free
Target users	Team of network specialist	Usually used by academicians	Anyone that installs the application
Measurement level	Radio level measurement, service level measurements	Radio level measurement, service level measurements	Radio level measurement, service level measurements and QoE (Quality of Experience)
Measurement Size	Measurements are only during the test drive	Measurements are only for a certain period	Measurements are continuous
Position accuracy	GPS, current cell	Current cell	GPS, current cell
Traffic Overhead	Little or no overhead traffic	High overhead	No overhead traffic
Requires human intervention	Trained users required (active)	Yes	No (passive)
Scalability	Reduced, more drive test requires more specialized equipment	Difficult, technology dependent	Handles all sizes of traffic/ measurements

2.0 PROBLEM STATEMENT

The problem of achieving quality of experience in telecommunication networks is a significant challenge faced by network operators and service providers. Despite advances in technology, network congestion, latency, and other factors can negatively impact the perceived quality of service by the user. This can lead to dissatisfaction, increased churn, and reduced revenue for service providers. Additionally, ensuring consistent quality of experience across different devices, applications, and locations presents a complex challenge. The problem requires careful consideration of factors such as network architecture, resource allocation, and user behavior to ensure that users receive high-quality service and have a positive experience with the network (Calle et al, 2015)

3.0 RELATED WORKS

A lot of study has been conducted on the subject of QoE in relation to telecommunication service, according to Timothy et al (2017) on service quality and customer satisfaction in Nigerian mobile telephony, The Nigerian Telecommunication industry has developed to be very competitive, as different Telecommunication companies jostle for the attention of subscribers. One of the key challenges confronting these Telecommunication companies is how they manage their service quality, which holds a great deal to customer satisfaction. Service quality and customer satisfaction are very essential in maintaining customer loyalty. Quality of Experience (QoE) in emerging mobile social network by Mianxiong et al (2015), The paper comprehensively surveys recent advances in MSNs and QoE issues addressed in various types of applications networks. From the lessons learned from the literature, it was found that most of the research proposals are dedicated to specific applications, network models and service scenarios. Regarding QoE monitoring studies in telecommunications network and mobile devices, there is an assorted list of tools to measure network performance in order to achieve a satisfactory QoE; some examples are MobiPerf (Xu et al, 2017), Mobilyzer (Kousias et al, 2017), Netalyzer (Apajalahti et al, 2018), in (Akpabio et al, 2020), (Fida et al, 2018) authors introduced YomoApp, an app to categorically monitor YouTube QoE related characteristics in mobile phones. QoE Doctor measures mobile application QoE using active measurement at both the application and network layers. While majority of the aforementioned only focused on QoE relevant objectives metrics such as rebuffing, page load time and interaction latencies, they lack a direct reference to user feedback e.g. mean opinion score (MOS). Where feedback is taken directly from real users and collects network measurements to provide a holistic perspective to the problem of QoE monitoring in network telecommunication and mobile network. This paper builds on past works on QoE achievement for telecommunications network in smartphones.

4.0 CONCLUSION

In this paper we have addressed QoE assessment, evaluation and achievement in network telecommunication. Also looking at how user end feedback can be exploited to achieve a desired and satisfactory QoE in mobile telecommunication network. All-in-all, the assessment, evaluation and implementation of QoE to better understand network telecommunication will provide future availability for other cellular users to have access to better telecommunications network provided by mobile network operators. A frame work to achieve QoE in telecommunications network was also discussed and looked into to enable achieving a desired QoE for better network.

ACKNOWLEDGEMENT

Firstly, I will like to praise the almighty Allah, Alhamdulillah for His mercy and wisdom, I will like to acknowledge Dr. (Mrs) C. O. Alenoghena for her immense contribution and guidance in seeing I achieve this work, her dedication is second to none, her patience and nurturing really made this work possible and for that I appreciate her. May God almighty bless you ma.

REFERENCES

A. Singh, A. Mahmoud, A. Koensgen, X. Li, C. Göerg, M. Kus, M. Kayralci and J. Grigutsch, Enhancing Quality of Experience (QoE) Assessment Models for Web Traffic," in 5th International Conference, Cork, Ireland, 2013

Apajalahti K, Walelgne EA, Manner J, Hyvönen E. Correlation-based feature mapping of crowdsourced LTE data. In: Proceedings of IEEE 29th Annual International Symposium on Personal, Indoor and Mobile Radio Communications; Bologna, Italy; 2018. pp. 1-7.

Akpabio, J. (2020). Quality of Experience and User Experiences in Telecommunication Services: A Study of Mobile Network Users in Nigeria. International Journal of Engineering and Technology (UAE)

Bartlett, J. (2021). 10 Best Practices for Improving Your Telecommunications Quality of Experience. Retrievedfrom https://www.ringcentral.com/updates/telecommunications-quality-of-experience.html

Cisco,"cisco visual networking index: global mobile data traffic forecast update, 2015-2020 white paper," 2015 [online]

C. Tsiaras, A. Sehgal, S. Seeber, D. Dönni, B. Stiller, J. Schönwälder and G. D. Rodosek, "Towards evaluating type of service related Quality-of-Experience on mobile networks," in 7th IFIP on Wireless and Mobile Networking Conference (WMNC), 2014

Dimitris. T, Nikos. P, Lazaros, M and Eirini. L, A survey on parametric QoE estimation for popular services. Article in Journal of Network and Computer Applications · January 2017

E. Ibarrola, J. Xiao, F. Liberal and A. Ferro, "Internet QoS Regulation in future networks: A user-centric approach," in ITU Kaleidoscope Conference, 2011

Fida M, Marina MK. Impact of device diversity on crowdsourced mobile coverage maps. In: Proceedings of 14th International Conference on Network and Service Management; Rome, Italy; 2018. pp. 348-352.

J. Shaikh, M. Fiedler and D. Collange, "Quality of Experience from user and network perspectives," Ann. Telecommun DOI: 10.1007/s12243-009-0142-x, Springer, pp. 47-57, 2010.

Kousias K, Midoglu C, Alay O, Lutu A, Argyriou A. The same, only different: contrasting mobile operator behavior from crowdsourced dataset. In: Proceedings of IEEE 28th Annual International Symposium on Personal, Indoor, and Mobile Radio Communications; Montreal, Canada; 2017. pp. 1-6.

M. A. Calle and J. G. Restrepo, "Quality of experience in telecommunication networks," in IEEE Latin America Transactions, vol. 13, no. 4, pp. 1024-1030, April 2015, doi: 10.1109/TLA.2015.7104132.

M. Rugelj, M. Volk, U. Sedlar, J. Sterle and A. Kos, "A novel user satisfaction prediction model for future network provisioning," Telecommunication system, 56 doi: 10.1007/s11235-013-9853-4 Springer, pp. 417-425, 2014.

M. Alreshoodi and J. Woods, "Survey on QOE\QOS corelation models for multimedia services," International Journal of Distributed and Parallel Systems (IJDPS) 4(3), pp. 53-72, 2013.

Mancuso V, Quirós MP, Midoglu C, Moulay M, Comite V et al. Results from running an experiment as a service platform for mobile broadband networks in Europe. Computer Communications 2019; 133: 89-101. doi: 10.1016/j.comcom.2018.09.004

Oluwole, T.O., & Adejumo, O.O. (2018). Quality of experience (QOE) of mobile and fixed broadband services in Nigeria. International Journal of Telecommunications and Network Security, 2(1), 6-12.

Mancuso V, Quirós MP, Midoglu C, Moulay M, Comite V et al. Results from running an experiment as a service platform for mobile broadband networks in Europe. Computer Communications 2019; 133: 89-101. doi: 10.1016/j.comcom.2018.09.004

P. Le Callet, S. Möller and A. Perkis, "Qualinet White Paper on Definitions of Quality of Experience Output version of the Dagstuhl seminar 12181," 2 June 2012. [Online]. Available: http://www.qualinet.eu/images/stories/whitepaper_v1.1_dagstuhl_output_co rrected.pdf.

R. Goleva, D. Atamin, S. Mirtchev, D. Dimitrova and L. Grigorova, "Traffic Sources Measurement and Analysis in UMTS," in the proceedings of the 1st ACM workshop on High Performance Mobile Opportunistic System, Paphos, Cyprus, 2012, pp 29-32.

S. Barakovic and L. Skorin-Kapov, "Survey and challenges of QoE management issues in wireless networks," Journal of conputer networks and communications, pp. 1-28, 2013

T. H. Falk and W.-Y. Chan, "Single-Ended Speech Quality Measurement Using Machine Learning Methods," IEEE Transactions on Audio, Speech, and Language Processing, 14(6), pp. 1935-1947, 2006.

Xu F, Li Y, Wang H, Zhang P, Jin D. Understanding mobile traffic patterns of large scale cellular towers in urban environment. IEEE/ACM Transactions on Networking (TON) 2017; 25 (2): 1147-1161. doi: 10.1109/TNET.2016.2623950

PAPER 31 – DEVELOPMENT OF TWO-LEVEL CONTROL TECHNIQUES FOR LOAD FREQUENCY CONTROL IN ISLANDED TWO-AREA MULTISOURCE MICROGRID

N. Abdulazeez[1], Musa Umar[2], I. N. Yakubu[2]

[1]Department of Electrical Engineering of Ahmadu Bello University, Zaria – Nigeria
[2]Department of Electrical and Electronics Engineering Technology, Federal Polytechnic Kaura Namoda
Email: abduazeeznurudeen224@gmail.com

ABSTRACT
Microgrid (MG) development has contributed to widespread connections among distributed generation (DG) units. In this paper, a two-area MG system comprise of different micro sources was developed. The dynamic nature of various renewable energy resources (RESs) wind power fluctuations, and changes in applied load are the significant challenges faced in an islanded microgrid (IMG) frequency control. With respect to this, two-level control technique-based load frequency control (LFC) was developed. The aim is to develop a control scheme that maintains zero steady-state errors for deviation in frequency and inter-area power flow within the acceptable limits in two-area IMG. The developed LFC was implemented using a PI controller at a lower level and a PID controller at a high level. Each controller measures and solve the integral of time multiplied absolute error (ITAE) to compute the optimal gain of the PI controller using the quasi-opposition Jaya algorithm (QOJAYA). At the same time, the PID coordinates the activities of the two-area and provides reference signals to the lower-level controllers. The feasibility of the developed scheme was verified through time-based simulations in MATLAB/Simulink environment. Its performances were compared with the Improved Salp Swarm Algorithm Type II fuzzy PID control scheme using settling time and maximum deviation as performance metrics.

KEYWORDS: Islanded microgrid, Microgrid, Load frequency control, Renewable energy Resources.

1. INTRODUCTION

Power energy is one of the key factors for any nation's growth and future prosperity, therefore, there is need to balance power generation and power demand, keeping in mind economic, technical, and environmental reasons for the choice of means of generation of electrical power. One of the major challenges of energy planners is to decide whether the investment in today's energy infrastructure should be based on emerging technology (RESs) or traditional fossil fuels. Renewable energy resources (RESs) are clean sources of energy that are increasingly displacing “dirty” fossil fuels in the power sector (Bayindir *et al*, 2014). The integration of RESs has considerably increased in recent years largely due to its environmental and economic friendly. This gives the concept of microgrid (MG) wider acceptability (Ravindra *et al*, 2014). It simply comprises distributed generators (DGs), energy storage devices, and load confined within an area with a small geographical spanning (Kortz, 2017). An MG can be operated in two modes: Islanded/off-grid mode and the grid-connected mode. Islanded microgrids (IMGs) power systems (PS) provide access to electricity to the rural and remote areas and isolated islands. IMGs differ from the central power grid, in structure, size, and functionality. IMGs consist of various RESs, like Wind and Photovoltaic (PV) which supply unstable power to MG. High penetration of RESs of inverter-based results in low system inertia. The reduced inertia in the MG lead to an increase in the rate of change of frequency, which may, in turn, lead to instability in the MG. Going by the factors mentioned above, IMG frequency control requires an intelligent and efficient controller (Palizban and Kauhaniemi, 2015; and Li *et al,* 2018).

The frequency of a PS depend on the active power balance. As the frequency is a common factor throughout the system, a change in active power demand at one point is reflected throughout the system by a change in frequency. In the islanded mode of operation, generation (having an intermittent source) and loads (demand-based) are varying continuously, so frequency control plays an important role in system stability (Li *et al*, 2018). Frequency control remains one of the most important issues in the power system. Future power systems need more robust and optimal LFC approaches that can handle new challenges posed by modern PS. By considering the aforementioned factors, IMG frequency control requires an intelligent and efficient controller (Palizban and Kauhaniemi, 2015).

To study the dynamic response of IMG against the change in load or source power various mathematical models of IMG have been reported in the literature. The designed of an optimal quasi-oppositional harmony search algorithm (QOHSA) based on a load frequency controller was discussed in (Shankar and Mukherjee, 2016), Kayalvizhi and Kumar, (2017) proposed a new centralized fuzzy adaptive MPC for LFC of an IMG, an intelligent ABC-Based terminal sliding mode controller for load-frequency control of islanded micro-grids was presented in (Bagheri *et al*,2020), in (Han *et al*, 2015), for load frequency in an autonomous MG, a μ-based robust controller

was proposed. Load frequency control method using PSO-based ANN control was presented in (Safari *et al.* 2018), an improved-salp swarm optimization (I-SSO) for LFC in IMG was discussed in (Prakash *et al*, 2018). However, the control strategies gave a good dynamic response, but they depend on the designer's experience. The aim of this paper is to develop a two-level supervisory load frequency control scheme for maintaining both frequency and tie-line power to their nominal values under different uncertainties. The two level control (i.e., lower level PI and higher level PID) controller is proposed to create necessary IMG control mechanism. The different gain parameters of proposed controllers are optimized by using Quasi-Oppositional JAYA (QO-JAYA) algorithm and finally to justify the supremacy of proposed two level control scheme its performances were compared with type-II fuzzy controller optimized using ISSO.

2 DESCRIPTION OF THE PROPOSED MODEL

For this study, the structure of IMG considered comprises of RESs like wind and PV source, storage sources like battery and flywheel and auxiliary sources like diesel engine generator (DEG), fuel cell (FC) and a micro-turbine (MT). The output of RESs is uncontrolled since it is weather dependent and highly stochastic in nature so there is a need for such controlled sources. These controlled sources i.e. MT, DEG, FC play an important role to stabilize the system when RESs' power is down to continuously supply the load demand. These controlled sources need some definite time to respond and feed the IMG, hence there is a need for such a source that can support the grid until the controlled sources are on. To fulfill this requirement, the storage system is applied which is charging during the normal case (power supply is equal to or more than demand). As soon as there is more demand than supply then storage sources immediately get activated for a shorter period and provide a huge amount of power to balance the demand and supply. The general schematic of the IMG is shown in Figure 1 which shows that distributed resources are integrated to ac bus through power converters.

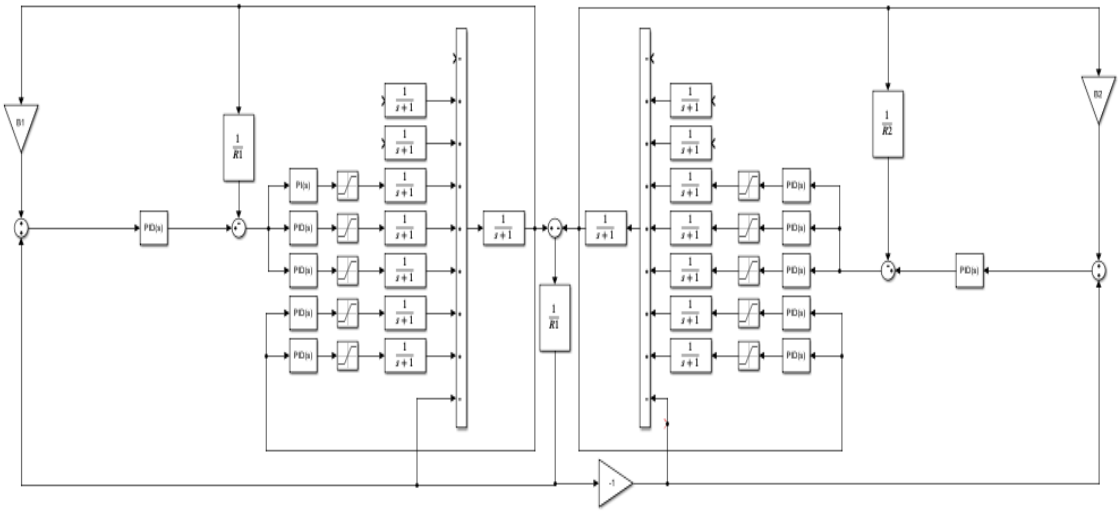

Figure 1: Configuration of a Two-area IMG system

The transfer function expression for the individual system is as shown in equation 1 to 8 (Prakash *et al*., 2018):

Wind turbine generator (G_{WT} (s)) = $\frac{1}{1+ST_{WT}}$ (1)

where T_{WT} is the time constant of the wind turbine

Photo Voltaic (PV) (G_{PV}(s)) = $\frac{1}{1+ST_{PV}}$ (2)

where T_{PV} is the time constant of the PV

Microturbine (G_{MT}(s)) = $\frac{1}{1+ST_{MT}}$ (3)

where T_{MT} is the time constant of the MT

Diesel Generator (G_{DG}(s)) = $\frac{1}{1+ST_{DG}}$ (4)

where T_{DG} is the time constant of the DG

Fuel Cell (G_{FC}(s)) = $\frac{1}{1+ST_{FC}}$ (5)

where T_{FC} is the time constant of the FC

Flywheel Energy Storage (G_{FES}(s)) = $\frac{1}{1+ST_{FES}}$ (6)

where T_{FES} is the time constant of the FES

Battery Energy Storage ($G_{BES}(s)$) = $\frac{1}{1+ST_{BES}}$ (7)

where T_{BES} is the time constant of the BES

The total power generation in each area of the MG system is

$P_{total} = P_{DG} + P_{MT} + P_{FC} + P_{WT} + P_{PV} \pm P_{BES} \pm P_{FES}$ (8)

2.1 Control Topology

In an interconnected (PS) with two or more interconnected control areas (CAs), the generation within each area must be controlled to maintain the load demand with that CA and schedule power interchange with its neighboring CAs. In the LFC problem, each area has its generator or coherent group of generators responsible for a generation. The tie-lines are the utilities through which the contracted and uncontracted (in abnormal conditions) energy exchange between the CAs is provided. In two areas islanding MG, the communication system is required to provide a means to exchange data and monitor various elements for control and protection purposes. In centralized control, a central controller (CC) acts as an interface between all the CAs and the distributed management system. Central control collects data and determines controlling actions for all units. Extensive communication and computation are required in centralized control, this requirement makes the centralized control infeasible (Singh *et al*, 2019). In decentralized control, each unit has a local controller (LC). The units are controlled independently by their LC because decentralized control assumes that the communication between subsystems is negligible. The controller does not rely on control of other controller's action. To achieve reliable and efficient control decentralized approach a strong coupling between the system units is required (Badal *et al*, 2019). As a result of the above situations, a two-level optimal coordination control method for the LFC of the multi-area IMG is preferred over the convention methods for load frequency control due to their computational efficiencies, solution accuracies, and improved reliability. Two-level load frequency control scheme, the lower control level comprised of proportional-integral (PI) to regulate each of the micro-source to control the MG's frequency and inter-MG power exchanges. At the higher control level, a proportional-integral-derivate (PID) will be applied in each MG as a supervisory controller to determine the set-points for the decentralized PI controllers in the lower layer. The control scheme is proposed to have the capability of switching from the two-level supervisory LFC to a decentralized LFC (i.e. comprising of only the local PIs) when the PIDs in the higher level (or communication between them) failed.

3 METHODOLOGY

The objective function for the two-level LFC problem are formulated as follows:

3.1 Formulation of Two-Level based LFC Objective Function

The lower control level comprises of proportional-integral (PI) to regulate each of the micro-source to control the MG's frequency and higher level comprises of PID controller to supervised the control activities of the two CAs. The Integral of Time multiplied Absolute Error (ITAE) criteria is used as the objective function for both the two control level as expressed in equation 9 and 10 respectively.

J_{LC} = ITAE = $min \int_0^T ACE_i = \int_0^T B\Delta f$ (9)

Where B denotes the biasing factor and Δf is the frequency deviation in p.u.

J_{HC} = ITAE = $\int_0^T ACE_i$, for i= 1,2 (10)

$ACE_1 = B\Delta f + \Delta P_{tie}$

where ΔP_{tiei} change in tie-line power between the ith area and the other area.

While minimizing ITAE the following constraints are need to be maintained

i. Load-generation balance as equality constraint as expressed in equation (11)

$\sum P_{Gi} = \sum P_{Di} + P_i^{tie}(t)$ (11)

ii. Frequency band: the frequency is constrained within the certain upper and lower band as;

$f_i^{min} \leq f_i \leq f_i^{max}$ (12)

iii. Controller gains constraints: the controller proportional, integral, and derivate gains are constrained with some upper and lower limits for practical considerations, as shown in (13-15);

$K_{pi}^{min} \leq K_{pi} \leq K_{Pi}^{max}$ (13)

$K_{Ii}^{min} \leq K_{Ii} \leq K_{Ii}^{max}$ (14)

$K_{Di}^{min} \leq K_{Di} \leq K_{Di}^{max}$ (15)

3.2 Quasi-Oppositional Jaya (QO-JAYA) Algorithm

QO-Jaya algorithm is developed for solving multi-objective optimization problems (Rao et al. 2017). In the QO-Jaya algorithm, the task of finding the best and worst solutions is accomplished by comparing the rank assigned to the solutions based on the non-dominance concept and the crowding distance value.

In the beginning, an initial population is randomly generated with a P number of solutions. Then a quasi-opposite population is generated which is combined with the initial population. This combined population is then sorted and ranked based on the non-dominance concept and the crowding distance value is computed for each solution. The quasi-opposite population is generated using equation (16).

$$X_{ij}^{q} = rand(a, b) \tag{16}$$

$$a = \frac{L+U}{2} \tag{17}$$

$$b = L + U - X_{ij} \tag{18}$$

Where L and U are the lower and upper bound of the variable; X_{ij}^{q} is the quasi-opposite value of X_{ij}.

Then P best solutions are selected from the combined population-based on rank and crowding distance. Further, the solutions are modified according to equation (19).

$$A(i+1, j, k) = A(i, j, k) + r(i, j, 1)(A(i, j, b) - |A(i, j, k|) - r(1, j, 2)(A(i, j, w) - |A(i, j, k)|) \tag{19}$$

Here b and w represent the index of the best and worst solutions among the current population. i, j, k are the index of iteration, variable, and candidate solution.

A(i, j, k) means the jth variable of kth candidate solution in an ith iteration. r(i, j, 1) and r(i, j, 2) are numbers generated randomly in the range of [0, 1]. The random numbers r(i, j, 1) and r(i, j, 2) act as scaling factors and ensure good diversification.

For this purpose, the best and worst solutions are to be identified. The solution with the highest rank (rank = 1) is selected as the best solution. The solution with the lowest rank is selected as the worst solution. The number of function evaluations required by the MOQO-Jaya algorithm = population size * no. of generations for a single simulation run.

i. Non-dominated Sorting of the Population

In this approach the population is sorted into several ranks (fronts) based on the dominance concept as follows: a solution x_i is said to dominate other solution x_j if and only if solution x_i is no worse than solution x_j concerning all the objectives and the solution x_i is strictly better than solution x_j in at least one objective. If any of the two conditions are violated, then solution x_i does not dominate solution x_j. Among a set of solutions P, the non-dominated solutions are those that are not dominated by any solution in the set P.

ii. Constraint-Dominance Concept

A solution i is said to constrained-dominate a solution j, if any of the following conditions is true. Solution i is feasible and solution j is not. Solutions i and j are both infeasible, but solution i has a smaller overall constraint violation. Solutions i and j are feasible and solution i dominates Solution j.

iii. Crowding Distance Computation

The crowding distance is assigned to each solution in the population to estimate the density of solutions surrounding a particular solution i. Thus, the average distance of two solutions on either side of solution i is measured along each of the M objectives. This quantity is called the crowding distance (CD_i).

$$CD_j = CD_j + \frac{f_m^{j+1} - f_m^{j-1}}{f_m^{max} - f_m^{min}} \tag{20}$$

where j is a solution in the sorted list, f_m is the objective function value of mth objective, f_m^{max} and f_m^{min} are the population-maximum and population-minimum values of the mth objective function.

i. Crowding-Comparison Operator

Crowding-comparison operator is used to identifying the superior solution among two solutions under comparison, based on the two important attributes possessed by every individual i in the population i.e. non-domination rank ($Rank_i$) and crowding distance (CD_j).

3.3 Algorithm for Optimal Tuning of PI and PID Controller Parameter Using QO-Jaya Algorithm

i. Read input data i.e., frequency, active power generation limits of all controllable DGs, and constraints.

ii. Read algorithm parameters i.e. population size, maximum number of iterations, and declaration of both upper bound and lower bound of variables.

iii. Generate quasi-opposite population using equation (16)

iv. Select good (P) solutions from initial population and quasi-opposite

v. Perform greedy selection to identify best and worst solutions in the selected population using equation (20) and compute new solution using equation (19).

vi. If the new position is better than old.

vii. Evaluate the objective function for the two control level

viii. Repeat steps (iv) to (vii) until a convergence criterion is met.

ix. Stop and print the result

4. RESULTS AND DISCUSSION

This section presents the two different analysis to validate the effectiveness of the proposed two-level control scheme upon the type II fuzzy controller based ISSO. The time-domain simulation results are presented to show the superiority of the developed scheme for the IMG system stability subjected to perturbation in ΔPL and ΔPW. The study of frequency deviation by changing the load and wind power has been recorded.

Case 1: Time-domain simulation results for frequency deviation against load power deviation ΔP_L by type II fuzzy controller based ISSO and two-level control scheme

In this case, the solar irradiation and wind speed are considered constant and a random pattern load as shown in Figure 2a is effected in the IMG at time t=0. In regard to this disturbance, the deviated responses of frequency and tie-line power resulted due to the two-level controller is depicted in this section. The deviation in frequency of area1 and area2 due to QO-Jaya optimized controllers are shown in Figure 2 (b-c) respectively. The tie-line power deviation is given in Figure 2 (d).

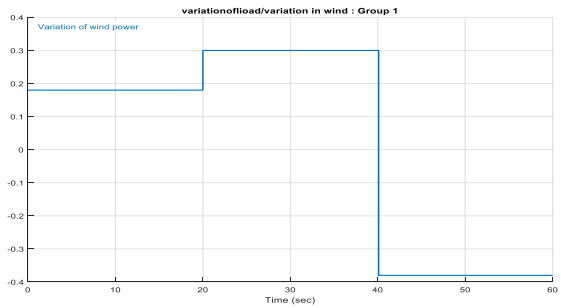

Figure 2a: Variation of load (ΔPL)

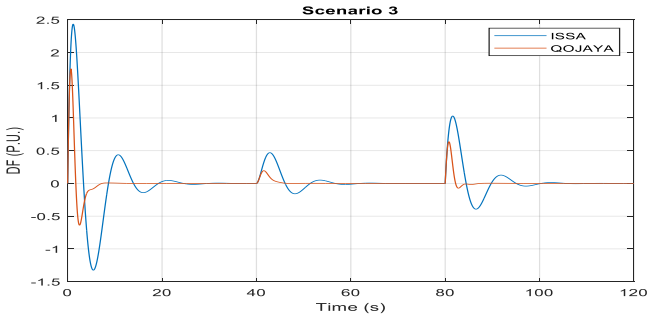

Figure 2b: Variation of area1 frequency due to ΔPL

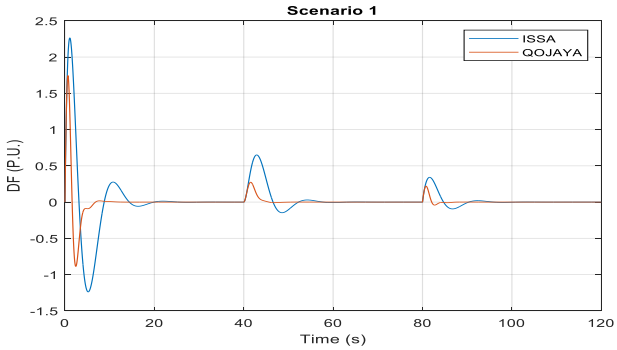

Figure 2c: Variation of area2 frequency due to ΔPL

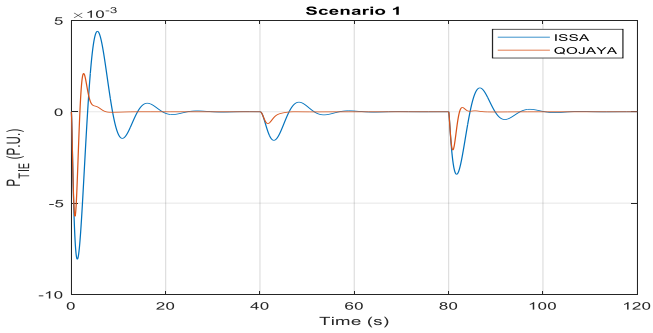

Figure 2d: Variation of tie-line power due to ΔPL

Case 2 Wind Power Fluctuation (ΔP_{Wind})

In this case, the wind turbine is considered as white noise since the environmental fluctuations are continuous and unstable. Figure 3a shows the wind power perturbation and Figure 3(b-c) represents the MG output frequency response by comparing the proposed controllers. The tie-line power deviation is given in Figure 3 (d).

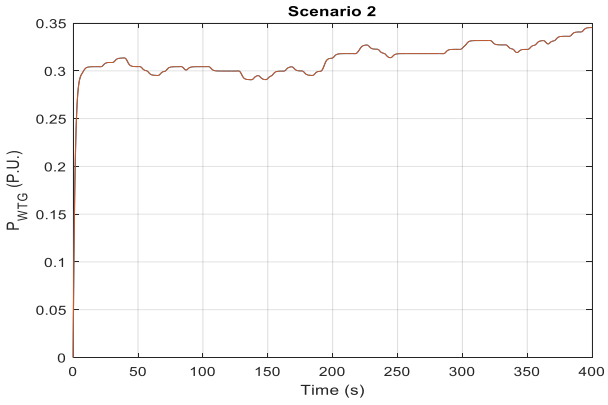

Figure 3a: Variation of wind power (ΔPW)

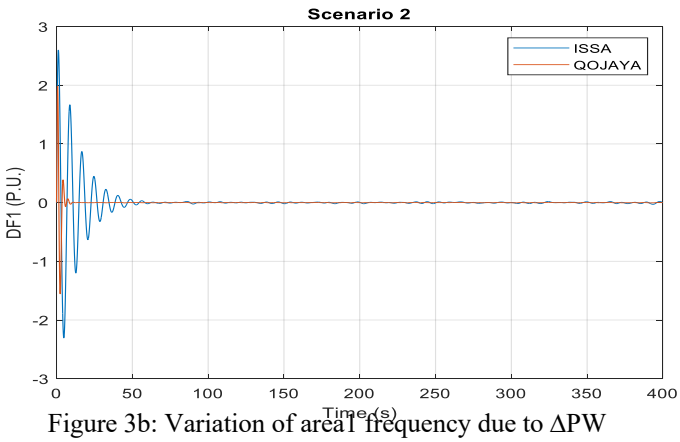

Figure 3b: Variation of area1 frequency due to ΔPW

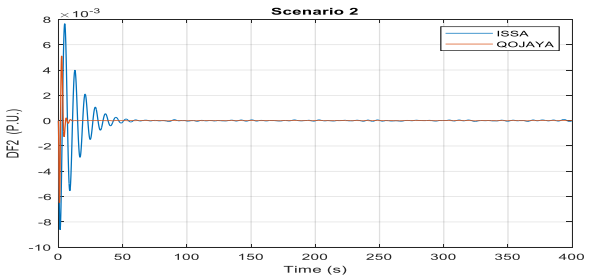

Figure 3c: Variation of area2 frequency due to ΔPW

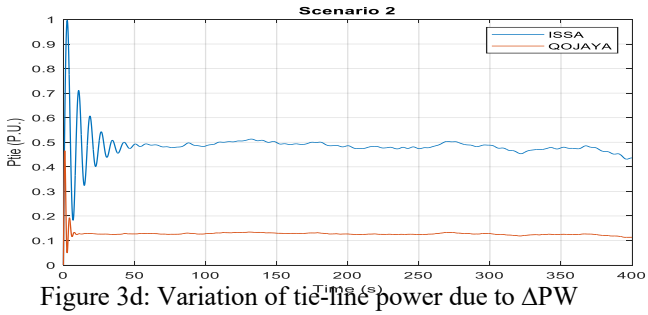

Figure 3d: Variation of tie-line power due to ΔPW

The critical analysis on dynamic responses and Table.1 reveals that, the proposed control scheme outperformed the ISSA tuned type-II fuzzy PID controller.

Table 1: Summary of two area IMG Response Following RLP with ISSA-Type II Fuzzy PID and Proposed Controller

States	**Controller**	**Performance**			
		Settling time (sec)	Improvement	Maximum deviation	Improvement
f_1 *(Hz)*	Proposed Control	4.79	29.556%	-0.0007	30%
	ISSA	6.80		-0.001	
f_2 *(Hz)*	Proposed Control	4.63802	25.161%	0.00	0%
	ISSA	6.20		0.00	
DPtie	Proposed Control	5.18	19.32%	0.00018	21.74%
	ISSA	6.42		0.00023	
ITAE	Proposed Control	8.2523	6.367%		
	ISSA	8.8312			

The dynamic responses has been depicted through different conditions reveal that proposed control scheme exhibits more effectiveness over ISSA optimized type-II fuzzy PID controller. Overall critical discussions on this section reveal that proposed control scheme exhibits superior performance in regard to LFC study of an islanded multi-area interconnected MG system.

5. CONCLUSION

In this work, a two level control scheme is proposed for the comprehensive LFC analysis of a multi-area multisource interconnected islanded microgrid system. The developed control schemes are meant to enable both centralization and decentralization of power system. The proposed controller simulation outcomes are compared with the Type II fuzzy PID control scheme under different scenarios. From the simulation outcomes of all scenarios, the proposed controller exhibits a better dynamic performance in terms of fast settling time, overshoot reduction and less frequency deviation error over Type II fuzzy PID controller.

REFERENCES

Annamraju A. and Nandiraju S. (2018): Robust Frequency Control in an Autonomous Microgrid: A Two-Stage Adaptive Fuzzy Approach, Electric Power Components and Systems, DOI: 10.1080/15325008.2018.1432723.

Bagheri, A., Jabbari, A., and Mobayen, S. (2020). An Intelligent ABC-Based Terminal Sliding Mode Controller for Load-Frequency Control of Islanded Micro-Grids. Sustainable Cities and Society, 102544. doi:10.1016/j.scs.2020.102544.

Bayindir, R., Hossain, E., Kabalci, E., and Perez, R. (2014). "A Comprehensive Study on Microgrid Technology. International Journal of Renewable Energy Research, 4(4),1094–1107.

Kayalvizhi S. and Vinod Kumar D. M., (2017) "Load Frequency Control of an Isolated Micro Grid Using Fuzzy Adaptive Model Predictive Control," in IEEE Access, 5,. 16241-16251, 2017, doi: 10.1109/ACCESS.2017.2735545.

Kortz D. (2017) Microgrids: reliable power is a small package. Barkely Lab Science Beat., http://www.lbl.gov/science-articles/Archieve/EETD-microgrids.html.

Li J., Liu Y., Wu L., (2018), Optimal Operation for Community-Based Multi-Party Microgrid in Grid-Connected and Islanded Modes, IEEE Transactions on Smart Grid. 9(2) (2018)756-765.

Mishra, D., Nayak, P. C., and Prusty, R. C. (2020). PSO optimized PIDF controller for Load-frequency control of A.C Multi-Islanded-Micro grid system. 2020 International Conference on Renewable Energy Integration into Smart Grids: A Multidisciplinary Approach to Technology Modelling and Simulation (ICREISG). doi:10.1109/icreisg49226.2020.9174552.

Palizban O., Kauhaniemi K., (2015) Hierarchical control structure in microgrids with distributed generation: Island and grid-connected mode, Renewable and Sustainable Energy Reviews. 44 (2015) 797-813.

Prakash C. S., Sonalika M., Ramesh C. P., Sidhartha P. (2018) Improved -salp swarm optimized type-II fuzzy controller in load frequency control of multi area islanded AC microgrid, Sustainable Energy, Grids and Networks (2018), https://doi.org/10.1016/j.segan.2018.10.003

Rao, R. V., and Rai, D. P. (2017a). Optimization of welding processes using quasi oppositional based Jaya algorithm. Journal of Experimental and Theoretical Artificial Intelligence, 29(5), 1099–1117.

Ravindra K. Kannan B. Ramappa. N (2014) "Microgrid a Value-Based Paradigin, the need for the redefinition of microgrids, IEEE Elect Mag 2(1); 20-29.

Sanjari M. J. and Gharehpetian G. B., (2013) Small Signal Stability Based Fuzzy Potential Function Proposal for Secondary Frequency and Voltage Control of Islanded Microgrid, Electric Power Components and Systems, 41:5, 485-499.

Shankar, G., and Mukherjee, V. (2016). Load frequency control of an autonomous hybrid power system by quasi-oppositional harmony search algorithm. International Journal of Electrical Power and Energy Systems, 78, 715–734.

APPENDICES

Di = damping coefficient ith area = 0,012 (pu/Hz); Mi = Inertia constant of ith area = 0.2 (pu/s); i= 1,2; TFC = Fuel Cell time constant = 4s; TBES = Battery energy time constant = 0.1s; TFES = Flywheel energy storage time constant =0.1s; TDEG = Diesel engine generator time constant = 2s; TMT = Microturbine time constant = 2s; TWTG = Wind turbine generator time constant = 1.5s; TPV = Photo Voltaic cell time constant = 1.8s. B = Frequency biasing factor = 0.425 pu MW /Hz. ; R = Regulation =0.05 Hz/Mw; T12 = Time coefficient=1.6 s.

PAPER 32 – Development of Fault Ride-Through Capability of Doubly Fed Induction Generator-Based Wind Turbine System under Fault Condition

Muhammad Abdulhadi, N. Abdulazeez, A. S. Abubakar, G. S. Shehu

Department of Electrical Engineering, Faculty of Engineering, Ahmadu Bello University, Zaria-Nigeria.

Email: abdulazeeznurudeen224@gmail.com

ABSTRACT The rapid growth in the wind power market among other Renewable energy sources (RES) is attracting the attention of scientists and researchers because the integration of Wind Turbine Systems (WTs) with the grid to complement the conventional sources in meeting up with global electrical energy demand is becoming a challenging task. The Doubly Fed Induction Generator (DFIG) has become very popular due to its low converter rating and flexible control of its active and reactive power, higher power quality, and better dynamic performance. Consequently, protecting the DFIG-based WTs from grid faults turn out to be indispensable. In this study, a 2 MW grid-connected DFIG-based WT model with a Hybrid scheme for Fault Ride-Through (FRT) capability and stability improvement was developed. The design and simulation were performed in MATLAB/Simulink (R2019b) software. The test system was subjected to disturbances leading to High Voltage Ride – Through (HVRT) by applying three–phase balanced fault without any compensation device than with conventional R-type SSFCL and finally with the Hybrid scheme. The performance of the Hybrid scheme shows fault current limitation and voltage compensation improvement over the R-type SSFCL. The THD of supply voltages with the Hybrid scheme is lower than 5%. This indicates that the Hybrid scheme complied with IEEE519 for harmonics content in power supplies.

KEYWORDS: DFIG, DC Chopper, Energy Storage, Fault current limiter (FCL), Fault Ride-Through, R-type SFCL,

1. INTRODUCTION

Wind energy amid several sustainable renewable energy sources (RES) that include hydro, solar (photovoltaic), tidal, biomass and geothermal, has become the most widespread energy source as a result of its cheap cost of maintenance, high production ability, availability in numerous parts of the world and absence of air pollution. Also, wind power is an intermittent energy source in the power system network but with this effect over 666GW of power would be generated worldwide using wind energy source in 2019 (Hossain, 2018). Electrical energy generation using Wind Turbine (WT) is accomplished by means of different configurations of induction or synchronous generators in connection with power electronic devices (Gardner *et al*., 2012). The most commonly used generator for wind turbine system are: Squirrel Cage Induction Generation (SCIG); Permanent Magnet Synchronous Generator (PMSG); Brushless Doubly Fed Induction Generator (BDIG; and Doubly Fed Induction Generator (DFIG). The DFIG becomes the most preferable for WT system owing to its merits which include reduced mechanical stress, pliable control of active and reactive power, variable speed operation, and low power rating of the connected power electronics converters (Amalorpavaraj *et al*., 2017). Conversely, one of the main drawback of the grid-connected DFIG-based WT is that it is very difficult to improve the performance of the DFIG via weakening the flux due to the fact that the stator of the DFIG is connected directly to the grid where the grid voltage directly controls the stator flux as such, a current surge is produced in rotor side converter (RSC) due to sudden change in machine magnetization caused by any voltage dip (Zhu *et al*., 2017). As a result of the large share of WT in supplying electric power to the grid and maintaining the overall system reliability, most countries necessitated that DFIG-based WT systems remain coupled to the grid in case of fault for certain period so as to satisfy condition of grid code (Fault Ride Through) (Xiao *et al*., 2018). Grid code states that wind farms must remain coupled to the grid for a certain period of time during fault and offer reactive power support to voltage dip (Alaraifi *et al*., 2013). Strictly, wind farm should adhere to the grid code since its disconnection leads to destabilization of the grid. The sensitivity of DFIG-based WT system due to the direct connection of its stator with the grid and the impact of fault current on the rotor, lead to large rotor current to be developed. The large current inrush in the rotor side causes the failure of the rotor side converter (RSC), destabilizes the DC-link voltage and DFIG eventually loses control (Uddin *et al*., 2017). The destabilized DC-link voltage decreases the life span of DC-link capacitor and reduces the efficiency of the converters (Amalorpavaraj et al., 2017).

Control improvement and hardware modification are the two existing method of enhancing the FRT (Xiao *et al*., 2018). Some techniques have been developed to minimize the overcurrent through grid fault or Transient stability (TS) of wind turbine by modelling grid side converter (GSC) or RSC control such as dual control and demagnetizing current control techniques (Alaraifi *et al*., 2013; Xiao *et al*., 2018).

Conventional crowbar is one of the hardware solutions that has been used to divert the overcurrent to power dissipated resistive circuit from RSC (Tohidi & Behnam, 2016; Uddin *et al*., 2017). Even though the current is diverted from converter using this method, but the generator acts as an induction machine that takes reactive power from the grid (Uddin *et al*., 2017). The DC chopper strategy is also commonly used to decrease the rotor overcurrent and to decrease the DC-link overvoltage for improving the operational safety of WT (Xiao *et al*., 2018). Conversely, this techniques is unable to arrest the oscillation of electromagnetic torque which might be destructive to the gearbox in some exciting situations (Nataraj *et al*., 2018; Yasoda *et al*., 2016).

DC chopper associated with storage system is implemented to prevent overvoltage in DC-link capacitor (Abbey & Joos, 2007; Uddin *et al*., 2017). A resistive type solid state fault current limiter (R-type SSFCL) is also used to enhance the capability of DFIG in FRT by withstanding fault up to a small duration but its limitation transpires during long duration faults (Dai *et al*., 2016; Uddin *et al*., 2017). Temporarily, R-type SSFCL scheme can only decrease the peak value of rotor fault current, but it doesn't have capability to remove the back EMF in rotor windings which is induced from transient stator flux and lead to a stator frequency plus rotor harmonics in rotor windings (Zou et al., 2016).

In order to decrease the negative impact of varying wind speed to DFIG output active power, shorten the recovery time after grid fault, limit the short-circuit current during faults and improve the transient stability of the system simultaneously, this paper implements a hybrid scheme which composes of R-type SSFCL, Energy Storage System (ESS) and DC chopper (DC-C) with modified control of RSC. The advantages of different schemes are combined to achieve a better response. The hybrid scheme aimed to have the ability of protecting RSC and DC-link capacitor by limiting the fault current and damp out the transients quickly. The scheme is also intended to smooth electromagnetic torque by reducing the mechanical stress on the WT.

2. THEORETICAL ANALYSIS

2.1 Concept of Doubly Fed Induction Generator DFIG

The DFIG is basically a wound rotor induction machine in which both stator and rotor are connected to electrical sources – thus the term 'doubly fed'. The dynamic model, operation and control of DFIG are discussed below.

Model of DFIG

The dynamic model of DFIG is fundamentally based on the general machine model in synchronous reference frame and all the system parameters and variables in per unit (p.u) and referred to the stator side (Rahimi & Parniani, 2010). Figure 1 shows the equivalent circuit of the DFIG in synchronous dq reference frame.

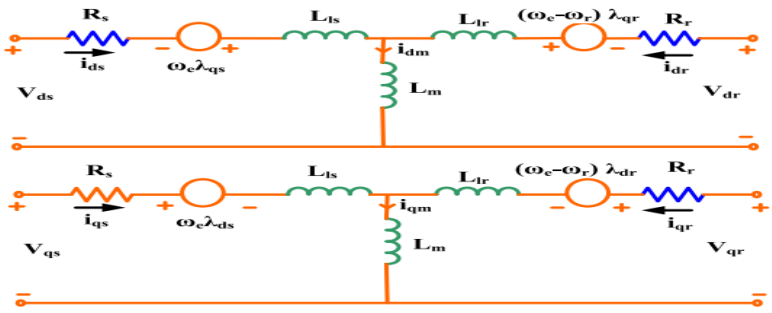

Figure 1: Equivalent Circuit of DFIG (Alaraifi *et al.,* 2013)

The dq voltage, current and flux equations of the equivalent circuit of DFIG are as follows (Amalorpavaraj *et al.,* 2017):

$$v_{ds} = R_s i_{ds} + \frac{d\lambda_{ds}}{dt} - \omega_e \lambda_{qs} \quad (1)$$

$$v_{qs} = R_s i_{qs} + \frac{d\lambda_{qs}}{dt} + \omega_e \lambda_{ds} \quad (2)$$

$$v_{dr} = R_r i_{dr} + \frac{d\lambda_{dr}}{dt} - (\omega_e - \omega_r)\lambda_{qr} \quad (3)$$

$$v_{qr} = R_r i_{qr} + \frac{d\lambda_{qr}}{dt} + (\omega_e - \omega_r)\lambda_{dr} \quad (4)$$

Where: $\mathbf{v_{ds}}$ and $\mathbf{v_{qs}}$ are dq stator voltages, $\mathbf{v_{dr}}$ and $\mathbf{v_{qr}}$ are dq rotor voltages; $\mathbf{i_{ds}}$ and $\mathbf{i_{qs}}$ are dq stator currents, $\mathbf{i_{dr}}$ and $\mathbf{i_{qr}}$ are dq rotor currents; ω_e is the supply angular frequency and ω_r is the rotor angular frequency; λ_{ds} *and* λ_{qs} are the dq stator flux linkages, λ_{dr} and λ_{qr} are the dq rotor flux linkages. $\mathbf{R_s}$ and $\mathbf{R_r}$ are the stator and rotor resistance respectively.

If L_s and L_r represent the stator and rotor inductance respectively, then the stator and rotor side inductances can be obtained using:

$$L_s = L_{ls} + L_m \quad (5)$$

$$L_r = L_{lr} + L_m \quad (6)$$

Where: L_{ls} and L_{lr} are the stator and rotor leakage inductance respectively and L_m is the magnetizing inductance.

The flux linkage equations for both stator and rotor are given by

$$\lambda_{ds} = L_s i_{ds} + L_m i_{dr} \quad (7)$$

$$\lambda_{qs} = L_s i_{qs} + L_m i_{qr} \quad (8)$$

$$\lambda_{dr} = L_m i_{ds} + L_r i_{dr} \quad (9)$$

$$\lambda_{qr} = L_m i_{qs} + L_r i_{qr} \quad (10)$$

The real power (P_s) and reactive power (Q_s) generated by DFIG are given by

$$P_s = \frac{3}{2}\left(v_{qs} i_{qs} + v_{ds} i_{ds}\right) \quad (11)$$

$$Q_s = \frac{3}{2}\left(v_{qs} i_{ds} - v_{ds} i_{qs}\right) \quad (12)$$

Operating Principle of DFIG

The operational analysis of DFIG in transient and steady state conditions is very significant to understanding its performance under grid faults. The fault analysis is essential for the implementation of FRT capability (Amalorpavaraj *et al.,* 2017). It has been stated that the stator of DFIG is directly connected to the grid while its rotor is connected to the grid through slip rings over a partial-scale back-to-back power converter. The back-to-back converter composed of a RSC and GSC connected to a dc-link. The dc-link is basically a capacitor which aids as energy storage and also serves as dc-link voltage ripples limiter. The converter converts within 20 – 30 % of total generated power. It also controls torque, speed and reactive power to or from the grid (Alsmadi *et al.,* 2018). The three-phase windings of the rotor are energized through three-phase current which is supplied via the RSC. Consequently, the rotor magnetic field interacts with stator magnetic field to develop torque as a vector product of the two vector fields (Fletcher *et al.,* 2010).

Control of DFIG

The control of DFIG functions essentially to regulate the power extracted from the WT, limit the power during high wind speed and to adjust the exchange of reactive power between the WT system and the grid. The control involves pitch control for the turbine, RSC and GSC control for the DFIG (Wessels *et al*., 2011). The rotor current controls the RSC which varies the torque and excitation while the GSC ensures constant dc-link voltage (Uddin *et al*., 2017). Figure 2 shows the control block diagram of DFIG. Many DFIGs deploy close-loop current control using Voltage Source Inverter (VSI) or vector-control technique.

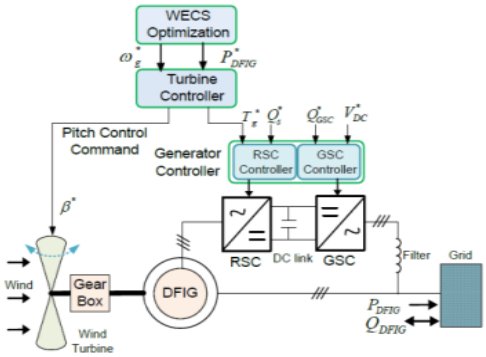

Figure 2: Control Block Diagram of DFIG-based WT (Wessels *et al*., 2011)

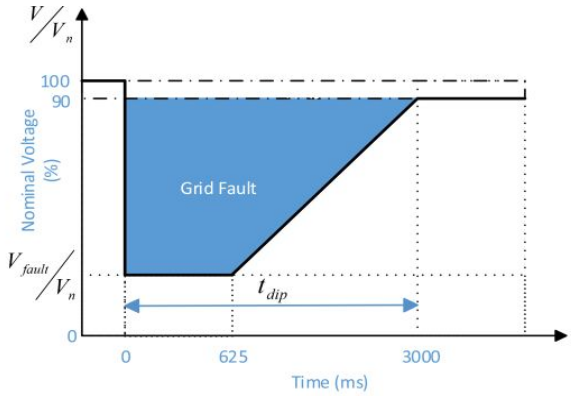

Figure 2: Figure 3: Grid Code FRT Requirement for WTs (Uddin *et al.,* 2017).

Grid Codes and FRT Requirement of DFIG

The requirements are as follows:

1. WT must stay connected to the grid for certain time (determined by the system specifications);
2. Active power must be restored immediately after the fault clearance; and
3. WT must provide reactive power thereby supporting the grid voltage during the fault (Ambati *et al.,* 2015).

Figure 3 shows the grid code FRT requirement.

3. Methodology

The methodology adopted in this research towards developing a hybrid scheme comprising of BSFCL, DC chopper and energy storage system for improving the fault ride through (FRT) and transient stability of grid connected DFIG-based WTs are discussed.

3.1 Modelling of the DFIG – Based WT

The DFIG model used in this paper was accomplished using equation (1 - 12). The DFIG Simulink model is as shown in Appendix B.

3.2 Modelling of the Grid

The DFIG – Based WT system integrated to the grid and its components were modelled as presented in Appendix C. In the model, bus 1 with nominal voltage of 600V was connected to the terminals of the DFIG. The 63kV/600V transformer was used to step up the voltage of the DFIG to a nominal grid voltage of 63kV for secondary transmission.

The grid taken as a 25km transmission line block was modelled with a single PI section. The model comprises of one set of RL series element connected between input and output terminals and two sets of shunt capacitances lumped at both ends of the line. RLC components are calculated using hyperbolic modifications to yield precise representations in zero and positive-sequence at specified frequencies. In order to achieve a stretched frequency response, a distributed parameter line was used in the model.

3.3 Energy Storage System and DC – Link Capacitor

The ideal dc voltage source and the dc – link capacitor parameters are, a 5000V was taken as the maximum voltage of the dc source with a 10Ω series resistance and 10000e-6 as the capacitance of the dc – link capacitor with an initial voltage of 1150V.

3.4 Fault Current Limiter (FCL)

The Fault Current Limiter employed has a switch model controlled by a gate signal and a virtual impedance. When in ON-state the switch model has an internal resistance (R_{on}). In OFF-state, this internal resistance is infinite. When the gate signal (g) is set to 1, the switch model is ON-state. A diode in parallel with a series RC snubber circuit having R_{on} and (L_{on}) at ON-state is also integrated. R_{on} being carefully chosen as $1 \times 10^{-3}\Omega$ and the Snubber resistance as $10^{3}\Omega$ were adopted from Beheshtaein et al., 2017 for both the controlled switch and diode respectively. The Diode impedance was infinite in OFF-state mode. The limiting fault current is expressed as (13).

$$I_{lim}^{m}(t) = \frac{U_s(t)}{Z_s + Z_{lim}} \approx \frac{U_s(t)}{Z_{lim}} \quad (13)$$

Where: Z_{lim} is the limiting impedance, $U_s(t)$ is the voltage of secondary transformer. It is assumed that $Z_s \ll Z_{lim}$.

A PI current controller and an active damping loop were realized to sense and trigger the control scheme. For mitigation, the current measurements was accomplished using Multiple Second – Order Generalized integrators PLL (MSOGI-PLL) for its fast response and less computational burden. Appendix D illustrates the employed FCL block with its components.

4. RESULTS AND DISCUSSION

The performance of the Hybrid scheme and the conventional R-type SSFCL in ensuring FRT ability was established by injecting grid faults (single-phase to ground faults) into the system. For fault considered in the work, the situation of voltage sag was accomplished by means of switching a highly inductive load at 0.3 seconds while the deeper voltage sag was achieved by means of a fault implementation block in MATLAB/Simulink environment. The fault was chosen between any phase and the ground. The switching time was also chosen between 0.4 to 0.6seconds while the fault resistance and ground resistance were both selected to be 0.0001Ω. Additionally, a snubber resistance of 1MΩ and infinite snubber capacitance were selected for a more severe fault condition. Lastly, a capacitive load was switched ON at 0.6 seconds to give the voltage swell. The supply voltage RMS values at PCC, the DFIG stator current response, DFIG electromagnetic torque, rotor speed of DFIG, DFIG rotor current response, and DC – Link voltage through Unbalanced Fault (Single-Phase to Ground) are shown in Figure 5-11 respectively.

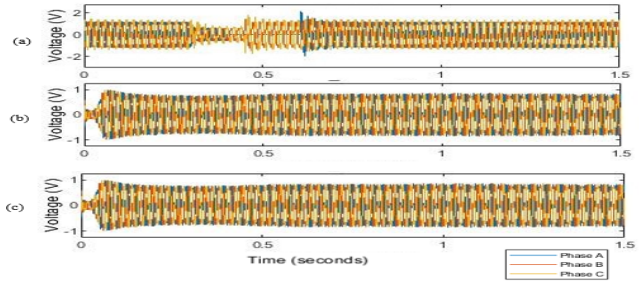

Figure 5: Unbalanced Fault (single phase to ground) supply Voltage

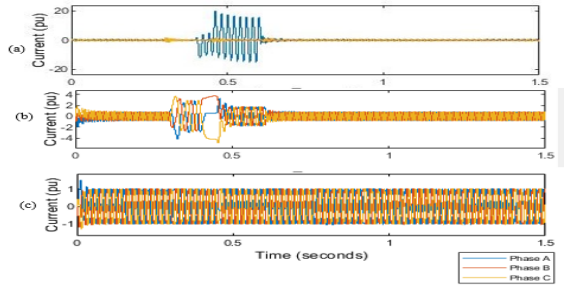

Figure 6: DFIG stator current response after applying a temporary unbalanced single-phase to ground fault

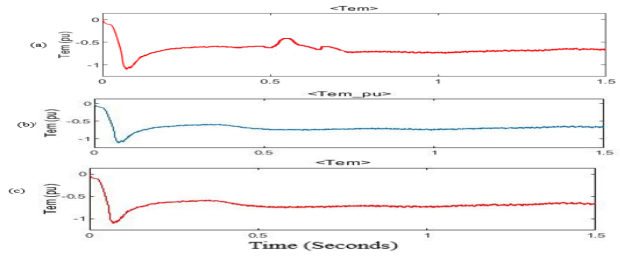

Figure 7: Electromagnetic Torque (Tem) response curves of the DFIG (single phase to ground) supply Voltage

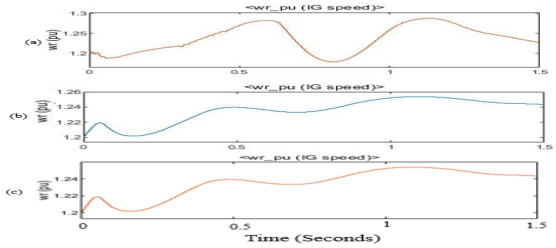

Figure 8: DFIG Rotor Speed under Unbalanced Fault (single phase to ground) supply Voltage

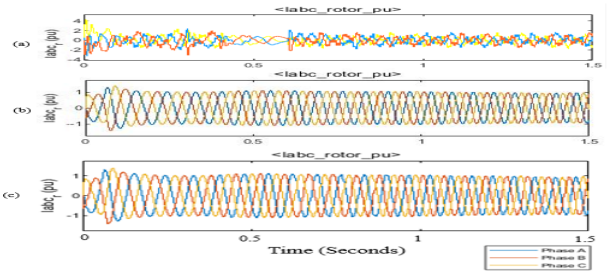

Figure 9: DFIG Rotor Current under Unbalanced Fault (single phase to ground) supply Voltage

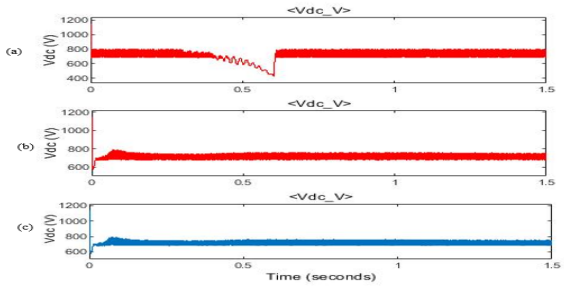

Figure 10: DC-link Voltage during Unbalanced Fault (single phase to ground) supply Voltage

It can be observed that the proposed hybrid scheme performed well and has the capability to improve the transient stability of the DFIG based variable speed WG system for unbalanced single-phase to ground faults as shown in Table 1-4. The voltage level is maintained at ±0.1 p.u. of the nominal value at PCC point and can mitigate the high current significantly during the fault time compared to R-type SSFCL scheme. The hybrid scheme also, stabilizes the machine speed during a fault, thus DFIG faces low stress and improves the transient stability. The THD (%) of supply voltage are 29.93pu, 4.01pu and 1.01pu without any compensation device, with R-type SSFCL and Hybrid scheme respectively. The percentage improvement in the voltage when Hybrid scheme was used was, 75.37% compared to that of R-type SSFCL. Correspondingly, the percentage decrease in output current profile was approximated to about 87.20%.

Table 1: Performance indices values for unbalanced single-phase to ground fault

Index Parameters	**Indices values for Unbalanced 1LG**		
	No Control	With R-type SSFCL	With Hybrid Scheme
Voltage (pu)	2.10	0.92	0.92
Speed (pu)	1.18	1.20	1.21
V_{dc} (V)	415	715	720

Table 2: Transient Stability Improvement for unbalanced single-phase to ground fault

Transient Criteria	**Improvement Comparison for Unbalance 1LG fault**	
	With R-type SSFCL	With Hybrid Scheme
Voltage	High	High
Speed	Moderate	High
Power	Moderate	High
DC link voltage	High	High

Table 3: Comparison among the series devices for the percentage of THD

Parameters	**Controller**	**Performance**	
		THD (%)	Improvement
Voltage	Hybrid Scheme	1.01	75.37%
	R-type SSFCL	4.10	

Table 4: Comparison among the series devices for the percentage TRD

Parameters	**Controller**	**Performance**	
		TRD (%)	Improvement
Current	Hybrid Scheme	1.01	87. 20%
	R-type SSFCL	7.89	

5. CONCLUSION

This paper developed a hybrid scheme consisting of Resistive-type Solid-state Fault Current Limiter (R-type SSFCL), Breaking Chopper (BC) and Energy Storage System (ESS) for Doubly-Fed Induction Generator (DFIG) based Wind Turbine (WT) system. The developed scheme focused on enhancing Fault Ride-Through (FRT) capability of DFIG based WT through the Hybrid scheme thus protecting the strict grid code requirements for the WT integration to grid networks. The scheme also guaranteed the protection of the converters against short-circuit currents. The Hybrid scheme performance indicates that there was an improvement in terms of fault current mitigation and voltage compensation over R-type SSFCL thus making the Hybrid scheme a better option for guaranteeing an improved DFIG-based WT systems FRT capability.

REFERENCES

Abbey, C., & Joos, G. (2007). Supercapacitor Energy Storage for Wind Energy Applications. *IEEE Transactions on Industry Applications*, *43*(3), 769–776. https://doi.org/10.1109/TIA.2007.895768

Alaraifi, S., Moawwad, A., El Moursi, M. S., & Khadkikar, V. (2013). Voltage Booster Schemes for Fault Ride-Through Enhancement of Variable Speed Wind Turbines. *IEEE Transactions on Sustainable Energy*, *4*(4), 1071–1081. https://doi.org/10.1109/TSTE.2013.2267017

Alsmadi, Y. M., Xu, L., Blaabjerg, F., Ortega, A. J. P., Abdelaziz, A. Y., Wang, A., & Albataineh, Z. (2018). Detailed Investigation and Performance Improvement of the Dynamic Behavior of Grid-Connected DFIG-Based Wind Turbines Under LVRT Conditions. *IEEE Transactions on Industry Applications*, *54*(5), 4795–4812. https://doi.org/10.1109/TIA.2018.2835401

Amalorpavaraj, R. A. J., Kaliannan, P., Padmanaban, S., Subramaniam, U., & Ramachandaramurthy, V. K. (2017). Improved Fault Ride Through Capability in DFIG Based Wind Turbines Using Dynamic Voltage Restorer With Combined Feed-Forward and Feed-Back Control. *IEEE Access*, *5*, 20494–20503. https://doi.org/10.1109/ACCESS.2017.2750738

Ambati, B. B., Kanjiya, P., & Khadkikar, V. (2015). A Low Component Count Series Voltage Compensation Scheme for DFIG WTs to Enhance Fault Ride-Through Capability. *IEEE Transactions on Energy Conversion*, *30*(1), 208–217. https://doi.org/10.1109/TEC.2014.2351799

Dai, S., Xiao, L., & Guo, W. (2016). Fault current limiter-battery energy storage system for the doubly-fed induction generator: analysis and experimental verification. *IET Generation, Transmission & Distribution*, *10*(3), 653–660. https://doi.org/10.1049/iet-gtd.2014.1158

Fletcher, D. J., Fletcher, D. J., & Yang, J. (2010). *Introduction to the Doubly-Fed Induction Generator for Wind Power Applications, Paths to Sustainable Energy*. 259. Retrieved from http://citeseerx.ist.psu.edu/viewdoc/summary?doi=10.1.1.725.7456

Gardner, P., Andrew, G., Lars, F. H., Colin, M., & Arthouros, Z. (2012). *Wind energy-the facts: a guide to the technology, economics and future of wind power*. New York: Earthscan.

Hossain, M. E. (2018). Improvement of transient stability of DFIG based wind generator by using of resistive solid state fault current limiter. *Ain Shams Engineering Journal*. https://doi.org/10.1016/j.asej.2017.03.014.

Nataraj, S. K.,. (2018). Improved fault ride through capability of DFIG-wind turbines using customized dynamic voltage restorer. *Sustainable Cities and Society*, *39*, 114–125. https://doi.org/10.1016/J.SCS.2018.02.008

Rahimi, M., & Parniani, M. (2010). Efficient control scheme of wind turbines with doubly fed induction generators for low-voltage ride-through capability enhancement. *IET Renewable Power Generation*, *4*(3), 242. https://doi.org/10.1049/iet-rpg.2009.0072

Tohidi, S., & Behnam, M. (2016). A comprehensive review of low voltage ride through of doubly fed induction wind generators. *Renewable and Sustainable Energy Reviews*, *57*, 412–419. https://doi.org/10.1016/J.RSER.2015.12.155

Uddin, W., Zeb, K., Tanoli, A., & Haider, A. (2017). Hardware-based hybrid scheme to improve the fault ride through capability of doubly fed induction generator under symmetrical and asymmetrical fault. *IET Generation, Transmission & Distribution*, *12*(1), 200–206. https://doi.org/10.1049/iet-gtd.2017.0578

Wessels, C., Gebhardt, F., & Fuchs, F. W. (2011). Fault Ride-Through of a DFIG Wind Turbine Using a Dynamic Voltage Restorer During Symmetrical and Asymmetrical Grid Faults. *IEEE Transactions on Power Electronics*, *26*(3), 807–815. https://doi.org/10.1109/TPEL.2010.2099133

Xiao, X.-Y., Yang, R.-H., Chen, X.-Y., Zheng, Z.-X., & Li, C.-S. (2018). Enhancing fault ride-through capability of DFIG with modified SMES-FCL and RSC control. *IET Generation, Transmission & Distribution*, *12*(1), 258–266. https://doi.org/10.1049/iet-gtd.2016.2136

Yasoda, K. G., Nanjundappan, D., & Boominathan, V. (2016). Enhancement of transient stability of distribution system with SCIG and DFIG based wind farms using STATCOM. *IET Renewable Power Generation*, *10*(8), 1171–1180. https://doi.org/10.1049/iet-rpg.2016.0022

Zhu, D., Zou, X., Deng, L., Huang, Q., Zhou, S., & Kang, Y. (2017). Inductance-Emulating Control for DFIG-Based Wind Turbine to Ride-Through Grid Faults. *IEEE Transactions on Power Electronics*, *32*(11), 8514–8525. https://doi.org/10.1109/TPEL.2016.2645791

Zou, Z.-C., Chen, X.-Y., Li, C.-S., Xiao, X.-Y., & Zhang, Y. (2016). Conceptual Design and Evaluation of a Resistive-Type SFCL for Efficient Fault Ride Through in a DFIG. *IEEE Transactions on Applied Superconductivity*, *26*(1), 1–9. https://doi.org/10.1109/TASC.2015.2507129

APPENDICES

Appendix A: Parameter of 2.0MW WT System

Items	Specifications
Generator Data	-
Synchronous speed (rev/min)	1500
Rated power (MW)	2.0
Rated line-to-line stator voltage (V_{rms})	575
Frequency (Hz)	50
Pole pair	4
Slip (s)	-0.2
R_s (pu)	0.023
L_{ls}(pu)	0.18
L_m(pu)	2.9
R'_r(pu)	0.016
L'_{lr}(pu)	0.16
Rotor nominal voltage (V_{rms}) (V)	1975
Inertia Constant H (s)	0.685
Friction factor (pu)	0.01
Converter Data	-
GSC Max. Current (pu)	0.8
GSC Coupling Inductor [L,R] (pu)	[0.3 0.003]
DC link voltage (V)	1150
DC link Capacitor (F)	10000e-6
Line filter Capacitor (for Q = 50Var) (F)	120e3
Turbine Data	-
Nominal Mechanical Output Power (MW)	2.0
Nominal wind speed at Cp Max (m/s)	11
Initial wind speed (m/s)	11
Cut in speed (m/s)	6
Cot out speed (m/s)	30

Appendix B: DFIG and Converters control parameters

Items	Specifications
Dc link regulator gains [kp, ki]	[8 400]
GSC regulator gains [kp, ki]	[0.83 5]
Speed regulator gains [kp, ki]	[3 0.6]
RSC regulator gains [kp, ki]	[0.6 8]
Q&V regulator gains [kp_Var, ki_V]	[0.05 20]
Pitch controller gain [kp]	[150]
Pitch compensation gains [kp, ki]	[3 30]
Frequency of GSC PWM carrier (Hz)	2700
Frequency of RSC PWM carrier (Hz)	1620

Appendix C: DFIG-Based Wind Turbine Simulink Model

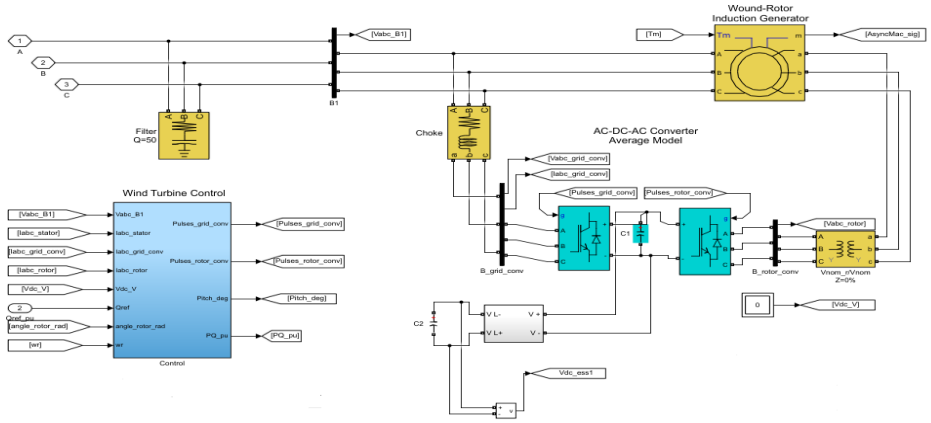

Appendix D: DFIG-Based WT System Grid Components

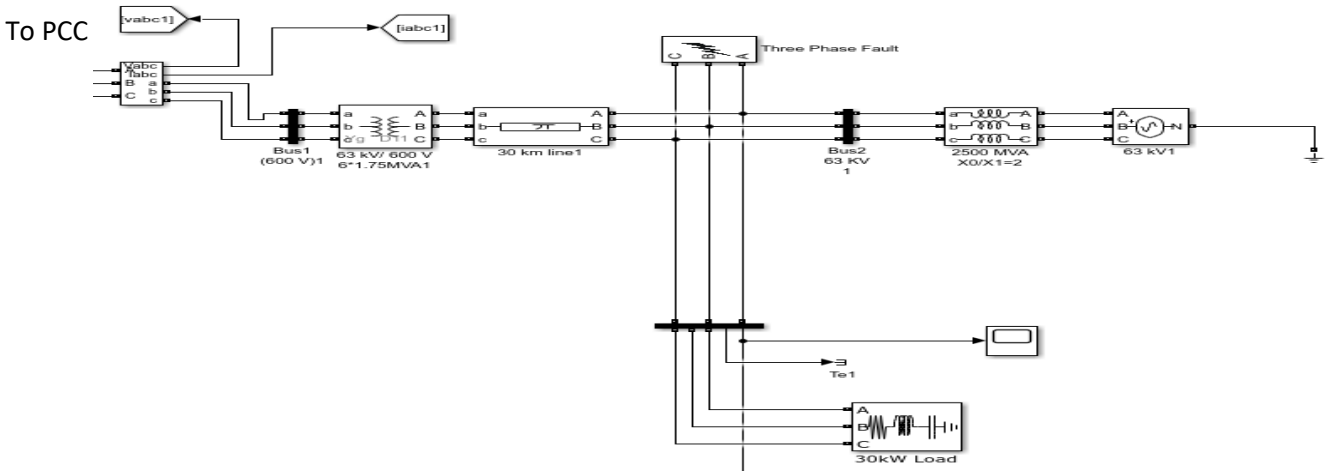

PAPER 33 – EFFECTS OF PROCESS PARAMETERS ON OIL AND BIODIESEL YIELD FROM SANDBOX (*HURA CREPITANS*) SEED

D. N. Onwe [1*], A. I. Bamgboye [2]

[1]Department of Agricultural and Food Engineering, Faculty of Engineering, University of Uyo, Nigeria.
[2]Department of Agricultural and Environmental Engineering, Faculty of Technology, University of Ibadan, Nigeria.
*Email: davidonwe@uniuyo.edu.ng

ABSTRACT
Multiple applications of vegetable oil for food, industrial applications and biodiesel production have necessitated the need to boost product yield. Process factors that influence oil and biodiesel yield were investigated. Factors studied for oil extraction were, moisture content (%wb), roasting temperature (°C), roasting time (min), extraction temperature (°C) and time (min). Reaction time (min), reaction temperature (°C), catalyst concentration (%wt) and molar ratio were investigated for biodiesel yield. Central composite rotatable design of response surface methodology experimental design was used for the study. Results obtained were analysed at ($p =\leq 0.05$). The oil yield from the sandbox seed ranged from 20.9-53.6%. The maximum oil yield of 53.6% was obtained at the processing conditions of 10.0%wb moisture content, 95 °C roasting temperature, 15 min roasting time, 65 °C extraction temperature and 90 min extraction time. The biodiesel yield ranged from 80.00-96.12% and, maximum biodiesel yield of 96.12% was extracted at 72.0 min reaction time, 50.0 °C reaction temperature, 0.9%wt catalyst concentration and 1:6 molar ratio. Mathematical models to predict sandbox seed oil and biodiesel yields at varying process conditions were developed. Coefficient of determination (R^2) relating the oil extraction and biodiesel production were 0.81 and 0.74, respectively. The results from the study provide data for equipment and process designs for oil extraction and biodiesel production from sandbox and other oilseeds.

KEYWORDS: *Hura crepitans*, Oil extraction, oil yield, biodiesel production, biodiesel yield.

1. INTRODUCTION

Sandbox **(***Hura crepitans* Linn.) is a dicotyledon tree of the (spurge) family Euphorbiaceae. It is a native tree of the tropical zones of the Amazon rainforest of North and South America (Adewuyi *et al.,* 2014). Sandbox seed has been suggested to contain a high oil content in addition to a number of important properties that can be useful for food and feed production, paints, and cosmetics amongst others industrial application and pharmaceutical potentials (Olatidoye *et al*., 2010; Onwe and Bamgboye, 2020; Basumatary, 2013). It is however grouped under underutilized species of plant (Adewuyi *et al.,* 2014). According to Idowu *et al.* (2012), sandbox is used as shade trees in many parts of the world because their wide spreading limb. In corroboration, Adewuyi *et al.* (2012) noted that sandbox is an underutilized plant in Nigeria and the seeds are unused. Solvent extraction has made it more profitable to recover most oil from seeds, nuts, and other materials with relatively low oil content, as up to 98% of oil can be recovered using solvent extraction (Matthäus, 2012). Oil is extracted from oil-bearing matters using crude liquids like acetone, ether, chloroform, petroleum, spirit, carbon tetrachloride, diethyl ether, and carbon tetra chloride. Various oilseeds have been studied to determine the best extraction conditions for the highest oil yield: sesame seed (Hashim *et al*., 2014; Elkhaleefa and Shigidi, 2015); rubber seed (Awais *et al.,* 2015); soybean seed (Lawson *et al.,* 2010); dried Bitter Gourd seed (Umamaheshwari and Dinesh Sankar Reddy, 2016); canola seed (Blake, 1982); un-sieved rice bran and sieved rice bran respectively (Sivala *et al.,* 1991); sunflower kernels (Southwell and Harris, 1992) and grated coconut (Hammonds *et al.*, 1991); Neem (*Azadirachta indica*) seed (Awolu *et al*., 2013); Sorrel (*Hibiscus sabdariffa*) seed (Betiku and Adepoju, 2013); almond seed (Akubude *et al.,* 2017); Dika nut (Abidakun *et al.*, 2012); groundnut (Olajide *et al.*, 2014); Shea kernel (Olaniyan and Oje, 2007); African star apple seed (Ajala and Adeleke, 2014); *Moringa* seed (Adejumo *et al.,* 2013). The global concern of the rapid depletion of the petroleum and its potential extinction, coupled to environmental pollution emissions from its combustion exhaust, has made biodiesel from organic lipids an available substitute to petroleum diesel (Reyes and Spulveda, 2006; Goering *et al.,* 1982). Organic lipids like vegetable oils, animal fats, waste oils, and recycled lubricants are combined with alcohol, primarily methanol or ethanol, in a displacement reaction known as transesterification to create fatty esters like methyl/ethyl ester (biodiesel). Factors that influence methyl ester yield from lipids have been studied (Zhang *et al.*, 2003; Ma and Hanna, 1999; Meher *et al.*, 2006; Van, 2005 and Schuchardta *et al.,* 1998)**.** Oil extraction by solvent extraction method from sandbox seed have been reported (Okolie *et al.,* 2012; Muhammed *et al.,* 2013; Adewuyi *et al.,* 2014; Shonekan and Ajayi, 2015; Nwanorh, 2015; Ottih *et al.,* 2015). Biodiesel was produced from sandbox seed oil (Adewuyi *et al.*, 2012; Adepoju *et al.*, 2013; Igbum *et al.*, 2012). The present work is focused on investigating the effects of process parameters on sandbox seed oil and biodiesel yield respectively.

2. MATERIALS AND METHODS

About 100 kg of mature sandbox fruits were collected from Uyo metropolis, Akwa Ibom State, Nigeria between (2016-2018). The fruits were cracked to remove the seeds and the seeds peeled to get the kernel (mesocarp) (Figure 2.1).

Figure 2.1 Sandbox seed processing

2.1. Solvent oil extraction from sandbox seed

Oil extraction was carried out according to the American Oil Chemists' Society (AOCS 5-04) standard procedure. A six-in-one Soxhlet apparatus was used for the extraction process. The experiments were carried out at varying processing conditions: moisture content, mc (4, 6, 8, 10 and 12% wet-basis), roasting temperature, $ϒ_{tp}$ (80, 85, 90, 95 and 100ºC) and time, $ϒ_{tm}$ (0, 5, 10, 15 and 20 min), extraction temperature, $ε_{tp}$ (60, 65, 70, 75 and 80ºC) and time, $ε_{tm}$ (60, 90, 120, 150 and 180 min). The sandbox seed oil (Figure 2.2) was weighed and taken as a fraction of the ground seed samples. The oil yield was calculated from Equation 2.1 as adopted by Bello and Daniel (2015) for determination of oil yield percentage.

$$Oil\ Yield\ (\%) = \frac{Wieght\ of\ oil\ extracted}{Wieght\ of\ sandbox\ seed\ sample\ used\ in\ the\ extraction} \times 100 \quad (2.1)$$

Figure 2.2 Biodiesel production

2.2. Biodiesel production from sandbox seed oil

The effects of process variables: reaction time (24, 48, 72, 96 and 120 min), reaction temperature (40, 45, 50, 55 and 60 ºC), catalyst concentration (0.3, 0.6, 0.9, 1.2 and 1.5 %wt) and molar ratio (1:2, 1:4, 1:6, 1:8 and 1:10 methanol: oil ratio) on the methyl ester yield were investigated. Two hundred millilitres (200 ml) of sandbox seed oil, amounting to 184 g in weight was used in each of the experiment. Other parameters were calculated as percentage weight or volume of the oil. Methanol was used as the alcohol in the transesterification reaction, and potassium hydroxide was used as the catalyst for the reaction. The Central Composite Rotatable Design (CCRD) of Response Surface Methodology was used for both experiments. Experiments were replicated thrice.

3. RESULTS AND DISCUSSION

The results of the sandbox oil and biodiesel yields at various process conditions are presented in Tables 3.1 and 3.2 respectively. Charts showing the effects of process parameters on oil and biodiesel yield are shown in Figures 3.1-3.4.

Table 3.1 Oil Yield from Sandbox Seed at Various Processing Conditions

Run	Factor 1 A: mc (%)	Factor 2 B: $ϒ_{tp}$ (%)	Factor 3 C: $ϒ_{tm}$ (min)	Factor 4 D: $ε_{tp}$ (ºC)	Factor 5 E: $ε_{tm}$ (h)	Response 1 Oil yield (%)
1	8	90	10	70	2.0	45.76
2	8	90	10	70	3.0	35.02

3	8	90	10	70	1.0	23.00
4	6	85	5	65	2.5	38.33
5	8	90	10	60	2.0	42.87
6	10	85	15	75	1.5	40.00
7	10	85	5	75	2.5	40.12
8	4	90	10	70	2.0	20.86
9	10	85	15	65	2.5	48.88
10	8	90	10	80	2.0	44.00
11	12	90	10	70	2.0	30.00
12	8	90	10	70	2.0	45.00
13	6	95	15	65	2.5	40.00
14	8	90	10	70	2.0	50.00
15	8	90	10	70	2.0	49.80
16	10	95	15	75	2.5	46.54
17	6	85	15	65	1.5	35.66
18	10	95	5	65	2.5	36.00
19	8	80	10	70	2.0	38.10
20	8	90	10	70	2.0	47.77
21	10	85	5	65	1.5	36.56
22	6	95	15	75	1.5	39.00
23	10	95	5	75	1.5	42.40
24	6	85	5	75	1.5	39.60
25	6	85	15	75	2.5	40.55
26	6	95	5	65	1.5	40.06
27	6	95	5	75	2.5	38.99
28	8	90	10	70	2.0	46.44
29	8	90	0	70	2.0	21.00
30	10	95	15	65	1.5	53.60
31	8	90	20	70	2.0	47.99
32	8	100	10	70	2.0	51.33

Where mc = moisture content of sandbox seed, γ_{tp} = Roasting temperature, γ_{tm} = Roasting time, ε_{tp} = Extraction temperature and ε_{tm} = Extraction time

The oil yield from the sandbox seed ranged from 20.86-53.60%. The highest oil yield of 53.60% obtained was similar to 53.61 and 53.81% obtained by Okolie *et al.*, (2012) and Muhammed *et al.* (2013), and higher than 37.75, 36.70 and 42.70% obtained by Adewuyi *et al.* (2014), Shonekan and Ajayi, (2015) and Nwanorh, (2015). The value was however lower than the 57.26% obtained by Ottih *et al.* (2015). According to Anwar *et al.* (2006); Orhevba *et al.* (2013), differences in oil yield during extraction are a function of extraction methods employed, and also biological and environmental conditions.

Increase in oil yield was observed as the moisture content increased from 4-10%wb, after which the yield declined (Fig. 3.1). The highest oil yield was obtained at 10% seed moisture; the decline in oil yield at moisture contents above 10%wb could be attributed to the observation that the ground sandbox seed forms a slurry paste at moisture contents above 10%, making further oil removal difficult. The trend is in agreement with reports on soybeans, and un-sieved and sieved rice bran (Lawson *et al.,* 2010; Sivala *et al.,* 1991) among others.

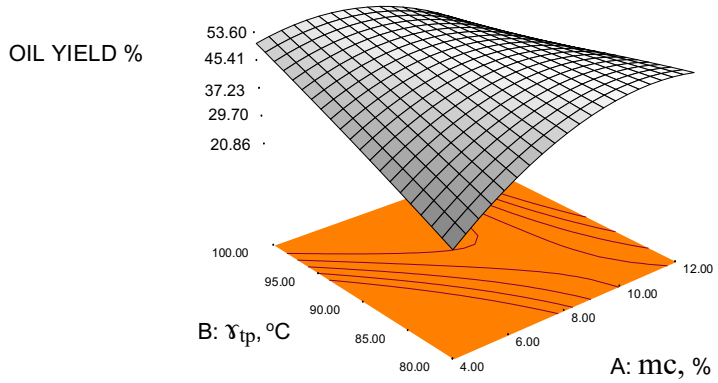

Figure 3.1. Oil yield against roasting time and moisture content

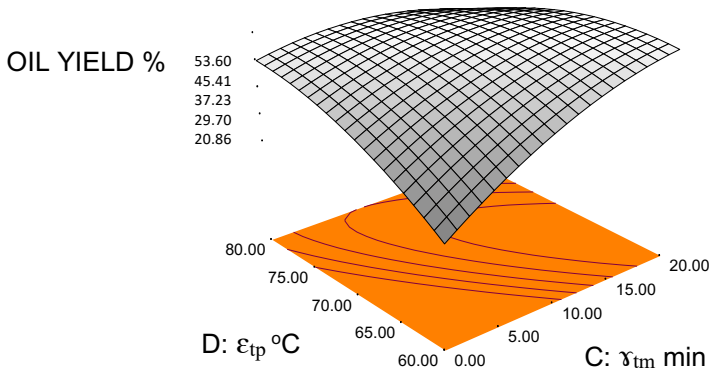

Figure 3.2. Extraction time and roasting temperature against oil yield

The sandbox oil yield increased as roasting temperature increased. The highest oil yield occurred at the roasting temperature region of 95-100°C (Figure 3.1). Due to the sandbox seed's softness, a seed similar to melon seed, roasting temperature around 100 °C was sufficient to penetrate the seed and release its oil. Similar roasting temperature of 100°C was obtained for maximum oil yield from *Moringa oleifera (*Adejumo *et al*. (2013). The unroasted samples at 0 min roasting time produced the lowest oil yield from the sandbox, and then the oil yield increased with an increase in roasting time up to 15 min beyond which the yield became constant (Figure 3.2). The sandbox oil yield increased with an increase in extraction temperature up to 75 °C, after which the oil yield decreased (Figure 3.2). Extraction temperature range of 60-90 °C has been reported to be suitable for maximum oil yield from seeds and nuts by solvent extraction. Solvent extraction temperature of 60 °C was reported by Asoiro and Akubuo (2012) as suitable for maximum oil extraction from *Jatropha curcas* L. Umamaheshwari and Dinesh Sankar Reddy (2016) obtaining maximum oil yield from bitter gourd at 98 °C extraction temperature and Elkhaleefa and Shigidi (2015) reported a lower extraction temperature of 40 °C for maximum oil yield from sesame seed. The sandbox oil yield increased with increase in extraction time up to 120 min, beyond which a decrease in oil yield was observed. It was observed that 2 hours reaction time was enough for complete oil removal from sandbox seed by solvent extraction. Lawson *et al.* (2010) obtained maximum oil yield from soybeans at an extraction time of 2½ hours.

Table 3.2. Biodiesel Yield from the Transesterification of Solvent Extracted Sandbox Seed Oil

S/N	Factor 1 A:τ_{tm} (min)	Factor 2 B:τ_{tp} (°C)	Factor 3 C:$\dot{c}_{cc}$ (% of oil wt)	Factor 4 D:η_{ra} (% vol. of oil)	Response Fuel yield (%)
1	48	45	0.60	8	86.20
2	96	45	0.60	4	86.12
3	48	55	0.60	4	88.65
4	48	55	1.20	4	81.02
5	48	45	1.20	8	83.79
6	48	45	0.60	4	86.25
7	96	45	0.60	8	87.16
8	72	50	0.90	6	94.55
9	72	50	0.90	6	94.89
10	72	50	0.30	6	89.48
11	72	50	0.90	2	80.11
12	72	50	0.90	6	91.99
13	96	55	0.60	4	88.01

14	96	55	1.20	4	82.36
15	96	45	1.20	4	83.88
16	72	50	0.90	10	87.98
17	72	40	0.90	6	88.42
18	120	50	0.90	6	92.68
19	48	55	0.60	8	91.23
20	72	60	0.90	6	96.12
21	48	55	1.20	8	83.33
22	24	50	0.90	6	81.65
23	72	50	0.90	6	86.99
24	96	55	1.20	8	81.22
25	72	50	0.90	6	87.98
26	96	45	1.20	8	82.63
27	48	45	1.20	4	80.11
28	72	50	0.90	6	92.65
29	96	55	0.60	8	85.00
30	72	50	1.50	6	80.00

Where r_{tm} = reaction time, r_{tp} = reaction temperature, $\dot{c}_{cc}$ = catalyst concentration (KOH) and η_{ra} = molar ratio

The biodiesel yield ranged from 80.00-96.12%. The maximum biodiesel of 96.12% was extracted at 72.0 min reaction time, 50.0 °C reaction temperature, 0.9%wt catalyst concentration and 1:6 molar ratio.
The biodiesel yield increased with increase in reaction time from 24 min to about 90 min before a decline in biodiesel yield was observed (Figure 3.3). This was an indication that transesterification reaction for sandbox seed oil requires about 1.5 hour to be completed. Similarly, Math *et al*. (2010) reported 90 min reaction time as optimum for maximum biodiesel yield from lipids with FFA. A lower reaction time of 40 min was obtained by Nakpong and Wootthikanokkhan (2010) for maximum biodiesel yield from crude *Jatropha curcas* oil. Reports have shown that transesterification process is spontaneous at the beginning of the reaction, converting approximately 80% of the reactants into ester fuels in the first 5 min and gaining approximately 93-98% conversion after 1 h of reaction period (Encinar *et al.,* 2005; Srivastava and Prasad, 2000; Alcantra, 2000; Shailendra *et al.,* 2008).

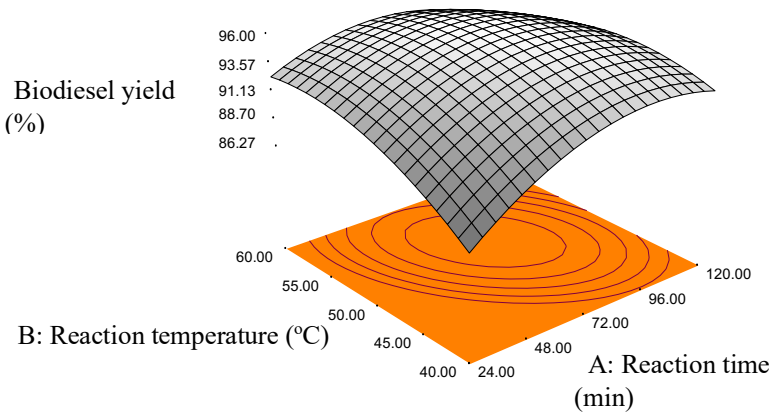

Figure 3.3. Reaction temperature and reaction time against fuel yield

The sandbox biodiesel yield increased with increase in reaction temperature from 40 °C to 50 °C after which the yield became steady (Figure 3.3). This indicates that 50-60 °C reaction temperature range is adequate for the

transesterification of sandbox seed oil. The reaction temperature was same with 60 °C obtained by Adepoju *et al.* (2013) for sandbox seed oil biodiesel and lower than 70 °C obtained by Adewuyi *et al.* (2014) for maximum biodiesel yield from transesterification of (H_2SO_4) acid pre-treated sandbox seed oil and but the. This difference in reaction temperature might be due to reaction process used. Similar reaction temperatures were reported by (Alhassan *et al.,* 2014 for *Gossypium Arboreum* seed oil; Anguebes-Franseschi *et al*., 2016 for crude palm oil of African origin; Nakpong and Wootthikanokkhan, 2010 for *Jatropha* seed; Singh *et al.,* 2006 for canola oil; Mansourpoor and Shariati, 2012 for sunflower oil).

The biodiesel yield increased as the catalyst concentration increased from 0.3% to 0.9% after which the yield dropped sharply. The value 0.9% g wt/wt of oil represents 0.5% weight of volume of oil used in the reaction (Figure 3.4). The result is average to 0.4% and 0.55% obtained by Adewuyi *et al.,* 2014 and Adepoju *et al.,* 2013 for sandbox seed. Similar result was obtained by Alhassan *et al.,* 2014 for *Gossypium Arboreum* seed oil, Anguebes-Franseschi *et al*., 2016 African palm oil and Mansourpoor and Shariati, 2012 for sunflower seed.

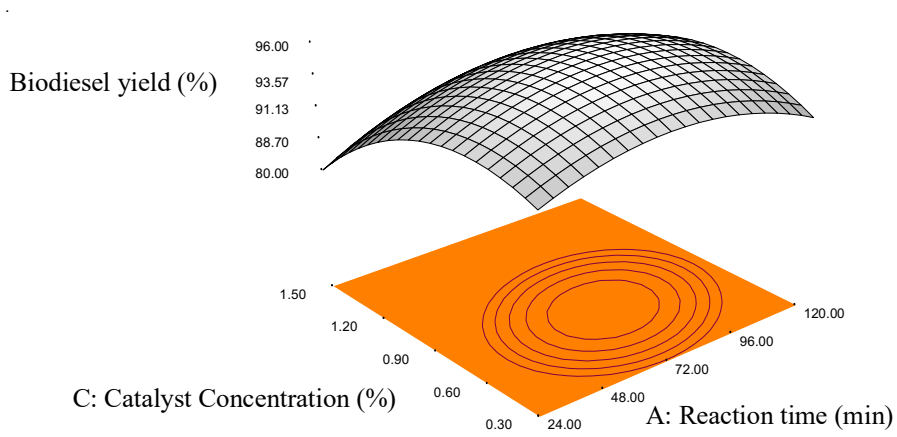

Figure 3.4. Catalyst concentration and reaction time against fuel yield

The sandbox biodiesel increased with increase in molar ratio from 1:2 up to 1:6 after which a decrease in yield was observed (Figure 3.4). Adewuyi *et al.* (2014) and Adepoju *et al.* (2013), obtained ratios of 1:6 and 1:5 respectively for maximum biodiesel yield from sandbox seed oil. Similar molar ratio was reported by Anastopoulos *et al.,* 2009; Alhassan *et al.,* 2014; and Nakpong and Wootthikanokkhan, 2010 as optimum for maximum biodiesel yield from four different vegetable oils, *Gossypium Arboreum* seed oil and *Jatropha curcas* seed oil respectively. The optimum molar ratio of 1:6 or less for other edible oils has been found to give the highest fuel yield (Encinar *et al.,* 2005; Vicente *et al.*, 2004; Dorodo, 2002).

a. Processes model equations

Mathematical relationship for predicting oil yield from sandbox relatively to the process factors is given in Equation 3.1. The coefficient of determination (R^2) relating the oil extraction process and oil yield was 0.81.

- $OY = 45.89 + 2.09mc + 1.81\text{ɤ}_{tp} + 3.59\text{ɤ}_{tm} + 0.013\varepsilon_{tp} + 1.10\varepsilon_{tm} - 1.91mc^2 - 0.88\text{ɤ}_{tp}^2 - 1.67\text{ɤ}_{tm}^2 + 0.56\varepsilon_{tp}^2 - 3.05\varepsilon_{tm}^2 + 0.57mc\text{ɤ}_{tp} + 2.23mc\text{ɤ}_{tm} - 0.63mc\varepsilon_{tp} - 0.29mc\varepsilon_{tm} + 0.70\text{ɤ}_{tp}\text{ɤ}_{tm} - 0.23\text{ɤ}_{tp}\varepsilon_{tp} - 1.85\text{ɤ}_{tp}\varepsilon_{tm} - 1.39\text{ɤ}_{tm}\varepsilon_{tp} + 0.80\text{ɤ}_{tm}\varepsilon_{tm} + 0.50\varepsilon_{tp}\varepsilon_{tm}$ (3.1)

Where, OY = Oil Yield (%), mc = moisture content of sandbox seed, ɤ_{tp} = Roasting temperature, ɤ_{tm} = Roasting time, ε_{tp} = Extraction temperature and ε_{tm} = Extraction time

Mathematical relationship for predicting biodiesel yield from sandbox relatively to the process factors is given in Equation 3.2. The coefficient of determination (R^2) relating the transesterification process and biodiesel yield was 0.74.

- $\text{Fuel Yield} = 91.51 + 0.74\text{ŕ}_{tm} + 0.84\text{ŕ}_{tp} - 2.47\dot{c}_{cc} + 0.83\text{ɱ}_{ra} - 1.46\text{ŕ}_{tm}^2 - 0.18\text{ŕ}_{tp}^2 - 2.07\dot{c}_{cc}^2 - 2.24\text{ɱ}_{ra}^2 - 0.69\text{ŕ}_{tm}\text{ŕ}_{tp} + 0.49\text{ŕ}_{tm}\dot{c}_{cc} - 0.81\text{ŕ}_{tm}\text{ɱ}_{ra} - 0.60\text{ŕ}_{tp}\dot{c}_{cc} - 0.17\text{ŕ}_{tp}\text{ɱ}_{ra} + 0.19\dot{c}_{cc}\text{ɱ}_{ra}$ (3.2)

Where ŕ_{tm} = reaction time, ŕ_{tp} = reaction temperature, $\dot{c}_{cc}$ = catalyst concentration (KOH) and ɱ_{ra} = molar ratio

4. CONCLUSION

Effects of process factors on oil and biodiesel yield from sandbox seed were investigated. Among the process factors studied, the oil yield from the sandbox seed ranged from 20.9-53.6%. The maximum oil yield of 53.6%

was obtained at the processing conditions of 10.0%wb moisture content, 95 ^{o}C roasting temperature, 15 min roasting time, 65 ^{o}C extraction temperature and 90 min extraction time. The biodiesel yield ranged from 80.00-96.12%. The maximum biodiesel of 96.12% was extracted at 72.0 min reaction time, 50.0 ^{o}C reaction temperature, 0.9%wt catalyst concentration and 1:6 molar ratio. Mathematical models to predict sandbox seed oil and biodiesel yields at varying process conditions were developed with 0.81 and 0.74 coefficient of determination (R^2).

REFERENCES

Abidakun O. A., Koya O. A., and Ajayi, O. O. (2012). *Effect of extraction conditions on the yield of Dika Nut (Irvingia gabonesis) oil under uniaxial compression.* Proc. ICCEM, 315-320.

Adejumo B. A., Alakowe A. T., and Obi D. E. (2013). *Effect of heat treatment on the characteristics and oil yield of Moringa oleifera seeds.* The International Journal of Engineering and Science (IJES), 2(1), 232-239.

Adepoju T. F., Abiodun A., Okunola A.A., and Dahunsi O. S. (2013). Experimental investigation of sand box biodiesel performance in an internal combustion engine. International Journal of Engineering Research & Technology (IJERT), 2(11), 3833-3855.

Adewuyi A., Paul O., Awolade, P. O., and Oderinde R. A. (2014). *Hura crepitans seed oil: an alternative feedstock for biodiesel production.* Journal of Fuels*,* 464590 (8).

Adewuyi A., Gopfert A., Wolff T. Rao B. V. S. K., and Prasad R. B. N. (2012). *Synthesis of azidohydrin from Hura crepitans seed oil: a renewable resource for oleochemical industry and sustainable development*. ISRN Organic Chemistry, 2012/ID 873046.

Ajala A. S., Adeleke S. A. (2014). *Effect of drying temperatures on physicochemical properties and oil yield of african star apple (Chrysophyllum alibidum) seeds*. Global Journal of Engineering Design and Technology (G.J. E.D.T.), 3(3), 12-16.

Akubude V. C., Maduako J. N., Egwuonwu C. C., Olaniyan A. M., Ozumba I. C., Nwosu C., and Ajala O. E. (2017). *Effect of process parameters on oil yield mechanically expressed from almond seed (Using Response Surface Methodology).* American Journal of Food Science and Nutrition Research, 4(1), 1-8.

Alcantra, R., *et al.* 2000*. Catalytic production of biodiesel from soy-bean oil used frying oil and tallow.* Biomass Bioenergy, 18, 515-527.

Alhassan, Y., Kumar, N., Bugaje, I. M., and Mishra, C. (2014). *Optimization of (Gossypium arboretum) seed oil biodiesel production by Central Composite Rotatable Model of Response Surface Methodology and evaluation of its fuel properties.* Journal of Petroleum Technology and Alternative Fuels, 5(1), 1-12.

Anguebes-Franseschi, F., *et al*. (2016). *Optimization of biodiesel production from African crude palm oil (Elaeis guineensis Jacq) with high concentration of free fatty acids by a two-step transesterification process.* Open Journal of Ecology, 6, 13-21.

Anwar F., Zafar S. N., Rashid U. (2006). *Characterization of Moringa oleifera seed oil from drought and irrigated regions of Punjab.* Pakistan Grasas Aceites, 57(2), pp. 60-168.

Asoiro F. U., Akubuo C. O. (2012). *Effect of temperature on oil extraction of Jatropha curcas L. kernel.* The Pacific Journal of Science and Technology, (2), 456-463.

Awais B., Suzana Y., and Murni M. A. (2015). *Optimization of the Parameters that Affects the Solvent Extraction of Crude Rubber Seed Oil Using Response Surface Methodology (RSM).* Recent Advances in Engineering, 28-33.

Awolu O. O., Obafaye R. O., Ayodele B. S. (2013). *Optimization of solvent extraction of oil from neem (Azadirachta indica) and its characterizations.* Journal of Scientific Research and Reports, 2(1), 304-314.

Basumatary S. (2013). *Non-conventional seed oils as potential feedstocks for future biodiesel industries*: *A Brief Review.* Research Journal of Chemical Sciences, 3(5), 99-103.

Betiku, E., and Adepoju, T. F. (2013). *Sorrel (Hibiscus sabdariffa) seed oil extraction optimization and quality characterization.* American Chemical Science Journal*,* 3(4), 449-458.

Blake J. A. (1982). *Evaluation of an On-farm Press. In: Vegetable oil fuels*. ASAE Publication, No. 482, MI 49055, 247-251.

Bello E. I., and Daniel F. (2015). *Optimization of groundnut oil biodiesel production and characterization.* Applied Science Report, 9(3), 172-180.

Dorodo, W., Ballesteros, E., De Almeida, J., Schellert, C., Lohrlein, H., and Krause, R. 2002. *An alkali-catalyzed transesterification process for high free fatty acid waste oils.* Trans ASAE, 45(3), 525-9.

Elkhaleefa A., Shigidi, Ihab I. (2015). *Optimization of sesame oil extraction process conditions*. Advances in Chemical Engineering and Science, 5, 305-310.

Encinar, J. M., Gonzalez, J. F., and Reinares, A. R. (2005). *Biodiesel from used frying oil: variables affecting the yields and characteristics of the biodiesel.* Ind. Eng. Chem. Res., 44, 5491-9.

Goering C. E., Schwab A. W., Daugherty M. J., Pryde E. H., and Heakin A. J. (1982). *Fuel properties of eleven oils.* Transactions ASAE, 25, 1472-1483.

Hammonds T. W., Harris R.V., and Head S. W. (1991). *The influence of moisture content on the extraction of oil from fresh grated Coconut.* Tropical Science, 31, 73-81.

Hashim, A. B., Giwa, S. O., Ibrahim, M., and Giwa, A. (2014). *Finding the optimum parameters for oil extraction from sesame seed using Response Surface Methodology*. International Journal of Scientific Research and Management Studies (IJSRMS), 2(1), 1-13.
Idowu D. O., Abegunrin T. P., Ola F. A., Adediran A. A., Olaniran J. A. (2012). *Measurement of some engineering properties of sandbox seeds (Hura crepitans)*. Agriculture and Biology Journal of North America, 8, 318-325.
Igbum O. G., Eloka-Eboka A. C and Nwadinigwe C. A. (2012). *Effects of transesterification variables on yields and properties of biodiesel fuels produced from four virgin tropical seeds oils*. International Journal of Environmental Bioenergy, l (1), 119-130.
Lawson O. S, Oyewumi A., Ologunagba F. O., Ojomo A. O. (2010). *Evaluation of the parameters affecting the solvent extraction of soybean oil. ARPN Journal of Engineering and Applied Sciences*, 5(10), 51-55
Ma F., and Hanna M. (1999). *Biodiesel production: A review.* Bioresource Technology, 70(1), 1-15.
Mansourpoor, M., and Shariati, A. (2012). *Optimization of biodiesel production from sunflower oil using response surface methodology*. *J. Chem Eng Process Technol*, 3(4), 5.
Math, M. C., *Sudheer, P. K., and Soma V. C. 2010. Optimization of biodiesel production from oils and fats with high free fatty acids. Indian Journal of Science and Technology, 3:3, 318-321.*
Matthäus B. Oil technology. S.K. Gupta (ed.), Technological Innovations in Major World Oil Crops, pp. 2.
Meher L. C., Sagar D. V., and Naik S. N. (2006). *Technical aspects of biodiesel production by Transesterification: A review.* Renewable Sustainable Energy Reviews, 10(3), 248-268.
Muhammed N. A., Isiaka A. A., and Adeniyi O. A. (2013). *Chemical composition of Hura crepitans seeds and antimicrobial activities of its oil.* International Journal of Science and Research (IJSR), 2(3), 440-445.
Nakpong, P., and Wootthikanokkhan, S. (2010). *Optimization of biodiesel production from Jatropha curcas L. oil via alkali-catalyzed methanolysis.* Journal of Sustainable Energy and Environment*,* 1,105-109.
Nwanorh K. O. (2015). Extraction and characterization of oil from Hura crepitans (sandbox tree). International Research Journal of Education and Innovation, 1-2(17), 60-62
Okolie P. N., Uaboi-Egbenni P. O., and Ajekwene A. E. (2012). *Extraction and quality evaluation of sandbox tree seed (Hura crepitan)*. Oil World Journal of Agricultural Sciences, 8(4), 359-365.
Olajide J. O., Afolabi J. O., and Adeniran J. A. (2014). *Optimization of oil yield from groundnut kernel (Arachis hypogeae) in an hydraulic press Using Response Surface Methodology*. Journal of Scientific Research and Reports, 3(14), 1916-1926.
Olaniyan A. M., Oje K. (2007). *Development of mechanical extraction rig for dry extraction of Shea butter from Shea kernel.* Journal of Food Science and Technology, 44(5), 465-470.
Olatidoye O. P., Adeleke A. E., Adegbite S. A., and Sobowale S. A. (2010). *Chemical composition and nutritional evaluation of sandbox (Hura crepitan) seed flour for domestic consumption and industrial*. Journal of Medical and Applied Biosciences, 2, 72-83.
Onwe, D. N., and Bamgboye A. I. 2020. *Effect of process conditions on sandbox seed oil yield by mechanical expression: A response surface approach*. Sci. J. Agric. Eng. 3, 70-81
Orhevba B. A., Chukwu O., Osunde Z. D., Ogwuagwu V. (2013). Influence of moisture content on the yield of mechanically expressed neem seed kernel oil. Academic Research International, 4(5), 252-257
Reyes J. F., and Sepulveda M. A. (2006). *PM-10 Emissions and power of a diesel engine fuelled with crude and refined biodiesel from salmon oil.* Fuel, 85, 1714-9.
Umamaheshwari P., Dinesh Sankar Reddy, P. (2016). *Effect of operating parameters on extraction of oil from bitter gourd seeds: a kinetic and thermodynamic study.* International Journal of Science and Research (IJSR), 5(2), 1243-1246.
Vicente, G., Martinez, M., and Aracil, J. (2004). *Integrated biodiesel production: a comparison of different homogeneous catalysts systems.* Biores Technol*,* 92, 297-305.
Shailendra S., Avinash, K. A., and Sanjeev, G. (2008). *Biodiesel development from rice bran oil: Transesterification process optimization and fuel characterization.* Elsevier; Energy Conversion and Management, 49, 1248-1257.
Shonekan F. O., and Ajayi J. O. (2015). The biochemical analysis of Hura crepitans (Sandbox Tree) seed oil and meal. Globalacademicgroup.com, Retrieved January 15, 2016.
Sivala K., Bhole N. G., and Mukherjee R. K. (1991). *Effect of moisture on rice bran oil extraction.* Journal of Agricultural Engineering Research, 1(50), 81-91.
Southwell K. H., and Harris, R. V. (1992). *Extraction of oil from oilseeds using the hot water flotation method.* Tropical Science, 2(82), 251-256.
Srivastava A., and Prasad R. (2000). *Triglycerides-based diesel fuels.* Renewable Sustainable Energy Rev, 4, 111-33.
Van Gerpen J. (2005). *Biodiesel processing and production.* Fuel Processing Technology, 86(10), 1097-1107.
Zhang Y., Dubé M. A., McLean D. D., and Kates M. (2003). *Biodiesel production from waste cooking oil: process design and technological assessment.* Bioresource Technology, 89, 1-16.

PAPER 34 – ASSESSING THE FEASIBILITY OF EXPLOITING HYDROPOWER RESOURCES OF UNDERUTILIZED WATER DAM

A. S. Akintaro[1], O. O. Olanrele[2*]

[1]Department of Mechanical Engineering, University of Ibadan, Ibadan, Oyo State, Nigeria.
[2]Department of Computer and Industrial & Production Engineering, First Technical University, Ibadan, Oyo State Nigeria.
[*]Email: Oladeji.olanrele@tech-u.edu.ng

ABSTRACT

The power sector in Nigeria faces significant challenges, with limited electricity access being a primary concern for stakeholders. Almost half of Nigeria's population has no access to electricity supply, notwithstanding the number of untapped energy sources in the country. However, integrating mini or micro hydropower plants into existing and underutilized water dams could help mitigate these challenges. This study evaluates the hydropower potential of the underutilized Eruwa (Opeki) dam to a 1MW mini hydropower plant. The Eruwa (Opeki) dam is a part of the Eruwa water scheme located at Eruwa a town in Oyo State, South West Nigeria. The methods adopted for the research are physical site inspection, data collection, engineering designs, and hydropower simulation. A 706.32kW theoretical power was achieved from the design with an annual energy generation of 4292.89MWh and projected investment and operation/maintenance cost ₦441,000,000 and ₦13,230,000/annum respectively. Annual revenue projection is ₦283,502,455.60, using the present electricity tariff of ₦66.04/kWh. The integration of mini hydropower plants into existing water schemes could increase electricity generation from renewable sources, reduce carbon footprint, and increase revenue for the scheme to prevent underfunding and facilities degradation.

KEYWORDS: Hydroelectric power, Renewable energy, Power generation capacity, Energy access, Energy economics, Dam infrastructure.

5 INTRODUCTION

Hydropower is a renewable energy source that generates power by using dams or diversion structures to alter the natural flow of a river or other body of water. It relies on the endless, constantly recharging system of the water cycle driven by the sun to produce electricity (U.S Office of Energy Efficiency and Renewable Energy, 2021). It is an environmentally friendly source of energy that has the potential to play a significant role in meeting the world's increasing demand for electricity. A hydropower plant is fueled by water, clean energy with lesser pollution in contrast to fossil fuels power plants. It is the most significant renewable energy for electricity generation, with a global installed capacity of 1307GW (Kumar, 2021). In addition, it is expected to remain the largest source of renewable electricity generation (IEA, 2021).

Nigeria, like many other developing countries, is facing an energy crisis with over 50% of its population lacking access to electricity. According to the International Energy Agency (IEA) (2020), Nigeria's energy poverty rate remains high, with an average electricity consumption of 146.84 kWh/capita, which is significantly lower than the global average of 3,074.04 kWh/capita. This is due in part to the poor exploration and exploitation of untapped hydropower potential and other renewable energy sources in the country.

This energy deficit has negatively impacted economic growth, social welfare, and sustainable development in the country. Despite its vast potential for hydropower generation, Nigeria's hydropower capacity remains vastly underutilized (Adewuyi, 2020; Emodi and Boo, 2015, Abban and Awopone, 2021). Nigeria's exploitable hydropower potential is estimated to be 14,120 MW, amounting to more than 50,800 GWh of electricity annually, however, less than 19% was tapped for electricity generation (IHA, 2018).

Furthermore, with over 734.2 MW of electricity generation potential from small hydropower, only 30 MW was produced, which is less than 5% of the potential (Odunfa et.al.,2019). Harnessing all the untapped energy sources through a decentralized grid system with multiple small and mini hydropower plant system could help mitigate energy poverty, increase the economic development of the country, and aids global energy transition plans. Given the increasing demand for electricity in Nigeria and the potential of hydropower as a clean and sustainable source of energy, there is a need to explore the feasibility of harnessing the hydropower potential of underutilized water reservoirs

The objective of this study is to evaluate the technical, economic, and environmental feasibility of harnessing the hydropower potential of the Eruwa (Opeki) Water Dam. The study will assess the potential for hydropower generation at the dam, taking into account factors such as water flow rate, turbine capacity, and power generation

capacity. The study will also evaluate the economic viability of hydropower generation from the Eruwa (Opeki) Water Dam, including the cost of infrastructure development, operations and maintenance, and revenue potential.

The Study area for this research is Eruwa (Opeki) dam, it was constructed in 1967 across the Opeki River sited in Eruwa, a town in Ibarapa East Local Government of Oyo State, Nigeria. The town falls on the 7.53° latitude and 3.42° longitude with an average topography of 149m. The dam has a height of 9.15m and a reservoir capacity of 2 million m³, covering approximately 92 hectares (Ogedengbe and Oke, 2004). It was built to function as a water supply source for the whole Ibarapa community causing the inclusion of a treatment plant capacity of 2.7 million liters/day. Opeki catchment falls within the humid tropical climate with wet seasons (March to November) and dry seasons (December to February) (Idowu and Matins, 2007). It is important to note that the dam and the water treatment facility are presently at 0% utilization. This is due to the degradation of the facility, and damaged distribution network resulting from road construction, all balls down to inadequate funding and maintenance of the scheme.

2. THEORETICAL ANALYSIS

2.1 Engineering calculation for hydroelectric power designs.

2.1.1 Flow rate

Since the maximum storage capacity head $= 8.80$m,

Dead storage head $= 3.16$m,

then gross head (H_g) $= 8.80 - 3.16 = 5.64$m

Due to low head, Kaplan turbine is selected.

Using the general hydropower formula in equation (1) below;

$$P = \cap \; x \; \rho \; x \; g \; x \; H_g \; x \; Q \tag{1}$$

Where, P is Power output (watts) =10^6, g is Acceleration due to gravity (m/s²) =9.81, H_g is Pressure head (m) =5.64, ρ is Water density (kg/m³) =1000, ∩ is Turbine efficiency = 90% and Q the Water flowrate (m³/s) is unknown. The water flow rate can be determined using equation (2) as stated below.

$$water\ flowrate\ Q\left(\frac{m^3}{s}\right) = \frac{p}{\cap \rho g H_g} \tag{2}$$

Applying equation (2), The water flow rate is;

$$Q = \frac{10^6}{0.9x1000x9.81x5.64} = 20.08\, m^3/s.$$

2.1.2 Penstock

Using Bernoulli's as stated in equation (3) below;

$$p_1 + \frac{1}{2}\rho {u_1}^2 + \rho g z_1 = p_2 + \frac{1}{2}\rho {u_2}^2 + \rho g z_2 \tag{3}$$

where ρ is water density, g is Acceleration due to gravity, p_1 is Pressure at penstock inlet, u_1 is Velocity at the dam, z_1 is Height at elevation 1(Head), p_2 is Pressure at turbine outlet, u_2 is Velocity in the turbine and z_2 is Height at elevation 2(Tail). At the same atmospheric pressure of p_1 and p_2, $z_2 = 0$ since elevation at the dam $z_1 = 5.64$, at the tail race is 0, and flow velocity in the dam is 0. Then the height at elevation 1(Head) is stated in equation (4), the flow velocity u was determined using equation (5), and the water flow rate (Q) is in equation (6);

$$z_{1=} {u^2}/{2g}, \tag{4}$$

$$flow\ velocity\ (u) = \sqrt{z_1 + 2g} \tag{5}$$

Then flow velocity u = $\sqrt{z_1 + 2g} = \sqrt{5.64x2x9.81} = 10.52 m/s^2$

$$water\ flowrate\ Q\left(\frac{m^3}{s}\right) = u\ x\ Area\ (A) \tag{6}$$

Then Area (A) $= \frac{Q}{U} = \frac{20.08}{10.52} = 1.91 m^2$

Since $A = \pi \frac{D^2}{4}$, Penstock diameter (D) = 1.56m.

Using Darcey Weibach equation as stated in equation (7) below; where h_f is Head loss due to friction, f is Friction factor, L is Length of penstock and D = Penstock diameter

$$h_f = f\left(\frac{l}{D}\right)\frac{u^2}{2g} \quad (7)$$

To get f, the reynold number (re) must be determined using equation (8)

$$Re = \frac{\rho uD}{\nu} \quad (8)$$

ν *is water viscocity* $= 0.001Pa.s$

Then, $Re = \frac{1000x10.54x1.56}{0.001} = 1.64\ x\ 10^7$, Reynold number (re) of 1.64 x 10^7 indicates high turbulence.

Moody Diagram was used since Reynolds number is available. Due to high turbulence, polyvinylchloride (PVC) pipe with loss roughness of 0.0025 is selected to reduce head loss due to friction. Equation (9) was used to determine the relative pipe roughness.

$$\text{Relative pipe roughness} = \frac{loss\ roughness}{D(mm)} \quad (9)$$

Then, the Relative pipe roughness = $\frac{0.0025}{1560} = 1.6x10^{-6}$

Tracing the moody diagram, friction factor (f) $= 0.007$

Therefore: head loss due to friction (h_f)as stated in equation (7) can be determined;

$h_f = 0.007\left(\frac{l}{1.56}\right)\frac{10.52^2}{2x9.81}$
@ $l = 100m$, $h_f = 2.53m$
@ $l = 50m$, $h_f = 1.27m$
@ $l = 30m$, $h_f = 0.76m$

30m PVC pipe was selected to have an adequate length and low head loss due to friction of 0.76m. The head loss at intake (h_t) is represented in equation (10), the head loss at gate valve h_v is in equation (11), and the net head (H_{net}) is in equation (12).

$$\text{head loss at intake } (h_t) = f\left(\frac{u^2}{2g}\right) \quad (10)$$

Then, the head loss at intake (h_t) $= 0.007\ \left(\frac{10.52^2}{2x9.81}\right) = 0.039m.$

$$\text{Head loss at gate valve } (h_v) = 0.15\left(\frac{u^2}{2g}\right) \quad (11)$$

Then, head loss at gate valve (h_v)$= 0.15\left(\frac{10.52^2}{2x9.81}\right) = 0.84m$, *taking o.15 friction of gate value.*

$$\text{Net Head}(H_{Net}) = H - (h_f + h_t + h_v) \quad (12)$$

Then, the Net head (H_{net}) $= 5.64 - (0.76 + 0.039 + 0.84) = 4.0m$

To get the thickness of the pipe, Diamond Plastic Corporation, Nebraska USA PVC pipe with the diameter of 60" (1524mm), thickness of 1.6" (40.64mm) and tensile strength of 7,000Psi was selected. The dimension of the pipe is equivalent to the required diameter.

Therefore, pressure wave velocity (C) is derived from Joukowsky equation and is stated in equation (13)

$$\text{Pressure wave velocity (C)} = \sqrt{\frac{10^{-3}K}{1+\frac{KD}{Et}}} \quad (13)$$

Kis the Bulk modulus of water $= 2.19x10^9 Nm^{-2}$
E is the young modulus of PVC $= 3.275x10^9 Nm^{-2}$
t is thickness of pipe (mm) $= 40.64$, *while D is pipe diameter* $(mm) = 1560m$

Then, Pressure wave velocity (C) is;

$$C = \sqrt{\frac{10^{-3}K}{1+\frac{KD}{Et}}} = \sqrt{\frac{10^{-3}\ X\ 2.19x10^{9}}{1+\frac{2.19x10^{9}x\ 1560}{3.275x10^{9}x\ 40.64}}} = \sqrt{82083.96} = 286.50\ m/s$$

Equation 14, 15, and 16 was used to determine the surge pressure, critical time, and net power output;

$$\text{Surge pressure} = c\ x\ \rho\ x\ u \quad (14)$$

$$\text{Critical time} = \frac{2L}{c} \quad (15)$$

$$\text{Net Power Output (P)} = \cap\ x\ \rho\ x\ g\ x\ H_{net}\ x\ Q \quad (16)$$

Then the Surge pressure $= 286.5x1000x10.52 = 3.01x10^{6}\ Pa = 437.14\ PSi$;

The Critical time $= \frac{2x30}{286.5} = 0.21s$;

And the Net power output (P) after considering accountable losses is given below;

$$P = 0.9\ x\ 1000\ x\ 9.81\ x\ 4.0\ x\ 20.08 = 709{,}145.28w = 709.14kW$$

3 METHODS

Physical site inspection was done, and dam data collected. Suitable hydropower equations, fundamental fluid property equations to cater for loses in the penstock system and simulation using Computer Aided Simulator System for Instream flow and Riparia (CASiMiR) was used. Furthermore, the dam head and the discharge rate of Opeki river form the basis of this study. The available average monthly discharge record of the Opeki River covering only nine years (between 1988 and 1996) shown in Table 1 was collected from Ogun Oshun River Basin Development Authority (Idowu and Matins, 2007). The most previous monthly data was used to evaluate and predict the annual energy generation potential of the dam based on the discharge rate of the river. The dam storage capacity of the reservoir is shown in Table 2.

Table 1: Average Monthly Discharge Rate of Opeki River (m³)

Years	Jan	Feb	Mar	Apr	May	Jun	Jul	Aug	Sep	Oct	Nov	Dec
1988	9.21	8.26	10.59	2.50	2.50	15.63	67.77	54.94	53.36	56.42	9.93	9.83
1989	12.32	16.42	12.13	17.88	26.81	23.54	46.22	77.81	87.70	63.58	26.79	9.37
1990	9.83	7.94	8.76	12.24	13.25	14.79	14.66	14.20	19.80	44.42	41.70	16.58
1991	2.50	2.50	2.50	8.19	2.88	3.58	27.63	99.06	35.64	42.40	7.36	3.62
1992	4.36	2.50	3.89	2.50	2.90	13.43	28.31	68.97	20.76	64.91	16.74	6.47
1993	7.06	6.65	3.75	2.93	2.89	4.86	14.65	11.69	25.10	44.14	9.07	44.14
1994	3.36	6.92	6.73	2.50	2.50	2.50	7.94	8.24	6.51	49.04	37.18	3.57
1995	6.25	5.97	7.88	11.50	17.87	34.33	49.89	29.35	31.23	65.90	34.87	15.34
1996	4.28	4.36	2.50	13.39	16.52	29.86	47.47	55.88	56.65	49.43	36.50	15.84

Table 2: Eruwa dam storage capacity

Storage capacity	Volume (m³)	Height (m)
Maximum Storage	2,000,000	9.15
Minimum Storage	1,780,000	8.8
Dead Storage	120,000	3.16

4 RESULTS AND DISCUSSION

The results were derived based on the dam data, Opeki river flow discharge, and engineering calculations from hydropower and fluid mechanics equations. Results were backed with Computer Aided Simulator System for Instream flow and Riparia (CASiMiR) as the hydropower simulation tool used for the study.

4.1 Penstock design

With the flow velocity of 10.52 m/s, the flow in the penstock results in turbulence flow at a Reynolds number of $1.64\ x\ 10^{7}$. To reduce head losses due to friction on the surface of the penstock material, Polyvinylchloride (PVC)

pipe is selected due to it smooth surface in contrast to steel or concrete. Table 3 below shows the penstock data selected.

Table 3: The Penstock data selected

S/N	Description	Dimension
1	Gross head	5.64m
2	Flow-rate	20.08 m/s
3	Flow velocity	10.52 m/s
4	Penstock diameter	1.56 m
5	Penstock length	30 m
6	Penstock thickness	0.04 mm
7	Penstock tensile strength	48.26 MPa (7000 Psi)
8	Head loss due to friction	0.76 m
9	Head loss due to intake	0.039 m
10	Head loss due to gate	0.84 m
11	Available net head	4.0 m
12	Pressure wave length	286.50 m/s
13	Surge pressure	3.01 MPa (437.14 Psi)
14	Critical time	0.21 Secs

4.2 Simulation Result

The annual data sheet for the hydropower simulation, and that of the daily power generation and discharge rate trend are shown in the appendices. The average daily and annual energy parameter projected by simulator (CASiMiR) is summarized in Table 4 Below.

Table 4: The average daily and annual energy parameter

S/N	Description	Capacity
1	Maximum Power Capacity	706.32 Kilowatt
2	Average Daily Power	490.06 Kilowatt
3	Average Daily Energy Generation	11,761.25 Kilowatt
4	Annual Energy Production	4292.89 Mega Watt Hour
5	Annual Discharge Volume	466,311,168.00 m^3

4.3 Investment Cost and Financial Return

The average total installation costs for new small hydropower projects commissioned between 2015 and 2021 in Africa is approximately $3500/KW. The operation and maintenance costs (O&M) varied between 1% and 3% of total installed costs per year. However, installing small hydropower plant on an existing dam built for other purposes yields an investment cost reduction of up to 70% compared with a new project (IRENA, 2022, IEA 2021).

4.4 Investment Cost.

The installation of hydropower is taking place on an existing dam built for other purposes.

Therefore, the investment costs per Kw is taken to be: $Installation\ cost$ x $(1 - 70\%\ \text{cost reduction})$

$$= 3500 \text{ x } (1 - 0.7) = \$\,1050$$

Investment cost of the project = $1050 \text{ x } 1000\text{KW} = \$\,1{,}050{,}000$

Converting to Naira (₦) at official rate of ₦420/\$1 $= \$\,1{,}050{,}000 \text{ x } 420 =$ ₦ $441{,}000{,}000$

Operation and maintenance (O&M) per annum is 3% of investment cost of the project;

Therefore, Operation and maintenance cost $= 0.03 \text{ x } 1{,}050{,}000 = \$\,31{,}500\ per\ annum$

Converting to Naira (₦) at official rate of ₦420/\$1, O&M cost $= \$\,31{,}500 \text{ x } 420 =$ ₦ $13{,}230{,}000$.

4.5 Financial Return**.**

The financial return is based on the total annual energy generation projected in the simulation, valued to be 4292.89MWh. According to Ibadan Electricity Distribution Company (IBEDC); the distribution company covering the project site, recent price per unit of energy for band B customer is ₦ 66.04/kWh.

Annual revenue from project per annum was derived from the total annual energy generated as calculated below:

Annual revenue $= Total\ annual\ energy\ generated\ (KWH)$ x $Price\ per\ unit$

$= 4292.89 \text{ x } 1000 \text{ x } 66.04 = ₦ 283{,}502{,}455.60.$

5. CONCLUSIONS

This study has evaluated the feasibility of harnessing the hydropower potential of the underutilized Eruwa (Opeki) Water Dam in Oyo State, Nigeria. The results indicate that the dam has significant untapped potential for hydropower generation, which could help to address Nigeria's energy deficit and contribute to sustainable development. The study found that the technical and economic feasibility of hydropower generation from the dam is high, with the possibility of converting it to a 0.71Mw mini hydropower plant with a projected annual energy generation of 4292.89MWh.

Given the potential benefits of hydropower generation from the Eruwa (Opeki) Water Dam and other underutilized water reservoirs in Nigeria, it is recommended that the government and private sector stakeholders invest in further exploration and development of hydropower resources. This could involve the deployment of new technologies and innovations that enhance the efficiency and sustainability of hydropower generation, as well as the implementation of policy and regulatory frameworks that incentivize private sector investment in the sector. Overall, the development of hydropower resources in Nigeria has the potential to create new economic opportunities, improve energy security, and contribute to the country's transition to a low-carbon, sustainable energy future.

REFERENCES

Abban, J., & Awopone, A. (2021). Techno-economic and environmental analysis of energy scenarios in Ghana. *Smart Grid and Renewable Energy*, *12*(06), 81–98. https://doi.org/10.4236/sgre.2021.126006.

Adewuyi, A. (2020). Challenges and prospects of renewable energy in Nigeria: A case of bioethanol and biodiesel production. *Energy Reports, 6*, 77-88. https://doi.org/10.1016/j.egyr.2019.12.002.

Emodi, N. V. and Boo, K. J. (2015). Sustainable energy development in Nigeria: Current status and policy options. *Renewable and Sustainable Energy Reviews*, Elsevier, 5, 356-381.

International Energy Agency (IEA). (2020). *World energy outlook 2020 – analysis*. IEA. Retrieved December 03, 2022, from https://www.iea.org/reports/world-energy-outlook-2020.

International Energy Agency (IEA). (2021). Climate Impacts on African Hydropower – Analysis - IEA. Retrieved December 16, 2022, from https://www.iea.org/reports/climate-impacts-on-african-hydropower.

International Hydropower Association (IHA) (2018). Nigeria. Retrieved February 25, 2023, from https://www.hydropower.org/country-profiles/nigeria.

IRENA. (2022), Renewable Power Generation Costs in 2021. International Renewable Energy Agency (IRENA). Retrieved January 05, 2023 from https://www.irena.org/publications/2022/Jul/Renewable-Power-Generation-Costs-in-2021.

Kumar Hemanth., 2021. World's biggest hydroelectric power plants. Power Technology. Retrieved December 15, 2021 from https://www.power-technology.com/analysis/worlds-biggest-hydroelectric-power-plants.

Odunfa, M. K., Saudu, T. C., & Oladimeji, T. E. (2019). Development of a small hydropower plant: Case of ikere gorge dam, Oyo State, Nigeria. *Journal of Power and Energy Engineering*, 07(03), 31–45. https://doi.org/10.4236/jpee.2019.73003.

U.S office of Energy Efficiency and Renewable Energy. 2021. How Hydropower Works. Retrieved February, 2020, from https://www.energy.gov/eere/water/how-hydropower-works.

Ogedengbe, K., & Oke, A. O. (2006). Studies on the potentials of the Opeki River Dam for water supply and Irrigation. *Moor Journal of Agricultural Research*, *5*(1). https://doi.org/10.4314/mjar.v5i1.31802.

Idowu, O. A., & Martins, O. (2007). Hydrograph analysis for groundwater recharge in the phreatic basement aquifer of the Opeki river basin, southwestern Nigeria. *ASSET, An International Journal of Agricultural Sciences, Environment and Technology*, (Series B), 6(1), 132 – 141. Retrieved December 21, 2022, from https://publications.unaab.edu.ng/index.php/Series_B/article/view/54/58.

Appendices

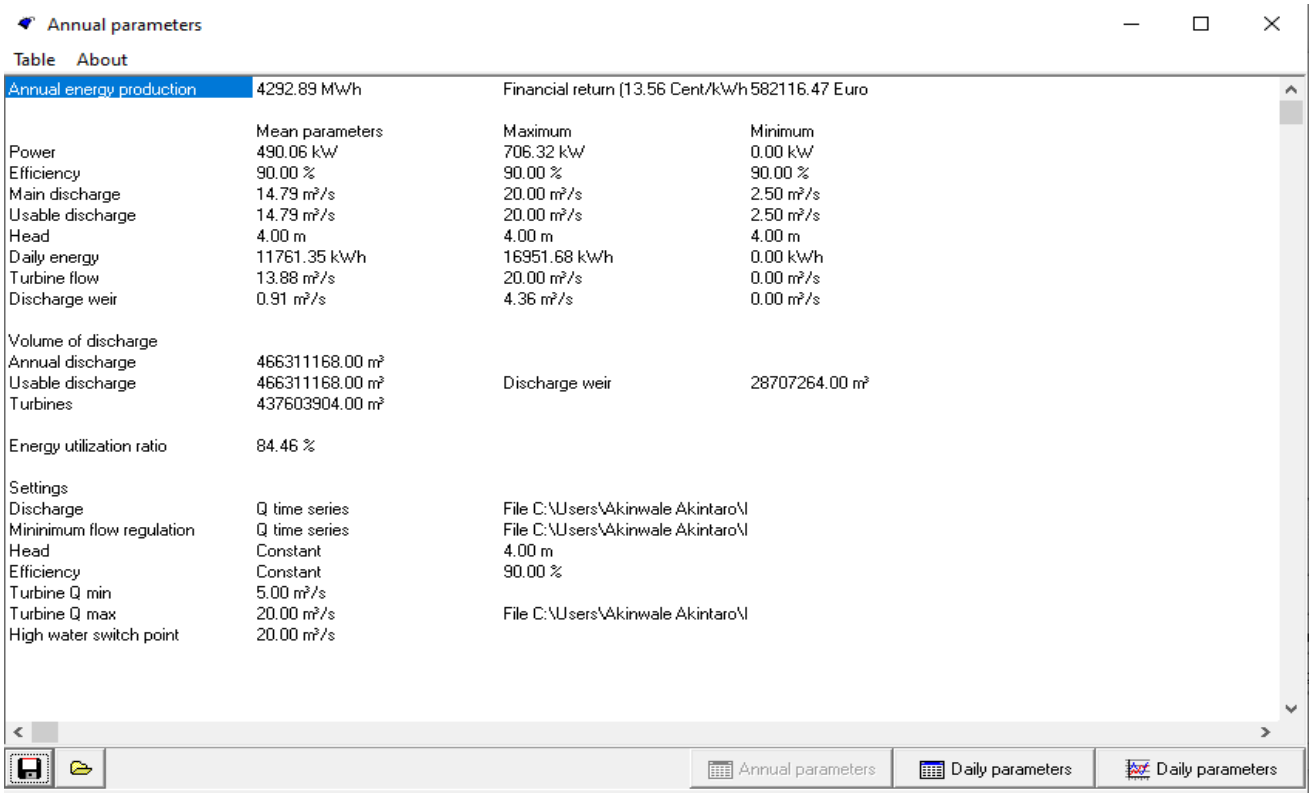
Annual parameters
Table About
Annual energy production 4292.89 MWh Financial return (13.56 Cent/kWh 582116.47 Euro
Mean parameters Maximum Minimum
Power 490.06 kW 706.32 kW 0.00 kW
Efficiency 90.00 % 90.00 % 90.00 %
Main discharge 14.79 m³/s 20.00 m³/s 2.50 m³/s
Usable discharge 14.79 m³/s 20.00 m³/s 2.50 m³/s
Head 4.00 m 4.00 m 4.00 m
Daily energy 11761.35 kWh 16951.68 kWh 0.00 kWh
Turbine flow 13.88 m³/s 20.00 m³/s 0.00 m³/s
Discharge weir 0.91 m³/s 4.36 m³/s 0.00 m³/s
Volume of discharge
Annual discharge 466311168.00 m³
Usable discharge 466311168.00 m³ Discharge weir 28707264.00 m³
Turbines 437603904.00 m³
Energy utilization ratio 84.46 %
Settings
Discharge Q time series File C:\Users\Akinwale Akintaro\I
Mininimum flow regulation Q time series File C:\Users\Akinwale Akintaro\I
Head Constant 4.00 m
Efficiency Constant 90.00 %
Turbine Q min 5.00 m³/s
Turbine Q max 20.00 m³/s File C:\Users\Akinwale Akintaro\I
High water switch point 20.00 m³/s
Annual parameters
Daily parameters
Daily parameters

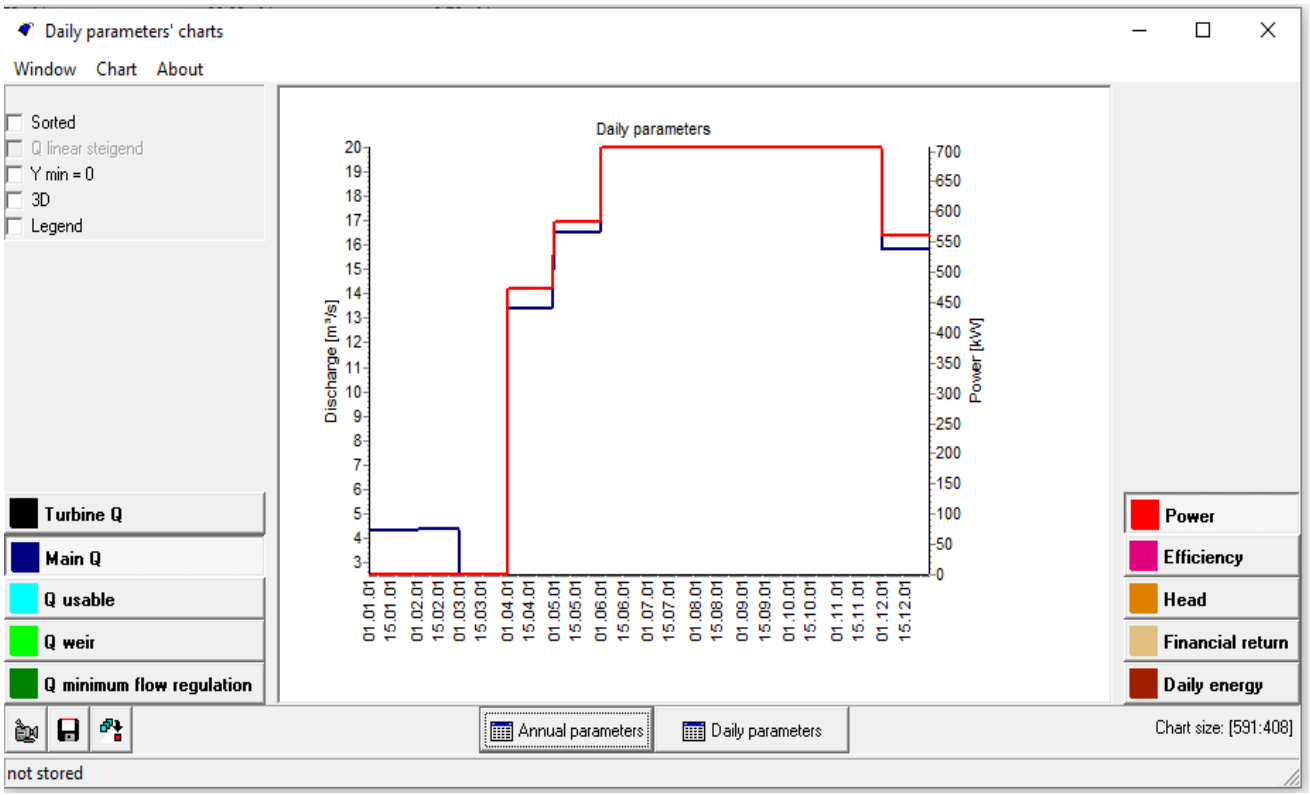
Daily parameters' charts
Window Chart About
Sorted
Q linear steigend
Y min = 0
3D
Legend
Daily parameters
Discharge [m³/s]
Power [kW]
Turbine Q
Main Q
Q usable
Q weir
Q minimum flow regulation
Power
Efficiency
Head
Financial return
Daily energy
Annual parameters
Daily parameters
Chart size: [591:408]
not stored

PAPER 35 – IMPACT OF THERMO-FLUID MODELLING AND SIMULATION FOR A TWO-SPOOL TURBOSHAFT GAS TURBINE CONFIGURATION

J. Elimian[1], A. Nasir[1]

[1]Department of Mechanical Engineering, Federal University of Technology, Minna, Nigeria.
Email: elimianjacob91@gmail.com

ABSTRACT
Gas turbines built in the tropics for power generation are made for other climate regions, thus their performance tends to be affected. This research aims to present the impact of thermo-fluid modelling for gas turbines on performance simulations of a two-spool turboshaft power-generating gas turbine configuration. The variation of operating conditions (compression ratio, turbine inlet temperature (TIT), and ambient temperature) on the performance of gas turbine (thermal efficiency, shaft power delivered, specific fuel consumption (SFC), heat rate (HR) and fuel flow (FF)) was investigated. The analysis of the cycle has been carried out using GASTURB 14. The off-design simulation is carried out for ambient temperature between 288K to 318K and TIT between 1400K to 1600K. As the ambient temperature increases for a given TIT, the thermal efficiency, shaft power delivered, and FF decrease while the SFC and HR increase; this is due to a decrease in mass flow rate to the compressor as a result of lower air density and a higher compressor work. There is a loss of 4.3% in thermal efficiency at TIT 1400K as ambient temperature increases from 288K to 318K, this loss decreases to 1.3% at TIT 1600K, which reveals that, as TIT increases percentage loss in thermal efficiency decreases on increasing ambient temperature. In addition to this, it was observed that there was an increase of 0.05 kg/kWh in SFC at TIT 1400K when the ambient temperature rises from 288K to 318K which in turn decreased to 0.01kg/kWh. As the TIT increases for a given compression ratio (design point) or an ambient temperature (off-design point), the thermal efficiency, shaft power delivered and FF increase while SFC and HR decrease. The simulation results obtained were validated using industry data and those obtained from other experimental methods and they showed acceptable agreement.

KEYWORDS: Ambient temperature, compression ratio, design and off-design point, turbine inlet temperature.

1. INTRODUCTION

Operators' top priority is to make sure gas turbines function as efficiently as possible. Gas turbines are designed to compress air with the least amount of effort possible while maintaining high levels of efficiency and aerodynamic stability. Anything that boosts productivity and profit in the current economic context is welcome (Ibrahim *et al.,* 2011a). The International Standard Organization (ISO) conditions for a gas turbine are 1.013 bar of atmospheric pressure, an ambient temperature of 15°C, and relative ambient humidity of 60% (ASME, 2015). In a gas turbine power plant, the output is sensitive to the surrounding environment (Xiaojun *et al.,* 2010). The performance of a gas turbine can be categorized according to its thermal efficiency, power production, specific fuel consumption (SFC), and work ratio. Its performance is affected by several factors, including the compressor pressure ratio (PR), combustion inlet temperature (TIT) and other operational factors such as ambient temperature, elevation and relative humidity (Thamir and Rahman, 2010). The best effective way for determining a gas turbine power plant's operation is a mathematical modelling strategy that makes use of computer tools (Barsali *et al.,* 2015). In this respect, quantitative modelling of gas turbine power plants is necessary. The conditions at a gas turbine power plant's inlet and exit determine its performance in terms of power production, thermal efficiency, and specific fuel consumption (Khaliq and Dincer, 2011). Hot days have significantly lower air density, pressure ratio, airflow, and power output. As a result, as ambient temperature rises, power output declines and specific fuel consumption (SFC) rises. Performance of gas turbines is strongly impacted by changes in the ambient conditions (Thamir et al., 2019). The ambient, which changes periodically, determines the gas turbine's performance (Nada, 2014). As the intake air temperature rises, the limiting air volume rises as well. As constant-volume engines, gas turbines continuously move the same volume of air at a specific shaft speed. Because combustion air in gas turbines is drawn directly from the atmosphere, weather conditions have a significant impact on how well they work (Saif and Tariq, 2017). The output power drops as the ambient temperature rises and rises with the turbine entry temperature (TET). To prevent early component failure and a shortened gas turbine's life, it is not possible to increase the TET indefinitely from a material standpoint (Nasir *et al.,* 2018). This research work investigates how operating conditions affect the performance calculations of gas turbines installed in Kogi State, central Nigeria with an altitude of more than 2000m above sea level. This research aimed to assess the impact of thermo-

fluid modelling for gas turbines on performance calculations, and this can be achieved through the following objectives:

i. to create a model to calculate gas turbine performance based on a chosen set of measurable parameters.
ii. investigating the operational factors (such as ambient temperature (AT)) that have an impact on gas turbine performance.
iii. validate model results with measure gas turbine performance.

2 THEORETICAL ANALYSES

2.1 Thermo-fluid Gas turbine component modelling

This dynamic thermo-fluid physics model, which consists of rotating and fluid elements, was developed as a starting point, using conservation principles and motion equations. Auxiliaries for the compressor, combustor, turbine, and engine are the gas turbine engine's key parts, and they all work together to produce the engine's total performance (Cohen *et al.,* 2017).

2.2 Modelling for Compressor

$$\dot{W}_c = \dot{m} \times h(T_{in}) - h(T_{out}) \quad (1)$$

$$PR_c = \frac{P_{out}}{P_{in}} \quad (2)$$

Equation (1), which reflects the compressor work but involves no heat transfer, is derived from energy conservation, equation (2) provides the compressor's pressure ratio relation (Thirunavukarasu, 2013).

2.3 Burner Modelling

$$\eta_b = \frac{1}{\dot{m}_f \times HV}(\dot{m}_{out} \times hT_{out} - \dot{m}_{in} \times hT_{in} \quad (3)$$

The combustion chamber efficiency is defined by equation (3).

2.4 Turbine Modelling

$$\dot{W}_T = m \times (h(T_{in}\dot{)} - h(T_{out})) \quad (4)$$

Turbine work is calculated by equation (4).

The rate of mass flow through the gas turbine is given as:

$$m \doteq \rho v \quad (5)$$

$$\frac{dm}{dt} = \frac{d}{dt}(\rho v) \quad (6)$$

$$\dot{m} = \rho v \quad (7)$$

The density of the working fluid (air) has an inverse relationship with the temperature

$$\rho = \frac{k}{T_1} \quad (8)$$

Where $T1$ is the ambient temperature, ρ is the density of air and k is the proportionality constant. The gas turbine's network (Wnet) is computed:

$$W_{net} = W_T - W_C \quad (9)$$

$$P = \dot{m}_a \times (W_{T-}W_C) = \dot{m}_a \times W_{net} \quad (10)$$

$$P = \rho v \times W_{net} \quad (11)$$

$$P = \frac{k}{T_1} v \times W_{net} \quad (12)$$

The specific fuel consumption (SFC) is expressed by Equation (13).

$$SFC = \frac{3600 \times \dot{m}_f}{W_{net}} \quad (13)$$

The heat supplied is written as:

$$Q_{add} = C_{pg}(TIT - T_1(1 + \frac{PR^{\frac{\gamma-1}{\gamma}} - 1}{\eta_C}) \quad (14)$$

The efficiency of the gas turbine (ηth) can be calculated by Equation (15). It is the proportion of heat input to work performed by the turbine.

$$\eta_{th} = \frac{W_{net}}{Q_{add}} \quad (15)$$

3. MATERIALS AND METHODS

3.1 Materials

3.1.1 GasTurb 14

GasTurb 14 has been used to analyze the gas turbine cycle and evaluate the plant's performance. GasTurb 14 (GASTURB GMBH MELATENER STRABE 7052074 AACHEN, GERMANY) is professional software for gas turbine performance calculations.

3.1.2 The two-spool turboshaft

Interest is only in the two-spool turboshaft in this work since gas turbines used for power generation are the focus.

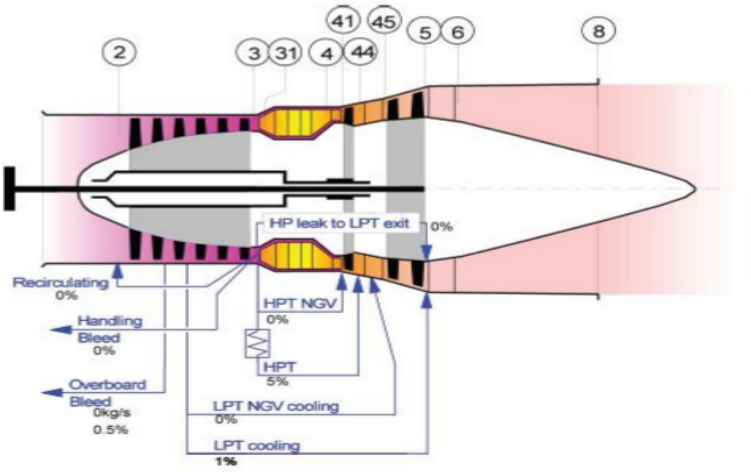

Figure 1. The state points in the GasTurb14 model of a two-spool turboshaft. The compressor entry (point 2), compressor outlet (point 3), high-pressure turbine entry (point 41), low-pressure turbine entry (point 45), and exhaust location (point 5) are the crucial points.

4. RESULTS AND DISCUSSION

4.1 Off-design point simulations

Table 1. Simulated results of the effect of ambient temperature and different turbine inlet temperatures on thermal efficiency

TIT(K)	1400	1500	1600
AMBIENT TEMPT(K)			

288	0.29015	0..29757	0.29652
293	0.28408	0.29537	0.29458
298	0.27770	0.29273	0.29257
303	0.27044	0.28947	0.29073
308	0.26283	0,28529	0.28885
313	0.25504	0.28028	0.28660
318	0.24719	0.27503	0.28396

The difference in thermal efficiency with ambient temperature at various TIT and a 60% relative humidity in the air is displayed in Table 1. It is evident that as the temperature of the turbine inlet increases from 1400K K to 1600 K, thermal efficiency also rises for a given ambient temperature until the turbine inlet temperature reaches 1650 K, at which point a sharp decline in thermal efficiency is seen (Ibrahim and Rahman, 2010). However, it is also established that the thermal efficiency will decrease for all ranges of TIT under consideration if the temperature of the ambient rises from 288K to 313K. Thermal efficiency rises at lower temperatures, but as the temperature rises, its value somewhat declines (Nasir *et al.*, 2018). Given that higher air density is derived from a lower ambient temperature and less compressor effort, improved gas turbine performance —which then results in greater thermal efficiency—is produced. Higher ambient temperatures, on the other hand, result in less air density and more compressor work. In this study, compressor work predominates over turbine work, resulting in a decline in net work done and a potential reduction in thermal efficiency at higher ambient temperatures (Saif and Tariq, 2017).

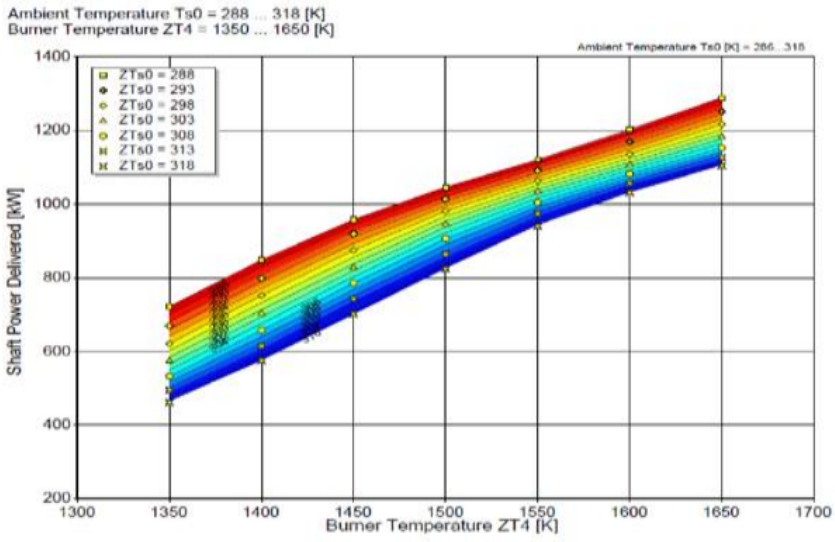

Figure 2. Shaft power delivered as a function of ambient temperature and TIT

The impact of the temperature of the ambient and TIT on shaft power is shown in Figure 2. It is clear that for a given ambient temperature, the shaft power provided increases when the TIT climbs from 1350K to 1650K (Nasir *et al.* 2018). However, it is determined that for all ranges of turbine inlet temperature being investigated, the shaft power provided decreases as the ambient temperature rises from 288K to 318K (Shi *et al.* 2010). At lower temperatures, the shaft power delivered is greater, but as the temperature rises, its value somewhat declines.

Table 2. Effect of ambient temperature and TIT on specific fuel consumption (kg/kWh)

AMBIENT TEMPT(K)	**TIT(K)**		
	1400	**1500**	**1600**
288	0.28772	0.28054	0.28154
293	0.29386	0.28263	0.28339

298	0.30062	0.28518	0.28533
303	0.30868	0.28839	0.28714
308	0.31762	0.29261	0.28901
313	0.32733	0.29785	0.29127
318	0.33772	0.30353	0.29398

Table 2 illustrates the change of ambient temperature and varied TIT on SFC. It has been found that when the turbine inlet temperature increases from 1350K to 1600K the significance of the specific fuel consumption decreases until the turbine inlet temperature of 1650K, where an abrupt rise in the value of the SFC is noticed. However, for a particular TIT, the value of a particular fuel consumption rises as the ambient temperature rises (Ibrahim and Rahman, 2010). This is because a change in ambient temperature produces an increase in the mass flow rate of air at the compressor's input (Saif and Tariq, 2017).

4.2 Model validation

The model developed in this study is validated by the actual data obtained from the gas turbine power plant. In this study, a GE LM6000pc gas turbine plant unit with an installed capacity of 45MW was selected for the study. The plant is owned by Dangote Cement Plc-Obajana Plant, Obajana, Kogi State, Nigeria. Operating data for the gas turbine unit were collected from the control room log sheet. A summary of the operating parameters of the GE LM6000pc used for this study is presented in Table 3.

Table 3. Operating parameters of GE LM6000pc

Time range	Ambient temperature (K)	Power output (MW)
04:00	295.4	38.87
06:00	295.4	36.76
08:00	297.1	31.17
10:00	297.1	31.08
12:00	297.6	37.99
14:00	298.2	37.86
16:00	299.8	37.25
18:00	299.8	32.78
20:00	299.3	33.41
22:00	295.9	39.33
24:00	295.4	38.88

The parameters considered in this study for the gas turbine engine during simulation are ambient temperature and turbine inlet temperature.

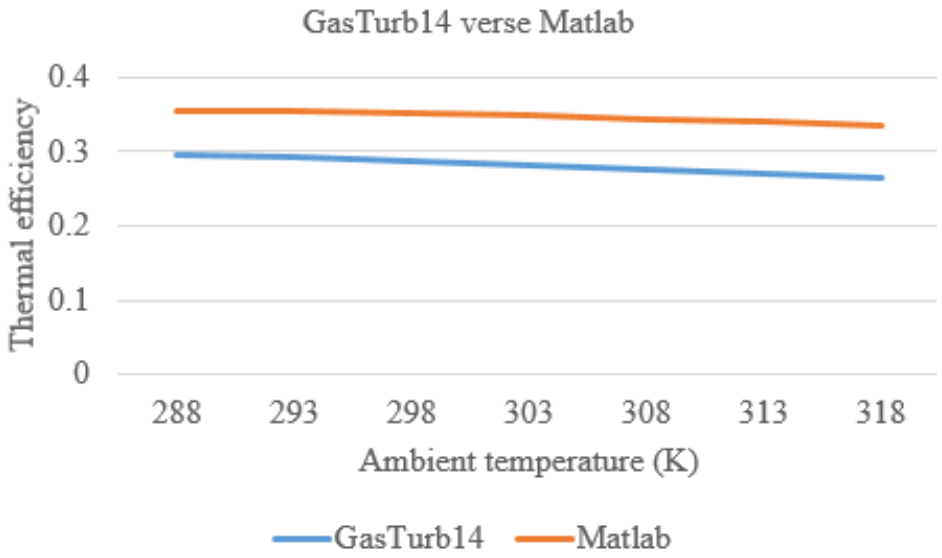

Figure 3. Comparison of the effect of ambient temperature on thermal efficiency

Figure 3 is a comparison between the results from the present study and that of previous work (Ibrahim *et al.,* 2016) and it reveals an acceptable agreement. It shows the effect of ambient temperature on the thermal efficiency of the gas turbine. As the ambient temperature increases for a given turbine inlet temperature, the ratio of the temperatures; $\frac{TIT}{T_1}$ reduces and this forces the thermal efficiency to decrease.

5.0 CONCLUSIONS

As the TIT increases for a particular ambient temperature (off-design point), the thermal efficiency and shaft power delivered increase while the SFC decreases. For a particular turbine inlet temperature at higher ambient temperatures (other than ISO conditions), the thermal efficiency and shaft power delivered decline while the specific fuel consumption rises. Lower air density and more compressor effort were the results of greater ambient temperature. The mass flow rate reduces because gas turbines are machines with a constant volume. The results of this study have been highlighted, but other areas of performance calculations should be carried out for other configurations of gas turbines.

ACKNOWLEDGEMENT

The authors acknowledge thankfully the effort and ideas of Engr. Prof A. Nasir.

REFERENCES

Barsali, S., De Marco, A., Giglioli, R., Ludovici, G., & Possenti, A. (2015). Dynamic modelling of biomass power plant using micro gas turbine. *Renewable Energy*, *80*, 806–818. https://doi.org/10.1016/j.renene.2015.02.064.

Cohen, H., Rogers, G. F. C., Saravanmuttoo, H. I. H., Straznicky, P. V., & Nix, A. C. (2017). *Gas turbine theory* (7th ed., p. 624). Pearson College Div.

Ibrahim, T. K., Rahman, M., & Abdalla, A. N. (2011). Gas Turbine Configuration for Improving the Performance of Combined Cycle Power Plant. *Procedia Engineering*, *15*, 4216–4223. https://doi.org/10.1016/j.proeng.2011.08.791.

Khaliq, A., & Dincer, I. (2011). Energetic and exergetic performance analyses of a combined heat and power plant with absorption inlet cooling and evaporative aftercooling. *Energy*, *36*(5), 2662–2670. https://doi.org/10.1016/j.energy.2011.02.007.

Nada, T. (2014). Performance characterization of different configurations of gas turbine engines. *Propulsion and Power Research*, *3*(3), 121–132. https://doi.org/10.1016/j.jppr.2014.07.005.

Nasir A., Mohammad A., & Jiya, J.Y. (2018). Design and Off-Design Operation and Performance Analysis of a Gas turbine. *Proceeding of the World Congress on Engineering*, 2, 978-988.

Saif, M. & Tariq, M. (2017). Performance analysis of gas turbine at varying ambient temperature. *International Journal of Mechanical Engineering and Technology* 8(1), 270 – 280.

Shi, X., Agnew, B., Che, D., & Gao, J. (2010). Performance enhancement of conventional combined cycle power plant by inlet air cooling, inter-cooling and LNG cold energy utilization. *Applied Thermal Engineering*, *30*(14–15), 2003–2010. https://doi.org/10.1016/j.applthermaleng.2010.05.005.

Ibrahim, K.T., Rahman, M.M., and Abdalla, A. N. (2010). Study on the effective parameter of gas turbine model with inter-cooled compression process. *Scientific Research and Essays*. 5(23), 3760 – 3770.

Thirunavukarasu, E. (2013). *Modelling and Simulation Study of a Dynamic Gas Turbine System in a Virtual Test Bed Environment. (Master' thesis)*. Retrieved June 20, 2022, from https://scholarscommons.sc.edu/etd/2254.

PAPER 36 – FLOOD FREQUENCY ANALYSIS OF RIVER NIGER AT LOKOJA GAUGE STATION: A MORPHODYNAMIC APPROACH

C. O. Onyike, A. O. Busari

Department of Civil Engineering, Federal University of Technology, Minna
Email: chubaonyike@yahoo.com

ABSTRACT
Flood frequency analysis is used by water resources professionals to estimate the probability of exceedance associated with a flood of a given magnitude. The estimation of flood frequencies is important because they are used for the planning and design of hydraulic structures. This study was carried out to understand the flood-generating processes and establish the reliability of different probability distribution models in predicting the bank-full discharge for selected return periods based on the available hydrometric dataset. The designed bank-full discharge and experimental results of the sampled bed materials at different chainages along the river reach being used to characterize the river bed materials by comparing the Eugelund & Hansen method, and Meyer-Peter & Muller method with their established criteria and finally obtain the sediment transport capacity of the River Niger at Lokoja. The results show that the flood magnitude is highly dependent on the sediment transport capacity of the river.

KEYWORDS: Bank-full discharge, Flood frequency, sediment transport capacity, morphodynamics, Probability distribution models

7. INTRODUCTION

Floods are the consequence of natural water exceeding the capacity of removal by the river channel or reservoirs (Knapp, 1979). Flood discharge in tropical regions is known to be a factor of intensity, extent and duration of rainfall, and the runoff characteristic of the basin. During precipitation, rainwater is absorbed by the soil, a part is lost through evapotranspiration and the remaining part is transported as runoff into rivers, streams, and reservoirs. The capacity of the drainage system of the catchment area to contain the excess runoff water in river channels, the catchment extent, the velocity of downstream discharge and the presence or absence or retention basins, determine if the flood water will overspread the natural banks and cause damage to adjoining areas. In the work of Busari et al. (2013), the Normal distribution model was found most appropriate for the prediction of yearly maximum daily rainfall in the Evaluation of Best Fit Probability distribution models. Another important aspect of the research presented here is the impact of deposition and erosion on the flow process. Prediction of the described process with its entire complexity requires the application of sophisticated mathematical models with several empirical or subjective assumptions (Brunner, 2016a; Kolerski, 2018; Parker, 2004; Popek, 2006; Wu, 2007). The most important assumptions seem to be the empirical formulae applied to complete the mathematical models of sediment routing (Beckers et al., 2018; Osidele et al., 2003; Parker, 2004; Popek, 2006; Radecki-Pawlik, 2014; Schmelter et al., 2012; Wu, 2007; Yang, 1996). Considerations of morphodynamical processes in the context of flood hazards are not very frequent. The rare examples found in the literature have been focused on short-term analyses of direct morphological responses to flood events. These are single-event computations based on simple deterministic modelling (Lane et al., 2008; Lane et al., 2007; Nones, 2019; Radice et al., 2013; Radice et al., 2016).

Hydrometric and climatic data are not enough for flood modelling and prediction. A good knowledge of land use patterns and the behaviour of our river systems is essential. The understanding of a riverbed material and its hydrology along with the selection of adequate modelling tools will yield a flood prediction of relatively low uncertainty.

8. THEORETICAL ANALYSIS

Sediment transport is the movement of solid particles driven by fluids like water or wind in rivers, lakes, reservoirs, and coastal waters. In the real world, the flow is unsteady like flood waves, tidal waves and wind waves as steady and uniform flows are very rare in reality. In the literature, many formulae use the boundary shear stress ĭ (= ρghS) to express sediment transport discharge, like Meyer – Peter and Muller, and Engelund and Hansen (Shu-Quing Yang, 2020). The maximum amount of sediment transported by a river as bed material load is the Sediment Transport Capacity (STC) and is related to the stream velocity, u. The general STC formula has the form:

$$qs = mu^b \quad (1)$$

where qs is the amount of bed material load per meter of river width (m^2/s), m is the proportionality coefficient, u is the local stream velocity and b is the exponent (values larger than 3). Meyer - Peter & Muller **(MPM)** equation is given as:

$$qsb = 8\sqrt{\Delta g D_m^3}\ \sqrt{(\mu\theta - 0.047)^3} \quad (2)$$

where qsb is the amount of sediment transported as bedload per meter of river width (m^2/s), D_m is the mean sediment grain size (m),

Bedform factor, $\mu = \sqrt{(C/C')^3}$

C = Chezy's coefficient ($m^{1/2}/s$) (3)

C' is the grain-related Chezy's constant given as:

$C' = 18\log(12h/D_{90})$ (4)

where D_{90} grain size of 90% passing (m).

Criteria for the characterisation of riverbed materials are given as

(a) $\frac{\omega s}{u*} > 1$; where ωs = fall velocity $\left(\frac{m}{s}\right)$, u = shear velocity $\left(\frac{m}{s}\right)$

(b) $D_m > 0.4$mm; D_m = mean sediment grain size (m)

(c) $\mu\theta < 0.2$ for Gravel – bed; μ = bed factor and θ = Shields parameter.

For Engelund and Hansen **(E-H)** equation. In equation (1), b = 5 and m is given by:

$$m = \frac{0.05}{C^3\left(\frac{\rho s - \rho}{p}\right)D_{50}\sqrt{g}} \quad (5)$$

where C is Chezy's coefficient ($m^{1/2}/s$), ρ_s is sediment density (kg/m^3) and D is median sediment grain size (50% of sediment material has a smaller diameter) (m). Criteria for the characterisation of riverbed materials are given as:

(a) $\frac{\omega s}{u*} < 1$;

(b) $0.19 < D_{50} < 0.93$mm;

(c) $0.07 < \theta < 6$ for Sand-bed.

9. MATERIALS AND METHODS/METHODOLOGY/EXPERIMENTAL PROCEDURE

3.1 Study Area

Lokoja is the capital city of Kogi State in the north-central part of Nigeria. It presents a very important hydro-geological feature and covers a land area of approximately 3180 km^2. The gauging station from which the data for this study was extracted is located along River Niger in Lokoja. Geographically, it is located at the following coordinates (08°40'N, 05°20''E and 07°20'N, 05°20'E, 07°20'N, 06°44'E) North of the equator and East of the meridian.

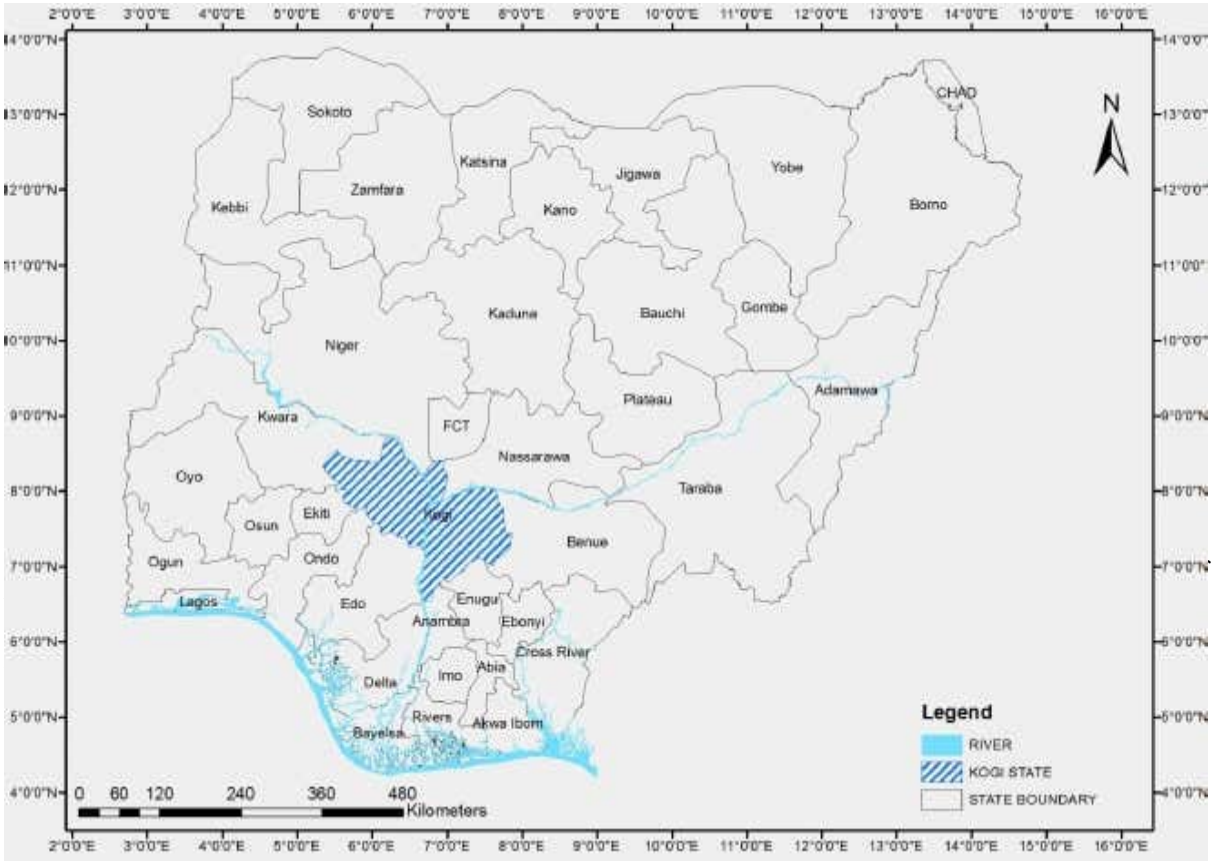

A total of twelve (12) bed material samples were collected from different locations at 50 m intervals downstream along the riverbed longitudinal profile commencing from the Lokoja Slipway herein designated as chainage 0 + 000. The soil samples were collected at an average depth of 0.5m by disturbed sampling method in accordance with BS 1377:1 (2016) standard procedure for sample collection. Water samples were also collected from the riverbed at 50m intervals along the river reach and the following tests were carried out: (a)Specific gravity, (b) Density of bed material and (c) Soil particle size distribution.

Calculation of Recurrence Interval T_p

The annual maximum flood discharge values have been arranged in descending order and the plotting position for the recurrence interval T_p for each discharge is obtained as:

$$T_p = \frac{N+1}{m} = \frac{22}{m} \quad (6)$$

Where m = order number and the discharge magnitude Q plotted against the corresponding T_p on EasyFit probability software shown in Figure 2.

The discharge and return period relationship is given in the plotted graph in Figure 2. The fitting equation (7) is shown as follows:

$$Q = -1.3194(T_p)^2 + 712.19(T_p) + 16476 \quad (7)$$

The degree of correlation between the parameters is high (R = 0.871)

Substituting the following return periods (30, 40, 50, 60, 70, 80, and 100) T_p values in equation (7) we have the maximum flood discharge (Q_{max}) corresponding to each return period.

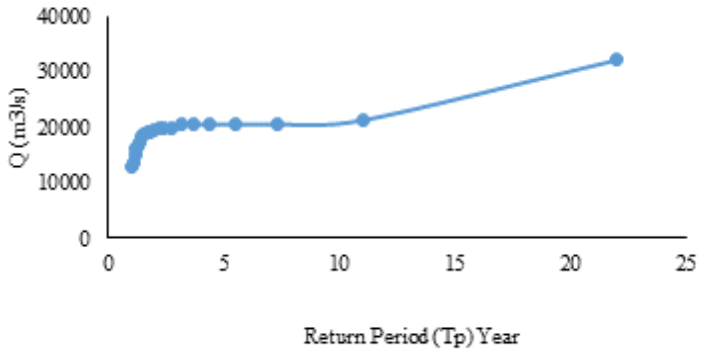

Figure 2. Graph of Discharge and Return Period

Table 1: (Q -Tp) Relationship

Return Period (Tp) years)	30	40	50	60	70	80	100
Flood discharge Q (m^3/s)	36654	42853	48787	54458	59864	65007	74501

10. RESULTS AND DISCUSSION

4.1 Results

Particle size analysis was conducted on the twelve (12 Nos.) material samples taken from the Lokoja gauge station, and the result so obtained for particle size (D_{50}) and Specific Gravity (GS) is presented in Table 2.

Table 2: Experimental results of soil sample

Sample No.	0+000	0+050 A	0+050 B	0+100	0+150 A	0+150 B	0+200	0+250 A	0+250 B	0+300	0+350	0+400
D_{50}	0.35	0.35	0.35	0.35	0.28	0.35	0.35	0.35	0.35	0.35	0.35	0.35
SG	2.44	2.75	2.42	2.6	2.66	2.67	2.52	2.68	2.21	2.63	2.63	2.62

The hydrometric dataset used in the research was extracted from the Nigerian Inland Water Authority (NIWA) and is presented under Appendix 1. The probability distribution function for the dataset comparing Cauchy, Gen. Logistic, Log-Logistic, Log-Logistic (3P), Log-Pearson 3 and Wakeby methods, is presented in Figure 3.

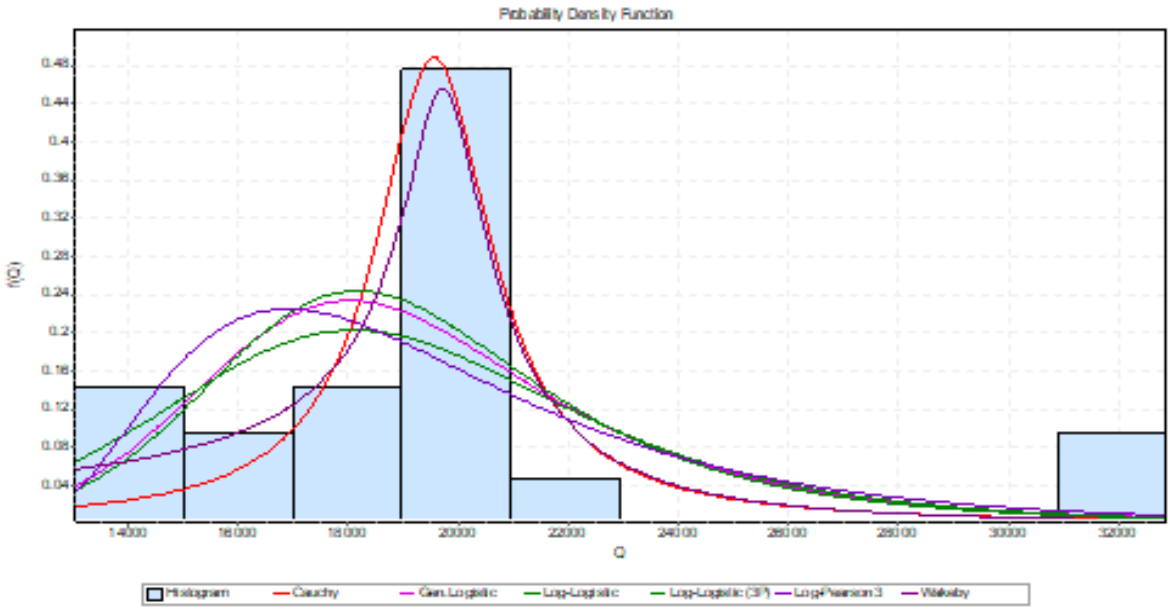

Figure 3: Probability distribution function for six (6) methods

Parameters for calculating the sediment transport and characterizing the riverbed channel by comparing the methods of Engelund & Hansen and Meyer-Peter & Muller with their established criteria are presented in Appendix 2. While the computed STC for the selected return periods and some river reaches is presented in Appendix 3.

4.2 Discussion of Results

The result of particle size distribution carried out on the 12 soil samples from the Lokoja gauge station shows that the bed materials are predominantly Sandy as a greater percentage of the materials fall within the region.

For the hydrometric data, the probability distribution for the selected recurrence intervals (Tp = 30, 40, 50, 60, 70, 80, and 100years) was plotted for six (6) models; Cauchy, Gen. Logistic, Log-Logistic, Log-Logistic (3P), Log-Pearson 3 and Wakeby. The reliability of the probability distribution as a fitting model has been tested using the statistical tests known as goodness of fit and found to be significantly correct. The statistical tools prescribed in the Easy Fit software have been used for the statistical analysis. The generated variables were used to determine how well the correlation coefficient and coefficient of determination best fit the models. From Figure 3, the best-fit model for the Lokoja gauge station is the Cauchy distribution model.

The parameters for calculating the sediment transport capacity (STC) were computed and presented in Appendix 2 for the selected recurrence intervals (return periods) and for the chainages according to the river reaches where samples were collected. For (Tp = 30) return period, the critical parameters for characterizing the river channel by methods of Eugelund & Hansen and Meyer-Peter & Muller with their established criteria are as follows:
$\omega s/u^* = 0.4720 < 1$; $D_{50} = 0.35 > 0.19$ and < 0.93mm; $\theta = 3.8588 > 0.17$ and < 6. These parameters satisfy the Eugelund & Hansen criteria for all the river reaches (chainages). Similarly, other selected return periods of 40, 50, 60, 70, 80, and 100 years also satisfy the E-H criteria and hence the channel is classified as a Sand-bed. Conversely,
the riverbed materials did not comply with MPM criteria.
From Appendix 3, the relationship between the selected return periods which is a function of the discharge, Q and the calculated sediment transport capacity is linear and therefore clearly indicates that the flood magnitude is highly dependent on the sediment transport capacity of the river.

5. CONCLUSION

Flooding in a river system can be better described by understanding the morphodynamics (bed-level formations and changes). With this research paper as reference material, a full understanding of fluvial flooding in Nigeria based on the morphodynamics of our river system is assured under the present-day climate change scenario. The results obtained from the computations show that the river flood magnitude is highly dependent on the sediment transport capacity of the river.

To understand the behaviour of our river system viz a viz the rainfall magnitude and discharge, it is worth noting that mining activities especially sand mining in our river channels cause a change in slope and thereby alter the behaviour of the river system. While erosion of the riverbed will translate to some advantage against flooding, the reverse is the case for huge and long-term deposition on the river floor bed which tends to reduce the river depth and by extension the carrying capacity of the river channel and thus leading to flooding.

Detailed studies are recommended on all the major rivers in Nigeria to characterize each river channel based on their discharge, slope, and bed materials (whether it is gravel-bed or sandy-bed material).
With this, we can fully estimate the sediment transport capacity of our rivers, predict erosion (or accretion), and deposition due to upstream release of water and propose viable river engineering measures rather than assuming dredging as usual. Flood intervention measures should be based on short and long-term assessments of the morphodynamics of the rivers, not by a mere assumption.

ACKNOWLEDGEMENT

The research work was carried out at the Federal University of Technology, Minna, Niger State, Nigeria. The authors are grateful to the Nigerian Inland Water Authority (NIWA) for making available the data set used as well as permitting the collection of soil and water samples from their dockyard.

REFERENCES

Beckers, F., Noack, M., & Wieprecht, S. (2018). Uncertainty analysis of a 2D sediment transport model: An example of the lower river Salzach. Journal of Soils and Sediments, 18(10), 3133- 3144.

Brunner, G. W. (2016a). HEC-RAS river analysis system hydraulic reference manual; US Army Corps of Engineers; Report No. CPD-69. Davis, CA: Hydrologic Engineering Center (HEC).

Busari, A. O., Mohammed, S., Ajibola O. (2013). Evaluation of Best Fit Probability Distribution Models for the Prediction of Rainfall and Runoff Volume (Case Study Tagwai Dam, Minna-Nigeria. International Journal of Engineering and Technology Volume 3 No. 2, 94 – 97.

Calenda, G., Mancini, C. P., & Volpi, E. (2009). Selection of the probabilistic model of extreme floods: The case of the river Tiber in Rome. Journal of Hydrology, 371(1 –4), 1 –11

Knapp, BJ (1979): Elements of Geographical Hydrology Geoge Allen and Uwin, London.

Kolerski, T. (2018). Mathematical modelling of ice dynamics as a decision support tool in river engineering. ater, 10(9), 1241.

Nones, M. (2019). Dealing with sediment transport in flood risk management. Acta geophysica, 67(2), 677–685. http://dx.doi. org/10.1007/s11600-019-00273-7.

Osidele, O. O., Zeng, W., & Beck, M. B. (2003). Coping with uncertainty: A case study in sediment transport and nutrient load analysis. Journal of Water Resources Planning and management, 129(4), 345 –355.

Parker, G. (2004). 1D sediment transport morphodynamics with Applications to Rivers and turbidity currents. In E-book available at Gary Parker's Morphodynamics. IL, USA: University of Illinois Available from http://hydrolab.illinois.edu/people/ parkerg/

Popek, Z. (2006). Bedload transport conditions in small lowland river. In Treatises and monograph (Vol. 300, p. 230). Warszawa, Poland: Publishing of Warsaw University of Life sciences —SGGW in Polish.

Pender, D., Patidar, S., Radecki-Pawlik, A. (2014). Hydromorphology of Mountain Rivers and streams. In Selected Topics in Environmental Management. Cracow, Poland: Publishing of Cracow University of griculture (In Polish).

Radice, A., Longoni, L., Papini, M., Brambilla, D., & Ivanov, V. I. (2016). Generation of a design Flood-event scenario for a Mountain River with intense sediment transport. Water, 8, 597. Radice, A., Rosatti, G., Ballio, F., Franzetti, S., Mauri, M., Spagnolatti, M., & Garegnani, G. (2013). Management of flood hazard via hydro-morphological river modelling. The case of the Mallero in Italian Alps. Journal of Flood Risk Management, 6(3), 197 –209.

Schmelter, M. L., Erwin, S. O., & Wilcock, P. R. (2012). Accounting for uncertainty in cumulative sediment transport using Bayesian statistics. Geomorphology, 175-176, 1 –13.

[15] Wu, W. (2007). Computational River dynamics. Leiden, The Netherlands: Taylor & francis/Balkema.

Yang, C. T. (1996). Sediment transport: Theory and practice. New York, NY: McGraw-Hill companies, Inc.

APPENDICES

Appendix 1. Annual Maximum Discharge (cumecs)

Year	July	August	September	October	November	December
2000	8188	14640	18225	16531	6073	3201
2001	0	0	17713	18885	7863	3364
2002	0	0	14939	13003	3201	3227
2003	9000	12123	18106	19025	13003	4265
2004	8625	13818	16098	15292	6724	2811
2005	7079	11062	13026	13792	9120	3392
2006	5422	8923	17599	19389	10710	3742
2007	7044	15650	19831	19831	10855	4110
2008	6759	14366	20426	19695	9920	4265
2009	9960	15140	19695	20534	15650	6481
2010	8311	14199	19806	21272	17940	5345
2011	4416	9080	16830	17340	14150	3915
2012	14102	18080	29815	32150	16079	4850
2013	8809	9120	15727	16396	9560	3582
2014	7560	14660	17512	19941	11376	4356
2015	7079	11062	13026	13792	9120	3393
2016	12079	17571	18225	19279	5826	3201
2017	8694	18139	19941	19941	10855	4110
2018	10360	18106	19695	20534	15446	6481
2019	10421	15652	32441	32860	16646	5171
2020	10887	14725	19520	20534	15650	3960

Source: Extracted from NIWA's gauge record in Lokoja and Adjusted with Rating Curves

Appendix 2. Parameters for calculating STC

Tp (yrs)	$u = Q/Bh^2$	$C = u/\sqrt{hi}$	μ	$\omega s/u^*$	D_m	$\mu\theta$	D_{50}	θ
30	24.766	203.577	3.8909	0.4720	0.0035	142791	0.35	3.8588
40	25.707	199.103	3.7004	0.4107	0.0035	14.2791	0.35	3.8588
50	26.443	194.675	3.5271	0,4227	0.0035	12.9117	0.35	3.6607
60	27.026	190.392	3.3698	0.4045	0.0035	13.4726	0.35	3.9980
70	27.498	186.371	3.2290	0.3892	0.0035	13.9475	0.35	4.3194
80	26.443	194.675	3.5271	0.4227	0.0035	12.9117	0.35	3.6607
100	28.478	176.078	2.8919	0.3550	0.0035	15.0104	0.35	5.1905

Appendix 3. STC (m^2/s) for Selected Return Periods and Reaches

Tp	River Reaches (Chainages)							
	0+000	0+050A	0+050B	0+100	0+150A	0+150B	0+200	0+250A
30	0.1255	0.2120	0.1396	0.1772	0.1526	0.1931	0.1399	0.1954
40	0.1617	0.2189	0.1441	0.1830	0.1182	0.1994	0.1544	0.2018
50	0.1992	0.2941	0.1937	0.2459	0.2117	0.2679	0.2219	0.2711
60	0.2375	0.3281	0.2160	0.2742	0.2361	0.2988	0.2646	0.3023
70	0.2761	0.4077	0.2684	0.3408	0.2935	0.3713	0.3076	0.3757
80	0.1992	0.2941	0.1937	0.2459	0.2117	0.2679	0.2219	0.2711
100	0.3900	0.4262	0.2806	0.3563	0.3068	0.3881	0.4346	0.3928

PAPER 37 – ASSESSMENTS OF METAL PARTICLES IN GROUND FOOD

Segun Isaac Talabi[1,*], Jamiu Kolawole Odusote[1], Jeleel Adekunle Adebisi[1], Ismaila Idowu Ahmed[1], Taiwo Yahaya[1], Modupe Rasheedat Mahamood[1], Lawrence Aderemi Olatunji[2], Mariam Kehinde Sulaiman[3], Suleaiman Abdulkareem[4]

[1]Department of Materials and Metallurgical Engineering, University of Ilorin, Ilorin, Nigeria.
[2]Department of Physiology, University of Ilorin, Ilorin, Nigeria.
[3]Department of Medical Microbiology and Parasitology, University of Ilorin, Ilorin, Nigeria.
[4]Department of Mechanical Engineering, University of Ilorin, Ilorin, Nigeria.
[*]Email: talabi.si@unilorin.edu.ng

ABSTRACT
Food processing encourages safe preservation and provides opportunities for the production of several types of diets. In Nigeria, some foodstuffs are commonly processed in the dried or wet form to powder or paste using an abrasive cutting process involving cast-iron discs. Despite the popularity of this method, metallic and non-metallic contaminants including heavy metals such as cadmium and lead that are detrimental to human health are introduced. Consequently, this study systematically determined the presence of metallic contaminants in ground maize grains, which were processed under dry and wet conditions. Locally available grinding discs manufactured using different furnaces were used to assess the quantity and composition of these contaminants. Irrespective of the disc type, different quantities of contaminants were found in the ground food grains. The discs manufactured using a pit and rotary furnaces generated the highest quantity under wet and dry grinding conditions, respectively. These metallic contaminants were found to contain heavy metals such as lead (≤ 0.316 mg/kg), cadmium (≤ 0.024 mg/kg), chromium (≤ 0.016 mg/kg), copper (≤ 0.880 mg/kg), manganese (≤ 0.624 mg/kg) and zinc (≤ 0.006 mg/kg).

KEYWORDS: contaminants, heavy metal, grinding, cast iron discs, metal particles, ground food

1. INTRODUCTION

Foods are edible materials that provide nutrients, energy, protein, vitamins, and minerals for human growth and development. They are essential for the replacement and repair of cells and provide the body with the necessary energy to function and fight against diseases. Food processing provides the opportunity to eat a greater variety of diets and encourages safe food preservation and packaging. Many dried or dehydrated food processing methods require milling (machining using rotary cutters) or grinding (abrasive cutting using grinding discs) the raw materials to flour/powder form under wet or dry conditions. Other methods involved crushing (pulverization by compression force), granulation (grains or granules formation from solid raw materials), pulverization (reduction to powder by hammering or grinding), and mixing (mechanical dispersion to attain homogeneity) (Gao et al., 2020, Ortega-Rivas et al., 2006). These methods offer the benefits and economic advantages associated with reduced volume/weight, convenience, packaging, handling and transportation, improved bioaccessibility, and greater nutritional value (Gao et al., 2020; Ortega-Rivas et al., 2006). More importantly, it ensures that the preserved food is maintained in dried form for future utilization. However, bad food processing strategies can be detrimental, leading to various challenges such as elevated cholesterol, obesity, certain cancers and digestive issues like Crohn's disease (Joardder and Masud, 2019).

Grinding is an ancient technique of particle size reduction that mechanically produces powders via impact, compression, shear, and cutting (Aradwad et al. 2021). It is an energy-intensive process in which solid food substances are broken down into fine particles (Jung et al., 2018). The food materials produced using this procedure are chemically and microbiologically stable and convenient for future use. The use of grinding machines equipped with cast iron discs is a popular method of food processing in Nigeria. Many households rely on this method to prepare grains as a paste or dried powder. Despite its commonality, this food processing method may not be safe as the grinding mechanism depends on the energized rubbing of two grinding discs, which often leads to the incorporation of metallic and non-metallic contaminants, and even heavy metals that are detrimental to human health (Cancer, 2012). This possible health risk, demands detailed quantitative and qualitative analyses of contaminants introduced into food prepared using such a procedure.

This present study involved a wholesome approach directed towards quantitative and qualitative assessment of metallic contaminants introduced into ground food under wet and dry grinding conditions. Moreover, the present

investigation considered the use of various grinding discs that are locally available for purchase in Nigeria, including imported ones. These discs are produced based on various manufacturing methods namely: cupola, pit and rotary furnaces. The selected discs were typically produced by semi-skilled artisans, who are not knowledgeable about the science of metallurgy and casting but possessed foundry experience, which has been acquired over a long period. Consequently, quality assurance of these locally produced discs is usually not carried out since the workers have no code of practice. Government regulations that are supposed to guide their production and usage are also not enforced. This may be due to a lack of adequate data, information and awareness on the nature of contaminants generated in food during processing with such grinding machines. In addition, previous investigations do not involve a systematic approach to the grinding procedure and retrieving of the metallic contaminants from the ground food. The information provided in this study is expected to prompt a series of other investigations to address the menace of food processing using grinding machines in line with SDG No. 9.

2. EXPERIMENTAL PROCEDURE

2.1 Materials

The grinding discs used in this study were sourced from local markets in the Southern region of Nigeria. Ten pairs of grinding discs produced using cupola, pit and rotary furnaces were purchased from six different manufacturers. The discs were designated as shown in Table 1.

Table 1. Different grinding discs and samples designation

Samples	Designation
RIL	Grinding discs produced using a rotary furnace and sourced from Ilorin
ROS	Grinding discs produced using a rotary furnace and sourced from Osogbo
RIW	Grinding discs produced using a rotary furnace and sourced from Iwo
PIL	Grinding discs produced using a pit furnace and sourced from Ilorin
CIW	Grinding discs produced using a cupola furnace and sourced from Iwo
ID	Imported grinding discs produced from India and sourced from Ilorin

2.2 Processing of maize grains under wet and dry conditions

The food grains were ground under wet and dry conditions. Regarding wet grinding, 10 kg of dried maize was soaked with deionized water for three days in a 30 litres capacity bucket. After three days, the water was decanted and the soaked weight of each food sample batch was determined as appropriately 10.3 kg. To ensure the reproducibility and uniformity of the grinding procedure, certain parameters including the discs' gap tightening sequence (using marked screw threads) and grinding time (18 minutes, 15 seconds) were kept constant. The grinding was done with 5 litres of water. A similar procedure and grinding conditions were employed to process the maize under a dry environment without soaking the maize in water or introducing water during grinding. Before installation and usage, the grinding discs' surfaces were grooved with the aid of a grinding disc, cleaned with a wire brush and later fixed on the locally fabricated grinding machine.

2.3 Quantification of magnetic contaminants

Scavenging devices were fabricated to trap magnetic contaminants from the ground food using the ferromagnetic principle as shown in Figure 1. The neodymium permanent magnets used were enclosed within the acrylic sheets to ensure they do not have any contact with the ground maize. Under the wet condition, the magnetic bed was kept below the flow of the food paste, while it was placed above the dry food powder. Each batch of ground food was run through the scavenger inclined at 23° for three cycles.

Regarding the scavenging process, the magnetic bed trapped the contaminants after which the device was dissembled with the magnetic bed initially in place to retain the scavenged particles at the upper layer of the curved acrylic sheet before it is removed. Thereafter, the contaminants were recovered using a neodymium permanent magnet wrapped with polyethylene film. The magnet was again separated from the film and the recovered contaminants were weighed after each cycle, kept in a sample bottle and later summed up to give the total amount of recovered magnetic contaminants per each grinding.

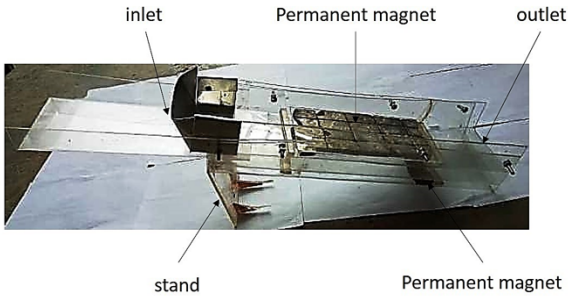

Figure 1. The scavenging device used for separating the magnetic contaminants from ground food.

Characterization of metallic contaminants

A BUCK Scientific ACCUSYS 211 Atomic Absorption Spectrophotometer was used to detect the presence of some heavy metals in the contaminants recovered from ground maize processed under dry grinding conditions. Regarding the analysis, a 10 ml mixture of concentrated HNO_3 and HCl in 3:1 was used to digest 0.05 g of contaminants scavenged from different batches of ground food. After digestion, the solution was diluted with the addition of 90 ml of distilled water and filtered with Whatman 1 filter paper. The filtered liquid solution was analyzed to detect the presence and relative quantity of Pb, Cd, Cr, Cu, Mn, and Zn. The analysis was conducted twice and the reported results represent an average value.

3. RESULTS AND DISCUSSION

3.1 Magnetic contaminants

Firstly, the efficiency of the scavenging devices used in the recovery of magnetic contaminants from the ground food was determined as approximately 85%. The determination was done by introducing a known quantity of metallic contaminants, which were previously generated from the discs during grinding into a known quantity of ground maize. Thereafter, the number of recovered contaminants after running the ground food through the scavenger three times was divided by the initial amount that was introduced into the food and multiplied by 100. Figure 2a shows the quantities of magnetic contaminants generated during the wet grinding of soaked maize grains with various cast iron discs that were produced using rotary, pit and cupola furnaces. Irrespective of the discs' type, significant amounts of contaminants were recovered after sequentially grinding the grains for 18.25 minutes.

PIL discs, which were produced using a pit furnace and sourced from Ilorin generated the highest quantity of contaminants. The smallest amount of such inclusions was recovered when ROS discs (sourced from Osogbo and produced using a rotary furnace) were used for grinding the grains. More so, one of the tightening nuts got loosed and was ground into the food while processing the grains with ROS discs. The nut contribution to the overall quantity of recovered contaminants during this batch of experiments was determined by subtracting the weight of the recovered nut from the initial nut weight. This scenario typically occurs during food processing with the locally fabricated grinding machine. The results obtained in this investigation reinforced earlier submissions about metallic inclusion in ground food (Normanyo *et al.*, 2010; Odusote J. K., 2017) and further assert that their presence is independent of the type of cast iron discs that may be installed on such grinding devices. Nevertheless, the results showed that the chemistry and structure can influence the number of metallic contaminants generated in the ground food. This observation was based on the difference in the number of recovered contaminants for the different discs type despite the similarity in grinding conditions. As expected the discs' structure and composition will affect properties such as wear and hardness (Kwofie S. and Chandler H. D., 2006), which will determine their performance in service. These contributions advance existing knowledge on the subject matter. Figure 2b is a representation of the contaminants which were recovered using a neodymium permanent magnet wrapped with polyethylene film.

However, under dry grinding conditions, the number of contaminants generated in the ground food increased (Figure 3). It should be noted that the comparison between the number of contaminants based on wet and dry grinding did not consider continuous usage over a long period. Under such circumstances, disc corrosion in synergy with wear may contribute to metal loss in a wet grinding condition. For all the investigated discs, the quantity of recovered magnetic particles/chips increased compared to when wet grinding was used to process the maize grains. Friction is the main mechanism responsible for food pulverization by grinding. In addition, the environment (grinding) plays a significant role in the abrasive wear rate of metallic materials (Gao *et al.*, 2020). Therefore, the presence of water during grinding serves as a lubricant, which reduced metal loss during the wet grinding operation (Wirojanupatump and Shipway, 1999). Consequently, the higher number of magnetic contaminants during the dry grinding can be attributed majorly to the lack of lubricating effect by water.

Nevertheless, some other factors such as an increase in temperature due to friction during grinding, and the constituents of the grinding discs could also influence the discs' wear performance. As expected, the quantity of magnetic contaminants generated into the ground food under dry grinding conditions varied for the different cast iron discs. In this instance, the least number of contaminants was introduced by PIL discs while the highest quantity was produced by RIL discs, which were manufactured using pit and rotary furnaces from Ilorin, respectively. It is not very clear why the discs produced using a pit furnace perform better under this condition. Nevertheless, the compositional analysis of contaminants resulting from the usage of these discs showed that the PIL disc has the highest amount of calcium. Calcium has been reported to possess the ability to induce spheroidal graphite generation in cast iron (Oluwole, 2007). The presence of graphite nodules within the microstructure of such cast iron will enhance its wear resistance. This observation may be responsible for the better performance exhibited by the discs (PIL discs).

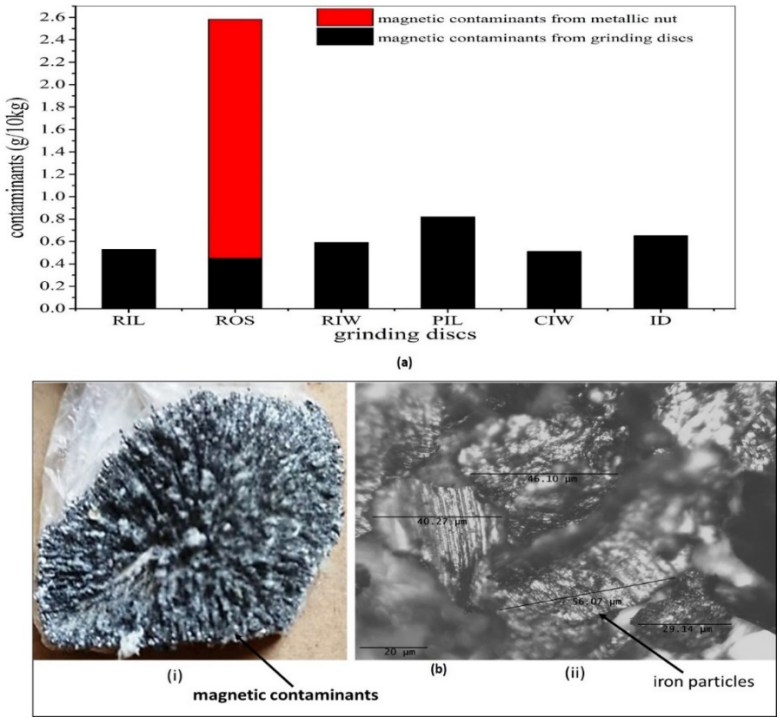

Figure 2. Magnetic contaminants generated from different locally sourced discs during wet grinding for 18.25 minutes (a), and a sample of magnetic contaminants recovered from ground food using a permanent magnet wrapped with a polyethylene sheet (i) and microstructural image (ii) obtained using an Amscope optical microscope (b).

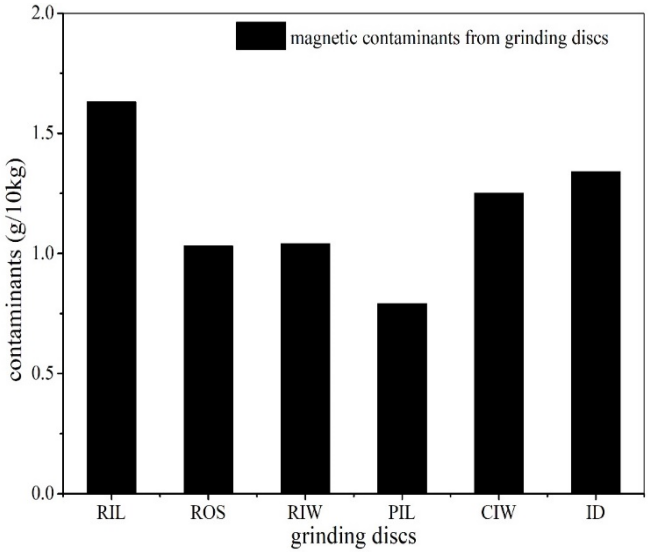

Figure 3. Magnetic contaminants generated from different locally sourced discs during dry grinding for 18.25 minutes.

3.3 Analysis of heavy metals in magnetic contaminants from ground food prepared using various grinding discs

There are about twenty-three heavy metals that in large quantities will be harmful to humans (Jaishankar *et al.*, 2014). Heavy metal toxicity can impair the functionality of some important organs such as the brain, lungs, kidneys and liver (Järup, 2003; Jaishankar *et al.*, 2014). Long-term exposure to them can cause neurological degenerative processes that can lead to multiple sclerosis, Parkinson's disease, Alzheimer's disease and muscular dystrophy while their compounds may be carcinogenic (Järup, 2003).

Table 2 shows AAS results for different samples of recovered magnetic contaminants. The results showed that food processed using locally fabricated grinding machines can be a contributory source of heavy metal intake in humans. Consequently, attention must be given to the processing of food grains with such machines having cast iron grinding discs installed in them. More so, the recovered metallic contaminants are not present in mineral or dietary form and may therefore constitute a major health hazard. Nevertheless, the analysis and comparison in this study were based on information available regarding the consumption of such heavy metals in their dietary form. Regarding this study, the presence of lead (Pb) was detected in contaminants generated from the usage of CIW, RIL and ROS discs. RIL contaminants presented the highest Pb value of about 0.3169 mg/kg. Sub-Saharan Africans consumed up to 450 g/person/day of maize (Ekpa *et al.*, 2019). Consequently, an adult in Nigeria may consume about 3.2 kg in a week. Based on earlier results (section 3.1), 0.5216 g of magnetic contaminants were recovered when 3.2 kg of maize grains were ground using RIL discs. This quantity of contaminants contained about 0.00016 mg of Pb. The tolerable weekly intake of Pb has been reported as 0.025 mg/kg body weight (Witkowska *et al.*, 2021). The average body weight of an adult in Nigeria is 72 kg, which implied that the maximum tolerable intake of Pb per week is 1.8 mg. This indicates that the detected Pb quantity is within the permissible limit. However, it must be noted that this is only coming from a single food source. Cadmium is another heavy metal that was detected during the analysis of contaminants recovered from food processed using all the investigated grinding discs. The maximum value of this metal was recorded in contaminants recovered from food processed using RIL discs. The tolerable weekly intake value of Cd has been reported as 0.007 mg/kg body weight (Witkowska *et al.*, 2021). According to the earlier submission, the detected value will imply a weekly consumption of 1.25×10^{-5} mg of Cd, which is within the permissible weekly consumption value. Chromium can exist in trivalent or hexavalent form in the environment and its hexavalent form has been reported to be toxic and carcinogenic (Gürkan *et al.*, 2017; Witkowska *et al.*, 2021). Nevertheless, the tolerable upper intake level of chromium has not been established. In this study, 0.01612 mg/kg and 0.00950 mg/kg of Cr were detected in ID and ROS contaminants, respectively. The recommended maximum daily intake of copper for adults, which is based on liver damage protection is 70 mg/week (Trumbo *et al.*, 2001). Similarly, the recovered contaminants will only contribute 0.00042 mg when an adult consumed 3.2 kg of maize ground under dry conditions using RIL discs whose contaminants contained the highest quantity of copper in this study. Compared to the permitted intake, copper consumption through food processed with the grinding machine that has these installed cast-iron discs is not significant. Manganese is another heavy metal that was detected in the recovered magnetic contaminants. This element was discovered in all the analyzed samples and the highest quantity was found in those recovered from food processed using ID discs. The tolerable intake level of zinc in the human body is 40 mg/day (Saper and Rash, 2009). This element was only detected in magnetic contaminants recovered from maize grains processed using ID discs and its value was not significant.

Table 2. Heavy metals present in recovered magnetic contaminants from ground food

Sample Code	Pb	Cd	Cr	Cu	Mn	Zn
	mg/kg					
CIW	0.08182	0.018182	0.00000	0.880165	0.20992	0.00000
ID	0.0000	0.021901	0.01612	0.607851	0.62479	0.00661
PIL	0.0000	0.014463	0.00000	0.715702	0.48760	0.00000
RIL	0.31694	0.023967	0.00000	0.80124	0.49298	0.00000
ROS	0.00579	0.018182	0.00950	0.564463	0.42314	0.00000
RIW	0.0000	0.021074	0.00000	0.500413	0.41901	0.00000

4. CONCLUSION

The presence and characteristics of magnetic contaminants recovered from maize processed under wet and dry grinding conditions using a locally fabricated grinding machine installed with cast iron grinding discs were investigated in this study. The results showed that the use of cast iron discs in food processing led to the introduction of metallic contaminants containing heavy metals such as lead, cadmium, chromium, manganese and zinc into the ground maize grains, which may be detrimental to human health. The presence of these contaminants was also found to be independent of the disc types, which were manufactured based on different production routes. More so, different quantities of contaminants were introduced into the processed food depending on the grinding conditions and type of discs. The highest quantity of contaminants was recovered from maize ground under dry conditions due to the lack of lubrication provided by wet grinding. Consequently, the study point to the need to regulate the production of cast iron discs that are used in food processing. Currently, there is no stipulation guiding important steps such as scrap selection and choice of melting furnace in the manufacturing of such grinding discs. The lack of regulation can constitute a major health hazard, which may hinder the realization of SDG No. 9 in developing nations like Nigeria.

ACKNOWLEDGEMENT

The funding of this research by the Nigeria National Research Fund (NRF) under the grant reference number TETF/DR&D-CE/NRF/2020/SETI/85/VOL.1, is duly acknowledged by the authors. The authors also appreciate the Department of Materials and Metallurgical Engineering for providing the spacing and some tools used in this experimental work.

REFERENCES

Ekpa, O., Palacios-Rojas, N., Kruseman, G., Fogliano, V., and Linnemann, A. R. (2019). Sub-Saharan African Maize-Based Foods - Processing Practices, Challenges and Opportunities. *Food Reviews International, 35*(7), 609-639. DOI:10.1080/87559129.2019.1588290

Gao, W., Chen, F., Wang, X., and Meng, Q. (2020). Recent advances in processing food powders by using superfine grinding techniques: A review. *Comprehensive Reviews in Food Science and Food Safety, 19*(4), 2222-2255. DOI:https://doi.org/10.1111/1541-4337.12580

Gürkan, R., Ulusoy, H. İ., and Akçay, M. (2017). Simultaneous determination of dissolved inorganic chromium species in wastewater/natural waters by surfactant sensitized catalytic kinetic spectrophotometry. *Arabian Journal of Chemistry, 10*, S450-S460. DOI:https://doi.org/10.1016/j.arabjc.2012.10.005

Jaishankar, M., Tseten, T., Anbalagan, N., Mathew, B. B., and Beeregowda, K. N. (2014). Toxicity, mechanism and health effects of some heavy metals. *Interdiscip Toxicol, 7*(2), 60-72. DOI:10.2478/intox-2014-0009

Järup, L. (2003). Hazards of heavy metal contamination. *Br Med Bull, 68*, 167-182. DOI:10.1093/bmb/ldg032

Kwofie S., and Chandler H. D. (2006). Potential health effects of locally-manufactured corn-mill grinding plates. *Journal of Science and Technology (Ghana), 26*(2), 137-147. DOI:10.4314/just.v26i2.32995

Normanyo, E., Esiam, E. K., Amankwa-Poku, K., and Adetunde, I. A. (2010). *Redesign Of A Grinding Mill For The Minimisation Of Iron Filing Production*.

Odusote J. K., G. A. S. I. I. A. S. A. K. A. A. (2017). Assessment of Metallic Contaminants in Grinded Millet using Domestic Grinding Machine. *Nigerian Journal Of Technological Development, 14*(1), 13-17.

Oluwole, O. O., Olorunniwo, O.E.,Ogundare, O.O., Atanda P.O. and Oridota, O.O. (2007). Effect of Magnesium and Calcium as Spheroidizers on the Graphite Morphology in Ductile Cast Iron. *Journal of Minerals & Materials Characterization & Engineering, 6*(1), 25-37.

Saper, R. B., and Rash, R. (2009). Zinc: an essential micronutrient. *Am Fam Physician, 79*(9), 768-772.

Trumbo, P., Yates, A. A., Schlicker, S., and Poos, M. (2001). Dietary reference intakes: vitamin A, vitamin K, arsenic, boron, chromium, copper, iodine, iron, manganese, molybdenum, nickel, silicon, vanadium, and zinc. *J Am Diet Assoc, 101*(3), 294-301. DOI:10.1016/s0002-8223(01)00078-5

Wirojanupatump, S., and Shipway, P. H. (1999). A direct comparison of wet and dry abrasion behaviour of mild steel. *Wear, 233-235*, 655-665. DOI:https://doi.org/10.1016/S0043-1648(99)00208-2

Witkowska, D., Słowik, J., and Chilicka, K. (2021). Heavy Metals and Human Health: Possible Exposure Pathways and the Competition for Protein Binding Sites. *26*(19). DOI:10.3390/molecules26196060

PAPER 38 – A SURVEY OF POWER AMPLIFIER SIGNAL LINEARIZATION TECHNIQUES IN COMMUNICATION NETWORKS

A. O. Ohida[1], J. Agajo[2], N. Salawu[2*]

[1-2]Department of Telecommunication Engineering, Federal University of Technology, Minna, Nigeria.
[1]ohida.pg916745@st.futminna.edu.ng
[2]james.agajo@futminna.edu.ng
[2*]nathsalawu@futminna.edu.ng

ABSTRACT
Radiofrequency power amplifiers are crucial components of communication networks. The inherent nonlinearity of these components causes in-band distortion, which worsens bit-error-rate performance, and spectrum regrowth, which causes interference in adjacent channels. Out-of-band emission requirements set by regulatory bodies are essentially violated by these distortions. At the output of the power amplifier (PA), crosstalk exists between the antenna branches due to mutual coupling and nonlinear distortion within the transmitted signal. Harmonic distortion is a result of the complexity of modern signal processing techniques and the nonlinear nature of PAs. For high spectral and power efficiency, PAs must operate linearly. Electronic isolators between PAs and antennas can prevent this crosstalk. However, they do not meet the design requirements of modern composite systems. They are rather avoided to achieve a suitable form factor. Very useful linearization strategies are therefore presented and discussed in this survey. The effectiveness of PAs, as well as the complexity and constraints of the system, are always taken into account while choosing the linearization approach. These are effective ways to linearize transmit signals from PA output. The techniques are found effectively suitable in all domains while maintaining the acceptable adjacent channel leakage ratio level.

KEYWORDS: Crosstalk, Distortion, Linearization, Massive MIMO, RF Power Amplifier, 3GPP.

1. INTRODUCTION

The escalating need for higher data rates, spectrum efficiency, and low cost have all been significant problems with cellular communication technology over the years. This demand is growing rapidly as wireless device deployments rise. Numerous radio technologies have also been created to manage the plethora of data-hungry applications that are constantly expanding. One of these essential technologies is massive MIMO (massive multiple input multiple outputs), also known as the advanced antenna system (AAS). Massive MIMO uses hundreds of small, tightly spaced antennas (Suryasarman & Springer, 2015). A representation of the layout is provided below in Figure 1.

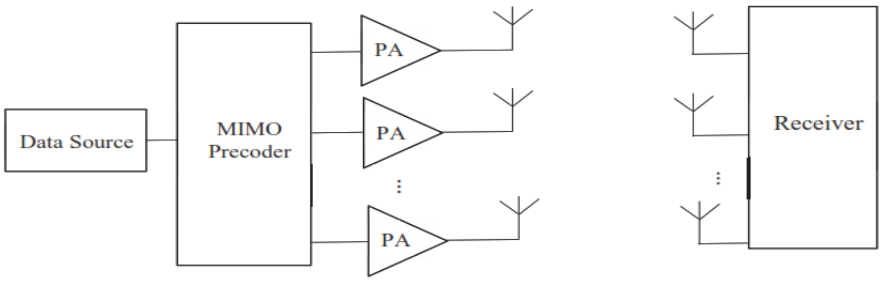

Figure 1. Multiple Input Multiple Output (MIMO) Structure

By using numerous transmitting and receiving antennas, multiple-input and multiple-output (MIMO) radio antenna technology makes use of multipath propagation. By establishing numerous signal paths to transmit the data and choosing specific paths for each antenna, a radio link's capacity can be greatly increased (Bland, 2016). In early developments, MIMO was initially defined as the use of numerous antennas at the transmitter and reception points. The concept is now acknowledged as a practical way to transmit and receive numerous data signals concurrently over a single radio channel using multipath propagation. High data rate broadcasting can be achieved by breaking a high-rate signal into several low-rate signals and sending them from transmitters that are spatially apart. Each receiver uses a variety of antennas to pick up the different cochannel signals that arrive from different angles. The radio frequency (RF) power amplifier (PA) of each transmitter branch, whose simple structure is shown in Figure 2, is crucial to the successful operation of numerous antenna systems. Its task is to increase the sent signal's power to a suitable degree for transmission. Due to its low strength, the produced signal needs to be amplified. This amplification is essential to account for channel route loss between the transmitter and the recipient.

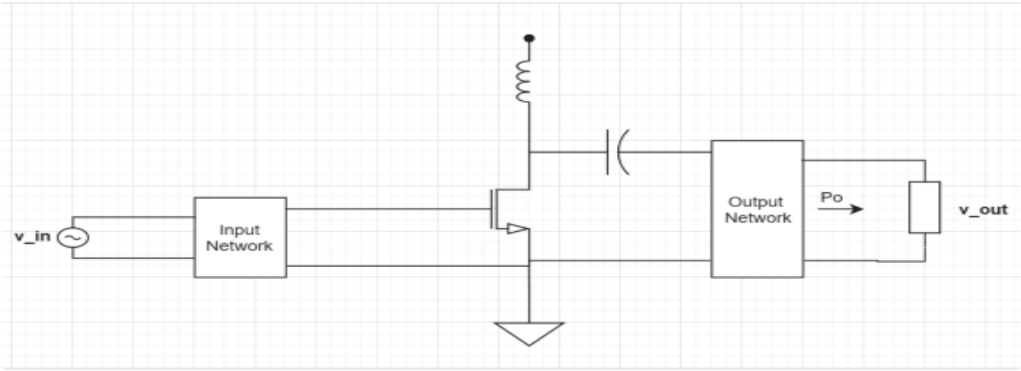

Figure 2. Radio Frequency Power Amplifier

Several technical issues arise at the power amplifier node in communication branches. These include nonlinear behaviour, perceptible signal distortions, and other kinds of interference that degrade the system's general functionality and the signal transmission's integrity (Brihuega et al., 2019). The distortions and irregular behaviour lead to crosstalk and mismatch (Hausmair et al., 2018).

2. THEORETICAL ANALYSIS

To handle both the high data rate and spectrum efficiency issues, newer modulation techniques like Wideband Code Division Multiple Access (WCDMA), Quadrature Amplitude Modulation (QAM), and Orthogonal Frequency Division Multiplexing (OFDM) have been developed. However, the result is a complex signal with a non-constant envelope, and a high peak-to-average power ratio (PAPR) (Jiang & Wu, 2018). At large PAPRs, power amplifiers exhibit nonlinear behaviour, as shown in Figure 3 as signal power fluctuation. The enhanced signal displays spectrum regrowth in such a case (Menon, 2016). This is considered a violation of the Third Generation Partnership Project (3GPP) specifications, which specify the highest allowed adjacent channel leakage ratio (ACLR) for mobile communication protocols (Al-qamaji & Abdalrahman, 2019).

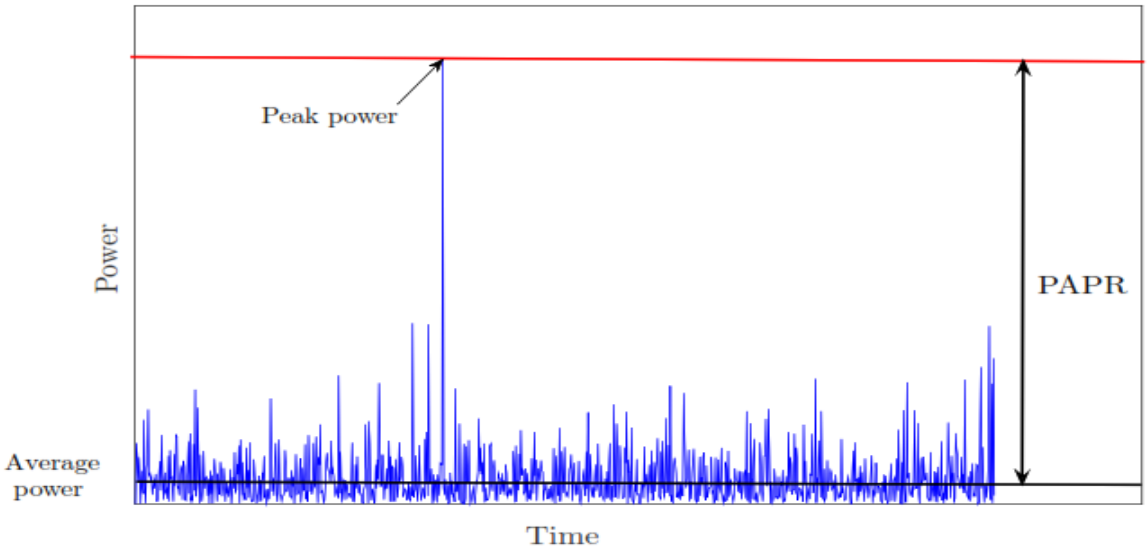

Figure 3. Power Fluctuation of Signal with High PAPR (Cheaito, 2017).

If the PAPR is strong, a high linear power amplifier is required at the transmitter. The linearity requirements can be met by lowering the PA far below its saturation limit. This leads to poor power efficiency which is especially unwanted in a mobile transmitter (Wan et al., 2015). Figure 4 below depicts the output response of PA.

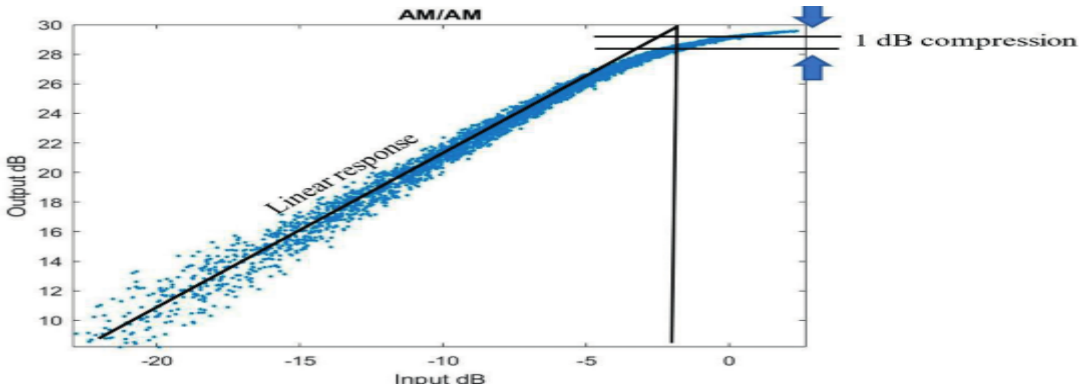

Figure 4. Power Amplifier Output Response.

When the PA is pushed above the linear zone, nonlinear distortion effects occur. Nonlinear distortion, which also creates harmonics and intermodulation signals outside of the intended frequency range, makes it more difficult to receive the signal. These unwanted distortion products, especially in adjacent frequency bands, conflict with other radio interface users (Jantunen, 2016). Both the 4G with MIMO and the 5G with massive MIMO have these naturally unfavourable effects, such as nonlinear before-PA, crosstalk on the transmitter side, and antenna crosstalk on both sides. Operation regions of the power amplifier are shown in the characteristics graph of figure 5. Power amplifiers must be run close to the compression region in order to achieve high power efficiency, which inevitably causes non-linear distortion of the output signal. Crosstalk is thus one of the challenges in the design of MIMO transceivers. It is present between different transmit and receive paths that are built in a single chipset (Bassam et al., 2019).

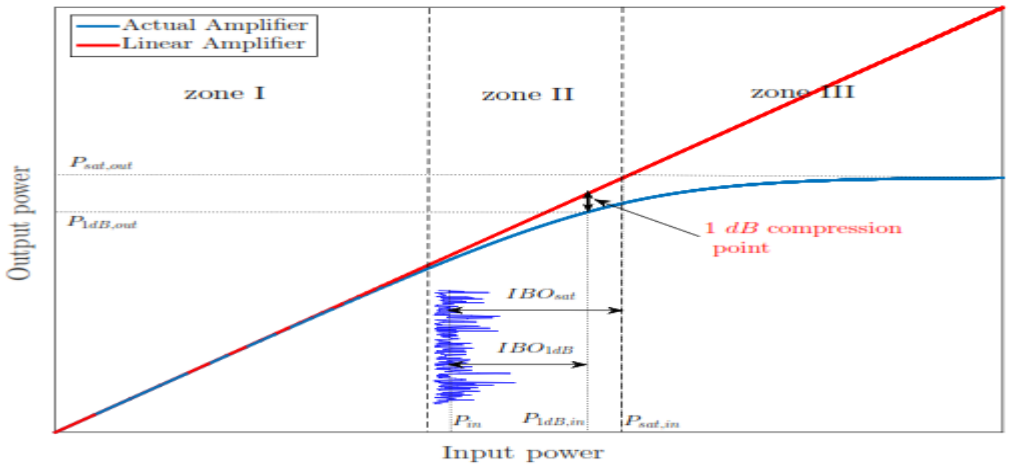

Figure 5. Power Amplifier Characteristics: Linear, Compression and Saturation Zones.

For situations where real antenna arrays driven by power amplifiers are not physically built, effective simulation environments are accessible. MATLAB, SIMULINK, and CADENCE are a few of them. These programming environments can be used to model, simulate, and evaluate dynamic systems and are all-purpose. Particularly for visualizing data and functions, working with matrices, and implementing algorithms, they offer a superior user interface. Mathematical tools as given below are some of the useful computational apparatus that can provide essential parameters where necessary:

i. Volterra Series: The finest methods for capturing and modelling the behaviours of nonlinear systems and functions are the Taylor and Volterra series. Taylor series can easily approximate the response of a nonlinear system to a specific input if the output of the system depends on the current value of the input. The Volterra Series is a functional extension of a dynamic, nonlinear, and time-invariant system. Because it can account for the memory effect, it is always simplified to a Memory Polynomial (MP) model equation.

ii. Normalized Mean Square Error, NMSE: This is a figure of merit that provides a measurement for the model accuracy and in-band distortion. It gives the difference between the actual measurement and the desired received signal. NMSE is determined using equation 1.

$$NMSE_{(Y_{desired}-Y_{actual})} = \frac{\sum_{n=0}^{N-1}|Y_d(n)-Y(n)|^2}{\sum_{n=0}^{N-1}|Y_d(n)|^2} \quad (1)$$

Y(n) denotes the measured signal at the output of the amplifier and Y_d (n) is the desired output signal.

iii. Adjacent Channel Leakage Ratio, ACLR: When a power amplifier is fed a wide band transmission signal, the output shows a noticeable frequency regrowth. This effect is also known as out-of-band distortion. This can be precisely captured and compared to known ACLR values from important performance indicators provided by standard organizations with the appropriate simulation tools. The ratio between the main signal and the power intermodulation signal is an indicator of quality. It can be defined as the ratio of the transmitted signal's power in the main or desired channel to that of the channel next to it as shown in equation 2.

$$ACLR = \frac{\int_{BW_{adj}}|Y(f)|^2 df}{\int_{BW_{main}}|Y(f)|^2 df} \quad (2)$$

Where Y(f) is the transmitted signal in the frequency domain, BW_{adj} is the signal bandwidth of the adjacent channel and BW_{main} is the signal bandwidth of the main channel. Both signals are assumed to have the same bandwidth.

iv. Least Square Method: This is generally a standard approach in regression analysis to approximate the solution of overdetermined systems by minimizing the sum of the square of the residuals made in the result of every single equation.

3. LINEARIZATION TECHNIQUES

Very nonlinear power amplifiers are used to drive the antenna components in communication systems and networks, resulting in significant nonlinear distortion (Brihuega et al., 2019). The radio frequency output signal exhibits spectrum regrowth due to the power amplifier's nonlinear behaviour in the frequency domain. Digitally modulated signals' spectrum widening creates neighbouring channel interference. In addition to spreading the transmitted spectrum, distortion also produces intersymbol interference, which increases the bit error rate (BER), thus contravening FCC regulations and 3GPP guidelines. This suggests that components such as power amplifiers and other parts must be linear. But for PA to display power efficiency, it must be operated in the nonlinear region. Using linearization techniques, this highly desired linear amplification is attained. The pre-distortion approach, the feedback method, and the feed-forward method are the three primary linearization techniques. These primary classes also have further variations as shown below. Figure 6 shows the linearization techniques.

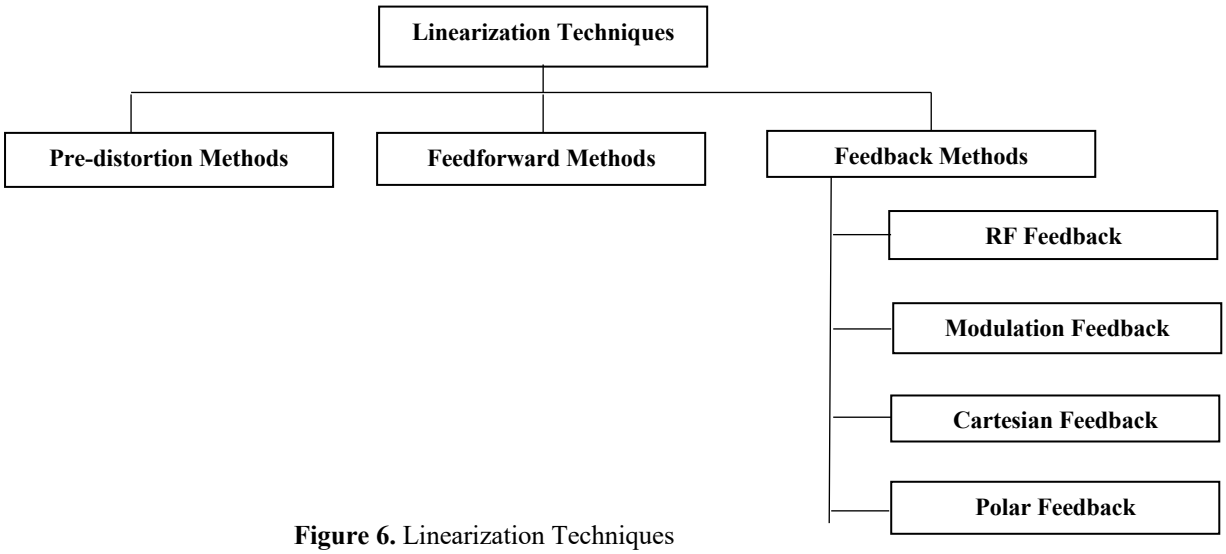

Figure 6. Linearization Techniques

3.1 FEEDFORWARD METHOD

This approach adds the radio frequency power amplifier output distortion to the PA output in the opposite phase after being extracted and amplified. Over time, this eliminates the distortion. Due to the error amplifier's high-power requirements and necessity for linearity, the approach has a low power efficiency (Goyal & Gupta, 2015). The couplers also cause a loss of power. The advantage, though, is in its capacity to lower distortion over a broad bandwidth. Also, the technique involves both phase and gain modifications, which makes implementation extremely challenging. The block diagram is displayed in figure 7.

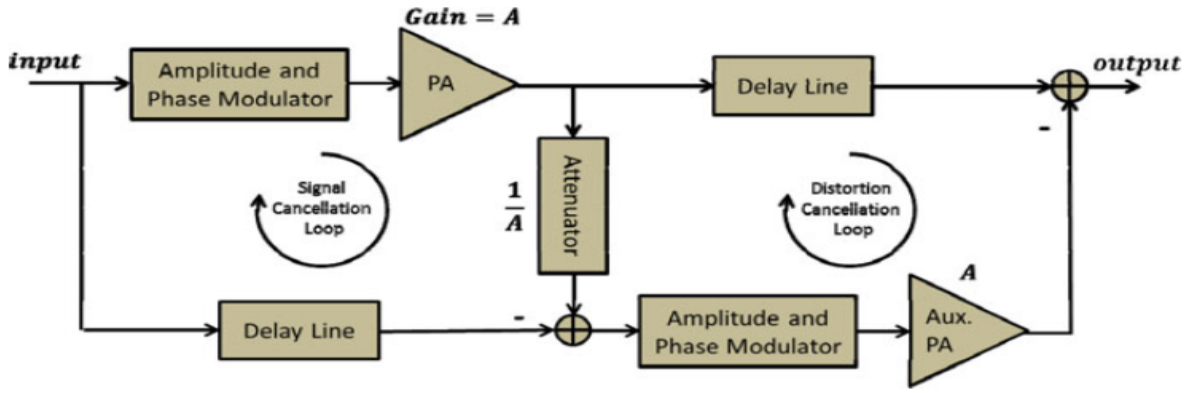

Figure 7. Block Diagram of Feedforward Linearization Technique (Cheaito, 2017).

3.2 FEEDBACK METHOD

One of the easiest methods for linearizing power amplifiers is the feedback technique. The goal is to make the output adhere to the PA's input. The controller, as depicted below, feeds back a portion of the output signal from the PA (Yadav, 2016). This is taken away from the power amplifier's input signal. As a result, the output is effectively optimized to be a linear and amplified representation of the input signal. Polar and Cartesian feedback are subtypes of the two fundamental types, RF feedback and modulation feedback as shown in Figure 8.

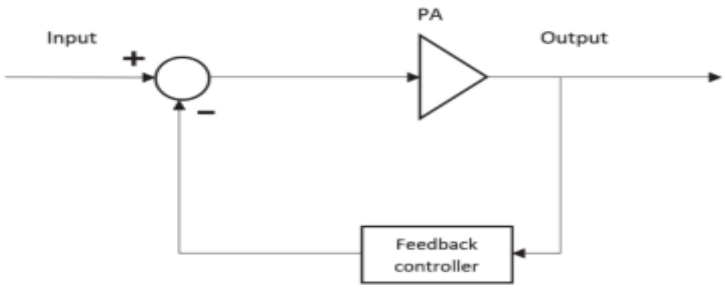

Figure 8. Feedback Linearization Method.

3.3 DIGITAL PRE-DISTORTION METHOD

The goal is to expand the input signal before the power amplifier so that the non-linearities caused by the PA can be balanced out (Kenney et al., 2015). To make the combined transfer characteristic of the RF power amplifier and the nonlinear device before it, linear, the notion entails the inclusion of the nonlinear element. Predistortion can be accomplished at either RF or baseband.

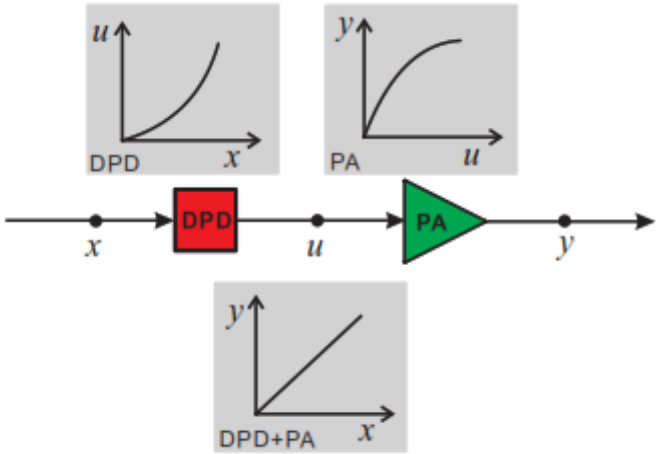

Figure 9. Principles of Pre-distortion Method (Guan & Zhu, 2017)**.**

4. CONCLUSION

The crucial and inherently nonlinear behaviour of radio frequency power amplifiers was examined in this paper, as well as the long-term impact on performance estimation of modern antenna systems used in communication networks. Power amplifiers are essentially nonlinear devices, and the signal processing methods also clearly show that there is signal distortion. The bit-error rate is lowered by the in-band distortion and out-of-band distortion results in spectrum broadening, which causes interference in adjacent channels. By correctly activating the power amplifiers in every transmitting branch such that their output signals are linear and amplified versions of the input RF signal, energy and spectrum efficiency as well as overall system performance are significantly improved.

A figure of merit called the adjacent channel leakage ratio (ACLR) shows the proportion between the main signal and the power intermodulation signal. Comparisons can be made between the out-of-band distortion measured using the proper simulation tool and data from common regulatory organizations like the third-generation partnership project (3GPP). The details presented in this paper adequately provide very insightful and generic linearization concepts to the researchers in the field. The strategies that were just explained have their respective pros and disadvantages. System complexity and application area are the deciding factors for any technique selection.

ACKNOWLEDGEMENT

I want to sincerely thank my supervisors, Engr. Dr. James Agajo and Engr. Dr. Nathaniel Salawu, for their continuous support of my work and related research, as well as for their persistence, inspiration, and wealth of knowledge.

REFERENCES

P. M. Asbeck, N. Rostomyan, M. Ozen, B. Rabet, J. A. Jayamon, (2019), Power Amplifiers for mm wave 5G Applications: Technology Comparisons and CMOS-SOI demonstration circuits, IEEE Transactions on Microwave Theory and Techniques, 67, 3099-3109.

Yufeng Wan, Tony J. Dodd, Robert F. Harrison, (2015), Modeling of Power Amplifier Nonlinearities using Volterra Series, IFAC Proceeding Volumes, 38, 785-790.

Ali Al-Qamaji, Fida Abdalrahman, (2019), Relaxed Isolation Based Linearization for Sub-6 GHz Advanced Antenna System, Faculty of Engineering, LTH, Lund University, Lund, Sweden.

P. M. Suryasarman and A. Springer, (2015), A Comparative Analysis of Adaptive Digital Predistortion Algorithms for Multiple Antenna Transmitters, IEEE Transactions on Circuits and Systems I: Regular Papers, 62(5), 1412-1420.

Alberto Brihuega, Mahmoud Abdelaziz, Matias Turunen, Thomas Erikson, Lauri Antilla, Mikko Valkama, (2019), Linearizing Active Antenna Arrays: Digital Predistortion Method and Measurements, arXiv: 1907.07959, 1, 6-8.

J. Stevenson Kenney and Jau-Homg Chen, (2015), Power Amplifier Linearization and Efficiency Improvement Technique for Commercial and Military Applications, IEEE International Conference on Microwave, Radar and Wireless Communications, 3-8.

Katharina Hausmair, Per N. Landin, Ulf Gustausson, Christian Fager, Thomas Eriksson, (2018), Digital Predistortion for Multi-Antenna Transmitters Affected by Antenna Crosstalk, IEEE Transactions on Microwave Theory and Techniques, 66(3):1524-1535.

Tao Jiang, Yiyan Wu, (2018), An Overview: Peak-to-Average Power Ratio Reduction Techniques for OFDM Signals, IEEE Transactions on Broadcasting, 54(2).

Lein Guan, Anding Zhu, (2017), Green Communications: Digital Predistortion for Wideband FR Amplifiers, IEEE Microwave Magazine.

Muhammad Furqan Haider, Fei You, Songbai He, Timo Rahkonen, Janne P. Aikio, (2022), Predistortion-Based Linearization for 5G and Beyond Millimeter-Wave Transceiver Systems: A Comprehensive Survey, IEEE Communications Surveys and Tutorials.

Yadav, S. P. and Bera, S. C., (2014), Nonlinearity Effect of High Power Amplifiers in Communication Systems, International Conference on Advances in Communication and Computing Technologies.

S. Bassam, M. Helaoui, and F. Ghannouchi, (2019), Crossover Digital Pre-distorter for the Compensation of Crosstalk and Nonlinearity in MIMO Transmitters, IEEE Transactions on Microwave Theory and Techniques, 57(5):1119-1128.

X. Bland, (2016), Modelling of Power Amplifier Distortion in MIMO Transmitters, Master's Thesis in Wireless, Photonics and Space Engineering, Chalmers University of Technology, Gothenburg, Sweden.

Menon Abilash, (2016), Power Amplifier Linearization Implementation Using A Field Programmable Gate Array, Master Thesis, University of Massachusetts Amherst.

Sonam Goyal, Jyoti Gupta, (2015), Review of Power Amplifier Linearization Techniques in Communication system, International Journal of Engineering Research and Technology (IJERT), 2:1897-1904.

Ali Cheaito, (2017), Analytical analysis of in-band and out-of-band Distortions for Multicarrier Signals: Impact of Non-linear Amplification, Memory Effects and Predistortion.

PAPER 40 – SEASONAL VARIATION AND HEALTH RISK ASSESSMENT OF GASEOUS AND PARTICULATE POLLUTANTS AROUND TRAFFIC HOTSPOTS OF A DENSELY POPULATED AFRICAN CITY

E. T. Odediran[1*], J. A. Adeniran[1], R. O. Yusuf[1]
[1]Environmental Engineering Research Laboratory, Department of Chemical Engineering, University of Ilorin, Nigeria.
[*]Email: odedirantolu@yahoo.com

ABSTRACT
Episodes of urban air pollution in Africa have received less attention than in the rest of the world. This study investigated the concentration variations of gaseous pollutants (CO, NO_2, SO_2, NH_3, TVOCs, and ground level O_3) and Particulate Matter (PM_1, $PM_{2.5}$, PM_{10} & TSP) during the rainy and dry seasons at 25 traffic intersections (TIs) within Ibadan. The daily rush and non-rush hour concentrations of pollutants were monitored. Cancer risks (CR_{inh}) and epidemiology-based mortality estimates using Relative Risk (RR) and Attributable Fractions (AF) linked with $PM_{2.5}$ and PM_{10} exposure were evaluated. The non-cancer risks via inhalation for CO, NO_2, SO_2 and ground level O_3 were assessed using Hazard Quotient (HQ). The mean concentrations of PM_1, $PM_{2.5}$, PM_{10} & TSP in the dry season were higher than in the rainy season by 53.24%, 132.20%, 360.49% and 365.83%, respectively. The dry season had the highest ER and AF mortality estimates from $PM_{2.5}$ and PM_{10} exposures compared to estimates during the rainy season. Health risk assessment over the study period showed that CR_{inh} of $PM_{2.5}$ was tolerable while HQ_{inh} of SO_2 was above 1 indicating significant non-cancer risks at TIs in Ibadan.

KEYWORDS: Gaseous Pollutants, Particulates, Traffic Intersection, Seasons, Rush and Non-rush hour, Health Risk.

1. INTRODUCTION

Air quality degradation in different cities in Africa impacts poor citizens more negatively due to urbanization, surge in population, industrialization and increased vehicular emissions (Anwar *et al.*, 2021; Das *et al.*, 2015; Delkash and Mir, 2016). Hence, this study investigated the variations in seasonal concentration levels and health risks associated with gaseous pollutants (CO, NO_2, SO_2, NH_3, TVOCs, and ground level O_3) and particulates (PM_1, $PM_{2.5}$, PM_{10} & TSP) in and around major traffic pollution hotspots of Ibadan metropolis.

2. MATERIALS AND METHODS

2.1 Study area

Ibadan city was chosen as the study area for this research because it is one of the biggest cities in Africa with rapid urbanization and industrialization. Ibadan is the third most populous city and the largest by geographical area in Nigeria. It is a major commercial and transportation hub with its strategic location on the country's railway line, an airport and expressways connecting it to many other major cities. Industrial, commercial, agricultural and residential activities were predominant in the study area. Ibadan is a prominent transit point between the coastal and hinterland regions of Nigeria. Gaseous pollutants and particulate matter (PM) were sampled in twenty-five major traffic Intersections (TIs) in Ibadan during rainy (wet) and dry seasons. The selected TIs (sampling sites) TIs are the major traffic hotspots, evenly and spatially distributed within the Ibadan metropolis. A Map of Ibadan with wind roses of rainy and dry seasons is presented as Figure S1 in the supplementary document.

2.2 Sampling protocol for PM and gaseous pollutants

Variations in rush and non-rush hour ambient concentrations of gaseous pollutants (CO, NO_2, SO_2, NH_3, TVOCs, and ground level O_3) and particulate matter (PM_1, $PM_{2.5}$, PM_{10} & TSP) were investigated simultaneously at 25 major TIs during rainy and dry seasons. Ambient concentration levels (in ppm) of six pollutant gases were monitored at TIs with Aeroqual S500 devices having 6 sensor heads while ambient PM concentrations of PM_1, $PM_{2.5}$, PM_{10} & TSP were monitored using Aerocet 531S.

2.3 Human exposure risks

In this study, the health risk assessment of $PM_{2.5}$, PM_{10}, CO, NO_2, SO_2 and ground level O_3 was investigated by applying the United States Environmental Protection Agency (USEPA) standard methods (Ostro, 2004; USEPA, 2011) which have been subsequently used in related studies (Chalvatzaki *et al.*, 2019; Feuyit *et al.*, 2019; Kim *et al.*, 2018; Kitwattanavong *et al.*, 2013; Morakinyo *et al.*, 2020). According to Ostro (2004) and Chalvatzaki *et al.* (2019), the relative risk (RR) for cardiopulmonary and lung cancer mortality connected with $PM_{2.5}$ exposure was estimated by:

$$RR = \left[\frac{(X+1)}{(X_o+1)}\right]^{\beta} \quad (1)$$

RR associated with all-cause mortality was calculated by:

$$RR = \exp[\beta(X - X_o)] \quad (2)$$

The Attributable Fractions (AF) for cardiopulmonary and lung cancer mortality connected with $PM_{2.5}$ and PM_{10} exposure were estimated using the:

$$AF = \frac{RR-1}{RR} \quad (3)$$

According to (USEPA, 2011), the non-cancer risks (hazard quotient-HQ) via inhalation of CO, NO_2, SO_2 and ground-level O_3 were examined using equations 4 and 5 (Morakinyo *et al.*, 2020).

$$ADD_{Inh} = \frac{C \text{ x } IR \text{ x } EF \text{ x } ED}{BW \text{ x } AT} \quad (4)$$

$$HQ_{inh} = \frac{ADD_{inh}}{RfC} \quad (5)$$

Cancer Risk (CR) for $PM_{2.5}$ through inhalation route (CR_{inh}) was calculated by using equation 6 (USEPA, 2011). The cancer Slope Factor (SF) of $PM_{2.5}$ were estimated using equation 7, respectively (Kim *et al.*, 2018; USEPA, 2011). Parameters for health risk assessment of particulates and gaseous pollutants are presented in supplementary Table S1. The definitions and values of parameters in equations 1 to 7 are detailed in the supplementary document.

$$CR_{inh} = ADD \text{ x } SF \quad (6)$$

$$SF = \frac{UR}{BW \text{ x } IR} \quad (7)$$

3. RESULTS AND DISCUSSION

Seasonal concentration levels of gaseous pollutants at 25 selected TIs are presented in Figures 1 and 2, respectively. Mean concentrations of CO, NO_2, SO_2, NH_3, TVOCs, and ground-level O_3 were higher in the dry season than rainy season by 28.76%, 33.33%, 20%, 136.31%, 126.08% and 66.67%, respectively (see supplementary Table S2). The seasonal variation in concentrations of gaseous pollutants at TIs in this study is attributed to changes in associated convective turbulence and atmospheric boundary layer dynamics, which to a higher vertical extent redistribute and mix pollutants expansively in the atmosphere during the different seasons (Adeniran *et al.*, 2017).

Similar to the Gaseous pollutant trends, the mean concentrations of PM_1, $PM_{2.5}$, PM_{10} & TSP in the dry season were higher than rainy season by 53.24%, 132.20%, 360.49% and 365.83%, respectively (see supplementary Table S2). Chowdhury *et al.* (2019) reported that seasonal variation effects usually influence outdoor PM concentration. Re-suspended particles have varied impacts at different times of the year, due to many factors including relative humidity, wind speed, rainfall, solar radiation intensity, population of on-road vehicles and traffic flow type (Adeniran *et al.*, 2018; Fernandez *et al.*, 2017). However, forced deposition of particles may be accelerated during the rainy season than the dry season because of heavy rainfall, higher relative humidity, temperature drop, wind speed and lush vegetation (Chate, 2005; Jones and Harrison, 2004; Ranjan *et al.*, 2016). Descriptive statistics of studied pollutants at Ibadan traffic intersections and their recommended limits are presented in supplementary Table S3.

Pearson's correlation indicated that a positive correlation existed between relative humidity and wind speed while temperature and relative humidity had a strong negative correlation of -0.82 (see supplementary Table S4). The correlations of total vehicle on-road with PM_1 and $PM_{2.5}$ were positive while relationships of total vehicle on-road with PM_{10} and TSP gave negative correlations. This suggests that emissions of ultrafine (PM_1) and fine ($PM_{2.5}$) particles from vehicle exhausts increase as vehicles spend more time in traffic congestion (rush hours) whereas coarse (PM_{10}) particles rise more from road dust resuspension caused by faster vehicular movement during free-flow traffic (non-rush hours).

A study of air masses backward trajectories using HYSPLIT (Hybrid Single-Particle Lagrangian Integrated Trajectory Model) suggested that prevailing air masses during the rainy season came from the south-west direction (supplementary Figure S2a) though the major air masses during the dry season in Ibadan were predominantly from both northeast and southwest paths (supplementary Figure S2b). HYSPLIT results were consistent with wind roses plotted with meteorological data of the twenty-five TIs.

3.1 Seasonal variation in concentration of gaseous pollutants at Tis

Figures 1(a) CO, (b) NO_2, (c) SO_2, (d) NH_3, (e) TVOCs and (f) O_3 show the seasonal concentration levels of gaseous pollutants at 25 traffic Intersections

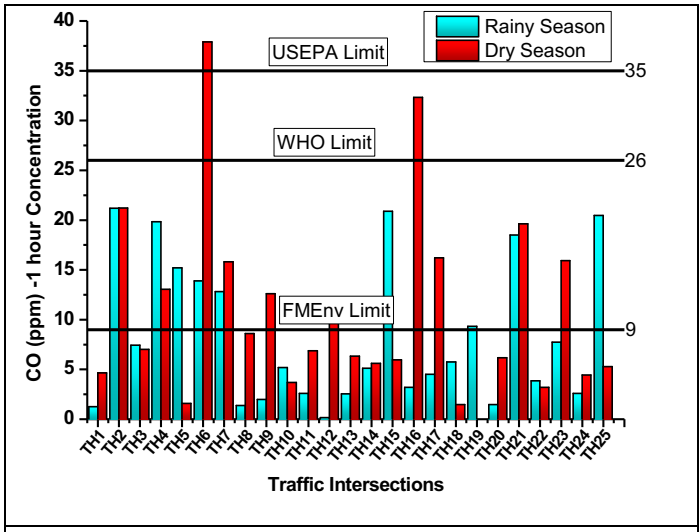
Rainy Season
Dry Season
USEPA Limit
35
WHO Limit
26
FMEnv Limit
9
CO (ppm) -1 hour Concentration
Traffic Intersections

(a)

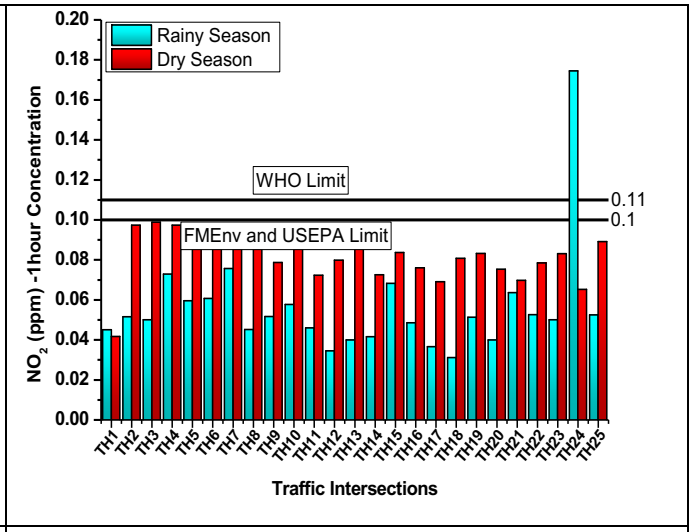
Rainy Season
Dry Season
WHO Limit
0.11
FMEnv and USEPA Limit
0.1
NO2 (ppm) -1hour Concentration
Traffic Intersections

(b)

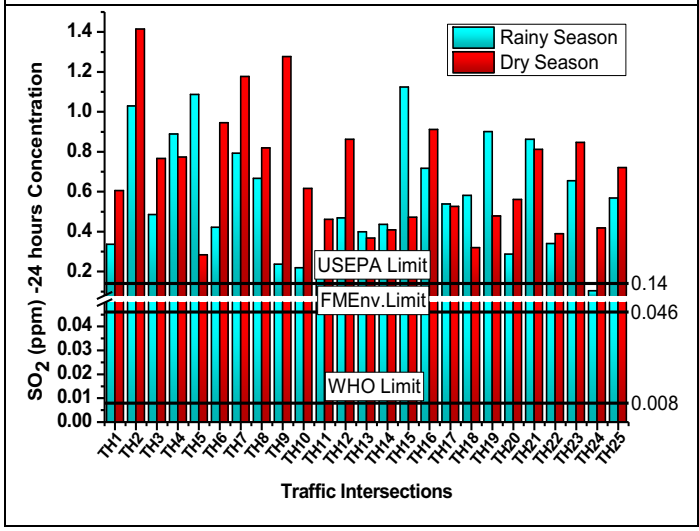
Rainy Season
Dry Season
USEPA Limit
0.14
FMEnv.Limit
0.046
WHO Limit
0.008
SO2 (ppm) -24 hours Concentration
Traffic Intersections

(c)

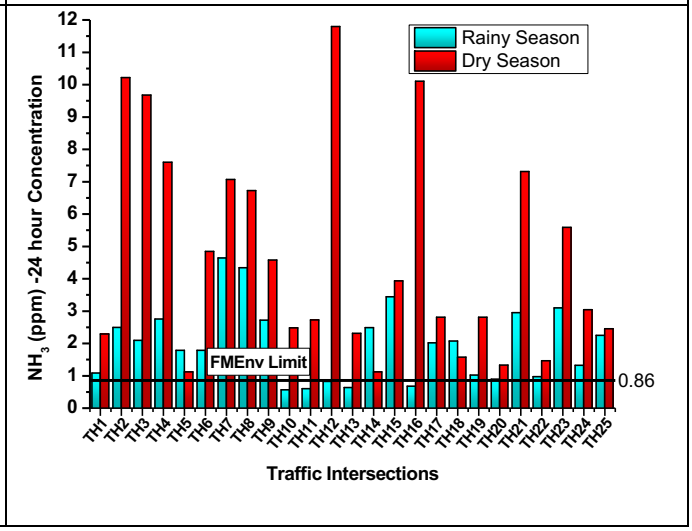
Rainy Season
Dry Season
FMEnv Limit
0.86
NH3 (ppm) -24 hour Concentration
Traffic Intersections

(d)

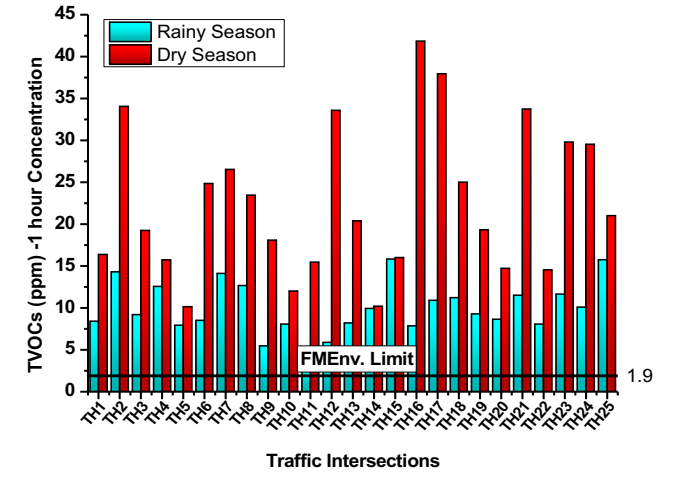
Rainy Season
Dry Season
FMEnv. Limit
1.9
TVOCs (ppm) -1 hour Concentration
Traffic Intersections

(e)

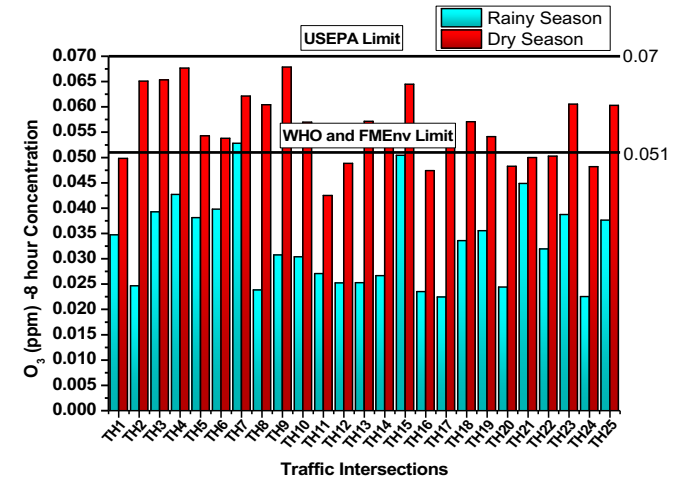
Rainy Season
Dry Season
USEPA Limit
0.07
WHO and FMEnv Limit
0.051
O3 (ppm) -8 hour Concentration
Traffic Intersections

(f)

Figure 1. Seasonal concentration levels of gaseous pollutants at 25 traffic Intersections (a) CO (b) NO_2 (c) SO_2 (d) NH_3 (e) TVOCs (f) O_3

3.2 Seasonal variation in concentration of particulates at Tis

Figure 2(a) PM_1 (b) $PM_{2.5}$ and (c) PM_{10} shows seasonal concentration levels of particulate matter at 25 traffic Intersections.

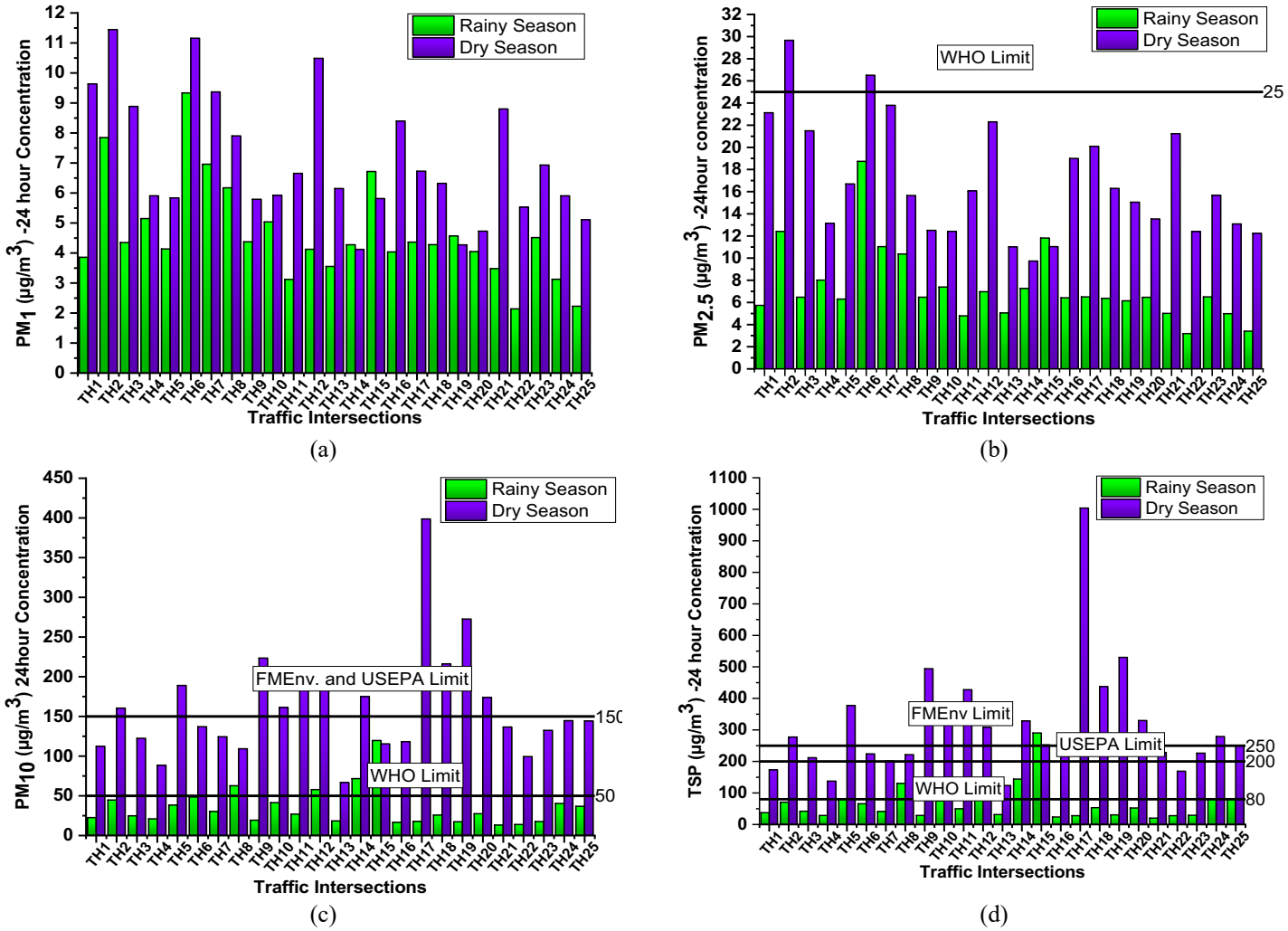

Figure 2. Seasonal concentration levels of particulate matter at 25 traffic Intersections (a) PM_1 (b) $PM_{2.5}$ (c) PM_{10} (d)TSP

3.3 Pollutants, recommended limits and effects on air quality

Employing the AQI ratings, Table 1 indicated that ambient air quality for $PM_{2.5}$, PM_{10}, CO and NO_2 were moderate, SO_2 was hazardous while ground-level ozone was good. This signifies that apart from SO_2, all other pollutants were within the acceptable range.

Table 1. AQI standards for atmospheric pollutants

Index Values	AQI Categories	$PM_{2.5}$ ($\mu g/m^3$) 24-hour	PM_{10} ($\mu g/m^3$) 24-hour	CO (ppm) 8-hour	NO_2 (ppm) 1-hour	SO_2 (ppm) 1-hour	O_3 (ppm) 8-hour

0-51	Good	0-12	0-54	0-4.4	0-0.053	0-0.035	0-0.054
51-100	Moderate	12.1-35.4	55-154	4.5-9.4	0.054-0.100	0.036-0.075	0.055-0.070
101-150	Unhealthy for Sensitive Groups	35.5-55.4	155-254	9.5-12.4	0.101-0.360	0.076-0.185	0.071-0.085
151-200	Unhealthy	55.5-150.4	255-354	12.5-15.4	0.361-0.649	0.186-0.304	0.086-0.105
201-300	Very Unhealthy	150.5-250.4	355-424	15.5-30.4	0.605-1.249	0.305-0.604	0.106-0.200
301-500	Hazardous	250.5-500.4	425-604	30.5-1004	1.250-2.049	0.605-1.004	>0.200
	Pollutants Mean Concentration	12.14	97.88	5.26	0.07	1.54	0.04
	Ibadan Overall AQI ranking	Moderate	Moderate	Moderate	Moderate	Hazardous	Good

3.4 Health Risk Assessment of TRAPs at Traffic Intersections

Table 2. Exposure Risk Assessment of Particulate and Gaseous Pollutants in Ibadan

Health Risk Parameters		Rainy Season	Dry Season	Rainy and Dry Seasons
$PM_{2.5}$: Cardiopulmonary mortality (%)	ER	0.27	0.44	0.37
	AF	0.21	0.31	0.27
$PM_{2.5}$: Lung cancer mortality (%)	ER	0.43	0.73	0.60
	AF	0.30	0.42	0.38
PM_{10}: All-cause mortality (%)	ER	0.06	0.36	0.20
	AF	0.06	0.26	0.17
$SF = UR/(BW \times IR) = 8.02 \times 10^{-6}$ (for $PM_{2.5}$)				
LADD		3.64	8.40	6.02
ELCR		2.92×10^{-5}	6.74×10^{-5}	4.83×10^{-5}
Hazard Quotient (HQ) via Inhalation				
CO		6.45×10^{-2}	8.31×10^{-2}	7.38×10^{-2}
NO_2		1.07×10^{-1}	1.56×10^{-1}	1.32×10^{-1}
SO_2		2.13	2.56	2.35
Ground level O_3		1.05×10^{-1}	1.77×10^{-1}	1.41×10^{-1}

Notably, overall AQIs of $PM_{2.5}$, PM_{10}, CO and NO_2 were acceptable despite recording high concentrations and breaching recommended limits at some TIs because of atmospheric dispersion and dilution of these pollutants concentration at the TIs. Pollutants dispersion is influenced by meteorological factors such as wind speed, wind direction, relative humidity, ambient temperature, rainfall and land topography (Ranjan *et al.*, 2016).

Table 2 indicated that AF for all-cause mortality due to PM_{10} exposure could be avoided by 0.06%, 0.26% and 0.17% during the rainy season, dry season and combined two seasons, respectively if PM_{10} were maintained at $10 \mu g/m^3$. The elevated AF (0.26%) during the dry season denotes a higher risk in the study area. Arranz *et al.* (2014) reported that exposure to particulate was responsible for all-cause mortality of 2% in Valladolid city of

Spain while Chalvatzaki *et al.* (2019) and (Odekanle *et al.*, 2020) revealed that 2.2% and 0.14% of all-cause mortality were preventable from exposure to PM_{10} in Lisbon (Spain) and Ile-Ife (Nigeria), respectively.

The CR_{inh} from $PM_{2.5}$ exposures (Table 2) indicated that the tolerable risk of cancer is higher during the dry season (6.74×10^{-5}) than during the rainy season (2.92×10^{-5}). In this study, cancer risk through inhalation increased by 130.69% during the dry season in comparison with the rainy season signifying that the dispersion rate and toxicity of $PM_{2.5}$ are higher in the dry season. HQ_{inh} results demonstrated that the probabilities that emissions of CO, NO_2 and ground level O_3 will pose non-cancer risks were all insignificant at TIs in Ibadan except SO_2 with HQ_{inh} values of 2.13, 2.56 and 2.35 for the rainy season, dry season and combined two seasons which were all greater than 1.0. This implies SO_2 emission at the studied TIs could cause adverse non-cancer ailments in Ibadan.

4. CONCLUSION

This study revealed the seasonal variation and health risks associated with exposure to gaseous pollutants (CO, NO_2, SO_2, NH_3, TVOCs, and ground level O_3) and particulate matter (PM_1, $PM_{2.5}$, PM_{10} & TSP) at and around traffic hotspots in a typical African urban environment. The concentration levels of studied pollutants measured at 25 major TIs in Ibadan were considerably more hazardous to public health during the dry season than the rainy season. Dispersion of pollutants was bolstered by prevailing meteorological conditions, the number of on-road vehicles, local activities at and around TIs and the dominating wind flowing from the southwest direction during the rainy season and the assortment of wind blowing from north-east and south-west direction during the dry season. The average concentrations of gaseous and PM pollutants exceeded the threshold limits set by WHO, National Ambient Air Quality Standards (NAAQS) of the United States and FMEnv at many TIs mostly in the dry season. Mortality estimates associated with $PM_{2.5}$ and PM_{10} exposures revealed that ER and AF during the dry season were above the estimates obtained during the rainy season and combined seasons. The AQI rating indicated that concentrations of $PM_{2.5}$, PM_{10}, CO and NO_2 were moderate, SO_2 was hazardous while ground-level O_3 concentration was good at the studied traffic hotspots. Health risk assessment of Ibadan TIs showed that CR of $PM_{2.5}$ was acceptable (tolerable) while the non-cancer risk of SO_2 was significant at the studied TIs. Pearson's correlation indicated that PM_1 & $PM_{2.5}$ emissions from vehicle exhausts increased as traffic congestion (rush hours) rose whereas PM_{10} emission increased with road dust re-suspension during traffic free-flow (non-rush hours). The results of this study are expedient in planning, designing and developing robust pollution mitigation strategies to control traffic air pollution in a typical African city. Alternative routes for vehicle decongestion, the use of cleaner fuel from renewables and the strengthening of mandatory vehicle inspection and maintenance programs could be integrated as basic solutions to urban air pollution in Africa.

REFERENCES

Adeniran, J. A., Aremu, A. S., Saadu, Y. O.& Yusuf, R. O. (2018). Particulate matter concentration levels during intense haze event in an urban environment. *Environmental monitoring and assessment, 190*(1), 41.

Adeniran, J. A., Yusuf, R. O.& Olajire, A. A. (2017). Exposure to coarse and fine particulate matter at and around major intra-urban traffic intersections of Ilorin metropolis, Nigeria. *Atmospheric Environment, 166*, 383-392. doi:10.1016/j.atmosenv.2017.07.041

Anwar, M. N., Shabbir, M., Tahir, E., Iftikhar, M., Saif, H., Tahir, A., Murtaza, M. A., Khokhar, M. F., Rehan, M.& Aghbashlo, M. (2021). Emerging challenges of air pollution and particulate matter in China, India, and Pakistan and mitigating solutions. *Journal of Hazardous Materials, 416*, 125851.

Arranz, M. C., Moreno, M. F. M., Medina, A. A., Capitán, M. A., Vaquer, F. C.& Gómez, A. A. (2014). Health impact assessment of air pollution in Valladolid, Spain. *BMJ open, 4*(10), e005999.

Chalvatzaki, E., Chatoutsidou, S. E., Lehtomäki, H., Almeida, S. M., Eleftheriadis, K., Hänninen, O.& Lazaridis, M. (2019). Characterization of human health risks from particulate air pollution in selected European cities. *Atmosphere, 10*(2), 96.

Chate, D. (2005). Study of scavenging of submicron-sized aerosol particles by thunderstorm rain events. *Atmospheric environment, 39*(35), 6608-6619.

Chowdhury, S., Dey, S., Di Girolamo, L., Smith, K. R., Pillarisetti, A.& Lyapustin, A. (2019). Tracking ambient PM2. 5 build-up in Delhi national capital region during the dry season over 15 years using a high-resolution (1 km) satellite aerosol dataset. *Atmospheric environment, 204*, 142-150.

Das, R., Khezri, B., Srivastava, B., Datta, S., Sikdar, P. K., Webster, R. D.& Wang, X. (2015). Trace element composition of PM2. 5 and PM10 from Kolkata–a heavily polluted Indian metropolis. *Atmospheric Pollution Research, 6*(5), 742-750.

Delkash, M.& Mir, H. M. (2016). Examining some potential actions in mitigating gaseous emissions from vehicles, case study: Tehran. *Air Quality, Atmosphere & Health, 9*(8), 909-921.

Fernandez, J.-M., Meunier, J.-D., Ouillon, S., Moreton, B., Douillet, P.& Grauby, O. (2017). Dynamics of suspended sediments during a dry season and their consequences on metal transportation in a coral reef lagoon impacted by mining activities, New Caledonia. *Water, 9*(5), 338.

Feuyit, G., Nzali, S., Lambi, J. N.& Laminsi, S. (2019). Air quality and human health risk assessment in the residential areas at the proximity of the Nkolfoulou landfill in Yaoundé Metropolis, Cameroon. *Journal of Chemistry, 2019*.

Jones, A. M.& Harrison, R. M. (2004). The effects of meteorological factors on atmospheric bioaerosol concentrations—a review. *Science of the Total Environment, 326*(1-3), 151-180.

Kim, H., Kang, K.& Kim, T. (2018). Measurement of particulate matter (PM2. 5) and health risk assessment of cooking-generated particles in the kitchen and living rooms of apartment houses. *Sustainability, 10*(3), 843.

Kitwattanavong, M., Prueksasit, T., Morknoy, D., Tunsaringkarn, T.& Siriwong, W. (2013). Health risk assessment of petrol station workers in the inner city of Bangkok, Thailand, to the exposure to BTEX and carbonyl compounds by inhalation. *Human and Ecological Risk Assessment: An International Journal, 19*(6), 1424-1439.

Morakinyo, O. M., Mukhola, M. S.& Mokgobu, M. I. (2020). Ambient gaseous pollutants in an urban area in South Africa: Levels and potential human health risk. *Atmosphere, 11*(7), 751.

Odekanle, E. L., Sonibare, O. O., Odejobi, O. J., Fakinle, B. S.& Akeredolu, F. A. (2020). Air emissions and health risk assessment around abattoir facility. *Heliyon, 6*(7), e04365.

Ostro, B. (2004). *Outdoor air pollution: assessing the environmental burden of disease at national and local levels*: World Health Organization.

Ranjan, O., Menon, J. S.& Nagendra, S. S. (2016). Assessment of air quality impacts on human health and vegetation at an industrial area. *Journal of Hazardous, Toxic, and Radioactive Waste, 20*(4), A4016002.

USEPA. (2011). Exposure factors handbook: 2011 edition: USEPA Office of Research and Development Washington.

PAPER 43 – UNCONFINED COMPRESSIVE STRENGTH OF BACILLUS *SPHAERICUS* INDUCED PRECIPITATE TREATED LATERITIC SOIL

[1]G. L. Yisa, [2]K. J. Osinubi, [2]A. O. Eberemu and [2]T. S. Ijimdiya

[1]Nigerian Building and Road Research Institute, Abuja, Nigeria
[2]Dept. Of Civil Engineering, Ahmadu Bello University, Zaria, Nigeria
Corresponding author: glyisa@abu.edu.ng

ABSTRACT

This study evaluated the potential of Bacillus *sphaericus* (B. *sphaericus*) in microbial-induced calcite precipitation improvement of the unconfined compressive strength (UCS) of lateritic soil. The soil, classified as A-2-6 (1) in the American Association of State Highway and Transportation Officials (AASHTO) system and SC in the Unified Soil Classification System (USCS), was treated with stepped B. *sphaericus* suspension of various densities of 0, 1.5 x 10^8, 6.0 x 10^8, 1.2 x 10^9, 1.8 x 10^9, 2.4 x 10^9 cells/ml at varying concentration of cementation reagents of 0.25, 0.5, 0.75 and 1 M. The cementation reagent used contained 3 g of Nutrient broth, 20 g of urea, 10 g of NH_4Cl, 2.12 g of $NaHCO_3$ and 2.8 g $CaCl_2$ per litre of distilled water. Soil specimens were prepared using bacteria to cementation reagent mix ratio of 25:75 with stepped B. *sphaericus* suspension density and compacted using three energy levels, namely, British Standard light (BSL), West African Standard (WAS) and British Standard heavy (BSH). The treated soil specimens were air-cured at an ambient laboratory temperature of 25 ± 2° C for 7, 14 and 28 days, respectively. Peak UCS values of 947.40, 989.28 and 1,240.82 kN/m^2 for BSL; 1,387.6, 1,481.72 and 1,743.43 kN/m^2 for WAS as well as 1,432.24, 1,598.34 and 1,835.98 kN/m^2 for BSH compaction were recorded at 7-, 14- and 28- days curing periods, respectively, for treatment with mix ratio B. *sphaericus* suspension density of (1.2 x 10^9 cells/ml): Cementation reagent (0.5 M). The UCS values of 1,743.43 and 1,835.98 kN/m^2 recorded for the specimens compacted with WAS and BSH energy at 28 days curing period meet the requirement for base material in the construction of low-volume roads.

Keywords: Bacillus *sphaericus*, Cementation solution, Lateritic soil, Unconfined compressive Strength

1. INTRODUCTION

Micro-organisms found in soil that are unicellular consist primarily of bacteria and archaea having a diameter range of 0.5 to 3 µm (Dejong et al., 2013; Sayed et al., 2019). They are present in the soil by entrapment during deposition (Sayed et al., 2019) or migration utilising the available pore spaces (Dejong *et al*., 2013).

Currently, soil improvement techniques such as chemical grouting or mixing with cement have over time been successful (Mahawish *et al.,* 2016). Grouting can be described as an artificial injection of chemical formulas that most times alter the soil pH level, and cause soil and groundwater contamination, which is not unconnected to their characteristics of being hazardous and toxic (Chittoori *et al*., 2019).

Microbial-induced calcite precipitation (MICP) is a bio-chemical process of soil strengthening that seeks to improve soil properties by enhancing its engineering properties, particularly strength and permeability. The MICP process is carried out by injecting micro-organisms which produce urease and also adding reagents for aiding cementation thereby producing a cementation compound generated to alter the engineering soil properties (Yang *et al.,* 2019). These micro-organisms are mostly not harmful and, as a result, will have little or no negative effect on the environment especially on humans (Umar *et al*., 2019). According to Dejong *et al*. (2010), MICP studies and application cuts across many disciplines from geotechnical engineering to sciences such as microbiology and geochemistry working together to achieve an environmentally friendly way of stabilizing soils.

Laterites are highly weathered soils formed by the concentration of hydrated iron and aluminium oxides and have no reasonable constant properties (Osinubi 2005). Laterites were first studied in humid tropics and mostly found where leached soils are predominant. They are formed in weathering systems by the process of lateralisation, which involves the breakdown of ferro-alumino silicate minerals and the permanent deposition of sesquioxides (Al_2O_3 and Fe_2O_3) within the profile to form the laterite horizon of material known as laterite.

Studies recently conducted on the application of the MICP technique which is still considered an innovation for the improvement of soils (Osinubi *et al*., 2019) have shown improvement in strength and hydraulic conductivity properties of the soils when used in the design of waste containment barrier systems. Other successful studies conducted using the MICP approach include; increasing liquefaction resistance (Montoya *et al*., 2013), improving the stability of slopes and foundation-bearing capacity (Whiffin *et al*., 2007), creating a water-impermeable crust on a sand surface (Stabnikov *et al*., 2011), crack healing in concrete and masonry (Amidi and Wang, 2015), treatment of waste (Chu *et al*., 2009), heavy metal immobilization (Fujita *et al*., 2010), shallow carbon sequestration (Washbourne *et al*., 2012), fine tailings consolidation (Liang *et al*., 2015), as well as shear strength and compressibility of organic soil (Canakci *et al*., 2015).

Previous research on soil improvement considered the use of conventional additives such as bitumen, lime, cement, pozzolanic material, agro-industrial waste, etc., which are either expensive or harmful to the environment and hence not sustainable. Therefore, this study is targeted at the assessment of UCS of lateritic soil treated with B. *sphaericus* (which is a more sustainable and environment-friendly approach to soil improvement) as the base material in the construction of low-volume roads. This involved treating the soil with B. *sphaericus* suspension density (i.e., 0, 1.5 x 10^8, 6.0 x 10^8, 1.2 x 10^9, 1.8 x 10^9, 2.4 x 10^9 cells/ml) at varying concentrations of cementation reagent (0.25, 0.5, 0.75 and 1 M). The soil specimens were prepared using bacteria to cementation reagent mix ratio of 25%:75% and compacted using three energy levels. The specific objectives were to assess the viability of B. sphaericus as an agent for lateritic soil strength development for use as the base material in the construction of low-volume roads as well as the morphological and microstructural arrangement of the natural and treated soil samples.

2. MATERIALS AND METHODS

2.1 Materials

2.1.1 Soil

The soil for the study was collected using the disturbed sampling method from the Abagana area of Anambra state, Njikoka Local Government Area. (Latitude 6°12′15″N and Longitude 7°0′40″E) sourced at depths between 0.5 and 3.0 m.

2.1.2 Bacteria

The Gram-positive micro-organism used in this research is *Bacillus sphaericus* rod-shaped bacterium with a 2 - 5 μm diameter size. The bacteria were isolated from the soil of which six (6) different samples were collected and used for the isolation, identification and characterisation of the *Bacillus sphearicus*. They were inoculated on Nutrient Broth, Yeast Extract Nutrient Agar, Nutrient Agar and MICP agar, respectively.

2.1.3 Cementation reagent

The cementation reagents were varied by using an equimolar concentration of urea and calcium chloride to produce cementation solutions of different molar concentrations (0.25M, 0.5M, 0.75M and 1M)

2.2 Methods

2.2.1 Index properties

The index property test was conducted according to BS 1377 (1990) and BS 1924 (1990) for natural and treated soils.

2.2.2 Sample preparation

The soil sample to be used was passed through a sieve of 425 μm aperture and mixed for the bacteria-cementation mix ratios of 25%:75% which gave the highest calcite value based on the calcite content test carried out. The composition ratio is based on the liquid limit of the natural soil. B. *sphaericus* was applied at suspension densities of 0, 0.5, 2.0, 4.0, 6.0 and 8.0 McFarland standards which is equivalent to 0, 1.5 x 10^8, 6.0 x 10^8, 12 x 10^8, 18 x 10^8 and 24 x 10^8 cells/ml, respectively, at a varying concentration of cementation reagent of 0.25, 0.5, 0.75 and 1M.

2.2.3 Atterberg limits

Atterberg limits (liquid limit, plastic limit, plasticity index test) are essential for soil classification and identification. The treated soil-bacteria-cementation reagent was air-dried, after which it was pulverised and passed through a sieve 425 μm aperture before testing.

2.2.4 Calcite content

For the calcite content determination, the acid-washing method was adopted as reported by (Osinubi et al., 2019). 5g of the treated soil was measured and mixed with 20 ml of 2M hydrochloric acid to dissolve $CaCl_2$. After that, the mixture was filtered with filter paper of pore size 200mm. The filtrate was rinsed and washed for 10 min using distilled water to remove any dissolved calcium from the soil. The particles on the filter were oven-

dried for 24 hours at a temperature of 105ºC and weighed. The difference in mass between the original sample A and the washed sample B was recorded as calcium carbonate (Calcite) mass. The percentage calcite content CC was computed using equation (1):

$$CC=100-\frac{B}{A}\times 100 \quad (1)$$

2.2.3 Unconfined compressive strength

Air-dried soil sample of 3 kg was mixed with optimum moisture content determined by dynamic compaction of the soil sample. The standard BS compaction mould was utilized. In the mould, the sample was placed and compacted in layers and blows corresponding to the energy level considered. The sample was then removed from the mould with the aid of a hydraulic lift and three samples of 38 by 76 mm were cored out and placed in a polythene bag for at least 48 hours before testing to allow for complete saturation. For the test, the axial load was gradually applied until shear failure occurred. For the test, failure is said to have occurred when two or three successive readings are equal or decreasing in descending sequence. The experiment was conducted with the addition of B. *sphaericus* suspension density (cells/ml) of 0, $1.5x10^8$, $6.0x10^8$, $12x10^8$, $18x10^8$ and $24x10^8$ at different concentrations of cementation reagent (0.25, 0.5, 0.75 and 1 M), respectively and compacted using three energy levels of BSL, WAS and BSH compaction loads all carried out in accordance with BS 1377 (1990) and BS 1924 (1990) for the natural and treated soils. The curing times for the samples were 7 days, 14 days and 28 days.

2.2.6 Microstructural analysis

A microanalysis test was carried out on the lateritic soil (natural and treated) to determine the change in morphology due to the formation of calcite bonds on the interparticle surface of the bio-treated soil. It was carried out using Phenom world pro desktop SEM (Phenom World, 2017).

3. RESULTS AND DISCUSSION

3.1.1 Index properties

The properties of the natural lateritic soil are classified as A-2-6 (1) in the AASHTO system and SC (clayey sand) in the USCS (AASHTO 1996 and ASTM 1992) are summarised in Table 1. The natural lateritic soil is reddish-brown, with 34.95 % passing through the BS sieve no. 200 size, with kaolinite being the dominant clay mineral.

Table 1. Natural properties of the soil

S/No.	Property	Quantity
1	Natural moisture content (%)	19.6
2	Percentage passing No. 200 sieve	34.95
3	Liquid limit (%)	36.5
4	Plastic limit (%)	20.06
5	Plasticity index (%)	16.44
6	Linear shrinkage (%)	8.37
7	Specific gravity	2.67
8	AASHTO classification	A – 2 – 6 [1]
9	USCS	SC
10	Colour	Reddish-brown
11	Dominant clay mineral	Kaolinite

3.1.2 Calcite content

The variation of the calcite content for the lateritic soil specimens prepared with stepped B. *sphaericus* suspension density at varying cementation reagents is presented in Figure 1. Generally, the calcite content of all the specimens increased as the cementation reagent concentration increased to peak values before decreasing. It was observed that the optimum calcium carbonate content values were 9.0%, for bacteria - cementation mix ratio of 25%:75% at B. *sphaericus* suspension density of 1.2 x 10^9 cells/ml and 0.5 M cementation reagent. This is not unconnected to the fact that the cementing reagent used in the MICP process plays a vital role in the precipitation of calcium carbonate, and excess usage of this calcium chloride could reduce urease activity (Soundara et al., 2020).

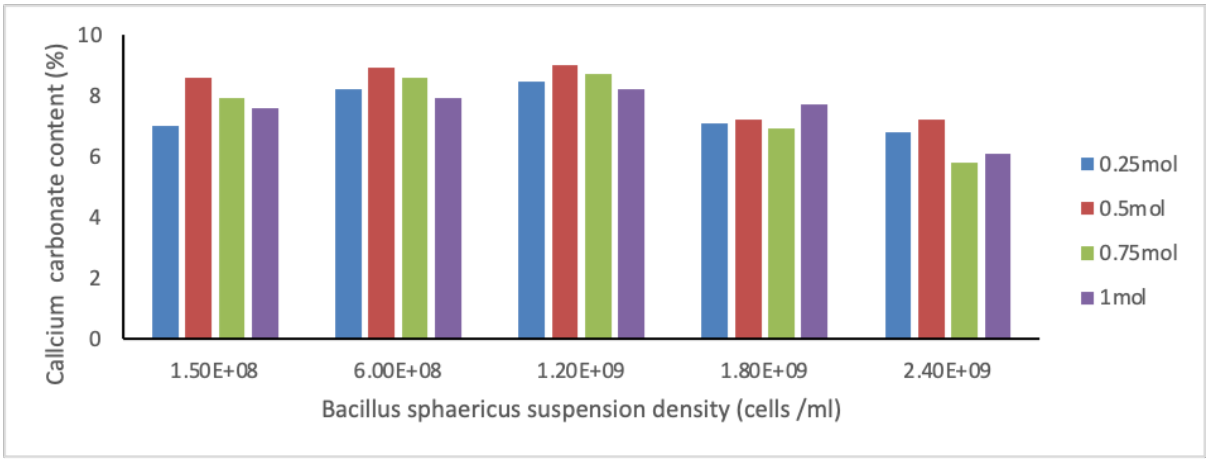

Figure 1. Calcite content of soil bacteria with varying cementation solutions mix (25%BS:75% cementation)

3.1.3 Atterberg limits

The variation of Atterberg limits (LL, PL, PI) of the lateritic soil treated with stepped suspension density of B. *sphaericus* of 0, 1.5 x 10^8, 6.0 x 10^8, 1.2 x 10^9, 1.8 x 10^9, 2.4 x 10^9 cells/ml using bacteria to cementation mix ratios of 25 %:75 % at the stepped concentration of cementation reagent of 0.25, 0.5, 0.75 and 1 M.
Generally, the increases in LL might result from the increase in water content needed for urea hydrolysis. Urease-positive enzymes were produced from the biochemical reaction, thereby hydrolysing urea into carbonate ions (CO_3^{2-}) and ammonium ions (NH_4^+). Generally, the increase in PL to peak values before decreasing could probably be due to an adequate amount of Ca^{2+} not being available on the calcite surface, thereby causing a reduction in the deposition of ion pairs (Dhami et al., 2016). The decrease in the PI values could probably result from calcite precipitation in the soil matrix voids. Generally, a decrease in PI values indicates soil improvement for any engineering use. The lateritic soil treated with B. *sphaericus* suspension density of 1.2 x 10^9 cells/ml and 0.5 M cementation reagent gave the best PI value indicating a better potential for soil improvement as presented in Figure 2.

The LL decreased from the natural value of 36.5 % to 34.2 % at 1.2x10^9 cells/ml before increasing to 37.20% at the highest treatment of 2.4x10^9 cells/ml. The PL increased from the natural value of 20.06% to 24.70% at the maximum treatment of 2.4x10^9 cells/ml. The PI value decreased from the natural value of 16.44% to 11.60% at 1.2x10^9 cells/ml before increasing to 12.50% at the treatment of 2.4x10^9 cells/ml.
The Atterberg limits findings in this study are consistent with the results reported by Moravej et al., 2018.

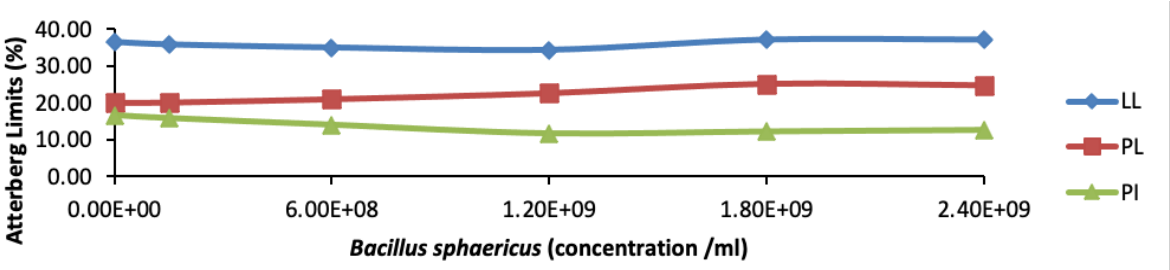

Figure 2. Variation of Atterberg limits of lateritic soil treated with B. *Sphaericus* suspension density at 0.5 M cementation reagent concentration

3.1.4 Unconfined compressive strength

The results of the UCS for BSL are presented in figures 3-5, the WAS are presented in figures 6-8 while that of the BSH are presented in figures 9-11, respectively, for the B. *sphaericus* suspension densities (i.e., 0, 1.5 x 10^8, 6.0 x 10^8, 1.2 x 10^9, 1.8 x 10^9, 2.4 x 10^9 cells/ml)) at a varying concentration of cementation reagent (0.25, 0.5, 0.75 and 1 M) using bacteria to cementation reagent mix ratio of 25%:75%, and compacted using three energy levels, namely, British Standard light, (BSL), West African Standard (WAS) and British Standard heavy (BSH). The treated soil specimens were air-cured at an ambient laboratory temperature of 25 ± 2° C for 7, 14 and 28 days,

respectively. Peak UCS values of 947.40, 989.28 and 1,240.82 kN/m^2 from natural values of 789.38, 803.20 and 900.28 kN/m^2 respectively, for BSL, 1,387.6, 1,481.72 and 1,743.43 kN/m^2 from natural values of 832.45, 848.64 and 999.89 kN/m^2 respectively, for WAS as well as 1,432.24, 1,598.34 and 1,835.98 kN/m^2 from the natural values of 928.03, 1030.08 and 1130.43 kN/m^2 respectively, for BSH compaction were recorded at 7, 14 and 28 days curing periods, respectively, for treatment with 1.2 x 10^9 cells/ml of B. *sphaericus* suspension density and 0.5M of cementation reagent. The values of the UCS obtained generally showed an increasing trend with an increase in compaction energy with BSH compaction energy showing the highest UCS values for all treatments evaluated. The results showed that the greater UCS value obtained is also a function of compaction load as well as the precipitations of calcites that were formed during the MICP process.
This result is consistent with the studies by Osinubi et al. (2017) and Osinubi et al. (2020).

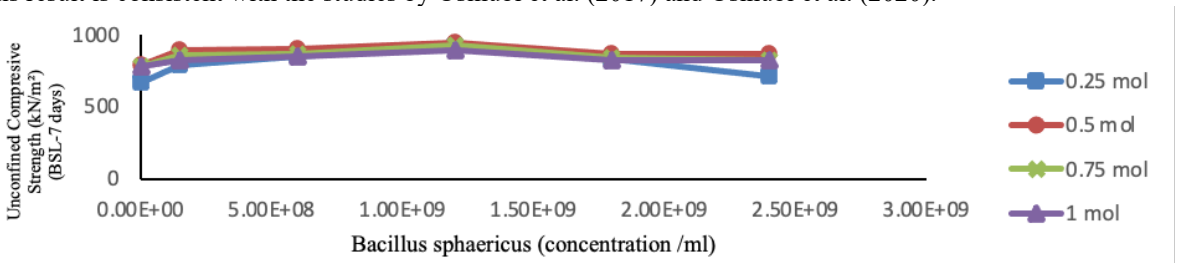

Figure 3. Graph of UCS of Lateritic soil treated with B. *sphaericus* suspension at varying cementation (BSL-7days curing)

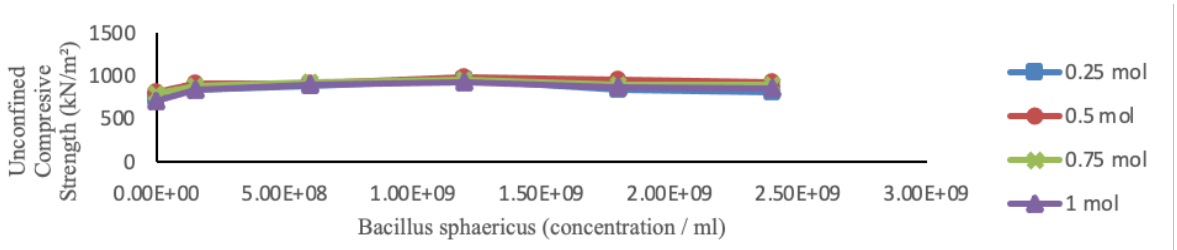

Figure 4. Graph of UCS of Lateritic soil treated with B. *sphaericus* suspension at varying cementation (BSL-14days curing)

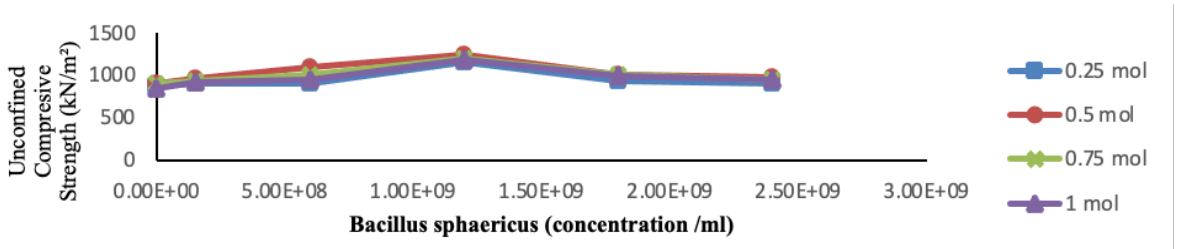

Figure 5. Graph of UCS of Lateritic soil treated with B. *sphaericus* suspension at varying cementation (BSL-28 days curing)

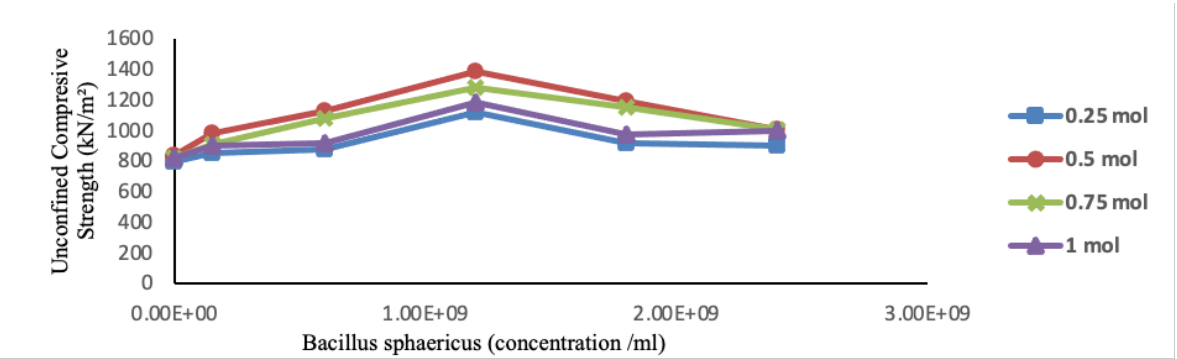

Figure 6. Graph of UCS of Lateritic soil treated with B. *sphaericus* suspension at varying cementation (WAS-7 days curing)

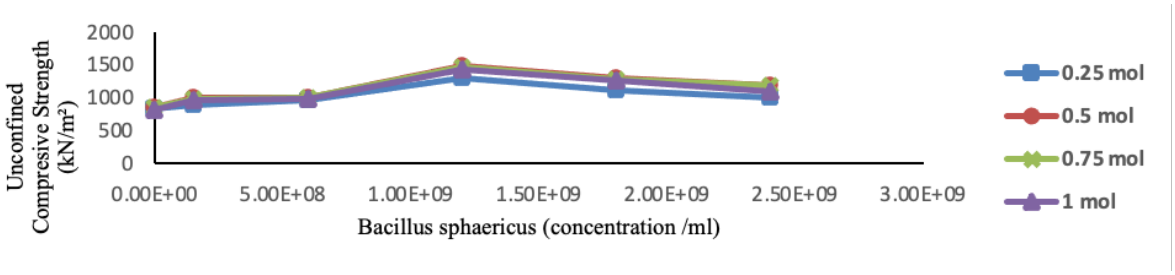

Figure 7. Graph of UCS of Lateritic soil treated with B. *sphaericus* suspension at varying cementation (WAS-14 days curing)

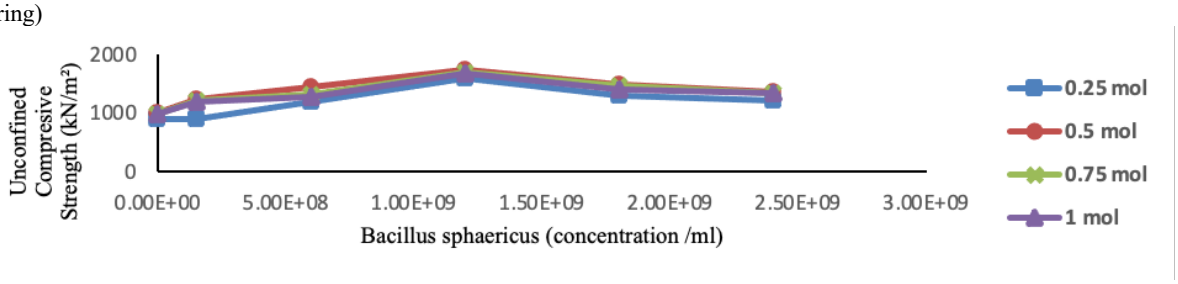

Figure 8. Graph of UCS of Lateritic soil treated with B. *sphaericus* suspension at varying cementation (WAS-28 days curing)

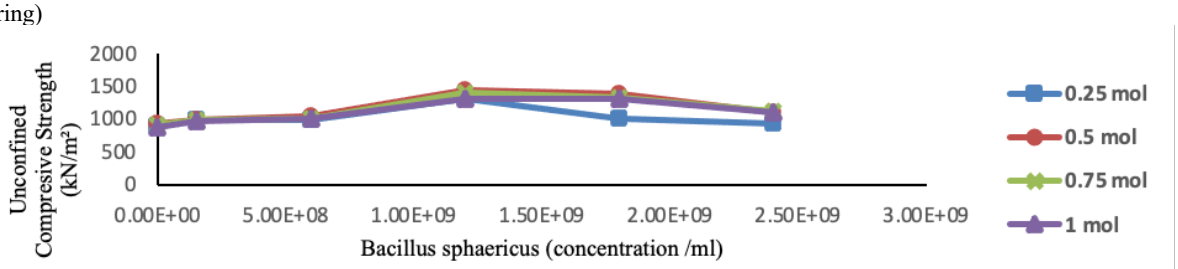

Figure 9. Graph of UCS of Lateritic soil treated with B. *sphaericus* suspension at varying cementation (BSH-7 days curing)

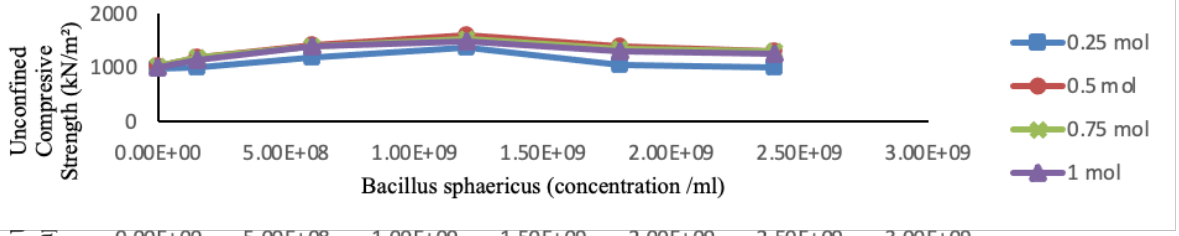

Figure 10. Graph of UCS of Lateritic soil treated with B. *sphaericus* suspension at varying cementation (BSH-14 days curing)

Figure 11. Graph of UCS of Lateritic soil treated with B. *sphaericus* suspension at varying cementation (BSH-28 days curing)

3.1.5 Microstructural analysis

The calcite crystals precipitation and growth on a micro-scale were examined by SEM micrographs of the soil (natural and treated soil specimens). Plates 1 and 2 (at x300 magnification) show a micrograph of the soil sample used for the UCS test for the 25% Bacteria and 75% cementation reagent mix at 0.5M concentration at a bacteria suspension density of 1.2 x 10^9 cells/ml. For the untreated UCS soil (Plate 1a), the thick lump particle could be attributed to the cohesive structure of the soil indicating that a thick diffuse double layer formed by the interaction of clay minerals and multivalent cations was still exerting a dominant impact on the soil-water combination. For the treated soil's microstructure (Plate 1b), the soil appears more uniform and consolidated resulting in a more bonded solid structure which possibly is a result of the calcite precipitate after the MICP process. This finding is in agreement with the findings by Cheng et al. (2013) and Al Qabany et al. (2012)

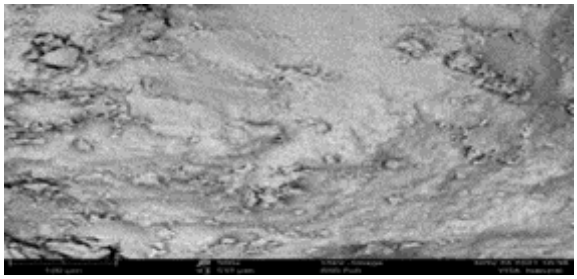

Plate 1a: Micrograph of Natural soil

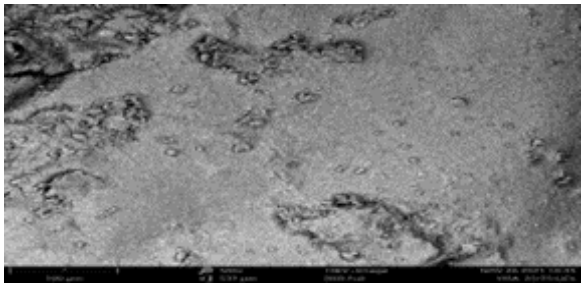

Plates 1b: Micrograph of treated soil

4. CONCLUSION

An evaluation of the influence of B. *sphaericus* in MICP technique improvement of the UCS of lateritic soil was carried out. The lateritic soil classified as A-2-6 (1) in the AASHTO and SC in the USCS was treated with stepped B. *sphaericus* suspension density (i.e., 0, 1.5 x 10^8, 6.0 x 10^8, 1.2 x 10^9, 1.8 x 10^9, 2.4 x 10^9 cells/ml) at a varying concentration of cementation reagent (0.25, 0.5, 0.75 and 1 M) using bacteria to cementation reagent mix ratio of 25% to 75% and compacted using three energy levels. MICP technique improved the Atterberg limits properties of the natural lateritic soil at B. *sphaericus* suspension density of 1.2 x 10^9 cells/ml and 0.5 M cementation reagent. Peak UCS values of 947.40, 989.28 and 1,240.82 kN/m^2 for BSL, 1,387.6, 1,481.72 and 1,743.43 kN/m^2 for WAS as well as 1,432.24, 1,598.34 and 1,835.98 kN/m^2 for BSH compaction were recorded at 7-, 14- and 28- days curing periods, respectively, for treatment with mix ratio B. *sphaericus* suspension density of (1.2 x 10^9 cells/ml): Cementation reagent (0.5 M). The UCS values of 1,743.43 and 1,835.98 kN/m^2 recorded for the specimens compacted with WAS and BSH energy at 28 days curing period did not meet the 7 days curing period criterion for cement treated soil of 1730 kN/m^2 requirement specified by TRRL (1977), However, the values of the UCS from the study were significantly improved.

RECOMMENDATION

Based on the findings in this study, it is recommended that to improve the UCS characteristics of an A-2-6(1) or SC soil, a bacteria-cementation mix ratio of 25 % and 75 % B. *sphaericus* suspension density of 1.2 x 10^9 cells/ml and 0.5 M cementation reagent, respectively can be used.

ACKNOWLEDGEMENT

The authors wish to acknowledge Ahmadu Bello University, Zaria for all the experiments conducted in the Civil Engineering Laboratory.

REFERENCES

AASHTO (1986).*Standard Specifications for Transport Materials and Methods of Sampling and Testing.* 14th Edition, American Association of State Highway and Transport Officials (AASHTO), Washington, D.C

Al Qabany A, Soga K and Santamarina C (2012). Factors Affecting Efficiency of Microbially Induced Calcite Precipitation. Journal of Geotech and Geoenv. Engrg, 138(8), pp. 992-1001. https://doi.org/10.1061/(ASCE)GT.1943-5606.0000666

Amidi, S. and Wang, J. (2015). Surface treatment of concrete bricks using calcium carbonate precipitation, *Construction Building Material,* Elsevier, 80:273–278

ASTM (1992).*Annual Book of Standards* Vol. 04.08, American Society for Testing and Materials, Philadelphia

BS 1377 (1990) Method of testing soils for civil engineering purposes. *British Standard Institute*, BSI, London.

BS 1924 (1990). Methods of Tests for Stabilized Soils. *British Standard Institute* (BSI) London.

Canakci, H, Sidik, W. and Kilic, I.H (2015) Effect of bacterial calcium carbonate precipitation on compressibility and shear strength of organic soil. *Soils and Foundations* 55(5): 1211-1221

Cheng L, Cord-Ruwisch R. and Shahin M.A. (2013) Cementation of sand soil by microbially induced calcite precipitation at various saturation degrees. Canadian Geotechnical Journal 50:81–90.

Chittoori, B.C.S, Burbank, M., Islam, M.T. (2018). Evaluating the effectiveness of soil-native bacteria in precipitating calcite to stabilise expansive soils. *ASCE IFCEE Geotech Special Publ*., https://doi.org/10.1061/97807 84481 592.007, 296:59–68

Chu, J., Ivanov, V., Lee, M., Oh, X., and He, J. (2009) Soil and waste treatment using biocement. In: *Proceedings of the international symposium on ground improvement technologies and case histories*, ISGI, vol 9, pp 165–170

DeJong JT, Mortensen BM, Martinez BC and Nelson DC (2010) Biomediated soil improvement. *Ecological Engineering, Elsevier,* 36(2): 197–210.

Dejong, J. T., Soga, K. S., Kavazanijian, E., Burns, S., Van Paassen, L., Al Qabany, A., Aydilek, A., Bang, S. S., Burbank, M., Caslake, L., Chen, C. Y., Cheng, X., Chu, J., Ciurli, S., Fauriel, S., Filet, A. E., Hamdan, N., Hata, T., Inagaki, Y., Jefferis, S., Kuo, M., Laloui, L., Larrahondo, J., Manning, D. A. C., Martinez, B., Montoya, B. M., Nelson, D. C., Palomino, A., Renforth, P., Santamarina, J. C., Seagren, E. A., Tanyu, B., Tsesarsky, M., & Weaver, T. (2013). "Biogeochemical processes and geotechnical applications: progress, opportunities and challenges*." Geotechnique*,[http://dx.doi.org/10.1680/geot.SIP13.P.017], 63(4): 287-301.

Dhami N.K, Mukherjee, A and Reddy, M.S (2016) Micrographical, mineralogical and nano-mechanical characterisation of microbial carbonates from urease and carbonic anhydrase producing bacteria, *Ecol Engrg* 94, 443–454. http://dx.doi.org/10.1016/j.ecoleng.2016.06.013

Fujita, Y., Taylor, J.L., Wendt, L.M., Reed, D.W. and Smith, R.W. (2010) Evaluating the potential of native ureolytic microbes to remediate a contaminated environment, *Environment Science Technology*, ACS Publ.,44:7652–7658

Liang, J., Guo, Z., Deng, L. and Liu, Y. (2015). Mature fine tailings consolidation through microbial-induced calcium carbonate precipitation. *Canadian Journal of Civil Engineering,* Can. Sci. Publ., 42:1–4

Mahawish, A., Bouazza, A. and Gates, W. P. (2016). Biogrouting coarse materials using soil-lift treatment strategy, *Can. Geotech. Journal*, https://doi.org/10.1139/cgj-2016- 0167, 53 (12): 2080–2085

Montoya B.M, DeJong J.T and Boulanger R.W (2013) Dynamic response of liquefiable sand improved by microbial-induced calcite precipitation, *Géotechnique*- ICE, https://doi.org/10.1680/geot.SIP13.P.019, 63(4): 302–312

Moravej, S., Habibagahi, G., Nikooee, E. And Niazi, A. (2018) Stabilisation of dispersive soils by means of biological calcite precipitation, Geoderma, Elsevier, https://doi.org/10.1016/j.geoderma.2017.11.037, 315(2018):130–137

Osinubi K. J. (2005). *Laterite Soils and Other Problem Soil of Africa*. Unpublished M.Sc.Lecture Notes. Ahmadu.Bello University, Zaria, Nigeria.-Personal communication.

Osinubi K.J, Eberemu A.O, Ijimdiya T.S, Yakubu S.E, Sani J.E (2017). Potential use of B. *Pumilus* in microbial-induced calcite precipitation improvement of lateritic soil. In: *Proceedings of the 2nd symposium on coupled phenomena in environmental geotechnics (CPEG2)*, Leeds, session: clean-ups, paper, vol 64, pp 1–6

Osinubi K.J, Yohanna P, Eberemu A.O, Ijimdiya T.S (2019) Evaluation of hydraulic conductivity of lateritic soil treated with *Bacillus Coagulans* for use in waste containment applications. In: Zhan L, Chen Y, Bouazza A (eds) *Proceedings of the 8th international congress on environmental geotechnics (ICEG 2018).*

Towards a sustainable geoenvironment Springer, Hangzhou, https://doi.org/10.1007/978-981-13-2227-3_50, vol. 3, pp 401-409.

Osinubi K.J, Eberemu A.O, Ijimdiya T.S and Yohanna P (2020) Interaction of landfill leachate with compacted lateritic soil treated with bacillus coagulants using microbial-induced calcite precipitation approach. *J Hazard Toxic Radioact Waste,* 24(1), 040190249. https://doi.org/10.1061/(asce)hz.21535515.0000465

Phenom World (2017) Fibermetric. https://www.phenom-world.com/software/fbermetric. Accessed 17 Sept 2018

Sayed M. A. Z., Hamideh, G, Brendan, C. O. (2019). Stabilisation of crustal sand layer using biocementation technique for wind erosion control, *Aeolian Research journals*, Elsevier publ., 40:34-41

Soundara, B., Kulanthaivel, P., Nithipandian, S., and Soundaryan, V. (2020) A Critical Review on Soil Stabilization using Bacteria, *IOP Conf. Series: Materials Science and Engineering,* 955, 012065, doi:10.1088/1757-899X/955/1/012065

Stabnikov V, Naeimi M, Ivanov V, Chu J (2011) Formation of water impermeable crust on sand surface using biocement, *Cement Concrete Researchs, Elsevier,* 41:1143–1149.

TRRL (1977). "A guide to the structural design of bitumen surfaced roads in tropical and sub-tropical countries." Transport and Road Research Laboratory, Road Note 31, H. M. S. O., London.

Umar, M., Kassim, K. A., Zango, M. U and Muhammed, A. S. (2019). Performance evaluation of lime and microbial cementation in residual soil improvement, *IOP Conf. Series: Materials Science and Engineering,* IOP publ., doi:10.1088/1757- 899X/527/1/012005, pp 1-10.

Washbourne, C. L, Renforth, P., Manning, D. (2012). Investigating carbonate formation in urban soils as a method for capture and storage of atmospheric carbon, *Sci Total Environ, Elsevier,* 431:166 175.

Whiffin VS, van Paassen LA and Harkes MP (2007) Microbial carbonate precipitation as a soil improvement technique*, Journal of Geomicrobiology* 24(5):417–423.

Yang Y., Jian, C., Yang, X., Hanlong L., Liang C. (2019). Seepage control in sand using bio-slurry, *Construction and Building Materials,* Elsevier publ., 212: 342-349.

PAPER 46 – NEED FOR EFFECTIVE EVALUATION OF WATER RESOURCES QUALITIES FOR SUSTENANCE AND ATTAINMENT OF CONSTRUCTION (ENGINEERING) DEVELOPMENT GOALS

K. C. Nwachukwu[1], B. O. Mama [2], I. S. Akosubo[3], O. Oguaghamba[4] and U.C. Onwuegbuchulem[5]

[1] Department of Civil Engineering, Federal University of Technology, Owerri, Imo State, Nigeria
[2, 4] Department of Civil Engineering, University of Nigeria, Nsukka, Enugu State, Nigeria
[3]Department of Civil Engineering, Nigeria Maritime University, Okerenkoko, Delta State, Nigeria
[5] Department of Building, Federal University of Technology, Owerri, Imo State, Nigeria
E-Mail: knwachukwu@futo.edu.ng

ABSTRACT

Water that is good for drinking is also good for construction purposes. Consequently, this study aims to evaluate the physicochemical qualities of water resources and to access their impact on the selected mechanical properties of concrete for sustainability and attainment of construction development goals. The water resource of interest here is the groundwater whose samples were collected in five locations in Owerri town of Imo state, Nigeria. The physicochemical parameters of the collected samples were analyzed in accordance with guidelines under the World Health Organization (WHO) standard. Thereafter, the analysed water samples were used to mix concrete where the compressive strength, flexural strength and split tensile strength were determined. The results from the quality analyses showed that the concentrations of the groundwater sampling fall within the WHO recommended standard. Similarly, the results of the compressive strength, flexural and split tensile strengths showed that analyzed water samples from the five locations which were used to mix concrete are capable of helping to produce concrete of excellent properties. Stakeholders are therefore advised to maintain the use of water resources that meet drinking standards as part of concrete ingredients to ensure sustenance of safety in the construction industry.

Keywords: Water Resources, Concrete, Compressive Strength, Flexural Strength and Split Tensile Strength

1. INTRODUCTION

Water resources is a term used to describe natural resources (bodies) of water that are potentially useful as a source of water supply. There are indeed three necessities of life which include water, food and shelter. That proves to a large extent the reason why water resources as natural elements are very essential and precious to life's existence. Two main classes of water resources can be identified as Groundwater and Surface water, but this recent work focuses on groundwater. Groundwater, according to Akpobori and Nfor (2007) has been the cornerstone of all rural and urban water supply development in Nigeria. As opined by Agunwamba (2000), two major sources of groundwater can be identified. Some are formed by rainwater which permeates into the ground through the pores of rock formation and finally reached the underground water table. There is the water from streams, lakes, and reservoirs which percolate through the soil to the underground water table. Thus, depending on the groundwater source, we can have Shallow well, Deep well and Boreholes as major sources of groundwater.

It is also important to note that water plays a crucial role in most human activities as well as the socio-economic development of any country, state, town or community. Its importance to mankind cannot be overemphasized. It is used for domestic purposes. The majority of city dwellers in Nigeria depend on groundwater as their source of water supplies. In the field of agriculture, water is used for irrigation and in the construction industry; it is a widely used raw material, especially as an ingredient in the concrete mixture for better workability, In a nutshell, it is those water samples whose physicochemical parameters meet the WHO recommended limits are eligible to be used in the construction works. This is one of the reasons why most of the specifications recommend the use of potable (treated) water for making concrete so that good mechanical properties of concrete can be sustained.

Owerri is the capital city of Imo State, Nigeria. Although, it consists of three local government areas which include Owerri Municipal, Owerri West and Owerri North, Owerri Municipal, which is the choice of our study in this present work constitute the majority of the state capital. With the presence of the majority of government activities, workers' activities, government facilities, federal and state institutions like Imo state university, Owerri, Alvan Ikoku Federal College of Education, state and federal agencies, notable establishment, industries and churches, the area has been one of the fastest developing LGA of the state. This means that there is always an increase in economic activities prompting an increase in water demand for any purpose. Sometimes, urbanisation might come with an acute shortage of water which might trigger many challenges like health-related issues or even building collapse. Though many factors may be responsible for building failures and collapse, the impact of poor water cannot be ruled out. According to Saravanakumar and Dhinakaran (2010), the use of poor-quality water in concrete leads to corrosion and ultimately causes failure in concrete, while the use of saline water in

concrete affects the properties of fresh and hardened concrete. Thus, the essence of this work is to develop a concept of ensuring that only portable water is always used in the construction industry as a way of ensuring the sustainability of quality concrete

In general, the assessment of Water Quality involves the overall process of evaluating the physical, chemical and biological nature of the water resources. Water Quality Assessments are normally based on five broad types of monitoring data: biological integrity, chemical, physical, habitat, and toxicity. This explains why the assessment of water qualities is of interest to many researchers across different fields of human endeavour/discipline. Geologists, Biologists, Crop Scientists/Technologists, Chemists, Civil Engineers, Environmentalists, agriculturists/Agricultural Engineers, physicists, Geographers as well as other water resources agencies have different interests and motives for the assessment of water resources qualities. However, for us in the Civil Engineering profession, our interest is mainly construction purposes, apart from the usual and general domestic purposes. Many researchers have done related works on the subject matter, but none have been able to deal substantially with the subject matter in the chosen area of study. For instance, Ijeh (2014) assessed groundwater quality in different parts of Owerri. His work is limited to groundwater water and for domestic purposes only. Olasoji and others (2019) assessed surface and groundwater qualities using Water Quality Index Method. Their area of interest was in Southwestern Nigeria. Also, the work of Okoro and others (2016) is limited to only groundwater. Eyankwere and others (2015) carried out both physicochemical and bacteriological assessments of groundwater quality in Ughelli and its environ. The work of Ihenetu and others (2020) majored on the pollution and health risk assessment of groundwater sources around a waste disposal site in Owerri West L.G.A. Nwosu and Nwosu (2016) carried out the physicochemical analysis of surface water and groundwater systems within the Federal University of Technology Owerri (FUTO). Their major interest as researchers from the physics department were to obtain the available geoelectric survey information. Nwachukwu and others (2020) carried out a comparative analysis of water quality from harvested rain and borehole water in Owerri West L.G.A. As expected, their research interest is limited to their field of career, biology. The work of Obi (2017) concentrated only on consumption purposes. On the effect of water sources on concrete and other construction materials, some authors have equally contributed enough to the literature. Al-Jabri and others (2011) have researched the effect of using wastewater on the properties of high-strength concrete. Nikhil and others (2014) have determined the impact of water quality on the strength properties of concrete. Their source of water was perhaps from the Indian country. Saravanakumar and Dhinakaran (2010) carried out work on the effect of acidic water on the strength, durability and corrosion of concrete. Finally, Nwachukwu and others (2022) assessed the suitability of Water Resources Qualities for Consumption and Construction purposes where some selected towns In Owerri West L.G.A, Imo State, Nigeria were used as Case Studies. Thus, from the foregoing, it can be envisaged that little or no work has been substantially done on the subject matter with respect to the area and present purpose of the study. Henceforth, the need for this recent research work.

2. MATERIALS AND METHODS

2.1. DESCRIPTION OF STUDY AREA

Owerri Municipal is the capital city as well as the center of attraction of Imo State. It is a Local Government Area in Imo State, Nigeria with Its headquarters in the city of Owerri. It has an area of between 58 km² and 60.5 km² and a population of over 127,213 according to the 2006 census. Its latitude and longitude are shown in Figure 1 (map of Imo state showing Owerri Municipal L.G.A.). The scope of the work is restricted to the main capital city.

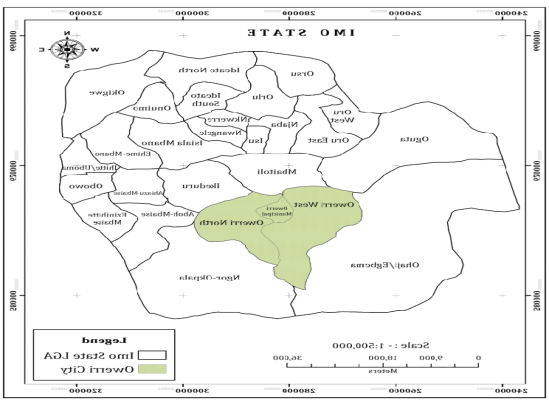

Figure 1. Map of Imo state showing the location of Owerri Municipal

2.2. COLLECTION OF GROUNDWATER DATA AND SAMPLING

The primary sources of data (physicochemical data) in this study were obtained through laboratory analysis of the groundwater from the five selected sample locations in Owerri Municipal L.G.A. of Imo state. The physicochemical data include the following: Sodium (Na), Potassium (k), Calcium (Ca), Magnesium (Mg), Chloride (Cl), Nitrite (NO_3), Bicarbonate (HCO_3), Sulphate (SO_4) Total Hardness (TH), Total Alkalinity (TA), Total Dissolved Solids (TDS) and pH. On the hand, the secondary data were obtained from extracts from WHO (World Health Organization) where the recommended limits for each groundwater resource for a particular purpose were selected. For the physicochemical parameters analysis, two 2-litre polyethene bottles were used to fetch two samples of water from the groundwater (borehole) in the five selected locations. The samples were then stored in a refrigerator at a temperature below 20 ^oC to prevent changes in the water sample between the time of collection and analysis. For assessment of the performance of the groundwater water in concrete production, two samples of groundwater per location were obtained for use in the mixing of concrete

2.3. PROCEDURE / METHOD OF LABORATORY ANALYSIS

In the first place, to assess the suitability of the groundwater qualities for drinking purposes, physicochemical analyses are carried out on the collected water samples. They are pH, Sodium (Na^+), Potassium (K^+), Calcium (Ca^{2+}), Magnesium (Mg^{2+}), Chloride (Cl^-), Sulphate (SO_4^{2-}), Nitrite (NO_3^-), HCO_3, Total Hardness (TH), Total Alkalinity(TA), and Total Dissolve Solids (TDS). Analyses of the majority of the parameters were done using the various standard methods for water analysis and in accordance with APHA (American Public Health Association), AWWA (American Water Works Association) and WPCF (Water Pollution Control Federation) (2005) guidelines. Specifically, the pH was determined using a pH meter. The cation concentrations were determined using atomic absorption spectrophotometer. Nitrate and sulphate concentrations were determined turbid metrically using a spectro-photometer at wavelengths of 410nm and 420nm, respectively. To ensure the correctness of chemical analysis of these water resources parameters, one must ascertain that the equality of the sum of the cations and anions expressed in terms of milliequivalents per litre satisfies the principle of electroneutrality. See the works of Nwachukwu and others (2022) for the steps involved.

Subsequently, the groundwater sample is assessed for its performance in the concrete mixture. In this section, the materials under investigation are a mixture of cement, fine and coarse aggregate and analysed water from the groundwater which was used in accordance with ASTM C1602/C1602M-22 (2022). Our attention here is to determine the compressive strength, flexural strength and split tensile strength of concrete cubes and cylinders. A total of thirty (30) cubes were prepared for compressive strength, flexural strength and split tensile strength. The procedure for compressive strength testing was done in accordance with BS 1881 – part 116 (1983) - Method of determination of compressive strength of concrete cube. Two samples were crushed for each mixture with groundwater per location. In each case, the compressive strength was calculated using Eqn. (1)

$$\text{Compressive Strength} = \frac{\text{Average failure Load (N)}}{\text{Cross– sectional Area (mm}^2\text{)}} = \frac{P}{A} \quad \textbf{(1)}$$

Flexural strength testing was done in accordance with BS 1881 – part 118 (1983) - Method of determination of Flexural Strength, ASTM C78/C78M-22 (2022) and ACI (1989) guideline. In this present study, two samples were crushed for each concrete cube. In each case, the Flexural Strength which is expressed as the Modulus of Rupture (MOR) was then calculated to the nearest 0.05 MPa using Equation 2.

$$\text{MOR} = \frac{PL}{bd^2} \quad \textbf{(2)}$$

Where b = measured width in cm of the specimen, d = measured depth in cm of the specimen at the point of failure, where L = Length in cm of the span on which the specimen was supported and P = maximum load in kg applied to the specimen.

The cylindrical split tensile test was done using the universal testing machine in accordance with BS EN 12390-6:2009 and ASTM C 496/ C 496 M-17 (2017). Two samples were crushed for each concrete cylinder and in each case, the Split Tensile Strength was then calculated using Eqn. (3)

$$F_t = \frac{2P}{\pi DL} \quad \textbf{(3)}$$

Where, F_t = Split Tensile Strength, MPa, P = maximum applied load (that is Load at failure, N) ; D = diameter of the cylindrical specimen (Diameter of cylinder, mm); and L = Length of the specimen (Length of the cylinder, mm),

3. RESULTS AND DISCUSSION

3.1 PRESENTATION OF RESULTS

The result of the physicochemical analysis obtained for the five selected locations (A - E) in Owerri Municipal L.G.A of Imo state for groundwater sampling as well as the result of the compressive strength (CS), flexural strength (FS) and Split tensile strength (STS) are presented in Tables 1 and 2.

Table 1. Presentation of Results of Physico-Chemical Analysis of The Groundwater Samples.

S/NO	LOCATION	Exp. No.	Ca^{2+} Mg/L (NA/*100-300)	Mg^{2+} (50)	N^{a+} (NA/*200)	K^{+} (NA)	HCO_3^- (<600)	Cl^- (250)	NO_3^- (50)	SO_4^{2-} (NA/*250)
1.	A	1A	34.7	8.9	24.9	0.40	35.0	65.8	9.4	57.2
		1B	35.5	9.0	25.5	0.42	36.5	65.9	9.5	60.0
		AV.	35.1	9.0	25.2	0.41	35.8	65.9	9.5	58.6
2.	B	2A	27.8	8.3	25.3	0.33	48.2	72.3	7.8	64.3
		2B	28.2	8.8	25.2	0.32	49.5	74.6	7.5	65.2
		AV.	28.0	8.6	25.3	0.33	48.9	73.5	76.5	64.75
3.	C	3A	34.6	9.3	39.8	0.24	50.0	75.0	8.3	70.8
		3B	35.8	9.5	39.1	0.28	50.3	75.9	8.4	72.7
		AV.	35.2	9.4	39.5	0.26	50.2	75.5	8.4	71.8
4.	D	4A	36.7	8.7	34.6	0.31	56.3	67.7	7.8	68.3
		4B	37.2	7.8	37.2	0.34	54.3	72.2	8.2	70.3
		AV.	37.0	8.3	35.9	0.33	55.3	70.0	8.0	69.3
5.	E	5A	29.6	7.5	40.3	0.40	48.9	75.0	7.6	81.2
		5B	30.5	7.6	39.3	0.34	48.2	80.0	8.5	79.4
		AV.	30.1	7.6	39.8	0.37	48.6	77.5	8.1	80.3

Table 2. Presentation Of Results Of Physico-Chemical Analysis (Contd), Compressive Strength (CS), Flexural Strength (FS) And Split Tensile Strength (STS) Of The Groundwater Samples.

S/NO	LOCATION	Expt. No.	TA Mg/$CaCo_3$ (200)	TH Mg/L $CaCo_3$ (NA/*100-500)	TDS Mg/L $CaCo_3$ (500)	pH (6.5 – 8.5)	CS (MPa) (20 -35)	FS (MPa)	STS (MPa)
1.	A	1A	54.32	98.76	267.9	7.1	27.13	8.48	5.03
		1B	54.76	97.89	271.0	7.3	28.03	8.52	5.05
		AV.	54.54	98.33	269.5	7.2	27.58	8.50	5.04
2.	B	2A	51.19	87.35	280.2	7.1	24.54	7.76	4.59
		2B	52.82	89.04	284.7	7.5	25.14	7.82	4.61
		AV.	52.01	88.20	282.5	7.3	24.84	7.79	4.60
3.	C	3A	52.43	88.65	273.2	7.2	26.37	6.77	5.05
		3B	53.12	89.23	269.9	7.4	25.83	6.96	5.09
		AV.	52.78	88.9	271.6	7.3	26.10	6.88	5.07
4.	D	4A	49.23	90.68	272.8	7.2	22.34	7.00	4.76
		4B	51.46	94.34	281.5	7.2	23.27	7.04	4.82

		AV.	50.35	92.51	271.2	7.2	22.81	7.02	4.79
5.	E	5A	50.09	89.03	255.8	6.5	24.28	7.65	5.89
		5B	50.21	88.28	261.0	6.5	25.18	7.71	5.88
		AV.	50.15	88.63	258.4	6.5	24.73	7.68	5.89

The following items describe the content in Tables 1 and 2: **i**. The procedures for checking the accuracy of the analysis and calculating the values of Total Alkalinity **(TA)**, Total Hardness **(TH)** and Total Dissolved Solids **(TDS)** have been demonstrated by the works of Nwachukwu and others (2022). **ii.** The values in the bracket represent WHO Standards. **iii. NA** implies that no health-based guideline value has been derived. **iv**. ***** indicate the taste threshold values.

3.2. DISCUSSION OF RESULTS

From the results of the physicochemical analyses for groundwater samples shown in Tables 1 and 2, the pH values of locations A to D indicate a neutral value which makes them fit for consumption. Of location, E shows a slightly acidic situation but somehow compares favourably with the WHO stipulated standards. The TDS values are also within the WHO recommended limit. For the anions, chloride concentration, nitrate (($N0_3$), Sulphate (SO_4), and HCO_3 levels are generally lower than the prescribed threshold level recommended by the WHO standard and therefore accepted. Similarly for the cations, Ca^{2+}.Mg^{2+}, Na^+ and K^+, the values also fall within the WHO stipulated standards. Although the values of TH in all selected locations fall within the WHO Taste Threshold stipulated standard, there is still the presence of hardness in these water sources, even though consumers can tolerate hardness up to 500 mg/L. However, their uses in the construction industries are guaranteed. Again, the result of the compressive strength for the groundwater in all selected locations shows that the values meet the minimum ACI (American Concrete Institute) standard (of 20MPa) for good concrete. Other design strengths conducted are also in good agreement with the production of concrete for sustainable construction development. Thus, water from the groundwater sources in these areas that satisfy the WHO standard, when used to mix concrete can positively impact the general strength of concrete cubes.

4. CONCLUSION

So far, the physicochemical analyses of samples of groundwater resources from the selected locations in Owerri Municipal L.G.A of Imo state, Nigeria have been presented. Also presented are the evaluation of the compressive strength, the flexural strength and the split tensile strength of the concrete mixed with samples of water from the selected locations. Both the cation and anion concentrations for the groundwater fall within the WHO recommended standard. Again, the total dissolved solids (TDS), fall within the WHO recommended standard. From the mechanical properties investigation, the compressive strength of concrete cubes mixed with water from the groundwater sources meets up with the minimum requirement of 20 MPa stipulated by ACI. Thus, to ensure the sustainability of good mechanical properties of concrete, there is a need for a prior physicochemical assessment of these water resources.

REFERENCES

ACI Committee 544. (1982). State-of-the-Report on Fibre Reinforced Concrete, (ACI 544.1R-82). Concrete International: Design and Construction. Vol. 4, No. 5: Pp. 9-30, American Concrete Institute, Detroit, Michigan, USA.

ACI Committee 544. (1989). Measurement of Properties of Fibre Reinforced Concrete, (ACI 544.2R-89). American Concrete Institute, Detroit, Michigan, USA.

Agunwamba (2000): "Water Engineering of And Management Tools"; Immaculate Publication Limited, Enugu.

Akpobori, I.A. and Nfor, B.N. (2007). The Development of Groundwater and the Practice of Hydrogeology in Nigeria: A New Paradigm. Journal of the Nigerian Association of Hydrogeologists, Vol.17, Pp. 70-76.

Al-Jabri, K.S., Al-Saidy, A.H., Taha, R and Al-Kemyani, A.J.(2011). Effects of Using Wastewater on the Properties of High Strength Concrete. The Twelfth East Asia – Pacific Conference on Structural Engineering and Construction, Vol.9, Pp.370- 376.

APHA, AWWA and WPCF (2005). Standard Methods for the Examination of Water and Wastewater, 21st Edition, American Public Health Association, American Water Works Association and Water Pollution Control Federation, Washington D.C.

ASTM C78/C78M-22 (2022). Standard Test Method for Flexural Strength of Concrete (Using Simple Beam with Third-Point Loading). ASTM International: West Conshohocken, PA, USA.

ASTM C496/C496M-17 (2017). Standard Test Method for Splitting Tensile Strength of Cylindrical Concrete Specimens. ASTM International: West Conshohocken, PA, USA.

ASTM C1602/C1602M-22 (2022). Standard Specification for Mixing Water Used in the Production of Hydraulic Cement Concrete. ASTM International: West Conshohocken, PA, USA..

British/European code (BS EN 12390-6) 2009.Testing concrete - Split tensile strength of test specimens. BSI - London.

British Standards Institution, BS 1881-Part 116 (1983). Methods of Determination of Compressive Strength of Concrete Cube, London.

British Standards Institution, BS 1881-Part 118 (1983). Methods of Determination of Flexural Strength of Concrete Cube, London

Eyankwere, M.O., Ufomata, D.O, Solomon, E.C. and Akakuru, O.C.(2015). Physico-chemical and Bacteriological Assessment of Groundwater Quality in Ughelli and its Environs, Delta State, Nigeria. International Journal of Innovation and Scientific Research, Vol.14, No.12, Pp.236- 243.

Ihenetu, S.C., Ochule, B.I., Enyoh, E.C., Ibe, F.C., Verla, A.W.and Isiuku, B.O.(2020). Pollution and Health Risk Assessment of Groundwater Sources Around a Waste Disposal Site in Owerri West Local Government Areas of Imo state. Journal of Material and Environmental Science (JMES), Vol.11, No.9, Pp.1560- 1573.

Ijeh, I.B. (2014). Groundwater Quality Assessment of Parts of Owerri, Southern Nigeria, IOSR Journal of Environmental Science, Technology and Food Technology (IOSR- JESTFT), Vol.8, No.2, Pp.63- 70.

Nikhil, T.R., Gooinath, S.M., Sushma, R.and Shanthappa, B.C. (2014). Impact of Water Quality on Strength Properties of Concrete. India Journal of Applied Research, Vol. 4, No. 7, Pp 197-199.

Nwachukwu, K.C, Okodugha, D.A, Uzoukwu, C.S., Okorie, P.O.and Egbulonu , B.A.(2022). Assessment of The Suitability of Water Resources Qualities For Consumption And Construction Purposes : A Case Study of Some Selected Towns In Owerri West L.G.A , Imo State, Nigeria; International Journal of Advances in Engineering and Management (IJAEM) , Vol. 4, No. 3.

Nwachukwu, M.O., Azorji, J.N., Nwachukwu, C.U., Adjeroh, L.A., Iheagwam, S.K. and Manuemelula, N.U. (2020). Comparative Analysis of Water Quality from Harvested Rain and Borehole Water in Owerri West, Imo State. International Journal of Environmental and Pollution Research, Vol. 8, No.2, Pp 13-28.

Nwosu, L.I. and Nwosu, B.O. (2016). Assessment of the Quality of Water Resources by Integrating Physico-Chemical Analysis Result with Geoelectric Survey Information in Federal University of Technology, Owerri, Nigeria. Indian Journal of Applied Research, Vol. 6, No. 11: Pp. 74-50

Obi, L.F. (2017). Comparative Quality Analysis Between Surface Water and Groundwater: A Case Study of Otamiri River and Boreholes in Owerri West, Imo state Nigeria"; International Journal of Advanced Technology and Engineering Exploration, Vol.4, No. 36.

Okoro, B.C., Uzoukwu, R.A.and Ademe, C.K. (2016). Quality Assessment of Groundwater Sources of Potable Water in Owerri, Imo State. Scientific Research Publishing Inc., Vol.3, No.3, Pp.1-6.

Olasoji, S.O., Oyewole, N.O., Abiola, B. and Edokpayi, J.N.(2019). Water Quality Assessment of Surface and Groundwater Sources Using a Water Quality Index Method: A case study of a Peri-Urban Town in South West, Nigeria. Journal of Environment, Vol.6, No.23, Pp.1- 11.

Saravanakumar, P. and Dhinakarana, G (2010). Effect of Acidic Water on Strength, Durability and Corrosion of Concrete. African Journal Online, Vol. 7, No. 2.

WHO (2011). Guidelines for Drinking Water Quality Recommendations: 4th Edition, Vol.1, World Health Organization, Geneva.

PAPER 49 – A SURVEY OF LOAD-BALANCING SCHEMES FOR HETEROGENEOUS NETWORKS

M. A. Idris[1*], A. O. Adejo[1], M. David[1], I. A. Yapati[2], M. Idris-Evuti[2]

[1]Department of Telecommunications Engineering, Federal University of Technology, Minna.
[2]Department of Computer Engineering Technology, Federal Polytechnic Bida.
[*]Email: idris.pg919359@st.futminna.edu.ng

ABSTRACT
Load-balancing is a critical aspect of heterogeneous networks (HetNets) aimed at achieving optimal network performance, resource utilization, and improved user experience. This survey presents an overview of load-balancing schemes in HetNets, categorizing them into reactive, proactive, and hybrid approaches. Reactive algorithms, such as Cell Breathing, User Offloading, Game Theory-Based, and Reinforcement Learning algorithms, focus on balancing load and enhancing network performance. Proactive algorithms, including Prediction-based, Proactive Handover, and Traffic-aware Resource Allocation algorithms, anticipate future network conditions and take pre-emptive actions to optimize resource allocation. Hybrid algorithms combine proactive and reactive strategies to achieve a balance between prediction-based optimization and real-time adaptation. The study highlights the performance metrics used to evaluate these algorithms, along with the challenges and future research directions for each category. Furthermore, it discusses the potential applications of load-balancing in 5G networks, which include edge computing, dynamic network slicing, multi-connectivity scenarios, and integration with machine learning and artificial intelligence techniques. Understanding and optimizing HetNet load-balancing schemes are crucial for the successful deployment and operation of future 5G and beyond networks, contributing to enhanced network performance, improved user experience, and efficient resource utilization in diverse use cases.

KEYWORDS: load-balancing , heterogeneous networks, algorithm, deployment, performance, metrics.

1. INTRODUCTION

Heterogeneous deployments are mixed deployments consisting of macro, pico, femtocells and relay nodes (Hu & Qian, 2013). Heterogeneous networks have revolutionized network deployment, especially in rural and remote areas with tendencies for low return on investment (ROI) for the deployment of Macro Base stations (MBS) (McGuire, 2014). Some of the demands the evolving fifth-generation (5G) network seeks to address are enhanced data rate, improved capacity, reduced latency and better quality of service (QoS). Heterogeneous networks (HetNets) are an effective means to achieve these key objectives (Liang, 2017).

Traditionally, inhomogeneous cellular networks, mobile User Equipment (UE) aligns with networks that guarantee the best performance in terms of RSRP. In Heterogeneous networks, this would lead to an imbalance in the system which may overburden the MBS while keeping other associated BS underutilized (Adiline Macriga & Surya, 2012). An unbalanced load causes performance degradation. Thus, load-balancing ensures a balanced distribution of network load among the different cell tiers to ensure optimal utilization of network resources and improved users' quality of experience.

2. LOAD-BALANCING IN HETEROGENEOUS NETWORKS

Load-balancing is essentially used in heterogeneous deployments to manage network load across different cell tiers to ensure optimal utilization of network resources (Ye et al., 2013). Load-balancing distributes network load across tiers reducing congestion, enhancing capacity and improving user experience and network management efficiency. Thus UEs are connected to the cell with the highest available capacity and data rates, providing a better quality of service (Duan et al., 2014). Load-balancing algorithms in HetNets are based on whether they are reactive, proactive, or hybrid (Salhani, 2019).

3. REACTIVE LOAD-BALANCING ALGORITHMS

Reactive load-balancing algorithms in heterogeneous networks encompass occurrence-based approaches aimed at balancing load, reducing congestion, improving resource utilization, and enhancing overall network performance in heterogeneous cellular networks. Studies on reactive load-balancing algorithms in heterogeneous networks (HetNets) have focused on improving the performance and efficiency of these algorithms by incorporating new metrics and techniques (Ali et al., 2007). Reactive load-balancing algorithms are based on

distance-aware cell association; optimization-based approach; and reinforcement learning. Some of these approaches are highlighted as follows:

3.1 Cell Breathing Algorithm

Cell breathing algorithm (also referred to as the Cell Range Expansion, CRE Algorithm). The algorithm is used to dynamically modify cell sizes and optimize resource allocation for load-balancing . It strives to maintain a fair distribution of load across the HetNet infrastructure. Cell breathing algorithms make adaptive adjustments in cell sizes, power allocation, and handover decisions based on criteria such as traffic demand, cell capacity, and interference levels. Studies by (Siomina & Yuan, 2012; Nyembe, 2015; Sasikumar et al., 2016; Zhang et al., 2018; Bakuza et al., 2021) all showed improved network performance in terms of throughput, spectral efficiency, user experience, significant energy savings without compromising the quality of service. However, work requires a high level of coordination and signalling overhead, which impacts network scalability and complexity; and the performance may vary in different network conditions. Additionally, the studies may require additional infrastructure deployment and cost, especially for deploying new small cells.

3.2 User Offloading Algorithm

The Distributed Optimization approach in load-balancing involves users making offloading decisions locally based on their information and interactions with neighbouring users or base stations. The principle is to optimize resource allocation and load-balancing while minimizing interference and maximizing individual utility. Evaluation metrics for this approach include overall system throughput, fairness, user satisfaction, convergence speed, and resource utilization efficiency. Works by (Kim et al., 2012; Ali et al., 2015) have shown that there are challenges associated with achieving convergence in distributed decision-making, handling selfish user behaviour, dealing with limited local information, and ensuring fairness and efficiency in resource allocation. Future research in this area could focus on developing efficient distributed algorithms with provable convergence guarantees, integrating machine learning and artificial intelligence techniques, and exploring incentive mechanisms to foster cooperative behaviour among users. By addressing these challenges, the Distributed Optimization approach holds promising prospects for more effective and efficient load-balancing in heterogeneous networks.

3.3 Game Theory-Based Algorithm

The Game-Theoretic Power Allocation algorithm is based on the principle of modelling user-base station interactions as a non-cooperative game, where each user strategically selects power allocation to maximize their utility. The algorithm as demonstrated by (Li et al., 2015; Al-Zahrani et al., 2016) takes into account factors such as interference, channel conditions, and fairness. Performance metrics for this algorithm include overall system throughput, fairness index, user satisfaction, and convergence speed of the game. However, there are challenges associated with formulating the game model, handling incomplete or imperfect information, and finding equilibrium solutions in large-scale networks. Future research in this area could focus on developing more realistic and scalable game models, considering network dynamics and user behaviour, and addressing challenges related to practical implementation and convergence analysis. By addressing these challenges, the Game-Theoretic Power Allocation algorithm has the potential to enhance power allocation strategies in heterogeneous networks, leading to improved network performance and user experience.

3.4 Reinforcement Learning Algorithm

The Q-Learning-based load-balancing algorithm is a value-based method that estimates the value of state-action pairs to optimize decision-making in load-balancing scenarios. It follows the principle of learning the optimal value function, specifically the Q-value, through iterative updates based on observed rewards and transitions. The algorithm is evaluated using performance metrics such as average reward, convergence rate, and the ability to find optimal or near-optimal policies. However, (Kudo & Ohtsuki, 2013; Lee et al., 2021; Samson, 2022) have shown that there are challenges associated with value-based methods, including handling large state spaces, tuning hyperparameters, and addressing overestimation bias. Future research in this area could focus on improving sample efficiency, mitigating overestimation bias, and developing algorithms that can handle continuous state and action spaces. By addressing these challenges, Q-Learning and similar value-based approaches hold promising prospects for more effective and efficient load-balancing algorithms in various domains.

4. PROACTIVE LOAD-BALANCING ALGORITHMS

Proactive Load-balancing Algorithms offer promising approaches to optimize load distribution in HetNets. They anticipate the network load imbalance and take corrective actions before the network becomes congested leveraging on predictions, mobility patterns, and real-time traffic conditions to proactively manage network resources (Manzoor et al., 2019). Proactive Load-balancing algorithms are designed to be more proactive and efficient than reactive load-balancing techniques that only react to the network congestion after it occurs. There are several types of load-balancing algorithms that use the PLB approach:

4.1 Prediction-based Algorithms

Prediction-based load-balancing algorithms in HetNets aim to anticipate future network conditions and traffic patterns by leveraging historical data and prediction techniques. These algorithms proactively adjust resource allocation and offloading decisions to prevent congestion and optimize network performance. Evaluation metrics for these algorithms include network throughput, latency, fairness index, user satisfaction, and prediction accuracy. However, works by (Xiao et al., 2017; Manzoor et al., 2019; Gures et al., 2022) show that challenges exist in accurately predicting future network conditions, handling dynamic and unpredictable traffic patterns, and efficiently utilizing prediction models. Future research in this area focuses on improving prediction accuracy through advanced machine learning techniques, incorporating real-time feedback into prediction models, and developing adaptive algorithms that can dynamically adjust load-balancing strategies based on changing network conditions.

4.2 Proactive Handover Algorithms

Proactive handover algorithms in HetNets anticipate future changes in user mobility patterns and make early handover decisions to redistribute users across cells. These algorithms aim to prevent congestion and improve user experience by maintaining optimal cell associations. Performance metrics for proactive handover algorithms include handover success rate, handover delay, network capacity utilization, and user satisfaction. However, (Yoneya et al., 2015; Alhabo & Zhang, 2018; Bitonti & Tropea, 2020) show that challenges do exist in accurately predicting user mobility, efficient handover decision-making, minimizing handover delay, and addressing signalling overhead. Research advancements in this area focus on incorporating machine learning techniques for mobility prediction, developing distributed handover algorithms, addressing the impact of handover on user quality of service, and exploring context-aware handover strategies for heterogeneous networks.

4.3 Traffic-aware Resource Allocation Algorithms

Traffic-aware resource allocation algorithms in HetNets consider real-time traffic demands and dynamically allocate network resources to balance the load across cells. These algorithms proactively monitor traffic conditions and adjust resource allocation based on changing demand patterns, aiming to optimize network capacity and minimize congestion. Performance metrics for traffic-aware resource allocation algorithms include network throughput, fairness, congestion rate, resource utilization efficiency, and user satisfaction. However, (Gong et al., 2010; Fan & Ansari, 2018; De Schepper et al., 2019; Jahid et al., 2021) highlight the challenges in accurately estimating traffic demands, adapting resource allocation in real-time, handling heterogeneous traffic types, and considering the Quality of Service (QoS) requirements. Advances in this area focus on developing intelligent resource allocation algorithms that adapt to dynamic traffic patterns, incorporating machine learning for traffic prediction and classification, addressing QoS constraints, and considering energy efficiency in resource allocation.

5. HYBRID LOAD-BALANCING ALGORITHMS

Hybrid load-balancing algorithms offer a versatile approach to address the complexities of load-balancing in heterogeneous networks by combining proactive and reactive strategies, they aim to achieve a balance between prediction-based optimization and real-time adaptation (Fan & Ansari, 2018). While challenges do exist in threshold determination, learning algorithms, and centralized-distributed coordination, Advancements in machine learning techniques, optimization algorithms, and communication protocols can enhance the performance, scalability, and efficiency of load-balancing in heterogeneous networks. Some of the techniques for load-balancing in heterogeneous cellular networks are:

5.1 Threshold-based Hybrid Algorithms

Threshold-based hybrid load-balancing algorithms combine proactive and reactive approaches by setting thresholds for various performance metrics. These algorithms as shown by (Getnet et al., 2019) monitor network conditions and trigger load-balancing actions when the predefined thresholds are crossed. The principle is to

proactively adjust resource allocation based on predicted load conditions, while reactively responding to real-time network events. Performance metrics for threshold-based hybrid algorithms include network throughput, latency, fairness, load-balancing efficiency, and resource utilization. Challenges include selecting appropriate threshold values, handling sudden changes in network conditions, and ensuring timely and effective load-balancing decisions. Future research in this area focuses on adaptive threshold determination algorithms, intelligent threshold adjustment mechanisms, and incorporating machine learning techniques to enhance prediction accuracy and decision-making.

5.2 Learning-based Hybrid Algorithms

Learning-based hybrid load-balancing algorithms leverage both historical data and real-time network feedback to make load-balancing decisions. These algorithms employ machine learning techniques to learn from past experiences and adapt load-balancing strategies accordingly. The principle as shown by (Ichkov et al., 2016; Fletscher et al., 2019; Alsuhli et al., 2021; E. Kim et al., 2022) combine proactive learning from historical patterns with reactive learning from current network conditions. Performance metrics for learning-based hybrid algorithms include network throughput, fairness, convergence speed, learning efficiency, and adaptability. Challenges include handling high-dimensional and dynamic data, designing efficient learning algorithms, and addressing the trade-off between exploration and exploitation. Future research in this area focuses on developing advanced machine learning models, incorporating deep reinforcement learning techniques, and exploring transfer learning and federated learning approaches for load-balancing in heterogeneous networks.

5.3 Centralized-Distributed Hybrid Algorithms

Centralized-distributed hybrid load-balancing algorithms combine centralized control with distributed decision-making. These algorithms have a central controller that collects network information, performs load-balancing analysis, and distributes load-balancing decisions to individual cells or users. The principle utilizes the centralized controller for global load-balancing optimization while allowing distributed entities to make local load-balancing decisions. Performance metrics for centralized-distributed hybrid algorithms include network throughput, fairness, scalability, convergence speed, and coordination efficiency. Challenges include designing efficient communication protocols between the central controller and distributed entities, ensuring synchronization and consistency in load-balancing decisions, and addressing the overhead of centralized control (Mahmudah et al., 2016; Saadoon, 2019; Yuanita et al., 2016). Future research in this area focuses on developing efficient distributed load-balancing algorithms, exploring coordination mechanisms for the central controller and distributed entities, and investigating the impact of communication delays and network dynamics on load-balancing performance.

6. FUTURE APPLICATIONS IN 5G AND BEYOND

Load balancing plays a vital role in optimizing network performance and ensuring efficient resource utilization in 5G networks. As 5G technology continues to evolve, load-balancing techniques are expected to find applications in various areas. Prominent application is in the context of edge computing, dynamic network slicing, multi-connectivity scenarios, machine learning and artificial intelligence. Overall, load-balancing in 5G holds immense potential for future applications, contributing to enhanced network performance, improved user experience, and efficient resource utilization in diverse use cases (Duan et al., 2015; Tsirakis et al., 2017; Furqan et al., 2019; E. Kim et al., 2022).

7. CONCLUSION

Load-balancing is a crucial aspect of optimizing network performance and resource utilization in heterogeneous networks (HetNets) within the 5G ecosystem. This study presented an overview of load-balancing algorithms categorized into reactive, proactive, and hybrid approaches. Reactive algorithms, such as Cell Breathing, User Offloading, Game Theory-Based, and Reinforcement Learning algorithms, focus on dynamically balancing load and improving network performance. Proactive algorithms, including Prediction-based, Proactive Handover, and Traffic-aware Resource Allocation algorithms, anticipate network conditions and take preventive actions to optimize resource allocation. Hybrid algorithms combine proactive and reactive strategies to strike a balance between prediction-based optimization and real-time adaptation.

Despite advancements in load-balancing algorithms, some challenges need to be addressed in each category. Reactive algorithms require coordination and may have signalling overheads, while proactive algorithms face difficulties in accurately predicting network conditions and efficiently handling dynamic traffic patterns. Hybrid

algorithms aim to overcome the limitations of individual approaches and present promising prospects for load-balancing in HetNets.

Looking ahead, load-balancing in 5G networks holds great potential for future applications. It can be leveraged in edge computing scenarios to distribute computational tasks and network traffic efficiently, reducing latency and improving overall system performance. Dynamic network slicing can benefit from load-balancing techniques to allocate network resources effectively among different virtual network slices based on their varying demands. Load-balancing algorithms can also optimize traffic distribution in multi-connectivity scenarios, where devices connect to multiple access points or networks simultaneously and enhance user experience. Integration of load balancing with machine learning and artificial intelligence techniques can enable intelligent decision-making and real-time optimization based on network conditions.

REFERENCES

Adiline Macriga, G., & Surya, V. S. (2012). Location Management and Resource Allocation Using Load-balancing in Wireless Heterogeneous Networks. In *Lecture Notes of the Institute for Computer Sciences, Social Informatics and Telecommunications Engineering* (pp. 383–393). Springer Berlin Heidelberg. https://doi.org/10.1007/978-3-642-27299-8_40

Alhabo, M., & Zhang, L. (2018). Load-Dependent Handover Margin for Throughput Enhancement and Load-balancing in HetNets. *IEEE Access*, *6*, 67718–67731. https://doi.org/10.1109/ACCESS.2018.2878489

Ali, K. A., Hassanein, H. S., & Mouftah, H. T. (2007, July). Directional Cell Breathing Based Reactive Congestion Control in WCDMA Cellular Networks. *2007 IEEE Symposium on Computers and Communications*. https://doi.org/10.1109/iscc.2007.4381553

Ali, Mohd. S., Coucheney, P., & Coupechoux, M. (2015). Load-balancing in heterogeneous networks based on distributed learning in potential games. *2015 13th International Symposium on Modeling and Optimization in Mobile, Ad Hoc, and Wireless Networks (WiOpt)*, 371–378. https://doi.org/10.1109/WIOPT.2015.7151095

Alsuhli, G., Banawan, K., Seddik, K., & Elezabi, A. (2021). *Optimized Power and Cell Individual Offset for Cellular Load-balancing via Reinforcement Learning*.

Al-Zahrani, A. Y., Yu, F. R., & Huang, M. (2016). A Joint Cross-Layer and Colayer Interference Management Scheme in Hyperdense Heterogeneous Networks Using Mean-Field Game Theory. *IEEE Transactions on Vehicular Technology*, *65*(3), 1522–1535. https://doi.org/10.1109/tvt.2015.2413394

Bakuza, E., Iddi, H. U., & Abdalla, A. T. (2021). Efficient Load-balancing Algorithm in Long Term Evolution (LTE) Heterogeneous Network Based on Dynamic Cell Range Expansion Bias. *Tanzania Journal of Science*, *47*(3), Article 3. https://doi.org/10.4314/tjs.v47i3.6

Bitonti, L., & Tropea, M. (2020). *Implementation and Simulation of Handover Techniques to Guarantee Service Continuity through Microservices at Edge*. *Simultech*, 287–293. https://doi.org/10.5220/0009971002870293

De Schepper, T., Latr\' e, S., & Famaey, J. (2019). Scalable Load-balancing and Flow Management in Dynamic Heterogeneous Wireless Networks. *Journal of Network and Systems Management*, *28*(1), 133–159. https://doi.org/10.1007/s10922-019-09502-2

Duan, X., Akhtar, A. M., & Wang, X. (2015). Software-defined networking-based resource management: Data offloading with load-balancing in 5G HetNet. *EURASIP Journal on Wireless Communications and Networking*, *2015*(1), 181. https://doi.org/10.1186/s13638-015-0405-3

Duan, X., Wang, X., & Akhtar, A. M. (2014, September). Partial mobile data offloading with load-balancing in heterogeneous cellular networks using Software-Defined Networking. *2014 IEEE 25th Annual International Symposium on Personal, Indoor, and Mobile Radio Communication (PIMRC)*. https://doi.org/10.1109/pimrc.2014.7136378

Fan, Q., & Ansari, N. (2018). Towards Throughput Aware and Energy Aware Traffic Load-balancing in Heterogeneous Networks with Hybrid Power Supplies. *IEEE Transactions on Green Communications and Networking*, *2*(4), 890–898. https://doi.org/10.1109/TGCN.2018.2837618

Fletscher, L. A., Suárez, L. A., Grace, D., Peroni, C. V., & Maestre, J. M. (2019). Energy-Aware Resource Management in Heterogeneous Cellular Networks With Hybrid Energy Sources. *IEEE Transactions on Network and Service Management*, *16*(1), 279–293. https://doi.org/10.1109/TNSM.2018.2866533

Furqan, M., Iqbal, S., Wasim, M., & Huang, Y. (2019, December). Load-balancing for Future 5G Network Communication: Performance and Trade-off. *2019 International Conference on Computational Intelligence and Knowledge Economy (ICCIKE)*. https://doi.org/10.1109/iccike47802.2019.9004407

Getnet, A., Beneyam, B., Flattie, A. G., Haile, B. B., & Hailemariam, D. (2019). *Capacity Demand-based Multiobjective Optimal Small Cell Placement under Realistic Deployment Scenario*. https://doi.org/10.1109/AFRICON46755.2019.9133900

Gong, J., Zhou, S., Niu, Z., & Yang, P. (2010). Traffic-aware base station sleeping in dense cellular networks. *2010 IEEE 18th International Workshop on Quality of Service (IWQoS)*, 1–2. https://doi.org/10.1109/IWQoS.2010.5542725

Gures, E., Shayea, I., Ergen, M., Azmi, M. H., & El-Saleh, A. A. (2022). Machine Learning-Based Load-balancing Algorithms in Future Heterogeneous Networks: A Survey. *IEEE Access*, *10*, 37689–37717. https://doi.org/10.1109/ACCESS.2022.3161511

Hu, R. Q., & Qian, Y. (2013). *HETEROGENEOUS CELLULAR NETWORKS* (First). Wiley & Sons, Ltd., Publication.

Ichkov, A., Atanasovski, V., & Gavrilovska, L. (2016). Hybrid access control with cell range expansion for LTE-A heterogeneous networks. *2016 IEEE International Black Sea Conference on Communications and Networking (BlackSeaCom)*. https://doi.org/10.1109/blackseacom.2016.7901560

Jahid, A., Alsharif, M. H., Uthansakul, P., Nebhen, J., & Aly, A. A. (2021). Energy Efficient Throughput Aware Traffic Load-balancing in Green Cellular Networks. *IEEE Access*, *9*, 90587–90602. https://doi.org/10.1109/ACCESS.2021.3091499

Kim, E., Jung, B. C., Park, C. Y., & Lee, H. (2022). Joint Optimization of Energy Efficiency and User Outage Using Multi-Agent Reinforcement Learning in Ultra-Dense Small Cell Networks. *Electronics*, *11*(4), Article 4. https://doi.org/10.3390/electronics11040599

Kim, H., Veciana, G. D., & Yang, X. (2012). *Distributed -Optimal User Association and Cell Load-balancing in Wireless Networks*. *20*(1), 177–190.

Kudo, T., & Ohtsuki, T. (2013). Cell range expansion using distributed Q-learning in heterogeneous networks. *EURASIP Journal on Wireless Communications and Networking*, *2013*(1), 61. https://doi.org/10.1186/1687-1499-2013-61

Lee, H., Kim, E., Kim, H., Na, J., & Choi, H. (2021). Multi-agent Q-learning based cell breathing considering SBS collaboration for maximizing energy efficiency in B5G heterogeneous networks. *ICT Express*, *xxxx*, 6–10. https://doi.org/10.1016/j.icte.2021.09.006

Li, M., Xu, X., Wang, Y., & Zhang, R. (2015, October). Game theory-based load-balancing in small cell heterogeneous networks. *2015 International Conference on Connected Vehicles and Expo (ICCVE)*. https://doi.org/10.1109/iccve.2015.67

Liang, Y. (2017). Interference Management in Heterogeneous Networks. In *Advances in Wireless Technologies and Telecommunication* (pp. 190–226). IGI Global. https://doi.org/10.4018/978-1-5225-1712-2.ch008

Mahmudah, H., Puspitorini, O., Wijayanti, A., Siswandari, N. A., & Yuanita, R. I. (2016). Performance Analysis of Cell Zooming Based Centralized Algorithm for Energy Efficient in Surabaya. *EMITTER International Journal of Engineering Technology*, *4*(2). https://doi.org/10.24003/emitter.v4i2.155

Manzoor, S., Mazhar, S., Asghar, A., Noor Mian, A., Imran, A., & Crowcroft, J. (2019). Leveraging mobility and content caching for proactive load-balancing in heterogeneous cellular networks. *Transactions on Emerging Telecommunications Technologies*, *31*(2). https://doi.org/10.1002/ett.3739

McGuire, C. (2014). *ENERGY EFFICIENT NETWORK FOR RURAL BROADBAND ACCESS*.

Nyembe, W. N. (2015). *Load-balancing using Cell Range Expansion in LTE Advanced Heterogeneous Networks*. University of Cape Town.

Saadoon, R. (2019). *Small Cells Deployment for Traffic Handling in Centralized Heterogeneous Network*. *August*.

Salhani, M. (2019). *Comparison of the proactive and reactive algorithms for load-balancing in UDN networks*. https://doi.org/10.12720/jcm.14.12.1119-1126

Samson, D. A. (2022). *Load-balancing and Optimization in LTE Network Using Fuzzy Logic and Q-Learning Techniques*. *6*(6).

Sasikumar, R., Ananthanarayanan, V., & Arumugam, R. A. (2016). An Intelligent Pico Cell Range Expansion Technique for Heterogeneous Wireless Networks. *Indian Journal of Science and Technology*, *9*. https://doi.org/10.17485/ijst/2016/v9i9/67610

Siomina, I., & Yuan, D. (2012, June). Load-balancing in heterogeneous LTE: Range optimization via cell offset and load-coupling characterization. *2012 IEEE International Conference on Communications (ICC)*. https://doi.org/10.1109/icc.2012.6364075

Tsirakis, C., Matzoros, P., Sioutis, P., & Agapiou, G. (2017). Load-balancing in 5G Networks. *MATEC Web of Conferences*, *125*, 03010. https://doi.org/10.1051/matecconf/201712503010

Xiao, Z., Li, S., Chen, X., Wang, D., & Chen, W. (2017). A Load-Balancing Energy Consumption Minimization Scheme in 5G Heterogeneous Small Cell Wireless Networks Under Coverage Probability Analysis. *International Journal of Pattern Recognition and Artificial Intelligence*. https://doi.org/10.1142/S0218001417590133

Ye, Q., Rong, B., Chen, Y., Al-Shalash, M., Caramanis, C., & Andrews, J. G. (2013). User Association for Load-balancing in Heterogeneous Cellular Networks. *IEEE Transactions on Wireless Communications*, *12*(6), 2706–2716. https://doi.org/10.1109/TWC.2013.040413.120676

Yoneya, R., Mehbodniya, A., & Adachi, F. (2015). Two Novel Handover Algorithms with Load-balancing for Heterogeneous Network. *2015 IEEE 82nd Vehicular Technology Conference (VTC2015-Fall)*, 1–5. https://doi.org/10.1109/VTCFall.2015.7391183

Yuanita, R. I., Puspitorini, O., & Mahmudah, H. (2016). Analysis technique of cell zooming using a lowerto-higher scheme on centralized algorithm towards green cellular network in surabaya. *2016 International Electronics Symposium (IES)*, 132–137. https://doi.org/10.1109/ELECSYM.2016.7860989

Zhang, Y., Cui, Z., Cui, Q., & Member, S. (2018). *Energy Efficiency Analysis of Heterogeneous Cellular Networks with Extra Cell Range Expansion*. 1–10.

PAPER 50 – EFFECT OF CURING AND TREATMENT METHOD ON ULTRASONIC PULSE VELOCITY OF COMPACTED LATERITIC SOIL TREATED WITH *BACILLUS THURINGIENSIS*

K. J. Osinubi[1], T. S. Ijimdiya[1], A. O. Eberemu[2] and I. M. Kanyi[3*]

[1]Department of Civil Engineering, Ahmadu Bello University, Zaria, Kaduna State, Nigeria.
[2]Department of Civil Engineering and Africa Centre of Excellence on New Pedagogies in Engineering Education (ACENPEE), Ahmadu Bello University, Zaria, Kaduna State, Nigeria.
[3]Department of Civil Engineering, Joseph Sarwuan Tarka University, Makurdi, Benue State, Nigeria.
*Email: wald2moris@gmail.com

ABSTRACT
The study used ultrasonic pulse velocity (UPV) to assess the integrity and apparent strength of compacted lateritic soil treated with Bacillus *thuringiensis* (Bt). The effect of treatment methods (mixing and injection methods) of cementation solution (C_s) applications and curing procedures (oven-cured at 30° C, wax-cured, and air-curing at 25 ± 2° C) on UPV was also investigated. Samples were treated with Bt suspension densities of 0, 1.5 x 10^8, 6.0 x 10^8, 12 x 10^8, 18 x 10^8 and 24 x 10^8 cells/ml and varying concentrations of C_s of 0.25, 0.5, 0.75 and 1 M. Specimens were compacted using British Standard light, West African Standard, and British Standard heavy energies, extruded, and cured using the procedures listed before the UPV tests. Results showed that UPV values increased as the compaction energy, Bt suspension density, and C_s concentration increased. The mixing method recorded higher UPV values relative to the injection method of treatment regardless of the curing procedure used. Air-cured specimens recorded higher UPV values in comparison to oven-cured and wax-cured specimens. It is recommended that treatment with Bt (24 x 10^8 cells/ml): C_s (0.75 M) by mixing method and air-curing at laboratory temperature can enhance the strength of lateritic soil for the embankment.

***Keywords*:** Bacillus *thuringiensis,* Curing method, Microbial-induced calcite precipitation, lateritic soil, Ultrasonic pulse velocity.

1. INTRODUCTION

The heterogeneous nature of soil makes it a complex material for erecting civil engineering infrastructure. The determination of *in situ* index and other engineering characteristics of soil is commonly achieved using direct methods that are usually destructive. For example, field density tests are carried out by destructive core cutter or sand replacement methods. The amount of time taken for these tests to be conducted and in most cases putting a temporal stop to construction activities is of grave concern (Yesiller *et al.*, 2000). Consequently, the non-destructive test (NDT) methods offer a faster assessment of soil and other material properties (Shi *et al.*, 2007; Slavova *et al.*, 2010). Some of the commonly used NDT methods include electrical resistivity, nuclear density, cone penetration and ultrasonic pulse velocity (UPV) tests (Leong *et al.*, 2004). However, there are accuracy concerns and operational difficulties associated with some of these methods that limit their usage in real-life engineering practice (Vinay *et al.*, 2019).

The wider utilization of UPV as an NDT method in assessing the quality of construction materials such as concrete, soil, metals and asphalt is due to its simple and quick approach to material quality and strength assessment (Shi *et al.*, 2007). In geotechnical engineering, UPV has been utilised to predict the density, water content, and strength as well as other soil parameters such as Young's modulus (E), shear modulus (G) and Poisson's ratio (ν) (Nakagawa *et al.*, 1996; Vinay *et al.*, 2019).

Soil improvement via soil microorganisms has opened up a new and reportedly viable alternative soil enhancement method for geotechnical engineers for over a decade (van Paassen *et al.,* 2010; Matthew *et al.,* 2012; Liu *et al.,* 2021; Yohanna *et al*., 2022; Etim *et al.,* 2022; Wang *et al*., 2022). This is achieved through the isolation and culturing of soil microbes with the potential of degrading urea into its constituent ions (NH_4^+ and CO_3^{2-}) by urease enzymes produced during the bacterial metabolic activities through a process known as urea hydrolysis. When this happens in an environment rich in calcium, a biogeochemical reaction occurs resulting in calcite precipitation. The precipitated calcite can clog soil particles thereby enhancing their strength. Building on this knowledge, the geo-environmental engineers have devised ways of intentionally creating scenarios that bring about the precipitation of this important mineral in the soil in sufficient amounts to enhance its engineering properties using urease-positive bacteria through a process referred to as microbial-induced calcite precipitation (MICP) (Osinubi *et al.,* 2021). MICP method of soil improvement is more compatible with nature (environment)

relative to the traditional use of chemicals in soil improvement since the latter is associated with carbon emissions contributing to global climate change concerns (Karol, 2003; DeJong *et al.,* 2006; Osinubi *et al.,* 2021).

The study was focused on the investigation of the coupled effect of the curing method and treatment procedure on UPV of compacted biotreated lateritic soil using the MICP technique. The UPV non-destructive test method was used to determine the strength of the compacted soil for use as embankment construction material.

2. MATERIALS AND METHODS

2.1 Materials

Soil: The lateritic soil was collected at Abagana in Anambra State, Nigeria, at a location (6° 12' 15" N and 7° 0' 40" E on latitude and longitude, respectively). Disturbed samples were collected at 0.5 - 3 m depth.

***Microorganism*:** Bacillus *thuringiensis* (*Bt*) was isolated from the soil and cultured using biochemical confirmatory test kits for identifying and characterising *Bt* in the laboratory and was used throughout the research.

***Cementation solution*:** The study utilised equimolar calcium chloride, and urea to obtain their mass concentration in solution as suggested by Murtala *et al.* (2016) in addition to constituents such as ammonium chloride (10 g), sodium bicarbonate (2.12 g) and nutrient broth (3 g) dissolved per dm^3 of de-ionized water for effective cementation solution suitable for MICP process (Stocks-Fisher *et al.,* 1999). Four different concentrations of cementation solutions (C_s) (i.e., 0.25, 0.5, 0.75 and 1 M) were used. The C_s is composed of nutrient broth, ammonium chloride (NH_4Cl), urea ($CO(NH_2)_2$), sodium bicarbonate ($NaHCO_3$) and calcium chloride ($CaCl_2$).

2.2 Methods

Index properties: Soil basic properties such as natural moisture content, specific gravity, consistency limits, sieve analysis and soil classification were determined following British Standard (BS) 1377 (1990) procedures for testing natural soils and BS 1924 (1990) procedures for testing stabilised soils.

***Preparation of sample*:** Lateritic soil was treated with *Bt* suspension densities of 0, 1.5 x 10^8, 6.0 x 10^8, 12 x 10^8, 18 x 10^8 and 24 x 10^8 cells/ml (equivalent to 0, 0.5, 2.0, 4.0, 6.0 and 8.0 McFarland Standards (MFS), respectively) and varying concentration of cementation solutions (C_s) of 0.25, 0.5, 0.75 and 1 M using mixing and injection methods of bacterial/cementation solution application. In the mixing method, 50 % of *Bt* solution (relative to natural soil optimum moisture as recommended by Osinubi *et al.,* 2019) was pre-mixed with the soil sample and kept for 6 hours in sealed polythene bags to maintain the prevailing moisture and allow for bacterial attachment to soil particles thereafter, 50 % of C_s was added, properly mixed and compacted with British Standard light (BSL), West African Standard (WAS) and British Standard heavy (BSH) energy, respectively. In the injection method, $\frac{1}{3}$ soil pore volume (PV) of *Bt* solution (relative to natural soil optimum moisture as recommended by Rowshanbakht *et al.,* 2016) was mixed with soil and compacted (using BSL, WAS and BSH energies). The compacted soil was then saturated by injecting $\frac{2}{3}$ PV of C_s under gravity in three cycles. In both cases, the compacted soils were extruded, trimmed and subjected to the three curing procedures (oven-cured at 30^0 C, wax-cured and direct exposure to room temperature) before carrying out the UPV test to assess the apparent strength.

2.3 Ultrasonic Pulse Velocity Measurement Procedure and Test Programme

In UPV measurement, two transducers (transmitter and receiver) are placed at both ends of the test samples with the aid of petroleum jelly (couplant) to eliminate the air gap between the test sample and the transducer surfaces to enhance the efficiency of the process as shown in Plate I. The transmitting transducer sends an ultrasonic wave signal through the test sample and this is detected at the other end by the receiving transducer over time. The UPV is therefore determined as the ratio of the travel distance (i.e., sample length, L) of the wave signal generated from the transmitting probe to the time, T when the signal is recorded at the receiving probe. This is represented mathematically in equation 1.

$$UPV = \frac{Sample\ length,\ L}{Time, T\ when\ the\ generated\ signal\ is\ recorded\ at\ the\ receiving\ probe} \quad (1)$$

Where:
UPV = Ultrasonic pulse velocity (m/s)

The test programme involved the determination of UPV for the treated and additive-free compacted lateritic soil. The UPV test was performed on the wax-cured, oven-cured at 30° C and air-cured samples after 7 days.

3. RESULTS AND DISCUSSION

3.1 Index Properties

Based on the laboratory index properties determined, the natural soil was classified as SC or A – 2 – 6 (2) using USCS (ASTM D 2487-06) and AASHTO (1986) systems of soil classification, respectively. These properties are summarised in Table 2. The particle size distribution of the natural soil is shown in Figure 1.

Table 2. Physical properties of the natural lateritic soil

Property	Quantity
Natural moisture content (%)	19.6
Specific gravity	2.67
Percentage passing No. 200 sieve	33.2
Liquid limit (%)	36.0
Plastic limit (%)	17.1
Plasticity index (%)	18.9
Linear shrinkage (%)	7.7
USCS	SC
AASHTO classification	A – 2 – 6 (2)
Gravel fraction (%)	0.1
Sand fraction (%)	66.7
Silt fraction (%)	18.0
Clay fraction (%)	15.2
Dominant clay mineral	Kaolinite
Colour	Reddish-brown

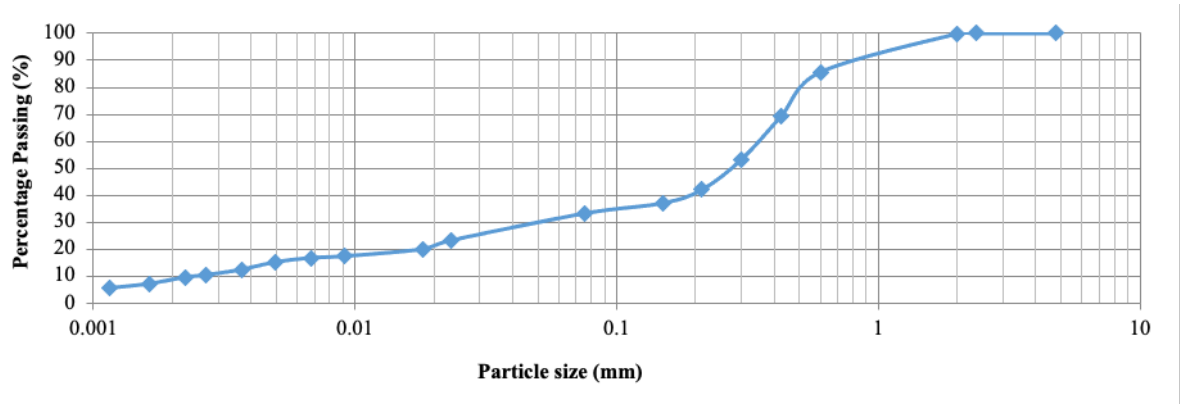

Figure 1. Particle size distribution curve of the natural lateritic soil

3.2 Effect of Curing Procedure and Bacillus *Thuringiensis* Density in Solution on UPV

The variation of UPV with the varying Bacillus *thuringiensis* densities in solution for the three curing procedures considered is shown in Figure 2. The UPV values increased as Bt population density in the mixture increased. The increasing trend was found to be similar when the compacted soils were subjected to different curing procedures (Figures 2a, b and c). The UPV values of 588, 618 and 634 m/s recorded for soil compacted with BSL energy and treated with C_s (0.25 M) after 7 days curing period increased to peak values of 634, 661 and 786 m/s for soil treated with Bt. (12 x 10^8 cells/ml) and C_s (0.25 M) for specimens wax-cured, oven cured and air-cured, respectively. Similarly, UPV values of 603, 636 and 858 m/s were recorded for specimens treated with C_s value of 0.75 M after 7 days of curing increased to peak values of 814, 1142 and 1219 m/s for specimens wax-cured, oven-cured and air-cured at room temperature, respectively. It was observed that UPV values increased as the C_s concentration increased. The increase in UPV values recorded could probably be attributed to the biogeochemical reaction involving Bt and the C_s in the soil mixture leading to the deposition of calcite in the matrix. The precipitated calcite filled voids and bridged particle contact points in the compacted soil (Osinubi *et al.,* 2021;

Wang *et al*., 2022) thereby enhancing the transmission of the pulse velocity signal and subsequently increasing UPV values (Shi *et al.*, 2007; Slavova *et al.*, 2010).

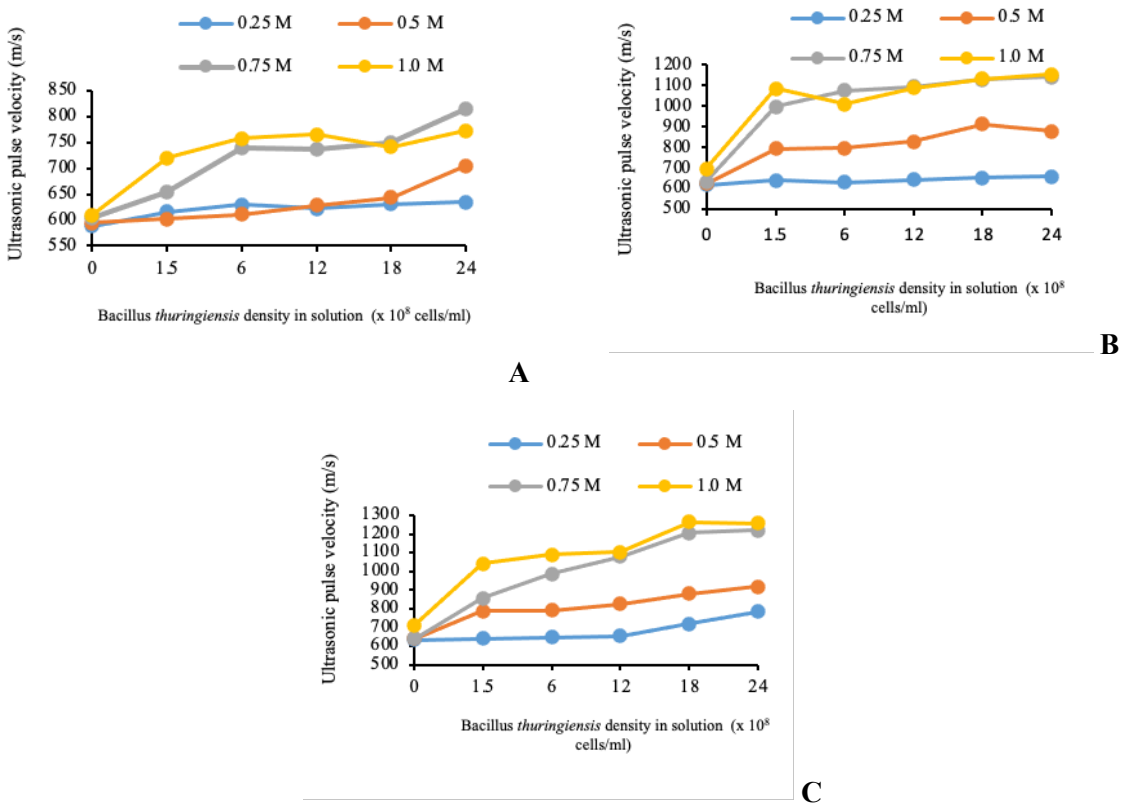

Figure 2: Variation of ultrasonic pulse velocity of compacted soil (BSL energy) with varying Bacillus *thuringiensis* density in solution for the three curing procedures: (A) 7 days wax-cured (B) 7 days oven-cured at 30° C (C) 7 days air-cured at ambient temperature.

A similar trend as discussed above was observed when the compacted soil was treated with 0.5 M and 1 M C_s with varying Bt density in solution. Also, the above results revealed that compacted soil specimens treated and air-cured at ambient temperature yielded higher UPV values. Least UPV values were recorded for wax-cured specimens while intermediate values were recorded for specimens oven-cured at 30° C. The increase in UPV values signifies an improvement in the strength of the bio-treated soil.

3.3 Effect of Treatment Method on UPV

The variation of UPV value of lateritic soil compacted using BSL energy with Bacillus *thuringiensis* suspension density for the treatment methods considered after 7 days of curing is shown in Figure 3. The UPV values increased as bacterial population density in the mixture increased irrespective of the treatment method (i.e., mixing and injection methods) used. However, the mixing method of C_s application during experimentation recorded higher UPV values. The mixing method presented a situation in which there were more bacterial interactions with the C_s thus leading to more calcite formed in the soil matrix. On the other hand, the injection method produced results that depicted limited bacterial interaction with the C_s since the movement of the organism within the soil matrix was dependent on the compacted soil pore throat and the ability of the Bt in the mixture to flow through the pore spaces (Rowshanbakht *et al.,* 2016; Etim *et al.,* 2022). The compacted soil pore throat did not offer a great chance for effective movement of the organism. According to Rebata-Landa (2007), the MICP process performs optimally for soil with grain size in the range of 50 and 400 µm. Therefore, bacterial activity is not usually effective in fine-grained soil. Thus, the observed variation in the UPV values in the injection method could be linked to this effect. Similar trends were also observed when higher compaction energy (i.e., WAS and BSH) was deployed.

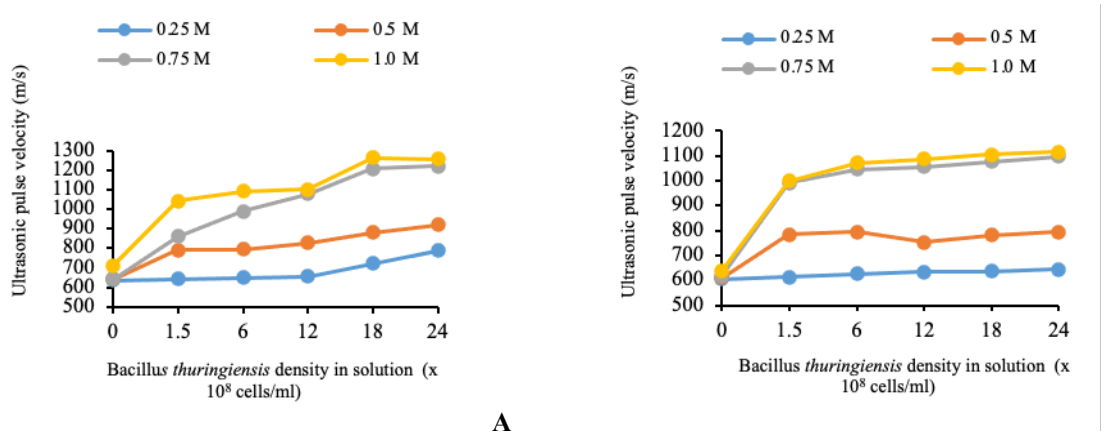

Figure 3: Variation of ultrasonic pulse velocity of compacted soil (BSL energy) with varying Bacillus *thuringiensis* density in solution for the treatment method: (A) 50 % Bt: 50 % Cs (mixing method) 7 days air-cured at ambient temperature (B) 1/3 PV (injection method) 7 days air-cured at ambient temperature.

3.4 Effect of Compaction Energy and Cementation Solution Concentrations on UPV

Variations of UPV of lateritic soil – C_s – Bacillus *thuringiensis* mixtures with compaction energy are shown in Figures 4 - 6. The UPV values increased as the compaction energy and C_s concentration increased. The trends of increase in the UPV values are similar irrespective of the curing procedure adopted. Although, maximum UPV values were obtained when treated specimens were cured by direct exposure to ambient conditions.

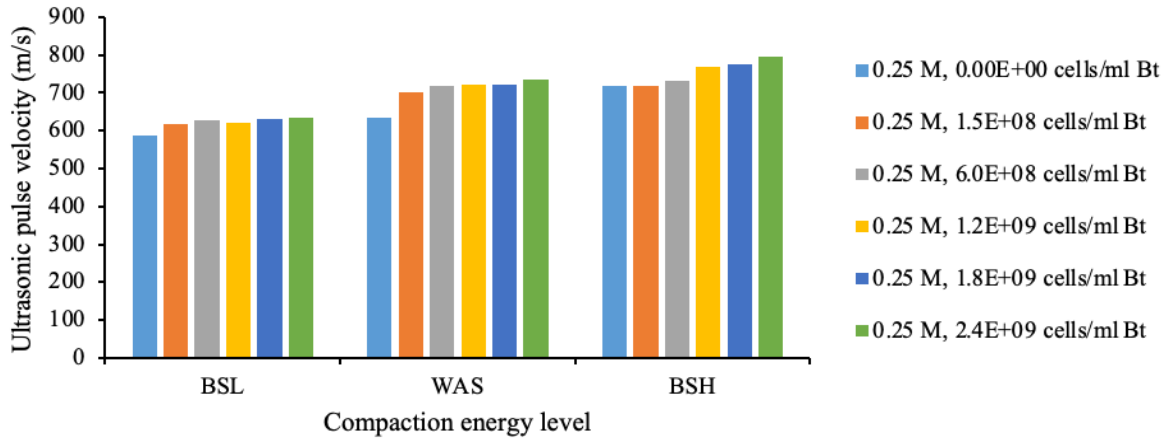

Figure 4. Variation of ultrasonic pulse velocity of lateritic soil – 0.25 M C_s – Bacillus *thuringiensis* mixtures with compaction energy (wax-cured).

The increase in UPV values with increment in C_s concentration may be attributed to greater quantities of urea and calcium chloride in the mixture at higher concentrations leading to increased urease activity that favoured the production of calcite in the soil matrix (Yohanna *et al*., 2022). The produced mineral (calcite) bound the particles together thereby improving the UPV values.

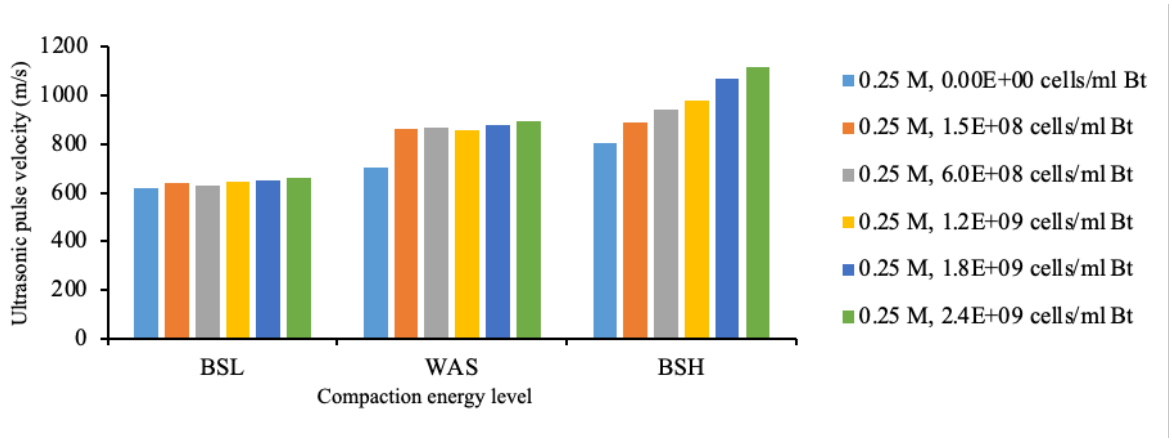

Figure 5: Variation of ultrasonic pulse velocity of lateritic soil – 0.25 M C_s – Bacillus *thuringiensis* mixtures with compaction energy (oven-cured).

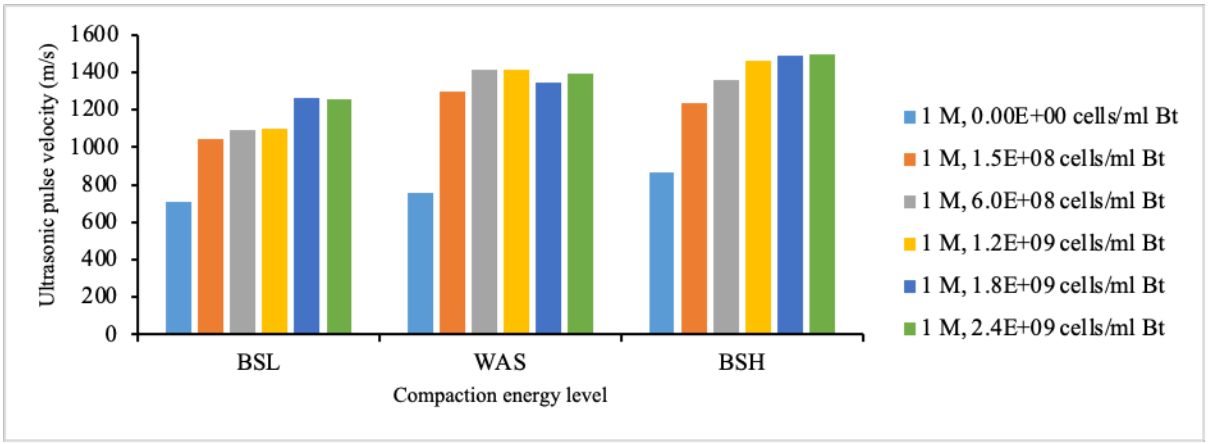

Figure 6: Variation of ultrasonic pulse velocity of lateritic soil – 1 M C_s – Bacillus *thuringiensis* mixtures with compaction energy (Air-cured at ambient temperature).

4. CONCLUSION

The study assessed the effect of curing and treatment procedures on UPV of MICP-treated compacted lateritic soil classified as A – 2 – 6 (2) and SC using the AASHTO and USCS systems, respectively. The results showed that:

i. The UPV values increased as Bt population density in the mixture increased. The UPV values of 588, 618 and 634 m/s recorded for compacted soil (BSL energy) treated with C_s (0.25 M) after 7 days of curing increased to peak values of 634, 661 and 786 m/s when treated with 12 x 10^8 cells/ml at 0.25 M for wax-cured, oven cured and air-cured samples respectively.
ii. The mixing method of C_s application recorded higher UPV values in comparison with the injection method irrespective of the curing procedure used.
iii. Specimens cured at ambient temperature recorded higher UPV values in comparison to oven-cured and wax-cured specimens.
iv. The UPV values increased as the compaction energy and C_s concentrations increased.

RECOMMENDATION

It is recommended that lateritic soil treated with Bt (24 x 10^8 cells/ml): 0.75 M C_s (0.75 M) mix ratio prepared using the mixing method and compacted with BSH energy when air-cured at ambient temperature can be used for embankment construction.

REFERENCES

AASHTO (1986). Standard Specification for Transportation, Material and Methods of Sampling and Testing. 14th Edition. American Association of State Highway and Transportation official Washington D.C.

ASTM D 2487 (2006). Standard practice for classification of soils for engineering purposes (unified soil classification system), American Society for Testing and Materials. Philadelphia.

BS 1377 (1990). *Method of Testing Soils for Civil Engineering Purpose*. British Standard Institute, BSI, London.

BS 1924 (1990). *Method of Test for Stabilized Soils. British* Standard Institute BSI London.

DeJong, J.T.,Fritzges, M.B.,Nusslein, K. (2006) Microbially induced cementation to control sand response to undrained shear. *Journal of Geotechnical and Geoenvironmental Engineering*-ASCE.132, 1381–1392.

Etim, R.K., Ijimdiya, T.S., Eberemu, A.O., Osinubi, K.J. (2022) Compatibility interaction of landfill leachate with lateritic soil bio-treated with Bacillus megaterium using MICP technique: criterion for barrier material in waste containment. Cleaner materials. https://doi.org/10.1016/j.clema.2022.100110

Karol, R.H. (2003) Chemical Grouting and Soil Stabilization.pp. 558 Marcel Dekker, New York.

Leong, E.C., Yeo, S.H. and Rahardjo, H., 2004, "Measurement of wave velocities and attenuation using an ultrasonic test system," *Canadian Geotechnical Journal*, Vol. 41, No. 5, pp. 844 – 860

Liu, B., Xie, Y. H., Tang, C. S., Pan, X. H., Jiang, N. J., Singh, D. N., Cheng, Y. J., Shi, B. (2021). Bio-mediated method for improving surface erosion resistance of clayey soils. *Engineering geology* 106295, 1-10.

Matthew, H. W.,Jason T. D.,Brian C. M., and Brina M. M (2012) Seismic and Resistivity Measurements for Real-Time Monitoring of Microbially Induced Calcite Precipitation in Sand. *Geotechnical Testing Journal*. 35(2):330-34.

Murtala U., Khairul A. K., Kenny T. P. C., (2016). Biological process of soil improvement in civil engineering: A review *Journal of Rock Mechanics and Geotechnical Engineering*-Elsevier, 8: 767-774.

Nakagawa, K., Soga, K., and Mitchell, J.K., 1996, "Pulse transmission system for measuring wave propagation in soils," *Journal of Geotechnical Engineering*, American Society of Civil Engineer, Vol. 122, No. 4, pp. 302 – 308

Osinubi, K. J., Eberemu, A. O., Gadzama E. W., J. E., Ijimdiya, T. S., (2019). Plasticity characteristics of lateritic soil treated with Sporosarcina pasteurii in microbial-induced calcite precipitation application. *SN Applied Sciences* 1:829 | https://doi.org/10.1007/s42452-019-0868-7

Osinubi, K. J., Eberemu, A. O., Ijimdiya, T. S., Etim, R. K. (2021). Microbial-Induced Calcite Precipitation Study on the Plasticity and Compaction Characteristics of Lateritic soil treated with Bacillus megaterium in Urea-CaCl2 Culture Medium. 2nd International Conference on Sustainable Infrastructural Development (ICSID), Theme: Sustainable Infrastructural Development (Virtual), Track 5: Geotechnics and Transportation Infrastructure, Covenant University, Ota, Ogun state, Nigeria, 27–28 July. *IOP Conference Series: Materials Science and Engineering* 1036 012031, pp 1-13. doi:10.1088/1757-899X/1036/1/012031

Rebata-Landa, V. (2007). Microbial Activity in Sediments: Effects on Soil Behaviour. Georgia Institution of Technology, PhD thesis.

Rowshanbakht, K., Khamehchiyana, M., Sajedib, R H and Nikudela, M. R. (2016). Effect of Injected Bacterial Suspension Volume and Relative Density on Carbonate Precipitation Resulting from Microbial Treatment. Journal of Ecological Engineering Vol 89, pp 49-55. https://doi.org/10.1016/j.ecoleng.2016.01.010

Shi, Q., Padilla, M. and Houston, W.N., 2007, "Comparison of field wave velocity and velocity of ultrasound through a soil specimen under laboratory condition," *Proceedings of the Sri Lankan Geotechnical Society's First International Conference on Soil & Rock Engineering*, Vol. 1.

Slavova, D.Z., Weidinger, D.M., Sevi, A.F. and Ge, L. (2010). "Evaluation of compacted silt characteristics by ultrasonic pulse velocity testing," *GeoFlorida 2010: Advances in Analysis Modeling & Design*, American Society of Civil Engineer, Geotechnical Special Publication No. 199, February, pp. 1284 – 1293. DOI: 10.1061/41095(365)128

Stocks-Fischer, S., Galinat, J.K. and Bang, S.S. (1999). Microbiological precipitation of $CaCO_3$. *Soil Biologyand Biochemistry*-Elsevier, 31 (11): 1563–1571.

van Paassen L. A., Ghose R, van der Linden TJM, van der Star WRL, van Loosdrecht M.C.M. (2010). Quantifying bio-mediated ground improvement by ureolysis: large-scale biogrout experiment. *Journal of Geotechnical and Geoenvironmental Engineering*- ASCE, 136(12):1721–1728.

Vinay M, Vinay A, A V Pradeep Kumar (2019). Ultrasonic Pulse Velocity Assessment of Cement Stabilized Soil. *International Journal of Scientific Research and Engineering Development* vol. 2(3): 901 – 905.

Wang Yuze; Charalampos Konstantinou; Kenichi Soga; Jason T. DeJong; Giovanna Biscontin; Alexandre J. Kabla (2022). Use of microfluidic experiments to optimize MICP treatment protocols for effective strength enhancement of MICP-treated sandy soils. Acta Geotechnica, 1-22. https://doi.org/10.1007/s11440-022-01478-9(0123456789.

Yesiller, N., Inci, G., and Miller, C. J., (2000), "Ultrasonic testing for compacted clayey soils," Advances in Unsaturated Geotechnics, ASCE GSP 99, C. D. Shackelford, S. L. Houston, and N.-Y. Chang, Eds., ASCE, 54-68.

Yohanna, P., Eberemu, A. O., Ijimdiya, T. S., Osinubi, K. J. (2022). The effect of Bacillus coagulans and moulding water content on the unconfined compressive strength of lateritic soil. Engineering Science & Technology 3(1) 69-83.

PAPER 51 – DEVELOPMENT OF SUSTAINABLE CONCRETING USING RHA BLENDED BIO SELF-COMPACTING CONCRETE INCORPORATING *Bacillus subtillis* AND DIFFERENT FILLERS

Taku, J. K[1*], Tyozenda, J. A.[2], Amartey, B.[3], Agber, T.[4]

[1]Department of Civil Engineering, Joseph Sarwuan Tarka University Makurdi
[2]ZwaTiF Engineers Ltd, Abuja
[3]Department of Civil Engineering, Ahmadu Bello University Zaria
[4]Directorate of Physical Planning, Benue State University Makurdi
[*]Email: kumataku@yahoo.com

ABSTRACT
Attaining a sustainable construction environment requires the use of readily available construction materials that are cheap and eco-friendly. This will make the attainment of the sustainable development goal of adequate mass infrastructure for all achievable. Self-Compacting Concrete is a special concrete that can be modified by the addition of fillers and supplementary cementitious materials to improve its overall properties and aid in its domestication in Nigeria. This research investigates the effect of the use of Rice Husk ash at 15% replacement of Portland Limestone Cement and incorporation of *bacillus subtilis* on the fresh state properties, and durability, measured using sorptivity and water absorption as well as the strength characterization at 7 and 28 days. The results showed an improvement in all the properties measured with the incorporation of bacteria and RHA. The use of fillers affected the microstructural characterization with the Limestone powder, crushed rock dust filler and cement kiln dust all having a positive impact on the microstructural and permeation properties of the SCC. It is concluded that the introduction of *bacillus subtilis*, into an RHA and LP, CKD or CRD ternary blended SCC improves its properties and its usage in concreting can impact positively sustainability in the built environment.

KEYWORDS: *bacillus subtilis,* Fillers, Rice Husk Ash, Self-Compacting Concrete, Sustainable Concreting

1. INTRODUCTION

Attaining a sustainable construction environment requires the use of readily available, affordable, and eco-friendly construction materials to achieve the sustainable development goal of providing adequate mass infrastructure for all, especially in less developed regions. Concrete is the most widely used construction material on earth, and there are continuous efforts to improve its strength and durability by incorporating materials that are readily available and can enhance its overall properties (Taku, et al 2021). One such special concrete that has revolutionized the construction industry is self-compacting concrete (SCC), which can be modified by adding fillers and supplementary cementitious materials to enhance its overall properties and facilitate its adoption in the Nigerian construction industry. Research has shown that the use of pozzolanic materials in the partial replacement of cement as well as the use of non-reactive fillers helps improve the basic properties of self-compacting concrete (Karatas, et al., 2020)

Ozawa and Maekawa (2001) studied the use of fly ash and limestone powder as supplementary cementing materials in self-compacting concrete, with a focus on the viscosity and hydration characteristics of the concrete and reported an overall improvement in the properties while. Khayat et al. (2003) investigated the performance of self-compacting concrete containing various supplementary cementing materials. Akbari and Ramezanianpour (2017) investigated the performance of self-compacting concrete containing RHA in terms of its resistance to chloride ion penetration and Liu and Li (2019) conducted a comprehensive review on the use of rice husk ash (RHA) in self-compacting concrete, highlighting its potential as a filler material. Calcined clay, Limestone Powder, Cement Kiln Dust, and crushed rock dust have variously been used in self-compacting concrete with exciting results (Siddique, et al.,2015; Siddique et al. 2019; Taku et al., 2022; Babatunde, et al. 2022). The self-healing property of concrete can be enhanced by the adoption of Microbial induced calcite precipitation (MICP) technology in concrete, whereby a rhyolitic bacterium, in the presence of nutrients and moisture, deposits calcium calcite in the concrete pores, thereby improving the overall properties of concrete and enhancing self-healing (Adepegba & Adegbola, 2021). Recent research on SCC using sporosarcina pasteurii shows an improvement in the permeation characterization and strength of self-compacting concrete at the early and later ages of the concrete

(Taku et al., 2023). Other research using other bacteria also reported similar improvements in concrete properties (Subramanian & Bose, 2010; Vijay & Murma, 2018; Osinubi et al., 2019; Alisha, et al., 2020; Luhar, et al., 2022)

This research investigates the effect of incorporating RHA at 15% replacement of Portland Limestone Cement and *bacillus subtilis* bacteria on the properties of self-compacting concrete using different fillers, namely limestone powder, crushed rock dust, and cement kiln dust. The study evaluates the fresh state properties, durability (measured using permeation properties of sorptivity and water absorption), microstructure, and strength characteristics of the SCC at 7 and 28 days.

4. METHODOLOGY

Portland Cement of grade 42.5N was used for this research work and the properties conform to the provisions of BS 12 (1991).
The grading and particle shapes of aggregates are significant factors in the production of SCC. Thus, the aggregates were carefully chosen to fit into the specifications for aggregates for Self-compacting concrete as stipulated by EFNARC (2005). Consequently, River sand from River Benue and crushed rocks of maximum particle size 10mm were used as fine and coarse aggregates respectively.

Sandcrete SPR-300 Super-plasticizer, manufactured by the WAFA group of companies was used for this research. The specific gravity, pH and chloride content of the SP are 1.08, 6.5 and less than 0.1% respectively.

The Bacteria (*bacillus subtilis*) was obtained from the soil while the calcium lactate was obtained at a local chemicals store in Makurdi. Both the Bacteria culture and preparation of the cementation reagent were carried out at the Microbial Laboratory in the Department of Microbiology, Joseph Sarwuan Tarka University Makurdi.

a. Fresh State Properties of Self-Compacting Concrete

The fresh state properties of the SCC were determined using the procedure stipulated in EFNARC (2005) to determine the flow time, the time taken to reach a diameter of 500mm, the flow diameter and the V-Funnel flow, while the L box and J rings were used to determine passing and filling ability of the concrete

b. Permeation and Strength properties

The permeation properties of the Self-Compacting Concrete were determined in accordance with the provisions of BS 1881-122 for sorptivity and water absorption of concrete. The test for sorptivity was carried out at 7 and 28 days for each mix to evaluate the effects of the bacteria, rice husk ash and filler on the rate of water absorption through interconnected capillary poles. The compressive and split tensile strengths were determined using 100x100x100mm^3 cubes and 100x200mm^3 respectively in accordance with the procedure set out in BS EN 12390-9 and BS EN 12390-10

c. Microstructural Characterization

The microstructural characterization was carried out using SEM and EDX at the Department of Chemical Engineering, Ahmadu Bello University Zaria

5. RESULTS AND DISCUSSION

a. Oxide Composition of Filler Materials

Table 1 gives the oxide composition of the materials used in the research. It can be seen that it is RHA and CRD has a combined SiO_2 + Al_2O_3 + Fe_2O_3 of over 70%, however, only the RHA is pozzolanic since the silica, aluminate and ferrite in the RHA exists in the amorphous state. The CRD exists in crystalline form and so the SiO_2 is non-reactive and hence does not possess pozzolanic properties (Kibriya & Tahir, 2017). LP and CKD contain more non-reactive calcite. Thus, while RHA is suited as a cement replacement material, CRD, CKD and LP can only serve as non-reactive fillers.

Table 1. Oxide Composition of Materials

Oxide	SiO_2	Al_2O_3	Fe_2O_3	CaO	MgO	Na_2O	K_2O	SO_3	LOI	Surface Area (cm^2/g)	Specific gravity
RHA	77.19	6.19	3.65	52.88	1.45	-	1.82	0.16	5.43	2400	2.20
OPC	10.41	6.10	3.18	70.26	4.09	0.57	1.17	3.04	6.72	3200	3.15

LP	8.97	1.02	0.37	46.77	2.38	0.02	0.13	-	39.5	1300	2.76
CKD	22.07	4.33	4.10	67.16	1.08	0.096	0.18	0.29	0.69	2065	1.15
CRD	58.4	15.9	8.1	3.42	1.98	4.14	2.82	-	2.82	2870	2.59

2.2 Fresh State Properties

The filling and passing ability, as well as the flowability characteristics of the ternary blended Bio-SCC were carried out to determine the effect of the RHA, Fillers and bacteria on the fresh state properties of the SCC. The result is presented in Tables 2 and 3 for filling and passing ability testing and flowability testing respectively

Table 2. Filling and Passing Ability Testing

	L-Box Test results						**J-Ring Tests results**		
ID mark	**Filler Material**	**H_1**	**H_2**	**H_2/H_1**	**T_{200} (s)**	**T_{400} (s)**	**d_{Jx} mm**	**d_{Jy} mm**	**SF_J - (mm)**
T1	0	7.7	7.4	0.96	0.80	1.93	630	630	630
T2	CRD	7.6	7.4	0.97	0.53	1.86	697	700	699
T3	CKD	7.3	7.2	0.99	0.40	1.13	700	700	700
T4	LP	7.4	7.1	0.96	0.67	1.40	700	706	703

Table 3: Flowability Testing – Slump Flow and V-funnel Testing

ID mark	**Filler Material**	**t_{500} (s)**	**Viscosity class**	**t_{flow} (s)**	**Slump flow (mm)**	**SCC class**	**V_{funnel} - time (s)**
T1	0	3.42	VS1/VF1	3.64	655	SF2	6.90
T2	CRD	4.72	VS1/VF1	4.48	710	SF2	8.30
T3	CKD	3.62	VS1/VF1	4.63	710	SF2	7.85
T4	LP	3.78	VS1/VF1	4.60	670	SF2	7.60

EFNARC (2005) specifies the following limits for the fresh state properties; Slump: 650 to 800mm; T_{500}: 3 to 7 seconds; V_{funnel}: 8-12 seconds; H_2/H_1: Closer to 1. It can be seen that all the samples met the flowability, passing ability and filling ability criteria, irrespective of the filler material used. Generally, the fines content and cementitious content determine the fresh state properties of the SCC. Research has shown that the bacterial content does not affect the fresh-state properties (Taku et al 2023). It can also be seen that even though all the samples met the specifications of EFNARC (2005), the higher the surface area of the particles of the filler, the less the flowability as the water demand is generally higher.

2.3 Permeation Characterization

The permeation properties were measured in terms of the water absorption and sorptivity in water and acidic environment. Figs. 1.0 presents the result of the Variation of water absorption with age for SCC containing the various filler. It can be seen that the water absorption decreased with age irrespective of the filler used. The same applies even when no filler was used. The absorption of water into the concrete depends on the pore spaces in the concrete. As the concrete ages, those spaces are filled up by the products of hydration, the products of the pozzolanic reaction, the calcium calcite precipitated by the bacteria and also the filler effect. Apart from filling the pore spaces, the fillers bring better packing and improve concrete durability (Kibriya & Tahir, 2017; Diagne, et al., 2021).

.

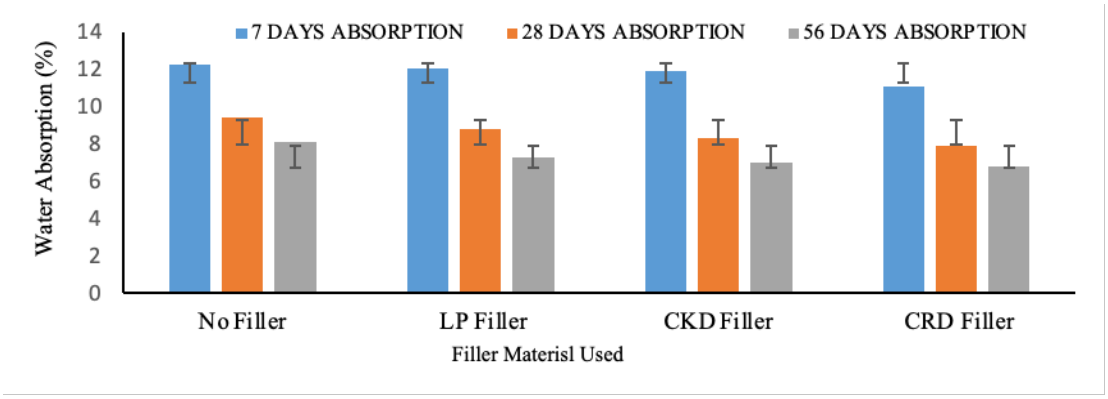

Figure 1: Variation of Water Absorption with Curing Age

The result of the Sorptivity behaviour of the ternary blended SCC in a normal curing environment and the acidic medium at different ages is given in Figure 2, where 7D-W, 14D-W, 28D-W, 56 D-W stands for curing age in days in normal water and 7D-A, 14D-A, 28D-A, 56D-A represents curing in acidic medium respectively.

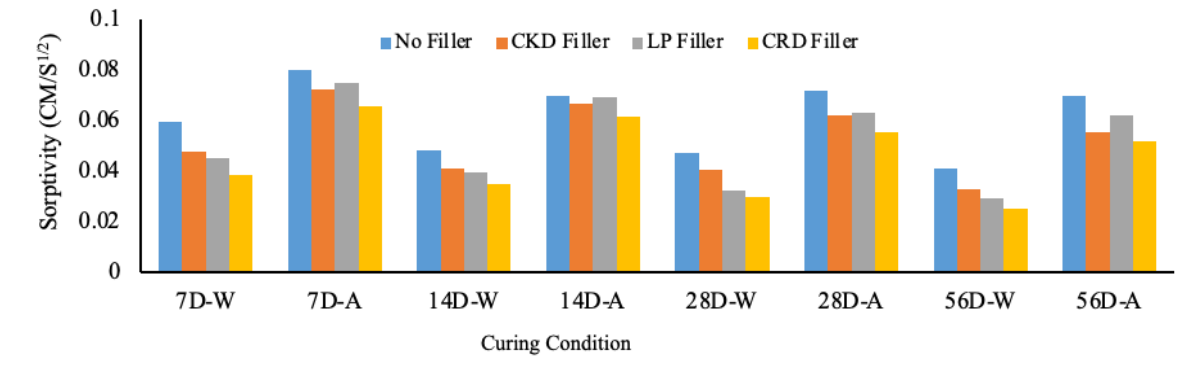

Figure 2: Variation of Sorptivity with Filler Type and Curing Condition

The sorptivity decreased with age as all the samples showed better permeation as they aged. The sorptivity performance for samples cured in the water proved better than that in Acid. This is a result of the inhibition of the calcite precipitation by the bacteria as well as the deterioration of the concrete matrix which leaves it more porous. The performance of the SCC incorporating filler is better than that without filler due to the filling of the pore spaces by the filler as well as the filler effect. Overall, CRD blended SCC showed better performance in normal conditions and acidic curing conditions. The result agrees with the works by El-Gamat, et al., (2012); Vaezi et al (2019) and Kaur et al (2021).

2.4 Strength Characterization

The effect of the RHA, *bacillus subtilis* and different fillers on the compressive, flexural and tensile strength was determined by testing samples at 7-, 28- and 56-days curing age for compressive strength and 7 and 28 days for split tensile and flexural strength. The result of compressive strength testing is presented in Figure 3.

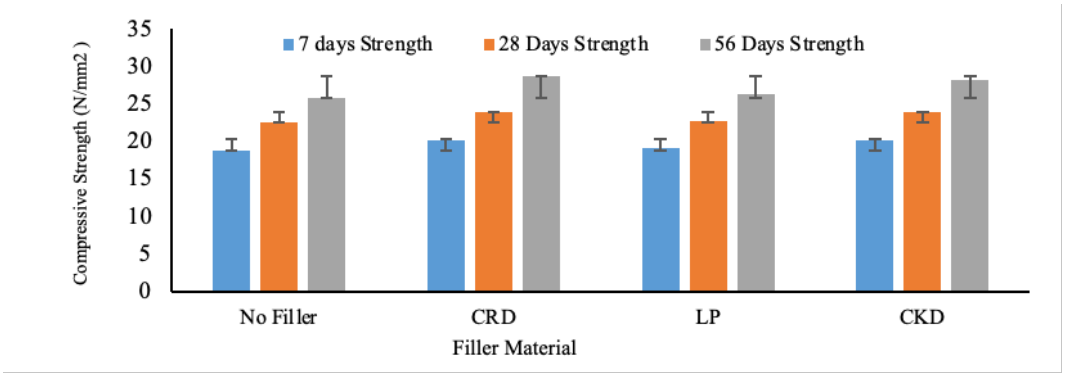

Figure 3: Variation of Compressive Strength with Age

The strength increased with age and the presence of filler, with the SCC containing the fillers showing higher strength development at all ages as compared to the without filler. Generally, the pozzolanic reaction, the hydration reaction and calcite deposition by the bacteria all contribute to strength development. In the case of the concrete with fillers, however, the fillers not only affect the porosity and microstructure of the concrete but also the reaction of cement. According to Moosberg-Bustnes et al (2004) and Diagne et al (2021), Fillers are materials whose function in concrete is based mainly on size and shape and they can interact with cement to improve particle packing and give the fresh concrete other properties, and even to reduce the amount of cement in concrete without loss of strength.

The result of split tensile and flexural strengths presented in Table 4 shows a similar pattern as the compressive strength.

Table 4. Flexural and Split-Tensile Strength Data

		Flexural Strength (N/mm^2)		Tensile Strength (N/mm^2)	
Mix	Filler Material	7 Days	28 Days	7 Days	28 Days
T1	No Filler	3.04	3.33	2.14	3.42
T2	CKD	3.11	3.38	2.17	3.44
T3	LP	3.07	3.35	2.22	3.48
T4	CRD	3.15	3.42	2.25	3.52

2.5 Microstructural Characterization

The Microstructural evolution of the SCC with the addition of RHA, *bacillus subtilis* and fillers was investigated using Standard Electronic Microscopy (SEM) analysis and the result for the microstructure at 28 days of curing is presented in Figure 5.

Figure 5: SEM Result for (a) CRD @ 28 days (b) LP at 28 days (c) CKD at 28 days

Figure 5 shows that the microstructural evolution of the SCC with the different fillers have distinct microstructures, due to the differing effect of each filler. This is due to the differences in particle sizes of the fillers as well as the effect on cement hydration.

6. CONCLUSION

The research shows that sustainable concreting can be achieved by the use of Rice Husk ash at 15% in replacement of Cement; the application of Microbial induced calcite precipitation and the use of readily available materials like limestone powder, Cement Kiln Dust and Crushed rock dust in Self-compacting concrete to improve the permeation and strength of SCC while also minimizing cost and ensuring environmental preservation. The SCC

properties are optimized by the combined pozzolanic action of RHA, the calcite precipitation by bacillus subtilis and the filler effect of the different fillers. It is also concluded that irrespective of the filler used, the filler particle size and shape are the determining factors of the level of effect the filler will have on the concrete properties.

ACKNOWLEDGEMENT

The Department of Microbiology and Department of Civil Engineering, JS Tarka University Makurdi are acknowledged for making their laboratories available for research.

REFERENCES

Adepegba, D., & Adegbola, O. (2021). Incorporation of Bio Materials for Sustainable Development in the Construction Industry: A Review. *Journal of Building Engineering*, 101105.

Akbari, R., & Ramezanianpour, A. A. (2017). Performance of self-compacting concrete containing rice husk ash subjected to chloride ion penetration. *Construction and Building Materials*, 151, 174-181.

Alisha, Sk., Rohit, P., Sachin, K. S. N., Rajesh, B. V. (2020): Self-healing Concrete using Bacteria, *The International Journal of Analytical and Experimental Model Analysis, 12(7): 3164-3170*

Babatunde, O. Y., Mvero, J., Muluku, R., et al. (2022): Effects of filler types on the microstructural and engineering properties of waste plastic binder composite for construction purposes, Civil and Environmental Engineering,19(1): 1-18, https://doi.org/10.1080/23311916.2022.2143057

Diagne, M., Dia, I. and Gueye, O. (2021) Influence of Types of Fillers on Workability, Bleeding, Compressive Strength, and Degree of Compaction of Hydraulic Concrete. *Materials Sciences and Applications*, **12**, 276-296. https://doi.org/10.4236/msa.2021.126019

EFNARC (2005): The European Guidelines for Self-Compacting Concrete Specification, Production and Use, www.efnarc.org

El-Gamal, S., Shaheen, Y., & Almusallam, T. (2012). The Effect of Nano-Silica on the Properties of Self-Compacting Concrete. *Construction and Building Materials*, 30:80-86.

Kibriya, T. and Tahir, L. (2017) Sustainable Construction—Use of Stone Dust as Plasticiser in High Strength SCC with Blended Cement. *World Journal of Engineering and Technology*, **5**, 412-420. https://doi.org/10.4236/wjet.2017.53035

Karatas, M., Benli, A., Arslan, F. (2020): The Effects of Kaolin and Calcined Kaolin on the Durability and Mechanical Properties of Self Compacting Concrete Mortars subjected to High Temperatures, Construction and Building Materials, 265: 1-12. https://doi.org/10.1016/j.conbuiltmat.2020.120300

Liu, J., & Li, Z. (2019). Application of Rice Husk Ash in Self-Compacting Concrete: A Review. *Construction and Building Materials,* 198: 365-376.

Okamura, H., & Ouchi, M. (2003). Self-Compacting Concrete. *Journal of Advanced Concrete Technology*, 1(1): 5-15.

Osinubi, K. J., Eberemu, A. O., Gadzama, E.W. *et al.* (2019): Plasticity Characteristics of Lateritic Soil treated with *Sporosarcina pasteurii* in Microbial-Induced Calcite Precipitation Application. *SN Appl. Sci. **1**(829): 1-12. https://doi.org/10.1007/s42452-019-0868-7*

Ozawa, K., & Maekawa, K. (2001). Study on Self-Compacting Concrete Containing Fly Ash and Limestone Powder–Viscosity and Hydration Characteristics. *Cement and Concrete Research*, 31(2): 193-198.

Siddique, R., Singh, M., & Kaur, I. (2015). Utilization of Rice Husk Ash as Partial Replacement with Cement in Self-Compacting Concrete. *Journal of Cleaner Production,* 92: 68-76.

Siddique, R., Singh, M., & Kaur, I. (2019). Application of Rice Husk Ash in the Self-Compacting Concrete: A Review. *Construction and Building Materials*, 198: 365-376.

Subramanian, K., & Bose, S. (2010). Microbially-Induced Calcite Precipitation in Construction Materials: A Review. *Construction and Building Materials*, 24(11): 2060-2071.

Taku, J. K., Amartey, Y., Ejeh, S., Lawan, A. (2021): Microstructural Characterization of Calcined Clay Blended Binary Self-Compacting Concrete, *Proceedings of the the 2021 Annual Conference of the School of Engineering, FUTA, Akure, (IARASETA 2021), October 6-8, 2021, pp290-313*

Taku, K., Amartey, Y., Ejeh, S., & Lawan, A. (2023). Properties of Calcined Clay and Limestone Powder Blended Bio-Self Compacting Concrete. *Journal of Civil Engineering and Materials Application*, *6*(4): https://doi.org/10.22034/jcema.2023.385305.1104

Vijay, K. & Murmu, M. (2018): Effect of Calcium Lactate on Compressive Strength and Self-Healing of Cracks in Microbial Concrete, *Frontiers of Structural and Civil Engineering https://doi.org/10.1007/s11709-018-0494-2*

PAPER 52 – CHARACTERIZATIONS OF SHEA BUTTER LEAF (VITTELLA PARADOXA) POWDER

Adesola, I. A[a], Yahya, M. D[b]

Department of chemical engineering, Federal university of technology, Minna Nigeria
Email: adesolaidowu77@gmail.com

ABSTRACT
The study investigated the phytochemical analysis, proximate composition, pH, and analytical enquiries of FT-IR, BET, and SEM-EDS of shea butter leaf powder. The leave was washed thoroughly under water to remove insoluble substances, later with distilled water, sundried for 14 days, ground and, sieved into powder by 60 um mesh size. The product was stored in an airtight container for further use. The qualitative analysis of the phytochemical study indicated 111.85mg/g flavonoid, 86.54mg/g tannins, 237.82mg/g phenol, 46.05mg/g alkaloids, and 535mg/g saponin. The proximate analysis shown 12.59% moisture content, 4.10% ash content, 12.34% crude fat, 12.25% crude protein, 17.80% crude fiber, and 40.92% carbohydrate content. The pH of the extract was 6.38. BET shown 182.5 area, 10.10cc/g pore volume, and 2.13nm pore size. FT-IR results indicated the presence of N-H, O-H, C-H, C N, C C, C O, C N, C C as functional groups present. SEM-EDS revealed the surface morphology. EDS shown the percentage in weight elemental compositions of the sample powder as 37.50% O_2, 29.64% Ca, 24.14% K, 6.07% Cl, and 2.65% Si. The results revealed the importance of Shea butter leave to process industries such as food processing industry, cosmetic and pharmaceutical industry, and as an adsorbent in waste water treatment.

KEYWORDS: Shea butter leaves, phytochemical screening, proximate analysis, and analytical studies

1.0 INTRODUCTION

The shea butter tree is otherwise called the Karite tree. It belongs to the family Sapotaciae, which comprises two major species. The two species are Vitellaria paradoxa, which was formerly called (i) Butyrospermum paradoxa, and (ii) Vitellaria parkii. It is perennial and peculiar to sub-Saharan Africa. The species of tree is found from Senegal to Uganda in Africa. This stretch can be described as a shea butter belt (Maanikuu & Peker, 2017). Solomon et al. (2017) established that *Butyrospermum paradoxa* (V. *paradoxa*) is more common in the western part of Africa, while the other species is prevalent in East Africa. Earlier in 2014, Obisesan et al. reported that the shea plant is mostly found in the wild in Nigeria. This could be found within Guinea, Sudan, and the Sahel.

2.0 MATERIALS AND METHODS

The fresh and health leaves of shea butter (V. *paradoxa*) was harvested in Gidan - kwano community, Minna in Bosso Local Government Area of Niger State, Nigeria. The plant part was identified at the department of Plant Biology, School of Life Science, Federal University of Technology, Minna, Niger state.

2.1 Preparation of Shea Butter Leave Powders

The harvested leaves were washed three times under running tap water and lastly with distilled water to remove any solid, dissolvable, or insoluble particles that were attached to the leaves. The thoroughly washed leaves were open-dried for two weeks, milled to a powder with a mechanical device, and sieved to remove any present shaft. The powder product was kept in an airtight container for further use.

2.2 Phyto – chemical Analysis

A phytochemical study was carried out to investigate the presence of some of the natural chemicals called polyphenols, which are antioxidants, in plant parts. These antioxidants are non-toxic, low-cost, helpful for traditional medicinal purposes, and, more recently, they serve as bio-reducing agents in the reduction of metallic salt to metallic ions during nanoparticle synthesis. The phytochemical study is carried out using the extract obtained from the plant powder.

2.3 Determination of pH

5 grams of shea butter leave powder were measured using a weighing balance and gently poured into a beaker containing 12.50 ml of distilled water. The two substances were mixed through a mechanical shaker for 15 minutes after the pH was measured using the pH meter (Akwu et al., 2019).

2.4 Proximate Analysis

Proximate analysis is a scientific and physical inquiry carried out to investigate the composition of micro- and macro-elements in a feed. The scientific tests include moisture content, ash content, crude fiber, crude protein, and crude fat. The analysis was done using the standard method of AOAC, 2000. The percentage composition of carbohydrates is determined by subtracting the sum of the values of moisture content, ash content, crude fiber, crude fats, and crude protein from 100. The percentage of dried matter is also obtained by deducting the percentage of moisture content from 100.

2.5 Analytical studies of Shea butter leave powder

The third goal of this objective is to characterize shea butter leave powder using the analytical instruments for FT-IR, BET, and SEM-EDS. FT-IR will be carried out to reveal the functional groups present in the leaf part of the plant. SEM will show the surface morphology; EDS will be used to determine the elemental composition; and BET will be carried out to reveal specific surface areas, pore sizes, and pore volume distributions of the material.

Phytochemical Screening

The results of the phytochemical study of shea butter leave extract presented in Table 1 indicated the presence of saponin, tannins, phenols, alkaloid and flavonoids.

Table 1. The qualitative and quantitative analysis of Shea butter leaf extract.

S /no	Phyto- chemical components	Test	Observation (coloration)	Inference	Mean values ±Sd (mg /g)
1	Phenol	Ferric Chloride	Brownish green / Black blue	P	233.8153 ±1.53
2	Flavonoids	Alkaline	Yellow	P	111.8455±1.48
3	Alkaloids	Mayer's	Cream/ Yellow precipitate	P	46.0512±0.78
4	Tannins	Ferric Chloride	Brownish green / Black blue	P	86.5382±0.61
5	Saponin	Foam	A foamy layer was observed	P	535. 8210±2.35

Gopalakrishnan K. et al. (2017) reported it to be a naturally occurring polyphenol in plants with the main characteristic of binding and precipitating proteins. Edem et al. (2016) also attributed its usage in the treatment of diseases to its antimicrobial properties. Agbo et al. (2014) submitted that compounds with high phenolic contents have a very good potential to neutralize free radicals. Hence, they are good antioxidants. The major reasons for the use of shea fruit ash in the local soap-making industry to cure skin-related diseases are discussed by Akoma et al. (2018).

3.2 Proximate Analysis

The results obtained from proximate analysis of shea butter leave powder indicated the various percentages compositions of the macronutrients found in the plant feed is shown in Table 2.

Table 2. Proximate Analysis of Shea Butter leaves Powder

S/No	Component	Shea Butter Leave Powder (%)
1	Moisture Content	12.59
2	Ash Content	4.10
3	Crude Fat	12.34
4	Crude Protein	12.25
5	Crude Fibre	17.80
6	Carbohydrate	40.92
	Total	**100.00**

The percentage of ash content in the leave part is carried out to reveal the mineral component in the organ. Lower report of ash content in plant species may suggest a low deposit of mineral elements in the plant. The carbohydrate content is reportedly higher in the leave of plants than in any other parts. This could have been to the fact that photosynthesis takes place in the plant – part Akwu et al., (2019). The percentage of composition of moisture content in a plant determines its absorption capacity and assimilation rate. According to Ngaha et al. (2016), plants with high moisture content have low storage ability, which gives them a higher advantage for industrial use. The result obtained using a pH meter to determine the hydrogen ion concentration of the extract shows that the pH is 6.38

3.4 Analytical Studies of Shea Butter Leave Powder

3.4.1 Fourier Transform Infrared (FT – IR)

Fourier transforms infrared spectral analysis carried out was aimed at identifying the presence of various functional groups present in shea butter leave powder. The functional groups which were revealed by the FT-IR include the O-H stretch, C-H stretch, C=O stretch, C-O stretch, C-C stretch, C=C stretch and the N-H stretch as shown in the FT -IR graph which shows the FT-IR spectra of shea butter

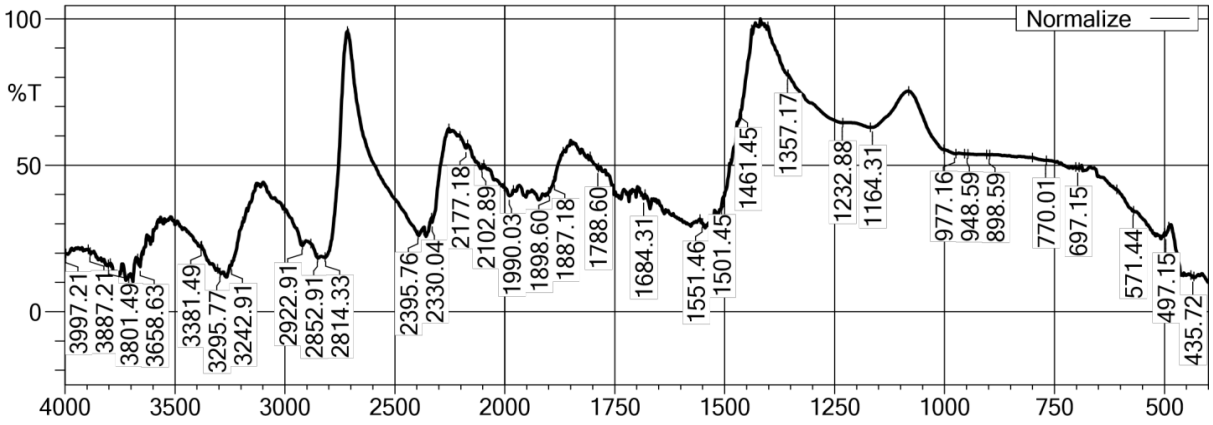

Figure 1. Fourier Transform Infrared (FT – IR)

3.4.2 Branauer-Emmett-Teller analysis (BET)

Bardestani et al. (2019) listed specific surface area and pore size as basic physical and chemical parameters that can be controlled while synthesizing adsorbents for environmental challenges. The specific surface area of an adsorbent plays a very vital role in the adsorption mechanism of heavy metals from aqueous solutions and, more importantly, in nanoparticle application. Based on the IUPAC classification of pore size, shea butter leaf powder falls under the mesopore grouping, which is recommended for bio-adsorbents. Table 3 shows the Branauer-Emmett-Teller analysis (BET)

Table 3. BET analysis of Shea butter leave powder

S/No	Characteristics	BET / BJH values
1	Surface Area (m^2/g)	182.5
2	Pore Volume (cm^3/g)	0.101
3	Pore Size (nm)	2.133

3.4.3 SEM- EDS

The results obtained for SEM revealed the surface morphology of the shea butter leaf powder. Unlike that of activated carbon or other carbonaceous materials, which reveal the presence of clogged pores and volatile organic compounds (VOC) on the surface of the raw adsorbent, Mohammad & Yahya (2021) found that the surface morphology of shea butter leave powder has irregular shapes with different dimensions and unequal pore sizes. Alhajali et al. (2022) revealed that the irregularities in the surface structure of plant part powder may have greatly contributed to removing heavy metal contaminants in wastewater. The quantitative tabulation of analytical EDS spectra as presented in Table 3.5 revealed the percentages in weight of 37.50% O2, 29.64% Ca, 24.14% K, 6.07% Cl, and 2.65 Si. The abundance of Ca, K, and Cl may favour the removal of heavy metals during effluent treatments. The presence of silicon may not be unconnected with the challenges of dust particles during open-air drying, which is still preferable to oven drying which can cause denaturalization of the organic matter that are present in leaves. Shown in Figures 2(a) and 2(b) are the surface morphology of shea butter leave powder and energy dispersive spectroscopy of shea butter powder, respectively.

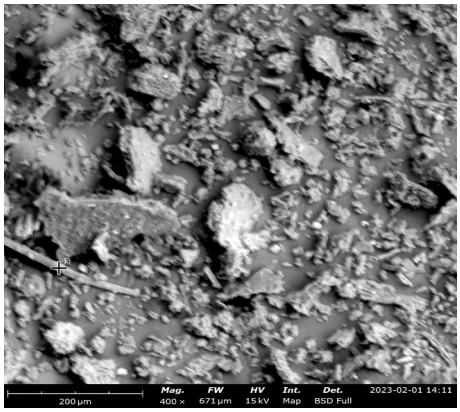

Figure 2. Surface Morphology of Shea butter leave powder

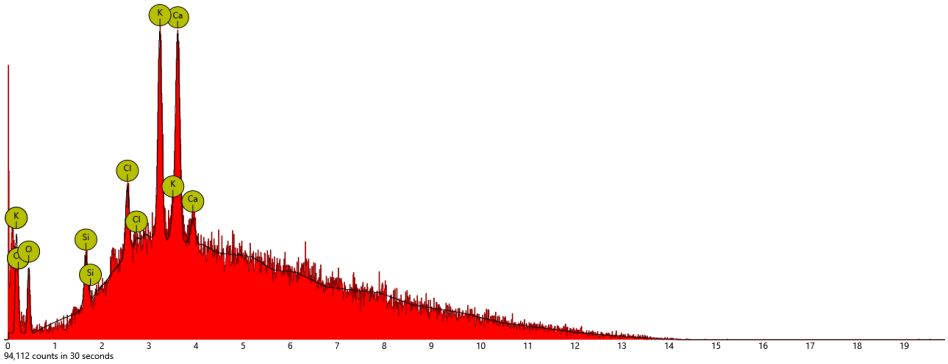

Table 5. Energy Dispersive Spectroscopy of Shea butter powder

Element Number	Element Symbol	Element Name	Atomic Conc.	Weight Conc.
8	O	Oxygen	59.09	37.50
20	Ca	Calcium	18.65	29.64
19	K	Potassium	15.57	24.14
17	Cl	Chlorine	4.32	6.07
14	Si	Silicon	2.38	2.65

4. CONCLUSION

Although many research studies have been reported on shea butter, most especially on the oil and the fruit, few have been reported on the leaf. This work-study examines the phytochemical screening, pH, proximate, and analytical studies of shea butter leaf powder. The results obtained in the phytochemical screening of shea butter leaves show that the plant part contains some natural chemicals called polyphenols, which are antioxidants and can be used in process industries such as food, cosmetics, pharmaceuticals, and in the preparation of nano-adsorbents for wastewater treatment. The results of pH show the extract is a good nano adsorbent. The results obtained from proximate analysis on moisture content composition show that the leave powder can be stored for industrial uses. The low percentage composition of ash content indicated that some elements were not present in the leaf powder. The results obtained for crude protein, crude fiber, crude fat, and carbohydrate content show that the leaf powder can be incorporated into animal feed compositions since its fruit is edible for humans and the shea butter is a natural antibiotic for humans, especially small children. The results of the analytical studies, as revealed by BET, show that both surface area and pore size of the leaf powder has physical and chemical properties that can be measured and controlled while synthesizing nano adsorbent. The results obtained from FT-IR reveal that shea butter leaf powder has an important chemical functional group that can aid adsorption techniques. The abundance of oxygen (O2) as shown by EDS confirms the presence of the hydroxy (OH) group. The presence of calcium (Ca) and potassium (K) tends to form complexes with heavy metals in water during the treatment process.

ACKNOWLEDGEMENT

This work was made possible by financial support from RONKEE Resources Ltd Abuja Nigeria.

REFERENCE

Abiodun B. A, Adewale A and, Abiodun O. O, (2019). Phytochemical And Proximate Analysis of Some Medicinal Leaves. *Clinical Medicine Research Volume 6 No 6 page* (209 – 214).

Agbo M. O, Uzor P. F, Akazie – Nneji U. N, Eze – Odurukwe C. U, Ogbatue U. B & Mbaoji (2014). Antioxidant, Total Phenolic and Flavonoid Content of Selected Nigeria Medicinal Plant.

Akoma O.A, Nma N.Y, Musa S.A and Salihu A.B (2018). Nutritional and phytochemical composition of Vitellaria paradoxa (Shea Fruit Pulp). International Journal of Biochemistry Research & Review.

Antia, B.S, Akpan E.J, Okon, P.A and Umoren, I.U (2006). Nutritive and anti- nutritive evaluation of sweet potatoes (Ipomoea batatas) leaves. Pakistan. J . Nutr. 5 (2) 166 – 168.

Alhajali, O, Ali Nizam A, Almostata R (2022). Application of Astacia Atlantica leaves powder As natural material to remove nitrate and phosphate ion from domestic wastewater by characterized Bio removal and phytotoxicity studies. *Journal of the Turkish Chemist. 9 (3)* 759 - 776

Asha S, Asha A and, Rajeshkumar S, (2016). Evaluation of Phytochemical Constituents and Antimicrobial Activity of Silver Nanoparticle Synthesized Ipomoea nil Against Selected Pathogens. Asian Journal of Pharmaceutical and Clinical Research

Akwu N.A, NaidooY, and, Singh M, (2019). A comparative Study of the Proximate, FTIR analysis and Mineral elements of the leaves and stem back of Grewia las

Akpoghelie J. O (2019). pH level, Ascorbic acid, Proline and, Soluble Sugar as Bio – indicator for Pollution. *Chemsearch Journal 8* (2) (41 – 49).

Bashiru .I, Umar A. I, Otitolaiye C.A and, Ayuba A.S (2019). Phytochemical screening, Proximate Analysis and Antioxidants Vitamins of Green Tea (Camellia simensis) Leaves consumed in Sokoto

metropolis Sokoto State Nigeria.Caliphate *Journal of Science and Technology Vol 1pp* (1 – 5).

Bardestani R, Gregory S.P and Serge K (2019). Experimental methods in Chemical Engineering: Specific surface area and pore size distribution measurement – BET, BJH, and DFT. *The Canadian Journal of Chemical Engineering Vol 97 (781 -2791)*

Caroling, G , Priyadhashini, M. N, Vinodhini, E, Ranjithan , A. M, Shanthi P (2015). Biosynthesis of Copper nanoparticle using aqueous guava extract of - characterization and study of antibacterial effect. *Int. J. Pharma Bio Sci* *5* (25 – 43).

Djekota C, Diouf D, Sane S, Mbaye M.S, Noba K (2014) Morphological Characterization of Shea Tree, (Vitellaria paradoxa subsp. paradoxa) population in the region of Mandoul in Chad. *Int. J. Biodiversity and Consevation*.

Edem B.E, Khan M.E, Ibok N.U & Dimlong L.I (2016). Qualitative & Quantitaive Phytochemical Screening and Proximate Composition of Bombax Buonopozense (Red Silk Cotton Tree) Stem back

Enaberuel L.O, Obisesan I.O, Okolo E.C, Akinwale R.O, Aisueni N.O and Ataya C.D (2014). Genetic Diversity of Shea Butter Tree (Vitellaria paradoxa) C.F Gaernt in the Guinea Savannah of Nigeria Based on Morphological Markers. *American –Eurasian Journal of Agric and Environmental Science 14* (7) 615 – 623.

Gautam, R. K., Mudhoo, A., Lofrano, G., & Chattopadhyaya, M. C. (2014). Biomass- Derived biosorbents for metal ions sequestration: Adsorbent modification and activation methods and adsorbent regeneration. *Journal of environmental chemical engineering*, *2*(1), 239-259.

Gopalakrishnan , K and Udayakumar, R. (2017). Phytochemical Content of leaf and stem of Marsilear quadrifolia (L.). *Journal of Plant Science and Phytopathology*

Ngaha N.M.I, Dahlan I, Massoma L.D, Mandengue S.H, and, Yusuf A.A (2016). Comparative Proximate Analysis of Leaves and Back of Alchornea Cordifolia. *Journal of Agriculture and Environmental Science Vol 5 N0 1,* page (200 – 216).

Nyarko G, Mahunu G.K, Chimsah F.A, Yidana J.A, Abubakari A.H, Abagali F.K, Quainou A,And Poudyal M (2012). Leaf and Fruit Characteristics of Shea (Vitellaria paradoxa) in Northern Ghana. *Research in Plant Biology, 2(3)* 38 - 45

Maanikuu, P. M. I and Peker, K (2017). Medicinal and Nutritional Benefits from Shea Tree – (Vitellaria *paradoxa*) *Journal on Biology, Agriculture and Healthcare Vol 7(22)*.

Muhammed, S.I and Yahya, M.D (2021). Removal of heavy metal ions from local Battery recycling wastewater using Functionalized corn husk derived activated carbon.

Kalu Achi. N ,Onyeabo .C, Ekeleme C.A – Egedigwe and, Onyeanula J.C (2017). Phytochemical, Proximate Analysis and Mineral composition of Aqueous extract of Ficus capensis leaves in south Eastern Nigeria. *Journal of Applied Pharmaceutical Science Vol 7* (03) pp 122.

Krstiv, V, Urosevic T, Pesovski B, (2018). A review on adsorbent for treatment of Water and wastewaters containing copper ions *Chemical Eng Sci*, 192, 273

Omoruyi B.O and Onyeneke E.C (2011). Proximate Composition, Phytochemical screening and Elemental Analysis of mistletoe (Tapinanthus bangwensis) leaves. *NISEB Journal Volume 11* No 3.

Pratap Chandran R (2017). Analysis of Proximate, Phytochemical Elemental composition and Antioxidant property of leaf of Alternanthera b*rasiliana* (I) kuntze MOJ *Food Processing and Technology Vol 4* Issue 3

Rajeswari A (2014). Evaluation of Phytochemical Constituents, Quantitative Analysi and Microbial Efficacy of Potential Herbs against Selected Microbes.

Sangoremi, A.A and Akens Hamilton A (2020). Elemental Composition and proximate Analysis of shea butter sold in Swali Market, Yenegoa Nigeria. International Journal of Environmental Agriculture and Biotechnology Vol 6 issue 1 Jan – Feb 2021.

Solomon O, Gold I. L, and Igene, L (2017). Assessment of Shea Fruit Processors in Niger State for Improved Livelihood and Entrepreneurial Activities. *Global Journal of Pure and Applied Science, Vol 24*, 17 – 23 doi: 10.4314/gjpas. V24i1.

Umar, A. Jimoh W.L.O, and Garba M.D (2011). Proximate analysis of Lepidium sativum leaves. Chem Search Journal Vol 2 No 1 – 2.

PAPER 53 – OPTIMIZING GEOPOLYMERIZATION PROCESS OF METABENTONITE-METAKAOLIN BASED GEOPOLYMER CONCRETE (BKGPC) USING RESPONSE SURFACE METHOD

A. Ahmed[1*], J. Abubakar[2], A. Lawan[3], A. Ocholi[4] and J. M. Kaura[5]

[1]Department of Civil Engineering, Federal University of Agriculture, Makurdi, Nigeria
[2]Department of Civil Engineering, Ahmadu Bello University, Zaria, Nigeria
[3]Department of Civil Engineering, Ahmadu Bello University, Zaria, Nigeria
[4]Department of Civil Engineering, Ahmadu Bello University, Zaria, Nigeria
Email: Amuinuahmed543@gmail.com

ABSTRACT
Carbon dioxide (CO_2) emissions from the production of Ordinary Portland Cement (OPC) contributed approximately 9% to greenhouse gases (GHGs) in the atmosphere which leads to global warming. Replacement of OPC in construction with supplementary cementitious materials (SCMs) is suggested by many researchers. Geopolymer concrete (GPC) strength characteristics for grades, mix proportions, and suitable precursors are major concerns in structural engineering. A mix design for a target compressive strength of 25 N/mm^2 with a Design of Experiment (DOE) using randomized block factorial design and laboratory investigations were conducted. Response Surface Method (RSM) analysis is employed for DOE and optimization of the geopolymerization process. Research findings in materials science and engineering led to the development of a mathematical model. The material was characterized using XRF and FTIR spectra, and the result of the XRF indicates that the chemical composition of the precursor conformed to BS EN 197:2011 for natural calcined pozzolans (Q). The FTIR result shows that polycondensation occurred at the end of the reaction and was accompanied by a water vaporization process. However, GPC exhibits a good compressive strength of 23.7 N/mm^2 with a NaOH molar concentration of 14 M and a Na_2Si_3O/NaOH ratio of 2.5 at a 28-day curing period.

Keywords: Geopolymer, Precursors, Alkaline, DOE, Optimization, Mathematical Model.

1. INTRODUCTION

Carbon dioxide (CO_2) emissions from the production of ordinary Portland cement (OPC) contributed approximately 9% to greenhouse gases (GHGs) in the atmosphere that lead to global warming (Mehta 2001; Lei et al., 2011). The replacement of OPC in construction with supplementary cementitious materials (SCMs) has been suggested by many researchers. Hafeez (2008); Karthikeyan et al. (2015) The geopolymerization process involves the activation of an alumino-silicate material or precursor from a geological source (meta bentonite, metakaolin) or an industrial by-product (fly ash, ground granulated blast furnace slag) with a strong alkali solution such as sodium silicates and sodium hydroxide, which is then mixed with aggregates to form a fresh geopolymer concrete (GPC) that is allowed to set, demoulded after 24 hours, and cured at 60 oC for another 24 hours (Xu and Van Deventer, 2000).

Researchers are suggesting partial or full replacement of ordinary Portland cement (OPC) in concrete construction with supplementary cementitious materials (SCMs) (Al-Bakri et al., 2011). Geopolymer is an emerging and innovative binder that can provide an environmentally friendly replacement for OPC (Bharat and Kamal, 2015). It has been estimated that geopolymer binder generates 85% less CO2 emissions and requires 60% less energy to manufacture than OPC (Duxson et al., 2007). Extensive research has been carried out on the development of geopolymer as a sustainable binder (Wallah and Rangan, 2021; Sumajouw and Rangan, 2006). Some recent studies have revealed that the positive effects of meta bentonite on the mechanical and microstructural properties of GPC are like those of conventional concrete with metabentonite or metakaolin. Mirza et al., 2009; Law et al., 2014). This study aimed at optimizing the geopolymer concrete strength parameters, and the following specific objectives were achieved: Establishing a mix design for a target compressive strength of 25 N/mm^2 and performing the design of experiment (DOE) using the Response Surface Method (RSM) conducting a laboratory experiment and using the exploratory data acquired from the lab to perform regression analysis and analysis of variance (ANOVA) to develop a mathematical model. Conducting microstructural characterization of the metabentonite/metakaolin-based geopolymer (BKGP) concrete products using Fourier transform infrared (FTIR) spectral Optimizing the response (compressive strength) properties of the BKGP concrete using RSM (Akbar et al., 2013)

2. THEORETICAL ANALYSIS

The polymerization process includes chemical reactions under highly alkaline conditions on Al-Si minerals, yielding polymeric Si-O-Al-O bonds as shown by equation (1), where M is the alkaline element, z is 1, 2, or 3, and n is the degree of polycondensation (Davidovits, 2008).

Mn [-(Si - O2) z - Al - O] n.H2O (1)

Figure 1 shows the optimization of the geopolymerization process by reshuffling the precursor (metabentonite and metakaolin) and the alkali solution (sodium silicates and sodium hydroxide) to form the best constituent combination and the optimum strength characteristic of the hardened geopolymer concrete (Lima-Guerra et al., 2014).

2.1 Response Surface Method (RSM):

In RSM, the standard factorial in a randomized block design, choosing a model type depends on the nature of accessible information and levels for each factor. For the most part, for an experiment matrix that has been as of now built up, the historical data or user-defined model is applied for the development and investigation of a model **(**Myers and Montgomery, 2002).

The polynomial equation of the correlation between the response variables and independent variables can be expressed in a general form as shown in equation 2.

$$Y = \beta_0 + \Sigma_{i=1}^{k}\beta_i X_i + \Sigma_{i=1}^{k}\beta_{ii}X_{ii}^2 + \Sigma_{j=2}^{k}\Sigma_{i\leq i\leq j}^{j=1}\beta_{ij}X_iX_j + \varepsilon \quad (2)$$

Where Y is the response, xi and xj are the independent variables (i and j are the range from 1 to k), β_o is the constant coefficient, β_i, β_{ii},β_{ij} are the coefficient for the linear, quadratic and interaction effects, and ε represent the error. The coefficient of correlation (R^2), ranging from 0 to 1 was employed to predict the fitness of the developed model. A highly significant and accurate model is indicated by R^2 close to 1 (Montgomery, 2017).

2.2 Optimization

The desirability function approach is one of the most widely used methods in the industry for the optimization of the response process. It is based on the idea that the "quality" of a product or process that has multiple quality characteristics, with one of them outside of some "desired" limits, is completely unacceptable. The method finds operating conditions ***x*** that provide the "most desirable" response values.

For each response, Yi(x), a desirability function di(Yi) assigns numbers between 0 and 1 to the possible values of Yi, with di(Yi) = 0 representing a completely undesirable value of Yi and di(Yi) = 1 representing a completely desirable or ideal response value. The individual desirabilities are then combined using the geometric mean, which gives the overall desirability D:

$$D = (d_1(Y_1) \times d_2(Y_2) \times \ldots \times d_k(Y_k))^{1/k} \quad (3)$$

with **k** denoting the number of responses. Notice that if any response ***Yi*** is completely undesirable **(*di*(*Yi*) = 0)**, then the overall desirability is zero. In practice, fitted response values ***i*** are used in place of the ***Yi***.
If a response is of the "target is best" kind, then its desirability function is with the exponents ***s*** and ***t*** determining how important it is to hit the target value. For ***s* = *t* = 1**, the desirability function increases linearly towards ***Ti***; for ***s* < 1, *t* < 1**, the function is convex, and for ***s*> 1, *t* > 1**, the function is concave.

$$d_i(\hat{Y}_i) = \begin{cases} 0 & \text{if } \hat{Y}_i(\boldsymbol{x}) < L_i \\ \left(\frac{\hat{Y}_i(\boldsymbol{x})-L_i}{T_i-L_i}\right)^s & \text{if } L_i \leq \hat{Y}_i(\boldsymbol{x}) \leq T_i \\ \left(\frac{\hat{Y}_i(\boldsymbol{x})-U_i}{T_i-U_i}\right)^t & \text{if } T_i \leq \hat{Y}_i(\boldsymbol{x}) \leq U_i \\ 0 & \text{if } \hat{Y}_i(\boldsymbol{x}) > U_i \end{cases} \quad (4)$$

If a response is to be maximized instead, the individual desirability is defined as with

$$d_i(\hat{Y}_i) = \begin{cases} 0 & \text{if } \hat{Y}_i(\boldsymbol{x}) < L_i \\ \left(\frac{\hat{Y}_i(\boldsymbol{x})-L_i}{T_i-L_i}\right)^s & \text{if } L_i \leq \hat{Y}_i(\boldsymbol{x}) \leq T_i \\ 1.0 & \text{if } \hat{Y}_i(\boldsymbol{x}) > T_i \end{cases} \quad (5)$$

T*i* in this case interpreted as a large enough value for the response.
Finally, if we want to minimize a response, we could use **T*i*** denoting a small enough value for the response.

$$d_i(\hat{Y}_i) = \begin{cases} 1.0 & \text{if } \hat{Y}_i(x) < T_i \\ \left(\frac{\hat{Y}_i(x) - U_i}{T_i - U_i}\right)^s & \text{if } T_i \le \hat{Y}_i(x) \le U_i \\ 0 & \text{if } \hat{Y}_i(x) > U_i \end{cases} \quad (6)$$

3. MATERIALS AND METHODS

3.1 Raw Materials

The bentonite clay used in this study was sourced, beneficiated, and heated at 105 °C for 24 h to remove the water content. The dried bentonite was crushed and ground (3000 cycles) in a ball mill to increase its fineness as cement (range of 100 m), calcined at 650 °C for two hours to improve its chemical composition, and acquired the metabentonite. Kaolin clay was sourced and processed, ball milled and calcined at 700 °C for two hours to improve its chemical composition and obtain the metakaolin.

Table.1 Chemical composition of Metabentonite and Metakaolin.

Components	SiO2	Al2O3	Fe2O3	Na2O	CaO	MgO	K2O
Metabentonite	51.10	26.01	13.89	0.01	6.04	0.02	0.43
Metakaolin	52.43	42.22	1.90	0.29	0.17	0.17	0.61

Fine aggregate was sourced locally and coarse aggregate was sourced from the quarry site and supplied to the laboratory and tests were carried out following BS EN 933-1 and BS EN 12620. Alkali (Sodium Hydroxide and Sodium Silicates**)** was sourced from a chemical supplier. The NaOH was in pellet form while Na_2SiO_3 was in the form of gel.

3.2 Mix Design:

In the study, 22-factor designs were considered to test two factors, A (bentonite) and B (alkali doss), each measured in percentage. If A has (a = 5; 10, 20, 30, 40, and 50) levels and B has (b = 5; 50, 60, 70, 80, and 90) levels, each complete replicate of the experiment will contain (a × b = 5 × 5 = 25) runs (or treatment combinations) is most commonly used for two-level factorial designs where the main effect can be estimated as the average change of the response variable (y) when the factor is changed from its low to its high level (Caijun, 1996). The interactions between the variables (bentonite, kaolin, and the alkaline activator) and responses (compressive strength) were determined from diagnostic, ANOVA, and 2D and 3D contour plots. The volumetric percentage of bentonite precursor and alkaline activator were selected as the factors and were coded as A and B, respectively, as shown in Table 1.

Table 1: Factors and Factor Levels Adopted

Factor	Name	Units	Type	Sub Type	Min.	Max.	Coded Low	Coded High	Mean	Std. Dev.
A	Metabentonite	%	Numeric	Discrete	10.00	50.00	-1	+1	30.00	14.19
B	Alkali Dosage	%	Numeric	Discrete	50.00	90.00	-1	+1	70.00	14.19

Twenty-five proportions of geopolymer concrete were used in this experiment for cube samples. The substitution of metakaolin by metabentonite was done in geopolymer concrete mixes at varying metabentonite proportions of (10 %, 20 %, 30%, 40% and 50 %) with five different volumetric percentages of alkaline activators of (50 %, 60 %, 70, 80, and 90 %) by mean DOE using randomized block factorial design in Design Expert 13.

3.3 Mixing Procedure for Geopolymer Concrete

The mixing method for geopolymer concrete was performed by adopting the traditional techniques used in the production of normal concrete. Firstly, all materials (bentonite, kaolin, fine aggregate, and coarse aggregate) were mixed in a dry condition in the concrete mixer for approximately three minutes (Pavithra et al., 2016). The alkaline solution was mixed for approximately two minutes. After that, the liquid activator component was added to the dry materials and mixed for four minutes in the concrete mixer (Rangan, 2011).

3.4 Preparation of Alkaline Solution for Geopolymer

The alkali activator materials (AAMs) are constituted of sodium silicate and sodium hydroxide and were mixed, stirred, and shaken for two minutes before use. The ratio of sodium silicates to sodium hydroxide (Na_2SiO_3/NaOH) used in this experiment was 2.5. Sodium hydroxide in pellet form has a high purity of more than 98% and could be dissolved in potable water 24 hours before use. The solutions had a suitable molecular concentration of 14 M. Twenty-four hours after preparation, NaOH solutions were added to the Na_2SiO_3 solutions for a 2.5 mix ratio.

3.5 Test Methods

The data to be followed in the developed models using RSM for optimization were evaluated in the laboratory analysis. To evaluate the mutual correlation with the variables, compressive strength at 28 days as a property of geopolymer concrete was taken as the response of interest. The geopolymer concrete specimens were cast, demolded after 24 hours, and oven dried at 600 °C for another 24 hours. The curing periods were 28 days for all the samples. The dry specimens were tested according to Provis and Van Deventer (2009) standards.

4. RESULTS AND DISCUSSION

4.1 Bonding Nature by FT-IR Spectra Analysis

Figure 2 shows the IR spectra of a metabentonite/metakaolin-based geopolymer (BKGP) concrete product with a 14 M molar concentration of NaOH and a Na_2SiO_3/NaOH ratio of 2.5. The IR spectral for BKGP concrete has the following bands: The vibrational frequency around 1006.4 cm-1 corresponding to the precursor material is shifted to 872 cm-1; this is due to the penetration of Al4+ atoms into the initial Si-O-Si-skeletal structures. The condensation of Si-O tetrahedra in geopolymer paste was confirmed. Symmetric stretching vibrations of -Si-O-Si- and -Al-O-Si- can also be identified near 730 cm1 and bending vibrations of -Si-O-Si- and -O-Si-O- in the 689 cm1 regions. The bending vibration of 1442.5 cm^{-1} corresponding to the CO_3^{2-} carbonate groups, 1651.2 cm-1 for H_2O crystallized, and 1792.8, 1919.6, 1979.2, 2102.2, and 2325.9 cm-1 vibrational plane Si-O

The absorption bands for BKGP concrete at (3194.3, 3254, 3339.7, 3432.9, 3466.4, 3567.1, 3645.3, 3675.2, and 3757.2 cm1) were observed due to the occurrence of stretching vibration of the -OH groups or bonded water. This result indicates that crystalline structures have been dissociated and changed due to the alkali activation process. The resulting silica-aluminium oxide species then reacted and formed oligomeric precursors. Furthermore, polycondensation occurs at the end of the reaction and is accompanied by the water vaporization process and this conforms to Brough and Atkinson (2002), Yang et al. (2020), and Fernandez-Jimenez and Palomo (2005).

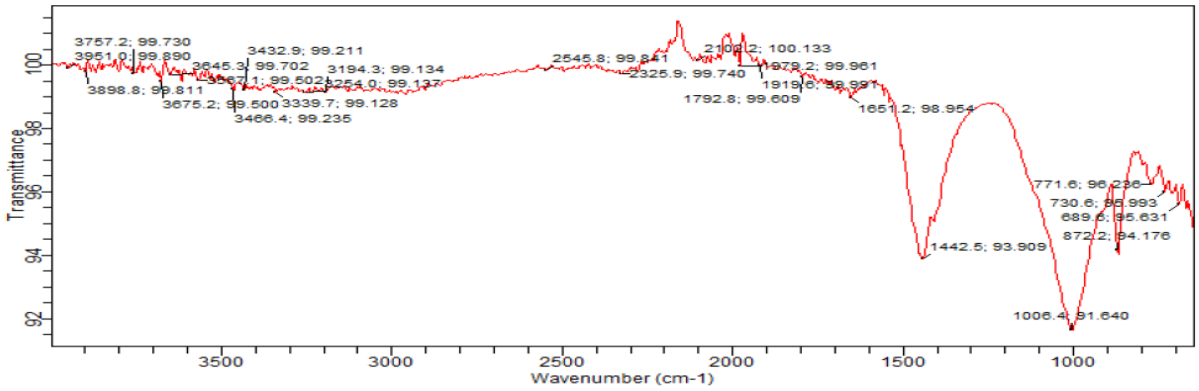

Figure 2: Shows the IR spectral for (BKGP) concrete product.

4.2 Response Surface Optimization:

The experimental data were made per the suggested DOE input from RSM. The resultant compressive strength of different mixes has been determined as a step for further analysis. The regression coefficient obtained for the experimental design, along with their corresponding p-values, are tabulated and shown in Table 2.

The p-value is 0.05, showing the high significance of all the input parameters, and it was considered for the construction of the RS model. The resulting regression model obtained an R-squared value of 84.54%, and the coefficients of determination (R-squared) are very near 100%, indicating the best fit of the data to the model assumed.

Table 2: Regression co-efficient for the RSM model.

Std. Dev.	0.84	**R^2**	0.85
Mean	20.28	**Adjusted R^2**	0.83
C.V. %	4.16	**Predicted R^2**	0.82
p-value	<0.01	**Adeq Precision**	37.87

The final model for 28 d compressive strength **CP8M2.0** of all mixes comprising all the terms is presented in Equation (7).

$$\textbf{(CP8M2.0)}^{1} = 22.84 + 0.6\ A + 1.02\ B + 2.56\ AB - 5.82\ A^2 - 2.33\ B^2 - 1.58\ A2B - 1.63\ AB^2 - 1.10\ A^2B^2 - 2.11\ A^3B - 2.84\ AB^3 + 4.19\ A^4 \quad (7)$$

The properties of formulated model for 28 d compressive strength **CP8M2.0** of the mix were presented in Table 2. The adequacy of the formulated models was validated by their degree of correlation (R^2). A high degree of correlation (R^2) was observed for the model based on their values being close to unity ($R^2 > 0.84$).

4.2 Analysis of Variance:

Diagnostic plots are vital to see if assumptions are met. Figure 3 shows the residual plot and regression diagram exhibiting the fits and the experimental observation for the attribute, compressive strength. As observed, there are no significant deviations from the normal probability line, and it can be fairly concluded that the assumptions of normality are satisfied.

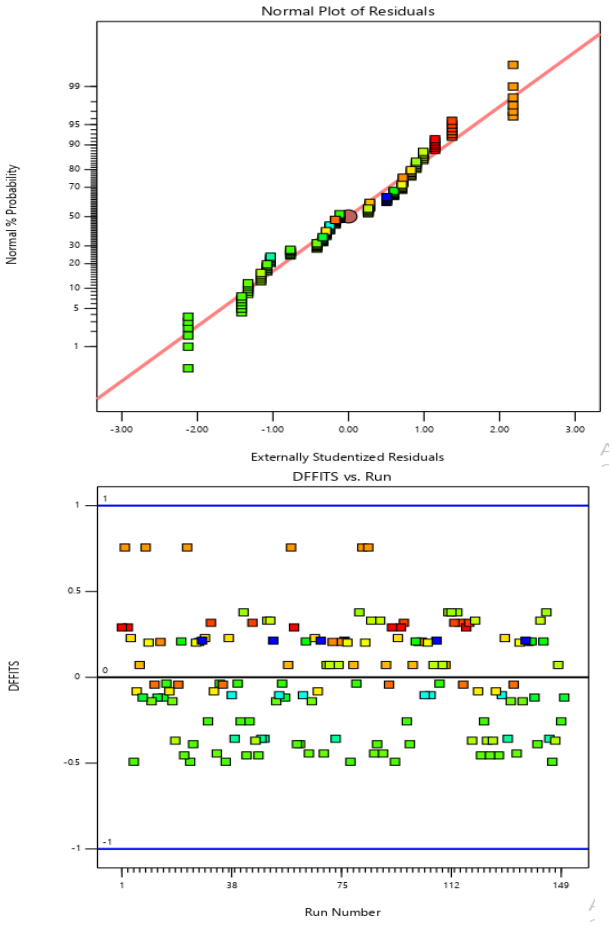

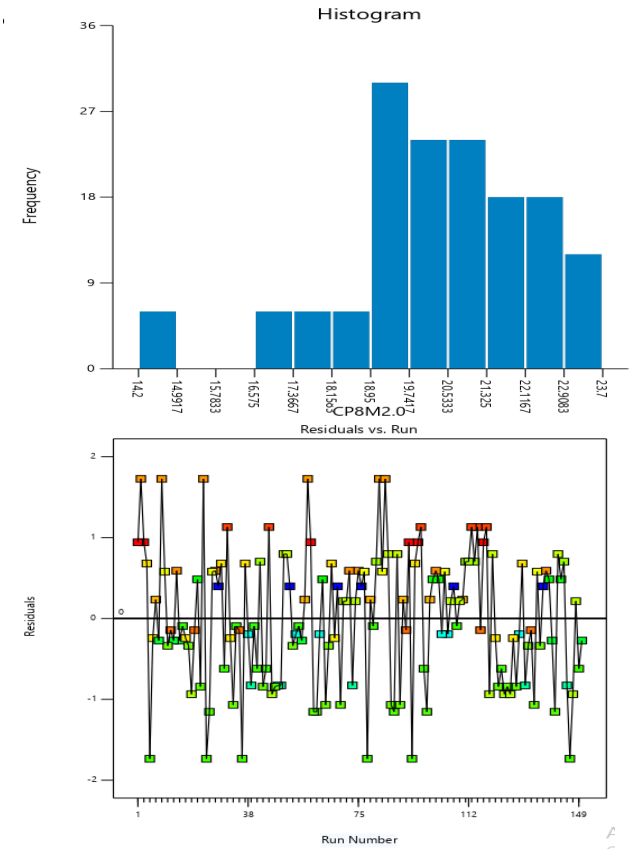

Figure 3. Residual plots for 28 d compressive strength **CP8M2.0** (Mpa) of BKGP concrete

The degree of influence on compressive strength and interactions among factors are described in Figure 4. The shape of the 3D response surface and contour can reflect the degree of interaction. Figure 4 is steep and elliptical as it represents significant interactions between the factors and this is similar to the result obtained by Petrus et al. (2016) and Danek et al. (2015).

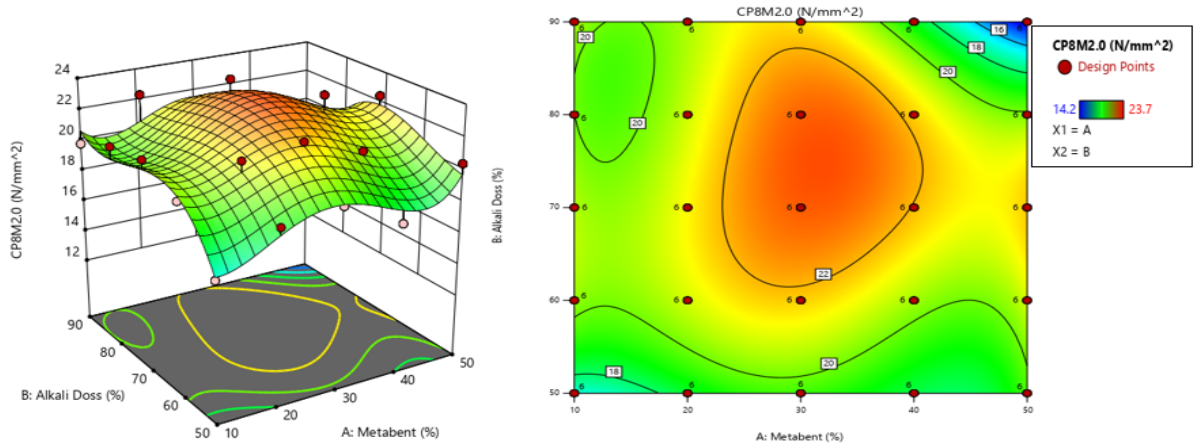

Figure 4. 3D-RS and contour plots showing the relation between Metabentonite, Alkaline dosage and strength

Figure 5 shows that the optimization of the 28-d compressive strength CP8M2.0 (Mpa) of BKGP concrete was at an optimum value of 23N/mm^2 and 96.8% desirability, and the percentage of metabentonite and alkaline dosage was 31.7% and 74.8%, respectively. This complies with Huang (2020).

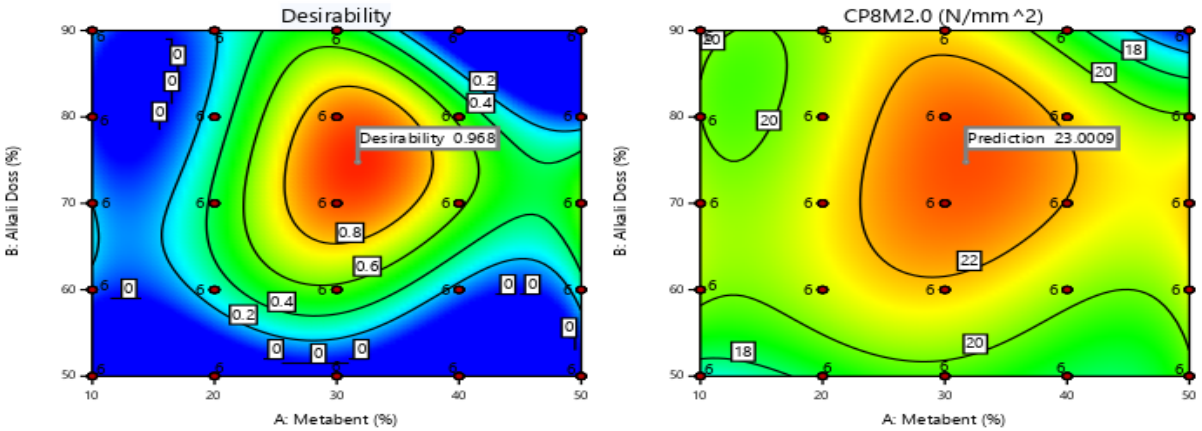

Figure 5: 2D-RS of Desirability and Optimum value of CP8M2.0 relations with factors (Metabentonite and Alkaline dosage)

5. CONCLUSIONS

Based on the experiments and analyses performed, the following conclusions were drawn:

i. The incorporation of metabentonite in metakaolin-based geopolymer concrete (GPC) is a step to further improve environmental sustainability. The formation of the matrix was due to the geopolymerization reaction that occurred.

ii. The mechanical properties of BKGP concrete are directly proportional to the bentonite substitution. About 31% of metabentonite showed maximum compressive strength among all BKGP concrete mixes due to the pozzolanic nature of the metabentonite/metakaolin-blend and alkali activation.

iii. The optimum preparation parameters are a metabentonite-metakaolin ratio of 31.7%, an alkali dosage of 74.8%, and a sodium silicate modulus of 2.5%. The maximum strength is predicted to be 23 MPa based on the optimum preparation parameters.

iv. The metabentonite/metakaolin-based geopolymer concrete with 23.6 MPa was prepared, which exhibited a relative error of 2.54%.

v. Metabentonite and metakaolin blended geopolymer BKGP concrete can be utilized as supplementary precursor material in geopolymer concrete upon thorough investigation (physical and chemical properties).

vi. BKGP concrete can be recommended as a sustainable concrete technology to reduce GHGs and global warming and can be utilized as a structural concrete material for residential construction and industrial infrastructure.

ACKNOWLEDGEMENT

The authors would like to thank every person or department that helped throughout the research. The supervisory team and the Civil Engineering Department, Ahmadu Bello University, Zaria Their careful reviews and constructive suggestions are gratefully acknowledged.

REFERENCE

Akbar. J, Bashir Alam, Muhammad Ashraf, Salman Afzal, Asfandyar Ahmad, and Khan Shahzada. (2013). "Evaluating the Effect of Bentonite on Strength and Durability of High PerformanceConcrete," *International Journal of Advanced Structures and Geotechnical Engineering*, vol. 02, no. 01, pp. 1–5.

Al-Bakri, M.M.; Mohammed, H.; Kamarudin, H.; Niza, I.K.; Zarina, Y. (2011). Review on fly Ash-based geopolymer concrete without Portland Cement. *J. Eng. Technol*. Res. 3, pp. 1–4.

Bharat B and Kamal K (2015) '' Geopolymer concrete-A Review'' *SSRG International Journal of Civil Engineering (SSRG-IJCE),* ISSN: 2348 – 8352, pp. 96-99.

Brough, A. R. and Atkinson, A. (2002). "Sodium silicate-based, alkali-activated slag mortars: Part I. Strength, hydration and microstructure. "*Cement and Concrete Research* 32(6), pp. 865-879.

Caijun, Shi. (1996). Strength, pore structure and permeability of alkali-activated slag mortars, *Cem. Concr. Res*. pp.

1789.

Danek, T.; Thomas, J.; Jelinek, J.(2015). Study of Interaction between Fly Ash-cement and Bentonite Matrices. *MATEC Web Conf*. 26, pp. 1003.

Davidovits, J., (2008). Geopolymer, Chemistry and Applications, *Institute of Geopolymer, 3rd(Ed),* France, Saint-Quentin. pp. 585.

Duxson, P.; Provis, J.L.; Lukey, G.C.; Van Deventer, J.S. (2007). The role of inorganic polymer technology in the development of green concrete. *Cem. Concr. Res.* 37, pp. 1590–1597.

Fernandez- Jimenez A. and J. Palomo, (2005*).* Composition and microstructure of alkali-activated fly ash mortar: effect of the activator, *Cem. Concr. Res*. pp. 1984.

Hafeez S.M., (2008). Preparation and Characterization of the Non-Portland Cement.*M.SC. Thesis, Zagazig Univ: Faculty of Science, Egypt*.

Huang, Y. (2020). Influence of Calcium Bentonite Addition on the Compressive Strength, Efflorescence Extent and Drying Shrinkage of Fly-Ash Based Geopolymer Mortar. *Trans. Indian Ceram. Soc*. 79, pp. 77–82.

Karthikeyan, M.; Ramachandran, P.R.; Nandhini, A.; Vinodha, R.(2015). Application of partial substitute of cement by bentonite in concrete. *Int. J. ChemTech Res*. 8, pp. 384–388.

Law, D., Adam, A., Molyneaux, T., Patnaikuni, I. and Wardhono, A. (2014*).* "Long-term durability properties of a class F fly ash geopolymer concrete." *Materials and Structures:* pp. 1-11.

Lei, Y. Zhang, Q. Nielsen, C., He, K.(2011). An inventory of primary air pollutants and CO2 emissions from cement production in China, 1990–2020. *Atmos. Environ*. 45, pp. 147–154.

Lima-Guerra, D.J.;Mello, I.; Resende, R.; Silva, R. (2014). Use of Bentonite and Organo bentonite as Alternatives of Partial Substitution of Cement in Concrete Manufacturing. *Int. J. Concr. Struct. Mater*. 8, pp. 15–26.

Mehta, P. K. (2001). *"*Reducing the Environmental Impact of Concrete" *ACI Concrete International* 23(10): pp. 61-66

Mirza, J.; Riaz, M.; Naseer, A.; Rehman, F.; Khan, A.; Ali, Q. (2009). Pakistani bentonite in mortars and concrete as low-cost construction material. *Appl. Clay Sci.* 45, pp. 220–226.

Montgomery DC (2017) *Design and Analysis of Experiments*, John Wiley and Sons.

Myers, R.H. and Montgomery, D.C. (2002) Response Surface Methodology: Product and Process Optimization Using Designed Experiments. 2nd Edition, John Wiley and Sons, New York

Pavithra, P.E.; Reddy, M.S.; Dinakar, P.; Rao, B.H.; Satpathy, B.; Mohanty, A. A (2016). Mix design procedure for geopolymer concrete with fly ash. *J. Clean. Prod*. 133, pp. 117–125.

Petrus, H.T.B.M.; Hulu, J.; Dalton, G.S.; Malinda, E.; Prakosa, R.A. (2016). Effect of Bentonite Addition on Geopolymer Concrete from Geothermal Silica. *Mater. Sci. Forum,* 841, pp. 7–15.

Provis, J. L. and Van Deventer, J. S. J. (2009). Geopolymer: structure, processing, properties and industrial applications. *J. L. Provis and J. S. J. Van Deventer. Boca Raton, Fla*: CRC

Rangan. B.V. (2011) ''Fly ash based geopolymer concrete'', *proceeding of International Workshop on Geopolymer cement and Concrete, Mumbai, India, December*, pp. 68-106

Sumajouw, M.; Rangan, B.V. (2006). Low-Calcium Fly Ash-Based Geopolymer Concrete: Reinforced Beams and Columns; *Curtin University of Technology: Perth, Australia*,

Wallah, S.; Rangan, B.V. (2021). Low-Calcium Fly Ash-Based Geopolymer Concrete: Long-Term Properties; *Curtin University of Technology: Perth, Australia, 2006.*Materials 14, 7790, pp. 21 of 23

Xu, H. and Van Deventer, J. S. J. (2000). "The geopolymerisation of alumino-silicate minerals." *International Journal of Mineral Processing* 59(3): pp. 247-266.

Yang, Y.; Jiang, J.; Hou, L.; Lu, Z.; Li, J.; Wang, J. (2020). Pore structure and properties of porous geopolymer based on pre-swelled bentonite. *Constr. Build. Mater*. 254, pp. 119-226.

PAPER 57 – ANALYSIS AND SIMULATION OF A ROTOR FLUX-ORIENTED CONTROL SCHEME FOR A THREE PHASE INDUCTION MOTOR AT VARIABLE SPEED

G. A. Olarinoye

Department of Electrical Engineering, Ahmadu Bello University, Zaria, Kaduna, Nigeria.
*Email: baolarinoye@abu.edu.ng

ABSTRACT
The performance of induction motor drives under variable speed conditions can be improved by computing the optimum flux that guarantees minimum loss and therefore maximum efficiency in the motor. In this paper, a method to optimize the flux and thereby minimize the losses in a three-phase induction motor under variable speed conditions was developed. Mathematical models for the conventional rotor flux-oriented control scheme, total power loss as a function of rotor flux and optimum flux as a function of operating speed and load torque were analytically derived. A MATLAB/Simulink model of the proposed rotor flux optimization scheme was developed, as well, to verify the analyses set forth for a typical three-phase Induction Motor. The results of the proposed method were compared with those of the conventional rotor flux control method and direct torque control method in terms of loss reduction and efficiency for the same induction motor. The proposed rotor flux optimization scheme achieved significant improvements in efficiency and power loss compared to the conventional rotor flux control scheme. It also achieved a 5.01% improvement in efficiency compared to the optimized DTC control scheme at a speed of 250 rad/s for a load torque of 3Nm. At a lower speed of 150 rad/s, power loss was reduced by 17.2% while efficiency increased by 5.7% for the same load torque under the proposed scheme as compared to the optimized DTC scheme.

KEYWORDS: Induction motor, rotor flux, control, optimum, variable speed.

11. INTRODUCTION

Rotor flux-oriented control strategy allows precise and rapid control of the electromagnetic torque and hence speed in the three-phase induction machine. The torque control is accomplished by varying the stator current in such a way as to produce the amount of torque and speed commanded while at the same time keeping the rotor flux constant. The *d*-axis of the synchronously rotating *q*-*d* reference frame is aligned with the rotor flux. With this alignment, the *q*-component of the rotor flux is set to zero thereby producing what is referred to as the rotor flux-oriented control. The scheme uses the *q* and *d*-axis components of the stator current to control the rotor flux and maintain its proper orientation in the *q*-*d* reference frame. The rotor flux can be regulated in the desired torque and speed operating range to increase motor drive efficiency. By proper computation of the flux level in the motor, it is possible to minimize the losses in the motor. The copper and core losses account for the largest amount of losses in induction motor and therefore explains the interest to use them in the analysis proposed in this paper. To increase the motor drive efficiency, the flux must be reduced and balance obtained between copper and core losses. In this paper, Loss based model approach that determines the optimal flux for loss minimization is analysed and implemented in MATLAB/Simulink.
Sruthi *et al.* (2017) formulated a loss minimization algorithm for energy saving and efficiency improvement in induction motor drives. The input voltage and frequency were optimized to reduce total losses. Eseosa & Christian (2018), Nam & Uddin (2006) and Laroui, *et al*. (2021) presented various approaches to optimization control techniques to improve the efficient operation of induction motors. Aygun & Aktas (2018) implemented a direct torque control (DTC) technique combined with an online loss minimization model-based controller (LMC) to minimize the losses of an induction motor applied in an Electric Vehicle (EV). The objective of this paper is to develop a rotor flux optimization control model for an existing three-phase induction motor and simulate its performances in MATLAB/Simulink for loss minimization under variable speed conditions.

12. THEORETICAL ANALYSIS

The dynamic model of the induction motor in *d*-*q* coordinates established in a rotor flux-oriented reference frame is provided in equations (1) – (10) (Sharma, Parashar and Chandel, 2020; Olarinoye *et al*., 2022).

$$V_{qs} = R_s i_{qs} + \omega_e \lambda_{ds} + p\lambda_{qs} \quad (1)$$

$$V_{ds} = R_s i_{ds} - \omega_e \lambda_{qs} + p\lambda_{ds} \quad (2)$$
$$V'_{qr} = R'_r i'_{qr} + (\omega_e - \omega_r)\lambda'_{dr} + p\lambda'_{qr} \quad (3)$$
$$V'_{dr} = R'_r i'_{dr} - (\omega_e - \omega_r)\lambda'_{qr} + p\lambda'_{dr} \quad (4)$$
$$\lambda_{qs} = (L_{ms} + L_{ls})i_{qs} + L_{ms} i'_{qr} \quad (5)$$
$$\lambda_{ds} = (L_{ms} + L_{ls})i_{ds} + L_{ms} i'_{dr} \quad (6)$$
$$\lambda'_{qr} = L_{ms} i_{qs} + (L_{ms} + L'_{lr})i'_{qr} \quad (7)$$
$$\lambda'_{dr} = L_{ms} i_{ds} + (L_{ms} + L'_{lr})i'_{dr} \quad (8)$$
$$T_e = \frac{p}{2}\frac{L_{ms}}{L'_r}\left(\lambda'_{dr} i_{qs} - \lambda'_{qr} i_{qs}\right) \quad (9)$$
$$T_e = \frac{2j}{p} P\omega_r + T_L \quad (10)$$

V_{ds} and V_{qs}, V'_{dr} and V'_{qr} are the direct axes and quadrature axes stator and rotor voltages, and i_{ds}, i_{qs}, i'_{dr} and i'_{qr} are stator and rotor currents, λ_{ds}, λ_{qs}, λ'_{dr} and λ'_{qr} are stator and rotor flux respectively. R_s and R_r are stator and rotor resistances respectively. ω_e is stator frequency and ω_r is the rotor's electrical speed.

2.2 R**otor flux-oriented control scheme for the three-phase induction motor**

The rotor flux-oriented control is derived from the rotor dynamic equations of the three-phase induction machine in the synchronously rotating reference frame represented by equations (3)-(4) and (7)-(8). The set of equations that establish this control scheme is given as follows; (Olarinoye *et al*., 2022)

$$\lambda'_{qr} = 0 \quad (11)$$
$$\lambda'_r = \sqrt{\lambda'^2_{qr} + \lambda'^2_{dr}} \quad (12)$$
$$\lambda'_r = \lambda'_{dr}. \quad (13)$$
$$0 = R'_r l'_{qr} + (w_e - w_r)\lambda'_r \quad (14)$$
$$0 = R'_r l'_{dr} + \rho\lambda'_{dr} \quad (15)$$
$$\lambda'_r = L_m l'_{ds} + L_r l'_{dr} \quad (16)$$
$$0 = L_m l_{qs} + L_r l'_{qr} \quad (17)$$
$$\frac{\tau_r d\lambda'_r}{dt} + \lambda'_r = L_m l_{ds} \quad (18)$$
$$\tau_r = \frac{L_r}{R_r} \quad (19)$$
$$w_s = w_e - w_r = \frac{R'_r L_m l_{qs}}{L'_r \lambda'_r} \quad (20)$$
$$\theta_e = \int \omega_e \, dt = \int \left(\omega_r + \frac{R'_r L_m l_{qs}}{L'_r \lambda'_r}\right) dt \quad (21)$$
$$T_{em} = \frac{3P}{4}\frac{L_m}{L_r}\lambda'_r i'_{qs} \quad (22)$$

$L_r$and L_m are the self and mutual inductances of the rotor circuit. The rotor flux magnitude λ'_r and its phase angle, θ_e are estimated from equations (18) and (21) respectively.

13. METHODOLOGY

The loss model and therefore, the optimum flux expression are formulated from the equivalent circuit model of the three-phase induction motor shown in Figure 1. The following voltage, flux linkage and current equations can be obtained from Figure 1 as follows;

$$V_{qs} = r_s i'_{qs} + \mathrm{k}\omega_e \lambda_{ds} + kp\lambda_{qs} \quad (23)$$
$$V_{ds} = r_s i'_{ds} - \mathrm{k}\omega_e \lambda_{qs} + kp\lambda_{ds} \quad (24)$$
$$0 = r_r{}' i'_{qr} + (\omega_e - \omega_r)\lambda'_{dr} + p\lambda'_{qr} \quad (25)$$
$$0 = r_r{}' i'_{dr} - (\omega_e - \omega_r)\lambda'_{qr} + p\lambda'_{dr} \quad (26)$$
$$i_{cq} = i_{qs} - i'_{qs} \quad (27)$$
$$i_{cd} = i_{ds} - i'_{ds} \quad (28)$$
$$i_{cq} = \frac{V_{qs}}{kr_c} \quad (29)$$
$$i_{cd} = \frac{V_{ds}}{kr_c} \quad (30)$$

$$k = 1 + \frac{r_s}{r_c} \tag{31}$$

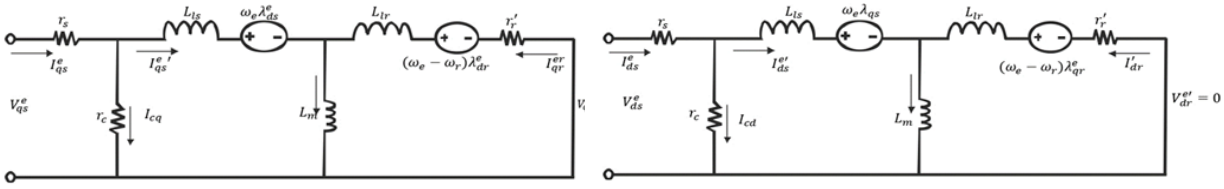

Figure 1: *q-d* equivalent circuit with core loss resistance

i_{cq} and i_{cd} are the currents flowing through the core loss branches of the *q* and *d* axes respectively. i'_{qs} and i'_{ds} are the torque currents responsible for producing electromagnetic torque in the motor as seen from the equivalent circuit. By applying equations (11) and (13) to the voltage equations (23) – (26), relationships between the applied stator currents and torque currents were obtained as follows;

$$\begin{bmatrix} i_{qs} \\ i_{ds} \end{bmatrix} = \begin{bmatrix} (1 + \frac{r_s}{kr_c}) & \frac{\omega_e L_s}{r_c} \\ -\frac{\omega_e L_x}{r_c} & (1 + \frac{r_s}{kr_c}) \end{bmatrix} \begin{bmatrix} i'_{qs} \\ i'_{ds} \end{bmatrix} \tag{32}$$

$$\begin{bmatrix} i'_{qs} \\ i'_{ds} \end{bmatrix} = \frac{1}{\left[1+\frac{r_s}{kr_c}\right]^2 + \frac{\omega_e^2 L_x L_s}{r_c^2}} \begin{bmatrix} (1 + \frac{r_s}{kr_c}) & -\frac{\omega_e L_s}{r_c} \\ \frac{\omega_e L_x}{r_c} & (1 + \frac{r_s}{kr_c}) \end{bmatrix} \begin{bmatrix} i_{qs} \\ i_{ds} \end{bmatrix} \tag{33}$$

The power loss model was formulated considering that the total electrical power loss is the sum of the copper and core losses in the motor. The expression of electrical power loss is obtained from the equivalent circuits as follows;

$$P_L = R_s\left(i_{qs}^2 + i_{ds}^2\right) + r'_r\left(i_{qr}^2 + i_{dr}^2\right) + r_c(i_{cq}^2 + i_{cd}^2) \tag{34}$$

A power loss model was derived by substituting current equations (29) – (33) into equation (34). It is given as follows;

$$\mathrm{P_L} = \frac{3}{2}\left[\frac{2\mathrm{T_e^2 L_r^2}}{\mathrm{k_t^2 L_m^2 \lambda_r^2}} + \frac{\mathrm{Z\lambda_r^2}}{\mathrm{L_m^2}} - \frac{\mathrm{r_r \lambda_r^2}}{\mathrm{L_r^2}} + \mathrm{kL_m^2}\left(\frac{\mathrm{r_r^2 + L_r^2 \omega_r^2}}{\mathrm{r_c L_r^4}}\right)\lambda_\mathrm{r}^2 - \ 2\mathrm{k}\lambda_\mathrm{r}^2\left(\frac{\mathrm{rr_r - \omega_e \omega_r L L_c}}{\mathrm{L_r^2 r_c}}\right) + \frac{2\mathrm{T_e}}{\mathrm{k_t r_c}}\left(\frac{\mathrm{k(\omega_e L r_r + \omega_r r L_r)}}{\mathrm{L_r}} + \mathrm{r_s \omega_e}\right)\right] \tag{35}$$

The optimum value of the rotor $\lambda_{r(opt)}$ flux for a given load torque and speed was obtained by differentiating equation (35) with respect to the rotor flux magnitude and equating the derivative to zero.

$$\lambda_{\mathrm{r(opt)}} = \sqrt{\frac{\mathrm{T_e L_r^3}}{\mathrm{k_t}}} \cdot \sqrt[4]{\frac{\mathrm{Zr_c}}{\mathrm{kL_m^2(\omega_r^2 L_m^2 L_r^2 + 2\omega_e \omega_r L L_r^3 + L_m^2 r_r^2) + ZL_r^4 r_c - r_r L_r^2 r_c L_m^2 - 2krr_r L_r^2 L_m^2}}} \tag{36}$$

With equation (36), it is possible to minimize total electrical losses, $\mathrm{P_L}$ in the motor. For controller design, the stator voltages are expressed as a function of the *d* and *q*-axis currents and the rotor flux by applying equations (5) - (8), (11) and (13) to equations (23) and (24). The following expressions were obtained;

$$V_{qs} = Kr'_s i'_{qs} + KLpi'_{qs} + K\omega_e L i'_{ds} + K\frac{L_m}{L_r}\omega_r \lambda'_r \tag{39}$$

$$V_{ds} = Kr'_s i'_{ds} + KLpi'_{ds} - K\omega_e L i'_{qs} - K\frac{L_m}{L_r^2} R_r \lambda'_r \tag{40}$$

$$L = L_s\left(1 - \frac{{L_m}^2}{L_s L_r}\right) \tag{41}$$

$$r'_s = r_s + \frac{L_m^2 R_r}{L_r^2} \tag{42}$$

Equations (39) and (40) are first-order non-linear systems for which V_{qs} and V_{ds} are inputs and i'_{qs} and i'_{ds} are outputs. The voltage commands needed to give the desired currents, i'_{qs} and i'_{ds}, are obtained with a feedback-based solution using current controllers. The formulation for the controller gains was performed using equations (39) and (40). The proportional and integral gains, k_{pi} and k_{ii} for the stator current controller were derived as;

$$k_{pi} = KL2\zeta\omega_n - Kr'_s \tag{43}$$

$$k_{ii} = KL\omega_n^2 \tag{44}$$

ζ is the damping ratio and ω_n is the natural frequency. The speed control and rotor flux control loops provide the *d* and *q*-axis current commands respectively according to equations (18), (22) and (10). PI controllers were also employed for the speed and flux control loops. The speed controller gains are obtained as;

$$k_{pw} = 2\frac{J}{p}\omega_n \tag{45}$$

$$k_{iw} = \frac{J}{p}\omega_n^2 \quad (46)$$

Similarly, the flux controller gains are obtained as;

$$k_{pf} = \frac{\tau_r}{L_m} 2\omega_n - \frac{1}{L_m} \quad (47)$$

$$k_{if} = \frac{\tau_r}{L_m}\omega_n^2 \quad (48)$$

The supply voltages in the synchronous reference frame are then calculated based on the following equations;

$$V_{qs} = \sigma_{qs} + K(\omega_e L i'^e_{ds} + \frac{L_m}{L_r}\omega_r \lambda'^e_r) \quad (49)$$

$$V_{ds} = \sigma_{ds} - K\left(\frac{L_m R_r}{L_r^2}\lambda'^e_r + \omega_e L i'^e_{qs}\right) \quad (50)$$

Figure 2 shows the block diagram of the drive scheme for the three-phase induction machine. The analysis set forth was programmed for simulation and verification in MATLAB/Simulink.

14. RESULTS AND DISCUSSION

The motor parameters utilized to verify the effectiveness of the proposed scheme are provided in Table 1.

Table 1: Induction Motor Parameters.

S/N	Parameters		S/N	Parameters	
1	Voltage	400V	7	R_r	1.52Ω
2	Frequency	50HZ	8	r_c	13400Ω
3	Synchronous speed	3000rpm	9	$L_s = L_r$	0.2405H
4	No of poles	2	10	L_m	0.2323H
5	Power	3kW	11	J	0.0044kgm^2
6	R_s	1.795Ω	12		

The computed controller gains are provided in Table 2.

Table 2: Current, speed and flux controller gains

Controller	**Proportional gain**	**Integral gain**
q-axis current controller (k_i, k_p)	639.4058	6.3958e+06
d-axis current controller (k_i, k_p)	639.4058	6.3958e+06
Speed controller (k_i, k_p)	1.76	176
Flux controller (k_i, k_p)	268.1424	2.7245e+04

The loss minimization program was set to trigger at 2.5s. With the reference speed and load torque set to 250 rad/s and 3Nm respectively, the rated flux was computed as 1Wb. The rotor flux-oriented control scheme enables the variation of motor speed. To this end, the motor speed was ramped down from 250 rad/s to 150 rad/s and maintained between 4 and 5s of simulation time. Figures 3-5 show the performances of the motor under the proposed scheme at variable speeds.

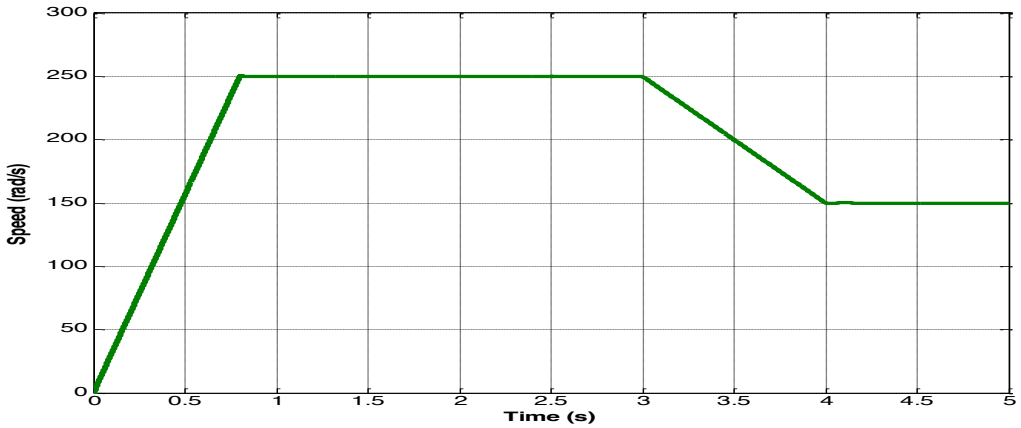

Figure 3: Variable speed profile of the induction motor

Figure 4 shows the plot of the rotor flux magnitude. It can be seen that the flux value is 1Wb until the proposed scheme is activated and the flux reduces significantly to its optimal value of 0.6357Wb for the given load torque.

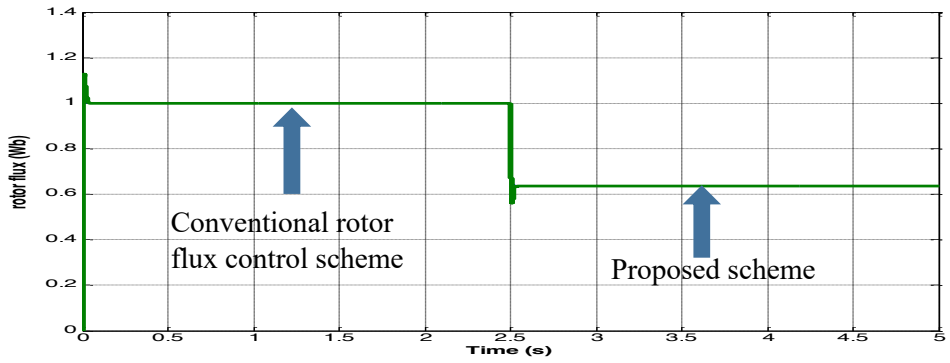

Figure 4: Rotor flux magnitude vs time

The total power loss is plotted in Figure 5. It can be seen that the conventional rotor flux control scheme produces a steady state power loss of 200W in the motor. The proposed scheme on the other hand, upon activation at a time of 2.5 s, produces a power loss of 108.04W in the same motor. The power loss further reduces to 83.645W because of the drop in speed. The total power loss therefore reduces by 22.6% and this implies that there is an opportunity to save power when the motor is driven at a lower speed.

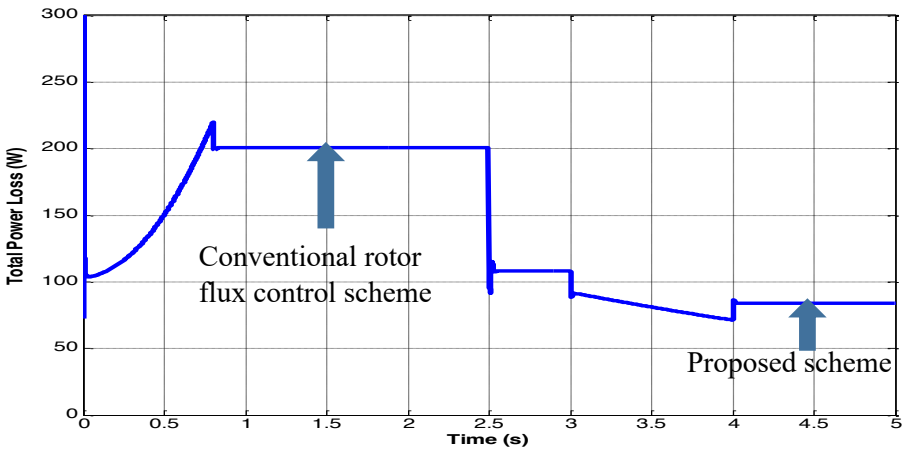

Figure 5: Total electric power loss under variable speed.

The efficiency of the motor is plotted in Figure 6. The motor efficiency rises from 78.9% for the conventional scheme to 87.41% for the proposed scheme at 250 rad/s as shown. It can also be seen to decrease to a value of 84.8% after the motor speed is dropped to 150 rad/s because the power output drops with speed. A table of comparison between these results and those obtained by Aygun and Aktas (2018) is provided in Table 2.

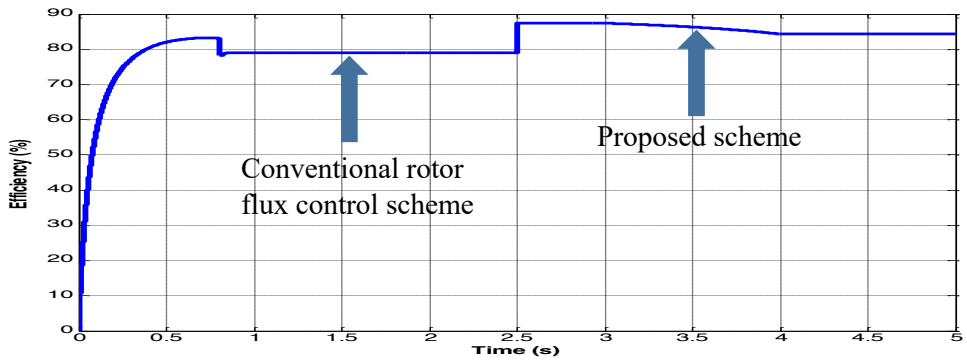

Figure 6: Efficiency of an induction motor under variable speed

Table 2: Comparison of results of the proposed rotor flux-oriented control scheme with those of the optimized DTC at variable speed

Scheme	Total power loss (W)	Efficiency (%)
Proposed scheme at 250 rad/s	108.04	87.41
Proposed scheme at 150 rad/s	83.645	84.8
Optimized DTC at 250 rad/s	166.28	82.4
Optimized DTC at 150 rad/s	101	79.1

Table 2 shows the superior performance of the proposed method at variable speed when compared with the performance of the optimized DTC method under the same operating conditions. At a lower speed of 150 rad/s, power loss reduces by 17.2% while efficiency is higher by 5.7% for a load torque of 3Nm under the proposed scheme as compared to the optimized DTC scheme developed in Aygun and Aktas (2018).

15. CONCLUSION

A rotor flux-oriented control model with optimization for a three-phase induction motor was analysed and simulated. The results obtained showed significant improvements over the conventional rotor flux control drive and the Direct torque control (DTC) drive of the same three-phase induction motor. A comparison of the conventional and proposed rotor flux-oriented control drive shows that when the reference speed was set to 250rad/s at a load torque of 3Nm, the rotor flux reduced from a rated value of 1Wb to an optimal value of 0.6357Wb thereby leading to a significant reduction of the total power loss from 200W to 108.04W and a consequential increase in efficiency from 78.9% to 87.41%. With the proposed drive scheme operating at variable speed mode in which motor speed was ramped down from 250rad/s to 150rad/s at a load torque of 3Nm, power loss is observed to further reduce significantly to 83.645W giving a reduction of 22.6%. A comparison between the results obtained and those obtained by Aigun and Aktas (2018) shows that the proposed rotor flux optimization control scheme is superior to the optimized Direct Torque Control (DTC) scheme for the same motor parameters. At a speed of 150 rad/s, power loss was reduced by 17.2% while efficiency increased by 5.7% for the same load torque under the proposed scheme as compared to the optimized DTC scheme.

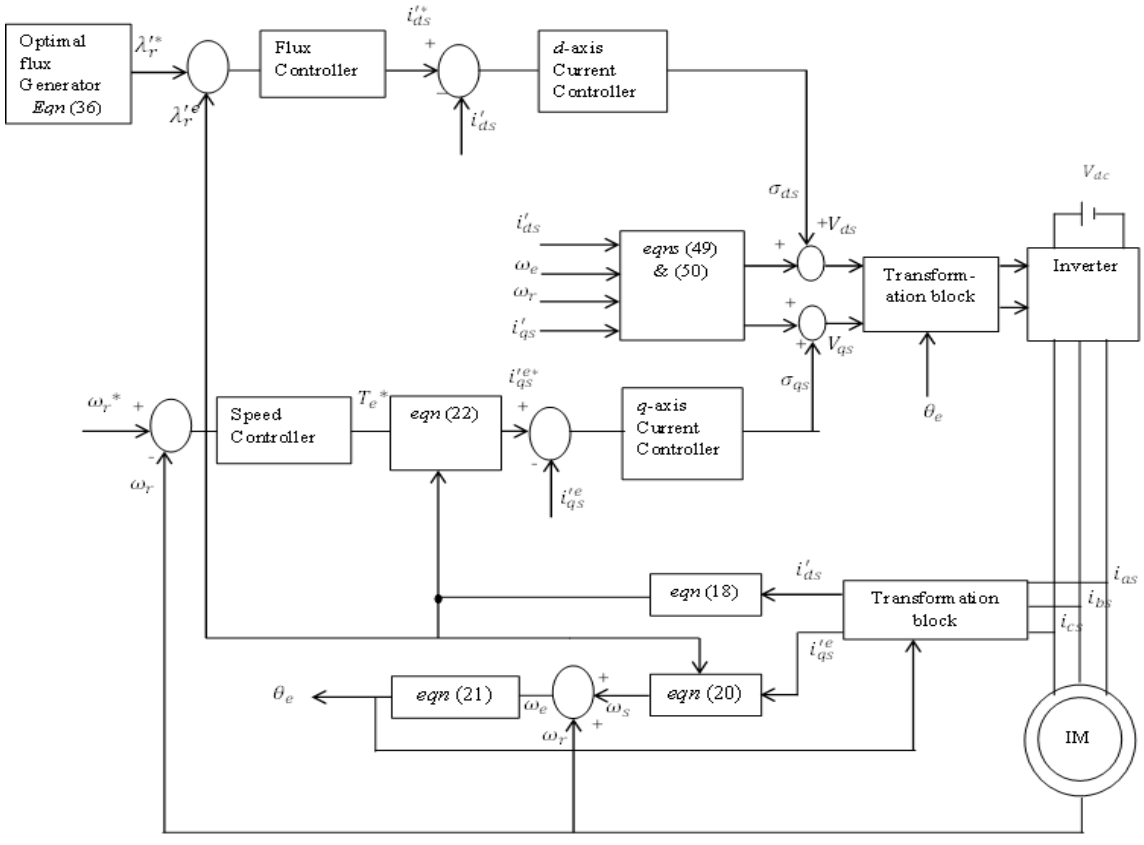

Figure 2: Block diagram of three phase induction motor drive scheme

REFERENCES

Aygun, H. and Aktas, M. (2018). A novel DTC method with efficiency improvement of IM for EV applications. Engineering, Technology & Applied Science Research, 8(5), 3456-3462.

Eseosa, O. and Christian, A. (2018). Energy Efficiency Optimization of Three-Phase Induction Motor Drives for Industrial Applications. Int. J. Eng. Appl. Sci, *5*(8).

Laroui, M.; Nour, B.; Moungla, H.; Cherif, M. A.; Afifi, H. and Guizani, M. (2021). Edge and fog computing for IoT: A survey on current research activities & future directions. Computer Communications, 180, 210-231.

Nam, S. W. and Uddin, M. N. (2006). Model-based loss minimization control of an induction motor drive. In IEEE International Symposium on Industrial Electronics. 3(1), pp. 2367-2372). IEEE.

Olarinoye, G. A.; Akorede, M.F and Akinropo, C. D (2022). Design and Simulation of a Three-Phase Induction Motor Speed Control System. FUOYE Journal of Engineering and Technology. Federal University Oye-Ekiti, Nigeria. 7(1), pp. 39 – 46.

Sharma, G.; Parashar, D. and Chandel, A. (2020). Analysis of Dynamic Model of Three Phase Induction Motor with MATLAB/SIMULINK. International Conference on Advances in Computing, Communication & Materials (ICACCM), Dehradun, India, pp. 51-58. IEEE.

Sruthi, M. P.; Nagamani, C. and Ilango, G. S. (2017). An improved algorithm for direct computation of optimal voltage and frequency for induction motors. Engineering Science and Technology, an international journal, 20(5), 1439-1449.

PAPER 58– MITIGATING DUST IMPACT: A COMPREHENSIVE OVERVIEW OF SOLAR PANEL CLEANING DEVICES FOR MAXIMIZED PERFORMANCE

M. A. Sanusi[1*], S. A. Adedayo[1], P. O. Omoniyi[1,3], R. M. Mahamood[2,3], TC. Jen[3], and E. T. Akinlabi[4]
[1] Department of Mechanical Engineering, University of Ilorin, P. M. B. 1515, Ilorin, Nigeria
[2] Department of Materials and Metallurgical Engineering, University of Ilorin, P. M. B. 1515, Ilorin, Nigeria
[3] Department of Mechanical Engineering Science, University of Johannesburg, P. O. Box 524, Johannesburg, South Africa
[6] Department of Mechanical and Construction Engineering, Northumbria University, Newcastle, NE18ST, United Kingdom
Email:18-30gd111@students.unilorin.edu.ng,

ABSTRACT

Solar energy usage is rapidly increasing as people become more aware of the limited availability of nonrenewable energy resources such as coal, wood, and gasoline. This review analyzes different solar panel cleaning systems, examining their technical aspects and efficiency. It explores challenges related to panel cleanliness, including dust accumulation, dirt deposition, and their effect on system performance. Thanks to technological advancements, solar panels can now be used in domestic and industrial applications. Rural areas that do not yet have proper electrical connections are now opting for solar panel installations and using solar panels on streetlights. This article gives an insight into the causes of the inefficiencies of solar panels. The main inefficiency was the system's inability to adapt to changes in the sun's position, for which solar tracking systems with solar panels were installed. Another issue that has caused some concern is the accumulation of dust clouds on solar panels. The accumulation of dust and dirt on these solar panels has been observed to reduce system efficiency by approximately 23-50%. This article highlights the performance of existing cleaning devices with their cleaning techniques and gives recommendations based on their design and efficiency improvement.

KEYWORDS: Cleaning Devices, Efficiency, Renewable Energy, Solar Energy, Solar Power

1. INTRODUCTION

The current global energy crisis has resulted in a heightened focus on utilizing clean energy sources instead of depending on fossil fuels. Solar power is among the potential renewable energy sources that show promise. Recent investments in renewable energy have underscored the appeal of solar energy, considered a highly attractive alternative, only behind wind power. Unfortunately, According to a study conducted by (Al-Otaibi et al., 2015), various environmental elements have the potential to impact the energy production of solar panels. One such factor is the accumulation of dust, which has been observed to substantially influence the overall efficiency of photovoltaic modules (Kumar et al., 2015). Studies by Nahar & Gupta (1990) demonstrated that the buildup of dust on unclean cell surfaces can cause performance to decline by as much as 20% each month. Additionally, (Goossens & Van Kerschaever 1999) experiments revealed that high wind speeds encourage dust accumulation on surfaces.

This research paper encompasses three main components, each addressing a distinct aspect of the technology under review. The first part delves into the issue of dust and its effects on solar technology. The second part focuses on the techniques employed for cleaning solar panels, and the third is the performance evaluation of existing solar panel cleaning mechanisms. The literature reviewed for this study covers the papers published from the 1990s to 2022. The methodology of this work revolves around a pair of key questions: (1) What consequences arise from dust accumulation on photovoltaic (PV) panels? and (2) What strategies exist for alleviating and cleansing dust buildup on PV panels?

2.0 CONCEPT OF DUST AND CHARACTERISTICS AND HOW DUST IS ACCUMULATED

"Dust" refers to any substance that becomes airborne, including dust and soil particles (suspended dust), fog, smoke, and particulate matter. These substances come from organic and inorganic land sources, such as sandstorms, volcanic emissions, forest fires, bacteria, pollen, factory emissions, and solid particles that persist in the atmosphere for extended periods and can travel long distances with wind movement are also included. Dust varies greatly in distribution, volume, concentration, and shape. Dust storms, being a natural phenomenon, extend beyond national boundaries, and there is a noticeable rise in their severity and occurrence frequency due to growing desertification and decreasing vegetation coverage, significantly negatively impacting human and socioeconomic development at both national and regional levels. (Guo et al., 2015; A. A. Kazem et al., 2014)

However, this dust buildup on solar panels, as shown in Figure 1, also termed "soiling," significantly affects the efficiency of PV systems, particularly in areas with little to no rainfall for several months during a dry season, in a study by El-Shobokshy & Hussein (1993). The effect of various particles commonly present in the atmosphere, including limestone, cement, and carbon particles of varying sizes, is considered. Studies have shown that fine carbon particulates with an average size of 5μm pose a substantial threat to the performance of PV panels. The accumulation of these carbon particles on the panel's surface leads to considerable power output losses. These particles primarily originate from combustion processes and are commonly found in carbon emissions.

Fig. 1 Dust accumulation on panel surface Source: (Walz et al., 2018)

2.1 EFFECT OF DUST ON SOLAR PANEL

The impact of dust accumulation on PV panels has been heavily researched due to its significant effect on efficiency, particularly in desert countries in the solar belt region. Mazumder et al. (2014) found that the deposition of only 4 g/m^2 of dust with particle diameters ranging from 0.5 to 10 mm can cause up to a 40% reduction in the electrical efficiency of the cell. Dorobantu et al. (2011) analyze the consequences of traffic-related pollution. Surprisingly, it was discovered that even a thin layer of dust and pollutants can result in a significant decline of up to 20% in PV performance, which may increase up to 40% with continued accumulation. Furthermore, Zorrilla-Casanova et al. (2011) examined the daily energy generation of a PV system throughout the year. The findings revealed an average daily energy loss of approximately 4.4% attributable to dust accumulation, which could increase to 20% in the absence of precipitation for extended periods.

Similarly, Rahman et al. (2012) conducted laboratory experiments with artificial dust and found that efficiency reduction could reach up to 50%. In hot climates with no precipitation, Kimber et al. (2006) found that daily efficiency reduction could be as much as 0.2%, resulting in up to a 56.2% decline in productivity annually, depending on the system's location. Generally, from the results discussed, photovoltaic cells are reduced by up to 40% as the area of dust deposition increases. However, the next section discusses techniques and technologies employed to prevent dust accumulation.

3.0 PV CLEANING TECHNIQUES: REVIEW AND CLASSIFICATION

Prior research has indicated that a rainfall amount of 5 mm is satisfactory for cleansing photovoltaic systems (Sulaiman et al., 2011). Nonetheless, our analysis of the systems revealed that certain designs necessitate a notably higher level of rainfall to achieve comprehensive module cleanliness. During rains, a thorough cleaning effect is observed, rejuvenating the performance of soiled cells to their initial levels. Surprisingly, even light rainfall below 1mm proves sufficient to cleanse the cover glass, reducing daily losses to less than 5% (Chen et al., 2020). However, dust accumulation can cause daily losses exceeding 20% in prolonged periods without rain, like summer. The mean daily energy loss in a year caused by dust is 4.4% (Moharram et al., 2013). Except for the summer months, where the scarcity of rainfall facilitates dust buildup, the monthly averages of daily energy losses remain below 2%. However, during this particular season, the absence of rain significantly increases losses, surpassing 15%. (Yao et al., 2022). Note that the summer months witness the peak of energy production, making the potential negative impact of dust particularly significant during this period. (Zorrilla-Casanova et al., 2011). Since natural cleaning system such as rainfall is not sufficient and efficient for cleaning the PV system, especially

in locations with low rainfall, researchers have devised various techniques to clean up the solar panel to increase their efficiency.

3.1 FORCED AIRFLOW OF AIR CONDITIONING SYSTEMS

Assi & Hassan (2012) proposed a method to increase the efficiency of solar panels by removing dust and reducing their temperature. The technique utilizes forced airflow from air conditioning systems to clean the panels. The airflow from the air conditioning system's fans is directed toward the solar panels to remove dust. This method has been implemented in the United Arab Emirates. It can also be used in other developed countries where air conditioning is widely used and has an efficiency of about 73%.

Similarly, the self-cleaning solar system developed by Tanesab et al. (2016) utilizes forced airflow from air conditioning systems to remove dust from solar panels. The system applies to all roofs and has proven effective in maintaining solar panels' efficiency. This method can reduce the maintenance cost of solar panels and increase their lifespan. However, this technique has not been proven to have high efficiency at cooling and cleaning photovoltaic cells.

3.2 NATURAL CLEANING USING RAIN AND WIND

The way rainwater falls on a tilted PV panel can be used to clean the surface naturally. PV panels are typically fixed at an angle to maximize exposure to sunlight. However, this cleaning method is imperfect because it does not entirely remove all the dust from the surface. As a result, some dust particles remain on the surface due to their interaction with atmospheric moisture. These particles can only be removed by heavy rain. However, this method can be unreliable in areas with severe pollution and insufficient rainfall. A study by Kimber (2007) found that after a light rain, a layer of clay is formed on the PV surface, causing a dramatic drop in electricity generation. Wind can also naturally clean PV surfaces exposed to it, especially when the wind is moderate in speed and does not produce dust. Although it is challenging to predict precipitation times and amounts, rainfall can increase the efficiency of the PV surface by preventing or reducing pollutant accumulation.

3.3 WATER CLEANING

In this method, a hose channel flows water to the PV surface, as shown in Figure 2, cleaning up the buildup of dust particles. Many water pumps are required to achieve the required high pressure. Modern methods sometimes mix compressed water with a special cleaning agent that aids efficient cleaning to enhance dust removal. Water can also be used to cool PV panels, similar to cleaning the panels with rainwater. However, one significant drawback of this method is water availability in areas where it is scarce (Deb & Brahmbhatt, 2018).

Furthermore, this situation leads to notable water depletion and the potential for chemical sedimentation along the edges of the PV panels. Employing high-pressure water pumps entails consuming PV-generated power, thereby reducing overall efficiency. Moreover, there exists a risk of water pipe obstruction or damage, along with the possibility of thermal shock to the heated PV panels when water descends, given that it will almost inevitably be cooler than the surface of the plates.

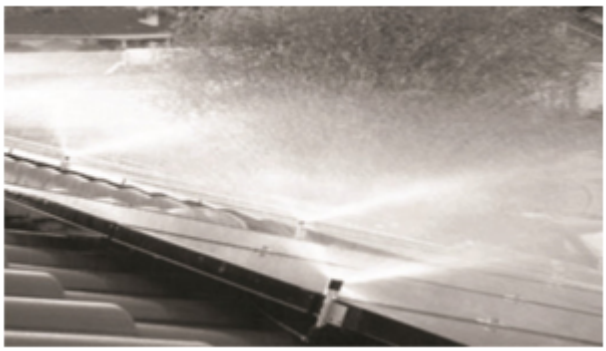

Fig. 2. Fully automated water cleaning system Source: (H. A. Kazem et al., 2020)

3.4 MANUAL CLEANING

This method involves using soft-bristled brushes, similar to those used for cleaning building windows, to eliminate accumulated dust from the PV panels, as shown in Figure 3. This method supplies washing water directly to the brushes, making it more efficient than the natural method of cleaning PV with rainwater or compressed air. However, there are some drawbacks to this method. Direct contact of the brush with the PV surface may result in

slurry, as the movement and pressure of the brushes cannot maintain equally across the entire surface. Additionally, this method is more expensive than other cleaning methods, requiring skilled labour to be effective (Deb & Brahmbhatt, 2018).

Fig. 3. Manual cleaning technique Source: (Khadka et al., 2020)

3.5 MECHANICAL CLEANING TECHNIQUE

The cleaning of photovoltaic (PV) panels is important for maintaining their efficiency, and several methods have been developed to remove accumulated dust and dirt. One such process involves using soft-bristled brushes similar to those used to clean building windows. However, direct contact between the brushes and the PV surface can result in slurry, which can be detrimental to the PV's efficiency. Al Shehri et al. (2017) conducted a practical examination to enhance PV efficiency by utilizing nylon, cloth, and silicone rubber foam brushes to address this issue. The study outcomes demonstrated that certain materials favourably impacted PV efficiency without any adverse long-term consequences. Figure 4 shows a mechanical PV cleaning device.

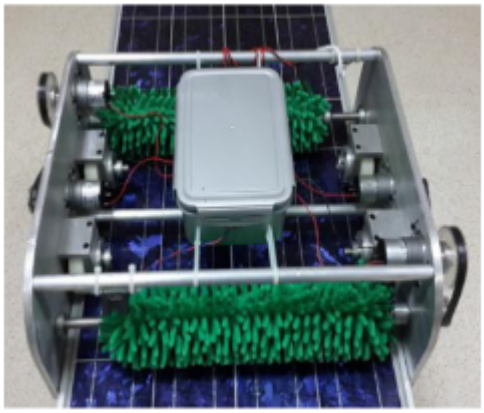

Fig. 4 Mechanical PV cleaning device Source: (Rai et al., 2019)

3.6 ELECTRICAL SCREENS (EDS)

An alternative approach to PV cleaning is using electro-dynamic display (EDS) technology, an innovative EDS system developed to efficiently eliminate accumulated dry dust without needing water or mechanical components.

This system utilizes a high-voltage electric field generated on a screen, effectively charging dust particles and facilitating their removal by propelling them beyond the edge of the plate surface. (Deb & Brahmbhatt, 2018). Even though the system is faster and more efficient, the system requires a high-voltage supply to power the system. And also It is ineffective for cemented or wet dust particles and is easily affected by ultraviolet rays (Deb & Brahmbhatt, 2018).

3.7 SELF-CLEANING ULTRASONIC

One effective cleaning method is standard high-frequency ultrasound, which operates at frequencies above human hearing and can reach up to 20 kHz. This technique is particularly useful for removing various water contaminants, such as polishing compounds, mould grease, dirt, and oil release agents. It can also clean materials such as metals, glass, and ceramics (Vasiljev et al., 2013).

3.8 ELECTROSTATIC CLEANING SYSTEM (ECS)

The automated cleaning technique known as the electrostatic cleaning system (ECS) offers a solution for maintaining the cleanliness of solar cell panels. In the presence of accumulated dust particles on the PV panel, the ECS employs electric charges to dislodge and effectively remove dust from the surface. Applying a high AC voltage to parallel screen electrodes on the panel generates electrostatic forces, which exert an influence on particles located in proximity to the electrodes. This doubles the electrostatic repulsion, effectively removing the dust particles without causing mechanical friction on the panel surface (Kawamoto & Shibata, 2015). Some drawbacks to this system include high voltage requirements in operating the system and the inability to clean tiny dust.

3.9 ROBOTIC CLEANING SYSTEM (RCS)

Robotic cleaning systems (RCS) are a viable alternative to manual cleaning, offering superior precision and accuracy without human intervention. RCS systems offer numerous benefits, such as minimal water usage, convenient control, and exceptional effectiveness. These systems can be seamlessly integrated with two primary cleaning approaches. The first method involves dry cleaning, while the second method entails wet cleaning, which incorporates water or other water-based liquids for effective cleansing. (Deb & Brahmbhatt, 2018). Overall, the system is automated and highly flexible (Farrokhi Derakhshandeh et al., 2021). Figure 5 shows a robotic PV panel cleaning device.

Fig. 5 Robotic PV cleaning device Source: (Moreno et al., 2006)

Table 1 summarizes the solar PV cleaning devices reviewed in several works of literature. The table summarizes the advantages and disadvantages of the techniques used in solar PV cleaning.

Table 1 Comparison of cleaning methods

S/N	Cleaning System	Advantages	Disadvantages
1	Forced airflow of the air	Carry out dry cleaning effectively. Do not require any power conditioning systems as it utilizes the rejected air from air conditioning units.	The operation of this system relies on AC power. Prolonged exposure to hot air can potentially diminish PV

			efficiency, making it crucial to minimize its duration.
2	Natural cleaning using rain	No cost or resources	It is weather related method.
3	Water cleaning (Heliotex cleaning system (HCS))	highly efficient in eliminating dust particles and effectively covering all areas of the PV panels. The cleaning process can be performed using either cooled or heated water, depending on the specific requirements.	This approach necessitates the utilization of water, a pump, and a controller. Depending on the circumstances, either stationary systems or designated vehicles are employed to carry out the cleaning process.
4	Manual cleaning	Environment-friendly, no electricity is needed,	human intervention is required, costly, and it needs water. Scratching happens sometimes.
5	Mechanical cleaning (Brush Cleaning System)	Mechanically remove the dust using a brush	Scratching happened sometime.
6	Electrical screens (EDS)	Effective and efficient dust particle removal with no moving part required.	It is costly and requires a high voltage, converter, and signal device.
7	Super-hydrophobic aircraft (SHOP)	No moving parts. However, natural rain or dew is useful. No need	No need for water or human intervention.
8	Super water jet (SHIP)	No moving parts are used majorly to break down dirt and dissolve it.	Reduce the screening efficiency due to coating
9	Self-cleaning ultrasonic	It's safe and reliable	It has some noises
10	Electrostatic cleaning system (ECS)	It has a high cleaning performance quickly while consuming little energy and power.	For large-scale commercial solar systems, it is not advisable to implement this method due to the need for a high-voltage function, which utilizes a powerful electric field.
11	Robotic cleaning system (RCS)	Offers superior precision and accuracy cleaning without human intervention.	They may not be suitable for cleaning large commercial solar systems, and the sensors used in RCSs may not be effective in all environments.

4.0 RECOMMENDATIONS FOR FUTURE RESEARCH

The preceding overview and discourse present a method for developing a suitable cleaning system by considering essential factors and characteristics when deciding on a recently developed and employed automated cleaning system, it is essential to carefully consider several significant factors to choose the most suitable technology from various mechanical cleaning systems. Depending on the solar farm's size, geographical location, and the prevailing environmental conditions such as pollutant levels, humidity, and temperature, a customized combination of cleaning methods can be devised and put into practice, such as using a combination of a mechanical cleaning system and a robotics cleaning system. An example would be designing a cleaning system that utilizes mechanical means, such as brushes powered by an Arduino board with a microcontroller that can be remotely operated.

5.0 CONCLUSION

This article discusses various automated methods for cleaning solar panels that have been studied. Solar panels experience a range of weather conditions throughout the year, which encompass factors like soil, dust buildup, air pollution, and avian excrement. Researchers have examined several cleaning methods for solar panels, which have positively impacted their performance. This paper indicates that the efficiency of Mechanical cleaning is moderate, with the lowest efficiencies being associated with forced airflow of air and water cleaning. Furthermore, the considerable disadvantages of RCSs include their expensive nature and the extensive duration required for the cleaning process. Therefore, engineers and designers should be mindful of these shortcomings in dusty regions when utilizing RCS, despite its typical robustness and suitability for large solar farms. If minimizing cleaning time is crucial, ECS may be a viable alternative with minimal time wastage. However, it may not be suitable for use in arid regions or where human intervention is restricted. Other cleaning mechanisms have demonstrated satisfactory labor and water usage indicators.

REFERENCES

Al-Otaibi, A., Al-Qattan, A., Fairouz, F., & Al-Mulla, A. (2015). Performance evaluation of photovoltaic systems on Kuwaiti schools' rooftops. *Energy Conversion and Management*, *95*, 110–119. https://doi.org/10.1016/j.enconman.2015.02.039

Al Shehri, A., Parrott, B., Carrasco, P., Al Saiari, H., & Taie, I. (2017). Accelerated testbed for studying the wear, optical and electrical characteristics of dry-cleaned PV solar panels. *Solar Energy*, *146*, 8–19. https://doi.org/10.1016/j.solener.2017.02.014

Assi, A., & Hassan, A. (2012). Removal of Air Blown Dust from Photovoltaic Arrays Using Forced Air Flow of Return Air from Air Conditioning Systems. *2012 International Conference on Renewable Energies for Developing Countries (REDEC)*.

Chen, J., Pan, G., Ouyang, J., Ma, J., Fu, L., & Zhang, L. (2020). Study on impacts of dust accumulation and rainfall on PV power reduction in East China. *Energy*, *194*, 116915. https://doi.org/10.1016/j.energy.2020.116915

Deb, D., & Brahmbhatt, N. L. (2018). Review of yield increase of solar panels through soiling prevention, and a proposed water-free automated cleaning solution. *Renewable and Sustainable Energy Reviews*, *82*(April 2017), 3306–3313. https://doi.org/10.1016/j.rser.2017.10.014

Dorobantu, L., Popescu, M. O., Popescu, C., & Craciunescu, A. (2011). The effect of surface impurities on photovoltaic panels. *Renewable Energy and Power Quality Journal*, *1*(9), 622–626. https://doi.org/10.24084/repqj09.405

El-Shobokshy, M. S., & Hussein, F. M. (1993). Degradation of photovoltaic cell performance due to dust deposition onto its surface. *Renewable Energy*, *3*(6–7), 585–590. https://doi.org/10.1016/0960-1481(93)90064-N

Farrokhi Derakhshandeh, J., AlLuqman, R., Mohammad, S., Al-Hussein, H., AlHendi, G., AlEid, D., & Ahmad, Z. (2021). A comprehensive review of automatic cleaning systems of solar panels. *Sustainable Energy Technologies and Assessments*, *47*(July), 101518. https://doi.org/10.1016/j.seta.2021.101518

Goossens, D., & Van Kerschaever, E. (1999). Aeolian dust deposition on photovoltaic solar cells: The effects of wind velocity and airborne dust concentration on cell performance. *Solar Energy*, *66*(4), 277–289. https://doi.org/10.1016/S0038-092X(99)00028-6

Guo, B., Javed, W., Figgis, B. W., & Mirza, T. (2015). Effect of dust and weather conditions on photovoltaic performance in Doha, Qatar. *2015 1st Workshop on Smart Grid and Renewable Energy, SGRE 2015*. https://doi.org/10.1109/SGRE.2015.7208718

Kawamoto, H., & Shibata, T. (2015). Electrostatic cleaning system for removal of sand from solar panels. *Journal of Electrostatics*, *73*, 65–70. https://doi.org/10.1016/j.elstat.2014.10.011

Kazem, A. A., Chaichan, M. T., & Kazem, H. A. (2014). Dust effect on photovoltaic utilization in Iraq: Review article. *Renewable and Sustainable Energy Reviews*, *37*, 734–749. https://doi.org/10.1016/j.rser.2014.05.073

Kazem, H. A., Chaichan, M. T., Al-Waeli, A. H. A., & Sopian, K. (2020). A review of dust accumulation and cleaning methods for solar photovoltaic systems. *Journal of Cleaner Production*, *276*. https://doi.org/10.1016/j.jclepro.2020.123187

Khadka, N., Bista, A., Adhikari, B., Shrestha, A., Bista, D., & Adhikary, B. (2020). Current Practices of Solar Photovoltaic Panel Cleaning System and Future Prospects of Machine Learning Implementation. *IEEE Access*, *8*(July), 135948–135962. https://doi.org/10.1109/ACCESS.2020.3011553

Kimber, A., Mitchell, L., Nogradi, S., & Wenger, H. (2006). The effect of soiling on large grid-connected photovoltaic systems in California and the Southwest Region of the United States. *Conference Record of the 2006 IEEE 4th World Conference on Photovoltaic Energy Conversion, WCPEC-4*, *2*, 2391–2395. https://doi.org/10.1109/WCPEC.2006.279690

Kumar, V., Shrivastava, R. L., & Untawale, S. P. (2015). Solar Energy: Review of Potential Green & Clean Energy for Coastal and Offshore Applications. *Aquatic Procedia*, *4*(Icwrcoe), 473–480. https://doi.org/10.1016/j.aqpro.2015.02.062

Moharram, K. A., Abd-Elhady, M. S., Kandil, H. A., & El-Sherif, H. (2013). Influence of cleaning using water and surfactants on the performance of photovoltaic panels. *Energy Conversion and Management*, *68*, 266–272. https://doi.org/10.1016/j.enconman.2013.01.022

Moreno, L., Cabás, R., & Fernández, D. (2006). Low mass dust wiper technology for MSL rover. *Proceedings of the 9th ESA Workshop on Advanced Space Technologies for Robotics and Automation*, *2*, 1–7.

Nahar, N. M., & Gupta, J. P. (1990). Effect of dust on the transmittance of glazing materials for solar collectors under arid zone conditions of India. *Solar and Wind Technology*, *7*(2–3), 237–243. https://doi.org/10.1016/0741-983X(90)90092-G

Rahman, M. M., Islam, M. A., Karim, A. H. M. Z., & Ronee, A. H. (2012). Effects of Natural Dust on the Performance of PV Panels in Bangladesh. *International Journal of Modern Education and Computer Science*, *4*(10), 26–32. https://doi.org/10.5815/ijmecs.2012.10.04

Rai, A. S. D., Shratriya, K., & Kurchania, A. (2019). Solar Panel Cleaning Device. *International Journal of Recent Technology and Engineering*, *8*(3), 6160–6161. https://doi.org/10.35940/ijrte.C5461.098319

Sulaiman, S. A., Hussain, H. H., Siti, N., Leh, H. N., & Razali, M. S. I. (2011). Effects of Dust on the Performance of PV Panels. *International Journal of Mechanical, Aerospace, Industrial, Mechatronic and Manufacturing Engineering*, *5*(10).

Tanesab, J., Parlevliet, D., Whale, J., & Urmee, T. (2016). Dust Effect and its Economic Analysis on PV Modules Deployed in a Temperate Climate Zone. *Energy Procedia*, *100*(September), 65–68. https://doi.org/10.1016/j.egypro.2016.10.154

Vasiljev, P., Borodinas, S., Bareikis, R., & Struckas, A. (2013). Ultrasonic system for solar panel cleaning. *Sensors and Actuators, A: Physical*, *200*, 74–78. https://doi.org/10.1016/j.sna.2013.01.009

Walz, K. A., Shoemaker, J. B., Scholes, A. J., Jiang, H., Silva, J. M. S., Sanfilippo, J., Zeltner, W. A., & Anderson, M. A. (2018). Experimental field trial of self-cleaning solar photovoltaic panels. *ASEE Annual Conference and Exposition, Conference Proceedings*, *2018-June*. https://doi.org/10.18260/1-2--30477

Yao, W., Han, X., Huang, Y., Zheng, Z., Wang, Y., & Wang, X. (2022). Analysis of the influencing factors of the dust on the surface of photovoltaic panels and its weakening law to solar radiation — A case study of Tianjin. *Energy*, *256*, 124669. https://doi.org/10.1016/j.energy.2022.124669

Zorrilla-Casanova, J., Piliougine, M., Carretero, J., Bernaola, P., Carpena, P., Mora-Lopez, L., & Sidrach-de-Cardona, M. (2011). Analysis of Dust Losses in Photovoltaic Modules. *Proceedings of the World Renewable Energy Congress – Sweden, 8–13 May 2011, Linköping, Sweden*, *57*, 2985–2992. https://doi.org/10.3384/ecp110572985

PAPER 59 – REVIEW ON MOBILE RADIO PROPAGATION

M. O. Afeare, A. U. Usman, S. Zubair

Telecommunication Engineering Department, Federal University of Technology Minna, Nigeria

E-mail address:afeare.pg916038@st.futminna.edu.ng

ABSTRACT

The behaviour of electromagnetic waves in a wireless channel is usually random and highly unpredictable. Its efficiency depends on the physical constituents of the propagation environment obstructing the direct line-of-sight (LOS) of radio signal transmission. Hence, transmitted radio signals often reach targeted receivers through different propagation mechanisms in non-line-of-sight (NLOS) scenarios called multipath resulting in path loss. Path loss is the signal intensity reduction that results from extensive fading throughout the transmission path. The placement of base stations (BS) requires the use of accurate path loss models. This paper describes the establishment of a basic mobile radio propagation model which at first presents communication services offered by the cellular telephone system limited to voice, it has gradually expanded to services other than voice such as data, image/video, human-to-human, human-to-machine and machine to machine communication making the mobile technology indispensable of our daily lives. Then it makes extensive reviews of the old traditional models (empirical models), and the new computational intelligence (CI) models and incidentally opens new research issues and future research directions. This review paper will serve as a reference material for researchers in the field of radio propagation and in particular for research in path loss prediction.

Keywords: Multipath, path loss, fading, traditional models, computational intelligence.

1. INTRODUCTION

Since the birth of communications, mankind has always depended on the presence of a communications channel (Faruk *et al.,* 2018 & 2019), even before the invention of modern technologies and techniques that replaced more traditional communication channels. The modern communication channel exists both in wired and wireless forms and a plethora of applications and technologies can use both communication media effectively (Matthews *et al,* 2017). The Basic elements of communication are represented in Figure 1.1

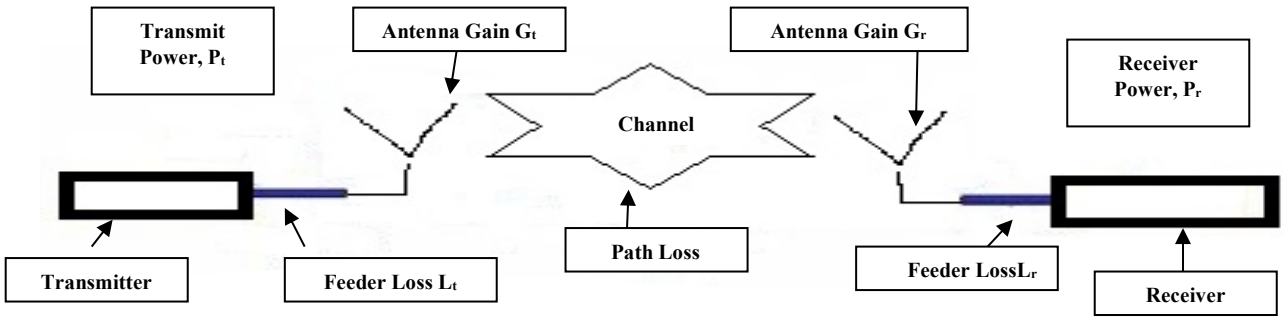

Figure 1.1 Elements of Communication System

The wireless form of communication techniques has enjoyed wide acceptance due to its support for mobility (Castaneda-Miranda, *et al*., 2020). Wireless devices and applications are used for different purposes in various sectors including health, education, e-commerce, transportation, smart agriculture, disaster, social networks, and many others. Wireless systems infrastructure has also been deployed to support broadcasting, public safety communications, and cellular mobile telephony. In particular, the most widely deployed technology is the cellular mobile communications networks. Broadband Internet provision is of particular interest in meeting the sustainable development goals (SDGs) (Wu *et al.,* 2018), particularly, in developing economies. (Aldossari *et al*., 2019).

1.1 Background to the Study

Path loss represents the reduction in signal strength of the transmitted signal caused by large-scale fading along the communication path (Rappaport, 2017). Hence, having accurate path loss models becomes essential during the deployment of wireless systems. Many different propagation models are available for different types of terrain, and their performances are location-dependent and site-specific. However, to obtain a dependable path loss model for a given area, a general model needs to be optimized and/or tuned. The optimized model can then be used by

engineers to determine the correct values of parameters such as base station (BS) location, transmitter and receiver antenna height, down tilt angle, transmitted power, and frequency (Adebowale *et al.,* 2021).
The inability of the traditional models in getting detailed information about the propagating environment leads to the adoption of heuristic models to predict path loss, including artificial neural networks (ANNs) and fuzzy systems (FSs). These methods learn and adapt to any changes in the environment, thus providing a better prediction when compared with the traditional models. Also, an addition to the heuristic models is the nature-inspired computational methodologies, also known as computational intelligence (CI), such as the genetic algorithm (GA), particle swarm optimization (PSO), and ant colony (AC), which provide a solution to the complex propagation environments where the traditional models failed (Faruk *et al*., 2019). In particular, these CI methods integrate neural networks, fuzzy logic, and other naturally inspired algorithms to optimize the path loss, thus reducing the errors and improving the prediction accuracy.

1.2 Theoretical Background

The Frequency Band

Radio waves are classified into different frequencies in the electromagnetic spectrum. The path of the spectrum that includes the radio spectrum extends from about 30kHz to 300GHz, although radio wave propagation is possible down to a few kilohertz. By international agreement, the radio frequency spectrum is divided into bands and each band is given a designation as represented in Table 1.1.

Table 1.1 The Frequency Band

Frequency Band	Frequency Range
Extremely low frequency (ELF)	< 3kHz
Very low frequency (VLF)	3-30kHz
Low frequency (LP)	30-300kHz
Medium frequency (MF)	300kHz – 3MHz
High frequency (HF)	3-30MHz
Very high frequency (VHF)	30-300 MHz
Ultra-high frequency (UHF)	300MHz -3GHz
Super high frequency (SHF)	3 -30 GHz
Extra high frequency (EHF)	30 - 300GHz

2. Theoretical Background

2.1 Radio Propagation

The study of the characteristics of radio waves in different propagation environments is needed for effective network planning and the deployment of wireless communication systems. The efficiency of a wireless system depends on the physical constituent of the propagation environment. The presence of building mountain billboards, foliage vehicles and other physical objects in a practical propagation environment usually obstructs the direct line-of-sight (LOS) of radio signal transmission. Hence, transmitted radio signals often reach targeted receivers through different propagation mechanisms in non-line-of-sight (NLOS) scenarios Nasir *et al*., (2019) as represented in Figures 2.1 and 2.2 respectively

2.2 Propagation Mechanisms

The electric field strength of signals radiated from a transmitter is subject to propagation loss due to reflection, refraction, diffraction, absorption and scattering. Weak received signals and path loss due to the reduction of the power density of an electromagnetic wave as it propagates from the transmitting antenna to the receiving antenna is of great concern in mobile communication. The major propagation mechanisms are refraction, reflection, diffraction, scattering and absorption (Surajudeen-Bakinde et al., 2018).
The propagation of electromagnetic waves is usually influenced by the atmospheric conditions of the propagation environment; different copies of transmitted radio waves arrive at the receiver using various propagation mechanisms. This phenomenon is known as multipath propagation and this causes signal fading at the receiver (Rappaport 2017). The large-scale fading concept is also referred to as *path loss*. Several propagation models have been developed for path loss estimations under different propagation scenarios.

2.3 The Path Loss Models

The path loss between a pair of antennas is the ratio of the transmitted power to the received power, usually expressed in decibels. It includes all of the possible elements of loss associated with interactions between the propagating wave and any objects between transmit and the receive antennas.

The power appearing at the receiver input terminals P_R can be expressed as

$$P_R = \frac{P_T G_T G_R}{L_T L L_R} \tag{2.1}$$

Where the parameters are defined in Fig. 1, with all gains G and losses L expressed as power ratios and powers expressed in watts. The antenna gains are expressed with references to an isotropic antenna, which radiates the power delivered to it equally in all directions. The values used are those corresponding to the direction of the other antenna and may necessarily be the maximum values. The effective isotropic radiated power (EIRP) is given by S. Saunders and A. Aragon- Zavala, (2007).

$$EIRP = \frac{P_R L_R}{G_R} \tag{2.2}$$

Where P_{TI} is the effective isotropic transmit power similarly, the effective isotropic received power is P_{RI} where

$$P_{RI} = \frac{P_R L_R}{G_R} \tag{2.3}$$

The advantage of expressing the powers in terms of EIRP is that the path loss, L, can then be expressed independently of system parameters by defining it as the ratio between the transmitted and the received EIRP, or the loss that would be experienced in an idealized system where the feeder losses were zero and the antennas were isotropic radiators($G_{T,R} = 1, L_{T,R} = 1$) S. Saunders and A. Aragon- Zavala, (2007) and Rappaport, (2002).

$$Pathloss, L = \frac{P_{TI}}{P_{RI}} = \frac{P_T G_T G_R}{P_R L_T L_R} \tag{2.4}$$

The main goal of propagation modelling is to predict L as accurately as possible, allowing the range of a radio system to be determined before installation. The maximum range of the system occurs when the received power drops below a level which provides just acceptable communication quality. This level is often known as the receiver s. The value of L for which this power level is received is the maximum acceptable path loss. It is usual to express the path loss in decibels, so S. Saunders and A. Aragon- Zavala, (2007).

$$L_{dB} = 10 \log \frac{P_{TI}}{P_{RI}} \tag{2.5}$$

2.4 Propagation Models

To solve the problem of capacity and coverage in cellular mobile networks, network operators develop propagation models in predicting receive signal strength in the world. Propagation models are mathematical attempts to model the real radio environment as closely as possible. The propagation path loss which is a major limiting factor to coverage prediction is derived from all losses encountered by the signal in its propagation from the base station (BS) tower to the mobile user or mobile station (MS)

Propagation models are useful for predicting signal attenuation or path loss which is the reduction in power of an electromagnetic wave as it propagates through space. It is a major component in the analysis and design of the link budget of a communication system. It depends on frequency, antenna height, receive terminal location relative to obstacles and reflectors, and link distance, among many other factors. Propagation models to be discussed include traditional propagation models such as geostatistical, geospatial, electrodynamic, statistical, empirical, deterministic and stochastic while the newer propagation models include heuristic models and computational intelligence.

2.5 LITERATURE REVIEW

In (Benmus *et al.,* 2015), an ANN was used to develop a model for estimating path loss in the Great Tripoli area considering five different area types (dense urban, urban, dense suburban, suburban, and rural) in the 900, 1800, and 2100 MHz frequency bands. Also in (Ofure *et al.,* 2016), an ANN was used to develop path loss propagation models that considered atmospheric parameters, relative humidity, and dew point, as input parameters. The models were used in estimating the reception power of GSM signals. An MLP network architecture and the weight and bias value were used in the development of the models. The performance of the proposed models was tested and found to be efficient with a mean squared error (MSE) of 0.056. In (Eichie *et al,* 2017), developed an ANN-based path loss model for signal quality estimation in rural and urban areas. They relied on a feed-forward network

topology and the Matlab Network Toolbox learning algorithm; specifically, they used the Levenberg–Marquardt approach with 31 to 39 neurons in incremental steps of 2. The model performance was then compared with existing techniques. Performance results show that the proposed model outperforms basic empirical models. The proposed method demonstrated significant improvements, comparable to analytical models, and revealed faster computation time due to the intrinsic parallelism of an ANN architecture. Neural network parameters were derived (Popoola *et al.,* 2019) for path loss prediction in VHF and UHF bands for wireless communications. Also, the developed model was compared with known empirical models, and it was observed that the model shows a better performance in prediction, accuracy, and generalization ability. Authors (Y. Zhang *et al.,* 2019) reported the principle, method, and data expansion methods of machine learning for path loss prediction for fifth-generation (5G) mobile networks. Measured data were used to estimate the performance of different propagation models such as the artificial neural network (ANN), support vector regression (SVR), and random forest (RF) alongside the log-distance model. Also, methods on how data expands to generate considering the amount of training samples for the system were presented. It was shown that the machine learning algorithms exhibit better performance than the log distance propagation model. However, open research areas to be exploited were also reported. In (Popoola *et al.,* 2019) conducted a study on the characterization of path loss in the very high frequency (VHF) band by exploiting the neural network modelling technique. The article reported how the propagation loss through frequency band 30–300 MHz is characterized based on the ANN algorithm and its attributes such as the activation functions and training algorithms based on the measured data at 203.25 MHz. The developed model was compared with the widely used empirical models, and it was observed that the ANN-developed model outperformed the empirical models based on the statistical analysis results which also recorded a correlation coefficient (R) of 0.95. 3.3. Evolutionary Computing. Evolutionary computing has also experienced significant attention from researchers within the path loss prediction area, where several works report the use of evolutionary algorithms. Similarly, in (Cavalcanti *et al.,* 2017) a genetic algorithm (GA) path loss models were developed for the prediction of losses for LTE and LTE advance networks. The GA was used in tuning the Free Space and Ericsson models. Findings from the work revealed a resemblance of the model's predictions with the actual measurement data. The swarm intelligence expression was introduced in the cellular robotic systems context by Beni and Wang in 1989. Swarm intelligence has also been utilized in various areas in which it has gained attention, including problem forecasting. Swarm intelligence is typically associated with three different algorithms. The most widely used, as found in the literature, is particle swarm optimization.

In (He et al., 2016). It was reported that the adoption of particle flight path information, which is used by the particle swarm optimization algorithm to train a radial basis function (RBF)-based neural network model to create a self-adaptive PSO-RBF NN algorithm for path loss estimation. Furthermore, in (Olukunle *et al.,* 2017), PSO was used to optimize some empirical path loss models for urban outdoor path loss estimation at the 2300 MHz frequency for LTE network systems. The measurement campaign was conducted in the urban areas of Port Harcourt, Nigeria. The modified model was compared with Okumura-Hata, COST 231, Ericsson 999, ECC-33, and Egli models for the specified environments. For the performance metrics, the RMSE and the MAE were used to gauge the models' efficacies. The results obtained were promising with RMSE and MAE values of 3.030 dB and 0.00162 dB, respectively. Hence, the PSO-modified model could be used for the deployment of the long-term evolution (LTE) wireless communication systems in the study locations.

Usman et al. (2015) examined the change in wireless mobile communication signal strength with weather and environmental factors in Bauchi. The investigation caused signal intensity to vary in different areas, although similar results were achieved at different times in the same location. Similarly, Ayekomilogbon et al. (2013) discovered seasonal variability in the influence of trees on radio waves due to variations in the electrical constants (conductivity and permittivity) of the trees in their research of signal degradation as a function of leaf density. Similarly, Nwawelu et al. (2012) discovered that trees and buildings have a considerable impact on wireless mobile network received power levels.

Ogbulezie et al. (2013) studied the applicability of two fundamental propagation models for GSM 900 and 1800MHz for the cities of Port Harcourt and Enugu, as well as Abuja, Kaduna, and Kano in Nigeria. Measurements from cities were compared to estimates from the Okumura Hata and COST-231 Hata models, and the classical models were shown to overestimate route loss in all cities. Similarly, due to the effect of terrain, the research indicated that route loss is not consistent at diverse sites for a constant distance surrounding the corresponding Base Transceiver Station (BTS) Benmus et al. (2016) used an ANN technique to construct an empirical model for predicting propagation path loss at 900MHz, 1800MHz, and 2100MHz in Tripoli, Libya. The results showed that the ANN path loss model agreed with the desired path loss with MSE values ranging from 3.7 to 6.7.

Recently, different ANN approaches were introduced to predict signal path loss in wireless communication networks Ayadi *et al.,* (2017) developed a new method for multi-band heterogeneous wireless network scenarios

using the ANN technique. In Eichie *et al*., (2017) Multilayer Perceptron (MLP) neural model was developed to predict path losses when radio signals are transmitted at frequencies within Global System for Mobile Communications (GSM) band. The developed neural network model predicts path loss based on three input variables namely: distance, transmit power and terrain elevation.

Angeles et al. (2015) used a three-stage technique to construct an ANN model for the GSM spectrum. The model included 33 neurons in the hidden layer, as well as a tansig (hyperbolic tangent sigmoid) transfer activation function.

Similarly, machine learning is a technique for enhancing system performance that is based on a flexible model architecture and a large amount of relevant data. Machine learning has recently acquired popularity in a variety of sectors, including autonomous driving, computer vision, and speech recognition. Previous research has looked into the feasibility of several machine-learning techniques for path loss prediction (Popoola et al., 2018). Finally the principle of ANFIS was introduced to path loss predictions to overcome the shortcomings of the empirical and deterministic models (Popoola *et al.,* 2019).

3. Review Methodology

This section describes the research processes used to review existing publications in the domain of mobile radio propagation for path loss prediction. In addition, we described how the selected papers were chosen using a set of inclusion and exclusion criteria.

3.1 Literature Search and Data Sources.

The systematic review was strategic in that the primary search terms were carefully chosen to find the appropriate works for the study. The following terms are specifically used to search for relevant research on mobile radio propagation for route loss prediction from relevant academic databases as they pertain to the study.

3.2. Study Selection Procedure.

The study selection approach was carefully developed to ensure a thorough examination of the literature. papers relevant to this study were acquired from several academic databases; specifically, 711 papers were retrieved and analyzed. This collection was reduced to 200 after a title check and 72 after an abstract check. Based on the full contents of the papers, 72 articles were thoroughly edited to provide a final list of 36 articles. Table 3.1 shows the database and its data sources.

3.3. Studies Inclusion/Exclusion Criteria.

Both inclusion and exclusion criteria were established to choose the most relevant publications for the investigation. The main literature elements were chosen by reading through the title, abstract, and complete content of the selected articles to arrive at the final list.

Table 3.1 Database Used as Data Source

Academic Database	URL Address
IEEE Explorer	http://ieeexplore.ieee.org/
Springer	http://www.springer.com/
Taylor & Francis	http://taylorandfrancis.com/
ISI Web of Science	https://apps.webofknowledge.com/
Science Direct	http://www.sciencedirect.com/
Scopus	https://www.scopus.com/
ACM Digital Library	https://www.dl.acm.org/
Google Scholar	https://scholar.google.com/

4. Results And Discussion

To pick the most relevant papers for the study, both inclusion and exclusion criteria were established. To arrive at the final list, the main literature aspects were chosen by reading the title, abstract, and complete content of the selected papers.

4.1. Application of Deep Learning. Deep learning is the new generation of the ANN which is currently attracting tremendous attention from the research community. However, surprisingly deep learning remains unexploited in propagation path loss prediction notwithstanding it is effectiveness, efficiency, and robustness in solving real-world problems. Empirical evidence from the literature has proven that deep learning architectures such as the deep belief network, convolutional neural network, attentive deep neural network, stack auto encoder, generative

adversarial network, deep reinforcement learning, deep long short-term memory, and deep recurrent neural network among many others can handle machine learning problems such as prediction, clustering, and classification better than the shallow ANN currently in use for propagation path loss prediction especially when the amount of the data size is large. As such, this survey suggests researchers explore these architectures of the new generation ANN in the domain of propagation path loss.

4.2. Multi-terrain Model. Observations from the survey pointed out that propagation path loss prediction is mainly conducted for a single terrain. Therefore, the model developed based on any CI algorithm for a particular terrain is limited for the prediction of path loss within the terrain. The result obtained from such a model cannot be generalized to other terrains. The multi-terrain propagation path loss prediction model remains an open issue. It is suggested researchers apply deep learning architecture because of its ability to handle large-scale data to investigate the possibility of propagation path loss prediction for multiple terrains.

5. Conclusion

This study presents a systematic literature review on mobile radio propagation path losses for different environments and spanning different operating frequencies. The literature review covered different classes of mobile propagation models as follows: fuzzy sets, artificial neural networks (ANNs), evolutionary algorithms, swarm intelligence (SI), and artificial immune systems (AISs). The current status of the application of AI and CI techniques for path loss prediction, research trends in the past few years, open research problems and future research areas and expectations are outlined in the paper. It was also discovered that the efforts made by researchers to propose a better model for the prediction of path loss in different terrains have at times led to the testing and simultaneous application of two different CI techniques in a specific environment. The comprehensive review presented in this paper can thus become a first point of reference for new researchers interested in radio propagation and channel modelling. Also, expert researchers in channel modelling or radio propagation can use this review to gain further insight when suggesting a novel approach for path loss prediction.

Acknowledgement

This research was conducted under the auspices of the Telecommunication Department of the Federal University of Technology Minna, Nigeria. The authors would like to express their sincere appreciation to the Federal University of Technology Minna for an up-to-date e-Library facility that enhanced the research for this study.

REFERENCES

Abraham U.U., Okpo U. O. & Elijah E. O. (2015) Macrocel Path Loss Prediction Using Artificial Intelligence Techniques. *International Journal of Electronics,* 101:4, 500-515, DOI:10.1080/00207217.2013.792040

Adebowale, Q. R., Faruk, N., Adewole, K. S., Abdulkarim, A., Olawoyin, L. A., Oloyede, A. A., Chiroma, H., Usman, A. D., &Calafate, C. T. (2021a). Application of Computational Intelligence Algorithms in Radio Propagation: A Systematic Review and Metadata Analysis. In *Mobile Information Systems* (Vol. 2021). Hindawi Limited. https://doi.org/10.1155/2021/6619364

Surajudeen-Bakinde, N. T., Faruk, N., Popoola, S. I., Salman, M. A., Oloyede, A. A., Olawoyin, L. A., & Calafate, C. T. (2018a). Path loss predictions for multi-transmitter radio propagation in VHF bands using Adaptive Neuro-Fuzzy Inference System. *Engineering Science and Technology, an International Journal*, *21*(4). https://doi.org/10.1016/j.jestch.2018.05.013

Rappaport T.S. (2017). Wireless Communications, Principles Practice. In *IBM technical disclosure bulletin* (Vol. 28, Issue 7).

Popoola, S. I., Misra, S., &Atayero, A. A. (2018e). Outdoor Path Loss Predictions Based on Extreme Learning Machine. *Wireless Personal Communications*, *99*(1), 441–460. https://doi.org/10.1007/s11277-017-5119-x

Popoola, S. I., Atayero, A. A., &Faruk, N. (2018b). Received signal strength and local terrain profile data for radio network planning and optimization at GSM frequency bands. *Data in Brief*, *16*, 972–981. https://doi.org/10.1016/j.dib.2017.12.036

Popoola, S. I., Atayero, A. A., Arausi, O. D., & Matthews, V. O. (2018b). Path loss dataset for modelling radio wave propagation in smart campus environment. *Data in Brief*, *17*. https://doi.org/10.1016/j.dib.2018.02.026

Ogbulezie, J. C., M. U. Onuu, J. O. Ushie, and B. E. Usibe, (2013) "Propagation models for GSM 900 and 1800MHz for Port Harcourt and Enugu, Nigeria," *Network and Communication Technologies*, Vol. 2, No. 2, 1–10, 2013b.

Oni, O. O., &Idachaba, F. E. (2017). Review of Selected Wireless System Path loss Prediction Models and its Adaptation to Indoor Propagation Environments. *Lecture Notes in Engineering and Computer Science*, *2228*

Nasir F., Segun I. P, Nazmat T. S., Abdulkarim A.O., Abubakar A., Lukman A. O., MaarufA., Caslos T. C. &Aderemi A. A. (2019). "Path Loss Predictions in VHF and UHF bands within Urban Environments: Experimental Investigation of Empirical, Heuristics and Geospatial Models" *IEEE Access*, (7),1-14, DOI: 10.1109/ACCESS.2019.2921411.

Matthews, V. O., Osuoyah, Q., Popoola, S. I., Adetiba, E., &Atayero, A. A. (2017). C-BRIG: A network architecture for real-time information exchange in smart and connected campuses. *Lecture Notes in Engineering and Computer Science*, *2229*.

Julia O. E., Onyedi D. O., Moses O. A. &Abiodun M. A. (2017).Comparative Analysis of Basic Modes and Artificial Neural Network-Based Mode for Path Loss Prediction. *Progress in Electromagnetics Research M*, (61), 133-146.

Malevich, E. S., Mikhailov, M. S., &Volkova, A. A. (2019). Comparison of the Results of an Experimental Research of the Radio Wave Propagation in the Forest with Numerical Simulation. *Conference Proceedings - 2019 Radiation and Scattering of Electromagnetic Waves, RSEMW 2019*.

Erunkulu, O. O., Zungeru, A. M., Lebekwe, C. K., &Chuma, J. M. (2020). Cellular Communications Coverage Prediction Techniques: A Survey and Comparison. In *IEEE Access* (Vol. 8, pp. 113052–113077). Institute of Electrical and Electronics Engineers Inc. https://doi.org/10.1109/ACCESS.2020.3003247

De Sousa, M. N., &Thomä, R. S. (2018). Mobile Station Localization Emitter in Urban NLoS using Multipath Ray Tracing Fingerprints and Machine Learning. *ICL-GNSS 2018 8th International Conference on Localization and GNSS: Seamless Indoor-Outdoor Localization, Proceedings*. https://doi.org/10.1109/ICL-GNSS.2018.8440898

Aldossari, S., & Chen, K. C. (2019). Predicting the Path Loss of Wireless Channel Models Using Machine Learning Techniques in MmWave Urban Communications. *International Symposium on Wireless Personal Multimedia Communications, WPMC*, *2019-November*. https://doi.org/10.1109/WPMC48795.2019.9096057

Bakare, B. I., Ngeri, T. E., &Orike, S. (2018). Comparative Analysis of Signal Strength of Some Cellular Networks in Port Harcourt, Nigeria. *European Journal of Electrical Engineering and Computer Science*, *2*(6). https://doi.org/10.24018/ejece.2018.2.6.33

Bailey, W. H., Cotts, B. R. T., &Dopart, P. J. (2020). Wireless 5G Radiofrequency Technology – An Overview of Small Cell Exposures, Standards and Science. *IEEE Access*, *8*. https://doi.org/10.1109/ACCESS.2020.3010677

Castañeda-Miranda, A., &Castaño-Meneses, V. M. (2020). Internet of Things for smart farming and frost intelligent control in greenhouses. *Computers and Electronics in Agriculture*, *176*. https://doi.org/10.1016/j.compag.2020.105614

Cheerla, S. (2020). Analysis of Different Path Loss Models in Urban Suburban and Rural Environment. *International Journal of Emerging Trends in Engineering Research*, *8*(7), 2972–2976. https://doi.org/10.30534/ijeter/2020/14872020

Eichie J. O., O. D. Oyedum, M. O. Ajewole, and A. M. Aibinu,(2017). ''Artificial neural network model for the determination of GSM level from atmospheric parameters,'' *Eng. Sci. Technol., Int. J.*, vol. 20, no. 2, pp. 795–804, Apr. 2017.

Cavalcanti B. J., d'Assunção A. G., and Mendon L. M., (2017) "Optimizing empirical propagation models for LTE and LTEA using genetic algorithms at 879 MHz," in Proceedings of the 2017 IEEE- APS Topical Conference on Antennas and Propagation in Wireless Communications (APWC), Verona, Italy,https://ieeexplore.ieee.org/author/37531408200.

Nwawelu, U. N., A. N. Nzeako, and M. A. Ahaneku, (2012) "The limitations of campus wireless networks: A case study of University of Nigeria, Nsukka," *International Journal of Networks and Communications*, Vol. 2, No. 5, 112–122, 2012.

Nwalozie, G. C., S. U. Ufoaroh, C. O. Ezeagwu, and A. C. Ejiofor, (2014) "Pathlossprediction for GSMmobile networks for the urban region of Aba, South-East, Nigeria," *International Journal of Computer Science and Mobile Computing*, Vol. 3, No. 2, 267–281, 2014.

Ogbulezie, J. C., M. U. Onuu, J. O. Ushie, and B. E. Usibe, (2013) "Propagation models for GSM 900 and 1800MHz for Port Harcourt and Enugu, Nigeria," *Network and Communication Technologies*, Vol. 2, No. 2, 1–10, 2013b.

Benmus T. A, R. Abboud, and M. K. Shatter,(2015) ''Neural network approach to model the propagation path loss for great Tripoli area at 900, 1800, and 2100 MHz bands,'' in *Proc. 16th Int. Conf. Sci. Techn. Autom. Control Comput. Eng. (STA)*, 2015, pp. 793–798

Benmus, T. A., R. Abboud, and M. K. Shater, (2016) "Neural network approach to model the propagation path loss for great Tripoli area at 900, 1800 and 2100MHz bands," *International Journal of Sciences and Techniques of Automatic Control and Engineering*, Vol. 10, No. 2, 2121–2126, 2016.

Ayekomilogbon, O., O. Famoriji, and O. Olasoji, (2013) "UHF band radio wave propagation mechanism forested environments for wireless communication systems," *Journal of Information Engineering and Applications*, Vol. 3, No. 7, 11–16, 2013.

Angeles J.C.D., E.P. Dadios, (2015) "Neural network-based path loss prediction for digital TV macrocells, Humanoid, Nanotechnology, Information Technology, Communication and Control, Environment and Management (HNICEM), 2015 International Conference on, IEEE.Ayadi M, A. B. Zineb, and S. Tabbane, (2017) ''A UHF path loss model using learning machine for heterogeneous networks,'' *IEEE Trans. Antennas Propag.*, vol. 65, no. 7, pp. 3675–3683, Jul. 2017.

PAPER 61 – MITIGATING INTERFERENCE AND IMPROVING RESOURCE USAGE IN A DOWNLINK MU-MIMO TRANSMISSION FOR B5G NETWORKS

D. U. Onyishi[1], A. A. Masud[1*]

[1]Department of Electrical and Electronics Engineering, Federal University of Petroleum, Effurun, Nigeria.
[*]Email: abdulmujeebakajewole@gmail.com

ABSTRACT
In this paper, an Enhanced Mechanism for Downlink Multi-User Multiple Output Multiple Input (EMD-MU-MIMO) was proposed to improve the resource usage of the resource blocks and mitigate interference in a 5G and Beyond (B5G) network. The modified algorithm considered the mobility of users in the system to make the proposed algorithm adaptable to practical environmental settings. Simulation results showed that the EMD-MU-MIMO algorithm mitigated interference by 7.47% and 2.01% when compared with the conventional IEEE 802.11ax standard and the existing MD-MU-MIMO algorithm, respectively. Additionally, the EMD-MU-MIMO algorithm showed a mean percentage reduction in unnecessary resource usage by 26.13% and 4.67% when compared with the conventional IEEE 802.11ax standard and against the MD-MU-MIMO algorithm, respectively. Future works would delineate the impact of the modified algorithm in mitigating outage probability and showing the general improvement in the spectral efficiency of the system.

KEYWORDS: Outage probability, MIMO, MU-MIMO, Interference, Resource Usage

1. INTRODUCTION

The mobility of users in a downlink MU-MIMO system can have a significant impact on the network, which highly reduces the Quality of Service (Hassan *et al.*, 2020; Adikpe *et al*., 2023). In this work, we restrict the discussion to the impact of mobile users on resource usage and interference. When users move around in the system, their channel conditions change, which affects the allocation of resource blocks (RBs) and the level of interference in the system (Zhang & Jiang, 2021). As such, it is essential that mobile users are allocated the appropriate number of RBs to maintain a certain quality of service while minimizing interference. If a user is moving away from the Next Generation Node B (gNB), the signal quality may degrade, and the system needs to allocate more RBs to maintain a certain level of quality. Similarly, if a user is moving towards the base station, the signal quality may improve, and the system can allocate fewer RBs to maintain the same quality (Barri *et al*., 2021).

Due to the randomness of users' movement, the behaviour of users is unpredictable during a defined time gap. If a user moves randomly during the time gap, the wireless channel between the moving user and the transmitting BS or receiving User Equipment (UE) changes with the location of the moving user (Zhang & Jiang, 2021). As such, the instantaneous wireless channel mismatches with the weight of beams derived from measured channel information. Hence, the beams for each receiving node may interfere with each other. The unpredicted inter-beam interference will degrade the performance of an MU-MIMO transmission and consequently increase the probability of an outage in the system. In the work of Lee *et al.*, (2018), the influence of inter-beam interference on the outage probability performance was exploited, but the randomness of interference was not considered. Hassan *et al*., (2020) proposed several techniques for joint transmit and receive beamforming in downlink multi-user MIMO systems under Rayleigh fading channel. Nonetheless, the mobility of users was not considered. Nalband *et al.*, (2020) evaluated the achievable sum rate and highlighted the energy efficiency properties of mmWave massive MIMO systems. The drawback of the work was that the effect of inter-beam interference was not considered. This could reduce the reliability of the approach in improving the spectral efficiency of the system. Arsal *et al*., (2021) identified that the computational complexity of expressions used to compute the outage probability and coverage probability increased as the number of transmit antennas and scheduled users on the same frequency response grew. A primary aspect of the work was focused on minimizing the computational complexity in computing the coverage probability, however, the SIR values of users connected to the same cell were not considered. These drawbacks are likely to reduce the approaches' performance in practical environments. The work of Huh *et al.*, (2021) utilized signal processing optimization to address digital federated learning and over-the-air compression schemes under muMIMO uplink systems. However, the drawback of the approach was that the computational complexity was high, which could affect the reliability of the communication link. In the work Barri *et al.*, (2021), the influence of interference and resource usage was considered, however, the mobility

of users was not taken into account. Kinol *et al*., (2022) proposed a novel low-complexity radix factorization-based fast Fourier transform multi-beam former and maximal likelihood –multi-user detection (MLMUD) techniques as signal detector and was customized with sub-detector systems which minimized complexity reduction with intolerable error rate performance. The shortcoming of the approach was that the computational complexity was high, which could affect the reliability of the communication link. For most of the literature, users were assumed to be stationary and if the mobility of the users was considered, the approach adopted was computationally complex.

Additionally, the mobility of users in an MU-MIMO system can also impact the channel estimation process. As users move, the channel conditions between the user and the base station change, and the channel estimation needs to be updated to ensure accurate signal transmission. The update rate of the channel estimation process needs to be carefully designed to balance the trade-off between accuracy and overhead. Overall, the mobility of users in a MU-MIMO system presents several challenges for resource usage and interference management. And proffering a balance to mitigate interference and improve resource usage is worth discussing.

Motivated by the discussion above, this paper considers the non-consideration of mobility in the work of Barri *et al*., (2021) and modifies the existing Mechanism for Downlink in a Multi-User MIMO (MD-MU-MIMO) algorithm to not only consider stationary users but also the randomness of mobile users. Furthermore, the modified algorithm is discovered to minimize unnecessary resources and mitigate interference in the system.

2. MATERIALS AND METHODS

This paper modifies the existing MD-MU-MIMO algorithm in the work of Barri *et al*., (2021) to improve resource usage and minimize interference in the MU-MIMO system. As such, this work develops a closed-form expression of the outage probability for both mobile and stationary UEs on the downlink MU-MIMO system. As such, it defines the events to identify mobile and stationary UEs at the start of the time frame, which would aid in evaluating the expected outage probability for the weighted probability of UE events on the downlink MU-MIMO as identified in the work of Masud *et al*., (2023).

In a real-world network environment, UE placement within a coverage area is random. In a MU-MIMO transmission, inter-beam interference and the number of received interference are innately influenced by the mobility state of the UEs. According to (Zhang & Jiang, 2021), continuous measurement of the channel state would probably be computationally challenging because the channel's state, the power delivered, etc., are all dynamic. In this paper, the data transfer to UEs is taken into account within a time frame to reduce this complexity. Additionally, the power transmitted and the channel's condition are thought to remain consistent during this time. These assumptions are adopted in this work. In this discrete time, it is easier to investigate the co-channel interference and inter-beam interference. Furthermore, this consideration makes allowance for the evaluation of a closed-form outage probability of an instantaneous MU-MIMO transmission. As a result, this work considers the placement of UEs in a coverage area to be randomly allocated according to Spatial Poisson Point Process (SPPP) with intensity ($\varkappa$). The set of BS is represented as $\Omega(\varkappa) = \{\mathrm{B_i}\}$, where Bi is the position of the BS, at an instant in time, *i*.

In the data transmission phase of MU-MIMO, the received signal of the receiving UE, k, is mathematically given as (Lee et al., 2018):

$$y_k = \sqrt{\frac{P_t}{K} D_k^{-\beta}}\, \boldsymbol{h}_k^H \boldsymbol{w}_k \boldsymbol{s}_k + \sum_{j \in K, j \neq k} \sqrt{\frac{P_t}{K} D_k^{-\beta}}\, h_k^H \boldsymbol{w}_j \boldsymbol{s}_j + \sum_{\tau \epsilon \Phi / T_k} \sqrt{P_t |\Omega_\tau|^{-\beta}}\, g_{\tau k} s_\tau + n_k \qquad (1)$$

where:

y_k denotes the receiving signal of the receiving UE
k is a receiving UE
P_t represents the transmit power
T_k depicts the BS
$\boldsymbol{h}_k \epsilon \mathbb{C}^{N_t \times 1}$ represents the channel gain vector between the k and T_k
$\boldsymbol{g}_{\tau,k} \epsilon \mathbb{C}^{1 \times 1}$ represents the channel gain vector between the k and τ
$\boldsymbol{S}_k \epsilon \mathbb{C}^{K \times 1}$ denotes the symbol transmitted from the BS
n_k depicts the additive white Gaussian noise (AWGN) with zero mean and variance of σ^2

$\sqrt{\frac{P_t}{K} D_k^{-\beta}} \boldsymbol{h}_k^H \boldsymbol{w}_k \boldsymbol{s}_k$ represents the desired signal

$\sum_{j \in K, j \neq k} \sqrt{\frac{P_t}{K} D_k^{-\beta}} h_k^H \boldsymbol{w}_j \boldsymbol{s}_j$ denotes the inter-beam interference signal

$\sum_{\tau \epsilon \Phi / T_k} \sqrt{P_t |\Omega_\tau|^{-\beta}} g_{\tau k} s_\tau$ depicts the co-channel interference signal

For the receiving UE, *k*, whether the inter-beam interference signal exists or not depends on whether the wireless channels change with respect to the location of the BS during the time frame or not. The orthogonality of the beams and the elimination of inter-beam interference are both possible in a scenario where the UEs remain stationary during a discrete time. In contrast, the beam for a moving UE interferes with the other beams while the beam for a stationary UE interferes with the beams for the moving UEs. To assess the effectiveness of a MU-MIMO transmission, the behaviour of UEs is divided into categories based on the presence or absence of inter-beam interference and the quantity of interference beams that have been received. This paper defines a number of events to illustrate the behaviour of UEs in the following manner, which simplifies the calculations. When the event $\mathcal{H}_2$ with 0 < M < K occurs, the beam for a motionless UE has interfered with the beams for M moving UEs, but the beam of a moving UE has interfered with the beams for K − 1 UEs. In light of the aforementioned, the proposed measurement of the instantaneous received SINR for motionless and moving UEs is represented as an event $\mathcal{H}_2^s$ and $\mathcal{H}_2^m$, respectively. As such, this paper considers two cases. The first case considers an event in which the UEs of an MU-MIMO system are both keep motionless during the time frame and is denoted as an event $\mathcal{H}_1$. For case two, an event that the $M(1 < M \leq K)$ UEs move during the time frame is denoted by the event $\mathcal{H}_2$.

The outage probability of an MU-MIMO transmission is defined as the probability that instantaneous received SINR does not exceed that required SINR threshold. The expected outage probability is the sum of the outage probability weighted by the probability of defined events. Assuming the SINR threshold is ξ_{thres}, hence, the expected outage probability proposed in this research work is given as:

$$P_k^{exp}(\xi_{thres}) = \sum_{i=1}^{2} \wp(\mathcal{H}_\mathrm{i}) \wp(\xi_{k,\xi_{thres}}^{ins})$$

$$= \wp(\mathcal{H}_1) \wp\left(\xi_{k,\xi_{thres}}^{ins}\right) + \wp(\mathcal{H}_2) \times \left[\wp(\mathcal{H}_2^s) \wp\left(\xi_{k,\mathcal{H}_2^s}^{ins} \leq \xi_{thres}\right) + \wp(\mathcal{H}_2^m) \wp\left(\xi_{k,\mathcal{H}_2^m}^{ins} \leq \xi_{thres}\right)\right] \quad (2)$$

where $\wp(\mathcal{H}_\mathrm{i})$ represents the probability of the event $\mathcal{H}_\mathrm{i}$ and $\xi_{k,\mathcal{H}_i^s}^{ins}$ depicts the instantaneous received SINR of the receiving node k when the event $\mathcal{H}_i$ occurs. The input parameters required to simulate and model the network topology of the wireless cellular network consider the variables for the mobile and stationary UEs. Before calculating each user's resource block, the work examines the mobility state of events for connected UEs. For the two states, the resources are calculated for one where the interference's impact, that is, when $\phi = 0$ is removed and another where the interference is taken into account, that is $\phi = 1$. The outage probability used to determine the latter and former aforementioned is delineated in (3) and (4), respectively.

$$P_k^{ins}(\xi_{thres}) = \varkappa Q \omega^{2/\beta} \left(1 + \sum_{m=1}^{N_t - K} \frac{1}{m!} \prod_{l=0}^{m-1} (m - \delta)\right) \quad (3)$$

$$P_k^{ins}(\xi_{thres}) = 1 - \frac{e^{-\varkappa Q \omega^\delta}}{(1 + 2\rho\omega)^U} \quad (4)$$

Where β Path loss exponent, N_t is the transmit antenna; *m* depicts the mobile receiving UEs, *K* is the receiving UEs, $\delta = 2/\beta$, $\mathrm{Q} = \mu\Gamma(\delta)\Gamma(1-\delta)$, $\rho = 1/\mathrm{KD}_\mathrm{k}^\beta$ and $\omega = \xi_{thres}/\rho$. $S_k = |\boldsymbol{h}_k^H \boldsymbol{w}_k|^2$

2.1 Proposed EMD-MU-MIMO Algorithm

Algorithm 1 delineates the EMD-MU-MIMO algorithm. The algorithm considers a network architecture that considers the mobility states of UEs. The mobility of UEs is an essential factor that influences the overall performance of the MU-MIMO system in a pragmatic environmental setting. As such, the proposed network model considers UEs to be randomly distributed around the coverage area of the BS. This case scenario for this extends the model in Barri *et al*., (2021). Algorithm 1 considers two cases in the EMD-MU-MIMO algorithm. The first event was denoted as $\mathcal{H}_1$ indicates that the UEs are stationary at the start of a set time frame and remain

stationary during a duration not less than T_{Frame}. In the second scenario, $\mathcal{H}_2$ considers the movement of the UE during T_{Frame}. The variables for these mobility events are considered in the input parameters that are needed to simulate and model the network topology of the wireless cellular network. For UEs that are connected to the gNB, the work checks the mobility state of events before computing each user's resource block. Concerning the two states, the resources are computed for one in which the effects of interference are removed, that is, where $\phi = 0$ and another in which the interference is considered, that is $\phi = 1$. The purpose of this modification is to minimize the processing time when considering the conditions to either include inter-beam interference or not. The proposed EMD-MU-MIMO algorithm would lower the probability of an outage in the network.

Algorithm 1 Proposed EMD-MU-MIMO algorithm

Input $\mathcal{H}_i, T_{Frame}, i,\ \mathcal{H}_2^s$ *and* $\mathcal{H}_2^m$

Input Number of MIMO layers, Bandwidth, frequency range, modulation type

Output RBs, SINR, and average data rate

For simulated network topology, users at time instant, U_i are uniformly or randomly distributed
  For each U_i
    If *i* is connected
      For each U_i trying to connect
        Calculate the maximum data rate the UE can achieve
        i ++
      End for
      Else
        i ++
        Evaluate the expected outage probability using equation (2)
        Compute PDF on events $\mathcal{H}_i$
        If $\phi = 0$
          Compute outage probability using equation (3)
          Compute Reach user's RB
        Else
        If $\phi = 1$ and 0 < M < K
          Compute outage probability using equation (4)
          Compute each user's RB
        End if
        End if
    End if
  End for
  For each cell topology
    Calculate BSs power allocated to the connected users
    Compare scenarios with conventional allocation
    K++
  End for
End for

The simulation parameters adopted for the EMD-MU-MIMO algorithm are as follows (Barri *et al*., 2021; Zhang & Jiang, 2021): Transmit antenna, $N_t = 25$; Receiving antenna, $N_r = 4$; Receiver Noise Power, P_{rn}=-32dBm; Link rate, $L_r = 867Mbits/s$; Resource block frames UL, $RB_{UL} = 275$; Resource block frames DL, $RB_{DL} = 275$; Users for each scenario, $U_i = 200, 250, 300$; Path loss exponent, β=4; SINR threshold, $\xi_{thres} = -30dB$; Average time interval, $\theta = 1s$; Number of discrete rates, L = 4. These values are used to evaluate the performance of the conventional IEEE 802.11ax approach, the mechanism for downlinking MU-MIMO, and the modified Efficient Mechanism for downlinking MU-MIMO (EMD-MU-MIMO) adopted in this work.

3. RESULTS AND DISCUSSION

This section presents and discusses the simulation results implemented to measure the performance of the EMD-MU-MIMO algorithm to mitigate unnecessary resource usage and interference in a MU-MIMO system adopted in the work of Barri *et al*., (2021). The results obtained using the proposed EMD-MU-MIMO system are compared against the conventional IEEE 802.11ax standard and the MD-MU-MIMO algorithm.

3.1 Interference

Figure 1 shows the result of the performance of the conventional IEEE 802.11ax standard, the MD-MU-MIMO algorithm, and the EMD-MU-MIMO algorithm in mitigating interference in an MU-MIMO system. In this paper, the interference is considered for three use case scenarios for each user. As in the work of Barri *et al.,* (2021) the three scenarios were designed to run at a total of fifty times. In these iterations, the mobility of the user was only considered for the EMD-MU-MIMO algorithm and the distribution of the users was considered to be random to make the scenario more realistic. This was compared against the interference observed from the conventional IEEE 802.11ax standard and the MD-MU-MIMO algorithm that considered the distribution of the UE to be uniform in the later and randomly distributed in the former. However, the mobility of the UE was not considered as in the work of Barri *et al*., (2021). On this premise, it was observed that the MD-MU-MIMO algorithm and the EMD-MU-MIMO had a mean percentage reduction of 5.56% and 7.47%, respectively, in the interference observed in the MU-MIMO system when compared with the conventional IEEE 802.11ax standard. Additionally, the average percentage improvement of the proposed EMD-MU-MIMO had a 2.01% improvement against the MD-MU-MIMO algorithm in the interference observed in the MU-MIMO system. In the subsequent report, this percentage improvement of the proposed EMD-MU-MIMO algorithm is expected to further increase when the mobility of the UE is also considered in the conventional IEEE 802.11ax standard and the MD-MU-MIMO algorithm.

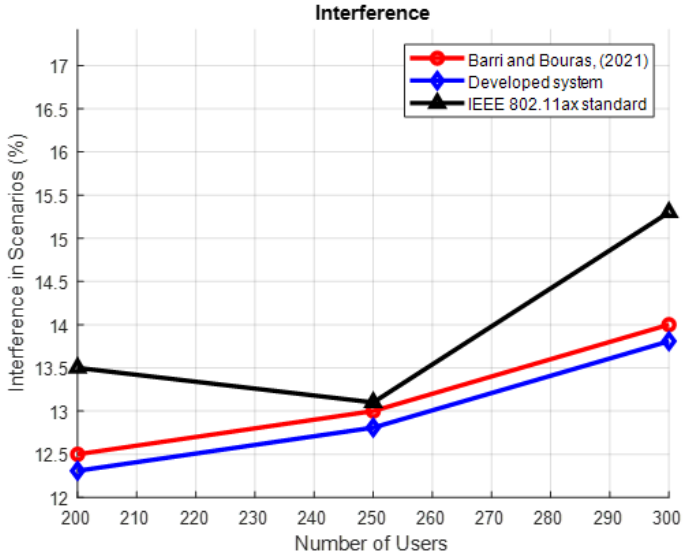

Figure 1: Interference for Three Use Case Scenarios for Each User

3.2 Resource Usage

Figure 2 shows the result of the performance of the conventional IEEE 802.11ax standard, the MD-MU-MIMO algorithm, and the EMD-MU-MIMO algorithm in improving resource usage in MU-MIMO. In this study, resource usage is considered for three use case scenarios for each user. The three scenarios were planned to run a

total of fifty times, similar to the research by Barri *et al*., (2021). The EMD-MU-MIMO algorithm was the only part of these iterations that took user mobility into account, and to make the scenario more plausible, the distribution of users was assumed to be random. This was compared to the observed resource utilization from the standard IEEE 802.11ax standard and the MD-MU-MIMO method, which assumed the distribution of the user equipment (UE) to be uniform in the latter and randomly distributed in the former. However, the mobility of the UE was not considered as in the work of Barri *et al*., (2021). On this premise, it was observed that the MD-MU-MIMO algorithm and the EMD-MU-MIMO had a mean percentage reduction of 29.36% and 26.13%, respectively, in the resource usage observed in the MU-MIMO system when compared with the conventional IEEE 802.11ax standard. In comparison, the average percentage improvement in the resource usage observed of the proposed EMD-MU-MIMO against the MD-MU-MIMO had a 4.67% improvement over the MD-MU-MIMO

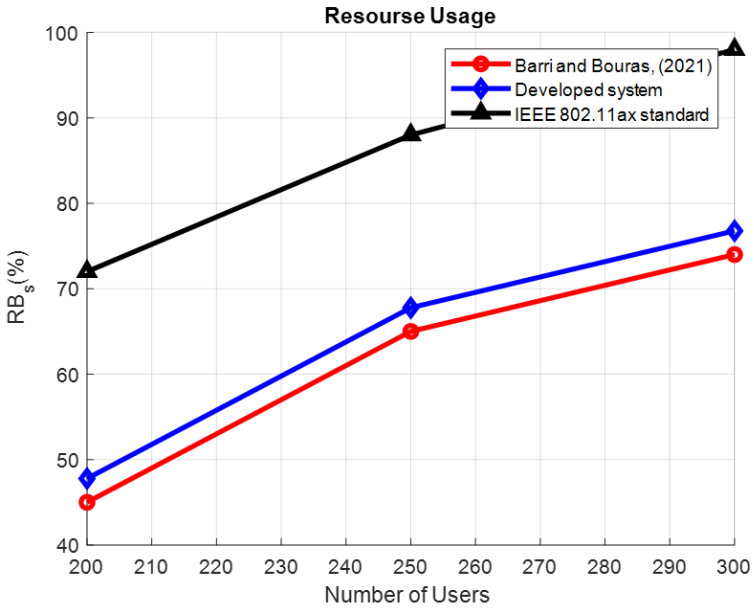

Figure 2: Resource Usage for Three Use Case Scenarios for Each User

4. CONCLUSION

This paper considers the mobility of users to modify an existing MD-MU-MIMO algorithm. As such, the modified algorithm termed EMD-MU-MIMO considers the mobile state of users in addition to the stationary state of users in the algorithm to minimize resources and mitigate interference in the MU-MIMO system. The developed algorithm was compared against the existing MD-MU-MIMO algorithm and the conventional IEEE 802.11ax algorithm. Results showed that the EMD-MU-MIMO algorithm mitigated interference by 7.47% and 2.01% when compared with the conventional IEEE 802.11ax standard and the MD-MU-MIMO algorithm, respectively. Additionally, the EMD-MU-MIMO algorithm showed a mean percentage reduction of 26.13% and 4.67% in resource usage when compared with the conventional IEEE 802.11ax standard and against the MD-MU-MIMO algorithm, respectively. Since mobility is a crucial part of this work, future works would also consider the mobility of the UE in the IEEE 802.11ax standard and the MD-MU-MIMO algorithm. This would aid in delineating the impact of the proposed EMD-MU-MIMO algorithm against the aforementioned algorithms in a more realistic scenario. Additionally, comparisons of the EMD-MU-MIMO algorithm against the conventional IEEE 802.11ax standard and the MD-MU-MIMO algorithm would be carried out with outage probability and spectral efficiency as performance metrics.

REFERENCES

Adikpe, A. O. Tekanyi, A. M. S. & Yaro, A. S. (2023). Mitigating the Signaling Resources Expended in 5G Location Management Procedures at Millimeter-Wave Frequencies. *Advances in Electrical and Electronic Engineering*, 20(4), 572-583.

Arsal, A., Civanlar, M. R., & Uysal, M. (2021). Coverage Analysis of Downlink MU-MIMO Cellular Networks. *IEEE Communications Letters*, *25*(9), 2859-2863.

Barri, E., Bouras, C., Kokkinos, V., & Koukouvela, A. (2021). A Mechanism for Improving the Spectral Efficiency in mu-MIMO for 5G and Beyond Networks. In *Proceedings of the 19th ACM International Symposium on Mobility Management and Wireless Access* (pp. 11-16).

Hassan, A. K., Moinuddin, M., Al-Saggaf, U. M., Aldayel, O., Davidson, T. N., & Al-Naffouri, T. Y. (2020a). Performance Analysis and Joint Statistical Beamformer Design for Multi-User MIMO Systems. *IEEE Communications Letters*, 24(10), 2152-2156.

Hassan, A. K., Moinuddin, M., Al-Saggaf, U. M., Aldayel, O., Davidson, T. N., & Al-Naffouri, T. Y. (2020a). Performance Analysis and Joint Statistical Beamformer Design for Multi-User MIMO Systems. *IEEE Communications Letters*, 24(10), 2152-2156.

Kinol, A. M. J., Nisha, A. S. A., Marshiana, D., & Krishnamoorthy, N. R. (2022). Hybrid Multi Beamforming and Multi-User Detection Technique for MU MIMO System. *Wireless Personal Communications*, *124*(4), 3375-3385.

Lee, S., Kim, S., Park, Y., Choi, S., & Hong, D. (2018). Effect of unpredictable interference on MU-MIMO systems in HetNet. *IEEE Access*, 6, 28870-28876.

Masud *et al*., (2023, April). Mitigating Interference and Improving the SINR in a Discrete Time Frame of a Downlink MU-MIMO Transmission in 5G and Beyond Wireless Networks. *Paper presented at the 2023 IEEE International Conference of Science, Engineering and Business for Driving Sustainable Development Goals, Omu-Aran, Kwara State.*

Nalband, A. H., Sarvagya, M., & Ahmed, M. R. (2020). Optimal hybrid precoding for millimeter wave massive MIMO systems. *Procedia Computer Science*, *171*, 810-819.

Zhang, W., & Jiang, S. (2021). Effect of Node Mobility on MU-MIMO Transmissions in Mobile Ad Hoc Networks. *Wireless Communications and Mobile Computing*, 2021.

PAPER 62 – DESCRIPTIVE ANALYSIS OF NASA WEATHER DATA USING MACHINE LEARNING ALGORITHM

Aneke Chikezie Samuel[1*], Philip Michael Asuquo[2], Simeon Ozuomba[3], Okechukwu Collins Eze[4], Chetachukwu P Ogbu[5]

[1,2,3]Department of Computer Engineering, University of Uyo, Akwa Ibom State, Nigeria
[4]Washington University in St Louis, Missouri, USA
[5]Verizon Business Group, Richardson, Texas, USA
*Email: anekechikezies@uniuyo.edu.ng

ABSTRACT
Descriptive Analysis of National Aeronautics and Space Administration (NASA) weather data using a machine learning algorithm is presented in this paper. NASA has provided a range of weather data capable of aiding in the prediction of various weather conditions. The paper looked at the prediction analysis of NASA weather data using 70128 entries from 2010 to 2017. Nine weather data were introduced and later scaled down to three namely Relative humidity, Temperature and Pressure. For temperature, the correlation coefficient between T2M and Next T2M, T2MWET and Next T2M, and RH2M and Next T2M is 0.96, 0.82 and -0.72 respectively. For Relative Humidity, the correlation coefficient between R2M and Next RH2M, Next RH2M and T2M is 0.96 and -0,7 respectively. For Pressure, the correlation coefficient between R2M and Next RH2M, Next RH2M and T2M is 0.96 and -0.7 respectively. This paper presented some machine learning algorithms to analyze NASA weather data in determining which algorithm is better suited for weather forecasting or prediction. Ridge Regression, Lasso Regression, Decision Tree Regression, and XGboost algorithm were used to validate their performances. The result showed that the XGboost algorithm performed better than the other algorithms with a root mean square error value (RMSE) of 0.26901and coefficient determination (R^2) value of 0.93385

KEYWORDS: Weather Forecasting, Machine learning, Algorithm, Performance, Temperature Prediction

1. INTRODUCTION

The study of weather is as old as creation itself, and it has always had a significant influence on people's environments and behaviour. The effects of disasters caused by weather and climate change can be lowered with prior knowledge of these factors. In this age of global warming, getting the most recent weather information and taking the necessary measures in light of recent environmental catastrophes brought on by climate change have become top priorities. The model that can forecast various weather data for any place on Earth, including those without weather stations, weather satellite coverage, or other weather measuring equipment, has been created. A lot of devices have been developed to aid in weather acquisition [1], [2].

Researchers have improved the accuracy of forecasts for a variety of important meteorological occurrences using machine-learning techniques. [3], [4], [5], [6]. By combining (i.e., ensemble) the results of different machine learning techniques in various domains, some researchers have recently tried to increase the performance of their predicting methods. [8], [9], [10].

The need for accurate meteorological forecasts is on the rise because some sectors need accurate weather prediction like the agriculture sector, maritime sector and the aviation sector. Correct weather prediction is very important in forecasting dangerous weather conditions to put up preventive measures. With regard to the measurement of atmospheric weather parameters, this research evaluates the forecasting accuracy of NASA data and also looked at the prediction analysis of NASA weather data.

To give clear guidance for predictive and prescriptive analyses, NASA weather data were examined through exploratory analysis and four machine learning algorithms were used for the analysis

2. THEORETICAL ANALYSIS

2.1 Data Cleaning and Pre-Processing

Although errors are frequently unavoidable, data cleaning might help to reduce them. An erroneous study conclusion might occur if these flaws are not corrected. Errors and inconsistencies are examples of dirty data. These data may result from any step in the study process, such as a defective research design, use of the wrong measurement tools, or incorrect data entry. While filthy data are faulty in one or more ways, clean data meet some criteria for high quality.

The NASA dataset was obtained in.csv format for analysis. The dataset is made up of nine (9) features which are Temperature, Dew Temperature, Wet Temperature, Specific Humidity, Relative Humidity, Precipitation, Surface Pressure, Wind Speed, and Wind direction. The dataset obtained from NASA does not require much pre-processing. The Year, Month, and Day columns were combined into a single column called Date.

	YEAR	MO	DY	HR	T2M	T2MDEW	T2MWET	QV2M	RH2M	PRECTOTCORR	PS	WS10M	WD10M
0	2010	1	1	0:00:00	24.37	21.81	23.09	16.30	85.56	0.0	100.66	1.79	240.97
1	2010	1	1	1:00:00	24.14	21.77	22.95	16.30	86.56	0.0	100.62	1.65	243.92
2	2010	1	1	2:00:00	23.99	21.75	22.87	16.24	87.19	0.0	100.58	1.47	250.12
3	2010	1	1	3:00:00	23.87	21.80	22.83	16.30	88.12	0.0	100.58	1.31	255.88
4	2010	1	1	4:00:00	23.74	21.85	22.80	16.36	89.12	0.0	100.60	1.19	263.58
...	...	...	...	...	...	...	...	...	...	...	...	...	...
70123	2017	12	31	19:00:00	25.40	20.30	22.85	14.83	73.25	0.0	100.65	1.75	298.86
70124	2017	12	31	20:00:00	25.11	19.84	22.48	14.40	72.56	0.0	100.73	1.73	295.75
70125	2017	12	31	21:00:00	24.87	19.41	22.14	14.04	71.62	0.0	100.78	1.66	296.93
70126	2017	12	31	22:00:00	24.74	18.89	21.82	13.55	69.88	0.0	100.78	1.48	303.61
70127	2017	12	31	23:00:00	24.62	18.39	21.51	13.18	68.25	0.0	100.75	1.28	317.23

70128 rows × 13 columns

Figure 1: Preview of the first five and last five of the NASA dataset

The table below shows the weather parameters used for the research, their description, and the international system of units.

Table1: Dataset Features Used for the Research

Weather Parameter	Feature Description	SI Unit
Date	This is the date each data was logged	second
Temperature	Normal Temperature value	^oC
Dew Temperature	Dew Temperature value	^oC
Wet Temperature	Wet Temperature value	^oC
Specific Humidity	Specific Humidity value	g/kg
Relative Humidity	Relative Humidity value	%
Precipitation	Precipitation value	m/Hr
Surface Pressure	Surface Pressure value	kPa
Wind Speed	Wind Speed value	m/s
Wind Direction	Wind Direction value	^{o}

3. METHODOLOGY

3.1 Descriptive Analysis

This part looks at the data visualization using the available dataset. Python libraries like Pandas, Matplotlib, Plotly, Seaborn, and NumPy were used for this analysis. Visualization is used to show the time series plots of the weather parameters for the NASA dataset.

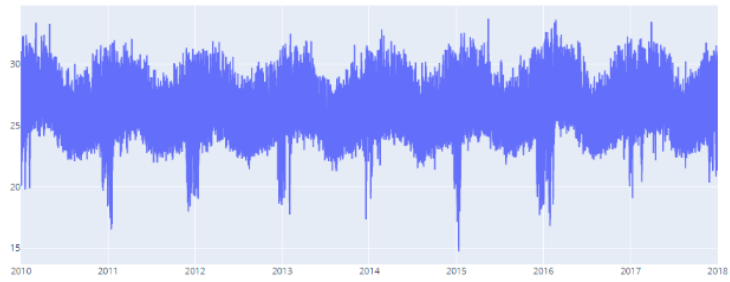

Figure 2: Time series plot of the T2M variable

A time series chart sometimes referred to as a times series graph or time series plot, is a data visualization tool that shows data points at progressively shorter time intervals. A measurement of a quantity and a time is represented by each point on the graph. This was done for all the variables used in this report with indications of signs of seasonality. Usually, there are annual changes in seasons precipitated by changes in the beginning, middle, and end of the season.

For temperature, there is an increase at the beginning of the year, a drop in the middle of the year, an increase from midyear to the third quarter, and a slight drop at the end of the year.

3.2 Predictive Analysis

Intelligent algorithms are used in predictive analysis to produce predictions based on patterns, trends, and correlations in historical data. Because predictive analytics is probabilistic, it cannot predict what will happen in the future but rather predictions of what might be.

A target variable *Next T2M* is created by shifting the value of the *T2M* variable by one step backwards

The Seaborn library is used to show the Pearson Correlation heatmap of the features of the dataset. Pearson Correlation is given as:

$$r = \frac{n(\Sigma xy) - (\Sigma x)(\Sigma y)}{\sqrt{[n\Sigma x^2 - (\Sigma x)^2][n\Sigma y^2 - (\Sigma y)^2]}}$$

Where,
n = total number of observations,
x = first variable
y = second variable
r = Pearson correlation value.

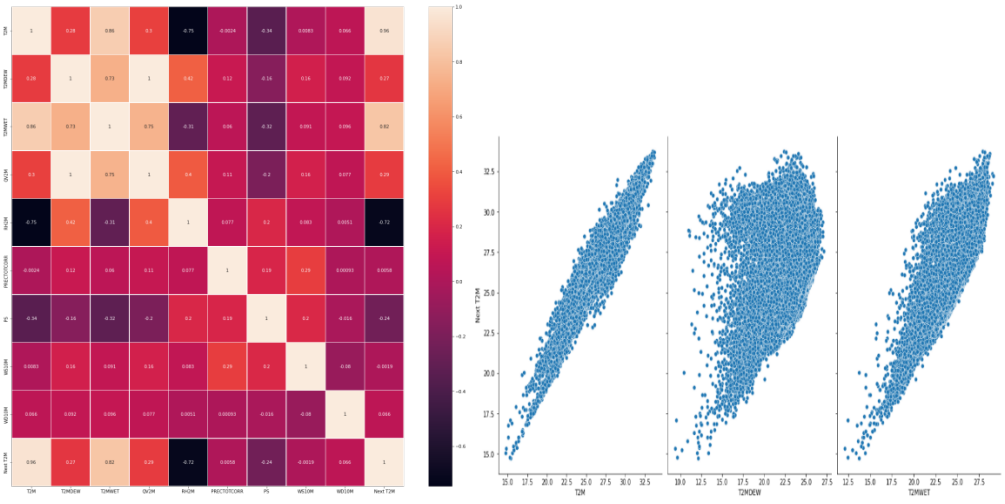

Figure 3: (a) Pearson Correlation Heatmap of Features in the Dataset (b) Scatter Plots of the Next T2M against T2M, T2MDEW, and T2MWET

Exploratory Data analysis shows that T2M and T2MWET are highly positively correlated with the Next T2M variable. Also, RH2M is highly negatively correlated with the Next T2M variable. The Pearson correlation coefficient between T2M and Next T2M is 0.96. The Pearson correlation coefficient between T2MWET and Next T2M is 0.82. The Pearson correlation coefficient between RH2M and Next T2M is -0.72.

A target variable Next RH2M is created by shifting the value of the RH2M variable by one step backwards.

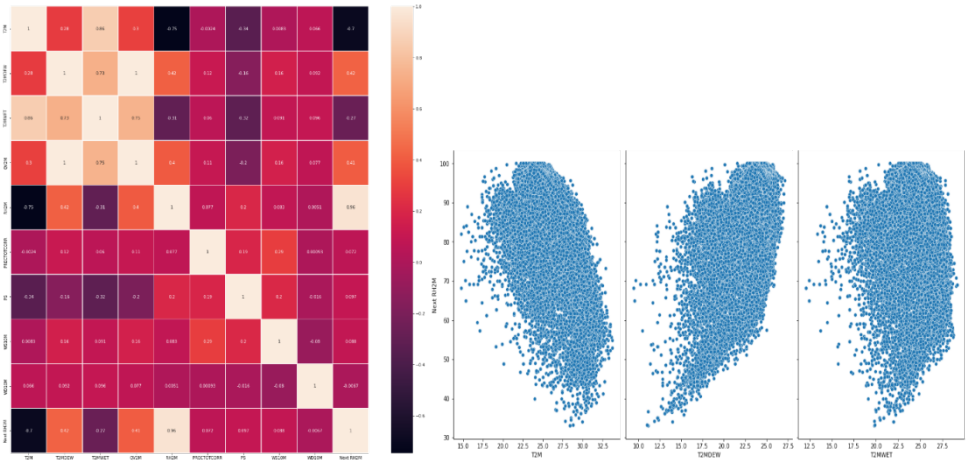

Figure 4: (a) Pearson Correlation Heatmap of Features in the Dataset (b)Scatter Plots of the Next RH2M against T2M, T2MDEW, T2MWET

Exploratory Data analysis shows that RH2M is highly positively correlated with the Next RH2M variable. Also, T2M is highly negatively correlated with the Next RH2M variable.
The Pearson correlation coefficient between R2M and Next RH2M is 0.96. The Pearson correlation coefficient between Next RH2M and T2M is -0.7.

The Scatter plot below was used for visualization to see which features correlate with the future temperature value.

3.3 Splitting Data into Training Set and Test Set

Before splitting the dataset, standardization is applied to it. This is to ensure all the variables are of the same variance.

The formula for standardization is:

$$x = x - \text{mean}(x)/\text{standard deviation}(x)$$

The dataset is split in the ratio of 75:25. The dataset is not shuffled because we are dealing with time-series data. We use 75% of the data for training, while we use 25% of the data for testing.

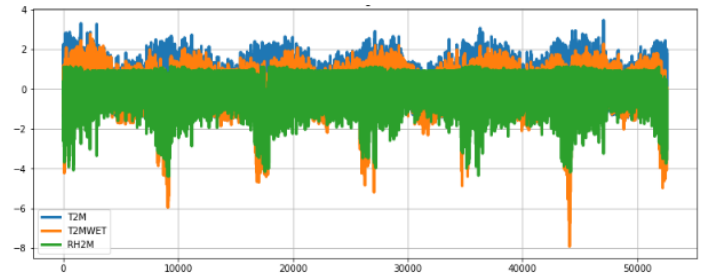

Figure 5: Line Plot of the T2M, T2MWET & RH2M features after applying standardization in the training dataset

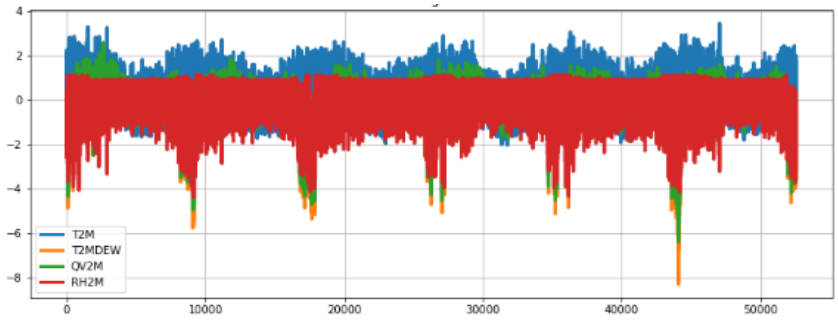

Figure 6: Line Plot of the T2M, T2MDEW, QV2M & RH2M features after applying standardization in the training dataset.

$$RMSE = \sqrt{\frac{\sum_{i=1}^{n}(P_i - O_i)^2}{n}} \qquad R^2 = 1 - \frac{\sum(y_i - \hat{y})^2}{\sum(y_i - \bar{y})^2}$$

Where, $\check{Y}$ - Predictive value of Y
$\bar{Y}$ - Mean value of Y

To model the training set for the prediction of future temperature, the following algorithms were used for the training; Ridge Regression, Lasso Regression, Decision Tree Regression, and XGBoostRegressor. This was also done for Relative Humidity and pressure.

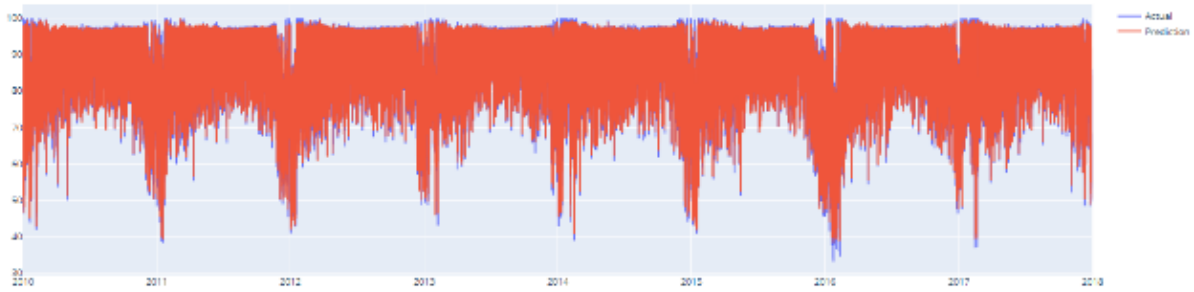

Figure 7: Line plot of actual result vs predicted result of the XGBoost regression model.

The table below shows the R Squared score and the Root Mean Squared Error on the test set of each algorithm.

Table 2: R Squared score and the Root Mean Squared Error of each Algorithm

Model	**R Squared**	**RMSE**
Ridge Regression	0.92599	0.28455
Lasso Regression	0.92580	0.28491
Decision Tree Regression	0.92519	0.28609
XGBoost Regression	0.93385	0.26901

4. RESULTS AND DISCUSSION

For temperature, the correlation coefficient between T2M and Next T2M, T2MWET and Next T2M, RH2M, and Next T2M is 0.96, 0.82, and -0.72 respectively. The analysis shows that T2M and T2MWET are highly positively correlated with the Next T2M variable. Also, RH2M is highly negatively correlated with the Next T2M variable. For Relative Humidity, the correlation coefficient between R2M and Next RH2M, Next RH2M, and T2M is 0.96 and -0.7 respectively. The analysis shows that RH2M is highly positively correlated with the Next RH2M variable. Also, T2M is highly negatively correlated with the Next RH2M variable.

For Surface pressure, the correlation coefficient between R2M and Next RH2M, Next RH2M, and T2M is 0.96 and -0.7 respectively. The analysis shows that RH2M is highly positively correlated with the Next RH2M variable. Also, T2M is highly negatively correlated with the Next RH2M variable.
The Scatter plot was used for visualization to see which features correlate with the future temperature value. From the exploratory data analysis, the three features used to predict the next hourly temperature are T2M, T2MWET, and RH2M.
The dataset was split and, standardization was applied to it. This is to ensure all the variables are of the same variance. The dataset is split in the ratio of 75:25. The dataset is not shuffled because we are dealing with time-series data. We use 75% of the data for training, while we use 25% of the data for testing. This was done for temperature, Relative humidity, and pressure.

Table 3: Predictive Algorithm deployed and their performance evaluation

Feature	Algorithm	R Squared	RMSE
Temperature	Ridge Regression	0.92321	0.27913
	Lasso Regression	0.92325	0.27908
	Decision Tree Regression	0.92149	0.28226
	XGBoost Regression	0.92308	0.27938
Relative Humidity	Ridge Regression	0.92599	0.28455
	Lasso Regression	0.92580	0.28491
	Decision Tree Regression	0.92519	0.28609
	XGBoost Regression	0.93385	0.26901
Pressure	Ridge Regression	0.92599	0.28455
	Lasso Regression	0.92580	0.28491
	Decision Tree Regression	0.92519	0.28609
	XGBoost Regression	0.93385	0.26901

5. CONCLUSION

Most previous studies that used machine learning approaches only applied single machine learning methods [5], [6]. In contrast, in this study, descriptive and predictive analysis of the NASA dataset was performed using four prediction models (i.e. Ridge Regression, Lasso Regression, Decision Tree Regression, and XGBoost regression) for performance analysis of NASA data. It reported a root mean square error (RMSE) value of between 0.27913 and 0.28455, 0.27908 and 0.28491, 0.28226 and 0.28609, 0.27938 and 0.26901 for Ridge Regression, Lasso Regression, Decision Tree Regression, and XGBoost regression respectively. The correlation analysis reported a coefficient of determination (R2) value of between 0.92321 and 0.92599, 0.92325 and 0.92580, 0.92149 and 0.92519, 0.92308 and 0.93385 for Ridge Regression, Lasso Regression, Decision Tree Regression, and XGBoost regression respectively.
XGBoost regression performed better than other algorithms with a root mean square error (RMSE) value of 0.26901 and a coefficient of determination (R2) value of 0.93385. For further improvements, a more predictive algorithm can be used to check for performance.

ACKNOWLEDGEMENT
I want to sincerely acknowledge the contributions of my co-authors in making this research a success. I want to thank the National Aeronautics and Space Administration for the dataset used in this research.

REFERENCES

[1] Aneke C.S, Asuquo P.M, and Ozuomba S. (2023)" Design and Implementation of a Microcontroller-based Weather Acquisition Device, "Journal of Engineering Research and Reports, Vol. 24, no. 6, Page 35-46, DOI: 10.9734/JERR/2023/v24i6823
[2] K. E. Ukhurebor, I. C. Abiodun, S. O. Azi, I. Otete and L. E. Obogai (2017) "A Cost Effective Weather Monitoring Device" Archives of Current Research International, Vol 7 no.4: page 1-9, DOI: 10.9734/ACRI/2017/32885

[3] Dongjin Cho, CheolheeYoo, JunghoIm, Dong-Hyun Cha. "Comparative Assessment of Various Machine Learning-Based Bias Correction Methods for Numerical Weather Prediction Model Forecasts of Extreme Air Temperatures in Urban Areas " Earth and Space Science
Vol 7, no. 4:2020 https://doi.org/10.1029/2019EA000740
[4] Kim, M., Im, J., Park, H., Park, S., Lee, M.-I., &Ahn, M.-H. (2017). "Detection of tropical overshooting cloud tops using himawari-8 imagery" Remote Sensing, Vol 9 no.7, Page 685.
[5] Lee, S., Han, H., Im, J., Jang, E., & Lee, M.-I. (2017). Detection of deterministic and probabilistic convection initiation using Himawari-8 advanced Himawari imager data. Atmospheric Measurement Techniques, 10 (5), 1859–1874
[6] Sim, S., Im, J., Park, S., Park, H., Ahn, M., & Chan, P. W. (2018). Icing detection over East Asia from geostationary satellite data using machine learning approaches. Remote Sensing,10 (4), 631
[7] Yoo, C., Im, J., Park, S., &Quackenbush, L. J. (2018). Estimation of daily maximum and minimum air temperatures in urban landscapes using MODIS time series satellite data. ISPRS Journal of Photogrammetry and Remote Sensing, 137, 149–162.
[8] Chou, J.-S, & Pham, A.-D. (2013). Enhanced artificial intelligence for ensemble approach to predicting high-performance concrete compressive strength. Construction and Building Materials, 49, 554–563.
[9] Healey, S. P., Cohen, W. B., Yang, Z., Kenneth Brewer, C., Brooks, E. B., Gorelick, N., et al. (2018). Mapping forest change using stacked generalization: An ensemble approach. Remote Sensing of Environment, 204, 717–728. https://doi.org/10.1016/j.rse.2017.09.02
[10] Ren, Y., Zhang, L., &Suganthan, P. N. (2016). Ensemble classification and regression-recent developments, applications, and future directions. IEEE Computational Intelligence Magazine,11 (1), 41–53

PAPER 65 – AN OVERVIEW OF APPLICATIONS OF COGNITIVE WIRELESS COMMUNICATION SIMULATORS

F. O. Ehiagwina[1,2*], N. T. Surajudeen-Bakinde[1], A. S. Afolabi[2], L. O. Afolabi[1], A. M. Usman[1,3]

[1]Department of Electrical and Electronics Engineering, University of Ilorin, Ilorin, Kwara State, Nigeria
[2]Department of Electrical/Electronic Engineering, The Federal Polytechnic Offa, Offa, Kwara State, Nigeria
[3]Department of Electrical & Electronic Engineering, Stellenbosch University, Stellenbosch, South Africa.
[*]Email: Frederick.ehiagiwna@fedpoffaonline.edu.ng

ABSTRACT
Cognitive radio is proposed in the literature to address the ironical problem of spectrum scarcity owing to inefficient utilisation. This idea has recently gained popularity because it provides wireless users with the ability to detect and efficiently adapt operating parameters based on interactions with the surrounding radio environment. In the evaluation of cognitive radio networks simulators are used. The simulators differ in terms of platforms and technicalities. Thus making selection process difficult. In this review, attention is paid to cognitive radio network simulators such as Network Simulator 2 and 3 (NS-2) and (NS-3), Java Simulator (J-Sim), Operations Network (OPNET) and MATLAB. In the selection of literature covered in this review, attention was paid to publications not later than 2017 from reputable databases. This review of cognitive radio network simulators will provide useful insights to new researchers in this field. Furthermore, a case study is reported on the application of the Monte Carlo simulation method to the cognitive radio network.

KEYWORDS: Cognitive radio, network simulators, random numbers, Monte Carlo simulation

1. INTRODUCTION

Cognitive radio is advocated in the literature to address the ironical problem of spectrum scarcity owing to inefficient utilisation. This idea has recently gained popularity because it provides wireless users with the ability to detect and efficiently adapt operating parameters based on interactions with the surrounding radio environment. In the last few years since the introduction of the concept by Mitola, there have been numerous significant advances in cognitive radios (Hu et al., 2018; Arjoune & Kaabouch, 2019). The structure of a typical CRN and the cognitive cycle are shown in Figures 1 and 2. The cognitive cycle is at the core of CRN operation.

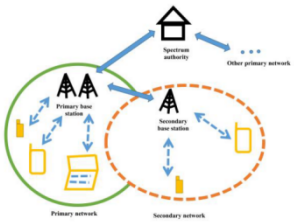

Figure 1: Architecture of a typical cognitive radio network

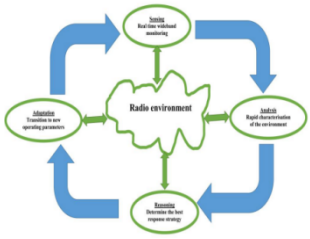

Figure 2: Cognitive cycle

It is crucial to have a complete grasp of CRNs via intense experimental analysis to gain deeper insight into CRNs and to create more reliable procedures. The two main categories of CRN experimental analysis techniques are platform-based emulation and computer-assisted simulation. Due to several benefits, computer-assisted simulation is used more frequently in CRN experimental analysis than platform-based experimental analysis. Some of the benefits include: 1) Computer-assisted simulators are more practical and less expensive than CRN platforms; whereas many simulators are open source and free to use or have academic versions that may be obtained from the Internet; 2) As the technology matures, computer-assisted simulators may be equipped with stronger technical assistance; yet, despite certain commercial CRN platforms having strong technical support, their lack of module libraries stems from the lengthy development process; and 3) The use of computer-assisted simulators, which allow for the adjustment of a wide range of CRN parameters without changing platform hardware architecture, makes them more appropriate for large-scale CRN experiments with fewer restrictions. Certain radio scenarios are difficult for radio platforms to simulate in the actual world, but computer-assisted simulation is completely relevant.

However, selecting a powerful and user-friendly simulator is still a challenge for many researchers due to the following reasons: 1) simulators are maintained by either commercial companies or open source communities;

historical technical development and current technique support (CRN patches, libraries, etc.) situations differ greatly among different simulators; and 2) CRN is a complex system, and some researches are typically undesirable to cover all functionalities; some simulators are not user-friendly while others are (Assegie & Nair, 2019; Dong et al., 2018; Kafetzis et al., 2022).

In contrast to conventional wireless networks, CRN is set up using a novel media access strategy. Via spectrum sensing, analysis, and cooperative decision-making, the transceiver uses dynamic spectrum access (DSA) to operate. The transceiver performs routing activities, QoS monitoring, and application management, as well as low-level coordination and configurations, in high-level functionality. When creating CRN simulators, each of these must be taken into account. Moreover, effective simulators should be able to replicate a flexible but controllable radio environment, be simple to install and setup, and be extendable with adaptive modular architectures (Agrawal et al., 2022; Aloqaily et al., 2020; Dong et al., 2018). There are also CRN simulators that are cloud-based. Examples of these are discussed in (Aron & Abraham, 2017; Campanile et al., 2020; Kafetzis et al., 2022).

The simulation platforms are described, coupled with studies deploying such a platform within the limitation of prescribed page numbers. Emphasis was placed on articles not later than 2017.

2. COGNITIVE RADIO NETWORK SIMULATOR

There are general-purpose simulators such as Network Simulator 2 and 3 (NS-2) (Patel et al., 2018; Sharma et al., 2019) and (NS-3), Java Simulator (J-Sim), Operations Network (OPNET), NetSim, Objective Modular Network Testbed (OMNEST) (Omnest, 2020), Objective Modular Network Testbed in C++ (OMNeT++), GNU and MATLAB. Others include Mininet (2020), Data Center Simulation tool (DCSim) (Byrne et al., 2017), and Cloud Simulator (CloudSim). In this section of the review, attention is paid to some cognitive radio network simulators based on the aforementioned platforms (Dong et al., 2018).

2.1. Cognitive Radio Network Simulation Based on NS-2 Simulator

NS-2 is an object-oriented simulator that has very detailed network modules. This simulator is usually used for designing protocols and new network architectures, comparing performances of various networks and studying network traffic. Further, NS-2 can be customized for specific simulation scenarios just like CRNs (Patel et al., 2018). On the contrary, this simulator suffers from its implementation complexity (Sharma et al., 2019). Figure 3 shows the architecture of the NS-2. It is a well-structured module that was mainly made to build Media Access Control (MAC) protocols.

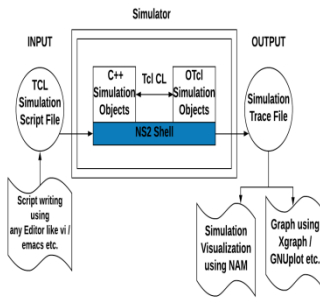

Figure 3: NS-2 Architecture (Patel et al., 2018)

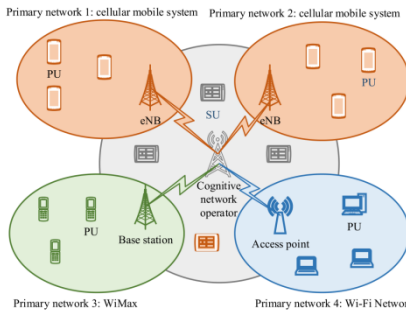

Figure 4: Cognitive Heterogeneous network

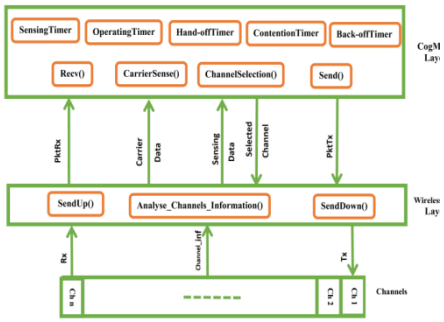

Figure 5: Structure of the CR node object in CogNS with accessories

Cognitive radio features can be incorporated into the NS-2. Examples of this include the CRCN, CRAHN and the CoGNS. All are at various stages of development (Darabkh et al., 2020). Research work on cognitive radio simulation based on NS-2 includes cognitive radio sensor network (Bukhari et al., 2018), channel selection/assignment, routing technique for multichannel cognitive radio networks, the effect of SU on the higher layers of the protocol stack and so on.

2.2. Cognitive Radio Ad Hoc Network (CRAHN)

Another NS-2-based emulator is the Cognitive Radio Ad Hoc Network (CRAHN), which detects primary user activity and pauses transmission when the principal user occupies the spectrum. Because nodes are always seeking vacant spectrum to communicate on, this simulator allows them to alter transmission and receiving channels. Examples of works on CRAHN include spectrum routing and aggregation (Ramkumar & Vadivel, 2018; Devapriya & Kannan, 2020; Singh & Dutta, 2020). Sridevi and Venkatesan (2017) and Devapriya and Kannan (2020) examined CRAHN as it relates to spectrum aggregation. According to Devapriya and Kannan (2020), the primary goal of a spectrum aggregation-based pleasant routing protocol for CRAHNS is to increase imperative

profitability, improve throughput and reduce framework delay for the cognitive heterogeneous network. A typical cognitive network operator-based 5G heterogeneous network is shown in Figure 4. The Stackelberg gaming hypothesis was used to realize high throughput and decreased delay, resulting in an improvement of the spectrum and energy efficiency.

2.3. Cognitive Network Simulator (CogNS)

CogNS is another NS-2-based simulator. It may be used to explore and assess the influence of lower-layer protocols, such as the MAC and physical layer, on transport and network layer protocols. Because packet loss probability, end-to-end delay and throughput are important QoS requirements in real-time dependable applications, the CogNS system evaluates these metrics over CRNs. However, CR-related characteristics such as primary user activity model, sensing time and frequency should be addressed while designing novel network and transport layer protocols over CRNs (Singhal & Thanikaiselvan, 2022; Hassani & Berangi, 2019).

Figure 5 shows the structure of each CogNS CR node object, as well as modules, timers and their relationships. Based on the topology of the mobile node object in NS2, the MAC layer, physical layer and channels are changed. The transmission of control information and data packets is shown by the arrows between different levels. The main change was made to the Mobile node's MAC layer. A cognitive CSMA/CA-based MAC protocol dubbed CogMAC is implemented in the MAC layer of CogNS.

Researches, where the CogNS is utilized, are in congestion control schemes for transport protocol and in the evaluation of the effect of secondary user block throughput of TCP in CRSN (Hassani & Berangi, 2018 and 2019).

2.4. Cognitive Radio Simulation Based on NS-3

Network Simulator 3 (NS-3) is not an evolution of NS2. Hence, it is not a backwards-compatible extension of NS2. Some models from NS2 have been ported to NS3. It is a discrete-event network simulator targeted primarily for research and educational use. The development of the open-source project began in 2006 (NS-3 Tutorial Release ns-3.18.1, 2013). The programme is written in C++ and Python. In general, NS3 has the advantage of supporting many radio models such as 802.11, 802.16, 802.15.3 and 802.15.4 and it has various options for network topologies and traffic patterns. This allows researchers to build different simulation scenarios to test their protocols. NS3 has three cognitive radio modules.

NS3 is created as a collection of libraries that may be integrated and used in conjunction with other software libraries. NS3 is more modular in this sense than certain simulation platforms, which offer customers a single, integrated graphical user interface environment where they can do all functions. NS-3 can be utilized with a variety of external animators, as well as data analysis and visualization tools. Users should anticipate working using C++ and/or Python software development tools and at the command line. NS3 is used on Linux operating systems. However, it can be utilized in FreeBSD and Cygwin (for Windows). The development of native Windows Visual Studio support is currently underway (Masek et al., 2019).

2.5. Cognitive Radio Emulator in NS-3 (CRENS3)

CRENS3 extension is written to add cognitive radio (CR) capabilities to the NS-3. CRENS3 follows the NS-3 standards in terms of documentation through the utilization of Doxygen. Khan and Islam (2019) incorporate the fee dBack-based approach to CRENS3 as a modifier. The authors noted that the existing cognitive module of CRENS3 made provision for three interfaces for each device. They are the transmitter interface, control interface and receiver interface. The block diagram of the CRENS3 extension in NS-3.17n is shown in Figure 6. In this case, the actual cognitive radio transceiver is being emulated by the transmitter and receiver interfaces of the module (Khan & Islam, 2019).

2.6. Cognitive Radio Simulation Based OMNeT++

Objective Modular Network Testbed in C++ (OMNeT++) is a general-purpose tool that has nested architecture for modelling networks. It also has a mobility extension for wireless networks named Mixed Simulator MiXiM. The Objective Modular Network Testbed in C++ (OMNeT++) is a well-designed open-source, component-based, discrete event-driven simulator written in C++. As an open-source network simulator, OMNET + + has plenty of public documents like NS-2 and NS-3 and it is also equipped with a powerful graphical user interface as OPNET does. Thus, OMNeT++ becomes successful in both industry as well as academia. OMNeT++ provides a hierarchically nested architecture for modelling. An OMNeT++ model is composed of many modules that pass messages back and forth for communication (Dong et al., 2018). Simple modules are the basic active elements used to model a system. They are programmed in C++ using the OMNeT++ simulation class library. Users can design new simple modules in OMNeT++ IDE. Meanwhile, a large number of simple modules are provided in the OMNeT++ library. Single modules can be assembled into more functional compound modules and so forth for compound modules with unlimited hierarchy levels. NED is the adhesive language in OMNeT++ for declaring simple modules, assembling compound modules and constructing network topologies. In the process of simulation and after, Then, an integrated GUI of OMNeT++, provides users with powerful features for ongoing animation

tracing, output tracing and synthesizing. It is convenient for users to look for the output results of the system or even each module.

On top of OMNeT++, MiXiM (Mixed Simulator) has been developed as a simulation framework for wireless and mobile networks. It provides wireless MAC protocols, as well as detailed models of radio wave propagation, interface estimation and radio transceiver power consumption. In the MAC layer, IEEE 802.11 and IEEE 802.15.4 protocols have been developed. Due to the component-based structure, it is relatively less time-consuming to implement a new CRN protocol via OMNeT++. To study cognitive radio, some reported efforts have built up proper framework and simulation models using OMNeT++, which shed light on developing CRNs efficiently (Dong et al., 2018). In smart home cognitive wireless sensor networks, a distributed cooperative spectrum resource allocation was simulated in OMNeT++ by Aroua et al. (2017).

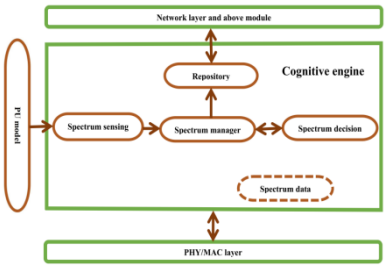

Figure 6: The block diagram of CRENS3 extension in NS-3.17 (redrawn by Dong et al., 2018)

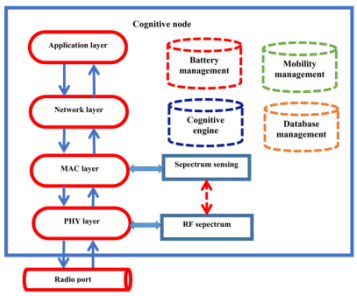

Figure 7: The node structure of CR Simulator in OMNeT++ (redrawn from Dong et al., 2018)

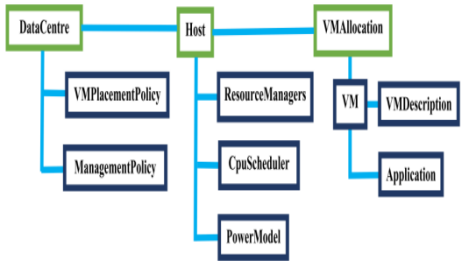

Figure 8: Data Center Simulation Architecture (redrawn from Byrne et al., 2017)

2.7. Cognitive Radio Simulation Based on Java (J-Sim)

J-Sim is another general-purpose simulator that was developed in Java. This simulator has a script interface that can run several script-based languages like Python or Perl. Further, J-Sim is described as neutral, extensible and reusable by authors. This is because it is closely coupled with autonomous component architecture, i.e., it relies on self-regulating, replaceable and linked components that help in managing complexity and inspiring reuse. More specifically, it uses a multi-agent-based computational model (MABM), which simulates the common interactions of a group of independent entities (agents) composing a system. This provides a perspective to study the agents' effects on the entire system. Interestingly, the MABM showed great efficiency in representing complex and dynamic systems. As for the weaknesses, MABMs, such as J-Sim, are inclined to be more resource and computational time exhaustive, less suitable for event-driven simulations and known to be fairly difficult to verify and validate.

2.8. Optimized Network Engineering Tool (OPNET)

Optimized Network Engineering Tool (OPNET) is a widely used object-oriented, discrete event-driven, general-purpose network simulation tool with many user-preferred features, tool sets and a huge library of available network protocols. It helps set up different network topologies and is convenient for users who need to design customized network protocols or applications. Generally speaking, using OPNET for the experimental study consists of three main procedures: modelling, simulating and analysis. In the simulation, all required models of protocols should be created and defined first. Then, the network is simulated based on the developed models with hierarchical structures. OPNET defines a network as a collection of submodels, in which the hierarchical structure is divided into the network, node and process domains. It runs in C/C++. It was initially free and made for multiple computer environments.

As a commercially supported software, OPNET has powerful graphical support of network topology, traffic flow control and various entities of network units. OPNET has a large user group and many discussion forums, so it is easy to be extended to implement CRNs. OPNET provides many integrated propagation models such as Free Space, Hata, CCIR, Longley-Rice, TIREM, Walfish-Ikegami and more added models such as Rayleigh, Ricean, two-ray and 802.15.4/ZigBee models from OPNET community (Dong et al., 2018).

3. COGNITIVE RADIO SIMULATION BASED ON MATLAB

GNU and MATLAB are signal processors that are easy to use, great in signal processing and support customized modules to mimic various functionalities. MATLAB is a software that is widely used with radio generation and network simulations; because of its rich mathematical library. In CRNs, MATLAB is used for signal analysis that exists in spectrum sensing and for modelling CRNs partially. As one of the most widely used scientific

experimental tools with powerful mathematical toolboxes and packages, MATLAB (Matrix Laboratory) is the pioneer of cognitive radio simulation because of its popularity in numerical computing and ease of use. Energy detection is the most fundamental technique in spectrum sensing in CRNs. To justify the feasibility and viability of energy detection, the PU signal is first generated with added noise in the radio environment. With a proper radio propagation model, the received signal can be simulated on the SU side and the energy detection technique is easily adopted by measuring the received signal level (Dong et al., 2018).

MATLAB is more than a signal processor; it is a comprehensive experiment tool that can be widely used in CRN studies. With a plethora of toolboxes, especially supported by Simulink, MATLAB can specify design details of network components as well as topology, which makes it ideal for operation on signal processing and spectrum management. Usually, Simulink is cooperatively used to drive CRN hardware platforms for experimental analysis. In the MATLAB/Simulink environment, software was created by Shuaibu-Sadiq and Anyasi (2020) to reuse a range of vacant frequencies using multiple model elements working together to produce spectrum sensing. A register transfer level - software-defined radio was used to interface the built Simulink model, which evaluates the estimated noise power of the received signal over a particular time and bandwidth. The threshold estimation produces a binary digit that can be used for decision and prediction. However, due to the lack of pre-defined network architecture, Matlab/Simulink is not convenient for higher-level network simulation or comprehensive construction studies (Dong et al., 2018).

4. EVALUATION OF SELECTED SIMULATION SCHEMES

A summary of some of the simulators discussed is presented in Table 1.

Table 1: Evaluation of selected network simulators

	Remark	Programme	CRN	Multiple Channel	Primary Receiver Activity
CogNS	Based on NS-2	C++/OTCL	Yes	Yes	No
CRAHN	Based on NS-2	C++/OTCL	Yes	No	Yes
CrSimulator	Based on OMNet++	C++/NED	Yes	Yes	No
J-SIM		Java	No	No	No
CRCN	Based on NS-2	C++/OTCL	Yes	No	No
MiXiM	Based on OMNet++	C++/NED	No	No	No

5. CASE STUDY: MONTE CARLO SIMULATION OF COGNITIVE RADIO NETWORK

A cognitive radio network involves a lot of dynamism. Given that, Monte Carlo simulation may be used to evaluate their performance. The probability of various outcomes in a process that cannot be easily anticipated due to the interference of random factors is modelled using a Monte Carlo simulation owing to ease of implementation and it is useful in simulating both deterministic and stochastic problems. It is a method for comprehending the effects of risk and uncertainty. In various disciplines, including finance, business, physics, and engineering, Monte Carlo simulation is used to solve a variety of issues (Makarfi et al., 2021; Helmy, Hassan & Ismail, 2022).

In this case study, a cognitive network was created to cover a 5000 by 5000 m^2 area and PU and SUs were randomly generated. It was observed that SU-to-SU calculations accounted for more than 96% of the collisions (Figure 12), hence the need for a spectrum decision manager to coordinate spectrum assignment to SUs.

The proposed algorithm for the CRN within the GSM 900/1800 Bands is shown in Table 2 (Ehiagwina et al., 2022). The simulation parameter for the case study is shown in Table 3.

Table 2: An adaptive spectrum decision algorithm for CRN simulation

1. Initialise the algorithm by specifying the spectrum band links, create a neural network (diagram), set constants and parameters

2. Perform spectrum sensing and acquire spectrum power densities $P(t_i, f_j)$ over time

3. Sort data into matrix form: $X = \begin{pmatrix} P(t_1, f_1) & \cdots & P(t_1, f_j) \\ \vdots & \ddots & \vdots \\ P(t_i, f_1) & \cdots & P(t_i, f_j) \end{pmatrix}$

4. Set decision threshold λ_k and $I_\phi(t_i, f_j)$: $P(t_i, f_j) \rightarrow \{0,1\}$ and apply the following rule:

$I_\phi(t_i, f_j) = \begin{cases} 1, & if P(t_i, f_j) \geq \lambda_k \\ 0, & if P(t_i, f_j) < \lambda_k \end{cases}$. Do for each entry on **3**. above

5. Determine the average spectrum duty cycle for each link using $\mu_j = N_f^{-1} \sum_{i=j=1}^{N_f} I_\phi(t_i, f_j)$

6. Obtain the spatio-temporal variations of duty cycles using $\mu_{(i,j)}(t) = N_f^{-1} \sum_{i=j=1}^{N_f} I_\phi(t_i, f_j)(t)$

7. From 6. above obtain CVDs according to $CVD_i = t_s(1-\mu_j)$

8. Use the outputs from **7**. as targets for the neural network with the data of **3**. as inputs

9. Develop an ANN-LSTM algorithm to obtain predicted CVDs, p_{CVD}

10. Is $p_{CVD} \geq k_{CVD}$, a defined threshold? If yes, proceed to the next step. If otherwise, proceed to step **13**. for a test of the existence of spatial opportunity using carrier-interference-ratio (CIR)

11. Compute the communicable area for the primary and secondary systems

12. Randomly generate the Locations of PR, ST and SR within the service area.

13. For an SU transmission, compute CIR_{PR} and CIR_{SR} then check if $CIR_{PR} > \lambda_2$ and $CIR_{SR} > \lambda_1$.

14. Check if the allowable number of trials has been reached, if no repeat steps 11 - 13 and if yes proceed to step 15.

15. Compute the probabilities where $CIR_{PR} > \lambda_2$ and $CIR_{SR} > \lambda_1$ are satisfied.

5.1. Performance Metrics for the Simulation

Making decisions is a crucial part of the CR's cognitive cycle. If the decision-making process is delayed, the quality of service (QoS) is negatively impacted; nevertheless, if the decision-making process is quick and the SU makes an incorrect conclusion, the SU may interfere with PU. Thus, the primary user interference probability (PUIP) will be evaluated to gauge the effectiveness of the created spectrum choice framework.

The ratio of the number of open slots found by the cognitive user to the total number of open slots present in the system over a limited period is known as spectrum utilization. This is expressed mathematically as in eqn. (1).

$$\eta_{SU} = \frac{number\ of\ vacant\ spectrum\ slot\ sensed}{total\ number\ of\ vacant\ slots\ in\ the\ spectrum\ fragment} \times 100\% \quad (1)$$

The PUIP is the ratio of the slots in which SU also uses the channel whereas a PU is transmitting. This is due to a false alarm. The PUIP is given as eqn. (2).

$$PUIP = \frac{total\ number\ of\ collision\ slots}{total\ number\ of\ PU\ activity\ slots} \quad (2)$$

The Simulation parameters for the hybrid spectrum opportunities extraction scheme may be seen in (Ehiagwina et al., 2022).

5.2. Result of the Case Study

The simulation revealed that over 96% of collisions were calculated from SU to SU interactions (Figure 11), demonstrating the necessity of a spectrum choice manager to coordinate SU spectrum assignment. As shown in the Figure, the percentage of PU to SU collision is quite low, with a maximum of 3. 456%.

The plot of users' collisions is shown in Figure 12. The results showed that SU-SU conflicts contribute to about 97% of the collisions, hence the development of the spectrum extraction decision algorithm to minimise these collisions.

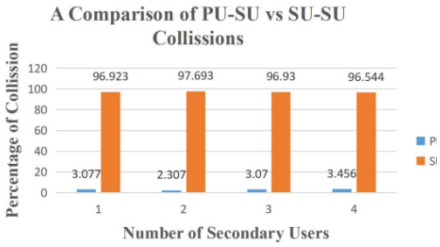

Figure 11: PU-SU vs SU-SU collisions

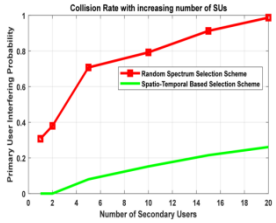

Figure 12: Collision rate with an increasing number of SUs

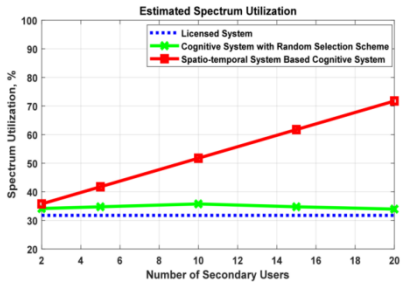

Figure 13: Spectrum utilization for the increasing number of SUs

About 4.5-fold reduction in collision rate was noticed when spatial and temporal-based spectrum selection scheme was used as against the random selection scheme. The estimated increase in spectrum utilization can be seen in Figure 13. Spectrum usage increased by more than a factor of two. This shows a preference for a spectrum extraction decision method that incorporates both spatial and temporal spectrum extractions and is adaptive.

6. CONCLUSION

It may be deduced from the foregoing overview of several of the existing CRN simulator that despite the much interest in CRN by researchers, who are keen on examining the various aspects, there seems to be no simulator robust enough to incorporate the various aspects and demands of cognitive radio networks. Several researchers are executing their algorithms via modifications of the existing simulators. In this study, we also reported on the case where Monte Carlo simulation was used for assessing the performance of CRN. The formulation and simulation of an adaptive algorithm for controlling the decision about the extraction of spectrum for CRN led to a reduction in PUIP and a rise in spectrum utilization. By creating an adaptive spectrum choice framework for the cognitive radio network, this research increased the efficiency of spectrum utilization.

ACKNOWLEDGEMENT

The Tertiary Education Trust Fund (TETFund) of Nigeria is acknowledged for supporting the study through the Academic Staff Training and Development (AST&D) program. We also thank the University of Ilorin's Department of Electrical and Electronics Engineering for supplying the measuring instrument utilized in the data collection phase of this investigation.

REFERENCES

Agrawal, S. K., Samant, A., & Yadav, S. K. (2022). Spectrum sensing in cognitive radio networks and metacognition for dynamic spectrum sharing between radar and communication system: A review. *Physical Communication*, 101673.

Aloqaily, M., Salameh, H. B., Al Ridhawi, I., Batieha, K., & Othman, J. B. (2020). A multi-stage resource-constrained spectrum access mechanism for cognitive radio IoT networks: Time-spectrum block utilization. *Future Generation Computer Systems*, *110*, 254-266.

Arjoune, Y., & Kaabouch, N. (2019). A comprehensive survey on spectrum sensing in cognitive radio networks: Recent advances, new challenges and future research directions. *Sensors*, *19*(1), 126.

Aron, R., & Abraham, A. (2022). Resource scheduling methods for cloud computing environment: The role of meta-heuristics and artificial intelligence. *Engineering Applications of Artificial Intelligence*, *116*, 105345.

Aroua, S., El Korbi, I., Ghamri-Doudane, Y., & Saidane, L. A. (2017, July). A distributed cooperative spectrum resource allocation in smart home cognitive wireless sensor networks. In *2017 IEEE Symposium on Computers and Communications (ISCC)* (pp. 754-759). IEEE.

Assegie, S., & Nair, P. (2019). Performance analysis of emulated software-defined wireless network. *Indonesian Journal of Electrical Engineering and Computer Science (IJEECS)*, *16*(1), 311-318.

Bukhari, S. H. R., Siraj, S., & Rehmani, M. H. (2018). NS-2-based simulation framework for cognitive radio sensor networks. *Wireless Networks, 24*(5), 1543-1559.

Byrne, J., Svorobej, S., Giannoutakis, K. M., Tzovaras, D., Byrne, P. J., Östberg, P. O., Gourinovitch, A., & Lynn, T. (2017). A review of cloud computing simulation platforms and related environments. *International Conference on Cloud Computing and Services Science, 2*, 679-691.

Campanile, L., Gribaudo, M., Iacono, M., Marulli, F., & Mastroianni, M. (2020). Computer network simulation with ns-3: A systematic literature review. *Electronics, 9*(2), 272.

Darabkh, K. A., Amro, O. M., Al-Zubi, R. T., Salameh, H. B., & Saifan, R. (2020). JavaSim-IBFD-CRNs: novel Java simulator for in-band full-duplex cognitive radio networks over the Internet of Things environment. *Journal of Network and Computer Applications, 172*, 102833.

Devapriya, S., Kannan, N. (2021). High energy and spectral efficiency analysis for CRAHN-based spectrum aggregation. *Journal of Ambient Intelligence and Humanized Computing, 12,* 6621–6628.

Dong, Q., Chen, Y., Li, X., & Zeng, K. (2018). A Survey on Simulation Tools and Testbeds for Cognitive Radio Networks Study. *arXiv preprint arXiv:1808.09858*.

Ehiagwina, F. O., Surajudeen-Bakinde, N. T., Afolabi, A. S., & Usman, A. M. (2022). A hybrid spectrum opportunities extraction scheme for cognitive wireless communication. *Telematics and Informatics Reports*, *7*, 100014.

Hassani, M. M., & Berangi, R. (2018). A new congestion control mechanism for transport protocol of cognitive radio sensor networks. *AEU-International Journal of Electronics and Communications, 85*, 134-143.

Hassani, M. M., & Berangi, R. (2019). Impact of Secondary User Block on the TCP Throughput in Cognitive Radio Sensor Networks. *Wireless Personal Communications, 109*(4), 2221-2238.

Hu, F., Chen, B., & Zhu, K. (2018). Full spectrum sharing in cognitive radio networks toward 5G: A survey. *IEEE Access*, *6*, 15754-15776.

Kafetzis, D., Vassilaras, S., Vardoulias, G., & Koutsopoulos, I. (2022). Software-defined networking meets software-defined radio in mobile ad hoc networks: State of the art and future directions. *IEEE Access*, *10*, 9989-10014.

Makarfi, A. U., Kharel, R., Rabie, K. M., Kaiwartya, O., Li, X., & Do, D. T. (2021, March). Reconfigurable intelligent surfaces-based cognitive radio networks. In *2021 IEEE Wireless Communications and Networking Conference Workshops (WCNCW)* (pp. 1-6). IEEE.

Masek, P., Stusek, M., Zeman, K., Drapela, R., Ometov, A., & Hosek, J. (2019, October). Implementation of 3GPP LTE Cat-M1 technology in NS-3: System simulation and performance. In *2019 11th International Congress on Ultra Modern Telecommunications and Control Systems and Workshops (ICUMT)* (pp. 1-7). IEEE.

Mininet. (2020).Mininet: An Instant Virtual Network on your Laptop (or other PC) - Mininet. http://mininet.org/. Accessed 22/11/2020.

Omnest. 2020. High-performance simulation for all kinds of networks. https://omnest.com/. Accessed 22/11/2020.

Patel, R. L., Pathak, M. J., & Nayak, A. J. (2018). Survey on network simulators. *International Journal of Computer Applications, 182*(21), 23-30.

Ramkumar, J., & Vadivel, R. (2018). Improved frog leap-inspired protocol (IFLIP)–for routing in cognitive radio ad hoc networks (CRAHN). *World Journal of Engineering*, *15*(2), 306-311.

Sharma, S., Mahajan, A. N., & Poonia, R. C. (2019). An Inclusive survey of Network Simulators. In *Proceedings of International Conference on Sustainable Computing in Science, Technology and Management (SUSCOM)*, pp. (2366-2372), Amity University Rajasthan, Jaipur-India.

Shuaibu-Sadiq, M., & Anyasi, F. I. (2020). Analysis of radio frequency spectrum usage using cognitive radio. *Journal of Electrical, Control and Technological Research*, *1*, 1-8.

Singhal, C., & Thanikaiselvan, V. (2022, August). Cross-Layer Design for Primary User Modeling in Cognitive Radio Ad-hoc Sensor Network. In *2022 3rd International Conference on Electronics and Sustainable Communication Systems (ICESC)* (pp. 577-582). IEEE.

Singh, L., & Dutta, N. (2020). Routing protocols for CRAHN: a comparative evaluation. In *Trends in Communication, Cloud and Big Data* (pp. 3-11). Springer, Singapore.

Sridevi, A., & Venkatesan, G. K. D. (2017). Certain investigations on high energy and spectral `efficient CRAHN-based spectrum aggregation. *Journal of Computational and Theoretical Nanoscience, 14*(8), 3861-3866.

PAPER 66 – CHARACTERIZATION OF ALUMINIUM-MATRIX COMPOSITE WITH ACID-TREATED CARBONIZED COCONUT HUSK REINFORCEMENT

J. A. Adebisi[1], M. O. Bello [1], O. J. Akinola[1,*], M. Ndagi[2], I. Ajigbon[3], I. I. Ahmed[1]

[1]Department of Materials and Metallurgical Engineering, University of Ilorin, Nigeria
[2]Department of Mechanical Engineering, University of Ilorin, Nigeria
[3]Advanced Composite Materials Research Laboratory, National Space Research and Development Agency (NASRDA), University of Ilorin Centre, University of Ilorin, Nigeria
[*]Email: 18-30gn019@student.unilorin.edu.ng

ABSTRACT
Aluminium alloys have been widely applied in the automobile, aerospace, defence, and other engineering sectors but low strength and low melting point were always seeming problematic. Many researchers have made use of synthetic reinforcement such as SiO_2 and SiC to solve the problem, but expensive. Similarly, many studies have been done on agricultural wastes as reinforcements with and without acid treatment. Considering the above, the effect of acid-treated carbonized coconut husk reinforcement on the properties of aluminium-matrix composites was studied. The stir-casting method was used to make composites with reinforcement ranging from 1.2 wt.% to 4.8 wt.% at a 1.2 wt.% interval. The mechanical, microstructural, thermal, and physical properties were investigated. The hardness and tensile strength of the composites increased from 9.40 BHN and 1200 MPa to 12.20 BHN and 1600 MPa in the sample containing 4.8 wt.% reinforcement, respectively. The newly developed aluminium metal matrix composite can find application in automobile parts production.

KEYWORDS: Reinforcement, carbonization, acid treatment, composite, coconut husk

1. INTRODUCTION

Aluminium and its alloys are commonly used as structural materials particularly in the aerospace industry due to their lightweight property (Dursun & Soutis, 2014; Georgantzia *et al.*, 2021; A. M. Usman *et al.*, 2014). The low strength, low melting point, and poor wear resistance are still a problem (A. Usman *et al.*, 2014). The use of reinforcements such as SiO_2, SiC particles and whiskers, or other elements or compounds as alloying elements was the common way of solving such problems (Arun *et al.*, 2013; Senapati *et al.*, 2014). The cheap way to improve aluminium's mechanical properties is to reinforce it with the available waste as reinforcement in the composite formulation. Research efforts have thus focused on the use of recycled wastes for composite development. Composite materials are materials made of two or more constituent materials with different physical or chemical properties that produce a material with different characteristics from the individual components when combined. Agricultural wastes are therefore the best substitute for expensive reinforcements because of increased farming activities and the deployment of modern technology resulting in vast renewable waste materials (Lancaster *et al.*, 2013).

Agricultural wastes are by-products or residues of agricultural processing. Bahrami *et al.* (2016) enumerated several benefits of using agro wastes as reinforcements including reduced production costs, availability, renewability, environmental conservation and safety. The use of naturally sourced particulates has been reported to offer good reinforcement constituents (Alaneme & Olubambi, 2013; Joseph & Babaremu, 2019; Nwobi-Okoye & Ochieze, 2018).

The present work focuses on the effect of treated carbonized coconut husk (TCCH) on the properties of aluminium matrix composites (AMCs)

2. MATERIALS AND METHODS

2.1 Materials

The materials used in this work include coconut husk (CH) which was sourced locally at Badagry, Lagos State. HCl was purchased at Tony Nigeria Enterprises, Ojota, Lagos. Aluminium scraps were obtained from the Materials and Metallurgical Engineering foundry. Some apparatus and equipment used include a muffle furnace, digital weighing balance, Whatman No.1 filter paper, sieve, laboratory blade mill, distilled water, carbonization chamber, oven, stirrer, and crucible furnace, available at the Department of Materials and Metallurgical Engineering, University of Ilorin, Nigeria. Equipment used for characterization includes Brinell hardness tester, and a Universal testing machine (UTM), both available at the Department of Mechanical Engineering, University

of Ilorin, Nigeria. Thermogravimetric analysis (TGA), X-Ray Diffractometry (XRD) and X-Ray Fluorescence (XRF) were carried out at the Centre for Solid Minerals Research & Development, Kaduna State Polytechnics, Nigeria. Scanning Electron Microscope (SEM) and Energy Dispersive X-ray Spectroscopy (EDS) at the Tshwane University of Technology, Department of Chemical, Metallurgical and Materials Engineering, Pretoria, South Africa.

2.2 Methods

The coconut husk was sorted to remove impurities, washed and sun-dried for 7 days to reduce the moisture content. This was carbonized at a temperature between 500 – 550 °C in a carbonization chamber for 60 minutes. The carbonized coconut husk (CCH) was pulverised using a laboratory blade mill and sieved to obtain particles below 100 µm. This was then leached with 0.5 M HCl for 120 minutes at laboratory temperature. This was filtered using Whatmann No.1 filter paper, rinsed several times with distilled water and thereafter dried in the oven to obtain TCCH.

The stir-casting method was used to produce specimens for characterization. Aluminium scrap was melted in a crucible furnace at a temperature of 700 °C. A measured amount of CCH was preheated to 300 °C for 3 hours in an electric oven to remove moisture. A calibrated pouring cup was used to tap 250 g of the molten metal and the preheated CCH was then mixed thoroughly for homogeneity. The mixture was poured into the preheated mould cavities at a maintained pouring temperature of 680 ºC. The composite was then allowed to solidify, and samples were removed, cleaned, labelled, and kept for characterization. The formulation of the composites is presented in Table 1.

Table 1: Weight percentage of aluminium scraps and carbonized coconut husk

SAMPLE ID	ALUMINIUM SCRAP (g)	CCH (g)	ALUMINIUM SCRAP (wt.%)	CCH (wt.%)
A	250	0	100	0
B	250	3	98.8	1.2
C	250	6	97.6	2.4
D	250	9	96.4	3.6
E	250	12	95.2	4.8

TGA, XRF and XRD were carried out on CH to determine its thermal stability up to 900 ºC, chemical composition and phase identification, respectively. Tensile, SEM/EDS, XRD and hardness of the composites were carried out to establish their mechanical and chemical properties.

3. RESULTS AND DISCUSSION

3.1 Treated Coconut Husk Features

The thermal characteristics of coconut husk by heating from room temperature to about 900 °C is presented in Figure 1. The thermal decomposition of agriculture was elucidated in Adebisi *et al.* (2019) as three stages of dehydration, volatilization and carbonization in an inert environment. The weight loss curve showed the first inflection at a temperature of 190 through 205 °C, which corresponds to the commencement of hemicellulosic compounds. This stage is more rapid from 280 to 375 °C. Cellulose decomposition occurred up to around 430 °C after which lignin and the main carbonization stage occurred. The first stage of dehydration is not pronounced in the TG curve, unlike the derivative (DTG) curve which indicated moisture loss up to around 100 °C. The derivative of the thermo-gravimetric analysis (DTG) curve shows the energy loss when the coconut husk was heated at room temperature, presenting a case of an exothermic process. The second stage of this thermal decomposition has been reported as the most crucial stage when all volatiles thermally left biomass to leave a residue of carbon char (Adebisi et al., 2019; Munir *et al.*, 2009; Nurhayati & Fauziah, 2013). The char left is principally the carbon skeleton of the biomass, which is about 20% as reported in Adebisi et al. (2019) to range between 18.60–29.40%. This carbon network is a ceramic with brittle nature and thus enhances the pulverization of the carbonized biomass.

As presented in Table 2, the compounds that constituted coconut husk are MgO, Al_2O_3, SiO_2, P_2O_5, SO_3, Cl, K_2O, CaO, TiO_2, V_2O_5, Cr_2O_3, MnO, Fe_2O_3, CuO, ZnO, SrO, BaO, and PbO. With carbon as the major element, silicon, iron, potassium, magnesium, and manganese also constitute about 95%. There is clear evidence of the removal of soluble silica from the TCCH. The presented elements are similar to the chemical composition obtained in coconut husk reported by Anuar *et al.* (2018), Anuar *et al.* (2020) and A. Usman et al. (2014). Phase identification of

compounds in a treated carbonized coconut husk, as shown in Figure 2, presented more crystalline reinforcement particles than untreated carbonized coconut husk. The XRD spectrum obtained for TCCH showed the most prominent peak at 27° as against 32° in TCC.

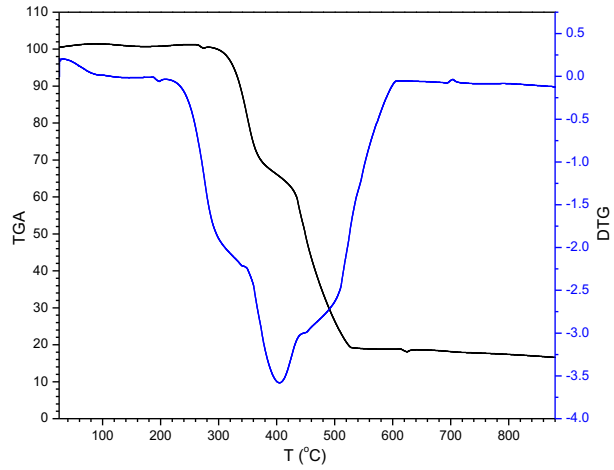

Figure 3: Thermogravimetric analysis of coconut husk

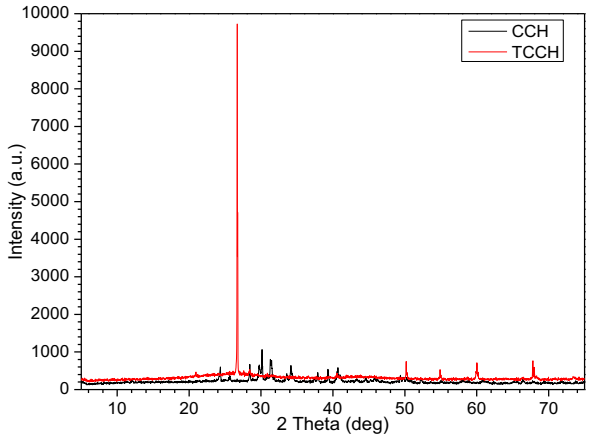

Figure 4: XRD of carbonized coconut husk and treated carbonized coconut husk

Table 2: Elemental composition of carbonized coconut husk and treated carbonized coconut husk

Compounds	MgO	Al_2O_3	SiO_2	P_2O_5	SO_3	Cl	K_2O	CaO	TiO_2	V_2O_5	Cr_2O_3	MnO	Fe_2O_3	CuO	ZnO	SrO	BaO	PbO
CCH (wt%)	4.16	0.16	72.13	0.49	0.24	1.28	6.89	1.24	0.09	0.06	0.06	3.27	8.78	0.43	0.02	0.01	0.80	0.74
TCCH (wt%)	4.20	1.43	61.95	1.02	0.29	1.28	8.37	5.38	0.13	0.07	0.09	4.07	8.16	0.31	0.41	0.01	2.10	0.73

3.2 Properties of Aluminium Treated Carbonized Coconut Husk Composites

The chemical composition of the aluminium scrap and composites produced showed that the addition of TCCH to the molten scrap increases the amount of almost all the constituting elements except silicon and titanium.

Table 3: Composition of the aluminium alloy and Composites Produced

Elements	**Al**	**C**	**Fe**	**Ag**	**Si**	**Ca**	**Cl**	**K**	**Mg**	**S**	**O**	**Ti**	**P**
0 wt%	89.66	2.93	2.11	1.59	1.03	0.64	0.57	0.48	0.27	0.24	0.20	0.19	0.08
2.4 wt%	85.70	4.42	2.51	2.55	1.00	0.76	0.64	0.59	0.35	0.45	0.75	0.00	0.28
4.8wt %	77.89	4.72	2.16	3.39	1.36	1.08	2.49	0.92	0.43	1.16	3.50	0.00	0.82

Figure 3 shows the XRD spectra for the scrap and composites. The addition of TCCH resulted in a shifting peak and lowered the intensity of the unreinforced aluminium. The strengthening of the produced composites is influenced by the nature of the reinforcing phases. The hardness values for the aluminium composites produced

are shown in Figure 4. The addition of TCCH slightly increases the hardness values of the composites. This may be a result of poor wettability of the reinforcement in the aluminium scrap used during casting.

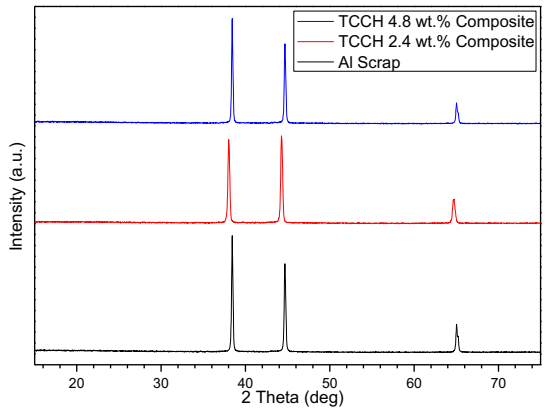

Figure 5: XRD patterns for unreinforced aluminium scrap and produced composites

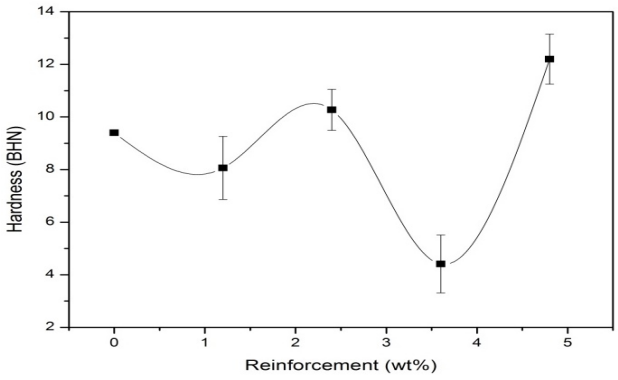

Figure 6: Hardness values for aluminium carbonized coconut husk composites

In Figure 5, tensile strength was observed to decrease by introduction of TCCH but later increased. The improved strength could be associated with the addition of TCCH well dispersed within the matrix. When the amount added exceeds a certain limit, agglomeration of the particles may be a source of stress raiser that will eventually result in failure (Oghenevweta *et al.*, 2016). The tensile strength improved from 1143 MPa to about 1600 MPa for 4.8 wt.% addition.

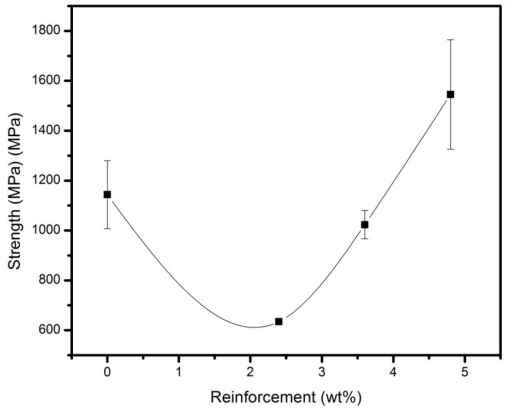

Figure 7: Ultimate tensile strength of the composites

4. CONCLUSION

This work has provided insight into the effect of introducing acid-treated carbonized coconut husk as reinforcement into the aluminium alloy. It was observed that:

1. The hardness of the composite materials increased from 9.40 BHN to 12.20 BHN.
2. The tensile strength of the composites increased from about 1200 MPa to 1600 MPa.
3. Microstructural analysis results show that Quartz (SiO_2) and Graphite (C) have the highest percentage among all the compounds and elements present in the reinforcement.

REFERENCES

Adebisi, J. A., Agunsoye, J. O., Bello, S. A., Kolawole, F. O., Ramakokovhu, M. M., Daramola, M. O., & Hassan, S. B. (2019). Extraction of Silica from Sugarcane Bagasse, Cassava Periderm and Maize Stalk: Proximate Analysis and Physico-Chemical Properties of Wastes. *Waste and Biomass Valorization, 10*(3), 617-629. doi: 10.1007/s12649-017-0089-5

Alaneme, K. K., & Olubambi, P. A. (2013). Corrosion and wear behaviour of rice husk ash—Alumina reinforced Al–Mg–Si alloy matrix hybrid composites. *Journal of Materials Research and Technology, 2*(2), 188-194.

Anuar, M. F., Fen, Y. W., Zaid, M. H. M., Matori, K. A., & Khaidir, R. E. M. (2018). Synthesis and structural properties of coconut husk as potential silica source. *Results in Physics, 11*, 1-4.

Anuar, M. F., Fen, Y. W., Zaid, M. H. M., Matori, K. A., & Khaidir, R. E. M. (2020). The physical and optical studies of crystalline silica derived from the green synthesis of coconut husk ash. *Applied Sciences, 10*(6), 2128.

Arun, L., Saddam, H., & Suneel, K. (2013). Dynamic behaviour of hybrid Aluminium6061 metal matrix reinforced with SIC and fly ash particulates. *International Journal of Innovative Research in Science, Engineering and Technology, 2*(6), 2501.

Bahrami, A., Soltani, N., Pech-Canul, M., & Gutiérrez, C. (2016). Development of metal-matrix composites from industrial/agricultural waste materials and their derivatives. *Critical Reviews in Environmental Science and Technology, 46*(2), 143-208.

Dursun, T., & Soutis, C. (2014). Recent developments in advanced aircraft aluminium alloys. *Materials & Design (1980-2015), 56*, 862-871.

Georgantzia, E., Gkantou, M., & Kamaris, G. S. (2021). Aluminium alloys as structural material: A review of research. *Engineering Structures, 227*, 111372.

Joseph, O. O., & Babaremu, K. O. (2019). Agricultural Waste as a Reinforcement Particulate for Aluminum Metal Matrix Composite (AMMCs): A Review. *Fibres, 7*(4), 33.

Lancaster, L., Lung, M., & Sujan, D. (2013). *Utilization of agro-industrial waste in metal matrix composites: towards sustainability.* Paper presented at the Proceedings of World Academy of Science, Engineering and Technology.

Munir, S., Daood, S. S., Nimmo, W., Cunliffe, A. M., & Gibbs, B. M. (2009). Thermal analysis and devolatilization kinetics of cotton stalk, sugar cane bagasse and shea meal under nitrogen and air atmospheres. *Bioresource Technology, 100*(3), 1413-1418. doi: https://doi.org/10.1016/j.biortech.2008.07.065

Nurhayati, A., & Fauziah, S. (2013). A Comparison Study on Oven and Solar Dried Empty Fruit Bunches. *Journal of Environment and Earth Science, 3*(2), 145-156.

Nwobi-Okoye, C. C., & Ochieze, B. Q. (2018). Age hardening process modelling and optimization of aluminium alloy A356/Cow horn particulate composite for brake drum application using RSM, ANN and simulated annealing. *Defence Technology, 14*(4), 336-345.

Oghenevweta, J. E., Aigbodion, V. S., Nyior, G. B., & Asuke, F. (2016). Mechanical properties and microstructural analysis of Al–Si–Mg/carbonized maize stalk waste particulate composites. *Journal of King Saud University - Engineering Sciences, 28*(2), 222-229. doi: https://doi.org/10.1016/j.jksues.2014.03.009

Senapati, A. K., Mishra, P. C., & Routara, B. C. (2014). Use of waste fly ash in the fabrication of aluminium alloy matrix composite. *Int. J. Eng. Technol, 6*, 905-912.

Usman, A., Raji, A., Waziri, N., & Hassan, M. (2014). Production and characterisation of aluminium alloy-bagasse ash composites. *IOSR Journal of Mechanical and Civil Engineering, 11*(4), 38-44.

Usman, A. M., Raji, A., Waziri, N. H., & Hassan, M. A. (2014). Aluminium alloy-rice husk ash composites production and analysis. *Leonardo Electronic Journal of Practices and Technologies, 25*, 84-98.

PAPER 67 – EXPERIMENTAL STUDY OF THE PRESSURE DROP AND FLOODING IN A ROTATING PACKED BED

U. Garba[1,2], D. Rouzineau[1], M. Meyer[1]

[1]Chemical Engineering Laboratory, University of Toulouse, CNRS, INPT, UPS, Toulouse, France
[2]Usmanu Danfodiyo University Sokoto, Nigeria
[*]Email: usman.garba@udusok.edu.ng

ABSTRACT
Embedded processes require compactness, low energy consumption, and insensitivity to gravity. Centrifugal processes respond to the last characteristic. Centrifugal force is used instead of the gravitational force with almost zero sensitivity to variations in the gravitational force. We studied a rotating packed bed (RPB) as a gas/liquid contactor for absorption. We focused our attention on the hydrodynamic behaviour of this device. Previous studies on RPB flooding and operating limits dwelled on virtual observations and pressure drop variations. However, physical visualizations are subjective because RPB pressure drop variations are too inconsistent to be used to determine the upper operating limit during RPB operations. A robust quantitative method of obtaining RPB flooding limits based on the flow rate of the ejected liquid, supported by visual observation and pressure drop measurement, was presented. The aim was to identify, with greater accuracy, RPB hydrodynamic characteristics and provide a more standard method of identifying the same.

KEYWORDS: Rotating packed bed, pressure drop, Flooding, Gas/liquid contactor, hydrodynamics,

1. INTRODUCTION

Reliance on gravitational force makes conventional packed columns for separation processes such as distillation and absorption has unimpressive sizes and physical footprints which makes them uneconomical, especially where space and weight are (Adekola et al., 2012; Hilpert & Repke, 2021). The operating ranges of non-rotating, conventional, packed bed columns (PBCs) are limited by gravitational and frictional forces acting in opposite directions on the down-flowing liquid and the gas flowing from the bottom of the column. An RPB, also called HIGEE (High g) contactor, is a compact process intensification equipment in which a combination of sizeable allowable gas and liquid flow rates is achieved by superimposing gravitational force with centrifugal force. In RPBs, the higher gravitational force factor employable raises the combined operating range of the throughputs in addition to their flexibility due to the additional degree of freedom offered by the rotation speed (Groß et al., 2018).

A fundamental aspect of the modelling, design, optimization, and implementation of pilot-scale and subsequent scale-up of RPBs is the clear understanding of the principles of its hydrodynamics via accurate prediction of the pressure drops and upper operating limits (Hendry et al., 2020; Neumann, et al., 2017a). Also, (Zhang et al., 2020) observed that the mass transfer performance and efficiency of an RPB, as reflected by its gas pressure drop, is closely linked to its hydrodynamic characteristics, operating costs, and energy requirements. Hydrodynamic characteristics such as the pressure drop of an RPB are a useful index in measuring its resistance and consequent energy consumption (Liu et al., 2018). Many studies were carried out to evaluate the influence of pressure drop in many RPB operations with empirical and semi-empirical models established (Jiao et al., 2010; Singh et al., 1992). RPB hydrodynamic parameters extensively reported in the literature include liquid holdup (Burns et al., 2000; Burns & Ramshaw, 1996), gas pressure drop (Neumann et al., 2017b; Pyka et al., 2022), liquid dispersion (Burns & Ramshaw, 1996; Xie, 2019) and, flooding (Hendry et al., 2020; Lockett, 1995). Although extensive research has been conducted and documented using RPBs, with many of its applications explored at the industrial scale, its design approach is still case-specific. It thus requires improvements (Neumann, et al., 2017a).

This work presents a robust quantitative method of obtaining RPB upper operating limit based on the flow rate of the ejected liquid, supported by visual observation and pressure drop measurements. This was achieved by connecting a hydrocyclone to the gas outlet. In addition, a comprehensive pressure drop behaviour and flooding for a countercurrent water-air system and a single-block stainless steel wire mesh packing using a double jet nozzle for the liquid inlet were used to study the hydrodynamics of the pilot-scale RPB. The aim was to improve further the understanding of RPB hydrodynamics for design, scale-up, and energy conservation purposes.

The relatively high rotation speeds of RPBs combined with the size of the equipment make it possible to implement forces more than 100 times greater than gravity, greatly intensifying the transfer phenomena between phases (Pan et al., 2017). Rapid contact surface replacement in RPBs allows for highly effective surface area packings of 2000 to 5000m^2/m^3 (Pan et al., 2017). This allows for higher mass transfer characteristics: gas-liquid interfacial area, gas-side and liquid-side volumetric mass transfer coefficients, and height of transfer unit (Cheng & Tan, 2011; Zhang et al., 2011). Also, this allows for the same separation performance in RPB to have much more flexible and compact equipment with a wider operating range than a gravity column used for absorption (L. L. Zhang et al., 2011). Overall, compared to conventional gravity columns, for a comparable processing capacity and efficiency, an RPB offers rotation as an extra degree of freedom, serves as the foundation of modular plants, and is more miniaturized with higher flexibility and energy efficiency (Neumann et al., 2018). The characteristics mentioned above make RPBs emblematic equipment for process intensification. Consequently, RPBs have been employed for various purposes in diverse fields such as separation processes, synthesis, and preparation of micro and nano-particles, petroleum products processing, biodiesel production, medical sciences, and pollution control (Hilpert & Repke, 2021; Neumann et al., 2018; L. L. Zhang et al., 2011).

A conventional, single-stage RPB is shown in Figure 1. It comprises a casing surrounding a rotor mounted on a shaft and rotated by a motor. The rotor is a motor-driven, ring-shaped cylinder that encloses an annular packing mounted on either a horizontal or a vertical shaft. In countercurrent operation mode, gas is introduced into the outer periphery of the packing from the casing. The liquid is usually introduced into the centre (or "eye") of the rotor via the liquid inlet through a stationary set of nozzles (liquid distributor) into the packing from the top of the RPB. After its transformation by centrifugal shear forces, the liquid flows in the form of rivulets, droplets, or films as determined by the rotation speed (Burns et al., 2000). The casing wall finally collects it and flows downwards under gravity, leaving the casing via the liquid outlet.

As equipment for efficient multi-phase mixing and mass transfer, (Yuan et al., 2022) identified RPB packing as its core component. Because of its excellent mass transfer characteristics, stainless steel wire mesh is commonly used as RPB packing (Chen et al., 2006). Conventional packed beds have constant cross-sections. Thus, their packing pores are nearly wholly filled throughout the column during flooding, causing a noticeable, steep rise in pressure drop.

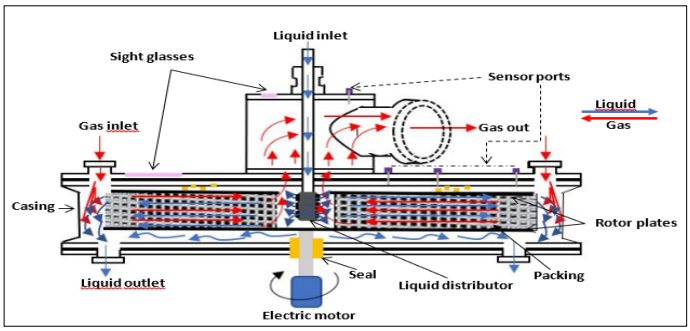

Figure 1: Schematic of a countercurrent flow RPB

However, due to the rotor geometry, RPB packings have variable cross-sections. The centrifugal forces are lowest at the centre (eye) of the rotor. Hence, RPB flooding occurs in the eye from where the liquid is ejected. Consequently, pressure drop variations during flooding in RPBs are not consistent as the sole indicator of flooding. (Neumann et al., 2017a), and Lockett (Lockett, 1995) also reported that in contrast to conventional columns, for RPBs, no sharp inflection in the total pressure drop or the holdup of the liquid with the gas velocity was observed during flooding. The procedure for visually determining the upper operating limit is to neutralize two operating variables and manipulate the third one (Groß et al., 2018). Therefore, it is possible to carry out two procedures to reconfirm the results. The speed of the rotor and the liquid flow rate may be set to a constant value then the gas flow rate gradually increases until an excessive splash of the liquid is observed in the eye of the rotor. Allowing the gas flow rate to increase beyond the upper operating limit will cause the liquid to accumulate in the eye of the rotor. (Groß et al., 2018; Neumann et al., 2017b) recommended the use of a combination of visual and quantitative approaches to adequately study the flow behaviour in RPBs, while (Groß et al., 2018) observed that due to observed inconsistencies, the use of physical and visual observations and the measurement of pressure drop variations alone are not sufficiently adequate to predict flooding behaviour in RPBs. (Burns et al., 2000) used

liquid holdup, while (Hendry et al., 2020) measured the flow rate of entrained liquid from the eye of the rotor to identify the upper operating limits in RPBs.

2. MATERIALS AND METHODS/METHODOLOGY/EXPERIMENTAL PROCEDURE

The experimental setup is shown in Figure 2. The RPB was a pilot-scale RPB 500 from ProCeller® located at the Laboratoire de Génie Chimique (LGC) in Toulouse (France). The RPB was a single-stage, vertical rotor type with a casing diameter of 0.676m, an inner rotor diameter of 0.160m, and an outer rotor diameter of 0.500m. The packing was a conventional, multi-layered, single-block, stainless steel wire mesh with an axial height of 0.040m, a specific surface of 2400 m^2/m^3, and a porosity of 86%. Visual observation was possible using two inspection glasses placed directly above the eye of the rotor and another on the casing (Figure 3a). To aid the systematic collection and subsequent measurement of ejected water from the eye of the rotor during flooding, a hydrocyclone was connected to the gas outlet. A countercurrent air-water system was used for all the experiments. The rotation speed of the rotor was selected and auto-controlled via a variable frequency drive. The liquid was pumped to the RPB using a peristaltic pump and controlled with a valve. The liquid flow rate was measured with a panel-type rotameter and sprayed from the centre of the RPB using a dual nozzle, flat fan liquid distributor. The liquid was recirculated to the feed tank using a bypass line. An air supply from the general laboratory compressor was used. The gas was introduced into the outside of the RPB into the casing through twin gas inlets and leaves after passing through the packing via the gas outlet. While the liquid sprays outwards from the centre of the packing to its periphery. A pressure sensor connected to a pressure transmitter was placed across the two points to measure the pressure drop between the packing periphery and the gas outlet. Pressure drop was measured in real-time by interfacing the sensor to a computer using a data acquisition system.

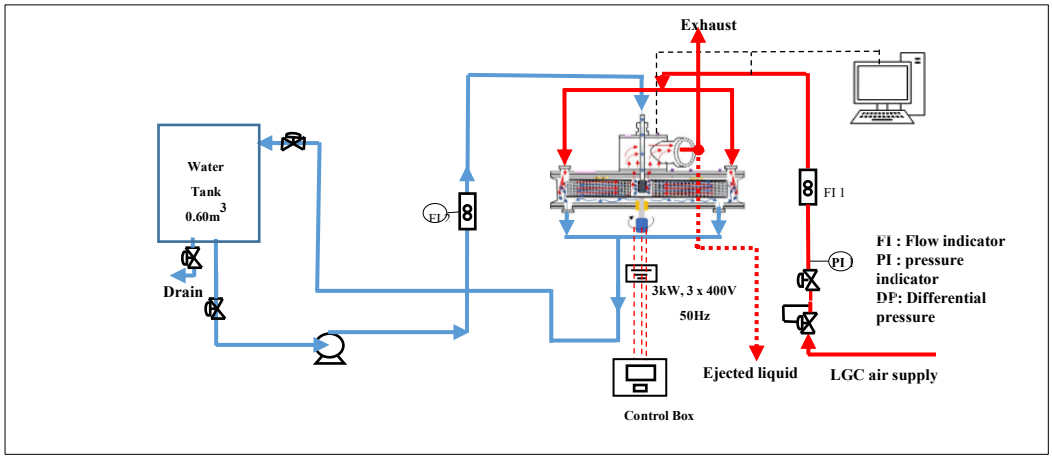

Figure 2: RPB countercurrent process flow diagram

The range of operating parameters studied was: gas flow rate (V_G), 0-400Nm^3/h; liquid flow rate (V_L), 0-0.75m^3/h and rotation speed 0-1500 revolutions per minute (RPM). Each experimental run was for 5 minutes. In the dry pressure drop measurements, the frictional pressure drop was first measured by passing air at 100Nm^3/h through the stationary rotor and then measuring the pressure drop. The experiment was repeated by increasing the airflow rate in steps of 50Nm^3/h. The same procedure was repeated with the rotor at various rotation speeds. Next, the effect of the rotation speed was investigated, initially via the centrifugal pressure drop. Without liquid and gas flow, the rotor was set to an initial speed of 100 rpm. The rotation speed was subsequently changed stepwise. The effect of rotation speed was further investigated by varying the rotation speed at constant gas flow rates. For the wet pressure drop, rotation speeds and liquid flow rates were kept while the gas flow rate was increased stepwise. This was followed by another set of experiments during which the gas flow rate and rotation speed were kept constant while the liquid flow rate was increased. The liquid flow rate and rotation speed were kept constant to determine the upper operating limit. In contrast, the gas flow rate was increased stepwise until the first drops of water were observed from the gas outlet according to the arrangement shown in Figure 3e. This point was taken as the upper operating limit of the RPB at the prevailing combination of operating factors. The reduction in rotation speed was continued gradually, with the amount of ejected water measured at each step after attaining a steady state of operation. Flooding points of the RPB operations were determined by visual observation of excessive water splashing at the RPB eye, with or without a sharp increase in pressure drop. The volume of water ejected at each step change of the gas flowrate was collected and measured using a measuring cylinder, and the flooding point was taken following the recommendation of (Hendry et al., 2020) when,

$$flowrate\ of\ ejected\ liquid \geq 8\%\ liquid\ flowrate \quad (1)$$

3.0 RESULTS AND DISCUSSION

Figure 3(a) shows that dry pressure drop increases with increased rotor speed. A slow increase in pressure drop was obtained at low rotational speeds from 100 to 550 RPM. Above 600 RPM, a rapid and almost linear increase in pressure drop was obtained. This phenomenon may be due to the greater need to overcome the pressure drop caused by rotation (centrifugal head) at higher rotational speeds, which consequently causes the air in the rotor and between it and the casing to rotate. The dry bed average increase in pressure drop per unit increase in rotation speed in the range investigated was 0.75Pa/rpm. This shows that centrifugal pressure contributes significantly to the total dry-packing pressure drop. Figure 3(b) also shows a substantially linear increase in pressure drop with increasing gas flow rate. The effects of gas inertia and friction primarily cause this. On average, Figure 3(b) shows that the average increase in pressure drop per unit increase in gas flow rate was 4.11Pa/Nm^{3}h^{-1} within the operating range investigated.

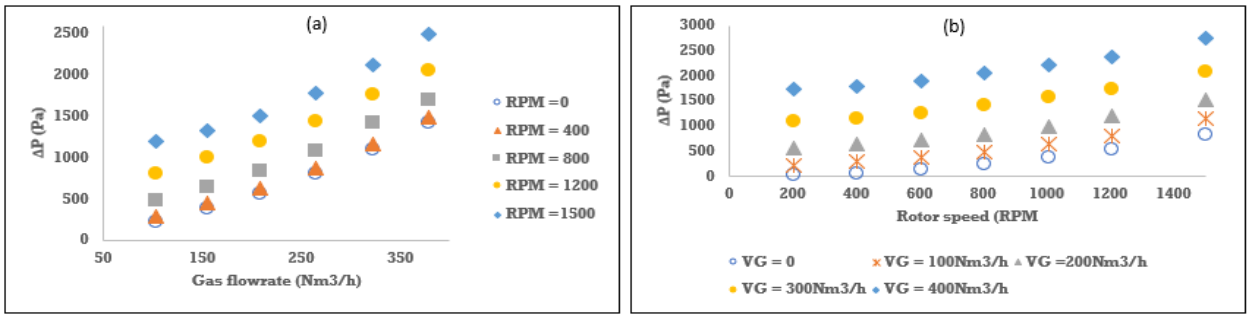

Figure 3: Dry bed pressure drop (a) effect of rotation speed (b) effect of gas flowrate

By comparing Figures 3(a) and (b), it can be seen that based on the sensitivity analysis mentioned above, the gas flow influences the dry pressure drop of the RPB more than the rotational speed. It can be deduced from Figures 3(a) and (b) that the range of dry pressure drops (20-2800Pa) in this work was comparable to the range obtained by (Liu et al., 2018) for the same range of rotation speed and comparable gas loads. The result is also comparable to that of (Neumann, Hunold, Skiborowski, et al., 2017) of 20-750Pa for similar rotation speed, RPB, and packing characteristics but using a lower gas flow rate of 15-60m^3/h. For the irrigated bed, Figures 4(a) and (b), as well as Figure 5(a), showed that the trend of the pressure drop variation was almost the same as that of the dry bed, with the pressure increasing with an increase in rotational speed and with the gas flow. (W. Zhang et al., 2020) identified the wetting of the packing surface, which affects the frictional pressure drop, and the blockage of the packing pores by the liquid to the passage of gas as the two principal contributors to the rise in pressure drop in wet RPBs. Figure 5(b) indicates the lower effect of liquid flow rate on the overall pressure drop in RPBs. For example, for a gas flow of 350Nm^3/h, the 50% increase in liquid flow rate from 0.3 to 0.6m^3/h produces small changes in the pressure drop with the increase in the speed of rotation, showing that the effect of the gas flow in the RPB is more than that of the liquid flows. This phenomenon is more visible when we represent this at constant rotational speeds with a variation of the gas flow (Figure 4a) or a variation of the liquid flow (Figure 4(b)). These results confirm the trends described by the reports of (Groß et al., 2018; Neumann, Hunold, Groß, et al., 2017). Additionally, in terms of liquid loading loads and gas capacities, it can be deduced that the ranges of the wet pressure drops in Figures 5(a) and (b) are comparable to the findings of (Liu et al., 2018).

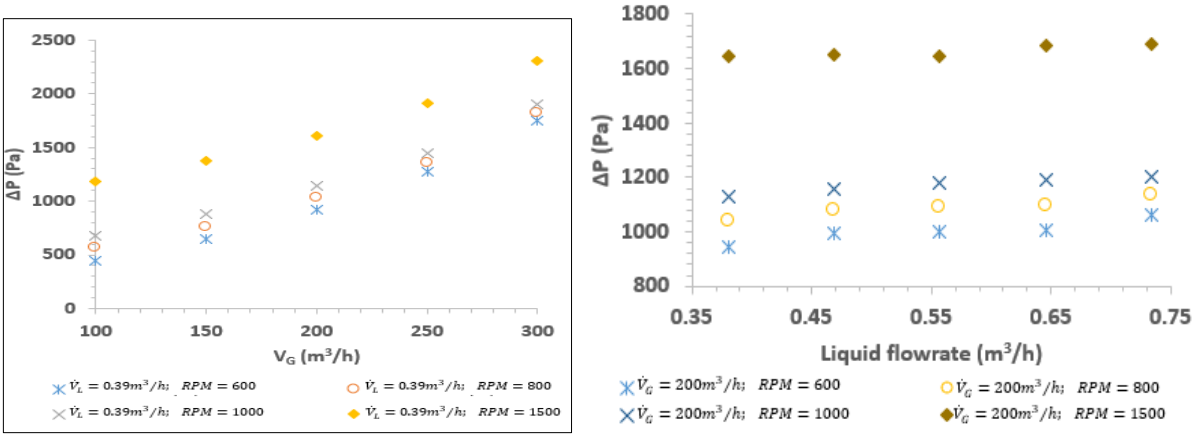

(a) (b)

Figure 4:

Figure 4 (a) shows that the flooding data follows a typical RPB equipped with a vertical axis pressure drop variation curve with rotation speed at constant gas and liquid flow rates, as highlighted by (Neumann, Hunold, Groß, et al., 2017). A lowering of centrifugal pressure drop is obtained at a decrease from the maximum rotation speeds. At the same time, liquid accumulation in the eye causes only slight increases in frictional pressure drop. Further decrease in the rotation speed will cause an accumulation of liquid in the eye of the rotor, which leads to an increase in the frictional pressure drop and a sharp

increase in the total pressure drop.

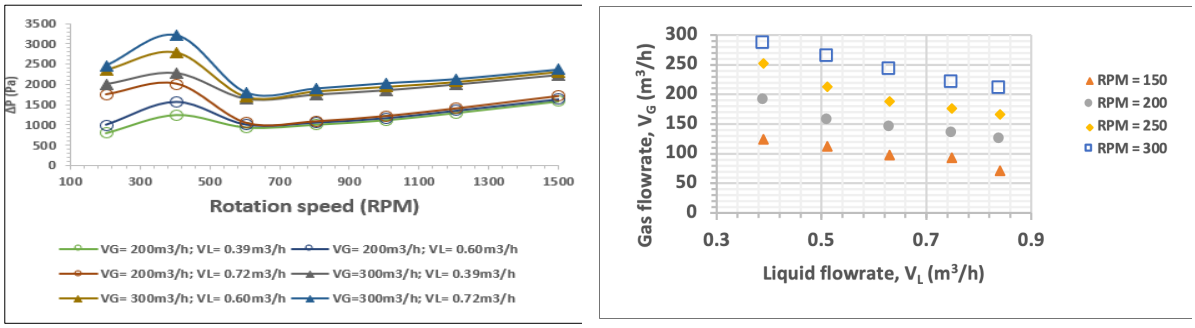

(a) (b)

Figure 5 (a) Effect of rotation speed at constant gas and liquid flow rates (b) upper operating points.

As the rotation speed is further decreased, rapid ejection of liquid from the eye of the rotor to the gas outlet is obtained due to the acceleration of the liquid droplets. The pressure drop increases significantly, and the presence of water is visually observable in the rotor eye. Figure 5(b) shows the upper operating limits of the system investigated. At a constant rotation speed, the gas flow rate at which the ejection of liquid droplets was observed and decreased with an increased liquid flow rate. Regular operation of the RPB without liquid ejection and possible high-pressure drops, which increase power consumption, is obtained by operating the RPB below the indicated points. The operating limit at a given condition can be improved by increasing the rotation speed from the given point. Based on a range of liquid loads and the gas capacity factor at the inner radius of the RPB, the trends and ranges of these operating limits are comparable to the results of (Groß et al., 2018).

4.0 CONCLUSIONS

This paper focused on furthering the understanding of the upper operating limits of RPBs as an essential aspect of its design, modelling, scale-up, and use for the intensification of mass transfer processes. The gas pressure drop of a pilot-scale RPB equipped with stainless steel wire mesh packing for an air-water system using a twin-nozzle liquid distributor was explored. A robust approach to determine RPB operating limits based on quantifying the volume of liquid ejected from the eye of the rotor was explored. The operating limits for RPBs are influenced mainly by the three operational parameters: gas flow rate, liquid flow rate, and rotational speed in that order.

ACKNOWLEDGMENT

This work was conducted under support funding from the Overseas Scholarship Scheme (OSS) of the Petroleum Technology Development Fund (PTDF), Nigeria (Grant Number: PTDF/ED/OSS/PHD/UG/1543/19).

REFERENCES

Adekola L., Meihong W., Peter S, O. O. (2012). Demonstrating full-scale post-combustion CO2 capture for coal-fired power plants through dynamic modelling and simulation. *Fuel*, *101*, 115–128.

Burns, J. R., Jamil, J. N., & Ramshaw, C. (2000). Process intensification: Operating characteristics of rotating packed beds - determination of liquid hold-up for a high-voltage structured packing. *Chemical Engineering Science*, *55*(13), 2401–2415. https://doi.org/10.1016/S0009-2509(99)00520-5

Burns, J. R., & Ramshaw, C. (1996). Process intensification: Visual study of liquid maldistribution in rotating packed beds. *Chemical Engineering Science*, *51*(8), 1347–1352. https://doi.org/10.1016/0009-2509(95)00367-3

Chen, Y. S., Lin, F. Y., Lin, C. C., Tai, C. Y. Der, & Liu, H. S. (2006). Packing characteristics for mass transfer in a rotating packed bed. *Industrial and Engineering Chemistry Research*, *45*(20), 6846–6853. https://doi.org/10.1021/ie060399l

Cheng, H. H., & Tan, C. S. (2011). Removal of CO2 from indoor air by alkanol amine in a rotating packed bed. *Separation and Purification Technology*, *82*(1), 156–166. https://doi.org/10.1016/j.seppur.2011.09.004

Groß, K., Neumann, K., Skiborowski, M., & Górak, A. (2018). Analysing the operating limits in high gravity equipment. *Chemical Engineering Transactions*, *69*, 661–666. https://doi.org/10.3303/CET1869111

Hendry, J. R., Lee, J. G. M., & Attidekou, P. S. (2020). Pressure drop and flooding in rotating packed beds. *Chemical Engineering and Processing - Process Intensification*, *151*(March), 107908. https://doi.org/10.1016/j.cep.2020.107908

Hilpert, M., & Repke, J. U. (2021). Experimental Investigation and Correlation of Liquid-Side Mass Transfer in Pilot-Scale Rotating Packed Beds. *Industrial and Engineering Chemistry Research*, *60*(14), 5251–5263. https://doi.org/10.1021/acs.iecr.1c00440

Jiao, W. Z., Liu, Y. Z., & Qi, G. S. (2010). Gas pressure drop and mass transfer characteristics in a cross-flow rotating packed bed with porous plate packing. *Industrial and Engineering Chemistry Research*, *49*(8), 3732–3740. https://doi.org/10.1021/ie9009777

Liu, X., Jing, M., Chen, S., & Du, L. (2018). Experimental study of gas pressure drop in rotating packed bed with rotational-stationary packing. *Canadian Journal of Chemical Engineering*, *96*(2), 590–596. https://doi.org/10.1002/cjce.22936

Lockett, M. J. (1995). Flooding of rotating structured packing and its application to conventional packed columns. *Chem. Eng. Res. Des.*, *73*, 379–384.

Neumann, K., Gladyszewski, K., Groß, K., Qammar, H., Wenzel, D., Górak, A., & Skiborowski, M. (2018). A guide on the industrial application of rotating packed beds. *Chemical Engineering Research and Design*, *134*, 443–462. https://doi.org/10.1016/j.cherd.2018.04.024

Neumann, K., Hunold, S., Groß, K., & Górak, A. (2017a). Experimental investigations on the upper operating limit in rotating packed beds. *Chemical Engineering and Processing: Process Intensification*, *121*(August), 240–247. https://doi.org/10.1016/j.cep.2017.09.003

Neumann, K., Hunold, S., Skiborowski, M., & Górak, A. (2017b). Dry Pressure Drop in Rotating Packed Beds - Systematic Experimental Studies. *Industrial and Engineering Chemistry Research*, *56*(43), 12395–12405. https://doi.org/10.1021/acs.iecr.7b03203

Pan, S. Y., Wang, P., Chen, Q., Jiang, W., Chu, Y. H., & Chiang, P. C. (2017). Development of high-gravity technology for removing particulate and gaseous pollutant emissions: Principles and applications. *Journal of Cleaner Production*, *149*, 540–556. https://doi.org/10.1016/j.jclepro.2017.02.108

Pyka, T., Koop, J., Held, C., & Schembecker, G. (2022). Dry Pressure Drop in a Two-Rotor Rotating Packed Bed. *Industrial & Engineering Chemistry Research*. https://doi.org/10.1021/acs.iecr.2c02500

Singh, S. P., Counce, R. M., Wilson, J. H., Villiers-Fisher, J. F., Jennings, H. L., Lucero, A. J., Reed, G. D., Ashworth, R. A., & Elliott, M. G. (1992). Removal of Volatile Organic Compounds from Groundwater Using a Rotary Air Stripper. *Industrial and Engineering Chemistry Research*, *31*(2), 574–580. https://doi.org/10.1021/ie00002a019

Xie, P. (2019). *Hydrodynamics and Mass Transfer of Rotating Packed Beds for CO 2 Capture*. *February*.

Yuan, Z.-G., Wang, Y.-X., Liu, Y.-Z., Wang, D., Jiao, W.-Z., & Liang, P.-F. (2022). Research and development of advanced structured packing in a rotating packed bed. *Chinese Journal of Chemical Engineering*, *49*, 178–186. https://doi.org/10.1016/j.cjche.2021.12.023

Zhang, L. L., Wang, J. X., Xiang, Y., Zeng, X. F., & Chen, J. F. (2011). Absorption of carbon dioxide with ionic liquid in a rotating packed bed contactor: Mass transfer study. *Industrial and Engineering Chemistry Research*, *50*(11), 6957–6964. https://doi.org/10.1021/ie1025979

Zhang, W., Xie, P., Li, Y., Teng, L., & Zhu, J. (2020). Hydrodynamic characteristics and mass transfer performance of rotating packed bed for CO2 removal by chemical absorption: A review. *Journal of Natural Gas Science and Engineering*, *79*(March), 103373. https://doi.org/10.1016/j.jngse.2020.103373

PAPER 68 – DEVELOPMENT OF ACTIVATED CARBONS FROM *PENTACLETHRA MACROPHYLLA* PODS AS HIGH-PERFORMANCE ADSORBENT FOR TREATMENT OF AZO DYE WASTEWATER

Gabriel O. Ogbeh[1*], Ayodele O. Ogunlela[2], and Raphael T. Iwar[1]

[1]Department of Agricultural and Environmental Engineering, Joseph Sarwuan Tarka University, P.M.B. 2373 Makurdi, Nigeria

[2]Department of Agricultural and Biosystems Engineering, University of Ilorin, Nigeria

[*]Email: gabriel.ogbeh@uam.edu.ng

ABSTRACT

This present study reports the preparation of activated carbons via facile pyrolysis using African oil bean (*Pentaclethra macrophylla*) pods as a potential carbon precursor. The experimental process parameters were optimized through a chemometric tool to produce activated carbons of high carbon yield and iodine numbers with H_3PO_4 and KOH as activating agents. The results indicated that the activated carbon obtained using KOH (KOH-$PMAC_{op}$) has a moderately higher surface area of 911.70 m^2/g than 527.59 m^2/g obtained using H_3PO_4 (H_3PO_4-$PMAC_{op}$) on almost the same set of optimum production parameters. It also exhibited the highest adsorption capacity of 148 mg/g for Congo red. Both activated carbons demonstrated evidence of extensive graphitic features from the analyses of the Raman spectroscopy and X-ray diffraction investigations conducted on them. The Fourier transform infrared (FT-IR) spectra of the KOH-$PMAC_{op}$ suggested a higher proportion of aromaticity than that of H_3PO_4-$PMAC_{op}$, which implies that it is likely to promote adsorption mechanisms like electrostatic and π-π interactions far better than that of H_3PO_4-$PMAC_{op}$. Both carbons, however, suggested their ability to support any rate-controlling chemisorption mechanism, as indicated by the Pseudo-second-order kinetic model obtained from the experimental data. Using African oil bean pods as a precursor for activated carbon offers another chance to develop sustainable and high-efficient adsorbents for wastewater treatment.

KEYWORDS: Activated carbons, Azo dye wastewater, Chemical activation, Chemometric tool, *Pentaclethra macrophylla* pods

1 INTRODUCTION

Wastewater from dyeing industrial processes constitutes one of the global environmental risk concerns. The discharge of dyeing wastewater into surface water resources impairs their quality parameters which are mostly occasioned by incomplete degradation of dye, as the inherent colour impedes light penetration into the water bodies (Karuppasamy *et al*., 2021; Yeow *et al*., 2021). The discharge of dyeing wastewater on soils also causes soil infertility, as the dye tends to stabilize and retain soils (Chandanshive *et al*., 2018; Hassan *et al*., 2022). Delays of seed germination and even plant growth inhibition on soils irrigated with dyeing wastewater have been reported (Chandanshive *et al.*, 2018; Khan & Malik, 2018). Many dyes are also known to be harmful to animal and human health, especially upon prolonged exposure, as they cause allergies, respiratory disorders, irritation, and even mutations or cancer risks in some cases (Chung, 2016; Kadhom *et al*., 2020). It is therefore imperative to facilitate the removal of dyes from wastewater at the source of generation before its eventual discharge into large bodies of water or on land. Although advanced treatment systems such as photocatalysis, the Fenton process, electrooxidation, and biological treatment have been successfully used to treat dye wastewaters, these treatment systems are often expensive to operate and maintain (Asaithambi *et al*., 2022; Bilińska & Gmurek, 2021; Solayman *et al*., 2023; Yeow *et al*., 2021). Due to its comparatively high efficiency, cost-effectiveness, and environmental friendliness, an activated carbon-based adsorption system has recently taken the lead as the preferred method for the treatment of dyeing wastewater.

Commercial activated carbons (ACs) are still expensive to buy, thus research on finding low-cost precursors for their synthesis has become more important (Ajaelu *et al*., 2022; Nindjio *et al*., 2022). The physical activation method, involves carbonization and activation in two steps (Ogungbenro *et al*., 2017; Yang *et al*., 2010), the chemical activation method, which transforms cellulose structures into carbonaceous material through simultaneous dehydration and carbonization (Jaria et al., 2019; Yorgun & Yildiz, 2015), the combined physical and chemical activation method, or the microwave-assisted activation method (Ao *et al*., 2018; Lam *et al*., 2017; Liew *et al*., 2018), are the different ways that activated carbons are produced. The chemical activation method offers the advantage of allowing the production of activated carbons of higher qualities at lower cost due to its lower power required to generate the needed activating temperatures, typically ranging from 400 to 700°C (Loredo-Cancino *et al*., 2013). The chemical activation method is, however, beset with the challenge of selecting the most appropriate optimal production conditions required to produce activated carbons of desired qualities. Because of their renewability and low cost, agroforestry wastes are appealing precursors for the sustainable

production of ACs. The creation of ACs with desirable qualities is influenced by a few factors, including the properties of the precursors, the manufacturing procedure, and the activation agents (Kwiatkowski & Broniek, 2017; Li *et al*., 2017). Depending on the content, stability, presence of heteroatoms, and functional groups of the plant waste, different ACs will be produced (Ekpete *et al*., 2017; Hidayu & Muda, 2016; Shamsuddin *et al*., 2016). Numerous widely available agroforestry residues have been explored for their potentials as ACs precursors. The pod of the African oil bean (*Pentaclethra macrophylla*) tree is one of such biomaterials. The African oil bean tree belongs to the Leguminoseae family and the Mimosoideae subfamily and grows approximately 6 meters in girth and 21 meters in height (Okpala, 2015). The most widely used part of the African oil bean tree is the seeds, which are usually enclosed in some flat pods that tend to burst once matured thereby dispersing the seeds. The pods are often considered waste and remain underused. The pods measure about 35 to 45 centimetres long by 5 to 10 centimetres broad, black in colour, quite hard, and woody in appearance.

There have been a few studies looking into the effects of preparation variables like temperature and impregnation ratio on activated carbons (ACs) from *Pentaclythra macrophylla* pods (PM_{ps}) (Abugu *et al*., 2015; Chimi *et al*., 2023), but none have shown that using a chemometric tool like Response Surface Methodology (RSM) to produce activated carbons from PM_{ps} allows for its structure to be well-developed for the removal of colour in dye wastewater. Therefore, it is suggested that PM_{ps} be used as a potential precursor for H_3PO_4- and KOH-activated carbons in this study. RSM was used as a chemometric technique to optimize the production parameters (activation temperature, activation time, and impregnation ratio) to create activated carbons with well-developed porous structures. The optimized ACs (H_3PO_4-$PMAC_{op}$ and KOH-$PMAC_{op}$) were then described and used to adsorb colour from a simulated azo dye wastewater.

2 THEORETICAL ANALYSIS

Conceptual basis of the chemometric tool

The chemometric tool employed for this study is the Central Composite Rotatable Design (CCD), which is a subset of the RSM. The CCD consisted of a full two-level factorial (2^3) coded as -1 and +1 at the lower and higher levels, six (6) central replicates located at the centre (0, 0, 0) to examine experimental error and reproducibility of the data, and six (6) axial points located at (±α, 0, 0), (0, ±α, 0) and (0, 0, ±α). Alpha (α) is the distance of an axial point from the centre which makes the design rotatable and has a value of 1.68. This gives a total of 20 experimental runs.

The Central composite design

The PMACs were prepared using three independent parameters namely the activation temperature (A), activation time (B), and impregnation ratio (C). The coded and real levels of these parameters are shown in Table 1. The responses of the design were the iodine number and the carbon yield. The attributes of the experimental responses were predicted from the second-order polynomial regression model generally described by Eq. (1).

$$Y_{I_n \text{ or } C_y} = \beta_o + \sum_{i=1}^{n} \beta_i X_i + \left(\sum_{i=1}^{n} \beta_{ii} X_i \right)^2 + \sum_{i=1}^{n-1} \sum_{j=i+1}^{n} \beta_{ij} X_i X_j \qquad (1)$$

where Y is the predicted response, β_o is the constant coefficient, β_I represents the linear term coefficients, β_{ij} represents the interaction coefficients, β_{ii} represents the quadratic coefficients, X_i, X_j are the coded values of the production parameters and n is the number of variables.

The experimental sequence was randomized to minimize the effects of the uncontrolled factors and outliers. The significance of each coefficient in the models was determined by F-test and *ρ*-values. The CCD of the RSM and its corresponding statistical analyses were done using Design-Expert (10.0.0 Stat-Ease Inc., Minneapolis, MN).

Table 1: Coded and Actual Levels of Production Factors used to produce the PMACs.

Production factor	**Coded levels**				
	-α (-1.68)	-1	0	+1	+α (+1.68)
	Actual values				
Activating temperature (°C), A	200	300	450	600	700
Activating time (min), B	20	60	120	180	210
Impregnation ratio (g/L), C	1	2	3	4	5

3 EXPERIMENTAL PROCEDURE

Materials

The *Penclethra macrophylla* pods (PM_{ps}) were harvested from Benue and Enugu States – Nigeria during their peak dispersal periods from December to January. The pods were cleaned to remove dirt and sun-dried for seven (7) days to reduce their moisture contents. The biomaterials were transformed into granules using a combination of manual and mechanical size reduction mechanisms – cutting, pounding, and grinding. The PM_{ps} were passed through sieves of size 50 – 80 meshes (0.180–0.300 mm) to achieve experimental uniformity. They were stored in jute bags and labelled appropriately. Also, standard analytical grades of orthophosphoric acid 85 wt% (H_3PO_4), potassium hydroxide (KOH), Congo red ($C_{32}H_{22}N_6Na_2O_6S_2$, CR) dye, iodine, hydrochloric acid, and sodium thiosulphate were purchased and used without any further purification.

Synthesis of the activated carbons

The 85 wt% mass fractions of H_3PO_4 and 50 mg of the PM_{ps} powder were mixed according to the designed ratios of 1:1, 2:1, 3:1, 4:1, and 5:1 (volume of H_3PO_4 to the mass of PM_{ps} powder) inside some sets of steel reactors that were agitated continuously at 1000 rpm on a centrifuge for 6 hours. The PM_{ps} were filtered out of the mixtures and the samples were dried using a thermostat oven set at 110 ^oC for 1 hour to prepare the impregnated samples. The reactors were placed inside a high carbonization temperature tube furnace and heated from ambient temperature to 200 ^oC for 30 minutes, followed by further heating at the different designed temperatures ranging from 200 to 700 ^oC and activation time ranging from 20 to 210 minutes for simultaneous carbonization and activation of the precursors (Jiang *et al.*, 2019). The air within the furnace was displaced by introducing a nitrogen gas stream at 60 mL/min into it for 20 min. Similar procedures were followed to produce ACs from the PM_{ps} using KOH powder. However, the chemical impregnation of the biomaterial was done by mixing the required mass of KOH and the PM_{ps} powder to attain the designed ratios inside separate steel reactors with 30 mL of deionized water (Jiang *et al*., 2019). After the samples were dried in a thermostat oven set at 110 ^oC for 1 hour, they were transferred inside the furnace to be pyrolysed at the different designed production conditions. All the carbonized chars were allowed to cool to room temperature and thereafter washed several times with 200 mL hot and cold distilled water to achieve a neutral pH, and then allowed to dry for 2 hours at 110 ^oC using the oven. The activated carbons were boiled with HCl solution under reflux to remove impurities and reduce their inherent ash contents (Figure S1). The products pounded in a laboratory mortar and sieved using Tyler's sieves and stored in airtight containers. The dried carbon yield was determined using Eq. (2).

$$\text{Carbonyield, } C_y = (1 - m_c/m_r)100 \qquad (2)$$

where C_y is the carbon yield (%), m_c is the mass of the carbonized product (g), and m_r is the mass of precursor (g).

Characterization of the activated carbons

Determination of the iodine number

The iodine numbers of the PMACs were determined using the standard test method established by the American Society for Test and Materials (ASTM D, 2006). A 1 litre stock solution of iodine-containing 2.70 g of iodine crystals and 4.10 g of potassium iodide (KI) was prepared. It was standardized by a standard solution of sodium thiosulphate. Also, starch solution, which served as the indicator reagent was prepared by dissolving 0.30 g of starch powder in 30 mL of deionized water, and 70 mL of boiled deionized water was added to it (Pongener *et al*., 2015). For each experimental run, 0.50 g of the PMACs and 10 mL of 5%v/v HCL were introduced into a 100 mL volumetric flask. The flask was stirred gently to wet the carbon, then 100 mL of the iodine stock solution was added to the mixture and the flask was shaken on a shaker for 1 hour. The mixtures were filtered using microfibre filters, and a 20 mL aliquot portion of the filtrate was titrated with 0.10 M sodium thiosulphate, and 2 to 3 pipette drops of the starch solution was also added as an indicator (Pongener *et al*., 2015). The mixture was stirred gently until it turned colourless. The initial and final volumes of the mixture and the titre value were recorded. A blank titration procedure was similarly performed with sodium thiosulphate solution but without the addition of the PMACs. The concentration of iodine adsorbed by the PMACs at room temperature was calculated using Eq. (3).

$$I_n = [((A - B)/A) \times ((V \times M)/W)] \times 253.81 \qquad (3)$$

where I_n was the iodine number (mg/g), and A and B were the volumes of sodium thiosulphate solution required for blank and sample titrations, respectively. W is the mass of the PMACs sample, M is the molar concentration of the iodine, V is the 20 mL aliquot, and 253.81 is the atomic mass of iodine.

Morphological Assessment of the PMACs

The organic structure of the PMACs were determined using a Thermo Nicolet Fourier transform infrared spectrometer (Nicolet 67, USA). The specific area was explored through nitrogen adsorption Brunauer-Emmett-Teller BET analysis using Micrometrics 3Flex version 5.02 equipment. The textural parameters and element

constitution of the carbon were determined using scanning electron microscopy combined with energy-dispersive X-ray spectroscopy EDX.

The batch adsorption and kinetic studies of PMACs

A stock solution of the Congo Red (CR) dye was prepared as the adsorbate solution for the batch experiments. The 1000 mg/l concentration of the CR stock solution was prepared by dissolving 1.0 g of the powdered dye in 1 litre of deionized water (Hammari *et a*l., 2021). The desired concentrations of the CR dye solution for the experiments were subsequently prepared via serial dilution of the stock solution. The batch adsorption of the dyes onto the activated carbons (H_3PO_4-$PMAC_{op}$ and KOH-$PMAC_{op}$) was performed to investigate the effects of initial concentration on the adsorption profile of the carbons. The amount of the dye adsorbed by the activated carbon at each initial concentration was calculated using Eq. 4. The experimental data obtained were subsequently analysed using Origin software (version 2022) by non-linear graphical plots of the Langmuir, Freundlich, and Temkin adsorption isotherms.

$$Q_e = (100 - C_e)V/w \quad (4)$$

The effects of contact time on the adsorption profile and the kinetic parameters of the activated carbon were evaluated at 15, 30, 60, 90, 120, 150 and 180 mins using 50 mg of each activated carbon and 100 ml of 100 mg/l of the CR solution in a set of flasks placed on a rotary shaker set at 200 rpm at ambient temperature of approximately 30±2ºC (Hammari *et al*., 2021). The amount of CR dyes adsorbed by the activated carbon at equilibrium at the different contact times were calculated using Eq. 5.

$$Q_t = (100 - C_t)V/w \quad (5)$$

The experimental data of the adsorption of the CR dye onto both activated carbons from the PM_{ps} was evaluated using the Pseudo-first-order (Eq. 6), Pseudo-second-order (Eq. 7), and the Elovich (Eq. 8) kinetic models to ascertain the rate-limiting profile of the adsorption process of the carbons. Nonlinear kinetics plots of the amount of CR dye adsorbed per time by both carbons were analyzed using Origin software (version 2022) as well as the experimental data and the theories of these kinetic models.

$$Q_t = Q_e(1 - e^{-K_t t}) \quad (6)$$

$$Q_t = K_2 Q_e^2 t/(1 + K_2 Q_e t) \quad (7)$$

$$Q_t = 1/\beta \ln t - 1/\beta \ln(\alpha\beta) \quad (8)$$

4 RESULTS AND DISCUSSION

Yields of the activated carbon

The optimum yields of the PMACs from the same quantity of the pods using H_3PO_4 and KOH activators differ significantly (51.10 and 39.15%, respectively). The lower AC yield of KOH-$PMAC_{op}$ is attributed to its tendency to promote intense volatilization of biomass through the breaking of C-O-C and C-C bonds (Yokoyama *et al*., 2019). Also, pyrolysis using KOH as an activator is favourable to the catalytic decomposition of heteroatoms within biomass, which promotes the increased release of gases like CO, CO_2, H_2O, and hydrocarbons, leading to lower carbon content of KOH-$PMAC_{op}$ than obtain with H_3PO_4-$PMAC_{op}$ (Jamnongkan *et al*., 2022).

Model Building and Optimization

Table 2 shows the CCD used for the experiments and the corresponding values of the responses (iodine number, I_n and carbon yield, C_y) at each experimental run for both H_3PO_4 and KOH activators. The effects of the principal factors and their interactions on each of the responses were analysed and optimized to obtain ACs with high adsorptive features. The results indicate that the three principal parameters (activation temperature, activation time, and impregnation ratio) have a high influence on the two responses for each activated carbon. The distinct variations of the I_n values, ranging from 454.74 to 1050.60 mg/g and C_y values, ranging from 29.34 to 51.30% for the KOH-PMACs and the I_n values, ranging from 217.37 to 810.06 mg/g and C_y values, ranging from 38.45 to 60.0% for H_3PO_4-PMACs are at the instant of the variations of each of these production parameters. The extent of the significant effects of these parameters on the responses is shown in Table S1. These parameters created both synergetic (positive coefficients) and antagonistic (negative coefficients) effects on the I_n and C_y values of both activated carbons, as indicated in Equations 9 to 12. However, any parameter found to be non-significant at $p>0.05$ on the ANOVA table was removed from each of the models.

$$I_{KOH} = -1108.06 + 1.52A + 6.66B + 629.66C - 2.42 \times 10^{-3}AB + 0.29AC - 1.43BC - 1.50A^2 - 88.00C^2 \quad (9)$$

$$I_{H_3PO_4} = -274.56 + 3.62A - 3.71B + 6.57 \times 10^{-3}AB - 0.17AC + 0.77BC - 3.17 \times 10^{-3}A^2 - 4.38 \times 10^{-3}B^2 - 11.35C^2 \quad (10)$$

$$C_{KOH} = 48.72 - 0.04A + 0.04B + 9.72 \times 10^{-5}AB - 3.58 \times 10^{-3}AC - 8.96 \times 10^{-3}BC - 3.38 \times 10^{-4}B^2 - 0.590C^2 \quad (11)$$

$$C_{H_3PO_4} = 46.42 - 0.02A + 0.16B - 6.17 \times 10^{-3}AC - 0.02BC - 5.02 \times 10^{-4}B^2 \quad (12)$$

With respect to the models for the iodine number of the KOH-PMACs and H_3PO_4-PMACs, the following can be inferred. Even though positive linear coefficients were clearly contributed by the three parameters to develop the KOH-PMACs of high iodine number (Equation 9), but that obtained from the impregnation ratio (+629.66) was much more profound, especially since the impregnation ratio was not significant in the preparation of the H_3PO_4-PMACs (Equation 10). Whereas the linear effects of both the activation temperature and impregnation ratio on the preparation of the KOH-PMACs and H_3PO_4-PMACs were positive coefficients, the reverse was noted for the coefficients of the interaction (AB) between these parameters. While negative coefficients of interaction between the temperature and impregnation ratio (AC) were needed to impact the iodine number of the KOH-PMACs, positive coefficients were useful to influence the iodine number of the H_3PO_4-PMACs. This implies that while a higher temperature maybe required for the simultaneous dehydration and carbonization of the KOH-impregnated PM_{ps}, a slightly lower temperature maybe needed to develop the H_3PO_4-impregnated PM_{ps}. The yields of both activated carbons were greatly influenced by both temperature and time than the impregnation ratio, as indicated by (Equations 11 and 12). Whereas both positive coefficients of interactions between temperature and time (AB) were needed to impact the yields of the KOH-PMACs and H_3PO_4-PMACs, the reverse was noticed for all the other interactions involving the impregnation ratio and the other two parameters (temperature and time), respectively.

The results (Table S2) of the numerical optimization analyses of the experimental data indicate that the PM_{ps} sample activated with H_3PO_4 at the optimum impregnation ratio of 3.7:1, temperature of 400°C, and activation time of 112 minutes recorded the highest predictive iodine number of 593.44 mg/g and carbon yield of 51.30%. The corresponding observed values recorded at these optimum conditions were 592.88 mg/g and 51.10%, respectively. For the PM_{ps} sample activated with KOH at an impregnation ratio of 3:1, temperature of 450°C, and activation time of 120 minutes, the highest predictive iodine number of 918.58 mg/g and carbon yield of 39.60% were obtained (Figure S2). An observed iodine number of 916.56 mg/g and a carbon yield of 39.15% were recorded. The specific surface areas obtained for the H_3PO_4-$PMAC_{op}$ and KOH-$PMAC_{op}$ were 527.59 and 911.70 m^2/g, respectively.

Table 2: The CCD for the Experiments and Actual and Predicted Data of the Responses obtained for both Carbons.

Run No.	A (°C)	B (min)	C (ml/g)	Iodine number, I_n (mg/g)				Carbon yield, C_y (%)			
	value & code	value & code	value & code	$PMAC_{KOH}$ observed	$PMAC_{KOH}$ predicted	$PMAC_{H3PO4}$ observed	$PMAC_{H3PO4}$ predicted	$PMAC_{KOH}$ observed	$PMAC_{KOH}$ predicted	$PMAC_{H3PO4}$ observed	$PMAC_{H3PO4}$ predicted
12	600 (+1)	180 (+1)	4 (+1)	991.96	987.62	810.06	809.83	29.43	29.52	36.37	36.34
4	600 (+1)	180 (+1)	2 (-1)	955.20	954.94	769.93	772.62	31.30	31.60	40.06	40.26
5	600 (+1)	60 (0)	4 (+1)	1026.42	1030.84	531.6	540.32	31.89	32.20	41.5	41.62
8	600 (+1)	60 (-1)	2 (-1)	653.72	656.10	683.3	687.11	32.05	32.14	40.66	40.57
6	300 (-1)	180 (+1)	4 (+1)	720.54	723.37	427.77	429.85	40.81	41.03	50.59	50.89
7	300 (-1)	180 (+1)	2 (-1)	861.11	861.91	292	289.17	40.97	40.96	51.02	51.11
2	300 (-1)	60 (-1)	4 (+1)	674.17	679.65	393.61	396.81	47.21	47.21	56.31	56.31
9	300 (-1)	60 (-1)	2 (-1)	466.57	476.13	434.01	440.13	44.78	45.00	51.33	51.57
16	700 (+1.68)	120 (0)	3 (0)	1011.64	1012.83	743.68	737.52	30.35	30.02	38.45	38.43
18	200 (-1.68)	120 (0)	3 (0)	651.34	642.64	217.37	215.06	50.44	50.33	60	59.72
20	450 (0)	210 (+1.68)	3 (0)	1050.60	1054.21	681.08	683.19	34.99	34.74	43.27	42.99
14	450 (0)	20 (-1.68)	3 (0)	794.51	784.08	591.2	581.01	39.65	39.41	46.65	46.58
19	450 (0)	120 (0)	5 (+1.68)	688.89	687.31	629.67	625.73	37.86	37.70	49.56	49.47
15	450 (0)	120 (0)	1 (-1.68)	454.74	451.11	633.79	631.84	37.72	37.57	48.76	48.64
3	450 (0)	120 (0)	3 (0)	911.43	915.95	632	644.11	39.40	39.20	46.97	47.98
10	450 (0)	120 (0)	3 (0)	950.38	915.95	658	644.11	39.33	39.20	48.41	47.98
11	450 (0)	120 (0)	3 (0)	911.43	915.95	668	644.11	39.33	39.20	48.51	47.98
1	450 (0)	120 (0)	3 (0)	911.43	915.95	642	644.11	39.98	39.20	48.86	47.98
13	450 (0)	120 (0)	3 (0)	911.43	921.21	658	674.22	39.45	40.00	48.56	49.21
17	450 (0)	120 (0)	3 (0)	911.43	921.21	668	674.22	39.30	40.00	49.01	49.21

Surface morphologies and properties of the activated carbons

The chemical activation of the PM_{ps} with H_3PO_4 and KOH showed relative variations in the textural structure of the material before and after the activation processes. The SEM micrographs of the PM_{ps} in Figure S3a revealed the large oval pores around 10 to 20 μm in diameter in the material were substantially transformed after the

chemical activation. Figure S3c for KOH-PMAC indicated its small pores while Figure S3b showed relatively larger pores in the H_3PO_4-$PMAC_{op}$. This is an indication that KOH-$PMAC_{op}$ structure contained a higher ratio of micropores than that of H_3PO_4-$PMAC_{op}$. The higher iodine numbers obtained with KOH-$PMAC_{op}$ depict availability of more microporous structure within the activated carbon and its greater affinity for the adsorption of small molecules (Karim *et al*., 2022). The extent of modification of the porous structure of the PMps and the carbons derived from them using H_3PO_4 and KOH as activating agents is shown in Figure 1a. The influence of the initial concentration of the CR dye solution on the adsorption mechanism is depicted in Figure 1b.

Adsorption study on Congo red dye

The reduction of CR dye in the solution increased with an increase in the initial concentration of the dye adsorbed onto the KOH-PMACop and H_3PO_4-$PMAC_{op}$. The obvious explanation for this phenomenon is largely that an increased concentration of the dye molecules in the solution offers them greater chance of being adsorbed onto the available adsorption sites on the carbons. This discovery is attributed to concentration gradient that drives the adsorption process (Chimi *et al*., 2023; Hammari *et al*., 2021).

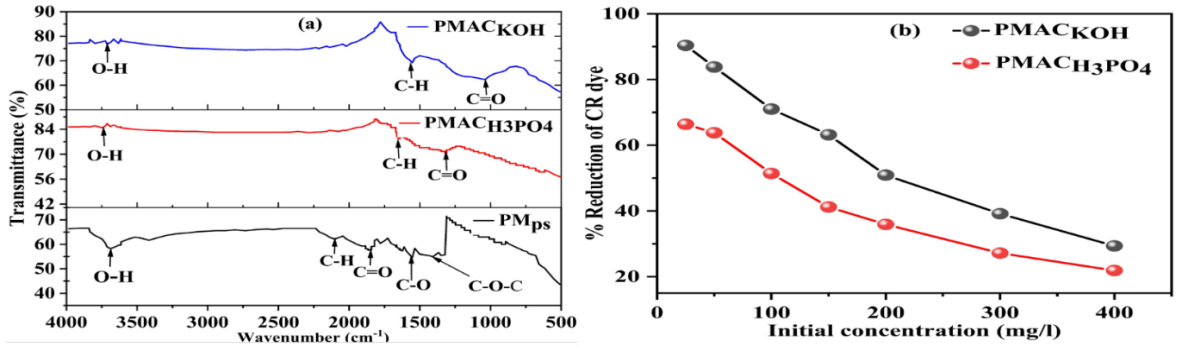

Figure 8: (a) FTIR of the PMps and the ACs by H_3PO_4 and KOH activators; (b) The effects of initial concentration on the adsorption profile of CR dye by the ACs

Also, the increased initial concentration of the CR dye solution caused the equilibrium adsorption capacities of both adsorbents to increase. This is expected, as the increased concentration of CR dye in the solution tends to overcome all resistances to mass transfer of the CR dye from the aqueous phase onto the solid phase (Hammari *et al*., 2021). The experimental data obtained for the KOH-$PMAC_{op}$ and H_3PO_4-$PMAC_{op}$ were best represented by the Langmuir isotherm (Figures 2a and b). Similarly, the Pseudo second-order kinetic model best represents the kinetic profile of the adsorption mechanism of both KOH-$PMAC_{op}$ and H_3PO_4-$PMAC_{op}$ (Figures 3a and b). The maximum amount of the CR dye adsorbed experimentally and theoretically by both activated carbons were nearly the same (Table S5).

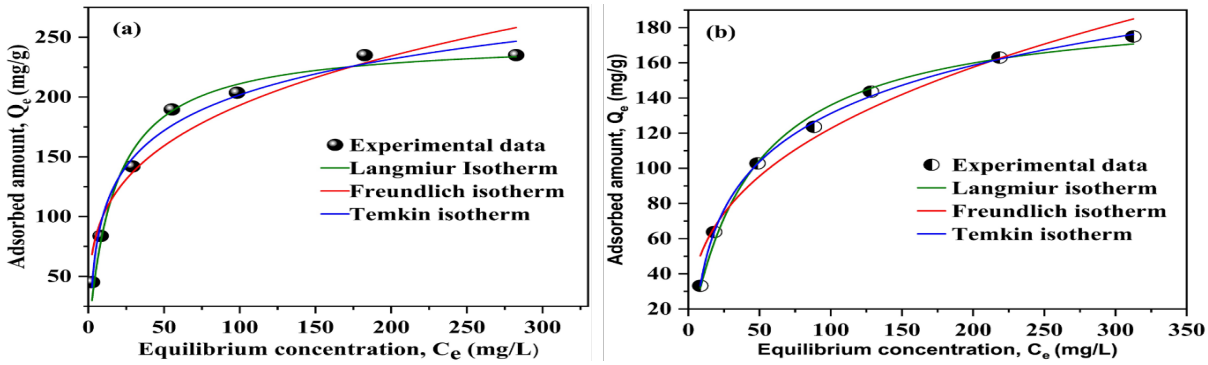

Figure 9: Adsorption isotherms of (a) KOH-$PMAC_{op}$ and (b) H_3PO_4-$PMAC_{op}$ at pH 6.8, 50 mg activated carbon, 32°C, 200 rpm and 120 minutes contact time

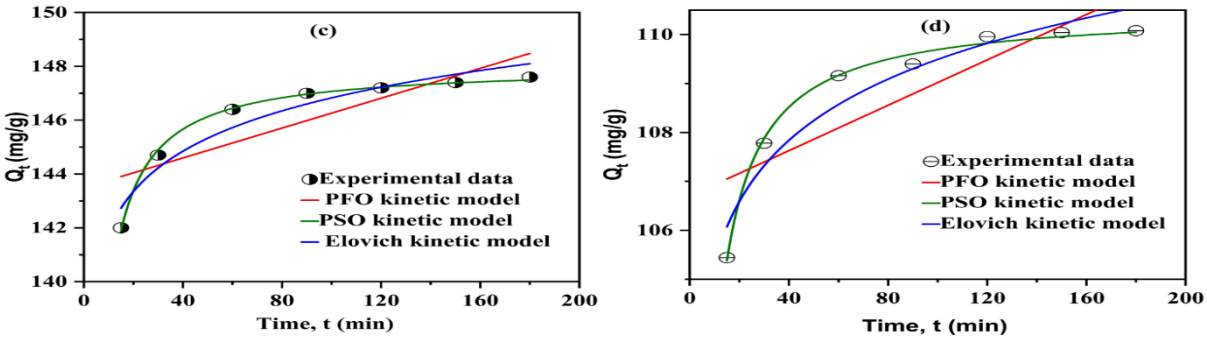

Figure 10: Adsorption kinetics of the (a) KOH-PMAC$_{op}$ and (b) H_3PO_4-PMAC$_{op}$

5 CONCLUSIONS

The RSM was used as a chemometric tool to produce activated carbons from PM$_{ps}$ with H_3PO_4 and KOH as the activating agents. The numerical optimization analyses of the experimental data indicate that the PM$_{ps}$ sample activated with H_3PO_4 at the optimum impregnation ratio of 3.7:1, temperature of 400^{o}C, and activation time of 112 minutes recorded the highest predictive iodine number of 593.44 mg/g, and carbon yield of 51.30%. The corresponding observed values recorded at these optimum conditions were 592.88 mg/g and 51.10%, respectively. For the PM$_{ps}$ sample activated with KOH at an optimum impregnation ratio of 3:1, temperature of 450^{o}C, and activation time of 120 minutes, the highest predictive iodine number of 918.58 mg/g and carbon yield of 39.60% were obtained. An observed iodine number of 916.56 mg/g and a carbon yield of 39.15% were recorded. The specific surface areas obtained for the H_3PO_4-PMAC$_{op}$ and KOH-PMAC$_{op}$ were 527.59 and 911.70 m^2/g, respectively. The Langmuir adsorption isotherm best interpreted the experimental data, and the Pseudo-second-order adsorption kinetics most suitably described the profile of the adsorption mechanism of Congo red removal by both activated carbons. The maximum amount of the CR dye adsorbed experimentally and theoretically by both activated carbons were nearly the same. Both activated carbons demonstrated evidence of extensive graphitic features from the analyses of the Raman spectroscopy and X-ray diffraction investigations conducted on them. The Fourier transform infrared (FT-IR) spectra of the KOH-PMAC$_{op}$ suggested a higher proportion of aromaticity than that of H_3PO_4-PMAC$_{op}$, which implies that it is likely to promote adsorption mechanisms like electrostatic and π-π interactions far better than that of H_3PO_4-PMAC$_{op}$.

ACKNOWLEDGEMENT

We appreciate most sincerely the technical assistance we received from the central laboratories of the Nigerian Stored Products Research Institute, Ilorin, Kwara State. We are also thankful for the support we received from the Departments of Chemistry and Animal Science, University of Agriculture, Makurdi.

REFERENCES

Abugu, H. O., Okoye, P. A. C., Ajiwe, V. I. E., Omoku, P. E., & Umeobika, U. C. (2015). Preparation and characterization of activated carbon produced from oil Bean (Ugba or Ukpaka) and snail shell. *Journal of Environmental and Analytical Chemistry*, *26*. https://doi.org/http://dx.doi.org/10.4172/jreac.1000165

Ajaelu, C. J., Oyedele, O., Ikotun, A. A., & Faboro, E. O. (2022). Safranin O dye removal using Senna fistula activated biomass: Kinetic, equilibrium and thermodynamic studies. *Journal of the Nigerian Society of Physical Sciences*, *5*, 951. https://doi.org/10.46481/jnsps.2023.951

Ao, W., Fu, J., Mao, X., Kang, Q., Ran, C., Liu, Y., & Zhang, H. (2018). Microwave assisted preparation of activated carbon from biomass : A review. *Renewable and Sustainable Energy Reviews*, *92*(July 2017), 958–979. https://doi.org/10.1016/j.rser.2018.04.051

Asaithambi, P., Yesuf, M. B., Govindarajan, R., Hariharan, N. M., Thangavelu, P., & Alemayehu, E. (2022). A Review of Hybrid Process Development Based on Electrochemical and Advanced Oxidation Processes for the Treatment of Industrial Wastewater. *International Journal of Chemical Engineering*, *2022*. https://doi.org/10.1155/2022/1105376

ASTM D, 4607-94. (2006). *Standard Test Method for Determination of Iodine Number of Activated Carbon.* West Conshohocken, PA: ASTM International.

Bilińska, L., & Gmurek, M. (2021). Novel trends in AOPs for textile wastewater treatment. Enhanced dye by-products removal by catalytic and synergistic actions. *Water Resources and Industry*, *26*(September). https://doi.org/10.1016/j.wri.2021.100160

Chandanshive, V. V., Kadam, S. K., Khandare, R. V., Kurade, M. B., Jeon, B. H., Jadhav, J. P., & Govindwar, S. P. (2018). In situ phytoremediation of dyes from textile wastewater using garden ornamental plants, effect on soil quality and plant growth. *Chemosphere*, *210*, 968–976. https://doi.org/10.1016/j.chemosphere.2018.07.064

Chimi, T., Hannah, B. U., Lincold, N. M., Jacques, M. B., Tome, S., Hermann, D. T., … Meva, F. E. (2023). Preparation, characterization and application of H3PO4-activated carbon from Pentaclethra macrophylla pods for the removal of Cr(VI) in aqueous medium. *Journal of the Iranian Chemical Society*, *20*(2), 399–413. https://doi.org/10.1007/s13738-022-02675-9

Chung, K.-T. (2016). Azo Dyes and Human Health: A Review. *Environ. Sci. Health Care*, *34*(4), 233–261. Retrieved from https://doi.org/10.1080/10590501.2016.1236602

Ekpete, O. A., Marcus, A. C., & Osi, V. (2017). Preparation and Characterization of Activated Carbon Obtained from Plantain (Musa paradisiaca) Fruit Stem . *Journal of Chemistry*, *2017*, 1–6. https://doi.org/10.1155/2017/8635615

Hammari, A. M., Misau, M. I., Aroke, U. O., Hamza, U. D., & Abdulkarim, A. (2021). Adsorption Equilibrium and Kinetics Studies of Congo Red Dye Using Groundnut Shell and Sorghum Husk Biosorbent. *Journal of Biochemistry, Microbiologiy, and Biotechnology*, *9*(1), 30–37.

Hassan, J., Rajib, M. M. R., Sarker, U., Akter, M., Khan, M. N. E. A., Khandaker, S., … Marc, R. A. (2022). Optimizing textile dyeing wastewater for tomato irrigation through physiochemical, plant nutrient uses and pollution load index of irrigated soil. *Scientific Reports*, *12*(1), 1–18. https://doi.org/10.1038/s41598-022-11558-1

Hidayu, A. R., & Muda, N. (2016). Preparation and Characterization of Impregnated Activated Carbon from Palm Kernel Shell and Coconut Shell for CO2Capture. *Procedia Engineering*, *148*, 106–113. https://doi.org/10.1016/j.proeng.2016.06.463

Jamnongkan, T., Intaramongkol, N., Kanjanaphong, N., Ponjaroen, K., Sriwiset, W., Mongkholrattanasit, R., … Huang, C. F. (2022). Study of the Enhancements of Porous Structures of Activated Carbons Produced from Durian Husk Wastes. *Sustainability (Switzerland)*, *14*(10). https://doi.org/10.3390/su14105896

Jaria, G., Silva, C. P., Oliveira, J. A. B. P., Santos, S. M., Gil, M. V., Otero, M., … Esteves, V. I. (2019). Production of highly efficient activated carbons from industrial wastes for the removal of pharmaceuticals from water—A full factorial design. *Journal of Hazardous Materials*, 212–218. https://doi.org/10.1016/j.jhazmat.2018.02.053

Jiang, W., Xing, X., Li, S., Zhang, X., & Wang, W. (2019). Synthesis, characterization and machine learning based performance prediction of straw activated carbon. *Journal of Cleaner Production*, *212*, 1210–1223. https://doi.org/10.1016/j.jclepro.2018.12.093

Kadhom, M., Albayati, N., Alalwan, H., & Al-Furaiji, M. (2020). Removal of dyes by agricultural waste. *Sustainable Chemistry and Pharmacy*, *16*(April), 100259. https://doi.org/10.1016/j.scp.2020.100259

Karim, A. Y. A., Balogoun, C., Avocefohoun, A. S., Prodjinonto, V., Gbaguidi, M. A. N., Dovonon, L. F., … Sohounhloue, D. C. K. (2022). Influence of Some Preparation Parameters on The Efficiency of Activated Carbons Prepared from Teak Wood Shavings (Tectona Grandis) and Coconut Shells (Cocos Nucifera) for The Treatment of Industrial Wastewater. *European Journal of Advanced Chemistry Research*, *3*(4), 1–9. https://doi.org/10.24018/ejchem.2022.3.4.121

Karuppasamy, K., Vikraman, D., Hussain, T., Hussain, S., Bose, R., Sivakumar, P., … Kim, H. S. (2021). Ternary Zn1-xNixSe nanostructures as efficient photocatalysts for detoxification of hazardous Congo red, methyl orange, and chrome yellow dyes in wastewater sources. *Environmental Research*, *201*(June), 111587. https://doi.org/10.1016/j.envres.2021.111587

Khan, S., & Malik, A. (2018). Toxicity evaluation of textile effluents and role of native soil bacterium in biodegradation of a textile dye. *Environmental Science and Pollution Research*, *25*(5), 4446–4458. https://doi.org/10.1007/s11356-017-0783-7

Kwiatkowski, M., & Broniek, E. (2017). An analysis of the porous structure of activated carbons obtained from hazelnut shells by various physical and chemical methods of activation. *Colloids and Surfaces A: Physicochemical and Engineering Aspects*, *529*. https://doi.org/10.1016/j.colsurfa.2017.06.028

Lam, S. S., Liew, R. K., Wong, Y. M., Yek, P. N. Y., Ma, N. L., Lee, C. L., & Chase, H. A. (2017). Microwave-assisted pyrolysis with chemical activation, an innovative method to convert orange peel into activated carbon with improved properties as dye adsorbent. *Journal of Cleaner Production*, *162*. https://doi.org/10.1016/j.jclepro.2017.06.131

Li, S., Han, K., Li, J., Li, M., & Lu, C. (2017). Preparation and characterization of super activated carbon produced from gulfweed by KOH activation. *Microporous and Mesoporous Materials*, *243*, 291–300. https://doi.org/10.1016/j.micromeso.2017.02.052

Liew, R. K., Azwar, E., Yek, P. N. Y., Lim, X. Y., Cheng, C. K., Ng, J. H., … Lam, S. S. (2018). Microwave pyrolysis with KOH/NaOH mixture activation: A new approach to produce micro-mesoporous activated carbon for textile dye adsorption. *Bioresource Technology*, *266*. https://doi.org/10.1016/j.biortech.2018.06.051

Loredo-Cancino, M. Soto-Regaldo, E. Cerino-Corfova, F.J. Garcia-Reyes, R.B., Garcia-Leon, A.M. and Garza-Gonzalez, M. T. (2013). Determining optimal conditions to produce activated carbon from barley husks using single or dual optimization. *Journal of Environmental Management*, *125*, 117–125. https://doi.org/10.1016/j.jenvman.2013.03.028

Nindjio, G. F. K., Tagne, R. F. T., Jiokeng, S. L. Z., Fotsop, C. G., Bopda, A., Doungmo, G., … Tonle, I. K. (2022). Lignocellulosic-Based Materials from Bean and Pistachio Pod Wastes for Dye-Contaminated Water Treatment: Optimization and Modeling of Indigo Carmine Sorption. *Polymers*, *14*(18). https://doi.org/10.3390/polym14183776

Ogungbenro, E.A., Quang, V.D., Al-Ali, K. and Abu-Zahra, R. M. M. (2017). Activated carbon from date seeds for CO2 capture applications. *Energy Procedia (13th International Conference on Green Gas Control Technologies GHGT-13, Lausanne, Switzerland)*, *114*, 2313–2321. https://doi.org/doi: 10.1016/j.egypro.2017.03.1370

Okpala, B. (2015). 18 reasons why you need the African oil bean (Ukpaka or Ugba). *Global Food Book*. Retrieved from https://globalfoodbook.com/health-benefits-of-african-oil-bean-seeds-ukpaka-ugba

Pongener, C., Kibami, D., Rao, K. S., Goswamee, R. L., & Sinha, D. (2015). Synthesis and Characterization of Activated Carbon from the Biowaste of the Plant Manihot Esculenta. *Chemical Science Transactions*, *4*(1), 59–68. https://doi.org/10.7598/cst2015.958

Shamsuddin, M. S., Yusoff, N. R. N., & Sulaiman, M. A. (2016). Synthesis and characterization of activated carbon produced from kenaf core fiber using H3PO4 activation. *Procedia Chemistry*, *19*, 558–565. https://doi.org/10.1016/j.proche.2016.03.053

Solayman, H. M., Hossen, M. A., Abd Aziz, A., Yahya, N. Y., Leong, K. H., Sim, L. C., … Zoh, K. D. (2023). Performance evaluation of dye wastewater treatment technologies: A review. *Journal of Environmental Chemical Engineering*, *11*(3), 109610. https://doi.org/10.1016/j.jece.2023.109610

Yang, K., Peng, J., Srinivasakannan, C., Zhang, L., Xia, H., & Duan, X. (2010). Bioresource Technology Preparation of high surface area activated carbon from coconut shells using microwave heating. *Bioresource Technology*, *101*(15), 6163–6169. https://doi.org/10.1016/j.biortech.2010.03.001

Yeow, P. K., Wong, S. W., & Hadibarata, T. (2021). Removal of azo and anthraquinone dye by plant biomass as adsorbent – a review. *Biointerface Research in Applied Chemistry*, *11*(1), 8218–8232. https://doi.org/10.33263/BRIAC111.82188232

Yokoyama, J. T. C., Cazetta, A. L., Bedin, K. C., Spessato, L., Fonseca, J. M., Carraro, P. S., … Almeida, V. C. (2019). Stevia residue as new precursor of CO2-activated carbon: Optimization of preparation condition and adsorption study of triclosan. *Ecotoxicology and Environmental Safety*, *172*(December 2018), 403–410. https://doi.org/10.1016/j.ecoenv.2019.01.096

Yorgun, S., & Yildiz, D. (2015). Preparation and characterization of activated carbons from Paulownia wood by chemical activation with H3PO4. *Journal of the Taiwan Institute of Chemical Engineers*, *53*, 122–131. https://doi.org/10.1016/j.jtice.2015.02.032

APPENDICES

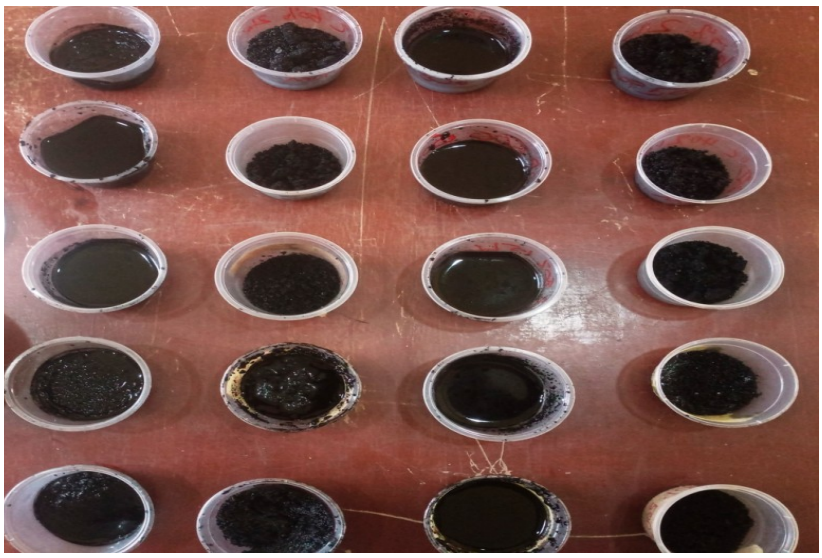

Figure S1: Acid treated and washed activated carbons

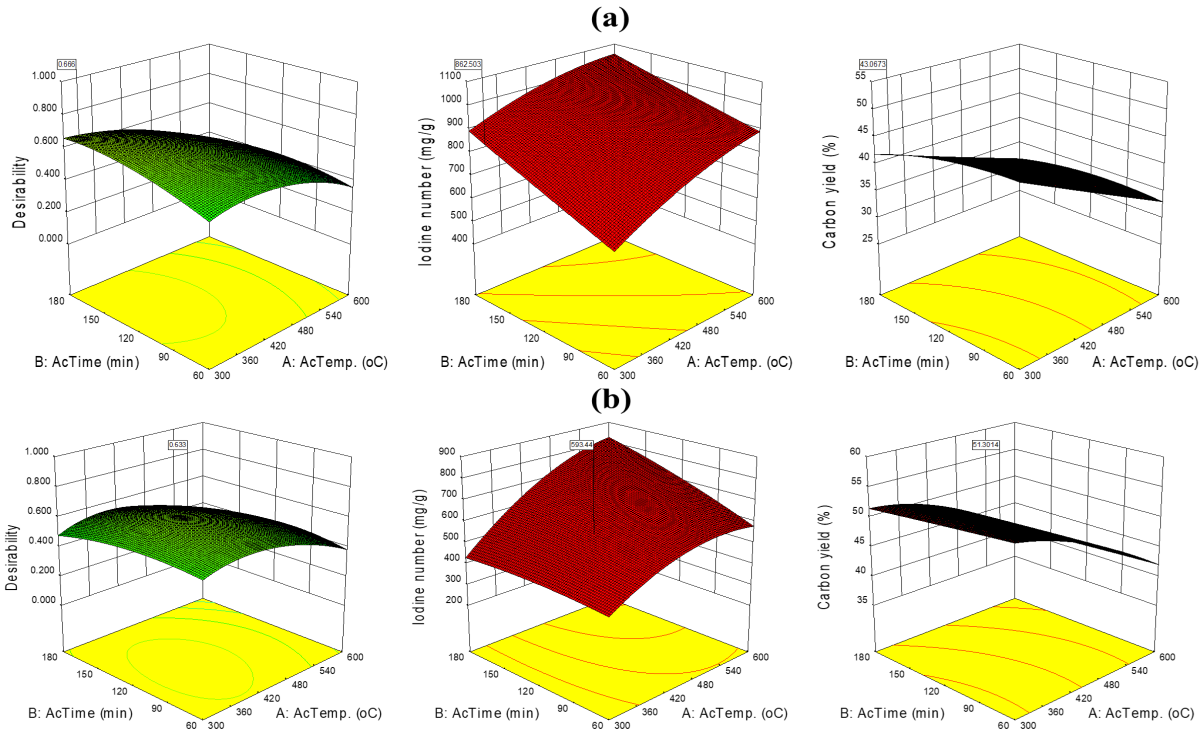

Figure S2: 3D Graphical Plots of the Effects of the pptimum production parameters on both responses (iodine number and Carbon yields) of (a) KOH-PMAC$_{op}$ and (b) H_3PO_4-PMAC$_{op}$.

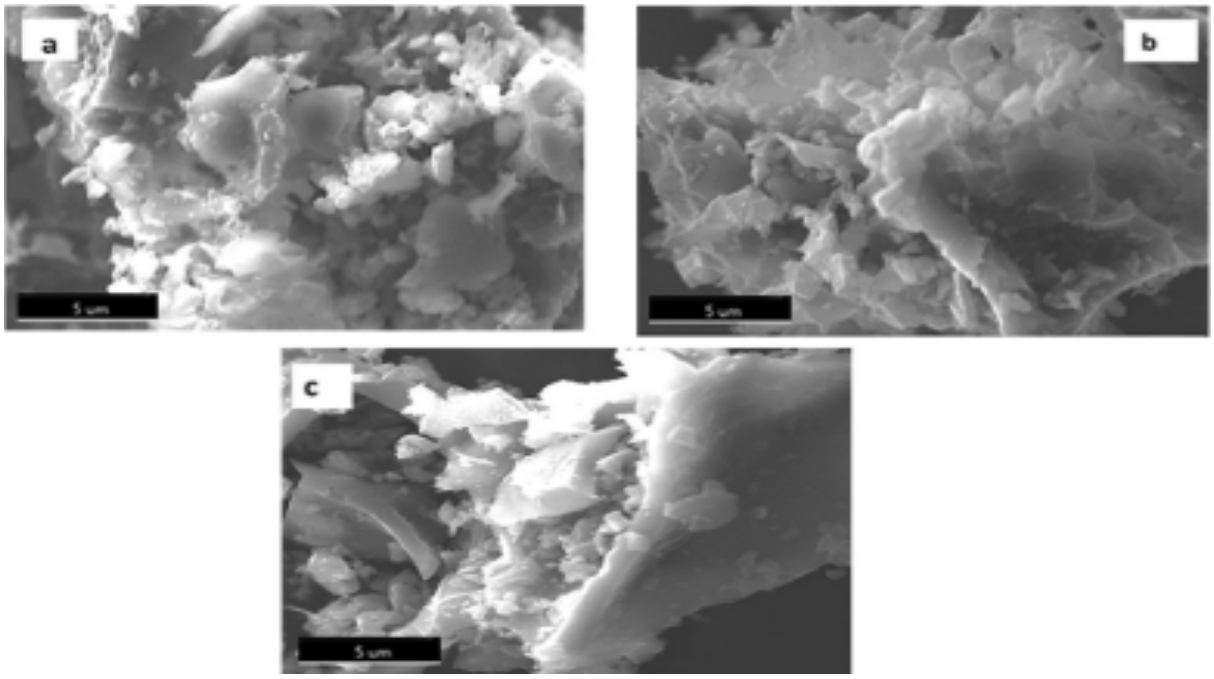

Figure S3: SE Micrographs of the (a) PMps precursor (b) H_3PO_4-$PMAC_{op}$ (c) KOH-$PMAC_{op}$

Table S3: Summary of the Results of the Analysis of Variances indicating the Significance of the Production Parameters on the Iodine number and Carbon yield of the Activated carbons

Source		Y_{In} (Iodine number)								Y_{Cy} (Carbon yield)							
	df	SS_K	SS_H	MS_K	MS_H	F_K	F_H	P_K	P_H	SS_K	SS_H	MS_K	MS_H	F_K	F_H	P_K	P_H
Model	9	598381.46	466637.83	66486.83	51848.65	327.60	302.04	0.00	4E-10	570.73	633.45	63.41	70.38	278.34	202.65	0.00	3E-09
A-act. Temp.	1	167183.06	333020.60	167183.06	333020.60	823.76	1939.97	0.00	8E-12	503.12	552.95	503.12	552.95	2208.32	1592.07	0.00	2E-11
B-act. Time	1	94734.59	11345.52	94734.59	11345.52	466.79	66.09	0.00	2E-05	36.43	26.53	36.43	26.53	159.92	76.40	0.00	1E-05
C-impreg. Ratio	1	55789.26	37.33	55789.26	37.33	274.89	0.22	0.00	7E-01	0.02	0.68	0.02	0.68	0.07	1.96	0.79	2E-01
AB	1	3779.72	27959.03	3779.72	27959.03	18.62	162.87	0.00	5E-07	6.13	0.01	6.13	0.01	26.88	0.03	0.00	9E-01
AC	1	14657.29	5353.02	14657.29	5353.02	72.22	31.18	0.00	3E-04	2.31	6.84	2.31	6.84	10.14	19.71	0.01	2E-03
BC	1	58500.81	16928.00	58500.81	16928.00	288.25	98.61	0.00	4E-06	2.31	12.35	2.31	12.35	10.14	35.56	0.01	2E-04
A2	1	15661.11	70225.26	15661.11	70225.26	77.17	409.09	0.00	8E-09	0.06	0.03	0.06	0.03	0.25	0.10	0.63	8E-01
B2	1	48.43	2958.79	48.43	2958.79	0.24	17.24	0.64	2E-03	17.64	38.92	17.64	38.92	77.42	112.07	0.00	2E-06
C2	1	197921.06	3297.18	197921.06	3297.18	975.22	19.21	0.00	2E-03	8.89	0.04	8.89	0.04	39.04	0.11	0.00	7E-01
Residual	9	1826.55	1544.96	202.95	171.66					2.05	3 Chart Area		0.35				
Lack of fit	5	688.73	718.96	137.75	143.79	0.48	0.70	0.78	7E-01	1.74	0.94	0.35	0.19	4.51	0.34	0.08	9E-01

Legend: SS_K and SS_H are the sum of square, MS_K and MS_H are the mean square, F_K and F_H are the F-calculated, and P_K and P_H are the P-values obtained from analyzing the iodine number and carbon yields of the KOH-PMAC and H_3PO_4-PMAC, respectively.

Table S4: Confirmation Tests of the Effects of the Optimum production parameters on the Activated Carbon Responses (Iodine number and Carbon yields)

Activated carbon	Parameter	Optimum	Lower	Higher	Surface area (m^2/g)
KOH-$PMAC_{op}$	Act. Temp., A	450	300	600	911.70
	Act. Time, B	120	60	180	
	Impre. ratio, C	3	2	4	
	I_n, predicted	918.58	476.13	987.6	
	I_n, observed	916.56	466.57	991.96	
	C_y, predicted	39.60	44.78	29.52	
	C_y, observed	39.15	45.00	29.43	
H_3PO_4-$PMAC_{op}$	Act. Temp., A	400	300	600	527.59
	Act. Time, B	112.45	60	180	
	Impreg. ratio, C	3.73	2	4	
	I_n, predicted	593.44	440.13	809.83	
	I_n, observed	592.88	434.01	810.00	
	C_y, predicted	51.30	51.57	36.34	
	C_y, observed	51.1	51.33	36.37	

Table S5: Effects of Initial Concentration on the Adsorption of Congo red dye from the solution

S/No.	C_o	KOH-PMAC$_{op}$		H_3PO_4-PMAC$_{op}$	
		C_e	Q_e	C_e	Q_e
1	25	2.4	45.2	8.4	33.2
2	50	8.1	83.8	18.1	63.8
3	**100**	**29**	**142**	**48.6**	**102.8**
4	150	55.2	189.6	88.2	123.6
5	200	98.2	203.6	128.2	143.6
6	300	182.5	235	218.5	163
7	400	282.5	235	312.5	175

Table S6: Effects of Contact time on the Adsorption of Congo red dye from the solution

Time (min)	C_o	KOH-PMAC$_{op}$			H3PO4-PMAC$_{op}$		
		C_t	%R	Qt	Ct	%R	2Qt
15	100	29. 00	71	142	47.28	76.36	105.44
30	100	27.65	72.35	144.7	46.11	76.945	107.78
60	100	26.80	73.2	146.4	45.42	77.29	109.16
90	100	26.50	73.5	147	45.3	77.35	109.4
120	100	26.40	73.6	147.2	45.02	77.49	109.96
150	100	26.30	73.7	147.4	44.98	77.51	110.04
180	100	26.20	73.8	147.6	44.96	77.52	110.08

Table S7: Parameters of the Theoretical Adsorption models of the isotherm and kinetics of the adsorption by both Activated Carbons

Adsorption model	Parameters	KOH-PMAC$_{op}$	H_3PO_4-PMAC$_{op}$
Langmuir	Q_m (mg/g)	248.265±8.77	194.081±5.466
	K_L (L/g)	0.057±0.009	0.0234±0.002
	R^2	0.984	0.993
	χ^2	109.906	22.407
Freundlich	K_F (L/g)	53.425±10.541	23.31±4.609
	n	3.584±0.529	2.774±0.303
	R^2	0.938	0.964
	χ^2	416.254	592.89
Temkin	A_T (L/g)	1.074±0.249	0.276±0.012
	ß	46.153±2.443	39.532±0.555
	b	54.94	64.145
	R^2	0.984	0.999
	χ^2	105.077	3.202
Pseudo-first-order (PFO) kinetic	Qe (mg/g)	143.487±0.871	106.700±0.728
	K_1 (min^{-1})	$-1.933x10^{-5}$	$-2.173x10^{-4}$
	R^2	0.7039	0.704
	χ^2	1.469	1.026
	S_{rate} ($mgg^{-1}min^{-1}$)	-0.003	-0.023
Pseudo-second-order (PSO) kinetic	Q_e (mg/g)	148.19±0.0628	110.491±0.071
	K_2 (mgg-1min-1)	0.0105	0.0124
	R^2	0.9974	0.995
	χ^2	0.0129	0.0162
	S_{rate} ($mgg^{-1}min^{-1}$)	230.583	151.38
Elovich kinetic	A_T (L/g)	$6.822x10^{-28}$	$8.051x10^{-25}$
	ß	0.4626±0.057	0.0692±0.049
	R^2	0.9309	0.9283
	χ^2	14.809	0.248

PAPER 69 – OPTIMIZING DEEP LEARNING FOR MEDICAL IMAGE CLASSIFICATION: A COMPARISON OF GRADIENT-BASED METHODS

Y. Ibrahim[1*], M. O. Momoh[2], K. O. Shobowale[3], Z. M. Abubakar[1], B. Yahaya[1], M. B. Mu'azu[1]

[1]Department of Computer Engineering, Ahmadu Bello University, Zaria, Nigeria.
[2]Department of Aerospace Engineering, Air Force Institute of Technology, Kaduna, Nigeria.
[3]Department of Mechatronics Engineering, Air Force Institute of Technology, Kaduna, Nigeria.
[*]Email: yibrahim@abu.edu.ng

ABSTRACT
Deep learning-based medical image classification has shown promising results in recent years with performance heavily reliant on choice of optimization schemes during training. In this paper, we present a comparative study of seven first-order stochastic gradient-based optimization schemes for a medical image classification task. A custom CNN architecture with convolutional layers and increasing number of filters followed by max-pooling and ReLU activation function with Dropout regularization were trained on a Tuberculosis Chest X-ray Database. The models were tested on a held-out test set to assess their performance in terms of accuracy, precision, recall, F1-score, and AUC score. Our experimental results demonstrate that Adamax achieves the highest accuracy and F1-score of 99.00% each and highest AUC score of 99.80%. Adadelta and Adagrad performed relatively poorly in comparison to other optimizers, achieving accuracies of 82.14% and 88.00% respectively. In terms of recall, both Adam and Nadam gave the highest recall scores of 98.86%. This suggests that the choice of optimizer plays a significant role in the performance of these models and provides valuable insights into the suitability of different optimizers for medical image classification. This will be beneficial for researchers and practitioners in the field of medical image analysis using deep learning.

KEYWORDS: Deep Learning, Convolutional Neural Networks, Optimizers, Medical Image Classification, Chest X-Ray Classification

1. INTRODUCTION

Medical image classification has nowadays become an increasingly important area of research, driven by advances in deep learning (DL) techniques and the growing availability of large-scale medical image datasets (Çallı *et al*., 2021). It is a critical task in healthcare and can assist professionals such as radiologists in detecting diseases and anomalies more accurately and efficiently. Among the various medical imaging modalities, X-ray is one of the most widely used *(Çallı et al*., 2021) due to its low cost and non-invasive nature with the ability to provide fast results. In particular, it has been used to detect Tuberculosis (TB), a chronic respiratory illness caused by bacterial infection which poses significant global health problem. According to the World Health Organization (WHO), TB is the 13th leading cause of death worldwide and the second leading infectious killer after COVID-19 (above HIV/AIDS)(Organization, 2022). In 2021, a total of 1.6 million people died from TB(Organization, 2022). Timely detection and accurate identification of TB are hence vital as delaying the diagnosis could be fatal, and prompt administration of appropriate medication can cure this lethal ailment (Sharma & Mohan, 2013).Therefore, there is need to develop schemes for accurate and timely diagnosis for effective treatment and control of these diseases, especially in low-resource settings where they are prevalent.

The traditional machine learning (ML) methods for medical image analysis typically involve hand-crafted extraction of features and feeding them to classical classification algorithms such as random forests (RF) (Melendez *et al.*, 2016), extremely randomized trees (ERT)(Melendez *et al.*, 2016), k-nearest neighbors (KNN) (Van Ginneken *et al*., 2002), etc. This approach relies on prior knowledge of the image content and may not generalize well to new datasets or imaging modalities (Melendez *et al*., 2016; Singh & Hamde, 2019; Van Ginneken *et al.*, 2002). These methods also require extensive manual annotation and may be prone to errors (Rahman *et al*., 2020), variability and subjective interpretation (Brady, 2017; Degnan *et al.*, 2019).

In contrast, the availability of extensive labeled datasets and deep convolutional neural networks (CNNs) has resulted in significant achievements in image recognition. CNNs can learn data-driven, highly descriptive, and hierarchical image features from a sufficient amount of training data. However, it is still challenging to acquire comprehensive annotations for medical imaging datasets like ImageNet (Greenspan *et al*., 2016; Shin *et al*., 2016). Furthermore, continued research in this area has led to significant advances in the diagnosis and treatment of a wide range of diseases.

Also, the effectiveness of these models is heavily reliant on the choice of optimization algorithms used during training. Gradient-based optimization algorithms have been widely adopted due to their efficiency and effectiveness in DL tasks (Dogo *et al*., 2018). However, selecting the optimal optimization scheme for a specific

task still remains a challenging and important problem especially for medical image detection and classification tasks.

This paper therefore presents a comparative study of popular first-order stochastic gradient-based optimization schemes for medical image classification, specifically focusing on optimizing DL models for TB Chest X-ray (CXR) Database. We analyze the performance of different optimizers in terms of accuracy, precision, recall, F1-score, and AUC score and provide insights into their suitability for medical image classification.

This study contributes to the growing body of literature on the utilization of DL models for medical image detection and classification. The findings of this study will be of great interest to researchers and practitioners in the field of medical image analysis using DL, as it provides valuable insights into the suitability of different optimizers for medical image classification. We evaluate our trained custom CNN models on a held-out test data and analyze their performance using various evaluation metrics and visualization techniques with a view to addressing the following research questions:

- How does the choice of gradient-based optimization schemes affect the performance of DL-based medical image classification models?
- Which first-order stochastic gradient-based optimization scheme performs the best on a custom CNN architecture for the TB CXR image classification in terms of accuracy, precision, recall, F1-score, and AUC score?
- What insights can be gained from comparing the performance of the various optimization schemes and how can this information be used to guide the selection of optimizers for medical image classification tasks?

The objectives of the study include providing an empirical evaluation of the impact of popular gradient-based optimization schemes on the performance of DL-based medical image classification models, designing and implementing a custom CNN architecture and comparing the performance of various first-order stochastic gradient-based optimization schemes. The paper also offers a benchmark for future researchers and practitioners to compare their results and select the most appropriate optimizer for their medical image classification task and provide guidance for the selection of optimization schemes for medical image classification tasks.

2. RELATED WORK

In various recent research, CNNs have been utilized to identify a number of lung ailments like TB and pneumonia through the analysis of chest X-ray (CXR) images. With the emergence of the COVID-19 pandemic in 2020, techniques based on CNNs have also been employed to detect the presence of the novel coronavirus by examining CXR images. The work of Sathitratanacheewin *et al*., (2020) highlights the limitations of using ML models for TB detection and surveillance, specifically with regards to the generalizability of the models. The study developed a Deep CNN model using a TB-specific CXR dataset from one population and tested it on a non-TB-specific CXR dataset from another population. The CCN model performed well in detecting TB in both the training and intramural test sets using the former, with AUC values of 0.9845 and 0.8502, respectively. However, the AUC dropped significantly to 0.7054 in the latter showing that a supervised DL model developed using the training dataset from one population may not have the same diagnostic performance in another population, indicating the importance of examining technical specifications of CXR images, disease severity distribution, dataset distribution shift, and overdiagnosis before implementing the model in other settings. The work of Rahman *et al*., (2020) developed a framework using CXR with DL, segmentation and visualization. The work was aimed to detect TB reliably from CXR images by utilizing image preprocessing, data augmentation, image segmentation, and deep-learning classification techniques. The study created a database of 3500 TB-infected and 3500 normal CXR images and utilized nine different deep CNNs for transfer learning. The study found that classification using segmented lung images outperformed that with whole X-ray images and achieved state-of-the-art performance with accuracy, precision, sensitivity, F1-score, and specificity of DenseNet201 being 98.6%, 98.57%, 98.56%, 98.56%, and 98.54% respectively. The proposed method could be useful in computer-aided faster diagnosis of TB. In their study, Tahir *et al*., (2021) achieved a sensitivity of over 90% in classifying several coronavirus families including SARS, MERS, and COVID-19 through transfer learning of various pre-trained CNN models. Chhikara *et al*., (2020) investigated whether CXR images could be used to identify cases of pneumonia. They assessed the effectiveness of several pre-trained models, including Resnet, Xception, and Inception, while also implementing various preprocessing techniques such as filtering and gamma correction. In several studies, deep ML algorithms have been utilized to detect TB by adjusting the parameters of deep-layered CNNs (Hooda *et al*., 2017; Lakhani & Sundaram, 2017; Nguyen *et al*., 2019; Pasa *et al*., 2019). Pre-trained models and their ensembles were utilized for TB detection using transfer learning in the DL framework, as explained in sources (Ahsan *et al*., 2019; Meraj *et al*., 2019). A DL approach was presented in (Hooda *et al*., 2017) to classify CXR images into TB and non-TB categories achieving an accuracy of 82.09% while Evalgelista & Guedes, (2018) reported an accuracy of 88.76% for an intelligent pattern recognition framework based on CNNs for TB detection from CXR images. The work of Pasa *et al*., (2019) suggested a deep neural network design that was enhanced for detecting TB, achieving an accuracy of 86.82%. Additionally, they presented a tool that allows for the interactive visualization

of cases of TB. In their study, Nguyen *et al*., (2019) assessed how well the pre-trained DenseNet model could classify images of normal and TB cases from two different databases. They used a fine-tuned version of the model and found that it achieved AUC scores of 0.94 and 0.82. In their research, Ahsan *et al*., (2019) put forth a CNN model that was pre-trained in a general manner to detect TB and achieved accuracies of 81.25% and 80% with and without the use of image augmentation techniques, respectively. Abbas *et al*., (2020) proposed a CNN design that applies a class decomposition method to enhance the efficiency of ImageNet pre-trained CNN models for transfer learning. This approach resulted in excellent accuracy for detecting TB on the Japanese Society of Radiological Technology (JSRT) database. Yadav *et al*., (2018) utilized transfer learning to identify TB and achieved a precision rate of 94.89%.

3. MATERIALS AND METHODS

3.1. Dataset description

We used the TB Chest X-ray Database made publicly available by Rahman *et al*., (2020) containing 7,000 CXR images (3500 TB, 3500 normal) labelled as either TB (positive) or Normal (negative). For our experiments, we utilized the dataset in an 80:10:10 split for the training, validation, and testing sets respectively. As a preprocessing step, we resized the images to 224x224 and normalized by scaling the pixel values to [0,1].

3.2 Architecture

We trained a custom CNN architecture consisting of four convolutional layers with increasing number of filters (32, 64, 128, 256) followed by max pooling layers of size 2x2, which reduces the spatial dimensions of the feature maps. The ReLU activation function is used for all convolutional layers to introduce non-linearity into the model. A flatten layer is added to convert the 2D feature maps into a 1D vector, which is then passed through two fully connected dense layers with 512 and 1 neurons respectively. The first dense layer uses the ReLU activation function while the last layer uses the sigmoid activation function, which outputs a probability value between 0 and 1 for the binary classification task. Dropout regularization with a rate of 0.5 was used in the first dense layer to prevent overfitting. The input shape of the model is defined as (224, 224, 3) to accommodate 3 colour channels. A summary of the network configuration is shown in Table 1.

Table1: Summary of the network configuration

Dataset: TB Chest X-Ray Database
Input image data - 224x224x3- channels RGB Images
Conv3x3-32; stride=1
ReLU (nonlinearity function)
Pooling layer: MaxPooling 2x2; stride= 1
Conv3x3-64; stride=1
ReLU (nonlinearity function)
Pooling layer: MaxPooling 2x2; stride= 1
Conv3x3-128; stride=1
ReLU (nonlinearity function)
Pooling layer: MaxPooling 2x2; stride= 1
Conv3x3-256; stride=1
ReLU (nonlinearity function)
Pooling layer: MaxPooling 2x2; stride= 1
Flattening (Input Layer of Neural Network)
FC-512 neurons
ReLU (nonlinearity function)
Dropout = 0.5 (regularization to prevent overfitting)
Final dense layer
Binary Cross entropy
Sigmoid Layer (ϕ)

3.3 First-order stochastic gradient-based optimization schemes

We explored a class of optimization algorithms that use the gradient of the loss function with respect to the model parameters to update the parameters iteratively during training. These methods differ in their approach to adaptively adjusting the learning rate, incorporating momentum, or scaling the gradient updates based on the history of the gradients or the model parameters. For the custom CNN architecture in Table 1, we experimented with seven gradient-based optimizers including Adaptive Moment Estimation (Adam), Adaptive Moment Estimation with an infinity norm extension (Adamax), Nesterov-accelerated Adaptive Moment Estimation (Nadam), Root Mean Square Propagation (RMSProp), Stochastic Gradient Descent (SGD), Adaptive Delta (AdaDelta), and Adaptive Gradient (AdaGrad). The learning rate was set as 0.001 with a batch size of 32 and each model was trained for 20 epochs. All other training parameters were set at their default settings.

3.4 Evaluation metrics

We evaluated the performance of the models using several standard evaluation metrics, including accuracy, precision, recall, and F1-score. The accuracy measures the overall classification performance, while precision and recall measure the performance of the model for the TB (positive) and Normal (negative) classes, respectively. F1-score is the harmonic mean of precision and recall and provides an overall measure of the model's performance. We also generated the Receiver Operating Characteristic (ROC) to visualize the model's performance and noted the Area under the curve (AUC) performance which measures the performance of the binary classifier.

4. RESULTS AND DISCUSSION

In this study, we trained and evaluated seven models (Models 1-7) corresponding to model trained with Adam, Adamax, Nadam, RMSprop, SGD, Adadelta, and Adagrad) on the TB Chest X-ray Database of 7,000 images of TB and Normal classes. All models were based on the CNN architecture described in Table I. The ReLU activation function is used for all convolutional layers to introduce non-linearity into the model and Dropout regularization with a rate of 0.5 was used in the first dense layer to prevent overfitting. The training and validation loss and accuracy for all the seven models are as shown in Figure 1.

Adam

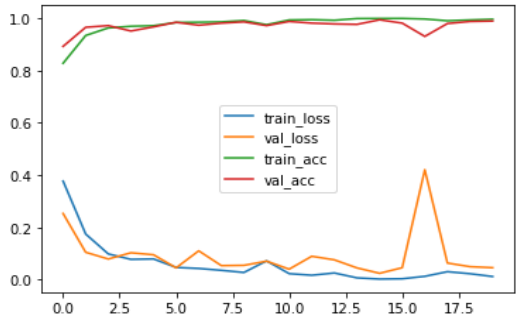

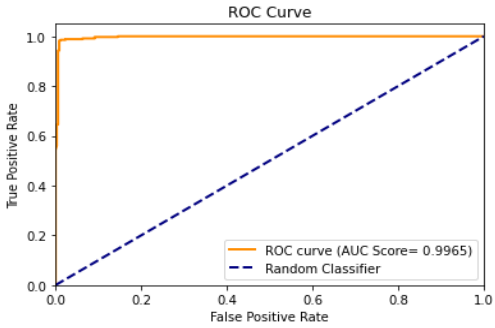

Adamax

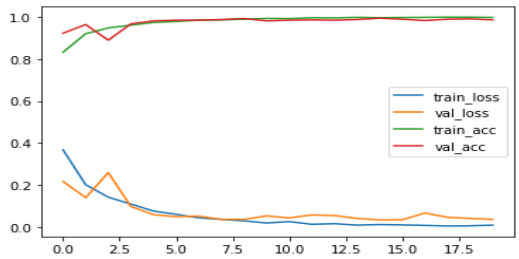

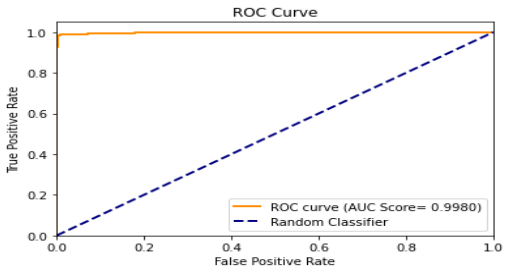

Nadam

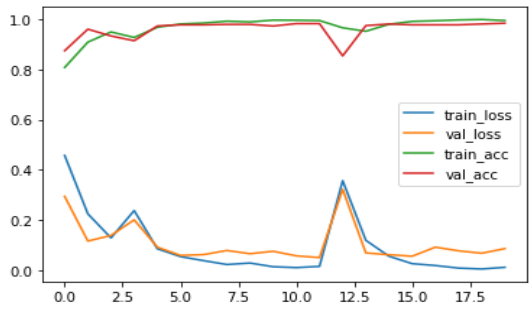

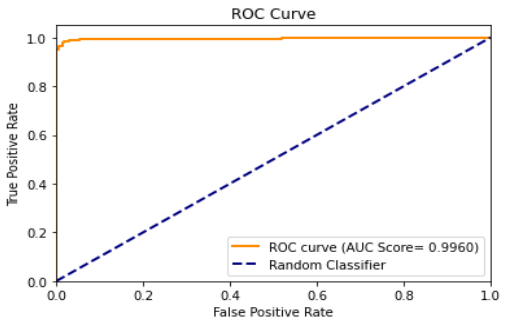

Sgd

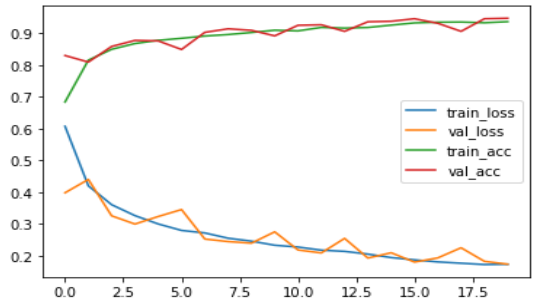

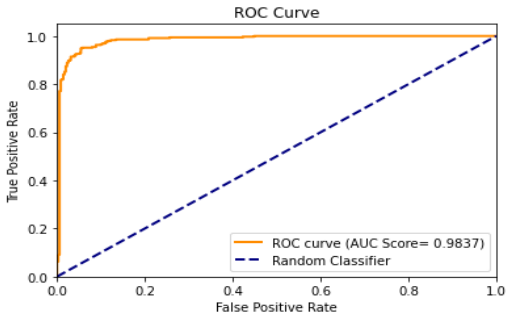

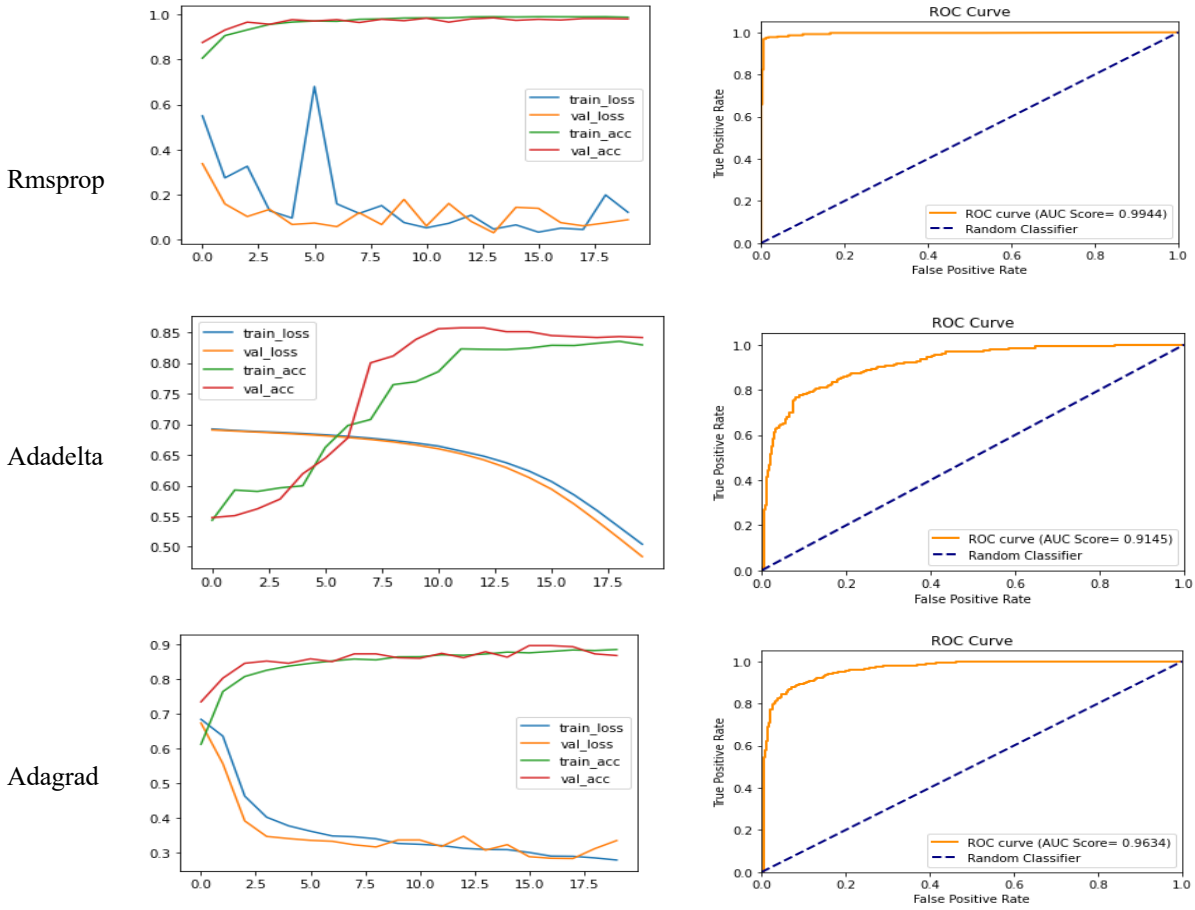

Figure 1: Training, validation, and testing performance of the various optimizers

Table 2 summarizes the performance of each optimizer in terms of the stated performance measures.

Table 2: Performance reports of various optimizers

Model	Optimizer	Accuracy	Precision	Recall	F1-Score	AUC score
Model 1	Adam	0.9800	0.9719	0.9886	0.9802	0.9965
Model 2	Adamax	0.9900	0.9942	0.9857	0.9900	0.9980
Model 3	Nadam	0.9757	0.9638	0.9886	0.9760	0.9960
Model 4	RMSprop	0.9786	0.9799	0.9771	0.9785	0.9944
Model 5	SGD	0.9414	0.9668	0.9143	0.9398	0.9837
Model 6	Adadelta	0.8214	0.7892	0.8771	0.8309	0.9145
Model 7	Adagrad	0.8800	0.9683	0.7857	0.8675	0.9634

Figure 2 shows the performance comparison of different optimizers based on several evaluation metrics (Accuracy, Precision, Recall, F1-Score and AUC Score.)

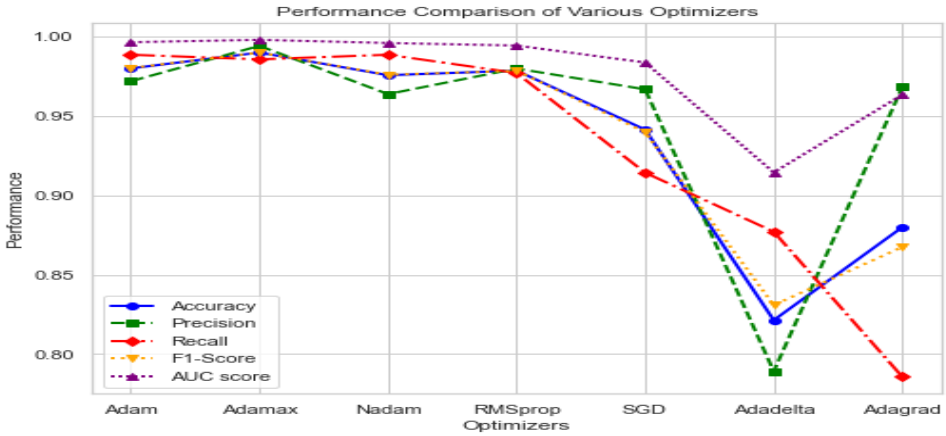

Figure 2: Comparison of optimizer performace

From the Figure 2, we can see that different optimizers perform differently for each evaluation metric. For example, Adamax and Adam appear to be the best optimizers for accuracy, while Adadelta gave the worst performance for precision, accuracy and f1-score. Specifically, the Adamax optimizer had the highest accuracy (99.00%) and performed best overall, with the highest precision (99.42%), F1-score (99.00%), and AUC score (0.9980) among all the tested optimizers. The Adam optimizer had the second-best accuracy (98.00%) and performed well, with a high precision (97.19%), recall (98.86%), and F1-score (98.02%). The RMSprop and Nadam optimizers also performed relatively well, achieving high accuracy, precision, recall, and AUC scores. However, the Adagrad and Adadelta optimizers were less effective, with lower accuracy (88% and 82.14%), F1-score (86.75% and 83.09%), and AUC scores (96.34% and 91.45%) respectively. The Adamax optimizer was the most effective in this study, achieving the highest scores across all metrics. The performance of our best-performing model (Model 2) is comparable to that of the state-of-the-art performance of Rahman *et al*., (2020) on the same dataset which achieved best accuracy of 98.6% despite utilizing DenseNet201 using transfer learning in classifying TB and normal images. We confirm that a less complex CNN architecture with proper parameter optimization can perform competitively with more complex state-of-the-art schemes.

5. CONCLUSION

In this study, we evaluated the performance of several popular first-order stochastic gradient-based optimization algorithms for optimizing a custom deep CNN weight for chest x-ray image classification. Our results demonstrated that a good choice of optimizer has a significant impact on the performance of DL models for CXR image classification with the best model achieving the highest testing accuracy and F1-Score of 99% each using Adamax optimizer. This is closely followed by Adam which recorded an accuracy and F1-Score of 98% and 98.02% respectively. In contrast, Adadelta and Adagrad optimizers resulted in comparatively poor performance, indicating that they may not be well-suited for this task. Interestingly, the AUC scores range from 0.9145 to 0.9980, indicating that the models built using these optimizers can distinguish between the positive and negative cases with varying degrees of accuracy. The highest AUC score achieved by the Adamax optimizer suggests that it is the most effective optimizer for this particular task. The study also suggests that the choice of optimizer should be based on the specific requirements of the task, and a thorough comparison of multiple optimizers should be conducted before making a final decision. The findings of this study provide useful insights for researchers and practitioners working on DL-based medical image analysis tasks. It would be of interest to investigate the effects of other CNN architectural designs and utilizing various medical datasets such as MRIs or CT scans for better generalization. We leave this exploration for future research. Other research directions could be developing explainability methods to aid physicians in interpreting the models' predictions and examining the models' impact on clinical outcomes in real-world settings to assess their efficacy in clinical practice.

REFERENCES

Abbas, A., Abdelsamea, M. M., & Gaber, M. M. (2020). Detrac: Transfer learning of class decomposed medical images in convolutional neural networks. *IEEE Access*, *8*, 74901-74913.

Ahsan, M., Gomes, R., & Denton, A. (2019). Application of a convolutional neural network using transfer learning for tuberculosis detection. 2019 IEEE International Conference on Electro Information Technology (EIT),

Brady, A. P. (2017). Error and discrepancy in radiology: inevitable or avoidable? *Insights into imaging*, *8*, 171-182.

Çallı, E., Sogancioglu, E., van Ginneken, B., van Leeuwen, K. G., & Murphy, K. (2021). Deep learning for chest X-ray analysis: A survey. *Medical Image Analysis*, *72*, 102125.

Chhikara, P., Singh, P., Gupta, P., & Bhatia, T. (2020). Deep convolutional neural network with transfer learning for detecting pneumonia on chest X-rays. Advances in Bioinformatics, Multimedia, and Electronics Circuits and Signals: Proceedings of GUCON 2019,

Degnan, A. J., Ghobadi, E. H., Hardy, P., Krupinski, E., Scali, E. P., Stratchko, L., Ulano, A., Walker, E., Wasnik, A. P., & Auffermann, W. F. (2019). Perceptual and interpretive error in diagnostic radiology—causes and potential solutions. *Academic radiology*, *26*(6), 833-845.

Dogo, E. M., Afolabi, O., Nwulu, N., Twala, B., & Aigbavboa, C. (2018). A comparative analysis of gradient descent-based optimization algorithms on convolutional neural networks. 2018 international conference on computational techniques, electronics and mechanical systems (CTEMS),

Evalgelista, L. G. C., & Guedes, E. B. (2018). Computer-aided tuberculosis detection from chest X-ray images with convolutional neural networks. Anais do XV Encontro Nacional de Inteligência Artificial e Computacional,

Greenspan, H., Van Ginneken, B., & Summers, R. M. (2016). Guest editorial deep learning in medical imaging: Overview and future promise of an exciting new technique. *IEEE transactions on medical imaging*, *35*(5), 1153-1159.

Hooda, R., Sofat, S., Kaur, S., Mittal, A., & Meriaudeau, F. (2017). Deep-learning: A potential method for tuberculosis detection using chest radiography. 2017 IEEE International Conference on Signal and Image Processing Applications (ICSIPA),

Lakhani, P., & Sundaram, B. (2017). Deep learning at chest radiography: automated classification of pulmonary tuberculosis by using convolutional neural networks. *Radiology*, *284*(2), 574-582.

Melendez, J., Sánchez, C. I., Philipsen, R. H., Maduskar, P., Dawson, R., Theron, G., Dheda, K., & Van Ginneken, B. (2016). An automated tuberculosis screening strategy combining X-ray-based computer-aided detection and clinical information. *Scientific reports*, *6*(1), 25265.

Meraj, S. S., Yaakob, R., Azman, A., Rum, S., Shahrel, A., Nazri, A., & Zakaria, N. F. (2019). Detection of pulmonary tuberculosis manifestation in chest X-rays using different convolutional neural network (CNN) models. *Int. J. Eng. Adv. Technol.(IJEAT)*, *9*(1), 2270-2275.

Nguyen, Q. H., Nguyen, B. P., Dao, S. D., Unnikrishnan, B., Dhingra, R., Ravichandran, S. R., Satpathy, S., Raja, P. N., & Chua, M. C. (2019). Deep learning models for tuberculosis detection from chest X-ray images. 2019 26th international conference on telecommunications (ICT),

Organization, W. H. (2022). *Tuberculosis Fact Sheet*. Retrieved 27 October 2022 from https://www.who.int/news-room/fact-sheets/detail/tuberculosis

Pasa, F., Golkov, V., Pfeiffer, F., Cremers, D., & Pfeiffer, D. (2019). Efficient deep network architectures for fast chest X-ray tuberculosis screening and visualization. *Scientific reports*, *9*(1), 6268.

Rahman, T., Khandakar, A., Kadir, M. A., Islam, K. R., Islam, K. F., Mazhar, R., Hamid, T., Islam, M. T., Kashem, S., & Mahbub, Z. B. (2020). Reliable tuberculosis detection using chest X-ray with deep learning, segmentation and visualization. *IEEE Access*, *8*, 191586-191601.

Sathitratanacheewin, S., Sunanta, P., & Pongpirul, K. (2020). Deep learning for automated classification of tuberculosis-related chest X-Ray: dataset distribution shift limits diagnostic performance generalizability. *Heliyon*, *6*(8), e04614.

Sharma, S. K., & Mohan, A. (2013). Tuberculosis: From an incurable scourge to a curable disease-journey over a millennium. *The Indian journal of medical research*, *137*(3), 455.

Shin, H.-C., Roth, H. R., Gao, M., Lu, L., Xu, Z., Nogues, I., Yao, J., Mollura, D., & Summers, R. M. (2016). Deep convolutional neural networks for computer-aided detection: CNN architectures, dataset characteristics and transfer learning. *IEEE transactions on medical imaging*, *35*(5), 1285-1298.

Singh, N., & Hamde, S. (2019). Tuberculosis detection using shape and texture features of chest X-rays. Innovations in Electronics and Communication Engineering: Proceedings of the 7th ICIECE 2018,

Tahir, A., Qiblawey, Y., Khandakar, A., Rahman, T., Khurshid, U., Musharavati, F., Islam, M., Kiranyaz, S., & Chowdhury, M. (2021). Coronavirus: Comparing COVID-19, SARS and MERS in the eyes of AI.

Van Ginneken, B., Katsuragawa, S., ter Haar Romeny, B. M., Doi, K., & Viergever, M. A. (2002). Automatic detection of abnormalities in chest radiographs using local texture analysis. *IEEE transactions on medical imaging*, *21*(2), 139-149.

Yadav, O., Passi, K., & Jain, C. K. (2018). Using deep learning to classify X-ray images of potential tuberculosis patients. 2018 IEEE International Conference on Bioinformatics and Biomedicine (BIBM),

PAPER 70 – H-Infinity Mixed Sensitivity Function for the DC Motor Control

A. Umar[1*], N.S Usman[1], S.M. Yusuf[1], Z. Haruna[1], A. Ore-Ofe[1], E.S. Jeffrey[1], S.A. Mikail[2]
[1]Department of Computer Engineering, Ahmadu Bello University, Zaria.
[2]Department of Electronics & Telecommunications Engineering, Ahmadu Bello University, Zaria.
[*]Email: abubakaru061010@gmail.com

ABSTRACT
This article presents an H-infinity mixed sensitivity function for the DC motor control. The main purpose of the DC motor is controlling the speed on a precise reference when uncertainties and disturbances act on it. Regulating the power supply of the DC motor in order to control the angular speed is a challenging task, this necessitates the use of H-infinity mixed sensitivity function, which is a robust technique to control the DC motor's speed in the presence of uncertainties and disturbances by the selection of appropriate weights for the plant. The DC motor was modelled, and simulation was done in MATLAB 2022b environment. The results showed that for the sensitivity function of the DC motor, the bode magnitude plot reduces from 35 dB to -35 dB with a frequency of 0.01 rad/secs to 1000000 rad/secs. Also, for the complementary sensitivity function of the DC motor, the bode magnitude plot reduces from 19 dB to -33 dB with a frequency of 0.01 rad/secs to 1000000 rad/secs. Taking the singular value plot into consideration, the magnitude of the DC servo motor reduces from -33 dB to -77 dB which showed good robust stability, performance and tracking capability when using H-infinity mixed sensitivity function.

KEYWORDS: DC Motor, H-infinity, Mixed Sensitivity Function, Robust Stability, Robust performance

16. INTRODUCTION

The Direct current (DC) motor is a device that converts electrical power to mechanical power. There exists numerous variants of DC motors which are; brushless (BLDC) motor, brushed DC motor, stepper motor and servo motor (Ma'arif & Setiawan, 2021). DC motors find applications in areas like pendulum, line follower robot, maze following robot and robot balancing (Covaci *et al.*, 2020; Hsu *et al.*, 2018; Tayal *et al.*, 2020). It possesses some advantages over the AC motors which are ease of control characteristics, low power consumption and better performance (Pandey *et al.*, 2020). The main purpose of the DC motor is controlling the speed on a precise reference when uncertainties and disturbances act on it (Taut *et al.*, 2018). The angular speed is regulated by adjusting the power supply of the motor, which is a challenging task, hence the need for a controller. However, the DC motor's speed robustness ensures that the system functions excellently in the presence of disturbance and uncertainty, while motors accuracy is being affected by its disturbance (Ahmed *et al.*, 2018). The accuracy and stability of the DC motor relates to the disturbance and uncertainty of the plant. There are some features like speed and torque nonlinearities which produces uncertainties in the rotational speed control system (Prakosa *et al.*, 2021b). The main disturbance occurs due to environmental circumstances and overload (Krishnan *et al.*, 2017). The position sensor's sensitivity causes uncertainty mainly in noise situations (Prakosa *et al.*, 2020). However, robust control provides a controller design which gives a tradeoff with uncertainty (Prakosa & Vtorov, 2019). H-infinity controller, which is a branch of robust controller gives a numerical optimization problem of stabilizing a plant in the presence of disturbance and uncertainties (Prakosa & Stotckaia, 2019). The H-infinity mixed sensitivity function is used for shaping the plant, in which the corresponding weights penalizes either the error signal, the input signal or the output signal through the use of augmented plant and weighting filters (Prakosa *et al.*, 2021a; Umar *et al.*, 2018).

There are some literatures done within the field of DC motor with respect to robust control technique. Dey *et al.* (2016) developed a robust H-infinity controller for the DC motor. The result was compared with the conventional PID controller, which performed better than the PID controller in terms of robust stability in the time and frequency domain. Also, (Vinida & Chacko, 2016) presented an H-infinity controller for the control of a sensorless DC motor. Particle swarm optimization (PSO) algorithm was used to optimize the H-infinity controller. The controller was also compared with PID controller, which showed better performance than the PID controller in terms of good disturbance rejection and reference tracking. The weights of the H-infinity controller were optimized in (Vinida & Chacko, 2021) using PSO, in which the DC motor was controlled using H-infinity controller. The experimental results of the controller were compared with proportional-integral (PI) controller. The H-infinity controller performed better during transient and sudden disturbances in the load. The DC motor's robustness was improved in (Prakosa *et al.*, 2022) using H-infinity mixed sensitivity synthesis technique to solve the problem of uncertainties and disturbances. The robustness of the DC motor's speed was improved because the system had a better overshoot and smoother signal.

This article proposes an H-infinity mixed sensitivity function for the DC motor control. The rest of the paper is structured as follows; the introduction is discussed in the first section, while in the second section, the DC motor model is presented. In section three, H-infinity mixed sensitivity function is designed and section four presents the simulation results. Finally, the last section gives the conclusion.

17. DC MOTOR MODEL

The DC motor considered in this article is the self-excited type. The motor is excited with a constant field current and a constant flux. The speed of the motor is regulated by changing the armature voltage. Hence, the motor is an armature based controlled motor (Porbiya & Kulkarni, 2021). The DC motor model parameters is adopted from (Akbar *et al.*, 2016).

The DC motor schematic diagram is given in Figure 1.

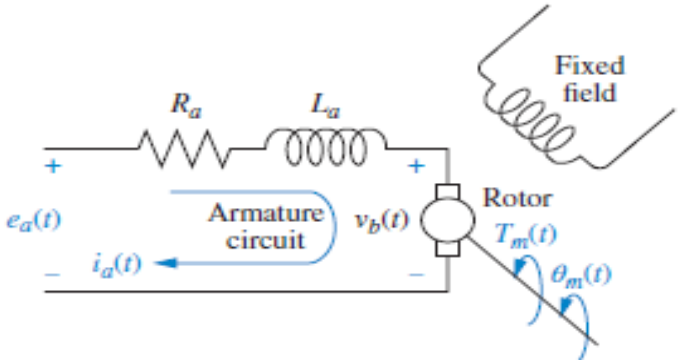

Figure.1. Schematic Diagram of the DC Motor (Nise, 2011)

The back electromotive force (emf) V_b is given by (Porbiya & Kulkarni, 2021):

$$V_b = K_b s\theta_m(s) \tag{1}$$

Where K_b is the back emf and θ_m is the maximum rotor shaft angle.

The armature voltage using Kirchoff's voltage law is written as (Porbiya & Kulkarni, 2021):

$$E_a(s) = R_a I_a + L_a s I_a(s) + V_b(s) \tag{2}$$

The developed motor torque is proportional to the armature current, which is written as (Porbiya & Kulkarni, 2021):

$$T_m(s) = K_t I_a(s) \tag{3}$$

Where T_m is the torque developed by the motor, K_t is the motor torque constant which depends on the magnetic field and motor characteristics.

Hence, the DC motor transfer function is written as (Porbiya & Kulkarni, 2021):

$$\frac{\theta_m(s)}{E_a(s)} = \frac{K_t/(R_a J_m)}{s\left[s + \frac{1}{J_m}\left(D_m + \frac{K_t K_b}{R_a}\right)\right]} \tag{4}$$

18. H-INFINITY CONTROLLER

The augmented plant model of the H-infinity controller is written as (Umar *et al.*, 2018):

$$P(s) = \left[\begin{array}{c|cc} A & B_1 & B_2 \\ \hline C_1 & D_{11} & D_{12} \\ C_2 & D_{21} & D_{22} \end{array}\right] \tag{5}$$

While the state space augmented model is written as (Umar, 2017):

$$\dot{x} = Ax + \begin{bmatrix} B_1 & B_2 \end{bmatrix}\begin{bmatrix} u_1 \\ u_2 \end{bmatrix} \tag{6}$$

$$\begin{bmatrix} y_1 \\ y_2 \end{bmatrix} = \begin{bmatrix} C_1 \\ C_2 \end{bmatrix} x + \begin{bmatrix} D_{11} & D_{12} \\ D_{21} & D_{22} \end{bmatrix}\begin{bmatrix} u_1 \\ u_2 \end{bmatrix} \tag{7}$$

The closed loop transfer function is given as (Umar, 2017):

$$Ty_1u_1(s) = P_{11}(s) + P_{12}(s)\left[I - F(s)P_{22}(s)\right]^{-1} F(s)P_{21}(s) \tag{8}$$

The objective of robust control is to find a stabilizing controller.

$$u_2(s) = F(s)\,y_2(s) \tag{9}$$

Given the condition (Umar, 2017):

$$\|Ty_1u_1\|_\infty < 1 \tag{10}$$

The design objective is to find a stabilizing controller $F_c(s)$, which guarantees the closed system bounded by an H_∞-norm that is given by a positive number

$$\|Ty_1u_1\|_\infty < \gamma \tag{11}$$

$$F_c(s) = \left[\begin{array}{c|c} A_f & -ZL \\ \hline F & 0 \end{array}\right] \tag{12}$$

The optimal criterion in designing an optimal H_∞ controller is written as (Umar, 2017):

$$\|Ty_1u_1\|_\infty < \frac{1}{\gamma} \tag{13}$$

3.1 H_∞ Mixed Sensitivity Problem

For the H_∞ optimal control, the weighting functions $W_1(s)$, $W_2(s)$ and $W_3(s)$ were used for shaping the plant model $G(s)$. $W_1(s)$ penalizes the error signal, $W_2(s)$penalizes the input signal and the output signal is been penalized by $W_3(s)$[22]. The H_∞ mixed sensitivity problem control structure is given in Figure 2.

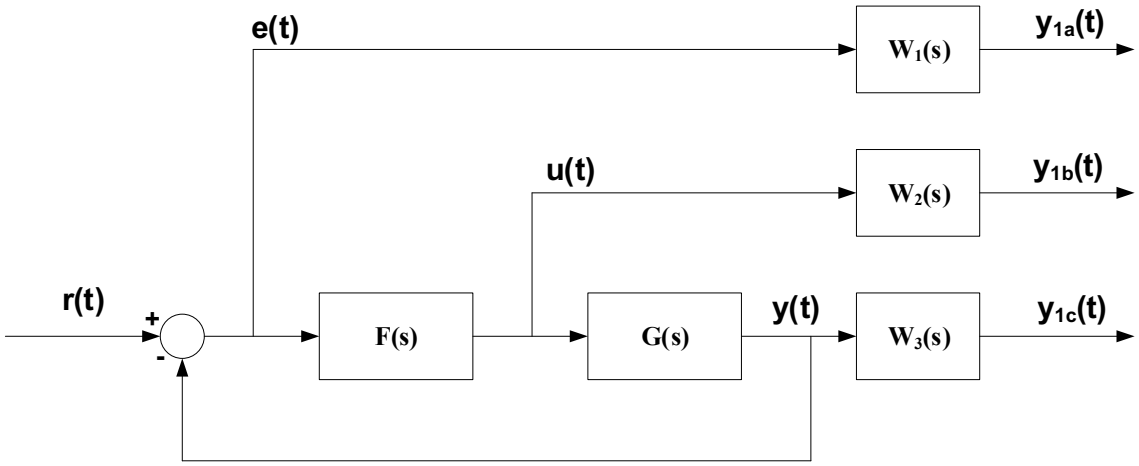

Figure 2: H_∞ Mixed Sensitivity Problem (Xue *et al.*, 2007)

The sensitivity transfer function $S(s)$and complementary sensitivity function $T(S)$ are written as:

$$S(s) = \left[1 + F(s)G(s)\right]^{-1} \tag{14}$$

$$T(s) = 1 - S(s) = F(s)G(s)\left[1 + F(s)G(s)\right]^{-1} \tag{15}$$

3.2 H_∞ Controller Selection

The selected weighting functions are written as:

$$W_1(s) = \frac{0.1011s + 1.352}{s + 0.02317} \tag{16}$$

$$W_2(s) = 0.0243 \tag{17}$$

$$W_3(s) = \frac{s + 206.5}{0.02157s + 1872} \tag{18}$$

19. SIMULATED RESULTS

This section discusses the results obtained from the simulation, which was done using MATLAB 2022b environment. The DC motor transfer function is written as.

$$G(s) = \frac{148}{s^2 + 201s + 6290} \tag{18}$$

However, the system has been proved to be observable and controllable, which paved way for other control analysis. The augmented H-infinity controller plant model is given as:

$$\begin{bmatrix} A_g & B_g \\ C_g & D_g \end{bmatrix} = \left[\begin{array}{cc:c} -201 & -6290 & 1 \\ 1 & 0 & 0 \\ 0 & 148 & 0 \end{array}\right] \tag{19}$$

The sensitivity and inverse sensitivity function bode magnitude and phase plot is given in Figure 3.

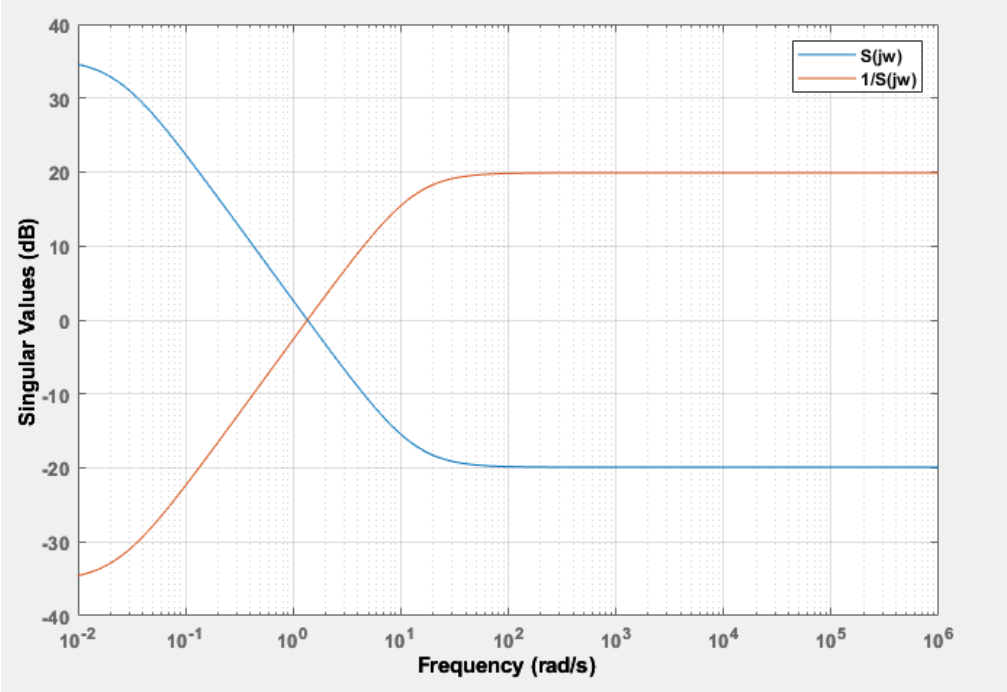

Figure 3: Sensitivity and Inverse Sensitivity Function Bode Plot

From Figure 3, it can be seen that as the frequency increases from 0.01 rad/sec to 10000000 rad/sec, the sensitivity function of the DC motor reduces from 35 dB to -35 dB. This can be deduced that at lower frequency, the sensitivity function is high, and at higher frequency, it becomes low. This shows the robustness of the H_∞ controller when applied to the DC servo motor.

The complementary and inverse complementary function bode magnitude and phase plot is shown in Figure 4.

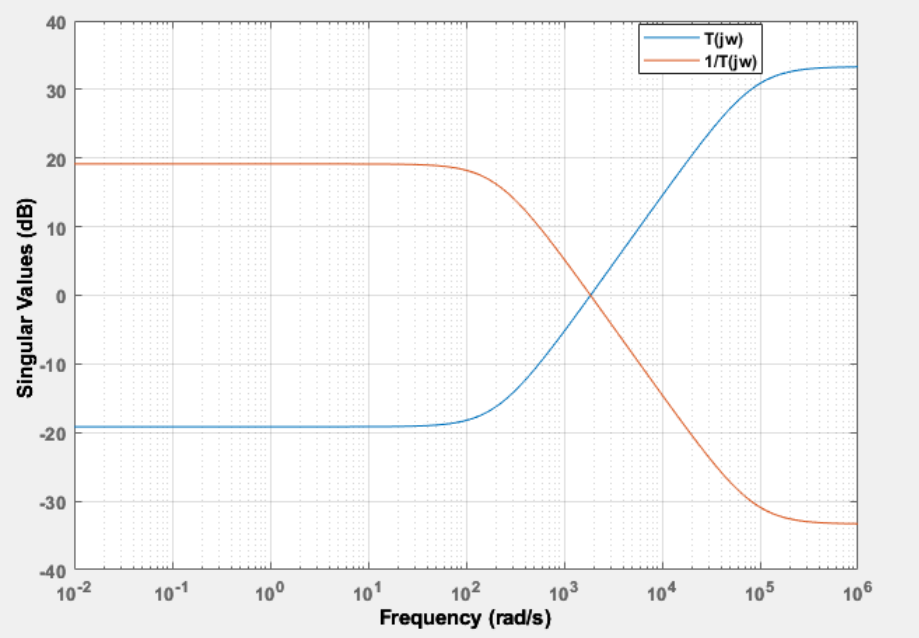

Fig. 4. Compelmentary and Inverse Complementary Function Bode Plot

From Figure 4, it can be seen that as the frequency increases from 0.01 rad/secs to 1000000 rad/secs, complementary function of the DC motor reduces 19 dB to -33 dB. This shows that at lower frequencies, the inverse complementary sensitivity function is high, and at low frequencies, the complementary sensitivity function is low. This shows the robustness of the H_∞ controller when applied to the DC servo motor.

Also, the singular value bode magnitude plot is shown in Figure 5.

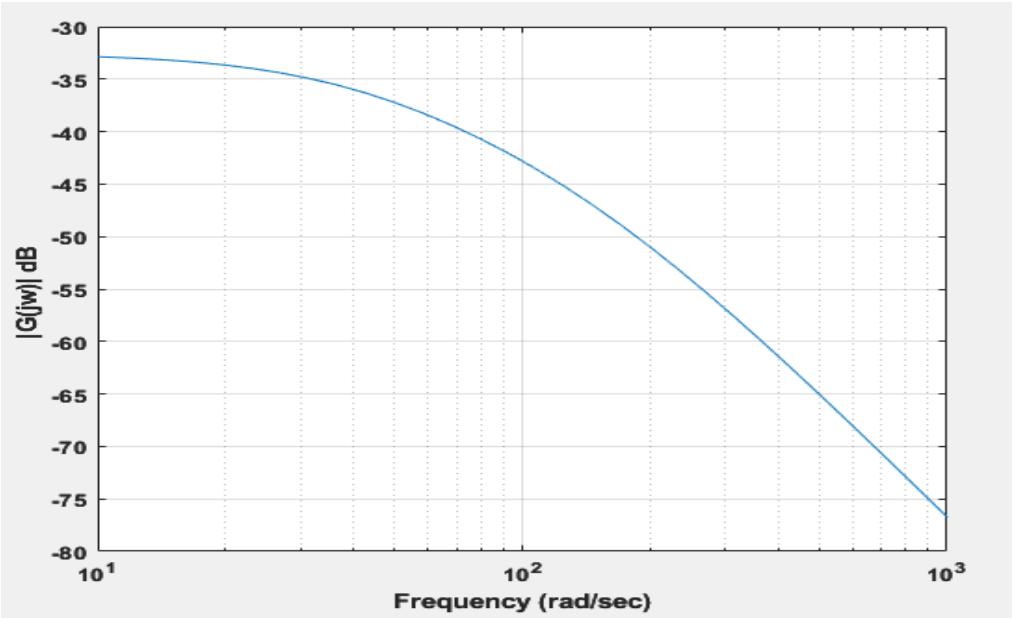

Figure. 5. Singular Value Bode Magnitude Plot

From Figure 5, it can be seen that as the frequency increases from 10 rad/secs, the magnitude of the DC servo motor also reduces from -33 dB to -77 dB, which clearly shows the robustness of using H_∞ controller of the DC servo motor.

The designed H_∞ controller is given as:

$$K = \frac{1356.1479s^3 + 117968874.8478s^2 + 23665484281.8058s + 740309658505.3711}{s^4 + 87020.4342s^3 + 20254139.9253s^2 + 1108802337.4526s + 25680077.8285} \tag{20}$$

With a γ value of 0.96094, which is less than 1.

20. CONCLUSION

This paper proposes an H-infinity mixed sensitivity function for the DC motor control. The main purpose of the DC motor is controlling the speed on a precise reference when uncertainties and disturbances act on it. Regulating the power supply of the DC motor in order to control the angular speed is a challenging task, hence H-infinity mixed sensitivity function was used for the control of the DC motor's speed because it takes into consideration uncertainties and disturbances, by selection of appropriate weights for the plant. Simulation was carried out in MATLAB 2022b environment, and the results obtained showed that for the DC motor's sensitivity function, the bode magnitude plots reduces from 35 dB to -35 dB with a frequency of 0.01 rad/sec to 1000000 rad/sec. Also, for the complementary sensitivity function of the DC motor, the bode magnitude plots also reduces from 19 dB to -33 dB with a frequency of 0.01 rad/sec to 1000000 rad/sec. However, for the singular value bode plot, the magnitude of the DC servo motor reduces from -33 dB to -77 dB which shows good robust stability, performance and good tracking capability when using H_∞ mixed sensitivity function. Future research will consider applying H_∞ mixed sensitivity function on other variants of the DC motor, by comparing both simulated and experimental results.

REFERENCES

Ahmed, A., Parmar, G., & Gupta, R. (2018). *Application of GWO in Design of Fractional Order PID Controller for Control of DC Motor and Robustness Analysis.* Paper presented at the 2018 International Conference on Advances in Computing, Communication Control and Networking (ICACCCN), Greater Noida, India.

Akbar, M. A., Naniwa, T., & Taniai, Y. (2016). *Model reference adaptive control for DC motor based on Simulink.* Paper presented at the 2016 6th International Annual Engineering Seminar (InAES), Yogyakarta, Indonesia.

Covaci, R., Harja, G., & Nascu, I. (2020). *Autonomous Maze Solving Robot.* Paper presented at the 2020 IEEE International Conference on Automation, Quality and Testing, Robotics (AQTR), Cluj-Napoca, Romania.

Dey, N., Mondal, U., & Mondal, D. (2016). *Design of a H-infinity Robust Controller for a DC Servo Motor System.* Paper presented at the 2016 International Conference on Intelligent Control Power and Instrumentation (ICICPI), PUNE, India.

Hsu, C.-F., Su, C.-T., Kao, W.-F., & Lee, B.-K. (2018). *Vision-Based Line-Following Control of a Two-Wheel Self-Balancing Robot.* Paper presented at the 2018 International Conference on Machine Learning and Cybernetics (ICMLC), Chengdu, China.

Krishnan, T. D., Krishnan, C., & Vittal, K. P. (2017). *Design of Robust H-infinity Speed Controller for High Performance BLDC Servo Drive.* Paper presented at the 2017 International Conference on Smart grids, Power and Advanced Control Engineering (ICSPACE), Bangalore, India.

Ma'arif, A., & Setiawan, N. R. (2021). Control of DC Motor Using Integral State Feedback and Comparison with PID: Simulation and Arduino Implementation. *Journal of Robotics Control, 2*(5), 456-461. doi:10.18196/jrc.25122

Nise, N. (2011). *Control System Engineering* (Vol. 7). Courier Kendallville: John Wiley & Sons, Inc, New York.

Pandey, S. K., Bera, C., & Dwivedi, S. S. (2020). *Design of robust PID controller for DC Motor using TLBO algorithm.* Paper presented at the 2020 IEEE International Conference on Advances and Developments in Electrical and Electronics Engineering (ICADEE), Coimbatore, India.

Porbiya, P., & Kulkarni, S. P. (2021). *Speed Control of DC Motor using MRAC, PSO and PSO Fuzzy Controller.* Paper presented at the 2021 International Conference on Smart Generation Computing, Communication and Networking (SMART GENCON), Pune, India.

Prakosa, J., & Stotckaia, A. (2019). The h-infinity robust control for optimization on low water flow application. *Journal of Advanced Research in Dynamical Control Systems, 11*(S4), 1995-2006.

Prakosa, J., & Vtorov, V. (2019). Experimental studies of adaptive control to stabilize the automatic unmanned mini quad rotor helicopter position. *Journal of Advanced Research in Dynamical Control Systems, 11*(S4), 1983-1994.

Prakosa, J. A., Gusrialdi, A., Kurniawan, E., Stotckaia, A. D., Adinanta, H. J. I. J. o. D., & Control. (2022). Experimentally robustness improvement of DC motor speed control optimization by H-infinity of mixed-sensitivity synthesis. *10*(6), 1968-1980.

Prakosa, J. A., Kukaev, A. S., Parfenov, V. A., & Venediktov, V. Y. (2020). Simple automatic fluid displacement measurement by time-of-flight laser sensing technology for volume calibrator need. *Journal of Optics, 49*(1), 69-75. doi:https://doi.org/10.1007/s12596-020-00596-5

Prakosa, J. A., Kurniawan, E., Sirenden, B. H., Adinanta, H., Afandi, M. I., Ula, R. K., & Pratomo, H. (2021xa). *Synthesis Method of Mixed Sensitivity for H-infinity Robust Control Optimization on DC Motor of*

Mechatronics Model. Paper presented at the 2021 International Conference on Radar, Antenna, Microwave, Electronics, and Telecommunications (ICRAMET), Bandung, Indonesia.

Prakosa, J. A., Widiyatmoko, B., Bayuwati, D., & Wijonarko, S. (2021b). *Optoelectronics of Non-Contact Method to Investigate Propeller Rotation Speed Measurement of Quadrotor Helicopter.* Paper presented at the 2021 International Symposium on Electronics and Smart Devices (ISESD), Bandung, Indonesia.

Taut, M., Chindris, G., & Pitică, D. (2018). *PID Algorithm used for DC Motor Control.* Paper presented at the 2018 IEEE 24th International Symposium for Design and Technology in Electronic Packaging(SIITME), Iasi, Romania.

Tayal, S., Rao, H. P. G., Bhardwaj, S., & Aggarwal, H. (2020). *Line Follower Robot: Design and Hardware Application.* Paper presented at the 2020 8th International Conference on Reliability, Infocom Technologies and Optimization (Trends and Future Directions)(ICRITO), Noida, India.

Umar, A. (2017). Development of a Position and Trajectory Tracking Control of Ball and Plate System using a Double Feedback Loop Structure. *(Masters of Science Thesis), Department of Electrical and Computer Engineering, Faculty of Engineering, Ahmadu Bello University, Zaria, Published*.

Umar, A., Muazu, M. B., Aliyu, U. D., Musa, U., Haruna, Z., & Oyibo, P. O. (2018). Position and Trajectory Tracking Control for the Ball and Plate System using Mixed H∞ Sensitivity Problem. *Covenant Journal of Informatics and Communication Technology, (CJICT), 6*(1), 1-15.

Vinida, K., & Chacko, M. (2016). *A novel strategy using H infinity theory with optimum weight selection for the robust control of sensorless brushless DC motor.* Paper presented at the 2016 IEEE symposium on sensorless control for electrical drives (SLED), Nadi, Fiji.

Vinida, K., & Chacko, M. (2021). Implementation of Speed Control of Sensorless Brushless DC Motor Drive using H-infinity Controller with Optimized Weight Filters. *International Journal of Power Electronics Drive Systems, 12*(3), 1379. doi:10.11591/ijpeds.v12.i3.pp1379-1389

Xue, D., Chen, Y., & Atherton, D. P. (2007). *Linear Feedback Control; Analysis and Design with MATLAB* (Vol. 3). 3600 Market Street, 6th floor, Philadelphia, PA 19104-2688, USA: Society for Industrial and Applied Mathematics.

PAPER 71 – ADVANCEMENTS IN COMPOSITE BRAKE PAD MATERIALS: A REVIEW OF THEIR TRIBOLOGICAL PROPERTIES AND PERFORMANCE.

Mojeed Okunlola[1]*, Peter Omoniyi[1,2], Kamaldeen Abdulrahman[1],
Tien-Chien Jen[2], Adebayo Adekunle[1]

[1]Department of Mechanical Engineering, University of Ilorin, Ilorin 240003, Nigeria.
[2]Department of Mechanical Engineering Science, University of Johannesburg, Johannesburg 2092, South Africa.
*Corresponding author's email: okunlolanrewajumojeed@gmail.com
Keywords: Brake Pad, Composite materials, Friction, Tribology, Wear

ABSTRACT
Composite brake pad materials have become increasingly popular due to their desirable properties; high strength, low weight, and excellent wear resistance. This review article provides a comprehensive overview of recent advances in composite materials for high-performance brake pads, focusing on their tribological properties and wear mechanisms. The article begins by introducing the importance of selecting suitable materials for brake pads. It then highlights the advantages and limitations of different composites used in brake pads, including ceramic matrix composites, carbon fiber-reinforced composites, and metal matrix composites. The article also discusses the mechanisms behind the wear and degradation of brake pads, such as abrasive wear, adhesion wear, and thermal degradation. Finally, the review concludes with a discussion of future research directions and potential improvements in the design of composite brake pads. This article provides a valuable resource for researchers and engineers in brake pad materials and tribology.

1 INTRODUCTION

A brake pad is the most crucial component of the disc braking system in which the life of the driver, passengers, and road users lies once the vehicle is set into motion [Borawski 2022]. A braking system's main function is to overcome the vehicle's momentum and stop the vehicle through friction [Milenković et. al. 2010]. The performance of the brake pad is greatly influenced by the friction material on the brake pad, which alters the vehicle's motion by converting the kinetic energy to thermal energy. Hence, this is achieved by the coefficient of friction, which accompanies the wear whenever the brake is engaged [Glisovic et. al. 2011]. These tribological properties are the most important to look into in the brake pad as a prerequisite to other properties because the lifespan of the brake is a function of how fast it fades during usage and how often the replacement will be done on the braking system. Figure 1 shows a typical automobile brake pad.

Figure 1: A typical brake pad [www.delphiautoparts.com. accessed 23/5/2023]

Tribology was coined from the Greek word *tribos,* which means "rubbing," translating the word literally into the "science of rubbing" [Al-Samarai et. al. 2012]. Tribology refers to the science and technology guiding the interaction of surfaces in relative motion. It also encompasses the study and application of wear, friction, and lubrication of parts [Archard 1986]. Friction and wear involves two or more bodies in contact, sliding, rolling, with respect to each other depending on the geometrical configuration of the objects, and the interfacial force produced in the process is known to as friction [Aadarsh 2014]. Friction and wear, as two kinds of responses from one tribo-system and are directly proportional to each other in every state of contact in the system. However, there are no simple, comprehensive relationship between them [Hsun-Yu et. al 2020]. Literature shows the recommended successful means of controlling wear irrespective of wear mechanisms by tribologists including soft or hard film coating, multi-phase alloying, and composite structuring in addition to the traditional lubrication method [Ostermeyer 2001].

Interactions among heat, wear, and friction characterises the tribological interface between the brake friction material and the brake disc. This results in continuous growth and destruction of smooth and hard surface structures [Ostermeyer and Mueller 2006], which is also achieved via modern automated methods [Bode and Ostermeyer 2009]. These interactions are influenced by the external load parameters, including normal force and sliding velocity, which dictates the life cycle and average size of the contact patches and the coefficient of friction over a period [Österle and Dmitriev 2016].

On the other hand, lubrication is a means of reducing the effect of friction and wear by incorporating a regulating film between the moving surfaces in contact. This film, known as a lubricant, can be in the form of solid, fluid, or

plastic substance but the most commonly used is oil and grease [Perez and Echeberria 2019]. The functions of lubricants, includes reduction of friction, wear and tear, corrosion prevention, temperature control and contamination, power transmission, and reduction in squealing or screeching noise due to vibration [Adeyemi et. al. 2016]. The addition of solid lubricant in the brake friction material helps modifies the effectiveness and harshness of the brake when applied. Also, it helps reduce the noise/squeal during braking.

2. PROPERTIES OF MATERIALS USED FOR BRAKE PADS

Friction material plays an important role in the braking system since it's the crucial part of the brake pad that decelerates and stop the wheel's rotation by transforming its kinetic energy to heat energy and dissipating it to the surrounding [Adekunle et. al. 2022, Lawal et. al. 2017]. Friction material is made from a blend of several raw materials because no single material can give all the properties required of friction material. Several researchers have worked on replacing carcinogenic asbestos (base material) lined brake pads in the market with eco-friendly materials such as palm kernel shell, periwinkle, sawdust, cow hooves, cow horn, banana peels, eggshell, and other agro-residue, together with other additives [Lawal et. al. 2019, Uzochukwu et. al. 2019]. The brake pad has been designed and formulated to maintain a steady frictional coefficient and should not decompose at high temperatures [Dineshkumar et. al. 2017]. There are three types of brake pads available on the market. Asbestos, metallic, and ceramic brake pads are available. Asbestos brake pads have good friction properties and thermal resistance, but they are carcinogenic. Because of this carcinogenic effect, the manufacturer decided to look for a more environmentally friendly alternative material [Blau 2001]. Ceramic brake pads generate less vibration, dust, and adequate disc or drum wear, whereas metallic brake pads provide a long service life with a reduced rotor life span. Ceramic brake pads generate less vibration, dust, and adequate disc or drum wear, whereas metallic brake pads provide a long service life with a reduced rotor life span [Verma 2016, Xingming et. al. 2016].

Under various velocities, frictional heat, and operating conditions such as mud, oil, and water, good friction material for brake pads maintains a coefficient of friction ranging from 0.2 to 0.4 [Yuji and Takashi 1998, Dineshkumar et. al. 2017]. The friction material for brake pad consists of more than ten elements in which solid lubricant is not left behind to increase the stability of the brake pad frictional coefficient and improve the thermal conductivity of the friction material.

Figure 2: Brake friction material [www.hella.com. accessed 23/5/2023]

Brake pads should be inspected every six months or every 16,000 to 80,000 kilometers drives for replacement, depending on the type of pad, weight of the vehicle, and driving terrain [Engberg 1995].

Recent Advances in Composite Materials for High-Performance Brake Pads: Eco-Friendly Materials Used for Brake Pads

Composite materials have been extensively used in manufacturing high-performance brake pads due to their superior mechanical and thermal properties. In recent years, several advancements have been made in composite materials for high-performance brake pads. Asbestos has been removed from brake pads, and there have been researches that have demonstrated that the removal can be replaced by eco-friendly composites such as seashells (base material), sawdust (fillers), and other additives such as Palm kernel shell (abrasive), charcoal (lubricant), metal chips (reinforcement) and epoxy resin (binder) [Adekunle et. al. 2022]. Agro-based materials have also demonstrated a promising prospect, as they have been used for production of brake pad. Lawal et. al. 2019 examined the production of automobile brake pads as well as the potential of agro-based composites of cashew nut shells and Nigerian gum Arabic binder. Steel dust, silicon carbide, and graphite were also used as additives. The produced friction material showed some favourable properties, such as improved hardness, compressive strength, frictional coefficient, wear rate, and good thermal capacity, in line with the work of Adekunle et al. 2022. Furthermore, agro-based materials, particularly plants fibers, are good replacements for asbestos for brake pad production as their coefficient of friction is reported to be 0.4848 and wear rate of 1.16mg/m. The tribological properties of the agro-based materials were in agreement with the commercial brake pads. They followed the trend in literature such as that of Adekunle et al. 2022, which had a 0.315 frictional coefficient and wear rate of 0.0614 mm^3/Nm. Other agro-based materials which have also been used as friction material is a coconut shell (base material), aluminum oxide (abrasive), graphite (friction modifier), and epoxy resin (binders). The coefficient of friction of 0.614 and the wear rate were found to be 0.03156 mg/m [Lawal et. al. 2019]. As a result, the developed friction material performs satisfactorily in terms of reduced brake noise and vibration during braking, as well as a low wear rate and stable frictional coefficient. The high wear resistance of the developed composite resulted

from the higher tensile strength leading to resistance of abrasive effect more than the reference sample with higher brittleness. Consequently, agro-based friction materials have substituted for asbestos in the production of brake pad friction material [Abutu et. al. 2018].

Metallic materials have also been used as friction materials, which produces improved performances compared to asbestos-based brake pads. Princa-Bretotean et al. 2018 replaced asbestos and its additives for brake friction material production with Aluminium, graphite, zirconium oxide, silicon carbide, titanium oxide, phenolic resin, Hexamethyl-tetramine, and coconut fibre. The coefficient of friction was determined to be 0.35; thus, the friction material with a wear value of 0.06 g is a good alternative to be used for small and medium vehicles, which is in accordance with technical literature on the tribological characteristic of the friction material produced from eco-friendly composite [Adeyemi et. al. 2016]. Similarly, Lawal et al. 2017 developed friction material from a blend of sawdust, steel dust, silicon carbide, graphite, and epoxy resin. The tribological property reported a wear rate of 3.23mg/m for the best sample produced. The composite brake friction material's higher wear resistance was attributed to the sample's higher compressive strength which indicates that there is proper bonding between the composite's particle arrangement and the intermolecular relation are firmly bonded with little pour spaces, which gives rise to low moisture absorption during the percolation test.

Polymer composites have also found their usefulness in producing friction material for brake pads. Afolabi et al. 2015 reinforced polymer with palm kernel shell and cow bone. The experimental matrix was palm kernel shell/epoxy resin and cow bone/epoxy resin at 30:70 formulation. A proper combination of PKS and cow bone as reinforced material showed excellent thermal resilience enough not to decompose at braking temperatures for long durations. The coefficient of friction test was performed with the aid of horizontal plane apparatus with a recorded value of 0.735 for palm kernel and 0.677 for cow bone with the wear rate of 9.57 x 10^{-7} and 1.44 x 10^{-6} g/m, respectively [Afolabi et al. 2015]. Table 1 gives the summary of the results of the tribological properties of friction material for brake pads reported in works of literature.

Table 1: Summary of works of literatures on tribological properties of brake pads.

Author (s)	Base Material	COF Produced/ control	Wear Produced/ control
Adekunle et. al. 2022	Seashell	0.315/ 0.318	0.0614/0.0812 mm^3/Nm
Lawal et. al. 2019	Cashew Nut Shells	0.4848/ (0.3-0.4)	1.16/3.80 (mg/m)
Abutu et. al. 2018	coconut shell	0.634/0.634	0.03156/ 0.04184 (mg/m)
Lawal et. al. 2017	Saw dust	-----	3.23 (mg/m)
Adeyemi et al. 2016	Palm kernel shell	0.37	3.040×10^{-6} (g/m)
Adeyemi et al. 2016	Cocoa beans shells	0.35	0.715×10^{-6} (g/m)
Adeyemi et al. 2016	Palm kernel shell	0.37–0.40/0.30–0.40	2.146/3.80 (mg/m)
Egeonu et. al. 2015	Palm kernel shell	0.349 /0.359	4.2547/3.2864 ($x10^{-10}$) (m^3 /m)
Bashir et. al. 2015	Banana peel	0.39/ (0.3-0.4)	0.038 /----- g
Afolabi et. al. 2015	Palm kernel shell	0.73/ (0.3-0.4)	$9.57E^{-7}$/ $1.85E^{-6}$ (g/m)
Afolabi et. al. 2015	Cow bone	0.677/ (0.3-0.4)	$1.44E^{-6}$/$1.85E^{-6}$ (g/m)
Mgbemena et. al. 2014	Palm kernel shell	---------	0.24/0.16 µm
Onyeneke et. al. 2014	Periwinkle	(0.4-.65)/ 0.45-0.65	0.025-0.06 (mm/min)
Aigbodion et. al. 2010	Bagasse	0.42/ (0.3-0.4)	4.20/3.80 (mg/m)

Wear and Degradation of Brake Pads

Figure 3a shows a typical brake pad without wear degradations. Figure 3b shows the wear tracks of the brake pad. Wear occurs as a result of interaction between brake pad and the rotating disc of the automobile's wheel. The material with less hardness, the brake pad, shows severe degradation with time. The disc's lifespan depends on the pad's aggressivity, determined by the friction material composition. A brake disc is majorly made of grey cast iron, and the brake pad should be made from lesser properties materials to promote long-term disc usage.

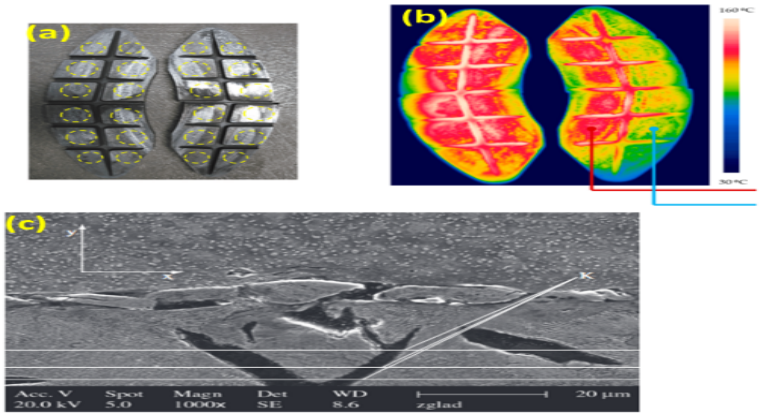

Figure 3: (a) A typical brake pad (b) worn brake pad (c) SEM image of worn brake pad [Polak and Grzybek 2005, Sawczuk et. al.2022]

There are various types of brake pad wear, which aids in the identification of the causes and the precise measurement toward accuracy in repairs, allowing for effective management of user time and money [Elzayady and Elsoeudy 2021, Li Xuewu et. al. 2020]. The wear on brake pads can be in any form; outer, inner, tapered, over-lapping pad wear, and a glazed or cracked pad surface with lifted edges. The glazed or cracked brake pad wear exhibits signs of physical damage and thermal tribulation to the friction material. Improper braking application of new pads and overuse are the common causes of this type of wear in brake pads [www.delphiautoparts.com. accessed 23/5/2023]. The major wear mechanisms, as shown in Figure 3c, occur as a result of delamination [Laguna-Camacho et. al. 2001 of filler particles from the organic binder and degradation of the phenolic resin during asperity heating [Manoharan et. al. 2019]. The primary dependants on the deformation of the friction pair parts are local friction intensity and heat due to thermal contact resistance [JIANG et. al. 2019]. Furthermore, braking force and brake pad vibrations [Perez and Echeberria 2019] Its wear was influenced by demonstrating that high weather temperatures result in rapid wear. The dominant wear modes were high sliding abrasion wear and fatigue cracks, and the friction behavior of automotive brakes is determined by the friction layers and friction films formed on the surface of the brake assembly [Bashir et. al. 2015, Elzayady and Elsoeudy 2021].

Based on the investigation conducted on a specific automotive vehicle's actual brake pad surface before and after the pad was subjected to usage for its wear mechanisms determination [Elzayady and Elsoeudy 2021]. Fiber delamination, as shown in Figure 4a, and fragmental wear, as shown by the large hole induced by particle removal from the material's surface in Figure 4b, are two possible wear mechanisms in brake pads. The most common type of wear that occurs during frictional motions between the brake lining and the disc surface is abrasive wear. The hole in the surface, as shown in Figure 4b, caused microcracks in the radial directions of the hole's circumference [Elzayady and Elsoeudy 2021, JIANG et. al. 2019], indicating non-uniformity of particle size in the sample. These cracks almost always appear when there is too much pressure applied to the pad, resulting in more working actions and stress. Other wear modes can be seen in large cracks in two perpendicular directions. Figure 4c depicts these cracks. They are most likely initiated in the sliding direction and then propagated, resulting in transverse sub-crack incidence. Thermal fatigue on the surface caused by working at a temperature range is the most common cause of these cracks. These wear modes occur in different ways and could be as result of mechanical damage due to friction action in the form of a glazed surface. It could also be wear due to abrasive which resulted in eroded phases. Furthermore, thermal fatigue which occurs due to thermo-mechanical (fatigue) wear and resulted to the formation of a large cracked surface. Finally, physical degradation by the rust layer formation and corroded surfaces which gives rise to diffused iron, oxygen, and carbon compounds, and could be thermo-chemical wear (phases pyrolysis) leading to phases fading [Elzayady and Elsoeudy 2021].

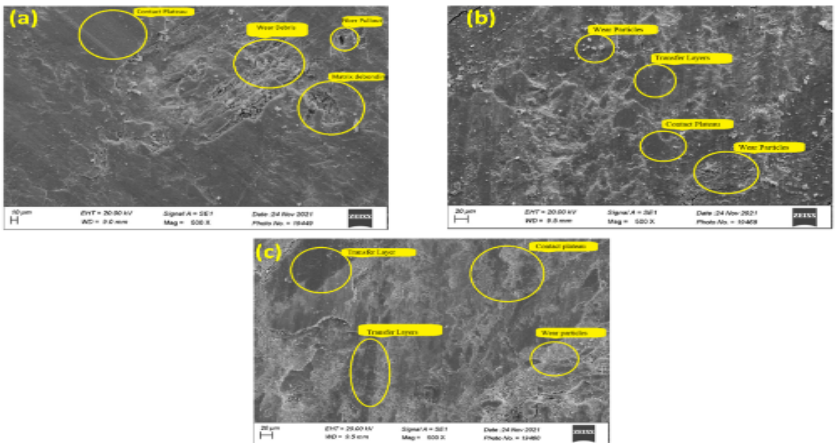

Figure 4: SEM images showing (a) voids (b) wear tracks (c) cracks of brake pad [Naidu et. al. 2022]

3 FUTURE RESEARCH DIRECTIONS

With the close correlation in the performance of the brake friction material produced from agro-waste, locally sourced eco-friendly composites, and conventional carcinogenic asbestos-lined ones, it is of great necessity to encourage the production of eco-friendly brake pads in replacement of asbestos-lined to provide a safe environment.

In determining the wear rate of the brake pad, the area of contact, the weight of the vehicle, and the sliding distance should be considered. Those are the parameters on which the braking performance depends.

4 CONCLUSION

Brake friction material should possess a moderately high coefficient of friction ranging between 0.2 to 0.4 for a lightweight vehicle, good thermal conductivity, good strength, and relatively high wear resistance under variable load and speed conditions. The Pin-on-disc apparatus is the most suitable, accurate, and mostly used method of determining the tribological properties (friction and wear) of friction material for brake pads. The velocity of sliding, sliding distance, and load acting on materials are the parameters on which the wear rate of friction material for brake pad depends. The tribological properties (friction coefficient and wear rate) of the brake pad are greatly influenced by the material composition and quantity of binder present in the composition, i.e., the higher the percentage of binder in the friction material composition led to corresponding higher hardness and wear resistance of the brake friction material.

REFERENCES

Aadarsh Mishra (2014). Analysis of relation between friction and wear. *International Journal of Mechanical* Engin*eering and Robotics Research, Volume 3*(3), (2278–0149). www.ijmerr.com

Abutu J. Lawal S. A., Ndaliman M. B., LafaAraga R. A., Adedipe O. and Choudhury I. A. (2018). Production and characterization of brake pad developed from coconut shell reinforcement material using central composite design, *SN Applied Sciences*, https://doi.org/10.1007/s42452-018-0084-x

ADEKUNLE Adebayo, OKUNLOLA Mojeed, OMONIYI Peter, ADELEKE Adekunle, IKUBANNI Peter, POPOOLA Tajudeen and IBRAHIM Hassan (2022). Development and analysis of friction material for eco-friendly brake pad using seashell composite. *International journal of science and technology*, scientiairanica.sharif.edu/article_23077, dio:10.24200/SCI2022.59835.6464

Adeyemi Ibukun Olabisi, Ademoh Nuhu Adam and Okwu Modestus Okechukwu (2016). Development and Assessment of Composite Brake Pad Using Pulverized Cocoa Beans Shells Filler. *International Journal of Materials Science and Applications*, *5*(2), pp. 66 -78.

Adeyemi, I. Olabisi, Ademoh A. Nuhu and Thankgod E. Boye (2016). Development of Asbestos-Free Automotive Brake Pad Using Ternary Agro-Waste Fillers. *Journal of Multidisciplinary Engineering Science and Technology (JMEST), Volume 3*(7), (2458-9403).

Afolabi Mayowa, Abubakre O.K., Lawal S.A. and Raji Abdulkabir (2015). Experimental investigation of palm kernel shell and cow bone reinforced polymer composites for brake pad production. *International Journal of Chemistry and Materials Research*, *Volume. 3*(2), 27-40. DOI: 10.18488/journal.64/2015.3.2/64.2.27.40

Aigbodion V. S., Akadike U., Hassan S.B., Asuke F. And Agunsoye J.O. (2010). Development of Asbestos - Free Brake Pad Using Bagasse. *Tribology in industry, Volume 32, No. 1.*

Al-Samarai Riyadh A., Haftirman Khairel Rafezi Ahmad and Al-Douri Y. (2012). Effect of Load and Sliding Speed on Wear and Friction of Aluminum–Silicon Casting Alloy. *International Journal of Scientific and Research Publications*, *Volume 2*, (2250-3153).

Archard J. F. (1986). Friction between metal surfaces. *Wear*, *Volume 1*, 54, (113).

Bashir Masrat, Saleem Sheikh Shahid and Bashir Owais (2015). Friction and wear behavior of disc brake pad material using banana peel powder. *International Journal of Research in Engineering and Technology,* Volume: 04, http://www.ijret.org

Blau Peter J. (2001). Compositions, Functions, and Testing of Friction Brake Materials and Their Additives. U.S. Department of Energy, http://www.osti.gov/bridge.

Bode Kai Henning and Ostermeyer Georg-Peter (2009). Simulations and Tests of Innovative Friction Laws in Brake Systems. P*roc. Appl. Math. Mech., Volume 9*, page 63 – 66. DOI 10.1002/pamm.200910017

Borawski Andrzej (2022). Testing Passenger Car Brake Pad Exploitation Time's Impact on the Values of the Coefficient of Friction and Abrasive Wear Rate Using a Pin-on-Disc Method. *Materials (Basel)*, *Volume 15*, p1–16.

Dineshkumar R., Ramanamurthy E. V. V. and Krishnapavanteja Ch. (2017). Development of friction material by using precast prefired (pcp f) blocks. *IOP Conf. Series: Materials Science and Engineering*, 197. doi:10.1088/1757-899X/197/1/012001

Engberg Catherine C. (1995). The Regulation and Manufacture of Brake Pads: The Feasibility of Reformulation to Reduce the Copper Load to the San Francisco Bay.

Egeonu Darlington and Okolo Chukwumaobi Oluah Patrick (2015). Production of Eco-Friendly Brake Pad Using Raw Materials Sourced Locally in Nsukka. *Journal of Energy Technologies and Policy*, *5*(11), (2224-3232), www.iiste.org

Elzayady Nagwa and Elsoeudy Ramadan (2021). Microstructure and wear mechanisms investigation on the brake pad. *Journal of materials research and Technology*, *Volume 11,* (2314-2335).

Glisovic J., Radonjic R., Babic M., Miloradovic D., Catic D. (2011). Design of vehicle road testing method for determination of brake pad friction characteristics. *Journal of the Balkan Tribological Association*, *Volume 17*(4), page 513–525.

Hsun-Yu Lin, Huy-Zu Cheng, Kuo-Jung Lee, Chih-Feng Wang, Yi-Chen Liu and Yu-Wei Wang (2020). Effect of Carbonaceous Components on Tribological Properties of Copper-Free NAO Friction Material. *Materials, Volume 13*, 1163. doi:10.3390/ma13051163

https://www.delphiautoparts.com/gbr/en/article/be-aware-brake-pad-wear#:-:text=Outer%20Pad%20Wear%3A%20If%20the,the%20brakes%20aren't%20applied. [Accessed 23 May 2023].

https://www.hella.com/partnerworld/us/Product-range/Brake-system/Brake-pads-2968/ [Accessed 23 May 2023].

https://www.google.com/search?client=ms-opera-mini-android&biw=360&bih=533&tbm=isch&sa=1&q=brake+pad%3A+understanding+friction+and+formulation&oq=brake+pad%3A+understanding+friction+and+formulation&aqs=mobile-gws-lite..#imgrc=m6Yeuin-MvCfEM [Accessed 23 May 2023].

JIANG Lan, YAN-LI Jiang, YU Liang, YANG Hong-Liang, Zi-Shen L., DING You-dong (2019). Fabrication, microstructure, friction and wear properties of SiC3D/Al brake disc graphite/SiC pad tribo-couple for high-speed train. *Trans Nonferrous Metals Soc China*, *29*, 1889e902.

Laguna-Camacho JR, Juarez-Morales a G, Calderon-Ramon a C, Velazquez-Martınez a V, Hernandez-Romero b I, Mendez-Mendez c JV (2001). A study of the wear mechanisms of disk and shoe brake pads. *Eng Fail Anal 2015*, https:// doi.org/10.1016/j.engfailanal.2015.01.004

Lawal S. S., Ademoh N. A., Bala K. C. and Abdulrahman A. S. (2019). Reviews in Automobile Brake Pads Production and Prospects of Agro Base Composites of Cashew Nut Shells and Nigerian Gum Arabic Binder. *Covenant Journal of Engineering Technology (CJET)*, *Volume 3*(2), (2682-5325).

LAWAL Sadiq Sius, BALA Katsina Christopher and ALEGBEDE Abdulkareem Tunde (2017). Development and production of brake pad from sawdust composite. *Leonardo Journal of Sciences*, pp. 47-56.

Li Xuewu, Liang Jingsong, TianShi, XinchunChen ChuanweiZhang, ZhaohuiLiu DianziLiu, QiaoxinZhang (2020). Tribological behaviors of vacuum hot-pressed ceramic composites with enhanced cyclic oxidation and corrosion resistance. *Ceram Int; 46*(9), 12911e20.

Manoharan S, Vijay R, Lenin Singaravelu D, Mohamed Kchaou (2019). Experimental investigation on the tribo-thermal properties of brake friction materials containing various forms of graphite: a comparative study. *Arabian J Sci Eng.*, *44*, 1459e73

Mgbemena Chinedum Ogonna, Mgbemena Chika Edith and Okwu Modestus Okechukwu (2014). Thermal stability of pulverized palm kernel shell (PKS) based friction lining material locally developed from spent, *ChemXpress*, *5*(4), 115– 122.

MILENKOVIĆ Predrag D., JOVANOVIĆ Saša J., JANKOVIĆ Aleksandra S., MILOVANOVIĆ Milan D., VITOŠEVIĆ Nenad D., DJORDJEVIĆ Milan V. and RAIČEVIĆ Mile M. (2010). The influence of brake pads thermal conductivity on passanger car brake system efficiency. *Thermal Science*, *Volume 14*, pp. S221-S230.

Naidu Mithul, Bhosale Ajit, Munde Yashwant, Salunkhe Sachin and Hussein Mohamed Abdelmoneam (2022). Wear and Friction Analysis of Brake Pad Material Using Natural Hemp Fibers. *Polymers*, *15, 188*. *https://doi.org/10.3390/polym15010188*

Onyeneke F. N., Anaele J. U. and Ugwuegbu C. C. (2014). Production of Motor Vehicle Brake Pad Using Local Materials (Perriwinkle and Coconut Shell). *The International Journal of Engineering and Science*. *Volume 3*(9), Pages 17-24.

Ostermeyer G.-P. (2001). Friction and wear of brake systems. *Forschung im Ingenieurwesen*, *Volume 66*, pp. 267-272.

Ostermeyer G.-P. and Mueller M. (2006). Dynamic Interaction of friction and surface topography in brake systems. *Tribology International*, *Volume 39*, page 370-380.

Österle Werner and Dmitriev Andrey I. (2016). The Role of Solid Lubricants for Brake Friction Materials. *Lubricants*, *Volume 4*(5) doi:10.3390/lubricants4010005.

Perez B, and Echeberria J. (2019). Influence of abrasives and graphite on processing and properties of sintered metallic friction materials. *Heliyon, Volume 5*, 2311. https://doi.org/10.1016/ j.heliyon.2019.e02311.

Pinca-Bretotean C., Josan A. and Birtok-Băneasă C. (2018). Laboratory testing of brake pads made of organic materials intended for small and medium vehicles, University Politehnica Timișoara, Faculty of Engineering Hunedoara, Revoluției 5, 331128 Hunedoara, *Romania IOP Conf. Series: Materials Science and Engineering*, doi:10.1088/1757-899X/393/1/012029

Polak Adam and Grzybek Janusz (2005). The Mechanism of Changes in the Surface Layer of Grey Cast Iron Automotive Brake Disc, *Materials Research*, *Volume 8*(4), (475-479).

Sawczuk Wojciech, Merkisz-Guranowska Agnieszka, Ulbrich Dariusz, Kowalczyk Jakub and Cañás Armando-Miguel Rilo (2022). Investigation and Modelling of the Weight Wear of Friction Pads of a Railway Disc Brake, *Materials*, *15*, 6312. https://doi.org/10.3390/ma15186312

Uzochukwu M.I, Aiyejagbara M.O, And Ugbaja M.I (2019). Property Investigation of Cowhorn/Prewrinkle Shell Epoxy Composite for Automobile Brake Pad Linings. *Journal of Emerging Trends in Engineering and Applied Sciences (JETEAS), Volume 10*(2), pp 48-53, (2141-7016).

Verma Piyush Chandra (2016). Automotive Brake Materials: Characterization of Wear Products and Relevant Mechanisms at High Temperature. Doctoral School in Materials Science and Engineering, Department of Industrial engineering, University of Trento, Itay.

Xingming Xiao, Yan Yin, Jiusheng Bao, Lijian Lu and Xuejun Feng (2016)., Review on the friction and wear of brake materials. *Advances in Mechanical Engineering*, *Vol. 8*(5), pp. 1–10. DOI: 10.1177/1687814016647300

Yuji Enomoto and Takashi Yamamoto (1998). New materials in automotive tribology. *Journal of tribology*, Tribology letters 5, pp. 13-24.

PAPER 72 – Exploration of Global Renewable Energy Statistics for Electricity Generation: A Case Study of Nigeria.

Y. A. Yisah[1], S. O. Anaza[1*], T. Abdulraheem[1], H. Otaru[1], M. Abdulazeez[1]. M. S. Salawu[1]

[1]Power Equipment and Electrical Machinery Development Institute, (PEEMADI) Okene, Kogi State, Nigeria
Email: sanaza@peemadi.gov.ng

Abstract:
In recent times, electricity has been the key driving factor in all aspect human life such as healthcare, transportation, entertainment and education. Providing this essential service to meet the ever growing universal energy consumption coupled with the fast exhaustion of fossil fuel reserves as well as the enormous environmental hazard associated with its consumption has necessitated substantial research consideration on clean energy sources. This study presents an exploration of global Renewable Energy (RE) statistics and its tendencies for electricity generation with particular emphasis on Nigeria. The exploration was based on the data obtained for all the various forms of RE data obtained from several RE data base. It also explores Nigeria RE potential, estimates the amount of electrical energy that can be generated from RE and the current status of their usage. Benefits and factors hampering the generation of electricity from RE sources were enumerated.The study unveils Nigeria RE potential with the annual average solar insolation ranging from 4.2kWh/m^2/day in the south to 5.9kWh/m^2/day in the north, wind energy ranging from 4.4 W/ m^2 to 35.2 W/m^2 (if the intensity is perpendicular to wind direction), and a hydro potential above 11,000MW.

Keywords: Electricity; Power generation; Renewable Energy;

1. Introduction

Energy is a vital constituent for growth and an influential engine of commercial and societal transformation in any nation. It is at the core of every quality life and an imperative factor for financial progress (Akorede *et al,* 2017). Electrical energy has become an essential product for a comfy life in both rural and urban areas. For this reason, its demand has been on the rise continuously universally at the rate of 3% per year. Worldwide, there is an estimation of above 1.5 billion people who lack access to electricity (Shaver, 2017). Nigeria is located in the western region of Africa (Adejumo and Suleiman, 2017) is the Africa's largest economy and home to approximately 10% of the un-electrified population of Sub-Saharan Africa (Maria *et al,* 2020, Komolafe *et al.* 2003, Lloyd 2007), with the majority of whom reside in the rural communities. (Diemuodeke *et al,* 2021). With a population of around 213 million(Nigeria population, 2021), the country barely generates meager 6000MW of electricity which by international standard is not adequate to cater for healthy living asides to support industrial development and infrastructure (Adhekpukoli, 2018: Eboibi *et al,* 2017).The energy mix of Nigeria electricity supply sector is dominated by fossil fuels with natural gas and hydro accounting for around 85% and 15% of grid-connected generation respectively (NPBR, 2015). Paradoxically, the country is endowed with huge fossil fuel reserve which according to Oyedepo *et al,* 2018 in 2017 her reserve are; Light Crude oil: 37.06 billion bbl, Natural gas: 5.284 trillion cubic meter and Coal and Lignite: 2.734 billion tones, though characterized by challenges such as depletion, high cost and greenhouse effect (Rana *et al,* 2017; Zubo *et al*, 2017).

2. Global Renewable Energy Statistics

Positive progress has been accomplished in the last decade which can be attributed to the combined effort of Engineer and scientists. Globally, several subsidies and policies have been established to assist the deployment of non-hydro RE sources and facilities, (Nadeeshani *et al,* 2015). It has yield result, the share of Net annual additions of renewable energy in power generation capacity in 2011 was less than 50% and increase to 84% in 2021(REN, 2022).

As depicted by Table 1, Total Annual Addition of Renewable Power Capacity (TAARPC) increased by 73.2% from 2016 to 2021, In order to achieve net zero scenarios for 2030 and 2050, the Table shows projected Value. Net Zero Scenario (NZS) denotes to the method of accomplishment a Net zero carbon footprint of methane, carbon dioxide (CO2), and other Greenhouse Gases (GHG) in the sky by eradicating all man-made GHG emissions from the air through reduction procedures (artificial

and natural sink), carbon-offsetting or by basically not radiating to reach net zero (Saheed and Hammed, 2020).

TABLE 8: Annual Additions of Renewable Power Capacity, by Technology and Total, 2016-2021, and to Achieve Net Zero Scenarios for 2030 and 2050 (GW) (REN, 2022)

	2016	2017	2018	2019	2020	2021	2030	2050
Total annual renewable power capacity additions	155.5	163.1	180.9	183.4	194.4	269.3	730.0	824.9
Hydropower	21.9	18.0	20.2	15.8	19.4	26.7	47.7	35.4
Wind power	54.9	53.5	50.7	60.8	95.3	93.6	236.4	253.1
Solar PV	77.0	103.0	104.0	111.0	145.0	175.0	421.9	459.6
Bio-power, geothermal, ocean power, CSP	9.3	6.4	8.5	6.8	9.6	11.8	24.0	76.9

To achieve NZS by 2030, the TAARPC is projected to increase by 171.1% from 2011 to 2030 and also projected to increase by 13%, from 2030 to 2050 to achieve NZS by 2050. Achieving NZS by 2030 will be difficult considering 73.2% increase in TAARPC over a span of five years (2016-2021) compared to projected increase of 171.1% over a span of 9 years (2021-2030). But if the increments of 74.9GW in TAARPC between 2020 to 2021 (A year) can be sustained annually, then the NZS 2030 can be achieved. It requires diligence and commitment of the entire stakeholder in RE business.

2.1. Solar PV

In terms of installed cumulative solar power, the top five countries as of 2022 are China, USA, Japan, Germany and India with installed capacity of 393,032MW, 113,015MW, 78,833MW, 66,554MW and 63,146MW respectively (IRENA, 2023). The installed solar power capacity in Germany alone (a country located in a temperate region), is more than 10times the highest peak total electricity generated from all sources in Nigeria, being 6000MW (Eboibi *et al,* 2017).

As depicted by Table 1, annual addition of solar PV has the highest increase rate of 127.3 % (from 77.0GW to 175GW) from 2016 to 2021. In order to achieve NZS for 2030 annual solar PV capacity is projected to increase by 246.9GW from year 2021 to 2030(9 years span). This will be tough to achieve unless the annual additions of solar PV Capacity increase from 2020 to 2021 (30GW) can be sustained. Annual increase of 30GW can easily be continued if tropical regions that have higher solar radiation (Bekele and Palm, 2010) can be encouraged to invest into solar PV project. Similarly to achieve NZS by 2050, the annual additions of solar PV Capacity is projected to increase by 8.9% from year 2030 to 2050.

2.2. Wind Power

As shown by Table 1, annual addition of wind power capacity increases from 54.9GW to 93.6GW (70.5% increase) from year 2016 to 2021. In order to achieve NZS by 2030, the annual addition of wind power capacity is projected to increase by 152.6% from 2021 to 2030 (9 years span). The task will be challenging unless the annual additions of wind power capacity increase from 2019 to 2020 (34.5GW) can be sustained. The annual additions of wind power Capacity is also projected to increase by 7.1% from year 2030 to 2050. In terms of installed cumulative solar power, the top five countries as of 2022 are China, USA, Germany India and Spain with installed capacity of 365,964MW, 140,862MW, 66,315MW, 41,930MW and 29,308MW respectively(IRENA, 2023).

2.3. Hydro power

Amongst the most clean sources of RE is Hydro power (Ravi and Tanweer, 2016). As shown in Table 1, annual addition of hydropower Capacity increases by 21.9% from 2016 to 2021, In order to achieve NZS by 2030, annual addition of hydro power capacity is anticipated to increase by 78.7%. Like other RE sources, it will be challenging to achieve, it is also projected to decrease by 25.8% within 2030 to 2050 to achieve NZS by year 2050. China, Brazil, Canada, US and Russia are the top five largest hydroelectric producers respectively It a major source of power generation in Brazil and Canada which constitute 64.7 and 59.0 percent respectively of their domestic electricity generation **(***IEA, 2020***)**..

2.4 Other Renewables

Generating electricity and thermal energy from biomass has the potential to help meet national goals for renewable energy (US department of Energy, 2010). As depicted by Table 1, annual addition

of other RE sources Capacity increases by 24.7 % from 2016 to 2021. It estimated that in order to achieve NZS by 2030 it should increase by 103.3% which will also be challenging unless the annual rise between 2020 and 2021 can be maintained over the nine years (2021-2030). An increase of 220.4% between year 2030 to 2050 is also required to achieve NZS by 2050. Geothermal can be categorize as RE source because the water is restocked by rainfall, thus the heat can be constantly created inside the earth (Ľudovít *et al,* 2010). In geothermal, US, Indonesia, Philippines, Turkey and New zealand are takes the leads with capacity of 2.57GW, 2.13GW, 1.93GW, 1.61GW and 0.98GW respectively. A country in Africa, Kenya was ranked 7 with geothermal electricity capacity of 0.82GW (The US information Administration, 2020).

In summary (Table 2), it can be deducted that some countries are in the forefront to achieve NZS. China are leading in 4 RE sources such as Solar PV, wind power, Bio-power and Hydropower. US are among the top five countries in virtually all the RE sources. Germany, Brazil and India can also be seen as among the countries taking advatages of the benefits of RE sources.

TABLE 2: Top Five Countries in RE Sources

S/N	Solar PV (IRENA, 2023).	Wind Power (IRENA, 2023).	Hydro power (*IEA, 2020*)	Geothermal (the US information Administration, 2020)	Bio –power (REN, 2021)
1.	China	China	China	USA	China
2.	USA	USA	Brazil	Indonesia	Brazil
3.	Japan	Germany	Canada	Philippines	United State
4.	Germany	India	USA	Turkey	Germany
5.	India	Spain	Russia	New zealand	India

3. Nigeria's RE Statistics for Electricity Generation.

Several aboriginal researchers have deliberated the possibility of Renewable Energy (RE) resources in Nigeria with a view of establishing their feasibility in the country. The country has installed capacity of 10,396MW, out of which 6,056MW is available. 82.5 % (4,996MW) of the available 6,056MW is from gas generating plants while the remaining 1,060MW is hydro (Stephen *et al,* 2022). A study conducted at the end of 2015 indicates that the segment of renewables in electric power generation (including off-grid) is around 23.7 % with 16.6% from hydropower, 3.7% from wind power while other renewables amount to 3.4% (Akorede *et al,* 2017). This necessitate the needs to access the RE potential of the country.

3.1 **Solar energy potential**

The information of the obtainable solar insolation at a place is crucial in choosing and planning proper solar energy systems and estimating the solar energy for that location (Okonkwo.and Nwokoye, 2014: Ilenikhena and Ezemonye, 2010). Nigeria by virtue of her location on the equator is around a high sunshine belt where solar insolation is equitably well distributed (Olayinka *et al,* 2014). A study conducted by Anaza *et al,* 2023 in as shown in Table 3.

Table 3: Solar Insolation of selected town in Nigeria (Anaza et al, 2023)

	Gombe (NE)	*Katsina(NW)*	*Abuja (NC)*	*Osogbo(SW)*	*Owerri(SE)*	*Port Harcourt (SS)*
January	5.6	*5.5*	*5.4*	*5.0*	*5.1*	*4.9*
February	6.0	*5.8*	*5.7*	*5.2*	*5.2*	*4.9*
March	6.4	*6.4*	*6.1*	*5.3*	*5.0*	*4.6*
April	6.3	*6.7*	*6.0*	*5.2*	*5.0*	*4.6*
May	6.1	*6.4*	*5.6*	*5.1*	*4.8*	*4.3*
June	5.8	*6.0*	*5.1*	*4.5*	*4.3*	*3.6*
July	5.3	*5.8*	*4.6*	*3.9*	*3.9*	*3.4*
August	5.0	*5.4*	*4.2*	*3.7*	*3.9*	*3.7*
September	5.5	*5.9*	*4.8*	*4.1*	*4.1*	*3.6*
October	5.9	*5.8*	*5.4*	*4.6*	*4.4*	*4.0*
November	5.8	*5.5*	*5.8*	*5.1*	*4.8*	*4.4*
December	5.5	*5.3*	*5.3*	*4.9*	*4.9*	*4.8*
Annual Avarage	5.8	*5.9*	*5.3*	*4.7*	*4.6*	*4.2*

From the Table 3, the annual average solar insolation ranges from 4.2kWh/m^2/day to 5.9kWh/m^2/day. Using an average solar irradiation 5.3kWh/m^2/day for Nigeria, the average annual irradiation will be around 1934.5 kWh/m^2. According to Bekele and Palm, 2010, the solar irradiation in tropical regions is greater than that of more temperate latitudes. Europe has an average annual irradiation of 1000 kWh/m^2, while that Middle East is around 1800 kWh/m^2 which are lower than Nigeria (Sunday *et al*, 2019). Unexpectedly according to IRENA 2023, Asia and Europe are in the fore front of annual additions of solar PV Capacity. According to Ani, 2014, Ebigenibo and Oluwasanmi, 2020, the hourly energy output of the PV generator E_{pv} can be calculated according to the equation 1.

E_{pv} = G (t) * A * P * η_{pv} ----------(1)

Where G (t) is the hourly irradiance in kWh/m^2, A is the surface area in m^2, P is the PV penetration level factor, and η_{pv} is the efficiency of PV generator.

Nigeria has a 923,768km^2 land area (Olayinka *et al,* 2014.), using an estimate of 1934.5 kWh/m^2 per year, an average of 178 7thosandTWh/year of solar energy is estimated to fall on the entire land area. Applying Equation (1), Using 15% conversion efficiency (solar panel conversion efficiency) and assuming 0.1% of its land is used, approximately 268.1TWh/year of electricity can be generated from solar PV, which is higher than her electricity demand estimate of 144.5 TWh/yr (Ezenanaya *et al,* 2014). Nigeria has an estimated population of 213.4 million (Nigeria population, 2021) as at December 2021. The W per capita is by this analogy from solar PV will be 1,256 which is higher than that of Germany (IRENA, 2023).

The Nation has no thorough project database of RE, no off-grid hybrid or grid connected solar projects, all existing projects are either stand-alone mini-grid or off-grid stand-alone lighting application of few kWp (Olayinka *et al,* 2014),

3.2 Wind energy potential.

The enthusiasm to address the country's energy and the zeal to maximize the numerous renewable energy benefits encouraged research into Nigeria's wind energy potential among which are Ajayi *et al,* 2011, Eboibi *et al,* 2017, Ajibola and Balogun 2019, Amadi 2018, Dioha *et al* 2016, Jasper and Bernard 2017, Joshua *et al,* 2015, Lawa and Isa 2013, Ogbeide *et al,* 2018, Yahaya *et al,* 2020. From their study it can be concluded that the average wind speed in Nigeria at 10m height lies between 1.9 m/s and 8 m/s depending on the location. From the wind map (Ikechukwu , 2016), it is clear that there are location such as Kastina, zamfara etc with very good wind potential having speed above 6m/s which is suitable for electricity generation. The wind potential in state like Kogi, Ekiti, Edo etc are only appropriate for water pumping.

The power generated p (t) by a wind turbine can be represented by

$$P(t) = \begin{cases} 0 & v(t) \leq V_{ci} \text{ or } v(t) \geq V_{co} \\ \frac{C\rho A(v(t))^3}{2} & V_{ci} < v(t) < V_r \\ p_r & V_r < v(t) < V_{co} \end{cases}$$.----------(2) (Agbetuyi *et al*, 2012; Eboibi *et al*, 2016).

Where: C is coefficient of power ρ is air density (1.1 kg/m^3) A is Area of wind turbine rotor. v(t) is wind speed at any time, V_{ci} is cut in wind speed, V_r is rated wind speed, V_{co} is cut out wind speed

Estimating from the above wind speed, the wind energy intensity perpendicular to the wind direction ranges between 4.4W/m^2 along the coastal areas to as high as 35.2W/m^2 to the extreme north (akinbulire *et al,* 2014). Currently, apart from the few stand-alone wind power plants which were installed in the 1960s in five northern states purposely for water pumping, there was no commercial wind power plants linked to the national grid. Additionally, a 5 kW wind turbine plant for electrification of a village was installed at Sayyan Gidan Gada, in Sokoto State (Uzoma *et al*, 2011: Sunday *et al,* 2019: Bamisile *et al,* 2017).

3.3 Hydro Energy Potential

Despite the Huge RE potential, at the moment hydropower is the only RE source used for saleable electricity generation in Nigeria (Olusola *et al,* 2020). The massive hydro potential source is demonstrated by her large rivers, small rivers and stream and the different river basin that were established. The country has substantial hydro potential sources spread in 13 States and in the river basin (Adebayo and peter 2014) with potential above 11,000MW (Akorede *et al,* 2017). The rivers were nearly evenly distributed all over the country with potential locations for hydropower scheme that can feed the rural, urban and isolated communities (Sunday *et al,* 2019).

The generation of electrical energy from Hydro power simply energy conversion. The turbine changes water energy into rotational energy at its shaft which the generator converted that rotational energy into electrical energy. The energy generated per year (KWH) can be calculated as:

$E = \rho * Q * H_n * g * \eta * n$ ---------- (3) (Bilal, 2013; Khizir *et al,* 2012)

Where: Q is flow rate (m^3/s), ρ is water density (1000 kg/m3), *n* is number of hours in year for which the specified flow occurs, H_n is net head (m), g is gravitational constant (9.8 m/s2), and η represent is efficiency which denote th e extent of energy conversion. Hydropower is the on RE sources is currently been used for commercial purpose, it 15% of grid-connected electricity generation (NPBR, 2015). A study estimated the small hydropower potential of country to be 3,500 MW (Oseni, 2012)

3.4 Other renewables

Thirty geothermal potential spots were discovered in the country. It is also estimated that about 2.10 x 10^9 GJ of biomass energy can be generated from waste and other sources yearly (Aliyu *et al*, 2015; Wole-Osho *et al,* 2014; Olusola *et al,* 2020). Though, there have not been commercial productions of electricity from Biomass and Geothermal.

4. Advantages and Challenges of RE

RE sources cause less environmental effect than other energy sources. The execution of RE technologies will assist to tackle the environmental concerns that developed due to greenhouse gas emissions such as oxides of nitrogen (NOx), carbon dioxide (CO_2), oxides of sulfur (SOx), and particulate matters that arise as a result to of power generation from natural gas, oil and coal. RE sources are clean energy system that has no consequence on the environment during or after generation. Variety of RE resources provides flexible sets of possibilities for their usage (Sunday 2012; Oisamoje and Oisamoje, 2013; Slootweg *et al,* 2001).

From literature surveyed, several factors have been attributed to the low pace of RE as it's relates to electricity generation, They includes: lack of consciousness and technical unskillfulness, high initial investment cost, inconsistency Regulatory framework and enticements, grid unpredictability and intermittency nature of RE sources. The latter can cause undesired effects in the structure, such as increased fault current, fluctuations in the voltage profile, readjustment of the control and protection systems, inversion in the flow direction, (Benvindo *et al* 2015, Kaabeche *et al*, 2011).

5. conclusion

Attentions have been focused on RE sources for electricity generation and other usage due to its enormous benefits and the challenges and hazards attributed to the use of fossil fuel. In this paper, global RE statistics were explored and its propensities for electric power generation highlighting Nigeria RE potentials. Data were obtained from several RE database and were analyzed, references were made to the leading countries to ascertain their growth and project the possible development in the near future. Nigeria RE potential was evaluated and estimates of electrical energy that can be generated from various RE were presented in conjunction to their current status for electricity generation. The study unveils that the country can resolve its electrical energy woes if it's RE sources are properly harnessed.

References

Adebayo C. and Peter M. (2014): "How is 100% renewable energy possible for Nigeria?", Global Energy Network Institute (GENI), www.geni.org peter@geni.org (619) 595-0139

Adejumo A.O. and Suleiman E.A. (2017): "Application of ARMA-GARCH Models on Solar Radiation for South Southern Region of Nigeria", Proceedings of International Conference on Science and Sustainable Development (ICSSD) Center for Research, Innovation and Discovery, Covenant University, Nigeria June 20-22, 2017, Journal of Informatics and Mathematical Sciences Vol. 9, No. 2, pp. 405–416, 2017

Adhekpukoli E. (2018): "The democratization of electricity in Nigeria," Electr. J., 2018. https://doi.org/10.1016/j.tej.2018.02.007

Agbetuyi, A. F., Akinbulire, T. O., Abdulkareem, A. and Awosope, C. O. A. (2012): "Wind Energy Potential in Nigeria", International Electrical Engineering Journal (IEEJ) Vol. 3 (2012) No. 1, pp. 595-601.

Ajayi, O. O., Fagbenle, R. O. and Katende, J. (2011): "Wind Profile characteristics and Econometrics Analysis of Wind Power Generation of a Site in Sokoto State, Nigeria", Energy Science and Technology, 1(2), 54-66.

Ajibola O. O. E., and Balogun O. J., (2019): "Stochastic Analysis of Energy Potentials of Wind in Lagos Metropolis", Proceedings of the World Congress on Engineering and Computer Science 2019 WCECS 2019, October 22-24, 2019, San Francisco, USA

Akinbulire, T.O, Oluseyi, P.O and Babatunde, O.M (2014): 'Techno-economic and environmental evaluation of demand side management techniques for rural electrification in Ibadan, Nigeria', Int. J Energy Environ Eng. 5(132): 1 – 11.

Akorede M. F., Ibrahim O., Amuda S. A., Otuoze A. O., and Olufeagba B. J. (2017). "Current Status and Outlook of Renewable Energy Development in Nigeria", Nigerian Journal of Technology (NIJOTECH) Vol. 36, No. 1,, pp. 196 – 212, www.nijotech.com, http://dx.doi.org/10.4314/njt.v36i1.25.

Ali, S., Zheng, Z., Aillerie, M., Sawicki, J. P., Péra, M. C. and Hissel, D. (2021): "A Review of DC Microgrid Energy Management Systems Dedicated to Residential Applications". Energies **2021**, 14, 4308. https://doi.org/10.3390/en14144308

Aliyu, A.K.; Modu, B. and Tan, C.W. (2018): "A review of renewable energy development in Africa: Afocus in South Africa, Egypt and Nigeria". Renew. Sustain. Energy Rev. **2018**, 81, 2502–2518.

Aliyu A. S., Dada J. O., and Adam I. K., (2015): "Current status and future prospects of renewable energy in Nigeria," Renew. Sustain. Energy Rev., vol. 48, pp.336–346, 2015.

Amadi H. N. (2018). "Wind Energy Potential Assessment of Coastal States in South-South Nigeria Based on the Weibull Distribution Model", EJECE, European Journal of Electrical and Computer Engineering Vol. 2, No. 7,. DOI: http://dx.doi.org/10.24018/ejece.2018.2.7.48

Anaza S. O. , Haruna Y. S., Amoo A. L., Sadiq A. A. and Yisah Y. A. (2023): "Potential of Renewable Energy Sources for Distributed Generations: An Overview", International Journal of Scientific Advances, Volume 4, Issue 1 Jan-Feb 2023 www.ijscia.com

Ani, V. A. (2014), "Feasibility and Optimal Design of a Stand-Alone Photovoltaic Energy System for the Orphanage", Research Article, Hindawi Publishing Corporation, Journal of Renewable Energy, Volume 2014, Article ID 379729, 8 pages http://dx.doi.org/10.1155/2014/379729

Atwa Y. M, El-Saadany E. F., Salama M. M. A., and Seethapathy R.,(2010): "Optimal Renewable Resources Mix for Distribution System Energy Loss Minimization", IEEE Transactions on Power Systems, VOL. 25, NO. 1, February 2010

Bamisile O., Dagbasi M., Babatunde A. and Ayodele O. (2017): "A review of renewable energy potential in Nigeria; solar power development over the years", Engineering and Applied Science Research, 44 (4): 242-248 https://www.tci-thaijo.org/index.php/easr/index, doi:10.14456/easr.2017.37

Bekele, G and Palm, B (2010): 'Feasibility study for a standalone solar–wind-based hybrid energy system for application in Ethiopia', Applied Energy 87: 487–495

Benvindo R. Pereira Jr., Geraldo R. Martins da Costa, Javier Contreras, and José R. Sanches Mantovani, (2015): "Optimal Distributed Generation and Reactive Power Allocation in Electrical Distribution Systems", accepted for inclusion in a future issue of IEEE Transactions on Sustainable Energy 2015

Bilal A. N. (2013): "Design of Micro - Hydro - Electric Power Station" International Journal of Engineering and Advanced Technology (IJEAT) Volume-2, Issue-5, pp 39-47

Diemuodeke, O.E., Mulugetta, Y., Njoku, H.I., Briggs, T.A. and Ojapah, M.M. (2021): "Solar PV Electrification in Nigeria: Current Status and Affordability Analysis",. Journal of Power and Energy Engineering, 9, 1-25. https://doi.org/10.4236/jpee.2021.95001 [24

Dioha M.O., Dioha I. J. And Olugboji O. A. (2016): "An Assessment of Nigeria Wind Energy Potential Based on Technical and Financial Analyses", Journal of Sustainable Energy VOL. 7, NO. 2, June, 2016

Ebigenibo G. S. and Oluwasanmi A. A. (2020): "The Economic Implications of Wind Energy and Solar Photovoltaic System Utilization for Electricity Generation in Nigeria". Saudi J Eng Technol, Dec, 2020; 5(12): 524-535

Eboibi B., Eboibi O., Okubio E. and Iyasele, C (2017): "Evaluation of wind energy potential in the south-south geopolitical zone of Nigeria", J. Appl. Sci. Environ. Manage. *Dec,* 2017, Vol. 21 (7) 1301-1306

Ezennaya O. S., Isaac O. E., Okolie U. O. and Ezeanyim O. I. C. (2014): "Analysis Of Nigeria's National Electricity Demand Forecast (2013-2030)," Int. J. Sci. Technol. Res., vol. 3, no. 3, pp. 333–340, 2014.

Gungah, A.; Emodi, N.V.; Dioha, M.O. (2019) "Improving Nigeria's renewable energy policy design: A case study approach". Energy Policy **2019**, 130, 89–100.

IEA 2020 "Key world energy statistics 2020 report". International Energy Agency. Retrieved 8th April 2023

Ilenikhena P.A. and Ezemonye L.I.N. (2010): "Solar Energy Applications In Nigeria", WEC Montreal 2010: Paper NO. 135 Revised [6 solar e]

IRENA 2023 "Renewable Capacity Statistics 2022" http://www.irena.org/Statistics/Download-Data retrieved 8th April 2023

Jasper A. and Bernard A. (2017): "Evaluation of Wind Energy Potentials in the Nigerian Onshore and Offshore Locations", FUPRE Journal of Scientific and Industrial Research, Vol.1, (2), 2017

Joshua O. O., Olayinka S. O. and Elizabeth T. O. (2015): "Assessments of Wind-Energy Potential in Selected Sites from Three Geopolitical Zones in Nigeria: Implications for Renewable/Sustainable Rural Electrification", Hindawi Publishing Corporation, Scientific World Journal, Volume 2015, Article ID 581679, 13 pages , http://dx.doi.org/10.1155/2015/581679

Kaabeche A., Belhamel M. and. Ibtiouen R (2011): "Sizing optimization of grid-independent hybrid photovoltaic/wind power generation system". Energy 36 (2011) 1214-1222, www.elsevier.com/locate/energy

Khizir M., Abu T. T. and Ashraful I. (2012) "Feasible Micro Hydro Potentiality Exploration in Hill Tracts of Bangladesh‖" Global Journal of Researches in Engineering Electrical and Electronics Engineering Volume 12 Issue 9 Version 1.0 pp 15-20

Komolafe, O.A., Omoigui, M.O. & Momoh, A. (2003): "Reliability investigation of the Nigerian Electric Power Authority transmission network in a deregulated environment". Conference Proceeding: 38th Industry Applications Conference, Retrieved from http://www.researchgate.net/institution/Obafemi_Awolowo_University/department/Department_of_Electronic 25th February, 2023

Lawa S. and Isa G. (2013), "Electricity Generation Using Wind in Katsina State, Nigeria", International Journal of Engineering Research & Technology (IJERT) Vol. 2 Issue 2, February – 2013

Lloyd, P. & Visagie, E. (2007). "The testing of gel fuels, and their comparison to alternative cooking fuels". In Domestic use of energy conference published 2007.

Ľudovít C., Vladimír K., Stanislav K., Matúš K. and Martin M. (2010): "A paper at Intensive Programme "Renewable Energy Sources"" University of West Bohemia, faculty of electrical engineering, department of electrical power and environmental engineering. https://api.core.ac.uk/oai/oai:dspace5.zcu.cz:11025/22539. retrieved April 16, 2023

Maurizio D., Davide F.,Marco M., and Gabriele M. (2014): "Distributed Generation Integration in the Electric Grid: Energy Storage System for Frequency Control". Hindawi Publishing Corporation, Journal of Applied Mathematics, Volume 2014, Article ID 198427, http://dx.doi.org/10.1155/2014/198427

Nadeeshani J., Mohammad A. S. M., and Peter J. W., (2015): "Optimal Operation of Distributed Energy Storage Systems to Improve Distribution Network Load and Generation Hosting Capability", accepted for inclusion in a future issue IEEE Transactions on Sustainable Energy 1 DOI10.1109/TSTE.2015.2487360

Nigeria population 2021, https://tradingeconomics.com/nigeria/population retrieved 16th April, 2023

NPBR 2015, "Nigeria Power Baseline Report",. Available from: http://www.nesistats.org/uploads/3/6/3/6/3636925/20150916_nigeria_energy_power_report_final.pdf (accessed February 02, 2023).

Ogbeide O. O., Akpala B., Igbinomwanhia N. O. and Azi S. O. (2018): "Statistical Quality Control Analysis of Wind Energy Potential for Power Generation in Benin", Journal of Energy Research and Reviews 1(2): 1-14, 2018; Article no.JENRR.42701

Oisamoje M. D. and Oisamoje E. E. (2013): "Exploring the Economic and Environmental Benefits of Solar Energy Generation in Developing Countries: The Nigerian Perspective". Journal of Energy Technologies and Policy, Vol.3, No.6, ISSN 2224-3232 (Paper) ISSN 2225-0573 (Online), www.iiste.org

Okonkwo G..N.and Nwokoye, A.O.C. (2014). "Analysis of Solar Energy Parameters in Bida, Nigeria". European Scientific Journal May 2014 edition vol.10, No.15, 116-131 ISSN:1857 – 7881 (Print) e - ISSN 1857- 7431

Olayinka S.O., Muyiwa S.A, Olanrewaju. M. O, Richard O. F (2014): "Solar energy applications and development in Nigeria: Drivers and barriers". Renewable and Sustainable Energy Reviews 32 (2014) 294–301

Olusola B., Qi H., Patrick A., Paul O.K. A., Serkan A. and Weihao H., (2020). "Analysis of Solar PV and Wind Power Penetration into Nigeria Electricity System", Conference Paper August 2020, DOI: 10.1109/ICPS48389.2020.9176822

Oseni, M. O. (2012): "Households Access to Electricity and Energy Consumption Pattern in Nigeria," Renewable and Sustainable Energy Reviews, vol. 16, pp. 990-995, 2012.

Oyedepo S. O. (2012): "Energy and sustainable development in Nigeria: the way forward". Energy, Sustainability and Society 2012, 2:15 http://www.energsustainsoc.com/content/2/1/15

Oyedepo, S. O., Babalola, O. P., Nwanya, S. C., Kilanko, O., Leramo, R. O., Aworinde, A. K., Adekeye, T., Oyebanji. J. A., Abidakun, A. O. and Agberegha, O. L. (2018): "Towards a Sustainable Electricity Supply in Nigeria: The Role of Decentralized Renewable Energy System". European Journal of Sustainable Development Research, 2(2), xx. https://doi.org/10.20897/ejosdr/xxxxx

Rana. H. A. Z., Geev M., Haile-Selassie R., Jamshid A., Taher N. and Prashant P.(2017) "Operation and Planning of Distribution Networks with Integration of Renewable Distributed Generators Considering Uncertainties: A Review", Renewable and Sustainable Energy Review, Volume 72, May 2017, Pages 1177-1198

Ravi S. M. and Tanweer D. (2016): "Spatial Technology for Mapping Suitable Sites for Run-of-River Hydro Power Plants" International Journal of Emerging Trends in Engineering and Development Issue 6, Vol. 4 http://www.rspublication.com/ijeted/ijeted_index.htm

REN21 (2021): "Renewables 2022 Global Status Report" [Online]. http://www.ren21.net/status-of-renewables/global-status-report/. (accessed on 16th April, 2023).

REN21 (2022): "Renewables 2022 Global Status Report" [Online]. http://www.ren21.net/status-of-renewables/global-status-report/. (accessed on 25th February, 2023).

Saheed M and Hammed A. S. (2020): "zero Emission" Encyclopedia of Sustainable Management, Springer Nature Switzerland AG 2020. https://doi.org/10.1007/978-3-030-02006-4_512-1

Shaver L. (2017): "Implementation of a DC Microgrid". Master's Degree, University of Wisconsin-Madison, USA, 2017.

Slootweg J.G., dc Haan S.W.H, Polinder H., and Kling W.L (2001): "Modeling Wind turbines in power system dynamics simulation" Power Engineering Society Summer meeting conference Vol.1 Proceedings (2001) Pp.22-26.

Stephen E. E., Oluwaseun K., Eeda A. N. and Amuda-Y. G. (2022): "Renewable Energy and Green Technology Adoption: A Viable Option for Efficient Energy Supply in Nigeria". Environ Anal Eco stud. 000728. 10(1). 2022. DOI: 10.31031/EAES.2022.10.000728

Sunday, O. O., Theophilus, U., Philip, O. B., Stephen C. N, Oluwaseun K., Richard, O. L., Abraham, K. A., Tunde, A., Joseph, A. O. and Olatunde, A. A. (2019): "Assessment of Decentralized Electricity Production from Hybrid Renewable Energy Sources for Sustainable Energy Development in Nigeria", S.O. De Gruyter, Open Eng. 2019; 9:72–89.

The U.S. Energy Information Administration 2020 "Geothermal electricity capacity - Country rankings" the global economy https://www.theglobaleconomy.com/rankings/geothermal_electricity_capacity/ retrived 10th April, 2023

UNEP, "Renewable Energy: Renewables on the rise.," United Nations, 2018. [Online]. Available: https://www.unenvironment.org/explore-topics/energy/what-we-do/renewable-energy. [Accessed: 23-02-2023].

US department of Energy (2010): "energy efficiency and renewable energy" www.eere.energy.gov/informationcenter retrieved April 16, 2023

Uzoma, C.C., C.E. Nnaji, C.N. Ibeto, C.G. Okpara, O.O. Nwoke, I.O. Obi and O.U. Oparaku, (2011): "Renewable energy penetration in Nigeria: A study of the South-East zone". Continental Journal of Environmental Sciences, 5(1): 1–5.

Wole-Osho I., Bamisile O., Adun H., and Yusuf I (2014): "Comparison of renewable energy potential in relation to renewable energy policy in ECOWAS countries," in 13th HONET-ICT International Symposium on Smart MicroGrids for Sustainable Energy Sources.

Yahaya, A. A., Bello, I. M., Mudassir, N., Mohammed, I. and Mukhtar, M. I. (2020): "Evaluation of Wind Potential for the Generation of Electricity in Aliero, Kebbi State", Asian Journal of Research and Reviews in Physics 3(1): 1-7, 2020; Article no. AJR2P.53791.

Zubo RHA, Mokryani G, Rajamani HS, Aghaei J, Niknam T, Pillai P. (2017): "Operation and planning of distribution networks with integration of renewable distributed generators considering uncertainties: a review. Renew" Sustain Energy Rev 2017; 72: 1177–98. http://dx.doi.org/10.1016/j.rser.2016.10.036.

PAPER 73 – COMMUNITY PARTICIPATION AND SUSTAINABLE OF WATER AND SANITATION SERVICES IN MUSANZE DISTRICT, NORTHERN PROVINCE OF RWANDA.

B. F. Sule[1*] and I. M. Bénigne[2]

[1*]Department of Civil & Environmental engineering, University of Ilorin, Ilorin, Nigeria. Email: bfsuleiman@gmail.com

[2]Pan African University Institute for Water and Energy Sciences (including Climate Change) – PAUWES, Abou Bekr Belkaid University of Tlemcen, Algeria. Email : mugwaneza.ben@gmail.com

ABSTRACT

Water-related diseases are closely linked to poverty and disproportionately affect vulnerable communities mainly in developing countries including Rwanda. Most development projects highlight community participation as one of the prerequisites for the improved performance of water and sanitation services. Three rural villages in Musanze District (Gataraga, Gitega, Rwinuma) in Rwanda were taken as a case study. Data were collected using questionnaires and analyzed using Statistical Package for the Social Sciences (SPSS). A total of 192 participants responded to the questionnaires of whom 189 were water and sanitation services beneficiaries. In addition, water and sanitation district and sectors officials were also interviewed. Our findings showed that sustainability issues were inadequately addressed at the planning and design stages, communities had no capacity to maintain the water and sanitation services and no sense of ownership. The study recommends the adoption and incorporation of the user centered design methodology at the initial stages of water and sanitation development programmes in order to produce interventions that fully solve community problems and to prioritize capacity building for operators and technical support at all levels for all other groups engaged in planning, implementation and maintenance of water and sanitation services.

Key words: Sustainability, Community Participation, User Centered Designs, user association, operation and maintenance

1 INTRODUCTION

In 2015, over 2.3 billion people all over the world still lacked basic sanitation service, 844 million people still lacked basic drinking water while only two out of five people using safely managed sanitation services (1.2 billion) lived in rural areas (UNICEF, 2017). This explains the need for SDG's 6 on ensuring availability and sustainable management of water and sanitation for all. Goal 6 includes the target of achieving universal and equitable access to safe and affordable drinking water for all and achieving access to adequate and equitable sanitation and hygiene for all and end open defecation, paying special attention to the needs of women and girls and those in vulnerable situations by 2030 (UN News Centre, 2015). In line with that, the Africa water vision aspires sustainable access to safe and adequate water supply and sanitation to meet the basic needs of all by 2025 (African Union, African Development Bank, & Economic Commission for Africa, 2009). In Africa, a considerable percentage of the population still lacks the basic need of safe drinking water. 89% of people have at least one basic water service globally, which mean an improved drinking-water source within a 30-minute round trip. In Africa, only six countries are above that threshold: Algeria, Tunisia, Seychelles, Libya, Egypt and Mauritius**.** Many countries are still far below the line; only 19.3 % of the population of Eritrea has access to a basic water service, followed by Uganda and Ethiopia, both with 39%. Nearly 40% of African countries currently provide basic drinking services to less two thirds of their people. Regarding sanitation, Africa has the lowest levels of basic sanitation services amongst world regions, although North African countries, Equatorial Guinea, and South Africa have coverage levels comparable to other regions. The proportion of the population with access to at least basic sanitation services in Africa increased from 25% in 2000 to 28% in 2015 (AU, ECA, AfDB, 2018) **.**

According to World Health Organization, around 3.4 million people die annually from water-related diseases (UNICEF, 2017). Waterborne diseases are a global issue which is affecting countries at different magnitude. The Rwanda Biomedical Center in 2016 confirmed outbreak of non-bloody diarrhea, typhoid, shigellosis and cholera cases in Rwanda. In 2008, Musanze district was among the least served districts in the country in terms of water, sanitation and hygiene (WASH) services (Murtaza et al., 2017). According to (MININFRA, 2017), Rwanda's main challenge to achieve its 2030 target of 100% access to basic water supply and sanitation is the funding gap

for WASH services in scattered settlements in difficult and hilly terrain. Most development projects donors identify community participation as one of the prerequisite for the improved performance of water and sanitation sector (Mdendemi, 2013).This puts into question the role of community participation in planning, implementing and maintaining water and sanitation services in rural areas of Rwanda to ensure their sustainability.

While assessing the effect of community participation on sustainability of rural water projects in Delta Central agricultural zone of Delta State, Nigeria, (Ofuoku, 2011) found a significant relationship between participation and sustainability of water projects and recommended that the level of participation should be increased, emphasizing on regular conference and institution of sanctions/rewards to encourage citizens to participate in development projects. Haq,et al., (2014) examined the relationship between the level of community participation and sustainability of the rural water supply programs in the rural area of Faisalabd district in Pakistan and their findings clearly demonstrated that community participation at all stages played a positive role in the ownership and sustainability of the rural water supply programs. The results also showed that there is a need of increased community participation in operation and maintenance of water supply projects in order to ensure the quality assurance of the programs. The study further suggested that local people should be involved before launching any development projects in communities.

These two studies have highlighted the importance of community involvement at the different stages of water and sanitation projects. The different stages include planning, design, construction, operation, maintenance and administration.

2. MATERIALS AND METHODS

2.1. Study Area

This research was conducted in Rwanda. Geographically located in Central Africa between 1°04’ and 2°51’ south latitude, and between 28°45’ and 31°15’ East longitude, Rwanda is a land-locked country, bordered by Burundi in the South; Tanzania in the East; Uganda in the North, and the Democratic Republic of Congo in the West. The borders of Rwanda stretched up to 900 kilometers. The country’s administrative division comprises of five provinces: Northern Province, Western Province, Southern Province, Eastern Province and the City of Kigali (MIDIMAR, 2015). Musanze district as the study focus is one of the 30 districts.. The district has an area of 530 km^2 and accounts for about 16% of the Northern Province of Rwanda (NISR, 2013). Based on the 2012 Census, the population of Rwanda was 10,515,973 comprising of which 52% female and 48% male. Since the 2002 Census, the population has increased by 2.4 million, which has represented an average annual growth rate of 2.6%.The population of Rwanda is still largely rural, with 83% living in rural areas (MIDIMAR, 2015).

2.2 Research Design

Primary data were obtained from the respondents directly in the study area of the three selected villages whose people are using public water and sanitation project of the village centre. Tools used in this group of respondents were filling questionnaires, interview and personal observation. Also other primary data sources were obtained from District water and sanitation officer and sectors’ land managers in charge of monitoring water and sanitation projects. Secondary data were obtained from different sources both published and unpublished documents and relevant literatures such as reports, journals, pamphlets, newspapers, publications and internet sources. These documents were obtained from libraries, different governmental and non- governmental institutions and offices.

The population of this study considered the respondents from the three selected villages in the rural area of Musanze (Gataraga, Gitega and Rwinuma). The respondents are residents of those villages, using public and water sanitation facilities that were visited. The exact location of conducting interviews were purposely chosen, near public water and/or sanitation facilities in order to give a sense to questions that were asked. Also, purposive sampling method was used for water and sanitation department official(s) and includes land managers in charge of monitoring the villages’ water and sanitation projects. Random sampling method was used to pick respondents at the village level.

2.3 Data Processing and Analysis

The collected data were edited, coded and processed by using Statistical Packages for Social Sciences (SPSS) Version 21.0. Under this, codes were developed and templates created (variables were designed and given labels). Editing and coding of the questionnaires was done and data were entered following the developed codes. Data analysis was done using Statistical Package for Social Science (SPSS) Version 21.0 and results are presented using percentages, tables, graphs and charts.

3. RESULTS INTERPRETATION AND DISCUSSION

3.1 Socio-Economic and Demographic Characteristics of Respondents

Respondents were both men (56.6%) and women (43.4%). Men and women were considered due to the fact that they are both involved in the different socio-economic activities that need water and sanitation facilities and are required to support water and sanitation schemes for their sustainability. In particular, women are the most affected by water and sanitation related problems in their areas. The majority (36.5%) of the respondents presented had secondary school level education (i.e. twelve years of basic education), (33.9%) had attained primary school education, 26.5% had not been to school while only 3.2% had attended a university. Thus, most of the respondents have basic knowledge of writing and reading, therefore can be selected for training on water and sanitation projects management. The major economic activity carried out in the study area is on farming (29.1%). Other economic activities include small scale businesses (10.6%), students (24.3%), Office workers (1.1%) while (34.9%) are unemployed or fully engaged in daily household activities. It should be highlighted that the collection of data was conducted in areas surrounding the water and sanitation facilities, which might explain the percentages of respondents' occupations.

3.2. Addressing sustainability during project planning

Districts and sectors water and sanitation officials revealed that community mobilization at initial planning is done to ensure that the people understand and accept the project while committing to safeguard it. Also, according to the policy of Government of Rwanda, (2016), the districts play an important role as asset managers and contract managers of water projects. They handle projects extensions, major repairs and rehabilitations, and manage project funds. Districts act as the contracting party for management contracts with private operators and ensure day-to-day supervision of contract compliance. Each district has a District Water Board in charge of those tasks and act as the same time as the contact point for water user committees, as the consumers' voice, as well as for reports and complaints received at village to sector level. The survey however, found that the totality of the respondents in the three villages claimed not to have participated in the initial stages of water supply and sanitation projects planning including design. Though, 98% responded positively that community participation in planning, implementation and management of water project can lead to the effective and sustainable of water and sanitation services.

3.3 Water Users Association

Concerning any water or sanitation user committee in the villages, only 38% of the respondents claimed they were of such committee while 62% of them did not know about user committees. Furthermore, among those who admitted to know of user committees, only 11% believed the committees work effectively, 21% did not think that the committees are working well while 58% did not have any idea of how the user committees work.

3.4 Water Quantity and Sanitation

On the quantity water available 96.5% said that the quantity of water at the public water pipes have reduced with time and that there were several times when water is completely off. On the public sanitation facilities 86% of the respondents said that the facilities are no longer as effective as they were, due to poor maintenance. The findings show that only 21.8% of the respondents said that they get enough water for their households from the water projects in the three villages, while for 78.2% of the respondents do not get enough water for their households. Among the reasons they gave included temporal water shortages, delays in maintenance in case of system failure, alternatives of free water sources, etc. Regarding sanitation facilities, 34, 7% of respondents said they were satisfied with the public sanitation facilities while 65.3% were not satisfied; the main reason was that the public toilets are no longer well maintained, therefore they are usually not clean.

3.5 Operations and Maintenance Cost

According to the National Sanitation Policy of Rwanda (MININFRA, 2016), in order to ensure cost recovery and financial sustainability; operation and maintenance costs of sanitation infrastructure shall be borne by the users. In addition, affordability shall be addressed by the choice of appropriate technologies and by enhancing efficiency, not only by granting subsidies. However, the polluter-pays and user-pays principles are to be applied in sewerage and waste management. Among the respondents, 19% revealed to have at least contributed to the maintenance of the projects, through labor work volunteerism or through collective community labor works "umuganda" which take place once every month. Moreover, in order to ensure cost recovery and financial sustainability, operation and maintenance costs of the water and sanitation infrastructure that were visited, the respondents affirmed that they pay a fee in order to use the services. For the public water station; a fee of 25 Rwandan Francs (approximately

USD 0.027) per 20 liters of water is paid, while for the public toilets a fee 50 Rwandan Francs (approximately USD 0.055) is paid to use the facility. The fee is collected by a member of the village who has a contract with the operator. Apart from collecting the user fees, the person also communicates to the operator in case of any unusual water shortage or pipe failure.

3.6 Capacity Building and Community Meetings.

According to Districts and Sectors' water and sanitation officers, only one capacity building workshop was conducted during the year in the sectors for water board members and water users' committee members on their roles and responsibilities in helping to manage community water and sanitation projects. It was found that 24% of the respondents regularly attend monthly community meetings and they stated that water and sanitation issues are among the issues discussed during the meetings. However, they revealed that the decisions on water and sanitation issues are just information to the community on actions taken to maintain services in the villages.

4 CONCLUSION

The failure of many development projects including that of water and sanitation is due to ineffective participation of key stakeholders including users, low capacity of the communities in operation and maintenance of water and sanitation systems as well as management of the resources. It has been highlighted that participation must take place at all stages of development of the water and sanitation schemes, from the planning stage, to implementation and management. Our findings showed that sustainability issues were inadequately addressed during initial stage of project development. This is corroborated by results from field observations and respondents claim of regular water systems breakdown caused by technical flaws in the designs and implementation, low technical capacities of water attendants and uncleanness of the public toilets due to poor designs and maintenance. Communities have no capacity to maintain the water and sanitation services and no sense of ownership. Community involvement in every step of the project is key because sustainability improves with greater community participation in all cycles.

REFERENCES

African Union, African Development Bank, & Economic Commission for Africa. (2009). The Africa Water Vision for 2025: Equitable and Sustainable Use of Water for Socioeconomic Development. *Economic Commission for Africa*, 1–34.

Andersson, K., Rosemarin, A., Lamizana, B., Kvarnström, E., McConville, J., Seidu, R., Dickin, S. and Trimmer, C. (2016). Sanitation, Wastewater Management and Sustainability: From Waste Disposal to Resource Recovery. UN Environment Programme and Stockholm Environment Institute. https://www.sei.org/publications/sanitation-wastewater-and-sustainability/

AU, ECA, AfDB (2018). *Africa Sustainable Development Report 2017*. *AfricaSustainable Development Report 2017*. https://doi.org/10.18356/3cff8bc0-en

Bamberger, M. (1986). The Role of Community Participation Planning and Project

Management FILE, (13), 1–50. Retrieved from

http://www.mapsofworld.com/thailand/provinces/krabi-map.html

Carter, C. R., & Rogers, D. S. (2008). A framework of sustainable supply chain management: Moving toward new theory. *International Journal of Physical Distribution and LogisticsManagement*, *38*(5), 360–387. https://doi.org/10.1108/09600030810882816

Carter, R. C., Tyrrel, S. F., & Howsam, P. (1999). The impact and sustainability of community water supply and sanitation programmes in developing countries. *Water and Environment Journal*, *13*(4), 292–296. https://doi.org/10.1111/j.1747-6593.1999.tb01050.x

Government of Rwanda (GOR). (2016). National Water Supply Policy, (December), 1–42.

GWP. (2011). Dublin-Rio Principles. *Water*, *46*(January 1992), 3–6.

Haq, M. A., Hassan, S. M., & Ahmad, K. (2014). Community Participation and Sustainabilitn of Water Supply Program in District Faisalabad, Pakistan. *Journal of Quality and Technology Management*, *X*(September), 125–137. https://doi.org/10.1182/blood-2014-01-553024

IWMI. (2003). How to establish a Water Users Association ? Practical steps for social mobilizers. http://www.iwmi.cgiar.org/regional-content/central_asia/pdf/wua_eng.pdf

Mdendemi, P. P. (2013). *Community Participation For Sustainability Of Rural Water Schemes*. https://doi.org/10.1016/S1473-3099(17)30118-4

MIDIMAR. (2015). The National Risk Atlas of Rwanda. https://www.gfdrr.org/sites/default/files/publication/National_Risk_Atlas_of_Rwanda_01.pdf

MININFRA. (2016). National Sanitation Policy, (December).

MININFRA. (2017). *Rwanda Overview : Water , Sanitation and Hygiene*. *Achieving the SDGs targets for water, sanitation and hygiene*.

Montgomery, M. A., Bartram, J., & Elimelech, M. (2009). Increasing Functional Sustainability of Water and Sanitation Supplies in Rural Sub-Saharan Africa. *Environmental Engineering Science*, *26*(5), 1017–1023. https://doi.org/10.1089/ees.2008.0388

Murtaza M., A. Muzola, S. James, F. N. (2017). Rural WASH programming : experiences from Rwanda, 40th WEDC International Confgerence, Loughborough, UK. https://www.academia.edu/34783828/Rural_WASH_programming_experiences_from_Rwanda

Ngirazie, L. A., Bushara, A. I., & Knox, J. W. (2015). Assessing the performance of water user associations in the Gash Irrigation Project, Sudan. *Water International*, *40*(4), 635–646. https://doi.org/10.1080/02508060.2015.1072677

NISR. (2013). EICV3 District profile, Musanze, 92.

NISR. (2014). *Fourth Population and Housing Census, Rwanda, 2012 , Population Projections*.

Ofuoku, A. U. (2011). Effect of community participation on sustainability of rural water projects in Delta Central agricultural zone of Delta State , Nigeria. *Journal of Agricultural Extension and Rural Development*, *3*(7), 130–136.

UN News Centre. (2015). UN adopts new Global Goals, charting sustainable development for people and planet by 2030. *United Nations Department of Economic and Social Affairs*. https://doi.org/10.1080/02513625.2015.1038080

UNDP - Global Centre for Public Service Excellence. (2016). Citizen Engagement in Public Service Delivery The Critical Role of Public Officials, 19. https://doi.org/http://dx.doi.org/10.1016/S1773-035X(15)30076-9

UNICEF, W. (2017). JMP launch version July 12 2017. Progress on Drinking Water, Sanitation and Hygiene - 2017 Update and SDG Baselines. *WHO Library Cataloguing-in Publication Data*. https://doi.org/10.1007/s12686-011-9397-4

Wang, J., Huang, J., Zhang, L., Huang, Q., & Rozelle, S. (2010). Water governance and water use efficiency: The five principles of WUA management and performance in China. *Journal of the American Water Resources Association*, *46*(4), 665–685. https://doi.org/10.1111/j.1752-1688.2010.00439.x

World Bank, (Zong-cheng Lin). (2003). Water User Associations Development in China: Participatory Management Practice under Bank-Supported Projects and Beyond. *Social Development Notes*, (83), 385–412. Retrieved from http://siteresources.worldbank.org/Intranetsocial development/873467

PAPER 74 – ACCURATE PREDICTION OF QUADCOPTER DYNAMICS THROUGH INCREMENTAL EVOLUTION OF GRNN MODEL DEVELOPMENT

A. G. Ibrahim[1*], J. D. Jiya[1], E. E. Omizegba[2], E. C. Anene[2], I. T. Balami[2]

[1]Department of Mechatronics and Systems Engineering, A.T.B. University, Bauchi, Nigeria
[2]Department of Electrical & Electronics Engineering, A.T.B. University, Bauchi, Nigeria.
[*]Email: agibrahim@atbu.edu.ng

ABSTRACT
This paper discusses the use of incremental evolution of generalized regression neural networks (GRNN) in the development of dynamic models of quadcopter systems. 11,835 flight datasets comprising attitude and altitude data were collected using quadcopter model F450 fitted with a PIXHAWK flight controller. The data were normalized and 70% was used for training and testing, while 30% was used for model validation. The results obtained show that for an MSE threshold of 0.1, a 98% reduction in the size of the hidden layer of the network is achievable for the attitude (roll, pitch and yaw) and altitude identification. The MSE values of 0.0268, 0.0514, 0.1627 and 0.2033 for the roll, pitch, yaw and altitude models respectively also indicated that the networks have higher accuracy compared with the GRNN models. Also, the R^2 values of 0.9732, 0.9484, 0.8373 and 0.7967 obtained for the validation of the roll, pitch, yaw and altitude models indicate that the models are well-fitted. The results showed that the incremental evolution-based GRNN algorithm reduces the size of the network's hidden layer by pruning neurons that do not contribute to error minimization between the actual flight output and the trained output, which results in higher accuracy compared to conventional GRNN models.

KEYWORDS: **Quadcopter, GRNN, System Identification, Incremental Evolution**

21. INTRODUCTION

The design of robust controllers for high performance operations of the quadcopter in constrained environments require an accurate model of the quadcopter system. These accurate models can also be used for design and development of advanced control strategies for trajectory planning control, fault-tolerant control, fault diagnosis and autonomous missions planning (Navarro et al., 2017). The development of a robust controller with the ability to adapt itself to the dynamic behaviour of the quadcopter system in the event of performance degradation of the actuators can be achieved with the aid of suitable system identification techniques, hence, an accurate identification of the system plays an important role in model reference adaptive control design. System identification and parameter estimation of any dynamic system produces a model of the system that can be used for the design, development and validation of control algorithms for the system. The mathematical model of quadcopter unmanned aerial vehicle systems derived from first principle contains un-modelled dynamics and model uncertainties arising from dynamic perturbations such as high frequency dynamics on parts of the system (Noormohammadi-asl *et al*, 2020). Furthermore, parametric and non-parametric uncertainties, noise and disturbances can affect the accuracy of models developed from experimental data. Neural networks are used in many applications including image recognition, classification, control and system identification, function approximation and regression (Tutunji, 2016). Neural identification offers a promising direction towards higher understanding of systems and the ability to solve some of the challenges in control design problems, especially in the determination of accurate dynamic models, and the development of intelligent control algorithms. Furthermore, there has been a paradigm shift in model identification of dynamic systems with the attention now focusing on the use of neural network techniques for improved accuracy in the determination of system models (Wang and Zhao, 2013).

Many researchers have worked on the development of neural networks for system identification. Abas *et al* (2011) investigated a method for parameter identification of a quadcopter using state estimation method with the implementation of Unscented Kalman Filter (UKF). In a related work, Navarro *et al* (2017) carried out a research on flight dynamics model development of a multi-copter using system identification techniques by using Comprehensive Identification from Frequency Response (CIFER) software for frequency response analysis. Al-Mahasneh *et al* (2017) carried out a study on the effect of evolutionary algorithms in improving neural network capabilities in identification of nonlinear multi input multi output dynamic systems such as quadcopters. Similarly, Al-Mahasneh *et al* (2018) carried out a comparative analyses between Generalized Regression Neural Network (GRNN) technique and Back Propagation Neural Networks (BPNN) technique in system identification and control of dynamic systems by comparing their training time and training error. Ives *et al* (2015) carried out system identification of the attitude of a quadrotor using experimental data. Furthermore, several other methods of system identification give better results, like the work of (Wang and Zhao, 2013) which is based on the white-

box technique, which requires a mathematical model of the system to be presented. Pairan *et al* (2020) carried out a review of neural network-based techniques for quadcopter dynamic modelling. Sa and Corke (2012) carried out system identification, estimation and control for a cost effective open-source quadcopter by using autoregressive moving average (ARMAX) model. Pairan and Shamsudin (2017) performed recursive system identification of a quadcopter based on radial basis function (RBF) neural network structure trained with constant trace (CT) and minimum resource allocation neural network (MRAN) algorithms for attitude model of quadcopters. The generated model was validated by checking the RMSE, training time and R^2 values. Salameh *et al* (2015) developed system models for a quadcopter hovering operation using experimental flight data. The models developed were autoregressive with extra input (ARX) – based models for the attitude and altitude single input single output. Filho *et al* (2016) developed a test bench to be used for identification of system parameters of a quadcopter. Chovancová *et al* (2014) carried out mathematical modelling and identification of parameters of the non-linear model of a quadcopter. Kantue and Pedro (2018) investigated the identification of unmanned quadcopter in accelerated flight using grey box modelling approach. Similarly, Kantue (2018) investigated nonlinear identification of an unmanned quadcopter rotor dynamics using radial basis function neural networks. Abdolahi and Rezaeizadeh (2018) carried out a black-box identification and iterative learning control of a quadcopter. Gandhi *et al* (2019) carried out a comparative analysis of multiple algorithms used for system identification of an unconventional UAV. Ayyad *et al* (2020) carried out a parametric system identification for linear system model of an unmanned aerial vehicle using deep learning and modified relay feedback test (MRFT). Amiruddin *et al* (2021) performed a comparative analyses of several deep learning techniques for system identification of quadcopter unmanned aerial vehicle. They compared gated recurrent units (GRUs), Long-short term memory and Convolutional neural networks (LSTM-CNN) in the identification of single-input-single-output (SISO) and multi-input-multi-output (MIMO) quadcopter system using a black-box approach.
This paper focuses on the development of black-box quadcopter dynamic models using incremental evolution of generalized regression neural networks with a view to reducing the size of the hidden layer of the network while improving the accuracy of the trained models.

22. THEORETICAL FRAMEWORK

The quadcopter is a four rotor fixed pitch propeller unmanned aerial vehicle. **Figure 1** shows the typical set-up of a quadcopter system.

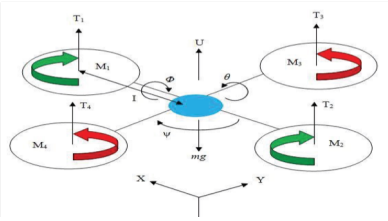

Figure 1: A Quadcopter Schematic Diagram

The thrust generation by the motors is directly proportional to the square of the angular speed as provided in equation (1)

$$T_i = c\omega_i^2 \qquad \ldots(1)$$

were T_i and ω_i are the thrusts and angular velocities exerted by the i^{th} motor respectively, and c is the drag coefficient of each of the identical propellers.

In the inertial frame, the acceleration of the quadcopter is due to thrust, gravity and linear friction. The thrust vector in the inertial frame can be obtained by using the rotation matrix R to map the thrust vector from the body frame to the inertial frame. The position and velocity in the inertial frame $X = (x, y, z)^T$ and $\dot{X} = (\dot{x}, \dot{y}, \dot{z})^T$, and the attitude in the body frame and the corresponding velocities $\Theta = (\phi, \theta, \psi)^T$ and $\dot{\Theta} = (\dot{\phi}, \dot{\theta}, \dot{\psi})^T$. The angular velocity in the body frame is given by;

$$\omega = \begin{bmatrix} 1 & 0 & -\sin\theta \\ 0 & \cos\phi & \cos\phi \\ 0 & -\sin\phi & \cos\phi \end{bmatrix} \quad \ldots (2)$$

The body and inertial frames are related by the rotation matrix *R*, which goes from the body frame to the inertial frame. Using the Z-Y-Z Euler angle conversion;

$$R = \begin{bmatrix} \cos\phi\cos\theta & \cos\psi\sin\theta - \sin\psi\cos\phi & \cos\psi\sin\theta\cos\phi + \sin\psi\sin\phi \\ \sin\psi\cos\theta & \sin\psi\sin\theta\sin\phi + \cos\psi\cos\phi & \sin\psi\sin\theta\cos\phi - \cos\psi\sin\phi \\ -\sin\theta & \cos\theta\sin\phi & \cos\theta\cos\phi \end{bmatrix} \quad \ldots (3)$$

The first set of differential equations that describe the acceleration of the quadcopter can be written as;

$$\begin{pmatrix} \ddot{x} \\ \ddot{y} \\ \ddot{z} \end{pmatrix} = g \begin{pmatrix} 0 \\ 0 \\ 1 \end{pmatrix} - R\frac{T}{m}\begin{pmatrix} 0 \\ 0 \\ 1 \end{pmatrix} \quad \ldots (4)$$

where T is the total torque generated by the quadcopter, m is the mass of the quadcopter system and g is the acceleration due to gravity.

With the inertia matrix *I*, which is a diagonal matrix with the inertias I_x, I_y and I_z on the main diagonal, the rotor inertia I_R, the vector *M* that describes the torque applied to the vehicle's body and the vector M_G of the gyroscopic torques, a second set of differential equations is obtained;

$$I\ddot{\omega} = -(\dot{\omega} \times I\dot{\omega}) - M_G + M \quad \ldots (5)$$

The vector *M* is defined as;

$$M = \begin{pmatrix} Lb(\omega_3^2 - \omega_4^2 \\ Lb(\omega_1^2 - \omega_2^2) \\ b(\omega_1^2 + \omega_2^2 - \omega_3^2 - \omega_4^2) \end{pmatrix} \quad \ldots (6)$$

Generalized Regression Neural Network (GRNN), also called general regression neural network, is a single pass associative memory feedforward type neural network, and uses normalized Gaussian kernels in the hidden layer as activation functions (Al-Mahasneh *et al* 2018). It is similar to radial basis function neural network, but the output is a special linear function. It is made up of the input layer, hidden layer, summation, division and output layer. **Figure 2** shows the structure of generalized regression neural network, unlike in feedback neural networks, the data in a GRNN can only flow from the input layer to the hidden layer and finally to the output layer. When GRNN is trained, it memorizes every unique pattern because it is a single pass network and does not require back propagation. After training GRNN with adequate training patterns, it will be able to generalize for new inputs. The output of GRNN can be calculated using equations (7) and (8).

$$D_i = \left(X - X_i\right)^T \left(X - X_i\right) \quad (7)$$

$$\hat{Y} = \frac{\sum_{i=1}^{N} Ye^{\left(-D_i/2\sigma^2\right)}}{\sum_{i=1}^{N} e^{\left(-D_i/2\sigma^2\right)}} \quad (8)$$

where D_i is the Euclidean distance between the input X_i and the training sample input *X* and *Y* is the training sample output, and σ is the smoothening parameter of the GRNN.

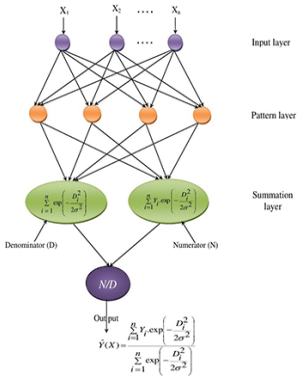

Figure 2: Structure of GRNN

23. MATERIALS AND METHODS

The quadcopter model F450 is a prototype quadcopter developed by Da-Jiang Innovations in Nanshan, Shenzen, China initially for hobbyists, but later, it became useful in many areas of application of UAVs including photography, search and rescue, agriculture and control design and validation. Its frame structure is rigid and light in weight, and can be assembled with less difficulty. It can accommodate a wide variety of off-the-shelf flight controllers like the PIXHAWK flight controller family, a wide range of GPS modules, electronic speed controllers, Lithium-Polymer (Li-Po) battery, and brushless DC motors. It has a diagonal length of 450mm from the centre of one DC motor to the other. **Plate 1** shows the quadcopter model F450 with the PIXHAWK 2.4.8 flight controller, the GPS module and the four propellers attached to the individual motors. The quadcopter has six degrees of freedom, three translational (movement along *x, y* and *z* directions) and three rotational (roll, pitch and yaw movements), making it an under-actuated system (Norouzi Ghazbi *et al*, 2016). There are two basic configurations of the quadcopter; the '+' configuration and the 'x' configuration. The 'x' configuration is considered more stable (Gupte *et al* 2012).

Plate 1: The Quadcopter Model F450

a. INCREMENTAL EVOLUTION ALGORITHM

The training of the neural network was carried out using MATLAB 2019b software. HP Pavillion 24 Intel(R) Core ™ i5 – 8400T CPU @1.70GHz, 1704MHz 6 cores logical processor and 12GB RAM was used for the simulation. Eleven Thousand, Eight Hundred and Thirty-Five (11,835) data sets were collected from attitude and altitude flight data, the data was divided in two with 70% for neural identification, 30% for model validation. The GRNN is initialized with one hundred (100) datasets of four (4) pulse with modulated (PWM) inputs and one (1) output each for the attitudes and altitude data of the quadcopter with a spread of 0.1. The GRNN inputs are the four plant inputs $u_1(k), u_2(k), u_3(k), u_4(k)$ and the target is the current plant outputs $y_1(k), y_2(k), y_3(k), y_4(k)$ for the roll, pitch, yaw and altitude respectively. The GRNN then predicts the next outputs $y_{1,2,3,4}(k+1)$ in a one-step-ahead mode as shown in **Figure 3(a)**, while **Figure 3(b)** shows the flowchart of the incremental evolution algorithm.

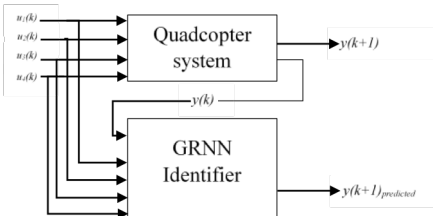

Incremental Algorithm for GRNN Model Development
Input: Input/target of attitude and altitude data
Output: Identified output

1. Initialize GRNN with the first 100 datasets
2. **Add** MSE threshold for training
3. For *i*=1 to *n* **do**
4. **Statements**
5. **If** (MSE(net(input(i), target(i))> threshold **then**
6. **Add 100 neurons to hidden layer**
7. **else;**
8. trained model=net(input(i))
9. **end** if
10. **end** for
11. **return** trained model=net(input(i))
12. **end**

Figure 3 (a) One-Step Ahead Prediction **(b)**. Flowchart of Incremental Algorithm

24. RESULTS AND DISCUSSION

The results shown in figures 4 and 5 of the identification of the quadcopter model F450 using GRNN and IE-GRNN. The results depict the predicted data and the target data. The GRNN takes 0.0244 seconds to train and generate the roll, pitch and yaw models, while the IE-GRNN takes 71.7300 seconds to train. The GRNN model is a forward path model, and a new node is assigned for every input/output data, that is why it takes only 0.0244 seconds to train, while the IE-GRNN trains the data in batches of 100 and discards any set of data which does not help improve the overall accuracy of the model. Hence the training time increases significantly

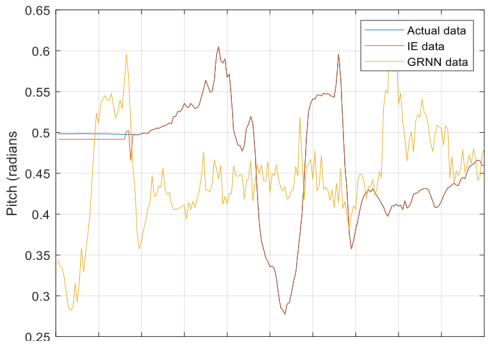

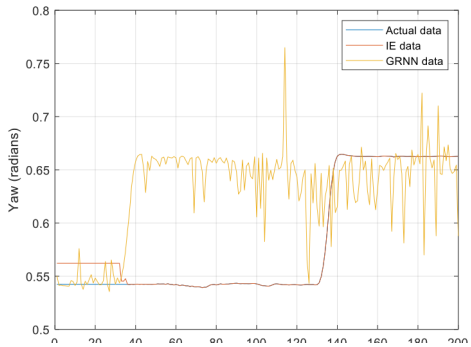

Figure 4(a) Pitch Identification for GRNN, IE-GRNN and Actual Data **(b).** Yaw Identification Responses for GRNN, IE-GRNN and Actual Data

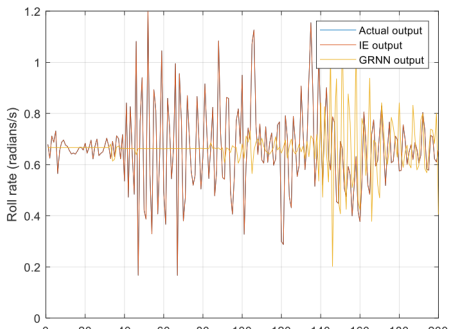

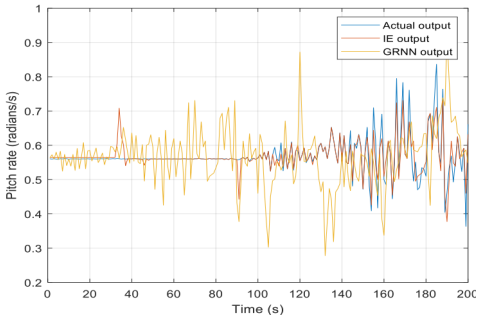

Figure 5 (a) Roll rate Identification comparison (b). Pitch rate Identification comparison

Furthermore, the mean squared error (MSE), root mean squared error (RMSE) and the R-squared values of the trained models in comparison with the actual data outputs are presented in table 1. The IE-GRNN provides better accuracy in terms of error minimization compared to the GRNN trained model. Also, the R^2 values closer to 1

also indicate that the models are well-fitted (Pairan & Shamsudin, 2017) (Dey et al., 2022) except for the altitude model, which has an R^2 value of 0.5. This is caused by the large disturbance experience while collecting data and the poor default controller developed for the quadcopter system which has poor disturbance rejection.

Table 1: Error Analysis of GRNN and IE-GRNN

Variable	MSE		RMSE		R^2	
	GRNN	**IE-GRNN**	**GRNN**	**IE-GRNN**	**GRNN**	**IE-GRNN**
Roll	0.0834	0.0268	0.29	0.16	0.9166	0.9732
Pitch	0.0691	0.0514	0.05	0.23	0.9975	0.9484
Yaw	0.9251	0.1627	0.10	0.40	0.9908	0.8373
Altitude	0.500	0.2033	0.71	0.45	0.7967	0.5000
Roll Rate	0.1570	0.0916	0.40	0.30	0.8430	0.9984
Pitch Rate	0.0857	0.0251	0.29	0.16	0.9143	0.9749
Yaw Rate	0.2330	0.1154	0.48	0.34	0.7670	0.8846

25. CONCLUSION

This work has shown the use of neural identification of quadcopters for large data samples and the impact of incremental evolution on generalized regression neural network with regards to over-fitting and under-fitting of the models. It also examined the accuracy of the developed models using the incremental evolution algorithm. The use of an improvised test bench for attitude data collection provides a cheap and alternative means to the use of expensive motion capture cameras, and the results obtained are comparable (Gandhi *et al*., 2019). Incremental evolution – based generalized regression neural network is suitable for offline black-box identification of quadcopter attitude and attitude rates dynamic models due to the reduced computational complexities and hardware requirements for its implementation. Incremental evolution – based generalized regression neural network – based models provide more accurate models compared to models developed using conventional generalized regression neural networks in terms of model fit, and error minimization. However, the longer training time required makes it unsuitable for online model identification.

ACKNOWLEDGEMENT

The first author would like to thank the department of Mechatronics and Systems engineering, Abubakar Tafawa Balewa University, Bauchi, for providing the environment and logistics to carry out the research work. The contributions of Prof. E. E. Omizegba and Prof. E. C. Anene both of the department of electrical and electronics engineering of the same university are also acknowledged

REFERENCES

Abas, N., Legowo, A., & Akmeliawati, R. (2011). Parameter identification of an autonomous quadrotor. *2011 4th International Conference on Mechatronics: Integrated Engineering for Industrial and Societal Development, ICOM'11 - Conference Proceedings*, *May*, 17–19. https://doi.org/10.1109/ICOM.2011.5937198

Abdolahi, Y., & Rezaeizadeh, A. (2018). Black-box identification and iterative learning control for quadcopter. *2018 6th International Conference on Control Engineering and Information Technology, CEIT 2018*, *October*, 1–5. https://doi.org/10.1109/CEIT.2018.8751795

Al-Mahasneh, A. J., Anavatti, S. G., & Garratt, M. A. (2017). Nonlinear Multi-Input Multi-Output System Identification using Neuro-Evolutionary Methods for a Quadcopter. *2017 Ninth International Conference on Advanced Computational Intelligence (ICACI)*, 2–7.

Al-Mahasneh, A. J., Anavatti, S. G., & Garratt, M. A. (2018). *Review of Applications of Generalized Regression Neural Networks in Identification and Control of Dynamic Systems*.

Amiruddin, B. P., Iskandar, E., Fatoni, A., & Santoso, A. (2021). *Deep Learning based System Identification of Quadcopter Unmanned Aerial Vehicle*.

Ayyad, A., Chehadeh, M., Awad, M. I., & Zweiri, Y. (2020). Real-Time System Identification Using Deep Learning for Linear Processes with Application to Unmanned Aerial Vehicles. *IEEE Access*, *8*, 122539–122553. https://doi.org/10.1109/ACCESS.2020.3006277

Chovancová, A., Fico, T., Chovanec, E., & Hubinský, P. (2014). Mathematical modelling and parameter

identification of quadrotor (a survey). *Procedia Engineering*, *96*, 172–181. https://doi.org/10.1016/j.proeng.2014.12.139

Dey, K., Kalita, K., & Chakraborty, S. (2022). Prediction performance analysis of neural network models for an electrical discharge turning process. *International Journal on Interactive Design and Manufacturing*, *17*(2), 827–845. https://doi.org/10.1007/s12008-022-01003-y

Filho, J. G. B. F., Dórea, C. E. T., Bessa, W. M., & Farias, J. L. C. B. (2016). Modeling, Test Benches and Identification of a Quadcopter. *Proceedings - 13th Latin American Robotics Symposium and 4th Brazilian Symposium on Robotics, LARS/SBR 2016*, 49–54. https://doi.org/10.1109/LARS-SBR.2016.67

Gandhi, M. S., Whitcher, L., Theodorou, E., & Johnson, E. N. (2019). *Practical System Identification for Small VTOL Unmanned Aerial Vehicle*. *January*. https://doi.org/10.2514/6.2019-1982

Gupte, S., Mohandas, P. I. T., & Conrad, J. M. (2012). A survey of quadrotor unmanned aerial vehicles. *Conference Proceedings - IEEE SOUTHEASTCON*. https://doi.org/10.1109/SECon.2012.6196930

Ives, N., Pacheco, R., De Castro, D., Resende, R., Américo, P., & Magalhães, A. (2015). Stability Control of an Autonomous Quadcopter through PID Control Law. *Journal of Engineering Research and Application Www.Ijera.Com ISSN*, *5*(54), 07–10.

Kantue, P. (2018). Nonlinear Identification of an Unmanned Quadcopter Rotor Dynamics using RBF Neural Networks. *2018 22nd International Conference on System Theory, Control and Computing (ICSTCC)*, 292–298.

Kantue, P., & Pedro, J. O. (2018). Grey-box modelling of an Unmanned Quadcopter during Aggressive Maneuvers. *2018 22nd International Conference on System Theory, Control and Computing, ICSTCC 2018 - Proceedings*, 640–645. https://doi.org/10.1109/ICSTCC.2018.8540761

Navarro, P., Cho, S., Rashid, A., Ruiz, A., & Bhandari, S. (2017). Flight testing, data collection, and system identification of a multicopter UAV. *AIAA Modeling and Simulation Technologies Conference, 2017*, *January*, 1–14. https://doi.org/10.2514/6.2017-1558

Noormohammadi-Asl, A., Esrafilian, O., Ahangar Arzati, M., & Taghirad, H. D. (2020). System identification and H∞-based control of quadrotor attitude. *Mechanical Systems and Signal Processing*, *135*, 106358. https://doi.org/10.1016/j.ymssp.2019.106358

Norouzi Ghazbi, S., Aghli, Y., Alimohammadi, M., & Akbari, A. A. (2016). Quadrotors unmanned aerial vehicles: A review. *International Journal on Smart Sensing and Intelligent Systems*, *9*(1), 309–333. https://doi.org/10.21307/ijssis-2017-872

Pairan, M. F., & Shamsudin, S. S. (2017). System identification of an unmanned quadcopter system using MRAN neural. *IOP Conference Series: Materials Science and Engineering*, *270*(1). https://doi.org/10.1088/1757-899X/270/1/012019

Pairan, Mohammad Fahmi, Shamsudin, S. S., & Zulkafli, M. F. (2020). Neural Network-Based System Identification for Quadcopter Dynamic Modeling: A Review. *Journal of Advanced Mechanical Engineering Applications*, *1*(2), 20–33. https://doi.org/10.30880/jamea.2020.01.02.003

Sa, I., & Corke, P. (2012). System identification, estimation and control for a cost effective open-source quadcopter. *Proceedings - IEEE International Conference on Robotics and Automation*, 2202–2209. https://doi.org/10.1109/ICRA.2012.6224896

Salameh, I. M., Ammar, E. M., & Tutunji, T. A. (2015). Identification of quadcopter hovering using experimental data. *2015 IEEE Jordan Conference on Applied Electrical Engineering and Computing Technologies, AEECT 2015*, 3–8. https://doi.org/10.1109/AEECT.2015.7360559

Tutunji, T. A. (2016). Parametric system identification using neural networks. *Applied Soft Computing Journal*, *47*, 251–261. https://doi.org/10.1016/j.asoc.2016.05.012

WANG, L.-Y., & ZHAO, W.-X. (2013). System Identification: New Paradigms, Challenges, and Opportunities. *Acta Automatica Sinica*, *39*(7), 933–942. https://doi.org/10.1016/s1874-1029(13)60062-2

PAPER 76 – IMPACT OF SUPPORT GEOMETRY ON THE PUNCHING SHEAR BEHAVIOR OF REINFORCED CONCRETE FLAT SLABS

M. A. Akinpelu[1], D. S. Gabriel[1], A. M. Salman[1]

[1]Department of Civil Engineering, Kwara State University, Malete, Kwara State, Nigeria. (10 points)
[*]Email: mutiu.akinpelu@kwasu.edu.ng

ABSTRACT
This study was carried out to assess the impact of support geometry on the punching behaviour of flat slabs using Abaqus Finite Element modelling software. The support geometrical constraint considered herein is strictly the column shapes. The first numerical specimen was developed using specifications of a previously tested experimental model and the simulation accuracy was validated by comparisons to experimental results. Three other variants of the validated model were developed by replacing the square column support with different shapes of column supports. The support shapes considered are L, T and Cruciform. The finite element analysis study showed that the influence of column geometry becomes visible only after the first initial crack had been developed in the slab. Although all simulated slabs indicated similar failure modes in the form of a sudden collapse at peak load signifying a typical shear failure. In conclusion, it was noted that the Cruciform shaped support column provided the highest shear resistance with a magnitude of 582.8 kN while 475 kN, 493.9 kN, and 502 kN were recorded in Square, L, and T-shaped support respectively.

KEYWORDS: Punching shear, Flat Slab, Column Shape, Finite Element.

1.0 INTRODUCTION

Flat slabs are primarily slabs that are without beams or any intermediate structural elements aiding in transferring loads to the columns. Hence, they have a direct transmission of loads and connection with columns. This system of flooring is becoming most adopted in various structures ranging from medium-rise to high risers and also in facilities such as garages, factories, airports, hospitals, multi-purpose buildings and skyscrapers. Their use is much more prevalent in skyscrapers and high risers which are sensitive to heights and the number of floors. As the number of floors increases, there is an inevitable need for machine floors which in turn reduces the number of available spaces. Therefore, a smaller headroom is readily adopted not only to reduce heights and increase the number of floors but also to ensure minimal barriers to the mechanical, electrical and all other servicing fittings.

On the other hand, one of the major structural sets for these types of slab is its inherent ability to fail in punching shear. Punching shear is caused by the concentration of loads from the supporting columns transferred to the slab in form of stress. This failure occurs as the slab gives way for the vertical bulging of the column through the slab in form of shear. Punching occurs both in axisymmetric and unsymmetric slabs. In the later cases, the stresses occur due to concentrated forces and moments induced by the eccentricity of reactions, while in the formal scenario failure and deformations are experienced mainly from the effects of concentrated force causing a trumpet or conical-shaped inclined cracks propagating through the slab around the perimeter of the column or wall at an angle between 20^{o}-30^{o}. (CEB-FIP, 1991).

However, over the decades punching shear behaviour has been an active field of interest and it has been investigated by various researchers. Varieties modelling methodology has been developed over time to simulate the behaviour of punching shear in slabs. Also, a series of databases has been initiated over the years to give a reference to the series of experimental tests carried out by different researchers. Whereas, they as much as possible try to postulate substantial possible scenarios, the research has been confined and some of the derived models are yet to be understood (Perez & Jalal, 2020).

The exact solution to most hands-on problems in engineering is very complex and the punching shear phenomenon is not exempted. The analytical approaches often involved the formation of mathematical models of the variables affecting the problem solution such as stresses and strain distribution in a solid structure. It is a common phenomenon in such procedures to replace the complex system with a simplified model that could be easily solved by an analytical approach (Akinpelu & Adedeji, 2018). Simplified models often come with many assumptions and uncertainties. Because of these, large "factors of safety" were introduced to ensure the safety of structures designed by this procedure. This is one of the reasons analytical results are highly conservative when compared to experimental results. However, with the advent of high-speed computers, the recent trend in the analysis of engineering problems embraced the use of more versatile numerical techniques. One of the most widely used numerical methods is Finite Element Method (FEM). To this end, in attaining the aim of this research, Abaqus finite element software 2021 was used to conduct all numerical analysis simulations.

2.0 THEORETICAL ANALYSIS

2.1 Abaqus Finite Element Methods

The governing equilibrium equation of discretized FE model derived from the principle of virtual work can be written symbolically in terms of displacement (*u)* as expressed in Equation 1:

$$F^N(u^M) = 0 \qquad \text{(Eqn 1)}$$

where F^N is the force component conjugate to the N^{th} variable and is the value of M^{th} variable displacement.

Due to the nonlinear stress-strain relationship of most engineering problems, the governing equation, Equation 1, emanated from the nonlinear equation of strains and thus, the function is nonlinear. Numerical methods are therefore required to solve the equation for a given set of forces. Besides, since the result of the governing equation is history-dependent, the solution must be sourced through incremental analysis of the external forces in order to capture the displacements, strains and stresses of time history along with the applied forces. Abaqus software basically utilises Newton-Raphson numerical procedure to solve the nonlinear equilibrium equation. The method is preferred to alternate procedures due to its high convergence rate.

2.2 Material Constitutive Model

2.2.1 Concrete Material

Numerous studies have supported the use of the Concrete Damage Plasticity Model (CPDM), which has been found to produce the most accurate results when compared to the experimental results and observations of reinforced concrete structure failure and post-failure (M. Akinpelu et al., 2021; Hafezolghorani et al., 2017; le Minh et al., 2021). The theory advanced by Lubliner et al., (1989) was applied to create the yielding criterion for this form model, along with modifications suggested by (Lee & Fenves, 1998) more details are found in (Dassault Systèmes, 2021). Three distinct stages of the concrete's plasticity, compressive behaviour, and tensile behaviour are taken into account during the calibration of CPDM. The sections below that follow discuss the theories and governing equations that were taken into consideration.

I) Concrete in Compression

The compressive stress characteristic data were generated using the (Eurocode 2, 2004) model for non-linear structural analysis.

The compressive stress and shortening strain for short-term uniaxial loading relationship was adopted from Equation 2 as defined in (Eurocode 2, 2004)

$$\frac{\sigma_c}{f_{cm}} = \frac{k\eta - \eta^2}{1+(k-2)\eta} \qquad \text{(Eqn. 2)}$$

The denotations in Eqn. 2 are as defined in Eqn. 3-8

$$\eta = \frac{\varepsilon_c}{\varepsilon_{c1}} \qquad \text{(Eqn. 3)}$$

$$\varepsilon_u = 0.0035\ (f_c < 50\ \mathrm{N/mm^2}) \quad \text{(Eqn. 4)}$$

$$\varepsilon_{c1} = \left(\frac{0.7 f_{cm}^{0.31}}{100}\right) < 2.8 \quad \text{(Eqn. 5)}$$

$$\varepsilon_{cu} = (2.8 + 27[(98 - f_c)/100]^4) \quad (f_c < 50\ N/mm^2) \quad \text{(Eqn. 6)}$$

$$k = 1.1 E_C \times \left(\frac{\varepsilon_u}{f_{cm}}\right) \quad \text{(Eqn. 7)}$$

$$f_{cm} = f_c + 8 \quad \text{(Eqn. 8)}$$

Where:
fc is the characteristic cylindrical compressive strength of concrete at 28 days.
$f$cm is the mean value of concrete cylinder compressive strength.
Ɛc is the strain at peak stress
Ɛc1 is the ultimate strain

II) Concrete in Tension

The following (Equation 9-10) describes analytical models are as defined suitable by (Cornelissen et al., 1986), with terms and symbols modifications from (Genikomsou & Polak, 2016)

$$\frac{\sigma}{f_t} = \left(\left(1 + \left(\frac{c_1}{w_c}\right)^3\right) e^{-\left(\frac{c_2 w}{w_c}\right)}\right) - \left(\left(\frac{w}{w_c}\right)(1 + c_1^3) e^{-c_2}\right) \quad \text{(Eqn. 9)}$$

$$w_c = 5.14\left(\frac{G_f}{f_t}\right) \quad \text{(Eqn. 10)}$$

Where; c_1 and c_2 are materials coefficients determined to be 3 and 6.93 respectively and w_c is the critical crack opening width, f_t is the tensile strength of concrete. While G_F is as established in (CEB-FIP, 1991) denoting the energy needed to propagate a tensile crack of a unit area given as;

$$G_F = G_{F0}(f_{cm}/f_{cmo})^{0.7} \quad \text{(Eqn. 11)}$$

f_{cmo} is taken as 10, and G_{F0} is expressed as a coefficient which is dependent on the maximum aggregate size. Hence the derived value of 0.065 J/m^2 were adopted as G_f assuming a maximum aggregate size d_{max} of 16mm

2.3 Steel Material

Steel Reinforcement Constitutive Model

The constitutive behaviour of steel material is identical in tension and compression. For this study, the stress-strain behaviour of reinforcing steel was modelled as a linear elastic, linear strain hardening material. The two elastic constants defined the linear elastic isotropic properties of the steel material while the plastic strains (obtained as total strains minus the elastic strains) and the yield strengths as presented in Table 1 defined the plastic property of the material adopted.

3.0 METHODOLOGY

3.1 Description of the Experimental Model

A flat slab specimen tagged RS, out of a series of test specimens experimented for punching at the University of Brasilia and reported by (Lima, 2021; R. de A. Palhares, 2018), was adopted. The tested specimen details is as presented in Fig. 2a and 2b. The slabs were loaded to failure by gradual increment through hydraulic jacks at 8 distinct points having radial dimensions of 1124 mm from the centre of the column as shown in Figure 3. The resulting mechanical properties of the materials are recorded in the adopted literature and presented in Table 1 and Table 2.

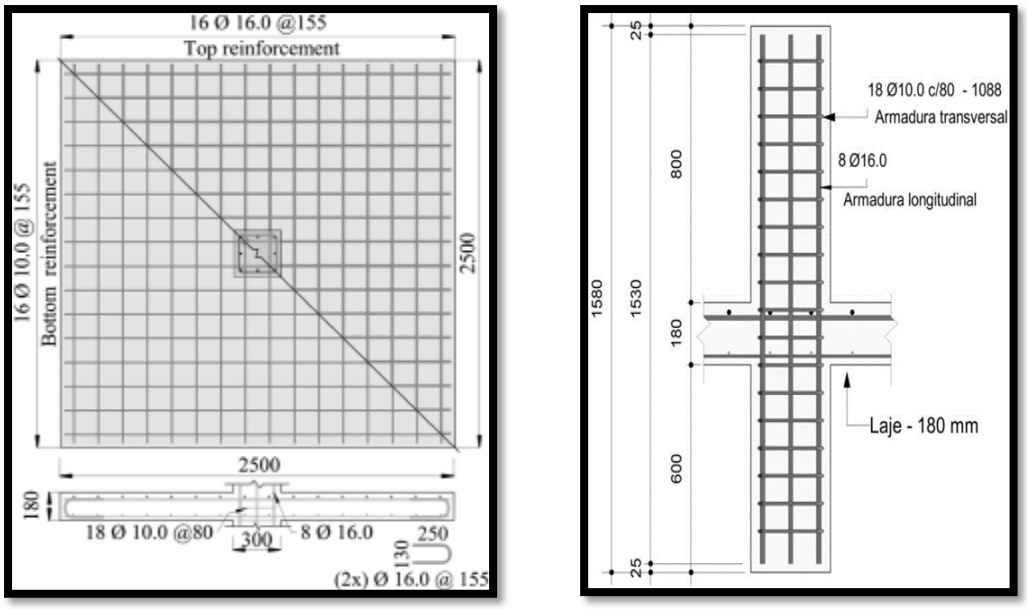

a) Slab reinforcement details b) Column reinforcement details

Fig. 1: Reinforcement arrangements in slab RS (all dimensions in mm)
(Lima, 2021; R. A. Palhares et al., 2022)

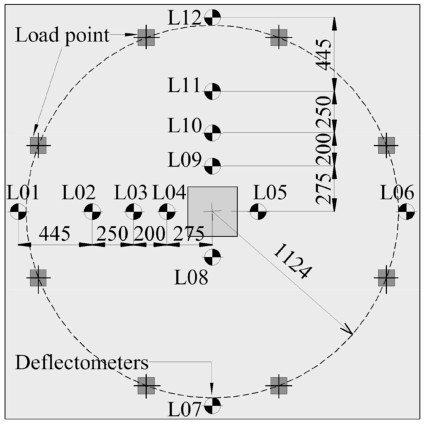

Fig. 2: Loading and deflectometer arrangements as used in the test system (all dimensions mm)
(Lima, 2021; R. A. Palhares et al., 2022)

Table 1: Mechanical Properties for the Reinforcement Steel

Bar diameter (mm)	Ultimate Yied stress (f_y) (N/mm^2)	Modulus of Elasticity (E_s) (N/mm^2)
16	549	196900
10	515	126600

(Source: (R. de A. Palhares, 2018)

Table 2: Mechanical Properties for the Concrete material

Slab	mean compressive strength, f_c (N/mm^2)	Average tensile strength*, f_{tm} (N/mm^2)	Modulus of Elasticity* (N/mm^2)
RS	29.9	2.89**	32,810*

(Source: (R. de A. Palhares, 2018)
*The average elastic modulus and tensile strength of concrete were calculated using Eurocode 2 (2004) as stated in Eqn 12 and 13 respectively.

$*E_C = 22\ [\ (f_c + 8)/10]^{0.3} * 10^3$ Eqn. 12

$**f_{tm} = 0.3 * f_c^{2/3}$ Eqn. 13

3.2 Description of Numerical models

The experimental model as defined in section 3.1 was used as a basis for the development and calibration of the control model (specimen with square support). The precision of the control model was validated by comparison with experimental results. The validated model was subsequently extended to develop other specimens by replacing the square support shape with L,T and cruciform consecutively. The calibrating parameters adopted in the numerical simulations are stated in Table 3. It is noteworthy that the columns were of the same surface area as that used in the experimental and control model even as the geometrical shape differs. The details of the substituting supporting columns are as shown in Fig. 3. Also, it was ensured that there was no moment inducing eccentricity via the support-slab connection, this implies that the slab was loading axially as the centroid of the slab was ascertained to coincide with that of the supporting column.

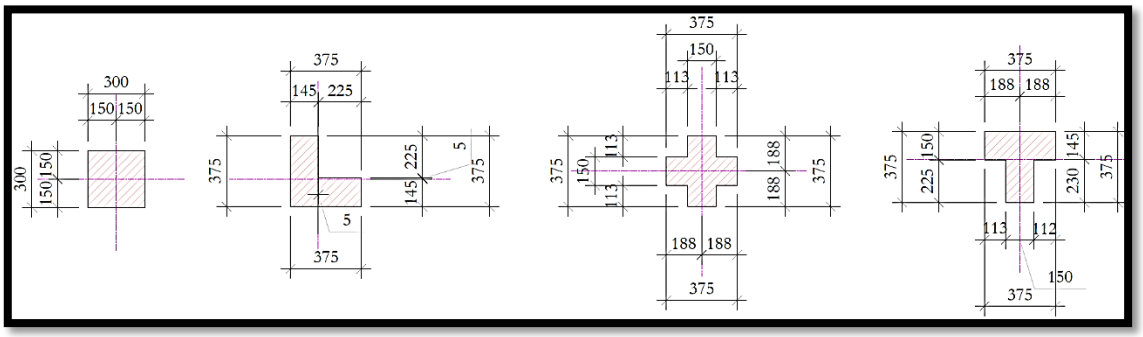

Fig. 3: Geometrical properties of different column shapes used in finite element simulations

Table 3: Material constitutive model parameters

Material	Parameter
Concrete	Model - CDPM Poisson ratio = 0.2 Young Modulus = 32,810 N/mm^2 (Eurocode 2, 2004) Dilation Angle, ψ = 25˚ (R. A. Palhares et al., 2022) Viscosity = 0.0001 (M. Akinpelu et al., 2021) Flow Potential Eccentricity = 0.1 (Default value) Stress ratio = 1.16 (Default Value) K = 0.667 (Default Value) Compressive stress-stress data = Eurocode 2, 2004 model Tensile stress-strain data = (Cornelissen et al., 1986) Element type =C3C8R Mesh Density 30x30mm (Wosatko et al., 2019)
Steel	Model – Linear elastic, linear strain hardening model Young modulus, Es = Experimental value (See table 1) Poisson ratio = 0.3 Element Type = T3D2

4.0 RESULT AND DISCUSSION

4.1 Model Validation

The load-displacement response graph (Figure 4) reveals that after the first crack was observed, the nonlinearity of the response to load is exhibited. However, there was continued resistance to the load effect but at a certain level of load exertion there is a sudden fall in the load resistance, this signifies the punching shear phenomenon. The aforementioned trend was similarly observed in the Finite element model and Experimental response signifying a good agreement between both models. Although there was a disparity in the initial stiffness behaviour, this has been attributed to microcracks development which could not be captured by the experimental instrumentation (M. A. Akinpelu & Adedeji, 2018).

The accuracy of the developed numerical model was further verified by comparison of the rupture surface deformation pattern in Fig. 5. Both models show correlating deformation pattern consistent with the conical shape formation as predicted by previous literature (R. A. Palhares et al., 2022).

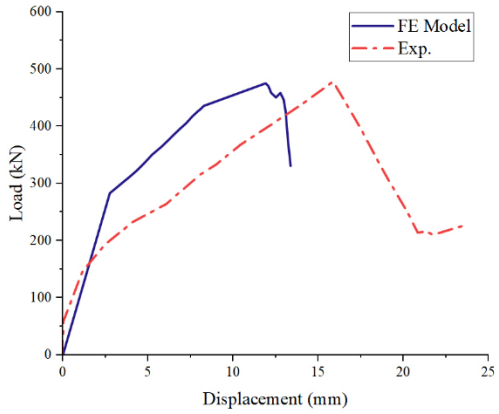

Figure 4: FEM versus experimental load-deflection response for the flat slabs

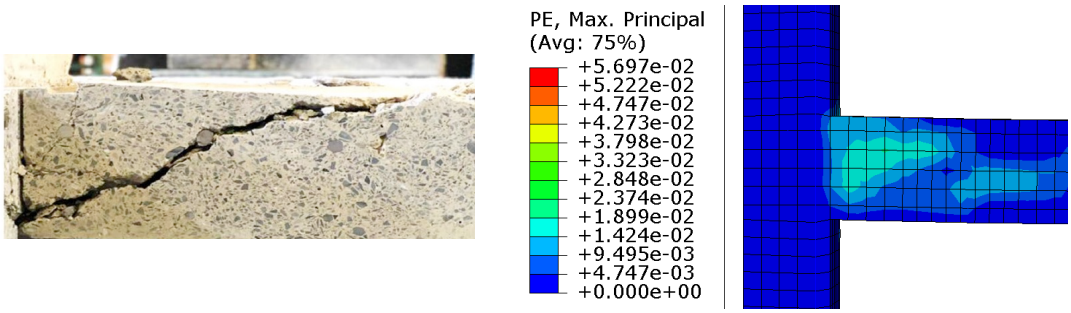

Figure 5: Experimental versus FEM rupture surface at failure.

4.2 Effect of Support Geometry of Punching shear behaviour of flat slabs

The load displacement response of the various considered model is as comparatively presented in Fig. 6. It can be observed that at the initial stages of loading where the structure is fully elastic and deformation is yet commence, the effect of variating column support shapes are negligible. However, after the initial stage where the response tends show nonlinearity given the development of tangential cracks within the model. It was observed that the stiffness response of various model differs and the magnitude of peak load resistance (Punching shear capacity) varies across the models considered (see Figure 7). Nevertheless, as discussed in Section 4.1 the failure mode (punching shear) of the various specimens is revealed to be insensitive to changing of the column shapes.

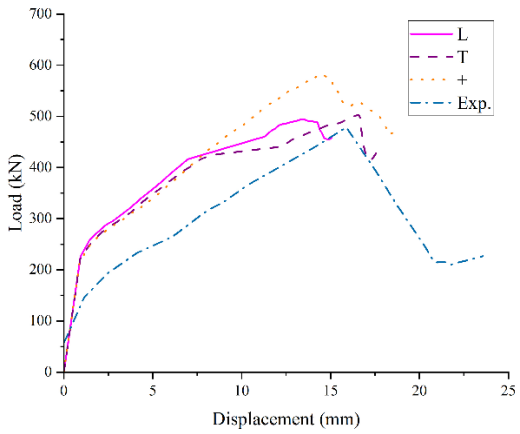

Figure 6 : Comparative graph showing the load-displacement response of various flat slab specimens

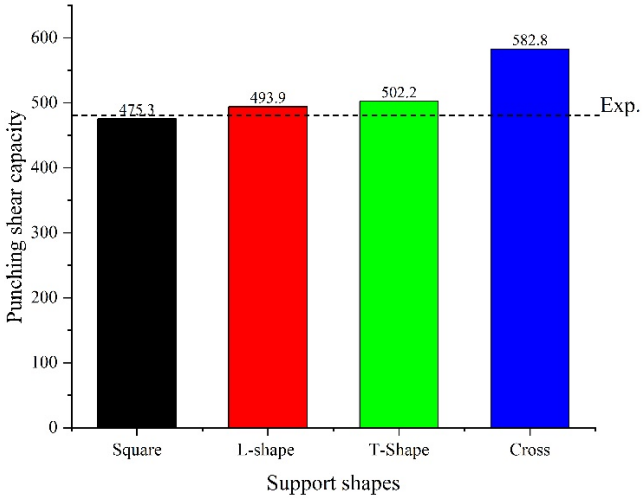

Figure 7: Comparative graph showing Punching shear capacity of various flat slab specimens

5.0 Conclusions

1. The developed finite element model precisely imitates the load-displacement behaviour of reinforced concrete flat slabs.
2. According to the results of the finite element analysis study, the influence of column geometry is only apparent after the slab has already developed its first crack. Despite that, all simulated slabs showed a similar failure mode in the form of a sudden, continuous drop in load resistance at a certain stage of load exertion representing a typical shear failure.
3. The finite element results reveal that the geometrical shape of the supporting column substantially influences the punching shear resistance of flat slabs. Deductively, cruciform shaped support column provided the highest shear resistance with a magnitude of 582.8 kN while 475 kN, 493.9 kN, and 502 kN were recorded in Square, L, and T-shaped support respectively.

References

Abaqus - SIMULIA User Assistance 2021. Retrieved February 14, 2023, from https://help.3ds.com/2021/english/dssimulia_established/SIMULIA_Established_FrontmatterMap/sim-r-DSDocAbaqus.htm?contextscope=all&id=b15ba98a76ce4305b417ecdd54e5394d

Akinpelu, M. A., & Adedeji, A. A. (2018). Structural Response of Reinforced Self-Compacting Concrete Deep Beam Using Finite Element Method. *Journal of Soft Computing in Civil Engineering*, *2*(1), 36–61. https://doi.org/10.22115/SCCE.2018.50115

Akinpelu, M., Ibitoye, B., Samson O., O., & Olorede, K. (2021). Numerical Verification of Strut and Tie Models and Failure Modes of Reinforced Self-Compacting Concrete Deep Beams. *International Journal of Engineering Research in Africa*, *53*, 76–100.

British Standards Institution, & European Committee for Standardization. *Eurocode 2 : design of concrete structures - part 1-1 :general rules and rules for buildings*. 226. Retrieved January 21, 2023, from https://www.en-standard.eu/bs-en-1992-1-1-2004-a1-2014-eurocode-2-design-of-concrete-structures-general-rules-and-rules-for-buildings/

CEB-FIP, C. (1991). Model Code 1990. *Comite Euro-International Du Beton, Paris*, 87–109.

Cornelissen, H. A. W., Hordijk, D. A., & Reinhardt Summary, H. W. (1986). Experimental determination of crack softening characteristics of normalweight and lightweight concrete.

HERON, 31 (2), 1986. https://repository.tudelft.nl/islandora/object/uuid%3A08c29b39-5c60-4ab6-b9d5-643d11007f7c

Genikomsou, A., & Polak, M. A. (2016). *Damaged plasticity modelling of concrete in finite element analysis of reinforced concrete slabs*. https://doi.org/10.21012/FC9.006

Hafezolghorani, M., Hejazi, F., Vaghei, R., Jaafar, M. S. bin, & Karimzade, K. (2017). Simplified damage plasticity model for concrete. *Structural Engineering International*, *27*(1), 68–78. https://doi.org/10.2749/101686616X1081

Institution, B. S., & Standardization, E. C. for. (2004). *Eurocode 2: Design of Concrete Structures : Part 1-1: General Rules and Rules for Buildings*. British Standards Institution. https://books.google.com.ng/books?id=DIw3AgAACAAJ

le Minh, H., Khatir, S., Abdel Wahab, M., & Cuong-Le, T. (2021). A concrete damage plasticity model for predicting the effects of compressive high-strength concrete under static and dynamic loads. *Journal of Building Engineering*, *44*, 103239. https://doi.org/10.1016/J.JOBE.2021.103239

Lee, J., & Fenves, G. L. (1998). Plastic-Damage Model for Cyclic Loading of Concrete Structures. *Journal of Engineering Mechanics*, *124*(8), 892–900. https://doi.org/10.1061/(ASCE)0733-9399(1998)124:8(892)

Lima, H. J. N. de. (2021). *Análise experimental da resistência a punção em lajes lisas com armadura de cisalhamento parcialmente ancorada*. https://repositorio.unb.br/handle/10482/41379

Lubliner, J., Oliver, J., Oller, S., & Oñate, E. (1989). A plastic-damage model for concrete. *International Journal of Solids and Structures*, *25*(3), 299–326. https://doi.org/10.1016/0020-7683(89)90050-4

Palhares, R. A., Rossignoli, F. W., Sales de Melo, G., & Lima, H. (2022). A numerical model capable of accurately simulating the punching shear behavior of a reinforced concrete slab. *Structural Concrete*, *23*(2), 1134–1150. https://doi.org/10.1002/SUCO.202100773

Palhares, R. de A. (2018). *Análise experimental da punção em lajes lisas de concreto armado com variação da ancoragem da armadura de cisalhamento*. https://repositorio.unb.br/handle/10482/34298

Perez, J. A., & Jalal, P. (2020). *Punching Shear in Concrete Flat Slabs Supported on Slender Edge Steel Columns* [Concrete Structures]. KTH Royal Institute of Technology.

Wosatko, A., Winnicki, A., Polak, M. A., & Pamin, J. (2019). Role of dilatancy angle in plasticity-based models of concrete. *Archives of Civil and Mechanical Engineering*, *19*(4), 1268–1283. https://doi.org/10.1016/J.ACME.2019.07.003

PAPER 77 – RECONFIGURATION OF UNBALANCED DISTRIBUTION NETWORK FOR IMPROVED VOLTAGE PROFILE AND POWER LOSS MITIGATION

A. S. MUSA[1], N. Abdulazeez[1], B Jimoh[2], Y. Jibril[2], A. S. Abubakar[2]
Department of Electrical Engineering, Ahmadu Bello University Zaria, Kaduna, Nigeria
Email: nuyor2019@gmail.com

ABSTRACT

The need for improved quality of services, and an increase in energy demand among others necessitated the urgent need for efficient utilization of the available energy via reducing technical losses in the network. This paper proposed a power loss mitigation scheme by developing an optimal reconfiguration for an unbalanced Distribution Network (DN) to reduce technical losses and improve system reliability. The various components that constitute the unbalanced networks were considered and the impedance of the line was modeled using modified Carson's equation. At the same time, a power flow based on the forward-backward sweep process was adopted to ascertain the base case losses. A composite load model was adopted. The optimal status of the switches in order to minimize the real power loss is found by Smell Agent Optimization (SAO) algorithm. The effectiveness of the proposed methodology is demonstrated on an unbalanced (123 Bus) radial distribution system. The active power loss in the base case of the IEEE 123 bus unbalanced network is 115.389KW whereas after reconfiguration the loss was reduced to 67.74kW representing a 41.30% reduction in power loss.

Keywords: Active power losses, Forward-backward sweep, Radial distribution system, Smell Agent Optimization algorithm, System reconfiguration

1. INTRODUCTION

A power system is an interconnected system that is composed of generating units/systems which convert other forms of energy into electricity, substations that distribute the generated power to the loads (consumers), and the transmission lines /systems that tie the generating stations and distribution substations together. According to voltage levels an electric power system can be viewed as consisting of a generating system, a transmission system and a distribution system (Ahmadi *et al* 2015). The transmission system is distinctly different, in both its operation and characteristics, from the distribution system. Whereas the later draws from a single source and transmit to individual loads, the transmission system not only handles the largest blocks of power but also the system. The main difference between the transmission and distribution system shows up in the network structure. The former tends to be looped and the latter generally, a radial structure (Tripathy *et al*, 1982). The modern power distribution network is constantly being faced with an ever-growing load demand (Yang *et al*, 2012). Distribution networks experience distinct change from a low to high load level every day (Rani *et al.*, 2015). In certain industrial areas, it has been observed that under certain critical loading conditions, the distribution network experience voltage collapse (Chakravorty & Das, 2001). The Distribution systems usually have system loses and poor voltage regulation because of the high current and low voltage levels in distribution systems (Nguyen *et al.*, 2016). The distribution losses can be divided into real and reactive power losses. Compared to the effect of reactive power losses in the system, the real power losses (I^2R) affect the efficiency of the power transfer while the reactive loss I^2X leads to poor voltage profile (Yuvaraj *et al.*, 2017). It is reported that as much as 13% of total power generated is wasted in the form of losses at the distribution level (Naik *et al.*, 2013). There are various techniques put in place to curtail these problems in the network. Among these techniques is the distribution network reconfiguration (DNR), distributed generation (DG), and optimal capacitor placement (Ali *et al*, 2017). The DNR is the most commonly used due to its cost effectiveness. The DNR is the process of readjusting or rearranging the network structure with the objectives to improve the power system conditions in the best possible way by opening and closing the available sectionalizing and tie line switches (Saonerkar *et al.*, 2016). Reconfiguration is applied for: service restoration under fault, load balancing to relieve overload on feeders ,improve voltage profile, planning outages for maintenance and power loss minimization (Kalambe & Agnihotri, 2014). Configuration of a power distribution system (PDS) is a complex activity which is important for electric power systems planning. Poor configuration leads to increased power losses, poor voltage profile (VP), and low power factor (PF) (Savier & Das, 2007). The modification of the switches depends on the type of objective function adopted therefore, the need to employ an efficient algorithm to implement an optimal NR having various perspectives such as objective function and constraints. Minimization of real power losses (RPLs) and improve voltage profile (VP) in order to improve distribution systems performance are the main objectives of DNR.

To solve DNR, numerous metaheuristics optimization algorithms have been explored and presented in the literature in the last two decades. (Esmaeilian *et al*., 2013) worked with Gravitational Search Algorithm (GSA) for optimal reconfiguration of a real distribution network to reduce energy loss and improve reliability. **(**Fathy *et al*., 2017**)** Presented a Binary Particle Swarm Optimization Gravity Search Algorithm (BPSOGSA) for optimal reconfiguration of distribution network to determine the positions of the sectionalizing and tie switches. A Cuckoo

search algorithm for distribution network reconfiguration to minimize the active power loss and maximizing the voltage magnitude deviation was presented by (Nguyen & Truong, 2015). (Tyagi, *et al.*, 2017)**,** developed an improved harmony search (IHS) for balanced and unbalanced distribution systems reconfiguration, while minimizing the real power purchase cost. Successfully implementation of the Runner Root Algorithm (RRA) to solve the distribution network reconfiguration problems with multi objectives was discussed in (Nguyen *et al.*, (2017)**.** (Kaur & Ghosh, 2016)**,** proposed a technique to optimize unbalanced distribution networks (UDNs) for keeping up the voltage profile with respect to the consequence of solving the multi-objective reconfiguration using the Firefly algorithm in a fuzzy domain with a load flow method. (Vasudevan & Sinha, 2017**)** put forward a distribution network reconfiguration method using Genetic Algorithm (GA) and Particle Swarm Optimization (PSO) to identify the optimum positions of the tie and sectionalizing switches. A hybrid intelligent method (comprising of Radial Basis Function Network (RBFN) of Artificial Neural Network (ANN) and Regression Tree of Data Mining) for estimating distribution network reconfigurations with the aim of reducing active losses were present in (Mori & Yokoyama, 2016)**.** (Dahalan *et al*., 2014) developed an algorithm for reconfiguration using fast and Non- elite Dominated Sorting Genetic Algorithm (NSGAII) to determine the optimal locations of the tie and sectionalizing switches within the network and the Backward Forward Sweep (BFS) algorithm was used to ascertain the base power loss. (Amini *et al*., 2018) proposed a non-iterative harmonic load flow (HLF) method based distribution network reconfiguration using backward/forward sweep technique. (Vasudevan and Sinha 2018)**,** used genetic algorithm(GA) and particle swarm optimization (PSO) to identify the optimum positions of the tie and sectionalizing switches to obtain a very efficient reconfigured distribution network. (Abdelaziz *et al.,* 2010), a reconfiguration of distribution systems using a modified Tabu Search (MTS) algorithm.

2. THEORETICAL ANALYSIS

2.1 Distribution Network

Distribution network is one of the main parts of power system as it is connected directly to the load centre. It is defined as a final stage in the delivery of electrical power. The primary purpose of an electricity distribution system is to meet the customer's demands for energy after receiving the bulk electrical energy from transmission or sub-transmission substation (Kansal *et al.*, 2016).

2.2 Radial Distribution Network

Generally, distribution networks are structured in mesh shape but operated in radial configuration by opening their tie-lines. In this type of topology, separate feeders radiate from the injection sub-station and feed the consumers. Radial distribution network is characterized by uncertainties and imperfection of network parameters such as: extremely large number of nodes and branches and unbalanced loads

2.3 Distribution system reconfiguration

Distribution Network reconfiguration (DNR) of the radial distribution network are employed for the purpose of loss minimization, voltage profile improvement, load balancing, and reliability enhancement. The distribution network reconfiguration is the most widely used method of improving reliability in distribution network by electrical distribution company because it allows the use of resources that already exist in the system. The DNR can be achieved by changing the status of the switches that connect/disconnect the branches of the system, in other to obtain a radial structure (Cruz, 2016).

The DNR problems can be formulated as a mono-objective (i.e., minimization of losses) or multi-objective optimization (i.e., minimization of losses, operating cost minimization, and maximization of the profit). The solution techniques applied to solve DR problems can be categorically classified into two: mathematical techniques and heuristic and metaheuristic techniques (Meneses *et al.,* 2015).

2.4 The Smell Agent Optimization Algorithm

The Smell Agent Optimization Algorithm is developed using three distinctive behaviors: the sniffing mode which is based on kinetic theory of gas. The trailing mode which is based on olfaction capacity of the agent and its ability to sniff the location of best and worst molecules of smell and a random behavior which is the strategy agent employs to escape from being trapped in a local minimum (Salawudeen *et al.*, 2018).

The initial position of the smell agent molecules was randomly initialized (generated) using the equations given below:

$$X_i^{(t+1)} = X_i^{(t)} + V_i^{(t+1)} \quad (1)$$

The fitness of the molecule was determined, and the molecule with best fitness is selected as the agent whose olfaction capacity is determined using the equation (2);

$$olf = \frac{f(x_{Agent})}{\sum_{i=1}^{N} f(x_i)/N} \quad (2)$$

The velocity of the molecule is updated and the sniffing mode is performed using the equations (3) and (4)

$$V_i^{(t+1)} = V_j^{(t)} + r_0 \times \sqrt{\frac{3kT}{m}} \quad (3)$$

$$X_i^{(t+1)} = X_j^{(t)} + \left(V_j^{(t)} + r_0 \times \sqrt{\frac{3kT}{m}}\right) \quad (4)$$

Then, the trailing mode of the agent is performed using equation (5)

$$X_i^{(t+1)} = X_i^{(t)} + r_1 \times olf \times \left(X_{agent}^{(t)} - X_{(i)}^{(t)}\right) - r_2 \times olf \times \left(X_{worst}^{(t)} - X_{(i)}^{(t)}\right) \quad (5)$$

The fitness of the trailing mode is evaluated and the position of the agent is updated until the best position is obtained. In a situation where the trailing mode failed to obtain the best solution, the agent goes into random mode hoping to obtain the better solution. If a better solution is obtained, the agent start trailing from this position again. If not, the agent goes back to the sniffing (default) mode and starts the SAO process all over again.

3. METHODOLOGY

3.1 Power Flow Method

Direct methods, Newton-Rapson (NR) methods, and Backward-Forward sweep methods are three methods proposed for solving distribution power flow analysis. The Backward-Forward Sweep method is an iterative means to solving the load flow equations of radial distribution systems which has two steps.

A. Backward sweep

The aim of backward sweep is to update branch currents in each section, by considering the previous iteration voltages at each node. During backward transmission, voltage values are held constant with updated branch currents transmitted backward along the feeder using backward path. The Backward sweep starts from the extreme end branch and proceeds towards the slack bus.

The branch currents preceding the end buses can be obtained using equation (6)-(7):

$$I_{ij}^{abc} = I_j^{abc} \quad (6)$$

$$I_{ik}^{abc} = I_k^{abc} \quad (7)$$

These are the currents in branches i-j or i-k, preceding end buses j or k respectively. For intermediate buses, the following equation (8-9) are used,

$$I_{hi}^{abc} = I_{ij}^{abc} + I_{ik}^{abc} + I_i^{abc} \quad (8)$$

$$I_{hi}^{abc} = \sum_r^{abc} I_{ir}^{abc} + I_i^{abc} \quad (9)$$

Where *r* are all those buses connected to *'i'* downstream, I_{hi}^{abc} is Branch current vector between bus *h* and *i*. I_{ij}^{abc} represent Branch current vector between bus *i* and *j*. I_{ik}^{abc} is the Branch current vector between bus *i* and *k*.

This analysis would assume a balanced network system, with (n-1) load buses which are treated as load buses and bus 1 as slack/swing bus. The general bus '*i*' current injection k^{th} iteration is given by the equation (10) (Alhaddad & El-Hawary, 2014b):

$$I_i^k = \left(\frac{S_i^{sch}}{V_i^k}\right) \quad (10)$$

Where S_i^{sch} is the scheduled complex power at bus *i*, V_i^k is the bus '*i*' voltage at the kth iteration. Now, the backward current sweep will apply Kirchhoff's current law (KCL) by starting from the last bus 'n' to the source bus 1 to obtain the branch currents.

B. *Forward sweep*

The aim of the forward sweep is to calculate the voltages at each node starting from the source node. The source node is set at unity and other node voltages are calculated as given in equation (11).

$$Vb_i = Vb_{i-1} - Ib_i \times z_i - Ib_i \times z_{mutuali} \quad (11)$$

Where Vb_i is the voltage of ith bus, Vb_{i-1} denotes voltage of (i-1)th bus and $z_{mutuali}$ is the mutual impedance. Mutual impedance will be present for both three phase and two phase, but it is absent for single phase.

For three phase unbalanced load, equation (12) was used to calculate the nodal voltage.

$$\begin{bmatrix}\dot{V}^{k}_{-abc}\\ \dot{V}^{m}_{-abc}\\ \dot{V}^{n}_{-abc}\end{bmatrix}=\begin{bmatrix}[A_1A_2A_3] & [0] & [0]\\ [0] & [A_1A_2] & [0]\\ [0] & [0] & [A_1]\end{bmatrix}\begin{bmatrix}\dot{V}^{Sw}_{-abc}\\ \dot{V}^{Sw}_{-abc}\\ \dot{V}^{Sw}_{-abc}\end{bmatrix}-\begin{bmatrix}[A_3A_2\dot{B}_1] & [A_3\dot{B}_2] & [\dot{B}_1]\\ [A_2\dot{B}_1] & [\dot{B}_2] & [0]\\ [B_1] & [0] & [0]\end{bmatrix}\begin{bmatrix}j^{e-1}_{-abc}\\ j^{e-2}_{-abc}\\ j^{e-3}_{-abc}\end{bmatrix}-$$
$$\begin{bmatrix}[0] & [A_3] & [0]\\ [0] & [I] & [0]\\ [0] & [0] & [0]\end{bmatrix}\begin{bmatrix}0\\ \dot{V}_{0}\\ 0\end{bmatrix} \quad (12)$$

3.2 Problem Formulation

The objective functions for the network reconfiguration considered in this paper are the active power loss reduction and voltage profile improvement.

$$Optimal\ Cost = \min\left(\sum_{i=1}^{Nbr} f_i\right) \quad (13)$$

$$fi = (w_1 f_{\text{loss}} + w_2 f_{\text{SAIFI}}) \times K_j \quad (14)$$

The total power loss of the *K*-th radial configuration is determined by the summation of losses in all line sections according to the following.

$$f_{loss} = P_{loss}^{(ASM)} = \sum_{j=1}^{Nbr} R_j \times \left(\frac{P_j^2+Q_j^2}{V_j^2}\right) K_j \quad (15)$$

Where: K_j is the switch state of j-th branch, with 0 indicating switch open and 1 indicating switch closed. Nbr is the number of the buses, Rj is the resistance of the j-th branch, Pj is the active power flowing through the terminal of j-th branch, Qj is the reactive power flowing through the terminal of j-th branch, Vj is the terminal node voltage of the j-th branch.

Subjected to constraints

The nodal voltage, branch power, and radial network are considered as the constraints as shown in equation (16-19).

a. Node voltage constraint

$$V_{min}(j) \le V(j) \le V_{max}(j) \quad (16)$$

b. Branch Power constraint

$$P_j \le P_{jmax} \quad (17)$$

$$Q_j \le Q_{jmax} \quad (18)$$

c. Radial Network constraint

$$\sum_{i=1}^{nl}\sum_{j=1}^{nbus} aij = 1 \text{ or } -1 \quad (19)$$

Where: *nbus* is the total number of buses, nl is the number of branches, aij is the elements of the incidence matrix A which has dimension of $nl \times nbus$.

3.3 Reconfiguration using SAO

The algorithmic steps to discover the optimal feeder reconfiguration in radial distribution system are discussed in this section. Let 'm' be the population size and 'N' be the number of decision variables in an optimization problem. For optimal feeder reconfiguration the number of open switch in a radial system is 'n1', Thus, the total number of variables in a particle is N = n1.

Step 1: Read RDS"s load and line data.

Step 2: Select reasonable esteems for SAO coefficients and set iteration index as t = 1.

Step 3: Arbitrarily arrange workable solution for all 'm' particles in vector form xi = [xi1, xi2,... xin1, xin1+1,], i = 1 to m; where xi1 to xin1 denotes the open switch position of feeder lines on the interim [2, nbus].

Step 4: For particle i, open the tie switch positions (xi1 to xin1) in the power distribution system,

Step 5: For particle i, execute backward/forward sweep power flow algorithm on radial distribution to estimate line flows, node voltage and active power loss using Eq. (13). Specify the estimated active power loss as fitness value to i th particle. Again go to step 4 for all remaining particles.

Step 6: Find the local optimum position pi for i th particle and the global optimum position pg among all particles on the basis of the minimal cost function.
Step 7: Modify SAO global and local parameters using Eq. (1) and Eq. (2).
Step 8: Carry out particle's velocity and position update using Eq. (3) and Eq. (4) respectively.
Step 9: Verify the modified particle's position meets the system constraints Eq. (17) to Eq. (20); if any particles violate the limits, arbitrarily allocate the random solution to the violated position as in step 3; otherwise move to step 10.
Step 10: Whether the halting conditions are met? i.e., is t == tmax?; if yes, ideal feeder reconfiguration in a system, and the load flow solutions are achieved; if no, increase the iteration count, and go to Step 4.
The flow chart for implementing the smell agent optimization is given in Figure 1.

4. RESULT AND DISCUSSION

The SAO optimization methodology is implemented in this study and analysed with the standard radial networks comprises of unbalanced IEEE 123 bus system. The BFS load flow analysis was carried out on the IEEE 123 bus distribution network first on the base case (with tie switches: 24 31 43 58 76) and then with SAO applied reconfiguration. Figure 2 show the optimally reconfigured IEEE 123-bus radial distribution system.

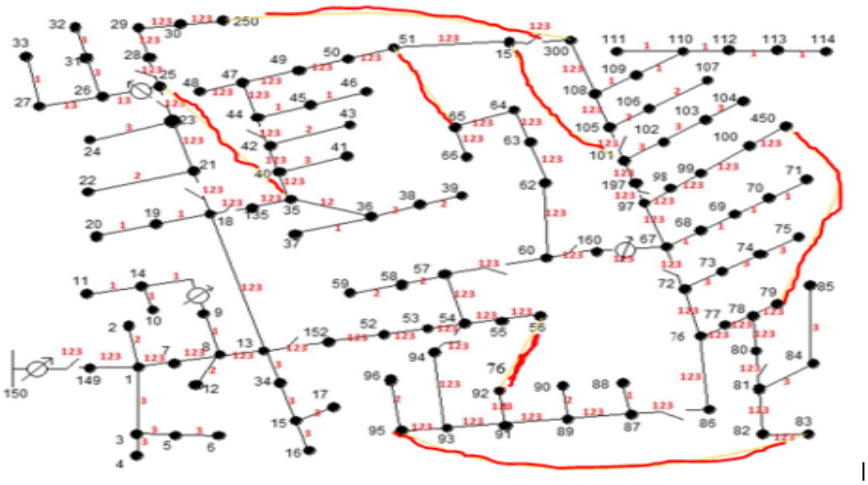

Figure 2: Optimally reconfigured IEEE 123-bus radial distribution system.

The voltage magnitude and active power loss are shown in Figures 3 and 4 respectively.

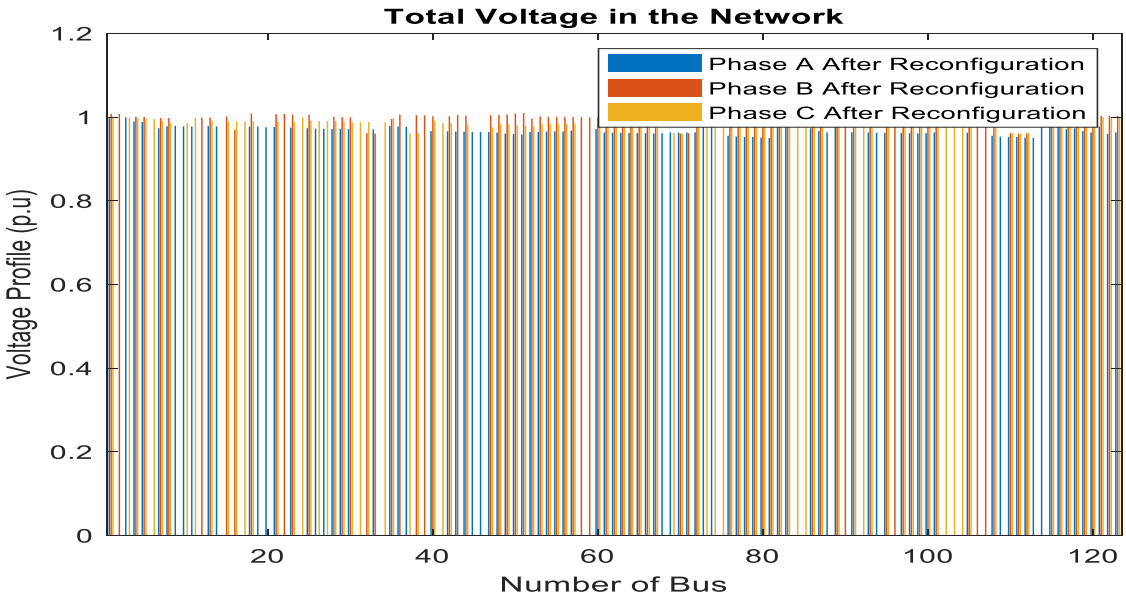

Figure 3: Total Voltage in the IEEE 123 bus Unbalanced Network for Base Case and Reconfiguration

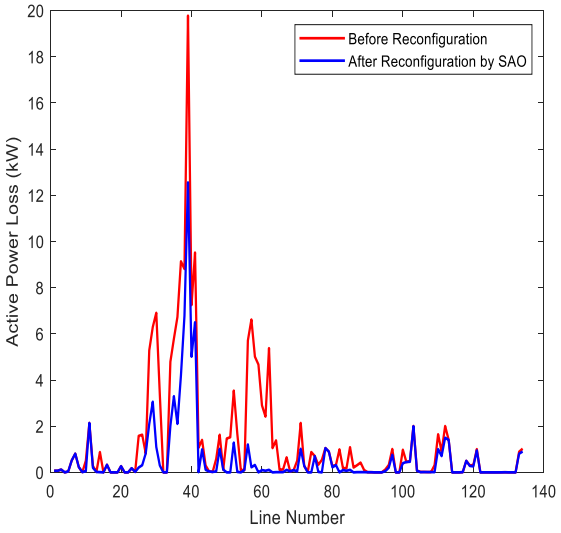

Figure 4: Active Power Loss in the IEEE 123 Bus Unbalanced Network for Base Case and Reconfiguration

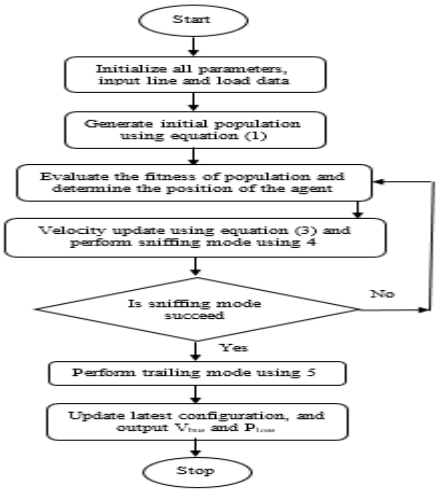

Figure 1: Flow Chart of Proposed SAO Method

The improvement in voltage profile and a reduction in active power loss is achieved as summarized in Table 1.

Table 1. Simulation result of IEEE 123-bus system

Items	Before Reconfiguration	After Reconfiguration
Tie Switches	24 31 43 58 76	28 42 61 72 118
Active Power Loss	115.389kW	67.74kW
Active Power Loss Reduction	----------	41. 30 %
Reactive Power Loss Reduction	----------	43.67%
Minimum Voltage	Phase A 0.9252pu	0.9584pu
	Phase B 0.9442pu	0.9582pu
	Phase C 0.9262pu	0.9873pu

The minimum bus voltage at phase A, B, and C of 0.8992pu, 0.8841pu, and 0.9241pu respectively (in the base case plot) which were improved to 0.998pu, 0.995pu, and 0.984pu after the application of reconfiguration. The tie switches after SAO driven reconfiguration is (28 42 61 72 118). The base case active loss is 115.389kW but with SAO applied reconfiguration the active power loss reduced to 67.74kW representing a 41.30% reduction of the active power loss. From the above test scenarios, it is observed that the SAO algorithm can improved voltage profile and obtain lower active power loss, thus resulting in higher quality solution.

5. Conclusion

This study presented a SAO algorithm for optimal network reconfiguration in for power loss minimization and voltage profile improvement in IEEE 123-bus radial distribution systems. The optimization algorithm consist of a multi-objective function and a number of constraints. Basic analyses carried out include load flow analysis, sensitivity factor analysis, and SAO. Backward and forward load flow analysis was used to compute all the required parameters in the test system. The outcomes obtained from the simulation studies manifest that the presented scheme has been superior in node voltage profile improvement and active power loss minimization.

REFERENCES

Abdelaziz, A. Y., Mohammed, F. M., Mekhamer, S. F., Badr, M. A. L. (2010) Distribution system reconfiguration using a modified tabu search algorithm. Electr. Power Syst. Res. 80(8), 943–953 (2010)

Ahmadi, H., & Martí, J. R. (2015). Minimum-loss network reconfiguration: A minimum spanning tree problem. *Sustainable Energy, Grids and Networks, 1*, 1-9.

Ali A. R., Medhat O. F. (2017) Modeling and Reconfiguration of middle Egypt Distribution Network. *Nine tenth International Middle East Power Systems Conference, Menoufia University,Egypt. 19 – 21 December 2017*

Chakravorty M., and Das D. (2001) Voltage Stability Analysis of Radial Distribution Networks. Electrical Power Energy System, 23, 129-135.

Cruz, M. R. M. (2016). Benefits of coordinating distribution network reconfiguration with distributed generation and energy storage systems.

Dahalan W. M., Mokhlis H., Ahmad R., Abu Bakar A. H., and Musirin I. (2014) "Simultaneous network reconfiguration and DG sizing using evolutionary programming and genetic algorithm to minimize power losses," Arab. J. Sci. Eng., vol. 39, no. 8, pp. 6327–6338, 2014.

Esmaeilian, H. R., Fadaeinedjad, R., & Attari, S. M. (2013). Distribution network reconfiguration to reduce losses and enhance reliability using binary gravitational search algorithm, 385.

Fathy, A., El-Arini, M., & El-Baksawy, O. (2017). An efficient methodology for optimal reconfiguration of electric distribution network considering reliability indices via binary particle swarm gravity search algorithm. Neural Computing and Applications, 1-16.

Kalambe S. and Agnihotri G. (2014) "Loss minimization techniques used in distribution network: bibliographical survey," Renewable and Sustainable Energy Renewable and Sustainable Energy Reviews, vol. 29, pp. 184–200, 2014.

Kansal, S., Kumar, V., & Tyagi, B. (2016). Hybrid approach for optimal placement of multiple DGs of multiple types in distribution networks. International Journal of Electrical Power & Energy Systems, 75, 226-235.

Kaur, M., & Ghosh, S. (2016). Network reconfiguration of unbalanced distribution networks using fuzzy-firefly algorithm. Applied Soft Computing, 49, 868-886.

Meneses P., de Quevedo, Contreras J., Rider M. J., and Allahdadian J. (2015) 'Contingency Assessment and Network Reconfiguration in Distribution Grids Including Wind Power and Energy Storage', IEEE Trans. Sustain. Energy, vol. 6, no. 4, pp. 1524–1533, Oct. 2015.

Nguyen, T. T., Nguyen, T. T., Truong, A. V., Nguyen, Q. T., & Phung, T. A. (2017). Multi-objective electric distribution network reconfiguration solution using runner-root algorithm. Applied Soft Computing, 52, 93-108.

Nguyen, T. T., & Truong, A. V. (2015). Distribution network reconfiguration for power loss minimization and voltage profile improvement using cuckoo search algorithm. International Journal of Electrical Power & Energy Systems, 68, 233-242.

Rani, D. S., Subrahmanyam N., & Sydulu, M. (2015). Multi-objective invasive weed optimization–an application to optimal network reconfiguration in radial distribution systems. International Journal of Electrical Power & Energy Systems, 73, 932-942.

Savier, J., & Das, D. (2007). Impact of network reconfiguration on loss allocation of radial distribution systems. *IEEE Transactions on Power Delivery, 22*(4), 2473-2480.

Tripathy, S., Prasad, G. D., Malik, O., & Hope, G. (1982). Load-flow solutions for ill-conditioned power systems by a Newton-like method. IEEE Transactions on Power Apparatus and systems (10), 3648-3657.

Vasudevan, B., & Sinha, A. (2017). Reliability improvement of reconfigurable distribution system using GA and PSO. Electrical Engineering, 1-13.

Yang, F., Stoupis, J., Donde, V.: (2012) Feeder automation for an electric power distribution system. US Patent 8121740, 21 Feb 2012

Yuvaraj T., Ravi K., Devabalaji K. R. (2017a) Optimal Allocation of DG and DSTATCOM in Radial Distribution System using Cuckoo Search Optimization Algorithm Hindawi Publ. Corp. Model Simul. Eng. 2017.

PAPER 78 – A PRELIMINARY EVALUATION OF THE CHALLENGES OF SUSTAINABLE CONSTRUCTION PRACTICES IN SOUTH AFRICA

J.O. Toyin[1*], M. C. Modupe[2]

[1]Department of Construction Management and Quantity Surveying, Durban University of Technology, Durban South 4001, South Africa
[*]Email: 22175967@dut4life.ac.za

ABSTRACT
The regular design and construction method negatively affect global sustainable development and project delivery. Its consequences on man and nature have advanced a serious global concern, necessitating the need to mitigate the negative impacts by adopting Sustainable Construction Practices (SCP). The South African construction industry has been compelled to adopt SCP to improve sustainable development. Notwithstanding, life evidence has shown that some challenges hinder the global adoption of SCP. Consequently, this paper aims to specifically investigate and evaluate challenges hindering the implementation of SCP among South African built environment professionals. The methodology approach involves a literature review and empirical field survey. The review found 20 challenges from published peered review articles which form the bases for the field survey questionnaire. 85 valid responses were received, the descriptive analysis classified the following 5 challenges as most critical: Additional cost on training: invite of ad-hoc; lack of awareness of sustainability principles; Employees' low knowledge and skills in sustainability; lack of client demand; and Lack of Standardization. The inferential analysis using factor analysis grouped the variables into 4 components: Planning related Challenges; Management and Contractual related challenges; Knowledge related factors; Financial related challenges. The study reveals the critical challenges facing the implementation of SCP adoption in the South African construction industry. The findings will promote and improve the adoption of SCP in South Africa and enhance global understanding of SCP.

KEYWORDS: Construction; Housing; Project management; Sustainability; South Africa.

26. INTRODUCTION

The huge to adopt sustainable construction practices in the built environment has received substantial attention, due to the global concern on the ecological system. An ecological system is a biological community made up of all the living things (including people) in a specific area as well as the non-living things that the living things interact with, such as the air, water, and mineral soil. The global concern on the ecosystem sustainability is a key driver that pushes every sector towards sustainability practices. Studies have proven that there are three pillars of sustainability. Those are planet or environment, social or people, and profit or economics. Several reviews on sustainability literature highlight the fact that more attention has been tailored towards the environmental aspect since it forms the base for the other aspects of sustainability. It is an evident that human activities have drastically affected the ecosystem, leading to environmental problems such as undue climate change, shortage of raw materials, and ecosystem degradation, among others. As a result, the construction industry has a severe impact on the environment as a major contributor to these problems. The industry's conventional approach has been founded on the idea that investments and innovations stimulate economic growth while also meeting the requirements and wants of consumers (Baloi 2003). Nonetheless, it is important to acknowledge that the industry's processes and products have negative effects on the environment. Water, energy sources, and natural resources are all heavily used during construction. Governments, environmentalists, and other stakeholder groups that are aware of sustainability practices' advantages frequently seek out sustainable construction approaches. Almost 171 nations have now implemented environmental management frameworks and systems using the ISO (International Organization for Standardization) 4000 standard to address environmental problems brought on by greenhouse gas emissions (Ayarkwa et al. 2022). However, understanding sustainable construction practices in South Africa is at its infant stage of research which requires further exploration and study. For instance, the concept of sustainable construction practices is a new notion in developing countries such as South Africa and is hardly practiced by the construction industry in the country. Evidence shows some challenges undermine the implementation of sustainable construction practices in developing countries. Therefore, this study aims to evaluate those challenges faced during the implementation of Sustainable construction practices among South African built environment professionals.

27. LITERATURE REVIEW

2.1 SUSTAINABILITY

To achieve sustainability, structures, organizations, and resources must be managed in a way that balances meeting present and future demands with resolving an array of issues that arise from managing resources for both the short and long term. (Ayarkwa et al. 2022).

2.1 SUSTAINABLE CONSTRUCTION PRACTICE

The goal of sustainable construction practices is to reduce the industry's negative environmental impact. Using recyclable and renewable materials, reducing overall waste generated on site, lowering the finished building energy usage, and safeguarding natural habitats both before and after construction. The usage of energy and emissions by the building industry have a big impact on the environment. In addition to the damage of natural habitats brought on doing the construction phase, energy is required on the project site.

Heavy construction equipment continues to rely significantly on fossil fuels. The energy contained in the building materials and the energy demands of the structures when they are in use are also the responsibility of the built environment.

The construction sector is responsible for 40% of CO_2 emissions and 36% of the world's energy consumption. At the same time, the production and delivery of materials can have a big impact on carbon emissions. Mining of raw resources can contaminate water streams. Because of this, the annual CO2 emissions from cement manufacturing are currently 2.8 billion tonnes worldwide, but if urbanization rates keep going at their current pace, they might reach over 4 billion tons. The International Council for Research and Innovation in Building and Construction published Agenda 21 for Sustainable Construction to minimize those impressions (Baloi 2003). Hence, the main principles of sustainable construction were highlighted as seen in figure 1.

Figure 1: Sustainable construction main principles

2.2 CHALLENGES OF SUSTAINABLE CONSTRUCTION PRACTICE

Over the years, there have been several difficulties with delivering sustainable construction projects. Insufficient awareness of sustainable construction procedures, employees' low knowledge, and skills in sustainability are the challenges that are frequently raised (Aghimien et al., 2019; Ogungbile and Oke 2018; Opoku and Ahmed, 2014). This resulted in hindrance to the rapid implementation of SCP in the construction industry. Notwithstanding, lack of support from the company managing board is another critical challenge Ahmed and El-Sayegh, 2022; Thomson and El-Haram, 2019; Zhou and Lowe, 2003). This will drastically hinder the adoption of SCP in such companies. In the same vein lack of standardization, and unclear contract requirements (Khalil et al. 2021; Ogungbile and Oke 2018; Opoku and Ahmed, 2014) may lead to mediocre quality control that could have a remarkable impact on the building and its environment. Table 1 reveals the summary of the challenges identified during the review process.

Table 1: Challenges of Sustainable construction practices adoption

Code	Challenges	Reference
CSCP1	Availability of sustainable construction materials.	(Abolore, 2012; Aghimien et al., 2018; Aghimien et al., 2019; Ahmed and El-Sayegh, 2022; Alqadami et al. 2020; Aigbavboa et al., 2017; Ayarkwa et al., 2022; Baloi, 2003; Hussin et al., 2013; Hwang and Ng 2013; Khalil et al. 2021;
CSCP 2	Lack of sustainability measures.	
CSCP 3	The cost associated with sustainability	
CSCP 4	Time constraints	
CSCP 5	Fear of return on investment in a short-term period	
CSCP 6	Incomplete complicated sustainable design	
CSCP 7	lack of performance information on sustainable buildings	
CSCP 8	lack of client demand	
CSCP 9	low profitability to the industry	

Code	Challenges	Reference
CSCP 10	Rigorous procurement process	Ogungbile and Oke 2018; Opoku and Ahmed, 2014; Thomson and El-Haram, 2019; Zhou and Lowe, 2003)
CSCP 11	Lack of sustainable product information	
CSCP 12	Lack of support from the company managing board	
CSCP 13	Employees low knowledge and skills in sustainability	
CSCP 14	Client requirement.	
CSCP 15	Contract requirement	
CSCP 16	Additional cost on training: ad-hoc invite	
CSCP 17	lack of awareness of sustainability principles	
CSCP 18	Technical difficulty during the construction process	
CSCP 19	Lack of budget to promote sustainability by the government	
CSCP 20	Lack of Standardization	

28. RESEARCH METHOD

The methodology approach adopted in this study is in two stages. The study begins by identifying the critical challenges hindering the adoption of sustainable construction practices in the construction sector using a qualitative method, by reviewing published empirical studies on the study focus. This included journal articles, book chapters, and conference papers discussing sustainable construction challenges. Studies were identified from the literature search for inclusion in the review using the following keywords string: "sustainable construction"; "challenges." These studies' titles and abstracts were then scrutinized to remove any irrelevant data, and the remaining articles were further screened by reading their full text to determine whether they met the study's goals. These resulted in the identification of 20 crucial challenges deterring the adoption of sustainable construction practices in the construction industry. The selected SCP challenges are those that have been given significant consideration in the studies carried out in many nations, Toyin and Mewomo (2022) and Chan et al. (2018) used a similar approach. The authors concurred that using well-known characteristics is preferable for a statistical research study since it makes it easier for respondents to answer and enables more accurate feedback.

Thereafter, a statistical web-designed survey questionnaire was compiled to collect quantitative data. In other to check the relevance and reliability of the questionnaire, two main steps were followed. Firstly, the questionnaire was reviewed by 3 sustainable environment specialist who is construction managers with over 5years of practicing experience and an academic who specializes in sustainable construction. The process enables them to scrutinize the questionnaire to confirm that unclear terminologies were not contained in the survey and that appropriate technical terms were used. The questionnaire covers the challenges and remedies to address those challenges. To choose the appropriate respondent, the snowballing sampling technique was used, which was a similar strategy to that used by Gledson et al. (2016) and Toyin and Mewomo (2022). In total 190 target professionals received the questionnaire, thus 85 survey questionnaires were dully filled and returned. Thus, representing a 45% response rate as seen in table 2.

On a five-point Likert scale, 1 being "not significant" and 5 being "strongly significant," the SCP difficulties were evaluated. Using Cronbach's α techniques is one of the effective ways to verify the validity of the quantitative questionnaire's reliability (Toyin and Mewomo, 2022). These techniques establish the typical link or internal regularity between the variables/factors in a questionnaire. The alpha (α) value for the 20 SCPC was obtained using IBM SPSS (Statistical Package for Social Scientists), and it was 0.916. Based on the five-point Likert scale, they show that the measuring scale is accurate at a 5% significant level. The statistical information gathered can thus be used to perform further descriptive and inferential analysis. In this study, part A sought the respondents' demographic data whereas section B sought the SCPC. The professionals that work in the built environment in South Africa are the target audience.

3.1 DESCRIPTIVE ANALYSIS

The SCPC variables were ranked using the mean item score (MIS), and their level of significance was ranked using the relative importance index (RII). To determine the significance of each component, the 5-point Likert scale was used to evaluate the variables.

3.2 INFERENTIAL ANALYSIS

The data analysis used is Factor Analysis (FA) through Principal Component. This analysis was used to evaluate the perceived cluster where each variable resonates, from which a concise component of those challenges can be formed for easy understanding. FA is a data reduction and analysis method; it is used to extract information

regarding interrelations among a set of variables (Ahmed and El-Sayegh 2022). FA has been used in previous studies related to construction management. Toyin and Mewomo 2023 used FA to categorize and group barriers hindering the implementation of Building Information Modelling (BIM) in the Lagos Nigeria construction industry. Ahmed and El-Sayegh 2022 also used FA to group the challenges of sustainable construction project delivery in the UAE. Similarly, Khalil et al. (2021) utilized FA to group challenges for the implementation of SCP in Libya. FA comprises three distinctive steps. Firstly, assessment of data suitability. This is when the Kaiser-Meyer-Olkin (KMO) measurement of sample adequacy is higher than the limit of 0.5 and Cronbach's α, reliability is greater than 0.7, and when Bartlett's test of sphericity has a significant level of 0.05. Secondly, factor extraction. In this study, the PCA (Principal Component Analysis) was employed to produce a straightforward solution with the fewest variables necessary to explain the substantial variance in the original data. Lastly, is the factor rotation which helps give a clearer picture of the extracted factors? The factors are provided by SPSS 29 as groups of variables, and the researcher interprets these groups based on theoretical knowledge and earlier research.

29. RESULTS AND DISCUSSION

4.1 RESPONDENT PROFILE

Table 1 show the profile of the built professionals in South Africa with experience in sustainable construction who voluntarily took part in the survey.

Table 2. Respondents' demography

Category		Respondent (Total 85)	
		Number	Percentage
Gender	Male	65	76.5%
	Female	20	23.5%
Race	South African	60	70.6%
	Indian	11	12.9%
	White	7	8.2%
	Others African	7	8.2%
	Other	0	0%
Years of experience	1-5	5	5.9%
	6-10	29	34%
	11-15	34	40%
	16-20	5	5.9%
	21 years and above	1	1.1%
Current role on project	Site Manager	18	21.1%
	Contractor	9	10.6%
	Project Manager	24	28.2%
	Consultant	22	25.9%
	Sub-contractor	12	14,1%
Profession	Architect	18	21.2%
	Construction Manager	26	30.6%
	Engineer	24	28.2%
	Quantity Surveyor	17	20%
Company sector	Private	54	63.5%
	Public	31	37.5%

4.2 DESCRIPTIVE DATA PRESENTATION AND DISCUSSION

Table 3 presents the descriptive analyses of the data received from the survey. From this table, it could be summarized that five out of the identified challenges were perceived to be strongly significant. Those are SCPC16: Additional cost on training: ad-hoc invite. The extra cost incurred in bringing SCP experts to train the company staff was unanimously ranked first among others. Thus, the cost becomes a burden on the firm, this will have an effect since it will reduce the expected profit from the project. SCPC17: lack of awareness of sustainability principles. It is important for professionals to be aware of the latest development in their field of practice, although the participants are aware of SCP, most of them lack an understanding of SCP principles. SCPC13: Employees' low knowledge and skills in sustainability. It is expected of the construction firm to engage in regular training and workshop for their employee in other to catch-up with the innovation in the industry. SCPC8: lack of client demand. This challenge was ranked 4th among others, this indicated that cl that client decisions cannot be neglected in the choice of design, nevertheless, it will significantly boost the implementation of SCP if client can quickly

realise the profound benefit during the lifecycle of the building. Lastly, SCPC20: Lack of Standardization. In the. In the construction industry, to curb differences in standards adopted, it is important to have a regulatory standard that will guide the professionals during the discharge of their duties. In the case of SCP, it is of important to have a regular standard that would guide the implementation of SCP in the South African construction industry.

Also, from Table 3, 3 (15%) of the variables were ranked least significant, those are SCPC10: Rigorous procurement process. At the present level of SCP adoption in South Africa, it can be reported that the procurement process is not really a significant challenge, notwithstanding, the mean weight is above the average mean, thus it condoles some level of importance. SCPC12: Lack of support from the company managing board. This was ranked 19th having a mean weight slightly above average, this evidence still indicates that there are some firm's board managers that still refused to fully embrace SCP. This could be because of several factors such as ignorance of acquiring desired Skills and competencies in their field of expertise (Toyin and Mewomo 2022). SCPC6: Lack of sustainability measures. This was ranked 20th which means is not much significant, also from the mean weight of 2.51 and Relative Importance Index (RII) of .05, it can be computed that the challenge is on the average bottom, thus regarded as neutral.

Table 3: Descriptive result

Code	Mean	Std. Dev.	RII	Ranking	Sig. Level
SCPC16	4.13	.768	0.83	1st	SS
SCPC17	4.07	.784	0.81	2nd	SS
SCPC13	4.06	.980	0.81	3rd	SS
SCPC8	4.05	.830	0.81	4th	SS
SCPC20	4.05	.785	0.81	5th	SS
SCPC19	3.85	1.102	0.77	6th	S
SCPC1	3.76	.972	0.75	7th	S
SCPC3	3.69	1.091	0.74	8th	S
SCPC2	3.68	.790	0.74	9th	S
SCPC5.	3.59	1.003	0.72	10th	S
SCPC18	3.54	.825	0.71	11th	S
SCPC14	3.51	.854	0.70	12th	S
SCPC7	3.47	.959	0.69	13th	S
SCPC9	3.44	.981	0.69	14th	S
SCPC11	3.31	.976	0.66	15th	S
SCPC15	3.20	.910	0.64	16th	S
SCPC4	3.06	1.028	0.61	17th	S
SCPC10	3.01	1.220	0.60	18th	N
SCPC12	2.85	1.086	0.57	19th	N
SCPC6	2.51	1.183	0.50	20th	N
SIGNIFICANT LEVEL RATING					
Descriptive Statistic N=85	**RII values**		**Significance level**		
	0.81≤RII≤1.00		Strongly significant (SS)		
	0.61≤RII≤0.80		Significant (S)		
	0.41≤RII≤0.60		Neutral (N)		
	0.21≤RII≤0.40		Less significant (LS)		
	0.00≤RII≤0.20		Not significant (NS)		

a. INFERENTIAL DATA PRESENTATION AND DISCUSSION

As previously explained, table 4 present the PCA of the variable, the principle is to reduce the factors into simple manageable clusters for proper understanding. Thus, the variables where then clustered into four components, namely: Planning related challenges; contractual and management related challenges; knowledge related challenges and financial related challenges.

Table 4: Rotated component cluster

	Component				
CODE	1	2	3	4	Communalities
Planning related Challenges					

SCPC10	Rigorous procurement process	**.768**			***.875***
SCPC8	lack of client demand	**.768**			***.716***
SCPC18	Technical difficulty during the construction process	**.698**			***.681***
SCPC19	Lack of budget to promote sustainability by the government	**.693**			***.717***
SCPC4	Time constraints	**.662**			***.884***
SCPC3	The cost associated with sustainability	**.636**			***.728***
Contractual and Management related challenges					
SCPC12	Lack of support from the company managing board		**.704**		***.819***
SCPC20	Lack of Standardization		**.685**		***.720***
SCPC6	Incomplete or complicated sustainable design		**.629**		***.566***
SCPC2	Lack of sustainability measures.		**.595**		***.790***
SCPC15	Unclear contract requirement		**.555**		***.730***
Knowledge related challenges					
SCPC11	Lack of sustainable product information			**.790**	***.807***
SCPC7	lack of performance information on sustainable buildings			**.773**	***.751***
SCPC13	Employees low knowledge and skills in sustainability			**.681**	***.699***
SCPC1	Unavailability of sustainable construction materials.			**-.663**	***.775***
SCPC17	lack of awareness of sustainability principles			**.639**	***.638***
Financial related challenges					
SCPC16	Additional cost on training: ad-hoc invite			**.652**	***.833***
SCPC9	Low profitability to the industry			**.592**	***.622***
SCPC5	Fear of return on investment in a short-term period			**.579**	***.590***
SCPC14	Client requirement			**.544**	***.726***

4.3.1 Planning related Challenges

The Six challenges under this component explain the planning-related challenges which affect the adoption of sustainable construction practices. These are rigorous procurement process; lack of client demand; Technical difficulty during the construction process; Lack of budget to promote sustainability by the government; Time constraints and the cost associated with sustainability. Adequate planning is important before embarking on any construction project. Aigbavboa et al. (2017) found that professionals in South Africa believe there is going to be increase in costs to comply with the standards of sustainability. This mind-set had a negative effect on the adoption of SCP in South Africa. As a result, it is expected the professionals are enlightening on the understanding of the long-time benefits that would be realised during the life circle of the project. Aghimien et al. 2019 suggested that to improve sustainable construction practices, a change from the norm to adopting innovative ideas is necessary for the construction industry. Thus, proper enlightenment of construction clients and professionals in terms of sustainable construction is needed to alienate the client's fear of an increase in investment cost and create a proper understanding of its inherent benefits. This will not only increase client interest, but it will also accelerate the provision of funds by the government and developers toward sustainable construction practices in South Africa.

4.3.2 Management and Contractual related challenges

The five challenges clustered under this component explain the contractual and management challenges hindering the quick acceptance of SCP in the South African construction environment. These are Lack of support from the company managing board; Lack of standardization; Incomplete or complicated sustainable design; Lack of sustainability measures; Unclear contract requirements. The acceptance of any innovative practice in the construction industry lies on the top management's decision. Therefore, it is important that such an idea is accepted by the managing board member. Khalil et al. (2021) opined that the leadership of any construction organisation should be at the forefront of enforcing sustainable construction practice. Contracts should also include incentives for the adoption of sustainable construction practices, according to Ahmed and El-Sayegh (2022); Ogungbile and Oke (2018). These authors recommended cost-plus-fee arrangements with special features that encourage contractors to submit bids for sustainable projects and do away with the requirement of including a green risk premium in contract.

4.3.3 Knowledge related factors

The five challenges extracted for factor 3 were Lack of sustainable product information; lack of performance information on sustainable buildings; Employees' low knowledge and skills in sustainability; Unavailability of

sustainable construction materials; lack of awareness of sustainability principles. This finding is in line with the findings of Ahmed and El-Sayegh (2022). Experience plays a key role in the construction industry. Being a knowledgeable skilled or unskilled labour in the construction process will aid smooth delivery of the project. Toyin and Mewomo (2022) found that construction management graduate finds it difficult to secure a job due to their low level of knowledge about innovative practices. Therefore, it is important to sensitize the workers and conduct training/workshops with SCP to ensure they understand the process and principles. Project managers should also schedule regular meetings to update the entire team on the status of the project.

4.3.4 Financial related challenges

The four extracted for factor 4 were the challenges that are cost related. This cluster explains the financial challenges encountered during the process of practicing sustainable construction. The need to hire experts to train the employee on the principle of SCP may have a significant implication on the budget of the project (Hussin 2013). Low profitability to the industry after investing heavily on the project tends to discourage the managing board from practicing sustainable construction (Alqadami et al. 2020). Fear of return on investment in a short-term period is a critical challenge that developers look at before investing in any innovative means of construction (Hwang and Ng 2013). Client requirements play a key role in the cost implication of the project. Introducing new principles or methods of construction as against what was initially agreed on before the start of the project may result in the abandonment of the project or increase the project's total cost.

30. CONCLUSION AND RECOMMENDATION

This study examines the challenges limiting the adoption of sustainable construction practices in the South African built environment. The study through the preliminary literature review highlights the challenges facing the acceptance of SCP. Through the empirical survey, the most critical challenges to South African built environment professionals were identified. The results of this study have important practical implications because they show that most employees have low knowledge and skills in sustainability, there is lack of awareness of sustainability principles, there is a lack of client demand for SCP, built professionals are unfamiliar with SCP, Additional cost on training: ad-hoc invite and Lack of Standardization are what majorly discourage the adoption of SCP in South Africa from a preliminary view. Those critical challenges were related to Planning; Knowledge; Management and Contractual; and Financial challenges.

The following recommendation could be suggested to enhance the future adoption of SCP in the South African construction industry and other related developing countries who also faces similar challenges:

- There may be a research focus on the development of SCP framework which will guide through the design and construction phases and also beyond those phases.
- The government may provide supporting funds towards sustainable practices: for materials, services and knowledge impacts to the workers.
- The top managers may organise regular training on the latest update as regards innovations towards sustainable development.

It is believed that the implementation of those recommendation will drastically provide an enable environment for the practice of sustainable construction practice in South Africa and beyond, thereby, contributing richly to the global sustainable development.

ACKNOWLEDGEMENT

I thank the DUT RESEARCH AND POSTGRADUATE SUPPORT Directorate and the conference funding committee who granted me the privilege to attend the FETiCON conference physically. The financial support is hereby appreciated.

REFERENCE

Abolore, A. A. (2012). Comparative study of environmental sustainability in building construction in Nigeria and Malaysia. Journal of Emerging Trends in Economics and Management Sciences, 3(6), 951-961.

Aghimien, D. O., Adegbembo, T. F., Aghimien, E. I., and Awodele, O. A. (2018). Challenges of sustainable construction: a study of educational buildings in Nigeria. International Journal of Built Environment and Sustainability, 5(1).

Aghimien, D. O., Aigbavboa, C. O., and Thwala, W. D. (2019). Microscoping the challenges of sustainable construction in developing countries. Journal of Engineering, Design and Technology, 17(6), 1110-1128.

Ahmed, S., and El-Sayegh, S. (2022). The challenges of sustainable construction projects delivery–evidence from the UAE. Architectural Engineering and Design Management, 18(3), 299-312.

Alqadami, A., Zawawi, N. A., Rahmawati, Y., and Alaloul, W. (2020, May). Challenges of implementing green procurement in public construction projects in Malaysia. In IOP Conference Series: Materials Science and Engineering (Vol. 849, No. 1, p. 012047). IOP Publishing.

Aigbavboa, C., Ohiomah, I., and Zwane, T. (2017). Sustainable construction practices:"a lazy view" of construction professionals in the South Africa construction industry. Energy Procedia, 105, 3003-3010.

Ayarkwa, J., Opoku, D. G. J., Antwi-Afari, P., and Li, R. Y. M. (2022). Sustainable building processes' challenges and strategies: The relative important index approach. Cleaner Engineering and Technology, 7, 100455.

Baloi, D. (2003, September). Sustainable construction: challenges and opportunities. In 19th Annual ARCOM Conference (Vol. 1, pp. 289-297). University of Brighton, Association of Researchers in Construction Management.

Chan, A P C, Darko, A, Olanipekun, A O and Ameyaw, E E (2018) Critical barriers to green building technologies adoption in developing countries: The case of Ghana, Journal of Cleaner Production, 172, 1067-1079.

Gledson, B, Hilton, D and Rogage, K (2016) Benchmarking BIM Levels of Training and Education amongst Construction Management Practitioners, In: Chan, P W and Neilson, C J (Eds.), Proceedings 32nd Annual ARCOM Conference, 5-7 September 2016, Manchester UK, Association of Researchers in Construction Management, 343352.

Hussin, J. M., Rahman, I. A., and Memon, A. H. (2013). The way forward in sustainable construction: issues and challenges. International Journal of Advances in Applied Sciences, 2(1), 15-24.

Hwang, B. G., and Ng, W. J. (2013). Project management knowledge and skills for green construction: Overcoming challenges. International journal of project management, 31(2), 272-284.

Khalil, A., Rathnasinghe, A. P., and Kulatunga, U. (2021). Challenges for the implementation of sustainable construction practices in Libya. Construction Economics and Building, 21(3), 243-261.

Ogungbile, A. J., and Oke, A. E. (2018). Sustainable construction practices in West African countries. In *Energy sustainability in built and urban environments* (pp. 3-15). Singapore: Springer Singapore.

Opoku, A., and Ahmed, V. (2014). Embracing sustainability practices in UK construction organizations: Challenges facing intra-organizational leadership. Built Environment Project and Asset Management, 4(1), 90-107.

Thomson, C. S., and El-Haram, M. A. (2019). Is the evolution of building sustainability assessment methods promoting the desired sharing of knowledge amongst project stakeholders?. Construction management and economics, 37(8), 433-460.

Toyin, J O and Mewomo, M C (2022) Building Information Modelling Core Competencies Expected of Construction Management Graduates: A Nigerian Construction Industry Case Study In: Tutesigensi, A and Neilson, C J (Eds) Proceedings of the 38th Annual ARCOM Conference, 5-7 September 2022, Glasgow, UK, Association of Researchers in Construction Management, 62-71

Toyin, J. O., and Mewomo, M. C. (2023). An investigation of barriers to the application of building information modelling in Nigeria. Journal of Engineering, Design and Technology, 21(2), 442-468.

Zhou, L., and Lowe, D. J. (2003, November). UK Building Procurement System and Sustainability. In First Scottish Conference of Postgraduate Researchers of the Built & Natural Environment (ProBE), 18th–19th November (pp. 29-40).

PAPER 83 – A REVIEW OF THE EFFECT OF EGGSHELL POWDER ON THE PROPERTIES OF RECYCLED POLYMERS

E. U. Inelo[1, a] G. O. Achurefe[1,b]

[1]Department of Chemical Engineering, University of Ilorin, Ilorin, Nigeria.

Email: [a] evelyninelo@gmail.com

[b] gloria.achurefe@gmail.com

ABSTRACT

Agricultural wastes have become a major source of environmental pollution as they have been implicated in the formation of greenhouse gases. Eggshell is a poultry waste that is available in large quantities and the disposal of has become a cause of pollution due to the generation of unpleasant odours and growth of microorganisms of which 6.4 million metric tonnes of eggshell waste are dumped globally in landfills. This paper reviews the effects of incorporating eggshell powder (ESP) on the properties of recycled polymers. It covers the preparation and characterisation of eggshell powder, its incorporation into recycled polymers, and the resulting changes in mechanical and thermal properties. In recycled low-density polyethene, a maximum tensile strength of 10.64Nm^{-2} was obtained at 10wt. % of ESP after which the tensile strength decreased at 12 wt%. For recycled High-density Polyethene/ethylene vinyl acetate (rHDPE/EVA) composite, a decrease in elongation at break and tensile strength were obtained with increasing ESP filler loading. However, the addition of a coupling agent (3- aminopropyltriethoxysilane) resulted in higher tensile strength and modulus. Another coupling agent (Benzyl Urea) was used on rHDPE/EVA composite and a significant improvement in tensile strength and modulus of elasticity was obtained.

KEYWORDS: Eggshell powder, Recycled polymers, Environmental pollution.

1. INTRODUCTION

Recycling polymers is a way to mitigate the environmental menace caused by heaps of polymeric waste produced from a continued increase in the consumption of polymers (mainly plastics) (Achilias et al., 2007) and also conserve natural oil and gas from which these polymeric materials are made (Hamad et al., 2013). The Food and Agriculture Organization of the United Nations (FAO) reported that landfills worldwide received 6.4 million tons of eggshell. This statistical information suggests that there is a significant opportunity to recycle and repurpose eggshell in polymer products (Bhagavatheswaran et al., 2019). The use of eggshells as an additive for concrete has been established (Hamada et al., 2020). Due to its rich $CaCO_3$ content which is a hard mineral (Ho et al., 2013), eggshell powders (ESP) are possible strengthening additives for recycled low-density polyethene (rLDPE) composites which are lightweight and a potential automobile component (Bello et al., 2021). This paper is focused on reviewing recycled High-density polyethene/ Eggshell powder (rHDPE/ESP) composite with their properties evaluations to establish their future applications.

2. THEORETICAL ANALYSIS

Recycled plastics are different from virgin raw material because it has been processed. This results in some level of deterioration and aggravated characteristics that make the starting raw material base plastic of lower grade properties (Golkaram et al., 2022). Also, the recycled polymers usually don't come from the precise plastic, resulting in incompatibility problems in the recycled plastic mix hence additives are important to improve their properties to make quality products within specifications that make them suitable for a range of applications (Vasudeo et al., 2016). Polymers can be recycled by reuse, mechanical recycling, and chemical recycling. However, reuse is not appreciably practised when it comes to plastics. Plastic products are generally dumped after first use or if reused do not continue for a long time, especially in food applications. A few examples of reuse can be seen in refilled drink bottles with washing liquids or consumers refilling and hence reusing their plastic bottles at home. Mechanical recycling involves grinding, reprocessing, and compounding the plastic to yield a new product that may or may not retain its former use. In chemical recycling, the polymer waste

is converted back into its oil/hydrocarbon component in the cases of polyolefins and monomers in the case of polyesters and polyamides, which can be used as raw materials for new polymer production and petrochemical industry, or into the pure polymers using suitable chemical solvents (Hamad et al., 2013; Khalid et al., 2022; Ncube et al., 2021; Ragaert et al., 2017).

3 METHODOLOGY

3.1 Preparation of eggshell powder

The eggshells were prepared differently by the authors:

Research by Farahana et al. (2014) on recycled high-density polyethene/ethylene vinyl acetate/eggshell powder (rHDPE/EVA/ESP) cleaned, dried, and ground the eggshell into a fine powder using a kitchen blender to an average particle size of 63µm. it was then dried in a vacuum oven at 80°C until a consistent weight was achieved.

Hanif et al. (2020) researched on rHDPE/EVA with uncarbonised and carbonised eggshell powder. The authors washed and dried the eggshell in a conventional oven at 80°C until a constant weight was achieved. The dried eggshells were crushed into smaller pieces and ground into powder using planetary ball mills set at 300rpm for 60 minutes and a kitchen blender. This was sieved to obtain a particle size of 63µm to remove coarse particles. A part of the eggshell was carbonised in a muffle furnace at 700°C for approximately 3 hours.

Farm et al. (2022) washed the eggshells and dried them at room temperature for 24 hours, it was ground using a blender and sieved to a mesh size of 32µm using a sieve shaker. Carbonised eggshell powder (CESP) was also prepared by thermally treating the eggshell at a low pyrolysis temperature of 400°C for one hour.

Bello et al. (2021) studied the effect of eggshells on recycled low density polyethylene (rLDPE). The eggshell was prepared using three different methods, which are manual crushing, disc grinding, and 70 hours of ball milling.

3.2 Preparation of recycled polymer composites

Farahana et al. (2014) prepared rHDPE composites by melt blending technique in an internal mixer. rHDPE was mixed at 160°C, 50 rpm for 4 minutes. Then, pre-determined quantities of EVA (Ethylene Vinyl Acetate), maleic anhydride (MA) which acted as a compatibilizer to enhance the interfacial interaction between the rHDPE and EVA matrix and ESP with filler loading of 0,5,10,15,20,25 wt.% wereadded and mixed for an additional 10 minutes. The composite matrix of rHDPE/EVA had a constant composition of 50wt.% each in all formulations. The resulting molten samples were then compressed into 2mm thick sheets using a hydraulic press at 160 °C for 2 minutes and cooled under pressure for 4 minutes.

In a related study by Farahana et al. (2015b), the compatibilizer used was Benzyl Urea (BU) with rHDPE/EVA (50/50 phr) composites. The composite was prepared through melt blending process in an internal mixer at a temperature of 190°C and a speed of 50rpm for 4 minutes. Pre-weighed amounts of EVA, BU, and ESP were then added to the mixer for an additional 6 minutes. The filler loading of ESP was 0,5,10,15,20,25 phr of the matrix composition. The resulting molten samples were compressed into 2mm

-thick sheets using a hydraulic press at a temperature of 190°C for 2 minutes and then cooled under pressure for 4 minutes.

In another study by Farahana et al. (2015a), 3-Aminopropyltriethoxysilane (APTES) was used as a coupling agent with rHDPE/EVA(50/50phr) composites. Melt blending was used to prepare the composites in an internal mixer at 190°C at a speed of 50rpm for 4 minutes. Pre-weighed EVA and ESP(filler loadings of 0,5,10,15,20,25 phr) or treated ESP(5,10,15,20,25 phr) were then added to the rHDPE, and the mixture was blended for another 10 minutes to obtain a homogeneous composite. The composite was then discharged from the mixer, pressed into round pieces and allowed to cool.

Hanif et al. (2020), prepared rHDPE/EVA (70/30) composites by melt blending at a temperature of 160°Cwithin 10 minutes at 50rpm. The composites were prepared by preheating rHDPE pellets for 2 minutes in a mixer, followed by EVA pellets and allowed to mix for 5 minutes. ESP (filler loading of 5-25 wt%) or carbonised ESP (CESP) with filler loading of 5-25 wt% were added afterwards for 3 minutes. The resulting blends were subjected to compression moulding for 10 minutes and cool pressed for 5 minutes.

Farm et al. (2022) prepared rHDPE by first cleaning the containers, cutting them into small pieces then melted in an internal mixer at 175°C at 32rpm. Eggshell powders were added to the melted HDPE at specific ratios for 8 minutes, after which the mixture was crushed and compressed using a hydraulic hot press. The compression moulding process involved preheating at 175°C for 3 minutes, followed by compression for 4 minutes. Each composite sample was prepared with a weight ratio of r-HDPE/filler varied at 90/10, 80/20, and 70/30.

Bello et al. (2021), prepared the rLDPE composites by dissolving 2 wt.% ESP in absolute ethanol, agitating the mixture in a ball mill, adding rLDPE to the mixture, heating and stirring until the ethanol vaporized, thereafter, palm kernel oil was added as a plasticizer after which the mixture was processed using a two-roll polymer mill. The resulting composite sheets were hot pressed and moulded using hydraulic compression to produce various samples for analysis. The process was repeated with increasing weight per cent of ESP up to 12 wt. %.

4 RESULTS AND DISCUSSION

4.1 Mechanical properties

4.1.1 Tensile strength

A study by Hanif et al. (2020) showed that the addition of ESP and CESP fillers decreased the tensile strength of the rHDPE/EVA blend composites. The author proposed the decrease in tensile strength was due to poor filler distribution and low interaction within the matrix. The increased filler concentration impeded good stress transfer between the matrix and the reinforcement filler when external stress was applied. However, rHDPE/EVA reinforced with CESP filler showed superior properties due to the removalof the spongy portion and the subsequent elimination of volatile matters during carbonisation. Results also showed that the tensile modulus increased for both composites when the amount of filler was increased. This was due to the presence of small and rigid filler particles that gave a better reinforcement structure in composites, improving stiffness and reducing the ductility of the blend composites. In general, the rHDPE/EVA/CESP composites had better filler particle dispersion andtended to form smaller agglomerates than the rHDPE/EVA/ESP composites. The author suggested that this was due to any separation in the ESP filler as a result of loose particles being removed when carbonising the ESP.

Farahana et al. (2015b) observed that the incorporation of ESP in the composite decreased its tensile strength and the author suggested that this was due to the non-polar and polar nature of the rHDPE and EVA polymer system, respectively, and the inability of ESP to support stress transfer. However, the addition of BU increased the tensile strength by facilitating stress transfer and improving interfacial adhesion. In a related study by Farahana et al. (2014), the compatibilizer used was maleic anhydride (MA) andresults showed that the tensile strength of the composites decreased with increasing ESP content which was proposed by the author to be due to poor interaction force between the components. However, the addition of MA improved the tensile strength by facilitating stress transfer between phases and increasing interfacial adhesion.

The effect of adding ESP filler to rHDPE/EVA matrices was studied by Farahana et al. (2015a) with and without APTES coupling agent and results on the tensile strength showed that the tensile strength of both composites decreased as the concentration of ESP increased due to weak interfacial adhesion. It was suggested that the addition of APTES coupling agent promoted better interfacial adhesion, resulting in improved stress transfer and higher tensile strength.

Bello et al. (2021) studied the effect of eggshell on RLDPE and observed that the addition of ESP increased the tensile strength up to 10 wt% at which tensile strength of $11mm^{-2}$ was obtained after which the tensile strength decreased to a value of $9mm^{-2}$ at 12 wt%, however, this value was higher than pristine rLDPE. According to the author, the increase in tensile strength was due to the structural integrity established by the individual ESP particles acting as load bearers and effectively transferring the load from the RLDPE matrix. The stress localisation is prevented due to the continuous and imperfection-free structure of the composite. Under load, the pores and crazes gradually stretch and fuse, forming cavities of different sizes until necking occurs, and the RLDPE/ESP attains ultimate tensile strength. The increase in the tensile strength with an increase in the wt% of ESP is due to a higher number of particles that offer a higher resistance to deformation before the composite necks. The decrease in tensile strength at 12 wt% is linked with defects and imperfections in the composite. Also, the study found that the tensile strength of rLDPE is comparable to that of pristine LDPE, with a difference of only 4%. The tensile strength of the pristine LDPE was $6.56 \pm 0.33\ Nmm^{-2}$ while that of rLDPE was $6.31 \pm 0.2\ nmm^{-2}$.

4.1.2 Flexural strength

A study on the effect of ESP and CESP on rHDPE showed the flexural strength of the composite at various filler loadings (Farm et al., 2022). The result showed that as the filler loading increased from 10 wt.% to 30 wt.% for ESP, the flexural strength increased. This finding is similar to previous research conducted by Siti Shuhada et al.(2009) and Buakaew et al. (2013). Buakaew et al. (2013) found that the maximum flexural strength and modulus for virgin HDPE/ESP were 31.2 MPa and 0.93 GPa, respectively at 30 wt. % of ESP. However, Farm et al. study showed even higher flexural strength and modulus at 32.21 MPa and 2.06 GPa for r-HDPE/CESP at 40 wt.% filler content. The results also showed that the flexural strength of CESP-reinforced r-HDPE is higher than ESP-reinforced r-HDPE. The author suggested that the weak bonding adhesion between the matrix and filler was attributed to the lack of chemical modification. The optimal filler loading was found to be 20wt.% for ESP and 30wt.% for CESP, beyond which agglomerationresulted in poor wetting and decreased stiffness.

The study of flexural strength for rLDPE by Bello et al. (2021) showed a higher value for rLDPE/ESP composite than pristine rLDPE polymer. An increase in flexural strength of up to 12 wt% was observed, with a slight decrease at 6 and 8 wt% ESP addition. The author proposed that the increase in flexural strength is attributed to the stiffening effect of eggshell nanoparticles, which form barriers that delay or block craze advancement during flexural loading. The addition of ESP creates multiple barriers that require additional stress for craze movement, resulting in higher flexural strengths of the rLDPE composites compared to the pristine rLDPE polymer. The number of barriers created by ESP is dependent on their weight fraction, with an expected increase in the number of barriers at higher weight fractions. However, the slight decrease at 6 and 8 wt% could be due to defects that cause discontinuity in the composites and reduce the degree of ESP networking within the matrix, leading to the composite's deformation at lower stress than expected.

4.1.3 Impact strength

Bello et al. (2021) research showed that the impact energy of the rLDPE composite decreased above 6 wt% ESP addition, which is a trade-off for an increase in hardness values, as harder materials absorb less impact. It is established that ESP addition to rLDPE increases impact energy up to 6 wt% while maintaining the hardness value of pristine rLDPE. However, above 6 wt%, there is a discernible improvement in the hardness of the composite. The author backed his findings with previous research that shows improvement in mechanical properties due to ESP addition. The author also proposed that the increase in impact energy up to 6 wt% could be attributed to the interaction between rLDPE and $CaCO_3$ of ESP, resulting in a less hard/soft structure that dampens the sudden impact of the hammer, leading to increased energy absorption. However, above 6 wt%, rLDPE-ESP interaction produces a hard/less soft structure that breaks easily upon sudden impact, resulting in smaller amounts of energy absorbed.

4.1.4 Thermal stability

Hanif et al. (2020) study showed that the addition of ESP or CESP fillers to the rHDPE/EVA blend composites improves their thermal stability. According to the author, the fillers decompose in the early stage and produce ash that absorbs heat generated during degradation, thereby delaying the thermal degradation process of the polymer matrix. Increasing the filler loading for both fillers also increased thethermal stability of the blend composites, as the degradation of the ESP or CESP filler constructs a barrier to the gas exhausted from the rHDPE/EVA matrix through heating. Furthermore, the residual mass of each blend composite showed an ascending trend with the addition of filler in the blend composites. CESP filler showed more thermal stability than ESP filler due to its carbonisation process, where the content of CESP filler is mostly carbon or ash, which enables it to withstand high temperatures.

4.2 Water absorption

A study by Farahana et al. (2015a) showed that water absorption increases with increasing ESP filler loading such that higher ESP loading showed more water absorption due to the higher content of filler in the composites. The author proposed that the presence of $CaCO_3$ in the ESP increased water absorption as the filler increased. The formation of agglomeration of the filler in composites also increases the water absorption due to difficulties in achieving a homogeneous dispersion of filler. Higher ESP loading results in greater water absorption because of increasing voids between ESP fillers and rHDPE/EVA matrices. Furthermore, the presence of the APTES coupling agent improved the interfacial adhesion between rHDPE/EVA matrices and ESP, resulting in lower percentages of water absorption compared to composites without APTES at similar filler loading.

5 CONCLUSION

This study shows the application of eggshells as a filler on recycled polymers. The composites were prepared through melt blending and hot compressed into thin sheets. The eggshell was processed depending on the author and was used in carbonised or uncarbonised form. The study found that the introduction of eggshell powder into composite materials resulted in enhancements in the properties of the composites. The usefulness of compatibilizer and coupling agents was also found to enhance the properties of the composites, especially in their mechanical properties by enhancing the interfacial adhesion between the polymer and the filler. Also, carbonised eggshell powder gave a better result on the properties of the recycled polymers than the uncarbonised eggshell powder.

REFERENCES

Achilias, D. S., Roupakias, C., Megalokonomos, P., Lappas, A. A., & Antonakou, E. V. (2007). Chemical recycling of plastic wastes made from polyethylene (LDPE and HDPE) and polypropylene (PP). Journal of Hazardous Materials, 149(3), 536–542.

Bello, S. A., Raji, N. K., Kolawole, M. Y., Adebayo, M. K., Adebisi, J. A., Okunola, K. A., & AbdulSalaam, M. O. (2021). Eggshell nanoparticle reinforced recycled low-density polyethylene: A new material for automobile application. Journal of King Saud University-Engineering Sciences.

Bhagavatheswaran, E. S., Das, A., Rastin, H., Saeidi, H., Jafari, S. H., Vahabi, H., Najafi, F., Khonakdar, H. A., Formela, K., Jouyandeh, M., Zarrintaj, P., & Saeb, M. R. (2019). The Taste of Waste: The Edge of Eggshell Over Calcium Carbonate in Acrylonitrile Butadiene Rubber. Journal of Polymers and the Environment, 27(11), 2478-2489. https://doi.org/10.1007/s10924-019-01530-y

Golkaram, M., Mehta, R., Taveau, M., Schwarz, A., Gankema, H., Urbanus, J. H., De Simon, L., Cakir-Benthem, S., & van Harmelen, T. (2022). Quality model for recycled plastics (QMRP): An indicator for holistic and consistent quality assessment of recycled plastics using product functionality and material properties. Journal of Cleaner Production, 362, 132311.

Farahana, R., Supri, A., & Teh, P. (2015a). Tensile and water absorption properties of eggshell powder filled recycled high-density polyethylene/ethylene vinyl acetate composites: effect of 3-aminopropyltriethoxysilane. Journal of Advanced Research in Materials Science, 5(1), 1-9.

Farahana, R., Supri, A., & Teh, P. L. (2015b). Effect of Benzyl Urea on Properties of Recycled High Density Polyethylene/Ethylene Vinyl Acetate/Egg Shell Powder Composites. Applied Mechanics and Materials,

Farahana, R. N., Supri, A., & Teh, P. L. (2014). Effect of maleic anhydride (MA) on properties of recycledhigh density polyethylene/ethylene vinyl acetate/egg shell powder (rHDPE/EVA/ESP) composites. Applied Mechanics and Materials,

Farm, Y., Sappa, A. M., Mustafa, Z., Muzammil, W., Ismail, M., Amaludin, N., & Kiring, A. (2022).

Mechanical properties of eggshells powder reinforced recycled high-density polyethylene. IOPConference Series: Materials Science and Engineering,

Hamad, K., Kaseem, M., & Deri, F. (2013). Recycling of waste from polymer materials: An overview of the recent works. Polymer Degradation and Stability, 98(12), 2801–2812.

Hamada, H. M., Tayeh, B. A., Al-Attar, A., Yahaya, F. M., Muthusamy, K., & Humada, A. M. (2020). Thepresent state of the use of eggshell powder in concrete: A review. Journal of Building Engineering, 32, 101583.

Hanif, M., Jalilah, A., & Naqiuddin, M. (2020). Effect of Uncarbonised and Carbonised Eggshell Powder on Mechanical and Thermal Properties of Recycled High Density Polyethylene/Ethylene Vinyl Acetate Blend Composites. IOP Conference Series: Materials Science and Engineering,

Ho, W.-F., Hsu, H.-C., Hsu, S.-K., Hung, C.-W., & Wu, S.-C. (2013). Calcium phosphate bioceramics synthesized from eggshell powders through a solid state reaction. Ceramics International, 39(6), 6467–6473.

Khalid, M. Y., Arif, Z. U., Ahmed, W., & Arshad, H. (2022). Recent trends in recycling and reusing techniques of different plastic polymers and their composite materials. Sustainable Materials and Technologies, 31, e00382.

Ncube, L. K., Ude, A. U., Ogunmuyiwa, E. N., Zulkifli, R., & Beas, I. N. (2021). An overview of plastic wastegeneration and management in food packaging industries. Recycling, 6(1), 12.

Ragaert, K., Delva, L., & Van Geem, K. (2017). Mechanical and chemical recycling of solid plastic waste.

Waste Management, 69, 24–58.

Vasudeo, R. A., Abitha, V. K., Vinayak, K., Jayaja, P., & Gaikwad, S. (2016). Sustainable development through feedstock recycling of plastic wastes. Macromolecular Symposia, 362(1), 39–51.

PAPER 84 – SMART FARMING FOR SUSTAINABLE RICE PRODUCTION IN NIGERIA

H. K. Muhammad, O. B. Sakariyau

Department of Entrepreneurship and Business Studies, Federal University of Technology, Minna
Email: halidumohammed08@gmail.com

ABSTRACT

Agriculture plays a significant role in Nigeria's economy, with rice being a staple food for millions of Nigerians. However, rice production in Nigeria has been faced with several challenges. Smart farming, an innovative agricultural approach, integrates advanced technologies such as precision agriculture, the Internet of Things (IoT), and big data analytics to enhance agricultural productivity, reduce environmental impacts, and increase food security. This study aims to explore the potential of smart farming in enhancing rice production in Nigeria. The study reviews the current status of rice production in Nigeria, identifies the challenges facing rice farmers, and explores the role of smart farming technologies in addressing these challenges. The study also examines the policy and institutional frameworks needed to promote smart farming in Nigeria. The study reveals that smart farming has the potential to revolutionize rice production in Nigeria by enabling farmers to optimize their crop yield, reduce water and fertilizer usage, and minimize the impact of climate change.

KEYWORDS**:** Smart farming, sustainability, Rice production and Nigeria

1.0 BACKGROUND INFORMATION ON THE IMPORTANCE OF RICE PRODUCTION IN NIGERIA

Rice is a staple food in Nigeria, and its production plays a critical role in ensuring food security and livelihoods for millions of Nigerians (Adewale, 2021). Nigeria is the largest producer of rice in West Africa, and the demand for rice has been steadily increasing due to population growth, urbanization, and changing dietary preferences (Omonona & Adewale, 2021). Rice production has significant economic implications for Nigeria as well. The rice sector contributes to rural development, poverty reduction, and employment generation along the value chain (Ibrahim & Badiru, 2021). The Nigerian government recognizes the importance of rice production and has implemented various policies and interventions to boost domestic production and reduce dependence on imports (Ogbonna et al., 2020).

However, despite the efforts to promote self-sufficiency in rice production, Nigeria still faces challenges in meeting the increasing demand. The country heavily relies on imports to bridge the supply gap, which puts pressure on foreign exchange reserves and affects the country's trade balance (Akerele et al., 2021). Additionally, traditional rice farming methods are often characterized by low productivity, limited access to modern inputs, and vulnerability to climate change and pests (Ibrahim & Badiru, 2021). Given the importance of rice as a staple food and the need for self-sufficiency, there is a growing emphasis on adopting innovative approaches such as smart farming to enhance rice production in Nigeria. Smart farming, which involves the integration of digital technologies and data-driven decision-making, has the potential to improve productivity, resource efficiency, and sustainability in agriculture (Ogbonna et al., 2020). By incorporating smart farming technologies and practices, Nigeria can enhance its rice production capacity, reduce post-harvest losses, optimize resource utilization, and increase farmers' income and welfare (Omonona & Adewale, 2021). Embracing smart farming in rice production can contribute to the overall goal of achieving food security, poverty reduction, and sustainable development in Nigeria (Adewale, 2021).

Rice is a vital crop in Nigeria as it serves as a major source of carbohydrates for the population (Olayemi & abdlazeez, 2022). The consumption of rice has been increasing steadily, driven by factors such as population growth, urbanization, changing dietary patterns, and the influence of globalization (Bolarinwa & Adeoye, 2021). As a result, rice has become a preferred staple food for many Nigerians, particularly in urban areas (Arokoyo et al., 2021). Nigeria's dependence on rice imports has significant economic implications. The country spends a substantial amount of foreign exchange on rice imports, leading to a strain on its foreign reserves and trade balance (Oni et al., 2021). Import dependence also exposes the country to market volatility, supply chain disruptions, and price fluctuations in the global rice market (Omotesho et al., 2020). Achieving self-sufficiency in rice production is, therefore, a priority for Nigeria to enhance its food security and reduce its reliance on imports.

Moreover, rice production has the potential to stimulate economic growth and rural development in Nigeria. It serves as a source of income for smallholder farmers, promotes job creation along the value chain, and contributes to poverty reduction (Ajibefun & Oyeyinka, 2022). Increased investment in rice production can create

employment opportunities, enhance farmers' income, and contribute to the overall economic development of rural communities (Ifejika et al., 2021).

However, traditional rice farming methods in Nigeria face various challenges, including low yields, inefficient use of resources, inadequate access to improved inputs, and post-harvest losses (Bolaji et al., 2021). Climate change impacts, such as erratic rainfall patterns and increased pest infestation, further exacerbate the challenges faced by rice farmers (Olayide & Abdulazeez, 2022).

To address these challenges and improve rice production, smart farming technologies offer promising solutions. Smart farming encompasses the use of precision agriculture techniques, data analytics, the Internet of Things (IoT) devices, and automation to optimize farming operations (Bolarinwa & Adeoye, 2021). By integrating these technologies into rice production, farmers can enhance productivity, reduce resource wastage, and make informed decisions for sustainable agriculture (Ajayi et al., 2021). By adopting smart farming practices, Nigeria can achieve multiple objectives simultaneously. It can increase rice production, ensure food security, enhance resource efficiency, mitigate environmental impacts, and improve farmers' livelihoods (Arokoyo et al., 2021). The integration of digital technologies and data-driven approaches can transform rice farming into a more efficient, profitable, and sustainable enterprise (Oni et al., 2021).

2.0 REVIEW OF EXISTING LITERATURE ON SMART FARMING TECHNIQUES AND THEIR APPLICATION IN AGRICULTURE.

Reviewing the existing literature on smart farming techniques and their application in agriculture reveals a wealth of research and practical implementation. Smart farming, also known as precision agriculture, involves the integration of advanced technologies, data analytics, and digital tools to optimize agricultural practices. Here is a summary of key findings from the literature:

Remote Sensing and Imaging Technologies: Remote sensing techniques, such as satellite imagery, drones, and ground-based sensors, play a crucial role in smart farming. These technologies provide real-time information on crop health, soil moisture, and nutrient levels, enabling farmers to make data-driven decisions for precision application of inputs (Biradar et al., 2021).

Internet of Things (IoT) and Sensor Networks: IoT devices and sensor networks are extensively used in smart farming applications. These devices monitor various parameters such as temperature, humidity, and soil conditions, allowing farmers to remotely track and manage their farms. IoT-based systems enable automated irrigation, climate control, and pest management, leading to resource optimization and improved crop productivity (Rasheed et al., 2020).

Data Analytics and Artificial Intelligence (AI): Data analytics and AI techniques have revolutionized agriculture by enabling predictive models, machine learning algorithms, and decision support systems. These technologies analyze large datasets to provide insights on crop growth, disease detection, yield prediction, and optimal resource allocation (Biradar et al., 2021). AI-based systems can also assist in weed detection, crop disease diagnosis, and personalized crop management recommendations (Goswami et al., 2020).

Precision Farming Techniques: Smart farming incorporates precision farming techniques such as variable rate application (VRA), site-specific nutrient management, and automated machinery guidance. VRA optimizes the application of fertilizers, pesticides, and water based on spatial variability within fields, reducing costs and environmental impacts (Rasheed et al., 2020). Site-specific nutrient management ensures precise fertilizer application based on soil nutrient levels, resulting in improved nutrient use efficiency (Goswami et al., 2020).

Big Data and Cloud Computing: The availability of big data and cloud computing has facilitated the storage, processing, and sharing of agricultural information. Farmers and researchers can access and analyze vast amounts of data collected from multiple sources, facilitating informed decision-making and collaborative research (Biradar et al., 2021).

Adoption and Barriers: Studies have highlighted factors influencing the adoption of smart farming technologies, including farmer education, access to information and training, cost-effectiveness, and policy support (Rasheed et al., 2020). Barriers to adoption include lack of awareness, inadequate infrastructure, and limited technical knowledge among farmers. Overall, the literature emphasizes the potential of smart farming techniques to improve agricultural productivity, resource efficiency, and sustainability. However, successful implementation requires addressing barriers to adoption, promoting capacity building among farmers, and developing supportive policies and infrastructure.

3.0 OVERVIEW OF THE CURRENT STATE OF RICE PRODUCTION IN NIGERIA.

Rice production plays a crucial role in Nigeria's agricultural sector and food security. Over the years, the country has made efforts to increase domestic rice production and reduce its reliance on imports. However, several challenges persist, affecting the overall state of rice production. According to Omonona and Adewale (2021), Nigeria is one of the largest rice-consuming countries in Africa, with high demand driven by population growth, urbanization, and changing dietary patterns. To meet this demand, the country has implemented various policies and initiatives to boost rice production, such as the Anchor Borrowers' Program and the Rice Transformation Agenda (Ogbonna et al., 2020).

Despite these efforts, Nigeria still faces challenges in achieving self-sufficiency in rice production. One of the key challenges is low productivity. Rice yields in Nigeria are below the global average due to several factors, including limited access to modern farming technologies, poor farm management practices, and inadequate infrastructure (Ajayi et al., 2021). Additionally, pest and disease outbreaks pose significant threats to rice production in Nigeria. Pests such as stem borers and diseases like rice blast can cause substantial yield losses (Sultan et al., 2022). Inadequate pest management practices and limited access to effective pesticides further exacerbate the problem.

Furthermore, limited access to credit and high production costs hinder the expansion of rice production in Nigeria. Smallholder farmers, who constitute a significant portion of rice producers, often face challenges in accessing affordable financing for agricultural inputs and machinery (Oni et al., 2021). High input costs, including seeds, fertilizers, and mechanization services, also impact the profitability and competitiveness of rice farming. Despite these challenges, Nigeria has shown progress in rice production. The country has witnessed an increase in domestic rice production, leading to a reduction in rice imports. The government's support for the rice value chain, including investments in irrigation infrastructure and the establishment of rice processing mills, has contributed to this progress (Ogbonna et al., 2020).

In summary, while Nigeria has made strides in increasing rice production, challenges such as low productivity, pest and disease management, and limited access to credit and inputs persist. Addressing these challenges through the adoption of modern farming technologies, improved extension services, and policy support is essential for enhancing the current state of rice production in Nigeria.

3.1 Brief overview of the challenges faced by traditional rice farming methods

Traditional rice farming methods in Nigeria face several challenges that hinder productivity and sustainability. These challenges include:

1. Low Yields: Traditional rice farming practices often result in low crop yields due to limited access to improved seeds, inadequate use of fertilizers, and suboptimal crop management techniques (Sultan et al., 2022). Low yields contribute to lower profitability and hinder efforts to achieve self-sufficiency in rice production.
2. Inefficient Resource Use: Traditional rice farming methods often involve inefficient use of resources, particularly water and fertilizers. Water management practices, such as flood irrigation, lead to water wastage and can contribute to environmental degradation (Omotesho et al., 2020) [^10^]. Improper fertilizer application and nutrient management can result in nutrient runoff, soil degradation, and water pollution (Bolaji et al., 2021).
3. Limited Access to Inputs and Technology: Smallholder rice farmers in Nigeria face challenges in accessing improved seeds, quality fertilizers, and mechanized farm equipment (Olayide & Abdulazeez, 2022). Limited access to modern agricultural technologies, such as machinery, irrigation systems, and precision farming tools, hampers productivity and efficiency in rice production.
4. Post-Harvest Losses: Traditional rice farming methods are associated with significant post-harvest losses, mainly due to inadequate storage facilities, pest infestation, and poor handling practices (Ajibefun & Oyeyinka, 2022). Post-harvest losses contribute to food insecurity; reduce farmers' income, and waste valuable resources.
5. Vulnerability to Climate Change: Climate change poses a significant challenge to traditional rice farming in Nigeria. Erratic rainfall patterns, increased temperature, and extreme weather events can negatively impact rice production (Olayide & Abdulazeez, 2022). Pests and diseases, which thrive under changing climatic conditions, can further affect crop health and yield.

3.2 Introduce the concept of smart farming and its potential for sustainable rice production

The following smart farming concepts are feasible to adopt by farmers:

1. Enhanced Farm Management: Smart farming enables farmers to improve their overall farm management practices. Through real-time monitoring and data-driven insights, farmers can track crop growth, soil conditions, and weather patterns, allowing for better decision-making and precise interventions (Ajayi et al., 2021). This helps optimize resource allocation, reduce waste, and increase overall farm efficiency.

2. Remote Monitoring and Control: Smart farming technologies offer remote monitoring and control capabilities, allowing farmers to manage their operations from a distance. IoT devices, such as soil moisture sensors and automated irrigation systems, can be accessed and controlled remotely, reducing the need for physical presence on the farm (Olayide & Abdulazeez, 2022). This feature enhances convenience, reduces labor requirements, and improves the timeliness of farm activities.

3. Data-Driven Decision Making: The collection and analysis of data in smart farming provide valuable insights for decision-making. By integrating data from multiple sources, such as weather forecasts, soil data, and historical crop performance, farmers can make informed decisions on planting schedules, pest control measures, and fertilization strategies (Sultan et al., 2022). This data-driven approach promotes precision and efficiency, reducing input costs and environmental impacts.

4. Improved Market Access and Traceability: Smart farming technologies facilitate improved market access and traceability of agricultural products. Through the use of block chain technology and digital platforms, farmers can establish transparent supply chains, ensuring product quality, authenticity, and origin (Ogbonna et al., 2020). This enhances consumer confidence, opens up new market opportunities, and supports fair pricing for farmers.

5. Capacity Building and Knowledge Transfer: The adoption of smart farming requires training and capacity building for farmers. By providing education and technical support on the use of smart farming technologies, farmers can effectively harness the potential of these tools (Ajibefun & Oyeyinka, 2022). Additionally, knowledge transfer among farmers and collaboration with research institutions and agricultural extension services can accelerate the adoption and diffusion of smart farming practices.

6. Sustainable Resource Management: Smart farming contributes to sustainable resource management in rice production. By optimizing water usage through sensor-based irrigation systems and data-driven decision-making, farmers can conserve water resources and reduce their environmental footprint (Bolaji et al., 2021). Efficient nutrient management, guided by soil sensors and precision application techniques, minimizes nutrient runoff and pollution, promoting soil health and ecosystem sustainability.

4.0 EXAMINATION OF SUCCESSFUL CASE STUDIES AND PROJECTS RELATED TO SMART FARMING IN RICE PRODUCTION

1. Digital Farming for Rice- Vietnam: The International Rice Research Institute (IRRI) collaborated with partners in Vietnam to implement a digital farming project focused on rice production. The project utilized remote sensing, satellite imagery, and data analytics to provide farmers with real-time information on crop health, water availability, and pest outbreaks. Farmers received personalized recommendations on optimal irrigation, fertilizer application, and pest control, leading to improved yields and resource efficiency (Nguyen et al., 2021).

2. Smart Rice Farming - Japan: The Japanese government initiated the Smart Agriculture Innovation Project, which included a smart rice farming initiative. The project integrated IoT devices, sensor networks, and data analytics to monitor and manage rice farms. Farmers received information on soil conditions, weather forecasts, and disease prevalence through a mobile application. This allowed them to make data-driven decisions for precision farming practices, resulting in increased yields and reduced resource usage (Yoshida et al., 2020).

3. Smart Irrigation Systems - India: In India, several projects have focused on smart irrigation systems in rice production. For example, the Kisan Suvidha project implemented IoT-based sensors and water management technologies to optimize irrigation in rice fields. The system monitored soil moisture levels and weather

conditions, enabling farmers to schedule irrigation based on crop needs. This resulted in significant water savings while maintaining or improving crop productivity (Paul et al., 2022).

4. Rice Crop Management using Data Analytic - Thailand: The Thailand Precision Agriculture Project (TPAP) used data analytics to enhance rice crop management. The project collected data from multiple sources, including sensors, satellites, and historical weather records. Machine learning algorithms were employed to analyze the data and generate customized recommendations for farmers regarding fertilizer application, pest control, and water management. The project achieved better crop performance, reduced costs, and improved environmental sustainability (Suwanprateeb et al., 2020).

5. Smart Farming in Rice Production - South Korea: The Rural Development Administration (RDA) of South Korea implemented smart farming technologies in rice production. The project integrated IoT devices, drones, and AI-based decision support systems. Farmers received real-time information on crop growth, soil conditions, and pest infestation. The system automatically controlled irrigation, fertilizer application, and pest management based on the collected data, resulting in increased productivity and resource efficiency (Park et al., 2021).

These case studies demonstrate the successful implementation of smart farming techniques in rice production. The integration of advanced technologies, data analytics, and decision support systems has proven effective in optimizing resource management, improving crop health, and enhancing yields. These initiatives have the potential to contribute to sustainable rice production and address challenges faced by traditional farming methods.

5.0 CONCLUSION

The adoption of smart farming technologies in rice production can revolutionize the sector, enhancing productivity, profitability, and sustainability. However, it is crucial to ensure that smallholder farmers, who constitute a significant portion of rice producers in Nigeria, have access to these technologies and the necessary support systems for successful adoption.

RERERENCES

Adewale, S. A. (2021). Enhancing food security and poverty reduction through smart farming in Nigeria. *Journal of Agricultural Science, 13*(4), 239-249.

Ajayi, C. A., et al. (2021). Determinants of agricultural technology adoption among rice farmers in Nigeria. *International Journal of Agricultural and Environmental Research, 7*(2), 102-116.

Ajibefun, I. A., & Oyeyinka, R. A. (2022). Post-harvest loss reduction strategies in the Nigerian agricultural sector. *Journal of Food Science and Technology, 59*(2), 803-814

Akerele, D. E., et al. (2021). Exploring the nexus between rice production and importation in Nigeria. *Journal of Agricultural Extension and Rural Development, 13*(2), 143-150. https://doi.org/10.17306/J.JARD.2021.01378

Biradar, C., et al. (2021). A review of the applications of unmanned aerial vehicle and remote sensing in precision agriculture. *International Journal of Advanced Remote Sensing and GIS, 10*(1), 247-269.

Bolaji, O. O., et al. (2021). Analysis of fertilizer use and determinants of rice yield in Nigeria. *Journal of Agricultural Economics, Extension and Rural Development, 3*(2), 119-129.

Goswami, R., et al. (2020). Smart farming: A review on IoT-based agriculture monitoring and automation system. *Computers, Materials & Continua, 65*(1), 1091-1107.

Ibrahim, A., & Badiru, I. (2021). Assessing the impact of agricultural policies on rice production in Nigeria. *African Journal of Agricultural Research, 16*(1), 1-10.

Jirgi, A. J., Oseghale, A. I., & Okafor, Q. E. (2021). Food Security Status Of Women Rice Farmers In Shiroro Local Government Area Of Niger State, Nigeria. *Nigerian Journal of Agricultural Economics*, *11*(1), 1-15. https://doi.org/10.22004/ag.econ.333598

Nguyen, H. T., et al. (2021). Enhancing rice production and farmers' income through digital farming in Vietnam. *Rice Today, 20(*1), 42-45.

Ogbonna, M. C., et al. (2020). Policy implications of rice production and importation in Nigeria. *Sustainable Agriculture Research, 9*(4), 42-51.

Oguntunde, P. G., et al. (2020). Smart agriculture in sub-Saharan Africa: Implications and challenges for sustainable crop production. *Environment, Development and Sustainability, 22*, 4611-4635.

Olayide, S. O., & Abdulazeez, B. B. (2022). Climate change adaptation strategies of small-scale rice farmers in Nigeria. *Journal of Agricultural Science, 14*(1), 96-112.

Omotesho, O. A., et al. (2020). Factors affecting rice production and farmers' adaptation strategies in Nigeria. *Journal of Agricultural Extension, 24*(2), 68-84.

Oni, O. A., et al. (2021). Analysis of the rice value chain and competitiveness in Nigeria. *Journal of Agricultural Extension and Rural Development Studies, 8*(1), 78-92.

Paul, K., Chatterjee, S. S., Pai, P., Varshney, A., Juikar, S., Prasad, V., ... & Dasgupta, S. (2022). Viable smart sensors and their application in data driven agriculture. *Computers and Electronics in Agriculture*, *198*, 107096.

Rasheed, A., et al. (2020). Applications of internet of things in smart agriculture: A comprehensive study. *Computers and Electronics in Agriculture, 177*, 105689.

Sultana, S., Khan, M. A., Hossain, M. E., Prodhan, M. M. H., & Saha, S. M. (2022). Yield gap, risk attitude, and poverty status of aman rice producers in climate-vulnerable coastal areas of Bangladesh. *Journal of Agricultural Science and Technology*, *24*(1), 83-95.

Yoshida, N., et al. (2020). Smart agriculture in Japan: Status, challenges, and potential. *Journal of Agricultural Informatics, 11*(3), 1-14

PAPER 85 – DEVELOPMENT OF AN IMPROVED FIBRE BRAGG GRATING SENSOR SENSITIVITY MODEL WITH TEMPERATURE COMPENSATION FOR STRUCTURAL HEALTH MONITORING

S.P. Obaje[1], E.E Agbon[1*], R. Ogwu[1], T.P. John[1], A. Umar[2], A.T Utev[1], I. Falalu[3], I. Abdulwahab[4]

[1]Department of Electronics and Telecommunications Engineering, Ahmadu Bello University, Zaria
[2]Department of Computer Engineering, Ahmadu Bello University, Zaria.
[3]Works Department, Nigerian College of Aviation Technology, NCAT, Zaria, Nigeria.
[2]Department of Electrical Engineering, Ahmadu Bello University, Zaria.
[*]Email: eagbonehime1@gmail.com

ABSTRACT
This research work presents an optimum Structural Health Monitoring (SHM) of composite structure using an improved Fibre Bragg Grating (FBG) sensor sensitivity model. Composite materials have been largely used in telecommunications, aerospace, marine, automotive, civil infrastructures, oil and gas, sports equipment, and in medical facilities due to their unique mechanical properties, namely strength and stiffness to weight ratios. However, these materials are subjected to deformation during loading and low velocity impact which may not be visible to the human sight and may lead to the failure of the composite structure. This poses a great challenge to manufacturing industries and presents a vital area of research. The improved FBG sensor sensitivity model eliminates cross sensitivity in the FBG measurement, determining the Poisson's ratio and the effective refractive index of the FBG sensor using a developed proportionality model to increase the FBG sensitivity to strain. Deploying the improved model will reduce fatigue failure on structures, network complexity and bulky sensor size due to the ability of the fibre optic cable to house several FBG sensors. The improved technique was implemented using MATLAB R2018a version. The result of the improved model was compared with that of the existing model. The simulation result shows that the improved FBG sensor sensitivity model performed better than the existing FBG model by 32.08% increment in sensitivity.

KEYWORDS: SHM, FBG, Sensitivity, Poisson's Ratio, Refractive Index

6. INTRODUCTION

Fibre Bragg grating sensing technology possesses a good multiplexing capability which enable it to accommodate many grading and different sensing like; strain, temperature, pressure, vibration just to mention a few in a fibre optic cable (Rani *et al.*, 2020). FBG is a type of reflector etching in the core of an optical fibre that reflects a particular wavelength of light and transmits others. This makes the FBG to be used as an optical sensor (Nicolas *et al.*, 2016). The centre of the fibre is enclosed by a silica cladding with slightly lower index of refraction than that of the core. Which is between 4µm and 9µm diameter this aid the coupled light into the fibre to propagates in the fibre core (Nicolas *et al.*, 2016). Each FBG is expressed with a definite wavelength that variations based on the physical parameters the sensor interact with (Nicolas *et al.*, 2016). The refractive planes in FBG are known as the Bragg planes. They are formed when two opposing light sources interfere constructively (Nicolas *et al.*, 2016). Stretching a FBG creates a change in the sensor's index of refraction (Nicolas *et al.*, 2016) as shown in Figure 1.

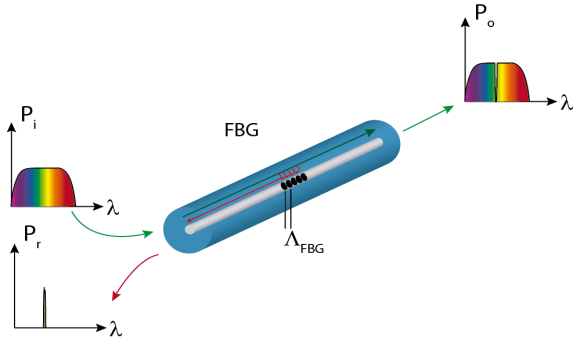

Figure 1: FBG Working Principle (Ganziy *et al.*, 2015)

7. RELATED WORKS

Ganziy *et al.* (2015) proposed an efficient fast detection technique for multimode fibre Bragg grinding sensor. The algorithm is based on a threshold detection window and a compensation centre of gravity for structural health

monitoring. This Dynamic Gate Algorithm exhibited high vigour with a profoundly improved wavelength fit resolution compared with the traditional techniques and the computational speed was better than the Gaussian Fitting Algorithm for better and precise peak identification. The analysed wavelength fit resolution of the Dynamic Gate Algorithm for various estimations of signal to noise ratios for various peak shapes. Liu *et al.* (2012) presented a distributed strain sensing using optical fibre sensing technology. Dynamic and distributed strains during the fatigue loading was quantified using the Brillouin Optical Correlation Domain Analysis technique. The evaluated measurement accuracy of Brillouin Optical Correlation Domain Analysis, measured strain values were compared with that of fibre Bragg grating sensors. The dynamic strain measurement positions of Brillouin Optical Correlation Domain Analysis were determined using by mean of measuring the length between the centre of the article and the fibre Bragg grating sensors using a tape measure. In other to verify the operability and measurement accuracy of the Brillouin Optical Correlation Domain Analysis for structural health monitoring, it was applied to a structural fatigue test using a full-scale horizontal tail plane article in corporation with Airbus. Capriotti *et al.* (2017) proposed a non-destructive assessment algorithm for the recognition of defects on composite airplane structures following High Energy Wide Area Blunt Impact procedure for ground service equipment. The work employed the waveguide geometry of these structures by using ultrasonic guided waves and a line scan method. The contact model and a non-contact model were created and tried on realistic test boards panels subjected to impact in the test bed. Two laboratory models for line checking were created, one utilizing contact piezoelectric transducers with a differential methodology and utilizing non-contact (air-coupled) transducers in a pitch–catch approach. Kumar and Chack (2018) presented a temperature non-sensitive strain measurement technique for Structural Health Monitoring. By deploying two conventional Fibre Bragg Grating (FBG) sensors to eliminate cross sensitivity to temperature and strain. The FBG which is operated at a central wavelength difference of 2 nm to eliminate the interfering of back reflected signals wavelength. The shift in wavelength of the two FBG are subtracted from one another to obtain the change in Bragg wavelength due to the applied engineering quantities. In this work a developed proportionality model is deployed to increase the sensitivity of FBG to induced strain.

8. THE EXISTING FBG MODEL

Shift in Bragg wavelength of an FBG sensor () due to engineering strain is calculated by Equation (1) (Kumar & Chack, 2018):

$$\Delta\lambda = \Delta\lambda_{fbg1} - \Delta\lambda_{fbg2} \tag{1}$$

Where $\Delta\lambda_{fbg1}$ is the change in wavelength of the FBG1 due to strain and temperature, while $\Delta\lambda_{fbg2}$ is the wavelength shift of FBG2 due to temperature (Kumar & Chack, 2018), the shift in FBG1 is expressed in Equation (2) (Ma & Chen, 2018):

$$\Delta\lambda_{fbg1} = \lambda_B\left(\alpha_f + \xi\right)\Delta T + \lambda_B\left(1 - P_e\right)\Delta\varepsilon \tag{2}$$

Where α_f is the thermal expansion coefficient of the FBG sensor, ξ is the thermal-optic coefficient of the FBG sensor and P_e is the effective strain optic coefficient. While the change in FBG2 due to change in temperature is expressed in Equation (3) (Ma & Chen, 2018):

$$\Delta\lambda_{fbg2} = \lambda_B\left(\alpha_f + \xi\right)\Delta T \tag{3}$$

where λ_B is the Bragg wavelength of FBG2 sensor and ΔT is the change in temperature, while Equation (4) is the expression for the sensitivity of FBG sensor to strain (Campanella *et al.*, 2018):

$$\Delta\lambda_B = \lambda_B\left[1 - P_e\right]\Delta\varepsilon \tag{4}$$

The expression for the strain optics coefficient is shown in Equation (5) (Campanella *et al.*, 2018):

$$P_e = \frac{n_{eff}^{\ 2}}{2}\left\{p_{12} - v\left[p_{11} + p_{12}\right]\right\} \tag{5}$$

where v is the Poisson's ratio and p_{11}, p_{12} are the Pockel's coefficient of the strain-optic (Campanella *et al.*, 2018).

9. THE IMPROVED FBG MODEL

The developed model in this work improves the sensitivity of the FBG sensors $(\Delta\lambda_{Bi})$ to engineering strain by varying the effective strain optics (p_e) parameters which are effective refractive index of the fibre (n_{eff}) and the Poisson's ratio (v). From Equations (4) and (5), Equations (6) to (11) are derived which gives the mathematical expressions on how the sensitivity of the FBG sensor can be improved. Equations (6) shows that FBG sensitivity $(\Delta\lambda_B)$ is inversely proportional to the effective strain optics coefficient (P_e):

$$\Delta\lambda_B \propto 1/p_e \tag{6}$$

Also, the effective strain optics coefficient (p_e) is inversely proportional to Poisson' s ratio (v) and directly proportional to the square of the effective refractive index of the fibre optic sensor $(n_{eff}{}^2)$ as shown in Equation (7):

$$p_e \propto n_{eff}{}^2 \times \frac{1}{v} \tag{7}$$

For the FBG sensitivity $(\Delta\lambda_B)$ is inversely proportional to the square of the effective refractive index of the fibre $(n_{eff}{}^2)$ and directly proportional to the Poisson's ratio as shown in Equations (8) to (11):

$$\Delta\lambda_B \propto \frac{1}{n_{eff}{}^2} \tag{8}$$

$$\Delta\lambda_B \propto v \tag{9}$$

$$p_{ei} = k_{pe} \times \frac{v}{n_{eff}{}^2} \tag{10}$$

$$\Delta\lambda_{Bi} = \lambda(1 - p_{ei})\Delta\varepsilon \tag{11}$$

where $\Delta\lambda_{Bi}$ is the improved FBG sensitivity, λ_B is the Bragg wavelength, $\Delta\varepsilon$ is the change in the induced strain on the FBG sensor, (n_{eff}) is the effective refractive index of the FBG sensor and k_{pe} is the proportionality constant of the effective strain optics coefficient of the FBG sensor and the value is 1.02. The flow chart of the improved FBG sensor sensitivity model is expressed in Figure 2.

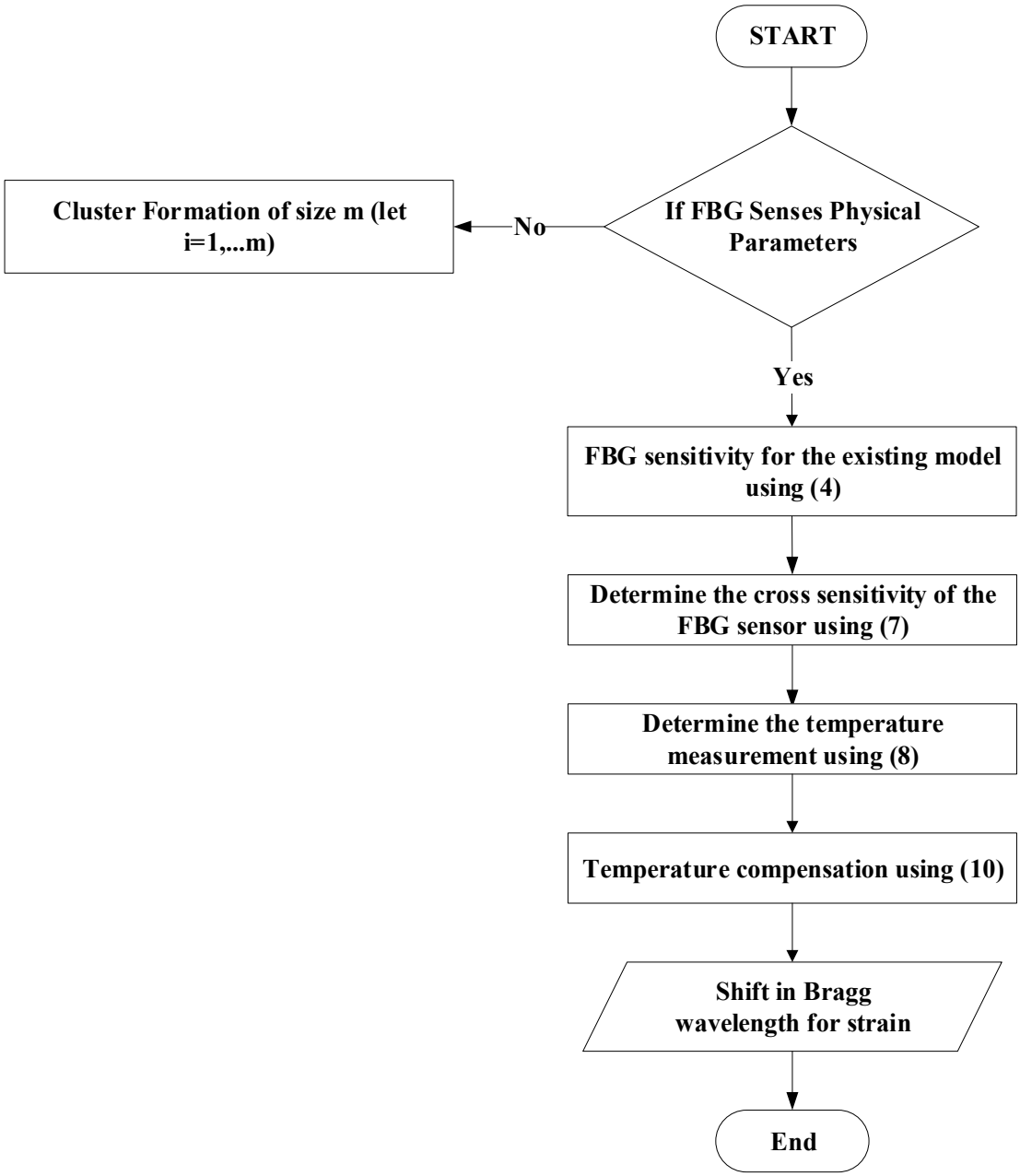

Figure 2: FBG Sensing of the Proposed Model

10. RESULTS

The result obtained from the simulation setup are discussed in this section. The following results are based on the shift in Bragg wavelength of the FBG sensor due to the induced physical parameter (strain) on the composite structure.

5.1 Shift in Bragg Wavelength Versus Induced Strain on the Composite Structure

In Fig. 3, the shifts in Bragg wavelength were plotted against the induced strain. The plot was obtained from the simulation values in Table 1. Table 1 was obtained from Equations (4) and (11).

Table 1: Induced Strain and Sensitivity of the Fibre Bragg Grating Sensor.

Strain (με)	*i*FBG (pm)	FBG (pm)
0	0	0
50	66.050	50.03
100	132.10	100.01

150	198.15	150.01
200	264.20	200.01
250	330.25	250.02

From the plots, it is observed that the improved fibre Bragg gating model sensitivity is higher when compared to the existing fibre Bragg grating model. This is due to the reduction in the value of the effective strain optics coefficient and the increment in the value of the Poisson's ratio of the FBG sensor respectively. The sensitivity of the improved fibre Bragg grating model increases as the induced strain on the composite structure increases. Furthermore, as it is observed from the plot, there is a corresponding increase in the shift in Bragg wavelength as the value of strain increases. The FBG sensitivity is the difference between the shift in Bragg wavelength and the Bragg wavelength of the FBG sensor. The improved FBG sensor model achieved 32.08% increment in sensitivity against the existing model. The percentage increment of the model was obtained using Equation (12):

$$Percentage\,increment = \frac{\sum iFBG - \sum FBG}{\sum FBG} \times 100\% \tag{12}$$

Where $\sum iFBG$ and $\sum FBG$ are the summation of the improved FBG sensor sensitivity values and the existing FBG sensor sensitivity values when the structure was subject to induced strain.

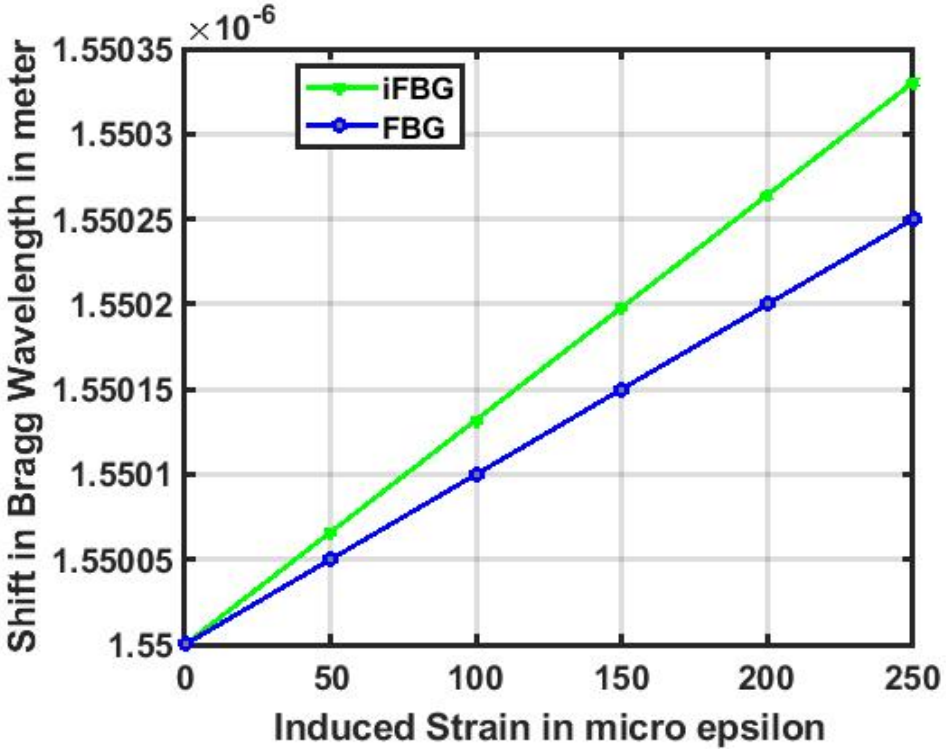

Figure 3: Shift in Bragg Wavelength against the Induced Strain on the Composite Structure

11. CONCLUSION

In this research, an optimum Structural Health Monitoring of composite structure using an improved Fibre Bragg Grating (FBG) sensor sensitivity model was presented. The improved FBG sensor sensitivity model eliminates cross sensitivity in the FBG measurement, determining the Poisson's ratio and the effective refractive index of the FBG sensor using a proportionality model to increase the FBG sensitivity to strain. The improved FBG sensor result in 32.08% increment in sensitivity when compared to the conventional FBG sensor.

REFERENCES

Campanella, C. E., Cuccovillo, A., Campanella, C., Yurt, A., & Passaro, V. M. J. S. (2018). Fibre Bragg grating based strain sensors: Review of technology and applications. *18*(9), 3115.

Capriotti, M., Kim, H. E., Lanza di Scalea, F., & Kim, H. J. M. (2017). Non-Destructive inspection of impact damage in composite aircraft panels by ultrasonic guided waves and statistical processing. *10*(6), 616.

Ganziy, D., Jespersen, O., Rose, B., & Bang, O. (2015). *An efficient and fast detection algorithm for multimode FBG sensing.* Paper presented at the 24th International Conference on Optical Fibre Sensors.

Kumar, J., & Chack, D. (2018). *FBG based strain sensor with temperature compensation for structural health monitoring.* Paper presented at the 2018 4th International Conference on Recent Advances in Information Technology (RAIT).

Liu, Y., Mejias, L., & Li, Z. (2012). Fast power line detection and localization using steerable filter for active UAV guidance.

Ma, Z., & Chen, X. J. S. (2018). Fiber Bragg gratings sensors for aircraft wing shape measurement: Recent applications and technical analysis. *19*(1), 55.

Nicolas, M. J., Sullivan, R. W., & Richards, W. L. J. A. (2016). Large scale applications using FBG sensors: determination of in-flight loads and shape of a composite aircraft wing. *3*(3), 18.

Rani, S., Haider, S., Masud, U., & Huda, A. B. J. S. L. (2020). Accurate Measurement of Gas Concentration Using Apodized Fiber Bragg Grating for Variation in Temperature and Presence of Noise. *18*(7), 530-537.

PAPER 86 – DEVELOPMENT OF AN AUTOMATED PLATE NUMBER RECOGNITION AND IDENTIFICATION SYSTEM

Z. Haruna, U. Abdulmalik*, N. S. Usman, A. Umar, Z. M. Abubakar

Department of Computer Engineering, Faculty of Engineering, Ahmadu Bello University, Zaria-Nigeria.

*Email: fabulouskaura@gmail.com

ABSTRACT

In this paper, an automated plate number recognition and identification system was developed to explore problems associated with many successful solutions in the field of computer vision. However, these solutions are typically tuned towards a particular environment due to the variations in the features of plate numbers across the universe. As such, a universal solution would be difficult to realize as the image analysis techniques used in developing this algorithm cannot generate a result with a hundred percent accuracy. Thus, this paper focuses on the development of an automated plate number recognition and identification system optimized for Nigerian plate numbers. The system comprises algorithms written in Python with the OpenCV library, canny edge detection, and feature detection techniques combined with the Tesseract optical character recognition engine to identify the characters on the plate. A Microsoft visual basic was used to develop a user interface for data presentation and MySQL server was used as a database. When a local image was tested using the developed recognition algorithm, the simulation result presented an accuracy of 90% at the localization stage and 70% for character extraction. This shows that the algorithm effectively localizes and extracts the characters on the plate number.

KEYWORDS: Plate number, OpenCV, canny edge detection, tesseract optical character recognition engine, MySQL.

1. INTRODUCTION

Modern intelligent transportation systems (ITS) rely heavily on vehicles. Plate characters offer a uniform method of identifying any vehicle. Vehicle License Plate Recognition (VLPR) has drawn a lot of interest from scientists. It can be utilized by government organizations to locate or identify stolen cars and to gather information for traffic management and planning. VLPR requires generalization and high accuracy in real-world applications due to its intimate ties to public security. Due to their diverse applications, such as electronic toll collection, highway surveillance, unattended parking lots and security monitoring of restricted areas, urban logistics, and traffic law enforcement, intelligent transport systems (ITS) significantly contribute to the advancement of smart cities (Ugwu *et al.*, 2022). Since each car's license plate is unique, automatic plate detection will have a wide range of uses. For instance, while employing intelligent parking, the entrance gate will only be opened and closed for allowed vehicles. Additionally, in vehicles, speed control operations and management of vehicles through tolls will be implemented (Akbarzadeh *et al.*, 2022). Different models were developed for various hardware configurations based on computational power and low cost using a novel set of neural networks. The suggested model precision, energy efficiency, communication latency, and computing delay are verified using various license plate datasets both during the day and at night as well as in real-time presented (Padmasiri *et al.*, 2022). Implemented automatic number plate recognition technology in police patrol cars to automate access control and security, such as identifying fast vehicles on highways and locating stolen cars in real time (Etomi & Onyishi, 2021). Using an automated license plate recognition (ALPR) system in resource-constrained contexts can help with the construction and management of smart cities as demonstrated by Padmasiri *et al.* (2022). This stage is heavily reliant on the number plate's specifications/characteristics. These characteristics include symmetry, spatial frequency, shape, color, height, and width. The conditions (lighting, visibility, image skew, and camera quality) under which the image was taken, as well as the characteristics of the image itself, determine the algorithm's capacity to recognize the plate. The majority of ANPR algorithms also include a pre-processing stage that gets the image ready using methods like grey scaling, thresholding, and noise removal. The most popular way to scale color pixels to grey is to simply average their RGB values (Etomi & Onyishi, 2021). It is impossible to overstate the importance of an automatic licensed plate detection system (ALPDS) in the modern world. This is because it is crucial to the development of smart cities' intelligent transportation systems. In both the academic and commercial sectors, there is growing interest in the field of license plate number detection (Ugwu *et al.*, 2022). Thus, this paper aimed at developing automated plate number recognition and identification system that explores different successful solutions in the field of computer vision. The system comprises stages: the input stage (camera for image acquisition), the processing stage (conversion to greyscale, filtering, contour detection, extraction, and recognition), plate number identification, and finally, the ticketing stage from a visual basic database.

2. THEORETICAL ANALYSIS

2.1 The overview of major keywords in this area of research.

Li and Wang (2022) presented Python as a powerful dynamic programming language that is free, open-source, and cross-platform. It features a vast number of potent built-in objects, standard libraries, and extension libraries, and it supports a variety of programming paradigms. By directly calling the built-in functions or standard libraries, powerful programming functionalities can be implemented. Students can expand their comprehension of the algorithm and principle by studying the source code, which will help them develop their programming skills and code quality (Li & Wang, 2022). Python is a reasonably simple language to learn. Dome and Sathe (2021) presented OpenCV as a library for many programming tasks with the main goal of offering real-time computer vision. Users can imports image, does image segmentation, and extracts the image (Li & Wang, 2022). Intel's research led to the creation of the OpenCV computer vision library's source code. The majority of image-processing software programs are developed in C/C++, and OpenCV is no exception. This is done to account for computing speed. It is a library built on the IPL that has more than 300 C functions and C++ classes (Image Processing Library). Thakare *et al.* (2018) presented an optical character recognition (OCR) tool for Python software called Python Tesseract. In other words, it will recognize and read any text that is embedded deeply within an image. Tesseract-OCR is implemented by the Python-Tesseract module in Python to transform the image into text. Utilizing a module to call the specified method, image to a string makes the implementation easier. Dome and Sathe (2021) use optical character recognition (OCR) to identify text contained in a digital image. It is mostly used to transform printed, handwritten, or transcribed text into editable and reusable text data. Alfath *et al.* (2022) referred to Visual Basic as a programming language, Visual Basic is also a tool for creating Windows-based application programs. A database is a collection of connected data that makes it simpler for activities to access information Wang *et al.* (2018). Setting the administrator permission enhanced the system's security. It was crucial to develop the database management system since it offered crucial technical support.

2.2 This section discusses related works done in this area of research

Mujawar and Vadi (2022) proposed a Raspberry Pi-based system for automatically identifying license plates that use image processing. In this system, a Raspberry Pi is coupled to a camera and an LCD circuit. The tool continuously looks for signs of license plates in the incoming camera footage. When it notices a number plate in front of the camera, it analyses the camera input and extracts the number plate component from the image. The extracted image is processed using OCR to get the license plate number. The program then displays the extracted number on an LCD. Mujawar and Vadi (2022) presented a system in which when it notices a number plate in front of the camera, it analyses the camera input and extracts the number plate component from the image. The extracted image is processed using OCR to get the license plate number. Etomi and Onyishi (2021) work on a Raspberry Pi, an automated system that makes use of the OpenCV library and py-tesseract-OCR demonstrated. After the camera takes a picture, the Raspberry Pi converts it to grayscale, applies filters, segments it, and recognizes characters before displaying the number plate on the console and then storing it in a database. Making sure the code is effective and that the computational complexity is reduced while improving flexibility is one of the trickiest parts of creating a portable program. The performance time is also shown, and it shows that there is a notable 3-second delay in the final output throughout the entire procedure. AG (2019) presented an Optical Character Recognition (OCR) on images and OpenCV techniques are used by the current Automatic Number Plate Recognition and Identification system to read and identify vehicle license plates. This work concentrated on license plate localization and extraction from images for use in various applications. It does this by utilizing several Python-developed OpenCV library techniques for image segmentation, from which some image segments were checked for characters. AG (2019) identifies the most likely license plate by using the characters on the plate's associated picture's height, width, aspect ratio, and other characteristics. Using these pixel properties, it was able to remove undesired contour lines and curves that stood out as noise while identifying the actual area of the image that contained the plate number. Following the acquisition of the region, OCR was used to extract the license plate text format using a trained template for various character styles. Akbarzadeh *et al.* (2022) developed an improved algorithm to carry out the plan. First, we go through many difficult steps. The placement of the plate is determined as the initial stage. In the second phase, an initial improvement to reduce the expected noise using a suitable filter, which is provided by the Gaussian function. The remaining stages of the program are: locating the edge of photographs, enhancing updated photos, and choosing the precise location of the plate. The study's ultimate step eventually entails several stages, such as using a neural network to automatically extract the characters from the plate. Padmasiri *et al.* (2022) provided an Automated License Plate Recognition (ALPR) solution for edge computing in situations with limited resources, which could enable the creation and administration of smart cities. The accompanying environmental restrictions, such as changing weather, plate variances among areas, vehicle speed, distorted characters, filthy plates, shadow, and reflection, make research

on ALPR tough even though it is a well-established area in the field of image processing. Ugwu *et al.* (2022) deliver a clever technique that uses computer vision to recognize car license numbers. Images of car license plates were used as training data for the system. Following the identification procedure, the trained images were pre-processed using the OpenCV library for image conversion and masking. The training images were initially annotated using the Visual Graphic Generator (VGG) annotation tool. Then, Tesseract-OCR was applied to isolate the texts from the photos. BC *et al.* (2022) presented a surveillance system that records images of moving targets and reads their license plates, which become a significant area of study this time. The dataset for Indian license plates was used in the study to identify license plates. Kaur *et al.* (2022) give an example of a successful ALPR system that recognizes characters with a CNN. The system efficiency was improved by applying a combination of pre-processing and morphological techniques to improve input image quality. The system can recognize license plates with several lines, slanted text, and multiple fonts, among other qualities.

3. MATERIALS AND METHODS

In this section, the procedure follow for the development of an automated plate number recognition and identification system was presented, which comprises some of the following interfaces as materials for both the hardware and software such as the programming language using Python, Pycharm IDE, Tesseract-OCR, USB camera, Microsoft visual basic, and SQL server management studio as the database in actualizing the research procedure. The methods used in achieving the objectives of this research are presented in this section as follows:

3.1 Implementation of plate number recognition and identification algorithm

Plate number recognition and identification algorithm was implemented on the pre-processed images using OpenCV and pytesseract. OpenCV was used for image processing tasks such as image filtering, edge detection, and extraction of contour image while pytesseract was used to extract the characters on the contour image. These tasks were programmed using Python with the aid of Pycharm IDE.

a. Local plate number images

In this paper, 115 local plate numbers were acquired by capturing images of vehicles with plate numbers using an Android mobile phone with the following specification: 1GBRAM, 2.0Hz*4 processor, 8MP camera, 2432x2432 image size. Some of the captured images are shown in Plate I as follows:

a. Front View b. Rear View

Plate I: Sample Local Captured Images

The acquired images were pre-processed by reducing the image size to 500x360 and cropping the image to view the front or rear area of the vehicle as shown in Plate II.

a. Front View b. Rear View

Plate II: Resizing and Cropping of Images

The next stage of image pre-processing is image conversion, i.e., converting an image from blue ray to grayscale to reduce the high resolution of the image. This is then followed by the final stage which is the image filtering, i.e., the stage at which noise is removed from the image with the aid of a bilateral filter (Blurring).

a. Image localization

In this step, the following processes were followed:

i. Canny edge detection technique was used to acquire the edges of the vehicle in the image and then used contours to ignore the unwanted contours in the image, such as the windscreen, spotlight, etc.
ii. Loop over contours was used to find the rectangle of the plate number.
iii. After localizing the plate number, the remaining background is negligible, then we proceed with removing the image except for the plate number contour.

b. Extract of character from a plate number

The following are the steps implemented for the extraction of characters from the localized plate number

i. Character segmentation cropped the image and save it with a new name.
ii. The last step is character recognition which reads the plate number character in the image and used a command to print the extracted character in the terminal.

The flowchart for the automatic plate number detection and recognition system for the plate number extraction from a captured vehicle image is presented in Figure 3.1 comprising of pre-processing of the captured image; conversion, contours detection, and also the plate number recognition:

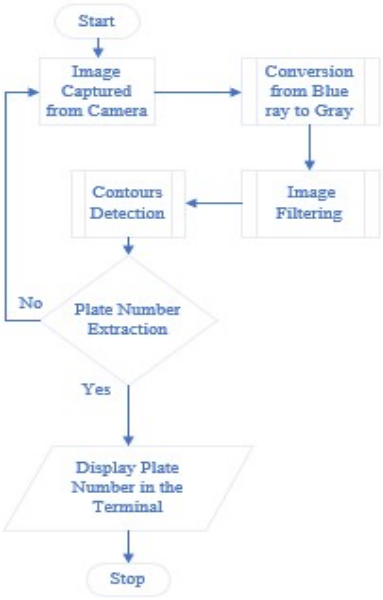

Figure 3.1: Vehicle Capture and Plate Number Recognition Algorithm

3.2 Development of desktop application and database

The design of a desktop software application using Microsoft visual basic and the development of a database using Microsoft SQL Server Management Studio is used in this research, the interface for both the front and back end are shown in the appendix that includes the authentication, vehicle user interface, daily access report, and database report for all entries.

4. RESULTS AND DISCUSSION

4.1 Detection Result

The following shows the result obtained when actualizing the plate number detection after a vehicle image is captured during the entrance. The processes below describe the steps for character recognition by capturing the vehicle image and then converting it to greyscale to reduce the image quality, dictating the vehicle edge for contour detection. After the detection of contour, tesseract-ocr was used to detect the character on the vehicle for daily entrance report by the developed program.

i. The original image captured from the vehicle

Plate III: Original Image

ii. Converting the original image from the actual image grayscale to help reduce the noise

Plate IV: Grayscale Image

iii. The image shows edge detection for the vehicle

Plate V: Canny Edge Image

iv. Contour edge detection

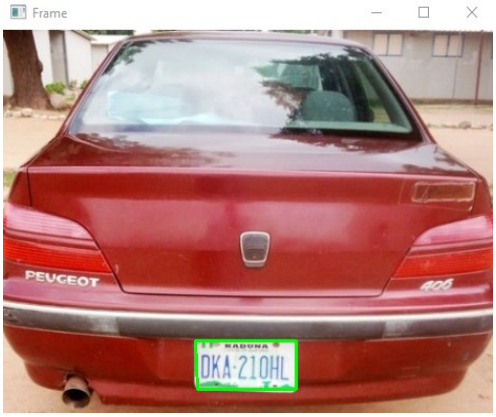

Plate VI: Contour Detection Image

v. Final result of extracted plate number

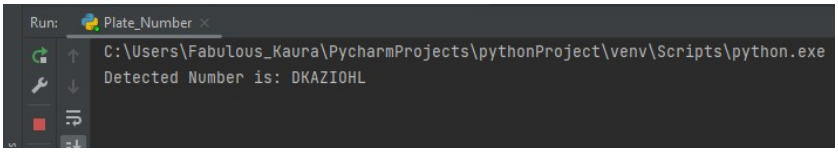

Plate VII: Result from Image

From the result in Plate VI, it is evident that the system recorded a good accuracy in plate number localization, while the result in Plate VII shows that the system can recognise 6 characters correctly out of the eight characters on the plate. This translates to 75%-character recognition accuracy

4.1.1 Analysis Table

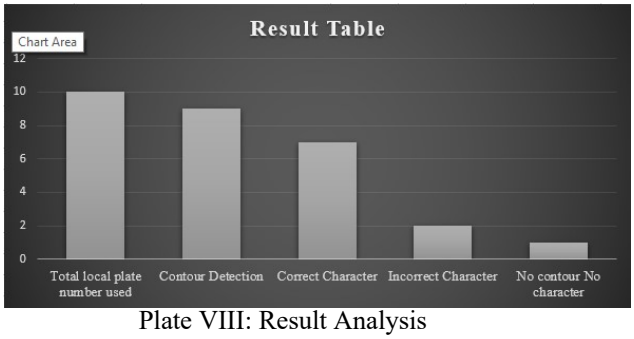

Plate VIII: Result Analysis

The above plate shows the local plate number sample tested on the algorithm. The total number of plates used is ten, only seven give correct characters, two of them incorrect characters, and only one does not have character or contour. Also, nine out of ten detect contour which gives us 90% contour detection and 70%-character recognition as the overall system performance.

4.2 Result Obtained from the Software Developed for Record Based

Below is the interface for the daily entrance report and the database entire report for daily entrance. The program is designed to accept information related to vehicle owners before gaining access to the daily entrance which captures the plate number, time, gate passing by, either staff, student, or visitor, and the security attending you during the entrance.

i. Daily entrance verification report

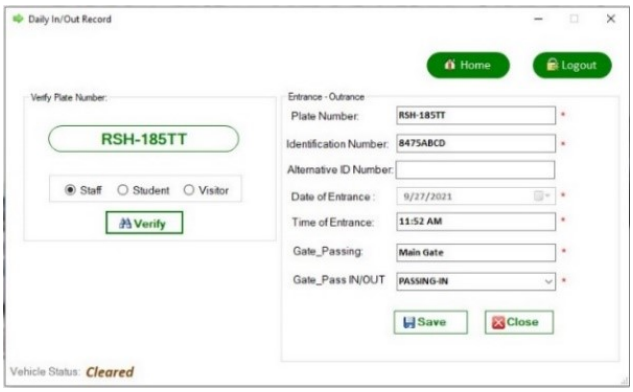

Figure 4.1: Daily Entrance Interface

ii. Database results obtained from daily report

	Plate_Numbr	Date_entmce	Time_entmce	ID_number	pass_gate	attdby	Pass_in_out	ID_Number2
1	seyhts	2021-07-29	8:42 PM	ghyjsdz	sdu	Label1	Entrance	hgjs
2	FGHJKH	2021-08-10	3:06 PM	qwety2376892	Main Gate	Label1	PASSING-IN	
3	FGHJKH	2021-08-10	3:06 PM	qwety2376892	Main Gate	Label1	PASSING-IN	
4	FGHJKH	2021-08-10	3:09 PM	qwety2376892	Main Gate	Label1		
5	JSJ332JKD	2021-08-10	3:27 PM	eshj8499	Main Gate	UMAR RIDWAN	PASSING-IN	
6	RSH-185TT	2021-09-29	1:34 PM	8475ABCD	North Gate	ABDULMALIK UMAR	PASSING-IN	
7	RSH-185TT	2021-09-29	1:50 PM	8475ABCD	Main Gate	ABDULMALIK UMAR	PASSING-IN	

Figure 4.2: Daily Entrance Report

5. CONCLUSION

The algorithm developed in this work for the extraction of Nigeria plate numbers proved quite effective and efficient. It had a 90% accuracy for license plate localization but a reading accuracy of 70%. MYSQL server database was used in this study which allows large storage of driver's particulars and vehicle data. With the output tied to a database, this system can be used as an automated process for managing a large number of vehicle user profiles as well as access control. Further work can be conducted to improve the accuracy of this system, using deep learning (tensor flow). Performance comparison for the captured plate number and the record stored in the database can be automated to make sure that each vehicle must be registered before accessing premises.

ACKNOWLEDGEMENT

I wish to express my profound gratitude to Almighty Allah; the Creator, Fashioner, without His mercies and favour I would certainly not exist. I would also like to express my profound gratitude to my supervisor Dr. Zaharuddeen Haruna for giving me the opportunity, for his patience, guidance, and careful instruction throughout the research, and a lot of others whom I cannot mention here whose hard work and dedication during this study assisted me with advice and encouragement. I have nothing to offer them but for Allah to reward them abundantly and enable them to succeed in all their endeavours. This acknowledgment would not be complete without expressing my sincere gratitude to my parents, brothers, and sisters for their love, patience, encouragement, and understanding which are the source of my motivation and inspiration throughout my work. May Almighty Allah in his abundance reward you all greatly, and then some more. I must in the final analysis not fail to appreciate all those special individuals, colleagues, family members, and friends whom I cannot mention here that have contributed in one way or another, in the course of my struggle and improved on my qualification. Thank you all.

REFERENCES

AG, S. F. (2019). Development of portable automatic number plate recognition (ANPR) system on Raspberry Pi. *International Journal of Electrical and Computer Engineering, 9*(3), 1805.

Akbarzadeh, O., Khosravi, M. R., & Alex, L. T. (2022). Design and Matlab simulation of Persian license plate recognition using neural network and image filtering for intelligent transportation systems. *ASP Transactions on Pattern Recognition and Intelligent Systems, 2*(1), 1-14.

Alfath, A. N., Taningngsih, I., & Suharto, E. (2022). Designed an Inactive Archives Management Information System Using Visual Basic 2010 at The Department of Community Empowerment and Village West Java Province. *Journal of Applied Engineering and Technological Science (JAETS), 3*(2), 105-115.

BC, M. H., Pukhrambam, S., Gokakakar, R. R., & Kaveri, B. (2022). YOLOV4 object detection for license plate detection.

Dome, S., & Sathe, A. P. (2021). *Optical character recognition using Tesseract and classification.* Paper presented at the 2021 International Conference on Emerging Smart Computing and Informatics (ESCI).

Etomi, E. E., & Onyishi, D. U. (2021). Automated number plate recognition system. *Tropical Journal of Science and Technology, 2*(1), 38-48.

Kaur, P., Kumar, Y., Ahmed, S., Alhumam, A., Singla, R., & Ijaz, M. F. (2022). Automatic license plate recognition system for vehicles using a CNN. *CMC-Computers, Materials & Continua, 71*(1), 35-50.

Li, F., & Wang, L. (2022). Application of Case-based Teaching in Computer Vision with OpenCV and Python. *environment, 5*, 8.

Mujawar, S. S., & Vadi, S. (2022). Raspberry Pi and OpenCV for license plate recognition in real-time.

Padmasiri, H., Shashirangana, J., Meedeniya, D., Rana, O., & Perera, C. (2022). Automated license plate recognition for resource-constrained environments. *Sensors, 22*(4), 1434.

Thakare, S., Kamble, A., Thengne, V., & Kamble, U. (2018). *Document Segmentation and Language Translation Using Tesseract-OCR.* Paper presented at the 2018 IEEE 13th International Conference on Industrial and Information Systems (ICIIS).

Ugwu, E. M., Taylor, O. E., & Nwiabu, N. D. (2022). An Improved Visual Attention Model for Automated Vehicle License Plate Number Recognition Using Computer Vision. *European Journal of Artificial Intelligence and Machine Learning, 1*(3), 15-21.

Wang, Y., Liu, J., He, X., & Wang, B. (2018). Design and realization of rock salt gas storage database management system based on SQL Server. *Petroleum, 4*(4), 466-472.

APPENDICES

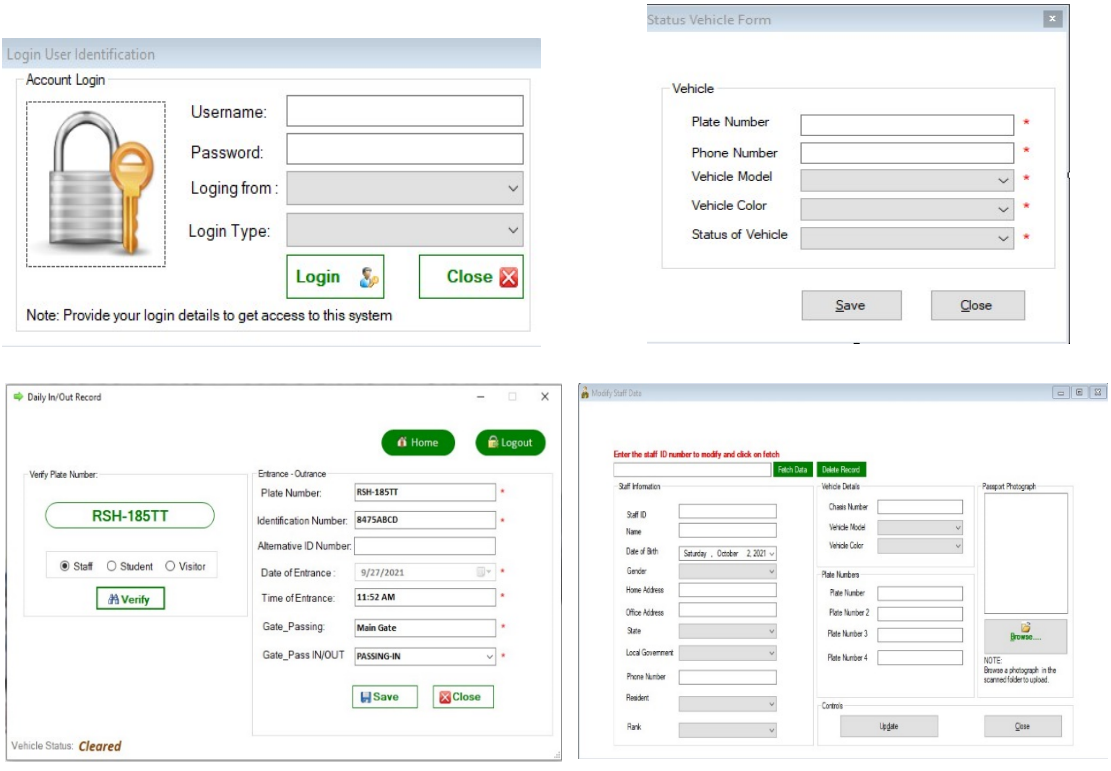


Main Form
File
Registration
Capture Vehicle
Report
Administration
Logout
Exit
AUTOMATIC NUMBER PLATE RECOGNITION
Current User: 0

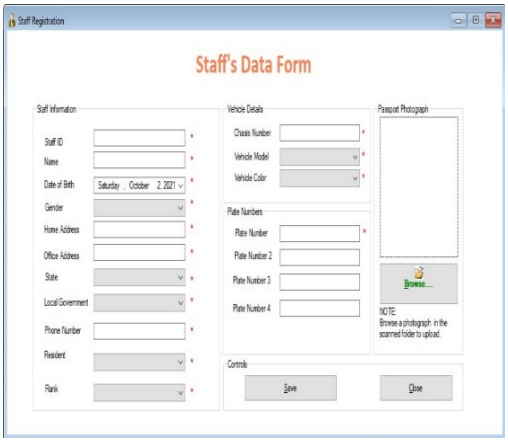
Staff Registration
Staff's Data Form
Staff Information
Staff ID
Name
Date of Birth
Gender
Home Address
Office Address
State
Local Government
Phone Number
Resident
Rank
Vehicle Details
Chasis Number
Vehicle Model
Vehicle Color
Plate Numbers
Plate Number
Plate Number 2
Plate Number 3
Plate Number 4
Passport Photograph
Browse...
NOTE:
Browse a photograph in the scanned folder to upload.
Controls
Save
Close

PAPER 87 – DEVELOPMENT OF FULLY BIOBASED MATERIALS FOR MEMBRANE INDUSTRY TRANSFORMATIONS IN THE LIGHT OF CIRCULAR ECONOMY

A.F. I. Akindele[1*], M. Ersöz[2]

[1]Department of Environmental Management and Toxicology, University of Medical Sciences, Ondo State
[2]Department of Chemistry, Secluk University, Konya, Turkey.
[*]Email: fakindele@unimed.edu.ng

ABSTRACT
Circular economy, a resource-efficient model emphasizes eliminating waste and making the entire economy more sustainable through waste reuse, reduction, and recycling. For economic and environmental concerns as well as to comply with the newly established reinforcements on green economy, circular strategies have been proposed in industrial sectors to realize the recovery of waste products that have potentials to be used as raw materials. The circular economy frameworks offer an opportunity for membrane technology innovation. Membrane technology has been applied across a broad spectrum of industrial and municipal installations and is currently popular for water treatment and reuse as well as water desalination, on account of its reliability, high-efficiency, and ease of operation. New membranes from renewable materials, including wood-based polymers (bio-based polymers) was innovated and it gave a membrane manufacturing by the green chemistry and green engineering principles and the life cycle analysis methodology realized green synthesis completely for membrane fabrications. This development solves seven out of seventeen of the sustainable development goal (SDG) No. 3, 6, 9, 12, 13, 14 and 15.

KEYWORDS: Circular economy, Green chemistry, Sustainable development goals, Wood-based polymers, Membrane technology, Life cycle analysis

INTRODUCTION

All sectors have virtually witnessed growth at different levels due to increased industrialization, agricultural and other human activities (Abu-Bakar et al., 2021; Muhammad, 2019; Mathai et al., 2021). Our daily activities and industrial processes generate a lot of waste with increase in the demand for products by the populace (Sharma et al., 2020). Consequently, there is increase in the challenges associated with resource management and the handling of waste. Improper disposal and management have continuously imposed negative impacts on human health (Rautela et al., 2021; Akan et al., 2021; Alshehrei and Ameen, 2021). This has led to more studies on sustainable use of cleaner resources and technology related to waste management, the circular economy and product life cycle assessment (Zhang et al., 2021; Sharma et al., 2021; Luttenberger, 2020). The circular economy is a resource-efficient model that emphasizes eliminating waste and making the entire economy more sustainable through waste reuse, reduction, and recycling. Circular strategies have been proposed in industrial sectors to realize the recovery of waste products that have potentials to be used as raw materials to find a lasting solution to economic and environmental challenges (Yaw Agyabeng-Mensah et al., 2012). New innovative ways of sourcing for safer raw materials have become the current trend in manufacturing industries. Interestingly, many unwanted wastes have now be converted into useful products thereby reducing the amount of waste getting into the landfills. The European Union's Waste Management Directive advocates the prevention of waste has the highest priority in a waste hierarchy system.

The present study work will address 7 sustainable development goals namely: SDG3 – good health and well-being in reducing harmful releases from chemical and biological processes; SDG6 – clean water and sanitation – in allowing water recycling, effluent treatment and desalination in both urban and rural environments; SDG9 - Industry, Innovation and Infrastructure – enabling cleaner technologies with less emissions, SDG12 – Responsible Consumption & Production – in enabling cleaner manufacturing; SDG13 – Climate Action – for new emission environment by adsorption or conversion from catalytic membranes; SDG14 – Life below Water – by preventing waste effluents and emissions entering water-ways and oceans; SDG15 – Life on Land – particularly through allowing increased land use efficiency within cleaner environments. This research work will involve development of new membranes from renewable materials, including wood-based polymers (bio-based polymers). Fully bio-based fibres for green membrane fabrication (This is a challenging problem because many polymer membranes have been developed to be chemically, thermally and mechanically robust (for process/product durability) and processed using low-cost, large-scale manufacturing solutions). Green-membrane research work will use a variety of approaches to these problems and will operate holistically to share knowledge across interest areas and

applications to allow new synthesis methods, testing/characterization and demonstration of feasibility for future development and exploitation; Re-use and recycling of biopolymers and LCA methodology to realize green membranes synthesis and production completely.

2. THEORETICAL ANALYSIS

2.1 Wood-based polymer

One option for lowering the environmental impact of plastics and timber debris is to use these wastes to make wood-polymer composites (WPC) goods, such as pallets, which are made of wood fiber and polymer. However, to evaluate the sustainability impact of WPC pallets, a comprehensive life cycle analysis must be performed. Aside from that, it is crucial to keep in mind that various commodities have varying lifespans, recycling abilities, and recycling potential. It is defined by the International Organization for Standardization (ISO) as being one of the environmental management techniques that addresses the social and environmental risks, ecological consequences throughout a product's life cycle from raw material obtaining through manufacturing, utilizing edge treatment, recycling, and disposal practices (Faggian et al., 2014; Zakariya, et al., 2022; Regulation (EC) No 1907/2006).

In recent years, WPC has also become interesting for other industries, namely the packaging and automotive sectors (Partanen and Carus, 2016). These are under increasing pressure to minimize the consumption of fossil-plastics. WPC saves petrochemical polymers, and this in the amount of the wood-fibers added. This leads to an almost balanced cradle-to-gate CO_2-balance. The reason for this is that during their growth, the wood fibers already absorbed exactly the amount of harmful greenhouse gases from the atmosphere, which is later emitted for production in the form of energy and fuel consumption

2.2 Raw material for membrane fabrication

Keratin, cellulose, and plastics can be widely found in domestic/industrial solid wastes and can be potentially used for liquid separation membrane fabrication.

2.2.1 Keratin

Keratin is a fibrous, structural protein commonly found in wool, hair, and poultry feather (Donato et al., 2020; Reddy et al., 2021). Wools obtained from textile fabric and hairy parts of animals are especially important keratin extraction sources, as it consists of ~95% raw keratin (Shavandi et al., 2017). Chicken feathers, which consist of ~90% protein keratin, are another major source for extracting keratin (Donner et al., 2019). The living-organism leftovers produced in tanning, slaughterhouse, and poultry industries are treated as waste, and their disposal often leads to vast environmental problems.

2.2.2 Cellulose

Cellulose is one of the most abundant biopolymers found in nature. Depending on the sources, lignocellulosic biomass typically contains cellulose, 40–60% and hemicellulose, 15–30% and lignin, 10–25%, which weave to each other to establish a strong-stretch network of recalcitrant biomass (Ariffin et al., 2008; Wang et al., 2017). Lignin is the main barrier in the deconstruction of lignocellulosic biomass; hence, lignin extraction during biomass pretreatment using solvent is required to ease the conversion of fibrous cellulosic materials (Tran and Mututuvari, 2016). Other sources, such as seaweed, are also gaining attention for cellulose extraction. The removal of lignin through harsh chemical treatment necessary for lignocellulosic biomass is not required for this alternative (Esparza et al., 2018).

2.2.3 Plastics and Rubber

The monomers of commonly used plastics are majorly derived from non-renewable fossil hydrocarbons, so these plastics are highly durable and generally not biodegradable. The share of plastics in municipal solid waste has increased tremendously. Nearly 80% of plastic debris from land-based sources ends up in the ocean as a result of mismanagement of the plastic waste throughout the plastic supply-chain life cycle, starting from production until post-consumer disposal (Li et al., 2016). The non-biodegradable nature of most commercially used plastics leads to their landfill accumulations for many years, hence resulting in direct plastic contamination (Kubowicz and Booth, 2017). On the other hand, the incomplete disintegration of durable plastics result in the formation of microplastic polymer particles of various morphologies that invade the environments and food chains. Therefore, efforts to recycle post-consumer plastics, such as polyethylene terephthalate (PET) bottles, which have been used as single-use packaging for beverages, are necessary to counter white pollution and the subsequent issues resulting from their disposal.

2.3 The Bio-based Economy

The seventh principle of Green Chemistry is "renewable rather than depleting raw materials". One of the great challenges of the twenty first century is the implementation from an unsustainable economy based on non-renewable fossil resources - oil, coal and natural gas – as raw materials to a bio-based economy with renewable biomass as the feedstock (Sheldon, 2018; Devi et al., 2022). The pressing need for climate change mitigation and the conservation of natural carbon resources is driving the switch to a carbon-neutral manufacture of commodity chemicals, materials and liquid fuels from renewable biomass in integrated biorefineries (Wang et al., 2021). However, the use of common and well-known biomass feedstocks, such as corn and edible oil seeds, won't continue to be a sustainable option in the longer term because of direct or indirect competition with food production.

2.4 Life Cycle Assessment

Full-scale LCAs are useful for comparing products and processes which have already been commercialized. Conducting a full scale LCA in the design or development phase is generally too difficult and time-consuming. In the final analysis, an assessment of the "greenness" of a process or product requires a multivariate approach that includes impacts across all the different metrics. However, the assessment tools for process industries can be simplified by splitting the system boundaries into two domains: the raw materials, production and supply domain and the gate-to-gate manufacturing domain (Sheldon, 2018).

3. MATERIALS AND METHODS

3.1 Methodological approach

The methodological approach applied in this work includes a stepwise methodology with three main building elements: identification of raw materials, (eco) toxicological assessment and Registration, Evaluation, Authorisation and Restriction of Chemicals (REACH) compliance analysis. The raw materials identified for the membrane production were then evaluated to focus on which chemicals are hazardous and for which endpoint there is a concern. While the production process and the final products were considered to identify to which REACH obligations the membranes manufacturer could be subjected.

3.1.1 Identification of raw materials

Regarding the manufacture of poly(vinylidene fluoride) (PVDF) and PES UF membrane, the dry-wet phase inversion process of GVS company was considered (GVS Group, Italy). In this process, a polymer solution will be prepared by mixing polymer and solvent. The solution is then filtered and cast onto the non-woven support. After a partial evaporation of the solvent, the cast film is immersed in a nonsolvent medium, called coagulation bath. Due to exchange of solvent and nonsolvent between polymer solution and coagulation bath, the composition in the film is changed and phase separation is induced, with the solidification of the polymer film. During the first step of desolvation by solvent evaporation, a thin skin layer of solid polymer is formed instantly at the top of the cast film due to the loss of solvent. In the solvent-nonsolvent exchange process that follows, the nonsolvent diffuses into the polymer solution film through the thin solid layer while the solvent diffuses out. Afterwards the membrane is washed and then lightly dried in an oven.

The raw materials used in phase inversion process will be identified through a visit to membrane manufacturer, by collecting the Material Safety Data Sheets (MSDS) of the chemicals used, as well as information about the uses, functions and amounts. Other suitable data and information were collected from supplier, project partner, and literature.

A special attention will be pose on impurities or residual undesired contaminants (free monomers) in polymers supplied, additives and solvents used and on their presence as residual contaminants in membranes, and on the use of other polymers/copolymers, in addition to those provided by polymers supplier.

3.1.2 (Eco) toxicological assessment of raw materials

A desk-based (eco) toxicological evaluation will be performed to identify the hazard profile of polymers, copolymers, polymeric additives and solvents used for the development of UF membrane. The evaluation was based on literature review and expert judgment.

3.2 Development and Performances of Waste-derived Polymeric

The bio-based polymers, which can be derived from natural sources such as cellulose and chitin or produced through biosynthesis, tend to have high hydrophilicity, biocompatibility, and biodegradability, as well as a low toxicity, carbon footprint, and environmental impact. The majority of bio-sourced polymers used for membrane fabrication are carbohydrates/polysaccharides and their derivatives. The origin of bio sourced materials possesses

a high degree of biodegradability that makes them attractive as green materials to be used for reducing pollution of the environment with plastic wastes. Cellulose is a linear polysaccharide primarily derived from many sources and has ordinary properties which are hydrophilicity and biocompatibility, exhibits excellent mechanical strength and perform chemical modifications with many functional groups. However, cellulose's high crystallinity and strong intermolecular hydrogen bonds make it difficult to dissolve in common solvents, which can hinder the production of cellulose-based membranes (Ariffin et al., 2008; Tran and Mututuvari, 2016; Wang et al., 2017; Esparza et al., 2018).

4. RESULTS AND DISCUSSION

The possibility of developing both design and functionality of the use of bio-sourced polymeric materials, nanofiber, recyclable polymers fully re-use and nanoparticles with well-defined mechanical stability, ensuring bio-compatibility and high flux rates. Stimulating new ideas in the field of innovative green membrane applications for different sectors through networking activities; contributing on the new innovative green methods for membrane manufacturing as re-use, renewable, recycling, and end-of-life management. Application of the "LCA methodology" to realize green synthesis completely for membrane fabrications will be adopted.

However, there are still some challenges and limitations associated with green or biodegradable membranes, including their degradation rate and composition with non-biodegradable materials, which can lead to waste disposal and secondary pollution. Further research is needed to understand the degradation mechanisms and behaviour of microorganisms and enzymes under different environmental conditions. Additionally, as green membranes are typically produced on pilot scales, more efficient scale-up models are needed to expand the production process.

5. CONCLUSION

Pertinence and innovative aspects of the research programme is that Green-Mem address completely the priorities for a European Union into first European Green Deal strategy, 2030 Climate action plan target directing towards finding an alternative green membrane system from bio-based materials which are sustainable, biodegradable, no toxicity and more eco-friendly. Moreover, membranes play a critical role in maintaining healthy air, land and aquatic environments. They are critical for capture of emissions, filtration of harmful substances and cleaning water sources and emissions.

ACKNOWLEDGEMENT

My appreciation goes to my mentor and collaborator Prof. ERSÖZ who has been a wonderful person to me. I also came to know about the conference through my friend Dr. J. A. Adeniran. The kind gesture is well appreciated.

REFERENCES

Abu-Bakar, H., Williams, L., & Hallett, S.H. (2021). A review of household water demand management and consumption measurement. *Journal of Cleaner Production, 292*, 125872. https://www.semanticscholar.org/paper/A-review-of-household-water-demand-management-and-Abu-Bakar-Williams/93c625376fb21ac82f762b92d0a6c7d461dd7869

Akan, O. D., Udofia, G. E., Okeke, E. S., Mgbechidinma, C. L., Okoye, C. O., Zoclancloun, Y. A. B., Atakpa, E. O., & Adebanjo, O. O. (2021). Plastic waste: Status, degradation and microbial management options for Africa. *Journal of environmental management*, *292*, 112758. https://doi.org/10.1016/j.jenvman.2021.112758

Alshehrei, F., & Ameen, F. (2021). Vermicomposting: A management tool to mitigate solid waste. *Saudi journal of biological sciences*, *28*(6), 3284–3293. https://doi.org/10.1016/j.sjbs.2021.02.072

Ariffin, H., Hassan, M. A., Shah, U. K., Abdullah, N., Ghazali, F. M., & Shirai, Y. (2008). Production of bacterial endoglucanase from pretreated oil palm empty fruit bunch by bacillus pumilus EB3. *Journal of bioscience and bioengineering*, *106*(3), 231–236. https://doi.org/10.1263/jbb.106.231

Devi, A., Bajar, S., Kour, H., Kothari, R., Pant, D., & Singh, A. (2022). Lignocellulosic Biomass Valorization for Bioethanol Production: a Circular Bioeconomy Approach. *Bioenergy research*, *15*(4), 1820–1841. https://doi.org/10.1007/s12155-022-10401-9

Donato, R.K.; Mija, A. Donato, R.K.; Mija, A. (2020). Keratin Associations with Synthetic, Biosynthetic and Natural Polymers: An Extensive Review. *Polymers* , *12*, 32. https://doi.org/10.3390/polym12010032.

Donner, M. W., Arshad, M., Ullah, A., & Siddique, T. (2019). Unravelled keratin-derived biopolymers as novel biosorbents for the simultaneous removal of multiple trace metals from industrial wastewater. *The Science of the total environment*, *647*, 1539–1546. https://doi.org/10.1016/j.scitotenv.2018.08.085

Esparza, Y., Bandara, N., Ullah, A., & Wu, J. (2018). Hydrogels from feather keratin show higher viscoelastic properties and cell proliferation than those from hair and wool keratins. *Materials science & engineering. C, Materials for biological applications*, *90*, 446–453. https://doi.org/10.1016/j.msec.2018.04.067

Faggian A., Scanferla P., Paulussen S., Zuin S. (2014). Combining the European chemicals regulation and an (eco) toxicological screening for a safer membrane development. *Journal of Cleaner Production*, 83, 404-412, ISSN 0959-6526,https://doi.org/10.1016/j.jclepro.2014.07.017.

Kubowicz, S., & Booth, A. M. (2017). Biodegradability of Plastics: Challenges and Misconceptions. *Environmental science & technology*, *51*(21), 12058–12060. https://doi.org/10.1021/acs.est.7b04051.

Li, W. C., Tse, H. F., & Fok, L. (2016). Plastic waste in the marine environment: A review of sources, occurrence and effects. *The Science of the total environment*, *566-567*, 333–349. https://doi.org/10.1016/j.scitotenv.2016.05.084.

Luttenberger, L. R. (2020). Waste management challenges in transition to circular economy–case of Croatia. *Journal of Cleaner production*, *256*, 120495. https://www.sciencedirect.com/science/article/pii/S0959652620305424

Mathai, M.V.; Isenhour, C.; Stevis, D.; Vergragt, P.; Bengtsson, M.; Lorek, S.; Mortensen, L.F.; Coscieme, L.; Scott, D.; Waheed, A.; Alfredsson E. (2021). The Political Economy of (Un)Sustainable Production and Consumption: A Multidisciplinary Synthesis for Research and Action. *Resources, Conservation and Recycling*, 167, 105265. https://www.sciencedirect.com/science/article/abs/pii/S0921344920305802

Muhammad, B. (2019). Energy consumption, CO2 emissions and economic growth in developed, emerging and Middle East and North Africa countries. *Energy*, 179, 232–245. https://www.sciencedirect.com/science/article/abs/pii/S0360544219305420

Partanen, A .and Carus, M. (2016). Wood and natural fiber composites current trend in consumer goods and automotive parts. *Reinforced Plastic*, 60, 170–173. https://www.sciencedirect.com/science/article/abs/pii/S0034361716000205

Rautela, R., Arya, S., Vishwakarma, S., Lee, J., Kim, K. H., & Kumar, S. (2021). E-waste management and its effects on the environment and human health. *The Science of the total environment*, *773*, 145623. https://doi.org/10.1016/j.scitotenv.2021.145623

Sharma, H. B., Vanapalli, K. R., Samal, B., Cheela, V. R. S., Dubey, B. K., & Bhattacharya, J. (2021). Circular economy approach in solid waste management system to achieve UN-SDGs: Solutions for post-COVID recovery. *The Science of the total environment*, *800*, 149605. https://doi.org/10.1016/j.scitotenv.2021.149605

Sharma, S., Basu, S., Shetti, N. P., Kamali, M., Walvekar, P., & Aminabhavi, T. M. (2020). Waste-to-energy nexus: A sustainable development. *Environmental pollution (Barking, Essex: 1987)*, *267*, 115501. https://doi.org/10.1016/j.envpol.2020.115501

Shavandi, A., Silva, T. H., Bekhit, A. A., & Bekhit, A. E. A. (2017). Keratin: dissolution, extraction and biomedical application. *Biomaterials science*, *5*(9), 1699–1735. https://doi.org/10.1039/c7bm00411g.

Sheldon R. A. (2018). Metrics of Green Chemistry and Sustainability: Past, Present, and Future. *ACS Sustainable Chemistry & Engineering*, 6 (1), 32-48. DOI: 10.1021/acssuschemeng.7b03505…….. https://pubs.acs.org/doi/10.1021/acssuschemeng.7b03505

Tran, C. D., & Mututuvari, T. M. (2016). Cellulose, Chitosan and Keratin Composite Materials: Facile and Recyclable Synthesis, Conformation and Properties. *ACS sustainable chemistry & engineering*, *4*(3), 1850–1861. https://doi.org/10.1021/acssuschemeng.6b00084

Reddy, C.C.; Khilji, I.A.; Gupta, A.; Bhuyar, P.; Mahmood, S.; AL-Japairai, K.A.S.; Chua, G.K (2021). Valorization of keratin waste biomass and its potential applications. Journal of Water Process Engineering. 40, 101707. https://www.sciencedirect.com/science/article/abs/pii/S2214714420305857

Regulation (EC) No 1907/2006 - Registration, Evaluation, Authorisation and Restriction of Chemicals (REACH). https://osha.europa.eu/en/legislation/directives/regulation-ec-no-1907-2006-of-the-european-parliament-and-of-the-council.

Wang, S., Dai, G., Yang, H., & Luo, Z. (2017). Lignocellulosic biomass pyrolysis mechanism: A state-of-the-art review. *Progress in Energy and Combustion Science, 62*, 33-86.

Wang, F., Harindintwali, J. D., Yuan, Z., Wang, M., Wang, F., Li, S., Yin, Z., Huang, L., Fu, Y., Li, L., Chang, S. X., Zhang, L., Rinklebe, J., Yuan, Z., Zhu, Q., Xiang, L., Tsang, D. C. W., Xu, L., Jiang, X., Liu, J., … Chen, J. M. (2021). Technologies and perspectives for achieving carbon neutrality. *Innovation (Cambridge (Mass.))*, *2*(4), 100180. https://doi.org/10.1016/j.xinn.2021.100180

Yaw Agyabeng-Mensah, Y. Agyabeng-Mensah, Liang Tang, L. Tang, Ebenezer Afum, E. Afum, Charles Baah, C. Baah, & Essel Dacosta, E. Dacosta. (2012). Organisational identity and circular economy: Are inter and intra organisational learning, lean management and zero waste practices worth pursuing?. *Sustainable Production and Consumption, 28*, 648-662. doi: 10.1016/j.spc.2021.06.018. https://pubag.nal.usda.gov/catalog/7440356

Zakariya, S.; Yeong, Y.F.; Jusoh, N.; Tan, L.S. (2022). Performance of Multilayer Composite Hollow Membrane in Separation of CO_2 from CH_4 in Mixed Gas Conditions. *Polymers*, *14*, 1480. https://doi.org/10.3390/polym14071480

Zhang, J., Qin, Q., Li, G., & Tseng, C. H. (2021). Sustainable municipal waste management strategies through life cycle assessment method: A review. *Journal of environmental management*, *287*,112238. https://doi.org/10.1016/j.jenvman.2021.112238

PAPER 88 – Effects of Surface Linings and Thickness of Lining on the Microbial Load of Stored Onion Bulbs (*Allium Cepa L.*)

O.V. Adeyinka-Ajiboye[1], M.O. Sunmonu[2], M. M. Odewole[2]

[1]Department of Agricultural & Biosystems Engineering, University of Ilorin, PMB 1515, Ilorin 240003, Nigeria
[2]Department of Food Engineering, University of Ilorin, PMB 1515, Ilorin 240003, Nigeria
Email: ajiboye.oa @unilorin.edu.ng

ABSTRACT

The study was done to investigate effects of surface linings (jute, foam and polypropylene) and thicknesses (single 2.1, 8.91 and 0.44mm, double 4.20, 17.82, 0.88 mm and triple 6.30, 26.73, and 1.32 mm) of lining on the microbial load of onions bulbs stored for 6 months in an instrumented wooden structure. Kano-Red variety of onions was used for the experiment. ANOVA was used to study the effects of types and thickness of lining layers on onion bulbs in storage. During storage, both the treated and the control onion bulbs showed a general rise in microbial load in storage. The control displayed a starting value of 10^3 CFU/g and a final value of 80.5 x 10^2 CFU/g. Polypropylene double had the lowest value of microbial load (11.5–54.75 10^2 CFU/g), while Jute single and Jute triple had equal values in the range of (10.75-71.75). Jute double had the highest initial and final values of (14.5 CFU/g -77.25 CFU/g). Conclusively, it can be said that despite the general increase in microbial load between the control and the treated, treated samples still had lower microbial load.

KEYWORDS*:* onion bulbs, storage condition, surface lining, lining thickness and microbial load

1. INTRODUCTION

Onion (*Allium cepa L.*) is a vegetable bulb crop that is popular all over the world and is known to most cultures. Its production is only second to that of tomatoes (FAO, 2012). Because of their particular flavour, onions are recognized by people as one of the vegetable crops with a wide range of uses (Emmanuel *et al.,* 2022). The health profits of onion are largely credited to its various bioactive components, such as organosulfur compounds, phenolic compounds, polysaccharides, and saponins (Marrelli *et al.,* 2019; Teshika *et al.,* 2019). The more potent onion varieties appear to provide the largest concentration of compounds that support health. According to the National Cancer Institute, onions are reported to contain antioxidants that may prevent cancer and lower cholesterol (Indu, 2017). Onions can be harvested in dry conditions, but they are more susceptible to disease following harvest after a rain or when the humidity is high.

Onions have long been grown for both food and profit across the savannas of West Africa (Kassam, 2011). Nigeria, a nation in sub-Saharan Africa, ranks among the top countries in the world for onion production (Jolayemi *et al*., 2018). The majority of the onion production in Northern Nigeria is done in the states of Kaduna, Kano, Jigawa, Katsina, Sokoto, Kebbi, Plateau, and Bauchi, specifically in the dry tropical zone (Anyanwu, 2003). Onion bulbs are so fragile and frequently suffer injury during preservation. Different types of onion bulbs require different storage temperatures, such as 0–5 °C for some and 25–30 °C for others, with an average relative humidity of 65% (Ayalew, 2018). Postharvest onion bulb losses from sprouting and rotting range from 46 to 56% depending on the storage environment and system used (Ayalew, 2018). Controlled environments can be utilized to store onions for a long time. Despite being more expensive than traditional storage, this method boosts crop value by increasing the product's window of opportunity for sale (Ayalew, 2018). During storage, onions are susceptible to rotting, sprouting, and physiological weight loss.

The strong demand for and popularity of this type are due to its superior shelf-life. It is well-established that proper aeration reduces storage losses in onion. Incorporating forced air in the storage will provide adequate ventilation (aeration) which subsequently reduces rotting and sprouting of the stored onions. Unexpectedly, over one-third of the food produced for human consumption worldwide is wasted or lost each year (Delgado *et al*., 2017). This is significant since it shows that food loss and waste in developing nations costs over $310 billion USD (FAO, 2011). Sadly, onions are one of the major crops affected. The (Allium cepa L.) plant's shelf life is essential to the onion industry.

The main objective of this research was to study the effects of lining layers of an onion storage structure on the shelf life and nutritional compositions of onion bulbs. The specific objectives of this study were to: design and

construct a forced air ventilated storage for onions as a test rig and investigate the effects of surface linings and thickness of surface lining on the shelf life and microbial load of stored onions.

2. MATERIALS AND METHODS

Experimental Location

The study was conducted at the Agricultural Storage Room of the Department of Agricultural and Biosystems Engineering (longitude 4º35´E and latitude 8º30´N), University of Ilorin, Ilorin, Kwara State between May 26 and November 26, 2022 (24 weeks). The agricultural warehouse has a storage capacity of 8.15 x 7.02 m^2. Jute, polypropylene and foam in different thicknesses were used as lining materials to line the boxes within the storage structure where the onion bulbs to be stored were kept. Fumigation of the outside surrounding was done to treat termites, pests and the likes from invading the store.

The Onion bulbs (Kano-Red) variety that was used for the storage experiment was purchased from National Horticultural Research Institute (NIHORT), Kano State, Nigeria. The onion bulbs were cleaned, sorted and graded according to their sizes hence, healthy, firm, matured and whole bulbs were used for the experiment.

The major piece of equipment for this experiment is the high-density fibreboard that was utilized to construct the storage structure containing the three boxes lined with materials. The equipment and supplies used for this experiment include an electronic platform weighing scale (TCS Series), a Model CL 201 scale (220g x 0.1g), a digital vernier calliper (0-150mm), a galaxy sensors thermometer (v1.8.10), a hygrometer (0-100% Tasjkovski Labs), suction fans, renewable energy source wattage (260 W) and onion bulbs (kano- red).

Design Calculations

Volume of Storage Structure

The volume of the structure was calculated using the formula below:

Volume of the upper section (internal) = (m^3) (1)

Volume of bottom section (internal) = (m^3) (2)

Total volume (internal) = Volume of the upper section (internal) + Volume of bottom section (internal) (m^3) (3)

Volume of the storage box (internal) = (m^3) (4)

Where,

a = internal long base edge of upper section, 0.945m , b = internal short base edge of upper section, 0.225 m

= internal height of upper section, 0.162m , = internal Length of upper section, 0.315m

= internal length of bottom section, 0.945m, = internal breadth of bottom section, 0.315m

= internal height of bottom section, 0.664m, = internal length of storage box, 0.282m

= internal breadth of storage box, 0.273m, = internal height of storage box, 0.127m

i. Volume of the upper section (internal) =

=

= =

= m^3

ii. Volume of bottom section (internal) =

=

= m^3

iii. Total volume (internal) = Volume of the upper section (internal) + Volume of bottom section (internal)

=

= m^3

iv. Volume of the storage box (internal) =

=

= m^3

Fan Selection

According to Bartok (2013), fan selection in a storage structure is calculated using Equation

(5)

Where; F_c is the fan capacity; and A is the floor area of the storage structure.

Since is calculated to be

Therefore,

However, a factor of safety is highly essential in the design of components. For the fan, a factor of safety of 10% was selected and the actual and required fan capacities are expressed in Equations 3.4 and 3.5, respectively

(6)

(7)

Where F_C is the fan capacity; F_A and F_F, are the actual fan capacity and the required fan capacity, respectively.

Substituting into Equation 3.4 and 3.5,

Experimental Procedure and Set Up

The storage structure that housed the onion bulbs is hexagonally-shaped with a height of 0.837 m and external base width is 0.975 mm. The storage box that is enclosed in the main structure is a rectangular-shaped box with dimensions of 0.282 x 0.273 x 0.127 m lined with jute, foam and polypropylene of single thicknesses 2.1, 8.91 and 0.44 mm, double thicknesses 4.20, 17.82, 0.88 mm and triple thicknesses 6.30, 26.73, and 1.32 mm per storage box respectively. A brushless suction fan DC Scirocco Ace Model: 109BF 12HA2, DC 12v = 0.6A was installed at the top of the storage structure to suck out the heat within the system. The surface speed of the fan when working on solar and direct electricity power was 134 and 169 r.p.m respectively. Five kilogrammes of forty onion bulbs were stored in each storage box of twenty-seven boxes and one control, which equals a total of one thousand, one hundred and twenty onion bulbs (1,120). Total weight of onion stored was one hundred and forty kilogrammes (140 kg). Powered by direct connection to electricity supply also to a solar with total wattage of 260 w. Each of the nine (9) high-density fibreboard constructions had three boxes, each lined with foam, jute, and polypropylene, and each contained a known quantity of clean onion bulbs weighing five kilogrammes (kg), which were stored inside the structure. To act as the experiment's control, five kilograms (5 kg) of onion bulbs was spread out on the floor.

The ambient temperature and relative humidity of the space where the storage structures were kept was monitored during the storage time.

Data Collection

Each month, samples of onion bulbs were taken for microbial analysis. Fungi count was carried out using potato dextrose agar. The results obtained for each count was recorded as colony forming unit per ml (cfu/ml) of sample as shown in equation (8). This involves the same procedures as bacterial count; however, Potato Dextrose Agar was used. After allowing the agar in the petri-dish to solidify, the plates were incubated at room temperature at 27 ºC for 48 hours. After the incubation period, the plates were counted and recorded.

Fungi count (cfu/ml) = (8)

Storage Procedure

The techniques utilized for storage included carefully labeling the storage structures according to type of lining material and thickness, assembling and storing the products in storage structures and at ambient condition. The structures were inspected for any undesirable openings that could allow pests like rodents and insects inside. Each storage structure in this investigation has two sets of 3" elevated castor legs that extend above the floor.

Statistical Analysis

Microsoft Excel 2010 was used to analyze the experimental data for analysis of variance (ANOVA). Model equations were generated with General Factorial Experiment module of the Design Expert Version 6.0.6. Furthermore, there was no meaningful comparison between the results because the difference in the results was so minimal. All of the model equations' sufficiency and validity were examined using numerical and graphical methods.

3. RESULTS AND DISCUSSION

The results presented in Figure 1 showed that both the treated and the control onion bulbs exhibited a general rise in microbial load in storage. The control displayed a starting value of 10^3 CFU/g and a final value of 80.5 x 10^2 CFU/g. Polypropylene double had the lowest value of microbial load (11.5–54.75 10^2 CFU/g), while Jute single and Jute triple had equal values in the range of (10.75-71.75). Jute double had the highest initial and final values of (14.5 CFU/g -77.25 CFU/g).

While from beginning to the end, foam triple had the value increase range of (10.25-71.00 CFU/g). Foam single had the initial fungi value range of (10.25–68.5), followed by foam double (9.75–66.75 CFU/g). Polypropylene triple revealed (11.75-69.5 CFU/g) and Polypropylene single (11.25-66.5 CFU/g). There is a concern to the public's health since onion bulbs contain large quantities of this fungus (Onuorah and Obika 2015). Commonly, growth of bacteria and fungi is confined to water activity (a_w) levels above 0.90 (Lund *et al.,* 2000). Unlike bacteria that cannot grow below 0.85 a_w, fungi are more tolerant to reduced a_w and can grow even below 0.80 (Lund *et al.,* 2000; Sagar and Suresh, 2010). While, the lowest a_w at which growth of bacteria has been reported was 0.75, fungal growth has been recorded at a_w levels as low as 0.61 (Lund *et al.,* 2000). Leistner (1992) reported that moisture content and water activity (a_w) of artificially dried fruits and vegetables range from 15 to 50% and 0.60 to 0.89, respectively. These conditions can only cause dormancy in bacteria and fungi until a favourable environment is attained (Prescott *et al.,* 2001; Sagar and Suresh, 2010).

Microbial counts and pathogens higher than international stipulated limits (10^3 CFUg-1 for fungi and 10^1 CFUg-1 for bacteria) in both commercially and conventionally produced fresh and dried fruits and vegetables have been reported (BarkaiGolan and Paster, 2011; Johannessen *et al.,* 2002; Mensah *et al.,* 2002; Witthuhn *et al.,* 2005). This assertion justifies the increase in total fungi count during the course of this study. The absence of the infrastructure required for the successful application of these technologies is a significant additional issue. Onion storage structures may be designed to maximize natural ventilation. Post-harvest management for agricultural products aims to achieve this by minimizing agricultural product loss or waste continues to be the main goal of post-harvest management systems. According to various studies that reported on onion postharvest technologies, using both conventional and innovative methods can effectively help to enhance the shelf life of onion produce.

The presence of these fungi in the onion bulbs is attributable to the environmental conditions, state of handling and processing, state of storage facility of the onions, the fungal load of the handlers and the quality of the onion bulbs. These fungi have been known to cause diseases of humans and animals. They may come from the air, water, soil and even the handlers. They are the sources of highly potent mycotoxins which are hazardous to health. The presence of these fungi in significant numbers in onion bulbs is therefore a public health risk. Fungal spoilage of onions also has a negative economic effect on the economy of the onion bulbs farmers in particular and the economy of the country in general. The control of the fungal spoilage of onion bulbs is therefore inevitable. Proper storage conditions, careful harvesting, protection of the bulbs from sunburn, provision of adequate ventilation and regular examination during storage will minimize the entry and proliferation of these organisms in the onion bulbs, thereby reducing the incidence of diseases they cause and also improve the economy by reducing wastes resulting from spoilages.

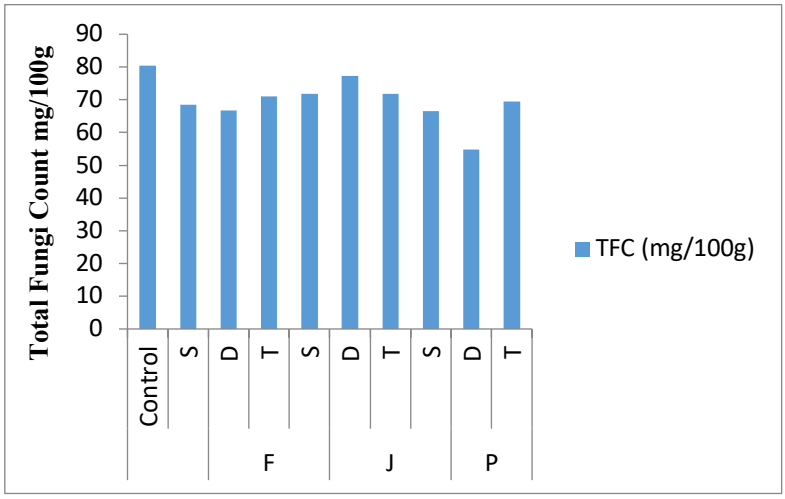

Figure 1: Graph of Total Fungi Count versus Lining Thickness

4. CONCLUSION

In conclusion, it can be said in terms of type of lining material and material thickness that onion bulbs stored were affected by an increase in total fungi count in this investigation which needs to be properly looked into and completely minimized in further investigations. The control exhibited the highest value 80.5 x 10^2 CFU/g of total fungi count in storage which means that for excellent postharvest management, keeping onion bulbs in the storage structure is safer for human health than just spreading on the floor. Other vegetable types could be researched on using the same storage structure and experiment done to check the effects of types of lining and lining layers on the shelf life and nutritional composition of the selected agricultural crop.

REFERENCES

Anyanwu, B. O. (2003). Agricultural Science for Schools and Colleges. Africa First Publishers, Onisha, Nigeria. In: Ojo, M. A, Mohammed, U.S, Adeniji, B and Ojo, A. O. Profitability and Technical Efficiency In Irrigated Onion Production Under Middle Rima Valley Irrigation Project In Goronyo, Sokoto State Nigeria. Continental *Journal of Agricultural Science 3*:7-14, 2009. © Wilolud Online Journals 2009.

Ayalew, D. (2018). Effect of storage temperature on physicochemical quality attributes of fresh Bombay red onion bulb (Allium cepal L.) doi:10.20944/preprints201803.0111v1

Barkai-Golan R, and Paster N (2011). Mycotoxins in Fruits and Vegetables, Elsevier Science.

Bartok, J. W. (2013). Fan and pad evaporative cooling system. Integrated pest management article from department of natural resources and the environment, University of Connecticut, Storrs CT.

Delgado, L., Schuster, M. and Torero, M. (2017). Reality of Food Losses: A New Measurement Methodology.

Emmanuel, O. Ajayi, Pamela E. Akin-Idowu, Olaide R. Aderibigbe, Dorcas O. Ibitoye, Gloria Afolayan, Oluyemisi M. Adewale, Esther A. Adesegun and Benjamin E. Ubi (2022). Nigeria Root Vegetables: Production, Utilization, Breeding, Biotechnology and Constraints. doi: 10.5772/intechopen.106861

Food and Agriculture Organization of the United Nations (2011). Global food losses and waste: Extent, Causes and Prevention. *Rome, Italy.*

Food and Agriculture Organization of the United Nations. (2012). World onion production. http://faostat.fao.org,accessedFebruary27,2017.

Indu, M. (2017). Origin and History of Onions. *IOSR Journal of Humanities and Social Science*, *22*(9): 7–10. https://doi.org/10.9790/0837-2209130710.

Johannessen, G., Loncarevic, S. and Kruse, H. (2002). Bacteriological analysis of fresh produce in Norway. Int. *J. Food Microbiol. 77*:199-203.

Jolayemi, O.S., Nassarawa, S. S., Lawal, O.M., Sodipo, M.A. and Oluwalana, I.B. (2018). Monitoring the changes in chemical properties of red and white onions (*Allium cepa*) during storage. *Journal of Stored Products and Postharvest Research, 9*(7): 78-86.

Kassam, A.H. (2011). Crops of the West Africa semi-Arid tropics. *International crop research institute for the semi-arid tropics 1*-11-256, Begumpet, Hydrabab, 500016, A.P. India.

Leistner, L. (1992). Food preservation by combined methods. *Food Res. Int. 25(2):*151-158.

Lund, B., Baird-Parker, T. and Gould, G. (2000). Microbiological Safety and Quality of Food, Maryland, Springer.

Marrelli, M., Amodeo, V., Statti, G. and Conforti, F. (2019). Biological properties and bioactive components of *Allium cepa* L.: focus on potential benefits in the treatment of obesity and related comorbidities. *Molecules.* (2019) *24*:119. doi: 10.3390/molecules24010119.

Mensah, P., Yeboah-Manu, D., Owusu-Darko, K. and Ablordey, A. (2002). Street foods in Accra, Ghana: How safe are they? B. World Health Organ. 80:546-554.
methods on the quality of onion bulbs Pak. *J. Agri., Agril. Engg., Vet. Sci., 2016, 32* (2): 221- 228 ISSN 1023-1072.

Onuorah Samuel and Obika Ifeanyi (2015). Fungi Associated with the Deterioration of Post-harvest Onion Bulbs Sold in Some Markets in Awka, Nigeria. *bioengineering and bioscience. 3. 90-94*. 10.13189/bb.2015.030503.

Prescott, L., Hardy, M. and Klein J (2001). Microbiology, New York, McGraw Hill.Rodrigues Ana, Almeida Domingos, Simal-Gandara Jesus and Perez, Rosa. (2017). Onions: A Source of Flavonoids. 10.5772/intechopen.69896.

Sagar, V., Suresh, K. (2010). Recent advances in drying and dehydration of fruits and vegetables: a review. *J. Food Sci. Technol. 47*(1):*15-26.*

Teshika, J.D., Zakariyyah, A.M., Zaynab, T., Zengin, G., Rengasamy, K.R.R. and Pandian, S.K. (2019). Traditional and modern uses of onion bulb (*Allium cepa* L.): a systematic review. *Crit Rev Food Sci Nutr.* (2019) 59:S39–70. doi: 10.1080/10408398.2018.1499074.

Witthuhn, R., Engelbrecht, S., Joubert, E.and Britz, T. (2005). Microbial content of commercial South African high-moisture dried fruits. *J. Appl. Microbiol. 98:722-726*.

PAPER 89 – STRUCTURAL INTEGRITY ASSESSMENT OF THE ACADEMIC AND HOSTEL BUILDINGS AT UNIVERSITY OF ILORIN USING NON_DESTRUCTIVE METHODS

I.T. Yusuf, A. O. Ibrahim, Y. O. Babatunde

Department of Civil Engineering, University of Ilorin, Ilorin, Nigeria.
*Email: ibnibrohim88@gmail.com

ABSTRACT

Quality and condition assurance assessment of concrete for structural adequacy have been performed by visual inspection and sampling by coring concrete using standard tests on specimens. They result in superficial local damage. Test methods that will not impair the function of structures and permit re-testing to measure their in-place properties at any time are, therefore necessary. Blocks 7-10 of the University of Ilorin, constructed with concrete walls and commissioned in 1980, were tested to determine the residual life of the buildings. The walls were subjected to non-destructive tests and a strength-Ultrasonic Pulse Velocity model in the form $a \ln x + c$ at R^2 of 96.5%. The resulting Pulse Velocities were then injected into the model to determine the residual life of the walls, and hence the buildings. The strength results were 21.81, 21.62, 21.65 and 21.35N/mm^2 for the blocks, respectively. These are less than 25N/mm^2 adopted for the structures at design stage, but greater than the expected remaining compressive strengths of 11.75N/mm^2 after 43 years of use, confirming that the conditions of the buildings are adequate. This method can be employed to identify dilapidated buildings to be demolished before sudden collapse to prevent loss of lives and properties.

KEYWORDS: Concrete blocks, Quality assurance, Ultrasonic pulse velocity, Compressive strength, Residual life

1. INTRODUCTION

Design of concrete requires an accurate knowledge of concrete properties under anticipated loading conditions. A large number of information is available on behaviour of concrete under static loading condition. However, when concrete is subjected to dynamic loadings, such as traffic on highway pavements and bridges, railroad bridges, building structures, airport pavements and marine structures, the fatigue behaviour/mechanism needs to be properly modelled. Fatigue is a process of progressive permanent internal changes in the materials that occur under the actions of cyclic loadings (Hiller and Roesler, 2016), which can cause progressive growth of cracks in the concrete and eventual failure of structures when high levels of cyclic loads (for shorter times) or low levels of loads (for longer times) are applied. Fatigue strength data of concrete and other materials that are used for development of load-induced stresses are needed for safe, effective and economical design. Indeed. fatigue cracking in concrete is a key failure mechanism and is the result of repeated applications of load at stress levels even below the flexural strength of the concrete slab (Roesler et al., 2013).

The mechanical response of a material is substantially altered by cyclic loadings. In the case of metals, it depends greatly on hardness of materials and experimental conditions. Under cyclic loading condition, a metal may harden, soften, remain stable or have mixed behaviour (soften or harden depending on strain level) (Bannantine et al., 2017). On the other hand, concrete which is a complex hybrid composite material under cyclic loading can experience fracture due to fracture of the cement paste, fracture of aggregate, failure of bond between the cement paste or combination of these mechanisms. Compared to metals, concrete is prone to have large number of flaws resulting from hydration, shrinkage and other causes. Mechanism of fatigue in concrete is not well established irrespective of the numerous hypotheses related to track initiation and propagation based on fracture of concrete mix (Bannantine et al., 2017).

Non-destructive test (NDT) methods are increasingly applied for the investigation of concrete for qualitative and quantitative explanation of the effects of structures due to (i) technological improvements in hardware and software for data collection and analysis, (ii) the economic advantages in assessing large volumes of concrete

compared with the acquisition of cores from existing structure, (iii) ability to perform rapid, comprehensive assessment of existing construction, and (iv) specification of NDT methods for quality assurance of deep foundations and concrete repairs (Verbeek and Stet, 2016). There has always been a need for test methods to measure the in-place properties of concrete. Ideally, these methods should be non-destructive so that they do not impair the function of the structure and permit re-testing at the same locations to evaluate changes in properties with time; and also serve as appropriate strength deterioration model for concrete design and maintenance purposes.

NDT methods, defined as testing that causes no structurally significant damage to concrete, are used to determine hardened concrete properties and to evaluate the condition of concrete in deep foundations, bridges, buildings, pavements, dams and other concrete construction. These test methods are applied to concrete construction for four primary reasons: (i) quality control of new construction; (ii) troubleshooting of problems with new construction; (iii) condition evaluation of older concrete for rehabilitation purposes; and (iv) quality assurance of concrete repairs. NDT emphasizes on methods that have been applied to measure physical properties other than the strength of concrete in structures with the later inferable from the former. The various NDT methods can be divided into two groups: those whose main purpose is to (a) estimate strength; and (b) evaluate conditions other than strength, that is to evaluate integrity. Generally, the most reliable tests for strength are those that result in superficial local damage. The integrity tests, on the other hand, are non-destructive and mostly based on visual inspections.

Ultrasonic Pulse Velocity (UPV) is a non-destructive technique that involves measuring the speed of elastic waves through materials in order to predict material strength, calculate low-strain elastic modulus and/or detect the presence of internal flaws such as cracking, voids, honeycomb, decay and other damages. The technique is found much applicable where intrusive (destructive) testing is not desirable and can be applied to concrete, ceramics, stone and timber. Absolute measurements need to be treated with caution. However, the UPV technique is not always practicable in testing sound concrete especially in the investigation of crack depth, where the crack is water-filled. The performance may also often be poor in very rough surface because sometimes good contact requires the use of a coupling gel between the transducer and the structure. This may be aesthetically unacceptable on some structures. Studies have proved the rational in using UPV for concrete testing. The studies concluded that for concrete with a particular mix proportion, there is a good correlation between UPV and the compressive strength; although there still exists a high uncertainty when one tries to make use of UPV to predict the strength of concrete in different mix proportions. It has also been established that UPV of hardened concrete is predictable based on its mix proportion. In addition, it has been shown that the compressive strength of concrete corresponds with the mix proportion (Mahure et al., 2018).

In taking measurements with the Pundit apparatus, pulses of longitudinal, elastic stress waves are generated by an electro-acoustical transducer that is hold in direct contact with the surface of the concrete under test (Komlos et al., 2016). After traversing through the material, the pulses are received and converted into electrical energy by a second transducer. The direction in which the maximum energy is propagated is at right angles to the face of the transmitting transducer; though, it is possible to detect pulses travelling through concrete in some other direction. In effect, it is possible to measure pulse velocity by placing the two transducers on either (a) opposite faces - direct transmission in accordance with BS 12504-4 (2004) as shown in Figure la; (b) adjacent faces - semi-direct transmission as shown in Figure lb; or (c) the same face - indirect or surface transmission as shown in Figure 1c. The direct wave transmission is the most sensitive, while the indirect is the least but most appropriate for in-situ testing for a slab (rigid pavement).

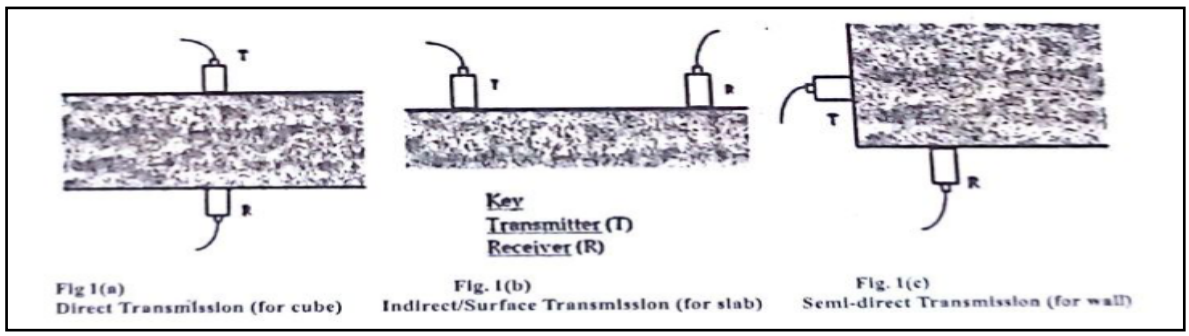

Figure 1: Methods of Propagation and Receiving Ultrasonic Pulses (BS 12504-4,2004)

Indirect transmission is used only when one face of the concrete is accessible, when the depth of a surface defect or crack is to be determined or when the quality of the surface concrete relative to the overall quality is of interest. The quality of concrete and concrete structure in terms of uniformity and incidence assessed shown in Table 1 (IS Code, BS 1881, 1986; BSI, 1986) evolved for characterizing of concrete structure in terms of ultrasonic pulse velocity. Ulucan et al. (2017), Mahure et al. (2018) and Lawson et al. (2015) explored the relationship between ultrasonic pulse velocity and compressive strength of concrete at various mix proportions and water/cement ratio at R^2 value ranging from 80-96.5%. Yusuf (2013) also noted that there is a unique relationship between strength and UPV logarithm model of the form $a \ln x + c$ that can be used to describe the strength of palm kernel shell concrete at R^2 value of 94.9-99.3%.

Table 1: Suggested Quality Criteria for Concrete

Pulse Velocity (m/sec)	Quality of Concrete (Grading)
Above 200	Very Good
100 – 200	Good
50 – 100	Medium
Below 50	Poor

The first set of buildings comprising ten blocks (Blocks 1-10) accommodating the Faculties of Science, Engineering and Technology, and seven Hostel Blocks at the then main campus of University of Ilorin, Ilorin, Nigeria, were commissioned for use in 1980. Over the past 43 years, various forms of rehabilitation exercises have been done on these buildings. Blocks I-10 were constructed with concrete walls; however, two of the engineering blocks (blocks 7 and 9) house machineries and equipment, experiencing various forms of vibrations.

Thus, the aim of the study reported on in this paper is to determine the residual life of blocks of Faculty of Engineering buildings (Blocks 7-10) as case study using UPV technique, which is a non-destructive method. The specific objectives are: (i) collection of data on the specifications (concrete mix proportion, 28-day concrete strength, water/cement ratio and workability) adopted for the design and construction of the buildings, (ii) measurement of the ultrasonic pulse velocity in the concrete walls using Pundit equipment, (iii) estimation of the remaining compressive strength in the concrete walls by employing an appropriate compressive strength-age transfer models, and (iv) determination of the residual life (integrity) of the concrete structures and compare with the expected value obtained from literature.

Traditionally, quality assurance of concrete construction for structural adequacy has been performed but does not provide data on the in-place properties of concrete. Coring to examine internal concrete conditions and obtain specimen for testing results in the introduction of weak spots to the whole structure. This approach also limits what can be detected; while the cores only provide information at core locations and core holes needed to be repaired. Furthermore, though assessment of in-situ compressive strength of a concrete structure plays a key role in the evaluation of its safety, strength integrity and concrete properties at the time of production, it does not adequately reflect actual loading forms on the concrete. NDT method however offer the advantage of providing information on the realistic in-plane properties of hardened concrete, such as the elastic constants, density,

resistivity, moisture content and hardness characteristics. Maintenance of concrete structures is more effective if the deterioration rate of the strength could be monitored as the concrete is being affected by load and weather conditions.

2. THEORETICAL ANALYSIS

Neville (2004) noted that the service life of concrete structures is affected by the exposure to severe environmental conditions, and that among the different types of attack of concrete structures, sulphate attack is the most destructive resulting in significant compressive strength reduction of concrete. The prediction of service life of concrete structures needs constant overview due to sulphate attack; and the long term assessment of concrete properties needs a more appropriate method (Cohen and Mather, 2011). Orejarena and Fall (2014) used numerical modelling methods, which are increasingly used in civil engineering applications, for the purpose of interpolating concrete properties. The authors noted that polynomial interpolation is inappropriate and may yield unsatisfactory results when used to predict intermediate values, and that linear regression can exclude illegitimate results. However, Savidemir (2016) stated that the expectation of long-term concrete properties is very difficult with this approaches; and to remove this subjectivity, some criterion must be advised to establish a basis for the prediction. He therefore suggested interpolation regression by employing a technique for accomplishing this objective as presented in Figure 2. The expected compressive strength loss percentage is estimated by inputting the required parameters, thereby predicting the service life of concrete structures.

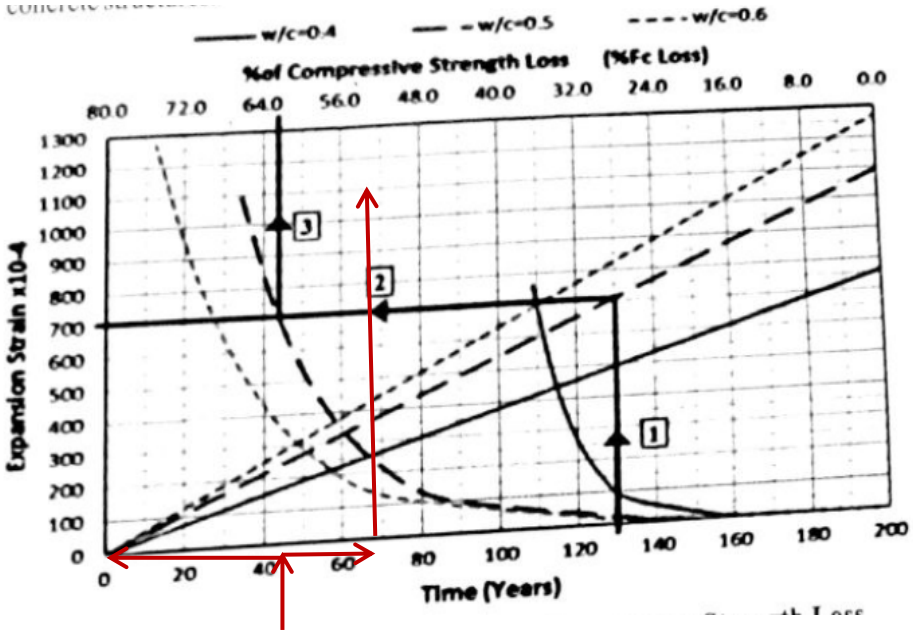

Figure 2: Expansion-Time and Expansion-Compressive Strength Loss Relationship of Concrete Structures

(Source: Savidemir, 2016)

3. METHODOLOGY

Generally, the residual lifespan of concrete is a necessary factor, and can only be deduced after an informed monitoring of strength subjected to many repetitions of loads. The influence of the frequency of loading on fatigue properties of the concrete buildings was examined with the PUNDIT apparatus. The NDT was performed using the experimental set-up shown schematically in Figure 3 in order to determine the ultrasonic pulse velocity of waves passing through the concrete walls. The Portable Ultrasonic Non-Destructive Digital Indicating Tester (PUNDIT, Model PC 1006), manufactured by CNS Farnell, London (Figure 4), was used to measure the velocity of propagation of a compression wave through a testing specimen. The dimension of the equipment which weighed 3kg was 185 x 130 x 185mm. The specified ambient temperature range of the equipment operation of 0 to 45C, which incidentally reflected the prevailing temperature in a tropical region, was ensured. The test equipment

provided a means of generating a pulse, transmitting it to the concrete walls, receiving and amplifying the pulse, measuring and displaying the time taken.

The concrete walls were subjected to the non-destructive test using the semi-indirect transmission. For each test procedure, the pulse velocity, transit time taken by the wave to pass through the PKS concrete and path length through the concrete wall were measured in accordance with the provisions of the British standard (BS EN12504-4, 2004). The 28-day compressive strength value of 25N/mm^2 adopted for the structures at design and construction stages were previously obtained from the Physical Planning Unit of University of Ilorin, Ilorin, Nigeria. The data set for the Ultrasonic Pulse Velocity (UPV), transit time and path length of the wave for each set of test was recorded. A logarithm compressive strength-UPV transfer model in the form $a \ln x + c$ at R^2 value of 96.5% was employed to determine compressive strengths in the concrete walls. The remaining compressive strength values were then compared with the expected values obtained from Figure 2.

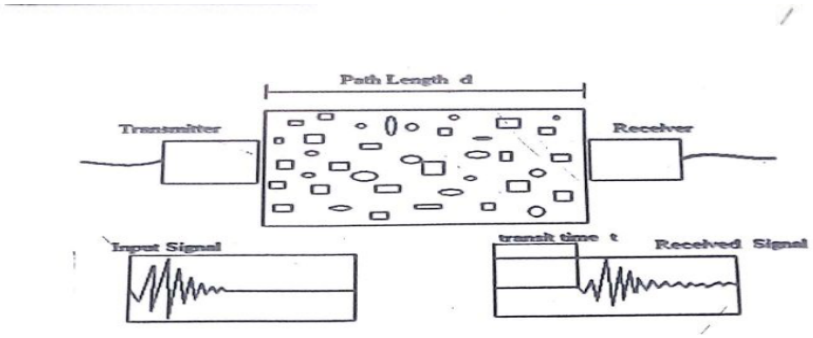

Figure 3: Ultrasonic Pulse Velocity Testing

Figure 4: The PUNDIT Plus Set (Source: Pundit, 1993)

4. RESULTS AND DISCUSSIONS

4.1 Results

The results of the average transit times, average path lengths and velocity of waves through the concrete walls of blocks 7- 10 of the Faculty of Engineering and Technology, University of Ilorin are presented in Tables 2--5.

Table 2: UPV Readings of Concrete Walls (Block 7)

Reading	Transit time (micro secs)	Path length (mm)	Velocity (m/sec)
1	206	22.50	109.2
2	210	22.79	108.5
3	209	22,78	109.0
Average	208.33	22,69	108.9

Table 3: UPV Readings of Concrete Walls (Block 8)

Reading	Transit time (micro secs)	Path length (mm)	Velocity (m/sec)
1	212	27.52	129.8
2	208	26.60	127.8
3	214	27.41	128.1
Average	211.33	27.18	128.6

Table 4: UPV Readings of Concrete Walls (Block 9)

Reading	Transit time (micro secs)	Path length (mm)	Velocity (m/sec)
1	211	22.13	104.9
2	208	21.99	105.7
3	204	21.54	105.6
Average	207.67	21.89	105.4

Table 5: UPV Readings of Concrete Walls (Block 10)

Reading	Transit time (micro secs)	Path length (mm)	Velocity (m/sec)
1	212	23.43	110.5
2	214	23.45	109.6
3	209	22.59	108.1
Average	211.67	23.16	109.4

Yusuf (2013) established a relationship between compressive strength (Y) and ultrasonic pulse velocity (x) as shown in Equation (1).

$$Y = 4.890\ln(x) + 0.869; R^2 = 0.965 \quad (1)$$

The residual compressive strengths of blocks 7-10, calculated from Equation (1) are as presented in Table 6.

Table 6: Computed Residual Compressive Strengths in the Walls of Blocks 7 - 10

Block	Property	
	Ultrasonic Pulse Velocity (m/sec)	Compressive strength (N/mm^2)
7	108.9	23.81
8	128.6	24.62
9	105.4	23.65
10	109.4	24.65

4.2 Discussions

The UPV is the measure of the quality of concrete. The UPV values of the concrete structures for the four blocks under study fall within 104.9 and 129.8 m/sec. Compared with the UPV values for quality criteria in the IS Code (Table I), the structures are still good.

The results show that the average UPV values for block 7, 8, 9 and 10 are 108.9, 128.6, 105.4 and 109.4 m/sec, respectively as presented in Tables 2 to 5. The corresponding compressive strengths obtained for the blocks when the UPV values were input in Equation (1) were 23.81, 24.62, 23.65 and 24.65 N/mm^2, respectively.

Figure 2 was used to validate the compressive strength results obtained for the blocks. This figure shows that, for the period of 43 years after the blocks were commissioned for use, the estimated expansion strain of the concrete structures is 300 x 10^{-4}. This produced an expected compressive strength loss of 53% implying that the structures should have lost 53% of its original strength, that is, 25 N/mm. This translates to I3.25 N/mm^2 lost by 2023, with

remaining strength of 11.75 N/mm^2. However, the residual compressive strengths obtained for the four blocks are much higher than 11.75 N/mm^2; thereby confirming the adequacy of the concrete structures.

5. CONCLUSIONS

Based on the outcome of the study, the following conclusions were drawn:

(a) The concrete walls of the Faculty of Engineering blocks, and hence the whole blocks in the academic and hostels of University of llorin, Nigeria, commissioned in 1980 are in good conditions.

(b) The ultrasonic pulse velocities of waves through the concrete material of blocks 7 to l0 are 108.9, 128.6, 105.4 and 109.4 m/sec, respectively.

(c) A logarithm relationship between compressive strength and UPV at R^2 value of 96.5% produced residual compressive strengths of 23.81, 24.62, 23.65 and 24.65 N/mm^2, respectively for blocks 7, 8, 9 and 10.

(d) The respective residual strength values are greater than the expected remaining life of 11.75 N/mm^2 for concrete structures of the same age (43 years). This confirms that the academic and hostel blocks of the University of llorin are still adequate for use.

RECOMMENDATIONS

From the study, the following recommendations are made:

(a) The UPV results should be used to (i) check the uniformity of concrete, (i) detect cracking and voids in concrete, (iii) control the quality of' concrete and concrete products by comparing results to a similar concrete, and (iv) detect the depth of a surface crack.

(b) For further studies, the effect of' changes in the volume fraction of cement paste, the source of coarse aggregate, the weather combined wth traffic, the UPV strength relationship should be examined for development of fatigue and other performance based characteristics of concrete.

ACKNOWLEDGEMENT

This paper cannot be put together without the tremendous background information made available by various research workers, authors of excellent books and articles, which have been referred to and listed in my references. I thank them.

REFERENCES

Bannantine, J.A., Comer, J.J., and Handrock, J.L. (2017). Fundamentals of Metal Fatigue Analysis, 3" Edition, Prentice Hall, Englewood Cliffs, New Jersey, pp. 273.

BS 1881 (1986). Method for Determination of Compressive Strength of Concrete Cubes. British Standards Institution, London, BS 1881: Part116.

BSI (1986). Recommendations for Measurement ofVelocity of Ultrasonic Pulses in Concrete. British Standards Institution, London, BS 1881: Part 203.

BS-EN 12504-4 (2004). Testing Concrete: Determination of Ultrasonic Pulse Velocity. British Standard BS EN 12504-4.

Cohen, M. D. and Mather, B. (2011). Sulfate Attack on Concrete -- Research Needs. ACI Mater Journal, Volume 3, No. 6. 62-69

Hiller, J. E. and Roesler, J.R. (2016). Transverse Joint Analysis for use in Mechanistic• Empirical Design of Rigid Pavements. Journal of Transportation Research Board 1809,TRB,National Research Council, Washington, D.C.,pp. 42--51.

Komlos, K., Popovics, S., Niimbergeroh, T, Babd, B. and Popovics, J. S. (2016). Ultrasonic Pulse Velocity Test of Concrete Properties as Specified in Various Standards. Cement and Concrete Composites, Vol. 18, pp. 357-364

Lawson, I, Danso, K.A., Odoi, H.C., Adjei, C.A., Quashie, F.K., Mumuni, II. and Ibrahim, I.S. (2015). Non Destructive Evaluation of Concrete using Ultrasonic Pulse Velocity. Research Journal ofApplied Sciences. Engineering and Technology 3(6): 499-504, ISSN: 2040-7467

Mahure, N. V., Vji h, G. K., Sharma, P., Sivakumar, N. and Ratnam, M. (2018). Correlation between Pulse Velocity and Compressive Strength of Concrete. International Journal of Earth Sciences and Engineering. ISSN 0974•5904, Volume 04, No 06 SPL, pp 871-874

Neville, A. (2004). The Confused World of Sulfate on Concrete. Cem. Coner. Res., 34(2004), pp.1275 1296

Orejarena, L. and Fall, M. 2010. The Use of Artificial Neural Networks to Predict the Effect of Sulfate Attack on the Strength of Cemented Paste Back fill Bull Fng Geol Environ,69(2010),pp. 659 670

Pundit, (1993) Manual of Portable Ultrasonic Non Destructive Digital Inheatrg Tester,C. N S Instruments, I London

Rosler, J. R., Hiller, J. E. and Litterton, P. C. (2013). Large Scale Airfield Concrete Slab. Fatigue Test. Accepted at 9th International Conference on concrete. Pp23

Saridemir, M. (2016). Prediction of the Compressive Strength of Mortars Containing Metakaolin by Artificial Neural Networks and Fuzzy Logic. Adv. Eng. Softw., 40(2009), pp.92092

Yusuf, I. T. 2013. A Study of Palm Kernel Shell Concrete Characteristics with Destructive and Nondestructive Methods. Ph.D. Thesis, University of Ilorin, Ilorin. Nigeria, 240pp

PAPER 90 – OPTIMIZATION OF CHARCOAL BRIQUETTES PRODUCTION PROCESS FROM RAFFIA PALM (Raphia Hookeri) EPICARP USING RESPONSE SURFACE METHODOLOGY

R. T. Iwar[1*], K. K. Katibi[2], G. O. Ogbeh[1]

[1]Department of Agricultural and Environmental Engineering, Joseph Sarwuan Tarka University, Makurdi, Nigeria.
[2]Department of Agricultural and Biological Engineering, Faculty of Engineering, Kwara State University, Malete, Nigeria
[*]Email: iwar.raphael@uam.edu.ng

ABSTRACT
In this study, charcoal briquettes were produced from carbonized raffia palm fruit shells using synthetic gum and cassava starch as binders. Response Surface Methodology (RSM) using rotatable Box-Benkhen Experimental Design (BBD) was used to optimize the briquette quality. The briquette samples were made by compressing the carbonized raffia palm fruit shells in an existing briquetting machine. The factors considered in the study were particle size, binder-substrate ratio, and drying time while relaxed density and the calorific value of the briquettes were the response variables. Statistical models were developed to predict the various responses. Results of the study indicated that a combination of 1.05 mm particle size, 29.41 % binder ratio, and 3 days drying time of synthetic gum bonded briquettes was optimum. Under the optimum settings of factors, the synthetic gum-bonded briquettes had a relaxed density of 451.99 Kg/m^3 and a calorific value of 21535.2 kJ/kg. The results also revealed that a combination of 1.99 mm particle size, 10 % binder ratio, and 3 days drying time of starch-bonded briquettes were optimum. Under the optimum settings of the factors, the starch-bonded briquettes had a relaxed density of 474.02 Kg/m^3 and a calorific value of 20185.5 KJ/Kg. Validation of the models indicated that there was no significant difference between the predicted and experimental values which implied that the models could reliably predict the responses.

KEYWORDS: Briquettes, Box Benkhen Design, Response Surface Methodology, Modelling & Optimization, Raffia Palm Epicarp.

1. INTRODUCTION

Briquetting is a process of binding together pulverized carbonaceous matter, often with the aid of a binder (Martin *et al.,* 2008). The common forms of briquettes are coal briquettes and biomass briquettes. Biomass briquettes originate from mostly agricultural residues. Briquettes may be produced with or without binders. The particles must bind properly during compression; otherwise, the briquettes might crumble easily. Pressure, heat, moisture, and size reduction are therefore necessary in the process of making high-quality briquettes. The binders can be organic or inorganic agents. Some of the identified binders of organic nature are heavy crude oil, starch, and molasses. The inorganic binders include clay, sodium silicate, and cement. The binder types, amount of binder agent and water addition, have significant effects on the thermal behaviour and combustion of the briquettes (Altun *et al.,* 2003). The combustion characteristics of the briquettes may be determined based on different parameters such as the reaction kinetics and the water boiling tests.

Most of the technologies for briquetting are expensive and unaffordable by the rural people, who need them most. It is pertinent, therefore, to design briquetting machines which are efficient but less expensive for the end users. In the current work, Raffia palm shells, an abundant agro-biomass in the tropics were carbonized using a laboratory muffle furnace for ease of experimentation. However, for the implementation of the technique in a rural setting, the authors proposed and tested the suitability of employing the drum method for the carbonization of the sample biomass material, while using the same biomass (raffia palm shells) as the primary energy source for carbonization. The briquette production process was done using a developed machine.

Although studies on the production of briquettes from agricultural waste biomass and its optimization using response surface methodology have been reported for rice husk (Musabbikhah *et al.,* 2017), palm kernel shells (Ugwu and Agbo, 2011), the mixture of Acarcia bark and Palm Kernel Shells (Kurnianwan *et al.,* 2017), corn cob residue mixed with macadamia shells (Suminya and Suchana, 2017), while studies on the production charcoal briquettes from Raffia Palm shells have only been reported in the literature by Iwar *et al*. (2018). To the best of the authors' knowledge, no previous studies have been conducted on the production and optimization of charcoal

briquettes from raffia palm shells using response surface methodology, which justifies the novelty of the current study.

Mathematical optimization is defined as the selection of best factors or elements (with regard to some set goals or constraints before the beginning of the selection) among some group of factors and elements considered. More generally, optimization includes finding the "best available" values of some objective function given a defined domain (or input), including a variety of different types of objective functions and different types of domains (Battiti *et al.,* 2008). Several mathematical approaches have been used to achieve optimization including Response Surface Methodology (RSM).

RSM can be described as a technique that involves complex calculations for the optimization process. This approach develops a suitable experimental design that integrates all of the independent variables and uses the data input from the experiment to finally come up with a set of equations that can give a theoretical value of an output. The outputs are obtained from a well-designed regression analysis that is based on the controlled values of independent variables. Thereafter, the dependent variable can be predicted based on the new values of independent variables. RSM involves the use of the following experimental designs: Box-Benkhen Design (BBD); Central Composite Design (CCD); Optimal Designs etc. (Khairul and Mohammed, 2015). For this study, the Box Benkhen design is preferred due to its flexibility and reduced experimental runs and its rotatable ability when blocking is not required.

The significance of this study lies in the fact that the optimal and most valid model can be used to predict the increase or decrease in the values of every dependent variable. Therefore, this work will contribute to giving significant impacts on society, by aiding the production of high-quality renewable fuel. Furthermore, the findings of this research could be seen as a step in the right direction toward curbing the menace of deforestation for the purpose of charcoal production and energy supplies.

2. MATERIALS AND METHODS

This section was divided into two namely: the briquetting process and experimental design.

2.1 Briquette Production Materials and Process Description

The materials and equipment used for the study include the fabricated briquette machine**,** black coated and covered drum (carbonizer), raffia palm shells, cassava starch, synthetic gum, bomb calorimeter, muffle furnace, set of mechanical sieves, electronic weighing balance, measuring cylinders, pressure gauge, vernier callipers, laboratory mortar and pestle and a mechanical hammer mill. Numerical designs and detailed descriptions of the machine are reported elsewhere in our previous study (Iwar *et al.,* 2018).

2.2 Biomass Feed Stock Preparation and Carbonization

Raffia palm fruits were collected from the neighbouring bushes in Nasarawa State Nigeria. The fruits collected were crushed and dried in the sun to reduce the moisture content of the feedstock to ensure effective carbonization. The dried raffia palm shells were shredded to small sizes using a laboratory mortar and pestle to provide more surface area for carbonization. A muffle furnace model SXL produced by Gallenkamp England, was used for the carbonization of the dried raffia palm shells. The biomass (raffia palm shells) was fed into the muffle furnace at a manageable batch of 100g at a time. 100g was weighed using a digital electronic weighing scale and put into crucibles. The crucibles were then loaded into a muffle furnace and ignited at a pre-set temperature of 450^{o}C for 45 min. The crucible and contents were unloaded and placed in desiccators to fully cool down as recommended by Martin *et al.,* (2008). The carbonized Raffia palm shells were then put in well-labelled plastic bags to avoid absorbing moisture from the atmosphere and were then ground into fine particles using laboratory mortar and pestle and kept for further processing.

2.3 Binder Preparation and Briquette Production Procedure

For the purpose of this research work, two binders were used, cassava starch (natural binder) and synthetic gum (synthetic binder). At first, the cassava starch of 0.25kg was dissolved in 0.5 litre of cold water to form a paste, and 2.5 litre of water was put to boil. The paste was gradually mixed with the boiling water and stirred gently

while hot until a smooth homogeneous gelatinized starch solution was obtained. The temperature of the stove heating the mixture was kept constant throughout the process and the mixture was continuously stirred for 5 to 10 minutes, until it turned slightly lumpy and rather viscous.

The pulverized carbonized raffia palm shells were then sieved using a mechanical sieve shaker into three different particle sizes of 0.3 mm, 1.15 mm, and 2.0 mm sieves. The different particle sizes were then put in labelled plastic bags for proper identification. The cooked cassava starch was poured into a mixer containing pulverized carbonized raffia palm shells at 10 %, 30 %, and 50 % binder levels and agitated properly to enhance proper blending prior to compaction because the optimum binder level required to produce briquettes with desirable properties was to be determined. Synthetic gum produced by dissolving a known weight (g) of waste polystyrene in a known volume (mL) of gasoline (synthetic binder) was prepared in the same way and mixed with the biomass sample as above. The biomass-binder mixture was manually fed into the moulds of the fabricated machine and was compressed using a 20-ton hydraulic jack (Iwar *et al.,* 2018). The compressed briquettes were then left to set for about five minutes according to the method of Osarenmwinda and Ihenyen, (2012), after which the lid of the machine was opened for ejection and sun-drying of the briquettes for 3 – 7 days to explore the effect of drying on the briquette physical and thermal properties (Fig. S1as provided in the appendix). The flow chart of the briquette production process is presented in Fig. S2 (See appendix).

2.4 Determination of Briquette Physical Characteristics

The relaxed density (density determined when dried) and relaxation ratio (ratio of compressed density to relaxed density) of the briquette was determined in the dry condition of the briquette after sun drying to a constant weight at an ambient temperature. The relaxed density was then calculated as the ratio of the briquette weight (kg) to the new volume (m^3). This indicates the relative stability of the briquette after compression (Oladeji, 2010). Similarly, the calorific values of the produced briquette samples were determined using Mahler-cook Bomb Calorimeter according to ASTM E711-87 standards (ASTM, 2004).

2.5 Experimental Design and Data Analysis

Box-Benkhen Design with 17 runs consisting of 12 actual design points and 5 centre points without replication for a rotatable design in Response Surface Methodology (RSM) was used to model the experimental factors and correlate the results with the responses (Marcos *et al.,* 2008). The factors considered were particle size, binder ratio, and drying time at three levels each. The responses were; relaxed density and calorific value of the briquettes. ANOVA tests at $p = 0.05$ level of significance were performed on the experimental results and significant factors and interactions were identified. The optimum factor conditions were also determined and verified experimentally. Quadratic models were developed to predict and correlate the responses. The same approach was used for briquette produced using both synthetic and organic binders.

3. RESULTS AND DISCUSSION

3.1 Modelling Experimental Factors of Briquette Production

Box-Benkhen Design with 17 runs in Response Surface Methodology (RSM) was used to model the experimental factors and correlate the results with the responses as shown in Tables S1 and S2 in the supplementary material (Appendices) for the synthetic gum and starch-based briquettes respectively. The factors considered were particle size at three levels (0.30 mm, 1.15 mm, and 2.0 mm), binder-to-substrate ratio at 10 %, 30 %, and 50 %, and drying time at 3 days, 5 days, and 7 days. The responses were relaxed density and calorific value of the briquettes produced.

3.1.1 Relaxed Density of the Produced Briquettes

From the analysis of Variance (ANOVA) carried out on the briquette samples, it was observed that particle size, binder ratio, and drying time had significant effect on the relaxed density of the briquette produced ($P \leq 0.05$). The ANOVA results also revealed that the interaction between the particle size and binder ratio on the relaxed density of the gum Arabic-bonded briquettes was significant, but the interaction between the particle size and drying time did not have significant effects on the relaxed density of the briquette as well as the interaction between the binder ratio and the drying time ($P \leq 0.05$)

Box Benkhen Design was used to relate particle size, binder ratio, and drying time as well as their interaction to develop a second-order regression model (equation) that can be used to evaluate the relaxed density as a response as shown in equation (1).

(1)

Where represent relaxed density, particle size, binder ratio and drying time respectively.

The studentized actual versus predicted values plot (Fig. 1A) is almost a straight line showing that the model can predict the response. The plot shows that the predicted values coincide with the model values and the points that were outside the model line were negligible signifying the model's adequacy. Thus the model is significant and can be used the move around the regions of the experimental design.

Similarly, it was observed that the model, particle size, binder ratio and drying time of the briquette produced using starch as binder had significant effect on the relaxed density of the briquettes ($P \leq 0.05$). A quadratic model for predicting the relaxed density of the briquettes produced with starch as binder was also developed and is as presented in equation (2). The model equation in terms of actual factors can be used to make predictions about the response (relaxed density) for given levels of each factor. The model equation is useful for identifying the relative impact of the factors by comparing the factor coefficients.

(2)

Where represent relaxed density, particle size, binder ratio and drying time respectively.

The studentized actual versus predicted values plot (Fig. 1B) is almost a straight line indicating that the model can predict the responses, thus errors in the model prediction ability may be due to noise. The plot shows that the predicted values coincide with the model values. The distance of the points from the model line is also lean, indicating that prediction error(s) in the model are negligible, which signifies the suitability of the model in predicting the response.

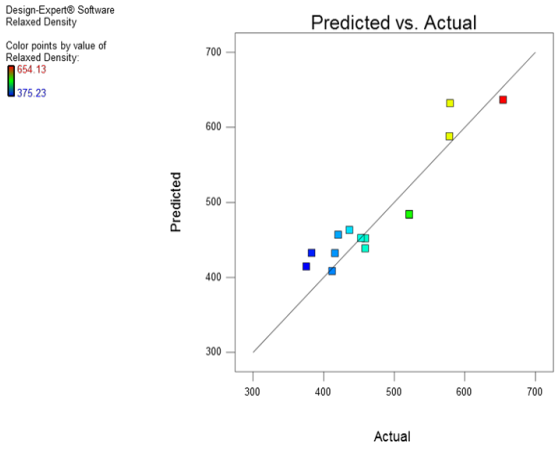

Figure 1 (A): Actual Versus Predicted Values plot for Relaxed Density of Synthetic Gum Based Briquettes

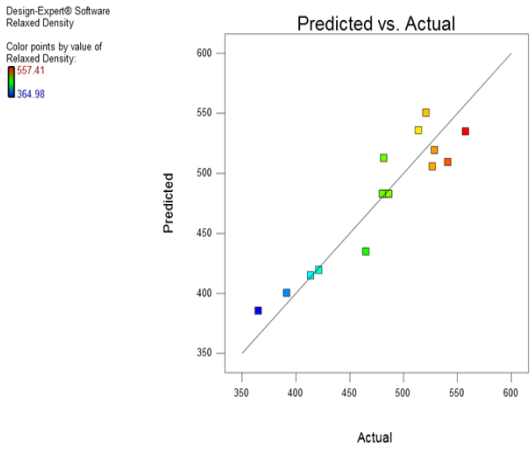

Figure 1 (B): Actual versus Predicted Plot for Relaxed Density of Starch Based Briquettes

3.1.2 Calorific Value of the Produced Briquettes

The results of ANOVA for the experiment on the calorific value of briquettes produced with synthetic gum revealed that the model and the binder ratio of the briquettes produced have significant effects on the calorific value of the briquettes, while the particle size and the drying time of the briquette had no significant effect on the calorific value of the briquettes ($P \leq 0.05$).

The results were used to develop a linear model for predicting the calorific value of the briquettes as given in equation (3). The model equation in terms of actual factors can be used to make predictions about the response (calorific value) for given levels of each factor. The model equation is useful for identifying the relative impact of the factors by comparing the factor coefficients.

(3)

Where represent the calorific value, particle size, binder ratio and drying time respectively.

The "Externally Studentized Residuals" plot (Fig. 2A) is almost a straight line indicating that the model has the ability to predict the responses, the error in the model was insignificant. The plot shows that the predicted values coincide with the model values and the points that are outside the model line are not much as well as the distance of the points from the model line, therefore the errors in the model are negligible, which means the model is significant. The studentized residual plots vs run plots are used to check the model accuracy. From Fig. 2A, it could be seen that the residuals for each run (1-17) were within the acceptable limits from the predicted values, which indicates that the model developed could accurately predict the responses based on the studied factors (independent variables).

Similarly, the results of calorific values of briquettes produced with starch binder reveal that the model and binder ratio have significant effects on the calorific value of the briquettes, while the particle size and the drying time of the briquette have no significant effect on the calorific value of the briquettes at $p \leq 0.05$ level of significance.

The results were also used to develop a linear model for predicting the calorific value of the briquettes as given in equation (4). The model equation in terms of actual factors can be used to make predictions about the response (calorific value) for given levels of each factor. The model equation is useful for identifying the relative impact of the factors by comparing the factor coefficients.

(4)

Where represent calorific value, particle size and binder ratio respectively.

Similarly, the "Studentized actual versus predicted" values plot (Fig. 2B) was almost a straight line showing that the model can predict the responses, with insignificant model errors. The plot shows that the predicted values coincide with the model values and the points that are outside the model line are not much as well as the distance of the points from the model line, therefore any errors in the model are negligible.

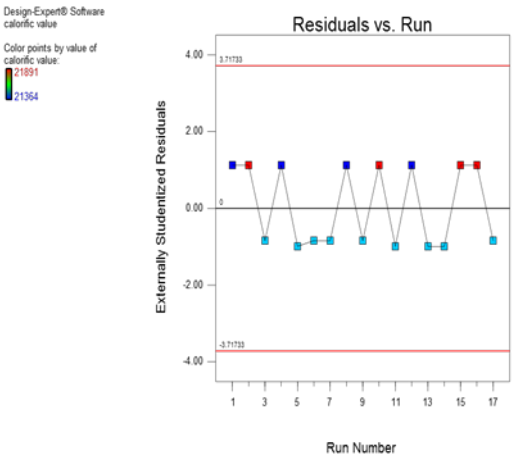

Figure 2 (A): Externally Studentized Residuals plot for calorific Value of Synthetic Gum-based Briquettes

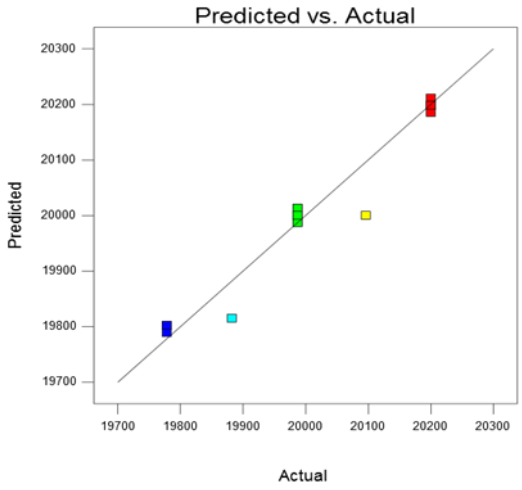

Figure 2 (B): Actual Versus Predicted Values plot for Calorific Value of Starch Based Briquettes

3.2 Optimization of the Briquette Quality

The result for the optimization reveals that a combination of the optimum values of particle size of 1.06mm, binder ratio of 29.41 % and the drying time of 3 days gives predicted values for the relaxed density and calorific value of the briquette produced with synthetic gum binder to be 451.99 kg/m^3 and 21535.3 KJ/kg respectively (Fig. S3 in appendix). The value of desirability at the optimum conditions was found to be 0.524, which is within an acceptable range of 0.50 to 0.90 in accordance with Munoz-Hernandez *et al.*(2004).

Similarly, for the starch-based briquettes, the results for the optimization revealed that a combination of the optimum values of particle size of 1.99 mm, binder ratio of 10 % and the drying time of 3 days gives predicted values for the relaxed density and calorific value of the briquette produced with the starch binder to be 474.01 kg/m^3 and 20185.5 KJ/kg respectively.

3.3 Experimental Validation

The correctness of the Box-Benkhen design (BBD) in design expert software was evaluated by producing briquettes from Raffia palm fruit shells at the given optimum factor conditions of 1.06 mm, binder ratio of 29.41 % and the drying time of 3 days for the synthetic gum based briquettes and 1.99 mm particle size, binder ratio of 10 % and the drying time of 3 days for the starch-based briquettes; The relaxed density and calorific value of both

briquettes produced using synthetic gum and starch binders was evaluated experimentally and the results compared with the predicted values as earlier given by the Box-Benkhen design (BBD) in RSM (Table 1).

For the synthetic gum-based briquettes the predicted result for the relaxed density and calorific value were 451.99 kg/m^3 and 21535.3 KJ/kg respectively while the experimental result for the relaxed density and calorific value were 452.07 kg/m^3 and 21620.6 KJ/kg respectively. For the starch-based briquettes the predicted result for the relaxed density and calorific value were 474.01 kg/m^3 and 20185.5 KJ/kg respectively while the experimental result for the relaxed density and calorific value were 470.98 kg/m^3 and 20200 KJ/kg respectively.

From the results, it was observed that there were little differences between the values predicted by the models developed and the experimental values but this may be due to the negligible errors made during the experimentation; since the differences between the predicted and experimental values can be seen as not being significant. It was also observed that both the predicted and experimental results fall within the acceptable standard values. This implies that, the models developed can be relied upon for the prediction of the desired responses.

3.4 Implication of Findings

The physical characteristics of charcoal briquettes including relax density and calorific value are critical factors for deciding on the quality and commercial value of briquettes. High relax density entails the transportability of the briquettes, while a high calorific value shows the energy content of the briquettes. These characteristics are influenced by variables such as the type and ratio of the binder, the particle size of the starting material, and the extent of drying which must be carefully optimized during the briquetting process (Gebresas *et al.,* 2015). Succinctly, increase in binder to substrate ratio lead to an increase in the relax density and calorific value of the briquette, while a decrease in the particle size encourages an increase in the relax density but does not alter the calorific value of the briquette. Such increased density is attributed to the release of pore space during the binder enrichment and compacting process, especially at miniature particle size of the precursor. Similar findings were reported by Fikri and Sartika (2018).

During optimization, the goals and constraints are associated with the responses and factors respectively. In this context both calorific value and relaxed density must be maximized as is desired of any energy material, the particle size was constrained in the range of the experimental levels chosen as guided by literature evidence (Aransiola *et al.,* 2019), while the binder ratio and drying time which are costly inputs were set to be minimized at the optimum conditions. Optimum calorific values of 20185.5 - 21535.3 KJ/kg as obtained in the current work are higher than those reported in previous studies (Mopoung and Udeye, 2017). This shows that both gum and starch are excellent binders for the production of charcoal briquettes and could separately be adopted in future research based on convenience and availability. Similarly, the relaxed density of the briquettes at optimum process conditions as stated earlier (451.99 – 474.01 kg/m^3) are comparable with that of wood-derived charcoal and those reported for charcoal briquettes of biomass origin (Aransiola *et al.,* 2019). These findings indicate that gum or starch-bonded charcoal briquettes at optimum preparation conditions highlighted are of commercial value as their relaxed density values provide room for its packaging, transport over long distances, storage, supply and their effective utilization by the end users. The findings of the current work are further consistent with those of Oladeji and Ekwerenmadu, (2012) and Yuliah *et al.,* (2017) in their separate works.

Table 1: Optimal Predicted and Experimental Values of Briquettes

	Synthetic Gum based Briquettes		**Starch Based Briquettes**		
Parameters	**Predicted**	**Experimented**	**Predicted**	**Experimented**	**Acceptable Standard Values**
Relaxed Density (kg/m^3)	451.99	452.07	474.01	470.98	200-2000 (ASTM, 2004)
Calorific value (kj/kg)	21535.3	21620.6	20185.5	20200	13000 AND ABOVE (ASTM, 2004)

4 CONCLUSION

Briquettes were produced from Raffia palm fruit shells using synthetic gum and cassava starch as binders. The briquette qualities were optimized by Response Surface Methodology (RSM) using rotatable Box-Benkhen Experimental Design (BBD). The raw material was carbonized and charcoal briquette samples were made by compressing the carbonized raffia palm fruit shells in the developed briquetting machine. The process factors considered for modelling and optimization were particle size, binder-to-substrate ratio and drying time. The relaxed density and the calorific value of the briquettes were the response variables. The study shows that raffia palm fruit shells can be optimally converted into durable briquettes that can be used to provide the energy required for both domestic and industrial use in Nigeria and elsewhere.

ACKNOWLEDGEMENT

The authors wish to acknowledge the Management of Dangote Cement Plc, Gboko, Nigeria for granting access to their Bomb Calorimeter which was used in the current study for the determination of briquette calorific values.

REFERENCES

Altun, N. E., C. Hicyilmaz and A. S. Bagci (2003). Combustion Characteristics of Coal Briquettes (Thermal Features)", *Energy and Fuels*, 17: 1266 - 1276.

Aransiola, E. F., T. F. Oyewusi, J. F. Osunbitan and L. A. O. Ogunjimi, "Effects of Binder Type, Binder Concentration and compacting Pressure on some Physical Properties of Carbonized Corncob Briquette". *Energy Reports,* 5: 909 – 918.

ASTM Standard E711-87 (2004). Standard Test Method for Gross Calorific Value of Refuse Derived Fuel by the Bomb Calorimeter, Annual Book of ASTM Standard, 2004.

Battiti, R., M. Brunato, and F. Mascia (2008). Reactive Search and Intelligent Optimization.Springer Velag. ISBN: 978-0-387- 09623-0.

Fikri, E. and C. Sartika (2018). Study on the Use and composition of Bio-charcoal Briquettes made of Organic Waste. *Journal of Ecological Engineering,* 19(12): 81 – 88.

Gebresas, A., H. Asmelash, H. Berhe and T. Tesfay (2015). Briquetting of Charcoal from Sesame Stalk. *Journal of Energy,* 2015: 757234

Iwar, R. T., K. Ogedengbe and L. A. Oparaku (2018). Comparing Optimally Produced Charcoal Briquettes from Raffia Palm Shells with Hard-wood based Charcoal. *American Journal of Energy Science*, 5(3): 29-35.

Khairul, A.M.S. and A.M.A. Mohammed (2015). Overview on the Response Surface Methodology (RSM) in Extraction Process. *Journal of Applied Science and Process Engineering*, 2(1): 8 - 17.

Marcos, A.B., E.S. Ricardo, P.O. Eliane, S.V. Leanardo and A.E. Luciane, "Response Surface Methodology as a Tool for Optimization in Analytical Chemistry. *Talanta*, 76(5): 965 - 977,doi:10.1016/j.talanta.2008.05.019.

Martin, J. F., R. M. A. Pineda, J. A. Manaay, S. R. A. Handa and A. B. Ocreto (2008). Design and Development of Charcoal Briquetting Machine. *Journal of Mechanical Engineering,* 16: 85 - 90.

Montgomery, D. C. (2002). Design and Analysis of Experiments, 5th Edition ed., John Wiley & Sons, New York, 2002.

Mopoung, S. and V. Udeye (2017). Characterization and Evaluation of Charcoal briquette using Banana Peel and Banana Bunch Waste for household Heating". *American Journal of Engineering and Applied Sciences,* 10(2): 353 – 365.

Munoz-Hernadez, G., M. Gonzalez-Valadez and J. Dominguez-Dominguez (2004). An Easy way to determine the Working Parameters of the Mechanical Densification Process. Agricultural Engineering International: *The CIGR Journal of Scientific Research and Development*. Manuscript FP 03 013. Vol. VI.

Musabbikhah, M., H. Saptoadi, S. Subarmono and M. A. Arifwibisono (2017). Modelling and Optimization of the Best Parameters of Rice Husk Drying and Carbonization by Using Taguchi Method with Mult-Response Signal to Noise Procedure. *International Journal of Renewable Energy Research*, 7(3): 1219 - 1227.

Oladeji, J. T. (2010). Fuel Characterization of Briquettes Produced from Corncob and Rice Husk Residues. *Pacific Journal of Science and Technology*, 11(1): 101 - 106.

Oladeji, J. T. and C.C. Ekwerenmadu (2012). The Effects of some Processing Parameters on Physical and Densification Characteristics of Corncob Briquettes. *International Journal of Energy Engineering,* 2(1): 22-27

Osarenmwinda, J.O. and O.I. Ihenyen (2012). The Preliminary Design and Fabrication of a Manually Operated Briquetting Machine. *Journal of Applied Science and Env. Management*, 16(2): 209 - 211.

Suminya, T., N. Mali, and W. Suchana (2017). Thermal Properties of Green Fuel Briquettes from Residue Corn Cob Material Mixed Macadamia Shell Charcoal Powder. *Journal of Physics: Conference Series*, 901 (1), 2017.

Ugwu, K. E. and K.E. Agbo (2011). Briquetting Palm Kernel Shells. *Journal of Applied Science and Environmental Management,* 15(3): 447 - 450.

Yuliah, Y., M. Kartawidjaja, S. Suryaningshih and K. Ulfi, (2017). Fabrication and characterization of rice husk and coconut shell charcoal based bio-briquettes as alternative energy source". *IOP Conference Series: Earth and Environmental Science*, 65(1):012021

APPENDICES

Figure S1: Optimally Produced Charcoal Briquettes

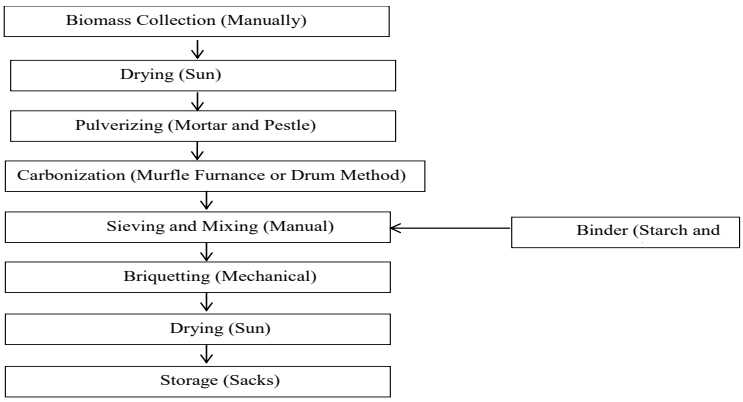

Figure S2: Process Flow Chart Diagram for Charcoal Briquette Production

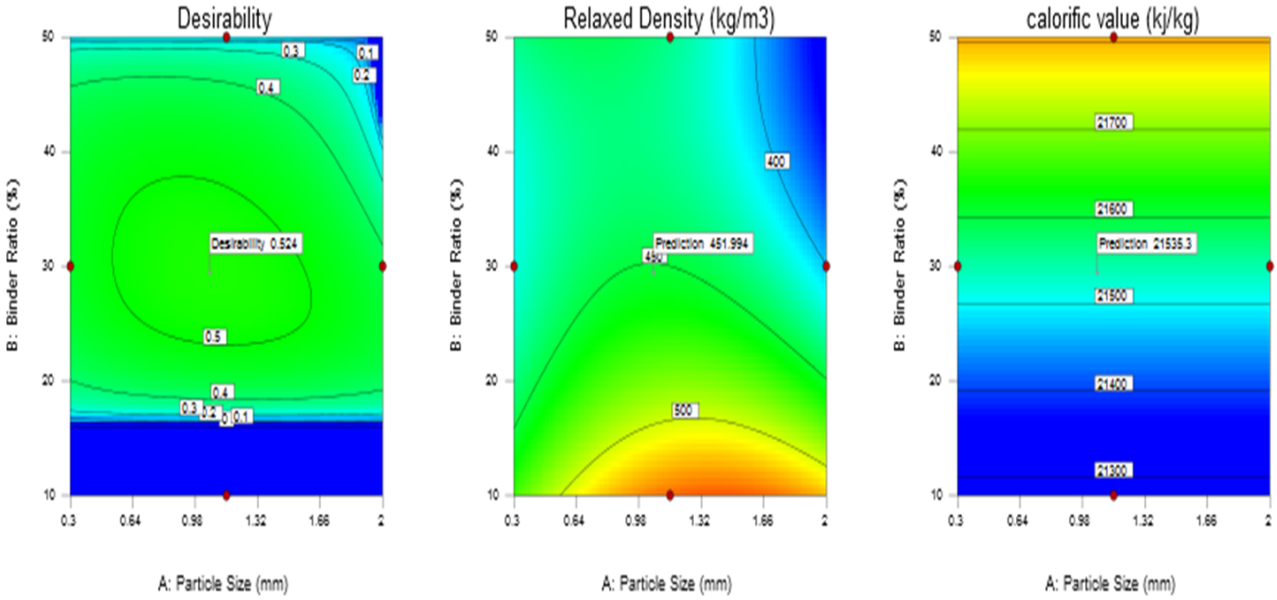

Figure S3: Response surface contour plots for optimization of synthetic gum-based briquettes

Table S1: Box-Benkhen Experimental Design for Synthetic Gum-based Briquette

Run	Parameters			Responses	
	Particle Size (mm)	Binder to substrate Ratio (%)	Drying Time (Days)	Relaxed Density (kg/m^3)	Calorific Value KJ/kg
1	0.3	30	7	528.63	21468
2	2	50	5	364.98	21891
3	1.15	30	5	481.43	21468
4	2	30	7	413.56	21468
5	0.3	50	5	481.43	21468
6	2	10	5	541.03	21364
7	1.15	30	5	486.11	21468
8	0.3	10	5	526.70	21364
9	2	30	3	391.39	21468
10	1.15	30	5	481.43	21468
11	0.3	30	3	421.18	21468
12	1.15	30	5	486.11	21468
13	1.15	50	3	464.81	21891
14	1.15	10	7	520.83	21364
15	1.15	50	7	557.41	21891
16	1.15	10	3	513.70	21364
17	1.15	30	5	480.11	21468

Table S2: Box-Benkhen Experimental Design (BBD) for Briquette Produced with Cassava Starch Binder

Run	**Parameters**			**Responses**	
	Particle Size (mm)	**Binder to substrate Ratio (%)**	**Drying Time (Days)**	**Relaxed Density (kg/m^3)**	**Calorific Value KJ/kg**
1	0.3	30	7	654.13	19987
2	2	50	5	411.81	19778
3	1.15	30	5	521.22	19987
4	2	30	7	375.23	19987
5	0.3	50	5	578.87	19882
6	2	10	5	458.72	20200
7	1.15	30	5	521.22	19987
8	0.3	10	5	420.42	20200
9	2	30	3	382.93	19987
10	1.15	30	5	521.22	20096
11	0.3	30	3	458.98	19987
12	1.15	30	5	521.22	19987
13	1.15	50	3	452.08	19778
14	1.15	10	7	436.30	20200
15	1.15	50	7	578.03	19778
16	1.15	10	3	415.90	20200
17	1.15	30	5	521.22	19987

PAPER 91 – PHYSICAL AND MECHANICAL PROPERTIES OF CONCRETE PRODUCED WITH PERIWINKLE SHELL ASH AND QUARRY DUST

C. E. Njoku[1]*, A. C. Ekeleme[2], B. N. Ekwueme[3] C. Onuoha[1], E. P. Onuzulike[1], W. Chibundu[1]

[1]Department of Materials and Metallurgical Engineering, Federal University of Technology Owerri, Nigeria
[2]Department of Civil Engineering, Abia State University Uturu, Abia State, Nigeria
[3]Department of Civil Engineering, Gregory University Uturu, Abia State
*Email: chiomanjoku211@yahoo.com

ABSTRACT
The usage of plentiful raw waste resources in the manufacturing of concrete has proven to be a sustainable and environmentally beneficial method of making concrete for a variety of purposes. In this study, the physical and mechanical features of concrete made by partially substituting fine aggregates and ordinary Portland cement with periwinkle shell ash and quarry dust (5%, 10%, 15%, and 20%), respectively, were examined. The water-to-cement ratio utilized for the concrete mixture of 1:2:4 was 0.60. Investigated were the constituent materials' physical and mechanical characteristics. Fresh concrete underwent a slump test, and then 150 mm cubes of cured concrete were subjected to density and compressive strength tests. The results revealed that the increase in the partial replacements with periwinkle shell ash and quarry dust, the more the slump increased from 1.2% to 3%. However, the concrete without the waste materials gave optimum compressive strength of 22.9 N/mm^2 as against those that were partially replaced having, 18.8 – 15.1 N/mm^2. The study showed that in other to produce concrete for pavements and other low-strength applications, replacements with periwinkle shell ash and quarry dust of up to 20% can be utilized.

***KEYWORDS*:** Concrete, Periwinkle shell ash, Quarry dust, Compressive strength, Partial replacement

1. INTRODUCTION

Concrete is used and applied in a wide variety of ways in the building sector. Cement, water, and aggregates are the three primary ingredients utilized in the manufacturing of concrete (Raheem et al., 2021). Sadly, the primary components utilized in the manufacture of conventional concrete are harmful to the environment. The manufacturing of ordinary Portland cement makes use of large amounts of energy and releases a high percentage of CO_2 into the atmosphere, which contributes to global warming. The excavation of the aggregates from the river might bring about aquatic pollution and an entire disruption of the ecosystem (Luhar et al., 2019). In order to produce eco-friendly and sustainable concrete, the waste materials which cause environmental pollution are used, most often partially in concrete production. Some of these waste materials include; sea shells, agricultural wastes, fly ash, quarry dust, waste plastics, steel slag, sawdust, and rice husk ash amongst others (Meko & Ighalo, 2021).

Periwinkle is a seafood and belongs to the gastropod molluscs. They are widely available in the rivers and coasts in Nigeria, and when eaten, their shells which are majorly composed of $CaCO_3$ (up to 96%) are thrown away as waste (Luhar et al., 2019). Periwinkle shell ash has been the subject of several studies looking at its potential use in concrete production as a partial replacement for fine aggregates, coarse aggregates, and cement. Bamigboye et al. (2016) employed periwinkle shell ash as a fractional substitute for both fine and coarse aggregates, reporting that up to 30 wt% of the periwinkle shell for the fine aggregate as well as the aggregates will result in non-compromising compressive strengths. In the investigation carried out by Afolayan et al. (2019) on the replacement of cement partially with periwinkle shell ash, their results showed an increase in compressive strength for 5 wt% periwinkle shell ash, after which the compressive strength decreased on the sisal fibre-reinforced concrete. Umoh & Ujene, (2015) revealed that the addition of sodium nitrate increased the compressive strength and splitting tensile strength of concrete that contains up to 30 weight percent of periwinkle shell ash in place of cement.

Some other studies have reported the blend of periwinkle shells and other agricultural waste; palm kernel shells (Ogundipe et al., 2021) and sawdust (Odeyemi et al., 2020). Quarry dust is released as a result of crushing operations, and they pose serious pollution to water, land and air. In a bid to put them to good use, they are utilized in replacing fine aggregates in concrete production. Scholars have reported enhancement in the mechanical properties of concrete that replaced fine aggregates with quarry dust (Febin et al., 2019; Oorkalan et al., 2020; Ponnada et al., 2020). There is a need to add to the existing knowledge to create enough data on the use of these agricultural wastes for concrete production because of how important concrete structures are to humans and the increasing population growth that places so much demand on their diverse applications. Thus, the study is aimed at ascertaining the physical and mechanical characteristics of concrete made by partially substituting fine aggregate with quarry dust (QD) and cement with periwinkle shell ash (PSA).

2. MATERIALS AND METHODS

The basic materials complied with the standards outlined in (BS 882: 1992, 2002). The binder used was Dangote ordinary Portland cement (OPC), grade 42.5R, with initial and ultimate settling times of 75 and 150 minutes, respectively, and a consistency of 28%. The materials utilized were granite, river sand, periwinkle shells from Owerri, Imo State, and quarry dust from Isiagu, Ebonyi State. The periwinkle shells were washed, sun-dried, calcined in a muffle furnace at 1000 ^{o}C for one hour, and then ground with a grinding machine at Eziobodo market in Owerri. Portable water was obtained from the Federal University of Technology Owerri, and it met the standard according to (BS:EN:1008:2002, 2002). The samples of the granite, river sand, quarry dust and periwinkle shells are shown in Figures 1 and 2.

Figure 1. (a) River sand (fine aggregate), (b) Granite (coarse aggregate)

Figure 2. (a) Quarry dust, (b) Periwinkle shells

The characteristic chemical compositions of the ordinary Portland cement, periwinkle shell ash, and the quarry dust used in the concrete production are presented in Table 1. While as the physical properties of the constituents are as shown in Table 2, and the sieve analysis of the aggregates were in line with and according to the limits specified by ASTM C33 (ASTM C33/C33M − 18, 2010).

Table 1 Chemical compositions of the constituent materials used

Constituents	Oxides and percentages									
	Al_2O_3	CaO	Fe_2O_3	K_2O	SiO_2	MgO	Na_2O	SO_3	MnO_3	TiO_2
Cement	3.91	66.55	3.62	0.39	19.21	1.17	0.40	3.23	-	-
Periwinkle shell ash	6.42	52.10	4.64	0.25	0.14	0.82	0.26	0.26	0.14	-
Quarry dust	15.52	14.30	6.53	4.35	45.4	3.54	-	0.55	-	2.65

(Kufre Etim et al., 2021; Sathiparan & De Zoysa, 2018; Umoh & Ujene, 2015)

Table 2. Physical properties of the constituents

Properties	Constituents				
	OPC	Periwinkle shell ash	Quarry dust	River sand	Granite
Specific gravity	3.13	2.00	3.21	2.60	2.60
Bulk density (kg/m^3)	830	727	2147	1397	2711
Particle size (mm)	5.00	4.50	7.50	6.80	20.00
Fineness modulus (%)	2.5	2.62	2.82	2.50	6.78
Colour	greenish-grey	white-ash	grey	pale green	grey/white/black

The Federal University of Technology Owerri in Nigeria's concrete laboratory of Civil Engineering Department, was where the materials were mixed, batched, and tested in accordance with standards. The batching and mix design of the material elements are presented in Table 3, and a mix ratio of 1 is to 2 is to 4 (cement/PSA to sand/QD to granite) and 0.60 water to cement ratio were employed. The concrete was cast in cubes using metallic moulds of 150 mm, then cured for 7, 14, 21 and 28 days.

Table 3 Mix design of the material constituents

Concrete designation	Constituents (%)				
	Cement	PSA	Sand	QD	Granite
A (Control)	100	0	100	0	100
B	95	5	95	5	100
C	90	10	90	10	100
D	85	15	85	15	100
E	80	20	80	20	100

The slump test was done on the fresh concrete in line with ASTM C-143 standard (Clason, 2022), the compressive strength test for the cured concrete was carried out in line with the standard specified by BS 12390 (BS-EN-12390-3-2009, 2009), and the density was done in line with the specified ASTM standard (ASTMC642-06, 2006). Results were presented as average values after triplicate runs.

3. RESULTS AND DISCUSSIONS

3.1 Slump Test Results

Slump test is carried out to understand the level of workability and consistency of the concrete mix. The results of the slump tests on the fresh concrete are shown in Table 4.

Table 4 Effect of PSA and QD partial replacements on the workability of the concrete

Concrete Designation	% Partial replacements		Slump (mm)
	PSA	QD	
A	0	0	66.1
B	5	5	67.0
C	10	10	67.0
D	15	15	68.0
E	20	20	68.2

The effect of percentage partial replacements with PSA and QD on the workability of the concrete is presented in Table 4. It could be seen that the increased percentage of replacements with PSA and QD yielded an increase in workability. This may be because it takes a long time for the PSA cement to chemically react with water (hydration), then in the case of OPC cement and water. The behaviour agrees with that reported by (Tayeh et al., 2020).

3.2 Unit weight of the concrete

The density test was used in measuring the unit weight of the concrete samples and the result is revealed in Figure 3. It could be understood that concrete A (control) without any partial replacements has density slightly higher (3 - 5%) than the other concrete mixtures that were partially replaced with PSA and QD. This implies that partially replacing river sand and OPC with 5%, 10%, 15%, and 20% PSA and QD respectively, slightly affects the concrete's unit weight. The result agrees with that reported by (Tayeh et al., 2020) Also, the concrete samples A to E, for all the days of curing (7, 14, 21, and 28 days) fit into the class of normal-weight concrete, as their densities are above 2000 kg/m^3 (Eziefula et al., 2018). Then as the days of curing increase, the unit weights for all the concrete samples increase, for more voids are filled with concrete mixes as the days of curing linger.

3.3 Compressive strength of concrete samples

Figure 4 gives the compressive strength of the investigated concrete samples that were cured for 7 days, 14 days, 21 days, and 28 days. For each concrete sample, the highest compressive strength was observed at 28-day curing, for the longer days of curing, the more compression force the concrete could carry. The concrete without waste addition showed the highest compressive strength, maybe there were more voids introduced in the bonds when the waste materials (PSA and QD) were added as against their non-inclusion (Kareem et al., 2022). However, the concrete cured at 28 days and with partial replacements of 5 to 20% of PSA and QD can be used in pavements and low-strength concrete applications as they belong to normal-weight concrete.

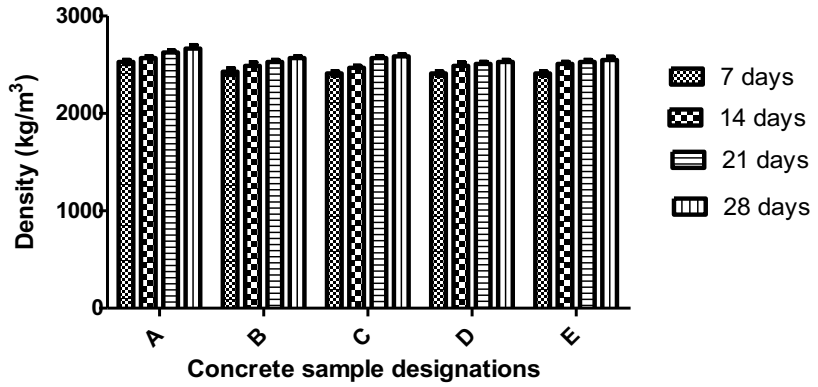

Figure 3 Unit weight of concrete samples

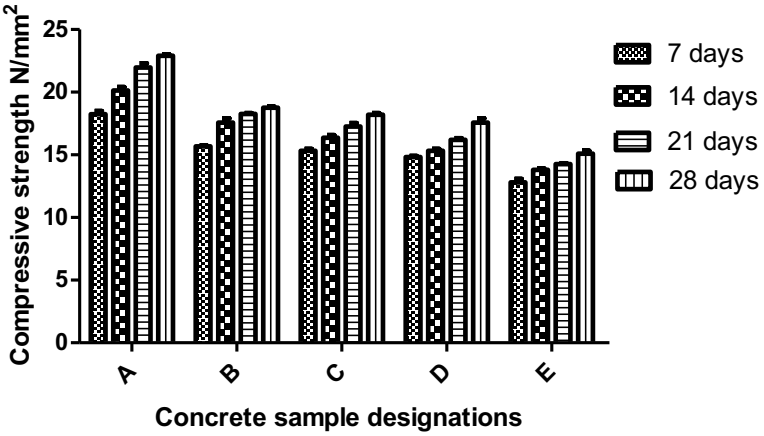

Figure 4 Average Compressive strengths of the produced concrete

4 CONCLUSION

The effect of partial replacement of ordinary Portland cement (OPC) with periwinkle shell ash (PSA), and river sand with quarry dust (QD), of varied weight percent (5, 10, 15 and 20) on the physical characteristics and mechanical characteristics of concrete was studied. The results showed that as there was increase in the partial replacements of OPC and sand gave rise to improvement of workability of the concrete. The unit weight of the concrete sample without partial replacement showed up to 3 to 5% higher than the ones with partial replacements. The control sample gave the optimum compressive strength of 22.9 N/mm2, higher than those that were partially replaced, ranging between 18.8 – 15.1 N/mm^2. It could be deduced that partially replacing with PSA and QD for up to 20 wt% can yield normal weight concrete for applications in pavements and other low-strength structures. Thus, converting the waste materials to very useful construction products.

REFERENCES

Afolayan, J. O., Wilson, U. N., & Zaphaniah, B. (2019). Effect of sisal fibre on partially replaced cement with Periwinkles Shell Ash (PSA) concrete. *Journal of Applied Sciences and Environmental Management*, *23*(4), 715. https://doi.org/10.4314/jasem.v23i4.22

ASTM C33/C33M − 18. (2010). *Concrete Aggregates 1*. *i*(C), 1–11. https://doi.org/10.1520/C0033

ASTMC642-06. (2006). C 642-06: Standard test method for density, absorption, and voids in hardened concrete. *ASTM International*, *March*, 11–13. https://doi.org/10.1520/C0642-21

Bamigboye, G. O., Soneye, T., Ede, A. N., & Olukanni, D. O. (2016). *The study of periwinkle shells as fine and*

coarse aggregate in concrete works. 361–364.

BS-EN-12390-3-2009. (2009). *BS-EN-12390-3-2009 Compressive strenght of test specimens.pdf.pdf*.

BS:EN:1008:2002. (2002). Mixing water for concrete. Specification for sampling, testing and assessing the suitability of water, including water recovered from processes in the concrete industry, as mixing water for concrete. *BSI Standards Publication*, *3*(December), 22. http://shop.bsigroup.com/en/ProductDetail/?pid=000000000019990036

BS 882: 1992. (2002). *Specification for aggregates from natural sources for concrete NO COPYING WITHOUT BSI PERMISSION EXCEPT AS PERMITTED BY COPYRIGHT LAW*.

Clason, M. (2022). ASTM Standard Test Method C143 : Slump of Hydraulic Cement Concrete. *ASTM International*, 1–11.

Eziefula, U. G., Ezeh, J. C., & Eziefula, B. I. (2018). Properties of seashell aggregate concrete: A review. *Construction and Building Materials*, *192*, 287–300. https://doi.org/10.1016/j.conbuildmat.2018.10.096

Febin, G. K., Abhirami, A., Vineetha, A. K., Manisha, V., Ramkrishnan, R., Sathyan, D., & Mini, K. M. (2019). Strength and durability properties of quarry dust powder incorporated concrete blocks. *Construction and Building Materials*, *228*. https://doi.org/10.1016/j.conbuildmat.2019.116793

Kareem, M. A., Raheem, A. A., Oriola, K. O., & Abdulwahab, R. (2022). A review on application of oil palm shell as aggregate in concrete - Towards realising a pollution-free environment and sustainable concrete. *Environmental Challenges*, *8*(August 2021). https://doi.org/10.1016/j.envc.2022.100531

Kufre Etim, R., Ufot Ekpo, D., Christopher Attah, I., & Chibuzor Onyelowe, K. (2021). Effect of micro sized quarry dust particle on the compaction and strength properties of cement stabilized lateritic soil. *Cleaner Materials*, *2*(September). https://doi.org/10.1016/j.clema.2021.100023

Luhar, S., Cheng, T. W., & Luhar, I. (2019). Incorporation of natural waste from agricultural and aquacultural farming as supplementary materials with green concrete: A review. *Composites Part B: Engineering*, *175*(May). https://doi.org/10.1016/j.compositesb.2019.107076

Meko, B., & Ighalo, J. O. (2021). Utilization of Cordia Africana wood sawdust ash as partial cement replacement in C 25 concrete. *Cleaner Materials*, *1*(August), 100012. https://doi.org/10.1016/j.clema.2021.100012

Odeyemi, S. O., Abdulwahab, R., Adeniyi, A. G., & Atoyebi, O. D. (2020). Physical and mechanical properties of cement-bonded particle board produced from African balsam tree (Populous Balsamifera) and periwinkle shell residues. *Results in Engineering*, *6*, 100126. https://doi.org/10.1016/J.RINENG.2020.100126

Ogundipe, K. E., Ogunbayo, B. F., Olofinnade, O. M., Amusan, L. M., & Aigbavboa, C. O. (2021). Affordable housing issue: Experimental investigation on properties of eco-friendly lightweight concrete produced from incorporating periwinkle and palm kernel shells. *Results in Engineering*, *9*(December 2020), 0–6. https://doi.org/10.1016/j.rineng.2020.100193

Oorkalan, A., Chithra, S., Balaji, R., Ganesh Kumar, S., Kishore Kumar, J., & Kishzore Kumar, T. (2020). Experimental study on high volume fly ash concrete made with coir pith and quarry dust. *Materials Today: Proceedings*, *21*, 833–836. https://doi.org/10.1016/J.MATPR.2019.07.588

Ponnada, S., Sankar Cheela, V. R., & Gopala Raju, S. S. S. V. (2020). Investigation on mechanical properties of composite concrete containing untreated sea sand and quarry dust for 100% replacement of fine aggregate. *Materials Today: Proceedings*, *32*, 989–996. https://doi.org/10.1016/j.matpr.2020.06.203

RAHEEM, A. A., ORIOLA, K. O., KAREEM, M. A., & ABDULWAHAB, R. (2021). Investigation on thermal properties of rice husk ash-blended palm kernel shell concrete. *Environmental Challenges*, *5*(September). https://doi.org/10.1016/j.envc.2021.100284

Sathiparan, N., & De Zoysa, H. T. S. M. (2018). The effects of using agricultural waste as partial substitute for sand in cement blocks. *Journal of Building Engineering*, *19*(April), 216–227. https://doi.org/10.1016/j.jobe.2018.04.023

Tayeh, B. A., Hasaniyah, M. W., Zeyad, A. M., Awad, M. M., Alaskar, A., Mohamed, A. M., & Alyousef, R.

(2020). Durability and mechanical properties of seashell partially-replaced cement. *Journal of Building Engineering*, *31*(March). https://doi.org/10.1016/j.jobe.2020.101328

Umoh, A. A., & Ujene, A. O. (2015). Improving the strength performance of high volume periwinkle shell ash blended cement concrete with sodium nitrate as accelerator. *Journal of Civil Engineering, Science and Technology*, *6*(2), 18–22. https://doi.org/10.33736/JCEST.147.2015

PAPER 92 – A HOSLISTIC APPROACH TOWARDS MODELLING, SYNTHESIS AND FABRICATION OF ORGANO-INORGANIC PEROVSKITE SOLAR CELL MODULE

B. Abdulkareem[1], A. U Alhaji[2], M. Mokoyo[3], S. Nurudeen[4], A. Farhana[5], O. Samuel[6]

[1]Department of Mechanical Engineering, Ahmadu Bello University Zaria, Kaduna State
[2,3]Department of Mechanical Engineering, Bayero University, Kano
[4]Department of Chemical Engineering, Bayero University, Kano
[5,6]Advanced Membrane Technology Research Center, Universiti Teknologi Malaysia, Malaysia, Johor Bahru

Email: ogabello2002@yahoo.com

ABSTRACT

The quest in searching for new material(s) for harvesting abundant solar energy in our society lead to the discovery of a perovskite family which possesses a photovoltaic effect. Halide perovskite solar cells (HPSCs) have become the next-generation solar technology due to their outstanding characteristics. Despite considerable improvements in the HPSCs' efficiency, there have been concerns about the conceptualization of the holistic approach involved in creating PSC modules from scratch. The overall performance of the OIHP solar cell module significantly relies on the material composition of the thin layers making up the module, their synthesis techniques, and the fabrication method employed. This paper provides a pathway for modelling, synthesis, and fabrication of solar cell module. The paper emphasized on modelling of chemical compositions of the light-absorbing layer using Goldsmith factors, synthesis techniques, device architectural configuration, and method of fabrication. Hence this review serves as a guide to a novice in the field of solar cell research in generating PSC modules from scratch.

KEYWORDS: Perovskite, Photovoltaic, Synthesis, fabrication, Goldsmith.

1.0 INTRODUCTION

1.1 Background of Study

A variety of scientific innovations, including solar power to produce electricity, solar thermal energy, and solar architecture, are employed to capture the radiant light and heat from the Sun. Solar energy, which is clean and reduces environmental pollution, can be used to generate a considerable amount of the energy required by human society. This will help to slow down the effects of climate change and global warming. There is a growing understanding that fossil fuel sources are rapidly depleting, or that they are not sustainable from an economic or environmental standpoint. The exponential growth of installed capacity for renewable energy power plants using sources like the sun and wind is self-sustaining due to constantly expanding economies of scale and supply chains, as well as a better understanding of the fundamental properties needed for both economical and efficient solar energy converters [1-3]. Kojima et al discovered in 2009 that the organic metal halide perovskite was comparable to dyes and could absorb sunlight. He claims that a liquid electrolyte and perovskite can be used in dye-sensitized solar cells to obtain a power conversion efficiency (PCE) of 3.8% [4]. A solid-state perovskite solar cell with a PCE of 9.7% was initially reported by Kim et al. in 2012 [5]. Perovskite solar cells have garnered the interest of numerous researchers worldwide in recent years due to their high efficiency and low cost. The amount of research published on this topic as well as the reported efficiencies have risen dramatically since the initial reports on solid-state perovskite solar cells with an efficiency of 10% in 2012 [5,6]. According to NREL, certified record efficiency now exceeds 22%. It is obvious that the perovskite solar cells (PSCs) record efficiency of 22.1% already outperform some of the well-established technologies, such as amorphous Si (13.6%), thin film and multi-crystalline Si (21.2% and 21.3%, respectively), and they are comparable to CdTe (22.1%) and CIGS cells (22.3%). Despite considerable improvements in the perovskite solar efficiency, there have been major concerns about the conceptualization of the holistic steps involve in generating PSC modules from scratch. This paper is focused in provide an overview of the modelling of PSC materials, synthesis and characterization of the PSC layers, device architectural configuration, and the method of fabrication. This review will hence provide a summary of practical details needed to pay attention to in developing, synthesis, and fabricating of PSC module.

2.0 METHODS AND MATERIALS

2.1 Modelling

Perovskite structure has an empirical formula ABX_3. The A and B-site are normally occupied with cation of different sizes such that A >B. For Organo-Inorganic halide perovskite, A- site is normally occupied with organic mono-cation and B-site occupied with divalent cation while X-site is occupied with halide ion as shown in Fig2.1.

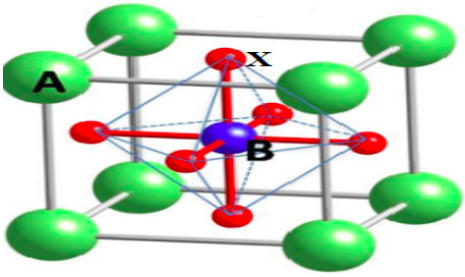

Fig 2.1: Crystal structure of a typical perovskite structure [7]

2.1.1 Structural Stability Modelling for Perovskite cluster

The first thing to do after conceiving the idea of generating a solar cell module from Organo-Inorganic Halid Perovskite (OIHP) is to carefully select the organic mono-cation, the divalent cation, and the appropriate halide anion. Many cations and anions have been modelled for this purpose as illustrated in Table 2.1. After this, the next is to model for stability of the structure using Goldsmith factors given in Equations 1, 2, 3, and 4. However, many theoretical modellings are used toward improving the efficiency of OIHP cluster which include viz; First principle density function model, Equivalent circuit model, Atomistic model, Opto-electronic modelling.

Table 2.1 Calculated effective ionic radii of A-organic cations, metal cations and halide anions [8,9]

A-Cation	r_A,eff	B-Cation	r_B,eff	B-Cation	r_B,eff	X-Anion	r_X,eff
Ammonium $[NH4]^+$	146	Be^{2+}	45	Ag^+	115	I^-	220
Hydroxylammonium $[NH3OH]^+$	216	Mg^{2+}	72	Cd^{2+}	95	Br^-	196
Methylammonium $[CH3NH3]^+$	217	Ca^{2+}	100	Ba^{2+}	135	Cl^-	181
Hydrazinium $[NH3NH2]^+$	217	Ti^{2+}	86	Eu^{2+}	117	F^-	133
Azetidinium $[(CH2)2NH2]^+$	250	V^{2+}	79	Tm^{2+}	103		
Formamidinium $[CH(NH2)2]^+$	253	Cr^{2+}	80	Yb^{2+}	102		
Imidazoline $[C3N2H5]^+$	258	Mn^{2+}	83	Pt^{2+}	80		
Ethylammonium $[CH3CH2)NH3]^+$	274	Fe^{2+}	78	Hg^{2+}	102		
Guanidinium $[(NH2)3C]^+$	278	Ni^{2+}	69	Np^{2+}	110		
Tetramethylammonim $[(CH3)4N]^+$	292	Cu^+	77	Ni^{2+}	69		
Thiazolium $[C3H4N5]^+$	320	Cu^{2+}	73	Sn^{2+}	115		
3-pyrollinium $[NC4H8]^+$	272	Zn^{2+}	74	Sb^{3+}	76		
Tropylium $[C_7H_7]^+$	333	Ge^{2+}	73				
Cesium $[Cs]^+$	167	Sr^{2+}	118				
Potassium $[K]^+$	138	Ag^{2+}	94				

The Goldschmidt Tolerance (GT) factor was used to determine the structural stability of perovskites. The GT factor (t) of ABX_3 is expressed in Equation (1), and the tolerance factor is given by

t= (1)

where r_A is the ionic radius of the A-cation, r_B is the ionic radius of the B-cation, and r_X is the ionic radius of the X-anion. The ideal cubic structure of the tolerance factor, t, is often between 0.9 and 1.0. A non-perovskite structure developed when the tolerance factor, t, was less than 0.71 or larger than 1.0 [10]. When t > 1, the A-

cation is fairly large, which could perhaps lead to the creation of non-perovskite. Conversely, when t 0.8, the A-cation is very little, which could potentially develop non- perovskite structure. Perovskite structures can often occur in the range of 0.8 to 1.0. A tolerance factor limit of 1.06 – 1.07 is considered for OIHP [11]. GT factor is unable to accurately forecast the ionic radius of organic cations in hybrid perovskite because of hydrogen bonds. Cheetham and colleagues used the rigid sphere model for organic cations, presupposed rotational freedom, and expanded the Goldschmidt Tolerance Factor equation to solve this difficulty is given in Equation (2).

t =(2)

r_{Aeff} is given as r_{mass} +r_{ion} [8].

According to reports, relatively few perovskite-type oxides exhibit an ideal cubic structure at ambient temperature, but many do so at higher temperatures.

However, an extended tolerance factor given by Equation (3) indicates the formability of the perovskite structure.

τ=--(3)

where nA is the oxidation state of A, r_X is the ionic radius of ion X, $r_A > r_B$ by definition and

τ < 4.18 indicates perovskite.

For stability of the structure, the octahedra factor which is defined as the ratio of the ionic radii of the B cation and the halide anion is given in Equation (4).

μ =

This indicates the stability of the BX_6 octahedron and it is limited within the range of

0.44 for a stable perovskite.

For example, to model $CH_3NH_2PbI_3$ cluster, the ionic radii of the constituent elements of the site A, B and X are needed. Here A site is occupied with CH_3NH_3 with ionic radius of 2.17A°. B-site is occupied with Pb with ionic radius of 1.19A° and ionic radius of I in X-site is 2.2A°

cluster in accordance with the Equation (2), the tolerance factor, t = 0.912

Which means the formation of $CH_3NH_2PbI_3$ is possible and it is within the tolerance factor for organic halide perovskite. Using the extended tolerance formula given in the Equation (3),

with n_A = 1, t` = 3.88 which is less than 4.18. This indicates that the structure chosen is a perovskite.

For stability of the structure, octahedra factor given in Equation (4) for $CH_3NH_2PbI_3$, μ is equal to 0.54 which is within the limit of stability of perovskite.

2.2 Selection of Synthesis Techniques

Chemical synthesis involves the artificial carrying out of necessary chemical reactions to produce one or more products [9]. Highlighted below are some of the most common techniques used for synthesizing perovskite materials;

Temperature-lowering crystallization: This includes the formation of crystals from a solution. It is a suitable approach for the crystal formation of hybrid-halide perovskites, whose temperature-dependent solubility in the associated acid halide solvents is mild at room temperature. The seed is inserted into the solvent to create high-quality single crystals, and crystal development occurs on the seed when the solution temperature is lowered. The precursor becomes saturated when the solution temperature is lowered. The method of solution growth with slow cooling is the most recommended, but it needs to be used with a range of temperatures. To counter this effect, a high volume of solution is needed because the allowable temperature range is often small and leaves a significant amount of the solute in the solution at the end of the growth run. A programmable temperature controller is also necessary [10].

The saturated solution must be kept at a chosen temperature and space must be made for evaporation to use the slow evaporation method. The reaction must be stabilized at a temperature of about 0.05°C and evaporation rates of just a few mm3/h. A limitation on the crystal development rate, however, is fluctuations within the small temperature differential between the reactants and the crystal zones [11].

Inverse temperature crystallization: Inverse temperature crystallization (ITC) method is used for synthesizing perovskites whose solubility is lost at an elevated temperature in a particular solvent, which favours their crystallization at elevated temperature. Most solids solubility increases as their temperature is elevated and hence, their crystallization is normally performed by lowering the temperature of the solution. To grow one crystal of organo-halide perovskite $CH_3NH_2PbI_3$ crystal using ITC, a calculated mass of CH_3NH_2PbI and PbI_2 is added to a glass vial that has been properly mixed with 5ml of Gamma-GBL. To completely dissolve the resulting combination, it is heated in an oil bath to 60°C. The perovskite solution is then heated for two hours at 152°C in an oil bath. After heating, the crystal will form and be filtered through a chosen Polytetrafluoroethylene (PTFE) filter with the required pore size. The temperature must be adjusted between 150 and 160°C because crystal growth is small and irregular at temperatures below 150°C and massive but irregular at temperatures over 160°C. Therefore, 152°C is the optimum and recommended temperature for growing a big, regular crystal. The benefit of this procedure is that crystallization can take place in the shortest possible (2- 3 h)

Ant-solvent vapour assisted crystallization: Anti-Solvent Assisted Inverse Temperature Crystallization is used for synthesizing a perovskite who's When a compound's concentration surpasses its solubility, precipitation in a

solution happens quickly. Gradual lowering of the temperature of the solution will bring about Super-saturation. Conventionally, as heat is added to a system, its solubility increases (Some perovskites-in-solvent systems are an exception to this rule) [12]. As a result, more solute can dissolve at high temperatures than at room temperature. This solution will become supersaturated if it is abruptly cooled at a rate faster than the rate of precipitation until the solute precipitates to the temperature-determined saturation point.

Solvent evaporation crystallization: When the concentration is increased to reach saturation, solvent evaporation may be a conventional approach to start crystallization. It takes a lot of time and is difficult to correctly control [13, 14]. Recently, Huang et al [13] reportedly used the solvent evaporation crystallization approach at higher temperatures (80°C) to synthesize a single-crystal perovskite thin film with the formula $(FAPbI_3)_{0.85}(MAPbBr_3)_{0.15}$ ($FA=CH(NH_2)^{2+}$). Such single-crystal perovskite thin films have lateral diameters ranging from 500 nm to 2 mm and micrometre-scale thicknesses (10–50 nm).

Hydrothermal Synthesis: Hydrothermal synthesis is a technique for creating crystals that relies on a substance's solubility in extremely hot water while under pressure. It entails selecting the reaction reagent as the first ingredient. Potassium hydroxide (KOH) or sodium hydroxide (NaOH) are frequently used as mineralizers. The chosen reaction reagents will be dissolved in deionized water to create a solution; KOH or NaOH will then be added to the resulting solution and will be agitated to control the solution's alkalinity. The initial reagent mole ratios will be chosen stoichiometrically. After being vigorously mixed, the reaction mixture will be placed into a Teflon vessel until 80% of its volume has been filled. For hydrothermal treatment operations, the vessel is often housed in a stainless-steel tank. Depending on the recipe, it is necessary to manage the crystallization temperature and time.

Device Architectural Configuration: Perovskite solar cells are still improving, which remarkably gives rise to the creation of new materials for usage in cells and the most current attempts to understand how perovskite devices function. The final product's electrical and optical characteristics are significantly influenced by the perovskite solar cell's overall architecture and material selection. The transparent conductive oxide (TCO) layer, the electron-transporting layer (ETL), the light-harvesting perovskite material, the hole-transporting layer (HTL), and the metal contact material are the five groups into which the materials used in perovskite solar cells can be categorized as shown in Fig 2.2

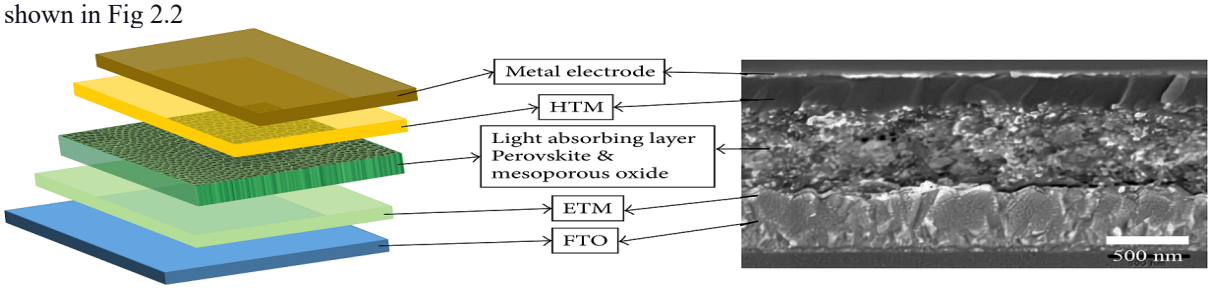

Fig 2.2 Typical SEM view of solar cell module [15]

There are two types of architectural configurations for solar cell modules. These include regular n-i-p and inverted p-i-n configurations.

Generally, the architecture of PSCs can be categorized as direct (n-i-p) and inverted (p-i-n) with either planar or mesoscopic structures, as depicted in Fig 2.3. The mesoscopic structure mainly contains a mesoscopic oxide scaffold, including titanium dioxide (TiO_2), which has been reported to obtain high device PCE [16] which is strongly related to the thickness of TiO_2 typically in the range 300-1000 nm.33 However, the mesoscopic oxide often needs high heat treatment [17, 18] which harms device performance and limits the industrial manufacturing roll-to-roll process toward the implementation of flexible devices. Hence, researchers are interested in exploring PSCs with planar structures, especially in inverted architecture. Inverted planar PSCs is a promising device as it offers excellent advantages such as owing low-temperature procedures that are compatible with large-scale production and suitable for flexible and wearable devices [19]

For the direct (n-i-p) architecture, the electron transport material (ETM) is fabricated above transparent conductive oxides (TCO) such as fluorine-doped tin oxide (FTO) or indium tin oxide (ITO) followed by perovskite layer, hole transport material (HTM), and top contact electrode. Meanwhile, in the inverted (p-i-n) configuration, HTM is deposited onto the TCO while ETM is layered onto the perovskite material before implementing the top contact electrode. The energy alignment is crucial in order to follow the device architecture, for instance, the conduction band (CB) of the electron transport layer (ETL) should be closer to that of perovskite in order to accept the photogenerated electron and the CB should be matched with top electrode for inverted device architecture whereby the CB of ETL should be matched with TCO for direct device architecture for efficient electron transport [20]

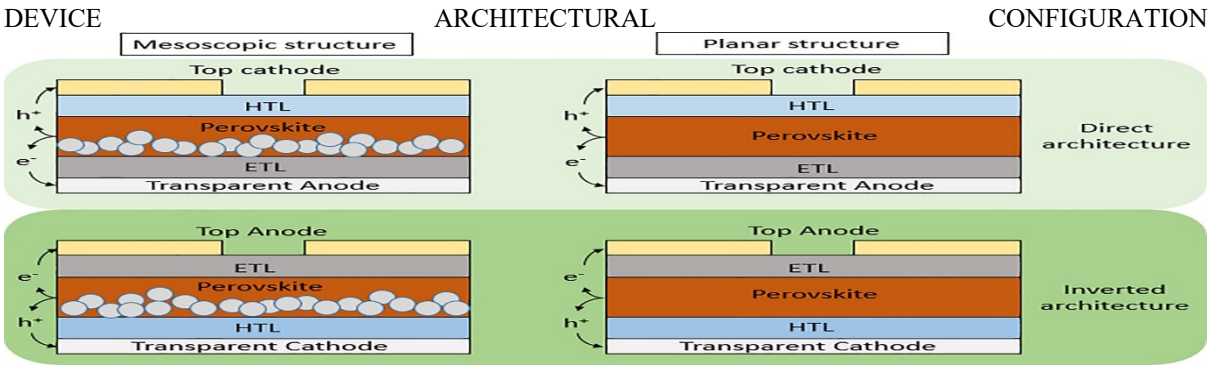

Fig 2.3 Schematic showing the device architecture of perovskite solar cells [21]

2.4 Fabrication Methods of Perovskite Solar Cell

Various deposition techniques have been employed in the fabrication of hybrid perovskite solar cells. The method for depositing perovskite thin films that uses solution processing is the most popular. Solution processing methods. Spin Coating: Spin coating is commonly used in the fabrication of organic-inorganic perovskite due to its low cost and easy processing. This is mainly for producing small-area solar cells at the research laboratory level. In this method, a small puddle of a solution is first deposited onto the centre of a substrate to fully cover the substrate and eventually spun to accelerate the evaporation of the solvent [22]. The substrate is accelerated to the final rotation speeds range from 500 – 10000 rpm. The rotation of the substrate at high-speed means that the centripetal force combined with the surface tension of the solution pulls the liquid coating into an even covering. During this time the solvent then evaporates to leave the desired material on the substrate in an even covering. The method could be further classified into; one-step deposition and two-step deposition methods. In the one-step deposition method, all the precursors of the perovskite (either in 1:1 stoichiometry or 3:1 non-stoichiometry ratio) are dissolved in a common solvent (such as DMF, DMSO, GBL, etc) in the same solution. In the two-step deposition method, a precursor of the metal halide is first deposited onto the prepared substrate usually by spin coating, and annealed to evaporate all the residual solvents. Then follow by dipping the coated substrate (at room temperature) into ammonium iodide solution (for a short period suitably 15 min) for the formation of the corresponding organic-inorganic halide perovskite layer. When the desired dipping time passed, the slide is subjected to annealing to evaporate the solvent. Two-step deposition provides better morphology control over one-step deposition [23].
Spray Coating: Spray coating is a productive solution-based method for making solar cells. Due to the liquid atomization effect, which results in a random spray of droplets of various sizes and increases series resistance, it is rarely reported [24]. The spray coating parameters; film drying time, substrate temperature, solvent engineering, and post-annealing conditions are required to be controlled to achieve high coverage perovskite films [18]. Spray coating expresses the advantage of producing solar cells on a large scale in contrast to spin coating which a thin film solar cell on a small-area thin film is fabricated in research laboratories.
Blade Coating Method: Using a blade coater applicator is one of the simplest, most eco-friendly, vacuum-free, and cost-effective solution-processed ways of manufacturing PSC on an industrial scale. The blade coater applicator is a conventional coating method that consists of a micrometer-sized screw used to control the blade's height with respect to the substrate surface [25]. In this method, airflow over the substrate can be modified to control the rate at which inks evaporate or the substrate can be heated to the solvent's boiling point to manage film uniformity and quality. Compared to spray coating and other roll-to-roll compatible methods, this process provides superior control over film shape. The manufacture of planar heterojunction PSCs is done using this method. Due to non-uniform deposition and the presence of moisture and air, the majority of perovskite deposition procedures typically cause pinhole formation in the perovskite layers, which frequently reduces the performance of solar systems. Blade coating is recommended as a means of overcoming these difficulties [26]. For the creation of self-assembled perovskite crystalline domains with features like homogeneous film coverage and enhanced device stability, it is one of the highly identified strategies. Additionally, the ease of application on flexible substrates and uniform, high-throughput deposition are benefits of this approach [27].
Screen Printing: Screen printing is a simple and promising technique for producing solar cells. In this method, a mesh with a desired printing design is placed over the substrate on which printing is designed. The mesh is pressed with the help of a moving blade or squeegee. The process starts with the printing of TiO_2 (electron transporting layer) followed by the printing of ZrO_2 (spacer layer) and carbon black/graphite top electrode. Then the perovskite solution is dropped onto the porous carbon electrode so that it infiltrates into the mesoporous TiO_2 and ZrO_2. The ZrO_2 as a porous insulating layer is used to prevent direct contact between the carbon electrode and the TiO_2/FTO substrate. The infiltration of the perovskite solution is the major challenge associated with this technique [28].
Slot-die Coating: The slot-die coating is a solution-processed method widely used for fabricating perovskite solar

cells. This method is almost similar to the blade-coating process but has the advantage of using less material. Slot-die coating resulted in poor film formation by the perovskite precursor solution and a two-step method is adopted to enhance good film formation. First, PbI_2 is applied using the slot-die coating. Then the PbI_2 was reacted with MAI solution and formed $MAPbI_3$. Also, the continuous flow of nitrogen gas on the surface of the substrate during deposition assists in the formation of uniform film and controls the solvent evaporation rate, and ensures pin-hole free [26].

Brush Painting: Brushing painting is one of the simplest techniques for creating perovskite solar cells is brush painting. It is a low-material loss, high-speed fabrication method. Since there is no annealing process involved, it is a faster procedure. It is a very economical approach that may be applied to flexible solar cells with a wide surface area. A high-efficiency solar cell can be produced by properly optimizing the solvent and perovskite material concentrations. Furthermore, this method eliminates the necessity for experimental condition control and other time-consuming steps [28, 29]. The lack of a vacuum and quick processing are two benefits of brush painting, making it a particularly economical approach. Brush-painted devices are more efficient than spin-coated ones since thermal annealing is not necessary. The difficulty of maintaining a consistent thickness when painting using brushes.

Electrodeposition: PSCs are produced using the adaptable, roll-to-roll compatible technology of electrodeposition. It is a preferred method for perovskite layer deposition due to its efficiency, speed, and high level of homogeneity [30]. The substrate is not heated during this process, in contrast to spin-coating, because heating creates a rough layer. On the substrate's surface, film breakdown and island creation occur at random when heat is applied [31]. Electrodeposition creates highly uniform thin layers, covers a broad area, and lacks sheer forces [32, 33]. It is a particularly intriguing method for manufacturing at a large scale since perovskite layer deposition on complex-shaped substrates is conceivable with this method rather than the other ways we've mentioned so far [31].

3.0 CONCLUSION

Perovskite solar cells have advanced rapidly, however, there are certain substantial constraints that could limit their advancement. Firstly, external environmental conditions (such as humidity, temperature, and ultraviolet light) have a significant impact on the stability of organic lead halide perovskite, which results in low device stability and significant issues encasing cells later on. Therefore, to increase the viability of such devices, it will be essential to develop a high-stability device composition that incorporates the light-absorbing layer, electron/hole transport layer, and electrode materials, as well as an affordable and efficient device packaging method. The overall performance of the OIHP solar cell module significantly relies on the material composition of the individual layer making up the module, their synthesis techniques, and the fabrication method employed. This paper hence gives an overview of pathways followed in modelling, synthesizing, and fabrication of solar cell modules. The paper emphasized the selection of chemical compositions of the light-absorbing layer and it modelling using Goldsmith factors, synthesis techniques, device architectural configuration, and method of fabrication. Hence this review will serve as a guide to a novice in the field of solar cell research.

ACKNOWLEDGEMENT

I wish to acknowledge the financial support given to me by Tertiary Education Fund (TETFUND) in carrying out this research work. My appreciation goes to my able and ever attentive supervisors in given me scholarly support.

REFERENCES

[1] Solar Cells: Materials, in: A. McEvoy, L. Castañer, T. Markvart (Eds.), Manufacture and Operation, second edition,Elsevier, Oxford, UK, 2012.

[2] A. Luque, S. Hegedus (Eds.), Handbook of Photovoltaic Science and Engineering, second edition,John Wiley & Sons Ltd., Chichester, UK, 2011.

[3] A. McEvoy, T. Markvart, L. Castañer (Eds.), Practical Handbook of Photovoltaics Fundamentals and Applications, Elsevier, Oxford, UK, 2012.

[4] Kojima A, K. Teshima, Y. Shirai, and T. Miyasaka, "Organometal halide perovskites as visible-light sensitizers for photovoltaic cells," Journal of the American Chemical Society, vol. 131, no. 17, pp. 6050-6051, 2009. View at Publisher · View at Google Scholar · View at Scopus

[5] Kim H.-S, C.-R. Lee, J.-H. Im et al., "Lead iodide perovskite sensitized all-solid-state submicron thin film mesoscopic solar cell with efficiency exceeding 9%," Scientific Reports, vol. 2, article 591, 2012. View at Publisher · View at Google Scholar · View at Scopus

[6] M.M. Lee, J. Teuscher, T. Miyasaka, T.N. Murakami, H.J. Snaith, Efficient hybrid solar cells based on meso-superstructured organometal halide perovskites, Science 338 (2012) 643–647.

[7] Green, M.A.; Baillie, A.H.; Snaith, H.J. The Emergence of Perovskite Solar Cells. Nat. Photonics 2014, 8, 506–514. [CrossRef]

[8] Kieslich, G.; Sun, S.; Cheetham, K. Anextended Tolerance Factor Approach for Organic-Inorganic Perovskite. Chem. Sci. 2015, 6, 3430–3433. [CrossRef] [PubMed]

[9] Anthony R. West, Wiley and Sons, 2005, "Solid State Chemistry and its Applications"

[10] Jiang Q, Y. Zhao, X. Zhang, X. Yang, Y. Chen, Z. Chu, Q. Ye, X. Li, Z. Yin, J. You, Nat. Photonics 2019, 13, 460.

[11] Zeng Q, X. Zhang, C. Liu, T. Feng, Z. Chen, W. Zhang, W. Zheng, H. Zhang, B. Yang, Sol. RRL 2019, 3, 1800239.

[12] Burschka J et al (2013) Sequential deposition as a route to high-performance perovskite-sensitized solar cells. Nature 499(7458):316–319

[13] Huang Y, L. Li, Z. Liu, H. Jiao, Y. He, X. Wang, R. Zhu, D. Wang, J. Sun, Q. Chen, H. Zhou, J. Mater. Chem. A 2017, 5, 8537.

[14] Liao W.O, Y. Zhang, C. L. Hu, J. G. Mao, H. Y. Ye, P. F. Li, S. P. D. Huang, R. G. Xiong, Nat. Commun. 2015, 6, 7338.

[15] Baikie T, Y. Fang, J. M. Kadro, M. Schreyer, F. Wei, S. G. Mhaisalkar, M. Graetzel, T. J. White, J. Mater. Chem. A 2013, 1, 5628.

[16] Chen D, Su A, Li X, et al. Efficient planar perovskite solar cells with low-temperature atomic layer deposited TiO2 electron transport layer and interfacial modifier. Sol Energy. 2019; 188:239-246.

[17] D'Innocenzo V, Grancini G, Alcocer MJ, et al. Excitons versus free charges in organo-lead tri-halide perovskites. Nat Commun. 2014;5(1):1-6.

[18] Kong M, Hu H, Egbo K, Dong B, Wan L, Wang S. Antisolvent assisted treatment for improved morphology and efficiency of lead acetate derived perovskite solar cells. Chin Chem Lett. 2019;30(6):1325-1328.

[19]. Kim S, Lee HS, Kim JM, et al. Effect of layer number on flexible perovskite solar cells employing multiple layers of graphene as transparent conductive electrodes. J Alloys Compd. 2018;744:404-411.

[20]. Bakr ZH, Wali Q, Fakharuddin A, Schmidt-Mende L, Brown TM, Jose R. Advances in hole transport materials engineering for stable and efficient perovskite solar cells. Nano Energy. 2017;34:271-305.

[21] https://onlinelibrary.wiley.com/doi/10.1002/er.5876

[22] Hoefler, S.F.; Trimmel, G.; Rath, T. Progress on Lead-Free Metal Halide Perovskite for Photovoltaic Applications: A review. Monatsh. Chem. 2017, 148, 795–826. [CrossRef] [PubMed]

[23] Kajal P, S. Powar, manufacturing technique of perovskite solar cell. 2018, 345-363

[24] Im S H, Kim H S, and Park N 2014 Organolead halide perovskite: new horizons in solar cell research J. Phys. Chem. C 140127150857007

[25] Razza S, Castro-Hermosa S, Di Carlo A, Brown TM (2016) Research update: large-area deposition, coating, printing, and processing techniques for the upscaling of perovskite solar

[26] Deng Y, Peng E, Shao Y, Xiao Z, Dong Q, Huang J (2015) Scalable fabrication of efficient organolead trihalide perovskite solar cells with doctor-bladed active layers. Energy Environ Sci 8(5):1544–1550

[27] Qiu, X.; Cao, B.; Yuan, S.; Chen, X.; Qiu, Z.; Jiang, Y.; Ye, Q.; Wang, H.; Zeng, H.; Liu, J.; et al. From Unstable CsSnI3 to Air Stable Cs2SnI6: A Lead Free Perovskite Solar Cells Light Absorber with Bandgap of 1.48 eV and high Absorption Coefficient. Sol. Energy Mater. Sol. Cells 2017, 159, 227–234. [CrossRef]

[28] Cai L, Liang L, Wu J, Ding B, Gao L, Fan B (2017) Large area perovskite solar cell module. J Semicond 38(1):14006

[29] Lee JW, Na SI, Kim SS (2017) Efficient spin-coating-free planar heterojunction perovskite solar cells fabricated with successive brush-painting. J Power Sources 339:33–40

[30] Kim H.-S, N.-G. Park, Parameters Affecting I–V Hysteresis of CH3NH3PbI3 Perovskite Solar Cells: Effects of Perovskite Crystal Size and Mesoporous TiO_2 Laye. J. Phys. Chem. Lett. **5**(17), 2927–2934 (2014)

[31] Chen H, Wei Z, Zheng X, Yang S (2015) A scalable electrodeposition route to the low-cost, versatile and controllable fabrication of perovskite solar cells. Nano Energy 15:216–226

[32] Huang J-, E, Qin T.W, Kim, D. Vak, C. Forsyth, C.R. McNeill, Y.-B. Cheng, Amorphous hole-transporting layer in slot-die coated perovskite solar cells. Nano Energy **31**, 210–217 (2017)

[33] Su T-S, Hsieh T-Y, Hong C-Y, Wei T-C (2015) Electrodeposited ultrathin TiO2 blocking layers for efficient perovskite solar cells. Sci Rep 5(1):16098.

PAPER 94 – SYNTHESIS AND CHARACTERIZATION OF CNTS/TIO_2 NANOCOMPOSITE FOR FORMULATION OF HYBRID NANOFLUID FOR MACHINING CFRPS

S. A. Lawal[1,6], R. O. Medupin[2*], U. G. Okoro[1], O. Adedipe[1], J. Abutu[3], J. O. Tijani[4], A. S. Abdulkareem[5], M. B. Ndaliman[1]

[1]Department of Mechanical Engineering, Federal University of Technology, Minna, Nigeria.
[2]Department of Materials and Metallurgical Engineering, Federal University of Technology, Owerri, Nigeria.
[3]Department of Mechanical Engineering, Taraba State University, Jalingo, Nigeria.
[4]Department of Chemistry, Federal University of Technology Minna, Nigeria.
[5]Department of Chemical Engineering, Federal University of Technology, Minna, Nigeria.
[6]Department of Mechanical Engineering, University of Mines and Technology, Tarkwa, Ghana
[*]Email: rasaq.medupin@futo.edu.ng

ABSTRACT
Removal of heat from cutting zones raises concerns in machining carbon fibre reinforced plastics (CFRPs). Therefore, this has necessitated increased search for sustainable and cost-effective cooling agents. In this study, carbon nanotubes (CNTs) and TiO_2 were synthesised using sol-gel and Central Composite Design and characterised to form different compositions of TiO_2/CNTs (9:1, 7:3, and 5:5) nanocomposites. The nanocomposites were characterized using Brunauer-Emmett-Teller (BET), HESEM/EDX, XRD and FTIR to investigate their stability as suitable fillers in base-oils. The FTIR spectra for TiO_2/CNTs revealed that the composites have absorption peaks corresponding to C=C and Ti-O bonds; giving rise to peaks assigned to Ti-O-C and C-O bonds. The diffraction peaks of anatase are clearly identified and the diffraction peaks assigned to CNTs are barely seen as a result of overlapping of the main peaks of CNTs with the peaks of TiO_2. The study established that the challenges common to individual NCs are sufficiently addressed with hybrid NCs TiO_2/CNTs (5:5) NC offering an overriding advantage over other nanocomposites as heat removing agent owing to its largest surface area, pore volume and as the most stable nanosuspension. It can, therefore, be concluded that TiO_2/CNTs nanocomposites have high prospect for reinforcing base oils for effective machining.

KEYWORDS: Synthesis, Characterisation, Carbon nanotubes, Titanium oxide, Nanocomposites, Machining

1. INTRODUCTION

Carbon fibre reinforced plastics (CFRPs) have been established as indispensable materials for many applications in engineering. Their outstanding performance in national defence, aerospace and upscale civilian products earns them their current status in manufacturing technology (Zheng et al., 2022). However, until recently, machining of CFRPs has received less attention than they actually deserve as a material with comparative advantages (Erturk et al., 2021). Researchers who have investigated machining of CFRPs with conventional cutting fluids decried the associated challenges and call for more studies to unravel the uncharted waters (Elgnemi et al., 2021; Wang et al., 2018; Zhang et al., 2017). Most of the orthodox cutting fluids are proven to have repeatedly fail to sustain their relevance in the current efforts towards achieving the UN's Sustainable Development Goals on responsible consumption and production (SDG #12).

Quick and easy removal of heat from cutting zones during machining affect the level of success of the process in terms of tool life, speed of cutting as well as surface finish. Sankaranarayanan et al. (2021) reported on the preference of bio-oil-based cutting fluids to proffer solutions to numerous health hazards associated with synthetic cutting fluids in pursuance of sustainable green manufacturing. Even though synthetic and vegetable oil perform excellent momentary cooling functions during machining, chemical imbalance which often triggers corrosion process renders them ineffectual in the present environmentally conscious world (Pimenov et al., 2021). Therefore, nanofluids are currently being advanced to address issues around quick heat removal from tool/workpiece interface by leveraging large surface areas provided by nanoparticles (NPs). This is expected to facilitate quick removal of heat and also help to reduce the quantity of fluids needed for a particular machining process (Patole et al., 2021). The volume of cutting fluids needed as well as the volume released to the immediate environment after being used are also significantly reduced; hence environmental pollution is effectively addressed in the same manner cost is also sufficiently managed (Ni et al., 2021; Haq et al., 2021). It is in line with this principle that the Minimum Quantity Lubrication (MQL) technique was established to further optimize machining parameters (Usha & Srinivasa Rao, 2019). MQL is an environment-friendly and cost-effective alternative to flooding and dry cutting fluid application (Agrawal & Patil, 2018). It is a machining process that is consistent with cleaner and responsible production in the context of sustainable production.

However, more recently, a more excellent way of performing the dual functions of heat removal and lubrication during machining has been launched and is currently receiving more attention from the research world (Gao et al., 2021). While the fluid lubricates the cutting interface, the nanofillers convey heat away from the cutting zone; making machining experience rather seamless and fast; thereby extending tool life and enhancing surface finish (Singh et al., 2021). This is termed nanofluid-MQL (nMQL). Kumar et al. (2023), in a recent study, described nMQL as the novel chapter of sustainable machining. The process involves spraying nanofluids mist on to the tool work interface during machining as the sliding friction between the tool work is converted to rolling friction and reduces friction coefficient significantly; hence giving rise to low cutting forces (Bai et al., 2019; Osman et al., 2020; Jamil MKhan et al., 2020; Lawal et al., 2023). Venkatesan et al. (2020) conducted a comparative study on certain machining parameters under dry and MQL. Their observation on turning operation under nMQL shows that MQL prevents wear mechanism which is a peculiar drawback with dry machining. This indicates that the use of nMQL is a step in the right direction in sustainable machining of difficult-to-machine materials for industrial applications. While also investigating the approach, Gao et al. (2021) observed that the optimization of the nanofluids under high pressure air flow addresses the problem of unsatisfactory heat transfer capacity of MQL in the machining zone and improves the lubrication performance of the interface between the tool and the workpiece. While acknowledging the possibility of taking advantage of different physical and chemical properties of NPs to form hybrid nanofluids, Gao et al. (2020) submitted that the use nMQL technique could lower processing damage such as resin coating, multi-fibre block pull-out, as well as pits. Therefore, it can be concluded that nMQL is the undisputable future of CFRPs machining.

Excellent as nMQL technique may seem, a number of challenges have been identified with the process of producing hybrid nanofluids. Production of standard nanosuspension remains an age-long procedural challenge. Abubakre et al. (2023) agreed with an earlier work by Urmi et al. (2021) on the difficulties associated with the attainment of long-term stability of hybrid nanofluids, which is one of the requirements of hybrid nanofluids applications. This quality of the nanofluids is important in that it improves its thermal behaviour during applications. Therefore, addressing the stability issue is vital to carrying out quality machining. From the literature, external force, stirring and ultrasonication can be deployed to break the bonds that hold NPs together provided the duration for each activity is addressed (Medupin et al., 2019; Ma et al., 2022). Hence the question of time remains a huge gap in the literature. Hence, given the vital role NPs play in the achievement of excellent clean machining via nMQL technique, the processes leading to the production of NPs deserves all the needed attention. It is in keeping with this, therefore, that this study is designed to synthesise and characterise high quality carbon nanotubes (CNTs), TiO_2 and their nanocomposites (NCs) for the development of hybrid nanofluids for CFRPs machining.

2. MATERIALS AND METHODS

All reagents used in this study were of analytical grade with percentage purity in the range of 95%-99.98%. They were sourced from Sigma Aldrich Chemicals Nigeria, a world class distributor of chemicals and other product and used without any further purification. The chemicals used in this experiment include titanium (IV) isopropoxide ($Ti\{OCH(CH_3)_2\}_4$, methanol (CH_3OH), sodium hydroxide pellets (NaOH), hydrochloric acid (HCl) and sodium dodecyl sulfate (SDS) as well as deionized and distilled water.

2.1 Synthesis of TiO_2 nanoparticles

Central Composite Design (CCD) based on Response Surface Method (RSM) was used for biosynthesis of TiO_2 NPs using sol-gel method as shown in Tables 1 and 2. A known volume of titanium isopropoxide was measured into a 250 cm^3 beaker containing a specific volume of extract from plant and stirred on a magnetic stirrer. The mixture was adjusted to the desired pH using NaOH and HCl solution under continuous stirring. The resulting mixture was washed with de-ionized water, dried at 105 ^oC in an oven for 12 h, and calcined at 450 ^oC for 3 h.

Table 1: 2^4 factorial design matrices

Coded value	Volume of extract (cm^3)	Volume of precursor (cm^3)	Stirring time (min)	pH
– Level	50	5	100	2
+ Level	80	8	200	12

Table 2: Experimental run for the biosynthesis of TiO_2 nanoparticles

Selected Run	Volume of extract (cm^3)	Stirring time (min)	Volume of precursor (cm^3)	pH	Crystallite size (nm)
3	65	100	6.5	12	18.92
6	50	100	6.5	7	10.20
9	80	150	6.5	12	16.41

13	65	200	6.5	2	8.09
15	65	200	8.0	7	11.05
17	65	100	8.0	7	9.70
19	65	150	5.0	2	7.64
21	50	150	6.5	12	14.09
25	65	200	5.0	7	10.15

2.2 Synthesis and purification of Carbon Nanotubes

A weight of 14.53 g of Ni and 20.2 g of Fe were dissolved in 100 ml of distilled water, and 10 g of kaolin was added to the mixture and shaken with orbital shaker at 200 rpm for 1 h. The mixture was allowed to cool before decanting and kept in the oven for 12 h at 120 ^{o}C to dry. The dried mixture was grounded and screened through a 150 μm sieve. The resulting fine powder (catalyst) was then calcined for 16 h at 500 ^{o}C to remove the nitrate content. Afterwards, the dried catalyst was then grounded to forestall the incidence of agglomeration that may hamper the interaction between carbon source and the surface mixture. Carbon nanotubes (CNTs) was then synthesized by decomposition acetylene (a carbon source) in a tubular quartz reactor placed horizontally in a furnace. The furnace was electronically controlled such that the heating rate, reaction temperature and gas flow rates were adequately regulated.

1.0 g of catalyst was spread in a quartz boat (11 cm × 2.6 cm) to form a thin layer and then placed in the centre of the quartz tube. The furnace was heated up at 10 °C/min while argon (Ar) was concurrently passed through the system at 30 ml/min. This was to ensure both inert contaminant-free furnace atmosphere and prevent oxidation of the samples before and after the reaction. Once the temperature reached the set reaction temperature of 750 ^{o}C, the argon flow rate was adjusted to 230 ml/min. C_2H_2 was then introduced at a flow rate of 150 ml/min and 200 ml/min in order to initiate CNTs growth. After 90 min reaction time, C_2H_2 flow was halted as the furnace cooled down to room temperature under a continuous flow of argon at 30 ml/min flow rate. The boat was withdrawn from the reactor to harvest the carbon deposit along with the catalyst. CNTs yield (%) was calculated based on the relationship expressed in Equation 1.

A 2.0 g measure of CNTs was loaded into a beaker containing 200 ml of 3M NaOH solution in order to remove the transition metal (Fe-Ni) catalysts and the support material (kaolin). The solution was then stirred using magnetic stirrer for 3 hours and allowed to settle. Subsequently, the solution was filtered and washed with distilled water to ensure a neutral pH. It was then dried at a temperature of 120 ^{o}C for 24 h. The CNTs was finally sonicated and kept in the shelf for further use.

2.3 Synthesis of nanocomposites

A known mass of synthesized CNTs and TiO_2 (TiO_2/CNTs) at different ratios were weighed in a ceramic mortar and crushed adequately with a pestle. The resulting mixtures for TiO_2/CNTs at 9:1, 7:3, and 5:5 ratios were compounded before analysis. In synthesising TiO_2/CNTs NCs, TiO_2/CNTs at 9:1, 7:3, and 5:5 ratios were compounded. At the same time, TiO_2 was dissolved in a suitable solvent and then added in droplets into the dispersed CNTs as sonication progresses and followed immediately with magnetic stirring. The suspension was transferred into round-bottom flask and refluxed at 200 ^{o}C in oil bath with magnetic stirring. Afterwards, the system was allowed to cool naturally to room temperature, filtered and washed with distilled water and ethanol several times. Subsequently, the resulted composite was dried at 100 ^{o}C and calcined at 550 ^{o}C.

2.4 Characterization of nanomaterials

Samples were characterized using Bruker AXS D8 Advance X-ray Diffractometer (XRD) with Cu Kα radiation to determine the phase and crystallite sizes of the NPs. Morphologies and structure of samples were characterized using Zeiss Auriga HRSEM with EDX. The EDX (operated at EHT for 20 kV), and the elemental composition of the samples was determined. The Brunauer-Emmett-Teller, BET surface area and pore size distributions of the samples were obtained from the plot of volume adsorbed versus relative pressure following the placement of 0.1 g sample in a tube after being degassed at 95 ^{o}C for 4 h to remove residual water and volatile compounds.

3 RESULTS AND DISCUSSION

2.2 XRD analysis of optimized CNTs, TiO_2 and TiO_2/CNTs

The factorial design of 2^4 factorials and experimental runs are presented in Tables 1 and 2 and used to investigate the influence of synthesis factors such as stirring time, pH, precursor volume, and extract volume on NPs yield. The crystallite size of TiO_2 is provided by XRD analysis. The phase composition estimated on the peak intensities was anatase, as presented in Fig. 1. Mean crystallite size was computed from full width at half maximum of related

diffraction anatase peak using Scherrer Debye equation (Equation 2). The smallest crystallite size was confirmed at an acidic medium (Table 2: run 19).

where is the crystallite size, is the shape factor (0.94), λ is the wavelength of the X-ray source, and is the full width at half maximum (FWHM).

Fig. 2 presents the XRD results of the CNTs, TiO_2, and TiO_2/CNTs NCs at different compounding ratios. XRD patterns reveal that mainly anatase peaks are found for the TiO_2 at 2 = 25.2°, 37.7°, 48°, and 54°. CNTs clearly displays two peaks at around 31.6° and 52.1°, which are indexed to the reflection of graphite of (002) and (100), respectively. For TiO_2/CNTs NCs, the diffraction peaks of anatase are clearly identified (Mustapha et al., 2020), and the diffraction peaks assigned to CNTs are barely seen (see Fig. 2(A)). This may be as a result of the overlapping of the main peaks of CNTs with the peaks of TiO_2 and is also attributable to the high intensity of the diffraction peaks of TiO_2 and low content of CNTs in the composites. Notably, the width of the XRD peaks at 35.03° and 57.5° was slightly broadened as CNTs were added to the NCs. This process implies that the introduction of CNTs markedly changes the NCs' crystalline size of TiO_2.

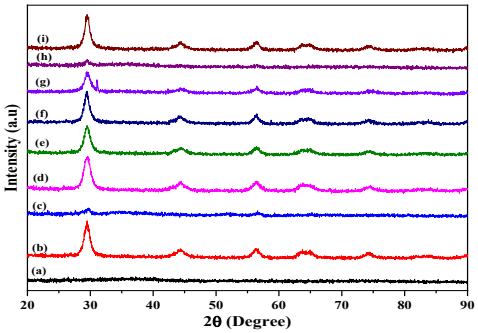

Fig. 1: XRD patterns of TiO_2 NPs for runs in Table 2

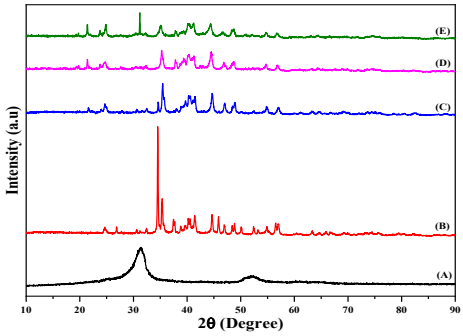

Fig. 2: XRD patterns of CNTs (A), TiO_2 (B), TiO_2/CNTs (9:1; 7:3; 5:5)

3.2 HRSEM/EDX of TiO_2, CNTs and TiO_2/CNTs

Fig. 3 presents HRSEM images of TiO_2, CNTs, and TiO_2/CNTs NCs at different ratios. The image shown in Fig. 3(a), the TiO_2 NPs, form a fleck-like structure and on the other hand, Fig. 3(b) reveals HRSEM image of tube-like CNTs with a diameter between 20 and 30 nm with a few agglomerated branches and tiny particles on the surface. The magnified images in Fig. 3(c-e) demonstrate that TiO_2 NPs are well dispersed on the surface of CNTs. The less identification of CNTs in the NCs was consistent with the TiO_2/CNTs content ratios in the samples, resulting in a well-homogeneous distribution of TiO_2 on the CNTs in TiO_2/CNTs (9:1) as shown in Fig. 3(c). Comparing the NCs with the TiO_2 NPs, the HRSEM image of TiO_2 presence voids or spaces between the particles; suggesting inter-particle porosity. The NCs suggest that the morphologies obtained for the NCs may be due to the interaction between TiO_2 and defect sites of the CNTs surface via binding by the intermolecular interaction.

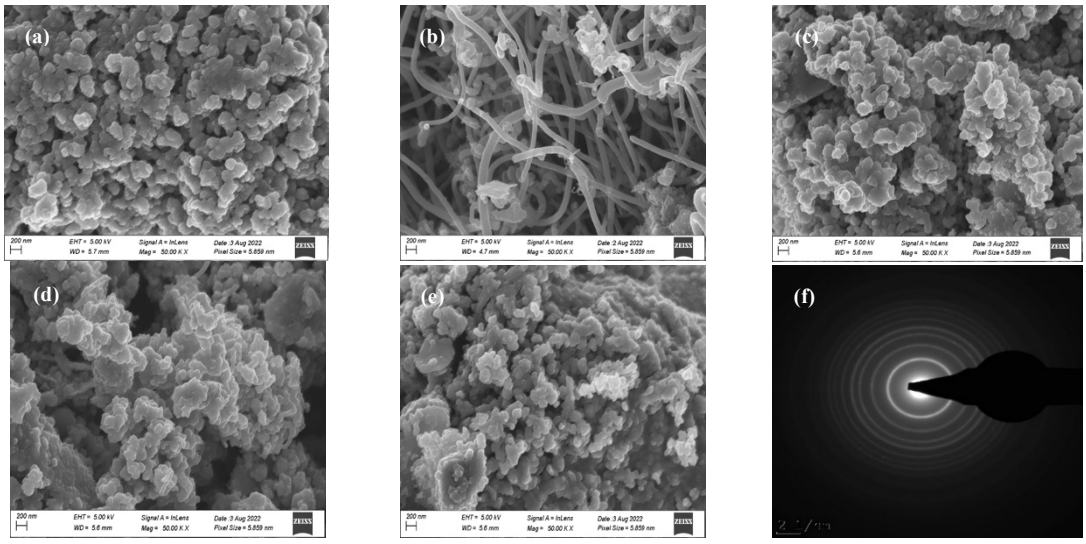

Fig. 3: HRSEM images of TiO_2 (a), CNTs (b), TiO_2/CNTs (9:1) (c), TiO_2/CNTs (7:3) (d), TiO_2/CNTs (5:5) (e)

The corresponding SAED pattern (Fig 3(f)) reflects MWCNTs, while the diffraction for anatase suggests the polycentric ring of TiO_2 as seen in the EDX spectra (Fig. 4). These were also confirmed by XRD analysis. The NCs also show polycentric rings of different reflection planes, which assume the nature of the TiO_2 dispersed in CNTs to form Ti-O-C and Ti-O-Ti networks. The EDX spectra (Fig. 4) indicate the Ti, C, and O are the predominant elements of the NCs in addition to trace elements from Ni salt and kaolin catalysts. The EDX analysis revealed that the presence of Ti content in the NCs composed followed the mass ratio of the composites.

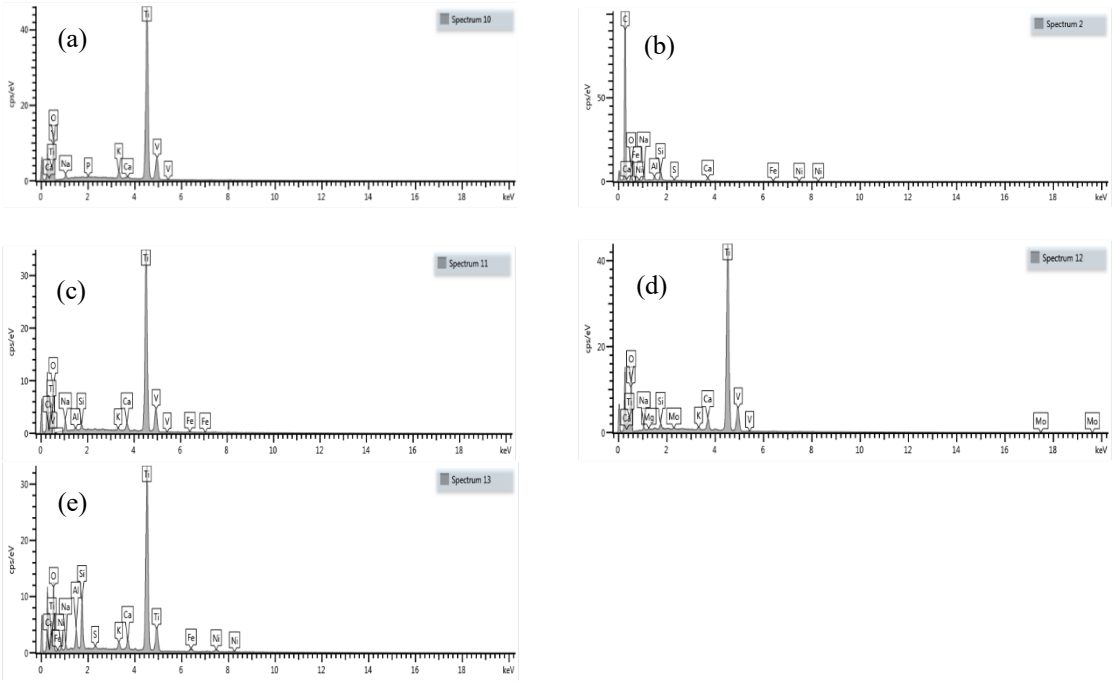

Fig. 4: EDX results of TiO_2 (a), CNTs (b), TiO_2/CNTs (9:1) (c), TiO_2/CNTs (7:3) (d), TiO2/CNTs (5:5) (e)

3.3 BET of TiO_2, CNTs and TiO_2/CNTs

Fig. 5 shows the N_2 adsorption-desorption isotherms of CNTs, TiO_2, and TiO_2/CNTs NCs while the BET-specific surface area, pore size, and pore volume are presented in Table 3. Based on the N_2 adsorption-desorption isotherm of TiO_2, the isotherms could be identified as the intermediate cases between hysteresis loop of type I where the two branches are almost vertical and parallel of a range of gas uptake and hysteresis loop of type IV where the branches stay nearly horizontal and parallel over a wide p/p^o range (D'Aloia et al., 2021). The isotherm identified for the CNTs is the type III isotherm as presented in Fig. 5(a). The isotherms resulting from the NCs are categorized as type II isotherms which can be ascribed to the combination of type I and type IV loops (Brockmann et al., 2020). This is explained by the fact that the isotherm of Fig. 5(e) is closer to type II than both TiO_2/CNTs (9:1) and TiO_2/CNTs. In Table 3, BET surface areas of the nanomaterials are presented. The surface area of TiO_2 is much higher than CNTs, indicating better textural properties and a wider range of applications. Also, the surface areas of the NCs increase as TiO_2 decreases relative to CNTs contents in the samples. This phenomenon could be caused by the separation of TiO_2 crystalline particles due to the addition of CNTs. Furthermore, the pore sizes reflect mesoporous nanomaterials which could favour mass transfer (Paumo et al., 2021). Pore volume of the NCs followed the same trajectory as the surface area and increase as CNTs content increases. This is attributable to the TiO_2 constantly occupying the reaction sites on the CNTs wall in accordance with an earlier work by Medupin et al. (2020).

Table 3: The summary of the BET results of CNTs, TiO_2, and TiO_2/CNTs

Sample	Surface area (m^2/g)	Pore size (nm)	Pore volume (cc/g)
CNTs	0.65	16.79	0.00276
TiO_2	127.62	6.648	0.296
CNTs/TiO_2 (1:9)	57.84	7.637	0.155
CNTs/TiO_2 (3:7)	71.19	8.412	0.195
CNTs/TiO_2 (5:5)	103.42	7.451	0.259

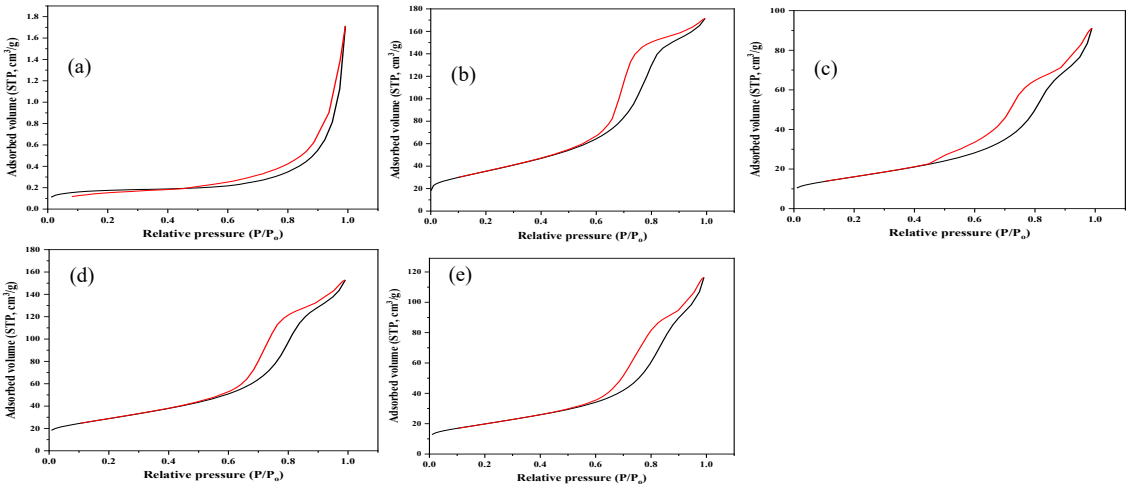

Fig. 5: N_2 Adsorption-desorption curves of CNTs (a), TiO_2 (b), TiO_2/CNTs (9:1) (c), TiO_2/CNTs (7:3) (d), TiO_2/CNTs (5:5) (e)

3.4 FTIR of TiO_2, CNTs and TiO_2/CNTs NCs

The FTIR spectra of TiO_2, CNTs, and TiO_2/CNTs are recorded and are shown in Fig. 6 to study the type of interactions that exist among the different constituents of the NCs and to determine their structure and functional groups. The absorption around 1630 cm^{-1} is assigned to the bending vibration of adsorbed water molecules (Fig. 6(a)). The broad band at the region of 950 cm^{-1} in the TiO_2 sample belongs to the characteristic vibration of the Ti–O–Ti network. It can be observed that the CNTs (Fig. 6(b)) show the C–C stretching bonds at 1650 cm^{-1} assigned as nanotube modes, and the peak in 1705 cm^{-1} is associated with C=O stretching of the carboxyl group as a characteristic of carboxyl functional groups (-COOH) (Medupin et al., 2017; Gopiraman et al., 2012; Shaban et al., 2020). The peaks around 3500-3300 cm^{-1} correspond to –OH stretching bond in hydroxyl and carboxyl groups indicative of the high presence of the groups. The FTIR spectra for the TiO_2/CNTs are shown in Fig. 6(c, d and e) reveals that the composites have absorption peaks corresponding to C=C and Ti-O bonds, giving rise to peaks assigned to Ti-O-C and C-O bonds (Pownraj & Valan Arasu, 2020; Khadom et al., 2022). These results demonstrate that the growth resulted in the formation of hetero-junction at the surface of the TiO_2 and CNTs, forming interfacial bonds in the matrices (Paumo et al., 2021).

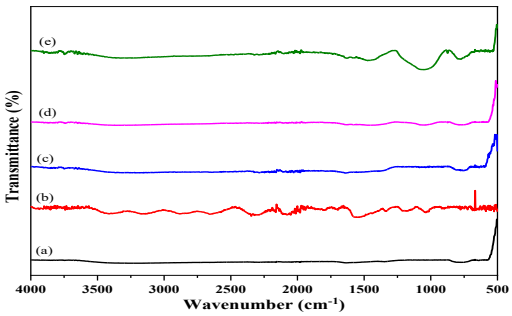

Fig. 6: FTIR spectra of TiO_2 (a), CNTs (b), TiO_2/CNTs (9:1) (c), TiO_2/CNTs (7:3) (d), TiO_2/CNTs (5:5) (e)

4 CONCLUSION

The results presented in this study showed that TiO_2/CNTs nanocomposites are reliable filler candidates for compounding hybrid nanofluids for machining processes. Characterisation results showed that the NPs are in good shape for the reinforcement base-oils from both organic and inorganic sources for the formulation of nanofluids meant for machining CFRPs. The sites created following the functionalization of CNTs (fibre) filled by TiO_2 (particles); making the formulation of nanosuspension system less challenging. The tendency of agglomeration in CNT system is significantly reduced as TiO_2 NPs occupy certain sites on the walls of CNTs and breaks the van der Walls attractions between individual CNTs. Three different nanofiller ratios were investigated under the same conditions and it was found that the stability of the nanofluids for machining application was significantly improved by the addition of fillers with TiO_2/CNTs (7:3) NCs being the most stably dispersed of the three as could be noticed with the HRSEM micrographs. The clustering simply indicates that the openings on the walls of CNTs attract TiO_2 in the suspension. Generally, however, the results from HRSEM/EDX, XRD and BET show that TiO_2/CNTs (5:5) NC offers an overriding advantage over other NCs as heat removing materials from the machining zone. The resulting nanosuspension is expected to be employed to reinforce base-oils for machining purposes.

ACKNOWLEDGEMENT

The authors thankfully acknowledge the support of the Tertiary Education Trust Fund, Nigeria, through the National Research Fund (NRF) with grant number: TETF/ES/DR&D/CE/NRF2020/SETI/113/VOL.1 for funding this research.

REFERENCES

Abubakre, O. K., Medupin, R. O., Akintunde, I. B., Tijani, J. O., Abdulkareem, A. S., Muriana, R. A., James, J. A., Ukoba, K. O., Jen, T-C., & Yoro, K. O. (2023). Journal of Science: Advanced Materials and Devices Carbon nanotube-reinforced polymer nanocomposites for sustainable biomedical applications: A review. *Journal of Science: Advanced Materials and Devices*, *8*(2), 100557. https://doi.org/10.1016/j.jsamd.2023.100557

Agrawal, S. M., & Patil, N. G. (2018). Experimental study of non-edible vegetable oil as a cutting fluid in machining of M2 Steel using MQL. *Procedia Manufacturing*, *20*, 207–212. https://doi.org/10.1016/j.promfg.2018.02.030

Bai, X.; Li, C.; Dong, L. & Yin, Q. (2019). Experimental evaluation of the lubrication performances of different nanofluids for minimum quantity lubrication (MQL) in milling Ti-6Al-4V. *International Journal of Advanced Manufacturing Technology*, 101, 2621–2632.

Brockmann, E. C., Pyykko, M., Hannula, H., Khan, K., Lamminmaki, U. & Huovinen, T. (2020). Combinatorial mutagenesis with alternative CDR-L1 and H2 loop lengths contributes to affinity maturation of antibodies, *New Biotechnology*, 60, 173-182, https://doi.org/10.1016/j.nbt.2020.09.002

D'Aloia, A. G., Di Fransesco, A. & De Santis, V. (2021). A novel computational method to identify/analyse hysteresis loops of hard magnetic materials, *Magnetochemistry*, 7(10), https://doi.org/10.3390/megnetochemistry7010010

Elgnemi, T. S. M., Jun, M. B. G., Songmene, V., & Samuel, A. M. (2021). Milling performance of CFRP composite and atomised vegetable oil as a function of fibre orientation. *Materials*, *14*(8). https://doi.org/10.3390/ma14082062

Erturk, A. T., Yarar, E., Vatansever, F., Sahin, A. E., Kilinçel, M., & Alpay, Y. O. (2021). A comparative study of mechanical and machining performance of polymer hybrid and carbon fiber epoxy composite materials. *Polymers and Polymer Composites*, *29*(9), S655–S666. https://doi.org/10.1177/09673911211020620

Gao, T. et al. (2020). Surface morphology assessment of CFRP transverse grinding using CNT nanofluid minimum quantity lubrication. J. Clean. Prod. 277, 123328. https://doi.org/10.1016/j.jclepro.2020.123328

Gao, T., Zhang, Y., Li, C., Wang, Y., An, Q., Liu, B., Said, Z., & Sharma, S. (2021). Grindability of carbon fiber reinforced polymer using CNT biological lubricant. *Scientific Reports*, *11*(1), 1–14. https://doi.org/10.1038/s41598-021-02071-y

Gopiraman, M., Selvakumaran, N., Kesavan, D., Kim, I. S., & Karvembu, R. (2012). Chemical and physical interactions of 1-benzoyl-3,3-disubstituted thiourea derivatives on mild steel surface: Corrosion inhibition in acidic media. *Industrial and Engineering Chemistry Research*, *51*(23), 7910–7922. https://doi.org/10.1021/ie300048t

Haq, M. A., Hussain, S., Ali, M. A., Farooq, M. U., Mufti, N. A., Pruncu, C. I., & Wasim, A. (2021). Evaluating the effects of nano-fluids based MQL milling of IN718 associated to sustainable productions. *Journal of Cleaner Production*, *310*(May), 127463. https://doi.org/10.1016/j.jclepro.2021.127463

Jamil MKhan, A. M. & Hegab, H. (2020). Milling of Ti–6Al–4V under hybrid Al_2O_3-MWCNT nanofluids considering energy consumption, surface quality, and tool wear: A sustainable machining, *International Journal Advanced Manufacturing Technology*, 107, 4141–4157.

Khadom, A. A., Abd, A. N., Ahmed, N. A., Kadhim, M. M., & Fadhil, A. A. (2022). Combined influence of iodide ions and Xanthium Strumarium leaves extract as eco-friendly corrosion inhibitor for low-carbon steel in hydrochloric acid. *Current Research in Green and Sustainable Chemistry*, *5*(December 2021), 100278. https://doi.org/10.1016/j.crgsc.2022.100278

Kumar, A., Sharma, A. K. & Katiyar, J. K. (2023). State-of-the-art in sustainable machining of different materials using nano minimum quality lubrication (NMQL), *Lubricants, 11, 64. https://doi.org/10.3390/lubricants11020064*

Lawal, S.A., Medupin, R. O., Yoro, K. O., Okoro, U. G., Adedipe, O., Abutu, J., Tijani, J. O., Abdulkareem, A. S., Ukoba, K., Ndaliman, M. B., Sekoai, P. T. & Jen, T-C. (2023). Nanofluids and their application in carbon fibre reinforced plastics: A review of properties, preparation and usage, *Arabian Journal of Chemistry*, 16, 104908, https://doi.org/10.1016/j.arabjc.2023.104908

Ma, C., Wen, R., Zhou, F., Zhao, H., Bao, X., Evelina, A., Long, W., Wei, Z., Ma, L., Liu, J., & Chen, S. (2022). Preparation and application of an environmentally friendly compound lubricant based biological oil for drilling fluids. *Arabian Journal of Chemistry*, *15*(3), 103610. https://doi.org/10.1016/j.arabjc.2021.103610

Medupin, R. O., Abubakre, O. K., Abdulkareem, A. S., Muriana, R. A., & Abdulrahman, A. S. (2019). Carbon Nanotube Reinforced Natural Rubber Nanocomposite for Anthropomorphic Prosthetic Foot Purpose. *Scientific Reports*, *9*(1). https://doi.org/10.1038/s41598-019-56778-0

Medupin, R. O., Abubakre, O. K., Abdulkareem, A. S., Muriana, R. A., Kariim, I., & Bada, S. O. (2017). Thermal and physico-mechanical stability of recycled high-density polyethylene reinforced with oil palm fibres. *Engineering Science and Technology, an International Journal*, *20*(6), 1623–1631. https://doi.org/10.1016/j.jestch.2017.12.005

Medupin, R. O., Abubakre, O. K., Abdulkareem, A. S., Muriana, R. A. & Lawal, S. A, (2020). Dimensional and Thermal Reliability of Multi-Walled Carbon Nanotube Filled Natural Rubber Nanocomposites, *International Journal of Engineering Research in Africa*, 51, 177-189

Mustapha, S., Ndamitso, M. M., Abdulkareem, A. S., Tijani, J. O., Shuaib, D. T., Ajala, A. O., & Mohammed, A. K. (2020). Application of TiO_2 and ZnO nanoparticles immobilized on clay in wastewater treatment: a review. *Applied Water Science*, 10(1). Springer International Publishing. https://doi.org/10.1007/s13201-019-1138-y

Ni, J., Cui, Z., Wu, C., Sun, J., & Zhou, J. (2021). Evaluation of MQL broaching AISI 1045 steel with sesame oil containing nano-particles under best concentration. *Journal of Cleaner Production*, 320(May), 128888. https://doi.org/10.1016/j.jclepro.2021.128888

Osman, K. A., Yılmaz, V., Ünver, H. Ö., ¸Seker, U. & Kılıç, S. (2020). Slot milling of titanium alloy with hexagonal boron nitride and minimum quantity lubrication and multi-objective process optimization for energy efficiency. *Journal of Cleaner Production*, 258, 120739.

Patole, P. B., Pol, G. J., Desai, A. A., & Kamble, S. B. (2021). Analysis of surface roughness and cutting force under MQL turning using nano fluids. *Materials Today: Proceedings*, *45*, 5684–5688. https://doi.org/10.1016/j.matpr.2021.02.501

Paumo, H.K., Dalhatou, S., Katata-Seru, L.M., Kamdem, B.P., Tijani, J.O., Vishwanathan, V., Kane, A., & Bahadur, I. (2021). TiO_2 assisted photocatalysts for degradation of emerging organic pollutants in water and wastewater. *Journal of Molecular Liquids*, 331, 115458. https://doi.org/10.1016/j.molliq.2021.115458

Shaban, M. M., Eid, A. M., Farag, R. K., Negm, N. A., Fadda, A. A., & Migahed, M. A. (2020). Novel trimeric cationic pyrdinium surfactants as bi-functional corrosion inhibitors and antiscalants for API 5L X70 carbon steel against oilfield formation water. *Journal of Molecular Liquids*, 305, 112817. https://doi.org/10.1016/j.molliq.2020.112817

Singh, Y., Negi, P., Yadav, A., & Tripathi, R. (2021). Euphorbia lathyris: A novel feedstock for bio based lubricant application with titanium dioxide nanoparticles as additives. *Materials Today: Proceedings*, 46, 10518–10522. https://doi.org/10.1016/j.matpr.2020.12.1237

Urmi, W. T., Shafiqah, A. S., Rahman, M. M., Kadirgama, K., & Maleque, M. A. (2021). Preparation Methods and Challenges of Hybrid Nanofluids: A Review. *Journal of Advanced Research in Fluid Mechanics and Thermal Sciences*, 78(2), 56–66. https://doi.org/10.37934/ARFMTS.78.2.5666

Usha, M., & Srinivasa Rao, G. (2019). Optimisation of Parameters in Turning Using Herbal Based Nano Cutting Fluid with MQL. *Materials Today: Proceedings*, *22*, 1535–1544. https://doi.org/10.1016/j.matpr.2020.02.115

Venkatesan, K., Devendiran, S., Sachin, D., & Swaraj, J. (2020). Investigation of machinability characteristics and comparative analysis under different machining conditions for sustainable manufacturing. *Measurement: Journal of the International Measurement Confederation*, 154, 107425. https://doi.org/10.1016/j.measurement.2019.107425

Wang, J. J., Zhang, J. F., Feng, P. F. & Guo, P. (2018). Damage formation and suppression in rotary ultrasonic machining of hard and brittle materials: A critical review. *Ceramic International,* 44(2), 1227–1239. https://doi.org/10.1016/j.ceramint.2017.10.050

Zhang, M.J. et al. (2017). Analysis of flow field in cutting zone for spiral orderly distributed fibre tool. *International Journal of Advanced Manufacturing Technology*, 92(9–12), 4345–4354. https://doi.org/10.1007/s00170-017-0471-2

Zheng, H., Zhang, W., Li, B., Zhu, J., Wang, C., Song, G., Wu, G., Yang, X., Huang, Y., & Ma, L. (2022). Recent advances of interphases in carbon fiber-reinforced polymer composites: A review. *Composites Part B: Engineering*, 233, https://doi.org/10.1016/j.compositesb.2022.109639

PAPER 95 – AN INTERNET OF THINGS (IoT) BASED PRECISION SYSTEM FOR IMPROVED IRISH POTATO PRODUCTION IN NIGERIA

C. M. Onuigbo[1] and O. E. Obieze[2]

[1]Department of Electrical/Electronic Engineering, Enugu State University of Science and Technology (ESUT), Enugu, Nigeria
[2]Digital Dynamics Systems Inc., Enugu, Nigeria
Email: onuigboch@gmail.com

ABSTRACT
There is a global concern regarding the increasing food scarcity caused by the current severe climate change, which has sparked research efforts to enhance food production. The Internet of Things (IoT) has emerged as a valuable tool in revolutionizing agriculture and improving food production. Food scarcity will definitely abate with the possibility of automated greenhouse smart farms. This research is aimed at developing an IoT-based precision monitoring system for improved greenhouse Irish potato production in Nigeria. The project focuses on three key metrics for optimal Irish potato yield: soil pH, temperature, and humidity. To achieve this, a model was developed in MATLAB/Simulink environment to monitor the greenhouse changes considering optimal yield values of the considered metrics. Simulation results showed changes in these metrics. Soil pH changed from an environmental value of 4.8 to 6.0, resulting in a percentage change of 20%, the temperature changed from 25°C to 18°C, at 28% percentage change while humidity changed from 70% to 85% producing a change of 21.43%, all driven by IoT sensors.

KEYWORDS: Internet of Things (IoT), Greenhouse Smart Farm, Greenhouse Irish potato, Precision Monitoring, MATLAB/Simulink.

1. INTRODUCTION

Potato is an essential crop for food security and income generation in Nigeria. However, the production of Irish potatoes, a variety grown in high altitude areas, is limited due to challenges such as pests and diseases, inadequate irrigation, and climate change. To address these challenges, an Internet of Things (IoT)-based precision system can be used to improve Irish potato production in Nigeria. According to a report by the Food and Agriculture Organization (FAO), precision agriculture, which utilizes IoT technologies, can improve crop production, resource use efficiency, and reduce environmental impact (FAO, 2018). This technology can be applied in Nigeria to enhance crop yield and quality of Irish potatoes. Soil moisture sensors can be used to determine the water content in the soil and provide real-time data on the plant's water status, allowing for optimal irrigation management (Fernandez-Getino et al., 2019). Temperature and humidity sensors can also be used to monitor the microclimate and help farmers make informed decisions regarding planting, harvesting, and pest control (Zhang et al., 2020). In addition, pest and disease detection can be done using sensors that can detect changes in the crop's physiology, allowing for early detection and intervention before it spreads (Wu et al., 2019). Furthermore, an IoT-based precision system can include irrigation control systems that automatically adjust water delivery based on the data collected by the soil moisture sensors (Zheng et al., 2019). An IoT-based precision system can provide farmers with real-time data that can be used to optimize their crop production, reduce waste, and increase their yield and profits. This paper discusses the potential of an IoT-based precision system for Irish potato production in Nigeria.

1.2 Brief Literature Review

Precision agriculture is an approach to farming that uses data analytics, machine learning, and IoT technologies to optimize agricultural practices for potato production. IoT-based precision agriculture systems with sensors for monitoring soil moisture, temperature, and humidity, as well as a data analysis platform for decision-making, have been explored in recent studies. These studies have shown the potential benefits of IoT-based systems for improving crop yield and resource efficiency, as well as reducing resource usage. Examples include the work by Liu et al (2020), Oyekanmi et al (2020), Osunmakinde and Oyekanmi (2021), Zhang et al (2021), and Abdelnasser et al (2021). These studies have demonstrated the effectiveness of IoT-based precision agriculture systems in improving crop yield and reducing resource usage in potato production. There is a scarcity of research specifically focusing on the application of precision agriculture and IoT technology for Irish potato production in Nigeria. Most existing studies tend to generalize findings from other crops or regions, neglecting the unique challenges and requirements of Irish potato farming in Nigeria. Therefore, there is a need for more targeted research that

investigates the specific benefits and feasibility of IoT-based precision agriculture in the context of Irish potato production in Nigeria.

2. THEORETICAL ANALYSIS

Precision agriculture revolves around the precise management of farming practices, taking into account variations in soil conditions, weather patterns, and crop requirements. By incorporating IoT technology, farmers can collect real-time data on various parameters. This data is then analyzed to make informed decisions and implement targeted interventions in a timely manner. IoT-enabled precision monitoring systems can provide valuable insights into the crop's growth and health. Sensors deployed in the fields and greenhouses can continuously measure critical factors such as soil pH, temperature, and humidity. These real-time measurements enable farmers to monitor the crop's environment closely and identify any deviations from optimal conditions. For instance, data on soil moisture levels can guide irrigation scheduling, ensuring that potatoes receive adequate water. Similarly, temperature and humidity data can inform climate control measures, creating optimal conditions for potato growth. This approach leads to improved resource efficiency and cost-effectiveness, maximizing the yield per unit of input. (Osunmakinde and Oyekanmi 2021).

3. MATERIALS AND METHOD

Materials: The materials used in this research were as follows:

- DHT11 Sensor: For temperature and humidity measurements.
- Sentek EnviroSCAN soil pH sensor: For soil pH level measurement.
- Laptop: This is a personal computer unit for performing multiple numerical and data applications.
- MATLAB Simulink: A "high- performance language" used in technical and engineering computing.
- GARMIN GPS 76 (Global Positioning System): A satellite navigation device that shows the location of the greenhouse for the smart farm in use for the study.
- Arduino: It is an open source electronics platform that is centered on easy-to-use hardware and software. It can read inputs such as a Twitter message, a light on a sensor, or a finger on a button and convert it to an output thus activating a motor, publishing something online and turning an LED on.
- ESP 8266 Wi-Fi Module: it is SOC (System On-chip) module integrated with a TCP/IP protocol stack for the provision of microcontroller access to any type of Wi-Fi network. It comes with the following features:
  - 2.4 GHz Wi-Fi (802.11 b/g/n, supporting WPA/WPA2);
  - General-purpose input/output (16 GPIO);
  - Inter-Integrated Circuit (I^2C) serial communication protocol;
  - Analog-to-digital conversion (10-bit ADC);
  - Serial Peripheral Interface (SPI) serial communication protocol;
  - I^2S (Inter-IC Sound) interfaces with DMA(Direct Memory Access) (sharing pins with GPIO);
  - UART (on dedicated pins, plus a transmit-only UART can be enabled on GPIO2); and
  - Pulse-width modulation (PWM).

3.1 Experimental Procedure**:** Developing an IoT-based precision system for improved Irish potato production in Nigeria as carried out in this research involved several steps as discussed:

- Identification of the requirements: The first step was to identify the requirements of the system, such as the sensors needed, the data that needed to be collected, and the communication protocol used. Three metrics were identified for evaluation: soil pH level, temperature and humidity. With good soil pH level, continuous availability of Nitrogen, Calcium and Potassium considered crucial for Irish Potatoes optimal yield will be maintained. To measure these metrics, the specific sensors for measuring them as specified in the materials used were also identified.
- Installation of the sensors: Next, sensors were installed in the potato fields to collect data on soil pH, temperature, humidity and other factors that affect potato growth. The sensors were installed by placing them in strategic locations on the farm to enable easy monitoring of the metrics measured.
- Connecting the sensors to the internet: The sensors were then connected to the internet to transmit data to the cloud for processing and analysis. The ESP 8266 Wi-Fi Module was used to achieve this objective.
- Processing and analysis of data: Once the data was collected, they were processed and analyzed using machine learning algorithms to provide insights into potato growth. The laptop computer unit was handy for this purpose.
- Providing real-time feedback: The insights were communicated to the farmers for implementation in a real-time mode so that informed decisions were made on potato farming practices.

- ❖ Implementation of actions: Based on the feedback received, required actions were taken in the farm resulting in improved potato yield.
- ❖ Monitoring the results: The system was monitored to evaluate its effectiveness in improving yield as the principal objective of the project.

3.2 Characterization of the Nigerian environment in comparison with standard metrics values

Soil pH in Nigeria varies depending on location and soil type, ranging from acidic to slightly alkaline. Some regions in the south-eastern and south-south parts of Nigeria have more acidic soil with a pH range of 4.5 to 6.0, while the soil in the northern parts of Nigeria is more alkaline with a pH range of 7.0 to 8.5. Soil pH can also vary within a small area due to factors such as vegetation, land use practices, and soil management techniques, so testing the soil pH in a specific area is recommended. Nigeria experiences hot and humid conditions throughout the year due to its location in the tropical zone. The average temperature varies by region and season, with coastal areas having an average temperature of 25-28°C and inland areas having a slightly cooler temperature of 21-27°C. During the dry season (Nov-Mar), temperatures can reach up to 40°C, while the rainy season (Apr-Oct) is generally cooler. Altitude, vegetation cover, and proximity to bodies of water can affect the actual temperature in a specific location.

The average environmental humidity in Nigeria varies by region and season. Coastal areas have high humidity levels ranging from 80% to 90% throughout the year, while inland areas have lower humidity levels ranging from 40% to 70%. During the rainy season, humidity levels are generally higher, ranging from about 70% to 90% or higher in some areas. However, during the dry season, humidity levels can be lower, ranging from about 20% to 50% in some parts of the country.

Table 1 shows the environmental and optimal metrics values which were used in modeling the IoT based model proposed in this work.

Table 1: Characterized Environmental and Optimal Yield Metrics Values

Metric	Environmental Values	Optimal Yield Values
Soil pH	4.5 to 6.0; 7.0 to 8.5	5.0 to 6.5
Temperature	78°F to 82°F; 25°C to 28°C	60°F to 70°F; 15.5°C to 21°C
Humidity	80% to 90% (PH); 40% to 70% (Abuja)	80% to 90%

Characterization was carried out using measurement equipment in Figure 1.

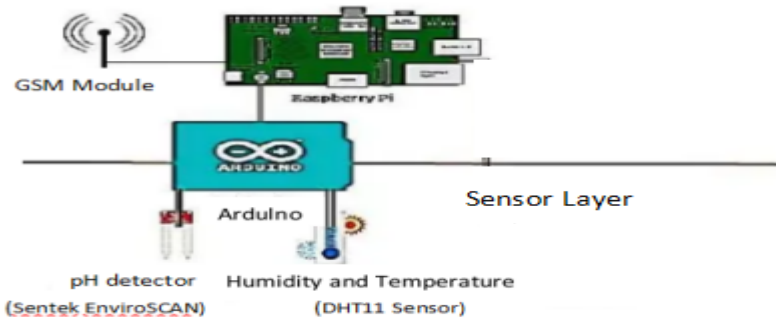

Figure 1: Measurement Equipment

3.2 Metrics Evaluated in this work

In this research, three metrics were assessed due to their invaluable relevance in ensuring optimal yield for Irish potatoes. These are, soil pH, temperature and humidity. An IoT-based precision system was used to coordinate the optimal amount of various metrics to ensure optimum Irish potato yield. The system used a combination of sensors, data analytics, and actuators to monitor and control key environmental factors, such as soil pH, temperature, and humidity, in real-time.

( ) Sentek EnviroSCAN soil pH sensor was used to measure soil pH levels. The sensor was installed in the soil, connected to a data logger and then calibrated. Measurements were then taken at regular intervals and collected data analyzed to determine the soil's pH level. The optimal soil pH for Irish potato

production is slightly acidic, with a pH range of 5.0 to 6.5, which allows for the optimal availability of essential nutrients. Soil pH affects the availability of nutrients in the soil, and adding organic matter or lime can help achieve the optimal pH. High pH levels in the soil can reduce Irish potato yield as they grow best in slightly acidic soils with a pH range of 5.0 to 6.0. High pH levels can decrease the availability of essential nutrients and facilitate the growth of soil-borne diseases.

(a) The DHT11 sensor, a low-cost temperature and humidity sensor, was used in the IoT-based system for monitoring environmental conditions in the potato farm. To measure temperature using the DHT11 sensor, three of the four connectors of the DHT11 sensor was linked to the Arduino microcontroller: the ESP 8266 Wi-Fi Module for data sensing, interpretation and communication. The program is uploaded and output is displayed on the Console or pushed to the cloud API platform. This was analyzed to identify patterns and trends in temperature fluctuations to optimize potato yield. The optimal temperature range for Irish potato production is between 60°F and 70°F (15.5°C to 21°C), with lower temperatures promoting vegetative growth and tuber development. Too low temperatures can slow growth and reduce yields, while too high temperatures can cause heat stress and decreased yields. The optimal temperature range can vary depending on the growth stage of the plant. An IoT-based precision system helps farmers monitor and optimize temperature levels for maximum potato production and quality. The data collected was analyzed to determine whether the temperature is within the optimal range for potato growth. If the temperature is too high or too low, the system activates cooling or heating systems, such as fans or heaters, to adjust the temperature.

- To measure humidity for optimal Irish potato yield using a DHT11 sensor in an IoT-based system, the sensor was connected to the microcontroller board, the ESP 8266 Wi-Fi Module. The humidity data was read. The IoT platform was used to send data to the cloud and was monitored remotely. The optimal humidity range for Irish potato production is between 80% and 90%. Low humidity can cause stunted growth and reduced yields, while high humidity can cause fungal diseases. Maintaining optimal humidity levels can be challenging, but farmers can use irrigation and other techniques to increase soil moisture and humidity levels. An IoT-based precision system helps farmers monitor and control humidity levels for maximum potato production and quality. The IoT sensors monitor humidity levels in the potato field, and the data analyzed to determine whether the humidity level is optimal for potato growth. If the humidity level is too low, the system activates a misting system to increase humidity levels. If the humidity level is too high, the system activates a ventilation system to reduce the humidity level. Since a properly configured GSM set can conveniently access cloud data, it can be used to monitor metrics measurement values and effect necessary real-time farm changes as desired for optimal crop yield on the go.

3.4 The Simulink Model of the proposed IoT System

The Simulink model of the proposed IoT system for precision monitoring and improving Irish Potato yield in greenhouse smart Farm is shown in Figure 2. To enhance the precision capability of the model, a fuzzy IF … THEN rule base was designed and imbibed in the model. The three metrics which were monitored for precision control were used in the fuzzy rule design conditions. This was done to add intelligence to the system so that precision could be achieved as desired. Achieving precision ensures optimal yield in Irish potato production in the IoT based precision model greenhouse smart farm.

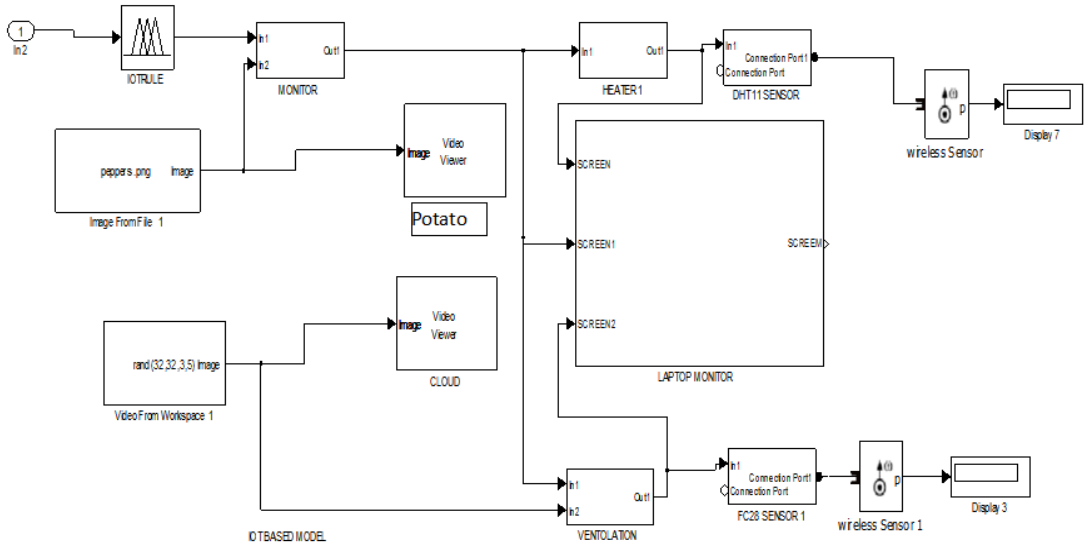

Figure 2: Designed IoT based Simulink model

The Simulink model of Figure 2 was designed bearing in mind the function of a basic wireless sensor node. The measured metrics were then fed into the model using a machine learning optimization algorithm after which it was simulated. Simulation results were used to evaluate and validate the proposed system for possible improvement in the continuous availability of the metrics for optimal Irish potato yield as expected.

4. RESULTS AND DISCUSSION

The following results shown in Table 2 were got from the simulation of the model in Figure 2.

Table 2: Metrics Values after Simulation compared to Characterized Values of the Nigerian Environment and Optimal Yield Values

Metrics	Environmental Values	Optimal Yield Values	Model Simulation Values
Soil pH	4.5 to 6.0; 7.0 to 8.5	5.0 to 6.5	6.0
Temperature	78°F to 82°F; 25°C to 28°C	60°F to 70°F; 15.5°C to 21°C	18°C
Humidity	80% to 90% (PH); 40% to 70% (Abuja)	80% to 90%	85%

Table 2 is an extension of Table 1, the additional information being the Model Simulation data values of the metrics got after the simulation of the model for the proposed system. The Simulink model is the IoT precision based system that monitors and controls the availability of the variable metrics such that optimal yield values are maintained at all times to ensure optimized Irish Potato yield. The precision control process provided by the proposed system is carried out as follows:

- Soil pH: With the proposed IoT system, an automated mechanism was used to maintain the soil pH level at 6.0 so that the optimal yield of Irish Potato would be guaranteed in most parts of Nigeria. In the environment where the research was carried out, the soil pH level was 4.8. With the IoT system, a difference of 1.2 was achieved. Thus, the percentage of improvement using the proposed system is then calculated as follows:

  Soil pH Percentage improvement: x 100% = 20%.

  Thus, 20% soil pH improvement was achieved using the IoT precision system proposed in this research.
- Temperature: In the proposed IoT system, results in table 2 showed a temperature model value of 18°C from an environmental value of 25°C. This gave a difference of 7°C. Improvement percentage computation is given as:

  Temperature Percentage improvement: x 100% = 28%.

  Thus, using the IoT precision system proposed in this research, 28% temperature improvement was achieved.
- Humidity: The humidity values in table 2 showed a change from 70% to 85%. This resulted in a difference of 15% achieved using the proposed IoT system in this research. The percentage of improvement from the simulation result using the proposed IoT based system in this research can be computed as follows:

  Humidity Percentage improvement: x 100% = 21.43%.

  This showed that using our proposed IoT based precision system, the percentage improvement in humidity for improved Irish potato yield is 21.43%.

  - Implication of Results to Irish Potato Yield

The foregoing percentage improvement results on soil pH, Temperature and humidity have far reaching implications for the overall improved yield in Irish Potato production. Given a specific farm size, the yield improvement will be to the magnitude of the average of the percentage improvements in soil pH, temperature and humidity. This can be calculated as follows:
Yield Improvement = Average (Soil pH Percentage Improvement + Temperature Percentage Improvement + Humidity Percentage Improvement) x Total yield (T). Thus,

If soil pH Percentage Improvement = S_p, Temperature Percentage Improvement = T_p,
Humidity Percentage Improvement = H_p and Yield Improvement = YI, Then,
YI = x T (1)
Thus, YI = x T (2)
YI = 23.14%T (3)

Total Cumulative Yield = 23.14T + T (4)

This means that applying our proposed IoT based system to a given Irish Potato farm will result in a yield improvement in the production of the crop. The demonstration in this work has shown how efficient this IoT system is and it can also be applied to the improvement in the yield of any tropical plant thereby increasing food production in the country. The information and knowledge gained from this work can be used to make decisions about soil management practices, such as adjusting fertilizer applications or selecting crops that are better suited for optimized yield and improved food production. The proposed IoT based system prototype in a real-time scenario is shown in Figure 3.

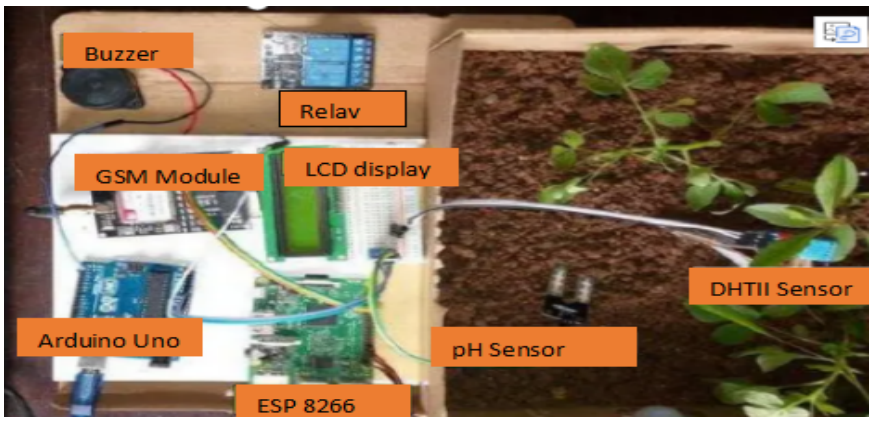

Figure 3: System Prototype

5. CONCLUSION

In conclusion, an Internet of Things (IoT) based precision system can significantly improve Irish potato production in Nigeria. With real-time data collection and analysis, farmers can make informed decisions about planting, irrigation, and fertilization, resulting in improved crop yields, reduced water usage, and increased profitability. The IoT-based precision system also has the potential to enhance the quality and safety of Irish potatoes, as it can detect and prevent disease outbreaks and pest infestations. Additionally, the system provides a platform for farmers to access information and expertise, facilitating knowledge sharing and collaboration within the agricultural community. Largely, an IoT-based precision system for Irish potato production in Nigeria has the potential to revolutionize the agricultural sector in the country, increasing productivity, reducing waste, and improving food security. With continued research and investment, this technology can be further developed and adapted to meet the unique needs and challenges of Nigerian farmers, paving the way for a sustainable and prosperous future.

REFERENCES

FAO. (2018). Precision agriculture and sustainable intensification. Retrieved from http://www.fao.org/3/i9024en/I9024EN.pdf

Fernandez-Getino, A. P., Sanchez-Perez, J. M., Navarro-Pedreno, J., & Gimenez, M. J. (2019). Effect of precision irrigation on potato growth and yield in semi-arid regions. Agricultural Water Management, 212, 166-174.

Wu, W., Zhang, X., Hu, L., Cao, Y., & Jin, S. (2019). A crop pest detection method based on deep learning and internet of things. Sensors, 19(16), 3611.

Zheng, D., Liu, F., Zhang, H., Zhang, X., & Wang, L. (2019). An Internet of Things (IoT)-based irrigation system for improving water use efficiency in greenhouse vegetable production. Agricultural Water Management, 221, 1-9.

Zhang, H., Wang, L., Liu, F., & Zheng, D. (2020). Precision agriculture based on the internet of things: A review. IEEE Access, 8, 52612-52624.

Liu, X., Zhang, S., Li, Y., & Li, H. (2020). A review of Internet of Things (IoT)-based precision agriculture technologies and their applications. Journal: Computers and Electronics in Agriculture, Volume 175, 2020 Link: https://doi.org/10.1016/j.compag.2020.105556

Oyekanmi, B. A., Oluwole, O. A., Olatunbosun, O. J., & Olayanju, T. M. A. (2020). An IoT-based smart agriculture system for improved crop management. Journal: 2020 6th International Conference on Advanced Computing and Communication Systems (ICACCS), 2020 Link: https://doi.org/10.1109/icaccs49037.2020.9074612

Osunmakinde, O. O., and Oyekanmi, B. A. (2021). IoT-based precision agriculture system for sustainable crop production. Journal: 2021 IEEE 11th International Conference on Advanced Computing (ICoAC), 2021 Link:

https://doi.org/10.1109/icoadvc51980.2021.9441812

Zhang, W., Liu, Y., Chen, X., & Zheng, Z. (2021). An IoT-based smart irrigation system for precision agriculture. Journal: 2021 IEEE 8th International Conference on Industrial Engineering and Applications (ICIEA), 2021 Link: https://doi.org/10.1109/iciea51579.2021.9474353

Abdelnasser, M. A., Fathy, A. F., & Alharbi, F. A. (2021). Design and implementation of an IoT-based smart irrigation system for precision agriculture. Journal: 2021 International Conference on Computer Applications Technology (ICCAT), 2021 Link: https://doi.org/10.1109/iccat53701.2021.9460911

Liu, J., Wang, H., Huang, J., & Xu, Z. (2020). An overview of IoT-based precision agriculture technologies and their applications. Journal of Sensors, 2020, 8817805. https://doi.org/10.1155/2020/8817805

Oyekanmi, S. A., Adeleke, A. O., Adegoke, B. M., & Adeniran, J. O. (2020). Design and implementation of an IoT-based smart agriculture system for improved crop management. SN Applied Sciences, 2(11), 1-9. https://doi.org/10.1007/s42452-020-03980-7

Osunmakinde, I., & Oyekanmi, S. A. (2021). An IoT-based precision agriculture system for sustainable crop production. Sensors, 21(4), 1275. https://doi.org/10.3390/s21041275

Zhang, Z., Li, Z., Li, J., & Cheng, Q. (2021). Design of smart irrigation system based on IoT technology. IEEE Internet of Things Journal, 8(9), 7662-7671. https://doi.org/10.1109/JIOT.2021.3078397

Abdelnasser, A., Sheta, W., & El-Khamy, S. (2021). Design and implementation of an IoT-based smart irrigation system for precision agriculture. IEEE Internet of Things Journal, 8(7), 5424-5435. https://doi.org/10.1109/JIOT.2021.3071768

PAPER 102 – MATERIAL SUSTAINABILITY IN NIGERIAN CONSTRUCTION ORGANIZATIONS: A PATHWAY TO ECONOMIC SUSTAINABILITY

S. A Mohammad[2*], M. M. Shafiei[1], and S. R. M. Riazi[1]

[1]School of Housing, Building and Planning, Universiti Sains Malaysia, Malaysia.
[2]Department of Quantity Surveying, Abubakar Tafawa Balewa University, Bauchi Nigeria.
[*]Email: msabubakar@student.usm.my/mohdsabubakar@gmail.com

ABSTRACT
Research on Material Sustainability in construction has been extended in literature to the public domain by examining how various constructs relate with the environmental dimension of sustainability Meanwhile, the current linear consumption of construction materials is economically unsustainable in the midst of growing financial fears. Given the crucial importance of construction firms in sustaining materials, this study aimed to examine the mediating effect of two extreme dimensions of organizational culture (OC) on material sustainability constraints (MSC) influencing the economic sustainability of construction projects (ESCP). A total of 359 responses from a cross-sectional survey from Nigerian construction firms were analyzed using Partial Least Squares-Structural Equation Modeling (PLS-SEM). The proposed research model was formulated largely under the premise of the Circular Economy (CE) theory. The main contribution of this study is to confirm the hypothesis that Hierarchical Culture (HC) diminishes the relationship between MSC and ESCP. This substantiates the need for construction firms to develop and adopt a more innovative culture, such as the Development Culture (DC), in order to drive circular practices and eventually contribute to the economic sustainability of Nigerian construction projects. The study also makes valuable contributions with regard to understanding the behavioral disposition of construction firms towards attaining sustainable outcomes.

KEYWORDS: Material Sustainability; Sustainable Material Management; Organizational Culture; Circular Economy; Economic Sustainability; Nigeria

3. INTRODUCTION

Being undoubtedly one of the rapidly urbanizing countries in sub-Saharan Africa, almost 50% of Nigeria's population now reside in urban settlements indicating the need for more infrastructure (Isa et al., 2013). Consequently, a lot of material resources are expected to become scarcer and hence expensive to use and a considerable number of these resources may not even be available for future utilization. The growing concern on population growth and resource scarcity has resulted in the concept of sustainability becoming more imperative over the past decades (Santoro, 2019). Being the foundation for most economic activities, the construction industry is hence plunged into the key role of ensuring sustainability. The current level of sustainability awareness is undoubtedly a crucial factor influencing the architectural tendencies and high resource consumption observed in developing countries (Kukah et al., 2022). Hence, this consumes a lot of energy and adds a lot of money to the construction process because it necessitates the importation of supplies and specialized labour. This is a problem given the ever increasing financial dilemma in Nigeria, where shortage of funds to execute construction projects (Taiwo & Misnan, 2020) is often highlighted.

Employing the use of "sustainable materials" in our construction practices to substitute "traditional materials" is believed to improve global dimensions of sustainability thereby reducing the ecological and economic effects in the course of the building's lifespan (Bribián et al., 2011). Additionally, it extends distinctive utility benefits to both clients and users. Nevertheless, most building endeavours still only patronize the so-called traditional materials as the use of sustainable materials in the industry is clearly enveloped by obstacles of adoption (Saleh & Alalouch, 2015; Darko & Chan, 2017). The question of sustaining materials viz-a-viz introducing new innovative ones is crucial due to the modern stride of high-tech innovations in every business domain (Esposito et al., 2018). According to Ritzén and Sandström, (2017), it is necessary to start from within the organization to understand the barriers faced by sustainable initiatives. The globally recognized idea of Organizational Culture (OC) of these organizations is at the heart of this argument. OC has been shown in prior research to be a background element or social context that impacts an organization's learning methods in acquiring and applying specialized expertise (Teräväinen et al., 2018). According to Owolabi et al., (2019), one of the primary impediments to creative applications in the Nigerian construction sector is the OC. Previous study in the Nigerian construction sector did not focus on the relationship between material sustainability in construction and economic

sustainability entirely in a way that integrated OC. Hence, this paper sought to address three major research questions to this effect: RQ1: What is the relationship between Material Sustainability Constraints (MSC) and OC in the Nigerian Construction industry RQ2: What is the relationship between MSC and Economic Sustainability of Construction Projects (ESCP) in the Nigerian Construction industry? RQ3: To what extent does OC mediate the relationship between MSC and ESCP in Nigeria?

4. THEORETICAL ANALYSIS

The world has relied on a linear economy ever since the advent of the industrial revolution (Esposito *et al*., 2018). Earth has become a "take, make, and dispose" realm as a result of our consumerist mentality and "single use" lifestyles. This indicates a linear progression of innovation: we obtain our inputs from the natural world, use them in the production of mass-produced items that we purchase, use once, and then throw away. Over the past three decades, there has been a growing movement toward increased circularity in many nations around the globe, which can now profit from increased incorporation and consistency. A number of researchers (Ghisellini et al., 2016; Geissdoerfer *et al*., 2017) sanction the initiation of the study of CE to Pearce and Turner, (1989). By examining the ways in which natural resources serve as both inputs for production and a sink for waste products, the authors demonstrated how modern economic systems combine linear and non-linear elements. According to Zadeh *et al*., (2016), empirical evidence that aids in the evaluation of sustainable methods will tremendously assist clients and can go a long way in paving the way for future sustainable products. Although the path to attainment of this objective is clearly identified by specified strategies, the process is quite often hindered by periodic constraints. This formed the basis for conceptualizing the relationship between the independent variable (MSC) and the dependent variable (ESCP). This concept is further explicated by Figure 1 below.

This study chose the development culture (DC) and hierarchical culture (HC) dimensions as mediating variables in order to effectively achieve the objectives set. The DC is one that strategizes on acclimatization to external forces by pre-empting the need to apply creative solutions (Patyal *et al.*, 2019). Its main feature is the flexibility to adapt to the naturally ever-changing consumer requirements (Zu *et al*., 2010). In contrast, the HC is well known for its qualities of bureaucracy, tendency for rigidity, tight restrictions and internal focus (Pakdil & Leonard, 2015). Innovative solutions wither in such environs. Hence, these culture types are deemed the most suitable to address MSC in the Nigerian construction sector. The conceptualization of the study variables also gave rise to the following research hypotheses;

H1: Material sustainability constraints have a negative impact on construction firms' development culture.
H2: Material sustainability constraints have a negative impact on construction firms' hierarchical culture.
H3: Material sustainability constraints have a negative impact on economic sustainability of construction projects.
H4: Development culture has a positive influence on economic sustainability of construction projects.
H5: Hierarchical culture has a positive influence on economic sustainability of construction projects.
H6: Development culture mediates the relationship between material sustainability constraints and economic sustainability of construction projects.
H7: Hierarchical culture mediates the relationship between material sustainability constraints and economic sustainability of construction projects

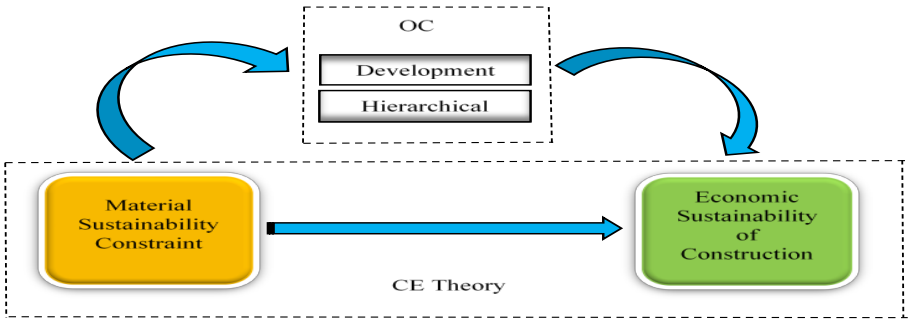

Figure 1: Research Framework

5. METHODOLOGY

3.1 Data Collection Process

For this study, the Positivist approach and Quantitative techniques were adopted as philosophy and design respectively in order to ascertain the mediating effects of OC on the relationship between MSC and ESCP in the Nigerian construction industry. This is to effectively analyze the causal relations and ascertain the level of direct and indirect relationship among all variables. A survey technique was used to ensure that the stated goals are satisfied. As a result of the background and scope provided, the target population for this study was all contracting and consulting firms in the study area. In total, 550 survey questionnaires were distributed to Construction Contracting and Consulting Companies in Nigeria, of which 390 were returned. Out of the returned questionnaires, 359 were used for data analysis. Data were obtained from Principal partners, Partners, Management staff, Project Managers and Regular staff of these organizations through the survey instruments.

3.2 Measurements

The measurement for MSC (7 items), OC (11 items) and ESCP (10 items) was done using a 5-point Likert scale. The Likert scale for MSC adopted ranged from "very less severe" denoted by 1, to "very highly severe" denoted by 5. The Likert scale for OC ranged from "strongly disagree" denoted by 1, to "strongly agree" denoted by 5. The Likert scale for ESCP indicators ranged from "very low" denoted by 1, to "very high" denoted by 5.

6. RESULTS AND DISCUSSION

4.1 Direct Relationships

Bootstrapping with a resample rate of 5000 was run to test the hypotheses of the study. To attain p-values, t-values and bootstrapped confidence intervals, Hair et al., (2019) suggested bootstrapping. Results for the five tested direct hypotheses are presented below in Table 1. Four hypotheses (H1, H2, H3, and H5) were found significant while H4 was not significant. Specifically, green job analysis and description with sustainable performance were not significant (β = 0.100, t = 1.581, p = 0.057, BCILL = -0.024, BCIUL = 0.190), explaining that development culture in Nigerian construction organizations is not significant thereby exposing it as responsible for not bringing the required sustainable economic performance to construction projects in the industry. Moreover, beta value is not significant, t-value is less than threshold value i.e., 1.645 and there is zero between upper and lower limit confidence intervals. Because this culture has the most tendency to support technology savvy or risk prone organizations due to their nature, where control is quite minimal due to demands for members to be experienced and enabled, its absence jeopardize the drive towards being entrepreneurial, creative and innovative to accommodate the dynamism, individuality and risky terrain of such organizations (Pakdil & Leonard, 2015; Patyal *et al*., 2019). Based on the above discussion, H4 is rejected.

Table 1: Hypothesis Testing for Direct Relationships

Hypothesis	Relationships	Std. Beta	T-values	P- values	BCI LL	BCI UL
H1	**MSC -> DC**	-0.308	7.573	**0.000**	-0.367	-0.234
H2	**MSC -> HC**	0.203	3.891	**0.000**	0.103	0.277
H3	**MSC -> ESCP**	-0.088	1.653	**0.049**	-0.169	0.006
H4	**DC -> ESCP**	0.100	1.581	**0.057**	-0.024	0.190
H5	**HC -> ESCP**	-0.219	3.800	**0.000**	-0.297	-0.110

4.2 Indirect Relationships

H6 was developed to investigate the mediating effect of DC on the relationship between MSC and ESCP. Analysis of the results revealed that the mediating effect of DC was found to be insignificant (β = -0.031, t = 1.524, p = 0.064, BCILL = -0.060, BCIUL = 0.008). Being a progressive culture, this implies that the concept of sustaining construction materials by organizations has not been fully embraced (Jones & Comfort, 2018). Hence, the justification for the outcome of this hypothesis can be explained in the scarcity of certain criteria necessary to attain minimum requirement to achieve a CE-based construction industry in Nigeria (Daniel et al., 2018; Ogunmakinde et al., 2019). Based on the discussion above H6 is rejected.

H7 was developed to investigate the mediating effect of HC on the relationship between MSC and ESCP. Analysis of the results revealed that the mediating effect of HC was found to be significant (β = -0.044, t = 2.925, p < 0.05, BCILL = -0.070, BCIUL = -0.022). This is a rational outcome and is in agreement with the findings of Büschgens et al., (2013), who reflect the difficulty of the HC to accommodate new inventions in its stringent and highly controlled setting. The results which are presented in Table 2 below also confirms that the current low state

of economic sustainability in the study area can be attributed to the most prevalent culture types in construction firms in the area; hierarchical culture. Based on the discussion above, H7 is accepted.

Table 2: Hypothesis Testing for Indirect Relationships

Hypothesis	Relationship	Std. Beta	T -values	P -values	BCILL	BCIUL
H6	**MSC -> DC -> ESCP**	-0.031	1.524	**0.064**	-0.060	0.008
H7	**MSC -> HC -> ESCP**	-0.044	2.925	**0.002**	-0.070	-0.022

7. CONCLUSIONS

For a while, policy makers and stakeholders have expressed interest in developing a sustainable model in the building industry. This trend hints to the questions of how construction firms (contracting and consulting) can adopt sustainable practices towards attaining sustainable material performance. Another question is whether OC mediates the relationship of the studied constructs within the Nigerian construction industry. The key contribution of this study is verification of MSC's influence on ESCP, and the discovery of partial effects of OC on ESCP in the Nigerian construction industry. As a mediator, HC lessens the link between MSC and ESCP. This signals that firms need to develop and switch to a more innovative culture like the DC to be able to drive sustainable practices and eventually contribute to economic sustainability of construction projects in Nigeria. Previous literature has highlighted these firms' reluctance in engaging these ideologies (Jones and Comfort, 2018) citing their organizational disposition as a probable reason for this shortcoming (Owolabi et al., 2019; Ritzén and Sandström, 2017). Based on the findings of this study, it is imperative on firm administrators to spearhead an organizational paradigm shift from the current stringent culture to a more flexible and innovative culture for the desired objective to be achieved. This could be done simultaneously with investments in innovations, sustainable skills and technology acquisitions to increase the economic performance of construction projects. When this is achieved, a more flexible and innovative culture (DC) will emerge within the industry and facilitate the attainment of ESCP in Nigeria.

REFERENCES

Büschgens, T., Bausch, A., & Balkin, D. B. (2013). Organizational culture and innovation: A meta-analytic review. In *Journal of Product Innovation Management* (Vol. 30, Issue 4, pp. 763–781). John Wiley & Sons, Ltd. https://doi.org/10.1111/jpim.12021

Daniel, E. I., Oshineye, O., & Oshodi, O. (2018). Barriers to sustainable construction practice in Nigeria. *Proceeding of the 34th Annual ARCOM Conference, ARCOM 2018*, *September*, 149–158.

Darko, A., & Chan, A. P. C. (2017). Review of Barriers to Green Building Adoption. In *Sustainable Development* (Vol. 25, Issue 3, pp. 167–179). John Wiley and Sons Ltd. https://doi.org/10.1002/sd.1651

David Taiwo, O., & Misnan, S. H. (2020). Factors Influencing Supply of Affordable Housing in Nigerian Cities Using Confirmatory Factors Analysis. *International Journal of Built Environment and Sustainability*, *7*(3), 11–21. https://doi.org/10.11113/ijbes.v7.n3.499

Esposito, M., Tse, T., & Soufani, K. (2018). Introducing a Circular Economy: New Thinking with New Managerial and Policy Implications. *California Management Review*, *60*(3), 5–19. https://doi.org/10.1177/0008125618764691

Geissdoerfer, M., Savaget, P., Bocken, N. M. P., & Hultink, E. J. (2017). The Circular Economy – A new sustainability paradigm? *Journal of Cleaner Production*, *143*, 757–768. https://doi.org/10.1016/j.jclepro.2016.12.048

Ghisellini, P., Cialani, C., & Ulgiati, S. (2016). A review on circular economy: The expected transition to a balanced interplay of environmental and economic systems. *Journal of Cleaner Production*, *114*, 11–32. https://doi.org/10.1016/j.jclepro.2015.09.007

Hair, J. F., Risher, J. J., Sarstedt, M., & Ringle, C. M. (2019). When to use and how to report the results of PLS-SEM. In *European Business Review* (Vol. 31, Issue 1, pp. 2–24). Emerald Group Publishing Ltd. https://doi.org/10.1108/EBR-11-2018-0203

Isa, R. B., Jimoh, R. A., & Achuenu, E. (2013). An overview of the contribution of construction sector to sustainable development in Nigeria. *Net Journal of Business Management*, *1*(1), 1–16. http://www.netjournals.org/pdf/NJBM/2013/1/13-017.pdf

Jones, P., & Comfort, D. (2018). The Construction Industry and the Circular Economy. *International Journal of Management Cases*, *20*(1), 4–15. https://doi.org/10.1057/9780230372481_3

Kukah, A. S. K., Blay Jnr, A. V. K., & Opoku, A. (2022). Strategies to Reduce the Impact of Resource Consumption in the Ghanaian Construction Industry. *International Journal of Real Estate Studies*, *16*(1), 51–59. https://doi.org/10.11113/intrest.v16n1.88

Muogbo, U. S., & Chuka, E.-U. (2019). Environmental Factors: A Panacea for Survival and Growth of Small and Medium Scale Businesses in Nigeria. *SSRN Electronic Journal*, *8*, 2319–2801. https://doi.org/10.2139/ssrn.3432188

Ogunmakinde, O. E., Sher, W., & Maund, K. (2019). An assessment of material waste disposal methods in the Nigerian construction industry. *Recycling*, *4*(1). https://doi.org/10.3390/recycling4010013

Owolabi, J. D., Faleye, D., Eshofonie, E. E., Tunji-Olayeni, P. F., & Afolabi, A. O. (2019). Barriers and drivers of innovation in the Nigerian construction industry. *International Journal of Mechanical Engineering and Technology*, *10*(2), 334–339.

Pakdil, F., & Leonard, K. M. (2015). The effect of organizational culture on implementing and sustaining lean processes. *Journal of Manufacturing Technology Management*, *26*(5), 725–743. https://doi.org/10.1108/JMTM-08-2013-0112

Patyal, V. S., Ambekar, S., & Prakash, A. (2019). Organizational culture and total quality management practices in Indian construction industry. *International Journal of Productivity and Performance Management*, *69*(5), 895–913. https://doi.org/10.1108/IJPPM-10-2018-0368

Pearce, D., Turner, R. (1989). *Economics of Natural Resources and the Environment*. https://scholar.google.com/scholar?hl=en&as_sdt=0%2C5&q=Pearce%2C+D.%2C+Turner%2C+R.%2C+1989.+Economics+of+Natural+Resources+and+the+Environment.+Johns+Hopkins+University+Press%2C+Baltimore.&btnG=

Ritzén, S., & Sandström, G. Ö. (2017). Barriers to the Circular Economy - Integration of Perspectives and Domains. *Procedia CIRP*, *64*, 7–12. https://doi.org/10.1016/j.procir.2017.03.005

Saleh, M. S., & Alalouch, C. (2015). Towards Sustainable Construction in Oman: Challenges & Opportunities. *Procedia Engineering*, *118*, 177–184. https://doi.org/10.1016/j.proeng.2015.08.416

Santoro, S. (2019). Guest Editorial Guest Editorial. *Stork Ibis and Spoonbill Conservation*, *8*(December), 8–9. https://doi.org/10.1177/146808740500600401

Teräväinen, V., Junnonen, J. M., & Ali-Löytty, S. (2018). Organizational culture: Case of the finnish construction industry. *Construction Economics and Building*, *18*(1), 48–69. https://doi.org/10.5130/AJCEB.v18i1.5770

Zabalza Bribián, I., Valero Capilla, A., & Aranda Usón, A. (2011). Life cycle assessment of building materials: Comparative analysis of energy and environmental impacts and evaluation of the eco-efficiency improvement potential. *Building and Environment*, *46*(5), 1133–1140. https://doi.org/10.1016/j.buildenv.2010.12.002

Zadeh, R. S., Xuan, X., & Shepley, M. M. (2016). Sustainable healthcare design: Existing challenges and future directions for an environmental, economic, and social approach to sustainability. *Facilities*, *34*(5–6), 264–288. https://doi.org/10.1108/F-09-2013-0067

Zu, X., Robbins, T. L., & Fredendall, L. D. (2010). Mapping the critical links between organizational culture and TQM/Six Sigma practices. *International Journal of Production Economics*, *123*(1), 86–106. https://doi.org/10.1016/j.ijpe.2009.07.009

PAPER 103 – MODELLING OF VOCS EMISSION AND TRANSPORT IN INDOOR ENVIRONMENT USING FINITE ELEMENT ANALYSIS

A. S. Atanda[1*], J. A. Adeniran[1], T. L. Adewoye[1]

[1]Department of Chemical Engineering, University of Ilorin, Ilorin, Nigeria.
[*]Email: sarat.morenikeji@gmail.com

ABSTRACT
The concentration of Volatile Organic Compounds (VOCs) in an indoor environment like beauty depends on its emission rate and transportation. Consequently, a better understanding of the dynamic behaviour of this pollutant in the indoor environment improves estimates of human exposure to indoor air pollutants**.** This study systematically evaluated the influence of four computational parameters on pollutant dispersion in a beauty shop. The computation parameters include turbulence models, grid resolution, and discretization of time step size and length of the sampling period. For concentration simulations, the Large Eddy Simulation (LES) and Detached Eddy Simulation (DES) models did not give any result because it had limitations in areas near the source, whereas the realizable k-ε turbulence model did gave a desirable result. An increase in the emission rate did not change the general dispersion characteristics, but it still affected the concentration distribution in the areas near the source and resulted in a larger polluted area. The findings of this study are intended to give a better understanding of the dynamic behaviour of VOCs in a beauty shop using CFD simulations, which will help develop a suitable control strategy.

KEYWORDS: Volatile Organic Compounds, indoor, beauty shop, ANSYS FLUENT, CFD, Modelling

12. INTRODUCTION

The quality of air in indoor environment is very important to work performance, productivity and the health of building users (Titiana, Andy, Marc, and Bluyssen, 2019). Although Indoor Air Quality (IAQ) is not usually monitored, it must be perceived as a relevant issue to follow up for the inhabitants' well-being and comfort for enhanced living environments and occupational health (Vilčeková *et al*., 017). The time spent in various types of indoor spaces depends on different social and environmental factors such as age, geographical latitude, occupation, lifestyle and quality of life (Śmiełowska, Marć, and Zabiegal, 2017). Common air pollutants in indoors are particulate matter, photochemical oxidants (including ozone), carbon monoxide, sulfur oxides, nitrogen oxides, VOCs and lead. A lot of research has shown that commonly used materials such as wood products, floor coverings, wall coverings, household spray products emits a variety of VOCs which reduces the quality of the indoor air (Hussain *et al*., 2015).

Volatile organic compounds (VOCs) are reactive organic compounds that are emitted into the atmosphere due to their high volatility at atmospheric conditions (Attia *et al*., 2019; Guerra *et al*., 2017; Tsai, 2016). They also have different types of reactive functional groups such as amines, amides, alcohols, carboxylic acids, aldehydes, and aromatic compounds (Attia *et al*., 2019). VOCs are considered to be important air pollutants because of their persistence in the atmosphere (Kumar *et al*., 2014) as well as their negative effects on respiratory and reproductive systems even at low levels of concentration (Tsai, Lu, Chung, and Chiang, 2020). The concentration of VOCs in the indoor environment depends on the pollutant emission sources, rate of removal, the air exchange rate with the outdoor air, and the outdoor VOCs concentrations (Guieysse *et al*., 2008).VOCs can be classified into several groups based on their properties. Based on the boiling point, the VOCs can be divided into Very Volatile Organic Compounds (VVOCs), VOCs, Semi Volatile Organic Compounds (SVOCs) and Particulate Organic Matters (POMs) by WHO. Based on molecular structure, it is classified as alkanes, alkenes, aromatic hydrocarbons, alcohols, aldehydes, ketones etc, and based on molecular polarity they can be the polar and nonpolar VOCs in indoor environments. A better understanding of the dynamic behavior through Computational Fluid Dynamics will help in designing suitable control strategies.
CFD simulation programs are a powerful tool for estimating the airflow patterns and thermal environment of various heating, ventilation, and air conditioning systems in a very detailed way. They have been used for the estimation and control of the indoor environment and space ventilation when using different ventilation systems (Szczepanik-Scislo and Lukasz Scislo, 2021). CFD divides a space into extremely fine grid cells, which can be used to predict the precise spatial distribution of target chemicals from spray products. Jung, Kim, Seol, Lee, and Kwon (2021) simulated inhalation exposure for an eight compartments room to an ethanol trigger and a propellant product. The well-mixed model overemphasized short-term exposure, particularly under the trigger spray scenario. The CFD based permeation model includes sorption/desorption, using a linear isotherm at inner and

outer surfaces and a blended wall function to account for the effects of near-wall turbulence. The model was used to show how vapor concentrations around a cardboard box containing a SVOC vary when some of the key input parameters are changed (Foat *et al*., 2021). Indoor environment like beauty shops where numerous essential oil and scented products are used depends on their emission rate, decay and transportation. Consequently, a better understanding of the dynamic behaviour of this pollutant in the indoor environment improves estimates of human exposure to indoor air pollutants.

13. THEORETICAL ANALYSIS

CFD solves Reynolds-Averaged Navier–Stokes Equations for turbulent buoyant flow, heat and mass transfer established based on conservation equations of mass, momentum, energy, turbulent kinetic energy equation, turbulent energy dissipation equation, and contaminants (Davardsoot and Kahfooroushan, 2018; Panagopoulos, Karayannis, Kassomenos, and Aravossis, 2021).

For the mass conservation as shown in Equation 1

$$\frac{\partial}{\partial x_i}(\rho u_i) = 0 \quad (1)$$

Equation 2 represents momentum conservation

$$\frac{\partial}{\partial x_i}\left(\rho u_i u_j\right) = -\frac{\partial P}{\partial x_i} + \frac{\partial}{\partial x_j}\left\{\left(\mu + \mu_t\right)\left(\frac{\partial v_i}{\partial x_i}\right)\right\} + \rho g_i \beta (T - T_m) \quad (2)$$

Turbulent kinetic Energy can be estimated with Equation 3

$$\frac{\partial}{\partial x_i}(\rho u_i k) = \frac{\partial}{\partial x_j}\left\{\left(\mu + \frac{\mu_t}{\sigma_t}\right)\left(\frac{\partial k}{\partial x_i}\right)\right\} + G_k + G_k - \rho\varepsilon \quad (3)$$

Equation 4 represents turbulent kinetic energy dissipation equation

$$\frac{\partial}{\partial x_i}(\rho u_i \varepsilon) = \frac{\partial}{\partial x_j}\left\{\left(\mu + \frac{\mu_t}{\sigma_\varepsilon}\right)\left(\frac{\partial \varepsilon}{\partial x_i}\right)\right\} + \frac{C_{1\varepsilon}\varepsilon}{k}(G_k + C_{3\varepsilon})G_b - C_{2\varepsilon}\rho\frac{\varepsilon^2}{k} \quad (4)$$

Energy conservation equation as indicated in Equation 5

$$\frac{\partial}{\partial x_i}(\rho u_i T) = \frac{\partial}{\partial x_i}\left\{\left(\frac{\mu}{P_r} + \frac{\mu_t}{P_r}\right)\left(\frac{\partial T}{\partial x_i}\right)\right\} + S_T \quad (5)$$

Contaminants conservation equations are indicated by Equation 6 -9;

$$\frac{\partial}{\partial x_i}(\rho u_i C) = \frac{\partial}{\partial x_i}\left\{\left(\frac{\mu}{\sigma} + \frac{\mu_t}{\sigma_T}\right)\left(\frac{\partial C}{\partial x_i}\right)\right\} + S_c \quad (6)$$

$$\mu_t = \rho C_\mu \frac{k^2}{\varepsilon} \quad (7)$$

$$G_k = \mu_t\left(\frac{\partial u_j}{\partial x_i} + \frac{\partial u_i}{\partial x_j}\right)\frac{\partial u_j}{\partial x_i} \quad (8)$$

$$G_k = -g_i\left(\frac{\mu_t}{\rho\sigma_h}\right)\frac{\partial u_j}{\partial x_i} \quad (9)$$

$C_{1\varepsilon} = 1.44\ C_{2\varepsilon} = 1.92 \quad C_{3\varepsilon} = 0.09$

$\sigma_k = 1.0\ \ \sigma_\varepsilon = 1.0$

Where ρ is the fluid density, u_i is the flow velocity vector field in x_i direction, P is the pressure, k is the turbulent kinetic energy, μ_t is the turbulent viscosity, μ molecular viscosity, g is acceleration due to gravity,C, $C_{1\varepsilon}$, $C_{2\varepsilon}$ and $C_{3\varepsilon}$ are coeficient in approximated turbulent transport equations, σ_h molecular prandtl number, σ_t is effective turbulent prandtl number, ε rate of dissipation of turbulence energy, T is the temperature, T_m is the reference temperature, G_k is the kinetic energy produced by buoyancy, C is molar concentration of the VOC.

14. METHODOLOGY

The transportation of VOCs in beauty shops was simulated using ANSYS Fluent (2016) which is an application-based software that helps in physical modelling. There are five major steps involve in the numerical simulation with ANSYS Fluent which describes flow of air pollutant include

(i) Geometry is set up according to the dimensions of the indoor space.
(ii) Setting up material properties and boundary conditions or a turbulent forced-convection problem, material properties considered/chosen were equivalent to n-butane (n-butane), which is selected from the gas list present in software.
(iii) Boundary condition for concentration change was considered zero at zeroth time, and change in the concentration with respect to time has been determined by mass flow equation through software.
(iv) Calculating a solution using the pressure-based solver wherein mass and energy balance equations are used.
(v) Examining the flow fields using ANSYS Fluent.

3.1 Geometry and Mesh generation

A 7.725 m × 6.000 m × 1.989 m (L ×H ×W) numerical model of the 3-D room as shown in Figure 1 was designed with SOLIDWORKs software and then saved in IGS format that is acceptable in ANSYS Fluent. The SOLID WORK modelled room has no furniture and occupants. The empty room as shown in Figure 1a was modeled to study indoor environmental conditions. An empty room consists of the glazed glass window, adiabatically insulated walls, and a source of aerosol placed on the table.

Meshing was carried with a high smoothing, slow transition and fine relevance center as shown in Figure 1b. The realizable k-ε turbulence model with standard wall functions in Fluent was used to model the effects of turbulence on airflow and aerosols transport.

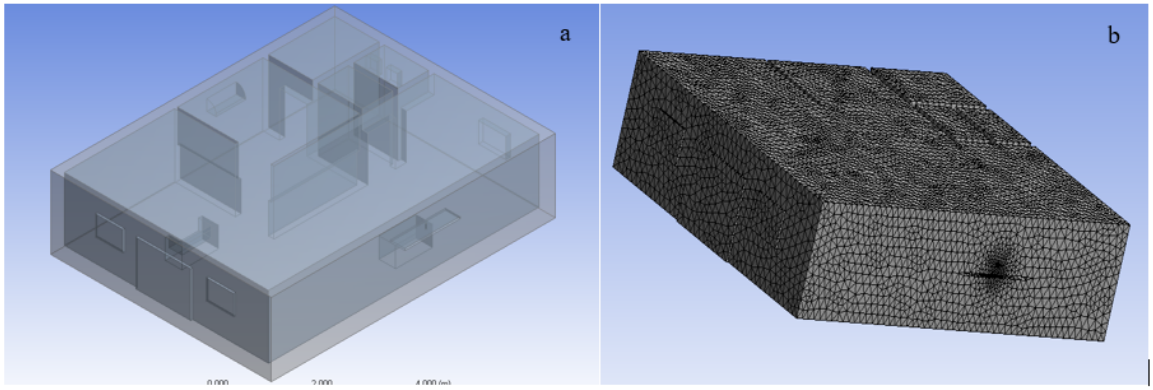

Figure 1: (a) geometry of modelled room (b) mesh generated

3.2 Setup and solution

The realizable k-ε turbulence model with standard wall functions in Fluent was used to model the effects of turbulence on airflow and aerosols transport (Adeniran *et al.,* 2021). The solver was set to be pressure based with two Eulerian phases with implicit body force. The VOCs was represented by n-butane which was chosen from the fluent data base. The VOCs inlet (Hair spray Bottle), wind inlet and outlet was specified to be velocity inlet and pressure outlet respectively in the software. The wind velocity was varied from 2 to 6 m/s. The solution of the model was initialized using the hybrid initialization

15. RESULTS AND DISCUSSION

Air flow velocity is an important parameter to be considered when studying airflow in an indoor environment wind velocity was varied from 2 to 6 m/s the result obtained for 2, 4, 6 m/s are presented in Fig. 2, 3 and 4 (Scenerio A, Scenerio B and Scenerio C) respectively.

Scenerio A

About one thousand (1000) iteration was carried out the volume fraction of VOCs emitted reduced swiftly with time and slightly reduced for some time until steady state was reached at about 800 iteration. The spread of the pollutant was not much this could be attributed to the wind velocity, which did not make the VOCs to spread to other part of the beauty shop. This can result excessive chemical exposure conditions in beauty shops that can lead include irritation to eyes and nose, headache, dizziness, drowsiness, *etc*. Therefore, the appearance of a mixture of compounds in high concentrations can cause similar symptoms to both employees and customers (Tsigonia, Lagoudi, Chandrinou, Linos, Evlogias, and Alexopoulos, 2010). For Scenerio B presented in Figure 3a and b there was a sharp decrease the volume fraction of the VOCs until uniform concentration is attained with the part of the room. A uniform spread was attained at a shorter time span around 700 iteration. When the wind velocity was increased to about 6 m/s the spread was very fast and steady state was attained at about 600 iteration. These findings predicts the highest concentration near the source of the pollutant concentration gradually decreases and then transported towards the direction of the wind this result corresponds to the findings of Mohammadi and Calautit (2021). Environmental conditions such as meteorology, temperature difference across the building, indoor activity, furnishings, etc., alter the rate of air exchange and consequent pollution transmission. For the model considered in this study it was observed that there was negligible spread of the VOCs to other compartment separated by walls.

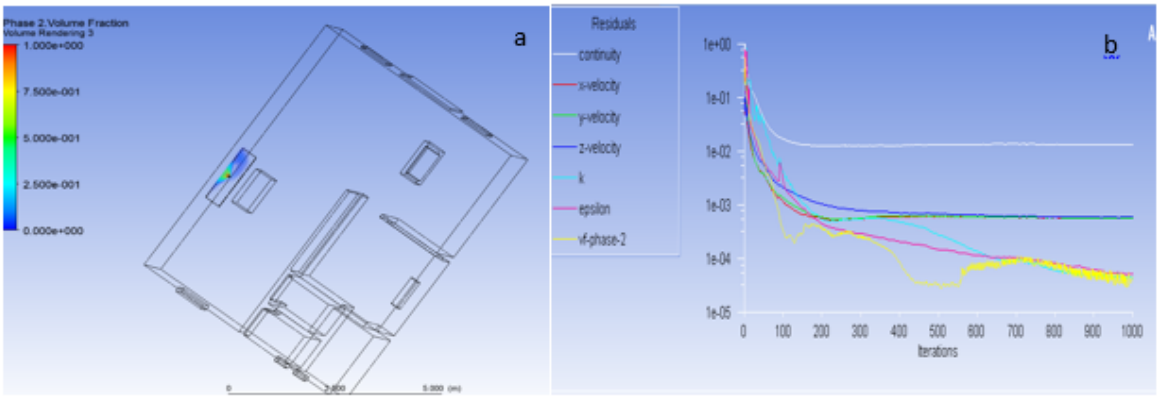

Figure 2:(a) Volume rendering of VOCs dispersion (b) decay of VOCs with time steps at wind velocity

Scenario B

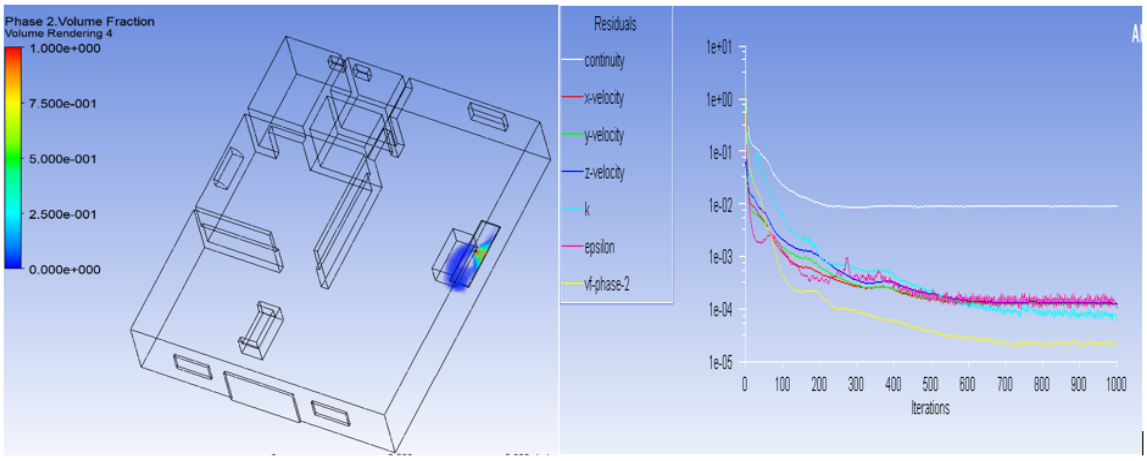

Figure 3:(a) Volume rendering of VOCs dispersion (b) decay of VOCs with time steps at wind velocity at 4 m/s

Scenerio C

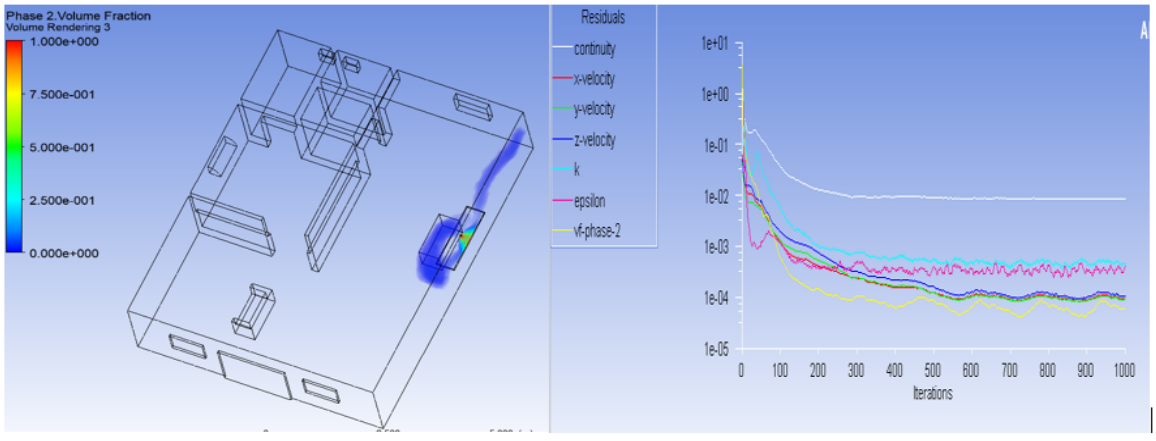

Figure 4: (a) Volume rendering of VOCs dispersion (b) decay of VOCs with time steps at wind velocity at 6 m/s

The emission rate of the pollutant was varied by increasing the emission rate thus altering the velocity of the VOCs inlet. It was found that an increase in emission rate did not affect the flow characteristics but increases the polluted area. The airflow velocity have impact on the transportation of the VOCs in the indoor environment.

16. CONCLUSIONS

This study concentrated on the transportation of VOCs in a beauty shop. The transportation pattern did not change an increase in emission rather there was a spread in the larger parts of the room. There was an increase in dispersion of the VOCs (n-butane) when the wind speed was increased from 2m/s to 6 m/s. Operation of saloons in confined places with poor ventilation leads to the emission of VOCs that might have pleasant smell in some cases but are actually deadly, poisonous, colourless, and odourless. Symptoms of poisoning are dull headache, blurred vision, shortness of breath, weakness, dizziness, and nausea or vomiting. Hence, this has adverse health effect on both the beauty shop operator and the customer. Measures must be taken in such indoor environment to reduce its impact on health and the environment. A great part of the effect of using spray products in beauty shop can be controlled by carrying out awareness campaigns, adopting air cleaning technology, introducing common house plants in work, proper engineering measures, and a well-designed awareness campaign. Where there is high usage of this hair product, which contains high concentration of VOCs, there should be a proper ventilation and vent can be installed around where these hair products are being used. However, a well-ventilated room with modern air purification systems should be used in most beauty shops

ACKNOWLEDGEMENTS

The authors would like to express our gratitude to all those who have contributed to this research paper.
Without your hardwork, expertise and dedication, this research would not have been possible.

REFERENCES

Adeniran, J. A., Mohammed, I. A., Muniru, O. I., Oloyede, T., Sonibare, O. O., Yusuf, M. N. O., ... and Sonibare, J. A. (2021). Indoor transmission dynamics of expired SARS-CoV-2 virus in a model African hospital ward. Journal of Environmental Health Science and Engineering, 19, 331-341.

Attia, M., Swasy, M., Ateia, M., Alexis, F., and Whitehead, D. (2019). Periodic mesoporous organosilica nanomaterials for rapid capture of VOCs. communication, 1-3.

Davardsoot, F., and Kahfooroushan, D. (2018). Modelling the dispersion of Volatile Organic Compounds in indoor environment. chemical engineering and technology, 1-22.

Foat, T., Drodge, J., Charleson, A., Whatmore, B., Pownall, S., Glover, P., . . . Marr, A. (2021). Predicting vapour transport from semi-volatile organic compounds concealed within permeable packaging. International Journal of Heat and Mass Transfer, 183(122012), 1-14.

Guerra, F. D., Campbell, M. L., Whitehead, D. C., and Alexis, F. (2017). Tunable Properties of Functional Nanoparticles for Efficient Capture of VOCs Energy Technology and Environmental Science 2, 9889–9894.

Guieysse, B., Hort, C., Platel, V., Munoz, R., Ondarts, M., and Revah, S. (2008). Biological treatment of indoor air for VOC removal: Potential and challenges. Biotechnology Advances, 26, 398–410.

Hussain, M., He, Y.-L., Mohamad, A. A., and Tao, W.-Q. (2015). A new hybrid algorithm for numerical simulation of VOC emissions using single-layer and multilayer approaches Taylor and Francis, 67, 211-229.

Jung, Y., Kim, Y., Seol, H.-S., Lee, J.-H., and Kwon, J.-H. (2021). Spatial Uncertainty in Modeling Inhalation Exposure to Volatile Organic Compounds in Response to the Application of Consumer Spray Products. International Journal of Environmental Research and Public health, 18(5334).

Kumar, A., Singh, B., Monika, P., Deepak, S., Krishan, K., and Jain, V. K. (2014). Assessment of indoor air concentrations of VOCs and their associated health risks in the library of Jawaharlal Nehru University, New Delhi. Springer, 2240-2243.

Mohammadi, M., and Calautit, J. (2021). Impact of ventilation strategy on the transmission of outdoor pollutants into indoor environment using CFD. Sustainability, 13(18), 10343.

Panagopoulos, I., Karayannis, A., Kassomenos, P., and Aravossis, K. (2021). A CFD simulation study of VOC and formaldehyde indoor air pollution dispersion in an apartment as part of an indoor pollution management plan. Paper presented at the 2nd International CEMEPE, SECOTOX Conference, Mykonos.

Śmiełowska, M., Marć, M., and Zabiegal, B. (2017). Indoor air quality in public utility

Szczepanik-Scislo, N., and Scislo, L. (2021). Comparison of CFD and Multizone Modeling from Contaminant Migration from a Household Gas Furnace. Atmosphere, 12(79), 1-11.

Titiana, A. M., Andy, V. d. D., Marc, O., and Bluyssen, P. M. (2019). A review of green systems within the indoor environment. Indoor and and Built Environment, 28(3), 298-306.

Tsai, J.-H., Lu, Y.-T., Chung, and Chiang, H.-L. (2020). Traffic-Related Airborne VOC Profiles Variation on Road Sites and Residential Area within a Microscale in Urban Area in Southern Taiwan. Atmosphere, 1-7.

Tsai, W.-T. (2016). Toxic Volatile Organic Compounds (VOCs) in the Atmospheric Environment: Regulatory Aspects and Monitoring in Japan and Korea. Environment, 3(23), 1-7.

Tsigonia, A., Lagoudi, A., Chandrinou, S., Linos, A., Evlogias, N., and Alexopoulos, E. C. (2010). Indoor air in beauty salons and occupational health exposure of cosmetologists to chemical substances. International journal of environmental research and public health, 7(1), 314-324.

Vilčeková, S., Kapalo, P., Mečiarová, Ľ., Burdová, E. K., and Imreczeová, V. (2017). Investigation of indoor environment quality in classroom-case study. Procedia engineering, 190, 496-503.

APPENDICES

The outer dimension of the geometry used for Figure A1

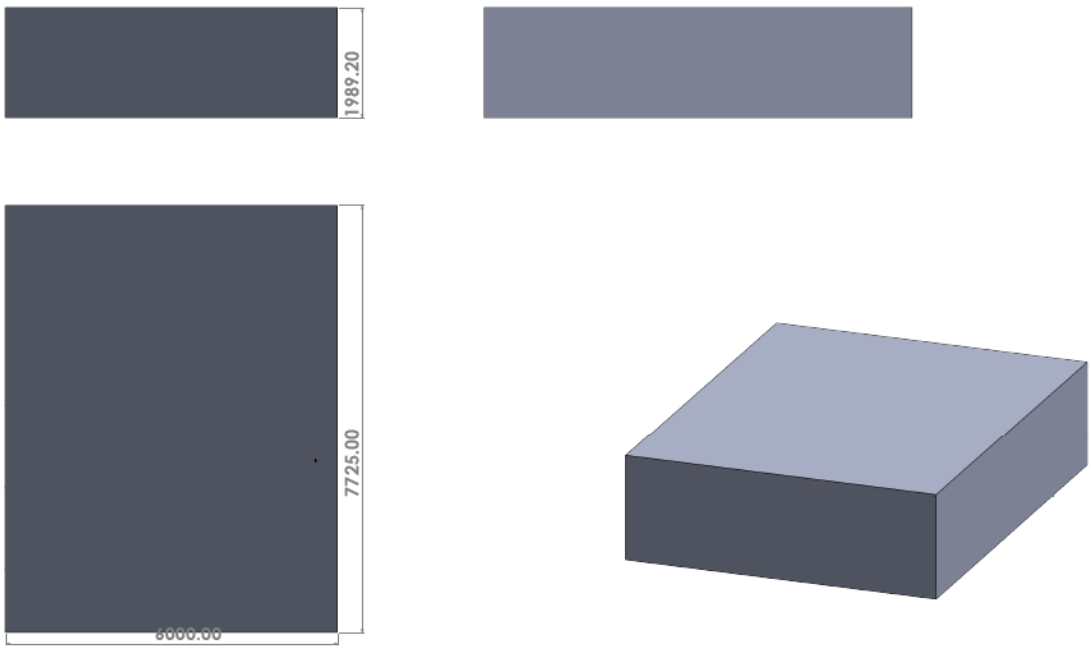

Figure A1: Dimension of the proposed geometry

PAPER 104 – VALUE-ADDED SESAME (*Sesamum indicum*) SEED CANDY QUALITY PREDICTION

O. A. Salihu[1*], S. T. Olorunsogo[1]

Department of Agricultural and Bioresources Engineering, Federal University of Technology, Minna, Niger State, Nigeria
[*]Email: onimisi.a.salihu@gmail.com

ABSTRACT
Sesame seed candy is a confection of sesame seeds and sugar or honey pressed into a bar or ball. This study focuses on the prediction of value-added sesame seed candy quality. Statistical design of experiment (DOE) method and response surface methodology (RSM) were adopted, mixture-process optimal design (I-optimal) was utilized to systematically vary the level of ingredients and processing parameters to identify the optimal combinations that leads to the highest quality of sesames seed candy. The proportion of ingredients (independent variables) taken were sesame seed (40 – 70%), ginger (10 – 30%), cinnamon (10 – 30%), and honey (10 – 30%) while the processing factor were roasting temperature (100 – 150ºC) and roasting time (10 – 30mins). Quality indexes of candy and sensory evaluation panels were used to evaluate the quality of the candy. Design Expert Software was used for the design and analysis of the experimental data. The qualities of the sesame seed candy are optimum at 62.133% sesame seed, 10% ginger, 15% cinnamon, 17.867% honey, 100ºC roasting temperature and 17.092 minutes of roasting time, the result obtained indicate that response surface methodology can accurately predict the quality of sesame seed candy.

KEYWORDS: Sesame seed candy, Quality prediction, Optimization, Quality indexes, Fortification

1. INTRODUCTION

Sesame (*Sesamum indicum*) is a flowering plant in the genus *Sasamum*, also called *beniseed*. It is cultivated for its edible seeds, which grow in pods. Sasame seed is one of the oldest oilseed crops known. It has one of the highest oil contents of any seed. Sesame has been regarded as a healthy snacks for aging prevention and energy increasing (Obiamaka, 2019). Candy is distinguished by the substantial use of sugar or sugar substitutes like honey. Sesame seed is rich in fat, protein, carbohydrates, fibre and some minerals. (Tunde-Akintunde *et al.*, 2012). As a deciding factor in snacks selection, quality is gaining importance. Snacks product quality is crucial in influencing whether consumers will repurchase a product. From a business perspective, it often makes sense to compete on quality rather than price. A quality-based approach, however, can only be effective if the business understands what the customers means by a high-quality product and can convert these requirements into product specifications. By understanding the relationship between perceived snacks quality and production and distribution processes, candy and other snack processing businesses will be able to predict, manage, and improve product quality.(Tijskens *et al.*, 2001).

Due to dietary, nutritional, or medical problems, many consumers also rely on manufacturing and processing standards, particularly to know what ingredients are there. In addition to ingredient quality, there are sanitary standards. To provide the safest possible snacks for the consumer, it is crucial to keep the environment where snacks is processed as clean as possible (Mayounga, 2018). Organoleptic properties are the characteristics and features of snacks that influence customer acceptability. Because everyone's definition of a good snack differs, it is hard to put a number on it. Snacks may be loved or disliked due to a variety of reasons, including certain expectations for its look, texture, flavor, and aroma as well as religious, cultural, social, psychological, or health-related considerations (Klaus, 2005). Customers are typically concerned that a snack product's quality meets a consistent level, which can be determined by looking at its organoleptic characteristics. Therefore, snacks makers, caterers, farmers, and producers must be able to uphold specific objective quality criteria (Schaschke, 2011).

Due to insufficient information about sesame seed candy quality, it can be challenging for modern snack processing companies to predict if sesame seed candy will be accepted by consumers. Unlike other common snack products, little is known about the manufacturing process, nutritional quality, and overall acceptability of sesame seed candy. Since sesame seed candy is made locally, neither the basic procedures nor the quantities of materials like sugar or honey are quantified. Therefore, it is necessary to design an experiment to determine the candy's quality and to research the impact of the mixture's ingredients and processing variables on that quality.

Sesame seed candy traditionally involve just three ingredients such as sesame seed, sugar and honey. However, this ingredient may not be enough to meet the dietary requirement of the consumer. Hence, there is need to fortify the product. Candy fortification is the practice of adding ingredients that will inject vitamins and minerals to commonly consumed candies during processing to increase their nutritional value (Olson *et al.*, 2021). It is a

proven, safe and cost-effective strategy for improving diets and for the prevention and control of micronutrient deficiencies. For the purpose of this research, ginger and cinnamon has been choosing as a fortifier for sesame seed candy production, the objective of this study was to determine the effect of mixture components and processing factors on the quality of value-added sesame seed candy as well as developing a model that can help to predict those quality.

2. THEORETICAL ANALYSIS

Response surface methodology (RSM) is concerned with the development of an empirical relationship between a response variable y and a set of control variables, x_1, x_2 …, x_k, that represents levels of quantitative factors believed to affect the response values. Such a relationship can be approximately represented by a polynomial model, typically of the first degree or the second degree in x_1, x_2, …, x_k. The model is then fitted to a data set generated by observing y at certain values of the control variables, referred to as locations, with an experiment region denoted by R (Andre & Siuli, 2015). If the fitted model is determined by an adequate representation of the response, then it can be used to predict the response at locations with R, that is, for given settings of the control variables.

3. MATERIALS AND METHODS

3.1 Materials

The materials used for this research are; Sesame (*Sesamum indicum*) seed, ginger, cinnamon and honey. The materials for this study were purchased from Kure market in Minna, Niger State. The preparation of sesame seed candy was carried out at the department of Agricultural and Bioresources Engineering laboratory, while the analysis was carried out at the department of Food Science and Technology laboratory at Federal University of Technology, Minna. Prior to the experiment, the sesame seed purchased was washed to remove foreign materials and clean the seed, it was then sundried to remove the water present after washing the seed.

3.2 Experimental Design

In this research work, a mixture-process optimal design was used for a mixture with four components (sesame seed, ginger, cinnamon and honey) and two factors (roasting temperature, z_1 and roasting time, z_2). Traditionally, the basic ingredients involved in the production of sesame seed candy are the sesame seed, sugar and/or honey, in this research work, ginger and cinnamon were added as a fortifier, honey was used as an alternative to sugar because of the adverse effect of sugar to human health, hence the ingredients that form the process variables are; sesame seed (x_1), ginger (x_2), cinnamon (x_3) and honey (x_4). The four ingredient forms 100% of the total mixture.

A unique type of response surface experiment known as a mixture experiment is one in which the product being studied consists of multiple parts or ingredients. Because many products design and development operations in an industrial setting include formulation or mixture, the design of these studies is beneficial. This research utilized a mixture-process (I-optimal) design, with the objective of selecting design points that sufficiently cover the design space. (Worrapson *et al.*, 2018).

3.3 Procedure for the production of sesame seed candy

The process involves washing of the sesame seed to remove foreign materials, after washing the seeds was sundried to remove the water left. The moisture content of the seed sample was determined. The total weight of the sample was taken as 250g (i.e., 100%), the weight of the ingredient was obtained by multiplying its percentage level by the total weight of the sample, each sample were roasted at a predetermine temperature for a period of time with reference to the experimental design. The honey was boiled, ginger, cinnamon and the roasted sesame seed were added to the honey syrup. The components were mixed together until a uniform sample was obtained. The prepared sample was allowed to cool and cut into shapes for analysis and sensory evaluation.

3.4 Proximate composition and chemical properties

AOAC standard method were used to determine the proximate composition and chemical properties, the quality indexes determined include; moisture content, dietary fibre, protein, carbohydrate, fat calcium, vitamin C, gross energy. The energy value of sesame seed candy was calculated based on the content of protein, fat and carbohydrate using the formula described by (Crisan & Sands, 2008). The gross energy is obtained using Equation 1.

$$\text{Gross energy (Kcal)} = (4 \times \%\ \text{protein}) + (4 \times \%\ \text{carbohydrate}) + (9 \times \%\ \text{fat}) \quad (1)$$

3.5 Sensory Evaluation

Fifty (50) sesame seed candy samples were subjected to sensory evaluation. Sensory evaluation is necessary as it help to determine the acceptability of the candy product. A total of thirty (30) untrained panelist majorly students of Federal University of Technology, Minna was used for the evaluation. The parameters that were evaluated

includes; hardness, taste, and overall acceptability. The 9-point hedonic scale was adopted for the evaluation and the resulting data were analyzed. (Sukanya & Michael, 2014).

3.6 Statistical Analysis

The obtained data were analyzed using Design Expert Software (v13.0). Each response variable will generate one model which is suggested by the program. The feasibility of the model is shown by coefficient of determination (R^2) and the significance of F-value of each variable factor. A good model has a significant value to the response and not significant value to the lack of fit, R^2 value and adjusted-R^2. In addition, the analysis of variance can also show the influence of combination to the factor by evaluating its F-value.

4. RESULTS AND DISCUSSION

Predictive models were generated for each response variables. The feasibility of the model is shown by coefficient of determination (R^2) and the significance of F-value of each variable factor. The analysis of variance also shows the influence of combination of the factors by evaluating its F-value. The greater the F-value, the more significant effect. The significant effect of variable factors to responses are characterized by p-value "Prob > F" which is less than 0.05. The statistical analysis on the proximate composition and sensory evaluation of the value-added sesame seed candy based on the experimental design are presented in the section. Backward elimination regression was used to choose the best model with p-value of 0.05 below as selection criteria.

4.1 Results

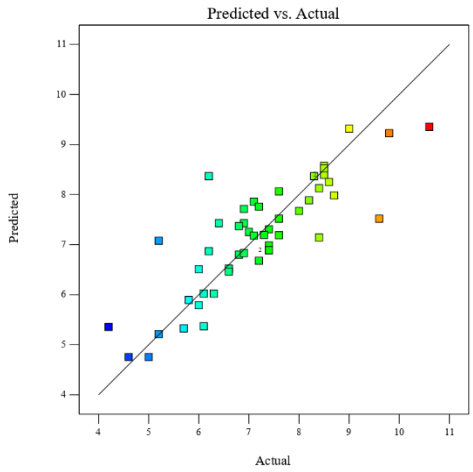

Fig 1(a): Moisture Content

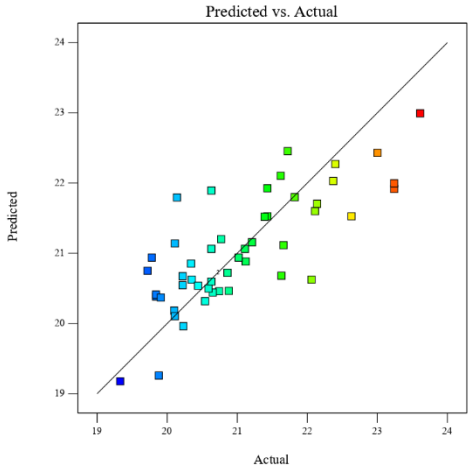

Fig 1(b): Dietary Fibre

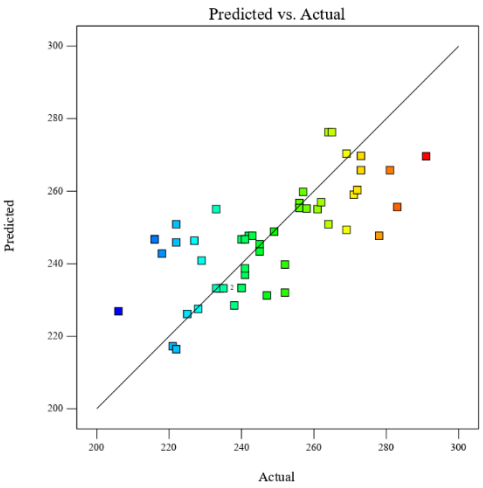

Fig 1 (c): Calcium

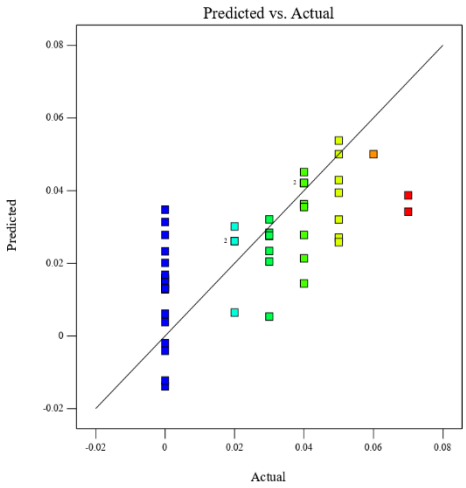

Fig 1(d): Vitamin C

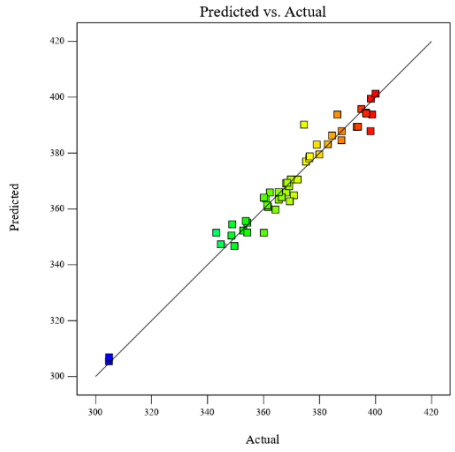

Fig 1(e): Energy Value

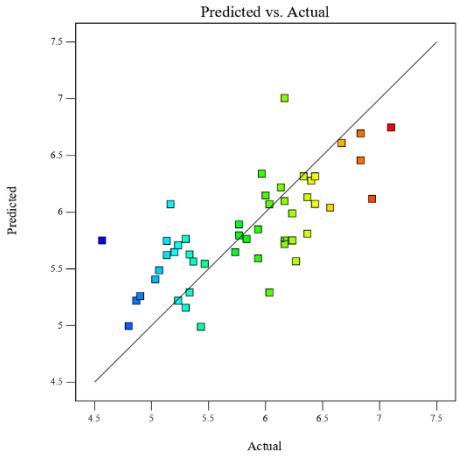

Fig 1(f): Hardness

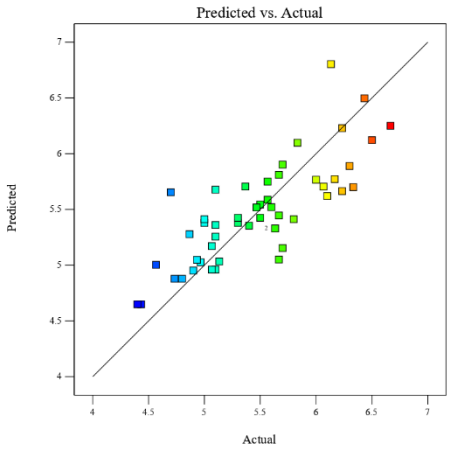

Fig 1(g): Taste

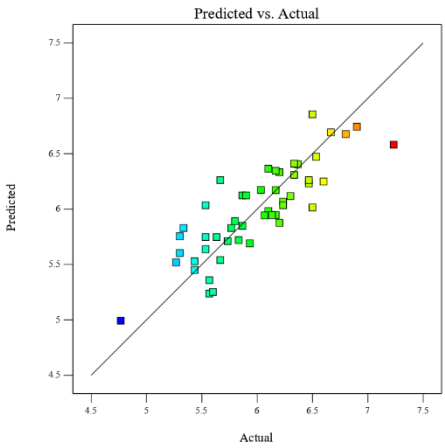

Fig 1(h): Overall acceptability

4.2 Discussion

From the analysis of variance, the F-value of 11.32 and p-value less than 0.0001 suggest that model terms (sesame seed, ginger, cinnamon, honey, roasting temperature and time) are significant since the p-value is less than 0.05. However, the interaction between the mixture components and the process variables do not have any significant effect on the moisture content. Equation 1 shows the model equation for the moisture content.

$$\text{Moisture Content} = 0.0643818\,x_1 + 0.0268625\,x_2 + 0.369692\,x_3 - 0.0414194x_4 \quad (1)$$

The R^2 value (0.7180) and Adjusted R^2 value (0.6545) indicate that the model is accurate enough to predict the responses. The difference between the actual moisture content and the predicted moisture content (i.e., residual) is low (Fig 1(a)), this also confirmed that the model equation can accurately predict the moisture content of the candy produced. High dietary fibre helps to reduce risk of some disease this can be achieved at 40% sesame seed, 10% ginger, 30% cinnamon, 20% honey, 150ºC roasting temperature and 10 minutes of roasting time (Ferreira *et al.*, 2018). Figure 1(b) is a graphical representation of the actual value and predicted value of the dietary fibre.

$$\text{Dietary Fibre} = -0.0799852x_1 + 0.0183948x_2 - 0.0830014x_3 - 0.186289x_4 \quad (2)$$

The R^2 value (0.6025) indicate that the model is accurate enough to predict the responses. The difference between the actual and the predicted dietary fibre (i.e., residual) is low, this also confirmed that the model equation can accurately predict the dietary fibre of the candy produced. High calcium content is good for children as it help to build the bone (Zeljka *et al.*, 2015). Highest calcium of the sesame seed candy was observed at 55.532% sesame seed, 11.6166% ginger, 22.8514% cinnamon, 10% honey, 100ºC roasting temperature and 30 minutes of roasting time. Figure. 1(c) is a graphical representation of the actual value and predicted value of the calcium. Equation 3 shows the model equation for predicting the response.

$$\text{Calcium} = 4.35989x_1 + 1.06765x_2 + 3.0605x_3 - 1.86931x_4 - 0.0119723x_1z_1 + 0.0322801x_4z_1 \quad (3)$$

The R^2 value (0.4999) indicate that the model is accurate enough to predict the calcium value. The residual value i.e., the difference between the predicted and actual value implies that the model equation is accurate to predict the calcium value. Highest vitamin C was observed at 40% sesame seed, 27% ginger, 10% cinnamon, 23% honey, 150°C roasting temperature and 10 minutes of roasting time. The longer duration of roasting at high temperature decreases the vitamin C value.

$$\text{Vitamin C} = 0.000261868x_1 + 0.00140136x_2 - 0.00308364x_3 - 0.00123507x_4 + 3.03199e^{-05}x_1z_2 + 0.000147085x_3x_4 + 4.37029e^{-05}x_3z_1 - 9.98588e^{-06}z_1z_2 \quad (4)$$

The R^2 value (0.4849) indicate that the model is accurate enough to predict the responses. There is a significance difference between the actual value and the predicted value of vitamin C (Fig. 1(d)), this may be due to insufficient data obtained for the vitamin C. The interaction between the mixture components and the processing factors are also significant as they have effect of the energy value. Highest energy value of the sesame seed candy was observed at 56.765% sesame seed, 20.235% ginger, 13% cinnamon, 10% honey, 150°C roasting temperature and 30 minutes of roasting time.

$$\text{Energy Value} = 25.738x_1 - 9.82589x_2 + 71.724x_3 + 54.8312x_4 - 0.401422x_1x_2 - 1.48519x_1x_3 - 1.18194x_1x_4 - 0.210086x_1z_1 - 0.70914x_1z_2 \quad (5)$$

The R^2 value (0.9575) and Adjusted R^2 value (0.8698) indicate that the model is accurate enough to predict the responses. There is an insignificance difference between the actual energy value and the predicted energy value (see Fig 1(e)), this implies that the model equation is very accurate to predict the energy value of the candy.
The model terms and their interaction are significant and can influence the hardness value. Highest hardness of the sesame seed candy was observed at 40% sesame seed, 10% ginger, 30% cinnamon, 20% honey, 150°C roasting temperature and 30 minutes of roasting time.

$$\text{Hardness} = 0.0575342x_1 - 0.0665569x_2 + 0.0420211x_3 - 0.0328615x_4 + 0.00328169x_1x_2 \quad (6)$$

The R^2 value (0.5204) indicate that the model is accurate enough to predict the responses. There is an insignificance difference between the actual hardness and the predicted hardness (see Fig 1(f)), this implies that the model equation will accurately predict the hardness with 52% confidence. At 40% sesame seed, 10% ginger, 30% cinnamon, 20% honey, 150°C roasting temperature and 30 minutes of roasting time high taste value was observed. Figure 1(g) is a graphical representation of the actual taste value and predicted taste value.

$$\text{Taste} = 0.0618701x_1 + 0.197294x_2 + 0.0966744x_3 + 0.0476478x_4 - 0.000318411x_1z_1 - 0.00438757x_2x_3 - 0.00542719x_2x_4 - 0.00175404x_2z_2 - 0.00325655x_3x_4 + 0.00161885x_3z_2 + 0.0010889x_4z_1 \quad (7)$$

The R^2 value (0.6329) indicate that the model is accurate enough to predict the responses. The difference between the actual taste value and the predicted taste value (see Fig. 1(g)), this implies that the model equation is adequate to predict the actual value. The R^2 value (0.7130) and Adjusted R^2 value (0.6093) indicate that the data obtain doesn't fit the regression model. There is an insignificance difference between the actual overall acceptability and the predicted overall acceptability (see Fig1(h)), this implies that the model equation is adequate to predict the overall acceptability.

$$\text{Overall Acceptability} = 0.257505x_1 - 0.24364x_2 + 0.149818x_3 + 0.723593x_4 + 0.00249526x_1x_2 - 0.00548263x_1x_3 - 0.0195558x_1x_4 - 0.00141764x_1z_1 - 0.00213239x_1z_2 \quad (8)$$

5. CONCLUSIONS

Sesame seed candy is one of the snacks that is highly consumed by children and adult in remote part of Nigeria. Knowing the quality of this candy and understanding the factor that influence its quality becomes significant. The result obtained show that vitamin C is affected by the roasting temperature, the higher the roasting temperature the smaller the vitamin C value, the result also indicate that Response Surface Methodology can be used to predict the quality of sesame seed candy. It's recommended that Artificial Neural Network (ANN) analysis should be used to further predict the quality of sesame seed candy and the result obtained should be compared with that of the Response Surface Methodology (RSM).

ACKNOWLEDGEMENTS

We sincerely appreciate Mr. Audu Yohanna, a laboratory technologist in faculty of Agriculture, Federal University of Technology, Minna for taking his precious time to assist us in carrying out the practical aspect of this research work.

REFERENCES

Andre, I. K., & Siuli, M. (2015). Response Surface Experiment and Design. In D. Angel, M. Max, S. John, & B. Derek (Eds.), *Handbook of Design and Analysis of Experiment* (pp. 198 - 230).

Crisan, E. V., & Sands, A. (2008). Nutritional value of Edible Mushroom," In: S. T. Chang and W. A. Hayer, Eds., Biology and Cultivation of Edible Mushrooms, . *Academic Press, New York*(137 - 168).

Ferreira, K. C., Bento, J. A. C., de Jesus, L. S., & Bassinello, P. Z. B. (2018). Dietary Fibers: Analysis Methods. *Multidisciplinary Journal*, *5*(3), 174 - 179. Retrieved from https://doi.org/10.29247/2358-260X.2018v5i3.p174-179

Klaus, G. G. (2005). Snacks Quality and Safety: consumer perception and demand. *European Review of Agricultural Economics*, *32*(3), 369-391.

Mayounga, A. T. (2018). "Antecedents of recalls prevention: analysis and synthesis of research on product recalls." Supply Chain Forum: . *An International Journal*, *19*(3), 1 - 10. Retrieved from https://doi.org/10.1080/16258312.2018.1530575

Obiamaka, A. U. (2019). Katun Ridi, the Snack enjoyed in Kaduna State. Retrieved from https://connectnigeria.com/articles/2019/08/katun-ridi-the-snack-enjoyed-in-kaduna-state/

Olson, R., Gavin-Smith, B., Ferraboschi, C., & Kraemer, K. (2021). Snacks Fortification: The Advantages, Disadvantages and Lesson from Sight and Life Programs. *nutrients*, *13*, 1118. Retrieved from https://doi.org/10.390/nu13041118

Schaschke, C. J. (2011). *Snacks Processing*. bookboon.

Sukanya, W., & Michael, O. M. (2014). The 9-point hedonic scale and hedonic ranking in snacks science: some reappraisals and alternatives. *Journal of Science. Snacks Agric*, 1 -12. Retrieved from https://wileyonlinelibrary.com

Tijskens, L. M. M., Hertog, M. L. A. T. M., & Nicolai, B. M. (2001). Snacks Process Modelling. In (pp. 367 - 374). Woodhead Publishing Limited, Abington Hall, Abington.

Tunde-Akintunde, T. Y., Oke, M. O., & Akintunde, B. O. (2012). Sesame Seed, Oil Seeds, Dr. Uduak G. Akpan (Ed).

Worrapson, W., Chayathach, P., Thongchai, K., & Surapol, N. (2018). An Extreme Vertices Mixture Design Approach to Optimization of Tyrosinase Inhibition Effects. *Engineering Journal*, *22*(1), 175 - 185. Retrieved from http://wwww.engj.org

Zeljka, R. M.-B., Vesna, R. A., Dijana, R. J., & Tanja, M. Z. (2015). Determination of Calcium Content of Dietary Supplements. *Hrana u zdravlju i bolesti, znanstveno-strucni casopis za nutricionizam i dijetetiku*, *4*(1), 28 - 33.

PAPER 105 – ADSORPTION OF PHENOLS FROM TANNERY WASTEWATER USING MANGANESE DIOXIDE-ALBIZIA LEBBECK COMPOSITE

T. L. Adewoye [1], A. S. Atanda[1*], S. I. Mustapha[1], O. A. A. Eletta[1], A.A. Oguntuase[1], J.J. Kure[1], F.A. Aderibigbe[1], I. A. Mohammed[1]

[1]Department of Chemical Engineering, University of Ilorin, Ilorin, Nigeria.
[*]Email: sarat.morenikeji@gmail.com

ABSTRACT
This study investigated the removal of phenols from Tannery wastewater by batch adsorption process using MgO-modified adsorbent synthesized from *Albizia lebbeck* pods, which is an agricultural waste. Brunauer–Emmett-Teller (BET), scanning electron microscopy (SEM), energy dispersive X-ray spectrometry (EDS) and X-ray diffraction (XRD), characterized the unmodified Albizia lebbeck (ALC) and modified Albizia lebbeck (MAL) adsorbents synthesized. The BET surface area of the ALC and MALC were 221.5 and 255.8 m^2/g, respectively. The batch adsorption studies were conducted to investigate the effect of contact time, temperature and adsorbent dosage on the uptake of Phenol from tannery wastewater onto the adsorbents. The adsorbents showed maximum adsorption efficiencies of 79.01 and 81.21% for ALC and MALC respectively. The result from this study showed that the synthesized adsorbents were found to be effective for the treatment of tannery wastewater as the residual concentration of phenolic of the treated wastewater was very low and falls within permissible limits for effluent discharge.

KEYWORDS*:* Adsorption, Tannery wastewater, Manganese dioxide, *Albizia lebbeck*, Composite.

1. INTRODUCTION

Effluent from Industries and urbanization are major sources of water pollution in Nigeria, as process industries place little emphasis on wastewater management (UN-Water, 2011; Fouda *et al*; 2021). Industrial wastewater is disposed into water bodies partially treated or untreated posing a threat to environmental health and safety (Akpor & Muchie, 2011). Tanneries generate a large quantity of wastewater which contain chemicals, residual dyes, heavy metals, surfactants, salts, chlorinated substances, and so on low biodegradability (Oladipo *et al*., 2017;Fouda *et al*; 2021). Tannery wastewater is characterised by high salinity, high pH, heavy metals, high biochemical oxygen demand (BOD), chemical oxygen demand (COD) and phenol content as a result of organic materials in the hides and skins processed in this industry (Mohammed *et al*., 2013; Nayl *et al*., 2017; Costa & Olivi, 2009).

Phenol is a persistent organic compound formed from leather tanning process (Chaudry *et al*., 2022) which pose threat to environmental safety and water quality. Phenol and its derivatives accumulate in the fatty tissues of living organisms and exhibit highly toxic effects because they do not degrade easily. Phenol has multiple human health issues such as damage to DNA, weakening of muscles, necrotic lesions and burning in the mouth, stomach and oesophagus as well as pulse fluctuations (Bhattacharya *et al*., 2015; Chaudry *et al*., 2022). With the increasing population of Nigeria, the demand for clean water sources to engage for personal, agricultural and industrial use has risen considerably. A means of supplying this demand is to reduce pollution of natural water bodies, and improve wastewater management (UN-Water, 2018).

Researchers have used conventional methods for the treatment of wastewater (Ademiluyi, Amadi, & Amakama, 2009; Badalians Gholikandi, Baneshi, Dehghanifard, Salehi, & Yari, 2010; Mustapha *et al*., 2019). Adsorption is a very versatile process for treating industrial effluents out of all the methods. Easy-to-use, low-cost, and achievable with a wide number of materials of either mineral, organic or biological origins (Crini *et al*., 2018). Activated carbon in particular, has received tremendous attention as an adsorbent material due to its effectiveness in the adsorption of organic and inorganic pollutants from aqueous solutions. Activated carbon has a high surface area, a microporous structure, and a high degree of surface reactivity making it one of the most important industrial adsorbent materials (Bansal & Goyal, 2005). The high cost of activated carbon, however, poses the greatest obstacle to its widespread industrial use, as a treatment method must not only be effective, but must also be technologically and economically feasible (Crini *et al*., 2018).

Agricultural waste materials have received a considerable amount of attention as adsorbent materials as they are low-cost, easy to obtain, have low toxicity, and can be used to remove a variety of pollutants from industrial wastewater (Van *et al*., 2021). The complete replacement of conventional adsorbents by agricultural waste materials has, however, been impeded by the reduced specific adsorption capacities of these materials in their unmodified form compared to that of the conventional adsorbents (Do *et al*., 2019).

Manganese dioxide nanoparticles are one of several nanomaterials, which have attracted the interest of researchers for years due to their unique properties as adsorbents. The high surface area (Do *et al*., 2019) and high electrochemical activity (Zhou *et al*., 2012) of manganese dioxide nanoparticles makes them ideal as adsorbent materials. The incorporation of nanoparticles such as manganese dioxide with agricultural waste materials combines the adsorption capacities of both materials and creates a composite material with the individual characteristic of the two materials.

The objective of this study is therefore to produce a cheaper and effective adsorbent material from an agricultural waste material, *Albizia lebbeck,* and improve its performance by incorporating manganese dioxide nanoparticles.

2. THEORETICAL ANALYSIS

The reduction efficiencies of the synthesized adsorbent was determined using Equation (1).

$$\%removal = \frac{C_0 - C_e}{C_0} \times 100 \quad (1)$$

Where, C_0 and C_e (mg/l) are the concentration of phenol present in the tannery wastewater sample at the initial stage and equilibrium, respectively. The equilibrium amount (Q_e) of phenol removed per mass of adsorbent was evaluated using Equation 2.

$$Q_e = \frac{(C_0 - C_e)V}{W} \times 100 \quad (2)$$

Where, Q_e (mg/g) is the amount of phenol adsorbed per unit mass of adsorbent at equilibrium. V(l) is the volume of the solution and W(g) is the mass of the adsorbent used.

3. MATERIALS AND METHODS

3.1 Characterisation of Tannery Wastewater

The Physico-Chemical Properties of the tannery wastewater were investigated, determined and recorded using standard procedures by Nayl *et al*., (2017). The colour and smell of the wastewater were investigated by visual and olfactory examinations respectively. A pH meter was used to determine the pH and Turbidimeter was used determine turbidity. The Total Dissolved Solids (TDS) and the conductivity were estimated with a TDS meter and a conductivity meter, respectively. The COD and the BOD were determined using titrimetric methods. The dissolved oxygen analysis during the BOD test was performed using a dissolved oxygen meter. The phenol content of the wastewater was determined using a colorimetric method.

3.2 Phenol test

The phenol test was performed according to the procedure described by (Kupina et al., 2018). About 0.1 mL of the tannery water sample was measured into a test tube using a micropipette. About 0.5 mL and 0.4 mL of Folin C reagent was measured and 7.5% sodium carbonate was added sequentially to the test tube. The sample changed to a blue colour indicating the presence of phenol. The solution was allowed to stand for 30 minutes before being transferred into a cuvette. The cuvette was inserted into a spectrophotometer, and the absorbance of the solution was measured at 760 nm. The absorbance value obtained was converted to mg/L of phenol content using Equation 3:

$$y = 0.9787x \quad (3)$$

Where, y is the absorbance value measured and x is the concentration of phenol in mg/L

3.3 Preparation of leaf extract

The leaf extract was prepared according to the method used by Manik *et al.* (2020). Neem leaves were collected from the university of Ilorin premises and washed thoroughly with distilled water to remove all adhering impurities. The washed leaves was air-dried in a room away from direct sunlight. About 10 g of the cleaned leaves were placed into a 500 mL beaker containing 150 mL distilled water. The mixture was boiled at 90ºC for 20 minutes. The mixture was then cooled to room temperature and the neem leaf extract was obtained by filtering the mixture using a filter paper. The filtrate obtained was used without further modification for the synthesis

3.4 Synthesis of manganese dioxide nanoparticles

MgO nanoparticles were synthesized by hydrothermal method described by Ahmed *et al*., (2020) and Paul *et al*., (2017). About 50 mL of 0.2 M aqueous solution of potassium permanganate was prepared and mixed with 5mL of the leaf extract at 70ºC for 60 minutes with continuous stirring A brown ring was formed around the walls of the conical flask at the top of the $KMnO_4$ solution which indicates the formation of precipitate. The precipitate was then centrifuged at 3000 rpm for 15 min, and the synthesized nanoparticles were collected after the supernatant had been removed. The nanoparticles were then washed with distilled water three times to remove all impurities. The nanoparticles were dried in an oven at 100ºC for 10 h to evaporate all water (Adewoye *et al*., 2021).

3.5 Preparation of agricultural waste material

The *Albizia lebbeck* seed pods used in this study were collected from Mimosa trees located at the Faculty of Pharmaceutical Sciences in the University of Ilorin. The pods were emptied of all seeds, washed with clean water to remove all adhering dirt and other impurities, and then subsequently cleaned using a brush and distilled water. The washed pods were sun-dried for 7 days to reduce the moisture content and render them brittle enough for grinding. The dried *Albizia lebbeck* pods were ground into smaller fractions using a mortar and pestle. The ground pods were then further reduced in size using a blender. The obtained powder was sieved with 0.75µm to obtain particles of uniform size distribution. A portion of the sieved powder was calcined in a muffle furnace at 300ºC for three hours to produce the carbonized *Albizia lebbeck* pods (CAL).

3.6 Synthesis of manganese dioxide-Albizia lebbeck composite

The uncalcined *Albizia lebbeck pod powder* was modified with manganese dioxide nanoparticles via wet impregnation according to the process described by Aslam *et al*. (2019). About 5 g of the carbonizeded *Albizia lebbeck* (CAL) was dispersed in a 150 mL ethanol solution and shaken in a water bath shaker at 40ºC for 1 hour. About 1.5 g of the manganese dioxide nanoparticles were dispersed in another 150 mL ethanol solution and shaken in a water bath shaker at 40ºC for 1 hour. Afterwards, both ethanol solutions were mixed together and shaken in a water bath shaker at 40ºC for 1.5 hours to impregnate the powdered *Albizia lebbeck* with the manganese dioxide nanoparticles. The ethanol solution was evaporated by placing the beaker in an oven at 80ºC. The material obtained was then calcined in a muffle furnace at 300ºC to produce modified *Albizia lebbeck* composite adsorbent (MALC). Both the produced CAL and MALC were used for both batch adsorption studies without further modification

3.7 Characterization of the prepared adsorbent

The adsorbents prepared was characterised to determine it properties. The formation of the manganese dioxide nanoparticles was confirmed using UV-visible spectroscopy. The surface morphology of each adsorbent material was determined using scanning electron microscopy (SEM). The surface area of the composite adsorbent was determined using Brunauer-Emmet-Teller (BET) surface area analysis, the functional groups on the adsorbent were determined using Fourier Transform Infrared Spectroscopy (FTIR), and the size distribution of the adsorbent was determined using Dynamic Light Scattering (DLS) analysis (Chen *et al*., 2020).

3.8 Batch adsorption experiments

Batch adsorption experiments were carried out to determine the performance and adsorption isotherms of both adsorbents by treating a sample of tannery wastewater using phenolic content as a marker. The experiment was conducted using a 250 mL Erlenmeyer flask and a water bath shaker. The effects of contact time, temperature, and adsorbent dosage on the adsorption equilibrium were investigated. About 50 mL of the wastewater sample are filled into each of the flasks. The flasks were shaken with a sonnicator at a constant rate, allowing for sufficient mixing of the adsorbent and wastewater sample. For the effect of time experiments, the duration of shaking was varied between 10 to 90 minutes, at 20-minute intervals. The effect of temperature experiments was conducted over a range of temperatures from 30 to 55°C, with an interval of 5°C at the equilibrium time obtained from the previous experiment. The dosage of the adsorbent was varied between 0.2 to 1 g at 0.2 g intervals, at the equilibrium time and temperature obtained from the previous experiments, to determine the optimum dosage. The mixture obtained was filtered, the residual concentration of the phenol content was then analysed, and the reduction efficiencies were determined using Equation (2) .The equilibrium amount (Q_e) of phenol removed per mass of adsorbent was evaluated using equation 3.The adsorption isotherms of the adsorption of phenol unto each adsorbent were analyzed using Langmuir, Freundlich, and Temkins models. The kinetics of the adsorption experiment were determined using Pseudo first order, pseudo second order, and Elovic models.

4. RESULTS AND DISCUSSION

4.1 Characterization of tannery water

The tannery wastewater sample collected in this research is a non-viscous liquid with a large quantity of visible suspended solids and a very offensive odour. The initial colour of the wastewater on agitation is dirty purple due to the circulation of several grey suspended solids but turned to light pink when clarified. The presence of suspended solids in the wastewater may be attributed to the deposition of solid matter from the animal hide treated in the collected water sample, while the pink colour that appears on clarification of the wastewater may be ascribed to the presence of a similarly coloured dyestuff applied to the processing water for colouring the treated leather.

Prior to the adsorption experiment, the wastewater was analysed to determine its physico-chemical properties. The chemical properties of the wastewater were quantitatively analyzed and expressed as a function of its pH,

conductivity, turbidity, TDS, BOD, COD, TOC, and phenol content using standard procedures from literature. The results of the analyses and the standards set forth in the Federal Environmental Protection Agency Act of 1999 are presented in Table 1.

The pH of the wastewater at 8.33, and the COD value of the wastewater, determined to be 160 mg/L, both fall at the edge, but still within the permissible limit for effluent discharge for tanneries. The BOD of the wastewater sample is very low at 0.35, indicating a very low quantity of oxidizable organic material (Von Sperling, 2007). The total dissolved solids of the wastewater was also determined to be vastly above the permissible limit. The quantity of phenols found in the wastewater, measured to be 0.918 mg/L which is above the permissible limit for effluent discharge for tanneries, was selected as the environmental marker for the treatment procedure being an indicator of a high concentration of phenolic compounds in the wastewater. The high concentration of phenolic in the wastewater being a threat to human health and the safety of the environment.

All variations in the results of this analysis for tannery wastewater that differ from the values reported in literature may be due to local variation in manufacturing methods, processes, and processing chemicals used.

4.2 Manganese dioxide nanoparticles synthesis

The manganese dioxide nanoparticles produced via green synthesis as discussed in the previous section were analyzed to confirm their formation. Physical examination showed a brown, ultrafine solid material. The absorbance spectrum of a colloidal sample of the synthesized material was analyzed within a range of 200 – 800 nm using UV spectroscopy. The absorption spectra obtained is presented in Figure 1.

The synthesised material shows an absorbance peak value of 413 nm, implying that the synthesised material absorbs radiation in this spectrum. This is similar to the peak absorbance value reported in literature by Hoseinpour *et al*. (2018) for manganese dioxide nanoparticles. This indicates the formation of manganese dioxide nanoparticles.

4.3 Characterisation of adsorbents

The surface morphology of the prepared adsorbents was analyzed using SEM and the images obtained are presented in Fig. 1 (a) – (c).

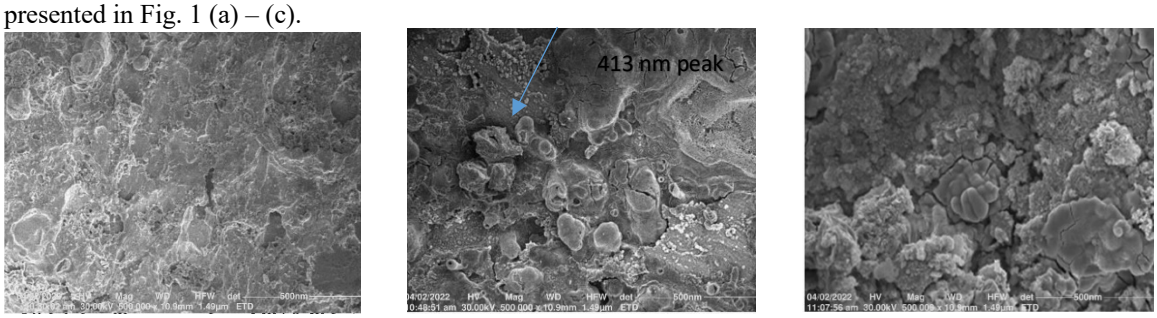

Fig. 1: SEM images for (a) manganese oxide nanoparticles (b) ALC adsorbent (c) MALC adsorbent

The images obtained from the SEM shows an enhanced image of the surface of each adsorbent. The manganese oxide nanoparticles show an almost unbroken surface as each particle is too small to be fully captured within the 500 nm range of the image. In the image for ALC and the composite, individual particles can be identified as the presence of the larger particles from the carbonized *Albizia lebbeck* are large enough to be seen individually. The surface image of ALC and MALC also bear a striking resemblance as the composite is modified from ALC.
The results obtained from the BET analysis are presented in Table 4.1.

Table 1: BET Analysis of the Prepared Adsorbents

Sample	Surface Area (m^2/g)	Pore Volume (cc/g)	Pore size (nm)
Manganese dioxide nanoparticles	127.8	0.04296	6.181
Carbonised *Albizia lebbeck* (ALC)	221.8	0.1011	6.929
Manganese dioxide-*Albizia lebbeck* composite (MALC)	255.1	0.08613	6.247

The result of the BET analysis showed a significant variation in the surface area of each adsorbent material. MALC is shown with the largest surface area, while the nanoparticle has the least. MALC is also observed to record a higher surface area than ALC, an increase that can be attributed to the additional surface area contributed by the nanomaterial added to ALC. These surface area values imply the availability of greater adsorption sites on MALC compared to ALC and the nanoparticle. Thus, in the absence of interference by functional groups on the surface of the composite, MALC was expected to perform better than ALC in an adsorption process.

There is also a variation in the pore size and pore volume of the adsorbent materials. The greatest pore volume and pore size recorded on ALC, with the lowest being recorded on the nanoparticle for both pore size and pore volume. MALC reported an intermediate value for pore size and pore volume, between the nanoparticle and ALC, which is as a result of the incorporation of the two materials. All three adsorbent materials are mesoporous, as the pore size of all three materials fall within the range of 2 – 50 nm (Zdravkov *et al*., 2007).

The results of the Dynamic Light Scattering analysis performed on each adsorbent material is recorded in Table 2.

Table 2: DLS analysis of the Prepared Adsorbents

Sample	Average hydrodynamic diameter (nm)
Manganese dioxide nanoparticles	Undefined (sample too polydispersed)
Carbonised *Albizia lebbeck* (ALC)	93.49
Manganese dioxide-*Albizia lebbeck* composite (MALC)	78.71

The DLS result revealed the average hydrodynamic diameter of each of the prepared adsorbents with the exception of the calcined manganese dioxide nanoparticles. The DLS analysis was unable to produce a definite average diameter for the nanoparticles as the sample was too polydispersed. This is one of the limitations of the DLS analysis, as a sample with widely varying size aggregates cannot be accurately measured through this technique (Tomaszewska *et al*., 2013). The dispersion of the manganese dioxide nanoparticles over a wide range of sizes is attributed to the aggregation tendency of manganese dioxide particles in solution. Individual particles clump together to form a larger particle. Thus, an additional technique may be required to accurately describe the size distribution of the manganese dioxide nanoparticles.

Both ALC and MALC report more favourable results in terms of the average hydrodynamic diameter, with both adsorbents showing a size distribution in the nanometre range. MALC reports the lower average diameter value of 78.71 nm, while ALC reports a slightly higher value of 93.49 nm. This is reasonable, as MALC is a composite of raw *Albizia lebbeck* and manganese dioxide nanoparticles. Thus, the lower average diameter may be attributed to the presence of the nanoparticles that was incorporated with the *Albizia lebbeck*.

4.4 Fourier Transform Infrared Spectroscopy (FTIR)

FTIR analysis revealed the functional groups present on each of the prepared materials. The results of the FTIR analysis performed on each adsorbent material is recorded in Figure A2. The FTIR spectra of the calcined manganese dioxide nanoparticle shows a broad absorption band between 3500 to 2500 cm^{-1}, with a peak at 3411.08 cm^{-1} which may be attributed to the stretching vibration of a hydroxyl group. The presence of the hydroxyl group is confirmed by the presence of a C-O group at 1052.24 cm^{-1}. The peaks appearing at the fingerprint region below 1500 cm^{-1} are compared to FTIR peaks obtained in the works of Hoseinpour *et al*. (2018) and Moon *et al*. (2015) to validate the appearance of an O-Mn-O bond. The peak at 526.65 cm^{-1} is related to the vibration of an O-Mn-O bond, the same bond reported by the two authors at 520 and 518 cm^{-1} respectively, indicating the formation of MnO_2 particles.

The calcined *Albizia lebbeck* displayed its first absorption peak at 3072.30 cm^{-1}, a region associated with a stretching C-H bond. The C-H bond is confirmed to be a C=C bond by the presence of weak absorption at 1,600 cm^{-1}. An absorption band at 2,211.08 cm^{-1} indicates the presence of a -C≡C- stretching bond. The presence of a C-O bond is observed by the presence of absorption at 1083.91, between 1000 to 1300 cm^{-1}. The sharp strong absorption band at 871.77 cm^{-1} is assigned to a C-H bending bond ($R_2C{=}CH_2$).

The absorption spectra of manganese dioxide-*Albizia lebbeck* composite displayed a similarity to the spectra of both the calcined manganese dioxide nanoparticle and to the calcined *Albizia lebbeck.* The first absorption band appeared at 3,411.08 cm^{-1}, a peak identical to that found on the nanoparticle spectra. This peak is assigned a stretching OH bond, whose presence is confirmed by the presence of a C-O bond at 1045.91 cm^{-1}. The presence of a -C≡C- stretching bond contributed by the *Albizia lebbeck* base is identified at 2195.25 cm^{-1}. A C=O stretching bond is attributed to a peak appearing at 1793.14 cm^{-1}, and the presence of a C-H bending bond caused by a methyl group is observed at 1460.69 cm^{-1}. The peak of the absorption band at 1045.91 cm^{-1} is attributed to the presence of a C-O bond, which could have been derived from the nanoparticles or the base compound. An absorption peak also exists at 878.10 cm^{-1}, a value similar to that on the *Albizia* lebbek spectra and denoting a C-H bending bond ($R_2C{=}CH_2$). The final significant peak appears at 507.65 cm^{-1}, a region close to the 526.65 cm^{-1} reported for the calcined manganese dioxide nanoparticles. This indicates the presence of an O-Mn-O bond in the modified material.

The work of Alabi *et al*. (2016) describes functional groups that facilitate the adsorption of phenols. This includes -$OH_{stretch}$ (hydroxyl), C=$C_{stretch}$ (aromatic), C-$H_{bending}$, and C-$H_{strecth}$. Several of these are present on the materials analysed above, with the CAL adsorbent having three of the recognised groups with the exception of the -OH stretching bond.

4.5. Batch adsorption studies

4.5.1. Effect of contact time

The effect of contact time was investigated on the adsorption of phenol unto MALC and ALC in the range of 10 -90 min using 0.2 g of adsorbent in 50 mL of wastewater at 30°C as presented in Figure 2a. The removal efficiency of the both ALC and MALC increased with an increase in contact time. The removal efficiency of both adsorbents steadily increased until equilibrium was attained at 70 minutes, after which there was a sharp decrease in the removal efficiency. The decrease in removal efficiency observed in Figure 2b may be due to the filling of pores of adsorbents with water molecules (Parlayici *et al*., 2015). Hence, the retention time of 70 mins was chosen as the optimum time in this study. More so, the removal efficiency of MALC is obtained to be higher than that of ALC lower contact times, with ALC having the highest removal efficiency at equilibrium. It was also observed in adsorption studies that ALC dispersed in the wastewater remains on the surface before adsorption and it settle in the bottom of the flask after adsorption. This could be due to the increase in mass of the ALC particles due to the adsorption of phenol fact that the adsorbent is completely saturated and becomes heavier in weight.

4.5.2. Effect of temperature

Temperature has strong effect on the intermolecular force between the adsorbate and the adsorbent particles. Effect of temperature on the adsorption process was investigated and the result obtained are presented in Fig. 2b. An increase in the temperature causes a decrease in the efficiency of both ALC and MALC for phenol removal as shown in Fig. 2c. This inverse relationship indicated that the adsorption process is an exothermic process (Edet & Ifelebuegu, 2020). The decrease in adsorption capacity is due to the fact that at low temperatures, the kinetic energy of the particle is low and the intermolecular attractive forces are strong, hence, the molecules of the adsorbate are easily and strongly attracted to the surface of the adsorbent which gives a higher adsorption efficiency and vice versa.

4.5.3. Effect of dosage on the removal of phenol.

The effect of ALC and MALC dosage on the percentage reduction of phenol was studied at 45°C for 70 min. The adsorbent dosage was varied from 0.2 – 1.0g/100 ml as shown in Figure 2b. It was observed that the reduction efficiency increased with increasing adsorbent dose until the optimum dosage of 0.8 g/50 ml for MALC and 0.8 g/50 ml for MALC and ALC and corresponding to 79.01 and 81.21%, respectively. The highest phenol removal occurred at 0.8 g in both MALC and ALC. The removal efficiency of each adsorbent increases as the dosage increases. This increase in the removal efficiency may be due to the increase in the available functional groups and the total surface area of the adsorbents. Thus, more active sites are present for the adsorption of phenol from the wastewater. ALC has a higher removal percentage than the MALC.

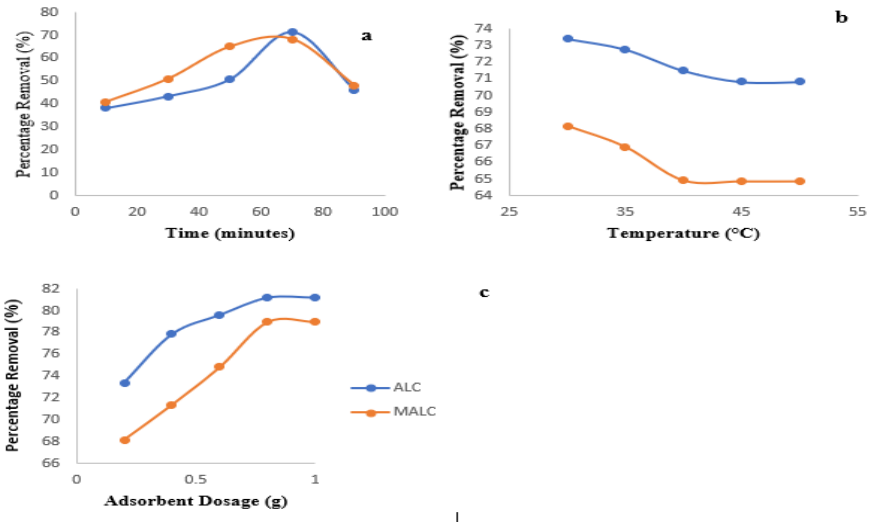

Fig. 2: Effect of (a) contact time, (b) temperature **(c)** dosage on the removal of phenol.

5. CONCLUSIONS

This study investigated the removal of phenol from Tannery wastewater by batch adsorption process using MgO-modified adsorbent synthesized from *Albizia lebbeck* pods, which is an agricultural waste. The un modified *Albizia lebbeck* (ALC) and modified *Albizia lebbeck* (MALC) adsorbent synthesized were characterized Brunauer–Emmett-Teller (BET), scanning electron microscopy (SEM), energy dispersive X-ray spectrometry (EDS) and X-ray diffraction (XRD). The BET surface area of the ALC and MALC were 221.5 and 255.8 m^2/g, respectively. The batch adsorption studies were conducted to investigate the effect of contact time, temperature and adsorbent dosage on the uptake of Phenol from tannery wastewater onto the adsorbents. The adsorbents showed maximum adsorption efficiencies of 79.01 and 81.21% for ALC and MALC respectively. The result from this study showed that the synthesized adsorbents were found to be effective for the treatment of tannery wastewater as the residual concentration of phenolic of the treated wastewater was very low and falls within permissible limits for effluent discharge.

ACKNOWLEDGEMENTS

We would like to express our gratitude to all those who have contributed to this research paper. Without your hardwork, expertise and dedication, this research would not have been possible.

REFERENCES

Achak, M., Elayadi, F., & Boumya, W. (2019). Chemical coagulation/flocculation processes for removal of phenolic compounds from olive mill wastewater: a comprehensive review. *Am. J. Appl. Sci*, *16*(3), 59-91.

Adewoye, T., Ogunleye, O., Abdulkareem, A., Salawudeen, T., & Tijani, J. (2021). Optimization of the adsorption of total organic carbon from produced water using functionalized multi-walled carbon nanotubes. *Heliyon*, *7*(1), e05866.

Ado, A., Tukur, A. I., Ladan, M., Gumel, S. M., Muhammad, A. A., Habibu, S., & Koki, I. B. (2015). A review on industrial effluents as major sources of water pollution in Nigeria. *Chemistry Journal*, *1*(5), 159-164.

Ahmed, M., Janyo, N., Sudi, I. Y., Gabriel, S., & Joh, I. (2020). Green Synthesis of Manganese Oxide Nanoparticles from Cassia ora Leaves and its Toxicological Evaluation. *Asian Journal of Applied Sciences*, *13*, 60-67. https://doi.org/10.3923/ajaps.2020.60.67

Akpor, O., & Muchie, B. (2011). Environmental and public health implications of wastewater quality. *African Journal of Biotechnology*, *10*(13), 2379-2387.

Al-Anber, M. A. (2011). *Thermodynamics approach in the adsorption of heavy metals*. IntechOpen.

Alabi, A. H., Buhari-Alade, A. I., Sholaru, F. O., & Awoyemi, R. F. (2016). Biosorption of phenols and dyes on Albizia lebbeck (Rattle seed) pod: equilibrium and kinetic studies. *International Journal of Environmental Sciences*, *5*(3), 154-165.

Alam, M. Z., Ahmad, S., & Malik, A. (2009). Genotoxic and mutagenic potential of agricultural soil irrigated with tannery effluents at Jajmau (Kanpur), India. *Archives of environmental contamination and toxicology*, *57*(3), 463-476.

Alam, M. Z., Ahmad, S., Malik, A., & Ahmad, M. (2010). Mutagenicity and genotoxicity of tannery effluents used for irrigation at Kanpur, India. *Ecotoxicology and Environmental Safety*, *73*(7), 1620-1628.

Ali Khan Rao, R., & Khatoon, A. (2017). Sorption studies for Cd (II) sequestration from aqueous solution on chemically modified Albizia lebbeck. *Separation Science and Technology*, *52*(3), 435-446.

Anku, W. W., Mamo, M. A., & Govender, P. P. (2017). Phenolic compounds in water: sources, reactivity, toxicity and treatment methods. *Phenolic compounds-natural sources, importance and applications*, 419-443.

Aslam, Z., Qaiser, M., Ali, R., Abbas, A., & Zarin, S. (2019). Al2O3/MnO2/CNTs nanocomposite: Synthesis, characterization and phenol adsorption. *Fullerenes, Nanotubes and Carbon Nanostructures*.

Awad, A. M., Jalab, R., Benamor, A., Nasser, M. S., Ba-Abbad, M. M., El-Naas, M., & Mohammad, A. W. (2020). Adsorption of organic pollutants by nanomaterial-based adsorbents: An overview. *Journal of molecular liquids*, *301*, 112335.

Ayub, S., Sharma, P. K., & Tripathi, C. N. (2014). Removal of hexavalent chromium using agro and horticultural wastes as low cost sorbents from tannery wastewater: A review. *International Journal of Research in Civil Engineering, Architecture & Design*, *2*(3), 21-35.

Bakar, A. F. A., & Halim, A. A. (2013). Treatment of automotive wastewater by coagulation-flocculation using poly-aluminum chloride (PAC), ferric chloride (FeCl 3) and aluminum sulfate (alum). AIP conference proceedings,

Bernard, E., Jimoh, A., & Odigure, J. (2013). Heavy metals removal from industrial wastewater by activated carbon prepared from coconut shell. *Res J Chem Sci*, *2231*, 606X.

Bhattacharya, A., Gupta, A., Kaur, A., & Malik, D. (2015). Simultaneous bioremediation of phenol and Cr (VI) from tannery wastewater using bacterial consortium. *International Journal of Applied Sciences and Biotechnology*, *3*(1), 50-55.

Bonilla-Petriciolet, A., Mendoza-Castillo, D. I., & Reynel-Ávila, H. E. (2017). *Adsorption processes for water treatment and purification*. Springer.

Chandra, R., Bharagava, R. N., Kapley, A., & Purohit, H. J. (2011). Bacterial diversity, organic pollutants and their metabolites in two aeration lagoons of common effluent treatment plant (CETP) during the degradation and detoxification of tannery wastewater. *Bioresource technology*, *102*(3), 2333-2341.

Chittoo, B. S., & Sutherland, C. (2020). Column breakthrough studies for the removal and recovery of phosphate by lime-iron sludge: Modeling and optimization using artificial neural network and adaptive neuro-fuzzy inference system. *Chinese Journal of Chemical Engineering*, *28*(7), 1847-1859.

Crini, G., Lichtfouse, E., Wilson, L. D., & Morin-Crini, N. (2018). Adsorption-oriented processes using conventional and non-conventional adsorbents for wastewater treatment. In *Green adsorbents for pollutant removal* (pp. 23-71). Springer.

Cueva-Orjuela, J. C., Hormaza-Anaguano, A., & Merino-Restrepo, A. (2017). Sugarcane bagasse and its potential use for the textile effluent treatment. *Dyna*, *84*(203), 291-297.

Do, Q. C., Choi, S., Kim, H., & Kang, S. (2019). Adsorption of lead and nickel on to expanded graphite decorated with manganese oxide nanoparticles. *Applied Sciences*, *9*(24), 5375.

Doble, M. (2007). Perry's chemical engineers' handbook. In: McGraw-Hill, New York, USA.

Durai, G., & Rajasimman, M. (2011). Biological treatment of tannery wastewater-a review. *Journal of Environmental science and Technology*, *4*(1), 1-17.

Ghosh, S., & Bandyopadhyay, A. (2017). Adsorption of methylene blue onto citric acid treated carbonized bamboo leaves powder: Equilibrium, kinetics, thermodynamics analyses. *Journal of molecular liquids*, *248*, 413-424.

Hadi, S. M., Al-Mashhadani, M. K., & Eisa, M. Y. (2019). Optimization of dye adsorption process for Albizia lebbeck pods as a biomass using central composite rotatable design model. *Chemical Industry and Chemical Engineering Quarterly*, *25*(1), 39-46.

Hoseinpour, V., Souri, M., & Ghaemi, N. (2018). Green synthesis, characterisation, and photocatalytic activity of manganese dioxide nanoparticles. *Micro & Nano Letters*, *13*(11), 1560-1563.

Jiang, J.-Q. (2015). The role of coagulation in water treatment. *Current Opinion in Chemical Engineering*, *8*, 36-44.

Joshi, N. C., Joshi, E., & Singh, A. (2020). Biological synthesis, characterisations and antimicrobial activities of manganese dioxide (MnO2) nanoparticles. *Research Journal of Pharmacy and Technology*, *13*(1), 135-140.

Karunarathne, H., & Amarasinghe, B. (2013). Fixed bed adsorption column studies for the removal of aqueous phenol from activated carbon prepared from sugarcane bagasse. *Energy Procedia*, *34*, 83-90.

Kupina, S., Fields, C., Roman, M. C., & Brunelle, S. L. (2018). Determination of total phenolic content using the Folin-C assay: Single-laboratory validation, First action 2017.13. *Journal of AOAC International*, *101*(5), 1466-1472.

Liu, C., Ding, R., & Xie, F. (2020). Facile synthesis of manganese dioxide nanoparticles for efficient removal of aqueous As (III). *Journal of Chemical & Engineering Data*, *65*(8), 3988-3997.

Luu, T. L., Tien, T. T., Duong, N. B., & Phuong, N. T. T. (2020). Tannery wastewater treatment after biological pretreatment by using electrochemical oxidation. In *Frontiers in Water-Energy-Nexus—Nature-Based Solutions, Advanced Technologies and Best Practices for Environmental Sustainability* (pp. 161-163). Springer.

Manasa, R. L., & Mehta, A. (2020). Wastewater: Sources of Pollutants and Its Remediation. *Environmental Biotechnology*, *2*, 197-219.

Manik, U., Nande, A., Raut, S., & Dhoble, S. (2020). Green synthesis of silver nanoparticles using plant leaf extraction of Artocarpus heterophylus and Azadirachta indica. *Results in Materials*, *6*, 100086.

Mariod, A. A., Saeed Mirghani, M. E., & Hussein, I. (2017). Chapter 41 - Albizia lebbeck (L. Benth.) Lebbeck Tree Seed. In A. A. Mariod, M. E. Saeed Mirghani, & I. Hussein (Eds.), *Unconventional Oilseeds and Oil Sources* (pp. 277-281). Academic Press. https://doi.org/https://doi.org/10.1016/B978-0-12-809435-8.00041-X

Masoud, M. S., El-Saraf, W. M., Abdel-Halim, A. M., Ali, A. E., Mohamed, E. A., & Hasan, H. M. (2016). Rice husk and activated carbon for waste water treatment of El-Mex Bay, Alexandria Coast, Egypt. *Arabian Journal of Chemistry*, *9*, S1590-S1596.

Mohammed, H., Hamza, A., Adamu, I., Ejila, A., Waziri, S., & Mustapha, S. (2013). BOD5 removal from tannery wastewater over ZnO-ZnFe2O4 composite photocatalyst supported on activated carbon. *Journal of Chemical Engineering and Materials Science*, *4*(6), 80-86.

Moon, S. A., Salunke, B. K., Alkotaini, B., Sathiyamoorthi, E., & Kim, B. S. (2015). Biological synthesis of manganese dioxide nanoparticles by Kalopanax pictus plant extract. *IET nanobiotechnology*, *9*(4), 220-225.

Mustapha, S., Shuaib, D., Ndamitso, M., Etsuyankpa, M., Sumaila, A., Mohammed, U., & Nasirudeen, M. (2019). Adsorption isotherm, kinetic and thermodynamic studies for the removal of Pb (II), Cd (II), Zn (II) and Cu (II) ions from aqueous solutions using Albizia lebbeck pods. *Applied water science*, *9*(6), 1-11.

Nayl, A. E. A., Elkhashab, R. A., Malah, T. E., Yakout, S. M., El-Khateeb, M. A., Ali, M. M. S., & Ali, H. M. (2017). Adsorption studies on the removal of COD and BOD from treated sewage using activated carbon prepared from date palm waste. *Environment Science Pollution Resources*, 1-10.

Okereke, J., Ogidi, O., & Obasi, K. (2016). Environmental and health impact of industrial wastewater effluents in Nigeria-A Review. *International Journal of Advanced Research in Biological Sciences*, *3*(6), 55-67.

Oladipo, A. A., Adeleye, O. J., Oladipo, A. S., & Aleshinloye, A. O. (2017). Bio-derived MgO nanopowders for BOD and COD reduction from tannery wastewater. *Journal of water process engineering*, *16*, 142-148.

Oubagaranadin, J. U. K., & Murthy, Z. (2011). Activated carbons: Classifications, properties and applications. *Activated Carbon: Classifications, Properties and Applications. Nova Science Publishers Inc, USA*, 239-266.

Patel, H. (2019). Fixed-bed column adsorption study: a comprehensive review. *Applied water science*, *9*(3), 1-17.

Ranade, V. V., & Bhandari, V. M. (2014). *Industrial wastewater treatment, recycling and reuse*. Butterworth-Heinemann.

Rocha, P. D., Franca, A. S., & Oliveira, L. S. (2015). Batch and column studies of phenol adsorption by an activated carbon based on acid treatment of corn cobs. *International Journal of Engineering and Technology*, *7*(6), 459.

Samarghandi, M. R., Al-Musawi, T. J., Mohseni-Bandpi, A., & Zarrabi, M. (2015). Adsorption of cephalexin from aqueous solution using natural zeolite and zeolite coated with manganese oxide nanoparticles. *Journal of molecular liquids*, *211*, 431-441.

Saxena, G., Chandra, R., & Bharagava, R. N. (2016). Environmental pollution, toxicity profile and treatment approaches for tannery wastewater and its chemical pollutants. *Reviews of Environmental Contamination and Toxicology Volume 240*, 31-69.

Sonune, A., & Ghate, R. (2004). Developments in wastewater treatment methods. *Desalination*, *167*, 55-63.

Tatah, V., Ibrahim, K., Ezeonu, C., & Otitoju, O. (2017). Biosorption kinetics of heavy metals from fertilizer industrial waste water using groundnut husk powder as an adsorbent. *J Appl Biotechnol Bioeng*, *2*(6), 221-228.

Tien, C. (2018). *Introduction to adsorption: Basics, analysis, and applications*. Elsevier.

Tomaszewska, E., Soliwoda, K., Kadziola, K., Tkacz-Szczesna, B., Celichowski, G., Cichomski, M., Szmaja, W., & Grobelny, J. (2013). Detection limits of DLS and UV-Vis spectroscopy in characterization of polydisperse nanoparticles colloids. *Journal of Nanomaterials*, *2013*.

UN-Water. (2011). *Policy brief: water quality* (United Nations. Available online at: http://www. unwater. org/downloads/waterquality_policybrief. pdf, Issue.

UN-Water. (2018). *Water Quality and Wastewater* (United Nations. Available online at: https://www.unwater.org/app/uploads/2018/10/, Issue.

Van, H. T., Nguyen, L. H., Dang, N., Chao, H.-P., Nguyen, Q. T., Nguyen, T. H., Nguyen, T. B. L., Van Thanh, D., Nguyen, H. D., & Thang, P. Q. (2021). The enhancement of reactive red 24 adsorption from aqueous solution using agricultural waste-derived biochar modified with ZnO nanoparticles. *RSC Advances*, *11*(10), 5801-5814.

Von Sperling, M. (2007). *Wastewater characteristics, treatment and disposal*. IWA publishing.

Worch, E. (2021). *Adsorption technology in water treatment*. de Gruyter.

Yi, Q. (2009). *Point Sources of Pollution: Local Effects and their Control-Volume II*. EOLSS Publications.

Zdravkov, B., Čermák, J., Šefara, M., & Janků, J. (2007). Pore classification in the characterization of porous materials: A perspective. *Open Chemistry*, *5*(2), 385-395.

Zekić, E., Vuković, Ž., & Halkijević, I. (2018). Application of nanotechnology in wastewater treatment. *Građevinar*, *70*(04.), 315-323.

Zhou, D., Liu, Q., Cheng, Q., Zhao, Y., Cui, Y., Wang, T., & Han, B. (2012). Graphene-manganese oxide hybrid porous material and its application in carbon dioxide adsorption. *Chinese science bulletin*, *57*(23), 3059-3064.

Edet, U. A., & Ifelebuegu, A. O. (2020). Kinetics, isotherms, and thermodynamic modeling of the adsorption of phosphates from model wastewater using recycled brick waste. *Processes, 8*(6), 665.

APPENDICES

Table A1: Comparison of the results of wastewater characterisation with set standards by FEPA

Parameters	Sample analysis values	Permissible limit (FEPA)
pH	8.33	6 – 9
Conductivity (mS/cm)	1.425	-
Turbidity (NTU)	3.808	-
TDS (mg/L)	715	30
TOC (%)	1	-
COD (mg/L)	160	164
BOD (mg/L)	0.35	50
Phenolics (mg/L)	0.918	0.2
Pb	1.132	-
Cd	1.002	-
As	0.487	-
Cr	1.477	-
Mn	0.252	-
Fe	0.864	-
Cu	0.132	-
Zn	0.434	-

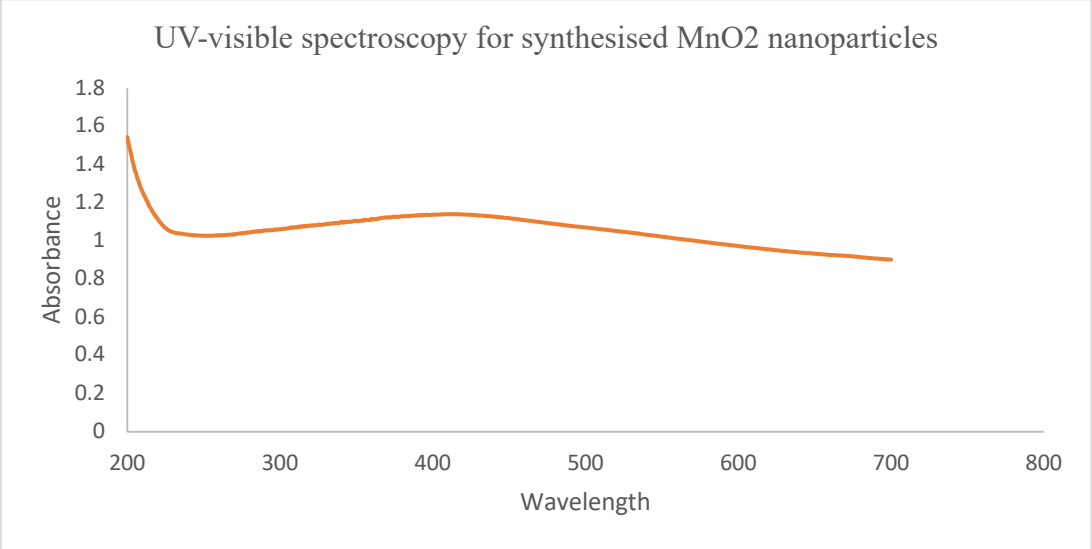

Fig. A1: UV-visible Spectroscopy for Synthesized MnO_2 Nanoparticles

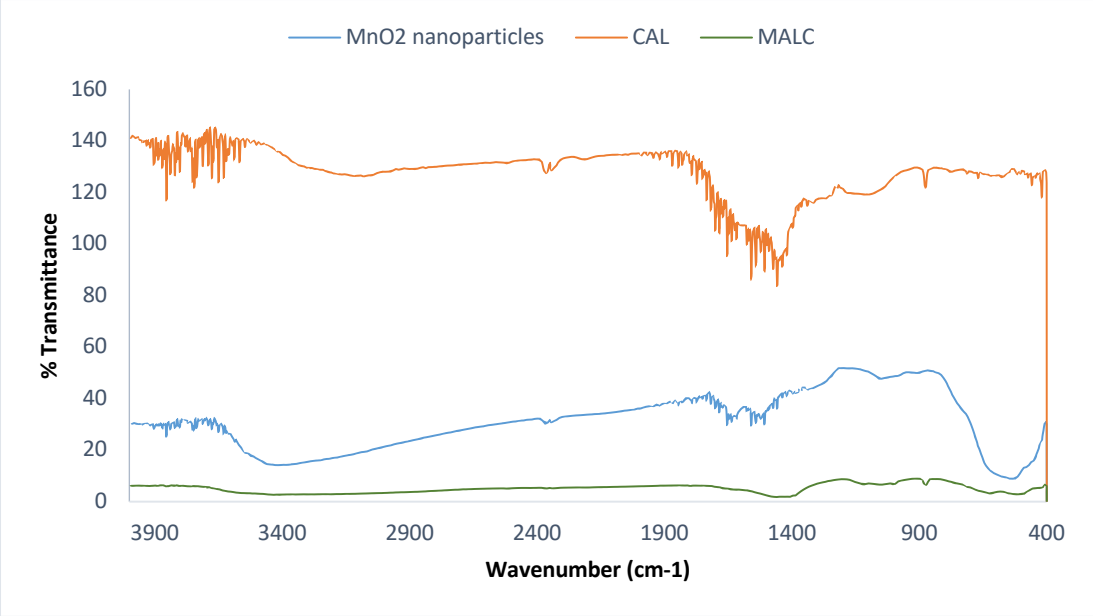

Figure A2: FTIR analysis of the MnO_2 nanoparticles, ALC and MALC

PAPER 106 – INFLUENCE OF STORAGE DURATION AND PACKAGING MATERIAL ON THE QUALITY OF VALUE-ADDED SESAME (*Sesamum indicum*) SEED CANDY

O. A. Salihu*, S. T. Olorunsogo

Department of Agricultural and Bioresources Engineering, Federal University of Technology, Minna, Niger State, Nigeria
*Email: onimisi.a.salihu@gmail.com

ABSTRACT
Sesame seed candy is a type of candy that is made by combining sesame seeds and either sugar or honey. These ingredients are then formed into a bar or ball shape through pressing. This study aimed to investigate the effect of storage duration and influence of three packaging material on the quality of value-added sesame seed candy. Sesame seed candy samples were packaged in different materials, including Aluminum Foil Laminated Pouches (AFLP), Low Density Poly Ethylene (LDPE, 400 gauges), High Density Poly Ethylene (HDPE, 700 gauges) and stored for 60 days at room temperature. Proximate analysis, sensory analysis and microbial analysis of the samples were carried out every 5 days. The storability analysis of the sesame seed candies shows that both storage duration and packaging material has influence on the total plate count with p-value less than 0.0001. The longer the duration of storage the more the growth of bacteria. The mold count is only affected by the packaging material. Based on the experimental result, aluminum foil laminated pouches are the best material to package the candy and it will still maintain some of its vital qualities over a period of time.

***KEYWORDS*:** Sesame seed candy, Storage duration, Quality indexes, Deterioration, Packaging materials.

1. INTRODUCTION

Sesame, also known as beniseed, is a flowering plant belonging to the *Sasamum genus*, and it is grown primarily for its edible seeds that develop inside pods. Sesame seeds are among the oldest oilseed crops and contain one of the highest oil contents of any seed. Sesame is widely considered a health food for promoting anti-aging and boosting energy levels.(Obiamaka, 2019). Sesame seeds are a rich source of fat, protein, carbohydrates, fiber, and several minerals. These seeds are widely known for their stability as they can resist oxidative rancidity effectively, even when they are exposed to air for extended periods (Tunde-Akintunde *et al.*, 2012). Sesame seed candy is a confectionary made by compressing sesame seeds with sugar or honey into the form of a bar or ball. It is a well-liked delicacy that is enjoyed across different regions spanning from the Middle East to East Asia, and its texture may vary between chewy and crispy (Richardson, 2002). In Nigeria, sesame seed candy is a popular snack among children. The primary components of this snack include sesame seeds, sugar, honey, and occasionally ginger, lime, orange, lemon, or cinnamon. Sesame seed candy comes in different shapes, such as

Plate 1: Sesame seed candy

cubes, cuboids, and spheres, and is commonly sold by teenage girls on the streets. Plate 1 is an image of sesame seed candy.

The production of sesame seed candy is primarily influenced by two essential factors - the roasting duration and temperature (Fernandez & DeLeon, 2017). Despite its effect on the quality of the candy, the impact of storage duration and packaging material has not been studied. Due to high demand for this product, especially among Nigerian children, and its high consumption rate, research on the shelf life of the product is necessary. This will enable the identification of an appropriate packaging material that can preserve consistent product quality and the acceptable duration for which the product can still be safely consumed.

Usually, sesame seed candy is prepared using three basic ingredients, which are sesame seeds, sugar, and honey. Nevertheless, these ingredients may not suffice to meet the dietary needs of consumers. As a result, fortification of the product is necessary. Candy fortification refers to the process of including vitamins and minerals in commonly consumed candies during processing to improve their nutritional value (Olson *et al.*, 2021). It is a well-established, safe, and economical technique for enhancing diets, preventing and managing micronutrient deficiencies. In this research, ginger and cinnamon have been selected as fortifiers for the production of sesame seed candy.

2. THEORETICAL ANALYSIS

Moisture content is a critical factor that affects the storability of agricultural commodities. High moisture content promotes the growth of microorganisms, leading to spoilage and degradation of quality. Therefore, it is essential to maintain the moisture content within the recommended range for each commodity. The percentage moisture will be calculated using the Equation 1 as given by (Christian *et al.*, 2019). This analysis will be carried out in triplicate and the average value will be recorded and used for moisture content calculation.

$$\%\ \text{Moisture} = \frac{W_1 - W_2}{W_1 - W} \times 100 \quad (1)$$

Where;

W = weight of empty crucible

W_1 = weight of sample and crucible before oven drying

W_2 = weight of sample and crucible after oven drying

3. MATERIALS AND METHODS

3.1 Materials

The materials that were used for this research are; Sesame (*Sesamum indicum*) seed, ginger, cinnamon and honey. The materials for this study were purchased from Kure market in Minna, Niger State. The storability analysis was carried out at the department of Food Science and Technology laboratory at Federal University of Technology, Minna.

3.2 Sample Preparation and production of sesame seed candy

The process involves washing of the sesame seed to remove foreign materials, after washing the seeds was sundried to remove the water left. The honey was boiled and the roasted sesame seed was added to the honey syrup. The components were mixed together until a uniform sample was obtained. The prepared sample was allowed to cool and cut into shapes for analysis and sensory evaluation. The candy samples were separated and packed in three packaging materials, the packaged samples were stored at room temperature and at an interval of 5days, the samples were taken out of the packaging materials and analyzed this process continue for 60days. Figure 3.1 is a flow chart showing the different processes involved in the production of sesame seed candy.

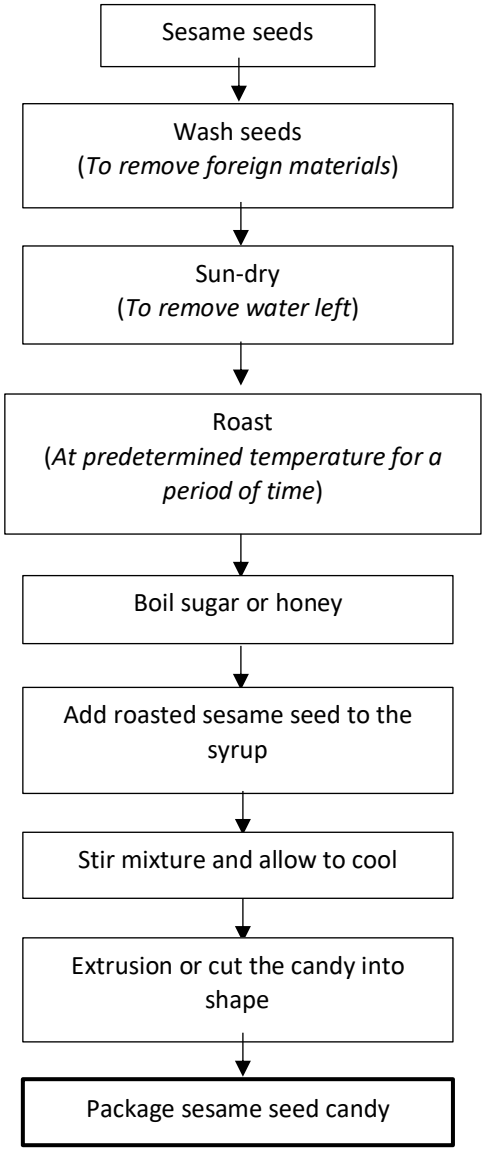

Figure 1: Sesame seed candy production process

3.3 Sensory Evaluation

Sensory evaluation of the samples was carried out every 5 days to determine the acceptability of the candy product. A total of thirty (30) untrained panelist majorly students of Federal University of Technology, Minna was used for the evaluation. The parameters that were evaluated includes; hardness, crispness and overall acceptability. The 9-point hedonic scale was adopted for the evaluation and the resulting data were analyzed. (Sukanya & Michael, 2014).

3.4 Statistical Analysis

In this research work, D-optimal point exchange design was used for a storage of 60 days with three different packaging material. The results obtained were analyzed using Design Expert Software (v13.0). The analysis of variance shows the influence of storage factors (duration of storage and packaging materials) on the candy quality by evaluating its F-value. The greater the F-value, the more significant effect. The significant effect of storage factors to the responses are characterized by p-value "Prob > F" which is less than 0.05.

4. RESULTS AND DISCUSSION

The storability analysis of the value-added sesame seed candy stored for about 60 days are presented in Table 4.1. The table shows the effect of the storage factors on the nutritional properties, microbial growth and sensory parameters, all the data presented are mean of the value obtained during experiment.

Table 1: Effect of factors on the quality of sesame seed candy

		Responses							
S_1: Storage Duration	**S_2: Packaging Materials**	**Moisture Content**	**Protein**	**Vitamin C**	**Water Activity**	**Mold Count**	**Total Plate Count**	**Hardness**	**Crispiness**
Days		%	%	mg/100g	%	CFU/g	CFU/g		
0	LDPE	4.570	17.250	0.002	8.620	0.0030	0.0000	3.500	5.000
0	HDPE	4.500	18.000	0.002	8.110	0.0040	0.0000	3.500	4.500
0	AFLP	4.460	17.630	0.001	8.310	0.0050	0.0000	4.000	4.500
0	AFLP	4.460	17.630	0.001	8.310	0.0050	0.0000	4.000	4.500
5	LDPE	4.750	17.230	0.002	8.710	0.0034	0.0000	4.000	4.000
5	HDPE	4.410	18.020	0.002	8.110	0.0042	0.0000	4.500	5.000
5	AFLP	4.480	17.610	0.002	8.130	0.0061	0.0000	5.000	4.000
10	LDPE	4.590	17.200	0.001	9.110	0.0040	0.0000	4.500	3.500
10	HDPE	4.620	18.000	0.001	8.070	0.0047	0.0010	4.500	4.000
10	AFLP	3.980	17.610	0.002	9.980	0.0068	0.0010	4.500	4.500
15	HDPE	4.470	17.980	0.001	8.280	0.0050	0.0011	4.000	4.000
15	AFLP	4.730	17.650	0.002	8.630	0.0063	0.0012	4.000	4.000
15	LDPE	4.680	17.180	0.001	9.330	0.0047	0.0016	4.000	4.000
20	HDPE	4.550	17.920	0.001	8.400	0.0055	0.0013	3.000	4.000
20	AFLP	4.980	17.830	0.001	8.710	0.0072	0.0014	3.000	4.000
20	LDPE	4.720	17.180	0.001	9.920	0.0046	0.0016	3.000	4.000
25	AFLP	4.970	17.800	0.001	8.810	0.0074	0.0014	4.500	4.500
25	LDPE	4.830	17.130	0.001	9.880	0.0042	0.0016	4.500	4.500
25	HDPE	4.590	17.720	0.001	8.450	0.0053	0.0017	4.000	4.500
30	HDPE	4.630	17.700	0.000	9.380	0.0048	0.0016	4.500	4.500
30	AFLP	5.040	17.630	0.000	8.820	0.0074	0.0016	4.000	4.500
30	LDPE	4.890	17.180	0.000	10.110	0.0050	0.0021	4.500	5.000
35	LDPE	5.060	16.150	0.000	10.240	0.0050	0.0015	4.000	4.500
35	AFLP	5.840	17.630	0.000	8.910	0.0075	0.0015	4.000	3.500
35	HDPE	5.710	17.080	0.000	10.980	0.0053	0.0027	4.500	4.000
40	AFLP	5.860	17.640	0.000	8.940	0.0069	0.0012	3.500	4.000
40	LDPE	5.490	16.000	0.000	11.210	0.0047	0.0018	4.000	4.000
40	HDPE	5.980	17.060	0.000	10.440	0.0043	0.0029	3.500	4.000
45	AFLP	5.860	17.610	0.000	10.000	0.0060	0.0013	4.000	4.500
45	LDPE	6.040	16.000	0.000	11.920	0.0050	0.0021	3.500	3.500
45	HDPE	6.980	17.000	0.000	11.240	0.0049	0.0030	4.000	4.000

50	AFLP	5.910	17.610	0.000	10.080	0.0042	0.0015	3.500	4.000
50	LDPE	6.930	15.980	0.000	13.140	0.0057	0.0028	4.000	4.000
50	HDPE	7.320	16.630	0.000	11.880	0.0040	0.0033	4.000	4.000
55	LDPE	6.970	15.330	0.000	14.720	0.0053	0.0021	4.000	4.500
55	AFLP	6.000	17.550	0.000	10.120	0.0038	0.0029	4.500	4.000
55	HDPE	7.480	16.600	0.000	12.110	0.0043	0.0033	4.000	3.500
60	LDPE	6.990	15.300	0.000	14.800	0.0053	0.0021	4.000	4.000
60	AFLP	5.920	17.500	0.000	12.250	0.0043	0.0029	4.000	4.000
60	HDPE	7.500	16.550	0.000	12.140	0.0045	0.0033	4.000	4.000

4.1 Effect of storage duration and packaging material on the quality of sesame seed candy.

The result shows that moisture content is significantly affected by storage duration and less affected by packaging materials with p-value less 0.05. However, moisture content tends to increase during storage period. Aluminum Foil Laminated Pouches gives the least moisture content of 3.98% while High Density Poly Ethylene gives the highest moisture content of 7.50% (Borchani *et al.*, 2010).

The effect of the storage condition on the protein value of the sesame seed candy is also presented in Table 4.1, the analysis of variance shows that the packaging material significantly affect the protein value of the candy with p-value less than 0.05. The result also shows that the packaging material that give high protein value is the high density poly ethylene (700 gauges) while low density poly ethylene (400 gauges) give the lease protein value. Sesame seeds is a good source of protein and a source of energy with rich assortment of minerals (Neha & Nandita, 2012).

For the vitamin C value, the result show that storage duration significantly affects the vitamin C value of the candy while the packaging material is less significant with a p-value greater than 0.05. The result also indicates that the value of vitamin C decrease consistently this may be due to exposure to oxygen during storage, trapped air in the packaging material can cause the Vitamin C value to decrease (Alvarez-Suarez *et al.*, 2015), beyond the 30th day vitamin C value were lost hence to maintain the vitamin C value the candy has to be store not beyond 30 days.

Both storage duration and packaging material significantly influence the water activity of the candy. From Table 4.1, the longer the storage duration the increase in water activity. Low density poly ethylene gives the highest water activity value of 14.8% while high density poly ethylene give the least water activity value of 8.07%.

The mold count is affected significantly by the packaging material. The storage duration does not have much influence on the bacteria growth. From Table 4.1, it is best to store the candy on low-density poly ethylene (400 gauges) as it gives the least mold count. Storing the candy on Aluminum foil laminated pouch will cause bacteria to grow and that could deteriorate the candy sample. Both storage duration and packaging material influence the total plate count. The longer the duration of storage the more the growth of fungi. Storing the candy on high density poly ethylene will encourage fungi growth as can be seen on Table 4.1. The said packaging material give a total plate count of 0.0033CFU/g.

From the Table it can be seen that the storage duration significantly affects the hardness of the candy, while packaging materials has no effect on the hardness. The longer the storage duration the harder the candy becomes. While both the storage duration and packaging materials do not have any significant effect on the crispiness of the candy. Crispness is associated with higher pitch sound made while eating a candy, it is important in candy acceptability. Thus, the food industry has to consider the necessity to control this characteristic both during production and storage (Roudaut *et al.*, 2002). Low Density Poly Ethylene material gives the lowest crispness of 3.500.

5. CONCLUSIONS

Sesame seed candy is one of the snacks that is highly consumed by children and adult in remote part of Nigeria. Knowing the quality of this candy and understanding the factor that influence its quality becomes significant. The storability analysis of the sesame seed candies also shows that both storage duration and packaging material has influence on the total plate count with p-value less than 0.0001. the longer the duration of storage the more the growth of bacteria. The mold count is only affected by the packaging material. Based on the experimental result, aluminum foil laminated pouches are the recommended material to package the candy and it will still maintain

some of its vital qualities over a period of time. Future studies can investigate the effect of other packaging materials and storage conditions on sesame seed candy quality.

ACKNOWLEDGEMENTS

We sincerely appreciate Mr. Audu Yohanna, a laboratory technologist in faculty of Agriculture, Federal University of Technology, Minna for taking his precious time to assist us in carrying out the practical aspect of this research work.

REFERENCES

Alvarez-Suarez, J. M., Giampieri, F., & Battino, M. (2015). Honey as a source of dietary antioxidants: Structures, bioavailability and evidence of protective effects against human chronic diseases. *Current Medicinal Chemistry*, *22*(34), 4279-4290. https://doi.org/doi: 10.2174/0929867322666150722105757

Borchani, C., Besbes, S., Blecker, C. H., & Attia, H. (2010). Chemical Characteristics and Oxidative Stability of Sesame Seed, Sesame Paste and Olive Oils. *Journal of Agriculture, Science and Technology*, *12*, 585 - 596.

Christian, E., E, Stanley, C., I, & Emmanuel, C., I. (2019). Proximate and Mineral Composition of Sesamum indicum L. Seed. *Medical & Analytical Chemistry International Journal*, *3*(4), 1 - 5.

Fernandez, E., & DeLeon, M. (2017). Effect of roasting conditions on sesame seed candy quality. *Journal of Food Science and Technology*, *54*(9), 2843-2849. https://doi.org/doi: 10.1007/s13197-017-2726-7

Neha, S., & Nandita, S. (2012). Wonders of Sesame: Nuteraceutical Uses and Health Benefits. 1 - 5

Obiamaka, A. U. (2019). Katun Ridi, the Snack enjoyed in Kaduna State. Retrieved from https://connectnigeria.com/articles/2019/08/katun-ridi-the-snack-enjoyed-in-kaduna-state/

Olson, R., Gavin-Smith, B., Ferraboschi, C., & Kraemer, K. (2021). Food Fortification: The Advantages, Disadvantages and Lesson from Sight and Life Programs. *nutrients*, *13*, 1118. Retrieved from https://doi.org/10.390/nu13041118

Richardson, T. H. (2002). Sweets: A History of Candy. 53 - 54. Retrieved from https://archive.org/details/sweets00timr/page/53

Roudaut, G., Dacremont, C., Valles Pamies, B., Colas, B., & Le Meste, M. (2002). Crispness: a critical review on sensory and material science approaches. *Trends inf Food Science & Technology*, *13*, 217 - 227.

Sukanya, W., & Michael, O. M. (2014). The 9-point hedonic scale and hedonic ranking in food science: some reappraisals and alternatives. *Journal of Science. Food Agric*, 1 -12. Retrieved from https://wileyonlinelibrary.com

Tunde-Akintunde, T. Y., Oke, M. O., & Akintunde, B. O. (2012). Sesame Seed, Oil Seeds, Dr. Uduak G. Akpan (Ed).

PAPER 107 – ENERGY ANALYSES OF BRIQUETTES PRODUCED FROM TORREFIED LOCALLY SOURCED GROUNDNUT SHELL

J.N. Gana[1*], J. O. Okafor[1], D. Paul[1]

Chemical Engineering Department, Federal University of Technology, PMB 65 Minna Niger State, Nigeria
*Email: jojoganny134@gmail.com

ABSTRACT
In this work, the energy analyses of Briquettes produced from locally sourced Groundnut Shell was determined and the proximate and ultimate analysis of the torrefied Groundnut Shell was carried out. In the preparation of the Briquettes (Groundnut Shell Briquette), cassava starch was used as a binder. The concentration of the binder was varied between 20 – 60 wt% while 70g of the sample was used throughout the experiment. The Calorific Values of the produced Briquettes were done using the Oxygen Bomb Calorimeter. Design Expert Central Composite design tool was used in the Design and Response Surface Methodology was used to optimize the Calorific Values of Groundnut Shell Briquettes. The Groundnut Shell Briquettes with optimized conditions were produced using 39.525 wt% binder concentrations, 57.512 seconds dwelling time and 4.316 MPa compaction pressure. The result showed that the Groundnut Shell Briquette gave 17.869 MJ/Kg Calorific Value. The Groundnut Shell Briquette gave the water boiling test and burning rate of 15.82 min and 0.22 g/min respectively. Therefore, Groundnut Shell briquette will be a good source of alternative energy since it is within the range of 17.00 MJ/kg – 24.00 MJ/kg.

KEYWORDS: Briquettes, Calorific Value, Water Boiling Test, Burning Rate, Dwelling Time.

1. INTRODUCTION

The decrease in the availability of fuel for domestic and cottage industries coupled with the ever-rising prices of non-renewable energies in developing countries such as Nigeria have necessitated alternative energy sources. Briquette is a good example of an alternative source of energy. This is because briquettes are very cheap and affordable (Ogwu *et al.*, 2014). Briquettes are produced from biomass. Biomass is a natural material of biological origin in abundance. Its abundance in nature makes it the best alternative energy source which is good for the mitigation of greenhouse gas emissions (Abdu and Sadiq, 2014). Biomass is usually plant based and popularly called cellulosic biomass (Shukla, 2015). Therefore, different types of waste have been used to form biomass briquettes. Some of the briquettes formed are briquettes from sawdust, date palm trunk, different plastic wastes, groundnut shell, coffee husk and pulp, rice husk and several other biomasses (Onukak *et al.,* 2017). Over 40 years ago, researchers have looked towards the area of biomass for its renewability, abundance and positive environmental impacts. Felling of trees poses a serious danger to the environment which should be highly discouraged and room be given to other sources of renewable energy like agricultural waste materials (Mba, 2019, Olowoyeye, 2021). Biomass in its original state is hard to handle, transport, store and use because of its high moisture content, irregular shapes, irregular sizes and low bulk density. In order to resolve these challenges, densification is adopted. Densification involves the production of densified products having uniform shapes and sizes, making it easier to handle, store and to be transported easily. This brings about cost reduction (Kumar *et al.,* 2017). This research seeks to treat, characterize, torrefy Groundnut Shell and also to optimize the Calorific Value from produced Groundnut Shell Briquettes using Design Expert after which the performance evaluation was carried out.

2. MATERIALS AND METHODS/METHODOLOGY/EXPERIMENTAL PROCEDURE

2.1 Materials

The materials used are Groundnut Shell which was obtained from Somazhiko Gboko Local Government, Niger State. Cassava Starch was used as the binder.

2.2 Equipment

Briquettes Rig, Oxygen Bomb Calorimeter, Grinding Machine, stop watch, Measuring Cylinder and Analytical Balance.

2.3 Methods

2.3.1 Treatment and characterization of the raw material

The initial treatments of the agricultural waste (Groundnut Shell) were carried out through sorting, drying, size reduction. The sorted feedstock was sun dried for 14 days and then taken for characterization: Proximate and

Ultimate analyses.

2.3.2 Torrecfaction of the treated Groundnut Shell

The agricultural wastes (Groundnut Shell) was torrefied at a temperature range of 240 – 260 ^{o}C using muffle oven for a period of an hour at NCRI Badeggi, Bida Niger State.

2.3.3 Optimization of the calorific value from produced briquettes using design expert

Design Expert Software was used for the optimization of the calorific value obtained from the briquettes which was produced from torrefied agricultural wastes. The Central Composite design (CCD), the experimental design in Response Surface Methodology (RSM) was used to obtain a second-order (quadratic) model. The design resulted in 20 Runs with Binder proportion, compaction pressure and dwelling time as independent variables and the Calorific Value of the briquettes as the response. Four replication of center points were used to predict a good estimation of errors and experiments were done in a randomized order. The actual and coded levels of each factor are shown in Table 1. The coded values were designated by -1(Minimum), 0 (Centre) and +1(Maximum) was used as adopted from (Ameh *et al.,* 2019).

Table 1 Factors for Central Composite Design for briquettes production

Factors	Units	-1	0	+1
Binding Ratio (A)	wt%	20	0	60
Dwelling Time (B)	Seconds	40	0	120
Compaction Pressure (C)	MPa	2	0	5

2.3.4. Determination of the Calorific Values of the produced Briquettes

The Calorific values of the produced briquettes (Groundnut Shell Briquettes) were determined by combusting the Briquettes with oxygen under pressure in a scaled bomb. The heat of the subsequent reaction was measured from the temperature rise of a surrounding water bath. By the calibration of the calorimeter system with thermochemical grade Benzoic Acid, the Gross Calorific value at constant volume was determined.

2.3.5 Briquetting of Pre-treated Samples

According to (Ameh *et al.,* 2019), a biomass mixture was prepared for briquettes production using a constant mass of biomass (Groundnut shells) of 70g and different concentration of binder; (20 to 60 wt.%), 145 ml of distilled water was used. Based on the design Expert used (CCD), twenty runs of briquettes of Groundnut Shells were also produced. Binders in form of paste were prepared using hot water of temperature 100^{o}C (20 to 60 wt % binder + 145 ml of hot water). At the start of the production of the briquettes, a hot water starch binder in the form of paste was added to biomass (torrefied Groundnut shells), stirred thoroughly for uniform mixture, the prepared mixture was charged into a laboratory hydraulic press machine. The briquettes mould consists of 12 dies arranged in three rows, each with dimensions of 11cm height and 7cm diameter. The mould was covered with a top plate and compressed manually at varying pressures of (2 – 5 MPa) and at varying dwelling time of (40 – 120 seconds) for briquette formation. The briquettes formed were sun dried for 14 days before further analyses.

2.3.6 Characterization of the Briquettes with optimum Calorific value

The following methods of analysis were used to characterize the briquettes:

Proximate and Ultimate analyses.

2.3.7 Thermal Analysis of the Produced Briquettes

The following analyses were carried out:

2.3.7.1 Burning rate

The burning rate was determined using insulated Biomass Stove, stopwatch and a fire source. Burning rate is the rate at which a known mass of briquette is allowed to burn completely in the presence of oxygen. The Briquette was placed in a biomass stove and lighted until it started burning. The time taken by the briquette to burn completely was recorded using the stopwatch as adopted by (Ameh *et.al.,*2019). The Burning Rate of the samples was determined using Eq. 1

$$\text{Burning Rate} = \frac{\text{Total weight of the burnt Briquettes}}{\text{Total time taken by the Briquettes}} \quad (1)$$

2.3.7.2 Ignition time

The ignition time was determined when a known mass of a briquette is ignited. This was determined using wire mesh grid, bursen burner and a fire source. The method used by (Onuegbu *et.al.*,2011) was adopted where 100 g of the Groundnut Shell briquettes was placed on a wire mesh grid in between two fire retardant bricks to allow free flow of air. A bursen burner was placed underneath the setup until the flame became blue. The burner was kept lighted until the briquettes were ignited. The ignition time was determined using Eq.2

$$\text{Ignition Time} = \text{Time the briquette is ignited} - \text{Time the burner was lighted} \quad (2)$$

2.3.7.3 Water Boiling Test

Water boiling test entails the time taken by a known mass of briquette to boil water. A biomass stove was loaded with a known mass of briquette and allow to heat water in a pot until it started boiling. The time taken by the briquettes to boil water was recorded according to (Yahaya and Ibrahim, 2012).

2.3.8 Evaluation of the produced briquette's performance

The produced briquettes were evaluated in order to examine its performance using biomass stove to cook. The Groundnut Shell Briquettes were used to cook a pot of food.

3. RESULTS AND DISCUSSION

The proximate analysis of the two samples (Groundnut Shell) is presented in the Table 2.

Table 2 Proximate Analysis of Groundnut shell

Samples	MC	AC	VM	FC
Groundnut Shell (%)	10.41	2.525	62.140	24.925

Table 2 indicates the percentage of moisture content, Ash content, volatile matter content and fixed carbon content. The table shows that Groundnut Shell volatile matter is quite high which implies that the combustion will be fast as well as the burning temperature. The groundnut shell has a very high fixed carbon content of 24.925% as compared to other agricultural wastes. This suggests that groundnut shells can be more exposed to solid combustion. This implies that groundnut shells will produce low amount of ash. This agrees with the findings of Chukwuneke *et al.* (2020)

The Ultimate analysis of the two samples (Groundnut Shell and Rice Husk) is presented in Table 2.

Table 3 Ultimate Analyses of Groundnut shell

Samples	C	H	N	O	S
Groundnut Shell (%)	62.337	5.920	1.892	27.328	0.275

Table 3 indicates the percentage of Carbon, Hydrogen, Nitrogen, Oxygen and Sulfur content. The amount of Carbon and Hydrogen content in the samples is very satisfactory as it signifies that the samples have high combustibility and can be used to produce briquettes.

3.1 Statistical and Optimization of the Calorific Value of Groundnut Shell Briquettes.

The design plan in Table 4 was employed for the statistical analysis and optimization of the calorific value of Groundnut Shell and Rice Husk Briquettes. The variables: Binding Ratio (A), Dwelling Time (B) and Compaction pressure (C) with Calorific value as the response were optimized using the coded values of the test variables.

Table 4 Results of Experimental Design Matrix for optimization of Calorific values for Groundnut Shell Briquettes

			F1	F2	F3	Response 1
Std	Run	Space Type	A: Binding Ratio	B: Dwelling Time	C: Compaction Pressure	Calorific Value
			Wt%	Seconds	MPa	MJ/kg
18	1	Center	40	80	3.5	18.7048
10	2	Axial	74	80	3.5	20.2376
11	3	Axial	40	40	3.5	15.5013
13	4	Center	40	80	3.5	18.6558
3	5	Factorial	20	120	2	17.7652
2	6	Factorial	60	40	2	19.2005
1	7	Factorial	20	40	2	12.9054

14	8	Axial	40	80	6	19.6422
5	9	Factorial	20	40	5	15.8764
20	10	Center	40	80	3.5	18.7048
15	11	Center	40	80	3.5	18.7048
7	12	Factorial	20	120	5	22.0926
6	13	Factorial	60	40	5	18.5959
19	14	Center	40	80	3.5	18.7048
17	15	Center	40	80	3.5	18.7048
12	16	Axial	40	147	3.5	18.9167
4	17	Factorial	60	120	2	18.5689
16	18	Center	40	80	3.5	18.7048
8	19	Factorial	60	120	5	18.5689
9	20	CentEdge	20	80	2	16.0987

The energy value depends on the significance of the variation of the results from process parameter combinations. The quadratic regression equation developed from the software is seen in Eq 3. This equation gives the optimum calorific value by relating it with the actual value.

$$y = -0.023911 + 0.268939A + 0.176056B + 1.74973C - 0.001834AB - 0.033082AC + 0.004085BC + 0.000396A^2 - 0.000506B^2 - 0.030206C^2 \quad (3)$$

where A = Binding Ratio; B = Dwelling Time; C = Compaction Pressure; Y = Calorific Value

The quadratic model shows how the three factors (A, B and C) affect the response (Calorific values). It comprises one-factor and multi-factor coefficients, which gives the effect of a single factor and combined effects of different factors respectively. The positive and negative terms represent synergistic and antagonistic effects respectively. In Table 4, the sequential model sum of squares gave a model F-value of 69.09 which implies that the model is significant. This level of significance justifies the fact that the proposed quadratic model is adequate. The Model is adequate since the statistic gave test of regression coefficient of R^2 = 0.9842 with adjusted R^2 value of 0.9699 and predicted R^2 value of 0.9071. The CV obtained was 1.83%. Since the Adeq Precision of 39.9650 is greater than 4, the signal is thus adequate; hence the design space can be navigated with the model (Chukwuneke *et al.*, 2020). Using the 5% significance p-value level for the analysis of variance (ANOVA), it can be seen from Table 5 that the terms A, B, C (Linear), AB, AC (Interactive) and B^2 (quadratic). Fig 1 shows the combined effect of two independent variables on the Caloric value as shown in the 3D surface plots. The interactive effect of dwelling time and binding ratio on the Calorific Value of Briquettes produced from Groundnut Shells shows that as the dwelling time and binding ratio increase, the calorific value also increases until it reaches the optimum point. The optimum point gives high quality briquettes according to the findings of Chukwuneke *et al.* (2020).

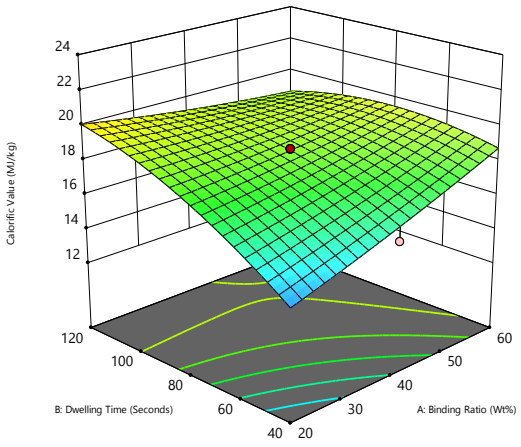

Fig. 1 Interaction effects of factors Dwelling Time and Binding Ratio

Fig 2 shows the perturbation plot where the dwelling time, binding ratio and compaction pressure influence the calorific value. Keeping the dwelling time (A) and the compaction pressure (B) constant, it was observed that as the binding ratio was increasing, the calorific value was also increasing but as soon as an optimum point was reached, the binding ratio started decreasing as well as the calorific value. This could be attributed to non-uniform

particle size of the treated groundnut shell used to produce the briquette which conforms to that of (Ameh *et al.,* 2019). Also, keeping the binding ratio and compaction pressure constant, it was observed that as the dwelling time was increasing, the calorific value was increasing. This implies that the longer the hydraulic jack presses the mixed sample, the better the calorific value. Finally, keeping the binding ratio and the dwelling time constant, the calorific values was observed to be increasing as the compaction pressure was increasing. This is a result of the particle size coming closer together to form a high quality briquette that can burn efficiently according to (Wilson *et al.*, 2017).

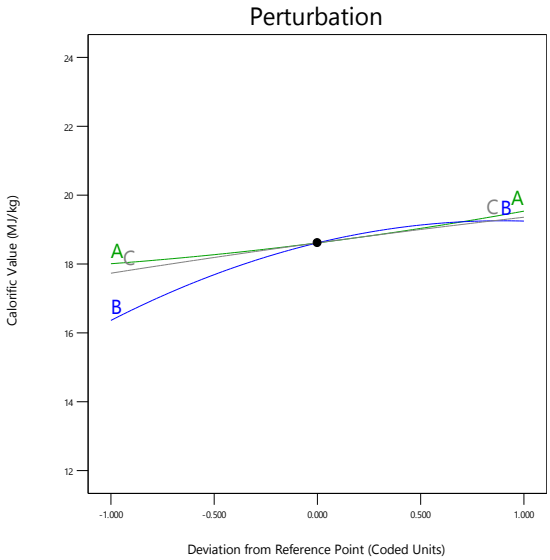

Fig 2 perturbation graphs showing the effects of the 3-factors on Calorific Value

Fig 3 shows the relationship between predicted energy value and actual energy value as given by the Design Expert software. Figure 3 gives a close distribution of the point along the straight line which implies agreement between the experimental and predicted energy values hence the developed quadratic model is justified.

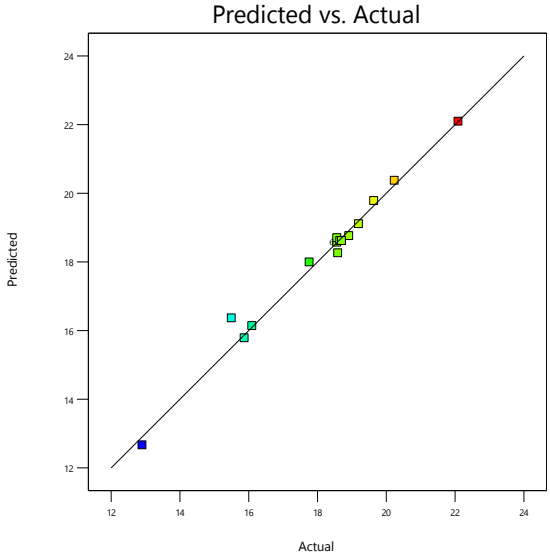

Figure 3 Graph showing the relationship between predicted values and actual values

Table 5. Significance of regression coefficients of Calorific value for Groundnut Shell briquettes

Source	Sum of Squares	df	Mean Square	F-value	p-value	
Model	69.23	9	7.69	69.09	< 0.0001	significant
A-Binding Ratio	5.60	1	5.60	50.31	< 0.0001	
B-Dwelling Time	22.01	1	22.01	197.65	< 0.0001	
C-Compaction Pressure	6.37	1	6.37	57.25	< 0.0001	
AB	17.21	1	17.21	154.60	< 0.0001	
AC	8.53	1	8.53	76.63	< 0.0001	
BC	0.4807	1	0.4807	4.32	0.0644	
A^2	0.1996	1	0.1996	1.79	0.2102	
B^2	5.66	1	5.66	50.88	< 0.0001	
C^2	0.0351	1	0.0351	0.3156	0.5866	
Residual	1.11	10	0.1113			
Lack of Fit	1.11	4	0.2778	810.01	< 0.0001	significant
Pure Error	0.0021	6	0.0003			
Cor Total	70.35	19				

The optimization process gave 17.869 MJ/kg of Calorific Value, 39.525 wt% Binding Ratio, 57.512 Seconds dwelling time and 4.316 MPa Compaction Pressure. These optimum values are shown in Table 6.

Table 6. Optimum values of Groundnut Shell Briquettes obtained from Design Expert Software

Binding Ratio wt% A	Dwelling Time (Sec) B	Compaction Pressure (MPa) C	Calorific Value (MJ/Kg)
39.09	57.512	4.316	17.869

4. CONCLUSIONS

The Groundnut shell briquettes have shown to be good source of an alternative energy. This research work was carried out to analyze the energy content of the briquettes produced from locally sourced groundnut shell. The optimization of the calorific value of the groundnut shell briquettes using cassava starch as binder was performed using response surface methodology (RSM). The groundnut shell briquettes were produced using optimized condition of values of 39.525 wt% binding ratio, 57.512 seconds dwelling time, 4.316 MPa compaction pressure. This gave the calorific value of 17.869 MJ/kg, burning rate of 0.22 g/min, water boiling time of 15.82 mins and ignition time of 15 mins. This value of the calorific value falls within the range of 17.00 MJ/kg and 24.00 MJ/kg making it a good energy source.

REFERENCES

Jasiczek, F. & Kwasniewski, D. (2020). Analysis of production Technology of Wood Briquettes, including costs and distribution. *24(1)*, 35 – 45.

Mba, H.N. (2018). Assessment of Environmental impact of deforestation in Enugu. *Resource and Environment. 8(4),* 207-2015.

Dhital, H.C. & Bajaracharya, T.R. (2016). Research on torrefaction and briquetting of biomass in Nepal. Proceeding of IOE Graduate Conference 1.

Young, P. & Khennas, S. (2003). Feasibility and Impact Assessment of a Proposed Project to Briquette Municipal Solid Waste for Use as Cooking Fuel in Rwanda.

Oyelaran, O.A., Olorunfemi, B.J., Sanusi, O.M., Fagbemigun, O.A. & Balogun, O.A. (2018). Enhancing the heating properties of agricultural waste briquettes. *1(32)*, 77- 92.

Thliza, B.A., Abdulrahman, F.I., Akan, J.C., Chellubi, Z.M. & Kime, B. (2020). Determination of Compressive Strength and Combustibilty Potential of Agricultural Waste Briquette. *Chemical Science international journal. 29(1).* 30-46.

Bogale, W. (2009). Preparation of Charcoal Using Agricultural Wastes. *Ethip J. Educ. & Sc. 5(1)* 79-91.

Ogwu, I.Y., Tembe, E.T. & Shomkegh, S.A. (2014). Comparative Analysis of Calorific Value of Briquettes Produced From Sawdust Particles of *Daniella Oliveri* and *Afzelia Africana* Combination at Binary And Tertiary Levels with Rice Husk. *Journal Of Research In Forestry, Wildlife And Environmental 6(2).*

Prasityousil, J. & Muenjina, A. (2012). Properties of solid fuel briquettes produced from rejected material of municipal waste composting. *Procedia Environmental Sciences*, 603-610.

Shahapur, A., Desai, N.R. & Kadar, A. (2017). Agricultural wastes as a supplementary source of energy: an economic assessment of a briquette making facility. *Journal of South Pacific Agriculture 20.*

Sharma, M.K., Priyank, G., & Sharma, N. (2015). Biomass Briquette Production: A Propagation of Non-Convention Technology and Future of Pollution Free Thermal Energy Sources.*American Journal of Engineering Research 4(2),* 44- 50

Ameh, O.A., Bello, T.K., Mohammed, F., & Onuh, T.U. (2019). Densification of *Khaya Senegalensis* Leaves for Green Coal Production. *Engineering, Technology, and Sustainable Development Journal, 1(1).*

Kumar, M.V., Vithyasagar, T. & Rajavel, R. (2018). Analysis of Biomass Briquettes by Using Different Agricultural Wastes.

Bhattacharya, S.C., Leon, A.M., & Rahman, M.M. (2000). A Study on Improved Biomass Briquetting. *Proceedings of the International Conference on Biomass-based Fuels and Cooking Systems*, 20-24. Stelte, W. (2013). Production Scale Briquetting of Torrefied Biomass. *Biomass*.

Gulhane, A.A. & Handa, C.C. (2017). A Review on Briquetting Machine for Agriwaste. *International Journal for Scientific Research & Development, 5(5),*664-666.

Lamido, S.I., Lawal, M., & Salami, H. (2018). Briquetting Business in Nigeria: A Solution to Unemployment. *International Journal of Engineering Development and Research,6(4),* 101-105.

Gajbhiye, N.J., & Raut, L.P. (2018). Briquettes making machine for industrial and agricultural purposes. *International Research Journal of Engineering and Technology, 5(2),* 594-597.

Suryaningsih, S., Nurhiul, O., Yuliah, Y., & Mulyana, C. (2017). Combustion quality analysis of briquettes from a variety of agricultural waste as a source of alternative fuels. *International Conference on Biomass: Technology, Application, and Sustainable Development.*

Olowoyeye, T. (2021). A Review of The Environmental Impact of Deforestation and Industrial Activities in Nigeria. 1-13.

Shahapur, A., Desai, M.N., & Kadar, M. (2017). Agricultural wastes as a supplementary source of energy: an economic assessment of a briquette making facility. *Journal of South Pacific Agriculture*, *20* 25-32.

Hibane, P.B., Ndiaye, L.G., Napoli, A. & Kobor, D. (2018). Physicochemical and mechanical properties of biomass coal briquettes produced by artisanal method. *African Journal of Environmental Scienceand Technology, 12(2),* 480-4486.

Shukla, S., & Vyas, S. (2015). Study of Biomass Briquettes, Factors Affecting Its Performance and Technologies Based On Briquettes. *Journal of Environmental Science, Toxicology and Food Technology*, *9(11),* 37-44.

Hersztek, M.M., Gondek, K., Jewiarz, M., & Dziedzic, K. (2019). Assessment of energy parameters of biomass and biochars, leachability of heavy metals and phytotoxicity of their ashes. *Journal of Material Cycles and Waste Management*, 786-800.

Ismail, A., Zakari, I.Y., Nasiru, R., Tijjani, B.I., Abdullahi, I., & Garba, N.N. (2013). Investigation of biomass briquettes as an energy source in relation to their calorific values and measurement of their total carbon and elemental contents for efficient biofuel utilization. *Advances in Applied Science Research*, *4(4),*303-309.

Borowski, G. (2014). Possibilities of Utilization of Energy Briquettes. *Electrical Engineering Research Report,1(27),* 48-50.

Zubairu, A. & Gana, S.A. (2014). Production and Characterization of Briquette Charcoal by Carbonization of Agro-Waste. *Energy and Power,4(2),* 41-47.

Onukak, I.E., Mohammed-Dabo, I.A., Ameh, A.O., Okoduwa, S.I., & Fasanya, O.O. (2017). Production and Characterization of Biomass Briquettes from Tannery Solid Waste. 2-19.

Chukwuneke J. L., Umeji A. C., Sinebe J. E. & Fakiyesi O. B. (2020). Optimization of Composition of Selected Biomass for Briquette Production. *Universal Journal of Mechanical Engineering*, 8(4), 227 – 236. DOI: 10.13189/ujme.2020.080408

Kpalo, S.Y., Zainuddin, M.F., Manaf, L.A., & Roslan,A.M. (2020). Production and Characterization of Hybrid Briquettes from Corncobs and Oil Palm Trunk Bark under a LowPressure Densification Technique. 2-16.

Okot, D.K. (2019). Briquetting and Torrefaction of Agricultural Residues for Energy Production. Wilson, M., Dick, K., Ochieng, A., Margret, N., and Flavia, N. (2017). Effect of Compaction Pressure, Particle Size and Binder Ratio on Thermo-Physical Properties of Maize Cob Briquettes. *International Journal of Scientific and Engineering,* 8(2), 329 – 338.

Onuegbu, T.U., Ekpunobi, U.E., Ogbu, I.M., Ekeoma, M.O. and Obumselu, F.O. (2011) Comparative studies of Ignition Time and water boiling test of coal and biomass briquettes blend. *International Journal of Recent Research and Applied Studies.* 7, 153- 159.

Yahaya, D.B., and Ibrahim, T.B. (2012). Development of Rice Husk Briquettes For use as fuel. *Research Journal of Engineering Applied Science.* 1(2), 130- 133.

PAPER 108 – IMPACT OF FISH FARMING ON THE WATER QUALITY OF RIVER CHANCHAGA, MINNA

G.M. Gomina

Department of Civil Engineering, Water Resources and Environmental Engineering.
School of Infrastructure Process Engineering and Technology.
Federal University of Technology Minna Nigeria
Email: mohammedganagomina6@gmail.com

ABSTRACT

This study aimed to assess the impact of effluent discharge from aquaculture fish farm on the water quality of a nearby receiving River Chanchaga Minna (9° 35′ 00" N, 6° 35′ 00"E) in Niger State. Some physiochemical water quality parameters of the effluent receiving stream were determined at seven selected sites, above and below the effluent discharge point into the stream to assess the effluent impact on the water body. The water quality parameters investigated include (water temperature, true color, turbidity and transparency), chemical parameters (pH, conductivity, TDS, total alkalinity, total hardness, ammonia and DO), major ions ($Ca^{2}+$, $Mg^{2}+$, Na+, K+, Cl−, $SO4^{2-}$ and HCO^{3-}), nutrient compound and heavy metals. Water samples were collected for: both rainy and dry season and analyzed in the laboratory using standard analytical methods. The effluent discharge from the investigated fish farm had a significant negative impact on the water quality of the receiving River and the indicator parameters comprised of ammonia, color and alkalinity.

KEYWORDS: Aquaculture, Water Quality, Nutrients, River, Wastewater, Environment.

1. INTRODUCTION

1.1 Background of the Study

Aquaculture plays an important role in the development of many national economies and a key role in the socio-economic resilience of rural areas, potentially offering valuable and skill-based employment opportunities and, in some cases, stabilizing the economic base of otherwise fragile communities (Edwards 1999; Muir 1999; Haylor and Bland 2001). Fish production is very important for many reasons. Fish is one of the most stable food items for man as it provides a rich source of essential protein for human consumption. carbohydrate diet, like in Africa (FAQ, 2005).

The common of discharge fish farming effluents among the local fish farmers in Nigeria are land disposal and dilution technique. Disposal effluent into a body of water or watercourses is known as disposal by dilution. There has been great concern about the level of safety of surface and underground waters, especially in developing countries (Nigeria) where there is an exponential increase in water pollution and an inefficient system of waste management. Hence, there is the need for continual research on the impact of pollution on aquatic. The toxic effects of fish pond effluents on surface water has been highlighted by Boyd (1990, 2001, 2003, 2005); Sticking, (2002); Omofunmi, (2014); Tucker and Robinson (1990), and Tomasso, (2002), that it produces offensive odour, impacts negatively on the aesthetic value of adjacent rivers. Characterization of fish farming effluents and quantification of their environmental impacts in aquaculture provides required information for effective waste management systems generation, collection, transportation, storage, treatment and ultimate disposal which are not currently coordinated in Nigeria. Almost all the fish farmers were not treating their effluents before discharging into the environment. Pond pisciculture affects the chemical composition of the water; depending on the season, species and size of fish stock (Boyd and Tucker 1998; Brune et al; 2003; Quant et al; 2009; Sidoruk, Assessing the impact of fish farming on the water quality of river Chanchaga. I. To determine the physico-chemical water quality parameters of the effluents receiving River. II. To determine the level of concentration of water quality parameters at each station of the river. III. To determine the causes of the environmental problem associated with flow through land-based fish farming facility

2. MATERIALS AND METHODS/METHODOLOGY/EXPERIMENTAL PROCEDURE

2.1 DESCRIPTION OF THE STUDY AREA

The investigated water body is River Chanchaga is located at the southern part of Minna, Niger State capital, and lies between latitudes 9^0 35^1 00^{11} N and longitudes 6^0 35^1 00^{11} E. The study area is predominantly underlain by the pre-cambrian basement complex rocks. The climate of the area is characterized by two distinct seasons: rainy season (may- October) and dry season (Nov-April) and it is warm throughout the year with average monthly temperature in the range of 28^0C and 35^0C while the relative humidity is in the range of 85 and 95%.

River Chanchaga servers as a major natural water source upon which members of the riparian communities depend, domestic water supply and some socioeconomic activities.

2 SAMPLING PROGRAM

Water samples for analysis was collected four times from each sampling station comprising two times in the dry season an two times in the rainy season. Sampling at each station was carried out at a fixed time of the day from about 0800h to 1800 h of each sampling date. At each sampling station, water samples were taken just below the water surface using uncontaminated 2.5-L plastic bottles.

3 LABORATORY ANALYSIS

The analyses was carried out within the holding time of each parameter, according to applicable standard methods (APHA 1995, 1998; Golterman et al. 1978; Willis and Savory 1995) the impact was determined by comparing the water quality of the unimpacted stations (A-B) with that of the impacted stations (E&F) as well as by comparing the latter stations with reference water (Stations G) and the Nigerian Standard for Drinking Water Quality (NSDWQ) and WHO Adequate quality control and quality

4 RESULTS AND DISCUSSION

Table 1. Mean values of water quality parameters of the investigated Chanchaga River compare

Parameter	USS (A-B)	EPP (C)	EDP (D)	ISS (E&F	RWB (G)	ANOVA F	ANOVA P
Channel characteristics							
River channel depth (cm)	19.78 (±1.92)	NA	33.93 (±2.66)	28.4 (±2.29)	NA	30.91	1.37E-05***
River channel width (cm)	66.2 (±27.16	NA	411.0 (±22.06)	298.68 (±25.73)	NA	38.62	2.96E-06***
Hydro-physical							
Water temp. (ºC)	26.46 (±0.32)	30.0 (±1.04)	28.0 (±0.82)	28.04 (±0.35)	30.0 (±2.7)	8.088	1.95E-03***
True color (Pt.Co.mg/L)	9.99 (±7.02)	60.91 (±8.63)	59.96 (±9.23)	53.64 (±13.0)	0.0 (±0.0)	8.73	7.33E-03***
Turbidity (NTU)	18.89 (±2.80)	40.86 (±7.23)	38.75 (±8.9)	33.05 (±3.5)	10.2 (±3.5)	9.18	1.02E-03***
General chemical							
pH	6.58 (±0.22)	7.96 (±0.4)	7.10 (±0.2)	7.20 (±0.09)	6.40 (±0.1)	4.66	1.90E-02***

Conductivity (µS/cm)	76.11 (±9.36)	74.65 (±6.36)	84.85 (±3.88)	87.41(±3.13)	19.80 (±1.99)	13.49	1.07E-04***
TDS (mg/L)	45.48 (±5.68)	48.1 (±16.22)	50.32 (±1.91)	51.79 (±2.03)	11.66 (±1.3)	12.78	1.5E-04***
Alkalinity (mg/L $CaCO_3$)	24.85 (±2.72)	78.1 (±15.22)	62.1 (±17.22)	58.43 (±6.8)	31.1 (±4.4)	12.19	2.01E-04***
Total hardness (mg/L$CaCO_3$)	48.95 (±5.14)	42.5 (±3.07)	44.5 (±4.07)	45.98 (±4.4)	40.0	0.26	0.769
Ammonia, NH_3 (mg/L)	0.17 (±0.05)	2.12 (±0.45)	1.625 (±0.375)	1.53 (±0.40)	0.0 (±0.0)	1.22	2.90E-03***
DO (mg/L)	5.43 (±0.55)	2.38 (±0.35)	3.38 (±0.55)	4.1 (±0.55)	5.5 (±1.24)	1.60	0.22
Major ions							
Ca^{2+} (mg/L)	7.67 (±0.81)	5.28 (±2.0)	6.38 (±1.0)	8.50 (±1.28)	2.8 (±1.2)	3.908	3.34E-02**
Mg^{2+} (mg/L)	2.44 (±0.33)	0.96 (±0.20)	1.48 (±0.40)	2.29 (±0.56)	1.24 (±0.2)	1.007	0.380
Na^{+} (mg/L)	5.25 (±0.26)	6.86 (±0.35)	6.61 (±0.25)	6.50 (±0.2)	3.10 (±0.2)	33.74	7.92E-08***
K^{+} (mg/L)	2.74 (±0.26)	5.91 (±0.24)	5.10 (±0.22)	5.31 (±0.21)	0.85 (±0.06)	63.7	1.49E-10***
CI^{-} (mg/L)	5.54 (±0.55)	8.02 (±0.46)	7.03 (±0.39)	6.88 (±0.48)	1.7 (±0.3)	14.07	8.06E-05***
$SO^{2-}4$ (mg/L)	2.26 (±0.38)	8.23 (±1.23)	7.43 (±1.53)	6.50 (±1.03)	0.49 (±0.32)	12.63	1.61E-04***
$HCO^{-}3$ (mg/L)	29.9 (±3.3)	82.43 (±22.12)	74.52 (±20.66)	70.1 (±8.2)	37.37 (±5.34)	12.14	2.07E-04***
Nutrient compounds							
$NO^{-}3$ (mg/L)	1.57 (±0.89)	4.5 (±1.20)	3.5 (±0.89)	1.63 (±0.54)	0.0 (±0.0)	0.023	0.095
$NO^{-}2$ (MG/l)	0.09 (±0.05)	1.36 (±0.40)	0.26 (±0.80)	0.13 (±0.4)	0.0 (±0.0)	0.309	0.584
$PO^{3-}4$ (mg/L)	0.34 (±0.14)	0.56 (±0.81)	0.51 (±0.29)	0.495 (±0.14)	0.31 (±0.26)	0.383	0.685
Heavy metals							
Hg^{2+} (mg/L)	0.03 (±0.006)	0.127 (±0.01)	0.03 (±0.006)	0.026 (±0.002)	0.005 (±0.005)	3.349	0.051

5

Mn^{2+} (mg/L)	1.39 (±0.15)	2.55 (±0.19)	1.55 (±0.19)	1.59 (±0.09)	1.63 (±0.19)	0.830	0.448
Fe^{2+} (mg/L)	1.87 (±0.13)	2.01 (±0.59)	2.12 (±0.49)	2.45 (±0.26)	2.39 (±0.30)	2.257	0.125
Cu^{2+} (mg/L)	0.054 (±0.02)	0.032 (±0.04)	0.054 (±0.03)	0.067 (±0.02)	0.134 (±0.08)	1.384	0.269
Zn^{2+} (mg/L)	0.147 (±0.09)	0.492 (±0.07)	0.292 (±0.21)	0.182 (±0.09)	0.178 (±0.084)	0.00	0.956

Table 2. Mean values of water quality parameters of the investigated Chanchaga River compare with WHO and NSDWQ standard

Parameter	**USS (A-B)**	**EPP (C)**	**EDP (D)**	**ISS (E&F**	**RWB (G)**	**WHO**	**NSDWQ**
Water temp (°c)	26.46	30.00	28.00	28.04	30.00	12-15	Ambient
True color (P6.CO.mg/L	9.99	60.91	59.96	53.64	0.00	15	15
Turbidity (NTU)	18.89	40.86	38.75	33.05	10.20	5	5
Ph	6.58	7.96	7.10	7.20	6.40	6.5-8.5	6.5-8.5
Conductivity (HIS/CM)	76.11	74.65	84.85	87.41	19.80	400	1000
TDS (mg/L)	45.48	48.10	50.32	51.79	11.66	500	500
Alkalinity (mg/L cab D3)	24.85	78.10	62.10	58.43	31.10	300	-
Total hardness mg/L ca cd3	48.95	42.50	44.50	45.98	40.00	500	150
Ammonia, NH3 (mg/L)	0.17	2.12	1.63	1.53	0.00	0.2	-
DO (mg/L)	5.43	2.38	3.38	4.10	5.50	6	5.0
Ca^{2+} (mg/L)	7.67	5.28	6.38	8.50	2.80	75	75
Mg^{2+} (mg/L)	2.44	0.96	1.48	2.29	1.24	30	20
Na^{2+} (mg/L)	5.25	6.86	6.61	6.50	3.10	50	200
K^{+} (mg/L)	2.74	5.91	5.10	5.31	0.85	20	-
CL^{-} (mg/L)	5.54	8.82	7.03	6.88	1.7	200	250
$SO4^{2-}$ (mg/L)	2.26	8.23	7.43	6.50	0.49	250	100
$HCO3^{-}$ (mg/L)	29.9	82.43	74.52	70.1	37.37	125-250	-
$NO^{-}3$ (mg/L)	1.57	4.5	3.5	1.63	0.0	50	50
$NO2^{-}$ (mg/L)	0.09	1.36	0.26	0.13	0.0	50	0.2
$PO4^{2-}$ (mg/L)	0.34	0.56	0.51	0.495	0.31	0.5	0.5
Hg^{2+} (mg/L)	0.03	0.27	0.03	0.026	0.005	0.001	0.001
Mn^{2+} (mg/L)	1.39	2.55	1.55	1.59	1.63	0.1-0.5	0.2
Fe^{2+} (mg/L)	1.87	2.01	2.12	2.45	2.39	0.1	0.3
Cu^{2+} (mg/L)	0.05	0.032	0.05	0.07	0.13	1	1
Zn^{2+} (mg/L)	0.15	0.492	0.29	0.18	0.18	5	3

Keys

USS: unimpacted sampling station **EPP:** effluent point from pond **EDP:** Effluent discharge point
ISS: impacted sampling station **RWB:** reference water body **WHO:** world health organization
NSDWQ: Nigeria's standard drinking water quality **NA:** not applicable

*Significant; P < 0.05
***Highly significant; P < 0.01*
****Very highly significant; P < 0.001*

Table 3. ANOVA statistics of Seasonal variations in the water Quality parameters of Chanchaga River.

Parameter	Dry season samples	Rainy season samples	ANOVA statistics	
	Mean ±SE	Mean ±SE	F	P
pH	6.53(±1.05)	7.64(±1.65)	10.43	0.015
TDS (mg/L)	36.15(±3.86)	50.56(±5.54	4.55	0.043
Water temp. (°c)	30.0(±3.24)	26.46(±2.41)	5.35	0.023
Turbidity (NTU)	18.34(±2.90)	29.09(±3.72)	5.188	0.031
Phosphate, PO_4^{3-} (mg/L)	0.72(±0.13)	0.08(±0.03)	22.79	6.1E-05***
Manganese, Mn^{2+} (mg/L)	1.20(±0.09)	1.82(±0.06)	32.34	5.5E-06***
Iron, Fe^{2+} (mg/L)	1.91(±0.18)	2.48(±0.18)	4.79	0.0379*
Dissolve Oxygen (mg/L)	5.43(±1.05	3.38	8.56	0.035
Mercury, Hg^{2+} (mg/L)	0.55(±0.17)	0.02(±0.003)	9.98	0.004**
Nitrate NO_3^- (mg/L)	1.57(±0.12)	3.5(±1.62)	18.62	0.046
Ammonia (mg/L)	2.12(±0.15)	0.17(±0.45)	5.21	0.041
Alkalinity (mg/L calo3)	78.1(±15.32	58.85(±12.3	25.31	0.024

* Significant; P < 0.05
***Highly significant; P < 0.01 ***Very highly significant; P < 0.001 SE-Std Error*

4 DISCUSSION

The results of the investigated physicochemical parameters in the sampling stations are presented in **Table 1 and 2** Generally most of the investigated parameters were of higher concentrations in the impacted section than in the unimpacted section, while the other parameters were higher in the unimpacted section than in the impacted section of the effluent receiving stream. Also a general pattern of progressive decrease in concentrations of investigated parameters (except DO, Cu2+, Fe2+ and Mg2+) was observed from the point of effluent discharge (Station D) into the stream to the last impacted sampling station F. according to Chapman (1992), effluent discharge would be deemed to impact a stream if the concentration of a given physicochemical variable is higher in the effluent or just below its point of discharge and decreases significantly with increasing distance downstream.

5. CONCLUSIONS

This study characterized some physico-chemical water quality parameters of the effluent receiving river chanchaga were determined at seven selected sites, above and below the effluent discharge point Table 1. The seven sampling stations comprised two stations (A-B) located upstream effluent discharge point (station D), effluent point from the ponds (Station C), two stations (E and F) located downstream of station D, while the seventh station (Station G) was a closed-by reference groundwater source.

The water quality parameter revealed the level of the mean concentrations of turbidity, true color, NH_3, PO^{3-}, Mn^{2+}, Fe^{2+}, and Hg^{2+} were above the FEPA (1991) effluent limitation standards. The difference between the water qualities of impacted and unimpacted stretches of the effluent receiving stream was significant ($P < 0.05$) for more than half of the parameters. All the investigated parameters (except total hardness, DO and Hg^{2+}) were higher in the impacted section than in the unimpacted section, thus indicating the negative impact on the receiving stream. The effluent qualities varied among the investigated parameters and decreased (except DO, Fe^{2+}, Mn^{2+} and Hg^{2+}) gradually from the outpour downstream. The pronounced increase

in ammonia, major ions and nutrient compounds indicated that the discharge from the fish farm is both inorganic and organic. The effluent discharge from the investigated fish farm had a significant negative impact on the water quality of the receiving River and the indicator parameters comprised of ammonia, color and alkalinity.

ACKNOWLEDGMENTS

This study is not funded by any organization. The author wishes to thank the Department of Civil Engineering, Water Resources and Environmental Engineering for providing the facilities to analyzed the samples and my supervisor Engr. Dr. M. Saidu whose experience, educative suggestions help this research work come to conclusion.

REFERENCE

APHA (American Public Health Association) (1995) Standard methods for the examination of water and wastewater. American Public Health Association, Washington, DC Boyd CE (1990) Water quality in ponds for aquaculture. Fisheries and Allied Aquacultures Departmental Series no. 3. Auburn University Press, Birmingham, Ala

Boyd CE, Tucker CS (2000) EPA rule-making for aquaculture effluents in the United States. Glob Aquac Advocate 3(6):81–82

Chapman DE (1992) Water quality assessments: a guide to the use of biota, sediments and water in environmental monitoring. UNESCO, World Health Organization, United Nations Environment Programme, London, p 585

Edwards P (1999) Aquaculture and poverty: past, present and future prospects of impact. Fifth Fisheries Development Donor Consultation, Rome, Italy, 22–24 February 1999. Rome, Italy.

FAO (2005) Inventory of fish farms in Nigeria. Aquaculture and inland fisheries Project of the National Special Programme for Food Security with State Agricultural Development Programme, pp 1–10

FEPA (1991) Guidelines and standards for environmental control in Nigeria. Federal Environmental Protection Agency (FEPA), Government Press, Lagos, p 238 Golterman HL, Clymo RS, Ohnstad MAM (1978) Methods for physical and chemical analysis of freshwater. IBP handbook No. 8. Blackwell Scientific Publication, Oxford

Haylor G, Bland S (2001) Integrating aquaculture into rural development in coastal and inland areas. In: Subasinghe RP, Bueno P, Phillips MJ, Hough C, McGladdery CE, Arthur JR (eds) Aquaculture in the third millennium technical. Proceedings of the conference on aquaculture in the third millennium, Bangkok, Thailand, 20–25 February 2000. Bangkok, Thailand and FAO, Rome, Italy: NACA and FAO, pp 73–81

NSDWQ (2007) Nigerian guidelines and standards for drinking water quality. Nigerian Industrial Standard Technical Paper No. 554

WHO (2014). water safety in distribution systems. Geneva: WORLD Health Organization (http:/apps.who.int/iris/bitstream/106655/204422/1/9789241548892_eng.pdf, accessed 7 June 2016).

Tucker CS, Hargreaves JA (2003) Management of effluents from channel catfish (Ictalurus punctatus) embankment ponds in the southeastern United States. Aquaculture 226:5–21.

Muir J (1999) Aquaculture and poverty: full baskets or empty promises? Perspectives from DFID aquaculture research programme. Paper presented at the Fifth Fisheries Development Donor Consultation, 22–24 February, FAO, Rome

Tucker CS, Hargreaves JA (2003) Management of effluents from channel catfish (Ictalurus punctatus) embankment ponds in the southeastern United States. Aquaculture 226:5–21. Willis MR, Savory J (1995) Water content of aluminum dialysis dementia and Ostemalacia. Environ Health Perspect 63:141–147.

PAPER 110 – DESIGN AND SIMULATION OF HYBRID POWER SUPPLY FOR RESIDENTIAL CONSUMER

D. E. Abah[1*], N. A. Iliyasu[1], A. J. Aliyu[1], A. Kabir[2]

[1]Department of Electrical Engineering, Ahmadu Bello University, Zaria, Nigeria.
[2]Department of Electrical and Electronics Engineering, Federal Polytechnic Kaura Namoda.
Email: deabah@abu.edu.ng

ABSTRACT

Hybrid Power System (HPS) is a combination of different renewable resources such as wind, solar, biomass, hydrogen fuel, hydro, with fossil fuel powered diesel generator to provide electric power. The objective of this work is to propose a methodology for designing a stand-alone hybrid PV/diesel/battery system minimizing the Cost of Energy (COE) and the CO_2 emission using HOMER (Hybrid Optimization of Multiple Electric Renewables) for a residence at Marcus Poli Estate Gwarinpa, Abuja, Nigeria. The capital cost, cost of energy, Net Present Cost (NPC) for different types of resources are determined from the load demand and optimized configuration of hybrid system are obtained. The analysis results show that, among five hybrid systems for supplying electrical requirements, the most economical is the PV - diesel -battery hybrid system, which has a total net present cost of US$118,771 and a cost of energy of US$0.340/kWh. The action plan is formed on the basis of cost-effective modelling that is minimization of energy production cost in a near future.

KEYWORDS: Cost of Energy; Hybrid Power System; MPPT; Net present Cost; Power Demand; Renewable Energy.

1. INTRODUCTION

In recent era there is a great scope for advancement in power generation considering environment friendly technology such as renewable energy technology is becoming, as technically viable and environmentally friendly. Around the world, effort is being made to study the viability of renewable energy incorporated hybrid system as alternative of diesel generator. The hybrid energy system generally works with primary renewable source in parallel combination of a standby secondary non-renewable module and storage unit (Ali *et al.*, 2017).

Main drawbacks of the standalone system considering solar as well as wind energy is the energy fluctuation, resulting in intermittent delivery of power and causing problems if reliable and continuous supply is required benefits. So, such types of problems can be overcome by the use of standalone hybrid systems. A hybrid power system can be defined as a combination of different source of energy, but complementary energy generation system can be provided by renewable energy or mixed (RES- with a backup of diesel generator set). Hybrid systems provides the better features of each energy resources as compared to conventional sources and also provide "grid-quality" electricity, with a power range of kilowatt to several hundred kilowatts (Iqbal & Khan, 2017; Zubo *et al*., 2018). Recent increase in power system complexity, rapid increased in energy demand, the requirement of secured and reliable power system, and power supply efficiency have made Hybrid Energy Systems (HES) development a major focus of the recent.

2 THEORETICAL ANALYSES

This section introduces the fundamental concepts relevant to this research. The review of literature is very important in establishing the basis and contemporaries of any research.

2.1 Component Modelling

The component of the system as discussed in previous sections consist of photovoltaic generator system, diesel generator system, grid, transmission system, control and communication system. Therefore, this section reviews the modelling techniques of the involving component of the Smart Grid (SG) technology.

2.1.1 Photovoltaic generator System (PGS)

PV farms are continuously being developing all over the world, usually having capacity up to the ranges of 1 MW to 500 MW (Singh *et al*., 2016). These PV farms could stand an alternative source of energy and improving the energy challenges of consumers. Grid connected PV system consist mainly of mechanical and electronic component.

2.1.2 PV System Module

Solar cell is an electronics component used for conversion of photon energy into pollution-free and green electric energy. Basically, the connection of the device in series and parallel pattern forms a PV module. Furthermore, to build PV arrays these modules are coupled in series and parallel forms to generate clean and green electric energy

(Iqbal & Khan, 2017). The solar cell process of capturing and converting sunlight energy into electricity is generally referred as photovoltaic conversion (Zubo *et al*., 2018).

2.1.3 MPPT

Maximum power point tracking (MPPT) is a control algorithm implanted in a DC–DC electronic power system converter with the function to extract maximum power from a PV array system. The main purpose of MPPT technique is to guarantee that the maximum power extracted from a PV system matches the optimum value of the power and voltage characteristic curve under sunlight irradiation (G) and temperature (T) variations. The function of the MPPT tracking algorithms is to latch the converter system operating voltage and current to the maximum power point (MPP) of the PV array.

2.1.4 Inverter System

MG as a novel technology that could immensely help to increase the reliability, resiliency and efficiency of power system grid network. Though, many challenging issues surrounding microgrid technology development are in existence and want to be carefully addressed in order to ensure the proper implementation and operation of the MG systems (Lasseter *et al*., 2003; Rocabert *et al*., 2012). One of those challenges is the stability of those systems throughout their smooth operation (Zamani-Gargari *et al*., 2018). The requirement to run AC Loads on solar energy leads necessitate the design of Solar Power Inverter system.

2.1.6 Dynamic Load

Ideally, Mega size electric power is generated in three phases, the three phases are inherently desired to be balance, even though attaining balance mode is difficult, but something close to the balance mode (symmetry) is always achievable (Amuta, 2019). An electric power system can be described to be symmetrical if the supply magnitudes are symmetrically equal and phase angles of the respective phases are spaced at an angle of 120 electrical degrees, otherwise the power systems network are termed asymmetrical. Research works on load modelling are significant in the sense that, power system operators require knowledge of the system dynamics under normal and faults operating conditions for decision making with regards to system stability margin and subsequently, control and or protection. Recently, different types of loads are continuously modelled and developed. dynamic loads are time dependent and are largely represented by Induction Motors (IMs) (Kontis *et al*., 2017). There exist two approaches of load modeling in the literature namely; component based and measurement-based approaches (Dong *et al*., 2012; Han, 2020; Saviozzi *et al*., 2018; Sharafi *et al*., 2019). The Component based load modeling requires knowledge of individual loads, acquisition of relationship between the voltage and or frequency dependency on real and reactive power of each component and then cumulate the results for all the components connected to the network.

3. MATERIALS AND METHODS

In this section, detailed procedures, methods and materials used in achieving the aim and objectives of this research are discussed.

3.1 Models of Hybrid power system Component

Electricity has been around us for centuries, growing and changing day by day. Without electricity the world would have not been the same. The human relies on electricity to be always available and to perform its functions. Usage of electricity has been increased every year since 1949. Not only has electricity usage been rapidly increasing, energy cost is rising and energy possibility is decreasing. With this consecutive growth in electricity usage as well as in its cost, new and unique methods of producing electricity are being developed constantly.
In this work, the energy sources considered are utility grid, diesel generator, and PV system.

3.2 Active PV Model

The mathematical description of PV cell has been studied over decades (Singh et al., 2016). The electrical circuit representation of the PV cell model, consisting of a photocurrent, diode, parallel resistor (leakage current) and a series resistor; is as shown in Figure 1. Based on PV cell circuit and Kirchhoff's circuit laws, the PV current can be modelled as in the following Equation 1.

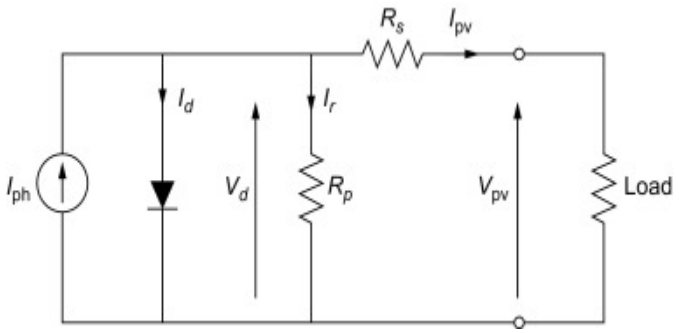

Figure 1: PV Model Electrical equivalent circuit

$$I_{pv} = I_{ph} - I_d - I_p = I_{ph} - I_0\left(e^{\frac{V_{pv}+R_sI_{pv}}{n_sV_tQ_d}} - 1\right) \quad (1)$$

Where; V_{pv} = PV- module Voltage, I_{pv}= PV Module Current, I_{pv}= Light current in (A), I_{pv} = Diode reverse saturation current, Q_d= Diode idealistic factor, R_p= Shun Resistance, R_s= series resistance, n_s= number of cells, $V_t = \frac{KT_c}{q}$ is the thermal voltage (V), k is Boltzmann's constant, T_c is the cell temperature, and q is the charge of an electron respectively.

3.3 Inverter System

Inverter system is an electrical device with related electronic components used to convert DC power into AC power within designed frequency and voltage magnitude. In system of microgrids architecture, an inverter system function to interfaces the DC sources of a renewable energy system to AC systems where the loads and utility grid are coupled. Technically, the inverter system is an important component in the microgrid system through which the voltage, frequency, active and reactive power can be controlled and stabilized. A typical three phase inverter system for PV interfacing to grid is as shown in figure 2.

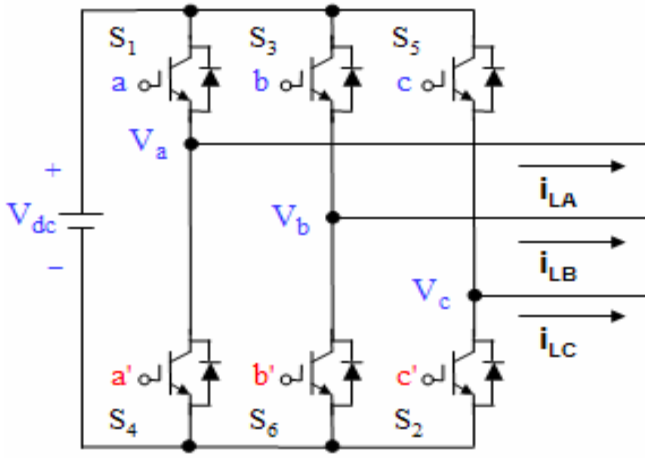

Figure 2: Inverter System Equivalent Circuit

The equivalent circuit system consists of three single phase inverter system cascaded together. The system operates like a single-phase inverter system but with 120° delay in the gating signals of each arm with respect to others. This is done to obtain a balanced three phase voltage from the output of the system. The technique is to controlled the operation of the transistor and diodes in the inverter circuit provided in any arm two switches are not ON or OFF simultaneously. The space vector equation representing this type of inverter can be expressed as in Equation 2.

$$V = \frac{2}{3}(V_a + aV_b + a^2V_c) \quad (2)$$

Moreover, this space vector formulation can be applied to both delta and star connected loads

Let Assume a star connected load, the total phase voltages at the star load for both balanced and unbalanced conditions is zero.

$$V_a + V_b + V_c = 0 \quad (3)$$

While, the phase voltage at the load point of coupling can be computed using Equation 4

$$V_i = V_j - V_{nk} \tag{4}$$

where i= a, b, c, j= A, B, C and n is the neutral point at the load point of interface k is the negative rail of the dc bus in the inverter Now, from Equation 4, Vnk can be expressed in terms of voltages at A, B and C as:

$$V_{nk} = \frac{V_{dc}}{3}(a^* + b^* + c^*) \tag{5}$$

Hence, the connection between the switching variable vectors a^*, b^*, c^* and phase to neutral output voltages vector can be mathematically expressed as:

$$\begin{bmatrix} V_a \\ V_b \\ V_c \end{bmatrix} = \frac{V_{dc}}{3}\begin{bmatrix} 2 & -1 & -1 \\ -1 & 2 & -1 \\ -1 & -1 & 2 \end{bmatrix}\begin{bmatrix} a \\ b \\ c \end{bmatrix} \tag{6}$$

While the phase-to-phase voltage can be computed as in Equation 7

$$\begin{bmatrix} V_{ab} \\ V_{bc} \\ V_{ca} \end{bmatrix} = \frac{V_{dc}}{1}\begin{bmatrix} 1 & -1 & 0 \\ 0 & 1 & -1 \\ -1 & 0 & 0 \end{bmatrix}\begin{bmatrix} a \\ b \\ c \end{bmatrix} \tag{7}$$

3.4 Utility Grid

To simulate microgrid in grid-connected mode, the grid side can be technically modelled as a three-phase power source, that is connected to distribution network lines through a step-down transformer (Craig et al., 2016).

3.5 Diesel Generator Model

Diesel generators are mainly used for off-grid supply, low installed capacity, high shaft efficiency, suitable for start-stop operation and high exhaust heat which are some advantages of diesel generator. In this work, the diesel generator is used as a standby power system. It is switched ON only when PV source is not able to meet the load demand. In this condition, a control system management block developed activate the selector switch automatically to alternative source of energy. The diesel generator is modelled to feed a load of 24kw (30kVA).

4. RESULTS AND DISCUSSION

This chapter provides the detailed results and discussion of the analysis carried out based on the theoretical concepts in the preceding chapters are presented.

4.1 Load Profile

The village considered to be electrified by Hybrid Energy Source is a residential building at Graceland, Zaria. The load profile of the residential was obtain from a survey as shown in Table 1.

Table 1: Electrical energy utilization data in kWh/day

Equipment	No.	Watt (W)	Total Power (W)	Time (Hr)	Energy (Wh)	Kwh
Fan	4	75	300	10	3000	3
AC	4	1500	6000	5	30000	30
Fridge	2	250	500	24	12000	12
Tv	2	75	150	9	1350	1.35
Pressing Iron	1	2000	2000	2	4000	4
Electric Cooker	1	6000	6000	2	12000	12
Decoder	2	150	300	9	2700	2.7
Laptop	2	78	156	3	468	0.468
Sound System	1	100	100	9	900	0.9
Light	25	26	650	10	6500	6.5
Toaster Machine	1	1200	1200	1	1200	1.2
Total			17356			**74.118**

The total load obtained from the residence per day was calculated to be **74.118kWh** and the daily load profile is shown in the Figure 3.

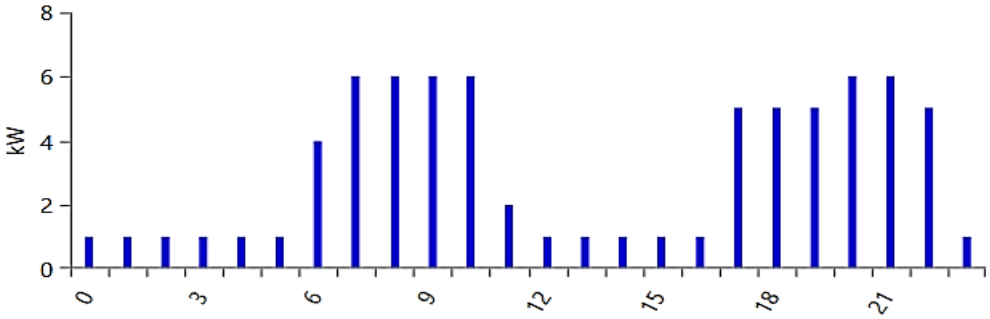

Figure 3: Daily Load profile

4.2 Resources assessment

We have considered sun powered, converter, battery and bio-diesel assets. The sun-based asset utilized Graceland, Zaria at **9° 4.3'N** and **7° 27.8E** was taken from NASA Surface Meteorology and Solar Energy site. The yearly normal sunlight-based radiation was scaled to be **4.93 kWh/m2/Day** and the normal clearness record was observed to be **0.483**. The sun-based radiation is accessible consistently; along these lines, a lot of PV power yield can be acquired is shown in Figure 4.

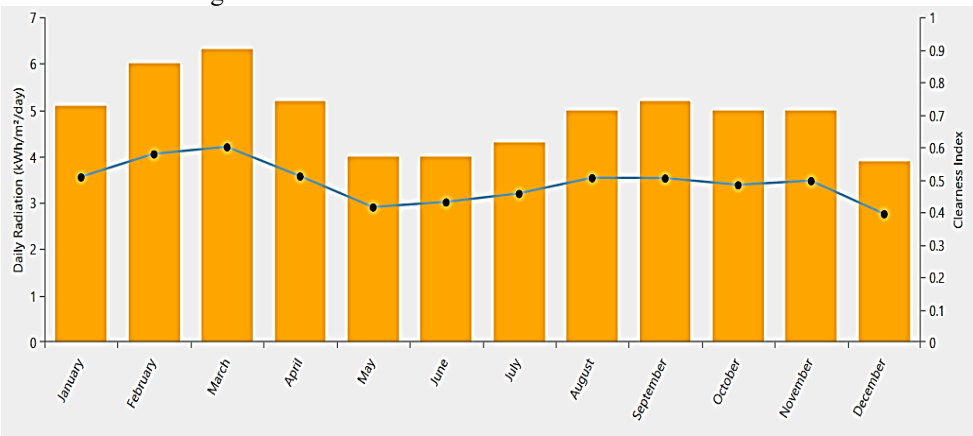

Figure 4: Solar radiation with clearness index

4.3 Complete System Model

The complete system model is depicted in Figure 5 showing the integration of all the system component and the control techniques deployed. The control strategy deployed is a combination of logic gates. The system is made to operate in two modes, the islanded mode and the grid connected mode.

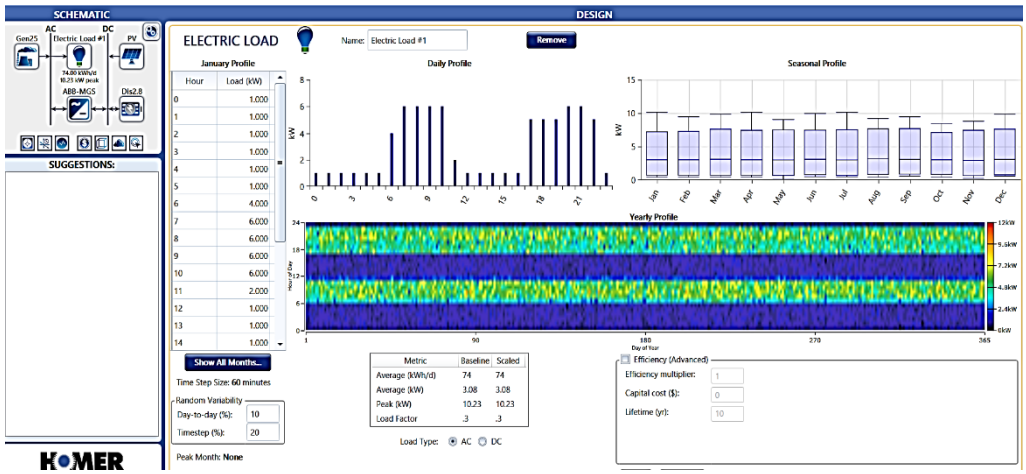

Figure 5: Complete System overview

4.4 Hybrid System Design and Analysis

In this work, we have considered a combination of the following technologies, namely solar PV systems, batteries, system converters and a bio-diesel generator for back-up. Figure 6 shows a schematic system configuration diagram. Generally, an ordinary move down diesel generator (DG) is utilized to supplement the renewable energy (RE) framework for pinnacle loads and amid poor asset periods. In this work, a bio-diesel generator is utilized in making the entire framework a clean and carbon impartial framework, with the end goal of power era **as well as for working successfully towards greenhouse gases (GHG) outflows moderation by not blazing any fossil fuels.**

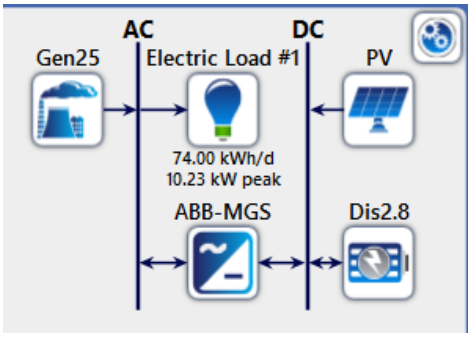

Figure 6: Schematic for the Hybrid Power system (HPS)

4.5 Optimization results

HOMER simulates system configurations with all of the combinations of components available in HOMER. The input data are analysed, characterized, and tabulated systematically so as to determine the most economic hybrid system that are proposed in this work. The PV-generator-battery-system converter hybrid system is the most economic system among the thousands of PV-generator-battery-system converter hybrid systems which were analysed with the HOMER software. A comparison of this system with a chosen representative of each of the systems is provided in table 2. The strategy taken in this simulation is to ensure the energy generator provide enough energy to meet the demand. The results in table.2 indicate that the PV-battery-system converter is the most economic system among the five selected systems with a renewable factor of **100%**. The system has a cost of energy (COE) of **US$0.340/kWh** and net present cost (NPC) of **US$118,771**. A PV-generator-battery-system converter is the second economic system for supplying the electrical energy demands for the resident. The COE and NPC of the system are **US$0.411/kWh** and **US$143,616** respectively. **The total simulating time step is 60 minutes. The analysis of the renewable energy resources data has been carried out using HOMER software.**

Table 2: Comparison of various hybrid power system

Architecture									Cost				
				PV (kW)	Gen25 (kW)	Dis2.8	ABB-MGS (kW)	Dispatch	COE ($)	NPC ($)	Operating cost ($/yr)	Initial capital ($)	Ren Frac (%)
				15.9		51	20.0	CC	$0.340	$118,771	$2,343	$88,489	100
				15.4	25.0	51	20.0	LF	$0.411	$143,616	$1,996	$117,816	99.9
					25.0	45	40.0	CC	$1.85	$646,967	$38,466	$149,700	0
				199	25.0		20.0	CC	$5.37	$1.88M	$118,127	$349,475	0
					25.0			CC	$7.92	$2.76M	$211,489	$30,000	0

5. CONCLUSIONS

The plenteous energy available in nature can be harnessed and utilized to provide source of electricity that is more sustainable than fossil fuels. Access to electricity is particularly important concern for people without access to the electricity grid. The economic feasibility of hybrid power systems integrating renewable energy to meet the load requirements of a residence in Marcus Poli Estate Gwarinpa, Abuja, Nigeria has been successfully investigated.

Using HOMER software for optimization, five different systems are proposed as somewhat optimal. For the proposed systems the following conclusions are drawn:

i. The most economic hybrid system is the solar pv-battery-power converter, with a net present cost (NPC) of **US$118,771** and a cost of energy (COE) of **US$0.340/kWh**.
ii. The second most economic hybrid system is the pv-diesel generator- battery-power converter, with COE and NPC **US$0.411/kWh** and **US$143,616** respectively.
iii. The diesel generator-battery-power converter is the third most economic hybrid system, with NPC of **US$646,967** and COE of **US$1.85/kWh**
iv. The fourth most economic hybrid system is the pv-diesel-power converter with NPC of **US$1.88M** and COE of **US$5.37/kWh**

17. The final most economic hybrid system is the diesel generator with NPC of **US$2.76M** and COE of **US$7.92/kWh**.
18. In this research work, the PV system is the only renewable power system considered. Therefore, it is recommended that more renewable energy sources can as well be incorporated so as to increase the power gotten from renewable energy sources.

REFERENCES

Ali Kadhem, A., Abdul Wahab, N. I., Aris, I., Jasni, J., & Abdalla, A. N. (2017). Reliability Assessment of Power Generation Systems Using Intelligent Search Based on Disparity Theory. *Energies*, *10*(3). https://doi.org/10.3390/en10030343

Craig, A., Li, X., Sesker, P., Mcinerny, A., DeAgostino, T., & Depcik, C. (2016, April). *Small-Scale Smart Electrical Grid Design, Construction, and Analysis*. https://doi.org/10.1115/IMECE2016-65219

Dong, Z. Y., Borghetti, A., Yamashita, K., Gaikwad, A., Pourbeik, P., & Milanović, J. (2012, April). *CIGRE WG C4.605 Recommendations on Measurement Based and Component Based Load Modelling Practice*.

Han, S. (2020). Three-Phase-Measurement-Based Load Modeling Technique Using Unbalanced Fault Data. *IEEE Access*, *8*, 83655–83662. https://doi.org/10.1109/ACCESS.2020.2992369

Iqbal, J., & Khan, Z. H. (2017). The potential role of renewable energy sources in robot's power system: A case study of Pakistan. *Renewable and Sustainable Energy Reviews*, *75*, 106–122. https://doi.org/https://doi.org/10.1016/j.rser.2016.10.055

Kontis, E. O., Papagiannis, G. K., Syed, M. H., Guillo-Sansano, E., Burt, G. M., Papadopoulos, T. A., & Chrysochos, A. I. (2017). Development of measurement-based load models for the dynamic simulation of distribution grids. *2017 IEEE PES Innovative Smart Grid Technologies Conference Europe (ISGT-Europe)*, 1–6. https://doi.org/10.1109/ISGTEurope.2017.8260251

Lasseter, R., Akhil, A., Marnay, C., Stephens, J., Dagle, J., Guttromsom, R., Meliopoulous, A. S., Yinger, R., & Eto, J. (2003). *Integration of distributed energy resources. The CERTS Microgrid Concept.*

Rocabert, J., Luna, A., Blaabjerg, F., & Rodríguez, P. (2012). Control of Power Converters in AC Microgrids. *IEEE Transactions on Power Electronics*, *27*(11), 4734–4749. https://doi.org/10.1109/TPEL.2012.2199334

Saviozzi, M., Silvestro, F., & Massucco, S. (2018). Implementation of Advanced Functionalities for Distribution Management Systems: Load Forecasting and Modeling through Artificial Neural Networks Ensembles. *Electric Power Systems Research*, *167*. https://doi.org/10.1016/j.epsr.2018.10.036

Sharafi, A., Vahidnia, A., & Jalili, M. (2019). Measurement-Based Identification of System Load Models for Low-Frequency Dynamics. *2019 9th International Conference on Power and Energy Systems (ICPES)*, 1–6. https://doi.org/10.1109/ICPES47639.2019.9105598

Singh, V. P., Kishor, N., & Samuel, P. (2016). Communication time delay estimation for load frequency control in two-area power system. *Ad Hoc Networks*, *41*, 69–85.

Zamani-Gargari, M., Kalavani, F., Abapour, M., & Mohammadi-Ivatloo, B. (2018). Reliability assessment of generating systems containing wind power and air separation unit with cryogenic energy storage. *Journal of Energy Storage*, *16*, 116–124. https://doi.org/https://doi.org/10.1016/j.est.2017.12.013

Zubo, R. H. A., Mokryani, G., & Abd-Alhameed, R. (2018). Optimal operation of distribution networks with high penetration of wind and solar power within a joint active and reactive distribution market environment. *Applied Energy*, *220*, 713–722. https://doi.org/https://doi.org/10.1016/j.apenergy.2018.02.016

PAPER 111 – DESIGN OF A LEUKEMIA DETECTION SYSTEM USING DIGITAL BLOOD SMEAR IMAGES

S. Saminu[1*], I. O. Muniru[1], S. A. Yahaya[1], A. J. Oladimeji[1], M. T. Ajibola[1], M. O. Ibitoye[1], Y. K. Ahmed[1], L. J. Jilantikiri[1]

[1]Department of Biomedical Engineering, University of Ilorin, Ilorin, Nigeria.
[*]Email: saminu.s@unilorin.edu.ng

ABSTRACT
Leukaemia is a fatal blood cancer that occurs due to the formation of abnormal and excessive increases in white blood cells in the bone marrow or blood. The traditional approaches used to diagnose the disease involve the manual analysis of blood sample images obtained from a microscope. This approach is tedious, slow, time-consuming, and prone to errors. Therefore, automatic detection of leukaemia based on the counting of the two blood cells is paramount for diagnosis and increasing the patient's survival rate. This paper presents a system that can detect each of the two blood cells needed through image processing, segmentation, and classification. The detection, classification, and counts are only limited to two of the cells present in the digital blood smear which are the white blood cells (WBCs) and red blood cells (RBCs). The model was evaluated with a collection of confirmed cases and normal cases to test its effectiveness in predicting the presence of Leukaemia by computing the ratio of WBC to RBC. The suggested model exhibits good performance results and can be utilized to make a reliable computer-aided diagnosis detection of leukaemia cancer.

KEYWORDS: Leukaemia, White Blood Cells (WBCs), Red Blood Cells (RBCs), Detection, Machine Learning, Blood Smear.

1. INTRODUCTION

Patients suffering from cancer that are dying due to the delay in discovering the cancerous cells in a blood smear is alarming, especially in developing countries. Cancer has been one of the leading causes of death among humans of all ages and gender according to research conducted by the Centre for Disease Control and Prevention in the United States (Bray *et al*., 2021). Leukaemia is a type of cancer that affects the White Blood Cells (WBCs) of the blood through malicious cloning of abnormal WBC; the bone marrow generates aberrant WBCs (Leukocytes). These aberrant cells should normally die after a while in normal circumstances, but, instead, their number increases. These aberrant WBCs prevent normal WBCs from carrying out their functions and as such cause Leukaemia disease. According to National Cancer Institute (USA), blood cancer is treatable if identified early (Sun, 2020). Leukaemia is detected by counting the corresponding blood cells in the suspected patient's blood sample under a microscope; however, this method can be tedious, time-consuming, and unsettling. One method of detecting blood cancer is by doing a complete cell or blood count to check for abnormalities in the blood which may indicate the presence of Leukaemia (Hegde, 2019). The complete blood count is performed by a haematologist who examines the blood sample under a microscope and checks for abnormalities as there is a normal range for both Red Blood Cell count and white blood cell count.

There are three types of cells in the human body; White blood cells, Red blood cells (RBCs) and, Platelets as depicted in Figure 1. The WBC are responsible for providing the necessary immune system required by the human body and it plays a pivotal role in protecting against the various diseases and infections by acting as a defence wall in the body (Shafique, 2018). The RBC is responsible for supplying oxygen to the body tissues from the heart (Fujita, 2021). According to Healthline, the normal RBC count range from 4.7 to 6.1 million cells per microliter μL) for men and 4.2 to 5.4 million cells per microliter (μL) for women and the normal number of White Blood Cells in the blood is 4,500 to 11,000 WBCs per microliter (4.5 to 11.0 × 10^3/μL). (Kannarkat, 2022). The nature of the disease can be determined using the correct counting and classification of these blood cells. This count is often tedious, hence the reason for the design of this system, which does the complete blood count automatically using image processing segmentation of blood smears and counting.

The design of a system that counts white blood cells and red blood cells in a sample digital blood smear and check for the presence of excessive white blood cells would reduce the manual work of medical practitioners, thus aids in the early detection and cure.

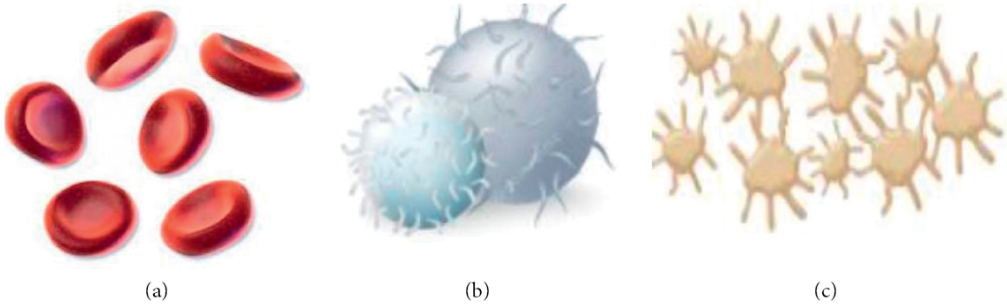

Figure 1. (a) Red blood cells (b) White blood cells (c) Platelets (Bukhari, 2022)

Several works have reported the segmentation of lymphocyte images as a region of interest for laboratory image analysis using computer-aided diagnostic and machine-learning techniques to improve the diagnosis and early detection of the disease (Jagadev, 2017). Cells in different types of leukaemia have been counted and differentiated based on the analysis of blood smear images (Wen, 2018; Xin,2016). (Ghaderzadeh, 2021) proposed a colour-based segmentation method that segment the lymphoblast and lymphocyte details of WBCs and eliminates extra elements contained in the blood. Generally, the segmentation of leukaemic disease is categorized into shape-based, region-based, and pixel-based approaches (Al-jaboriy, 2019). Edge-based and k-means were applied by (Sarder, 2020) to segment several smears of blood. The hybrid technique based on morphological and thresholding were proposed to segment the smears of blood with high accuracy (Bukhari, 2022). Most of the reported works in the literature employed complex machine learning and deep learning approaches that require sophisticated, higher memory processing units for algorithms execution. Therefore, this work aims to design a system that aids the detection of leukaemia (excessive presence of white blood cells) using image processing and Hough transform to count red blood cells and white blood cells in a digital blood smear based on low complexity and low-cost resources. This work only encompasses the complete blood count using digital image processing to detect whether there is a presence of leukaemia or not, the design does not tell which type of Leukaemia is present, its stage or the method of treatment.

The objectives of this work are to:

1. Analyze and extract both red blood cells and white blood cells using colour segmentation in MATLAB environment.
2. Design a system that can count the extracted entities i.e. (WBCs and RBCs count)
3. Ensure the accuracy of design results by testing against both confirmed Leukaemia blood smear samples and normal blood smear samples.
4. Deploy on a portable hardware that interfaces the user with the model.

The rest of this paper is organized as follows: section two discusses the methodology and materials used in this study. section three provides the results and a discussion of the results obtained. Finally, section four presents the conclusion of the study.

2. MATERIALS AND METHODS

2.1 Dataset

The dataset used in this work was obtained from the American Society of Hematology (ASH) image bank, a web-based image library that offers a comprehensive collection of images relating to a wide range of hematologic topics. It is a publicly available database that can be accessed via “https://imagebank.hematology.org/”.

2.2 METHODOLOGY

A MATLAB-based system was developed to ease the task of automatic classification of blood smear samples as having leukaemia or not. The system is a graphical user interface designed using GUIDE, an interactive design tool in MATLAB. The implementation process follows a typical image analysis pipeline. The block diagram

depicting the stages followed to achieve the proposed system is shown in Figure 2. It consists of image acquisition, image pre-processing, image segmentation, cell counting, and performance analysis. The main idea followed to achieve the desired result is that for any blood smear sample, the normal ratio of white blood cells to red blood cells should not be greater than 10%. The system is designed to generate an output "POTENTIAL LEUKEMIA DETECTED" if the ratio is more than 10%.

.

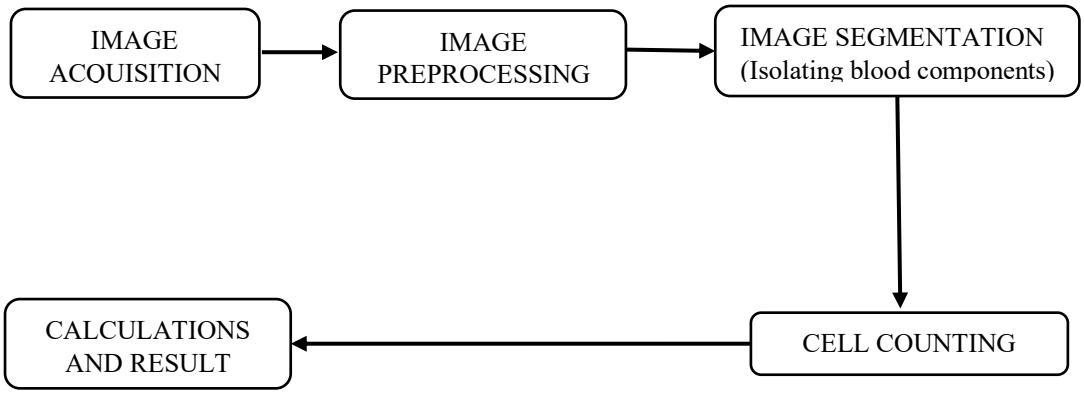

Figure 2. Block diagram of the proposed system

2.2.1 IMAGE ACQUISITION: In this study, the actual capturing of the microscopic images of the blood smear was not carried out. Rather, images downloaded from the ASH database were used. The image analysis process commences by loading an image into the MATLAB application built for this study.

2.2.2 IMAGE PREPROCESSING: The main goal of image preprocessing is to enhance the quality of the image by removing noise, correcting distortions, improving contrast, adjusting brightness and colour balance, and removing unwanted artefacts**.** Doing this can help to improve the accuracy of the subsequent image analysis steps. The final task then involves the conversion of the image to three common colour models used in image processing namely RGB, CYMK, and YCbCr. RGB is an additive colour model used in digital imaging systems that combines red, green, and blue colour channels to describe colours, with a range of intensity levels for each channel between 0 and 255. CMYK, on the other hand, is a subtractive colour model used in printing that describes colours by the amount of cyan, magenta, yellow, and black needed to produce a colour. Meanwhile, YCbCr is a colour space used in digital video and image processing that separates colour information from brightness information, with three channels: Y for brightness, and Cb and Cr for colour. YCbCr is often used in digital video and image formats such as JPEG and MPEG due to its efficient compression.

The reason for this is to determine which of the colour scales gives the best performance.

2.2.3 IMAGE SEGMENTATION:

This function allows the application to segment the image into its constituent cells using image processing techniques such as thresholding and morphological operations. Whereas thresholding is used to separate two or more images by setting an intensity threshold, a morphological operation is used to manipulate the shape and size of objects in an image. This step separates the white blood cells, red blood cells, and platelets from each other. The outcome of this function is that rectangular bounding boxes are placed around the WBCs and RBCs to enhance visual counting

2.2.4 CELL COUNTING: In this part, the bounded cells per group are counted automatically using the Hough transform. The ratio of the WBCs to the RBCs is then computed. An output is generated based on the value of the ratio.

3 RESULTS AND DISCUSSION

The range of WBCs and RBCs for a healthy adult is between 4,500 µL-11,000 µL and 4,500 µL – 5,900 µL respectively (Sun, 2020). µL pronounced as microliter is one-millionth of a litre, and is commonly used as a unit of measurement for blood components. In a sample of the portion of a regular arrangement of red blood cells, it is considered that if the ratio of WBCs to RBCs is 8% or more (Li, 2020), the outcome of such is regarded as "POTENTIAL LEUKEMIA DETECTED".

3.1 MODEL PERFORMANCE

The system is meant for counting components in blood smear samples. To test for performance, the model is supplied with various images of confirmed cases of leukaemia in blood smears and normal blood smears without any presence of excessive white blood cells.

3.1.1 Performance of the system with T-cell prolymphocytic leukaemia digital blood smear

T-cell prolymphocytic leukaemia (T-PLL) is an extremely rare and typically aggressive malignancy (cancer) that is characterized by the out-of-control growth of mature T-cells (T-lymphocytes). T-cells are a type of white blood cell that protects the body from infections. T-PLL affects older adults with a median age at diagnosis of 61 years, and it is more common in men than in women. (Castorvy et al, 2012). A typical T-Cell prolymphocytic blood smear sample used for the test is shown in Figure 3.

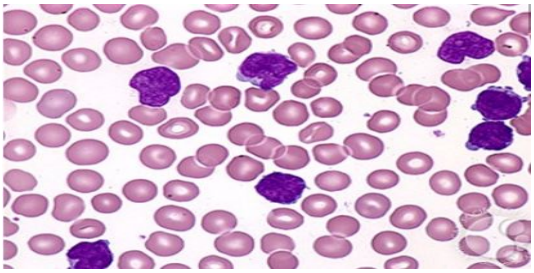

Figure 3. T-cell prolymphocytic leukaemia blood smear

The output from input the above image into the design is shown as follows:

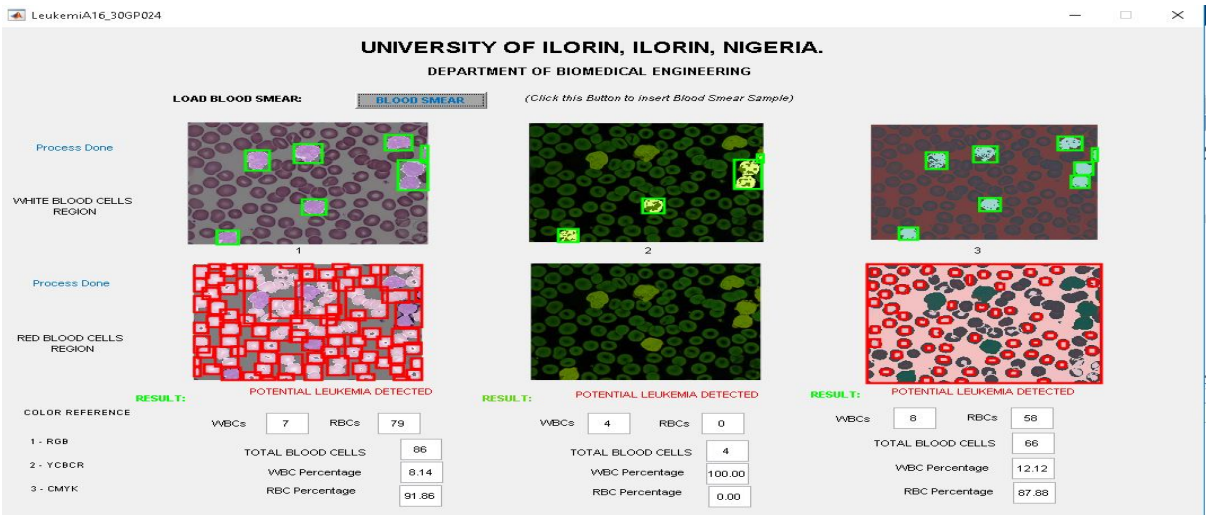

Figure 4. Result output for T-cell prolymphocytic leukaemia blood smear

The processed T-cell Prolymphocytic Leukaemia blood smear image shown in Figure 3 is transformed within 3 colour spaces to isolate overlapping cells into individual cells. There is a presence overlapping of white blood cells in the RGB regions of Figure 3 which alters the output of the result for processing in Figure 4. For the YCbCr colour space conversion of Figure 4, the overlapping cells are well isolated and the end user decides on

which colour space result to use. The CYMK colour region fails to identify red blood cells and can therefore be ignored in this result.

3.1.2 Performance of the system with normal cells from digital blood smear

A sample image of a normal blood smear with no Leukaemia shown in Figure 5 is tested against the design to ensure accurate performance of the design.

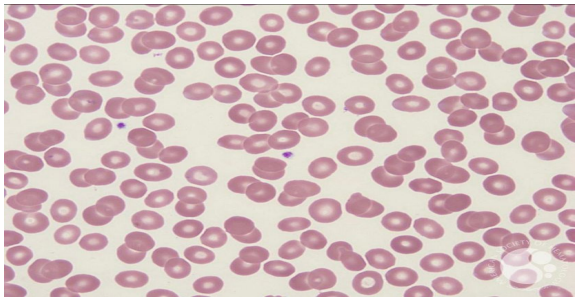

Figure 5. Normal blood smear

The output of the above image supplied to the designed system gives an output shown in Figure 6 which corresponds to the expected result for a normal blood smear

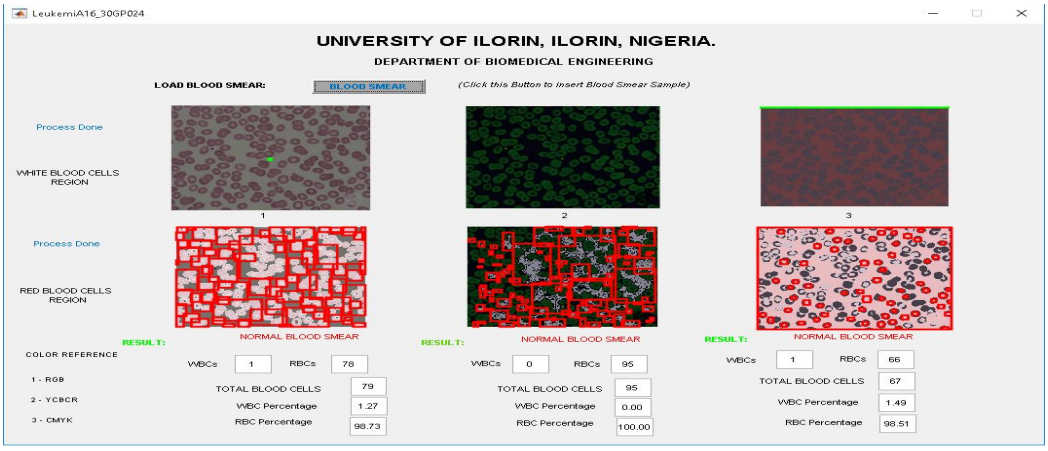

Figure 6. Result of normal blood smear from design output

The design runs the supplied image across three colour spaces, as sources and pixels of images differ, the best output which best selects the needed component should be used for result. It is discovered that the result correctly predicts the presence of a normal blood sample.

3.1.3 Performance of the system based on accuracy

To check if the design predicts the required result, series of tests were carried out by running the design against confirmed blood smear samples of both normal and leukemic blood smears. Two samples relating the actual expected result, also known as MANUAL COUNT and the results acquired from the design "DESIGN COUNT" for both normal and leukemic blood smear are presented in Tables 1.1 and 1.2.

Table 1.1. Test of design result against manual count for a sample Leukaemia blood smear

	WBCs	RBCs	PREDICTION
MANUAL COUNT	7	82	LEUKEMIA Present.

	COLOUR SPACES	WBCs	RBCs	PREDICTION
DESIGN COUNT	RGB	7	79	Potential Leukaemia Detected
	CMYK	4	0	Potential Leukaemia Detected
	YCbCr	8	58	Potential Leukaemia Detected

Table 1.2. Test of design result against manual count for a sample Normal blood smear

	WBCs	RBCs	PREDICTION
MANUAL COUNT	1	98	Normal

	COLOUR SPACES	WBCs	RBCs	PREDICTION
DESIGN COUNT	RGB	1	78	Normal Blood Smear
	CMYK	0	95	Normal Blood Smear
	YCbCr	1	66	Normal Blood Smear

4 CONCLUSION

A system that can count both RBCs and WBCs using image processing and segmentation will go a long way in relieving the stress put on the haematologist during the analysis of digital blood smear for leukaemia presence. The design proposed in this paper is suitable for quick counting of digital blood smear rather than having haematologist do it manually which can be stressful and contribute to errors. Although a haematologists still have to select the best suitable segmentation out of the 3 colour spaces used in this design, which are either RGB, CYMK or YCbCr , the performance results presented is still promising. A design that can classify the different types of Leukaemia detected by means of machine learning algorithm is required, as after using this design to count the various blood cells to determines excesses in the presence of white blood cells. There is still a need to study the shape of the corresponding cells to diagnose the type of Leukaemia present.

REFERENCES

Al-jaboriy, S.S. Sjarif, N.N. Chuprat, S. and Abduallah, W.M. (2019), Acute lymphoblastic leukaemia segmentation using local pixel information, Pattern Recognition Letters, 125, 85–90.

Bray, F., Laversanne, M., Weiderpass, E., & Soerjomataram, I. (2021), The ever-increasing importance of cancer as a leading cause of premature death worldwide. Cancer, 127(16), 3029-3030.

Bukhari, M. Sadaf, Y. Saima, S. and Ahmed, A. (2022), A Deep Learning Framework for Leukaemia Cancer Detection in Microscopic Blood Samples Using Squeeze and Excitation Learning, Mathematical Problems in Engineering, 2022, Article ID 2801227, 18 pages.

Catovsky, D. Dearden, C. (2012), Treatment of T cell prolymphocytic leukaemia. In UpToDate. https://www.uptodate.com/contents/treatment-of-t-cell-prolymphocytic-l Dearden C. How I treat prolymphocytic leukaemia. Blood, 120(3), 538-551.

Fujita, T.C. Sousa-Pereira, N. Amarante, M.K. and Watanabe, M.A. (2021), Acute lymphoid leukaemia etiopathogenesis, Molecular Biology Reports, 48(1), 817–822.

Ghaderzadeh, M. F. Asadi, A. Hosseini, D. Bashash, H. Abolghasemi, and A. Roshanpour, (2021), Machine learning in detection and classification of leukaemia using smear blood images: a systematic review," Scientific Programming, 2021, Article ID 9933481.

Hegde, R.B. Prasad, K. Hebbar, H. Singh, B.M.K. and Sandhya, I. (2019), Automated decision support system for detection of leukaemia from peripheral blood smear images, Journal of Digital Imaging, 33, 361–374.

Jagadev, P. and Virani, H. (2017), Detection of leukaemia and its types using image processing and machine learning, in Proceedings of the 2017 International Conference on Trends in Electronics and Informatics (ICEI), IEEE, Tirunelveli, India, 522–526.

Kannarkat, G. T., Darrow, J., & Moghekar, A. (2022). Reassessing accuracy of blood cell correction factor for traumatic lumbar puncture. Journal of the Neurological Sciences, 432, 120097.

Li, L. and Wang, Y. (2020), Recent updates for antibody therapy for acute lymphoblastic leukaemia, Experimental Hematology & Oncology, 9, 33–11.

Sarder, M.A. Maniruzzaman, M. and Ahammed, B. (2020), Feature selection and classification of leukaemia cancer using machine learning techniques, Machine Learning Research, 5(2), p. 18.

Shafique, S. and Tehsin, S. (2018), Acute lymphoblastic leukaemia detection and classification of its subtypes using pretrained deep convolutional neural networks, Technology in Cancer Research & Treatment, 17, Article ID 1533033818802789.

Sun, L., Yu, Y., Niu, B., & Wang, D. (2020). Red blood cells as potential repositories of microRNAs in the circulatory system. Frontiers in genetics, 11, 442.

Wen, J. Xu, Y. Li, Z. Ma, Z. and Xu, Y. (2018), Inter-class sparsity based discriminative least square regression Neural Networks, 102, 36–47.

Xing, F. and Yang, L. (2016), Robust nucleus/cell detection and segmentation in digital pathology and microscopy images: a comprehensive review

PAPER 112 – SUSTAINABLE SOLID WASTE MANAGEMENT AT GREGORY UNIVERSITY UTURU

A. C. Ekeleme[1], C. E. Njoku[2], B. N. Ekwueme[3], C. Onuoha*[2], V. E. Amuluku[3]

[1]Department of Civil Engineering, Abia State University Uturu, Abia State, Nigeria
[2]Department of Materials and Metallurgical Engineering, Federal University of Technology Owerri, Imo State Nigeria
[3]Department of Civil Engineering, Gregory University Uturu, Abia State, Nigeria
*Email: chukwudikeonuoha@gmail.com

ABSTRACT
As man carries out his daily activities, waste is generated leading to pollution; and the associated challenges in the proper and sustainable management of the waste. The universities are in no wise exempted from the rapid pollution from municipal solid wastes. In this study, the wastes generated at the Gregory University Uturu campus were quantified and classified according to standards, and possible strategies suggested for sustainable waste management. During the study, an average of 449.8 kg/day (0.45 tons/day) were generated, with plastics and polythene wastes having the largest proportions of 35% and 25% respectively. Whereas other waste categories which include paper, organic, metal, e-waste, medical waste, textile, and others resulted in 15%, 12%, 4%, 2%, 1%, 1%, and 2% respectively. The campus generates waste at approximately 0.21 kg/capita/day and about 82% of the waste can be recycled. Using the waste-to-energy approach, a minimum of 22.kWh of electricity can be generated per day. The study recommends the adoption of the waste management hierarchy (reduction, reuse, anaerobic digestion, incineration, and landfilling) as a sustainable approach to managing waste in the University.

***KEYWORDS*:** Solid waste management, Pollution, Sustainable approach, Universities

1. INTRODUCTION

The swift growth of the world population, perpetually growing living standards, and massive technological innovations are constantly increasing the multiplicity and quantity of solid waste. Virtually everything man does results in some form of waste (Saleh & Koller, 2019). In fact, global solid waste (SW) released in 2010 was estimated at about 10.4 billion tons and is envisaged to stand at 148 billion tons by 2025 (Alam & Qiao, 2020). Therefore, waste is inescapable as it is an outcome of daily human activities.

Waste is any solid, fluidy, gaseous, radioactive substance, the release, disposal, and throwing away of which may cause deadly changes to the environment (Ashikuzzaman & Howlader, 2019). Generation of municipal solid waste, coupled with the high organic content present in solid waste and its often inadequate disposal, results in extensive environmental pollution, via the emission of gases such as methane (CH_4) and carbon monoxide (CO) that contribute to the greenhouse effect. As a result of this environmental menace, municipal authorities are presently charged with the responsibility of discovering and implementing techno-economic and political solutions of greater efficiency to manage the growing quantities of municipal solid waste (Saleh & Koller, 2019). Administration of waste encompasses the gathering, transporting, treating or dumping of rejected materials. Justifiable solid waste management is one of the fundamentals for workable environmental running as the careless disposal of solid waste contaminates the environment and endangers human wellbeing (Ashikuzzaman & Howlader, 2019).

In prehistoric cities, wastes were managed by discarding on top of unpaved streets and thoroughfares, where they were abandoned to accrue (Abdel-Shafy & Mansour, 2018; Briney, 2020). It was in 320 BCE in Athens that the first recognized law forbidding this exercise was instituted. In Greece and in the Greek-dominated cities of the eastern Mediterranean, in ancient Rome, and in most other parts of the world, methods of disposal were very rudimentary, which included open pits situated within the vicinity. As the number of residents increased, plans were directed towards conveyance of waste further away from the cities (Omang *et al*., 2021). As at 2018, the speed of waste production in Nigeria was valued at 0.65-0.95 kg/capita/day which translates to an average of 42 million tonnes of wastes annually. This is more than half of 62 million tonnes of waste generated in sub-Sahara Africa annually and the problem is the where and how to channel these wastes.

Several research works have investigated municipal solid waste management, (Abdel-Shafy & Mansour, 2018; Oji Iheukwumere *et al*., 2020; Omang et al., 2021; Ugwu *et al*., 2021; Zadawa *et al*., 2015). Challenges and conceivable panacea to the municipal solid wastes management in Nigeria was investigated by (Amuda *et al*.,

2014), They discovered that, with the global population explosion, unplanned urbanization, climate change, combined with existing un-sustainability features; cities in developing countries are certainly going to encounter difficulties in proficiently dealing with municipal solid waste which will undeniably lead to enormous glitches on They further recommended combined efforts of local, state and federal government, the stakeholders, non-governmental organizations and the private sector in tackling this menace. The research focused on the need for efficient solid waste management. However, (Sembiring & Nitivattananon, 2010) that studied the integration of the informal sector in sustainable solid waste management, posited that effective and efficient waste management will lead to unemployment of the scavengers and waste pickers who also need to survive in the society.

Due to lax environmental regulations, insufficient resources, and unchecked rapid urbanization and industrialization, indiscriminate dumping is the primary disposal method in developing countries such as Nigeria (Ugwu *et al*., 2021). More so, the Federal Government of Nigeria has promulgated various laws and regulations to safeguard the environment. This effort of the Federal Government is left on the shoulders of the Federal Ministry of Environment, empowered to administer and enforce environmental laws in Nigeria. However, in Nigerian universities, waste composition and generation patterns have received little or no attention. Universities are tasked with the critical responsibility of promoting safe and friendly environments by adopting responsible waste management policies.

Gregory University Uturu (GUU) is sited at Uturu, Abia State in Nigeria. It is a Private University named after Pope Gregory I. The staff and students' population as at the period of this study (in the year 2022) is about 2100. Gregory University, Uturu (GUU) has about eight colleges and fifty-seven departments. The colleges include; College of Medicine and Health Sciences, College of Law, College of Engineering, College of Agriculture, College of Environmental Sciences, College of Humanities, College of Natural and Applied Sciences, Joseph Bokai College of Social and Management Sciences, and College of Education. The appalling situation in Nigeria is exactly what is obtainable at Gregory University and other Nigerian universities in terms of waste management. Most tertiary institutions in the country lack data on the quantity and composition of waste generated, making it difficult to design a waste management system. Thus, this research is intended to identify the causes of waste generation, determine the amount of waste generated daily and design an effective waste management model for Gregory University; so as to provide the needed data for efficient solid waste management.

2. MATERIALS AND METHODS

The materials used for this study comprise weigh balance (200kg scale) for weighing samples, spade for mixing and leveling waste during sorting, personal protective equipment (nose mask, coverall, safety boots, hand gloves, eye protection) worn during field work, oven for drying the waste to get some of the generated waste's chemical and physical properties. Others include litter pickers for picking and sort the waste, plastic containers for collecting samples and for sorting and polythene bags for samples packaging after weighing.

In this study, solid waste were collected from selected sites which include each faculty, hostel, and cafeterias. Sampling and analysis were performed as stipulated by (*ASTM D5231-92(2016) - Standard Test Method for Determination of the Composition of Unprocessed Municipal Solid Waste*, n.d.). The sampling of the waste was done day-to-day in a space of eight days. In order to find out the quantity of waste produced, waste was taken and retained in large bags. Labels of activity area and dates were placed on the large bags, and kept outside the building for a while, to resume taking of weight later. The average weights of each component were added to determine the total amount of solid waste at each waste dump point. The weight of waste generated at each dump point was recorded for all the eight days. The different waste components were characterization by sorting and separating into several categories (leaves, food waste, paper, cardboard, plastics, metal, and others). Quartering method was used in reducing the homogeneously mixed waste to a size that can be tested in the laboratory. The obtained sample was placed plastic bags, closed and taken to the laboratory for tests.

Furthermore, the solid wastes were differentiated into recyclable and non-recyclable categories. The recyclable wastes for which there is a market include metals, polythene bags, paper, and plastic while those for which there is no market are e-waste, glass, leather, organic waste, and textile. Non-recyclable category includes wastes such as sanitary waste. Food scraps, garden wastes, wood, textiles, newspaper, packaging material, magazines, office paper, and cardboard were classed as recyclable organics. Animal excreta, miscellaneous paper, cellophane, miscellaneous cardboard, waxed paper, and plasticized paper were classed as non-recyclable organics.

The weight of the solid waste generated within the campus per day was determined by subtracting the weight of the empty collection tank or the previous weight recorded from the weight of the waste generated on a particular day. The waste generated per capita per day was the obtained by dividing by the population of students and staff in the university.

Samples were analyzed for moisture content, in that a portion of the waste was placed in a clean and dry container weighing W_1 and the weight of the sample and container, W_2 was recorded. The container with the sample was then oven-dried at a temperature of about 110 degrees Celsius for about twelve hours until a constant mass was reached. The sample was taken out of the oven, cooled, and and then re-weighed (W_3). The percentage moisture content was obtained using equation (1) (HAYAKAWA & TSUBAKI, 1998).

$$M = \frac{W_2 - W_3}{W_2} x\ 100\% \quad \text{.....(1)}$$

where M is the moisture content, W_2 is the initial weight and W_3 is the final weight.

3. RESULTS AND DISCUSSION

3.1 Waste characterization

The essence of waste composition is to predict the waste management strategy to be adopted in a particular location. For example, organics served as food for pests, insects and rodents and hence need to be disposed of regularly since controlled biological treatment facilities for its conversion to wealth are lacking. Figure 1 shows the waste composition by weight of municipal solid waste generated at Gregory University Uturu. Plastics make up most of the waste generated on campus, accounting for 38 percent (Figure 2(a)). Polythene ranks with 25 percent (Figure 2(b)), followed by paper (Figure 2(c)) and organic materials with 15 percent and 12 percent, respectively. Others include textile waste materials (2 %), E-waste (2 %), medical waste (1 %) and metal trash (Figure 2(d)) (4 %). The quantity of the recyclables like paper and plastic is an indication of immediate monetary value to the collectors. (Ranjith Kharvel Annepu Advisor & Themelis Stanley-Thompson Professor Emeritus, 2012) made similar observations in their work on sustainable solid waste management in India. The reason for this high percentage of plastics is because Gregory University Uturu is a Private University where the main food types as provided by the school cafeterias are such foods and drinks that are contained in plastic disposable containers. Polyethylene bags ranked second due to their high use for sachet waster due to scarcity of drinkable water on campus. Paper is also a prevalent waste category in universities due to massive administrative and academic activities. Metal waste consist of aluminium tin, can drink containers, and other metal scraps from the mechanical metal workshop located at the school.

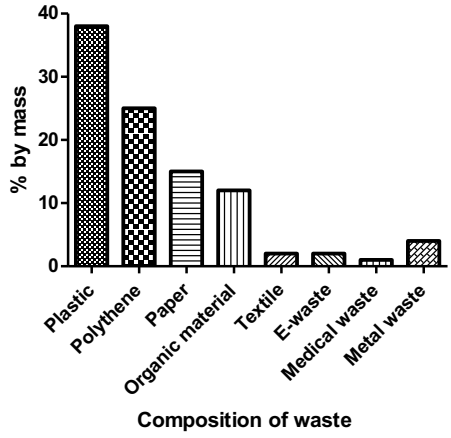

Figure 1 Composition of the waste in percentage

Figure 2 Grouping of major waste materials (a) plastic (b) polythene (c) paper and (c) metal waste

3.2 Estimation of daily waste generated

The average waste generation of 449.8 kg/day (0.45 tons) was obtained from this investigation, giving a per capita generation rate of 0.21 kg/capita/day. Most of the organic waste was from staff quarters, cafeterias, and garden waste, while the inorganic waste was primarily plastic waste from the hostels and paper waste from educational and administrative activities. Table 1 is a display of the average waste generated from different dump sites in the campus. The hostel and residential areas generated the highest amount of waste with 324.2kg/day, followed by the academic zones with 52.7kg/day and the cafeterias with 48kg/day. Other supporting areas like the security posts, sport area and university clinic generated 11.4kg/day, school auditorium area 7.5kg/day, and the religious area generating the least amount of waste, 6kg/day. The quantity of waste generated in a particular area is largely dependent on the degree of human activities in that area, as can be seen from the result.

Table 1 Average waste generation from different dump sites

Dump site	Average waste generation/day	Percentage by weight
Academic areas; colleges, administrative buildings, library	52.7	12
Residential area; hostels, staff quarters, chancellor villa	324.2	72
Cafeterias	48	10
Religious areas	6	1
School auditorium/ amphitheatre	7.5	2
Other areas; security post & clinic	11.4	3
Total	449.8	100

3.3 Optimization of collection points

The reconnaissance survey carried out to determine the current number of collection points in GUU showed that the current number of primary collection points is inadequate to cater for the amount of waste generated by the university. The result showed that currently, we have 25 primary collection points in GUU and these primary collection points were also found to be unevenly distributed over the university area leading to waste being indiscriminately dumped and open-burnt in certain areas, actions that harm the environment. The number of primary collection points was increased to an optimized value of 97 collection points with an addition of 55 extra collection points to the existing number currently in the university. The primary collection points were placed at not more than 15m apart in areas where there are a lot of activities and to enhance the ease of access to the collection points as well as the route for transportation to the secondary collection points. Figure 3 is the map of GUU showing optimization of waste collection points.

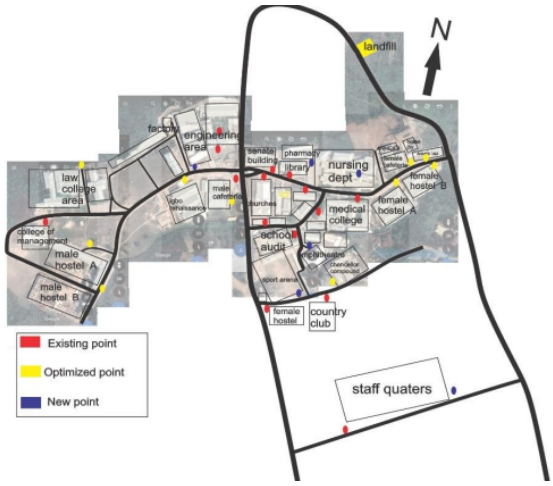

Figure 3: Map of GUU showing optimized collection points

3.4 Moisture content of the waste

The moisture content of a waste stream is a crucial parameter for the degradation of biodegradable waste in landfills, and it is also a key determinant in the production of landfill gas like methane. Moisture content is also used to determine the calorific value of waste applied in incineration and waste-to-energy generation. In this work, the average moisture content of the waste stream was obtained to be 16.15% (using Equation 1) which is slightly less than the average moisture content in waste streams in Nigeria (20%) as stated by (Zadawa et al., 2015) and even lower than observed by other researchers (Ranjith Kharvel Annepu Advisor & Themelis Stanley-Thompson Professor Emeritus, 2012), (Ugwu et al., 2021).

3.5 Recyclable potential of waste

A reasonable proportion of the waste generated in the GUU campus is recyclable or is potentially recyclable. It shows that 82% of the waste streams are recyclable while 15% are potentially recyclable. The GUU campus has a lower non-recyclable waste of 3%. GUU is not able to recycle, reuse or recover energy from any of its waste categories. Figure 4 shows the potential recycling rating for waste generated in the university; it shows that 82% of the waste can be recycled, 15% has the potential of being recycled, while as 3% cannot be recycled. Thus, a

large percentage of the waste stream can be recycled if proper channels are put in place to segregate waste at the source.

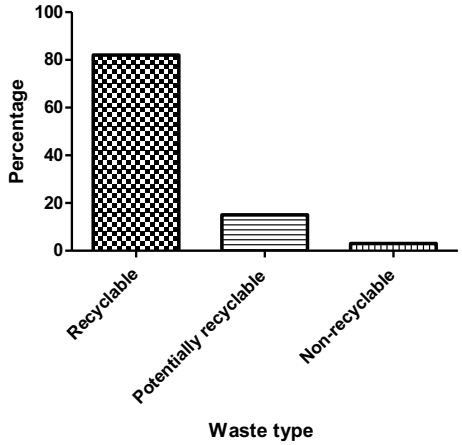

Figure 4 Level of recyclability in percentages

3.6. Sustainable management strategies

Universally, the initiative for workable measures and approaches to solid waste management is on the increase. Appropriate sustainability measures are necessary in order to prevent the attendant health implications of indiscriminate dumping of waste in the society. Conventionally, the most prevalent sustainability measures in use include the 3Rs (i.e. reduce, re-use and recycle), composting, open burning, anaerobic digestion (incineration) sanitary landfilling, etc. Most of these measures are capital intensive and can only be efficiently practiced in advanced economies. This study has revealed that there is high percentage of recyclable waste at the university but at present, the University has no existing recycling facilities probably due to lack of funds and expertise. Hence, the best approach remains reduction at source and re-use.

3.6.1 Reduction, Re-use and recycle

Source reduction focuses on minimization of generation of waste. Efforts should be made to prevent unnecessary waste generation. This could be achieved by enhancing public awareness on the dangers of municipal solid waste, which will in turn change the consumption pattern of the citizens. Again, the essence of the re-use strategy cannot be over-emphasized. As uncovered in the Gregory University Uturu, there is large proportion of plastic containers generated as a result of the feeding pattern in the university. Staff and students should be encouraged to go for returnable and re-usable containers. Secondary usage of waste is also to be encouraged as far as it can be done in a hygienic manner. Since, the university does not have facilities for recycling, the informal sector can be engaged for the collection of recyclable wastes while market for recyclables are explored for sale of such items. This will go a long way in tackling the menace.

3.6.2 Utilization of Bio-Gas

Energy can be derived from the enormous waste generated on campus. This can be obtained by the decomposition of organic waste anaerobically to generate methane gas. This gas can be used as fuel to power automobiles, generate electricity and also serve as cooking gas for domestic use. Though the waste generated by Gregory University contains a low proportion of organic waste (12 percent), the waste to energy prospects of the school can be increased by considering other energy-generating management methods like incineration. The campus can produce at least 225 kWh of electricity per day from its 0.45 tons of waste generated daily. When this amount of energy is properly harnessed and distributed to campus users, significant savings on-grid electricity can be realized in addition to a cleaner environment. Additionally, methane can be produced via anaerobic composting of agricultural and human wastes in digesters. In biogas digesters, waste can be fermented to produce a gas rich in methane. The gas can be harnessed to generate enough energy for electricity, cooking, lighting, and a variety of other energy-intensive applications.

3.6.3 Incineration

Incineration is primarily the process of destroying waste in a furnace by controlling combustion at high temperatures to generate steam, which is then used to generate electricity via steam turbines. By incinerating waste, approximately 70% of the total waste mass and 90% of total volume can be reduced, leaving a small residue of waste to be disposed of in a landfill. If this is done, the pressure demand on landfills will be removed and the huge cost associated with waste disposal will be saved. The waste stream in GUU is rich in combustible materials like paper (15%), polythene (25%), plastic (38%) and medical waste all of which can easily be taken care of by incineration. Incineration not only reduces waste volumes but also provides alternative energy sources. However,

incineration plants are typically among the most expensive SWM options, requiring highly skilled personnel and meticulous maintenance. Hence, it is recommended that incineration be used only when other simpler and less expensive options are unavailable.

3.6.4 Landfilling

Sanitary landfilling is the most common method of disposing of municipal solid waste globally and the cheapest and most convenient method adopted by developing countries, where 65 to 80 percent of collected solid waste is disposed of. Other methods cost largely more than landfilling and as such, landfilling is no longer the preferred option only in developing countries. After considering all other options in the waste hierarchy system, the final point of disposal of the waste generated in GUU should be an engineered landfill. An engineered landfill also known as a sanitary landfill which the school is currently using should be improved to manage the waste generated in the school.

4. CONCLUSION

The status of waste generation on campus, its composition, and the possibility for sustainable management was determined in this study with Gregory University as case study. The amount of waste generated by various parts of the university and the associated student and staff population were also estimated. During the study period, Gregory University generated an average of 449.8 kg of solid waste per day, with polythene and paper waste accounting for the largest proportions at 26 percent and 24 percent, respectively. The waste generation was approximately 0.21 kg/capita/day. The university can generate approximately 225 kWh of electricity per day if appropriate waste-to-energy (WTE) technologies are implemented. The in-depth understanding of waste generation trends in GUU and how this should result in more sustainable waste management strategies on campus is expected to spur similar studies in Nigerian universities.

ACKNOWLEDGEMENTS

The authors acknowledge Gregory University Uturu for providing the facilities used in this investigation.

REFERENCES

Abdel-Shafy, H. I., & Mansour, M. S. M. (2018). Solid waste issue: Sources, composition, disposal, recycling, and valorization. In *Egyptian Journal of Petroleum* (Vol. 27, Issue 4, pp. 1275–1290). Egyptian Petroleum Research Institute. https://doi.org/10.1016/j.ejpe.2018.07.003

Alam, O., & Qiao, X. (2020). An in-depth review on municipal solid waste management, treatment and disposal in Bangladesh. In *Sustainable Cities and Society* (Vol. 52). Elsevier Ltd. https://doi.org/10.1016/j.scs.2019.101775

Amuda, O. S., Adebisi, S. A., Jimoda, L. A., & Alade, A. O. (2014). *Journal of Sustainable Development Studies Challenges and Possible Panacea to the Municipal Solid Wastes Management in Nigeria*. *6*(1), 64–70.

Ashikuzzaman, M., & Howlader, M. H. (2019). *Sustainable Solid Waste Management in Bangladesh* (pp. 35–55). https://doi.org/10.4018/978-1-7998-0198-6.ch002

ASTM D5231-92(2016) - Standard Test Method for Determination of the Composition of Unprocessed Municipal Solid Waste. (n.d.).

Briney, A. (n.d.). *An Overview of Municipal Waste and Landlls How Cities Deal With Garbage, Recycling, Landlls, and Dumps PRINT By SHARE FLIP EMAIL*. https://www.thoughtco.com/municipal-waste-and-landfills-overview-1434949

HAYAKAWA, O., & TSUBAKI, J.-I. (1998). 粒子の形態分析 3. 粒子径分析 : 3. 3 レーザ回折・散乱法, 光子相関法. *Journal of the Society of Powder Technology,Japan*, *35*(12), 866–875.

M. Saleh, H., & Koller, M. (2019). Introductory Chapter: Municipal Solid Waste. In *Municipal Solid Waste Management*. IntechOpen. https://doi.org/10.5772/intechopen.84757

Oji Iheukwumere, S., Friday Nkwocha, K., & Patrick Nwabudike, C. (2020). Schematic Modelling of Sustainable Solid Waste Management in Nigeria. *International Journal of Sustainable Energy and Environmental Research*, *9*(2), 98–109. https://doi.org/10.18488/journal.13.2020.92.98.109

Omang, D. I., John, G. E., Inah, S. A., & Bisong, J. O. (2021). Public health implication of solid waste generated by households in bekwarra local government area. *African Health Sciences*, *21*(3), 1467–1473. https://doi.org/10.4314/ahs.v21i3.58

Ranjith Kharvel Annepu Advisor, by, & Themelis Stanley-Thompson Professor Emeritus, N. J. (2012). *Sustainable Solid Waste Management in India*.

Sembiring, E., & Nitivattananon, V. (2010). Sustainable solid waste management toward an inclusive society: Integration of the informal sector. *Resources, Conservation and Recycling*, *54*(11), 802–809. https://doi.org/10.1016/j.resconrec.2009.12.010

Shekdar, A. V. (2009). Sustainable solid waste management: An integrated approach for Asian countries. *Waste Management*, *29*(4), 1438–1448. https://doi.org/10.1016/j.wasman.2008.08.025

Ugwu, C. O., Ozoegwu, C. G., Ozor, P. A., Agwu, N., & Mbohwa, C. (2021). Waste reduction and utilization strategies to improve municipal solid waste management on Nigerian campuses. *Fuel Communications*, *9*, 100025. https://doi.org/10.1016/j.jfueco.2021.100025

Zadawa, A. N., Omran, A., & Robinson, G. M. (2015). Challenges in developing and threshold countries to facilitate the NSP: Innovative sustainable solid waste management in Nigeria. In *Strategies Towards the New Sustainability Paradigm: Managing the Great Transition to Sustainable Global Democracy* (pp. 155–169). Springer International Publishing. https://doi.org/10.1007/978-3-319-14699-7_13

PAPER 113 – SOLID WASTE MANAGEMENT IN A NIGERIAN UNIVERSITY HOSTELS

Mokuolu O.A*, Alabi K.A

Department of Water Resources and Environmental Engineering, Faculty of Engineering and Technology, University of Ilorin, Ilorin, Kwara state, Nigeria
*Email: mokuolu.oa@unilorin.edu.ng

ABSTRACT

Waste generation rate and characterization are prerequisites for developing a sustainable solid waste management system. This study presents the generation rate and characterization of solid waste within the hostels in University of Ilorin Campus. The study was aimed to determine the amount of waste generated and propose better disposal method. Structured questionnaires were administered both physically and online with 400 and 157 respondents obtained respectively. Data was analyzed using statistical tools. Quantification and characterization were also carried out in the 38 hostels within the campus. A total of 1528 Kg/day were generated in the hostels out of the 3255 Kg/day generated in the University. Methods of disposal observed were open burning (32.7%), open dumping (26.2%), Incineration (20.3%), burial in a pit (14.5%), others (6.3%). Food, polythene, plastic, glass, and metal wastes were major categories found. The study revealed 100% recyclable materials. It is therefore recommended that University of Ilorin school management take immediate action by educating the entire populace within the school premises on the concept of 7R's or creating awareness and/or other waste to wealth initiatives in their solid waste management system. It is also recommended that there should be sanction(s) for mismanagement of solid waste within the hostels on campus.

***KEYWORDS*:** Waste generation, Waste characterization, Hostel, waste disposal/ end point, Ilorin

1. INTRODUCTION

Solid waste is a complex mixture of different substances that are discarded by household, individual or organizations that are harmful to the environments and health (Rushton, 2003). Umeh *et al.*, (2019) also described wastes as: "unwanted or unusable materials from industry and agriculture, businesses and other household items and can be liquid, solid or gaseous in nature, and hazardous or non-hazardous". In a simple approach, waste is an irresistible material that emanates in daily activities. However, solid waste is neither liquid nor gaseous material that has performed primary functions and not useful again to its handler.

Solid waste management can simply be defined as the control of solid waste from birth to burial. The term "from birth to burial" in this context means from the point of generation, storage, collection, transfer and transport, processing and to the final point which is disposal. The fundamental target of solid waste management is to protect the health of the population, promote environmental quality, develop sustainability and provide support to economic productivity through utilization of waste as a resource (Dong *et al.,* 2005). Waste management is an important element of environmental protection (Igbinomwanhia & Olanipekun, 2009). Waste management is important as improperly handled waste can have devastating effects on both the environment of its surroundings as a whole, and on the health of people in places where poor waste management occur (Cogut, 2016). Solid waste management problem has been a reoccurring issue in most developing countries higher institutions, especially in our dear country, Nigeria. In most Nigeria universities, solid waste management issue emerged every year as more students are being admitted.

University of Ilorin is located in Ilorin, the capital city of Kwara State on latitude 8.4799° N and longitude 4.5418° E, covering an approximate land mass of 5,000 hectare. Currently there are 38 hostels on the university campus. University of Ilorin, Ilorin is a federal government university, with potentials for massive growth and expansion for the fact that the institution remains the most sought after. Physical development and population increase yearly in the institution and these lead to increment in solid waste generation. According to Hakami and Seif (2015),

development does not come without environment burdens, generation of waste is one among them. The persistence of solid waste management menace is due to lack of generation rate data, proper characterization, knowledge on health and environmental effect, knowledge on Waste to Wealth, sensitization, intensive institutional research and adequate budgetary.

As University of Ilorin is known to be one of the largest institutions in Nigeria, there is no existing data for waste generated per day per capita which implies that there is no efficient solid waste management body. Most of the generated solid wastes are openly burnt in the university dump site which is harmful to public health and the environment. This work will ultimately make a revelation of the amount of waste being generated in the university hostels and characterization of the waste to propose efficient disposal method to the management.

2. METHODOLOGY

The techniques that were employed in the study involved the collection of first-hand data from the porters, cleaners, waste collectors and students within the study area. The data collection techniques include the following:

2.1 Site Visitations

This is the physical visitation to the study area to carry out reconnaissance survey

2.2 Questionnaire

Structured questionnaires were administered both physical and online. Minimum sample size of 384 were obtained using Wayne (2007) formula. 400 were obtained in physical while 157 were obtained online.

The questionnaires were designed in a simple and clear manner to obtain accurate information from students. The questionnaire was targeted to obtain the following:

(i) Types of waste generated daily
(ii) Availability of waste bin for storage
(iii) Method of collection
(iv) Frequency of collection
(v) Method of disposal

These questionnaires were administered in two forms which include the following:

(i) Self-administered: Questionnaires were delivered to the targeted group of people to fill themselves.

(ii) Online survey: Google form was designed to reach out to more students on campus. This was done also to reduce the amount of waste that will be generated from printing questionnaires.

2.3 Characterization

This is a process of sorting out solid waste into different components. Characterization of solid waste is used to enhance processing, recovering, and proper management of solid waste. Waste characterization method of Bernache-Pérez *et al.,* (2001) which was used by Oyelola and Babatunde (2008), was applied in this study. The method involves measurement, classification and weighing of solid waste from specific sources. This method was also used by Okeniyi and Anwan, (2016). Thus, the solid waste was characterized in accordance with College and University Recycling Council (CURC) grouping system with modifications by Oladejo *et al.,* 2018 accommodate peculiar waste stream generated on campus. Plate 1 shows characterization process in a male hostel and plate 2 shows the open burning method on campus.

Solid waste in this study was categorized into the following components: paper, food, plastic (food packs, pet bottles, etc.), polyethylene (water sachets, nylon, etc.), metals (can drinks, etc.), glass, and sanitary (diapers, pads, and rags).

3. MATERIALS AND METHODS/METHODOLOGY/EXPERIMENTAL PROCEDURE

(i) Mechanical weighing scale

(ii) Personal protective equipment/tools (PPE)
(iii) Shovels, rakes, dust pans, hand brooms, magnets, and other necessary tools

4. RESULTS AND DISCUSSION

The data was analyzed using the following tools:

(i) SPSS 26
(ii) Microsoft Excel

Plate 1: Characterization at a male Hostel

Plate 2: Open burning on campus

The mass-based distribution of the quantified wastes in different hostels within the university campus is presented in Table 1. The table shows that Hall B generated the highest amount of waste daily.

Table 1: Amount of waste generated per day per hall

S/N	Hostel	Day 1	Day 2	Day 3	Day 4	Average (Kg)
1	Hall A	41.27	40.90	16.70	38.03	**34.23**
2	Hall B	60.83	41.77	46.95	62.71	**53.07**
3	Hall C	50.23	39.11	75.45	31.88	**49.17**
4	Hall D	64.55	47.39	42.32	26.94	**45.30**
5	Hall E	53.77	41.35	26.95	42.80	**41.22**
6	Hall F	35.95	39.19	53.98	50.86	**45.00**
7	Hall G	29.91	36.73	62.19	37.79	**41.66**
8	Hall H	42.99	32.36	37.41	53.54	**41.58**
9	Hall I	35.59	58.12	53.75	35.22	**45.67**
10	Hall J	21.75	33.14	33.85	66.69	**38.86**
11	Hall K	43.72	34.87	44.88	13.96	**34.36**
12	Hall L	40.54	23.86	30.54	53.56	**37.13**
13	Hall M	39.37	23.08	54.57	46.79	**40.95**
14	Hall N	47.90	49.83	0.00	37.26	**33.75**
15	Hall O	32.64	26.92	39.85	23.44	**30.71**
16	Hall P	45.92	30.27	33.18	50.49	**39.97**
17	Hall Q	52.70	14.61	56.49	64.66	**47.12**
18	Hall R	28.45	56.34	26.94	28.24	**34.99**
19	Hall S	32.55	58.35	55.83	34.02	**45.19**
20	Hall T	25.60	39.32	47.10	54.39	**41.60**
21	Hall U	18.22	18.95	49.43	27.27	**28.47**
22	Hall V	37.00	48.03	22.06	37.25	**36.09**
23	Hall W	29.23	46.57	44.31	43.76	**40.97**
24	Hall X	24.39	54.03	24.00	39.78	**35.55**
25	Hall Y	64.22	28.49	43.82	48.90	**46.36**
26	Hall Z	54.48	23.07	50.50	39.42	**41.87**
27	Hall AA	14.00	52.54	51.33	32.37	**37.56**
28	Hall AB	58.19	36.01	37.33	57.88	**47.35**
29	Hall AC	52.78	54.48	27.90	43.89	**44.76**

30	Hall AD	35.94	11.52	26.99	42.67	**29.28**
31	Hall AE	70.56	32.58	48.77	32.07	**46.00**
32	Hall AF	71.12	40.48	35.85	55.32	**50.69**
33	Hall AG	42.60	38.84	47.92	72.53	**50.47**
34	Hall AH	42.89	27.81	61.38	35.07	**41.79**
35	Hall AI	24.52	33.46	58.38	33.64	**37.50**
36	Hall AJ	48.17	16.94	25.68	38.08	**32.22**
37	Hall AK	34.26	17.85	34.95	33.41	**30.12**
38	Hall AL	30.55	25.65	25.45	32.24	**28.47**

The average mass-based distribution of different components of waste in hostels within the university campus is presented in Table 2. The table shows that the most generated waste is food (169.61kg), followed by polythene (161.32kg), and plastic (158.41kg) while the least is metal (29.11kg) within the hostels. The characterization was done in accordance with the work of (Okeniyi & Anwan, 2012) at Covenant University, Ota, Nigeria with a little modification.

Table 2: Average daily generated solid waste per hall

Hostel	Paper(kg)	Plastic(kg)	Metal(kg)	Food (kg)	Polythene(kg)	Glass(kg)	Other(kg)
Hall A	1.28	5.30	1.20	7.58	5.67	1.10	1.35
Hall B	1.50	4.30	0.95	4.55	4.65	1.32	0.90
Hall C	2.15	5.74	0.89	8.54	6.93	0.95	2.00
Hall D	2.47	2.57	0.35	3.53	3.53	0.35	0.70
Hall E	2.10	3.30	1.25	3.75	2.65	0.80	0.67
Hall F	1.37	2.55	0.25	2.65	2.45	0.75	0.20
Hall G	1.54	4.00	0.70	2.18	3.84	1.25	1.20
Hall H	1.66	4.71	0.50	3.16	4.68	1.35	1.90
Hall I	2.45	4.50	1.20	3.35	4.56	1.20	1.16
Hall J	1.30	4.25	0.60	3.40	4.68	1.45	0.20
Hall K	1.30	3.81	0.61	4.71	4.05	0.91	0.80
Hall L	0.90	1.82	1.06	4.83	7.33	1.43	0.00
Hall M	1.33	3.30	0.71	3.81	6.08	0.55	1.22
Hall N	1.12	6.13	0.00	3.50	1.20	0.85	0.44
Hall O	2.36	4.34	1.44	1.15	4.62	0.73	1.31
Hall P	1.46	4.67	0.81	2.74	4.73	1.30	1.13
Hall Q	2.12	3.63	0.84	5.21	3.18	1.03	1.12
Hall R	2.00	3.66	0.73	6.77	6.70	2.14	0.80
Hall S	1.54	4.27	0.81	4.78	3.30	1.04	0.43
Hall T	1.93	4.21	1.56	6.50	4.51	1.43	0.42
Hall U	1.13	5.20	0.43	6.74	7.00	0.84	0.92
Hall V	1.47	1.70	0.53	4.00	6.04	0.85	1.62
Hall W	0.78	3.20	1.00	2.03	3.02	1.25	1.16
Hall X	1.97	3.82	0.65	5.05	3.08	0.60	0.40
Hall Y	1.73	3.82	0.26	3.14	3.86	1.00	2.24
Hall Z	2.15	3.83	0.52	3.54	3.92	0.71	0.00
Hall AA	1.50	4.45	0.90	1.87	2.57	1.00	0.00
Hall AB	1.11	3.72	0.56	4.05	4.06	1.52	0.73
Hall AC	1.80	3.90	1.57	4.60	4.73	1.27	1.13
Hall AD	2.01	3.53	0.40	4.67	3.10	1.00	1.26
Hall AE	2.84	3.36	0.97	4.84	5.50	1.07	0.61

Hall AF	1.32	4.00	0.56	2.93	4.89	0.55	1.00
Hall AG	0.76	4.10	1.11	9.30	4.43	0.70	0.02
Hall AH	1.46	6.71	0.94	4.80	0.37	1.08	0.00
Hall AI	1.42	6.32	0.78	5.72	5.05	0.62	1.52
Hall AJ	1.41	5.88	0.05	2.73	4.10	1.13	0.63
Hall AK	2.14	4.45	0.27	6.33	3.10	1.05	2.31
Hall AL	1.54	5.36	1.15	6.58	3.16	1.40	1.20
TOTAL	**62.42**	**158.41**	**29.11**	**169.61**	**161.32**	**39.57**	**34.70**

The summary of the responses of students from the questionnaire on solid waste disposal practices in their various hostels are presented in Table 3. 32.7% and 26.2% of all respondents agreed open burning and open dumping respectively are the solid waste disposal methods adopted in their various hostels.

Table 3: Methods of solid waste disposal

	Frequency	Percent	Valid Percent
Open burning	182	32.70	32.70
Open dumping	146	26.20	26.20
Incineration	113	20.30	20.30
Burial in a pit	81	14.50	14.50
Other	35	6.30	6.30
Total	557	100.00	100.00

5. CONCLUSIONS

Quantification and characterization of solid wastes generated in University of Ilorin has been carried out. The quantification identified Hall A, Hall AF, and Hall AG as the highest solid waste generation hostels amongst others as shown in table 1. It was also revealed from the study that recyclable materials are the most generated solid wastes on the university campus hostels as shown in table 2. The study also revealed that open burning and open dumping are mostly adopted amongst the hostels on campus as shown in figure 3. It was also revealed that most of the solid waste generated in the school are being burnt except plastic wastes being recycled by Vicfold Recycler. Hence it can be concluded that the solid waste management in the university is substandard and needs urgent intervention.

REFERENCES

Bernache-Pérez, G., Sánchez-Colón, S., Garmendia, A. M., Dávila-Villarreal, A., & Sánchez-Salazar, M. E. (2001). Solid waste characterisation study in the Guadalajara Metropolitan Zone, Mexico. *Waste Management & Research, 19*(5), 413-424.

Cogut, A. (2016). Open burning of waste: a global health disaster. *R20 Regions of climate action*.

Dong, J., Rotich, K., & Zhao, Y. (2005). Municipal solid waste management challenges in developing countries—Kenyan case study. *Changchun, pp92–100*.

Hakami, B. A., & Seif, E.-S. S. A. (2015). Household solid waste composition and management in Jeddah City, Saudi Arabia: A planning model. *International Research Journal of Environment Sciences, 4*(1), 1-10.

Igbinomwanhia, D., & Olanikpekun, J. (2009). *Solid waste crisis in Nigeria–A case study of the constraint to effective private sector participation (PSP) on solid waste management in lagos metropolis.* Paper presented at the Advanced Materials Research.

Okeniyi, J. O., & Anwan, E. U. (2012). Solid wastes generation in Covenant University, Ota, Nigeria: Characterisation and implication for sustainable waste management. *J. Mater. Environ. Sci, 3*(2), 419-424.

Oladejo, O. S., Adamu Mathew, A., Ibikunle, P. D., & Omamofo, E. K.-W. (2018). Solid waste generation, characteristics and material recovery potentials for landmark university campus. *International Journal 9*(9), 1071-1082.

Oyelola, O., & Babatunde, A. (2008). Characterization of domestic and market solid wastes at source in Lagos metropolis, Lagos, Nigeria. *African Journal of Environmental Science and Technology, 2*(12), 430-437.

Rushton, L. (2003). Health hazards and waste management. *British medical bulletin, 68*(1), 183-197.

Umeh, P. P., Friday, K., & Oji, S. (2019). Geographical Analysis of Household Waste Generation and Disposal in Taraba State, Northeast Nigeria. *International Journal, 8*(2), 58-68.

Wayne, W.D. 2007. Biostatistics. A foundation for analysis in the health sciences, John Wiley and sons (Asia) PTE LTD.183-184

PAPER 114 – DISTURBANCE OBSERVER FOR HARMONIC SUPPRESSION OF A Z-SOURCE INVERTER FED THREE-PHASE INDUCTION MOTOR DRIVE

I. V. Friday, G. S. Shehu

Department of Electrical Engineering, Ahmadu Bello University, Zaria, Nigeria.
*Email: p17egee8014@abu.edu.ng

ABSTRACT
To minimize the detrimental effects of the pulse-width modulated (PWM) voltage and harmonics of a non-linear load, a second-order inductor-capacitor (LC) low-pass smoothing filter is usually added between the inverter and the drive. However, the output voltage drop via the filter inductor and resonance frequency effects are taken into consideration while designing the filters, as a result, baseband harmonics, which make up the majority of the harmonics produced by the frequency converter, are not completely removed. This paper proposes a control system for an impedance source inverter (ZSI)-driven three-phase induction motor drive to minimize AC-side voltage and current harmonics. The control system uses an observer-based output feedback servomechanism controller designed using linear quadratic techniques and linear matrix inequalities, which ensures closed-loop stability and asymptotic tracking regulation regardless of disturbances. A speed adaptation mechanism is added to the observer to enable speed-sensorless operation. The controller is evaluated using several MATLAB/Simulink simulations, which demonstrate perfect tracking, good disturbance rejection, and low voltage and current total harmonic distortions (THD).

KEYWORDS: Linear Matrix Inequality, Induction Motor, Robust Servomechanism, Observer, Harmonics, Stability

1. INTRODUCTION

Estimation techniques such as Extended Kalman Filter (EKF) and Unscented Kalman Filter (UKF) are used to replace measuring signals in a drive system equipped with an LC filter (Akin et al., 2003; Janiszewski, 2012), the observer with disturbance estimation developed for a continuous system can also be implemented in a discrete system. However, there are some significant differences between the two. In a discrete system, the observer frequency response is heavily dependent on the adopted reference system. It is noteworthy that state variables are computed in a stationary reference frame for observers with disturbance estimation, the variables that are estimated by the discrete observer in the stationary αβ reference frame have larger errors than variables estimated by the observer calculated as a continuous system (Rothenhagen & Fuchs, 2007). To minimize this large error, an observer with a convex optimization is developed. The convex optimization allows the observer to consider both the state variables and the disturbance estimates. By using the convex optimization, the observer can estimate the state variables more accurately and with less error than a traditional discrete observer. Additionally, the convex optimization can be used to improve the accuracy of the disturbance estimates. In order to improve the performance of the induction motor drive, this paper proposes the use of robust servomechanism control combined with a disturbance observer based on linear matrix inequalities optimization to detect and compensate for external disturbances, which is a challenging task due to its non-linearities. Low order harmonics have been successfully eliminated for linear time invariant systems using the robust servomechanism controller (Karimi-Ghartemani & Karimi, 2021; Marwali & Keyhani, 2004), which combines the internal model principle and the optimal control theory. However, results for nonlinear load systems were not at acceptable THD levels, and their configuration necessitates mounting the induction motor on the transformer which makes the system complex and overparameterized. There was also a robust servo controller design method for AC induction motor speed control using polynomial differential operator (D. H. Kim et al., 2017), which outperformed standard PI controllers; however, obtaining those nominal values for induction motors may be impossible due to the system being linearized at an equilibrium point on which the accuracy of the linear time-invariant model developed is heavily reliant.

This paper proposes a discrete-time state-space machine model to robustly control an induction motor drive and update the time-varying rotor speed term every sampling time. It also proposes to develop a disturbance observer based on linear matrix inequalities to detect and compensate for external disturbances. The proposed design approach will be tested on a 2.2 kW three-phase induction motor, with the only measurements being the dc-link voltage and the inverter output current. The results will be compared to existing control methods for accuracy of tracking, robustness, harmonic distortion, and system stability.

2. THEORETICAL ANALYSIS

For the simplicity of modeling, the AC- and DC-sides of the circuit are considered separately, and the converter is assumed to operate in continuous conduction mode (CCM).

2.1 System Model for the AC Side.

The inverse Γ-model (Slemon, 1989), a commonly used and somewhat accurate compromise, was chosen for use in this study. It is an accurate representation that does not involve the complex mathematics of the other models, yet still provides a reasonable representation of the machine's performance. The AC side of the system is represented in fig.1 and the state space equations of the system are given as follows:

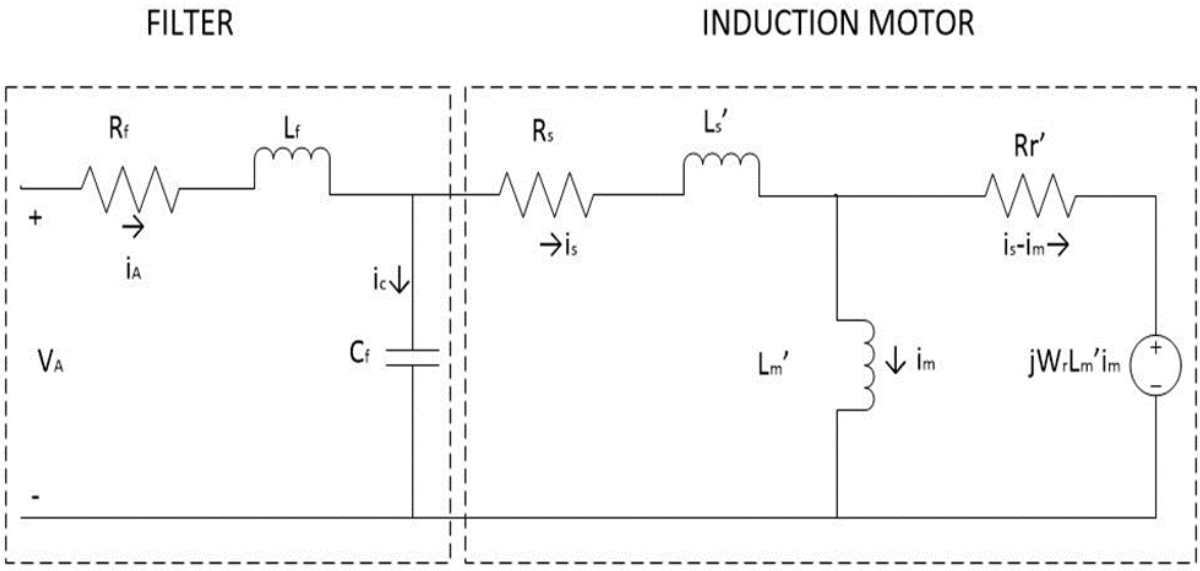

Fig.1. An equivalent circuit of the Inverse Γ model of the Induction Motor connected to an Inverter Output LC filter in a (α - β) stationary reference frame.

Where (Rasmussen, 2002);

$$L_s = L_m + L_{ls},\ L_r = L_m + L_{lr},\ \varphi_s = L_s i_s + L_m i_r,\ \varphi_r = L_m i_s + L_r i_r, \sigma = 1 - \frac{{L_m}^2}{L_s L_r}, {R_r}' = (L_m/L_r)^2 R_r,$$

$${L_s}' = \sigma L_s,\ {L_m}' = (1-\sigma)L_s, \varphi_r = L_m i_m,\ T_r = {L_r}/{R_r},\ Sig_m = \sigma L_s\, L_r/L_m,\ J = [0-1;1\ 0]$$

With States as: $\left(i_{A\alpha}, i_{A\beta}, V_{s\alpha}, V_{s\beta}, i_{s\alpha}, i_{s\beta}, \varphi_{r\alpha}, \varphi_{r\beta}\right)$ and input, $U = V_A, y = i_A$

Taking Kirchhoff's Current Law (KCL) and Kirchhoff's Voltage Law (KVL) around the loops of fig.1, the open loop state space model can be formed:

$$A_p = \begin{bmatrix} \frac{-R_f}{L_f} I_{2\times2} & \frac{1}{L_f} I_{2\times2} & 0_{2\times2} & 0_{2\times2} \\ \frac{1}{C_f} I_{2\times2} & 0_{2\times2} & \frac{-1}{C_f} I_{2\times2} & 0_{2\times2} \\ 0_{2\times2} & a_4 I_{2\times2} & a_1 I_{2\times2} & a_2 I_{2\times2} - a_3 W_r J \\ 0_{2\times2} & 0_{2\times2} & a_6 I_{2\times2} & -a_5 I_{2\times2} + W_r J \end{bmatrix}$$

Where $a_1 = \frac{-\left(R_s + \frac{{L_m}^2 R_r}{{L_r}^2}\right)}{\sigma L_s}$, $a_2 = \frac{1}{Sig_m}\left(\frac{1}{T_r}\right)$, $a_3 = \frac{1}{Sig_m}$, $a_4 = \frac{1}{\sigma L_s}$, $a_5 = \frac{1}{T_r}$, $a_6 = \frac{L_m}{T_r}$

$$B_p = \left[\frac{1}{L_f} I_{2\times2}\ 0_{2\times2}\ 0_{2\times2}\ 0_{2\times2}\right]^T,$$

$$C_p = [I_{2\times2}\ 0_{2\times2}\ 0_{2\times2}\ 0_{2\times2}],$$

$D_p = [0_{2\times2}]$, where I_n denotes an n dimensional identity matrix.

Taking away the varying part of the state matrix, which is updated at each sampling time, A_p is further divided into

linear time-invariant A, and linear time varying matrices A_w.

$$A = \begin{bmatrix} \frac{-R_f}{L_f} I_{2\times2} & \frac{1}{L_f} I_{2\times2} & 0_{2\times2} & 0_{2\times2} \\ \frac{1}{C_f} I_{2\times2} & 0_{2\times2} & \frac{-1}{C_f} I_{2\times2} & 0_{2\times2} \\ 0_{2\times2} & a_4 I_{2\times2} & a_1 I_{2\times2} & a_2 I_{2\times2} \\ 0_{2\times2} & 0_{2\times2} & a_6 I_{2\times2} & -a_5 I_{2\times2} \end{bmatrix}, \qquad A_w = \begin{bmatrix} 0_{2\times2} & 0_{2\times2} & 0_{2\times2} & 0_{2\times2} \\ 0_{2\times2} & 0_{2\times2} & 0_{2\times2} & 0_{2\times2} \\ 0_{2\times2} & 0_{2\times2} & 0_{2\times2} & -a_3 W_r J \\ 0_{2\times2} & 0_{2\times2} & 0_{2\times2} & W_r J \end{bmatrix}$$

Which yields

$$x = (A + w_r A_w)x_p + B_p u \quad (1)$$

$$y(k) = C_p x_p + D_p \quad (2)$$

2.2 Plant Discretization

The system equations generated from (1) to (2) is not stabilizable and detectable under continuous mode except it is scaled, hence the need to operate in discrete mode. Explicit (forward) Euler method of discretization which helps the fast discretization of the varying part of A matrix at every sampling interval is used (Kullick & Hackl, 2018; Unbehauen, 2009).

2.3 Robust Servomechanism Controller

The controller has two parts: a servo-compensator which ensures the asymptotic tracking of the reference signals in the presence of disturbances, and a stabilizing compensator which must, as its name suggests, stabilize the augmented model with the dynamics of the servo-compensator. The stabilizing compensator selected is a linear quadratic (LQ) optimal state feedback to which an observer is added in order to dispense with additional sensors and estimate the immeasurable states.

2.3.1 Servo-compensator

Keyhani & Marwali, (2012), clearly outlined principles of this approach as follows. If the tracking/disturbance poles to be considered are ±jω1, ±jω5, and ±jω7, etc., where $f = 50hz, \omega1 = 2\pi \times 50$ rad/s, $\omega5 = 5\omega1$, and $\omega7 = 7\omega1$, etc., the servo-compensator is represented as,

$$\dot{\eta} = A_c\eta + B_c e \quad (3)$$

Where $e = V_{ref,\alpha\beta} - V_{s,\alpha\beta}$ is the estimated load voltage tracking error;

$\eta = [\eta_1\ \eta_2 \dots \eta_i]^T,\ i = 1,2, \dots n$

$A_c = block\ diag[A_{c1}, A_{c2}, .., A_{cn}]$

$B_c = [B_{c1}, B_{c2}, \cdots, B_{cn}]^T$

With $A_{ci} = \begin{pmatrix} \vec{0}_{2\times2} & \vec{I}_{2\times2} \\ -{w_i}^2\vec{I}_{2\times2} & \vec{0}_{2\times2} \end{pmatrix}$

$B_{ci} = (\vec{0}_{2\times2} \quad \vec{I}_{2\times2})^T$

Which depicts the continuous transfer function, $1/(s^2 + {w_i}^2)$ representation in a state space.

2.3.2 Observer - Stabilizing Compensator

The stabilizing compensator is, however, not unique (Davison & Ferguson, 1981); there are various classes of stabilizing compensators that can be used in a robust servomechanism controller. One of them, adopted is the observer-based stabilizing compensator. This type of compensator uses an observer to estimate the system states $\hat{x}_p$, both available and unavailable and then uses the estimated states to design a stabilizing compensator.

The stabilizing compensator may be formed in the presence of the servo compensator by augmenting the system matrices of both the plant (1&2) and the servo-compensator (3), which is expressed as,

$$\begin{bmatrix} \dot{X} \\ \dot{\eta} \end{bmatrix} = \begin{bmatrix} (A + w_r A_w) & 0 \\ -B_c C_p & A_c \end{bmatrix} \begin{bmatrix} X \\ \eta \end{bmatrix} + \begin{bmatrix} B_p \\ -B_c D_p \end{bmatrix} u,$$

$$\begin{bmatrix} y_m \\ \eta \end{bmatrix} = \begin{bmatrix} C_m & 0 \\ 0 & I \end{bmatrix} \begin{bmatrix} X \\ \eta \end{bmatrix} + \begin{bmatrix} D_m \\ 0 \end{bmatrix} u \quad (4)$$

The stabilizing compensator, with the control signal,

$$u = K_0\hat{x}_p + K_1\eta = [K_0 \quad K_1]\check{x} = K\check{x} \quad (5)$$

ensures the stability of the augmented model, via a feedback gain K that minimizes the linear quadratic performance index (i.e., the optimization criterion) in (6).

$$J_{\epsilon} = \sum_{k=0}^{\infty} \left(z(k)' Q z(k) + \mu(k)' R \mu(k) \right) \quad (6)$$

Consequently, the feedback gain K is obtained from Matlab function dlqr (),

Now, consider a load torque which causes disturbance to the motor speed and in turn cause the inverter to generate more voltage or current in order to maintain the desired motor speed, (1) – (2) can be re-written in the discrete form as follows considering the input as disturbance:

$$\dot{x}_p(k+1) = A_d x_p(k) + B_{d1} w(k)$$
$$y(k) = C_{d2} x_p(k) \quad (7)$$

where $x \in R^n$ and is the state vector, $A \in R^{n \times n}$ and is the state matrix, $B \in R^{n \times r}$ and is the input matrix, $w \in R^r$ and is the exogenous input, $C \in R^{m \times n}$ and is the output matrix, $y \in R^m$, and it is assumed that (A_d, C_{d2}) is detectable.

A Luenberger observer of the form is to be designed (Caverly & Forbes, 2019):

$$\dot{\hat{x}}_p(k+1) = A_d \hat{x}_p(k) + L_d(y(k) - \hat{y}(k))$$
$$\hat{y}(k) = C_{d2} \hat{x}_p(k) \quad (8)$$

The gain L_d is determined by minimizing standard $H_2 (or\ H_\infty)$ norm of the transfer function between e and w_k while also stabilizing the dynamics of the estimate error, and ensuring the sub-system T(z) (11) meets the requirements for disturbance attenuation performance.

The error state is defined as:

$$e(k) = x_p(k) - \hat{x}_p(k) \quad (9)$$

The error dynamics is derived as,

$$\dot{e}(k) = \left(A_d - L_d C_{d2}\right) e(k) + B_{d1} w(k) \quad (10)$$

The observer gain, L_d is to be designed in such a way that the H_2 norm provided by the transfer function (11) of the input $w(k)$, on the output e, to minimize model deviation and the effect of the disturbance w(k) to the estimated error.

$$T(z) = (ZI - (A_d - L_d C_{d2}))^{-1} B_{d1} \quad (11)$$

This amounts to solving an optimization problem whose constraints are formulated using Linear Matrix Inequalities (LMIs), if there exist a symmetric matrix X and a matrix Y satisfying the transfer function (11) which is equivalent to minimizing $\mathcal{J}(\gamma) = \gamma^2$ subject to (Caverly & Forbes, 2019; Duan & Yu, 2013)

$$\left[{A_d}^T X + A_d X + C_{d2} Y + Y^T C_{d2} + I_8 \right] < 0 \quad (12)$$

$$\begin{bmatrix} -Z & X{B_{d1}}^T \\ XB_{d1} & -X \end{bmatrix} < 0 \quad (13)$$

$$trace(Z) < \gamma^2 \quad (14)$$

Where ${C_{d2}}^T = {C_{d2}}^{-1}$ is a special case of congruence transformation., It is desired to stabilize the poles of the observer matrix $(A_d - L_d C_{d21})$ in a vertical strip region defined by $\mathbb{D} = \mathbb{H}_{\alpha,\beta} = \{z = x + iy : \alpha < x < \beta \mid z \in \mathbb{C}^{-\infty} \cap \mathbb{C}^{\beta},\ \alpha < Re(z) < \beta\}$, where $\mathbb{D}$ is the open unitary disk centered at the origin (Marx et al., 2003), where $\mathcal{J}_{H_2}(L_d) = \left|\left|T(z)\right|\right|_2$ is minimized, the resulting constraints are:

$$XA_d + YC_{d2} + (XA_d + YC_{d2})^T + 2\alpha X < 0 \quad (15)$$

$$XA_d + YC_{d2} + (XA_d + YC_{d2})^T + 2\beta X > 0 \quad (16)$$

$$\begin{bmatrix} -X & XA_d \\ {XA_d}^T & -X \end{bmatrix} \quad (17)$$

$$\begin{bmatrix} -X & XA \\ {A_d}^T X & -X - \gamma {C_{d2}}^T C_{d2} \end{bmatrix} < 0 \quad (18)$$

where X and Z are symmetric matrices, and Y = $-{L_d}^T X$ is a "change of variable" matrix. Once the problem is solved using convex optimization algorithm, the full-order observer gain with pole location limitations is retrieved thus

$$L_d = -(X^{-1}) Y^T \quad (19)$$

3. EXPERIMENTAL PROCEDURE

The design of the control system is carried out using MATLAB R2022a software at a switching frequency of 5 kHz with the PowerGUI set to a sampling rate of 2 e-06. An MSi GE620DX computer with an Intel (R) Core i7-2670QM CPU @ 2.20GHz processor was used to perform the simulation. The Control system comprises of blocks such as the Discrete PI DC-link Controller, modified space vector modulation, coordinate transforms, etc.

The simulation follows a three-step approach: modeling, parameter identification, and control design. The mathematical model of the system was created in the Simscape Electrical domain and was simulated in Simulink. The parameters of the model were identified based on the operating data of the system.

Simulation parameters for the drive are as follows:

3hp, 415 V, 4.6 A, four-pole, 50 Hz, 1435 rpm star connected, three-phase Squirrel Cage Induction Motor (SQIM)
Induction motor parameters
R_s = 4.55 Ω, R_r = 1.39 Ω, L_s= 281.9 µH, L_r = 281.9µH, L_m = 267.8µH, J = 0.089 Kg·m²
Filter parameters
C_f = 40 µF, L_f = 2.6 mH, R_f = 1Ω
Z-source parameters
L1= L2 = L = 500µH, C1 = C2 = C= 500µF
where R_f, L_f, and C_f are the per-phase ac resistance of the filter inductors, the inductance of the filter-inductors, and the capacitance of the filter-capacitors, respectively. Also, R_s, R_r, L_s, L_r, L_m, and J are respectively Per-phase stator resistance, Per-phase rotor resistance, Per-phase stator inductance, Per-phase rotor inductance, magnetizing inductance, and the moment of inertia.
After parameter identification, the control system was designed based on the mathematical model of the system. The Discrete PI DC-Link Voltage Controller was designed to keep the DC-Link voltage constant irrespective of fluctuations from intermittent sources. The modified space vector modulation technique was developed to maintain the switching frequency, modulation index, and pulse duration constant.

4. RESULTS AND DISCUSSION

.4.1 System Harmonics
The (IEC 61000-3-2 and IEEE 519) standards recommend that electric drives have a total harmonic distortion (THD) of less than 5%. This sub-section evaluates the effectiveness of the robust servomechanism controller in eliminating baseband harmonics and, in general, the harmonics of the entire system to a globally acceptable standard.
The corresponding THD at 8sec. is 1.87% for 4 cycles as shown in provided in fig.2.

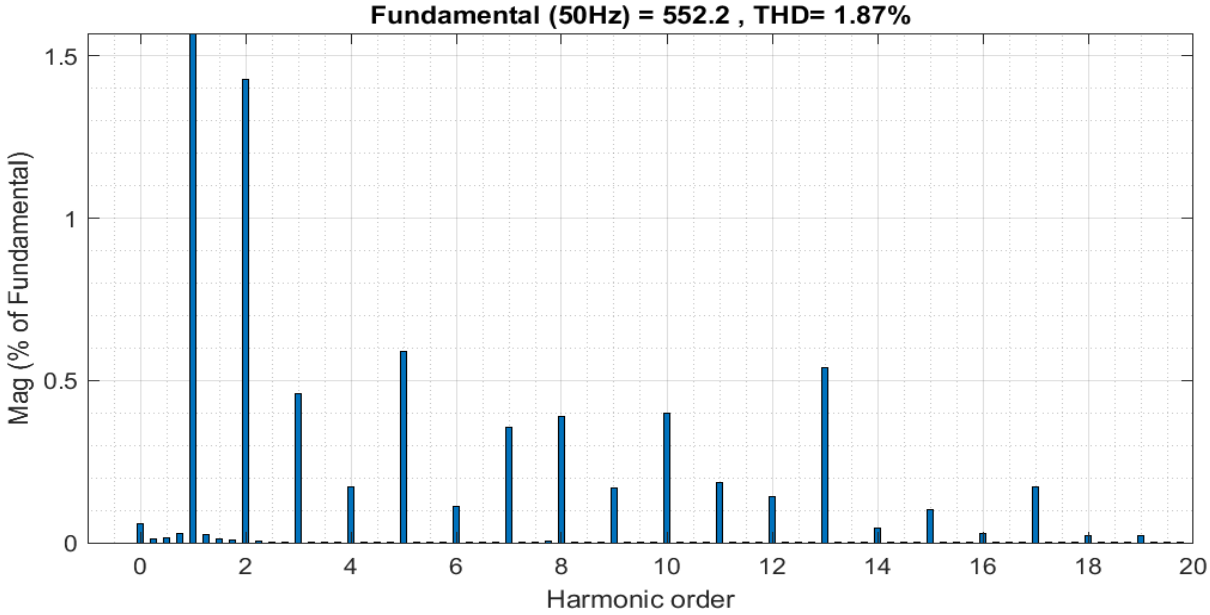

Fig.2: Harmonic spectrum for the stator voltage

Figure .3 is the harmonic spectrum for the stator current which shows a THD of 4.5% at 8.5sec. and 4 cycles

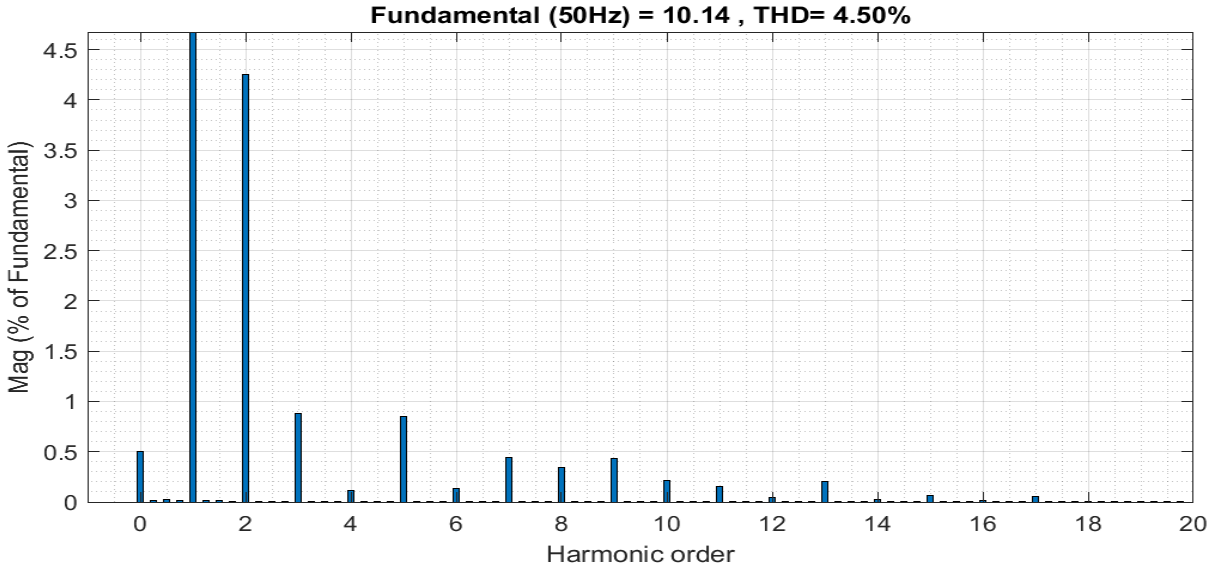

Fig.3: Stator current harmonic profile

4.2.1 Comparison of Harmonic Result

Sivakumar et al., (2023), used a fuzzy logic controller-based shunt active filter (SAF) to reduce the THD of the source current to 2.66%, but did not reveal the voltage of the power grid with a 3-phase induction motor drive (IMD). Nishizawa et al., (2019), introduced a space vector pulse width modulation technique for reducing inverter input current harmonics, but with an exponential increase in THD in over-modulation mode. Voltage harmonics were not examined in depth.

5. CONCLUSION

The outcome for the simulated system met the IEC 61000-3-2 and IEEE 519 standards, demonstrated an excellent harmonic profile for the induction motor drive, and had good stability margins and robustness, which will be revealed in later publications. Overall, the simulation showed good performance that met the desired requirements for the induction motor drive system. To ensure that the induction motor drive system meets the desired requirements, further tests need to be conducted under real-time conditions. This will allow for the evaluation of the system's robustness and operating performance. To maintain steady-state operation during these tests, it is recommended that the changes in stator resistance caused by temperature and load variations be modeled in the system. Additionally, a control modification or advanced ZSI design can be implemented in order to further improve the system's performance and energy efficiency.

ACKNOWLEDGEMENTS

The authors would like to thank Dr. Michael Ajeni from the University of Manchester for his valuable insights and feedback.

The authors would also like to thank the anonymous reviewers for their helpful comments and suggestions, which significantly improved the quality of the paper.

Finally, the authors would like to thank the Ahmadu Bello University Department of Electrical Engineering staff for their contributions toward the success of this research.

REFERENCES

Akin, B., Orguner, U., & Ersak, A. (2003). State estimation of induction motor using unscented Kalman filter. *IEEE Conference on Control Applications - Proceedings*, *2*, 915–919. https://doi.org/10.1109/cca.2003.1223132

Caverly, R. J., & Forbes, J. R. (2019). *LMI Properties and Applications in Systems, Stability, and Control Theory*. http://arxiv.org/abs/1903.08599

Davison, E. J., & Ferguson, D. I. J. (1981). The Design of Controllers for the Multivariable Robust Servomechanism Problem Using Parameter Optimization Methods. *IEEE Transactions on Automatic Control*, *vol.26*, 93–110. https://doi.org/10.23919/acc.1982.4787986

Duan, G.-R., & Yu, H.-H. (2013). *LMIs in Control Systems Analysis, Design and Applications* (1st ed.). CRC Press Taylor & Francis Group. http://www.taylorandfrancis.com

Janiszewski, D. (2012). Unscented Kalman Filter for sensorless PMSM drive with output filter fed by PWM converter. *IECON Proceedings (Industrial Electronics Conference)*, *June*, 4660–4665. https://doi.org/10.1109/IECON.2012.6389495

Karimi-Ghartemani, M., & Karimi, H. (2021). A robust multivariable approach for current control of voltage-source converters in synchronous frame. *IEEE Journal of Emerging and Selected Topics in Power Electronics*, *9*(5), 6174–6183. https://doi.org/10.1109/JESTPE.2020.3031206

Keyhani, A., & Marwali, M. (2012). Smart power grids 2011. In *Power Systems* (Vol. 53). https://doi.org/10.1007/978-3-642-21578-0

Kim, D. H., Nguyen, T. H., Pratama, P. S., Kim, H. K., Jung, Y. S., & Kim, S. B. (2017). Servo system design for speed control of AC induction motors using polynomial differential operator. *International Journal of Control, Automation and Systems*, *15*(3), 1207–1216. https://doi.org/10.1007/s12555-015-0215-8

Kullick, J., & Hackl, C. M. (2018). *Speed-sensorless state feedback control of induction machines with LC filter*. *i*, 1–9. http://arxiv.org/abs/1807.11799

Marwali, M. N., & Keyhani, A. (2004). *Control of Distributed Generation Systems — Part I : Voltages and Currents Control*. *19*(6), 1541–1550.

Marx, B., Koenig, D., & Georges, D. (2003). Robust pole-clustering for Descriptor systems, A strict LMI Characterization. *European Control Conference (ECC)*, 1117–1122.

Nishizawa, K., Itoh, J. I., Odaka, A., Toba, A., & Umida, H. (2019). Current Harmonic Reduction Based on Space Vector PWM for DC-Link Capacitors in Three-Phase VSIs Operating over a Wide Range of Power Factor. *IEEE Transactions on Power Electronics*, *34*(5), 4853–4867. https://doi.org/10.1109/TPEL.2018.2859763

Rasmussen, H. (2002). A new observer for speed sensorless field oriented control of an induction motor. *IECON Proceedings (Industrial Electronics Conference)*, *1*, 420–425. https://doi.org/10.1109/IECON.2002.1187545

Rothenhagen, K., & Fuchs, F. W. (2007). Implementation of state and input observers for doubly-fed induction generators. *EUROCON 2007 - The International Conference on Computer as a Tool*, *1*, 2110–2117. https://doi.org/10.1109/EURCON.2007.4400532

Sivakumar, A., Thiyagarajan, M., & Kanagarathinam, K. (2023). Mitigation of supply current harmonics in fuzzy-logic based 3-phase induction motor. *International Journal of Power Electronics and Drive Systems*, *14*(1), 266–274. https://doi.org/10.11591/ijpeds.v14.i1.pp266-274

Slemon, G. R. (1989). Modelling of Induction Machines for Electric Drives. *IEEE TRANSACTIONS ON INDUSTRY APPLICATIONS*, *25*(6), 1126–1132.

Unbehauen, H. (2009). *Regelunkstechnik II:Zustandsregelungen, digitale und nichtlineare Regelsysteme.*

PAPER 115 – THE DESIGN OF ENGINE WITH REDUCED EMITTED POLLUTANTS ON THE ENVIRONMENT

P.S.Abam. Y.Y.Adajah, R.I. Tamuno. S.O.Anaza, A. A. Adelere

Power Equipment Electrical Machinery Development Institute, Okene.

Email: paulsotoye@gmail.com.

ABSTRACT

Two major emitted gases from the combustion engines which pollute the environment are nitrogen oxide (NO_X) and Carbon iv oxide (CO_2). In this study, a redesign engine is presented which extract nitrogen from the air before combustion and Carbon iv after combustion. The components of the redesign engine include the nitrogen extractor chamber, the combustion chamber, the cyclone and the carbon iv oxide absorption chamber will be modeled in order to obtained the relationship between the input and output parameters in each section. These parameters which will be the basis for designing the model include the airflow rate, pressure, temperature, as well as the chemical combustion of the gases at each stage. For the absorption of nitrogen Al_2SiO_5 was use while KOH was used at the exhaust end to absorb the carbon iv oxides. For the four stroke petrol engine used for the experiment, the exhaust temperature at normal working condition using oxidant containing nitrogen was 200^oC, but when the air was bubbled through Al_2SiO_5 at a concentration of 40g/dm^3 the exhaust temperature increased to 300^oC which is about 50% increase. At the exhaust the CO_2 produced was 6.66 but upon passing the exhaust gas through KOH after using the redesign engine, the percentage reduction at 67% KOH was 64%.

KEYWORDS: Pollution, gases, combustion, re- design engine.

1. INTRODUCTION

The issue of global warming is a result of burning of fossil fuel as carbon iv oxide and nitrogen oxide are continuously being released into the atmosphere. The nitrogen oxide that is emitted, the effluent eat up the ozone layer thereby exposing the earth to more radiation from the sun. On the other hand, if carbon iv oxide that is released , due to ongoing deforestation there are fewer plants now available to convert carbon iv oxide to oxygen and as a result of this the temperature of the environment rises. Using electrical cars cannot be a solution to this as the battery being used are produced through combustion (Derek, 2017). Charging the battery is another problem which has to be done by means of electricity produced by combustion. It is in this circumstance that this study is centred on how to remove nitrogen before combustion from the air and carbon iv oxide has to be absorbed from product of combustion before being disposed into the atmosphere .however the issue of chemistry of combustion will be avoided in this presentation (Libin and Sajunla, 2018).

The same space the engine is to occupy within the vehicle is to remain. The retrofitted engine is to have the nitrogen absorbing device before combustion and carbon iv oxide absorbing reagent after combustion. Provision will be made

to ensure the elimination of nitrogen as a moderant is taken care of by cooling (by adding dopant to the coolant). (Baskar et al, 2021) investigated the effect of oxygen enriched combustion on pollution performance characteristics of spark ignition engine and reported a high value of nitrogen oxide emission with increasing oxygen concentration as a drawback of the technology.

(Zhou et al, 2020) carried out research on combustion, performance and emission analysis of an oxygen controlling downsize spark ignition engine and found that increasing the oxygen percentage in the air and decreasing the equivalent ratio, lower fuel consumption.

2. MATERIALS AND METHODS/METHODOLOGY/EXPERIMENTAL PROCEDURE

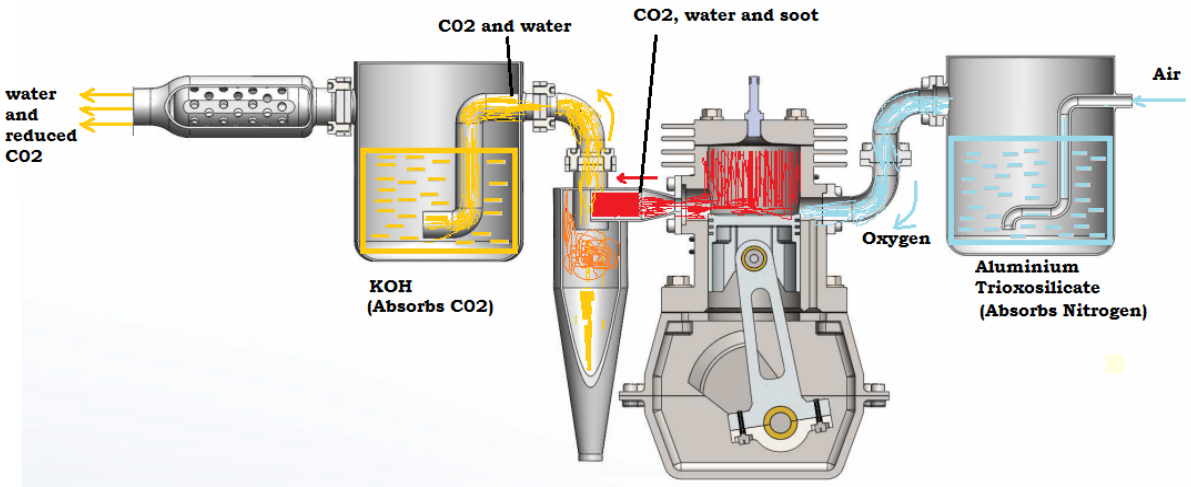

Fig 1: Design Engine with Three combustion Chamber.

A four stroke, single cylinder gasoline engine is used Yamaha 125. The materials for the redesign engine with reduced pollutant emitted to the environment are: Engine type 125 Yamaha engine four stroke one cylinder, displacement 29.87dm^3, stroke 155.5mm, bore 174.5mm, power 860kw, rated torque 11.88Nm at 6500rpm others are compression ratio 17.5, specific fuel consumption 235kg/h and the reagents are potassium hydroxide (KOH) and Aluminum silicate (Al_2SiO_5).The nitrogen absorbed consist of Aluminum silicate and carbon iv oxide absorbed consist of potassium hydroxide, other accessory are thermocouple, measuring cylinder and gas analyzer. The nitrogen extractor is attached

at the entrance of the air and the carbon iv oxide absorbed at the exhaust pipe. A drill was made to accommodate the thermocouple within the engine. The exhaust gas analyzer is placed at the exit of the exhaust pipe.

The experimental setup mainly consist of four stroke one cylinder spark ignition engine, exhaust gas analyser, flow meter and thermometers. It is an already existing engine which is restructured to consist of three combustion chambers and a post combustion chamber. The pre- combustion chamber is to accommodate nitrogen extracting substance. The engine used in this research has 174.5mm, stroke 155.5mm and rated power of 860Kw at 6500rpm. The engine was coupled with exhaust gas analyser and a thermocouple. The gasoline used in this work was obtained from a petrol station. The experiment was carried out with 10g/dm^3, 20g/dm^3, 30g/dm^3, 50g/dm^3 0f Aluminium silicate (Al_2SiO_5) and potassium hydroxide (KOH).The engine experiment was conducted under constant spark timing and compression ratio (17.5:1). During the experiments, all data were taken after steady–state condition were reached and all measurements were repeated at least four times at each test point and the average value were used to minimize systematic errors. Exhaust gas emission such as nitrogen oxide (NO_X), carbon iv oxide ($C0_2$) and hydrocarbon (HC) were measured using the exhaust gas analyzer. Technical specification such as measurement ranges and accuracy of the exhaust gas analyzer are taken.

3. RESULTS AND DISCUSSION

Table 1: Technical specification of exhaust gas analyzer

	Emission	Measuring range	Accuracy
1	$C0_2$	0- 20%	0.01%
2	NO_X	0- 40%	1ppm
3	HC	0- 40ppm	1ppm

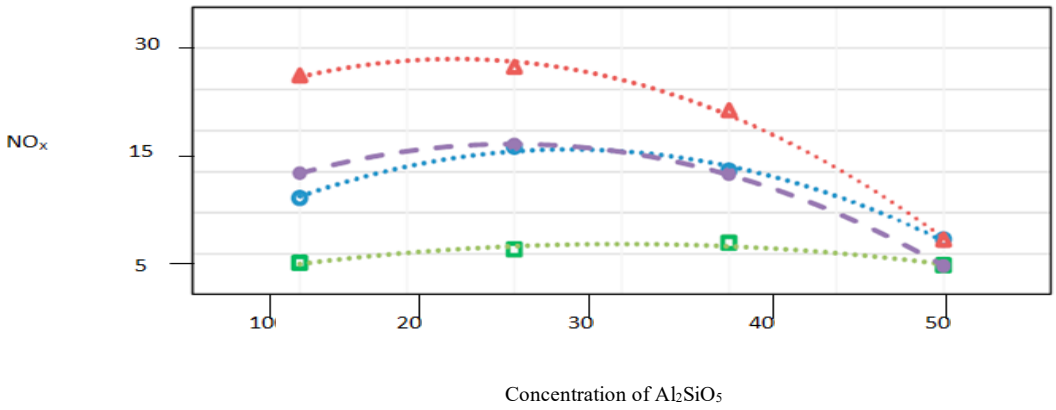

Fig 2: Variation of NO_X with Al_2SiO_5

The effect of NO_X as pollutant emission of the test engine was investigated. There was a significant decrease in NO_X emission at 20gdm^3 of aluminum silicate. This is a promising result since nitrogen oxide is a greenhouse gas and that is why we reduced NO_X emission level. In the case of 30g/dm^3, NO_X emissions were reduced by 10.3% and 11.2% respectively.

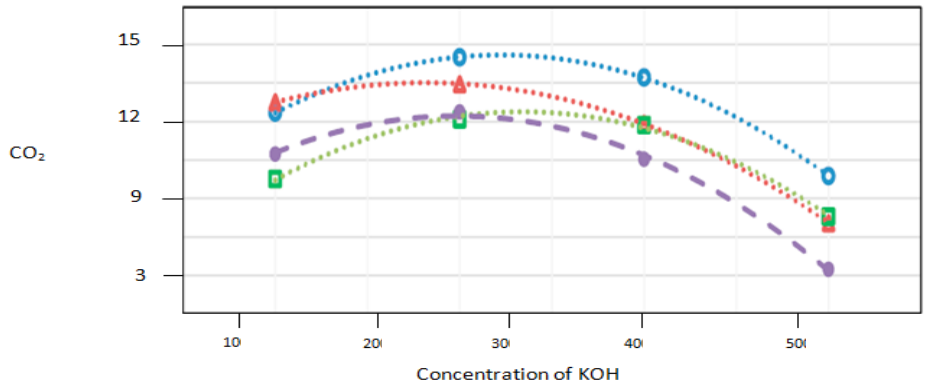

Fig 3: Variation of CO_2 being absorbed by KOH

The results obtained shows that there was maximum absorption of carbon iv oxide by potassium hydroxide at 30g/dm^3 and 40g/dm^3. Therefore the possible reason for the maximum absorption at 40g/dm^3 is due to increase in combustion temperature.

The absorption process was analysed using a reagent tank in which the exhaust gas was bubbled through. In the column, an aqueous solution of KOH will react with CO_2 in the exhaust gas. The absorption reaction of KOH and CO_2 usually leads to the production K_2CO_3 according to the stoichiometric equation

$$2KOH + CO_2 \rightarrow K_2CO_3 + H_2O$$

In the case of excess of concentration of KOH, it leads to the increased production K_2CO_3 over a long period of time but if the advert of complete usage of KOH and CO_2 become in excess, an undesirable product is formed

$$K_2CO_3CO_2 \rightarrow 2K\,HCO_3$$

Therefore, obtaining the right percentage to absorb the CO_2 adequately over a long period of time is the aim of the phase of the experiment.

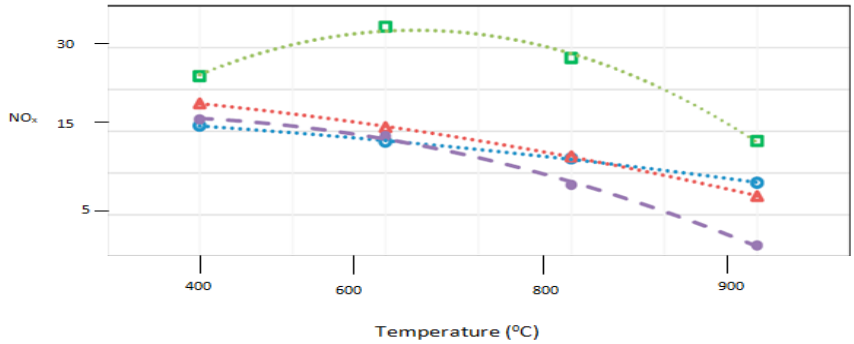

Fig 4: Effect of combustion temperature on the engine

The extraction of nitrogen from the oxidant increases the temperature. Maximum temperature is obtained at 50g/dm^3, but the metrological temperature of the engine is not exceeded. Dopant was added to reduce the temperature of the engine.

4. CONCLUSIONS

The redesign engine developed works by reducing the nitrogen content in the air which enters the inlet manifold of the engine thereby increasing the percentage of oxygen available in a given air fuel ratio and reducing the percentage of NOx produced at the exhaust at elevated temperatures. The results indicatd that extracting nitrogen from the oxidant with aluminum silicate at 20g/dm^3 to 40g/dm^3 shows reduction of N0$_X$ at the effluent. Carbon iv oxide emission was also absorbed using potassium hydroxide. Maximum absorption occur at 40g/dm^3. The reduction of NO_X and CO_2 were tested with exhaust gas analyzer. It is concluded that aluminum silicate is used to extract nitrogen from air which lead to reduction in nitrogen oxide emission while carbon iv oxide absorbed by potassium hydroxide which enable us to reduce global warming. The work will make available a system to reduce the depletion of the ozone layer which shields the earth from harmful ultra- violet radiation of the sun. Determination of the time with which the nitrogen absorption reagent becomes saturated and cannot further absorb the nitrogen and the effect of the volume and temperature on the absorption decay time. For the exhaust system, the temperature has the tendency of boiling up the KOH and at higher temperatures it may even completely evaporate, so there is need to either look for a medium to increase the operating temperature of KOH, or check for the effectiveness of using solid state of KOH as the reagent. Also, there would be a need to determine the time for complete saturation of the KOH at the selected optimal state.

ACKNOWLEDGEMENT

I wish to express my profound gratitude to Almighty God whose love and guidance led to the completion of this project and course in general

My gratitude also goes to my mentor Engr. Prof. A.S. Adavbiele for his advice, keen scrutinization of my work.

My very big thanks are expressed to a senior friend, Engr. Dr S. O. Ogbeide and the former Postgraduate coordinator Mechanical Engineering department, Ambrose Alli University Ekpoma, Engr. Prof. O. Obodeh.

I owe so much thanks to my dearly beloved wife Mrs. H. Abam for her understanding and support during the period of this study, may God reward her abundantly.

REFERENCES

Baskar, J.; Robert,W. and Zhijum.W. (2021). Carbon capture for Automobiles using internal Combustion Rankine cycle engine, Journal of engineering for gas turbine and power, 3:35 -41

Bosch,M,; Serras,F. and Bagguna.J. (2015). Synthesis of new oxadiazole derivatives as Inflammatory analgesic and antimicrobial agents, International Journal on medical chemistry 4: 16- 22

Derek, M.S.(2017 September 7). Carbondioxide Removal Option: A Literature Review Identifying Carbon Removal Potentials and Cost, Master's Thesis at the University of Michigan.

Hitesh, B.P. and Suple,Y.R. (2018). Experimental investigation of exhaust emission of four stroke spark ignition engine by using direct injection of LPG and it's analysis, International journal of modern engineering research, 3: 2600- 2605.

Krishnamoorthy, G. and Sami, M. (2017). Radiating Modelling in Oxy- Fuel Combustion Scenarios, America society of Mechanical Engineers, Power Division Publication, 7: 615-621

Libin,P and Sajunulai, F. (2014), A Comparison of emission of SI and CI engine in a lownitrogen oxy-combustor environment, International Journal of advance research in science and Engineering, 7:78-85.

Longwell, J.P; Frost, E.E.and Weiss, M.A. (2013) Flame Stability in Bluff – Body Recirculation Zones, Journal of Industrial and Engineering Chemistry, 45: 29 -33.

Maher, A.R and Baghdadi, S.A. (2013). Performance study of a four stroke spark ignition engine working with hydrogen and ethanol as supplementary fuel, International Journal of Hydrogen energy 3: 1005- 1009.

P.S. Micheal, and Fusoil, P.U. (2013). Development of a Combustion Chamber Design Methodology and Automation of the Design Process, International Journal of Aeronautical Sciences, 4: 5- 10

Prasad,T, Yassodam, S and Latha.P. (2010). Effects of Nanoscalezinic oxide particles on the Germinating, growth and yield of Peanuts, A Journal of Agricultural chemistry 9: 2-6.

Yinghui,G; Canbing,L. and Yijia. C. (2016) Cost Analysis of air Capture driven by Wind Energy Under Different Scenarios, Journal of Modern Power System and clean energy, 4: 275- 281.

Zhou,S; L.Yin,F.D and QianqianJia, G.A, (2020), Computational study of a vertical plunging still water, A Journal of chemical science engineering 1 : 72- 79.

PAPER 116 – PROBABILISTIC MODELLING OF FLOOD FLOW ALONG MGENI RIVER AT TABLE MOUNTAIN, SOUTH AFRICA

O. O. Olofintoye[1*], B. F. Bakare[2], A. W. Salami[1,3], A. M. Ayanshola[1], S. O. Bilewu[1], T. S. Abdulkadir[1,4], M. O. Jimoh[5], O. Oyebode[6]

[1]Department of Water Resources and Environmental Engineering, University of Ilorin, Ilorin, Nigeria.
[2]Department of Chemical Engineering, Mangosuthu University of Technology, Durban, South Africa.
[3]National Centre for Hydropower Research and Development, University of Ilorin, Ilorin, Nigeria.
[4]Department of Civil Engineering, Kabale University, Republic of Uganda.
[5]School of Engineering, University of Warwick, Coventry CV4 7AL, United Kingdom.
[6]Department of Civil Engineering, University of South Africa, Johannesburg, South Africa.
[*]Email: olofintoye.oo@unilorin.edu.ng

ABSTRACT
Accurate flood prediction is indispensable for effective environmental protection. This study establishes best-fit probability distribution models for estimating annual maximum flows at Table Mountain along the Mgeni River. Six probability distribution functions (Normal, Log-Normal, Pearson III, Log-Pearson III, Gumbel and Log-Gumbel) were fitted to the annual maximum flow series of the river. Reliability of raw data was verified using the Spearman-brown reliability check. The non-parametric Chi-square goodness-of-fit statistical test was employed to determine the suitability of the functions in representing the observed data at a specified level of significance. The Kruskal-Wallis non-parametric H-Test was employed to determine if there were significant differences in the performances of the models. Finally, a test score statistics was used to establish the most appropriate model for application in the study area. It was found that the Log-Pearson III probability distribution function, which is a 3-parameter model taking cognizance of a skew coefficient in estimation, is the most suitable model. The Log-Normal and Pearson III models were also found suitable while the Normal, Gumbel and Log-Gumbel models were not suitable at the tests' level of significance. The models found suitable are recommended for predicting flood flows in the study area.

KEYWORDS: Annual maximum flow, Probability distribution function, Flood prediction, Goodness of fit test, H-test, Test score

8. INTRODUCTION

Disasters result in loss of lives, destruction of infrastructure, damaged ecosystems and undermined societal development (Sudmeier-Rieux et al., 2019). Floods are natural disasters resulting from unusual surplus or excess of water in which the resulting higher than usual water levels extend out onto the floodplains. They occur in river basins, usually as the result of a lot of rain (Loucks & Bee, 2005). These natural events have always been a part of the geologic history of the earth, and because human settlements and activities have always tended to use floodplains, their uses has frequently interfered with the natural processes in the floodplain, causing inconvenience and catastrophe to humans (Mays, 2011).

According to Witwatersrand (2022), flooding events in areas around the Mgeni River in the KwaZulu-Natal province in South Africa have doubled over the last century. Noteworthy is the disastrous flood that hit Durban city in the province in April 2022. This is considered the most catastrophic natural disaster yet recorded in the region in collective terms of lives lost, homes and infrastructure destroyed and economic losses. The calamitous flood in its wake resulted in loss of 459 human lives, 88 people still missing by the end of May 2022, and over 4000 destroyed homes rendering 40,000 people homeless and 45,000 people temporarily unemployed. Also, substantial damages were caused to some of Mgeni raw water abstraction and conveyance infrastructure resulting in shortfall in potable water supply in some districts (Umgeni, 2022). The cost of infrastructure and business losses amounted to an estimated 2 billion USD. Several historical flooding events have been recorded in the region notable among which are the Durban flood in September 1987 and the great Deluge of 1856.

Studies suggest that an increase in the severity and frequency of extreme hydrological events is expected worldwide. Recent anthropogenic global climate warming may have contributed to the trend in increased flooding and this trend may continue into the future (NZCCO, 2008; Witwatersrand, 2022). Hence, it is pertinent to establish or re-establish accurate flood prediction models for effective environmental protection in flood prone areas through frequency analysis of flows, to establish best-fit probability distribution functions that can facilitate the prediction of future flood events.

Several researchers (Topaloglu, 2002; Olukanni, 2003; Khudri & Sadia, 2013; Paul et al., 2014) have analysed historical hydrologic events using methods of statistical frequency analysis, and developed appropriate best-fit models to forecast extreme events. For instance, Salami (2007) developed probability distribution models

for predicting annual peak and low flows at selected gauging stations along some South-West Rivers in Nigeria. Probability distribution functions such as Gumbel, Normal, Log-Pearson type III and Log-normal distributions were fitted to the flow series. The Gumbel (Extreme value type I) and Log-normal models were found suitable for estimating flows in the study area. Adeyemo and Olofintoye (2014) demonstrated the application of the parametric Normal, Lognormal, Pearson III, Log-Pearson III, Gumbel and Log-Gumbel probability distribution models in estimating monthly river flows into the Vanderkloof dam in South Africa. The models were found appropriate for flow computations in the reservoir.

This study analyzes the frequency distribution of flood flows along the Mgeni river in South Africa using data obtained from the Table Mountain gauging station. It employs statistical methods to determine the fitness of the developed models. Establishing relevant functions for predicting flood flow in the river is germane in articulating proactive measures towards addressing the challenges associated with flooding in the watershed.

9. THEORETICAL ANALYSIS

Statistical methods were adopted for the analysis in this work. The mathematical principles applicable are discussed in the following subsections.

2.1 Data Reliability Check:

The Spearman-Brown coefficient was used to check the reliability of data. Formula for computing the coefficient is given in Equation 1 as:

$$r_{SB} = \frac{2 \times r}{1 + r} \qquad (1)$$

Where r_{SB} is the Spearman-Brown correlation coefficient and r is the Pearson Moment correlation coefficient between the data set split in half. A value of the coefficient greater than 0.8, implies good reliability of data.

2.2 Probability Curve Fitting:

Six probability curves were fitted to flow data in the study area. The probability density functions and the generalized equations of the models are presented in Table 1.

Table 1: Probability density functions and generalized models of fitted curves.

SN.	Distribution	Probability density function	Generalized model equation
1	Normal	$f(x) = \frac{1}{\sigma\sqrt{2\pi}} e^{(x-\mu)^2/2\sigma^2}$	$Q_T = Q_{av} + k\sigma$
2	Log-Normal	$f(x) = \frac{1}{x\sigma\sqrt{2\pi}} e^{(\ln x - \mu_{\ln x})^2/2\sigma^2_{\ln x}}$	$\log Q_T = \overline{\log Q} + k\sigma_{\log Q}$
3	Pearson III	$f(x) = \frac{1}{\beta\Gamma(p)}\left(\frac{x-\alpha}{\beta}\right)^{p-1} e^{-(x-\alpha)/\beta}$	$Q_T = Q_{av} + k'\sigma$
4	Log-Pearson III	$f(x) = \frac{1}{x\beta\Gamma(p)}\left(\frac{\ln x-\alpha}{\beta}\right)^{p-1} e^{-(\ln x-\alpha)/\beta}$	$\log Q_T = \overline{\log Q} + k'\sigma_{\log Q}$
5	Gumbel	$f(x) = \beta \exp\{-\beta(x-u) - e^{-\beta(x-u)}\}$	$Q_T = Q_{av} + \sigma(0.78Y_T - 0.45)$
6	Log-Gumbel	$f(x) = (\beta/x)\exp\{-\beta(\ln x - u) - e^{-\beta(\ln x - u)}\}$	$\log Q_T = \overline{\log Q} + \sigma_{\log Q}(0.78Y_T - 0.45)$

Source: Olofintoye (2007).

Where x is the standardized variate, μ, u and α are location (mean) parameters while σ and β are scale parameters (variance). $\Gamma()$ is the gamma function and p is a shape parameter. Q_{av} is the mean of the observed data while Q_T is the estimated flow for a specified return period T. Y_T is the reduced variate computed for a specified return period. The variable k is a frequency factor obtained from Normal distribution tables while k' is obtained from tables of frequency factors for the Pearson distribution.

2.3 Goodness-of-fit Test:

The Chi-square (χ^2) goodness-of-fit test was used to check if an experimental distribution follows a hypothesized one. This test is based on the sum of the squares of differences between the observed and estimated frequencies. Equation 2 may be used to compute a χ^2 value.

$$\chi^2 = \sum_{j=1}^{N} \frac{(o_j - e_j)^2}{e_j} \qquad (2)$$

Where o_j is the observed frequency, e_j is the estimated frequency, and N is the total frequency. If the calculated value is greater than the critical value at the specified level of significance, then the null hypothesis of a good fit is rejected.

10. METHODOLOGY

Details on the methodologies applied herein are presented in the following sub-sections.

3.1 Data and Validation:

Annual maximum flow data at Table Mountain gauging station, along the Mgeni River was collected from the Department of Water and Sanitation (DWS), Pretoria, South Africa. DWS is the custodian of hydrological data in the study area. The unit of the data is cubic metres per second. Sixty (60) years of data (1951 – 2022) was used for the analyses in this study. Statistics were computed to provide an insight into the nature of the data and the Spearman-Brown split-half technique was used to check the validity of the data.

3.2 Fitting Probability Distribution Functions:

The flow series was ranked according to Weilbull's plotting position and the corresponding return periods were estimated. Weibull's plotting position is an efficient formula for computing plotting position for unspecified distribution (Viessman et al., 1989). The Weibull plotting position may be computed using Equation 3 as:

$$P = \frac{m}{n+1} \quad (3)$$

Where m is the series of event ranking, 1 for highest value and so on in descending order, n is the number of events and P is an estimate of the probability of values being equal or greater than the ranked value. The return period T is estimated as the reciprocal of the probability using Equation 4 as follows:

$$T = \frac{1}{P} \quad (4)$$

The flow series was evaluated using six methods of probability distribution functions, Normal, Log-Normal, Pearson III, Log-Pearson III, Gumbel and Log-Gumbel. Curve fitting was carried out following standard procedure (Topaloglu, 2002; Salami, 2007; Olofintoye & Adeyemo, 2012; Khudri & Sadia, 2013; Adeyemo & Olofintoye, 2014; Paul et al., 2014).

3.3 Evaluating the Suitability of the Developed Models:

The suitability of the established probability models was examined using the statistical non-parametric chi-square (χ^2) goodness-of-fit test. If the computed value of the statistics using Equation (2) is greater than the corresponding critical value (or if the ratio $\chi^2_{Computed}/\chi^2_{Critical}$ is greater than one), the null hypothesis is rejected at the specified level of significance and it is concluded that there is significant discrepancy between experiment and theory (Olofintoye, 2007; Gupta, 2013). A 10% level of significance was adopted for the test in this study following the suggestion of (Haktanir et al., 2012).

3.4 Comparison of Flood Flow Models:

Since flood flow data are known to be skewed and generally not to follow a Normal distribution, comparisons between the performances of the models were made using the Kruskal-Wallis H-Test. This is the non-parametric equivalence of the Analysis of Variance (ANOVA) technique. The H-Test was performed at 5% level of significance as suggested by (Gupta, 2013). Only models that were found suitable by the Chi-square test were included in this test. Probability plots were also made to aid in visual inspection of model fit.

3.5 Test Scoring and Selection of the Most Suitable Flood Flow Model:

A test scoring scheme that has been successfully applied in the literature (Olofintoye, 2007; Olofintoye et al., 2009; Khudri & Sadia, 2013; Paul et al., 2014) was adopted to evaluate the fitness of a model relative to the others. Scoring of models was based on the Mean Relative Deviation (MRD), Mean Square Relative Deviation (MSRD) (Jou et al., 2009) and $\chi^2_{Computed}/\chi^2_{Critical}$ fit statistics. Lower values of these statistics indicate better fit. In the scheme, the assessment of a model is based on total test score obtained on all the fit statistics. A maximum score of six (6) is awarded a function best supported by a fitness test while a minimum of one (1) is awarded to the least performing model. A zero (0) score is awarded in all cases when the chi-square test indicates that a model is inappropriate. The model with the maximum overall score is selected as the most suitable model. Elaborate information on statistical test scoring may be found in the mentioned literature and other statistical texts.

11. RESULTS AND DISCUSSION

The flood data collected was analyzed in order to determine its reliability. The correlation coefficient (r) was computed and adjusted for the split half method using the Spearman's brown correlation coefficient (r_{SB}). The value of r was found to be 0.86 while r_{SB}= 0.92. These values lie in the excellent range and suggest that the data

is reliable within the acceptable limits. A summary of statistics of the annual maximum flow series in the study area is present in Table 2.

Table 2: Summary of statistics of annual maximum flows in Mgeni River at Table Mountain (1951 – 2022)

Mean value $\bar{x}$, (m^3/s)	*Median* (m^3/s)	*Standard deviation* σ, (m^3/s)	*Skewness coefficient, G*	*Minimum* (m^3/s)	*Maximum* (m^3/s)
135.29	94.19	134.18	2.42	8.82	760.82

It is observed from examination of statistics in Table 2, that the range and standard deviation of the series are high. Also, the mean lies to the right of the median with a positive coefficient of skewness. This indicates that the frequency distribution of maximum annual flow in the river is positively skewed. This corroborates the observations of Viessman et al. (1989) and other pundits who have noted that the distribution of flood flows are generally markedly right skewed partially due to the influence of natural phenomena.

The developed model equations, results of chi-square goodness-of fit test and its significance status and the computed values of the fit statistics of each function are presented in Table 3. The test scores obtained on each fit statistic are emphasized in italics and enclosed in parentheses. The probability fitness plots for the models are presented in Figure 1.

Table 3: Summary of developed probability distribution models and statistical tests

		Test Statistics				
Model	*Model Equation*	*MRD*	*MSRD*	$\chi^2_{Computed}$ / $\chi^2_{Critical}$	*Total Test Score*	*Significance Status*
Normal	Qp = 135.29 + 134.18K	5.8050 *(0)*	105,273.76*(0)*	1.0120 *(0)*	0	Significant
Log-Normal	Qp = Antilog (1.93 + 0.45K)	3.6659 *(5)*	303.30*(5)*	0.7836 *(6)*	16	Not Significant
Pearson III	Qp = 135.29 + 134.18K'	2.8938 *(4)*	1,631.63*(3)*	0.9107 *(4)*	11	Not Significant
Log-Pearson III	Qp = Antilog (1.93 + 0.45K')	2.8613 *(6)*	202.82*(6)*	0.7772 *(5)*	17	Not Significant
Gumbel	Qp = 74.91 + 104.66YT	3.0927 *(0)*	2,854.19*(0)*	0.7507 *(0)*	0	Significant
Log-Gumbel	Qp = Antilog (1.73+ 0.35YT)	3.4269 *(0)*	1,504.36*(0)*	0.4575 *(0)*	0	Significant

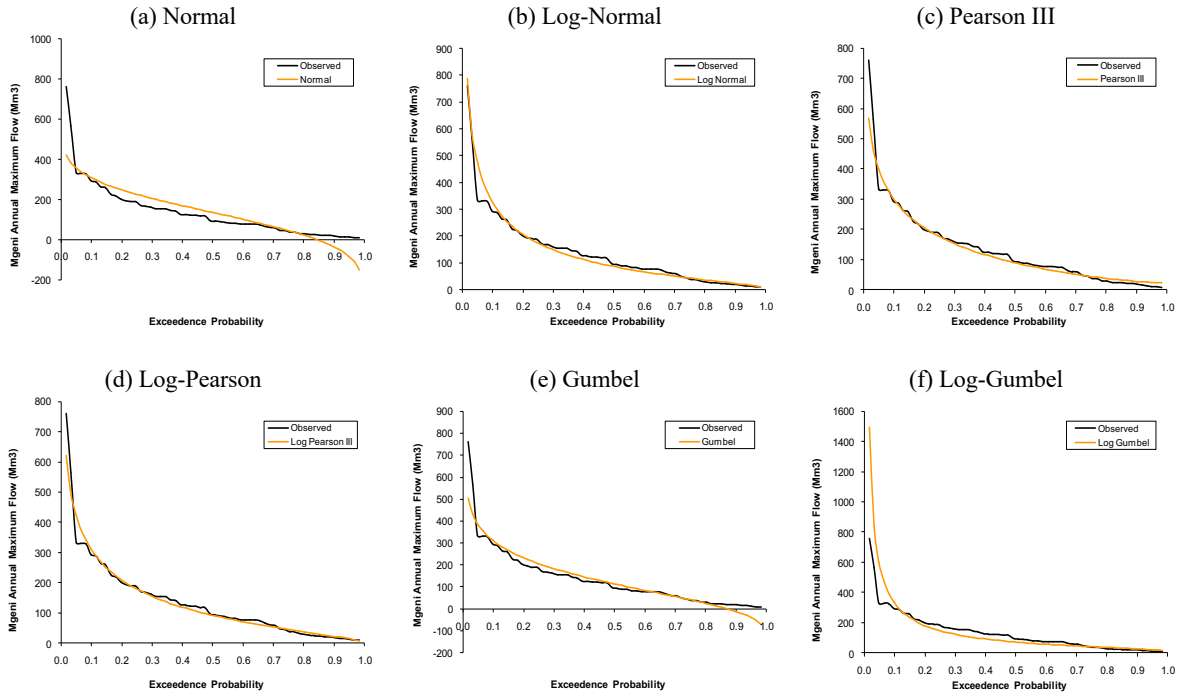

Figure 1: Fitness plots for Models

It is evident from Table 3 and Figure 1 that only 3 models viz. Log-Normal, Pearson III and Log-Pearson III distributions exhibited good fit to the data at the level of significance, and are therefore suitable for predicting flood flows in the study area. The Normal and Gumbel curves showed large deviations at the tails of the distribution. Also, some part of the curves lies in the negative range below the horizontal axis (Figures 1a and 1e).

While the Log-Gumbel was entirely restricted to the positive range of estimation, it showed very large deviation at the left tail of the distribution which rendered it unsuitable. Consequently, the Normal, Gumbel and Log-Gumbel distribution models were not compared further in the Kruskal-Wallis Test.

The Normal distribution is generally known to provide reasonable approximation in the centre of a distribution but is often inadequate at one or both tails of skewed distributions (Olofintoye, 2007; Salami, 2007). This is evident from the results in this study as the Normal distribution model produced a poor fit and exhibited significant deviations at the tails of the model (Figure 1a). This phenomenon has also been observed by Olofintoye et al. (2009) who reported that hydrologic series are generally skewed and found the Normal distribution model inadequate at most of the hydrologic stations in the study. Applications of normalization procedures before fitting Normal models to flow series may however be beneficial in resolving this problem in future studies.

The significance statuses of the Log-Normal, Pearson III and Log-Pearson III models indicate that they are suitable for estimating future flood flow in the study area. Based on total test scores obtained (Table3), Log-Pearson III is the best performing model, Log-Normal the second and Pearson III the third best. However, the value of the computed H-statistic in the Kruskal-Wallis test (H = 0.064) was less than the critical value of the statistic ($H_{critital}$ = 5.99) at the 5% level of significance. This suggests that there are no significant differences in the performance of the models and hence the 3 models are applicable in estimating flood flow in the area.

Since flood flow data are known to be generally skewed, 3-parameters distributions like the Pearsonian models, which employ the computation of a skew coefficient in estimation of hydrologic random variables, are often found to provide good fits in flood modelling. The selection of Log-Pearson III function as the best-fit model in this study further corroborates the findings of (Olofintoye, 2007; Olofintoye & Sule, 2009; Olofintoye et al., 2009) that the distributions hydrologic data are positively skewed and Log-Pearson III probability distribution model may conveniently be used to estimate future events.

In particular, the United States (U.S.) Interagency Advisory Committee on Water Data has recommended the use of Log-Pearson III distribution in calculating flood recurrences. It is also the default distribution adopted by the U.S. Geological Survey for flood studies. Likewise, the U.S. Water Resources Council (WRC) has also recommended that Log-Pearson III distribution be used as a base method for flood flow frequency studies in an attempt to promote a consistent, uniform approach to flood flow frequency determination for use in all federal planning involving water related land resources (Mays, 2011). Therefore, the findings in the study are in accord with international suggestions.

12. CONCLUSION

The need for reliable hydrologic studies cannot be overemphasized particularly in this era of climatic vicissitude. Increases in severities and frequencies of extreme daily rainfall events with attendant flooding are speculated worldwide due to recent anthropogenic global warming (IPCC, 2011). Therefore, establishing methods germane in effective management of hydrologic events is of great practical value in flood control.

Frequency analysis of annual maximum flow of Mgeni River measured at Table Mountain Gauging Station was performed to establish probability distribution models apposite in estimating flood. Six probability curves were fitted. It was found that the Log-Normal, Pearson III and Log-Pearson III distribution models were suitable for modelling flood flow in the area. These models may be useful in developing strategies for mitigating the adverse effects of floods experienced in the Mgeni watershed in South Africa.

A 3-parameter Log-Pearson III model which takes cognizance of a skew coefficient in estimations was found to be most appropriate in modelling flood flow in the study area. This is consistent with results from earlier studies and in accord with suggested international standards. Also, the length of data used in the analyses is statistically large and sufficient to provide good approximations to the population parameters and support the various statistical tests (Gupta, 2013). This suggests that the established models are appropriate and are therefore recommended for estimating flood flows in the Mgeni watershed, South Africa.

ACKNOWLEDGEMENT

The authors acknowledge the Department of Water and Sanitation, South Africa for making river flow data available for this study.

REFERENCES

Adeyemo, J., & Olofintoye, O. (2014). Optimized Fourier Approximation Models for Estimating Monthly Streamflow in the Vanderkloof Dam, South Africa. In A. Tantar, E. Tantar, J. Sun, W. Zhang, Q. Ding, O. Schütze, M. Emmerich, P. Legrand, P. D. Moral, & Coello Coello C.A. (Eds.), *EVOLVE - A Bridge between Probability, Set Oriented Numerics, and Evolutionary Computation V* (pp. 293-306). Springer International Publishing.

Gupta, S. C. (2013). *Fundamentals of Statistics* (I. Gupta, Ed. Seventh ed.). Himalaya Publishing House.

Haktanir, T., Bajabaa, S., & Masoud, M. (2012). Stochastic analyses of maximum daily rainfall series recorded at two stations across the Mediterranean Sea. *Arabian Journal of Geosciences*, *2012*, 1 - 16. https://doi.org/10.1007/s12517-012-0652-0

IPCC. (2011). *Managing the risks of extreme events and disasters to advance climate change adaptation*.

Jou, P. H., Akhoond-Ali, A. M., Behnia, A., & Chinipardaz, R. (2009). A Comparison of Parametric and Nonparametric Density Functions for Estimating Annual Precipitation in Iran. *Research Journal of Environmental Sciences*, *3*(1), 62-70.

Khudri, M. M., & Sadia, F. (2013). Determination of the Best Fit Probability Distribution for Annual Extreme Precipitation in Bangladesh. *European Journal of Scientific Research*, *103*(3), 391-404. http://www.europeanjournalofscientificresearch.com

Loucks, D. P., & Bee, E. v. (2005). *Water Resources Systems Planning and Management: An Introduction to Methods, Models and Applications*. UNESCO and Delft Hydrualics.

Mays, L. W. (2011). *Water Resources Engineering* (Second ed.). John Wiley & Sons, Inc.

NZCCO. (2008). *Climate change effects and impacts assessment: a guidance manual for local governments in New Zealan–2nd edition, .*

Olofintoye, O., & Adeyemo, J. (2012, 05 – 09 May, 2012). Development and Assessment of a Fourier Approximation Model for the Prediction of Annual Rainfall in Ilorin, Nigeria. Water Footprint: Water Institute of Southern Africa Biennial Conference and Exhibition, International Conference Center, Cape Town.

Olofintoye, O. O. (2007). *Frequency Analysis of Maximum Daily Rainfall for Selected Urban Cities in Nigeria* [M.Eng Thesis, University of Ilorin]. Ilorin, Nigeria.

Olofintoye, O. O., & Sule, B. F. (2009). Best–Fit Probability Distribution Model for Peak Daily Rainfall in Southern Nigeria. 1st Annual Civil Engineering Conference University of Ilorin, Department of Civil Engineering, University of Ilorin, Nigeria.

Olofintoye, O. O., Sule, B. F., & Salami, A. W. (2009). Best–fit Probability distribution model for peak daily rainfall of selected Cities in Nigeria. *, New York Science Journal*, *2*(3), 1-12.

Olukanni, D. O. (2003). *Development of Statistical Model for Reservoir Inflow at Kainji, Jebba, and Shiroro Hydropower Stations* University of Ilorin]. Ilorin, Nigeria.

Paul, S., Hasan, M. A., & Shopan, A. A. (2014). *AN ASSESSMENT OF BEST FITTED RAINFALL DISTRIBUTION FOR PROJECTED CLIMATE CHANGE OVER BANGLADESH USING STATISTICAL DOWNSCALING METHOD* 2nd International Conference on Civil Engineering for Sustainable Development, KUET, Khulna, Bangladesh.

Salami, A. W. (2007). Fitting probability distribution models to peak and low flows in selected rivers in South-West Nigeria. *Nigerian Journal of Technological Development*, *5*, 50-63.

Sudmeier-Rieux, K., Nehren, U., Sandholz, S., & Doswald, N. (2019). *Disasters and Ecosystems, Resilience in a Changing Climate - Source Book* (U. N. E. Programme, Ed.). UNEP and Cologne: TH Köln - University of Applied Sciences.

Topaloglu, F. (2002). Determining Suitable Probability Distribution Models for Flow and Precipitation Series of the Seyhan River Basin. *Turk Journal of Agric*, *26*, 189 - 194.

Umgeni. (2022). *STATEMENT: Heavy downpours cause damage to Umgeni Water infrastructure*. Retrieved 24th April, 2023 from https://www.umgeni.co.za/statement-heavy-downpours-cause-damage-to-umgeni-water-infrastructure/

Viessman, W., Krapp, J. W., & Harbough, T. E. (1989). *Introduction to Hydrology* (Third ed.). Harper and Row Publishers Inc.

Witwatersrand. (2022). *The 2022 Durban floods were the most catastrophic yet recorded in KwaZulu-Natal*. Retrieved 24th April, 2023 from https://www.wits.ac.za/news/latest-news/general-news/2023/2023-04/the-2022-durban-floods-were-the-most-catastrophic-yet-recorded-in-kwazulu-natal.html

PAPER 117 – AFFORDABLE HOUSING USING INDIGENOUS BUILDING MATERIALS

J. Sule[1], S. Duna[1], A. M. Abdulmumin[2], A. Halidu[3]

[1]Building Research Department, Nigerian Building and Road Research Institute, Abuja, Nigeria.
[2]Civil Engineering Department, University of Ilorin, Ilorin, Nigeria.
[3]Civil Engineering Technology Department, Federal Polytechnic Nasarawa, Nasarawa, Nigeria.
*Email: jibrinsule2005@yahoo.com

ABSTRACT
Provision of Housing in Nigeria has been overwhelmed by many challenges over a long time. These setbacks have been categorized as both qualitative and quantitative. The challenges have continued to become a nightmare, which has affected the socio-economic aspect of Nigerian, even though some efforts have been made to curb these lapses such as the Presidential Executive Order No. 5 to improve local content in public procurement with science, engineering and technology components. One of the major challenges is the high cost of building materials. These high cost of building materials has become a bottle-neck to developers trying to make profit off their investments thereby increasing the cost of the houses being constructed for the masses. It has become paramount for the Nigerian government to curtail the crisis resulting to the high cost of housing in Nigeria which calls for innovative solutions, and more funding for research institutes to drive the Research and Development sector to develop and improve an indigenous building technology to ease housing development in Nigeria. This paper, therefore, tends to explore indigenous building materials and technologies that are cheap and readily available to ease housing construction in Nigeria.
KEYWORDS: Affordable, Indigenous Materials, Housing Deficit, Sustainability.

1. INTRODUCTION

Housing plays a predominant role in the well-being, economy, education, environmental, political and social life of any nation (Alaghbari, et *al.* 2011). Despite this role, many people in the low-income categories in developing countries such as Nigeria found it difficult to have buildings of their own due to high cost of conventional materials used in constructing the building. Like many urbanised societies, Nigeria is not an exception in experiencing acute difficulties in the provision of adequate housing for her citizens. The lack of access to adequate housing, which is priced out of the economic reach of the poor, is sometimes so serious that some are forced to construct shacks on pirated land with all manners of refuse materials (Olotuah, A, 2000; UNCHS (Habitat), 1992). Research shows that increasing demand for wood for housing construction is considered to contribute severely to the adverse environmental effects attributed to the building sector in most nations. Although according to (Alam and Starr, 2009; Duguma and Hager, 2010), the effects vary from one country to the other, as policy strategies and regulatory reforms have been proposed to encounter such problems in most developing countries. For example, in Sub-Saharan Africa, building developers are encouraged to switch from the use of conventional clay burnt bricks to alternative building materials to minimise the inefficient wood consumption mostly for brick making (GoM, 2004).

Provision of adequate and quality housing units, is among the role of any government, since, housing is one of the human fundamental needs. This indicator signifies, among other factors, the standard of living of a country's populace. It can also be used to measure the economic viability of a nation. Housing deficit, when left to persistent, could lead to increase in crime, outbreak of diseases, unaffordable house prices, poor standards of living as well as high mortgage payments, just to mention but few (Henilane, I., 2016).

Research by Anderson, L.M. et'al. (2003), further explained that when low-income households do not have affordable housing, family resources needed for food, medical or dental care, and other necessities are diverted to housing costs. The consequence of the above turns out to be a cost worry or overburden, especially where 50% or more of household income is expended on housing rent.

However, the use of alternative building materials has been advocated by the United Nations Commission for Human Settlement since the early 1990s (UNCHS, 1993). The use of alternative building materials is also considered as a means of enhancing the housing stock for low-income populations by using local and affordable materials and methods available. Although, the perception of using alternative building materials has highly been criticised by previous authors such as Myers, G. A.,1999 for a number of reasons. In addition, the structures built using alternative building materials are considered as structurally poor in terms of durability due to the lack of technological knowhow during material manufacturing or house construction process (Wells et al., 1998b).

Despite all the criticism the use of alternative building materials is gaining more favour as most of the problems highlighted are being addressed through research and development. (Kuchena and Usiri, 2009; Venkatarama 2007a and b; and Acosta, 2000)

1.1 Affordable Building

In most developed economies, the housing sector is seen as an important sector for stimulating economic growth. In Nigeria, however, access to affordable housing has largely, remained an unfulfilled dream to many numbers of people, especially, the middle and the lower earners.

Affordable building has been defined in various forms by scholars in building industry. However, others are of the believe that housing is considered affordable if it consumes 30% or less of a household's income (Community Tool Box. 2018). In other word, affordable building may be referring to as house that can be acquired by median group whose income is below middle-class income in the society. The choice of an affordable house goes beyond having a roof over one's head; it involves choosing your neighbourhood, amenities, and services that come (or don't come) with it (Wilson, K. 2018). The ability to access wealth by the majority of the citizen often puts upward pressure and competition from high-income masses on housing prices, thereby posting a higher risk for low-income masses (Community Tool Box. 2018).

Globally, affordable housing is defined in many ways, and one of such definition is that affordability which takes into consideration the degree of spending on housing to income of the house hold. However, one of the major challenges of the low-income group is the affordability of building home of their own due to high cost of building materials for house construction (Saad, T.,1992). Hence the need to know what is building materials.

1.2 Building Materials

The cost of building materials and components are known to constitute about 60-70% of the cost of the buildings. Currently, the gap between the rising demand and declining production levels is widening at an alarming rate. This will lead to the increase of prices of building materials in Nigeria, which will seriously affect the affordability of housing for the vast majority of the population. Building materials are the essential components of buildings construction and these materials must be sustainable for both the present and future generations (Usman, A. U.2018; CIB, 2011). As a result, there has been a surge of interest in developing Alternative Building Materials which are capable of meeting our structural needs with lower energy and material consumption (Usman, A. U., 2018). The global trend towards increased environmental awareness and climate change has also resulted in a surge of interest in ecologically friendly building materials known as alternative building materials.

1.3 Alternative Building Materials.

Alternative building materials can play a vital role in the Nigerian building construction industry, however; there is the need to understand what constitutes the term "Alternative Building Materials". Alternative building materials are building materials that are developed through modifying conventional industrial materials or unconventional/indigenous/traditional materials or modifying unconventional /traditional/indigenous materials which are particularly attractive for housing (Anigbogu, N. A., 1999).

The major advantages of these materials over conventional materials typically include a low embodied energy (often leading to reduced embodied greenhouse gas emissions), ease of construction, widespread availability and low cost, they are ozone-friendly, they are reusable, as well as biodegradable. These properties make alternative housing technologies attractive not only for housing in developed countries but also for use in humanitarian engineering projects in developing countries (Sharman, J., 2016). Despite its advantage, it was established that building constructed with natural material is associated with problems of acceptability, low strength, high level of maintenance and deforestation among other issues. It is on this basis that the Nigerian Building and Road Research Institute (NBRRI) is making effort in contributing it quota to the development of affordable housing in the country.

2. NIGERIAN BUILDING AND ROAD RESEARCH INSTITUTE (NBRRI) AS A CONTRIBUTOR TO THE PROVISION OF AFFORDABLE HOUSING

The Nigerian Building and Road Research Institute (NBRRI) is one of the parastatals under the Federal Ministry of Science, Technology and Innovation (FMSTI), whose mandate is to conduct integrated Research and Development activities into the varied aspects of the Building and Road construction industries, build capacity and set the pace in indigenous construction technology development to improve the quality of life of Nigerians in the areas of affordable housing and increased economic empowerment.

2.1 Nbrri Technology and Innovation

The need to adopt measures for economic growth as well as provide adequate housing for the Nigerian is paramount, as such there is a growing awareness for the utilization of locally sourced materials especially in the deployment of mass housing construction schemes. For the materials to be appropriate to the needs of developing countries, they must be indigenous, locally available in abundance with low energy input in terms of production, maintenance and transportation costs, and labour intensive.

2.2 Some Research Carried Out By The Institute

This section intends to highlight some of the achievements recorded in the past few years by the Institute. The highlight cut across Building Research Department, Road Research Department and Engineering Materials Research Department as it mandates. They are as follows:

2.2.2 NBRRI Pozzolana

In line with the current thrust of the Institute to boost local content and produce a cheap, qualitative and yet highly competitive alternative to the conventional Portland cement, a product known as NBRRI Blended (Pozzolana) Cement as shown in Figure 1 was been produced and will soon be available in the market. It is locally sourced due to its availability all over the country and can be used with Portland cement at a ratio depending on raw material but varying from 20:80 to 50:50. This will reduce the cost of housing provision as well as provide employment for skilled, semi-skilled and unskilled. Pozzolanas are very good innovations in material production and utilisation in the building industry, they are siliceous and aluminous materials which in themselves possesses little or no cementitious value but will, in finely divided form and in the presence of moisture, chemically react with calcium hydroxide at ordinary temperatures to form compounds possessing cementitious properties. The utilisation of pozzolans brings about economic, environmental and technical advantages. The technical advantages involve the improvement of the quality of concrete i.e improved workability, improved resistance to sulphate attack, reduced alkali-aggregate reaction, reduced heat of hydration and thermal shrinkages and increase in water tightness.

Fig 1: NBRRI Blended Pozzolana

2.2.3 NBRRI Compressed Stabilised Earth Blocks

Walling takes up about 40% of construction costs, therefore it becomes imperative to explore cheaper means of wall construction materials such as drywalls and earth walls. Extensive research has been undertaken to produce quality and acceptable compressed stabilized earth blocks (CSEB) for low-cost housing. Paul O. A. and Isaac I. A. 2014; Patowary et.al, 2015, in their work evaluated the compressive strength of lateritic bricks stabilized with cement, lime and termite-hill.

The breakthrough in the design and production of interlocking Compressed Stabilized Earth Blocks (CSEBs) at 5% cement stabilization by the Nigerian Building and Road Research Institute as shown in Figure 2a, has made a giant achievement towards achieving the Sustainable Development Goals. These NBRRI CSEBs have under gone several tests such compressive strength and moisture absorption and have met the standard required for construction purposes. With cement stabilisation, the blocks must be cured for 28 days weeks after manufacturing. After this, they can dry freely and be used like common bricks with a soil cement stabilised mortar. Figure 2b shows the installation of CSEBs while 2c shows complete single bedroom using CSEBs.

Fig 2: Compressed Stabilized Earth Block (a) the CSEB (b) Installation of the CSEB (c) Single Bedroom

2.2.4 NBRRI Interlocking Block Making Machines and Laterite Grinding Machine

The Interlocking block making machines show in Figure 3a were designed and fabricated specifically for the production of laterite blocks shown in Figure 2(a) while the laterite grinding machine in Figure 3b, grinds laterite to required mesh size for block production. The laterite grinding machine eliminates materials wastes and guarantees high productivity. The Interlocking block making machines are simple and robust and produce a minimum of 500 blocks per day depending on the power source. They are ideal for mass housing delivery and can also serve as a means of economic empowerment.

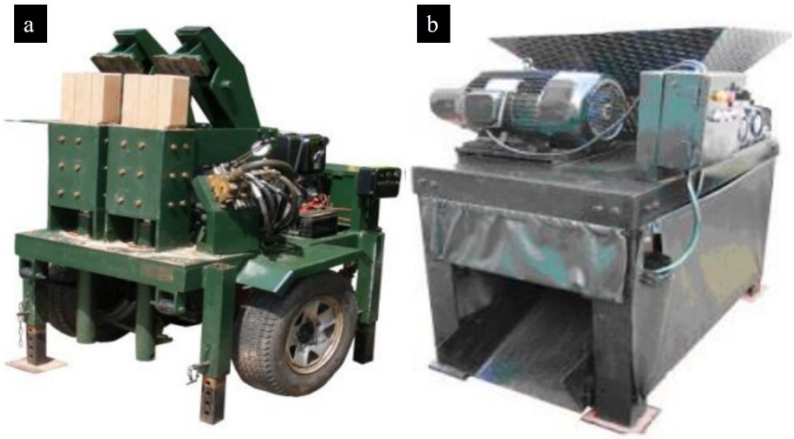

Fig 3: (a) Interlocking Blockmaking Machine -(Diesel) (b) Laterite Grinding Machine

2.2.5 NBRRI Laminated Bamboo Panals

The Bamboo plant is rated as the fastest growing plant on Earth. It has played an important role in the livelihood of millions around the world which has become a replacement for timber (Liese & Köhl ,2015).

One of the major problems is that it attracts living organism when is not treated. In Nigeria, Bamboo is an under-utilized raw-material (Ogunsanwo et' al. 2015). It is most commonly used as follows; scaffolding, supports (studs), fencing, fuel, ladders, Yam Stakes and frames for mud houses in rural areas in the south east and south-south states of the country. Hence NBRRI has developed bamboo laminated penal used for ceiling and floor finishes. This new development will help cut down the cost of walling, ceiling and floor finishes during construction. The major raw materials required for the production of the laminated bamboo floor finishes are recycled bamboo used as scaffold which qualifies it to be sustainable. Figure 4a shows the Laminated Bamboo Panel produced. Figure 4b and 4c show how they are applied on floor and ceiling finishes.

Fig 4: (a) Laminated Bamboo Panel (LBP) (b) Installation of LBPs as Floor Finish (c) Installation LBPs fitted as Ceiling Finish

2.2.6 NBRRI Mador Tiles as Roofing Materials

Roof coverings also play a major role in the high cost in construction which are mostly imported into Nigeria. With the desire to lower construction cost, building professionals have been on the search for cost effective and light roofing which are durable and are less labour intensive. Coir is a green building material and has potential as a raw material for the production of roofing materials like corrugated sheets and tiles (Darsana P et' al, 2016). This is why NBRRI research team were able to innovate a fibre concrete roofing tiles (called MADOR tiles) with locally sourced raw materials and manufactured with specially fabricated machine in order to cut down production cost. The raw materials required for the production of the NBRRI MADOR tiles are all locally sourced and are readily available, the materials used includes fiber from plants such as coconut and a small amount of port-land cement. The machine required for the production of the tiles were also locally fabricated which makes all the production processes indigenous. Figure 5 show the production stage of mador tiles.

Fig 5: (a) Placing the mix on the Vibrating Machine (b) Mador Tiles as Produced (c) Application of the Mador Tiles

2.2.7 NBRRI Rubberized Asphalt Mat (RAM)

Based on studies from other parts of the world, the use of rubberized asphalt can improve pavement performance and serve as a better method of road maintenance for the safety of transport services and better service life of the pavement. The material used for the NBRRI RAM are aggregates, bitumen and Crumb rubber. Crumb rubber is a term usually applied to recycled tyres from automotive and truck scrap tires which are derived by reducing the rubber into uniform granules with reinforcing materials such as steel and fiber being removed along with any other type of inert contaminants such as dust and glass. There are two processes of incorporating crumb rubber into bitumen and these processes are the wet process and the dry process. However, the wet process was adopted in this study which involved incorporating the crumb rubber into the bitumen as part of the binder and the modified binder was mixed with aggregate and shaped in form of a mat to produce a rubberized asphalt mat (RAM).

A rubberized Asphalt mat is a mixture of crumb rubber derived from waste tyres as fine particles, aggregates of different sizes with bitumen as the binding agent. The use of crumb rubber for the modification of bitumen will not only reduce the environmental problems associated with its disposal but can also enhance the elastic responses of bitumen at higher ambient temperatures. Figure 6 shows the production stages of RAM.

Fig 6: Stages of production of NBRRI Rubberised Asphalt Mat

2.2.8 NBRRI Dismantlable House (NDH)

In a bid to demonstrate the application of NBRRI innovations and its potential for modular construction, the NBRRI dismantlable house was designed. The modular prefabricated housing technology is still nascent in the Nigerian Construction Industry despite having been in existence for at least 25 years. The NBRRI dismantlable house presents a hybrid of innovative building construction technologies such as dry construction, indigenous materials, green and recycled materials, and emerging technologies and composites. It is a quick assembly of affordable housing model that addresses the Nigerian housing needs as well as having the potentials to respond to emergency needs for temporary housing provision using the prefabrication technology while incorporating strategic NBRRI R&D outputs in materials and technological processes.

The NDH is a housing model that has evolved over the years from a simple One-Bedroom to a more robust Three-Bedroom structure. The NDH is 100% indigenous from design (spatial considerations, aesthetics and function), and materials selection (locally sourced), to construction (dry stacked/mortar-less) which has been tailored to suit the socio-economic peculiarities of the Nigerian climate. Its application is not restricted to only residential buildings; it can also be satisfactorily applied to the construction of schools, hospitals, shops, warehouses, etc. Furthermore, the building's aesthetics, especially on the facade, was achieved through appropriate proportioning of elements, highlighting and detailing of fenestrations, while the finesse was achieved through competent craftsmanship and appropriate colour complementation.

Fig7: (a) NBRRI Dismantleable One-Bedroom (b) NBRRI Dismantleable Three-Bedrooms

2.2.9 NBRRI Technology Village

In line with the housing challenges as well as NBRRI's R&D outputs in the housing sector, NBRRI technology village was set up to fill this gap by taking practical measures that will ensure a paradigm shift from the era of theoretical analysis to justifiable actions. This concept was also borne out of a desire to project the totality of NBRRI innovations for full visibility to the entire country and beyond in projects that display the entirety of NBRRI innovations in one location. Considering the materials and methodology adopted the approach is in line with the Sustainable Development Goals (SDGs) for sustainable affordable housing in Nigeria. This project is aimed at building confidence in the general populace to adopt NBRRI innovations in line with Presidential order and Federal Government's drive toward promoting local content.

3. CONCLUSION AND RECOMMENDATIONS

3.1 Conclusion

Due to the large housing deficit of about 17 million in Nigeria housing problems has continue to become a nightmare which has affected the socio-economic aspect of Nigerian, even though some efforts have been made to curb these lapses such as the Presidential Executive Order 5 to improve local content in public procurement with science, engineering and technology components. It has become paramount for the Nigerian government to curtail the crisis resulting to the high cost of housing in Nigeria which calls for innovative solutions, and more funding for research institutes such as Nigerian Building and Road Research institute to drive the Research and Development sector to develop and improve on alternative building technologies to ease housing development in Nigeria. Home grown technologies that are sustainable will help curtail the menace of building collapses which is as a result of poor workmanship and compromise by contractors trying to make maximum profit due to the high cost of building materials in Nigeria. Alternative building techniques are excellent strategy to solving the high cost of housing provision and should be considered as they are much simpler and cheaper to implement which will help boost the Nigerian Housing industry.

3.2 Recommendations

Some of the measures to be put in place to provide decent accommodation for Nigerian citizens include:

(i) Government should deliberately explore alternative and innovative ways of cost-effective, quality, healthy, large-scale housing stock delivery programmes that are achievable within short delivery duration; and hinged on NBRRI Dismantlable House concept, across the country. This could be within its housing programmes or in response to emergencies or crises.

(ii) Government should as a matter of deliberate policy promote and adopt the use as well as encourage direct patronage of NBRRI innovations

(iii) Reduce the dependency on imported machines by fabricating and using locally-made ones

(iv) Making raw materials for building cheap and affordable e.g. cement, sand, laterite, roofing materials, ceiling materials, glass window materials, plumbing materials

(v) Capacity building in terms of artisan training, e.g. masonry, carpentry, Tiling, iron binding, plumbing and electrical training.

(vi) Restructure and adequately fund the Nigerian Building and Road Research Institute (NBRRI) to perform its statutory role.

ACKNOWLEDGMENTS

The authors wish to acknowledge the contribution made by the Nigerian Building and Road Research Institute for the support rendered to us in the process of collecting and writing this paper.

REFERENCE

Acosta, D. (2000). Soil-cement block masonry: An appropriate technology for massive production of low-cost housing? In Proceedings of the 12th IB2Mac. Twelfth Int.Brick/Block Masonry.1(pp. 27-45). Madrid: Caracas, IDEC.

Alaghbari, W., Salim, A., Dola, K., & Abdullah Abang Ali, A. (2011). Developing affordable housing design for low income in Sana'a, Yemen. International Journal of Housing Markets and Analysis, 4(1), 84–98. https://doi.org/10.1108/17538271111111857

Alam, S. A., and Starr, M. (2009). Deforestation and greenhouse gas emissions associated with fuelwood consumption of the brick making industry in Sudan. Science of the Total Environment, 407, 847-852.

Anderson, L.M., Charles, J.S., Fullilove, M.T., Scrimshaw, S.C., Fielding, J.E., & Normand, J. (2003). Providing Affordable Family Housing and Reducing Residential Segregation by Income: A Systematic Review. American Journal of Preventive Medicine, 24(3), 47–67. https://doi.org/10.1016/S0749-3797(02)00656-6

Anigbogu, N. A (1999). Economics of Alternative construction materials: Some Conceptual Issues. Nigerian Journal of Construction Technology Management. Vol.2, issue 1, pp. 93-96,

CIB (International Council for research and innovation in Building and construction), (2011). Agenda 21on sustainable construction. Association of Research in Construction Management, vol. 2, pp 49, http://www.cibworld.nl:600/pages/begin/A21SCDC.ht ml

Community Tool Box. (2018). Providing affordable housing for all. Center for community health and development. http://communityhealth.ku.edu/

Darsana P, Ruby A , Anu J, Arakkal J, Binuraj P.R , Jithin Sarmaa. (2016). Development of Coir-Fibre Cement Composite Roofing Tiles. International Conference on Emerging Trends in Engineering, Science and Technology (ICETEST - 2015) pp. 169-178.

Duguma, L. A., and Hager, H. (2010). Consumption and species preference for house construction wood in central highlights of Ethiopia-implications for enhancing tree growing. Journal of Forestry Research, 21 (1), 104-110.

Government of Malawi (GoM). (2004). Environmental Policy. Lilongwe: Environmental Affairs Department, Ministry of Natural Resources and Environmental Affairs.

Henilane, I. (2016). Housing Concept and Analysis of Housing Classification. Baltic Journal of Real Estate Economics and Construction Management, 4(1), 168–179. https://doi.org/10.1515/bjreecm-2016-0013

Kuchena, C. J., and Usiri, P. (2009). Low cost construction technologies and materials - case study Mozambique. In Proceedings of the 11th International Conference on Non-Conventional Materials and Technologies, 6-9 September 2009. Bath, UK: NOCMAT.

Liese, Walter & Köhl, Michael. (2015). Bamboo -The Plant and its Uses. 10.1007/978-3-319-14133-6.

Myers, G. A. (1999). Political ecology and urbanisation. Zanzibar's construction materials industry. Journal of modern African Studies, 37 (1), 83-108.

Ogunsanwo, O.Y.; Terziev, N.; Panov, D.; Daniel, G. 2015. Bamboo *(Bambusa vulgaris Schrad.)* from Moist Forest and Derived Savanna Locations in South West Nigeria-Properties and Gluability. *BioResources* 10(2): 2823-2835.

Olotuah, A (2000). The Challenge of Housing in Nigeria. Effective Housing In The 21st Century", 1(1), 16-19.

Patowary B. N., Nath N., Hussain I. ,& Kakoti H. J. (2015). Study of Compressed Stabilized Earth Block. International Journal of Scientific and Research Publications, 5(6), 2250-3153.
Paul O. Awoyera and Isaac I. Akinwumi. (2014). Compressive Strength Development for Cement, Lime and Termite-hill Stabilised Lateritic Bricks. International Journal of Engineering and Science (IJES). Vol 3(2), pp.37 – 43.
Saad, T (1992). Implementation of the New National Housing Policy: Problems and Prospects Housing Today., 8 (2), 11-23.
Sharman, J. (2016). Alternative housing: a different approach to materials, styles and community thinking (Part one).
UNCHS (Habitat) (1992). Building Materials for Housing Nairobi: UNCHS (Habitat).
UNCHS. (1993). Building materials for housing: Report of the Executive Director, United Nations Commission on Human Settlements. Habitat International, 17 (2), 1-20.
Usman, A. U.; M. F. Khamidi & T. Hassan, (2018). Sustainable building material for green building construction, conservation and refurbishing. Management in Construction Research Association (MiCRA) Postgraduate Conference.
Venkatarama Reddy, B. V. (2007a). Enhancing bond strength and characteristic of soil-cement masonry. Journal of Materials in Civil Engineering, 19 (2), 164-172.
Venkatarama Reddy, B. V. (2007b). Optimum soil grading for soil cement blocks. Journal of Materials in Civil Engineering, 19 (2), 139-148.
Wells, J., Sinda, S. H., and Haddar, F. (1998b). Housing and building materials in low-income settlements in Dar es Salaam. Habitat International, 22 (4), 397-409.
Wilson, K. (2018, April 11). 4 Factors that can Make Affordable Housing not so Affordable—Strong Towns. https://www.strongtowns.org/journal/2018/4/10/4-factors-that-can-makeaffordable-housing-not-so-affordable

PAPER 118 – HYDROGEN ECONOMY: PANACEA TO AIR POLLUTION PROBLEMS AND PROSPECTS FOR A CLEANER PLANET EARTH

E.I Muhibbu-Din[1]*, M Sanni[1]

[1]Clean Energy/Environmental Research Laboratory (CE[2]RL), Department of Chemical Engineering, University of Ilorin, Nigeria
*Email: muhibbudin.ei@unilorin.edu.ng

ABSTRACT
One of the biggest issues facing planet Earth is environmental degradation brought on by human activities. Studies have shown that 89% of the pollution that exists on Earth today is due to the use of fossil fuels. To green the world and provide clean, sustainable energy, engineers and scientists have been looking for a pollution-free, readily available fuel choice for the transportation and industrial sectors. The hydrogen gas economy has been chosen as the greatest solution. This hydrogen economy has the potential to displace the need for fossil fuels. This review study discourses the possibility of using hydrogen gas as an energy source to create a cleaner planet through decarbonization. The role of hydrogen as the foundation for greener and cleaner energy in the industrial and transport sectors, utilizations on its zero emissions, increasing electrification through fuel cell technology, and profits of hydrogen economy on the environment were substantially discussed. With a hydrogen economy, planet earth will reach its natural state of equilibrium.

KEYWORDS: Climate Change: Cleaner Earth: Clean Energy: Clean Environment: Pollution Free

1. INTRODUCTION

Globally, air pollution has detrimental consequences on the environment, human health, other living things, and materials. In particular in industrialized and emerging nations, it is a serious and widespread public health issue. Industrial and transportation emissions are significant sources of poor urban air quality in both industrialized and developing nations. (Balat, 2008). Despite the implementation of sound and strategic environmental policies, ongoing air monitoring, and evaluation, the issue of air pollution remains a critical problem that has yet to be fully addressed on both regional and global scale. This is because strict adherence to environmental laws and regulations has failed in light of the current state of global climate change, unpredictable weather patterns, ongoing environmental degradations, and imbalances in equilibrium. Additionally, the diversity in air pollution patterns highlights the need for workable solutions that aim to significantly reduce air pollution (De Nicola, 2016).

According to the World Health Organization (2020), air pollution is the leading environmental health concern in the world and is directly linked to seven million annual fatalities, mostly from cancer and cardiopulmonary/kidney illness (Silva, R. A., et al., 2013). Air pollution has been related to cognitive health impairments such as accelerated cognitive aging and decreased memory and intellect, in addition to its well-known impact on disease burden (Clifford, A., Lang, L., Chen, R., Anstey, & K. J. & Seaton, 2016). Additionally, a recent body of economics study has shown how these negative health effects manifest themselves in economic outcomes (Zivin, J. G. & Neidell, 2018). He, J., (2019) discovers evidence of diminished output at two industrial facilities in China as a result of elevated air pollution. A refinery's closure in Mexico City is also used by Hanna, R., and Oliva, P. (2015) to demonstrate how air pollution decreased as a result. Fossil fuel consumption results in the release of various poisonous gases, dangerous hydrocarbons, and airborne particles during industrial processes, transportation, electricity generation, and other activities. As a result of human activity, this pollution has expanded globally and continues to exist. These pollutions can be sporadic or seasonal, and they are typically restricted to particular locations within communities that are influenced by geological and geographical variables. It is a specific type of pollution that is of interest and concern since its constituent parts and amounts have become exceedingly diverse and substantial, creating a noticeable imbalance in the typical composition of the air. The most prevalent air pollutants include sulfur oxides, nitrogen, greenhouse gases, particulate matter (such as dust and smoke), and various chemical compounds (hydrocarbons). These pollutants are primarily produced by the combustion of fossil fuels (coal, oil, and natural gas), as well as biomass, such as bush or forest or wood burning, and agricultural residues.

2. IMPACTS OF THE HYDROGEN ECONOMY ON REGIONAL AIR POLLUTION, ALTERNATIVE ENERGY, AND CLIMATE CHANGE

Numerous studies and evaluations of industrial and transportation-related emissions from the environment center on three main problems: air pollution, energy security, and climate change.

2.1. Climate Change

Since publishing its first report in 1989, the Intergovernmental Panel on Climate Change (IPCC) of the United Nations has propagated the theory that climate change is causing persistent global warming because greenhouse gases (GHG), particularly anthropogenic carbon dioxide and ozone in the atmosphere, are preventing heat from radiating into space. (IPCC, 2014)

The Arctic is one of the regions on the planet that is most vulnerable to climate change. The Arctic Climate Assessment report of 2004, which was conducted by leading scientists from countries that border the Arctic Circle, warned that the warming over Greenland could result in the complete melting of the Greenland Ice Sheet, leading to a sea level rise of about seven meters (23 feet) (IASC & Committee, 2004). More recent studies suggest that this process may occur faster than anticipated. According to a study by the Arctic Monitoring and Assessment Programme, the Arctic has been warming at a rate of nearly twice the global average in the last decade (AMAP, 2021). This warming trend has already had significant impacts on the region, including melting permafrost, changing sea ice patterns, and altering ocean currents.

One of the primary drivers of climate change is the increasing concentration of greenhouse gases in the atmosphere, particularly carbon dioxide. These gases trap heat and prevent it from escaping into space, leading to a warming planet. Carbon dioxide concentrations have been increasing at an accelerating rate in recent years and are now at their highest levels in more than three million years. In 2017, atmospheric concentrations of carbon dioxide surpassed 400 parts per million (ppm), a level that is considered dangerous for the long-term stability of the planet's climate (NASA, 2018). The continued burning of fossil fuels for energy, along with deforestation and other human activities, is responsible for the majority of these emissions.

It is now widely accepted that human-made gases are the predominant cause of observed global warming. According to the Intergovernmental Panel on Climate Change (IPCC), the major climatic changes already taking place may be "irreversible" for centuries to come if strong and sustained reductions in carbon dioxide and other greenhouse gas emissions are not achieved (IPCC, 2021). The IPCC has recommended a range of mitigation and adaptation measures to address the impacts of climate change, including reducing emissions, transitioning to renewable energy sources, and investing in infrastructure and technology to adapt to changing conditions.

One promising solution for reducing carbon emissions is the transition to a hydrogen economy and fuel cell technology. Hydrogen is a clean-burning fuel that can be produced from renewable sources, such as wind or solar power. When used in fuel cells, hydrogen produces electricity with only water and heat as byproducts. According to the Hydrogen Council, if governments and industry work together to scale up the production and use of hydrogen, it could account for up to 18% of the world's total energy demand by 2050 and reduce global CO_2 emissions by up to six gigatons per year (Hydrogen Council, 2021). This transition would not only reduce carbon emissions but also create new job opportunities and stimulate economic growth.

In summary, the urgency of addressing climate change has become increasingly clear in recent years. The consequences of inaction are severe and potentially irreversible, particularly in vulnerable regions like the Arctic. It is critical to take bold and immediate steps to reduce carbon emissions and transition to cleaner, more sustainable energy sources. The transition to a hydrogen economy and fuel cell technology is one promising solution that could help address this urgent problem. Apart from major effects on CO_2 emissions, non-CO_2 emissions spread into the environment will also be drastically reduced on adoption of hydrogen gas technology (hydrogen economy) in the transportation sector (cars, light-duty vehicles, heavy trucks). The forecasts for the emission levels of CO, NOx, volatile organic compounds (VOCs), and particulate matter will be dramatically decreased by more than 70% for NOx and other pollutants (Muhibbu-din, I.,2020).This will undoubtedly help and enhance the planet Earth's air quality, recover, and revitalize good air quality life on the planet. [Osama et al, 2020).Worldwide economic transition to hydrogen economy is anticipated.

2.2. Alternative Energy

The world continues to face an energy crisis due to the depletion of fossil fuel resources and the increasing problem of environmental pollutions (Ullah et al., 2019; Mannan et al., 2018). In addition to the decreasing supplies of crude oil and political instability in regions with significant oil reserves, the demand for alternative fuels is driven by increasingly stringent pollution regulations (Mannan et al., 2018). Many alternative fuels have been proposed, including biodiesel, methanol, ethanol, hydrogen, boron, natural gas, liquefied petroleum gas (LPG), and Fischer-Tropsch fuel, p-series. Among these, hydrogen gas energy is the most abundant and prevalent element in the universe (Wang et al., 2020). It also has the highest specific energy content of all conventional fuels. Among others, hydrogen economy is technically possible, economically viable, environmentally acceptable, and widely accessible as an alternative fuel (Muhibbu-Din et al., 2022) (Meher LC, Sagar DV, & Naik SN,2006).The potential of hydrogen gas as an energy carrier gained significant attention following the global energy crisis of 1974 (Meher et al., 2006, Muhibbu-Din et al,2021). Although hydrogen is not readily available in a usable form, it possesses exceptional properties that make it a promising energy carrier (Mazloomi & Gomes, 2019). These qualities include being lightweight, abundant, and ecologically friendly. Hydrogen gas energy is not an inherent primary energy found in nature. An additional energy source must be available before hydrogen can be produced, just like

electricity. Hydrogen burns cleanly and produces just water and a negligible quantity of nitrogen oxides as waste products. Because of its quick burning speed, high effective octane rating, lack of toxicity and inability to generate ozone, hydrogen is an extremely unique fuel for use in transportation and industrial sectors (Muhibbu-din et al., 2020).

Compared to methane and gasoline, it has substantially greater air flammability boundaries. A combination of clean coal, fossil fuels (with carbon sequestration), nuclear energy, and large-scale renewables can be used to make hydrogen, which could eventually overtake other fuels as the primary source for transportation and industry. On a longer time period, large-scale hydrogen generation will likely occur. The alternatives for producing hydrogen in the short and medium term are first focused on distributed hydrogen generation from electrolysis of water with sunshine (Muhibbu-din et al., 2021) and natural gas reformation. A total of 40 million tons of hydrogen may be produced annually using each of the centralized or decentralized hydrogen production technologies. Because it may be produced indefinitely in the future using renewable energy sources, hydrogen will play a significant role in the development of sustainable, clean energy (Muhibbu-din et al., 2021)

The world stands to gain from a hydrogen economy in a number of ways, including energy security with no or less reliance on oil imports, sustainability by utilizing clean, renewable energy sources, improved urban air quality due to emissions of almost no carbon, hydrocarbon, heavy metals, greenhouse gases, NO_X, and other pollutants at the point of use, and economic viability by potentially influencing the future.

When generated from clean sources, which are now being prioritized as governmental goals, hydrogen will offers a variety of advantages as a clean energy carrier. The development of a sizable market for hydrogen as an energy source offers practical answers for both the security of the energy supply and the reduction of emissions. Because hydrogen emits no pollutants when it is used up, it prevents emissions caused by the transportation and industrial sectors. In contrast to other alternative fuels, hydrogen as a secondary energy carrier that can be produced from any (locally available) primary energy source, which can help diversify the sources and supplies of automotive fuel while also providing the long-term possibility of being entirely produced from renewable energies. Through the utilization of fuel cells, hydrogen might also be utilized as a medium for storing electricity. Various techniques are being used to mass-produce hydrogen. Due to its abundance, hydrogen can be created using a variety of techniques, some of which are clean and green, or extracted from a wide range of substances and molecules. Various feed stocks, including fossil and renewable resources, can be used to make it. Hydrogen can be produced using a variety of process technologies, including chemical, biological, electrolytic, photolytic, and thermo-chemical. According to Muhibbu-din et al. (2020), common ways for producing hydrogen include steam methane reforming, gasification of coal and other hydrocarbons, electrolysis of water, hydrogen from biomass, and hydrogen from nuclear energy.

2.3. Regional Air Pollution

The adoption of hydrogen fuel vehicles might dramatically reduce regional or local air pollutants, which are the source of noise, ozone, and acid rain as well as particle matter (Balat, 2008). As opposed to fossil fuels, emissions of NOx, SO_2, and particulates can be decreased by 70-80%. This is a significant advantage of hydrogen, particularly in heavily populated places. The need for enhancing urban air quality is expanding and becoming more important as there are more megacities around the world.

Various world energy scenarios have a wide range of expectations for the future contribution of hydrogen to the global energy system. In the future energy scenarios, hydrogen gas energy will play a significant role as an energy transporter. With stringent climate regulations, fluctuating oil and gas prices, and technology advancements in hydrogen vehicles, fuel cells, and carbon capture and storage, hydrogen gas energy will become a feasible choice. Recent studies suggest that hydrogen vehicles are expected to be adopted by 70% of the world's population by 2050, leading to a significant global demand for the fuel under favorable conditions (Li et al., 2018; Wang et al., 2020)) and a large increase in renewable energy sources, especially solar energy that will be used to produce hydrogen, will also occur. (Muhibbu-din et al. 2022).

3. CONCLUSIONS

In conclusion, the hydrogen economy offers the chance to solve all of the major energy policy objectives in the industrial and transportation sectors and has significant potential to mitigate the consequences of climate change and address the problem of air pollution. Additionally, the hydrogen economy produces electricity using hydrogen fuel cells to create power. However, utilizing hydrogen as a fuel will be the most straightforward method to accomplish carbon capture and storage without upsetting the balance of the earth's CO_2 consumption. The hydrogen economy holds the key to resolving the air pollution problem, aiding in the global clean-up, and reconciling planet earth with nature.

ACKNOWLEDGMENT

We are grateful for the enormous efforts made by every member of the Clean Energy and Environmental Research Laboratory (CE^2RL), Department of Chemical Engineering, University of Ilorin, Nigeria, to the advancement of Hydrogen Energy in the country.

REFERENCES

1. Balat, M. (2008) Potential Importance of Hydrogen as a Future Solution to Environmental and Transportation Problems. International Journal of Hydrogen Energy, 33, 4013-4029. http://dx.doi.org/10.1016/j.ijhydene.2008.05.047
2. Clifford, A., Lang, L.,, Chen, R., Anstey, & K. J. & Seaton, A. (2016). Exposure to air pollution and cognitive functioning across the life course–a systematic literature review. Environmental research , 383–398.
3. De Nicola, F., Adamo, P., & Giordano, S. (2016). Comparison of lichen and moss bags as monitoring devices of airborne trace elements and PAHs. In Biomonitoring of Air Pollution Using Mosses and Lichens, A Passive and Active Approach, State of the Art Research and Perspectives.. Nova Science Publishers.
4. Hanna, R., & Oliva, P. (2015). The effect of pollution on labor supply: Evidence from a natural experiment in mexico city. Journal of Public Economics 122, 68–79.
5. He, J.,, Liu, H., & Salvo, A. (2019). Severe air pollution and labor productivity: Evidence from industrial towns in china. American Economic Journal: Applied Economics, 173–201.
6. IASC, & Committee, I. A. (2004). Impacts of a Warming Arctic. Cambridge University Press, New York, NY, USA .
7. IPCC. (2014). AR5 Synthesis Report: Climate Change.
8. Meher LC,, Sagar DV,, & Naik SN. (2006). Technical aspects of biodiesel production by transesterification. Renew Sustain Energy, 10:248.
9. Muradov, N.Z. and Veziroglu, T.N. (2008) “Green” Path from Fossil-Based to Hydrogen Economy: An Overview of Carbon-Neutral Technologies. International Journal of Hydrogen Energy, 33, 6804-6839. http://dx.doi.org/10.1016/j.ijhydene.2008.08.054
10. World Health Organization, W. H.O (2020). World health statistics 2020: monitoring health for the SDGs, sustainable development goals.
11. Osama R. Shaltami , Namat M. Hamed , Fares F. Fares , Hwedi Errishi , Farag M. EL Oshebi1 and Elena Maceda (2020). AIR POLLUTION – A REVIEW. Conference: Virtual Conference on Environment and Health (VCEH)
12. Romm, J. (2007). Energy Myth Four–The Hydrogen Economy Is A Panacea To The Nation’s Energy Problems. Energy and American Society–Thirteen Myths, 103-124.
13. Silva, R. A., West, J. J., Zhang, Y., Anenberg, S. C., Lamarque, J. F., Shindell, D. T., ... & Zeng, G. (2013). Global premature mortality due to anthropogenic outdoor air pollution and the contribution of past climate change. Environmental Research Letters, 8(3), 034005.
14. Woodward, C. (2005). "The Big Meltdown",E/The Environmental Magazine,. www.emagazine.com/view/?2302&printview&imagesoff , online.
15. Zivin, J. G., & Neidell, M. (2018). Air pollution's hidden impacts. Science, 359(6371), 39-40.
16. Muhibbu-Din,. E.I OLARENWAJU, A. M., MUBARAK, S., VICTOR, O., & ASUQUO, B. D. (2020). Prevalence of Covid-19 Pandemic: A Paradigm Shift to Hydrogen Economy. Engineering & Technology Research Journal Volume 5(2) pp. 81-92 .
17. Muhibbu-Din,. E.I. E., Ebube, O. V., Asuquo, B. D., Adepoju, M., & Mubarak, S. (2021). Generation of Solar Hydrogen Gas Energy from Water Splitting Process as an Alternative to Fossil Fuel. Adeleke University Journal of Engineering and Technology, 4(2), 13-19.
18. Muhibbu-din, I., Ebube, O. V., Asuquo, B. D., Muheez, A., & Mubarak, S. (2022). Photoelectrochemical Process of Producing Hydrogen Gas Energy from Brewery Wastewater. Malaysian Journal of Applied Sciences, 7(1), 58-65.
19. Sharma, S. and Ghoshal, S.K. (2015) Hydrogen the Future Transportation Fuel: From Production to Applications. Renewable and Sustainable Energy Reviews, 43, 151-1158.
20. Muhibbu-din, I. (2020). Investigation of Ambient Aromatic Volatile Organic Compounds in Mosimi Petroleum Products Depot, Sagamu, Nigeria. Anthropogenic Pollution, 4(1), 65-78.
21. Mazloomi, K., & Gomes, C. (2012). Hydrogen as an energy carrier: Prospects and challenges. Renewable and Sustainable Energy Reviews, 16(5), 3024-3033.
22. Li, M., Liao, R., Wu, T., Wu, J., & Wei, D. (2018). The prospect and challenges of hydrogen energy development in China: A review. Renewable and Sustainable Energy Reviews, 91, 995-1006.

23. Wang, Y., Zhang, J., Wang, S., Song, C., & Wang, R. (2020). Recent advances in hydrogen production technologies by bioreactors: A review. International Journal of Hydrogen Energy, 45(54), 28863-28876.
24. Mazloomi, M., & Gomes, C. (2019). An overview of hydrogen production methods. Renewable and Sustainable Energy Reviews, 107, 581-597.
25. Ullah, K., Ahmed, S., Sarwar, W., Ahmed, I., & Saba, T. (2019). Renewable energy technologies for sustainable development goals: A review. Renewable and Sustainable Energy Reviews, 105, 393-406.
26. Mannan, H. A., Rasul, M. G., Khan, M. M. K., & Sharif, A. (2018). Renewable energy: An overview of resources and technologies. Sustainable Cities and Society, 31, 183-200.
27. Wang, Y., Zhang, J., Wang, S., Song, C., & Wang, R. (2020). Recent advances in hydrogen production technologies by bioreactors: A review. International Journal of Hydrogen Energy, 45(54), 28863-28876.
28. NASA. (2018). The consequences of greenhouse gas. Retrieved from https://climate.nasa.gov/effects/.
29. Intergovernmental Panel on Climate Change. (2021). Global warming of 1.5°C. Retrieved from https://www.ipcc.ch/sr15/.
30. Intergovernmental Panel on Climate Change. (2019). IPCC Special Report on the Ocean and Cryosphere in a Changing Climate. Retrieved from https://www.ipcc.ch/srocc/.
31. Hydrogen Council. (2021). Path to hydrogen competitiveness: A cost perspective. Retrieved from https://hydrogencouncil.com/en/path-to-hydrogen-competitiveness/.
32. AMAP, 2021. Impacts of Short-lived Climate Forcers on Arctic Climate, Air Quality and Human Health. Summary for Policy Makers

PAPER 119 – MAXIMUM POWER TRACKING OF PHOTOVOLTAIC UNDER PARTIAL SHADING WITH SPRING SEARCH ALGORITHM INTEGRATED WITH PERTURB AND OBSERVE

Yusuf Elijah[1], A. S. Abubakar[2], G. S. Shehu[3]

[1]Department of Electrical Engineering, Ahmadu Bello University, Zaria, Nigeria.
[2]Department of Electrical Engineering, Ahmadu Bello University, Zaria, Nigeria.
[3]Department of Electrical Engineering, Ahmadu Bello University, Zaria, Nigeria.
[*]Email: yusufelijah360@gmail.com

ABSTRACT
Solar power generation is perfectly suited for clean energy and meeting the increasing energy demands owing to its abundance and easy maintenance. However, it has low efficiency as maximum power is not extracted from the photo-voltaic panel due to solar irradiance obstruction causing partial shading condition. This condition creates multiple power peaks of which the maximum power peak is selected for maximum power utilization. To achieve this, a tracker based on spring search algorithm integrated with perturb and observe algorithm (SSA-PO), and operationally tied with DC-DC boost converter was developed for maximum power point tracking of the photovoltaic system at constant solar irradiance and during partial shading conditions. This generated a tracking efficiency of 97.8% at PSC1, 96.3% at PSC2 and 96.9% at PSC3, therefore, yielding an improvement of 0.15% and 2.29% during constant and partial shading conditions, and tracking time was 6.8% and 2.5% improvement when compared with the result of artificial bee colony algorithm with perturb and observe (ABC-PO).

KEYWORDS: Boost converter, MPPT, Partial shading, Photovoltaic, Tracking efficiency.

1 INTRODUCTION

The demand for energy world-wide is rapidly increasing, the International Energy Agency (IEA) predicted the world energy consumption will increase by 44% from 2006-2030 (A. K. Pandey et al., 2016). The conventional way of power generation that uses fossil fuel still provide the larger part of energy demand and has the challenges of carbon emission, installation cost and is being depleted (Başoğlu, 2022),(Li et al., 2018), thus, the need for renewable energy. Solar photovoltaic (PV) is widely applied in standalone and on-grid application as a result of its easy maintenance, low cost of installation, absence of noise, and free from pollution(Dileep & Singh, 2017).
In PV system sunlight is converted into direct current without any green-house gas emission which is widely advocated by governments (Ali & Mohamed, 2022). The current-voltage (I-V) curve of PV depends on temperature and irradiance. Under constant temperature and increase in irradiance, the PV current increases in direct proportion with negligible effect on PV voltage (Ahmad et al., 2019). The efficiency of the solar power generation needs to be improved, thus, several MPPT methods are developed to extract maximum power from the PV system (Dileep & Singh, 2017),(Rezk & Eltamaly, 2015). Conventional MPPT methods include, Incremental conductance technique (Mao et al., 2020)(Putri et al., 2015), Perturb and Observe techniques (Mo et al., 2022) etc. Perturb and observe method is the simplest method among the various methods. Conventional MPPT methods are effective under uniform irradiance conditions but are ineffective under changing atmospheric conditions and partial shading condition (PSC) (Liu et al., 2008),(A. Pandey et al., 2008). Thus, under PSC, to track the MPP, the conventional methods should be integrated with soft computing algorithms for better efficiency.
Photovoltaic arrays are connected in series or parallel so as to obtain required amount of voltage and current, and there is possibility of partial shading condition as a result of shadow of buildings, trees, moving clouds etc. The panels will receive a varying solar irradiation, which will give rise to partial shading condition (Ram et al., 2017). Under PSC the power vs voltage curve produces multiple peaks with only one peak which represent the true MPP, known as Global MPP (GMPP) and local MPP (LMPP). The conventional methods can only track the LMPP and are unable to track the GMPP due to system non-linearity. This will lead to power loss and low efficiency of the system. To improve the efficiency a soft computing method is fused with the P&O technique or other conventional methods (Zainuri et al., 2014).

The aim of this research is to develop a PV array MPPT model under partial shading with boost converter by developing a spring search algorithm integrated with perturb and observe (SSA-PO) and apply on PV system configured with boost converter, and evaluating its performance based on tracking efficiency and time.

2 THEORETICAL ANALYSIS

In this section the theoretical background to the study is going to be discussed.

2.1 Photovoltaic Cell Model

In solar cell modelling, single diode and double diode model methods are used, also organic cell modelling apart from the silicon cell model is being developed over the years (Mazhari, 2006) and is the basic energy conversion unit of the PV system (Tayeb et al., 2022). However, the double diode method is complex (Ram et al., 2017). To predict the energy generation of photovoltaic cell, the single diode circuit model is used as represented in Figure 1.

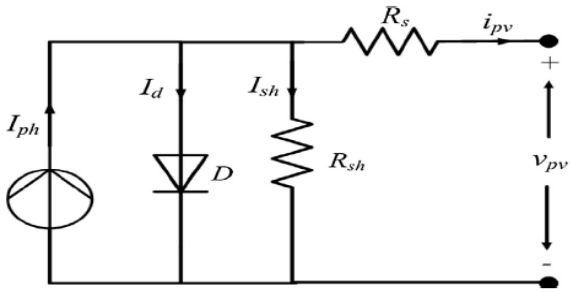

Fig 1: Circuit Diagram of PV Cell Model

The characteristic equation of the one diode model could be obtained from Kirchhoff's current law using:

$$I_{pv} = I_{ph} - I_d - I_{sh} \tag{1}$$

Where, I_{ph} is Photons current, I_d is Diode current, I_{pv} is Photovoltaic current and I_{sh} is shunt resistor current

The characteristic equation in (1) is also expressed using:

$$I_{pv} = N_p \left\{ I_{ph} - I_o \left[exp\left(\frac{q(V_{pv} + I_{pv}R_S)}{N_S AkT} \right) - 1 \right] \right\} - \frac{V_{pv} + I_{pv}R_S}{R_p} \tag{2}$$

Where, I_o is saturation current, N_p is number of parallel cell, N_s is number of series cell, q is electron charge, A is ideality factor, k is Boltzmann constant and T *is* cell temperature.

The saturation current which is dependent on temperature variation and the photon current are expressed using (Dileep & Singh, 2017):

$$I_o = I_{rs} \left(\frac{T}{T_{ref}} \right)^3 exp\left[\frac{qE_g}{Ak} \left(\frac{1}{T_{ref}} - \frac{1}{T} \right) \right] \tag{3}$$

$$I_{ph} = (I_{sc} + (T - Tref)\, K_i) \frac{G}{1000} \tag{4}$$

Where, G is irradiance, E_g is band gap energy, I_{rs} is reverse saturation current, K_i is short circuit current temperature coefficient and T_{ref} is the reference temperature.

Modules are also connected in series and parallel to meet power demand. A standard panel has 36 or 72 number of cell arrangement (Tey et al., 2018).

2.2 PV Array with Partial Shading

The solar array performance is often affected by partial shading as solar irradiance is obstructed from fully reaching the panels, which drastically reduce the output power. Figure 2, shows the diagram of PV array under partial shading. The array is receiving a varying solar irradiance, which will create multiple local maximum power point and global maximum power point (Pal & Mukherjee, 2020).

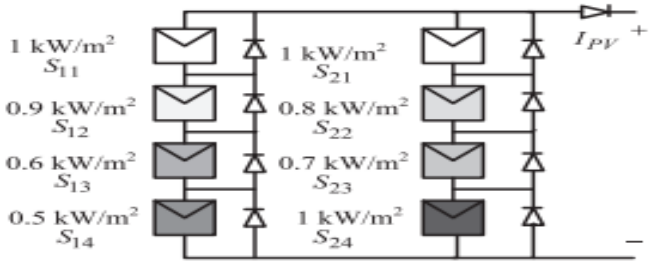

Figure 2: PV Array with partial shading

2.3 Spring Search Algorithm (SSA)

The principle behind this optimization technique is based on hooks law. Equation (5) is the expression of Hooke's law (spring force).

$$F_s = -KY \tag{5}$$

Where, F_s is spring force, K is a constant and Y is the stain or compression of the spring.

3.0 MATERIAL AND METHODS

The objectives of this research were realized through the implementation of spring search algorithm with boost converter using MATLAB/Simulink.

3.1 Objective Function and Constraints

The problem presented in this research is non-linear, as such, in this research the maximum power point of the PV array is to be optimized. Therefore, the power is the objective function that the algorithm is required to optimize while voltage and current are the decision variables, this is expressed using:

$$P_m = \sum_{z=1}^{n} V_{mz} I_{mz} \tag{6}$$

Where, n is the number of the solar panels, V_{mz} is maximum voltage of solar panel numbered z, I_{mz} is the maximum current of solar panel numbered z.

3.2 Pv Array Specification

The parameters of a single PV module at standard temperature of 25°C and insolation of 1000W/m^2 is shown in table 1. In this work, the PV array is made up of 2 modules connected in series (Pilakkat & Kanthalakshmi, 2019). To generate the required P-V and I-V curve, three shading conditions PSC1, PSC2, PSC3 are presented, which are:

i. When the PV array has pattern 1000W/m^2 and 1000W/m^2 (PSC 1)
ii. When the PV array has a shading pattern of 1000W/m^2 and 500 W/m^2 (PSC2)
iii. When the PV array has a shading pattern 300W/m^2 and 800W/m^2 (PSC3)

Table 1: PV Module Specification of Vikram Eldora-37

Parameter	***Value***
Maximum power (P_{max})	37W
Voltage at MPP (V_{mpp})	17V
Current at MPP (I_{mpp})	2.25A
Open circuit voltage (V_{oc})	21.8V
Short circuit current (I_{sc})	2.8A
Module efficiency	10.10%
Short circuit current temperature coefficient	0.04%/°C

3.3 Development of SSA-PO Algorithm for PV MPPT Model under PSC with Boost Converter

The implementation of PV MPPT model under partial shading condition using SSA-PO is described using the flow chart in Figure 3.

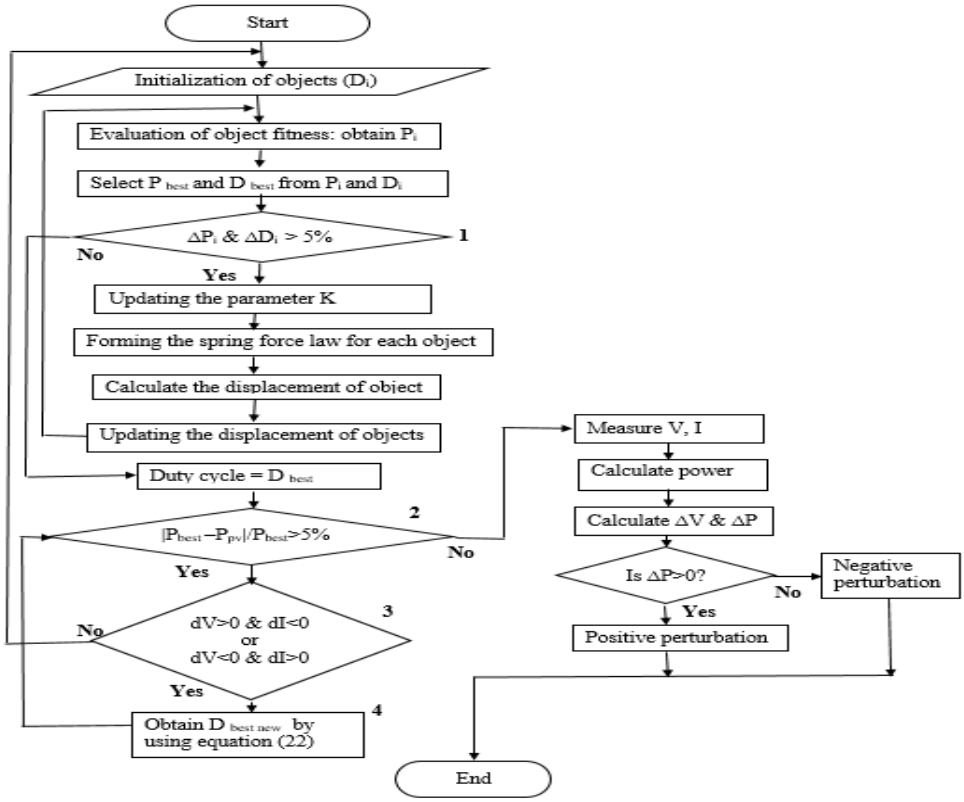

Figure 3: Flow-chart of SSA-PO Algorithm

Figure 4, shows the developed Simulink model of the proposed SSA-PO algorithm connected to the switching device of the boost converter, which has wide acceptance in PV power system as it has good efficiency (Fathabadi, 2016). The algorithm generates the duty cycle that controls the converter, as such, maximum power tracked by the algorithm is supplied to the resistive load at the output terminal of the converter.

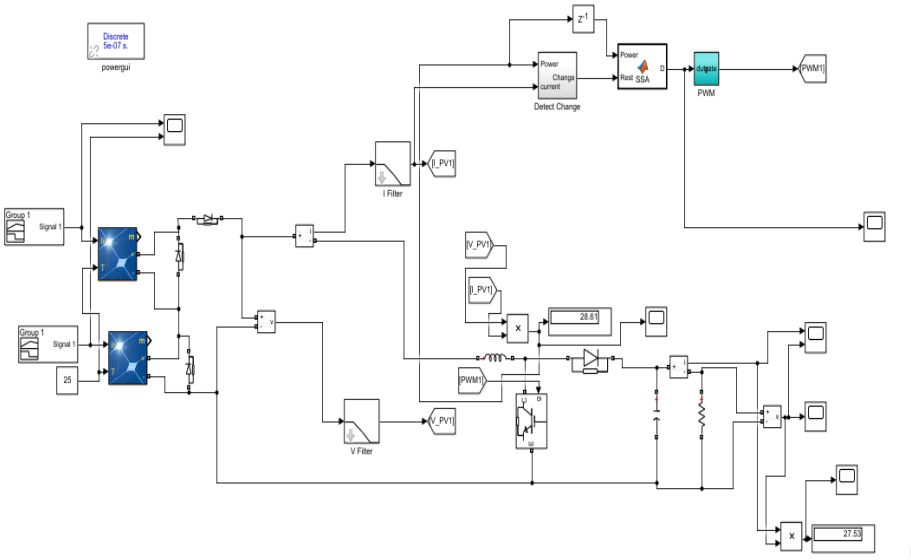

Figure 4: Developed Simulation Model of SSA-PO with Boost converter

4.0 RESULT AND DISCUSSION

In this section, the implementation was carried out in MATLAB/SIMULINK and the result compared with ABC-PO algorithm with boost converter, using efficiency and tracking time as performance metrics.

4.1 Result obtained with ABC-PO Method

Table 2 shows the result obtained with ABC-PO method. The power (P) is tracked at 69.06W at time (T) 0.16 seconds as compared to 70.72W of the photovoltaic power of the system at constant irradiance (1000W/m^2 and 1000W/m^2) from 3.2. Therefore, with ABC-PO method, the efficiency is found to be 97.65% with a tracking error of 2.3% at constant solar irradiance. At time 1 second, the photovoltaic power of the system dropped to 30.63W due to irradiance change from 1000W/m^2 to 500W/m^2. The ABC-PO tracked the power (P) to be 29.7W at time (T) 1.04 second with tracking efficiency of 96.9% and tracking error of 3.03%.

At partial shading conditions of PSC2 (1000W/m^2 and 500W/m^2) and PSC3 (800W/m^2 and 300W/m^2) as shown in 3.2. From table 2, the ABC-PO tracked the power to be 16.13W at time 0.09s. However, at time 1 second the irradiance changed and the power output increases due to increase in solar irradiance on the PV array. The ABC-PO tracked the power to be 21.76W at time 1.056 second.

4.2 Result obtained with SSA-PO Method

In this section the developed technique is used to track the GMPP from the solar array at constant and partial shading condition. From table 2, it shows the power tracked when the solar array is under PSC1 and PSC2 as shown in 3.2. When the PV array has irradiances of 1000W/m^2 and 1000W/m^2, the SSA-PO tracked the power to be 73.55W at time 0.149 second as compared to the 75.19W of the photovoltaic system at constant irradiance. The tracking efficiency was found to be 97.8% with tracking error of 2.18% at constant solar irradiance.

Furthermore, at time 1 second the irradiance changed from 1000W/m^2 to 500W/m^2 hence the power dropped. The SSA-PO tracked the GMPP and the power was found at 27.5W at time 1.075 seconds compared to 28.55W of the photovoltaic system during partial shading condition. This reduction in power output was due to the reduction in solar irradiance received by the solar array. The tracking efficiency was 96.3% with tracking error of 3.6%.

At partial shading conditions PSC2 (1000W/m^2 and 500W/m^2) and PSC3 (800W/m^2 and 300W/m^2) as shown in3.2. From Table 2, the SSA-PO tracked the power to be 19.95W at time 0.1s. However, at time 1 second the irradiance changed and the power output increased due to increase in solar irradiance on the PV array. The SSA-PO tracked the power to be 27.51W at time 1.029 second, which indicated power increase due to solar irradiance increase.

Table 2: Results obtained from developed method and ABC-PO method at partial shading condition PSC1, PSC2 and PSC3.

Parameter Description	*ABC-PO (PSC1, PSC2, PSC3)*	*Developed method (PSC1, PSC2, PSC3)*	*% Improvement (PSC1, PSC2 ,PSC3)*
Tracking Time (sec)	*0.16, 1.04, 1.056*	*0.149, 1.075, 1.029*	*6.8, 3.3, 2.5*
Open-circuit Voltage (V)	*36.24, 23.69, 20.05*	*37.23, 22.83, 22.8*	*0.99, 0.86, 2.75*
Short-circuit Current (A)	*1.907, 1.2, 1.09*	*1.96, 1.204, 1.207*	*2.78, 0.33, 10.7*
Maximum Power point (W)	*69.06, 29.7, 21.76*	*73.55, 27.5, 27.51*	*6.5, 7.4, 26.4*
Relative Error (%)	*2.3, 3.03, 2.32*	*2.18, 3.6, 0.01*	*0.12, 0.57, 2.31*
Tracing Efficiency (%)	*97.65, 96.9, 94*	*97.8, 96.3, 96.29*	*0.15, 0.6, 2.29*

5. CONCLUSION

This research presents the development of maximum power tracking method of a PV system under and varying solar irradiance with SSA-PO method. In this work, a DC-DC boost converter was modelled and employed between the PV array and the load. A spring search algorithm integrated with Perturb and observe (SSA-PO) MPPT was developed to determine the duty-cycle of the boost converter for maximum power tracking under partial and constant irradiance. Finally, the developed method result was compared with the performance of ABC-PO using tracking efficiency and time as performance metrics.

The developed work obtained 0.15% and 2.29% improvement in tracking efficiency compared with ABC-PO respectively under constant and partial shading condition. Also, the developed method obtained 6.8% and 2.5% improvement in tracking time under constant and partial shading condition compare with ABC-PO method.

The developed work employed boost converter to enable maximum power tracking, I recommend further work should employ Zeta converter with the developed technique.

ACKNOWLEDGMENT

I wish to express my sincere gratitude to God almighty for His love, faithfulness and guidance during this work. I also want to express my profound gratitude to Dr. A.S. Abubakar and Dr. G.S. Shehu, for there unrelenting effort, guidance and time to go through all the manuscripts despite tight schedules.

REFERENCE

Ahmad, R., Murtaza, A. F., & Sher, H. A. (2019). Power tracking techniques for efficient operation of photovoltaic array in solar applications–A review. *Renewable and Sustainable Energy Reviews*, *101*, 82–102.

Ali, A. I. M., & Mohamed, H. R. A. (2022). Improved P&O MPPT algorithm with efficient open-circuit voltage estimation for two-stage grid-integrated PV system under realistic solar radiation. *International Journal of Electrical Power & Energy Systems*, *137*, 107805. https://doi.org/10.1016/J.IJEPES.2021.107805

Başoğlu, M. E. (2022). Comprehensive review on distributed maximum power point tracking: Submodule level and module level MPPT strategies. *Solar Energy*, *241*, 85–108. https://doi.org/10.1016/J.SOLENER.2022.05.039

Bendib, B., Belmili, H., & Krim, F. (2015). A survey of the most used MPPT methods: Conventional and advanced algorithms applied for photovoltaic systems. *Renewable and Sustainable Energy Reviews*, *45*, 637–648.

Bouaouadja, N., Bouzid, S., Hamidouche, M., Bousbaa, C., & Madjoubi, M. (2000). Effects of sandblasting on the efficiencies of solar panels. *Applied Energy*, *65*(1–4), 99–105. https://doi.org/10.1016/S0306-2619(99)00044-6

Dileep, G., & Singh, S. N. (2017). An improved particle swarm optimization based maximum power point tracking algorithm for PV system operating under partial shading conditions. *Solar Energy*, *158*, 1006–1015. https://doi.org/10.1016/J.SOLENER.2017.10.027

Esram, T., & Chapman, P. L. (2007). Comparison of photovoltaic array maximum power point tracking techniques. *IEEE Transactions on Energy Conversion*, *22*(2), 439–449.

Fathabadi, H. (2016). Novel high efficiency DC/DC boost converter for using in photovoltaic systems. *Solar Energy*, *125*, 22–31. https://doi.org/10.1016/J.SOLENER.2015.11.047

Gevorkian, P. (2011). *Large-scale solar power system design: an engineering guide for grid-connected solar power generation*. McGraw-Hill Education.

Kiriş, B., Bingöl, O., Şenol, R., & Altintaş, A. (2016). Solar array system layout optimization for reducing partial shading effect. *Acta Physica Polonica A*, *130*(1), 55–59.

Li, L.-L., Lin, G.-Q., Tseng, M.-L., Tan, K., & Lim, M. K. (2018). A maximum power point tracking method for PV system with improved gravitational search algorithm. *Applied Soft Computing*, *65*, 333–348.

Liu, F., Kang, Y., Zhang, Y., & Duan, S. (2008). Comparison of P&O and hill climbing MPPT methods for grid-connected PV converter. *2008 3rd IEEE Conference on Industrial Electronics and Applications*, 804–807.

Mao, M., Cui, L., Zhang, Q., Guo, K., Zhou, L., & Huang, H. (2020). Classification and summarization of solar photovoltaic MPPT techniques: A review based on traditional and intelligent control strategies. *Energy Reports*, *6*, 1312–1327.

Mazhari, B. (2006). An improved solar cell circuit model for organic solar cells. *Solar Energy Materials and Solar Cells*, *90*(7–8), 1021–1033. https://doi.org/10.1016/J.SOLMAT.2005.05.017

Mo, S., Ye, Q., Jiang, K., Mo, X., & Shen, G. (2022). An improved MPPT method for photovoltaic systems based on mayfly optimization algorithm. *Energy Reports*, *8*, 141–150. https://doi.org/10.1016/J.EGYR.2022.02.160

Mohapatra, A., Nayak, B., Das, P., & Mohanty, K. B. (2017). A review on MPPT techniques of PV system under partial shading condition. *Renewable and Sustainable Energy Reviews*, *80*, 854–867.

Pal, R. S., & Mukherjee, V. (2020). Metaheuristic based comparative MPPT methods for photovoltaic technology under partial shading condition. *Energy*, *212*, 118592. https://doi.org/10.1016/j.energy.2020.118592

Pandey, A., Dasgupta, N., & Mukerjee, A. K. (2008). High-performance algorithms for drift avoidance and fast tracking in solar MPPT system. *IEEE Transactions on Energy Conversion*, *23*(2), 681–689.

Pandey, A. K., Tyagi, V. V., Selvaraj, J. A., Rahim, N. A., & Tyagi, S. K. (2016). Recent advances in solar photovoltaic systems for emerging trends and advanced applications. *Renewable and Sustainable Energy Reviews*, *53*, 859–884. https://doi.org/10.1016/J.RSER.2015.09.043

Pilakkat, D., & Kanthalakshmi, S. (2019). An improved P&O algorithm integrated with artificial bee colony for photovoltaic systems under partial shading conditions. *Solar Energy*, *178*, 37–47.

Putri, R. I., Wibowo, S., & Rifa'i, M. (2015). Maximum power point tracking for photovoltaic using incremental conductance method. *Energy Procedia*, *68*, 22–30.

Ram, J. P., Babu, T. S., & Rajasekar, N. (2017). A comprehensive review on solar PV maximum power point tracking techniques. *Renewable and Sustainable Energy Reviews*, *67*, 826–847.

Rezk, H., & Eltamaly, A. M. (2015). A comprehensive comparison of different MPPT techniques for photovoltaic systems. *Solar Energy*, *112*, 1–11.

Tayeb, A. M., Solyman, A. A. A., Hassan, M., & Abu el-Ella, T. M. (2022). Modeling and simulation of dye-sensitized solar cell: Model verification for different semiconductors and dyes. *Alexandria Engineering Journal*, *61*(12), 9249–9260. https://doi.org/10.1016/J.AEJ.2022.02.057

Tey, K. S., Mekhilef, S., Seyedmahmoudian, M., Horan, B., Oo, A. T., & Stojcevski, A. (2018). Improved differential evolution-based MPPT algorithm using SEPIC for PV systems under partial shading conditions and load variation. *IEEE Transactions on Industrial Informatics*, *14*(10), 4322–4333.

Wu, L., Chen, Z., Long, C., Cheng, S., Lin, P., Chen, Y., & Chen, H. (2018). Parameter extraction of photovoltaic models from measured IV characteristics curves using a hybrid trust-region reflective algorithm. *Applied Energy*, *232*, 36–53.

Zainuri, M. A. A. M., Radzi, M. A. M., Che Soh, A., & Rahim, N. A. (2014). Development of adaptive perturb and observe-fuzzy control maximum power point tracking for photovoltaic boost dc–dc converter. *IET Renewable Power Generation*, *8*(2), 183–194.

PAPER 120 – SHORT-TERM LOAD FORECASTING FOR MICROGRID SYSTEM BASED ON ARTIFICIAL INTELLIGENCE TECHNIQUES

B.I Gwaivangmin[1], G.A Bakare[2], Y.S Haruna[3] and A.L Amoo[4]

Department of Electrical and Electronics Engineering
Abubakar Tafawa Balewa University, Bauchi
bgwaivangmin@gmail.com

ABSTRACT
Microgrids are becoming increasingly popular as a means of providing localized and reliable electricity supply, particularly in remote or isolated areas. Accurately forecasting short-term electricity load demand is essential for effective microgrid management and optimal resource allocation. In this study, we present a short-term electricity load demand forecast for a microgrid system with an 11 kV dedicated feeder of the University of Jos, Plateau State, using three machine learning techniques: Adaptive Neuro-Fuzzy Inference System (ANFIS), Particle Swarm Optimization-ANFIS (PSO-ANFIS), and Support Vector Machine (SVM). The study utilizes five years of historical load demand data obtained from the Jos Electricity Distribution Company (JEDC) and weather data, including temperature, humidity, wind speed, and solar radiation, obtained from NASA for January 2018 to January 2022, with data distribution of 80%, 10%, and 10% for training, testing, and validation. The results show that PSO-ANFIS outperforms, ANFIS and SVM, with RMSE, MSE, and MAPE of 3.0372, 8.2478, and 1.7868 for PSO-ANFIS,3.1663, 10.0254, and 3.1511 for ANFIS, while SVM yields an RMSE, MSE, and MAPE of 6.9721, 24.4407, and 4.6789 respectively. This study demonstrates the effectiveness of PSO-ANFIS in forecasting short-term electricity load demand for microgrid systems, providing valuable insights for energy management and decision-making.
KEYWORDS: Energy, Forecasting, Load demand, Management, Microgrid, and Optimal

1. INTRODUCTION

1.1 Background of the Study

Microgrids are becoming increasingly popular as a means of providing localized and reliable electricity supply, particularly in remote or isolated areas. These systems, which operate independently and sometimes in parallel with the main grid, can enhance energy security, reduce power outages, and optimizes the utilization of renewable energy sources. However, effective microgrid management requires accurate prediction by optimizing the allocation of resources, reducing operational costs, and ensuring grid stability of the short-term electricity load demand.

To this end, various machine learning techniques have been developed to forecast electricity load demand, including Expert systems, Fuzzy systems, and Adaptive Neuro-Fuzzy Inference Systems (ANFISs). ANFIS and PSO-ANFIS, have shown promise in accurately predicting load demand for microgrid systems among these techniques. ANFIS integrates the merits of fuzzy logic and neural networks to provide a hybrid modeling approach that can handle complex and uncertain systems. The incorporation of Particle Swarm Optimization (PSO) into ANFIS results in the enhancement of its performance, leading to improved model accuracy as PSO optimizes the learning process.

1.2 Aim and Objectives

In this study short-term electricity load demand prediction for a microgrid system with an 11 kV dedicated feeder of the University of Jos, Plateau State, using three machine learning techniques is the aim.

The objectives of the study can be inferred from the methodology described in the abstract and include:

i. To apply three machine learning techniques, which include; Adaptive Neuro-Fuzzy Inference System (ANFIS), Particle Swarm Optimization-ANFIS (PSO-ANFIS), and Support Vector Machine (SVM)regression, to predict short-term electricity load demand.
ii. To contrast the key performance index of the three machine learning techniques in terms of their prediction ability of short-term electricity load demand.
iii. To provide valuable insights for energy management and decision-making regarding microgrid systems.

1.3 Literature Review

Khantach *et al.* (2019), in their study, proposed a load forecast model by decomposing the historical period and analyzing the historical evolution of 24 hours. PSO-trained ANFIS is expected to give a better result. Park *et al*. (2020), in their proposal, suggest an algorithm that uses a back propagation neural network (BPNN) as well as a reinforcement learning-based load demand forecasting model to select similar days. Butt *et al*. (2020), in their

study, utilized load data from a feeder to predict short-term and medium-term load demands for the next one day, three days, seven days, fourteen days, and thirty days.

Adebunmi *et al*. (2021), in their study, using the Neuro-fuzzy model for load forecasting and compared three models (ANFIS, ANN, and MLR) using RMSE and MAE as metrics.

Agboola *et al*. (2021), in their study, presented an ANN-based approach for LTLF of the Trans-Amadi industrial feeder under the PHEDC network from 2020 to 2029.

Niu *et al*. (2021), in their research, developed a machine-learning model to improve short-term electricity load forecasting accuracy.

Omitaomu and Niu (2021) presented a survey of existing research on the application of artificial intelligence techniques to load forecasting, power grid stability assessment, faults detection, and security problems in smart grid and electrical power utility systems.

Thomas and Okafor (2021) explored the use of stochastic/probabilistic extrapolation to forecast Nigeria's electricity demand from 2020-2040, using MATLAB for computation. The authors suggest that the use of artificial intelligence techniques would lead to even better results.

Ul Islam, *et al* (2022) provided a review of hybrid deep learning models for short-term load forecasting (STLF) in smart power grids based on nature-inspired metaheuristic techniques. STLF is essential for load scheduling, unit commitment, and cost-effective operation of smart power grids.

Atanasovski *et al* (2022) in their work compared different practical procedures for short-term load prediction and their application on primary load demand and temperature data for the Republic of North Macedonia

Stamatellos and Stamatellos (2023) discussed the significance of short-term load prediction in electrical power system planning, operation, and control.

2.0 THEORETICAL ANALYSIS

2.1 Factors Affecting Electrical Load Demand Forecasting

Weather is one of the crucial factors that can affect electricity load demand forecasting. Here are some of the major weather factors that can impact electricity demand:

(i)Temperature(ii) Humidity (iii) Precipitation(iv)Wind(v)Storms(vi) Solar Radiation(vii) Extreme Weather Events(viii)Economic Conditions.

2.2 ANFIS Model

The mathematical depiction of an Adaptive Neuro-Fuzzy Inference System (ANFIS) is presented below:

i. To start, the input signals (x_1, x_2, ..., x_n) are converted into fuzzy values utilizing fuzzy membership functions ($\mu_{A1}(x_1)$, $\mu_{A2}(x_2)$, ..., $\mu_{An}(x_n)$) for each input variable. These membership functions decide the extent to which each input signal is associated with each fuzzy set.

ii. The rule in the ANFIS model can be represented as follows: "IF x_1 is A_1 AND x_2 is A_2 AND ... AND x_n is A_n THEN y is $f(x_1, x_2, ..., x_n)$", where A_1, A_2, ..., A_n are the fuzzy sets associated with the input signals x_1, x_2, ..., x_n, and f is the consequent of the rule that represents the output variable y.

iii. The ANFIS algorithm calculates the firing strength of each rule by multiplying the degree of membership of each input signal to its corresponding fuzzy set. Specifically, the firing strength of rule i is denoted as w_i and computed as follows:

$$w_i = \mu_{A1i}(x_1) * \mu_{A2i}(x_2) * ... * \mu_{Ani}(x_n)$$

iv. The calculation of the normalized firing strength of each rule can be expressed as follows: $w_{i'} = w_i / (w_1 + w_2 + ... + w_k)$

where k is the total number of rules and w_i is the firing strength of the *ith* rule.

v. The ANFIS system computes the output as a weighted sum of the consequents of all the rules, where the weight of each consequent is its normalized firing strength. Mathematically, it can be expressed as:

$$y = (w_{1'} * f_1 + w_{2'} * f_2 + ... + w_{k'} * f_k) / (w_{1'} + w_{2'} + ... + w_{k'})$$ Here, f_i represents the consequent of rule *i,* and $w_{i'}$ is the normalized firing strength of rule *i,* calculated as:

$$w_{i'} = w_i / (w_1 + w_2 + ... + w_k)$$

The value of k is the total number of rules.

2.3 PSO-ANFIS Model

Salisu et al (2019) The PSO-ANFIS algorithm combines the capabilities of Particle Swarm Optimization (PSO) and Adaptive Neuro-Fuzzy Inference System (ANFIS) to optimize ANFIS parameters.

One can express the mathematical formulation of PSO-ANFIS as follow:

$$y = f(x) = G*(a_1x_1 + a_2x_2 + ... + a_n*x_n + b)$$

Here is the given information:

- The output variable is represented by y.
- The input variables are $x_1, x_2, ..., x_n$.

- The optimized parameters obtained from the PSO algorithm are $a_1, a_2, ..., a_n$.
- The constant bias term is denoted by b.
- G is the scaling factor that ANFIS calculates.
- ANFIS model function is represented by $f(x)$.

By utilizing the PSO algorithm, the optimal values of $a_1, a_2, ..., a_n$ are determined so as to minimize the discrepancy between the predicted output of the ANFIS model function and the actual output. The ANFIS network is used to calculate the scaling factor G based on the input variables. The output y is determined by summing the input variables and optimized parameters, each of which is multiplied by a specific weight, and then adding the bias term to the result.

2.4 SVM Regression Model

The SVM regression model makes predictions based on the following equation:

$f(x) = \Sigma_i \alpha_i K(x_i, x) + b,$

where $f(x)$ represents the predicted output for input vector x, α_i denotes the Lagrange multipliers, x_i represents the support vectors, $K(x_i, x)$ is the kernel function that measures the similarity between x_i and x, and b is the bias term. During training, the Lagrange multipliers and bias term are determined by minimizing the cost function:

minimize:

$$\frac{1}{2} \Sigma_i \Sigma_j \alpha_i \alpha_j y_i y_j K(x_i, x_j) - \Sigma_i \alpha_i$$

subject to:

$$\Sigma_i \alpha_i y_i = 0 \text{ and } 0 \leq \alpha_i \leq C$$

Here, y_i represents the output value of the i-th training example, C is the regularization parameter that determines the trade-off between maximizing the margin and minimizing the training error. The Lagrange multipliers, α_i, are optimized subject to the constraint that the sum of their products with the corresponding output values is zero, and their values are limited to be between zero and C.

2.5 Data Normalization.

Data normalization is important because some of the data were not available or recorded as zero because of power outages due to faults online, load shedding system collapse, and maintenance to mention a few

The normalization formula is:

$$x' = \{x - min(x)\} / \{max(x) - min(x)\}$$

Here, x represents the original value that needs to be normalized. $min(x)$ is the smallest value present in the range of x, $max(x)$ is the largest value present in the range of x, and x' represents the normalized value.

By applying this formula, the original values are transformed to a new scale that ranges from 0 to 1, where 0 corresponds to the minimum value in the range of the original values, and 1 corresponds to the maximum value.

2.6 Model Statistical Evaluators

There are several statistical evaluators that could be used to assess the performance of a normalized 6-year historical load data and weather data made up of temperature, humidity, solar irradiation, precipitation, and wind speed, for training, testing, and validation.

In this study, the following statistical evaluators for the model were utilized.

(i) Root-mean-square error (RMSE)

The equation for RMSE is:

$RMSE = sqrt\{(1/n) * Sum (y_i - x_i)^2\}$

In this context, "y_i" represents the estimated value and "x_i" represents the observed value, given that "n" refers to the total number of samples.

(ii) Mean Square Error (MSE)

The equation for MSE is:

$MSE = (1/n) * Sum (y_i - x_i)^2$

Assuming "n" represents the total number of instances, "y_i" is the projected value, and "x_i" is the factual value.

(iii) Mean Absolute Percentage Error (MAPE)

The equation for MAPE is:

$MAPE = (1/n) * Sum (| (y_i - x_i) / x_i|) * 100\%$

In the given context, "n" denotes the total number of examples, "y_i" represents the anticipated value, and "x_i" signifies the factual value.

Typically, reduced values of RMSE, MSE, and MAPE imply superior performance since they indicate that the model is generating more precise predictions.

3.0 MATERIALS AND METHODS

3.1 Materials

The components employed in predicting the load demand are:

i. Load demand data: Load demand data is the 6-year historical primary input data from the Jos Electricity Distribution Company (JEDC) .
ii. Weather data: temperature, humidity, solar insolation, wind speed, and precipitation from the NASA website.
iii. ANFIS, PSO-ANFIS, and SVMR software: ANFIS, PSO-ANFIS, a software package which was developed by Yapiz *et al* (2015) and SVM Regression in MATLAB

3.2 Method

The methods used for load demand forecasting using ANFIS, PSO-ANFIS, and SVMR were as follows:

(a) Data collection and pre-processing
(b) Model development
(c) Model evaluation
(d) Model selection.

3.3 Implementation of Short-term Load Forecasting based on PSO-ANFIS

The execution of PSO-ANFIS for Short-term Load Forecasting

3.3.1 Data Collection and Pre-processing

Data collection

Primary data on the load demand on the 11kV dedicated feeder was collected using the digital logger for 6 years (January 2014 - January 2019) from the 11kv JEDC substation is situated at the Naraguta campus of the University of Jos.

The temperature, humidity, solar insolation, wind speed, and precipitation records for the designated duration were acquired from NASA as weather data.

Data pre-processing

The gathered data underwent pre-processing via the subsequent procedures:

Data cleaning

The following steps were carried out to clean the load demand and weather data:

i. Removal of duplicates
ii. Checked for missing values
iii. Checked for formatting errors
iv. Checked for consistency
v. Checked for accuracy.

3.4 PSO-ANFIS Short-Term Implementation

In order to execute short-term load forecasting using PSO-ANFIS, the following steps were followed:
(i)Collect and pre-process the data (ii) Design the PSO algorithm(iii)Develop the ANFIS model(iv)Train the PSO-ANFIS model(v) Validate the model(vi)Forecast the load demand(vii) Evaluate the performance(viii) Refine the model.

3.5 SVM Regression Short-Term Implementation

In order to execute short-term load forecasting using SVM regression, use the following procedure:
Data collection (ii) Data pre-processing(iii). Feature selection (iv) Model training (v) Model evaluation(vi) Hyperparameter tuning(vii) Model deployment.

4.0 RESULTS AND DISCUSSION

The results obtained for PSO-ANFIS were compared with ANFIS and SVM. Tables and Graphs for the 24-hour ahead prediction are also presented from the analysis carried out.

4.1 Simulation Results of the ANFIS Model

The data collected were simulated using, ANFIS for MATLAB
The data was split into three groups, with 70% of it allocated for training, 20% for testing, and 10% for validation purposes.
The outcomes of the load demand using ANFIS-trained data, test data, and load demand are illustrated in Figures 1,2 and 3.

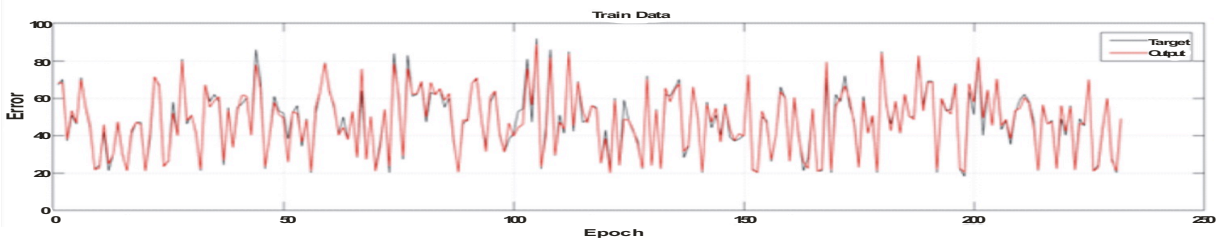

Fig 1: ANFIS Trained Data for Load Demand

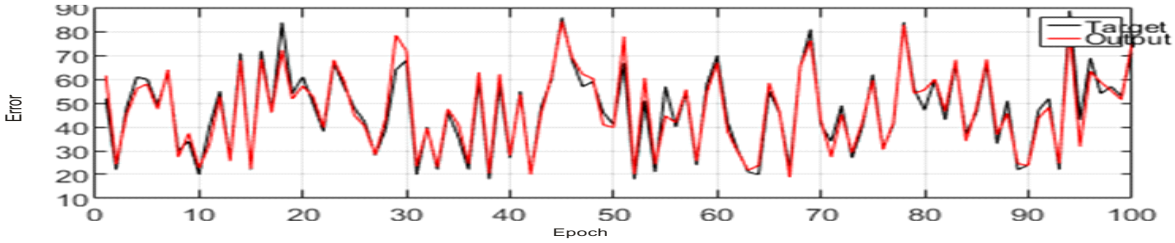

Fig 2.: ANFIS Test Data for Load Demand

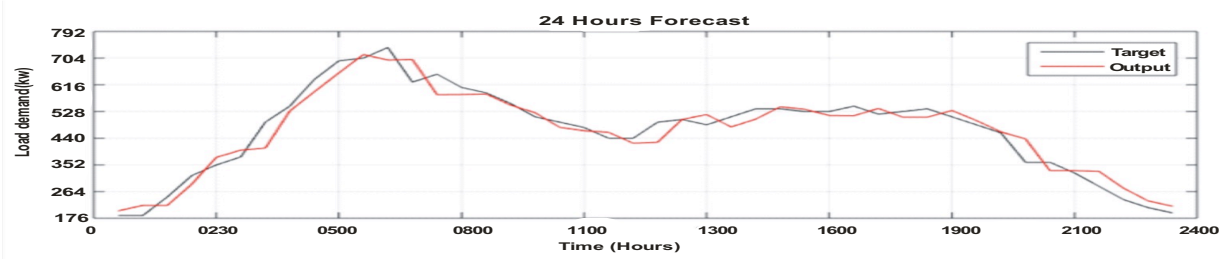

Fig 3: Load Demand Curve for 24Hours 11kV dedicated Feeder using ANFIS.

The ANFIS KPI for the 24-hour load demand was MSE of 10.0254, RMSE of 3.16663, and MAPE of 1.8627.

4.3 Simulation Results of PSO enhanced ANFIS model.

The data collected were simulated using, PSO enhanced ANFIS on the MATLAB platform. The data was split into three groups, with 70% of it allocated for training, 20% for testing, and 10% for validation purposes. Figure 4, 5, and 6 shows the simulation of PSO enhance ANFIS(PSO-ANFIS) train, test, and load demand forecast for the next 24 hours.

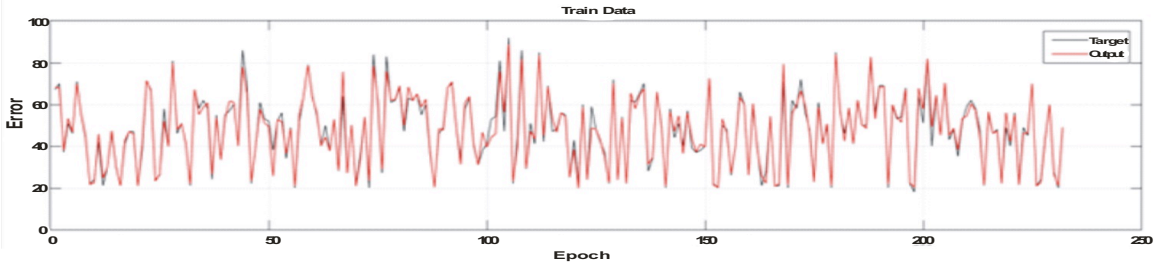

Fig 4: Trained Data for PSO-ANFIS

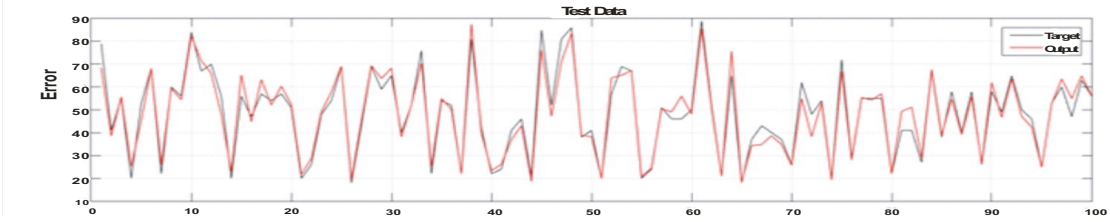

Fig 5: Test Data PSO-ANFIS

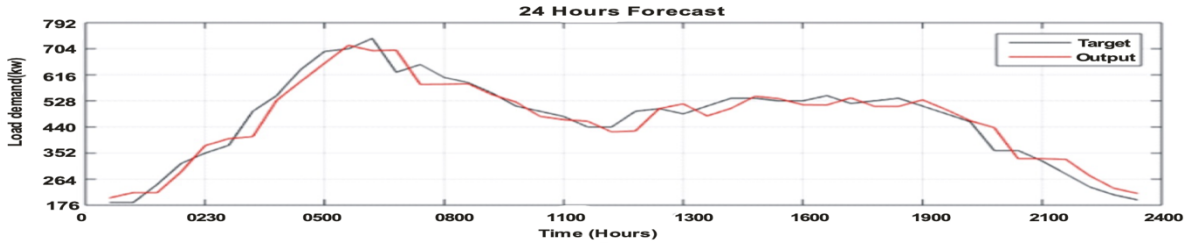

Fig 6: Load Demand Curve for 24 Hours Load Demand Forecast for the 11kV Dedicated Feeder using PSO-ANFIS

By employing PSO-ANFIS, the load demand data was examined, and a 24-hour forecast was conducted. As depicted in Figure 6, the forecast resulted in an MSE of 8.2478, RMSE of 3.0372, and MAPE of 1,7868. Table 1 indicates that the forecasting performance of PSO-ANFIS is superior to that of ANFIS.

4.3 Simulation Results using SVMR.

Support vector machine regression simulation was carried out and the Predicted versus actual load demand forecast was plotted as shown in Figure 7. With an RSME of 6.9721; MSE of 24.4407, and MAPE of 4.7623.

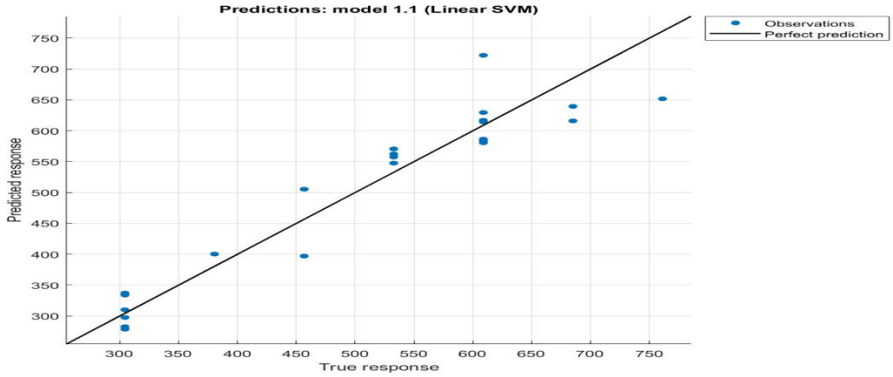

Fig 7: 24 Hours Load Demand Forecast for the 11kV Dedicated Feeder using SVMR.

.

4.4 Analysis of the Results

According to Table 1 analysis, the PSO-ANFIS model outperformed the other models in terms of forecasting performance. Specifically, at a 24-hour forecast, From the results, PSO-ANFIS is seen to be a better Forecasting Model compared to ANFIS and SVMR in this study It has an RMSE of 3.0372, MSE of 8.2478, and MAPE of 1.7868 as compared to ANFIS; 3.1663,10.0254, 1.8627 and SVMR of 6.9721, 24.4407 and 4.7623 respectively. Therefore, based on this analysis, it can be concluded that the PSO-ANFIS model is more effective and accurate than the ANFIS and SVMR models for short-term load forecasting.

Table 1: Comparison of ANFIS, PSO-ANFIS, and SVMR Performance Index

Method	RMSE	MSE	MAPE
ANFIS	3.1663	10.0254	1.8627
PAO-ANFIS	3.0372	8.2478	1.7868
SVMR	6.9721	24.4407	4.7623

5.0 CONCLUSION

The study utilized three machine learning methods, namely Adaptive Neuro-Fuzzy Inference System (ANFIS), Particle Swarm Optimization-ANFIS (PSO-ANFIS), and Support Vector Machine (SVM) regression, to forecast short-term electricity load demand. The study evaluated and compared the prediction capabilities of three machine learning techniques for short-term electricity load demand forecasting, namely Adaptive Neuro-Fuzzy Inference System (ANFIS), Particle Swarm Optimization-ANFIS (PSO-ANFIS), and Support Vector Machine (SVM) regression. The study's results provide valuable insights for microgrid system energy management and decision-making. The PSO-ANFIS model was identified as the most efficient and accurate technique for short-term load forecasting based on the findings. The study enhances the field of energy management by offering a dependable and efficient approach for forecasting short-term load demand.

REFERENCES

Atanasovski, M., Kostov, M., Veljanovski. G and Popovski, P (2022) "Short-Term Load Forecast in Power Systems: A Comparison of Different Practical Algorithms," *18th International Conference on the European Energy Market (EEM)*, Ljubljana, Slovenia, pp. 1-5, doi: 10.1109/EEM54602.2022.9921172.

Butt, F.M., Hussain,L., Mahmood, A and Lone, K.J (2020) Artificial Intelligence Based Accurately Load Forecasting System to Forecast Short and Medium-Term Load Demands. MBE, 18(1): 400–425

Khantach,A., Hamlich, M and Belbounaguai, N (2019)Short Term Load Forecasting using Machine Learning and Periodicity Decomposition.AIMS Energy, Vol.7 issue 3.pp.382-394.

Park, R.B., Song, K.B and Kwon, B.S (2020) Short-Term Load Forecasting Algorithm Using a Similar Day Selection Method Based on Reinforcement Learning. Energies, Vol.13, 2640; doi:10.3390/en13102640 www.mdpi.com/journal/energies

Salisu.S., Mustafa, M.W., Mustafa.M., Otuoze A.O and Mohammed, O.M (2019) A Hybrid PSO-ANFIS Approach for Horizontal Solar Radiation Prediction in Nigeria. Elektrika Journal of Electrical Engineering. Vol.18, No2, pp.23-32.

Stamatellos, G and Stamatelos, T (2023) Short-Term Load Forecasting of the Greek Electricity System. *Appl. Sci. 13*(4), 2719; https://doi.org/10.3390/app13042719

ul Islam, B., Rasheed, M and Ahmed, S. F (2022) Review of Short-Term Load Forecasting for Smart Grids Using Deep Neural Networks and Metaheuristic Methods. Mathematical Problems in Engineering Volume 2022, Article ID 4049685, 14 pages https://doi.org/10.1155/2022/4049685

Yapiz (2015) Multi-objective PSO in Matlab.www.yarpiz.com

PAPER 122 – EXTRACTION AND CHARACTERIZATION OF KERATIN PROTEIN FROM CHICKEN FEATHERS USING ALKALINE HYDROLYSIS METHOD: EFFECTS OF SODIUM SULPHIDE CONCENTRATION AND SHELF-LIFE EVALUATION

Z. Aliyu[1], A. D. Mahmud[1]*, A. B. Oluwatoyin[1], A. Aliyu[1], A. S. Yahaya[1], A. M. Saleh[1]

[1]Department of Chemical Engineering, Ahmadu Bello University, Zaria, Nigeria.
*Email: admahmud@abu.edu.ng

ABSTRACT
This study investigated the extraction of keratin protein from chicken feathers through alkaline hydrolysis using sodium sulphide as a digesting agent. The protein was precipitated using hydrogen chloride and confirmed through biuret test, solubility test, sulfur test, and FTIR analysis. The effect of varying sodium sulphide concentrations (0.5 M, 0.75 M, and 1 M) on the extracted keratin was evaluated. Results showed that a higher concentration of sodium sulphide produced a higher yield of keratin, with 1 M producing 65.8% yield. However, the shelf-life of wet keratin extracted using 1 M concentration was four weeks, compared to six weeks for 0.5 M and 0.75 M concentrations. The dried keratin was unaffected after six weeks. The study suggests that a higher concentration of the reducing agent produced a higher yield of keratin protein but with a shorter shelf-life if drying was not carried out. The utilization of abundant waste generated by poultry industries is crucial in reducing pollution and creating opportunities for valuable product development. The extraction of keratin from chicken feathers provides an eco-friendly approach to waste management and creates opportunities for product development.

KEYWORDS: Keratine, Chicken feathers, Shelf-life, Yield, Drying, Hydrolysis

13. INTRODUCTION

Keratin is a vital and abundant structural protein in humans and animals, which can be found in various industrial wastes such as slaughterhouse by-products, skin remains, animal hair, horns, hooves, and feathers (Idris *et al.,* 2012; Kalia, 2019; Reddy, 2017; Teresa & Justyna, 2011). These wastes are considered environmental pollutants due to their resistance to physical, chemical, and biological agents (Kumawat *et al.,* 2015). α-keratins and β-keratins are the two most abundant forms of keratins, with the former occurring in mammals and the latter in birds and reptiles (Barone et al., 2006; Sharma & Gupta, 2016). This work focuses on the extraction of keratin from chicken feathers, which have received significant attention in various applications, such as cosmetics, tissue engineering, and regenerative medicine, due to their biocompatibility, biological function, and biodegradability (Agarwal *et al.,* 2019).

Chicken feathers are a rich source of keratin, with a large quantity being produced as a by-product of the poultry industry each year (Ji *et al.,* 2014; Olonilebi, 2017). However, conventional methods of extracting keratin, such as acidic hydrolysis, can cause damage to some amino acids and consume a large quantity of reagents, which cannot be recycled (Wang & Cao, 2012). Therefore, alternative methods, such as enzymatic hydrolysis and chemical-enzymatic treatment, have been proposed to produce hydrolyzed feather protein (Alahyaribeik & Ullah, 2020). Ionic liquids (ILs) have also been studied for their potential to dissolve biopolymers, including keratin, into useful materials for industrial applications (Idris *et al.,* 2012).

Alkaline extraction using sodium sulphide has been shown to be an efficient and economically favorable method that preserves the secondary structure of the protein, while the addition of an ionic surfactant such as sodium dodecyl sulfate can prevent the aggregation of keratin polypeptide chains (Ji *et al.,* 2014). Enzymatic catalysis hydrolysis is a promising alternative method, but its industrial application is hindered by the outer protective film and compact structure of the feather (Alahyaribeik & Ullah, 2020). Therefore, developing effective and eco-friendly processes to extract keratin from poultry feathers is desirable from both environmental and economic perspectives (Ji *et al.,* 2014).

14. THEORETICAL ANALYSIS

Keratin is a type of protein that is particularly abundant in feathers, hair, and nails. Keratin from chicken feathers is a particularly interesting protein because it has a unique structural feature that allows it to be used in a variety of applications. Keratin is a type of protein with a complex hierarchical structure that can be classified into primary, secondary, and tertiary structures. The primary structure of keratin is determined by the specific sequence of amino acids that make up the polypeptide chain. This sequence of amino acids determines the folding pattern of the keratin molecule and its final structure (Rao & Georgopoulos, 2006).

In the case of chicken feather keratin, the primary structure consists of a repeating pattern of four amino acids: glycine, alanine, serine, and tyrosine. This pattern is repeated many times to form a long polypeptide chain. This unique sequence of amino acids gives chicken feather keratin its unique properties, including its strength, flexibility, and resilience. The secondary structure of keratin is characterized by alpha-helices, which are formed when the polypeptide chain twists around itself. The alpha-helices then associate with one another to form coiled-coil structures, which in turn associate to form protofilaments. The protofilaments then bundle together to form intermediate filaments, which are the structural components of keratin fibers.The tertiary structure of keratin involves the folding and packing of the intermediate filaments into a three-dimensional structure. This three-dimensional structure gives keratin its unique properties and allows it to form strong and resilient fibers (De Guzman & Tomalia, 2011).
Chicken feather keratin is particularly interesting because it has been found to have a number of practical applications. For example, it has been used to create biodegradable plastic alternatives, wound dressings, and as a component in hair care products. By understanding the structure and properties of chicken feather keratin, scientists and engineers can develop new and innovative uses for this versatile protein.

15. MATERIALS AND METHODS

The use of chemical (alkaline) hydrolysis was employed in the extraction process with sodium sulphide as the reducing agent. The extraction method was carried out by different stages of experimental procedures as listed below and all the chemicals used were of analytical grade requiring no further purification.

3.1 Collection and Pretreatment of Waste Chicken Feathers

Chicken feathers were collected from Samaru market, latitude **11.1617 ˚N and longitude 7.6479 ˚E. The feathers were washed with distilled water to remove all the accompanied blood and dirt. It was then soaked in detergent for 2 hours, and washed with distilled water, after which it was oven dried at 60 ˚C for 12 hours. The dried feathers were soaked in diethyl ether for 12 hours to cleanse it from stain, oil and grease, then washed with hot water (100 ˚C) followed by distilled water and then oven dried at 60 ˚C for 48 hours to remove its moisture content. The dried chicken feathers were ground using a laboratory milling machine at mesh size 0.25 mm and stored in a sealed plastic bag at room temperature.**

3.2 **Keratin Protein Extraction**

1 L of 0.5 M sodium sulphide solution was prepared in a 2000 ml beaker. 25 g of the ground CF was weighed and added to the sodium sulphide solution. The solution was heated to the temperature of 60 ˚C at a pH of 10 and stirred continuously for 6 hours using a magnetic stirrer. The solution was centrifuged at 10,000 rpm for 10 minutes. The supernatant liquid was carefully collected then filtered using the burchner funnel with filter paper of 110 mm to make it particle free.

3.3 Protein Precipitation

After the extraction process, the pH of the keratin solution was adjusted to 3.5 by addition of HCl to precipitate the protein. The solution was then centrifuged at 10,000 rpm for 6 minutes and the solid particles carefully collected**.**

3.4 **Protein purification**

400 ml distilled water was added to the keratin protein collected and stirred (washing). The solution was centrifuged at 10,000 rpm for 6 minutes and the solid particles collected carefully for further analysis and characterization.

The above steps were repeated for sulphide concentration 0.75 M and 1 M.

a. Analysis and characterization of the keratin protein

3.5.1 General Test (Biuret Test)

5 % sodium hydroxide solution and 1 % copper sulphate solution were prepared. 2 ml of each keratin solution (0.5 M, 0.75 M, 1 M) was mixed with the sodium hydroxide solution in the ratio 1:1. Three drops of the copper sulphate solution were added to the mixture solutions. Changes in the solution were observed and recorded.

3.5.2 Differentiating Test (Solubility Test)

10 ml of distilled water was added to each keratin protein in a test tube. The test tubes were then shaken vigorously for a minute and observations recorded.

3.5.3 Confirmatory Test (Sulfur Test)

40 % sodium hydroxide solution and 2 % lead acetate solution were prepared. 2 ml of each keratin protein was mixed with the sodium hydroxide solution in the ratio 1:1. The solution in the test tubes were held on flame and boiled for 1 minute, then cooled under tap. 5 drops of the lead acetate solution were added to the mixture solution and changes observed and recorded.

3.5.4 Fourier Transform Infrared Spectroscopy

Functional groups of the extracted protein were investigated by mixing samples into KBr pellets using fourier transform infrared (FT-IR) absorption spectrum Agilent spectrometer (30 scans with 8 cm^{-1} resolution) in the wavenumber range of 650 – 4,000 cm^{-1}.

3.5.5 Shelf-Life

A sample of the wet keratin extracted was segregated and kept in a sealed container, while some part was shadow dried for 72 hours at room temperature, crushed into fine powder and kept in another sealed container. Both samples were then observed for 6 weeks (Fig 1).

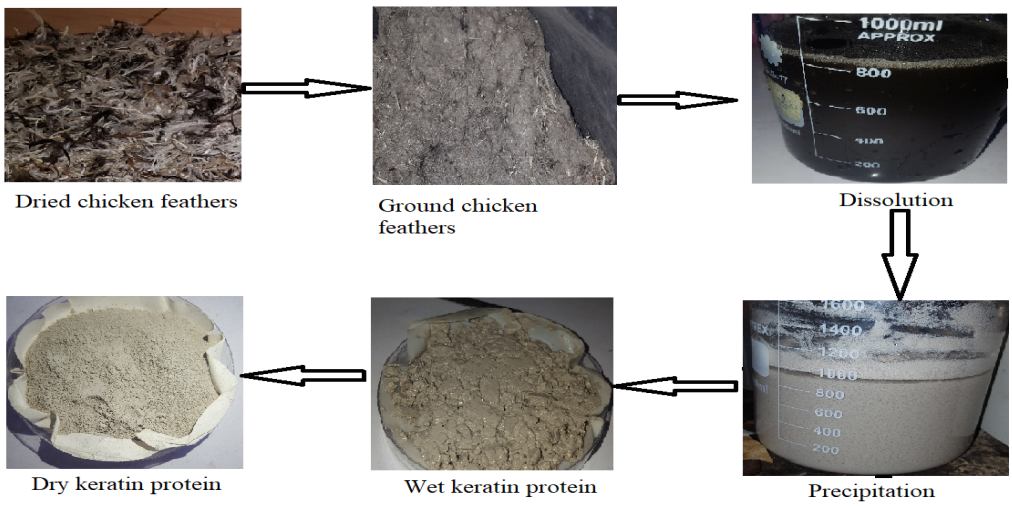

Fig 1: Schematic diagram of the keratin extraction process

16. RESULTS AND DISCUSSION

4.1 Extraction of Keratin from Chicken Feathers

Alkaline hydrolysis was carried out to extract keratin from chicken feathers using 0.5 M, 0.75 M and 1 M concentration of the reducing agent, sodium sulphide (Na_2S). Table 1 shows the physical observation, moisture content, yield and shelf-life after extraction.

Table 1: Physical appearance of extracted keratin

Concentration	0.5 M	0.75 M	1 M
% Moisture Content (MC)	70	74.5	78.1
% Protein Yield	55.7	61.6	65.8
Shelf-life (weeks)	4	6	6
Physical Appearance	Most compacted	Moderately compacted	Least compacted with a smoother appearance

The wet keratin (keratin before drying) extracted for the 1 M concentration appeared to be smoother and loose indicating high amount of water present. While the 0.5 M concentration was the least loose, showing low amount of water. According to Abebe (2017), the solubility of the feathers is dependent on the concentration of Na_2S, temperature and process time.

As seen in table 1, the concentration of the reducing agent affects the appearance, associated water as well as the yield of the extracted protein. The amount of keratin yield in the final product depends on the degree of hydrolysis of the feather. Hence, the 1 M concentration shows the highest degree of hydrolysis. This contradicts the work of Gindaba *et al.,* 2019 which says that at 0.5 M the yield decreases on increasing concentration of the solvent. The

increasing pattern of keratin yield is caused by peptide and disulphide bonds cleavage. The **effect of concentration of sodium sulphide at constant temperature and pH is shown in Figure 2.**

The samples of wet and dried keratin proteins were observed for 6 weeks under atmospheric conditions. At week 4, the 1 M wet keratin was observed to have some microbial growth while the 0.5 M, 0.75 M and all the dried keratins appeared the same. At week 6, there was some microbial growth on the 0.5 M and 0.75 M wet keratin and none for the dry keratins of all concentration. The onset of the contamination for the 1 M keratin was due to the high amount of moisture present providing the environment for the growth.

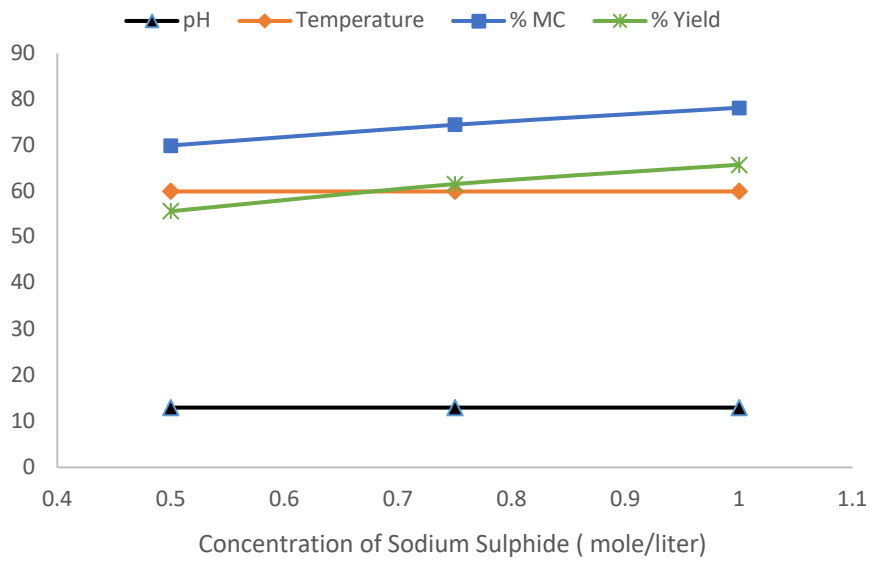

Fig 2: **Effect of concentration of sodium sulphide at constant temperature and pH**

4.2 Characterization of the Extracted Protein

4.2.1 Biuret test

The protein solution remained its usual color (ash) on the addition of the NaOH solution. It turned purple however on the addition of the copper sulfate solution indicating the presence of peptide linkage as shown in Figure 3. This is a general test for all types of protein where the Cu^{2+} ions react with the nitrogen of the peptide bond to form a purple color complex.

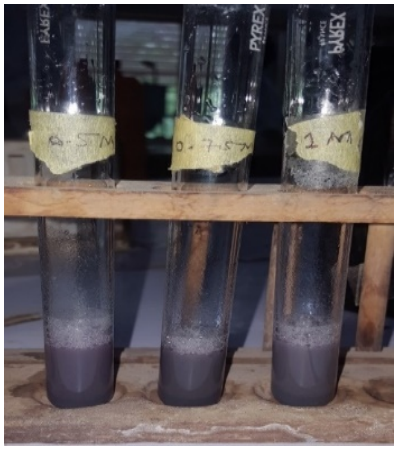

Fig 3: Biuret test for extracted protein from chicken feather

4.2.2 Solubility test

On addition of water, the keratin was observed to be insoluble as shown in Figure 4. This is due to the presence of the disulphide bonds present making it insoluble. It differentiates it from the rest of the proteins that are highly soluble owing to the hydrophilic amino acids present in them.

Fig 4: Solubility test for extracted protein from chicken feather

4.2.3 Sulphur test

The protein solution turned black on the addition of the lead acetate shown in Figure 5, confirming the presence of cysteine which is a major component of keratin. Upon boiling of the keratin solution with sodium hydroxide, the sulphur present in its amino acids i.e. cysteine is converted to inorganic sodium sulphide. It then reacts with lead to form lead sulphide that forms black colored pigments inside the solution.

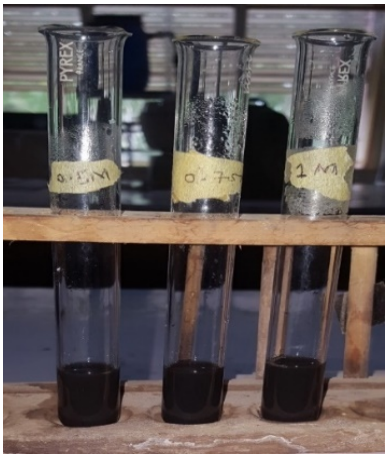

Fig 5: Confirmatory test for extracted protein from chicken feather

4.3 Fourier Transform of Infrared

Keratin is a natural polymer with a complicated structure, hence the need for Fourier Transform of Infrared (FTIR) to understand all details of structure of keratin. The **characteristic bands and signals from these spectra was analyzed in order to confirm the products as keratin. Figure 6-9 shows the characteristic absorption bands for the keratin extracted.**

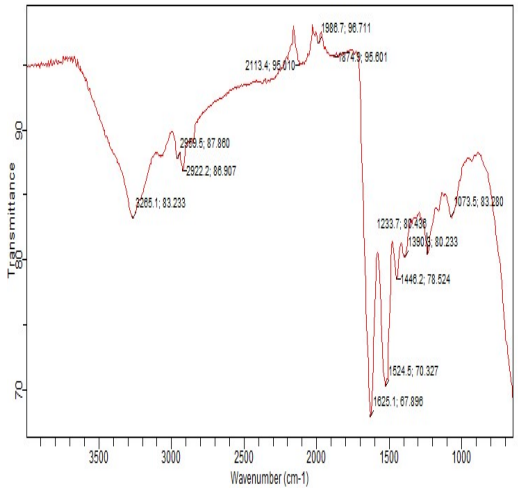

Fig 6: FT-IR of chicken feathers

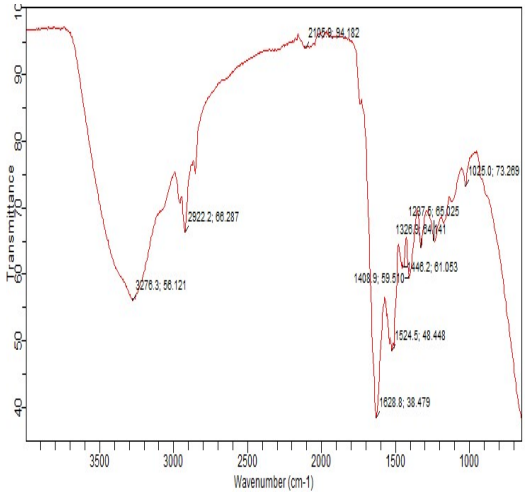

Fig 7: FT-IR of Extracted Protein of 0.5 M

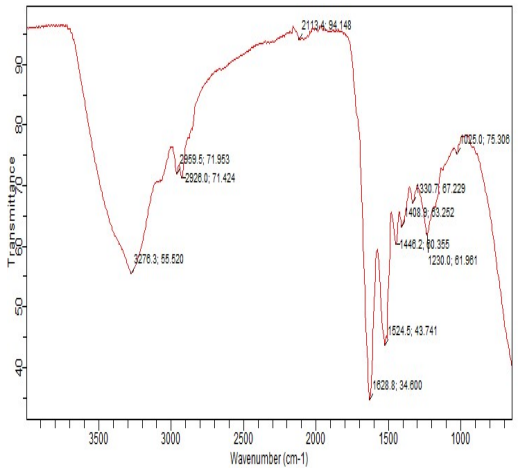

Fig 8: FT-IR of Extracted Protein of 0.75 M

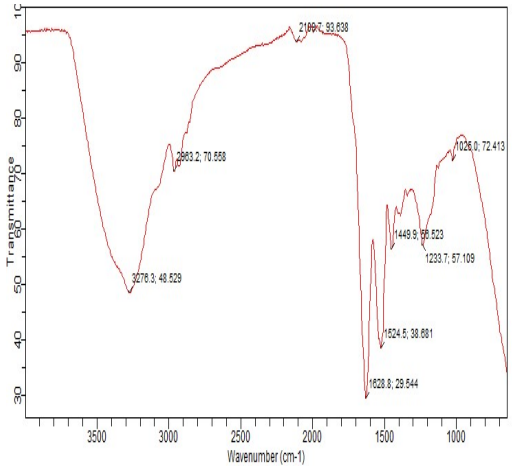

Figure 9: FT-IR of extracted protein of 1 M

17. CONCLUSION

Sodium sulphide proved to be a highly effective dissolution agent, while hydrogen chloride demonstrated excellent precipitating properties. Notably, at a concentration of 1 M alkalis, the extracted keratin exhibited a loose appearance, with a moisture content of 78.2%, a yield of 65.8%, and a shelf-life of only 4 weeks. These findings suggest that higher concentrations of the dissolution agent lead to greater keratin extraction. Furthermore, this extraction process is suitable for scaling up from the laboratory to the industrial level.

ACKNOWLEDGEMENT

The research team will like to acknowledge Ahmadu Bello University Zaria **and** Petroleum Technology Development Funds for providing research laboratories.

REFERENCES

Abebe, T. (2017). *Extraction and Optimization of Natural Protein (Keratin) from Waste Chicken Feather for the Development of Anti-Ageing Cream*. ADDIS ABABA UNIVERSITY, SCHOOL OF CHEMICAL AND BIO-ENGINEERING BIOCHEMICAL.

Agarwal, V., Panicker, A. G., Indrakumar, S., & Chatterjee, K. (2019). Comparative study of keratin extraction from human hair. *International Journal of Biological Macromolecules*, 27. https://doi.org/10.1016/j.ijbiomac.2019.04.098

Alahyaribeik, S., & Ullah, A. (2020). Methods of keratin extraction from poultry feathers and their effects on antioxidant activity of extracted keratin. *International Journal of Biological Macromolecules*, 31. https://doi.org/10.1016/j.ijbiomac.2020.01.144

Barone, J. K., Schmidt, W. F., Gregoire, N. T. (2005). Extrusion of Feather Keratin. *Journal of Applied Polymer Science, 100,* 1432–1442. https://doi.org/10.1002/app.23501

De Guzman, R. C., & Tomalia, D. A. (2011). Chapter Two - Keratin: Intermediate Filament System of Wool, Hair, Nails and Other Keratinized Tissues. In Advances in Clinical Chemistry (Vol. 55, pp. 75–96). Academic Press. https://doi.org/10.1016/B978-0-12-385855-9.00002-1

Idris, A., Vijayaraghavan, R., Rana, U. A., Fredericks, D., Patti, A. F., & MacFarlane, D. R. (2012). *Dissolution of keratin in ionic liquids*. *207890*, 12. https://doi.org/10.1039/b000000x

Ji, Y., Chen, J., Lv, J., Li, Z., Xing, L., & Ding, S. (2014). Extraction of keratin with ionic liquids from poultry feather. *SEPARATION AND PURIFICATION TECHNOLOGY*, *2013*, 31. https://doi.org/10.1016/j.seppur.2014.05.049

Kalia, S. (2019). *Keratin as a Protein Biopolymer; Etraction from Waste Biomass and Applications* (S. Sharma & A. Kumar (eds.)). Springer Nature Switzerland AG. https://doi.org/10.1007/978-3-030-02901-2

Kamarudin, N. B., Sharma, S., Gupta, A., Kee, C. G., Chik, S. M., & Gupta, R. (2017). *Statistical investigation of extraction parameters of keratin from chicken feather using Design-Expert*. *2016*. https://doi.org/10.1007/s13205-017-0767-9

Kumawat, T. K., Sharma, A., Sharma, V., & Chandra, S. (2015). *Keratin Waste: The Biodegradable Polymers*. 23. http://dx.doi.org/10.5772/intechopen.79502

Olonilebi, J. O. (2017). Fast Foods Consumption And Well-Being Degeneration In Humans. *Journal of Food and Quality Control, 2*(3), 1-8. https://doi.org/iiardpub

Ramakrishnan, N., Sharma, S., Gupta, A., & Alashwal, B. Y. (2018). Keratin based bioplastic film from chicken feathers and its characterization. *Biological Macromolecules*, 31. https://doi.org/10.1016/j.ijbiomac.2018.01.037

Rao, J. R., & Georgopoulos, M. (2006). Keratin-based biomaterials and biomedical applications. In Biomedical applications of natural proteins (pp. 127-150). Springer, Boston, MA.

Reddy, N. (2017). *Keratin-based Biomaterials and Bioproducts*. Smithers Rapra Technology Ltd. http://www.polymer-books.com

Sharma, S., Kumar, A. (2019). Keratin as a Protein Biopolymer. *Extraction from Waste Biomass and Applications*. Springer Nature Switzerland.

Teresa, K., & Justyna, B. (2011). Biodegradation of keratin waste : Theory and practical aspects. *Waste Management*, *31*, 1689–1701. https://doi.org/10.1016/j.wasman.2011.03.024

Wang, Y., & Cao, X. (2012). Extracting keratin from chicken feathers by using a hydrophobic ionic liquid. *Process Biochemistry*, *47*(5), 896–899. https://doi.org/10.1016/j.procbio.2012.02.013

PAPER 123 – DEVELOPMENT OF A KERATIN-BASED HAIR CREAM FORMULATION FOR REPLENISHING DAMAGED HAIR: A RESPONSE SURFACE METHODOLOGY APPROACH

A. B. Oluwatoyin[1], A. D. Mahmud[1]*, Z. Aliyu[1], A. Aliyu[1], A. S. Yahaya[1], A. M. Saleh[1]

[1]Department of Chemical Engineering, Ahmadu Bello University, Zaria, Nigeria.
*Email: admahmud@abu.edu.ng

ABSTRACT
This study aimed to develop a hair cream formulation that can replenish damaged keratin in hair caused by various hair treatments and activities. The active ingredient used in the hair cream was keratin extracted from chicken feathers. The hair cream formulations were designed and optimized using simplex lattice response surface methodology. Ten samples were produced by varying the percentage of distilled water, keratin protein, and emulsifier, while keeping all other ingredients constant, and the responses were pH and viscosity. The optimal percentage of the varied ingredients was determined as 54.54% distilled water, 2.59% keratin protein, and 7.87% emulsifying wax, with a pH of 6.0 and viscosity of 21,222cps. The selected optimal solution had a desirability value of 0.92. Stability assays were conducted to study the organoleptic properties, pH, phase separation, and spreadability of the hair cream formulations. The formulations exhibited great stability at room temperature (25°C) and -5°C, but were unstable at 50°C. The pH range of the formulations was adjusted to be within the isoelectric pH range of the hair. Therefore, the use of keratin extracted from chicken feathers as the active ingredient has a high potential to replenish damaged hair and provides a sustainable approach to hair care.

KEYWORDS: Hair, Keratine, Isoelectric pH, Viscosity, Chicken feathers, response surface methodology

18. INTRODUCTION

Hair is a unique pigmented filament of keratin that grows from follicles located in the dermis of the skin. It serves as a protective layer against mechanical stress and aids in regulating body temperature (Buffoli *et al.,* 2013). Hair is made up of two distinct parts; the follicle, which is the internal part, and the hair shaft, which is the external part and comprises of the cortex, cuticle, and medulla (Leeson *et al.,* 1985). The duration of hair growth is coordinated by various hormones and cytokines and is influenced by factors such as location of hair growth on the body, age, nutritional habits, and environmental factors (Wolfram, 2003; Mathew, 2016). Hair growth occurs in three phases; anagen, catagen, and telogen (Wolfram, 2003; Mathew, 2016). The keratin proteins, which are responsible for the strength and stability of hair, are produced during the hair growth process and are controlled by over 30 growth factors and cytokines (Erdogan, 2017; Hill *et al.,* 2010). These proteins are categorized into two families; the acidic type I keratins and the basic-neutral type II keratins (Erdogan, 2017; Hill *et al.,* 2010).

Keratin proteins in hair are classified into three broad groups: Alpha (α) keratin, which is found in the hair fiber cortex and has low sulfur content with an average molecular weight of 60-80 kDa; β-keratin, which forms the majority of the hair cuticle and is difficult to extract; and gamma (γ) keratin, which has a molecular weight of 15 kDa, is usually globular and is high in sulfur content (Hill *et al*., 2010). The major proteins synthesized in the hair shaft include alpha-keratin, intermediate filaments, and keratin-associated proteins (KAP). There are approximately 54 functional alpha-keratin genes, of which 28 are acidic type I keratins, and 26 are basic-neutral type II keratins (Wu *et al.,* 2008; Swain *et al.,* 2008).

Activities such as styling and exposure to environmental factors can weaken the keratin disulfide bonds in hair, leading to hair damage such as breakage, porosity, and frizziness (Pressly et al., 2016). Incorporating hydrolyzed keratin into hair care products can repair and restore the texture, luster, and manageability of hair. Keratin creams can be formulated as hair straightening creams or keratin treatment creams. Hydrolyzed keratin is usually added to the cool down phase of the formulation, in proportions ranging from 0.5wt% to 15wt% of the formulation, with a preference of 0.5wt% to 15wt% of the formulation (Michael & Marie, 2016). Keratin treatment creams aid in repairing disulfide bond damages resulting from various hair beautification activities, and may also contain other active ingredients along with cosmetically approved excipients (Ursula *et al.,* 2002).

19. THEORETICAL ANALYSIS

The formulation and composition of hair creams containing keratin proteins. Two types of hair creams, namely hair straightening creams and keratin treatment creams, are formulated using hydrolyzed keratin. Hair straightening creams break the disulfide bonds in hair keratin, whereas keratin treatment creams repair the

damage caused to the disulfide bonds. The composition of a hair cream formulation includes diluents, active agents, preservatives, and emollients. The ingredients should be safe for use on human hair and scalp and must not cause any adverse reactions or damage to hair. The preferred diluent is water, whereas the preferred preservatives include glycerin compounds, parabens, and essential oils. The amount of each ingredient ranges from 0.1wt% to 50wt% of the formulation, depending on the ingredient. Emollients are added in an amount ranging from 0.5wt% to 15wt% of the formulation. Suitable emollients include silicone compounds, polyols, triglycerides, and fatty acid esters (Santos *et al.,* 2017).

20. MATERIALS AND METHODS/METHODOLOGY/EXPERIMENTAL PROCEDURE

The hydrolyzed keratin (Table 1) was extracted from chicken feathers in the research laboratory of chemical engineering Ahmadu Bello University Zaria, Kaduna Nigeria. The reagents and other ingredients used in the formulation were gotten from Steve Moore Chemicals and local stores from Sabon Gari and Samaru market. The ingredients are shown in Table 1. Design expert version 13 was used to vary the solvent (distilled water), active ingredient (keratin protein) and emulsifier (emulsifying wax NF), using simplex lattice mixture design. The equipment and instruments used were gotten from the research laboratory and the PTDF laboratory in the department of Chemical Engineering Ahmadu Bello University Zaria Kaduna, Nigeria.

Table 1: Ingredients in the Formulations

Ingredients	Quantity (g)	Quantity wt%	Functions
1. Glycerin	6	6	Emollient
2. Sweet almond oil	6	6	Conditioning agents
3. Shea butter	15	15	Plant extracts
4. Coconut oil	6	6	
5. Vitamin E	0.5	0.5	Anti-oxidant
6. Sodium benzoate	1	1	Preservative
7. Citric acid	q. s	q. s	pH modifier

3.1 Experimental design

Design Expert version 13 was used to design the experiment varying the amount (percentage) of diluent (distilled water), active ingredient (keratin protein) and emulsifier (emulsifying wax) in each formulation using simplex lattice mixture design. Ten samples of 100 wt% hair cream were generated and formulated. The pH and viscosity of each sample were the responses analyzed. All other ingredients were kept constant in the 10 formulations.

3.2 Preparation of Ingredient

The ingredients were measured using beakers and weighing scale, and it was ensured all the ingredients sum up to 100 wt% of each formulation. They were further separated into three phases which are the water phase (phase A), oil phase (phase B) and cool down phase (phase C) as shown in Table 2. Sodium benzoate (preservative) solution was prepared by dissolving 30g of sodium benzoate powder in 47.8ml of distilled water at 15^{o}C. Citric acid solution (pH modifier) was also prepared by dissolving 50g of citric acid powder in 50ml of distilled water.

Table 2: Phases in the Formulation

Phase A (water phase)	**Phase B (oil phase)**	**Phase C (cool down phase)**
Water	Shea butter	Hydrolyzed keratin
Glycerin	Coconut oil	Vitamin E
	Emulsifying wax NF	Sodium benzoate
	Sweet almond oil	Fragrance

3.3 Formulation of the Hair Cream

Phase B was heated using a hot plate and stirred with a spatula till it completely melted. Phase A was then prepared by adding glycerin to distilled water and heated to 75ºC using a hot plate. Using a thermometer, it was ensured that phase A and B were at the same temperature (75ºC) before proceeding with the formulation, this is to enable easy mixing of the two phases.
Phase B was added to phase A and stirred thoroughly with a magnetic stirrer. Once the mixture cooled down to 40ºC the ingredients in phase C (cool down phase) were added individually to the mixture and stirred continuously. A laboratory emulsion mixer was then used to mix the formulation till all the ingredients were well blended as. The hair cream was transferred into jars and sealed properly.

3.4 Physicochemical Analysis

Before testing the formulation, the appearance, color, odor and homogeneity of the hair cream were observed and noted after preparation. Afterwards each sample was subjected to a centrifugation cycle of 3000 rpm for 30 minutes using a centrifuge and were observed for phase separation according to the ANVISA guide. The organoleptic parameters were observed.
The samples were further subjected to pH analysis using a pH meter at room temperature. The pH meter was calibrated with pH buffer 7 solution, it was then inserted into the formulation for 1 minute, the reading on the device was noted and recorded.
An NFV-E1 intelligent viscometer was used to measure viscosity of the formulations at room temperature using spindle number 4 at full scale rotation of 12 rpm for 30 seconds.
The spreadability of each formulation was determined using glass slides. O.5 g of the sample was placed on a glass slide and a second glass slide was placed on it. A 250 g weight glass load was placed on the upper slide for 5 minutes. The load was removed and the spreading diameter was measured and recorded. The spreadability of the samples was calculated using Equation 1;

$S = d^2 \frac{\pi}{4}$ ..... 1 (Viviane *et al.*, 2009).

3.5 Preliminary Stability Test

The stability test was carried out at varying temperatures, each sample was placed in transparent glass containers and were properly sealed with a lid. 10 g of each sample was subjected to stability test at 50 ºC in an oven for 7 days, changes were observed at day 7. 20 g of each sample were also subjected to stability test at -5 ºC for 15 days and the remaining bulk samples were stored at room temperature (25 ºC) for 15 days. The changes were observed at an interval of 5 days. Changes in appearance, color, odor, phase separation, pH and spreadability were observed and noted at 5 days intervals (5, 10 and 15 days).

3.6 Adjusting the pH of the Samples

The pH of hair care formulations should be around the isoelectric pH of hair (Michael and Marie, 2016). The pH of the formulations was adjusted with citric acid at room temperature (25ºC) on completion of the stability test. This is done by adding quantum sufficit (q.s) amount of citric acid to each formulation and stirred properly with spatula, a pH meter was used to heck the pH of the formulation till it reaches the isoelectric pH.

21. RESULTS AND DISCUSSION

On formulation, the hair cream appeared to have a smooth texture with no sedimentation or coalesces. The color of the cream is slightly off white, this is because the Keratin protein used was ash color. The formulations had a characteristic pleasant odor of the fragrance used. There was no phase separation which means that the ingredients were well mixed and compatible.

4.1 Physico Chemical Properties of the Formulations

On preparation of the hair cream the following organoleptic properties were observed and stated in Table 3;

- Appearance: Formulations all had smooth texture, and there were no sedimentation or coalescence.
- Color: The color is off white
- Odor: Formulation had a pleasant odor
- Phase Separation: No phase separation, the two phases were well blended and the hair cream formulation was homogeneous.

Table 3: Physico-Chemical Properties of Hair Cream Formulations

Sample	pH	Viscosity (cp)	Spreading Diameter (cm)	Spreadability (cm)	Mass (g)
1	6.0	8390	6	28.28	76.81
2	5.9	24300	5.7	25.52	78.29

3	5.8	13940	5.9	27.34	85.53
4	6.0	24250	6.0	28.28	95.86
5	5.9	28100	5.7	25.52	108.61
6	6.0	21600	5.1	20.43	85.13
7	5.9	14180	5.4	22.90	88.08
8	5.9	24800	5.9	27.34	83.14
9	5.9	26400	6	28.28	89.57
10	5.9	26260	5.5	23.76	84.74

4.2 Design of Experiment Results

The responses of the experimental design are shown in Table 4. Other results obtained from design expert include the model summary statistics, the analysis of variance, fits statistics. These results are given for the pH and viscosity respectively. The numerical optimization solution and the graphical representation of the design were also obtained.

Table 4: Experimental Design Matrix

		Component 1	Component 2	Component 3	Response 1	Response 2
Std	**Run**	**A: Distilled water %**	**B: Keratin protein %**	**C: Emulsifying wax %**	**pH**	**Viscosity cps**
7	1	55	3.5	6.5	6.0	8390
3	2	53.5	3.5	8	5.9	24300
4	3	55	5	5	5.8	13940
1	4	55	3.5	6.5	6.0	24250
6	5	52	5	8	5.9	28100
5	6	55	2	8	6.0	21600
10	7	55	5	5	5.9	14180
9	8	53.5	3.5	8	5.9	24800
8	9	53.5	5	6.5	5.9	26400
2	10	53.5	5	6.5	5.9	26260

It is evident that the variation of water, keratin protein and emulsifying wax have substantial effect on the viscosity of the formulations but not on the pH of the formulations. Sample 1 have the lowest viscosity this is because it has maximum amount of water and intermediate amount of keratin and emulsifying wax. Sample 5 have the highest viscosity which is as a result of it minimum amount of water content and maximum amount of keratin protein. It also gave the highest yield in terms of mass. Sample 3 and 7 have lesser viscosity compared to the remaining samples, this is because they have maximum amount of water and keratin protein but minimum amount of emulsifying wax.

4.2 pH analysis results

Table 5, 6 and 7 gives the model summary statistics, analysis of variance and the fit statistics for the pH response. A 3D graphical representation of the response is shown in Figure 4.1. Figure 4.2 shows the graph relating the predicted and the actual value.

Table 5: Model Summary Statistics

Source	**Std. Dev.**	**R^2**	**Adjusted R^2**	**Predicted R^2**	**PRESS**	
Linear	**0.0422**	**0.7201**	**0.6401**	**0.4025**	**0.0267**	**Suggested**
Quadratic	0.0255	0.9418	0.8690			
Special Cubic						Aliased

Linear model was suggested for the pH analysis which gave the difference between **Adjusted R^2 and the Predicted R^2 as 0.24** ≈ 0.2 which is the acceptable value for **R^2.**

Table 6: ANOVA for Linear Model

Source	Sum of Squares	Df	Mean Square	F-value	p-value	
Model	0.0321	2	0.0161	9.00	0.0116	Significant
Linear Mixture	0.0321	2	0.0161	9.00	0.0116	
Residual	0.0125	7	0.0018			
Lack of Fit	0.0099	3	0.0033	5.07	0.0753	not significant
Pure Error	0.0026	4	0.0007			
Cor Total	0.0446	9				

The ANOVA gave a Mixture Component coding as **L_Pseudo with a F-value** of 9.00 and **P-values** less than 0.0500 which indicates that the model terms are significant.

Table 7: Fit Statistics

Std. Dev.	0.0422	**R^2**	0.7201
Mean	5.91	**Adjusted R^2**	0.6401
C.V. %	0.7144	**Predicted R^2**	0.4025
		Adeq Precision	7.4903

The **Lack of Fit F-value** is 5.07 which is significant, this is good because the model needs to fit. The **Adeq Precision** measures the signal to noise ratio of 7.490 which indicates an adequate signal. Thus, the model can be used to navigate the design space.

4.3 Viscosity analysis results

Table 8, 9, and 10 gives the model summary statistics, analysis of variance and the fit statistics for the viscosity response. Figure 4.3 and 4.4 gives a 3D graphical representation of the response and a graph relating the predicted and the actual value.

Table 8: Model Summary Statistics

Source	Std. Dev.	R^2	Adjusted R^2	Predicted R^2	PRESS	
Linear	**4857.03**	**0.5855**	**0.4670**	**0.2731**	**2.896E+08**	**Suggested**
Quadratic	5611.00	0.6839	0.2887			
Special Cubic						Aliased

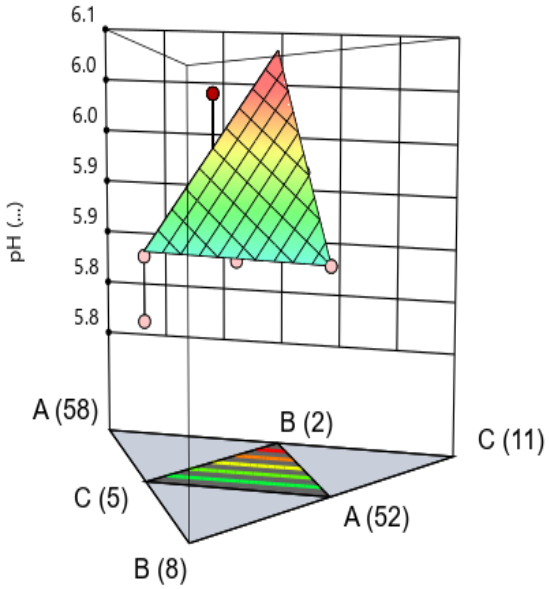

Fig 1: 3D Representation of pH Model

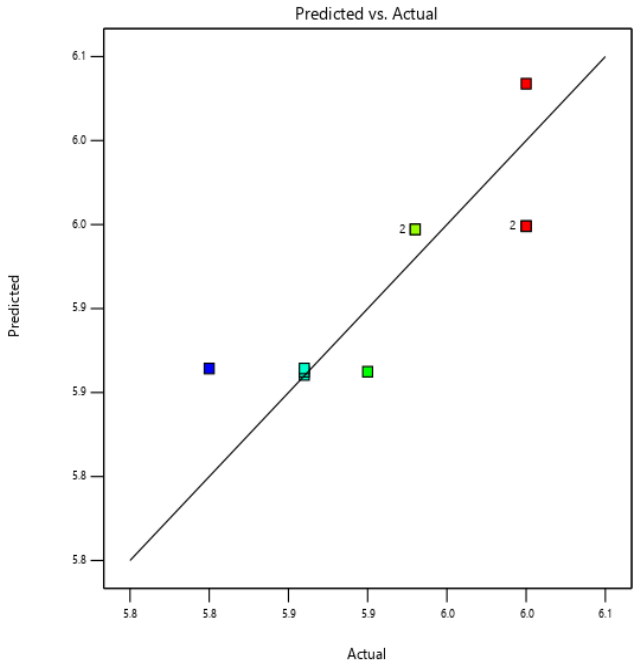

Fig 2: Representation Predicted vs. Actual pH value

The suggested model for the viscosity is a linear model. The **Model F-value** is 4.94 and **P-values is** less than 0.0500 which indicates that the model terms are significant.

Table 9: ANOVA for Linear Model

Source	**Sum of Squares**	**df**	**Mean Square**	**F-value**	**p-value**	
Model	2.332E+08	2	1.166E+08	4.94	0.0459	Significant
Linear Mixture	2.332E+08	2	1.166E+08	4.94	0.0459	
Residual	1.651E+08	7	2.359E+07			
Lack of Fit	3.920E+07	3	1.307E+07	0.4151	0.7520	not significant
Pure Error	1.259E+08	4	3.148E+07			
Cor Total	3.984E+08	9				

The **Lack of Fit F-value** of 0.42 implies the Lack of Fit is not significant relative to the pure error which is good since the model needs to fit.

Table 10: Fit Statistics

Std. Dev.	4857.03	**R^2**	0.5855
Mean	21222.00	**Adjusted R^2**	0.4670
C.V. %	22.89	**Predicted R^2**	0.2731
		Adeq Precision	5.8593

The **Predicted R^2** of 0.2731 is in reasonable agreement with the **Adjusted R^2** of 0.4670; i.e. the difference is less than 0.2. **Adeq Precision** measures the signal to noise ratio, a ratio of 5.859 indicates an adequate signal which is desirable. This model can be used to navigate the design space.

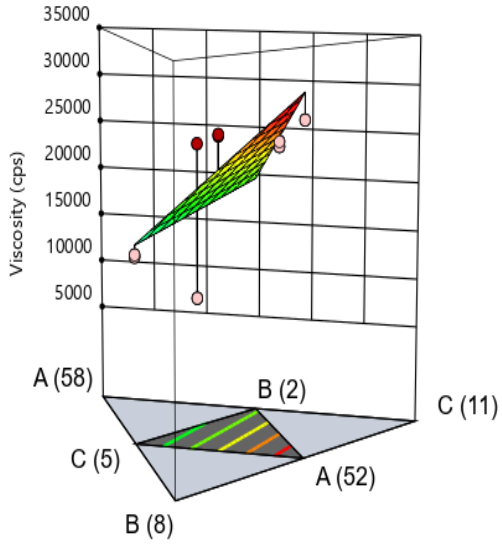

Fig 3: 3D Representation of Viscosity Model

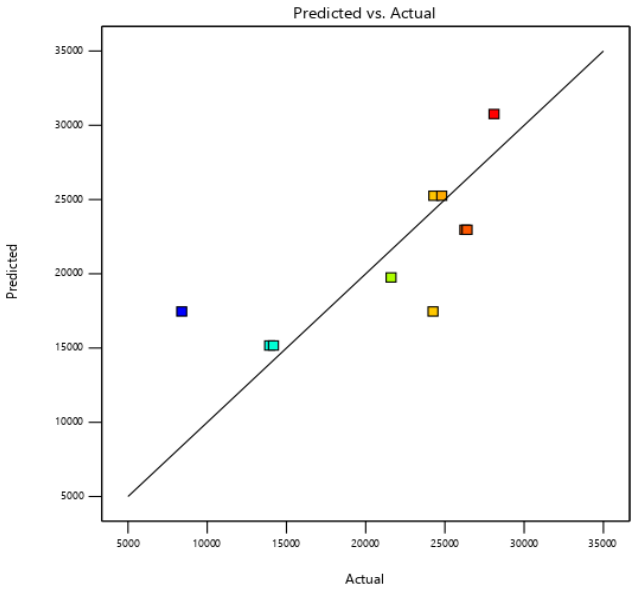

Fig 4: Representation Predicted vs. Actual viscosity values

4.4 Numerical optimization solution

Equations 2 and 3 gives the final mathematical representations of the pH and Viscosity response model respectively in Terms of L_Pseudo Components.

$$pH = 6.04A + 5.69B + 6.03C \quad \ldots\ldots 2$$

$$Viscosity = 4164.76A + 26278.10B + 35340.00C \quad \ldots\ldots 3$$

Where;

A= Distilled water; B = Keratin Protein and C=Emulsifying wax

Table 4.9: Numerical Optimization Solutions

Distilled water	Keratin protein	Emulsifying wax	pH	Viscosity	Desirability	
54.544	**2.588**	**7.868**	**6.0**	**21222.041**	**0.920**	**Selected**

For the numerical optimization the amount of distilled water was kept in range, keratin protein was minimised and the emulsifying wax was maximised. These ranges give the highest desirabiblity of 0.91% for the model as shown in Figure 5. Figure 6 shows the graphical optimization representation of the model.

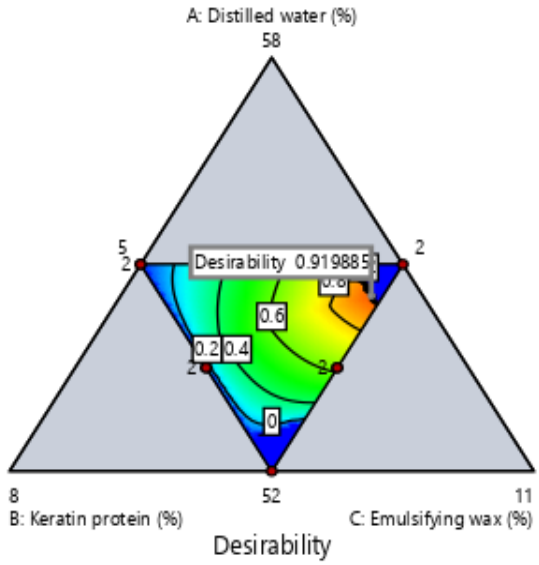

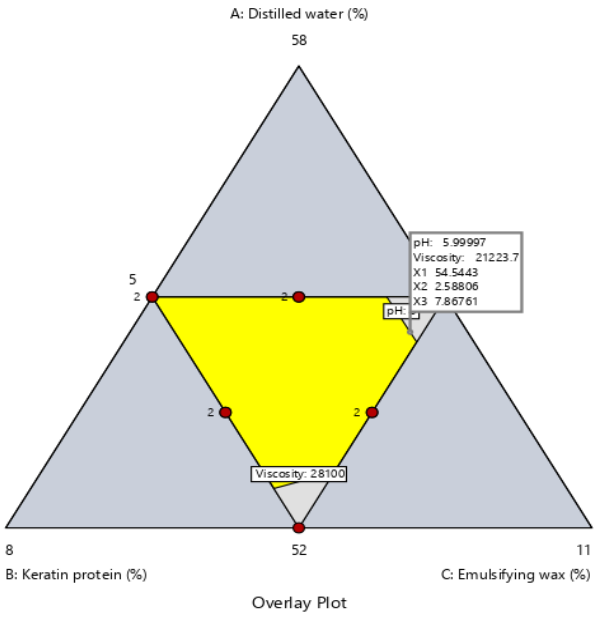

Fig 5: Contour Graph for Numerical Optimization Desirability

Fig 6: Graphical Optimization Representation

4.5 Stability Assay Results

The centrifugation test shows that each sample was stable enough to go through the preliminary stability analysis since no phase separation was observed after subjecting the formulations to a centrifugation cycle of 3000 rpm for 30 minutes, this is in accordance with ANVISA (2004) guidelines. The formulations were analyzed in the

laboratory for changes in organoleptic properties, phase separation, pH and spreadability during the stability assay. The physico-chemical properties of the formulations are stated in Table 11. Table 12 to 14 shows the results for the stability analysis of the formulations at day 5, 10 and 15 respectively. Table 15 shows the stability tests result at 50°C on day 7. There was no microbial growth observed throughout the duration of the stability test, which indicates that the preservative used was effective and stable.

Table 11: Stability Tests Result at Day 5

At 25°C	**S1**	**S2**	**S3**	**S4**	**S5**	**S6**	**S7**	**S8**	**S9**	**S10**
Appearance	NC	NC	NC	NC	NC	NC	NC	NC	NC	NC
Color	NC	NC	NC	NC	NC	NC	NC	NC	NC	NC
Odor	NC	NC	NC	NC	NC	NC	NC	NC	NC	NC
Phase separation	NC	NC	NC	NC	NC	NC	NC	NC	NC	NC
Spreadability (cm)	25.52	24.63	27.34	28.28	25.52	20.43	20.43	21.23	27.34	28.28
pH	6.1	6.0	5.9	6.0	6.0	6.0	6.0	5.9	6.0	5.9
At -5°C										
Appearance	NC	NC	NC	NC	NC	NC	NC	NC	NC	NC
Color	NC	NC	NC	NC	NC	NC	NC	NC	NC	NC
Odor	NC	NC	NC	NC	NC	NC	NC	NC	NC	NC
Phase separation	NC	NC	NC	NC	NC	NC	NC	NC	NC	NC
Spreadability (cm)	27.34	23.76	25.52	24.63	25.57	21.23	21.23	23.76	25.52	28.28
pH	6.0	5.9	5.8	6.0	5.9	6.0	5.9	5.9	6.0	5.9

Where NC signifies no change and S1 to S10 stands for sample 1 to 10.

At 25°C, all 10 formulations showed no change in appearance, color and odor. There was also no phase separation. The change in pH and spreadability was also not significant. At -5°C there was also no change in color, odor, appearance and pH. The change in spreadability was also minute.

Table 12: Stability Tests Result at Day 10

At 25°C	**S1**	**S2**	**S3**	**S4**	**S5**	**S6**	**S7**	**S8**	**S9**	**S10**
Appearance	NC	NC	NC	NC	NC	NC	NC	NC	NC	NC
Color	NC	NC	NC	NC	NC	NC	NC	NC	NC	NC
Odor	NC	NC	NC	NC	NC	NC	NC	NC	NC	NC
Phase separation	NC	NC	NC	NC	NC	NC	NC	NC	NC	NC
Spreadability (cm)	28.28	25.52	27.34	28.28	27.34	21.23	21.23	23.76	28.28	27.34
pH	6.1	6.0	6.1	5.9	5.9	6.1	6.1	6.0	5.9	6.0
At -5°C										
Appearance	NC	NC	NC	NC	NC	NC	NC	NC	NC	NC
Color	NC	NC	NC	NC	NC	NC	NC	NC	NC	NC
Odor	NC	NC	NC	NC	NC	NC	NC	NC	NC	NC
Phase separation	NC	NC	NC	NC	NC	NC	NC	NC	NC	NC
Spreadability (cm)	28.28	24.63	25.52	25.52	27.34	23.76	21.23	27.34	28.28	27.34
pH	6.0	5.9	5.8	6.0	5.9	6.0	5.9	5.9	6.0	5.9

Where NC signifies no change and S1 to S10 stands for sample 1 to 10.

At 25°C and -5°C respectively on day 10 of the stability analysis. At 25°C, all 10 formulations showed no change in appearance, color and odor. There was also no phase separation. The change in pH and spreadability was also not significant. At -5°C there was also no change in color, odor, appearance and pH. The change in spreadability was also minute.

Table 13: Stability Tests Result at Day 15

At 25°C	**S1**	**S2**	**S3**	**S4**	**S5**	**S6**	**S7**	**S8**	**S9**	**S10**
Appearance	NC	NC	NC	NC	NC	NC	NC	NC	NC	NC
Color	NC	NC	NC	NC	NC	NC	NC	NC	NC	NC
Odor	NC	NC	NC	SC	SC	NC	NC	SC	NC	SC
Phase separation	NC	NC	NC	NC	NC	NC	NC	NC	NC	NC
Spreadability (cm)	27.34	27.34	28.28	27.34	28.28	22.90	23.76	25.52	27.34	28.28

pH	6.0	6.1	5.9	5.9	6.0	6.1	6.1	5.9	6.0	6.1
At -5°C										
Appearance	NC	NC	NC	NC	NC	NC	NC	NC	NC	NC
Color	NC	NC	NC	NC	NC	NC	NC	NC	NC	NC
Odor	NC	NC	NC	NC	NC	NC	NC	NC	NC	NC
Phase separation	NC	NC	NC	NC	NC	NC	NC	NC	NC	NC
Spreadability (cm)	27.34	28.28	27.34	27.34	27.34	23.76	25.52	28.28	27.34	28.28
pH	6.0	5.9	5.8	6.0	5.9	6.0	5.9	5.9	6.0	5.9

Where NC is no change SC is slight change and S1 to S10 stands for sample 1 to 10

On day 15, at 25°C all 10 formulations shows no change in appearance, color, and phase separation. Sample 4,5,8 and 10 shows a slight change odor, this could be as a result of the fragrance wearing off. At -5°C there was also no change in color, odor, appearance and pH. The change in spreadability was also minute, this is shown in table.

Table 14: Stability Tests Result at 50°C on Day 7

Day 7	**S1**	**S2**	**S3**	**S4**	**S5**	**S6**	**S7**	**S8**	**S9**	**S10**
Appearance	SVC	SVC	SVC	SVC	SVC	SVC	SVC	SVC	SVC	SVC
Color	SVC	SVC	SVC	SVC	SVC	SVC	SVC	SVC	SVC	SVC
Odor	NC	NC	NC	NC	NC	NC	NC	NC	NC	NC
Phase separation	NC	NC	NC	NC	NC	NC	NC	NC	NC	NC
Spreadability (cm)	9.62	9.34	8.55	9.46	9,62	8.92	9.72	8.55	9.34	9.62
pH	6.1	6.0	6.1	5.9	6.1	6.1	6.0	6.1	6.0	6.1

Where NC is no change, SVC is severe change and S1 to S10 stands for sample 1 to 10

All 10 formulations showed severe change in color, appearance and spreadability. There was no separation of the oil and water phases in the formulation and showed only slight change in the color and pH. This implies that the formulations are not stable and should not be stored at elevated temperature at high temperature.

4.6 Adjusting the pH of the formulations

As stated in literature, it is very rare to formulate cosmetics at the just the right pH, hence the need for the adjustment.

Table 15. pH Adjustment to Isoelectric pH of Hair

Samples	**Quantity of Citric Acid Solution (ml)**	**Initial pH**	**Adjusted pH**
1	0.5	6.0	3.9
2	0.5	6.1	4.1
3	0.5	5.9	4.3
4	0.5	5.9	4.0
5	0.5	6.0	4.2
6	0.5	6.1	4.3
7	0.5	6.1	4.5
8	0.5	5.9	4.2
9	0.5	6.0	4.0
10	0.5	6.1	4.1

The adjusted pH of the formulation using citric acid. The adjusted pH fell between the range of 3.9 to 4.5 which is in range as stated by Ursula *et al.,* 2002 and Michael & Marie, 2016. Which is acceptable and considered safe because it is between the isoelectric pH range of hair.

22. CONCLUSION

The results of the study demonstrate excellent compatibility among the ingredients in the hair cream formulations. The response surface models developed using Design Expert Version 13 were found to be linear and significant for both responses. Numerical optimization solutions revealed the optimal amounts of distilled water, keratin protein, and emulsifying wax to be 54.54%, 2.59%, and 7.87%, respectively, with a desirability score of 0.92. The formulations exhibited good stability at room temperature (25°C) and -5°C, but showed instability when exposed to high temperature (50°C), suggesting that storage above room temperature is not recommended. Throughout the stability analysis, there was no evidence of microbial growth, and the pH of the formulations fell within the isoelectric pH range of hair. Based on these results, the hair cream formulations can be considered both safe and effective for use.

ACKNOWLEDGEMENT

The research team will like to acknowledge Ahmadu Bello University Zaria and **Petroleum Technology Development Funds** for providing research laboratories.

REFERENCES

ANVISA (2004). "Cosmetics Products Stability Guide" Volume 1, National Health Surveillance Agency, Quality in Cosmetics Series.

Barbara B., Fabio R., Mauro L., Elisabetta S., Anna T., Elena G., Rita R., and Luigi F.R., (2013), "The human hair: from anatomy to physiology, Section of Anatomy and Physiopathology" Department of Clinical and Experimental Sciences, University of Brescia, Brescia, Italy and Studio Rinaldi & Associati, Milan, Italy.

Bilgen E. (2017). "Anatomy and Physiology of Hair" http://dx.doi.org/10.5772/67269.

Eric D.P. and Craig J.H., (2016) "Keratin Treatments Formulations and Methods" United States Patent, US 9,326,926 B2.

Roland C.L. and Thomas S.L, (1985), "Textbook of Histology"

Hill P., Brantley H., and Van Dyke M., (2010), "Some Properties of Keratin Biomaterials: Kerateines. Biomaterials".

Marc M.B. and Janellele M. B. (2016), "Keratin Based Hair Straightening Formulations, Methods and Systems", United States Patent Application Publication, US 2016/ 0158138 A1.

Mathew G. (2016), "A Brief Introduction to Hair and Science of Hair Care Products".

Niharika S., Samapika R., Rashmi M.H., Janaki I. and Mansee T. (2008). "Keratin".

Santos, R. C., Silveira Jr, R. F., Marques, L. A., Silva, A. F., & Almeida, R. B. (2017). Formulation and characterization of hair creams containing keratin proteins. Journal of cosmetic science, 68(3), 175-186.

Ursula H., Herbert D., Petra B and Ernst F. (2002). "Method and Composition Adjusted to the Isoelectric Point of Hair for Conditioning of Oxidatively Dyed Hair''. United States Patent Application Publication, US 2002/0122783 A1.

Viviane C.K.N.D, Regis A.N.D., Mariana R.B. and Margereth L.A. (2015), "Physical Chemistry Evalauation of Stability, Spreadability, In Vitro Antioxidant, and Photo-Protective Capacities of Topical Formulations Containing Calendula *officinalis* L. leaf extract", Brazilian Journal of Pharmaceutical Sciences vol. 51, n. 1

Wolfram L.J., (2003), Human hair: "A Unique Physicochemical Composite". Journal of Am Academic Dermatol.

Wu D.D., Irwin D.M. and Zhang Y.P. (2008). "Molecular Evolution of the Keratin Associated Protein Gene Family in Mammals, Role in the Evolution of Mammalian Hair". BMC Evol Biol.

PAPER 124 – OPTIMAL SITING AND SIZING OF D-STATCOM FOR POWER LOSS REDUCTION IN DISTRIBUTION NETWORKS USING BACTERIAL FORAGING ALGORITHM

Alex Aligbe[1*], P.E. Orukpe[2], and Samuel O. Igbinovia[2]

[1]Department of Electrical and Electronics Engineering, Air Force Institute of Technology, Kaduna, Nigeria.
[2]Department of Electrical/Electronics Engineering, University of Benin, Benin City, Nigeria.
[*]Email: a.aligbe@afit.edu.ng and aligbealexprof@gmail.com

ABSTRACT
This paper describes the optimization operation of a distribution network for the purpose of reducing operational expenses and increases the performance of the entire system. The objective of this research is to optimally allocate and size the required kVAr for a Distributed Static Synchronous Compensators (D-STATCom) for a distribution network in order to improve the voltage profile and reduce the total line losses. D-STATCom is a shunt compensating device which is connected to voltage control converter. Bacterial Foraging Algorithm (BFA) was deployed for allocating and sizing of the D-STATCom. BFA is a natural inspired Algorithm that allow bacterial to search for food and avoid harmful substances. The proposed algorithm was demonstrated in IEEE 33 bus and Irrua Distribution Network (IDN). It was observed that the proposed algorithm sited D-STATCom at bus 14 with kVAr value of 3350 and reduces the kW and kVAr losses by 56.61% and 54% respectively for IEEE 33 bus and sited D-STATCom at bus 38 with kVAr value of 5090 and reduces the kW and kVAr losses by 46.7% and 43.4% for IDN. The proposed algorithm was compared with other existing algorithm; the proposed algorithm gave a better result in term of power loss reduction. The optimal siting of D-STATCom devices and proper sizing was able to reduce the total line losses and improve the voltage profile of the networks.

KEYWORDS: D-STATCom, power loss, distribution network, and voltage profile.

23. INTRODUCTION

In recent years, because of the rapid growth in power electronics due to its low cost, fast switching ability and low losses makes the control and operation of power system more flexible and economical [1]. The maximum operating capacity of power system can be exploited by installing Flexible AC Transmission system (FACTs) devices on the network. Installing FACTs devices in distribution network makes the operation more reliable [2]. A distribution system is the network that link the transmission system (high voltage) and the final consumers (low voltage), they have high R⁄X ratio, which makes the power losses to be high [3]. In a distribution system, there is need to provide the required power to the entire loads and maintain the voltage magnitude at an accepted range which is one of the main constraint of the system [4].

FACTs device technology was design initially for transmission network, due to the advancement in technology; the idea was now gaining ground for distribution network application. There are FACTs devices that are suitable for improving voltage level, minimize power loss, and improve power quality in distribution system; these devices are Solid State Transfer Switch (SSTS), Static VAR Compensator (SVC), Unified Power Quality Conditioner (UPQC), Dynamic Voltage Restorer (DVR) and Distributed Static Synchronous Compensator (D-STATCom). D-STATCom is a shunt compensating device connected to a voltage source DC/AC converter, used to resolve power quality related issues such as voltage sag, unbalance load, power loss, voltage instability, operational cost and harmonics distortion. Installation of D-STATCom on all the buses in a distribution network is not economical and therefore unnecessary, there is need to optimally place this devices on the network.

There are several novel techniques that have been deployed in reaching for the optimal location of D-STATCom devices in a distribution network. In [5], immune Algorithm was used to optimally site and size D-STATCom in IEEE-33 and 69 bus networks for multi-objective function, the performance of the network was examined under different load conditions. The author in article [6], optimally sized and sited shunt FACTS devices in a standard IEEE-14 and 57 bus network using fuzzy-Genetic Algorithm (FGA) for multi-objective function. In [7], the authors optimally sited and sized FACTS devices on IEEE-30 bus network using Success History based Adaptive Differential Evolution (SHADE) and Superiority Feasible solution (SF) to solve optimal power flow problem when wind turbines was integrated into the network. The placement and size of SVC was demonstrated in radial distribution system to influence the performance of the network after installing renewable energy sources on the network in [8]. Particle Swarm Optimization (PSO) Algorithm was deployed in [9] to optimally site and size D-STATCom for power quality improvement on a radial distribution network. The study of various load impact when D-STATCom are optimally allocated in a distribution network was demonstrated in [10-11]. In [12], grey

wolf optimization was proposed to reconfigure and allocate D-STATCom in radial distribution network for multi-task functions. Authors in article [13] reconfigured the network by optimally allocating a D-STATCom in order to save energy. JAYA Algorithm was deployed to optimally allocate D-STATCom in a distribution system to enhance the voltage profile and minimizes the total line losses in [14]. Ant Colony Algorithm (ACA) was used to site and size D-STATCom in a radial IEEE 33 bus network in [15]. A Modified Sine Cosine Algorithm (MSCA) was used to optimally site and size D-STATCOM in a distribution network in [16]. In [17], Multi-objective Genetic Algorithm (MGA) was used to optimally allocate and size D-STATCom for Total Harmonic Distortion (THD) mitigation and cost reduction in operation. In this paper, Bacterial Foraging Algorithm (BFA) is propose for optimal siting and sizing of D-STATCom in IDN and IEEE 33 bus Network with the purpose of improving voltage profile and reducing power losses.

24. OVERVIEW OF D-STATCOM MODEL AND THE RESEARCH OBJECTIVE FUNCTION

2.1 Mathematical Model of D-STATCom

D-STATCom belongs to the family of Distributed Flexible AC Transmission System (DFACTs), which comprises of Voltage Source DC/AC Converter (VSC), power transformer and DC capacitor to store energy. D-STATCom has the capacity to absorb or inject kW and kVAr when sited on a network; the amount of power injected or absorbed will depend on the capacity of the energy storage device. D-STATCom can monitor the line voltage and compare it with the reference AC voltage, and provide the required leading or lagging reactive current in order to improve the network voltage. Figure1 shows the steady state connection of D-STATCom to bus m in a distribution network.

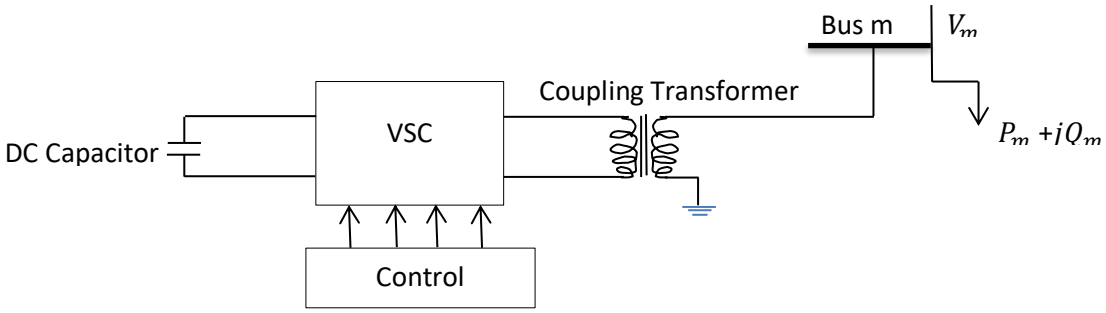

Fig 1: D-STATCom connected to a Distribution Network.

Let consider the schematic diagram shown in figure 1 as a two bus network represented as bus m and m+1, where the line resistance and reactance between the two buses are R_m and X_m respectively. The voltage on bus m and m+1 are V_m and V_{m+1}. After installing D-STATCom on bus m, the voltages on bus m and m+1 changes to V'_m and V'_{m+1}, likewise the injected current by D-STATCom is $I_{DSTATCOM} < (\alpha' + 90^0)$ and the line current is $I_L < \emptyset_L$.

The new voltage on bus m can be calculated after installing D-STATCOM on the network as;

$$V'_m < \theta' = V_m < \delta - (R_m + JX_m) * I_L < \emptyset_L - (R_m + JX_m) * I_{DSTATCOM} < (\alpha' + 90^0) \quad (1)$$

where; $V'_m = V'_m < \theta'$ (2)

The injected kVAr at bus m is given as;

$$jQ_{DSTATCOM} = V'_m * I_{DSTATCOM} < (\alpha' + 90^0)^* \quad (3)$$

Where * denote conjugate of complex variable.

2.2 The Research Problem Formulation

A. Load Flow Analysis

Backward/Forward Sweep Algorithm (BFSA) was used to analyze the load flow in this research work. Kirchhoff's voltage and current law are applied to BFSA method. Let's consider a two-bus one line diagram for a distribution system as shown in figure 2.

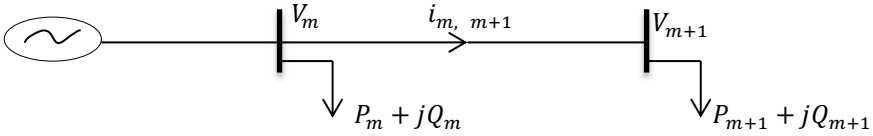

Fig 2: One line diagram for a two-bus distribution System.

The steps required to calculate load flow using BFSA are listed as follows;
Step 1: calculate the bus current.
The current generated at bus m can be calculated as;

$$i_m = \frac{P_m + jQ_m}{V_m^*} \quad (4)$$

where V_m represent the voltage magnitude at bus m, P_m and Q_m are the kW and kVAr at bus m. According to Kirchhoff's current law, the summation of all the current that flow in and out of the bus must be equal to zero.
***Step 2*:** calculate the branch current.
The amount of current that flows between bus m and m+1 is given as;

$$J_{m,m+1} = i_m + i_{m+1} \quad (5)$$

***Step 3*:** representing the bus current injected and the branch current in matrix form;

$$[J] = [BIBC]\,[I] \quad (6)$$

Where, $[BIBC]$ matrix represents the line data of the network.
***Step 4*:** calculate the bus voltage.
The voltage on bus V_{m+1} can be calculated by applying Kirchhoff' voltage law and is given as;

$$V_{m+1} = V_m - i_{m,\ m+1}(R_m + jX_m) \quad (7)$$

where; R_m *and* X_m are the line resistance and reactance.
***Step 5*:** calculate the power losses on the lines.
For kW loss is given as;

$$P_{Loss(m,m+1)} = \left(\frac{P_{m,m+1}^2 + jQ_{m,m+1}^2}{|V_{m,m+1}|^2}\right) * R_m \quad (8)$$

While for kVAr loss is given as;

$$Q_{Loss(m,m+1)} = \left(\frac{P_{m,m+1}^2 + jQ_{m,m+1}^2}{|V_{m,m+1}|^2}\right) * X_m \quad (9)$$

The total kW and kVAr loss on the entire network can be calculated as;

$$P_{TLoss} = \sum_{m=1}^{N} P_{Loss(m,m+1)} \quad (10)$$

Similarly,

$$Q_{TLoss} = \sum_{m=1}^{N} Q_{Loss(m,m+1)} \quad (11)$$

B. The Research Objective Function

This research is carried out to solve two major problems in Irrua distribution network which are, voltage profile improvement and reduction in power losses;

i. Total Power Losses

This objective function min(F) can be determine by referring to the two bus single line distribution network diagram shown in figure 2;

$$\text{min(F)} = min\left(P_{Loss(m,m+1)} + (V_m - V_{m+1})\right) \quad (12)$$

ii. Inequality Constraints

- Bus Voltage Constraints
  The voltages on every bus on the network should be within the accepted range, that is, $\pm 5\%$ of its nominal values as expressed in eq.(13).
  $$0.95pu \leq 1pu \leq 1.05pu \quad (13)$$
- D-STATCom Size Constraints
  The kVAr that will be injected by the installed D-STATCom into the network should not exceed the required kVAr value, as expressed in eq.(14)
  $$Q_m^{min} \leq Q_{D-STAT} \leq Q_m^{max} \quad (14)$$
  Where, Q_{D-STAT} is the kVAr injected at bus m.

25. PROPOSED METHOD FOR THE RESEARCH

3.1 Description of Bacterial Foraging Optimization Algorithm

Bacterial Foraging Algorithm (BFA) is a biological inspired swarm intelligence algorithm that is driven by stochastic search approach developed by Passino. This algorithm has been used by different researchers in finding solutions to optimization problems in power system. The concept of BFA is based on the foraging behavior of Escherichia coli bacterial that reside in human intestine. A set of tensile flagella helps the bacterium to perform two basic operations which are swimming and tumbling during foraging. Whenever each flagellum pulls out a cell, the flagella will rotate in a clockwise direction making the movement of flagella to be independent and cause bacterium to tumble less but when found in a harmful place, it will tumble several times to get a nutrient gradient.

There are basically four steps for BFA, they are Chemotaxis, Swarming, Reproduction, and Elimination and Dispersion. These four steps are applied in solving objective functions either singular or multiple.

3.2 The proposed Algorithm for optimal placement and sizing of D-STATCom

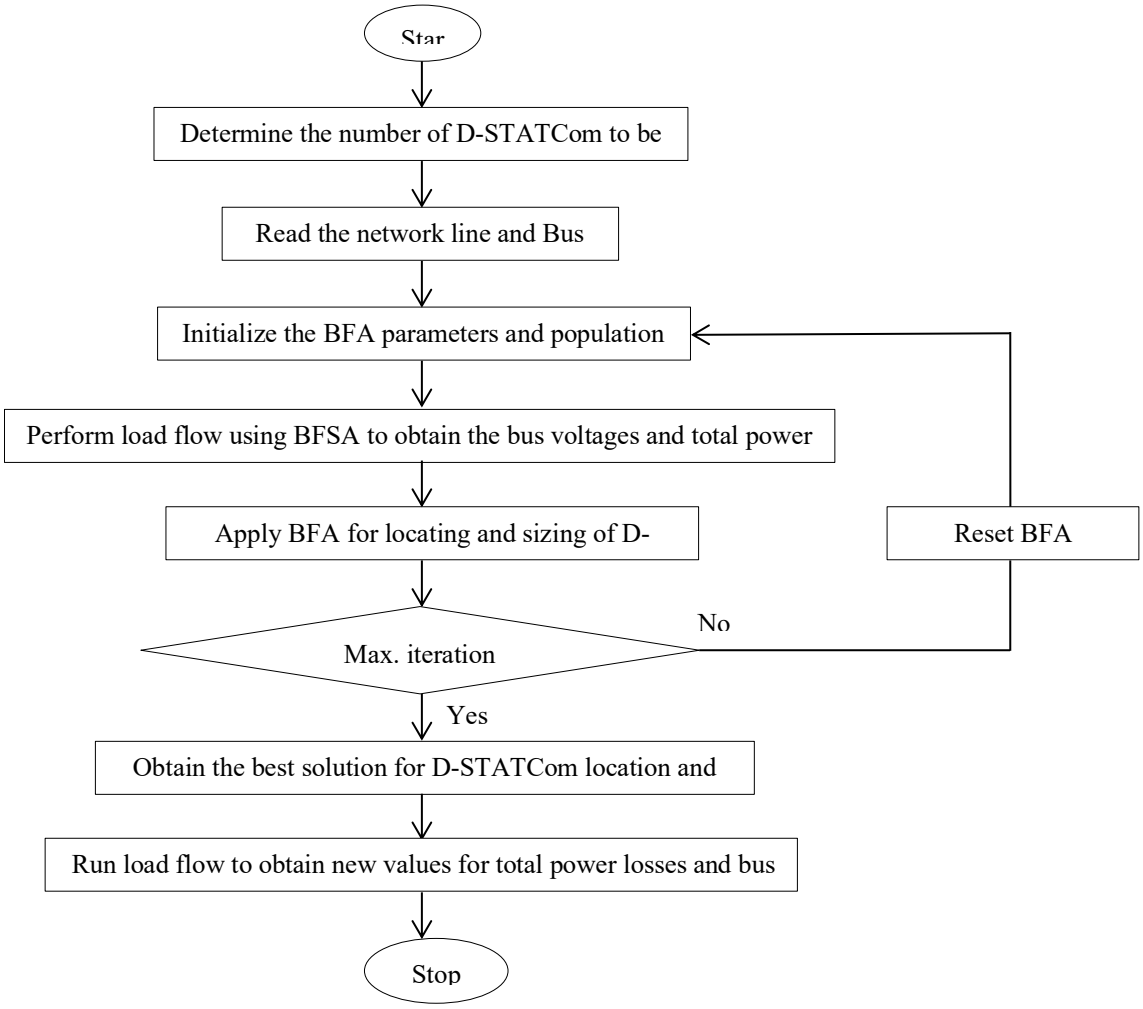

Fig 3: Flow chart for the optimal placement and sizing of D-STATCom using proposed Algorithm.

26. SIMULATION RESULTS AND DISCUSSION.

The proposed Algorithm was demonstrated on IEEE 33 bus network before deployed on Irrua distribution Network. The research work was simulated using MATLAB R2020a environment, the parameter used for both networks are similar.

4.1 Simulation Results for IEEE 33 Bus Network

IEEE 33 bus network consists of 33 buses, 32 lines with a total kW and kVAr load of 3715 and 2295 respectively. The total reactive power flowing through the network is 2487.96kVAr. Backward and forward sweep algorithm (BFSA) was used to analyse the load flow in order to identify weak buses while BFA was used to site and size D-STATCom on the network. The proposed method placed D-STATCom on bus 14 with a kVAr value of 3349.840. Figure 4a shows the improvement in the voltage profile after the installation of D-STATCom. It was observed that kW and kVAr losses were reduced by 56.61% and 54% respectively as shown in figure 4b. The proposed method was compared with other existing methods; it was observed that proposed method gives a better total power loss reduction as shown in table 1

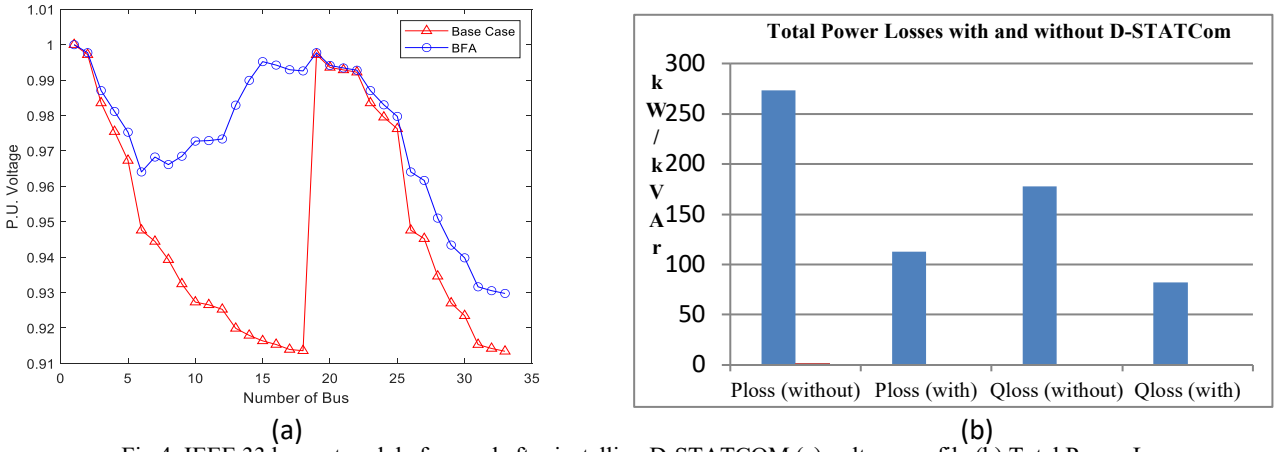

Fig 4: IEEE 33 bus network before and after installing D-STATCOM (a) voltage profile (b) Total Power Losses

Table 1: A comparison between the proposed method and existing methods for IEEE 33 bus system.

Parameter	proposed Method	In [18]	In [10]
Without D-STATCom installation (kW) /(kVAr)	273 / 178	211/ 143	210.98
With D-STATCom installation (kW) /(kVAr)	113 / 82	151.5 / 103.4	151.37
Optimum size of D-STATCom (kVAr)	3349.840	1144	1250
Optimum location of D-STATCom	14th bus	30th bus	30th bus
% loss reduction	56.61 / 54	28.19 / 27.7	28.25

4.2 Irrua Distribution Network (45-bus) Simulation Results

IDN consists of 45 buses, 44 lines with a total load of 8817 kW and 5596 kVAr. Backward and forward sweep algorithm (BFSA) was used to analyse the load flow in order to identify weak buses. BFA was used to site and size D-STATCom on the network. The proposed algorithm placed D-STATCom on bus 38 with a kVAr value of 5090. Figure 5a shows the improvement in voltage profile after the installation of D-STATCom. It was observed that kW and kVAr losses were reduced by 46.7% and 43.4% respectively after installing D-STATCom as shown in figure 5b.

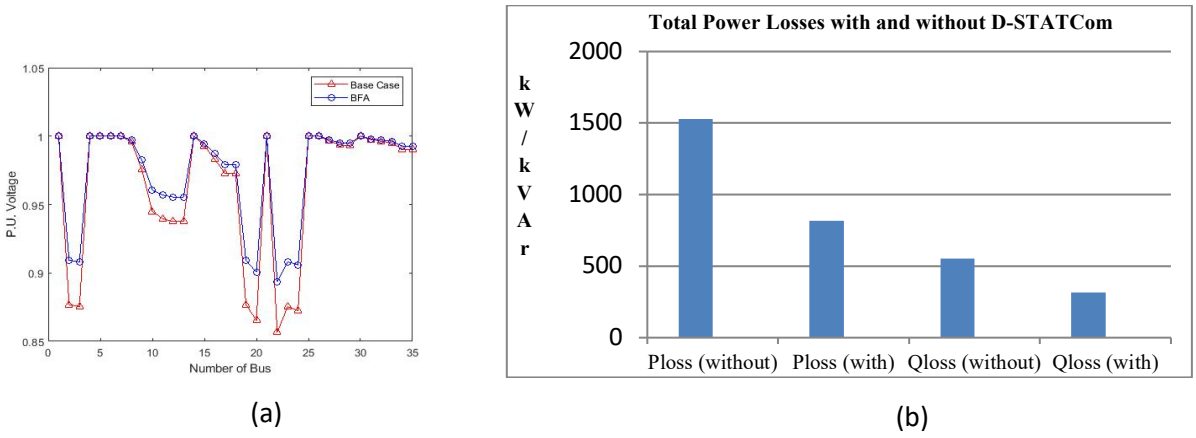

Fig 5: IDN network before and after installing D-STATCom (a) Voltage profile (b) Total power losses

27. CONCLUSION

In the research work, BFA was used to optimally placed and sized D-STATCom on both IEEE 33 bus and IDN. BFSA was used to carry out the load flow analysis while BFA was used to perform the optimal placement and sizing of D-STATCom. The results show that D-STATCom was properly sited and sized on both networks which lead to the significant minimization of total power losses and improvement in the voltage profile when compared to the base case. Some of the benefit of the proposed method is that; it was able to minimize power losses, improve the network voltage profile and the simulation time was short. For future research; D-STATCom should be optimally sited alongside Distributed Generators (DGs) using novel Optimization techniques for multi-objective

function which include costing, voltage stability index, power losses and so on. Artificial Intelligent (AI) should be considered for controlling D-STATCom in a distribution network.

REFERENCES

[1] A. Aligbe , A. E. Airoboman, A.S. Uyi, and P.E. Orukpe "Microgrid , Its Control and Stability : The State of The Art," *International Journal of Emerging Scientific Research*, vol. 3. January, 2021, doi: 10.37121/ijesr.v3.145.

[2] A. Samimi, and M. A. Golkar "A Novel Method for Optimal Placement of STATCOM in Distribution Networks Using Sensitivity Analysis by DIgSILENT Software," *IEEE Conference*, 2011.

[3] P.E. Amaize, A. E. Airoboman, A.Aligbe, K.T. Abayomi and K.O.Okokpujie "An Assessment of Renewable Energy Potentials in Nigeria Using Biogas," *International Journal of Civil Engineering and Technology (IJCIET),* vol. 9, no. 11, pp. 2938–2948, 2018.

[4] S. M. S. Hussain and M. Subbaramiah "An Analytical Approach for Optimal Location of DSTATCOM In Radial Distribution System," *IEEE (2013) Conference,* pp. 1365–1369, 2013.

[5] S. A. Taher and S. A. Afsari, " Optimal location and sizing of DSTATCOM in distribution systems by immune algorithm," *Int. J. Electr. Power Energy Syst.(Elsevier)*, vol. 60, pp. 34–44, 2014, doi: 10.1016/j.ijepes.2014.02.020.

[6] A. R. Phadke, M. Fozdar, and K. R. Niazi, " A new multi-objective fuzzy-GA formulation for optimal placement and sizing of shunt FACTS controller," *Int. J. Electr. Power Energy Syst.(Elsevier)*, vol. 40, no. 1, pp. 46–53, 2012, doi: 10.1016/j.ijepes.2012.02.004.

[7] *P. P. Biswas, P. Arora, R. Mallipeddi, P. N. Suganthan, and B. K. Panigrahi, "Optimal placement and sizing of FACTS devices for optimal power flow in a wind power integrated electrical network," pp. 1–27.

[8] F. Reli, P. Mari, H. Glavaš, and I. Petrovi´c "Influence of FACTS Device Implementation on Integrated Renewable Energy Sources," *mdpi energies*, vol. 13, pp. 1–15, 2020. doi:10.3390/en13205516

[9] S. Devi and M. Geethanjali, "Optimal location and sizing of Distribution Static Synchronous Series Compensator using Particle Swarm Optimization," *Int. J. Electr. Power Energy Syst.(Elsevier)*, vol. 62, pp. 646–653, 2014, doi: 10.1016/j.ijepes.2014.05.021.

[10] A. R. Gupta, and A. Kumarb, " Impact of various load models on D-STATCOM allocation in DNO operated distribution network ," *6th International Conference on Smart Computing and Communications (Elsevier)*, 2018, doi: 10.1016/j.procs.2017.12.110.

[11] A. Jain, A. R. Gupta, and A. Kumar, "An Efficient Method for D-STATCOM Placement in Radial Distribution System," *IEEE Conference* ,2014.

[12] G. Selvaraj, and K. Rajangam "Multi-objective grey wolf optimizer algorithm for combination of network reconfiguration and D - STATCOM allocation in distribution system," *Int Trans Electr Energ Syst (john wiley)*, pp. 1–21, 2019, doi: 10.1002/2050-7038.12100.

[13] A. R. Gupta, and A. Kumar, "Energy saving using D-STATCOM placement in radial distribution system under reconfigured network," *5th International Conference on Advances in Energy Research (Elsevier)*, vol. 90, pp. 124–136, 2016, doi: 10.1016/j.egypro.2016.11.177.

[14] A. A. A. El-ela, M. T. Mouwafi, and A. S. Shammah "Optimal Placement of D-STATCOM in Distribution Systems Using JAYA Algorithm," *IEEE 2018 Twentieth International Middle East Power Systems Conference (MEPCON), Cairo University, Egypt*, pp. 834–838, 2018.

[15] A. Oloulade, A. M. Imano, A. Viannou, and H. Tamadaho, "Optimization of the number , size and placement of D-STATCOM in radial distribution network using Ant Colony Algorithm," *American Journal of Engineering Research and Reviews (AJOERR)*, pp. 1–13, 2018, doi: 10.28933/AJOERR.

[16] M. Ebeed, S. Kamel, and A. Youssef, "Optimal Integration of D-STATCOM in RDS by a Novel Optimization Technique," *IEEE 2018 Twentieth International Middle East Power Systems Conference (MEPCON), Cairo University, Egypt*, pp. 638–642, 2018.

[17] M. H. Nazari, A. Khodadadi, A. Lorestani, S. H. Hosseinian, and G. B. Gharehpetian, "Optimal multi-objective D-STATCOM placement using MOGA for THD mitigation and cost minimization," *Journal of Intelligent & Fuzzy Systems*, vol. 35, pp. 2339–2348, 2018, doi: 10.3233/JIFS-17698.

[18] M. O. Okelola, S. A. Salimon, O. A. Adegbola, E. I. Ogunwole, S. O. Ayanlade, and B. A. Aderemi, "Optimal Siting and Sizing of D-STATCOM in Distribution System using New Voltage Stability Index and Bat Algorithm," vol. 2, no. 2, pp. 2–6, 2021.

PAPER 125 – ANALYSING GENE EXPRESSION DATA OF PATIENTS WITH AND WITHOUT OVARIAN CANCER USING DYNAMIC MODE DECOMPOSITION

A. M. Usman[1,3*], N. T. Surajudeen-Bakinde[1], F. O. Ehiagwina[1,4], A. S. Afolabi[1], A. A. Oloyede[2], O. S. Zakariya[1]

[1] Department of Electrical & Electronics Engineering, University of Ilorin, Ilorin, Nigeria.
[2] Department of Telecommunication Science, University of Ilorin, Ilorin, Nigeria.
[3]Department of Electrical & Electronic Engineering, Stellenbosch University, Stellenbosch, South Africa.
[4]Department of Electrical & Electronic Engineering, The Federal Polytechnic, Offa, Nigeria.
[*]Email: usman.am@unilorin.edu.ng

ABSTRACT
Machine learning (ML) algorithms have been deployed in recent years as models for the analysis of complex data. The ubiquity of ML algorithms stems from their ability to learn the patterns and structures inherent in data. In addition, they are adaptable to a wide range of data types, irrespective of size, which allows them to learn and predict the future pattern of data. In this work, dynamic mode decomposition (DMD), an ML algorithm, is deployed to analyse the pattern of gene expression data from patients with and without ovarian cancer. Ovarian cancer is one of the deadliest gynaecologic cancers in the world. The obscure nature of the symptoms makes early detection of ovarian cancer difficult. If the disease is diagnosed early, the chance of survival increases for patients. In this work, DMD is applied to analyse gene expression data from patients with and without ovarian cancer to understand the spatiotemporal patterns of the data. The DMD modes captured the prevalent structures and predicted the future state of the data. The results obtained show that DMD is a promising algorithm that can predict the features inherent in gene expression for patients with and without ovarian cancer. The DMD modes can further be applied as features to train detection and classification models that can assist health practitioners in the quest for early detection of ovarian cancer through gene expression data.

KEYWORDS: DMD, eigendecomposition, eigenvalues, eigenvectors, ML, ovarian cancer, SVD

28. INTRODUCTION

Ovarian cancer, a disease often known as a silent killer, is the deadliest gynaecologic malignancy worldwide. It is frequently not diagnosed at the early stage until it has reached an advanced stage because of its generally elusive symptoms. Thus, making it challenging to treat on a medicinal basis (Stewart et al., 2019). Early detection of ovarian cancer in patients increases the chances of survival to 90% at stage 1, 70% at stage 2, and 20% or less survival rate for stages 3-4. Unfortunately, only 20% of ovarian cancers are detected in stage 1 or stage 2 (Elias et al., 2018). In order to achieve accurate early detection of the disease, detection and classification models must show high sensitivity and accuracy in performance, because of the cryptic nature of the symptoms of the disease at the early stages (Elias et al., 2018; Stewart et al., 2019).

Machine learning (ML) algorithms have greatly transformed the way complex data are analysed in recent years. ML algorithms have been deployed in recent years as models for the analysis of complex data. The ubiquity of ML algorithms stems from their ability to learn the patterns and structures inherent in data that may not be feasible for humans to learn. Besides, ML algorithms are applicable to a wide range of data types, regardless of the dimension of the data, whether structured, unstructured, or semi-structured. Interestingly, ML algorithms are also flexible and easily adaptive to variations in data, thereby allowing them to continuously learn the patterns as they evolve and improve prediction along the way. ML algorithms have been used to solve complex problems in different fields of applications which include but are not limited to weather forecasting, marine mammal species detection and classification, financial market analyses, and disease modelling among others (Brunton et al., 2016; Kutz et al., 2016; Usman et al., 2020).

ML algorithms have been deployed for the analysis of different cancer-related datasets. Akazawa & Hashimoto, (2020) deployed five ML algorithms (support vector machines (SVM), random forest, naive Bayes, logistic regression, and XGBoost) to predict the pathological diagnosis of ovarian tumours using patient information and data from preoperative examinations. Diagnostic results were derived from 16 features that were commonly available from blood tests, patient background, and imaging tests. XGBoost provided the best accuracy of 80% among the other classifiers. Prabhakar & Lee, (2020) proposed an ML-based model for classifying ovarian cancer. To choose the most pertinent features for classification, the authors used a variety of datasets, including gene expression data and clinical data, and employed a stochastic optimisation technique. Different feature selection techniques were used to select the most important genes among thousands of other sampled genes in order to

avoid computational complexity. The selected features were passed into different classifiers, and the combination of the genetic bee colony optimisation (GBCO) feature selection technique and the SVM-radial basis function (RBF) kernel technique classifier gave the highest classification accuracy of 99.48%. Wang et al., (2023) proposed a novel strategy for ovarian cancer detection utilising deep learning methods and second harmonic generation (SHG) imaging. A convolutional neural network (CNN) was used to determine whether ovarian cancer is present or absent from SHG photos as input. A dataset of SHG images of ovarian tissue was used to test the model, and an average classification accuracy of 99.7% was reported.

In this research, dynamic mode decomposition (DMD), an ML algorithm, is deployed to analyse the pattern of gene expression data of patients with or without ovarian cancer. Four thousand gene expression data were collected for each patient. This is a high-dimensional dataset with 4000 likely feature-set per patient. DMD is an entirely data-driven ML algorithm that can analyse the spatiotemporal structure of data and thereafter, make a prediction about the future behaviour of the data. Initially developed for the analysis of experiments and simulations in the field of fluid mechanics, DMD has since been used for the analysis of several complex time-varying datasets (Kutz et al., 2016). Thus, the power of DMD is used to extract the patterns of gene expression in order to use it to predict the future state of the data.

29. DESCRIPTION OF THE ALGORITHM

Dynamic mode decomposition (DMD) is an ML algorithm that is enjoying a wide range of applications in different fields of study. DMD has been deployed for weather forecasting, marine mammal species detection, financial market analysis, and disease modelling (Brunton et al., 2016; Ogundile et al., 2021; Proctor & Eckhoff, 2015; Usman & Versfeld, 2022). DMD is entirely an *equation-free*, data-driven algorithm that does not rely on the mathematical equation governing a system. Rather, DMD relies on raw data to determine the structure that describes the behaviour of the system to be modelled. This property makes DMD attractive for applications with different types of data. DMD is deployed to analyse the pattern of gene expression data of patients with and without ovarian cancer.

The DMD algorithm gives the accurate eigendecomposition of a dataset into the dominant spatiotemporal patterns that best explain the behaviours of the system. The patterns are thus used to construct a model of the process being observed. The data collected are arranged as *m* snapshots in a large, tall skinny matrix $\boldsymbol{X}$, represented as (Kutz et al., 2016):

$$\boldsymbol{X} = \begin{bmatrix} | & | & \dots & | \\ \boldsymbol{x_1} & \boldsymbol{x_2} & \dots & \boldsymbol{x_m} \\ | & | & \dots & | \end{bmatrix}, \tag{1}$$

where the snapshots, $\boldsymbol{x_1}, \boldsymbol{x_2}, \cdots, \boldsymbol{x_m}$, represent the observations in the dataset and *m* is the number of snapshots. Each snapshot, $\boldsymbol{x}$, contains *n* numbers of spatial points saved per time snapshot, with $n \gg m$. The data are then split into two matrices:

$$\boldsymbol{X_1} = \begin{bmatrix} | & | & \dots & | \\ \boldsymbol{x_1} & \boldsymbol{x_2} & \dots & \boldsymbol{x_{m-1}} \\ | & | & \dots & | \end{bmatrix} \in \boldsymbol{X}, \tag{2}$$

$$\boldsymbol{X_2} = \begin{bmatrix} | & | & \dots & | \\ \boldsymbol{x_2} & \boldsymbol{x_3} & \dots & \boldsymbol{x_m} \\ | & | & \dots & | \end{bmatrix} \in \boldsymbol{X}. \tag{3}$$

$\boldsymbol{X_1}$ and $\boldsymbol{X_2}$ are subsets of the dataset as indicated, and $\boldsymbol{X_2}$ is the exact data matrix $\boldsymbol{X}$, only starting from the second column. The DMD algorithm gives a spatiotemporal decomposition of the dataset into a set of dynamic modes. It does this by finding a best-fit operator, ζ, that would produce the leading eigenvalues, ν and eigenvectors, ϕ, of the dataset.

The best-fit operator, ζ, can be expressed in terms of the data matrices as defined by:

$$\boldsymbol{X_2} \approx \zeta \boldsymbol{X_1} \implies \zeta \approx \boldsymbol{X_2 X_1^{\dagger}}, \tag{4}$$

where $\boldsymbol{X_1^{\dagger}}$ is the Moore-Penrose pseudoinverse of $\boldsymbol{X_1}$. DMD efficiently computes the leading eigenvalues, ν and eigenvectors, ϕ of the best-fit operator, ζ. The DMD modes, **M**, are the eigenvectors of ζ and each mode has a corresponding eigenvalue of ζ.

However, the algorithm avoids the direct computation of ζ, because the data matrices, $\boldsymbol{X_1}$ and $\boldsymbol{X_2}$ are high-dimensional, which makes them inflexible for the computation of ζ. Instead, the dataset is projected onto a low-rank subspace and then an approximate low-dimensional best-fit operator, $\bar{\zeta}$, defined by:

$$\bar{\zeta} = \boldsymbol{X_2 X_1^{\dagger}}, \tag{5}$$

is introduced for the reconstruction of the leading ν and ϕ of ζ, without overtly computing ζ. The cost of the DMD algorithm is the singular value decomposition (SVD), an effective matrix factorisation technique for high-dimensional datasets (Kutz, 2013).

Thus, given the data matrices, $\boldsymbol{X_1}$ and $\boldsymbol{X_2}$, the DMD modes, **M**, are computed as follows (Tu et al., 2013):

1. The *economy* singular value decomposition (SVD) of $\boldsymbol{X_1}$ is calculated:

$$\boldsymbol{X_1 = U \sum V'}, \tag{6}$$

where $\boldsymbol{U} \in \mathbb{R}^{n \times h}$ is the matrix of the left singular vectors of $\boldsymbol{X_1}$, $\Sigma \in \mathbb{R}^{h \times h}$ is a diagonal matrix containing the singular values of $\boldsymbol{X_1}$, and $\boldsymbol{V'} \in \mathbb{R}^{m \times h}$ is the matrix of the right singular vectors of $\boldsymbol{X_1}$. h denotes the rank of the reduced *economy* SVD approximation of $\boldsymbol{X_1}$.

2. The approximate best-fit operator, $\bar{\zeta}$ is calculated:

$$\boldsymbol{X_2} \approx \boldsymbol{X_1}\bar{\zeta} \;\Rightarrow\; \boldsymbol{U \sum V'}\bar{\zeta}, \tag{7}$$

$$\bar{\zeta} = \boldsymbol{U' X_2 V \sum^{-1}}. \tag{8}$$

3. The leading eigenvalues, ν and eigenvectors, ϕ are derived from the computation of the eigendecomposition of $\bar{\zeta}$:

$$\bar{\zeta}\,\phi = \phi\,\nu. \tag{9}$$

4. The modes, **M**, are calculated as defined by:

$$\mathbf{M} = \mathbf{X_2} \boldsymbol{V \sum^{-1}}\,\phi. \tag{10}$$

30. MATERIALS AND EXPERIMENTAL PROCEDURE

a. Data Description

The proposed model is tested on a dataset containing the gene expression data of 216 patients. The gene expression samples are two separate surface-enhanced laser desorption and ionization-mass spectrometry (SELDI-MS) data, one containing proteomic cancerous serums while the other containing normal serums (Conrads et al., 2004). The data was accessed using MathWorks R2021b edition. For each patient, 4000 gene expression data is collected. 121 of the patients are confirmed to have ovarian cancer while 95 are normal patients with no ovarian cancer.

b. Dataset Pre-processing

The data is preprocessed and structured to fit into the DMD architecture. The gene expression for each patient is arranged column-wise as a snapshot and each snapshot contains 4000 samples (gene expressions) representing the number of rows of the data matrix. Consequently, the raw data is represented in the form of a 4000×216 large, tall skinny matrix to represent $\boldsymbol{X}$ in Equation (1). Thus, each column is a snapshot of 4000 gene expressions of a particular patient while the rows represent specific gene expressions at a given spatial point.

c. Performing DMD on the newly formed data matrix *X*

The newly formed 4000×216 data matrix $\boldsymbol{X}$ is used to derive the two observation matrices, $\boldsymbol{X_1}$ and $\boldsymbol{X_2}$ as defined in Equations (2) and (3). The DMD modes are thus computed as enumerated from Equations (6) to (10). The eigenvalues, ν and the DMD modes, **M** derived from the DMD operation represent the spatiotemporal coherent

patterns in the gene expression data. The ν gives the dynamic characteristics and behaviour of each mode (columns of **M**), i.e. $\mathbf{M}_\mathrm{i}$ corresponds to eigenvalue, ν_i.

The predicted future solution can be produced for all time in the future using **M**. The approximate solutions of the data for all future are computed as defined by:

$$\boldsymbol{X_f} = \mathbf{M}\exp(\boldsymbol{\Omega}\mathrm{t_f})\,\boldsymbol{s}, \tag{11}$$

where $\boldsymbol{\Omega} = \log(v)\,/(\Delta \mathrm{t_f})$, is the diagonal matrix of the eigenvalues, t_f is the predicted future time, and $\boldsymbol{s} = \mathbf{M}^{\dagger}\boldsymbol{x_1}$, is the initial amplitude of the modes, † is the Moore-Penrose pseudoinverse operator. Equation (11) is the low-rank representation of the original data. The reconstruction of Equation (11) follows Theorem 1 as defined in Tu et al. (2013) which states that each pair of DMD modes, $\mathbf{M}_\mathrm{i}$ and eigenvalue, ν_i correspond to the eigevectors and eigenvalues of ζ, i.e.:

$$\zeta\mathbf{M}_\mathrm{i} = \mathbf{M}_\mathrm{i}\,\nu_i. \tag{12}$$

d. Data Reconstruction from the Modes

Following the decomposition of the data with the DMD operation, the level of correlation in the gene expression of patients with ovarian cancer and those without ovarian cancer was investigated. This was done using the first three $\boldsymbol{V'}$ modes as depicted in Figure 1. As can be observed, Figure 1 demonstrates that the gene data is significantly correlated indicating that many patients have considerable overlap in gene expression.

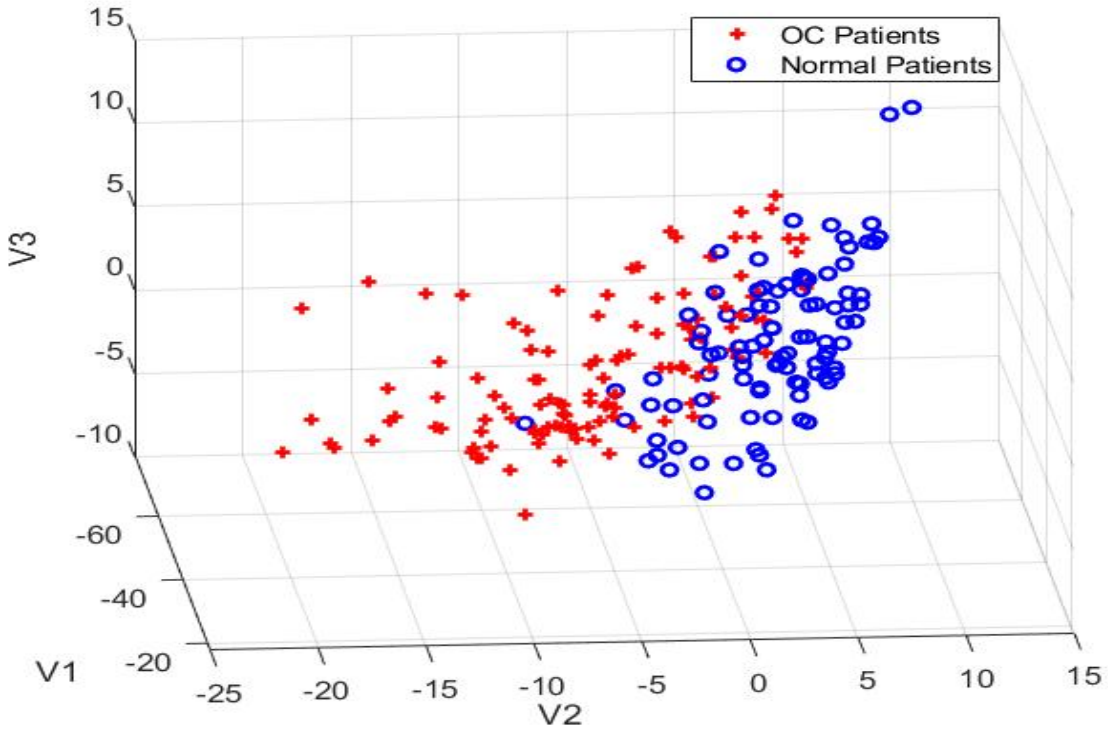

Fig 1: Visualisation of correlation patterns of the gene expression data of patients with and without ovarian cancer in lower-dimensional space.

The computed DMD modes are compared with the gene expression of randomly picked observation (equivalent to the modes positions) to gain an intuition of the accuracy of the computed modes as shown in Figure 2.

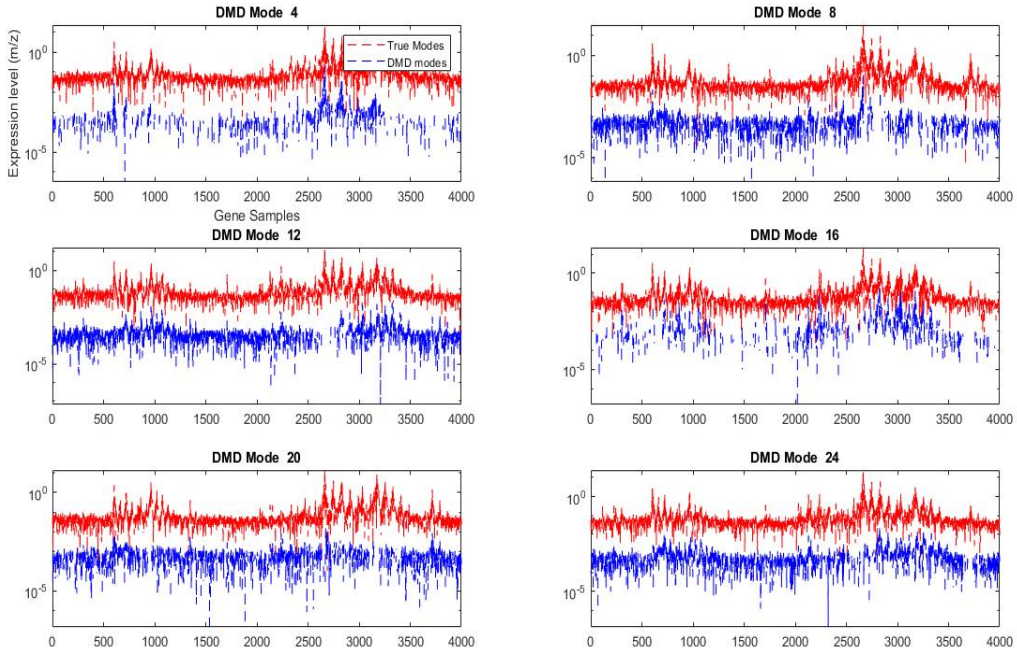

Fig 2: Comparison of the computed modes, **M** with the gene expression samples (True modes).

RESULTS AND DISCUSSION

The rank decomposition level, represented with h, and simulated at different values was implemented. This was done to know the point at which the dominant underlying patterns of the data can be represented with the modes. From the simulated results (at $h = 30$), the computed modes, **M** were randomly picked and compared with the observation snapshots of the original data (true modes) to gain intuition into the accuracy of the DMD. The comparison as depicted in Figure 2 shows that rank-30 decomposition was able to characterise the spatiotemporal pattern of the original data. The predicted data is shown in Figure 3.

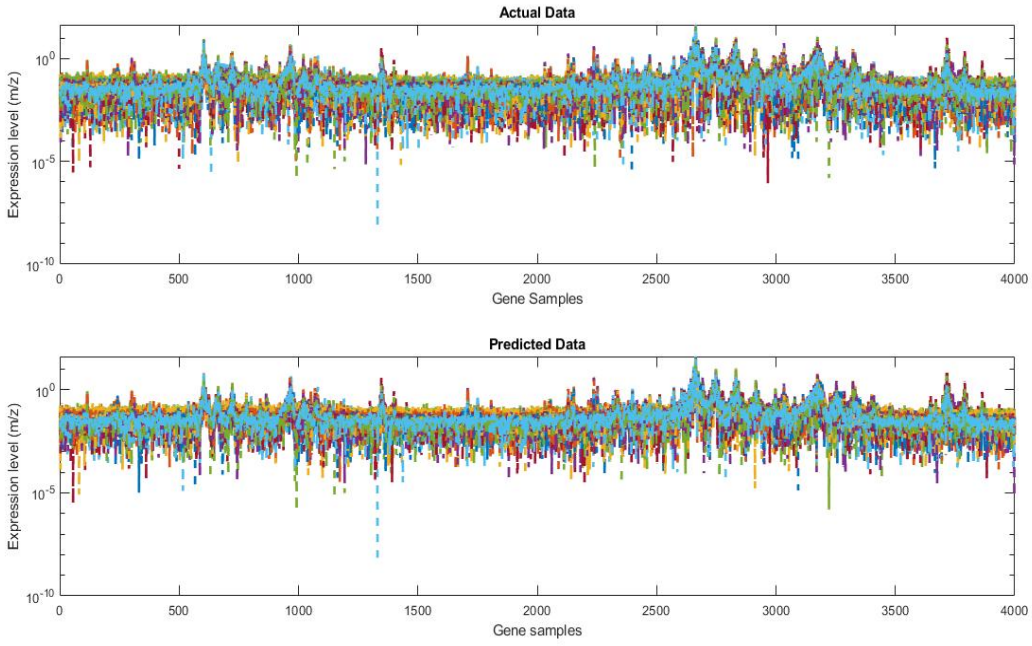

Fig 3: Comparison of the original data and the predicted data (reconstructed using the DMD modes, **M**.

The reconstructed (predicted) patterns demonstrate the effectiveness of DMD in capturing the underlying dynamics that exist in the gene expression data. As can be observed in Figures 2 and 3, the modes and the reconstructed data closely match the original data, thus, indicating that the DMD modes, **M,** capture the majority of the variations that dominate the structure of the original data.

Moreover, the patterns derived from the DMD operation can be interpreted to give insights into the dynamics of the gene expression for patients with and without ovarian cancer. Interestingly, DMD was able to reproduce the dominant structure of the original ovarian cancer data. The ability to reconstruct the original data from the modes provides confidence in the accuracy of the DMD analysis. The benefits of DMD therefore centre on the fact that it is an *equation-free* architecture and that a future-state prediction may be created for any time t (of course, provided the DMD approximation holds).

Therefore, the DMD modes, **M,** can be used as features set to train detection and classification models for accurate detection and classification of gene expressions as either having cancerous cells or not. As earlier noted, the cryptic symptoms of ovarian cancer make early detection difficult. However, ML algorithms can be used to model detection and classifying tools with high performance in terms of sensitivity, accuracy, specificity, and precision. The higher the performance of any of these metrics, the better the chance for early detection of genes that may be carrying the ovarian cancer disease.

Furthermore, it can be observed that despite the original data being of high dimension (4000 x 216), the model can identify patterns and correlations between the gene expression of the patients as depicted in Figure 1 in lower-dimensional space. It is noteworthy that the first three V' modes were plotted in the space encompassed by those modes, patients with ovarian cancer form a discrete cluster distinct from the cluster created by patients without cancer. This shows that high-dimensional data can be effectively analysed in lower-dimensional space. The insights gained from such visualisations can help improve clinical understanding of the disease and its underlying mechanisms.

31. CONCLUSION

The early detection of ovarian cancer among patients could significantly increase the rate of survival. However, detection at the early stage is cryptic due to the elusive nature of the symptoms of ovarian cancer. In this study, DMD was deployed for the analysis of the spatiotemporal coherent patterns that exist in gene expression data of patients with and without ovarian cancer to observe and understand the dominant patterns in the data. An understanding of the patterns can lead to effective feature extractions for training detection and classification models. The DMD modes were used to predict the future state of the data and a closely matched reconstructed pattern of the original data was achieved. The next phase in the work is to deploy the DMD modes as features to train different detection and classification models for the early detection of ovarian cancer tumours from the gene expression data of patients.

ACKNOWLEDGEMENTS

The Federal Government of Nigeria's NEEDS assessment programme through the University of Ilorin is acknowledged for partly supporting this research. MathWorks R2021b© is acknowledged for the ovarian cancer data deployed in this research. Stellenbosch University is acknowledged for providing access to the MATLAB edition (R2021b) used for the research.

REFERENCES

Akazawa, M., & Hashimoto, K. (2020). Artificial intelligence in ovarian cancer diagnosis. *Anticancer Research*, *40*(8), 4795–4800. https://doi.org/10.21873/anticanres.14482

Brunton, B. W., Johnson, L. A., Ojemann, J. G., & Kutz, J. N. (2016). Extracting spatial--temporal coherent patterns in large-scale neural recordings using dynamic mode decomposition. *Journal of Neuroscience Methods*, *258*, 1–15.

Conrads, T., Fusaro, V. A., Ross, S., Johann, D., Rajapakse, V., Hitt, B. A., Steinberg, S. M., Kohn, E. C., Fishman, D. A., Whitely, G., & And, O. (2004). High-resolution serum proteomic features for ovarian cancer detection. Endocrine-related cancer. *Endocrine-Related Cancer*, *11*(2), 163–178. https://doi.org/10.1677/erc.0.0110163

Elias, K. M., Guo, J., & Bast, R. C. (2018). Early Detection of Ovarian Cancer. *Hematology/Oncology Clinics of North America*, *32*(6), 903–914. https://doi.org/10.1016/j.hoc.2018.07.003

Kutz, J. N. (2013). *Data-driven modeling \& scientific computation: methods for complex systems \& big data*.

Oxford University Press.

Kutz, J. N., Brunton, S. L., Brunton, B. W., & Proctor, J. L. (2016). *Dynamic mode decomposition: data-driven modeling of complex systems*. SIAM.

Ogundile, O. O., Usman, A. M., Babalola, O. P., & Versfeld, D. J. J. (2021). Dynamic mode decomposition: A feature extraction technique based hidden Markov model for detection of Mysticetes' vocalisations. *Ecological Informatics*, *63*, 101306.

Prabhakar, S. K., & Lee, S. W. (2020). An Integrated Approach for Ovarian Cancer Classification with the Application of Stochastic Optimization. *IEEE Access*, *8*, 127866–127882. https://doi.org/10.1109/ACCESS.2020.3006154

Proctor, J. L., & Eckhoff, P. A. (2015). Discovering dynamic patterns from infectious disease data using dynamic mode decomposition. *International Health*, *7*(2), 139–145.

Stewart, C., Ralyea, C., & Lockwood, S. (2019). Ovarian Cancer: An Integrated Review. *Seminars in Oncology Nursing*, *35*(2), 151–156. https://doi.org/10.1016/j.soncn.2019.02.001

Tu, J. H., Rowley, C. W., Luchtenburg, D. M., Brunton, S. L., & Kutz, J. N. (2013). On dynamic mode decomposition: theory and applications. *ArXiv Preprint ArXiv:1312.0041*.

Usman, A M, & Versfeld, D. J. J. (2022). Detection of baleen whale species using kernel dynamic mode decomposition-based feature extraction with a hidden Markov model. *Ecological Informatics*, 101766.

Usman, Ayinde M, Ogundile, O. O., & Versfeld, D. J. J. (2020). Review of automatic detection and classification techniques for cetacean vocalization. *IEEE Access*, *8*, 105181–105206. https://doi.org/https://doi.org/10.1109/ACCESS.2020.3000477

Wang, G., Zhan, H., Luo, T., Kang, B., Li, X., Xi, G., Liu, Z., & Zhuo, S. (2023). Automated Ovarian Cancer Identification Using End-to-End Deep Learning and Second Harmonic Generation Imaging. *IEEE Journal of Selected Topics in Quantum Electronics*, *29*(4). https://doi.org/10.1109/JSTQE.2022.3228567

PAPER 126 – Production of Biogas from Anaerobic Co-Digestion of Pineapple Crown and Cattle Dung in A Batch Digester

K. O. Oladosu[1, 2], A. B. Ajala[1*], A. Amidu[1], O. R. Jimoh[1], A. I Joseph[3].

[1,2]Department of Mechanical Engineering, Kwara State University, Malete, Nigeria

[2]Centre for Sustainable Energy, Kwara State University, Malete, Nigeria

[3] Department of Chemical Engineering, University of Ilorin, Ilorin, Nigeria

*Email: ajaladeji1@gmail.com

ABSTRACT

Biogas production from agricultural waste is gaining more attention from researchers in the biofuel industry. However, many of the findings from biogas production have not been implemented, especially in the rural area wherethe agricultural waste is mostly available. This study was aimed at the determination of the influence of biochar (BC) on biogas yield from anaerobic co-digestion of pineapple crown (PC) and cattle dung (CD) using a domestic batch digester. Thefeeds where characterize to determine moisture content, ash yield, total solid, volatile solid, fixed solid content, and pH. The nanoparticle size of biochar was determined using Dynamic Light Scattering (DLS) instrument. In the first experimentalsetup, biogas was produced from anaerobic co-digestion of PC and CD in the fabricated batch digester, while biogas was also produced in the anaerobic co-digestion of PC and CD in the presence of BC. Biogas was collected at 30- and 45-days hydraulic retention time (HRT). The gas analyzer revealed the major composition of the incombustible biogasfrom PCCD at 30 days HRT to be CH_4 (50.38 %), while PCCDBC has CH_4 (40.38 %). At forty-five days HRT, a combustible biogas was produced from PCCD with 59.42 % CH_4 and 54.2 % CH_4 as major gas composition in PCCDBC. Forty-five days HRT is more suitable for the production of combustibles biogas from both PCCD and PCCDBC using locally fabricated batch domestic co-digester. The biogas produced in this study is suitable for domestic cooking.

KEYWORDS: Agricultural wastes, Biochar, Biogas, Cattle dung, Co-digestion, Pineapple crown

32. INTRODUCTION

A large proportion of global gas consumption is derived from naturally occurring sources that are not readily available and accessible by a common man in the street. This has continued to pose serious challenges to researchers in the development of suitable alternatives to the naturally occurring source of gas supply (Hamzah *et al.,* 2020; Cavali *et al.,* 2022). A notable problem associated with the use of gas from natural sources is that it contributes to global warming as a result of the release into the environment of the associated by products from its exploration, production, and usage. It is on record that not less than 10.9×10^9 tons of carbon per year are released into the environment due to the utilization of fossil energy (Cavali *et al.,* 2022). In an attempt to providing cleaner energy sources, gas production known as biogas from plants and animal wastes is fast gaining the attention of researchers. Biogas is a form of renewable fuel and an energy source, it is a combustible gas mixture produced during the anaerobic fermentation of biomass by bacteria (Adebayo *et al.,* 2013; Kulichkova *et al.,* 2020*).*

In European countries, up to 70 % of the feedstock used for biogas production comes from the agricultural sector such as dedicated energy crop (DEC), manure, and agricultural residues. According to the European Biogas Association, DEC constitutes 50 or more percent as a substrate for biogas production in Austria, Cyprus, Germany, and Latvia; for comparison, agricultural residues account for 40-60% of biogas generation in Cyprus, Germany, Denmark, France, Italy, and Poland (Kulichkova *et al.,* 2020).

Nigeria as a country is blessed with about 1.42 million metric tonnes per year of pineapple production (Efunwoye *et al.,* 2019; Baidhe *et al.,* 2021). The pineapple crown has continued to constitute a serious environmental problem which includes landfilling and blockage of the drainage. This pineapple crown can be used for biogas synthesis (Efunwoye *et al.,* 2019). With an estimated 20.7 million cattle herds in Nigeria, the country has been ranked 5th in cattle population in Africa. By the year 2050, the Nigerian cattle population is expected to be about 53.6 million (Ripples Nigeria, 2021). On average, a cow produces 5.4 kg of dung per day, poor management of the cow dung can result in environmental pollution (Yusuf *et al.,* 2020). The use of Pineapple crowns and cow dung for biogas production could be a big opportunity for Nigeria to be enlisted among the biogas producer in the world. Considering the huge waste generation from both pineapple crowns and cow dung in Nigeria, this study was therefore aimed at the fabrication of an anaerobic co-digester for biogas synthesis from these wastes.

33. MATERIALS AND METHODS

2.1 Materials

Pineapple crown was sourced from Lapi Market, Niger State, Nigeria and it was ground with locally fabricated grinding machine to particle size ≤ 0.425 mm. Cow dung was collected from Mandate Market, Ilorin, Nigeria and it was ground with locally fabricated grinding machine to particle size of ≤ 0.425 mm. Bio-char was obtained from Mechanical Engineering Department, Kwara State University, Ilorin, Nigeria.

2.2 Methods

2.2.1 Description and Design of the Digester

The construction of batch biogas digesters was done using a 170 L high-density polyethylene (HDPE) drum. A manual stirrer was fabricated and attached at the bottom, while a digital thermometer, pressure gauge, gas outlet tap, and 2" ball valve (for loading the digester) were attached at the top cover. A stand for the digester was also constructed using a 1"x 6mm flat bar and 1" square pipe.

2.2.2. Anaerobic Co-Digestion Mechanisms

The digesters were incubated at mesophilic (25–35 °C) conditions for a certain period of time. It is a multi-step biological process where the organic carbon is mainly converted to carbon dioxide and methane. The process can be divided into four steps: hydrolysis/liquefaction, acidogenesis, acetogenesis and methanogenesis (Al-Kanmun and Torii, 2015).

2.2.3. Biogas production setup

The biogas production setup in this study is divided into two stages:

2.2.3.1 First Stage Digestion (A)

Modification of the method described by Hamzah *et al.* (2020) was used for the biogas production in this study. Both the dry cow dung and dry pineapple crown were moisturized by adding water by weight of 17.1 kg and 7 kg respectively. The digester was first washed and allowed to dry. 12 % pineapple crown slurry was prepared by measuring 1.4 kg of ground pineapple crown into 10.2665 kg of water in the digester and mixed with the help of the stirrer (XI). 5.833 kg of cow dung was measured into the digester and also mixed with the help of the stirrer, the mixing ratio of pineapple slurry to cow dung is 1:2. The pH of the content in the digester was monitored using a Universal pH paper. The digester was covered and the co-digestion process was allowed to continue for 21 days. The temperature of the digester was monitored with the aid of the digital thermometer while the pressure of both the digester and the gas storage tank was monitored with a pressure gauge. The biogas produced was pumped into the storage tank with the aid of the evacuation pump.

2.2.3.2 Second Stage Digestion (B)

The whole procedure in the first stage of digestion was repeated with the addition of 349.99 g of biochar by 20 g/L reported by Rasapoor *et al.* (2020).

Plate XIV: Experimental Setup for Biogas production by Co-digestion Process

2.2.4 Sample Characterization

The determination of moisture content, total solid, volatile solids, fixed solids, ash content, pH were done according to the reported methods by Jeppu *et al.* (2022). The average size of the biochar was determined according to the method described by Guo *et al*. (2020). The biogas composition was determined using gas analyzer.

34. RESULTS AND DISCUSSION

3.1 Characterization of Feedstocks for Biogas Generation

The result of the analysis for both pineapple and cow dung are presented in Table 1.

Table 1: Characterization of Cow Dung and Pineapple Crown

Parameter	Cow Dung	Pineapple Crown
Moisture (%)	6.00	5.00
Ash (%)	15.00	5.20
Total solid (%)	94	95
Volatile Solid (%)	80.00	89
Fixed Solid (%)	20.00	11.00
pH	8.1	6.6

3.1.1 Moisture Content

The moisture content provides relevant information on the amount of water that is present in semisolid or solid material. The knowledge of the moisture content serves as the basis for the amount of water that is required to prepare the substrate for the co-digestion process. The moisture content of cow dung (6 %) is higher than that of pineapple crown (5 %) The low moisture content indicates that the samples can be preserved over a long period without much deterioration.

3.1.2 Ash Content

The ash content of any organic material is the inorganic or mineral component left after the material has been subjected to elevated temperature. The ash content of cow dung of 15 % in this study is higher than the 5.2 % of pineapple crown. The ash content of the cow dung in this study is within the 11.62 to 32.16 % reported by Maj *et al.,* 2021, while the ash content of pineapple crown in this study is close to the 4.5 % reported by Daud *et al.* (2014).

3.1.3 Total solid

A high total solid value indicates that there is a low water content in the sample, while low total solid content shows that there is high water content. The 94 % total solid in cow dung is much higher than the 15.32 % reported by Anhuradha and Mullai (2010) but is slightly above the 81.86 % reported by Hamzah *et al.* (2020). The total solid of 95 % of pineapple crown in this study is above 79.35 % for pineapple waste by Hamzah *et al.* (2020). The total solid in cow dung in this study is slightly above that of pineapple crown.

3.1.4 Volatile Solids (%)

Substances that can be easily converted directly from the solid phase to the vapour phase without passing through the liquid phase are referred to as volatile solids. The volatile solids of 89 % of pineapple crown and 80 % of cow dung in this study are considerably high, however, the volatile solids in pineapple are slightly higher than that of cow dung. The 80 % volatile solid in this study is in total agreement with the report by Hamilton and Zhang (2023) that fresh manure is 80 % volatile. The volatile solid of pineapple crown in this study is much higher than the 4.95 % for pineapple waste reported by Hamzah *et al.* (2020) but slightly lower than the 95.9 % for pineapple (Rani and Nand, 2004). The volatile solid of cow dung in this study is very close to the 77.5 % reported by Anhuradha and Mullai (2010), but is much higher than the 6.25 % for cow dung reported by Hamzah *et al.* (2020).

3.1.5 Fixed Solids (%)

Fixed solids, otherwise known as inorganic ash is the measure of solid matter that remains after the total dissolved solids have been evaporated (Omondi 2021). The 20 % fixed solids content of cow dung is in total agreement with the report by Hamilton and Zhang (2023) that fresh manure has 20 % fixed solids. However, the value of the fixed solids of cow dung is above 11 % for pineapple crowns.

3.1.6 pH

The methane producing bacteria live best under neutral to slightly alkaline conditions, the required pH for anaerobic digestion ranges between 6.8 and 8.5. The pH values for cattle dung used in this experiment is 8.1 which is slightly alkaline and pineapple crown is 6.6 which is acidic. The pH of the mixture of PCCD is 7.4 and PCCDBC is 7.6 which is within the required pH for Biogas generation, with that the method of anaerobic co-digestion employed in this experiment was able to produce a more desired pH for biogas generation.

3.1.7 Particle size determination of Bio-Char using Dynamic Light Scattering

Bio-char is stable carbon-rich material (Guo *et al.,* 2020). The average particle size distribution by intensity was investigated by Dynamic Light Scattering (DLS) and the result is presented in Figure 4.1, while the other data generated is presented in Appendix. The Z-Average of 75.68 nm represent the average particle size of the bio-char. Nanoparticle are particle with size ranging from 1-100 nm, this gives an indication that the bio-char used for the co-digestion in this study is nanoparticle in size. The nanoparticle size in this study is much higher than the 4 nm and 5 nm for cattle manure and soybean reported by Guo *et al.* (2020).Nanopaticle size between 2 nm and 50 nm is called mesopores and is considered Type IV isotherm (*Thommes et al.,* 2015). Highly developed mesoporous carbon material are more suitable for adoption of larger molecules such as dyes (Kumar and Jena *et al.,* 2016).

3.2 Characterization of Biogas from PCCD AND PCCDBC

The biogas collected from the co-digestion of pineapple and cow dung as well as the one from the co-digestion of pineapple, cow dung, and bio-char in this study is categorized into combustible and non-combustible biogas.

3.2.1 Incombustible Biogas from the Co-digestion of PCCD and PCCDBC

Biogas collection was first carried out on the fifteenth day of co-digestion. The collected biogas was ignited, but it does not support combustion. Another biogas collection was done on the thirtieth day of co-digestion but it does not still support combustion. Analysis of the biogas from 30 days of co-digestion by Bio Portable Gas Analyzer revealed the composition of the biogas produced as shown in Table 2. Ten different gases were identified from both PCCD and PCCDBC co-digestion systems. Gases such as carbon monoxide (CO), nitrogen oxide (NO), nitrogen dioxide (NO_2), sulphur dioxide (SO_2), and hydrogen sulphide (H_2S) are considered to be impurities. However, the gases may not result in any serious environmental pollution as their presence is only in trace amounts. The addition of the bio-char was to minimize the formation of H_2S, however, there was no positive contribution of the bio-char to the biogas composition within the first thirty days of the gas production.

Table 2: Biogas Composition for 30 days Co-digestion from PCCD and PCCDBC

S/N	Gas	PCCD (%)	PCCDBC (%)
1	O_2	1.621	1.213
2	CO	0.0037	0.00427
4	CO_2	2.100	3.200
5	NO	0.00116	0.00132
6	NO_2	0.00033	0.00037
7	NOX	0.00149	0.00169
8	SO_2	0.00006	0.00003
9	CH_4	50.38	40.38
10	H_2S	0.00015	0.001827

Figure 1 present the plot of the results of the major biogas composition which are methane (CH_4), carbon dioxide (CO_2), and oxygen (O_2). Oxygen is a combustible gas but its presence is low in biogas. There is not much significant difference in the oxygen content of the biogas from both the PCCD (1.621 % O_2) and PCCDBC (1.213 % O_2). CO_2 is a non-combustible gas, hence its presence might further be a setback to the combustion of the biogas produced. The CO_2 content of 2.1 % recorded in PCCD is lower than 3.2 % in PCCDBC. PCCD has a higher methane (CH_4) content of 50.38 % compared with the 40.38 % from the PCCDBC process route. This might be due to higher carbon content that might likely result from the addition of bio-char, thereby causing an imbalance in the carbon-to-nitrogen ratio (Omondi *et al.,* 2019). The non-combustibility of the biogas from both PCCD and PCCDBC at 30-day co-digestion is in agreement with the report by Agunwamba (2001) that for any biogas mixture to be combustible, the methane content must be more than 50 %.

In another study by Omondi *et al.* (2019) on biogas production from the co-digestion of water hyacinth (WH) and ruminal slaughterhouse waste (RSW), biogas production was collected for 60 days HRT. Co-digestion of WH with RSW at 1:4 and 1:5 RSW: WH ratio improved the startup rate above that for both biomass. At the 1:4 of RSW to WH ratio and 60 days residence time, there was an increase in biogas production from 87 % to 90 %. However, the percentage methane content of the biogas was not reported and it was not also documented that the biogas combusted.

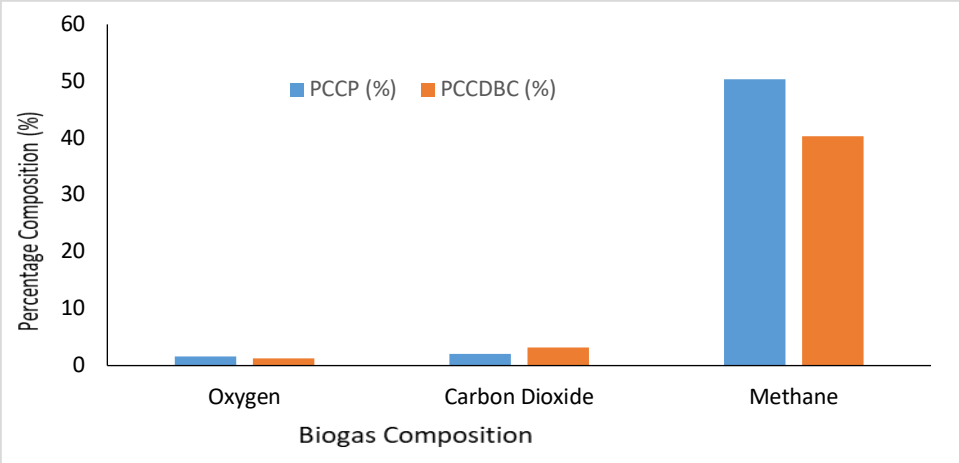

Fig 1: Biogas Composition from PCCD and PCCDBC after 30 Days of Co-digestion

3.2.2 Combustible Biogas from the Co-digestion of PCCD and PCCDBC

The third biogas collection was carried out at the forty-fifth day of co-digestion. The biogas collected from PCCDBC (Plate II) and PCCD (Plate III) combusted on espouse to fire. The biogas from PCCDBC burns with almost complete blue flame while that of PCCD burns blue and traces of yellow flames.

Plate II: Combustion of biogas from PCCDBC

Plate III: Combustion of biogas from PCCD

Analysis of the biogas from 45 days of co-digestion by Bio Portable Gas Analyzer revealed the composition of the biogas produced as shown in Table 3. Four different gases were identified from both PCCP and PCCDBC co-digestion systems. The percentage composition of H_2S in PCCD (0.000242 %) and PCCDBC (0.000246 %) is relatively small. Hence there will be minimal environmental pollution from H_2S during the usage of the biogas. The O_2 from both PCC (0.00022 %) and in PCCDBC (0.000229 %) is considerably low, this does not constitute any challenge to the biogas combustion as sufficient O_2 from the air will combine with the biogas during its usage.

Table 3: Biogas Composition for 45 days Co-digestion from PCCD and PCCDBC

Gas	**PCCD (%)**	**PCCDBC (%)**
H_2S	0.000242	0.000246
O_2	0.00022	0.000229
CO_2	35.94	41.15
CH_4	59.42	54.2

Figure 2 present the plot of the results of the major biogas composition at 45 days of co-digestion which are methane (CH_4) and carbon dioxide (CO_2). The amount of CO_2 in both PCCD (35.94 %) and PCCDBC (41.15 %) is considerably high. It could therefore be inferred that a longer period of co-digestion enhances the biochemical conversion of the carbon content of the substrate into the CO_2. The presence of biochar in PCCDBC indicates higher carbon content which might also be converted to CO_2 during the co-digestion, thereby accounting for higher CO_2 in PCCDBC compared to PCCD. The CH_4 content in PCCD (59.42 %) is slightly higher than in PCCBC (54.2 %). The presence of CH_4 in both PCCD and PCCDBC is more than the required amount of >50 % CH_4 for any biogas to combust. This is the main reason for the combustibility of the synthesized biogas after 45 days.

The methane content in this study is slightly lower than the 69.89 % methane content reported by Al-Mamun and Torrii (2019) for the co-digestion of cafeteria, vegetable and fruit wastes, at mixing ratio of 1.5:0.5:1.0 and 21 days of HRT. The higher methane content by Al-Mamun and Torrii (2019) could be attributed to difference in substrate composition.

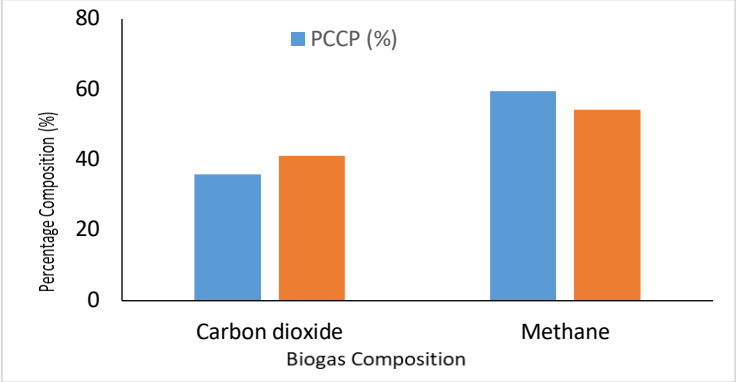

Fig 2: Biogas Composition from PCCD and PCCDBC after 45 Days of Co-digestion

The addition of bio-char did not show any significant effect on the methane content, this could be because the nanoparticle is mesoporous which is more suitable for the adsorption of bigger molecular substances (Kumar and Jena *et al.,* 2016). It is also possible that the bio-char was in excess (Torri and Fabbri, 2014).

In a study by Torri and Fabbri (2014), biochar made from maize was added to an anaerobic digestion system. The results showed that the addition of bio-char not only significantly boosted the cumulative methane yield but also enhanced the reaction rate. Similar to this, it was discovered that 10.0 g L^{-1} of biochar was the ideal quantity and that higher levels decreased the methane output. This was primarily because moderate bio-char addition effectively reduced VFA buildup, leading to increased levels of methanogenic activity, whereas higher biochar concentrations caused more propionic acid to collect in the digester, decreasing the stability of the anaerobic digestion process.

35. CONCLUSION

It can be concluded in this study that the cow dung used in this study consists of 6 % moisture, 15 ash, 96 total solid, 80 % volatile solid, 8.1 pH and 20 % fixed solid. The result of the characterization revealed 5 % moisture, 5.2 % ash, 95 % total solid, 89 % volatile solid, 6.6 pH and 11 % fixed solid. The pH of the mixture of PCCD is 7.4 and PCCDBC is 7.6 which is an improvement to the individual pH of cattle dung and pineapple crown. Hence, both cow dung and pineapple crown are suitable for biogas production. The major composition of biogas produced at 30 days hydraulic retention time for PCCD is 2.1 % CO_2 and 50.38 % CH_4, while that of PCCDBC are 3.2 % CO_2 and 40.38 % CH_4. At 30 days of hydraulic retention time, an incombustible gas was produced. The major composition of biogas produced at 45 days hydraulic retention time for PCCD is 35.94 % CO_2 and 59.42 % CH_4, while that of PCCDBC is 41.15 % CO_2 and 54.2 % CH_4. At 45 days of hydraulic retention time, a combustible gas was produced which is suitable for domestic uses.

REFERENCES

Adebayo, A. O., Jekayinfa, S. O., & Linke, B. (2013). Effect of co-digestion on anaerobic digestion of cattle slurry with maize cob at mesophilic temperature. *Journal of Energy Technologies and Policy*, *3*(7), 47-54.

Agunwamba, J. C. (2001). Analysis of socioeconomic and environmental impacts of waste stabilization pond and unrestricted wastewater irrigation: interface with maintenance. *Environmental Management*, *27*(3), 463-476.

Al-kamun, M. R., & Torii, S. (2014, October). Anaerobic co-digestion of cafeteria, vegetable and fruit wastes for biogas production. In 2014 International Conference on Renewable Energy Research and Application (ICRERA) (pp. 369-374). IEEE.

Anhuradha, S., & Mullai, P. (2010). Kinetics and bioenergy conversion studies of mango pulp industry solid wastes. *World Applied Sciences Journal*, *9*(8), 950-956

Baidhe, E., Kigozi, J., Mukisa, I., Muyanja, C., Namubiru, L., & Kitarikawe, B. (2021). Unearthing the potential of solid waste generated along the pineapple drying process line in Uganda: a review. Environmental Challenges. 2, 100012.

Cavali, M., Junior, N. L., de Almeida Mohedano, R., Belli Filho, P., da Costa, R. H. R., & de Castilhos Junior, A. B. (2022). Biochar and hydrochar in the context of anaerobic digestion for a circular approach: An overview. *Science of the Total Environment*, 153614.

Efunwoye, O. O., & Oluwole, O. R. (2019). Bioethanol production from pineapple waste by solid state fermentation method. *Nigerian Journal of Microbiology*, *33*(2), 4811-4820.

Guo, F., Bao, L., Wang, H., Larson, S. L., Ballard, J. H., Knotek-Smith, H. M., & Han, F. (2020). A simple method for the synthesis of biochar nanodots using hydrothermal reactor. *MethodsX*, *7*, 101022.

Hamzah, A. F. A., Hamzah, M. H., Mazlan, F. N. A., Man, H. C., Jamali, N. S., & Siajam, S. I. (2020). Anaerobic co-digestion of pineapple wastes with cow dung: effect of different total solid content on bio-methane yield. *Advances in Agricultural and Food Research Journal*, *1*(1).

Jeppu, G. P., Janardhan, J., Kaup, S., Janardhanan, A., Mohammed, S., & Acharya, S. (2022). Effect of feed slurry dilution and total solids on specific biogas production by anaerobic digestion in batch and semi-batch reactors. *Journal of Material Cycles and Waste Management*, *24*(1), 97-110.

Kulichkova, G. I., Ivanova, T. S., Köttner, M., Volodko, O. I., Spivak, S. I., Tsygankov, S. P., & Blume, Y. B. (2020). Plant feedstocks and their biogas production potentials. *The Open Agriculture Journal*, *14*(1).

Maj, I., Kalisz, S., Szymajda, A., Łaska, G., & Gołombek, K. (2021). The influence of cow dung and mixed straw ashes on steel corrosion. *Renewable Energy*, *177*, 1198-1211.

Omondi, E. A., Ndiba, P. K., & Njuru, P. G. (2019). Characterization of water hyacinth (E. crassipes) from Lake Victoria and ruminal slaughterhouse waste as co-substrates in biogas production. SN Applied Sciences, 1, 1-10.

Rani, D. S., & Nand, K. (2004). Ensilage of pineapple processing waste for methane generation. *Waste management*, *24*(5), 523-528.

Rasapoor, M., Young, B., Asadov, A., Brar, R., Sarmah, A. K., Zhuang, W. Q., & Baroutian, S. (2020). Effects of biochar and activated carbon on biogas generation: A thermogravimetric and chemical analysis approach. *Energy Conversion and Management*, *203*, 112221.

Thommes et al., 2015

Torri, C., & Fabbri, D. (2014). Biochar enables anaerobic digestion of aqueous phase from intermediate pyrolysis of biomass. Bioresource technology, 172, 335-341.

Yusuf, S. S., & Jibrin, I. M. A. (2020, October). Assessment of Cattle Dung Availability and its Energy Potentials in Funtua, Katsina State, Nigeria. In *Proceedings of 7th NSCB Biodiversity Conference*.

PAPER 134 – EXPERIMENTAL EVALUATION AND OPTIMIZATION OF ORGANIC MATERIALS FOR THE DEVELOPMENT OF FREE-ASBESTOS BRAKE PADS

AElakhame Z. Uwagbai[1], Shuaib–Babata Y. Lanre[2], Busari O. Yusuf[2], Ajao K. Suleiman[2]

[1]Department of Prototype Design and Development, Federal Institute of Industrial Research, Oshodi, Lagos, Nigeria.
[2]Department of Minerals and Metallurgical Engineering, Faculty of Engineering, University of Ilorin, Kwara, Nigeria.
[*]Email: ezeberu@yahoo.com

ABSTRACT
This study presents evaluation and optimization of locally available organic materials for the development of asbestos free brake pads. Some eco-friendly materials for automobile brake pads selected locally are rice husk fibres, gum Arabic, graphite, quartz and steel dust were processed and evaluated for possible asbestos replacement in comparison with the commercial brake pad materials. The material was processed and characterised for elemental composition, microstructural analysis phase presents and observe chemical properties. Using scanning electron microscope (SEM) equipped energy dispersive x-ray spectroscopy (EDX), x-ray diffractometer (XRD) spectrometer and Fourier transform Infrared Spectrophotometer (FTIR) respectively. Commercial brake pad XRD spectrum consist of three compounds exhibit a sharp, tight peak and wagging movement to attest that, the compounds are crystallite and amorphous. While, all the selected materials are also crystallite, excluding gum Arabic and rice husk that are amorphous. Characterization of SEM-EDX shows that, the commercial brake pad has similar element composition with the selected reinforcement materials, except barium oxide find out to be the based materials in the commercial brake pad that was alternatively replaced by rice husk in the new laboratory formulation. Also, it was determined that FTIR analysis of the commercial brake pad has common functional group of 1, 3 – disubstitution (meta) (C-H), alkyl-substituted ether (C – O) stretch, skeletal (C-C) vibrations aromatic tertiary amine (CN) stretch and vinyl (C-H) in-plane bend molecules with the selected materials for new laboratory formulation. Hence, this is accentuating that, the materials can be alternative use for production. It can be finally concluded that the locally available raw materials selected has been evaluated with higher quality than the existing properties of the commercial brake pad which can definitively leads to its low cost of its production.

KEYWORDS**:** Brake pad; Microstructure; Rice Husk; Scanning Electron Microscope; Asbestor

1. INTRODUCTION

Brake pads is an essential component of the braking systems in automobiles to control the speed by converting kinetic energy of the vehicles to heat which is dissipated to the atmosphere. Brake pads are composed of steel backing plates with friction material bound to the surface that faces the disc brake rotor. (Bekir *et al*., 2022). Brake pad materials generally are classified into four principal categories, as Non-metallic materials, semi-metallic materials, fully metallic materials and ceramic materials. The requirements for friction material design includes stable friction force, reliable strength and good wear resistance over a wide range of braking condition. Moreover, the friction material must be compatible with a composite disc brake by forming reliable friction film (stable third-body layer) at the friction surface (Sathyamoorthy *et al*., 2022)

Composition of brake pads has rapidly changed, as a result of the ban on asbestos fibres and the heat being generated during braking causes reduction in braking efficiency (Durowaye et al., 2020). (Najmuddin *et al*., 2021). However, some less thermally stable resins in brake pads were identified as producing oily residues that contributed to brake fade (Abutu *et al*., 2018). All epoxy and certain phenolic resins were identified as evolving volatile gases during degradation causing a back pressure on the brake pad also resulting in brake fade (Heerok *et al*., 2021).

Recently, concerted effort to address environmental issues and the need to protect the environment has drawn research focus to the use of natural fibers in several applications, including brake pads (Najmuddin *et al*., 2021). Dalibor *et al*. (2022) evaluated palm kernel fibers (PKFS) for production of asbestos-free automotive brake pads and the findings concluded that PKF can be effectively used as replacement to asbestor. Nwogu *et al.*, (2021) studied physic-mechanical properties of basalt-based brake as alternative to ceramics brake pad following the standard procedures employed by commercial manufacturer and the result obtained showed that the properties of palm kernel shell-based brake pad wholly satisfied the recommendation of the Standard Organization of Nigeria (SON). Lawal *et al*. (2020) produced brake pad of agro based composits of cashew nut shells and Nigerian gum Arabic binder. The studied concluded that cashew nut shell can be used in placement of materials in commercial brake pad. Furthermore, the morphology and wear properties of palm ash and Polychlorinated Biphenyls (PCB)

waste brake pad further justify the potential of biomass (Ammar *et al.,* 2023). Also, was reported by Güney *et al.,* (2019). Performance evaluation of brake pads development using two different manufacturing methods employed for the design and production of asbestos free brake pad using cashew nutshell by Adekunle *et al.,* (2023). The results of the studies indicated that palm slag can be used effectively as an alternative to brake pad composites. Nwogu *et al.* (2021) embarked on microstructure and wear mechanisms investigation on the brake pad. The brake pad when compared with asbestos-based commercial brake pad they was found to perform effectively.
Hence, this work aimed at producing eco-friendly friction composite brake pads produced from local available raw materials and compare it with the commercial brake pad by using powder metallurgy method to develop samples for characterization.

2. MATERIALS AND METHODS

2.1. Materials

The raw composite materials used in this study were rice husk, quartz, steel slags, graphite and gun arabic were s ourced from Ofada, Ogun State; Okpila, Esako, Edo State; Africa Foundry, Ogijo, Shagamu, Ogun State; Sama-Borkono, Warji, Bauchi State; a local vendor within the industrial raw materials supplier trade group registered b ut were harvested in Kano State Nigeria respectively as shown in Figure 2.

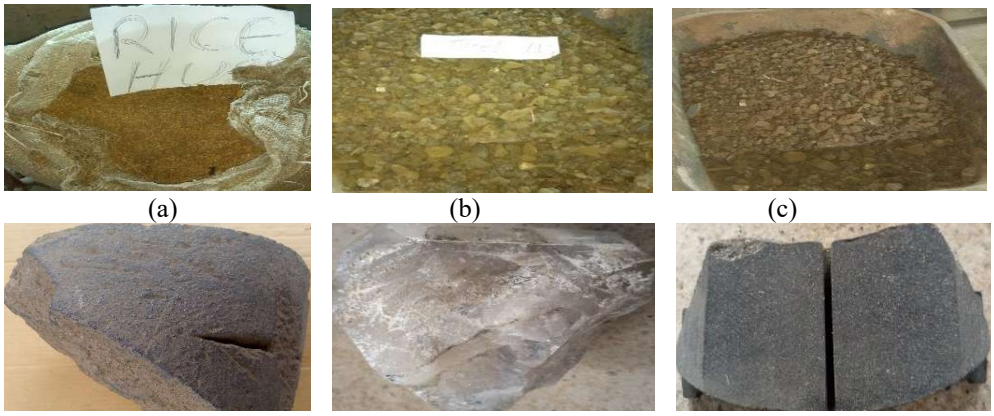

(a) (b) (c)

(d) (e) (f)

Fig 2: Photographs of raw materials (a) Rice Husk, (b) Gum Arabic, (c) Steel Slags, (d) Graphite ore, (e) Quartz ore and (f) Commercial brake pad

2.2. Materials Milling

A 5kg of the Rice Husk (HR) particles was sun dried for one week and charged into a ball milling machine (Model 87002 Limoges - France, A50 – 43, at 250 rpm) shown Figure 2b for 48 hours, with 25kg pebbles of different size (Dia 46.5mm, 39mm and 30mm of Big, medium and small) respectively; to form fine powder. The produced powder was later sieved with 75 µm (X), 100 µm (Y) and 150 µm (Z) sieve size aperture, using a vibro sieve machine (Vibro sieve machine Bs 410 standard sieves Endecotts Limited, London). While that of Steel slags, Quartz and graphite were pulverized using hammer mill, Model 000T, Puissance: 1.5KV, No 13634 (figure 2b) and then charged into milling machine to form fine powder and sieved to 100 µm particles size. The procedures were in line with the practice of Elakhame *et al.* (2020). The samples of the milled sieved materials are presented in Figure 3.

(a) (b) (c)

(d) (e) (f) (g)

Fig 3: The various machines used and processed raw materials (a) Hammer Mill (b) Ball Milling Machine (c) Rice Husk (d) Processed Gum Arabic (e) Steel Slags (f) Graphite (g) Quartz.

2.3. Evaluation Properties of the raw Materials.

The elemental composition and phases present in the materials were determined with the accordance of ASTM standard.

I. **X-ray Diffractometer (XRD)**

XRD experiments were performed by (MiniFlex 600, Rigaku, Japan) diffractometer with Cu Kά based on ASTM E2860 – 20(2021)The experimental conditions were as follows: 45 kV, 40 mA, 21-23^{o}C, divergent beam slits 2 and 3 mm, receiving slits 1 and 0.2 mm, 2θ = 5-70^{O}C, and continuous scan with a scan rate of 2^{O}C/min.

II. **Scanning Electron Microscope and Energy Dispersive X-Ray Spectroscopy (SEM-EDS)**

The Scanning Electron Microscope with energy dispersive X-ray spectroscopy (SEM-EDS) (Phenom Prox model, phenomWorld, Eindhoven) based on test procedure in ASTM C1255 – 18(2018) and ASTM E2809 – 13(2019) Sample was placed on the Aluminium holder stub using sticky carbon tape. The sample was insulated using gold and then grounded electrically. The samples (each) where then labeled on their stub, then dried in the oven at 60^{O}C. Nitrogen line was opened at 50 psi and the vent button is pressed to fill the area with nitrogen for proper purging of the chamber.

III. **Fourier Transform Infrared Spectrophotometer (FTIR).**

For functional unit determination, the Fourier transform Infrared Spectrophotometer- (8400 S, Shimadzu, Japan) was used. Samples were weight-in at 0.01 g and homogenized with 0.01 g KBr anhydrous by mortar agate. The mixtures were pressed by vacuum hydraulic (Graseby Specac) at 1.2 psi to obtain transparency pellet. The procedure in American Society for Testing and Materials (ASTM) ASTM D6348 - 12(2020) standards were adopted to evaluate the raw materials.

3. RESULTS AND DISCUSSION

3.1. Elemental Compositions of the Raw Materials Specimens.

Table 1 shows the elemental composition of Commercial Brake Pad (CBP), Graphite (G), Quartz (Q), Steel Dust (SD), Rice Husk (RH) and Gum Arabic (GA)**.** The **results** revealed that the materials mainly contain metallics, semi-metallic and non-metals. It can be seen that G, Q, SS, RH & GA have similar composition of elements compared to the commercial specimen and equally found in asbestors. This suggested that the materials selected can be used as fibres in the development of brake pads. The amount of Fe, Ca, S, P, Mg and Na in G, Q, SS, RH and GA are comparable to the amounts present in the commercial specimen. All the raw materials have higher amounts of C and Si compared to the commercial specimen. Correspondingly, their properties are similar to commercial specimen, except the present of Ba only in the commercial specimen. These results are in lie with earlier confirmed by Durowaye *et al.* (2020).

Table 1: Comparison of EDX Results Showing Elemental Compositions of Commercial brake pad, graphite, quartz, steel dust, rice husk and Nig gum Arabic.

S/N	*Element Symbol*	*Element Name*	*CBP Weight Conc.*	*Graphite Weight Conc. (G)*	*Quartz Weight Conc. (Q)*	*Steel Slsg Weight Conc. (SS)*	*Rice Husk Weight Conc. (RH)*	*Gum Arabic Weight Conc. (GA)*
1	Ba	Barium	26.96	-			-	-
2	C	Carbon	19.51	74.06		5.24	49.21	55.52
3	Fe	Iron	17.46		1.47	33.53		-
4	Ca	Calcium	7.11	5.08	2.04	2.35	11.82	11.28
5	Ti	Titanium	5.83			0.56	0.42	0.74
6	S	Sulfur	5.07	1.29	0.78	0.44	3.83	1.56
7	Si	Silicon	3.58	8.01	76.72	52.07	16.83	3.18
8	Ag	Silver	3.48	3.12		1.14		-
9	K	Potassium	2.32	2.20	2.49	0.49	2.20	8.66
10	Mn	Manganese	2.14			1.61		-
11	P	Phosphorus	1.66	0.87	0.17	0.46	5.47	1.80
12	Mg	Magnesium	1.53	0.61	0.37	0.28	0.70	2.04

13	Al	Aluminium	1.27	2.51	3.58	1.25	1.51	-
14	V	Vanadium	1.14		0.30			-
15	Na	Sodium	0.57	0.31	0.22	0.07	0.22	0.37
16	N	Nitrogen	0.19	0.94			0.79	2.01
17	O	Oxygen	0.18	0.35			1.41	3.67
18	Cl	Chlorine	-	0.65				
19	**Ag**	Silver			4.51		2.34	6.07
20	**Y**	Yttrium			3.34		3.26	
21	**Cr**	Chromium			1.23	0.51		
22	**Zn**				2.75			

3.2. Scanning Electron Microscopy (SEM) of the Raw Materials Specimens.

In the spectrum of commercial specimen (Fig 4). It's evidenced that barium and iron powders are uniformly distributed in the resin. Graphite particles are evenly spread in the matrix. Clusters of Magnesium, Aluminum, Silica, Sulfur and other are seen at random locations Ossia *et al*. (2021). It is observed in Figure (4b) that silicon and calcium powders are distributed uniformly, while graphite particles are evenly spread in the matrix. Clusters of phosphorus, sulfur, yttrium, silver and aluminum are seen at random location (Yezhe *et al*., 2020).

The surface topography in (Figure 4c) was observed and the exterior surface of the gum arabic appears as irregular rocky surface and clearly different from that of the parent gum arabic, which has spherical shape with many dents on the surface (Nwogu *et al*., 2021). It is also observed that the spectrum had regular edges and homogenous structure (Figure 4d) (Oktem *et al*., 2021). The presence of large and spherical particles of silicon in (Figure 4e) indicate the rounded nature of quartz particles while the spherical grains indicate recycled nature and maturity of sediment accumulation. Quartz particle at higher magnification shows spongy surface and microcracks (Ahmad *et al*., 2021). (Figure 4f) shows that graphite has a wide and thick particle size indicated at 1000× magnification. The distance between the graphite particles looks wider with a far position and the existence of many stacks in the graphite structure indicating that graphite has a layered structure (Seckley, *et al*., 2020).

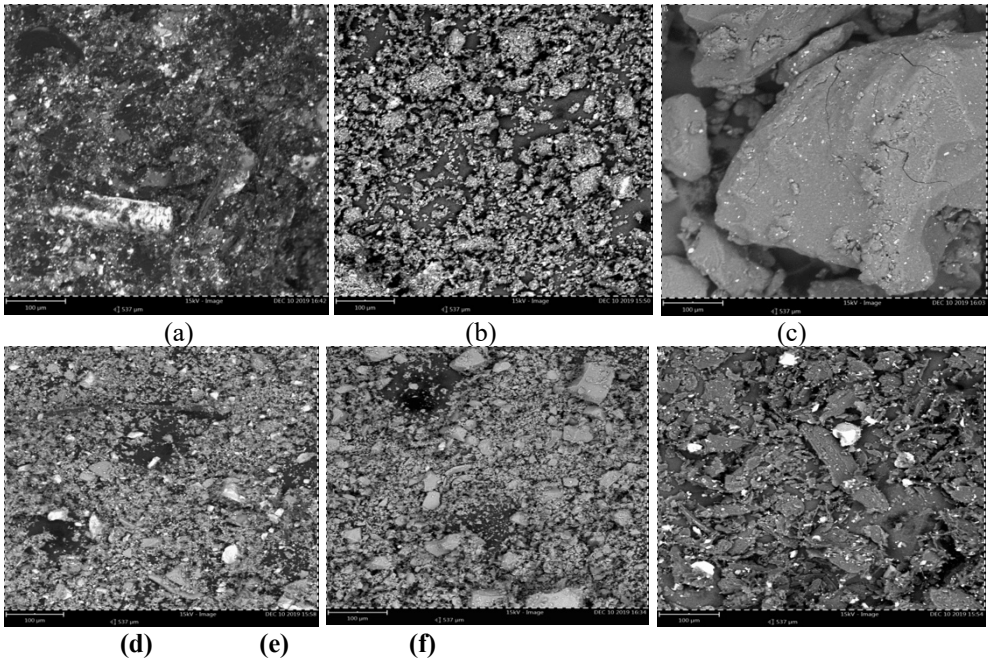

(a) (b) (c)

(d) (e) (f)

Fig 4: SEM micrograph of the samples (a) Commercial brake pad (b) Rice husk (c) Gum Arabic (d) Steel dust (e) Quartz (f) Graphite.

3.3 X-Ray Diffraction (XRD) Results of the Raw Materials Specimens.

The phase purity and crystallinity of the commercial pad was examined by X-ray diffraction techniques (XRD). Figure 5a consists of three phase compounds namely Graphite (C), Barite (BaO_4S) and Calcite ($Ca_6\ C_6\ O_{18}$). The

three compounds exhibit a sharp and tight peak at 2θ equal 20 and 30^{O} above 50% intensity Siburian *et al.* (2018). Figure 5b reveals that the optimal sharp peak occurred at 2θ angle equivalent 27^{O} with 100% intensity' the presences of sharp crystalline peaks all-round suggest that the graphite specimen is a predominantly crystallite (Obidiegwu *et al*., 2020). Figure 5c shows the amorphous nature of Nig gum arabic, the maximum intensity was obtained at 2θ angle equal 75^{O} Atmika *et al*. (2019). The absence of sharp crystalline peaks indicates that the specimen is amorphous in nature with an interesting feature of intensity distribution due to it wagging shape. Figure 5d consist of phase compound namely Quartz (Si_3C_6). The hexagonal crystal system exhibits a sharp and tight peak at 2θ equivalent 27^{O} with 100% intensity (Ammar *et al*, 2023). Figure 5e indicate the broad peaks at 2θ equals 75^{O} and low intensity counts confirmed the RH to be largely amorphous silica. Suggesting, the presence of quartz as crystalline phase. While Figure 5f shows the mineral phases of (silicon, graphite, magnetite, wuestite and ferdisillicite) were determined at higher and lower phases due to the very complex mineralogical composition of BOF steel slag, with many overlapping peaks and different solid solutions of oxides are (FeO, Fe_3O_4), silicon, Ferdicillicite (Fe) and graphite (Viderscak *et al.*, 2022). The purity crystal system exhibits a sharp and tight peak at 2θ equals 29^{O} with 100% intensity. This result shows that the steel slag is best suitable for thermal, abrasive and hardness enhancement properties in brake pad (Lyu *et al*., 2020).

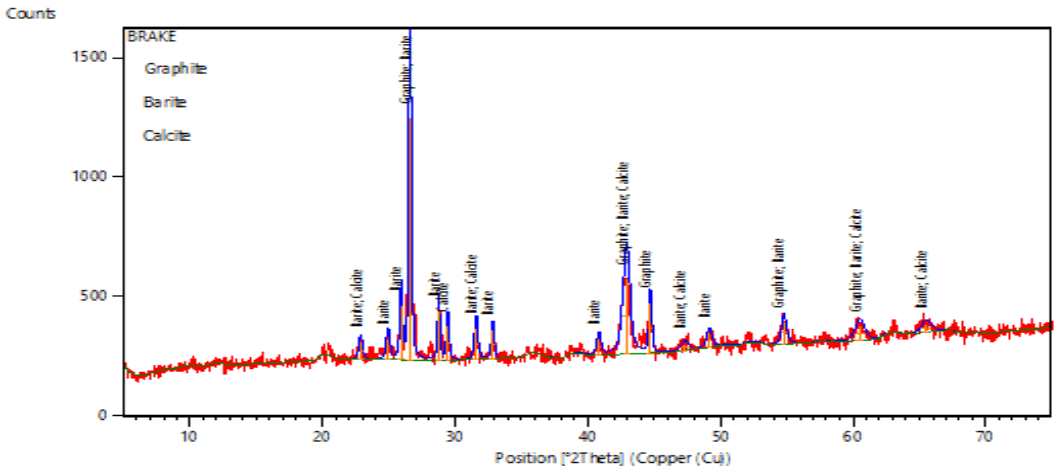

(a).

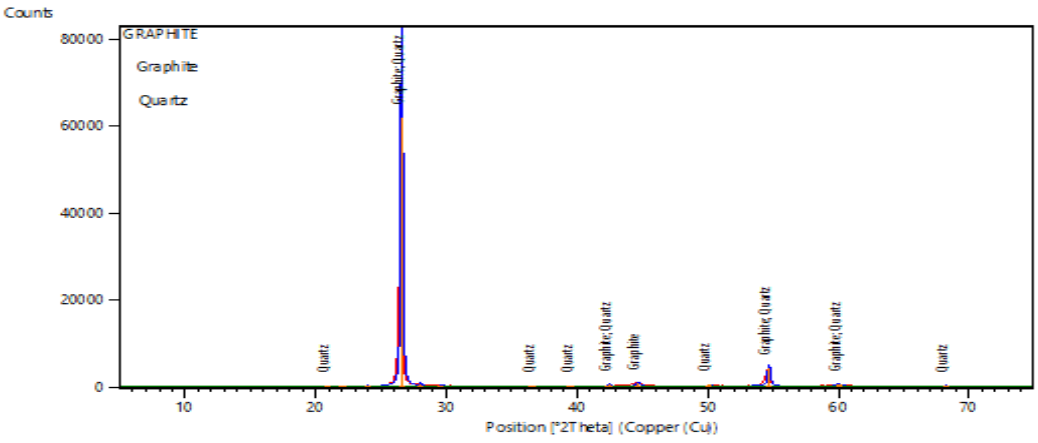

(b).

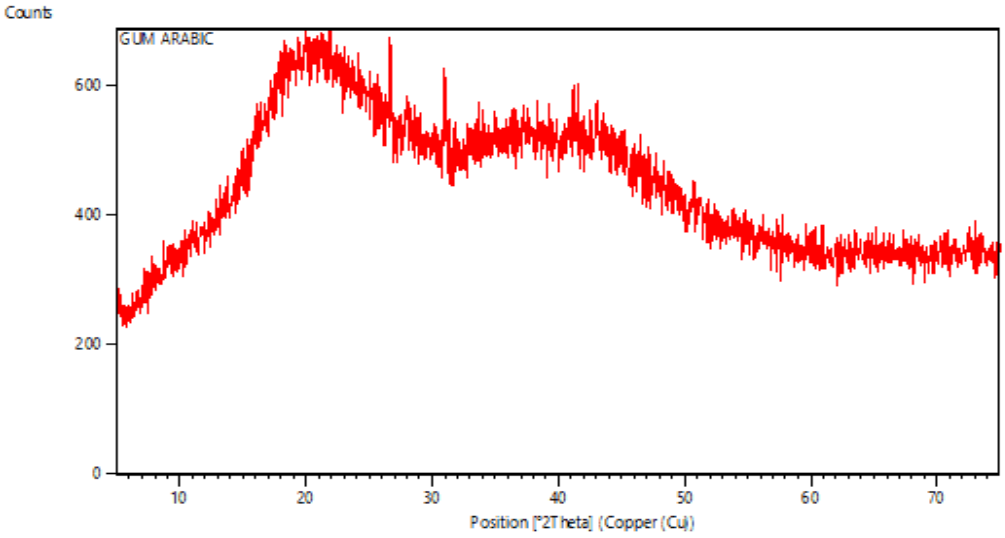
Counts
GUM ARABIC
600
400
200
0
10
20
30
40
50
60
70
Position [°2Theta] (Copper (Cu))

(c)

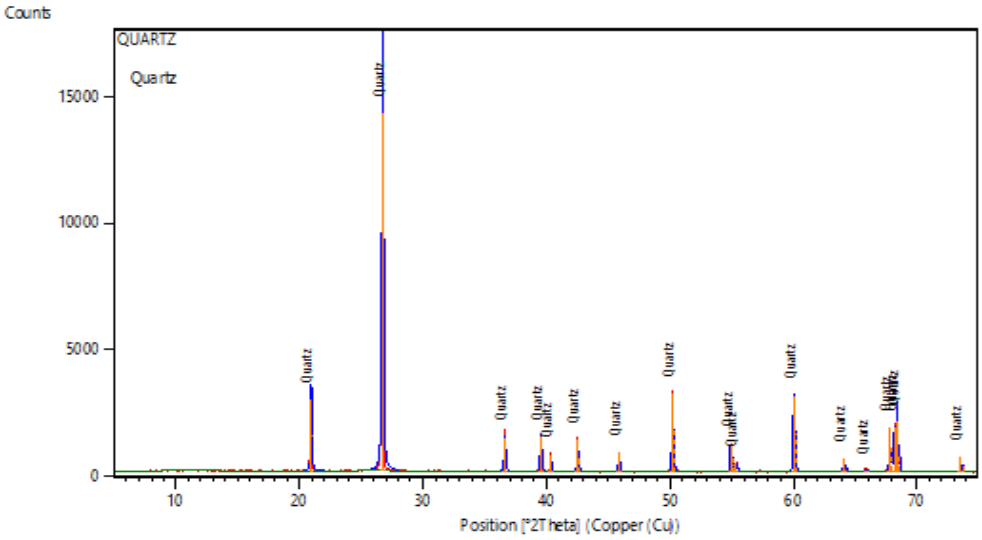
Counts
QUARTZ
Quartz
15000
10000
5000
0
Quartz
10
20
30
40
50
60
70
Position [°2Theta] (Copper (Cu))

(d)

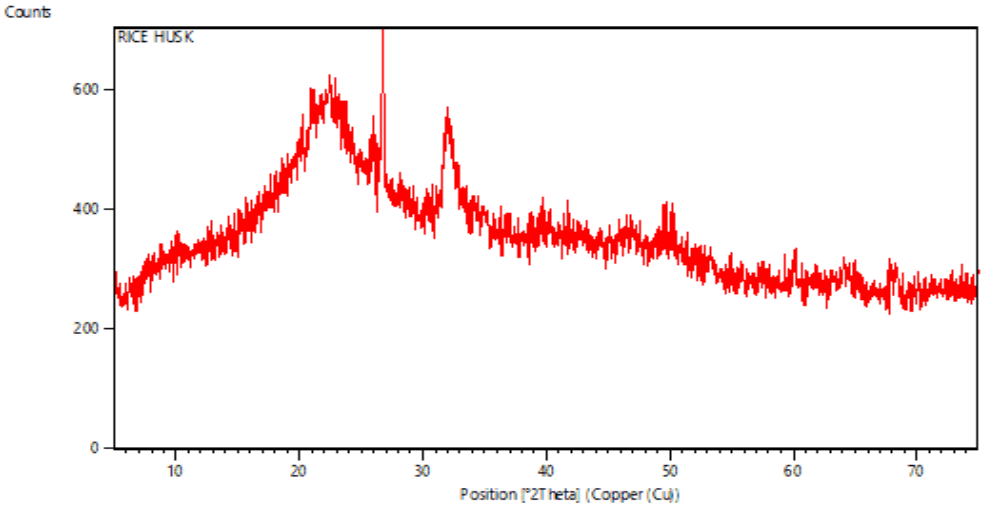
Counts
RICE HUSK
600
400
200
0
10
20
30
40
50
60
70
Position [°2Theta] (Copper (Cu))

(e)

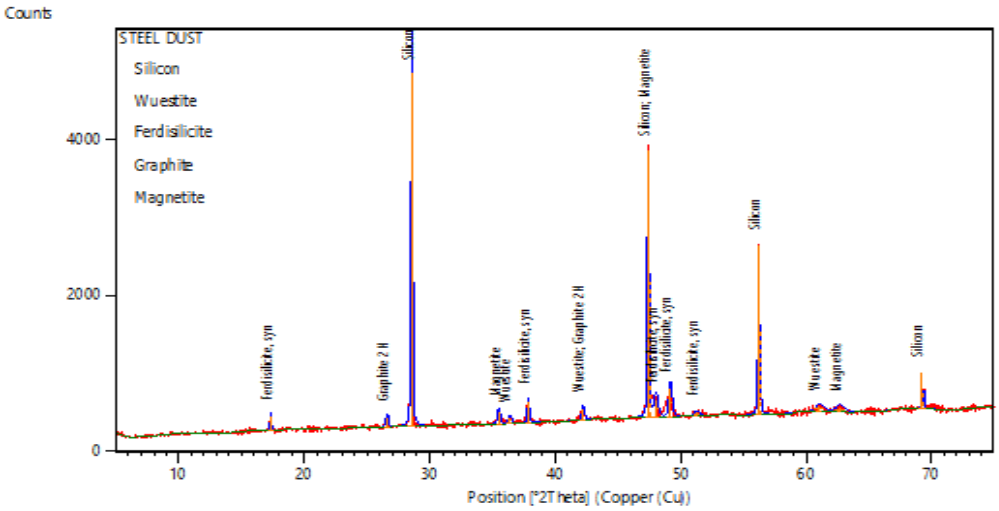

(f)

Fig 5. XRD spectrum of the samples (a) Commercial brake pad (CBP), (b) Graphite (c) Nig. Gum Arabic (d) Quartz (e) Rice husk (f) Steel dust.

3.4 Fourier Transform Infrared (FTIR) Spectrometer Results of the Raw Materials Specimens.

According to the peak values shown in Figure 6a the peaks at 887.28, 1419.66 and 2438.1 cm-^{1} band range show vinylidene (C-H) out of plane bend stresses in the structure. This indicates the presence of the CH molecule called Methylene. The peaks of organic silicone (Si-C-O) stretching at 3691 cm-^{1}indicate the presence of SiO_2 and SiC molecules in the structure Viderscak *et al*. (2022) and Heerok et al. (2021). Figure 6b shows finger print, peaks at 925.86, 1080.17 and 1388.79 cm-^{1} bands in the range of C-H and C-O indicate the presence of cyclohexane ring vibrations (C6-H12), cyclic ethers/large rings (CO_2CH_3) stretch and trimethyl or "tert-butyl" (multilplet) ($C_7H_{18}Sn$) molecules respectively (Oberdörster *et al*., 2005). The peak of 1535.39 and 1666.55 cm^{-1} bands corresponded to C-H-NO and N-H indicates the presence of aromatic nitro compounds ($C_6H_5NO_2$) and amide (NH_2) molecules respectively. The FTIR spectral of gum Arabic is displaced in Figure 6c. The peaks at finger print zone at 786.98, 1080.17, 1211.34, 1319.35 and1411.94 cm-^{1} bands in the range of C-H, C-O, P-O-C, C-N, C-H and C-H indicate the present of 1, 3 distribution (meta) ($C_6H_4N_2O_4$), cyclic ethers, large rings (CO_2CH_3) stretch, aromatic phosphates (PO_4) stretch, aromatic, aromatic tertiary amine (C3H6N) stretch and vinyl (CH_2) inter-plane bend molecules respectively (Lyu *et al*., 2020). According to the peak values of steel particles elements shown in Figure 6d, the peaks at 786.98, 1057.03, 1327.07 and 1411.94 cm-^{1} bands in the range of C-H, C-O, O-H and C-H indicate the presence of (CH) 1, 3 distribution (meta) ($C_6H_4N_2O_4$), alkyl-substituted ether (CHO_2) stretch, phenol or tertiary alcohol (R $_3$COH) bend, Vinyl (C6H6) in-plane bend molecules respectively (Güney *et al*., 2019). The FTIR spectral of quartz is shown in Figure 6e. The peaks of 786.98, 1057.03, 1226.77, 1319.35 and 1411.94 cm-^{1} bands in the range of C-H, C-O, C-C, C-N and C-H indicate the present of 1, 3 – disubstitution (meta) (C-H), alkyl-substituted ether (C – O) stretch, skeletal (C-C) vibrations aromatic tertiary amine (CN) stretch and vinyl (C-H) in-plane bend molecules respectively. The peaks of 1519.96, 1697.41 and 1797.72 cm-^{1} bands in the range of C-H, C-O, C-C, C-N and C-H indicate the present of aromatic nitro compounds ($C_6H_5NO_2$), aromatic combination bands (C_6H_6) and five – membered ring anhydride (C_4O) molecules respectively (Oktem *et al*., 2021). Figure 6f shown the peaks at 794.7, 887.28, 949.01, 1064.74, 1211.34, 1334.78, 1334.78 and 1411.94 cm-^{1} bands in the range of C-H, C-H, C-H, C-O, C-C, C-H, C-H and C-H, indicate the present of 1, 3-disubstitution (meta) (C-H), vinylidence (C-H) out of plane bend, cyclohexane ring vibrations (C_6H_{12}), alkyl-substituted ether C-O stretch, skeletal (C-C) vibrations, methyne (C-H) bend, methyne (C-H) bend, vinyl (C-H) in-plane bend molecules respectively Viderscak *et al*. (2022).

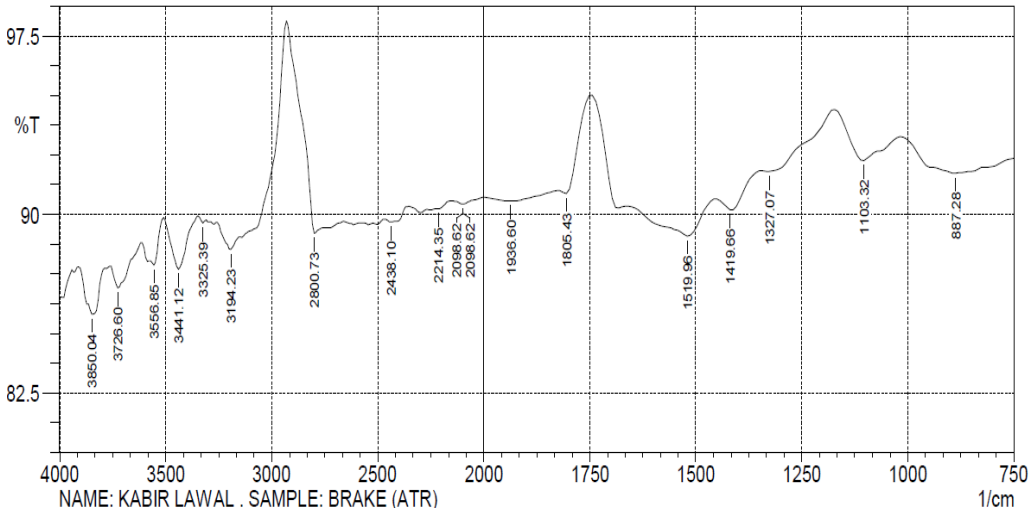
97.5
%T
90
82.5
3850.04
3726.60
3556.85
3441.12
3325.39
3194.23
2800.73
2438.10
2214.35
2098.62
2098.62
1936.60
1805.43
1519.96
1419.66
1327.07
1103.32
887.28
4000
3500
3000
2500
2000
1750
1500
1250
1000
750
NAME: KABIR LAWAL . SAMPLE: BRAKE (ATR)
1/cm

(a)

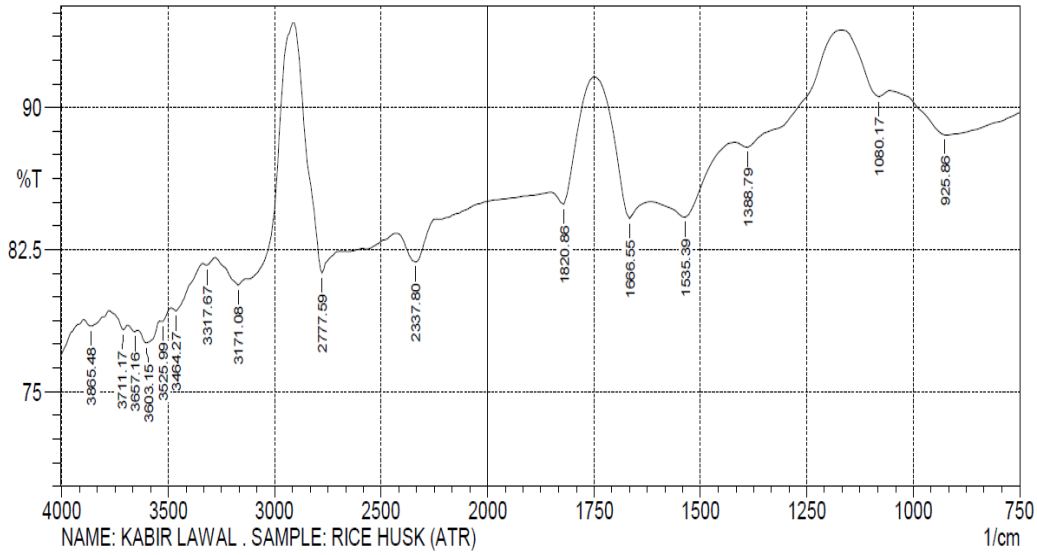
90
%T
82.5
75
3865.48
3711.17
3657.16
3603.15
3525.99
3464.27
3317.67
3171.08
2777.59
2337.80
1820.86
1666.55
1535.39
1388.79
1080.17
925.86
4000
3500
3000
2500
2000
1750
1500
1250
1000
750
NAME: KABIR LAWAL . SAMPLE: RICE HUSK (ATR)
1/cm

(b)

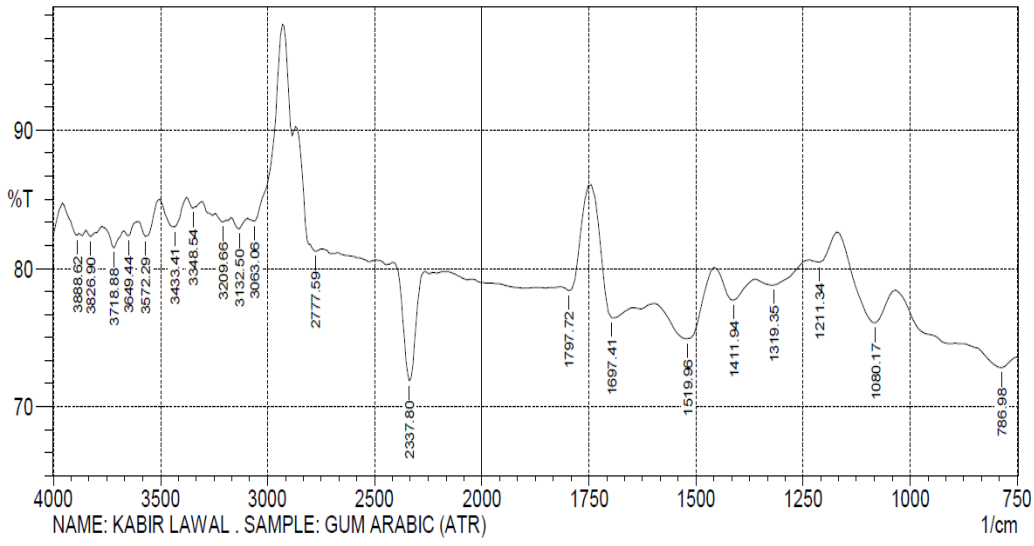
90
%T
80
70
3888.62
3826.90
3718.88
3649.44
3572.29
3433.41
3348.54
3209.66
3132.50
3063.06
2777.59
2337.80
1797.72
1697.41
1519.96
1411.94
1319.35
1211.34
1080.17
786.98
4000
3500
3000
2500
2000
1750
1500
1250
1000
750
NAME: KABIR LAWAL . SAMPLE: GUM ARABIC (ATR)
1/cm

(c)

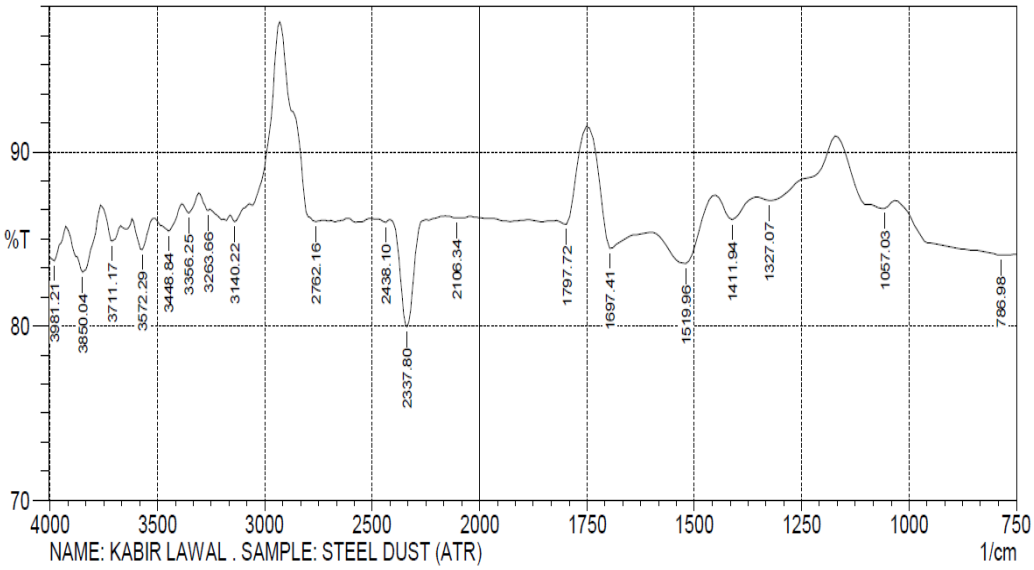

(d)

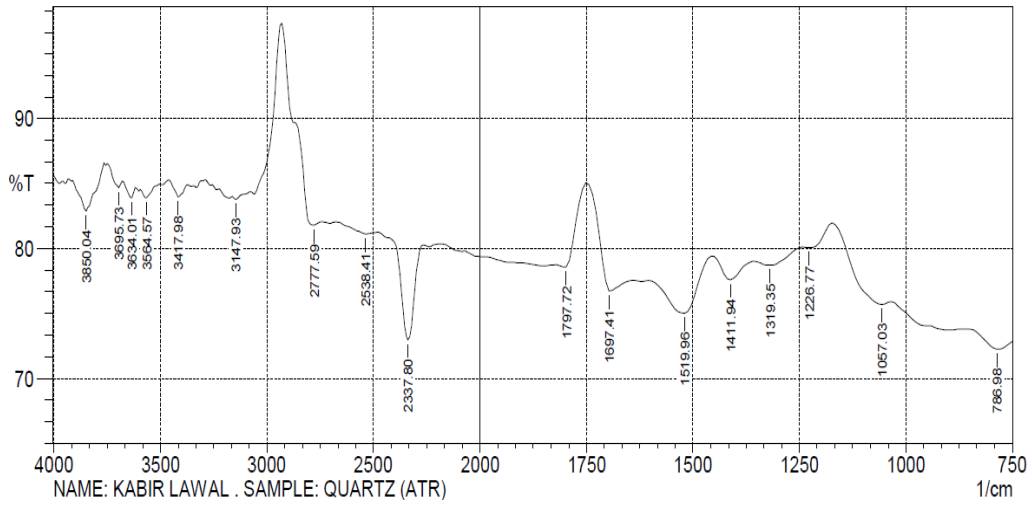

(e)

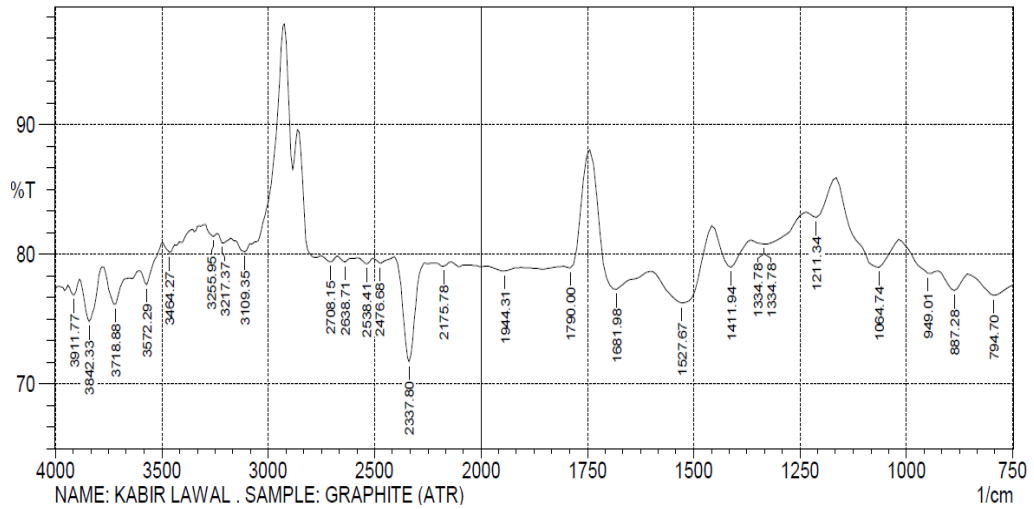

(f)

Fig. 6: FTIR spectrum of the samples (a) Commercial brake pad (b) Rice husk (c) Nig. Gum Arabic (d) Steel dust (e) Quartz (f) Graphite.

4 CONCLUSION

The evaluation of locally available raw materials selected for the development of brake pad were determined and the conclusions are summarized as follows:

1. That values of the necessary parameters obtained from the raw specimens are within the standard requirement for commercial specimen.
2. Chemical composition of all the raw material specimens exhibited most of the elements within the commercials specimen and even have higher wt% of C at Q (76.72)%, S.S (52.07)% and R.H (16.83)%; and Si at G (74.06)%, R.H (49.21)% and G.A (55.52)% compared to the commercial specimen at C (19.51)% and Si (3.58).
3. The spectrum of commercial specimen figure 3a exhibited uniformly distributed of both Barium and Iron in the resin and in comparison to the selected raw materials specimens that gave a better properties of evenly spread of particles in the matrix. Clusters of Magnesium, Aluminum, Silica, Sulfur, phosphorus, yttrium, silver and other are seen at random locations. Except, the surface topography in Figure 3c appeared as irregular rocky surface and clearly different from that of the parent gum Arabic with spherical shape and many dents on the surface. The presence of large and spherical particles of silicon in Figure 3e indicate the rounded nature of quartz particles.
4. The phase purity and crystallinity of the commercial specimen Figure 4a consists of three phase compounds namely Graphite (C), Barite (BaO_4S) and Calcite ($Ca_6\ C_6\ O_{18}$). The three compounds exhibited a sharp and tight peak at 2θ equal 20 and 30^O above 50% intensity, The selected raw materials specimens gave a better optimal sharp peak in Figure 4b at 2θ angle equivalent 27^O with 100% intensity; Figure 4c shows the amorphous nature of Gum Arabic, the maximum intensity was obtained at 2θ angle equal 75^O; Figure 4d exhibited a sharp and tight peak at 2θ equivalent 27^O with 100% intensity; Figure 4e indicate the broad peaks at 2θ equals 75^O and low intensity counts confirmed the RH to be largely amorphous silica. While Figure 4f exhibited a sharp and tight peak at 2θ equals 29^O with 100% intensity appropriately. This result shows that the steel slag is best suitable for thermal, abrasive and hardness enhancement properties in brake pad (Menezes *et al*., 2005).
5. FTIR analysis of the commercial brake pad has a common functional group of 1, 3 – disubstitution (meta) (C-H), alkyl-substituted ether (C – O) stretch, skeletal (C-C) vibrations aromatic tertiary amine (CN) stretch and vinyl (C-H) in-plane bend molecules which also displaced better in the selected materials for new laboratory formulation accentuating that, the materials
6. It can be finally concluded that the locally available raw materials selected has been evaluated with higher quality than the existing properties of the commercial specimen which can definitively leads to its low cost and can be alternative use for production.

REFERENCE

Achebe C.H, Chuckwuneke JL, Amone F.A and Ewulonu CMA Metrofit for abestor based brake pad employing Palm Kernel fibre as the base filler material, journal of material design and application. 7(27) (2018).

Adekunle n. o., ismaila s. o., kuye s. i., adetunji r., olamide o. o. and tomori o. design and production of asbestos free brake pad using cashew nutshell, lautech journal of engineering and technology 17 (1) 2023: 8-17.

Assoc. Prof. Nagwa Ahmed Elzayady, Ramadan Elsoeudy. Microstructure and Wear Mechanisms Investigation on the brake pad. Journal of Materials Research and Technology 11(5).(2021).

Atmika I.K.A, Subagia IDGA, Surata IW and Sutantra I.N Hardness and wear rate of basalt\ alumina in shellfish powder, reinforce phenolic rosin matrix hybrid composite brake lining pads. Material science and engineering 539{2019} 012012

Bekir Guney, Ibrahim Mutlie, Hanifi Kucuksariyildiz. The effect of flame spray coating on the tribological properties of Brake Disc. Journal of Polythenic, Volume: 23 Issue: 3, 755-761(2020).

C.U Ossia, Akuro Big- Alabo. Development and Characterization of Green Automotive Brake pads from waste shells of Giant African Snail (Achatina Achatina L.). International Journal of Advanced Manufacturin Technology. 114, 2887 – 2897(2021).

Dalibor Viderscak, Zdrauko Schauperl, Krunoslau Ormuz, Sanja Solic, Mladen Niksic, Drana Milcoc, Pavao Ormuz. Influence of Brake Pad Properties to Braking Characteristics. Promet-Traffic and transportation vol 34 No 1 (2022)

E.O. Obidiegwu, H.E. Mgbemere,E.F. Ochulor and P.A. Ajayi. Characterization of train brake blocks composite reinforced with aluminium dross. Nigerian Journal of Technology (NIJOTECH) Vol 39 No.4, October 2022.

Elakhame Z. U, Shuaib-Babata, Y. L, Jimoh S. O, Bankole L.K., Ambali, I.O., Production and Characterization of Asbestos Free Brake Pads From Kenaf Fiber Composite, Adeleke University Journal of Engineering and Technology [AUJET] Vol. 3, No 1, 69-78 (2020).

G. Sathyamoorthy, R. Vijay, D. Lenin Singaravelu. Brake friction composite materials: A review on classsifications and influences of friction materials in braking performance with characterizations. Proceeding of the institute of Mechanical Engineers. Part J: Journal of Tribology, Volume 236, Issue 8(2022).

Gai, Peter Friday, Adisa, Ademola Bello, Tokan Aje, Bawa, Mohammed A. Economic viability of basalt based brake pad in Nigeria. International Journal of Engineering Technologies and Management Research. 8(12), 26-41 (2021).

Güney, B., & Mutlu, I. (2019). tribological properties of brake discs coated with cr2o3–40% tio2 by plasma spraying. *Surface Review and Letters*, *26*(10), 1950075.

Hasan Oktem, Ilyas Uygur, Murat Cevik. Design, Construction and Performance of a novel brake pad friction tester. Science direct Volume 115, 2018.

Heerok Hon, Gyeongpil Kim, Junghwan Lee, optimal location of pad for reduction of temperature deviation on brake disc during high-energy braking, journal of mechanical science and technology, 35, 1109-1120 (2021).

J. Abutu, S.A. Lawal, M.B. Ndaliman, R.A. Lafia Araga, O.Adedipe, I.A. Choudhury, Production and characterization of brake pad developed from coconut shell reinforcement material using central composite design, SN Applied Science, (2019) 1:82.

Joseph Abutu, Sunday Albert Lawal, M. B. Ndaliman, Imtiaz Choudhury, Effects of process parameters on the properties of brake pad developed from seashell as reinforcement material using grey relational analysis, Engineering Science and Technology an International Journal 21(4) (2018).

M.I.M. Ahmad, M. Zahri, M.Z. Nuawi, M.F.M. Tabir and M.A. Selamat, Characterization based physical and mechanical properties of brake pad materials for railway vehicle applications, Journal of Materials and Enviroment Science, ISSN: 2028-2508.

Najmuddin M Jamadar and Himmat T Jadhav. A review on braking control and optimization techniques for electric vehicle, Proceedings of the Institution of Mechanical Engineers Part D Journal of Automobile Engineering 235(1):095440702199690 (2021).

Nwogu, C. U and Osarenwinda, J. O. Response Surface Modelling of an Automobile Brake Pad Made from a new- fangled composite material. NIPES Journal of Science and Technology Research 3(3) (2021).

S. S. Lawal, N .A Ademoh, K. C. Bala and A. S. Abdulrahman. A review of the compositions, processing, materials and properties of Brake Pad production. Journal of Physics: Conference series, Volume 1378, Issue 3 (2019).

Yezhe Lyu, Mara Leonard, Jens Wahlstrom, Stefano Gialanella, Ulf Olofsson. Friction wear and airborne particle emission from Cu- free brake materials. Tribology International 141 (2020).

Zeina ammar, hamdy ibrahim, mahmoud adly, ioannis sarris and sherif mehanny. Influence of natural fiber content on the frictional material of brake pads—a review, journal of composite science, and composite 7(1) {2023): 72.

PAPER 135 – A BRIEF REVIEW OF WATER PUMPS CATEGORY AND THEIR POWER SOURCES

M.S. Ayuba[1*], S.S. Lawal[2]

[1,2]Department of Mechanical Engineering, Federal University of Technology, Minna, Minna Nigeria.
[*]Email: damakan2016@gmail.com

ABSTRACT
Water is the driving force of nature, without it, life will mean nothing. Ground water provides about half of the water requirements for human existence. This paper presents a review of different groundwater pump categories and their power sources available from literature. The review covers positive displacement pumps and centrifugal pumps. The power sources for the groundwater pumps reviewed includes manual, electric and fuel sources. The merits and de-merits of the different category of pumps reported by different authors was also highlighted. It was concluded that manually powered borehole water pumps are the cheapest and the most widely acceptable water pumps especially in rural communities of developing countries while the fuel powered pumps is the most expensive power source.

KEYWORDS: *Borehole, Ground water, Manual power, Pumps*

1. INTRODUCTION

Access to portable drinking water and sanitation has been recognised by the United Nations general assembly as a human right and as a necessity for the fulfilment of many other human rights (United Nations, 2010). Water is the lifeblood of all humans, it is the driving force of all nature; without water, life will mean nothing. Millions of people are dying in places where access to portable water supply is a challenge, and these places are especially in rural areas of underdeveloped and developing in nations (WHO, 2022; Cronin*, et al*., 2008). According to estimates, groundwater provides about half of the world's drinking water, and 2.5 billion people rely primarily on this resource to meet their daily water needs (Gronwall and Danert, 2020). Nigeria has grown increasingly reliant on groundwater, which today is thought to supply drinking water to over 100 million people. The popularity of borehole water (a ground water) for drinking water has grown tremendously which were used by 32% of Nigerians in 2011 compared to 10% in 1999 (NBS, 2013). Ground water represents a large portion of water supplies used for different applications. To make quality ground water supply physically available, sufficient in terms of quantity and to guarantee its availability and affordability when required, water lifting devices were invented (Yannopoulos *et al*., 2015).

Water lifting devices have been in existence since around 3000BC (Yannopoulos *et al*., 2015). According to the Mateo-Sagasta *et al.* (2017), Animals muscles were employed to convert their efforts to the energy needed to move the wheels in early devices like water wheels and chutes. Up to the last century, various kinds of lifting devices like indigenous water lifts have been extensively utilised for irrigation and other water lifting purposes. However, Pumps were developed and is still in use today due to advancement in technology and its ease of operation. People in rural area frequently find it difficult to afford a typical water supply that is connected to the grid to meet their water demands, mostly because of the associated cost, lack of appropriate technology and trained technicians. Most times, even if they can afford the initial set up cost of the pump's energy costs keep increasing and, they are usually unable to match these operating costs hence this paper reviews ways to obtain ground water especially using borehole pump for people in these areas lagging behind. different types of pumps and their power sources were considered to address the problems of water shortage in rural areas, at the same time, improvements in the most prominent and conventional type of pump (manually powered borehole water pumps) in the rural areas was discussed to take advantage of appropriate technologies in the water and sanitation sector so as to guide researchers and stakeholders on technical alternatives to water pumping systems and its power sources to ensure the increase in reliable water supply to areas in need with less expenses and energy requirements.

2. PUMPS

A pump is a device that moves liquid from one place to another or from bottom to the top surface, typically by converting mechanical energy into fluid flow energy (Miao *et al.,* 2018). Pumps serve as a great blessing for these people who fervently need assistance in meeting their water needs for irrigation, village water supply and for livestock watering purposes (Bhatia, 2014). They are used in households in many locations to convey water and other liquid.

2.1 Types of pumps

According to Kassab (2017), pumps can be categorised based on the manner in which they add energy to the working fluid into two categories namely:

1. The centrifugal (rotodynamic) pumps
2. Positive displacement pumps (PDP).

While the positive displacement pumps were developed long before the centrifugal pumps, its capacity is not affected by pressure which it operates (Stewart, 2018). The centrifugal pumps was later developed and put into to address the problems of highly transferring viscous fluids which the PDP was faced with. The centrifugal pump is usually affected by pressure and other parameters. These two pump categories are discussed forthwith.

Centrifugal pump. Centrifugal pumps are used for moving liquids by increasing a specific volume flow to a specified pressure level (Gulich, 2014). The centrifugal pumps as shown in figure 2 also called rotodynamic pumps consists of one or more impellers which is completed by blades, which is installed on moving shafts and receives energy from pumps motor and is covered by a casing. They add kinetic energy to the fluid using a spinning impeller where the energized fluid enters the impeller axially and then fluid leaves the impeller with high relative speed and collected in volute or diffuser and then conversion of velocity head to pressure head occurs which is followed by decreasing velocity. These types of pumps can be divided into two namely: centrifugal pumps (axial, radial and mixed) and special effect pumps (jet and airlift pumps). The centrifugal pumps are used where low pressure is required. The benefit of centrifugal pumps is that they are simple to operate, they are long lasting and they are reliable. However, this category of pumps has the disadvantage of susceptibility to cavitation, internal recirculation and, seal or packing wear (Abelin, et al., 2006).

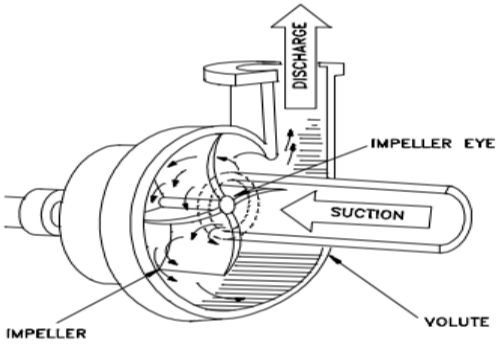

Fig 1: A Centrifugal Pump (United State Department of Energy, 2015)

Positive displacement pump (PDP). Positive displacement pumps add energy to a fluid by applying force to the liquid with a mechanical device such as piston or plunger (Stewart, 2019).The positive displacement pumps as shown in figure 3 pressurises the fluid with a collapsing volume action thereby squeezing and amount of the fluid equal to the displacement volume of the system with each piston stroke or shaft rotation (Abelin, et al., 2006). it uses energy periodically by application of force to one or more movable boundaries of any desired number of enclosed fluids containing volumes resulting in direct increase in pressure up to the value required to move the fluid through the valves or ports into the discharge line. Most manual pumps fall into this category of pumps (Savva and Frenken, 2001). according to (Abelin, et al., 2006)The positive displacement pumps are also divided into two: the reciprocating pumps and the rotary pumps. The reciprocating pumps are those in which linear motion of a piston or plunger in a cylinder causes the displacement, it is consisting of piston, plunger and, diaphragm. While the rotary pumps are those in which the circular motion causes the displacement, it consists of gear, lobe, screw and vane, a disadvantage of the positive displacement pump is that it can potentially over pressurise system piping and some components of the pump and, it requires more system safeguard such as relief valve. The cyclical nature of pumping action can cause fatigue in the components.

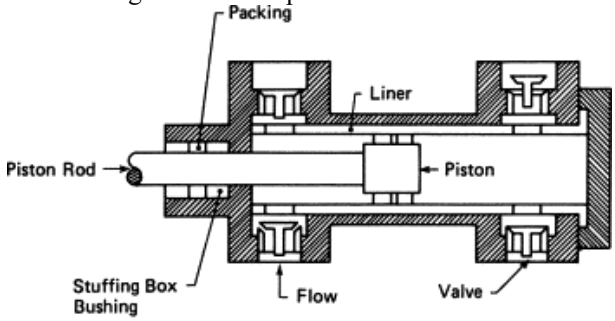

Fig 2: Positive displacement pump (Stewart, 2019).

2.2 Working principle of positive displacement pumps

According to Hussey (2007), positive displacement pumps work using two basic principles of operation, namely:

1. The direct lift principle, where a reciprocating rod, piston and valves lift water and,
2. The screwing principle where a rotating rod and rotor moves water through a screwing process.

In the direct lift principle as shown in figure 5, water is either raised through direct lift or suction. The direct lift pumps are either with pistons pumps or through direct action pumps. In direct lift pump (piston pumps), a piston is raised by a rod which sucks water into the cylinder through an inlet check valve or non-return valve on the upstroke which is opened by the vacuum created. On this stroke, water is discharged from pump head and on the downward stroke, the lower valve closes and water flows through the valve in the piston to the upper part of the cylinder for the process to be repeated. Pumps operating using this principle are generally used in rural communities on deep wells and boreholes where pistons can be installed below the residual water level. They are mostly more suitable than deep well pumps and easy to maintain.

Pumps operating on the suction principle use, a direct lift where the piston is situated above the water level. The pump here is primed to displace air from the pump cylinder, pump column or connecting pipes so that water is forced into the pump cylinder by atmospheric pressure. Suction pumps can either be with lift or force pumps or with diaphragm pumps. In the lift or force pumps, a suction pump with two valves, one-foot valve and one side valve where water does not pass through the piston is used. Water is drawn into the cylinder by a piston through a lower valve as the piston is raised. As the piston descends, it closes the lower valve and forces water out of the pump through a valve and delivery pipe. It is mostly suitable for direct connection to well points due to its similarity with other suction displacement pumps. The suction pump (diaphragm pump) on the other hand uses a flexible diaphragm to provide an alternative to a reciprocating piston to move water.an upward movement of the diaphragm increases the volume of a pump chamber. In the absence of air, water will flow into the chamber through an open valve. A downward movement of the diaphragm will reduce the volume of the pump chamber and consequently the valve closes and water will be expelled through another valve and a discharge pipe (Practical Action Group, 2008). Table 1 shows the merits and demerits of the different category of pumps.

Table 1: Merits and de-merits of different category of pump as reported by authors

Author	Category of Pump	Merits	Demerits
Savva and Frenken, (2001)	Centrifugal pump	Gentle and relatively quiet system.	No suction power
Mobley (2001)	Reciprocating Positive displacement pump	High pressure at outlet	High wear and tear
Islam *et al*. (2007)	Positive displacement pump	Easy to maintain	Stressful to operator
Nwoha (2016)	Centrifugal pump	Can be applied in many fields where high pressure is required.	Difficult to monitor
Bajpal (2018)	Dynamic pumps	Small in size	Cannot be used on highly viscous fluid
Koukouvinis and Gavaises, (2021)	Positive displacement pump	Can control flow rates hence, can be used as metering pumps	It is complex and difficult to maintain
Hellemans (2022)	Positive displacement pumps	Provides a constant flow of fluid at a given speed	Pump gets damaged If pressure relieving devices (PRD) isn't used.

2.3 Power Sources for Pumps

Water pumps are powered by a rotary or reciprocating mechanism that consumes energy while performing mechanical work of moving the fluid from one location to another. (Martin et al., 2011) opines that the optimal type of energy for pumps depends on the long-term relative price of one energy source compared to another. The energy sources required by water pumps thus include:

- Fuel engine power source
- Electrical power source
- Manual power source (Dey, 2022)

The most common source of power for water pumps is fuel and electricity. Diesel (fuel) powered pumps is a commonly used water pumping system in many areas where grid supply is difficult to reach (ISA, 2015). Resources used to generate energy, such as coal, gasoline and natural gas have become environmentally unfriendly, paving the way for alternative energies (Becenen and Eker, 2005). The shortcomings of the fuel source of energy for pumping systems include:

- Fuels sources produces fumes and noise which can cause environmental pollution
- Fuel engines need periodic maintenance to avoid breakdown and also require parts replacement occasionally.
- There is always need to transport fuel to the engines location which could waste time due to the state of roads especially in rural areas.
- Fuels could result in increased cost and spillage of these fuels could leads to land contamination (Eker, 2005).

However, the continuous use of fossil fuels and their negative impact on the environment has made researchers look out for clean sources like solar and manual power. Solar powered pumps are powered by the sun. A photovoltaic (PV) array, also known as solar modules or panels, converts solar energy directly into electricity to power a water pump in a solar-powered water pumping system. water pumps designed specifically designed for solar power and PV modules are available to meet a wide range of head discharge requirements (Wijetunge *et al.,* 2006). The advantages of solar powered pumps are that it is environmentally friendly as there is no pollution caused by them, and cost effective than internal combustion engine powered pumps and is easy to operate, while the disadvantage of solar water pumping systems is their relatively high initial cost when compared to other alternative energy sources. Table 2.0 shows the contribution of authors using different power sources for groundwater pumps. However, manual power is abundant almost everywhere, it is simple, cost effective and can be utilized without negative environmental effects: it is eco-friendly because no waste is produced which makes it a good source of power.

Table 2: contribution of authors using different power sources for groundwater pumps

Author	Power source	Contribution
Savva and Frenken (2001)	Multiple power source	Discussed different power sources for irrigation water pumps
Short and Oldach (2003)	Electrical Solar power	Addressed some issues associated with solar powered water pumping system.
Wijetunge *et al.* (2006)	Electrical Solar power	Evaluated the performance of solar water pumps
Islam *et al*. (2007)	Pedal pump (Manual)	Designed and developed a pedal pump for low lift irrigation purpose
Takacs (2014)	Electrical power	Developed and artificial liquid system using electrical submersible pumps (ESP)
Uche *et al.* (2014)	Dual power	Designed and fabricated a dual powered (manual pedal and DC motor) water pump
Waghmare *et al.* (2015)	Manual power	Designed a model for manually operated spiral tube water wheel pump
Nwoha (2016)	Manual power	Developed a manually operated centrifugal water pump to assist farmers and as a teaching aid for students.
Armanous *et al*. (2016)	Diesel fuel and Solar power	Used the life cycle of diesel fuel and solar pumps to assess the environmental impact of groundwater pumping system
Vartak (2017)	-	Applied the benefits of PD pumps in the chemical industry
Pawlick *et al.* (2018)	Hydraulic pump	Provided a manual that would serve as a guide for ram pump design and installation for use in developing countries.
Koukouvinis and Gavaises (2021)	Fuel(petrol)	Reported the factors that affect performance and cavitation formation in pumps

3. CONCLUSION

A variety of pumps and other water lifting devices are available for transferring water from one point to another, however, the main categories of pumps were considered in this review due to the available literature. From the papers reviewed, the centrifugal pumps appear to be applied in areas involving low viscous fluids while the positive displacement pumps appear to be utilized in areas where fluid flow rates need to be controlled by changing the speed of the pump. The manual power source if improved using the latest available technology is a viable (in terms of cost and ease of operation) power source for groundwater pumps to transfer water to areas not connected to the grid.

REFERENCES

Abelin, S. M., Asdal, R., Beekman, W., Block, H., Bolles, S., Buscher, K., et al. (2006). *Improving Pumping system performance* (Second ed.). Barkekey, Carlifonia: U.S Department of Energy.

Armanous, A., EL-Tahan, A. M., & Negm, A. (2016). Life Cycle Assessment of Dielsel fuel and Solar Pumps in Operation Stage for Rice Cultivation in Tanta, Nile, Delta, Egypt. *Procedia Technology*, 478-485.

Ashiedu, F. I., Nwoha, T. C., & Izelu, C. O. (2016). Design and development of a manually operated pump for Agrarian communities. *International Journal of Current Research, 8*(3), 27378-27382.

Bajpal, P. (2018). Hydraulics. In *Biermanns Handbook of Pulp and Paper* (Third ed., Vol. 2, pp. 455-482). Kanpur, India: Elsevier.

Becenen, I., & Eker, B. (2005). Powering of water pumps by alternative energy sources in Thrace region. *Triakia Journal of Sciences, 3*(7), 28-31.

Bhatia, S. C. (2014). Solar Devices. *Advances in Reneable Energy Syetems*, 733-743.

Cronin, A. A., Shrestha, D., Cornier, N., Abdalla, F., Ezard, N., & Aramburu, C. (2008). A review of water and sanitation provision in refugee camps in association with selected health and nutrition indicators- the need for integrated service provision. *Jounal of wate and health, 6*(1), 1-12.

Dey, A. K. (2022). *Pump: Defination, Types, Advantages, Applications.* India: Learn Mechanical.

Eker, B. (2005). Solar Powered Water Pumping Systems. *Trakia Journal of Sciences, 3*(7), 7-11.

Gronwall, J., & Danert, K. (2020). Regarding Groundwater and Drinking Water Access through a Human Rights Lens: Self-Supply as a Norm. *Water, 12*(2), 419.

Gulich, J. F. (2014). Pump types and performance data. In *Centrifugal pumps* (pp. 43-47). Berlin, Heidelberg: Springer.

Hellemans, M. (2022). Overpressure Scenarios. In *Overpressure Protection in the process industry* (pp. 203-270). Elsevier.

Hussey, S. W. (2007). Pump Technology. In *Water From Sand and Rivers* (pp. 85-99). Loughborough: Water Engineering and Development Centre.

ISA. (2015). *Solar Water Pumping System.* Internations Solar Aliance.

Islam, M. S., Hossain, M. Z., & Abdul-Khair, M. (2007). Design and Devlopment of Pedal Pump for Low-Lift Irrigation. *Journal of Agriculture and Rural Development, 5*(1&2), 116-126.

Kassab, S. K. (2017). *The Pumps, The Heart of the Circuit.* Egypt: Alexandria Univerty.

Koukouvinis, P., & Gavaises, M. (2021). Cavitation in positive displacement pumps. *Cavitationa and Bubble Dynamics*, 303-329.

Martin, D. L., Dorn, T. W., Melvin, S. R., Corr, A. J., & Kranz, W. L. (2011). Evaluating Energy use for Pumping Irrigation Water. *Proccedings of the 23rd annual central plains irrigation conference* (pp. 104-116). Colby, Kansas: Burlinton.

Mateo-Sagasta, J., Zadeh, S. M., & Turral, H. (2017). *Water pollution from agriculture: a global review.* Rome: Food and Agricultural Organization of the United Nations.

Miao, S., Yang, J., Shi, F., Wang, X., & Shi, G. (2018). Research on energy conversion characteristics of pump as turbine. *Advances in Mechanical Engineering, 10*(4), 1-10.

Mobley, K. R. (2001). Vibration Monistory and Analysis. In *Plant Engineers Handbook* (pp. 757,759-811). India: Elsevier.

NBS. (2013). *National Household Survey 2009-2012, Uganda Bureau of Statistics, In JMP. Estimates on the use of water sources and sanitation facilities. Joint monitoring programme of UNICEF and WHO.*

Pawlick, M., Chesser, C., Grguras, C., & Benson, A. (2018, August 16). *Ram pump design and installation manual for use in developing countries.* India.

Practical Action Group. (2008). *Human Powered Hand Pumps for Water Lifting.* Warwickshare: The Schumacher Centre for Technology and Development.

Savva, A., & Frenken, K. (2001). *Irrigation pumping plant.* Harare: Food and Agricultural Organization (FAO).

Short, T. D., & Oldach, R. (2003). Solar Powered Water Pumps: The Past, the Present and the Future? *J.Sol. Eng, 125*(1), 76-82.

Stewart, M. (2018). Reciprocating Pumps. In *Surface Production Operations* (pp. 311-414). Elsevier.

Stewart, M. (2019). *Pump fundamentals.* Gulf Professional Publishing.

Takacs, G. (2014). *Electrical Submersible Pumps (ESP): Manual design operations and maintainance.* Burlington, USA: Gulf Professional Publishers.

Uche , R. R., Oguoma, O., & Godfrey, E. (2014). Design and Fabrication of a Dual Powered Water Pump. *Innovative Systems Design and E ngineering, 5*(6), 7-19.

United Nations. (2010). *Resolution A/RES/64/292.* New York, USA: United Nations General Assembly.

United State Department of Energy. (2015). *Fundamentals of Pumps.* Washinton D.C.

Vartak, A. R. (2017). Positive displacement pumps used in the chemical industry. *Conference seminar by department of Dyestuff Technology* (pp. 1-11). Mumbai: Institute of chemical technology.

Waghmare, S. N., Mestri, M. M., Lavekar, P. V., Misal, T. S., & Nalawade, P. C. (2015). Manually operated spiral tube water pumps. *International Research Journal of Engineering and Technology, 2*(1), 167-169.

WHO. (2022). *Drinking-water.* Manilla: World Health Organization.

Wijetunge, J. J., Chandrarathna, J. T., & Lanka, S. (2006). Performance Evaluation of Solar Water Pumps. *WEDC International Conference , Colombo.*, (pp. 421-424). Colombo, Sri Lanka.

Yannopoulos, S., Lyberatos, G., Theodossiou, N., & Li, W. (2015). Evolution of water lifting devices over the centuries worldwide. *Water, 7*, 5031-5060.

PAPER 136 – CHARACTERIZATION OF PIT SAND OBTAINED FROM SELECTED LOCATIONS IN THE SOUTH WESTERN ZONE OF NIGERIA

S. S. Omopariola[1]* and A. A. Jimoh

[1]Civil Engineering Department, Federal Polytechnic, Ilaro,
[2]Civil Engineering Department, University of Ilorin, Ilorin
*Email: samuel.omopariola@federalpolyilaro.edu.ng

ABSTRACT
Sand is about the commonest fine aggregate available in South Western Nigeria. Of the various types of natural sand, pit sand is the most readily available and most widely used. However, not all available Pit – sand is fit for concreting works. This study focusses on the characterization of Pit sand obtained from selected locations across the South Western zone of the Country. From the values obtained the conformity with relevant standards and the suitability for concreting works was determined. Samples of Pit – sand were collected from three different locations from each of the five states in the zone. Sieve analysis test were carried out on all the samples and the values of fineness modulus (FM), coefficient of uniformity (Cu) and coefficient of curvature (Cc) were determined. Other properties considered are specific gravity (SG), water absorption (WA), and percentage silt content (SC). These values were compared with values stipulated in British standards and other relevant literatures. The range of the values of FM, Cu and Cc SG, WA, and SC are 4.16 – 4.68, 2.63 – 10, and 0.53 – 2.56 2.67 – 2.86, 0.67 – 2.04 and 5.4 – 18.18 respectively. Conclusively, while some of the samples are suitable, some are not.

KEYWORDS: Characterization, Pit – Sand, Selected, Locations

1. INTRODUCTION

Building construction is a major component of the sustainable cities and communities which is one of the seventeen goals of Envision 2030 sustainable development goals. However, the incessant report of building collapse constitutes an impediment to the achievement of this goal if not addressed. Alsadey and Omran (2021) opined that various studies have been carried out that shows that the use of poor-quality material is one of the major factors responsible for the collapse of buildings. Concrete is the most widely used building materials. It consists of water, cement, fine and coarse aggregate. Its failure in service is one of the major factors responsible for building collapse. This is as a result of the use of poor quality constituent materials for its production. Hannah et. al. (2014) stated that the physical and strength properties of concrete are highly dependent on the quality of constituent materials used in its production. Savitha, 2012 affirms that it is necessary to confirm the quality of building materials before their use so as to build strong, durable and cost-effective structures.

Sand is about the commonest fine aggregate available in South – western Nigeria. Orchard, et. al. (1979) described sand as a natural fine aggregate that is used in production of concrete. Of the various types of natural sand, pit sand is the most readily available and most widely used in this part of the country. However, not all available Pit – sand is fit for concreting works. According to Omopariola and Jimoh (2023), the durability and structural performance of concrete is greatly influenced by the properties of sand that is one of its major constituent materials. It should be noted that sand constitutes between 27 to 30 percent of the constituent materials of concrete by volume. Hence it was advocated that good quality sand of known properties should be used I the production for concrete production. Olanitori (2006) opined that the use of sand with high proportion of clay and silt content results in the production of concrete with low compressive strength. Hence it was therefore recommended that relevant tests should be carried out to check the effect of impurities in building sands on performance of concrete.

This study therefore focusses on the characterization of pit sand obtained from selected locations across the South – Western zone of the Country so as to assess its conformity with relevant standard. Laboratory tests were carried out on the various properties of sand that can influence the properties, durability and structural performance of concrete. This will assist in determining its suitability for concreting works.

2. THEORETICAL ANALYSIS

The mathematical principles used in the determination of the various properties of the samples collected from all the locations are stated below.

2.1. Fineness Modulus

The fineness modulus was obtained by divide the cumulative percentage passing the recommended sieve sizes by 100.

2.2. Coefficient of uniformity and Coefficient of Curvature

These were determined by obtaining the values of D10, D30 and D60 from the sieve analysis curve and applying equations (1) and (2) respectively.

$$Cu = \frac{D60}{D30} \quad (1)$$

$$Cc = \frac{(D30)^2}{(D60)(D10)} \quad (2)$$

2.3. Specific gravity

The specific gravity of the samples was determined using Equation (3)

$$Gs = \frac{M2 - M1}{(M4 - M1) - (M3 - M2)} \quad (3)$$

Where; M1 is the weight of pycnometer, M2 is the weight of pycnometer and oven dried sample of sand, M3 is the weight of pycnometer, sand and water and M4 is the weight of pycnometer and water

2.4. Water Absorption

Water Absorption value was obtained using Equation (4)

$$A(\%) = \frac{Wsat - Wdry}{Wsat - Wwet} * 100 \quad (4)$$

Where: A – Water absorption (%), Wsat - weigh of the saturated sample, Wdry- weigh of the dry sample and Wwat– weigh of the saturated sample immersed in water.

2.5. Moisture Content

The value of moisture content for all the samples was determine from Equation (5)

$$M = \frac{M1}{M2} * 100 \quad (5)$$

Where; M is the moisture content (%), M1 is the weight of water from the samples the weight of water from the sample and M2 is the weight of oven dried sample.

2.6 Percentage silt content

Percentage silt content was carried out according to [4] and the result was obtained from the expression

$$V = \frac{V1}{V2} * 100 \quad (6)$$

Where; V is the percentage Silt content, V1 is the volume of the silt layer and V2 is the sand level below the silt

3. MATERIALS AND METHODS

Samples of pit sand were collected from three locations in each of the five states of the South Western States. The states are Ekiti, Ogun, Ondo, Osun ad Oyo States. The locations and their GPS are presented in Table 1

Table 1: Locations, Location codes and GPS of Locations of collection of Sand

STATE	LOCATION CODE	LOCATION	GPS

EKITI	FA 01	Ayedun	7.86°N, 5.52°E
	FA 02	Efon	7.66°N, 4.92°E
	FA 03	Ijan	7.61 °N, 5.50 °E
OGUN	FA 01	Abeokuta	7.16 °N, 3.34 °E
	FA 02	Ishara	6.98°N, 3.68 °E
	FA 03	Ogbere	6.96 °N, 3.20 °E
ONDO	FA 01	Akure	7.25 °N, 5.21 °E
	FA 02	Ondo	7.10 °N, 4.84 °E
	FA 03	Owo	7.20 °N, 5.59 °E
OSUN	FA 01	Ede	7.73 °N, 4.43 °E
	FA 02	Ikire	7.37 °N, 4.19 °E
	FA 03	Ipetu	7.82 °N, 4.74 °E
OYO	FA 01	Ibadan	7.40 °N, 3.92 °E
	FA 02	Igboora	7.43°N, 3.29 °E
	FA 03	Iseyin	7.97 °N, 3.60 °E

3.1. Sieve Analysis of Fine Aggregate

Samples of sand obtained from all the locations were oven dried to constant weight at about 110 ± 5°C I accordance with BS EN 933 – 1: 1997. The oven dried samples were then placed a set of standard 8-inch sieve were arranged in descending order of sizes from top down and the lid of the sieve was closed. The set of sieves and then placed in a mechanical shaker which was made to run for about 10 minutes. Separate weighing of materials retained on any one screen was done for each of the sieve sizes and recorded. Cumulative weight retained each of the sieves were converted into percentages of the total weight. Finally, the cumulative percentage of samples passing each sieve size was obtained and the result was plotted in the sieve analysis graph.

3.2. Specific Gravity and Water Absorption of Fine Aggregate

The test was carried out in accordance with BS EN 1097 – 6: 2000. 500g of the sample was placed in a pycnometer was partially filled with water. The pycnometer was then filled to approximately 90% of capacity and placed in a vacuum flask to eliminate air bubbles. The pycnometer was then filled with water to full capacity. The total weight of water introduced into the glass graduate was determined and the sample was then removed from the pycnometer and dried in the oven to a constant weight at 110 ± 5°C. It was allowed to cool in air at room temperature for 1-2 hours and then weighed to the nearest 0.1g. The weight of the pycnometer filled to its calibration capacity with water was determined and the specific gravity and absorption was then calculated using equation and 3 and 4 respectively.

3.4 Moisture Content

The container was first dried and weighed to the nearest 0.1g and the weight was recorded as M1. The samples then scooped into the container and the weight of the container with the sample were obtained to the nearest 0.1g and recorded as M2. The container and the samples were placed in an oven and dried to constant weight at a temperature of 105+/-5°C for a period of 24 hours as stipulated in BS 812:109 1990. The container and the oven dried sample were then removed from the oven and allowed to cool for about 1hour. The container and the oven dried sample were weighed again to the nearest 0.1 and the weight was recorded as M3. The moisture content of the samples were the calculated using equation

4.4 Percentage Silt Content

1% solution of salt was prepared and poured into the 250ml measuring cylinder up to the 50ml as stipulated in B.S. 1881 – 1:1975. This was followed by the addition of the sample of sand to the solution up to the 100ml line of the cylinder I the first instance and then increased to the 150ml line. The cylinder was shaken thoroughly and left to settle for 3 hours. Measurement of the silt layer was obtained and recorded as V1, while the sand level below the silt was recorded as V2.

4 RESULTS AND DISCUSSION

From the sieve analysis carried out on all the samples, the following discoveries were made:

1. The percentage passing the 4.75mm sieve for the samples from all the three locations (Ayedun, Efon and Ijan) in Ekiti State falls below the stipulated lower limit of 89% (see Table 2). Furthermore, the percentage passing the 2.36mm sieve for Efon and Ijan also falls below the lower limit of 60%. However, the percentage

passing the other sieve sizes are within the lower and upper limits and falls into class C as stated in Table 4 of BS 882:1992 (see Table 2).

2. In the case of samples from Ogun State, only the sample from Abeokuta falls short of the grading limit of 60% in sieve size of 2.36. Samples from the two other locations Ishara and Ogbere are within the stipulated lower and upper limits in all the sieve sizes. Additionally, they satisfy the grading limits for class C.
3. Samples from all the three locations in Ondo State (Akure, Ondo and Owo) had lower percentage passing the 4.75mm sieve, additionally, samples from Akure and Ondo also had lower percentages in 2.36mm sieve.
4. Result of the sieve analysis of samples from Osun State indicates that the percentage passing the 4.75 and 2.36mm sieve sizes are lower than89% stated in BS 882:1990. However, they all conform to the overall grading limits in the rest of the sieve sizes.
5. The sample from Ibadan in Oyo State has a lower value of percentage passing the 4.75mm sieve size. It however conforms to the required specification and falls within the limit of class C in the rest of the sieve sizes. Samples from the remaining 2 locations are within the overall limits in all the sieve sizes. Additionally, they both are within the limits of class C in all the sieve sizes.

From all of the above, it ca be inferred that the lower values of percentage passing any of the sieve sizes implies that they are coarser materials. This does not prevent their use in concreting works. Moreover, the footnote of Table 4 BS 882:1990 states that where sands do not comply with values in the Table, an agreed grading envelope may also be used provided that the supplier can satisfy the purchaser that such materials can produce concrete of the required quality.

Table 2: Grading Limits for Fine Aggregates

Sieve Size	Percentage by mass passing BS sieves			
	Overall Limits	Additional Limits for grading		
		C	M	F
10.00mm	100	—	—	—
5.0mm	89 to 100	—	—	—
2.36mm	60 to 100	60 to 100	65 to 100	80 to 100
1.18mm	30 to 100	30 to 90	45 to 100	70 to 100
600 µm	15 to 100	15 to 54	25 to 80	55 to 100
300 µm	5 to 70	5 to 40	5 to 48	5 to 70
150 µm	0 to 15	—	—	—

NOTE Individual sands may comply with the requirements of more than one grading. Alternatively, some sands may satisfy the overall limits but may not fall within any one of the additional limits C, M or F. In this case and where sands do not comply with Table 4 an agreed grading envelope may also be used provided that the supplier can satisfy the purchaser that such materials can produce concrete of the required quality. an Increased to 20 % for crushed rock fines, except when they are used for heavy duty floors.

Source Table 4 BS 882:1992

Table 3: Table of values of Sieve Analysis of Samples of Sand from Ekiti State

Sieve Sizes	Lower limit	EKS01	EKS02	EKS03	Upper Limit

9.5	100	100	100	100	100
4.75	89	82	84	84	100
2.36	60	66	42	54	100
1.18	30	63	38	52	100
0.6	15	20	17	16	100
0.3	5	19	16	14	70
0.15	1	7	6	5	15

Table 4: Table of values of Sieve Analysis of Samples of Sand from Ogun State

Sieve Sizes	Lower limit	0GS01	0GS02	OGS03	Upper Limit
9.5	100	100	100	100	100
4.75	89	91	90	97	100
2.36	60	54	69	96	100
1.18	30	51	49	87	100
0.6	15	17	20	51	100
0.3	5	16	18	46	70
0.15	1	5	6	3	15

Table 5: Table of values of Sieve Analysis of Samples of Sand from Ondo State

Sieve Sizes	Lower limit	ODS01	ODS02	ODS03	Upper Limit
9.5	100	100	100	100	100
4.75	89	60	87	88	100
2.36	60	50	51	73	100
1.18	30	48	49	33	100
0.6	15	33	21	18	100
0.3	5	31	20	12	70
0.15	1	8	6	1	15

Table 6: Table of values of Sieve Analysis of Samples of Sand from Osun State

Sieve Sizes	Lower limit	OSS01	OSS02	OSS3	Upper Limit
9.5	100	100	100	100	100
4.75	89	66	82	75	100
2.36	60	54	53	49	100
1.18	30	51	52	46	100
0.6	15	17	17	22	100
0.3	5	15	16	7	70
0.15	1	8	5	1	15

Table 7: Table of values of Sieve Analysis of Samples of Sand from Oyo State

Sieve Sizes	Lower limit	OYS01	OYS02	OYS3	Upper Limit
9.5	100	100	100	100	100
4.75	89	85	93	90	100
2.36	60	79	88	65	100
1.18	30	77	85	60	100
0.6	15	22	22	36	100
0.3	5	21	21	17	70
0.15	1	6	8	14	15

4.2. Fineness Modulus

The fineness modulus is a representative of the mean size of particles of sand. The range of values according to Anupoju (2016) is 2.2 – 3.2. From 2.2 to 2.6 is classified as fine sand, 2.6 – 2.9 as medium and 2.9 – 3.2 as coarse sand. From the results presented in Table 8, it follows that only the sample from Ogbere in Ogun State is slightly lower that the code's requirement. All others are okay and can be classified as coarse sand.

4.3. Coefficient of Uniformity and Coefficient of Curvature

According to Nenu (2019), the Coefficient of Uniformity (Cu) and Coefficient of Curvature (Cc) are parameters used to determine the grading characteristics of sand. Cu values between 4 and 6 are classified as well graded, while less than 4 are regarded as uniformly graded or poorly graded. Higher values are indications of materials with different size ranges. From the result presented in Table 8, samples from Owo in Ondo State, Ipetu in Osun State, Ibadan and Igboora in Oyo State are poorly graded while all others are well graded. It was also stated that Cc values of 1 – 3 implies a well graded sand. From the results in Table 8, samples from Akure in Ondo state, Ibadan, Igboora and Iseyin all in Oyo State have Cc values of less than 1, hence they can be classified as poorly graded. However all other samples have their values within the range of 1 and 3 and ca thus be classified as well graded.

Table 8: Table of Value of Fineness Modulus, Coefficient of Uniformity and Coefficient of Curvature of Pit Sand from all locations.

PROPERTIES	FINENESS MODULUS			COEFFICIENT OF UNIFORMITY			COEFFICIENT OF CURVATURE		
LOCATION	FA01	FA02	FA03	FA01	FA02	FA03	FA01	FA02	FA03
EKITI	4.19	4.46	4.37	5	5	5.6	1.8	1.25	1.21
OGUN	4.23	3.23	2.16	6.5	5.5	4.67	2.16	2.56	1.52
ONDO	4.53	4.28	3.34	10	4.83	2.63	0.32	1.13	2.38
OSUN	4.68	4.4	4.11	5	4.67	3.33	0.8	0.86	0.53
OYO	3.98	3.72	3.77	3.6	3.6	6.67	1.6	1.6	1.67

4.4 Specific Gravity

The values of the specific gravity of the samples from all the locations as indicated in Table 9 are between 2.67 and 2.86. This is within the range of values specified in BS 882:1990 and some other literatures. This implies that the specific gravity of all the samples are okay ad fit for use as concreting materials. The value of specific gravity of aggregates is of paramount importance ad very useful I concrete mix design (Bahabri, 2016). It is also an indication of the strength as well as the quality of the material.

4.5 Water Absorption

The water absorption values of all the samples presented in Table 9 are from 0.67 – 2.04 %. The specification in BS 8007 is 3%, while BS 6349 specifies maximum of 2% in case of critical conditions. It implies that the values of water absorption for all the samples are ok even for critical conditions.

4.6 Moisture Content

The recommended value of moisture content of fine aggregate according to ASTM C 128 – 15 is 0.2 – 2% with proviso that sand can contribute up to 6% free moisture. The range of values of moisture content for all the samples in the study are between 0.45 and 5%. This implies that the moisture content of all the samples are okay for concreting. It should be noted that the need for the determination of moisture content in sand is so as to make provision for the quantity of water required to maintain the water cement ratio.

4.7 Percentage Silt Content

The presence of high percentage of silt in sand results in the reduction of concrete strength. The maximum amount of silt require in sand for concreting work is 8%. Results from the study shows that only the samples from Ijan in Ekiti State, Obere in Ogun State and Ibadan in Oyo state meet this conditions. Samples from all other locations possess higher values.

TABLE 9: Table of Values of Specific Gravity, Water Absorption, Moisture Content and Percentage Silt Content of Pit Sand from all the locations.

PROPERTIES	SPECIFIC GRAVITY			WATER ABSORPTION			MOISTURE CONTENT			PERCENTAGE SILT CONNTENT		
LOCATION	FA01	FA02	FA03	FA01	FA02	FA03	FA01	FA02	FA03	FA01	FA02	FA03
EKITI	2.81	2.78	2.84	0.67	1.01	1.01	1.12	5	1.06	11.11	8.89	5.35
OGUN	2.67	2.86	2.71	0.67	1.26	0.98	5	0.75	2.5	8.89	18.18	5.4
ONDO	2.86	2.83	2.81	2.04	1.35	2.04	1.32	1.12	1.35	11.32	9.62	10.91
OSUN	2.75	2.69	2.72	1.35	0.67	1.69	1.44	1.12	0.3	10.42	10	12
OYO	2.85	2.73	2.77	0.67	1.01	1.01	3.17	0.45	1.44	8	16	8.33

5. CONCLUSION

In conclusion, the result of the sieve analysis from which grading parameters such as the coefficient of uniformity and coefficient of curvature indicates that samples from some locations are poorly graded. Sands from such locations by combining samples from different locations at appropriate proportions to obtain desired gradation. The values of specific gravity, water absorption and moisture content for all the samples indicate that all of them are suitable for concrete production. However, the major set – back to the use of these samples is the presence of high percentage of silt.

ACKNOWLEDGEMENT

The assistance rendered by Messrs Olaseinde Adeyanju and Femi Solomon in the collection of samples for the research work is duly acknowledged

REFERENCES

1. Alsadey Salahaldein and Omran Abdelnaser , 2021, Effect of the Type of Sand on the Properties of Concrete, Journal of Engineering and Applied Scence, 16 (3): 111-113, 2021
2. Anupoju Sadanandam, (2016), https://theconstructor.org.finenessmodulus Accessed on 08/05/2023
3. ASTM C128-15, Standard Test Method for Relative Density (Specific Gravity) and Absorption of Fine Aggregate
4. Bahabri A. A., (2016), Textural Characteristics of Fine Aggregate Efficiency on Concrete Strength,
i. *American Journal of Materials Science*, 6(3): 73-78, 2016
5. BS 812-109: 1990: "Methods for determination of moisture content", British Standards Institution London.
6. BS EN 882: 2004: Specification for aggregates from natural sources for concrete, British Standards Institution London.
7. BS EN 933 – 1:1997, Test for Geometrical Properties of Aggregates "Determination of Particle Size Distribution – Sieving Method", British Standards Institution London.
8. BS EN 1097 – 6: 2020, Test Method for Density, Relative Density (Specific Gravity), and Absorption of Fine Aggregate.
9. BS 1881-120 (1983) Testing Concrete Method for Determination of Compressice Strength of Concrete Cores. British Standards Institute, London.
10. BS 6349-1-4-2021 pdf free download.Maritime works Part 1-4: General—Code of practice for materials
11. BS 8007:1987, *Code of practice for the design of concrete structures for retaining aqueous liquids*
12. Hannah Nyambara Ngugi, Raphael Ndisya Mutuku, Zachary Abiero Gariy, 2014, Effects of Sand Quality on Compressive Strength of Concrete: A Case of Nairobi County and Its Environs, Kenya, Open Journal of Civil Engineering, Vol.4 No.3(2014),
13. Nenu S. K. https://theconstructor.org.uniformitycoefficient.com Accessed on 08/05/2023
14. Olanitori, L.M., 2006. Mitigating the effect of clay content of sand on concrete strength. Proceedings of the 31st Conference on Our World in Concrete and Structures, August 16-17, 2006, CI-Premier PTE Ltd,

Singapore, pp: 15-17.

15. Omopariola And Jimoh (2023), The Evaluation of Engineering Properties of Some SelectedAggregates in South Western Nigeria for Concrete Production, Nigerian Journal of Technology (NIJOTECH), Vol. 42, No. 1, March, 2023, pp.92 - 98
16. Orchard, D.F., A. Curran and R. Hearne, 1979. Concrete Technology-Volume 1-Properties of Materials. 4th Edn., Applied Science Publishers Ltd., London, England, UK.,
17. Savitha, R., 2012. Importance of quality assurance of materials for construction work. Building Materials Research and Testing Division, National Building Research Organization, Colombo, Sri Lanka.

PAPER 137 – COMPUTATIONAL DEVELOPMENT AND AERODYNAMIC ANALYSIS OF A SINGLE-STAGE LAUNCH VEHICLE TO SUBDUE POST-LAUNCH RISK

A. Jinadu[1*], A. M. Oluwatofunmi[1], O. A. Olayemi[1], T. Dmytro[2], V. Koloskov[3]

[1]Department of Aeronautical and Astronautical Engineering, Faculty of Engineering, Kwara State University, Kwara State, Nigeria.
[2]Nanjing University of Aeronautics and Astronautics, Nanjing, China.
[3]National University of Civil Defence of Ukraine, Ukraine.
[*]Email: abdulbaqi.jinadu@kwasu.edu.ng

ABSTRACT
The aerospace industry has prioritized reducing fatalities and failure rates after the launch of a vehicle resulting from system or engine failure. Rocketry has been difficult over the years, and international players in the industry are constantly attempting to learn from any failures. This paper aims to decrease material, resource, and payload waste while ensuring crew safety by focusing on the computational modelling and aerodynamic analysis of a single-stage launch vehicle. CATIA V5 was utilized to create the computational model of a triggered nose cone rocket booster while ANSYS was used to analyse the trigger nose cone at different angles of attack and determine how the trigger nose cone will behave in case of emergencies such as system or engine failure, which could lead to the complete explosion of the launch vehicle. Based on the current findings, the trigger nose cone is not in the safe zone when ejected at an angle of attack greater than 20° due to the shockwave's effect on its surface when ejected from the main body of the launch vehicle.

KEYWORDS: Post-launch, Engine failure, Single-stage launch vehicle, Trigger nose cone, Combustion chamber.

1. INTRODUCTION

The mission of humans and payloads to space, though quite involving, has been a success story in the recent and distant past. In earlier years, there was little need for such skills in spaceflight. This changed dramatically in 1986 with the loss of the Space Shuttle Challenger and was perpetuated by the loss of Space Shuttle Columbia in 2003 (Banks et. Al 2019). However, a lot of failures in the journey of man and payload to space via launch vehicles, space shuttles, and spaceships, has been recorded in the past which have resulted in fatalities of the crew and other things on board, wastage of resources, time, and capital spent on building each of the launch vehicles that failed. Comparing the costs of different launch vehicles, the possibility of the risk of failure is assumed to be accounted for by the cost of insurance (Parkinson, 1999).
According to Chang (1996), The failure of a Launch Vehicle is attributed to associated problems such as structures and propulsion. It was also brought to notice by Gorbenko et al. (2009) in a study of Orbital Carrier Rocket and Spacecraft Failure: 2000-2009 that the probability of fatal and partial spacecraft failure and mechanical damage increased from 0.059 to 0.073.
Karacalioglu & Bukley (2015) cited that some of these failures are due to system failures. Fernández et al. (2022) noted that trajectory and attitude control and the separation systems account for over a 90% of space launch vehicle failures. System failure may occur before, during, or after the launch of any launch vehicle, such as a single-stage, two-stage, or three-stage launch vehicle. Failure could happen during the separation of the nose cone of a single stage to orbit (SSTO) launch vehicle or when each stage detaches itself from the preliminary stage of such a launch vehicle, which could lead to loss of control and navigation of the launch vehicle by the ground station or astronaut on board. In a time in which a significant number of launch vehicles are being developed, boosted by numerous new space actors demanding cheaper access to space, the need to ensure the reliability of launch vehicles and the performance of a successful Post-Mission Disposal (PMD) is undeniable (Fernández et al. 2022).
Furthermore, failures as a result of human error, such as with Electron Szondy, (2017), Falcon 9 etc., may occur during the preliminary stage of the launch vehicle's design, which may not only lead to the launch vehicle's failure but also affect things present on board such a launch. Wrong input of data by the ground station can also lead to the failure of the launch vehicle, which may lead to the malfunction of the launch vehicle's peripheral systems such as the propulsion system, control system, and re-entry system, which could jeopardize the survivability of the crew on board.
Other failures, such as Astra's Launch Vehicle 0010 and Rocket Lab (2021) may be due to engine malfunction. Such a failure makes it impossible for the launch vehicle to be successful in its mission. This failure may lead to the failure of the propulsion system because of the failure in the combustion process and cycle that occur between LOX (liquid oxygen) and LH2 (liquid hydrogen) or kerosene or any kind of liquid fuel-based combustion system,

or because of the failure that occurs in the ignition process of the solid fuel system, which leaves no space for the crew and things present on board to escape from such a launch vehicle.
On Analysis of Space Launch Vehicle Failures and Post Mission Disposal Statistics, most of these failures are not limited to but mostly occur within the propulsion, separation, trajectory and, attitude control systems (Ayala et al., 2022). Based on the conclusion of the research, these three subsystems alone account for 90% of launch failures, with 54% corresponding to the propulsion system. Mathematical model approach has helped to improve the level of safety (Melnikov & Davydova 2018).

4. THEORETICAL ANALYSIS

2.1 Six Degrees of freedom (6DOF) solver theory

The six-degree of freedom solver in ANSYS Fluent uses the object's forces and moments to compute the translational and angular motion of the center of gravity of an object. The governing equation for the translational motion of the center of gravity is solved in the inertial coordinate system.

$$\dot{\overrightarrow{v_G}} = \frac{1}{m}\sum \overrightarrow{f_G} \tag{1}$$

where $\overrightarrow{v_G}$ is the translational motion of the center of gravity, m is the mass, and $\overrightarrow{f_G}$ is the force vector due to gravity. The angular motion of the object, $\overrightarrow{\omega_B}$, is more easily computed using body coordinates:

$$\dot{\overrightarrow{\omega_B}} = L^{-1}\left(\sum \overrightarrow{M_B} - \overrightarrow{\omega_B} \times L\overrightarrow{\omega_B}\right) \tag{2}$$

where L is the inertia tensor, $\overrightarrow{M_B}$ is the moment vector of the body, and $\overrightarrow{\omega_B}$ is the rigid body angular velocity vector. The moments are transformed from inertial to body coordinates using equation (3)

$$\overrightarrow{M_B} = R\overrightarrow{M_G} \tag{3}$$

where R represents the following transformation matrix:

$$\begin{matrix} C_\theta C_\varphi & C_\theta C_\varphi & -S_\theta \\ S_\emptyset S_\theta C_\varphi - C_\emptyset S_\varphi & S_\emptyset S_\theta S_\varphi + C_\emptyset C_\varphi & S_\emptyset C_\theta \\ C_\emptyset S_\theta C_\varphi + S_\emptyset S_\varphi & C_\emptyset S_\theta C_\varphi - S_\emptyset C_\varphi & S_\emptyset C_\theta \end{matrix} \tag{4}$$

where in generic terms, $C_x = \cos(x)$ *and* $S_x = \sin(x)$. The angles $\emptyset, \theta$ *and* φ are Euler angles.
The angular and translational velocities are used in the dynamic mesh calculations to update the rigid body position (Ahamed et al., 2014).

2.2 Rocket Equation

The change in mass of launch vehicle as it accelerates is given by Equation (5) (Lepsch Jr et al., 1995).

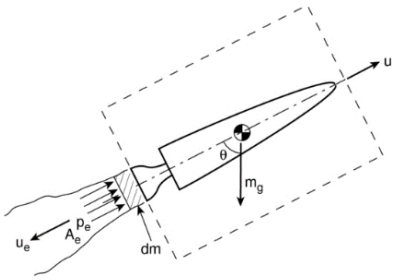

Fig 1. Schematic for application of the momentum theorem (Tartabini et al., 2015)

As shown in Figure 1, by considering a small mass, dm, expelled from the trigger nose cone during time dt, the initial momentum of the mass in the control volume is, $m\text{-}v.du$. The final momentum of mass in the control volume is

$$(M_v - dm)(u + du) + (u - u_c)dm = m_v u + m_v du - udm - dudm + udm - u_c dm \tag{5}$$

The change in momentum during the interval dt is

$$\text{momentum}_{\text{final}} - \text{momentum}_{\text{initial}} = m_v du - u_e du \quad (6)$$

The net force acting on the system is given by Equation (7)

$$\sum F = (p_e - p_o)A_e - D - mg\cos\theta. \quad (7)$$

Applying conservation of momentum, the resulting impulse, $\sum Fdt$, must balance the change in momentum of the system:

$$m_v du - dmu_e = \left[(p_e - p_o)A_e - D - m_v g\cos\theta\right]dt \quad (8)$$

Then since

$$dm = \dot{m}dt = -\frac{dm_v}{dt}dt, \quad (9)$$

where $\dot{m}$ is the propellant mass flow rate, the equation reads:

$$m_v du = \left[(p_e - p_o)A_e + \dot{m}u_e - D - m_v g\cos\theta\right]dt \quad (10)$$

For $p_e = p_o$,

$$du = -\frac{u_e dm_v}{m_v} - \frac{D}{m_v}dt - g\cos\theta dt \quad (11)$$

Eq. (11) is known as the Rocket/launch vehicle Equation. It can be integrated as a function of time to determine the velocity of the rocket/launch vehicle.

If $u_e = constant$, assuming that at $t = 0, u = 0,$ neglecting drag, and assuming $\theta = 0$, then the rocket equation can be simplified as

$$du = -u_e\frac{dm_v}{m_v} - gdt, \quad (12)$$

which can be integrated to give

$$u = -u_e In\left(\frac{m_v}{m_{vo}}\right) - gt, \quad (13)$$

where m_{vo} is the initial mass of the rocket/launch vehicle. Equation (12) can be re-written as

$$u = g\left[In\left(\frac{m_v}{m_{vo}}\right) - t\right], \quad (14)$$

This equation (14) can be likened to the Breguet Range Equation for aircraft. It shows the overall dependence of the primary performance parameter for a rocket (velocity, u) on propulsion system efficiency (Isp) and structural design.

Assuming the rate of fuel consumption is constant, the mass of the rocket or launch vehicle varies over time as

$$m_v(t) = m_{vo} - (m_{vo} - m_{v,final})\frac{t}{t_b} \quad (15)$$

where t_b is the time at which all propellants are used. This expression can be substituted into the equation for velocity and then integrated to find the height at the end of burnout:

$$h_b = \int_0^{t_b} udt, \quad (16)$$

which for a single-stage sounding rocket with no drag and constant gravity yields

$$h_b = g\left[-t_b Isp\frac{In\left(\frac{m_{vo}}{m_{v,final}}\right)}{\left(\frac{m_{vo}}{m_{v,final}} - 1\right)} + t_b Isp - \frac{1}{2}{t_b}^2\right] \quad (17)$$

The final height of the rocket can then be determined by equating the kinetic energy of the vehicle at burnout with its change in potential energy between that point and the maximum height.

5. MATERIALS AND METHODS

The computational setup for the aerodynamics analysis in this experiment was carried out using Ansys Fluid Fluent. Given the fluidic nature of the analysis, a suitable computational domain was constructed to ensure accurate results. The adopted computational domain, mesh, and boundary conditions are illustrated in figure 2 below.

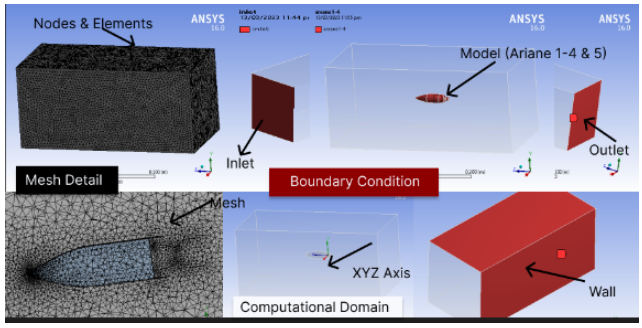

Fig 2: Computational domain, mesh and boundary condition (Author).

The computational domain was constructed in the form of a wedge geometry, representing a 14.940° section of the corresponding 3D domain. The property volume of the computational model is 0.1642 m^3, with a bounding box measuring 0.225 m in length on the X and Y axis and 0.48753 m in length on the Z axis.
To ensure reliable results, a uniform computational mesh was used. The Ariane 5 prototype's mesh consists of 29,299 triangular nodes and 160,880 elements. The Ariane 1-4 series prototype's mesh consists of 92,207 triangular nodes and 374,333 elements.
This made it possible to accurately analyze the aerodynamics of the prototypes under consideration. In addition, the initial conditions used for the validation case were summarized in Table 1, providing a comprehensive overview of the experimental conditions and results.

Table 1: Input Parameters (validation case)

Parameter	Value	Units
Fluid Density	1.225	Kg/m^3
Temperature	288.16	K
Viscosity	1.7894e-05	Kg/m^{-s}
Specific Heats Ratio	1.4	-

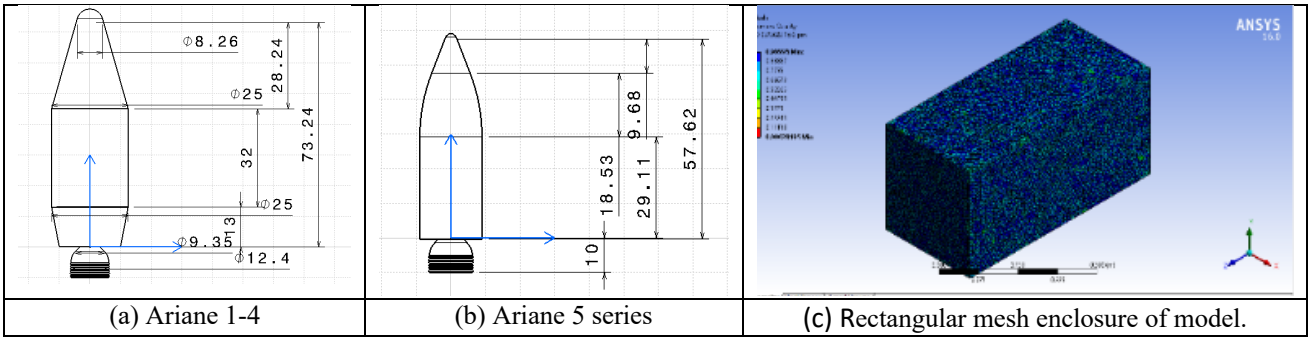

(a) Ariane 1-4 | (b) Ariane 5 series | (c) Rectangular mesh enclosure of model.

Fig 3(a-c): Schematic diagram of Ariane 1-4 and Ariane 5 series and the mesh of a rectangular enclosure around the trigger nose cone model on ANSYS (Author)

The schematic diagram of the models and its rectangular mesh are seen in Figure 3(a-c) above. The tank, nozzle system, combustion system, and trigger nose cone were modeled using CATIA. The choice of CATIA was based on its interface, which supports computational modeling, while Ansys was used for Computational Aerodynamics analysis, as it has a suitable interface for this purpose. Figure 4 shows the meshing and boundary conditions applied using ANSYS Fluid Flow (Fluent).

6. RESULTS AND DISCUSSION

The stress impact of air velocity at Mach 0.6 is shown in figure 4(a-n) after some simulations of the proposed CAD models using the ANSYS CFD FLUENT workbench to carry out the aerodynamics analysis of the model to know how they react at different angles of attack.

4.1 Fluid Flow Fluent

When a trigger nose cone is discharged from a launch vehicle for an emergency case, the effect of drag force is plotted using the ANSYS Fluid Fluent. Its response to its surrounding medium while ejecting and re-landing in a secure environment at Mach 0.6 will be observed from various angles of attack.

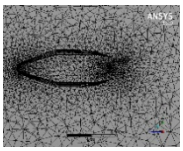

a) (Ariane 1-4 series) at 0º angle of attack

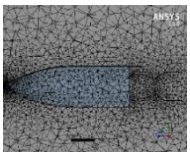

(b) (Ariane 5) at 0º angle of attack

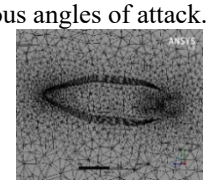

c) (Ariane 1-4 series) at 5º angle of attack

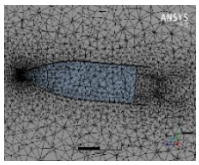

d) (Ariane 5) at 5º angle of attack

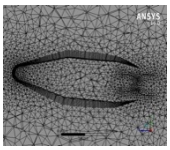

e) (Ariane 1-4 series) at 10º angle of attack

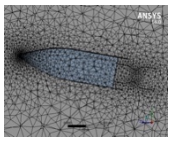

(f) (Ariane 5) at 10º angle of attack

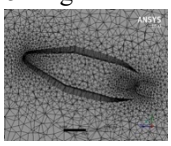

g) (Ariane 1-4 series) at 15º angle of attack

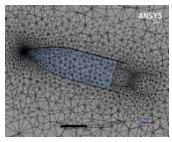

(h) (Ariane 5) at 15º angle of attack

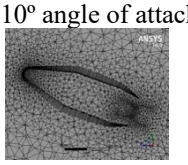

i) (Ariane 1-4 series) at 20º angle of attack

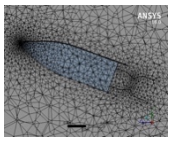

(j) (Ariane 5) at 20º angle of attack

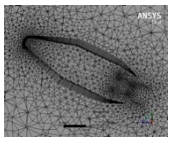

k) (Ariane 1-4 series) at 25º angle of attack

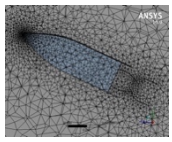

(l) (Ariane 5) at 25º angle of attack

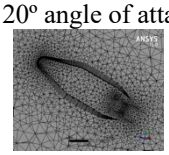

(m) (Ariane 1-4 series) at 30º angle of attack

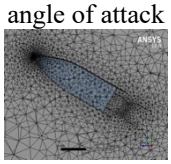

(n) (Ariane 5) at 30º angle of attack

Fig 4(a-n): Mesh cross-section view of trigger nose cone at various angles of attacks (Author)

It is observed that the convergence history of Ariane 1-4 differs from that of current study (Ariane 5). This shows that the stability of the trigger nose cone at different angles of attack varies based on its shape. It is also observed that each model tends to be unstable at the first stage of being ejected from the main body of the launch vehicle due to the viscous and pressure forces generated as each component tends to interact with their immediate environment.

Table 2 The Viscous and Pressure Convergence History for Trigger Nose Cone of current study (Ariane 5)

Angle of Attack (º)	Viscous (Pa. s)	Pressure (Pa)	Angle of Attack (º)	Viscous (Pa. s)	Coefficient of Pressure
0	0.000173489	-0.032071135	0	0.000283247	-0.052361361
5	-0.000199944	0.029084287	5	-0.000326438	0.047484551
10	-0.000199944	0.029084287	10	-0.000326438	0.047484551
15	-0.00118218	0.068081288	15	-0.001719448	0.11115312

20	0.000913956	0.046168723	20	0.001492172	0.075377506
25	0.000347398	0.016404732	25	0.000567181	0.026783236
30	0.000347398	0.016404732	30	0.000567181	0.026783236

Table 3 The Viscous and Pressure Convergence History for Trigger Nose Cone (Ariane 1-4 series)

Angle of Attack (°)	Viscous (Pa. s)	Pressure (Pa)	Angle of Attack (°)	Viscous (Pa. s)	Coefficient of Pressure
0	0.00017348892	-0.032071135	0	0.00028324722	-0.052361037
5	-0.00019994352	0.029084287	5	-0.0003264384	0.047484551
10	-0.00019994352	0.029084287	10	-0.0003264384	0.047484551
15	-0.0011021804	0.068081288	15	-0.0017994782	0.11115312
20	0.0011727725	0.051545741	20	0.000191966	0.084156311
25	0.0024728612	0.032727325	25	0.0040373245	0.053432368
30	-0.0006705494	-0.087020394	30	-0.0010947745	-0.14207411

The values of the viscous and pressure forces tend to differ depending on the angle of attack of the trigger nose cone. As a result, the influence viscosity of the fluid (air), pressure drag, and normal force have on the surface of the nose cone at different angles of attack results in positive and negative values. This positive and negative viscosity indicates the resistivity and the acceleration of each model at different angles of attack as shown in Table 2 and Table 3.

4.2 The velocity plane view of a trigger nose cone angle of attack

Based on the computational aerodynamic analysis presented in Figures 5(a-n) below, it can be inferred that, in the Ariane (1-4 series), the effect of shock waves and aerodynamic disturbances is relatively insignificant within the 0-15° angle of attack range when compared to the 20°-30° range. This is observable by the light yellow and green colours in the images below. As a precaution, it is advisable to eject each triggering nose cone within an angle of attack range of 0°-15°. Any angle beyond this range poses a certain degree of risk.

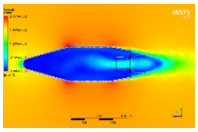

(a) (Ariane 1-4 series) at 0° angle of attack

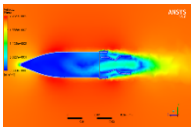

(b) (Ariane 5) at 0° angle of attack

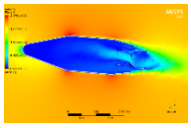

(c) (Ariane 1-4 series) at 5° angle of attack

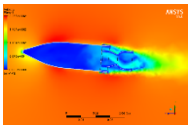

(d) (Ariane 5) at 5° angle of attack

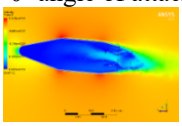

(e) (Ariane 1-4 series) at 10° angle of attack

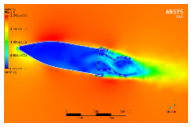

(f) (Ariane 5) at 10° angle of attack

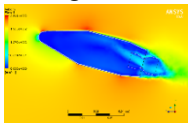

(g) (Ariane 1-4 series) at 15° angle of attack

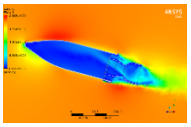

(h) (Ariane 5) at 15° angle of attack

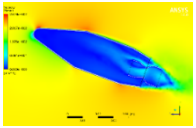

(i) (Ariane 1-4 series) at 20° angle of attack

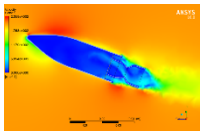

(j) (Ariane 5) at 20° angle of attack

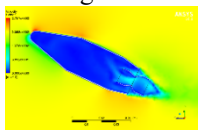

(k) (Ariane 1-4 series) at 25° angle of attack

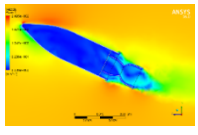

(l) (Ariane 5) at 25° angle of attack

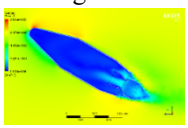

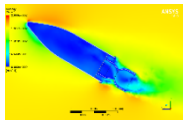

(n) (Ariane 5) at 30° angle of attack

(m) (Ariane 1-4 series) at 30º angle of attack

Fig. 5(a-n). The velocity plane view of trigger nose cone at various angles of attacks (Author).

During the research conducted on the Ariane 5, it was discovered that the impact of shock waves and aerodynamic disturbances was significantly lower within the 0-15º angle of attack range compared to the 20-30º range. As a safety precaution, it is recommended that trigger nose cones be ejected within the 0-15º angle of attack range, which has been determined to be the safest zone for ejection. It is advised to eject the trigger nose cone within a range of 0-15º angle of attack, with a minimum of 0º and a maximum of 15º, to ensure maximum safety.

7. CONCLUSION

a. In the range of 0º angle of attack to 30º angle of attack at Mach 0.6, the stability of the trigger nose cone varies based on its shape.
b. It confirms the standard safe zone for each trigger nose cone lies in the range of 0–15º angles of attack.
c. Any zone with an angle of attack greater than 20º is a no-go zone because the shock waves have a larger effect on the surface, which could lead to a loss of control of the trigger nose cone.

ACKNOWLEDGEMENT

This research was supported by Kwara State University, Malete. Gratitude to Olalekan Adebayo Olayemi and Ayinde Marvelours Oluwatofunmi who provided expertise that greatly assisted the research.
Appreciation to Tiniakov Dmytro and Volodymyr Koloskov for moderating the manuscript.

REFERENCES

1. Banks, R., Auñón, S. M., Harding, R., & Mumbower, A. (2019). Spacecraft Accident Investigation. Principles of Clinical Medicine for Space Flight, 885-904. https://doi.org/10.1007/978-1-4939-9889-0_30
2. Parkinson, R. C. (1999). The hidden costs of reliability and failure in launch systems. Acta Astronautica, 44(7-12), 419-424. https://doi.org/10.1016/S0094-5765(99)00093-4
3. Chang, I. S. (1996). Investigation of space launch vehicle catastrophic failures. Journal of spacecraft and rockets, 33(2), 198-205. https://doi.org/10.2514/3.26741
4. Gorbenko, A., Kharchenko, V., Tarasyuk, O., & Zasukha, S. (2009). A study of orbital carrier rocket and spacecraft failures :179–198. https://doi.org/10.11610/isij.2815
5. Karacalioglu, A. G., & Bukley, A. (2015). Examining the Underlying Causes of Space Launch Failures. In Space Safety is No Accident: The 7th IAASS Conference (pp. 179-188). Springer International Publishing. https://doi.org/10.1007/978-3-319-15982-9_21
6. Fernández, L. A., Wiedemann, C., & Braun, V. (2022). Analysis of Space Launch Vehicle Failures. In XXVI International Congress 31st August–3rd September 2021 On-line event hosted by the Tuscany AIDAA Section in Pisa. https://doi.org/10.24355/dbbs.084-202202091543-0
7. Fernández, L. A., Wiedemann, C., & Braun, V. (2022). Analysis of Space Launch Vehicle Failures and Post-Mission Disposal Statistics. Aerotecnica Missili & Spazio, 101(3), 243-256. https://doi.org/10.1007/s42496-022-00118-5
8. Szondy, B. D. (2017). Electron rocket failure caused by ground error.
9. Rocket Lab identifies cause of Electron failure. (2021). 2021–2022.
10. Ayala, L. F., Carsten, W. &, Viatli, B. (2022). Analysis of Space Launch Vehicle Failures and Post - Mission Disposal Statistics. Aerotecnica Missili & Spazio, 243-256. https://doi.org/10.1007/s42496-022-00118-5
11. Melnikov, B., & Davydova, E. (2018). Mathematical modeling of increasing the level of safety in case of failures of space technology. International Journal of Open Information Technologies, 6(5), 1-6.
12. https://www.popularmechanics.com/space/rockets/g18751736/rocket-launch-failures/
13. Ahamed, S. N., Kumar, J. V., Mushraffuddin, M., & Shrawini, P. (2014). Modeling And Analysis of

Rocket Outer Shell. International Journal of Scientific & Technology Research, 3(4) 270–280.

14. Lepsch Jr, R. A., Stanley, D. O., & Unal, R. (1995). Dual-Fuel Propulsion in Single-Stage Advanced Manned Launch System Vehicle. NASA Technical Reports Server Journal of Spacecraft and Rockets. 32(3) 417–425. https://doi.org/10.2514/3.26631.
15. Tartabini, P. V., Beaty, J. R., Lepsch, R. A. & Gilbert, M. G. (2015) Payload Performance Analysis for a Reusable Two-Stage-to-Orbit Vehicle. No. NASA/TM-2015-218760.
16. Bussler, L., & Sippel, M. (2017). Comparison of Reusable First Stage Return Options, 21st AIAA International Space Planes and Hypersonics Technologies Conference 1-15. https://doi.org/10.2514/6.2017-2137.

PAPER 141 – COMMUNICATION RANGE ASSESSMENT OF LORA-BASED IOT SENSOR NODE FOR SMART CITY APPLICATIONS

Wali Samuel[1], Simeon Ozuomba[2*], Philip Michael Asuquo[3]

[1,2,3]Department of Computer Engineering, University of Uyo, Akwa Ibom State, Nigeria
*Email: simeonoz@yahoo.com

ABSTRACT
In this paper, communication range assessment of LoRa-based IoT sensor node for smart city application is presented. Specifically, the effect of Degree of Urbanisation (DoU), payload size and bit error probability (BEP) on the sensor node communication range are considered. Semtech SX1272 LoRa transceiver operating in the EU868 (863–870/873 MHz) frequency band with spreading factor of 12 and transmitter power of 13 dBm, was used for numerical computations using Visual Basic for Applications (VBA) as implementation tool. The results show that for rural area with building coverage of 3 %, the communication range are 16.854 km and 16.338 km while BEP are 5.186×10^{-04} and 1.307×10^{-04} at payload size of 5 bytes and 51 bytes respectively. Similarly, DoU corresponding to urban area with building coverage of 16 %, gave communication range of 4.994 km and 4.841 km with BEP of 5.186E-04 and 1.307E-04 at payload size of 5 bytes and 51 bytes respectively. Specifically, based on the results, a minimum payload size of 26 bytes was selected and it has transmission range of 16.519 km for PB of 3 %, 8.100 km for PB of 8 % and 4.895 km for PB of 16 %. In any case, although the lower payload size gives higher communication range, small payload size requires higher percentage of overhead bits and also has higher bit error rate which leads to lower data delivery success ratio. As such, in practice, careful compromise is required between payload size and communication range.

KEYWORDS: Bit Error Probability, Communication Range, LoRa, Sensor node, Internet of Things, Smart City Application

1. INTRODUCTION

Nowadays, advancements in embedded systems, sensors, communication and Internet technologies have given rise to proliferation of smart systems for diverse applications such as smart agriculture, smart homes, smart transportation system and smart city applications [1,2]. Particularly, smart city applications require deployment of sensor nodes with requisite wireless communication capabilities that will enable data collection from various locations within the area of interest. Such wireless sensor network coverage is dependent on several factors and mostly propagation loss models are used to estimate the communication range [3,4].
Notably, in wireless sensor communication applications, long range (LoRa) transceiver technologies are popular because of their low power consumption and long range communication capability [5,6]. Also, for LoRa transceivers, apart from the environmental factors which are captured in the propagation model, the communication range is also affected by the payload size. As such, determination of the achievable communication range for a LoRa-based sensor node requires careful selection of the payload size for any give set of LoRa sensor node parameter configuration. Accordingly, this paper presents the requisite analytical models and algorithm that can be used to determine the communication range of LoRa-based IoT sensor node for smart city applications. Particularly, the paper presented approaches to select the minimum payload size that can be used to achieve a given communication range while satisfying the required sensor data capacity and duty cycle requirements. Sample numerical computations are implemented using Visual Basic for Applications (VBA).

2. METHODOLOGY

In this section, analytical expressions for computing the sensor node bit error rate and transmission range based on expected data delivery success ratio and Comit´e International des Radio-Communication (CCIR) path loss model are presented. According to **[7]** energy per useful (payload) bit or energy efficiency, EC_{ppldb} for a sensor node is given as;

$$EC_{ppldb} = \frac{(I_{avg})(V)(t_{cycl})}{B_{pldb}} \qquad (1)$$

where I_{avg} is the average current drawn per cycle, V is the operating voltage and tcycle is the cycle time of the sensor node. Also, according to **[7]**, B_{pldb} is the fraction of the payload data that is successfully delivered and it is given as;

$$B_{pldb} = (B_{payL})\left((1-\text{BER})^{\left(\left(\frac{5}{4}\right)(B_{dataL}-B_{headL})\right)}\right)(1-P_{coll}) \qquad (2)$$

where $B_{payL}$is the actual payload data size; B_{pldb} is the portion of the payload data that is successfully delivered, B_{dataL} is the total size of the data packet including the payload and the header bits , B_{headL} is the packet header which is 20-bits and R_{Succ} is the data delivery success ratio, where R_{Succ} is given as,

$$R_{Succ} = \frac{B_{pldb}}{B_{payL}} = \left((1 - \text{BER})^{\left(\left(\frac{5}{4}\right)(B_{dataL} - B_{headL})\right)}\right)(1 - P_{coll}) \qquad (3)$$

where P_{coll} is the probability of packet collision at the media access control layer. Notably, the concept of data delivery success ratio, R_{Succ} is used to sum up the impact of packet collision probability (Pcoll) that occurs due to the media access control protocol and the packet loss that occur due to error which is captured using the bit error probability (BEP, also referred to as bit error rate, BER), where;

$$\text{BER} = 1 - \left(\left[\frac{R_{Succ}}{(1 - P_{coll})}\right]^{\left(\left(\frac{5}{4}\right)(B_{dataL} - B_{headL})\right)^{-1}}\right) \qquad (4)$$

For LoRa transceiver with spreading factor, SF and bit error rate, BER, the operating energy per bit to noise power spectral density, ${E_b}/{N_O}$ is computed as follows;

$${E_b}/{N_O} = \frac{erfinv(1 - 2(BER))}{\left(\frac{\log_{12}(SF)}{\sqrt{2}}\right)} \qquad (5)$$

The value of ${E_b}/{N_O}$ expressed in dB is denoted as $\left.\frac{E_b}{N_0}\right|_{dB}$, where;

$$\left.\frac{E_b}{N_0}\right|_{dB} = 10\,Log\left({E_b}/{N_O}\right) \qquad (6)$$

In order to determine the LoRa transceiver Operating Link Margin, OLM, the required signal to noise ratio, SNR_{rq} is needed and it is given as;

$$SNR_{rq} = S_{sensitivity} + 174 - 10\log_{10}(BW) - NF \qquad (7)$$

where $S_{sensitivity}$the LoRa receiver sensitivity, BW is the bandwidth and NF is is the noise figure. The operating signal to noise ratio, SNR_{op} is given as;

$$SNR_{op} = \left.\frac{E_b}{N_0}\right|_{dB} + 10\log_{10}(SF) + 10\log_{10}\left(\frac{4}{4+CR}\right) - 10\log_{10}(2^{SF}) \qquad (8)$$

where CR is the coding rate. The Operating Link Margin, OLM is equal to $SNR_{op} - NR_{rq}$. The achievable transmission range (d) for a LoRa transceiver based on Comit´e International des Radio-Communication (CCIR) path loss model is defined as follows;

$$d = 10^{\left(\frac{P_t - S_{sensitivity} - (SNR_{op} - SNR_{rq}) - A + \text{DoU}}{B}\right)} \qquad (9)$$

where

$$A = 69.55 + 26.16 * \log_{10}(f) - 13.82 * \log_{10}(h_b) - a(h_m) \qquad (10)$$

$$a(h_m) = [1.1 * \log_{10}(f) - 0.7] * h_m - [1.56 * \log_{10}(f) - 0.8] \qquad (11)$$

$$B = 44.9 - 6.55 * \log_{10}(h_b) \qquad (12)$$

$$\text{DoU} = 30 - 25(\log_{10}(PB)) \qquad (13)$$

where P_t represents the transmitter power in dBm, DoU represents the degree of urbanization and PB represents the percentage of the signal propagation area that is covered by building (note, PB is the degree of urbanization determining factor). The value of PB is such that $PB \geq 16$ % for urban area, $PB < 16$ % for sub-urban area (with typical value of $PB = 8$ %) and $PB < 8$ % for rural area (with typical value of $PB = 3$%). Also, d is the communication distance in km and f is the frequency in MHz, where 150 MHz≤ f ≤ 1000MHz; 40m ≤ h_b ≤ 200m; 1m≤ h_m≤ 10 m and 1 km ≤ d ≤ 20km.

3. SIMULATION PROCEDURE AND INPUT DATASET

The algorithm for computing the sensor node bit error rate (BER), and transmission range (d) based on expected data delivery success ratio (R_{Succ}) is presented in Procedure 1. The use case multisensor node adopted for the simulation has four sensors comprising of MQ-4 natural gas and methane (CH4) sensor, MQ-7 carbon monoxide (CO) sensor, DS 18S20 temperature sensor and Sensirion DS 18S20 relative humidity sensor. As regards the transceiver and microcontroller, the WM-SG-SM-42 LoRa module [8,9] which consist of Semtech SX1272 LoRa transceiver and STMicro STM32L0 series 32 bit microcontroller unit (MCU) was used. Specifically, the Semtech SX1272 LoRa transceiver operating in the EU868 (863–870/873 MHz) frequency band with spreading factor of 12 was used for the numerical computations implemented using Visual Basic for Applications (VBA). Other data input for the simulation includes: the bandwidth, BW=125Khz; the Code Rate, $\boldsymbol{CR}$=1 ; the transmitter power ($\boldsymbol{P_t}$) = 13 dBm; the signal frequency, f = 863 MHz; the payload size, $\boldsymbol{B_{payL}}$ = 5 bytes to 51 bytes; packet collision probability, $\boldsymbol{P_{coll}}$ = 0; the total data frame header size, $\boldsymbol{B_{headL}}$ = 20 bits; the degree of urbanization determining factor, PB, 3% for rural area, 8 % for sub-urban area and 16 % for urban area; LoRa transceiver sensitivity,

$S_{sensitivity}$ = -137 dBm; data delivery success ratio, R_{Succ} = 0.99 and the Noise Figure, NF = 6 . For every payload, B_{payL} in bytes the overhead size is 13 bytes, hence, the total size of the data packet including the payload and the header, B_{dataL} is given as;

$$B_{dataL} = B_{payL} + 13 \quad (14)$$

PROCEDURE 1: The algorithm for computing the sensor node bit error rate (BER), packet loss probability (Ploss), operating link margin (OLM) and transmission range (d) based on expected data delivery success ratio (R_{Succ})

Step 1: Input the following LoRa-based sensor node parameters values:

i. The Bandwidth, BW
ii. The total data frame header size, B_{headL}
iii. The Code Rate, CR
iv. The degree of urbanization determining factor, PB
v. The transmitter power (P_t)
vi. The total data frame size, $B_{dataL} = B_{payL} + 13$
vii. The signal frequency, f
viii. Lora Transceiver Sensitivity, $S_{sensitivity}$
ix. The total payload size, B_{payL}
x. Data delivery success ratio, R_{Succ}
xi. Packet collision probability, P_{coll}
xii. The Noise Figure, NF (Note, NF= 6)

Step 2: Set LoRa modulation spreading factor, SF =12

Step 3: Compute the successfully delivered payload data, $B_{pldb} = (R_{Succ})B_{payL}$

Step 4: Compute the Packet Loss Probability (P_{Loss}): $P_{loss} = 1 - \left(\frac{R_{Succ}}{(1-P_{coll})}\right)$

Step 5: Compute the sensor node bit error rate (BER):

Step 6 $$\text{BER} = 1 - \left(\left[\frac{R_{Succ}}{(1-P_{coll})}\right]^{\left(\left(\frac{5}{4}\right)(B_{dataL}-B_{headL})\right)^{-1}} \right)$$

Step 7 $$SNR_{rq} = S_{sensitivity} + 174 - 10\log_{10}(BW) - NF$$

Step 8: $$E_b/N_O = \frac{erfinv(1-2(BER))}{\left(\frac{\log_{12}(SF)}{\sqrt{2}}\right)}$$

Step 9: $$\left.\frac{E_b}{N_0}\right|_{dB} = 10\,Log\left(E_b/N_O\right)$$

Step 10: $$SNR_{op} = \left.\frac{E_b}{N_0}\right|_{dB} + 10\log_{10}(SF) + 10\log_{10}\left(\frac{4}{4+CR}\right) - 10\log_{10}(2^{SF})$$

Step 11: $$\text{OLM} = SNR_{op} - SNR_{rq}$$

Step 12: $$A = 69.55 + 26.16 * \log_{10}(f) - 13.82 * \log_{10}(h_b) - a(h_m)$$

Step 13: $$a(h_m) = [1.1 * \log_{10}(f) - 0.7] * h_m - [1.56 * \log_{10}(f) - 0.8]$$

Step 14: $$B = 44.9 - 6.55 * \log_{10}(h_b)$$

Step 15: $$\text{DoU} = 30 - 25(\log_{10}(PB))$$

Step 16: $$d = 10^{\left(\frac{P_t - S_{sensitivity} - OLM - A + \text{DoU}}{B}\right)}$$

Step 17: Output B_{payL}, R_{Succ}, B_{pldb}, P_{loss}, BER, OLM, d

Step 18: Stop

Furthermore, based on the selected parameter settings of the four sensors in the multisensor node used in the simulation, the multisensor node generates 206 bytes per cycle with cycle time of 30 minutes or 1800 seconds (1,800,000 ms). The simulation is conducted for the following payload sizes 5, 11, 21, 31, 41 and 51 bytes and the corresponding packet time on air for each payload size is determined. Also, for each payload size, the number of transmission required per cycle to effectively transmit all the 206 data bytes generated per cycle by the multisensor is determined. Notably, the transmission repeat time is selected based on the packet time on air for the given payload size, the number of required transmission per cycle for delivering the 206 bytes in 1800 seconds and the 1 % duty cycle restriction imposed on LoRa transceiver technologies. The essence of the simulation is to determine the bit error rate (BER) and transmission range (d) for a given expected data delivery success ratio (R_{Succ}) and payload size, as well as the number of payload transmissions required per sensor node cycle time of 1800 seconds and the percentage of overhead bits per payload size. The results are required to make informed decision on the selection of the minimum payload size for any desired communication range.

Let PToA(k) denote the packet time on air for payload size k. The PToA for each of the payload size is computed using an online tool located at https://avbentem.github.io/airtime-calculator/ttn/eu868. Again, let ntrx_TTLPLD be the required number of transmissions to deliver all the 206 bytes generated by the sensor node per cycle and let trxcycle_TTLPLD in seconds be the required transmission cycle time if ntrx_TTLPLD transmissions are to be carried out in the 1800 seconds sensor node cycle time. Then;

ntrx_TTLPLD = 206 bytes / Payload size in bytes (15)

trxcycle_TTLPLD in seconds = 1800 s /(206 bytes / Payload size in bytes) (16)

Also, let trxcycle_ PToA &DC in seconds be the required transmission cycle time if the payload size with packet time on air (PToA in seconds) is used for the transmission and let ntrx_ PToA &DC be the required number of transmissions to deliver all the 206 bytes if the trxcycle_ PToA &DC in seconds transmission cycle time is used. Then;

trxcycle_ PToA &DC in seconds = 100*PToA in seconds (17)

ntrx_ PToA &DC = 1800 seconds/ (100*PToA in seconds) (18)

Any payload size for which trxcycle_ PToA & ≤ trxcycle_TTLPLD is appropriate for the sensor node. Likewise, any payload size for which ntrx_TTLPLD & ≤ ntrx_ PToA &DC is also considered appropriate for the sensor node.

4. RESULTS AND DISCUSSION

The simulation results for the transmission cycle time and number of required transmissions per sensor node cycle time of 1800 seconds and payload size are shown in Figure 1 and Figure 2. Notably, in Figure 2, payload sizes that have transmission cycle time based on total payload per cycle (trxcycle_TTLPLD) greater or equal to the transmission cycle time based on packet time on air and duty cycle (trxcycle_ PToA &DC) are selected as those that can be used for the use case multisensor node. Those are the payload sizes that can deliver the total of 206 bytes generated by multisensor node in each sensor node cycle time of 1800 seconds and also satisfy the 1% duty cycle restriction. Accordingly, payload size of 26 and above can be used for the use case multisensor node since such payload sizes will satisfy both the duty cycle requirement and the total number of payload data required to be transmitted in the given multisensor cycle time.

Again, the simulation results for the transmission range, d and bit error probability, BER, versus payload size in byte are shown in Figure 3. The results showed that the transmission range decreases as the payload size increases. Particularly, the highest transmission range of 16.854 km occurred for payload size of 5 bytes operated in the rural area with urbanisation determining factor of 3 % whereas the same payload size has transmission range of 16.338 km in the same rural area for a payload size of 51 bytes. Also, the transmission range degreases as the degree of urbanization determining factor, PB increases from 3% for the rural area to 16 % for the urban area. Specifically, the maximum transmission range for PB =8 % is 8.264 km while that of PB = 16 % is 4.994 km for payload size of 5 bytes.

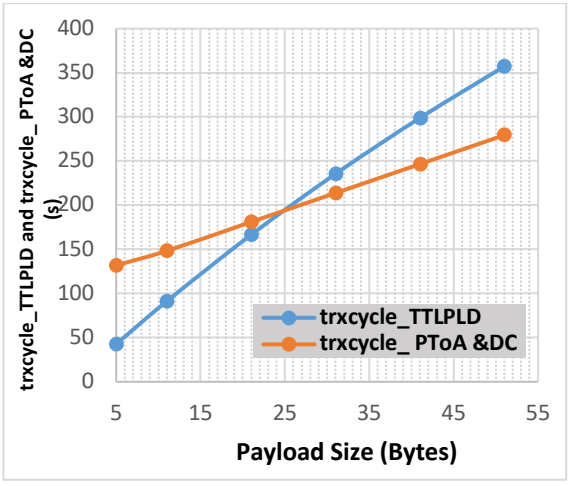

Fig 1: Transmission cycle time based on total payload per cycle (trxcycle_TTLPLD) and transmission cycle time based on packet time on air and duty cycle (trxcycle_ PToA &DC) versus payload size

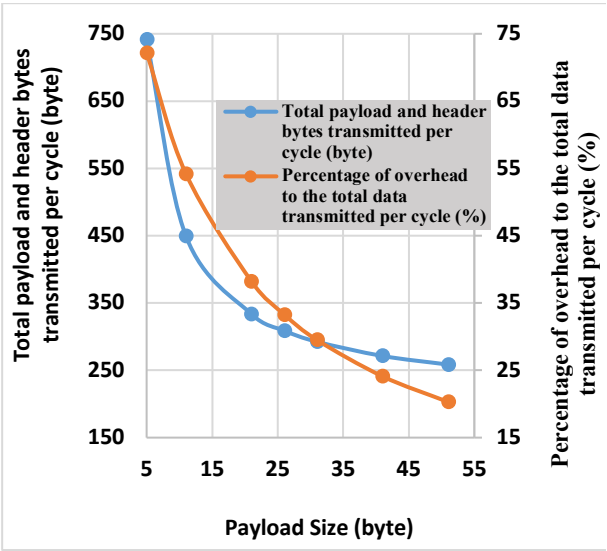

Fig 2: Total payload and header bytes transmitted per cycle and Percentage of overhead to the total data transmitted per cycle

Furthermore, based on the results in Figure 2, the minimum payload size that can be applied in the use case multisensor node is 26 and this gives a transmission range of 16.519 km for PB =3 %, 8.100 km for PB =8 %, and 4.895 km for PB =16 %. In any case, while the smaller payload size has higher transmission range, the bit error probability (BER), as shown in Figure 3 and the percentage of overhead bits, as shown in Figure 2 are highest for the smallest payload size. In essence, while small payload size can give longer transmission range, it also has very high bit error rate or bit error probability which will lead to higher probability of packet loss due to error and

hence the need to retransmit the packet. Such retransmission of packet will required additional time and energy consumption in the sensor node. In addition, the total number of data bytes (including the payload and overhead bits) transmitted per cycle is highest (741.6 bytes) for the smallest payload size of 5 bytes and the percentage overhead bit is 72 2 % whereas the total data bytes transmitted for payload size of 51 bytes is 258.5 bytes and the percentage overhead bit is 20.3 %.

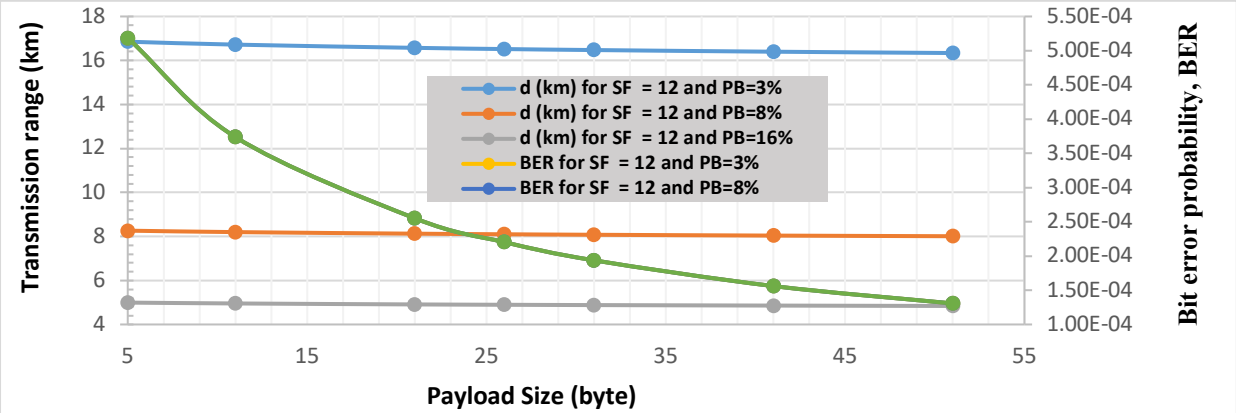

Fig 3: Transmission range (km) and bit error probability, BER, versus payload size in byte

5. CONCLUSION

Analytical expressions and algorithm for computing LoRa-based Internet of Things (IoT) sensor node bit error rate and transmission range based on expected data delivery success ratio and Comit´e International des Radio-Communication (CCIR) path loss model are presented. Also, presented are analytical expressions for determining the number of transmissions required per sensor node cycle and the transmission cycle time required for the LoRa transceiver, as well as the percentage of overhead bits for any given payload size. In all, the results show that the transmission range is inversely related to the payload size; the transmission range decreases as the payload size increases. Similarly, the bit error probability and percentage of overhead bits to the total transmitted data packets per cycle decrease with increase in payload size. Essentially, small payload size can be used to achieve higher transmission range, but its downside is that it is more susceptible to bit error and also more overhead bits are transmitted which will require higher energy consumption in the sensor node. As such, in practice, careful compromise is required between the payload size and desired transmission range.

REFERENCES

1. Midhila, P., Manjushree, M., Raajasubramanian, D., Srinivasan, S., Chalwadi, H., Devi, R., ... & Narendra, K. (2023). Importance and Applications of Internet of Things (IoT). *Internet of Things: Applications for Sustainable Development*, 1.
2. Hashem, I. A. T., Usmani, R. S. A., Almutairi, M. S., Ibrahim, A. O., Zakari, A., Alotaibi, F., ... & Chiroma, H. (2023). Urban Computing for Sustainable Smart Cities: Recent Advances, Taxonomy, and Open Research Challenges. *Sustainability*, *15*(5), 3916.
3. Jondhale, S. R., Maheswar, R., & Lloret, J. (2022). *Received signal strength based target localization and tracking using wireless sensor networks* (pp. 1-202). Springer.
4. Majid, M., Habib, S., Javed, A. R., Rizwan, M., Srivastava, G., Gadekallu, T. R., & Lin, J. C. W. (2022). Applications of wireless sensor networks and internet of things frameworks in the industry revolution 4.0: A systematic literature review. *Sensors*, *22*(6), 2087.
5. Malik, P., Bilandi, N., & Gupta, A. (2022). Narrow band-IoT and long-range technology of IoT smart communication: Designs and challenges. *Computers & Industrial Engineering*, 108572.
6. John, S. T., Sarkar, P., & Davis, R. (2022). Energy-efficient long range wide area network for construction industry applications. *Automation in Construction*, *136*, 104150.
7. Lluís Casals, Bernat Mir, Rafael Vidal and Carles Gomez (2017) Modeling the Energy Performance of LoRaWAN Sensors 2017, 17, 2364
8. USI (2018) Product SPEC of WM-SG-SM-42 LoRa Module, data sheet Mar.22 2018 Rev 0.5 . Available at http://edworks.co.kr/wp-content/uploads/2020/12/WM-SG-SM-42_Product-SPEC_Rev05_20180322.pdf
9. Gaitan, N. C. (2021). A long-distance communication architecture for medical devices based on LoRaWAN protocol. *Electronics*, *10*(8), 940.

PAPER 142 – SYNTHESIS AND CHARACTERIZATION OF ZEOLITE A FROM ALOJI KAOLIN VIA HYDROTHERMAL METHOD

V. C. Eluwa[1*]

[1]Department of Chemical Engineering, Federal University of Technology, Minna
*Email: Victoria.eluwa@futminna.edu.ng

ABSTRACT
This study focused on the synthesis and characterization of Zeolite A from Aloji kaolin via the hydrothermal method. The effect of short crystallization times (0.5h, 1h, 1.5h, 2h, and 3h) and high crystallization temperature of 115℃ on the formation of Zeolite A as the final product was investigated. The characterization of the synthesized Zeolite A was conducted using Scanning electron microscope (SEM), X-ray diffraction (XRD), and Brunauer- Emmett- Teller **(**BET) analysis. The results showed a well-developed Zeolite A with cubic morphology and a crystallinity of 78.12%, as well as a surface area and pore size of 18.8832 m^2/g and 178.461 Å respectively was successfully synthesized using high alkali concentration (5 mol/L) and a crystallization time of 3h. The findings provide a valuable insight into the synthesis of Zeolite A from kaolin and its potential application in various fields.

KEYWORDS: Kaolin, Zeolite, Crystallization, Temperature, Hydrothermal.

1. INTRODUCTION

Increase in global population as well as rapid industrialization has resulted in depletion of non-renewable resources, increasing pollution and thus various ecological and environmental problems. These problems have greatly transcended to degradation of the environment and human health which has greatly stared people to become inquisitive about current model of industrialization procedure and production. Due to improvement in regulations and emergence of new policies there is a shift in the regular mode of pollution first then treatment later to a cleaner method of production. In the clean production methods harmful and very toxic substances that cause pollution are either avoided or reduced to the barest minimum. (He *et al.,* 2021).

Zeolites are porous materials that consist of a three-dimensional framework structure of crystalline aluminosilicate materials. Zeolites have uniform sized pores and usually known as molecular sieves (Johnson & Arshad, 2014). Zeolites have a very wide range of applications and have been applied in fields such as catalysis, adsorption processes, bacterial adhesion water treatment, air pollution remediation, detergent making, fuel cell and ion exchange. (Hartarti *et al.,* 2020). Zeolites exist in two categories, both as natural and synthetic. The natural occurring ones are mined from the earth while the synthetic zeolites are produced in the laboratory. Natural zeolites are found in sedimentary rocks that are near the earth's crust. Commonly found natural zeolite includes Clinoptilolite, Analcime, chabazite, heulandite, erionite, laumontite, and mordenite (Derbe *et al.,* 2020; Nasief *et al.,* 2021). Natural zeolites are known to contain contaminants like Fe^{2+}, SO_4^{2-}, SiO_2, and sometimes other zeolites, these impurities tend to reduce their pores and channels thereby making them unsuitable for commercial use where purity and uniformity are highly essential.

In order to eliminate the limitations associated with natural, it has prompted researchers to investigate the synthesis of synthetic zeolite. (Yoldi *et al.,* 2019). Synthetic zeolites are generally preferred due to the homogeneity in their composition (particle size and shape) as well as high crystallinity in comparison to the natural zeolite. This is majorly due to the ease with which desired structural properties and chemical compositions can be manipulated by varying the parameters during the synthesis operation. (Lim *et al.* 2021)

Synthetic zeolite preparation and synthesis are very challenging and the common synthesis methods involves using alumina and silica obtained from analytical/ synthetic chemicals to form aluminosilicate hydrogel which is then crystallized to obtain zeolite. This source of alumina and silica is very expensive and leads to high cost of zeolite in addition to causing several environmental burdens due to pollution. (Otieno *et al.,*2019; Kumar and Jena 2022). In an attempt to reduce the cost of zeolite and pollution associated with using analytical grade chemicals, several other alternative sources of alumina and silica have been explored and are still currently being investigated. Kaolin has been found to be an alternative source for alumina and silica because of its low-cost benefit and it has a Si/Al ratio of 1 which suitable for the synthesis of low silica zeolites. (Lim *et al.* 2021; Binay, *et al*. 2019). Low silica zeolites like zeolite A also known as zeolite LTA are of very special interest due their high adsorption and ion exchange properties. (Arasi *et al.,* 2021; Kirdeciler & Akata 2020; Kamyab & Williams 2021).

In this work Aloji kaolin was used as an alternative source for alumina and silica because of its low-cost benefit and it has a Si/Al ratio of 1 which is suitable for the synthesis of low silica zeolites. The work involves the synthesis of zeolite A from Aloji kaolin. This will be achieved by refining raw kaolin and then converting this to metakaolin by calcination. The metakaolin will then be used in synthesizing zeolite A.

2.MATERIALS AND METHODS

2.1 Materials

Raw Kaolin was obtained from Aloji in Kogi state, Nigeria. The only chemical reagent used was analytical grade sodium hydroxide (NaOH) pellet obtained from Sigma Aldrich. Also, the deionized and distilled water used were all obtained within Chemical Engineering Laboratory of the Federal University of Technology, Minna and were used as at when received.

2.2 Method

2.21 Refining and Metakaolinization of Kaolin clay

Raw Aloji kaolin was crushed mildly and sieved using an 850µm sieve mesh. This was then transferred into a 1000ml beaker where it was soaked using deionized water for 12h. The mixture was then stirred continuously for about 30 minutes after which the lighter fraction (supernatant) was collected. After sedimentation the Kaolin was decanted and dried in the oven. The refined Kaolin was then calcined in a muffle furnace at 850℃ for 2h to obtained metakaolin which is a more reactive form of Kaolin.

2.2.2 Synthesis of Zeolite A

Zeolite A was synthesized from Aloji kaolin using the conventional hydrothermal method. Refined Kaolin was converted to metakaolin at 850℃. The metakaolin obtained were then mixed with 5M concentration of sodium hydroxide and the resulting mixture was stirred using a magnetic stirrer. The homogenous solution was aged and then heated in a Teflon lined stainless steel autoclave at 115 ˚C for 0.5h, 1h, 1.5h, 2h and 3h. The resultant product obtained was continuously washed with deionized water until a pH of 7 was obtained, after which the zeolite sample was dried in an oven at 100℃ for 8h and the zeolite crystals obtained stored in an air tight container.

2.3Zeolite Characterization

2.3.1 X-Ray Diffraction (XRD).

X-ray diffraction (XRD) is an efficient and effective technique that is used to identify crystallographic structure of solids. XRD can be used to determine the crystal size of zeolites, study the crystal structure of zeolite, as well as determine the crystallinity of zeolites. The XRD analysis was performed using an **Ultima IV, Rigaku, UK and with Cu-Kα radiation having a fixed power source (40 kV, 40 mA), and** a diffraction angle (2Θ) in the range of 5-90^0 and these were detected at a scan rate of 0.01.the percentage crystallinity was calculated using Equation 1

$$Percentage\ crystalinity = \frac{\text{Sum of relative intensities } of\ synthesized\ zeolite}{\text{Sum of relative intensities of standard zeolite}} \times 100 \quad \text{.....1}$$

2.3.2 Scanning Electron Microscopy (SEM).

Scanning electron microscope (SEM) is a technique that is used to study the surface of solids (zeolite crystals) as it shows the crystal shape and size. It also provides various signals that describe the morphology and topology of the zeolite.

2.3.3. Brunauer- Emmett- Teller (BET).

Nitrogen adsorption_ desorption isotherms were observed using Quantachrome Corporation instrument. The specific surface area was calculated using Brunauer- Emmett- Teller equation. The pore volume was obtained based on the amount of nitrogen adsorbed at P/P$_\circ$ 0- 0.99.

3.0 RESULT AND DISCUSSION

3.1 XRD ANALYSIS

XRD analysis was carried out for the metakaolin and each of the zeolite samples synthesized at various crystallization times during zeolite synthesis. This is because the phase composition was obtained from the XRD analysis would determine the success of the synthesis of Zeolite A. The XRD pattern shown in Figure 1 gives the analysis of result for the metakaolin used in the Zeolite A synthesis. The diffraction pattern obtained shows that peaks associated with kaolinite mineral can be seen at 2Θ values of 12.38 and 24.94. The metakaolin also contains impurities like quartz and mica as seen by the diffraction peaks at 26.67 and 20.84respectively.

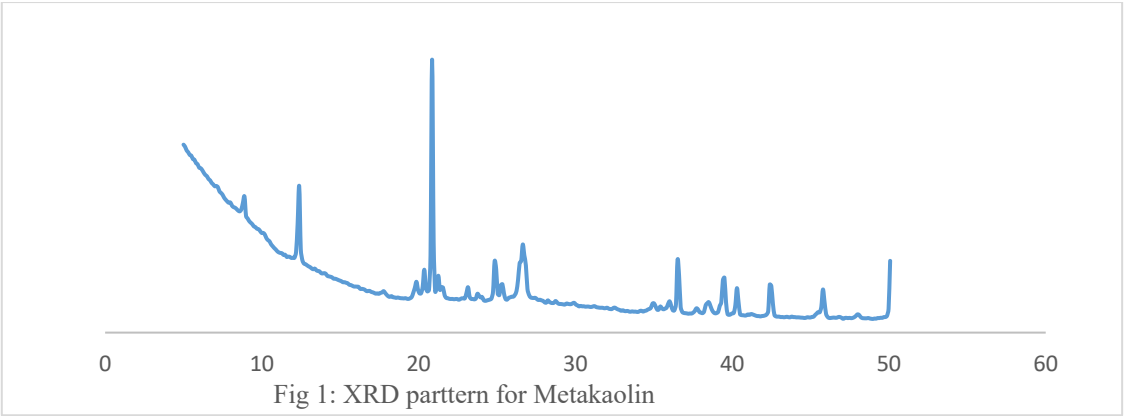

Fig 1: XRD parttern for Metakaolin

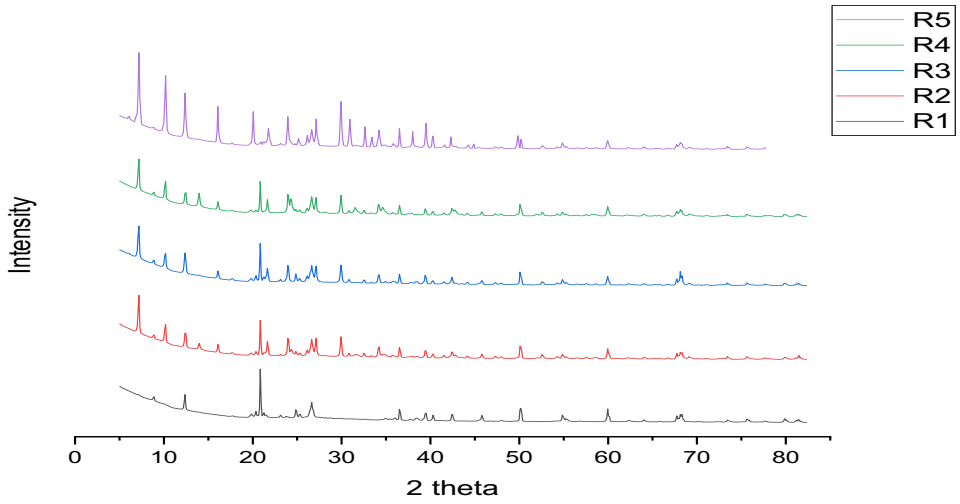

Fig 2: XRD pattern for synthesized zeolite at various crystallization times

In the study of zeolite synthesis, XRD analysis was carried out. Figure 2 shows the XRD pattern for the zeolite synthesized at various crystallization time. It can be seen from the result that the XRD obtained after 0.5h of crystallization (R1) showed peaks only similar to those found in the metakaolin. These are kaolinite peaks at 2 theta values of 12.51, 24.64 and quartz peaks at 26.67. However, at a crystallization time of 1h as indicated by plot R2, other diffraction peaks became visible. Here peaks characteristic of zeolite A began to emerge. The diffraction peaks at 2Θ values of 7.18, 10.24, 12.49, 16.04, 20.46, 30.89, and 34.21 were obtained. Similarly, a peak characteristic of faujesite was obtained at 2 Θ value of 14.21; this readily disappeared as crystallization time increased to 1.5h. The diffraction peaks obtained at 1.5h (R3) has similar peaks as those at 1h. it was observed that more peaks characteristic to zeolite A were added and the faujesite peak disappeared. New peaks that emerged at 1.5h were obtained at 2Θ values of 19.98, 24.13, 36.67, 39.65, 42.31 and 42.74. The diffraction peaks obtained after2h (R4) crystallization time were seen at 2 theta values of 7.18, 10.24, 12.49, 16.04, 20.46, 24.13,30.89, 34.21, 36.67, 39.65, 42.31, 42.74. 44.25 and 47.34. These peaks are characteristic peaks obtained for zeolite A according to Tracey and Haggins (2001). This confirms that zeolite A formation begins even after 1h crystallization time and continues to new peaks emerges with increasing time. The peaks obtained for zeolite synthesized at 3 h in this study gave the highest crystallinity of 78.12 % and the diffraction peaks were observed at 2Θ values of 7.18, 10.24, 12.49, 16.04, 20.46, 21.71, 24.04, 25.15, 30.01, 30.89, 32.68, 34.21, 36.64, 38.04, 39.62, 40.27, 42.38, 44.20, 44.85, and 49.83. These peaks obtained from this work were in close agreement with to that obtained from the works of Yusriadi *et al.,* (2020); Maia *et al.,* (2019) and Vegree *et al.* (2020). Furthermore, it can be seen from Figure 2 that diffraction peaks obtained from the zeolite crystallized at 3h had peaks of higher intensities than the other zeolites synthesized, this may explain the reason for a higher percentage crystallinity obtained by this zeolite.

3.2. SEM ANALYSIS

The zeolite samples synthesized were viewed under the microscope to study the changes occurring as the synthesis time was increasing. Figure 3a-f gives the micrographs for the changes in the morphology of the zeolite during synthesis. It was observed from the micrographs that the metakaolin used as shown in Figure 3a were flat plated and had hexagonal shaped particles scattered within the plates. With a crystallization time of 0.5h, the micrograph in Figure 3b still depicted dominantly flat plated hexagonal shaped morphology. This goes to confirm the XRD pattern that at this crystallization time the XRD pattern was similar to that obtained for metakaolin having peaks only characteristic of kaolinite at 2 theta values of 12.51, 24.64 and quartz peak 26.67.

The micrograph in Figure 3c gives the zeolite sample formed at 1h crystallization time. The figure shows a mixture of both cubic and hexagonal shaped morphology for samples. However, the micrograph also showed an improvement from the originally flat plated metakaolin to transforming cubic shape (Gougazeh & Buhl, 2014). In a similar manner it agrees with the XRD result that peaks characteristic of zeolite was formed, since cubic shaped crystals were observed. Furthermore, in Figure 3d for 1.5h crystallization time and a similar pattern was identified as samples were seen to contain crystals of both cubic and hexagonal crystals.

In Figure 3e, the micrographs showed crystals that have predominantly cubic morphology, with very few flat plated and hexagonal shaped crystals present. The XRD result obtained confirms that zeolite samples crystallized for 2h produced more peaks that are characteristic of zeolite A than those crystallized at lesser time. The micrograph was almost similar to that of zeolite sample crystallized at 3h. Although the sample crystallized at 3h showed better formed cubes. This is clearly shown in figure 3f image cubic morphology for zeolite LTA using kaolin as starting raw material.

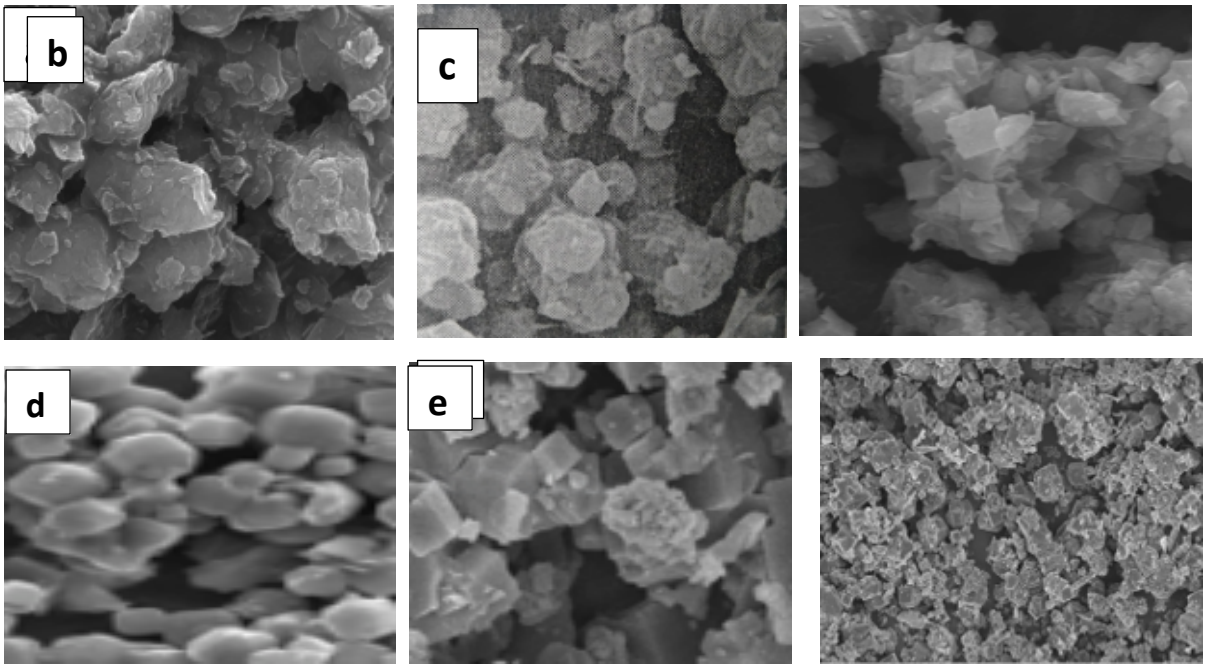

Fig 3: SEM images for zeolite A obtained at various crystallization times

The morphology of the synthesized zeolite A after 3h crystallization time with higher magnification is shown in Figure 4. The micrograph depicts some well-developed cubic crystals that is typical of zeolite A. This shape is in conformity with Kirdeciler *et al.,* (2020) and Salimkhani *et al.* (2021) that reported obtaining image cubic morphology for zeolite LTA using kaolin as starting raw material.

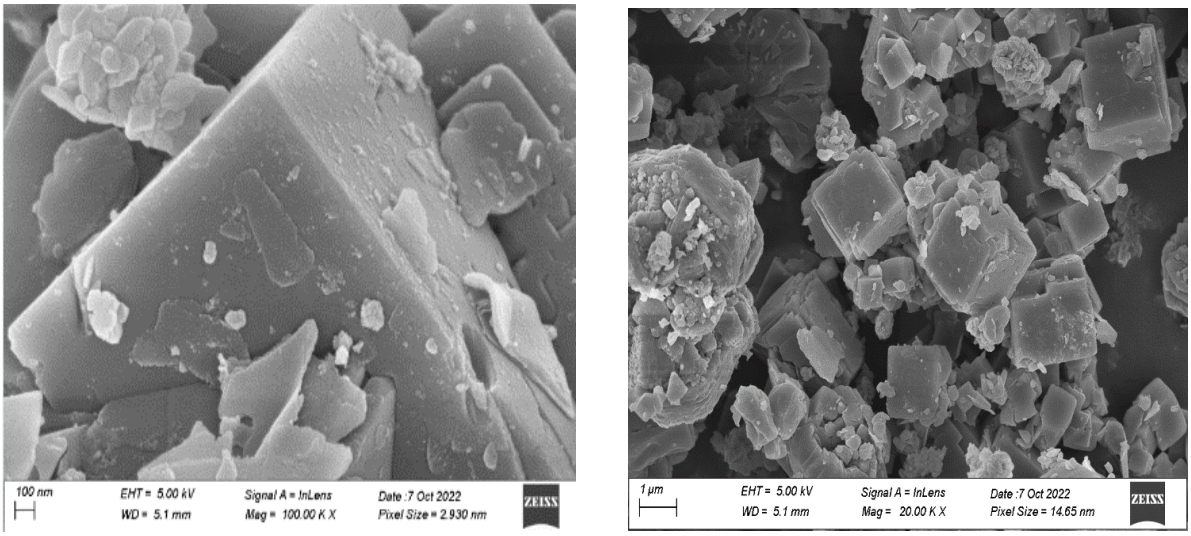

Fig 4: SEM images for zeolite A obtained at 3h crystallization time.

3.3 BET RESULTS

The pore size, pore volume as well as the surface area of the zeolite with the best crystallinity (R5) was determined using BET. The BET results show that the surface area pore size and pore volume of the synthesized zeolite was obtained as 18.8832 m^2/g, and 178.461 Å, and 0.070864 cm^3/g respectively, thus, the synthesized zeolite has pore size in the mesoporous range. The values were a much better and different than the values obtained as surface area, pore size and pore volume for the refined kaolin. These values were obtained as14.15 m^2/g, 166.593 Å, and 0.001326 cm^3/g respectively. This also shows that the synthesis process resulted in an increase in surface area, pore size and the pore volume of the final product zeolite A.

4. CONCLUSION

In conclusion, the present study has demonstrated the successful synthesis of zeolite A from Aloji kaolin via hydrothermal method. The effect of varying crystallization times and temperature on the synthesis of zeolite A was investigated, and it was found that a crystallization time of 3 h on an alkali concentration of 5 mol/L resulted in a well-developed zeolite A crystal with high crystallinity and desirable morphological and textural properties. The characterization results obtained through XRD, SEM, and BET analysis confirmed the formation of Zeolite A with a cubic morphology, high surface area and pore size. These findings suggest that Aloji kaolin can serve as a potential source of raw material for the synthesis of zeolite A which could have potential application in various fields such as catalysis, separation and adsorption.

REFERENCES

Arasi, M. A., Salem, A., & Salem, S. (2021). Production of Mesoporous and Thermally Stable Silica Powder from Low Grade Kaolin Based on Eco-Friendly Template free Route via Acidification of Appropriate Zeolite Compound for Removal of Cationic Dye from Wastewater. *Sustainable Chemistry and Pharmacy* 19.

Binay, M.I., Kirdeciler, S.K., &Akata, B. (2019). Development of antibacterial powder coatings using single and binary ion-exchanged zeolite A prepared from local kaolin. *Applied Clay Science,* 182

Derbe, T., Temesgen, S., and Bitew, M. (2021). A Short Review on Synthesis, Characterization, and Applications of Zeolites. *Advances in Materials Science and Engineering.*

Hartati, Prasetyoko, D., Mardi Santoso, M., Qoniah, I., Leaw, W. L., Firda, P. B. D., and Nur, H (2020)A review on synthesis of kaolin-based zeolite and the effect of impurities. *Journal of the Chinese Chemical Society,* 1–26.

He, Y., Tang, S., Yin, S., & Li, S (2021). Research progress on green synthesis of various high-purity zeolites from natural material-kaolin. *Journal of Cleaner Production,* 306 (2021) 127248.

Johnson, E. B. G. & Arshad, S.E. Hydrothermally synthesized zeolites based on kaolinite: A review. *Applied Clay Science*. 97–98 (2014) 215–221

Gougazeh. M & Buhl. J. (2014). Synthesis and characterization of zeolite A by hydrothermal transformation of natural Jordanian kaolin. Journal of the Association of Arab Universities for Basic and Applied Sciences. 15, pp.35–42

Kamyab, S. M., & Williams, C. D. Pure zeolite LTJ synthesis from kaolinite under hydrothermal conditions and its ammonium removal efficiency. *Microporous and Mesoporous Materials*. 318(2021)111006

Kirdeciler, S. K. &Akata, B. One pot fusion route for the synthesis of zeolite 4A using kaolin. *Advanced Powder Technology,* 31 (2020) 4336–4343

Kumar, M.M & Jena, H (2022). Direct single-step synthesis of phase pure zeolite Na–P1, hydroxy sodaliteand analcime from coal fly ash and assessment of their Cs+ and Sr2+ removal efficiencies. *Microporous and Mesoporous Materials,* 333 (2022) 111738.

Lim, W., Lee, C., & Hamm. S. Synthesis and characteristics of Na-A zeolite from natural kaolin in Korea. *Materials Chemistry and Physics*, 261(2021)124230

Maia, A. B., Dias, R. N., Rômulo, S. A., and Neves, R.F. (2019). Influence of an aging step on the synthesis of zeolite NaA from Brazilian Amazon kaolin waste. *Journal of Material Research and Technology*; 8(3):2924–2929

Nasief, F.M., Shaban, M., Alamry, K.A., Abu Khadra, M.R., Khan,A.A.P., Asiri, A.M., & Abd El-Salam, H.M. Hydrothermal synthesis and mechanically activated zeolite material for utilizing the removal of Ca/Mg from aqueous and raw groundwater. *Journal of Environmental Chemical Engineering,* 9 (2021)105834

Otieno, S.O., Kengara, F.O., Kemmegne-Mbouguen, J.C., Langmi, H.W., Kowenje, C.B.O., & Mokaya, R. The effects of metakaolinization and fused-metakaolinization on zeolites synthesized from quartz rich natural clays. *Microporous and Mesoporous Materials,* 290 (2019) 109668

Salimkhani, S., Siahcheshm, K., Kadkhodaie, A., &Salimkhani, H (2021). Structural analysis and the effect of the chromium on LTA (Na) zeolitesynthesized from kaolin.*Materials Chemistry and Physics*, 271 (2021) 124957.

Vegere, K., Kravcevica, R., Krauklis, A.E., &Juhna, T. (2020). Comparative study of hydrothermal synthesis routes of zeolite A. *Materials Today: Proceedings* https://doi.org/10.1016/j.matpr.2020.06.326

Yoldi, M., Fuentes-Ordonez, E.G., Korili, S.A., & Gil, A. (2020). Zeolite synthesis from industrial wastes. *Microporous and Mesoporous Materials*, 287 (2019) 183–-191.

Yusriadi, Y., Sulastri, E., & Lembang, N.P (2020). Synthesis of Type A Zeolite from Rice Husk Ash and Its Application as a Builder on Effervescent Tablet Form Detergent. *TensideSurfantant Detergent,* 57 (2020) 3.

PAPER 143 – PARAMETERS CHARACTERIZATION OF WIRELESS TECHNOLOGIES: AN INDOOR LOCALIZATION PERSPECTIVE

S. L. Ayinla[1,3*], A. A. Aziz[1], M. Drieberg[1], M. Susanto[2], T. I. Amosa[1], A. O. Yusuf[3], H. O. Mahmud[3]

[1]Department of Electrical & Electronic Engineering, Universiti Teknologi PETRONAS, Perak, Malaysia.
[2]Department of Electrical Engineering, University of Lampung, Bandar Lampung, Indonesia.
[3]Department of Computer Engineering, University of Ilorin, Ilorin, Nigeria.
[*]Email: ayinla.sl@unilorin.edu.ng

ABSTRACT
The persistent rise in demand for affordable indoor localization systems and technologies capable of accurately predicting the real-time location of targets has been observed. While the Global Navigation Satellite System (GNSS) has proven its reliability in outdoor, it falls short of the required accuracy for indoor environments. In response, multiple wireless technologies have been proposed as potential alternatives to deliver location-based services in indoor settings with minimal errors. However, studies that comprehensively analyze and evaluate the parameter characteristics of these evolving technologies in indoor applications remain rare. In this regard, this paper assesses and characterizes different wireless technologies based on six parameters. Our study examines four short-range including WiFi, BLE, Zigbee and UWB, and the two long-range wireless technologies such as LoRa and WiFi Halow. The selected technologies are characterized using available information and distance-dependent models in terms of frequency band, data rate, coverage area, power consumption, signal-to-interference-plus-noise ratio, smartphone availability and deployment cost, and application. Result indicates that UWB is suitable for small indoor environment because of wide frequency band, this is followed by WiFi, BLE and Zigbee while LoRa is ideal for large indoor environment. LoRa has the least energy consumption followed by BLE. The energy consumed by Zigbee and UWB are considerably low while WiFi consumes the most energy. WiFi, BLE and UWB are smartphone accessible, hence they have the lowest cost while other technologies need extra hardware for deployment. These findings can be used as a guideline in selecting a wireless technology for an indoor localization system based on application requirements.

KEYWORDS**:** Indoor localization, WiFi, BLE, Zigbee, UWB, LoRa and WiFi Halow

36. INTRODUCTION

Location-based services (LBSs) have grown in popularity due to technological advancements and increase in the number of Internet of Things (IoT) devices. An IoT is a collection of interconnected end devices, including sensors and software, that are embedded in a specific environment with the capacity to sense, communicate, process, and store data without the need for human interaction. However, the collected environmental data remains insignificant until the precise location of its acquisition is determined. Thus, localization is a key step towards developing smart and IoT applications. Localization is the process of using available information and algorithms to determine the location of a target (Sadowski & Spachos, 2018a). Localization can be in outdoor or indoor scenarios. Outdoor localization has been achieved successfully using various types of regional-based Global Navigation Satellite System (GNSS). However, using GNSS in indoor scenario is accompanied by a lot of environmental and economic challenges. Furthermore, people tend to spend about 87-90% of their time indoors (Klepeis et al., 2001; Sarigiannis, Gotti, & Karakitsios, 2019; Wang, Shang, & Wu, 2023). Therefore, alternative solutions to locating people and objects in indoor environments need to be explored.

The use of wireless technologies has increased in the last decades in our daily lives. Wireless Access points (WAPs) have been deployed in a multitude of indoor environments for provision of internet connection. Although these technologies were designed for communication, the transmitted signal can be used to estimate the location of a target in the satellite denied environments (Asaad & Maghdid, 2022). However, the environmental constraints need to be overcome with proper analysis of the signal propagation to achieve accurate and robust indoor localization services. During signal propagation in a medium, there is signal degradation as the signal travels from the transmitter to the receiver. This signal loss increases exponentially as the distance between the transmitter and receiver increases. Besides the medium loss, presence of obstacles such as walls, stationary and moving objects also pose a challenge to accurate signal-to-distance estimation. The presence of obstacles along the signal propagation direction causes signal impairments such as reflection, refraction, absorption, and scattering (Farahsari, Farahzadi, Rezazadeh, & Bagheri, 2022). Various wireless technologies commonly used for communication have been employed in the design of indoor localization models.

The study in this paper is structured as follows: Section II reviews the relevant work, followed by an extensive overview of wireless technology in Section III. Section IV presents the system distance-dependent model, and Section V addresses the wireless technology's appropriateness. Section VI brings the study to a conclusion.

37. RELATED WORK

The task of indoor localization presents more difficulties compared to its outdoor counterpart due to the presence of environmental obstacles. Numerous studies have been conducted to determine the parameter characterization of various wireless technologies (Sadowski & Spachos, 2018a, 2018b, 2019) (Khan, Awais, Rasheed, Masood, & Ghadi, 2021; Sadowski, Spachos, & Plataniotis, 2020; Simka & Polak, 2022; Tabaa & Hachimi, 2022). Nevertheless, each of these technologies exhibits its unique strengths and limitations in the context of localization. The study in (Sadowski & Spachos, 2018a) compared the accuracy and power consumption of Zigbee, BLE, and WiFi for the development of an indoor positioning system. WiFi was the most accurate system, followed by BLE. BLE was discovered to use the least amount of power. When Line of Sight (LoS) is available, Zigbee transmit up to 100 m. Similarly, the study in (Sadowski & Spachos, 2018b) evaluates the accuracy and power consumption of WiFi, BLE, Zigbee, and LoRa. The tests were carried out using a trilateration technique in two different environments. WiFi proved to be the most accurate also, followed by BLE. BLE was discovered to consume the least amount of power. When operating at maximum transmission power, LoRa has the longest range.

The study presented by Sadowski and Spachos (2019) verify the maximum number of beacons required in indoor localization to optimize accuracy. The result showed that placing six beacons and using nonlinear least algorithm with three closest references and a moving average filter yields the optimal result. Sadowski et al. (2020), performance of two memoryless localization techniques with trilateration on three technologies using RSSI was described. Results established that k-Nearest Neighbours (k-NN) with k = 4 was the most accurate. Khan et al. (2021), evaluation of WiFi, BLE and LoRa for suitability in a particular indoor localization domain was carried out with Pycom's LoPy. WiFi exhibited the highest level of accuracy, followed by LoRa, while BLE had the lowest accuracy.

Simka and Polak (2022), present the evaluation of different configuration modes of LoRa at 2.4 GHz in three different environments. Trilateration was setup to determine the location of an object using RSSI. The results indicate that the performance of LoRa was influenced by factors such as signal configuration, node positioning, and the characteristics of the indoor environment. The performance of LoRa was also evaluated under both LOS and NLOS indoor environments in the study conducted by Tabaa and Hachimi (2022). Results show improved performance of LoRa as the spreading factor increases from 7 to 12.

In this paper, detailed parameter characteristic of these wireless technologies from indoor localization perspective was analysed. Additionally, wireless technology recently incorporated into smartphone was compared with the existing ones. The comparison was based on using available information and distance-dependent models.

38. WIRELESS TECHNOLOGIES

Indoor localization schemes require wireless communication technology for the transmission and reception of data from one device to another. The most popular short and long-range technologies are WiFi, BLE, Zigbee, UWB, WiFi Halow and LoRa. This section focuses on their suitability in the development of indoor localization models and presents a comparison of these technologies.

3.1 WiFi (IEEE 802.11)

WiFi is one of the most used wireless technologies because it is compatible with a lot of portable devices from laptops to smartphones and smartwatches. It was first released in 1997 and later clarified in 1999. It works in the industrial scientific and medical (ISM) band of 2.4 or 5 GHz. It is commonly used to create a Wireless Land Area Network (WLAN) and largely used to link various devices to the internet in private and public settings. Due to the advancement in smart applications, there has been an exponential growth in the number of WiFi-enabled devices. This growth has inspired several researchers to use this technology for the development of affordable indoor localization services in recent years (Grgić, Balić, Križanović, & Žagar, 2022; Kargar-Barzi, Farahmand, Mahani, & Shafique, 2023; Zhou, Meng, Zhou, & Teng, 2022). WiFi networks are primarily designed for communication purposes, and thus, efficient algorithms are required to enhance their accuracy for localization purposes (Martin-Escalona & Zola, 2020).

The IEEE 802.11 standard has undergone continuous improvements, starting from its initial release as IEEE 802.11b in 1999, which operated at a frequency of 2.4 GHz, to IEEE 802.11g (2003) and IEEE 802.11n (2008), operating at 2.4 or 5 GHz, offering improved data rates, bandwidth, and coverage area. The IEEE 802.11ah standard (2017), also known as WiFi low power or WiFi Halow, was developed specifically for IoT device connectivity at sub-1-GHz frequency, providing an extended transmission range of approximately 1 km. The advent of IEEE 802.11ac (2014) and its more recent successor, IEEE 802.11ax (2020), which operate at the 6

GHz frequency band, have led to improved throughput, particularly in high-density environments. Furthermore, the forthcoming IEEE 802.11be (2024), which is slated to operate at 2.4/5/6 GHz frequency bands, will be specially designed to cater for WLAN indoor and outdoor localization operations. Table 1 presents an overview of the various generations of WiFi technologies, along with their distinctive key characteristics.

TABLE 1: Generation of WiFi (IEEE 802.11) Wireless Technology Standards

WiFi Generation	IEEE Standard	Release Date	Frequency Band (GHz)	Data Rate	Coverage Range (m)	Max. Transmission Power (mW)
WiFi	802.11	1997	2.4	1 - 2 Mbps	20-100	100
WiFi-1	802.11b	1999	2.4	1 - 11 Mbps	35-140	100
WiFi-2	802.11a	1999	5	6 - 54 Mbps	35-120	100
WiFi-3	802.11g	2003	2.4	6 - 54 Mbps	38-140	100
WiFi-4	802.11n	2008	2.4/5	72 - 600 Mbps	70-250	100
WiFi-Gig	802.11ad	2012	60	Up to 6.7 Gbps	1-10	10
WiFi-5	802.11ac	2014	5	433 - 6.933 Gbps	35-70	160
WiFi-Halow	802.11ah	2017	0.9	Up to 347 Mbps	100-1,000	100
WiFi-6/6E	802.11ax	2019/2020	2.4/5/6	574 - 9.608 Gbps	30-120	100
WiFi-EDMG	802.11ay	2021	60	Up to 20 Gbps	10-100	10,000
WiFi-7	802.11be	2024	2.4/5/6	1.376-46.120 Gbps	30-120	Not yet defined

3.2 BLE (IEEE 802.15.1)

Bluetooth Low Energy (BLE) is a Wireless Personal Area Network (WPAN) technology for low-power and short-range communication. It was intended for energy-constrained devices, and it operates at 2.4000 – 2.4835 GHz frequency bands. BLE was introduced by Bluetooth Special Interest Group (SIG) in 2010. Compared to older versions, BLE offers higher energy efficiency, an improved data rate of 24 Mbps, and a coverage range of 30-60 meters (Martin-Escalona & Zola, 2020). However, the most recent Bluetooth version (5.3) launched in 2021 has a transmission rate and range of about 2-50 Mbps and 240 meters, respectively.

There has been a drastic improvement from Bluetooth classic and BLE. The former refers to versions 1.0 in 1999 to 3.0 in 2009, while the latter includes versions 4.0 in 2009 to the most recent versions 5.3 launched in 2021 with two-fold increase in transmission range and rate. Classic Bluetooth suffers from short battery lifetime, making it impractical for IoT applications while BLE was introduced to meet the demand for wireless connectivity of small devices. Due to low power usage of BLE, it's ideal for IoT devices (Andy 2023). Table 2 summarizes the various improvements in BLE versions from Bluetooth classic to BLE.

TABLE 2: Improvement in Bluetooth Technology

Versions / Factors	Bluetooth v1	Bluetooth v2	Bluetooth v3	Bluetooth v4	Bluetooth v5
Data Rate	732.2 kbps to 1 Mbps	2.1 Mbps Enhanced Data Rate	800 kbps - 24 Mbps (via WiFi) (EDR)	1 Mbps (LE), 25 Mbps (EDR)	2 Mbps (LE), 50 Mbps (EDR)
Range	10 m	30 m	30 m and 10 m indoors	60 m and 40m indoors	240 m
Compatibility	N/A	Ok for any mobile phone, little sound sync issues	Ok for any mobile phone	Best for models with the same version	Best for newer phone models
Power	High	High	High	Mid-high	Low
Reliability	Low	Low	Low	Mid-high	High

a. Zigbee (IEEE 802.15.4)

Zigbee is a popular wireless technology designed to enable low-cost, low-power machine-to-machine (M2M) communication in sensor networks. It operates at 868 MHz band in Europe, 915 MHz band in the US and Australia, and 2.4 GHz in other regions (Obeidat, Shuaieb, Obeidat, & Abd-Alhameed, 2021). Zigbee is used for long-distance communication between devices in wireless sensor network. Although Zigbee is cost-effective, energy-efficient, and suitable for sensor localization in Wireless Sensor Networks (WSNs), it is not commonly found on most user devices, making it unsuitable for indoor localization of targets. Additionally, since it operates without a license in ISM bands, it is susceptible to interference from other signals operating in the same spectrum, such as WiFi and BLE.

b. UWB (IEEE 802.15.4a)

Ultra-Wideband (UWB) is a promising low energy, short-range radio-based technology that enables quick and reliable transmission of pulses at the speed of light (0.3m/ns) and larger bandwidth (<500MHz) in the frequency range of 3.1 to 10.6 GHz. This technology is particularly well-suited for the development of advanced micro-location-based systems that require secure and real-time positioning information, regardless of whether they are used indoors or outdoors (Kinexon, 2022). The standard was designed to be both low-power and low-cost while also being capable of supporting many connected devices.

Although UWB has been incorporated into some new smartphones from Apple, Samsung, Google, and Xiaomi like WiFi and BLE, it differs because it operates at a very high frequency and thus uses a wide spectrum of several GHz. Wireless technologies are often limited to narrow bands to avoid interference with each other. However, UWB technology addresses this issue by using extremely low power levels that fall within the noise floor of other wireless applications. Essentially, the UWB spectrum is wide enough to be easily detectable, but low-powered enough to prevent interference with other signals. Fig. 1 shows the spectrum of common wireless technologies. UWB technology is becoming increasingly popular, with the Apple AirTag being one of its most common applications. Its ability to track the location of objects makes it useful in various scenarios, and it holds promise for secure car unlocking and smart homes in the future (Viot, Bizalion, & Seegars, 2021). In contrast to WiFi and BLE, which rely on RSSI for distance estimation, this technology utilizes time of flight (ToF) multiplied by the speed of light in air to determine both distance and direction from the transmitter. The pulse-based nature of UWB technology enables this significant advantage.

Technologies that rely on RSSI can yield misleading distance and location measurements in indoor environments. The multipath effects can be ignored in UWB because the technology uses the shortest distance to calculate the ToF even if the direct signal is weaker than the obstructed signals. In addition, it only requires a single measurement to determine position accurately and reliably, while other technologies may require multiple samples with filtering to determine location (Viot et al., 2021).

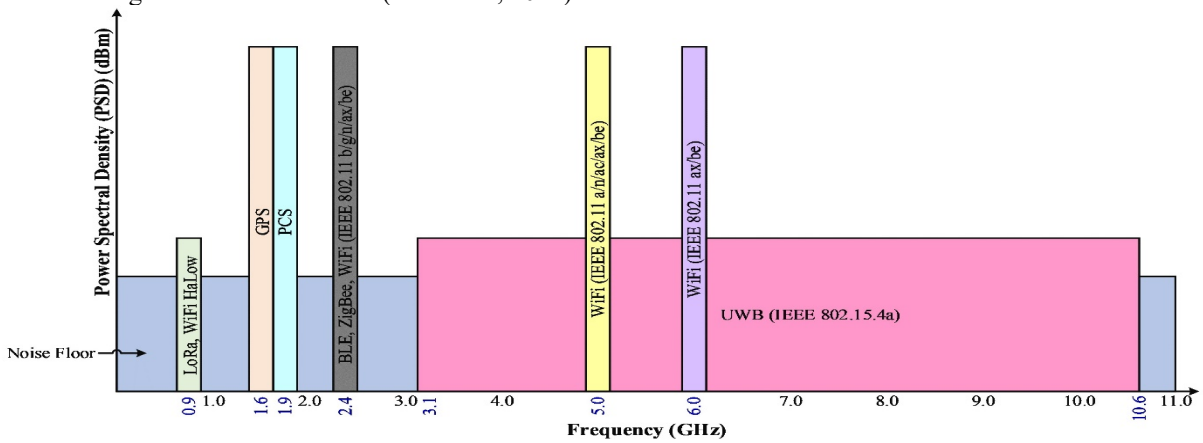

Fig 1: Spectrum used by common Wireless Technologies.

c. LoRa (Long Range)

LoRa is a wireless technology that has emerged as one of the most frequently utilised long range and Low-Power Wide-Area Network (LPWAN) technology in a variety of IoT applications. LoRa operates at frequencies of 868 MHz and 915 MHz in the unlicensed ISM bands in Europe and America, respectively, providing a range of around 5 km in urban areas and up to 15 km in rural areas (Al Khattat, Anas, & Saif, 2022). The low power, low data rate and long range makes it the ideal technology for IoT and smart applications, unlike other technologies transmitting more data and hence consumes more power. LoRa uses a Chirp Spread Spectrum (CSS) modulation to improve robustness against noise and bandwidth of 125, 250 or 500 kHz to transmit small data packet (0.3-50 kbps) on the sub-1 GHz bands.

The important parameters of LoRa are Bandwidth (BW), Spreading Factor (SF) and Code Rate (CR). These parameters influence its bit rate, resistance to interference and receiver or decoder sensitivity (Tabaa & Hachimi, 2022). An increase in BW lowers the receiver sensitivity, increases the data rate, whereas an increase in SF increases the receiver sensitivity, increases power consumption, lower data rate and its resistance to interference.

39. SYSTEM DISTANCE-DEPENDENT MODEL

Considering an indoor environment where there is LOS between a transmitter and a receiver at a distance of $d = 100\ m$ apart, the carrier frequency f_c, and the path loss exponent n. Path loss of any wireless technology can be defined in (Ghosh et al., 2022):

$$PL_{wt}[dB] = 2n \log_{10}\left[\frac{4\pi d}{f_c}\right] + 10 \log_{10}\left[\frac{4\pi}{\lambda}\right]^2 \quad (1)$$

Where wt is refers to any of the wireless technology, λ is the wavelength and is related to frequency and speed of light c by

$$\lambda = \frac{c}{f_c} \tag{2}$$

The received power is related to the transmitted power Pt_{wt} , transmitter and receiver gains ($Gt_{wt}\ and\ Gr_{wt}$) and system loss L_{wt} by:

$$Pr_{wt}[dBm] = Pt_{wt} + Gt_{wt} + Gr_{wt} - PL_{wt} - L_{wt} \tag{3}$$

The noise spectral density is given as:

$$N_{0-wt} = -174 + 10\,log_{10}\,BW_{wt} \tag{4}$$

Signal-to-interference-plus-noise ratio (SINR) is related to the received power Pr_{wt} , Bandwidth BW_{wt} and noise spectral density N_{o-wt} by:

$$SINR_{wt}[dB] = Pr_{wt} - N_{0-wt} - 10\log_{10} BW_{wt} \tag{5}$$

Data rate of the wireless technology is related to the bandwidth and SINR by Shannon Hartley equation (Ghosh et al., 2022) as:

$$R_{b-wt}[bps] = BW_{wt} \times log_2(1 + 10^{\frac{SINR_{wt}}{10}}) \tag{6}$$

Coverage range is also related to gains, receiver sensitivity by Friis equation (Augustin, Yi, Clausen, & Townsley, 2016) as:

$$Range_{wt}[m] = \frac{\lambda}{4\pi}\sqrt{\frac{Pt_{wt}\times Gt_{wt}\times Pt_{wt}}{P_{min-wt}\times Gr_{wt}}} \tag{7}$$

40. RESULTS AND DISCUSSION

Some underlying factors need to be considered for a wide-scale adoption of any of these technologies in indoor localization systems. The factors are frequency band, coverage range, Signal-to-Interference-plus-Noise Ratio, power consumption, deployment cost and smartphone accessibility and applications. Table 3 summarizes these factors. The parameters in Table 3 assumed the devices are transmitting with maximum power and LOS is maintained between the devices.

Table 3: Parameter characteristics of different Wireless Technologies in Indoor Environment

Technology / Metrics	WiFi	BLE	Zigbee	UWB	WiFi Low Energy	LoRa
Frequency (GHz)	2.4/5/6	2.4-2.48	2.4	3.1-10.6	0.9	0.915
Coverage (m)	~100	30-60	10-30	10-30	100-1,000	2,000-5,000
Data rate (Mbps)	2-600	1-2	0.25-1	53.3-480	8.67-347	0.3-50 kbps
Consumption	Medium	Very low	Low	Low	Low	Extreme low
Smartphone availability	Yes	Yes	No	Partial	No	No
Applications	Smart cities	IoTs	WSN	LBS, Smart Car Access	IIoTs	IoTs, Smart farming
Advantages	Widely available, low cost and portable	Widely available, low cost and portable	Low-cost and power consumption	Accurate, reliable, and low power consumption	Wide range, low power consumption	Wide range, low power, and low-cost
Disadvantages	Prone to noise, signal blockage	Prone to noise, signal blockage	Limited range and data rate	Limited adoption and range, Require LOS	Prone to noise, Extra HW, not suitable for higher BW applications	Limited data rate and BW, Require Extra HW

Frequency band and coverage area: the frequency of the wireless technology can affect the coverage of the system. Lower frequency signals tend to have a longer range and are better suited for large indoor spaces such has LoRa and WiFi Halow, while higher frequency signals tend to have a shorter range and are better suited for smaller indoor spaces. Data Rate: Higher data rate improves system capacity but at the expense of energy consumption. Most indoor LBSs does not need to transfer large amount of data. UWB, WiFi and BLE uses tens of Mbps while the data rate of LoRa, WiFi Halow and Zigbee is in the order of tens of kbps as shown in Fig. 2. SINR: A higher SINR means that the received signal is stronger relative to the interference and noise, which reduces the probability of errors and increases the capacity of the network as seen in Fig. 3. Power Consumption: The consumption should be low to support battery-operated devices and enable long lifetime. LoRa, BLE and WiFi

Halow are the most appropriate technology with least power consumption. Zigbee and UWB are suitable for devices that may need to work for few months with medium power consumption. WiFi technology has the highest energy consumption, but common WiFi-based APs are usually powered from the main supply. Smartphone accessibility and deployment cost: Both parameters are interwoven. Lower deployment cost can make indoor localization systems more accessible and affordable for a wider range of applications and users. WiFi and BLE tend to have lowest cost because they are readily available on smartphones. Recently, UWB technology is also available on smartphones from vendors like Apple, Samsung, Google Pro and Xiaomi Mix. LoRa, Zigbee and WiFi Halow requires special hardware (HW), but the range of LoRa can be compensated with the cost of the HW. Applications: Wireless technology-based indoor localization is a cost-effective and precise solutions for a variety of satellite-denied applications such as healthcare, industries, logistics, context-aware marketing, and emergence response.

Based on Equations (1-7), the estimated data rate and quality of the received signal can be measured by SINR for the wireless technologies as illustrated in Figures 2 and 3. The results in Figure 3 indicate that UWB and WiFi have significantly higher data rates compared to BLE and Zigbee which have relatively low data rates, and LoRa has the lowest achievable data rate. UWB and WiFi are suitable for real-time applications. SINR is a metric used to determine the signal quality relative to noise and interference in the environment. UWB provides the best signal quality, followed by WiFi, while LoRa exhibits the least signal quality. Zigbee and BLE have relatively good signal quality. It is important to note that the actual signal strength may vary greatly depending on the environment, such as the presence of walls, humans, other wireless devices, interference, and other factors.

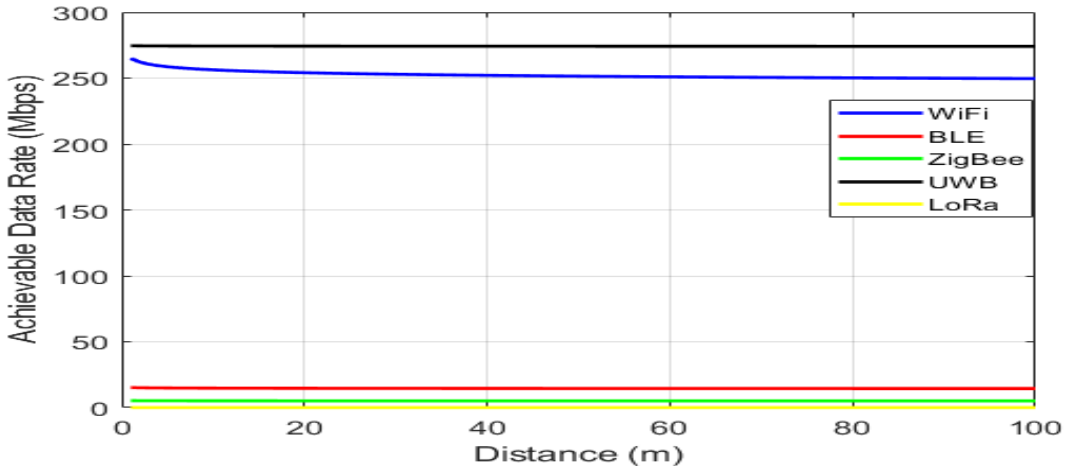

Fig 2: Data Rate of the Wireless technologies

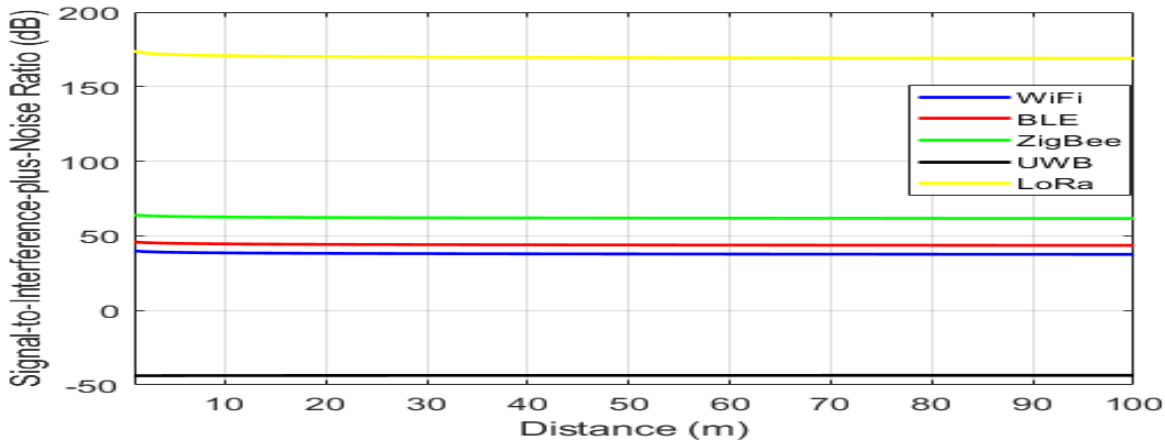

Fig 3: SINR of the Wireless technologies

41. CONCLUSION

In this study, we characterize and analyse the performance of several wireless communication technologies in term of frequency band, data rate, SINR, energy consumption, smartphone availability, deployment cost and application areas. The essence of the characterization is to help us to decide the appropriate wireless technology for a specific indoor localization application. In the analysis, UWB is found to be suitable for small indoor environment because of the wide frequency band, followed by WiFi, BLE and Zigbee while LoRa and WiFi

Halow are suitable for large indoor environment. LoRa has the least energy consumption followed by BLE and WiFi Halow. The energy consumed by Zigbee and UWB are relatively low while WiFi consumes the most energy. WiFi, BLE and recently UWB are smartphone accessible, hence they have the lowest cost while others wireless technologies need extra hardware for deployment.

However, it is important to note that the accuracy of this analysis can be affected by a variety of factors, including environmental conditions and device heterogeneity. Future study should consider experimental evaluation of the wireless technologies in different environments with different interference level using robust indoor localization techniques.

ACKNOWLEDGEMENT

This study was funded by International Collaborative Research Fund (ICRF) between Universiti Teknologi PETRONAS, Perak, Malaysia and University of Lampung, Bandar Lampung, Indonesia.

REFERENCES

Al Khattat, V. H. F., Anas, S. B. A., & Saif, A. (2022). *An Efficient 3D Indoor Positioning System Based on Visible Light Communication.* Paper presented at the 2022 2nd International Conference on Emerging Smart Technologies and Applications (eSmarTA).

Andy G., Different Bluetooth Versions: What you need to know, updated on 01/03/2023, accessed on 20/03/2023, available at https://www.headphonesty.com/2021/01/bluetooth-versions/.

Asaad, S. M., & Maghdid, H. S. (2022). A Comprehensive Review of Indoor/Outdoor Localization Solutions in IoT era: Research Challenges and Future Perspectives. *Computer Networks*, 109041.

Augustin, A., Yi, J., Clausen, T., & Townsley, W. M. (2016). A study of LoRa: Long range & low power networks for the internet of things. *Sensors, 16*(9), 1466.

Farahsari, P. S., Farahzadi, A., Rezazadeh, J., & Bagheri, A. (2022). A Survey on Indoor Positioning Systems for IoT-based Applications. *IEEE Internet of Things Journal, 9*(10), 7680-7699.

Ghosh, J., Haci, H., Kumar, N., Al-Utaibi, K. A., Sait, S. M., & So-In, C. (2022). A novel channel model and optimal power control schemes for mobile mmWave two-tier networks. *IEEE Access, 10*, 54445-54458.

Grgić, K., Balić, L., Križanović, V., & Žagar, D. (2022). *An Example of Indoor Positioning Possibility Using WiFi Network and Mobile Phone.* Paper presented at the 2022 International Conference on Smart Systems and Technologies (SST).

Kargar-Barzi, A., Farahmand, E., Mahani, A., & Shafique, M. (2023). CAE-CNNLoc: An Edge-based WiFi Fingerprinting Indoor Localization Using Convolutional Neural Network and Convolutional Auto-Encoder. *arXiv preprint arXiv:2303.03699*.

Khan, F. U., Awais, M., Rasheed, M. B., Masood, B., & Ghadi, Y. (2021). A comparison of wireless standards in iot for indoor localization using loPy. *IEEE Access, 9*, 65925-65933.

Kinexon. (2022). UWB Technology. Everything you need to know about UWB technology (kinexon.com), accessed on 20/03/2023, available: https://kinexon.com/uwb-technology/.

Klepeis, N. E., Nelson, W. C., Ott, W. R., Robinson, J. P., Tsang, A. M., Switzer, P., . . . Engelmann, W. H. (2001). The National Human Activity Pattern Survey (NHAPS): a resource for assessing exposure to environmental pollutants. *Journal of Exposure Science & Environmental Epidemiology, 11*(3), 231-252.

Martin-Escalona, I., & Zola, E. (2020). Passive round-trip-time positioning in dense IEEE 802.11 networks. *Electronics, 9*(8), 1193.

Obeidat, H., Shuaieb, W., Obeidat, O., & Abd-Alhameed, R. (2021). A review of indoor localization techniques and wireless technologies. *Wireless Personal Communications, 119*(1), 289-327.

Sadowski, S., & Spachos, P. (2018a). *Comparison of rssi-based indoor localization for smart buildings with internet of things.* Paper presented at the 2018 IEEE 9th Annual Information Technology, Electronics and Mobile Communication Conference (IEMCON).

Sadowski, S., & Spachos, P. (2018b). Rssi-based indoor localization with the internet of things. *IEEE Access, 6*, 30149-30161.

Sadowski, S., & Spachos, P. (2019). *Optimization of BLE beacon density for RSSI-based indoor localization.* Paper presented at the 2019 IEEE International Conference on Communications Workshops (ICC Workshops).

Sadowski, S., Spachos, P., & Plataniotis, K. N. (2020). Memoryless techniques and wireless technologies for indoor localization with the internet of things. *IEEE Internet of Things Journal, 7*(11), 10996-11005.

Sarigiannis, D. A., Gotti, A., & Karakitsios, S. P. (2019). Indoor air and public health *Management of Emerging Public Health Issues and Risks* (pp. 3-29): Elsevier.

Simka, M., & Polak, L. (2022). On the RSSI-based indoor localization employing LoRa in the 2.4 GHz ISM band. *Radioengineering, 31*(1), 135-143.

Tabaa, M., & Hachimi, H. (2022). Experimental test and performance of RSSI-based indoor localization in LoRa Networks. *Procedia Computer Science, 203*, 420-425.

Viot, M., Bizalion, A., & Seegars, J. (2021). Exploring Ultra-Wideband Technology for Micro-Location-Based Services. *Microwave Journal, 64*(6).

Wang, L., Shang, S., & Wu, Z. (2023). Research on indoor 3D positioning algorithm based on wifi fingerprint. *Sensors, 23*(1), 153.

Zhou, R., Meng, F., Zhou, J., & Teng, J. (2022). A Wi-Fi Indoor Positioning Method Based on an Integration of EMDT and WKNN. *Sensors, 22*(14), 5411.

PAPER 144 – ASSESSMENT OF THE SIGNIFICANCE OF GIS-BASED WATERSHED ANALYSIS FOR EFFECTIVE WATER RESOURCES MANAGEMENT

M. I. Alfa[1*], A. Ismail[2], R. E. Daffi[1], H. I. Owamah[3], D. B. Adie[2] and B. Abdulraham[1]

[1]Department of Civil Engineering, University of Jos, Jos, Nigeria
[2]Department of Water Resources & Environmental Engineering, Ahmadu Bello University, Zaria, Nigeria
[3]Department of Civil Engineering, Delta State University, Abraka, Oleh Campus, Delta State, Nigeria
[*]Email: meshilalfa@gmail.com

ABSTRACT
Traditional techniques have been used over the years for the determination of watershed characteristics and runoff. Technological advancements in the area of remote sensing and Geographic Information Systems have proven to be more effective techniques that can produce more accurate results, save time and remove most human errors. The efficiency of using GIS-based techniques for watershed analysis was explored in this study, using the Galma River catchment as a case study. Characteristics such as Area, perimeter, time of concentration, length of overland flow, longest flow path, time to recession, and peak discharge amongst others were determined using traditional manual techniques and GIS-Based techniques. The results from both methods were compared using the student's t-test. In addition to a strong correlation of 0.98 observed for results from both methods, the results showed that the difference in the estimates from both techniques was not statistically significant at a 95% confidence level since the *t stat* (1.528) is less than the *t critical-two tail* (2.120) and the *P (T<=t) value* of 0.266 is greater than 0.005. It was concluded that the GIS-Based techniques for watershed analysis are reliable, accurate, and time-saving methods that should be explored in Water resources studies.

KEYWORDS: Discharge, Flood, Gamji catchment, GIS, Watershed analysis, Water resources

1. INTRODUCTION

Water resources management-related problems are central determinant for the attainment of a number of the Sustainable Development Goals (SDGs). Accurate determination of watershed characteristics and the resultant runoff from them is essential for optimum design and planning of water resource infrastructure (Boulos, 2017).
While traditional technique has been used extensively over the years for delineation of watershed, determination of the characteristics and estimation of design flood especially for ungauged catchments, the method has become greatly undesirable. This is because of the amount of time spent, the great propensity for human errors amongst other factors. The advancement of technology especially in the area of remote sensing and Geographic Information systems have provided more effective techniques that can produce more accurate results, save time and remove most human errors (Dongquan *et al.,* 2009; Widaningrum *et al.,* 2015; Radwan *et al.,* 2017).
Notwithstanding the aforementioned advantages of the GIS-based system, it becomes necessary to compare the output with that of the traditional system since it is significantly dependent on remotely sensed data. The efficiency of using GIS-based techniques for watershed analysis was therefore explored in this study, using Galma River catchment in Kaduna State, Nigeria as a case study.

2. THEORETICAL ANALYSIS

The comparison of the two methods was based on the morphometric and hydrologic characteristics of the Galma basin. The various mathematical principles are summarized in Table 1.

Table 1: Methods used for Estimation of Morphometric Parameters

Parameter	Symbol	Formula	Reference
Area	A	GIS Analysis	-
Perimeter	P	GIS Analysis	-
Longest Flow Path	L_{fp}	GIS Analysis	-
Basin Slope	S	*GIS Analysis*	-
Stream Number	N_u	*GIS Analysis*	Horton (1945)
Stream Length	L_u	*GIS Analysis*	Horton (1945)
Mean Stream Length	N_{um}	$L_{um} = L_u / N_u$	Strahler (1964)
Stream frequency	F	$F = \Sigma N_u / A$	Horton (1945)
Drainage Density	D_d	$D_d = \Sigma L_u / A$	Horton (1932; 1945)
Length of Overland Flow	L_o	$L_o = 1/2D_d$	Langbein & Leopold (1964)
Form factor	F_f	$F_f = A/L_b^2$	Horton (1932)
Compactness coefficient	C_c	$C_c = 0.282038P/A^{0.5}$	Horton (1945)
Elongation ratio	R_e	$R_e = 2\sqrt{(A/n)}/L_b$	Schumm (1956)
Circularity ratio	R_c	$R_c = 4nA)/P^2$	Miller (1953)
Time of Concentration	T_c	$T_c = 0.000323{L_{fp}}^{0.77}S^{-0.385}$	Kirpich (1940)
Time to Recession	N	$N = 0.84A^{0.2}$	Mustafa & Yusuf, 2012

3. MATERIALS AND METHODS

3.1 Study Area

The area for this study is the Galma River Basin in Kaduna State, Nigeria (Figure 1). It is bounded by Longitudes 337152.18 - 473052.91 m and latitudes 1156258.19 - 1262840.39 m in UTM Zone 32. The Galma river drains parts of Kaduna, Kano and Katsina states with a significant portion of the catchment area (92.99%) in Kaduna State, 4.54% in Kano state and 2.47% in Katsina state.

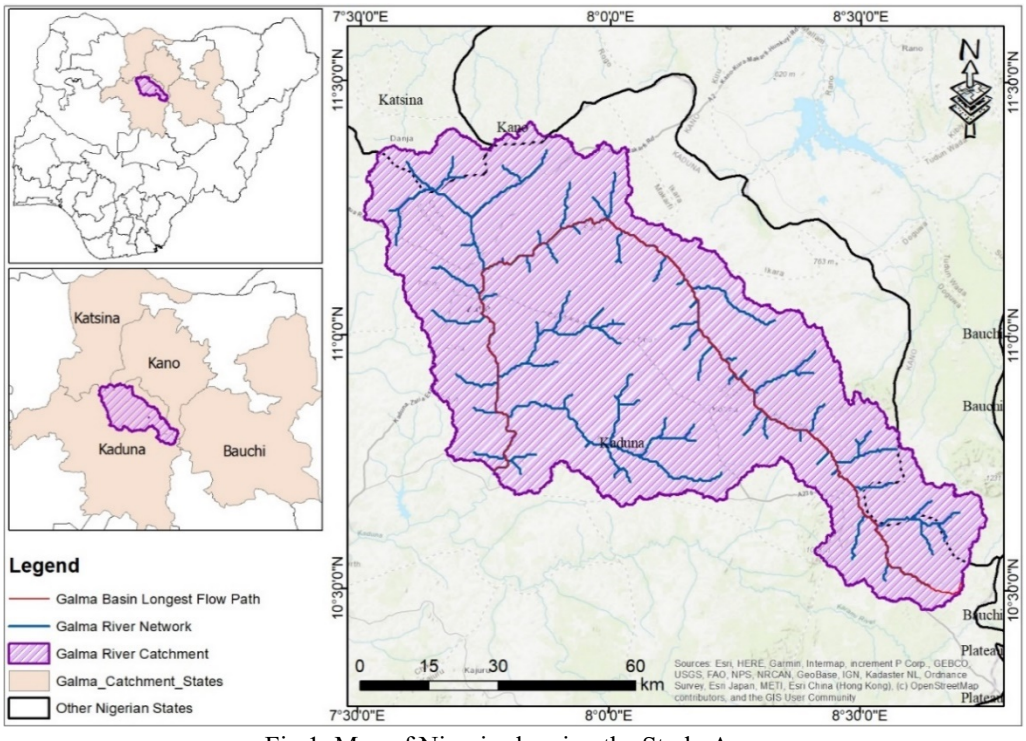

Fig 1: Map of Nigeria showing the Study Area

3.2 Determination of Morphometric Characteristics of the Catchment

The equations summarized in Table 1 were used to determine the respective morphometric characteristics of the watershed. These methods have been applied previously to other watersheds such as the Ofu River catchment in Kogi State, Nigeria (Alfa *et al.,* 2019).

3.3 Method of Determination of Peak Discharge

The rational equation method was applied for the estimation of the peak runoff for the galma river catchment. The rational equation has been described previously by various authors (Wang *et al.,* 2011; Wang *et al.,* 2012; Baiamonte, 2020). The method was recommended in and has been comprehensively described in the Federal Republic of Nigeria Highway Design Manual Part 1 (2013): Volume IV (Drainage Design). The rational equation is expressed by equation 1.

$$Q = 0.278CIA \quad (1)$$

In which, C is the composite runoff coefficient of the catchment, I is the rainfall intensity expressed in millimetres per hour for a certain time of concentration and A is the catchment area in square kilometres.

The runoff coefficient, C was estimated following the methods described previously in Alfa *et al.,* (2018). It combines the terrain slope (Figure 2), the land cover characteristics (Figure 3) and soil characteristics (Figure 4) to develop a composite runoff coefficient for the entire catchment.

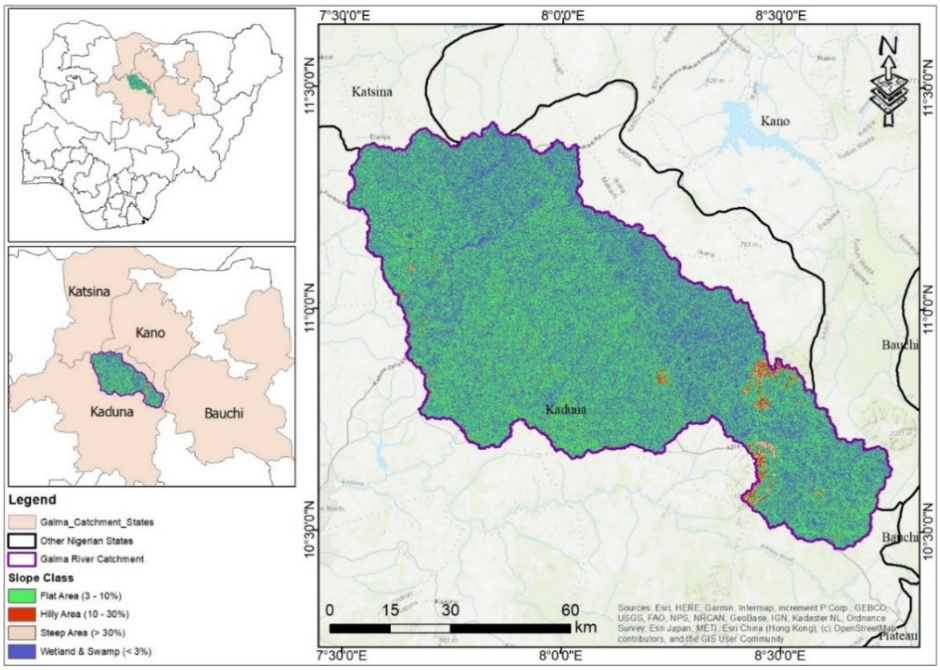

Fig 2: Terrain Slope Map of the Study Area

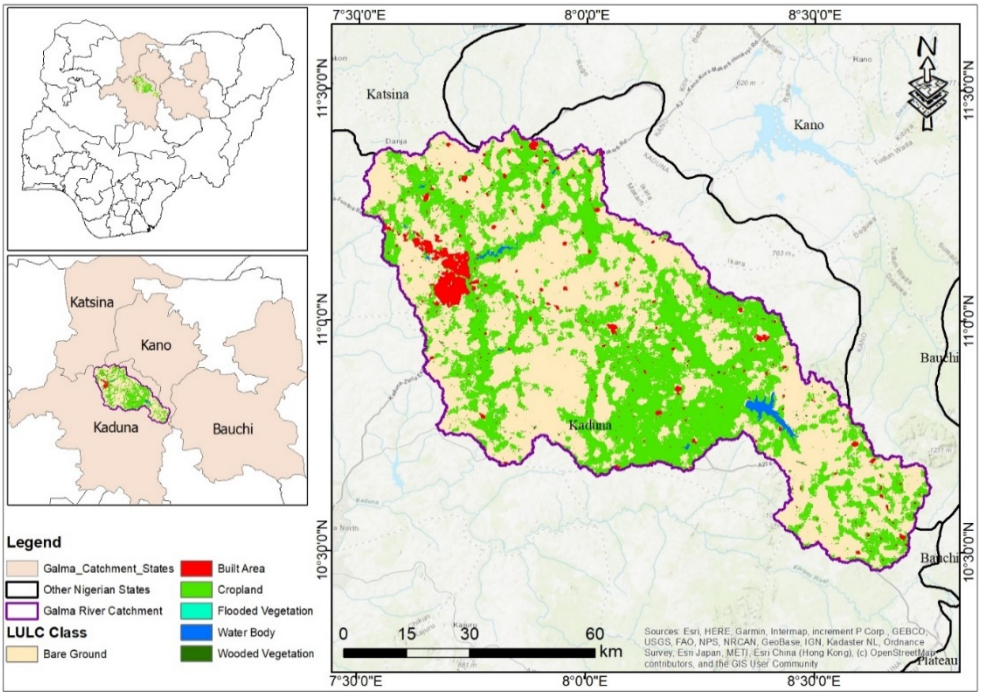

Fig 3: Land use/Landcover Map of the Study Area

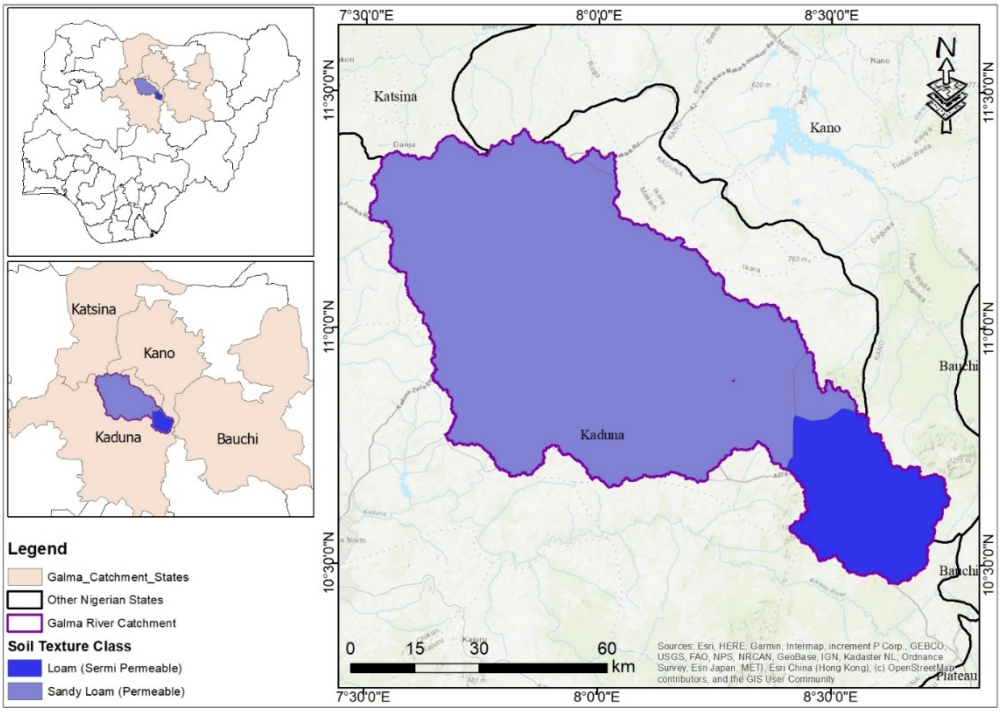

Fig 4: Soil Map of the Study Area

The slope was generated from the Shuttle Radar Topographic Mission digital elevation model (SRTM DEM) obtained from the *earthexplorer* portal of the United States Geological Survey, the land cover data was obtained from Environmental Systems Research Institute (ESRI) while the soil map was extracted from the FAO's digital soil map of the world.

3.4 Statistical Analysis

The student's t test was used to compare the catchment characteristics obtained using both methods at 95% confidence level.

4. RESULTS AND DISCUSSION

4.1 Runoff Coefficient

The composite runoff coefficient for galma river catchment is presented in Table 1. The composite value of 0.57 was obtained.

Table 1: Runoff Coefficient for Galma River Catchment

Class	Area (m^2)	Runoff Coefficient, C	
		Value	Composite
Land use/Landcover			
Water Body	43.97	0.3	0.18
Wooded Vegetation	12.44	0.05	
Flooded Vegetation	0.14	0.3	
Cropland	2,710.00	0.015	
Built Area	205.73	0.3	
Bare Ground	3,591.50	0.3	
Slope			
Wetland & Swamp (<3%)	2,828.68	0.05	0.09
Flat Area (3 - 10%)	3,584.12	0.11	
Hilly Area (10 - 30%)	107.58	0.2	
Steep Area (<30%)	26.19	0.3	
Soil			
Sandy Loam (Permeable)	5,562.67	0.1	0.12
Loam (Semi Permeable)	1,001.12	0.2	
Catchment Value			**0.38**

4.2 Morphometric and Discharge Characteristics

The morphometric and discharge characteristics of the galma river catchment are presented in Table 2.

Table 2: Morphometric and Hydrologic Characteristics of Galma Basin

Parameter	Category	Manual	GIS-Based
Area (km^2)	Areal (Basic)	6,781.00	6563.795
Perimeter (km)	Areal (Basic)	451.00	807.99
Longest flow path (km)	Areal (Basic)	115.00	256.97
Basin Slope	Relief	0.02	0.04
Stream Number	Linear	673.00	149.00
Stream Length (km)	Linear	2,266.40	917.09
Mean Stream Length (km)	Linear	3.367608	6.154938
Stream Frequency	Linear	0.10	0.02
Drainage Density	Areal (Derived)	0.33	0.14
Length of Overland Flow	Areal (Derived)	1.50	3.58
Form factor	Areal (Derived)	58.97	25.54
Compactness coefficient	Areal (Derived)	1.54	2.81
Elongation ratio	Areal (Derived)	0.81	0.36
Circularity ratio	Areal (Derived)	0.42	0.13
Time of Concentration	Areal (Derived)	15.00	17.27
Time to Recession from peak	Areal (Derived)	4.90	4.87
Peak discharge	Hydrologic	3,613.99	3,498.23

Similarly, the results of the statistical comparison of the characteristics of the catchment obtained using both methods is presented in Table 3.

Table 3: Results of Statistical Analysis

Statistics	*Manual*	*GIS-Based*
Mean	822.7850038	720.822612
Variance	3334012.226	3004452.887
Observations	17	17
Pearson Correlation	0.980344979	
Hypothesized Mean Difference	0	
df	16	
t Stat	1.152813806	
P(T<=t) one-tail	0.132959805	
t Critical one-tail	1.745883676	
P(T<=t) two-tail	0.26591961	
t Critical two-tail	2.119905299	

The results showed that a strong correlation (0.98) exist between the catchment characteristics obtained using both methods. More so, the results showed that the difference in the estimates from both techniques was not statistically significant at a 95% confidence level since the *t stat* (1.528) is less than the *t critical-two tail* (2.120) and the *P (T<=t) value* of 0.266 is greater than 0.005. The results obtained herein corroborates previous findings on the reliability of using GIS-based techniques for catchment-wide hydrological studies that can save time and produce more accurate results (Dongquan *et al.,* 2009; Widaningrum *et al.,* 2015; Radwan *et al.,* 2017).

5. CONCLUSION

It was concluded that the GIS-Based techniques for watershed analysis is a reliable, accurate and time saving methods that should be explored in Water resources studies. With a correlation coefficient of 0.98 and a P-value of 0.266, it can be concluded that the results obtained from the GIS-based study can be a safe replacement for the traditional manual techniques.

REFERENCES

Alfa, M. I., Ajibike, M. A., Adie, D. B., & Mudiare, O. J. (2018). Assessment of the effect of land use/land cover changes on total runoff from Ofu River catchment in Nigeria. *Journal of Degraded and Mining Lands Management*, *5*(3), 1161-1169.

Alfa, M. I., Ajibike, M. A., Adie, D. B., & Mudiare, O. J. (2019). Hydrologic and morphometric analysis of Ofu River Sub-Basin using remote sensing and Geographic Information System. *Nigerian Journal of Technological Development*, *16*(2), 49-55.

Baiamonte, G. (2020). A rational runoff coefficient for a revisited rational formula. *Hydrological Sciences Journal*, *65*(1), 112-126.

Boulos, P. F. (2017). Smart water network modeling for sustainable and resilient infrastructure. *Water Resources Management*, *31*(10), 3177-3188.

Dongquan, Z., Jining, C., Haozheng, W., Qingyuan, T., Shangbing, C., & Zheng, S. (2009). GIS-based urban rainfall-runoff modeling using an automatic catchment-discretization approach: a case study in Macau. *Environmental Earth Sciences*, *59*, 465-472.

Horton, R. E. (1932). Drainage-basin characteristics. Eos, Transactions American Geophysical Union, 13(1), 350-361.

Horton, R. E. (1945). Erosional development of streams and their drainage basins; hydrophysical approach to quantitative morphology. Geological society of America bulletin, 56(3), 275-370.

Kirpich, Z. P. (1940). Time of concentration of small agricultural watersheds. Civil Engineering, 10(6), 362.

Langbein, W. B., & Leopold, L. B. (1964). Quasi-equilibrium states in channel morphology. American Journal of Science, 262(6), 782-794.

Miller, V. C. (1953). A quantitative geomorphic study of drainage basin characteristics in the clinch mountain area virginia and tennessee (No. CU-TR-3). Columbia University New York.

Mustafa S. and Yusuf M. I. (2012). A Textbook of Hydrology and Water Resources, Revised Edition. Abuja. Topsmerit Page Publishing Company.

Radwan, F., Alazba, A. A., & Mossad, A. (2017). Watershed morphometric analysis of Wadi Baish Dam catchment area using integrated GIS-based approach. *Arabian Journal of Geosciences*, *10*, 1-11.

Schumm, S. A. (1956). Evolution of drainage systems and slopes in badlands at Perth Amboy, New Jersey. Geological society of America bulletin, 67(5), 597-646.

Strahler, A. N. (1964). Quantitative geomorphology of drainage basin and channel networks. Handbook of applied hydrology, Ed. Ven Te Chow, 04, 9 - 76.

Wang, X., Liu, T., Li, C., Zhu, Z., Zhang, S., & Melesse, A. M. (2011). Development of a modified rational equation for arid-region runoff estimation. In *World Environmental and Water Resources Congress 2011: Bearing Knowledge for Sustainability* (pp. 4702-4716).

Wang, X., Liu, T., & Yang, W. (2012). Development of a robust runoff-prediction model by fusing the rational equation and a modified SCS-CN method. *Hydrological Sciences Journal*, *57*(6), 1118-1140.

Widaningrum, D. L. (2015). A GIS–based approach for catchment area analysis of convenience store. *Procedia Computer Science*, *72*, 511-518.

PAPER 147 – STORAGE STABILITY OF OPTIMIZED FOAM-MAT DRIED TOMATO-PEPPER-ONION POWDER UNDER DIFFERENT PACKAGING CONDITIONS

A. Sadiq[1*], S. T. Olorunsogo[2]

Department of Agricultural and Bioresources Engineering, Federal University of Technology, Minna, Niger state, Nigeria

*Email: sadiqabbas032@gmail.com

ABSTRACT

The storage stability of optimized foam-mat dried tomato-pepper-onion powder was evaluated under different packaging conditions. The powder was prepared using a foam-mat drying technique and optimized using response surface methodology. The levels for various input variables were tomato (5 – 76%), pepper (5 – 78%), onion (5 – 80%), egg white (2 - 15%), carboxymethyl cellulose (0.15 - 0.75%) & Drying temperature: 50-80°C. Laminated aluminium foil, high density polyethylene and medium density polyethylene were three distinct packaging types used to package the optimized powder. Every five days, the storage stability of the powders was checked while they were kept at room temperature for 30 days. The amount of MC, lycopene, protein, and microbial growth were assessed in the powder sample. The findings demonstrated that, in comparison to the control group, all packing options considerably increased the powder's storage stability. The LAF was the most effective in keeping moisture from entering the package and was also able to preserve the most lycopene content (10.40%) as compared to the control value of 10.21%, while also having the lowest moisture content over the course of storage at 4.39 percent.

***KEYWORDS*:** Storage Stability, Foam-mat Drying, Tomato-pepper-onion Powder, Packaging Conditions, Compositional Changes, Viable Load

1. INTRODUCTION

In many cuisines around the world, vegetables like tomatoes, peppers, and onions are crucial. Lycopene, a carotenoid with antioxidant qualities, is abundant in tomatoes. Lycopene, which gives tomatoes their red color, has been linked to a lower risk of some malignancies, cardiovascular illnesses, and age-related macular degeneration (AMG) (Hossain *et al.,* 2021). Vitamin C, carotenoids, and capsaicin, a bioactive substance with anti-inflammatory and analgesic qualities, are all abundant in peppers. Quercetin, a flavonoid with anti-inflammatory and antioxidant effects, is abundant in onions. (Iqbal *et al.,* 2021). These three veggies are combined to give varied dishes flavor and aroma as well as a balanced nutrient content.

Food processing and preservation are crucial for guaranteeing food safety, accessibility, and availability. Different techniques for food preservation have been created over time and implemented on a global scale. The techniques that are most frequently utilized are drying, canning, freezing, and irradiation. The nature of the product, the preservation criteria, and the planned use all factor into the preservation method selection (Liu *et al.,* 2022).

One of the earliest and most popular ways of food preservation is drying, which is how those vegetables are preserved. It entails drying out food products to eliminate moisture and stop microbial development and enzymatic activity, which could lead to spoiling. Drying is economical, uses little energy, and keeps the vegetables' nutritious content.

Traditional drying techniques including sun, air, and oven drying take a long time to dry, are of poor quality, and result in deteriorated products. As a result, the food sector has created and embraced cutting-edge drying techniques like freeze-drying, spray drying, and foam-mat drying (Bhatkar *et al.,* 2021). Foam-mat drying is a relatively new technology that has attracted attention due to its ability to produce high-quality, nutritious and shelf-stable food powders.

Proteins, surfactants and other foaming ingredients are used in foam-mat drying to create stable foam. After regulated drying, the foam transforms into a porous, stable powder. A variety of food powders, including milk, egg, fruit, and vegetable powders, have been produced using the method (Kilicli *et al.,* 2022).

However, nothing is known about the foam-mat dry tomato, pepper, and onion powder's storage stability under various packing scenarios. Therefore, it is necessary to research how different packaging materials and storage settings affect the quality indices of foam-mat dried tomato-pepper-onion powder while it is being stored. This study intends to fill up this information gap and offer important insights into the creation of packaging techniques that would increase the storage stability and shelf life of dried tomato, pepper, and onion powder packaged in foam-mats.

2. THEORETICAL ANALYSIS

Examining the effects of various packaging materials on the compositional changes and viable load in the powder during storage is a part of the theoretical analysis of the research on the storage stability of optimized foam-mat dried tomato, pepper, and onion powder under various packaging conditions. The study makes use of food science and technology principles, particularly those relating to drying and packing. Theoretical ideas like the mechanics of foam-mat drying and the elements influencing food product shelf life are also taken into account.

In order to ascertain the impacts of packing on the stability of the powder, the research also analyzes the lycopene content, moisture content, protein and the microbial growth.

3. MATERIALS AND METHODS

The tomatoes, onions, and peppers were gathered from the Kure market in Minna, Niger State, and the defective ones were separated out. The tomatoes, onions, and peppers had a diameter of 65 to 80 mm and weighed 80 to 110 g. The biomaterials were soaked in a salt solution containing 1 percent $CaCl_2$ and 0.2 percent potassium metabisulphite (KMS) for 10 minutes at room temperature after being cleaned with distilled water. The Federal University of Technology, Minna's department of Agricultural and Bioresources Engineering laboratory handled the preparation of the foam-mat dry powder, while the department of Food Science and Technology of Federal University of Technology Minna handled the analysis.

3.1 Experimental Design

Combining mixture variables and process variables allowed the experimental design to be constructed. The drying process for foam mats is typically impacted by a number of factors, including drying temperature (^oC). The levels of these variables (drying temperature, foaming agent and binder) were collected from the literature for the current research. Different drying temperatures might result in radically different outcomes even when using the same ingredients (such as tomato, onion, and pepper). With three main components—tomato (,x-1), pepper (,x-2), and onion (,x-3), as well as egg white (,x-4) as a foaming agent and carboxyl methyl cellulose (CMC) (,x-5) as a stabilizer—D-optimal design is employed in this study.

Table 3.1: Experimental Design for the Formulation Experiment

Run	**X_1:Tomato**	**X_2:pepper**	**X_3:Onion**	**X_4:Egg White**	**X_5:CMC**	**Z_1:Drying Temp**
	%	%	%	%	%	^0C
1.0	36.1	51.5	5.0	7.3	0.2	65.0
2.0	20.3	56.5	21.0	2.0	0.2	57.8
3.0	5.0	74.6	5.0	15.0	0.4	50.0
4.0	25.8	67.0	5.0	2.0	0.2	80.0
5.0	45.3	28.6	21.5	4.2	0.4	50.0
6.0	22.6	70.2	5.0	2.0	0.2	50.0
7.0	74.3	5.0	5.0	15.0	0.7	80.0
8.0	63.9	6.4	27.5	2.0	0.2	80.0
9.0	9.4	41.8	40.9	7.2	0.7	65.0
10.0	5.0	14.6	78.2	2.0	0.2	80.0
11.0	61.9	18.0	5.0	15.0	0.2	80.0
12.0	7.2	78.5	11.5	2.0	0.7	65.0
13.0	62.1	11.5	10.7	15.0	0.7	50.0
14.0	76.5	5.0	5.0	13.3	0.2	50.0
15.0	15.9	5.0	76.3	2.0	0.7	50.0
16.0	15.3	46.4	35.5	2.0	0.7	50.0
17.0	69.0	16.3	8.1	5.9	0.8	65.0
18.0	69.7	17.1	10.4	2.1	0.7	80.0
19.0	7.0	5.0	72.8	15.0	0.2	80.0
20.0	23.1	5.3	55.9	14.9	0.7	65.0

21.0	5.7	9.6	70.8	13.2	0.7	50.0
22.0	52.6	26.6	5.0	15.0	0.8	65.0
23.0	41.7	42.0	9.7	5.8	0.8	50.0
24.0	76.3	5.1	16.5	2.0	0.2	50.0
25.0	5.0	74.3	18.5	2.0	0.2	65.0
26.0	56.3	5.0	36.5	2.0	0.2	57.5
27.0	62.7	5.0	23.2	8.3	0.7	50.0
28.0	29.0	50.3	5.0	15.0	0.7	80.0
29.0	26.4	13.7	51.3	8.4	0.2	80.0
30.0	47.6	21.4	28.9	2.0	0.2	65.0
31.0	54.0	32.9	5.0	7.6	0.6	80.0
32.0	26.1	15.8	55.6	2.0	0.4	65.0
33.0	5.0	26.2	53.0	15.0	0.7	80.0
34.0	37.8	40.3	19.4	2.0	0.5	80.0
35.0	73.4	11.9	8.4	6.2	0.2	65.0
36.0	61.9	18.0	5.0	15.0	0.2	80.0
37.0	5.0	31.4	48.4	15.0	0.2	65.0
38.0	13.9	6.6	73.8	5.5	0.2	65.0
39.0	5.0	26.2	53.0	15.0	0.7	80.0
40.0	27.8	37.8	19.2	15.0	0.2	50.0
41.0	32.4	5.3	59.4	2.1	0.7	65.0
42.0	29.0	50.3	5.0	15.0	0.7	80.0
43.0	24.2	5.0	55.7	15.0	0.2	50.0
44.0	5.0	74.9	5.0	15.0	0.2	80.0
45.0	48.8	13.6	22.1	15.0	0.5	72.8
46.0	13.7	65.4	14.5	5.7	0.8	80.0
47.0	12.3	5.0	80.0	2.0	0.7	80.0
48.0	66.7	19.1	11.5	2.0	0.7	50.0
49.0	42.9	9.5	35.7	11.7	0.2	65.0
50.0	5.0	74.3	5.0	15.0	0.7	65.0
51.0	5.0	12.9	80.0	2.0	0.2	50.0

3.2 Procedure for the production of optimized foam-mat dried tomato-onion-pepper powder.

The procedure involves blanching the tomato, pepper and onion samples in boiling water for 30 seconds to stop enzymatic action. Next, a home blender was used to chop and grind the biomaterials into pulp for 4minutes, until a smooth, uniform mixture was formed. Following that, according to the combinations of the experimental treatment, 100ml of the pulp was poured into 51 small containers, and various concentrations of egg white (5%, 10 % and 15%), carboxymethyl cellulose (CMC) (0.15% 0.45% and 0.75%), tomato (5-76.5%), pepper (5-78.5%), and onion (5-80%) were added. A 400 W jug-type blender (model number FPO12A) was then used to agitate (whip) the mixture for 7 minutes to create foam. To let air into the foam, the top of the mixer was opened. The mixture was then dried using a foam-mat drying technique to form the powder.

3.3 Storage of tomato-pepper-onion composite powder in different packaging materials

This study was conducted to find out suitable packaging materials for the storage of the foam-mat dried tomato-pepper-onion powder. The powder was packed in Laminated Aluminium Foil (LAF), High Density Polyethylene (HDPE), and Medium Density Polyethylene (MDPE) and stored for 30 days. Some selected quality indices of the powder such as protein, moisture content, lycopene content and microbial loads (fungal and bacterial loads) were conducted at an interval of 5 days during the storage period of 30 days and the values of their microbial loads were recorded.

3.4 Statistical Analysis

D-optimal point exchange design was used for a storage period of 30 days with three different packaging material. The results obtained were analyzed using Design Expert Software (v13.0). The analysis of variance shows the influence of storage factors (duration of storage and packaging materials) on the foam-mat dried powder. The greater the F-value, the more significant effect. The significant effect of storage factors to the responses are characterized by p-value "Prob > F" which is less than 0.05.

4. RESULTS AND DISCUSSION

Table 4.1: Effect of Three Packaging Materials on Some Selected Quality Indice and Viable Loads of Tomato-Pepper-Onion Powder: tomato:67.25% pepper: 5.0%. onion: 20.0% egg white: 7.59% , CMC: 0.150% DT: 61.93^{o}C

Run	Storage Duration (Days)	Packaging Materials	Moisture Content %	Protein %	Lycopene mg/100g	Viable Load (cfu/g) Bacteria	Fungal
1	0	Laminated Aluminium Foil	5.38	11.47	10.21	2.46×10^2	5.53×10^2
2	0	High Density Poly Ethylene	6.95	9.02	9.8	3.24×10^2	6.5×10^2
3	0	High Density Poly Ethylene	6.92	10.38	10	3.15×10^2	8.32×10^2
4	0	Medium Density Poly Ethylene	6.03	11.64	10.43	1.69×10^2	2.25×10^2
5	0	High Density Poly Ethylene	6.23	11.64	10.43	1.69×10^2	2.25×10^2
6	5	Laminated Aluminium Foil	5.75	11.61	10.35	2.3×10^2	3.39×10^2
7	5	Laminated Aluminium Foil	4.65	10.98	10.12	3.03×10^2	7.84×10^2
8	5	Medium Density Poly Ethylene	6.82	9.55	10.15	4.78×10^2	5.9×10^2
9	5	Medium Density Poly Ethylene	6.07	11.5	10.42	1.85×10^2	2.86×10^2
10	5	Laminated Aluminium Foil	4.39	10.98	10.12	3.86×10^2	7.99×10^2
11	10	High Density Poly Ethylene	6.59	11.42	10.29	2.19×10^2	3.88×10^2
12	10	Medium Density Poly Ethylene	6.65	9.89	10.21	4.43×10^2	7.81×10^2
13	10	Medium Density Poly Ethylene	6.84	9.21	10.11	6.04×10^2	9.44×10^2
14	10	Laminated Aluminium Foil	5.35	11.14	10.18	2.72×10^2	5.37×10^2
15	10	Medium Density Poly Ethylene	6.16	10.98	10.39	1.99×10^2	2.76×10^2
16	15	Laminated Aluminium Foil	6.3	11.64	10.43	1.23×10^2	2.25×10^2
17	15	Laminated Aluminium Foil	5.31	11.46	10.21	2.5×10^2	4.93×10^2
18	15	Medium Density Poly Ethylene	6.22	10.5	10.39	2.54×10^2	2.68×10^2
19	15	Laminated Aluminium Foil	6.13	10.82	10.37	1.67×10^2	3.01×10^2

20	15	Medium Density Poly Ethylene	6.57	10.36	10.3	2.83×10^2	3.45×10^2
21	20	Medium Density Poly Ethylene	6.34	10.31	10.28	3.23×10^2	1.92×10^2
22	20	Laminated Aluminium Foil	5.14	11.05	10.15	2.96×10^2	6.11×10^2
23	20	High Density Poly Ethylene	6.58	11.55	10.3	1.86×10^2	3.65×10^2
24	20	Laminated Aluminium Foil	5.22	11.12	10.18	2.78×10^2	5.39×10^2
25	20	Medium Density Poly Ethylene	6.61	9.86	10.26	3.74×10^2	4.1×10^2
26	25	Laminated Aluminium Foil	5.96	10.8	10.36	1.89×10^2	3.26×10^2
27	25	High Density Poly Ethylene	6.58	11.53	10.29	2.1×10^2	3.92×10^2
28	25	Laminated Aluminium Foil	5.05	11.01	10.15	3×10^2	6.45×10^2
29	25	High Density Poly Ethylene	6.51	11.62	10.38	1.79×10^2	2.75×10^2
30	25	High Density Poly Ethylene	6.86	9.1	9.89	3.2×10^2	6.33×10^2
31	30	Medium Density Poly Ethylene	6.79	9.46	10.19	2.85×10^2	7.46×10^2
32	30	Laminated Aluminium Foil	5.42	11.51	10.25	2.41×10^2	4.72×10^2
33	30	Medium Density Poly Ethylene	6.63	9.8	10.26	4.1×10^2	4.28×10^2
34	30	High Density Poly Ethylene	6.78	10.75	10.15	2.86×10^2	4.54×10^2
35	30	Laminated Aluminium Foil	6.25	11.24	10.4	1.45×10^2	2.63×10^2
36	35	High Density Poly Ethylene	6.92	10.44	10.02	3.13×10^2	5.64×10^2
37	35	Medium Density Poly Ethylene	6.84	9.21	10.08	6.35×10^2	9.95×10^2
38	35	High Density Poly Ethylene	6.86	10.75	10.13	2.95×10^2	4.75×10^2
39	35	Medium Density Poly Ethylene	6.81	9.27	10.13	5.43×10^2	7.86×10^2
40	35	High Density Poly Ethylene	6.61	11.37	10.0	2.25×10^2	4.53×10^2

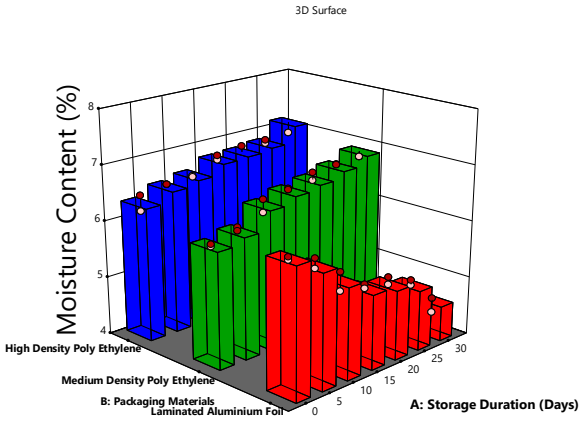

Fig 4(a): 3D Surface Diagram showing the effect of different packaging materials on the Lycopene Content of Powder tomato-pepper-onion mix during storage.

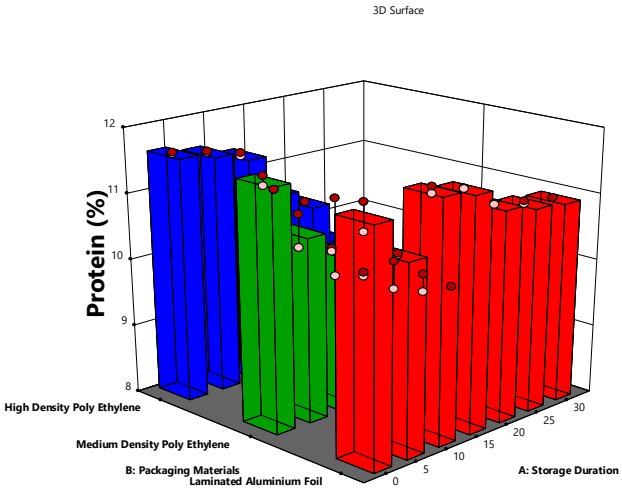

Fig 4(b): 3D Surface Diagram showing the effect of different packaging materials on the Fungal load of Powder tomato-pepper-onion mix during storage.

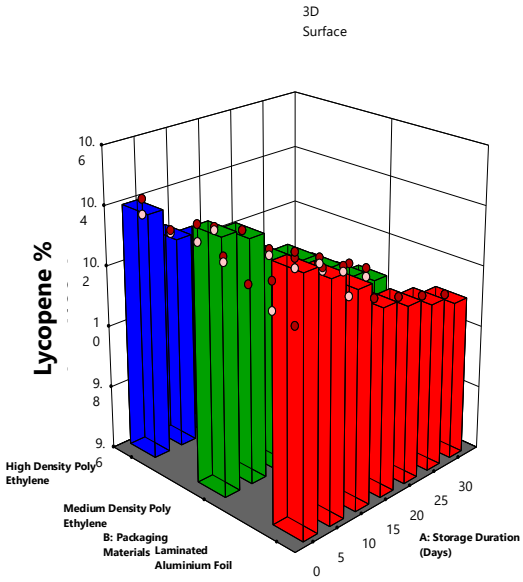

Fig 4(c): 3D Surface Diagram showing the effect of different packaging materials on the Lycopene Content of Powder tomato-pepper-onion mix during storage

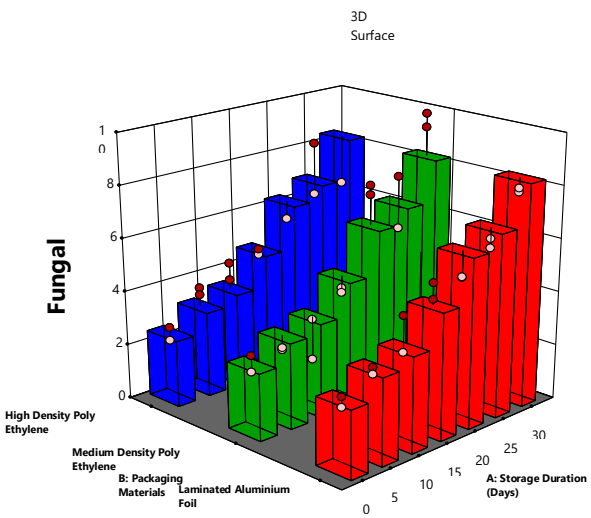

Fig 4(d): 3D Surface Diagram showing the effect of different packaging materials on the Fungal load of Powder tomato-pepper-onion mix during storage.

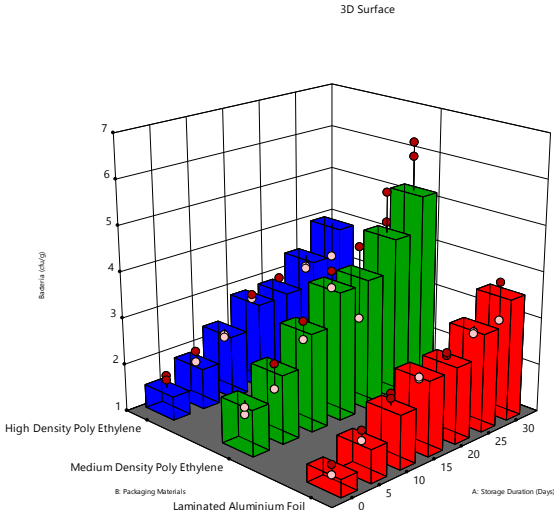

Fig 4(e): 3D Surface Diagram showing the effect of different packaging materials on the Bacterial load of Powder tomato-pepper-onion mix during storage.

4.2 Discussion

The optimized results of the foam-mat dried powder showed that 67.25% of tomato, 5.0% of pepper, 20.0% of onion, 7.59% of egg white, 0.150 of CMC with a drying temperature of 61.93^{O}C produced foam-mat dried powder of 0.5972 desirability index. The optimized result of foam-mat dried tomato-pepper-onion powder was further subjected to storage analysis as shown in Table 4.1. Table 4.1 Shows the moisture content, protein content, lycopene and viable loads of the powdered tomato-onion-pepper stored in each packaging material was measured at different time intervals (days 0, 5, 10, 15, 20, 25, and 30). The results show that the moisture content increased over time from 5.38 to 6.92% in all the three packaging materials, but the rate of increase was higher in the MDPE compared to the other two packaging materials (LAF and HDPE). The LAF had the lowest moisture content throughout the storage period, indicating that it was the most effective in preventing moisture from entering the package. From the table, it can be observed that there is a gradual decrease in protein content over time in all three packaging materials. However, the rate of decrease is slightly different for each packaging material. The protein content in MDPE decreases more rapidly compared to HDPE and LAF. This could be due to the lower oxygen and moisture barrier properties of MDPE compared to HDPE and LAF. LAF shows the least decrease in protein content over time, which could be attributed to its high barrier properties. Overall, the results suggest that LAF is the most effective packaging material for maintaining the protein content of powdered tomato-onion-pepper during storage, followed by HDPE and MDPE. Similarly, it can be seen that the lycopene content of the powder tomato pepper and onion decreases over time. The rate of degradation varies depending on the packaging material used. The LAF packaging was able to preserve the lycopene content the most, while the HDPE packaging was the least effective in preserving the lycopene content. The MDPE packaging was also able to preserve the lycopene content to a certain extent but was not as effective as the LAF packaging.

Table 4.1 also showed that the viable load of bacteria and fungi varied throughout the 30-day storage period. The bacterial counts ranged from 1.23 to 6.35 log cfu/g, while the fungal counts ranged from 1.92 to 9.95 log cfu/g. However, the microbial counts in the product samples remained within acceptable limits for most food products throughout the storage period. These findings are consistent with previous studies that have reported that the microbial counts in dehydrated vegetables are generally low, and the storage period has a limited effect on their microbial load (Sarker et al., 2014).

5. CONCLUSION

The evaluation of the various packaging materials revealed that LAF (Laminated Aluminum Foil) packaging offered the best moisture barrier qualities, maintaining the powder's antioxidant activity and microbial loads. Although to a lesser extent than LAF packaging, HDPE (High-density Polyethylene) packaging was also helpful in maintaining the powder's quality qualities. In addition, it was discovered that MDPE (Medium-density Polyethylene) packaging performed the least well in maintaining the powder's quality attributes. To ensure the

quality and shelf life of foam-mat dried tomato-pepper-onion powder, LAF or HDPE packaging for storage and transportation are recommended. Overall, the findings of this study indicate that foam-mat drying is a promising method for processing vegetables into powder form.

ACKNOWLEDGEMENT

We greatly appreciate Mr. Audu Yohanna, a laboratory technician at the Federal University of Technology, Minna's faculty of agriculture, for giving up his valuable time to help us carry out the practical component of our research endeavor.

REFERENCES

Bhatkar, N. S., Shirkole, S. S., Mujumdar, A. S., & Thorat, B. N. (2021). Drying of tomatoes and tomato processing waste: a critical review of the quality aspects. Drying Technology, 39(11), 1720-1744.

Hossain, M. A., Mitra, S., Belal, M., & Zzaman, W. (2021). Effect of foaming agent concentration and drying temperature on biochemical properties of foam mat dried tomato powder. *Food Research*, *5*(2), 291-297.

Iqbal, M. J., Shukat, R., Farooq, M., Solangi, I. A., Ilyas, N., Ullah, R., ... & Ahmed, F. (2021). Drying of onion paste to develop powders by foam-mat drying process using egg albumin as foaming agent. *Pakistan Journal of Agricultural Research*, *34*(2), 431-437.

Kilicli, M., Erol, K. F., Toker, O. S., & Tornuk, F. (2022). Production of tomato powder from tomato puree with foam-mat drying using green pea aquafaba: drying parameters and bioaccessibility of bioactive compounds. Journal of the Science of Food and Agriculture

Liu, Y., Zhang, Z., & Hu, L. (2022). High efficient freeze-drying technology in food industry. Critical Reviews in Food Science and Nutrition, 62(12), 3370-3388.

Sarker, M., Hannan, M. A., Quamruzzaman, M. A., & Khatun, H. (2014). Storage of tomato powder in different packaging materials. *Journal of Agricultural Technology*, *10*(3), 595-605.

PAPER 148 – EXPERT SYSTEM FOR TROUBLESHOOTING AND REPAIR OF COMPUTER ENGINEERING LABORATORY EQUIPMENT

K. A. Sodiq[1*], S. O. Abdulsalam[2], O. L. Lawal[3], L. A. Saliu[3], A. T. Otapo[4], H. Ojo[5]

[1]Department of Computer Engineering, Yaba College of Technology, Yaba, Nigeria.
[2]Department of Computer Science, Kwara State University, Malete-Ilorin, Nigeria
[3]Department of Computer Technology, Yaba College of Technology, Yaba, Nigeria.
[4]Department of Computer Engineering, Yaba College of Technology, Yaba, Nigeria.
[5]Department of Computer Engineering, Yaba College of Technology, Yaba, Nigeria.
[6]Department of Electrical/Electronics Engineering, Federal Polytechnic Ilaro, Ilaro, Nigeria.
[*]Email: kazeem23@yahoo.com

ABSTRACT
Technologists and Technicians in Computer engineering Laboratories have been conducting practicals for students with a number of equipment, maintenance of such equipment and detection of faults on them are being carried out with a conventional approach. However, with advancement in Computer Technology and Artificial Intelligence, there exists few or no expert system that can be used in troubleshooting and repair of equipment in Computer Engineering Laboratories. This research proposed expert system for the maintenance and repair of equipment in the Computer Engineering Laboratories. Data was collected on five (5) equipment in the three (3) Computer Engineering Laboratories: Computer Technology Laboratory, Control Engineering Laboratory and Basic Electricity/Measurement and Instrumentation laboratory from three (3) higher educational institutions in southwestern areas of Nigeria. The data was encoded into If-then -rules, programmed with Python programming language and My Sql. A user interface was designed to guide users through the use of the system and display appropriate outputs. A test was carried out by four (4) users in one of the institutions to get their remarks and feedback on the Expert System. It was concluded that the expert system can be used to troubleshoot, repair and maintain computer engineering laboratory equipment by the Technologists and Technicians.

KEYWORDS: Computer Engineering, Equipment, Expert system, Laboratory, Technologists

1. INTRODUCTION

Expert Systems are artificial intelligence technology designed to mimic the judgment skills of human decision-makers. An expert system is created to record the knowledge and skill of human experts, then use it to give wise counsel or make choices in a certain field (Jackson and Peter,1998). Expert Systems are utilized in many different industries, such as health, finance, engineering, and others, to automate decision-making and solve complicated problems.

The creation of expert systems for equipment diagnosis and repair in computer engineering labs has the power to completely alter how equipment is maintained and repaired. These solutions can reduce machine downtime, lower repair expenses, and improve system maintainability. Expert systems can quickly and accurately diagnose faults, suggest fixes, and even foresee equipment problems before they happen by utilizing artificial intelligence and machine learning. Expert Systems are utilized in many industries, such as health, finance, engineering, and others, to automate decision-making and solve complicated problems. Systems for knowledge automation offer a very effective and efficient approach to give customers, staff members, and even advisors themselves access to top-tier expert decision-making information and counsel for particular challenges (Exsys Corvid, 2011).

Every laboratory in the world has an expert when it comes to the detection of faults and providing solution to those faults but over the years the world has seen those experts die with such knowledge. Hence it is against this backdrop that this research seeks to implement an expert system for the maintenance, repair and troubleshooting of equipment in Computer Engineering Laboratories. There is a need to build a computer program that represents and reasons with knowledge of experts in the computer engineering field with a view of maintaining computer laboratory equipment by detecting and analyzing faults related to the equipment. This is justified by the importance of such expert system in the field of computer engineering as there are fewer or no expert system available. Another importance reason is that the expert system will make maintenance of computer engineering laboratory equipment more efficient by reducing the time needed to solve problems.

The research therefore proposed an expert-based system for the troubleshooting, repair and maintenance of equipment present in Computer Engineering Laboratory. This paper will specifically design and implement a prototype expert system and assess the efficiency of the system in identifying and fixing equipment issues.
Amanuel (2016) worked on the computer troubleshooting expert system that self-learns, He introduced an expert system that is specialized to detecting computer errors and suggesting viable solutions for the faults found. The expert system's conceptual model was created utilizing a decision tree form, which makes the reasons involved in computer troubleshooting simple to understand and analyze. The expert system was built using 'if – then' rules based on the conceptual model. Backward chaining was utilized to infer the rules and make relevant recommendations in the produced system.

Youssef (2012) developed an expert PC troubleshooter by employing rule-based methods and fuzzy systems to identify POST beep faults. He also employed an intelligent agent that aids in self-learning and knowledge acquisition. Using the MS.NET Framework 4.0 and MS Visual Studio 2010, ASP.NET 4.0 and C#.NET 4.0 are used to develop the Expert PC Troubleshooter. Using MS Office Access 2010, the rule-base is implemented as a relational database.

Aaron (2011) proposed an expert system algorithm for diagnosing faults in computer systems. The system uses a knowledge-based approach, where the knowledge is represented as a set of rules that capture the expertise of human experts in the field of computer engineering. The system is designed to be user-friendly, where the user can interact with the system using natural language, and the system provides recommendations for fault diagnosis and repair based on the symptoms reported by the user. The authors evaluated the effectiveness of the system using a dataset of computer system faults, and reported an accuracy rate of 90.5%, indicating the potential of the system to improve the efficiency of fault diagnosis and repair in computer systems. The authors also compared the performance of their system with other existing diagnostic tools and reported that their system outperformed the other tools in terms of accuracy and speed.

(Sourav et al., 2013) proposed an expert system for diagnosing and fixing computer faults using a knowledge-based approach that captures the expertise of human experts in computer engineering. The system is user-friendly and provides recommendations for fault diagnosis and repair based on reported symptoms. The study evaluated the system's accuracy using a dataset of computer faults, reporting an accuracy rate of 91%. Additionally, the study compared the system's performance with other diagnostic tools, demonstrating its superior accuracy and speed.

(Piotr & Przemyslaw, 2015) studied the application of expert systems in aircraft maintenance. The authors developed a knowledge-based system that collected the expertise of human maintenance personnel to provide recommendations for diagnosis and repair of faults. The system used a rule-based approach to identify faults based on symptoms and provides detailed instructions for repair. The effectiveness of the system was evaluated using a set of maintenance tasks, which reported a high success rate in identifying and fixing faults. The authors concluded that the system has been successfully implemented in the maintenance of the M-28 aircraft and has resulted in improvements in maintenance efficiency and accuracy.

(Sylvester and Adeola, 2015) presented an expert system called the Computer Fault Diagnosis and Troubleshooting System (CFDTS) designed to help non-expert users diagnose and repair computer faults. The system used a knowledge-based approach to diagnose computer faults, relying on a set of rules generated from expert knowledge of computer troubleshooting. The CFDTS has a user-friendly interface that guides users through the troubleshooting process. Additionally, the system has a database of known computer faults and solutions which can be updated as new faults are identified. The study evaluates the effectiveness of the CFDTS using a set of test cases and reports a high success rate in diagnosing and fixing computer faults. The authors concluded that the CFDTS could improve the efficiency of computer maintenance.

2. THEORETICAL BACKGROUND

The process of building expert systems is often called knowledge engineering. The knowledge engineer is involved with all components of an expert system. Building expert systems is generally an iterative process. The components and their interaction will be refined over the course of numerous meetings of the knowledge engineer with the experts and users. The various components of expert system are presented in Figure 1.

i. Knowledge Base
ii. Inference Engine
iii. User Interface

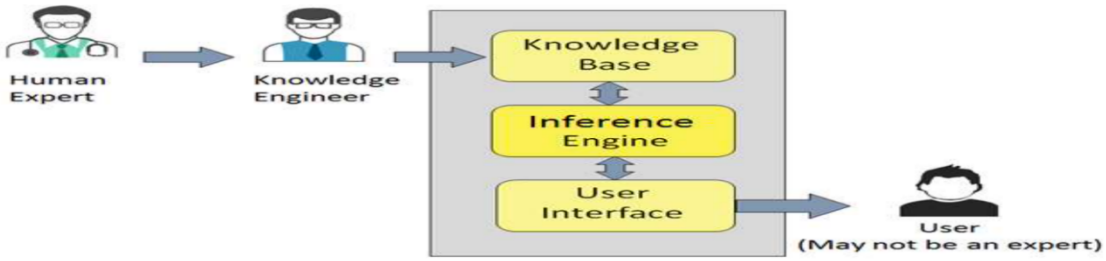

Figure 1: Component of Expert System Source: Tutorial Point

Knowledge Base: It contains domain-specific and high-quality knowledge. Knowledge is required to exhibit intelligence. The success of any ES majorly depends upon the collection of highly accurate and precise knowledge.
Knowledge Acquisition: The knowledge acquisition component allows the expert to enter their knowledge or expertise into the expert system, and to refine it later as and when required. Historically, the knowledge engineer played a major role in this process, but automated systems that allow the expert to interact directly with the system are becoming increasingly common.
Representing and Using Domain Knowledge: Expert system is built around a knowledge base module. Expert system contains a formal representation of the information provided by the domain expert. This information may be in the form of problem- solving rules, procedures, or data intrinsic to the domain. To incorporate this information into the system, it is necessary to make use of one or more knowledge representation methods. Three common methods of knowledge representation evolved over the years are IF-THEN rules, Semantic networks and Frames.
IF-THEN rules: Human experts usually tend to think along: condition ⇒ action or Situation ⇒ conclusion Rules. "if-then" are predominant form of encoding knowledge in expert systems.
These are of the form: If a1, a2, ..., a Then b1, b2, ..., bn: where each aI is a condition or situation, and each bi is an action or a conclusion.

The Inference Engine: This interprets and evaluate facts in knowledge base to provide answer.

The User Interface: The Expert System user interface usually comprises of two basic components:

i. The Interviewer Component: this controls the dialog with the user and/oral lows any measured data to be read into the system.
ii. The Explanation Component: this gives the system's solution, and also makes the system's operation transparent by providing the user with information about its reasoning process.

3. METHODOLOGY

This research work involves data collection, data processing, expert system development. A standard validated techniques was employed in the procedure of collecting, measuring and analyzing data for this study. Human experts in three (3) higher institutions in Southwestern region of Nigeria were met in their various laboratories to gather enough raw data which are the symptoms, faults, causes and possible solutions for the equipment. Data was collected on five (5) equipment each of three (3) Computer Engineering Laboratories namely, Computer Technology Laboratory, Control Engineering Laboratory and Basic Electricity / Measurement and Instrumentation laboratory. The raw data gathered from the data collection phase were processed and analyzed to produce meaningful information for this study. The development of the expert system was implemented on Intel duo core computer with a minimum processor speed of 900 mHz. A minimum Random-Access Memory (RAM of 4MB) and A minimum hard disk space of 10MB. Web-based system for system for computer engineering laboratory equipment was implemented with web-based application for information storage, a middleware application and a client-side application. Specifically, a browser Graphics and text browser is preferable e.g Internet Explorer, A text editor and Windows Apache, Pycharm (WAMP server).

3.1 System Design

This is the section that traps user input; the input will be supplied via a keyboard into the database. The following are the various forms that will be used to trap data from the user. The forms are admin registration form, application form, application status, user form and faults, symptoms and possible solution.

The output design varies based on the criteria of selection. The output data can be on screen display from the database (data storage). The output design comprises of the name of equipment search, list of fault display and

general information about the fault. The flowcharts used in the development of the proposed system are shown in Figures 3, 4, and 5 for Admin, user and fault search respectively.

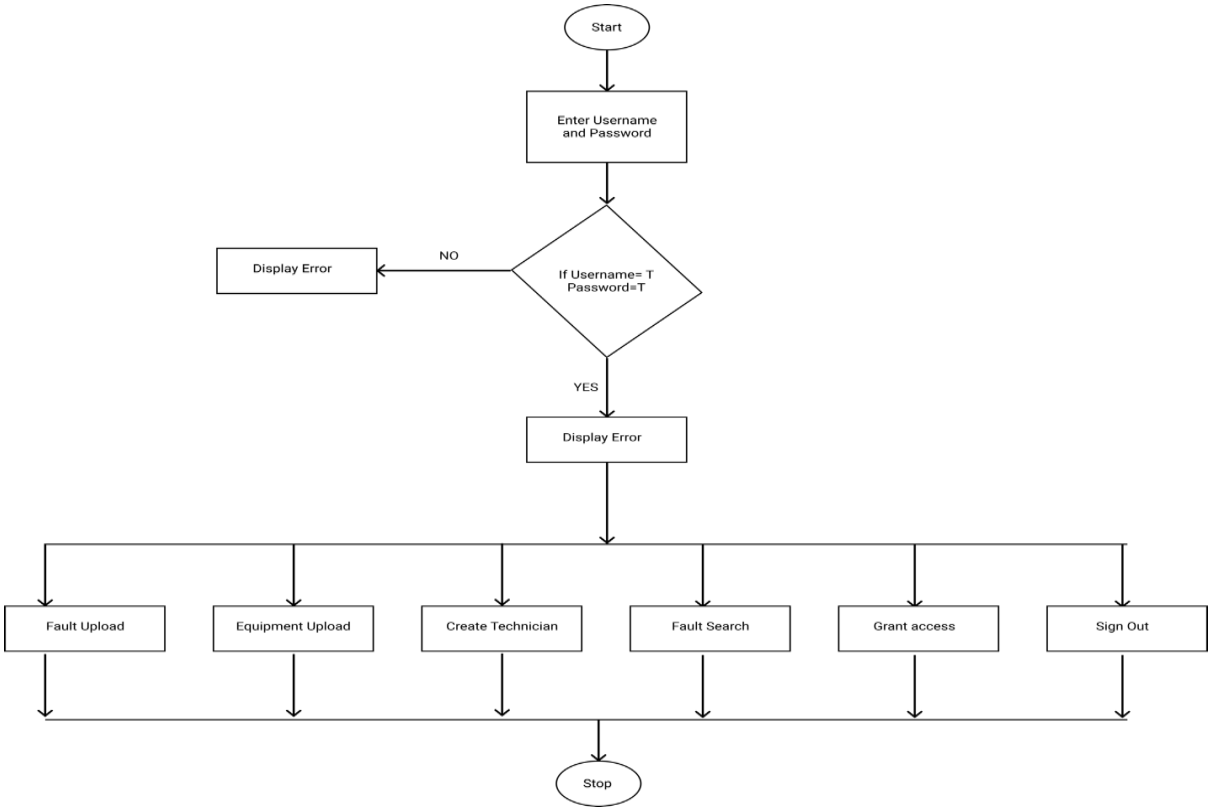

Figure 3: Admin Flowchart

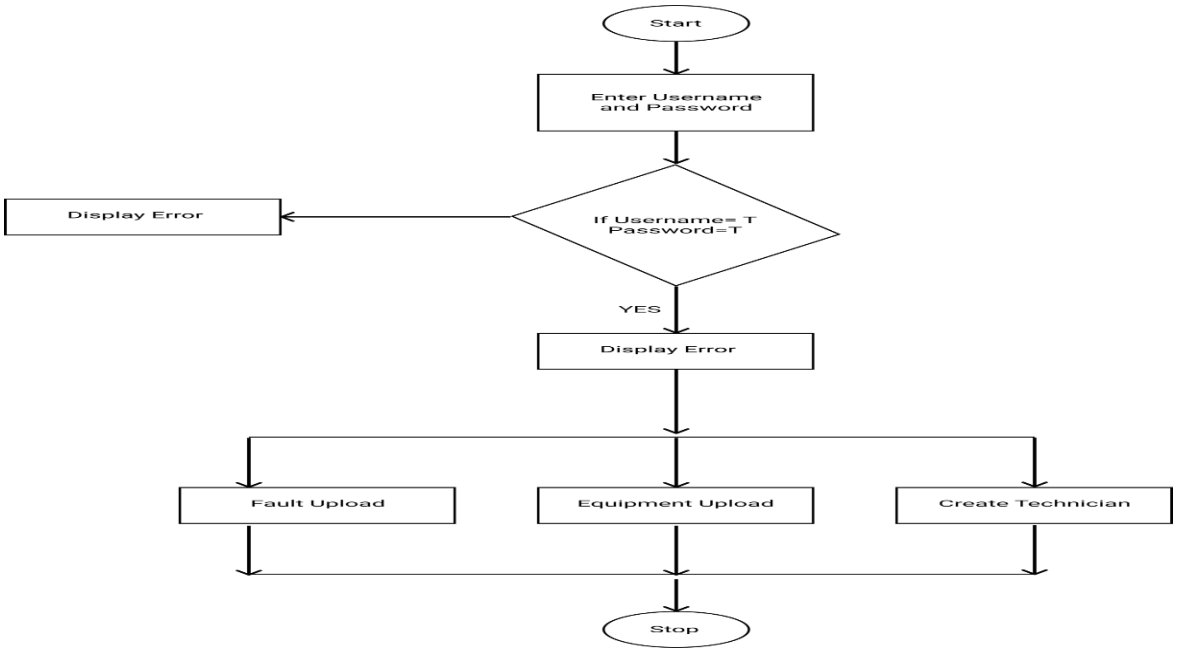

Figure 4: User Flowchart

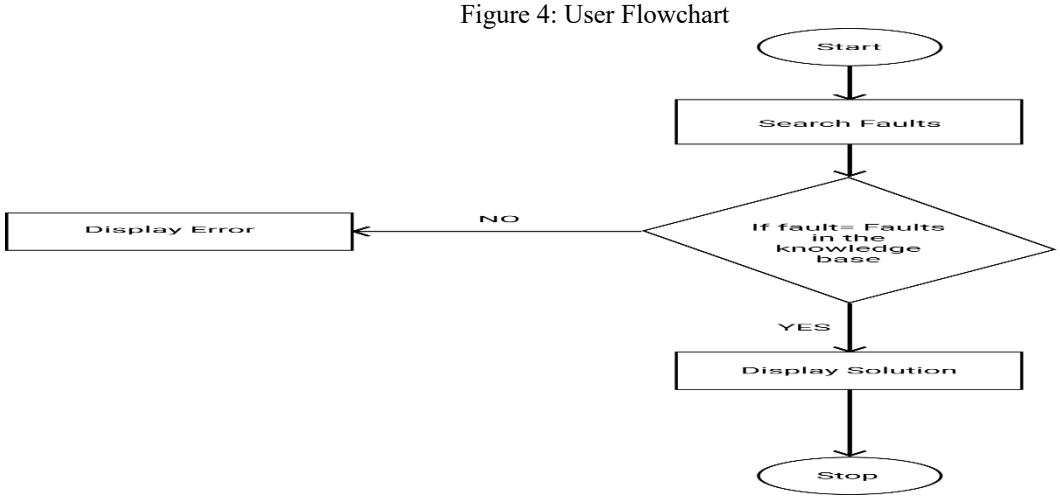

Figure 5: Fault Search

4. RESULTS AND DISCUSSION

4.1 System Output

The proposed web-based system is accessible to the users via any device that can be used to access the web. The steps taken for a user to search for faults are explained below in form of images. The figure 6 shows the sample output generated from the system.

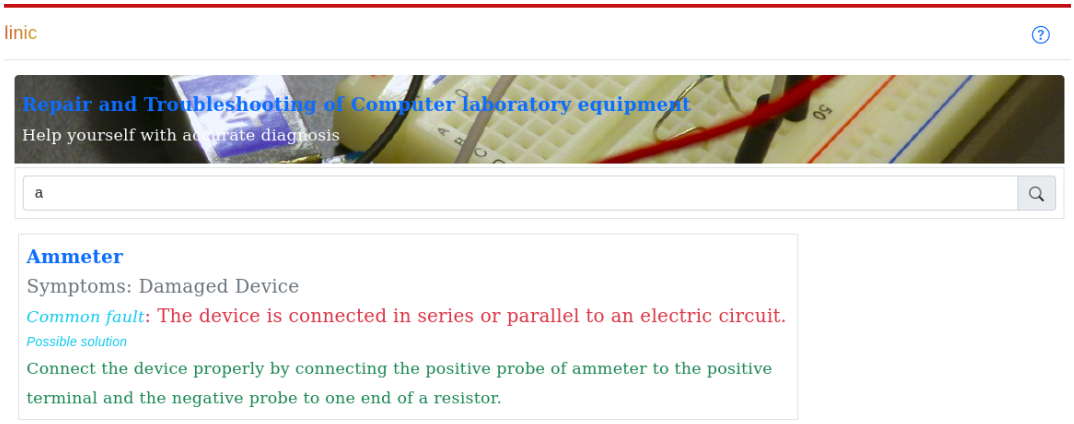

Figure 6: Results generated from the interface.

3.2.SystemTesting

Testing was conducted at different times taking records of the search inputs and observe the response from the system. It was observed that in as much as the search input matches what was in the knowledge base, a response will always be generated by the system. A continuous testing and adding of knowledge to the knowledge base over a long period of time will provide enough insight and data for troubleshooting and repair of computer engineering laboratory equipment.

The tests were conducted stage by stage. The first stage was conducted during the completion of the first draft. The second and third stage were conducted after the testing from the first stage and the last stage of the testing was conducted after final iteration has been made to the system. The recorded stages of the testing of the system are presented in Table 1.

Table 1: Recorded Stages of the Testing of the System

User	User Interface	Interactivity of System
User 1	Not Satisfactory	Not interactive enough
User 2	Slightly satisfactory	Not interactive enough
User 3	Satisfactory	Slightly Interactive
User 4	Satisfactory	Interactive

The performance of the system was carried out in one of the laboratories by 2 technicians and 2 students, the results and outcome obtained are similar amongst all the testers, that is the expert system can troubleshoot and repair computer engineering laboratory equipment.

4.3 Discussion

From the test carried out, we discovered that there is a certain level of expectation from the user for the accurate result of the fault that was searched for. The remarks of these users were based on the complexity of the fault and the solution provided. For the first user, the remarks were not satisfactory because the system was not that easy to interact with because the search results were not that informative enough. The second user who was slightly satisfied with the system interface also complained about the interactivity of the system. The third and fourth user were pretty satisfied but still suggested that they would love if the results are well detailed for easy understanding. The test was taken in a similar format to an already existing expert system for troubleshooting which can be read in (Amanuel , 2016).

CONCLUSION

There are different types of expert system for troubleshooting of faults, but this study presents the design and implementation of expert-based system for the troubleshooting and repair of computer laboratory equipment. The system was tested and can be used in different computer engineering laboratories and still gives a satisfactory result. Therefore, it is concluded that the expert system can be used for the troubleshooting, repair and maintenance of computer engineering laboratory equipment by Technologists. Further research is needed to develop expert system for other equipment used in other computer engineering laboratories and support can be integrated into the system to allow users to contact specialists in case of any difficulty that may not be considered in the system.

REFERENCES

Aaron, D. M. A. (2011). An Expert System Algorithm for Computer System Diagnostics. International Journal of Engineering (IJE), 5(5), 435-467.

Amanuel, A.E.(2016). Self Learning Computer Troubleshooting Expert System. International Journal of Artificial Intelligence & Applications, 7(1):45-58.

Exsys Corvid Quick-Start Guide - Fundamentals & Tutorials (2011). Available at:
. http://www.exsys.com/PDF/ExsysCORVID_QuickStartGuide.pdf . Accessed on February 23, 2023.

Jackson and Peter, (1998). Introduction to Expert Systems, 3rd ed, Addison Wesley.

Piotr G. & Przemysław, M.(2015). Use of the expert methods in computer-based maintenance support of the M-28 aircraft. Scientific. Journal of Polish Naval Academy, 2(201), 5-12.

Sourav, M. , Sumanta, C. & Biswarup, N. (2013). Diagnosis and Troubleshooting of Computer Faults Based on Expert System and Artificial Intelligence. International Journal of Pure and Applied Mathematics, 83(5), 717-729.

Sylvester,I.Ele and Adesola, W.A. (2013). Design of Computer Fault Diagnosis and Troubleshooting System (CFDTS). West African Journal of Industrial and Academic Research, 9(1), 43-53.

Tutorial Point (n.d). Artificial Intelligence – Expert Systems. Available at:
https://www.tutorialspoint.com/artificial_intelligence/artificial_intelligence_expert_systems.htm . Accessed on February 23, 2023.

Youssef Bassil (2012). Expert PC Troubleshooter with Fuzzy-Logic and Self-Learning Support. International Journal of Artificial Intelligence & Applications (IJAIA), Vol.3, No.2, March 2012.

PAPER 152 – A REVIEW OF WATER ABSORPTION IN WATER HYACINTH REINFORCED HIGH DENSITY POLYPROPYLENE (HDPP) COMPOSITE

Ojomu, G.O., Adegbuyi, P.A.O., Adefuye, A.O., Raji, N.A., Adedeji, K.A

Lagos State University, Department of Mechanical Engineering, Lagos, Nigeria.

ABSTRACT

Natural plant fibre-reinforced composites have been in use as engineering materials in recent times. They are advantageous because of their light weights, biodegradability, cost and are environmentally friendly. In this paper, a composite of size 75mm x 3.77mm x 20.65mm was developed from 55 grammes of high-density polypropylene (HDPP), 35 grammes of water hyacinth, and 10 grammes of aluminium powder used as a binder. A second sample was produced in the same quantity but was coated with 0.05 micron-film of zinc primer (which weight is negligible). The weights of the composites were initially weighed in the dry forms and recorded. Each of the samples was immersed in same quantity of distilled water for 35 days while the differences in weight percentage in their dried forms and wet forms were noted at intervals of five (5) days by a weighing/timing sensor attached to immersion apparatus for the period. It was noted that the sample with zinc primer weighed less at each measuring interval than the one without; this suggested that water absorption can be minimized with the application of zinc primer or other materials that are waterproofed. Fibre loading was also varied in the composites at 10, 15, 20, 25, 30, 35 and 40 weight percentage (Wt. %) to investigatewater absorption as the loading was increasing; water absorption increased as the load increased but less in the sample with zinc primer.

KEYWORDS: Fibre-Reinforment, Water Hyacinth, Water Absorption, High-Density Polypropylene (HDPP), Composites, Zinc Primer.

1. INTRODUCTION

Plant fibres and their polymer composites have been found to possess mechanical properties comparable to some engineering materials. In this group of plants is water hyacinth (Eichhornia Crassifies). Water hyacinth is found abundantly on waterways. It has high specific stiffness than other plant fibres like kenaf, jute, sisal, coir, pine apple leaf, cotton, etc, Dhakai, Zhang and Richardson, (2006). The plant constitues nuisance to fishing expeditions and marine transport. Composites from the plants are lighter in weight; this is a major advantage to other composites. Reinforced plastics and fibre reinforced plastics consists of the fibre, which is the discontinuous or dispersed phase in a polymer matrix (the composition phase). The fibres are the reinforcement and the main source of strength while the matrix transfers stresses between the reinforcing fibres; the fibres carry the loads along their longitidunal direction, Ekundayo and Adejuyigbe, (2019). Sometimes, fillers are added to smooth the production process and impact special mechanical properties to the composites. In this type of composite materials, the low modulus and temperature limitations of the plastics are overcome by reinforcement with fibres of high modulus. Therefore, harvesting this plant and using it as components in fibre-reinforced composites is of more advantage; however, composites from natural plant fibres are hydrophilic as they age in use (Chikol, Teshapa and Bharath 2012); this reduces the their service durability.

2. THEORETICAL ANALYSIS

Investigation into the behavior of water hyacinth fibre-reinforced composites was reviewed by Rahman and Afsar (2011); in their research, they developed fibre-reinforced polyethylene composites using water hyacinth, varying the weights of the fibre at 15, 20, 25, 30 and 35 grammes. The fibre was initially treated with sodium hydroxide; another part was not treated with the alkali. Water absorption on the composites was conducted by immersion method on both treated and untreated fibre-reinforced composites. Results of their findings showed that the treated fibre-reinforced samples absorbed less water than the untreated samples; this suggested the treatment with alkali helped in more interfacial bonding between the fibre and matrix than in the untreated one; also, traces of cellulose in the fibre might have added to the bonding, (Begun et al; 2021). The treatment reduced voids and porosity in the treated composites, thereby allowing less water molecules into it; this improved performance in the mechanical properties in the treated than the untreated samples. However, water absorption increased in the composite as the fibre loading increased in the composites. It is therefore necessary to look into this gap and reduce it to a certain degree. Meenalochani and Reddy (2017) also worked on the

principle that water absorption behavior of natural fibre-reinforced composites can be reduced through the removal of OH groups from fibres according to the following equation:

$$\longrightarrow \text{Fibre} - OH + NaOH \longrightarrow \text{Fibre} - O^{-}Na^{+}H_2O \quad (1)$$

The authors worked on jute-hemp reinforced hybrid polymer composites. This enhanced inter-bonding between the matrix and fibre. The hybrid material act as skin protection, slowing down water intake from 21% to 6%. Fick's law of diffusion plays a major role in the process; it shows that the diffusion coefficient is an important factor. Therefore for diffusion that obeys Fick's law, diffusion coefficient (or moisture intake) can be expressed as the following equation:

$$M = \frac{4Mm}{h}\left(\frac{t}{\pi}\right)^{0.5} * Dx^{0.5} \quad (2)$$

Where M_m=equilibrium moisture content of the sample

h=thickness of the composite sample

t=time of immersion/diffusity and

D_x= mass diffusity in the composite.

3. MATERIALS AND METHODS

3.1 Materials

1.Water Hyacinth plant. Source: Lagos lagoon, Nigeria.

2. High density polypropylene (HDPP). Source: Exxon Mobil, Lagos, Nigeria

3. Aluminium powder. Source: ALLUMACCO, Agege, Lagos, Nigeria

4. Zinc primer. Source: Berger Paints. Lagos, Nigeria.

5. Clean basin

6. Distilled water

3.2 Equipment

1. Grinding machine

2. Digital weighing balance

3. Sensory weighing/timing machine

3.3 Method

Water hyacinth was harvested from lagos lagoon and washed with clean water to remove dirts; the bulk of the fibre was treated with dilute sodium hydroxide (NaOH) to improve adhesion between the fibre and high-density polypropylene matrix. It was thereafter dried in the sun for fifteen (15) days. After this process, the fibre was grinded into powder by a grinding machine. A composite was developed from the fibre and matrix using a 2-Roll mill and compounding moulding machines with a mould size designed to a rectangular size of 75mm x 22mm x 7mm; the high-density polypropylene (HDPP) was first charged into the mill at a temperature of 167 degree centigrade which melted it into liquid form. After this, mixture of the dried water hyacinth and aluminium powder was sprinkled into the melted HDPP and rolled along the mill until the mixture formed homogenous solid mixture. The solid composite was then transferred to the compression moulding machine where it was moulded into the required rectangular shape; this was labeled sample A. Another composite was developed in the same process but was dipped into 2 micron-film of zinc primer and labeled as sample B (the weight of the micron-film zinc primer was assumed negligible). All samples are shown in figures 1 and 2. The samples were first weighed in their dried forms and the weights recorded; they were then immersed in distilled water for thirty five (35) days during which time they were weighed separately again at intervals of five (5) days with a

weighing/timing sensor; the differences in weight were noted at each of the five (5) day intervals with the process of weighing performed three (3) times and the mean values recorded; this was done in order to use the parameters calculate the equilibrium moistures in the composites. Water hyacinth fibre loading was varied in the composites at 10, 15, 20, 25, 30, 35 and 40 weight percentage (Wt. %) to investigate water absorption as the loading was increasing. Since water absorption is measured by measuring the increase in mass as a percentage of dry mass, then it is equivalent to the increase in weight percent as specified in equation 3 below:

Increase in weight = $\frac{W_f - W_i}{W_i} \times 100\%$ (3)

Where W_f= weight of sampled in distilled water after specific (determined) days and Wi= initial weight of sample before immersion in distilled water in the specific (determined) days; this is predetermined by the porosity, P:

Porosity (P) = $\frac{\Delta W}{T}$ (4)

$\Delta W = W_2 - W_1$

W_2 = weight of composite at time t

W_1 = initial weight of composite at time t

Composites Developed

Sample A

Figure 1: Composite without zinc primer

Sample B

Figure 2: Composite with zinc primer

Data from experiment

Weight (Wt) of sample A in dried form= 100 gms

Weight (Wt.) of sample B in dried form= 100 gms

Using equation 1, the water intake per cent (water absorption) was calculated for samples A and B as shown in table 1 below:

SAMPLE A (without zinc primer) **SAMPLE B (zinc primer)**

Table 1: Water absorption values for samples A and B/days of immersion

DAYS	Wt in wet form	Water Absorption	Wt. in wet form	Water Absorption
5 Days	100.23	0.23	100.21	0.21
10 Days	100.60	0.60	100.43	0.43
15 Days	100.82	0.82	100.62	0.62
20 Days	101.10	1.10	100.81	0.81
25 Days	100.45	1.45	101.15	1.15
30 Days	101.74	1.74	101.48	1.48
35 Days	101.83	1.83	101.63	1.63

Table 2: Fibre loading/water absorption for samples A and B

Fibre Loading (Wt. %)	Sample A Water Absorption	Sample B Water Absorption
10	0.25	0.23
15	0.40	0.38
20	0.68	0.60
25	1.25	0.80
30	1.31	1.11
35	1.40	1.25
40	1.48	1.35

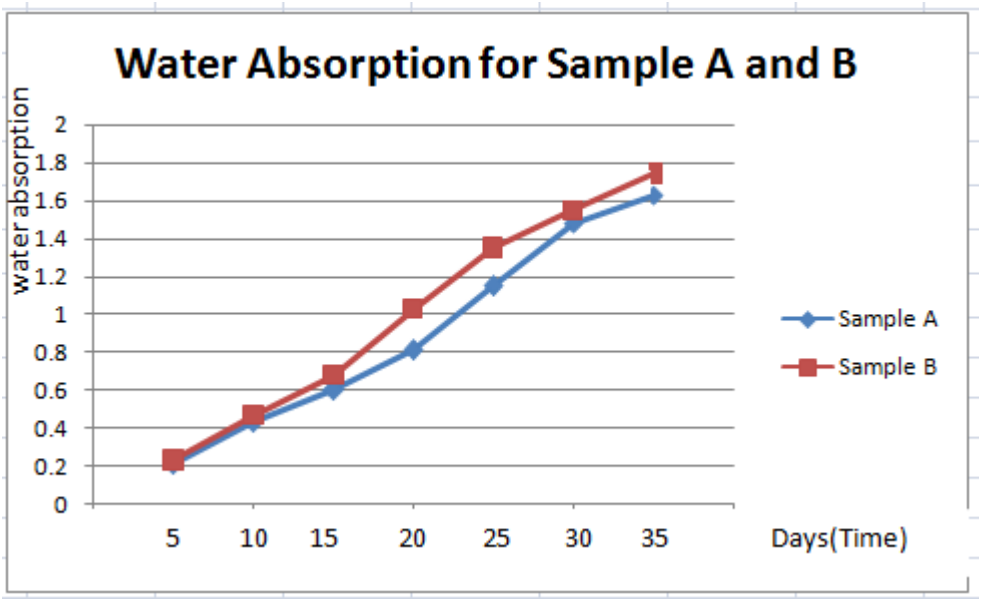

Figure 3: Graph of Water Absorption/Days of Immersion

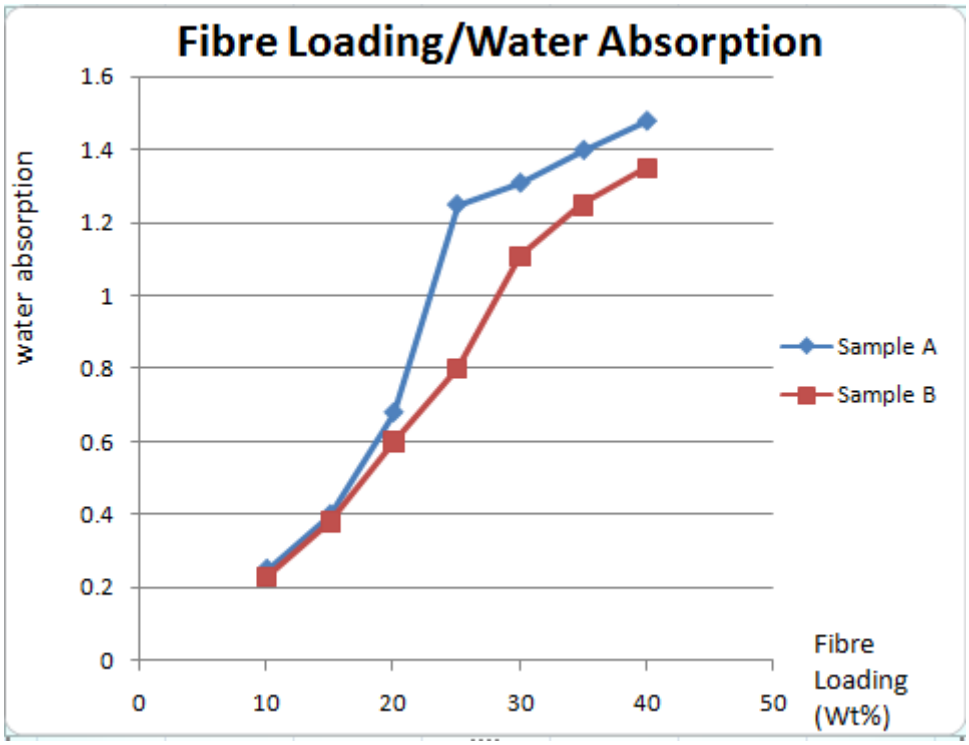

Figure 4: Graph of fibre loading/water absorption

RESULTS AND DISCUSSION

From the results in Table 1, all the samples absorbed water molecules; however, water absorption was less in the sample with the zinc primer because it was less porous because of the 'skin' protection of zinc film; this suggests that coating natural fibre-reinforced composites with zinc primer can reduce water intake, thus reducing the hydrophilic nature of the composites. From 20th to 25th day of immersion in figure 3, there is significant difference between the samples; this significance decreased between day 30 and 35, suggesting saturation was beginning to set in. For fibre loading: in Figure 4, as the fibre loading in the composite samples increased, water absorption increased. When natural fibre is exposed to water molecule (or a humid condition), the cellulose in it is attracted by the humid environment. Between 25 and 40% fibre loading, water absorption increased; this weakens the adhesion in fibre-matrix surface, resulting in brittleness of the composites. However, the sample with the zinc primer (sample B) absorbed less water as shown in the figure (Figure 4).

5.0 CONCLUSION

The research showed that coating fibre reinforced polymer composites reduced moisture intake.

6.0 ACKNOWLEDGEMENT

The author acknowledged the management committee of FETiCON for this conference.

REFERENCES

Begum, H.A., Tanni, T.R., & Shahid, A. Md. (2021). Analysis of water absorption in natural fibre composites. *Journal of Textile Science and Technology,7(4):1-14. DOI:104236/jltt.2021.74013*

Chikol, S.V.,Teshapa, & V.,Bharath, K.N. (2012). Water Absorption behavior of Areca fibre reinforced composites. *International Journal of Materials and Biomaterials Applications, 2(2):12-14* http://www.urpjournals.com

Saha, M., Rahman, & H., Ali, A. (2011). Effect of fibre loadings on mechanical properties of water hyacinth fibre reinforced polypropylene composites. *Proceedings of the International Conference on Mechanical Engineering (ICME2011), 18-20 December, Dhaka, Bangladesh, 1-6*

Ekundayo, G., & Adejuyigbe, S. (2019). Reviewing the development of natural fibre polymer composites: *A case study of sisal and jute. International journal of computer engineering and science research, 1(1): 7-17.*

Huner, U. (2015). Effect of water absorption on the mechanical properties of flax fibre reinforced epoxy composites. *Advanced in Sciences and Technology Research Journal, 9(26):1-6. DOI:10.12913/22998624/2357*

Saha, M., & Afsar, A.M. (2018).Thermo-Mechanical and morphological properties of water hyacinth reinforced polypropylene composite. International Journal of Engineering Materials and Manufacture, 3(3):151-161. DOI:10.26776/ijemm.03.03.2018.04

Dhakai, H.N., Zhang, Z.Y., & Richardson, M.O.W. (2014). Investigation of the surface morphology and structural characterization of palm fibre reinforced acrylonitrile butadiene styrene (PF_ABS) composites. *Materials Sciences and Applications, 5(6):1-6*

Priyanka, L., Singh, R., & Kapur, G.S. (2019). Development of polypropylene/banana peel (treated and untreated) composites with and without compatibilizer and their studies. *Materials Research Express. 6(9):1-8. DOI 10.1088/2053-1591/ab2eea*

Lashumu, A.N., & Raman. P.R. (2016). A review of chemical behavior of natural fibre composites. *International Journal of Chemical Science, 14(4):2223-2238*

Meenalochani, K.S., & Reddy, B.G.V. (2017). A review on water absorption behavior and its effect on mechanical properties of natural fibre reinforced composites. *Materials Science and Engineerig,Corpus ID: 212488926, 1-5.*

PAPER 154 – THE IMPLICATIONS OF LOW SHORT-CIRCUIT CAPACITY ON THE STRENGTH OF POWER GRID: A NIGERIAN CASE STUDY

S. O. Sanni[1,2*], A. I. Abdullateef[1], O. O. Mohammed[1]

[1]Department of Electrical & Electronics Engineering, University of Ilorin, Ilorin, Nigeria.
[2]Department of Electrical & Electronics Engineering, Federal University Oye Ekiti, Nigeria.
[*]Email: shereefdeen.sanni@fuoye.edu.ng

ABSTRACT
The quest to integrate renewable energy sources (RES) into power grids arises from the need to adopt a sustainable source of energy while achieving energy security. RES such as solar photovoltaic (PV) and wind energy systems are also called inverter-based generators (IBGs) because of their inverter-interfaced connections with the grid. The inverter's quick dynamic response and low short-circuit capacity (SCC) can cause distress to the grid and potentially result in power system stability problems. This paper has assessed the SCC and system strength of the Nigerian grid based on proposed IBG integrations in the northern part of the country. A short-circuit study was conducted, system strength was evaluated using the Network Response Short Circuit Ratio (NRSCR), and a dynamic voltage stability analysis was performed. These studies revealed that most of the proposed points on the grid have low SCC but suitable for the size of IBG integration; however, some identified weak points may affect the stability of the grid. The results of this investigation provide valuable insights on the impact of IBG integration in renewable energy-rich, SCC-deficient areas of a grid.

KEYWORDS: Renewable energy resources; Inverter-based generators, Short-circuit capacity; Solar PV; System strength; Wind energy system; Voltage stability

1. INTRODUCTION

The Nigerian power grid, like many others around the world, is struggling to meet the increasing demand for energy due to inadequate generation. But then, the adoption of renewable energy sources (RES) has provided an alternative source, largely owing to its reduced marginal costs and a drive for low-carbon generation (Gordon et al., 2022). RES popularity has been further supported by government incentives and advancements in technological breakthroughs, and it is projected that Nigeria's energy mix will increasingly incorporate renewable energy sources, as shown in Figure 1 (International Renewable Energy Agency, 2023).

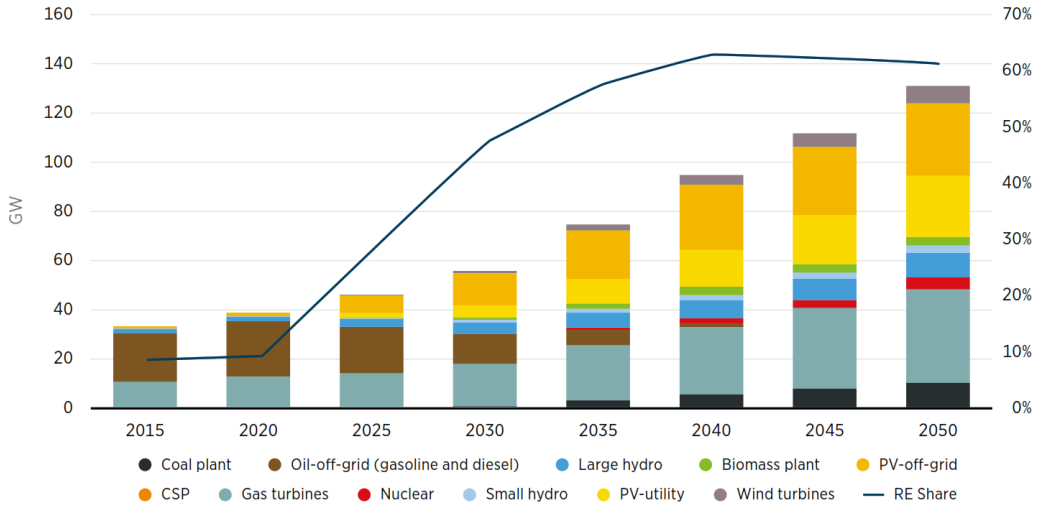

Fig. 1. Electricity generation based on generation technology under current plans and policies

Although RES technologies such as solar photovoltaic and wind energy systems, which are within a larger group of generators known as inverter-based generators (IBGs), are the most prevalent, their power electronics inverter interface may pose a challenge to the stable operation of power grids. Traditionally, synchronous generators (SGs) are the primary sources of short-circuit current, which ensures power grid resilience during system disturbances.

The large-scale integration and preference of IBGs over SGs in power systems, however, leads to low short-circuit current, which can make a power grid vulnerable. The strength of the grid at a specific point in the network is one such vulnerability and is characterized by the size of the short-circuit capacity (SCC). IBGs are typically located in remote regions of an electric power grid, where they are connected to the main grid by long transmission lines and are not supported by SGs, which provide short-circuit services (Ekic et al., 2018). As the penetration level of IBGs increases in some areas and the commitment to synchronous resources falls, these areas become weak. The weakness is aggravated by the rapid dynamic response of the inverter controller, which responds quickly to any slight deviation from normal operating conditions (Mohammed et al., 2019). Moreover, having a large concentration of these IBGs within an area will allow them to interact with each other, causing significant weak grid issues.

System strength assessment is an essential requirement for power system operators and planners to provide adequate understanding of potential weak grid areas prior to the integration of an IBG. The system strength of a power grid with IBG is quantified by the short-circuit ratio (SCR) (North American Electric Reliability Corporation, 2017). It estimates how rigid the grid is to disruptions such as changing power injection or equipment switching. Although SCR's computation is based on the steady state parameter, it is an indicator of a bus's resilience to disturbance during dynamic conditions (Goud et al., 2019). SCR computation, however, does not consider the impact of interactions between IBGs, which can lead to inaccurate estimates of the grid's strength at the PoIs for IBG (North American Electric Reliability Corporation, 2017; Zhang et al., 2014). Other available methods, such as the weighted short-circuit ratio (WSCR) developed by ERCOT (Zhang et al., 2014) and the composite short-circuit ratio (CSCR) developed by GE (GE Energy, 2014), do consider the effects of IBG interactions on grid strength but fail to account for the electrical connections between IBGs, which can result in an inaccurate representation of the grid's strength at PoIs. Moreover, both the CSCR and WSCR methods mainly provide the combined strength of a power grid in the area where the IBGs are interconnected, but they do not compute the strength of the grid at each individual PoI within an area (Aldaoudeyeh et al., 2019). The network response short-circuit ratio (NRSCR) proposed by Sanni et al. (2022) addresses these limitations and provides a more accurate assessment of the grid's strength at PoIs by accounting for both the interactions among IBGs and their electrical connections.

This paper presents an investigation into the impact of low SCC on system strength at the PoI when IBGs are integrated. The Nigerian transmission grid is used as the case study based on the proposed integration of IBGs in the grid.

2. METHODOLOGY

2.1 Power System model

The Nigerian transmission grid system being studied is presented in Figure 2. It comprises 71 buses, including 19 conventional generators, 43 loads, and 79 overhead transmission lines. Power transmission occurs at two voltage levels: 330 kV and 132 kV. Thermal power plants serve as the primary sources of conventional generation in the southern part of the country, whereas hydroelectric power plants dominate the northern part. The northern region also has abundant renewable energy resources, such as wind and solar, with available land for utility-scale deployment. In 2016, Nigerian Electricity Bulk Trading (NBET) Plc signed a power purchase agreement (PPA) with several investors (see Table 1) interested in harnessing this resource for utility-scale systems. Accordingly, this study incorporates renewable generation, which includes nine solar PV plants and one type III wind turbine generator, based on the NBET's PPA.

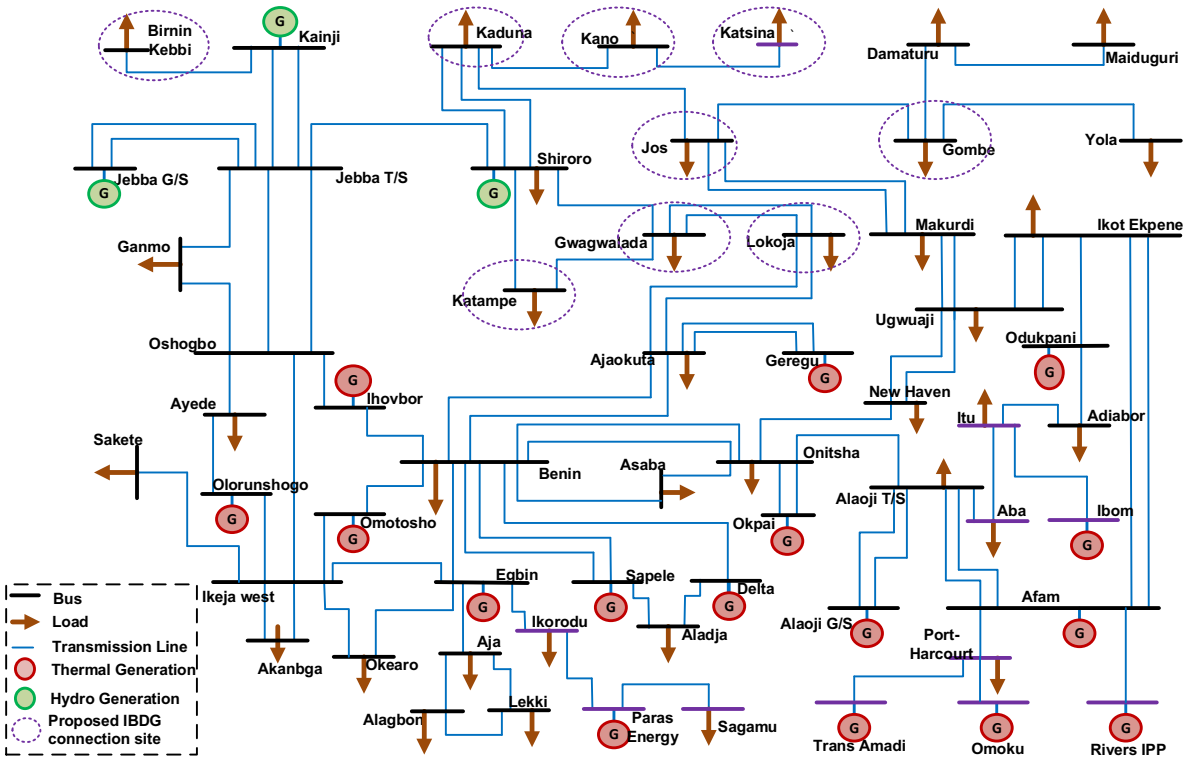

Fig. 2. Single-line diagram of case study Nigerian transmission network.

Table 1. Proposed solar PV and wind energy projects in northern Nigeria

Project / Project Company	Type	PoI	Equivalent Capacity (MW)
KVK Power Limited	Solar	Birnin Kebbi	55
Nigerian Solar Capital Partners	Solar	Gombe	100
LR Aaron Power	Solar	Gwagwalada	100
CT Cosmos	Solar	Jos	220
Quaint Abiba Power	Solar		
Anjeed Innova Group	Solar		
EN Africa	Solar	Kaduna	50
Novia Scotia Power Development Company	Solar	Kano	130
Oriental Renewable Solutions	Solar		
Afrinegia Power Limited	Solar	Katampe	50
Pan Africa Solar	Solar	Katsina	175
Nova Solar 5 Farm Limited	Solar		
Vergnet	Wind (Type 3)	Katsina	10
Middle Band Solar One	Solar	Lokoja	100
Total			**990**

b. Short-circuit studies

The short-circuit current is the current at a given point in the power system during a short-circuit fault based on the equivalent source impedance and nearby sources of fault current. Short-circuit studies use static computational methods involving various factors to model the contribution of synchronous and asynchronous machines. The short-circuit capacity (SCC) at a bus is the short-circuit current expressed as power (Urdal et al., 2015). This information is also used to classify power grids without IBGs as either weak or strong. In fact, the terms "SCC" and "system strength" are sometimes used interchangeably (Gordon et al., 2022). Although there is no predefined threshold for SCC, the higher the SCC of a bus, the stronger the bus. Short-circuit analysis was conducted in this study using the IEC 60909 standard, which expresses the short-circuit power as shown in equation (1). It involves applying a balanced three-phase fault to the bus of interest first, and thereafter computing short-circuit capacity based on the symmetrical short-circuit current and pre-fault voltage of the bus.

$$S_i^{''} = \sqrt{3} V_n I_i^{''} \tag{1}$$

where $S_i^{''}$ is the short-circuit capacity to be computed for bus *i*, $I_i^{''}$ and V_n are the short-circuit current and the bus nominal voltage, respectively.

c. Grid Strength Assessment

When IBGs are integrated into a power grid, the short circuit ratio (SCR) given by equation (2) is a common measure used to assess the strength of the PoI and to evaluate its ability to operate under different system conditions. A lower SCR is associated with a weaker system, while a higher SCR indicates a strong system that can easily recover from major disturbances. It is defined as the ratio of the short-circuit capacity at the PoI to the rated capacity of the IBG. It is mathematically expressed as given in Equation (2) (Sanni et al., 2022).

$$SCR_i = \frac{\left|S_i^{''}\right|}{P_{\mathrm{IBG},i}} \tag{2}$$

where $P_{IBG,i}$ is the rated power of the IBG.

However, the accuracy of the SCR only applies to a single IBG in a single PoI, as it does not account for the effects of interactions caused by close-by IBGs (Fernandes et al., 2015; Kim et al., 2020; Wu et al., 2018). To address this, a previous work by the author proposed the network response short-circuit ratio (NRSCR) (Sanni et al., 2022), which captures the interactions among IBGs to evaluate system strength. Equation (3) shows the expression for computing NRSCR.

$$NRSCR_i = \frac{S_i^{''}}{\left(P_{DG,i} + \sum_{j \in D, j \neq i} \left[P_{DG}^{C}\right]_{j,i}\right)} \tag{3}$$

Where S_i'' is the short-circuit capacity at the i^{th} PoI; $P_{DG,i}$ is the rated capacity of the IBG connected at bus *i*; $\left[P_{DG}^{C}\right]_{j,i}$ is the fraction of neighbouring IBG injection at bus *j* interacting with the IBG at bus *i*; and *D* is the total number of IBG in the network. Typically, system strength evaluated either with SCR or NRSCR classifies a system as strong for value greater than 3, weak for value between 2 and 3, and very weak for value less than 2.

Although this study involves multiple IBG integrations, both the SCR and NRSCR measures are evaluated to provide a proper perspective on the accuracy of the latter.

d. Dynamic analysis

This study conducts dynamic simulation studies is to assess how the IBGs respond to a sudden disturbance at the PoIs with different system strength values. To achieve this objective, a solid three-phase short circuit fault is simulated in this test network, which lasts for 0.3 seconds before clearing. The response of the IBG during and after fault clearance is then evaluated with respect to the NRSCR values in the PoIs. This study utilized the industry-standard Power System Simulation for Engineering (PSS/E) software to model and simulate the Nigeria 330 kV network.

3. RESULTS AND DISCUSSION

This section describes the results of short-circuit studies, system strength evaluation, and dynamic analysis of the system response to disturbance.

Figure 3 presents the results of the short-circuit studies conducted on the Nigerian transmission grid to assess the strength of the network without any IBG integration using the IEC 60909 standard. It was observed that buses in the southern part of the grid had significantly higher SCC values than buses in the northern region. The highest SCC value of 19,888 MVA was recorded at the Benin bus, while the lowest value of 378 MVA was at the Maiduguri bus. The reason is due to the higher concentration of synchronous generators in the south than in the north. Selected buses in the northern region (coloured red), including Birnin Kebbi, Gombe, Jos, Kano, and Katsina, are the proposed PoI for IBG integration based on the NBET PPA agreement. It is observed that these PoIs have very low SCC compared to most buses in the grid. This should be of concern for future integration of IBG into the grid in this region.

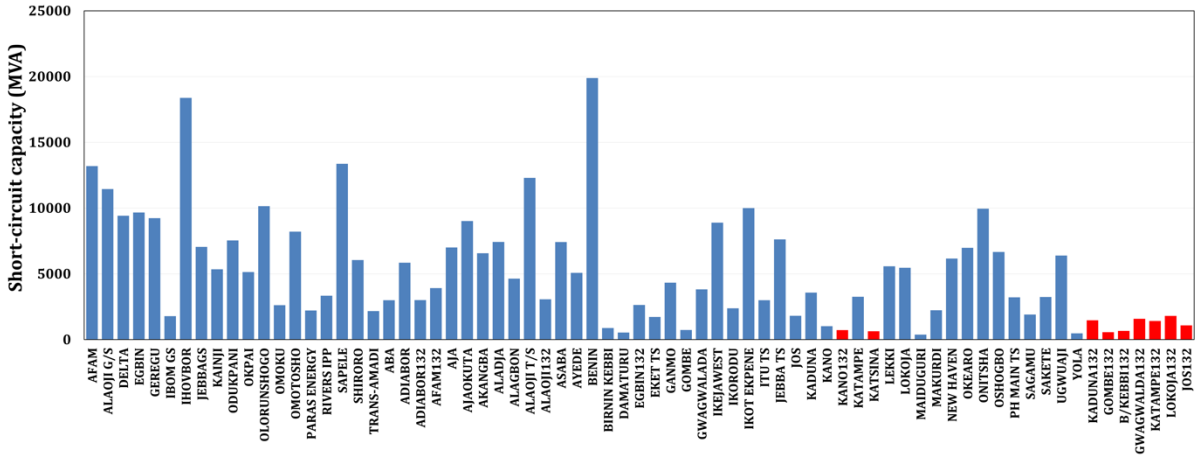

Fig. 2. Short-circuit capacity profile of the Nigerian transmission grid.

The SCC value at the proposed PoIs shows that it ranges from 571.77 MVA at Gombe to 1805.67 MVA at Lokoja. These SCC values are used to evaluate the system's strength using SCR and NRSCR metrics. Table 1 presents the results of the SCR and NRSCR values computed using Equation (2) and (3), respectively, with the rated power output of the IBGs. It is observed that the result of the SCR estimates is generally higher than that produced by NRSCR. While the rated power at the PoIs ranges from a minimum of 50 MW at Kaduna and Katampe to 220 MW at Jos, SCR identified all the PoIs as strong (i.e., > 3), with Kaduna (SCR = 29.44) as the strongest. This is contrary to the NRSCR measure which suggests Katampe (NRSCR = 19.01) as the strongest, while the buses at Kano (NRSCR = 2.05) and Katsina (NRSCR = 1.93) are identified as weak and very weak, respectively. Moreover, both measures identified Katsina as the weakest PoI. This confirms the suggestion that the SCR metric is unsuitable as a metric of choice in a multi-IBG-penetrated power grid. Furthermore, the PoIs at Kano, Katsina, Kaduna, Gombe, and Jos all have NRSCR values less than 10, with Kano and Katsina posing a potential concern for the grid due to their closeness and interaction between the two PoIs. All other buses have NRSCR values greater than 10 and may not be of concern to the grid.

Table 4. System strength evaluation result for IBG integrated Nigerian transmission grid

PoI	Short-circuit power at PoI (MVA)	Rated Power injection of IBG (MW)	SCR	NRSCR
Kano	735.01	130	5.65	2.09
Katsina	650.33	185	3.51	1.96
Kaduna	1472.13	50	29.44	7.31
Gombe	567.77	100	5.68	2.94
Birnin kebbi	664.41	55	12.08	12.08
Gwagwalada	1581.97	100	15.82	13.48
Katampe	1415.51	50	28.31	19.01

Lokoja	1805.67	100	18.06	16.49
Jos	1085.71	220	4.94	3.23

To confirm the validity of result and presence of interaction based on the system strength values indicated in Table 1, a dynamic simulation is conducted to assess the dynamic voltage stability of the Nigerian power grid. A credible disturbance by way of a three-phase fault is simulated at the Shiroro bus for 300 ms, and the Shiroro-Jebba transmission line is tripped to clear the fault. Figure 4 illustrates the voltage response of the PoIs in relation to the system strength, which is evaluated using NRSCR. The simulation is conducted first with all the IBGs connected (Scenario A). Thereafter, the simulation is repeated by disconnecting the IBG at Kano (scenario B).
For scenario A, it is observed that the bus voltages in Kano, Katsina, Kaduna, Gombe and Jos displayed some transients during fault conditions. The response can be attributed, among other things, to the proximity of the two weakest buses (Kano and Katsina), to the fact that the short-circuit power of these buses is low in comparison to the rated capacities of the IBGs, and to the fact that the control action of the IBG power electronic systems at these PoIs interacts with one another in an attempt to maintain a stable system operation. This demonstrates that the IBG voltage controller's quick dynamic response has a significant impact on grid stability in locations with low SCC. In contrast, Birnin Kebbi, Gwagwalada, Katampe, and Lokoja buses' voltage responses did not experience similar transients, despite Katampe and Gwagwalada's nearness to the fault location.
In scenario B, where the generator at Kano was disconnected, none of the PoIs experienced any transients during the fault as recorded in scenario A. This confirms that the absence of interactions among multiple IBGs at a weak PoI is will not impact grid operation negatively.

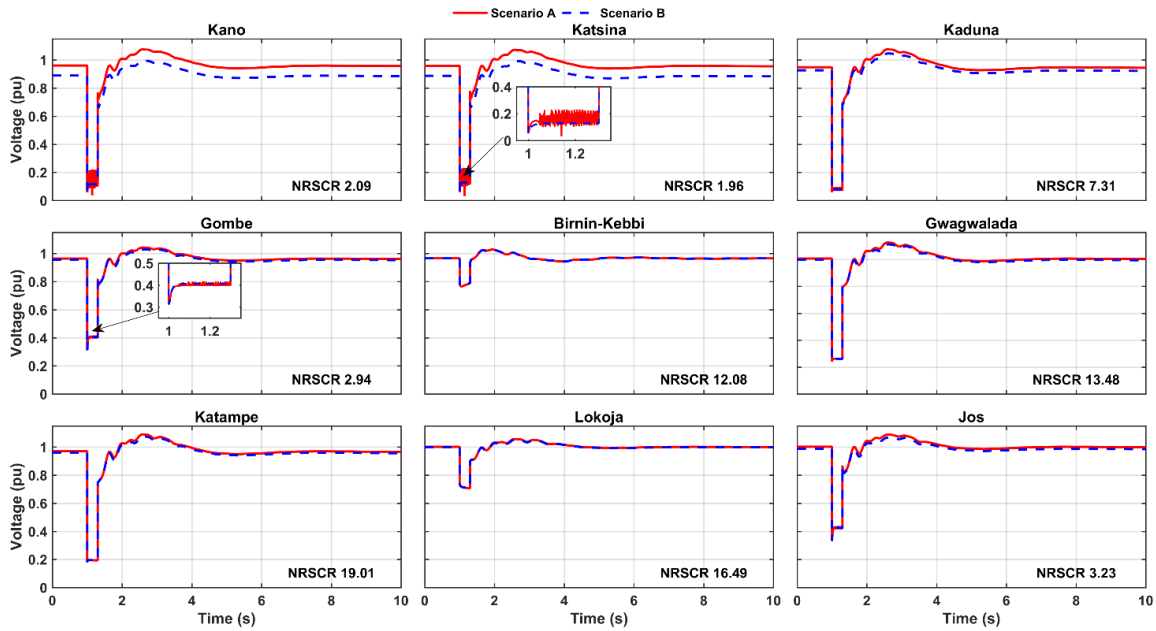

Fig. 3. voltage response to system disturbance

4. CONCLUSION

The existence of low SCC in the Nigerian transmission grid and its impact on system strength when integrated with IBGs has been examined. Without IBG, the short circuit studies indicates that the most buses in the northern part of the grid are weak. With the integration of IBGs, the system strength measured by NRSCR shows that some of the proposed PoI based on the NBET PPA are not entirely weak, with some strong PoIs. However, the presence of few buses with NRSCR value less than 3 may be a source of concern in ensuring operational stability. Dynamic voltage stability analysis shows that PoIs with system strength less than 10 may require close attention and adequate planning to integrate IBGs. In this regard, this study will help the system operators and the concern stakeholders to have the knowledge of the system strength for immediate and future system planning. Nevertheless, additional studies will be required to establish a threshold NRSCR value to differentiate a weak

grid condition and a strong grid. Future studies will investigate the impact of IBG integration on frequency stability of the grid.

ACKNOWLEDGEMENT

The lead author received support from the Tertiary Education Trust Fund (TETFund) through the Academic Staff Training and Development (AST&D) Grant of the Federal University Oye-Ekiti, Nigeria.

REFERENCES

Aldaoudeyeh, A. M., Wu, D., & Jiang, J. J. (2019, August). Identification of Critical Branches for Improving Weak Grid with Large-scale Integration of Inverter-based Resources. *2019 IEEE Power & Energy Society General Meeting (PESGM)*. https://doi.org/10.1109/pesgm40551.2019.8974106

Ekic, A., Fischer, A., Eisenbeisz, A., Lind, G., Aldaoudeyeh, A. M., & Wu, D. (2018, September). Impact Analysis of Power Network Structure on Grid Strength. *2018 North American Power Symposium (NAPS)*. https://doi.org/10.1109/naps.2018.8600573

Fernandes, R., Achilles, S., & MacDowell, J. (2015). *Report to NERC ERSTF for Composite Short Circuit Ratio (CSCR) Estimation Guideline*.

GE Energy, C. (2014). *Minnesota Renewable Energy Integration and Transmission Study (Final Report)*. http://www.minnelectrans.com/documents/mrits-report.pdf

Gordon, S., Bell, K., & Hong, Q. (2022). Implications of reduced fault level and its relationship to system strength: a Scotland case study. *CIGRE Session 2022*.

Goud, R. D., Rayudu, R., Mantha, V., & Moore, C. P. (2019, September). Impact of Short-circuit Ratio on Grid Integration of Wind Farms-A New Zealand Perspective. *2nd International Conference on Large-Scale Grid Integration of Renewable Energy in India (RE Grid Integration Conference India 2019)*.

International Renewable Energy Agency. (2023). *Renewable Energy Roadmap: Nigeria*.

Kim, D., Cho, H., Park, B., & Lee, B. (2020). Evaluating Influence of Inverter-based Resources on System Strength Considering Inverter Interaction Level. *Sustainability 2020, Vol. 12, Page 3469*, *12*(8), 3469. https://doi.org/10.3390/SU12083469

Mohammed, O. O., Otuoze, A. O., Salisu, S., Ibrahim, O., & Rufa'i, N. A. (2019). Virtual synchronous generator: an overview. *Nigerian Journal of Technology*, *38*(1), 153–164.

North American Electric Reliability Corporation. (2017). *Integrating Inverter-Based Resources into Low Short Circuit Strength Systems*. https://www.nerc.com/comm/PC_Reliability_Guidelines_DL/Item_4a._Integrating _Inverter-Based_Resources_into_Low_Short_Circuit_Strength_Systems_-_2017-11-08-FINAL.pdf

Sanni, S. O., Akorede, M. F., & Olarinoye, G. A. (2022). Strength assessment of electric power systems containing inverter-based distributed generation. *Electric Power Systems Research*, *207*. https://doi.org/10.1016/j.epsr.2022.107825

Urdal, H., Ierna, R., Zhu, J., Ivanov, C., Dahresobh, A., & Rostom, D. (2015). System strength considerations in a converter dominated power system. *IET Renewable Power Generation*, *9*(1), 10–17. https://doi.org/10.1049/iet-rpg.2014.0199

Wu, D., Li, G., Javadi, M., Malyscheff, A. M., Hong, M., & Jiang, J. N. (2018). Assessing Impact of Renewable Energy Integration on System Strength Using Site-Dependent Short Circuit Ratio. *IEEE Transactions on Sustainable Energy*, *9*(3), 1072–1080.

Zhang, Y., Huang, S. H. F., Schmall, J., Conto, J., Billo, J., & Rehman, E. (2014). Evaluating system strength for large-scale wind plant integration. *IEEE Power and Energy Society General Meeting*, *2014-Octob*(October), 1–5. https://doi.org/10.1109/PESGM.2014.6939043

PAPER 155 – BAMBOO AVAILABILITY AND LAND USE PATTERN IN THE SURROUNDING SIX LOCAL GOVERNMENT AREAS TO IBADANLAND METROPOLIS, NIGERIA

W. B. Adebosin[1]; N. A. Adewole [2]* & A. O. Olorunnisola[2]

Ogun State Forestry Plantation Project, Area J4, Ogun State, Nigeria
Department of Wood Products Engineering, Faculty of Technology, University of Ibadan, Oyo State, Nigeria
*Email: nureniadedapoadewole@gmail.com

ABSTRACT
Quests for mitigating wood scarcity in Nigeria is further promoting the use of bamboo as substitute in the production of wide range of products while its short gestation period is a cash-in for its sustainable uses. This study investigated bamboo status cum land-use patterns in six of the eleven Local Government Areas 'LGA' outside Ibadanland metropolis in Oyo State, Nigeria to generate baseline data. With Graphics Peripheral Interface Standard 'GPIS' tool, Landsat imageries for year 2000, 2015 and 2020 were generated for the study locations. Bamboo species identification, characteristics cum sample collection were carried out during on-the-spot assessment. The common land-use in the six LGAs are built-up-areas, thick-vegetation, farmlands and sparse vegetation. In year 2000, 2015 and 2020 the built-up-areas, thick-vegetation, farmlands and sparse vegetation covered 20.02%, 30.07% and 30.39%; 10.74%, 25.72% and19.19%, and, 30.78%, 12.19% and 30.39%, respectively, while bamboo covered 1189.59 km^2 (36.46%), 990.49 km^2 (32.02%) and, 1003.63 km^2 (32.45%), respectively. Open farmland exists for bamboo cultivation across the six LGAs while existing bamboo stocks, grows naturally, matured, intact, harvested with little royalty payment or free. This study established that a species of bamboo: *Bambusa vulgaris* Schrad grows in abundance with wide distribution across Akinyele, Egbeda, Ido, Lagelu, Oluyole and Ona-Ara LGAs in Ibadanland.

KEYWORDS: Bamboo species, Availability, Distribution, Land-use pattern, Ibadanland

1. INTRODUCTION

Anthropogenic activities have contributed in no small measure to the dwindling of forest resources globally (FAO, 2010; Mmom and Mbee, 2013). It appears an un-ending growth in the world population cum technological advancement are stimulating conversion of more forest land to meet provision for shelter, agricultural and commercial activities requests of the world population. These needs of man were found to be major drivers in forest depletion by plethora of literature (Gadallah *et. al.*, 2019; Taylor, 2019; Zar *et. al.,* 2017). Nigeria's experience is not difference in that Fasoro and Ajewole (2019) reported that Nigeria's natural forest has, over the past years, experiencing a remarkable degradation and depletion. The forest land encroachment for the identified needs of man is increasingly posing considerable challenge to retaining forest land for sustenance of economic tree species in Nigeria. Also, scarcity of reserve land cum long gestation period required to raise economic tree species plantation have also been identified as critical bane to the regular supply of wood from these categories of trees to wood industrial sector in Nigeria (Damenortey, 2018; Fasoro and Ajewole, 2019).

The worsening scarcity of wood of economic tree species has encourage indiscriminate logging of lesser known trees species, so much so, that fruit trees are now been sourced for their wood. To mitigate this critical gap in wood supply to Nigeria wood industries, attention has been shifted to promotion of cultivation and use of bamboo, a presumably abundant Non-Timber Forest Products (NTFPs) in Nigeria because of its suitability for replacing wood (Omiyale, 2003; Onilude, 2006). Adewole (2009), Ladapo *et. al.,* (2017), Damenortey (2018) noted that dwindling in supply of wood raw material to industry has encouraged promotion of bamboo as a suitable alternative/complementary raw material. Other factors that have endeared bamboo as a replacement for wood in Nigeria are un-ending population increase, depletion of natural forest resource and its short harvesting period on marginal land (Adewole, 2019). In fact Bamboo is a hard, strong, flexible and renewable grass with growth rate of about 1metre/day (Scurlock *et. al.,* 2000; Igbokwe *et. al.*, 2016). It includes over 1000 species of woody perennial grasses in more than 100 genera and can be managed on marginal agricultural land. (Sewanon *et. al.,* 2015)

The culm been suitable for conversion into various modern and specialized intermediate products to replace wood but still mostly used *in-situ* for scaffolding, as column, pedestal bridge, farm structure material, poultry feed trough among other in traditional ways of using its culm (Adewole and Olayiwola, 2011; Adewole and Bello, 2013; Adewole and Udele, 2021). Now that Bamboo is been promoted for use as raw material for modern

products in Nigeria, there is need to validate the veracity of claim of its abundance availability vis-à-vis availability of marginal farm land with proximity to sub-urban area in Nigeria. It is for these reasons among other relevant needs that this study was initiated to generate planning prone data on bamboo availability and pattern of land uses in the six sub-urban Local Government Area 'LGA' in Ibadan, Oyo State, Nigeria.

2. METHODOLOGY

This study was conducted between May and July, 2021 to obtain preliminary information on bamboo type, availability, abundance and distribution at the six LGAs that lie outside the metropolis areas in Ibadanland. The study locations were purposefully selected because they host the fringe secondary forests that exist in Ibadanland. The current forest transition and land use cover maps of the respective LGAs was acquired through satellite imageries and mapping with Graphics Peripheral Interface Standard (GPIS) tool. The imageries considered were for the year 2000, 2015 and 2020, for the entire six LGAs. The imageries indicated locations, bamboo distributions and other land uses. Comparison of current satellite images of the forest depletion ratio and the rate of bamboo availability, distribution and changes availability across the six LGAs was assessed. The six LGAs fringe forest areas were visited during the-on-spot-assessment to ascertain the veracity of the imageries findings and to ascertain mode of bamboo stock accessibility cum bamboo culm characteristics. Culm and leaves sample specimens collected from all the six LGAs were taken to the Herbarium Unit of the Department of Botany, University of Ibadan for identification.

3. RESULTS AND DISCUSSION

3.1 Study Location: Description and Characteristics

The six LGAs selected for the study are *Akinyele, Lagelu, Egbeda, Ona-Ara, Oluyole* and *Ido.* These LGAs surrounds the five LGAs that fell within the Ibadan metropolis. The fringe forests in Ibadanland only that exists at the selected six LGAs. These six LGAs are fast growing in number of new settlement enclaves and the push from the metropolis continue to encourage large population of low income earners to migrate daily to these six LGAs contrary to the conventional rural to urban drift. There are fringe farm lands and it appears there are abundant human resources to drive bamboo plantation cultivation if relevant bodies drive policy along the line.

3.2 Bamboo Status in the Six LGAs and Stock Characteristics

The status in respects of bamboo availability, distribution and variation over twenty years, starting from year 2000 for the six LGAs are represented in Figure 1. It could be inferred from the yellow color indicating the bamboo abundance in Figure 1 that bamboo actually can be found in all the six LGAs with varying densities and different distribution patterns. However, the Figure 1 (a) revealed that Egbeda LGA has the lowest density of bamboo abundance while bamboo is most prevalent in Oluyole and Ona-Ara as at year 2000. The scenario has changed in the Year 2015 and 2020 in that the imageries shows that Akinyele and Lagelu has the high density of bamboo abundance while Oluyole and Ona-Ara appeared to have lost considerable density of bamboo. This observation was most of the bamboo stocks being concealed rather as undergrowth as was later found out through on-the-spot assessment as shown in Plate 1. Bamboo is very lowly patronized, even for traditional uses. The bamboo stocks that exist in all the six LGAs grow naturally and are largely remain un-tapped. Matured Bamboo culms are available in each of the six LGAs and harvesting them by any user is hardly ever charged for fee. The cost associated in procuring bamboo culm length in each of the six LGAs is determined by labour incurred in harvesting and the cost of transporting to where it will be used. Only in two occasions and in Ona-Ara LGA was there indication that a peanut royalty may have to be paid to land owner on whose land bamboo is growing before the culm can be harvested. This observation agrees with the earlier findings by Adewole (2017). The bamboo species growing in all the six LGAs considered were identified as *Bambusa vulgaris* Schrad Ex.J.C.Wendl.

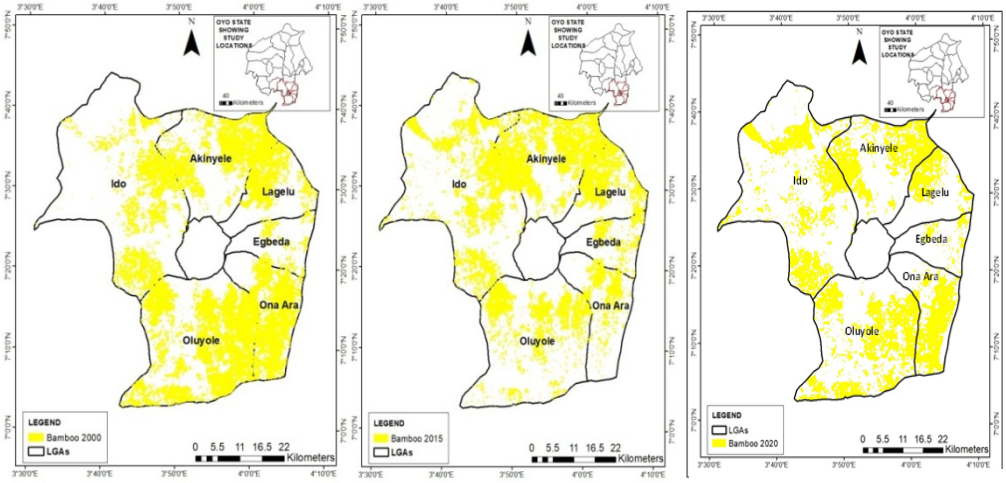

a) Status of Bamboo at the Six LGAs in Year 2000

b) Status of Bamboo at the Six LGAs in Year 2015

c) Status of Bamboo at the Six LGAs in Year 2020

Figure 1: Bamboo Status at the Six LGAs from the Year 2000 to Year 2020

3.3 Land Use Patterns in Relation to Bamboo Availability in the Six LGAs

The form of land uses in relation to the portion of the land where bamboo stocks occupied in each of the six LGAs and for the years under considerations are shown in Figure 2. It was evident that the lands in each of the LGAs were partitioned into four major forms of uses: the built-up-areas, thick-vegetation, farmlands and sparse vegetation. In year 2000 the built-up-areas, thick-vegetation, farmlands and sparse vegetation covered 20.02%, 30.07% and 30.39% respectively. This implies that areas where bamboo could be found were in higher proportion in terms of land uses at the six LGAs as at the Year 2000. In the Year 2015 and 2020 respectively, the land use distributions among these four critical use components: the built-up-areas, thick- vegetation, farmlands and sparse vegetation are 10.74%, 25.72%, 19.19%, and, 30.78%, 12.19% and 30.39%, respectively. The areas designated built up area appears shrink in Year 2015 but with Year 2020 the statistics was clearer that there have been considerable encroachment into the fringe forest areas in all the six LGAs due to continuous growth of emerging settlement. The low cost of acquiring landed properties for shelters must have attracted many of the hitherto residents in the most of the metropolis LGAs to migrate to actualize the dream of owning personal houses within the enclaves of the six LGAs in Ibadanland.

Meanwhile the portion of the land covered in each of the six LGAs relative to other four critical land uses over the period considered by this study is presented in Table 1. There are fluctuations in the areas covered by bamboo but with further growth in Year 2020. The study noted that that the vast areas of farm lands and sparse vegetation that exist in all the six LGAs can serve as veritable sites for bamboo plantation. Ido LGA is particularly mostly blessed with expanded farm land cum sparse vegetation when compared with other LGAs considered for the study. Since the soil readily supports bamboo growth and the turnaround time for raising bamboo plantation is less than 5 years for the culms that are even suitable for processing, the findings of this study suggest that exploitation of bamboo culms for modern application can be practiced with assured sustainability.

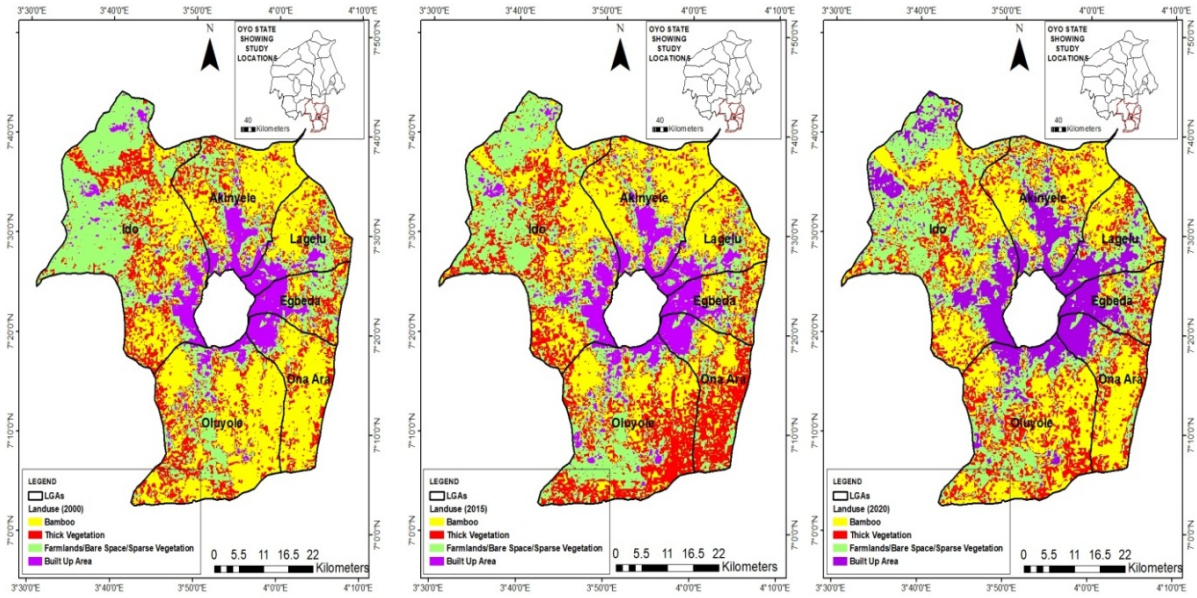

a) Land Uses at the 6 LGAs in b) Land Uses at the 6 LGAs in c) Land Uses at the 6 LGAs in 2020

Figure 2: Patterns of Land Uses in Relation to Bamboo Availability in Each of the Six LGAs

Table 1: Landuse Spatial Pattern in 2000, 2015 and 2020 for the Six LGAs

Landuse	2000		2015		2020	
	(km^2)	(%)	(km^2)	(%)	(km^2)	(%)
Bamboo	1189.59	38.46	990.49	32.02	1003.63	32.45
Thick Vegetation	619.30	20.02	795.52	25.72	617.72	19.97
Farmlands/ Bare lands/Sparse Vegetation	952.10	30.78	930.08	30.07	939.93	30.39
Built Up Area	332.26	10.74	377.16	12.19	531.97	17.20
Total Landed Area	**3093.25**	**100.00**	**3093.25**	**100.00**	**3093.25**	**100.00**

4. CONCLUSION AND RECOMMENDATION

This study confirmed that bamboo exists in Akinyele, Lagelu, Egbeda, Ona-Ara, Oluyole and Ido Local Government Areas of Ibadanland. It grows easily on the six LGAs soils and naturally too. Though bamboo is widely available, but it is in relative abundance in respect of the six LGAs with Oluyole and Ona-Ara LGAs having the highest density. The bamboo stocks were largely matured, resources remain intact and can be harvested by stranger free most of the time and occasionally with little royalty payment to land owners. This study established that a species of bamboo: *Bambusa vulgaris* Schrad grows in abundance with wide distribution across Akinyele, Egbeda, Ido, Lagelu, Oluyole and Ona-Ara LGAs in Ibadanland. The species of bamboo that grows in all the six LGAs is the same: *Bambusa vulgaris* Schrad Ex.J.C.Wendl. Land resources in all the six LGAs were shared among four main uses: the built-up-area, thick-vegetation, farmland and sparse vegetation. The areas covered by bamboo have not significantly changed over the space over the past 20 years. The Ido LGA was noted to have the largest land areas that can be exploited for bamboo plantation for sustainability purpose.

Arising from this finding, it is recommended that a critical appraisal of the characteristics properties of the bamboo resources in the six LGAs should be investigated. Also that appropriate bodies in Oyo State gear-up to harness the potentials of the abundance bamboo resources for modern application and to mitigate wood supply shortage while enunciating appropriate policies that will encourage bamboo plantation cultivation to plan for its sustainable uses.

REFERENCES

Adewole N. A. and Udele, K. E. (June, 2022) Failure Load Comparison of Joints Secured with Gusset-Plate and Adhesive in 5-Web-Pratt Trusses Made of Bambusa vulgaris, Chrysophylum albidium and Tectona

grandis Laminates. African Journal of Agriculture, Technology and Environment (AJATE) Volume 11 Number 1. 20-29 June, P-ISSN: 2315-8042; E-ISSN: 2346-7290

Adewole, N. A. (2009). Bamboo Resource in Ibadan and Environs: Utilizations, Opportunities and Challenges. Journal of Tropical Forest Resources 25(1):42-51.

Adewole, N. A. (2019). Pathway to sustainable Social and Economic Development through Apposite Use of Nigeria's Forest and Forest Products Resources. Published by Forestry Association of Nigeria, in V. A. J. Adekunle and A. O Akinwole. (Eds) Sustainable Development Through Appropriate Forest Management Strategies: Exotic Dezines Ltd., Ibadan. 209-238pp. ISBN 978-978-310-842-0.

Adewole, N. A. and Bello, K. O. (2013). Recycling of Bamboo (Bambusa vulgaris Schrad) Recovered from Scaffold into Material for Furniture Production. Innovative Systems Design and Engineering 4(9):73-79 www.iiste.org

Adewole, N. A. and Olayiwola, H. A. (2011). Production of Bamboo-Lam from Flat Bamboo Strip Prepared from Bambusa vulgaris Schrad. In A. T. Oyeyemi, B. O. Adewuyi and D. A .Palemo (Eds.). Materials Processing for Sustainable Environment and National Development.Proceedings of Combined Proceedings of the Nigerian Materials Congresses [NIMACON-2010 and NIMACON-2011]. 21-24 November, 2011. 346-350pp.

Adewole, N.A (2017): Technical Issues in Adapting Roadside Carpentry Workshop facilities for Harnessing Modern Products Sustainably from Bamboo Resource in Ibadan. Proceeding of the 39th Annual Conference of Forestry Association of Nigeria held in Lagos, 20-24 February, 2017.pp 672-687.

Damenortey R.A. (2018):Bamboo an alternative wood to reducing tropical deforestation in Ghana. Proceedings of DIl-2018 Con. On Infrastructure Development and investment strategies for Africa, Reading Africa for sustainable development, A capacity building/empowerment and strategy discourse. Living stone Zambia 11-13 July,2018.

FAO(2010): Global Forest Resources Assessment.378pp.

Fazoro O.A. and Ajewole (2019). Investment analysis of small scale private forest plantation development in Ogun State, Nigeria. Asian Jour. of adv. Agric. Research 10(1):1-8, 155N 2A56-8864.

Gadallah, N. A., Adewole, N. A., & Ajayi, D. D. (2019). Potential of agroforestry as forest landscape restoration tool to solve forest cover loss cum food security in Sennar and Gedaref States, Sudan. International Journal of Development and Sustainability, 8, 199-210.

Ladapo, H.L, Oyegoke, O.O, and Bello, R.O (2017): Utilization of vast Nigeria's Bamboo Resources for Economic Growth: A Review. Journal of Research in Forestry, Wildlife and Environment, Vol.9, No 2, June 2017.

Mmom P.C and Mbee D.M. (2013):Population pressure and forest resources depletion in Gelegele forest reserve of Edo State . vol 3,No 3,pp31-42.Published by European centre for research training and development United Kingdom.12pp

Omiyale, O. (2003): Bamboo and Rattan: Vehicle for Poverty Alleviation in Nigeria, Paper Presented at the World Forestry Congress Quebec City Canada.

Onilude M.A. (2006). Potential of bamboos as raw materials for the wood industries in Nigeria. Dept. of Agricultural and Environmental Energy, University of Ibadan.

Scurlock, J. M., Dayton, D. C., & Hames, B. (2000). Bamboo: an overlooked biomass resource?. Biomass and bioenergy, 19(4), 229-244.

Sewanon H.H and Chenangnon F (2015):Traditional ecological knowledge and use value of bamboo in southern Benin: implication for sustainable management. Ethnobotany research and application vol 14 pp139-153.

Taylor Meek (2019): Effects of Deforestation: How does Agriculture cause Deforestation. Scientist Media pp30-35.

Zar C.H; Chilo K.Y and Osamu S. (2017): Interaction between rural people's basic needs and forest: A case study of Katha District of Myanmar. International Journal of Forest Research, vol 2017.

PAPER 156 – PREDICTION OF NO_X EMISSION IN GAS TURBINE POWER PLANT WITH HARRIS HAWKS OPTIMIZED ARTIFICIAL NEURAL NETWORK

T. I. Amosa[1], O. Ibrahim[2], S. L. Ayinla[1,3], A. Bahashwan Abdullah Omar[1], F. Mochammed[4]
A. O. Yusuf[3], H. O. Mahmud[3]

[1] Department Electrical & Electronics Engineering, Universiti Teknologi PETRONAS, Bandar Seri Iskandar, Malaysia.
[2]Department of Electrical & Electronics Engineering, University of Ilorin, Ilorin, Nigeria.
[3]Department of Computer Engineering, University of Ilorin, Ilorin, Nigeria.
[4]Department of Chemical Engineering, Universiti Teknologi PETRONAS, Bandar Seri Iskandar, Malaysia.
[*]Email: amosatemitopeibrahim@gmail.com

ABSTRACT
Predictive emission monitoring systems (PEMS) are critical instruments for verifying and strengthening the reliability of costly continuous emission monitoring systems used in gas-turbine power facilities. PEMS is built on the premise of predictive models that are trained on historical data to estimate emission components. The availability of a relevant and environmentally friendly dataset for gas turbine processes has prompted an investigation into the efficacy of models derived from different machine learning techniques. This inquiry aims to develop a predictive model for CO and NOx emissions based on both ambient variables and technological process parameters. In the present study, a new machine learning-based model is proposed for the prediction of NOx emissions in natural gas turbines. The model utilizes an Artificial Neural Network (ANN) that is optimized with the Harris Hawks Optimizer (HHO). The model is trained and validated on a dataset obtained from the University of California at Irvine (UCI) open data repository. The effectiveness of the proposed algorithm was evaluated by comparing it with conventional ANN. The proposed model obtained R^2 = 90.36%, RMSE = 3.9276, and MSE = 15.4260. The results showed that the proposed approach is effective and demonstrates competitive performance over ANN.

KEYWORDS: NOx emissions, exhaust emission prediction, Intelligent emission monitoring, Harris hawk optimizer, Gas turbine combined cycle

19. INTRODUCTION

More energy consumption has a twofold detrimental impact on the environment, causing increased deforestation as well as increased carbon and flue gas emissions (Kaya et al., 2019). Air pollution is a significant problem that encompasses all components that have the potential to harm living things. The combustion process in the power sector is one of the primary sources of hazardous pollutants (NOx and CO) emitted into the atmosphere. The nitrogen dioxide (NO_2) and nitric oxide (NO) emissions that arise from nitrogen and oxygen gas interactions in the air during combustion are referred to as NOx. NOx (NO_2 + NO) is regarded as the principal pollutant of the atmosphere because it causes tropospheric ozone, ozone layer depletion, photochemical smog, acid rain, and eventually global warming. Several agreements have been adopted in different United Nations (UN) climate change conventions by participating nations to raise environmental awareness in both public and political spheres. The Paris Climate Change Agreement and the Glasgow Climate Pact are two of such agreements that have established alternative roadmaps for achieving environmental sustainability. The Glasgow Climate Pact was adopted, with the goal of making the 2020s a decade of climate action and support. In this convention, several themes have been agreed upon in the decision package, including greater steps to strengthen climate change resilience and reduce greenhouse gas emissions. They also committed to working together to close the gap between existing emission reduction plans and what is needed to cut emissions so that global average temperature rises are restricted to 1.5 degrees. In fact, for the first time, countries are being urged to reduce unabated coal power and wasteful fossil fuel subsidies, in addition to the extant severe environmental laws, and tax implementation for carbon emissions.

In compliance with these resolutions, there is a specific focus on lowering emissions from power plants, as the combustion process in the power sector is a major source of hazardous pollutants (NOx and CO) emitted into the atmosphere (Korpela et al., 2015; Skalska et al., 2010). In some regions of the globe, strong environmental restrictions limit these emissions to particular levels (Shakil et al., 2009). The Large Combustion Plant Directive and its replacement, the Industrial Emissions Directive (IED), which went into force in 2016 for

power plants with a capacity of more than 50 MW, is the European union regulations that limit flue gas emissions (NOx, CO, and dust) (Kaya et al., 2019). The flue gas contents of NOx and CO must be regularly monitored from any combustion plant surpassing a total capacity of 100 MW, according to IED (Korpela et al., 2017). Furthermore, when natural gas is utilized as a fuel, NOx and CO emissions are regulated to 25 ppmdv (parts per million by dry volume) by the EU.

Since it has become mandatory for power plant operators to monitor the NOx and CO pollutants emitted during combustion operations in a power plant, three solutions for monitoring flue gas emissions from a combustion unit have been developed: i) intermittent measurements, ii) continuous emission monitoring system (CEMS), or iii) predictive emission monitoring system (PEMS) (Kaya et al., 2019). Emission testing facilities typically perform "intermittent measurements" with calibrated equipment at reasonable expenses. The emission monitoring equipment (such as a sensor set) is placed on-site in CEMS. CEMS delivers real-time emissions data collected directly from sensors. The accuracy of these measurements is dependent on adequate maintenance and calibrations of the equipment, which should be carried out according to industry standards (Kaya et al., 2019). PEMS, conversely, is an expert system that employs predictive models based on historical data to estimate emission components using some process variables like ambient temperature, turbine inlet temperature, etc. PEMS is regarded by many scholars as a backup, or alternative to CEMS for monitoring (Chien et al., 2005). Analytical equations derived from thermodynamic (or first) principles, mass and energy balance, and data-driven models, which include statistical and machine learning methods, are the two basic approaches to model development for PEMS. CEN/TC 264/WG 37 contains the standardization and technical specifications required for PEMS software certification, as well as performance and quality assurance for a PEMS to demonstrate suitability for its measuring task and to ensure that the PEMS continues to perform within the specified performance during operation.

For several decades, low research consideration has characterized the development of data-driven models for PEMS due to lack of applicable and ecologically valid datasets. However, the publication of an open source flue gas emission dataset (Kaya et al., 2019) on the University of California, Irvine, open data repository has prompted a challenge to develop and assess the performance of different models built using various machine learning algorithms. This paper presents a novel data-driven approach for learning PEMS model which is known for its promising solution for handling massive data (Sherstinsky, 2018). The primary aim of this study is to employ the Harris Hawks Optimized Artificial Neural Network (ANN-HHO) algorithm to develop a model capable of predicting NOx emissions from gas turbines. The implementation and training were performed using MATLAB software. Using the Neural Net Tuning tool, ANN models was created, and HHO was applied to enhance model performance. Various statistical metrics, including MSE, RMSE, and R^2 were utilized to assess the models' performance.

The rest of this paper is structured as follows: Section 2 discussed various related works. Section 3 provides a detailed description of the materials and methods utilized to apply the ANN-HHO design in a power plant, including theoretical concepts. Experimental results are presented in Section 4, while Section 5 summarizes the study's conclusions.

20. RELATED WORKS

Over the last five decades, PEMS models have progressed from first principle-based models to AI-based models. AI-based models can be applied to process more data than traditional approaches and have been gaining popularity because of the advancements in computer technology and availability of larger datasets for training. Because AI-based PEMS models must employ process data linked to NOx emission, this gives them greater flexibility in selecting and processing process data than the first principle or statistical models. In 1973, the first PEMS was developed and published (Hung, 1975). PEMS studies and commercial applications for a variety of sources and sectors have been extensively investigated since 1990. PEMS describe a relationship between a set of emission source process parameters (e.g., air pressure, turbine exhaust pressure) and the resulting flue gas emissions. However, lack of largescale datasets for training has been a major limitation for learning robust and accurate AI-based PEMS models for several decades.

The largest flue gas emission dataset was introduced by researchers in (Kaya et al., 2019). This data was collected over a five-year period to further PEMS research. Researchers were able to start an open discussion on the features of data and the quality of models derived from various machine learning methods to predict CO and NOx emissions after the dataset was published in the open data repository of the University of California, Irvine (UCI) in 2019. The authors provide the first attempt in literature to use extreme learning machine regressors (ELMs) to solve this challenge. The best result has a coefficient of determination $R^2 = 0.56$ and mean absolute error (MAE) 0.97 mg/m3 for CO prediction and R = 0.67 and MAE = 4.57 mg/m3 for NOx prediction. The study conducted by Li et al. in 2015, identified two notable limitations associated with ELM. Firstly, the inherent randomness in ELM results in amplified uncertainty during both approximation and learning processes. Secondly, if an inappropriate activation function is used, ELM is prone to experiencing generalization degradation (Lin et al., 2015). The author in (Wood, 2023) employed a set of twelve models, including multi-linear regression (MLR) and machine learning (ML) techniques, to accurately predict CO and NOx emissions in combined cycle gas turbines. Using Artificial Neuro Fuzzy Inference System (ANFIS) optimized with GA, the author in reference (Dirik, 2022) predicts the NOx emission in a combined cycle power plant. The performance obtained in this study improved due to the replacement of gradient-based backpropagation learning algorithm with meta-heuristic optimizer (GA) for learning the ANFIS model. Motivated by this, we also proposed to learn a prediction model for NOx emission in a combined cycle power plant using ANN optimized by HHO.

21. MATERIALS AND METHODS

In this section, we described the ANN and HHO algorithms, as well as the machine learning approach employed in this study to predict greenhouse gases emitted in power plants. This study followed a data driven approach that uses historical data obtained from a combined cycle power plant. A combined cycle power plant is composed of gas turbines, steam turbines, and steam generators with heat recovery, where electricity is generated by combining gas and steam turbines in a single cycle (Dirik, 2022). The electricity is then transmitted from one turbine to the next, which can produce hazardous gaseous pollutants such as CO (carbon monoxide) and NOx (nitrogen oxides). NOx refers to a group of pollutants that include nitric oxide (NO_2) and nitrogen monoxide (NO), which are typically generated during the combustion process. This article is focused on NOx emissions from gas-fired power plants, which contribute to smog, acid rain, and tropospheric ozone pollution. By predicting the peak levels of such emissions, adequate preventive action is planned. To address this problem, ANN-HHO is employed to predict combined cycle emissions and their reductions, and to simulate NOx-level pollutant emissions based on environmental and control factors.

3.1 Artificial Neural Network

An artificial neural network is a biological-inspired computational intelligence algorithm that draws inspiration from human brain, and it is comprises of numerous artificial neurons. These neurons are linked by coefficients, known as weights, that form the neural structure of the network (refer to Fig. 1). Each neuron processes information by utilizing its weighted inputs, activation function, and one output. Essentially, a neuron is black-box model that determines what the outputs will be given the inputs. ANNs are sometimes referred to as connectionist models since the connection weights symbolize the memory of the system (Agatonovic-Kustrin & Beresford, 2000). While a single neuron can execute basic information processing tasks, the true strength of neural computing is derived from the interconnection of neurons within a network.

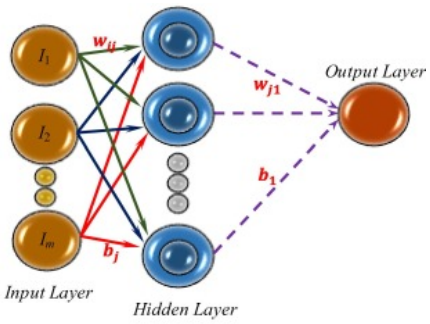

Figure 1. Illustration of ANN Structure.

The crucial characteristic of ANN is their capability to improve in a task through learning from experience. This feature enables ANN to be applied in a broad range of applications such as classification, prediction, detection, image processing, and pattern recognition. By minimizing the error between actual and expected outputs during training, ANN parameters, such as bias and weight, can be optimized (Khatir et al., 2021). While supervised, unsupervised, and reinforcement are the three learning approaches in machine learning, the most often used ANN is a fully connected, supervised network with backpropagation learning rule. However, it suffers from several limitations, particularly in their sensitivity to noisy data and vanishing gradient problem. Thus, there is a need to complement or replace this learning algorithm.

3.2 Harris Hawk Optimization Algorithm

Harris Hawks Optimization (HHO) algorithm was proposed in 2019 by Heidari et al.(Heidari et al., 2019), and has since then received huge research attention. HHO simulates collaborative behaviour and hunting style of the Harris Hawks in nature, i.e., surprise pounce. Harris's hawks employ the "surprise pounce" tactic, also referred to as the "seven kills" strategy, as their primary method of capturing prey. This strategy involves several hawks working together to attack a detected escaping rabbit from different directions, converging on it simultaneously outside of its cover. While the attack can be completed quickly in a matter of seconds, it may also involve multiple short-length, quick dives near the prey over several minutes, depending on the prey's escaping capabilities and behaviors. The Harris's hawks have the ability to imitate various hunting techniques depending on the situation and the fleeing patterns of their prey. In particular, researchers have identified four chasing tactics employed by these birds, namely, soft besiege, hard besiege, soft besiege with progressive rapid dives, and hard besiege with progressive rapid dives, as described in (Heidari et al., 2019).

3.3 Optimizing ANN with Harris Hawk Optimizer

HHO is a population-based gradient-free meta-heuristic optimization algorithm inspired by the collaborative conduct and hunting style of Harris Hawks. Stimulating the dynamic pattern and behaviours of this intelligent specie of bird via mathematical model, an optimization an algorithm is generated. HHO is well suited for improving ANN by optimizing the error function. However, HHO was used in this work to address the drawbacks of backpropagation learning algorithm in ANN, such as slow convergence and the tendency to be trapped in local minima. HHO is a stochastic search technique for optimization based on the concepts of harmonized foraging of one of the most intelligent birds, Harris' Hawks in hunting escaping preys (rabbits in most cases). In the HHO algorithm, the Harris's hawks serve as the candidate solutions, with the best solution in each step being identified as the intended prey or close to the optimum. These hawks randomly perch on various locations and employ two strategies to detect prey. In Table 1, we present the setting/parameters of the proposed hybrid algorithm.

Table 1. ANN-HHO Parameters setting for the proposed ANN-HHO algorithm.

Algorithm	Setting/Parameters	Types/value
HHO	Number of search agent	30
	Maximum iteration	100
	Lower bound	-10
	Upper bound	10
	default constant	1.5
ANN	Input layer	9
	hidden size	10
	Output layer	1
	Epoch	1000
	Activation function	Sigmoid

3.4 Datasets

This study makes use of the Gas Turbine CO and NOx Emission Dataset from the University of California at Irvine (UCI) open data repository (Kaya et al., 2019). The data was obtained in northwestern Turkey during a five-year period, and it consisted of hourly average sensor readings of eleven variables (nine input and two target

variables) with a total of 36,733 occurrences. The nine independent variables may be divided into two categories: environmental variables (such as temperature, humidity, and pressure) and process factors (such as turbine energy yield and air filter difference pressure). Table 2 summarizes the engine variables names, acronyms, and basic statistics of the variables contained in dataset utilized in our study. For this study, we use the data obtained between 2011-2013 for training and validation, and only the first 6-month data from 2014 for testing.

Table 2. Summary of the features contained in the UCI CO and NOx emission dataset.

Variable name	Acronym	Unit	Mean	Min	Max
Ambient Temperature	AT	deg. Celsius	17.71	–6.23	37.10
Ambient Pressure	AP	mbar	1013.07	985.85	1036.56
Ambient Humidity	AH	%	77.87	24.08	100.20
Air Filter Difference Pressure	AFDP	mbar	3.93	2.09	7.61
Gas Turbine Exhaust Pressure	GTEP	mbar	25.56	17.70	40.72
Turbine Inlet Temperature	TIT	deg. Celsius	1081.43	1000.85	1100.89
Turbine After Temperature	TAT	deg. Celsius	546.16	511.04	550.61
Compressor Discharge Pressure	CDP	mbar	12.06	9.85	15.16
Turbine Energy Yield	TEY	MWH	133.51	100.02	179.50
Carbon Monoxide	CO	mg/m^3	2.37	0.00	44.10
Nitrogen Oxides	NO_x	mg/m^3	65.29	25.90	119.91

22. RESULTS AND DISCUSSION

In this section, we discuss the result of the prosed ML-based modelling and prediction of NOx emission from gas turbine power plant using ANN and the proposed ANN-HHO. The obtained result is summarized in Table 3.

Table 3: Simulation result of ANN and ANN-HHO model

Model	Data split		Performance metrics					
	Train	Test	MSE		RMSE		R^2	
ANN	65	35	20.1687	20.3097	4.4910	4.5066	0.9140	0.9119
	70	30	19.5909	19.2445	4.4262	4.3846	0.9169	0.9156
	80	20	19.1679	21.1168	4.3781	4.5953	0.9180	0.9091
ANN-HHO	65	35	13.5591	18.3471	7.3643	9.5712	0.9153	0.8854
	70	30	12.9506	15.4260	3.5987	3.9276	0.9191	0.9036
	80	20	14.6665	18.2373	3.8297	4.2705	0.8310	0.7899

Table 3 shows the results of various training-testing dataset split ratios for the conventional ANN and ANN-HHO models. The ANN model shows the best result with a split ratio of 70-30%, with MSE, RMSE, and R^2 values of 19.2445, 4.3846, and 90.56%, respectively. In comparison, the ANN-HHO model shows values of 15.4260, 3.9276, and 90.36% for MSE, RMSE, and R^2, respectively. Although the R^2 value does not change significantly, the proposed model exhibits a lower MSE and RMSE, indicating lower overall error and a closer fit to the actual data. Therefore, the ANN-HHO model gave a robust NOx emissions prediction in a gas turbine process based on ambient variables and technological process parameters.

Since the accurate prediction of NOx emissions is crucial in industries that rely on gas turbines, such as power generation or aerospace, the proposed model can used to optimize emissions and avoid regulatory penalties, leading to more efficient and environmentally friendly engine design. Therefore, the significance of the proposed model is its usefulness in accurately predicting NOx emissions, making it a valuable tool for industries that depend on gas turbines.

23. CONCLUSION

The aim of this research is to create an ANN-based model using a publicly available dataset on combined cycle power plant exhaust, and to improve its performance through HHO algorithm to accurately predict NOx levels. The study utilizes a machine learning approach to develop a data-driven model for estimating NOx emission

concentrations in exhaust gases. The performance of the constructed models was evaluated based on statistical metrics such as R^2, MSE, and RMSE. The ANN model achieved R^2 = 90.56%, RMSE = 4.3846, and MSE = 19.2445 on the test data, while the ANN-HHO model attained R^2 = 90.36%, RMSE = 3.9276, and MSE = 15.4260. The results demonstrate that the hybrid ANN-HHO model outperforms the ANN model in predicting NOx, as evidenced by lower system error values. The result indicates that the proposed model has the potential to accurately predict NOx levels in exhaust emissions.

REFERENCES

Agatonovic-Kustrin, S., & Beresford, R. (2000). Basic concepts of artificial neural network (ANN) modeling and its application in pharmaceutical research. *Journal of pharmaceutical and biomedical analysis*, *22*(5), 717-727.

Chien, T., Chu, H., Hsu, W., Tu, Y., Tsai, H., & Chen, K. J. A. E. (2005). A performance study of PEMS applied to the Hsinta power station of Taipower. *39*(2), 223-230.

Dirik, M. (2022). Prediction of NOx emissions from gas turbines of a combined cycle power plant using an ANFIS model optimized by GA. *Fuel*, *321*, 124037. https://doi.org/https://doi.org/10.1016/j.fuel.2022.124037

Heidari, A. A., Mirjalili, S., Faris, H., Aljarah, I., Mafarja, M., & Chen, H. (2019). Harris hawks optimization: Algorithm and applications. *Future Generation Computer Systems*, *97*, 849-872. https://doi.org/https://doi.org/10.1016/j.future.2019.02.028

Kaya, H., Tüfekçi, P., & Uzun, E. J. T. J. E. E. C. S. (2019). Predicting CO and NOxemissions from gas turbines: novel data and abenchmark PEMS. *27*, 4783-4796.

Khatir, S., Tiachacht, S., Le Thanh, C., Ghandourah, E., Mirjalili, S., & Abdel Wahab, M. (2021). An improved Artificial Neural Network using Arithmetic Optimization Algorithm for damage assessment in FGM composite plates. *Composite Structures*, *273*, 114287. https://doi.org/https://doi.org/10.1016/j.compstruct.2021.114287

Korpela, T., Kumpulainen, P., Majanne, Y., Häyrinen, A., & Lautala, P. (2017). Indirect NOx emission monitoring in natural gas fired boilers. *Control Engineering Practice*, *65*, 11-25.

Korpela, T., Kumpulainen, P., Majanne, Y., & Häyrinen, A. J. I.-P. (2015). Model based NOx emission monitoring in natural gas fired hot water boilers. *48*(30), 385-390.

Lin, S., Liu, X., Fang, J., & Xu, Z. (2015). Is Extreme Learning Machine Feasible? A Theoretical Assessment (Part II). *IEEE Transactions on Neural Networks and Learning Systems*, *26*(1), 21-34. https://doi.org/10.1109/TNNLS.2014.2336665

Shakil, M., Elshafei, M., Habib, M. A., & Maleki, F. (2009). Soft sensor for NOx and O2 using dynamic neural networks. *J Computers Electrical Engineering*, *35*(4), 578-586.

Sherstinsky, A. (2018). Fundamentals of Recurrent Neural Network and Long Short-Term Memory Network.

Skalska, K., Miller, J. S., & Ledakowicz, S. J. S. o. t. t. e. (2010). Trends in NOx abatement: A review. *408*(19), 3976-3989.

Wood, D. A. (2023). Long-term atmospheric pollutant emissions from a combined cycle gas turbine: Trend monitoring and prediction applying machine learning. *Fuel*, *343*, 127722.

PAPER 157 – EFFECT OF ROASTING TIME ON THE PROXIMATE AND ANTI-NUTRITIONAL COMPOSITIONS OF DELONIX REGIA SEED FLOUR

A.L. Adepoju[1], B.A. Adejumo[2], T.B. Idowu[2]

[1*]Department Food Engineering, University of Ilorin, PMB 515, Ilorin 240003, Nigeria.
[2]Department of Agricultural and Bioresources Engineering, Federal University of Technology Minna, Nigeria.
[*]Email: adepoju.al@unilorin.edu.ng

ABSTRACT
This study aimed at investigating the effects of roasting time on proximate and anti- nutritional compositions of *Delonix regia* seed flour. The seeds were divided into four samples (A-D) of 1kg each. Sample A served as the control (not roasted) while samples B, C and D were roasted for 30, 60 and 90 minutes respectively at a temperature of 150^{o}C. All the samples were afterwards dehulled and milled into a coarse particle size of about 3mm. The proximate and anti-nutritional properties were determined using standard analytical procedures. The results showed that the moisture and ash contents were reduced to 5.90% and 6.26% respectively with an increase in roasting time. The protein content of the flour increased with roasting time with the highest value of 31.52% recorded at 60 minutes. The highest value (10.70%) of fat was observed at 30 minutes roasting time while for crude fibre and carbohydrate contents, roasting reduced their values when compared with the control sample. All anti-nutritional properties evaluated (tannin, phytate, saponin, cyanide and oxalate) reduced with an increase in roasting time. Roasting of *Delonix regia* seeds can therefore help to reduce the anti-nutritional factors while enhancing some proximate qualities of the flour which in turn, can be explored as a protein source for animals' feed.
KEYWORDS**:** *Delonix regia*, roasted seed flour, proximate composition, anti-nutritional composition

1. INTRODUCTION

Delonix regia, is a wild, deciduous and ornamental tree belonging to the legume family (*Fabaceae*). It is called different names in different parts of the world where it is being grown, for instance, it is usually referred to in English as flame of the forest, peacock flower, flamboyant or flame tree; as Krisnachura in Bangladesh, in Bengali as chura or Radha and in French, as poinciana. The Hindus referred to it as gul mohr, shima or sunkesula and mayirkonrai, panjadi in Tamil (Ebada et al., 2023; Mayuri et al., 2022). Though the Delonix tree has its origin in Madagascar, it is widely cultivated in many tropical and subtropical countries (Sharma & Arora, 2015; Tura et al., 2015). Under favourable conditions*, Delonix regia* grows to a height of more than 15 m and produces pods which are 5 cm broad and 30-60 cm long, containing several seeds during the fruiting season (Alagbe et al., 2020; Umanah et al., 2019).

In fact, as reported in the literature, all the parts of the *Delonix regia* tree possess beneficial effects. The leaves, bark, flowers, root, fruit and seed have been reported to have anti-inflammatory, anti-microbial, anti-ulcer, anti-diarrheal, hepatoprotective, anti-diabetic, gastroprotective and antioxidant properties (Adejumo et al., 2019; Alagbe et al., 2020; Oyedeji et al., 2017; Umanah & David, 2021; Wang et al., 2016). This is because the plant is rich in phytochemicals and bioactive compounds such as phenolic compounds, flavonoids, tannins, steroids and carotenoids (Alagbe et al., 2020; Shewale et al., 2012). A study carried out by Ebada et al. (2023) recommended the use of pigment extracted from the flower of Delonix regia as additives in food formulation as colourants and sweeteners. This plant, especially the seed oil also has potent insecticidal activity as reported by Tura et al., (2015).

Delonix regia seed is another useful part of the plant, though it is often underutilized. Certain studies have shown that the seeds contain up to 36% crude protein and 9.39% lipids (Bake et al., 2016; Umanah et al., 2019). This can be a very good boost in the diet of both animals and man alike if adequately explored. However, proper utilization could be limited due to the presence of antinutrients in the seed which interfere with the bioavailability of nutrients in the body and can pose serious physiological and pathological dangers (Umanah & David, 2021). These anti-nutrients such as oxalic acid, phytates, phytic acid, lectins, and saponin which are present in the seed can be eliminated or reduced drastically by appropriate processing methods like cooking, boiling, roasting or germination. This will enhance the potential of the seed as flour, meal and diet formulation for livestock and probably human beings. Therefore, this study was aimed at investigating the effects of roasting time on the proximate and anti-nutritional composition of *Delonix regia* seed flour with a view to enhance its utilization.

2. MATERIALS AND METHODS

2.1 Sample Preparation and Production of Delonix regia Seed Flour

Four (4) kg of *Delonix regia* seeds were obtained from the Federal University of Technology, Minna and conveyed to the laboratory for analysis, the seeds were collected manually, sorted and washed to remove contaminants. Other materials used include; a conical flask, Soxhlet apparatus, distil water, weighing balance, Kheldjal apparatus, measuring cylinder (200 ml), oven, air circulated oven, filter paper, volumetric flask (250 ml), heating mantle, burettes, milling machine. The seeds were divided into four samples A, B, C and D. Sample A was used as control (raw) and the initial moisture content was determined. Samples B, C and D were roasted in an oven at a temperature of 150ºC for 30, 60 and 90 minutes, respectively, and then de-hulled and milled into a coarse particle size of about 3 mm and packaged for further analysis.

2.2 Proximate and Anti-nutrient Contents

Association of Analytical Chemists, AOAC (AOAC, 2005) standard procedures were used for the analysis of the proximate composition (moisture, fat, protein, ash, and crude fibre) and the antinutrients (tannin, phytate, saponin, cyanide and oxalate) of the seed flour samples and carbohydrate content was calculated by difference. All analyses were carried out in triplicate. The methods used were similar to the ones reported by Oyedeji et al., (2017)

3. RESULTS AND DISCUSSION

3.1 Effect of Roasting Time on the Proximate Composition of Delonix regia Seed Flour

The effect of roasting time on the proximate composition of *Delonix regia* seed flour is presented in Table 1. The moisture contents of roasted *Delonix Regia* seed flour range from 8.10 % in sample B which was roasted for 30 minutes to 5.90% in sample D (roasted for 90 minutes). Both roasted samples and the control had moisture contents that are within the safe range (14% or less) for dried agro-products (Vera Zambrano et al., 2019). It was observed from the study that the higher the roasting time of the seeds, the lower the moisture content of flour obtained. These values were lower than those recorded for raw and cooked *Delonix regia* seed meal incorporated in fish feed (Umanah & David, 2021) and for *Delonix regia* seeds (Oyedeji et al., 2017). However, almost the same range of values of moisture content obtained in this study were reported by Alagbe et al., (2020) for Delonix regia leaves and roots. The variations in the moisture content obtained may be due to the season of harvest, processing methods, varietal differences or temperature of processing. The ash content of roasted *Delonix regia* seed flour of samples B, C and D is 8.81%, 6.55% and 6.26% with a control (sample A) of 9.2% respectively. Sample D which was roasted for 90 minutes had the lowest ash content. The results of the ash content obtained were higher than the 4.14% (toasted sample at temperature between 60 and 80ºC) and 6.35% (raw sample) reported by Bake et al., (2016) and 5.93% (raw sample) reported by Abulude & Adejayan, (2017). Similarly, the highest fat content obtained in this study (10.70% for sample B which was roasted for 30 minutes) was higher than the value obtained by Bake et al., (2016) for toasted *Delonix regia* seed. These varying values obtained for the roasted samples compared to that obtained by Bake et al., (2016) may probably be due to the difference in roasting temperature and time used for processing the *Delonix regia* seed flour.

A reduction in the crude fibre content of roasted *Delonix regia* seed flour was observed from 8.57% in the control sample to 7.92% in sample B (30 minutes roasting time) and then an increase from this value to 8.21% at 90 minutes roasting time. However, this value is lower than the one for the control sample; so, it can be concluded that roasting *Delonix regia* seed reduces the crude fibre content of the flour. Higher values of crude fibre were reported by Olufayo & Falola, (2018) for raw, soaked and roasted *Delonix regia* seed. Increasing the roasting time of *Delonix regia* seed flour resulted in a rise in protein content. At 60 minutes of roasting, the protein content increased from 21.01% in the control sample to 31.52%, but it later declined to 28.01% at 90 minutes of roasting. It can be deduced that an increase in the roasting time of *Delonix regia* seed above 60 minutes will negatively affect the protein content of the flour. The protein values obtained from this study are higher than those reported for soaked, cooked, parboiled and roasted *Delonix regia* seed (Lamidi & Evien, 2019); *Delonix regia* leaves and roots (Alagbe et al., 2020); raw and cooked *Delonix regia* seed used for fish meal (Umanah & David, 2021). The highest carbohydrate content (47.93 %) obtained from this experiment was observed in the control sample and reduced to 42.49% in sample D. However, these values are higher than the 30.10% obtained by Abulude & Adejayan, (2017) but lower than 48.34% reported by (Oyedeji et al., 2017) for raw *Delonix regia* seed.

Table 1: The effect of roasting time on the proximate composition of *Delonix regia* seed flour.

Roasting Temperature	**150ºC**			
Sample Label	**A**	**B**	**C**	**D**
Roasting Time	**Control**	**30min**	**60min**	**90min**
Moisture Content (%)	8.50	8.10	6.15	5.90
Ash (%)	9.20	8.81	6.55	6.26
Fat (%)	4.79	10.70	8.70	9.13
Crude Fibre (%)	8.57	7.92	7.99	8.21
Protein (%)	21.01	24.51	31.52	28.01
Carbohydrate (%)	47.93	39.96	39.09	42.49

3.2 Effect of Roasting Time on the Anti-Nutritional Composition of Delonix regia Seed Flour

Anti-nutrients, just like the name implies, hinder or go against the actions of nutrients in the body of both humans and animals. They are chemical substances found in plants that have the capability of affecting the availability of nutrients by interfering with metabolic processes (Okezie et al., 2017). The effect of roasting time on some anti-nutritional composition of *Delonix regia* seed flour is presented in Table 2.

Table 2: The effect of roasting time on some anti-nutritional composition of *Delonix regia* seed flour.

Roasting Temperature	**150**^{o}C			
Sample Label	**A**	**B**	**C**	**D**
Roasting Time	**Control**	**30 min**	**60 min**	**90 min**
Phytate (mg/100g)	634.90	410.86	402.39	392.43
Tannin (mg/100g)	1224.20	561.21	560.90	550.68
Cyanide (mg/100g)	551.28	228.21	213.33	203.46
Saponin (mg/100g)	746.92	560.40	521.60	490.74
Oxalate (mg/100g)	550.29	222.21	210.08	201.78

The phytate content of roasted *Delonix regia* seed flour reduces from 634.90 mg/100g in the unroasted sample to 392.43mg/100g after roasting the seeds for 90 minutes. The values were higher than those reported for selected green vegetables in Afaha Eket, Akwa-Ibom State, Nigeria (Okezie et al., 2017) and for *Delonix regia* seeds incubated in vitro with *Pennisetum purpureum* (Olufayo & Falola, 2018). The obtained tannin contents of roasted *Delonix regia* seed flour are 1224.20 mg/100g, 561.21 mg/100g, 560.90 mg/100g and 550.68 mg/100g for samples A, B, C and D respectively. It was observed that the tannin in the seed flour of *Delonix regia* reduced

as the roasting time increased. Sample D which was roasted for 90 minutes has the lowest tannin content. The results of the tannin content obtained were lower than the 882 mg/100g (roasted) and 2274 mg/100g (raw) reported by Bake et al., (2016). This may probably be due to the difference in roasting temperature and time used for processing the *Delonix regia* seed. There was a reduction in the cyanide content of roasted *Delonix regia* seed flour from 551.28 mg/100g in sample A to 203.46 mg/100g in sample D. The results of the cyanide content obtained were higher than the 7.15 mg/100g and 19.45 mg/100g reported for toasted and raw Delonix regia seed meal in the diet of *Clarias gariepinus* fingerlings (Bake et al., 2016). The saponin contents of roasted *Delonix Regia* seed flour obtained in this study are 746.92 mg/100g, 560.40 mg/100g, 521.60 mg/100g and 490.74 mg/100g for samples A, B, C and D respectively. The lowest saponin content was observed in sample D which was roasted for 90 minutes. The results of the saponin content obtained were higher than those reported for raw *Delonix Regia* seed (Oyedeji et al., 2017) and *Delonix regia* seeds which were roasted, soaked, parboiled and cooked (Lamidi & Evien, 2019). The oxalate content of roasted *Delonix regia* seed flour varied between 550.29 mg/100 in the control sample and 201.78 mg/100g in sample D which was roasted for 90 minutes. The results of the oxalate content obtained were higher than the 10.15 mg/100g (roasted) and 45.46 mg/100g (raw) reported by Bake et al., (2016) and 2.57 mg/g (raw sample) reported by Oyedeji et al., (2017).

4. CONCLUSION

The effects of roasting time on proximate and anti- nutritional compositions of *Delonix regia* seed flour were studied. It can be concluded from the study that roasting time has varying effects on the proximate composition of Delonix regia seed flour while decreasing the anti-nutritional factors present in the *Delonix regia* seed flour. It was also observed that the protein content increased with an increase in roasting time. *Delonix regia* seed flour can therefore be incorporated into certain animal feed to boost the protein content.

5. REFERENCES

Abulude, F. O., & Adejayan, A. W. (2017). Nutritional values of flamboyant (Delonix regia) seeds obtained in Akure, Nigeria. *PeerJ Preprints*, 1–18. https://doi.org/10.30809/phe.1.2017.21

Adejumo, B. A., Adepoju, A. L., Ojetunde, E. ., & Adeyinka-Ajiboye, V. . (2019). Yield and characteristics of Delonix regia seed oil as influenced by cooking time. *40th Annual Conference and 20th International Conference of the Nigerian Instiution of Agricultural Engineers*, 333–338.

Alagbe, J. O., Adeoye, A., & Oluwatob, i A. O. (2020). Proximate and Mineral Analysis of Delonix regia Leaves and Roots. *Annals of Nutrition & Food Science*, *4*(1), 1–4.

AOAC. (2005). *Official method of Analysis.* (Method 935.14 and 992.24; 18th Editi). Association of Officiating Analytical Chemists.

Bake, G., Yusuf, I., & Sadiku, S. (2016). Evaluation and Nutrient Quality of Toasted Flamboyant Seed (Delonix regia) Meal in the Diet of Clarias gariepinus Fingerlings. *Journal of Agriculture and Ecology Research International*, *5*(2), 1–9. https://doi.org/10.9734/jaeri/2016/21687

Ebada, D., Hefnawy, H. T., Gomaa, A., Alghamdi, A. M., Alharbi, A. A., Almuhayawi, M. S., Alharbi, M. T., Awad, A., Al Jaouni, S. K., Selim, S., Eldeeb, G. S., & Namir, M. (2023). Characterization of Delonix regia Flowers' Pigment and Polysaccharides: Evaluating Their Antibacterial, Anticancer, and Antioxidant Activities and Their Application as a Natural Colorant and Sweetener in Beverages. *Molecules*, *28*(7), 1–19. https://doi.org/10.3390/molecules28073243

Lamidi, A. A., & Evien, E. E. (2019). Chemical composition and anti-nutritional factors of underutilized (Delonix regia) seeds processed with different methods for sustainable ruminant production. *Nigerian Journal of Animal Science and Technology*, *2*(2), 56–62.

Mayuri, G., Reshma, D., & Dipika, F. (2022). The flamboyant Delonix regia (Gulmohar). *International Journal of Creative Research Thoughts*, *10*(3), 586–593.

Okezie, E., Ugbogu, A. E., Odungide, A. A., & Atani, C. S. (2017). Proximate , Antinutritional and Mineral Estimation of Some Selected Consumed Green Vegetables in Afaha Eket, Akwa-Ibom State, Nigeria. *American Journal of Food Science and Technology*, *5*(5), 182–191. https://doi.org/10.12691/ajfst-5-5-3

Olufayo, O. O., & Falola, O. O. (2018). Nutritional Contents of Processed Delonix regia Seeds Incubated In Vitro with Pennisetum purpureum. *Nigerian Journal of Animal Production*, *44*(4), 1–9.

Oyedeji, O. A., Azeez, L. A., & Osifade, B. G. (2017). Chemical and nutritional compositions of flame of forest (Delonix regia) seeds and seed oil. *South African Journal of Chemistry*, *70*, 16–20. https://doi.org/10.17159/0379-4350/2017/v70a3

Sharma, S., & Arora, S. (2015). Phytochemicals and pharmaceutical potential of delonix regia (Bojer ex hook) raf a review. *International Journal of Pharmacy and Pharmaceutical Sciences*, *7*(8), 21–33.

Shewale, V. D., Deshmukh, T. A., Patil, L. S., & Patil, V. R. (2012). Anti-inflammatory activity of Delonix regia

(Boj. Ex. Hook). *Advances in Pharmacological Sciences*, *2012*. https://doi.org/10.1155/2012/789713

Tura, A. M., Kebede, B. H., & H/marian, M. (2015). Physiochemical Characterization and Evaluation of Insecticidal Activities of Delonix Regia Seed oil against Termite, Ticks and Cockroach. *Journal of Natural Sciences Research*, *5*(15), 40–46.

Umanah, S. I., & David, G. S. (2021). Implications of dietary Delonix regia seed meal on growth , feed utilization , haematology and fillet yield of red Nile tilapia Oreochromis niloticus. *World Journal of Advanced Research and Reviews*, *12*(01), 140–154.

Umanah, S. I., George, E. M., & David, G. S. (2019). Growth Performance and Feed Utilization of Heterobranchus bidorsalis Fed with Flamboyant Seed Meal Substituted for Wheat Offal. *Asian Journal of Biological Sciences*, *12*(4), 842–850. https://doi.org/10.3923/ajbs.2019.842.850

Vera Zambrano, M., Dutta, B., Mercer, D. G., MacLean, H. L., & Touchie, M. F. (2019). Assessment of moisture content measurement methods of dried food products in small-scale operations in developing countries: A review. *Trends in Food Science and Technology*, *88*, 484–496. https://doi.org/10.1016/j.tifs.2019.04.006

Wang, L. S., Lee, C. T., Su, W. L., Huang, S. C., & Wang, S. C. (2016). Delonix regia leaf extract (DRLE): A potential therapeutic agent for cardioprotection. *PLoS ONE*, *11*(12), 15–17. https://doi.org/10.1371/journal.pone.0167768

PAPER 158 – INFLUENCE OF WATERSHED DELINEATION ON HYDROLOGICAL PROCESSES UPSTREAM WATERSHED OF ASA DAM RIVER, ILORIN, KWARA STATE, NIGERIA

A. A. Bello[1], A. G. Adeogun[1*], H. Solihu[1], Adebayo, H.O[2].

[1]Deparment of Civil Engineering, Kwara State University, PMB 1530 Malete, Kwara State, Ilorin, Nigeria.
[2]Deparment of Agricultural and Bioresources Engineering, University of Abuja, Abuja, Nigeria.
*Email: adeniyi.adeogun@kwasu.edu.ng

ABSTRACT
This study assessed the impact of watershed delineation on the estimation of water quality parameters in the Asa River in Ilorin, Nigeria. MAPWindow GIS interfaced with Soil and Water Assessment Tools (SWAT) and was used to pre-process the spatial data. The model was used to simulate water quality parameters such as organic phosphorus and nitrate at subbasin level of the study area. The watershed was delineated into 5, 9, 13, 15, 17, and 29 sub-basins, and each delineated sub-basin was modelled for 19 years (January 2001 to December 2019). The results showed that predicted values of organic phosphorus and nitrate concentrations ranged from 731607.04 mg/l to 6764932.7mg/l and from 1441992.79 mg/l to 3575204.59 mg/l respectively. The lowest annual predicted values of sediment yield, sediment concentration, and streamflow were obtained for a watershed delineation into 5 sub-basins. The highest predicted values, however, were obtained when the watershed was delineated into 29 sub-basins. The number of sub-basins however, had little or no influence on the average monthly predicted values of water quality parameters in the watershed. It could be inferred from the result that the number of sub-basins delineated in the watershed directly influence the predicted values of water quality parameters.

KEYWORDS: Asa Dam River, Hydrological process, Soil and Water Assessment Tools (SWAT), Sub-basins, Watershed delineation and Water quality parameters

1. INTRODUCTION

The process of delineating watersheds plays a significant role in the study of hydrological processes, as it affects the prediction and management of water resources in a given area. Hydrological cycle research, centred on the assessment of water resources through the quantifiable investigation and evaluation of the hydro-meteorological factors that control the circulation and transfer of water in all of its processes (Shiklomanov, 2011). It is concerned with the components of the water balance and its quantitative estimation, which comprises the following phases: the transfer of water from the atmosphere to the soil via precipitation, the settlement of water from the soil and open surface water into the atmosphere via evaporation and transpiration; the variation in the distribution and storage of water in multiple reservoirs, namely surface and groundwater reservoirs; and the distribution and redistribution of water on the land surface (Ngasoh, et. al., 2022).

Watershed delineation is a critical step in any spatial hydrological modelling. Watershed modelling has grown in importance as a method for evaluating the impacts of climate change and human impacts on water resources and the hydrologic cycle. However, the impact of watershed delineation is the capability of a model to adequately reflect the spatial variability of a river basin factor for the hydrological process. There is need to study the effects of several delineation of water production, as well as the watershed delineation in modelling, determine the precision required to obtain an accurate simulation modelling result.

The main objective of this study is to analyse the extent to which the watershed has affected the hydrological processes in Asa Dam, Kwara state of Nigeria. To achieve this objective, the following specific objectives have been identified: first, to delineate selected watershed into sub-basins for the purpose of hydrological modelling; secondly, modelling and to predict selected hydrological processes in the watershed through the application of Soil and Water Assessment Tool (SWAT) and using various watershed delineation of the watershed.

2. THEORETICAL ANALYSIS

The simulation of hydrologic cycle by SWAT is based on the water balance Equation;

$$SW_t = SW_o + \sum_{i=1}^{t}(R_{day} - Q_{surf} - E_a - W_{seep} - Q_{gw})_i \quad (1)$$

where SW_t is the final soil water content (mm water), SW_o is the initial soil water content in day i (mm water), t is the time (days), R_{day} is the amount of precipitation in day i (mm water), Q_{surf} is the amount of surface runoff in day i (mm water), Ea is the amount of evapotranspiration in day i (mm water), W_{seep} is the amount of percolation

and bypass flow exiting the soil profile bottom on day i (mm water), and Q_{gw} is the amount of return flow in day i (mm water).

Soil erosion rates on cultivated land was modeled in SWAT by using the Universal Soil Loss Equation developed by Wischmeier and Smith in 1978 (Neitsch et al.,2011). This method is based on statistical analyses of data from 47 locations in 24 states in the Central and Eastern United States. The Universal Soil Loss Equation can be written as in Equation 2

$$A = R * K * L * S * C * P0.11 \qquad 2$$

In Equation 2, A is the computed soil loss in tons/acre/year, R is rainfall factor, K is the soil-erodibility factor, L, slope-length factor, S, slope-steepness factor, C, cropping-management factor, and P, erosion-control practice factor.

3. MATERIALS AND METHODS/METHODOLOGY/EXPERIMENTAL PROCEDURE

3.1 Description of case study area

Asa Dam is located between latitudes 8° 36′ N and 8° 24′ N and longitudes 4° 36′ E and 4° 10′ E in Ilorin. Ilorin is the capital of Kwara State in Nigeria, West Africa. A geographical map of Nigeria showing the location of Study area in Nigeria is presented in Fig. 1. Asa Dam was built in 1984 on River Asa. It is a composite dam with an earth embankment. The dam is about 600 m long, 25 ft (7.5 m) high at its deepest section and has a crest width of 6 ft (1.8 m). The embankment is made of in situ soil overlay by clay seal and concrete material. The foundation is made of 4-ft-thick compacted soil and clay overlayed by 4-ft-thick concrete cement. The maximum water level at the upstream is 20 ft (7.5 m) while the downstream water level can be as low as 2 m in the peak of the dry season. Asa River is approximately 56 km long and has a maximum width of about 100 m. The river lies within Oyo and Kwara states in Nigeria, with a total catchment area of 1037 km^2 (Balogun and Ganiyu 2017). The tributaries of Asa River in Ilorin include Rivers Aluko, Agba, Odota, Okun, Osere, Atikeke, and Mitile. Asa River in turn empties its water into River Niger. The annual rainfall ranges between 75 and 112 cm, humidity and means annual temperature range from 60 to 89% and 27 to 30°, respectively (Ilorin Meteorological Stations).

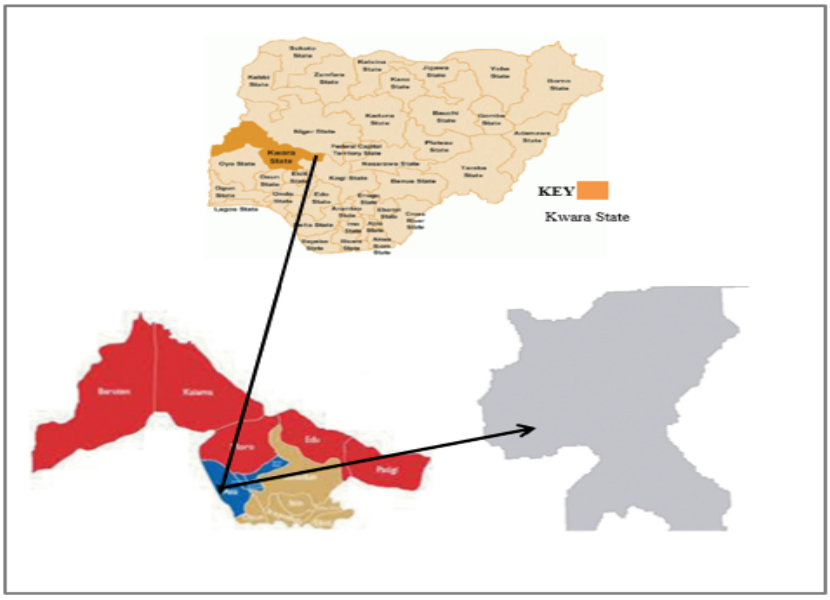

Figure 1: Map of Nigeria showing Kwara location of study area, Asa dam (Adeogun, et. al.2020)

3.2 Model Selection and Description

The Soil and Water Assessment Tool (SWAT) integrated with map window GIS was chosen as the model for this study, based on previous research on its efficacy as reported in many studies (Ayana et.al., 2012; Betrie et.al.,2011, Omani et al., 2007). Moreover, the model has a user-friendly interface, and its results are easy to visualize. SWAT

is a continuous daily step process-based model that was created to predict the impact of land management practices on water, sediment, and agricultural chemical yields over extended periods in vast, intricate watersheds with different soils, land use, and management conditions. The tool has been used and accepted by many researchers previously (Adeogun et al., 2022).

3.3. Model Data Requirements

SWAT modelling requires spatial data and temporal data for model parametrization. The spatial data encompass the Digital Elevation Model (DEM), soil and land use maps, while the temporal data, which is also known as weather data, comprises maximum and minimum temperature, humidity, wind, and solar radiation.

Digital Elevation Model (DEM): is one of the principal inputs of the SWAT model. Topography was delineated using a DEM, which describes the elevation of any point in a given area at a particular spatial resolution. A 90 m grid DEM was obtained from STRM (Shuttle Radar Topography Mission). The DEM was used to establish the boundary of the watershed and analyze the drainage patterns of the land surface terrain. Terrain parameters, such as slope gradient and slope length, as well as stream network characteristics, such as channel slope, length, and width, were derived from the DEM. Figure 2 displays the DEM of the study area.

Soil map: The soil textural and physicochemical properties necessary for the SWAT model include soil texture, available water content, hydraulic conductivity, bulk density, and organic carbon content for each soil type. Soil data was obtained from the harmonized digital soil map of the world (HWSD) produced by the Food and Agricultural Organization of the United Nations (Adeogun et al.., 2022). Table 1 displays the soil map and its information for the study area.

Land use map: The land use of an area is a critical factor that impacts groundwater flow, surface erosion, and evapo-transpiration in a watershed during simulation. The land-use map for this study was obtained from the Global Land Cover Characterization (GLCC) database and was used to estimate vegetation and other parameters representing the watershed area (GLCC, 2012). The GLCC database, which has a spatial resolution of 1 km and 24 classes of land use representation, was used to obtain the land-use map for the study area (GLCC, 2012). The database was developed by the United States Geological Survey. Figure 2 presents the DEM and the land-use map for the study area.

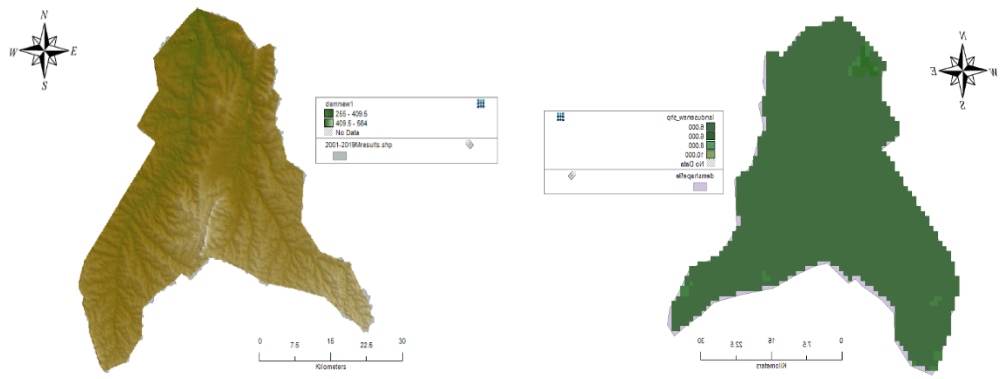

Figure 2: Digital Elevation Model (DEM) and Land map of the study area

Weather data: The required climatic data for the SWAT model simulation was obtained from the Nigeria Meteorological Agency (NIMET) station in Ilorin. The collected data consists of daily precipitation, maximum and minimum temperature, solar radiation, relative humidity, and wind speed for the period between January 2021 to December 2019. These weather variables were utilized to regulate the hydrological balance in the watershed. In the event of missing data, a weather generator integrated into the SWAT model was employed to estimate the missing values.

Creation of Hydrological Response Units (HRU): The HRU approach facilitates the modelling of hydrologic behaviour in a unit that is easy to represent. In this study, HRUs were delineated in a basin with high spatial heterogeneity by utilizing basin characteristics such as physiography, land use, soil, elevation, and slope in a geographical information system. The hydrologic behaviour of each HRU was analyzed based on basin characteristics, which can be incorporated in a physically based or conceptual hydrologic model for simulating groundwater and water yield.

3.4. Model Parametrization and Prediction of water quality parameters

The SWAT model can predict water quality parameters such as Nitrate, Organic phosphate, and sediment concentration. In this study, the prediction of water quality parameters in sub-basins of the watershed was conducted using spatial and temporal data for the study area. The obtained results were analyzed using Microsoft Excel software and the spatial and temporal variations of water quality parameters were visualized using the GIS component of the model.

4. RESULTS AND DISCUSSION

4.1. Delineation of watershed into sub-basins

The watershed was delineated into different sub-basins area, As explained earlier, the number of sub basins to be delineated can be varied by either increasing or decreasing the area of watershed within the boundary as specified in the automatic watershed delineation. Based on the division, the minimum number of delineations was 5 while the highest number of divisions was 29. Other subdivisions are 9, 13, 15, and 17. Figures 3 to 5 depict the various divisions of the watershed's delineation.

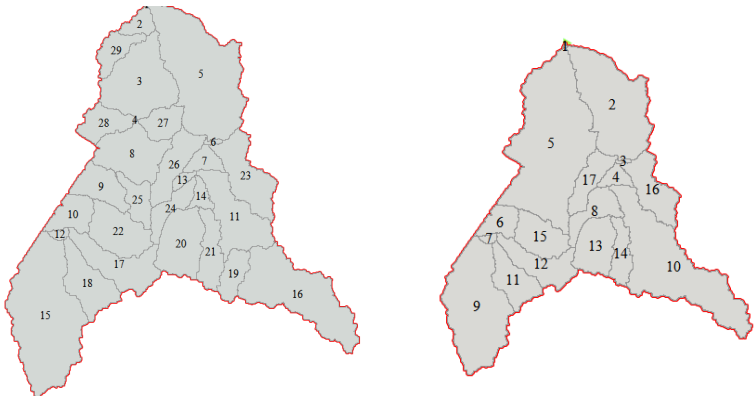

Figure 3: watershed delineated into (i) 29 sub basins and (ii) 17 sub basins.

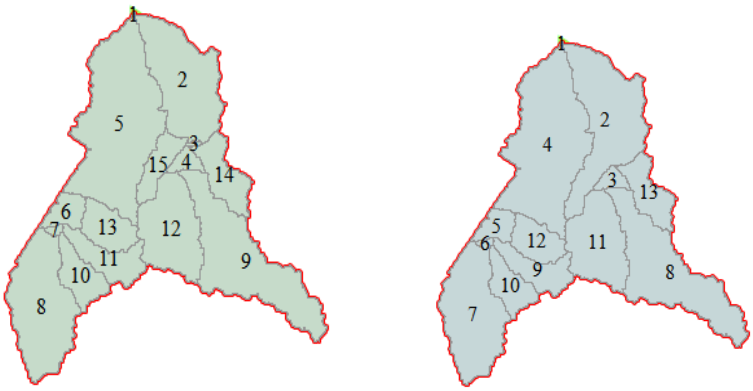

Figure 4: watershed delineated into (i) 15 sub basins and (ii) 13 sub basins.

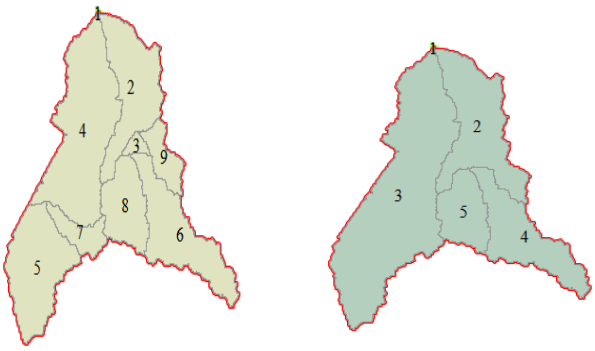

Figure 5: watershed delineated into (i) 9 sub basins and (ii) 5 sub basins.

4.2. Effects of watershed delineation on water quality parameters

The results of the model prediction on water quality parameters (sediment yield, flow, Nitrate, Organic phosphate and sediment concentration) using different numbers of delineated sub basins were compared. Generally, the results showed there is an increase in the value of water quality parameters as the number of sub-basins increases. For sediment concentration, SEDCON (see Figure 6). The result showed that the least annual predicted value of 54,119.96 mg/L, 635.04 m^3/s, 1441,992.97 t/ha, 98.20 ha and 731,607.04 mg/L for Sediment concentration, Stream Flow, Nitrate Concentration, Sediment yield and Organic Phosphorous respectively was obtained when the number of sub-basins was five (5). However, a higher predicted values was also obtained when the watershed was delineated into 29 sub basins with Sediment concentration of 304,713.25 Mg/L, Sediment yield of 977.46 t/ha , Organic Phosphorous of 6764932.7 mg/l, Stream flow of 1900.22 m3/s and Nitrate concentration of 3575204.59 mg/l. This result indicated that the predicted values of water quality parameters are directly proportional to the number of sub basins. However, it has little or no influence on the average monthly predicted values of water quality parameters in the watershed.

The result from this work is in tandem with a previous study conducted by Thushapan et al (2020) on the effects of watershed delineation on hydrological processes modeling. In his work, the study area was divided into eight sub catchments and concluded that the number of sub-catchments was increasing as the model performance was also increasing. The work of Adeogun et al. (2022) on the effects of watershed delineation on the prediction of water quality parameters in Gaa Akanbi Area Ilorin using SWAT with a physically based semi-distributed hydrological model interfaced with mapwindow GIS software also revealed that there was no noticeable change on the water quality parameters as the number of sub basins delineation increases in the watershed. He also recommended that the threshold value for deciding on the required number of watershed drainage density for the prediction of water quality parameters should be evaluated by trial-and-error procedure.

5. CONCLUSION

Watershed delineation is a critical process in hydrological modelling, and its accuracy has a significant impact on the estimation of hydrological processes such as runoff, evapotranspiration, and groundwater recharge. The accuracy of watershed delineation is influenced by various factors such as the quality and resolution of input data, the methodology used, and the spatial scale of delineation. Accurate watershed delineation is critical for effective water management and conservation, and therefore, careful consideration of the data sources and methodology is necessary for accurate watershed delineation. This study aimed to assess the impact of watershed delineation on the estimation of water The watershed was delineated into different numbers of sub-basins, and the results showed that the number of sub-basins directly influenced the predicted values of water quality parameters.

The study found that the lowest annual predicted values of sediment yield, sediment concentration, and streamflow were obtained for a watershed delineation into 5 sub-basins, while the highest predicted values were recorded when the watershed was delineated into 29 sub-basins. However, the number of sub-basins had little or no influence on the average monthly predicted values of water quality parameters in the watershed. This study highlights the importance of watershed delineation in accurately predicting water quality parameters, and the number of sub-basins used in the delineation process can have a significant impact on the predicted values. These findings could be useful for water resource management and policy development in the region, especially in addressing water quality concerns in the Asa Dam River watershed.

REFERENCES

Adeogun, A. G., Ganiyu, H. O., Adetoro, A. E. and Idowu, B. S. (2022). Effects of Watershed Delineation on the Prediction of Water Quality Parameters in Gaa Akanbi Area, Ilorin. LAUTECH Journal of Civil and Environmental Studies.

Ayana, A.B., Edossa, D.C, and Kositsakulchai, E. (2012). Simulation of Sediment Yield Using SWAT Model in Fincha Watershed, Ethiopia. Kasetsart Journal of Natural Science,Vol 46: 283 - 297

Balogun, O.S., Ganiyu HO (2017). Study and analysis of Asa River hypothetical dam break HEC-RAS. Nigeria Journal of Technology, 36:315–321

Betrie, G.D., Mohammed, Y.A., van Griensven and A, Srinivasan,R.(2011). Sediment Management Modelling in the Blue Nile Basin using SWAT. *Hydrology and Earth System Sciences* Vol. 15: 807-818

Ifabiyi and Eniolorunda. (2012). Watershed Characteristics and Their Implication for Hydrologic Response in the Upper Sokoto Basin, Nigeria. Journal of Geography and Geology. 4. 10.5539/jgg.v4n2p147

Neitsch, S.L, Arnold,J.G., Kiniry,J.R and Williams, J.R. (2011). Soil and Water Assessment Tool Theoretical Documentation Version 2009 Grassland, Soil and Water Research Laboratory – Agricultural Research Service Blackland Research Center – Texas AgriLife Research

Ngasoh, F. G. Mbajiongu, C. C., Istifanus, A. B., Vinking, J. M. (2022). Design, Development and Testing of a Hydrological Process Demonstration System. Sch J Eng Tech, 6, 111-120.

Omani, N., Tajrishy, M. and Abrishamchi, A. (2007). Modelling of a River Basin Using SWAT Model and SUFI-2, Paper presented at the 4th International Conference of SWAT Model UNESCO-IHE Delft, Netherlands, 4-6 July 2007

Shiklomanov, I. A. (2011). The Hydrological cycle. Encyclopedia of life support system (EOLSS), Vol. 1, pp. 1-9.

Thushapan K., & Wickramaarachchi, Thushara. (2020). Effect of Watershed Delineation on Hydrologic Processes Modeling. Confererence : Proceedings of Undergraduate Research Symposium on Recent Advances in Civil Engineering at Faculty of Engineering, Univeristy of Ruhuna, Hapugala, Galle.

PAPER 159 – EFFECT OF CALCINATION PARAMETERS ON CHEMICAL COMPOSITION OF BEANS POD ASH FOR POZZOLANIC ACTIVITY

O. P. Joseph[1*], A. A. Adedeji[1], O. A. Mokuolu[2], J. A. Alomaja[1]

[1]Department of Civil Engineering, University of Ilorin, Ilorin, Nigeria.
[2]Department of Water Resources and Environmental Engineering, University of Ilorin, Ilorin, Nigeria.
[*]Email: joseph.oluwatoyin@adelekeuniversity.edu.ng

ABSTRACT
Beans Pod Ash (BPA) can be utilized as partial replacement of cement for the production of cement pozzolanic concrete, due its pozzolanic characteristics. This will significantly lower construction cost and environmental pollution connected with the usage and production of cement. This study aims at modelling the effect of calcination parameters (burning temperature and dwelling time) on the chemical composition of BPA for optimum pozzolanic properties. The central composite design (using 2-factors, 5-levels) of response surface method was adopted. The two (2) factors considered include burning temperature at 500°C, 600°C, 700°C, 800°C, 900°C, and dwelling time at 1, 2, 3, 4, 5 hours. Responses were obtained from the resulting chemical properties of BPA. The results of chemical analysis which include Silicon oxide (SiO_2), Aluminum oxide (Al_2O_3), ferric oxide (Fe_2O_3), Calcium oxide (CaO), Magnesium oxide (MgO), Potassium oxide (K_2O) and lots more and loss on ignition (LoI), were modelled and optimized. The optimum combined composition of silica, alumina and ferric oxide (54.14%), signifying a good pozzolanic property, was obtained and an optimum loss on ignition of 6.16%, at a burning temperature of 738.38°C and a dwelling time of 3.45-hours, conforming to ASTM C618-12a Class C pozzolan.

KEYWORDS: Beans Pod Ash, Calcination, Temperature, Dwelling Time, Pozzolanic Properties

1. INTRODUCTION

Concrete is a composite manmade building material that looks like stone. Combining cement with both fine and coarse aggregate, sufficient water and sometimes additives, like pozzolans, plasticizers, etc, makes concrete. Water allows it to set and bind the materials together. Different mixtures are added to meet specific requirements. Concrete can be engineered to satisfy a wide range of performance specifications and is typically reinforced with steel bars due to its very low tensile strength when compared with compressive strength. Known as the strongest building material, concrete has found major uses in dams, highways, buildings and many different kinds of building and construction (Jezek, 2009). Portland cement is the most common type of cementiteous material used in concrete production and was discovered by Joseph Aspdin in 1824. Other cementiteous materials include lime, pozzolan and any combination of these materials. Richness of concrete mix is one of the major factors that affect the rate of strength development in concrete and is determined by the quantity and quality of cementiteous materials (Joseph and Raymond, 2014). Cement paste is formed when cement mix with water and this paste serves as binder for other constituent materials in concrete production.
Concrete properties depend largely on the properties of its aggregate constituents because it constitutes typically 75% or more of the concrete volume. Hence, for strong and durable concrete, aggregate has to be strong, durable and washed before use in order to prevent impurities from slowing down hydration process among the concrete constituents. Water is another key ingredient in the production of concrete, which when mixed with cement, forms a paste that binds the aggregate together. Water causes the hardening of concrete through a process called hydration. The role of water is important because the water to cement ratio is the most critical factor in the production of concrete. A careful balance in water to cement ratio in concrete production makes the concrete workable and strong (Shi *et al,* 2012).

Ghassan and Mouin (2016) defined pozzolan as a siliceous material used as a partial replacement for cement in concrete production. ASTM C618 (2005) also defined pozzolans as “siliceous and aluminous material which ordinarily have little or no cementiteous properties but in finely divided form and in the presence of moisture can react with calcium hydroxide liberated during the hydration of ordinary Portland cement to form compounds possessing cementiteous properties”. Pozzolans react with calcium hydroxide and other alkalis in a cementiteous reaction in order to reduce the resultant heat of hydration generated from concrete production, thereby improving concrete workability and durability. Pozzolans also help concrete to develop resistance to sulphate attack and alkali-silica reaction, thereby making concrete with pozzolana fitting for concrete structures

like dams and bridges. Tijani *et al* (2018) and Altwair *et al* (2011) affirmed that pozzolanic activity in pozzolans are better enhanced at optimum burning temperature and time. Pozzolans can be cheaply sourced from volcanic mineral deposits, fly ash, fired and crushed clay and ash of some agricultural wastes, amongst others.

Fakayode *et al* (2014) and Ajeigbe *et al* (2010) affirmed that Nigeria contributes at least 45% of cowpea production per annum worldwide; amounting to over 3.4 million tons of dried cowpea in various varieties like Glycine Max (Soya Beans), Vigna Vexillata (Otili), Stenocarpastylosa (Feregede), Phaseolus Vulgaris (Kokondo) and Vigna Unguiculata (Big White, Small White, Oloyin and Drum). Vigna Unguiculata, also known as beans is a species of cowpea locally referred to as big-white-beans, small-white-beans, oloyin-beans and drum-beans, based on their physical properties. Beans pod is the protective outer covering of beans seed and proper burning of beans pod will result into beans pod ash. Due to ever increasing quantities of waste from beans production annually as beans pod and or beans pod ash, there exist an ever increasing cost of waste management. Hence, utilization and recycling of beans pod and or beans pod ash surfaced as the only economical alternative; as it help in reducing disposal concerns (Siddique, 2012).

This objective this study is to determine the effect of calcination temperature and dwelling time on the chemical composition of beans pod ash for optimum pozzolanic activity and characterization of beans pod ash based on performance parameters of pozzolanicity.

2. MATERIALS AND METHODS

Beans (vigna unguiculata) Pod Fodder is an agricultural waste obtained from the production of beans and is being cheaply used as animal feed. Nevertheless, the need to see how it can be better utilized economically, like ashes of other agricultural wastes as pozzolans in concrete production, necessitated the urgency of this study. Beans Pod is that part of beans plant that housed beans seed. It is greenish when growing but yellowish brown when fully matured and dry. A beans pod contains an average of four (4) beans seeds. The pod were sourced from Igbaja – Oke-Ode axis in Irepodun Local Government of Kwara State. The pod were sun dried, separated from impurities (like grasses, leaves, etc), crushed to about 0.5 mm size using the jaw crusher and burnt locally using gas-burner at the department of Civil Engineering shed, Adeleke University, Ede. The ashes were milled and processed into fine particle using hammer mill at the department of Agricultural Engineering, Adeleke University, Ede. The calcination process was carried out at the department of Chemical Engineering laboratory, Afe Babalola University, Ado-Ekiti (ABUAD) using a muffle furnace at temperature varying from 500^{o}C to 900^{o}C for dwelling time varying between 1-hour to 5-hours. Determination of the chemical components of calcined ash was also carried out at ABUAD.

Response surface method (RSM) of experimental design was adopted because of its ability to investigate the effects of the independent variables over the response, either as individual or combined variables (Al-kahtani *et al,* 2023). Also, RSM requires less input in order to save time and money with the capacity of providing maximum output (Singh *et al,* 2018). RSM has two (2) distinct design approach namely, central composite design (CCD) and box-behnken. The choice of CCD for this study over Box–Behnken was as a result of its ability to fit a full quadratic model, able to run design where all variables are at their maximum or minimum setting and ability to have up to five (5) levels per variable. Statistical analytical software known as Design Expert (10.0.1 version) was used for this study. The two independent variables for this study include calcination temperature and dwelling time with their corresponding five (5) levels each – 500^{o}C, 600^{o}C, 700^{o}C, 800^{o}C, 900^{o}C and 1 hour, 2 hours, 3 hours, 4 hours, 5 hours, respectively. At the end of design of experiment, thirteen (13) runs was obtained for the design.

Samples calcined at different calcination temperature and times were analyzed using the energy-dispersive X-ray fluorescence analysis (ED-XRF) and the machine model used to determine the basic chemical composition of the samples is the Shimadzu EDXRF-702HS. This machine was used to perform nondestructive chemical analysis of elemental oxides present in differently calcined samples of pozzolan used.

In order to correlate dependent variables to the independent variables, response surface plots and mathematical model equations were developed. The empirical data was used to predict the relationship between burning temperature, burning time and oxides of the resulting ash, by applying multiple linear regressions. Eight (8) different models (namely mean, linear, two factor interaction (2FI), quadratic, cubic, quartic, fifth and sixth interaction) were used to analyze the response of pozzolanic performance of BPA to changes in calcination temperature and time. The models were fitted into the experimental data using Design Expert Software and the appropriate model chosen based on the lowest standard deviation values, selection of the highest order polynomial, where the additional terms are significant and the model not aliased, with

insignificant lack of fit and the maximization of "Adjusted R^2 value" and the "Predicted R^2 value"; and linear and or quadratic models were suggested. But, in terms of higher R^2 and lower standard deviation values, either linear or quadratic model was finally chosen for each of the responses to predict the pozzolanic quality of BPA. Adequacy of models were authenticated by the determination of coefficient of R^2 and probability of prediction *F ratio test*.

In order to obtain the optimum calcination temperature and dwelling time for a good pozzolanic reactivity based on the percentage content of chemical compounds in BPA, CCD of RSM was set to maximize or minimize percentage content of these chemical compounds, as the case may require, based on the influence of such compounds on pozzolanic quality of BPA. The criteria used for the optimization process is shown in Table 1. Optimum conditions obtained were used to carry out experiment, the actual values obtained were compared with the predicted values and Chi-square test was carried out to ascertain the validity of models for the experimental and predicted values.

Table 1: RSM-CCD Optimization Criteria

Name	Goal	Lower Limit	Upper Limit	Lower Weight	Upper Weight	Importance
Calcination temp	is in range	500	900	1	1	3
Calcination time	is in range	1	5	1	1	3
SiO_2	maximize	30.46	35.02	1	1	3
Al_2O_3	maximize	9.86	12.98	1	1	3
Fe_2O_3	maximize	8.27	11.8	1	1	3
CaO	maximize	12.59	15.03	1	1	3
MgO	minimize	6.02	7.74	1	1	3
K_2O	minimize	5.33	7.37	1	1	3
Pb_2O_5	minimize	6.52	8.11	1	1	3
LOI	minimize	2.35	8.72	1	1	3
$SiO_2 + Al_2O_3 + Fe_2O_3$	maximize	53.44	55.24	1	1	3

3. RESULTS AND DISCUSSION

Effect of calcination temperature and time on the chemical composition of calcined BPA

Table 2: CCD-RSM Results of Pozzolanic Chemical Properties of Calcined BPA

Runs	X_1	X_2	Temp (°C)	Time (hr)	SiO_2 (%)	Al_2O_3 (%)	Fe_2O_3 (%)	CaO (%)	MgO (%)	K_2O (%)	Pb_2O_5 (%)	LOI (%)	$SiO_2 + Al_2O_3 + Fe_2O_3$ (%)
01	1	1	800	4	34.74	10.68	8.94	15.03	6.05	7.15	7.33	8.34	54.36
02	0	0	700	3	34.20	10.33	9.31	13.80	6.11	5.40	7.92	5.08	53.84
03	-α	0	500	3	30.46	12.98	11.80	12.59	7.74	6.42	8.11	2.35	55.24
04	α	0	900	3	34.41	9.86	10.02	13.37	6.94	7.37	6.52	8.72	54.29
05	0	α	700	5	34.08	10.38	9.29	13.82	6.02	5.33	7.96	5.31	53.75
06	0	0	700	3	34.20	10.33	9.31	13.80	6.11	5.40	7.92	5.08	53.84
07	0	0	700	3	34.20	10.33	9.31	13.80	6.11	5.40	7.92	5.08	53.84
08	-1	1	600	4	32.13	11.06	10.92	12.88	7.03	6.28	7.95	3.72	54.11
09	0	-α	700	1	34.64	10.21	9.68	13.84	6.20	5.51	8.00	4.73	54.53

10	-1	-1	600	2	32.84	11.20	10.96	12.91	7.26	6.84	8.00	3.35	55.00
11	1	-1	800	2	35.02	10.15	8.27	14.76	6.13	7.02	7.94	8.03	53.44
12	0	0	700	3	34.20	10.33	9.31	13.80	6.11	5.40	7.92	5.08	53.84
13	0	0	700	3	34.20	10.33	9.31	13.80	6.11	5.40	7.92	5.08	53.84

The results of CCD-RSM experimental design and energy-dispersive X-ray fluorescence (ED-XRF) analysis is presented in Table 2. BPA exhibited a maximum total of 55.24% for combined oxides composition of silica, alumina and iron (SiO_2 + Al_2O_3 + Fe_2O_3) at a calcination temperature and dwelling time of 500°C and 3-hours respectively, which complies with the ASTM C618-12a, of at least 50% for Class C Pozzolan. BPA calcined at 800°C for a period of 2-hours possessed the highest amount of silica content (35.02%) and loss on ignition (LoI) of 8.03%, which is slightly more than the maximum 6% specified by ASTM C618-12a for class C pozzolan.

Silicon Dioxide (SiO_2)

The silica content of BPA ranged between 30.46% - 35.02%, in conformity to BS EN 197-1:2000, which states that reactive silicon dioxide content shall be not less than 25.0% by mass. Silica content was found to increase with increase in calcination temperature (increasing from 30.46% to 35.02% as calcination temperature increases from 500°C to 800°C); a similar trend was observed by Altwair *et al* (2011) for palm oil waste; and quadratic model (Equation 1) was chosen. Since high silica content is favourable in pozzolanic reaction (Lowe, 2012 and Malvar and Lenke, 2006) and pozzolanic activity also strongly depends on the amount of reactive silica (Setina *et al,* 2013), RSM was set to maximize silica content in BPA resulting in an optimum value of 34.05% (Figure 1)

$$\text{Silicon Oxide} = 8.17293 + 0.069406*BT - 1.15631*DT + 0.001075*BT*DT - 0.0000443254*BT^2 + 0.037996*DT^2 \quad \ldots\ldots (1)$$

(Std Dev. = 0.16, R^2 = 0.9903, Mean = 33.79, Adj. R^2 = 0.9834, Pred. R^2 = 0.9080, Prob>F < 0.0001)

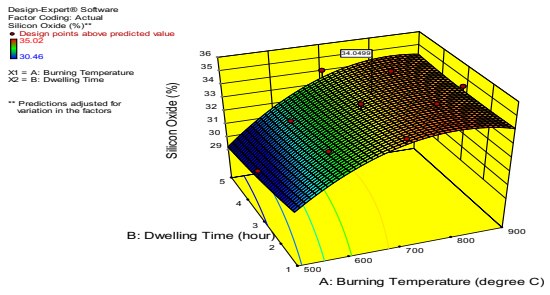

Figure 1: Response of Silica Content to Variations in Calcination Temperature and Dwelling Time

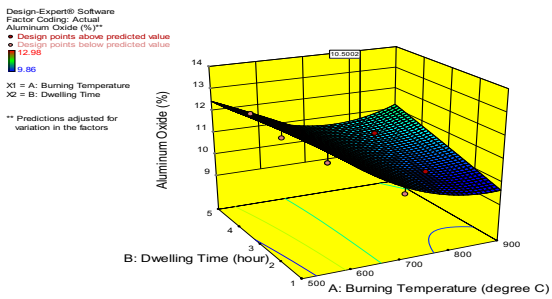

Figure 2: Response of Alumina Content to Variations in Calcination Temperature and Time

Aluminum Oxide (Al_2O_3)

The alumina content of BPA ranged between 9.86% - 12.98%. Alumina content was found to be indirectly proportional to calcination temperature but without a clear pattern of proportionality for dwelling time, as shown in the quadratic model (Equation 2) chosen. RSM was set to maximize alumina content in BPA, since the presence of alumina in concrete mitigate against corrosion (Tijani *et al,* 2018) and because pozzolanic reaction is largely controlled by its alumina and silica content (Walker and Pavi'a, 2011). An optimum value of 10.50% alumina content was obtained (Figure 2)

$$\text{Aluminum Oxide} = 31.64098 - 0.049998*BT - 1.07766*DT + 0.001675*BT*DT + 0.0000275582*BT^2 - 0.0056681*DT^2 \quad \ldots\ldots (2)$$

(Std Dev. = 0.29, R^2 = 0.9242, Mean = 10.63, Adj. R^2 = 0.8700, Pred. R^2 = 0.2673, Prob>F = 0.0009)

Ferric Oxide (Fe_2O_3)

The content of ferric oxide, which is said to be responsible for compressive strength, soundness and setting in concrete (Tijani *et al,* 2018), ranged between 8.27% - 11.80% in BPA. Quadratic model given in Equation (3)

was chosen to analyze ferric oxide in BPA. Since it positively contribute to concrete properties, RSM was set to maximize the quantity of ferric oxide in BPA and optimum value of 9.59% ferric oxide was obtained (Figure 3).

Ferric Oxide = 37.89351 – 0.068229*BT – 1.51944*DT + 0.001775* BT* DT
+ 0.0000400323* BT^2 + 0.044073* DT^2 ..... (3)

(Std Dev. = 0.47, R^2 = 0.8593, Mean = 9.73, Adj. R^2 = 0.7855, Pred. R^2 = -0.4324, Prob>F = 0.0068)

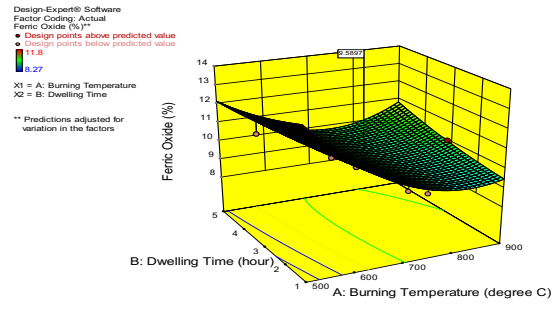

Figure 3: Response of Ferric Oxide to Variations in Burning Temperature and Dwelling time

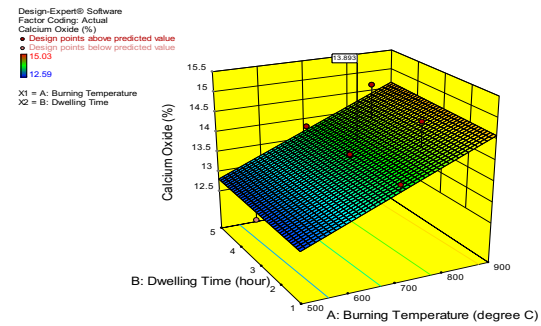

Figure 4: Response of Calcium Oxide to Variations in Burning Temperature and Dwelling Time

Calcium Oxide (CaO)

The percentage composition of calcium oxide in BPA ranged between 12.59% - 15.03%, which is similar to what was presented by Supic *et al* (2021) for soybean straw ash and in conformity to ASTM C618 (2019), which states that the amount of calcium oxide in a class C pozzolana shall not be less than 10.0% by mass. However, linear model given in Equation (4) was chosen to analyze calcium oxide in BPA. Being a major constituent material in both pozzolanic and cementiteous reactions (Lowe, 2012), RSM was set to maximize the quantity of calcium oxide in BPA and optimum value of 13.89% calcium oxide was obtained (Figure 4).

Calcium Oxide = 10.41436 + 0.00463333*BT + 0.016667*DT..... (4)

(Std Dev. = 0.55, R^2 = 0.4595, Mean = 13.71, Adj. R^2 = 0.3514, Pred. R^2 = -0.2754, Prob>F = 0.0461)

Magnesium Oxide (MgO)

The percentage composition of magnesium oxide in BPA ranged between 6.02% - 7.74%, which is similar to what was presented by Supic *et al* (2021) for soybean straw ash. However, quadratic model given in Equation (5) was chosen to analyze magnesium oxide in BPA. Gonçalves *et al* (2019) mentioned that the development of a less resistant microstructure, as a result of a lesser quantity of C-S-H, was likely caused by the dilution of cement with progressively larger replacement levels of MgO. Hence, RSM was set to minimize the quantity of magnesium oxide in BPA and optimum value of 6.39% magnesium oxide was obtained (Figure 5).

Magnesium Oxide = 24.55184 – 0.047749*BT – 0.33902*DT + 0.000375* BT* DT
+ 0.0000310948* BT^2 + 0.00344828* DT^2 ..... (5)

(Std Dev. = 0.24, R^2 = 0.8998, Mean = 6.46, Adj. R^2 = 0. 8282, Pred. R^2 = 0.0731, Prob>F = 0.0022)

Potassium Oxide (K_2O)

The percentage composition of potassium oxide in BPA ranged between 5.33% - 7.37% and was referred to as impurities in pozzolanic ash by Olawale and Oyawale (2012). However, quadratic model given in Equation (6) was chosen to analyze potassium oxide in BPA. Smith *et al* (2020) mentioned that the presence of higher percentage of alkali, such as potassium oxide and sodium oxide, in pozzolanic concrete may adversely affect early curing age strength, due to the difficulty experienced in the formation of calcium trisilicates in concrete. Hence, RSM was set to minimize the quantity of potassium oxide in BPA and optimum value of 6.26% potassium oxide was obtained (Figure 6).

Potassium Oxide = 27.18960 – 0.057561*BT – 1.41131*DT + 0.001725* BT* DT
+ 0.0000391746* BT^2 + 0.022996* DT^2 ..... (6)

(Std Dev. = 0.66, R^2 = 0.6042, Mean = 6.07, Adj. R^2 = 0. 3215, Pred. R^2 = -1.7028, Prob>F = 0.1750)

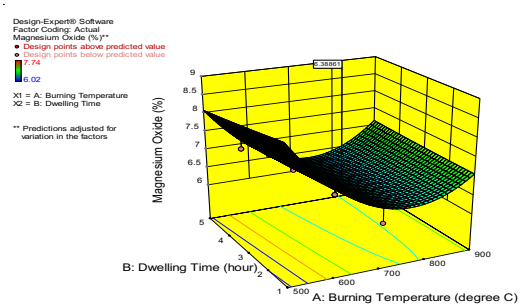

Figure 5: Response of Magnesium Oxide to Variations in Burning Temperature and Time

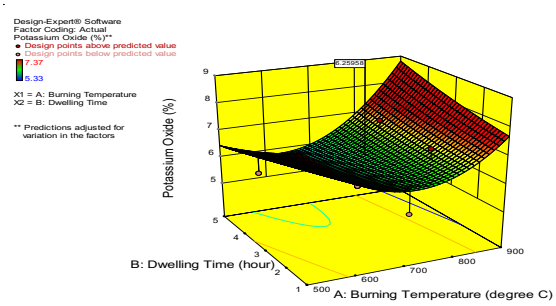

Figure 6: Response of Potassium Oxide to Variations in Burning Temperature and Time

Combined Effects of Silicon, Aluminum and Iron Oxides

ASTM C618 characterized pozzolanic materials based on the percentage composition of the silicon, aluminum and iron oxides. The combined percentages of silicon, aluminum and iron oxides in BPA ranged between 53.44% - 55.24%; this is in conformity to ASTM C618 (2012a), which states that the combined percentages of silicon aluminum and iron oxides in a pozzolanic material shall be not less than 50.0% for a Class C pozzolan. However, quadratic model, given in Equation (7) was chosen to analyze these combined oxides in BPA. Since higher percentage of these oxides in BPA is favourable in pozzolanic reaction and in the classification of pozzolanic materials (ASTM C618, 2012a), RSM was set to maximize the quantity of these oxides in BPA and the optimum value of 54.14% combined silicon, aluminum and iron oxides was obtained (Figure 7).

$$SiO_2 + Al_2O_3 + Fe_2O_3 = 77.70741 - 0.048821*BT - 3.75341*DT + 0.004525*BT*DT + 0.0000232651*BT^2 + 0.076401*DT^2 \quad \ldots\ldots (7)$$

(Std Dev. = 0.15, R^2 = 0.9543, Mean = 54.15, Adj. R^2 = 0.9217, Pred. R^2 = 0. 5536, Prob>F = 0.0001)

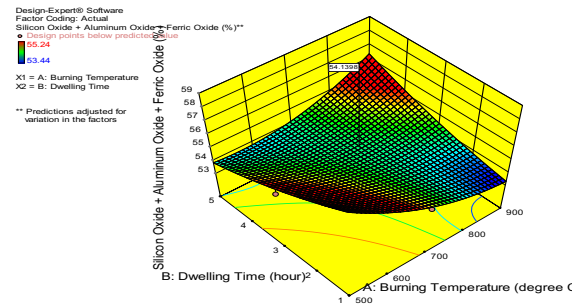

Figure 7: Response of $SiO_2 + Al_2O_3 + Fe_2O_3$ to Variations in Burning Temperature and Time

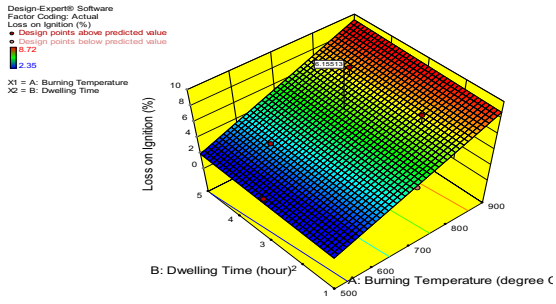

Figure 8: Response of Loss on Ignition to Variations in Burning Temperature and Time

Loss on Ignition (LoI)

Before employing ashes of any agricultural by-products for pozzolanic reaction, loss on ignition (LoI) of such material must be considered (Altwair *et al,* 2011). It is well known that a high LoI results in increased water consumption and superplasticizer dosage (Sata *et al,* 2007). The quantity of LoI in BPA ranged between 2.35% - 8.72%; this is in conformity to ASTM C618 (2012a), which states that the quantity of LoI in a pozzolanic material shall not be more than 10.0% for a Class N and 6.0% for both Class F and Class C pozzolan. However, linear model given in Equation (8) was chosen because it has the highest R-squared, lowest standard deviation, highest order polynomial with significant additional terms and model not aliased. RSM was set to minimize the value of LoI in BPA and the optimum value of 6.16% LoI was obtained (Figure 8).

$$\text{Loss on Ignition} = -7.9359 + 0.018367*BT + 0.15333*DT \quad \ldots\ldots (8)$$

(Std Dev. = 0.56, R^2 = 0.9291, Mean = 5.38, Adj. R^2 = 0.9149, Pred. R^2 = 0. 8618, Prob>F < 0.0001)

Validation of Optimization Process

The models developed were validated in accordance with Algaifi *et al* (2021) and Mohammed *et al* (2017). Values for estimated R^2 and adjusted R^2 in Table 3 confirms the conclusion of Algaifi *et al* (2021) that when the difference between the adjusted R^2 and estimated R^2 is less than 0.2, a model is regarded reasonable and accurate; likewise, when the ratio between R^2 and adjusted R^2 is high, a good agreement and fitness can be reached.

Table 3: Model Validation Based on Estimated R-Square and Adjusted R-Square

Models/Responses	Estimated R^2	Adjusted R^2	Difference btw Estimated R^2 and Adjusted R^2	Ratio of Estimated R^2 and Adjusted R^2
SiO_2	0.9903	0.9834	0.0069	1.01
Al_2O_3	0.9242	0.8700	0.0542	1.06
Fe_2O_3	0.8593	0.7855	0.0738	1.09
CaO	0.4595	0.3514	0.1081	1.31
$SiO_2 + Al_2O_3 + Fe_2O_3$	0.9543	0.9217	0.0326	1.04
LoI	0.9291	0.9149	0.0142	1.02

4. CONCLUSION

In order to characterize the ash of Beans Pod as a pozzolan, some pozzolanic properties of calcined BPA were investigated through the use of XRF and XRD laboratory method of analysis to determine the chemical and mineral composition that are present in calcined BPA. It can be concluded that calcined BPA exhibits a class C pozzolanic properties based on ASTM C618-12a specifications and that the amount of silica present and the LoI on BPA are greatly affected by calcination temperature and dwelling time. Optimum pozzolanic properties of calcined BPA, based on XRF method of analysis, was obtained at 738.38^oC burning temperature and 3.45-hours of dwelling time. Also, the models developed were validated with empirical data and the coefficient of determination indicates adequate representation of the real relation with the independent variables.

REFERENCES

Ajeigbe, H. A.; S. G. Mohammed; J. O. Adeosun and D. Ihedioha. (2010). Farmers' Guide to Increased Productivity of Improved Legume–Cereal Cropping Systems in the Savannas of Nigeria. IITA, Ibadan, Nigeria. 104 pp.

Algaifi, H.A.; M. A. Mustafa; E. Alsuhaibani; S. Shahidan; F. Alrshoudi; G. F. Huseien and S. A. Bakar. (2021). Optimisation of GBFS, Fly Ash, and Nano-Silica Contents in Alkali-Activated Mortars. Polymers, Vol. 13, 26 pp.

Al-kahtani, M. S. M.; H. Zhu; S. I. Haruna and J. Shao. (2023). Evaluation of mechanical properties of polyurethane-based polymer rubber concrete modified ground glass fiber using response surface methodology. Arabian Journal for Science and Engineering, 48(4), 4695-4710.

Altwair, N. M.; M. A. M. Johari and S. F. S. Hashim. (2011). Influence of Calcination Temperature on Characteristics and Pozzolanic Activity of Palm Oil Waste Ash. Australian Journal of Basic and Applied Sciences, Vol. 5, Issue 11, pp 1010-1018.

ASTM Standard C618, (2005). Standard Specification for Coal Fly Ash and Raw or Calcined Natural Pozzolan for Use in Concrete. ASTM International, West Conshohocken, PA, USA.

ASTM Standard C618, (2012a). Standard Specification for Coal Fly Ash and Raw or Calcined Natural Pozzolan for Use in Concrete. ASTM International, West Conshohocken, PA, USA.

ASTM Standard C618, (2019). Standard Specification for Coal Fly Ash and Raw or Calcined Natural Pozzolan for Use in Concrete. ASTM International, West Conshohocken, PA, USA.

Barbir, D.; P. Dabic and P. Krolo. (2013). Hydration Study of Ordinary Portland Cement in the Presence of Lead (II) Oxide. Chemical and Biochemical Engineering Quarterly, Q. 27 (1), pp 95-99.

Fakayode, B. S.; A. O. Omotesho and T. Z. Adebayo. (2014). An Economic Survey of Cowpea (Vigna Unguiculata) Storage Practices in Kwara State, Nigeria. Bangladesh J. Agril, Res. 39(1), pp 47-57.

Ghassan, K. A. and Mouin, A. (2016). Natural Pozzolan as a Partial Substitute for Cement in Concrete. US Army Corps of Engineers, Construction Engineering Research Laboratory, Champaign, IL

Gonçalves, T.; R.V. Silva; J. De-Brito; J.M.F. Rodriguez and A.R. Esquinas. (2019). Hydration of Reactive MgO as Partial Cement Replacement and Its Influence on the Macroperformance of Cementitious Mortars. Advances in Materials Science and Engineering, Vol. 2019, 12 pp.

Jezek, G. (2009). (http://www.concrete.com/history of concrete)

Joseph, A. A. and Raymond, M. D. (2014). Rate of Strength Development Of Concrete Made Using Selected Nigerian Cement Brands. International Journal of Technology Enhancements and Emerging Engineering Research, Volume 2, Issue 12, pp 48 – 51.

Keppert, M.; L. Scheinherrová; M. Jerman; B. Doušová; L. Kobera; J. Brus and R. Cern. (2019). Hydration of Ordinary Portland Cement in Presence of Lead Sorbed on Ceramic Sorbent. Materials, 12(1), 14 pp.

Lowe, R. D. (2012). Pozzolanic Properties of Biomass Fly Ash. A Thesis Presented to the Graduate School of Clemson University, 74 pp.

Malvar, L. J. and Lenke, L. R. (2006). Efficiency of fly ash in mitigating alkali-silica reaction based on chemical composition. ACI Materials Journal, 103(5), pp. 319-326.

Mohammed, B.S.; C. K. Veerendrakumar and M. F. Nuruddin. (2017). Rubbercrete Mixture Optimization Using Response Surface Methodology. Journal of Cleaner Production.

Olawale, O. and Oyawale, F.A. (2012). Characterization of Rice Husk via Atomic Absorption Spectrophotometer for Optimal Silica Production. International Journal of Science and Technology, Volume 2 No.4, pp 210-213.

Sata, V.; C. Jaturapitakkul and K. Kiattikomol. (2007). Influence of pozzolan from various by-product materials on mechanical properties of high-strength concrete. Construction and Building Materials 21(7), pp 1589-1598.

Setina, J.; A. Gabrene and I. Juhnevica. (2013). Effect of Pozzolanic Additives on Structure and Chemical Durability of Concrete. 11th International Conference on Modern Building Materials, Structures and Techniques, Procedia Engineering 57, pp 1005-1012.

Shi, C., F. He and Y. Wu. (2012). Effect of pre-conditioning on CO2 curing of lightweight concrete blocks mixtures. Construction and Building Materials, 26(1), 257-267.

Siddique, R. (2012). Utilization of wood ash in concrete manufacturing. Resources, conservation, and recycling, Vol. 67, pp 27-33.

Singh, Y.; A. Sharma; G. K. Singh; A. Singla and N. K. Singh. (2018). Optimization of performance and emission parameters of direct injection diesel engine fuelled with pongamia methyl esters-response surface methodology approach. Industrial crops and products, 126, 218-226.

Smith, A. S. J.; G. Xu; M. J. Garba and M. Y. Aliyu. (2020). Pozzolanic and Mechanical Properties of Date Palm Seed Ash (Dpsa) Concrete. Nigerian Journal of Technology, Vol. 39, No. 3, pp. 680-686.

Šupić, S.; M. Malešev; V. Radonjanin; V. Bulatović and T. Milović. (2021). Reactivity and Pozzolanic Properties of Biomass Ashes Generated by Wheat and Soybean Straw Combustion", Materials, Vol. 14, 20 pp.

Tijani, M. A.; W. O. Ajagbe and O. A. Agbede. (2018). Modelling the Effect of Burning Temperature and Time on Chemical Composition of Sorghum Husk Ash for Optimum Pozzolanic Activity. FUTA Journal of Engineering and Engineering Technology, Vol. 12, Issue 2, pp 273-281.

Walker, R. and Pavı´a, S. (2011). Physical properties and reactivity of pozzolans and their influence on the properties of lime–pozzolan pastes. Materials and Structures, Vol. 44, pp 1139-1150.

PAPER 161 – STATISTICAL OPTIMIZATION OF THE SYNTHESIS OF CALCIUM OXIDE FROM DOLOMITE FOR CARBON DIOXIDE CAPTURE

I. A. Joseph[1*], E. O. Ajala [1], A. Ahmed El-Imam [2], M. A. Ajala [1], E. O. Babatunde[1], C. T. Are[3]

[1]Department of Chemical Engineering, University of Ilorin, Ilorin Nigeria
[2]Department of Microbiology, University of Ilorin, Ilorin Nigeria
[3]Department of Chemistry, Prince Abubakar Audu University, Anyigba, Nigeria
* Email: isaacchemeng@yahoo.com

ABSTRACT
Dolomite is a double carbonate mineral of calcium and magnesium that can serve as raw material for the synthesis of calcium oxide. In many industrial chemical processes, carbon dioxide (CO_2) is an undesired by-product that is required to be removed for the smooth running of the process. X-Ray Diffraction (XRD) analysis revealed that dolomite ore collected in Okere, Kwara State has the major mineral phase of dolomite with 94 % purity. Following the dissolution of dolomite in hydrochloric acid, calcium hydroxide [$Ca(OH)_2$] precipitation using ammonium hydroxide (NH_4OH) was optimized. For the precipitation study, the temperature was varied between 10 to 50 ^oC, the time between 2 to 10 Minutes, and volume ratio of the filtrate to NH_4OH between 1:0.8 to1:3 ml:ml. $Ca(OH)_2$ obtained at optimum conditions (40 ^oC, 2 minutes and Vol:Vol of 1:2.5 ml:ml) was calcined at 700 ^oC to obtain CaO. Dynamic Light scattering of CaO shows an average particle size of 49.46 nm, FTIR was used to confirm CaO at wavelength of 1394 cm^{-1} and 872 cm^{-1}. CO_2 capture was done by exposing the synthesized CaO at room conditions for 30 days. XRD analysis shows the new mineral phase of 78 % calcite and 9.42 % lime. This is an indication that the synthesized CaO is suitable for CO_2 capture.

KEYWORDS: Calcium oxide, Calcite, Carbon dioxide, Dolomite, Optimum

1. INTRODUCTION

Calcium oxide is a basic inorganic metal oxide with the chemical formula CaO (Sun *et al.,* 2018; Khine *et al.,* 2022,). Due to technological advancement, the use of CaO has continued to gain wider applications such as catalyst, glass making, bleaching powder, mortars and cement, carbon capture, calcium carbide, and treatment of acidic soil (Gupta and Agarwal, 2016; Sun *et al.,* 2018; Khine *et al.,* 2022). CaO has been reportedly produced from naturally occurring minerals such as calcite, limestone, gypsum aragonite, and marble. Other reported non-mineral sources of calcium oxide production are seashells, cow born, eggshell, and crab shell (Mohadi *et al.,* 2016). Another neglected important raw material that could be suitable for CaO production is dolomite. Dolomite is a naturally occurring basic mineral with calcium carbonate (54.35 %) being a major constituent followed by magnesium carbonate (45.65 %) (Ajala *et al.,* 2019; Joseph *et al.,* 2022). Nigerian abundant dolomite deposit in Edo, Kogi, Ogun, Kwara, and the Federal Capital Territory is yet to explore for CaO production (Are *et al.,* 2022; Joseph *et al.,* 2022).

Different reported methods of CaO synthesis are thermal decomposition, biogenic method, hydrothermal technique, multi-component synthesis, combustion method, two-step thermal decomposition technique,sol–gel, microwave synthesis, co-precipitation technique, precipitation method (Gupta and Agarwal, 2016; Mohadi *et al.,* 2016; Sun *et al.,* 2018; Aseel *et al.,* 2018; Szalai *et al.,* 2019; Habte *et al.,* 2019; Khine *et al.,* 2022). CaO synthesis is usually obtained by calcination of $Ca(OH)_2$ between 450 -650 ^oC temperature (Karami *et al.,* 2012; Mirghiasi *et al.,* 2014; Khine *et al.,* 2022).

Carbon dioxide (CO_2) has been reported to be one of the leading greenhouse gas resulting in global warming (Tian *et al.,* 2016; Liu 2016). Several industrial processes such as cement, ammonia, nitric acid, iron, aluminum, and steel manufacturing have a high contribution to CO_2 emission (Liu 2016; Nasr *et al.,* 2015). CO_2 as a byproduct in the biological process such as in biohydrogen production usually leads to a decrease in the microorganism population that is responsible for the biosynthesis of the main product (Park *et al.,* 2005; Nasr *et al.,* 2015; Vasiliadou *et al.,* 2020). CO_2 is considered a strong metabolic poison that causes inhibition due to the disruption of the cell wall structure of microorganisms (Martirosyan *et al.,* 2012). This study was aimed at the synthesis of CaO for CO_2 capture from locally sourced dolomite from Oreke, Ifelodun Local Government Area of Kwara State, Nigeria. The precipitation of $Ca(OH)_2$ was optimized via Box-Benken Design.

2. MATERIALS AND METHODS

2.1 Materials

Dolomite ore sample was collected from Oreke, Ifelodun local Government area of Kwara State, Nigeria. For effective dissolution of dolomite, particle size ranging from 0.15 mm to 0.3 mm was used in this study. This was archived through the size reduction of the dolomite rock by cruising, grinding, and sieving. Analytical grade of hydrochloric acid (35 -38 %) by Central Drug House (P) Ltd and ammonium hydroxide was used in this study.

2.2 Methods

A slight modification of the dissolution method reported by the same author, Joseph *et al.* (2022) in an earlier study was done. This involved the dissolution of 6 g of dolomite in 100 ml of 2 M HCl at 50 °C for 10 minutes, followed by filtration. For the Box-Behnken Design, precipitation time was varied between 2 to10 Mins, a ratio of the volume of the filtrate to the volume of precipitant was studied between 1:0.8 and 1: 1:3 ml/ml, and the temperature was varied between 10 to 50 °C (Table 1). 6 M NH_4OH precipitant was added to the filtrate according to volume to volume ratio in the optimization 2. The precipitate was filtered and oven dried at 60 °C for 4 hours. The whole process was repeated for other experimental runs. At the optimum precipitation, the raffinate was tested for reuse to precipitate another fresh filtrate from dolomite dissolution. The synthesized $Ca(OH)_2$ was calcined in a mulfu furnace at 700 °C for 120 Mins. CO_2 capture was done by exposing the synthesized CaO at room conditions for 30 days.

3. RESULTS AND DISCUSSION

3.1 Stage-wise Reaction Mechanism

The mechanism for the synthesis of CaO via a precipitation reaction and CO_2 capture pathway developed in this study is presented in equations 1 to 14.

$$CaMg(CO_3)_2 + 4HCl \rightarrow CaCl_2 + MgCl_2 + H_2O + CO_2 \quad (1)$$

A detailed mechanism of the dissolution of dolomite in hydrochloric acid (HCl) was reported by the same author, Joseph *et al.* (2022). The detailed reaction mechanism for the precipitation of calcium hydroxide using ammonium hydroxide as precipitant is presented in equations 2 to 6. The developed reaction mechanism for the calcination of calcium hydroxide to produce CaO is shown in equations 7 to 10. CO_2 capture using CaO is a chemical process, the developed reaction mechanism backing up the process is represented in equations 11 to 14.

Reaction mechanism of calcium hydroxide precipitation using ammonium hydroxide:

$$CaCl_2 + 2NH_4OH \rightarrow Ca(OH)_2 + 2NH_4Cl \quad (2)$$
$$CaCl_2 \rightarrow Ca^{2+} + 2Cl^- \quad (3)$$
$$NH_4OH \rightarrow NH_4^+ + OH^- \quad (4)$$
$$Ca^{2+} + OH^- \rightarrow Ca(OH)_2 \quad (5)$$
$$NH_4^+ + Cl^- \rightarrow NH_4Cl \quad (6)$$

Reaction mechanism of thermal treatment of calcium hydroxide

$$Ca(OH)_2 \rightarrow CaO + H_2O \quad (7)$$
$$Ca(OH)_2 \rightarrow Ca^{2+} + OH^- \quad (8)$$
$$2OH^- \rightarrow H_2O + O^{2-} \quad (9)$$
$$Ca^{2+} + O^{2-} \rightarrow CaO \quad (10)$$

Reaction mechanism of CO_2 capture

$$CaO + CO_2 \rightarrow CaCO_3 \quad (11)$$
$$CaO \rightarrow Ca^{2+} + O^{2-} \quad (12)$$
$$CO_2 + O^{2-} \rightarrow CO_3^{2-} \quad (13)$$
$$CO_3^{2-} + Ca^{2+} \rightarrow CaCO_3 \quad (14)$$

3.2 Application of Statistical Tools in Chemical Synthesis of $Ca(OH)_2$ from Dolomite

The actual and the predicted precipitation yield from the seventeen experimental runs from Box-Behnken Design is presented in Table 2. From the precipitation study, 36.6 % actual yield and a close predicted yield of 37.83 % was achieved at precipitation time of 6 Mins, 10 °C, and 0.8 Vol/Vol ratio of pregnant solution from the dissolution of dolomite in HCl to NH_4OH as precipitant. Both the experimental conditions at run 12 (2 Mins, 1.9 Vol/Vol, and 50 °C) as well as at run 16 (10 Mins, 3 Vol/Vol, and 30 °C) have the highest actual yield of 70 %. However, run 16 has a much closer predicted yield of 69.17 % than run 12 with a predicted yield of 68.66 %. The total residual sum of 0.004 is an indication that the predicted values are much close to the experimental value.

Table 1: Factors Influencing the Precipitation of $Ca(OH)_2$ using NH_4OH

Factor	Name	Minimum	Maximum	Coded Low	Coded High	Mean	Std. Dev.
A	Time (Mins)	2.00	10.00	-1 ↔ 2.00	+1 ↔ 10.00	6.00	2.83
B	Vol./Vol. (mL:ml)	0.80	3.00	-1 ↔ 0.80	+1 ↔ 3.00	1.90	0.7778
C	Temperature (°C)	10.00	50.00	-1 ↔ 10.00	+1 ↔ 50.00	30.00	14.14

Table 2: Experimental Conditions for the precipitation of $Ca(OH)_2$ using NH_4OH

Run	A:Time (Minutes)	B:Vol./Vol (mL:mL)	C:Temperature (°C)	Yield (%)		Residual
				Actual	Predicted	
1	6	3	10	53.33	52.17	1.164
2	6	1.9	30	66.67	62.66	4.01
3	10	1.9	10	53.33	54.66	-1.33
4	6	3	50	66.67	65.50	1.17
5	6	0.8	50	50	51.17	-1.17
6	6	1.9	30	66.63	62.66	3.97
7	6	0.8	10	36.67	37.83	-1.16
8	2	0.8	30	56	55.50	0.50
9	2	1.9	10	53.33	51.10	1.33
10	10	1.9	50	63.33	64.66	-1.33
11	6	1.9	30	60	62.66	-2.66
12	2	1.9	50	70	68.66	1.33
13	6	1.9	30	60	62.66	-2.66
14	10	0.8	30	56.67	54.84	1.84
15	2	3	30	66.67	69.84	-3.17
16	10	3	30	70	69.17	0.83
17	6	1.9	30	60	62.66	-2.66
Total						**0.004**

The statistical analysis of the reduced quadratic model of $Ca(OH)_2$ precipitation is presented in Table 3. The goal of developing any statistical model is to be able to accurately predict the outcome of any experiment without necessarily going through the tedious process of conducting such an experiment (Joseph *et al.,* 2022). Based on the experimental data, a quadratic model (equation 15) under the Box-Behnken Design was developed in this study for the prediction of precipitation yield of $Ca(OH)_2$ from a pregnant solution of leached dolomite in HCl. Analysis of Variance (ANOVA) revealed that the quadratic model with R^2 of 0.9326, adjusted R^2 of 0.8802, and predicted R^2 of 0.8802 is most appropriate for model prediction. The adequate prediction value of 15.6517 further shows the model has high prediction efficiency as its value is much higher than the least value of 4 for any model to be significant. A maximum probability (P) value of 0.05 has been set for the determination of model significance. The developed model with a P-Value of 0.0001 is significant, while model terms such as B, C, A^2, B^2, and C^2 are also significant.

Table 3: ANOVA for Reduced Quadratic model of $Ca(OH)_2$ Precipitation

Source	Sum of Squares	df	Mean Square	F-value	p-value	Remarks		
Model	1106.67	7	158.10	17.80	0.0001	significant	R^2	0.9326
A-Time	0.8911	1	0.8911	0.1003	0.7587		Adjusted R^2	0.8802
B-Vol./Vol.	410.84	1	410.84	46.25	< 0.0001		Predicted R	0.7676
C-Temperature	355.64	1	355.64	40.04	0.0001		Adequate Precision	15.6517
AC	11.12	1	11.12	1.25	0.2921			
A^2	67.45	1	67.45	7.59	0.0223			
B^2	78.85	1	78.85	8.88	0.0155			
C^2	187.04	1	187.04	21.06	0.0013			
Residual	79.95	9	8.88					
Lack of Fit	26.88	5	5.38	0.4052	0.8257	not significant		
Pure Error	53.07	4	13.27					
Cor Total	1186.62	16						

Final Equation in Terms of Actual Factors

$$Yield\ (\%) = +18.12784 - 2.46Time + 20.1052Vol./Vol + 1.45819Temperature - 0.020844Time * Temperature + 0.250156Time^2 - 3.57645Vol./Vol.^2 - 0.01662Temperature^2 \quad (15)$$

3.2.1 Single Effect of the Process Variables on the Precipitation of $Ca(OH)_2$

The graphical representation of the process variable is shown in Figure 1. The precipitation shows a decline in the yield from 67.0 % to 62.66 % when the precipitation time increases from 2 to 6 Mins, However, as the single effect of time increases further to 10 Mins, the yield also increases to 66.33 %. This implies that the precipitation is best favoured by a minimum time of precipitation as the precipitate might dissolve into the solution. The single effect of Vol./Vol. ratio on the precipitation shows a positive effect as the yield increased from 51.16 % to 65.50 % when the concentration was increased from 0.8 to 3 ml:ml. This implies that the more precipitant added was able to force the $Ca(OH)_2$ out of the pregnant solution. The single effect of temperature also shows a significant positive contribution to the precipitation as the yield increases from 49.61 % to 62.74 % when the temperature was raised from 10 ^oC to 50 ^oC. It could be inferred that the rise in the temperature of the reaction promotes the bond formation of $Ca(OH)_2$ from the pregnant solution.

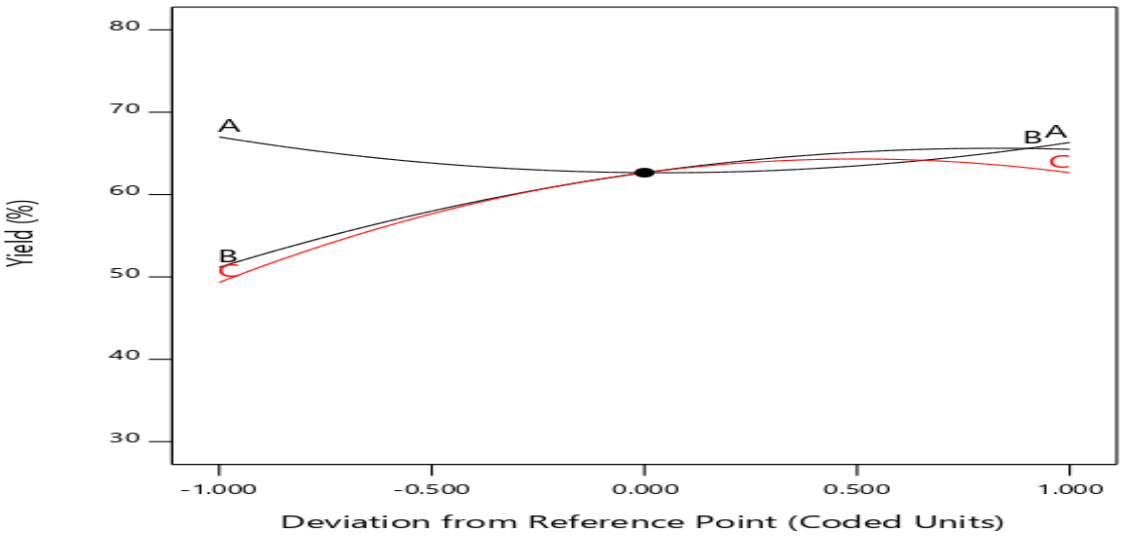

Figure 1: Effect of Time, Vol/Vol. Ratio of Precipitant and Temperature on the Precipitation of $Ca(OH)_2$ from Dissolved Dolomite

3.2.2 Optimum Predicted Points for the Precipitation of $Ca(OH)_2$ from Aqueous Dolomite

The numerical optimization method of point prediction predicted 72.12 % yield of $Ca(OH)_2$ at the optimum operating conditions of 2 Mins, 2.5 ml;ml and 40 ^oC, while the experimental validation gave a much closer yield of 72.10 %.

3.3. Sample Characterization

X-Ray Diffraction (XRD) was used for mineral phase identification and quantification. In Figure 2, the most prominent Oreke dolomite phase of 94 % purity is present at a diffraction angle between 30 to 32 ^oC (Fahad *et al.,* 2011; Baba *et al.,* 2014), while quartz (2.8 %) and muscovite (3.1 %) are present as an impurity in trace amount. Following the calcination of $Ca(OH)_2$ at optimum conditions, the synthesized CaO that was left open for CO_2 capture at room temperature for 30 days was subjected to XRD analysis (Figure 3) and the result shows that a mineral phase transition occurred with end product showing 78 % calcite, and 9.42 % lime at a diffraction angle of 29^o to 31^o and 39^o respectively, while quartz is present in trace amount as an impurity. Dynamic Light scattering of CaO shows an average particle size of 49.46 nm, FTIR was used to confirm CaO at wavelength of 1394 cm^{-1} and 872 cm^{-1}.

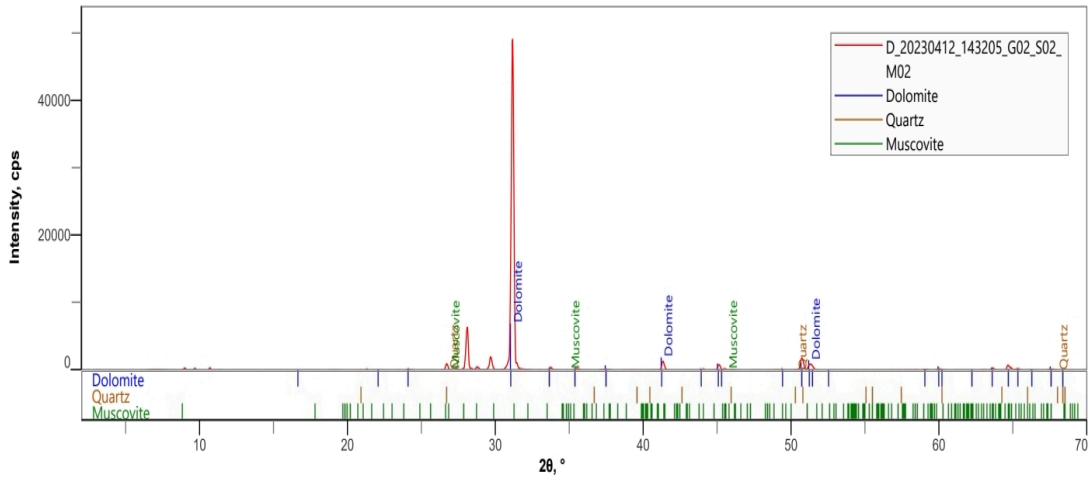

Figure 2: XRD Spectral of Oreke Dolomite Ore

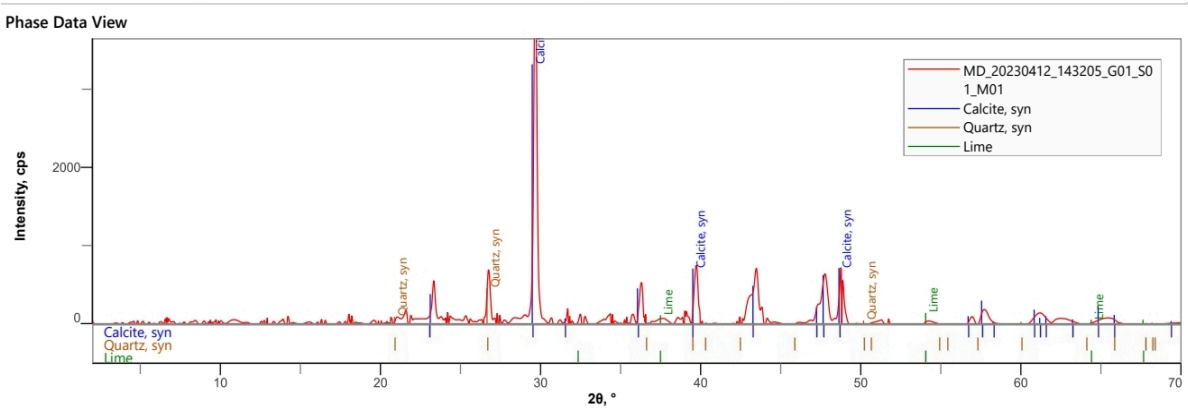

Figure 3: XRD Spectral of Synthesized CaO after CO_2 Capture

4. CONCLUSION

Following the dissolution of dolomite in HCl, the optimization of the process condition of precipitation of $Ca(OH)_2$ from pregnant solution using Box-Behnken Design was achieved at the optimum point of 2 Mins, 2.5 ml;ml and 40 ^oC with 72.12 % predicted optimum yield of $Ca(OH)_2$ and 72.10 % validated yield. From XRD analysis, Oreke dolomite has 94 % purity. XRD analysis confirmed the high CO_2 captured using the synthesized CaO in this study to calcite and lime. The high CO_2 capture could be attributed to the small average particle size (49.46 nm) of CaO as identified by Dynamic Light scattering. Oreke dolomite is a suitable raw material for CaO synthesis with a high potential for CO_2 capture.

REFERENCES

Ajala, E. O., Ajala, M. A., Odetoye, T. E., & Okunlola, A. T. (2019). Synthesis of solid catalyst from dolomite for biodiesel production using palm kernel oil in an optimization process by definitive screening design. *Brazilian Journal of Chemical Engineering*, *36*, 979-994.

Are, C. T., Yisa, J., Suleiman, M. A. T., Auta, M., & Joseph, I. A. (2022). Optimization of the calcination of brucite for the production of magnesia using response surface methodology. *Chemical Data Collections*, *40*, 100895.

Aseel, M. A., Itab, F. H., & Ahmed, F. M. (2018, May). Producing high purity of metal oxide nano structural using simple chemical method. In *Journal of Physics: Conference Series* (Vol. 1032, No. 1, p. 012036). IOP Publishing

Baba, A. A., Omipidan, A. O., Adekola, F. A., Job, O., Alabi, A. G., Baral, A., & Samal, R. (2014). Optimization study of a Nigerian dolomite ore dissolution by hydrochloric acid. *Journal of Chemical Technology and Metallurgy*, *49*(3), 280-287.

Gupta, J., & Agarwal, M. (2016, April). Preparation and characterizaton of CaO nanoparticle for biodiesel production. In *AIP conference proceedings* (Vol. 1724, No. 1, p. 020066). AIP Publishing LLC.

Habte, L., Shiferaw, N., Mulatu, D., Thenepalli, T., Chilakala, R., & Ahn, J. W. (2019). Synthesis of nano-calcium oxide from waste eggshell by sol-gel method. *Sustainability*, *11*(11), 3196.

Fahad, M., Iqbal, Y., & Ubic, R. (2011). Characteristics of dolomite from swabi, khyberpakhtunkhwa for its use as a raw material in fertilizer production. In *JPMS Conference Issue Materials*.

Joseph, I. A., Ajala Elijah O., Ahmed E. A., Ajala M. A. (2022a). Optimization and Kinetics Studies of the Dissolution of Dolomite in Sulphuric Acid (H_2SO_4) Via Box Behnken *Experimental Design. Southern Journal of Sciences*. 30(34), 69-81.

Joseph, I. A., Ajala E. O., Ahmed E. A., Ajala M. A. (2022b). Application of Box-Behnken Design in the Leaching Kinetics of Dolomite in Hydrochloric Acid (HCl). 52nd Nigerian Society of Chemical Engineering Conference and AGM.

Khine, E. E., Koncz-Horvath, D., Kristaly, F., Ferenczi, T., Karacs, G., Baumli, P., & Kaptay, G. (2022). Synthesis and characterization of calcium oxide nanoparticles for CO2 capture. *Journal of Nanoparticle Research*, *24*(7), 139.

Liu, Z. (2016). National carbon emissions from the industry process: Production of glass, soda ash, ammonia, calcium carbide and alumina. Applied Energy, 166, 239-244.

Mirghiasi, Z., Bakhtiari, F., Darezereshki, E., & Esmaeilzadeh, E. (2014). Preparation and characterization of CaO nanoparticles from Ca (OH) 2 by direct thermal decomposition method. *Journal of Industrial and Engineering Chemistry*, *20*(1), 113-117.

Mohadi, R., Anggraini, K., Riyanti, F., & Lesbani, A. (2016). Preparation calcium oxide from chicken eggshells. *Sriwijaya Journal of Environment*, 1(2), 32-35.

Nasr, N., Velayutham, P., Elbeshbishy, E., Nakhla, G., El Naggar, M. H., Khafipour, E. & Hafez, H. (2015). Effect of headspace carbon dioxide sequestration on microbial biohydrogen communities. *International Journal of Hydrogen Energy*, *40*(32), 9966-9976.

Park, W., Hyun, S. H., Oh, S. E., Logan, B. E., & Kim, I. S. (2005). Removal of headspace CO2 increases biological hydrogen production. *Environmental science & technology*, *39*(12), 4416-4420.

Sun, H., Wu, C., Shen, B., Zhang, X., Zhang, Y., & Huang, J. (2018). Progress in the development and application of CaO-based adsorbents for CO2 capture: A review. *Materials Today Sustainability*, *1*, 1-27.

Szalai, A. J., Manivannan, N., & Kaptay, G. (2019). Super-paramagnetic magnetite nanoparticles obtained by different synthesis and separation methods stabilized by biocompatible coatings. *Colloids and Surfaces A: Physicochemical and Engineering Aspects*, *568*, 113-122.

Tian, H., Lu, C., Ciasis, P., Michalak, A. M., Canadell, J. G., Saikawa, E., & Wofsy, S. C. (2016). The terrestrial biosphere as a net source ogf greenhouse gases to the atmosphere. *Nature,* 531(7593), 225-228.

Vasiliadou, I. A., Melero, J. A., Molina, R., Puyol, D., & Martinez, F. (2020). Optimization of H_2 production through minimization of CO_2 emissions by mixed cultures of purple phototrophic bacteria in aqueous samples. Water, 12(7), 2015.

PAPER 162 – EFFECT OF RESAMPLED DIGITAL ELEVATION MODEL (DEM) ON FLOW AND SEDIMENT LOADING PREDICTION UPSTREAM OF OYUN RIVER CATCHMENT IN KWARA STATE

M. A. Wopa[1], A. G. Adeogun[2*], A. Sanni[1], H. Soliu[2]

[1]Deparment of Civil Engineering, Kwara State Polytechnic, Kwara State, Ilorin, Nigeria.
[2]Department of Civil Engineering, Kwara State University, Malete, Ilorin, Nigeria.
Corresponding Author's Email: adeniyi.adeogun@kwasu.edu.ng

ABSTRACT
This study investigates the effect of resampled Digital Elevation Model (DEM) on the prediction of flow and sediment loading upstream of Oyun River catchment in Kwara State. To delineate the watershed, a DEM of 90-meter resolution was sourced from the space Shuttle Radar Topography Mission (SRTM), and the ASTER global DEM data sources. The 90-meter resolution was resampled to four different resolutions which are 75-meter, 60-meter, 45-meter, and 30-meter resolutions. The watershed and streamline were delineated, and the hydrologic simulation was performed using Soil and Water Assessment Tool (SWAT). The results show an insignificant effect on flows for all the resampled DEMs as against the results obtained with the prediction of sediment concentration. The 90-meter resolution DEM has the lowest predicted value of sediment concentration 228,899.70mg/l while the 30-meter resampled DEM has the highest predicted value of 521,246.94 mg/l. Similarly, the sediment yield (SYLD t/ha) for 90-meter resolution DEM has the least value of about 528.90 t/ha while the 30-meter resampled DEM has the highest value of 2145.57 t/ha. Results obtained in this study can be a decision support tool for researchers when selecting an appropriate DEM resolution to simulate sediment loading in the watershed.

KEYWORDS: Resampled DEM; Sediment Concentration; Sediment Yield; SWAT; Model; Flow.

1. INTRODUCTION

Accurate estimation of water yield and water balance in a river catchment is essential for sustainable management of water resources at the watershed level. To achieve this, hydrological modelling is necessary, and the application of Geographical Information Systems (GIS) combined with Digital Elevation Model (DEM) has significantly improved this process. The integration of GIS with DEM has enhanced hydrological modelling in various areas, including data management, parameter extraction and interpolation, visualization, and interface development.

Digital Elevation Models (DEMs) are essential tools for studying land surface processes and modelling the flow of water and sediment in river catchments (Viglione et al., 2013). DEMs provide a digital representation of the elevation of the land surface, typically at a spatial resolution ranging from several meters to several kilometers (Tarboton et al., 2015). DEMs can be used for a wide range of applications, including terrain analysis, land use planning, environmental monitoring, and hydrological modelling (Su et al., 2017). The development of DEMs has revolutionized hydrological modelling by providing a detailed and accurate description of the topography of river catchments (Wu et al., 2013). The resolution of a Digital Elevation Model (DEM) can have a significant effect on flow and sediment loading predictions upstream of a river catchment. When a DEM is resampled to a lower resolution, it loses some of the fine-scale details that may have been present in the original data. This loss of detail can result in a coarser representation of the terrain, which can affect the accuracy of the flow and sediment predictions. Resampling a DEM can also introduce errors in the calculation of slope and drainage area, which are important parameters in predicting flow and sediment loading.

Based on the foregoing, it is common to resample DEMs to a coarser resolution to reduce computational requirements (Choi et al., 2015). Resampling involves averaging or aggregating elevation values over larger grid cells, which can result in a loss of fine-scale terrain details (Tarboton et al., 2015). However, high-resolution DEMs can also pose computational challenges due to their large file size and processing requirements.. Therefore, it is essential to carefully consider the effects of DEM resolution on the accuracy of predictions and to use appropriate methods to account for errors introduced by resampling.

2. THEORETICAL ANALYSIS

The simulation of hydrologic cycle by SWAT is based on the water balance Equation 1

$$SW_t = SW_o + \sum_{i=1}^{t}(R_{day} - Q_{surf} - E_a - W_{seep} - Q_{gw})_i \quad 1$$

where SW_t is the final soil water content (mm water), SW_o is the initial soil water content in day i (mm water), t is the time (days), R_{day} is the amount of precipitation in day i (mm water), Q_{surf} is the amount of surface runoff in day i (mm water), Ea is the amount of evapotranspiration in day i (mm water), $W_{seep}$is the amount of percolation and bypass
flow exiting the soil profile bottom on day i (mm water), and Q_{gw} is the amount of return flow in day i (mmwater).

The estimation of erosion/soil loss and sediment yield for each Hydrologic Response Unit (HRU) is carried out using the Universal Soil Loss Equation and Modified Universal Soil Loss Equation (MUSLE) (Williams, 1975) respectively. The current version of SWAT model uses simplified stream power Equation 3.8 derived by Bagnold (1977) to route sediment in the channel.

$$S_{ed} = 1.292EI_{USLE}K_{USLE}C_{USLE}P_{USLE}LS_{USLE}CFRG \quad 2$$

Where S_{ed} is the sediment yield on a given day (metric tons), EI_{USLE} is the rainfall erosion index (0.017 m-metric ton cm/(m^2hr)), other factors are as defined in Equation 3.7. The value of EI_{USLE} for a given rainstorm is the product of total storm energy (E_{storm}) times the maximum 30 minutes intensity (I30)

3. MATERIALS AND METHODS

3.1 Description of the study area

The study area is the Oyun River Basin, which has a terrain elevation of 259 meters above sea level and can be found between latitudes 9^0 $5^0$1 and 8^0 24^1North and Longitudes 4^0 38^1 and 4^0 03^1East. The river Oyun, which starts near Ila Oragun at an elevation of 465.003m above the sea level, flows for about 80 kilometres to the northeast and converges with River Asa in Ilorin, Kwara State. The watershed area of Oyun River in Kwara State is located southeast of Ilorin and is known for its open and undulating terrain, rocky outcrops, and varying slopes. The area is mostly used for farming with only a small section of forest reserve.

River Oyun is a major water source for Offa town and its neighbouring areas, and it also supplies raw water for the University of Ilorin water supply scheme. Figure 1 shows a map of the Oyun River basin, which includes a network of rivers and catchment areas, with the catchment area of interest being enclosed within the thick black boundary line.

Figure 1: Location map of the study area.

3.2. Modelling Tool and GIS interface

The modelling tool selected for this study is the Soil and Water Assessment Tool (SWAT). SWAT was developed by the United States Department of Agriculture (USDA) to predict the impact of land management practices on water, sediment, and agricultural chemical yields in large un-gauged basins (Arnold, et al.,1995). The creation of the sub catchment and other geo-processing of the spatial data were carried out using Map window GIS. Map window-GIS was developed by Leon (2011) and is a compact tool for the delineation of watershed from Digital Elevation Model. It is a window based, open-source GIS client which can be used to visualize, manage, edit, analyse data, and compose printable maps. It includes powerful analytical functions through integration with GEOS and GDAL (Geospatial Data Abstraction Library).

3.3. Digital Elevation Model (DEM)

Digital elevation model (Figure 2) used in this study is of resolution 90m and was obtained from online database developed by CGIAR (2012). The DEM provides the basis for watershed delineation into sub-basins. Also, topographic parameters such as terrain slope, channel slope and reach length are derived from the DEM. A resolution of 90m x90m was resampled into other resolutions (75m x 75m,60m x 60m, 45m x 45m, 30m x 30m) using the GIS component of the model.

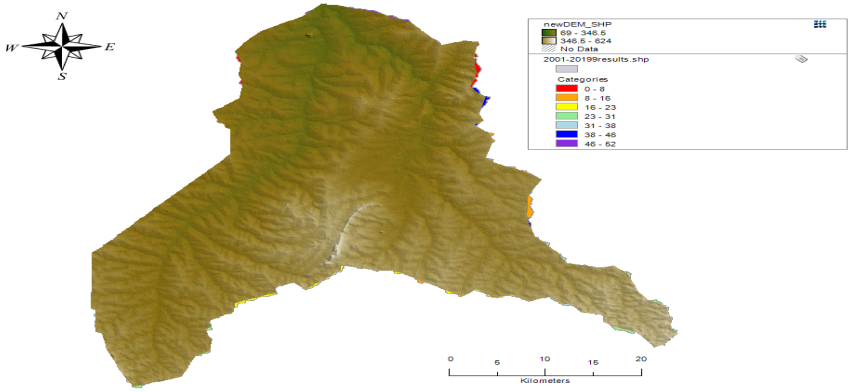

Figure 2: DEM map of the study area

3.4. Land Use and Soil data

The Land use map that is needed to run SWAT was extracted from the Global Land Cover Characterization (GLCC) database, and it is also used to estimate vegetation and other parameters representing the watershed area. The GLCC database was developed by United State Geological Survey and has a spatial resolution of 1Km and 24 classes of land use representation (GLCC, 2012). The digital soil data for the study was extracted from harmonized digital soil map of the world (Harmonized World Soil Database (HWSD)) produced by Food and Agriculture Organization of the United Nations, Rome (Nachtergaele et al., 2009).

3.5. Weather Data

Meteorological data necessary to run the SWAT model was obtained from Nigeria Meteorological Agency (NIMET) station based in Ilorin, Kwara State. The data collected includes daily precipitation, maximum and minimum temperature, solar radiation, relative humidity, and wind speed, in order to perform the hydrological analysis. The collected weather variables for driving the hydrological balance within the watershed were for a period of Nineteen (19) years i.e. (January 1, 2001, to December 31, 2019).

3.6. Watershed delineation into sub-basins and Hydrologic Response Units (HRUs)

The delineation of the watershed was achieved using reprojected DEM of the study area. In the Automatic Watershed Delineation (AWD) of the GIS interface, network delineation by threshold method was adopted. For uniformity, a threshold value of 20km^2 was adopted for all the resampled DEM resolutions. A total of 55 sub-basins were created in the watershed and was subdivided into 61 hydrologic response unit (HRUs). The HRU is the smallest spatial unit needed for running the hydrological model. Figure 3 shows the delineated subbasins in the study area.

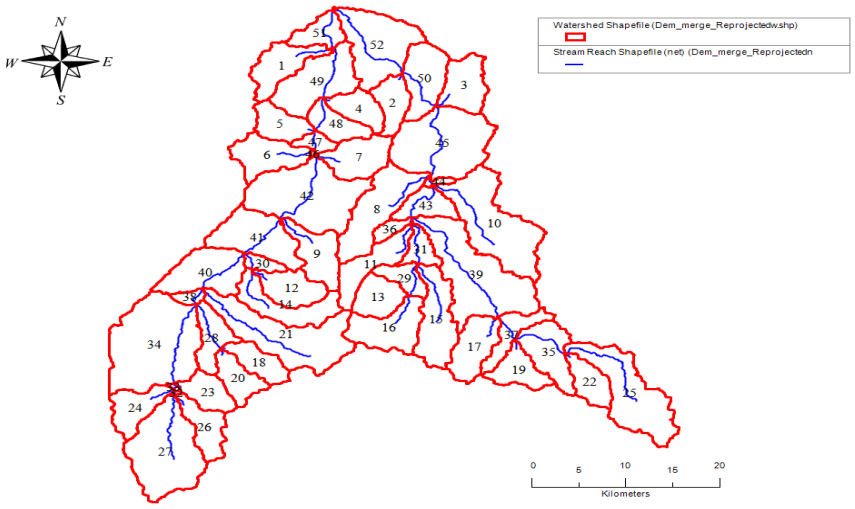

Figure 3: Watershed Delineation and Hydrological Response Unit (HRU)

3.7. Swat setup and run

SWAT was executed using the Soil Conservation Service (SCS) Runoff Curve Number method for estimating surface runoff from precipitation. The SCS curve number method is a rainfall-runoff model that was designed for computing excess rainfall (direct runoff). This method assumes an initial abstraction before ponding that is related to curve number. The daily weather (precipitation, wind, solar radiation, relative humidity and daily minimum and maximum temperature) data were prepared in the appropriate file format (as Microsoft excel file) required by the model and imported into the model. The resampled DEMs of the study area were used in turn for the prediction of flow and the sediment loadings. The simulation period is from 01 January 2001 to Dec 31, 2019. All necessary files needed to run SWAT were written, and the appropriate selection of weather sources done before running the model.

4. RESULTS AND DISCUSSION

4.1 Prediction of stream flow

The lowest predicted value of 2229.91m^3/s was observed at a lower resolution of 90m by 90m used for the hydrological modelling of the study area. However, this value increased to a maximum value of 2345.14m^3/s when the DEM was resampled to a resolution of 75m. It was also noticed that the value of stream flow predicted was a bit stable with values hovering between 2333.02m^3/s to 2344.19m^3/s. At a finer resolution of 45m and 30m respectively. It can also be inferred from the result that decreasing the resolution of the DEM above 60m does not have substantial effect on the predicted values of stream flow of the river. This result compared well with the findings of Ghaffari (2011) and Mou, et.al. (2015) with the conclusion that DEM resolutions impacted the predicted values of runoff, sediment yield and stream flow. These findings highlight the significance of considering the impact of flow on hydrological processes and the importance of optimizing DEMs resolution for accurate flow measurement and prediction. The results could have important implications for a range of applications, including water resource management, flood forecasting, and erosion control.

4.2 Prediction of sediment concentration and sediment yield

The study showed that the value of predicted sediment concertation increased as the DEM resolution becomes finer from 90m x90m towards 30m x 30m. DEM of 30m resolution has the highest predicted value of 521,246.94 mg/l while the least predicted value of 228,899.70mg/l was observed with a 90m DEM resolution. The result indicated that resolution of the DEM can significantly influence sediment concentration prediction. It was further discovered that the predicted sediment concentration is inversely proportional to the resolution of the DEM as shown in Figure 7. While the prediction of sediment yield in the study area showed a linear relationship between the DEM resolution and the predicted sediment yield and a similar pattern as it was obtained for stream flow. The result showed that as the predicted values of sediment yield and concentration increases as the resampled DEM decreases and tends to be stabilised at a higher resolution (45m, 30m). The sediment yield (SYLD t/ha) for 90m resolution DEM has the least value of about 528.90 t/ha while the 30m resampled DEM has the highest value of 2145.57 t/ha. This finding is significant because it suggests that the accuracy of sediment yield estimates can be influenced by the resolution of the DEM used. Details information about the predicted values

of sediment yield and concentration could be obtained from Table1 and graphically from Figure 4 to Figure 6. The spatial distribution of predicted sediment yield in the watershed and sediment concentration along the river reach is shown in Figure 7.

Table 1: Details information about predicted flow and sediment loading by each of resampled DEM.

S/N	DEM Resolution (m)	Flow (m^3/s)	Sediment Concentration (mg/l)	Sediment Yield (t/ha)
1	90 x 90	2229.91	228,899.70	528.90
2	75 x 75	2345.14	503,842.25	1,926.14
3	60 x 60	2338.02	486,447.25	1,965.07
4	45 x 45	2341.29	506,174.80	2,079.96
5	30 x 30	2341.19	521,246.94	2,145.57

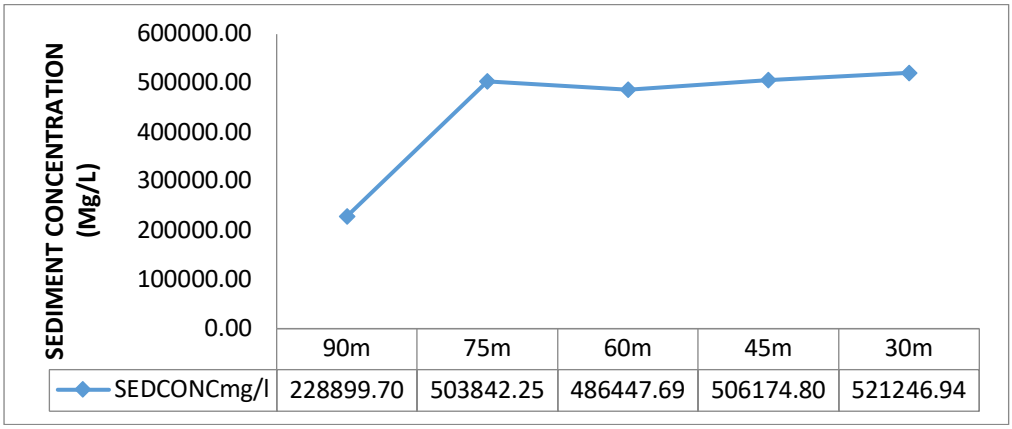

Figure 4: A plot of DEM resolution against the predicted sediment concentration

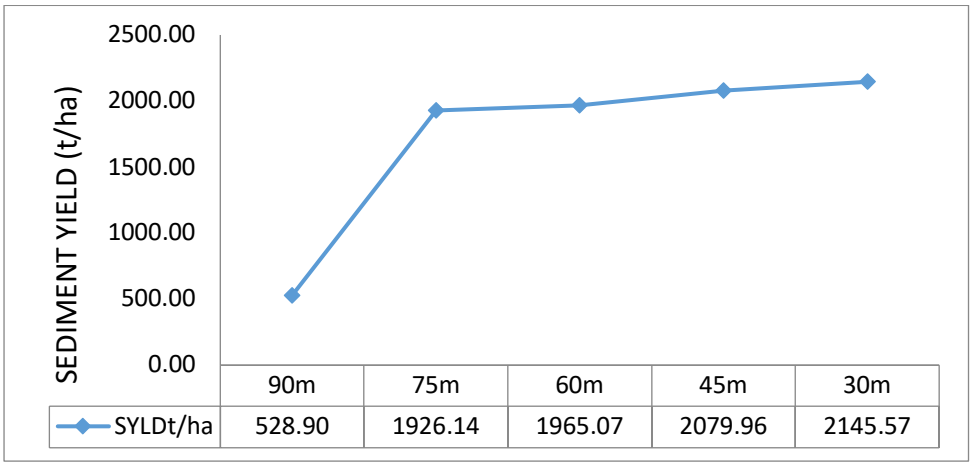

Figure 5: A plot of DEM resolution against the predicted sediment yield

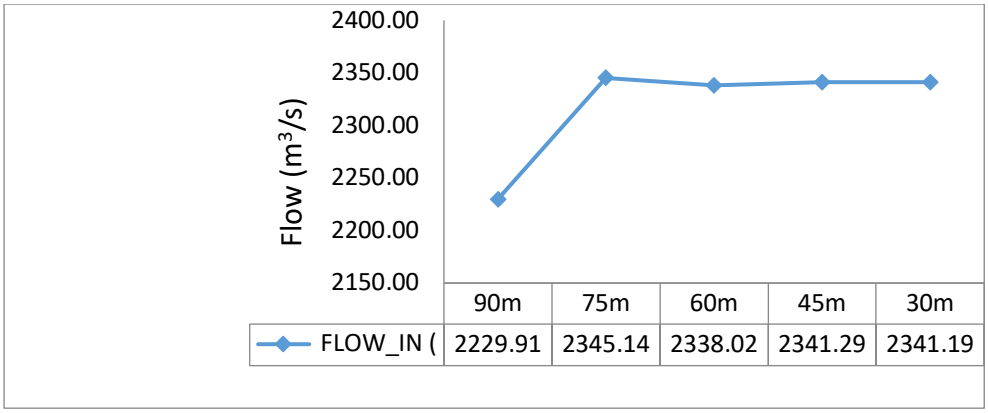

Figure 6: A plot of DEM resolution against the predicted stream flow

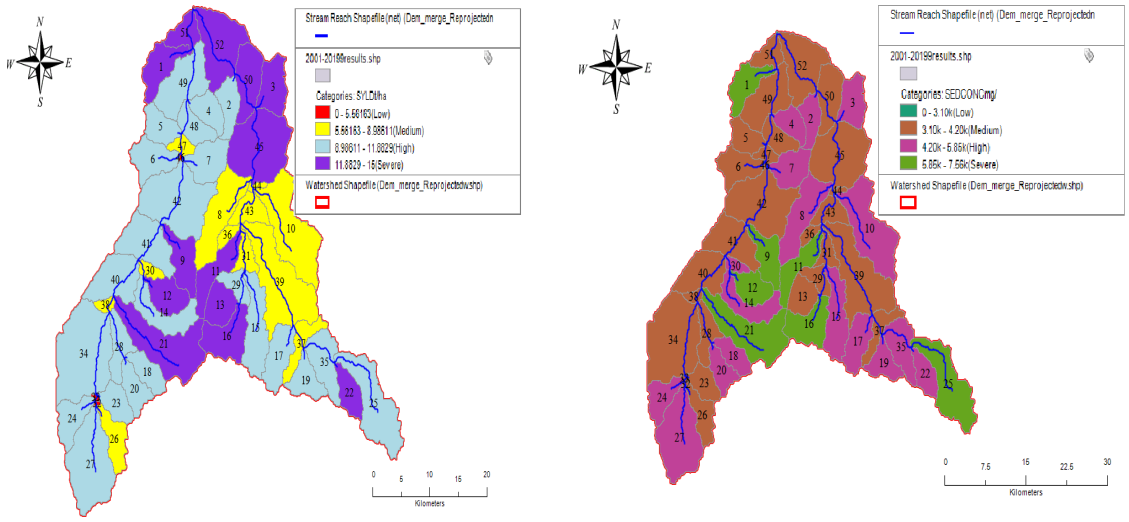

Figure 7: Spatial Variation of Sediment yield and Concentration in the Watershed

5. CONCLUSION

The study investigated the impact of Digital Elevation Models (DEMs) on the simulation of sediment loading, taking into consideration three parameters. The results revealed a similar pattern in the prediction of stream flow, sediment yield and sediment concentration and that the DEM with a resolution of 60m produced the best value when all three parameters were considered. These findings suggest that the choice of DEM resolution has a significant impact on the accuracy of sediment loading simulation. Therefore, this study could serve as a valuable decision support tool for researchers in the selection of an appropriate DEM resolution for stream flow sediment loading simulations. The importance of accounting for the effect of resampled DEMs on simulation accuracy cannot be overstated and the implications of these findings could extend to a range of applications in various fields.

REFERENCES

Arnold, J.G, Williams, J.R, Maidment, D.R (1995) Continuous-time Water and Sediment-routing Model for Large Basins. . Journal of Hydraulic Engineering, 121(2): 171-183.

Choi, H.-K., Kim, D., & Lee, S. (2015). Optimal digital elevation model (DEM) grid size for terrain analysis in a mountainous watershed. Geocarto International, 30(5), 530-545. doi: 10.1080/10106049.2014.899283

CGIAR (2022) SRTM 90m Digital Elevation Data, available at http://srtm.csi.cgiar.org/, accessed on 23rd December 2022

GLCC (2022) Global Land Cover Characterization, available at http://edc2.usgs.gov/glcc/glcc.php, Cited on 13/10/2022

Ghaffari.G (2011) The impact of DEM resolution on Runoff and Sediment Modelling Result Research Journal of Envieonmental Science 5(8), 691-702

Leon, L.F. (2011), MapWindow Interface for SWAT (MWSWAT). Available at http://www.waterbase.org/docs/MWSWAT%20Setup.pdf accessed on 24th April,2023

Mou, L. T.; Darren, L. F.; Barnali, D.; Ab Latif, I, Zulkifli, Y.; Vincent C.(2015). Impacts of DEM resolution, source, and resampling technique on SWAT-simulated streamflow, Applied Geography, Volume 63,Pg 357-368,

Su, Z., Wen, J., & Li, X. (2017). Remote sensing of hydrology: A review of achievements and challenges. Remote Sensing, 9(10), 1032. doi: 10.3390/rs9101032

Tarboton, D. G., Sadler, J. M., & Ahlfeld, D. P. (2015). Hydrologic modeling using geospatial data: A review. Vadose Zone Journal, 14(1). doi: 10.2136/vzj2014.10.0159

Viglione, A., Parajka, J., Rogger, M., Salinas, J. L., Laaha, G., Sivapalan, M., & Blöschl, G. (2013). Comparative assessment of predictions in ungauged basins – Part 1: Runoff-hydrograph studies. Hydrology and Earth System Sciences, 17(5), 2071-2087. doi: 10.5194/hess-17-2071-2013

Wu, Q., Liu, J., Liang, E., Li, X., & Zhang, X. (2013). Advances in digital elevation model research: A review. Journal of Geographical Sciences, 23(6), 1007-1020. doi: 10.1007/s11442-013-1044-4

PAPER 163 – GREY-BASED TAGUCHI ANALYSIS FOR TRIPLE OBJECTIVE OPTIMIZATION OF TIG WELDED LOW CARBON STEEL

C. S Abima* and N. Madushele

Mechanical Engineering Science, University of Johannesburg, South Africa
*Email: cynthias@uj.ac.za

ABSTRACT
The welding process remains one of the most value-adding techniques in the industry, especially for fabrication and repair purposes. Present scenario report that increasing hardness reduces ductility and percentage elongation properties which are equally essential for structural integrity. Against this backdrop, this study adopts the grey base-Taguchi method to investigate the process parameters combination that results in an optimum balance of tensile strength, hardness, and elongation at break point for the Tungsten Inert Gas welding of low-carbon steel joints. L9 Taguchi matrix is adopted towards maximizing the triple functions. A single grade for the responses was established, followed by ANOVA and signal-to-noise ratio analysis. A confirmatory test followed by a repeat showed a 0.257 improvement in the grey relational grade which validates the effectiveness of the method in achieving the triple-objective functions. The study benefits the scientific and industrial bodies by providing the process window for maximizing the tensile strength and hardness properties of welded joints in a way that the increased hardness properties do not compromise the elongation at break hence making the joint susceptible to brittle failure.

KEYWORDS: Grey-based Taguchi, Triple objective optimization, Tensile strength, Hardness and Percentage elongation

1. INTRODUCTION

Welding is an efficient metal joining process widely used in various sectors, such as automobiles, aircraft, buildings, marine etc. (Vidyarthy & Sivateja, 2020). It is one of the most value-adding processes in the manufacturing industry, especially for repair and fabrication purposes. The integrity of the welded assembly or repaired components depends on the resultant mechanical properties of the joints (C. Abima et al., 2021). These mechanical properties are influenced by numerous factors, including welding technique, heat input, temperature gradient, microstructural presentation and weld defects (C. S. Abima et al., 2021; Nguyen & Kim, 2020; Pan et al., 2022). Of the numerous welding techniques, tungsten inert gas (TIG) is widely used due to its ability to weld a wide range of materials, high efficiency, high-quality joints, high deposition rate, easy operating principle, and lower cost. The tensile and hardness properties of TIG welded joints have been investigated by several studies in a bit to determine the influence of process parameters on the resultant joint quality. For instance, (İrsel, 2022) has reported increased yield strength and tensile strength for low carbon steel (S235JR) welded by TIG welding with ER30L filler wire. The authors attributed these strength improvements to an increase in hardness properties as a result of delta-ferrite phase formation. Another author reported that the tensile strength and elongation decrease as preheat temperature increases but increase as the welding current increases (Kumar & Singh, 2019). Still, in the pursuit for better mechanical properties, several researchers have adopted various optimization methods such as Taguchi, response surface methodology, etc. (Ghuge et al., 2022). For example (Shanmugasundar et al., 2019) optimized the TIG welding process by considering the gas flow rate, current and nozzle distance for optimal tensile strength. Their result shows that the welding current mainly influences the ultimate tensile. Taguchi optimization analysis of TIG welded joints reported by (Ghumman et al., 2022) shows that the hardness values and tensile strength were mostly influenced by increased arc current as gas flow rate. The study of (Joseph et al., 2017) also showed that the tensile strength of the welds were most influenced by the welding voltage and current. Lower level settings of these parameters matrix by Genetic algorithm and response surface methodology favourd the tensile strength.

Because the structural integrity of weldment is judged by combined mechanical properties rather than single responses, it became imperative to adopt a system capable of optimizing multiple objective properties. To achieve this, the grey-based Taguchi method was introduced. This method overcomes the limitation of a single function or response per an analysis of the conventional Taguchi method (Wakchaure et al., 2018). For example, the grey-based approach was adopted by (Mohanty et al., 2021) to optimize the tensile and hardness properties

of 0.002% C steel welded via the TIG welding process on a higher the better criteria. The tensile strength and hardness value increase with increased current, voltage and speed. Another study reports the parameter optimization of pulsed TIG welded Monel 400 AISI and AISI 304 steel dissimilar joints to maximize the tensile strength and percentage elongation and minimize the heat-affected zone (Avinash et al., 2019). The authors reported that the pulse frequency most influenced the grey relational grade (GRG) and that a confirmatory test showed an increase in the percentage elongation, tensile strength and a reduced heat-affected zone of the weldment. (Vinoth et al., 2021) reported that lower current welding speed with intermediate gas flow rate gave the optimal result for grey relational grade analysis of TIG welded 316 for improved corrosion, impact and tensile strength.

Although a variety of TIG welding process parameters have been investigated to optimize dual objectives such as tensile strength and elongation or tensile strength and hardness, reports show that the hardness of steel increases with increasing tensile strength (Angst et al., 2001) (Zhang et al., 2011). However, increasing hardness reduces percentage elongation and thus leads to brittle failure, which is detrimental to structural members. For structural applications, these three qualities are required at their optimum (Zhang et al., 2011) without an appreciable trade-off. Following this, the Grey-based Taguchi optimization is adopted in this study to optimize the triple functions for the structural integrity of AISI 1008 TIG welded joints.

2. MATERIALS AND EXPERIMENTAL PROCEDURE

2.1 Materials and equipment

The welding procedure was carried out with 100 x 100 x 6 mm AISI 1008 plates welded by the conventional TIG welding machine and a 2.4 mm diameter ER70S/6 filler electrode in a butt joint configuration. The elemental weighted composition of AISI 1008 and the filler electrode are presented in Table 1.

Table 9 Chemical composition of AISI 1008ER70S/6 filler metal

Element symbol	C	S	P	Mn	Si	Cr	Mo	Ni	Al	Fe	V	Cu
AISI 1008	0.072	0.009	0.001	0.32	0.07	0.042	0.005	0.006	0.042	Bal	-	-
ER70S/6	0.06	0.035	-	1.4	0.8	0.15	0.15	0.15	-	-	0.03	0.5

2.2 Welding parameters, responses and design matrix

Three factors in three levels were selected for the experimental design matrix to optimize the triple functions. A thorough literature survey aided the choice process parameters adopted in this study. Welding voltage (levels- 10, 15, 20), current (levels- 140, 160, 180), and gas flow rate (levels- 15, 17, 19) were the selected process parameter and their respective levels. On the other hand, the desired output responses are the tensile strength, percentage elongation and hardness. The design matrix was achieved by adopting the Taguchi statistical method. In contrast to the traditional trial-and-error approach, the Taguchi method enables limited experimental runs to provide ideal and optimal results. Table 2 shows the L9 orthogonal matrix of the welding process parameters.

Table 10 Matrix design for Experimental run

Sample Run	Input process parameters		
	Voltage (V)	Current (A)	Gas flow rate L/mm
T-L1	10	140	15
T-L2	10	160	17
T-L3	10	180	19
T-L4	15	140	17
T-L5	15	160	19
T-L6	15	180	15
T-L7	20	140	19
T-L8	20	160	15
T-L9	20	180	17

2.3 Welding and mechanical test procedures

The rust layer due to oxidation was removed by surface grinding and cleaned by acetone a few minutes before the welding operation. Shielding of the weld pool was achieved by crystal argon gas. Following the completion of the welding, test pieces for tensile and hardness analysis are cut off. Three replicate specimens were machined for each parameter in accordance with ASTM standards E8/E8M and tested using an axail testing machine. The weld hardness properties were tested using the digital Indentec Vickers microhardness test machine according to ASTM E384 standard, at a dwell time of 15 seconds, and a 300N impression force by a diamond indenter travelling a distance of 0.2mm for each indent across the sample length.

2.4 Analytical methods

The TIG welding process parameters were multi-objectively optimized for maximum tensile strength, percentage elongation, and hardness value using the grey-based Taguchi technique. When evaluating the strength of the links between sequences, grey relational analysis is helpful. It combines many output responses into a single output response by assigning Grey Relational Grade (GRG) values to discrete output responses. The signal-to-noise ratio (S/N) and the ANOVA analysis were computed using the Minitab 17 application.

3. RESULTS AND DISCUSSION

3.1 Physical observation of welds

All welds have good front and rear bead appearance, as shown in Figure 1. There were no physical flaws like pores, splatter, or fractures. The backside of every weld bead had likewise fused completely.

3.2 Tensile and Hardness Results

The ultimate tensile strength (UTS) and percentage elongation (% Ɛ) of the welded specimen under loading conditions have been determined using axial tensile testing. These properties are crucial as they determine the strength and the stress-strain relationship of components and structures. All tested specimens failed at the base material region, indicating strong joint connections. Only the hardness values (HV) for the heat-affected zone is taken into account in this study. The result (Table 3) presents an average of the three replicate tested samples.

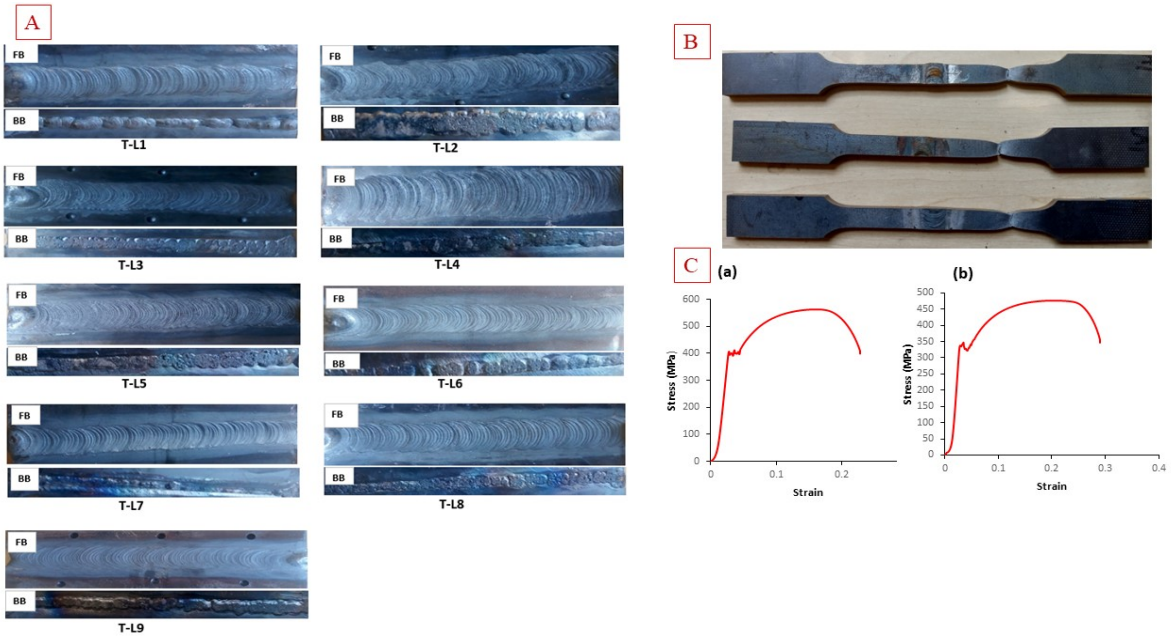

Figure 11 (A) welded specimens (B) fractured specimens (C) representative stress-strain

Table 11 Results from the experiment

Input Parameters						Experimental outcomes		
Sample runs	Voltage (V)	Current (A)	Gas flow rate (L/min)	Welding speed	Heat input	UTS (MPa)	% Ɛ	HV

T-L1	10	140	15	36.93	1592.2	389.0	23.6	159.7
T-L2	10	160	17	36.93	1819.7	338.3	28.3	126.9
T-L3	10	180	19	38.72	1952.5	399.0	24.1	150.8
T-L4	15	140	17	35.30	2498.6	386.0	21.5	133.7
T-L5	15	160	19	33.33	3024.3	389.5	25.5	134.7
T-L6	15	180	15	30.00	3780	476.6	24.1	154.8
T-L7	20	140	19	34.28	3430.6	306.2	23.4	153.2
T-L8	20	160	15	35.30	3807.4	394.7	25.1	152.8
T-L9	20	180	17	40.00	3780	335.5	25.2	131.6

3.3 Grey relational analysis

The ideal process parameter combination that maximizes the intended responses based on larger-is-better criteria is found using the grey-based Taguchi approach. Equation 1 is used to first normalize the experimental data before Equation 2 computes the data set's deviation sequence. Finally, Equations 3 and 4 are used to derive the grey relational coefficient and the grey relational grades (GRG). The data for the grey-relational analysis are shown in Table 4.

$$x_i^*(k) = \frac{x_i(k) - \text{Min}\, x_i(k)}{\text{Max}\, x_i(k) - \text{Min}\, x_i(k)} \qquad \text{Data normalization (the larger-the-better)} \qquad (1)$$

where = $x_i^*(k)$ is the normalized value, $x_i(k)$is the target value, $\text{Min}\, x_i(k)$ is the lowest value of $x_i(k)$, and $\text{Max}\, x_i(k)$ is the highest value of $x_i(k)$

i = 1, 2, 3…,m. and k =1, 2, 3…,n. m and n are the number of experimental data and the number of responses, respectively.

$$\xi_i(k) = \frac{\Delta_{Min} + \xi\Delta_{Max}}{\Delta_{oi} + \xi\Delta_{Max}} \qquad \text{Grey relational coefficient} \qquad (2)$$

where $\xi_i(k)$ = grey coefficient, Δ_{oi} = deviation sequence, $\Delta_{Min}\ and\ \Delta_{Max}$ = minimum and maximum values of Δ_{oi} for all the sequences, and ξ = the identification coefficient. The identification coefficient of 0.5 is utilized to produce equal weightage for both quality response factors.

$$\Delta_{oi} = \|x_o(k) - x_i(k)\| \qquad \text{Deviation sequence} \qquad (3)$$

$$y_i = \frac{1}{n}\sum_{k-1}^{n} \xi_i(k) \qquad \text{Grey relational grade} \qquad (4)$$

where y_i is the GRG for the ith experimental run, and n is the number of characteristic response

Table 12 Grey relational analysis

Runs	Sequence deviation			Grey relational coefficient			GRG	Ranking
	UTS	% Ɛ	HV	UTS	% Ɛ	HV		
T-L1	0.514	0.691	0.000	0.493	0.420	1.000	0.638	2
T-L2	0.812	0.000	1.000	0.381	1.000	0.333	0.572	4
T-L3	0.455	0.618	0.271	0.523	0.447	0.648	0.540	5
T-L4	0.532	1.000	0.793	0.485	0.333	0.387	0.402	9
T-L5	0.511	0.412	0.762	0.494	0.548	0.396	0.480	7
T-L6	0.000	0.618	0.149	1.000	0.447	0.770	**0.739**	**1**
T-L7	1.000	0.721	0.198	0.333	0.410	0.716	0.486	6
T-L8	0.481	0.471	0.210	0.510	0.515	0.704	0.576	3
T-L9	0.829	0.456	0.857	0.376	0.523	0.369	0.423	8

Minitab 17 software has been used to calculate the main effect plots for the signal-to-noise ratio (S/N) and the mean effect plot for means. The response table for means corresponding to the values of the GRGs (Table 5) shows that the optimum parameter set is Voltage 1 - Current 3 – Gas flow rate 1, i.e. voltage = 10 V, current = 180 A, gas flow rate = 15L/min. The ranking shows that the gas flow rate had the most influence on the GRG, followed by the welding voltage.

Table 13 Response table for means

Level	Voltage (V)	Current (A)	Gas flow rate L/min
1	**0.5833**	0.5087	**0.6510**
2	0.5403	0.5427	0.4657
3	0.4950	**0.5673**	0.5020
Delta (Max-Min)	0.0883	0.0587	0.1853
Rank	2	3	1

The overall grade for grey relations = 0.5396

Figure 2 shows that a change in any of the process parameters affects the output response. The GRG decreases with increasing voltage and increases with increasing current. On the other hand, the GRG first decreased and then increased slightly with an increased gas flow rate. Changes in the gas flow made a significant change in the GRG.

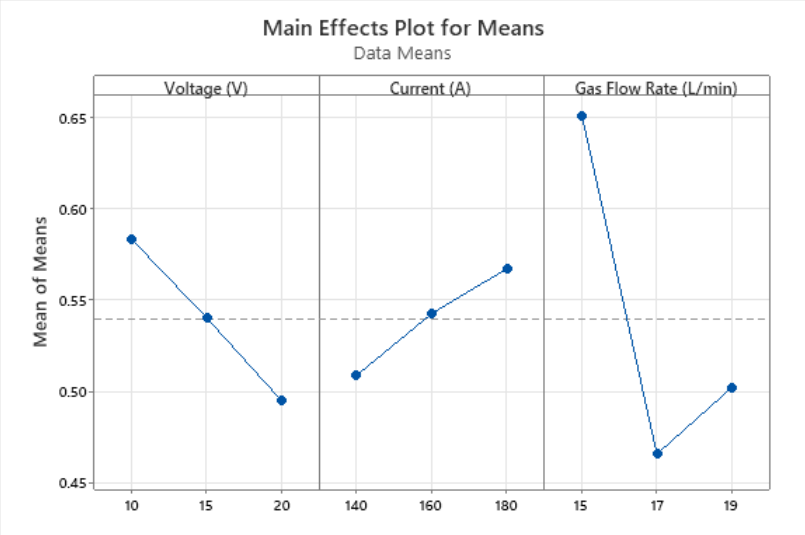

Figure 12 The main effects plot for means

3.5 Analysis of Variance

Analysis of variance (ANOVA) demonstrates the relative percentage contribution and level of significance of each parameter's influence at a 95% confidence level. Table 6 shows that the flow rate had the most influence on the GRG, with a 36.69% contribution, followed by the welding voltage with 12.89%.

Table 14 ANOVA for the transformed response

Source	DF	Seq SS	Contribution	Adj SS	Adj MS	F-Value	P-Value
Regression	3	0.050168	55.27%	0.050168	0.016723	2.06	0.224
Voltage	1	0.011704	12.89%	0.011704	0.011704	1.44	0.284
Current	1	0.005163	5.69%	0.005163	0.005163	0.64	0.461
Gas Flow Rate	1	0.033301	36.69%	0.033301	0.033301	4.10	0.099

Error	5	0.040604	44.73%	0.040604	0.008121
Total	8	0.090772	100.00%		

3.6 Confirmatory experiment

With the values of the optimum set of process parameters (Voltage 1 - Currentn 3– Gas flow rate 1, i.e. voltage = 10 V, current= 180 A, gas flow rate = 15L/min) acquired for the GRG, a confirmation experiment was carried out to validate predicted against experimental results. The obtained tensile strength, percentage elongation and hardness values for these optimum set of parameters are 486 Mpa, 25.3% and 158 HV, respectively. These values are compared with the initially obtained optimum parameters with the highest ranking for the GRG, i.e. voltage = 15 V, current= 180 A, gas flow rate = 15L/min). The GRG value obtained for the predicted optimal parameters is 1.0485, suggesting a high level of similarity. In the confirmation experiment, which incorporated the initial data and confirmation test results, a GRG value of 1.000 was achieved, indicating a perfect match. Both experiments demonstrated favourable and accurate outcomes, reinforcing the validity of the predicted optimal parameters and the success of the confirmation experiment.

$$\hat{y} = y_m + \sum_{i=1}^{n}\left(\hat{y} - y_m\right), \quad (5)$$

where y_m is the total mean GRG, $\hat{y}$ is the GRG at the optimal level of each process parameter, and n is the number of significant parameters.

The confirmation test results in Table 7 reveal a close match between the predicted and experimental GRG values. The optimal parameter settings significantly enhance the grey relational grade of the responses, particularly the tensile strength and yield strength, by a notable improvement of 0.0489. This indicates the effectiveness of the chosen parameter combination in improving the desired mechanical properties.

Table 15. Confirmation results

	Initial optimal parameters	Optimal parameters from S/N of GRG	
		Predicted	Experimental
level	Voltage 2- Current 3- Gas flow rate 1	Voltage 1- Current 3 - Gas flow rate 1	Voltage 1- Current 3- Gas flow rate 1
UTS (MPa)	476.6		396
% Ɛ HV	24.1		25.3
HV	154.8		153
GRG	0.739	0.5968	0.854

Improvement in GRG = 0.257

4. CONCLUSION

Grey-based Taguchi optimization technique for triple function optimization of process parameters in TIG welding for AISI 1008 is reported for a total of nine runs produced following the L9 orthogonal matrix. The study show that obtaining a high strength and hardness weldment that exhibit favourable percentage elongation to avoid brittle joints is possible by adopting the grey-based Taguchi method.

To attain optimal tensile strength, percentage elongation, and hardness, the recommended parameters are voltage at 10 V, current at 180 A, and gas flow rate at 15 L/mm. More so, the set of optimal parameters resulted in higher values for all the measured outcomes. According to the ANOVA analysis, the gas flow rate is the mos program influential parameter impacting the ultimate tensile strength.

This result also shows that high-level current, low voltage, and low gas flow settings gave the best tensile, hardness, and ductile behaviour suitable for industrial applications.

ACKNOWLEDGEMENT

The authors acknowledgement the University of Johannesburg for granting a research fund.

REFERENCES

Abima, C., Akinlabi, S., Madushele, N., & Akinlabi, E. (2021). Process Parameters Optimization for GMA Welding of AISI 1008 Steel Joints for Optimal Tensile Strength Revue des Composites et des Matériaux Avancés-

Journal of Composite and Advanced Materials Process Parameters Optimization for GMA Welding of AISI 1008 S. *Revue Des Composites et Des Matériaux Avancés*, *6*(December), 349–354. https://doi.org/10.18280/rcma.310606

Abima, C. S., Akinlabi, S. A., Madushele, N., Fatoba, O. S., & Akinlabi, E. T. (2021). Multi-objective optimization of process parameters in TIG-MIG welded AISI 1008 steel for improved structural integrity. *International Journal of Advanced Manufacturing Technology*, *https://doi.org/10.1007/s00170-021-08181-1*. https://doi.org/10.1007/s00170-021-08181-1

Angst, J., Sellar, R., & Merikangas, K. R. (2001). On the tensile strength and hardness relation for metals. *Journal of Materials Engineering and Performance*, *10*(6), 718–722. https://doi.org/10.1361/105994901770344601

Avinash, S., Balram, Y., Sridhar Babu, B., & Venkatramana, G. (2019). Multi-response optimization of pulse TIG welding process parameters of welds AISI 304 and Monel 400 using grey relational analysis. *Materials Today: Proceedings*, *19*, 296–301. https://doi.org/10.1016/j.matpr.2019.07.211

Ghuge, N. C., Palande, D. D., & Belkhode, P. B. (2022). Optimization of Cutting Parameters using the RSM-Desirability Approach in the MQL-Assisted Turning of AISI 4130. *Nigerian Journal of Technological Development*, *19*(4), 316–323. https://doi.org/10.4314/njtd.v19i4.4

Ghumman, K. Z., Ali, S., Din, E. U., Mubashar, A., Khan, N. B., & Ahmed, S. W. (2022). Experimental investigation of effect of welding parameters on surface roughness, micro-hardness and tensile strength of AISI 316L stainless steel welded joints using 308L filler material by TIG welding. *Journal of Materials Research and Technology*, *21*, 220–236. https://doi.org/10.1016/j.jmrt.2022.09.016

İrsel, G. (2022). Study of the microstructure and mechanical property relationships of shielded metal arc and TIG welded S235JR steel joints. *Materials Science and Engineering A*, *830*. https://doi.org/10.1016/j.msea.2021.142320

Joseph, J., Muthukumaran, S., & Joseph, J. (2017). Optimization of activated TIG welding parameters for improving weld joint strength of AISI 4135 PM steel by genetic algorithm and simulated annealing. *Int J Adv ManufTechnol*, *93*, 23–34. https://doi.org/10.1007/s00170-015-7599-8

Kumar, S., & Singh, R. (2019). Optimization of process parameters of metal inert gas welding with preheating on AISI 1018 mild steel using grey based Taguchi method. *Measurement*, *148*, 106924. https://doi.org/10.1016/j.measurement.2019.106924

Mohanty, S., Mohanta, G. K., Senapati, A. K., & Rath, K. C. (2021). Taguchi grey relational analysis for optimal process parameter of low carbon steel welded by GTAW by using ER309L filler material. *Materials Today: Proceedings*, *44*, 2556–2561. https://doi.org/10.1016/j.matpr.2020.12.631

Nguyen, N. V., & Kim, S. E. (2020). Experimental study to investigate microstructure and continuous strain rate sensitivity of structural steel weld zone using nanoindentation. *International Journal of Mechanical Sciences*, *174*. https://doi.org/10.1016/j.ijmecsci.2020.105482

Pan, M., Li, Y., Sun, S., Liao, W., Xing, Y., & Tang, W. (2022). A Study on Welding Characteristics, Mechanical Properties, and Penetration Depth of T-Joint Thin-Walled Parts for Different TIG Welding Currents: FE Simulation and Experimental Analysis. *Metals*, *12*(7). https://doi.org/10.3390/met12071157

Shanmugasundar, G., Karthikeyan, B., Santhosh Ponvell, P., & Vignesh, V. (2019). Optimization of process parameters in TIG welded joints of AISI 304L -austenitic stainless steel using taguchi's experimental design method. *Materials Today: Proceedings*, *16*, 1188–1195. https://doi.org/10.1016/j.matpr.2019.05.213

Vidyarthy, R. S., & Sivateja, P. (2020). Influence of activating flux tungsten inert gas welding on mechanical and metallurgical properties of the mild steel. *Materials Today: Proceedings*, *28*, 977–981. https://doi.org/10.1016/j.matpr.2019.12.335

Vinoth, V., Sudalaimani, R., Ajay, C. V., Kumar, C. S., & Prakash, K. S. (2021). Materials Today : Proceedings Optimization of mechanical behaviour of TIG welded 316 stainless steel using Taguchi based grey relational analysis method. *Materials Today: Proceedings*, *45*, 7986–7993. https://doi.org/10.1016/j.matpr.2020.12.1002

Wakchaure, K. N., Thakur, A. G., Gadakh, V., & Kumar, A. (2018). Multi-Objective Optimization of Friction Stir Welding of Aluminium Alloy 6082-T6 Using hybrid Taguchi-Grey Relation Analysis- ANN Method. *Materials Today: Proceedings*, *5*(2), 7150–7159. https://doi.org/10.1016/j.matpr.2017.11.380

Zhang, P., Li, S. X., & Zhang, Z. F. (2011). General relationship between strength and hardness. *Materials Science and Engineering A*, *529*(1), 62–73. https://doi.org/10.1016/j.msea.2011.08.061

PAPER 164 – ADDITIVE MANUFACTURING IN MODERN DENTISTRY: STATE OF THE ART AND FUTURE PROSPECT

C. S Abima[1*] and N. Madushele[2]

[1]Mechanical Engineering Science, University of Johannesburg, South Africa
[2]Biomedical Engineering and Healthcare Technology Research Centre (BEAHT RC) University of Johannesburg, South Africa

*Email: cynthias@uj.ac.za, oyamacythia@gmail.com

ABSTRACT
The adoption of additive manufacturing in dentistry has initiated sufficient growth in the manufacturing of dentures. Despite the potential for improving healthcare at a low cost, the integration of additive manufacturing in dentistry has been deemed to be slow. The call for research and development to improve its adoption in the delivery of dental treatment is evident in past studies. This paper reviews recent studies on additive manufacturing in dental treatment. A scientometric review is presented to identify the different research trends and the current research focus through Voswier visualization software using a bibliometric approach. The findings revealed that only developed and a few developing countries are actively involved in research publications in this field. This result is worrisome as the cases of dental disease and people needing denture replacement continue to rise across the globe. The root cause of this has also been studied and evaluated in this study. This research contributes to the existing body of knowledge by synthesizing state-of-the-art research on additive manufacturing in modern dentistry. Furthermore, the study highlights the sustainable benefits of additive manufacturing in prosthodontics.

KEYWORDS: 3D printing, additive manufacturing, CAM/CAD, modern dentistry, digital dentistry, dentures, prosthodontic

1. INTRODUCTION

Complete removable dentures have been used to reinstall patients with edentulism for a long time (Arutyunov et al., 2022; Pradhan et al., 2022). Before the introduction of advanced manufacturing processes, dentures were fabricated by conventional methods such as milling and lost-wax techniques (Anadioti et al., 2020). Technological advancement led to the introduction of digital dentistry in the 1980s (T et al., 2009). After the first attempt at fabricating dentures by developing a computer-aided-design/computer-aided manufacturing (CAD/CAM) model in 1994 (Tamburrino et al., 2022), (Goodacre et al., 2012) launched the construction of digital dentures. Since then, digital dentistry has changed the practice of dentistry in many areas. For instance, 3D printers can produce models for patients before surgery, allowing them to visualize the operation and result, enhancing patient compliance and acceptability. In addition, digital manufacturing procedures in dentistry improve patient healthcare in the early treatment phase and guarantee accurate capturing of patient diagnoses with the help of dental scanners (Hoang et al., 2016), (Güth et al., 2017). Patient data obtained by precise scanning is now further transferred to CAD/CAM programming software to plan and fabricate required dentures models and structures (Stanley et al., 2018; Tamburrino et al., 2022). Interestingly, manufactured dentures are more affordable for patients since employing CAD/CAM lowers the cost of dental restoration, eliminating the need for temporary crowns and bridges during treatment and reducing the number of doctor appointments. Therefore, the patient can replace dentures within a short time frame at a lower cost and zero risk.

The frameworks for removable dentures, and temporary and fixed bridge dentures have traditionally been fabricated using formative manufacturing approaches (such as the lost-wax technique, alginate impression and flasking methods). These conventional formative techniques are manual, laborious, material and time-consuming, involving several steps where mistakes are likely to happen. In modern/digital dentistry, subtractive and additive manufacturing processes are employed for dental fabrication. The traditional subtractive method becomes unsuitable when fabricating tin and complex shapes with undercut areas. Moreso, the efficient removal of material from a workpiece in milling operations requires heavy cutting forces. These heavy forces produce vibrations that place the workpiece under some degree of thermal and mechanical stress. This, especially with thin parts, may lead to dimensional distortion (Hagman & Svanborg, 2022).

These challenges, coupled with numerous discomfort, urgently necessitated an automatic procedure for dental manufacturing. The huge amount of waste associated with subtractive processes (Kalberer et al., 2019; Srinivasan et al., 2021) and the unaesthetic appearance (Li et al., 2020) of the manufactured product makes additive manufacturing a better choice (Awasthi et al., 2021; Rouf, Malik, et al., 2022).

Additive manufacturing is a layer-by-layer deposition of materials to create a piece (Čretnik & Fekonja, 2022; Ferchow et al., 2022; Galante et al., 2019; Rekow, 2020; Su et al., 2020). Among the numerous advantages of additive manufacturing in dental applications are the speed and accuracy offered by dental 3D printers. Multiple parts can be printed simultaneously once the digital copies are available and can fit on the bed. This means that technicians begin part production once the scan copy arrives [26], reducing delivery time for patient treatments and improving data retention (Anadioti et al., 2020). These advantages promotes additive manufacturing in dentistry ranging from prosthodontics, maxillofacial surgery, and oral implantology to orthodontics, endodontics, periodontology, biomedical and pharmaceutical markets (Al-Dulimi et al., 2021; Sheoran et al., 2020; Silva et al., 2017; Singh & Ramakrishna, 2017). Several researchers have studied various aspects of 3D printing in dentistry. For instance, (Punia et al., 2022) elaborated on various 3D printing techniques and the materials used in dental applications. (Rouf, Raina, et al., 2022) further studied the mechanical properties of 3D printed parts for dental applications. (Tian et al., 2021) also presented a classification and characteristics of additive manufacturing technologies adopted in dentistry. The authors also highlighted the factors affecting 3D printing technology. (Osman et al., 2017) also reported that digital light processing of zirconia dental implants presented desirable dimensional accuracy and excellent surface finish. The market for dental 3D printing is anticipated to grow from USD 3.2 billion in 2022 to USD 7.9 billion in 2027 at a CAGR of 20.2% (Tamimi & Hirayama, 2019). American College of Prosthodontists record reveals that about 120 million Americans are missing at least one tooth, and over 36 million are completely edentulous (Akl & Stendahl, 2022). Over 200 million Americans are anticipated to have partial dentures in the next 15 years, and 2.3 million implant-supported crowns are created each year.

Currently, North America dominates the 3D printing market, having above 35 per cent of the market share, followed by Europe (Akl & Stendahl, 2022). North America takes the lead due to the growing incidence of dental caries & gum disease, the ageing population, the high cost of oral care, the increasing demand for aesthetic dentistry, and the expanding acceptance of digital dentistry. African countries are still at the bottom of this list due to slow growth resulting from limited funding for establishing digital manufacturing stations or laboratories (Campbell et al., 2019). (Tiwari et al., 2021) reported an increased burden of dental diseases in South Africa. The authors stated that limited dental specialists and dental services are available to care for the increased dental issues in South Africa. (Dizon et al., 2018) also estimated a 22.3% increase in the adoption of additive manufacturing processes in the next few years.

It becomes crucial to evaluate the research associated with additive manufacturing in dentistry, the organizations involved, regional and international contributions to the field, and priority themes that are likely to influence the agendas for research advancements to visualize the application of additive manufacturing in dentistry. A road map of knowledge areas through the identification of research patterns is needed to future broaden the growth of additive manufacturing in dental applications. Therefore, using the VOSviewer program, the study objective is to undertake a scientometric examination of the scholarly output on the subject of 3D printing in dentistry between 2008 and 2022.

2. RESEARCH METHODOLOGY

The data used for this study was retrieved on the 7th of April 2023 from the University of Johannesburg Library Scopus database. Published articles were sourced using the following terms “dentistry, 3D printing, additive manufact*”. The Boolean operators “OR” and “AND” were used to connect the search queries. The search period ranges from 2008 to 2022, a period of 15 years. The initial search within the year range resulted in a total of 286 documents. After filtering to limit the search terms to dentistry application, document type and limited to English language, a total number of 188 documents (146 journal articles (77.7 %), 26 (13.8%) conference proceedings and 16 (8.5%) book chapters) were obtained. Their full records, including authors, article titles, affiliation countries, document sources and abstracts, were downloaded in CSV format. The VOSviewer software was used to map out the study themes and interrelationships of the various themes. Curve lines and circles

represent these interrelationships between themes. Greater relationship strength is indicated by a thicker line and verse visa. The more significant an item is the bigger its circles.

3. RESULTS AND DISCUSSION

a. Growth Trend Analysis

Table 1. shows exponential growth over the last five years from 2018 to 2022. The fast growth over this period is attributed to the increased demand for eco-friendlier and customized dental treatment. Very slow growth was observed from 2008 to 2016. Research growth on this subject peaked up in 2017 and has been on the increase yearly.

Table 1. The growth trend of publications and citations on additive manufacturing in dentistry

Year	Number of publications
2022	48
2021	32
2020	28
2019	26
2018	21
2017	12
2016	7
2015	2
2014	3
2013	3
2012	1
2011	2
2010	1
2009	1
2008	1
Total	188

b. Journal Source Analysis

Of the 188 working documents, 83 document sources published articles on additive manufacturing in dentistry. Out of these 83 document sources, only 6 met the threshold at the defect setting of a minimum of 5 documents per source and zero citations. For this reason, the minimum number of documents per source was reduced to 3. With this new setting, 14 sources met the threshold. The analysis shows that the journal of prosthetic dentistry had the highest number of publications and was closely followed by the journal of prosthodontics. The top 14 most published journal sources are presented in Table 2. A similar trend was reported by (Kamali et al., 2022).

Table 2: Top Active journals publishing on additive manufacturing in dentistry

Source	Documents	Citations
Journal of prosthetic dentistry	8	310
Journal of prosthodontics	7	144
Dental materials	6	1049
Materials today: proceedings	6	49
International journal of computerized dentistry	5	101
Rapid prototyping journal	5	29
Journal of aesthetic and restorative dentistry	4	91
Journal of the mechanical behavior of biomedical materials	4	41
Lecture notes in mechanical engineering	4	3

Processes	4	35
Archives of materials science and engineering	3	15
Clinical epidemiology and global health	3	155
Metals	3	9
Polymers	3	23

3.3 Keyword Analysis

In scientometric studies, keywords are used to identify trends in a particular field or application (Adekunle et al., 2021; D. Aghimien et al., 2022; D. O. Aghimien et al., 2020; Nyika et al., 2021). In this study, the co-occurrence of keywords on the search query and their interrelationship has been analyzed by VOSviewer software and presented in Fig. 1. Of the retrieved 1348 keywords, 78 keywords met the set threshold of a minimum of 5 occurrences per keyword. Keywords such as 3D printing, computer-aided design, additive manufacturing, prosthesis design, digital dentistry, rapid prototyping, and dental implant. The co-occurrence map of keywords identified four clusters represented by the red, green, blue and yellow colours. The red cluster reflected keywords describing the industrial research focus of additive manufacturing, including the type of materials, mechanical properties, biocompatibility and material characterization techniques. The green cluster had keywords related to design and procedures for product optimization through computer-aided design and case documentation. While the blue clustered keywords focused on the additive manufacturing procedures for digital dentistry. The yellow-clustered words described the use of additive manufacturing in orthodontics, prosthesis and rapid prototyping of dentures.

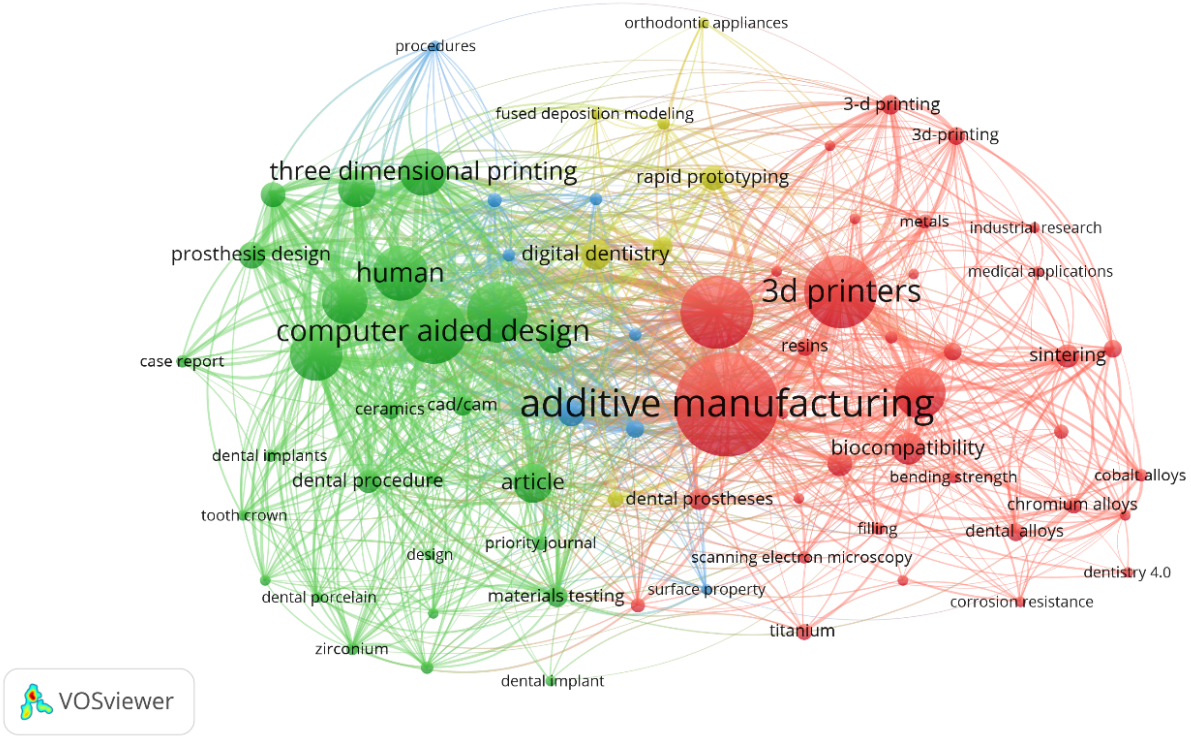

4. Figure 1. Co-occurrence of keywords on additive manufacturing in modern dentistry

3.4 Countries Analysis

For the bibliometric analysis of countries, the precondition was set at a minimum number of 5 documents per country and 2 citations. The database retrieved 55 countries actively publishing within the search query. From preconditions, 14 out of 55 countries meet the threshold. Table 3 shows that the United States of America (USA), India, Germany, Spain and Switzerland are the top publishers on additive manufacturing in dentistry, followed by Poland, Australia, China etc. Developed nations in Europe and the USA as well as fast-developing countries such as China, India, Brazil and Romania made up the list.

Table 3. Countries analysis

Country	Documents	Citations
United States	32	1489
India	23	265
Germany	11	81
Spain	10	134
Switzerland	9	133
Poland	8	67
Australia	7	55
China	7	42
United Kingdom	7	51
Romania	6	10
Slovenia	6	14
Sweden	5	105
Brazil	4	29
Slovakia	4	15

These nations now have the technical and human resources necessary to switch from traditional production methods to additive methods, in contrast to poor underdeveloped countries. (Nyika et al., 2021) reported a similar trend in a scientometric analysis on the environmental effects of additive manufacturing, where institutions of developed countries were active publishers on the subject. The bibliographic coupling of countries presented in Fig 2 reveals a strong interrelationship and collaboration between the United States, Switzerland and Spain. It also shows a robust partnership between USA and India. Strong partnerships also exist between Switzerland and Brazil. It is, therefore, safe to say that collaborative efforts contributed significantly to the advances in research studies in these countries. Sadly no African country was identified to be carrying out significant research in dentistry as it relates to additive manufacturing.

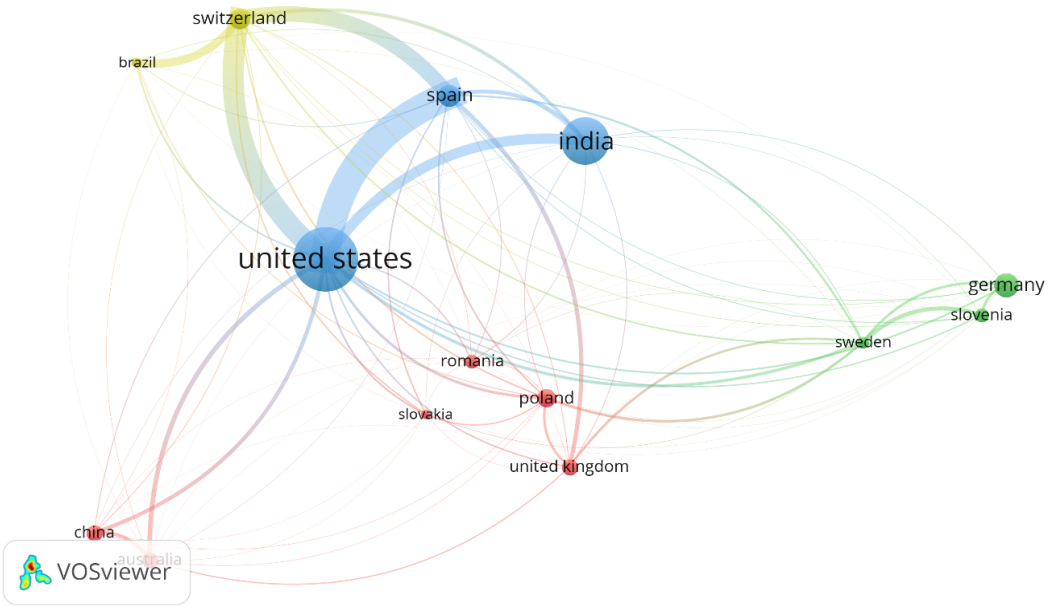

Figure 2. The bibliographic coupling of countries

4. FUTURE PROSPECT OF ADDITIVE MANUFACTURING IN MODERN DENTISTRY

Customized medication delivery systems for individuals with dental disorders may be made using 3D printing in addition to dental prosthesis and orthodontic. Additionally, 3D printing could make dental research and development more productive and efficient. In order to more accurately evaluate novel therapies and technologies, researchers may be able to employ 3D printing technology to produce more precise replicas of teeth, gums, and other oral components.

Additive manufacturing produces dental prosthesis with minimum waste since it only employs the precise quantity of material required to construct the desired piece. This decreases the amount of material waste generated throughout the production process. Another long-term advantage of AM in dentistry is the reduction in the requirement for inventory storage and transportation. Additive manufacturing can be more energy-efficient than traditional manufacturing procedures since it requires less energy to manufacture the same or better-quality dental prosthesis. Finally, dental prostheses made with additive manufacturing technology can have a longer lifespan than traditional dental prostheses, minimizing the need for frequent replacements and the environmental effect of dental waste.

5. CONCLUSION

The application of additive manufacturing in dentistry, especially in the production of dentures, helps to improve patent treatment through custom-made dentures. It is imperative to explore the extent of the adoption of additive manufacturing in denture manufacturing. The study shows that the journal of prosthetic dentistry and journal of prosthodontics had the highest publication and that USA and India are the most active publishing countries in the subject area. This bibliometric analysis has revealed a rising trend in research, publications, and citations on additive manufacturing in dentistry, with a significant upshot from 2017 upwards. However, the technological capacity and uses of 3d printers must be extended to many nations by providing the personnel and financial resources required to implement the technology. In addition, more collaboration between authors and institutions is required in the field to share ideas and advance technological knowledge in dentistry. Indeed, an automatic procedure for dental manufacturing is the way forward, especially in South Africa, where a report has it that dental issues among 6-year-old children seem to be increasing, and it's currently around 40%. Of this, almost 80% of cases are untreated, and many of these children require restorations and possibly extractions (Wyk et al., 2004). Dulimi et al. (Srinivasan et al., 2021) relate that 3D printing and rapid prototyping can greatly change people's lives if implemented on a wider scale (Al-Dulimi et al., 2021). The study indicated that intensive research is needed on additive manufacturing of dentures considering the rising pollution of patients needing tooth replacement.

ACKNOWLEDGEMENT

Authors are grateful to University of Johannesburg for funding this research

REFERENCES

Adekunle, S. A., Ejohwomu, O., & Aigbavboa, C. O. (2021). Building information modelling diffusion research in developing countries: A user meta-model approach. *Buildings*, *11*(7), 1–20. https://doi.org/10.3390/buildings11070264

Aghimien, D., Aigbavboa, C. O., Oke, A. E., Edwards, D., Thwala, W. D., & Roberts, C. J. (2022). Dynamic capabilities for digitalisation in the AECO sector – a scientometric review. *Engineering, Construction and Architectural Management*, *29*(4), 1585–1608. https://doi.org/10.1108/ECAM-12-2020-1012

Aghimien, D. O., Aigbavboa, C. O., Oke, A. E., & Thwala, W. D. (2020). Mapping out research focus for robotics and automation research in construction-related studies: A bibliometric approach. *Journal of Engineering, Design and Technology*, *18*(5), 1063–1079. https://doi.org/10.1108/JEDT-09-2019-0237

Akl, M. A., & Stendahl, C. G. (2022). Removable Partial Denture Frameworks in the Age of Digital Dentistry : A Review of the Literature. *Prosthesis*, *4*, 184–201.

Al-Dulimi, Z., Wallis, M., Tan, D. K., Maniruzzaman, M., & Nokhodchi, A. (2021). 3D printing technology as innovative solutions for biomedical applications. *Drug Discovery Today*, *26*(2), 360–383. https://doi.org/10.1016/j.drudis.2020.11.013

Anadioti, E., Musharbash, L., Blatz, M. B., Papavasiliou, G., & Kamposiora, P. (2020). 3D printed complete removable dental prostheses: a narrative review. *BMC Oral Health*, *20*(1), 1–9. https://doi.org/10.1186/s12903-020-01328-8

Arutyunov, S., Kirakosyan, L., Dubova, L., Kharakh, Y., Malginov, N., Akhmedov, G., & Tsarev, V. (2022). Microbial

Adhesion to Dental Polymers for Conventional, Computer-Aided Subtractive and Additive Manufacturing: A Comparative In Vitro Study. *Journal of Functional Biomaterials*, *13*(2), 1–12. https://doi.org/10.3390/jfb13020042

Awasthi, A., Saxena, K. K., & Dwivedi, R. K. (2021). An investigation on classification and characterization of bio materials and additive manufacturing techniques for bioimplants. *Materials Today: Proceedings*, *44*, 2061–2068. https://doi.org/10.1016/j.matpr.2020.12.176

Campbell, R. I., Beer, D. J. de, & Pei, E. (2019). Additive manufacturing in South Africa : building on the foundations. *Figshare*, 1–18.

Čretnik, A., & Fekonja, A. (2022). The Use of Selective Laser Melting in Mandibular Retrognathia Correction. *Metals*, *12*, 1–10. https://doi.org/10.3390/met12091544

Dizon, J. R. C., H, A., Jr, E., Chen, Q., & Advincula, R. C. (2018). Mechanical characterization of 3D-printed polymers. *Additive Manufacturing*, *20*, 44–67.

Ferchow, J., Bühler, M., Schlüssel, M., Zumofen, L., Klahn, C., Hofmann, U., Kirchheim, A., & Meboldt, M. (2022). Design and validation of a sheet metal clamping system for additive manufacturing and post-processing. *International Journal of Advanced Manufacturing Technology*, *119*(11–12), 7947–7967. https://doi.org/10.1007/s00170-022-08773-5

Galante, R., Figueiredo-Pina, C. G., & Serro, A. P. (2019). Additive manufacturing of ceramics for dental applications: A review. *Dental Materials*, *35*(6), 825–846. https://doi.org/10.1016/j.dental.2019.02.026

Goodacre, C. J., Garbacea, A., Naylor, W. P., Daher, T., Marchack, C. B., & Lowry, J. (2012). CAD/CAM fabricated complete dentures: concepts and clinical methods of obtaining required morphological data. *The Journal of Prosthetic Dentistry*, *107*(1), 34–46.

Güth, J. F., Runkel, C., Beuer, F., Stimmelmayr, M., Edelhoff, D., & Keul, C. (2017). Accuracy of five intraoral scanners compared to indirect digitalization. *Clinical Oral Investigations*, *21*(5), 1445–1455. https://doi.org/10.1007/s00784-016-1902-4

Hagman, C., & Svanborg, P. (2022). Additive Manufacturing of a Removable Partial Prosthesis in Titanium Using Binder Jetting Technology : A Brief Research Report. *Frontiers in Manufacturing Technology*, *2*(l), 1–7. https://doi.org/10.3389/fmtec.2022.863593

Hoang, D., Perrault, D., Stevanovic, M., & Ghiassi, A. (2016). Today surgical applications of three-dimensional printing: A review of the current literature & how to get started. *Annals of Translational Medicine*, *4*(23). https://doi.org/10.21037/atm.2016.12.18

Kalberer, N., Mehl, A., Schimmel, M., Müller, F., & Srinivasan, M. (2019). CAD-CAM milled versus rapidly prototyped (3D-printed) complete dentures: An in vitro evaluation of trueness. *Journal of Prosthetic Dentistry*, *121*(4), 637–643. https://doi.org/10.1016/j.prosdent.2018.09.001

Kamali, A. H., Moradi, M., Goodarzian, F., & Ghasemi, P. (2022). A discrete event simulation method for performance analysis of an additive manufacturing in the dental clinic. *International Journal of Advanced Manufacturing Technology*, *118*, 2949–2979. https://doi.org/10.1007/s00170-021-08135-7

Li, C., Pisignano, D., Zhao, Y., & Xue, J. (2020). Advances in Medical Applications of Additive Manufacturing. *Engineering*, *6*(11), 1222–1231. https://doi.org/10.1016/j.eng.2020.02.018

Nyika, J., Mwema, F. M., Mahamood, R. M., Akinlabi, E. T., & Jen, T. (2021). A five-year scientometric analysis of the environmental effects of 3D printing. *Advances in Materials and Processing Technologies*, *DOI: 10.10*, 1–11. https://doi.org/10.1080/2374068X.2021.1945267

Osman, R. B., Van Der Veen, A. J., Huiberts, D., & Wismeijer, D. (2017). 3D-printing zirconia implants; a dream or a reality? An in-vitro study evaluating the dimensional accuracy, surface topography and mechanical properties of printed zirconia implant and discs. *Journal of the Mechanical Behavior of Biomedical Materials*, *75*, 521–528.

Pradhan, S. R., Singh, R., & Banwait, S. S. (2022). On 3D printing of dental crowns with direct metal laser sintering for canine. *Journal of Mechanical Science and Technology*, *36*(8), 4197–4203. https://doi.org/10.1007/s12206-022-0737-y

Punia, U., Kaushik, A., Garg, R. K., Chhabra, D., & Sharma, A. (2022). 3D printable biomaterials for dental restoration: A systematic review. *Materials Today: Proceedings*, *63*, 566–572. https://doi.org/10.1016/j.matpr.2022.04.018

Rekow, E. D. (2020). Digital dentistry: The new state of the art — Is it disruptive or destructive? *Dental Materials*, *36*, 9–24. https://doi.org/10.1016/j.dental.2019.08.103

Rouf, S., Malik, A., Singh, N., Raina, A., Naveed, N., Siddiqui, M. I. H., & Haq, M. I. U. (2022). Additive manufacturing technologies: Industrial and medical applications. *Sustainable Operations and Computers*, *3*(May), 258–274. https://doi.org/10.1016/j.susoc.2022.05.001

Rouf, S., Raina, A., Irfan Ul Haq, M., Naveed, N., Jeganmohan, S., & Farzana Kichloo, A. (2022). 3D printed parts

and mechanical properties: Influencing parameters, sustainability aspects, global market scenario, challenges and applications. *Advanced Industrial and Engineering Polymer Research*, *5*(3), 143–158. https://doi.org/10.1016/j.aiepr.2022.02.001

Sheoran, A. J., Kumar, H., Arora, P. K., & Moona, G. (2020). Bio-medical applications of additive manufacturing: A review. *Procedia Manufacturing*, *51*, 663–670. https://doi.org/10.1016/j.promfg.2020.10.093

Silva, M., Felismina, R., Mateus, A., Parreira, P., & Malça, C. (2017). Application of a Hybrid Additive Manufacturing Methodology to Produce a Metal/Polymer Customized Dental Implant. *Procedia Manufacturing*, *12*, 150–155. https://doi.org/10.1016/j.promfg.2017.08.019

Singh, S., & Ramakrishna, S. (2017). Biomedical applications of additive manufacturing: Present and future. *Current Opinion in Biomedical Engineering*, *2*, 105–115. https://doi.org/10.1016/j.cobme.2017.05.006

Srinivasan, M., Kamnoedboon, P., McKenna, G., Angst, L., Schimmel, M., Özcan, M., & Müller, F. (2021). CAD-CAM removable complete dentures: A systematic review and meta-analysis of trueness of fit, biocompatibility, mechanical properties, surface characteristics, color stability, time-cost analysis, clinical and patient-reported outcomes. *Journal of Dentistry*, *113*(August). https://doi.org/10.1016/j.jdent.2021.103777

Stanley, M., Paz, A. G., Miguel, I., & Coachman, C. (2018). Fully digital workflow, integrating dental scan, smile design and CAD-CAM: Case report. *BMC Oral Health*, *18*(1), 4–11. https://doi.org/10.1186/s12903-018-0597-0

Su, C. Y., Wang, J. C., Chen, D. S., Chuang, C. C., & Lin, C. K. (2020). Additive manufacturing of dental prosthesis using pristine and recycled zirconia solvent-based slurry stereolithography. *Ceramics International*, *46*(18), 28701–28709. https://doi.org/10.1016/j.ceramint.2020.08.030

T, M., Y, H., J, K., Kuriyama S, T., & Y, T. (2009). A review of dental CAD/ CAM: current status and future perspectives from 20 years of experience. *Dental Materials Journal*, *28*(1), 44–56.

Tamburrino, F., Aruanno, B., Razionale, A. V., Barone, S., Martini, M., & Bordegoni, M. (2022). A Digital Process for Manufacturing Customized Trays for Dental-Whitening Treatments. *Processes*, *10*(7), 1–11. https://doi.org/10.3390/pr10071232

Tamimi, F., & Hirayama, H. (2019). *Digital Restorative Dentistry*.

Tian, Y., Chen, C., Xu, X., Wang, J., Hou, X., Li, K., Lu, X., Shi, H., Lee, E., & Jiang, H. B. (2021). A Review of 3D Printing in Dentistry : Technologies , Affecting Factors , and Applications. *Scanning*, *2021*, 1–19.

Tiwari, R., Bhayat, A., & Chikte, U. (2021). Forecasting for the need of dentists and specialists in South Africa until 2030. *Plos One*, *16*(5), 1–14.

Wyk, P. J. Van, Wyk, C. Van, & Africa, S. (2004). Oral health in South Africa. *International Dental Journal*, *54*, 373–377.

PAPER 165 – SUSTAINABLE MANAGEMENT OF STORM WATER GENERATION IN A FAST-URBANIZING RESIDENTIAL AREA OF MALETE, KWARA STATE, NIGERIA

A. Sanni[1,2]; A. G. Adeogun[1]; H. Solihu[1], M.A. Wopa[1,2]

[1]Department of Civil Engineering, Kwara State University, PMB 1530, Ilorin, Kwara State, Nigeria
[2]Department of Civil Engineering, Kwara State Polytechnic, Ilorin, Kwara State, Nigeria
Email: adeniyi.adeogun@kwasu.edu.ng

ABSTRACT
An alteration in the natural land cover characteristics of the environment due to the high rate of urbanization globally has created a large span of impervious surfaces that resist the infiltration rate but encourage runoff from precipitation. This phenomenon affects the natural environment. To mitigate the effect of storm water generation, Low Impact Development (LID) techniques was developed as a means of storm water management. In this study, Storm Water Management Model (SWMM) in conjunction with MAPWindow GIS was used to simulate the effects of selected LIDs embedded in the SWMM to mitigate storm water generated in the study area. The study area was delineated into six sub-basins in the GIS environment and imported into the SWMM to study the effect of some selected LIDs which are green roofs, rain gardens, vegetative swale, and permeable pavement. The results show that the permeable pavement has the highest reduction value of about 50% across all sub-basins while Green Roof has the least reduction value of 0.003%. Outcome of this study can be a decision support tool that can be adopted by different stakeholders and relevant authorities in the selection of appropriate LIDs practices to mitigate the urban impact of storm water generation in the study area.

KEYWORDS*:* Storm water; Mitigation; SWMM; LIDs; Sub-catchment; MAPWindow

1.0 INTRODUCTION

Storm water is the precipitation generated from rain, sleet, or melting snow. In a natural setting, only a small percentage becomes surface run off. This runoff usually flows into the nearest stream, creek, river, lake, or wetland. Due to the rapid urbanization around the world, the natural land covers characteristics are changing into impervious surfaces and degrading the natural environment. These adverse effects include the increase runoff and peak flows that cause flash flooding and water quality degradation and other water related problems (Dientz, 2007). In addition, climate change is another big challenge that is making our towns and cities vulnerable to erosion and incessant flooding. Climatic change and growth in the major cities have altered hydrological pattern and increases runoff volumes resulting into erosion, flooding and degradation of ecosystem. Low impact development (LID)s advocates the design of a decentralized storm water control system above centralized location in the catchment area. The benefit of LIDs is to control the amount storm runoff, improve storm water quality and river, reduced the flood peak, increases the infiltration rate and base flow and to restore water cycle systems distorted by urbanization to their pre-development state Kim et al., (2021).

In the past, the control schemes of urban flooding were focused on the construction of drainage channels to convey the generated runoff. However, construction of drainages in our towns and cities can only achieve a certain effect in the short term but cannot solve the problem fundamentally. In recent time, applications of Low Impact Development (LID) practices have proved as the sustainable solutions to mitigate the adverse effects of urbanization and to retrieve the natural hydrology of urban areas. The impact of various LIDs can be simulated using various hydrological models such as Storm Water Management Model (SWMM) which can simulate the natural hydrological conditions as much as possible.

Malete is one of the fastest growing towns in Kwara State Nigeria and this might not be unconnected with to the recent citing of Kwara State University in the town. In the past ten (10) years of establishing the University, the number of students admitted for different programs has geometrically increased while the academic and non-academic staff of the university has also shot up. Hence, there is a rapid growth in the construction of buildings for student hostels at different locations around the town to cater for the housing need of the student and staff populace. This rapid urban growth has increased the generation of urban storm water runoff, and this may be accompanied by associated effects such as water logging resulting in ground flooding, traffic jams, underground submerging, and interruption of utilities pipeline such as gas and electricity. Urban water logging seriously impacted on people's life and property safety.

Therefore, this research aimed at studying the effect of the application of different Low Impact Development (LID) in managing storm water generation in the study area. Outcome of the study can be an eye opener and decision support tool to develop and other relevant authorities in selection of best alternatives LIDs for storm water management in the area.

2. THEORETICAL ANALYSIS

The modeling tool adopted in this research was Storm Water Management Model (SWMM). It is a comprehensive hydrological and water quality simulation model used for single or continuous events of runoff in urban areas (Rossman, 2005). SWMM comprises four computational blocks, namely RUNOFF, STORAGE/ TREATMENT, TRANSPORT and EXTRAN. Hydrograph and pollutograph were generated by the RUNOFF block. The basic input parameters required to simulate hydrograph were rainfall hyetograph and the sub-catchments physical characteristics. The infiltration loss on pervious area was estimated by Horton equation (Equation 1) because of the availability of soil data. The EPA SWMM is a physically based, deterministic model that simulates water inflows, outflows, and storages within a sub-catchment.

$$F = ff + (fo - ff)\, e - kt \qquad \text{Equation 1}$$

where f_o: the initial infiltration rate (capacity)
f_f: the final rate (almost equal to percolation rate)
k: Constant (depend on soil type and vegetation)
t: time from the beginning of the rain

3.0 METHODOLOGY

3.1 Description of the study area

The study area is in Malete Town which is located between latitude $8^0$36' and $8^0$24' North and Longitudes $4^0$36' and $4^0$10' east. Its total area is 1230.0 km^2 and it is a small town in Moro Local Government Area of Kwara State. The headquarter of the town is in Bode Saadu, a town situated along Jebba road, Moro Local Government is made up of five districts namely Lanwa, Ejidongari, Olooru, Malete and Ipaye. The topography of the area is a fair representative of surrounding plains which can be described as undulating with very broad and gentle slopes. The town is characterized with combination of open storm water drainage system and earth drain for the conveyance of generated storm water from the environment. The town is the custodian of the Kwara State University which was established in 2009. The main occupation of Malete inhabitant are farming, trading and hunting. Figure 1 shows the Google Earth imagery of Malete Town while Figure 1 shows the location of Malete Town in Kwara State Map.

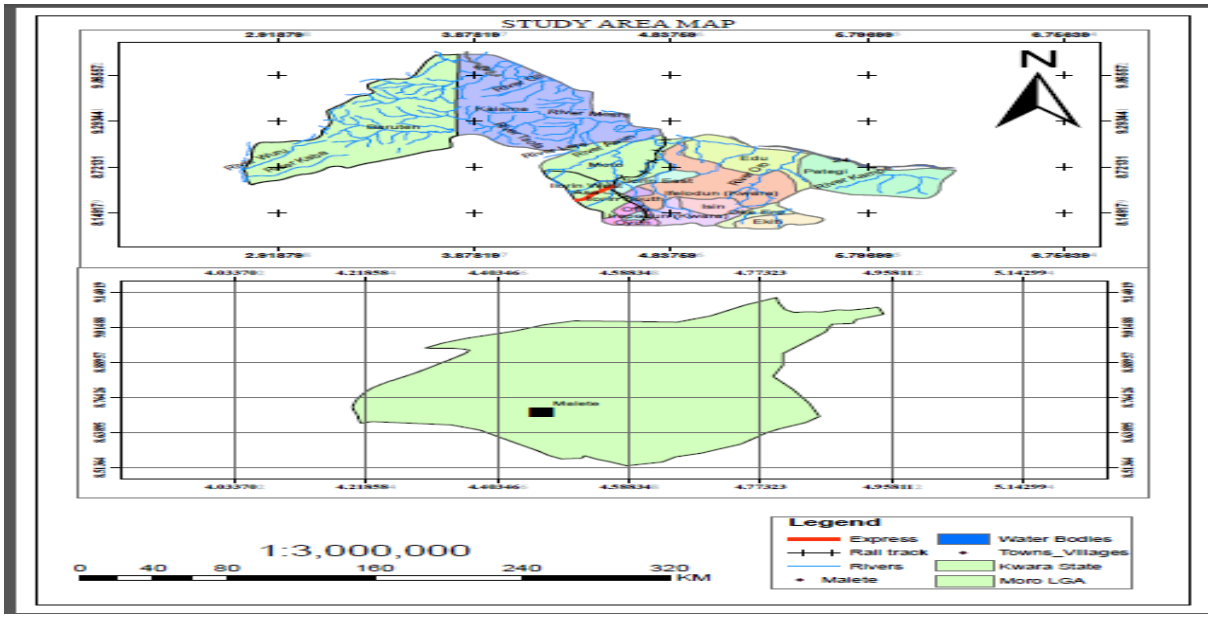

Figure 1: shows the location of Malete Town in Mooro Local Government of Kwara State

3.2 Model Selection, Data Requirements and Geoprocessing of Spatial Data

The modeling tool adopted in this research was Storm Water Management Model (SWMM). It is a comprehensive hydrological and water quality simulation model used for single or continuous events of runoff in urban areas (Rossman, 2005). The basic input parameters required to simulate hydrograph were rainfall hyetograph and the sub-catchments physical characteristics. The infiltration loss on pervious area was estimated by Horton equation

because of the availability of soil data. The EPA SWMM is a physically based, deterministic model that simulates water inflows, outflows, and storages within a sub catchment.

Spatial data required for the modelling exercise include the Digital Elevation Model (DEM) of the study area. The DEM of resolution 90 m x 90 m was extracted from online database of Shuttle Radar Topographical Mission (SRTM) website of United State Department of Agriculture (CGIAR, 2012). The DEM was geo-processed using the Automatic Watershed Delineation (AWD) dialogue box from the Mapwindow GIS interface (Leon, 2011). AWD was prepared by setting the elevation units, threshold size and creating an outlet for the watershed. Other spatial data used in the delineation of the watershed into subbasins include the land use map which was extracted from Global Land Cover Characterization (GLCC) database and used to estimate parameters such as vegetation representing the study area. The land use database was prepared by United States Geological Survey (USGS) and has a spatial resolution of 1km. The soil data required for the study was obtained from harmonized digital soil map of the world (HWSD v1.1) produced by Food and Agriculture Organization of the United Nations (Nachtergaele et al., 2009). The daily weather (precipitation, wind, solar radiation, relative humidity and daily minimum and maximum temperature) data of the study area were obtained from Nigerian Meteorological Agency (NIMET) Ilorin and were prepared in the appropriate file format by the model and imported into the model. The study area was divided into six subbasins and 11 Hydrologic response unit (HRU). The HRU is the smallest spatial unit of the model. The total catchment includes 6 sub catchment, 10 junctions, 10 conduit links, 1 outfall, and 1 rain gage station (Figure 1). SWMM was used for obtaining quantity of runoff generated within each sub catchment and the flow rate, flow depth, in conduit during a stimulation period and comprised of multiple time step.

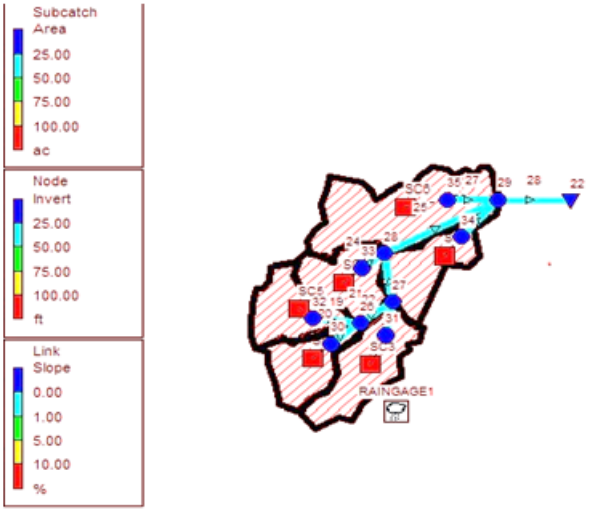

Figure 2: Delineation of the Watershed into Sub basins

3.3 Selection and Modelling of Low Impact Developments

There are different LID components that can be simulated in SWMM model. However, LIDs simulated in this research are (i) Rain Garden (ii) Permeable Pavement (iii) Vegetative Swales and (iv) Green Roof. Different scenarios were created for simulations which include the combination of LIDS to evaluate their efficiency in the reduction of the amount of total runoff from each of the sub catchment area.

4. RESULTS AND DISCUSSION

The outcome of the study is as presented in Table 1 and figure 3. The result shows that all LIDs modelled reduced the storm water generation across the sub basins of the study area. However, the percentage runoff reduction using permeable pavement as LID in the six sub-catchment of the study area was highest among the other LIDs considered to reduce surface runoff, flood peak and delay peak flow with average storm water reduction of about 50 %. This result is higher when compared with the results obtained by Arora, et al (2023) that investigated the effectiveness of permeable pavement at the basin scale under a variety of design rainfall and land-use situations. Their results indicated that the incorporation of permeable pavements in urban settings is effective in reducing storm water in a developed catchment by decreasing the peak flow by 7–16%.

The application of vegetative swale has a runoff reduction percentage in the sub-catchment between 13.95% - 15.56% which makes it to be the second most effective in storm water management in the study area. This outcome is lower than the result obtained by Bailee (2017) which indicated that 87.2 % of runoff volume was reduced by the swale. Conversely, Qinghua *et al.* (2017) also corroborated that vegetative swale as an effective low impact

development procedure in mitigating runoff. A very low runoff percentage reduction was observed in the application of Rain garden with the value ranging from 0.0003% to 0.31%. Though, this agreed with Derek (2011) who reported that rain gardens can help the existing developments by mitigating storm water volume and peak flow and provide a dynamic internal saturation zone with the potential for water quality benefits, the percentage reduction is low compared with a similar study in Nepal by Neupane *et.al.*, (2020) where the rain garden reduced the runoff generated by about 42%. The green roof has the lowest storm water reduction of 0.0003 % in reducing storm water and Aruna *et al.*, (2012) confirmed the efficacy of green roof as an alternative procedure for runoff reduction in watershed.

Table 1: - Summary of Rainfall Runoff Reduction by Low Impact Development

Sub-catchment	Low Impact Development	Area Covered (%)	Number of Units per LID (sc)	Initial storage (in)	Final storage (in)	LID performance differences	LID performance (%)
Sc1	Green Roof	10	10	669199.56	669197.65	1.91	0.0003
	Vegetable swale	10	10	669199.56	565156.19	104,043.37	15.55
	Permeable pavement	10	10	669199.56	334112.46	335,087.10	50.07
	Rain garden	10	10	669199.56	667112.86	2,086.70	0.31
Sc2	Green Roof	10	10	668743.35	668741.44	1.91	0.0003
	Vegetable swale	10	10	668743.35	564710.93	104,032.42	15.56
	Permeable pavement	10	10	668743.35	333884.36	334,859.00	50.07
	Rain garden	10	10	668743.35	667605.45	1,137.9	0.17
Sc3	Green Roof	10	10	666689.18	666687.26	1.92	0.0003
	Vegetable swale	10	10	666689.18	571731.36	94,957.82	14.24
	Permeable pavement	10	10	666689.18	332848.50	333,840.62	50.07
	Rain garden	10	10	666689.18	665522.62	1,166.56	0.17
Sc4	Green Roof	10	10	668585.18	668583.26	1.92	0.0003
	Vegetable swale	10	10	668585.18	565564.86	103,020.32	15.41
	Permeable pavement	10	10	668585.18	333804.74	334,780.44	50.07
	Rain garden	10	10	668585.18	667445.57	1,139.61	0.17
Sc5	Green Roof	10	10	665467.68	665465.76	1.92	0.0003
	Vegetable swale	10	10	665467.68	563056.22	102,411.46	15.40
	Permeable Pavement	10	10	665467.68	332245.18	333,222.50	50.07
	Rain garden	10	10	665467.68	664325.43	1,142.25	0.17
Sc6	Green Roof	10	10	666206.33	666204.41	1.92	0.0003
	Vegetable swale	10	10	666206.33	573246.62	92,959.71	13.95
	Permeable pavement	10	10	666206.33	332604.45	333,601.88	50.07
	Rain garden	10	10	666206.33	665032.15	1,174.18	0.18

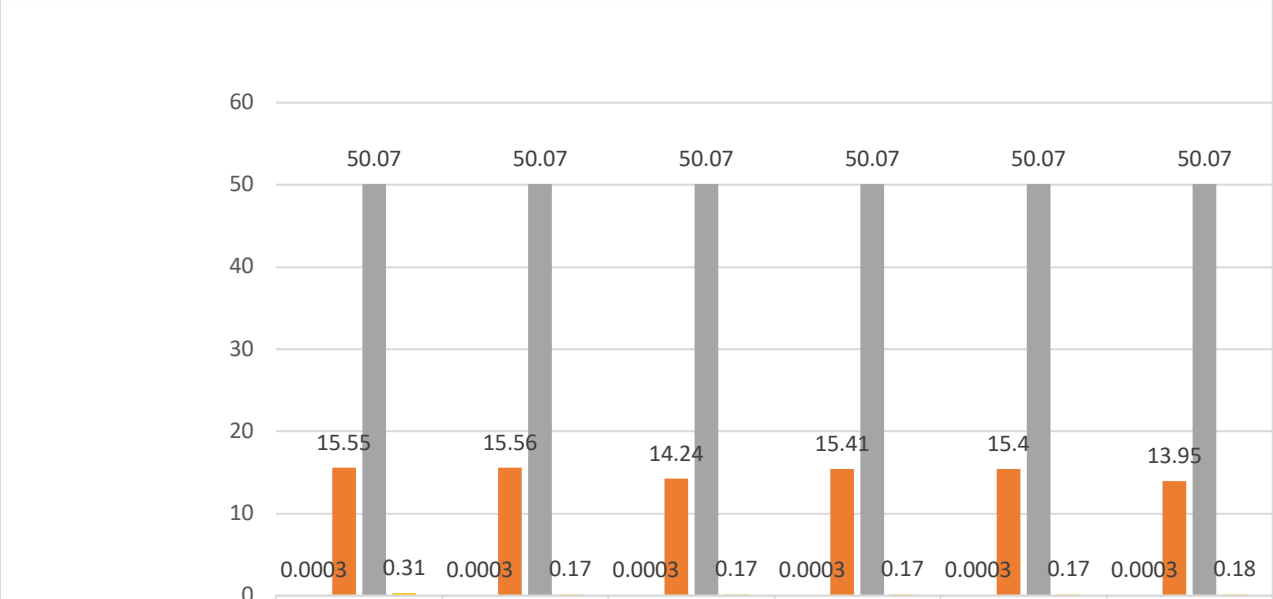

	Sub -catchment 1	Sub -catchment 2	Sub -catchment 3	Sub -catchment 4	Sub -catchment 5	Sub -catchment 6
Green roof	0.0003	0.0003	0.0003	0.0003	0.0003	0.0003
vegetative swale	15.55	15.56	14.24	15.41	15.4	13.95
permeable Pavement	50.07	50.07	50.07	50.07	50.07	50.07
Rain garden	0.31	0.17	0.17	0.17	0.17	0.18

Figure 3: Percentage runoff reduction by selected LIDs in the watershed

5. CONCLUSION

The findings indicate that all the four LIDs examined through model simulation were means of controlling and managing the effects of storm water on environment and water quality. It was also discovered that Permeable pavement and Green roof have the highest and lowest percentage runoff reduction respectively in the study area. Therefore, the outcome of this study can be a decision support tool that can be adopted by different stakeholders and relevant authorities in the area while selecting appropriate LIDs practice to mitigate urban impact of storm water generation.

ACKNOWLEDGEMENT

I sincerely appreciate Almighty Allah for the opportunity given to carry out this research work. I would also like to express my sincere gratitude to my supervisor in person of Dr. A. G Adeogun for his guidance and constructive criticism. I am grateful to my parents, siblings, colleagues and friends for their support and encouragement through this research work.

REFERENCES

Arora, M.; Chopra, I.;Nguyen, M.H.; Fernando, P.; Burns, M. J.; Fletcher, T.D (2023) Flood Mitigation Performance of Permeable Pavements in an Urbanised Catchment in Melbourne, Australia (Elizabeth Street Catchment): Case Study. Water 2023, 15, 562. https://doi.org/10.3390/w1503056

Aruna, V. , Suja, R. and Rajalakshmi, C.R. (2021) Effectiveness of Permeable Pavements and Vegetative Swales for Developing Sponge Cities. DOI: https://doi.org/10.21203/rs.3.rs-501295/v1

Bailee, Y (2017) Examining the Runoff Reduction Potential of Highway Swales Master of Science Thesis, University of Tennessee, USA

CGIAR (2012) SRTM 90m Digital Elevation Data, available at http://srtm.csi.cgiar.org/, accessed on 23rd December, 2013

Derek A. S. (2011) Retention and management of storm water runoff with rain gardens and rainwater harvesting systems. a Thesis on Partial Fulfillment of the Requirements for the Degree Master of Science in the Graduate School of The Ohio State University.

Leon, L.F. (2011), MapWindow Interface for SWAT (MWSWAT). Available at http://www.waterbase.org/docs/MWSWAT%20Setup.pdf accessed on 24th September,2022

Nachtergaele, F. and Velthuizen, H.V., and Verelst, L. (2009), Harmonized World Soil Database (HWSD). Food and Agriculture Organization of the United Nations, Rome

Neupane, A ; Lamichhane, S; Shrestha, S; Ghimire, A. (2022). Evaluation of runoff reduction after the deployment of lid through swmm: a case study in suryabinayak municipality in Nepal. WASH Journal 19., published by Society of Public Health Engineers, Nepal (SOPHEN)

Qinghua Luan, Xiaoran Fu, Cuiping Song , Haichao Wang, Jiahong Liu and Ying Wang (2017),Runoff Effect Evaluation of LID through SWMM in Typical Mountainous, Low-Lying Urban Areas:A Case Study in China,Water 9,4

Yiran Bai, Na Zhao , Ruoyu Zhang and Xiaofan Zeng (2018) Storm Water Management of Low ImpactDevelopment in Urban Areas Based on SWMM, School of Hydropower and Information Engineering, Huazhong University of Science and Technology,pp 1-1.

PAPER 167 – ASSESSMENT OF AUTOMOBILE USERS' PERCEPTION OF VIABILITY OF PRODUCING SPARE PARTS FROM BIOMATERIAL COMPOSITES IN NIGERIA

A. A. Ojetoye[1], R. Abu[2]*and N.A. Adewole[3]

[1]Department of Mechanical Engineering, Faculty of Engineering, Adeleke University, Ede, Nigeria.
[2]Department of Mechanical Engineering, Faculty of Technology, University of Ibadan, Nigeria.
[3]Department of Wood Products Engineering, Faculty of Technology, University of Ibadan, Nigeria.
*Email: aburahaman@yahoo.com

ABSTRACT

The use of composite in automotive parts production engenders lightweight and fossil fuel consumption thereby promoting reduction of volume of gas released into the atmosphere by automobiles. The perception of automobile users on viability of producing spare parts from composite of biomaterials origin in Nigeria was investigated. Google tool was used to share structured questionnaires on 60 WhatsApp groups and responses of 227 respondents were validated with oral interview conducted with 30 car users drawn from Osogbo, Osun State with all respondents randomly but purposively selected. There is general awareness among respondents in respect of promotion of local capacity and content input in commercial production of automobile parts globally. About 89% of the total respondents agreed that development of local capacity and the use of bio-material can reduce the high cost of spare parts. Bumpers, fenders, door handles and doors were indicated by 73.5%, 63.4%, 57.6% and 30.7% respondents, respectively as outer parts made with composite while 82.1%, 46.3%, 44.3%, 36.2% and 34.2% respondents agreed that dashboard, door handle, glove box, clutch pedal and door panel, respectively were interior parts made with composite. This study affirmed the positive disposition of automobile users to buy spare parts made with biomaterials composite.

KEYWORDS: Automotive parts production, Biomaterial composites, Light weight, Green environment, Nigeria

1. INTRODUCTION

The rising challenge of greenhouse gas emissions and improvement in fuel economy are important factors that have been motivating automobile manufacturers to shift attention to producing lightweight vehicles. These factors have stimulated substantial transformation in automobile industries globally to address consumers' complaints about vehicles that minimize energy consumption, issues on climate change, reduction in vehicles weight among others (Zhang *et. al.,* 2022; Wasser *et. al.,* 2023). The continuing quest by automobile industries to meet consumers new demands have influenced automobile manufacturers to keep exploring the use of new materials. It has also encouraged the modification of conventional materials (Fetahun and Ahsen, 2018) since material plays a significant role in determining the overall performance of the vehicle (Hambali *et. al.,* 2023).

A wide range of conventional materials: steel, plastic, aluminum, copper, magnesium and carbon fiber have been employed for vehicle manufacturing. The choice of any of these conventional materials is often done with due consideration to their physical, thermal, mechanical, and chemical resistance, durability, and ease of manufacturing (Tador, 2023). However, the paradigm shifts in the material choice for automotive parts manufacturing in this era of pursuit of lightweight and consideration for the environment have favored the use of composite material. Composite material inherently engendered improved mechanical characteristics as it often combines two or more materials in one (Kumar *et. al.,* 2013). Composites are easier to produce and provide innovative design opportunities that would be difficult to realize with conventional materials. Composite forming results in a material with high specific strength, high dimensional stability, and lessened weight (Singh *et. al.*, 2021). Composites can be created to satisfy certain geometrical, mechanical, structural, chemical and aesthetic requirements. Composites are generally classified according to their matrix into fiber-reinforced composites, which are formed by nearby fibrous materials with a matrix such as metal. Polymer or ceramic, particle reinforced composites where short particles serve as reinforcements and structural composites are designed by gently arranging a system of other composites and binding them with a homogenous adhesive material (Lee, 1990; Egbo, 2020).

Natural fibre is a better alternative to synthetic fiber composite and it appears to be gaining more popularity globally because of new environmental regulations and its friendliness to the environment. They are also capable of reducing vehicle weight for better performance, have low manufacturing cost and good weight resistance ratio, and are readily available (Chauhan *et. al.*, 2019; Sharma *et. al.*, 2020). This growing trend in adapting natural fibre in the form of composite for vehicle part production is yet to gain attention in Nigeria neither is there information on the perception of vehicle users on the readiness to patronize the such product. This was why this study was initiated to investigate the perception of automobile users in Nigeria on the viability of producing a non-structural automotive part with a composite made from biomaterial to reduce the automotive part cost, and weight and aid fuel consumption reduction.

2. METHODOLOGY

The survey tools used are a structured questionnaire that was shared via Google link, and oral interviews conducted on thirty automotive users selected randomly but with a bias for car brands from Osogbo, Osun State, Nigeria. While the structured questionnaire was shared on 60 separate WhatsApp platforms, the oral interview was conducted to complement the responses from the structured questionnaire to validate claims and evaluate outlier data. All the responses obtained were statistically analyzed using Microsoft Excel App.

3. RESULTS AND DISCUSSION

3.1 The Vehicle and Respondents Consciousness on Material of Production

The car users that were involved in the oral interview drive the range of vehicles indicated in Table 1. These vehicle models were (Not older than 20 years). The vehicles were largely none commercial and included saloon cars, spot cars and sport utility vehicles. The results emanated from the structural questionnaire indicated that a total of 257 respondents responded through various WhatsApp outlets. Of these total respondents, 85% were male while 14% indicated that they were female. This perhaps indicated that female has apathy in responding to issues and request on WhatsApp outlets. However, the majority of the respondents (90.6%) were of the opinion that car cost often dictates its

Table1: Types and Models of Vehicles involved in the Study

SN	Type	Model	Frequency
1	Toyota	Toyota Corolla, Toyota Carina, Toyota Camry, Toyota Land Cruiser, Toyota Yaris, Toyota Supra	6
2	Benz	Mercedes Benz	1
3	Mazda	Mazda3, Mazda Cx5	2
4	Honda	Honda CRV, Honda Civic, Honda Accord, Honda Pilot, Honda City	5
5	Nissan	Nissan	1
6	Volkswagen	Golf, Volkswagen	2
7	Mitsubishi	Mitsubishi	1
8	Volvo	Volvo	1
9	Kia	Kia	1
10	Hyundai	Hyundai	1
11	Lexus	Lexus IS, Lexus RX, Lexus LS, Lexus LX,	4
12	Ford	Ford	1
13	BMW	BMW	2
14	Chevrolet	Chevrolet	1
15	Audi	Audi	1
			30

quality. It was evidenced from physical interaction with some car users that they are concerned about the type of material that their vehicles are made from while 93% of the online respondents were conscious of the materials that their cars were made from. Though their concern may be borne out of curiosity rather than informed knowledge of the material suitability. This contradicts the position reported by (Teli *et. al.*, 2013;

Amineba and Kosacha, 2016) that car users mostly pay attention to quality criteria rather than the knowledge of materials that their car was made from.

3.2 Use of Biomaterial for Automobile Parts Production

Literature [Pruez et al., 2013] indicated that composites have been introduced into the automobile industries over 6 decades ago. Large numbers of vehicle users (86%) indicated that they have either driven or seen cars with parts manufactured with composites. The components indicated to have been made from composite materials by the respondents represented in the pie-chart in Figure 1 are the body, engine and interior parts of the automobiles. Their observations agreed with the findings of (Ortega *et. al.,* 2012; Pruez, *et. al.,* 2013; Hăloiu, and Iosif, 2013; John and Alex, 2014; Prodanovic and Milutinovic, 2017; Gheorghe *et. al.,* 2021; Fisher, 2022). The distribution of engine components indicated to have been noticed to be made from composite materials by respondents is presented in Figure 2. The overriding members made of composite material according to respondents are the oil filter (23%) and transmission system (20%). Auto manufacturers consider polymer composites in making light engine parts without ignoring the reliability of the parts (Pruez, *et. al.,* 2013; Prodanovic and Milutinovic, 2017).

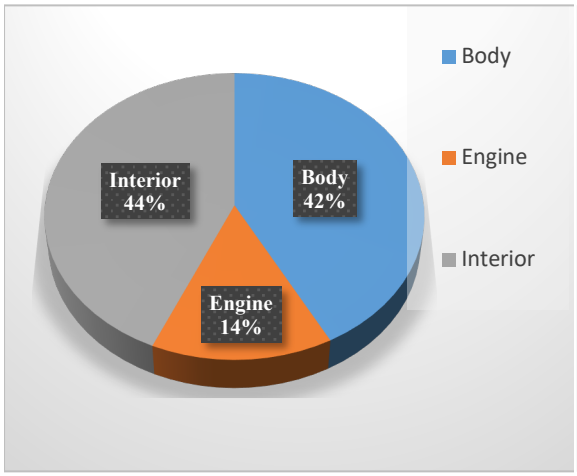

Fig. 1: Car Parts Made of Composites

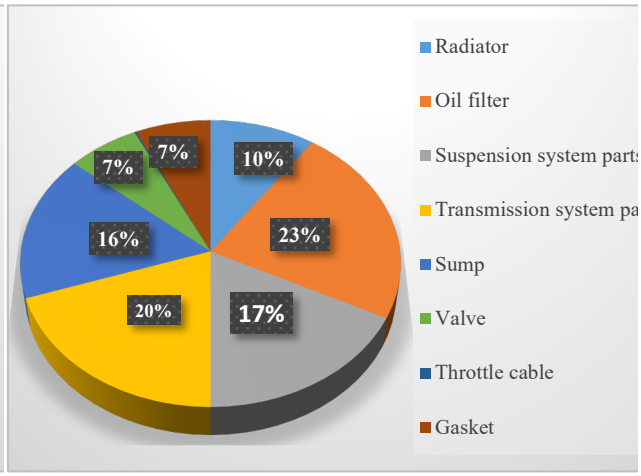

Fig. 2: Engine Parts Made of Composites

The vehicle body and interior parts that were indicated by users as parts made from composites to their knowledge are represented by Pie-charts in Figures 3 and 4. The vehicle bumper (20%) was indicated as the parts that were mostly made from composites followed by Bonnet and Fender that were (17%) each. Most of these parts are made of carbon and natural fibers (Ortega *et. al.,* 2012; John and Alex, 2014; Vieyra *et. al.,* 2022; Ford, 2023). In the same vein, Dashboard was indicated as the parts that were made from composites. Literature shows that all these parts can be made from natural fibers and compared reasonably with plastics used traditionally (Hăloiu, and Iosif, 2013; Riyardi, 2019; Fisher, 2022).

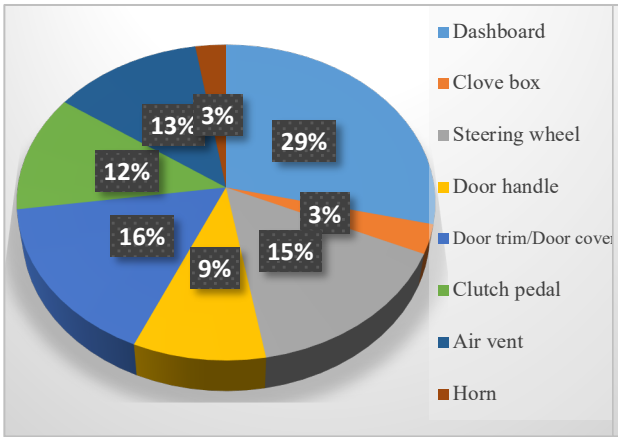

Fig. 3: Body Parts Made of Biomaterials

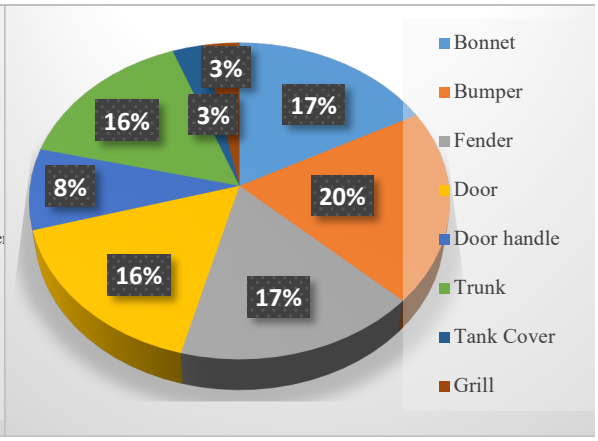

Fig. 4: Interior Parts Made of Biomaterials

3.3 Frequently Changed Automotive Parts

Responses from the surveyed automobile users indicated Bumpers, Fenders, Grills and side Mirrors as the most frequent parts that they often repair or replace as presented in Figure 5. Making auto parts from biomaterial was strange to few respondents; large numbers of the respondents were of the opinion that vehicle parts can be made from any material. And this category indicated readiness to patronize parts made with new bio-composite materials. As for those who believed that biomaterials can be used to produce the body parts they replace regularly, their beliefs align with the reported opinion of Prodanovic and Milutinovic (2017). There was a consensus among respondents on the willingness to buy locally manufactured automotive spare parts from biomaterials. This position is a ready impetus needed to stimulate the development of local capacity in automotive spare parts manufacturing in Nigeria. The motivation of the overwhelming respondents (96.1%) is that manufacturing automotive spare parts from biomaterials will almost certainly lead to a considerable reduction in the price of these spare parts and the cost of car maintenance.

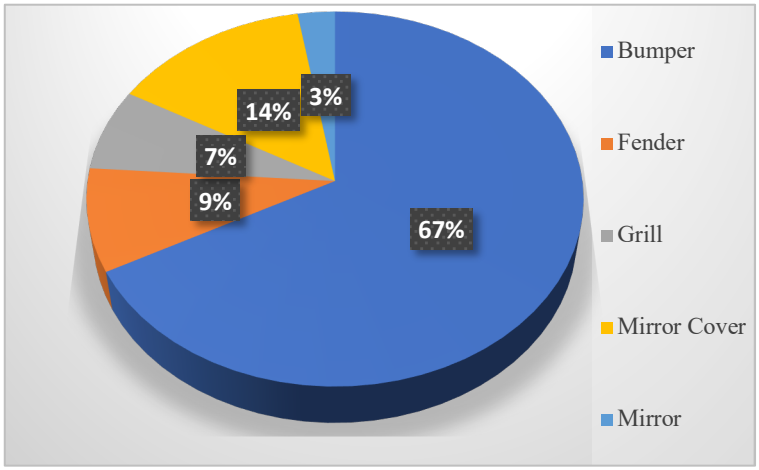

Fig. 5: Body parts that require replacement often

4. CONCLUSION

The study noted that there was general awareness among the vehicle users on the material that their vehicle parts were produced from. There was general knowledge that composite materials are involved in the production of automotive parts among users in Nigeria. The non-structural members were chosen as the most probable parts that will attract production with bio-composite materials while the majority of automobile users will readily patronize locally manufactured automobile parts made of biomaterials. It was evidenced that Nigerian vehicle users will be motivated to patronize automotive parts made locally with biomaterial composites if it has the propensity to reduce the spare parts and vehicle maintenance costs.

REFERENCES

Amineha, H. and Kosacha, N. (2016) Assessment of Consumers' Satisfaction with the Automotive Product Quality. International Journal of Environmental & Science Education, vol. 11, no. 16, 8726-8739.

Chauhan, V. Kärki, T. and Varis, J. (2019) Review of natural fiber-reinforced engineering plastic composites, their applications in the transportation sector and processing techniques. J. Thermoplast. Compos. Mater.

Egbo, M.N. (2020) A Fundamental Review on Composite Materials and Some of their Applications in Biomedical Engineering. J. King Saud Univ. 33(8). https://doi.org/10.1016/j.jksues.2020.07.007

Fentahun, M.A and Ahsen, M. (2018). Materials Used in Automotive Manufacture and Material Selection Using Ashby Charts. International Journal of Materials Engineering 2018, 8(3): 40-54 https://dOI:10.5923/j.ijme.20180803.02

Fisher, G. (2022) Automotive Interiors Setting the Pace for Vehicle Design. (Accessed: 2023-04-05). URL https://www.fiberjournal.com/automotive-interiors-setting-the-pace-for-vehicle-design/

Ford (2023). Ford develops prototype carbon composite bonnet - materials today (Accessed: 2023-04-05). URL http://www.materialstoday.com/composite-applications/news/ford-develops-prototype-carbon-composite-bonnet/

Gheorghe, V.; Scutaru, M.L.; Ungureanu, V.B.; Chircan, E.; Ulea, M. (2021) New Design of Composite Structures Used in Automotive Engineering. Symmetry 2021, 13, 383. https://doi.org/10.3390/sym13030383

Hăloiu, A. and Iosif, D. (2013) Bio-source composite materials used in automotive industry. Scientific Bulletin, Automotive series, no.24(1).

Hambali, A., Sapuan, S.M., Ismail, N. and Nukman, Y. (2023). Material selection of polymeric composite automotive bumper beam using analytical hierarchy process. (Date Retrieved: April 2, 2023)

John, A., and Alex, S. (2014) A Review on the Composite Materials used for Automotive Bumper in Passenger Vehicles. International Journal of Engineering and Management Research (IJEMR): 98-101.

Kumar, A., Lal, S. and Kumar, S. (2013) Fabrication and characterization of A359/Al2O3 metal matrix composite using electromagnetic stir casting method. J Mater Res Technol 2013;2(3):250–4.

Lee, Stuart M. (1990) International Encyclopedia of Composites, Historical Perspectives of Composites ed. Delmonte, J. New York: VCH Publishers.

Ortega, Z., Monzón, M.D., Soto, P., Guinea, I., Suárez, L. and Hernández, P.M. (2012) Use of Banana Fiber in Injection – Moulded Parts for the Automotive Sector. ECCM15 - 15TH European Conference on Composite Materials, Venice, Italy, 24-28 June.

Prodanovic, S. and Milutinovic, M. (2017) Some Applications of Biomaterials in Automotive Industry. In: Advances in Applications of Industrial Biomaterials. https://dOI.org/10.1007/978-3-319-62767-0_1

Pruez, J. C., Shoukry, S. N., William, G. W., and Shoukry, M. S. (2013) Lightweight Composite Materials for Heavy Duty Vehicles. West Virginia University.

Riyadi, S. (2019) Development of Composite Fiber Materials for Prototype of Car Components. Chemistry and Materials Research, ISSN 2224- 3224 (Print) ISSN 2225- 0956 (Online). Vol.11 No.1. https://dOI.org/10.7176/CMR

Sharma, S.; Sudhakara, P.; Misra, S.; Singh, J. (2020) A comprehensive review of current developments on the waste-reinforced polymermatrix composites for automotive, sports goods and construction applications: Materials, processes and properties. Mater. Today Proc. 33, 1671–1679.

Singh H, Brar GS, Kumar H, Aggarwal V. (2021) A review on metal matrix composite for automobile applications. Mater Today Proc 2021; 43:320–5.

Tador, M.P. (2023). Systematic approach on materials selection in the automotive industry for making vehicles lighter, safer and more fuel–efficient. (Date Retrieved: April 2, 2023).

Teli, S.N., Majali, V.S., Bhushi, U.M., Gaikwad, L.M. and Surange, V.G. (2013) Cost of Poor-Quality Analysis for Automobile Industry: A Case Study. J. Inst. Eng. India Ser. C https://dOI.org/10.1007/s40032-013-0091-z

Vieyra, H., Molina-Romero, J.M., Calderon-Najera, J.D. and Santana-Diaz, A. (2022) Engineering, Recyclable, and Biodegradable Plastics in the Automotive Industry: A Review. Polymers, 14(16), 3412. https://doi.org/10.3390/polym14163412

Wazeer, A., Das, A., Abeykoon, C., Sinha, A. and Karmakar, A. (2023) Composites for electric vehicles and automotive sector: A review. Green Energy and Intelligent Transportation 2, 100043. https://doi.org/10.1016/j.geits.2022.100043

Zhang, W. and Xu, J. (2022) Advanced lightweight materials for Automobiles: A review. Materials & Design 221, 110994. https://doi.org/10.1016/j.matdes.2022.110994

PAPER 169 – DEVELOPMENT OF ULTRA-HIGH-PERFORMANCE CONCRETE (UHPC) USING LOCALLY AVAILABLE MATERIALS: A REVIEW

Odeyemi, S.O[1] and Olorunfemi, K.O.[2*]

[1]Department of Civil Engineering, Kwara State University, Malete, Nigeria.
[2]Department of Civil Engineering, Kwara State University, Malete, Nigeria; Department of Civil Engineering, Kwara State Polytechnic, Ilorin, Nigeria.
[*]Email: olorunfemikenny@gmail.com

ABSTRACT
The need for high-strength concrete is on the increase for good workability, high strength, and better durability. Supplementary Cementitious Materials (SCM) are finely ground substances that are used in concrete to replace a part of cement in a Mix. These SCM may be natural, manufactured or natural waste which is abundantly available in a locality. Various types of SCM have been in use. This paper reviews the use of these materials in the UHPC. It was concluded that if locally available materials are capable of producing UHPC that exhibit comparable properties of commercial mixtures, it would significantly lead to reduced costs and acceleration of its field application.

KEYWORDS: Durability, Super-plasticizer, Supplementary Cementitious Materials, Workability.

1. INTRODUCTION

Concrete is one of the most consumed materials that is widely used in the construction industries in the world (Naik, 2008). Sustainable development is fast becoming a global issue and has led to the development of various systems in the construction industry with new technology which comes with various challenges (Hani et al., 2022; Hrabova et al., 2020). Efforts have been made to reduce the cost of cement to improve profitability (Ghana et al., 2020), ensure affordability (Olutoge and Oladunmoye, 2017) and increased availability (Suhendro, 2014). Attempts have also been made to use locally available materials especially waste in conventional concrete and this effort is also made on HPC and UHPC. The materials used are generally compatible to cement since they are finally in ground form and when mixed with water they react with calcium oxide $Ca(OH)_2$ to form a hydrated phase possessing cementing properties at room temperature. These materials include Pozzolana like rice ash, fly ash, limestone etc which are locally available to meet the increasing demand for sustainable supplements for cement in concrete (McCarthy et al., 2017). The supplementary cementitious materials like silica fume, fly ash, rice husk ash and ground granulated blast slag are believed to modify the hydration and microscopic development of UHPC (Zhang et al., 1996).

Advances in the science of concrete have led to the development of a new class of cementitious composite called Ultra-High-Performance Concrete (UHPC). The Concept of UHPC was first initiated by De Larrard and Sedan in 1994 (Weina, 2017). UHPC is defined as that concrete that has a minimum specified compressive strength of more than 120 MPa with specified durability, tensile strength, ductility and toughness requirements. Fibres are generally included to achieve specified requirements (ACI 239 C, 2018). UHPC commonly consists of cement, silica fume, fine quartz sand and high range water reducing admixtures, steel fibres and low water–cement ratio ranging from 0.15 - 0.25 with a post-cracking tensile strength greater than 5MPa. It is superior to ordinary concrete because the pores are discontinuous which declines liquid penetration. It is used in the construction of highway structures, water retaining structures, bridges, hydro-power structures, pavements, offshore platforms, noise and vibration damping, tunnels and high-rise structures (Graybeal, 2011). Microstructural properties of UHPC as a notable representative of UHPC have now been highly investigated by government agencies and universities (Chegqing et al., 2018). The dense microstructure of UHPC can be attributed to its mix typically with a very low water binder ratio, mix design and composition of materials (Onkar & Singh, 2019).

Ultra-high-performance concrete (UHPC), also known as reactive powder concrete, is a new cementitious composite characterized by excellent mechanical properties and durability performance (Meng & Khayat, 2016). Ultra-high-performance concrete (UHPC) may be in demand because of its high strength, good workability and better durability. The common strategy used in increasing the strength properties of high-performing concrete is to lower the water-cement ratio and increase the cement content (Mahmud et al., 2016; S. O. Odeyemi, Anifowose et al., 2020). Ultra-high-performance concrete (UHPC) is a cement-based composite that can exhibit high strength and advanced durability properties as a result of its low water/binder ratio and fine-rich design. (Richard, 1999). Generally, the cement content required for the production of UHPC (600-1000 kg/ m^3) is approximately twice the amount of cement required in ordinary concrete (Shweta & Renisha, 2020). All the cement particles do not react due to the low water-cement ratio, leftover unhydrated cement behaves inertly and will be used in particle packing (Graybeal, 2007). Due to its high cement content, the hydration heat of UHPC can be relatively large compared to that of conventional concrete.

2. APPLICATIONS OF LOCAL MATERIALS IN UHPC

The rising trend in the use of conventional local materials adopted for construction worldwide is largely attributed to the continuous growth in the global economy and standard of living (S. O. Odeyemi, Atoyebi, et al., 2020). Figure 1. shows the percentages of the most used locally available materials in concrete industries. Fly ash, 20%, Slag (12%) and Silica fume (9%) for special projects. The physical and chemical analyses of mineral admixtures provided by the manufacturer are given in Table 1.

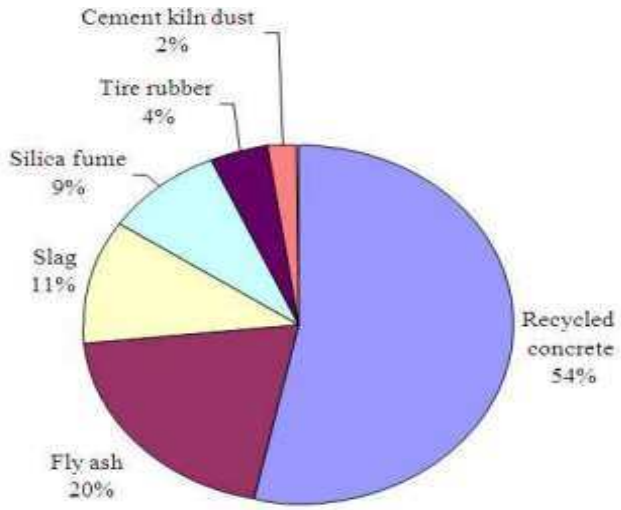

Figure 1: Most used locally available material in concrete (Ibrahim et al. 2015)

Table 1: Physical and chemical analysis of mineral admixtures

Oxide component (%)	PC	FA	SF	GGBFS	MK
CaO	62.58	4.24	0.45	34.12	0.78
SiO_2	20.25	56.2	90.36	36.41	52.68
Al_2O_3	5.31	20.17	0.71	10.39	36.34
Fe_2O_3	4.04	6.69	1.31	0.69	2.14
MgO	2.82	1.92	-	10.26	0.16
SO_2	2.73	0.49	0.41	-	-
K_2O	0.92	1.89	1.52	0.97	0.62
Na_2O	0.22	0.58	0.45	0.35	0.26
Loss of ignition	3.02	1.78	3.11	1.64	0.98

Physical Properties					
Specific gravity	3.15	2.25	2.2	2.79	2.5
Blaine Fineness(m^2/kg)	3260	287	21080	418	12000

(Source: Ibrahim et al. 2015)

Many studies have been conducted over the years to know the influences of natural admixtures on the strength properties of conventional concrete. Based on environmental and economic consequences associated with the continuous use of conventional materials, various natural admixtures such as rice husk ash, corn cob ash, eggshell ash, guinea corn husk etc. are found to replace cement adequately (Odeyemi et al., 2022).

In Germany, as a result of an extensive research project financed by the government, technical criteria and measures have been put in place to use available raw materials for UHPC, to reduce the cement content and to use fibre mixtures and non-corrosive high-strength plastic fibres to control the strength and the ductility depending on the requirements given by an individual design and construction (Fehling et al., 2003; Schmidt et al. 2003). A hybrid bridge was also constructed (Fehling et al., 2004) for pedestrians and bicycles with a length of about 135m and a maximum span of 40m consisting of precast prestressed chords and precast bridge deck elements made of UHPC with a maximum grain size of 2 mm using local materials.

Breakthroughs in the application were the very first prestressed hybrid pedestrian bridge at Sherbrooke in Canada in 1997. The replacement of steel parts of the cooling tower at Cattenom and two 20.50 and 22.50 m long road bridges used by cars and trucks at Bourg-lès-Valence in France was built in 2001 (Hajar et al, 2014, Dembovska, et al., 2017). In addition, coarse-grained UHPC with artificial or natural high-strength aggregates were developed for highly loaded columns and extremely high-rise buildings (Schmidt et al., 2003). Wang et al., (2012) reported the advantages of UHPC to include the reduced cross-sectional area, protection against rebar corrosion, reduction of thermal, shrinkage-induced cracks and disabling ingress of harmful ions due to dense cementitious matrix.

2.1 GROUND GRANULATED BLAST SLAG (GGBS) & GROUND GRANITE POWDER (GGP)

Ground Granulated Blast Slag are residues from metallurgical processes from the production of metals from ore or refinement of impure metals. They are explored from lime-based inorganic fluxes. The slags used in concrete come from the blast furnace production of iron from ore. The iron ore is fed into the furnace with coke and limestone while the slag is produced at 1300-16000 as a liquid layer floating on the top of liquid iron. It is then collected and cooled (Lee, 1974). The speed of cooling affects the properties of the slag. If allowed to cool slowly, it crystallizes to give a material having virtually no cementing materials. If cooled sufficiently rapidly to below 800 temperatures, it forms a glass which is latent hydraulic cement. This substance is then ground into a very fine powder with a minimum of 80% less than 45 microns in size. This is the cementitious material called ground granulated blast furnace slag (GGBS). GGBFS has been used for many years as a supplementary cementitious material in Portland cement concrete, either as a mineral admixture or as a component of blended cement.

Hongru et al., (2020) studied the properties of ultra-high-performance concrete (UHPC) with ground granite powder (GGP) to replace cement by different ratios from 0 - 25%. The hydration products and pore structure on the micro-scale, and the compressive and flexural strength as well as chloride permeability on the macro scale, were studied and the influence of curing conditions, i.e., standard curing (SC), warm water curing (WWC), and autoclaved curing (AC), was also explored. It was found that though the replacement of cement by GGP did not influence the morphology and chemical compositions of hydration products, however, the pore structure changed significantly over the replacement ratio, i.e., GGP

2.2 EFFECT OF GGBS IN UHPC CONCRETE

Yakinkaya & Copuroql (2021) investigated the effect of ground granulated blast furnace slag (GGBS) replacement of cement at 0%, 30% & 60% on the hydration heat, strength and microstructural characteristics of UHPC. The result showed that UHPC with GGBS is more sensitive to ambient temperature from cumulative heat. 60% replacement reduces cumulative heat released by 36% and 28% at 20 0C and 35 0C respectively. That is, as a result of high Portland cement dosage, the hydration of heat of UHPC can be relatively high compared to conventional concrete. Ground Granulated Blast Furnace Slag (GGBS) can be used in UHPC formulation for reducing Portland cement dosage thereby limiting hydration.

2.3 SILICA FUME (SF)

Silica fume, a by-product obtained from the reduction of high-purity quartz with coal or coke and wood chips in an electric arc furnace during the production of silicon metal or ferrosilicon alloys. Silica fume condensed from the gases escaping from the furnaces has a very high content of amorphous silicon dioxide and consists of very fine spherical particles. Ferrosilicon alloys are produced with nominal silicon contents of 61 to 98%t. When the silicon content reaches 98 %, the product is called silicon metal rather than ferrosilicon. As the silicon content increases in the alloy, the SiO2 content will increase in the silica fume. (ACI 234 R., 1996). Most silica fumes range from light to dark grey in colour. Because SiO_2 is colourless, the colour is determined by the non-silica components, which typically include carbon and iron oxide (Aitcin, 1998).

2.4 EFFECT OF SILICA IN UHPC CONCRETE

Kamal et al., 2020 reported that with the current search for the possibility of producing UHPC using locally available material in Egypt, the effect of silica fume, quartz powder, steel powder and fibre type and dosage of superplasticiser were investigated in 49 types of concrete mixes. The effects of the variables were considered and investigated. Three percentages of silica fumes 10%, 15% and 20% were used as replacements for cement content. Quartz powder and steel powder with a percentage of 10% of sand was also used. Different type of high-range water reducer from 0% -2% by weight of powder was used. the weight of steel fibre was 40-80kg/m^3 water to powder ratio was 0.2-0.45. The results showed that it is possible to use local material to produce UHPC and that the use of 10% silica filling as replacement of cement content at 10% water per power resulted in compressive strength increase of 43N/mm^2, 67.4 N/mm^2, 127 N/mm^2 at 3, 7 28 days respectively while the inclusion of steel fibres with 40 kg/m^3 increase the compressive strength to 64.3 N/mm^2, 88N/mm^2 and 135N/mm^2 at 3,7 days and 21 days respectively. Hunchate (2014) studied the incorporation of silica fume and superplasticizer on concrete and observed that the compressive strength increased as the proportion of silica fume rises to 15%.

2.5 EFFECT OF AVAILABLE AGGREGATE IN UHPC

Alsaman, (2018) also reported in research where three gradations of Arkaneses river sand were used for the production of UHPC. Sand A had a natural graduation that was distributed from the 4.75um Sieve to the 75um sieve. Sand B had a smaller particle size which range from the 600um sieve to being retained on the 300um while the Type C sand passed the sieve 75um, These were used to evaluate the effect of curing regimes on the compressive strength of concrete using silica fume. A 90-day compressive strength of 155MPa was obtained with a total binder of 1,009 kg/m^3, 5% silica fume and type Sand A.

Hani et al., (2022) studied the influence of lightweight aggregate (LWA) on the strength properties and microstructure of UHPC, enhancing the spalling resistance by the elevated temperature of 100 ºC and 200 ºC, prepared four different mixtures of UHPC with 0.2 water-binder ratio and varying percentages of LWA at partial replacement of 0%, 5%, 10% and 15%. The ingredient of UHPC i.e. cement, silica fume, silica sand, and LWA was mixed with water and superplasticizer until a viscoplastic liquid is obtained and steel fibre was finally added. The results showed that the compressive strength of the UHPC specimen was reduced with increasing the content of LWA at ambient temperature, but the

compressive strength of the UHPC specimens prepared with LWA improved when exposed to elevated temperatures. The replacement of 10% of the silica sand with LWA led to an increase in the compressive strength from 100 MPa to 110 MPa after exposure to 200 °C; however, the flexural strength decreased from 23.6 MPa to 18.3 MPa. On the contrary, the flexural strength of UHPC increased with the inclusion of LWA at an ambient temperature but reduced with high-temperature exposure. respectively.

2.6 EFFECT OF STEEL FIBRE IN UHPC

Haitham et al. (2020) concluded that the ability to produce UHPC depends on available materials and optimises the proportion of these materials. Four fraction volume of steel fibre content was adopted which were 0%, 1.5%, 3%, and 4.5%. The results showed that UHPC reaching 150 N/mm^2 is possible and every increase in steel fibre content will improve the compressive strength by about 40% of the steel fibre content of 4.5%. The increments of the steel fibre are needed to study its effect on the mechanical properties of ultra-high-performance concrete.

Chujie et al., (2020) studied the combinations of single fibres and nine combinations of hybrid fibres to analyse the mechanical properties and crack propagation behaviour of ultra-high-performance concrete (UHPC) by digital image correlation. He found out that in comparison to single fibres, the long fibres had a more pronounced effect than short fibres and a hybrid combination of medium-length fibre (Vf = 0.5%) and long fibre (Vf = 1.5%) generated a better flexural behaviour in terms of post- crack strength, deflection, toughness, than the other hybridization series. A digital image correlation (DIC) technique was applied to record the evolution of surface deformation. The hybrid use of longer fibre replaced the shorter fibre, long fibre replaced medium length fibre and short fibre, medium length fibre replaced short at lower replacement ratios (0.5% and 1.0%), the crack shapes were presented linear variation and showed an abrupt change and did not have a constant increment at higher replacement ratios (1.5% and 2.0%).

3. CONCLUSION

Various researchers who have investigated the use of local materials in UHPC discovered that if locally available materials are capable of producing UHPC that exhibits comparable properties of commercial mixtures, it would significantly lead to reduced costs and acceleration of its field application.

ACKNOWLEDGEMENT

The Authors acknowledge the input of the academic staff of the Department of Civil and Environmental Engineering, Kwara State University, Malete.

REFERENCES

ACI 239 C. (2018). Minutes of SubCommittee Meeting. Structural Design of UHPC.

ASTM C311/C311M-18. (2018). American Society Testing Materials, C618, Specification For Fly Ash and Raw or Calcined Natural Pozzolana for use as Mineral/admixture in Portland cement concrete.

Aïtcin, P. (1998). High-Performance Concrete. CRC Press: Boca Raton, FL, USA.

Alsalman et al., 2020. Development Of Ultra-High-Performance Concrete With Locally Available Materials. Construction And Building Materials Journal. Vol 133. Pg 135-145.

Chegqing, W., Jun, L., & Yu, S. (2018). Develpoment of Ultra High Performance Concrete against Blast. Science Publishing in Civil & Structural Engieering.

Dembovska, L., Bajare, D., Pundiene, I., Vitola, L., 2017. Effect of pozzolanic additives on the strength development of high performance concrete. Procedia Eng 172, 202–210. https://doi.org/10.1016/j.proeng.2017.02.050.

Gana, A.J., Atoyebi, O.D., Ichagba, R.B., 2020. Effect of different brands of Nigerian cement on the properties of pervious concrete Effect of different brands of NigerianNcement on the properties

of pervious concrete. IOP Conf. Ser. Earth Environ. Sci. 445 https://doi.org/10.1088/1755-1315/445/1/012029.

Graybeal, B. A. (2007). Compressive Behavior of UHP Fibre Reinforced Concrete. ACI Materias Journal, 104(2), 146.

Graybeal, B. A. (2011). Material Property Characteraisation of UHPC. U.S Federal Highway Administration.

Hani, A., Saleh, A. ., Oussuama, E., Musa, A., Yasser, I., Aref, A. ., & Abdulrahman, F. . (2022). Mechanical and Microstrucural Properties of UHPC with Light Weight Aggregate. Building MDPL, 1782–1795.

Hajar Z., Simon A., Lecointre D., Petitjean J., "Construction of The First Road Bridges Made of UHPC". 3rd International Symposium on HPC, Orlando 2003.

Hongru, Z., Tao, J., Bingjian, H., & Hungwei, H. (2020). Performance of UHPC with Cement partially Replaced by Ground Granite Powder (GCP) under Different Curing Condition. Construction Building Materials. https://en.wikipedia.org/wiki/Cement

Hrabova, K., Teply, B., & Vymazal, T. (2020). Sustainability Assessment of Concrete Mixes. IOP Conf. Ser. Earth Environ. Sci., 444(012021).

Ibrahim A. S AL-Jumailya , Nahla Najib, Qays: (2015); An overview on the Influence of Pozzolanic Materials on Properties of Concrete, International Journal of Enhanced Research in Science Technology & Engineering, Vol. 4 Issue 3, March-2015, pp: (81-92),

Kamal, M. .M., Safan, M. A., Etman, Z. A. and Salam, R. A. (2013) "Production Of Ultra High-Strength Concrete Using Local Materials" Engineering Research Journal, Minoufia University, Vol. 36, No. 1. PP: 91-100

Lee, M.G., and Wang , Y.C., "A Preliminary Study of Strengthening Concrete Members using Reactive Powder Concrete," Journal of Chinese Civil and Hydraulic Engineering, Vol. 16, No. 4, (2004), pp. 715-721.

Liu, Y., & Wei, Y. (2021). Internal Curing by Porous Calcined Bauxite Aggregate in Ultrahigh-Performance Concrete. Journal of Materials in Civil Engineering., 33.(04020497.).

McCarthy, M.J., Robl, T.L., Csetenyi, L.J., 2017. Recovery, processing, and usage of wet stored fly ash. In: Coal Combustion Products (CCP's) Characteristics, Utilization and Beneficiation, pp. 343–367. https://doi.org/10.1016/B978-0-08-100945-1.00014-9.

Mahmud, H., Bahri, S., Yee, W., & Yeap, Y. (2016). Effect of Rice Husk Ash on the Strength and Durability of High Strength-High Performance Concrete. International Journal of Civil & Enviromental Engineering, 10(3), 390–395.

Meng, W., & Khayat, K. (2016). Mechanical properties of ultra-high-performance concrete enhanced with graphite nanoplatelets and carbon nanofibres. Compos. Part B Eng., 107, 113–122.

Naik, T. . (2008). Sustainability of Concrete Construction. Practice Periodical on Structural Design and Construction, https://doi.org/10.1061/(ASCE)1084-0680(2008)13:2(98), 98–103

Odeyemi, S.O, Mukaila, A., Bello, A., Giwa, Z., & Wilson, N. (2022). Strength Properties and Microstructure of Sandcrete Blocks Incorporated with Maize Straws. Advance Engineering Forum, 46, 71–78.

Odeyemi, S. O., Anifowose, M., & Oduoye, W. (2020). Mechanical Properties of High-Performance Concrete with Guinea Corn Husk Ash as Addictive. LAUTECH Journal of Civil and Enviromental Studies, 50(0131).

Odeyemi, S. O., Atoyebi, O. D., & Ayo, E. K. (2020). Effect of Guinea Corn Husk Ash on the Mechanical Properties of Lateritic Concrete. IOP Conference Series: Earth and Environmental Science, 445(1). https://doi.org/10.1088/1755-1315/445/1/012034

Olutoge, F.A., Oladunmoye, O.M., 2017. Bamboo leaf ash as supplementary cementitious material. Am. J. Eng. Res. 6, 1–8.

Onkar, M., & Singh, P. (2019). An Overview of Microstructural & Material Properties of UHPC. Journal of Sustainable Cement- Based Materials, 8(3), 1–47.

Richard, I. (1999). The Nature of C-S-H in Hardened Cement. Cement and Concrete Research, 29(8), 1131–1147.

Schmidt, M., Fehling, E., Teichmann, T., Bunje, K., & Bornemann, R. (2003). Ultra-high-performance concrete: Perspective for the precast concrete industry. Beton Und Fertigteil-Technik, 3, 16–29.

Shweta, M., & Renisha, M. (2020). Reviewing Some Properties of UHPC. International Journal of Research and Technology, 09(06), 14–135.

Suhendro, B., 2014. Toward green concrete for better sustainable environment. Procedia Eng 95, 305–320. https://doi.org/10.1016/j.proeng.2014.12.190.

Wang, C., Yang, C., & Liu, F. (2012). Preparation of UHPC with Common Technology and Materials. Cement and Concrete Conposite, 34(4), 533–544.

Weina, M. (2017). Design and performance of cost-effective ultra-high-performance concrete with prefabricated elements. Missouri University of Science and Technology.

Yakinkaya, C., & Copuroqlu, O. (2021). Hydration Heat, Strength and Microstructure- Characteristic of UHPC Containing Blast Furnace Slag. Journal of Building Engineering, 34.

Yakinkaya, C., & Copuroqlu, O. (2021). Hydration Heat, Strength and Microstructure- Characteristic of UHPC Containing Blast Furnace Slag. Journal of Building Engineering, 34.

Zhang, M., Lastra, R., & Malhotra, V. (1996). Rice-Husk Ash Paste and Concrete: Some Aspects of Hydration and the Microstructure of the Interfacial Zone between the Aggregate and Paste. Cement and Concrete Research, Vol 26(6), 963–977.

PAPER 170 – PLANT DISEASE DETECTION USING CNN WITH SPATIAL ATTENTION

A .Ridwanullah [*], O .Abdulbasit,O . Enoch,A. Ameenullah[1]

[1]Department of Agricultural and Biosystems Engineering, University of Ilorin, Ilorin, Nigeria.
[*]Email: 17-30ga004@students.unilorin.edu.ng

ABSTRACT
Agriculture is one of the most significant contributors to the Nigerian economy. According to statistics by Statista, agriculture contributed about 30% to the country's GDP between July and September 2021, making it the second-largest contributor after oil. However, a significant problem of crop production is pests and disease. Late detection of plant disease causes huge losses to farmers through low returns and depreciated farm produce. The detection of disease is widely done manually by farmers on farms through physical inspection, the result of which may be inaccurate. This paper presents a novel approach to plant disease detection using a Convolutional Neural network (CNN) with spatial attention. The proposed method is applied to a dataset consisting of images of sample leaves of various plants, including apple, blueberry, cherry, corn, grape, orange, peach, potato, raspberry, soybean, squash, strawberry, and tomato. The CNN model was built using transfer learning. The pre-trained EfficientNet80 model was used as the base model, with the final classification layer replaced with a new dense layer and an output layer for binary classification. The model achieved an accuracy of 85%, making the proposed method a better method for detecting plant diseases at an early stage, improving crop yields, and reducing the need for pesticides. It can also be extended to other types of plant diseases and integrated into existing agricultural systems.

KEYWORDS: Plant Disease, Convolutional Neural Network Spatial Attention, Deep Transfer Learning

1. INTRODUCTION

The world's population is growing at an exponential rate, and this necessitates the need for massive food production in order to reduce the rate of hunger (Paymode & Malode, 2022). Due to the challenge of food insecurity ravaging the globe, resulting from inappropriate control of crop pests and diseases, researchers have sought several ways to find lasting solutions to this effect. According to a report from the State of Food Security and Nutrition Report (FAO, 2022), an estimated 29.3 percent of the global population of 2.3 billion people were moderately or severely food insecure in 2021. Healthy plants have the power to help end hunger, reduce poverty, protect the environment, and boost economic development. Plant disease causes damage to farmland and has a detrimental effect on the quality of agricultural produce. In agriculture, it's important to keep an eye on the condition of farm crops (Chaitanya P. *et al*., 2023). The ability to monitor vast fields of crops and see disease symptoms as soon as they appear on plant leaves makes the detection and recognition of crop diseases a significant research topic. Finding a quick, efficient, least expensive, and effective method to identify crop disease occurrences is therefore crucial (Paymode & Malode, 2022). Visual inspection of plants by experienced experts has been the most definitive means of disease diagnosis, which is time-consuming and expensive. Alternately, with the growing use of digital cameras, automated diagnostic technologies that analyze digital pictures of plants and identify plant diseases and pests have been created to increase the precision and effectiveness of plant disease and pest diagnosis (Han et al, 2021).

Nigeria is a nation with a fast-growing population and a noteworthy agricultural industry, with agriculture contributing significantly to the nation's GDP. Over 70% of Nigerians engage in the agricultural sector, mainly at a subsistence level (FAO, 2022). The development of the nation's agricultural industry depends on disease-free crop output. Plant disease causes damage to farmland and has a detrimental effect on the economy. In agriculture, it is important to keep an eye on the condition of farm crops (Chaitanya P. e*t al.,* 2023). The ability to monitor vast fields of crops and see disease symptoms as soon as they appear on plant leaves makes the detection and recognition of crop diseases a significant research topic. Finding a quick, efficient, least expensive, and effective method to identify crop disease occurrences is therefore crucial (Paymode & Malode, 2022). Visual inspection of plants by experienced experts has been the most definitive means of disease diagnosis, which is time-consuming and expensive. Alternately, with the growing use of digital cameras, automated diagnostic technologies that analyse digital pictures of plants and identify plant diseases and pests have been created to increase the precision and effectiveness of plant disease and pest diagnosis (Han *et al*., 2021).
In recent years, the invention of deep learning has gained massive recognition and has done better in several applications than the current methods (Liu & Wang, 2021). Researchers have introduced the use of convolutional neural networks (CNNs), which have displayed astounding performance in picture identification and detection

tasks. Without the assistance of a human, a CNN is capable of categorising an input item into the appropriate category and extracting visual information through a sequence of convolution and pooling processes. For the identification of diseases and pests in agriculture, a number of deep learning techniques built around CNN have been developed. These outperform traditional machine learning methods (Han *et al.*, 2021). Saleem *et al*. (2019) reported that CNNs achieved high levels of accuracy in identifying plant diseases from images, outperforming other machine learning models.

Golhani *et al.* (2018) discussed various advanced neural network techniques that can be used for processing hyperspectral data, with a special focus on plant disease detection. The article highlighted the use of CNNs for classifying hyperspectral images of diseased plants and emphasised the need for developing robust and efficient CNN models for plant disease detection. Controlling damaged leaves during crop growth is an important step. Early disease identification, classification, and analysis of sick leaves, as well as potential remedies, are always beneficial to agriculture. Plant disease and pest identification can be carried out by means of digital image processing. In recent years, deep learning has made breakthroughs in the field of digital image processing that are far superior to traditional

A study published in 2019 highlighted the potential of deep learning models, including CNNs, for the detection and classification of plant diseases. The study reported that CNNs achieved high levels of accuracy in identifying plant diseases from images, outperforming other machine learning models (Saleem *et al.,* 2019). Furthermore, advanced neural network techniques can be used for processing hyperspectral data, with a special focus on plant disease detection. use of CNNs for classifying hyperspectral images of diseased plants and the need for developing robust and efficient CNN models for plant disease detection.

Singh *et al*., (2020) provides a state-of-the-art survey of various techniques for plant disease detection and discusses the use of CNN for identifying different plant features based on varied statistics. The study concludes that CNN-based models have shown promising results for detecting plant diseases with high accuracy rates. In addition to CNN, other machine-learning techniques have also been utilised for plant disease detection. For example, one study (Singh *et al.,* 2020) discusses the use of SVM (Support Vector Machine) and ANN (Artificial Neural Network) in addition to CNN. These studies suggest that CNNs are a promising approach for plant disease detection, offering high accuracy and robustness in identifying diseased plants. However, further research is needed to develop more efficient and accurate CNN models for plant disease detection and to explore the potential of other machine-learning techniques for this application (Saleem *et al.,* 2019). Therefore, the aim of this study was to develop a model for recognizing and identifying plant diseases using convolution neural networks with spatial networks.

2. METHODOLOGY

2.1 Datasets

The data used for this research was obtained from the Kaggle.com website. The dataset is titled "Plant Village Dataset," and it consists of 70,000 high-quality images of diseased and healthy plant leaves from different species, including apple, blueberry, cherry, corn, grape, orange, peach, potato, raspberry, soybean, squash, strawberry, and tomato. Each species has three data splits (train, test, and validation), with consistent categories across all splits.

2.2 Data Pre-processing

Before training the model, the dataset is pre-processed to prepare it for use. This involves resizing the images to a fixed size of (256, 256) pixels, normalising the pixel values to a range of [0, 1], and performing data augmentation techniques such as rotation, flipping, and zooming to increase the dataset size and improve model generalisation. The data augmentation helps to create new samples of photos from the available photos, which thereby increases the dataset size. The proposed method for training the model in the subsequent stage subsequently incorporates the photographs as input. The newly-trained architectural model is then used to predict the never-before-seen visuals.

2.3 Transfer Learning

The proposed plant disease detection model is built using transfer learning, specifically the pre-trained EfficientNet80 model. The pre-trained model is used as a feature extractor, and only the final fully connected layer is modified for our specific task. The transfer learning approach takes advantage of the pre-trained model's ability to recognize general features in images while allowing us to fine-tune the model for our specific task.

2.4 CNN Architecture

The CNN model was built using transfer learning. The pre-trained EfficientNet80 model was used as the base model, with the final classification layer replaced with a new dense layer and an output layer for binary classification (diseased or healthy plant). The model was then fine-tuned with the pre-processed dataset. The CNN architecture is given in figure 1 below.

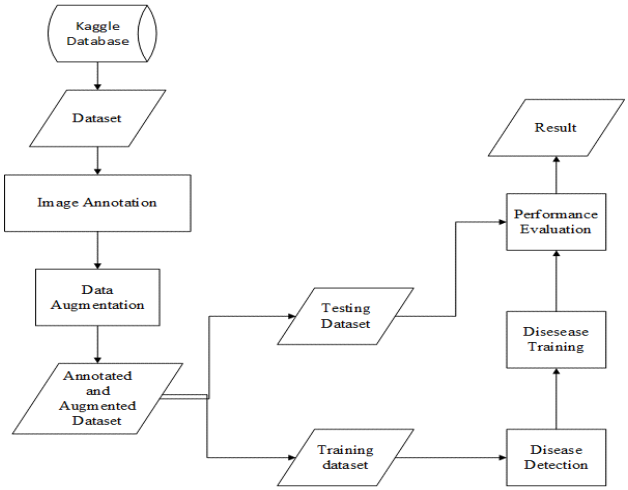

Figure 1: overview of deep-learning approach to plant disease detection (adapted from*(Fuentes et al., 2017)*)

2.5 CNN with Spatial Attention

To further improve the model's performance, CNN with spatial attention was used. Spatial attention focuses on the most informative regions of an image, allowing the model to better identify important features related to plant diseases. Spatial attention was implemented in the CNN model to improve its performance in detecting plant diseases. The CNN model's convolution and pooling layers were combined with a spatial attention module to achieve this. In summary, the spatial attention module was designed to attend to the most important features in the image and suppress less important features.

Specifically, spatial attention module used took the output feature maps of the last convolution layer as input and generated attention maps that are multiplied with the feature maps to produce weighted feature maps.

2.6 Training and Validation

The model was trained on a system of available RAM of 12.0 GB using the pre-processed training set with a batch size of 32 and for a total of 50 epochs. During training, the model was optimised using the Adam optimizer and a categorical cross-entropy loss function.

2.7 Testing and Evaluation

The performance of the CNN model was evaluated using the pre-processed testing set. The model was evaluated using the accuracy as the metric. The model's performance was measured and verified with training, testing, and validation sets and the accuracies and losses were determined as in Figures 2 and 3.

3. RESULTS AND DISCUSSION

The result, as in fig 2 and fig 3, shows that the training and validation accuracies become higher with the number of epochs while the losses in both the training and validation sets decreases with the number of epochs. The number of epochs denotes the number of times the entire datasets is worked through in the learning algorithm. This is due to the fact that the model produces a lot of errors in the early epochs as it attempts to identify the fundamental patterns in the data. However, when the model is trained for more epochs, the more complex patterns in the data it can recognize and the more accurate it becomes. Overall, the model gave an evaluation accuracy of 85%.

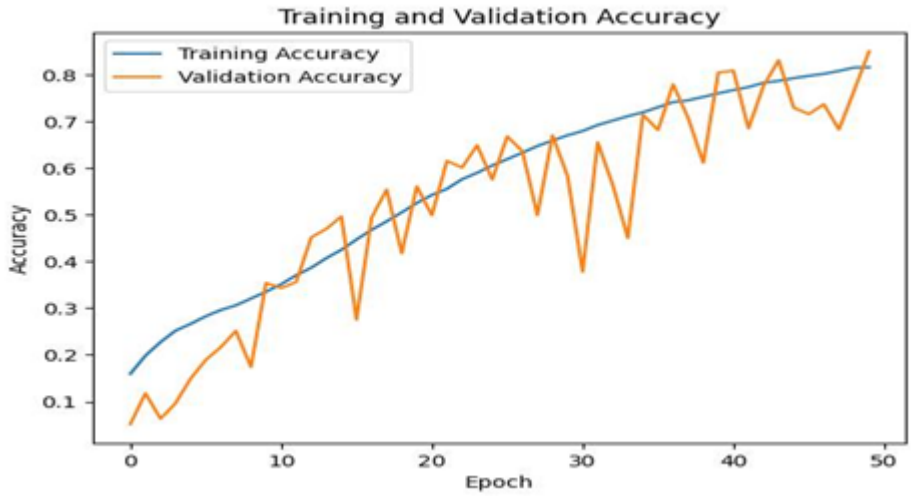

Fig. 2: Training and Validation accuracy

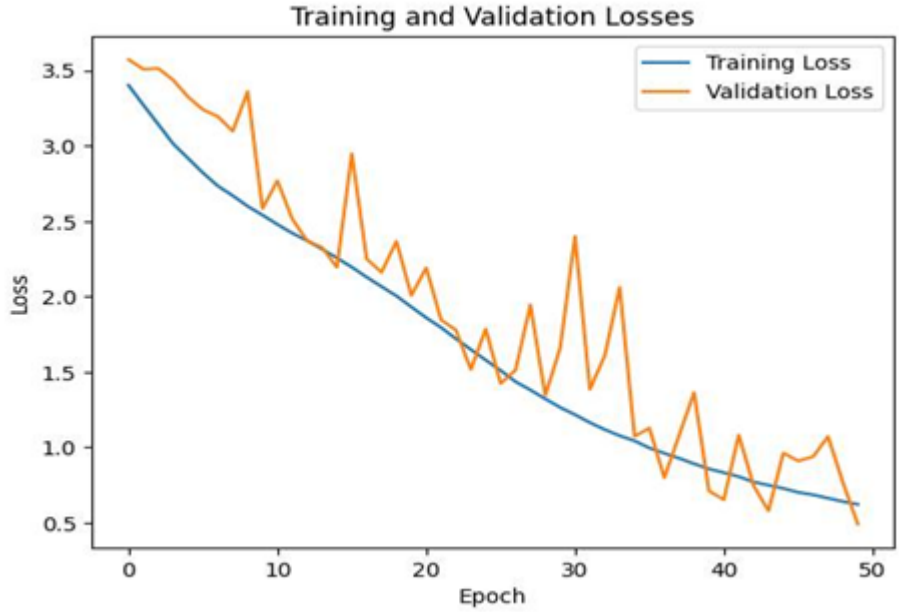

Fig 3: Training and Validation Losses

4. CONCLUSION

In conclusion, this study showed that a CNN model with spatial attention can effectively detect plant diseases with high accuracy. The use of transfer learning and spatial attention improved the performance of the model, resulting in high accuracy and performance metrics. This study provides a useful framework for future research in the area of plant disease detection using deep learning.

ACKNOWLEDGEMENT

Authors gratefully recognize the immense support received from Adeyi Qudus Babatunde and Samuel Aregbesola who are both alumni of the Department of Agricultural and Biosystems Engineering, University of Ilorin, Nigeria.

REFERENCES

1. Chaitanya P, S., K, H., Priyanka K, M., Sri K, P., & D, P. (2023). Plant disease detection using cnn. In S. Jagannath Nanda & R. Prasad Yadav (Eds.), *Data Science and Intelligent Computing Techniques* (2023rd ed., pp. 47–54). Soft Computing Research Society. https://doi.org/10.56155/978-81-955020-2-8-5

2. Paymode, A. S., &Malode, V. B. (2022). Transfer learning for multi-crop leaf disease image classification using convolutional neural network vgg. Artificial Intelligence in Agriculture, 6, 23–33. https://doi.org/10.1016/j.aiia.2021.12.002

3. Liu, J., & Wang, X. (2021). Plant diseases and pests detection based on deep learning: A review. Plant Methods, 17(1), 22. https://doi.org/10.1186/s13007-021-00722-9

4. Han, C. H., Kim, E., Doan, T. N. N., Han, D., Yoo, S. J., &Kwak, J. T. (2021). Region-aggregated attention CNN for disease detection in fruit images. PLOS ONE, 16(10), e0258880. https://doi.org/10.1371/journal.pone.0258880

5. Saleem, M. H., Potgieter, J., &Arif, K. M. (2019). Plant disease detection and classification by deep learning. Plants, 8(11), 468. https://doi.org/10.3390/plants8110468

6. Golhani, K., Balasundram, S. K., Vadamalai, G., & Pradhan, B. (2018). A review of neural networks in plant disease detection using hyperspectral data. Information Processing in Agriculture, 5(3), 354–371. https://doi.org/10.1016/j.inpa.2018.05.002

7. Chen, Junde, et al. "Using Deep Transfer Learning for Image-Based Plant Disease Identification."*Computers and Electronics in Agriculture*, vol. 173, June 2020, p. 105393. *DOI.org (Crossref)*, https://doi.org/10.1016/j.compag.2020.105393.
8. Singh, V., Sharma, N., & Singh, S. (2020). A review of imaging techniques for plant disease detection. Artificial Intelligence in Agriculture, 4, 229–242. https://doi.org/10.1016/j.aiia.2020.10.002
9. *Nigeria at a glance | fao in nigeria | food and agriculture organization of the united nations*. (n.d.). Retrieved 12 May 2023, from https://www.fao.org/nigeria/fao-in-nigeria/nigeria-at-a-glance/en/

10. Fuentes, A., Yoon, S., Kim, S., & Park, D. (2017). A robust deep-learning-based detector for real-time tomato plant diseases and pests recognition. *Sensors*, *17*(9), 2022. https://doi.org/10.3390/s17092022

PAPER 172 – SELECTION AND PORE DISTRIBUTION ANALYSIS OF BIOCOMPOSITE IMPLANTS FOR LOAD-BEARING BONE REPLACEMENT

H. K. Ibrahim [1,3*], M. S. Abolarin[1], A. S. Abdulrahman[2], O. Adedipe[1], U. G. Okoro[1]

[1]Department of Mechanical Engineering, School of Process, Infrastructure and Technology, Federal University of Technology Minna, Nigeria.
[2] Department of Material and Metallurgical Engineering, School of Process, Infrastructure and Technology, Federal University of Technology Minna, Nigeria.
[3] Department of Mechanical Engineering, Faculty of Engineering and Technology, University of Ilorin, Nigeria.
*Email: Ibrahim.kh@unilorin.edu.ng

ABSTRACT
Fabrication of biocomposites to promote bone growth through pore distribution and gradient formation for load-bearing bone replacement have gained attention due to their excellent mechanical properties and biocompatibility. This research study aims to investigate the selection and pore distribution analysis of homogenous, porous, and gradient biocomposite implants for load-bearing bone replacement. The study utilises powder metallurgy, scanning electron microscopy (SEM) and Image J software to produce and characterise the pore size distribution of the biocomposites, respectively. The software can segment the image to isolate the pores from the rest of the implant, measure the size of individual pores, and generate pore size distribution plots. The radar chart was adopted to compare and evaluate the mechanical strength of various biocomposite implants to identify the most suitable implant for load-bearing bone replacement. The findings of this study revealed the gradient and porous biocomposites exhibited desired mechanical properties with porosity of 20.67 and 27.72 % pore size up to 134 and 256 **μ**m, compressive strength of 162 and 95 MPa and compressive modulus of 30.42 and 28.3 GPa respectively**.** The SEM analysis, coupled with pore size distribution and porosity percentage measurements, offers valuable information for optimising the design and fabrication of biomaterials with enhanced properties. Radar chart analysis further contributes to a comprehensive evaluation of the implants' mechanical and physical characteristics.

KEYWORDS: Biocomposite, Pore, Mechanical, Properties, Selection and Image J

1. INTRODUCTION

Bone atrophy, also known as bone loss or osteoporosis, is a common condition characterised by decreased bone mass and deterioration of bone tissue. This condition often leads to weakened bones, increased fracture risk, and reduced quality of life for affected individuals (Poliakov *et al.,* 2019). In severe cases, load-bearing bones may become significantly compromised, necessitating implants for bone replacement (Bahraminasab and Farahmand, 2017). Traditional implants for load-bearing bone replacement are typically made from metallic materials such as titanium, cobalt chromium alloy or stainless steel. While these implants provide structural support, they often lack the necessary biological properties to promote bone growth and integration with the surrounding tissue (Cabezas-Villa *et al.,* 2018). Consequently, researchers and medical professionals have focused on developing biocomposite implants as an alternative solution to tailor the structural material for required mechanical and physical properties (Krishna and Suresh, 2022).

Biocomposite implants are engineered materials composed of organic and inorganic components. These materials possess a unique mechanical strength, biocompatibility, and bioactivity, making them ideal for load-bearing bone replacement and repair (Oshkour *et al.,* 2015). Biocomposite implants can provide both mechanical support and a favourable environment for new bone formation by mimicking the natural structure of bone. The selection of appropriate mechanical, physical properties and pore distribution is crucial for optimising the performance and functionality of these implants. A radar chart, a spider chart, is a graphical method utilised to select materials and process parameters in machining and manufacturing industries (Holota *et al.,* 2015; Wan *et al.,* 2013; Porter and Niksiar, 2018). This chart displays multivariate data as a two-dimensional chart of three or more quantitative variables represented on axes starting from the same point (Wan *et al.,* 2013). The relative position and angle of the axes in the radar chart provide the deviation degree of the actual value and the reference value of each index as required for the selection implant in the load-bearing application.

In selecting a load-bearing implant, biomechanical properties play a vital role in determining the implant's ability to withstand the mechanical stresses encountered during normal physiological activities. The implant's mechanical strength, stiffness, and fracture toughness must be carefully considered to ensure long-term stability and durability

(Mantripragada *et al.,* 2012; Moghadasi *et al.,* 2022). Additionally, the implant should have a similar or close modulus to the natural bone to minimise stress-shielding effects and promote proper load transfer to the surrounding tissue (Bahraminasab and Farahmand, 2017). The physical properties of biocomposite implants, including density, porosity, and surface characteristics, have been reported to be essential for bone integration (Jawad *et al.,* 2015). The implant should possess an appropriate density to match that of the host bone, which allows for efficient load transfer and prevents stress concentration at the implant-bone interface. The porosity in the implant facilitates nutrient diffusion, vascularisation, and cell infiltration, promoting bone ingrowth and enhancing the implant's long-term stability (Wo *et al.,* 2020).

Choy *et al.* (2015) revealed Ti/CaP biocomposites with a 1.67 atomic ratio have a porosity of 26%, pore size up to 152 um, compressive strength of 212 MPa and compressive modulus of 12 GPa. Wo *et al.* (2020) reported the micro-pore structure of porous Ti-6Al-4V scaffolds (pTi) produced 3D printing. The average pore size and porosity of pTi were obtained in the range of 300 ± 9 µm - 804 ± 10 µm and 42.7 ± 1.1 - 58.9 ± 1.3%, respectively. The pTi facilitated the adhesion and differentiation of osteoblast when pore size decreased, or porosity increased. Taniguchi *et al.* (2016) reported that the porous Ti-6Al-4V (pTi) implants fabricated from additive manufacturing with a porosity of 65% and pore size of 600 µm had better fixation ability and more significant bone ingrowth than those with pore sizes of 300 and 900 µm. Cetinel *et al.* (2019) fabricated Ti foams using the space holder method for bone substitute materials. The result shows that the foam samples with ~60% porosity had compressive strength comparable to that of cortical bone, and the samples with ~80% porosity displayed compressive strength similar to that of cancellous bone.

However, the pore size and distribution complexity affected the strength, especially the implants applied for load-bearing bone replacement. The Pore distribution analysis is a critical aspect of designing biocomposite implants. It is considered a key measure in many engineering calculations to quantify the complex geometry of the pore space (Oliveira *et al.,* 2020**;** Safari *et al.,* 2021). An optimal pore distribution allows for uniform bone ingrowth and vascularisation, enhancing the implant's integration with the host bone. Many researchers focused mainly on manufacturing implants with porosity percentages that revealed similar stiffness and bone ingrowth properties without considering another design pattern to correct the strength and stability of the implants. Therefore, this study aims to conduct a selection and pore distribution analysis of biocomposite implants for load-bearing bone replacement.

2. MATERIALS AND METHOD

2.1 Fabrication of Biocomposite Implants

The biocomposite specimens were produced in different design patterns, including dense, porous and gradient biocomposites using the powder metallurgy technique. The biocomposite samples were fabricated based on formulation compositions of pure titanium (P-Ti), cow bone-based hydroxyapatite (Ha), $CaCO_3$ (61.23Ti-18.41Ha-15.2$CaCO_3$) and constant volume fraction of Polyvinyl Alcohol (PVA) as binder and stabiliser. The biomaterial powders were mixed and blended using a Jar mixer for 20 min. Subsequently, the powder blends were poured into the fabricated cylindrical die with dimensions of 30mm height, 20mm internal diameter and 30mm outer diameter. The mixtures were uni-axially compacted using WEIBER P100HE electrically operated hydraulic press under a pressure of 400 MPa for 30 min. The compacted sample was ejected to obtain green biocomposite and preheated at a temperature of 200 ºC to remove binder PVA), and lubricant as reported by Mara (2015). The wall of the circular die mould and top punch of the hydraulic press was adequately lubricated to avoid agglomeration of the specimen during ejection. The ejected samples were sequentially cleaned in deionised water containing several drops of acetone to eliminate contaminants. The preheated green biocomposite samples were further sintered under sintering temperatures of 800 ºC for two hours in Murfle Furnance, and the heating rate was 10 °C/min. Similar procedures were adopted for the fabrication of porous biocomposite specimens. However, the space holder (SH) method was utilised to fabricate porous biocomposite samples with reported ranges of space holders in the literature for optimal porosity (Cetinel et al. 2018). The fabrication involves mixing of biomaterial compositions of 59.31Ti-16.19 (Ha+$CaCO_3$)-9.4 % of Ammonium Bicarbonate with 100 um particle size as space holder (SH) material and decomposed at 110 ºC. Followed by the addition of binder, stabiliser and lubricant and poured in cylindrical die mould. The green porous samples were compacted and sintered. The gradient biocomposite (GB) sample was produced from the different compositions (100Ti, 61.23Ti-18.41Ha-15.2$CaCO_3$ and 59.31Ti-16.19 (Ha+$CaCO_3$)-9.4SH) biomaterial powders and separately poured in the die mould of 20mm internal diameter and 30mm height dimensions after blending processes using SNE FOURE 28A2092 Jar Mixer, for 20 minutes. Three separate layers formed were stacked and compacted uni-axially using WEIBER P100HE electrically operated hydraulic press with 400 MPa to obtain green-gradient composite biomaterial samples. The wall of the circular die mould and the top punch of the hydraulic press was lubricated correctly to avoid

agglomeration of the specimen during ejection. The green-graded biocomposite samples were finally sintered at 800 ºC temperatures for two hours in Muffle electric furnace.

2.2 Characterisation and Pore Distribution Investigation

The samples were characterised on Zeiss Ultra PLUS FEG scanning electron microscope (SEM) using the Oxford instruments detector and Aztec 3.0 software SP1. The SEM micrographs were imported for the analysis and examined for porosity and pore size distribution analysis using an open-source image processing software (ImageJ 1.42). And the porosity is determined by using the image volume method to sum up the porosity pixels of all analysed images and by dividing that value by the sum of the areas observed in these images. Then this obtained value was multiplied by 100%. These calculations have been conducted without taking into account those areas which are revealed in the segmented images. Image processing has been utilised to evaluate the biophysical parameters such as porosity and pore size distribution (Safari *et al.* 2021). By establishing porosity from routine core analysis as expected results, the porosity volume obtained from image processing is compared with the pore volume of bone established in the literature (Morgan *et al.* 2018).

2.3 Determination of Biomechanical and Physical Properties of Biocomposites

The compression test was conducted following ASTM 3039-79 standards using a 100KN capacity computerised Testometric universal testing machine (UTM) with specifications: UTM Testometric FS5080, DBBMTCL-5000Kg, Serial No: 38140, Rochdale England). The specimens were cut to a standard dimension of 3.142 x 20^2 mm x 10 mm to conform to the instrument's specification. Three specimens were tested per sample, and the loads at which failure occurred and the deflections shown on the output display unit of the machine, were recorded. An average value of the results was calculated for each test sample. The load and deformation readings were automatically recorded until the rupture of the sample occurred. The specimen's total surface area, compressive strength and modulus were calculated using a formula adopted by Li and Zhou (2021); Abutu *et al.* (2019) as follows, respectively.

$$Compressive\ Strenght\ (CS) = \frac{Max.Applied\ Load\ (AL)}{Total\ Crossectional\ Area\ (CA)} \quad (MPa) \qquad (1)$$

$$Total\ Crossectional\ Area\ (CA) = \pi r^2 h \qquad (2)$$

$$Modulus\ (E) = \frac{Compressive\ Stress\ \ (CS)}{Compressive\ Strain\ (\varepsilon)} \quad (GPa) \qquad (3)$$

Hardness was carried out to determine resistance to the indentation following ASTM E-92 wih using Digita Micro Vickers Hardness Tester, HVC-30E, shown in Plate X. The test was carried out at three different points for each specimen, and the average value was recorded, which is similar to the method adopted by OKtem et al., (2015). The tester is equipped with a monitor to display the microscopic view of the sample surface to accurately determine the indentation surface area that is impressed on the sample. The load of 2 kg was gradually applied and sustained for 15 s, after which the load was automatically removed, and the stage clamp holding the sample was returned to the microscope measuring objective. Impact test was carried out using a Charpy impact testing machine with a capacity of 150J/300J and 2 Joules of minimum value of scale graduation (Avery-Denison, model No: 6705U/33122, Leeds, LS102DE England). The Specimens were then subjected to a machining process for using according to the ASTM E23 testing procedure, with a specimen size of 55 X 10 X 10 mm with a notch angle of 45, 2 mm depth and 0.25 mm radius along the base, as shown in Figure 3.6 (Li and Zhou 2021). The impact strength values were considered the initiation fracture toughness (IS), and the plane strain fracture toughness (FT) was estimated using the single specimen method described in ASTM E1820-08. The fracture toughness (FT) was calculated from the expression in equation 4 that links the impact strength (energy release rate) IS in (KJ/m^2) with other properties of materials (modulus and poison ratio) (Jelito and Schneider, 2019; Čamagić et al., 2019):

$$FT = \sqrt{\frac{IS \cdot E}{1-\nu^2}} \qquad (4)$$

The density of the sintered samples was investigated using Archimedes' principle in accordance with ASTM B962, and the porosity will be calculated with mathematical expressions (Zakaria *et al.,* 2021). Suitable biocomposites were selected for application in load-bearing bone replacement using a radar chart component.

3. RESULTS AND DISCUSSIONS

3.1 Microstructure of the Biocomposites

The microstructures of the dense, porous and gradient biocomposites examined by SEM analysis are shown in Figure 1. The dense biocomposite microstructure revealed some scratches with little pores due to the reaction of $CaCO_3$ at very sintering temperatures that usually give up CO_2 and then form pores on the surface of the biocomposite (Choy *et al.,* 2015). The porous and gradient samples showed relatively large irregular pores, with some fine spherical pores uniformly distributed along the surface of the first and second layers of the gradient sample, as shown in Figure 1C. The findings were also confirmed on Image J software by applying a threshold to reveal the porosity and pore distribution pattern shown in Figure 2. Figures 3A, 3B and 3C summarise the measured porosity and average pore size obtained from image J software for three biocomposites. The porosity increased with the addition of SH. The measured porosities of the biocomposites were 9.2, 25.72 and 20.62%, respectively, and were significantly higher than the pure titanium implant with a porosity of 1.46 as obtained by Mara (2015).

Regarding dense Ti-Ha-$CaCO_3$ biocomposites, the emphasis is on achieving a minimum pore size and high density for load-bearing applications. The implant exhibited less than 5% porosity and had a pore size distribution within the submicron to micron range. The average pore sizes of the fabricated porous biocomposites were reported to range from 100 μm to 300 μm. The specific pore size was adjusted by varying the particle size of $CaCO_3$ and the processing parameters (Choy *et al.,* 2015).

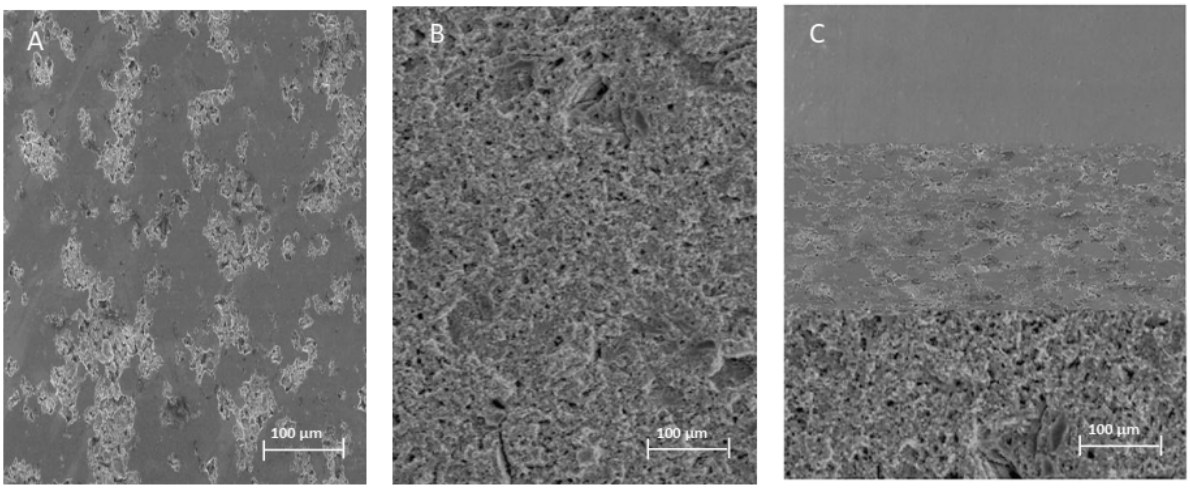

Figure 1: SEM for the Biocomposite Samples: Dense (A), Porous (B) and Gradient (C)

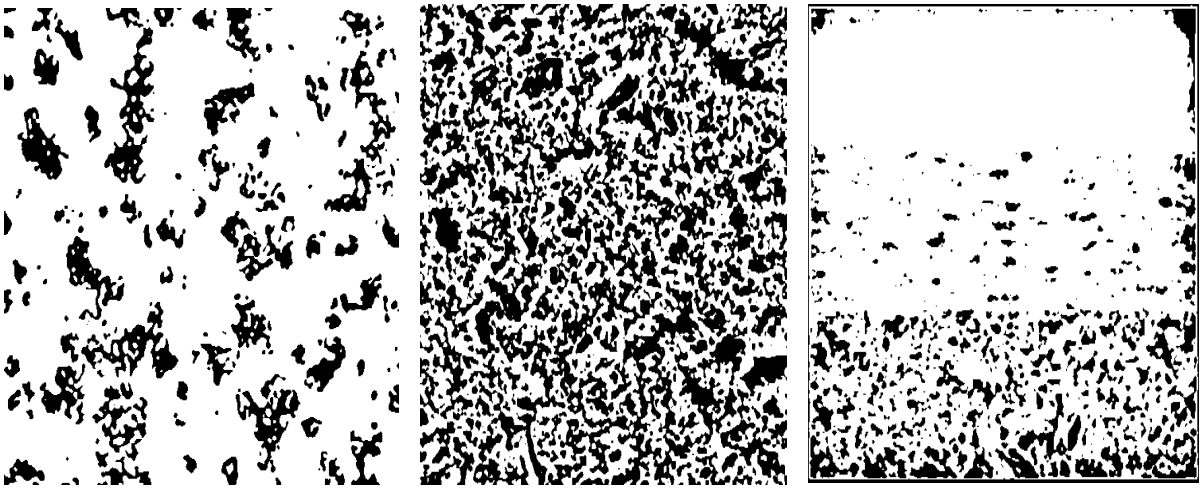

Figure 2: Threshold image of Biocomposites SEM obtained from Image J Software

It can be observed from Figure 3 (A, B, C) that there are some large irregular pores in the porous and gradient biocomposite with pore sizes of 252 and 135 μm. The formation of the large pores may be due to the space holder

and emission of CO2 gases produced by the reactions between $CaCO_3$ and Ti-Ha powders during the sintering process (Choy *et al.,* 2015). Moreover, the pore structure of the implant, including porosity and pore size, is an important characteristic that influences the physical performance of a biomaterial since it allows the migration and proliferation of osteoblasts, mesenchymal cells and vascularisation (Cetinel *et al.,* 2019); Wo *et al.* 2020;). The results showed that increasing the porosity of the scaffolds led to decreased mechanical strength but improved the implant's ability to support cell ingrowth and vascularisation. Several studies have investigated the effect of porosity and pore size on the biological behaviour of calcium-phosphate bone grafts, suggesting that the optimal porosity for the bone implant is about 30%. In contrast, a pore size larger than 100 µm is considered most satisfactory for bone graft substitutes to promote implant stabilisation (Choy *et al.,* 2015).

This result suggests the closeness of the modulus prevents bone resorption resulting from stress shielding (Cabezas-Villa *et al.,* 2018). The results indicated that a gradient in pore size reduced stress concentrations at the implant-bone interface, leading to improved load transfer and reduced risk of implant failure. The study emphasised optimising the pore size distribution in functionally graded implants to enhance their mechanical performance. These findings contribute to developing biocomposite implants that can effectively replace load-bearing bones while promoting osseointegration and long-term functionality. Gradient biocomposites exhibit a gradual transition in material properties, including porosity and pore size, along their structural gradient. The compressive strength of functionally graded biocomposites can vary based on the specific design and material composition (Matula *et al.,* 2021).

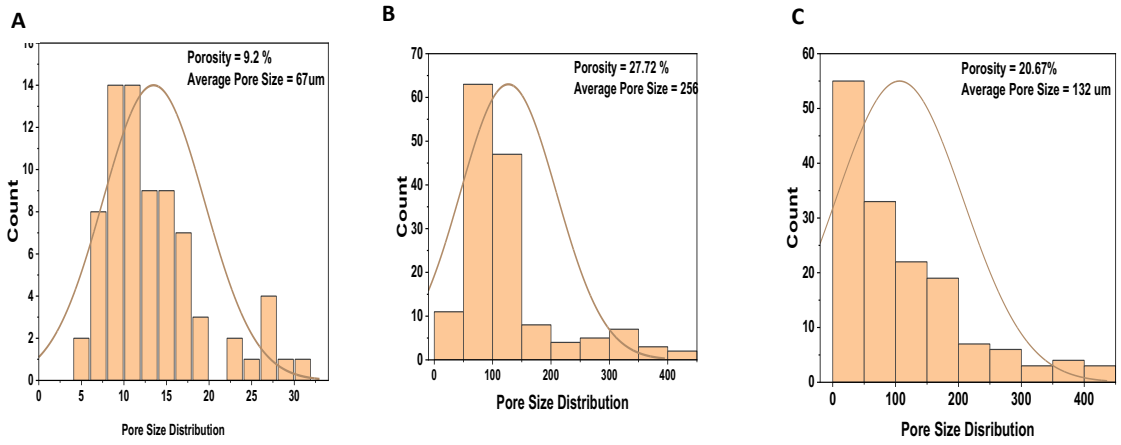

Figure 3: Pore Size Distribution of Ti-Ha-CaCO3 Biocomposite obtained from Image J Software; Dense (A). Porous (B) and Gradient (C).

3.2 Biomechanical and Physical Properties of Biocomposites

The biomechanical properties of dense, porous, and gradient biocomposites are crucial in determining their suitability as implants to replace bone. The results of various biomechanical properties, including compressive strength, modulus, hardness, impact strength, and fracture toughness, are shown in Figure 4. The dense biocomposites exhibited higher mechanical properties with 174 MPa than porous biocomposites obtained at 95 MPa. In contrast, porous biocomposites tend to have lower compressive strength due to the presence of voids. The findings were consistent with (Mara, 2015) for biocomposite compressive strength obtained as 167 MPa. The compressive strength of porous biocomposites can vary depending on the porosity and pore size distribution, ranging from tens to a few hundred megapascals.

The presence of pores in porous biocomposites can act as stress concentrators, making them more susceptible to crack propagation. The fracture toughness of biocomposites can be influenced by factors such as pore size, porosity, and the presence of toughening agents or reinforcement phases. It is important to note that the specific values of biomechanical properties mentioned above can vary depending on factors such as material composition, fabrication techniques, and processing parameters. Customisation of these properties is often necessary to match the requirements of specific bone replacement applications.

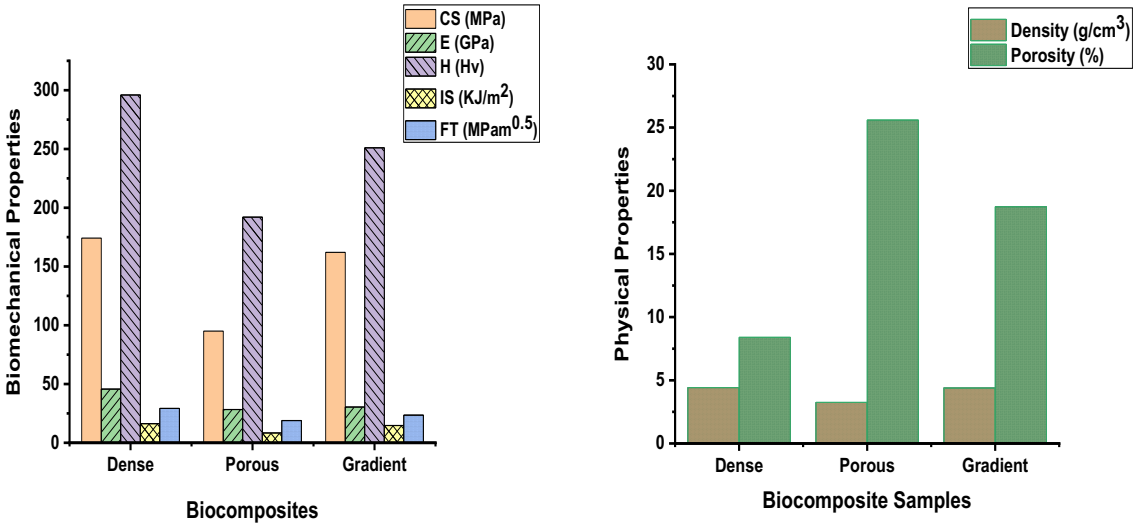

Figure 4: Biomechanical and Physical Properties of Different Structure Ti-Ha-$CaCO_3$ Biocomposites

A high level of material density and minimal porosity typically characterises dense biocomposites. These characteristics contribute to their superior compressive strength, making them suitable for load-bearing applications. Due to their high compressive strength, dense biocomposites provide stability and support for bone replacement. In a study by Qian *et al.* (2015), a functionally graded biocomposite composed of titanium and hydroxyapatite demonstrated compressive strength ranging from 100 to 300 MPa, depending on the gradient profile. The transition from dense to porous regions in functionally graded biocomposites allows for a controlled distribution of mechanical properties, enabling optimised load transfer and stress distribution (Bahraminasab and Farahmand, 2017).

3.3 Selection Analysis of Biocomposite Implants

A radar chart component was applied to manufactured biocomposite implants with biomechanical and physical properties obtained for the specimens (Dense, Porous and Gradient Biocomposites). In selecting biocomposites, the data obtained for biocomposite mechanical and physical properties were compared with the cortical bone and titanium data obtained from the literature, as shown in Table 1. However, the radar charts are effective only if they check limited samples' properties, not more than 8 (Holota *et al.,* 2015). After obtaining the properties of both the biocomposites, cortical bone and titanium, the intervals of physical variables for used materials were set for compressive strength (CS), modulus (E), hardness (H), impact strength (IS), fracture toughness (FT), density (D) and porosity (P). The prepared table of intervals for the individual parameters of the materials with the respective markings (1 to 5) is shown in Table 2. The first column indicates the *marking of a variable*. The marking range of variables was determined from 1 to 5 (dimensionless number), where 1 represents the lowest value of individual variables, and 5 represents the highest value of variables. According to Table 2, the individual parameter values of used materials with appropriate markings from 1 to 5 were transferred. The same markings are applied for the required (Titanium and Cortical Bone properties) material from Table 1. As follows, obtained data were written down in Table 3, from which data were used for the construction of radar chart Figure 5 to 7.

Table 1: Required Biomechanical Properties of Cortical Bone and Titanium Implants

Properties	Titanium	Cortical bone
CS (MPa)	250-600 (Tharaknath *et al.,* 2016)	100-230 (Nawawi *et al.,* 2011; Prasad *et al.,* 2017)
E (GPa)	100-110 Petersen (2014)	7-30 (Nawawi *et al.,* 2011; Prasad *et al.,* 2017)
H (Hv)	244.7-275.3 (2400-2700 MPa) Kaivosoja *et al.,* 2013)	50-100 (Hamandi *et al.,* 2022)
IS (KJ/m^2)	25 (Jelitto and Schneider 2019)	6 (Abdel-Wahab and Silberschmidt, 2011)]
FT ($MPam^{1/2}$)	60 (Nawawi *et al.,* 2011)	2-12 (El-Hajje *et al.,* 2014; Nawawi *et al.,* 2011; Nurul Amin *et al.,* 2022)
D (g/cm^3)	4.4-4.51 (Petersen, 2014)	1.8-2.1 (Zakaria *et al.,* 2018; Nurul Amin *et al.,* 2022)
P (%)	0-1.46 (Prakash *et al.,* 2016; Mara, 2015)	5-15 (Morgan *et al.,* 2018)

Table 2: Intervals and ranges according to individual Biomechanical and Physical parameters

Node	CS (MPa)	E (GPa)	H (Hv)	Jc (KJ/m^2)	K_{IC} (MPa$m^{\frac{1}{2}}$)	ρ (g/cm3)	P (%)
1	0-99	1-30	1-60.9	1.0-7.5	1-12	0-1.5	1-15
2	100-230	31-60	61-120.9	7.6-14.0	13-25	1.6-3.0	16-30
3	231-360	61-90	121-180	14.1-20.5	26-38	3.1-4.5	31-45
4	361-490	91-120	181-240	20.6-26.0	39-52	4.6-6.0	46-60
5	491-620	121-150	241-300	26.1-32.5	53-65	6.1-7.5	61-75

Table 3: Marking of parameters for individual materials based on their values.

Parameters	Dense	Porous	Gradient	Titanium	Cortical Bone
CS (MPa)	2	1	2	5	2
E (GPa)	2	1	1	5	1
H (Hv)	5	4	5	5	2
Jc (KJ/m^2)	3	2	3	4	1
K_{IC} (MPa$m^{\frac{1}{2}}$)	3	2	2	5	1
ρ (g/cm3)	3	3	3	3	2
P (%)	1	2	2	0	1

In the evaluation of the radar chart, it can be observed that the biocomposites have different biomechanical and physical parameters. Dense, porous and gradient materials are similar only in one or two of the required parameters with cortical bone (required) characteristics defined in Table 1. In the selection of biocomposite for replacement of bone or titanium implant, the mechanical and physical properties of dense Ti-Ha-CaCO3 biocomposite were compared with cortical bone and titanium implant shown in Figure 5. It can be observed that the dense biocomposite compressive strength (174 MPa) and porosity of 8.8 percentage values were within the range of cortical bone compressive strength and porosity properties, as reported in Table 1. Although the biocomposite hardness is within the range of the hardness value of titanium implants, its properties are lesser than the value of titanium. These characteristics contribute to their superior compressive strength, making them suitable for load-bearing applications. And the high impact strength of dense biocomposites ensures their ability to withstand sudden loads and impacts encountered in load-bearing bone replacement applications. Choy *et al.* (2015) reported a similar result.

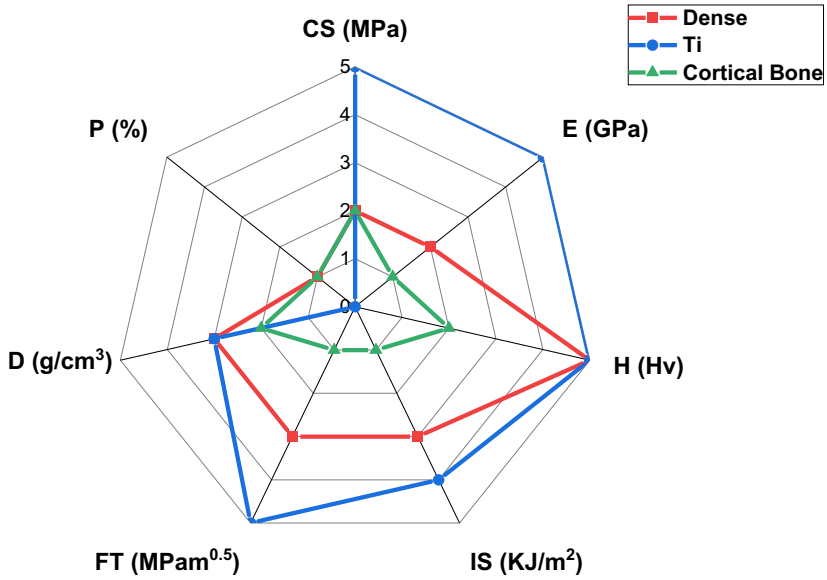

Figure 5: Radar Component Chart for Selection Analysis of Dense Ti-Ha-CaCO3 Biocomposites

Figure 6 displayed the radar component plot to compare porous Ti-Ha-CaCO3 biocomposite properties with cortical bone and Titanium implant properties. The plot revealed that the compressive strength (95 MPa) of porous biocomposite is lower and is not within the range of cortical bone porosity percentages, making it less suitable for replacing load-bearing bone such as femoral, knee and ankle bone. However, the presence of pores often leads to a reduction in compressive strength compared to dense biocomposites cortical bone. The compressive strength of porous biocomposites varies depending on the porosity and pore size. The mechanical strength of porous biocomposites may be adjusted by optimising the porosity and pore size using a space holder to balance mechanical properties and biological performance. Cetinel *et al.* (2019) reported porous titanium possesses a porous structure with interconnected voids, which can facilitate tissue ingrowth and promote osseointegration. However, the composite can be applied to replace the cancellous bone with wide ranges of compressive strength (0.2-500 MPa) as reported by

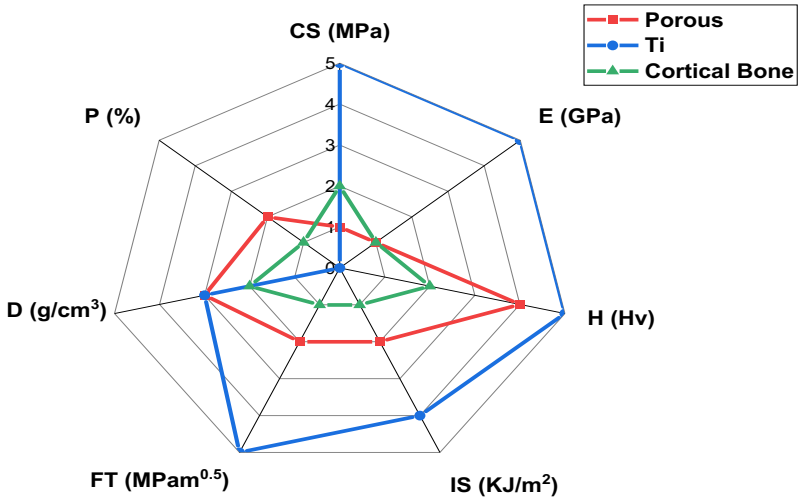

Figure 6: Radar Component Chart for Selection Analysis of Porous Ti-Ha-CaCO3 Biocomposite

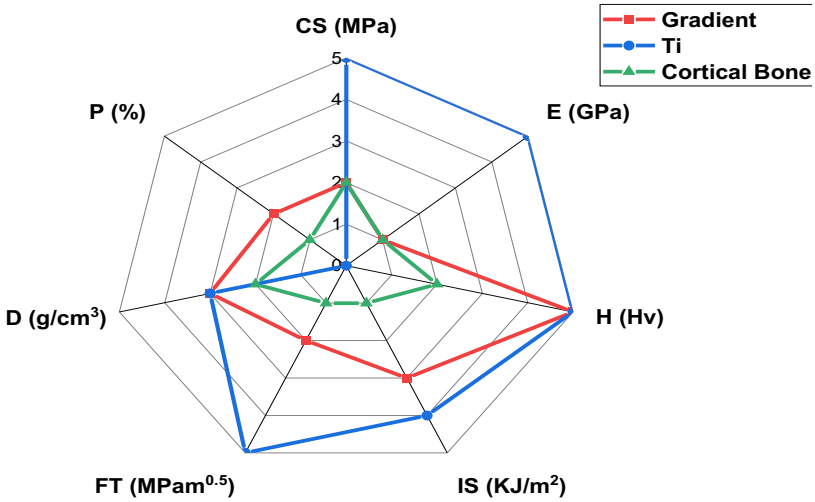

Figure 7: Radar Component Chart for Selection Analysis of Gradient Ti-Ha-CaCO3 Biocomposite

According to the results from the selection analysis in Figure 7, gradient biocomposite has proved to be the most suitable for replacing titanium implants as alternative biocompatible implants, about reported parameter values which most closely approximate cortical bone set parameters. And the strength, stiffness, fracture toughness, density and porosity as crucial properties in load-bearing bone replacement, selection of gradient biocomposite in the radar plot has excellent strength, hardness, fracture toughness and optimal porosity as established by (Adoba *et al.,* 1997). However, it is interesting that the biocomposite has a stiffness value within the cortical bone modulus range.

This result suggests the closeness of the modulus prevents bone resorption resulting from stress shielding (Cabezas-Villa *et al.,* 2018). The results indicated that a gradient in pore size reduced stress concentrations at the implant-bone interface, leading to improved load transfer and reduced risk of implant failure. The study emphasised optimising the pore size distribution in functionally graded implants to enhance their mechanical performance. These findings contribute to developing biocomposite implants that can effectively replace load-bearing bones while promoting osseointegration and long-term functionality. Gradient biocomposites exhibit a gradual transition in material properties, including porosity and pore size, along their structural gradient. The compressive strength of functionally graded biocomposites can vary based on the specific design and material composition (Sedighi *et al.* 2017).

4. CONCLUSION

The SEM analysis revealed that the Ti-Ha-CaCO3 biocomposite implants exhibited a well-defined interconnected porous structure, especially for porous and gradient biocomposites, essential for promoting cell adhesion, proliferation, and nutrient transport within the implant. Moreover, the study measured the porosity percentages of the implants, which demonstrated an optimal porosity range suitable for load-bearing bone replacement. The controlled porosity contributes to improved mechanical properties, such as load-bearing capacity and elasticity, necessary for withstanding physiological forces and ensuring long-term implant stability. Additionally, the investigation of the mechanical and physical properties of the Ti-Ha-CaCO3 biocomposite implants through radar chart analysis provided a comprehensive understanding of the material's performance. It favourably showcased a combination of properties in selecting and analysing the pore distribution of biocomposite implants for load-bearing bone replacement. The insights from this research can potentially drive the development of novel biomaterials with improved performance, leading to more successful and durable orthopaedic implants for patients needing load-bearing bone replacements.

ACKNOWLEDGEMENTS

The authors thank the University of Ilorin and the Tertiary Education Trust Fund (TETFund) Nigeria for supporting this research.

REFERENCES

Abdel Wahab, A. A. & Silberschmidt, V. V. (2011). Journal Of Theoretical And Applied Mechanics, 49, 3, pp. 599-619, Warsaw 2011.

Abutu, J., Lawal, S. A., Ndaliman, M. B., Lafia-Araga, R. A., Adedipe, O., & Choudhury, I. A. (2018). *Effects of process parameters on the properties of brake pad developed from seashell as reinforcement material using grey relational analysis. Engineering Science and Technology, an International Journal, 21(4), 787–797.* doi:10.1016/j.jestch.2018.05.014

Adoba, A. E., McShane, H. B., Rawlings, R. D. & Rehman, I. U. (1997). A Study Of The Mechanical Properties And Bioactivity Of Functionally Graded Titanium Matrix Composites Reinforced With Bioactive Particles, Volume I: Composites Applications and Design, Proceedings of ICCM–11, Gold Coast, Australia, pp. 496-508.

Bahraminasab, M., and Farahmand, F. (2017). State of the art review on design and manufacture of hybrid biomedical materials: Hip and knee prostheses. ProcIMechE Part H: J Engineering in Medicine 1–29. DOI: 10.1177/0954411917705911

El-Hajje, A., Kolos, E. C., Wang, J. K., Maleksaeedi, S., He, Z., Wiria, F. E., … Ruys, A. J. (2014). *Physical and mechanical characterisation of 3D-printed porous titanium for biomedical applications. Journal of Materials Science: Materials in Medicine, 25(11), 2471–2480.* doi:10.1007/s10856-014-5277-2

Hamandi, F.; Tsatalis, J.T.; Goswami, T. (2022). Retrospective Evaluation and Framework Development of Bone Anisotropic Material Behavior Compared with Elastic, Elastic-Plastic, and Hyper-Elastic Properties. Bioengineering 2022, 9, 9. https://doi.org/10.3390/ bioengineering9010009

Jawad K. O., Rana A. A. & Sura A. M. (2015). Fabrication, characterization and Physical Properties of Functionally Graded Ti/HAP bioimplants, Wulfenia Journal Vol 22, No. 7 pp. 336-348.

Jelitto, H., & Schneider, G. A. (2019). *Fracture toughness of porous materials – Experimental methods and data. Data in Brief, 103709.* doi:10.1016/j.dib.2019.103709

Kaivosoja, E., Tiainen, V.-M., Takakubo, Y., Rajchel, B., Sobiecki, J., Konttinen, Y. T., & Takagi, M. (2013). Materials used for hip and knee implants. Wear of Orthopaedic Implants and Artificial Joints, 178–218. doi:10.1533/9780857096128.1.178

Krishna, E. S. & Suresh, G. (2022). Bioactive Titanium-Hydroxyapatite Composites by Powder Metallurgy Route, Volume 12, Issue 4, 2022, 5375 – 5383 https://doi.org/10.33263/BRIAC124.53755383

Li, C.; Zhou, Z. (2021). Charpy Impact Behavior of a Novel Stainless Steel Powder Wire Mesh Composite Porous Plate. *Materials*, *14*, 2924. https://doi.org/10.3390/ma14112924

Mantripragada, V. P., Lecka-Czernik, B., Ebraheim, N. A., & Jayasuriya, A. C. (2012). *An overview of recent advances in designing orthopedic and craniofacial implants. Journal of Biomedical Materials Research Part A, NA–NA.* doi:10.1002/jbm.a.34605

Mara, F. C. V. T. (2015). Mechanical Characterisation of Porous Titanium Implant Materials, PhD thesis, Universidade do Minho, Escola de Engenharia.

Matuła, I.; Dercz, G.; Sowa, M.; Barylski, A.; Duda, P. Fabrication and Characterization of New Functional Graded Material Based on Ti, Ta, and Zr by Powder Metallurgy Method. *Materials* **2021**, *14*, 6609. https://doi.org/10.3390/ma14216609.

Moghadasi, K., Isa, M. S. M., Ariffin, M. A., Mohd jamil, M. Z., Raja, S., Wu, B., Yamani, M., Muhamad, M. R., Yusof, F., Jamaludin, M. F., Ab Karim, M. S., Abdul Razak, B. & Yusoff, N. (2022). A review on biomedical implant materials and the effect of friction stir-based techniques on their mechanical and tribological properties, Journal of Materials Research and Technology, Volume 17, pp. 1054-1121, ISSN 2238-7854, https://doi.org/10.1016/j.jmrt.2022.01.050.

Morgan, E. F., Unnikrisnan, G. U., & Hussein, A. I. (2018). *Bone Mechanical Properties in Healthy and Diseased States. Annual Review of Biomedical Engineering, 20(1), 119–143.* doi:10.1146/annurev-bioeng-062117-121139

Nawawi, N. A., Alqap, A. S. F. & Sopyan, I (2011). Recent Progress on Hydroxyapatite-Based Dense Biomaterials for Load Bearing Bone Substitutes, Recent Patients on Materials Science, Volume 4, pp. 63-80.

Nurul Amin, A. K. M., Nasir, S. N. M., Khalid, N. S., & Arif, M. D. (2012). *Comparison of Surface Roughness Attainable in High Speed End Milling of Silicon with Air Blowing on Conventional and CNC Milling Machines. Advanced Materials Research, 576, 1922.* doi:10.4028/www.scientific.net/amr.576.19

Oshkour, A. A., Pramanik, S., Mehrali, M., Yau, Y. H., Tarlochan, F., & Abu Osman, N. A. (2015). *Mechanical and physical behavior of newly developed functionally graded materials and composites of stainless steel 316L with calcium silicate and hydroxyapatite. Journal of the Mechanical Behavior of Biomedical Materials, 49, 321–331.* doi:10.1016/j.jmbbm.2015.05.020

Petersen, R. (2014). Titanium Implant Osseointegration Problems with Alternate Solutions Using Epoxy/Carbon-Fiber-Reinforced Composite. Metals, 4(4), 549–569. doi:10.3390/met4040549

Poliakov A., Pakhaliuk V., and Popov V. L. (2019) Current Trends in Improving of Artificial Joints Design and Technologies for Their Arthroplasty. *Front. Mech. Eng.* 6:4. doi:10.3389/fmech.2020.00004.

Prakash, K. S., Gopal, P. M., Anburose, D., & Kavimani, V. (2016). *Mechanical, corrosion and wear characteristics of powder metallurgy processed Ti-6Al-4V/B4C metal matrix composites. Ain Shams Engineering Journal.* doi:10.1016/j.asej.2016.11.003

Prasad, K., Bazaka, O., Chua, M., Rochford, M., Fedrick, L., Spoor, J., … Bazaka, K. (2017). *Metallic Biomaterials: Current Challenges and Opportunities. Materials, 10(8), 884.* doi:10.3390/ma10080884

Qian, C., Zhang, F., & Sun, J. (2015). *Fabrication of Ti/HA composite and functionally graded implant by three-dimensional printing. Bio-Medical Materials and Engineering, 25(2), 127–136.* doi:10.3233/bme-151263

Saraf, S., Singh, A., & Desai, B. G. (2019). *Estimation of Porosity and Pore size distribution from Scanning Electron Microscope image data of Shale Samples: A Case Study on Jhuran Formation of Kachchh Basin, India. ASEG Extended Abstracts, 2019(1), 1–3.* doi:10.1080/22020586.2019.12073197.

Oliveira, T. J. A., Cássaro, F. A. M. & Pires, L. F. (2020). The porous size distribution obtained and analysed by free access software. Revista Brasileira de Ensino de Física, vol. 42, e20200192: 1-4, DOI: https://doi.org/10.1590/1806-9126-RBEF-20200192.

Sedighi, M., Omidi, N. & Jabbari, A. H. (2017). Experimental Investigation of FGM Dental Implant Properties Made from Ti/HA Composite, Mechanics of Advanced Composite Structures 4 (2017) 233-237.

Tharaknath, S., Ramkumar, R. &. Lokesh, B. (2016). Middle-East Journal of Scientific Research 24 (Recent Innovations in Engineering, Technology, Management & Applications): 124-132, DOI: 10.5829/idosi.mejsr.2016.24.RIETMA120.

Zakaria, M.Y., Sulong, A.B. Ramli, M.I. Ukwueze B. Harun W.S.W. & Mahmun, R.L. (2018). Fabrication of Porous Titanium hydroxyapatite Composite Via Powder Metallurgy With Space Holder Method *Journal of Advanced Manufacturing Technology (JAMT),* Vol. 12 No. 1, pp. 37-48

PAPER 173 – BUILDING OF MACHINE LEARNING PREDICTIVE MODEL FOR SIMULATING BIODIESEL YIELD

E.O. Babatunde[1*], F. A. Aderibigbe[1], T.M. Busari[1], F.B. Owoyale[1], J.A. Adeyoola[1]

[1]Department of Chemical Engineering, University of Ilorin, Ilorin, Nigeria.
*Email:babatunde.eo@unilorin.edu.ng

ABSTRACT
Continuous exploration, refining, and transportation of fossil fuels resulting in environmental pollution, and harm to man, animals (terrestrial and aquatic) and plants has led to the search for alternative fuel sources. In addition, an increase in the population of men globally has resulted in overdependence and high consumption of fuel. This has led to the release of harmful materials to the ecological system hence the search for more eco-friendly alternatives leading to the production of biodiesel among others. The availability of feedstock required for the production of biodiesel encourages reliance on it as a source of fuel for general usage. The high yield of biodiesel depends on factors such as the type of feedstock, catalyst employed, operating temperature and reaction time. In this paper, a machine learning predictive model was developed which could accurately predict the quality of biodiesel generated from various sources of biomass, including vegetable oils, animal fats, and algae. The model was trained using historical data on biodiesel quality and process conditions and was tested using new data to evaluate its accuracy and performance. The resulting predictive model was used to optimize biodiesel production, reduce cost, and promote the use of renewable energy sources.
KEYWORDS: Machine learning; Predictive model; Pollution; Biomass; Simulation.

1. INTRODUCTION

Due to the prominent application of biodiesel in our various day-to-day activities such as heavy road traffic, shipping and aviation which entails the powering of heavy vehicles and various machines, the use of biodiesel in many sectors especially in the transportation sector which is the major consumer of biofuel, would be essential in order to achieve a sustainable way of living. According to (Commission. 2022), the demand for biofuel has been forecasted to rise from 146 billion litres in 2020 to 186-342 billion litres in 2026. As a result, the need for the production of biodiesel for our various day-to-day activities is on the rise. Hence, it is important to have a solid plan for the sustainable production of this fuel. In recent years, there has been a growing interest in the production of biodiesel from different types of biomass as the more sustainable option to conventional fossil fuels.

However, the production process can be challenging and lengthy due to various factors such as feedstock type, reaction conditions, and conversion efficiency. Biodiesel is an alternative fuel option for diesel engines that is created by chemically reacting vegetable oil or animal fat with an alcohol such as methanol or ethanol is the most commonly used alcohol (Yusuf et al. 2011; Liu et al. 2021). While other alcohols, like propanol, butanol, isopropanol, tert-butanol, branched alcohols, and octanol, can also be used, they are more expensive (Yusuf et al. 2011). Methanol is generally preferred due to its affordability, high reactivity, and the fact that the resulting fatty acid methyl esters (FAMEs) are more volatile than fatty-acid ethyl esters (FAEE) produced using ethanol (Senders et al. 2018; Yusuf et al. 2011). However, ethanol is less toxic and considered more renewable, as it can be produced through fermentation from renewable sources. FAME and FAEE have slight differences as fuels, with FAEE having slightly higher viscosities and slightly lower cloud and pour points than FAME (Bozbas 2008).
One of the major disadvantages of using biodiesel is that it delivers less energy than fossil fuels hence necessitating the use of more energy to produce the same amount of energy. If this strategy is to be successful over the long term, it is critical to evaluate how efficiently biomass-based biodiesel is produced. Biodiesel production from different types of biomass is gaining popularity as a sustainable alternative to fossil fuels (Liakos et al.2018; Vicente et al. 1998). However, the process can be complex and time-consuming due to factors like feedstock type, reaction conditions, and conversion efficiency.
The use of Artificial Intelligence (AI) has the potential to significantly enhancing the biodiesel production process by automating and improving different aspects of the process, leading to better optimization and efficiency. It could help to optimize and streamline various aspects of the process, leading to better efficiency and cost savings. AI can optimize reaction conditions by analysing large data sets from previous experiments to predict optimal conditions for specific feedstock. This approach minimizes the trial-and-error involved in traditional methods and also improves efficiency.

Machine Learning (ML) is a type of artificial intelligence (AI) that enables computers to learn from data without being explicitly programmed (Senders et al. 2018; Allogbani et al. 2020). The ML approach has been widely used

in various fields, including agriculture (Liakos, Busato et al. 2018), healthcare (Burkart and Huber, 2021; Char, et al. 2020), finance (Goodell et al. 2021; Anderson and Whitcomb, 2016), and energy (Liu, et al. 2021), among others. In biodiesel production, the yield of the final product is a crucial factor that affects the profitability and sustainability of the process. Therefore, developing a predictive model for simulating biodiesel yield using ML could help to optimize the production process and reduce cost.

This paper aims to explain how a machine learning predictive model could be used to simulate biodiesel yield, with response surface methodology as the ideal optimization tool. The use of machine learning is possible to create models that predict the yield of biodiesel by analysing data from past production processes. The model could be trained to recognize the connections between input variables like the type of feedstock, the amount of catalyst and solvent, reaction temperature and time, and the output variable - biodiesel yield. These models can then forecast the yield of biodiesel for new input data.

2. MATERIALS AND METHODS

2.1 Materials and Data Collection

In this study, data collection was obtained on different types of biomass feedstocks and oil sources for biodiesel production from previous studies (Czitrom 1999; Hahne et al. 2008; Lenth, 2010; Nesteski et al. 2017; Van-Gerpen et al. 2005). In order to identify relevant sources, an online database such as Google Scholar, and ScienceDirect was searched using keywords such as "biodiesel," "biomass feedstock," "oil source," "transesterification," and "yield." The quality of the sources was evaluated by checking the author's credentials, the publication date, and the reputation of the journal or publisher. After identifying relevant sources, the relevant data related to the characteristics of different biomass feedstocks and oil sources were extracted. This included data on the fatty acid composition, viscosity, density, and other properties that can affect the yield and quality of biodiesel produced. The data was then organized and analysed using Excel to identify patterns and trends. By following the aforementioned guidelines, reliable sources related to the characteristics of different biomass feedstocks were identified.

2.2 Data Preparation

The data preparation commenced with the use of 'Exploratory Data Analysis (EDA). The data was cleaned by removing any duplicate or missing data, some errors or inconsistencies were also corrected using a method in pandas, known as the drop function; a popular Python library for data manipulation and analysis, that allows the removal of specific rows or columns from data frame based on their labels or indexes. and the data was transformed into a consistent format. Thereafter, the relevant variables that are likely to influence the biodiesel yield were carefully selected; the type of feedstocks, reaction temperature, reaction time, and the molar ratio of alcohol to oil. These data were visualized to help identify patterns and relationships between the variables while making use of a scatter plot. The data was then normalized as the variables being considered to have different units such as time, temperature, catalyst loading and molar ratios. Hence, the data were rescaled to a standard range to ensure that each variable contributes equally to the model.

2.3 Process Optimization

In this step, useful data was extracted from the various data available for use in predicting the yield of biodiesel. This involved calculating ratios of the oil to methanol used in the transesterification process of biodiesel production, the residence time of the oil and methanol in the reactor vessel and different operating temperatures of various reactants.

2.4 Model selection

Out of the several types of predictive models that can be used to simulate the yield of biodiesel, the use of line regression was adopted in this work for the model selection. Linear regression involves fitting a linear equation to the data, where the independent variables are used to predict the value of the dependent variable. The equation takes the form:

$$y = \beta_0 + \beta_1 x_1 + \beta_2 x_2 + ... + \beta_n x_n + \varepsilon$$

where y is the dependent variable, x_1, x_2, ... x_n are the independent variables, β_0, β_1, β_2, ... β_n are the regression coefficients, and ε is the error term. The regression coefficients were estimated using the least squares method, which minimizes the sum of the squared errors between the predicted and actual values of the dependent variable. Figure 1 shows the block diagram of the process.

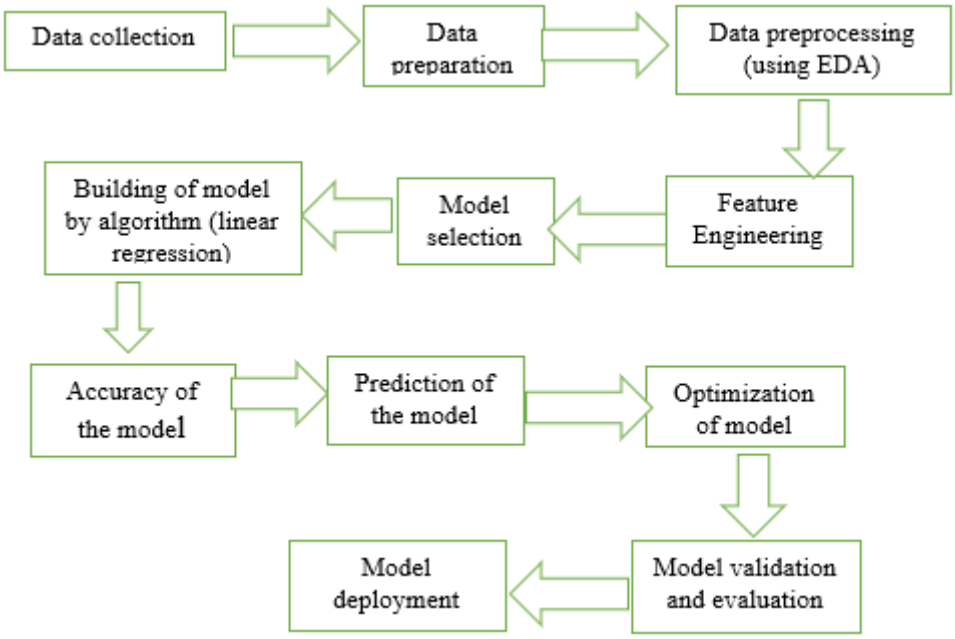

Figure 1: The block diagram of the process

2.5 Model Training

After the best model had been selected, it was then trained using the prepared data for the fitness of purpose. This involves fitting the model to the data and adjusting its parameters to minimize the error between the predicted values and the actual values. Out of the different methods of training a model which include supervised learning, unsupervised learning, semi-supervised learning and reinforcement learning, the use of supervised learning was adopted in this work because it involves training the model using a labelled dataset, where the input variables are associated with the corresponding output variable.

2.6 Model Evaluation

After training the model, it was then evaluated using the cross-validation technique to check its performance and to determine how well it would predict the yield of biodiesel. Cross-validation is a technique used to evaluate the performance of a model by partitioning the data into several folds and training the model on different combinations of the folds. It is commonly used to estimate the generalization performance of a model.

2.7 Model Deployment

Finally, after the performance of the model was satisfied, the model was deployed for use in predicting the yield of biodiesel under different conditions.

3. RESULTS AND DISCUSSION

The experimental yield and the machine learning (ML) predicted yield for 27 different sets of conditions are shown in Table 1. It is essential for evaluating the performance model to contrast the anticipated values of the ML model with the experimental yield.

Table 1: Experimental runs with the Response Variables

Methanol/Oil Ratio (ml/ml)	Time (min)	Catalyst loading (wt%)	Temperature (°C)	Experimental Value, Yield (%)	Machine Learning Yield (%)
3	60	1	55	80	96
4.5	75	0.8	48	65	94
4.5	45	1.2	48	79	95
7.5	75	1.2	62	85	78
7.5	45	1.2	62	85	78
7.5	75	0.8	62	70	78
4.5	75	0.8	62	66	88
9	60	1	55	72	77
6	60	1	55	86	86
4.5	45	0.8	48	68	95
4.5	75	1.2	48	80	95
6	60	0.6	55	51	86
6	60	1	55	86	86
6	60	1	69	73	80
4.5	45	0.8	62	84	88
6	60	1	55	86	86
4.5	75	1.2	62	83	88
6	60	1.4	55	88	87
7.5	45	0.8	48	70	85
6	60	1	55	86	86
6	60	1	55	86	86
7.5	75	0.8	48	66	85
7.5	75	1.2	48	85	85
6	30	1	55	88	86
6	60	1	55	86	87
6	60	1	41	70	93
6	90	1	55	79	86

The experimental yield and the ML anticipated yield are generally extremely similar. Nevertheless, it is frequently the case that the ML projected yield is a little higher than the observed yield. For instance, in the 7th and 8th sets of conditions, the experimental yield was 66%, whereas the ML estimated yield was 88%. The 15th set of conditions is similar to the 1st with an experimental yield of 84% while the ML anticipated value is 88%.

The ML model is overfitted because of its training on a limited dataset. An overfit model is one that performs well on training data but poorly on test data. Validating the ML model with additional experimental data is essential to ensure its accuracy and reliability.

4. CONCLUSIONS

Finally, the goal of this research was to create a machine-learning model for forecasting biodiesel yield. On the basis of the experimental findings and analysis, it could be said that the machine learning model created to forecast biodiesel yield exhibits good agreement with the experimental values, despite having a tendency to slightly overestimate the yield. The model's ability to correctly forecast yield is a promising finding, and it may have important practical implications for optimizing biodiesel manufacturing procedures. Because it is based on sparse data, the model's accuracy and reliability must be confirmed with additional experimental data. As a result, further experimental analysis is required to confirm the precision and viability of the machine-learning model.

Therefore, additional research is necessary to confirm the precision and viability of the machine-learning model. Future work should concentrate on refining the model's parameters and taking into account more sophisticated algorithms to boost performance. This study, therefore, shows the potential of machine learning to accurately predict yields in biodiesel production processes. It also emphasizes the necessity of further testing the precision and dependability of the machine learning model to guarantee its suitability for a wider range of situations. The results of this study add to the growing body of knowledge on the application of machine learning in Chemical Engineering and may have significant ramifications for the design of more effective and environmentally friendly biodiesel production methods.

REFERENCES

Alloghani, M., Al-Jumeily, D., Mustafina, J., Hussain, A., & Aljaaf, A. J. (2020). A systematic review on supervised and unsupervised machine learning algorithms for data science. *Supervised and unsupervised learning for data science*, 3-21.

Anderson, M. J., & Whitcomb, P. J. (2016). *RSM simplified: optimizing processes using response surface methods for the design of experiments*. Productivity press.

Bozbas, K. (2008). Biodiesel as an alternative motor fuel: Production and policies in the European Union. *Renewable and Sustainable Energy Reviews*, *12*(2), 542-552.

Burkart, N., & Huber, M. F. (2021). A survey on the explainability of supervised machine learning. *Journal of Artificial Intelligence Research*, *70*, 245-317.

Char, D. S., Abràmoff, M. D., & Feudtner, C. (2020). Identifying ethical considerations for machine learning healthcare applications. *The American Journal of Bioethics*, *20*(11), 7-17.

Commission, A. T. (2022). How biofuels and rising incomes impact grain and oilseed demand. https://www.austrade.gov.au/news/insights/insight-how-biofuels-and-rising-incomes-impact-grain-and-oilseed-demand

Czitrom, V. (1999). One-factor-at-a-time versus designed experiments. *The American Statistician*, *53*(2), 126-131.

Goodell, J. W., Kumar, S., Lim, W. M., & Pattnaik, D. (2021). Artificial intelligence and machine learning in finance: Identifying foundations, themes, and research clusters from bibliometric analysis. *Journal of Behavioral and Experimental Finance*, *32*, 100577.

Hahne, F., Huber, W., Gentleman, R., Falcon, S., Gentleman, R., & Carey, V. (2008). Unsupervised machine learning. *Bioconductor case studies*, 137-157.

Lenth, R. V. (2010). Response-surface methods in R, using RSM. *Journal of Statistical Software*, *32*, 1-17.

Liakos, K. G., Busato, P., Moshou, D., Pearson, S., & Bochtis, D. (2018). Machine learning in agriculture: A review. *Sensors*, *18*(8), 2674.

Liu, Y., Esan, O. C., Pan, Z., & An, L. (2021). Machine learning for advanced energy materials. *Energy and AI*, *3*, 100049.

Nasteski, V. (2017). An overview of the supervised machine learning methods. *Horizons. b*, *4*, 51-62.

Senders, J. T., Zaki, M. M., Karhade, A. V., Chang, B., Gormley, W. B., Broekman, M. L., Smith, T. R., & Arnaout, O. (2018). An introduction and overview of machine learning in neurosurgical care. *Acta neurochirurgica*, *160*, 29-38.

Van Gerpen, J. (2005). Biodiesel processing and production. *Fuel Processing Technology*, *86*(10), 1097-1107.

Vicente, G., Coteron, A., Martinez, M., & Aracil, J. (1998). Application of the factorial design of experiments and response surface methodology to optimize biodiesel production. *Industrial crops and products*, *8*(1), 29-35.

Yusuf, N., Kamarudin, S., & Yaakub, Z. (2011). Overview of the current trends in biodiesel production. *Energy Conversion and Management*, *52*(7), 2741-2751.

PAPER 174 – EXPERIMENTAL DETERMINATION OF COMMINUTION PARAMETERS OF ZANKAN SPODUMENE

U.M. Akindele[1,3*], A.J. Adebisi[2], I.A. Talabi[2], Y. Taiwo[2], R.M. Mahamood[2], S. Abdulkareem[1] and I.I. Ahmed[2,4]

[1]Department of Mechanical Engineering, University of Ilorin, Ilorin.
[2]Department of Materials and Metallurgical Engineering, University of Ilorin, Ilorin.
[3]Department of Mineral and Petroleum Resources Engineering, Kaduna Polytechnic, Kaduna.
[4]Air Force Institute of Technology, Kaduna.
*Email: usmanakindele@kadunapolytechnic.edu.ng

ABSTRACT

Samples of Spodumene obtained from Zankan Village, Nigeria were subjected to grindability test using granite and magnetite as reference ores, from which work index was determined, in line with Bond modified energy equation. Sieve analysis was carried out using laboratory sieve shaker and lastly, homogenized samples obtained using Coning-quartering and riffle splitter methods. The homogenized-samples were processed for Chemical compositional analysis using atomic absorption spectroscopy (AAS). Grindability tests showed that 80% passing size fraction of the "Feed" for Spodumene, Granite and Magnetite was 553.82, 357.68 and 418.85 µm respectively, while, those of the "Product" were 257.02, 177.42 and 242.67 µm respectively. Hence, the work index of the Zankan Spodumene determined from the 80% passing size fraction of the feed and product, was 13.27 kWh/ton. The study showed that spodumene with liberation size of 75 µm has the highest-grade value of 3.02% lithium oxide. The experimental parameters obtained from this study will be relevant to commercial exploitation of the Zankan Spodumene for lithium battery production.

KEYWORDS: Spodumene; Comminution; Grindability; Liberation; Zankan

1. INTRODUCTION

The growing projection of lithium resources has necessitated the development of an efficient process route to recover lithium products from its host rocks (Tian et al., 2018), particularly the comminution process and its parameters. Comminution being a process in which solid materials is reduced in size as a sequence of crushing and grinding to reduce the particle size of run-of-mine to desired level (Wills and Napier – Munn, 2006, Obassi et al., 2015b) (Obassi et al., 2015a). Hence, it is an important test in the proper design of beneficiation plants (Abdul Mwanga et al., 2015). Comminution parameters provide information about the particle size distribution that leads to mineral liberation. It equally to determine the energy needed for particle size reduction and its cost implication (Dirk and Jens, 2013); (Wang et al., 2013) (Weedon et al., 1990)

However, these parameters (work index and liberation size determination) are energy intensive process which amounted to 30-50% of the total power consumption in mineral processing plants (Egbe et al., 2013); (Napier-Munn et al., 1996) while 30-70% of the overall energy used goes to mining operations (Stefon et al., 2014)

This paper considered comparative grindability test (Olatunji and Durojaiye, 2010, Obassi et al., 2015a) (Umar et al., 2016) (Egbe et al., 2013) for the determination of work index of an ore. Also, determination of Liberation size which has to do with deportment of mineral of interest across the particle size determine by chemical compositional examination (Gay, 2004) (Obassi et al., 2014); Nuhu, 2017). Therefore, this study focuses on the evaluation of Work Index of Zankan lithium ore as well the liberation size for the applicability and potentiality in the concentration and pilot scale projection.

2. EXPERIMENTAL PROCEDURE

2.1 Sample Collection and preparation

The samples used for experimental work were obtained from Zankan village, Jemaa LGA of Kaduna state, Nigeria. Figure 1, showing the location where the spodumene samples were obtained. Ore Samples collected at five different pits were crushed and pulverized using Jaw crusher and Ball Mill operated at 415V, 50Hz, 4000w, 8.1A and 220-240V, 50Hz, 370W,3.8A respectively. The ore sample were then homogenized and sampled using coning- quartering and riffle splitter methods to achieve representative sample for physical, chemical and work index determination. Granite and Magnetite obtained from Kaduna and Kogi States respectively were used as reference materials for determination of work index.

Fig. 1: Google Map showing the location of Zankan in Kaduna state, Nigeria; $9^{o}23^{II}15^{III}$N; $8^{o}11^{II}30^{III}$E.

2.2 Methodology

The chemical characterizations of the different sieve apertures were performed using atomic absorption spectrophotometer (AAS; Shimadzu model 7000). Sieve size analysis was conducted on the samples and the distribution weighed and recorded. The work index of the Zankan spodumene was determined using Berry – Bruce method which entails milling two mineral samples of the same weight, a reference material of known work index, Granite, with theoretical work index of 15.13 Kwh/ton and magnetite of 15.86 Kwh/ton (Umar et al., 2016) (Yaro, 1997); (Weiss, 1985). The work index of the test material (Zankan spodumene) was thereafter computed using the Bond's energy equation… see Eq. (2) (Wills and Napier – Munn, 2006)

3. RESULTS AND DISCUSSION

3.1 Work index determination

Tables 1 shows the cumulative weight percentage passing of the particle sizes of the test material (Spodumene) and a reference materials, Granite and Magnetite (Feed and Product). From the results, the particle size fractions of the test material and the reference materials show a normal distribution pattern, indicating that the particle size fractions of the three materials respond to the theories of comminution. That is, the energy consumed in size reduction is proportional to the area of new surface produced. The 80% passing for the "Feeds" and "Products" were obtained according to Gaudin-Schuhman equation, see Eq. (1)

$$80\ \%\ Cum\ Passing\ Size\ =\ (80\ \%\ /\ \%\ passing\ size\ 1)2x\ size\ 1 \ldots\ldots\ldots\ldots\ldots\ldots\ldots\ldots\ldots\ldots\ (1)$$

which are 553.82 µm F_t, 257.02 µm P_t, 357.68 µm F_{rG}, 177.42 µm P_{rG}, 418.85 µm F_{rM}, 242.67 µm P_{rM} for the reference and test materials respectively, these could as well be obtained from Figure 2-7.

Table 1: Result of sieve size analysis of the "Feed" and "Product" for all the materials

Sieve size Range (µm)	CWP of Granite as Feed (%)	CWP of Magnetite, as Feed (%)	CWP of Spodumene as Feed (%)	CWP of Granite as product (%)	CWP of Magnetite as product (%)	CWP of Spodumene as product (%)
+1000	98. 56	97.45	99.20	99.00	99.30	99.65
-1000+710	98.00	95.55	92.95	98.90	98.70	98.50
-710+500	85.50	80.25	85.25	97.85	91.25	93.60
-500+355	79.70	73.65	78.05	96.90	88.10	88.50
-355+250	69.50	61.70	65.70	94.90	86.85	78.90
-250+180	41.35	38.15	48.55	80.80	68.90	65.25
-180+125	30.40	29.45	35.25	67.15	58.65	45.40
-125+90	16.40	11.10	19.25	45.10	37.40	33.50
-90+63	13.45	10.05	14.25	26.75	24.80	25.50
-63+45	07.50	06.80	08.75	22.20	18.50	18.65
-45 (Pan)	00.00	00.00	00.00	00.00	00.00	00.00

CWP; Cumulative Weight Passing

$$W_{it} = W_{ir}\left({}^{10}\!/_{(pr)^{\frac{1}{2}}} - {}^{10}\!/_{(Fr)^{\frac{1}{2}}}\right) / \left({}^{10}\!/_{(pt)^{\frac{1}{2}}} - {}^{10}\!/_{(Ft)^{\frac{1}{2}}}\right) \ldots\ldots\ldots\ldots\ldots\ldots\ldots\ldots\ldots\ldots\ (2)$$

Where;

W_{ir} = work index of the reference ore

W_{it} = work index of the test ore

P_r = 80% of the product (reference material)

P_t = 80% of the product (test material)

F_r = 80% of the feed (reference material)

F_t = 80% of the feed (test material)

F_t = 553.82 µm; P_t = 257.02 µm; F_{rG} = 357.68 µm; P_{rG} = 177.42 µm; F_{rM} = 418.85 µm; P_{rM} = 242.67 µm

$$W_{it} = W_{ir}\left(10/(pr)^{\frac{1}{2}} - 10/(Fr)^{\frac{1}{2}}\right) / \left(10/(pt)^{\frac{1}{2}} - 10/(Ft)^{\frac{1}{2}}\right)$$

Therefore;

$$W_{it} = W_{ir}\left(10/(177.42)^{\frac{1}{2}} - 10/(357.68)^{\frac{1}{2}}\right) / \left(10/(257.02)^{\frac{1}{2}} - 10/(553.82)^{\frac{1}{2}}\right)$$

W_{it} = 1.077 x 15.13

W_{it} = 16.3kWht (with Granite as reference material)

Also;

$$W_{it} = W_{ir}\left(10/(242.67)^{\frac{1}{2}} - 10/(418.85)^{\frac{1}{2}}\right) / \left(10/(257.02)^{\frac{1}{2}} - 10/(553.82)^{\frac{1}{2}}\right)$$

W_{it} = 0.646 x 15.86

W_{it} = 10.24kWht (with magnetite as reference material)

Average work index of Zankan Spodumene is 13.27kWh/ton

Therefore, amount of energy required to comminute Spodumene is 16.3Kwht (with Granite as reference material) and10.24Kwht (with magnetite as reference material) to 80% passing. Average work index of Zankan Spodumene is 13.27Kwh/ton in contrast to 14.5kWh/ton of spodumene by (Oliazadeh et al., 2018).

3.2 Sieve Size/ Assay Analysis

Table 2 shows the results of Sieve analysis of the head sample and the assay grade of lithium in the various sieve sizes. The first column shows the various sieve size in µm used in the sieve test. The coarsest sieve size used was 150 µm and the finest was 38 µm. The results had shown the 75 µm sieve size as the liberation size, having the highest-grade value of 3.02% lithium oxide.

Table 2: Particle Size Analysis of Zankan Spodumene and assay analysis

Sieves (µm)	Wt (g)	Wt (%)	CWR (%)	CWP (%)	AAS (% Li_2O)
150	184.50	18.45	18.45	81.55	2.11
106	373.01	37.30	55.75	44.25	2.84
75	252.72	25.27	81.02	18.98	3.02
50	104.63	10.46	91.48	08.52	2.65
38	61.49	6.15	97.63	02.37	2.04
pan	23.65	2.37	100	0	-

Wt; Weight, CWR; Cumulative Weight Retained, CWP; Cumulative Weight Passing

4. CONCLUSIONS

Based on the experimental results obtained from the work carried out, the Liberation study shows 75 µm sieve size as the liberation size, having the highest-grade value of 3.02% lithium oxide and this value is good percentage

of Feed to Concentrator or extraction unit for significance upgrade and high lithium products. An average work index of the Zankan Spodumene computed to be 13.27Kwh/ton, the amount of energy required to comminute one ton of the test material. Spodumene which is high in lithium content, is the most common lithium bearing minerals that serves as alternative source to brine. Nigeria, has several spodumene deposits across her state of federation, yet to be fully explored, hence its potential to become a major stakeholder in lithium production industry could be fully enhanced, if technical informations are established

ACKNOWLEDGEMENT

The research work was funded by Tertiary Education Trust Fund (TETFUND) under the auspices of National Research Fund (NRF) with Grant Reference: TETF/DR&D-CE/NRF/2020/SETI/31/ Vol.1.The financial support is duly acknowledged.

REFERENCES

ABDUL MWANGA, JAN ROSENKRANZ & LAMBERG, P. 2015. Testing of Ore Comminution Behavior in the Geometallurgical Context—A Review. *Minerals,,* 5**,** 276-297.

DIRK, S. & JENS, G. 2013. Use of Mineral Liberation Analysis (MLA) in the Characterization of Lithium-Bearing Micas. *Journal of Minerals and Materials Characterization and Engineering,* 1**,** 285-292.

EGBE, E. A. P., MUDIARE, E., ABUBAKRE, O. K. & OGUNBAJO, M. I. 2013. Determination of the Bond Work Index of Baban Tsauni (Nigeria) Lead-Gold ore. *European Scientific Journal,,* 9.

GAY, S. L. 2004. liberation Model for Communition based on probability theory,. *Mineral Engineering,* 17**,** 525-534.

NAPIER-MUNN, T. J., MORRELL, S., MORRISON, R. D. & KOJOVIC, T. 1996. Mineral Comminution Circuits Their Operation and Optimization;. *JKMRC Monograph Series in Mining and Mineral Processing; Julius Kruttschnitt Mineral Research Centre: Brisbane, Australia,,* 2.

OBASSI, E., GUNDU, D. T. & AKINDELE, U. M. 2014. liberation size and beneficiation of Arufu Lead Ore, Nasarawa State, North-Central Nigeria. *International Journal of Engineering and Research.,* 3.

OBASSI, E., GUNDU, D. T. & AKINDELE, U. M. 2015a. Determination of Work index of Arufu Lead Ore, Nasarawa State, North-Central Nigeria. *International Journal of Engineering and Sciences.,* 4.

OBASSI, E., GUNDU, D. T. & AKINDELE, U. M. 2015b. Liberation Size and Beneficiation of Enyigba Lead Ore, Ebonyi State, South-East Nigeria. *Journal of Minerals and Materials Characterization and Engineering,* 3**,** 125.

OLATUNJI, K. J. & DUROJAIYE, A. G. 2010. Determination of Bond index of Birnin- Gwari Iron Ore in Nigeria. *Journal of Minerals & Materials Characterization & Engineering,* 9**,** 635-642.

OLIAZADEH, M., AGHAMIRIAN, M., ALI, S., LEGAULT, E., GIBSO, C. & 2018. Flowsheet Development for Benefication of Lithium Minerals from Hard Rock Deposit. *The Minerals, Metals & Materials Series,.*

STEFON, N., BERN, K., AMIT, K. & ZORIGTKHUU, D. 2014. An Energy Benchmarking Model for Mineral Communition. *Mineral Engineering,* 65**,** 178-186.

TIAN, J., XU, L., WU, H., FANG, S., DENG, W., PENG, T., SUN, W. & HU, Y. 2018. A novel approach for flotation recovery of spodumene, mica and feldspar from a lithium pegmatite ore. *Journal of cleaner production,* 174**,** 625-633.

UMAR, A. H., YARO, S. A., ABDULWAHAB, M. & DODO, M. R. 2016. Characterization of Sokoto Phosphate Rock for Beneficiation. *Journal of Raw Materials Research,* 10**,** 74-93.

WANG, C., NADOSKI, S., MEJIA, O., DROZDIAK, J. & KLEIN, B. Energy and Cost Comparisons of HPGR based circuits with the SABC circuit installed at the Huckleberry Mine. 45th Canadian Mineral Processors Conference Proceedings, Ottawa, Canada., 2013.

WEEDON, D. M., NAPIER-MUNN, T. J., EVANS, C. L., GRAY, M. J., BOWYER, G. J., CASTLE, J. F., VAUGHAN, D. J. & WARNER, N. A. 1990. Studies of mineral liberation performance in sulphide comminution circuits. In Sulphide Deposits—Their Origin and Processing. *Springer: Berlin, Germany.*

WEISS, N. L. 1985. *Mineral Processing Handbook,.*

WILLS, B. A. & NAPIER – MUNN, T. J. 2006. *Mineral Processing Technology*.

YARO, S. A. 1997. *Development of Process Route for the Beneficiation of MallamAyuba Manganese deposits to Ferromanganese feed grade,.*

APPENDICES

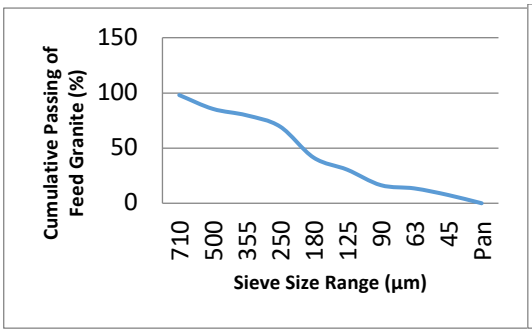

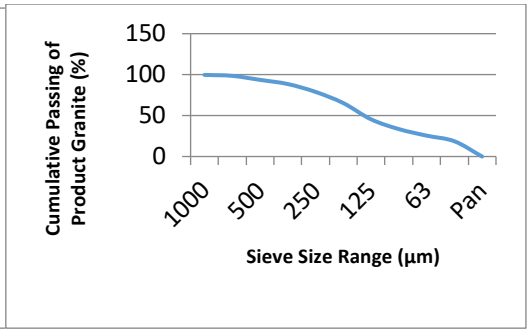

Fig. 2 Size distribution of the "feed" reference material (Granite) **Fig. 3** Size distribution of the "Product" reference material (Granite)

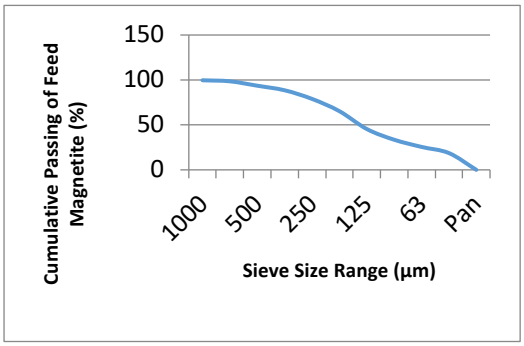

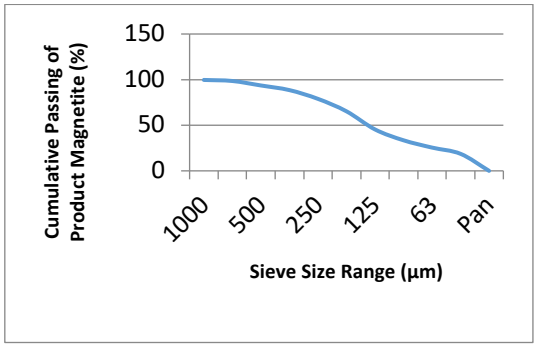

Fig. 4 Size distribution of the "feed" reference material II (Magnetite) **Fig. 5** Size distribution of the "product" reference material II (Magnetite)

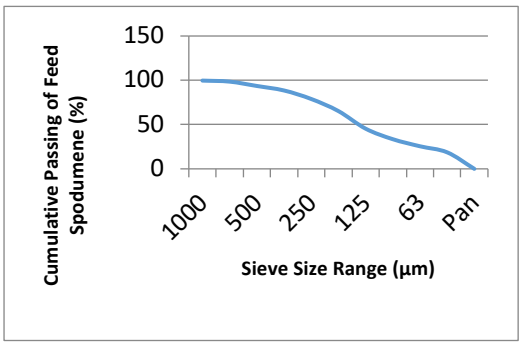

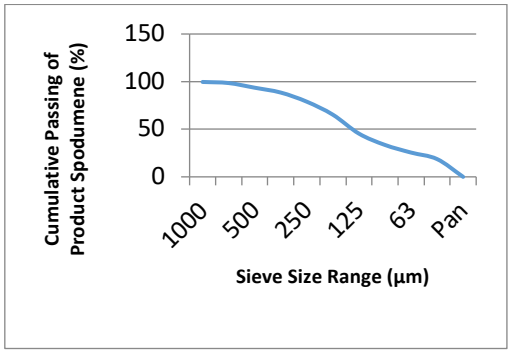

Fig. 6 Size distribution of the "feed" test material **Fig. 7** Size distribution of the "product" test material

PAPER 175 – RESEARCH FINDINGS IN GEOTECHNICAL PRACTICES FOR CONSIDERATION IN ROCK FORMATION

E. O. Adebiyi[1*], B. A. Morenikeji[2*], J. O. Babalola[2], T. K. Amaechi [3], O. S. Familua[4]

[1]Department of Mining Engineering, Federal University of Technology, Akure, Nigeria.
[2]Department of Mineral & Petroleum Engineering, Yaba College of Technology, Lagos, Nigeria.
[3]Department of Metallurgical Engineering, Yaba College of Technology, Lagos, Nigeria.
[4]Department of Architectural Technology, Kwara State Polytechnic, Ilorin, Nigeria.
[*]Email: bilorite2@gmail.com benmore80@gmail.com

ABSTRACT
The practice of geotechnical engineering is a field that requires rock and soil mechanics principles. In an environment due to the effects of unconformities and the irreversible result of failures within the rock formation, such as faults, joints, earthquakes, and other environmental problems. The study aided in classifying methods of mineral evaluation and rock formation on the earth's surface. The information was based on reviewed techniques with aided tools using geological surveys, geophysical investigations, and drilling methods as means of exploration operations. The exploration operation on the rock formation investigated surface and subsurface conditions using equipment such as a gravimeter, seismometer, and drilling machine on site. The methods of classifying rocks by mass were determined by the findings from the study, fieldwork, and laboratory experiments. The research findings have been stated for the application of civil and mining engineering, including related geological engineering aspects of the rock formation to be achieved. The study also showed that the engineering qualities of rock and soil materials, such as color, shape, texture, and origin of formation, are connected. Rock mass rating, rock quality designation, and geological strength index were also mentioned as three more ways to classify rock masses.

KEYWORDS: Geological, Geophysical, Drilling, Exploration, Investigation.

1. INTRODUCTION

Geotechnical engineering can be referred to as a relatively new engineering field that has evolved rapidly over the past few years. The basics of geotechnical engineering can be viewed as surface and underground, civil, and mining engineering works, whereas the challenge had to be corrected in a practical and effective manner. Geotechnical Engineering (rock) has concern with the engineering behavior of earth materials, which apply the principles of rock mechanics and soil mechanics for the remedy of respective engineering constraints but differ in the application (DIR, 1997). The field of study has knowledge areas that overlap in specialty with the related sub-disciplines such as civil engineering, geological engineering, hydrology, soil mechanics, rock mechanics, geophysics, mining engineering, and military, petroleum engineering, coastal engineering, seismology, and offshore construction (DIR, 1997). This is to provide information on the physical properties of rock and soil underlying and subsurface conditions, including surface and subsurface exploration of a site with various methods. Surface exploration can be done using geologic mapping, geophysical methods, and photogrammetry to observe the physical condition of the site. The work requires mapping and interpretation of geomorphology through geophysical techniques applied for subsurface exploration, such as the measurement of seismic waves, surface waves, and Rayleigh waves, which can be observed with the downhole method and electromagnetic survey. Subsurface exploration requires in situ testing, which is a standard penetration test and a cone penetration test, often subsurface sampling, and laboratory testing of the rock and soil materials. Rock is a naturally formed aggregate of minerals that forms part of the earth's surface. Rocks are grouped into igneous rock, sedimentary rock, and metamorphic rock, which are based on chemical composition, geological age, origin, structure, and texture mineralogy. The aggregate materials, which are rocks, are weathered by erosion and denudation processes from the parent rock to soil materials (Obasi, 1999).

2. THEORETICAL ANALYSIS

2.1 Principle and Theory

The analytical approach to the interpretation of the research findings was reviewed through the adoption and observations of the principles of electromagnetic, gravitational, and mechanics theories for engineering application on intact rock masses.

2.2 Expression of Term Representation

The research findings were given written expression in some definitions such as ground control, ground conditions on rock stress and excavation, ground or rock support and reinforcement, core recovery (CR), fracture frequency (FF), uniaxial compressive strength (UCS), rock mass rating (RMR), rock quality designation (RQD), and geological strength index (GSI). In addition, methods of rock mass classification were presented in formulas 1, 2, and 3, respectively.

3. MATERIALS AND METHODS

3.1 Research Equipment and Materials

The geotechnical practice was described as having qualitative and quantitative effects on the review of the mineral evaluation and rock formation. The equipment with materials required for the research work, such as rock or soil materials, shovel, geological hammer, Schmidt impact hammer, compass clinometer, mineralogical microscope, survey instrument, gravimeter, seismometer, and drilling machine This is an effort to explore, based on analysis, characterization, guidelines, and interpretation of rock and soil formation and hazards, the engineering properties (DIR, 1997).

3.2 Methods of Data Collection

3.2.1 Geological method: This is working on regional geology Information for geological mapping to generate topographical and position of the site of subsurface materials, description of overburden and bear rock or investigation. This is method of mapping investigation and techniques to explore the earth surface for studying the sediment that hardened into rock materials through field and recording geological information. Geological structure refers to all natural planes of weakness in the rock mass to pre-mining activity comment on rock formation (Priest, 1993). The basic instrument applied for the geological features such as optical ore microscope. Effect of geologic features on design for a range of characteristics such as geological structure, orientation and spacing, persistence, and roughness, wall strength and aperture, filling and seepage, and several sets.

3.2.2 Geophysical method: This method of investigation and techniques work to explore the earth's surface and subsurface conditions for detecting and surveying ground control vibration. This is a method applied to an area that has environmental conditions such as electromagnetic conductivity, ground, penetration radar, resistivity, seismicity, and gravity. This is working on physical and quantitative predictions with electromagnetic field principles and laws. The bore holes characterized on the geophysical survey required additional data collected from drilling exploration to aid in identifying an area for detailed investigation, as presented in Table 1. The site purpose of the geophysical survey done on bore holes or sinkholes and voids below with subsurface depth to bedrock or rock layers (Wightman et al., 2004) was described.

Table 1: Applicability of geophysical methods (ASTM D6429, 2011)

Method	Applicability Rating for Voids and Sinkholes	Applicability Rating for Depth to Bedrock
Ground Penetrating Radar	A	A
Gravity	A	A
Seismic Reflection/Refraction	B	B
Resistivity	B	N/A
DC Resistivity	N/A	B
Frequency Domain Electromagnetics	B	B
Time Domain Electromagnetics	B	B

*Note: A - preferred methods; B – alternative method; N/A – not applicable

3.2.3 Drilling method: This method was described as boring and sampling with coring investigations taken from the bore holes on the earth's surface and subsurface exploration. This is a method of using techniques to explore the penetration of the ground and the extraction of rock materials at depth beneath the surface of the earth using a drilling machine. The specification for codes and standard measures was itemized with aided tests such as boring tests, sampling tests, penetration tests, index tests, in situ tests, groundwater investigations, triaxial shears tests with strain, and the determination of the California bearing ratio. The work was examined on the technical description of the geotechnical investigation as described by Moytec (2016), as presented in Table 2.

Table 2: The codes and standard measures (Moytec, 2016)

Codes	Standard
IS: 1888	Plate load test
IS: 1892	Boring test
IS: 2131	Standard penetration test
IS: 2720	California bearing ratio
IS: 3043	Soil resistivity test
IS: 3048	Soil drilling test
IS: 4968	Static cone penetration test.

4. RESULTS AND DISCUSSIONS

4.1 Geological Survey Information for Geotechnical Practice

The research findings revealed geological mapping and the position of a location on the earth's surface of rock and soil. These are derivatives of geological characteristics, composition, features, and properties of rock and soil on the earth's surface, such as rock types and rock strength. This is the basis for classification in intact rock: a rock type, which can be examined by petrographic method and analysis; guideline practice on rock types itemized on physical characteristic efforts to engineering behavior. Rock type is initially grouped by identification of the intact rock, such as igneous rock, sedimentary rock, and metamorphic rock, with characteristics and features such as chemical composition, geological age, minerals, origin, structure, and texture, whereas Obasi (1999) described the combination of geological features.

Table 3: Characteristics and Features of Common Rock Formation

Rock Type	**Rock Class**	**Common Rocks**	**Primary Minerals**	**Secondary Minerals**	
	Intrusive	**Igneous**			
Granite	✓	✓	Quartz, K - Feldspar	Plagioclase, Mica, Amphibole, Pyroxene	
Quartz Diorite	✓	✓	Quartz, Plagioclase	Hornblende, Pyroxene, Mica	
Diorite	✓	✓	Plagioclase	Mica, Amphibole, Pyroxene	
Gabbro	✓	✓	Plagioclase, Pyroxene	Amphibole Olivine	
	Extrusive				
Rhyolite	✓	✓	Quartz, K - Feldspar	Plagioclase, Mica, Amphibole, Pyroxene	
Dacite	✓	✓	Quartz, Plagioclase	Hornblende, Pyroxene, Mica	
Andesite	✓	✓	Plagioclase	Mica, Amphibole, Pyroxene	
Basalt	✓	✓	Plagioclase, Pyroxene	Amphibole Olivine	
	Clastic	**Sedimentary**	**Primary Mineral**	**Original Sediment**	
Conglomerate	✓	✓		Sand, gravel, cobbles	
Sandstone	✓	✓		Sand	
Siltstone	✓	✓		Silt	
Claystone	✓	✓		Clay	
Shale	✓	✓		Laminated clay & silt	
	Non-clastic				**HCI Reaction**
Limestone	✓	✓	Calcite		Strong
Dolomite	✓	✓	Dolomite		Weak
Chert	✓	✓	Quartz		None
	Foliated	**Metamorphic**	**Primary Minerals**	**Formed from**	**Texture**
Slate	✓	✓	Quartz, Mica	Shale, Clay stone	Platy, fine-grained

Phyllite	✓	✓	Quartz, Mica	Shale, Clay stone, Fine-grained Pyroclastic	Platy, fine-grained with a silky sheen
Schist	✓	✓	Mica, Quartz, Feldspar, Amphibole	Sedimentary & Igneous Rocks	Medium-grained with irregular layers
Gneiss	✓	✓	Mica, Quartz, Feldspar, Amphibole	Sedimentary & Igneous Rocks	Layered, medium to coarse-grained
	Non-Foliated				
Greenstone	✓	✓	Mica, Hornblende, Epidote	Intermediate Volcanic & Mafic Igneous	Crystalline
Marble	✓	✓	Calcite & Dolomite	Limestone & Dolomite	✓
Quartzite	✓	✓	Quartz	Sandstone & Chert	✓
Amphibole	✓	✓	Hornblende & Plagioclase	Mafic Igneous & Calcium-Iron Bearing Sediments	✓

According to DIR (1997), igneous rock is the solidification of molten magma or material and features items on mineralogical composition such as color, texture, and method of placement, e.g., intrusive and extrusive. Sedimentary rock originated from the process of deposition and lithification of sediment materials through chemical precipitation with the solution or secretion of organisms. Sedimentary rock is featured itemized and may originate from either clastic or non-clastic sediments or materials precipitated by organisms. Metamorphic rock originated in pre-sedimentary rock materials due to changes that are metamorphosed based on changes in temperature and pressure. Metamorphic rock is featured itemized on its foliated or non-foliated that is massive as presented in Table 3. The summary features of common rocks such as igneous, sedimentary, and metamorphic rocks were described as the identification of rock type and rock class with primary and secondary minerals. In addition, intact rock can be grouped into relative rock with characteristics and the identification of rock type with the quality of the intact rock. Relative rock strength is designated by a series of items such as degree of cementation, mineral type, and weathering. Also, the recorded data was compared with the International Standard Rock Method (ISRM) (DIR, 1997).

4.2 Geophysical Investigation and Survey in Geotechnical Operation

The preferred research methods were stated to determine the geophysical feature of the site such as ground Control including components for the appropriate method. Ground control is a main part of underground mining operations which is primarily concerned with the preferred method of rock stability and instability from mine development and economics for ore exploitation. The geotechnical conditions in the rock mass were surveyed with observations to the geophysical method such as ground penetrating radar and gravity to determine mining operations and ground conditions with degree of accuracy (Laubscher, 1990) was stated. The types of ground control are micro scale and macro scale. The main components of ground control such as ground conditions, mine planning and design, and ground or rock support and reinforcement. The ground control can be written as stated;

Ground Control	=	Ground Conditions	+	Mine Planning and Design	+	Ground Support and Reinforcement

4.2.1 Ground Conditions in Rock Stress for Geotechnical Operations

The ground condition of rock stress can be referred to as the basic geotechnical properties of the rock mass. The features determine ground conditions such as geological structure, rock stress, rock strength, groundwater, blast damage, and the size, number, shape, type, and orientation of openings with their interaction (Dunnicliff, 1993; Hoek et al., 1995). The rock stress field is based on magnitude and orientation, which can be described as a pre-mining stress field and disturbance effects due to excavation (DIR, 1997). This is written as stated:

Rock stress around and excavation	=	Pre-mining stress	+	Disturbance

Field Effects

The pre-mining stress field consists of components such as forces generated by the weight of overlying rock masses and large horizontal forces (tectonic forces) in the Earth's crust. The significance of rock stress and its effects on underground mining work should be considered and specified. The rock stress field around an excavation is impacted by dynamic forces that can cause rock instability or consistent failure (Amadel and Stephansson, 1997). The types of rock stress measurements include absolute rock stress measurements and stress change measurements.

4.2.2 Ground or Rock Support and Reinforcement in Geotechnical Practice

Rock support and reinforcement are properly designed, planned, and installed to be achieved during geotechnical operations. Ground support was applied to the surrounding area of the excavation to limit the movement of the rock mass, such as concrete lining, timber props, shotcrete, and steel sets. Ground support and reinforcement were involved in all the stages, and the approaches measured were used to react to the stability of the ground. However, the number, size, shape, orientation, and ground conditions of the excavations were observed when planning for the most adequate ground support and reinforcement work (DIR, 1997; Hutchinson et al., 1996).

4.3 Drilling Operation in Geotechnical Practice

This was described with drilling techniques such as rock coring and mud rotary drilling. The drilling technique and model instrument were used for downward force or thrust, penetration distance, drilling fluid, pressure, time, and torque, with penetration rate and energy features outlining the subsurface conditions. The drilling parameters were recorded to ensure adequate uniformity in rock transition from soil to the eroded rock of the parent rock in the difference of rock layer properties such as uniaxial compressive strength. The rock and soil characteristics resulting from the drilling index tests are stated in the aspect of geotechnical design. The codes of standard tests were adopted in stated drilling tests such as the bore test, California bearing ratio, plate load test, penetration standard test, and soil resistivity test. The measures that were required, such as the Atterberg limit test, water content, unit weight, abrasive, durability, hardness-size distribution, and specific gravity, were examined on rock core. In situ tests of rock and soil revealed the index properties for effective measures of engineering behavior (Barton et al., 1974). The index properties can be measured and classified into samples collected from one borehole to another and can be registered as a stratigraphic unit (Bieniawski, 1973). The procedures for rock cored boreholes value were collected during coring and handled appropriately as a basic index property for bulk or disturbed rock masses. In addition, downhole information was adopted for functional effects on discontinuities in a sinkhole. Measurement Whole Drilling (MWD) was applied to drilling rigs for intact rock and rock mass (Savidge et al., 2006; ASTM D2113 and D5079).

4.4 Methods or Systems of Rock Mass Classification in Geotechnical Practice

The observations were adopted to reveal geological properties, geophysical ground control, and boring with coring and penetration systems. The degree of characterization was described in measurements on rock core, such as core recovery (CR), rock quality designation (RQD), and fracture frequency (FF). The methods of research revealed the geotechnical practice in rock mass of the application in the construction field, and design work was determined as stated, such as rock mass rating, rock quality designation, and geological strength index.

4.4.1 Rock Mass Rating System

The system was initiated for application in tunnel design, with an approach adopted on rock as a treatment for structural ability in the construction field. The parameters for the Rock Mass Rating (RMR) Classification System Valve for specific site investigation include uniaxial compressive strength (UCS), rock quality designation (RQD), discontinuity conditions, discontinuity spacing (S), and orientation of discontinuities. The last parameter is stability for specific constraints with the design of mined slopes and bedrock foundations; other parameters measure numeric valves for components (Laubscher, 1990) as presented in formula 1.

$$RMR = \sum_{i=1}^{5} R_i \qquad 1$$

Where Ri is the reflected value recorded for R_1- R_5

R6 is the basic RMR value for certain types of features (such as slope, foundation, and tunnel) and strikes and dips of discontinuities. The orientation valve of R6 ranges from 0 for the most favorable condition to -60 for an unfavorable discontinuity orientation mined slope. The RMR system ranges between 0 and 100, where 0 reflects very poor rock masses and 100 reflects excellent rock masses. The RMR value system is adopted as the parameters for specific design methods (Bienlawski, 1989; Hoek et al., 1995; Wyllie, 1999).

4.4.2 Rock Quality Designation

The core recovery parameter was described as basic to examine the rock mass quality (Deere and Deere, 1988), and the rock mass quality was observed on the Rock Quality Designation (RQD) as presented in Table 5. Also, the ratio of the sum of the total length of sound pieces sized of intact rock greater than 4 inches (100mm) in length to the addition of the total length of the core run (Deere et al., 1967; ASTM 6032, 2011) as presented in formula 2

$$RQD = \frac{\sum length\ of\ sound\ pieces > 4\ inches}{Total\ length\ of\ core\ run} \times 100\% \quad 2$$

RQD was adopted by the recommendation for a mix size of 2 to 16 inches' diameter core, whereas larger with smaller core sizes were observed through adequate drilling operations. The mechanical break's fault caused by drilling or boring of the core was not observed in the deduction for RQD. The RQD number of core pieces was summed, and the length of the core greater than 4 inches was noted on the log data. RQD should be recorded as a core run to 5 feet with 4 pieces' length to 125 feet as a correlate to core values recovered to a piece of 5 feet' length as presented in Table 4.

Table 4: Rock Quality based on Rock Quality Designation (RQD), (Deere and Deere, 1988)

RQD	Rock mass quality
0 – 25	Very poor
25 – 50	Poor
50 – 75	Fair
75 – 90	Good
90 – 100	Excellent

4.4.3 Geological Strength Index System

This was developed for geotechnical design properties for rock masses, whereas empirical design formulas such as RMR, CSIR, or Q systems Therefore, the design of a rock mass classification method for transportation application recommendations (Hoek, 1994; Hoek and Brown, 1997; Marinos and Hoek, 2001) was described. The GSI system was recently adopted to measure the strength and stiffness of rock masses. The GSI system has two basic features that control the mechanical behavior of rock masses, such as the degree of interlocking of blocks and the condition of discontinuity surfaces on intact rock and within the rock mass. The GSI system has revealed the qualitative and quantitative analysis approach to borehole or sinkhole investigation (Hoek et al., 2013), which has been heavily altered, such as consistent conditions with the lower row method. The GSI system was described as heterogeneous rock masses, such as alternating series or layers of harder and softer rock materials (Marinos and Hoek, 2001), as presented in formula 3.

$$GSI = 1.5 \cdot JCond_{89} + \frac{RQD}{2} \quad 3$$

Where $JCond_{89}$ is referred to as a joint condition rating (Bieniawski, 1989).

5. CONCLUSION

The research work on geotechnical practice has aided the mineral and petroleum industries in achieving optimization guidelines for extraction and drilling operations on the earth's surface and subsurface conditions. The geotechnical practice has revealed interrelationships with various fields such as civil, mining, petroleum, and geological engineering and geosciences in the application of rock and soil mechanics investigation. The practice of geotechnical work has revealed the classification and identification of minerals and types of rock and soil formations, as presented in Table 3. The geotechnical investigation has revealed the difference between rock and soil properties as engineering materials and their application to rock and soil mechanics for design work to solve engineering constraints.

ACKNOWLEDGEMENT

The paperwork is essential to the aspect of geotechnical work on earth's surface and subsurface conditions. The authors appreciated the support from the Faculty of Engineering and Technology, University of Ilorin, for accepting the paperwork. Also, we would like to thank the authors for the materials used as sources of information in this paper.

REFERENCE

Amadei, B, and Stephansson, O, 1997. Rock Stress and its Measurement, 490 p (Chapman & Hall: London).

ASTM D5092 (2010), Standard Practice for Design and Installation of Groundwater Monitoring Wells, ASTM International. DOI: 10.1520/D5092-04R10E01

ASTM D5878 (2008), Standard Guides for Using Rock-Mass Classification Systems for Engineering Purposes, ASTM International. DOI: 10.1520/D5878-08

ASTM D6429 (2011), Standard Guide for Selecting Surface Geophysical Methods, ASTM International. DOI: 10.1520/D6429-99R11E01

Barton, N, Lien, R and Lunde, J, 1974. Engineering classification of rock masses for the design of tunnel support, in Rock Mech, 6:183-236.

Bieniawski, Z T, 1989. Engineering Rock Mass Classifications, 251 p (John Wiley & Sons: New York).

Bieniawski, Z T, 1973. Engineering classification of jointed rock masses, in Trans S Afr Inst Civ Eng, 15:335-344.

Deere, D.U., A.J. Hendron, F.D. Patton, and E.J. Cording (1967), "Design of surface and near-surface construction in rock," Proceedings of the 8th U.S. Symposium on Rock Mechanics – Failure and Breakage of Rock, American Institute of Mining, Metallurgical and Petroleum Engineers, Inc., pp. 237-302.

Deere, D.U., and D.W. Deere (1988), "The Rock Quality Designation (RQD) Index in Practice," Rock Classification Systems for Engineering Purposes, Louis Kirkaldie, Ed., American Society for Testing and Materials, ASTM STP 984, pp. 91-101.

Department of Industry & Resources (1997). Geotechnical consideration in underground mines, Mine Occupational Safety and Health Advisory Board, Australia (MOSHAB) Approved pages 9, 23, 27, 148, 149.

Dunnicliff, J, 1993. Geotechnical Instrumentation for Monitoring Field Performance, 577 p (John Wiley & Sons: New York).

Hoek, E. (1994), "Strength of Rock and Rock Masses," ISRM News Journal, Vol. 2, No. 2, pp. 4-16.

Hoek, E., T.G. Carter, and M.S. Diederichs (2013), "Quantification of the Geological Strength Index Chart," Proceedings of 47th U.S. Rock Mechanics/Geomechanics Symposium, San Francisco, American Rock Mechanics Association, Paper 13-672.

Hoek, E, Kaiser, P K and Bawden, W F, 1995. Support of Underground Excavations in Hard Rock, 215 p (Balkema: Rotterdam).

Hoek, E., P.K. Kaiser, and W.F. Bawden (1995), Support of Underground Excavations in Hard Rock, A.A. Balkema, 215 pp.

Hoek, E., and E.T. Brown (1997), "Practical estimates of rock mass strength," International Journal of Rock Mechanics and Mining Sciences, Elsevier, Vol. 34, No. 8, pp. 1165-1186. DOI: 10.1016/S1365-1609(97)80069-X

Hutchinson, D Jean and Diederichs, Mark S, 1996. Cable bolting in Underground Mines, 406 p (BiTech Publishers: Richmond, British Columbia).

Laubscher, D H, 1990. A geomechanics classification system for the rating of rock mass in mine design, in J S Afr Inst Min Metall, 90(10):257-273.

Marinos, P., and E. Hoek (2001), "Estimating the geotechnical properties of heterogeneous rock masses such as flysch," Bulletin of Engineering Geology and the Environment, Springer-Verlag, Vol. 60, No. 2, pp. 85-92. DOI: 10.1007/s100640000090.

Moytec Consultant (2016): Technical specification for Geotechnical investigation, Rabindra Bharati University at 24 Ganapati Sur Sarani (South Sinthi at BT Road, Kolkata 700050) Ward No .02. Page 9-17.

Obasi Romanus (1999). The foundation to Engineering Geology Kenlua paperback and omobala publishers Nigeria Page 24 – 27.

Priest, S D, 1993. Discontinuity Analysis for Rock Engineering, 473 p (Chapman & Hall: London).

Savidge, J., K. Bennett, A. Lutenegger, and C-J Hung (2006), Subsurface Investigation Qualification: Participant Workbook," Participant workbook for NHI Course 132079, National Highway Institute, Federal Highway Administration, Publication FHWA-NHI-05-035, 838 pp.

Wightman, W.E., F. Jalinoos, P. Sirles, and K. Hanna (2004), Application of Geophysical Methods to Highway Related Problems, Federal Highway Administration, Central Federal Lands Highway Division, FHWA-IF-04-021, 742 pp.

Wyllie, D.C. (1999), Foundations on Rock, E&FN Spon, Second Edition, 401 pp.

PAPER 176 – DEVELOPMENT AND CHARACTERIZATION OF SAWDUST/*PROSOPIS AFRICANA* LEAF SILVER-ZINC NANOPOROUS ADSORBENT

J. A. Adeniran*, B. T. Ogunlade, A. K. Oyeneye, E. T. Odediran, S. A. Atanda

[1]Department of Chemical Engineering, University of Ilorin, Ilorin, Nigeria.
*Email: adeniran.ja@unilorin.edu.ng

ABSTRACT
This study focused on the green synthesis and characterization of sawdust/*Prosopis africana* leaf silver-zinc nanoporous (SD/PAL Ag-ZnNPs) adsorbent for air pollution control. Sawdust was carbonized at 450 °C for 1 hour with a conversion yield of 28%. PAL Ag-ZnNPs solution was produced from *Prosopis africana* leaf extract. Bi-metallic PAL nanoparticle extract and the activated carbon from sawdust were hybridized to produce SD/PAL Ag-ZnNPs adsorbent. Characterization results using Ultraviolet-Visible (UV-VIS) spectroscopy indicated the presence of phytoconstituents which acts as capping and stabilizing agents, Fourier Transform Infrared (FT-IR) spectroscopy analysis showed the presence of a carbonyl group in the sample which reduces Ag^+ in the sample to silver nanoparticles, Scanning Electron Microscopy (SEM) confirmed the porosity of the sample, Energy Dispersive Spectroscopy (EDS) showed carbon and oxygen as the major components with atomic weight percentages of 83.54% and 15.51% respectively. Transmission Electron Microscopy (TEM) analysis confirmed the presence of nanoparticles, and X-Ray Diffraction (XRD) analysis indicated the presence of face-centered cubic crystal. Overall analyses showed that SD/PAL Ag-ZnNPs adsorbent exhibited high adsorption capacity which may be useful for air pollution control. This study showed the potential of producing low-cost adsorbents from agricultural and wood processing wastes.

KEYWORDS: Nanoparticles; Green synthesis; Bimetallic; *Prosopis africana*

1. INTRODUCTION

The adverse effect of air pollution has been felt by both human health and the environment, it has led to a lot of problems for living things and the ecosystem. Air pollution ranks third in the top 10 risk factors contributing to disabilities and death in Nigeria between 2007 and 2017 (Pona *et al.*, 2021). Nigeria has the highest number of premature deaths in the Sub-Saharan Africa region in 2017, this is due to ambient $PM_{2.5}$ pollution with 49,100 death (Croitoru *et al.*, 2020).

The health effect of pollution is not only determined by the level of the pollution but also by the period people spend inhaling polluted air (the exposure level) (Manisalidis *et al.*, 2020). Exposure has to do with the concentration of pollutants in the immediate breathing environment for a specified amount of time. This can be measured either by combining information on pollutant levels in each micro-environment where people spend time with information on activity patterns or directly through personal monitoring.

In the past, outdoor air pollution has been the major attention of scientists. But recently, many studies have been conducted on indoor air pollution because most people spend between 80 to 90% of their time indoors giving them greater exposure to indoor pollution than outdoor ones. Furthermore, the concentration of air pollutants is much higher indoors than outdoors (Gonzalez-Martin *et al.*, 2021; Lu *et al.*, 2019).

In the last few decades, air quality has improved in several countries due to emission reduction strategies and legislation, but there is not much difference in some other countries. Industrialisation and urbanisation frequently result in air and environmental pollution at large, which results in lowers life expectancy and harms people's well-being. Public awareness of environmental pollution and issues with environmental regulations vary greatly around the world since different countries are going through different stages of industrialization (Zeng *et al.*, 2019). In Africa, about 3 billion people still rely on solid fuels, of which 2.4 billion of them on biomass, and the rest on coal. In most African countries, biomass is the major source of fuel for most rural households (Benti *et al.*, 2021; Stoner *et al.*, 2021). During the 1990s, the use of biomass as the traditional fuel in Sub-Saharan Africa increased as a percentage of total energy use, while in most other parts of the world, the trend has been the reverse (Doggart *et al.*, 2020; Makonese *et al.*, 2018). 3.55 million death are attributed to high levels of indoor air pollution each year as a result of the inefficient and incomplete combustion of solid fuel (Ali *et al.*, 2021).

The specific objectives of this study are to: (i) synthesize Silver-Zinc nanoparticles with *Prosopis africana* leaves (PAL Ag-ZnNPs) using green synthesis method; (ii) produce activated carbon (micro-adsorbent) from sawdust; (iii) hybridize PAL Ag-ZnNPs solution and activated carbon produced from sawdust to form nanoporous adsorbent; and (iv) characterize SD/PAL Ag-ZnNPs adsorbent.

2. THEORETICAL ANALYSIS

2.1 Percentage yield for carbonization

The weight difference of the sample before and after carbonization gives the weight loss and the percentage yield of the material calculated as a percentage (Equation 1).

$$Percentage\ yield\ (\%) = \left(\frac{W_F}{W_I}\right) \times 100 \qquad (1)$$

Where $W_F =$ weight of the sample after carbonization
$W_I =$ weight of the sample before carbonization

3. MATERIALS AND METHODS

3.1 Materials

The agricultural waste used to produce hybridized nanopourous adsorbent is *Prosopis africana* leaves (PAL) which was obtained from the environment of the University of Ilorin, Ilorin, Nigeria, and the wood processing waste is sawdust. All chemicals/reagents used throughout the experiment were of analytical grade; they include silver nitrate (95% pure), zinc nitrate (hexahydrate) (96% pure), and deionized water. The apparatus that was used during the course of this research study are test tubes, measuring cylinder, weighing balance, beakers, muffle furnace, centrifuge, funnel, camera, stopwatch, filter paper, oven, water bathe, and spectrometer.

3.2 Preparation of *Prosopis africana* Nanoparticles (PAL Ag-ZnNPs)

3.2.1 Preparation of feedstock

Fresh leaves were collected, washed to remove dirt and sun-dried under normal atmospheric conditions. On complete dryness, the dried leaves were milled to a powder using a mortar and a pestle and sieved.

3.2.2 Extraction stage

Prosopis africana leaves (PAL) extract was obtained using the methods described by Lateef *et al.*, (2015). About 10 g of the PAL powder was weighed and suspended in 1,000 mL of deionized water, followed by heating in a water bath at 60 ℃ for 1 hour. The extract was filtered and then centrifuged at 4,000 rpm for 30 minutes. The final clear extract was collected and stored in a refrigerator at 4 ℃ for further use (Lateef *et al.*, 2015).

3.2.3 Green synthesis of PAL Ag-ZnNPs

About 45 mL of 1mM silver nitrate ($AgNO_3$) solution and 45 mL of zinc nitrate solution was added to 10 mL of the extract to reduce the amount of silver and zinc ions to silver/zinc nanoparticles. The solution was placed in the sunlight and agitated to speed up the rate of reaction. Once the solution changes from golden brown colour to colourless, it indicates the formation of PAL Ag-ZnNPs. The solid residue was then dried at 60 ℃ for 1 hour which then formed the PAL Ag-ZnNPs pellets; the solution absorbance is measured with a Ultraviolent-visible spectrometer (Lateef *et al.*, 2015).

3.3 Preparation of Adsorbent

3.3.1 Preparation of feedstock

The sawdust used for adsorbent was gathered at a sawmill in Ilorin, dried in the sun at the normal atmospheric condition and weighed before carbonizing.

3.3.2 Carbonization of adsorbent

The prepared sample of sawdust was placed in a muffle furnace and carbonized at 450 ℃ for 1 hour, to achieve good yield and porosity (Chowdhury *et al.*, 2016). The resulting material was cooled at room temperature, weighed and stored in a clean, dry container.

3.4 Hybridization of Nanoporous Adsorbent

50 g of adsorbent was added to 1,000 ml of PAL Ag-ZnNPs solution. This mixture was subjected to continuous stirring for 2 hours. The mixture was then filtered resulting in a residue (hybridized nanoporous adsorbent) and a clear filtrate. The residue was heated at about 110℃ for 10 hours to reduce its moisture content forming SD/PAL Ag-ZnNPs adsorbent (Peternela et al., 2017).

4. RESULTS AND DISCUSSION

4.1 Production of Nanoporous Adsorbent

PAL Ag-ZnNPs nanoparticles were produced using green synthesis. This was observed by the solution changing from golden brown colour to colourless shown in figure 1, further confirmation was done with UV-VIS analysis.

Figure 1: (a) PAL extract solution, and (b) PAL Ag-ZnNPs nanoparticles solution

Percentage yield for carbonizing sawdust at 450 ℃ for 1 hour was calculated for different batches using equation 1:

$$percentage\ yield\ (\%) = \left(\frac{196}{700}\right) \times 100$$

$$percentage\ yield\ (\%) = 28\%$$

$$percentage\ yield\ (\%) = \left(\frac{213}{750}\right) \times 100$$

$$percentage\ yield\ (\%) = 28.4\%$$

$$percentage\ yield\ (\%) = \left(\frac{210.75}{750}\right) \times 100$$

$$percentage\ yield\ (\%) = 28.1\%$$

$$percentage\ yield\ (\%) = \left(\frac{210}{750}\right) \times 100$$

$$percentage\ yield\ (\%) = 28\%$$

4.2 Characterization of Nanopourous Adsorbent

4.2.1 Ultraviolet-Visible (UV-VIS) Spectroscopy Analysis

The wavelength of spectral region of UV-VIS spectrometer ranged between 190 – 900 nm. The UV-VIS spectrum of *Prosopis africana* leaf extract in figure 2a shows bands at λ_{max} = 400 nm, 260 nm, and 205 nm with absorbance of 0.099, 0.255, and 1.069 respectively. PAL AgNPs graph in figure 2b shows bands at λ_{max} = 450 nm, 275 nm, and 215 nm for the peaks with absorbance of 0.128, 0.063, and 2.172 respectively, and λ_{min} = 245 nm for the valley with absorbance of -0.006. PAL Ag-ZnNPs graph in figure 2c shows bands at λ_{max} = 470 nm, and 220 nm with an absorbance of 0.126 and 3.277 respectively.

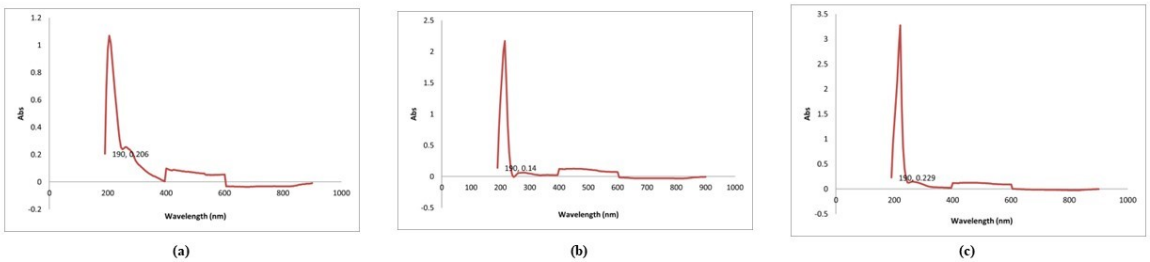

Figure 2: UV-VIS Spectrum of (a) *Prosopis africana* leaves (PAL) extract, (b) PAL AgNPs, and (c) PAL Ag-ZnNPs

4.2.2 Fourier Transform Infrared Spectroscopy (FT-IR) Analysis

The FT-IR spectrum of SD/PAL Ag-ZnNPs adsorbent is shown in figure 3f. the different adsorption bands in the graph indicate the presence of mercaptans, thiophenols, thiolacids, phosphine, phosphine oxides, anhydrides, acid

halides (halogenides), carboxylic acid salts, alkenes, boron compound, thioamides, thioureas, sulphonamides, phosphorus compounds, aromatic compounds, trisubstituted alkenes, chlorohydrocarbons sulphur compounds, bromohydrocarbons, iodohydrocarbons.

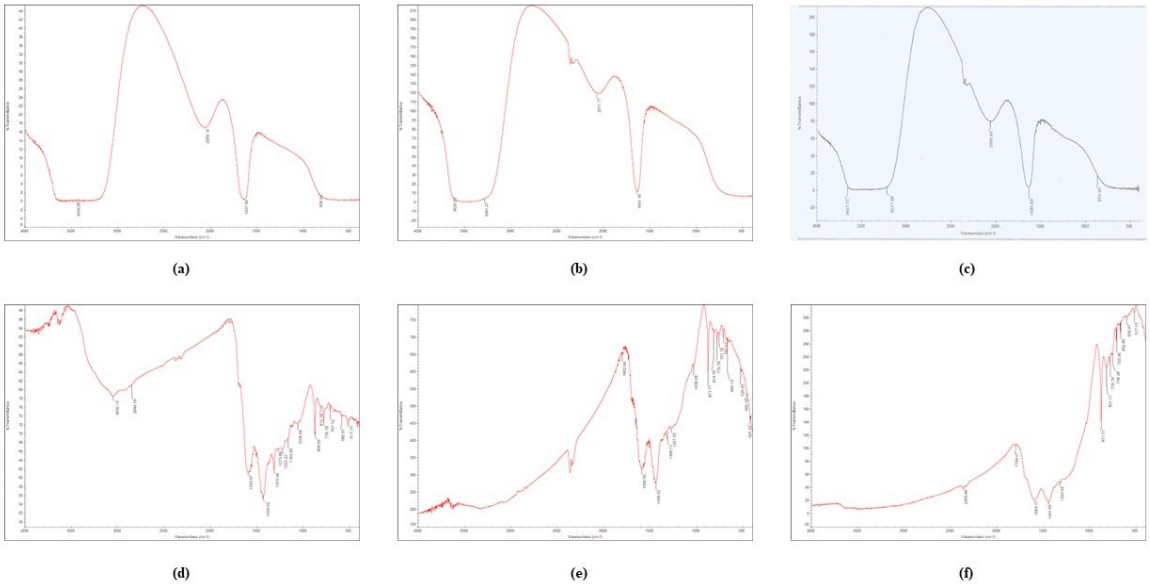

Figure 3: FT-IR Spectrum of (a) *Prosopis africana* leaves (PAL) extract, (b) PAL AgNPs, (c) PAL Ag-ZnNPs, (d) sawdust adsorbent, (e) SD/PAL AgNPs adsorbent, and (f) SD/PAL Ag-ZnNPs adsorbent

4.2.3 Scanning Electron Microscopy (SEM) Analysis of SD/PAL Ag-ZnNPs adsorbent

Pores were identified in the SD/PAL Ag-ZnNPs adsorbent at 10 μm and 20 μm using a scanning electron microscope with magnification of 1000 X and 200 X respectively (Figure 4).

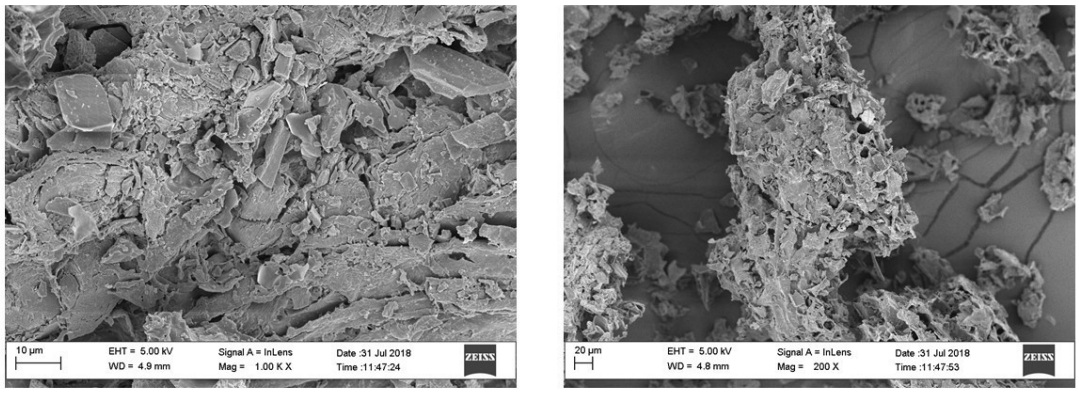

(a) **(b)**

Figure 4: SEM Micropraph of SD/PAL Ag-ZnNPs adsorbent at (a) 10 μm, 1000 X magnification, and (b) 20 μm, 200 X magnification

4.2.4 Scanning Electron Microscopy (Energy Dispersive Spectroscopy) Analysis of SD/PAL Ag-ZnNPs Adsorbent

Scanning Electron Microscopy (Energy Dispersive Spectroscopy) analysis was done to identify particular elements and their relative atomic proportion in SD/PAL Ag-ZnNPs adsorbent sample. Table 1 shows carbon and oxygen as the major components with atomic percentages of 83.54% and 15.51% respectively.

Table 1: Table of SEM (EDS) of SD/PAL Ag-ZnNPs adsorbent

S/N	Element Identified	Atomic %	Weight %	Weight % Sigma
1	C	83.54	78.16	0.55
2	O	15.51	19.32	0.55
3	Mg	0.35	0.67	0.06
4	K	0.19	0.56	0.06
5	Ca	0.41	1.28	0.08
	Total	100	100	1.30

4.2.5 Transmission Electron Microscopy (TEM) Analysis

The transmission electron microscopy was used to check the lattice arrangement and crystallinity of the SD/PAL Ag-ZnNPs adsorbent. Figure 5 shows the structure of the sample at a nano level confirming the presence of nanoparticles.

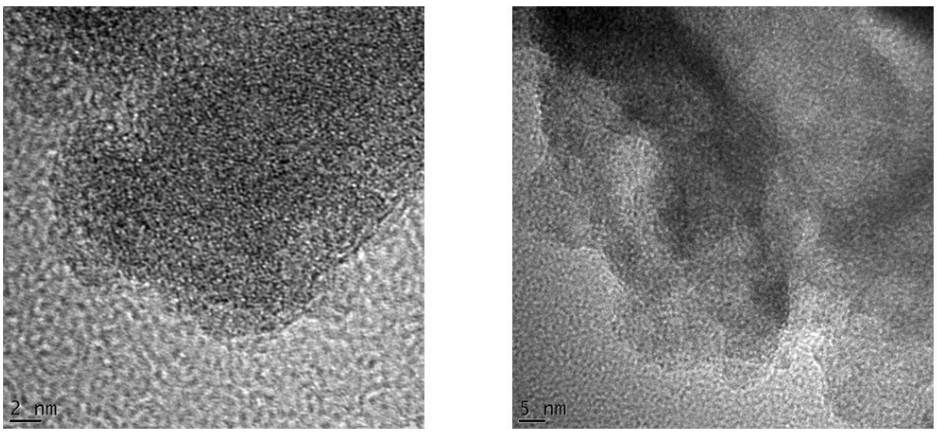

(a) **(b)**

Figure 5: TEM analysis of SD/PAL Ag-ZnNPs adsorbent at (a) 2 nm, and (b) 5 nm

4.2.6 Transmission Electron Microscopy (Energy Dispersive Spectroscopy) Analysis

The Energy Dispersive Spectroscopy reflects the bimetallic nature and atomic ratio between the elements present in the hybridized adsorbent. The EDS pattern also indicated the presence of K, Ca, O, Cu, Mg, P, and S. The energy required by the Spectroscopy for the analysis of TEM (EDS) ranges from 0-10 KeV.

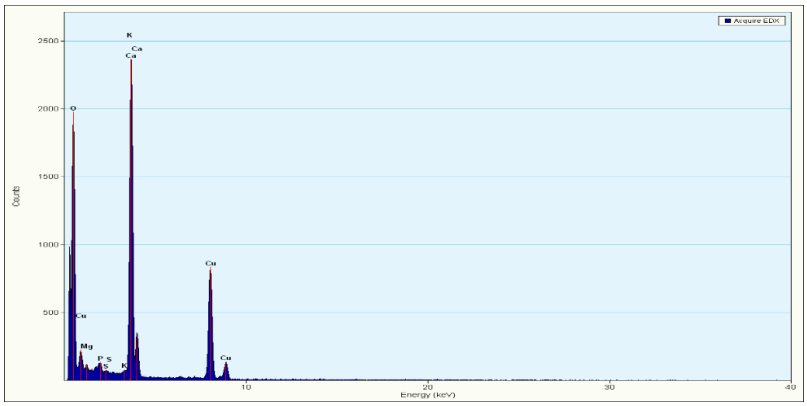

Figure 6: Graph showing the energy level for the elemental constituent for SD/PAL Ag-ZnNPs adsorbent

4.2.7 X-Ray Diffraction (XRD) Analysis

X-ray diffraction was used to identify the composition of the molecules on an atomic scale. The red line in the graph represents quartz crystalline structure, the blue line indicates cristobalite structure and the black line indicates glass structure.

Ag exhibits a single face-centred cubic (fcc) geometry. The peaks observed at 2θ values of 29.4°, 39.3° and 48.2° which correspond to crystallographic planes of (104), (113), and (116) and can be ascribed to the composition of

PALE that are acting as capping and stabilizing agents for SD/PAL Ag-ZnNPs adsorbent, thus preventing agglomeration.

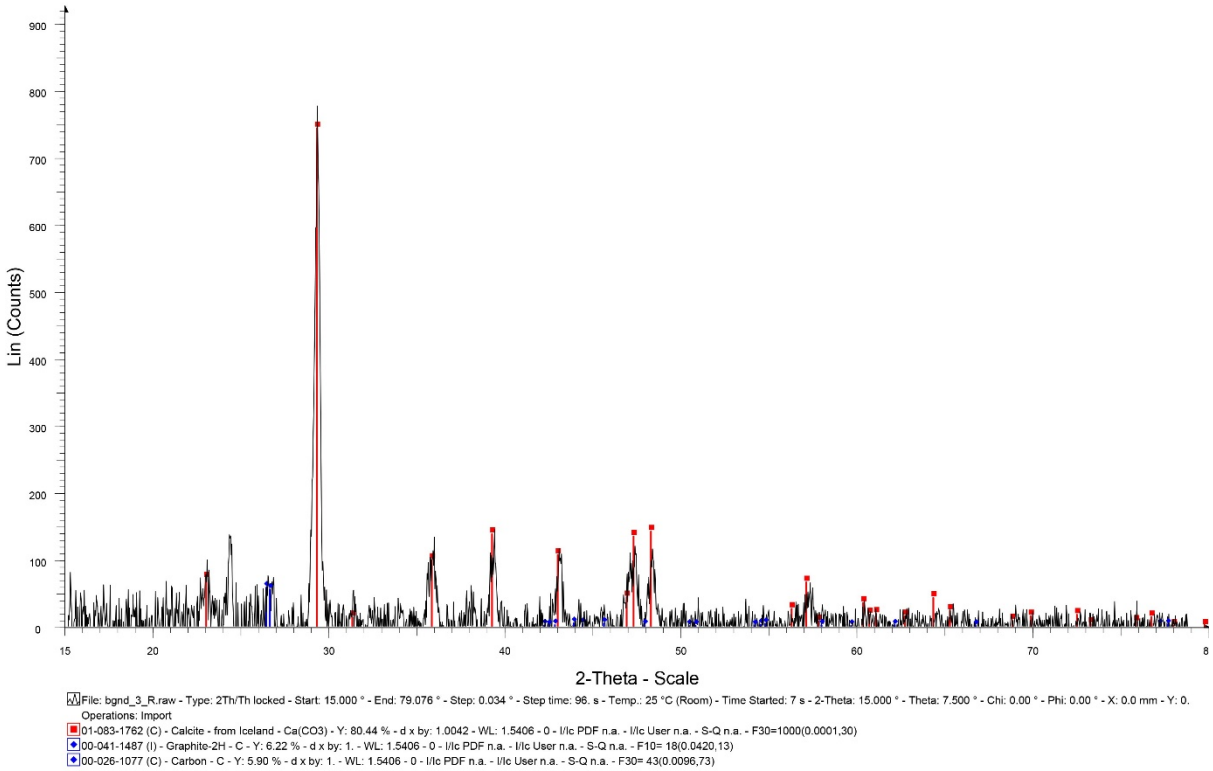

Figure 7: Graph of XRD showing peaks observed

5. CONCLUSION

Silver-zinc nanoparticles were produced with *Prosopis africana* leaf extract and hybridized with carbonized sawdust which is an economical, efficient, and eco-friendly process. The study showed that bimetallic Ag-ZnNPs could be prepared by *Prosopis africana* leaf extract. The silver and zinc ions were reduced to silver-zinc nanoparticles when added to *Prosopis africana* leaf extract; it was observed that the colour of the solution turned from golden brown colour to colourless. After the carbonization of sawdust, around 28% yield was gotten.

The UV-VIS spectra of PAL Ag-ZnNPs solution showed the presence of phytoconstituents (such as amino acid) in the extract which acts as a capping and stabilizing agent making it suitable for the adsorption process. FT-IR spectroscopy analysis on SD/PAL Ag-ZnNPs adsorbent showed the presence of a carbonyl group in the sample which confirmed that Ag+ ions in silver nanoparticles by capping material of plant extract. SEM confirmed the porosity of the nanoporous adsorbent while SEM (EDS) identified the major and trace components in the adsorbent. TEM confirmed the presence of nanoparticles while TEM (EDS) indicated the presence of K, Ca, O, Cu, Mg, P, and S in the adsorbent. The X-ray diffraction analysis confirmed that the peaks observed at 2θ values of 29.4°, 39.3°, and 48.2° can be attributed to the composition of PAL that are acting as stabilizing and capping agent. The result obtained showed that SD/PAL Ag-ZnNPs adsorbent will be a good adsorbent for air pollution control.

REFERENCES

Ali, M. U., Yu, Y., Yousaf, B., Munir, M. A. M., Ullah, S., Zheng, C., Kuang, X., & Wong, M. H. (2021). Health impacts of indoor air pollution from household solid fuel on children and women. *Journal of hazardous materials*, *416*, 126127.

Benti, N. E., Gurmesa, G. S., Argaw, T., Aneseyee, A. B., Gunta, S., Kassahun, G. B., Aga, G. S., & Asfaw, A. A. (2021). The current status, challenges and prospects of using biomass energy in Ethiopia. *Biotechnology for Biofuels*, *14*(1), 1-24.

Chowdhury, Z. Z., Karim, M. Z., Ashraf, M. A., & Khalid, K. (2016). Influence of carbonization temperature on physicochemical properties of biochar derived from slow pyrolysis of durian wood (Durio zibethinus) sawdust. *BioResources*, *11*(2), 3356-3372.

Croitoru, L., Chang, J. C., & Akpokodje, J. (2020). The health cost of ambient air pollution in Lagos. *Journal of Environmental Protection*, *11*(09), 753.

Doggart, N., Ruhinduka, R., Meshack, C. K., Ishengoma, R. C., Morgan-Brown, T., Abdallah, J. M., Spracklen, D. V., & Sallu, S. M. (2020). The influence of energy policy on charcoal consumption in urban households in Tanzania. *Energy for Sustainable Development*, *57*, 200-213.

Gonzalez-Martin, J., Kraakman, N. J. R., Perez, C., Lebrero, R., & Munoz, R. (2021). A state–of–the-art review on indoor air pollution and strategies for indoor air pollution control. *Chemosphere*, *262*, 128376.

Lateef, A., Ojo, S. A., Akinwale, A. S., Azeez, L., Gueguim-Kana, E. B., & Beukes, L. S. (2015). Biogenic synthesis of silver nanoparticles using cell-free extract of Bacillus safensis LAU 13: antimicrobial, free radical scavenging and larvicidal activities. *Biologia*, *70*(10), 1295-1306.

Lu, F., Shen, B., Yuan, P., Li, S., Sun, Y., & Mei, X. (2019). The emission of PM2. 5 in respiratory zone from Chinese family cooking and its health effect. *Science of the total environment*, *654*, 671-677.

Makonese, T., Ifegbesan, A. P., & Rampedi, I. T. (2018). Household cooking fuel use patterns and determinants across southern Africa: Evidence from the demographic and health survey data. *Energy & Environment*, *29*(1), 29-48.

Manisalidis, I., Stavropoulou, E., Stavropoulos, A., & Bezirtzoglou, E. (2020). Environmental and health impacts of air pollution: a review. *Frontiers in public health*, 14.

Peternela, J., Silva, M. F., Vieira, M. F., Bergamasco, R., & Vieira, A. M. S. (2017). Synthesis and impregnation of copper oxide nanoparticles on activated carbon through green synthesis for water pollutant removal. *Materials Research*, *21*.

Pona, H. T., Xiaoli, D., Ayantobo, O. O., & Tetteh, N. D. (2021). Environmental health situation in Nigeria: current status and future needs. *Heliyon*, *7*(3), e06330.

Stoner, O., Lewis, J., Martínez, I. L., Gumy, S., Economou, T., & Adair-Rohani, H. (2021). Household cooking fuel estimates at global and country level for 1990 to 2030. *Nature communications*, *12*(1), 5793.

Zeng, Y., Cao, Y., Qiao, X., Seyler, B. C., & Tang, Y. (2019). Air pollution reduction in China: Recent success but great challenge for the future. *Science of the total environment*, *663*, 329-337.

PAPER 177 – DEVELOPMENT AND CHARACTERIZATION OF NANOPOROUS ADSORBENT FROM AGRICULTURAL WASTE

J.A. Adeniran[1*], A.K. Oyeneye[1], B. T. Ogunlade[1], E. T. Odediran[1], S. A. Atanda[1]

[1]Department of Chemical Engineering, University of Ilorin, Ilorin, Nigeria.
[*]Email: adeniran.ja@unilorin.edu.ng

ABSTRACT
This study focused on the production and characterization of flamboyant pod/banana peel silver-zinc nanoporous (FP/BPE Ag-ZnNPs) adsorbent for air pollution control. The flamboyant pod was carbonized at 450°C for 1 hour with a conversion yield of 27.48%. Extract from banana peel was used to synthesise Ag-ZnNPs solution. The nanoparticle extract and the carbonized flamboyant pod were hybridized to produce FP/BPE Ag-ZnNPs adsorbent. Characterization results using Ultraviolet-Visible (UV-VIS) spectroscopy indicated the presence of unsaturated hydrocarbon absorbing compounds which acts as stabilizing agent, Fourier Transform Infrared (FT-IR) spectroscopy analysis showed the presence of carbonyl group which acts as a reducing agent for reducing silver ions present in the sample to silver nanoparticles. Scanning Electron Microscopy (SEM) confirmed the porosity of the sample, Energy Dispersive Spectroscopy (EDS) showed carbon and oxygen as the major components with atomic weight percentages of 82.52% and 11.88% respectively. Transmission Electron Microscopy (TEM) analysis confirmed the presence of nanoparticles, and X-Ray Diffraction (XRD) analysis indicated the presence of face-centred cubic crystal. Overall analyses showed that FP/BPE Ag-ZnNPs adsorbent exhibited high adsorption capacity which may be useful for air pollution control. This study showed the potential of producing low-cost, non-toxic, and environmentally friendly adsorbents from agricultural wastes.

KEYWORDS: Volatile Organic Compounds, Green Synthesis of Nanoparticles, Indoor Air Pollution

1.0 INTRODUCTION

The effect of indoor air pollutants on human health has been of interest for many years. According to the report from the United States environmental protection agency (US EPA), the risks purported by indoor air pollution are highly greater than that of outdoor air (Kester & Morgott, 2023). Over the years, much emphasis has been laid on outdoor air quality control. Nevertheless due to improvements in the standard of living, it has become imperative to eradicate pollution caused due to indoor air. Certain factors are responsible for degrading indoor air quality, the factors ranging from; Modern buildings are designed and constructed with high thermal insulation and air tightness to optimize the air conditioning processes and thus saving cost and energy (Arumugam et al., 2022). There are a large number of consumer spray products (insecticides, air fresheners); paints and asbestos that may release chemical compounds into the surrounding indoor environment. These released chemicals may be accumulated thereby reaching unhealthy concentrations. It is also evident that in most societies, people spend more time doing activities in the indoor environment than in the outdoors.

Volatile organic compounds VOCs are emitted as gases from certain solids or liquids. On combination with nitrogen results in the formation of ground-level ozone and particulate matter which are the main component of smog. Airborne particulate matter is associated with various adverse health effects (Adebiyi, 2022). VOCs are known to be mutagenic and carcinogenic (Tsai, 2023).

Delonix regia (flamboyant tree) is mostly grown as ornamental trees but due to its large production of flowers, pods and leaves, it resulted in the menace of environmental pollution. Hence there is need for the conversion of the waste to useful material. It has therefore been adopted primarily for economic and ecological advantages (Shadman et al., 2022). This study focused on the production and characterization of flamboyant pod/banana peel silver-zinc nanoporous (FP/BPE Ag-ZnNPs) adsorbent for air pollution control

2.0 THEORETICAL ANALYSIS

The percentage yield of the flamboyant pod carbonized adsorbent was estimated by comparing the difference between the weight of the sample before and after carbonization. This gives the weight loss of the sample and the percentage yield of the material calculated as follows

$$percentage\ yield\ (\%) = \left[\frac{W_F}{W_I}\right] \times 100 \qquad (2.1)$$

Where; $W_F$and $W_I$are the weight of the sample after and before carbonization respectively.

3.0 MATERIALS AND METHODS

3.1 Materials

The natural precursors that were used to synthesize the nanoparticle and adsorbents are banana peel (BP) and flamboyant pod (FP). The reagents employed include; zinc nitrate hexahydrate ($Zn(NO_3)_2.6H_2O$) silver nitrate ($AgNO_3$), and deionized water. laboratory apparatus used during the research include beakers; measuring cylinder; weighing balance; centrifuge; filter paper; funnel; muffle furnace; stop-watch; camera; oven; water bathe.

3.2 SYNTHESIS OF NANOPARTICLES

3.2.1 Preparation of Feed stock

Fresh, green banana peels were carefully collected from self-consumed banana bought from the local market in Ilorin. The banana peels were washed to remove dirt and other extraneous substances. These washed peels were then air dried at room temperature ($30 \pm 2c$). On complete dryness, the dried banana peels were milled to powder form using mortar and pestle.

3.2.2 Extraction Stage

Banana peels extract (BPE) was obtained using the methods described by Lateef *et al.*, (2015) by weighing 10 g of the BP powder and suspending it in 1000 ml of deionized water, then heated in a water bath at 60 °C for 1 h. The extract was filtered using Whatman No. 1 filter paper and then centrifuged at 4000 rpm for 30 minutes. After which final clear extract was collected and stored in a refrigerator at 4°C for further use. Fourier transform infrared (FTIR) spectroscopic analysis was carried out on the extract sample. It was used to know the functional group of the crude extract (Lateef et al., 2015).

3.2.3 Green synthesis of BPE-Ag/ZnNPs) and Characterization

About 40 ml of 1 mM silver nitrate ($AgNO_3$) solution was added to 5 ml of the extract at room temperature (30 ± 2℃).) to reduce the amount of silver ions. Similarly 45 ml of Zinc nitrate hexahydrate $Zn(NO_3)_2.6H_2O$ was added to 5 ml of the extract at room temperature (30 ± 2℃).) to reduce the amount of zinc ion. The reaction mixture was allowed to settle for some minutes observing the visual change of the mixture until a stable color was observed. The color stability indicates the formation of the desired silver/zinc nanoparticles (Ag/ZnNPs). The Ag/ZnNPs solution was centrifuged at 10,000 rpm for 1 hour. The solid residue was then dried at 60 ℃ for 1 hour. The solution absorbance was measured using an Ultra-violent spectrometer (Lateef et al., 2015)

3.3 PREPARATION OF ADSORBENTS

Preparation of adsorbent from a flamboyant pod requires various stages of pod preparation;

3.3.1 Feed stock preparation

The flamboyant pods were sourced at the campus of the University of Ilorin, Ilorin, Kwara State. They were carefully washed to remove all forms of dirt. The washed pods were then sun-dried, oven dried and subsequently, ground (to reduce the size and increase the surface area) to micro molecules using the milling machine.

3.3.2 Carbonization of Adsorbent

1 kg of the prepared sample was placed in a muffle furnace and carbonized at 400 ℃ for 2 h (Chandrakala & Upadhyay, 2018). The resulting material was cooled at room temperature and stored in a cleaned, dried container.

3.4 Hybridization of Nano-porous Adsorbent

Unlike the common procedure of activating adsorbents which mostly require an aqueous solution of acidic compounds, the carbonized flamboyant pod was activated by hybridizing with BP-Ag/ZnNPs. 50 g of adsorbent was soaked in 500 ml BP-Ag/ZnNPs solution for 3 hours. The resulting solution was stirred for 2 h using magnetic stirrer at an agitation speed of 1500 rpm. It was then sieved using the whatman filter paper, the residue was oven dried at a temperature of 100 ^{0}C thereby resulting in BP-Ag/ZnNPs activated Carbon. The hybridized activated carbon was then collected, allowed to cool and stored in an air tight container (Shankar et al., 2004).

4.0 RESULTS AND DISCUSSION

4.1 Fourier Transform Infrared Spectroscopy (FTIR) Investigation for the Samples

The analysis for banana peel extract reveals the presence of hydroxyl (free, sharp and alcohol), amines, alkynes, oximes, alkenes, aromatic tertiary amine, secondary amine, phosphine oxide, and compounds of sulphur. Figure 1b shows the FT-IR spectra of Banana Peel silver nanoparticles. The adsorption band showing at 3651.7 cm^{-1} is ascribed to O-H stretching, the band at 3198.94 $cm^{-1}$is due to N-H and O-H stretching, and the band at

2062.27 cm^{-1} shows $C \equiv C$ functional group. The peak at 1631.66 cm^{-1} indicates that there may exist $C = N$ and C=C functional group, the band at 833.77 cm^{-1} indicates C-H stretching. Thus, the presence of hydroxyl (free, sharp and alcohol), amines, alkynes, oximes, and alkenes, compounds in the Banana peel silver nanoparticles is confirmed.

Figure 1c shows the FT-IR spectra of Banana peel silver-zinc nanoparticles. The adsorption band showing at 3572.56 cm^{-1} is ascribed to O-H stretching vibration. The band at 3331.93 $cm^{-1}$is due to N-H and O-H stretching, and the band at 2068.60 cm^{-1} shows $C \equiv C$ functional group. The band at 1625.33 cm^{-1} indicates that there may exist $C = N$ and C=C functional group, the band at 1302.37 cm^{-1} indicates C-N stretching. The band appearing at 1178.89 cm^{-1} indicates C-N stretching and $P = O$ functional group, the band 688.13 cm^{-1} shows C-S stretching. These confirm the presence of hydroxyl (free, sharp and alcohol), amines, alkynes, oximes, alkenes, aromatic tertiary amine, secondary amine, phosphine oxide, and sulphur compounds in the Banana peel Silver-Zinc nanoparticles (BPE Ag/Zn). Figure 1d shows the FT-IR spectrum of the Flamboyant Pod adsorbent. The adsorption band showing at 3145.12 cm^{-1} is ascribed to N-H stretching vibration and O-H stretching, the band at 1694.99 $cm^{-1}$is due to $C = O$ stretching, the band at 1574.67 cm^{-1} indicates $C = C$ functional group. The band appearing at 1413.19 cm^{-1} indicates C-H deformation vibration and $S = O$ functional group, the band at 1118.73 cm^{-1} also shows $C = S$ functional group. The bands at 874.93 cm^{-1} and 827.44 cm^{-1} reveal C-H deformation vibration, the band 694.46 cm^{-1} shows C-H deformation, C-Br stretching and C-S stretching, the band 615.30cm^{-1} show C-H bending, and C-S stretching, and the band at 520 cm^{-1} indicates S-S and C-I stretching. Hence it can be inferred from this analysis, the presence of amides, amine sulphate, alcohol, sulphonic acid, unsaturated and aromatic aldehydes, alkenes, alkanes, sulphate, thioacids, meta-disubstituted benzene, bromohydrocarbon, alkynes, and sulphur compounds in the flamboyant pod adsorbent. Figure 1e which represents the FTIR analysis of BPE AgNPs Hybridised adsorbent confirms the presence of alkenes, alkanes, oximes, thioamides, ethers, bromohydrocarbon, sulphate, and sulphur compounds in the Banana peel silver nanoparticles hybridized adsorbent. Figure 1e represents the FTIR spectral for banana peel silver-zinc nanoparticles hybridized adsorbent. The spectral revealed the presence of phosphine, boron compounds, oximes, aromatic, and alkene in the Banana peel silver-zinc nanoparticles hybridized adsorbent

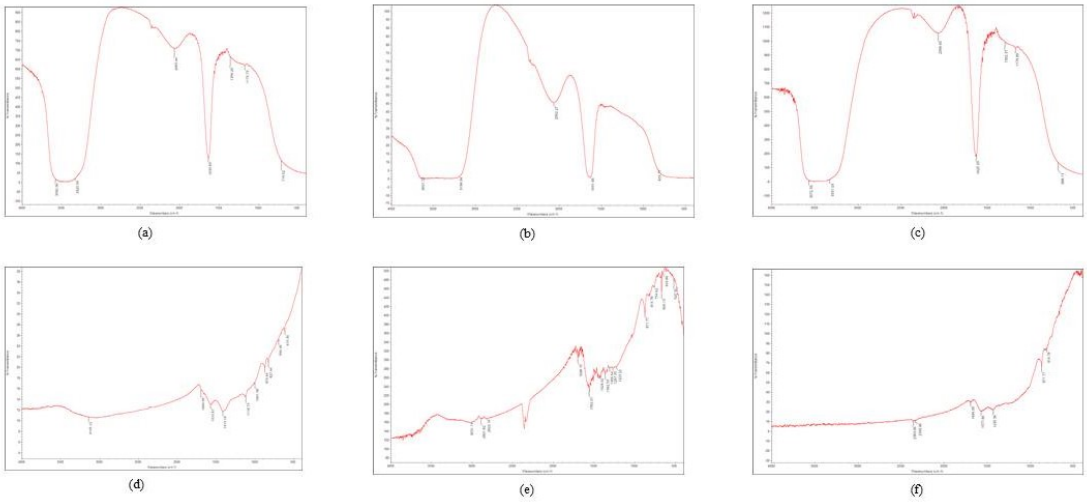

Figure 1: FTIR Spectrum of (a) Banana Peel Extract (BPE) (b) BPE AgNPs before Hybridization (c) BPE Ag/ZnNPs before Hybridization (d) Flamboyant Pod Adsorbent (e) BPE AgNPs Hybridized Adsorbent (f) BPE Ag/ZnNPs Hybridized Adsorbent

4.2 Analysis of Ultraviolet-Visible (UV-VIS) Spectrometer

The UV-VIS spectra for Banana Peel extract is shown in Figure 2a. The UV spectrum shows various bands at the following wavelengths of 400 nm, 285 nm, 205 nm and 245. The band at 285 nm is due to n $\rightarrow\sigma^*$ transitions or the combination of both n $\rightarrow\pi^*$ transitions and $\pi \rightarrow\pi^*$ transitions linked by double band, these fall in the ultraviolet region. No particular chromophore exists at the band 285 nm. The band at 205 nm can be due to either n $\rightarrow\sigma^*$ transitions or the combination of both n $\rightarrow\pi^*$ transitions and $\pi \rightarrow\pi^*$ transitions linked by double band, this also falls in the ultraviolet region. The band at 245 nm is due to either n $\rightarrow\sigma^*$ transitions or the combination of both n $\rightarrow\pi^*$ transitions and $\pi \rightarrow\pi^*$ transitions linked by double band, and it falls in the ultraviolet region. The conjugated dienes present at 245 nm are parent acyclic triene compounds and the chromophore existing is α,β-γ,δ-diene ketone. The

band at 400 nm are due to n $\rightarrow\sigma^*$ transitions, and it requires less energy (longer wavelength) compared to $\pi \rightarrow\pi^*$ transitions. This region falls within the ultraviolet and visible regions. The absorbance recorded for bands 400 nm, 285 nm, 205 nm and 245 nm, are 0.137, 0.518, 1.529, and 0.371 respectively. Figure 2b shows the UV-VIS spectra for Banana Peel silver nanoparticles. The UV spectrum shows various bands at the following wavelengths; 400 nm, 275 nm, and 215 nm and the following absorbance; 0.150, 0.222, and 3.069. The band at 400 nm and 275 nm are due to n $\rightarrow\sigma^*$ transitions which require less energy (longer wavelength) compared to $\pi \rightarrow\pi^*$ transitions. The band at 215 nm can be due to either n $\rightarrow\sigma^*$ transitions or the combination of both n $\rightarrow\pi^*$ transitions and $\pi \rightarrow\pi^*$ transitions linked by double band, these fall in the ultraviolet region. The chromophore existing at 215 nm is β-unsaturated six ring ketones, and the conjugated dienes present are acyclic and transoid compounds. Similarly Figure 2c shows the UV-VIS Spectrum of the Banana peel silver/zinc nanoparticles at various bands of wavelengths 400 nm, 270 nm, 215 nm and 245 having absorbance values of 0.216, 0.295, 2.776, and 0.215 respectively. The band at 400 nm and 270 nm are due to n$\rightarrow\sigma^*$ transitions which require less energy (longer wavelength) compared to $\pi\rightarrow\pi^*$ transitions. The band at 215 nm can be due to either n$\rightarrow\sigma^*$ transitions or the combination of both n$\rightarrow\pi^*$ transitions and $\pi\rightarrow\pi^*$ transitions linked by double band, these fall in the ultraviolet region. The chromophore existing at 215 nm is α,β-unsaturated six ring ketones, and the conjugated dienes present are acyclic and transoid compounds. The band at 245 nm will also be due to either n$\rightarrow\sigma^*$ transitions or the combination of both n$\rightarrow\pi^*$ transitions and $\pi\rightarrow\pi^*$ transitions linked by double band, and it falls in the ultraviolet region. The conjugated dienes present at 245 nm is parent acyclic trienes compounds and the chromophore existing is α, β-γ,δ-diene ketone. It was observed that for all the spectra, an increase in wavelength leads to a decrease in absorbance which follows Beer Lambert's law.

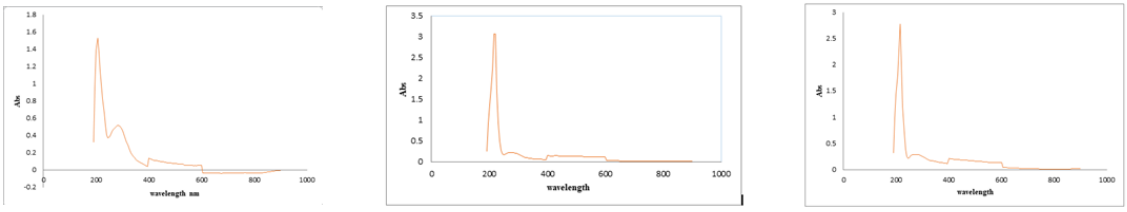

Figure 2: UV-VIS Spectrum of (a) Banana Peel Extract (BPE) (b) BPE AgNPs (c) BPE Ag/ZnNPs

4.3 Scanning Electron Microscope (SEM) Analysis For BPE Ag/ZnNPs Hybridized Adsorbent

SEM was used to know the surface texture and porosity of the sample. The BP-Ag/ZnNPs was observed at an accelerating voltage of 5.00 kV and working distance of 5.0 mm, it was observed under different focal lengths and magnification. Pores were identified for particle size 20 μm at 200k x magnification and 200 nm at 20. k x magnification.

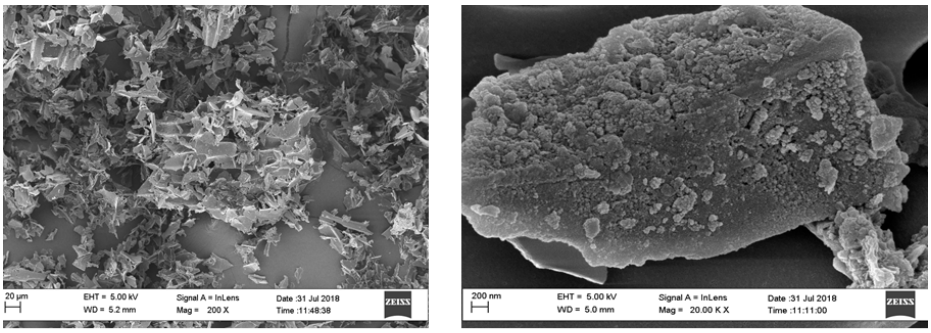

Figure 3: SEM Micrograph of BPE Ag/ZnNPs at (a) 20 μm (200k x magnification) (b) 200 nm (20.k x magnification)

4.4 Analysis Of scanning electron microscopy energy dispersive spectroscopy for BPE Ag/ZnNPs Hybridized Adsorbent

The SEM-EDS analysis shows the component elements present in the banana peel silver/zinc nanoparticles hybridized adsorbent. From Table 4.1, it can be deduced that carbon and oxygen are the major components (elements with more than 10% atomic weight) present. Potassium and calcium are identified as the minor components (Elements with an atomic weight between 1-10%), and magnesium, silicon and copper are the trace components (elements with less than 1% atomic weight).

Table 4.1: Components present in BPE Ag/ZnNPs hybridized adsorbent

S/N	Elements	Weight %	Weight % Signal	Atomic %

1	Carbon	82.52	0.65	88.59
2	Oxygen	11.88	0.62	9.58
3	Magnesium	0.32	0.07	0.17
4	Silicon	0.18	0.07	0.08
5	Potassium	2.3	0.11	0.76
6	Calcium	2.15	0.12	0.69
7	Copper	0.65	0.21	0.13
	Total	100.00	1.85	100.00

4.5 Transmission Electron Microscopy (TEM) Analysis for BPE Ag/ZnNPs Hybridized Adsorbent

Transition electron microscopy was used to ascertain the lattice structure and crystallinity of banana peel-silver-zinc nanoparticles hybridized adsorbent. Figure 4 shows the sample structure at nano levels that is 20 nm and 200nm which confirms the presence of nanoparticles

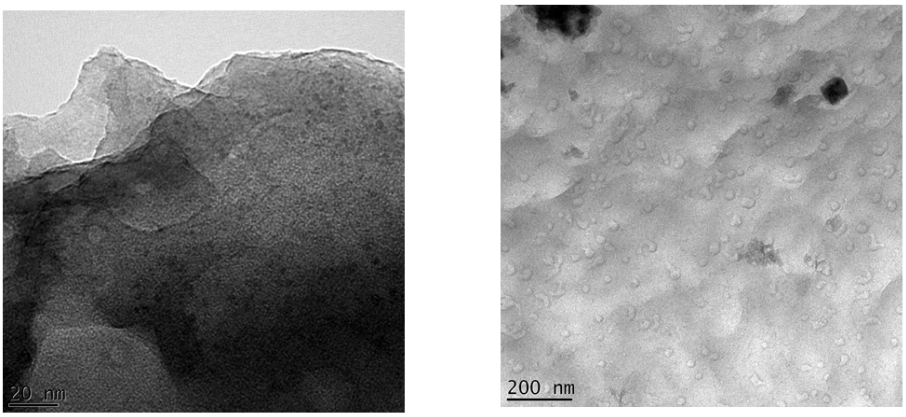

Figure 4: TEM micrographs of the Banana peel extract Ag/Zn Hybridized Adsorbent showing result for (a) 20nm (b) 200nm

4.6 X-RAY Diffraction (XRD) Analysis for BPE Ag/ZnNPs Hybridized Adsorbent

X-ray diffraction analysis result is shown in Figure 5. The red line in the graph represents quartz crystalline structure, the blue line indicates cristobalite structure and the black line indicates glass structure. Silver exhibits a single face-centred cubic (fcc) geometry. The peaks observed at 2θ values of 29.4°, 39.2° and 48.2° which correspond to crystallographic planes of (104), (113) and (116) can be ascribed to the composition of BPE that are acting as capping and stabilizing agents for hybridized bimetallic BPE Ag/ZnNPs hybridized adsorbent, thus preventing agglomeration.

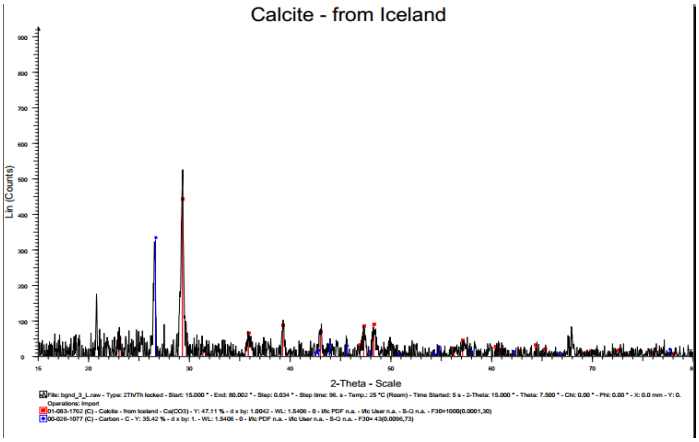

Figure 5: Graph for XRD showing peaks observed

5. CONCLUSION

Banana peel extract was used to produce the silver-zinc nanoparticle which is then hybridized with carbonized flamboyant pod. It can be inferred from the study that bimetallic Ag-ZnNPs could be prepared with banana leaf extract. The silver and zinc ions were reduced to silver-zinc nanoparticles when added to the banana peel extract; it was observed that the colour of the solution turned from golden yellow to a colourless precipitate solution. The carbonized flamboyant pod has a yield of 28 per cent. The UV-VIS spectra of BP Ag-ZnNPs solution showed the presence of phytoconstituents (such as amino acid) in the extract which acts as a capping and stabilizing agent making it suitable for the adsorption process. FT-IR spectroscopy analysis on FP/BP Ag-ZnNPs adsorbent showed the presence of a carbonyl group in the sample which confirmed that silver ions in silver nanoparticles by capping material of plant extract. The porosity and surface structure of the adsorbent was investigated through the SEM analysis, while SEM (EDS) identified the major and trace elements present in the adsorbent. The TEM analysis confirmed the presence of nanoparticles. The X-ray diffraction analysis confirmed the peaks observed at 2θ values of 29.4°, 39.2° and 48.2° which correspond to crystallographic planes of (104), (113) and (116) can be ascribed to the composition of BPE that are acting as capping and stabilizing agents for hybridized bimetallic BPE Ag/ZnNPs hybridized adsorbent, thus preventing agglomeration. Conclusively hybridized flamboyant pod banana peel silver/zinc nanoparticle is an economical, efficient, and eco-friendly alternative to the conventional carbon activation method employed in air pollution control.

REFERENCE

Adebiyi, F. M. (2022). Air quality and management in petroleum refining industry: A review. *Environmental Chemistry and Ecotoxicology*.

Arumugam, P., Ramalingam, V., & Vellaichamy, P. (2022). Effective PCM, insulation, natural and/or night ventilation techniques to enhance the thermal performance of buildings located in various climates–A review. *Energy and Buildings*, 111840.

Chandrakala, M., & Upadhyay, A. (2018). Preparation of nontoxic activated charcoal from gulmohar (Delonix regia) shell. *International Journal of Science, Environment and Technology*, *7*(2), 689-695.

Kester, J. E., & Morgott, D. A. (2023). Ethylbenzene exposure in North America-an update. *Journal of Environmental Exposure Assessment*, *2*(1), 1.

Lateef, A., Ojo, S. A., Akinwale, A. S., Azeez, L., Gueguim-Kana, E. B., & Beukes, L. S. (2015). Biogenic synthesis of silver nanoparticles using cell-free extract of Bacillus safensis LAU 13: antimicrobial, free radical scavenging and larvicidal activities. *Biologia*, *70*(10), 1295-1306.

Shadman, S., Khalid, P. A., Hanafiah, M. M., Koyande, A. K., Islam, M. A., Bhuiyan, S. A., Woon, K. S., & Show, P.-L. (2022). The carbon sequestration potential of urban public parks of densely populated cities to improve environmental sustainability. *Sustainable Energy Technologies and Assessments*, *52*, 102064.

Shankar, S. S., Rai, A., Ahmad, A., & Sastry, M. (2004). Rapid synthesis of Au, Ag, and bimetallic Au core–Ag shell nanoparticles using Neem (Azadirachta indica) leaf broth. *Journal of colloid and interface science*, *275*(2), 496-502.

Tsai, W.-T. (2023). A Survey on Toxic Volatile Organic Compounds (VOCs): Toxicological Profiles, Health Exposure Risks, and Regulatory Strategies for Mitigating Emissions from Stationary Sources in Taiwan. *Atmosphere*, *14*(2), 242.

PAPER 178 – DEVELOPMENT OF A SMART TRAFFIC CONTROL MODEL USING DEEP LEARNING TECHNIQUE

T. M. Adepoju[1]*, A. A. Badrudeen[2]*, M. O. Oladele[2], T. A. Abdul-Hameed[3], C. V. Anyanwu[2]and O. A. Akobi[2],

[1]Computer Engineering Technology Department, Federal Polytechnic, Ayede, Nigeria,
[2]Computer Engineering Technology Department, Federal Polytechnic, Ede, Nigeria,
[3]Electrical and Electronic Engineering Technology Department, Federal Polytechnic, Ayede, Nigeria,
Email: atemilola@gmail.com

ABSTRACT
In recent times, ineffective traffic light control has been the cause of numerous problems such as delay on the highway as well as waste of energy and resources. To improve the effectiveness, taking the traffic data as input and intelligently adjusting the traffic light duration accordingly has become pertinent. Therefore, an improved traffic light control system is required so as to address the traffic delay-based problems. The application of artificial intelligence has recently gained widespread attention due to its capability to be able to solve complex problems such as in signal and traffic light control. Hence, this study developed an improved traffic signal model exploiting Deep Neural Network tool. The performance evaluation of the developed model shows that isolated intersection and coordinated intersections (Deep Learning) approach is superior to that of the fixed-time signal control method.

KEYWORDS: Control system, Data, Deep neural network, Optimization, Signal, Traffic.

1. INTRODUCTION

The increase in the population of urban areas and its attendant effect on traffic congestion makes it urgent to develop improved traffic control systems. As traffic volume continues to increase, the highways become more and more congested. One of the most cost-effective measures for dealing with this congestion is traffic signal control. Traffic signal retiming and coordination of existing signals have been proven to bring about substantial reductions in traffic delay, considerable energy savings, and consequently, huge reduction in travel time and increased safety for the public (Lee and Park, 2017). Many frameworks for traffic light detection using machine learning have been proposed in the past but were rather time inefficient in either the reduction of the dimension or in terms of the efficiency of the machine learning algorithms used.

Also, the development of the Smart Traffic Control System based on traffic environment using deep learning is required as the current traffic lights are making use of technologies that are using much older microcontrollers providing low efficiency and no flexibility. Such traffic light management systems suffer from problems as they execute certain previously defined lines of code that cannot offer the adjustability that occurs in real-life scenarios. The current traffic management systems provide hard-coded and previously set intervals of time for different signals, and that makes the system very rigid. The smart traffic control system based on traffic environment using deep learning neural network algorithm delivers excellent results on various parameters like performance, efficiency, and along with the superb flexibility and sustainability (Arel, 2018). Therefore, the need for better approaches that can improve the computational problems is crucial. Therefore, this study aims to provide solution to problems identified with the conventional traffic light control system by developing a deep neural network model for effective and efficient traffic light control system.

2. RELATED WORKS

According to De Schutter (2015), Manual traffic control management involves a traffic policeman standing on each and every cross-section of the roads and controls flow of traffic by using sign board. If density of traffic is more on the road, then traffic police gives signal to the vehicle driver whether to drive or stop. He or she can also recognize emergency vehicles on the road and give first priority to the lane on which emergency vehicle is passing. But in case of multiple emergencies the police officer gets confused and becomes unable to manage the traffic flow.

In order to eliminate most weakness of the manual traffic control system, an automatic traffic management method was recommended (Chiu and Chand, 2017). The system includes simple three color traffic signal which are red, green and yellow. Before green light, yellow light glow for less than 20 seconds; indicating to start your vehicle

and be ready to move. For all the time red light is on, indicating each vehicle to stop. This system cannot identify emergency vehicles like ambulance and VIP car. It treats all vehicles and emergency vehicles in the same way, because they have fixed the timings for red and green signals (Badrudeen, *et al.*, 2014; Badrudeen, Akanni, and Kawonise, 2016). At the night time, both red and green signals are manually switched off while the yellow signal is left for traffic control in that scenario. In this regard, the probability of delay in emergency services in peak hours results in high value using this technique, which can be inefficient for practical scenario.

Hartenstein and Laberteaux (2018) developed an Intelligent Traffic Management Technique based on Image Processing, which uses cameras to capture image of the traffic density on road. Image captured by camera is analyzed by a computer chip in order to detect vehicles on road. The computer will calculate the timings for red and green signals to control the traffic density and send the data to traffic signals controller to enable red and green signal dynamically change the timings. Sometimes this technique is not efficient because camera cannot cover long distances during heavy traffic jam and during heavy rain, when image captured by camera is not clear.

Casas (2017) proposed a biologically-inspired neural network for traffic signal control and validated it with comparative simulations. Li, Lv and Wang, 2016) developed a management system using Wireless Technologies. In this technique emergency vehicle is equipped with RF transmitter and RF-receiver mounted on a signal pole. As emergency vehicle is approaching the intersection, a signal is sent to the RF receiver and to the main control system. The control system calculates the approximate amount of time for green signal where emergency vehicle moves and keeps red light to remaining lanes. Then emergency vehicle can pass easily. This technique controls traffic flow in an efficient way and also gives solutions for emergency vehicles.

IRIS (Intelligent Roadway Information System) is an open-source Advanced Traffic Management System (ATMS) software project developed by the Minnesota Department of Transportation. It is used by transportation agencies to monitor and manage interstate and highway traffic. IRIS provides real-time information on high way conditions to detect traffic incidents, manage the flow of traffic, and broadcast traveler information. IRIS uses the GPL license, Advanced Traffic Management System (ATMS) software tool. ATMS helps to reduce traveling times, maximize highway ability, and generally afford safer travelling directions.

3. MATERIALS AND METHODS

Traffic Volume Data Collection

Oke-fia intersection at Osogbo, Osun State Nigeria, was used as a case study for this study. Two dual carriage roads and three single carriage roads form the intersection at Oke-fia, and this make traffic management at the intersection a big challenge. The traffic volume data for 24 hours for each day of the week were collected via questionnaire with a sample in Table 1. The traffic volume represents the number of vehicles arriving the intersection; and the traffic volume is classified into four types namely; Low (L), Moderate (M), Heavy (H) and Very Heavy (VH) as shown in Table 2 with the number of vehicles that represents each class of traffic volume. The traffic volumes were collected at different period of day for each road that make the intersection. The traffic type according to Table 2 will determine the duration of the traffic signal or light that controls the vehicle coming into and going out of the junction. Directed Acyclic Graph Deep Neural Network (DAG-DNN) model was employed for the study. DAG-DNN was trained with the traffic type of each road such that the model can predict the traffic volume of each road for period of the days of the week. The predicted traffic volume was used to control the traffic lights in order to reduce unnecessary delay of vehicles; which characterize the conventional fixed-delay traffic control system.

Table 1: Traffic (volume) types on each road

Traffic (volume) type	**Number of vehicles**
Low (L)	0 – 50
Moderate (M)	51 – 100
Heavy (H)	101 – 300
Very Heavy (VH)	301 – 1000

Data Pre-processing

Because Directed Acyclic Graph Deep Neural Network (DAG-DNN) requires large data; thus the traffic volume data obtained from the questionnaires was augmented to produce sufficient amount of data required to train for training. The processed data were divided into training dataset and testing dataset. The training dataset consist of 80% of the whole data while the testing dataset consist of 20% of the whole data.

The flow chart of the DAG-DNN model is shown in Figure 1. DAG-DNN loaded and trained 80% of the dataset. During the training the DNN automatically extracts relevant features need to classify the traffic type (Low, Moderate, Heavy and Very Heavy) for each period of days for the week.

Table 2: Traffic Volume at Oke-fia Intersections in Osogbo per day

Period of day (Hour)	**Sunday**	**Monday**	**Tuesday**	**Wednesday**	**Thursday**	**Friday**	**Saturday**
12am- 3am	L	L	L	L	L	L	L
3am- 6am	M	M	M	L	L	M	M
6am -9 am	H	M	M	M	M	M	M
9am -12 pm	H	H	H	H	H	H	H
12 pm - 3 pm	H	H	VH	H	H	H	H
3 pm - 6 pm	M	VH	H	VH	VH	VH	VH
6pm - 9 pm	VH	VH	VH	VH	M	M	M
9pm -12 am	M	L	L	L	L	L	L

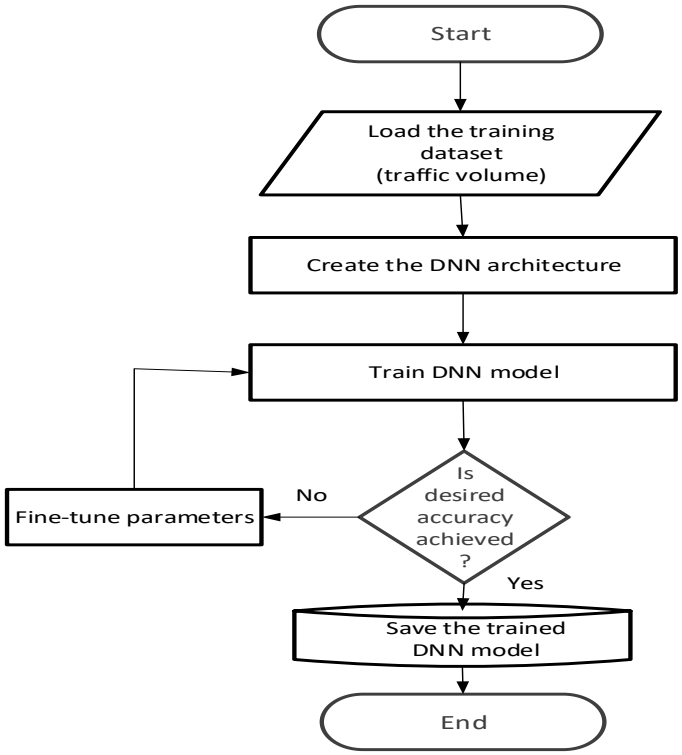

Figure 1: Flow chart of DAG-DNN model

The training of the DAG-DNN stop after the desired level of validation accuracy has been achieved during the learning process. Thereafter, the trained DAG-DNN model was saved for future prediction or classification of traffic type (or volume) needed for the traffic control system to make appropriate decision on duration of traffic lights for each road.

Performance Metric

The performance metrics used the study are True Positive Rate, False Positive Rate and Accuracy. DAG-DNN model is evaluated using accuracy as shown in equation (1).

$$Accuracy = \frac{Correct\ classification}{Total\ number\ of\ tested\ samples} \times 100\% \quad (1)$$

4. RESULTS AND DISCUSSION

Traffic Lights Control by the DAG-DNN model

The results of DAG-DNN prediction for traffic control at Oke-fia junction, Osogbo, in different period of the day (Monday to Sunday) are presented in Figure 2. Notably, the four roads intersection consists of: Road 1, namely the road from Iwo to Oke-fia, Road 2, namely the road from Olaiya to Oke-fia, Road 3, and Road 4 are single carriage leading to Ilobu town and Ikirun town, respectively. Since Road 1 and Road 2 are the two major roads that are dual carriage meeting at the Oke-fia junction, the DAG-DNN traffic controller is configured for only Roads 1 and 2. It can be observed from the Figure 2 that the DAG-DNN yields 100% accuracy for other five days of the week excluding Tuesday and Wednesday with the accuracy results of 87.5%. Table 3 the results obtained for True Positive Rate (TPR) and False Positive Rate (FPR) for the traffic types for period of the day, with testing time of 0.85 s. It was revealed that the DAG-DNN model was able to identify Very Heavy traffic volume better than the others.

Table 4 is the Comparison of the total moving time and the total waiting time for the developed DAG-DNN based traffic light control system and that of fixed-delay based traffic light control system. Table 4 reveals that results of the DAG-DNN model has appropriate moving time and waiting time for all the traffic types. Also, when the traffic is low the waiting time allocated is minimal while the moving time is high and vise-versa for other traffic types. The fixed-delay-based traffic light control system always allocates the same waiting and moving times but increased values as the traffic volume increases.

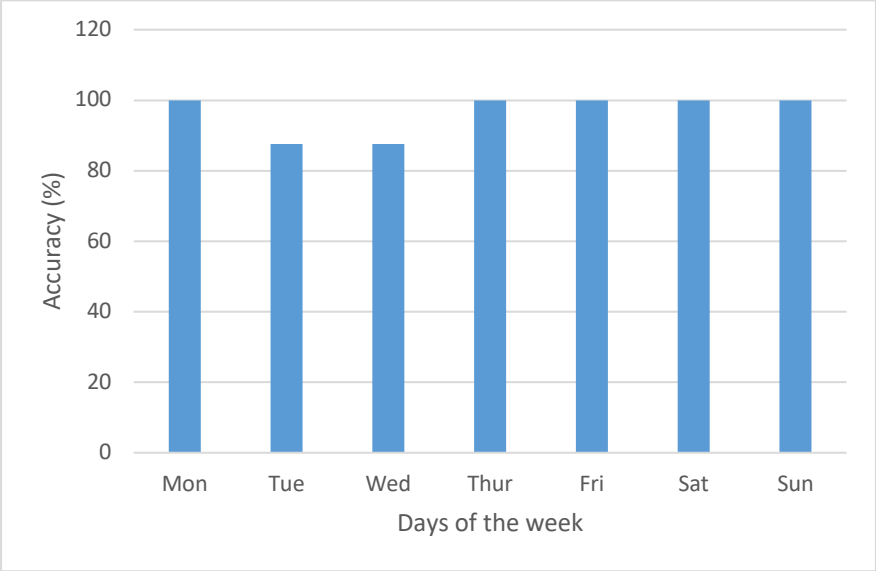

Figure 2: Bar Chart for accuracy of DAG-DNN model

Table 3: Results of the DAG-DNN model for traffic type

Traffic type	**True Positive Rate (TPR)**	**False Positive Rate (FPR)**
Low	80.30 %	19.70 %
Moderate	85.50 %	14.50 %
Heavy	91.90 %	8.10 %
Very Heavy	93.78 %	6.22 %

Table 4: Comparison of the Developed traffic light control method with the existing fixed time method

Traffic volume	Developed traffic control (DAG-DNN)		Existing traffic control	
	Total moving time (s)	**Total waiting time (s)**	**Total moving time (s)**	**Total waiting time (s)**
Low	600	54000	5400	5400
Moderate	516	138240	10800	10800
Heavy	384	278640	16200	16200
Very Heavy	300	432000	21600	21600

Therefore, the developed DAG-DNN proves to be a better option for traffic control at any road intersection and recommended for a smart traffic control system.

5. CONCLUSION

In this study, a Directed Acyclic Graph Deep Neural Network (DAG-DNN) model was developed for intelligently controlling traffic at Oke-fia junction Osogbo. The results obtained from the test of the DAG-DNN model showed that it gives acceptably high accuracy. The developed DAG-DNN will help to proportionately allocate moving time and waiting time for each road based on their traffic volume; and eliminate unnecessary delay associated with the conventional traffic light control system.

REFERENCES

Arel, C. Liu, T. Urbanik, and A. Kohls (2010). "Reinforcement learning-based multi-agent system for Network traffic signal control," *IET Intelligent Transport Systems*, Vol. 4, no. 2, pp. 128–135.

Badrudeen A. A., Akanni A. A., and Kawonise, K. (2016). "Effect of Emergency Interrupt Complexity on the Performance of Adaptive Network Based Fuzzy Inference Traffic Light Control System," Journal of Information Engineering and Applications, *6*(8) pp. 84-94.

Badrudeen A. A., Akanni A. A, Ajayi O. O. Adepoju T. M. and Sobowale A. A. (2014). "Traffic Light Control Using Adaptive Network Based Fuzzy Inference System" *Proceedings of International Conference on Artificial Intelligence & Manufacturing Engineering (ICAIME), Dubai*, pp. 156-161.

Casas, N. (2017). "Deep deterministic policy gradient for urban traffic light control," *arXivpreprintarXiv:1703.09035.*

Chiu and Chand S. (2017). "Adaptive traffic signal control using fuzzy logic," in *The First IEEE Regional Conference on Aerospace Control Systems*, pp. 1371–1376.

Gokulan, Y. Shen, J., Liu, M. Ito, and Shiratori, N. (2017) "Adaptive traffic signal control: Deep reinforcement learning algorithm with experience replay and target network," *arXiv preprintarXiv:1705.02755*.

Hartenstein and L. Laberteaux, "A tutorial survey on vehicular adhoc networks," *IEEE Communications magazine*, vol. 46, no. 6, June 20018.

Li, Y. Lv, and F.-Y. Wang, (2016). "Traffic signal timing via deep reinforcement learning," *IEEE/CAA Journal of Automatic aSinica*, vol. 3, no. 3, pp. 247–254.

Schutter, (2015). "Optimal traffic light control for a single intersection," in *American Control Conference*, vol. 3, pp. 2195–2199.

PAPER 179 – ANALYSIS OF LOCALLY PRODUCED ALUMINIUM OXIDE FOR THE PRODUCTION OF WASTEWATER TREATMENT FILTER USING XRF, SEM/EDX

A. A. Olatunji[1,2*], A. M. Ayanshola[2], E. O. Ajala[3], M. A. Ajala[3], I. O. Lamidi[1]

[1]Department of Civil Engineering, Federal Polytechnic Ede, Nigeria.
[2]Department of Water Resources and Environmental Engineering, University of Ilorin, Ilorin, Nigeria.
[3]Department of Chemical Engineering, University of Ilorin, Ilorin, Nigeria.
[*]Email: olatunji.abass@federalpolyede.edu.ng

ABSTRACT
Aluminium oxide (Al_2O_3) an inorganic chemical reagent with chemical name Aluminium oxide. It is also called as Alpha-Alumina, Alumina, Alundum or Aloxide. It is mostly used in wastewater treatment. Water pollution due to industrial, agricultural and domestic activities has caused a significant threat to human as well as surrounding environment. The quest towards mitigating the environmental hazard and making use of waste (waste to wealth), finding alternative, locally available and more economical way of treating wastewater has motivated this research. The Aluminium oxide was extracted from waste Maltina Can using alkali method and the Laboratory Developed Aluminium oxides (LDA) was characterized by XRF. EDX analysis of the LDA was done and Image J software was used to analyze SEM images. The LDA contained 69.70% of Al_2O_3, an indication of higher percentage of aluminium oxide (78.4% threshold) present in the Malt Can. The LDA SEM analysis indicated 1.435µm, 33.421µm, 24.757µm, and 11.237 µm for an average Area, Mean, Standard deviation, and Length respectively. The Aluminium oxide developed in the laboratory is pure enough to be used for the development of composite filter for effective treatment of wastewater.

KEYWORDS: Aluminium Oxide, EDX, SEM, Waste Can, Wastewater Treatment, XRF

24. INTRODUCTION

Water pollution due to industrial, agricultural and domestic activities has caused a significant threat to human as well as surrounding environment (Schwarzenbach, 2010). Adsorption continues to be the most effective method for removing pollutants from water and wastewater among the many water treatment technologies that have been developed over the past 20 years (Anastopoulos et al., 2017); this is because it is straightforward to design, simple to use, and affordable (Abdolali et al., 2017).

Aluminum cans and other packaging are the main sources of aluminum in municipal solid waste (MSW) (EPA, 2021). Water companies all over the world have employed aluminum as a crucial pre-treatment in water purification processes (Dassanayake et al., 2015). With 3.9 million tons produced in 2018, aluminum accounted for 1.3 percent of all MSW production. This comprised two million tons found in both durable and nondurable goods, as well as 1.9 million tons of aluminum containers and packaging. In 2018, almost 2.7 million tons of aluminum were dumped in landfills. This accounted for 1.8% of all MSW dumped that year (EPA, 2021).

Aluminum Cans shield its contents from the damaging effects of the elements while preserving their flavor. It is long-lasting and extremely durable. Additionally, the can itself never rusts or loses any of its characteristics. These are most likely the key explanations for why aluminum is so commonly utilized in food packaging (Ajibola, 2015).

One of the main problems that cause pollution in the environment is the use of Aluminum Waste Cans. Many of these Cans end up in landfills or lying on the ground since they cannot decompose naturally and require a very long time to do so. Like other non-biodegradable materials, it further obstructs drainage, leading to floods, and creates stagnant water, which fosters additional health problems like malaria and cholera, among others (Ajibola, 2015).

Al_2O_3 is the chemical name for aluminum oxide, an inorganic chemical reagent. Alpha-Alumina, Alumina, Alundum, or Aloxide are some of its alternate names. Its Molar Mass/Molecular Weight is 101.96 g/mol. It is used to take water out of the gas streams during the water purification process. In the production of adsorbents and catalysts, aluminum oxide, a very effective ceramic oxide, finds numerous significant applications (Byjus, 2022). Aluminum Waste Cans and Foil paper both contain aluminum oxide and can be extracted from them. Additionally, it can be produced by calcining Gibbsite, which has the chemical formula $Al(OH)_3$ (Byjus, 2022).

According to Hassan Basri et al. (2019), the effectiveness of ammonium removal in water treatment increases as aluminum concentration does. Aluminum oxide nanoparticles were utilized by Tabesh et al. (2018) to remove cadmium and lead, with adsorption capabilities of 78 and 217 mg/g, respectively. Another study opined that the maximum adsorption capacity of aluminum oxide nanoparticles to remove methylene blue was 2:5 * 10x5 mol/g (Banerjee et al., 2015). Aluminum oxide nanoparticles were also used to remove fluoride, and their adsorption capability was 65 mg/g (Liu et al., 2016). Safwat et al. (2022) has also studied its ability in the phenol removal and found it to be effective. Therefore, aluminium oxide is more effective in the treatment of wastewater.

Aluminum Waste Can is ubiquitous in Nigeria and constitute environmental hazard such as blockage of drainage system thereby causing flood, which may result to death. The use of AWC in wastewater treatment has a potential to reduce cost of treatment and mitigate their environmental nuisance. The research will proffer solution to the problem of high cost of wastewater treatment as aluminium oxide is expensive, producing it locally will save the cost and also provide employment.

25. MATERIALS AND METHODS

2.1 MATERIALS

Materials used are Aluminium Waste Can, Concentrated Sodium Hydroxide (NaOH), Distilled Water, Concentrated Hydrogen Peroxide (H_2O_2), Concentrated Hydrochloric Acid (HCl), Concentrated Nitric Acid (HNO_3). Equipment used are Oven, Furnace, Grinder, Pipette Filler, Hot Plate, Filtered Paper.

2.2 METHODS

The Aluminium oxide was extracted from waste Maltina Can using alkali method. Precisely 5g of aluminium sheet (Plate 1) was taken and it is reacted with 9g of NaOH and diluted with 250 ml distilled water (Eqn. 1). NaOH is reacted with aluminium sheet to form sodium aluminate. Then this solution was filtered to remove foreign particles. After heating (until boiling), about 4ml H_2O_2 was added to this solution and kept for 24 hours to settle ferric oxide which was brick red in colour. After settlement, clear solution was picked up by the pipette filler and filtered. About 80ml 1:1 HCl was added in the filtrate to form aluminium hydroxide.

$$Al(OH)_3 + NaOH \rightarrow NaAlO_2 + 2H_2O \qquad \text{Eqn. 1}$$

Then the aluminium hydroxide was kept in an oven at 105^{o}C temperature for drying. Again, it was kept in a furnace at about 800^{o}C temperature to form aluminium oxide. This aluminium oxide was grinded in a grinder and allowed to pass through 100 meshes and final product, aluminium oxide was obtained.

After the final product of aluminium oxide was obtained, scanning electron microscopy with energy dispersive X-ray detection (SEM-EDX), and XRF analysis of the product were conducted.

Plate 1: Aluminium Sheet

26. RESULTS AND DISCUSSION

3.1 XRF

The elemental oxides composition of both PA and LDA are provided in Table 1. In comparison, it could be observed that the Silicon Oxides (SiO_2) for LDA and PA were 15.75% and 4.60% respectively. Higher percentage of silicon oxide in LDA could be attributed to the dissolved colour pigment in the malt Can used for the process, this would however, be an advantage if use for the development of composite filter for wastewater treatment as silicon oxide will increase the capacity of clay in the wastewater treatment.

Table 1: XRF Result for Aluminium Oxides (Developed and Pure)

	SiO_2 (%)	Al_2O_3 (%)	Fe_2O_3 (%)	CaO (%)	K_2O (%)	TiO_2 (%)	Na_2O (%)	MgO (%)	Cl (%)	LOI (%)
LDA	15.75	69.70	2.34	5.80	0.35	0.12	0.002	3.07	0.20	0.77
PA	4.60	88.90	0.40	1.82	0.33	0.12	0.002	1.25	0.22	0.80

LDA = Laboratory Developed Al_2O_3, PA = Pure Al_2O_3

LDA and PA comparison in term of Aluminium Oxide (Al_2O_3), it was observed that LDA percentage was 69.70% while that of PA was 88.90%. Though, the percentages were not equal but very close, an indication of higher percentage of aluminium oxide (78.4% threshold) present in the Malt Can.

Comparison in term of Iron Oxide (Fe_2O_3), Calcium Oxide (CaO), and Magnesium Oxide (MgO), LDA has higher percentages in these oxides than PA. These may be due to impurities in LDA as it was not subjected to further refine for commercial purpose as the case was for the PA. Titanium oxide (TiO_2) and sodium oxide (Na_2O) seems to have the same values for both LDA and PA.

3.2 EDX

The material composition information of both PA and LDA are provided in Figure 1 and Figure 2. It measures the atomic concentration within aluminium oxides compounds.

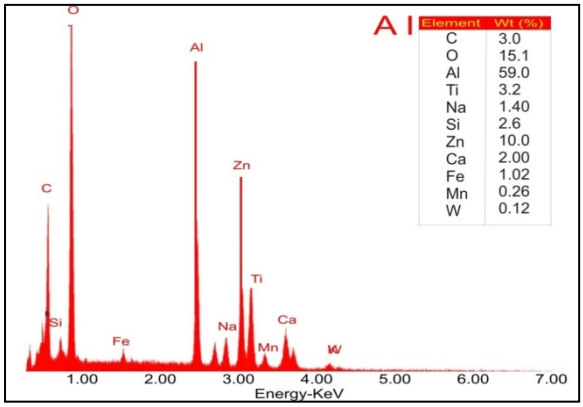

Fig. 1: EDX Result of LDA

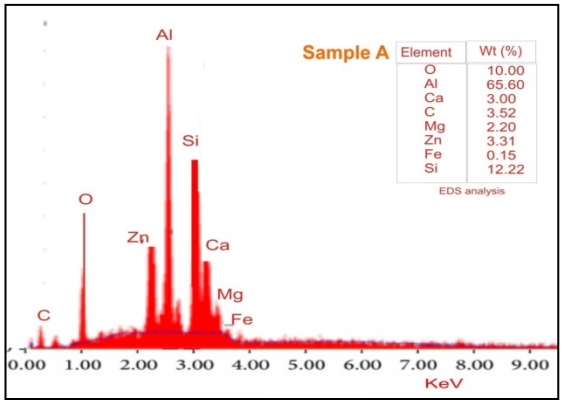

Fig. 2: EDX Result of PA

From the EDX analysis as shown in Figure 1 and Figure 2, the Aluminium percentage of LDA was 59.0% while that of PA was 65.6%. It could be seen that the percentage of aluminium was lower in LDA than PA, but the value was higher than that of Sheel *et al*. (2016) who used the same method for Waste Can and their value was 48.71% of Aluminum. The likely reason for this wide margin could be as a result of different Can used in their country, as the composition of various Can slightly different from each other.

The oxygen (O) percentage in LDA was 15.1% which was higher than the PA of 10%. Similarly, the percentages of zinc (Zn) and iron (Fe) were higher in LDA (10.0% and 1.02% respectively) when compare with that of PA (3.31% and 0.15% respectively). However, calcium (Ca – 2.0%), carbon (C – 3.0%), and silicon (Si – 2.6%) were lower in LDA compare to 3.0%, 3.52% and 12.22% respectively in PA. This will not have any negative effect as the clay and bagasse to be used with already contains higher percentage of these elements.

It could be seen that the LDA contained Sodium (Na) due to available NaOH which was used for the development. The presence of titanium (Ti) and manganese (Mn) in LDA could be attributed to the impurity that may have occurred during the process. In Figure 3, it could be observed that the different in Al level are not that much and one hardly notice differences in C, Ca and Fe level. It is only in Si that the difference was evidently noticed.

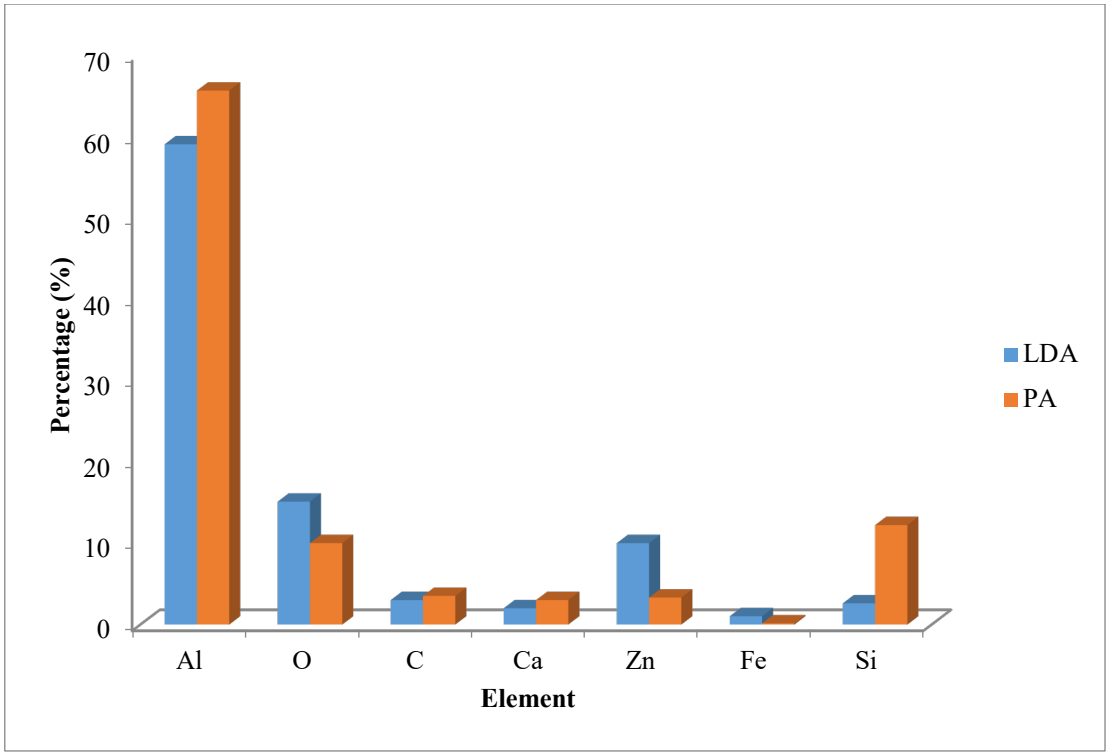

Fig. 3: EDX Result Comparison of Elements in LDA and PA

3.3 SEM

Figure 4 and Figure 5 shows SEM image of both LDA and PA respectively. The images produced structural information and provide images of the surface of LDA and PA at extremely high magnifications (10,000 times).

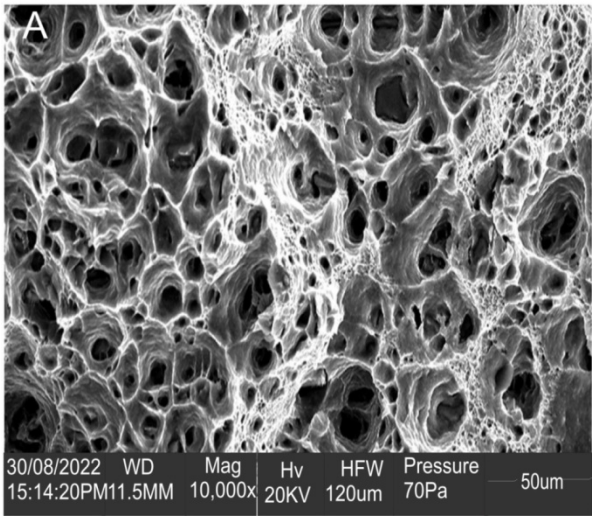

Fig. 4: SEM 10,000 Times Magnification of LDA

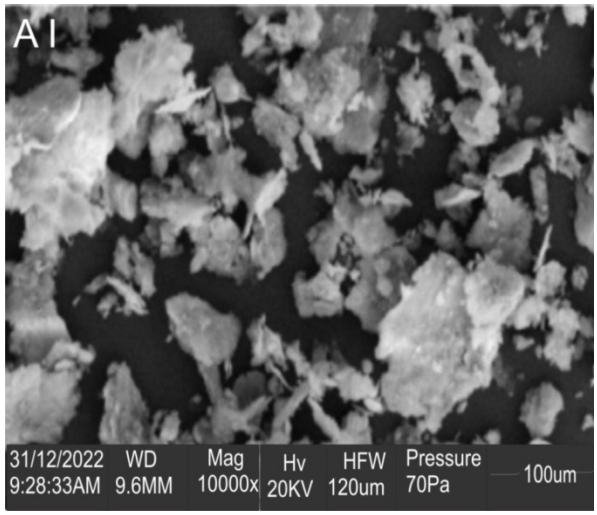

Fig. 5: SEM 10,000 Times Magnification of PA

Table 2: SEM Analysis of LDA and PA using Image J

	LDA				PA			
S/N	**Area**	**Mean**	**StdDev**	**Length**	**Area**	**Mean**	**StdDev**	**Length**
1	1.419	68.135	102.001	11.111	7.487	27.140	10.169	29.851
2	0.972	19.262	27.548	7.576	6.559	20.708	15.784	26.119
3	0.845	59.887	22.198	6.566	11.571	19.262	7.859	46.269
4	1.164	67.781	9.514	9.091	13.799	41.072	6.109	55.224
5	0.781	43.408	15.863	6.061	3.960	17.922	10.094	15.672
6	1.419	33.360	24.066	11.111	4.888	32.177	5.451	19.403
7	1.674	41.610	14.946	13.131	5.817	36.447	12.430	23.134
8	0.845	58.057	12.069	6.566	2.290	34.324	13.258	8.955
9	0.717	37.511	8.218	5.556	25.309	46.002	7.730	101.493
10	1.291	19.235	18.049	10.101	15.841	26.168	5.703	63.433
11	1.610	49.218	32.113	12.626	5.260	37.788	8.338	20.896
12	2.120	35.248	24.032	16.667	33.663	34.893	10.693	135.075
13	4.352	37.231	35.264	34.343	14.913	24.805	2.571	59.701
14	0.590	15.757	36.441	4.545	24.381	34.812	5.011	97.761
15	0.845	28.358	36.195	6.566	6.002	21.742	11.757	23.881
16	1.355	3.694	7.520	10.606	18.997	34.655	3.252	76.119
17	1.801	16.726	20.115	14.141	4.146	25.000	14.951	16.418
18	1.993	18.608	26.091	15.657	1.733	29.786	24.835	6.716
19	1.801	4.230	9.044	14.141	2.846	34.630	4.144	11.194
20	1.100	11.101	13.855	8.586	4.146	36.358	23.750	16.418
Average	**1.435**	**33.421**	**24.757**	**11.237**	**10.680**	**30.785**	**10.195**	**42.687**

Image J software was used to analyzed SEM images shown in Figures 4 and 5 and twenty pores on each image were chosen and the software was used to determine the Area, Mean, Standard Deviation and Length for each pore as shown in Table 2 above. Twenty pores were selected on each image in order to completely cover the entire image hence, ensured true analysis. For LDA, the average Area was 1.435µm, average Mean was 33.421µm, average standard deviation was 24.757µm while average Length was 11.237. PA on the other hand has average Area of 10.680µm, average Mean of 30.785µm, average standard deviation of 10.195µm and average Length of 42.687µm.

The average Area of pores in LDA was 1.435µm while that of PA was 10.680µm; this is an indication that the pores in PA are bigger than that of LDA. Similarly, the average Length of pores in LDA was 11.237µm while that of PA was 42.687µm, an indication of longer pores in PA. This could be summarized that the particle grain size of LDA was finer than that of PA; this is because the LDA product was sieved through sieve 100 micron, hence,

making it finer. This make the LDA to be more nanoparticles than PA, hence, LDA will be more effective in wastewater treatment.

27. CONCLUSION

Aluminium oxide has been developed in the laboratory, various tests were carried out. From the results and analysis carried out, it can be concluded that: The Aluminium oxide developed in the laboratory is pure enough to be used for the development of composite filter for wastewater treatment, as it has 78.4% Al_2O_3 threshold when compare with the commercial pure Aluminium oxide. LDA has smaller pores, shorter grains and finer particle grain size. It will aid the capacity of clay in the treatment of wastewater since it contains more silicon oxide, as this will be an advantage for the purpose. The Aluminium oxide that was developed in the laboratory should be used for the development of composite filter. It could be subjected to further refine to meet up with the commercial standard, especially, in removal of titanium and manganese impurities if to be used for other purpose.

ACKNOWLEDGEMENT

The Authors acknowledged Ass. Prof. L.A. Azeez of Pure and Applied Chemistry Department, Osun State University, Osogbo, Nigeria. Mrs Ikimat Bello (Lab. 1) and Mr Damilare (Lab. 2) of the same department for their assistance during the course of this research.

REFERENCES

Abdolali, A., Ngo, H.H., Guo, W., Zhou, J.L., Zhang, J., Liang, S., Chang, S.W., Nguyen, D.D., and Liu, Y. (2017). Application of a Breakthrough Biosorbent for Removing Heavy Metals From Synthetic and Real Wastewaters In A Lab-Scale Continuous Fixed-Bed Column, *Journal of Bioresources Technology.* 229, 78–87.

Ajibola Ameerah. (2015). Recycling Aluminium Cans: Problems Associated with Improper Disposal of Aluminium Cans. From http://blog.wecyclers.com/2015/09/29/recycling-aluminium-cans-problems-associated-with-improper-disposal-of-aluminium-cans/ (Accessed on April 14, 2023).

Anastopoulos, I., Bhatnagar, A., Hameed, B.H., Ok, Y.S., and Omirou, M. (2017). A Review on Waste-derived Adsorbents from Sugar Industry for Pollutant Removal in Water and Wastewater. *Journal of Molecular Liquids 240,* 179–188.

Banerjee, S., Gautam, R.K., Jaiswal, A., Chattopadhyaya, M.C., and Sharma, Y.C. (2015). Rapid Scavenging of Methylene Blue Dye from A Liquid Phase by Adsorption on Alumina Nanoparticles. *RSC Advances*, Vol. 5, No. 19, pp. 14425–14440.

Byjus. (2023). Aluminium Oxide – Al_2O_3. Accessed on 29/03/2023. Retrieved from https://byjus.com/chemistry/al2o3/

Dassanayake, K.B., Jayasinghe, G.Y., Surapaneni, A., and Hetherington, C. (2015). A Review on Alum Sludge Reuse with Special Reference to Agricultural Applications and Future Challenges. *Waste Management. 38***,** 1 p. 321–335.

EPA. (2021). Facts and Figures About Materials, Waste and Recycling: Recycling Aluminum: Material-Specific Data. https://www.epa.gov/facts-and-figures-about-materials-waste-and-recycling/aluminum-material-specific-dataaluminum-material-specific-data (Accessed on May 23, 2021).

Hassan Basri, M.H., Mohammad Don, N.N., Kasmuri, N., Hamzah, N., Alias, S., and Azizan, F.A. (2019). Aluminium Recovery from Water Treatment Sludge Under Different Dosage of Sulphuric Acid. *Journal of Physics: Conference Series 1349,* 012005 doi:10.1088/1742-6596/1349/1/012005

Liu, L., Cui, Z., Ma, Q., Cui, W., and Zhang, X. (2016). One-step Synthesis of Magnetic Iron-Aluminum Oxide/Graphene Oxide Nanoparticles as a Selective Adsorbent for Fluoride Removal from Aqueous Solution. *RSC Advances*, Vol. 6, No. 13, pp. 10783–10791.

Safwat M.S., Mohamed, N.Y., Mohamed N. A., Meshref, and Elawwad, A. (2022). Adsorption of Phenol onto Aluminum Oxide Nanoparticles: Performance Evaluation, Mechanism Exploration, and Principal Component Analysis (PCA) of Thermodynamics. *Adsorption Science & Technology*, Volume 2022, Article ID 1924117, 14 pages https://doi.org/10.1155/2022/1924117

Schwarzenbach, R.P., Egli, T., Hofstetter, T.B., Von Gunten, U., and Wehrli, B. (2010). Global Water Pollution and Human Health. *Journal of Annual Review of Environment and Resources,* 35, 109–136.

Sheel, T.K., Poddar, P., Murad, A.B.M.W., Neger, A.J.M.T., and Chowdhury, A.M.S. (2016). Preparation of Aluminum Oxide from Industrial Waste Can Available in Bangladesh Environment: SEM and EDX Analysis. *Journal of Advanced Chemical Engineering*, 6: 152. Doi: 10.4172/2090-4568.1000152

Tabesh, S., Davar, F., and Loghman-Estarki, M.R. (2018). Preparation of γ-Al_2O_3 Nanoparticles using Modified Sol-Gel Method and Its Use for the Adsorption of Lead and Cadmium ions. *Journal of Alloys and Compounds*, vol. 730, pp. 441–449.

PAPER 180 – IMPACT ASSESSMENT OF A SOLID WASTE DUMP SITE ON ITS OST ENVIRONMENT: PARTICULATE MATTER

D. O. Oke[1,2,3], J. A. Sonibare[2], E. L. Odekanle[3, 4], F. A. Akeredolu[2], A. T. Olayanju[3, 5], C. O. Aremu[3, 6] and B. S. Fakinle[1,3]

[1]Department of Chemical Engineering, Landmark University Omu-Aran, Nigeria.
[2]Department of Chemical Engineering, Obafemi Awolowo University, Ile-Ife, Nigeria.
[3]Landmark University SDG 13 (Climate Action Research Group), Omu-Aran, Nigeria
[4]Department of Chemical and Mineral Resources Engineering, First Technical University, Ibadan, Nigeria
[5]Department of Agricultural and Biosystems Engineering, Landmark University, Kwara State, Nigeria
[6] Department of Crop Science, Landmark University, Omu-Aran, Nigeria.

ABSTRACT
Burning of solid waste openly has contributed greatly to the degradation of ambient air quality, thus having a harmful effect on environment, animals, materials and humans. This study employs a mass-based solid waste characterization method and also looks at the parameter such as ash content of the solid waste. Met One GT 331 mass monitor was employed to assess the levels of particulate matter and Total suspended particles (TSP) at ten sampling points on a dumpsite when the solid wastes were combusted. The study characterized 35.151 kg of solid waste with food waste, nylon, plastic, metals, paper and textile contributing to the major components in the study area with 23.46%, 27.64%, 7.30%, 3.29%, 24.32%, and 13.98% respectively. The percentage ash content was 7.12%, 7.09%, 21.41%, 29.16%, 8.88% and 7.58% respectively for food waste, nylon, plastic, paper, textile and composite waste. The 24 hr extrapolated concentrations for $PM_{2.5}$, PM_{10} and TSP ranged from 1.97 – 23.48 µg/m^3, 12.70 – 796.62 µg/m^3 and 17.38 - 882.27 µg/m^3 respectively. The extrapolated concentration for TSP breach the standard limit by FEPA for two days of the study.

KEYWORDS: Solid waste, Air emission, Climate action, Particulate matter.

1. INTRODUCTION

Open burning of solid waste in a dumpsite is a large source of air pollutants which is of huge concern to the quality of air (Angaye and Abowei, 2018). Open burning is harmful to human health and the environment. The solid waste burnt is released in its raw form into the atmosphere, they pose not only a great danger to the environment but also become a health concern for life (Weli *et al.*, 2014). The effects of open burning can lead to breathing difficulties, eye irritation, threat to normal functioning of the liver, kidney, heart and lungs of humans (Peter *et al.*, 2018). Open burning is a daily activity that kills the environment. The adverse effects of pollutants are largely dependent on their concentration and exposure rate (Barakat-Haddad *et al.*, 2015). Literature review on air quality around solid waste dumpsites in Nigeria showed values higher than the standard limit by the Federal Ministry of Environment (FMEnv) (Tariwari and Jasper, 2017). This is largely attributed to the unsafe management of waste including open-air burning of waste. Air pollution associated with solid waste has become a major source of greenhouse gases emission including particulate matter during openair burning (EZEKWE *et al.*, 2016). Suspended Particulate matter released during the burning of waste contain anthropogenic substance that causes irritation to the naval cavity and causes infections. Several studies have confirmed the consistent relationship between mortality and PM exposure (Angaye and Abowei, 2018). Exposure to airborne particulate matter is of increasing concern to the general public and its assessment is necessary from time to time (Power *et al.*, 2018; Uba, 2015). Exposure to high concentrations of PM_{10}, and $PM_{2.5}$ particles can cause health-related problems in humans in both short and long term (Chen *et al.*, 2018). WHO (2014) attributed more than 7 million death due to exposure to PM both indoors and outdoors. The ratio of $PM_{2.5}/PM_{10}$ is crucial to identify emission sources of PM. A high ratio of $PM_{2.5}/PM_{10}$ shows that fine particles dominate while a low ratio value indicates domination of coarse particles. Meteorological parameters such as temperature and relative humidity affect the movement of air contaminants (Karagulian *et al.*, 2015) . These parameters are directly or inversely related with the concentration of air pollutants (Zhou *et al.*, 2018). Wu *et al.* (2014) established that meteorological parameters have great effect on movement of PM as well as the concentration levels.

The increase in population pressure in the university community has increased the amount of solid waste generated; proper characterization of the waste is needed for effective decisions and management policy. This paper sets out to quantify and characterize the solid waste generated within the university community and assess the impact of particulate matter ($PM_{2.5}$ and PM_{10}) and Total suspended particles (TSP) around the open burning site as this would provide reliable data on the composition of waste generated and the ambient air quality around the open burning site with specific reference to $PM_{2.5}$, PM_{10} and TSP.

2. METHODOLOGY

2.1 Description of sampling /study area

Obafemi Awolowo University (OAU), Ile-Ife is situated on 13000 Acres (53km) of land. The university community comprises the central campus (academics and administrative buildings), student residential area, staff quarters and central market.

Three solid waste sample collection points were chosen for this study; a student residential hall (Awolowo Hall), Environmental and Design Management (EDM) faculty and Student Union Building (SUB). Ten sampling points were taken at the open burning site (Tonkere) of the University for the Assessment of particulate matter. The total area of the dump site was measured to be 74.041m (breadth) x 107.061m (length). Five points ($S_1 – S_5$) were taken on the site while five points ($S_6 – S_{10}$) were taken around the waste dump site.

2.2 Methods

2.2.1 Waste Characterization

The indirect method of waste disposal is in use in the university community. The solid waste generated was obtained from the central waste disposal bins from the three selected collection points (Awolowo Hall, EDM Faculty and SUB). Mass-based characterization was used in this study, the samples were taken before the delivery of the waste materials to landfills by the university-operated truck disposal system. The waste collected was sorted according to their composition type (food waste, Nylon, plastic, metal, paper and textile). Each of these characterized wastes is weighed and recorded. Waste samples were collected for seven days.

2.2.2 Determination of Ash Content of Solid Waste

The ash content of the characterized solid waste was determined using the *Muffle furnace* (electric furnace), a furnace fitted with an indicating pyrometer so that the desired temperature can be maintained.

10 grams of each of the characterized solid waste was weighed with the analytical balance into the aluminium crucibles. The crucible was marked with a unique identification number using a porcelain marker before being placed in the furnace until the weight becomes constant by igniting at a temperature of 575±25^{o}C for three hours. The crucible was removed and placed in a desiccator which is allowed to cool to room temperature before weighing it to determine its weight. After weighing, the crucible was returned to the furnace for one hour at 575±25^{o}C, cooled again in the desiccator, and re-weight. This step was repeated until the weight of the crucible is constant and the final weight was recorded. The percentage ash content of characterized waste was calculated using equation (1);

$$\text{Percentage Ash Content} = \frac{Initial\ Weight}{Final\ Weight}\ X\ 100 \quad (1)$$

2.2.3 Measurement of Particulate Matter

Opening Burning of solid waste generated in the university community takes place at Tonkere, a superb of the university community. Ambient concentrations of Particulate Matter and Total Suspended Particles were monitored for seven days. Met One GT331 mass monitor was used to measure the concentrations of particulate matter and TSP. It is a full-featured, battery-operated, portable laser particle counter that provides the functionality of a bench unit with the convenience of a handheld. It can data log particle counts continuously and it measures five mass ranges of particulate: PM_1, $PM_{2.5}$, PM_7, PM_{10} and Total Suspended Particulate (TSP) with a flow rate of 2.83 l/min. To measure the ambient PM and TSP, the GT 331 monitor is switched on in the environment of interest and the measured concentration is read directly on the LCD. During this field study, the particulate monitor was positioned 1 m above ground level to prevent the measurement of fugitive dust mobilized by tides. Measurement was carried out during open burning of the solid waste with an average time of 15 minutes for 7 days. Kestrel 4000 meter was used to measure the meteorological parameters such as the relative humidity and barometric pressure. Digital Sound Level Meter was used to measure the noise levels of the sampling points. The 24-hr averaging period extrapolated concentrations of the measured PM and TSP were subsequently computed using an atmospheric stability formula (Fakinle *et al*., 2018) given in equation (1):

$$C_o = C_1 \times F \quad (2)$$

where C_o = the concentration at the averaging period t_o

C_1 = the concentration at the averaging period t_1

F = factor to convert from the averaging period t_1 to the averaging period $t_o = (t_1/t_0)^n$

n = 0.28, the stability-dependent exponent

2.2.4 Evaluation of Air Quality Implication

The evaluation of air quality implication of the temperature, PM and TSP concentrations obtained from the study areas were compared with the ambient air quality standards of the Federal Ministry of Environmental

Protection Agency (FEPA, 1991). The ratio of $PM_{2.5}/PM_{10}$ is also calculated to ascertain the nature of the particulate matter source that dominates the solid waste dumpsite. The relationship between the meteorological parameters and suspended particulate matter was also established in the study. The standard limit set for total suspended particles (TSP) by FEPA is 250 $\mu g/m^3$.

3. RESULTS AND DISCUSSION

3.1 Determination of Solid Waste Characteristics

A total of 35.151kg of solid waste were characterized, the percentage composition was 23.46%, 27.64%,7.30%, 3.29%, 24.32%, and 13.98%, for food waste, nylon, plastic, metals, paper and textile were recorded respectively as shown in Figure 3. From the physical characterization carried out on the solid waste samples from the three sampling locations, The percentage composition for SUB Car Park in the seven days sampling period was food waste 28.5%, Nylon 33.6%, plastic 7.2%, metal 3.1%, paper 25.5% and textile 2.1%. For EDM, the percentages of 19.8%, 20.5%, 10.1%, 5.8%, 37.5%, and 6.3%, for food waste, nylon, plastic, metals, paper and textile were recorded respectively. Awolowo Hall, the percentage compositions were 21.8%, 27.5%,5.6%, 1.9%, 15.0%, and 28.3%, for food waste, nylon, plastic, metals, paper and textile were recorded respectively (Table 3). Figure 1 shows the percentage distribution of waste collected while Figure 2 shows the plot of the compositions of the characterized components of the waste.

Table 3: Total composition of waste collected over 7 days in different collection points

COLLECTION POINTS	FOOD WASTE(kg)	NYLON(kg)	PLASTIC(kg)	METAL(kg)	PAPER(kg)	TEXTILE(kg)
SUB CAR PARK	3.268	3.850	0.827	0.350	2.925	0.237
EDM	1.827	1.892	0.932	0.539	3.456	0.583
AWOLOWO HALL	3.158	3.973	0.808	0.268	2.166	4.092

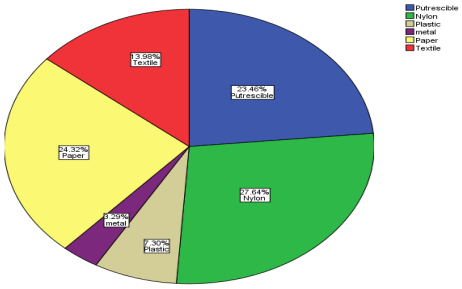

Figure 1: Percentage composition of the solid waste collected

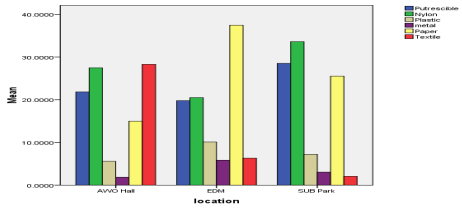

Figure 2: Total Composition of Waste Collected in the three collection points

3.2 Determination of Ash Content

The experimental procedure embarked upon for the determination of the ash content of the characterized solid waste samples yielded the following results, the percentage composition were 7.12 %, 7.09 %, 21.41 %, 29.16 %, and 8.88 %, for food waste, nylon, plastic, paper and textile were recorded respectively (Table 4). When the mixture of all five waste samples (composite) was taken, a percentage ash composition of 7.58% was obtained.

Table 4: Ash Content Analysis of solid waste

Solid waste Composition	Initial Value(g)	Final Value(g)	Percentage Ash Composition
Putrescible	10.025	0.718	7.12

Paper	10.003	2.917	29.16
Plastic	10.051	2.152	21.41
Composite	10.029	0.760	7.58
Nylon	10.032	0.711	7.09
Textile	10.017	0.890	8.88

3.3 Meteorological Parameters

The average values for the meteorological parameters in the study area for seven days in 10 sampling points, (Temperature, Relative humidity and pressure) are shown in Table 5. The temperature measured ranges between 27.42°C to 29.76 °C with an average of 28.24 °C. The acceptable limit for ambient temperature is 30 ^{0}C by FEPA (1991). The measured temperature of the study is below the standard value. The reading for the relative humidity is between 51.40 % - 66.80 % with an average of 58.43%. The barometric pressure measured for seven days ranges between 976.32 hpa - 979.23 hpa with an average of 973.3167 hpa.

Table 5: Measured Meteorological Parameters

Day/Parameters	D_1	D_2	D_3	D_4	D_5	D_6	D_7	**Mean value**
Temperature (^{O}C)	**27.65**	**28.53**	**29.76**	**27.42**	**28.21**	**27.87**	**28.21**	**28.24**
Relative humidity (%)	**54.30**	**66.80**	**52.50**	**61.40**	**60.20**	**62.40**	**51.40**	**58.43**
Pressure (HPA)	**976.32**	**979.23**	**976.48**	**977.19**	**976.59**	**975.34**	**975.6**	**973.32**

3.4 Measured Ambient Concentrations of Particulate Matter

The particulate levels of the sampling area were done for seven (7) days in the university dumpsite. The measured ambient concentration was extrapolated to 24 hours, for day one of the samplings the concentration ranged from 2.11 – 11.33 µg/m^3, 16.10 – 48.92 µg/m^3 and 24.99 – 100.43 µg/m^3 for $PM_{2.5}$, PM_{10} and TSP respectively. Concentration ranged from 3.03 – 378.88 µg/m^3, 25.96 – 814.34 µg/m^3 and 33.20 – 821.67 µg/m^3 for $PM_{2.5}$, PM_{10} and TSP respectively. The third-day extrapolated concentration was in the range of 6.68 – 40.89 µg/m^3, 40.31 – 119.15 µg/m^3 and 45.66 – 133.28 µg/m^3 for $PM_{2.5}$, PM_{10} and TSP respectively. The fourth-day extrapolated levels ranged from 1.97 – 122.75 µg/m^3, 12.70 – 215.99 µg/m^3 and 17.38 – 224.94 µg/m^3 for $PM_{2.5}$, PM_{10} and TSP respectively. Concentrations for day five ranged from 5.12 – 72.16 µg/m^3, 43.62 – 116.98 µg/m^3, and 54.63 – 243.15 µg/m^3 for $PM_{2.5}$, PM_{10} and TSP respectively. The concentration level for day six ranged from 15.65 – 35.82 µg/m^3, 95.22 – 359.09 µg/m^3 and 109.68 µg/m^3 for $PM_{2.5}$, PM_{10} and TSP respectively. The seventh-day concentration was 23.48 – 78.62 µg/m^3, 210.48 – 796.62 µg/m^3 and 255.61 – 882.27 µg/m^3 for $PM_{2.5}$, PM_{10} and TSP respectively. Figure 4 shows the concentration of $PM_{2.5}$, PM_{10} and TSP for the 7 days of sampling.

The ratio of $PM_{2.5}/PM_{10}$ computed from the study (Table 7), shows a value ranging between 0.087 - 0.789 for sapling point one (SP_1), 0.098 – 0.666 for SP_2, 0.07 – 0.909 for SP_3, 0.080 – 0.409 for SP_4, 0. 064 – 0.214 for SP_5, 0.062 – 0.129 for SP_6, 0.084 – 0.368 for SP_7, 0.081 – 0.568 for SP_8, 0.074 – 0.357 for SP_9 and 0.046 – 0.424 for SP_{10}.

Table 7: Computed Ratio of $PM_{2.5}/PM_{10}$ from the Solid Waste dumpsite

Sampling Points/ Days	**DAY ONE**	**DAY TWO**	**DAY THREE**	**DAY FOUR**	**DAY FIVE**	**DAY SIX**	**DAY SEVEN**
SP_1	0.167	0.126	0.087	0.789	0.272	0.271	0.083
SP_2	0.134	0.666	0.496	0.389	0.393	0.210	0.098
SP_3	0.07	0.607	0.193	0.191	0.253	0.084	0.119
SP_4	0.329	0.025	0.231	0.195	0.409	0.080	0.114
SP_5	0.129	0.064	0.107	0.141	0.149	0.214	0.107
SP_6	0.120	0.065	0.062	0.037	0.129	0.077	0.114
SP_7	0.368	0.106	0.186	0.116	0.084	0.164	0.095
SP_8	0.231	0.160	0.198	0.568	0.081	0.168	0.116
SP_9	0.357	0.166	0.144	0.170	0.074	0.144	0.126
SP_{10}	0.424	0.292	0.134	0.046	0.104	0.124	0.114

3.5 Discussion of Results

Solid waste management in the university community is through open dumping and landfilling. There is no formal recycling scheme within the community, however, scavengers often visit the dumpsite to pick things that can be recycled such as plastics and metals. The waste disposal methods in the study area include collection points, usage of waste disposal trucks and landfilling. Major compositions of waste collected in this study are food waste, nylon, plastic, metal, paper and textile. In the collection point within the academics area, the highest percentage of waste is paper due to students' activities and high usage of paper in many offices. However, at the student residential, textile waste had the highest percentage. Results obtained in this study show a similar trend with the characterization of solid waste in other Nigerian universities as presented in Figure 5. The Ash content of solid waste shows the amount of material left after burning of waste which is usually in the form of ash, this usually poses another danger to the ambient environment and air quality if not properly managed. In this study, paper waste has the highest ash content value of 29.16 % with nylon having the lowest value.

Based on the air quality index, the particulate levels and TSP were fairly clean when there is no open burning of waste and were heavily polluted during the burning of waste. During the study for seven days, $PM_{2.5}$, PM_{10} and TSP were very high in concentrations for day two, day six and day seven of the study due to the burning of waste and vehicular movement. Day two and Day seven of the study area were observed to breach the FEPA standard for 24 hrs concentration for $PM_{2.5}$, PM_{10} and TSP. $PM_{2.5}$ breached the standard but PM_{10} and TSP were within the acceptable limit. Day One and Day six for all particulate levels were well within the acceptable limit

4. CONCLUSION

The study provides useful information on the nature of solid waste generation and the composition of the study area. It also investigates particulate matter levels associated with open burning of solid waste generated within the university community. Results obtained in this study could help the university management on effective ways to handle the solid waste generated. From the particulate matter measurement, it can be concluded that open burning of solid waste increases the concentrations of these air pollutants and thus affect the ambient environment and human life. The data obtained is expected to influence the policy on proper management of solid waste and air quality around the study area. Proper and effective handling of waste within the university community is urgently needed to be put in place. The university management should also invest in converting this enormous waste generated daily into useful energy. The study recommends against open burning of solid waste at any collection points within the academic environment and students' hostels.

REFERENCES

Angaye, T., and Abowei, J. J. M. T. (2018). Evaluation of suspended particulate matter (SPM) around municipal solid waste dumpsites in yenagoa metropolis, Nigeria. *4*(2), 54-57.

Barakat-Haddad, C., Zhang, S., Siddiqua, A., Dghaim, R. J. J. o. e., and health, p. (2015). Air quality and respiratory health among adolescents from the United Arab Emirates. *2015*.

Chen, G., Jin, Z., Li, S., Jin, X., Tong, S., Liu, S., Yang, Y., Huang, H., and Guo, Y. J. E. i. (2018). Early life exposure to particulate matter air pollution (PM1, PM2. 5 and PM10) and autism in Shanghai, China: A case-control study. *121*, 1121-1127.

Ezekwe, C. I., Agbakoba, A., And Igbagara, P. W. J. G. (2016). Source Gas Emission And Ambient Air Quality Around The Eneka Co-Disposal Landfill In Port Harcourt, Nigeria. *2*(1).

Fakinle, B. S., Oni, O. S., Olalekan, A. P., Sonibare, J. A., Okedere, O. B., & Odunlami, O. A. (2018). Total suspended solids and volatile organic compounds in the airshed of a reconstructed road along Lagos-Ibadan expressway. International Journal of Civil Engineering and Technology, 9(11), 2420–2427.

FEPA. (1991). Guidelines to standards for environmental pollution control in Nigeria. Federal Environmental Protection Agency (FEPA). Lagos.

Karagulian, F., Belis, C. A., Dora, C. F. C., Prüss-Ustün, A. M., Bonjour, S., Adair-Rohani, H., and Amann, M. J. A. e. (2015). Contributions to cities' ambient particulate matter (PM): A systematic review of local source contributions at global level. *120*, 475-483.

Peter, A. E., Nagendra, S. S., and Nambi, I. M. J. A. P. R. (2018). Comprehensive analysis of inhalable toxic particulate emissions from an old municipal solid waste dumpsite and neighbourhood health risks. *9*(6), 1021-1031.

Power, M. C., Lamichhane, A. P., Liao, D., Xu, X., Jack, C. R., Gottesman, R. F., Mosley, T., Stewart, J. D., Yanosky, J. D., and Whitsel, E. A. J. E. h. p. (2018). The association of long-term exposure to particulate matter air pollution with brain MRI findings: the ARIC study. *126*(2), 027009.

Uba, S. (2015). *Environmental Impact Assessment of Dumpsites in Zaria Metropolis, Kaduna State, Nigeria.* M. Sc Thesis, Ahmadu Bello University, Zaria Nigeria.

Weli, V. E., Adekunle, O. J. J. o. E., and Science, E. (2014). Air Quality in the Vicinity of a Landfill Site in Rumuolumeni, Port Harcourt, Nigeria. *4*(10), 1-9.

Wu, S., Deng, F., Hao, Y., Wang, X., Zheng, C., Lv, H., Lu, X., Wei, H., Huang, J., and Qin, Y. J. C. (2014). Fine particulate matter, temperature, and lung function in healthy adults: findings from the HVNR study. *108*, 168-174.

Zhou, X., Cai, J., Chen, R., Wang, C., Zhao, A., Yang, C., Li, H., Liu, S., Cao, J., and Kan, H. J. E. P. (2018). Estimation of residential fine particulate matter infiltration in Shanghai, China. *233*, 494-500.

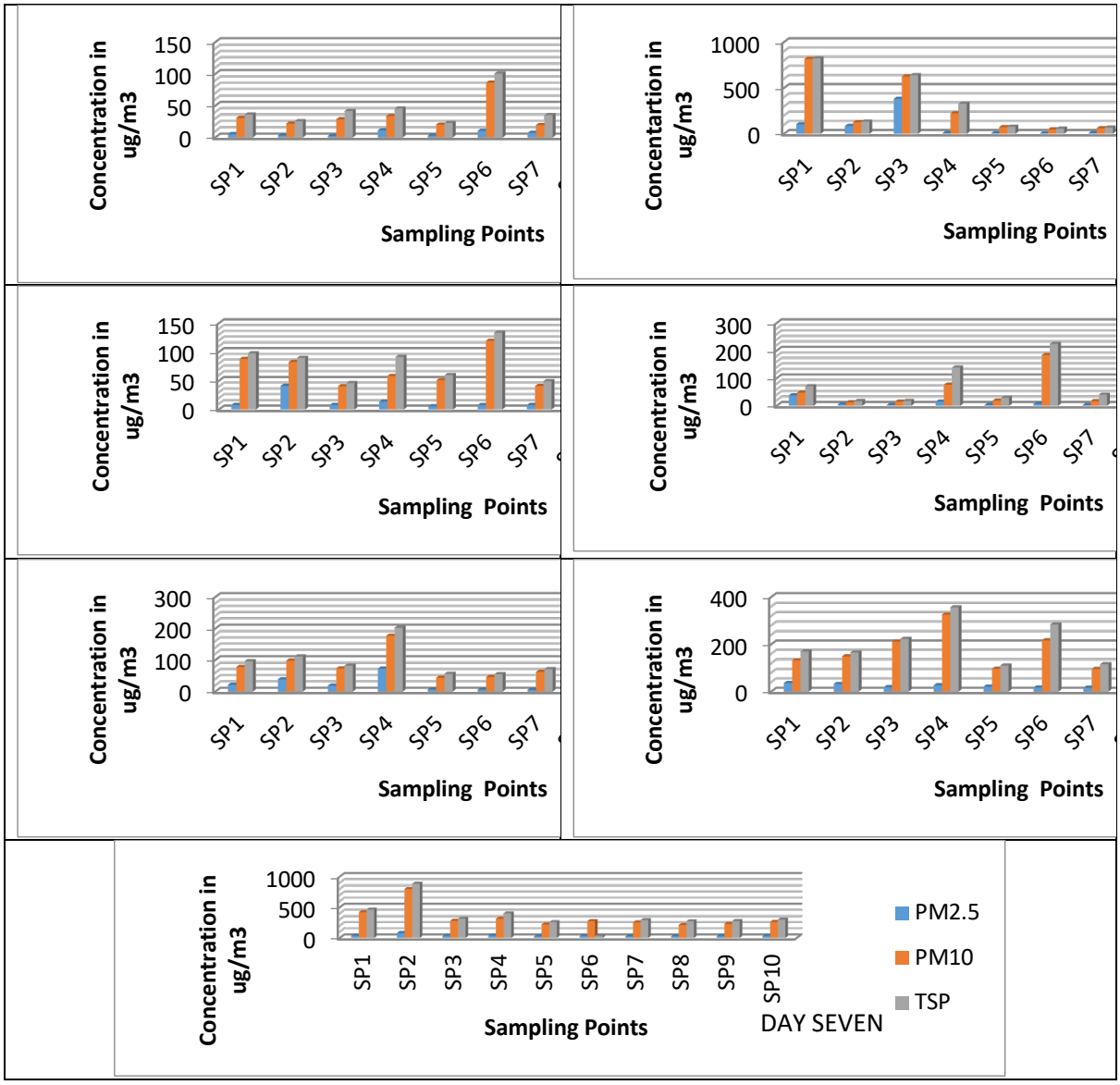

Figure 4: Concentrations of particulate matter level and TSP from the study area

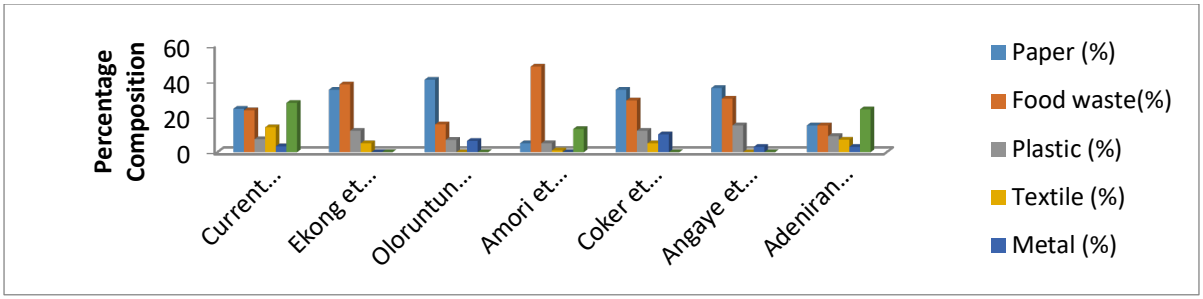

Figure 5: Comparison of Solid waste characterization from study and previous studies

PAPER 183 – EFFECT OF CARBURIZATION TIME AND TEMPERATURE ON HARDNESS PROPERTIES OF MILD STEEL

O. Adedipe[1], A.A. Adeyemo[1], I.C. Ugwuoke[1], S.A. Lawal[1], N.A. Agbo[2], V.S. Aigbodion[3], O.W. A. Oyeladun[4], A. J. Owoeye[1], J.B. Mokwa[5], E.T. Dauda[6]

[1]Department of Mechanical Engineering, Federal University of Technology, Minna, Nigeria.
[2] Defence Industries Cooperation of Nigeria (DICON), Kaduna Nigeria
[3]Africa Centre of Excellence, ACE-SPEC, University of Nigeria, Nsukka, Nigeria
[3]Faculty of Engineering and Built Environment, University of Johannesburg, South Africa
[4]Department of Mineral and Petroleum Resources Engineering, Kaduna Polytechnic, Zaria, Nigeria
[5]Department of Mechanical Engineering, Federal Polytechnic Bida, Nigeria
[6]Department of Metallurgical and Materials Engineering, Ahmadu Bello University, Zaria, Nigeria

ABSTRACT
The service conditions of automobile steel components such as crankshaft, gears and cams to mention but a few require high hardness to enable them satisfy their design requirements when in operation. In this study, hardness properties of carburized mild steel rods were investigated to determine the impact of carburization parameters on the steel. Mild steel rods were carburized using coconut charcoal powder and periwinkle shell powder. The samples were carburized at temperatures of 850°C, 900°C and 950°C respectively; and were soaked for 1 hour, followed by water quenching. Leeb hardness tester was used to determine the hardness values of the carburized mild steel rods. The highest hardness value of 774 HL was obtained with carburization parameters of 436.80g of coconut shell charcoal, 150.23g of periwinkle shell powder, carburization temperature of 900^0C and at a soaking time of 109 minutes. It was established that locally sourced materials (Carburized coconut shell and periwinkle shell) could serve as effective carburization ingredients for mild steel due to the improvement in hardness of the mild steel.

1. INTRODUCTION

Carburization is a surface-hardening heat treatment process which is carried out to enhance the performance of parts such as bearings and gears in order to improve the hardness of the surface to resist wear and the toughness of the interior to resist impact during service (Binzhou et al., 2018). This is due to the loads arising from vibration, speed of rotation and the nature of applied stresses they experience in service (Salawu et al., 2019). Case hardening has also been described as the process of hardening the surface of steel by infusing elements into the metal surface forming a hard, wear resistance skin but preserving a tough and ductile interior (*Metals Handbook, 1981)*. The various case hardening processes are carburizing, cyaniding, citrating, carbonitriding and flame/Induction hardening. The focus of this study is carburization which improves specific mechanical properties of low carbon steel by the addition of carbon materials at elevated temperature (Orisanmi et al., 2017). Carburization has proved very effective in improving mechanical properties of mild steel and increase in thickness of surface layers (Afolalu et al., 2018). Several materials have been used in the literature for carburization process. These include egg shell, periwinkle shell, coconut shell, palm kernel shell, cow bones and horns. The processing time and bonding efficiency of these materials are subjects for discussion with respect to different steels (Sanni and Fayomi 2018). The effect of soaking time on mechanical properties of mild steel subjected to packed carburization at temperatures of 850°C, 900°C and 950°C using pulverized bone as the carburizer was investigated in (Aramide et al., 2010). After quenching in oil and tempered at 250°C, better mechanical properties were revealed for samples that were soaked at the carburizing temperature of 900°C for 15 minutes and 30 minutes respectively.

A study carried out using combined coconut shell charcoal and periwinkle shell as carburization materials was reported in (Agbo et al., 2017) where carburizing time, case depth and carburizing materials (75% weight of pulverized coconut shell charcoal and 25% weight of pulverized periwinkle shell) were used for the carburization of 18 samples of 0.08% carbon content mild steel rods of length 55 mm and 14 mm diameter. The carburization temperature was maintained at 900^oC and it was found that case depth and hardness values increased with increase in different carburizing time (1, 2 and 3 hours). Periwinkle shell was also found to be a good cost effective

carburizer when used with $BaCO_3$ as energizer in the improvement of hardness and impact strength of low carbon steel with 0.182% carbon (Adzor et al., 2016).

The use of wood charcoal as carburizer and $BaCO_3$as energizer in the carburization of mild steel with carbon content of 0.17% at different temperatures (750-950^oC) and different times (1-3 hours) revealed that the hardness and tensile properties of the material were improved (Obolo et al., 2017). Pulverized wood charcoal (70% weight) and (30% weight) egg shell also proved useful in the carburization of grey cast iron at 700^oC, 800 ^oC and 900^oC respectively (Salawu et al., 2019). Increase in hardness of the samples was revealed with respect to carbon concentration at different carburizing temperatures.

Efforts have been made to investigate the suitability of locally sourced organic carburizers and energizers as replacement to commercially available chemical ones. For example in (Ihom & Azoro, 2019; Ihom et al., 2012; Ihom et al., 2013), the effects of charcoal carburizer and periwinkle shells, cow bones, banana peels (Ihom and Azoro 2019); and rice husk, sugar cane, melon shell, egg shell energizers (Salawu et al., 2019; Umunakwe et al., 2017) on case depth and hardness of mild steel enhanced the case depth and hardness of the material compared to use of chemical energizers ($BaCO_3$, Na_2CO_3, $CaCO_3$). The suitability of palm kernel shell and coconut shell mixture was investigated for the carburization of low carbon steel (0.16% C), energized with 20% by weight of $CaCO_3$ (Umunakwe et al., 2017). The hardness and tensile properties were enhanced by an order of magnitude using the mixed carburizers compared to the use of the carburizers individually. Charcoal carburizer and mixture of cow bone and coconut shell using different carburizing temperatures (900^oC, 950^oC and 1000^oC) were found to improve the hardness property of low carbon steel (Miswanto et al., 2019).

In a recent study, the tensile and fatigue strengths of low carbon steel were improved by carburization using coconut shell charcoal as carburizer (Syahid et al., 2020). At pack carburizing temperature of 900^oC, the tensile strength increased from 356.66 N/mm^2 to 541.15 N/mm^2 while the fatigue strength increased from 161 MPa to 232 MPa. These results have shown the reliability of coconut shell charcoal as carburizer.In this study, mild steel was carburized using coconut shell charcoal and periwinkle shell powder as carburizing ingredients in order to investigate the suitability of these materials for carburization of mild steel and their effect on hardness properties of the steel.

2. THEORETICAL ANALYSIS

During carburization, the residual air in the carburizing box combines with carbon to produce CO gas. Carbon monoxide gas which is unstable at the process temperature decomposes as it contacts the iron surface. The process is governed by the following reactions (*Metals Handbook, 1981)*:

$$2C + O_2 = 2CO$$

$$2CO = C + CO_2$$

The atomic carbon enters the steel through the following reactions:

$$Fe + 2CO = Fe(C) + CO_2$$

$$C + CO_2 = 2CO$$

Where Fe(C) is carbon dissolved in austenite. Carbon is absorbed by the steel surface, and subsequently diffuses towards the centre of steel sample. CO_2 thus formed reacts with the carbon (C) of the carburizing medium to produce CO, and thus, the cycle of the reaction continues. Charcoal is the basic source of carbon during solid carburization (*Metals Handbook, 1981)*. As entrapped air inside the box may be less to produce enough CO_2 particularly in the beginning of the carburization, it is thus common practice to add energizer usually $BaCO_3$ which decomposes during the heating up period as:

$$BaCO_3 = BaO + CO_2$$

The CO_2 formed then reacts with the carbon of the carburizer to produce CO gas. Thus, $BaCO_3$ makes CO_2 available at an early stage of carburization and hence it is called energizer. The case depth increases with rise in carburization temperature and time.

3. MATERIALS AND METHODS

The materials used for this study include mild steel, coconut shell and periwinkle shell; details can be found in (Adedipe et al., 2023a; Adedipe et al., 2023b). The as-received mild steel rods were carburized using different weights of coconut shell charcoal and pulverized periwinkle shell powder at temperatures of 850, 900 and 950oC respectively; and at different times (1 to 3 hours). The equipment used are muffle furnace (Model: HSX-2-6-13), ultrasonic sieve shaker (Model: DYS-1000), purposed developed carbonization chamber, grinding machine (Model: TW-IP-12), Ball mill (Model: XMQ 240 X 30), digital weighing balance (Model: I-JA503) and Leeb hardness tester. The equipment are located at Mechanical Engineering Department, Federal University of

Technology Minna, Nigeria, where the experiments were carried out. Experimental design considering the different weights of carburizing ingredients, carburization time and temperature was carried out using design expert. A total of 31 mild steel samples of 100 mm length were carburized. The as-received samples are shown in Figure 3.1.

Figure 3.1: As received mild steel rods

The coconut shells were sun dried to remove the moisture content and was later carbonized in the carbonization chamber. The carbonized coconut shells were grinded to powered form using Pulverizer or grinding machine. The periwinkle shells were also sun dried and grinded using the ball mill. To obtain the periwinkle shell in powder form, further grinding was done using the grinding machine. The periwinkle shell powder was then sieved into finer particles using the ultrasonic sieve shaker. Carburization boxes of dimensions 140mm x 80mm x 60mm were fabricated with stainless steel to contain the carbonized coconut shell powder, periwinkle shell powder and the mild steel rods. The lids of the boxes were sealed with mixture of clay and sodium silicate (Figure 3.2) before the carburization process.

Figure 3.2: Carburization box sealed with clay and sodium silicate

Prior to carburization, the mild steel rods were polished to remove rust and different weights of samples of carbonized coconut shell powder and periwinkle shell powder were measured using the digital weighing balance. The mild steel rods were inserted inside the carburization boxes and the boxes were sealed before loading them in the furnace for carburization process (Figure 3.3).

Figure 3.3: Mild steel rod in carburization materials arranged in the furnace

A laboratory muffle furnace was used to carry out the heat treatment process. The carburization boxes housing the mild steel rods and carburizing materials were loaded in the furnace as shown in Figure 3.3. The carburizing temperatures used were 850^0C, 900^0C and 950^0C at different times ranging from 1 hour to 3 hours as stated in the design of experiment. After carburization, the samples were removed from the cans and were allowed to cool in air. After cooling, the samples were heated in the furnace at temperature of 900^0C for 1 hour, followed by quenching in water and tempering at a temperature of 200^0C for1 hour. The hardness of the samples was measured using the Leeb Hardness tester.

4. RESULTS AND DISCUSSION

The chemical composition of the mild steel sample is shown in Table 4.1 as investigated in recent studies (Adedipe et al., 2023a; Adedipe et al., 2023b) where carburization of mild steel samples was carried out using coconut shell charcoal and nanoparticles derived from periwinkle shell.

Table 4.1: Chemical composition of mild steel

Elements	*C*	*Mn*	*Si*	*P*	*S*	*Zn*	*Al*	*Ni*	*Fe*
%	0.16	0.35	0.15	0.0031	0.021	0.034	0.005	0.075	Balance

The coconut shell charcoal is shown in Figure 4.1 while the sample of periwinkle shell powder is shown in Figure 4.2. Samples of the carburized mild steels are shown in Figure 4.3 where it can be seen that the surface appearance of the samples are darker compared to in Figure 4.1, which implies the deposit of carburizing materials on the surface at the test temperatures.

Figure 4.1: Carbonized coconut shell powder

Figure 4.2: Periwinkle shell powder

Figure 4.3: Carburized mild steel

The hardness values of the 31 carburized samples and that of as-received sample are set out in Table 4.2. Hardness measurements were taken on each sample five times. The average hardness values are shown in the table. The obtained hardness values are related to the carburization parameters as generated from the design of experiment. It can be seen that the sample with serial number 22 had the highest hardness value of 774 HL, which corresponds to carburization parameters of 436.80g of coconut shell charcoal, 150.23g of periwinkle shell powder, carburization temperature of 900^0C and at a soaking time of 109 minutes. However, the hardness value of the as-received sample was found to be 501 HL, which when compared to hardness value of 774 HL implies a significant improvement in hardness of the material, due to the deposit of carbon from coconut shell charcoal and periwinkle shell powder which functioned as the catalyst or energizer.

The improvement in hardness value is in agreement with those obtained from other organic carburization ingredients (Ihom et al., 2013; Ihom and Azoro 2019; Miswanto et al., 2019). The implication of the results is that improved hardness does not only depend on carburization time and temperature, but also on the optimum quantity of carburization ingredients. In similar works (Adedipe et al., 2023a; Adedipe et al., 2023b), hardness value of mild steel was found to increase by 114.1% at ratio 3:7 of nano particles of periwinkle shell powder and coconut shell charcoal respectively. This implies that the hardness properties of mild steel could be effectively influenced using organic carburizing materials such as coconut shell and periwinkle shell. In Table 4.2, the least hardness value was found to be 365 HL in sample with serial number 17. The carburization parameters of the sample were 436.80g of carburized coconut shell and 150.23g of periwinkle shell powder at a carburization temperature of 850^0C and at a soaking time of 135 mins. The lower hardness value may be as a result of the carburization temperature use.

Table 4.2: Hardness values of carburized mild steel

		Hardness values (HL)				
Samples	***Average***	***1***	***2***	***3***	***4***	***5***
1	624	481	591	674	688	687
2	622	540	587	697	623	664
3	655	605	582	621	725	744
4	764	663	712	797	840	810
5	703	556	684	710	745	823
6	570	396	623	606	568	658
7	723	688	755	748	632	796
8	695	624	721	743	673	717
9	724	651	732	743	745	750
10	675	590	719	708	658	702
11	533	531	531	604	568	432
12	678	643	676	670	676	727
13	571	551	584	539	577	605
14	592	496	531	593	647	694
15	687	581	595	768	729	762
16	674	612	631	651	705	772
17	365	338	393	408	348	339
18	667	559	644	709	654	772
19	591	518	577	676	543	644
20	692	569	664	716	747	767
21	688	597	650	690	781	726
22	774	664	773	787	835	815
23	695	584	612	714	777	791
24	562	536	592	557	676	452
25	698	588	711	755	700	740
26	654	610	579	695	708	678
27	644	560	627	624	676	733
28	581	579	617	553	606	553
29	510	420	428	518	571	616
30	742	651	737	743	786	796
31	700	672	674	713	725	718
As received Sample	501	331	440	556	549	632

5. CONCLUSION

Mild steel samples were carburized at temperatures of 850^{0}C, 900^{0}C and 950^{0}C and at various times ranging from 1 to 3 hours. The following conclusions can be drawn from this study:

1. The surface hardness of mild steel can be enhanced by organic carburizing materials such as coconut charcoal and periwinkle shell.
2. Highest hardness value of 774 HL was obtained using carburization parameters of 436.80g of carburized coconut shell and 150.23g of periwinkle shell, carburization temperature of 900^{0}C and at a soaking time of 109 minutes.
3. Hardness properties of mild steel depend on several factors ranging from carburization ingredients, time and temperature. Hence, locally sourced organic materials have been found to be effective materials in carburization of mild steel.

ACKNOWLEDGEMENT

Authors acknowledge the financial support given by the National Research Fund (NRF) under the aegis of the Tertiary Education Trust Fund (TETFund), Nigeria (TETF/ES/DR&D-CE/NRF2020/SETI/87/VOL.1).

REFERENCES

Adedipe, O., Aigbodion, V. S., Lawal, S. A., Oyeladun, O. W., Mokwa, J.B & Dauda, E. T. (2022a). Unveiling High-Performance Carburized Mild Steel Using Coconut Shell Ash and CaCO3 Nanoparticles Derived from Periwinkle Shell. The International Journal of Advanced Manufacturing Technology, Springer. Pp. 1-11.

Adedipe, O., Aigbodion, V. S.,Lawal, S. A., Oyeladun, O. W., Mokwa, J. B. Dauda, E.T. (2023b). Explicit Microstructure and Electrochemical Study of Value- Added Carburized Mild Steel with Coconut Shell Ash and CaCO3 Nanoparticles Derived from Periwinkle Shell Chemical Data Collection. *Elsevier*, (101028: 1-10).

Adzor, S. A., Nwoke, V. U., & Akaluzia. (2016). Investigation of Suitability of Periwinkle Snail Shell as Carburizing Material for The Surface Hardness Improvement of Low Carbon Steel. *European Journal of Material Science*. 3(2). PP. 13-23.

Afolalu, S. A., Abioye, O. P., Salawu, W. T., Okokpujie, A. A., Abioye, A. A., Omotosho, O. A. & Ajayi, O. O. (2018). Impact of Heat Treatment on HSS Cutting Tool (ASTM A600) and it's Behavior During Machining of Mild Steel (ASTM A36) in Aip Conference Proceedings. PP. 1-6.

Agbo, N. A., Dauda, E. T., Awe, T. & Oyeladun, O. A. (2017). The Suitability of Periwinkle as Energizer in Case Hardening of 0.08 Mild Steel Using Coconut Shell as Carburized at 900 c. In 33 Annual Conference of Nigerian Metallurgical Society. Vol 2. PP. 45-53.

Aramide, F. O., Ibitoye, S. I., Oladele, I. O. & Borode, J. O. (2010). Pack Carburization of Mild Steel Using Pulverized Bone as Carburizer Optimizing Process Parameter. *Leonard Electronic Journal of Practice and Technologies*. Vol. (16). PP. 1-12.

Binzhou, Li., Changsheng, Li., Zhenxing, Li. & Dong, J. (2018). Microstructure and Mechanical Properties of Fe-Cr-2Ni-Mo-V Steel in a Carburizing Process. *Procedia Manufacturing*. Vol. (15). PP. 1612-18.

Ihom, P. A. & Azoro, K. U. (2019). The Development of Eco-friendly Energizer as Replacement for Industrial Chemical Energizers in the Casehardening of Mild Steel Materials. *International Journal of Mechanical and Civil Engineering*. 2(2). PP. 11-22.

Ihom, P. A., Nyior, G. B., Alabi, O. O., Segun, S., Nor, I. J. & Ogbodo, N. J (2012). The potentials of Waste Organic Materials in Surface Hardness Improvement of Mild Steel. *International Journal of Science and Engineering Research*. 3(11). PP. 1-10.

Metals Handbook (1981). Heat Treatment. Vol (4)., 1981. 9th Edition. American Society of Metals (ASM).

Miswanto, T. O., Rajaguguk, O. & Sumandi, S. (2019). The Study of.Low Carbon Steel Pack Carburizing Using Cow Bone and Coconut Shell. IOP conference Series: *Material Science and Engineering*. DOI: Doi: 10.1088/1757-899X/478/1/012037.

Obolo, O. E., Barnabass, A. A., Umar, S. & Jafar L. (2017). Investigating the Mechanical Properties of Carburized Mild Steel(0.18%C). Cost of Corrosion of Metallic Products in Federal University of Abeokuta. *International Journal of Applied Engineering Research*. 12(24): PP.41- 47.

Orisanmi, B. O., Afolalu, O. R., Adetunji, O. R., Salawu, E. Y, Okokpujie, I. P., Abioye, A. A., Akinyemi, O. O. & Abioye, O. P. (2017). Cost of Corrosion of Metallic Products in Federal University of Agriculture, Abeokuta. *International Journal of Applied Engineering Research*. 12(24). PP. 41-47.

Salawu, E. Y., Oluseyi, O. A., Inegbenebor, A. & Akinlabi, S. (2019). Microstructural and Mechanical Characterization of Pulverised Wood Charcoal and Egg- Shell as Organic Carbon Additives for Grey Cast Iron Carburization. *International Journal of Mechanical and Production*. 9(6): PP. 391-98.

Sanni, O. & Fayomi, O. S. (2018). The inhibitive Study of Eggshell Powderon Uns n08904 Austenitic Stainless-Steel Corrosion in Chloride Solution. *Defence Technology*. 14(5). PP. 463-68.

Syahid, M. A., Hayat, A., Arief, S. & Rudi, A (2020). Fatigue strength Improvement of Low Carbon Steel through Carburizing Process with Coconut Shell Charcoal. IOP Conference Series: *Material Science and Engineering* 575 (012064): 1-7. Doi: 10.1088/1757-899X/875/12064.

Umunakwe, R., Okoye, O. C., Madueke, C. I. & Komolafe (2017). Effect of Carburization with Palm Kernel/Coconut Shell Mixture on the Tensile Properties and Case Hardening of Low Carbon Steel. *Fuoye Journal of Engineering and Technology*. 2(1): 101-5. Doi: 10. 46792/fuoye.et v2i.83.

PAPER 185 – GREEN HYDROGEN PRODUCTION FROM PHOTOVOLTAIC POWER STATION AS A ROAD MAP TO CLIMATE CHANGE MITIGATION

K. R. Kamil[1*], A. Regillo[2], A. O. Yusuf[3]

[1]Fellow, Open Africa Power (OAP 2022), Enel Green Power, Rome, Italy.
[2]Head of Enel Open Innovation, Hubs and Startups, Enel Green Power, Enel Foundation, Rome, Italy.
[3]Department of Electrical and Electronics Engineering, Faculty of Engineering and Technology, University of Ilorin, Ilorin, Nigeria.
[*]Email: kehinde.kamil@nbrri.gov.ng

ABSTRACT
Hydrogen is increasingly recognized as a critical element in the global net-zero transition. Addressing climate change is increasingly urgent, and hydrogen's role as a decarbonisation vector in hard-to-abate sectors is clear. Africa enjoys high renewable energy capacity factors ranging from 28% to 36% for solar according to global solar irradiance index report. According to IRENA, 96% of all hydrogen produced today comes from fossil fuels. Only 4% is produced by water electrolysis. Realizing green hydrogen fuel ambition would have significant positive socio-economic effects across the continent. This study discusses the Africa green hydrogen production industry using Nigeria as a case study to enunciate the possibility of generating clean hydrogen vectors from a percentage of the Photovoltaic power output of a standalone solar grid electrification project in different regions in the country. The usage analysis and effectiveness of the produced hydrogen fuel in each region is carried out with the highest region having an annual output of 12,247,278 kg of green hydrogen and 8,573,094 kg of ammonia, expected production from the proposed usage of 50 % of the power generation output of the installed 1.6 MWp solar power mini-grid in the region. The analysis was repeated for the other considered regions in the country. The results showcased the enormous advantages of electrolytic production of hydrogen and how the greener economy project can play a major role in mitigating climate change effects and overreliance on fossil fuels as the driver of the economy in many Africa countries.

KEYWORDS: renewable energy, photovoltaic, climate change, green hydrogen vector, fossil fuels, electrolysis

4. INTRODUCTION

The increasing reliance on fossil fuels and the associated problems have spurred a greater interest in the production and utilization of clean energy sources (IEA G20, 2020). Non-renewable energy sources like gas, oil, and coal make up a significant portion of total energy consumption, which can lead to various economic, political, and environmental issues (IEA Renewable, 2023). Therefore, in recent years, there has been a growing focus on hydrogen as an efficient and clean energy source, which has the potential to mitigate the negative impacts of fossil fuel usage on the environment (Fereidooni et al, 2018). Although the primary applications of hydrogen currently include the production of ammonia, soil enrichment, and the production of methanol and other chemical compounds, it is increasingly being recognized as a viable source of clean energy (Mostafaeipour et al, 2020).

The competitiveness of producing green hydrogen can vary depending on several factors, including local resources, proximity to demand, and infrastructure availability, at regional, national, and project-specific levels. Sunlight represents a crucial and sustainable energy source, and the energy it provides to the Earth's surface is many times greater than the total energy consumption of humans (RAYmaps, 2022). The issue of global warming and the affordability of modern photovoltaic (PV) systems, as opposed to traditional ones, have encouraged the use of PV cells to increase the production of clean energy. While there has been substantial progress in the efficiency of PV cells, with current efficiency reaching around 29%, their efficiency in commercial applications remains in the 10-20% range, and they are not yet capable of fully replacing fossil-fuel-based electricity. Factors such as temperature and shading can affect the efficiency of PV cells, and thus, it is critical to accurately forecast and estimate the efficiency of PV systems under realistic weather conditions (Yohannes et al, 2022).

1.1 Solar Renewable Resources Potentiality in Africa Countries

The Sustainable Energy for All (SE4All) initiative, led by the United Nations (UN) and the World Bank in partnership with other organizations, aims to ensure access to sustainable energy for all by 2030, as part of a global effort. Sub-Saharan Africa's geographic location offers the potential for a significant contribution to global energy supply through solar energy, provided that adequate infrastructure is available (Climate-Champion, 2023 and Siemens Gamesa, 2023).

Nigeria, located in West Africa and with a landmass of 923,768 square kilometers, benefits from abundant sunshine throughout the year, as it is situated just above the equator. On average, Nigeria receives 6.5 hours of sunshine per day, with an average flux of 5.55 kWh per square meter per day. This means that Nigeria receives 4.851 x 10^{12} kWh of energy per day from the sun. Solar radiation intensities range from 3.5-7.0 kWh per square meter per day, increasing from south to north. This energy source could be available for 26% of the day, from 9:00 am to 4:00 pm. Given these facts and figures regarding Nigeria's geographic location, the potential for significant generation of electrical energy from solar power is very high in Nigeria (Kamil et al, 2021).

1.2 Relevant Properties of Hydrogen

Hydrogen contains more energy per unit of mass than natural gas or gasoline, making it attractive as a transport fuel. Nevertheless, being the lightest element, hydrogen has a lower energy density per unit of volume. Therefore, more significant volumes of hydrogen are required to meet the same energy demands as other fuels.

The different types of hydrogen vectors, classified by color, have varying degrees of CO2 emissions and environmental impact. Green hydrogen, obtained from water electrolysis powered by renewable energy, has a very low environmental impact and generates zero CO2 emissions. The colors classification of hydrogen vectors is as shown in Table 1.

Table 1. Type and properties of hydrogen vectors (Ferrara et al, 2023).

Hydrogen Vector Type	Properties
Brown Hydrogen	Obtained from coal gasification with more than 20 kg of CO2 emitted for every kg of hydrogen produced.
Grey Hydrogen	Obtained from steam reforming of natural gas with more than 9 kg of CO2 emitted for every kg of hydrogen produced.
Blue Hydrogen	Obtained with the same production method of grey hydrogen but with a partial capture, transport and storage of CO2. It emits up to 5kg of CO2 not captured for every kg of hydrogen produced
Pink Hydrogen	Obtained from the water electrolysis powered by nuclear energy. It has high environmental impact due to the production of nuclear waste even if it does not emit CO2.
Green Hydrogen	Obtained from the water electrolysis powered by renewable energy. It has very low environmental impact and generates zero CO2 emissions.

1.4. Green Hydrogen as a pathway to Sustainable Power Generation in Africa

Africa, as a continent, has a comparatively low contribution to global warming, responsible for less than 3% of the world's energy-related carbon dioxide (CO2) emissions to date. It also has the lowest emissions per capita of any continent (IEA, 2022). Despite this, Africa is among the most severely affected by the consequences of climate change, including increased frequency of extreme weather events, such as drought, delayed rainy seasons, or flooding due to excessive rains. Table 2 shows some of the pioneering green hydrogen production projects in Africa (Piebalgs et al, 2023).

Table 2. Pioneering Investments of African countries in Green Hydrogen generation (Piebalgs et al, 2023)

Country	Project Partner and Capacity	End Use
Egypt	100-3000 MW Renew Power	Mobility and Export
	4GW Masdar Project	Export and Industrial Feedstock
	100-3000 MW Siemens Project	Mobility and Export
	10MW Alfarnar green Ammonia	Industrial Feedstock
Namibia	100-3000 MW Daures Green Village	Various uses and Export
	10 MW Hydrogen Refueling Station	Mobility
South Africa	10MW Anglo American Mining Truck	Mobility
	ArcelorMittal DRI MoU	Industry Feedstock

Morocco	3 GW HEVO Ammonia	Industrial Feedstock and Export
Algeria	Sonatrach and Eni Hydrogen pilot project	Various Use
Mauritania	3GW AMAN Ammonia 3MW Total and Chariot Nour Green Hydrogen Project	Various Use and Export Industrial Feedstock and Export

By exploiting the abundant renewable resources of the continent to produce GH2, Africa can stimulate local socio-economic growth, strengthen regional energy security, and help ease poverty. The development of green hydrogen in Africa can bring substantial benefits to the continent, such as the building of a green economy in African countries, the improvement and acceleration of access to energy, the creation of jobs, and potentially improving access to power and fresh water.

This study uses Nigeria, a country in the western hemisphere of Africa, as the case study to examine the possibility of producing and using green hydrogen from commissioned photovoltaic grid systems in different regions of the country. It discusses how the generated hydrogen fuel can service numerous industrial and commercial needs as an alternative to fossil fuels. The study will expose how green hydrogen can act as an enabler for climate change mitigation and a carbon-free energy ecosystem. This study aims to exploit the probability of producing green hydrogen from proliferating renewable photovoltaic grids in different regions in Nigeria to showcase the countries' potential to join African hydrogen-producing nations.

5. METHODOLOGY

2.1. Case Study Analysis and PV System Simulation

Renewable electrification projects from solar have started to make noticeable impact in the rural and alternative electrification of provinces in many African Countries. This section examines system design towards the production of green hydrogen from photovoltaic power plant. The availability of renewable power to support this concept will be carefully examined. By the end of 2019, Nigeria's estimated installed mini-grid capacity was about 2.8MW, with 59 projects serving rural consumers. These are mostly residential-based mini-grids with some developed for specific productive uses. If fully commercial-served mini-grids are included, the number is expected to be significantly higher (Bloomberg and SEforALL, 2020).
According to a spotlight report published by Rural Electrification Agency in Nigeria showcasing some mini-grid photovoltaic projects commissioned across the country. This study utilizes the information in proposing using a percentage of the photovoltaic electrical power outputs to generate sustainable green hydrogen in the same ecosystem (REA, 2022).

Table 3 shows the specifications and locations of the solar grid projects considered in this study. The photovoltaic solar potential in the considered regions is obtained from Global Atlas SolarGIS of different countries. The webpage provides an aggregated and harmonized solar resource and PV power potential from the perspective of different countries and their regions. Solar Irradiance is the quantity of power received from the sun at a point on the Earth's surface measured in Wh/m^2 or kWh/m^2.

Table 3. Considered Photovoltaic Stand-alone Grid and their Capacity (REA, 2022 and Global Atlas, 2023)

Country Location (PV Grid Region)	**Size of the Photovoltaic mini-grid Project**	**SolarGIS Annual Photovoltaic**
North Central Region **(PV Grid Region A)**	80 kWp solar mini-grid at an isolated community in Ajaokuta, Kogi State.	1448.3 kWp
South South Region **(PV Grid Region B)**	100 kWp solar hybrid LGA Akwa Ibom State community in Onna	1168 kWp
South East Region **(PV Grid Region C)**	100 kWp solar mini-grid at Eka-Awoke community, Ikwo LGA- Ebonyi State.	1314 kWp

North West Region **(PV Grid Region D)**	1.6 MWp of solar power Sabon Gari Market Grid Project.	1607 kWp
North East Region **(PV Grid Region E)**	85 kWp solar mini-grid at Dakiti community in Akko LGA - Gombe State	1753 kWp
North East Region **(PV Grid Region F)**	91 kWp solar mini-grid in sarkin Kudu community, Taraba State.	1557.5 kWp

2.2. Simulation for the expected Annual Power Generation in PV Region A

The annual performance of individual photovoltaic power projects will be used in estimating the quantity of green hydrogen produced through electrolysis. In the electrolysis process, water molecules will split into their constituent elements.

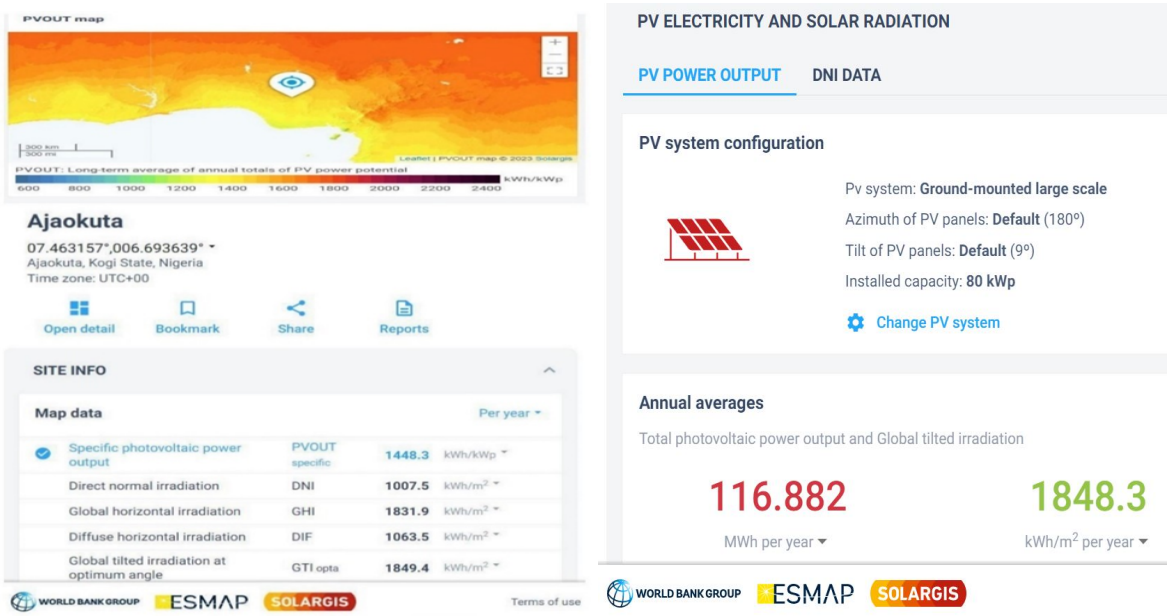

Fig. 2. SolarGIS Annual Specific Photovoltaic Power output in PV Grid Region A and the simulation result for the for 80kWp grid system

Estimating for the power generation for the first considered PV grid system installed in Region A, an 80 kWp solar mini-grid at an isolated community in Kogi State using the available photovoltaic resources from SolarGIS of the region. The site specific PV potentiality obtained from SolarGIS was used in the design simulation carried out on Global Solar Atlas, as shown in Fig .2. To start with, it is important to stress that the efficiency of a solar panel is a matter of area, not power. Let us assume we want to install 300 Wp solar panels. We would need 267 numbers of solar panels to achieve 80kWp. The simulation result for the case study PV Region A in Ajaokuta, Kogi State, Nigeria, where the grid has been commissioned. The grid configuration in the simulated design is ground-mounted as installed on the site. The simulation result shows that a total of 116.882 GWh or 116,882 kWh per year is the expected generation. The system design will be in a hybridized form whereby an equal percentage of the generated photovoltaic power in the considered regions will service the province's primary need and supply the proposed green hydrogen generation plant in the area. Fig .3. shows the monthly and daily photovoltaic generation from the stand alone PV grid system. The highest generation is in November with a peak hourly photovoltaic power output of 55.1 kWh.

Fig. 3. The monthly and hourly distribution of the photovoltaic power output in PV Grid Region A

Green hydrogen production, as proposed in this study, helps in creating carbon-free sustainable energy. According to the obtained result of the annual generation from the photovoltaic power station. Utilizing 50% of the photovoltaic power output to produce hydrogen through electrolysis. In the process of electrolysis, water molecules splits into their constituent elements as shown in (Eq. (1).

$$H_2O\ (liquid) \rightarrow H_2\ (gas) + 1/2O_2\ (gas) \qquad (1)$$

Electrolysis requires electrical power to split apart the water molecules. In other words, generating 1 gram (1 kg) of hydrogen requires 9 grams (9 kg) of water based on the stoichiometric values with the assumption of no losses in the electrolysis process. The amount of power needed is defined by the higher heating value (HHV) of hydrogen divided by the electrolyze system efficiency (Goldmeer, 2019)

$$Electrolyzer\ Power = \frac{HHV}{System\ Efficiency} \qquad (2)$$

The HHV for hydrogen is 12,756.2 kJ/Nm3 (141,829.6 kJ/kg); this is equivalent to 3.54 kWh/Nm3 (39.39 kWh/kg). Assuming a 70% efficiency of PEM electrolyzer system, which represents commercially available technology. The photovoltaic power will be used as a clean alternative power in servicing the power requirement of the electrolyzer (Goldmeer, 2019 and Patrik et al, 2016).

Therefore, in PV Grid Region A using 50 % of the power output of the 80kWp PV grid system for hydrogen production will be:

$$116882\ kWh\ x\ 50\% = 58441\ kWh \qquad (3)$$

The formula for calculating hydrogen production from electrolysis can be given as:

$$m = \frac{z * F * I}{96485 * V} \qquad (4)$$

Where m is the mass of hydrogen produced (in grams), z is the number of electrons involved in the electrolysis reaction, F is the Faraday's constant (96485 C/mol), I is the current flowing through the electrolytic cell (in Amperes), and V is the voltage applied across the electrodes (in Volts). The formula assumes 100 % Faraday efficiency that is not realistic in industrial production of hydrogen. Since we have the photovoltaic energy output instead, hydrogen production can be given as:

$$m = \frac{P}{\eta * E\_H} \qquad (5)$$

Where m is the mass of hydrogen produced (in grams), P is photovoltaic energy input (in kWh) and E_H is the energy required to produce one mole of hydrogen (in kJ/mol).

$$E\_H = \frac{\Delta H°f}{\eta_{electrolysis} * \left(\frac{1}{molar} mass\ of\ hydrogen\right)} \qquad (6)$$

ΔH°f = standard enthalpy changes of formation of hydrogen (approximately 285.8 kJ/mol), efficiency (η) of a Proton Exchange Membrane (PEM) electrolyzer can be assumed to be 70% depending on the operating condition of the temperature of the electrolysis water, pressure, and current density. The molar mass of hydrogen is in grams/mol (approximately 1.0079 g/mol) (Goldmeer, 2019).

$$E\_H = \frac{285.8}{0.7 * \left(\frac{1}{1.0079}\right)} = 411.52kj/kg \quad (7)$$

Therefore, calculating the hydrogen production in region A with the photovoltaic power out of 58441 kWh or 210,387,600 kJ as we are working with energy value from direct source and the standard unit of energy in the International System of Units (SI) is the joule.

$$m = \frac{58441 * 3600}{411.52} = 511{,}245\ kg \quad (8)$$

Using photovoltaic energy of 58,441 kWh, we can estimate the production of approximately 511,245 kg of green hydrogen from PEM electrolysis. Since the electricity for the electrolysis process comes from renewables (solar), there is no 'direct' release of CO2 when generating or burning hydrogen. The schematic in Figure 4. shows how the produced hydrogen gas can be utilized in different sectors of the country's economy.

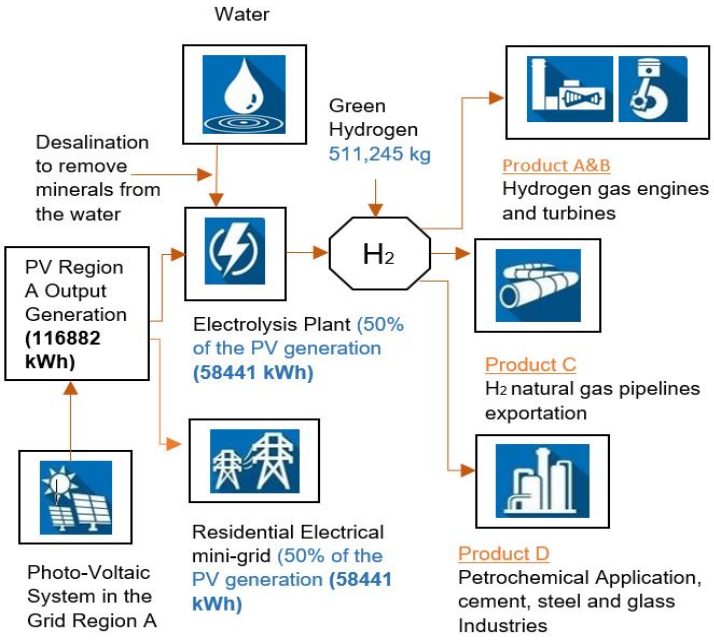

Fig. 4. The schematic showing the distribution of PV Grid Region A power output

Hydrogen production for the conventional steam methane reforming (SMH) and electrolysis of water involves the release of carbon dioxide to the atmosphere during the process. Green hydrogen production from electrolysis of water as proposed in this study will help in alleviating the environmental treats associated with Hydrogen production for commercial and industrial use (Masdar, 2022).

The procedure was repeated for the other commissioned solar grid projects in the remaining five (6) geopolitical zones. The Table. 4 below gives the output green hydrogen generation when 50 % of the annual output photovoltaic power output was used for hydrogen production.

Table 4. Green Hydrogen gas production from PV output in different region.

Photovoltaic Project	**Expected Annual PV e lectricity utilized (50% of the total PV output)**	**Expected Hydrogen production (kg)**
80 kWp solar mini-grid at an isolated community Ajaokuta, in Kogi State	58441 kWh	511,245 kg in PV Grid Region A
100 kWp solar hybrid LGA - Akwa Ibom State community in Onna	63899 kWh	558,992 kg in PV Grid Region B

100 kWp solar mini-grid at Eka-Awoke community, Ikwo LGA- Ebonyi State.	63899 kWh	558,992 kg in PV Grid Region C
1.6 MWp of solar power Sabon Gari Market Grid Project.	1400 MWh	12,247,278 kg in PV Grid Region D
85 kWp solar mini-grid at Dakiti community in Akko LGA - Gombe State	72182 kWh	631,452 kg in PV Grid Region E
91 kWp solar mini-grid in sarkin Kudu community, Taraba	71373 kWh	624,375 kg in PV grid Region F

3.0 RSULTS AND DISCUSSION

3.1. Hydrogen gas as a motor fuel (Product A)

When comparing hydrogen and diesel as motor fuels, various factors must be taken into account, including their energy content, efficiency, and emissions (Milan, 2021).

- Energy Content: On a mass basis, diesel fuel has a higher energy content than hydrogen, with an energy density of approximately 44 kWh/kg compared to around 33 kWh/kg for hydrogen. However, since hydrogen is a gaseous fuel, it can be stored in larger volumes, thus increasing its energy content compared to liquid fuels like diesel.

- Efficiency: Regarding efficiency, fuel cell vehicles utilizing hydrogen can be more effective than diesel vehicles. Hydrogen fuel cell vehicles can transform a larger portion of the stored energy in hydrogen into useful work compared to diesel vehicles, which usually experience energy losses due to factors such as friction.

- CO_2 emissions: In the studied regions analyzed, hydrogen produced from renewable energy sources is considered a green fuel due to its zero greenhouse gas emissions during combustion, while diesel fuel releases CO_2 and other harmful pollutants into the atmosphere when burned.

Deducing from the established relationship, 537,869 kg of hydrogen produced from PEM electrolysis in PV Grid Region A can provide more energy compared to the equivalent amount of diesel fuel and the use of hydrogen as a motor fuel has a lower environmental impact, as it produces no greenhouse gas emissions during combustion.

3.2. Green Hydrogen in the production of Ammonia (Product D)

Most hydrogen generated globally for ammonia production for fertilizers or petrochemicals comes from steam methane reforming, which releases carbon dioxide. However, the production of green ammonia involves a 100% renewable and carbon-free process. The Haber-Bosch process is a commonly used method for producing ammonia from hydrogen and nitrogen, where they are reacted under high pressure and temperature conditions to yield ammonia. The reaction can be expressed as follows:

$$N_2 + 3H_2 \rightarrow 2NH_3 \qquad (9)$$

Where N_2 represents nitrogen, H_2 represents hydrogen, and NH3 represents ammonia. The conversion efficiency of the Haber-Bosch process is typically around 70-80%. This means that for every 100 kg of hydrogen, 70-80 kg of ammonia can be produced (Guerra et al, 2019 and Yohannes et al, 2022).

Given the amount of green hydrogen from produced in Grid Region A form PEM electrolysis is 511,245 kg, the amount of green ammonia that can be produced using the Haber-Bosch process can be calculated as follows:

$$Green\ ammonia\ = 0.70\ to\ 0.80\ *\ 511{,}245\ kg \qquad (10)$$

$$Green\ ammonia\ = 376{,}810.3\ to\ 454{,}095.6\ kg \qquad (11)$$

Table 5. Ammonia production from the available hydrogen gas in each region

Green Hydrogen Produced	**Green Ammonia Equivalent Production (kg)**
PV Grid Region A production of 511,245 kg of Hydrogen	357,871.5 to 408,996 kg
PV Grid Region B production of 558,992 kg of Hydrogen	391294.4 to 447193.6 kg
PV Grid Region C production of 558,992 kg of Hydrogen	391294.4 to 447193.6 kg
PV Grid Region D production of 12,247,278 kg of Hydrogen	8,573,094 to 9,797,822.4 kg
Grid Region E production of 631,452 kg of Hydrogen	442,016.4 to 505,161.6 kg
Grid Region F production of 624,375 kg of Hydrogen	437,062.5 to 499,500 kg

3.3. Green Hydrogen usage in Gas Turbine Engines (Product B)

Gas turbine engines that are powered by green hydrogen have a higher energy efficiency than those fueled by fossil fuels. This is because hydrogen has a higher energy density per unit of volume and a lower ignition temperature, resulting in a more efficient combustion process. However, operating a gas turbine on a hydrogen/natural gas blend instead of using 100% hydrogen reduces the required amount of hydrogen flows (Goldmeer, 2019).

In terms of power generation volumes, a single General Electric (GE) 6B.03 gas turbine operating 8,000 hours annually would require approximately 33 million kg of H2 per year. If the hydrogen were generated via steam methane reforming, it would produce around 178,000 metric tons of CO2 annually (GE, 2023).

3.4 Economic Viability of Green Hydrogen Production Plant

3.4.1. Availability of Water Source to support Electrolysis Process

Enormous availability of water resources in Nigeria favors the consideration of green hydrogen projects in the country. However, it advisable to extract the water required from the wide spread streams and rivers in different regions of the country to avoid water resources competition with residential usage of water at any point of construction of a green hydrogen plant projects. As shown in the schematic in Figure 4, the desalination process helps in removing impurities or minerals that may be present in the water, as these can have a negative impact on the efficiency and performance of the electrolysis process.

PV Grid Region A is located in Ajaokuta, where there are abundant water bodies, including rivers and streams. Some of the major rivers in the area include the Niger River and its tributaries, such as the Anambra River and the Benue River. Furthermore, PV Grid Region B is located in Onna, Akwa Ibom where some of the major rivers in the area include the Cross River, which is the largest river in the region, and its tributaries, such as the Kwa River and the Imo River. These rivers provide a source of water for domestic, agricultural, and can serve industrial usage in green hydrogen production plant.

In general, it is estimated that to produce 1 gram of hydrogen through electrolysis, around 9 grams of water is required based on stoichiometric values and assuming no losses in the process This is because the reaction of splitting water into hydrogen and oxygen requires a certain amount of energy, and the amount of water used in the process reflects the amount of energy required (Vaughan et al). However, the actual energy consumption may be higher due to the energy losses during the process, so the energy efficiency of electrolysis can vary.

4.0 CONCLUSION

Electrolysis is not a new idea, but the use of renewable energy sources to power the electrolytic production of hydrogen is gaining investment interest in various countries worldwide. So as not to fall behind, African nations must also begin exploring opportunities in this area. Many African countries have an abundance of renewable photovoltaic energy resources, and they should take a cue from developed countries and invest in green hydrogen production. Nigeria, as discussed in this study, has yet to consider this direction. The study's analysis reveals that the countries viability of generating green hydrogen in different regions of the country.

This study analysed six different regions for green hydrogen production and found that PV Grid Region D, situated in the northern part of the country where solar intensity is highest, produced the greenest hydrogen among the

regions studied. This region has an annual output of 12,247,278 kg of green hydrogen and 8,573,094 kg of ammonia can be produced from it. Considering the abundant availability of water resources in African countries and the continuous fall in the price of deploying renewable energy projects, Nigeria and other African countries should consider investing more in this sector to promote carbon neutrality.

REFERENCES

A. Mostafaeipour, M. Khayyami A. Sedaghat, . Sedaghat (2020). Evaluating the Wind Energy potential for hydrogen production" International Journal of Hydrogen Energy pp 1-11.

A. Piebalgs, E. Zigah (2023). Has COP27 accelerated the development of Green Hydrogen in Africa?" Energy and Climate, Florence School of Regulation, https://fsr.eui.eu/has-cop27-accelerated-the-development-of-green-hydrogen-in-africa/ (accessed:2023).

A. Vaughan (2016). Almost 90% of new power in Europe from renewable sources in 2016" The Guardian,https://www.theguardian.com/environment/2017/feb/09/new-energy-europe-renewable-sources-2016?_sm_au_=icH71r6FFm6sl06H. pp. 345-247.

Bloomberg, SEforALL (2020). State of the Global Mini-grids Market Report, 2020. https://www.seforall.org/publications/state-of-the-global-mini-grids-market-report-2020 (accessed: 2020).

B. Milan, H. Catlyne, J. Page (2018). Green Industrialisation and Entrepreneurship in Africa". The Global Commission on the Economy and Climate, The New Climate Economy. pp. 4-6.

B. Yohannes, A. Diedou, (2022). Africa Renewal E-Magazine Green Hydrogen, A viable option for transforming Africa's energy sector, 2022.

C. Ferrara (2023). From Green to Sustainability, Enel Green Power Learning Hub" https://www.enelgreenpower.com/learning-hub/renewable-energies/hydrogen.

Climate Champion (2023). Green Hydrogen Catapult, Race to Zero and Race to Rsilience", www.climatechampions.unfccc.int/ (accessed January, 2023).

GE Future of Hydrogen Gas Power "Hydrogen and CO2 Emmission Calculator" https://www.ge.com/gas-power/future-of-energy/hydrogen-fueled-gas-turbines/hydrogen-calculator (accessed: 2023).

Global Solar Atlas (2023). Energy Data Info" https://globalsolaratlas.info/download/nigeria (accessed: 2023).

Guerra, O. J., Eichman, J., Kurtz, J., Hodge, B. M (2019). "Cost competitiveness of electrolytic hydrogen". J.Joule 3, pp. 2425–2443.

J. Goldmeer (2019). POWER TO GAS: HYDROGEN FOR POWER GENERATION, Fuel Flexible Gas Turbines as Enablers for a Low or Reduced Carbon Energy Ecosystem" General Electric Power (GEA33861), 2019.

K. Kamil, A. Yusuf, A. Sharif, S.B Seriki, (2021). Renewable Energy Hybridization as an Efficient and Cost-Effective Alternative for Electrification. Nigerian Journal of Technology Development. Vol. 19. pp. 2437-2110.

IEA for the G20, (2020). The Future of Hydrogen, Seizing todays Opportunities, Report prepared by the IEA for G20, Japan Technical Report TR-95-012.

IEA Renewable, 2022. How much will renewable hydrogen production drive demand for new renewable energy capacity by 2027" Fuel Report prepared by IEA Analysis and Statistics.

Masdar, (2022). "AFRICA'S GREEN ENERGY REVOLUTION Hydrogen's role in unlocking Africa's untapped renewables" Abu Dhabi Sustainability Week (2022). pp 12-13.

M. Fereidooni, A Mostafaeipour, V. Kalantar (2018). A Comprehensive evaluation of Hydrogen Production from Photovoltaic Power Station" Renewable and Sustainable Energy Reviews 82(2018) pp. 414-423.

M. Patrik (2023). Run on Less with Hydrogen Fuel Cells" RMI Energy Transformed. https://rmi.org/run-on-less-with-hydrogen-fuel-cells/.

Siemens gamesa renewable Energy (2023). Green Hydrogen Fuel for the Future, Siemens Gamesa pilot Project www.siemensgamesa.com/en-int.

RAYmaps (2020). How to calculated the surface area required by Solar Panels, www.raymaps.com (accessed 2022).

Rural Electrification Agency (REA) (2022). 'NEP's achievement in the last two years, Spotlight on Rural Electrification Agency https://rea.gov.ng/reference-document/ (accessed: 2022).

PAPER 187 – CORROSION SUSCEPTIBILITY OF FOOD GRINDING DISCS IN GASTRO-INTESTINAL ENVIRONMENT

I.I. Ahmed[1,5], R. A. Yahya[1], T. Yahaya[1], S. I. Talabi[1], J. A. Adebisi[1], R. M. Mahamood[1], J. K. Odusote[1], M. K. Sulaiman[2], L. A. Olatunji[3], S. Abdulkareem[4]

[1]Department of Materials and Metallurgical Engineering, University of Ilorin, Ilorin, Nigeria.
[2]Department of Parasitology, University of Ilorin, Ilorin, Nigeria.
[3]Department of Anatomy, University of Ilorin, Ilorin, Nigeria.
[4]Department of Mechanical Engineering, University of Ilorin, Ilorin, Nigeria
[5]Department of Metallurgical and Materials Engineering, Air Force Institute of Technology, Kaduna, Nigeria
[*]Email: ahmed.ii@unilorin.edu.ng

ABSTRACT
The need for food size reduction before consumption has led to the use of motorized grinding machine which operates on energized rubbing of two grooved cast-iron discs, and this unintentionally results in tribological degradation and corrosion of grinding discs into the ground food. Six grinding discs from three states in Nigeria were selected for this study, based on manufacturing methods namely: rotary, cupola and pit furnaces, for assessment of their corrosion susceptibility in a simulated gastro-intestinal environment. The electrolyte used contained 2 g/L NaCl acidified to pH of 1.7 with HCl and regulated at 37°C. Experimental techniques used for the study included: XRF for chemical composition and XRD for phase identification. Corrosion susceptibility of discs in pseudo-body fluid was studied using potentiodynamic polarisation scan and gasometric methods in simulated gastro-intestinal environment, as electrolyte. Key finding from the study was that all grinding discs contain iron and silicon as dominant alloys, which existed as iron carbide and ferrosilicon phases. Corrosion of discs in simulated gastric solution was well profound irrespective of the manufacturing method, though, with varying degrees among the discs. The outcome of this study is applicable to food industries to minimise the risk of food contamination from corrosion.

KEYWORDS**:** grinding disc, corrosion, potentiodynamic, gasometry, gastric, food contamination

1. INTRODUCTION

Size reduction is a food processing technique often carried out before consumption, particularly grains and vegetables. The traditional tools often used for the processing include stones (Anthony et al., 2013), pestle and mortar (Nnaji & Emmanuel, 2016), which are relatively effective but inefficient and time-consuming. The ever-increasing population further demanded faster and more efficient processing methods. This resulted in development of age long technology which operates on energized rubbing of two grooved cast-iron discs, that still dominates food grinding hitherto. The mode of its operation results in tribological degradation and galvanic corrosion of discs when in contact with water. Hence, persistent wearing and corrosion of the grinding discs during food processing may end up contaminating ground food with far reaching implications on health and safety of citizenry feeding on ground foods. Data from the World Health Organization affirms, that approximately 10% of individuals fall ill globally from eating contaminated food thus leading to 420,000 deaths annually (World Health Organization, 2015). Hence, consumption of processed foods laden with metal chips and corroded particles, in most households which rely on grinding machine for processing staples grains (such as millets and sorghum) particularly in Africa and Asia, may constitute health risk that requires urgent attention. The aim of the research was to conduct assessment of corrosion susceptibility of food grinding discs in gastro-intestinal environment, a bid to understand the chemical interaction of ingested disc particles with food into human alimentary canal system.

2. MATERIALS AND EXPERIMENTAL PROCEDURE

2.1 Materials

The cast iron grinding discs (Figure 13) used for the study were sourced from two states in Nigeria (Osun and Kwara) and one imported from India based on manufacturing methods namely: rotary, cupola and pit furnaces. Traditionally, food grinding discs are often produced from scrap cast irons with little or no quality control measures. A total of six samples used for the research and nomenclature adopted for each are shown in Table 16

Figure 13: Grinding disc

Table 16: disc nomenclature and source location

Disc Name	Production furnace	Source location
ROS	Rotary	Osun
RIL	Rotary	Kwara
RIW	Rotary	Osun
PIL	Pit	Kwara
CIW	Cupola	Osun
ID	N/A	India

EXPERIMENTAL PROCEDURE

2.2 Determination of Chemical Composition

Elemental chemical composition analysis was carried out on disc samples using XRF Mini Pal 4 version PW 4030 operated at 30 keV. Samples subjected to metallographic sample preparation were examined using XRF spectrometer installed with Mini Pal analytical software designed for detection and measurement of elements in samples for qualitative and quantitative chemical composition analyses.

2.3 Phase Identification with XRD

X ray diffraction was carried out on cast samples using Panalytical Empyrean X-ray Diffractometer for identification of metallurgical phases present in the samples. XRD data were collected with a copper (Ka-XRD-740) anode radiation tube. A divergence and scatter slit of 1.0° each and a receiving slit of 0.3 mm were used. The power rating of the X-ray generator used was 40 mA and 45 kV. Six samples from different manufacturing methods were examined at ambient temperature. X-ray intensities were measured at Bragg angle 2θ (Ahmed et al., 2018) between 15° and 80 ° and at a continuous scanning speed of 10°/min. A sampling pitch of 0.1° and the preset time of 0.6 s were used for all the samples.

2.4 Potentiodynamic Polarisation Scan and Gasometry

Corrosion susceptibility of samples were assessed using potentiodynamic polarization scan in line with ASTM G61 standard and gasometry methods. Polarization scan was conducted in a 170 ml standard three-electrode electrochemical cell using Corrtest EIS Potentiostat/Galvanostat model CS150 installed with analytical software. Each sample of 1 cm^2 was spot welded with conducting wire and then mounted in cold resin. Metallographic sample preparation was done prior to polarization scan. The sample was connected to Potentiostat through the working electrodes terminal, while platinum wire was used as a counter electrode and saturated calomel (Ag/AgCl in KCl) electrode was used as reference electrode. The Simulated gastro-intestinal solution used as electrolyte contained 2g/L of sodium chloride (NaCl) acidified to pH of 1.7 with HCl and maintained at 37 °C which is typical of the human body system. Open circuit potential (OCP) was carried out for 300 seconds and then polarization scan at the rate of 0.2 mV/s between 0.1 to OCP and 0.3 V to OCP.

The measurement of corrosion product by gasometric measurement of hydrogen gas evolution from samples immersed in a simulated solution over a given time was also carried out. The surface area of the samples was measured before insertion into the conical flask containing 100 ml of simulated solution for 120 minutes, in line with the method and setup reported elsewhere (Huang et al., 2007).

3. RESULTS AND DISCUSSION

3.1 Chemical composition Analysis with XRF

The results of X-ray Fluorescence spectroscopy are shown in Table **Error! Reference source not found.**. The r esults showed iron as the dominant element in their alloy composition. The exceptionally low Fe composition of 65.169 and 57.423 wt% in RIL and CIW sample respectively could be attributed to high amount of oxygen probably from oxides which amount to 29.593 and 23.617 wt% respectively.

Table 17: Elemental chemical composition (wt%)

Element	Fe	Si	Al	Mg	Ca	Cr	Mn	O	Co	Cu	Sn
ROS	88.86	4.22	3.53	0.65	0.25	0.17	0.59	0.00	0.29	0.15	0.00
RIL	65.17	0.96	1.92	0.02	0.85	0.00	0.03	29.59	0.04	0.05	0.52
RIW	92.52	2.09	2.98	0.00	0.61	0.13	0.07	0.00	0.26	0.04	0.05
PIL	92.97	1.47	2.30	0.00	0.68	0.11	0.26	0.00	0.22	0.23	0.06
CIW	57.42	3.80	1.91	2.29	4.34	0.01	0.08	23.62	0.01	0.04	2.03
ID	92.08	2.04	2.63	0.00	0.58	0.27	0.64	0.00	0.19	0.12	0.31

The rest four samples (ROS, RIW, PIL and ID) contain Fe composition which ranges between 88.855 and 92.966 wt%. Aluminum and Silicon alloy elements were also observed to be present in considerable proportion. The elemental chemical composition is characteristic of cast iron particularly the ROS, RIW, PIL and ID.

3.2 X-Ray Diffraction

The results of XRD are shown in Figure 14 containing diffraction spectra of disc samples. All the six samples revealed the presence of iron carbide (Fe_3C) and significant amount of ferroalloys, which was observed in four of the samples tested except PIL and ID. This is an indication that all the discs are cast iron. There was also a spectrum of magnetite (Fe_3O_4) observed in CIW sample. This observation is consistent with the XRF result which showed a significant amount of oxide in CIW sample.

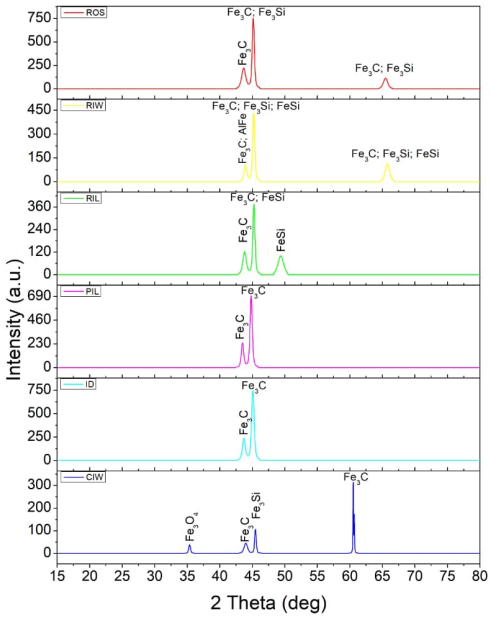

Figure 14: X-ray diffractometry of grinding disc samples

3.3 Corrosion Test Open Circuit Potential

The results of open circuit potential of all the discs are shown in the Figure 15 as a plot of potential vs reference electrode (saturated calomel electrode) against time. The results showed the order of nobility of the tested discs based on their respective OCP and then benchmarked with austenitic stainless steel; type 304 (ASS 304) widely used globally for food processing. Expectedly, ASS 304 appeared as the most noble with OCP of -0.374V after 300s. The order of nobility of all the disc tested including stainless steel, was ASS>PIL>ROS>RIW>CIW>RIL>ID. Among the cast iron disc tested, PIL and ID disc was ranked highest and lowest in order of nobility with OCP of -0.432 and -0.446 V respectively. The order of nobility suggests that PIL is likely to be more resistant to corrosion susceptibility and ID appeared to be most vulnerable to corrosion

degradation into the ground food. However, there was no significant indication of the effect of disc manufacturing method on the observed results.

3.4 Potentiodynamic Polarisation Scan and Gasometry

The results of potentiodynamic polarization scan carried out on disc sample is shown in Figure 16. The ASS 304 used as benchmark showed corrosion potential which is significantly higher that cast irons samples with corrosion potential measured at - 0.36387 V. ID sample observed to have the least nobility with corrosion potential of -0.44288 V. This is consistent with result of the OCP although slight difference in order of nobility based on marginal difference in their respective corrosion potential. The order of nobility of the overall samples is ASS>RIW>ROS>PIL>CIW>RIL>ID. On the transpassive region of the polarisation curve, the observed order of nobility was ASS>PIL>ROS>CIW>RIL>ID>RIW. This is a region that characterise the localised corrosion where corrosion rate is more potent probably due to presence of aggressive corrosion species including chloride ion.

The results of gasometric tests are shown in Figure 17. The hydrogen evolution from the reaction between the metallic materials and acidic gastric solution caused water displacement which was measured. The early and consistently higher evolution of hydrogen gas from cast iron discs is an indication of higher corrosion rate occurring on cast iron discs compared to the stainless steel which is an alloy steel. Chromium in steels is reputed for formation of Cr-oxide film that protects subcutaneous layer from aggressive environment (Ahmed et al., 2017).

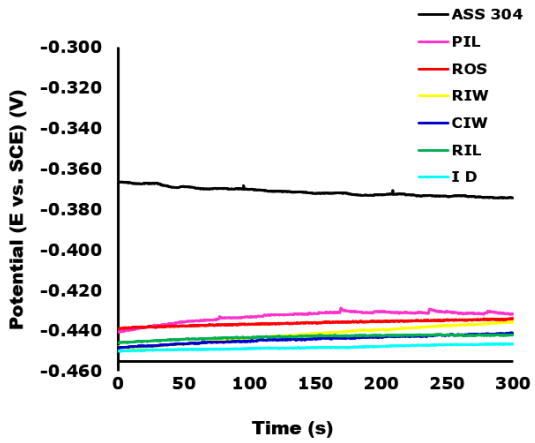

Figure 15: Result of open circuit potential of disc in simulated gastro-intestinal solution

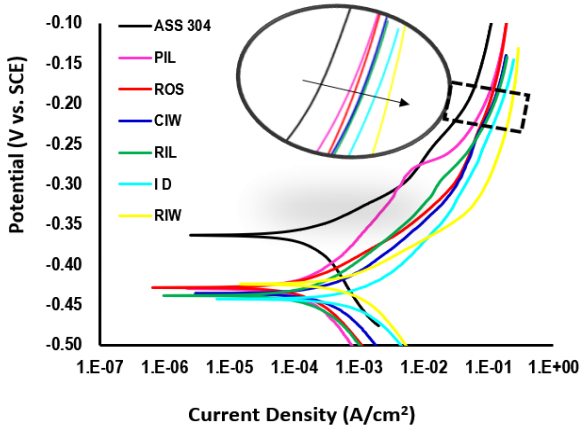

Figure 16: Potentiodynamic polarisation scan of ASS 304 and cast iron samples

The order of corrosion susceptibility from the plot of hydrogen evolution against the time at immersion time of 120 minute (Figure 17), is CIW>ID>RIL=CIW>ROS>PIL>ASS 304. The results of gasometric study are consistent with transpassive corrosion in potentiodynamic polarization scan of the discs when exposed to simulated gastric solution for 300 second.

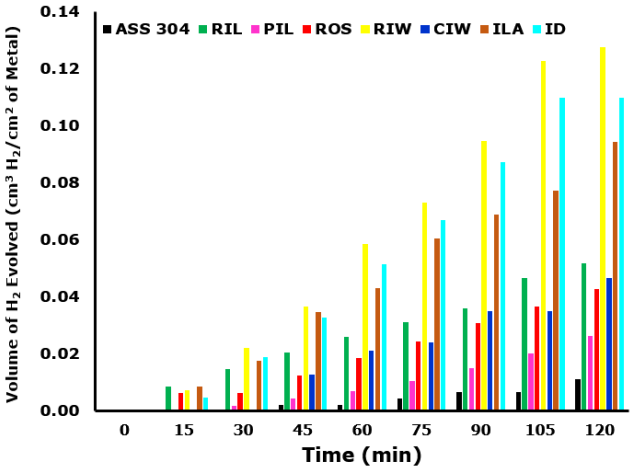

Figure 17: Gasometric study of discs in simulated gastro-intestinal solution at regular interval

4. CONCLUSIONS

The research on corrosion susceptibility of the food grinding discs in gastro-intestinal environment have been carried out and the following are the conclusions at the end of the study: Chemical composition showed significant amount of iron, silicon and aluminum which appeared as iron carbide and ferroalloys, an indication that all discs tested are cast irons. Corrosion test on the disc by open circuit potential (OCP), potentiodynamic polarization scan and gasometry did not show any indication of effect of manufacturing method on corrosion susceptibility of the discs. The ranking order of nobility of the grinding discs based on marginal difference in electrode potential showed ID and RIW as the most susceptible to corrosion, while PIL was found to be more noble.The nobility of austenitic stainless steel (ASS 304) compared to cast iron disc, suggests prevalence of galvanic corrosion between the grinding discs and other steel materials rather than between the discs.

ACKNOWLEDGEMENT

This research was funded by Tertiary Education Trust Fund under the auspices of National Research Fund with Grant Reference: TETF/DR&D-CE/NRF/2020/SETI/85/ Vol .1. The financial support is duly acknowledged.

REFERENCES

Ahmed, I. I., Adebisi, J. A., Abdulkareem, S., & Sherry, A. H. (2018). Investigation of surface residual stress profile on martensitic stainless steel weldment with X-ray diffraction. *Journal of King Saud University - Engineering Sciences*, *30*(2), 183-187. https://doi.org/https://doi.org/10.1016/j.jksues.2016.01.004

Ahmed, I. I., Adebisi, J. A., Sulaiman, A., & Andrew, H. S. (2017). Analysis of Intergranular Carbide Precipitate in HAZ of Martensitic Stainless Steel. *Journal of Engineering Science and Technology*, *12*(4), 1037-1047. http://jestec.taylors.edu.my/Articles%20in%20Press/12_10_8.pdf

Anthony, B., Ojekale, C., Chukwu, G., Oladipupo, L. O., & Titilola, S. (2013). Some Nigerian Traditional Food Milling Techniques and Cookware Increase Concentrations of Some Heavy Metals in Lycopersicon Esculentum and Citrullus Lanatus. *Iosr Journal Of Pharmacy*, *3*(3), 6-13.

Huang, J., Fisher, P. R., & Argo, W. R. (2007). A gasometric procedure to measure residual lime in container substrates. *HortScience*, *42*(7), 1685-1689.

Nnaji, J. C., & Emmanuel, P. N. (2016). Trace Metals in Food Condiments Processed with Manual Metallic Grinders. *The Phamaceutical and Chemical Journal*, *3*(1), 172-177.

World Health Organization. (2015). *Disease Outbreak News: Cholera – United Republic of Tanzania*. WHO. Retrieved 15/10/2020 from https://reliefweb.int/report/united-republic-tanzania/disease-outbreak-news-cholera-united-republic-tanzania

PAPER 190 – CORRELATION BETWEEN PRODUCTION METHODS AND TRIBOLOGICAL DEGRADATION OF FOOD GRINDING DISCS

J. A. Adebisi[1*], T. Yahaya[1], S. I. Talabi[1], R. M. Mahamood[1], I. I. Ahmed[1,5], J. A. Odusote[1], M. K. Sulaiman[2], L. A. Olatunji[3], S. Abdulkareem[4]

[1]Department of Materials and Metallurgical Engineering, University of Ilorin, Ilorin, Nigeria.
[2]Department of Parasitology, University of Ilorin, Ilorin, Nigeria.
[3]Department of Anatomy, University of Ilorin, Ilorin, Nigeria.
[4]Department of Mechanical Engineering, University of Ilorin, Ilorin, Nigeria
[5]Department of Metallurgical and Materials Engineering, Air Force Institute of Technology, Kaduna, Nigeria
[*]Email: adebisi.ja@unilorin.edu.ng

ABSTRACT
Staple foods consumed in Africa and Asia often require size reduction with the aid of grinding machine which operates on energized rubbing of two grooved cast-iron discs. This eventually results in tribological degradation of grinding discs into the ground food. In this study, six grinding discs from two geopolitical zones in Nigeria were considered based on four melting furnaces namely: rotary, cupola, pit and induction furnaces, to assess the correlation between their production methods and tribological degradation. Techniques used for the study included: X-Ray Fluorescence spectroscopy for determination of elemental composition; X-Ray Diffractometry was used for identification of phases; Vickers hardness test was carried out to determine hardness values of the discs and lastly, pin on disc wear tribometer was used to measure wear mass loss from discs. The study revealed that all grinding discs contain iron, carbon and silicon as dominant alloy elements, which existed predominantly as iron carbide and ferrosilicon phases. The hardness values measured ranged between 239-455 Hv20 with highest and lowest hardness values recorded in rotary and induction samples, respectively. Least and highest wear was observed in rotary and induction samples, respectively. Hence, strong correlation exits between hardness values and mass losses observed in tribological test. Findings from this study is relevant to food industries where control measures on materials selection and production routes may be adopted to minimise the risk of food contamination from tribological degradation.

KEYWORDS: grinding disc, hardness, wear, tribological degradation, friction, food contamination

1 INTRODUCTION

Foods grinding have always been necessary to achieve size reduction before consumption particularly grains and vegetables. The traditional tools often used for food grinding include stones (Anthony et al., 2013), pestle and mortar (Nnaji & Emmanuel, 2016), which are relatively effective but inefficient and time-consuming. The ever-increasing population further demanded faster and more efficient grinding methods, which resulted in development of grinding machine. Grinding machine operates on energized rubbing of two grooved cast-iron discs, which periodically wear out due to tribological degradation, and are still widely used in Asia and sub-Sahara Africa. The operation of grinding machine results in tribological degradation of pair of discs used for grinding due to frictional contact between one fixed and other rotating disc. Hence, persistent wearing of the grinding discs during food processing may end up contaminating ground food with far reaching implications on health and safety of citizenry feeding on ground foods. Data from the World Health Organization affirms, that approximately 10% of individuals fall ill globally from eating contaminated food thus leading to 420,000 deaths annually (World Health Organization, 2015).

The cast iron discs used by the grinding machine is a metallic alloy typically produced by artisan in metallurgical foundry from iron scraps which could be melted using different furnaces namely: Rotary, Cupola, Pit and Induction. The melt is then cast in disc shape by sand casting technique. The furnaces operate differently on the basis of energy source (fuel or electricity) used, and these may impact the quality of the cast produce, its alloy composition and performance in service. Hence, the aim of this research was to investigate if there is any correlation between the production methods and tribological degradation of the food grinding disc.

2 MATERIALS AND EXPERIMENTAL PROCEDURE

2.1 Materials

The cast iron grinding discs (Figure 13) used for this study were sourced, from 3 states in Nigeria (Osun, Kwara & Lagos) and one imported from India, based on manufacturing methods namely: rotary, cupola and pit furnaces.

Traditionally, food grinding discs are often produced from iron scraps with little or no quality control measures. A total of six samples used for the research and nomenclature adopted for each are shown in Table 16.

Figure 18: Grinding disc

Table 18: disc nomenclature and source location

Disc Name	Production furnace	Source location
ROS	Rotary	Osun
RIL	Rotary	Kwara
RIW	Rotary	Osun
PIL	Pit	Kwara
CIW	Cupola	Osun
ILA	Induction	Lagos
ID	N/A	India

Experimental Procedure

Determination of Chemical Composition

Elemental chemical composition analysis was carried out on disc samples using XRF Mini Pal 4 version PW 4030 operated at 30 keV. Samples subjected to metallographic sample preparation were examined using XRF spectrometer installed with Mini Pal analytical software designed for detection and measurement of elements in samples for qualitative and quantitative chemical composition analyses.

Phase Identification with XRD

X ray diffraction was carried out on cast samples using Panalytical Empyrean X-ray Diffractometer for identification of metallurgical phases present in the samples. XRD data were collected with a copper (Ka-XRD-740) anode radiation tube. A divergence and scatter slit of 1.0° each and a receiving slit of 0.3 mm were used. The power rating of the X-ray generator used was 40 mA and 45 kV. Six samples from different manufacturing methods were examined at ambient temperature. X-ray intensities were measured at Bragg angle 2θ (Ahmed et al., 2018) between 15° and 80 ° and at a continuous scanning speed of 10°/min. A sampling pitch of 0.1° and the preset time of 0.6 s were used for all the samples.

Hardness Test

The Vickers hardness test was carried out following ASTM E384 testing procedures. Metallographic sample preparations were carried out on test specimens to obtain a smooth surface prior to hardness test. The diamond indenter makes indention with applied load of 30 kgf on the test specimens for 10s. The average of the two diagonals of indentation produced was measured for calculation of Vickers Hardness Number (VHN) in kgf/mm^2 according to Equation 1.

$$\boldsymbol{Vicker\ Hardnss\ Number\ (HV)} = \frac{1.854\,P}{d^2} \qquad (1)$$

P = load (kgf), d = average of two diagonals of indentation (mm)

Wear Test

The wear test was carried out according to ASTM G99 standard procedure (ASTM, 2004) using a rotary stage pin on disc Anto Paar tribometer equipped with Instrum X analytical software. Metallographic sample preparations were carried out on test specimens to obtain a smooth surface. The specimen was mounted on the rotating spindle of the machine. A ball pin of 6mm diameter made of corundum ruby was used under a normal load of 10N. The test was done over a radius of 3.5 mm at a linear speed of 10 cm/s and the test ran for a duration of 600 sec in a dry condition at ambient temperature. The wear mass loss, V_{disk} from specimens after test was evaluated from Equation 2 on assumption there was significant pin (ball) wear.

$$\boldsymbol{V_{disk} = 2\pi R\left[r^2 sin^{-1}\left(\frac{d}{2r}\right) - \left(\frac{d}{4}\right)\left(4r^2 - d^2\right)^{\frac{1}{2}}\right]} \qquad (2)$$

d = wear track width, R = wear track radius, r = ball pin radius, e according to

3 RESULTS AND DISCUSSION

Chemical composition Analysis with XRF

The results of X-ray Fluorescence spectroscopy are shown in Table 19. The results showed iron as the dominant element in their alloy composition. The exceptionally low Fe composition of 65.169 and 57.423 wt% in RIL and CIW sample respectively could be attributed to high amount of oxygen probably from oxides which amount to 29.593 and 23.617 wt% respectively.

Table 19:Elemental chemical composition (wt%)

Element	Fe	Si	Al	Mg	Ca	Cr	Mn	O	Co	Cu	Sn
ROS	88.86	4.22	3.53	0.65	0.25	0.17	0.59	0.00	0.29	0.15	0.00
RIL	65.17	0.96	1.92	0.02	0.85	0.00	0.03	29.59	0.04	0.05	0.52
RIW	92.52	2.09	2.98	0.00	0.61	0.13	0.07	0.00	0.26	0.04	0.05
PIL	92.97	1.47	2.30	0.00	0.68	0.11	0.26	0.00	0.22	0.23	0.06
CIW	57.42	3.80	1.91	2.29	4.34	0.01	0.08	23.62	0.01	0.04	2.03
ID	92.08	2.04	2.63	0.00	0.58	0.27	0.64	0.00	0.19	0.12	0.31

The rest four samples (ROS, RIW, PIL and ID) contain Fe composition which ranges between 88.855 and 92.966 wt%. Aluminum and Silicon alloy element were also observed to be present in significant proportion. The elemental chemical composition is characteristic of cast iron particularly the ROS, RIW, PIL and ID.

X-Ray Diffraction

The results of XRD are shown in Figure 19 containing diffraction spectra of disc samples. All the six samples revealed the presence of iron carbide (Fe_3C) and significant amount of ferroalloys, which was observed in four of the samples tested except PIL and ID. This is an indication that all the disc are cast iron. There was also spectrum of magnetite (Fe_3O_4) observed in CIW sample. This observation is consistent with the XRF result which showed significant amount of oxide in CIW sample.

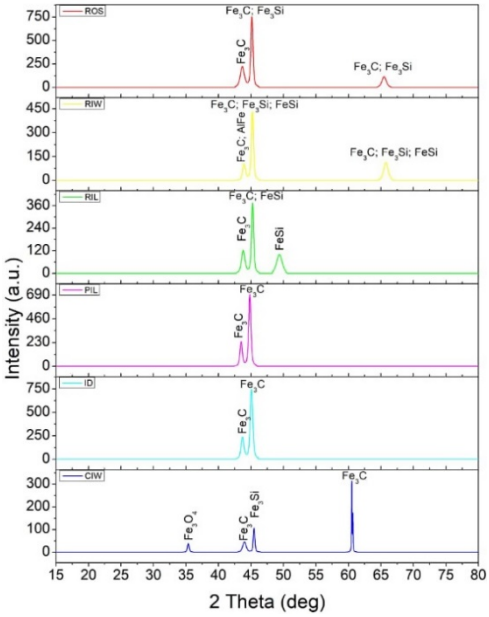

Figure 19: X-ray diffractometry of grinding disc samples

Hardness Test

The results of Vickers hardness test are shown in Figure 20. The Rotary furnace product, RIL, RIW and ROS disc has hardness values of 455, 452 and 443 HV respectively while induction furnace product, ILA disc was observed to have least hardness value of 239 HV. The cupola furnace product, CIW has hardness value of 447, which is marginally higher than rotary product, ROS. PIL disc produced by Pit furnace has a hardness value of 415 HV and the foreign disc from whose production method was not clearly understood has hardness value of 366 HV. The induction furnace products hardness values fair closely with typical austenitic stainless steel, 304 plotted as benchmark for comparison. The high hardness exhibited by rotary and cupola products may be attributed to lack quality control particularly on carbon, which may be introduced to melt from oil or diesel fuel used to fire rotary

furnace. In contrast, induction furnace used electric power supply and offers relatively good control of melt chemical composition by not introducing additional carbon into the melt. The hardness test therefore suggests possible correlation between production furnace and mechanical properties of the disc produced.

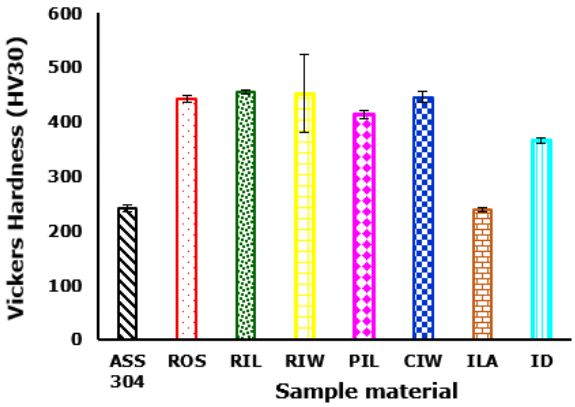

Figure 20: Vickers hardness values

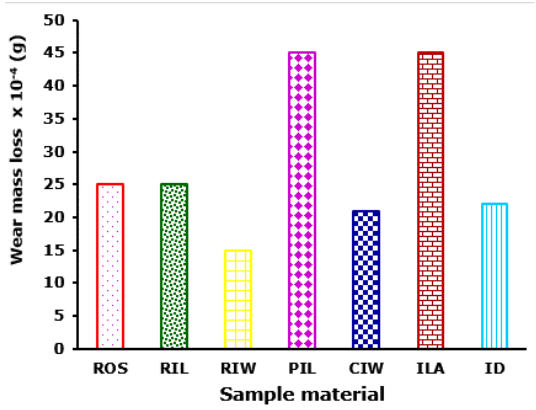

Figure 21: Wear mass loss

Wear Test

The results of wear mass loss are shown in Figure 21. The rotary furnace products, RIW, RIL and ROS were observed to have relatively lower wear mass loss of 15 x 10^{-4}, 25 x 10^{-4} and 25 x 10^{-4} g respectively, and in contrast, induction furnace product, ILA has the highest wear mass loss of 46 x 10^{-4} g at 10 min. The result of wear test is consistent with hardness test result. It therefore appears like production furnace as an observable effect on tribological degradation of the discs. Hence, this study agreed with earlier researchers (Bressan et al., 2008; ELSawy et al., 2017) that tribological degradation of the grinding discs decreases when the hardness value increases. This is corroborated by the hardness and mass wear loss of the sample ILA compared to the hardness value and wear mass loss of RIW disc sample.

4 CONCLUSIONS

The research study on investigation of correlation between production methods and tribological degradation of food grinding discs has been completed and the following are the conclusions at the end of the study:

- Chemical composition showed significant amount of iron, silicon and aluminum which appeared as iron carbide and ferroalloys, an indication that all discs tested are cast irons.
- Higher hardness value observed in rotary and cupola furnaces products compared to induction furnace is an indication of correlation between tribological degradation of the grinding discs.
- The relatively lower wear mass loss observed in rotary furnace products, compared with higher wear mass loss in induction furnace product is an indication of quality control including carbon composition peculiar to induction furnace.
- Consequently, lower hardness value of induction furnace product is attributable to its relatively higher wear mass loss. Therefore, tribological degradation of the disc can be mitigated with increase in hardness values.

ACKNOWLEDGEMENT

This research was funded by Tertiary Education Trust Fund under the auspices of National Research Fund with Grant Reference: TETF/DR&D-CE/NRF/2020/SETI/85/ Vol .1. The financial support is duly acknowledged.

REFERENCES

Ahmed, I. I., Adebisi, J. A., Abdulkareem, S., & Sherry, A. H. (2018). Investigation of surface residual stress profile on martensitic stainless steel weldment with X-ray diffraction. *Journal of King Saud University - Engineering Sciences*, *30*(2), 183-187. https://doi.org/https://doi.org/10.1016/j.jksues.2016.01.004

Anthony, B., Ojekale, C., Chukwu, G., Oladipupo, L. O., & Titilola, S. (2013). Some Nigerian Traditional Food Milling Techniques and Cookware Increase Concentrations of Some Heavy Metals in Lycopersicon Esculentum and Citrullus Lanatus. *Iosr Journal Of Pharmacy*, *3*(3), 6-13.

ASTM. (2004). Standard Test Method for Wear Testing with Pin-on-Disk Apparatus. In *Designation: G99-04*. West Conshohocken, USA: ASTM International.

Bressan, J., Daros, D., Sokolowski, A., Mesquita, R., & Barbosa, C. (2008). Influence of hardness on the wear resistance of 17-4 PH stainless steel evaluated by the pin-on-disc testing. *Journal of Materials Processing Technology*, *205*(1-3), 353-359.

ELSawy, E., EL-Hebeary, M., & El Mahallawi, I. (2017). Effect of manganese, silicon and chromium additions on microstructure and wear characteristics of grey cast iron for sugar industries applications. *Wear*, *390*, 113-124. https://doi.org/https://doi.org/10.1016/j.wear.2017.07.007

Nnaji, J. C., & Emmanuel, P. N. (2016). Trace Metals in Food Condiments Processed with Manual Metallic Grinders. *The Phamaceutical and Chemical Journal*, *3*(1), 172-177.

World Health Organization. (2015). *Disease Outbreak News: Cholera – United Republic of Tanzania*. WHO. Retrieved 15/10/2020 from https://reliefweb.int/report/united-republic-tanzania/disease-outbreak-news-cholera-united-republic-tanzania

PAPER 191 – EFFECTS OF PROCESSING ROUTES ON THE PHYSICOCHEMICAL PROPERTIES OF RECYCLED CARBONATED CAN

J. A. Adebisi[1], A. A. Abdulkareem[1], K. O, Olubajo[1,*], E. O. Falodun[2], M. I. Adewoye[3], I. I. Ahmed[1]

[1]Department of Materials and Metallurgical Engineering, University of Ilorin, Nigeria
[2]Department of Mechanical Engineering, Covenant University, Ota, Nigeria
[3]Advanced Composite Materials Research Laboratory, National Space Research and Development Agency (NASRDA), University of Ilorin Centre, University of Ilorin, Nigeria
[*]Email: 17-30gn053@student.unilorin.edu.ng

ABSTRACT
Recycling of aluminium cans and other scraps are secondary sources of aluminium alloys and composites to ensure healthier environment and low cost of production. Aluminium cans were processed into different casts; whole can, can bodies, and can lids with or without paints. The casts include whole cans, cans without paint, cans without paint and lid, and the lid. Microstructural examination and chemical analysis of the casts were studied using Scanning Electron Microscope (SEM) and Energy Dispersive Spectrometry (EDS), respectively. Tensile and hardness properties of the casts were also examined. The chemical analysis revealed that the can body and lid contain Al, C, Mg and O but the lid contains more trace elements. Mn, Fe and Si were observed to be pronounced when paint is removed prior to casting, thus reducing some elements migration to the slag phase. The hardness test showed the lids alone had the highest hardness value but casts without paint has least hardness. The tensile result showed that the lid had the highest tensile strength value of about 240 MPa with least observed in can without paint. Removal of paints prior to casting aluminium cans has no significant effects on the physicomechanical properties of aluminium casts.

KEYWORDS: Recycling, aluminium can, paint, processing routes, casting

28. INTRODUCTION

Aluminium and its alloys are materials utilised in various sectors, such as aerospace, automobiles, food packaging, cosmetics, household utensils, construction, and pharmaceutical industries. Aluminium-based alloys are employed because of their unique properties, basically lightweight and corrosion resistance. Its major use for food packaging is because it met basic requirements for food preservation such as protection to gas and light barriers, as well as versatility, post-consumer material recycling and corrosion resistance (Soares *et al.*, 2019). The use of aluminium cans in packaging has almost replaced the traditional glass bottle packaging system. The rate at which people consume packaged drinks with aluminium cans has increased the number of aluminium cans littering the environment. Indiscriminate dumping of aluminium cans has contributed to environmental pollution. Efforts have been made in recycling aluminium cans to minimize their environmental pollution (Bello et al., 2017; Bulei et al., 2018; Risonarta et al., 2018). The aluminium beverage can consist mostly of aluminium with a little amount of other metals such as magnesium (Mg), manganese (Mn), iron (Fe), silicon (Si), and copper (Cu). The lid is made up of a slightly different alloy than the main body. The beverage cans are made up of two aluminium alloys (3004 ASTM for the main body and 5182 ASTM for the lid) having different compositions (Valik, 1982).

The aluminium cans are also coated both in and out to prevent corrosion (Soares et al., 2019). In the recycling efforts reviewed so far, no efforts have been made to study the effects of these coatings on the properties of recycled products. Hence, this work investigated effects of recycling routes on the physical, chemical, and mechanical properties of carbonated drink cans.

29. MATERIALS AND METHODS

2.1 Materials

The materials used in this work include aluminium cans, collected from a local market (Oja tun-tun) in Ilorin, metropolis Kwara state. 220-800 grade emery papers, polishing cloth, electric muffle furnace, steel crucible, knife and scissors. Nitrocellulose thinner was used for removal of coatings. Equipment used includes Instron testing machine at Kwara state University Malete, Ilorin. Scanning Electron Microscope (SEM) and Energy dispersive x-ray spectroscopy (EDS) at the Department of Chemical, Metallurgical and Materials Engineering, Tshwane University of Technology, Pretoria, South Africa.

2.2 Methods

The aluminium cans were washed thoroughly with tap water and soap to remove the soil and other contaminants. They were rinsed thoroughly and left to dry. 400 g was measured and labelled, "whole can". The remaining cans were cleaned with nitrocellulose thinner to remove their paints. Traces of remnants of paints were removed using emery paper and polishing prior to washing slightly with thinner again. These were rinsed with water and dried. Another 400 g was measured and labelled "can without paint". The remainder were separated with knife and scissors into body and lids and labelled "can without paint and lid", and "lid", respectively. Average weights of each group were taken and recorded.

The muffle furnace was set to a temperature of 800 °C at average heating rate of 16.5 °C/min. The whole cans were crushed to reduced their volume before charging into a steel crucible and soaked at 800 °C for 15 minutes in the furnace. The aluminium melt was poured into the prepared mould. This was repeated separately for can without paint, can without paint and lid, and lid. Specimens were prepared for SEM/EDS, tensile, and hardness tests.

30. RESULTS AND DISCUSSION

Figure 1 shows the scanning electron micrographs of casts aluminium. Figure 1(a) shows a uniform phase of aluminium without grain boundaries. This may be as a result of reduced alloying element that have interacted with paint in the slag phase. Remnants of paints are ceramic that could be reactive with the melt. Figure 1(b) represents the image for the lid which is usually stronger with higher tensile strength than the body due to load bearing nature during packaging and transportation. The grain boundaries in Figures 1 (c and d) show second phase grain boundary phases of other elements present in the cast.

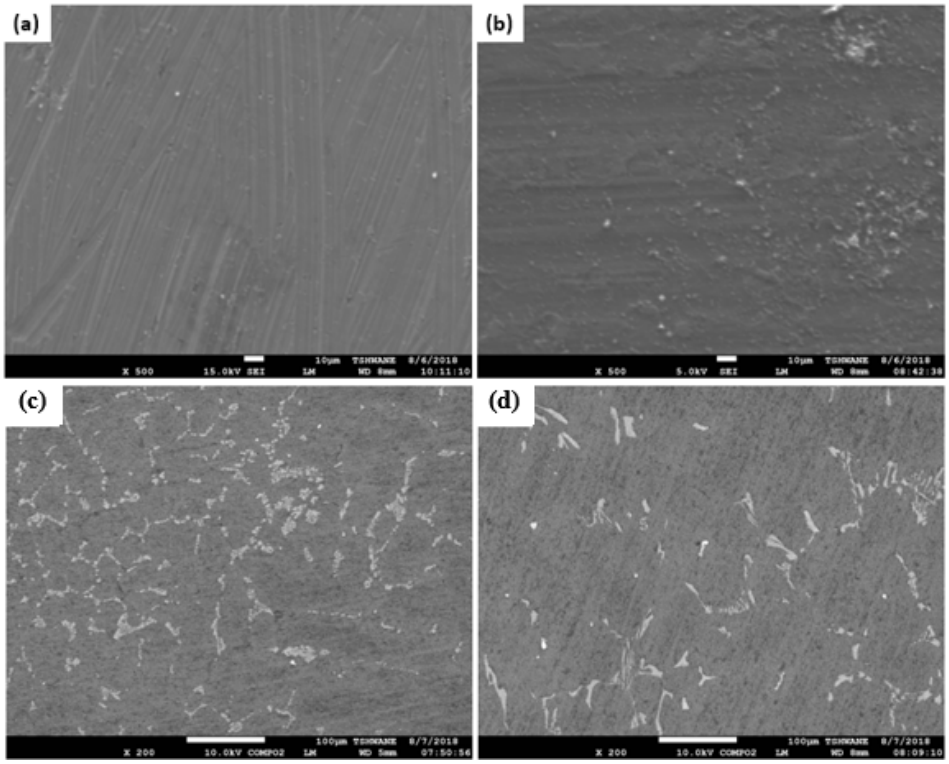

Figure 22: SEM images of (a) whole can, (b) lid, (c) can without paint, and (d) can without paint and lid

Figure 2 presents the chemical compositions of samples produced from the casts. The whole can, Figure 2(a) has the highest proportion of aluminium as a result of the diminished alloying elements due to reactivity of the melt with the slag phase. However, Figure 2(b) which is the lid presents the highest number of alloying elements and thus stronger for load bearing purposes. The secondary phases manoeuvres stresses generated in the materials.

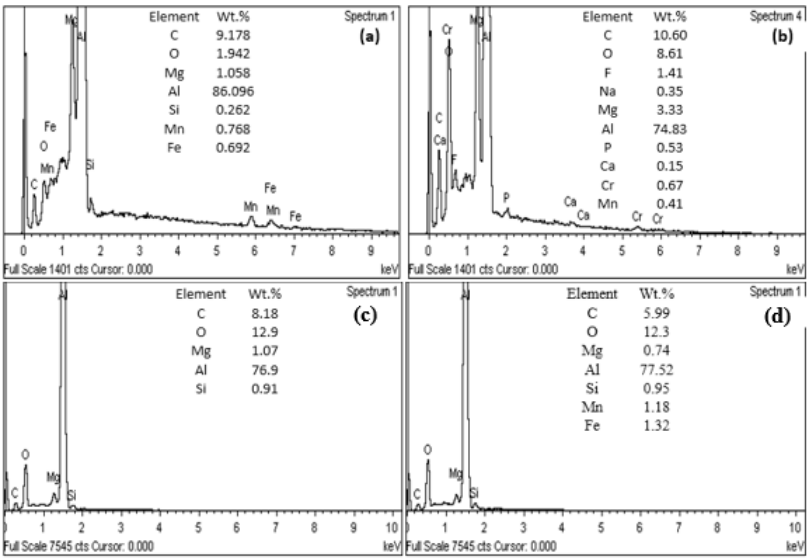

Figure 23: Chemical composition and EDS spectra of (a) whole can, (b) lid, (c) can without paint, and (d) can without paint and lid

The hardness values for the casts are presented in Figure 3. The lid has the highest hardness which may be as a result of secondary phases formed during the casting as revealed in Figure 2(b). It can be deduced that hardness in aluminium alloys depends on the phases present within the matrix under investigation.

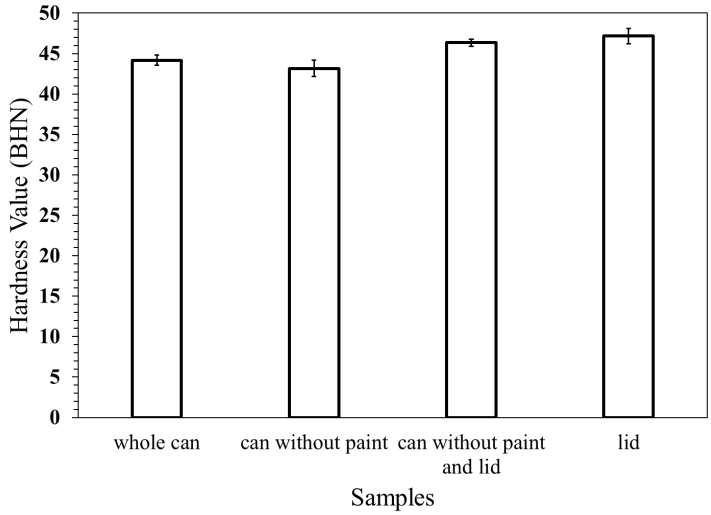

Figure 24: Brinell hardness values for the casts

The results of tensile tests carried out on aluminium casts are presented in Figure 4. The lid possesses the highest tensile strength from the casts. This is followed by the whole can due to presence of the lid.

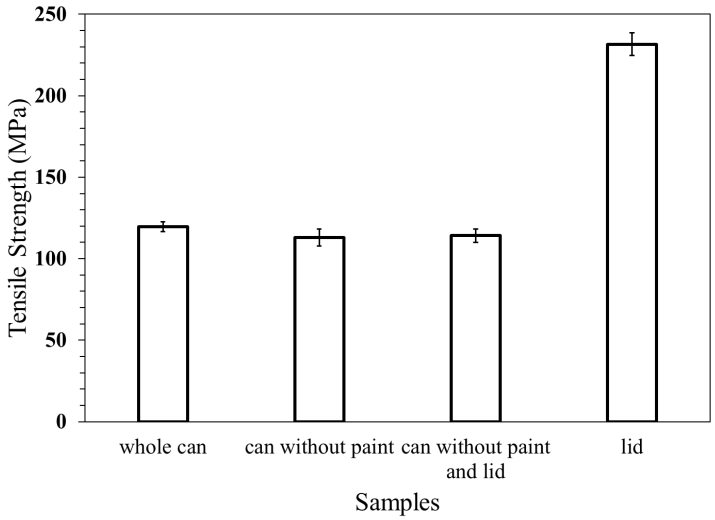

Figure 25: Tensile strength for the casts

31. CONCLUSION

It can be concluded that aluminium beverage cans consist of two main alloys with different chemical and mechanical properties due to their area of applications. The lid contains more F and Mg along with other elements in the body of the cans. The lid has the highest hardness value and tensile strength.

REFERENCES

Bello, S. A., Agunsoye, J. O., Adebisi, J. A., & Hassan, S. B. (2017). Effect of aluminium particles on mechanical and morphological properties of epoxy nanocomposites. *Acta Periodica Technologica*(48), 25-38.

Bulei, C., Todor, M., Heput, T., & Kiss, I. (2018). *Recovering aluminium for recycling in reusable backyard foundry that melts aluminium cans.* Paper presented at the IOP Conference Series: Materials Science and Engineering.

Risonarta, V. Y., Anggono, J., Suhendra, Y. M., Nugrowibowo, S., & Jani, Y. (2018). *Strategy to improve recycling yield of aluminium cans.* Petra Christian University.

Soares, D. S., Bolgar, G., Dantas, S. T., Augusto, P. E., & Soares, B. M. (2019). Interaction between aluminium cans and beverages: Influence of catalytic ions, alloy and coating in the corrosion process. *Food Packaging and Shelf Life, 19*, 56-65.

Valik, L. H. V. (1982). *Material for Engineering*: Addison Wesley Publishing Company, inc.

PAPER 192 – DEVELOPMENT OF AN ARTIFICIAL INTELLIGENCE BASED SYSTEM FOR NUTRIENT DELIVERY TO GREENHOUSE GROWN CROPS

M.O. Omobowale[1]*, I.O. Medebem[1], T.O. Sijuade[1]

[1]Department of Agricultural and Environmental Engineering, Faculty of Technology University of Ibadan Nigeria.
*Email: mo.omobowale@ui.edu.ng

ABSTRACT
Applying nutrients to crops either on the field or in a greenhouse has been a manual process, especially in developing countries where farmers or greenhouse attendants introduce nutrients based on intuition, or at specific intervals, not knowing exactly when a crop requires the said nutrients. This is one of many reasons why artificial intelligence has been introduced into the agricultural sector. This project was designed to develop an artificial intelligence-based system for the automatic delivery of nutrients to greenhouse-grown crops. The system was built with an Arduino microcontroller serving as the brain box of the system, a soil Nitrogen, Phosphorus and Potassium (NPK) sensor for reading nutrients level, an organic light-emitting diode which displays the specific nutrient level in mg/kg, while a solenoid valve was incorporated into the delivery mechanism. The data was logged onto a secure digital (SD) card via SD module installed on the Arduino board. The microcontroller was configured to interpret the varied states of the soil as relayed by the soil sensor; and this involved data capture from NPK sensor, data processing to determine when to release nutrients, and delivery of nutrients if the solenoid valve is activated. The system was evaluated on soil whose nutrients were leached out, placed in a greenhouse, and the performance was satisfactory.

KEYWORDS: Nutrients, Arduino microcontroller, NPK sensor, Organic Light-Emitting Diode, Secure digital module.

1. INTRODUCTION

The optimal population that the planet Earth can sustainably support is approximately 1.9 billion people (Daily et al., 1994). However, with an estimated global population of about 8 billion people, it is evident that the Earth is currently experiencing overpopulation (Prosekov& Ivanova, 2018). Furthermore, it is projected that by the end of this century, the world's population may increase up to 16 billion people (Pison, 2019). With this constantly growing population, the available land for agriculture decreases rapidly due to; urbanization, increased demand for food supply, and the genuine effects of global warming. It is now known that the agricultural sector is facing a severe crisis.

A solution needs to be proffered to meet this ever-growing demand, and in a constantly evolving world, the need to always be one step ahead is the new normal. One of the solutions is the implementation of Artificial Intelligence (AI) into the day-to-day agricultural processes (Talaviya et al., 2020). Artificial Intelligence technology has an abundance of potential in meeting the increased demands of the agricultural sector (Khan, 2021). This technology can increase not only the output of desired crops but also their quality. With improved crop production, monitoring, harvesting, processing, and marketing, AI as an emerging technology has done a good thing for the agricultural sector. In addition to aiding with crop production and all its derivatives, it also calculates and senses temperature, water content, precipitation, wind speed, solar radiation, and various other factors (Kim et al., 2008).

As it stands, agriculture in Nigeria currently contributes about 40% to the gross domestic product (GDP). Also, about 70% of the working population is involved with agriculture to varying extents (CIA 2012). This shows to a large extent how the country is dependent on agriculture for survival. It is for this reason that the exploration into artificial intelligence, which has been dormant in this part of the world, should be an achievable goal for the next ten years. Artificial intelligence applications in greenhouse agriculture, such as irrigation, weeding, and spraying, include sensors and other techniques incorporated into robots and drones. These technologies reduce water, pesticides, and herbicides, maintain soil fertility, and aid in the efficient use of manpower, increases productivity and improves quality (Talaviya et al., 2020).

Greenhouse conditions are already among the most mechanized and controlled globally, but artificial intelligence (AI) technologies are now taking control to unprecedented levels, similar to what is happening in many other industries (Bhardwaj et al., 2021). AI systems are beginning to give greenhouse operators a variety of production-related benefits due to their ability to process massive volumes of data and make minor constant modifications. With the dawn of the 21st century, fine-tuning existing agricultural processes for farmlands and greenhouses was

paramount. The world had entered a digital age, and agriculture could not be left behind. Drones for fertilizer distribution were introduced, intelligent sensor irrigation systems for efficient water supply, satellite imagery, navigation systems to increase agricultural output, artificial intelligence for nutrient delivery processes and computer vision for the harvesting of matured or ripe fruits (Talaviya et. al, 2020).

2. MATERIALS AND METHOD

2.1 Design and Implementation of Nutrient Delivery System

The design of the nutrient delivery system ensures that the system can read and determine the soil nutrient level. Upon determination of the nutrient level, the system can either allow the flow of the nutrient mixture or remain closed. The system is made up of the hardware and software components working hand in hand. The system consists of the Control unit, Sensing Unit and Output Unit.

i. **Control Unit:** This was made up of an Arduino Nano V3 microcontroller board. This unit controls the readings that were obtained through the course of various experiments. It consists of analogue pins for the input of data and digital pins for the output of information. To this board, the sensor and organic light-emitting diodes (OLED) indicator were connected.
ii. **Sensory Unit:** Here, the soil nutrient sensor was connected to the Arduino microcontroller board. Depending on the number of nutrients available, this unit reads the data and transmits it to the Arduino board. The program which is interfaced with the Arduino board determines what information to send to the output unit.
iii. **Output unit:** This unit comprises the organic light-emitting diodes (OLED) indicator that displays the nutrient level for Nitrogen, Potassium and Phosphorus, respectively. Also, this unit consists of the solenoid valve that controls the distribution of the fertilizer mixture into the irrigation pipes.

2.2 Block Diagram of the System

The general block diagram of the system is shown below. It shows the schematic form of the general arrangement of the components of the nutrient delivery system. The block diagram consists of three stages; The reading stage, processing, and delivery stages (Figure 1). In the reading stage, the sensor is stuck into the soil sample. The level is then read and transmitted to the Arduino board. The processing stage involves converting the information retrieved by the soil sensor to a readable output on the OLED. The delivery stage involves the solenoid valve opening or not based on the information determined in the processing stage.

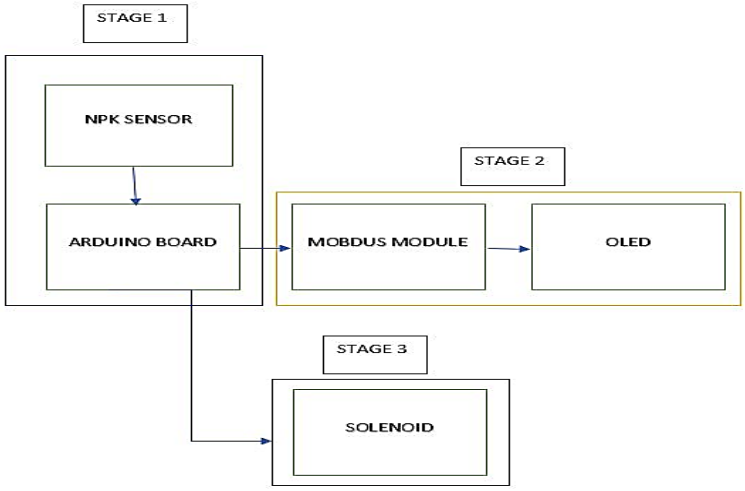

Figure 1. Block Diagram of the System

2.3 Hardware Design Configuration

The hardware configuration depicts all the connections needed in the different delivery system units.

2.3.1 Control Unit: ATMega328 microcontroller on Arduino platform

The control unit of the microcontroller is the ATMega328 microcontroller on the Arduino platform. Through the course of this experiment, several digital pins on the Arduino board were used (Figure 2).

2.3.2 Sensing Unit: JXCTIOT Soil NPK Sensor connection to Arduino

Using Software Serial, the R0 and DI pins of the Modbus are connected to D2 and D3 Arduino. Similarly, DE & RE was set to a designated level. Due to the DE and RE pins being connected to the digital pins, there are only two levels: high or low. Thus, the DE and RE pins are set to a high level. The DE and RE pins are connected to the D7 and D8 pins on the Arduino. The NPK Sensor is made up of four wires. VCC is the brown one, and it requires a 9V-24V power supply. The GND pin is a black-coloured pin; as a result, it is attached to the Arduino's GND. The B pin of the RS485 Modbus board is linked to the B pin of the wire, and the A pin of the wire is connected to the A pin of the RS485 (Figure 3).

2.3.3 Output Unit: OLED interface with Arduino

A 0.96 Organic light-emitting diode (OLED) is chosen for the display. In a 4-bit mode setup, OLED pins D4, D5, D6, and D7 are used as data lines. These pins are wired to pins 5, 4, 3, and 2 on the Arduino. VCC is linked to pin 15 (A), and GND is connected to pin 16 (K). The organic light-emitting diodes (LEDs) installed on the circuit board are connected to these pins (A and K). The OLED's pin E (Enable) is connected to the Arduino board's digital pin 11. On the OLED, pin RS (Register Select) is connected to Arduino digital pin 12. The OLED's R/W pin is connected to GND (ground) (Figure 3).

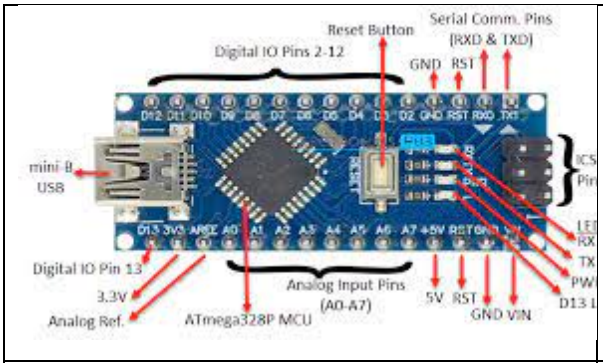

Figure 2 Connection Points of Arduino Nano Board

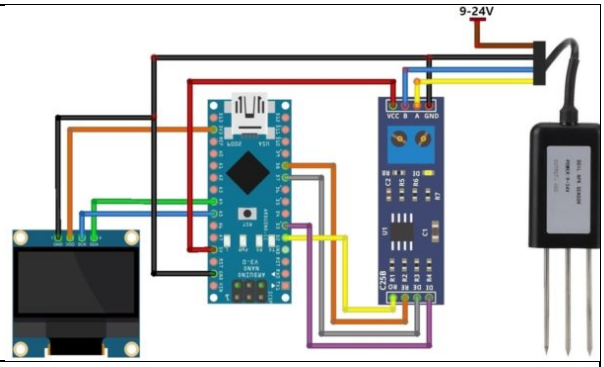

Figure 3. Circuit Diagram for Sensor Connection

2.3.4 Solenoid Valve Connection to the Arduino

The solenoid valve was used to control the flow of the fertigation process. The Vin and GND pins of the Arduino board were initially connected to the breadboard's positive (+) and negative (-) rails. The Solenoid was connected to the breadboard with connecting wires. A snubber diode was introduced to prevent damage to the system that transient voltages may cause. This occurs when the magnetic coil suddenly loses power. The snubber was placed from the negative side of the coil to the positive side. A TIP122 Transistor and a base resistor control and limit the electric current. The base resistor is connected to the Arduino board's digital pin 6. The solenoid's negative terminals are connected to the collector on the transistor. Then the transistor's emitter is connected to the GND rail of the breadboard. (Figure 4)

2.3.5 RTC Module and SD Card Module Connection to the Arduino

The I2C communication (SCL, SDA) is used to connect the RTC module DS3231 to Arduino, and the SPI communication is used to connect the SD card module to Arduino (MISO, MOSI, SCK, CS). Pins 4 and 7 are designated as the CS and output pins, respectively. The SCL and SDA pins take up pins A4 and A5. Because the OLED monitor is also interfaced with the A4 and A5 pins, 2 resistors were introduced to serve as pull-up resistors so that both the RTC module and the OLED monitor will be able to read and display their values respectively (Figure 5 and Figure 6).

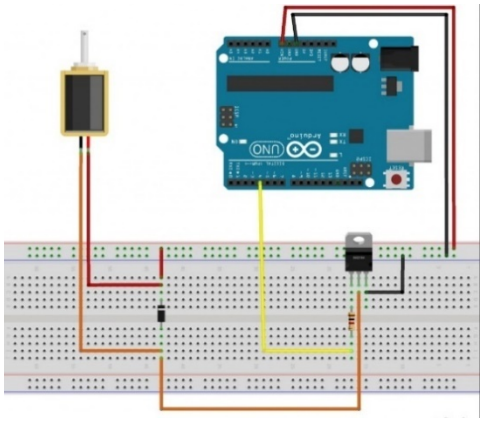

Figure 4. Circuit Connection for Solenoid Valve

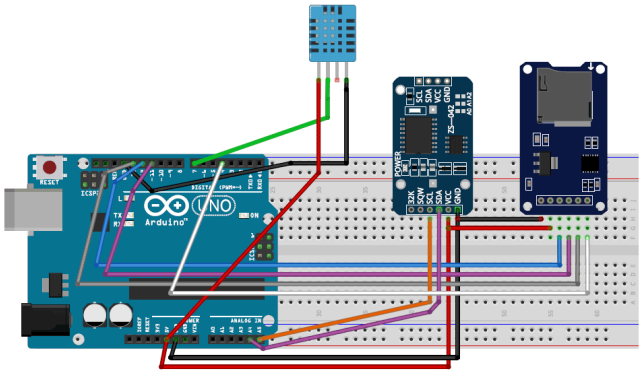

Figure 5. Circuit Connection for RTC and SD Card Modules

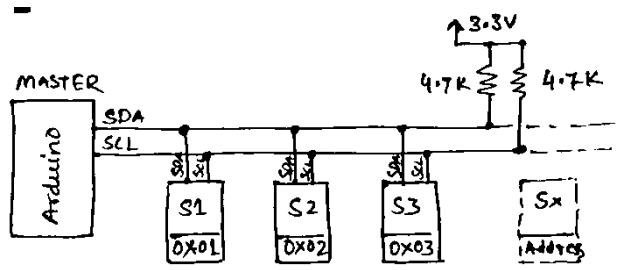

Figure 6. Circuit Connection of Resistors with RTC Module and OLED Monitor

2.4 Software Design

The microcontroller is configured to interpret the varied states of the soil as suggested by the soil sensor. The Integrated Development Environment (IDE) for Arduino was used.

Program Pseudo Code

READ sensor value

COMPARE sensor value with the set threshold

DISPLAY soil nutrient value on OLED

IF sensor value < maximum predetermined value TURN-ON pump

ELSE IF sensor value> maximum predetermined value > TURN OFF pump

Figure 7 shows the flowchart of the process.

2.5. Evaluation

Prelimnary evauation of the AI-based fertigation system was performed on leached soil without crops.

3. RESULTS AND DISCUSSION

3.1 System Performance

The performance of the nutrient delivery system depends on the following;

i. The quality of the NPK Sensor: The NPK sensor used for this project has an efficiency of 70 percent (Manufacturer Specification).

ii. The inlet pressure: 20.7 kPa pressure was applied to the solenoid valve which was the recommendation of the manufacturer.

iii. The threshold value programmed into the algorithm was 40 mg/kg

3.2 Evaluating the Performance of Nutrient Delivery System with Time

Figures 8 and 9 show the levels of Nitrogen and Phosphorus measured throughout the study. From the figures, an increase in the trend line indicates that nutrients were added at that point to the sample, while the decrease in the trend line implies the plant continuously utilizes the nutrients until it goes below the threshold value. The graphical trends observed were similar, and this indicates that the system delivers the nutrients in corresponding proportions. The nitrogen level does not drop below the threshold value (40 mg/kg) incorporated into the system as shown in Figure 8. This implies that the delivery system performed in accordance with the set objective of the project. There was no need to change or replenish the nutrient solution during the study, which is similar to previous experiments carried out by Pardossi *et al*. (2002).

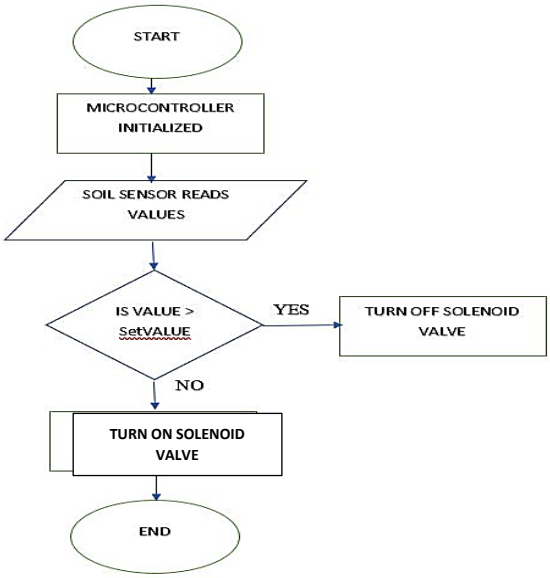

Figure 7. Flowchart of the System

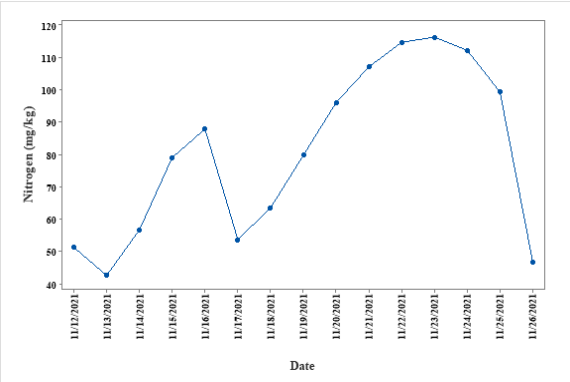

Figure 8. Mean Nitrogen Plot

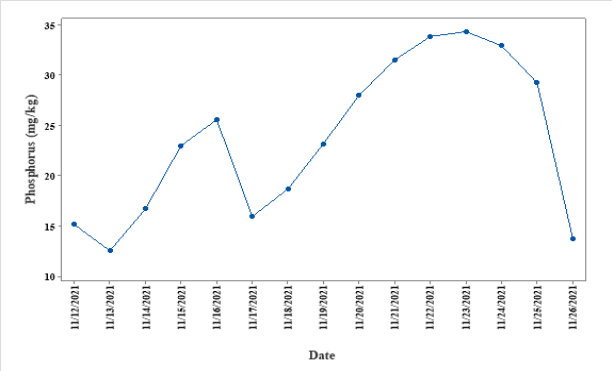

Figure 9. Mean Phosphorus Plot

3.3 Descriptive Statistics and Z-test Result

Table 1 presents the descriptive statistics of the nutrients. The values obtained for Nitrogen are similar to results obtained from previous experiments where the average value for Nitrogen were 100 mg/kg, while the same cannot be said for phosphorus and potassium, which had average values of 12 and 160 mg/kg, respectively (Pardossi *et al*., 2002). Table 2 shows the Z-test results from the analysis of the nutrient levels against the hypothesized value of the same nutrient.

From Table 2, it shows that Nitrogen is 'Not Significant' when compared with an allowable nitrogen value 75 mg/kg (Carson and Phillips, 2021), this indicates that the values measured by the sensor were within the range of nitrogen adequate for plants growth. The results of Phosphorus and Potassium were both significant, when compared with an allowable phosphorus value of 25 mg/kg (Kreuser, 2015) and an allowable potassium value of

40 mg/kg (Li *et al*., 2018). This indicates that the values of Phosphorus and Potassium measured by the sensor during the study do not fall within the range of adequate values of both Phosphorus and Potassium, respectively. The overall performance shows that the system can deliver the nutrients when the sensor reads below the set threshold.

Table 1. Descriptive Statistic of the Nutrients

Nutrient	Mean	StDev	Minimum	Maximum	Mode
Nitrogen	82.663	27.317	0.000	149.000	108
Phosphorous	24.278	8.036	0.0000	60.000	32
Potassium	33.015	11.048	0.0000	60.000	43

Table 2. Z-test Results

Nutrient	Test Value (mg/kg)	Z-value	P-value	Sig
Nitrogen	75	54.11	1.000	Not Sig
Phosphorous	25	-17.34	0.000	Sign
Potassium	40	-121.94	0.000	Sign

4. CONCLUSION

The research was able to develop an artificial intelligence-based system for nutrient delivery to greenhouse-grown crops. The Arduino-based sensing system was able to communicate its output from the soil to the OLED display. The delivery system uses Nitrogen as a threshold value as it is the most important component in fertilizer. Once the sensor reaches the value of 40 mg/kg, the Arduino board triggers the solenoid valve to shut off the operation. The system setup is cost-effective as it uses simple hardware architecture consisting of the Arduino nano board, the solenoid valve, the NPK sensor and the OLED module. It reduces the need to constantly be in the greenhouse to supply nutrients to the growing crops due to its automation. The system can be improved by installing a moisture content sensor to prevent the system from drowning the crops and be scaled for commercial purposes with additional sensors and improved pipe systems

REFERENCES

Bhardwaj, H., Tomar, P., Sakalle, A., & Sharma, U. (2021): Artificial Intelligence and Its Applications in Agriculture With the Future of Smart Agriculture Techniques. In *Artificial Intelligence and IoT-Based Technologies for Sustainable Farming and Smart*

CIA. (2012): The World Fact Book. Retrieved May 27, 2021, from https://www.cia.gov/library/publications/the-world-factbook/geos/ni.html

Daily, G., Ehrlich, A., & Ehrlich, P. (1994): Optimum Human Population Size. *Population and Environment, 15*(6), 469-475. https://doi.org/10.1007/BF02211719.

Khan, I. (2021): *Artificial Intelligence (AI) as Sustainable Solution for the Agriculture Sector : Findings from Developing Economies*. *January*.

Kim, Y.J., Evans, R.G., & Iversen, W.M., (2008): Remote sensing and control of an irrigation system using a distributed wireless sensor network. *IEEE Transactions on Instrumentation and Measurement*. 57 (7),1379–1387.https://doi.org/10.1109/TIM.2008.917198.

Kreuser, W. C. (2015). Simplifying soil test interpretations for turf professionals. *G2265: http://turf. unl. edu/NebGuides/g2265. pdf (accessed December 5, 2021)*.

Pardossi, A., Malorgio, F., Incrocci, L., Campiotti, C. A., &Tognoni, F. (2002). *A comparison between two methods to control nutrient delivery to greenhouse melons grown in recirculating nutrient solution culture. Scientia Horticulturae, 92(2), 89–95.* doi:10.1016/s0304-4238(01)00292-8

Pison, G. (2019): How many humans tomorrow? The United Nations revises its projections. *The Conversation*, 2–7. http://theconversation.com/how-many-humans-tomorrow-the-united-nations-revises-its-projections-118938

Prosekov, A. Y., & Ivanova, S. A. (2018): Food security: The challenge of the present. *Geoforum*, *91*(February), 73–77. https://doi.org/10.1016/j.geoforum.2018.02.030

Talaviya, T., Shah, D., Patel, N., Yagnik, H., & Shah, M. (2020): Implementation of artificial intelligence in agriculture for optimisation of irrigation and application of pesticides and herbicides. *Artificial Intelligence in Agriculture*, *4*, 58–73. https://doi.org/10.1016/j.aiia.2020.04.00

PAPER 193 – LEARNING FROM EXAMPLES PARADIGM FOR THE DESIGN OF FUZZY CONTROL FOR A REACTIVE DISTILLATION PROCESS

*Giwa, Samuel Boluwatife[1]; Araromi, Dauda Olurotimi[1], Sulayman, Aminah Abolore[1] and Salami, Kolapo Kaz-eem[1]

[1]Department of Chemical Engineering, Ladoke Akintola University of Technology, Ogbomosho, Oyo State.
*Email: sbgiwa@student.lautech.edu.ng

ABSTRACT
The successful implementation of process intensification techniques, such as reactive distillation (RD), often requires tight control of the process. Tight control refers to the need to closely monitor and regulate process parameters such as temperature, pressure, flow rate, and reactant concentrations, among others, to maintain optimal performance. However, RD is highly nonlinear due to complex interactions between vapor-liquid equilibrium, vapor-liquid mass transfer, and chemical kinetics arising from the concurrent separation and reaction and hence making its control challenging. In this work, a generic nonlinear two-reactant-two product reactive distillation process model was used to design a fuzzy controller based on the 'learning from examples' paradigm for RD closed loop system. The performance of the fuzzy controller was compared with Proportional Integral (PI) controller. The results showed that the fuzzy controller outperformed the PI controller in terms of setpoint tracking with no overshoot.

KEYWORDS: process intensification, Reactive Distillation, Nonlinear, Fuzzy controller, Proportional integral control

1. INTRODUCTION

This should include the background to the study, a brief review of literature and clearly stated objectives. The section and others should be in single-line spacing. Reactive distillation has been employed in many industrial processes (Luyben, 2009). The growing application of reactive distillation processes has necessitated a better understanding of its process dynamics and control. The integration of separation and reaction presents a very complex control strategy, this is a result of the nonlinear coupling of chemical reaction, and phase equilibrium as the design of reactive distillation processes is significantly more complex than the design of conventional distillation processes (Keller, 2014). This makes the control of RD systems challenging as the process objectives such as obtaining product purity specification (separation performance) while maximizing reactant conversion (reaction performance) must be fulfilled. These are translated into achievable control objectives, which are then integrated into the overall control strategy (Baur et al., 2000).

Reactive distillation columns are generally modelled by a set of highly nonlinear first-order differential equations (Olanrewaju & Al-Arfaj, 2005). However, many model-based controllers use linear models because they are easier to analyse and require fewer computational recourses than nonlinear models (Kawathekar, 2021) but the highly non-linear nature of RD makes linear controllers difficult in capturing and controlling its complex dynamics (Fedor & Perduková, 2017). Moreover, for effective control, nonlinear controllers show high superiority over linear controllers(Kawathekar & Riggs, 2007). This introduces us to a special type of controller called the fuzzy logic controller which can combat this problem of non-linearities as it is not based on a mathematical model and is mostly used to solve the problem with a high degree of uncertainty or fuzziness. This type of controller is based on fuzzy logic and it behaves like a man-in-the-loop(Al-Odienat & Al-Lawama, 2008).

In a study conducted by Tian et al. (2003), the reliability of the fuzzy logic controller was demonstrated through the successful implementation of a pattern-based predictive control scheme that was developed to maintain the required purity in the distillation ethyl tert-butyl ether (Tian et al., 2003). Kapoor et al. (2011) conducted a study to compare the performance of a PID and fuzzy controller in a reactive distillation column using a generic mathematical model and found that the deviation of temperature from steady state error was less with the use of the fuzzy controller and it also reached a steady state faster.

2. THEORETICAL ANALYSIS AND METHODOLOGY

2.1 Modelling Reactive Distillation Process

In this study, the reactive distillation process was modelled using the principles of mass and energy balance based on the assumptions presented by Bamikole & Taiwo(2018). Figure 1 shows a schematic diagram of a typical reactive distillation column with the column considered to have N number of stages with the reboiler and the condenser being the 1 and N stages respectively.

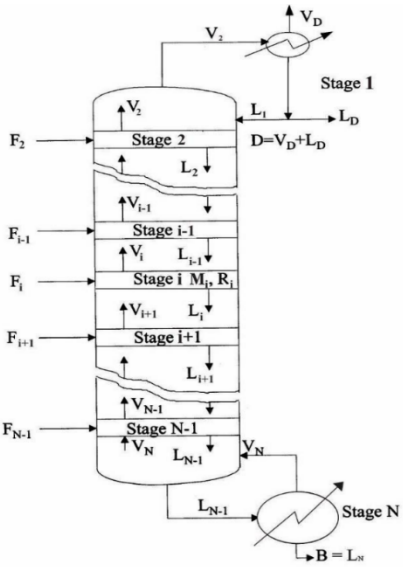

Figure 26: A schematic diagram of reactive distillation (Bamikole & Taiwo, 2018)

The reactive distillation column is comprised of three main sections. The first section called the reactive section, is where the chemical reaction occurs. The second section called the stripping section, is located between the condenser and the reactive section. The third section called the rectifying section, is located between the reactive section and the reboiler.

Equation 1 to 9 shows various equations modelling the column with the various parameters defined in section 2.2

Material balance around the reboiler:

$$\frac{M_N\, dx_N}{dt} = L_{N-1}x_{N,j} - Bx_{N,j} - v_{v_1}y_{N,j} \text{ where } L_{N-1} = B + V_N \quad (1)$$

j is the number of components

$$\frac{M_i\, dx_{1,j}}{dt} = L_{i-1}x_{i-1,j} - L_i x_{i,j} + V_{i+1}y_{i+1,j} - V_i y_{i,j} - F_i z_{1,j} + \delta_i v_j r_{i,j} \quad (2)$$

$$V_i = D(r+1) + \sum_{i=2}^{i}\left(1 - q_i\right)F_i \quad (3)$$

Material balance around the condenser:

$$\frac{M_1\, dx_{1,j}}{dt} = V_2 y_{2,j} - L_i x_{I,j} - Dx_{i,j} \quad \text{where } V_2 = L_1 + D \quad (4)$$

Material balance in the liquid phase:

$$L_i = \sum_2^i q_i F_i + \sum_1^i R_i + rD \quad (5)$$

The equation showing the vapor flowrate from other stages:

$$V_i = D(r+1) + \sum_{i=2}^{i}\left(1 - q_i\right)F_i \quad (6)$$

The reaction rate equation is given as

$$R_{i,j} = r_{i,j} * M_i \qquad where\ r_{i,j} = 3.255 * 10^{12} e^{-\frac{9547}{T_i}} x_A x_B \quad (7)$$

Equations 8 and 9 are derivation from the vapor-liquid equilibrium and Raoults law

$$\sum_{j=1}^{nc} y_{i,j} = \sum_{j=1}^{nc} \frac{\gamma_{i,j} P_{i,j}^0 x_{i,j}}{\emptyset_{i,j} P} = 1 \text{ where } \sum_{j=1}^{nc} x_{i,j} = 1 \quad (8)$$

$$T_i = \frac{1}{ln\left(P_{i,j}^0\right)}\left(A_j - B_j ln\left(P_{i,j}^0\right)\right) \quad (9)$$

The resulting equations above were solved using the semi-implicit Runge-Kutta in MATLAB workspace using relevant parameters presented by Olanrewaju & Al-Arfaj(2005).

2. Parameters nomenclature

In this section, all the parameters and variables utilized in equations 1 through 9 are explicitly defined.

B is the bottom flow rate, V_N is the Vapor flow rate coming from stage N, L_N is the Liquid flow rate coming from stage N

D is the distillate flow rate, $x_{i,j}$, $y_{i,j}$ is the Liquid and vapor mol fraction of the ith component at the ith stage respectively.

q_i is the Vapor quality (the fraction or percentage of vapor in a two-phase mixture of a liquid and a vapor) at the ith stage, $r_{i,j}$ is the Rate of production of the jth component in the ith stage, F_i is the Feed flow rate at the ith stage.

M_i is the Liquid hold-up at the ith stage, R is the Reflux ratio, δ_i Checks if the reaction is taking place at the ith stage where it takes a value of 1 if the reaction occurs else 0, k_0 is the Arrhenius constant, and E is the activation energy.

R is the universal gas constant, $R_{i,j}$ is the Rate of production of jth component in the ith stage, and N is the total number of stages including the reboiler and the reflux drum.

x_A is the mol fraction of water in the liquid phase, x_B is the mole fraction of ethylene oxide in the liquid phase, nc is the Number of components,

A_j, B_j is the Antoinne Parameters, $P_{i,j}^0$ is the Saturated vapor pressure of the jth component in the ith stage, $\emptyset_{i,j}$ is the Fugacity coefficient of the jth component at the ith stage.

T_i is the Temperature at the ith stage, $\gamma_{i,j}$ is the Activity coefficient of the jth component in the ith stage, $P_{i,j}^0$ is the saturated vapor pressure of the jth component in the ith stage, Vs is the Vapor flow rate from the reboiler.

3. Fuzzy controller

According to Nizami (2011), the use of a fuzzy logic system is a key feature of the fuzzy controller, which gained widespread attention when Mamdani designed a control system for a laboratory-scale steam engine boiler using fuzzy algorithms (Mamdani, 1974). Fuzzy control provides a formal framework for representing, manipulating, and implementing a human's heuristic knowledge of system control (Ibarra & Webb, 2016) as it is based on the concept of fuzzy logic, which allows for degrees of truth between true and false. The use of fuzzy control provides a flexible and adaptive approach to system control, accounting for uncertainty and complexity (Zadeh, 2009). Additionally, incorporating human expertise into the control system leads to improved system performance and efficiency (Heras-Cervantes et al., 2019). The fuzzy controller is integrated into a closed-loop control system, as shown in the block diagram in Figure 2.

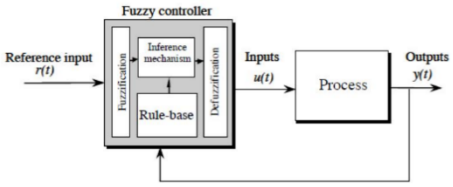

Figure 2: A typical fuzzy controller

The fuzzy controller has inputs (r(t)) and outputs (u(t)), similar to a regular PID controller. The plant outputs are represented by y(t) (Matko & Kavšek-Biasizzo, 2000). The design of a fuzzy controller involves selecting inputs and outputs, filtering them, and designing each of the four components of the controller as shown in Figure 2.

4. Construction of fuzzy rules from the "Learning from examples" algorithm

In their 1992 article, Wang and Mendel introduced the learning-from-examples approach, which involves that involves constructing a fuzzy rule-based system from a set of example cases. This method allows for the creation of a fuzzy inference system without the need for prior knowledge of the system's underlying dynamics or structure (Wang & Mendel, 1992). The learning from examples algorithm is described by the following key steps

1. Defining the lower and upper bound of output and input
2. Input Data: Start with a labeled dataset called "examples" where each data point consists of input features and corresponding output labels.
3. Setting up fuzzy membership function for set of input and output
4. Construction of rules using training data
5. Check if similar rule exists; if no, go to step 8 else move to step 6

6. Compare the degree of attainment
7. Select rule with the highest degree of attainment and discard the other rule
8. Add to rules

Our objective is to achieve servo responses in the RD system's top and bottom product compositions by controlling the reflux flow rate and vapor boil-up rate, using proportional integral control (PI) triggered by the error signal as shown in equation (10)

$$u(t) = k_p * e(t) + k_i * \int e(t)dt \quad (10)$$

k_p and $k_i$are the proportional constant and integral constant respectively, e is the magnitude of the error signal at time t and u is the output signal from the controller.

Simulation of the closed-loop of the RD model under PI control and Tyreus-Luyben parameter settings generated a dataset for fuzzy rule construction. Fuzzy membership functions assigned to regions in the input and output domains represented linguistic values, with triangular membership functions used. The dataset was used to obtain fuzzy rules, with premises formed from the input portion and consequents from the output portion. The rule base for the two-input two-output system has the form described in Equation 11(Passino & Yurkovich, 1998).

$$R_i = if\ u_1 is\ X_1^j\ and\ u_2 is\ X_2^k\ Then\ y\ is\ Y^l \quad (11)$$

The ith rule has "degree" defined by equation (12) for output y

$$degree\left(R_i^y\right) = \mu_{A_1^j}(u_1) * \mu_{A_1^k}(u_2) * \dots * \mu_{A_n^l}(u_n) * \mu_{B_1^p}(y) \quad (12)$$

where, $u_1 and\ u_2$ denote reflux rate and vapor boil-up rate, respectively, y denote either top and bottom product composition, j, k, l, and q can be any of linguistic values (S, C, B), $X_m^j and\ Y_m^j$ denote the fuzzy sets with associated membership functions $\mu_{X_k^j}(u_k)$ and $\mu_{Y_m^j}\left(y_m\right), m = 1,2$

Through rules embedded in the inference mechanism, the appropriate rule was determined by computing $\mu_i(u_1, u_2, \dots, u_n)$ for all rules in the rule base as described by Equation 13.

$$\mu_i(u_1, u_2, \dots, u_n) = \mu_{A_1^j}(u_1) * \mu_{A_1^k}(u_2) * \dots * \mu_{A_n^l}(u_n) \quad (13)$$

The largest value of $\mu_i(u_1, u_2, \dots, u_n)$ fixes the appropriate rule.

5. Defuzzification Stage

This is the stage to convert the fuzzy set quantification of the conclusions to a discrete value that will serve as input to the plant(Matko & Kavšek-Biasizzo,2000). The defuzzification strategy used in this work is the centroid method given in Equation 14 (Nizami, 2011; Ibarra & Webb, 2016).

$$y_q^{crisp} = \frac{\sum_{i=1}^{R} b_i^q \mu_i(u_1,u_2,\dots,u_n)}{\sum_{i=1}^{R} \mu_i(u_1,u_2,\dots,u_n)} \quad (14)$$

where R is the number of rules and b_i^q is the center of the area of the membership function $\mu_{B_q^k}\left(y_q\right)$

3. RESULTS AND DISCUSSION

To simulate the system, the fourth order Runge-Kutta method was utilized with a sampling interval of 3 minutes. For the LFE algorithm, three membership functions were selected for each input and output, which represent three linguistic values. The fuzzy control employed four input linguistic variables; top error, integral of top error, bottom error, and integral of bottom error, where the error indicates the difference between each product composition and the desired value. Reflux rate and vapor boil-up rate were selected as output linguistic variables. The fuzzy rule base was generated using 2000 data sets, and the rule base was used to generate a surface plot for the bottom and top composition fuzzy controllers (Figures 4a and 4d) respectively.

The fuzzy controller's information is compactly represented by a surface created from rules and membership functions.

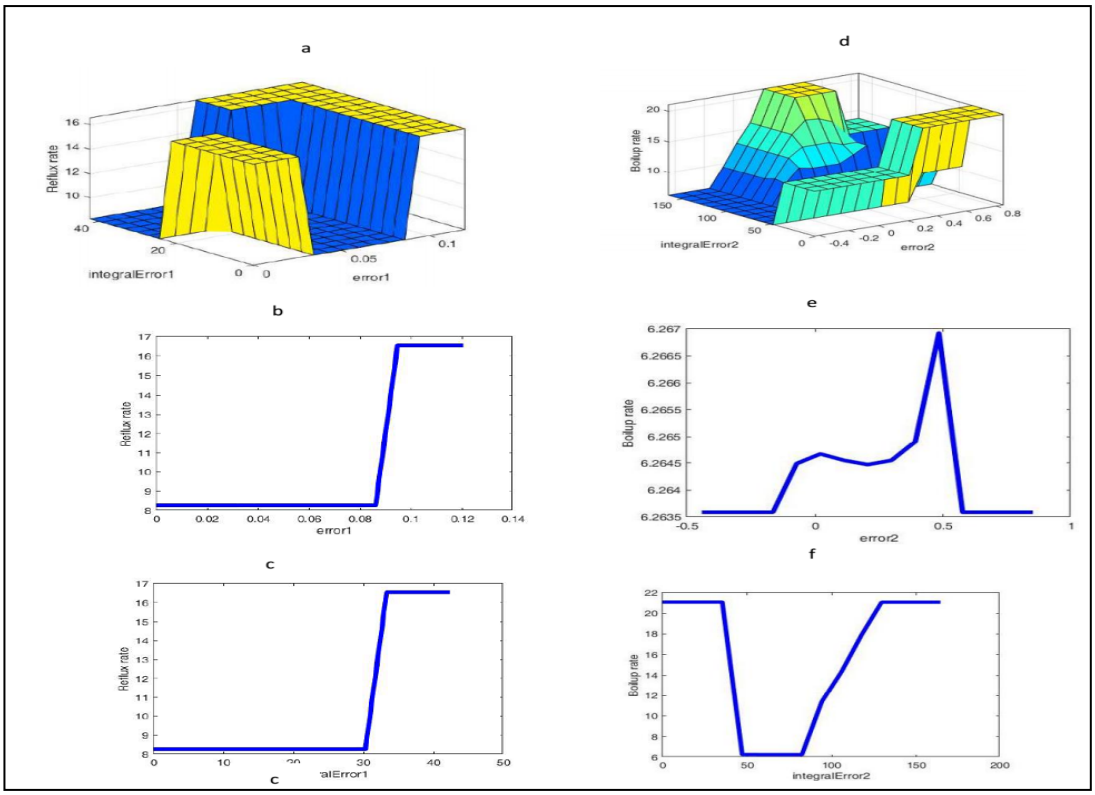

Figure 4: Surface plot for the control surface represented in both 3-D and 2-D

The top composition fuzzy controller exhibits a discontinuous control surface in the form of a plane. Figures 4b and 4c show quasi-linear relationships between the input and controller output. The control surface for the bottom composition is rippled and exhibits a non-linear relationship between the inputs and controller output.

The designed fuzzy controllers for top and bottom compositions are tested and the results are shown in Figure 5. The controllers can effectively control the RD system by tracking set points. The response is smooth and without oscillations.

In Figure 5, the performance of the fuzzy controller and PI controller based on Tyreus-Luyben settings in tracking set point variables is shown with continuous and dotted lines, respectively. Both controlled outputs and manipulated variables are displayed. Multiple simulations were conducted with incremental set point values up to 0.98, beyond which the system became unstable. The PI controllers exhibited oscillatory behaviour and unreasonable overshoot, while the Fuzzy controllers had smooth responses and were able to track all setpoints tested. Overall, the Fuzzy controllers outperformed the conventional PI controllers.

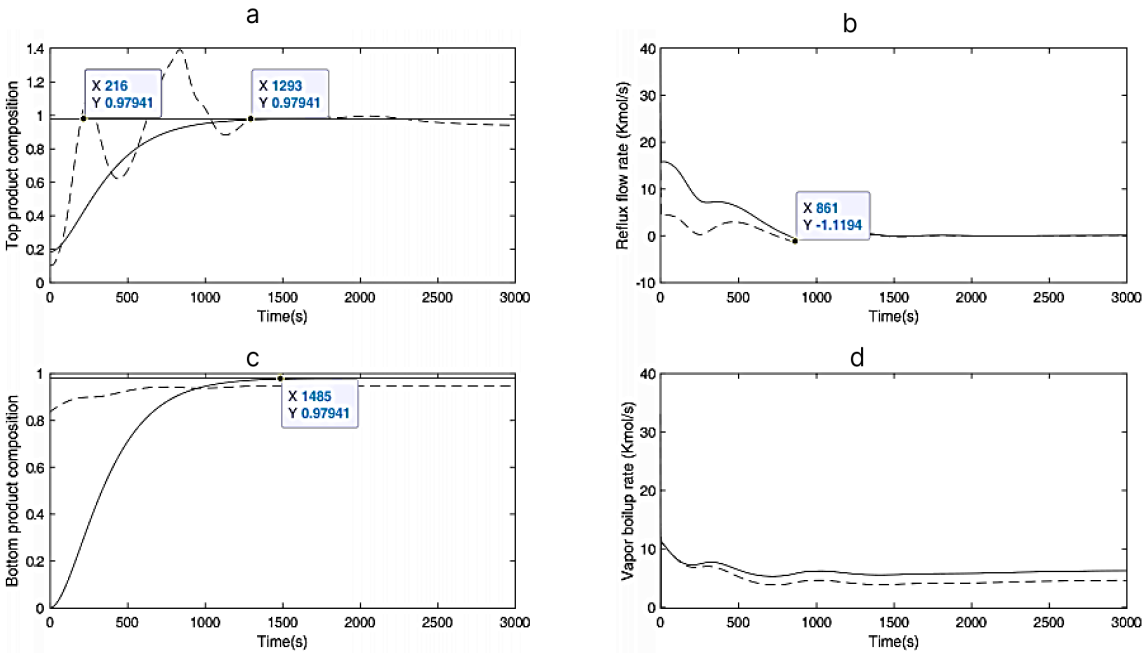

Figure 5: Closed-loop responses of RD process

The responses of the fuzzy controllers were slow and overdamped compared to conventional PI controllers. The rise time for the fuzzy controller's top product response is significantly longer, as seen in Figure 5a. However, the rise times for both PI controllers are unreasonably short for practical implementation of the cascade process plant, which has inherent transportation lag due to simultaneous reaction and separation. Therefore, the rise time obtained for the Fuzzy control system is reasonable in a practical sense.

The output of the controller for reflux and vapor boil-up rates are similar, as shown in Figures 5b and 5d. The Fuzzy controller initially sends a large feedback signal, while the PI controller exhibits unreasonable behaviour with negative values. Both controllers initially provide the same rate for vapor boil-up, but they later diverge, with the fuzzy controller having a higher rate. The findings suggest that high flow rates are necessary during start-up, followed by a steady supply at lower rates once steady states have been established for both products.

To ensure balance, the study focused on the reaction, which is a reversible elementary reaction involving four reacting species with unity stoichiometric coefficients. The components' relative volatilities are $\alpha_C > \alpha_A > \alpha_B > \alpha_D$, with A and C being the main components of the top product, while B and D are present in larger quantities in the bottom product. After simulations, both top and bottom products reached a purity of 0.98, leading to an overall conversion of 98% using the designed fuzzy controllers for the RD process.

Our approach surpassed the method utilized by Olanrewaju and Al-Arfaj(2005) which assumed a linear system and utilized a robust linear state estimator for the modelling and control of reactive distillation. By achieving higher product purities, our approach demonstrated its superiority and potential to enhance process performance. Our approach achieved higher product purities, demonstrating its effectiveness and potential for improving process performance. In 2.4 hours, a composition of 97.9% was reached for the x_d composition in the bottom product, while Olanrewaju and Al-Arfaj's method took 4 hours to reach a steady state composition of 95%. Similarly, for the top product, we achieved 97.9% purity was achieved in 2.8 hours, compared to Olanrewaju and Al-Arfaj's method which took 1.5 hours to reach 95%. Although our approach has a minor drawback in achieving a steady state for the x_c composition, its ability to achieve higher purities in a shorter time frame makes it a promising avenue for further development.

3. CONCLUSION

An uncoupled fuzzy rule-based controller for a generic nonlinear reactive distillation model was developed using a "Learning from Example" algorithm. This algorithm employed data obtained from simulated closed-loop control schemes of the RD, which utilized PI-type controllers with parameters obtained from Tyreus-Luyben parameter settings. Using three triangular membership functions for both the antecedent and consequent parts of the If-Then rules, sixteen rules were derived for each control scheme. The resulting fuzzy controller was able to track all the setpoints used in the simulations, achieving a purity of 98% for each output. Moreover, the overall fractional conversion for the RD was found to be 98%.

REFERENCES

Al-Odienat, A. I., & Al-Lawama, A. A. (2008). The advantages of PID fuzzy controllers over the conventional types. *American Journal of Applied Sciences*, *5*(6), 653–658. https://doi.org/10.3844/ajassp.2008.653.658.

Bamikole, J. O., & Taiwo, O. (2018). *Journal of the Nigerian Society of Chemical Engineers, 33 (1), 2018 Modelling And Simulation Of Reactive Distillation Systems Using Matlab And Aspen Plus*. *33*(1), 129–142.

Fedor, P., & Perduková, D. (2017). Use of Fuzzy Logic for Design and Control of Nonlinear MIMO Systems. *Modern Fuzzy Control Systems and Its Applications*. https://doi.org/10.5772/68050.

Heras-Cervantes, M., Marx Chávez-Campos, G., Javier Vergara Hernández, H., del Carmen Téllez-Anguiano, A., Anzurez-Marin, J., & Espinosa-Juárez, E. (2019). Fuzzy Logic Modeling and Observers Applied to Estimate

Compositions in Batch Distillation Columns. Distillation - Modelling, Simulation, and Optimization. https://doi.org/10.5772/intechopen.83479.

Ibarra, L., & Webb, C. (2016). Advantages of Fuzzy Control While Dealing with Complex/ Unknown Model Dynamics: A Quadcopter Example. *New Applications of Artificial Intelligence*. https://doi.org/10.5772/62530.
Kapoor, U., Rani, A., Singh, V., & Gupta, J. R. P. (2011). Simulation and control of reactive distillation column. *India International Conference on Power Electronics, IICPE 2010*. https://doi.org/10.1109/IICPE.2011.5728067

Kawathekar, R. (2021). Nonlinear Model Predictive Control. In *Advances in Industrial Control*. https://doi.org/10.1007/978-3-030-68010-7_5.

Kawathekar, R., & Riggs, J. B. (2007). *Nonlinear model predictive control of a reactive distillation column*. *15*, 231–239. https://doi.org/10.1016/j.conengprac.2006.07.004.

Keller, T. (2014). Reactive Distillation. In *Distillation: Equipment and Processes*. https://doi.org/10.1016/B978-0-12-386878-7.00008-5.

Luyben, W. L. (2009). Control of a column/pervaporation process for separating the ethanol/water azeotrope. *Industrial and Engineering Chemistry Research*, *48*(7), 3484–3495. https://doi.org/10.1021/ie801428s.

Matko, D., & Kavšek-Biasizzo, K. (2000). Generalized Predictive Control of a Nonlinear Process using Fuzzy Model. *IFAC Proceedings Volumes*, *33*(25), 83–88. https://doi.org/10.1016/S1474-6670(17)39320-5

Mamdani, E. H. (1974). Application of fuzzy algorithms for control of simple dynamic plant. Proceedings of the Institution of Electrical Engineers, 121(12), 1585-1588.

Nizami, M. S. (2011). *Development of a Fuzzy Logic Controller for a Distillation Column Using Rockwell Software by Master of Applied Science*.

Olanrewaju, M. J., & Al-Arfaj, M. A. (2005). Development and application of linear process model in estimation and control of reactive distillation. *Computers and Chemical Engineering*, *30*(1), 147–157. https://doi.org/10.1016/j.compchemeng.2005.08.007

Passino, K. M., & Yurkovich, S. (1998). *Fuzzy control*. 475.

Tian, Y. C., Zhao, F., Bisowarno, B. H., & Tadé, M. O. (2003). Pattern-based predictive control for ETBE reactive distillation. *Journal of Process Control*, *13*(1), 57–67. https://doi.org/10.1016/S0959-1524(02)00011-2

Wang, L. X., & Mendel, J. M. (1992). Generating Fuzzy Rules by Learning from Examples. *IEEE Transactions on Systems, Man, and Cybernetics*, *22*(6), 1414–1427. https://doi.org/10.1109/21.199466

Zadeh, L. A. (2009). Position Paper: Toward extended fuzzy logic; A first step. Fuzzy Sets and Systems, 160(21), 3175-3181. Retrieved 5 9, 2023, from https://sciencedirect.com/science/article/pii/s0165011409002140

PAPER 194 – REMEDIATION OF SPENT ENGINE OIL-CONTAMINATED SOIL BY THE USE OF BIOMATERIALS

J. M Stephen[1*], A. S Mohammed[1], B. O Atteh[1]

[1]Department of Agricultural and Bioresource Engineering, Federal University of Technology Minna, Niger State Nigeria
[*]Email: Stevejay62@gmail.com

ABSTRACT
This experiment was carried out in metropolitan Minna, the capital of Niger State. The study aimed to assess the effects of soil contamination with spent engine oil on some selected soil physiochemical properties. The experiment was set up in a completely randomized design in 3 replicates. The treatments consisted of 3 kg soil samples contaminated with 50, 100, 200 and 300 milliliters of spent engine oil, while the control sample was soil without added engine oil. The physicochemical properties of the soil samples before and after remediation were analyzed using standard methods. The contaminated soils showed a significant ($P<0.05$) increase in soil pH, bulk density and organic carbon (OC) contents compared to the control sample, while nitrogen, phosphorus and potassium decreased significantly ($P<0.05$). However, the pH, organic carbon, phosphorus and potassium values of each contaminated soil samples decreased significantly ($P< 0.05$) while the nitrogen content increased significantly after remediation of the contaminated soil samples using the biomaterials. The bulk density of the of the contaminated soil samples also decreased when treated with rice husk but increased when treated with sawdust.

KEYWORDS**:** spent engine oil, physicochemical properties, remediation, rice husk, sawdust.

1. Introduction

Soil serves as the primary recipient of waste products and chemicals utilized in modern industrial society (Brady and Weil, 2002). The prevalence of land contamination with spent engine oil is mainly observed in developing countries worldwide, primarily due to ineffective environmental laws (Adams et al., 2004). This ineffectiveness directly impacts the rate at which spent engine oil enters the environment, leading to pollution. The increased utilization of automobile engines and machinery has consequently resulted in higher rates of environmental contamination by used engine oil (Abioye et al., 2012). Spent engine oil contains hazardous substances, including heavy metals, aliphatic and aromatic hydrocarbons, benzenes, as well as sulphur and nitrogen (Mohammed and Amnah, 2012). These substances have detrimental effects on soil and soil microflora, such as reduced growth rate and reproduction, compromised health, and mutagenesis. As a result, they alter population dynamics, disrupt trophic relationships, and impact the structure of natural communities within ecosystems.

According to Tudararao-Aherobo and Mesogboriwon (2020) spent engine oil can be defined as used lubricating oils obtained after servicing and subsequently drained from automobile and generator engines. Spent oils contain a high percentage of aromatic and aliphatic hydrocarbons, nitrogen and sulphur compounds as well as metals such as Manganese, Calcium, Zinc and Lead. In contrast, fresh oils do not contain these contaminants. The impact of contamination by spent automobile oil in the environment has been shown to be more widespread than contamination by crude oil (Nwite, 2013). For instance, Nigeria was reported to account for more than 87 million litres of spent oil waste annually, yet sufficient attention has not been given to its disposal (Anoliefo and Vwioko, 2001). Large amounts of spent oil are released into the environment during manual oil changing operations, either intentionally by automobile and generator mechanics or accidentally through spills. The oil is dumped into water bodies, farmlands and open vacant plots use as mechanic workshops, resulting in pollution of both soil and water (Ikhajiagbe and Anoliefo, 2011). Osubor and Anoliefo (2003) conveyed that approximately 20 million gallons of spent oil are accumulated every year from mechanic workshops across Nigeria and disposed of carelessly into the environment.

When spent engine oil is introduced into the soil, it not only eradicates microbial life but also renders the soil inhospitable for worms and other small organisms. This inactivity leads to inadequate aeration in the soil, which can ultimately suffocate soil, reducing it to little more than dust. Soil polluted in this manner becomes unsuitable for any growth, requiring years of specialized treatment to restore its fertility.

Soil polluted in this manner becomes unsuitable for any form of growth, requiring years of specialized treatment to restore its fertility in contaminated areas.

Spent engine oil causes great damage to soil and soil microflora. It creates unsatisfactory conditions for life in the soil due to poor aeration, immobilization of soil nutrients and lowering of soil pH (Ugoh and Moneke, 2011). It has been shown that marked changes in properties occur in soil contaminated with hydrocarbon; this affects the

physical, chemical and microbiological properties of the soil (Okonokhua et al., 2007). At low concentrations, some of these heavy metals are essential micronutrients for plants, but they can cause metabolic disorders and growth inhibition when the concentration is high. Therefore, there is a need for remediation of spent engine oil-contaminated soil by the use of biomaterials.

2. MATERIALS AND METHODS

2.1 Study area

The study area for this research was the metropolitan Minna, the capital of Niger State. Niger State is located in the North Central Zone of Nigeria, while Minna town is located in the Eastern Senatorial district with a landmass of 1664km2. According to the 2006 census, Minna town had a human population of 3,488,180 persons (National Population Commission, 2006).

2.2 Sample collection

Soil samples with a long history of spent engine oil contamination were collected from a mechanic workshop located at Ketaren Gwari, Minna, Niger State, Nigeria. The samples were collected at a depth of 0-20 cm.
The contaminated soil samples were collected from eight (8) spots, each located 30 meters away from each other. These samples were then pooled together to obtain a composite sample. In contrast, the second control soil sample was obtained from Federal University of Technology, Minna, Niger State, which has no previous history of oil pollution.

.3 Collection of spent engine oil

Freshly drained used engine oil was obtained during motor service from a mechanic workshop located at Ketaren Gwari, Minna, Niger State, Nigeria. The oil was collected into a clean six-litre gallon and transported to soil and water laboratory (agricultural and bioresource engineering department).

2.4 Collection and processing of Amendment biomaterials

The biomaterials used as amendments are rice husk and sawdust. The rice husk was obtained from a rice mill located along Gidan Mango Road, Minna. The agricultural wastes (rice husk) were collected using a rack and shovel, air dried, ground and kept in clean polythene bags, while the sawdust was collected into a pan using a trowel, dried under the sun-dried for three (3) days and store in a plastic container. All processed samples were transported to the laboratory for further analysis.

2.5 Experimental Design

The experiment consisted of five samples, each weighing 3kg, and these samples were replicated three times. One of the samples served as a control, where no engine oil was added to the soil. The remaining four samples were mixed with varying amounts of used engine oil. Additionally, each soil samples mixed with spent engine oil was treated with the collected biomaterial at a ratio of 10:1.

C1 = Control (soil sample without used engine oil
E50 = Soil sample mixed with 50 millilitres of used engine oil
E100 = Soil sample mixed with 100 millilitres of used engine oil
E200 = Soil sample mixed with 200 millilitres of used engine oil
E300 = Soil sample mixed with 300 millilitres of used engine oil

2.6 Physicochemical analysis of the soil

The bulk density of the soil was determined through the core sampler method (George et al., 2013). The pH was determined using the glass electrode pH meter (1:1) (George et al., 2013). The total nitrogen was determined using the micro-Kjeldhal distillation method according to Bremner (1996). Available Phosphorus was determined by the Bray-1 method as described by George et al., (2013). The soil organic carbon was determined by the Walkley and Black wet dichromate oxidation method (George et al., 2013). Potassium was extracted with 1N ammonium acetate solution (NH_4OAC) and quantified using the flame photometer National Research Council (NRC, 1993).

2.7 Statistical analysis

The experimental data sets were collected in replicates, and the mean of the replicated measurements was used for further analysis. Descriptive statistics and the statistical significance at a 5% level of significance using one-way ANOVA were determined with IBM SPSS Statistics 20.

3. RESULTS AND DISCUSSION

3.1 Results

The physicochemical properties of the contaminated soil and the effect of the biomaterials on some selected physicochemical properties of the contaminated soil were analysed and are presented in Tables 1, 2 and 3.

Table 1: Effect of soil contamination with used engine oil on some selected soil Physicochemical properties

Samples	pH	BD (g/cm^3)	C (%)	N (%)	P (mg/kg)	K (mg/kg)
C1	6.22±0.01a	0.95±0.01a	1.35±0.02a	0.64±0.02d	33.93±0.02e	0.81±0.01e
E50	6.34±0.02b	1.24±0.02b	1.55±0.02b	0.35±0.03b	25.84±0.02d	0.76±0.02d
E100	6.67±0.02c	1.42±0.01d	1.66±0.02c	0.42±0.03c	20.12±0.01c	0.54±0.03c
E200	6.93±0.01d	1.37±0.03c	1.67±0.03c	0.24±0.02a	17.37±0.02b	0.46±0.02b
E300	7.34±0.03e	1.64±0.02e	1.87±0.02d	0.21±0.02a	14.73±0.03a	0.42±0.02a

Note: * Values followed by same superscript alphabet are not significantly different at (P<0.05) along the columns. Values are Mean ± SEM of triplicate determination.

Table 2: Effect of rice husk on some selected soil physicochemical properties of the contaminated soil

Samples	pH	BD (g/cm3)	C (%)	N (%)	P (mg/kg)	K (mg/kg)
C1	6.22±0.01a	0.95±0.01a	1.35±0.02a	0.64±0.02e	33.93±0.02e	0.81±0.01e
E50	6.27±0.03b	1.12±0.01b	1.51±0.02b	0.51±0.01d	28.56±0.02d	0.67±0.01d
E100	6.44±0.03c	1.25±0.02c	1.56±0.01b	0.44±0.02c	23.97±0.01c	0.56±0.02c
E200	6.58±0.01d	1.34±0.02d	1.62±0.02c	0.25±0.02b	20.02±0.01b	0.47±0.02b
E300	6.84±0.04e	1.46±0.02e	1.75±0.02d	0.19±0.01a	17.48±0.02a	0.32±0.01a

Note: * Values followed by same superscript alphabet are not significantly different at (P<0.05) along the columns. Values are Mean ± SEM of triplicate determination.

Table 2: Effect of sawdust on some selected soil physicochemical properties of the contaminated soil

Samples	pH	BD (g/cm^3)	C (%)	N (%)	P (mg/kg)	K (mg/kg)
C1	6.22±0.01a	0.95±0.01a	1.35±0.02a	0.64±0.02c	33.93±0.02e	0.81±0.01d
E50	6.32±0.01b	1.78±0.03b	1.40±0.02b	0.32±0.03b	29.68±0.03d	0.70±0.03c
E100	6.54±0.04c	1.82±0.03c	1.46±0.03c	0.29±0.04b	25.08±0.02c	0.44±0.01b
E200	6.62±0.04d	1.75±0.01b	1.51±0.01d	0.25±0.03a	21.12±0.02b	0.35±0.02a
E300	7.12±0.04e	1.75±0.02b	1.69±0.04e	0.25±0.01a	18.54±0.04a	0.36±0.01a

Note: * Values followed by the same superscript alphabet are not significantly different at (p<0.05) along the columns. Values are Mean ± SEM of triplicate determination.

3.2 Discussions

The results presented in Table 1 clearly demonstrate a significant increase in soil pH, bulk density, and organic carbon (OC) content when the soil was mixed with spent engine oil compared to the control sample without added engine oil. Conversely, other properties such as nitrogen, phosphorus, and potassium showed significant decreases. Additionally, with an increase in the concentration of spent engine oil, there was a gradual rise in pH, carbon, and phosphorus levels. Among the soil samples, E300 recorded the highest values of 7.34 for pH, 1.64 for bulk density, and 1.87 for carbon.

This finding regarding soil pH aligns with the results of Diana et al. (2004), who observed significantly higher pH values in hydrocarbon oil-contaminated soils. Bulk density is considered crucial for bioremediation because soil physical properties, directly and indirectly, influence factors affecting the degradation process, such as soil aeration, movement of nutrients through soil pores, and water-holding capacity (Vidali, 2001).

.

The increased carbon level in the contaminated soil may be a result of both the addition of used engine oil to the soil and the presence of hydrocarbons in the used engine oil (Tanimu et al., 2019). Conversely, the decrease in nitrogen, phosphorus, and potassium levels may be attributed to the increased concentration of spent engine oil. Kayode et al. (2009) observed a reduction in nitrogen content in soil treated with spent lubricant oil, and several authors have demonstrated that pollution by petroleum products can lead to decreased nitrogen levels in plants (Wyszkowski and Wyszkowska 2005). Phosphorus was also found to be reduced in oil-contaminated soils compared to the control, which aligns with the findings of Okonokhua et al. (2007). In their study, the phosphorus content decreased progressively from 5.76 ppm in the control to 4.85 ppm in the soil samples. Regarding exchangeable cations, potassium levels were generally higher in the control group than in the different levels of spent engine oil application.

The results of the effect of rice husk and sawdust on the physicochemical properties of contaminated soil are presented in Table 2 and Table 3. The pH, organic carbon, phosphorus, and potassium values of the contaminated soil samples significantly decreased, while the nitrogen content increased significantly after remediation using the two different biomaterials (rice husk and sawdust). The bulk density of the contaminated soil samples decreased

when treated with rice husk but increased when treated with sawdust. The significant increase in bulk density of spent engine oil-treated soil using sawdust could be attributed to compaction resulting from oil contamination as well as reduced porosity.

4. CONCLUSION

Spent engine oil pollution alters the pH of the soil and impacts its physiochemical properties. As the level of spent engine oil in the soil increases, several soil properties undergo changes. Specifically, properties like pH, bulk density, and organic carbon tend to increase, while nitrogen, phosphorus, and potassium levels tend to decrease. The results obtained indicated a significant improvement in the rate of remediation of contaminated soil through the application of biomaterials. Rice husk, which is known for its high nitrogen and phosphorus content, made a substantial contribution to the availability of these elements in the remediated soils. Additionally, the study revealed that rice husk outperformed sawdust in the remediation processes.

REFERENCES

Abioye, O.P., Agamuthus, P. & Abdul-Aziz, A.R. (2012). Biodegradation of used Motor Oil in soil using organic waste Amendments. *Biotechnology Research International*, 201(587), 115-122.

Adams, G.O., Tawari, P. & Igelenyah, E. (2014). Bioremediation of Spent Oil Contaminated Soils using Poultry Litter. *Research Journal in Engineering and Applied sciences*, 3(2), 118-124.

Anoliefo G.O., & Vwioko, D.E. (2001). Tolerance of chromolema odorota (L.) K and R grown in soil contaminated with spent lubricant oil. *Journal of Tropical Bioscience*, 1, 20-24.

Brady, N.C., & Weil, R.R. (2002). The Nature and Properties of Soils. New Jersey, *Pearson Education*, Inc. 837 pp.

Bremner, J. M. (1996). Nitrogen- Total. In: Sparks, D. L. (ed), Methods of Soil Analysis. Part 3, Chemical Methods. *American Society of Agronomy*, 5, 1086 – 1121

Diana B.R, Knight, J.D., Richard E.F, & James J.G (2004). Natural revegetation of hydrocarbon-contaminated soil in semi-arid grasslands. *Canadian Journal of Botany*, 82, 22-30.

George, E., Rolf, S., & John, R. (2013). Methods of Soil, Plant and Water Analysis: *Manual for West Asia and Africa Region, Third Edition*. International Center for Agricultural Research in the Dry areas (ICARDA).

Ikhajiagbe, B. & Anoliefo, C.O. (2011). Natural attention of a 14-month old waste engine oil polluted soil. *Journal of Basic and Applied Sciences*, 5(6): 925-930.

Kayode, J., Olowoyo, O., & Oyedeji, A. (2009) The effects of used engine oil pollution on the growth and early seedling performance of Vignauniguiculata and Zea mays. Research Journal of Soil Biology, 1,15–19

Mohammed, A.E. & Amnah, K.A. (2012). Bioremediation of contaminated soils with petroleum Hydrocarbons and their suitable *Environmental and biological conditions -2nd international conference on Ecological, Environmental and Biological sciences (EEBS)*. Bali Indonesia.

National Research Council (NRC). (1993). Committee on oil. Fate and Effects. Sources and Impacts of Contaminants in Soils. *National Academies Press*, 9p.

Nwite J. N. (2013). Evaluation of The Productivity of a Spent Automobile Oil Contaminated Soil Amended with Organic Wastes in Abakaliki, South Eastern Nigeria. Ph. D Thesis, Department of Soil Science, Faculty of agriculture, University of Nigeria, Nssuka. Pp 3.

Osubor, C.C. & Anoliefo, G.O. (2003). Inhibitory effect of spent lubricating oil on the growth and respiratory function of ArachushypogenaL. *Benin Science Digital*, 1, 73-79

Tanimu, J., Michael, G.I, & James, P.A. (2019) Effects of Contamination of Soil with Used Engine Oil on Some Soil Properties and Microbial Growth in Wukari, North Eastern Nigeria. *East African Scholars Journal of Agriculture and Life Sciences*, 2(6), 358-363

Tudararao-Aherobo, L., & Mesogboriwon, S. (2020). Bioremediation of Spent Engine Oil Contaminated Soils Using Indigenous Fungi Species. *International Journal of Scientific Research in Science and Technology (IJSRST)*, 7(2), 445-461.

Ugoh, S.C, & Moneke, L.U. (2011). Isolation of Bacteria from Engine Oil Contaminated Soils in Auto-mechanic Workshops in Gwagwalada, Abuja, FCT-Nigeria. *Academia Arena*, 3, 1-10.

Vidali, M. (2001). Bioremediarion: An overview. *Journal of Applied Chemistry*, 73(7),163-172.

Wyszkowski, M., & Wyszkowska, J. (2005). Effect of enzymatic activity of diesel oil contaminated soil on the chemical composition of oat (Avena sativa L.) and maize (Zea mays L). *Plant Soil Environment*, 5,360–367

PAPER 195 – EFFECTS OF IRON ORE TAILINGS (IOT) ON THE MECHANICAL PROPERTIES OF CONCRETE

F. Balarabe[1*], A. Mahmud[2]

[1,2]Department of Civil Engineering, Federal University of Technology, Minna, Nigeria
*Email: phartymah36@gmail.com

ABSTRACT
A lot of research has shown that iron ore tailings (IOT) is not only a source of pollutant but also has good pozzolanic properties. However, the behaviour of IOT concrete in service is yet to be fully reported. This research investigates the effect of IOT on the mechanical properties of concrete whose fine aggregates is partially replaced with IOT. Fine aggregates content in concrete of mix ratio 1:2:4 of 10 to 40% was replaced with IOT. Young's modulus and Poisson ratio of the resulting concrete beams were determined by compression test. The results showed that 20% replacement of fine aggregates by IOT in the concrete mix gave the best mechanical properties of the resulting concrete. The Young's modulus of the concrete was seen to increase by 26.53% when with 20% IOT content when compared to that without IOT. The Poisson ratio at 20% IOT content was seen to also decrease by 61.54% when compared to that without IOT. As such, 20% IOT for fine aggregate content replacement in concrete mix 1:2:4 is recommended for structural uses.

***KEYWORDS*:** Concrete, Fine aggregates, Iron ore tailings, Poisson ratio, Young's modulus

1. INTRODUCTION

The high demand of sand for construction purposes is increasing daily and the process of mining these aggregates from rivers and flood plains has led to environmental problems, which includes: water pollution, deforestation, collapsing of river banks, destruction of landscape and reduction of farm and grazing lands (Ako et al., 2014). Currently, one of the fundamental issues worldwide is achieving a sustainable environment and eco-friendly community through effective recycling of waste materials in the construction industries. Various research have broadly proven that waste materials from industries such as foundry sand, copper tailings, iron ore tailings, recycled concrete, fly ash, and ceramic waste can be utilized in the production of sustainable concretes (Obinna and Özgur, 2012; Sada et al., 2013; Adesina, 2018; Yufeng et al., 2019; Auta & Kabiru, 2020); Pinchi et al., 2020). Aggregates occupies 60%-80% of concrete's volume by mass and strongly influence the freshly mixed and hardened concrete's properties, mix proportions and economy. Aggregates are classified into two groups: fine and coarse. Fine aggregates consist of natural sand, manufactured sand or a combination of both with most particles smaller than 5 mm (Abdullahi, 2006). Aggregates must satisfy certain standards for optimum engineering use: they must be clean, hard, strong, durable particles free of absorbed chemicals, coatings of clay and other fine materials in amounts that could affect hydration and bond of the cement paste. The most suitable aggregate would appear to be one that is well graded with a balance between rounded and angular particles and a surface texture that is not too smooth (Abdullahi, 2006). Fine aggregates, being a major component of concrete, play a major role in determining the quality of concrete to be produced. Hence it is required to be of good physical properties.

Ineffective agricultural, urban and industrial wastes disposal have been shown to be a major environmental and health issue (Obinna and Özgur, 2012; Sada et al., 2013; Adesina, 2018; Yufeng et al., 2019; Auta & Kabiru, 2020); Pinchi et al., 2020). The results from previous research have demonstrated that effective utilization of these wastes in production of concrete is cost efficient, with reduced permeability, increased strength, will reduce the effects of environmental issues and loss of life of human and aquatic animals. These waste materials to name a few are: iron ore tailings (Yufeng et al., 2019); copper tailings (Obinna and Özgur, 2012); locust bean pod ash

(Auta and Kabiru, 2020); rice husk (Adesina, 2018); groundnut husk (Sada et al., 2013); crushed waste rocks (Li and wang, 2017); broken bricks (Pinchi et al., 2020); scrap tires (Sofi, 2018); plastics (Karthikeyan et al., 2019); crushed glass (Anju et al., 2017); blast furnace slag (Mujedu et al., 2018) and silica fume (Shanmugapriya and Uma, 2013) which are used either as a binder to partly or fully replace cement, used in varying combinations with fine or coarse aggregate in concrete, in their natural or processed states.

Elinwa and Maichibi (2014) evaluated the feasibility of utilizing Itakpe iron ore tailings (IOT) to replace sand and cement in concrete production. It was shown that Itakpe IOT has pozzolanic properties and can be used as retarders for hot water concreting. It was also shown that at 20% replacement for sand and cement in conventional concrete mix of 1:2.14:4.88 and water-cement ratio of 0.5, strength increase of 10% and 30% were observed for sand and cement respectively. It was noted that replacing IOT for sand in concrete up to 20% can be used with confidence for long term higher strength as the compressive strength of all the resulting concrete were higher than 20 kN/m^2.

Yufeng et al. (2019) investigated the properties of fresh and hardened concrete produced by incorporating iron ore tailings as a partial replacement for 10%-60% of fine aggregates for the preparation of high tensile-compressive strength concrete of C35 grade. It was maintained that addition of IOT beyond 30% resulted in low quality fresh concrete. From the hardened properties, only at 30% replacement level was the 28- and 90-days curing ages of the compressive strength of the concrete excellent when compared to the control. Percentage Increase of 4.90 and 4.61 were reported for both days respectively. This increase in strength was reportedly due to the pore filling ability of the IOT containing a good portion of particles passing sieve size 300 μm. Also, the tensile and flexural strength at all the replacement levels were investigated and found to be best at 30% IOT content. An increase of 76.32% and 40.38% was observed at 28- and 90-days curing ages respectively when compared to those at the control stage. For good shrinkage and crack property, IOT replacement for sand was recommended not to exceed 40%.

Effects of partial replacement of sand by iron ore tailings on the compressive strength of concrete was investigated by Shivam et al. (2017) and Mohamed et al. (2022). Grade M25 concrete was produced by Shivam et al. (2017) using a mix ratio of 1: 1.458: 2.529, water cement ratio of 0.45 by substituting iron ore tailings in proportions of 5% up to 20% for fine aggregates in the mix. The compressive strength of the hardened concrete showed a gradual improvement as the addition of IOT increased up to 15%. At 20% IOT content, the compressive strength decreased and this suggest usage of IOT only up to 15% if strength improvement is the only target. Mohamed et al. (2022) similar to Shivam et al. (2017) incorporated up to 40% IOT into concrete mix to replace fine aggregate. Mohamed et al. (2022) maintained that concrete mechanical and durability properties improved with IOT content obtained up to 14% strength improvement with 20% IOT content and recommended that the optimum percentages of IOT for fine aggregate replacement is between 30 and 40%.

Anju et al. (2017) investigated the compressive strength of grade M25 concrete produced by using a mix ratio of 1:1.7:2.5, water cement ratio of 0.45, iron ore tailings and glass powder for the partial replacement of fine aggregate at 10%, 20%, 30%, and 40% respectively. The compressive strength of the hardened concrete with 30% waste glass and IOT content at 28 days curing showed 5.8% increment when compared to the control but at 40% waste glass and IOT content, the compressive strength decreased which implies that 30% waste glass and IOT content replacement for fine aggregates in concrete mixes is the optimum replacement to achieve high strength concrete.

Zhao et al. (2014) reported that 100% replacement of natural aggregate with iron ore tailings in ultra-high-performance concrete resulted in decreased workability and compressive strength of the material. It also indicated that for 90 days standard cured specimens when the replacement level was not beyond 40%, the mechanical behaviour of the iron ore tailing (IOT) replaced concrete was comparable to that of the control mix. The specimens that were steam cured for 2 days, had reduction in the compressive strengths for the IOT replaced concrete to be less than 11% while there was up to 8% increase in flexural strength when compared to the control mix.

Ugama et al. (2014) investigated the properties of a rigid pavement using iron ore tailing (IOT) as fine aggregate for the replacement of sand (RS) by 20%, 40%, 60%, 80% and 100% respectively. In terms of density, iron ore tailings were classified as a heavy aggregate resulting in concrete pieces of heavier weight and thus recommended for use in concrete production for pavement with higher self-weight and smaller deformation under external loads. It was observed that with increasing IOT percentage, the workability of concrete reduced and at 20% IOT content, compressive strength of the concrete at 28 days curing decreased by 3.09%, the splitting tensile strength improved by 1.89% more than the control. Thus, the optimum replacement level for IOT content in concrete beam production is about 20%.

The foregoing shows that the incorporation of wastes into concrete mixes is not a new technology. In order to increase utilization of IOT, there is need to carry out extensive research on the effects of IOT on the mechanical properties of concrete to increase the percentage of tailings utilization and clear the suspicion of long-term effect. This research would focus on the compressive strength, modulus of elasticity and Poison ratio of concrete produced by partially replacing its fine aggregates contents with IOT.

2. MATERIALS AND METHODS

Many materials were used in the laboratory experiments conducted in this research in order to determine the physical properties of constituent materials for the production of concrete whose sand percentage is partially replaced by iron ore tailings and to determine the mechanical properties of the resulting hardened concrete.

2.1 Materials

The materials used in this research include:

i. Cement: Grade 43 Dangote Portland Cement, obtained from a cement depot at Mando area of Kaduna, Kaduna State was used for this work.

ii. Fine aggregates: Clean sharp sand all of which passed sieve size 5 mm obtained from a local dealer at Mando Roundabout in Kaduna, Kaduna State was used for this work.

iii. Iron Ore Tailings (IOT): Clean iron ore tailings all of which passed sieve size 5mm obtained from Itakpe in Kogi State was used for this work.

iv. Coarse aggregates: Crushed granites all of which passed sieve size 20 mm obtained from a local dealer at Mando Roundabout in Kaduna, Kaduna State was used for this work.

v. Water: Potable water from a bore hole located at the Civil Engineering laboratory at Nigerian Defence Academy Afaka, Kaduna was used for this work.

2.2 Methods

The data obtained from the specific gravity and bulk density tests carried out on the aggregates and iron ore tailings were used to batch the concrete.

Absolute Volume Method was used to prepare the concrete mix as shown in Table 1. The concrete was cast into 150 mm × 150 mm × 150 mm and 150 mm x 150 mm x 700 mm cast iron moulds in three levels with adequate tamping to remove trapped air and slump tests were conducted on the fresh concrete to check workability. Water curing method was used to cure the concrete produced. Compressive strength test was carried out on the 28 days curing 150 mm × 150 mm × 150 mm hardened concrete cubes. Modulus of elasticity and Poisson ratio of the hardened 150 mm x 150 mm x 700 mm concrete were also investigated from readings obtained while loading the beam to failure after three cyclic loadings from a predetermined basic stress to a predetermined upper stress according to the requirements of BS 1881 (1983).

The modulus of elasticity and Poisson ratio were determined from:

Modulus of elasticity, E_c =

Poisson ratio, μ =

Where;

σ_a is the upper loading stress (N/mm^2) ($\sigma_a = f_c/3$);

σ_b is the basic stress (i.e 0.5 N/mm^2);

ε_{aa} is the mean axial strain under the upper loading stress;

ε_{at} is the mean transverse strain under the upper loading stress;

ε_{ba} is the mean axial strain under the basic stress.

ε_{bt} is the mean transverse strain under the basic stress.

Table 1: Matrix of Concrete Ingredients for Concrete with IOT for Fine Aggregates

Concrete Type	Quantity of Fine Aggregates (kg)	Quantity of IOT (kg)	Quantity of Coarse Aggregates (kg)	Quantity of Cement (kg)	Quantity of Water (l)
0% IOT	16.09	0	32.18	8.04	4.82
10% IOT	14.54	1.62	32.30	8.08	4.85
20% IOT	12.97	3.24	32.43	8.11	4.87
30% IOT	11.39	4.88	32.55	8.14	4.88
40% IOT	9.80	6.54	32.68	8.17	4.90

3. RESULTS AND DISCUSSION

The result of mechanical properties experiments carried out on the IOT concrete produced are summarized and discussed below.

Compressive Strength

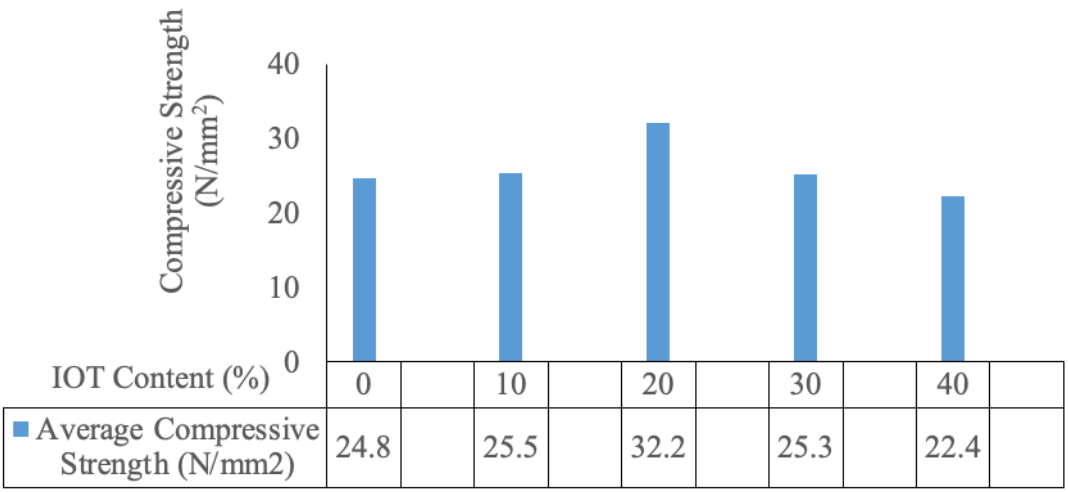

Figure 1: 28-Day Compressive Strength of IOT Concrete

The compressive strengths of the resulting concrete from incorporating IOT into concrete mix to replace fine aggregates is shown in Figure 1 above. It can be observed that the average 28-day compressive strength of the concrete without IOT is 24.76 N/mm^2. This is relatively adequate for a 1:2:4 concrete mix ratio with a target strength of 20 N/mm^2. The strength of the concrete without IOT was seen to increase from 24.76 N/mm^2 by 2.9% to 25.47 N/mm^2 with the replacement of 10% fine aggregates with IOT in the concrete mix. At 20% IOT for fine aggregates replacement in the mix, the strength gain of 30% was seen in the concrete's strength without IOT with 32.18 N/mm^2 28-day compressive strength value. This value was seen to further reduce with further IOT content beyond 20%. This suggests that 20% IOT replacement for fine aggregates is recommended for use in concrete mix of 1:2:4. This result is consistent with the work of Elinwa and Maichibi (2014); Mohamed et al. (2022); Ugama et al. (2014); and Yufeng et al. (2019).

Modulus of Elasticity

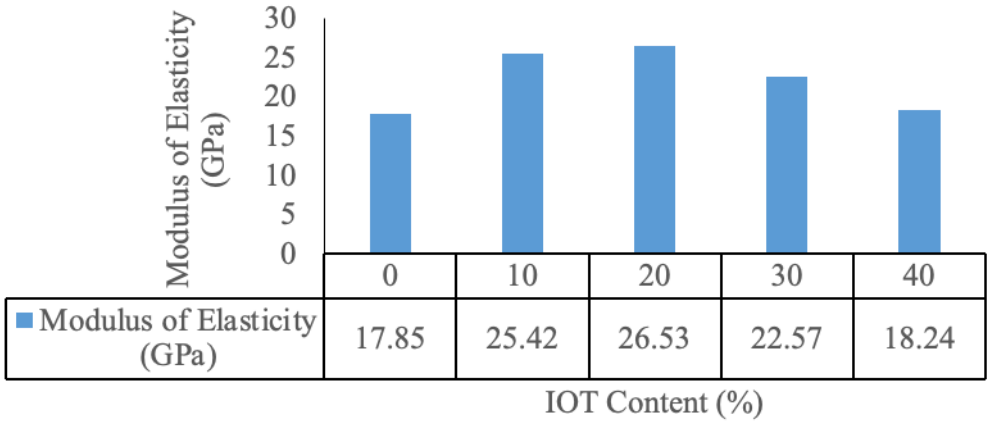

Figure 2: Modulus of Elasticity of IOT concrete

The modulus of elasticity of the IOT concrete is shown in Figure 2. From the figure, the modulus of elasticity is seen to increase from 17.85 GPa for concrete without IOT to 25.42 GPa for concrete with 10% IOT content. This represents a 42.41% increment in the strength capacity of the concrete without IOT by the replacement of 10% fine aggregate content with IOT. With IOT for fine aggregate content of up to 20%, the modulus of elasticity is seen to further increase to 26.53% indicating 48.63% increment to the strength capacity of the concrete without

IOT and 4.37% increment to that at 10% IOT content. Further additions of IOT beyond 20% resulted in lower modulus of elasticity below than that with 10% IOT. Modulus of elasticity of 30% and 40% IOT content concrete were obtained as 22.57 GPa and 18.24 GPa respectively. These indicate 26.44% and 2.18% increment respectively to the strength capacities of the concrete without IOT content and 14.92% and 45.45% decrement respectively in strength capacities to the concrete with 20% IOT content. Contrary to the behaviour of concrete containing 10% steel reported by Esfahani et al. (2016), the modulus of elasticity of the concrete can be optimally improved by the addition of 20% IOT for fine aggregates.

Poisson Ratio

The Poisson ratio of the IOT concrete is shown in Figure 3. From the figure, the Poisson ratio of 0.21 for concrete without IOT content increased to 0.23 when 10% portion of the fine aggregate in the concrete mix was replaced by IOT. This represents 9.52% increment in the Poisson ratio when 10% fine aggregate was replaced by IOT represents a proportional increase in the deformation ability of the concrete when 10% IOT was introduced. With 20% IOT for fine aggregate in the concrete mix, the Poisson ratio decreased from 0.21 to 0.13. This represents 61.54% decrease in the deformation of the concrete when 20% IOT was introduced in the mix. With 30% and 40% IOT substitution for fine aggregate in the concrete mix, the Poisson ratios were 0.25 and 0.28 respectively. These represent 19.05% and 33.33% increments respectively in the deformation ability when compared to the concrete without IOT content. When compared to the concrete with 20% IOT content, they further increased by 92.31% and 115.38% respectively. This result shows a decrease in Poisson ratio which indicates improved deformation ability of the IOT concrete was observed only at 20% IOT content.

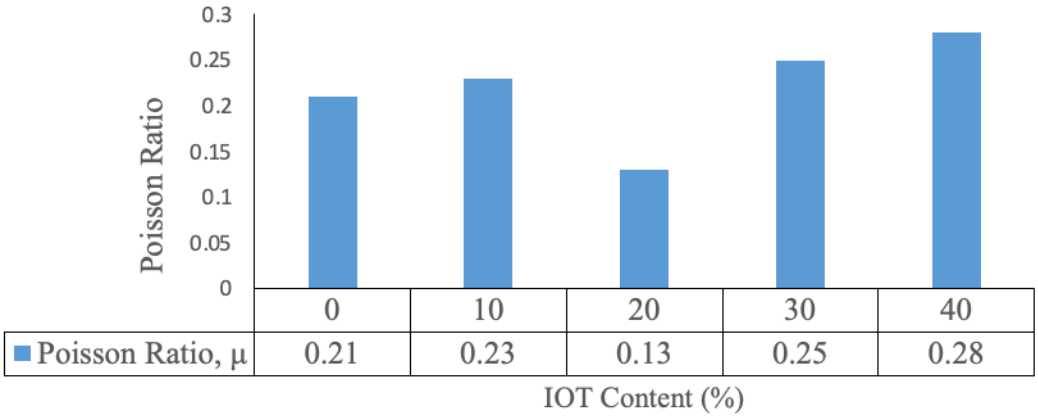

Figure 3: Poisson Ratio of IOT concrete

4. CONCLUSION

The effects of iron tailings (IOT) on the mechanical properties of concrete have been carried out and the results have been presented, analysed and discussed. From the study, the following conclusions were drawn:

i. The mechanical properties of the IOT concrete used in this research showed that the day 28 water cured compressive strengths of the concrete without (0%) IOT, and those with 10%, 20%, 30% and 40% IOT replacement for fine aggregates are 24.76 N/mm^2, 25.47 N/mm^2, 32.18 N/mm^2, 25.29 N/mm^2 and 22.36 N/mm^2 respectively.

ii. The modulus of elasticity obtained from the concrete without (0%) IOT, and those with 10%, 20%, 30% and 40% IOT replacement for fine aggregates are 17.85 GPa, 25.42 GPa, 26.53 GPa, 22.57 GPa and 18.24 GPa. Their Poisson ratio are also 0.21, 0.23, 0.13, 0.25 and 0.28 respectively.

iii. The mechanical properties of the IOT concrete were observed to be best at 20% IOT for fine aggregates replacement in the mix. As such, 20% IOT content for fine aggregates can be incorporated into structural concrete mix

ACKNOWLEDGEMENT

The authors are especially grateful to the Department of Civil Engineering, Nigerian Defence Academy, Kaduna, Nigeria for providing the laboratory and equipment for carrying out this research.

REFERENCES

Abdullahi, M. (2006). Properties of Some Natural Fine Aggregates in Minna, Nigeria and Environs. *Leonardo Journal of Sciences, 5*(8), 1-6.

Adesina, A. (2018). Use of Rice Husk in Concrete: Review of Mechanical Properties. 15-52.

Ako, A. T., Onoduku, S. U., Oke, A. S., Essien, I. B., Idris, N. F., Umar, N. A. and Ahmed, A. A. (2014) Environmental Effects of Sand and Gravel Mining on Land and Soil in Luku Minna, Niger State, North Central Nigeria. *Journal of Geosciences and Geomatics. 2*(2), 42-49.

Anju, M. T., Abhishek, V., Albin S., and Jerison, S. J. (2017). Partial Replacement of Fine Aggregate with Iron ORE Tailings & Glass Powder. *International Journal of Science Technology & Engineering (IJSTE)*, *3*(11), 351-357.

ASTM C33-03 (2001). Standard Specifications for Concrete Aggregates, Annual book of ASTM Standards, American Society for Testing and Materials, Philadelphia, PA.

Auta, S. M., and Kabiru, A. (2020). Effect of Locust Bean Pod Epicarp Ash (LBPEA) on the Compressive Strength of Revibrated Concrete. *Construction of Unique Buildings and Structures*, *90*(9002) https://doi.org/10.18720/CUBS.90.2

BS 1881 part 121 (1983). Method for Determination of Static Modulus of Elasticity in Compression, British Standard Institute (BSI), 2 Parks Street, London.

Elinwa, A. U., and Maichibi, J. E. (2014). Evaluation of the Iron Ore Tailings from Itakpe in Nigeria as Concrete Material. *Science Publishing Group, Advances in Materials*, *3*(4), 27-32. https://doi.org/10.11648/j.am.20140304.12

Esfahani, M. S. Janbaz, S. Mirmazhari, S. (2016). Effect of Various Types of Fillers on Mechanical Properties of Concrete. International Journal of Civil Engineering, Construction and Estate Management, 4(3), 20-28.

Karthikeyan, M., Balamurali, K., Barath, K. V., Manoj, P. S., and Janarthanan, R. (2019). Utilization of Waste Plastic in Concrete. *International Research Journal of Engineering and Technology (IRJET), 6*(4), 1400-1405.

Li, B., and Wang, W. (2017). Assessment of Mechanical and Durability Properties of High Strength Concrete Using Iron Ore Tailings and Waste Rock as Aggregates. *International Journal of Civil & Environmental Engineering (IJCEE)*, *17*(1), 1-9.

Mohamed, M. A., Muwaffaq, A., Ali, M., Jawad, A., and Ahmed, F. D. (2022). Concrete made with Iron ore Tailings as a Fine Aggregate: Step towards Sustainable Concrete. *Materials,* 15, 6236. https://doi.org/10.3390/ma15186236

Mujedu, K. A., Lamidi, I. O., Familusi, A. O., and Olatunji, A. A. (2018). Utilization of Blast Furnace Slag as Coarse Aggregate in Concrete Production. *The International Journal of Engineering and Science (IJES)*, *7*(11), 50-57. https://doi.org/10.9790/1813-0711025057

Obinna, O., and Özgur, E. (2012). Copper Tailings as a Potential Additive in Concrete: Consistency, Strength and Toxic Metal Immobilization Properties. *Indian Journal of Engineering and Materials Sciences*, 79-86.

Pinchi, S., Ramírez, J., Rodríguez, J., and Eyzaguirre C. (2020). Use of Recycled Broken Bricks as Partial Replacement of Coarse Aggregate for the Manufacturing of Sustainable Concrete. IOP Conf. Series: *Materials Science and Engineering.* https://doi.org/10.1088/1757-899X/758/1/012039. 1-5.

Sada, B. H., Amartey, Y. D., and Bako, S. (2013). An Investigation into the Use of Groundnut Shell as Fine Aggregate Replacement. *Nigerian Journal of Technology* (NIJ*OTECH)*, *32*(1), 54–60.

Shanmugapriya, T., and Uma, R. N. (2013). Experimental Investigation on Silica Fume as Partial Replacement of Cement in High Performance Concrete. *The International Journal of Engineering and Science (IJES)*, *2*(5), 40-45.

Shivam, T., Anubhav, R., and Bajpai, Y. K. (2017). Effect of Partial Replacement of Sand by Iron Ore Tailings on the Compressive Strength of Concrete. *International Research Journal of Engineering and Technology (IRJET)*, *4*(12), 1169-1173.

Sofi, A. (2018). Effect of Waste Tyre Rubber on Mechanical and Durability Properties of Concrete. *Ain Shams Engineering Journal, 9*(2018), 2691–2700. https://doi.org/10.1016/j.asej.2017.08.007

Ugama, T. I., Ejeh, S.P., and Amartey, D. Y. (2014). Effect of Iron Ore Tailing on the Properties of Concrete. *International Institute for Science, Technology and Education (IISTE). Civil and Environmental Research, 6*(10), 7-13.

Yufeng, J., Hao, W., Yue, C., Min, R., and Wen, L. (2019). Preparations of Composite Concretes Using Iron Ore Tailings as Fine Aggregates and Their Mechanical Behaviour. *Materials and technology, 53*(4), 467–472.

Zhao, S., Fan, J., and Sun, W. (2014). Utilization of Iron Ore Tailings as Fine Aggregate in Ultra-High-Performance Concrete. *Construction and Building Materials*, *50*, 540–548. https://doi.org/10.1016/j.conbuildmat.2013.10.019

PAPER 196 – OVERVIEW STORAGE TECHNIQUES AND QUALITY EVALUATION OF FRUITS AND VEGETABLES FOR MINIMA POSTHARVEST LOSSES

S.E. Chukwu[1], A. A. Nworji [2], A.I. Oyebanji[1], E. K. Gbabe[1], A.O. Usman[1]

[1]Department of Postharvest Engineering Research, Nigerian Stored Product Research Institute,Ilorin, Nigeria.

[2]Department of Research Outreach, Nigerian Stored Product Research Institute, Ilorin, Nigeria.

Email: obanjiometer87@gmail.com

ABSTRACT

Appropriate Storage techniques and quality evaluation constituted two major phases in any postharvest, as it determines the degree of probable loss likely to experience in any postharvest. Harvesting is considered as the first step in the vegetable and grain supply chain and it is a criticaloperation in deciding the overall crop quality, due to inadequacy in post- harvest practices 30 to 43 percent of agricultural product are often lost. The motivation for this research was strengthenby the fact that postharvest storage techniques and concomitant quality evaluation are seldom treated and less than 5% research funding has been allocated for this issue in previous years. Related few literatures on spotlight were relative old and lack technical innovations. Thus, attemptwas made in this paper to write a overview on various storage techniques and it corresponding quality impactas it concern fruits and vegetables for minima postharvest losses. Finding here indicates that eachmeasure taken to reduce postharvest losses has a direct impact on the nutritional and sensory quality of produce. All pre and postharvest practices directly affect produce quality and therefore should be evaluated from a plant physiology and pathology point of view in addition to food chemistry and food nutrient aspects.

KEYWORDS**:** Storage, Techniques, Quality Evaluation, Minimal, Fruits and Vegetables, Postharvest Losses

1. Introduction

Fruits and vegetables are important sources of vitamins, minerals, and fibers. Including, fruits and vegetables in diet, add to healthy living fights and retard speedily development of several diseases(Adhikari, 2021). Increased consumption of fruits and vegetables has been associated with a reduced risk of cancer and heart diseases in many epidemiological studies, thus highlighting theirbeneficial health properties. In the accordance with the findings of Gamrasni *et al.,* (2020) fruits and vegetables qualities refer to extrinsic characteristics such as size, shape, color, and firmness. These visual attributes, together with sensorics parameters such as scent and taste, affect consumers' acceptance, and thus have a direct economic implication. However, in recent years there has been a growing awareness of the intrinsic factors of nutritional and functional attributesrelated to phytonutrient content, such as minerals, vitamins, dietary fibers, and other phytochemicals that determine the nutritional values of fresh produce and directly or indirectly affect consumers' health.

In addition, postharvest loss includes the food loss across the food supply chain from harvesting of crop until its consumption (Aulakh *et al.,* 2013). The losses can broadly be categorized as weightloss due to spoilage, quality loss, nutritional loss, seed viability loss, and commercial loss (Boxall,2001). Magnitude of postharvest losses in the food supply chain vary greatly among different crops, areas, and economies. In developing countries, eagerness to make the best use of the food produced is well profound. However, a significant amount of produce is lost in postharvest operations due to a lack of knowledge, inadequate technology, evidently poor storage infrastructure. Later submission of FAO (2011) estimated postharvest losses in fresh produce to be 5% to 25% in developed countries and 25% to 50% in developing countries which is debilitatingand scaring. Therefore, pleading remedies and thorough investigation, such a menace

constitute strongly the basis of this research. In the last few decades, most of the countries have focused on improving their agricultural production, land use, and population control as their policies to cope with this increasing food demand. Thus, downplayed postharvest loss (PHL) as well as the best candidate techniques employable for identified grains, fruit, or vegetable. It important to bring to the fore the implication of such a negligence which constitute a critical issue. This assertion was further strengthened by the claims of Deepak and Prasanta (2017) affirmed that postharvest storage technique were seldomly researched and less than 5% research funding has been allocatedfor this issue in previous years. Deepak and Prasanta (2017) further reiterated that current literatures on subject of reckon where relatively old (Bourne, 1977; Greeley, 1986 and Pantenius,1988) and lack technical innovation needed for dynamic and revolving agricultural system.

In recent years, the field of postharvest handling of fresh produce faced few technological advances, that lunch the combination online monitoring of the environment or produce state and active modulation of storage conditions with the emerging discipline of modelling based on big data and artificial intelligence (AI) tools both introduces opportunities and challenges to the field.This research will provide insights and gives thorough overview of storage techniques and qualityevaluation of fruits and vegetables for minima postharvest Losses.

2. MATERIALS AND METHODS

This study employed desktop analysis which was conducted by extensive literature review from available documents and reports from current journals, textbooks on pre-harvest and post-harvestfood safety programmes of selected developed and developing nations.

3. RESULTS AND DISCUSSION

3.1 Synopsis of Postharvest Activities

Sorting and grading fruits and vegetables are necessary for selling the products at the appropriateprice in the market. Sorting is done as it helps in the removal of diseased, damaged products fromthe healthier ones. The chance of the spread of disease and infection from infected products to healthier ones is avoided through sorting (Prasad and Paul, 2021).

Pre-cooling is defined as the removal of field heat carried out after the harvest of the crop to slowdown the rate of metabolism and to reduce the rate of deterioration. It is the first step carried out in temperature management. Pre-cooling methods like room cooling, forced air cooling, hydro cooling, ice-cooling, and vacuum cooling can be used for fresh produce based on the characteristicsof produce (Mercier *et al.,* 2019). For instance, pre-cooling process gained reasonable measure ofacceptance in fruit and vegetable handling. Table 3.1 drew attention on sub-component of pre- cooling and latent strength of each identify method. Thus, the main objective of pre-cooling is to minimize the effect of microbial activity, ethylene production, and the rate of respiration.

Table 3.1. Composite Pre-cooling Method

Pre-cooling methods	Description	Suitable for Fruits/Vegetable
Room cooling	Crops are placed in a cold room where cold air passes through a fan which servesas a unit of refrigeration.	Cabbage, tomato, pumpkin, Squash, raw mango.
Forced air cooling	Crop receives cold air directly at highvelocity. There is a high chance of desiccation of crops	Cabbage, carrot, cauliflower, strawberries.
Hydro cooling	Crops are submerged in cold water. The heat exchanger is used to maintain water temperature. It helps in faster cooling andis mainly used for vegetable.	Pomegranate, asparagus, beans, cucumber.

Ice cooling	Crops packed in boxes are cooled by this method.	Asparagus,	broccoli, greenonions
Vacuum cooling	Crops that don't have thick wax cuticles are cooled by this method. The main disadvantage of this method is crop weight is reduced by 1% for every 5 or 6 reductions in temperature.	Lettuce,	leeks, Chinesecabbage

Source: Gross *et al.,* (2016)

However, the important of packaging can never be overemphasis. Packaging materials are used towrap the fresh produce to save them from mechanical, biological damage during handling operations of fruits and vegetables. The packaging requirements depend on various factors such as susceptibility to water loss, microbial infections, heat accumulation, and primary consideration onthe type of package needed. Suffice to know, that choose of packaging material have a reserve effect as it was brought to fore in Table3. 2. Plastic bags (polyethylene films) are mainly used for the packaging of fruits and vegetables as film bags are clear, less expensive, and allow easy inspection of the items. Cabbage, potatoes, citrus, apples can be shipped easily in corrugated fiberboard boxes. Oranges, onions, are transported using jute sacks/bags woven from propylene whereas basket woven from palms is used for tomatoes packaging **(**Idah *et al.,* 2007). As further elaborated by Table3.2.

Table 3.2. Effect of packaging materials and methods on the shelf life of fruits and vegetables

Food/Treatment	Packaging materials	Shelf life	Reference
Peach, Cauliflower, Truffle	Tray: polypropylene Cover: PE-LD/PET(40 µm),0- 14 micro perforated package, all wrapped in PE	4 days at 4 °C	Gonzalez-Buesa *et al*.,2009`
Strawberry	stretch PVC	8 days at 1 °C	Nunes *et al.,* 1995
Minimally Processed fruits (kiwi, banana and prickly pear)	1) PE/Al/PET 2) Coex.polyolefinic high permeable film	4-12 days at 5 °C	Del Nobile *et al*., 2007
Sweet cherry	5 % O2 + 10 % CO2	80 days at 1 °C	Ai-Li *et al.* 2002
	PE: 13-18 % O2 + 2-4 % CO2	40 days at 1 °C	
	70 % O2 + 0 % CO2	20 days at 1 °C	

	Air	30 days at 1 °C	
Cactus pear fruits	Cryovac MY 15	9 days at 4 °C	Piga *et al*., 2003
	Plastic box		

* PE-LD: low-density polythene, PVC: poly (vinyl chloride), PE:Polyethylene, PP: Polypropylene, OPS: oriented polystyrene and MAP: Modified atmosphere packaging

3. 2 Postharvest Storage Techniques and Quality Implication

Generally, fruit and vegetable are metabolically active, even after harvest, until they are either processed or consumed as opined by Ziv and Fallik (2021). However, depends on the storage conditions, various physiological processes, such as respiration, ripening, and senescence, can significantly impact on the quality and shelf life of fruits and vegetables. Since fresh produce is not sterile, the storage time of fresh produce also largely depends on interactions with other organisms in its environment, namely pathogenic microorganisms, insects, and other pests. The two major, processes causing fruit and vegetable deterioration is tracing to the physiological deterioration, which involves water loss, softening, ripening, and shedding of leaves and microbial

decay, caused by pathogenic bacteria, yeasts, or molds. All are dependent on environmental conditions and greatly interact with one another.

The most prevalent approach to preserve fruit quality and to reduce produce loss after harvest is to delay ripening and senescence. Fruit ripening involves several metabolic processes that differ between 'climacteric' and 'non-climacteric' fruits. During the ripening of climacteric fruit, respiration increases until it reaches a peak, which is accompanied by an increase in ethylene production. In contrast, respiration of non-climacteric fruit does not increase during ripening, andethylene is not required in order to complete the ripening process. Regardless of the type of ripening, this process, as well as other metabolic processes that lead to deterioration, are driven byrespiration. After harvest, the fresh produce continues to respire—utilising food reserves taking inoxygen, and releasing carbon dioxide and heat from stored carbohydrates. For that reason, postharvest treatments that reduce respiration will delay deterioration processes, prolong shelf life, and help to maintain produce quality (Ai-Li *et al*., 2002).

Consequently, Cold storage is the most frequently used practice to decrease metabolic activity. However, low-temperature (LT) storage conditions must be adjusted and optimized for each specific type of produce. Additionally, other storage conditions such as humidity and air composition should be adjusted for the best results (Adeeko *et al.,* 2020).Thus, it is necessary to determine the optimal storage conditions to prolong fruit and vegetables' storage time for instance Paulauskiene *et al.,* (2020) specifically indicated controlled atmosphere (CA) for kiwifruit storedin an atmosphere containing 2% oxygen (O_2) and 5% carbon dioxide (CO_2) at 0 °C led to the greatest increase in the soluble solids content and dry matter content after 6 weeks of storage in fruit of all cultivars. Paulauskiene *et al.,* (2020) further reiterated that different air parameters in the storage chambers had different effects on the synthesis of pigments in fruit, but the content ofpigments increased most in fruit stored in the chamber with atmospheric parameters 0.5% O_2 + 1% CO_2. More recent research has shown that dynamic controlled atmosphere (DCA) or ultra-low oxygen (ULO) for apples, are increasingly gaining acceptance as a chemical-free process to prolong storage time. Koricanac *et al.,* (2020) observed that various qualitative parameters changed differently, depending on the applied storage technique. 'Golden Delicious' apples fromthe ULO chamber had a lower weight loss and significantly higher content of total phenols, flavonoids, and antioxidant capacity, compared with fruit stored in normal atmosphere (NA). However, 'Idared' apples stored under NA conditions exhibited better quality traits during shelf life in comparison with fruit from the ULO chamber.

Ethylene is the plant hormone best-known for its effect on fruit ripening. The inhibition of ethylene synthesis is advantageous because inhibiting ethylene production delays processes related to fruitripening, that is softening, chlorophyll degradation, and the breakdown of complex sugars, for instance, breaking down of starch, into simple sugars. Reducing ethylene synthesis by LT/CA storage and/or by application of the competitive ethylene antagonist, 1-methylcyclopropene (1- MCP), which blocks the response of plants to ethylene, can greatly delay the ripening of climacteric fruits, and additionally alleviate physiological

disorders such as scald in apples (Dällenbach *et al.,* 2020). However, treatment of 1-MCP for late-harvested apples stored in CA increased flesh browning (Jung and Cho, 2020). Indication that more work is required to optimizeperformance of this treatment. Interestingly, co-regulation of methionine biosynthesis, ethylene production, and respiration in 1-MCP-treated tomatoes has shed new light on the effect of this treatment on fruit physiology and may facilitate the improvement of its implementation (Gamrasni*et al.,* 2020). While manipulating ethylene production is a common practice, the increase in applications of other growth regulators, such as salicylic acid and the polyamine putrescine, holdsgreat promise to extend the repertoire of postharvest treatments and resultantly prolong the storagetime of non-climacteric fruits, such as mandarins (Gamrasni *et al*., 2020).

It pertinent to know that, both genetic background and environmental parameters can significantlyaffect postharvest performance. Genotypic background and pre-harvest climatic conditions were found to affect the head quality and post-harvest performance of freshly cut broccoli (Conversa *et al.,* 2020**)**. Similarly, cultivars and cultivation seasons were found to have a significant effect onthe postharvest quality and shelf lives of baby leaves (spinach and 'wild' rocket) while maturity atharvest, the weather during the growing season, and orchard management greatly affected the flesh-browning of apples stored at CA (Koukounaras *et al.,* 2020) . Another example of the geneticeffect on shelf life was demonstrated in the fruit quality of six different cultivars of mangoes as well as for three acorn squash cultivars that were found to differ in susceptibility to cold storage temperatures and fungal decay (Adeeko *et al.,* 2020). In addition, agrotechnical practices such asthe grafting of cucurbitaceae vegetables such as watermelons, or the training and pruning of fruit trees such as mangoes were shown to significantly affect fruit quality and postharvest performance (Sharma *et al.,* 2018). Furthermore, the pre-harvest application of pro hydro jasmon (PDJ) or abscisic acid (ABA) induced a red colour in mango fruits that were exposed to sunlight at the orchard, which consequently reduced their susceptibility to fungal decay during storage (Kumar *et al.,* 2020). All of these parameters for preharvest handling play important roles and affect the postharvest performance of fresh produce; thus, methods for controlling and manipulating these parameters have great potential to be used as part of an integrated management system.

4. CONCLUSION

Suffices to note that while the shelf lives of horticultural commodities is dependent on postharvest handling, shelf life is also significantly affected by a wide range of pre-harvest factors. it is important to note that each measure taken to reduce postharvest losses has a direct impact on the nutritional and sensory quality of fresh produce. All pre and postharvest practices directly affect produce quality and therefore should be evaluated from a plant physiology and pathology point ofview in addition to food chemistry and food nutrient aspects. Specifically, as integrated approachesincreasingly become a common practice, a standard evaluation of fruit and vegetable sensory andnutritional quality is essential, in parallel with the development of high-throughput evaluation means for the chemical composition of fresh produce. Two examples demonstrating such efforts include the evaluation of mineral (calcium) content in apples by the use of X-ray fluorescence, andthe use of an ultrasound-assisted extraction method for extracting antioxidants in chokeberries to provide a more accurate quality evaluation.

REFERENCES

Adeeko, A., Yudelevich, F., Raphael, G., Avraham, L., Alon, H., Presman, M.Z., Alkalai-Tuvia, S., Paris,H.S., Fallik, E., Ziv, C.(2020). Quality and Storability of Trellised Greenhouse-Grown,Winter- Harvested, New Sweet Acorn Squash Hybrids. *Agronomy* 2020, 10, 1443

Adhikari, B. (2021). Post-harvest practices of horticultural crops in Nepal: Issues and management. Archives of *Agriculture and Environmental Science,* 6(2), Pp. 227–233. https://doi.org/10.26832/24566632.2021.0602015.

Ai-Li, J., Sjhi-Ping T., Yong, X. (2002) Effects of Controlled atmosphere with high-O2 or high-CO2 concentrations on postharvest physiology and storability of Napoleon sweet cherry, *Acta Botanica*Sinica, 44(8), pp. 925—930

Aulakh, J., Regmi, A., Fulton, J.R., Alexander, C. (2013) Estimating post-harvest food losses: Developinga consistent global estimation framework; Proceedings of the Agricultural & Applied EconomicsAssociation's 2013 AAEA & CAES Joint Annual Meeting; Washington, DC, USA. 4–6 August 2013.

Bourne, M. (1977) Post Harvest Food Losses—the Neglected Dimension in Increasing the World Food Supply. Department of Food Science and Technology, Cornell University; Ithaca, NY, USA: 1977.

Boxall, R.A. (2001). Post-harvest losses to insects: A world review. International Biodeterior. Biodegrad. 2001;48:137–152. doi: 10.1016/S0964-8305(01)00076-2.

Conversa, G., Lazzizera, C., Bonasia, A., Elia, A. (**2020).** Harvest Season and Genotype Affect Head Quality and Shelf-Life of Ready-to-Use Broccoli. *Agronomy* **2020**, 10, 527.

Dällenbach, L.J., Eppler, T., Bühlmann-Schütz, S., Kellerhals, M. and Bühlmann, A. (2020). Pre- and Postharvest Factors Control the Disease Incidence of Superficial Scald in the New Fire Blight Tolerant Apple Variety "Ladina". *Agronomy* 2020, 10, 464.

Deepak and Prasanta (2017) Reducing Postharvest Losses during Storage of Grain Crops to Strengthen Food Security in Developing Countries. PubMed Center. Published online 2017 Jan 15. doi: 10.3390/foods6010008

Food and Agriculture Organzation (2011). Global Food Losses and Food Waste–Extent, Causes and Prevention; FAO: Rome, Italy, 2011.

Gamrasni, D., Feldmesser, E., Ben-Arie, R., Raz, A., Tabatznik Asiag, A., Glikman, M., Aharoni, A. andGoldway, M. (2020). Gene Expression in 1-Methylcyclopropene (1-MCP) Treated Tomatoes during Pre-Climacteric Ripening Suggests Shared Regulation of Methionine Biosynthesis, Ethylene Production and Respiration. *Agronomy* 2020, 10, 1669..

Gross, K. C., Wang, C. Y., and Saltveit, M. E., 2016. The commercial storage of fruits, vegetables, and florist and nursery stocks. Agricultural Research Service, United States Department of Agriculture,66(66), Pp. 68–70. www.ntis.gov.

Idah, P. A., Ajisegiri, E. S. A., and Yisa, M. G. (2007). Fruits and Vegetables Handling and Transportationin Nigeria. *Au Journal of Technology,* 10(3), Pp. 175–183.

Jung, S.K. and Choi, H.S. (2020). Browning of Early and Late-Harvested 'Empire' Apples Affected by Cold Storage and 1-MCP. Agronom**2020**, 10, 1050.

Koricanac, A., Miletic, N., Popovic, B., Mitrovic, O., Lukic, M., Pešakovic, M and Tomic, J. (2020**)** TheEffect of ULO and NA Storage on Changes in the Quality of Apple Fruit (Malus domestica Borkh.)during Shelf Life. *Agronomy* **2020**, 10, 25.

Koukounaras, A., Bantis, F., Karatolos, N., Melissas, C., Vezyroglou, A. (2020). Influence of Pre-HarvestFactors on Postharvest Quality of Fresh-Cut and Baby Leafy Vegetables. *Agronomy* 2020, 10, 172.

Kumar, S.P., Maurer, D., Feygenberg, O.,Love, C., Alkan, N. (2020) Improving the Red Color and FruitQuality of 'Kent' Mango Fruit by Pruning and Preharvest Spraying of Prohydrojasmon or AbscisicAcid. *Agronomy* **2020**, 10, 944.

Mercier, S., Mondor, M., McCarthy, U., Villeneuve, S., Alvarez, G., and Uysal, I. (2019). Optimized coldchain to save food. Saving Food: Production, Supply Chain, Food Waste and Food Consumption, Pp. 203–226. https://doi.org/10.1016/B978-0-12-815357-4.00007-9.

Pantenius, C. (1988) Storage losses in traditional maize granaries in Togo. *International Journal of Tropical Insect Science.* 1988;9:725–735. doi: 10.1017/S1742758400005610.

Paulauskiene , A., Taraseviciene, Z., Zebrauskiene, A., Pranckietiene, I. (**2020**). Effect of Controlled Atmosphere Storage Conditions on the Chemical Composition of Super Hardy Kiwifruit. *Agronomy* **2020**, 10, 822.

Prasad, K., and Paul, J. R., 2021. Postharvest Losses of Papaya and Practice for Management. Food and Scientific Reports, 2(February), Pp. 7–11.

Sharma, S., Barman, K., Siddiqui, M.W., Nath, V. (2018) Chapter 10-Training and Pruning for ImprovedPostharvest Fruit Quality. In Preharvest Modulation of Postharvest Fruit and Vegetable Quality; Siddiqui, M.W., Ed.; Academic Press: Cambridge, MA, USA, 2018, pp. 257–276.TX, USA.

Ziv, C. and Fallik, E. (2021). Postharvest Storage Techniques and Quality Evaluation of Fruits and Vegetables for Reducing Food Loss. *Agronomy* 2021, 11, 1133. https://doi.org/10.3390/agronomy11061133.

PAPER 197 – TECHNO-ECONOMIC ANALYSIS OF WIND ELECTRIC ENERGY GENERATION IN BENIN CITY

T. Abdulraheem[1], Y. A. Yisah[1], S.O. Igbinovia [2], S.O. Anaza[1], & O.S. Imadu[1]

[1]Power Equipment and Electrical Machinery Development Institute, Okene, Kogi State.
[2]Department of Electrical and Electronics Engineering, University of Benin, Edo State.
Email: mytajuddeen@gmail.com

ABSTRACT
All over the world, attention is now being focused on producing electricity from renewable energy sources rather than the conventional use of fossil fuel. Nigeria is not an exception in this regard, especially when supply is grossly inadequate to meet the demands of her growing population. This study presents a techno-economic analysis for generating electricity from wind in Benin City, Edo State. Wind speed data was obtained from Nigerian Meteorological Agency, Edo State. Analysis of the wind data obtained shows that due to the low wind speed, the size of a unit wind turbine appropriate for installation in Benin City is 1kW. The economic analysis of installing wind turbine of 1kW considering a lot of variables such as cost of turbine, exchange rate, current cost of energy per kWh and depreciation indicates that the total expenditure made cannot be recovered within 20 years of the expected life span of a wind turbine. Hence, making wind turbine installation in Benin City technically feasible but not economically and commercially viable.

KEYWORDS: electricity, wind turbine, economically viable, wind speed.

1. INTRODUCTION

The amount of electricity a nation can produce for its citizens is one of the indices for measuring how developed that country is. Nigeria's electricity deficit challenge is no doubt one of the major problems facing the country. The conventional means of using fossil fuel to generate electricity appears not to be yielding the desired result. Hence, the need to explore other alternatives (Olagbegi et al, 2014). Using renewable sources such as wind would not only help in addressing this challenge, but also lead to a reduction in the amount of greenhouse gases emission that accompanies the use of fossil fuel (Aidan and Ododo, 2010). Wind energy is one the renewable energy that is yet to be given the desired attention and fully harnessed in Nigeria (Aliyu and Mohammed, 2014). A lot of countries have taken advantage of this renewable energy resource in forming part of the solution to their power problem. Although, the Federal Government had made effort in that regard with the installation of 10MW wind turbine in Katsina State (Oluleye and Ogungbenro, 2011). This work provides a technical-economic analysis of wind electric energy potential in Benin City, Edo State.

2. THEORITICAL ANALYSIS

2.1 Wind

Wind is air in motion produced due to the difference in atmospheric pressure and an irregular heating of the surface of the earth by the sun. Air has certain mass (kg) and mass density (kg/m^3). Flow of air leads to the flow of mass. The flowing mass has kinetic energy which can be converted to mechanical or electrical energy depending on how it is to be used (Kalekirstos, 2013).

2.2 Power in wind

The Kinetic energy K.E of an air flowing with a mass, m and velocity, v is given in equation (1)

$$\text{K.E} = \frac{1}{2}\ \text{m}\ v^2 \qquad (1)$$

The mass of air, m passing through the wind turbine in unit time is $\rho \text{A} v$ (Ajao, 2009).
Therefore, power P, which is the kinetic energy passing through an area in unit time is given as:

$$\text{P} = \frac{1}{2}\rho A\ v^3 \qquad (2)$$

Where;
P is the power in wind; m is mass of air and A is the rotor area interacting with air flow
ρ = air density in kg/m^3 (taken as 1.225kg/m^3)
v =wind speed in m/s

2. 3 Power in wind turbine

Not all the power available in wind can be converted to electric power because air is continuously moving. According to Albert Betz the maximum fraction of achievable electric energy from wind is 0.59. This is called the power coefficient. Therefore, the electric wind power is given by equation (3) (Kalekirstos, 2013).

$$P_e = \frac{1}{2}\rho A v^3 C_p \quad (3)$$

Where

P_e = wind electric power in Watts

C_p= power coefficient.

3. METHODOLOGY

Wind data for five years (2011-2015) was collected from the Nigerian Meteorological Agency (NIMET) located in Benin City. The wind speed was measured at an altitude of 10m.

4. RESULTS AND DISCUSSION

4.1 WIND DATA

Table 1 shows the average monthly wind run data obtained from NIMET for five years (2011-2015). The cell with XX indicates the month in which measurements was not possible due to the measuring instrument that was faulty. The raw data obtained was in wind run. The wind run was converted to wind speed in m/s, because the data required for this work is wind speed. The wind run measured in km was from 9:00hr to 9:00hr the next day.

Table 1: Monthly wind run for Benin City (2011-2015)

Monthly Wind Run(km)					
Month	**Year**				
	2011	**2012**	**2013**	**2014**	**2015**
Jan.	93.38	94.18	98.85	101.90	121.95
Feb.	124.08	103.29	114.53	94.96	116.32
Mar.	121.15	121.70	121.65	104.68	90.32
Apr.	96.57	113.74	101.70	102.27	67.70
May	100.51	97.46	99.77	89.90	97.24
Jun.	94.78	96.83	100.00	90.52	87.31
Jul.	102.31	103.58	103.40	93.81	102.02
Aug.	118.24	136.40	124.83	114.50	111.66
Sep.	106.50	94.63	XX	95.49	99.95
Oct.	77.52	68.71	92.58	77.32	72.82
Nov.	69.96	71.96	81.35	67.85	66.47
Dec.	92.53	64.76	87.93	62.85	73.39

$$\text{Wind speed (m/s)} = \frac{\text{wind run in meters}}{\text{duration of wind run in seconds}} \quad (4)$$

Duration of wind run is 24 hours, Therefore,

Duration of wind run in seconds = 24 x 60 x 60

Duration of wind run in seconds = 86400 seconds

Therefore,

$$\text{Wind speed (m/s)} = \frac{\text{wind run in meters}}{86400} \quad (5)$$

For instance, the average monthly wind speed for the month of January, 2011 can be calculated as follows:

$$\text{Wind speed (m/s)} = \frac{93.38\ X\ 1000}{86400}$$

Wind speed (m/s) = 1.08 m/s

Table 2: Monthly wind speed in m/s for Benin City (2011-2015)

monthly Wind Speed (m/s)						
Month	**Year**					
	2011	**2012**	**2013**	**2014**	**2015**	**Average**
Jan.	1.08	1.09	1.14	1.18	1.41	1.18
Feb.	1.44	1.20	1.33	1.10	1.35	1.28
Mar.	1.40	1.41	1.40	1.21	1.05	1.29
Apr.	1.12	1.32	1.18	1.18	0.78	1.12
May	1.16	1.13	1.16	1.04	1.13	1.12
Jun.	1.10	1.12	1.16	1.05	1.01	1.01
Jul.	1.18	1.20	1.20	1.09	1.18	1.17
Aug.	1.37	1.58	1.45	1.33	1.29	1.40
Sep.	1.23	1.10	XX	1.11	1.16	1.15
Oct.	0.90	0.80	1.07	0.90	0.84	0.90
Nov.	0.81	0.83	0.94	0.79	0.77	0.83
Dec.	1.07	0.75	1.02	0.73	0.85	0.88
					Average	**1.11**

4.2 WIND SPEED AT VARYING HEIGHTS

Wind speed measurements for wind resource assessment are basically measured at a base height of 10 m above the ground. Depending on the type and capacity of the turbine, its installation height is generally above 10 m. Wind speed closer to the ground changes with height due to resistance and roughness of the terrain. The estimation of wind speed at any height can be estimated using the power law relationship as given in equation (6) (Kalekirstos, 2013).

$$V = Vref\,[\frac{H}{H_{ref}}]^{\propto} \quad (6)$$

Where

V= calculated wind speed

Vref = measured wind speed

H = height for which the wind speed is to be estimated

H_{ref} = height at which wind is measured

$\propto$= friction coefficient or Hellman exponent. It is a function of the topography. Friction coefficient of 0.4 was used because of the high rise buildings present in the City.

The wind speed at heights of 20m, 30 m and 50 are presented in Table 3

Table 3: Estimated average monthly wind speed at varying heights for Benin City.

Average Wind Speed(m/s)				
Months	**10m**	**20m**	**30m**	**50m**
Jan.	1.18	1.56	1.83	2.25
Feb.	1.28	1.69	1.99	2.44
Mar.	1.29	1.70	2.00	2.46
Apr.	1.12	1.48	1.74	2.13
May	1.12	1.48	1.74	2.13
Jun.	1.01	1.33	1.57	1.92
Jul.	1.17	1.54	1.82	2.23
Aug.	1.40	1.84	2.17	2.67
Sep.	1.15	1.52	1.79	2.19

Oct.	0.90	1.19	1.40	1.68
Nov.	0.83	1.10	1.29	1.71
Dec.	0.88	1.16	1.37	1.68

4.3 WIND ELECTRIC ENERGY DENSITY

Wind electric power density = $\frac{1}{2}\rho v^3$Cp (7)

The wind electric density for Benin City assuming an installation height of 20m and using Cp of 0.45 is presented in Table 4

Table 4: Wind electric energy density for Benin City at an installed altitude of 20m

Month	Wind speed at 20 m (m/s)	Electric power Density(W/m^2)
Jan.	1.56	**1.04**
Feb.	1.69	1.33
Mar.	1.70	1.35
Apr.	1.48	0.89
May	1.48	0.89
Jun.	1.33	0.65
Jul.	1.54	1.01
Aug.	1.84	1.72
Sep.	1.52	0.97
Oct.	1.19	0.46
Nov.	1.10	0.37
Dec.	1.16	0.43

4.4 COST OF WIND TURBINE AND ITS ECONOMIC VIABILITY

Because of the low wind profile of the City, wind turbine with very low cut-in speed is to be used. Many commercially available wind turbines have their cut-in speed not below 2.5m/s. However, a 1kW wind turbine with a cut-in speed of 1m/s and rated speed of 12m/s is available. Installing this wind turbine at a height of 20m and considering that the available wind speed is around one sixth of the turbine rated speed, the power obtainable is an average of 100W.

Generally, the cost of electricity generation is primarily affected by three main components:

i. Total Capital cost
ii. Operation and Maintenance cost
iii. Fuel cost (Ragheb, 2015)

Capital cost consists of the cost of wind turbine which accounts for 75% and installation which could be taken as 25% of capital cost. The operation and maintenance cost is 1.5% of the turbine cost (Ragheb, 2015).

Since wind is free, the fuel cost is nil.

The price of the 1kWind turbine is $1,000 (₦500, 000), taking exchange rate at ₦500 to a dollar.

Since 75% of the total capital cost makes up the cost of the turbine, Therefore,

Total capital cost = $\frac{turbine\ cost}{0.75}$

Total capital cost = $\frac{500000}{0.75}$

Total capital cost = ₦666, 666.67

Also

Total capital cost = turbine cost + installation cost

Installation cost = total capital cost- turbine cost

Installation cost = ₦666,666.67 – ₦500, 000

Installation cost = ₦166,666.67

Operation and maintenance cost per annum = 1.5% of turbine cost

Operation and maintenance cost per annum = $\frac{1.5}{100}$ x 500000

Operation and maintenance cost = N7, 500/year

If 100W is the average power generated by the turbine, the annual energy expected to be produced is

100 x 24x 365 = 876 kWh

The current price of electricity from power distribution companies in Nigeria is ₦34.00/kWh.

Gross yearly income from the sale of 876 kWh at the rate of ₦34.00/kWh = 876 x 34
= ₦29,784

Net income per year = gross income – operation and maintenance cost
= ₦29,784 – ₦7,500

Net income per year = ₦22, 284

Using an average useful lifetime of 20 years for the wind turbine as being documented by many manufacturers (Jurgen, 2018) , the cumulative net income over this period of 20 years is expected to be greater than the total capital cost in order to make the project viable. Table 5 shows the yearly expenditure, the gross and net income, as well as the cumulative net income of the 1 kW wind turbine

Table 5: Estimated yearly expenditure and cumulative net income of 1kW wind turbine for Benin City

Year	Expenditure (₦)	Gross Income(₦)	Net Income(₦)	Cumulative Net Income
0	666, 666.67	-	-	-
1	7,500	29,784	22, 284	22, 284
2	7,500	29,784	22, 284	44,568
3	7,500	29,784	22, 284	66,852
4	7,500	29,784	22, 284	89,136
5	7,500	29,784	22, 284	111,420
6	7,500	29,784	22, 284	133,704
7	7,500	29,784	22, 284	155,988
8	7,500	29,784	22, 284	178,272
9	7,500	29,784	22, 284	200,556
10	7,500	29,784	22, 284	222,840
11	7,500	29,784	22, 284	245,124
12	7,500	29,784	22, 284	267,408
13	7,500	29,784	22, 284	289,692
14	7,500	29,784	22, 284	311,976
15	7,500	29,784	22, 284	334,260
16	7,500	29,784	22, 284	356,544
17	7,500	29,784	22, 284	378,828
18	7,500	29,784	22, 284	401,112
19	7,500	29,784	22, 284	423,396
20	7,500	29,784	22, 284	445,680

From Table 5, the total income at the end of 20 years is ₦ 445,680. This amount is less than the total capital cost of ₦666, 666.67. From this analysis, it can be said that wind turbine installation in Benin City is not economically viable.

4.5 DEPRECIATION COST

Due to wear and tear as well as other factors, wind turbine depreciates on the average of 3.5% of the total capital cost per year (Ragheb, 2015). Table 6 shows the yearly residual value for the 1kW turbine.

Table 6: Yearly residual value of the 1kW wind turbine

Year	Percentage Depreciation	Amount of depreciation (₦)	Residual value (₦)
1	3.5	17,500	482,500
2	3.5	17,500	465,000
3	3.5	17,500	447,500
4	3.5	17,500	430,000
5	3.5	17,500	412,500
6	3.5	17,500	395,000
7	3.5	17,500	377,500
8	3.5	17,500	360,000
9	3.5	17,500	342,500
10	3.5	17,500	325,000

11	3.5	17,500	307,500
12	3.5	17,500	290,000
13	3.5	17,500	272,500
14	3.5	17,500	255,000
15	3.5	17,500	237,500
16	3.5	17,500	220,000
17	3.5	17,500	202,500
18	3.5	17,500	185,000
19	3.5	17,500	167,500
20	3.5	17,500	150,000

After 20 years of usage, the residual value of the turbine would be ₦150, 000. This amount, in addition to the total income of ₦ 445,680 that would be made at the end of 20 years is still less than the total capital cost of the turbine.

5. CONCLUSION

A technical and economic analysis of wind electric energy potential for Benin City has been carried out. The result indicates a low wind profile for the city (recording 1.4m/s and 0.83m/s as the highest and lowest average monthly wind speed respectively at an altitude of 10m), which would yield 1.72W/m^2 and 0.37W/m^2 as the largest and smallest wind electric power density respectively, if a wind turbine is installed at a height of 20m. From the analysis of result made, one can conclusively assert that the wind electric power for Benin City is not economically viable. This is because the money that would be spent in the installation of a wind turbine in the City cannot be recovered over its useful life, leading to a negative return on investment. Solar energy can be explored instead.

ACKNOWLEDGEMENT

The authors appreciate the Nigerian Meteorological Agency for making the data for this work available.

REFERENCES

Ajao, K. R & Adegun I. K. (2009).“Development and Power Performance Test of Small Three- Blade Horizontal Axis Wind Turbine” Heat transfer research, Vol. 40, No. 8.

Aidan , J. & Ododo, J. C. (2010). “wind speed distributions and power densities of some cities in northern Nigeria”
journal of engineering and applied sciences, vol. 5, No. 8,

Aliyu, D. G. & Mohammed O. (2014) “Assessment of Wind Energy Alternative in Nigeria from the Lessons of the
Katsina Wind Farm” Civil and Environmental Research, vol. 6 , No.4, pp

Jurgen, H. (2016) “ Analysis of the Lifetime of a Wind Turbine-Operation Past Design Life”, Wind Europe Summit,
Hamburg, Germany, 27th -29th September, 2016.

Kalekirstos, G. G. (2013) “Feasibility Study of Small Scale Standalone Wind Turbine for Urban Area” KTH Industrial Engineering and Management.

Oluleye A. & Ogungbenro S. B. (2011) “Estimating the wind energy potential over the coastal
stations of Nigeria using power law and diabatic methods” African Journal of Environmental Science
and Technology Vol. 5.

Olagbegi, P.O., Kwasi-Effah, C. C., & Ugbi, B. A. (2014)” Preliminary Investigation of the effect of wind speed on
output performance of a wind electric generator ” Global Journal of Advanced Engineering Technologies
vol. 3, No. 2.

Ragheb, M (2013) “Economics of wind power generation” Handbook for onshore and off shore wind turbines,
University of Illinious, Urbana, United States.

PAPER 198 – DEVELOPMENT AND PERFORMANCE EVALUATION OF A FACULTATIVE STABILISATION POND FOR FISH WASTEWATER TREATMENT

E. P. Lydia*, P. A. Adeoye, I. M. Muhammed, M. Y. Otache

Department of Agricultural & Bioresources Engineering, Federal University of Technology Minna
E-mail: lydia.pam63@gmail.com

ABSTRACT

Wastewater is characterized by high concentration of nutrients and solid materials which are usually discharged into water Streams, Environment and Rivers without any form of treatment. This practice causes pollution and changes in river hydrology and other environmental issues such as eutrophication of receiving water and environment. Thus, the search for effective method for the control or removing pollutant from wastewater. To this end waste treatment using stabilisation pond has become a preferred alternative waste stabilisation pond is a relatively shallow body of wastewater contained in an earthen man-made basin into which wastewater flows and from which after a certain retention time, a well-treated effluent is discharged. The study aimed at developing and evaluating the performance of a facultative wastewater stabilisation pond for the fish wastewater treatment. The objectives of the study are to: Design a facultative wastewater pond, construct the designed facultative stabilisation pond, and carry out performance evaluation on some physicochemical parameters using the efficiency removal formula % removal = $\frac{c1-cf}{cf}$ x 100. The aerial loading rate formula was used for the design of facultative pond. The result of experimental analysis reveals BOD_5 in all instances in terms of whether the pond was screened or covered that there was significant reduction in concentration. The entire configuration allowed for average reduction in concentration by 53%, PH in the other hand in all instances had slight increases, for TDS, TSS, EC with exemption of TSS there was reduction in concentration of 50% irrespective of whether the pond is covered, screened or covered plus screened.

KEYWORDS: Wastewater, BOD_5, retention time.

1. INTRODUCTION

Aquaculture has witnessed tremendous growth during the past decades (FAO, 2004); this has culminated to the increasing trend and interests over time in fish farming for both commercial and domestic purposes. Fish produced by farming activities currently accounts for over one third of all fish directly consumed by Human (FAO ;2004). This large growth resulted in competition for natural water (Piedratha, 2003); this has consequently led to intensification of aquaculture system and environmental problems

Aquaculture, similar to other animal production system, generates waste; the amount and quantity of these wastes depend on the production system and feed quality (Keramat, 2008). Such wastewaters are characterized by high concentrations of nutrients and solid materials which are usually discharged into water streams, environment and rivers without any form of treatment (Sandra *et al.;*2018). The discharge of such wastewater forms a major environmental concern because they cause eutrophication of receiving water and environment; thus, the search for effective method for the control or removing pollutants from wastewater has attracted a lot of research concern. Fish farmers have used different kinds of chemicals, mechanical means with differing degrees of limitations or success, adverse effect, and cost implications. In the face of all this, hence the recourse to the idea of employing natural methods that might be more appropriate in varying measures; for instance, treatment that will produce an effluent which may meet the recommended effluent discharge limit. To this end, waste treatment through the use of stabilisation ponds has become the preferred alternative. Waste stabilisation pond is a relatively shallow body of wastewater contained in an earthen man-made basin into which wastewater flows and from which after a certain retention time (time which takes the effluent to flow from the inlet to the outlet), a well-treated effluent is discharged (Ukpong, 2012).

2 METHODOLOGY

The Aerial loading rate formula was used for the design of facultative pond proposed by (Mara, 1997) and adopted by (Raji et al., 2017). According to Mara the equation uses the mean temperature of the air in the coldest month.

2.1 Design consideration for the pond

The basic design criteria for the development of the facultative pond were adopted from Metcalf and Eddy (1993). They are; optimal depth (m) of 1.2 -2.5, surface loading (kg/ha) 60 -200, detention time (days) 5 -30, BOD (%) 80 -95, optimal temperature 20^0C, TSS (%) 70 – 80.

2.2 Design Preliminaries

Influent flow rate (Q) = 2mg/l, BOD_5 Organic Loading (BOD_5) = 55mg/L, Average air Temperature = 23^0C, Organic Loading rate = 80kg/ha/day, Sludge depth = 0.7 ,Assume seepage rate and evaporation = 2.0mm, Pond depth = 1.1m

2.3. Design Equations

$$A = \frac{Q\,(BOD)}{(LR)(1000)} \quad (2.1)$$

$$\text{Detention Time} = \frac{V}{Q} \quad (2.2)$$

$$HRT = \frac{V}{Q - V'} \quad (2.3)$$

Storage Volume = (Water Depth-Sludge Depth) x Pond Area (2.4)

Water Loss = Assumed Seepage rate x volume (2.5)

2.4 Design Calculations

Pond size determination from Equation. 2.1

$$A = \frac{Q\,(BOD)}{(LR)(1000)}$$

$$A = \frac{2(55)}{80\,X\,1000} = 1.375 \text{ X } 10^{-2}\ (3.39 \text{ x } 10^{-3}) = 13.7m^2$$

Applying the length to breadth ratio 2:1, Length is twice width, if width = w then length = 2w, Area is therefore

$A = L \text{ x } W = 2W \text{ x } W = 2W^2$

If Area = $13.7m^2$

$$= \sqrt{6.85}$$

W = 2.6 But length is 2xW

L = $5.2m^2$

Using ratio 1.1

Surface Length = 5.2 +1x1.1= 6.3m

Surface width = 2.6 + 1 x 1.1 = 3.7m

Bottom Length = 5.2 - 1 x 1.1 = 4.1

Bottom Width = 2.6 – 1 x 1.1 = 1.5

Calculate Storage Volume from Equation. 2.4

V = (Pond depth – Average Sludge depth) x Pond Area

V = (1.1 – 0.7) x 13.7m^2

V = 5.48m^3

Water Loss from Equation. 2.5

V' = (Assumed Seepage – Average Sludge depth) x Area

V' = (0.02 - 0.7) x 13.7

V' = -9.316

Hydraulic retention time from equation 2.3

$$\text{HRT} = \frac{5.2}{2-(-9.316)} = 0.48$$

Detention time from Equation. 2.2

$$\textbf{Detention time} = \frac{\boldsymbol{Area\ of\ pond\ x\ operating\ depth}}{\boldsymbol{flow\ rate}}$$

$$\text{Detention time} = \frac{13.7\ x\ 1.1}{2} = 7.5\ day$$

3. RESULTS AND DISCUSSION

3.1 Performance of the designed Wastewater stabilisation pond (WSP)

The performance of a facultative waste stabilisation pond WSP) depends on a host of factors and by extension, on the intended purpose. Generally, facultative WSP could be either be an oxidation or anaerobic pond; they are intended merely as waste-holding devices. The objective is to produce suitable effluent for discharge to surface waters or the environment. Based on its structure, ample dissolved oxygen may exist and aerobic metabolism may take place in the upper portion of the pond whereas there may be little or no dissolved oxygen in the lower depths. Thus, its performance can be hampered by temperature, light, organic loading, size and shape, and hydraulic considerations. The interplay of these factors can affect the process from attaining natural purification. Despite all this, the overall performance of WSP can be tied to two basic factors; in this regard, the assumed seepage and water loss regime which derive directly from the hydraulic considerations. In specific terms, the design considerations which took into cognisance the effect of optimal depth, detention time, ambient temperature fluctuation, surface loading and BOD concentration impacted positively on the WSP performance. The concrete flooring of the WSP mitigated against the possibility of soil erosion while the trapezoidal shape allowed for maximum surface loading condition as well depth. The design allows for 80-95 % BOD removal efficiency with a concentration of 55mg/l; though, BOD concentration of 20-40 mg/l is considered adequate. On the other hand, the large surface area with the corresponding depth allowed for high rate of energy conversion for optimal

temperature regime. Since the efficiency of a WSP cannot be discussed in isolation of overhead cost, it suffices to note that the WSP design allowed for non-prohibitive (minimum) operational and maintenance costs, relatively.

3.2 Physico-chemical parameter analysis and removal efficiency

(a) Physico-chemical parameter behavioural pattern

Table 3.1 below shows the behavioural pattern of the parameters under different pond configurations. For BOD_5, it is seemingly clear in all instances, in terms of whether the pond is screened or covered that there was significant reduction in concentration. In the overall, the entire configuration allowed for an overall average reduction in BOD concentration by 53 %. This result is in agreement with the findings of Mahsssen *et al*. (2008) though lower than that of Oke *et al*. (2006) who obtained 95 % removal efficiency. Despite this, the concentration is below the allowable threshold as prescribed by FEPA (2012) for fresh water fish farming; this implies that it can safely be discharged to the environment. However, the marginal difference in performance brings to the fore that if BOD reduction is the primary objective of the WSP, pond configuration in terms of whether it is covered, screened or both, has no serious impact on the outcome. Similarly, the concentration of DO is within the allowable range and also attest to the marginal relative importance of the nature of the pond with respect to overall effectiveness. It suffices to be cognisant of the fact that decreases in BOD_5 regime provide no tangible information of the changes in specific organic compounds. Despite this though, it measures the effect of a waste under conditions approximating natural stream conditions. In respect of the results here as in **Table 3.1**, it is glaring that the 5-day BOD cannot be considered a quantitative result without an approximation of the rate of oxidation and the BOD_5 to the ultimate oxygen demand. This is relevant considering that in facultative ponds or WSP, particulate matter is the main source of BOD in the effluent since the influent wastes may have been converted to bacteria or algal protoplasm. On the other hand, there was slight increases in pH, the overall pH in all instances connotes that the water may not portend any deleterious hazard and thus could be discharged into the environment and safe for fish farming. The pH regime for a time period of experiment has to do with carbon dioxide removal; the removal of carbon dioxide from the pond waters may invariably result in an increase in the pH of the waters. The trend is repeated for TDS, TSS and EC with exemption of increases in TDS as in when the pond is screened; though, the average 10 % reduction is almost in accord with the findings of Gopolang and Letshwenyo (2018) who obtained 8.5 %. However, reduction in TDS is not effective as the overall water quality is heavily impacted; this is evident by comparatively juxtaposing it with the recommended water quality standard for fish farming.

Table 3.1: Reduction pattern of the Physico-chemical parameters on the basis of nature of pond

Parameters	Initial concentration (mg/l)	Final effluent concentration (mg/l)	Percentage Increase/Reduction (%)	FEPA (2012) mg/l	Fish farming quality standard (mg/l)
BOD_5	7.45				
A		3.4	54.0		
B		3.6	51.0	30	5.0
C		3.4	54.0		

DO	7.41				
A		4.3	41.9		
B		4.5	39.0	Not < 2	5.0
C		4.5	39.0		
pH	7.18				
A		8.74	21.7		
B		8.76	-22.0	6-9	6-9
C		8.77	-22.0		
TDS	114.13				
A		101.80	10.8		
B		173.84	-52.0	< 2000	0.13
C		101.65	10.0		
TSS	0.57				
A		0.31	45.0		
B		0.28	50.0	30	10-20
C		0.26	54.0		
EC	178				
A		158	11.0		
B		160	10.0	2000 (µs/cm)	NA
C		158	11.0		

a, b, and c represents screened, pond covered and screened + pond covered, respectively; NA: Not applicable

4. CONCLUSIONS

Difficulties in obtaining precise relationships between agricultural practices and environmental problems occur because of the diffuse source of residuals from agriculture and the many factors that are involved. Some of which are not controllable by man, in this regard, the variability of waste discharges complicates assessment of the environmental impact of agricultural production; for instance, excessive amounts of nutrients and the conditions they can cause; as superfluity of amounts in surface waters can result in over fertilisation and can accelerate the process of eutrophication. Against the backdrop of these facts and the findings in this study, the following specific and general conclusions were drawn; viz: Optimal residence time varies across the pond configuration with respect to the parameters. For both BOD and DO, the best resident time is seven (7) days for effective load reduction if the pond is screened; also for TDS and EC but at fourteen (14) days. For both pH and TSS, the optimal reduction time is twenty-one (21) days by applying a combination of screened with the pond covered currently. For screened, covered, screened and covered pond configurations, the optimal removal efficiency can be obtained in seven (7) days followed by twenty-one (21) days.

REFERENCES

Ukpong E.C (2012) Variation of some waste stabilization pond parameters with shape

*Journal of Engineering Research*11 (2) 107 – 121.

FAO, (2004). The state of world fisheries and Aquaculture. 1st Edu, FAO, Rome. Italy.

Federal Environmental Protection Agency (2012) Guidelines and standards for environmental pollution in Nigeria.

Gopolang O. P and Letshwenyo O (2018) Performance Evaluation of Waste Stabilisation ponds. *Journal of Water Resources and Protection* (10) 1129-1147

Raji S.A, Olusanya S.O, Olokoba S.O, Olodo A.A, (2017) Waste stabilisation pond design for university of *Illorin, International Journal of Science and Technology Research* (6) 6.2277-8

Metcalf and Eddy Inc. Wastewater engineering treatment disposal and reuse (1991) 3 New York;McGraw-Hill Book Company

Mahassen M.E.G, Waled M.S, Azza M. A and Mohammed K (2008) Performance Evaluation of a waste stabilisation pond in a rural area in Egypt. *American Journal of Enviromemtal Sciences* 4(4) 316-326

Oke I.A, Olun J.A, Okuofu C.A and Olarinoye N.O (2006) Effiency of a biological treatment plant at Ahmadu Bello University, Zaria, *Research Journal of Agriculture and Biological Sciences* 2(6) 452-459

Piedratha, R.H. (2003); Reduction of Potential Environmental impact of Tank Aquaculture Effluent through Intensification and Recirculation: 1226: 35-44

Sandra Chinenyenwa Amijiofor, Nik Norsyahariati, Nik Daud, Syazwani Idrus and Hasfalina Che man (2018) Recycling of fish pond wastewater by absorption of pollutants using aged refuse as an alternative low cost adsorbent. Journal of sustainable environment research (28) 315 – 321.

Shun Darlin (2007) water and waste water calculation manual (2) 73 – 74 New York m c Graw. 11.11

PAPER 199 – ANALYSIS OF FIVE-PHASE SYNCHRONOUS RELUCTANCE MOTOR UNDER MULTI-PHASE FAULTS

G. D. Umoh[1], E. G. Ekpo[2]

[1]Dept of Electrical Engineering, Maritime Academy of Nigeria, Oron, Akwa-Ibom State – NIGERIA.
[2]Dept of Electrical/Electronics Engineering, Akwa Ibom State Polytechnic Ikot Osurua, Ikot Ekpene, Akwa Ibom State
Email: umohgideon@gmail.com

ABSTRACT

A model of a five-phase synchronous reluctance motor is presented. The machine is modelled for a five-phase supplied, with ACEBD winding configuration. The model considers the utilization of the third harmonics of the air-gap MMF as well the fundamental component, and a neglect of the third harmonics. These two models speed performance characteristics are monitored for multi-phase faults and their subsequence restorations. The fault pattern of losing $\frac{2\pi}{5}$phases from the first faulty before the $\frac{4\pi}{5}$ radian phase and the losing of $\frac{4\pi}{5}$ phase radian first before the $\frac{2\pi}{5}$ Radian phase. These phases were subsequently restored according to the considered fault patterns. The machine was then monitored on load and on no load using MATLAB/SIMULINK software for the analysis. The effect of the utilization of the third harmonic of the air-gap MMF is pronounced especially at fault and restorations.

KEYWORDS: Finite Element Analysis, Five-Phase, Harmonics, Multi-phase fault, Synchronous Reluctance Machine**.**

1. INTRODUCTION

The synchronous reluctance machine has found prominence especially in high-speed drives. Its various advantages include reduces losses especially when using a squirrel cage rotor, and fault tolerances especially with the multi-phase system.

The high cost of permanent magnet machine, as well as other disadvantages of the switch reluctance machine has led researchers to consider the Synchronous reluctance Machine (SYNRM) as a viable alternative to the Induction motor.

The SYNRM has the ability to utilize the reluctance torque for energy conversion in additional to the torque developed by the magnetizing component of the circuit [1]. Improvement in the machine saliency of the rotor increases to availability of reluctance torque for energy conversion, and the rotor can be modelled in the simplest form [2, 3, 4].

Various models by many researchers have contributed to an acceptable representation of the performance characteristics of the machine for further research and improvement. Winding function (WF) model [2, 5], phase variable models [2, 6, 7], d-q model [1] [8]Finite Element Model [2] etc.

The FE model has been used to verify a used of a combination of the direct-phase variable model and winding function model, proving to give a more accurate result than the d-q model [2, 9, 10].

The use of the direct-variable model for the multi-phase system does not necessitate the transformation to the d-q frame, as was applicable due to high computational requirements. In fault predictions and analysis of machine performance during the unbalance conditions, the direct-phase variable model is greatly appreciated [2].

The utilization of the multi-phase system in fault analysis gives a wider degree of freedom as losses of up to n-1phases can be considered. In addition, the additional harmonics are available for torque production as phase increases [6, 11, 12]

This study analyses a five-phase Synchronous Reluctance Motor characteristic performance during fault and unbalanced conditions, operating on load and no load. Model of not utilizing and utilizing the third harmonics of

the air-gap MMF are considered for different fault pattern of successive loss of $\frac{2\pi}{5}$ rad phases and $\frac{4\pi}{5}$Rad phase loss pattern.

2. MODEL OF FIVE-PHASE SYNCHRONOUS RELUCTANCE MOTOR

The machine was modelled using the direct-phase variable model as a 40 slots, 4-pole, 5-phase synchronous reluctance motor, with cage rotor.

The machine has a $\frac{2\pi}{5}$Radian separation for the windings.

The general voltage equation SYNRM is given in (1).

Where,

$$p = \frac{d}{dt} \qquad \square\square\square$$

Where λ is the flux linkage, V is the voltage matrix, R is the resistance matrix and I is the current matrix.

$$pI = [L(\theta_r)]^{-1}\left(V - \left\{R + \omega_r\left[\frac{dL(\theta_r)}{d\theta_r}\right]\right\}I\right) \qquad (3)$$

$$\omega_r = \frac{d\theta_r}{dt} \qquad (4)$$

$$I = \left[i_{as}; i_{bs}; i_{cs}; i_{ds}; i_{es}; i_{kq}; i_{kd}\right] \qquad (5)$$

$$V = \left[v_{as}; v_{bs}; v_{cs}; v_{ds}; v_{es}; v_{kq}; v_{kd}\right] \qquad (6)$$

$$L(\theta_r) = \begin{bmatrix} L_{ss} & L_{sr}{}' \\ \frac{2}{5}(L'_{sr})^T & L'_r \end{bmatrix} \qquad (7)$$

$$L_{ss} = \begin{bmatrix} L_{asas} & L_{asbs} & L_{ascs} & L_{asds} & L_{ases} \\ L_{bsas} & L_{bsbs} & L_{bscs} & L_{bsds} & L_{bses} \\ L_{csas} & L_{csbs} & L_{cscs} & L_{csds} & L_{cses} \\ L_{dsas} & L_{dsbs} & L_{dscs} & L_{dsds} & L_{dses} \\ L_{esas} & L_{esbs} & L_{escs} & L_{esds} & L_{eses} \end{bmatrix} \qquad (8)$$

The self-inductances are arranged on the leading diagonal of the matrix of (8).

$$L_r^{'} = \begin{bmatrix} L_{lkq}^{'} + L_{mq} & 0 \\ 0 & L_{lkd}^{'} + L_{md} \end{bmatrix} \qquad (9)$$

$$L_{sr}^{'} = \begin{bmatrix} L_{mq}cos\theta_r & L_{md}sin\theta_r \\ L_{mq}cos\left(\theta_r - \frac{2\pi}{5}\right) & L_{md}sin\left(\theta_r - \frac{2\pi}{5}\right) \\ L_{mq}cos\left(\theta_r - \frac{4\pi}{5}\right) & L_{md}sin\left(\theta_r - \frac{4\pi}{5}\right) \\ L_{mq}cos\left(\theta_r + \frac{4\pi}{5}\right) & L_{md}sin\left(\theta_r + \frac{4\pi}{5}\right) \\ L_{mq}cos\left(\theta_r + \frac{2\pi}{5}\right) & L_{md}sin\left(\theta_r + \frac{2\pi}{5}\right) \end{bmatrix} \qquad (10)$$

Where $L_{ss}$is the stator inductance matrix, $L_r^{'}$ is the rotor inductance matrix referred to the stator and $L_{sr}^{'}$ is the mutual inductances between the stator and the rotor referred to the stator.

$$R = \begin{bmatrix} R_{as} & 0 & 0 & 0 & 0 & 0 & 0 \\ 0 & R_{bs} & 0 & 0 & 0 & 0 & 0 \\ 0 & 0 & R_{cs} & 0 & 0 & 0 & 0 \\ 0 & 0 & 0 & R_{ds} & 0 & 0 & 0 \\ 0 & 0 & 0 & 0 & R_{es} & 0 & 0 \\ 0 & 0 & 0 & 0 & 0 & R_{kq} & 0 \\ 0 & 0 & 0 & 0 & 0 & 0 & R_{kd} \end{bmatrix} \quad (11)$$

R is the resistance matrix. The electromagnetic torque is given in (12)

$$T_e = \frac{1}{2} {I_s}^T \frac{\partial [L_{ss}(\theta_r)]}{\partial \theta_r} I_s + {I_s}^T \frac{\partial L_{sr}(\theta_r)}{\partial \theta_r} I_r \quad (12)$$

$$I_s = [i_{as},\ i_{bs},\ i_{cs},\ i_{ds}, i_{es}]^T \quad (13)$$

$$I_r = \left[i_{qr},\ I_{dr}\right]^T \quad (14)$$

$$T_e = J\left(\frac{p}{2}\right)\frac{d\omega_r}{dt} + T_l \quad (15)$$

Where,

$I_s$is the stator current matrix and I_r is the rotor current matrix.

J is the inertia expressed in kilogram-meter square (kg-m2) or joule-second square (J.s2), while p is the no of poles of the machine.

A general sinusoidal form approximation of the inductances as given in (16) [8, 11].

$$L_{xy} = LA_{xy} + LB_{xy}\cos(2\theta \pm \theta_p) \quad (16)$$

$$LB_{xy} = C_{a\theta_p} LB \quad (17)$$

$$LA_{xy} = C_{b\theta_p} LA \quad (18)$$

Where $C_{a\theta_p}$, $C_{b\theta v}$ are the phase dependent parameter, and depends on the phase shift θ_p.

From a generalized equation of inductances, as given by [8]

$$L_{s5} = L_{ls} I + L_{A5} M_{a5} + L_B M_{b5} \quad (19)$$

Where the expression for M_{a5} and M_{b5} are given in [11].

$$L_{mq} = \frac{5}{2}(L_A + L_k) \quad (20)$$

$$L_{md} = \frac{5}{2}(L_A - L_k) \quad (21)$$

Where,

$$L_k = L_B\left(\frac{1}{2}C_{b\theta 0} + C_{b\theta 1} + C_{b\theta 2}\right) \quad (22)$$

When considering only the fundamental of the winding function,

$$L_k = \frac{5}{2} L_B C_{b\theta} \quad (23)$$

3. SIMULATION OF THE DYNAMIC PROCESS

The machine parameters for the considered machine are given in table I

The speed characteristics of the model was investigated using MATLAB/SIMULINK, creating loss of phases fault, and subsequent restoration in the order of fault occurrence. The machine was loaded with a load torque of 5Nm after synchronism at 2.5 seconds, after which the four phases fault is subsequently created. The model was also modified to accommodate the 3rd harmonics of the air-gap MMF, and subjected to the same fault conditions.

Based on the configuration of the windings and the power supply, $\frac{2\pi}{5}$rad and $\frac{4\pi}{5}$Rad phase shift exists between the phases of interest.

The machine was wound as ACEBD configuration with$-\frac{2\pi}{5}$,$-\frac{4\pi}{5}$, $\frac{4\pi}{5}$, $\frac{2\pi}{5}$ arrangement.

The fault pattern was created with e-phase as the first faulty phase before the subsequent phases.

The EDAC fault pattern shows a $\frac{4\pi}{5}$ radian phase loss after the e-phase fault, while ECBA fault pattern shows a $\frac{2\pi}{5}$ Radian phase loss after the e-phase fault. The EADC fault pattern considers the loss of a positive $\frac{4\pi}{5}$ Radian phase immediately after an e-phase fault.

The fault occurrences and restoration patterns are tabulated in table II.

TABLE I. 5-PHASE MACHINE PARAMETERS

Quantities	**Value**
Stator Outer / inner radius	105.02 / 67.99mm
Rotor Radius	67.69mm
Effective stack length	160.22mm
Number of slot	40
Number of turns	48
Main air-gap length g_a	0.4mm
Inter polar slot space g_b	21.3mm
Stator slot depth	18mm
phase voltage	370 v
Number of poles	4
Frequency	50Hz
The stator resistance R_s	0.83Ω
Stator leakage inductance L_{ls}	10.98mH
rotor q-axis leakage inductanceL_{lqr}	6.2mH,
Rotor q-axis leakage inductance L_{ldr}	5.5mH
Rotor q-axis resistance R_{qr}	0.25 Ω
rotor d-axis resistance R_{dr}	0.12 Ω
moment of inertia J	0.089kg/m2

TABLE II. FAULT AND RESTORATION PATTERN FOR THE 5-PH SYNRM

Fault and Restoration Pattern				
Time (Seconds)		Fault and Restoration Pattern		
Fault	Restoration	Phase	Phase	Phase
3	25	E	E	E
5	26	D	A	C
7	27	A	D	B
9	28	C	C	A

SPEED CHARACTERISTICS FOR EDAC FAULT PATTERN WITHOUT LOAD

The Speed characteristic of the EDAC fault and restoration pattern was monitored without load for both the models without the 3rd harmonics of the air-gap MMF (model A) and with the 3rd harmonics of the air-gap MMF (Model B).

At fault 1, model B show a higher transient rise of 345.719 rad/s as compared to a value of 321.200 rad/s for model A. during the subsequent faults, model B still record a greater value than model A.

O the loss of the 4th phase, the speed of Model A drop to 55.72% of the synchronous speed of the machine, and rises to 66.13% of the synchronous speed on first phase restoration. On the restoration of the second phase, the speed of Model A returned to the synchronous speed of the machine as seen Fig. 1. Speed performance characteristics of on no load with and without 3rd harmonics.

For Model B, despite the loss of all the four phases, the machine still maintains synchronism. It can be noted that, on the first phase loss, the machine operates with an unbalance four-phase system and as a result, greater oscillation is observed. On the loss of the second phase, the 5 phase machine is supplied by a 3-phase supply, and as a result, a reduction in the oscillation is observed. Conversely, on the loss of an additional phase, an increase in the oscillation is also recorded, which still increased as the 4th phase is lost. The speed performance characteristics on no load for EDAC fault pattern is shown in Fig. 1, while the transient characteristics of the speed are tabulated in table III.

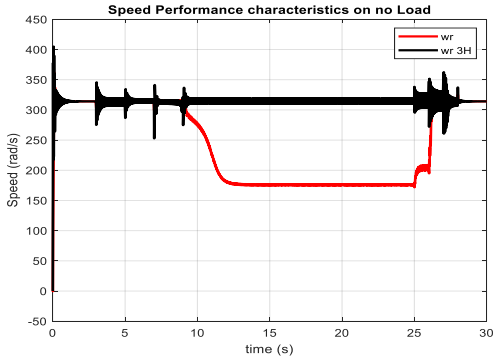

Fig. 1 Speed performance characteristics load with and without 3rd harmonics

FIVE-PHASE SPEED CHARACTERISTICS ON LOADED

For the loaded machine of both model A and model B, the machine still runs with oscillations at synchronous speed when three of the phases are lost, but drops to a negative value of the synchronous speed on the loss of the fourth phase. The machine does not return to the positive speed value even when the 1stphase fault is cleared, but on an additional phase restoration, it returns to positive speed value and records a gradual decrease in oscillation as faults are cleared. The speed characteristics of model A and Model B, when loaded with a load torque of 5Nm is presented in Fig. 2, while

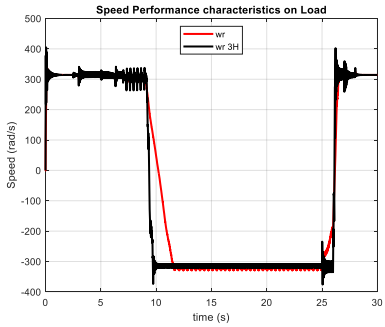

Fig. 2 Speed performance characteristics on load with and without **3rdharmonics**

TABLE III. SPEED TRANSIENT CHARACTERISTICS FOR EDAC FAULT PATTERN.

SPEED TRANSIENT CHARACTERISTIC (RAD/SEC) EDAC CONFIGURATION (WITH AND WITHOUT 3RD HARMONICS)					
Quantity		**On no Load**		**On Load**	
		Max val.	Min val.	Max val.	Min val.
Without 3rd Harmonics (Model A)	Start	362.287	284.785	314.435	311.496
	Fault 1	321.2	303.192	320.6	302.797
	Fault 2	320.639	303.352	319.4	303.453
	Fault 3	320.422	299.344	316.437	291.185
	Fault 4	315.466	175.766	313.995	-327.848
	Restore 1	208.629	171.788	-273.745	-328.801
	Restore 2	329.224	194.88	325.771	-1.88.993
	Restore 3	327.328	306.471	327.338	306.067
	Restore 4	325.179	310.3	325.179	310.301
With 3rd Harmonics (Model B)	Start	404.303	-1.6e-18	321.544	305.985
	Fault 1	345.719	275.066	340.871	279.048
	Fault 2	334.512	286.59	329.867	298.163
	Fault 3	341.342	252.799	335.364	265.032
	Fault 4	336.772	276.166	319.871	-373.151
	Restore 1	338.279	295.371	-234.99	-375.853
	Restore 2	351.66	272.041	402.239	-334.958
	Restore 3	362.603	260.842	359.405	258.739
	Restore 4	337.26	307.183	337.137	311.541

SPEED CHARACTERISTICS ON LOAD WITH FAULT PATTERNS (WITHOUT 3RD HARMONICS)

The Machines models were loaded at 2.5 seconds with a load torque 5N before the introduction of faults as stated in table 2.

The speed characteristics of model A is shown in Fig. 3. It can be observed that on the loss of the second phase 'D' in EDAC and 'A' in EADC, the machine still operates with $\frac{4\pi}{5}$Rad phase shift from the reference phase 'B' for both EDAC and EADC. Conversely, for the ECBA fault pattern, on the loss of the

second phase the machine operates with a $\frac{2\pi}{5}$Rad phase shift from the reference phase 'D'. The ECBA fault pattern shows a drop in speed 173.815 rad/s before dropping to the negative value of the synchronous speed at the loss of the 4th phase.

On restoration of last lost phase, the ECBA fault pattern model, show a sharp rise to the synchronous speed, while the EDAC and EADC rises to -273.745rad/s and -279.879 rad/s respectively, before rising to the synchronous speed on the restoration of additional phase.

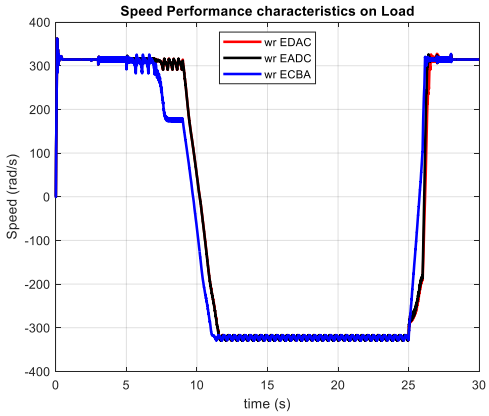

Fig. 3 *Speed performance characteristics on load without 3rdharmonics (EDAC, EADC and ECBA fault pattern)*

SPEED CHARACTERISTICS ON LOAD WITH FAULT PATTERNS (WITH 3RD HARMONICS)

The speed characteristics of model B is shown in Fig. 4, as a co-plot of all the considered faults pattern. It can be observed that on the loss of the phases, reluctance characteristics still sustain the machine in synchronism for all the fault pattern until a loss of synchronism is experienced at the loss of the fourth phase. After loss of synchronism, the speed of the models, drops to a negative synchronous speed with a recorded oscillation. On restoration of last lost phase, no fault pattern return to positive synchronous speed until the restoration of an additional phase. However, the EADC fault pattern only returned to the positive synchronous speed on the restoration of the third lost phase, while the ECBA pattern had settled at 290.742 rad/s on second restoration and returned to a positive synchronous speed on the restoration of the third phase.

On complete restoration, the observed oscillation settles at the synchronous speed. The transient of these characteristics are tabulated in table 4.

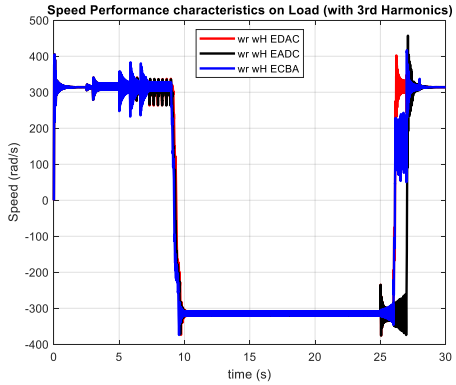

Fig. 4 Speed performance on load with 3rdharmonics (EDAC, EADC and ECBA fault pattern) showing faults

SPEED TRANSIENT CHARACTERISTIC (RAD/SEC)							
CONFIGURATIONS ON LOAD							
Quantity		**EDAC**		**EADC**		**ECBA**	
		Max val.	Min val.	Max val.	Min val.	Max val.	Min val.
Model A	Start	362.287	284.785	362.287	284.785	362.287	284.785
	Fault 1	320.6	302.797	320.6	302.797	320.6	302.797
	Fault 2	319.4	303.453	322.767	295.562	320.952	282.4
	Fault 3	316.437	291.185	313.879	290.742	304.768	173.815
	Fault 4	313.995	-327.848	311.507	-3.29.452	179.46	-328.884
	Restore 1	-273.745	-328.801	-279.879	-329.174	110.757	-328.366
	Restore 2	325.771	-1.88.993	326.109	-185.645	320.169	110.757
	Restore 3	327.338	306.067	324.241	306.019	321.397	307.183
	Restore 4	325.179	310.301	325.179	310.339	327.076	308.804
Model B	Start	321.544	305.985	404.303	-1.6e-18	404.303	-1.6e-18
	Fault 1	340.871	279.048	340.871	279.048	340.871	279.048
	Fault 2	329.867	298.163	343.111	287.949	383.246	232.338
	Fault 3	335.364	265.032	337.235	265.798	342.44	286.042
	Fault 4	319.871	-373.151	335.808	-372.139	326.845	-374.183
	Restore 1	-234.99	-375.853	-234.732	-372.555	--287.997	-346.333
	Restore 2	402.239	-334.958	-260.704	-374.3	243.052	-346.333
	Restore 3	359.405	258.739	457.189	-374.3	416.962	233.228
	Restore 4	337.137	311.541	329.706	309.407	333.239	306.997

4. CONCLUSION

The Synchronous reluctance machine models of ignoring the third harmonics of the Air-gap Magneto Motive force (MMF) as well as utilizing the MMF model, considered for multi-phase fault show similar characteristics of dropping to a negative synchronous speed at phase loss of up to four phases. The Synchronous reluctance motor has the ability to utilize it reluctance torque as a contribution to the electromagnetic torque. The effect of this reluctance torque is greatly observed.

On no load, Model A (not utilizing the 3rdharmonics of the Air gap MMF (Model A) remains on synchronism until the loss of the fourth phase, as a drop to 55.72% of the synchronous speed of the machine is recorded. On restoration of a phase fault, a rises to 66.13% of the synchronous speed is recorded, and returns to synchronous speed on additional phase restoration.

For Model B (ignoring the 3rdharmonics of the Air-gap MMF), despite loss of all the four phases, synchronism is maintained but with oscillations.

In Model A of not utilizing the 3rd harmonics of the air-gap MMF, the ECBA drops to a speed of 173.815 rad/s and restores to a speed of 233.228 rad/s before settling at synchronism on additional phase restoration in Model B.

The effect settling at a speed other than the synchronous speed or it negative synchronous speed is only observed in the ECBA fault pattern which considers a $\frac{2\pi}{5}$Radian loss of phase with respect to the first lost phase.

When two of the phases were lost, the machine assumed an uneven three phase arrangement as fewer oscillations were observed, as compared to a phase, three phases and four phases loss.

These two models of A and B and can be used to predict the nature of the phase fault experience by the machine.

These characteristics of the machine can be harnessed for variable drives and regenerative breaking.

REFERENCES

[1] P. Krause, O. Wasynczuk, and S. Sudhoff, , Analysis of Electric Machinery and Drive Systems, New York: IEEE press, 2013.

[2] E. Obe, and A. Binder, , "Direct-phase-variable model of a synchronous reluctance motor including all slot and winding harmonics," Energy Conversion and Management, vol. 52, pp. 284-291, 2011.

[3] E. S. Obe, "Direct Computation of AC machine Inductances based on winding function Theory," Energy Conversion and Management, vol. 50, pp. 539-542, 2009.

[4] T. Matsuo and T. A. Lipo, "Rotor Design Optimization of Synchronous Reluctance Machine," IEEE Transaction on Energy Conversion, vol. 9, no. 2, pp. 359-365, June 1994.

[5] H. A. Toliyat, L. Xu and T. A. Lipo, "A Five-Phase Reluctance Motor with High Specific Torque," IEEE Transactions on Industry Applications, vol. 28, no. 3, pp. 659-667, May/June 1992.

[6] H. A. Toliyat, S. P. Waikar and T. A. Lipo, "Analysis and Simulation of Five-Phase Synchronous Reluctance Machine Including Third Harmonic of Airgap MMF," IEEE Trans. on Ind. Applicat., vol. 34, no. 2, pp. 332-339, March/April 1998.

[7] G. Umoh, G. Ekpo and A. Akhikpemelo, , "Beyond Phase Dependent Coefficients in the Modelling and Analysis of Five-Phase Synchronous Reluctance Machine," International Research Journal of Engineering and Technological, vol. 9, no. 8, pp. 1970-1977, August 2022.

[8] T. Camarano, T. Wu, S. Rodriguez, J. Zumberge, and M. Wolff, , "Design and Modeling of a Five-Phase Aircraft Synchronous Generator with High Power Density," IEEE Energy Conversion and Exposition (ECCE), pp. 1878-1885, 2012.

[9] G. Umoh, C. Ogbuka, and E. Obe., "Modelling and Analysis of Five-Phase Permanent Magnet Synchronous Motor in Machine Variables," Przegląd Elektrotechniczny, vol. 96, no. 1, pp. 87-92, 2020.

[10] G. Umoh, C. Obe , C. Ogbuka , G. Ekpo, , E. Obe , "Direct-Phase Variable Modelling and Analysis of Five-Phase Synchronous Reluctance Motor for Direct-On-Line Starting," Przegląd Elektrotechniczny, vol. 97, no. 1, pp. 24-29, 2020.

[11] G. Umoh, E. Obe, and O. Okoro, "The Effect of Third-Harmonics of the Air-gap MMF on Inductance Determination in five-phase Synchronous Reluctance Motor," IEEE 3rd Conference on Electro-Technology for National Development (NIGERCON), pp. 795-801, 2017.

[12] H. A. Toliyat, M. M. Rahimian and T. A. Lipo, "DQ Modeling of Five Phase Synchronous Reluctance Machine Including Third Harmonic of Air-Gap MMF," IEEE Industry Applications Society Annual Meeting, vol. 1, pp. 231-237, Sep 28-Oct 4,1991.

PAPER 201 – REACTION KINETICS OF CORNCOB HYDROLYSIS OF A MAGNETIC SULFONATED SOLID ACID CATALYST

O. A. Falowo[1,*], B. Oladipo[2], O. O. Oyekola[2], J. O. Obemme-Nmom[1], A. Ilesanmi[1], O. Davies[1]

[1]Department of Chemical Engineering, Landmark University, P.M.B. 1001, Omu-Aran, Kwara State, Nigeria
[2]Department of Chemical Engineering, Cape Peninsula University of Technology, Bellville Campus, Symphony Way, Bellville, Cape Town 7535, South Africa
[*]Email: falowo.olayomi@lmu.edu.ng

ABSTRACT
The study investigated the kinetics of corncob hydrolysis into glucose using a synthesized magnetic sulfonated solid acid catalyst. A core nanomagnetic particle was modified using SiO_2 from calcined rice husk ash to generate grafting nanoparticles that accommodate sulfonic groups from concentrated sulfuric acid. The magnetic sulfonated solid acid catalyst was applied in the hydrolysis of corncobs at 100, 110, and 120 °C. Glucose recovery from batch hydrolysis was fitted into Saeman's, first-order and second-order reaction models. Results showed that the magnetic sulfonated solid acid catalyst possessed excellent catalytic properties and was effective in corncob hydrolysis. Among the equations used for the kinetic modeling, Saeman's model perfectly fitted the experimental data at all temperatures investigated. Reaction kinetic was consistent for the hydrolysis yield at 110 °C in all the models. Activation energy of corncob hydrolysis was 10.45 kJ/mol and 69% of sugar was recovered from the hydrolysate. Hence, this study could help to achieve optimal operation in a biorefinery to sustain sugar availability for chemical and fuel production.

KEYWORDS: Hydrolysis, Corncobs, Kinetics, Solid acid catalyst

1. INTRODUCTION

The consideration for the environment and the commitment to a circular economy has led to a coordinated effort in maximizing lignocellulose biomass as raw materials in the process industry. Due to the availability of lignocellulose biomass on a large scale, they can contribute substantially to the production of chemicals, biofuels, adhesives, resins, activated carbon, aromatics, etc. Lignocellulose feedstock is projected to replace petroleum feedstock in producing value-added chemicals.

The polymeric substances (lignin, cellulose, hemicellulose) in lignocellulose biomass are decomposed through pretreatment to release fermentable sugars. A physical or chemical pretreatment method disintegrates the crystalline structure, removes lignin, and opens up the complex structure of the material for hydrolysis to form monomeric sugars (Yat *et al.*, 2008). However, there are various associated problems with the hydrolysis process depending on the catalyst used or the operational conditions. Several homogeneous catalysts commonly used are sulfuric acid, maleic, and oxalic acids (Lee & Jeffries, 2011). Solid catalysts can address challenges associated with producing eco-friendly and economically viable products from lignocellulose. The catalyst can also be used under mild operating conditions, and it is highly selective and efficient. To improve the separation of the product mixture and reuse the catalyst for subsequent hydrolysis, carbonaceous solid acid catalyst functionalized with the SO_3H group offers a promising strategy for cellulose hydrolysis (Guo *et al.*, 2012). Gill *et al.* (2007) prepared four different sulfonic acids attached to silica-coated magnetic nanoparticles; it was reported that the prepared catalyst exhibited comparable or better catalytic activity to commercial solid acid catalysts such as Amberlyst A-15, Nafion, and sulfonic acid.

Hydrolysis is vital to release fermentable sugars locked up in the biomass, and could potentially serve as raw material in the process where sugar solution is needed. The amount of reducing sugars present in the liquid phase after hydrolysis is dependent on the selected operational conditions (Gámez *et al.*, 2004). Sugars in lignocellulose biomass fundamentally correspond to the homopolymers in the original material. For example, glucan corresponds to glucose while araban, xylan, and acetyl groups are linked to hemicellulose (Gámez *et al.*, 2004). In addition to a detailed theoretical model capable of predicting the reaction behaviour of biomass hydrolysis before production, process engineer, as well as practitioners need extensive data and empirical rate models to explore possible processing schemes. The objective of studying the kinetic models is to optimize the hydrolysis process as well as to obtain equations useful for reactor design and economic consideration (Xiang *et al.*, 2004).

There is information in the literature on the hydrolysis of corncob using dilute mineral acids, but there is little quantitative work describing the kinetics of corncob hydrolysis in the presence of a magnetic solid acid catalyst at moderate temperatures. Lin *et al.* (2020) reported that increasing the temperature range between 100 and 140ºC

leads to a high kinetic rate and favors sugar formation. This study seeks to establish the kinetic behaviour of corncob hydrolysis in the presence of a magnetic sulfonated solid acid catalyst at a moderate temperature.

2. MATERIALS AND METHODS

2.1 Materials

Corncobs and rice husks used in the experiment were collected from Landmark University Teaching Farm, Omu-Aran, Kwara State, Nigeria. The collected corncobs were washed and oven-dried for 6 h at 105 °C. The dried corncob was pulverized, passed through an 80 µm mesh sieve, and stored in a desiccator prior to hydrolysis. Other chemicals and reagents used are ferric chloride hexahydrate ($FeCl_3.6H_2O$), ferrous sulfate heptahydrate ($Fe_2SO_4.7H_2O$), ammonia solution (NH_4OH), ethanol, hydrochloric acid, acetone, sulfuric acid, and citric acid.

2.2 Physicochemical analysis of the corncob

Proximate analysis of the used corncob was carried out according to NREL protocols. On a dry basis, the potential concentration of glucose in corncob was calculated by assuming a total conversion of polysaccharides to sugars without degradation. The potential maximum sugar concentration was calculated according to Eq. (1) (Gámez *et al.*, 2004).

$$S_P\left(\frac{g}{L}\right) = F \times \frac{CPn}{LSR} \times 10 \quad (1)$$

where F is the factor of hydration, LSR is the liquid-to-solid ratio, and CP_n is the composition of each sugar in the polysaccharide.

2.3 Development of magnetic sulfonated solid acid catalyst

The magnetic core (Fe_3O_4 nanoparticles) of the acid catalyst was prepared by co-precipitation according to Esfahani *et al*., 2014. The SiO_2 nanoparticles synthesized from acidified calcined rice husks ash were added by wet impregnation to the magnetic core to activate the support for sulfonic group. Subsequently, a sulfonated solid acid catalyst was prepared by following the steps described in Safari and Zarnegar (2013) using concentrated sulfuric acid. The prepared catalyst was washed, dried, and stored for analysis and hydrolysis.

2.4 Hydrolysis of milled Corncob

The modified hydrolysis process of corncob in this study was carried out according to method reported in Qi *et al.* (2019). A known mass (2 g) of milled corncob was added to water in the liquid-solid ratio of 10:1. The reaction medium in a two-necked reactor was heated to a selected temperature, and 0.5 g magnetic solid acid catalyst was added to the mixture. Batch hydrolysis of corncob was conducted at different temperatures of 100, 110, and 120 °C, with the view of reducing energy demand and inhibitory by-product formation (Lin *et al.*, 2020). As the reaction progresses, 1 ml of the hydrolysate was taken from the mixture at 20 min intervals for 120 min. The absorbance of the reducing sugar on the basis of glucose was determined by the dinitrosalicylic acid (DNS) method at a wavelength of 540 nm. The yield of reducing sugar at any time (t) was calculated using Eq. (2) (Aguilar *et al.*, 2002):

$$\%\, Total\ reducing\ sugar = \frac{moles\ of\ reducing\ sugar\ in\ the\ hydrolysate}{moles\ of\ reducing\ sugar\ in\ corncob} \times 100 \quad (2)$$

2.5 Kinetic modelling of corncob hydrolysis

The hydrolysis of lignocellulosic materials has been described by Saeman's model. This model uses a pseudo-homogenous irreversible first-order reaction to describe the hydrolysis of cellulose to glucose. The generalized form of Saeman's model is shown in Eq. (3) (Saeman, 1945).

$$polymer \xrightarrow{k_1} monomer \xrightarrow{k_2} decomposition\ products$$

$$Cellulose\ [C] \xrightarrow{k_1} Glucose\ [G] \xrightarrow{k_2} 5-HMF\ [H] \quad (3)$$

The analytical expressions of the resulting differential equation can be used to determine the concentrations of cellulose (C), glucose (G), and 5-hydroxymethylfurfural (H) as a function of time at an isothermal reaction. This is shown in Eqs. (4)–(6)

$$C = C_0 e^{-k_1 t} \quad (4)$$

$$G = \frac{C_0 k_1}{k_2 - k_1}\left(e^{-k_1 t} - e^{-k_2 t}\right) \quad (5)$$

$$H = \left\{1 + \frac{k_1 e^{-k_2 t} - k_2 e^{-k_1 t}}{k_2 - k_1}\right\} C_0 \quad (6)$$

where, C_0 represents the theoretical potential glucose amount available in corncob (g/L), the rate constants k_1 (min^{-1}) and k_2 (min^{-1}) are zero under the initial concentration of products. If G_0 is very close as assumed, Eqn. 5 can be simplified as;

$$\frac{G}{C_0} = \frac{k_1}{k_2 - k_1}\left(e^{-k_1 t} - e^{-k_2 t}\right) \quad (7)$$

The Seaman's model was also applied to the hydrolysis of the hemicellulose fraction.

Assuming an irreversible reaction and negligible mass transfer rate effect across the catalyst surface, the experimental data were fitted into unimolecular first-order reaction and second-order reaction models as represented in Eq. (8) and (9).

$$\ln\left(\frac{1}{1-X_C}\right) = kt \quad (8)$$

$$\frac{X_C}{C_{A0}(1-X_C)} = kt \quad (9)$$

where X_C, k, C_{A0}, and t are the fractional conversion of cellulose to reducing sugar, the reaction rate constant, quantitative initial glucose concentration, and reaction time, respectively.

Activation energy of the corncob hydrolysis process was determined from the natural logarithm of Arrhenius equation as given in Eq. (10).

$$ln\, k = ln\, A - \frac{E_a}{RT} \quad (10)$$

where, k is the reaction rate constant (min^{-1}), A is the frequency factor (min^{-1}), E_a is the activation energy (kJ/mol), R is the universal gas constant (8.314 J/mol.K), and T is the absolute temperature (K).

2.6 Statistical Analysis

All experimental data were determined in triplicate, and an average value was presented. Experimental data were analyzed using non-linear regression and fitted to the kinetic models using OriginPro 9.0 software.

3. RESULTS AND DISCUSSION

The composition obtained for corncob (wt.% on a dry basis) is 47.36% of cellulose, 38.26% of hemicellulose, and 10.41% of lignin. The values were within the range reported by Wang *et al.* (2019).

The elemental composition of the magnetic sulfonated acid catalyst showed that it contains 26.93 wt.% of carbon, 36.59 wt.% of oxygen, 13.91 wt.% of silicon, 2.64 wt.% of sulfur, and 19.93 wt.% of iron (Fig. 1). The synthesized catalyst is amorphous in structure with a surface area of 72 m^2/g and an acid density of 0.96 mmol/g.

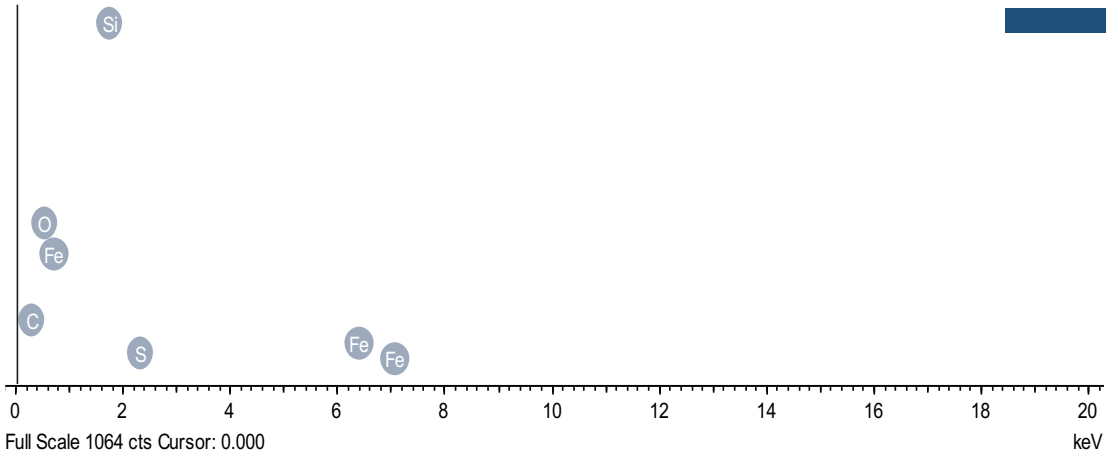

Figure 1: Pictograph of the elemental composition of magnetic sulfonated solid acid catalyst

The increase in temperature by 10 °C had a significant effect on the yield of glucose recovery from the hydrolysate (Table 1). The general trend shows a significant increase in total reducing sugar with time for all temperatures investigated. However, as the hydrolysis proceeded to the completion time at the highest temperature, reducing sugar yield marginally decreased from 69.25 % to 69.21%, which could be due to the increase in the rate of glucose decomposition.

Table 1: Percentage yield of glucose formation at different temperatures

Time	Total Reducing sugar yield (%)		
(min)	100 °C	110 °C	120 °C
20	3.69	3.93	19.08
40	4.26	11.04	26.40
60	5.16	16.47	43.95
80	7.36	21.51	45.63
100	11.13	23.79	69.25
120	15.91	35.61	69.21

Non-linear regression analysis of experimental data was carried out using Origin 9.0 by fitting the experimental results into Saeman's model, first-order, and second-order kinetic models. The statistical parameters and ANOVA of the Saeman model is presented in Table 2. Considering the values of rate constants in this study, the rate constant of glucose decomposition K_2 is negative at 100 and 110 °C while it was positive at 120 °C. At the highest temperature of hydrolysis, the ratio K_1/K_2 is 3.5 which indicates that glucose formation proceeds faster than the rate it is degraded. It is clear that the rate of decomposition of glucose is negligible compared to the rate at which glucose is formed but K_2 increases with temperature and concentration of catalyst. The same behaviour was reported by Aguilar *et al.* (2002).

Table 2. Nonlinear curve fit for Saeman's model analysis

	Hydrolysis Temperature		
	100 °C	110 °C	120 °C
Statistics			
Number of points	7	7	7
Degree of Freedom	5	5	5
Reduced Chi-Square	0.2809	0.098487	0.62751
Residual sum of squares	0.14045	0.47436	3.13755
R-square	0.96524	0.97898	0.9683
Adj R-square	0.95829	0.97476	0.96196
Parameters			
K_1	4.8025 E-4	0.00115	0.00397
K_2	-0.00406	-0.0041	0.00115
t-value	5.05996	6.4556	6.5011
prob>|t|	0.0039	0.00133	0.00129
ANOVA			
Regression (Sum of squares)	12.4487	66.92857	362.198
F value	221.51782	352.7334	288.600
Prob>F	1.3157E-5	4.151E-6	6.835E-6

As shown in Saeman's model plot (Fig. 2), the reducing sugar yield obtained at 100 °C ranged from 0.55 to 2.35 g/L. Likewise, the reducing sugar obtained at 110 °C increased from 0.61 g/L at 20 min to 5.63 g/L at 120 min. At a temperature of 120 °C, the reducing sugar amount was at the highest in the hydrolysate, ranging from 3.01 to 10.93 g/L at the end of 2 h. Generally, the formation of glucose is expected to increase as the reaction temperature increases (Wang *et al.*, 2019). Gámez *et al.* (2004) reported a sugar yield of 21.4 g/L at 6% phosphoric acid, 300 min, and at a temperature of 100 °C from sugarcane bagasse. The study observed a very low glucose concentration (1.60 g/L) in the first 1 h of the hydrolysis. Similarly, hydrolysis of sugarcane bagasse using 2% H_2SO_4 yielded 3 g/L glucose and 21.6 g/L xylose at 122 °C for 24 min (Aguilar *et al.*, 2002). The yield corresponds to the amount of glucose recovered from the hydrolysate at 120 °C for 20 min.

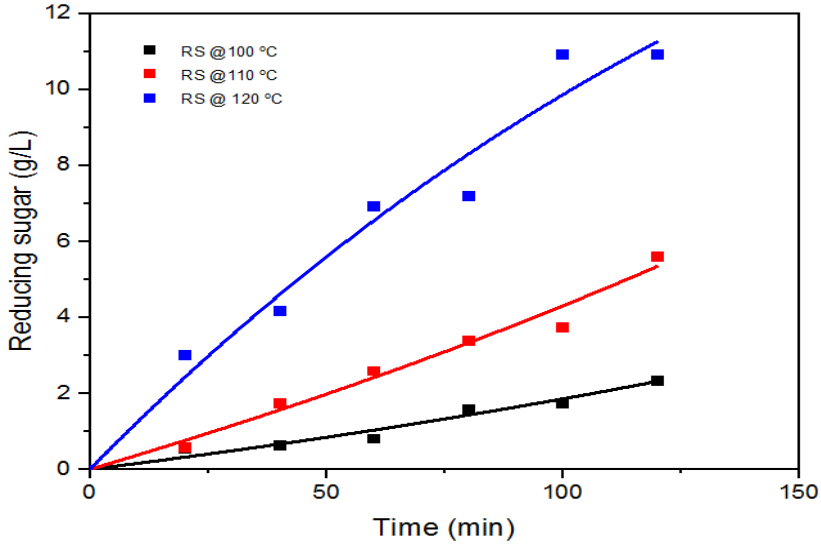

Figure 2: Plot of experimental data using Saeman's model

The R^2 of the kinetic statistics at 100, 110, and 120 °C was 0.9652, 0.9748, and 0.9683, respectively. All R^2 showed a good agreement between the actual glucose yield and predicted data using Saeman's model. Hydrolysis conducted at 110 °C had the highest R^2, which indicates that the experimental data obtained at this temperature is consistent with the expected data using Saeman's model. The fitness of experimental data to the first-order and second-order kinetic models followed similar behaviour based on R^2 value. Fitted data using the first-order reaction model showed a high and approximate value of R^2 (Fig. 3). On the contrary, based on R^2 values, the second-order reaction model showed a significant deviation at high temperature (120 °C) (Fig. 4), which suggest that glucose formation from lignocellulose biomass cannot be described by the second-order reaction model.

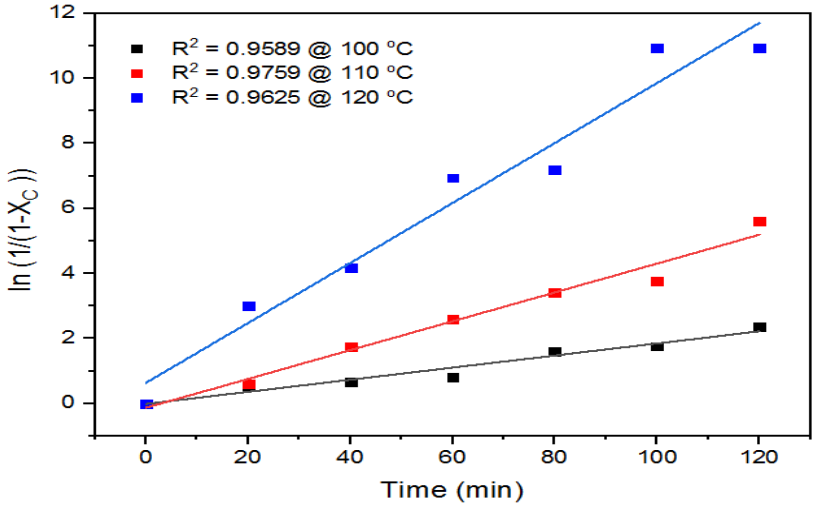

Figure 3: Plot of glucose formation using a first-order reaction model

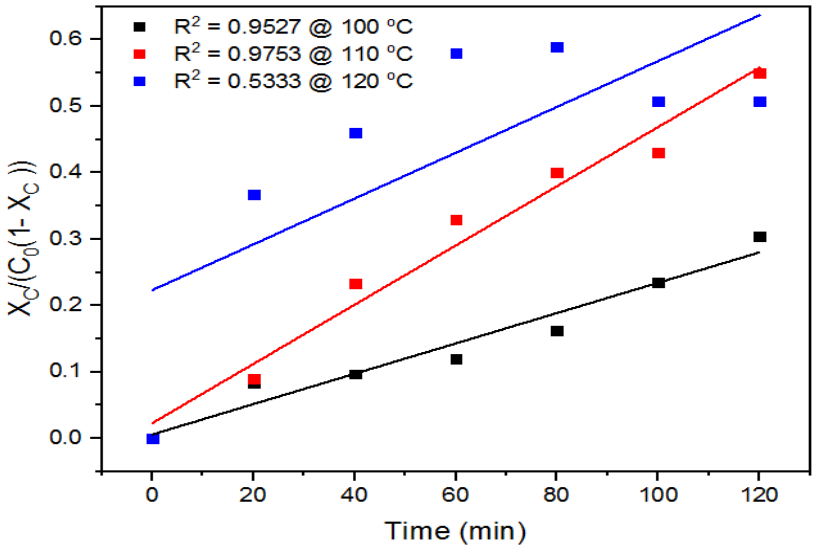

Figure 4: Plot of glucose formation using a second-order reaction model

Kinetic parameters were obtained from the plot of the natural logarithm of rate constants against the reciprocal of temperature (Fig. 5). Using Arrhenius expression, the frequency factor (*A*) from Saeman's model was 127.32 $Lmol^{-1}s^{-1}$ and the activation energy was 10.45 $kJmol^{-1}$. Activation energy for cellobiose hydrolysis to glucose was 111 kJ/mol, and the maximum glucose yield obtained was 68% (Vanoye *et al.*, 2009).

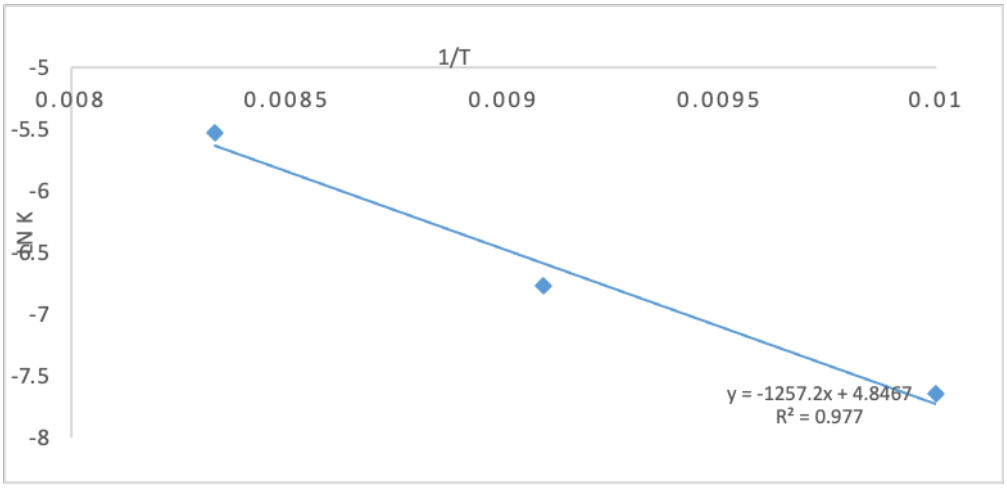

Figure 5: Plot of the natural logarithm of rate constants against the reciprocal of absolute temperature

The rate constants of glucose degradation were negative except at the temperature of 120 °C. This made it difficult to calculate the activation energy of glucose degradation. The temperature region might have to be extended in order to understand the rate of glucose degradation with respect to the catalyst used. Vanoye *et al.* (2009) claimed that the rate of two competing reactions (glucose formation and glucose decomposition) varies with acid strength. A catalyst having a pKa close to zero would have a dominating glucose formation with minimal glucose degradation. It was also reported that sugar degradation becomes significant at high temperatures for solid acid-catalyzed hydrolysis (Zhou *et al.*, 2021).

At the end of the batch hydrolysis of corncob, magnetic sulfonated catalysts were recovered from the product mixture using an external catalyst. The catalyst was washed and reapplied in another batch of hydrolysis at 110 °C. As shown in Fig. 6, the magnetic sulfonated solid acid catalyst can expedite the hydrolysis of corncob up to 5 cycles.

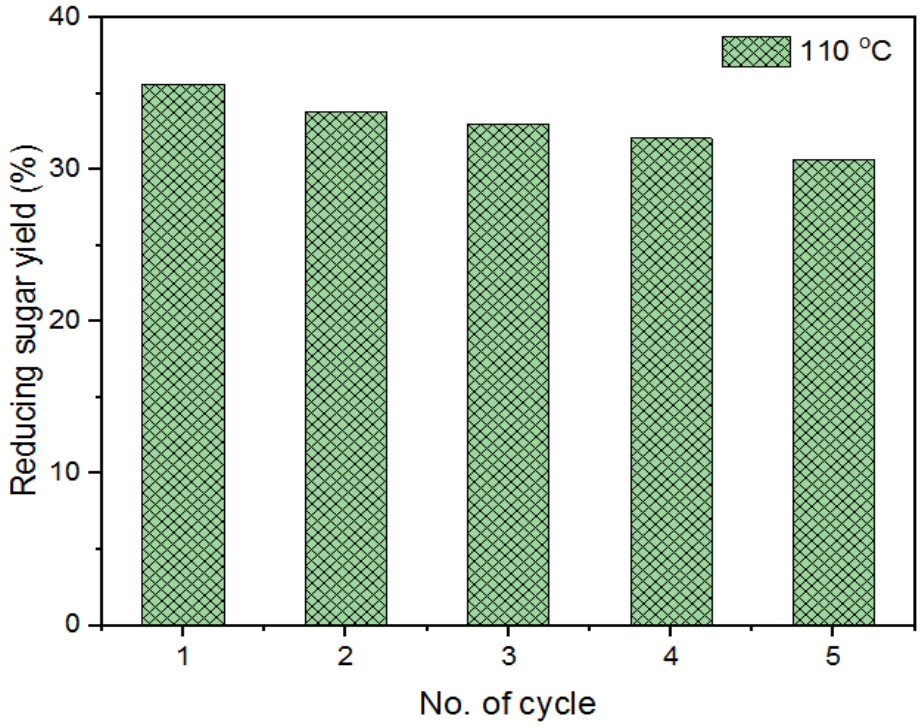

Figure 6: Reusability performance of magnetic sulfonated solid acid in corncob hydrolysis

4. CONCLUSION

The study conducted corncob hydrolysis at moderate temperatures and successfully fitted the experimental data into Saeman's model, first-order and second-order reaction models. It was observed that the value of R^2, Saeman's model accurately fitted the glucose yield better than the other models. The second-order model is not suitable for describing hydrolysis of lignocellulose biomass, particularly at high-temperature since large deviation of predicted

results from experimental results were observed. The sugar produced is stable and degradation of glucose into hydroxymethylfurfural, levunic acid, and formic acid is unlikely. Activation energy for glucose formation from corncob was 10.45 kJ/mol, and the synthesized magnetic sulfonated solid acid catalyst can be reused up to 5 times in the hydrolysis process after being separated with an external magnet.

ACKNOWLEDGEMENT

The authors of this work want to appreciate the technologists in the Department of Chemical Engineering for their technical assistance. The authors are grateful to the LUCRID, Landmark University, Omu-Aran for sponsoring this work for FETICON 2023 conference.

REFERENCES

Aguilar, R., Ramırez, J., Garrote, G., & Vázquez, M. (2002). Kinetic study of the acid hydrolysis of sugar cane bagasse. *Journal of food engineering, 55*(4), 309-318.

Gámez, S., Ramírez, J. A., Garrote, G., & Vázquez, M. (2004). Manufacture of fermentable sugar solutions from sugar cane bagasse hydrolyzed with phosphoric acid at atmospheric pressure. *Journal of Agricultural and Food Chemistry, 52*(13), 4172-4177.

Gill, C. S., Price, B. A., & Jones, C. W. (2007). Sulfonic acid-functionalized silica-coated magnetic nanoparticle catalysts. *Journal of Catalysis, 251*(1), 145-152.

Guo, F., Fang, Z., Xu, C. C., & Smith Jr, R. L. (2012). Solid acid mediated hydrolysis of biomass for producing biofuels. *Progress in energy and combustion science, 38*(5), 672-690.

Lee, J.-W., & Jeffries, T. W. (2011). Efficiencies of acid catalysts in the hydrolysis of lignocellulosic biomass over a range of combined severity factors. *Bioresource technology, 102*(10), 5884-5890.

Lin, R., Deng, C., Rajendran, K., Bose, A., Kang, X., & Murphy, J. D. (2020). Competing reactions limit production of sugars in hydrothermal hydrolysis of grass silage: an assessment of the effect of temperature on sugar production and parasitic energy demand. *Frontiers in Energy Research, 8*, 575523.

Qi, W., Liu, G., He, C., Liu, S., Lu, S., Yue, J., . . . Hu, J. (2019). An efficient magnetic carbon-based solid acid treatment for corncob saccharification with high selectivity for xylose and enhanced enzymatic digestibility. *Green chemistry, 21*(6), 1292-1304.

Saeman, J. F. (1945). Kinetics of wood saccharification-hydrolysis of cellulose and decomposition of sugars in dilute acid at high temperature. *Industrial & Engineering Chemistry, 37*(1), 43-52.

Safari, J., & Zarnegar, Z. (2013). A highly efficient magnetic solid acid catalyst for synthesis of 2, 4, 5-trisubstituted imidazoles under ultrasound irradiation. *Ultrasonics sonochemistry, 20*(2), 740-746.

Vanoye, L., Fanselow, M., Holbrey, J. D., Atkins, M. P., & Seddon, K. R. (2009). Kinetic model for the hydrolysis of lignocellulosic biomass in the ionic liquid, 1-ethyl-3-methyl-imidazolium chloride. *Green chemistry, 11*(3), 390-396.

Wang, C., Yang, G., Zhang, X., Shao, L., Lyu, G., Mao, J., . . . Xu, F. (2019). A kinetic study on the hydrolysis of corncob residues to levulinic acid in the FeCl 3–NaCl system. *Cellulose, 26*, 8313-8323.

Xiang, Q., Lee, Y. Y., & Torget, R. W. (2004). *Kinetics of glucose decomposition during dilute-acid hydrolysis of lignocellulosic biomass.* Paper presented at the Proceedings of the Twenty-Fifth Symposium on Biotechnology for Fuels and Chemicals Held May 4–7, 2003, in Breckenridge, CO.

Yat, S. C., Berger, A., & Shonnard, D. R. (2008). Kinetic characterization for dilute sulfuric acid hydrolysis of timber varieties and switchgrass. *Bioresource technology, 99*(9), 3855-3863.

Zhou, Z., Liu, D., & Zhao, X. (2021). Conversion of lignocellulose to biofuels and chemicals via sugar platform: an updated review on chemistry and mechanisms of acid hydrolysis of lignocellulose. *Renewable and Sustainable Energy Reviews, 146*, 111169.

PAPER 204 – EFFECT OF SALINITY ON THE GROWTH PARAMETERS OF OKRA PLANT IN TUNGAN KAWO IRRIGATION SCHEME

M.A. Mohammed[1*], J.J. Musa[1]

Department of Agricultural and Bioresource Engineering, Federal University of Technology Minna, Niger State, Nigeria.
Email: usmanbabaaminu@gmail.com

ABSTRACT
Wushishi (Tungan Kawo) irrigation scheme is located in Niger State, Nigeria and it serves as the study area for this experiment. Beds were prepared and plots were marked out according to the design before planting, so as to ensure a proper and conducive environment for easy germination of the okra plant. Varying amounts of salt water concentration of 5 g/L, 10 g/L, 15 g/L and also fresh water (non-salt concentrated water) were used to irrigate the okra plant. The effect of the planting period and the various salt concentration on height, leaf dry matter, leaf area and leaf number of the okra plant was determined. The varying levels of salt concentration had no negative impact on the growth of the crops at a point, while after while crop growth was negatively impacted indicating crop stress. These were evident after the twelfth week of growth as there was decrease in the growth parameter of most crops irrigated with the 5 g/L and 10 g/L salt concentrated water application compared to the crops that were irrigated with fresh water.

KEYWORDS: Tungan Kawo, Salinity, okra, growth parameters

1. INTRODUCTION

Soils with high amounts of soluble salts are called saline soils. They often exhibit a whitish surface crust when dry. The solubility of calcium sulphate or gypsum ($CaSO_4$) is used as the standard for comparing solubility's of salts (Seelig, 2000). Salts more soluble than gypsum are considered to be soluble and cause salinity. Salts less soluble than gypsum are considered insoluble and do not cause salinity. Sodium (Na^+) is a positively charged component, or cation, of many salts. If 15% or more of the clay sites are occupied by sodium (sodium-clay), the poor physical condition of the soil often restricts root growth and makes tillage difficult (Seelig, 2000). Thus, Soils high in sodium (sodic soils) may present physical restrictions to plant growth and increased plant stress, because of the complex nature of salts which cover the pore spaces and also hold water tighter for plant root uptake due to surrounding osmotic forces. Increasing soil salinity is a serious land degradation issue, with the area affected by dry land salinity estimated to be approximately 4 million hectares (ha) in 2000, and is predicted to increase to 20 million hectares (ha) by 2020 (National Land and Water Resources Audit (NLWRA)).

Agriculture-induced salinity and sodicity not only influence the chemical and physical characteristics of soils but also greatly affect soil microbial and biochemical properties (Rietz and Haynes, 2003). Soil salinization is a major factor contributing to land degradation and a decrease in crop yield (Anjum *et al*. 2005). It was reported that salinity in the arid and semi-arid regions of the world is a serious threat to agriculture (Rao *et al*. 2002). Production of grain legumes is severely reduced in salt-affected soils because their ability to form and maintain nitrogen-fixing nodules is impaired by both salinity and sodicity. Shah and Shah (2011) found that salinity is usually combined with high pH conditions, due to the presence and enrichment of calcium carbonate in the upper most soil layers in the arid and semi-arid regions of Pakistan evaluated by the impacts of groundwater on soil and crops in District Karak (arid region) (Khattak *et al*. 2002). Soil deterioration and reduction in crop yield were noted due to water salinization. Tavakkoli *et al* (2010) concluded that multiple factors contributing to subsoil constraints include salinity, sodicity, and high chloride concentrations present in many rain-fed farming soils of Southern Australia. Moradi and Abdelbagi (2007) found that salinity is a widespread soil problem limiting the productivity of cereal crops worldwide.

Increased soil salinity makes it difficult for plant roots to extract water from the soil and some salts are known to be toxic when present in high concentrations in the soil. Soil salinity is also known to degrade soil properties by weakening the bond between soil particles. It also leads to dense, cloddy and structureless soil, as it destroys aggregation. Soil salinity also causes dispersion in the subsoil, accelerating erosion, which can also cause the appearance of gullies and tunnels. The objective of this study was to evaluate the effect of salinity on the growth parameters of okra plant in Tungan Kawo irrigation scheme

2. MATERIALS AND METHODS

2.1 Study Area

Wushishi (TunganKawo) irrigation scheme is located within Niger State, Nigeria. Niger state lies in the Savannah zone of the tropics between latitudes 8°10'N and 11°3'N and longitude 3° 20'E and 7°30'E. Wushishi local government has a total population of 81783 (NPC, 2006) with a projected population of 98796 as of 2012. It is bordered by Gbako Local Government to the south, Rafi and Bosso Local Government Areas to the east, Mariga Local Government Area to the north; Mashegu and Lavun Local Government Areas to the west (Makusidi, 2015).

2.2 Site description

Three areas were chosen for the experiment with locations of (9° 39'42" N 6°5'56" E; 9°41'22" N 6°5'35" E; 9°44'33" N 6°5'25" E), respectively. The sites are located at Kanko which is one of the closest settlement to the dam.

2.3 Land Preparation and planting

The entire site was harrowed to a depth of 40 cm. Beds were prepared and sixteen (16) plots were marked out according to the design before planting, so as to ensure a proper and conducive environment for easy germination.

2.4 Irrigation of the plots and Salt concentration

Irrigation was done for a period of 90 days, and each of the plots was irrigated daily in the evening (5:00pm) Varying amounts of water from the dam (saline water of 10.0 mmhos/cm electrical conductivity) of 5 g/L, 10 g/L, 15 g/L and also fresh water (non-salt concentrated water) was used. The saline irrigation water was divided into 16 portions according to the number of plots. Watering cans were used for the watering of the plots.

2.5 Growth Parameters

For the computation of the growth parameters of plants, intervals of 30, 60, 90 days were used after the sowing of crops. Plant samples were collected, the leaf area and fresh weight of the samples were recorded (average measurement of three plants). The samples were dried in the oven at 70°C-80°C for 3 days and the dry weight was recorded. The data obtained on growth parameters, namely leaf area and dry matter were subjected to computation for different growth functions in accordance with the procedure by Das, (2011). While the plant height and leaf number data were gotten in accordance with the procedure of Wood *et al,* (2000).

3. RESULT

Table 1: Determination of salinity in the soil and water

Sample description	EC (mmhoscm-1) Reading	Presence of salinity
Dam site soil	0.5	Highly saline
Okra irrigation soil	0.7	Strongly saline
Freshwater	0.3	Moderately saline
Dam site water	10.0	Very strongly saline

3.1 Effect of planting period and water concentration on the plant height of Okra

From the result obtained in Figure 1**,** the 10 g/L irrigation water showed the highest height of 17 cm in the first four weeks. This trend continued to the eighth and twelfth week, which made it have the highest height of 50.95 cm and 81.6 cm, respectively. The fresh irrigation water also showed significant growth with plant height of 16.2 cm, 47.8 cm, and 67.5 cm, respectively, for the first four weeks, the eighth week and the twelfth week. The plots where 5 g/L and 15 g/L saline irrigation water were applied showed the least plant height in the first four weeks attaining almost the same plant height of 11.8 cm and 11.6 cm. Also, the 5 and 10 g/L saline irrigation water showed heights of 39.8 cm and 42.1 cm after 8 weeks, respectively, and 67.5 cm to 69.5 cm in the twelfth week of growth, respectively. The salt water concentration has significant effect on the plant height of okra. This was because it had a better growth than the fresh water (no salt) application despite its salt concentration.

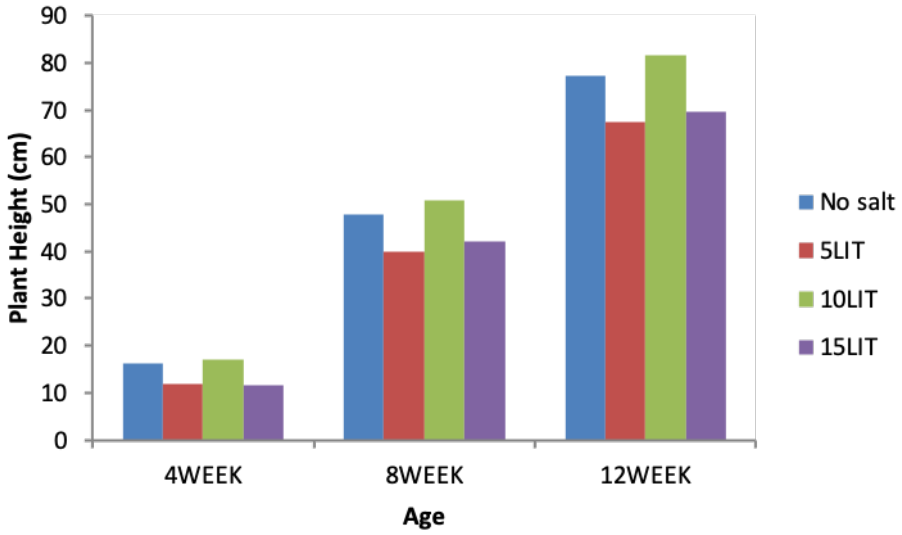

Figure 1. Effect of planting period and water concentration on plant height of Okra

3.2 Effect of planting period and salt concentration on the leaf dry matter

In the first four weeks to the eighth and twelfth week, the dry matter for fresh water was found to be the highest at 0.8 g, 1.7 g and 2.4 g, respectively (figure 2) compared to the other three saltwater concentrations which had almost the same dry matter contents of 0.8 g for the 5 g/L, 10 g/L and 15 g/L saline irrigation water respectively, in the first four weeks. Both 10 g/L and 15 g/L saline irrigation water had 1.6 g in the eighth week, while the 5 g/L saline irrigation water had 1.4 g in the eighth week. In the twelfth week, the 5 g/L, 10 g/L and 15 g/L saline irrigation water all showed dry matter content of 1.8 g, 2 g and 1.6 g, respectively.

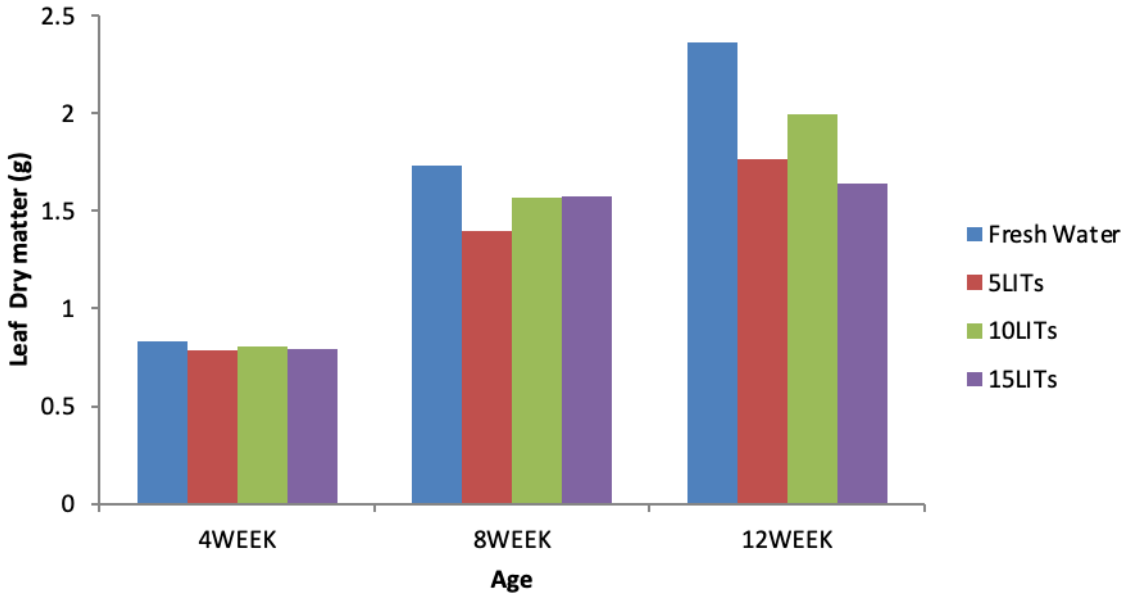

Figure 2: Effect of planting period matter and salt concentration on the dry matter of leaf

Effect of planting period and salt concentration on the number of leaves

Figure 3 shows that for the first four weeks, both the freshwater plot and 10 g/L saline irrigation water plots showed the highest number of leaves of 5 per plant. The 5 g/L and 15 g/L saline irrigation water plots showed the same number of leaves, 3 leaves per plant in the first four weeks. For the eighth week, both the freshwater plot and 15 g/L saline irrigation water plot showed the highest number of leaves, 9 leaves per plant. In the eighth week growth stage, both the 5 g/L, and 10 g/L salt water plots showed the same number of leaves 8 leaves per plant. And in the twelfth week, the 10 g/L plot showed the second highest growth after the freshwater plot had 13 leaves per plant. The 15 g/L plot followed with 10 leaves per plant. The 5 g/L salt water plot recorded 8 leaves per plant

in the twelfth week. These results show similarities with the study carried out by Ghoulam, (2002) who reported that saline water has effect on the agro-physiological parameters five varieties of sugar beet. Salinity affected all of the considered parameters (plant height and number of leaves per plant). Thus, high NaCl concentrations caused a great reduction in growth parameters such as leaf area, and fresh and dry weight of leaves and roots, but the leaf number was less affected.

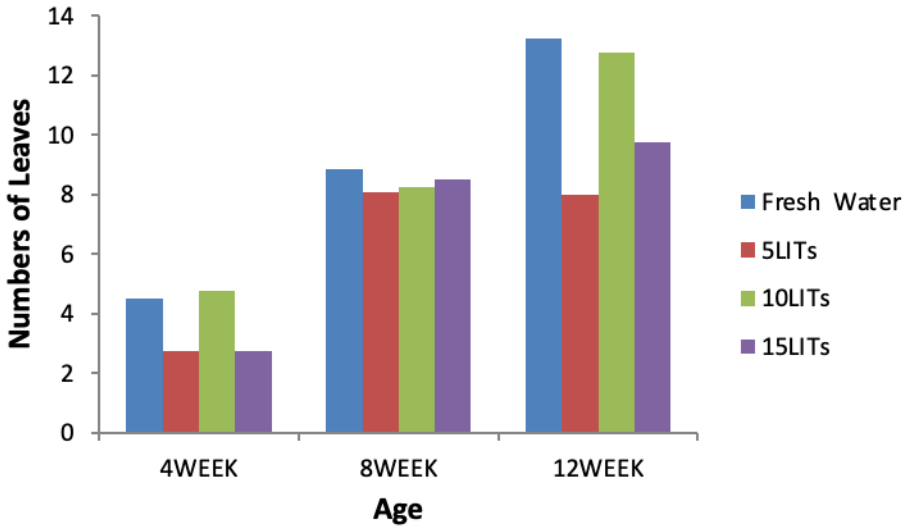

Figure 3. Effect of planting period and salt concentration on the number of leaves Okra

3.3 Effect of planting period and salt concentration on the leaf area of Okra

From figure 4, the freshwater, 5 g/L, 10 g/L, and 15 g/L showed almost the same leaf area of 373 mm^2, 367 mm^2, 363 mm^2, and 367 mm^2, respectively, for the first four weeks of growth. For the eight week, the freshwater plot recorded leaf area of 475.2 mm^2 which was greater than the leaf area recorded in the three salt water concentration plots. For the eight week, the 5 g/L, 10 g/L, and 15 g/L recorded leaf area of 434.8 mm^2, 442.8 mm^2, and 449 mm^2, respectively. For the twelfth week the freshwater plot maintained the highest leaf area of 792.3 mm^2, followed closely by the 5 g/L, 10 g/L and 15 g/L plot with leaf area of 751.2 mm^2, 744.2 mm^2 and 709.8 mm^2, respectively.

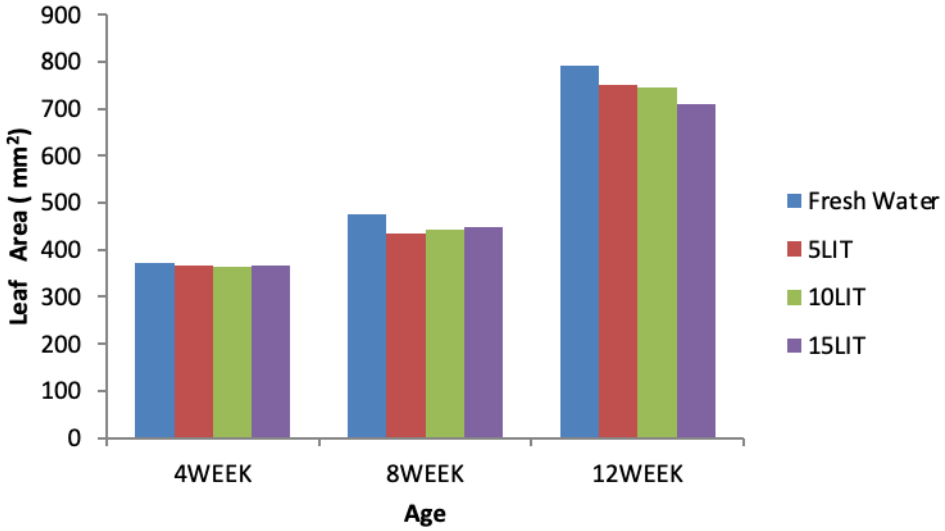

Figure 4. Effect of planting period and salt concentration on leaf area of Okra

4. CONCLUSION

From the results obtained showed that the treatments had effects on the growth parameters on the okra plants investigated. The varying levels of salts concentration either showed normal growth after 4 weeks on most of the crops or decreased crop yield indicating crop stress in some crops. These were evident after the twelfth week of growth as there was decrease on the growth parameter of most crops in the 5 g/L and 10 g/L salt water compared to that of freshwater, even though the 10 g/L salt water showed stable growth parameters of the crops. While the result of the freshwater application showed the best growth parameter as there was significant increase on the plants growth parameters after the twelfth week. The freshwater application indicated that water low in salinity was the most effective and most favourable water to be used for irrigation practice so as to ensure optimum crop growth and development.

REFERENCE

Anjum, R. Ahmed, A. Rahmatullah, Jahangir, M. and Yousif, M. (2005). Effect of soil salinity /sodicity on the growth and yield of different varieties of cotton. International Journal of Agriculture and Biology, 4, 606-608.

Das, T (2011). Jain Brothers (New Delhi) weed science basics and applications pp 791-797

Ghoulam, C. (2002) Effects of salt stress on growth, inorganic ions and proline accumulation in relation to osmotic adjustment in five sugar beet cultivar, Environmental and Experimental Botany, 47(1), 39 -50

Khattak, A, Michael, D., Reginald R., & Shauna L. (2002). Factors Related to More Severe Older Driver Traffic Crash Injuries. Journal of Transportation Engineering. 128(3), 243-249

Makusidi, M (2015). Impact of Tungan-Kawo Dam IrrigationProject on Rice Production Among Small Holder Farmers in Wushishi Local Government Area of Niger State-Nigeria. International Journal of Scientific and Research Publications, 5(10), 428-432

Moradi, F., & Abdelbagi, M. (2007). Responses of Photosynthesis, Chlorophyll Fluorescence and ROS-Scavenging Systems to Salt Stress During Seedling and Reproductive Stages in Rice. Annals of Botany 99: 1161–1173

Rao, D., Giller, K, Yeo, R., & Flowers J. (2002). The effect of salinity and sodicity upon nodulation and nitrogen fixation in chickpea. Annals of Biology, 89, 563 – 570.

Rietz, D.N. & Haynes, R. (2003). Effect of irrigation-induced salinity and sodicity on soil microbial activity. Soil Biology and Biochemistry, 35:845-854.

Shah, S.A. & Shah, Z. (2011). Changes in soil microbial characteristics with elevated salinity. Sarhad Journal of Agricultural 27(2): 233-244

Tavakkoli, E, Rengasamy, P & Glenn K. (2010) High concentrations of Na+ and Cl– ions in soil solution have simultaneous detrimental effects on growth of faba bean under salinity stress. Journal of Experimental Botany, 61(15), 4449–4459.

Wood, T.F, Rose, D.M, & Chung, M. (2000). "A Simple and Non-destructive Technique for Measuring Plant Growth and Development." American Biology Teacher, 62(3), 215-217

PAPER 206 – DEVELOPMENT OF BIO-NANOCOMPOSITE FILMS FROM SWEET POTATO FOR ACTIVE FOOD PACKAGING

O.K. Omiwole[1*], M. A. Olutoye[1], E.O. Babatunde[2]

[1]Department of Chemical Engineering, Federal university of Technology, Minna, Nigeria.
[2]Department of Chemical Engineering, University of Ilorin, Ilorin, Nigeria.
[*]Email: omiwole.kehinde@gmail.com

ABSTRACT

Continuous use of synthetic polymers in food industries constitutes threat in terms of pollution of our environment and micro-plastic pollution of living cells. This has driven diverse innovations in bio-plastics productions; however, most bio-plastics typically have poor barrier, mechanical and thermal properties making it difficult to replace synthetic plastics. This work proposed development of reinforced nanocomposite films as alternatives for petroleum-based polymers in food packaging. Potato starch nanocomposite films were prepared by solution casting method with cellulose nanofibers (CNF) isolated from Oil Palm Empty Fruit Bunches mechanically as reinforcement agent. 20 wt% of silver nanoparticles (AgNPs) were incorporated as an antimicrobial agent while 20 wt% glycerol was added as plasticizer. The effects of the plasticizer, AgNPs and CNF contents on the mechanical, thermal and antimicrobial properties of the films were investigated. Increase in CNF increased the film's tensile strength and the rate of water vapor transmission was reduced. Incorporation of 20 wt% glycerol, however, decreased the tensile strength of the composite films by 14%. Bio-assay tests revealed the antimicrobial activity of the films. However, increase in CNF did not translate to higher thermal stability as previously reported in some findings. This could be attributed to the ultrasonication method used.

KEYWORDS: Bio-nanocomposite, Cellulose nanofiber, silver nanoparticles, Films, bio-plastics, reinforcement

1. INTRODUCTION

Packaging protects the food and offers consumers hygienic security. (Wang *et al*. 2015). It facilitates handling, transportation, and storage of food materials by shielding them from physical, chemical, and biological harm. (El-Wakil,*et al*. 2015). Additionally, it provides crucial details regarding the product's properties, nutritional value, and ingredient composition (Tunc *et al*. 2007). Over the past decades, the food industries have been using petroleum-based plastic materials owing to their attractive properties, such as flexibility, safety, versatility, and low cost (Gil-López *et al*, 2019; Hassan et al. 2018). However, there are significant worries about the economic, environmental and public health that accompany continuous uses of these materials.

There has been increase in the demand for biodegradable packaging materials as an alternative to synthetic ones from consumers, food processors, environmentalists and government bodies particularly for use in short-term packaging and disposable applications such as fast-food restaurants, disposable cutlery, drinking straws, cups, plates, and utensils (Makaremi *et al*., 20l7). Using biopolymer-based food packaging materials, our environment becomes more sustainable because packaging made of biopolymers can be disposed in bio-waste collections for further composting, leaving behind recyclable organic byproducts like carbon dioxide and water.

Sadly, compared to typical non-biodegradable materials made from petroleum, the use of biopolymers as food packaging materials has limitations such as weak in mechanical, thermal, and barrier properties. As a result, numerous research projects were conducted to enhance the biopolymers' qualities. Among these is the application of nanocomposite idea. According to research, nanocomposite is an effective method for improving the mechanical and barrier properties of biopolymers (Quifer-Rada *et al*. 2016). Biopolymers may have their mechanical and barrier properties improved by the addition of nanofillers including silicate, clay, and titanium dioxide (TiO_2), as well as additional uses as an antibacterial agent, biosensor, and oxygen scavenger in food packaging. (Osman*et a*l., 20l9). The bio-nanocomposite can be used as an active food packaging that can interact with food in a variety of ways, such as by releasing advantageous components like antibacterial agents and antioxidant agents or by removing unfavorable elements like oxygen or water vapor. The bio-nanocomposite can also be used as smart food packaging, able to recognize characteristics of the packaged food like microbial contamination or expiration date and employ a mechanism to record and transmit data about the food's quality and safety.

This study is concerned with the production of bio-nanocomposite films with addition of cellulose nanofibers from Oil Palm Empty Fruit Bunches (OPEFB) as reinforcing agent and glycerol as plasticizer. In this study, cellulose nanofibers from OPEFB were isolated by mechanical treatment using ultrafine-grinder and

ultrasonicator. The effect of cellulose nanofibers content and glycerol on the properties of the matrix was evaluated by characterizations and tests.

2.0 THEORETICAL ANALYSIS

2.1 Extraction

Cellulose Nanofibres were extracted from a lignocellulosic biomass. A complex and compact hetero-matrix structure of Oil Palm Empty Fruits Bunches (OPEFB) was used. The cellulose is protected from isolation by lignin, hemicellulose, and their physical-chemical interactions. (Hassan *et al*. 2020; Zhao *et al*. 2015). The two-step multistage process for isolating cellulose nanoparticles from the biomass is acquired. In Figure 1, the first step is the fragmentation of lignocellulosic material to recover cellulose, and the second step is the treatment of cellulose to obtain its nanoscale dimension. Nanofibrillated cellulose was produced by defibrillation using mechanical processes such as high-intensity ultrasonication and grinding which produced 40-100 nm-diameter nanofibrillated cellulose.

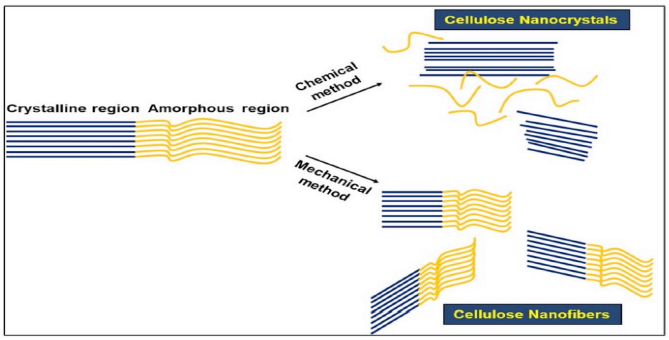

Figure 1: Methods in the Production of Nanomaterial from Biomass (Wyman, 2010)

2.2 Working Principle in OPEFB's Ultrasonication

The act of agitating the particles in solutions using sound vibrations is known as ultrasonication. These disturbances are used to combine the solutions, quicken the rate at which a solid dissolve in a liquid and remove dissolved gases from the liquids. Ultrasonic sound pulses were used during the sonication procedure of OPEFB. Due to the pressure being applied, thousands of tiny vacuum bubbles were produced in the fluid during the procedure. The process of cavitation causes the created bubbles to burst into the fluid. In the cavitation field, bubbles collapse, creating ripples in the process that releases a tremendous amount of energy. The molecular connections between the water molecules are broken down as a consequence. The sound waves discharge energy, causing friction in the solution as a consequence (Wyman, 2010). Figure 2 demonstrates the sound wave's propagation in the liquid resulting in the formation of bubbles and their collapse.

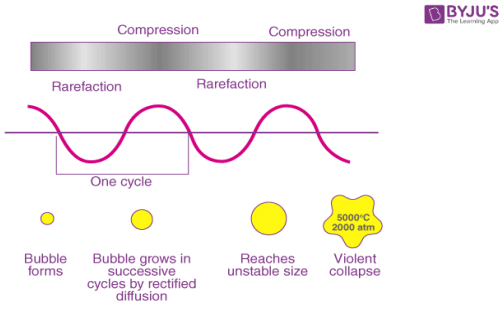

Figure 2: Working Principle of Ultarsonication (Wyman, 2010)

3.0 MATERIALS AND METHODS

3.1 Materials.

Sweet Potato was purchased from market. OPEFBs were collected from Palm Oil Refinery in Ondo State to obtain nanofibers. Glycerol (commercial grade product), PVA (produced by Calvon Sekisui Chemical Co. ltd), Sodium hydroxide (NaOH), and sodium hypochlorite (NaOCl) were used as received without any further purification.

3.2 Pretreatment and Isolation of Cellulose Nanofibers (CNF)

To eliminate impurities, dry OPEFBs were sliced to a length of about 1cm and boiled in water for 1hr at 100° C. After being submerged in a 1000 ml solution of 6% NaOH for 12 h at room temperature, 50 g of sliced OPEFBs were rinsed to a pH neutral state. OPEFBs were bleached by immersing them in 12% hypochlorite solution at ambient temperature for 5 h. Before creating cellulose nanofibers, the acquired cellulose pulp was rinsed to neutral pH and placed in a refrigerator. Using a mixer, the cellulose material was mixed with water. The mixture was then run 30 times at 1500 revolutions per minute through an ultrafine-grinder. Thereafter, the suspension was processed using ultrasonicator for 3 hr at 40 Amplitude.

3.3 Preparation of Silver Nanoparticles

Fresh Aloe vera leaves were cleaned with distilled water, thereafter, 10 g of leaves were immersed in 100 ml of distilled water and heated for 12 min. The extract was then gathered, put in a container, and sieved through Whatman filter paper. An aqueous solution (0.01M) of silver nitrate ($AgNO_3$) with different concentrations of Aloe Vera extract ranging from 1 to 5 ml were prepared separately. 10 ml of 0.01M $AgNO_3$ was added to every concentration of the leaf extract, after 20 min, the colour of the solution changed from light brown to dark brown, which indicated formation of AgNPs. The final colloidal solution of silver nanoparticle was later analyzed using UV–Vis spectrophotometer.

3.4 Preparation of Reinforced Active Bio-nanocomposite Films.

By using solution casting technique, reinforced composite films with the incorporation of cellulose nanofibers were produced. In a ratio of 4:1, Potato Starch extracted from sweet potato tubers and PVA were combined and diluted in water. The mixture was heated for 10 min at 90 ºC while being stirred. Granular flour undergone gelatinization at this stage. Glycerol as a plasticizer (0 and 20 wt%), 20 wt% AgNPs solution, and cellulose nanofibers (0, 2, 4, and 6 wt%) were added to the mixture, which was then agitated for 15 min. The composite was then molded in a Teflon mold and dried in an oven for 48 h at 45 °C. SPG-aNF-b is the designation for a set of PS/PVA cellulose nanocomposite materials. In this notation, S stands Starch, P for PVA, G for glycerol, ‘a’ for the glycerol percentage, NF for nanofibers, and ‘b’ for the weight percentage of nanofibers in each sample.

3.5 Characterization of Bio-nanocomposite

The CNF, and AgNPs were characterized using standard methods such as Scanning Electron Microscopy (SEM), used to view the surface morphology of the CNT, on a TA Q500 TGA, thermogravimetric analyses were carried out, SPG20NF6 and SPG0NF0 Control films' FTIR spectra were acquired using a Perkin Elmer FTIR/NIR Frontier model (Waltham, MA, USA) with a precision of 4 cm^{-1} between 4500 and 500 $cm^{-1}$and UV-Vis spectrometer was used to analyze the silver colloidal fluid that resulted. Using a UV-Vis spectrophotometer Shimadzu-UV 1800 and distilled water as a standard, the absorbance spectrum of the colloidal material was measured.

3.6 Determination of Antibacterial Activity

Using disc diffusion technique, the antibacterial effects of the SPG20NF6 and reference films were evaluated against Staphylococcus aureus and Escherichia coli. In Mueller-Hinton agar dishes that were incubated at 37°C for 24 h, a 6 mm film disc was utilised. By quantifying the zone of inhibition around the circumference of the disc (millimeter) after incubation, the antibacterial efficacy of the films was ascertained. As a control, Cefotaxime antibiotic disc was used.

3.7 Mechanical properties of Bio- Nanocomposite films

Using a micrometer, the thickness of films was determined at eight distinct places. (Pisttsburg, USA). Using Instron Universal Testing 3367, the films' tensile strength (TS) and percent elongation at break (E%) were calculated. Each film was divided into 15 mm x 100 mm strips and stored at 25 °C and 50% RH until analysis. Bluehill 2 software (Norwood, MA, USA) was used to calculate the strain at fracture as well as the maximum force applied to the specimen at the moment of fracture.

4.0 RESULTS AND DISCUSSION

4.1 Scanning Electron Microscopy (SEM) of Cellulose Nanofiber.

The SEM micrograph in Figure 4 shows that raw OPEBF cellulose size (Figure 3) was reduced after 3.5 - 4 hr of ultrasonication and cellulose fibers with average size of approximately 40 to 900 nm were produced. This has indicated that the hydrogen bonding between the CNF was lower after ultrasonication and smallest diameter of CNF can be obtained after 4 h of treatment. This proved that ultrasonication can break the relatively weak interfaces among cellulose fibers, which are bonded to each other by H-bonds. Thus, it has the ability to disintegrate the micro-size cellulose fibers into nano-sized cellulose fibers (Ojogbo *et al*, 2020).

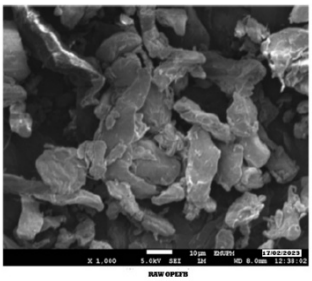

Figure 3: SEM of Raw OPEBF

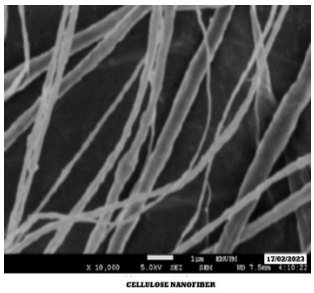

Figure 4: SEM of CNF

4.2 UV-Vis spectrum of Green synthesized Silver Nanoparticles (AgNPs)

The UV–visible absorption spectra of the silver nanoparticles with different concentrations of Aloe Vera leaf extract (1, 2, 3, 4 and 5 ml) are recorded and depicted in Figure 5 with absorbance intensities of 0.6, 0.8, 1.15, 1.3 and 1.75 respectively (Suvith *et al*., 2108). The formation of AgNPs during the reduction process is indicated by change in the colour of the reaction solution from light brown to dark brown which can be visually observed. Metal nanoparticles have free electrons, which yield a varied surface plasmon resonance (SPR) absorption band, due to the mutual vibration of electrons of metal nanoparticles in resonance with light wave (Wang *et al*., 2015). The the peaks in Figure 5 show the characteristics of surface plasmon resonance (PSR) of silver nanoparticles. The increase in the concentration of the leaf extract increases the absorbance intensity.

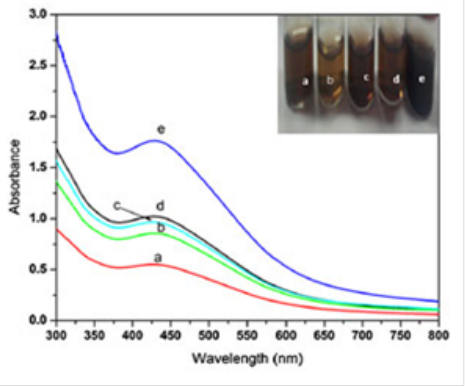

Figure 5 :UV-Vis Spectra of AgNPs at Different Aloe Vera Concentrations

4.3 FTIR Analysis of the Potato Starch Nanocomposite Film

The FTIR spectra obtained for the SPG0NF0 control and SPG20NF6 films are shown in Figure 6. The presence of characteristic bands of the methylcellulose structure can be seen in all films. Bands at 1460 cm^{-1}, 1377 cm^{-1}, 1325 cm^{-1}, and 947 cm^{-1} are characteristic of C-H stretches of CH_2 and CH_3. Bands at 1050 cm^{-1} are characteristic of C-O-C bonds of ethers present in methylcellulose. The bands at 2900 cm^{-1} are due to the C-H stretches and the stretches of the O-H bond of the hydroxyl groups present in the methylcellulose structure (Ramezanzade, 2017). The presence of the phenolic compounds from the Aloe Vera extract in the SPG25NF6 films was detected with the appearance of a band at 1595 cm^{-1} , which is characteristic of C=C-C stretches of the aromatic ring. This information is corroborated by the appearance of a small band at 1410 cm^{-1} characteristic of C=C stretches. This confirms the incorporation of the bioactive compounds into the methylcellulose matrix.

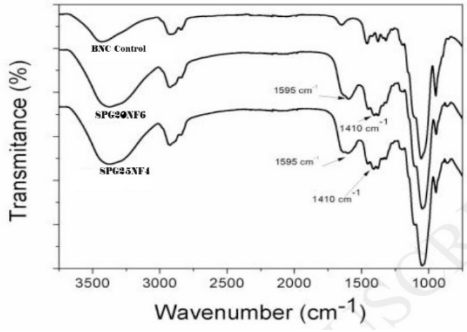

Figure 6: FTIR Spectra of Bio-nanocomposite films

4.4 Determination of Antibacterial activity

The antimicrobial activity of the films was tested by the growth of the inhibition zone of the gram positive bacteria S. aureus and gram-negative bacteria E. coli. In Figure 7, it was observed that the BNC Control sample showed no activity. The film containing Aloe Vera extract, is unable to inhibit microbial growth to a large extent under the conditions tested, due to the low concentration of the bioactive compounds (Mackevica et al. 2016). The SPG25NF6 films containing the silver nanoparticles presented a better antimicrobial activity for the two bacteria tested. An inhibition zone of 8.0 ± 0.5 mm was observed for, E. coli. For S. aureus, a zone of 7.0 ± 0.3 mm was observed. The antibiotic Cefotaximewas used as a reference and showed an inhibition zone of 14 ± 0.3 mm for E. coli and 14 ± 0.4 mm for S. aureus. This result is in agreement with the results obtained by Hemmati *et al*, (2018).

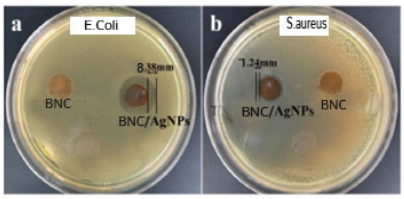

Figure 7: Incubation of Ecoli , S.aureus with BNC control and BNC/AgNP

4.5 Mechanical Tests

The tensile strength of Potato Starch Bio-nanocomposite films can be seen in Figure 8. The tensile strength of neat PS/PVA film was 47.3 MPa. Obviously, the addition of cellulose nanofibers improved tensile strength of the film. With increasing cellulose nanofibers content up to 7%, tensile strength of PS/PVA films without glycerol improved from 47.70 MPa to 60.72 MPa. Both matrix PS/PVA and cellulose nanofibers as filler have identical chemical nature, that is, hydroxyl groups.

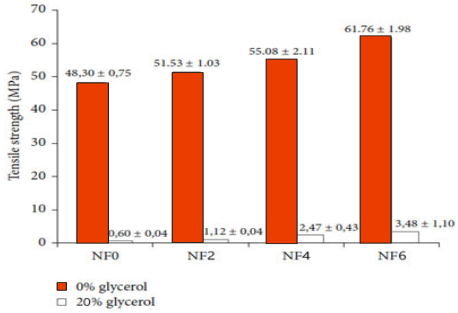

Figure 8: Films Tensile Strength

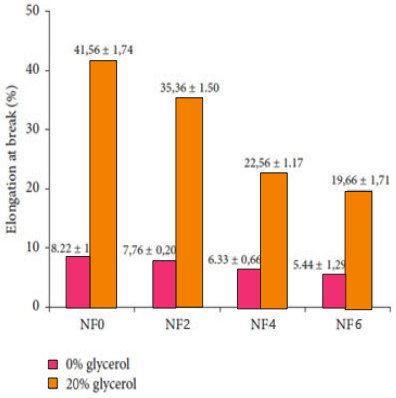

Figure 9: Films Elongation at Break

The increase of tensile strength due to the addition of cellulose nanofibers indicated that interfacial adhesion between PS/PVA as polymer matrix and cellulose nanofibers occurred. Figure 8 exhibits that there is difference in the tensile strength between nanocomposite films with glycerol and the films without glycerol. Glycerol reduces the inter-molecular and intra-molecular forces of the polysaccharide chain so that the film structure becomes more flexible (Hassan, 2018). Addition of glycerol caused tensile strength to decrease significantly. Figure 9 shows that with increasing cellulose nanofibers content the elongation at break decreased. The film without the addition of glycerol has a lower elongation value compared to the film with the addition of glycerol.

4.6 Thermogravimetric Analysis of the Films

Figure 10 shows the TGA curve of the bio-nanocomposite film for each treatment. The gradual loss in weight at around 80–120°C is attributed to the vaporization of bound water. The abrupt loss in weight, started around 250°C and ended at approximately 350°C, is due to the pyrolysis of thermoplastic starch and cellulose. This stage corresponds to the major weight loss of the film. Further loss in weight beyond 350°C could be ascribed to the decomposition of the remaining carbonaceous material (Suvith *et al*, 2018). The temperature at maximum rate of degradation of the films decreased by the addition of CNF. This indicated that the thermal stability of the reinforced films decreased as CNF quantity increases. This result is contrary to those reported in literature that

addition of crystalline cellulose could enhance thermal stability of the films. This can be attributed to ultrasonication process employed (Biji *et a*l, 2015).

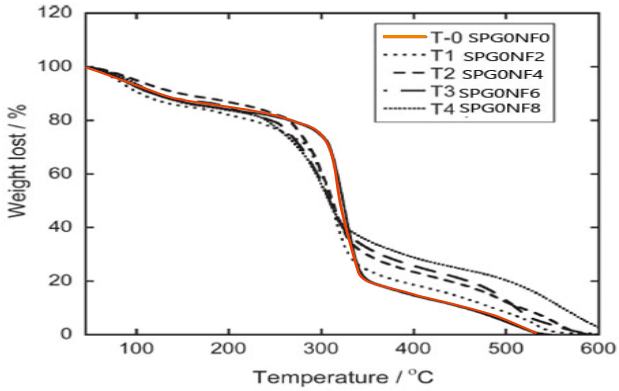

Figure 10: TGA Curves of bio-nanocomposite films with Varied CNF wt%

5.CONCLUSION

Isolation of Cellulose Nanofiber from OPEFB was accomplished mechanically using grinding and ultrasonication processes yielding nano-sized fibers of diameter40-900 nm. Bio-reduction of $AgNO_3$ using Aloe Vera extract as the reducing and capping agent was successfully accomplished as confirmed by the UV-Vis spectrum of the green synthesized AgNPs, Reinforced and Active Bio-nanocomposite films were formulated at an optimum condition of 45 °C within 48 h using wet processing method incorporated with CNF for reinforcement, glycerol as plasticizer and silver nanoparticles as antimicrobial agent.

The film without glycerol exhibited better tensile strength, but the elongation at break was reduced and this made the film brittle. The addition of cellulose nanofiber also resulted into the reduction of the film elongation at break while its increase increased the film crystallinity. Glycerol incorporation lowered the film's crystallinity when compared to the film without glycerol. The presence of the phenolic compounds from the Aloe Vera extract is responsible for the reduction of $AgNO_3$, capping of AgNPs and antimicrobial activity of AgNPs in the film. Finally, thermal stability of the reinforced film did not increase with increase in cellulose nanofiber content. However, more investigations are recommended on safety use of nanomaterials in food packaging materials

REFERENCES

Biji, K.B., Ravishankar, C.N., Mohan, C.O., Srinivasa Gopal, T.K., 20l5. Smart packaging systems for food applications: a review. J. Food Sci. Technol. 52, 6l25– 6l35.

Echegoyen, Y., Rodríguez, S., Nerín, C., 20l6. Nanoclay migration from food packaging materials. Food Addit. Contam. 33, 530–539.

El-Wakil, N.A., Hassan, E.A., Abou-Zeid, R.E., Dufresne, A., 20l5. Development of wheat gluten/nanocellulose/ titanium dioxide nanocomposites for active food packaging. Carbohydr. Polym. l24, 337–346.

Gil-López, D. L., Lois-Correa, J. A., Sánchez-Pardo, M. E., Domínguez-Crespo, M. A., Torres-Huerta, A. M., Rodríguez-Salazar, A. E., and Orta-Guzmán, V. N. (2019). "Production of dietary fibers from sugarcane bagasse and sugarcane tops using microwave-assisted

Hassan, E. A., Fadel, S. M., & Hassan, M. L. (2018). Influence of TEMPO-oxidized NFC on the mechanical, barrier properties and nisin release of hydroxypropyl methylcellulose bioactive films. International Journal of Biological Macromolecules, 113, 616-622.

Hemmati, F., Jafari, S. M., Kashaninejad, M., & Barani Motlagh, M. (2018). Synthesis and characterization of cellulose nanocrystals derived from walnut shell agricultural residues. International Journal of Biological Macromolecules, 120(Pt A), 1216-1224.

Makaremi, M., Pasbakhsh, P., Cavallaro, G., Lazzara, G., Aw, Y. K., Lee, S. M., & Milioto, S. (2017). Effect of Morphology and Size of Halloysite Nanotubes on Functional Pectin Bionanocomposites for Food Packaging Applications. ACS Applied Materials & Interfaces, 9(20), 17476-17488.

Osman, T.,; Alvarez V A; Cyras V P; Vzquez A. Extraction of cellulose and preparation of nanocellulose fromsisal fibers. Cellulose. 2019; 15:149-159.

Ojogbo, E., E.O. Ogunsona, T.H. Mekonnen, Chemical and physical modifications of starch for renewable polymeric materials, Mater. Today Sustain. 7–8 (2020) 100028. https://doi.org/10.1016/j.mtsust.2019.100028.

Quifer-Rada, P., Choy, Y. Y., Calvert, C. C., Waterhouse, A. L., & Lamuela-Raventos, R. M. (2016). Use of metabolomics and lipidomics to evaluate the hypocholestreolemic effect of Proanthocyanidins from grape seed in a pig model. Molecular Nutrition & Food Research, 60(10), 2219-2227.

Ramezanzade, L., Hosseini, S. F., & Nikkhah, M. (2017). Biopolymer-coated nanoliposomes as carriers of rainbow trout skin-derived antioxidant peptides. Food Chemistry, 234, 220-229.

Suvith VS, Philip D (2018) Catalytic degradation of methylene blue using biosynthesized gold and silver nanoparticles. Spectrochim Acta A Mol Biomol Spectrosc 118:526–532

Torstensen, J. O., Liu, M., Jin, S. A., Deng, L., Hawari, A. I., Syverud, K., . . . Gregersen, O. W. (2018). Swelling and Free-Volume Characteristics of TEMPO-Oxidized Cellulose Nanofibril Films. Biomacromolecules, 19(3), 1016-1025.

Tunc, S., Angellier, H., Cahyana, Y., Chalier, P., Gontard, N., & Gastaldi, E. (2007). Functional properties of wheat gluten/montmorillonite nanocomposite films processed by casting. Journal of Membrane Science, 289(1-2), 159-168.

Vijaykumar M, Priya K, Nancy FT, Noorlidaha A, Ahmed ABA (2013) Biosynthesis, characterization and anti-bacterial effect of plant-mediated silver nanoparticles using Artemisia nilagirica. Ind Crops Prod 41:235–240

Wang, Z., Xia, T., & Liu, S. (2015). Mechanisms of nanosilver-induced toxicological effects: more attention should be paid to its sublethal effects. Nanoscale, 7(17), 7470-7481.

Wyman C., van der Heide, T. Zhang, D. LiuX. Zhao, E. v. d. H., T. Zhang and D. Liu, Delignification of Sugarcane Bagasse with Alkali and Peracetic Acid and Charecterization of the Pulp. Bio-resources 2010, 5 (3), 1565-1580

Zhao. X., E. van der Heide, T. Zhang, D. LiuX. Zhao, E. v. d. H., T. Zhang and D. Liu, Delignification of Sugarcane Bagasse with Alkali and Peracetic Acid and Charecterization of the Pulp. Bio-resources 2015, 5 (3), 1565-1580

PAPER 208 – Influence of Carbonized Plantain Peel Addition on The Properties of Aluminium Matrix Composite

J. A. Adebisi[1], D. J. Afolabi[1], M. O. Oseni[1,*], S. I. Talabi[1], K. P. Odimayomi[3], S. Sulaiman[2], I. I. Ahmed[1]

[1]Department of Materials and Metallurgical Engineering, University of Ilorin, Nigeria
[2]Department of Mechanical Engineering, University of Ilorin, Nigeria
[3]Advanced Composite Materials Research Laboratory, National Space Research and Development Agency (NASRDA), University of Ilorin Centre, University of Ilorin, Nigeria
[*]Email: 18-30gn072@student.unilorin.edu.ng

ABSTRACT
Current applications in engineering require high-strength, lighter and inexpensive materials. Aluminium alloys and composites have been extensively used for engineering applications because of their good specific strength. Unfortunately, synthetic materials like silicon carbide that are used to reinforce aluminium are expensive. In this work, aluminium matrix was reinforced with a cheap carbonized plantain peel (CPP) selected among three agricultural wastes based on their thermal stability. Less than 100 µm CPP powder (0 – 4.8wt %) was incorporated in molten aluminium using the stir-casting method. TGA analysis was carried out on plantain peel. Tensile, hardness, XRD, and SEM/EDS of the specimens were carried out. From the results obtained, there was an increase in strength from 1280.1113 N/mm^2 to 4373.25 N/mm^2. Hardness number of the pure aluminium casting at 9.4 increased to 26.76 of the reinforced casting (4.8 wt.%). This new class of material can be used in automobile industry.

KEYWORDS: plantain peel, carbonization, reinforcement, aluminium, composite

1. INTRODUCTION

Aluminium is abundant in the earth crust and quite easy to recycle due to its low melting point. However, it has low strength which makes its applications challenging in engineering. Aluminium alloys have compelling properties such as electrical and thermal conductivities, and high reflectivity to both heat and light (Vijaya & Srinivas, 2018). They have been identified as structural materials in automobile and aerospace industries owing to their lightweight (Dursun & Soutis, 2014; Georgantzia *et al.*, 2021; Usman *et al.*, 2014b). Nonetheless, aluminium alloys have challenges of low wear resistance and relatively low strength (Usman *et al.*, 2014a). These challenges have been improved by alloying and composite development. Aluminium composites have been reported to offer remarkable uplift of these challenges by the introduction of reinforcements that impede early dislocations (Arun *et al.*, 2013; Senapati *et al.*, 2014). Composite material is a combination of two or more distinct basic materials (metal, ceramic and polymer), with conspicuous interface between them, and their properties differ abruptly from the constituting components.

Aluminium matrix composites (AMCs) have been developed to improve the performance of conventional aluminium alloys that cannot meet modern engineering product requirements. They have high strength, high elastic modulus and good wear resistance. The cost of their production remains high due to use of conventional reinforcements such as silicon carbide, alumina, and titanium carbide. This restriction has been minimized by the use of inexpensive natural reinforcements and thus lowering materials costs and increasing their usage (Gladston *et al.*, 2015). Farming and processing of agricultural produce generate by-products and residues that could be harnessed for production of natural reinforcing phase in AMCs. The wastes constitute environmental pollution when indiscriminately disposed and burning enhance greenhouse gas emissions which invariably increase global warming. The use of naturally sourced particulates (biomass based) has been reported to offer hybrid reinforcements with low cost and renewability (Alaneme & Olubambi, 2013; Joseph & Babaremu, 2019; Nwobi-Okoye & Ochieze, 2018).

This work investigates the effect of carbonized plantain peel (CPP) on AMC's properties. Thermal stability of plantain peel was enhanced prior to pulverization and subsequent use as reinforcement in AMC production. This approach encourages generation of wealth from wastes.

2. MATERIALS AND METHODS

2.1 Materials

Plantain peel was obtained at ITEM-7 eatery, Tanke, Ilorin. Aluminium scraps were obtained from Materials and Metallurgical Engineering foundry. Some apparatus and equipment used include muffle furnace, digital weighing balance, sieve, laboratory blade mill, carbonization chamber, oven, stirrer, and crucible furnace, available at the Department of Materials and Metallurgical Engineering, University of Ilorin, Nigeria. Equipment used for characterization include Brinell harness tester, Universal testing machine (UTM), both available at Department of Mechanical Engineering, University of Ilorin, Nigeria. Thermogravimetric analysis (TGA), X-Ray Diffractometry (XRD) and X-Ray Fluorescence (XRF), were carried out at Centre for Solid Minerals Research & Development, Kaduna State Polytechnics, Nigeria. Scanning Electron Microscope (SEM) and Energy Dispersive X-ray Spectroscopy (EDS) at Tshwane University of Technology, Department of Chemical, Metallurgical and Materials Engineering, Pretoria, South Africa.

2.2 Methods

The plantain peel (PP) was washed and rinsed with water to remove dirt. It was sun-dried for 14 days for moisture content reduction. This was carbonized at a temperature between 500 – 550 °C in a carbonization chamber with limited air for 60 minutes. The carbonized PP (CPP) was pulverised using laboratory blade mill and sieved to obtain particles below 100 μm.

Stir casting method was used to produce specimens for characterization. Aluminium scrap was melted in a crucible furnace at a temperature of 700 °C. A measured amount of CPP was preheated to 300 °C for 3 hours in an electric oven to remove moisture. A calibrated pouring cup was used to tap 250 g of the molten metal and the preheated CPP was then mixed thoroughly for homogeneity. The mixture was poured into the preheated mould cavities at a maintained pouring temperature of 680 ºC. The composite was then allowed to solidify, and samples removed, cleaned, labelled and kept for characterization. The formulation of the composites is presented in Table 1.

Table 4: Weight percentage of aluminium scraps and carbonized plantain peel

SAMPLE ID	ALUMINIUM SCRAP (g)	CPP (g)	ALUMINIUM SCRAP (wt.%)	CPP (wt.%)
A	250	0	100	0
B	250	3	98.8	1.2
C	250	6	97.6	2.4
D	250	9	96.4	3.6
E	250	12	95.2	4.8

TGA of the PP, XRF and XRD of CPP were carried out. Tensile, SEM/EDS, XRD and hardness of the composites were carried out to establish their physical, mechanical, and chemical properties.

3. RESULTS AND DISCUSSION

3.1 Plantain Peel Features

The thermal decomposition profile of plantain peel by heating from room temperature to about 900 °C is presented in Figure 1. Thermal decomposition of agricultural wastes was explained in Adebisi *et al.* (2019) as a three stages of dehydration, volatilization and carbonization in inert environment. The weight loss curve showed rapid decomposition at 280 °C, which corresponds to hemicellulosic compounds vapourization, up to 360 °C. Cellulose decomposition occurred up to around 414 °C after which lignin, at 478 °C decomposes as the main carbonization stage. The derivative of thermo-gravimetric analysis (DTG) curve shows the energy gain from heat supplied when the plantain peel was heated from room temperature, presenting a case of endothermic process. The second stage of this thermal decomposition has been reported as the most crucial stage when all volatile matters thermally left the biomass to leave a residue of carbon char (Adebisi et al., 2019; Munir *et al.*, 2009; Nurhayati & Fauziah, 2013). The char left is principally carbon skeleton of the biomass, which is about 18.89% as reported in Adebisi et al. (2019) to range between 18.60–29.40%. This carbon network is a ceramic with brittle nature and thus enhances pulverization of the carbonized biomass.

As presented in Table 2, the compounds that constituted CPP are MgO, Al_2O_3, SiO_2, Cl, K_2O, CaO, Cr_2O_3, MnO, Fe_2O_3, BaO, and PbO. With carbon as the major element, silicon, iron, potassium, calcium, magnesium, aluminium, and manganese also constitute about 91%. The presented elements are similar to chemical composition obtained in plantain peel reported by Ogbodo *et al.* (2021). Phase identification of compounds in CPP, as showed in Figure 2, revealed presence of $KAlCl_2O$, PbO, Ba_2FeO_4, SiO_2, MnSi, Cr_2O_3, $Mg_2Al_4Si_5O_{18}$. The XRD spectrum obtained for CPP is similar to that reported by Hemalatha and Lakshmi (2021) for raw plantain peel as against carbonized in this present work.

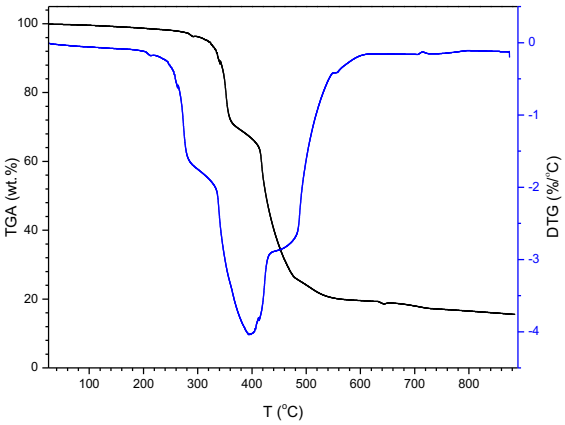

Figure 27: Thermogravimetric analysis of plantain peel

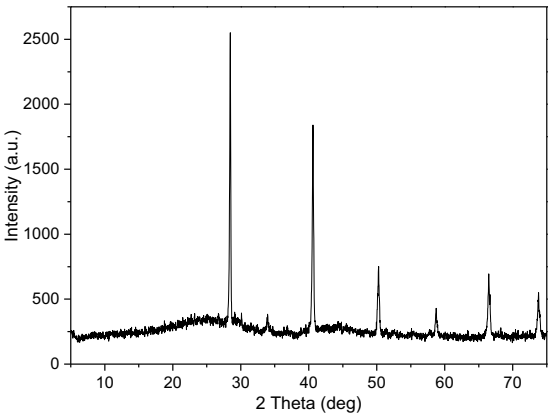

Figure 28: XRD of carbonized plantain peel

Table 5: Elemental composition of plantain peel

ELEMENT	MgO	Al_2O_3	Cr_2O_3	SiO_2	Cl	K_2O	CaO	MnO	Fe_2O_3	BaO	PbO	LOI
COMPOSITION (wt%)	3.34	1.75	0.05	62.11	1.36	4.32	3.15	3.81	12.46	0.65	0.67	6.31

3.2 Properties of Aluminium Carbonized Plantain Peel Composites

The chemical composition of the aluminium scrap and composites produced showed that addition of CPP to the molten scrap increases the amount of carbon, silver, silicon, calcium, chlorine, potassium, magnesium, sulphur and phosphorus. This is in tandem with the theory of composite formulation.

Table 6: Composition of the aluminium alloy and composites produced

Elements	Al	C	Fe	Ag	Si	Ca	Cl	K	Mg	S	O	Ti	P
0 wt%	89.66	2.93	2.11	1.59	1.03	0.64	0.57	0.48	0.27	0.24	0.20	0.19	0.08
2.4 wt%	79.68	4.50	1.39	3.03	1.40	0.90	2.95	0.70	0.49	1.07	3.35	0.00	0.54
4.8wt %	81.21	7.01	2.19	2.44	1.52	1.00	1.16	0.83	0.27	0.37	1.70	0.00	0.28

Figure 3 shows the XRD spectra for the scrap and composites. Addition of CPP enhances the peaks and conform to simple rule of mixture without altering the peak positions in the unreinforced aluminium alloy.

The hardness values for the aluminium composites produced is shown in Figure 4. Addition of CPP increases the hardness in the composites but decreases when the amount of reinforcement exceeds 1.2 wt.%. This may be as a result of poor wettability of the reinforcement in the aluminium scrap used during casting.

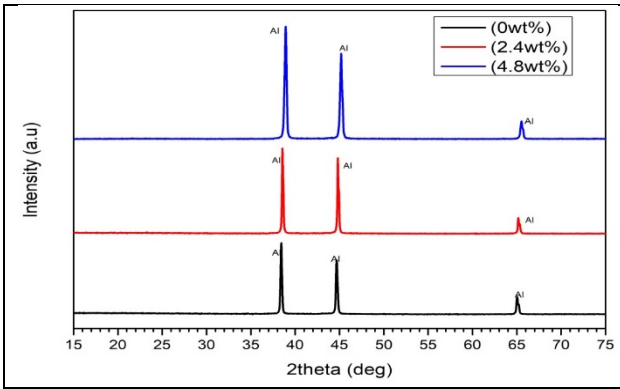

Figure 29: XRD patterns for unreinforced aluminium scrap and produced composites.

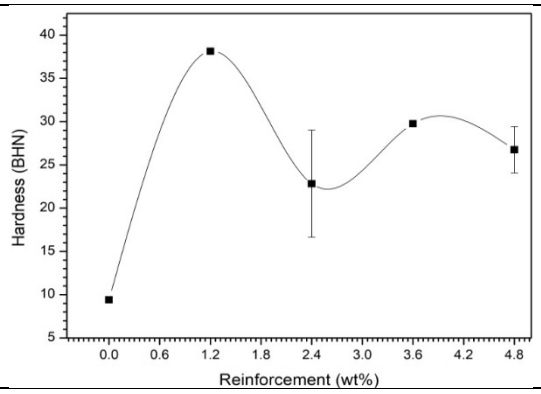

Figure 30: Hardness values for aluminium carbonized plantain peel composites

Figures 5 shows the tensile strengths of the composites produced which increase in all the samples. The decrease in the values at points 2.4 and 3.6 wt.% may be attributed to presence of defects during casting, which could be nonhomogeneous mixing and agglomeration as a result of excess reinforcement loading. It was reported by Oghenevweta *et al.* (2016) that agglomeration of the particles may be a source of stress raiser that will eventually results in failure when amount added exceeds a certain limit. The tensile strength improved from 1143 MPa to above 4500 MPa, representing an increment of about 300%.

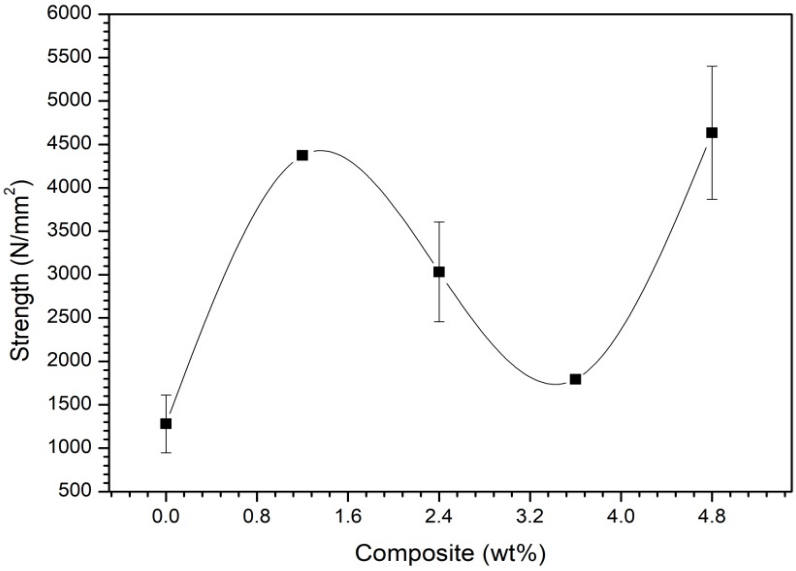

Figure 31: Ultimate tensile strength of the composites

4. CONCLUSION

Carbonized plantain peel has improved the properties of composites produced. The resulting composite shows increment in strength from 1143 MPa of the pure aluminium (0wt %) casting to 4373 MPa of the reinforced sample (4.8wt %). Hardness number of the pure aluminium casting at 9.4 increased to 26.76 of the reinforced casting (4.8wt %). This new class of material can be used in aerospace and automobile industry.

REFERENCES

Adebisi, J. A., Agunsoye, J. O., Bello, S. A., Kolawole, F. O., Ramakokovhu, M. M., Daramola, M. O., & Hassan, S. B. (2019). Extraction of Silica from Sugarcane Bagasse, Cassava Periderm and Maize Stalk: Proximate Analysis and Physico-Chemical Properties of Wastes. *Waste and Biomass Valorization, 10*(3), 617-629. doi: 10.1007/s12649-017-0089-5

Alaneme, K. K., & Olubambi, P. A. (2013). Corrosion and wear behaviour of rice husk ash—Alumina reinforced Al–Mg–Si alloy matrix hybrid composites. *Journal of Materials Research and Technology, 2*(2), 188-194.

Arun, L., Saddam, H., & Suneel, K. (2013). Dynamic behaviour of hybrid Aluminium6061 metal matrix reinforced with SIC and fly ash particulates. *International Journal of Innovative Research in Science, Engineering and Technology, 2*(6), 2501.

Dursun, T., & Soutis, C. (2014). Recent developments in advanced aircraft aluminium alloys. *Materials & Design (1980-2015), 56*, 862-871.

Georgantzia, E., Gkantou, M., & Kamaris, G. S. (2021). Aluminium alloys as structural material: A review of research. *Engineering Structures, 227*, 111372.

Gladston, J. A. K., Sheriff, N. M., Dinaharan, I., & Selvam, J. D. R. (2015). Production and characterization of rich husk ash particulate reinforced AA6061 aluminum alloy composites by compocasting. *Transactions of Nonferrous Metals Society of China, 25*(3), 683-691.

Hemalatha, M., & Lakshmi, B. (2021). Valorization of fruit waste using DES pretreatment and hydrolysis over a heterogeneous catalyst for bioethanol production. *Biomass Conversion and Biorefinery*, 1-11. doi: 10.1007/s13399-021-01669-6

Joseph, O. O., & Babaremu, K. O. (2019). Agricultural Waste as a Reinforcement Particulate for Aluminum Metal Matrix Composite (AMMCs): A Review. *Fibers, 7*(4), 33.

Munir, S., Daood, S. S., Nimmo, W., Cunliffe, A. M., & Gibbs, B. M. (2009). Thermal analysis and devolatilization kinetics of cotton stalk, sugar cane bagasse and shea meal under nitrogen and air atmospheres. *Bioresource Technology, 100*(3), 1413-1418. doi: https://doi.org/10.1016/j.biortech.2008.07.065

Nurhayati, A., & Fauziah, S. (2013). A Comparison Study on Oven and Solar Dried Empty Fruit Bunches. *Journal of Environment and Earth Science, 3*(2), 145-156.

Nwobi-Okoye, C. C., & Ochieze, B. Q. (2018). Age hardening process modeling and optimization of aluminum alloy A356/Cow horn particulate composite for brake drum application using RSM, ANN and simulated annealing. *Defence Technology, 14*(4), 336-345.

Ogbodo, N. O., Asadu, C. O., Ezema, C. A., Onoh, M. I., Elijah, O. C., Ike, I. S., & Onoghwarite, O. E. (2021). Preparation and Characterization of activated carbon from agricultural waste (Musa-paradisiaca peels) for the remediation of crude oil contaminated water. *Journal of Hazardous Materials Advances, 2*, 100010. doi: https://doi.org/10.1016/j.hazadv.2021.100010

Oghenevweta, J. E., Aigbodion, V. S., Nyior, G. B., & Asuke, F. (2016). Mechanical properties and microstructural analysis of Al–Si–Mg/carbonized maize stalk waste particulate composites. *Journal of King Saud University - Engineering Sciences, 28*(2), 222-229. doi: https://doi.org/10.1016/j.jksues.2014.03.009

Senapati, A. K., Mishra, P. C., & Routara, B. C. (2014). Use of waste flyash in fabrication of aluminium alloy matrix composite. *Int. J. Eng. Technol, 6*, 905-912.

Usman, A., Raji, A., Waziri, N., & Hassan, M. (2014a). Production and characterisation of aluminium alloy-bagasse ash composites. *IOSR Journal of Mechanical and Civil Engineering, 11*(4), 38-44.

Usman, A. M., Raji, A., Waziri, N. H., & Hassan, M. A. (2014b). Aluminium alloy-rice husk ash composites production and analysis. *Leonardo Electronic Journal of Practices and Technologies, 25*, 84-98.

Vijaya, M., & Srinivas, K. (2018). Development and Mechanical Properties of SiC Reinforced Aluminium Metal Matrix Composites. *J. Rec. Act. Prod, 3*(1).

PAPER 209 – APPLICATION OF SUPPORT VECTOR REGRESSION MODELLING FOR THE PREDICTION OF IMPACT ATTENUATION OF 3D PRINTED HIP PROTECTORS

S. A. Yahaya[1,2*], I. O. Muniru[1], S. Saminu[1], M. O. Ibitoye[1], T. M. Ajibola[1], L. J. Jilantikiri[1], Z. M. Ripin[2], M.I.Z. Ridzwan[2]

[1]Department of Biomedical Engineering, University of Ilorin, Ilorin, Nigeria.
[2]School of Mechanical Engineering, Universiti Sains Malaysia, Malaysia.
[*]Email: yahaya.say@unilorin.edu.ng

ABSTRACT
3D printed thermoplastic polyurethanes of different shore hardness were used to make hip protectors for the prevention of osteoporotic hip fracture, which was then tested. The result was used to develop a support vector regression model to estimate the effect of the protector shore hardness, shell thickness, and infill density on the impact attenuation capacity at different energy levels. The results from the model show that the impact attenuation ability of a hip protector is significantly dependent on the infill density of the hip protector and its shore hardness. Excellent agreement was found between the model results and test results.

KEYWORDS: 3D print, thermoplastic polyurethane; hip protector; impact attenuation; support vector regression; performance prediction.

1. INTRODUCTION

The enormous benefits of additive manufacturing over conventional manufacturing methods cannot be overemphasized (Parandoush and Lin, 2017). This benefit is due to its ability to significantly help in creating intricates part that would otherwise be very challenging to produce using other techniques, reduce the number of distinct parts needed for an assembly, reduce material waste, reduce the number of production steps and reduce the amount of inventory being held (Sendel et al., 2015).

Advancement has led to the application of 3D human body scan data to surface pad modeling to create custom-fit hip protectors, reportedly to have influenced adherence in a wearer test (Park and Lee, 2019). However, optimizing 3D printed hip protectors' mechanical performance requires careful study on the thickness of the printed intervention capable of restraining shock propagation to the vulnerable site in sideways fall, yet ensuring the protector aesthetic and fitness towards maintaining adherence (Holzer et al., 2009). Also, acquiring the impact attenuation data of a 3D printed hip protector is intensely demanding, from the making and remaking of a model, printing such model, to the biomechanical impact testing to acquire the force attenuation data. Most hip protector research has understandably not considered models fitting for impact attenuation because of the strain of the laboratory time and effort it represents in acquiring huge experimental data as seen in other fields where models are usually demanding enormous data (Van Der Ploeg et al., 2014). Consequently, test systems with subjective experimental models have been used in most studies to quantify various hip protectors' impact attenuation properties.

Moreso, artificial neural networks (ANN) have been demonstrated to predict composite plates' absorbed energy under low-velocity impact load due to their ability to efficiently learn the input-output relations of non-linear problems (Malik and Arif, 2013). However, the high generalization of performance and the ability to model non-linear relationships uniquely and globally make support vector regression (SVR) particularly appealing, justifying its growing adoption in various science and engineering fields (Üstün et al., 2007).

In this study, SVR has been chosen to develop a robust model with which a 3D printed hip protector's impact attenuation capability could be estimated. SVR expunges the difficulties of using linear functions in the high-dimensional feature space and ensures the transformation of optimization problems into dual convex quadratic programs (Roy et al., 2015). Support vector machines have been used extensively in computational biology to classify vectors derived from different features with great accuracy (Cohen and Widdows, 2013).Moreover, the use of SVR in performance prediction in biomechanical impact problems has not been reported in previous hip protectors optimization research. Therefore, there is an opportunity to explore the benefit of the reported performance edge of a promising statistical algorithm SVR over ANN (Akande et al., 2014)

2. METHODOLOGY

a. THE DATASET

ii. Experimental data acquisition

The proposed computational intelligence-based SVR model was developed using the experimental data derived from impact force attenuation testing of the 3D printed hip protectors using a biofidelic drop towers testing system (Yahaya et al., 2020). The hip protector (Figure 1) was modelled from the 3D surface geometry of the human hip scan, and the hip geometry data were applied to develop the inner surface of the hip protector in contact with the human body.

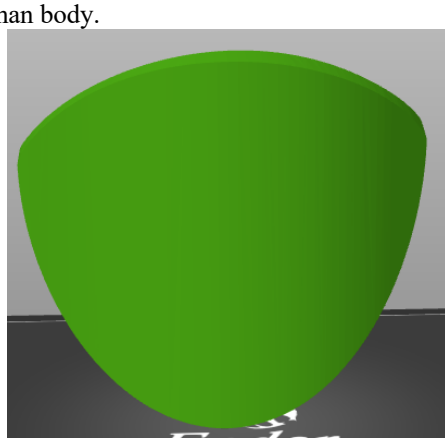

Fig. 1. The 3D printed hip protector.

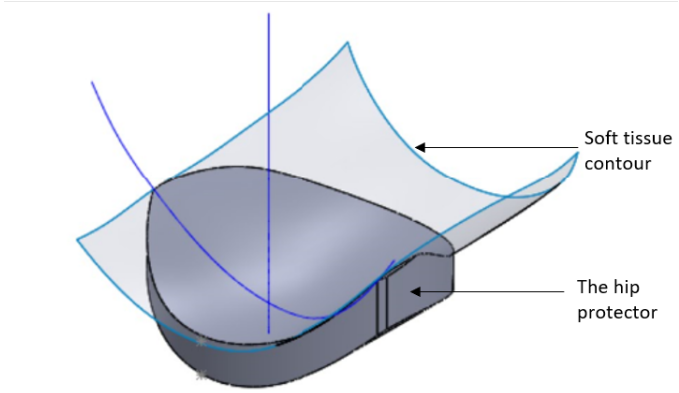

Fig. 2. The 3D printed hip protector modeled according to a hip surface geometry.

The outer surface was created with a shield-like shape projected to the inner surface at a thickness of 10.2 mm(Figure 2). It bears the dimension of the hip protector with the maximum height taken at the greater trochanter. When the cut was extruded to finalize the model, the protector's structural information conforming to the desired pad outline was extracted.

Three protectors of different shore hardness but having a similar characteristic and structural information were printed and subsequently subjected to drop towers impact test to measure each of the protectors' impact attenuation properties. An average of 5 impact tests was done per sample at different energy levels and recorded. The impact mass of 6.57 kg was dropped from heights of 300 mm and 400mm, simulating impact to the sideways when a human falls to the ground. The forces were recorded first without the hip protecting pads and subsequently with the hip protectors in place. The attenuation rate was determined using the ratio of forces at the femoral neck when the soft tissue was not protected, termed the unprotected force, F_u, andF_p is the impact recorded at the same point when the hip protector was in place to protect the soft tissue

iii. Description of dataset

Four descriptors, namely, pad thickness, impact energy, unprotected impact force, and maximum impact force, were used to train and test 18 experimentally acquired datasets in building a predictive model using SVR. Table 1 shows the training and testing dataset of the developed SVR model. To determine the impact force attenuation rate of the 3D printed hip protector, the above-mentioned descriptors were used to build the SVR model. The result of a statistical analysis of the acquired experimental data is also presented in Table 2. The mean, maximum, minimum, and standard deviation helps to describe the disparities in the dataset..

Additionally, Table 2 also shows the correlation of each of the descriptors and the target - impact force attenuation. The impact energy and maximum impact force are positively correlated with the target. However, the degree of correlation of the impact energy is higher than that of the correlation of the maximum impact force to the impact force attenuation rate. The pad shell thickness and infill density show a negative correlation to the target (impact force attenuation rate). These correlation results demonstrate the need to seek a nonlinear model to represent the descriptors' various effects since their degree of linear relationship is very weak and suggests a simple linear model cannot efficiently capture the existing relationship.

Table 1. Descriptor and target dataset.

Sample name	Impact attenuation	Shore hardness (%)	Shell thickness (L)	Infill density (%)	Impact energy (J)	Base impact force (N)	Impact force (N)
25_2L_85A	0.55	85	2	25	19.34	6,271.26	2,792.04
25_3L_85A	0.50	85	3	25	19.34	6,271.26	3,157.91
25_4L_85A	0.49	85	4	25	19.34	6,271.26	3,184.28
50_2L_85A	0.49	85	2	50	19.34	6,271.26	3,175.49
50_3L_85A	0.49	85	3	50	19.34	6,271.26	3,196.97
75_4L_85A	0.49	85	4	75	19.34	6,271.26	3,210.89
100_4L_85A	0.49	85	4	100	19.34	6,271.26	3,172.19
100_2L_95A	0.53	95	2	100	19.34	6,271.26	2,958.07
25_3L_95A	0.53	95	3	25	19.34	6,271.26	2,923.76
25_4L_95A	0.51	95	4	25	19.34	6,271.26	3,084.54
25_2L_75A	0.53	75	2	25	19.34	6,271.26	2,947.20
25_2L_85A_2	0.69	85	2	25	25.78	11,531.83	3,542.33
50_3L_85A_2	0.62	85	3	50	25.78	11,531.83	4,428.86
75_4L_85A_2	0.60	85	4	75	25.78	11,531.83	4,585.73
50_2L_95A	0.64	95	2	50	25.78	11,531.83	4,199.48
25_3L_95A_2	0.67	95	3	25	25.78	11,531.83	3,856.31
25_4L_95A_2	0.64	95	4	25	25.78	11,531.83	4,142.46
25_2L_75A	0.68	75	2	25	25.78	11,531.83	3,730.70

Table 2. Statistical analysis of the acquired dataset.

	Shore hardness	Shell thickness	Infill density (%)	Impact energy (J)	Maximum impact F_p (N)	Attenuation rate (%)
Mean	87.22	2.94	44.44	1.84	3,460.51	56
Maximum	95.00	4.00	100.00	25.78	4,585.73	69
Minimum	75.00	2.00	25.00	19.34	2,792.04	49
Standard deviation	6.29	0.85	25.76	3.14	543.01	7
R	7	-30	-30	93	68	

iv. Description of SVR computational intelligence technique

This study predicts 3D printed hip protectors' impact attenuation rate from the impact response value acquired from the dataset to train the SVR model. The main idea is to find a function $f(x, \alpha)$ (that predicts the impact attenuation based on SVM approach) that approximates the original dataset $(y_1, \ldots, y_k)$ with the at most ε (margin) derivation from the actual obtained values y_i (impact attenuation based on biomechanical test). To construct the linear model f(x) presented in Eq 1, the input dataset is mapped to a k-dimensional feature space with the aid of non-linear mapping function, and a soft margin concept was introduced by relaxing the ε deviation constrain to ensure the existence of the solution. The soft margin imposes a penalty cost using the slack variables ξ and ξ^* if the ε deviation setting is not met.

$$f(x) = w \cdot \phi(x) + b \qquad 1$$

where w is the weight vector, $\phi(x)$ represents a set of non-linear transformation which maps the input vector to a higher dimensional feature space from a lower dimension and b is the bias constant (Salami et al., 2019). The loss function that controls the ability of the SVR to estimate the impact attenuation is given by Eq. 2

$$L(y, f(x)) = \begin{cases} 0 & \text{if } |y - f(x)| \leq \varepsilon \\ |y - f(x)| - \varepsilon & \text{otherwise} \end{cases} \qquad 2$$

by solving the primal optimization problem in Eq. 3, the optimal w can be obtained.

$$\text{Minimise } \frac{1}{2}||w||^2 + C\sum_{i=1}^{k}[\xi_i + \xi_i^*] \qquad 3$$

Subject to:

$$\begin{aligned} y_i - f(x) &\leq \varepsilon + \xi_i^* \\ f(x) - y_i &\leq \varepsilon + \xi_i^* \\ \xi_i \xi_i^* &\geq 0 \quad i = 1, \ldots, k \end{aligned} \qquad 4$$

where ξ_i and ξ_i^* are the non-negative slack variables that represent the magnitude of the soft margin outside the ε deviation and C is the regularization factor. The non-negative slack variable is assigned to each instance if the data is not linearly separable to avoid misclassification. It can be seen as the distance from the separating hyperplane if an instance is misclassified and $||\omega||^2$ is the Euclidian norm.

It is more effective to solve the primal problem by transforming it to a primal-dual setting with the inclusion of a non-linear mapping function known as the Kernel function, which is a dot product in some feature space described by Eq.5.

$$K(x, x_i) = \phi(x) \cdot \phi(x_i) \qquad 5$$

Eq.6 is the reformulated solution of f(x) obtained without directly operating $\phi(x)$ and calculating the weight vector w by using the kernel trick, f(x) can be obtained.

$$f(x) = \sum_{i=1}^{k} (\alpha_i - \alpha_i^*) K(x, x_i) + b \qquad 6$$

where k is the index of the data points, α_i and α_i^* are the Lagrangian multipliers which are greater than or equal to zero and must be less than C, and $K(x, x_i)$ is the result of the kernel function in Eq.6.

v. Description of the computational methodology

The SVR model's computational development was done using the training dataset,and the testing dataset with the aid of a test-set cross-validation technique was used to evaluate the accuracy of the generalization and predictive ability of the developed model. The computational methodology entails; data partitioning into training and testing datasets; selection of initial kernel parameters for a particular kernel function to create support vectors using the training dataset; estimation of the target in the testing dataset using the support vector and the testing dataset descriptors; evaluation of the model's estimation accuracy during the training and testing stage by comparing the impact attenuation of the 3D printed hip protector with the estimated values.

b. Optimal parameters search technique

To obtain the optimum kernel parameters, the test-set cross-validation optimization technique was employed. A computational efficient selection procedure for these optimized parameters requires multiple modelling iterations dependent on the nature and size of the dataset. This entails the initial selection of kernel parameters, deployment of test-set cross-validation technique, varying and altering kernel parameters combination for Kernel type in every run, identifying the model parameters' optimum values, and subsequently deploying them to train the final SVR algorithm. The optimum values were judged by the observed correlation coefficient (R^2) and the RMSE for each kernel parameters combination. The value of the kernel option characterize the mapping of the kernel function in the transformation of the data to high-dimensional feature space. The hyper-parameter controls the choice of the hyperplane that ensures minimal error, the maximum allowed deviation of the estimated value from the actual target is controlled by the epsilon (ε). In contrast, the trade-off between the complexity of the model and the maximum allowed deviation of the target's estimated value from the experimental or actual value of the target is controlled by the regularisation factor or penalty factor, C.

c. Evaluation of the predictive capacity of the proposed SVR-based model

The statistical performance of the proposed SVR model was evaluated using the correlation coefficient (R^2), and the root means square error (RMSE) to determine the predictive and generalization capacity of the model. These parameters show the estimation quality of the model by revealing the associated error of estimation between the experimental and estimated values of impact force attenuation. Eq.**Error! Reference source not found.** shows t he correlation coefficient and Eq. **Error! Reference source not found.** shows the RMSE, respectively.

$$R^2 = \frac{\sum_{i=1}^{n} (A_{r(\exp)} - A'_{r(\exp)})(A_{r(\text{est})} - A'_{r(est)})}{\sqrt{\sum_{i=1}^{n} (A_{r(\exp)} - A'_{r(\exp)})^2 \sum_{i=1}^{n} (A_{r(est)} - A'_{r(est)})^2}} \qquad (8)$$

$$RSME = \sqrt{\frac{1}{n} \sum_{i=1}^{n} (A_{r(\exp)} - A_{r(est)})^2} \qquad (9)$$

where $A_r(exp)$ is experimental attenuation rate, $A'_r(exp)$ is mean experimental attenuation rate, $A_r(est)$ is estimated attenuation rate, $A'_r(est)$ mean estimated attenuation rate.

3. RESULTS AND DISCUSSION

The identified optimum values of the model parameters deployed to train the final SVR algorithm are presented in Table 3.

Table 3. Optimum kernel parameters for the developed SVR-based model.

Kernel Function	Gaussian
Kernel scale	2.8284
Regularization factor	8
Gamma (G)	0.1250
Epsilon (ε)	9.7656×10^{-4}

The generalisation and predictive accuracy of the SVR model to estimate the impact attenuation of a 3D printed hip protector in a simulated sideways fall was evaluated. The model uses the pad's shore hardness, shell thickness, infill density, base impact force, maximum impact force and impact energy as input descriptors and the impact force attenuation as the target output. The impact force attenuation was either influenced by the input variables or is correlated with their data. The acquired support vectors during the training stage were utilized by the model to estimate the impact attenuation of the hip protecting pad in the testing dataset. Figures 3 and 4 present the correlation cross-plots for the training and testing datasets of the Gaussian kernel functions compared in terms of their estimation accuracy using the optimal SVR modelling parameters gotten from the search approach.

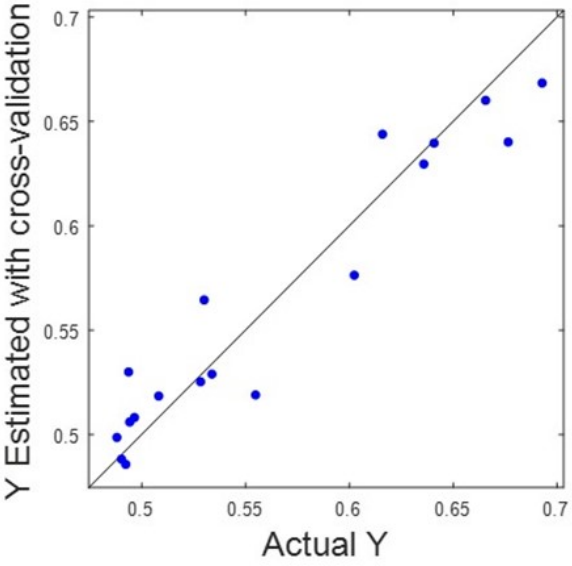

Fig. 3. Correlation cross-plot between experimental and estimated impact attenuation rate of 3D printed hip protectors for the training dataset.

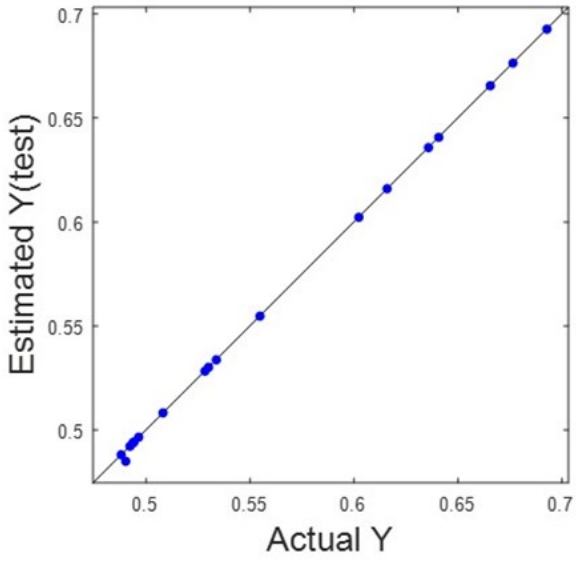

Fig. 4.Correlation cross-plot between experimental and estimated impact attenuation rate of 3D printed hip protectors for testing dataset.

There exists a close relationship between the experimental and estimated impact force attenuation of the training and testing dataset of the hip protector for the selected kernel type – Gaussian Kernel, The R2 value of 91.5% (with RMSE = 0.0208) and 99.9% (with RMSE = 0.0012) obtained for the training and test sets respectively showed the proposed model is an excellent fit since it performed superbly in the phase that involved unseen data. The obtained RMSE values, which are measures of the proximity of the data points to the regression line, ranged from 0.0012 - 0.0208, indicating a good fit and showing that the developed model has good performance and can potentially be generalized. The implemented model produces results using the acquired support vectors that were in good agreement with the experiment result when only the descriptors were supplied to the model without the target. The measured impact attenuations were effectively tracked, as shown in Figure 5.

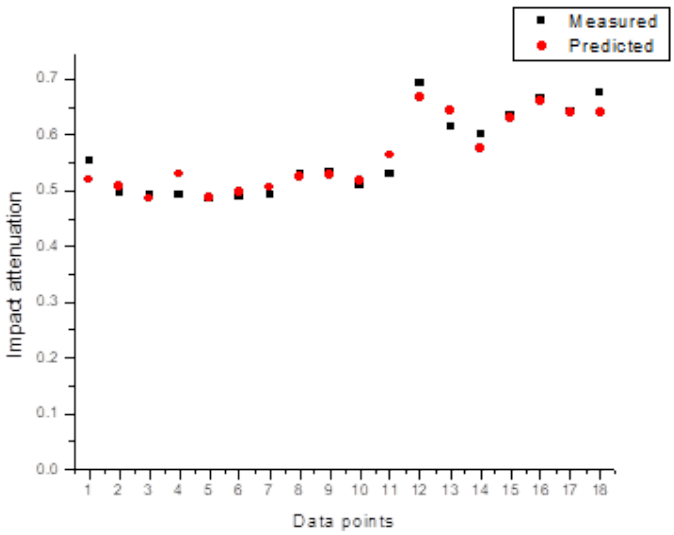

Fig. 5.Tracking of measured impact attenuation by SVR (Testing data).

4. CONCLUSION

This study has investigated the effect of shore hardness, infill density, and shell thickness on the impact attenuation of 3D printed TPU hip protectors using SVR. The impact attenuation of 3D printed hip protector has a highly non-linear dependency on the various factors that influence the material's stiffness, making it very difficult to model. Based on the result of the analysed data, the SVR-based model accurately estimated the impact attenuation of hip protector with an accuracy of over 99% and 0·002 based on R2 and RMSE between the experimentally obtained impact force attenuation and the corresponding estimated values. The proposed model help reduce the experimental cost of examining variability in design parameter yet quantify their performance. The results from the model demonstrate that SVR is viable in predicting the impact attenuation of 3D printed hip protectors. In addition, important new information is hereby provided regarding the influence of infill density and material shore hardness on the impact attenuation rate of a hip protector. This SVR model will find significant application in fracture prevention study because of its ability to predict novel hip protectors' impact attenuation capability

ACKNOWLEDGEMENT

The authors would like to acknowledge technical assistance from Mr. Wan Mohd Amri Wan Mamat Ali, Mr. FakruruziFadzil, and Mr. Baharom Awang of the School of Mechanical Engineering, USM. The financial support provided under USM RUI grant (1001/PMEKANIK/8014070). The authors also thank the Tertiary Education Trust Fund (TETFUND) through University of Ilorin, Ilorin, Nigeria for financial support of S.A Yahaya.

REFERENCES

Akande KO, Owolabi TO, Twaha S, et al. (2014) Performance Comparison of SVM and ANN in Predicting Compressive Strength of Concrete. IOSR Journal of Computer Engineering. Ver. I. DOI: 10.9790/0661-16518894.

Cohen T and Widdows D (2013) Geometric Representations in Biomedical Informatics: Applications in Automated Text Analysis. In: Methods in Biomedical Informatics: A Pragmatic Approach. Elsevier Inc., pp. 99–139. DOI: 10.1016/B978-0-12-401678-1.00005-1.

Holzer LA, von Skrbensky G and Holzer G (2009) Mechanical testing of different hip protectors according to a European Standard. Injury 40(11): 1172–1175. DOI: 10.1016/j.injury.2009.02.005.

Malik MH and Arif AFM (2013) ANN prediction model for composite plates against low velocity impact loads using finite element analysis. Composite Structures 101. Elsevier Ltd: 290–300. DOI: 10.1016/j.compstruct.2013.02.020.

Parandoush P and Lin D (2017) A review on additive manufacturing of polymer-fiber composites. Composite Structures. DOI: 10.1016/j.compstruct.2017.08.088.

Park JH and Lee JR (2019) Developing fall-impact protection pad with 3D mesh curved surface structure using 3D printing technology. Polymers 11(11). DOI: 10.3390/polym11111800.

Roy K, Kar S and Das RN (2015) Selected Statistical Methods in QSAR. In: Understanding the Basics

of QSAR for Applications in Pharmaceutical Sciences and Risk Assessment. Elsevier, pp. 191–229. DOI: 10.1016/b978-0-12-801505-6.00006-5.

Salami BA, Johari MAM, Ahmad ZA, et al. (2019) Modelling the early strength of alkali-activated cement composites containing palm oil fuel ash. Proceedings of Institution of Civil Engineers: Construction Materials 172(3): 133–143. DOI: 10.1680/jcoma.16.00052.

Sendel F, Allison-Hope D and Morris J (2015) 3D Printing Sustainability Opportunities and Challenges. Bsr.

Üstün B, Melssen WJ and Buydens LMC (2007) Visualisation and interpretation of Support Vector Regression models. Analytica Chimica Acta. DOI: 10.1016/j.aca.2007.03.023.

Van Der Ploeg T, Austin PC and Steyerberg EW (2014) Modern modelling techniques are data hungry: A simulation study for predicting dichotomous endpoints. BMC Medical Research Methodology. DOI: 10.1186/1471-2288-14-137.

Yahaya S., Ripin M. and Ridzwan MI. (2020) Assessment of the force attenuation capability of 3D printed hip protector in simulated sideways fall. Materials Research Express. DOI: https://doi.org/10.1088/2053- 1591/abd2f7.

PAPER 210 – INFLUENCE OF CARBONIZED COCONUT HUSK ADDITION ON THE PROPERTIES OF ALUMINIUM MATRIX COMPOSITE

J. A. Adebisi[1], S. O. Ogbemudia[1], R. O. Idowu[1*], Y. O. Busari[1], K. P. Odimayomi[3], S. Sulaiman[2], I. I. Ahmed[1]

[1]Department of Materials and Metallurgical Engineering, University of Ilorin, Nigeria
[2]Department of Mechanical Engineering, University of Ilorin, Nigeria
[3]Advanced Composite Materials Research Laboratory, National Space Research and Development Agency (NASRDA), University of Ilorin Centre, University of Ilorin, Nigeria
[*]Email: 17-30gn038@student.unilorin.edu.ng

ABSTRACT
The use of different kinds of metal-matrix composite (MMC) materials is growing rapidly over the last decades because they offer a better combination of properties. Research attempts have been previously made to reduce the cost of composite processing, weight reduction, and improved desired performance. The properties of aluminium matrix composites reinforced with carbonized coconut husk (CCH) were investigated. The composite samples were produced by stir-casting methods using varying percentages of carbonized coconut husk. Tensile, hardness, EDX, XRD, and XRF were carried out on the composites. The results showed that the tensile strength of the composite increased with the addition of carbonized coconut husk. The composite sample with 3.6 wt.% CCH showed the highest tensile strength of 85 MPa and hardness also increases with reinforcement. The composite can be utilized in automobiles where high strength is required.

KEYWORDS: coconut husk, carbonization, reinforcement, aluminium, composite

1. INTRODUCTION

Aluminium has low strength and low melting point, which makes it difficult for use in engineering applications. Aluminium and most of its alloys have good electrical and thermal conductivities, and high reflectivity to both heat and light (Vijaya & Srinivas, 2018). Aluminium alloys are commonly used as structural materials in the aerospace industry due to their lightweight (Dursun & Soutis, 2014; Georgantzia *et al.*, 2021; A. M. Usman *et al.*, 2014). The low strength and low wear resistance, however, have always been a problem (A. Usman *et al.*, 2014). These challenges have been improved by alloying and composite development. Aluminium composites have been produced by the incorporation of reinforced particles in aluminium (Arun *et al.*, 2013; Senapati *et al.*, 2014). Composite materials are materials made of two or more constituent materials with different physical or chemical properties that produce a material with different characteristics from the individual components when combined. Agricultural wastes are by-products or residues of agricultural processing. Examples include maize cob, maize stalk, groundnut pod, bagasse and coconut shell. They constitute environmental pollution and enhance greenhouse effects when burnt. The quest for the utilization of these products has birthed a lot of scientific research. The use of naturally sourced particulates (agro waste) has been reported to offer good reinforcement constituents, owing to their availability and immensely low cost (Alaneme & Olubambi, 2013; Joseph & Babaremu, 2019; Nwobi-Okoye & Ochieze, 2018).

The present work focuses on the effect of carbonized coconut husk (CCH) on the properties of novel aluminium matrix composites (AMCs). The thermal stability of coconut husk was enhanced before pulverization and subsequent use as reinforcement in AMC production. The use of waste materials in composite manufacture overrides waste into wealth.

2. MATERIALS AND METHODS

2.1 Materials

The materials used in this work include coconut husk (CH) which was sourced locally at Badagry, Lagos State. Aluminium scraps were obtained from Materials and Metallurgical Engineering foundry. Some apparatus and equipment used include muffle furnace, digital weighing balance, sieve, laboratory blade mill, carbonization chamber, oven, stirrer, and crucible furnace, available at the Department of Materials and Metallurgical Engineering, University of Ilorin, Nigeria. Equipment used for characterization include Brinell harness tester, Universal testing machine (UTM), both available at Department of Mechanical Engineering, University of Ilorin, Nigeria. Thermogravimetric analysis (TGA), X-Ray Diffractometry (XRD) and X-Ray Fluorescence (XRF), were carried out at Centre for Solid Minerals Research & Development, Kaduna State Polytechnics, Nigeria. Scanning

Electron Microscope (SEM) and Energy Dispersive X-ray Spectroscopy (EDS) at Tshwane University of Technology, Department of Chemical, Metallurgical and Materials Engineering, Pretoria, South Africa.

2.2 Methods

The coconut husk was sorted to remove impurities, washed and sun-dried for 7 days to reduce the moisture content. This was carbonized at a temperature between 500 – 550 °C in a carbonization chamber for 60 minutes. The carbonized coconut husk (CCH) was pulverised using a laboratory blade mill and sieved to obtain particles below 100 µm.

Stir casting method was used to produce specimens for characterization. Aluminium scrap was melted in a crucible furnace at a temperature of 700 °C. A measured amount of CCH was preheated to 300 °C for 3 hours in an electric oven to remove moisture. A calibrated pouring cup was used to tap 250 g of the molten metal and the preheated CCH was then mixed thoroughly for homogeneity. The mixture was poured into the preheated mould cavities at a maintained pouring temperature of 680 ºC. The composite was then allowed to solidify and samples removed, cleaned, labelled and kept for characterization. The formulation of the composites is presented in Table 1.

Table 7: Weight percentage of aluminium scraps and carbonized coconut husk

SAMPLE ID	ALUMINIUM SCRAP (g)	CCH (g)	ALUMINIUM SCRAP (wt.%)	CCH (wt.%)
A	250	0	100	0
B	250	3	98.8	1.2
C	250	6	97.6	2.4
D	250	9	96.4	3.6
E	250	12	95.2	4.8

TGA, XRF and XRD were carried out on CH to determine its thermal stability up to 900 ºC, chemical composition and phase identification, respectively. Tensile, SEM/EDS, XRD and hardness of the composites were carried out to establish their mechanical and chemical properties.

3. RESULTS AND DISCUSSION

3.1 Coconut Husk Features

The thermal characteristics of coconut husk by heating from room temperature to about 900 °C is presented in Figure 1. Thermal decomposition of agricultural was elucidate in Adebisi *et al.* (2019) as a three stages of dehydration, volatilization and carbonization in inert environment. The weight loss curve showed first inflection at a temperature of 190 through 205 °C, which corresponds to the commencement of hemicellulosic compounds. This stage is more rapid from 280 to 375 °C. Cellulose decomposition occurred up to around 430 °C after which lignin and main carbonization stage occurred. The first stage of dehydration is not pronounced in the TG curve unlike the derivative (DTG) curve which indicated moisture loss up to around 100 °C. The derivative of thermo-gravimetric analysis (DTG) curve shows the energy loss when the coconut husk was heated from room temperature, presenting a case of exothermic process. The second stage of this thermal decomposition has been reported as the most crucial stage when all volatiles thermally left biomass to leave a residue of carbon char (Adebisi et al., 2019; Munir *et al.*, 2009; Nurhayati & Fauziah, 2013). The char left is principally carbon skeleton of the biomass, which is about 20% as reported in Adebisi et al. (2019) to range between 18.60–29.40%. This carbon network is a ceramic with brittle nature and thus enhances pulverization of the carbonized biomass.

As presented in Table 2, the compounds that constituted coconut husk are MgO, Al_2O_3, SiO_2, P_2O_5, SO_3, Cl, K_2O, CaO, TiO_2, V_2O_5, Cr_2O_3, MnO, Fe_2O_3, CuO, ZnO, SrO, BaO, and PbO. With carbon as the major element, silicon, iron, potassium, magnesium, and manganese also constitute about 95%. The presented elements are similar to chemical composition obtained in coconut husk reported by Anuar *et al.* (2018), Anuar *et al.* (2020) and A. Usman et al. (2014). Phase identification of compounds in carbonized coconut husk, as shown in Figure 2, revealed presence of MnS, KCl, $Al_3Ti_{0.75}Fe_{0.18}V_{0.06}$, TiO_2, $KCr(SO_4)_2$, $CaMgP_2O_7$, $Ca_3(SO_3)_2SO_4$, SiO_2, $Ca_3Al_2Si_2$, and $SrAl_4O_7$. The XRD spectrum obtained for CCH is similar to those reported by Anuar et al. (2018) with the most prominent peak occurring at 32° diffraction angle.

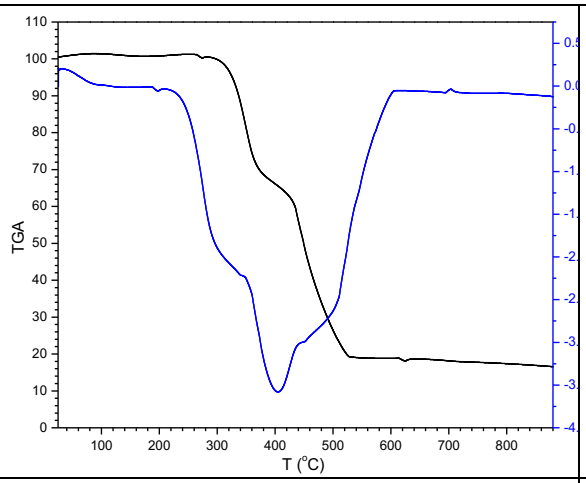

Figure 32: Thermogravimetric analysis of coconut husk

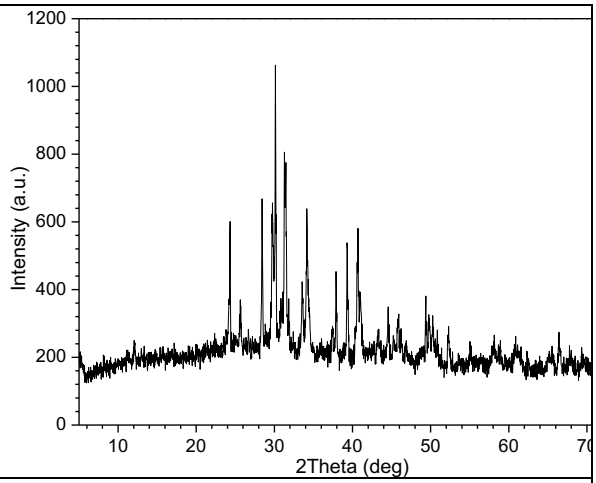

Figure 33: XRD of carbonized coconut husk

Table 8: Elemental composition of coconut husk

ELEMENT	MgO	Al_2O_3	SiO_2	P_2O_5	SO_3	Cl	K_2O	CaO	TiO_2	V_2O_5	Cr_2O_3	MnO	Fe_2O_3	CuO	ZnO	SrO	BaO	PbO
COMPOSITION (wt%)	4.161	0.163	72.133	0.490	0.238	1.280	6.891	1.236	0.094	0.063	0.063	3.270	8.780	0.433	0.019	0.006	0.803	0.741

3.2 Properties of Aluminium Carbonized Coconut Husk Composites

The chemical composition of the aluminium scrap and composites produced showed that addition of CCH to the molten scrap increases the amount of carbon, silicon, calcium, chlorine, potassium magnesium and sulphur. This is in tandem with the theory of composite formulation as an additive manufacturing process.

Table 9: Composition of the aluminium alloy and Composites Produced

Elements	Al	C	Fe	Ag	Si	Ca	Cl	K	Mg	S	O	Ti	P
0 wt%	89.66	2.93	2.11	1.59	1.03	0.64	0.57	0.48	0.27	0.24	0.20	0.19	0.08
2.4 wt%	75.00	6.24	1.61	3.48	1.76	1.20	3.09	1.66	0.30	1.07	4.03	0.00	0.55
4.8wt %	78.68	7.38	3.54	2.23	1.62	1.53	1.47	1.36	0.92	0.70	0,29	0.28	0.00

Figure 3 shows the XRD spectra for the scrap and composites. Small addition of CCH resulted in shift peak while further addition lowered the intensity of the unreinforced aluminium. The strengthening of the produced composites is influenced by the nature of the reinforcing phases.

The hardness values for the aluminium composites produced are shown in Figure 4. Addition of CCH initially increases the hardness of the composite but decreases when the amount of reinforcement exceeds 1.2 wt.%. This may be as a result of poor wettability of the reinforcement in the aluminium scrap used during casting.

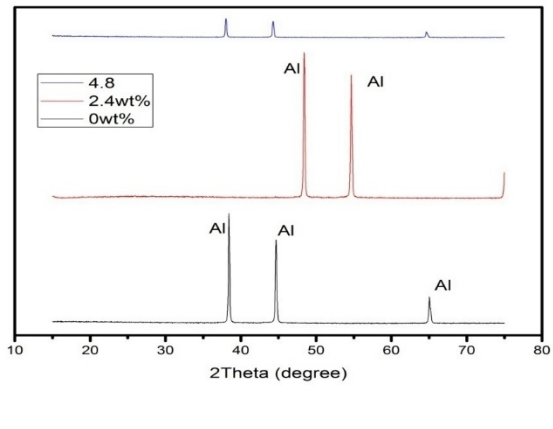

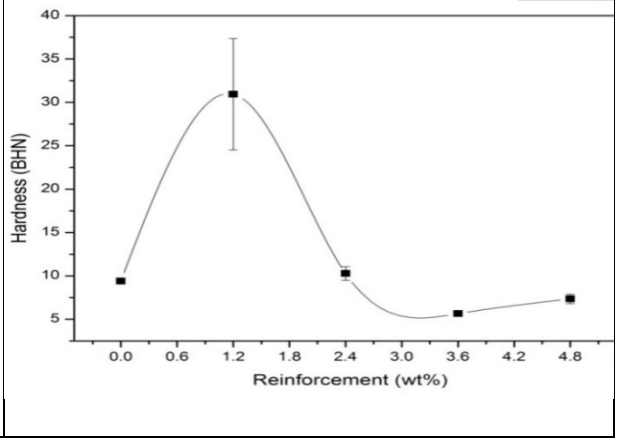

Figure 34: XRD patterns for unreinforced aluminium scrap and produced composites	*Figure 35: Hardness values for aluminium carbonized coconut husk composites*

Figures 5 and 6 showed tensile strengths and stress – strain curves of the composites produced. In Figure 5, tensile strength was observed to increase with increase in reinforcement up to 3.6 wt.%. The improved strength could be associated with the addition of CCH well dispersed within the matrix. When the amount added exceeds a certain limit, agglomeration of the particles may be a source of stress raiser that will eventually fails (Oghenevweta *et al.*, 2016). The tensile strength improved from 1143 MPa to 4485 MPa, representing an increment of 292%.

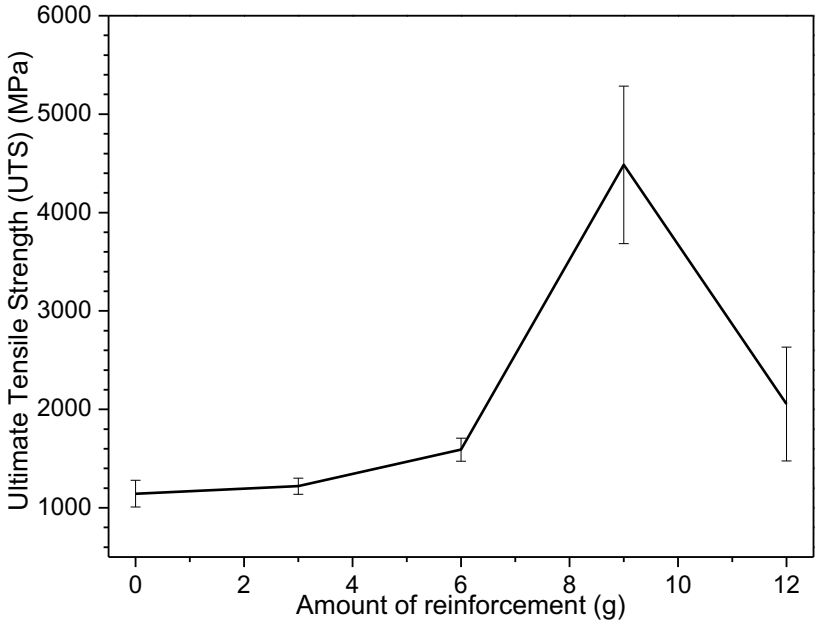

Figure 36: Ultimate tensile strength of the composites

5. CONCLUSION

Aluminium based composites reinforced with carbonized coconut husk particles were produced using the stir casting process and the hardness, tensile test and micro structure of the fabricated MMC according to the working conditions were evaluated. The results showed that

1. Addition of amorphous reinforcement to aluminium alloy may cause peak shift and reduction in intensity of the crystalline aluminium phase.
2. The hardness of the composite decreased slightly with the comparison of aluminium scrap.
3. Tensile strength increased up to 3.6 wt.% CCH after which agglomeration may result in decrease in strength.
4. Improved ultimate tensile strength of up to 292% was achieved.

REFERENCES

Adebisi, J. A., Agunsoye, J. O., Bello, S. A., Kolawole, F. O., Ramakokovhu, M. M., Daramola, M. O., & Hassan, S. B. (2019). Extraction of Silica from Sugarcane Bagasse, Cassava Periderm and Maize Stalk: Proximate Analysis and Physico-Chemical Properties of Wastes. *Waste and Biomass Valorization, 10*(3), 617-629. doi: 10.1007/s12649-017-0089-5

Alaneme, K. K., & Olubambi, P. A. (2013). Corrosion and wear behaviour of rice husk ash—Alumina reinforced Al–Mg–Si alloy matrix hybrid composites. *Journal of Materials Research and Technology, 2*(2), 188-194.

Anuar, M. F., Fen, Y. W., Zaid, M. H. M., Matori, K. A., & Khaidir, R. E. M. (2018). Synthesis and structural properties of coconut husk as potential silica source. *Results in Physics, 11*, 1-4.

Anuar, M. F., Fen, Y. W., Zaid, M. H. M., Matori, K. A., & Khaidir, R. E. M. (2020). The physical and optical studies of crystalline silica derived from the green synthesis of coconut husk ash. *Applied Sciences, 10*(6), 2128.

Arun, L., Saddam, H., & Suneel, K. (2013). Dynamic behaviour of hybrid Aluminium6061 metal matrix reinforced with SIC and fly ash particulates. *International Journal of Innovative Research in Science, Engineering and Technology, 2*(6), 2501.

Dursun, T., & Soutis, C. (2014). Recent developments in advanced aircraft aluminium alloys. *Materials & Design (1980-2015), 56*, 862-871.

Georgantzia, E., Gkantou, M., & Kamaris, G. S. (2021). Aluminium alloys as structural material: A review of research. *Engineering Structures, 227*, 111372.

Joseph, O. O., & Babaremu, K. O. (2019). Agricultural Waste as a Reinforcement Particulate for Aluminum Metal Matrix Composite (AMMCs): A Review. *Fibers, 7*(4), 33.

Munir, S., Daood, S. S., Nimmo, W., Cunliffe, A. M., & Gibbs, B. M. (2009). Thermal analysis and devolatilization kinetics of cotton stalk, sugar cane bagasse and shea meal under nitrogen and air atmospheres. *Bioresource Technology, 100*(3), 1413-1418. doi: https://doi.org/10.1016/j.biortech.2008.07.065

Nurhayati, A., & Fauziah, S. (2013). A Comparison Study on Oven and Solar Dried Empty Fruit Bunches. *Journal of Environment and Earth Science, 3*(2), 145-156.

Nwobi-Okoye, C. C., & Ochieze, B. Q. (2018). Age hardening process modeling and optimization of aluminum alloy A356/Cow horn particulate composite for brake drum application using RSM, ANN and simulated annealing. *Defence Technology, 14*(4), 336-345.

Oghenevweta, J. E., Aigbodion, V. S., Nyior, G. B., & Asuke, F. (2016). Mechanical properties and microstructural analysis of Al–Si–Mg/carbonized maize stalk waste particulate composites. *Journal of King Saud University - Engineering Sciences, 28*(2), 222-229. doi: https://doi.org/10.1016/j.jksues.2014.03.009

Senapati, A. K., Mishra, P. C., & Routara, B. C. (2014). Use of waste flyash in fabrication of aluminium alloy matrix composite. *Int. J. Eng. Technol, 6*, 905-912.

Usman, A., Raji, A., Waziri, N., & Hassan, M. (2014). Production and characterisation of aluminium alloy-bagasse ash composites. *IOSR Journal of Mechanical and Civil Engineering, 11*(4), 38-44.

Usman, A. M., Raji, A., Waziri, N. H., & Hassan, M. A. (2014). Aluminium alloy-rice husk ash composites production and analysis. *Leonardo Electronic Journal of Practices and Technologies, 25*, 84-98.

Vijaya, M., & Srinivas, K. (2018). Development and Mechanical Properties of SiC Reinforced Aluminium Metal Matrix Composites. *J. Rec. Act. Prod, 3*(1).

PAPER 211 – CFD ANALYSIS OF A 3-BLADED NACA 0018 VERTICAL AXIS WIND TURBINE FOR DEPLOYMENT IN ILORIN, KWARA STATE, NIGERIA

Olalekan Adebayo Olayemi[1]*, Tomisin Favour Ajide[1], Adebowale Martins Obalalu[2], Segun Emmanuel Ibitoye[3], Abdulbaqi Jinadu[1], and Benjamin Elochukwu Anyaegbuna[4]

[1]Department of Aeronautics and Astronautics, Faculty of Engineering and Technology, Kwara State University, Malete, Kwara State, Nigeria.
[2]Department of Physics, Augustine University, Ilara-Epe, Lagos State, Nigeria.
[4]Department of Mechanical Engineering, Bells University of Technology, Ota, Ogun State, Nigeria.
*__Email__: olalekan.olayemi@kwasu.edu.ng

ABSTRACT

During the last few years, vertical axis wind turbines have evolved as a suitable supplement to energy production worldwide. There has been a lot of interest in vertical axis wind turbines as a small-scale renewable power converter because they can be used in places where the wind speeds are turbulent or unsteady. When investigating the aerodynamic characteristics of vertical axis wind turbines, computational fluid dynamics has been shown to be one of the most effective methods. There is a need for better knowledge of the factors that influence the accuracy of computational fluid dynamics. The aim of this paper is to demonstrate the influence of these factors on the simulation of a low-speed turbine to guide the execution of accurate computational fluid dynamics simulations of vertical axis wind turbines at varying tip speed ratios and solidities. To simulate the turbulent, unstable fluid flow around the turbine, we used a 2D SIMPLE approach with the help of ANSYS FLUENT. In the study, it was found that when the tip speed ratio is low, the result is largely dependent on the azimuthal increment, and a fine azimuthal increment of 0.1 is usually better for low tip speed ratios.

***KEYWORDS*:** Aerodynamic performance, CFD, vertical axis wind turbine, wind energy

1. INTRODUCTION

One of the most important raw materials in modern civilization is energy. Energy has become a key factor in the standard of living and the development of the community. Almost 90% of the world's energy comes from burning fossil fuels such as coal, oil, and natural gas (Wenehenubun et al., 2015). People use fossil fuels to meet almost all their energy needs, such as powering vehicles, offices, and home lighting. The demand for and cost of energy increase daily due to population growth and technological advancement. Meanwhile, energy resources from the Earth's fossil fuels are limited, and at the same time, there are problems with global climate change (American et al., 1990). There has been a lot of interest in clean and renewable energy over the last few decades because people are becoming more concerned about their well-being. In the renewable energy industry, wind energy for power generation is now the fastest-growing, with an annual growth rate of over 30% in view of its long-term viability and low cost (Bangga et al., 2017). There are generally two types of wind turbines: vertical axis (VAWT) and horizontal axis (HAWT). Vertical Axis Wind Turbines (VAWT) have recently sparked lots of attention both for offshore applications (Rezaeiha et al., 2017) and in the built environment, like cities and towns, due to some of their advantages, such as omnidirectional capabilities, low maintenance costs, and low noise when compared to Horizontal Axis Wind Turbines (HAWT) (Kooiman & Tullis, 2010).

2. LITERATURE REVIEW

Despite the advantages provided by vertical axis wind turbines (VAWT), they still contribute little to the amount of electricity used in the world. Because of that, a lot of research has been carried out to improve the efficiency of vertical axis wind turbines (VAWT). Mahmoud et al. (2012) carried out some studies on different parameters that influence the performance of vertical axis wind turbines (VAWT). One of the parameters being studied is the addition of an endplate to the rotor of a vertical axis wind turbine (VAWT). The author concluded that a rotor with an endplate gives better performance than one with none. Lee et al. (2016), using wind turbines and numerical analysis, observed the influence of helical angles on the power coefficient using various tip speed ratios. The authors concluded that helical angle 45 gives the maximum Cp. Tartuferi et al. (2015) proposed a way of improving the efficiency of the Savonius wind turbine by introducing a new aerofoil-shaped blade and a Savonius wind turbine that self-aligns itself to the direction of the freestream wind. The proposed Savonius turbine was found to have better efficiency than a normal Savonius turbine. Mohamed et al. (2011) introduced an optimized

aerofoil blade shape to improve the power output of a Savonius wind turbine. At a tip speed ratio (TSR) of 0.7, the design was found to provide a 40% increase. Saad et al. (2021) carried out an analysis of a new proposed idea of using a twisted blade for the development of a multistage Savonius wind turbine. The results were compared with available numerical results, and the twisted-bladed Savonius rotor was found to give more power output. Supradeepan (2021) carried out an analysis to increase the performance of a duct wind turbine. It was found that an aerofoil cross-section with a cowl gives better performance with a reduced load. Jang et al. (2021), using computational fluid dynamics (CFD) and direct simulation Monte Carlo (DMSC), compared the estimated power of an H-Darrieus turbine in terms of electrical efficiency and found that it corresponded to the power performance measured. Ramlee et al. (2020), using various solidities, analyze the power performance of a vertical axis wind turbine (VAWT). The result shows that turbines with high solidities perform better at a low tip speed ratio (TSR).

Due to the high cost of using a wind tunnel, a lot of experiments have been carried out using computational fluid dynamics (CFD). Some of the experiments include Pope et al. (2010), who used fluent to analyze two different types of aerofoil blades while keeping the first and second laws of thermodynamics in mind. The results show that the second law of thermodynamics provides more insight than the first law. De Tavernier et al. (2019), using computational fluid dynamics (CFD), investigated the effect of the shape of an aerofoil on the performance of vertical axis wind turbines (VAWT). The author concluded that there is a need for proper selection of an aerofoil to obtain good performance from vertical axis wind turbines (VAWT). Li & Li (2010), using numerical computation, observed the influence of solidity on the performance of vertical axis wind turbines (VAWT). From the results, it was concluded that an increase in solidity results in a corresponding increase in the static torque coefficient. Aliet al. (n.d.) observed the influence of the blade on the efficiency of vertical axis wind turbines (VAWT) using the MATLAB program. It was observed that S1046 gave a better performance.

Some of the research was also based on the effect of Reynolds number. Chamorro et al. (2012), using wind turbines, investigated the influence of Reynolds number on the mean velocity, velocity skewness, and kinematic shear stress and discovered that at high Reynolds numbers greater than or equal to 9.3 x 104, Reynolds number influence can be neglected. Kamoji et al. (2009) observed the effects of Reynolds number, aspect ratio, and overlap ratio on the efficiency of two wind turbines: a modified wind turbine with no center shaft and a conventional wind turbine. The Savonius rotor without a shaft was found to have the highest coefficient of power. Roh & Kang (2013) studied the effects of Reynolds number and blade profile on the efficiency of straight-blade vertical axis wind turbines (VAWT). The author concluded that power production is dependent on the blade profile.

Dabiri (2011) investigated the use of two vertical axis wind turbines (VAWT) rotating in opposite directions to each other to improve the efficiency of power generated on a farm by wind turbines. The result shows that more power can be generated using an arrangement that allows the vertical axis wind turbines (VAWT) to extract energy from a neighboring VAWT wake, thereby reducing the cost of operation. Migliore (1983) compared the NACA 6 series to the NACA 4 series to determine the best selection for the H. Darrieus blade. The author concluded that the NACA 6 series has the same maximum power coefficient as the NACA 4 series. Sharma & Gupta (2014), using a wind turbine, investigated the performance of a two-staged Savonius turbine. The result shows that at a 9.37 percent overlap condition, a maximum Cp is obtained.

3. METHODOLOGY

3.1 Description of the model

The vertical axis wind turbines (VAWT) and the wind tunnel domain were represented using a two-dimensional computational fluid dynamics (CFD) model, as seen in Fig. 2. This was based on previous literature that has proven that a 2D model is sufficient for identifying the factors that impact the VAWT's performance. The wind turbine is an H-type vertical-axis wind turbine with three symmetrical NACA0018 airfoil blades. The turbine has a shaft radius of 0.02 m and a turbine radius of 0.5 m. As shown in Fig. 1, the shaft and the turbine both revolve at the same counterclockwise speed. Using the freestream velocity of 3 m/s and the rotational speed of the turbine of 27 m/s as described in Table 1, the tip speed ratio for the reference case was calculated to be 4.5. Using equation (1) and a chord length of 0.06 m, the solidity of the blade is calculated to be 0.18.

3.2 Computational domain and grid

Previous research has demonstrated that a blockage ratio of less than 5% (a minimum domain width of 20 D) is necessary for computational fluid dynamics (CFD) simulations of VAWTs to limit the influence of side

boundaries on the results. The blockage ratio in 2D simulations is D/W, where D and W are the turbine diameter and domain width, respectively. The blockage ratio is considered unaffected by the turbine tip speed ratio and solidity since it is calculated based on the complete diameter of the turbine. As a result, a domain width of 20 D is used in this investigation, and the diameter of the rotating domain is 1.5 D. Using the sliding mesh technique, the rotating domain is connected to the stationary domain. The stationary domain is rectangular in shape, and the rotating domain is circular, as shown in Fig. 2. As seen in Table 2, the distance from the center of the turbine to the inlet and outlet of the domain is 5D and 25D, respectively. Four quartiles are defined in the plane around the blades, i.e., 315 ° ≤ θ <45 °, upwind 45 ° ≤ θ <135 °, leeward 135 ° ≤ θ <225 °, and downwind 225 ° ≤ θ ° 315 °. The position of the upper blade is used to define the azimuthal angle θ.

Time-dependent Reynolds-averaged Navier-Stokes (U-RANS) is solved using ANSYS FLUENT. The freestream velocity is modeled arriving from the left with a standard ambient condition and 299. Temperature Menter's shear stress transfer (SST) model, developed from the k-two-equation formulation, is employed to accomplish turbulence closure. Both temporal and spatial discretization are accomplished using second-order schemes. For pressure-velocity coupling, the SIMPLE approach is utilized. The meshing was carried out using Ansys, as shown in Fig. 3.

$$\sigma = \frac{nc}{D} \tag{1}$$

Table 1 describes the parameters of the vertical axis wind turbine, and some of the salient input parameters are highlighted in Table 1.

Table 1: Parameters for Reference Case

Parameters	Value	Parameters	Value
Aerofoil profile	NACA0018	Rotational speed [rad/s}	27.00
Aerofoil chord length {m}	0.06	Tip speed ratio	4.50
Swept area [m2]	1.00	Free stream velocity[m/s]	3.00
Diameter	1.00	Shaft diameter[m]	0.04
Numbers of blade	2.00		
	3.00		

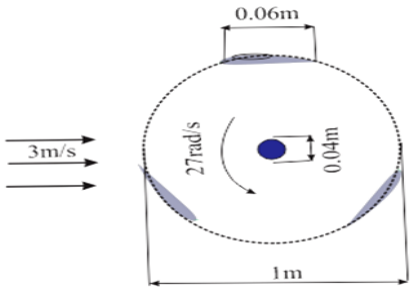

Fig. 1: Schematics of the reference case

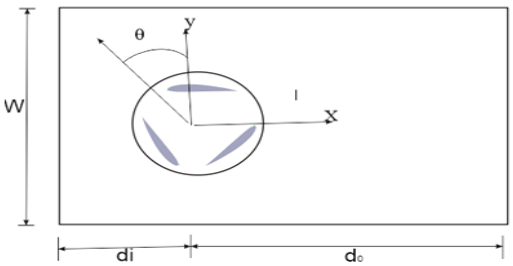

Fig. 2: Schematics of the computational

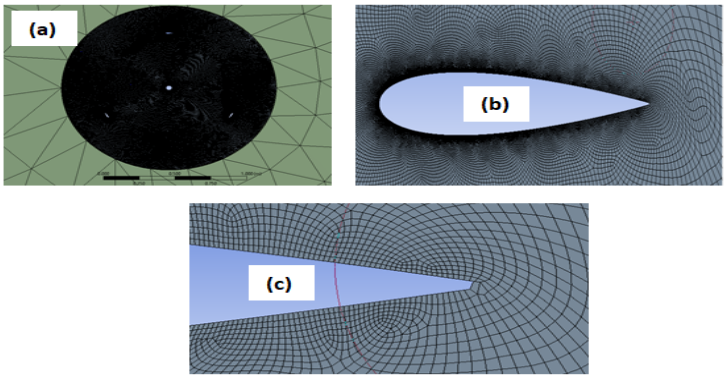

Fig. 3(a-c**):** (a) mesh near the rotating core, (b) mesh near the aerofoil, (c) mesh near the trage

4. RESULTS AND DISCUSSION

4.1 Results validation

Computational Fluid Dynamics (CFD) has been frequently used to predict the performance of vertical axis wind turbines (VAWT). In the previous study, the results were compared to determine the accuracy of the results. In the present study, parameters that affect the accuracy of results gotten from computational fluid dynamics (CFD) using low wind velocity The figure compares the result gotten by Rezaeiha et al. using the same parameter.

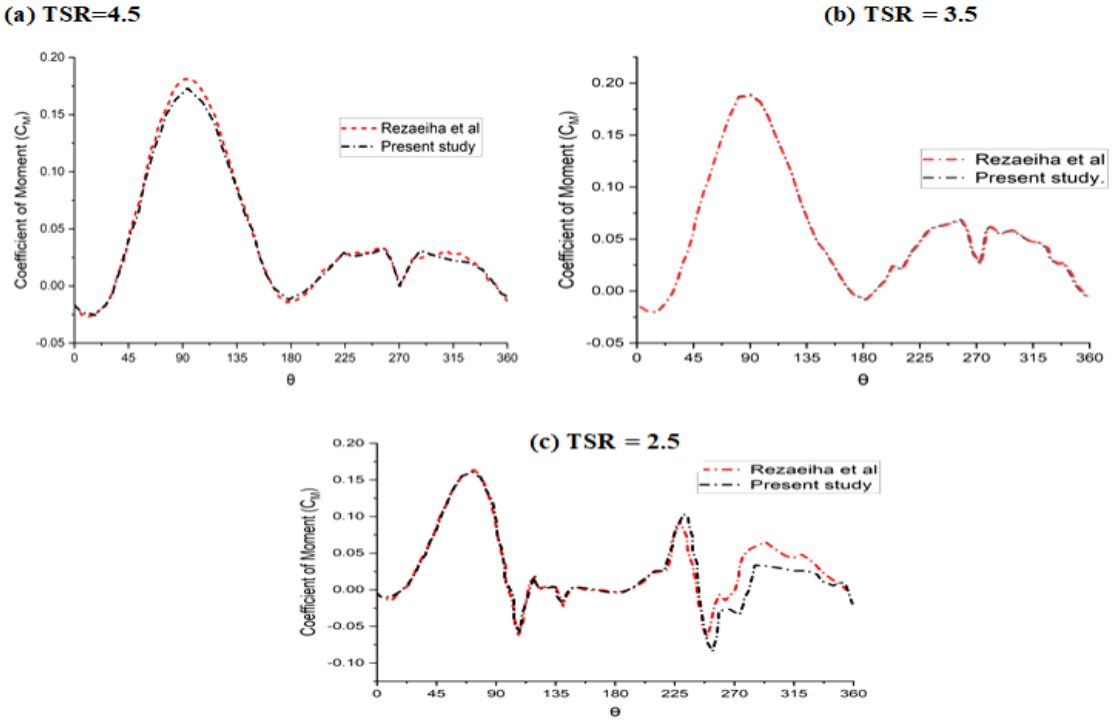

Fig. 4: Validation of the Results from the Present Study with those of Rezaeiha et al. [19] a) Tsr = 4.5; b) 3.5; c) 2.5

Table 2 displays the simulation parameters for the reference case.

Table 2: Reference case

d_i	d_0	W	d_c	Dθ	Turbine revolution
5.0D	25.0D	20.0D	1.5D	0.1	20.0

4.2 Azimuthal increment (dθ)

In the case of wind turbines, the time step is often associated with the turbine revolution and expressed as an azimuthal increment. The number of degrees that the turbine rotates every time step is thus specified as an azimuthal increment. Fig. (5) displays the instantaneous moment coefficient vs. azimuth increment () for the range of tip speed ratios of 1.5–5.5, using azimuthal increments of 0.1, 0.5, and 1.0. The solidity of the turbine is 0.18, which is the same as in the reference scenario. It can be seen clearly in Figs. 5(a) and 5(b) that the difference between the findings for d = 0.5° and 0.1° is insignificant at high tip speed ratios of 4.5 and 5.5. The fundamental reason for this is that moderate to high tip speed ratios of 4.5 and 5.5 correspond to a regime in which the flow is generally connected, as well as a change in the angle of attack on the blades during the turbine that is below the stall angle. As a result of the absence of dynamic stall and the wake-blade interactions of the blades, the flow is less complicated than that at a lower tip speed ratio. A closer look at Figs. 5(a) and 5(b) reveals modest variations when the azimuthal angle = 1.0° on the downwind side is about 270°, corresponding to the shaft's wake [Rezaeiha, Montazeri, and Blocken 2018].

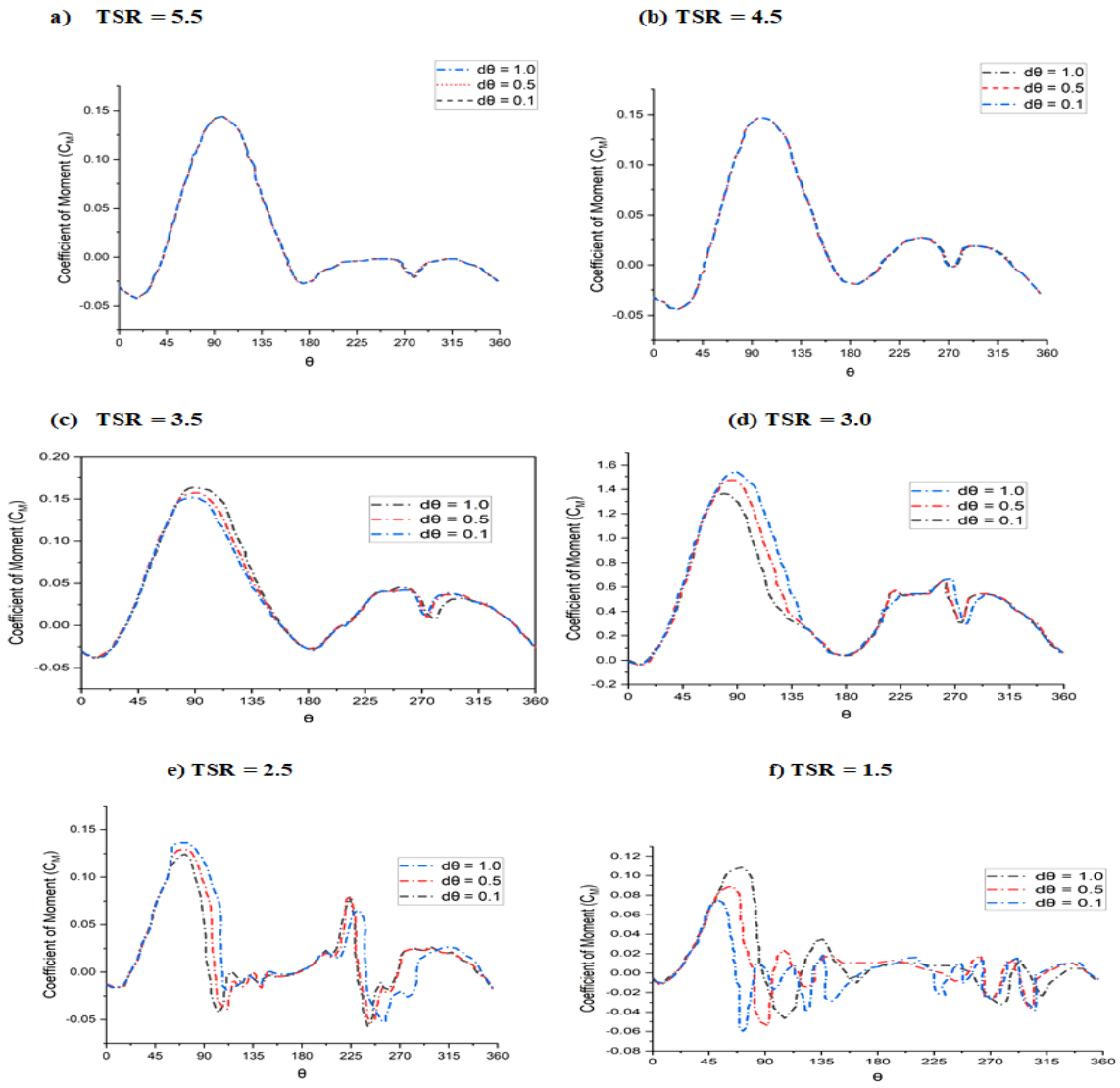

Fig. 5: (a) TSR 5.5 (b) TSR 4.5 (c) TSR 3.5 (d) TSR 3.0 (e) TSR 2.5 (f) TSR 1.5

This demonstrates that, even at relatively high levels, the interactions between the vortices shed from the shaft and the blades traveling in the shaft wake (the shaft's wake-blade interaction) may make flow calculations more difficult. In this instance, finer azimuthal increments are necessary.

For tip speed ratios less than 4.5, where the changes in the angle of attack on the blades are more pronounced, results are significantly reliant on azimuthal increments because blade-wake interaction occurs and the stall angle might be reached. This is most noticeable in two areas: upwind (67.5°–135°) and downwind (225°–315°).The former is linked to the occurrence of the dynamic stall, which occurs at such azimuthal angles and results in an abrupt reduction in C_M. The latter relates to the interactions of the vortices shed by the blades in the upwind region and the shaft with the downwind blades (blade-wake interactions), resulting in large changes in C_M(Rezaeiha, Montazeri, and Blocken 2018). Due to the complexity of the flow, a finer azimuthal increment is needed in predicting the flow.

Table 3 displays the parameters used in carrying out the study of the influence of azimuthal increment on solidity.

Table 3: parameters for solidity

d_i/D	d_0/D	L ×W	Dθ	Λ	Σ
5.0	25.0	30.0 × 20.0	0.1, 0.5	4.5	0.06, 0.12, 0.24

4.3 Solidity

The parameters used for the study are described in Table 3. Using azimuthal increments of 0.1 and 0.5, the instantaneous coefficient of the moment can be seen plotted against θ for a set of solidities of 0.06, 0.12, and 0.24. It can be noted that for the solidities of 0.12 and 0.24 (Figs. 6(a) and 6(b)), no substantial change in azimuthal increments is detected.

For a solidity of 0.06, significant changes in CM (Fig. 6(c)) are detected for an azimuthal increment of 0.5°. The difference in C_M is most noticeable in two areas: 90°–150° and 225°–305°, where the former corresponds to the azimuthal angles where dynamic stall may occur and the latter relates to the region where the resulting blade–wake interactions would occur.

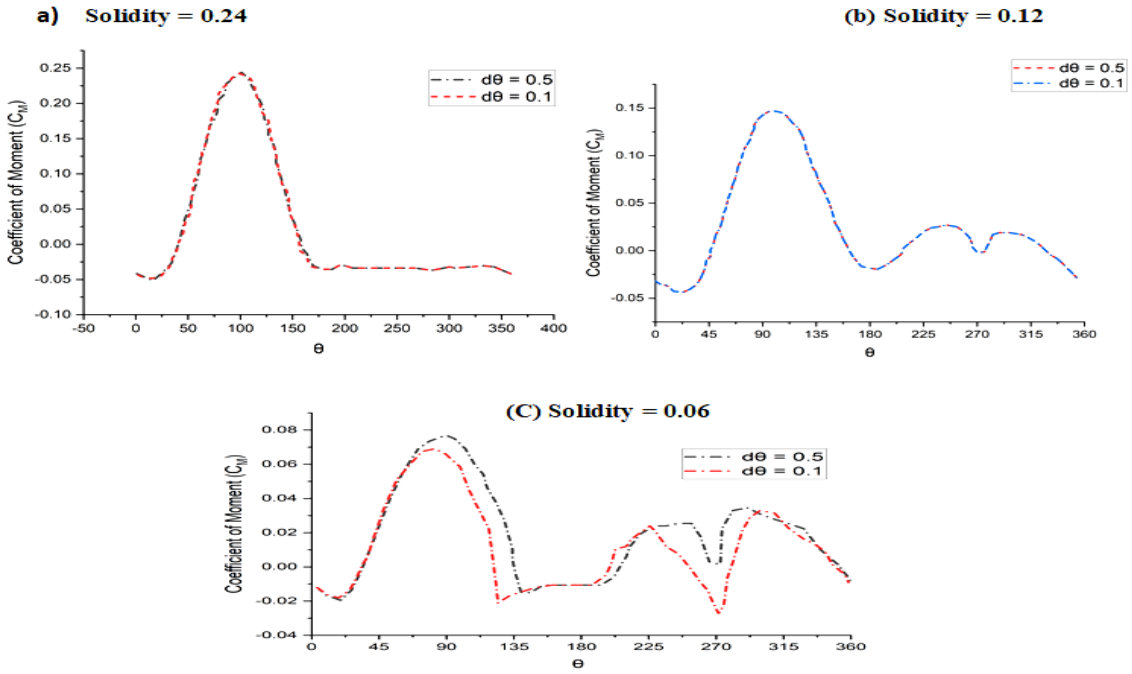

Fig. 6: (a) solidity 0.24 (b) solidity0.12 (c) solidity 0.06

4.4 Coefficient of performance (Cp)

The predicted turbine coefficient of performance (C_P) shown in Fig. 7 demonstrates the deviation between the results of simulations using fine (0.1°) and coarse (0.5°–1.0°) azimuthal increments. For tip speed ratios (TSR) of 4.5 and 5.5, the deviation can be said to be insignificant. At 3.5, the results begin to diverge.

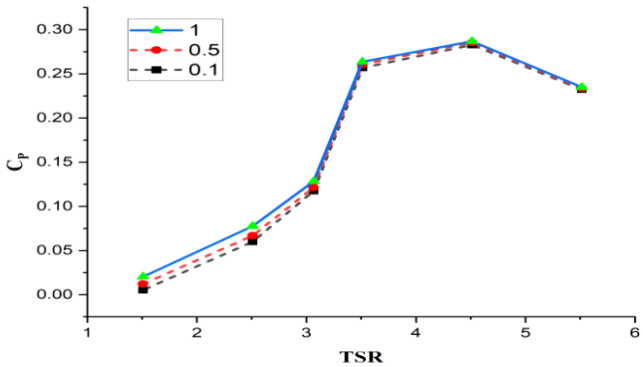

Fig. 7: power coefficient along each Tip Speed Ratio (TSR) using different azimuthal increment.

When the coefficient of performance (C_P) is reduced to 2.5, the deviation in terms of the coefficient of performance (C_P) rises, and the deviation reduces when the coefficient of performance (C_P) is reduced further to 1.5. This indicates that at a tip speed ratio (TSR) of 2.5–3.5, the separation on the blades is still growing.

5. CONCLUSION

Computational Fluid Dynamics (CFD) simulations were conducted to determine the minimal requirements for the azimuthal increment criteria used in the Computational Fluid Dynamics (CFD) modeling of Vertical Axis Wind Turbines (VAWT) with varying tip speed ratios and solidity. The following results were obtained:

1. The tip speed ratio is critical in defining the minimal requirements for azimuthal increment since it is the primary element influencing changes in the angle of attack of the turbine blades.
2. Low-to-moderate tip speed ratios often put turbines in a "blade-wake interaction" condition, where changes in blade angle of attack exceed stall angles and cause blade-wake interactions.
3. Conversely, tip speed ratios ranging from moderate to high correspond to a regime in which fluctuations in the blade's angle of attack are less than the static stall angle and the flow is more or less continuously attached to the blade.
4. Therefore, it is determined that for a low to moderate tip speed ratio, an azimuthal increment of 0.1 is the best choice, while for a high tip speed ratio, an azimuthal increment of 0.5 is the best choice to decrease simulation time while still maintaining accuracy.

REFERENCES

Ali, A. M., Mohamed, M. H., & Hafiz, A. A. (n.d.). *Theoretical Investigation of H-rotor Darrieus Turbine Performance with Different Airfoil Shapes*.

American, S., America, N., & American, S. (1990). *Energy from Fossil Fuels Author (s): William Fulkerson , Roddie R . Judkins and Manoj K . Sanghvi (SEPTEMBER 1990), pp . 128-135 Published by : Scientific American , a division of Nature America , Inc . Stable URL : https://www.jstor.org/stable/10.230*. *263*(3), 128–135.

Bangga, G., Lutz, T., Dessoky, A., & Krämer, E. (2017). Unsteady Navier-Stokes studies on loads, wake, and dynamic stall characteristics of a two-bladed vertical axis wind turbine. *Journal of Renewable and Sustainable Energy*, *9*(5). https://doi.org/10.1063/1.5003772

Battisti, L., Brighenti, A., Benini, E., & Castelli, M. R. (2016). Analysis of Different Blade Architectures on small VAWT Performance. *Journal of Physics: Conference Series*, *753*(6). https://doi.org/10.1088/1742-6596/753/6/062009

Chamorro, L. P., Arndt, R. E. A., & Sotiropoulos, F. (2012). Reynolds number dependence of turbulence statistics in the wake of wind turbines. *Wind Energy*, *15*(5), 733–742. https://doi.org/10.1002/we.501

Dabiri, J. O. (2011). Potential order-of-magnitude enhancement of wind farm power density via counter-rotating vertical-axis wind turbine arrays. *Journal of Renewable and Sustainable Energy*, *3*(4). https://doi.org/10.1063/1.3608170

De Tavernier, D., Ferreira, C., & van Bussel, G. (2019). Airfoil optimisation for vertical-axis wind turbines with variable pitch. *Wind Energy*, *22*(4), 547–562. https://doi.org/10.1002/we.2306

Eboibi, O. (n.d.). *A Numerical Investigation into the Effects of Fluctuating Wind on the Performance of a Small Scale Vertical Axis Wind Turbine*. https://www.researchgate.net/publication/269761823

Hamada, K., Smith, T., Durrani, N., Qin, N., & Howell, R. (2008). *Unsteady Flow Simulation and Dynamic Stall around Vertical Axis Wind Turbine Blades*. http://www.sandia.gov/wind/other/VAWThist.pdf

Islam, M., Ting, D. S. K., & Fartaj, A. (2008). Aerodynamic models for Darrieus-type straight-bladed vertical axis wind turbines. *Renewable and Sustainable Energy Reviews*, *12*(4), 1087–1109. https://doi.org/10.1016/j.rser.2006.10.023

Jang, H., Hwang, Y., Paek, I., & Lim, S. (2021). *Performance Evaluation and Validation of H - Darrieus Small Vertical Axis Wind Turbine*. 1687–1697.

Kadam, A. A., & Patil, S. S. (n.d.). A Review Study on Savonius Wind Rotors for Accessing the Power Performance. In *IOSR Journal of Mechanical and Civil Engineering*. www.iosrjournals.org

Kamoji, M. A., Kedare, S. B., & Prabhu, S. V. (2009). Experimental investigations on single stage modified Savonius rotor. *Applied Energy*, *86*(7–8), 1064–1073. https://doi.org/10.1016/j.apenergy.2008.09.019

Kooiman, S. J., & Tullis, S. W. (2010.). *Response of a Vertical Axis Wind Turbine to Time Varying Wind Conditions found within the Urban Environment*.Wind Engineering, 34(4), 389–401

Lee, J. H., Lee, Y. T., & Lim, H. C. (2016). Effect of twist angle on the performance of Savonius wind turbine. *Renewable Energy*, *89*, 231–244. https://doi.org/10.1016/j.renene.2015.12.012

Li, S., & Li, Y. (2010). Numerical study on the performance effect of solidity on the straight-bladed vertical axis wind turbine. *Asia-Pacific Power and Energy Engineering Conference, APPEEC*, *1153*, 1–4. https://doi.org/10.1109/APPEEC.2010.5449269

Mahmoud, N. H., El-Haroun, A. A., Wahba, E., & Nasef, M. H. (2012). An experimental study on improvement of Savonius rotor performance. *Alexandria Engineering Journal*, *51*(1), 19–25. https://doi.org/10.1016/j.aej.2012.07.003

Migliore, P. G. (1983). COMPARISON OF NACA 6-SERIES AND 4-DIGIT AIRFOILS FOR DARRIEUS WIND TURBINES. *Journal of Energy*, *7*(4), 291–292. https://doi.org/10.2514/3.48083

Mohamed, M. H., Janiga, G., Pap, E., & Thévenin, D. (2011). Optimal blade shape of a modified Savonius turbine using an obstacle shielding the returning blade. *Energy Conversion and Management*, *52*(1), 236–242. https://doi.org/10.1016/j.enconman.2010.06.070

Pope, K., Dincer, I., & Naterer, G. F. (2010). Energy and exergy efficiency comparison of horizontal and vertical axis wind turbines. *Renewable Energy*, *35*(9), 2102–2113. https://doi.org/10.1016/j.renene.2010.02.013

Ramlee, M. F., Fazlizan, A., & Mat, S. (2020). *Performance Evaluation of H-Type Darrieus Vertical Axis Wind Turbine with Different Turbine Solidity*. *17*(2), 833–839. https://doi.org/10.1166/jctn.2020.8726

Rezaeiha, A., Montazeri, H., & Blocken, B. (2018). Towards accurate CFD simulations of vertical axis wind turbines at different tip speed ratios and solidities: Guidelines for azimuthal increment, domain size and convergence. *Energy Conversion and Management*, *156*(September 2017), 301–316. https://doi.org/10.1016/j.enconman.2017.11.026

Rezaeiha, A., Pereira, R., & Kotsonis, M. (2017). Fluctuations of angle of attack and lift coefficient and the resultant fatigue loads for a large Horizontal Axis Wind turbine. *Renewable Energy*, *114*, 904–916. https://doi.org/10.1016/j.renene.2017.07.101

Roh, S. C., & Kang, S. H. (2013). Effects of a blade profile, the Reynolds number, and the solidity on the performance of a straight bladed vertical axis wind turbine. *Journal of Mechanical Science and Technology*, *27*(11), 3299–3307. https://doi.org/10.1007/s12206-013-0852-x

Saad, A. S., Elwardany, A., El-sharkawy, I. I., Ookawara, S., & Ahmed, M. (2021). *Performance evaluation of a novel vertical axis wind turbine using twisted blades in multi-stage Savonius rotors*. *235*(March).

Sharma, K., & Gupta, R. (2014). *Performance Measurement of a Two-Stage Two-Bladed Savonius Rotor* (Vol. 4, Issue 1).

Supradeepan, L. R. K. (2021). *Performance evaluation of cowl - augmented wind turbine*.

Tartuferi, M., D'Alessandro, V., Montelpare, S., & Ricci, R. (2015). Enhancement of savonius wind rotor aerodynamic performance: A computational study of new blade shapes and curtain systems. *Energy*, *79*(C), 371–384. https://doi.org/10.1016/j.energy.2014.11.023

APPENDICES

NOMENCLATURE

c	blade chord length	ω	rotational speed
c_m	coefficient of moment	R	radius of Turbine
c_p	power coefficient	P	turbine power
c_t	thrust coefficient	T	thrust coefficient
D	diameter of turbine	$\underline{u}$	free stream velocity
d_c	diameter of rotating core	W	width
d_0	distance from turbine center to domain outlet	σ	solidity
dθ	azimuthal increment	λ	tip speed ratio
d_i	distance from turbine center to domain inlet		

PAPER 212 – DEVELOPMENT OF AN APPLICATION SOFTWARE FOR DESIGN OF OFF-GRID PHOTOVOLTAIC ENERGY SYSTEMS

O. M. Tijani[1*], M. F. Akorede[2], T. A. Abdul-Hameed[3], T.M Adepoju[4]

[1]Department of Electrical & Electronics Engineering, Federal Polytechnic Ayede, Nigeria.
[2]Department of Electrical & Electronics Engineering, University of Ilorin, Ilorin, Nigeria.
[3]Department of Electrical & Electronics Engineering, Federal Polytechnic Ayede, Nigeria.
[4]Department of Electrical & Electronics Engineering, Federal Polytechnic Ayede, Nigeria.
[*] Email: tijanimo@federalpolyayede.edu.ng

ABSTRACT

The task of sizing solar PV system using manual method is time consuming and susceptible to error. This may lead to poor design that cumulate to in-efficient solar PV installation and waste of scarce resources. The solar PV system is the cleanest and cheapest source being the energy from the sun. A system of this type has a high initial setup cost, but has little or no ongoing operating costs over an extended period of time. In this research, a software was developed to give the specification of the components that constitute solar PV system, thus avoiding oversized or undersized solar PV system installation.
The work was carried out using a residential building as a case study. The peak sun hour considered is 7 hours, which is subject to change as it depends on the location. The developed software is a GUI tool, easy to use, and vary fast to give accurate results unlike the manual sizing calculation method. Three different input data and sized output interface are developed for the software tool; load demand module, battery size module, and PV array module. The software operation was validated with manual other existing application to establish it accuracy and correctness.

KEYWORDS: Solar PV System, Peak Sun Hour, Load Demand, Battery Size, PV Array Size, GUI-Based Tool

1.0 INTRODUCTION

A technology known as photovoltaic (PV) turns solar energy into direct current electricity without using any combustion processes that could result in negative byproducts for the environment (Singh, 2018). Solar power is the best renewable energy sources available because it is the cleanest of all (Merts, 2019). Solar power has many applications like in residential, commercial and industrial areas (Oghogho & Ikponmwosa, 2014). Due to its sustainability, regenerative nature, and ability to reduce emissions, solar electricity is a viable option.. Effective and efficient software tools are critical in ensuring proper design which reduces cost and wastage. Therefore, it is an economically viable option. (Klaus, 2017), to create the PV sizing system GUI-based application, several software solutions are available. Examples are: RETScreen, PV F-Chart, HOMER Pro, Solar Design Tool, INSEL, TRNSYS, NREL Solar Advisor Model, ESP-r 11.5, PVSYST 4.33, Solar Pro, PV Design Pro-G, PV-SOL Expert and so many others (Tamer *et al*.,2012). The aim of this study was to create a software application that could accurately calculate the size of a standalone photovoltaic (PV) system. The objectives were to:

1. develop the load demand and load curve module;
2. develop the solar PV system components module;
3. simulate and evaluate the performance of the developed tool using a case study.

1.1 Related Works

A brief review of some prominent solar sizing tools is presented example which include among the following; Hybrid Optimization Model for Electric Renewables (HOMER) Software created with certain goals in mind. HOMER input window is developed to minimize the effort required to enter load data, component data, standard and cost (Oulis R.A. *et al.,* 2018). HOMER provides reasonable default value for some of the needed data to enhance quick start of the main analysis. The challenge of comparing designs of both off-grid and grid-connected power systems for different applications is made easier by this software tool, called a micro power optimization model embeded in HOMER (Bhandari, R. *et al*., 2014). In Homer, quality input data for the resource are not always readily available; there are no detailed input data for configuration; and a laborious criterion is required to make the solution of the optimization converge with the optimum region, making the selection of this criterion difficult.

Renewable Energy Technologies Screen (RETScreen), a distinctive decision-support tool for analyzing clean energy. The software is available in multiple languages, thus allowing it expanded user data base. This software

can simulate a wide range of applications, including industrial remote wind PV-gen set hybrid power supply, standalone battery storage systems for lighting, massive multi-array central power plants, and distributed power systems installed on residential and commercial buildings (Lalwani *et al.,* 2010). However, the software tool has its own limitation; for example, having data being added manually, lack of reporting functions facility, and absence of scope of adding other data sources or customized data to the software interface

Transient Systems Simulation (TRNSYS) is a software , which is based on graphics and is incredibly versatile, is used to model the behaviour of transient systems. The simulation tool was created in 1975 and is available for purchase (Lalwani *et al.,* 2010). TRNSYS has a large library of parts, each of which simulates the performance of a single system component (Aristide. *et al.* ,2018).It can be ported to work with other simulation software as well. Just as RETscreen, the software is updateable. The software tool is not free, and it is also not very flexible or user-friendly.

Photovoltaic Systems (PVsyst) is suitable for grid-connected, standalone, pumping, and DC-grid systems. It is a PC software program for studying, sizing, simulating, and analyzing data on solar systems. It is an updatable software tool. This application falls short when it comes to handling shadow analysis thoroughly. Due to deficiencies identified in the previous software solutions, an attempt towards remedifying such deficiencies are made using a proposed GUI-based tool for Solar PV design. The development platform is National Instrument LabVIEW.

2.0 A CASE STUDY FOR THE DEVELOPED GUI-BASED SOFTWARE

The case study to validate the use of the software is a residential building with the appliances in a given quantity and wattage rating as stated in table 3.1. The appliances are most common household electrical appliances. They are necessary as the basic electrical services needed for the comfort of a user or occupants of the typical residential building.

Table 2.1: Appliances Data

S/N	APPLIANCE	QUANTITY	WATTAGE(W)	HOUR OF USE (Hrs)
1	External Bulb	20	25	12
2	Interior Bulb	15	20	16
3	Refrigerator	1	2500	8
4	Washing Machine	1	1500	1
5	Home Theatre System	1	200	10
6	Toasting Machine	1	1500	1
7	Air Conditioning System	4	1200	5
8	Standing Fan	5	70	8
9	Laptop	3	90	3

3.0 DESIGN AND DEVELOPMENT OF THE SOLAR SIZING APPLICATION TOOL

The overall steps for the implementation of the proposed software tool begins with collection of appliances data, and ends with evaluation and analysis of the performance of the GUI tool developed. The tool comprises four modules. They include, load demand, load curve module, battery size module, and solar PV array size module (Mohd *et al*., 2015).

3.1 Development of Load Demand Module

The demand load as given in eqn. (3.1) is the sum of the operational load and non-operational demand loads. It is determined by applying the proper adjustment factor to the sum total. Proven mathematical equations for solar sizing were appropriately adopted in programming the GUI interface.

$$P_a = \frac{\sum_{j=1}^{n} P_j}{A.F} \tag{3.1}$$

where P_a is the adjusted power in watt, $P_{J\ is\ the}$ active power of the jth appliance in watt . $A.F$ is the Adjustment Factor, 0.85 for AC loads while 1.0 for DC loads. P_a in eqn. (4.1) is the sum of the wattage of each appliance under test, A.F is the adjustment factor to present the load (watt) for DC loading or AC loading. The Energy

Demand is the product of each adjusted power and the hours of use of such appliance. The summation of such energy demand in eqn (4.2) is the total energy demand per day.

$$E_{total} = \sum_{a=1}^{n} (P_a \times T_j) \tag{3.2}$$

where, $E_{total}$is the total energy demand per day in watt-hour, *n is the* the number of appliances under consideration and T_j is the time of use of the jth appliance in hours(hrs)

$$Ah_{est} = \frac{E_{total}}{BB_v} \tag{3.3}$$

where Ah_{est} = estimated battery amp-hour capacity. BB_V is the battery bus voltage which ranges from 12V, 24V , 48V, etc

$$Ah_{total} = \frac{(Ah_{est} \times n)}{DoD} \tag{3.4}$$

where Ah_{total} is the total ampere-hour due to the PV array. *DoD* is the depth of discharge of the battery

3.2 Battery Sizing GUI Interface Development

To accurately determine the battery size, the daily Ampere-hour capacity is required. The expected size for this battery module includes the following: battery capacity in (Ah), selected battery capacity (Ah), total battery power(kW), average depth of discharge (avg. DOD), the total battery capacity (Ah), number of batteries in parallel (NoB_P), number of battery in series (NoB_S), and the total number of batteries. The expected battery sized parameters, depend on a number of configured input parameters which include: the days of autonomy, depth of discharge (DoD), selected battery capacity (AH) and the system voltage (Vdc or Vac).

$$RBC_{Ah} = \frac{Ah_{est} \times DoS}{DoD} \tag{3.5}$$

where RBC_{Ah} is the required battery capacity in Amp-hour, Ah_{est} is denoted as the estimated Ampere-hour capacity of the PV required per day. *DoS* is regarded as the days of storage for the battery. *DoD* is the depth-of –discharge of the battery.

$$NoB_p = \frac{RBC_{Ah}}{S_{Ah}} \tag{3.6}$$

where NoB_P is the number of batteries in parallel, NoB_S is the number of batteries in Series. S_{Ah} is the selected Amp-hour capacity of the battery.

$$NoB_s = \frac{BB_v}{SD_v} \tag{3.7}$$

where BB_v is the battery bus voltage (dcV), SD_v is the selected system design voltage (dcV/acV).

$$NoB_T = NoB_p \times NoB_s \tag{3.8}$$

Here, the NoB_T is the total number of batteries to be specified. Other expressions for the development of the battery module GUI interface are eqns (3.9) and (3.10)

$$E_{Ah} = NoB_p \times S_{Ah} \tag{3.9}$$

$$ET_{(kwh)} = \frac{E_{Ah} \times BB_v}{1000} \tag{3.10}$$

where E_{Ah} is the total Ah required. $ET_{(kwh)}$ is the total energy capacity of the battery bank in kwh.

4.4 Solar PV Array Module Development

The PV array GUI interface will be designed based on tested solar sizing equations, similar to existing developed module interfaces. The input requirements are as follows; battery round trip efficiency ($BRT_{efficiency}$), selected PV module maximum voltage at STC (SPV_{max}) in volts, nominal rated PV module output power (NPV_{output}) in Watt, and energy output per module (EM_{output}) in Watt-hour.
The module energy output at operating temperature (ME_{output}) in Watt-hour is computed by given eqn. in (3.11)

$$EM_{output} = SPV_{gp} \times P_h \quad (3.11)$$

where EM_{output} is the energy output per module in Watt-hour. $SPVg$ is the selected PV module guaranteed power at STC in Watt. P_h *is* defined as the peak sun hour for the geographical location.
The module energy output at operating temperature (MEoutput) in Watt-hour in eqn (4.12) is the product of the de-rating factor (D.F) and the module energy output.

$$ME_{output} = D.F \times EM_{output} \quad (3.12)$$

The total energy demand (E_{total}) divided by the battery trip efficiency($BRT_{efficiency}$) gives the array output power (RA_{output}) in eqn. (3.13).

$$RA_{output} = \frac{E_{total}}{BRT_{efficiency}} \quad (3.13)$$

The number of modules required ($NoM_{required}$) is function of both eqn (3.12) and (3.13), as given in eqn. (3.14)

$$NoM_{required} = \frac{RA_{output}}{ME_{output}} \quad (3.14)$$

The number of modules in string (NoM_{string}) as given in eqn (3.15) is determined by dividing the designed system voltage (usually determined by the battery bank) by the nominal module voltage at standard test condition (STC) (Sharma. D. *et al.,*2014).

$$NoM_{series} = \frac{BB_v}{SPV_{\max}} \quad (3.15)$$

The number of modules in parallel in eqn (3.16) is determined by dividing the designed required number of modules ($NoM_{required}$) by number of modules in series (NoM_{string}). (Sharma. D. *et al*.,1986)

$$NoM_{parallel} = \frac{NoM_{required}}{NoM_{series}} \quad (3.16)$$

The total number of module purchased ($NoM_{purchased}$) is computed using eqn. (3.17) as given:

$$NoM_{purchased} = NoM_{series} \times NoM_{parallel} \quad (3.17)$$

The nominal array output (NRA_{output}) is computed as given in eqn. (3.18)

$$NRA_{output} = NRPV_{output} \times NoM_{purchased} \quad (3.18)$$

4.0 SIMULATION RESULTS AND DISCUSSION

Load Curve and Load Demand Module

On simulation, the load curve in Figure 4.1 as well as the load demand in Figure 4.2 are displayed. Figure 4.2 which is the load demand module has the following expected outputs; the total ampere-hour per day for the load demand is 3108.333 AH, total energy per day is 63.41 kW-hr, total AC power per day is 11.92 kW and total DC power per day of 14.02 kW.

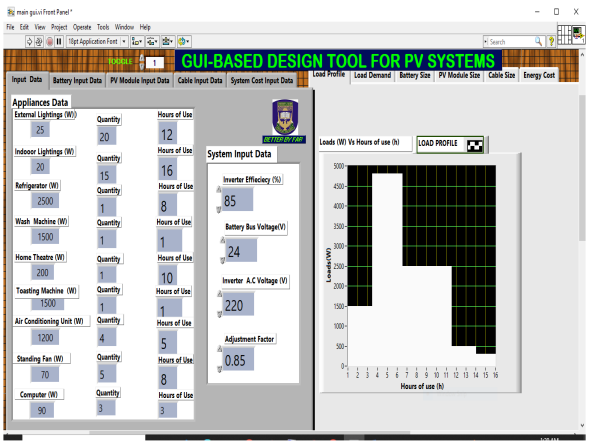

Figure 4.1 Appliance Data and Load Curve Module

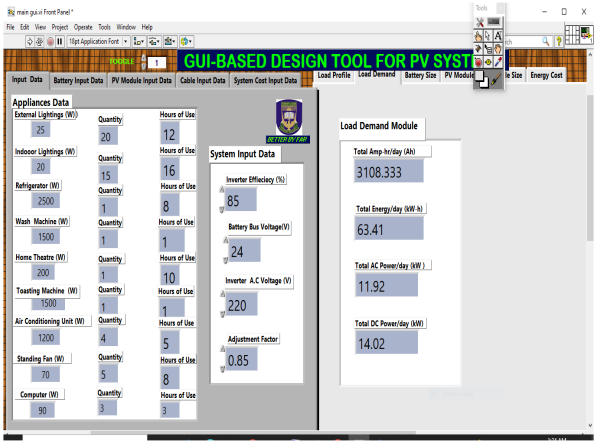

Figure 4.2 Appliance Data and Load Demand Module Module

The Battery Size Module

The battery size module in. Figure 4.3 shows the number of batteries in series is 2 while, the number of batteries in parallel is 118, and the total number of batteries is 236. The total battery energy of 652.75 kW-h and the required capacity of the battery of 27197.9 Ah were established.

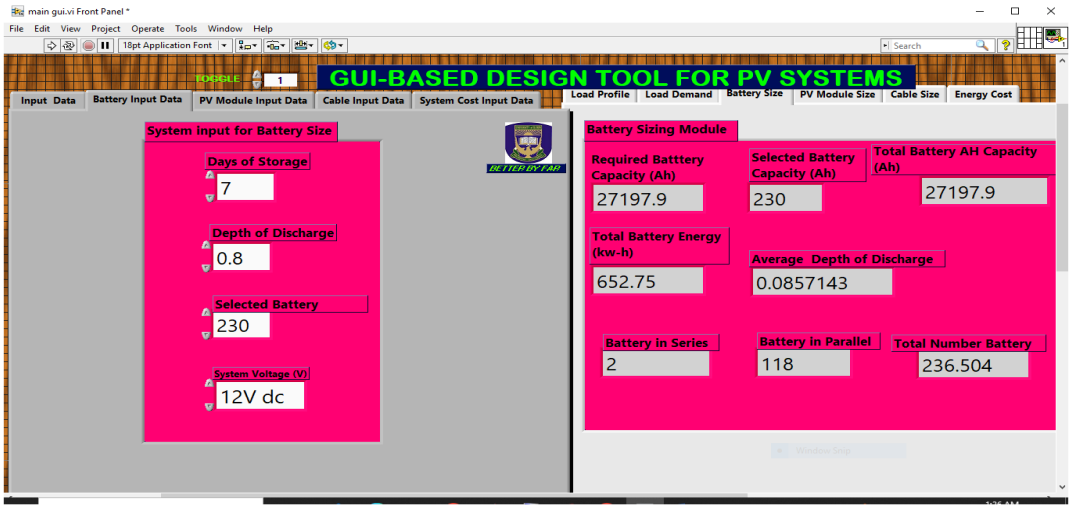

Figure 4.3: Simulated Battery Size Module

PV Components Sizing Module

The PV module size requires some data inputs for its development. The type of climate (tropical or moderate) under consideration determines the de-rating factor. For moderate weather, it 0.8 while for tropical weather, it is 0.9. Figures 4.4 and 4.5, show 40 and 45 number of solar panels for moderate and tropical climate conditions respectively.

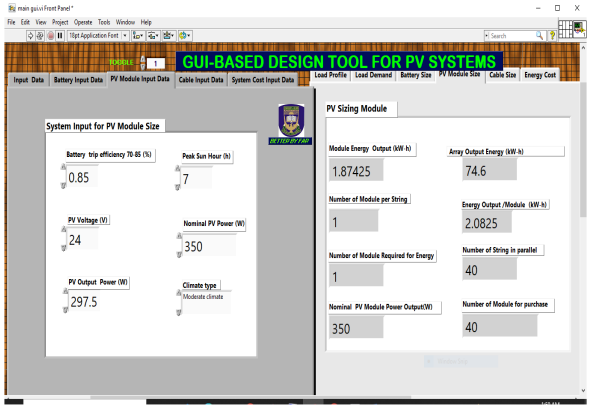

.4: PV Component Sizing Module for Moderate Climate

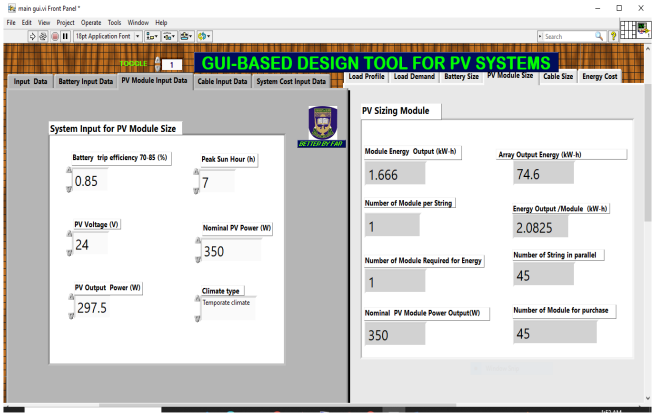

Figure 4.5: PV Component Sizing Module for Tropical Climat

5.0 CONCLUSION

This application software tool consists of 3 modules that are interactive and friendly to the users. The developed tool was evaluated to be robust and effective to provide timely solar PV sizing design via GUI.

ACKNOWLEDGEMENTS

The authors would like to acknowledge the personnel of the Department of Electrical & Electronics Engineering, University of Ilorin, Ilorin, Nigeria, who not only provided the enabling environment that helped to sustain our interest in this work but also made laudable criticism and observations in a Departmental seminar presentation.

REFERENCES

Aristide, Houngan & Anjorin, Malahimi & Obahoundje, Salomon & Sadate, Dankoro & Morel, Nepo & Vianou, Antoine & Gerald, Degan. (2018). TRNSYS Software Used for the Simulation of the Dynamic Thermal Behavior of a F2-building in Lokossa City in Benin Republic. 1-7. *10.23919/ICUE-GESD.2018.8635689.*

Bhandari, R., (2011). Electrification Using Solar Photovoltaic Systems in Nepal. *Applied Energy*, 88(2), 458-465.

HOMER Energy (2011). *Getting Started Guide for HOMER Legacy (Version 2.68),*

Homer Energy and National Renewable Energy Laboratory, Colorado. http://www.ecowrex.org/document/getting-started-guide-homer-legacy-version-268

Lalwani M., Kothari D.P., & Singh, M. (2010). Investigation of solar photovoltaic simulation softwares. Review article. *International Journal of Applied Engineering Research*, 3, 585-601.

Mert, G., (2019). Economic Feasibility of Solar Power Plants Based on PV Module with Levelized Cost Analysis, *Energy*, 171, 866-878.

Sharma, Dinesh. (2014). Review and analysis of solar photovoltaic software. *International Journal of Engineering and Technology.* 4. 725-731.

Oulis R.A., Tzelepis D., Konstantelos,I., & Booth, C., & Strbac, G. (2018). Design of a Hybrid AC/DC Microgrid Using HOMER Pro: Case Study on an Islanded Residential Application. *Inventions.* 3.55. *10.3390/inventions3030055*.

PAPER 213 – DEVELOPMENT AND PERFORMANCE EVALUATION OF A SCREW PRESS BRIQUETTING MACHINE

Mopah, E. J[1], Idah, P.A[1], Gbabo, A[1], Lawal, S. A[2]

[1]Department of Agricultural and Bioresources Engineering, Federal University of Technology, P.M.B 65, Minna, Niger State, Nigeria.
[2]Department of Mechanical Engineering, Federal University of Technology, P.M.B 65, Minna, Niger State, Nigeria.

ABSTRACT
Nigeria produces a massive amount of crop residue with high bulk volume and low density, most especially, rice husk. This low-density, high-volume agro residue is difficult to handle, transport, and store. A briquetting machine was developed and it was used to produce briquettes from rice husk. The feedstock was formulated for briquetting using rice husk of varying particle sizes (2mm, 3mm, 4mm), conditioned to varying moisture (10%, 12%, 14%), starch was obtained from the by-product of the rice colour cortex (rejections) and was processed into gel and added in proportion of 40, 50 and 60% by weight to 1 kg each of samples of rice husk as binder and was fed into screw press machine, which was operated at varying die diameter (30mm, 40mm, 50mm) and barrel temperature (100 ºC, 120 ºC, 150 ºC). The analysis of variance indicate that the machine produced rice husk briquette of 3.4087×10^{-4}kg/m^3 density, calorific value of 14.235 MJ/kg having a durability of 77.27% and hardness of 31.49HVN respectively, while the efficiency and capacity of the machine were 87 % and 192.74 kg/h, respectively. The machine would be useful for compacting quality solid fuel of crop residue that would aid handling, transportation and storage challenges.

KEYWORDS: Briquette; renewable resources; development and rejected rice powder.

1. INTRODUCTION
Energy is crucial for every country to achieve real economic and social growth (Deepak and Jnanesh, 2015). The increasing degradation of different non-renewable energy resources worldwide, as well as the greenhouse gas impact, demands increasing interest in sustainable energy. Briquetting is a solid fuel production technique that compacts biomass to produce fuel that may be used in both rural and semi-urban areas (Obi, 2015). Briquette has been proven to be a significant and cost-effective renewable energy source. In light of the technical considerations inherent in the technological adaption of this concept to local conditions, briquetting technology has been unable to achieve a solid footing in many developing nations (Ikubanni *et al.,* 2019). Hence, providing solutions to the operational challenges connected with this briquette technology and assuring the quality of the raw materials utilized are critical variables in determining its economic viability (Adeleke *et al.,* 2019). In view of the above, this work is organized into two main sections: the development of the machine and its performance evaluation.

2. MATERIALS AND METHODS
Design calculations for essential components were done to determine the strength of the materials and their appropriate sizes.

2.1 Machine design requirement and specification

The design of the machine was based on the following assumptions and requirements, namely:

a. The pressure adopted for the design is 30 MPa (Khurmi and Gupta (2008)
b. The minimum capacity of the machine (200 kg/hr)
c. The density of biomass 80 kg/m^3-130 kg/m^3 (Tumuluru, *et al* 2010)
d. The expected density of the briquettes ≤ 1000 kg/m^3 according to Khurmi and Gupta (2008)
e. The die diameter for briquettes (30 mm – 50 mm) and Length for the briquette (50 mm)

2.2 Machine design consideration

The machine designed for briquetting is a single extrusion heated-die screw-press type. The machine components are divided into the following units: (i) the feed unit, (hopper) (ii) compression/extrusion unit (Barrel, screw and dies) (iii) power unit and (iv) the support unit.

- Hopper volumetric flow

The hopper serves as a holding bin, to hold the required quantity of the feedstock expected to be processed into briquettes per batch (200 kg/hr).

Density is given as: $\rho = m/v$ (1)

The required density of the briquette is 1000 kg/m^3

$V_{fs} = \frac{200\ \text{Kg/hr}}{130\ \text{Kg/m}^3} = 1.54\ \text{m}^3/\text{hr}$

Since the machine is expected to produce 200 kg briquette per hour, the volume of feedstock required per hour i.e., Vol. flow rate (*VFR*) will be

$200\ (\text{kg/hr}) \times \frac{1.54\ (\text{m}^3)}{1000\ \left(\frac{\text{kg}}{\text{m}^3}\right)} = 0.31\text{m}^3/\text{hr}$

But Mass flow rate of the feedstock (MFR) = Density of biomass x VFR (2)

$\text{MFR} = 130\ \left(\frac{\text{kg}}{\text{m}^3}\right) \times 0.31\ \left(\frac{\text{m}^3}{\text{hr}}\right) = 39.99\ \text{kg/hr}$

In other to take care of contingencies, 40 kg is taken as the MFR and for convenience, the hopper will be refilled every 12 minutes i.e., 5 times within one-hour of operation. Therefore, the MFR per batch is:

$$= \frac{40}{5} = 8\ kg/batch$$

The volume of 40 kg biomass is $= \frac{8}{130} = 0.061\ m^3$ approximately 0.1m^3

The hopper volume from the design requirement and specification above (2.1b and c) was calculated as $1.54\text{m}^3/\text{hr}$ to accommodate this volume of biomass.

(b) Determination of the hopper radius

To design a hopper to accommodate the above volume of biomass the following considerations were made:

- The hopper is a cut-off cone (frustum) ii. The diameter of the neck of the hopper is equal to the diameter of the barrel.

The volume of a frustum as shown below is

$$V = \frac{\pi h}{3}(R^2 + Rr + r^2) \quad (3)$$

Where V is the volume of the required hopper (0.1m^3), h is the height taken to be 0.5 m ; Therefore, R is 0.5m.

(c) Volume of the barrel

The cylindrical barrel is made of mild steel pipe of thickness 3 mm, diameter (D) 100 mm and height (h) 680 mm.

The volume of the barrel V_b is given as,

$V_b = \pi r^2 h$ (4)

Where r =D/2 $V_b = 3.142 \times 0.05^2 \times 0.68\text{m} = 1.53 \times 10^{-3}\text{m}^3$

(d) Screw shaft diameter

The diameter of the shaft was computed using an established formula stated by Khurmi and Gupta (2005)

$$d^3 = \frac{16}{\pi s_s}\sqrt{(K_{bM_b})^2 + (KtM_t)^2} \quad (5)$$

Where, d = expected diameter of the shaft (m) ; Mt = torque moment (Nm); Mb = bending moment (Nm) ; d = diameter of the screw shaft (m) ; Kb = shock and fatigue factor applied to bending moment ; Kt = shock and fatigue factor applied to torsional moment

Ss = permissible shear stress of the shaft ; Shaft diameter = 4.95cm – 1.16cm = 3.79cm

The nearest commercially available shaft diameter is 40 mm in accordance with IS3688-1977. (Spotts, 1991). Therefore, a shaft of 40 mm diameter is appropriate for the screw.

(e) Determination of the Screw Flight (Blade Height)

The last turn must yield 9 cm^3 of biomass at 60 rpm.

Volume = Cross-sectional Area of the Barrel × Pitch length of the screw auger (6)

Assumed clearance = 0.05

Barrel diameter = 5 cm, the cross-sectional area will be 5 cm – 0.05 cm = 4.95 cm^2

where, *qm* = weight of the biomaterials to be briquetted (kg m^{-1}), *n* = number of screw rotations and dependent on the nature of the bio-material. For dense (coarse) material *n* = 0.8-1.5

(f) The prime mover

From the screw shaft flight design, the diameter of the last flight of the compression zone is shaft diameter (38 mm) plus the flight (19 mm) i.e. (38+19) 57 mm. We also know that the pressure required to compact biomass up to 1000 kg/m^3 is 30 MPa (Muhammad *et al*. 2016) the speed of the screw was calculated as 46.7 rpm.

The coefficient of friction (*f*) between the screw and feeding material was given by Khurmi, & Gupta, (2005) to be between 0.32-0.58. For this study, 0.58 was used.

$$P_{avg} = \frac{Work}{time} = \frac{Fcos\theta}{t} \quad (7)$$

Equation (7) can be rearranged in the form:

$$P_{avg} = Fcos\theta v_{avg} \quad (8)$$

The instantaneous power can be calculated from the expression:

$$P_{instanteneous} = Fcos\theta v \quad (9)$$

Equation (8) is a scalar product in a vector notation hence,

$$P = F_0' \cdot v \quad (10)$$

Therefore, the minimum power required to drive the auger is

$= 284.03 \times 8.77 = 2490.94\ Nms^{-1}$ Approximately 3.3 HP

The reduction ratio is 1:30 m ; The driver speed = 1,400/30 = 46.7rpm

(f) Die diameter

The die is the mold for the densified biomass. The die geometry is an important parameter to be varied for this research work. A solid shaft of mild steel of 70 mm diameter is machined to form three (3) different cylindrical shape dice of the same length with diameters 30 mm, 40 mm and 50 mm. The density of each of the briquettes extruded is dependent on the volume of each die.

Therefore, the volume of die is equal to the volume of the briquette as given in equation (4)

$$V_b = \pi r^2 h$$

(g) Machine description

The machine components are divided into the following units: (i) the feed unit, (ii) the compression/extrusion unit (iii) the power unit and (iv) the support unit. The machine designed for briquetting rice husk is a single extrusion heated-die screw-press type. The other parts of the machine are the motor, pulleys and belts, screw, barrel and briquette dies. Power is transmitted through direct coupling from the electric motor to the screw. The outer surface of the barrel is fixed with an electrical coil to heat the biomass between 100 - 150ºC. The temperature of the heater is maintained by the thermostat. The temperature is varied at 100ºC, 120ºC and 150ºC to help in melting the lignin in the biomass thereby binding the granules together.

- Choice and preparation of binders

Binders are substances capable of holding materials together by surface attachment based on their cohesive and adhesive properties. To achieve this work, 40%, 50% and 60% by weight of discoloured rice (reject) powder obtained from rice colour sorter was used as a binding agent in line with the works of Musa, (2007) and Olorunnisola, (2007). The powder was made into a gel and added to 1 kg of each of the samples of rice husks. The rejected rice gel in it require proportion 0.4, 0.5 and 0.6 by weight of the husk per sample

- Production of the briquette from residue

A measured quantity of rice husk with a varying moisture content of 10%, 12% and 14% was collected from the boiler husk room of the designated rice mill, sieved using 2mm, 3mm and 4mm particle size based on ASAE 424.1 (2003). For this work, starch was obtained from the by-product of the rice cortex (rejections), processed into a gel and added in a proportion of 40, 50 and 60% by weight to 1 kg each of samples of rice husks, mixed vigorously using a domestic blender (as feedstock mixer). The feedstock is fed into the screw press barrel to produce the desired briquettes. A measured quantity of the biomass feedstock was fed into the developed screw press machine, where briquettes were extruded in batches, cooled, packaged and stored for a while (1 week) before the quality test was conducted.

2.5 Machine extrusion efficiency and capacity performance evaluation

The extrusion efficiency performance evaluation reported by (Onu and Simonyan, 2015) in equation (11) below was used. The briquetting machine was subjected to the test. The input mass of the biomass and the output mass of the briquette formed was measured using a weighing balance. The processing time of the biomass to form a briquette was recorded for each test using the stopwatch. The biomass loss was calculated and results are shown in Table 6. The extrusion efficiency and the capacity performance were evaluated using equations 10, 11 and 12 below

Extrusion efficiency

$$O_E = \frac{100\ W_{oE}}{W_{Fs}}\ \% \qquad (11)$$

Note: O_E = *extrusion efficiency*, W_{oE} = *weight of extrude*, W_{Fs} = *weight of feed sample*

Machine capacity

$$MC\ (kg/h) = BFR \times 1\ hour \qquad (12)$$

However,

$$BFR = \frac{Average\ mass\ of\ output\ briquette\ (kg)}{Average\ processing\ time\ (s)} \qquad (13)$$

Note: MC and BFR are the machine capacity and briquette forming rate

2.6 Experimental design

Experiments were conducted using Taguchi method. The results are shown in Tables 1. The Taguchi experimental design layout and matrix specified 27 trials. The average of three samples per experiment was considered with the results shown in Table 1. Analysis of variance was carried out on the experimental data to show how the process and the feedstock parameters significantly affect the briquette quality indices using 5% significance level and the result for each of these quality indices.

➢ RESULTS AND DISCUSSION

The results obtained from various tests performed on the briquettes produced from the developed briquetting machine were analyzed.

(a) Briquette Quality Attributes

The results of the quality attributes (density, durability, hardness and calorific value) of the briquettes are shown in Table 1

Table 1: Briquette Quality Attributes

RUNS	D (10^{-4}kg/m^3)	DR (%)	CV (MJ/kg)	HD (HVN)
1	2.65	93	19.34	45.7
2	2.48	86	19.41	45.1
3	2.48	79	19.21	44.9
4	2.30	100	21.35	46.2
5	2.48	86	21.43	45.9
6	2.83	69	21.01	46.0
7	3.01	76	19.83	46.4
8	2.48	93	19.35	46.8
9	2.83	94	19.72	46.5
10	4.28	60	16.13	40.6
11	3.38	53	16.06	41.3
12	4.08	49	16.45	40.9
13	2.79	50	23.10	47.1
14	2.79	64	22.95	46.9
15	2.69	52	23.20	47.8
16	1.89	63	17.61	46.8
17	1.69	65	17.44	46.5
18	1.49	73	17.49	46.3
19	2.80	89	17.96	37.4
20	2.87	76	17.16	37.3
21	2.87	98	17.45	36.9
22	2.48	95	18.14	35.7
23	2.36	92	18.42	35.5
24	2.23	94	18.72	35.7
25	2.04	91	15.50	33.8
26	1.91	47	15.25	33.6
27	2.04	88	15.04	33.8
Average	**2.60**	**76.85**	**18.69**	**42.13**

Note: D-Density, DR-Durability, CV-Calorific value, HD-Hardness

(b) Analysis of variance

Tha analysis of variance of the responses showed that the process and the feedstock parameters (die diameter (DD), temperature (TT), moisture content (MC), particle size (PS) and binder ratio (BR)) significantly affect the briquette quality indices. This analysis was conducted using 5% significance level, the result for each of these quality indices is as presented below:

i. Density of briquette

Table 2: ANOVA for the results of density of briquette

Factor	DOF	SS	MS	F	p-value
DD	2	0.68	0.34	8.62	0.439
MC	2	4.06	2.03	51.73	0.002
PS	2	2.23	1.12	28.44	0.052
TT	2	2.33	1.17	29.75	0.044
BR	2	0.18	0.09	2.33	0.805
Error	18	0.71	0.04		
Total	26	10.19	0.39		

The ANOVA for density of the briquette showed that, moisture content, particle size and temperature were statistically significant at 5%. The result in table 1 is in conformity with the work carried out by Waweru and Chirchir (2016) which F-value for moisture content was 49.00. In transport, handling and storage briquettes, high density and mechanical strength are desirable (Sahin, 1998). The density of biowaste briquettes depends on the

density of the original biowaste, the pressure, temperature and time of densification. The higher the density, the higher is the energy.

ii. Durability of briquette

Table 3: ANOVA for the results of durability of briquette

Factor	**DOF**	**SS**	**MS**	**F**	**p-value**
DD	2	4812	2406	142.33	0.439
MC	2	420.5	210.26	12.44	0.002
PS	2	922.7	461.35	27.29	0.052
TT	2	698.7	349.35	20.67	0.044
BR	2	571.2	285.60	16.89	0.805
Error	18	304.3	16.91		
Total	26	7729.4	297.29		

The ANOVA for durability of the briquette shown in Table 2 indicates that die diameter was statistically significant at 5%, followed by particle size. Briquettes with high durability are desirable to minimise breakage and dust formation during transporting and conveying. Though, there are no recommended standards for biomass briquettes, other researchers (Haykiri-Acma *et al*., 2013; Antwi-Boasiako & Acheampong, 2016) have reported that durability of 80 - 90 % or over 90 % is required for better handling and transportation.

iii. Hardness of briquette

Table 4: ANOVA result for the result of hardness of briquette

Factor	DOF	SS	MS	F	p-value
DD	2	593.53	296.77	3604.79	0.000
MC	2	15.81	7.91	96.02	0.757
PS	2	54.96	27.48	333.79	0.368
TT	2	22.03	11.02	133.79	0.677
BR	2	0.05	0.03	0.33	0.999
Error	18	1.48	0.08		
Total	26	687.81	26.45		

The ANOVA for hardness of the briquette (Table 4) showed that, die diameter was statistically significant at 5%. Ndindeng *et al*., (2015) reported that briquettes should be produced using fine and medium-sized particles, since large-particle briquettes crumbled when they were ejected from the machine due to the elastic nature of the husk. Fine particles usually absorb more moisture than large particles and, therefore, undergo a higher degree of conditioning (hardness) (Kaliyan and Morey, 2009).

iv. Calorific value of briquette

Table 5: ANOVA for the results of calorific value of briquette

Factor	DOF	SS	MS	F	p-value
DD	2	41.33	20.67	77.48	0.018
MC	2	67.41	33.71	615.68	0.001
PS	2	29.13	14.57	266.05	0.067
TT	2	5.83	2.92	53.25	0.61
BR	2	0.12	0.06	1.13	0.99
Error	18	0.99	0.06		
Total	26	144.69	5.57		

The ANOVA for calorific value of the briquette (Table 5) indicated that, die diameter and moisture content were statistically significant. The calorific value of briquettes is one of the most influential factors affecting the burning rate of a briquette. The calorific value of rice husk briquette was in the range of 15.04 to 23.2 MJ/kg. This was also in line with previous researchers Oladeji and Oyetunji (2013), who reported calorific values of 2,765 kJ/kg and 17,348 kJ/kg for cassava and yam peels briquettes.

3.3 Performance evaluation of the machine

The efficiency and capacity of the machine were determined through the experimental tests as shown in Table 6.

Table 6: Performance evaluation of the briquetting machine

Run	Pt (s)	Mi (kg)	Mo (kg)	Loss (kg)
1	12	0.8	0.69	0.11
2	13	0.8	0.69	0.11
3	12	0.8	0.69	0.11
4	14	0.8	0.69	0.11

5	12	0.8	0.69	0.11
6	13	0.8	0.69	0.11
7	12	0.8	0.69	0.11
8	12	0.8	0.69	0.11
9	14	0.8	0.68	0.12
10	14	0.8	0.68	0.12
11	13	0.8	0.68	0.12
12	13	0.8	0.68	0.12
13	14	0.8	0.68	0.12
14	15	0.8	0.68	0.12
15	13	0.8	0.68	0.12
16	12	0.8	0.68	0.12
17	12	0.8	0.68	0.12
18	12	0.8	0.69	0.11
19	14	0.8	0.69	0.11
20	12	0.8	0.69	0.11
21	13	0.8	0.69	0.11
22	12	0.8	0.69	0.11
23	11	0.8	0.69	0.11
24	13	0.8	0.69	0.11
25	12	0.8	0.69	0.11
26	12	0.8	0.69	0.11
27	12	0.8	0.69	0.11
Average	**13**	**0.8**	**0.69**	**0.11**

Note: Pt-Processing time; Mi-Mass of biomass input; Mo- Mass of briquette output

From Table 6, the average mass of the briquette formed was 0.69 kg while the loss was 0.11 kg. Also, the average processing time for the machine to transform from biomass to solid fuel (briquette) was 13 seconds. The efficiency of the machine was calculated to be 87% and the capacity of the machine was 192.74kg/h which is closely related to the established capacity (200 kg/h) in our machine design requirement and specification (section 2.1). The machine production capacity and efficiency are greater than 122.928 kg/h and 85.7%, and 43 kg/hr reported by Pelumi *et al., (*2019) and Obi *et al*., (2013) respectively. The findings of this study has shown that composite briquette of rice husk would produce good biomass solid fuel. There is a great tendency that the briquettes are environmentally friendly based on the elemental compositional values of the briquette.

➢ CONCLUSION

The press screw machine attained a high production capacity of 192.74 kg/h which makes it suitable for small-scale entrepreneurs in rural areas. All the briquettes extruded were well-dense, hard, durable free of damage and had good geometry for convenience which implies that they are convenient for handling, storage and transportation for further use with desirable quality.

REFERENCES

Adeleke, A.A. Odusote, J.K. Malathi, M. Lasode, O.A. and Paswan. D. Influence of torrefaction on lignocellulosic woody biomass of Nigerian origin, J. of Chem. Tech. and Metall. 2019; 54(2): 274

Antwi-Boasiako, C.; Acheampong, B. Strength properties and calorific values of sawdust-briquettes as wood-residue energy generation source from tropical hardwoods of different densities. Biomass-Bioenergy 2016, 85, 144–152.

ASAE, S269.4 (2003) – Cubes, pellets and crumbles – definitions and methods for determining density, durability and moisture content. 567 – 569. St. Joseph, Mich.: U.S.A

Deepak K.B. and Jnanesh, N.A. (2015). Investigation of areca leaves as a biomass fuel by the method of briquetting. International Journal of Mechanical Engineering. 3(6) 16-21.

Haykiri-Acma, H. Yaman, S. Kucukbayrak, S. "Production of biobriquettes from carbonized brown seaweed, Fuel Process". Technol. 106 (2013) 33–40.

Ikubanni, P.P. Omololu, T. Ofoegbu, W. Omoworare, O. Adeleke, A.A. Agboola, O.O. and Olabamiji. T.S. (2019). Performance Evaluation of briquette Produced from a Designed and Fabricated Piston-Briquetting Machine. Intl. J. of Eng. Res. and Tech.; 12(8): 1227-1238

Kaliyan, N. and Morey, R. V. (2009), "Factors affecting strength and durability of densified biomass products" Biomass and Bio-energy 33, 337-359

Khurmi, R. S., & Gupta, J. K. (2005). a Textbook of Machine Design,. Eurasia Publishing Home (PVT) Ltd. Pp

1-1251

Muhammad, S.N. Muhammad, A. A. Abdul, N. and Anjum M. (2016). "Design and Fabrication of Biomass Extruder of 50 mm Diameter Briquette Size" Innovative Energy & Research.

Musa, N.A. (2007). "Comparative Fuel Characterization of Rice husk and Groundnut shell Briquettes". NJRED. 6(2), pp. 23-26

Ndindeng, s.a., manful, j.t., futakuchi, k., mapiemfu-lamare, d., akoa-etoa, j.m., bigoga, j., Graham-acquaah, s. And moreira, j. 2015. A novel artisanal parboiling technology for rice processors in sub-Saharan Africa. Food Sci Nutr. (under review)

Obi, O.F. (2015) "Evaluation of the effect of palm oil mill sludge on the properties of sawdust briquette,

Renewable and Sustainable Energy Reviews". 52 1749-1758.

Obi, O.F.; Pecenka, R.; Clifford, M.J. (2013). A Review of Biomass Briquette Binders and Quality Parameters. Energies, 15, 2426

Oladeji, J. T., and Oyetunji, O. R. (2013). Investigations into Physical and Fuel Characteristics of Briquettes Produced from Cassava and Yam Peels. Journal of Energy Technologies and Policy, 3(7), 40 -47

Olorunnisola, A. (2007) 'Production of fuel briquetting from wastepaper and coconut admixtures', Agricultural Engineering Journal, Vol. 9, No. 6, pp.1–15

Onu olughu, Onu & Simonyan, Kayode. (2015). African Journal of Agricultural Research Performance evaluation of a motorized ginger juice expression machine. African Journal of Agricultural Research. 10. 3662-3670. 10.5897/AJAR2015.9928.

Pelumi, I. P. Tobiloba, O. Wallace, O. Oluwatoba, O. Akanni, A. A., Oluwole A. O and Sola. O. T. (2019) "Performance Evaluation of Briquette Produced from a Designed and Fabricated Piston-Type Briquetting Machine". International Journal of Engineering Research and Technology. ISSN 0974-3154, Volume 12, Number 8, pp. 1227-1238

Sahin, A. 1998) "Evaluation of biomass residue 1. Briquetting waste paper and wheat straw mixtures, Fuel Process". Technol. 55 (175–183.

Waweru, J. and Chirchir D. K. (2017). "Effect of the Briquette Sizes and Moisture Content of Combustion Characteristics of Composite Briquettes" *IJISET –International Journal of Innovative Science, Engineering and Technology, Volume 4, Issue, 102-111*

PAPER 214 – CONSOLIDATION CHARACTERISTICS OF ROAD SOILS AT DIFFERENT COMPACTION ENERGIES AND MOISTURE

S. T. Oyewo[1*], Y. A. Jimoh[2], O. O. Adeleke[3], O.J. Olatoyan[4], and O. K. Olayanju[5]

[1,4,5] Department of Civil Engineering, Redeemers University, P.M.B 230, Ede, Nigeria.
[2,3] Department of Civil Engineering, University of Ilorin P.M.B 1515, Ilorin, Nigeria.
*Email: oyewos@run.edu.ng

ABSTRACT

Road construction material samples were sourced from two borrows pits at Ogbondoroko and Ogele in Kwara State, Nigeria. The samples were subjected to conventional roadwork tests according to British International testing procedure BS1377:2000 and Nigerian General Specification for Road and Bridges (1997). The tests include index properties, compaction, and consolidation (when saturated). The moisture contents for the Ogbondoroko soil ranged from 3.47 to 21.10% and Ogele from 6.79% to 20.65%. Ogbondoroko road Soil Gs = 2.47, PL = 23%, LL = 37%, Ip = 14% GI = 1; and the soil was grouped as A-2-6(1) according to AASHTO (M145-91) and was classified as a good subgrade material. Ogele Soil has Gs = 2.53, PL = 18%, LL = 36%, Ip = 18% with GI = 0 and was grouped as A-2-6(0), the soil was classified as a good subgrade material. The compaction characteristics are 15% and 6% Optimum Moisture Content (OMC) while the Maximum Dry Density (MDD) are 1.58g/cm^3 and 1.62g/cm^3 for the Ogbondoroko and Ogele soil samples respectively. The consolidation characteristics of the selected soil samples for Ogbondoroko: Cc = 0.055, Cv = 2.08mm^2/minutes, av = 0.0023, Mv = 0.0014, t90 = 163.3 minutes, e_o= 0.674, e_f = 0.573 while for Ogele: Cc = 0.20 , Cv = 1.77mm^2/minutes, av = 0.062, Mv = 0.039, t90 = 191.9 minutes, e_f = 0.573, e_o = 0.674. It is concluded that the soils of the two borrow pits are not suitable as road construction material and should be delisted for road works development in the State, except as subgrade.

***KEYWORDS*:** consolidation characteristics, road soils, moisture contents, quality control, pavement failure, stability

1.0 INTRODUCTION

Soil consists of the different phases of nature; solid, liquid, and gas, and whose characteristics depend on the interactive placement of the phases when stress is applied. The particulate solid medium forms the real properties in bearing the load, which is dependent on the type of mineralogy of the soil skeleton, the surrounding fluid, and open spaces (voids). The physical structure, chemistry, and properties of the minerals present in the soil structure constitute other influences on the general soil behavior under load. The compressibility of soil is termed consolidation as a saturated soil mass subjected to a compressive force, and its volume decreases. The strength of soil is determined by compacting energy, degree of compaction, and consolidation related to prevailing moisture content. Moisture content influences the physical properties of soil, such as weight, density, viscosity, and conductivity, so it is important to establish the amount of moisture content present in the soil.

Pavement is a typical structure of various layers resting over the soil, either in embankment or cutting, meant to sustain vehicular or other movements. The foundation of the road is the subgrade which can be made of a remaining bed of cuttings or on top of the fill of embankments. Subgrade soil is an integral part of the road, which provides support to the pavement structure as the foundation and for all the imposed loads from traffic, including the overburdened layers of surface, base, and subbase. The four distinct layers of the road are termed (bottom to top) sub-base, base (also known as road base), binder course (base course), and surface course (wearing course). As the stress transmitted through the road structure from the vehicles above spreads and lessens with depth, more substantial and more expensive materials are needed in the upper levels. Thus material layers are usually arranged within a pavement structure in order of descending load-bearing capacity, with the highest load-bearing capacity material (and most expensive) on the top and the lowest load-bearing capacity material (and least expensive) on the bottom (Pavement Interactive, 2008). The consolidation test is one of the quality control and assurance tests of materials used for road construction, and any inadequacies in the quality of the material will result in pavement failure. Also, consolidation is significant in analyzing the stability of embankment and pavement structures. Pavement design aims to provide a structural and economical combination of materials to serve the intended traffic volume in a given climate over the existing soil conditions and for a specified time interval.

The study aims to determine the suitability of burrow pit materials for road construction. The study's specific objectives are to i. Determine the consolidation characteristics of road soils at different compacting energies and moisture and ii. Characterize the effectiveness of the soils for road construction.

2.0 THEORETICAL ANALYSIS

The load was converted to the corresponding pressure in kN/m^2 using Eq. 1:

$$P = wg/A \quad (1)$$

Where P is pressure in kN/m^2, g is the acceleration due to gravity, w is the weight in kg, and A is the area in square meters.

The final void ratio corresponding to the complete swelling condition was determined using Eq. 2:

$$et = (Gs/\gamma d) - 1 \quad (2)$$

Where et = final void ratio of the soil sample after consolidation, Gs = the specific gravity of the soil, and γd is the max dry density of the soil.

The change in void ratio (Δe) was calculated using Eq. 3:

$$\Delta e = ((1+e_t)/Ht)) \Delta H \quad (3)$$

Where e_t is the final void ratio after consolidation, Ht is the final thickness after consolidation, ΔH is the change in dial gauge reading for each pressure increment at 24hrs.

Thus, the void ratio (e) under each pressure increment was calculated from Eq. 4 after swelling.

$$e = e_t + \Delta e \quad (4)$$

The curve between stress ($\bar{\sigma}$) (as abscissa) and void ratio (e) (as ordinate) for the determination of the Coefficient of compressibility (av) and Coefficient of volume change (mv) was plotted. Similarly, the graph of log$\bar{\sigma}$ (as abscissa) and void ratio e (as ordinate) was plotted to determine the Compression Index (Cc) using Eq.5.

$$Cc = -de/(\log_{f0}\ \bar{\sigma}) \quad (5)$$

Where de is the change in void ratio and log $\bar{\sigma}$ is the log of stress for the soil sample. The corresponding mathematical definitions of the change in void ratio and stress are given as Eq. 6 and 7 respectively.

Coefficient of compressibility (av),

$$av = \Delta e/\Delta\sigma \quad (6)$$

Where Δe is the change in void ratio and Δσ is the change in stress

Coefficient of volume change (Mv)

$$Mv = av/(1 + e) \quad (7)$$

Where av is the Coefficient of compressibility and e is the void ratio of the soil sample

Coefficient of consolidation (C_V) was computed using Taylor's √t model: for each load increment, √t was plotted (as abscissa), and the dial gauge reading at each load increment (as ordinate). The value of T90 (time at 90% degree of consolidation) from the plot was determined from which Coefficient of consolidation(C_V) was obtained for soil samples at (35kg ≡ 77.68kN/m^2) percentage of water content using the square-root of time fitting method in Eq. 8.

$$C_V = T_{90}H^2/t_{90} \quad (8)$$

Where C_V= coefficient of consolidation (mm^2/minutes), T_{90} = 0.8480 time factor of 90% consolidation, H = height of the specimen (mm), and t_{90} = is the time taken to reach 90% degree of consolidation.

Imputing T_{90} = 0.8480 into Eq. 8 give rise to Eq. 9 and t_{90} was determined from the test curve.

$$C_V = 0.848H^2/t_{90} \quad (9)$$

Model in Eq.10 that was developed by Terzaghi and Peck (1967) was used to predict compression index, and the value was compared with that observed in the laboratory.

$$Cc = 0.009(w_L - 10) \quad (10)$$

Where Cc is the compression index and W_L is the liquid limit

3.0 MATERIALS AND METHOD

Road construction materials were sourced from two borrows pits at Ogbondoroko and Ogele, Kwara State Ministry of Works construction sites located around Ilorin township, in the North-central geo-political zone of Nigeria. The open pit method was used by digging at a depth of 1.2m, and disturbed soil samples of 100kg were collected inside sealed bags from each of the burrow pits. Soil samples were taken at the four edges and the center of the borrow pit and put inside sealed bags to prevent moisture. The test was carried out on disturbed soil samples.

3.1 METHODOLOGY

The laboratory tests conducted on the samples were: the Atterberg limits test, specific gravity test, sieve analysis test, moisture content test, compaction test, and consolidation test as specified by the British International testing procedure BS1377:2000 and Nigerian General Specification for Road and Bridges (1997).

3.2 APPARATUS AND EQUIPMENT SET UP

Consolidometer accessories include consolidation ring, porous stones, consolidation cell, dial gauge, loading devices. Consolidometer accessories testing procedure include: positioning the dial gauge, measurement of weight, height, diameter of confining ring, measurement of height and diameter of aluminum sample, trimming specimen into the confining ring, take water content measurement from trimming and weighing soil sample and confining ring.

3.3 LABORATORY INVESTIGATION

The samples were subjected to all conventional tests for road works which include index, compaction, and consolidation (when saturated) test. The characteristics determined were: specific gravity, maximum dry density, stress, log of stress, initial void ratio, final void ratio, coefficient of compressibility (av), coefficient of volume change (mv), coefficient of consolidation (Cv) and compression index (Cc).

4.0 RESULTS AND DISCUSSION

Tables 1 and 2 are the consolidation result and void ratio respectively for the Ogbondoroko site. The result of the consolidation shows that at 2hrs for 5kg loading, the soil was stable throughout; at 1hr for 10kg and 15kg loading, the soil was stable throughout; at 4mins for 35kg loading, the soil was stable and at 0sec up to 24hrs, the soil was stable. At 35kg of loading, the soil was stable for 24hrs, the final void ratio was 0.573, and the initial void ratio was 0.674, which shows that the void ratio reduced at 35kg loading for 24hrs. The final void ratio corresponding to swelling, the change in the void ratio (after swelling), and the void ratio was calculated for each pressure increment at 24hrs using Eq. 2, 3 and 4 respectively.

Table 3 is the consolidation result for Ogbondoroko soil showing the square root time at 35kg loading. This shows the dial gauge reading for the pressure loading of 35kg was constant, which shows that there was no compression throughout the 24hrs. This study used Table 3 to plot the graph of dial guage reading against square root time and the Coefficient of consolidation was determined using Eq. 9.

Tables 4 and 5 are the consolidation result and void ratio respectively for Ogele site. This table showed that the soil was stabled between 8hrs to 24hrs loading for 25kg, 30kg and 35kg respectively. The final void ratio was 0.573, and the initial void ratio was 0.674, showing that the void ratio reduced 35kg loading between 8hrs to 24hrs. The final void ratio corresponding to swelling, the change in the void ratio (after swelling) and the void ratio for each pressure increment at 24hrs were calculated using Eq. 2, 3 and 4 respectively.

Table 6 of the consolidation result for Ogele soil shows the square root time at 35kg loading. The study used Table 3 to plot the graph of dial guage reading against square root time and Coefficient of consolidation was determined using Eq. 9.

TABLE 1: Consolidation of Ogbondoroko Soil

Consolidation of Ogbondoroko Soil								
Time	Sqrt Time (Min)	5kg	10kg	15kg	20kg	25kg	30kg	35kg
0sec	0.00	0.00	58.90	108.20	131.90	149.00	160.00	163.00

5secs	0.28	5.00	85.00	115.00	132.00	149.00	161.00	163.00
10secs	0.41	7.00	90.00	118.00	134.00	149.50	161.00	163.00
15secs	0.50	8.00	92.00	119.00	135.00	149.50	161.20	163.00
30seccs	0.71	10.00	93.00	121.00	137.00	150.00	161.20	163.00
1mins	1.00	20.00	95.00	122.00	140.00	150.70	161.50	163.00
2mins	1.41	30.00	101.00	124.00	141.00	151.30	162.00	163.00
4mins	2.00	36.00	103.00	127.50	143.00	153.20	163.00	163.00
8mins	2.82	54.50	105.00	129.00	145.00	155.00	163.00	163.00
15mins	3.87	58.50	107.00	130.20	146.50	156.50	163.00	163.00
30mins	5.48	58.50	107.90	131.00	148.00	157.90	163.00	163.00
1hr	7.75	58.80	108.00	131.90	148.50	158.50	163.00	163.00
2hrs	10.95	58.90	108.00	131.90	149.00	159.00	163.00	163.00
4hrs	15.49	58.90	108.20	131.90	149.00	159.50	163.00	163.00
6hrs	18.97	58.90	108.20	131.90	149.00	160.00	163.00	163.00
8hrs	21.91	58.90	108.20	131.90	149.00	160.00	163.00	163.00
24hrs	37.95	58.90	108.20	131.90	149.00	160.00	163.00	163.00

TABLE 2: Void Ratio of Ogbondoroko Soil

Observation of Ogbondoroko soil						Calculation of Ogbondoroko soil		
Vertical Load (kg)	Vertical Load (kN)	Stress kN/m^2	Log kN/m^2	Dial reading at 24hrs	Change in Thickness (ΔH)mm after consolidation	Thickness of soil (H)mm after consolidation	Δe	e
0.00	0.00	0.00	0.00	0.00		20.00		0.674
5.00	49.05	11.10	1.05	58.90	0.589	19.41	0.0507	0.623
10.00	98.10	22.19	1.35	108.20	0.493	18.92	0.0421	0.615
15.00	147.15	33.29	1.52	131.90	0.237	18.68	0.0206	0.594
20.00	196.20	44.39	1.65	149.00	0.171	18.51	0.0146	0.588
25.00	245.25	55.49	1.74	160.00	0.110	18.39	0.0095	0.583
30.00	294.30	66.58	1.82	163.30	0.330	18.37	0.0028	0.576
35.00	343.35	77.68	1.89	163.30	0.000	18.37		0.573

Figure 2a shows the void ratio against stress for Ogbondoroko burrow pit, while Figure 2b shows the void ratio plotted against log of stress. The graph in Figure 2a shows a linear graph which is the relationship between void ratio and the stress. The slope of this graph is the coefficient of compressibility (av) which is 0.0023. The value gotten for coefficient of compressibility was substituted into Eq. 7 to calculate the coefficient of volume change (Mv) which is 0.0014.The rsquare value for the graph is 0.8192 which is close to 1, this shows that there is a strong correlation between the void ratio and the stress of the soil. The graph in Figure 2b shows a linear graph which is the relationship between void ratio and the log of stress. The slope of this graph is the compression index (C_c) which is 0.055. The rsquare value for the graph is 0.9813 which is close to 1, this shows that there is a strong correlation between the void ratio of the soil and the log of stress. Eq.10 was used to predict compression index (Cc) as 0.243.

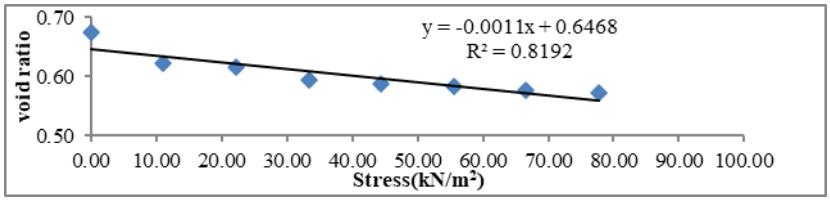

Fig. 2a: Void ratio of Ogbondoroko against the stress

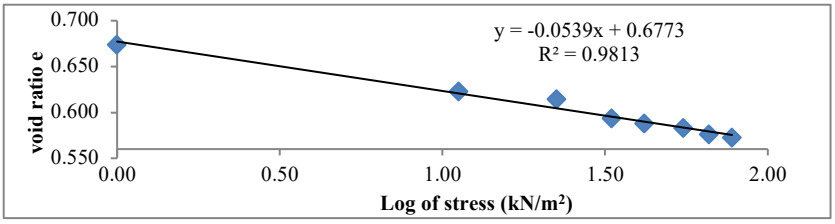

Fig. 2b: Void ratio of Ogbondoroko against the log of stress

TABLE 3: Square root time for Ogbondoroko Soil

Ogbondoroko	
Sqrt Time (Min)	35kg
0.000	163.300
0.288	163.300
0.409	163.300
o.498	163.300
0.706	163.300
1.000	163.300
1.414	163.300
2.000	163.300
2.828	163.300
3.873	163.300
5.477	163.300
7.745	163.300
10.951	163.300
15.491	163.300
18.971	163.300
21.910	163.300
37.947	163.300

The graph in Fig 3A shows a linear graph which is the relationship between dial guage reading and square root of time. t_{90} was determined from the graph i.e. the time taken to reach 90% consolidation which is 163.3 and t_{90} was inputted into Eq. 9 to determine coefficient of consolidation (C_v) which is 2.08mm^2/minute.

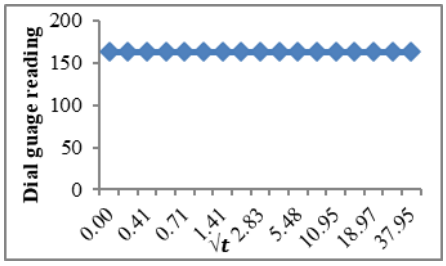

Fig.3A: Dial Guage reading against $\sqrt{t}$ for Ogbondoroko Soil

Table 4: Consolidation of Ogele Soil

Consolidation of Ogele Soil								
Time	Sqrt	5kg	10kg	15kg	20kg	25kg	30kg	35kg
0sec	0.00	0.00	60.50	117.50	146.00	164.20	178.50	188.00
5sec	2.24	52.00	95.00	125.00	147.00	164.50	179.00	188.50
10sec	3.16	58.00	100.00	128.00	148.00	165.50	179.00	188.90
15sec	3.87	59.00	102.00	130.00	148.00	166.00	179.50	188.90
30sec	5.48	60.00	108.00	135.00	148.00	167.00	179.80	188.90
1min	7.75	60.00	110.00	137.00	150.00	167.50	180.00	189.00
2min	10.95	60.00	111.50	139.00	152.00	167.50	180.00	189.00
4min	15.49	60.00	114.50	141.00	155.00	168.00	180.00	189.00
8min	21.91	60.00	115.50	142.50	159.00	170.10	180.50	189.10
15min	30.00	60.00	116.00	143.50	161.00	172.00	181.00	189.50
30min	42.43	60.00	116.50	144.50	162.20	174.10	182.10	190.00
1hr	60.00	60.00	116.50	145.00	163.20	175.30	183.00	190.80
2hrs	84.58	60.00	117.00	145.00	163.50	176.10	184.00	191.90
4hrs	120.00	60.50	117.00	145.50	164.00	177.00	184.90	193.50
6hrs	146.97	60.50	117.20	146.00	164.20	177.50	185.50	195.00
8hrs	169.71	60.50	117.50	146.00	164.20	178.50	188.00	198.00
24hrs	293.94	60.50	117.50	146.00	164.20	178.50	188.00	198.00

Table 5: Void Ratio of Ogele Soil

Observation of Ogele Soil						Calculation of Ogele soil		
Vertical load (kN)	Vertical Load (kN)	Stress kN/m^2	Log kN/m^2	Dial Reading at 24hrs	Change in Thickness (mm) after consolidation	Thickness of soil(H)mm after consolidation	Δe	e
0.00	0.00	0.00	0.00	0.00		20.00		0.674
5.00	49.05	11.10	1.05	58.90	0.59	19.41	0.051	0.623
10.00	98.10	22.19	1.35	108.20	0.49	18.92	0.042	0.615
15.00	147.15	33.29	1.52	131.90	0.24	18.68	0.021	0.594
20.00	196.20	44.39	1.65	149.00	0.17	18.51	0.015	0.588
25.00	245.25	55.49	1.74	160.00	0.11	18.39	0.010	0.583
30.00	294.30	66.58	1.82	163.30	0.33	18.37	0.003	0.576
35.00	343.35	77.68	1.89	163.30	0.00	18.37		0.573

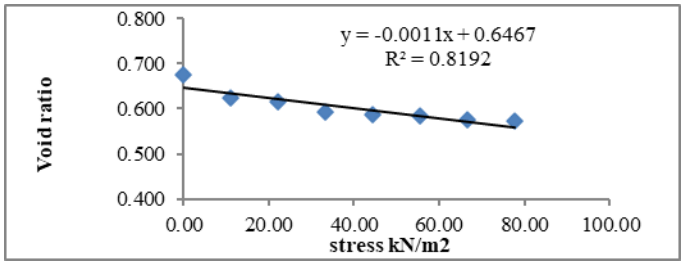

Fig 5A: Void Ratio against Stress of Ogele Soil

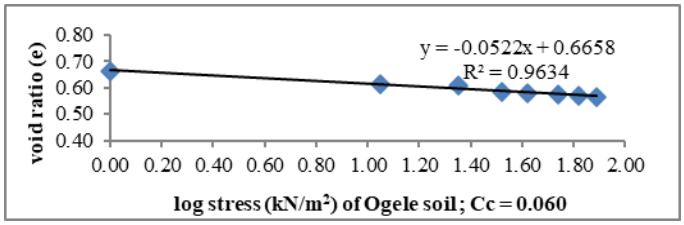

Fig 5B: Void Ratio against log Stress of Ogele Soil

Figure 5a shows the void ratio against stress for Ogele burrow pit while Figure 5b shows the void ratio plotted against stress for Ogele burrow pit. The graph in Figure 5a shows a linear graph which is the relationship between void ratio and the stress. The slope of this graph is the coefficient of compressibility (av) which is 0.062. The rsquare value for the graph is 0.8192 which is close to 1, this shows that there is a strong correlation between the void ratio and the stress of the soil. The value gotten for coefficient of compressibility was substituted into Eq. 7 to calculate the coefficient of volume change (Mv) which is 0.039.The graph in Figure 5b shows a linear graph which is the relationship between the void ratio and log of stress of Ogele soil. The slope of this graph is the compression index (C_C) which is 0.20. The rsquare value for the graph is 0.9634 which is close to 1, this shows that there is a strong correlation between the void ratio of the soil and the log of stress. The compression index (Cc) is 0.234 from Eq. 10.

Table 6: Coefficient of Consolidation for Ogele Soil

Ogele	
Sqrt Time(min)	35kg
0.00	188.00
0.29	188.90
0.41	188.90
0.50	188.90
0.71	189.00
1.00	189.00
1.41	189.00
2.00	189.00
2.83	189.10
3.87	189.50
5.48	190.00
7.75	190.80
10.95	191.90
15.49	193.50
18.97	195.00
21.91	198.00

37.95	198.00

The graph in Fig 6 shows a linear graph which is the relationship between dial guage reading and square root of time. t_{90} was determined from the graph as 191.9 and t_{90} was inputted into Eq. 9 to determine Coefficient of consolidation (C_V) which is 1.77mm^2/minute.

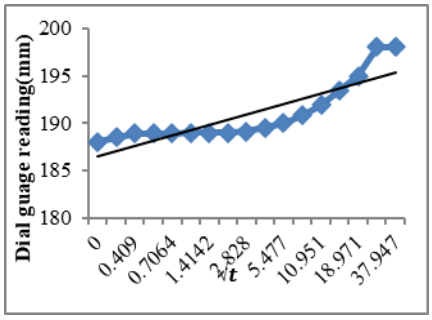

Fig.6: Coefficient of Consolidation for Ogele Soil

5.0 CONCLUSION

Road construction materials were sourced from Kwara State Ministry of Works borrows pits at Ogbondoroko, and Ogele. The consistency limit parameters of the samples from the two locations are for Ogbondoroko road Soil: P.L. is 23%, L.L. is 37%, Ip is 14%. The Group index (GI) = 1. The soil was grouped as A-2-6(1) according to AASHTO (M145-91) and the soil was classified as good subgrade material. The corresponding results for Ogele Soil: PL = 18%, LL = 36%, Ip = 18% and GI = 0. The soil was grouped as A-2-6(0) and classified as a good subgrade material. The soil is suitable as a good subgrade road construction material but not as a subbase or base material. Good quality road construction materials in the two burrow pits have been exhausted; as such, the sites should be delisted for road works development in the State, except as subgrade.

ACKNOWLEDGEMENT

I am very grateful to God almighty, to my supervisor Prof. Y.A Jimoh during my master programme for his fatherly approach, help and advice during the this project. My appreciation also goes to the Head of Departments of Engineering, lecturers and all staffs of Civil Engineering Department for their moral support, Mr femi and all Civil Engineering laboratory instructors of the University of Ilorin for their assistance during the practical work.

REFERENCES

AASHTO (1986) *Guide for design of pavement structures*, American Association of State Highway and Transportation Officials, Washington, DC**.**

AASHTO (1993) *Guide for design of pavement structures* – Google Books, American Association of State Highway and Transportation Officials, Washington , DC**.**

AASHTO M145-91 (1991) *Specification for classification of Soils and Soil-Aggregate Mixtures for Highway Construction Purposes.* Washington DC: American Association of State Highway and Transportation Officials.

Ahmed, M.Y, Nury A.H.,Islam F. and Alam, M.J.B.,(2012).*Evaluation of geotechnical properties and structural strength enhancing road pavement failure.,*Bangladesh Civil and Environmental Engineering Department,Shahjala University Science and Technology, Bangladesh.

BS 1377 (2000). *Methods of testing soils for civil engineering purposes,* British Standards Institute London.

Day, R. W.(2001). *Soil Testing manual:* procedures, classification data, and sampling practices. New York:McGraw Hill,Inc.pp 293-312

Federal Ministry of Works &Housing (1997) *Specification for Roads and Bridges* Vol.II.FMW&H, Ministry of Works, Abuja.

Pavement interactive (2008). *Pavement structure*. Accessed 27th May 2014 .Website: http://www.pavementinteractive.org<http://www.pavementinteractive.org/article/structural-designpavement-structure/

Kalu A.Ugwa (2012). Mathematical Modeling as a Tool For Sustainable Development: International Journal of Academic Research in Progressive Education and Development, Vol.1 ,No 2.2 ISSN:2226-6348.

Terzaghi, Karl (1967), *Theoretical soil mechanics*, John Wiley & Sons, Inc., p. 265.

PAPER 215 – DEVELOPMENT OF A FUZZY LOGIC BASED OFFLINE HANDWRITTEN CHARACTER RECOGNITION SYSTEM

A.R. Ajayi[1*], A.T. Ajiboye[1], O.A. Yusuf[1], O.F. Adebayo[1], E.T. Olawole[1]

[1]Department of Computer Engineering, University of Ilorin, Ilorin, Nigeria.
[*]Email: ajayi.ra@unilorin.edu.ng

ABSTRACT
Offline character recognition is a technique that allows computers to read letters, numbers, and other symbols and convert them into digital form that can be used by computers. Existing fuzzy logic based recognition systems have employed transition data and other features to recognize alphabets. In this study, geometrical features of the alphabet character contour, based on the basic line types that form the character skeletons are used. The selected features are the number of vertical lines (VL), the number of left diagonal lines (LD), number of intersection points (IP) and the sum of pixel (SOP) values. The fuzzy logic model takes these inputs and outputs numbers corresponding to the recognized alphabets. The fuzzy system actual outputs have been compared with the reference outputs; the maximum error observed was 0.45 which is considerably minimal. The mean absolute percentage error (MAPE) value obtained for the model was 1.72%. The MSE and RMSE are 0.03 and 0.16 respectively.

KEYWORDS: Fuzzy logic, Handwritten, Recognition, Geometric

1 INTRODUCTION

Character recognition is a technique that allows computers to read letters, numbers, and other symbols and convert them into digital form that can be used by computers. Machine recognition of handwritten characters has gained much attention over the decades, this is due to its application in various automation processes such as digital character conversion, meaning translation, content based image retrieval, keyword spotting, signboard translation, Text-to-Speech Conversion, Scene Image Analysis, intelligent paper marking, Reading postal addresses and signature verification (Hamdan, 2021; Manisha et al., 2016; Shen et al., 2023).

Character recognition can be classified into two categories: offline recognition and online recognition. Offline character recognition system accepts images of machine printed and handwritten characters as input and gives as output the recognized characters in machine editable text. The online handwritten recognition system receives dynamic signals from electronic devices such as digital pen, digital stylus like devices (Pugazhenthi & Vallarasi, 2015), smartphone and tablet, and gives the recognized characters in machine editable format as output (Manisha et al., 2016). Although deep learning techniques have proved to be highly efficient in recognition systems, but it comes with high computational cost (Wang et al., 2021). It is therefore, expedient to employ methods that can achieve efficient result at a very low computational cost. This study will recognize offline handwritten English Alphabets based on the geometrical properties of handwritten images using a fuzzy logic model. The objectives of this study are to: recognize offline handwritten alphabets using fuzzy logic; compare the actual results with the system's fuzzy logic outputs and evaluate the performance of the developed fuzzy logic model.

2 THEORETICAL ANALYSIS

Fuzzy logic is a soft computing approach based on the degree of truth of membership rather than the classical true or false approach (Alhassan & Hagras, 2020). The fuzzy logic system consists of the fuzzifier, the fuzzy inference engine, the rules base system, and the defuzzifier as shown in Figure 1 (Mohammed & Hagras, 2020). The fuzzifier takes the crisp inputs and converts them to fuzzy sets using fuzzy linguistic variables, fuzzy linguistic terms, and membership functions. The fuzzified inputs and the fuzzy rule base serves as input to the fuzzy inference engine where inferences are made based on a set of rules and produce an output. The resulting fuzzy output is then mapped to a crisp output using the membership functions by the defuzzifier.

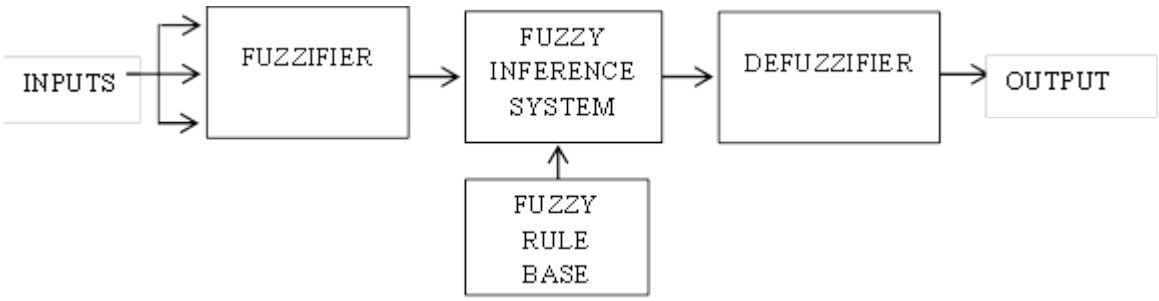

Figure 1: Block Diagram of a Fuzzy Logic System

3 METHODOLOGY

This section describes the stages of the developed fuzzy logic based character recognition system.

3.1 Data Samples

A feature extraction technique based on character geometry for character recognition was reported by (Dileep & Ramesh, 2012). In the study, a feature vector was formed from each zone of uppercase offline handwritten alphabets. The feature vector has a length of 8. Four of these features with distinct or unique values were selected and modeled as variables to the fuzzy logic system. The features are: number of vertical lines (VL), number of left diagonal lines (LD) and the number of intersection points (IP). The mean value of each extracted features for five image samples of each alphabet was computed as shown in Table 1. To ensure that each alphabet appears exclusively within a fuzzy set with no overlap, the sum of pixels of the image (SOP) was computed and added as a distinguishing feature. The average of the minimum and maximum SOP value for each alphabet category was computed and the result is as shown in Table 1.

Table 1: Selected Features of Offline Handwritten Alphabets

VL	LD	IP	SOP
0.05	0.03	0.04	25.00
0.09	0.02	0.03	25.00
0.08	0.05	0.01	26.06
0.10	0.03	0.03	35.64
0.09	0.03	0.03	34.57
0.14	0.03	0.00	13.30
0.19	0.05	0.03	32.45
0.02	0.03	0.02	43.09
0.08	0.05	0.01	22.87
0.20	0.00	0.02	26.06
0.14	0.03	0.00	22.87

3.2 Fuzzification of Input Data

The selected features of the offline handwritten alphabet of Table 1 are taken as the input to the fuzzy inference system, while the English alphabet (A – K) are considered as the output. The maximum and minimum values of the parameters were first studied, and these were used for the fuzzification process. From the obtained data, the fuzzy sets for VL, LD, IP and SOP were defined and are as shown in Table 2.

Table 2: Fuzzy Set for Offline Handwritten Alphabet Parameters

Parameter	Parameter specification	Notation	Range
Number of vertical lines (VL)	Positive Very Small	PVS	0 – 0.09
	Positive Small	PS	0.08 – 0.2
Number of left diagonal lines (LD)	Positive Very Small	PVS	0 – 0.03
	Positive Small	PS	0.02 – 0.05
Number of intersection points (IP)	Positive Very Small	PVS	0 – 0.03
	Positive Small	PS	0.02 – 0.05
Sum of Pixel (SOP)	Positive Very Small	PVS	0 – 15
	Positive Small	PS	14 – 25
	Positive Medium	PM	23 – 35
	Positive Large	PL	32 – 43
	Positive Extra Large	PXL	42 – 50

3.3 Fuzzy Logic Membership Function

Membership functions (MF) are used in the fuzzification and defuzzification steps of a Fuzzy Logic System, to map the non-fuzzy input values to fuzzy linguistic terms. It quantifies a linguistic term with each point in the input space mapped to a membership value between 0 and 1. The common fuzzy logic membership functions are the triangular, trapezoidal, and the Gaussian MF (Walia et al., 2015). In this study, the trapezoidal membership function was employed in the fuzzification of input variables and the triangular MF for the output. The Trapezoidal MF mappings for the fuzzy sets VL and SOP, in the MATLAB environment are shown in Figures 2 and 3 respectively.

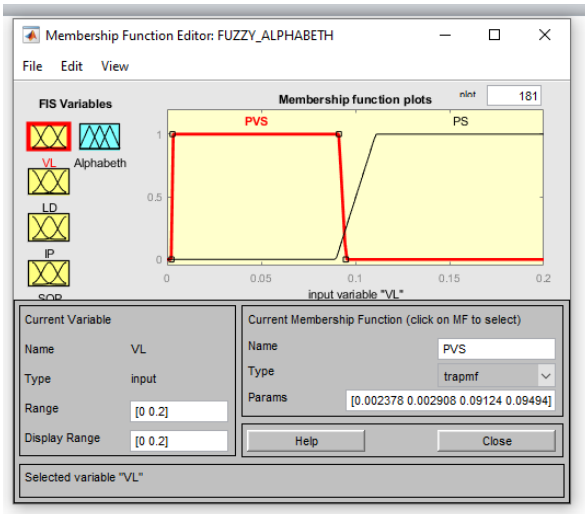

Figure 2: Membership function for VL parameter parameter

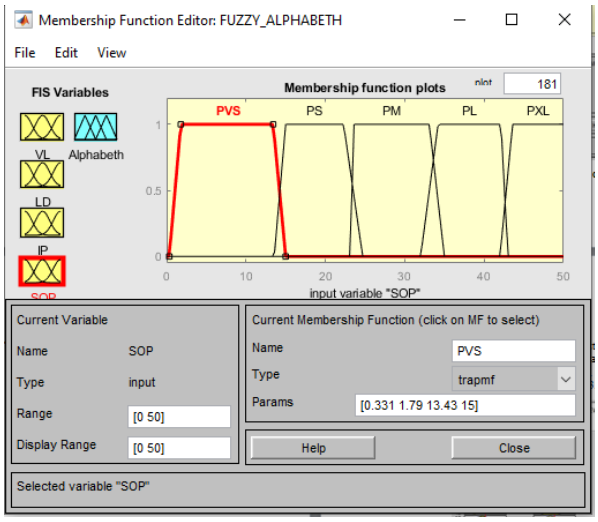

Figure 3: Membership function for SOP

3.4 Fuzzy Rule Base

In a Fuzzy Logic System, a rule base is constructed to control the output variable. A fuzzy rule is a simple IF-THEN rule with a condition and a conclusion(Iancu, 2018). Eleven (11) different rules were formulated for this model as shown in Figure 6. Sample fuzzy rules for the recognition of offline handwritten alphabets are shown in Table 3.

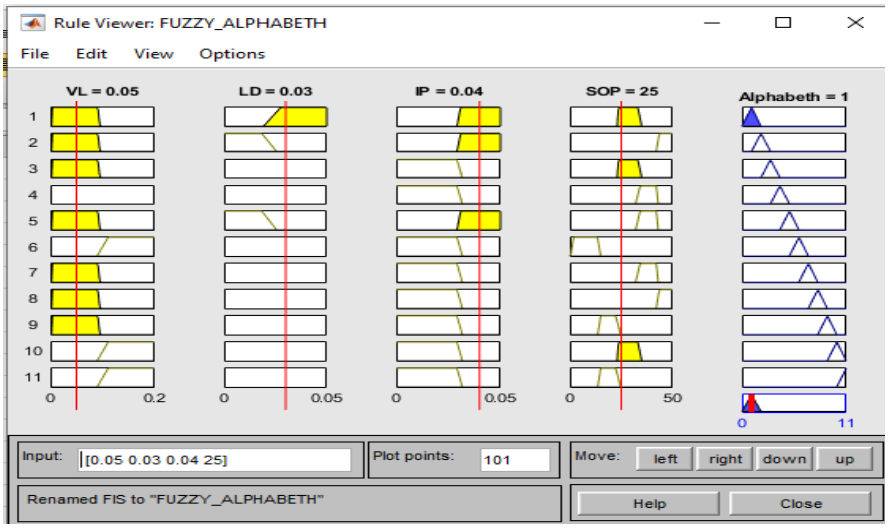

Figure 4: Rule viewer for the developed fuzzy model

Table 3: Sample Fuzzy Rules for the Developed Model

Fuzzy Rules
1. If (VL is PVS) and (LD is PS) and (IP is PS) and (SOP is PM) then (Alphabet is A)
2. If (VL is PVS) and (LD is PVS) and (IP is PS) and (SOP is PXL) then (Alphabet is B)
3. If (VL is PVS) and (IP is PVS) and (SOP is PM) then (Alphabet is C)
4. If (IP is PVS) and (SOP is PL) then (Alphabet is D)
5. If (VL is PVS) and (LD is PVS) and (IP is PS) and (SOP is PL) then (Alphabet is E)

The developed fuzzy logic model has one output variable named Alphabet. The variable is assigned the alphabets A – K, the first eleven alphabets considered in this study. The range of the output variable is between 1 and 11 corresponding to eleven triangular membership functions for alphabets A – K. The fuzzified output Alphabet Triangular MF is as shown in Figure 7. This is then defuzzified to obtain a single crisp output for each of the recognized alphabet.

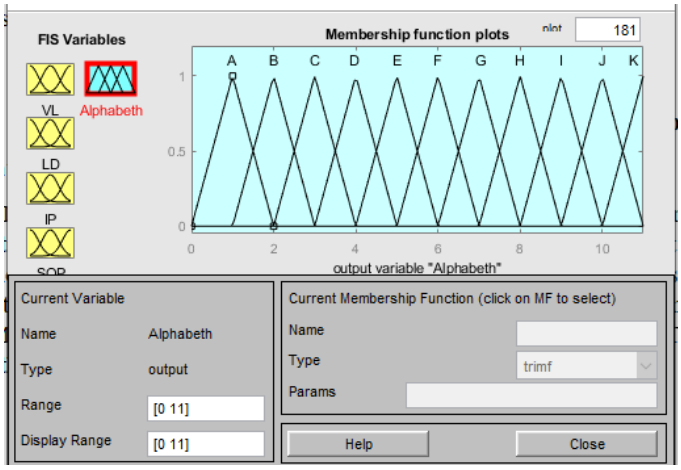

Figure 5: Membership function for Alphabet Output parameter

3.5 Defuzzification

The Fuzzy Inference engine gives a fuzzy output which is defuzzified to obtain a crisp output. Defuzzification is performed according to the membership function of the output variable, in this case, the Alphabet MF. A number of defuzzification methods exists, these include: centroid method, bisector method, mean of maximum method, last of maximum (Chakraverty, Sahoo, & Mahato, 2019). For this study, the centroid method was employed. The equation for calculating the centroid is given in equation 1

$$W^* = \frac{\sum_{i=1}^{n} j_i . A_i}{\sum_{i=1}^{n} A_i} \quad (1)$$

Where: W* is the centroid position, j_i is the center of the area of the fuzzy set at instant i, while A_i is the area of the fuzzy set at instant i, n is the number of elements in the fuzzy set and i =1, 2...n (Ibrahim et al., 2021).

3.6 Model Error Analysis

The statistical methods such as absolute percentage error (APE), mean absolute percentage error (MAPE) are popular method for testing model performance (Tofallis 2015, Kim & Kim 2016). The Absolute percentage error (APE) was used to compute the percentage deviation between the actual and system alphabet recognition output shown in Equation 2 (Ibrahim, et al. 2021).

$$\text{APE } (\%) = \left| \frac{actual\ output\ (i) - predicted\ output(i)}{actual\ output\ (i)} \right| \times 100 \quad (2)$$

$$\text{MAPE } (\%) = \frac{1}{n} \sum_{i=1}^{n} APE(i) \quad (3)$$

where:
n is the number of fitted points,
The recognition efficacy of the model was further analyzed using Mean square error (MSE) and Root Mean square error (RMSE) evaluation metrics as shown in equations 4 and 5 respectively.

$$MSE = \frac{1}{n} \sum_{i=1}^{n} (e_i)^2 \quad (4)$$

$$RMSE = \sqrt{\frac{1}{n} \sum_{i=1}^{n} (e_i)^2} \quad (5)$$

4 RESULTS AND DISCUSSION

In this study, a fuzzy logic model for the recognition of offline handwritten alphabet by considering the geometrical features and sum of pixel of the handwritten images has been implemented in the MATLAB environment. In order to test the developed model, random positive numbers corresponding to the fuzzy input variables for each of the alphabets were generated; these numbers were fed into the fuzzy logic model and the results were recorded as shown in Table 4. The recognized output was compared with the actual output, the percentage error between the actual alphabet number and the predicted alphabet number showed the effectiveness of the recognition model; the smaller the percentage error the better the accuracy of the recognition system. It was observed from Table 4 that the APE between the actual and system output varied between 0% minimum to 7% maximum. The MAPE obtained for the model was 1.72% which is considerably low.

With a high degree of closeness between the actual and values, the suitability of the developed fuzzy logic model for recognition of offline handwritten alphabet is established. The absolute error of the system output from the actual output was computed and plotted as shown in Table 4, it was deduced from the chart that the error margin between the actual and system output is maximum at 0.45 when the recognized alphabet is 5 which represents the alphabet E and minimum at 0, when the alphabets A, C, D, F, H, I, J are recognized. This shows a significant and minimal error value for the fuzzy model. Further model evaluation gave an MSE of 0.03 and RMSE of 0.16 respectively.

Table 4: Result of Actual and Recognition Output for Offline Handwritten Alphabets

Reference Output	Input Variables						
	VL	LD	IP	SOP	Recognition Output	Error	APE
1	0.09	0.04	0.05	28.08	1.00	0.00	0
2	0.04	0.02	0.03	28.85	2.14	-0.14	7
3	0.07	0.04	0.02	31.15	3.00	0.00	0
4	0.16	0.05	0.02	41.92	4.00	0.00	0
5	0.09	0.03	0.03	34.23	4.55	0.45	9
6	0.15	0.04	0.00	8.85	6.00	0.00	0
7	0.14	0.03	0.03	33.46	6.99	0.01	0.14
8	0.07	0.04	0.02	45.77	8.00	0.00	0
9	0.07	0.05	0.03	19.62	9.00	0.00	0
10	0.16	0.00	0.01	29.62	10.00	0.00	0
11	0.17	0.04	0.00	20.38	10.70	0.30	2.73
							1.72
							MAPE

5 CONCLUSION

A fuzzy logic based model for the recognition of offline handwritten English alphabet has been developed. The model uses the geometrical features extracted from pre-processed alphabet images as input. The features are the number of vertical lines (VL), the number of left diagonal lines (LD), the number of intersection points (IP) and the sum of pixel (SOP) values. The system output are numbers corresponding to the recognized alphabets. The fuzzy system actual outputs have been compared with the reference outputs; the maximum error observed was 0.45 which is considerably minimal. The MAPE value obtained for the model was 1.72 %. The MSE and RMSE are 0.03 and 0.16 respectively. The method is simple to implement, requires a very low computational cost and reliable.

ACKNOWLEDGEMENT

The author would like to thank Dr. A.T. Ajiboye of the department of Computer Engineering, University of Ilorin and Prof. A.S. Falohun of Computer Engineering Department, LAUTECH Ogbomoso for their valuable guidance and support for this work.

REFERENCES

Alhassan, M. S. E., & Hagras, H. (2020). A congestion control approach based on weighted random early detection and Type-2 fuzzy logic system. *Int. J. Comput. Sci. Trends Technol.(IJCST), 8*(4), 83-94.

Chakraverty, S., Sahoo, D.M., Mahato, N.R. (2019). Defuzzification. In: Concepts of Soft Computing. Springer, Singapore. https://doi.org/10.1007/978-981-13-7430-2_7

Dileep, G. D., & Ramesh, R. (2012). A feature extraction technique based on character geometry for character recognition *arXiv preprint, arXiv* (pp. 1202-3884).

Hamdan, Y. B. (2021). Construction of statistical SVM based recognition model for handwritten character recognition. *Journal of Information Technology, 3*(02), 92-107. https://doi.org/10.36548/jitdw.2021.2.003

Iancu, I. (2018). Heart disease diagnosis based on mediative fuzzy logic. *Artificial Intelligence in Medicine, 89*, 51-60. https://doi.org/10.1016/j.artmed.2018.05.004

Ibrahim, O., Owonikoko, W. O., Abdulkarim, A., Otuoze, A. O., Afolayan, M. A., Madugu, I. S, Adedayo, K. E. (2021). Performance Evaluation of Different Membership Function in Fuzzy Logic Based Short-Term Load Forecasting. *Pertanika Journal of Science & Technology, 29*(2). http://dx.doi.org/10.47836/pjst.29.2.14

Kim, S. and H. Kim (2016). A new metric of absolute percentage error for intermittent demand forecasts. *International Journal of Forecasting, 32*(3): 669-679. https://doi.org/10.1016/j.ijforecast.2015.12.003

Manisha, C. N., Reddy, E. S., & Krishna, Y. (2016). Role of offline handwritten character recognition system in various applications. *International Journal of Computer Applications, 135*(2), 30-33. https://doi.org/10.5120/ijca2016908349

Mohammed, H. A., & Hagras, H. (2020). A Type 2 Fuzzy Logic Based System for Basal Metabolic Rate Prediction of Diabetes Patients in Sudan. *International Journal of Computer Science Trends and Technology (IJCST),* 8(3), 95-104.

Pugazhenthi, D., & Vallarasi, S. A. (2015). Offline character recognition of printed Tamil text using template matching method of Bamini Tamil font. *Indian Journal of Science and Technology, 8*(35), 1-4. DOI: 10.17485/ijst/2015/v8i35/86811

Shen, L., Chen, B., Wei, J., Xu, H., Tang, S.-K., & Mirri, S. (2023). The Challenges of Recognizing Offline Handwritten Chinese: A Technical Review. *Applied Sciences, 13*(6), 3500. https://doi.org/10.3390/app13063500

Tofallis, C. (2015). "A better measure of relative prediction accuracy for model selection and model estimation." *Journal of the Operational Research Society, 66*(8): 1352-1362. https://doi.org/10.1057/jors.2014.103

Walia, N., Singh, H., & Sharma, A. (2015). ANFIS: Adaptive Neuro-Fuzzy inference system-a survey. *International Journal of Computer Applications, 123*(13). https://doi.org/10.5120/ijca2015905635

Wang, Y., Xiao, W., & Li, S. (2021). *Offline handwritten text recognition using deep learning: A review.* Paper presented at the Journal of Physics: Conference Series. DOI 10.1088/1742-6596/1848/1/012015

PAPER 216 – DEVELOPMENT OF HARMONIC PERIOD-BASED TASK SET SCALING MECHANISM FOR REAL TIME TASK SCHEDULING ALGORITHM BASED ON THE RBOUND UTILIZATION BOUND APPROACH

Ogbonna Chima Otumdi[1*], Simeon Ozuomba[2], Philip Michael Asuquo[3]

[1,2,3]Department of Computer Engineering, University of Uyo, Akwa Ibom State, Nigeria
*Email: otumdii@yahoo.com

ABSTRACT
In this paper, development of harmonic period-based task set scaling mechanism for real time job scheduling based on the Rbound utilization bound approach applicable to single core and multicore systems is presented. The solution includes selection and broadcasting of harmonic task period by the computing platforms, harmonic period-based traffic shaping at the clients and harmonic period-based Task Set Scaling (hpenTSS) at the computing platforms. Relevant analytical expressions and corresponding algorithms are developed in respect of the solution. A case study harmonic period shaped task set, Γ with six tasks was used for numerical examples and the results of the hpenTSS mechanism was compared with two other RBound task set scaling methods identified as TSSmax and TSSrand. The results show that the task set with system utilization of 0.91 and Rbound(Γ') of 1.30 is not schedulable with the TSSmax approach because the r-value is greater than 2. Similarly, the task set is not schedulable with the TSSrand approach because the utilization of 0.91 is greater than the Rbound(Γ') of 0.74 obtained from the TSSrand mechanism. However, the task set is schedulable with the hpenTSS approach since the r-value is 1 which satisfies the condition $1 \leq r < 2$ and also the utilization of 0.91 is less than Rbound($\vec{\Gamma}$) of 1 obtained from the hpenTSS mechanism. In all, the combination of traffic shaping and hpenTSS mechanisms guarantees improved system utilization performance when compared with the existing RBound based TSSmax and TSSrand mechanisms for real time task scheduling on single core and multicore systems.

KEYWORDS: Harmonic Period, Real Time Task, Task Set Scaling Mechanism, Fog Computing, Task Scheduling Algorithm, Rbound Utilization Bound Approach, Single Core System.

1 INTRODUCTION

Single core and multi-core real time task scheduling problems have been projected as one of the fundamental problems in real-time embedded system design (Marwedel, 2021; Dhanesh *et al*., 2020; Jadon & Yadav 2021). Also partitioned scheduling, which is one of the main types of scheduling algorithm in multi-core system design is very important for fog-cloud platforms with distributed task execution (Sun *et al.*, 2020; Memari *et al.*, 2022). More especially on the fog nodes which are usually identified as resource constrained, efficient scheduling algorithm is required to maximize the system utilization (Saha *et al.*, 2020; Pallewatta *et al.*, 2019).
In any case, achieving high system utilization is more difficult with real time tasks since they require stringent timing conditions in terms of meeting task deadlines and task execution times. Accordingly, some utilization bound task scheduling approaches like LLbound, Kbound, Rbound and Cbound has been developed for task scheduling on both single core and multi core platforms. However, some issues relating to limited system utilization performance has been identified in those approaches (Fan *et al.*, 2015). As such, in this paper, a solution that enhances the achievable system utilization based on the RBound approach is presented. The solution introduced the concept of harmonic task period, harmonic period-based traffic shaping and harmonic period-based task set scaling. Appropriate combination of the three concepts is used to develop a solution that enhances the system utilization of harmonic period–based RBound real time task scheduling algorithm. The requisite analytical expressions and algorithms are presented. Numerical examples are also presented based on a case study task set consisting of six tasks.

2 REVIEW OF RELATED WORKS

Generally, periodic real time task set, denoted as Γ and consisting of N tasks, each denoted as t_i can be characterised by the tuple (C_i, T_i) where C_i is used to indicate the worst-case execution time for task t_i and T_i is used to indicate the minimum inter-arrival time between two consecutive jobs of t_i, where;

$$\Gamma = \{t_1, t_2, \dots, t_N\} \quad (1)$$

Also, in task set, Γ the task period, T_i is used to determine the priority of the task, t_i. Hence, the tasks are sorted such that for two consecutive tasks, t_i and t_j, we have $t_i\ t_j \in \Gamma, T_i \leq T_j$ if $i < j$. Again, task, t_i utilization, u_i is defined as (Fan *et al.,* 2015);

$$u_i = \frac{C_i}{T_i} \tag{2}$$

The task set, Γ utilization $U(\Gamma)$ is defined as;

$$U(\Gamma) = \sum_{t_i \in \Gamma} u_i \tag{3}$$

When periodic real time task set, Γ is scheduled, the feasibility of the scheduler meeting the deadline of all the tasks in the task set can be determined using some approaches of which $RBound$ utilization bound approach is of the widely used method and it is given as [8];

$$RBound(\Gamma) = \begin{cases} (N-1)\left(r^{1/(N-1)} - 1\right) + \frac{2}{r} - 1 \\ 1 \leq r < 2 \\ r = \frac{maximum\ (Ti)}{minimum\ (Ti)} \end{cases} \tag{4}$$

Where $maximum\ (Ti)$ is the maximum task period and $minimum\ (Ti)$is the minimum task period in the task set, Γ. Remarkably, the RBound task set transformation approach is applicable for task set that satisfy the condition $1 \leq r < 2$ In order to improve on the achievable $RBound$ utilization bound based on the RBound approach, a Task Set Scaling (TSS) mechanism was applied whereby the task set Γ with the tuple (C_i, T_i) is transformed to a new task set Γ' with the tuple $\left(C_i', T_i'\right)$ using the Task Set Scaling (TSS) algorithm. One of such TSS algorithm is given as Algorithm 1 $TSS(\Gamma, t_k)$ [8];

Algorithm 1 $TSS(\Gamma, t_k)$

Require: (1)Γ: input task set, sorted with non-decreasing period order and selected the k^{th} task in Γ for the scaling.

1: $N = |\Gamma|$
2: $T_k' = Z_k = T_k$ and $C_k' = C_k$
3: //step 1: transform LOWER-priority tasks into harmonics
4: **for** $i = k + 1$ to N **do**
5: $Z_i = Z_{i-1} \cdot \left\lfloor \frac{T_i}{Z_{i-1}} \right\rfloor$
6: **end for**
7: **for** $i = 1$ to $k - 1$ **do**
8: $R_i = 2^{\left\lfloor \log_2 \frac{T_k}{T_i} \right\rfloor}$
9: $T_i' = T_i \cdot R_i$
10: $C_i' = C_i \cdot R_i$
11: **end for**
12: **for** $i = k + 1$ to N **do**
13: $R_i = {}^{Z_i}/_{T_k}$
14: $T_i' = {}^{Z_i}/_{R_i}$
15: $C_i' = {}^{C_i}/_{R_i}$
16: **end for**
17: **return** Γ'

3 METHODOLOGY: DEVELOPMENT OF THE ENHANCED RBOUND TASK SET SCALING MECHANISM

Notably, one of the three approaches currently employed to perform the TSS task transformation according to RBound approach uses the maximum period of a task in the task set to scale up all the task period in the task set. This first task transformation approach is defined in Equation 5 and can be referred to as TSSmax approach. On the other hand, the second approach perform the task transformation according to RBound approach by using the minimum period of a task in the task set to scale down all the task period in the task set. This second task transformation approach is defined in Equation 6 and can be referred to as TSSmin approach. However, studies have shown that the two approaches cannot guarantee the schedulability of the original task set from which the transformed task set is obtained. The third TSS approach method, (given as Algorithm 1 $TSS(\Gamma, t_k)$), is based on the period of a randomly selected task in the task set which is guaranteed that the original task set is schedulable if the new task set is schedulable. This third approach can be referred to as TSSrand approach.

However, after evaluating the achievable system utilization bound based on the RBound approach with the three different TSS approaches (TSSmax , TSSmin and TSSrand), it is discovered that the use of the third TSS mechanism to transform the task set, Γ with tuple (C_i, T_i) to task set, Γ′ with the tuple (C_i', T_i') increased the achievable system utilization bound of Γ′ (Fan *et al*., 2015). However, the task set, Γ′ with the tuple (C_i', T_i') is still limited in the achievable utilization bound for cases where the task periods do not have harmonic relationships. In this case, harmonic relationship among the task periods is where the task periods are integer multiple of a given task period in the task set. Specifically, maximum achievable system utilization can occur when r =1 and that is when the task period, T_i are harmonic and then the TSS transformation can realised a single harmonized task period, T_i' for all the tasks in the task set (Fan *et al.*, 2015).

$$\begin{cases} C_i' = C_i \cdot 2^{\left\lfloor \log \frac{T_{max}}{T_i} \right\rfloor} \\ T_i' = T_i \cdot 2^{\left\lfloor \log \frac{T_{max}}{T_i} \right\rfloor} \end{cases} \tag{5}$$

$$\begin{cases} C_i' = C_i \cdot 2^{\left\lfloor \log \frac{T_{min}}{T_i} \right\rfloor} \\ T_i' = T_i \cdot 2^{\left\lfloor \log \frac{T_{min}}{T_i} \right\rfloor} \end{cases} \tag{6}$$

Each of the three TSS approaches transforms the task set Γ with the tuple (C_i, T_i) to a new task set Γ′ with the tuple (C_i', T_i') and the task set schedulability is feasible if these conditions are satisfied (Fan *et al.*, 2015);

$$\begin{cases} U(\Gamma) \leq RBound(\Gamma') \\ 1 \leq r < 2 \\ r = \frac{maximum\ (T_i')}{minimum\ (T_i')} \end{cases} \tag{7}$$

3.1 Harmonic Period-Based Traffic Shaping

Most importantly, in this paper, the harmonized task period, T_i' is referred to as the harmonic period, and it is denoted as Ť. Consequently, the concept of traffic shaping is employed in this research such that the task periods of each of the incoming tasks are transformed to be integer multiple of the harmonic period, Ť. Each of the computing or task processing platform, such as the fog node or cloud computing platform will indicate its harmonic period, Ť and this information is broadcast in the fog-cloud network. Every edge device and other fog nodes or cloud servers that intend to send task to the network will adjust their period, T_i and execution time, C_i such that the transformed period, $\vec{T}_i$ is a perfect (or integer) multiple of the harmonic period, Ť. Next, the harmonization factor, $\vec{K}_i$ is determined and then used to determine the harmonic transformed period, $\vec{T}_i$ and the harmonic transformed execution time, $\vec{C}_i$ by using the following analytical expressions and associated algorithm presented in this paper. Given a task set, Γ with tuple (C_i, T_i) and harmonic period, Ť, the harmony period shaped task set, $\vec{\Gamma}$ with tuple $(\vec{C}_i, \vec{T}_i)$ is obtained as follows;

$$\vec{K}_i = \left\lfloor \frac{T_i}{\check{T}} \right\rfloor \tag{8}$$

More precise transformation is given as;

$$\vec{K}_i = \begin{cases} \left\lfloor \frac{T_i}{\check{T}} \right\rfloor \ if \ \frac{T_i}{\check{T}} - \left\lfloor \frac{T_i}{\check{T}} \right\rfloor \leq 0.5 \\ \left\lceil \frac{T_i}{\check{T}} \right\rceil \ if \ \frac{T_i}{\check{T}} - \left\lfloor \frac{T_i}{\check{T}} \right\rfloor > 0.5 \end{cases} \tag{9}$$

$$\vec{T}_i = \vec{K}_i(\check{T}) \tag{10}$$

$$\vec{C}_i = \mathrm{C_i}\left(\frac{\vec{T}_i}{T_i}\right) \tag{11}$$

Hence, the original task set traffic with tuple (C_i, T_i) is transformed to harmonic period shaped task set, $\vec{\Gamma}$ with tuple $(\vec{C}_i, \vec{T}_i)$. In practice, the clients that originates the task C_i, T_i will shape their task using the harmonic period, Ť broadcasted by the fog node. Hence, the task coming to the fog nodes are already in the harmonic period shaped format characterized with the tuple $(\vec{C}_i, \vec{T}_i)$.

The algorithm for the harmonic period traffic shaping ***hpenTSHP*** method is given in Algorithm 2 as follows;

Algorithm 2: *hpenTSHP* algorithm

//The algorithm for harmonic period traffic shaping method

Require: Γ: input task set, (C_i, T_i) sorted with non-decreasing period order, that is in ascending order of task period, T_i and t_1: the 1^{st} task in Γ, according to the task set that is scaled.

1: **for** $i = k + 1$ to N **do**

2: $\vec{K}_i = \begin{cases} \left\lfloor \frac{T_i}{\check{\Upsilon}} \right\rfloor \ if \ \frac{T_i}{\check{\Upsilon}} - \left\lfloor \frac{T_i}{\check{\Upsilon}} \right\rfloor \leq 0.5 \\ \left\lceil \frac{T_i}{\check{\Upsilon}} \right\rceil \ if \ \frac{T_i}{\check{\Upsilon}} - \left\lfloor \frac{T_i}{\check{\Upsilon}} \right\rfloor > 0.5 \end{cases}$

3: $\vec{T}_i = \vec{K}_i(\check{\Upsilon})$

4: $\vec{C}_i = \frac{\mathrm{C_i}}{\mathrm{K_i}}$

5: **end for**

6: **return** $\vec{\Gamma}'$

3.2 Harmonic period enhanced task scaling (hpenTSS) mechanism

In this paper a Harmonic period enhanced task scaling (hpenTSS) mechanism is developed and it is presented in Algorithm 3. The hpenTSS mechanism is applied to the task set obtained from the traffic shaping *hpenTSHP* algorithm. At the end of implementation of the hpenTSS algorithm, all the task period will become equal to the harmonic period, as shown in Step 5 of Algorithm 3.

Algorithm 3: hpenTSS algorithm //Algorithm for the harmonic period enhanced task scaling (hpenTSS) mechanism

Require:

1) $\vec{\Gamma}$: input task set, $\left(\vec{C}_i, \vec{T}_i\right)$ sorted with non-decreasing period order of task period, $\vec{T}_i$

1: **for** $i = k + 1$ to N **do**

2: $\mathrm{K_i} = \frac{\vec{T}_i}{\check{\Upsilon}}$

3: $Z_i = \mathrm{K_i}(\check{\Upsilon})$

4: $R_i = \frac{\mathrm{Z_i}}{\check{\Upsilon}} = \frac{\mathrm{K_i}(\check{\Upsilon})}{\check{\Upsilon}} = \mathrm{K_i}$

5: $\vec{T'}_i = \frac{\mathrm{Z_i}}{\mathrm{R_i}} = \frac{\mathrm{K_i}(\check{\Upsilon})}{\mathrm{K_i}} = \check{\Upsilon}$

6: $\vec{C'}_i = \frac{\vec{C}_i}{\mathrm{K_i}} = \frac{\vec{C}_i}{\left(\frac{\vec{T}_i}{\check{\Upsilon}}\right)} = \vec{C}_i\left(\frac{\check{\Upsilon}}{\vec{T}_i}\right)$

7: **end for**

8: **return** $\vec{\Gamma}'$

The Rbound task set scaling mechanism uses the Rbound schedulability test model to determine the schedulability of any given task set. The Rbound schedulability test model determines the maximum achievable system utilization attainable for any given task set. In all, it has been found that the maximum attainable system utilization based on the Rbound schedulability test model is 1. The various task set scaling (TSS) mechanism in available published works try to improve on the attainable system utilization by scaling the task periods in any given task. However, the system utilization attained by those mechanisms are still very low compared with the value that can be achieved if traffic shaping is introduced before the TSS. Accordingly, in this paper, the traffic shaping approach is adopted before the TSS mechanism is employed. The traffic shaping is implemented using a harmonic period published by the computing platform that will schedule the task set. In summary, the method adopted in this work is as follows;

- ✓ The computing platform publish its harmonics period
- ✓ The clients shape their traffic with respect to the harmonics period
- ✓ The computing platform transform the task set period using the TSS implemented using the harmonics period
- ✓ The Rbound task scheduling algorithm is implemented based on the TSS modified tasks set

In order to evaluate the proposed approach, a test set is used. The existing TSS methods are applied to the task set along with the approach presented in this paper. The system utilization attained by the various methods are compared.

4 RESULTS AND DISCUSSION

The TSSmax, TSSrand, and hpenTSS approaches along with traffic shaping mechanism are applied to a case study harmonic period shaped task set, Γ with six tasks and the results are presented in Table 1, Table 2, Table 3 and Table 4

Table 1. The results of schedulability test for the TSSmax Transformed Task Set, Γ' and the TSSrand Transformed Task Set, Γ' based on a given case study task set, Γ

	Case Study Task Set, Γ			TSSmax Transformed Task Set, Γ'			TSSrand Transformed Task Set, Γ'		
	Ci (s)	Ti (s)	Ui	Ci'(s)	Ti' (s)	Ui'	Ci'(s)	Ti' (s)	Ui'
1	0.5	4	0.125	1	8	0.125	2	16	0.125
2	1	8	0.125	1	8	0.125	2	16	0.125

3	1.5	10	0.15	1.5	10	0.15	1.5	10	0.15
4	2.5	16	0.15625	2.5	16	0.15625	2.5	16	0.15625
5	4	20	0.2	4	20	0.2	4	16	0.25
6	6	40	0.15	6	40	0.15	3	16	0.1875
		U(Γ)	**0.91**		**U(Γ')**	**0.91**		**U(Γ')**	**0.99**
	U(Γ)	**0.91**		**U(Γ')**	**0.91**		**U(Γ')**	**0.99**	
	Tmax (s)	**40.00**		**Tmax (s)**	**40.00**		**Tmax (s)**	**16.00**	
	Tmin (s)	**4.00**		**Tmin (s)**	**8.00**		**Tmin (s)**	**10.00**	
	r	**10.00**		**r**	**5.00**		**r**	**1.60**	
	N	**6.00**		**N**	**6.00**		**N**	**6.00**	
	Rbound(Γ)	**2.12**		**Rbound(Γ')**	**1.30**		**Rbound(Γ')**	**0.74**	

Table 2. The results of the harmonic period traffic shaping of the given case study task set, Γ with harmonic period of 4 seconds.

Case Study Task Set, Γ				Harmonic Period Shaped Task Set, $\vec{\Gamma}$			
Task Set, Γ	Ci (s)	Ti (s)	Ui	Task Set, $\vec{\Gamma}$	$\vec{C}$ (s)	$\vec{T}_i$ (s)	Ui'
1	0.5	4	0.125	1	0.5	4	0.125
2	1	8	0.125	2	1	8	0.125
3	1.5	10	0.150	3	1.2	8	0.150
4	2.5	16	0.156	4	2.5	16	0.156
5	4	20	0.200	5	4	20	0.250
6	6	40	0.150	6	6	40	0.188
		U(Γ)	0.906			**U(Γ)**	0.994

Table 3. The results of schedulability test for the TSSmax Transformed Task Set, Γ' and the TSSrand Transformed Task Set, Γ' based on a given case study task set, Γ

	Case Study Task Set, Γ			**Harmonic Period Shaped Task Set, $\vec{\Gamma}$**			**hpenTSS Transformed Task Set, $\vec{\Gamma}'$**		
Task Set Γ, ti	**Ci (s)**	**Ti (s)**	**Ui**	**$\vec{C}$i (s)**	**$\vec{T}$i (s)**	**$\vec{U}$i**	**$\vec{C}$i'(s)**	**$\vec{T}$i' (s)**	**$\vec{U}$i'**
1	0.5	4	0.125	0.5	4	0.125	0.500	4	0.125
2	1	8	0.125	1	8	0.125	0.500	4	0.125
3	1.5	10	0.150	1.2	8	0.150	0.600	4	0.150
4	2.5	16	0.156	2.5	16	0.156	0.625	4	0.156
5	4	20	0.200	4	20	0.200	1.000	4	0.250
6	6	40	0.150	6	40	0.150	0.750	4	0.188
			0.906			0.906			0.994
	U(Γ)	0.91		U(**Γ'**)	0.91		U(**Γ'**)	0.99	
	Tmax (s)	40.00		Tmax (s)	20.00		Tmax (s)	4.00	
	Tmin (s)	4.00		Tmin (s)	4.00		Tmin (s)	4.00	
	r	10.00		r	5.00		r	1.00	
	N	6.00		N	6.00		N	6.00	
	Rbound(Γ)	2.12		Rbound($\vec{\Gamma}$)	1.30		Rbound($\vec{\Gamma}'$)	1.00	

Table 4. The results of schedulability test for the TSSmax and TSSrand approaches applied to the harmonic period shaped task set, $\vec{\Gamma}$

	Case Study Task Set, Γ	TSSmax Transformed Task Set, Γ'	TSSrand Transformed Task Set, Γ'

	Ci (s)	Ti (s)	Ui	Ci'(s)	Ti' (s)	Ui'	Ci'(s)	Ti' (s)	Ui'
1	0.5	4	0.125	1.000	8	0.125	2.000	16	0.125
2	1	8	0.125	1.000	8	0.125	2.000	16	0.125
3	1.2	8	0.150	1.200	8	0.15	2.400	16	0.150
4	2.5	16	0.156	2.500	16	0.15625	2.500	16	0.156
5	4	20	0.200	4.000	20	0.2	4.000	16	0.250
6	6	40	0.150	6.000	40	0.15	3.000	16	0.188
			0.906			0.91			0.994
	$U(\vec{\Gamma})$	0.91		$U(\vec{\Gamma}')$	0.91		$U(\vec{\Gamma}')$	0.99	
	Tmax (s)	40.00		Tmax (s)	40.00		Tmax (s)	16.00	
	Tmin (s)	4.00		Tmin (s)	8.00		Tmin (s)	16.00	
	r	10.00		r	5.00		r	1.00	
	N	6.00		N	6.00		N	6.00	
	Rbound($\vec{\Gamma}$)	2.12		**Rbound($\vec{\Gamma}'$)**	1.30		**Rbound($\vec{\Gamma}'$)**	1.00	

When the TSSmax and TSSrand approaches are applied to a case study period shaped task set, Γ with six tasks, as presented in Table 1 and Table 2, the results showed that;

- ✓ With TSSmax transformed task set, Γ', (shown in Table 1) even though U(Γ) of 0.91 < Rbound(Γ') of 1.30 the task set is not schedulable since r > 2
- ✓ With TSSrand transformed task set, Γ', (shown in Table 1) even though r value of 1.6 is less than 2, the task set is not schedulable since U(Γ) of 0.91 > Rbound(Γ') of 0.74.

The case study period shaped task set, Γ with six tasks, are shaped by using the harmonic period traffic shaping mechanism presented in this paper. The traffic shaping is conducted with a harmonic period of 4 seconds. The results show that in the harmonic period shaped task set, $\vec{\Gamma}$ (presented in Table 2) all the task periods are integer multiple of the harmonic period of 4 seconds.

The hpenTSS approach is applied to the harmonic period shaped task set, $\vec{\Gamma}$ and the results showed that with hpenTSS transformed task set, (shown in Table 3) every task in the transformed task set, $\vec{\Gamma}'$ has a period, $\vec{T}$i' (s) = 4 which is the harmonic period. Also, r = 1 and the task set is schedulable since $1 \leq r \leq 2$ and U($\vec{\Gamma}$) of 0.91 < Rbound($\vec{\Gamma}'$) of 1.0 . Hence, while the TSSmax and TSSrand approaches could not achieve schedulaility of the given case study task set, Γ the combination of the traffic shaping mechanism and hpenTSS approach are able to make the scheduling of the case study task set feasible.

Furthermore, the TSSmax and TSSrand approaches are applied to the harmonic period shaped task set, $\vec{\Gamma}$ and the results showed that;

- ✓ With TSSmax approach, (shown in Table 4) even though U(Γ) of 0.91 < Rbound(Γ') of 1.30 the task set is not schedulable since r > 2 (r =10).
- ✓ With TSSrand approach, (shown in Table 4) the task set is schedulable since r=1 < 2 and U($\vec{\Gamma}$) of 0.91 < Rbound($\vec{\Gamma}'$) of 1.0 .

Essentially, when the traffic is shaped using harmonic period, both the TSSrand and hpenTSS give the same result. However, the algorithm for hpenTSS has less computational resource demand than the TSSrand algorithm. In all, the approach presented in this paper enhanced the schedulability bound achievable in periodic real time task scheduling.

5 CONCLUSION

An approach for improving the system utilization for RBound-based real time task scheduling algorithm applicable in single core and multicore systems is presented. The approach is based on selection of a harmonic period at the computing platforms, broadcasting the selected harmonic period and then mandating all client tasks to be shaped by the client such that their real time task period is integer multiple of the harmonic period of the computing platform. Notably, the computing platform in this case can be single core or multicore systems on a fog node or on a fog-cloud computing platform. The harmonic period shaped traffic is further transformed at the fog node or cloud computing platform using Task Set Scaling (TSS) mechanism which in this case ensures that all the task periods become equal to the harmonic period and the task execution times are scaled with respect to the single harmonic period in the platform. The schedulability test for the TSS transformed task set is conducted using the RBound utilization bound approach and the results show that the combination of harmonic period-based traffic shaping and harmonic period-based TSS mechanisms, enhances the achievable system utilization of the real time task scheduling algorithm.

REFERENCES

Marwedel, P. (2021). *Embedded system design: embedded systems foundations of cyber-physical systems, and the internet of things* (p. 433). Springer Nature.

Dhanesh, L., Deepa, S., Elangovan, P., & Prabhu, S. (2020). Enhanced and Energy-Efficient program scheduling for heterogeneous multi-core processors system. In *Advances in Electrical Control and Signal Systems: Select Proceedings of AECSS 2019* (pp. 737-747). Springer Singapore.

Jadon, S., & Yadav, R. S. (2021). Deadline-Constrained Tasks' Scheduling in Multi-core Systems Using Harmonic-Aware Load Balancing. *Arabian Journal for Science and Engineering*, *46*, 3099-3113.

Sun, H., Yu, H., & Fan, G. (2020). Contract-based resource sharing for time effective task scheduling in fog-cloud environment. *IEEE Transactions on Network and Service Management*, *17*(2), 1040-1053.

Memari, P., Mohammadi, S. S., Jolai, F., & Tavakkoli-Moghaddam, R. (2022). A latency-aware task scheduling algorithm for allocating virtual machines in a cost-effective and time-sensitive fog-cloud architecture. *The Journal of Supercomputing*, *78*(1), 93-122.

Saha, R., Misra, S., & Deb, P. K. (2020). FogFL: Fog-assisted federated learning for resource-constrained IoT devices. *IEEE Internet of Things Journal*, *8*(10), 8456-8463.

Pallewatta, S., Kostakos, V., & Buyya, R. (2019, December). Microservices-based IoT application placement within heterogeneous and resource constrained fog computing environments. In *Proceedings of the 12th IEEE/ACM International Conference on Utility and Cloud Computing* (pp. 71-81).

Fan, M., Han, Q., Liu, S., Ren, S., Quan, G., & Ren, S. (2015). Enhanced fixed-priority real-time scheduling on multi-core platforms by exploiting task period relationship. *Journal of Systems and Software*, *99*, 85-96.

PAPER 217 – OCCUPATIONAL SAFETY PRACTICES AND ATTAINMENT OF SUSTAINABLE DEVELOPMENT GOALS AMONG TRICYCLE RIDERS IN MINNA

Ramatu Hamidu

Department of Entrepreneurship and Business Studies, Federal University of Minna, Minna, Nigeria.
Email: hameedu.rahmatu@gmail.com

ABSTRACT
This conceptual review article explores the relationship between occupational safety practices and the attainment of sustainable development goals among tricycle riders in Minna. Tricycle riders are a significant mean s of transportation in Minna, providing affordable transportation to many people. However, the nature of their work exposes them to various hazards, including road accidents, environmental pollution, and poor working conditions. The article reviews the literature on the importance of occupational safety practices in the transportation sector, with a particular focus on tricycle riders. It discusses the potential impact of unsafe working conditions on the attainment of sustainable development goals, such as poverty reduction, environmental protection, and economic growth. The article also discusses various strategies that can be used to promote occupational safety practices among tricycle riders. Overall, the article concludes that promoting occupational safety practices among tricycle riders is crucial for the attainment of sustainable development goals in Minna.

KEYWORDS: Occupational safety practices; Sustainable Development Goals; Tricycle riders; Minna

1.0 INTRODUCTION

Tricycle riders play a crucial role in the transportation sector in Nigeria, particularly in cities like Minna, where they provide affordable and accessible transportation to many citizens. However, their work is associated with occupational safety risks, including road accidents, exposure to environmental hazards, and health issues (Aloba et al., 2021; Igwegbe et al., 2018). Furthermore, the United Nations Sustainable Development Goals (SDGs) call for the promotion of sustainable cities and communities, which includes ensuring safe and sustainable transportation systems (United Nations, 2015). Therefore, there is a need to examine the relationship between occupational safety practices and the attainment of sustainable development goals among tricycle riders in Minna.

The use of tricycles for transportation in Nigeria is associated with several challenges, including overloading, poor road infrastructure, and inadequate regulation (Onifade et al., 2018). Recent research has shown that occupational safety practices among tricycle riders in Minna are inadequate, leading to high rates of accidents and injuries (Aloba et al., 2021; Igwegbe et al., 2018). Additionally, the attainment of sustainable development goals is hindered by the lack of adequate transportation infrastructure and systems (World Bank, 2018). Therefore, there is a pressing need to investigate the relationship between occupational safety practices and the attainment of sustainable development goals among tricycle riders in Minna.

Furthermore, Sustainable development is defined as development that meets the needs of the present without compromising the ability of future generations to meet their own needs (World Commission on Environment and Development, 1987). The attainment of sustainable development goals requires the integration of economic, social, and environmental considerations in all decision-making processes (United Nations, 2015).

Transportation is a crucial element of sustainable development, and it plays a vital role in improving access to education, healthcare, and employment opportunities (World Bank, 2018). The SDGs aim to achieve sustainable and inclusive transportation systems that are safe, affordable, and accessible to all (United Nations, 2015). In Nigeria, the transportation sector accounts for a significant portion of greenhouse gas emissions, and sustainable transportation is critical to achieving the country's climate change targets (Federal Ministry of Environment, 2015).

The transportation sector in Nigeria faces several challenges that hinder the attainment of sustainable development goals. These challenges include inadequate transportation infrastructure, lack of regulation, and inadequate implementation of policies (Federal Ministry of Environment, 2015).

In conclusion, tricycle riders play a critical role in the transportation sector in Nigeria, particularly in cities like Minna. However, their work is associated with occupational safety risks, and the attainment of sustainable development goals in the transportation sector is hindered by several challenges.

A comprehensive review of the literature reveals that occupational safety practices and sustainable development goals are critical issues in the transportation sector, particularly for tricycle riders the key findings from recent studies on this topic are presented in the subsisting paragraphs;

A study by Okafor and Agumba (2020) examined the relationship between occupational safety practices and sustainable development goals among tricycle riders in Nigeria. The study found that tricycle riders face numerous occupational hazards, including road traffic accidents, exposure to air pollution, and inadequate safety equipment. The study also found that sustainable development goals, such as environmental sustainability and social responsibility, are important considerations in ensuring the safety and well-being of tricycle riders. The authors recommended that policymakers adopt a holistic approach that balances economic, social, and environmental objectives to promote sustainable development goals and improve the safety of tricycle riders.

Another study by Olajide et al. (2018) explored the factors affecting the occupational safety practices of tricycle riders in Nigeria. The study found that lack of awareness, inadequate training, and non-compliance with safety regulations were significant factors that affect the safety practices of tricycle riders. The study also found that the lack of enforcement of safety regulations and inadequate provision of safety equipment by government agencies contribute to the poor safety practices among tricycle riders. The authors recommended that policymakers should adopt a comprehensive approach that includes awareness campaigns, training, and the provision of safety equipment to improve the occupational safety practices of tricycle riders.

A study by Etchie et al. (2019) investigated the environmental impact of tricycles on the SDGs in Nigeria. The study found that tricycles contribute significantly to air pollution, which can lead to respiratory diseases and other health problems. The study also found that tricycles contribute to congestion and noise pollution, which can affect the well-being of residents and hinder economic activities. The authors recommended that policymakers should adopt policies that promote the use of cleaner fuels, improve road infrastructure, and regulate the operations of tricycles to reduce their environmental impact and achieve the SDGs.

Another study by Ibrahim et al. (2019) examined the knowledge and perception of tricycle riders on road safety regulations in Nigeria. The study found that tricycle riders had a low level of awareness of road safety regulations, which contributes to the poor safety practices among tricycle riders. The study also found that the lack of effective enforcement of safety regulations and inadequate provision of safety equipment by government agencies were significant factors that contribute to poor safety practices among tricycle riders. The authors recommended that policymakers should adopt a comprehensive approach that includes awareness campaigns, training, and the provision of safety equipment to improve the knowledge and compliance of tricycle riders with road safety regulations.

A study by Umar et al. (2017) investigated the factors affecting the health and safety of tricycle riders in Nigeria. The study found that tricycle riders face numerous occupational hazards, including exposure to air pollution, road traffic accidents, and physical strain due to the nature of their work. The study also found that inadequate provision of safety equipment, such as helmets and reflective vests, contributes to the poor safety practices among tricycle riders. The authors recommended that policymakers should adopt a comprehensive approach that includes awareness campaigns, training, and the provision of safety equipment to improve the health and safety of tricycle riders.

Additionally, a study by Ogbuabor and Onukwube (2021) found that occupational safety practices among tricycle riders in Nigeria are inadequate, with many riders not using appropriate safety gear such as helmets and reflective jackets. The study highlights the need for improved safety practices and regulations in the sector.

Therefore, there is a pressing need to investigate the relationship between occupational safety practices and the attainment of sustainable development goals among tricycle riders in Minna. This gap in the literature highlights the need for further research in this area hence the purpose of this study seeks to bridge this important gap by exploring the relationship between occupational safety practices and the attainment of sustainable development goals among tricycle riders in Minna. The specific objectives of the article are as follows:

- To examine the current state of occupational safety practices among tricycle riders in Minna.
- To suggest policy interventions that can improve the occupational safety practices of tricycle riders in Minna and promote the attainment of sustainable development goals in the transportation sector.

By achieving these objectives, the article seeks to contribute to the body of knowledge on occupational safety practices and sustainable development goals among tricycle riders in Nigeria, specifically in the context of Minna.

This knowledge can be useful in informing policy decisions and interventions that prioritize the safety and well-being of tricycle riders while promoting sustainable development goals in the transportation sector.

2.0 THE THEORETICAL CONCEPTS AND FRAMEWORKS THAT UNDERPIN THE RELATIONSHIP BETWEEN OCCUPATIONAL SAFETY PRACTICES AND SUSTAINABLE DEVELOPMENT GOALS

The relationship between occupational safety practices and sustainable development goals can be understood through several theoretical concepts and frameworks. One such framework is the Sustainable Development Goals (SDGs) framework, which was adopted by the United Nations in 2015 to provide a comprehensive framework for sustainable development. The SDGs framework comprises 17 goals and 169 targets that address various aspects of sustainable development, including economic growth, social inclusion, and environmental sustainability (United Nations, 2015). The framework recognizes that sustainable development is a multi-dimensional and interconnected concept that requires integrated approaches and partnerships among different stakeholders.

Another theoretical concept that underpins the relationship between occupational safety practices and sustainable development goals is the triple bottom line (TBL) framework. The TBL framework recognizes that sustainable development requires balancing economic, social, and environmental objectives (Elkington, 2004). According to this framework, organizations and societies should aim to achieve economic prosperity, social equity, and environmental sustainability simultaneously, rather than focusing solely on economic growth at the expense of social and environmental objectives. Occupational safety practices can contribute to the social and environmental dimensions of the TBL framework by promoting the health and well-being of workers and reducing environmental pollution.

In the specific context of tricycle riders in Minna, the concept of vulnerable road users (VRUs) is relevant to understanding the relationship between occupational safety practices and sustainable development goals. VRUs refer to road users who are at higher risk of road accidents and injuries, such as pedestrians, cyclists, and tricycle riders (World Health Organization, 2018). Tricycle riders in Minna can be considered VRUs due to their exposure to road accidents and occupational hazards. Occupational safety practices that prioritize the safety and well-being of tricycle riders can contribute to the social and environmental dimensions of sustainable development by reducing the incidence of road accidents and injuries.

In conclusion, several theoretical concepts and frameworks underpin the relationship between occupational safety practices and sustainable development goals. These frameworks emphasize the importance of integrated approaches and partnerships among different stakeholders in achieving sustainable development objectives

3.0 METHODOLOGY

To achieve the objectives of this study, the researcher reviewed the research trends in the area of occupational safety practices and sustainable development. High impact papers were downloaded with the key words" Occupational safety practice", Sustainable development", "Sustainable Development Goals (SDGs)" and "Tricycle Riders Nigeria". 317 papers were downloaded out of which 23 were relevant to the research objectives. They findings and recommendations on the relationship between occupational safety practice where summarized and presented in the succeeding paragraph.

4.0 RESULTS AND DISCUSSIONS

The study found that tricycle riders in Minna face various challenges related to occupational safety practices and achieving sustainable development goals. These challenges include poor road infrastructure, lack of safety equipment, limited access to healthcare, and inadequate social protection. These challenges have significant implications for the wellbeing of tricycle riders, their families, and the wider community.

The study also found that implementing occupational safety practices and sustainable development goals can have significant positive impacts on the livelihoods of tricycle riders. This can include improved safety practices, increased earnings, and better access to healthcare and social protection. The study highlights the need for interventions that address the specific challenges faced by tricycle riders in Minna, including improving road infrastructure, providing safety equipment and training, and enhancing access to healthcare and social protection.

5.0 CONCLUSIONS

In conclusion, the literature highlights the importance of occupational safety practices and sustainable development goals among tricycle riders. Poor safety practices and inadequate regulations in the sector can lead to accidents and fatalities, while failing to address sustainable development goals can result in poor working conditions and economic inequality. Addressing these issues requires a multi-sectoral approach, involving

government agencies, private sector stakeholders, and civil society organizations. The implementation of training programs and awareness campaigns can also play a crucial role in promoting safety practices and achieving sustainable development goals among tricycle riders.

This study clearly identified the key role of stakeholders (Governmental, private and civil societies) in the sensitization, implementation and monitoring of safety practices in ensuring sustainability among tricycle riders. This is emphasized considering the low rate of information dissemination which has resulted in the need for the adoption of safety practices in the past, stakeholder's involvement will create better chances for sustainability among the study's population.

Based on the key findings of the study, here are some recommendations for improving occupational safety practices and achieving sustainable development goals among tricycle riders in Minna are put forward:

Improve road infrastructure: The government should prioritize improving the road infrastructure in Minna to make it safer for tricycle riders. This can include repairing potholes, installing speed bumps, and creating dedicated lanes for tricycle riders.

Provide safety equipment: Tricycle riders should be provided with safety equipment such as helmets, reflective jackets, and gloves. This will help to reduce the risk of accidents and injuries on the road.

Increase access to healthcare: Tricycle riders should have better access to healthcare services. This can be achieved by establishing health clinics and mobile health units that can provide medical care and emergency services to tricycle riders.

Provide social protection: Tricycle riders should be provided with social protection such as insurance, pensions, and other benefits. This will help to protect their income and improve their overall well-being.

Promote awareness and training: The government and other stakeholders should promote awareness and training programs to educate tricycle riders on safe driving practices, health and safety, and sustainable development.

Engage stakeholders: The government should engage with relevant stakeholders such as tricycle riders' associations, civil society organizations, and the private sector to develop policies and programs that address the specific needs of tricycle riders.

REFERENCE

Adekoya, A. F. (2016). Occupational health and safety practices among commercial motorcyclists in Lagos, Nigeria. Journal of Environmental and Public Health, 2016, 1-7. https://doi.org/10.1155/2016/2082450

Adeyemi, A., & Afolabi, A. (2018). Occupational safety practices among tricycle riders in Ibadan, Nigeria. Journal of Community Health, 43(5), 975-981. https://doi.org/10.1007/s10900-018-0523-3

Akande, T. M., Okorie, N. N., & Nwagbara, U. (2018). Occupational safety and health risks among commercial tricycle riders in Nigeria: A case study of Nnewi metropolis. Journal of Environmental and Public Health, 2018, 1-8. https://doi.org/10.1155/2018/2352469

Ayodeji, S. O., & Ogunlade, O. A. (2019). Occupational safety and health practices among tricycle operators in Nigeria. Journal of Health and Medical Sciences, 2(1), 38-48.

Federal Republic of Nigeria. (2015). Sustainable Development Goals: Nigeria's implementation framework 2016-2030. http://www.ng.undp.org/content/nigeria/en/home/library/poverty/nigeria-sdgs-implementaion-framework-2016-2030.html

International Labour Organization. (2019). Safety and health at the heart of the future of work: Building on 100 years of experience. https://www.ilo.org/global/topics/safety-and-health-at-work/lang--en/index.htm

Minna, N. (2018). Minna: A vision of a smart and sustainable city. https://www.nigeriaworld.com/articles/2018/may/042/minna-a-vision-of-a-smart-and-sustainable-city.html

National Bureau of Statistics. (2019). Road transport data (Q4 2018). https://www.nigerianstat.gov.ng/pdfuploads/Road%20Transport%20Data%20Q4%202018.pdf

National Bureau of Statistics. (2020). Labor force statistics: Unemployment and underemployment report - Q4 2019. https://www.nigerianstat.gov.ng/pdfuploads/Q4_2019_UNEMPLOYMENT_REPORT.pdf

World Health Organization. (2021). Global status report on road safety 2018. https://www.who.int/publications/i/item/9789241565684

Elkington, J. (2004). Enter the Triple Bottom Line. In Henriques, A. and Richardson, J. (Eds.),The Triple Bottom Line, Does It All Add Up? Assessing the Sustainability of Business and CSR(1-16). London: Earthscan.

Ilah, S. K., & Ahmad, I. T. An Evaluation of Occupational Hazards among Tricycle Drivers in Tarauni Local Government Area, Kano State, Nigeria.

Etchie, T. O., Etchie, A. T., Adewyi, G. O., Pillarisetti, A., Sivanesan, S., Krishnamurthi, K. & Arora, N. K. (2019). The gains of life expectancy by ambient PM2.5 pollution reductions in localities in Nigeria.Environmental Pollution 236: 146-157.

Oni-Jimoh, T., Liyanage, C., Oyebanji, A., & Gerges, M. (2018). Urbanization and meeting the need for affordable housing in Nigeria. *Housing, Amjad Almusaed and Asaad Almssad, IntechOpen*, *7*(3), 73-91.

PAPER 218 – ENHANCING FOOD SAFETY AND QUALITY WITH EDIBLE COATINGS: A REVIEW

Y. Sayuti[1], S. E Adebayo[1] and B.O Atteh[1]

[1]Department of Agricultural and Bioresource Engineering, Federal University of Technology Minna, Minna 920101, Nigeria
*Email:engnryasman@gmail.com

ABSTRACT
The edible coating is utilized to prolong the post-harvest lifespan of fresh food while simultaneously enhancing the visual appeal property and ensuring food safety. These coatings can be derived from both animal and plant sources. Edible coatings come in various forms such as proteins, lipids, polysaccharides, resins, or combinations thereof. Edible coatings act as a protective barrier which effectively prevents moisture and gas exchange whenever food is processed, handled or stored. They effectively mitigate food spoilage and promote protection by either their inherent properties or the inclusion of antimicrobial compounds. In addition to their protective qualities, edible coatings offer several other advantages such as minimizing packaging material wastage, prolonging the lifespan of fresh and slightly treated products, and shielding fresh foods against detrimental atmospheric factors. By facilitating the controlled spread of gas, water, aroma, and taste components within the food structure, these coatings play a vital role in preserving product quality.

KEYWORDS: Edible coating, Fruits, Vegetables, shelf life

1.0 INTRODUCTION

The role of edible coatings is vital in food protection by forming a thin consumable layer that acts as a protective barrier against oxygen, external microbes, moisture, and solutes (Baldwin et al., 1996). These coatings create a semi-permeable barrier, with the primary objective of lengthening the lifespan of food products. By minimizing moisture and solute migration, gas exchange, oxidative reactions, and respiration, edible coatings help maintain the freshness of fruits and reduce physiological disorders (Park, 1999). Edible coatings offer an alternative approach to prolonging the postharvest lifespan of fresh fruits, whether stored at low temperatures or not. They mimic the effects of improved atmosphere storage by modifying the inner gas configuration surrounding the food (Park, 1999). Acting as semi-permeable barriers, Arvanitoyannis and Gorris, (1999) noted that edible coatings effectively reduce the respiration level, moisture loss, and oxidation reactions, thus maintaining the inner value and features of the food. In recent years, the usage of edible coatings has garnered significant consideration due to several factors. There is an increasing awareness of decreasing ecological degradation resulting from plastics, driving the exploration of edible coatings as a more sustainable option. Additionally, the necessity to prolong the shelf life of food products and meet the mandate for better and ecologically friendly diets has further emphasized the importance of edible coatings (Espino-Diaz et al., 2010)

1.1 Edible coating history

When consumers purchase fruits and vegetables, they often assess the freshness and quality based on appearance (Kader, 2002). One of the commonly experienced and challenging issues in the fresh-cut food sector is preserving and managing the freshness of produce while preventing the development of putrefaction and pathogenic microbes. Edible coatings provide an extra defensive layer for fresh food and can even replicate the effects of improved atmosphere storage by altering the centre gas configuration (Rojas-Grau et al., 2007). Various edible coatings have been successfully used in preserving several varieties of fruits and vegetables, including oranges, apples, grapefruits, cherries, cucumbers, strawberries, tomatoes, and capsicums. The achievement of edible coatings in preserving fruits and vegetables is largely influenced by controlling the centre gas structure of the food (Salleh, 2013).

1.2 Application of edible coating

The advancement of polysaccharide edible coatings has had a significant impact on the utilization of edible coatings in the food production sector. Among these polysaccharide materials, carrageenan and carboxymethylcellulose (CMC) have gained particular attention for their ability to form a continuous network and

establish polymer interactions, leading to the functional properties of the coatings (Min and Krochta, 2005). Carrageenan and CMC are effective walls against oxygen, aroma, and oil, thereby providing value and reliability to the coatings. Their firmly filled, ordered hydrogen-bonded system arrangement and little solubility contribute to their excellent oxygen barrier properties (Banker, 1966). Carrageenan-based coatings have been useful for an extensive variety of foods and have been used as carriers for antimicrobials or antioxidants, as well as for reducing water loss, oxidation, or breakdown in food products (Lacroix and Le Tien, 2005).

Furthermore, edible coatings have the benefit of being able to integrate useful ingredients which include antioxidants, antimicrobials, nutrients, and flavours. This capability allows for the enhancement of food stability, value, functionality, and safety (Min and Krochta, 2005; Lin and Zhao, 2007). The use of antimicrobial mediators, such as important oils, in edible coatings has been shown to effectively prolong the postharvest lifespan of foods. These agents are released slowly on the fruit's surface, maintaining a high concentration, thereby, providing protection against microbial agents (Ouattara et al., 2000; Xing et al., 2011). Incorporating oils into edible coatings offers a potential solution for controlling postharvest diseases and enhancing fruit preservation. Tufan et al. (2021) summarized the application of edible coatings to fresh fruits and vegetables (Table 1).

In recent literature, various instances of edible coatings used for fresh vegetables and fruits have been reported. Edible coatings can be used for both fresh-cut and complete fruits and vegetables, offering a versatile approach to preservation (Tufan et al., 2021).

Table 1. Edible coatings used for fresh fruits and vegetables

Product	**Coating substance**	**Coating Technique**	**Vital Effects**
Baby carrot	Chitosan	Spraying and dipping	Avoiding outward fading, Guaranteeing colour protection, keeping food textural and organoleptic qualities in the course of storage
Banana	Rice starch	Spraying	Prolonging lifespan, decreasing mass loss, helps in hardness, affecting oxygen and carbon dioxide mass transfer
Carrot/zucchini	Whey protein	Dipping	Preventing deterioration throughout storage, decreasing mass reduction, inhibiting microorganisms development, promotes antioxidant action
Tomato	Iodide-doped chitosan	Dipping	gives vital nutritive components without any alteration in antioxidant action, prolonging lifespan
Guava	Chitosan-cassava starch	Dipping	Outstanding microbiological qualities
Pomegranate aril	Chitosan	Dipping	Visible colour feature, prolonging lifespan, keeping nutritive and organoleptic properties
Mango	Corn starch	Extrusion	Gives good mechanical and barrier characteristics, preserving physical and chemical properties
Pumpkin	Modified starch	Dipping	Enhanced colour, increased pro-vitamin A quality
Tomato	Mango kernel starch	Dipping	Lengthening lifespan
Avocado	Moringa leaf extract, chitosan and carboxymethyl cellulose	Dipping	Reduce respiratory level, advanced developed property quality, protects fruit value, extended lifespan
Huanghua pears	Shellac and Semperfresh (sucrose-polyester based coating)	Dipping	Variations in fragility and firmness, lesser actions of cell wall hydrolases

Cashew apples	Corn starch	Dipping	Suspending damage features, prolonging lifespan in low-temperature storage
Strawberry	Chitosan	Casting	Fleshly and microbiological safety of food, outstanding bactericide and fungicide actions.
Guava	Hydroxypropyl methylcellulose and beeswax	Dipping	Inhibiting ripening, lengthening lifespan
Blueberry	Sodium alginate, pectin	Dipping	Constructive influence on hardness and microorganism development, decreasing development kinetics of yeast and mesophilic aerobic bacteria
Mushroom	Chitosan/Zein	Casting	Prolonging lifespan, suspending mass loss, inhibiting dimming, preserving colour and decreasing respiration level.
Apple	Soy protein isolate	Dipping	Prolonging lifespan by regulating mass loss and firmness
Pineapple	Chitosan, pullulan, flaxseed, nopal cactus and aloe gum	Dipping	Preserving quality, lengthening lifespan, decreasing mass loss, suspending the alteration of entire soluble solid quality and colour

Source: Tufan et al (2021)

Dehydration and drying processes are commonly utilised to increase the lifespan of perishable products through the removal of moisture. However, these techniques can negatively impact the structure and properties of heat-sensitive food (Song et al., 2017). To address this issue, researchers have found that applying edible coatings to foods before drying would improve their nutritional and sensory properties, prevent vitamin losses, and inhibit oxidation (Song et al., 2018; Garcia et al., 2014). According to Gonzalez-Aguilar et al. (2010), the combination of edible coatings and reduced-temperature storage promising in preserving the freshness of tomatoes. Edible coatings function by producing an improved surrounding around the food, acting as a temporal barricade to gas, moisture, and aroma elements. This helps reduce the fruit's respiration level, minimize moisture loss, and preserves its texture and sensory properties (Olivas et al., 2008).

In addition to their barrier properties, edible coatings can be supplemented with food additives to control detrimental reactions in plant-based foods (Rojas-Grau et al., 2009). These barriers are typically made of hydrocolloids, hydrophobic compounds, or a mixture of both in the form of composite coatings, which enhance their coating properties for optimal handling (Espino-Diaz et al., 2010). Edibility is one of the main advantages of edible coatings, as they can be consumed along with the coated food. According to Prasad and Batra (2015), edible coatings are also safe and economical compared to synthetic coatings.

2.0 EDIBLE COATING FORMATION METHOD

The dipping technique is widely used for forming edible coatings and its involves submersing the product in a coating solution, draining off the excess solution, and allowing the coating to dry (Parreidt et al., 2018; Suhag, 2020). This technique is suitable for coarse and uneven surface products and allows for the recovery of excess coating material (Dangaran, 2009). It produces a thin layer on the product surface, providing effective coverage.

The fluidized bed coating method is used to fix an extremely thin layer to very minor or less dense substances. The process involves fluidizing the particles with hot air while simultaneously spraying a liquid binder. This promotes particle agglomeration, enhancing the dispersal and solubility of the coating substance. The agglomerates are then been dried in batch or continuous processing systems (Debeaufort and Voilley, 2009).

Spraying is employed when a thin and selective coating is desired on a single surface. It offers more control compared to pan or fluidized bed coating methods. Though, after coating and drying the upper surface, a separate process is required to cover the lower surface. To achieve uniform coverage, the product must be rotated during the coating process. Spray coating is particularly suitable for products with bulky surface areas. The spray nozzle's design parameters which include flow rate, droplet mass, spray space and angle, and overlap speed are crucial in

the efficiency of the coating process. Factors such as coating fluid pressure, viscosity, temperature, surface tension, and nozzle design impact spraying efficiency (Debeaufort and Voilley, 2009).

The pan coating is utilized for applying tinny or dense coatings on rigid and nearly round particles. It helps prevent water and fat loss while adding aroma to the coated product. The pan-coating technique is commonly employed in the pharmaceutical and confectionery industries. It involves placing the product in a revolving bowl and adding the coating substance either by ladle or spray. The rotation of the pan ensures an even distribution of the coating substance on the surface of the product (Dangaran, 2009).

Advantages of edible coatings
The advantages of edible coatings as listed by Park 1999 are that edible coatings:

(i). enhance the preservation of acids, colour, flavour, and sugar in food.
(ii). aid maintain the properties of food during preservation.
(iii). lessen mass loss and loss of firmness in produce.
(iv). cause a decrease in the need for polymer packaging and leads to waste reduction.
(v). are consumable and contain health-beneficial nutrients, making them a beneficial addition to fruits and vegetables.

Disadvantages of edible coatings (Ghaouth *et al*., 1991)
Despite the numerous advantages of edible coatings, Ghaouth et al (1991) reported the following disadvantages of edible coatings:

(i). dense coating can restrict the exchange of oxygen, leading to the growth of off-flavours in foods.
(ii). edible coatings with excellent gas barricade properties can disrupt the normal ripening process in fruits and vegetables by promoting anaerobic respiration.
(iii). certain edible coatings have hygroscopic properties, which can contribute to increased microbial growth

2.1 Herbal Edible Coatings

The food industry has embraced a novel technique known as the herbal edible coating. This technique involves the utilization of herbs either individually or in combination with other edible coatings. Widely used herbs in these coatings include Aloe vera gel, Neem, Lemon grass, Rosemary, Tulsi, and Turmeric. Herbs possess antimicrobial qualities which are rich in vitamins, antioxidants, and vital minerals (Douglas et al., 2005). Aloe vera gel, in particular, has gained widespread use in coating food due to its antimicrobial characteristics and its ability to reduce moisture and moisture loss (Chauhan et al., 2014). Substances such as ginger, essential oils like clove bud oil and mint oil, extracts from turmeric and neem, and various other essential oils and extracts are also employed in the edible coating of food (Nasution et al., 2015). Herbs serve as natural sources of vitamins, minerals, antioxidants, and offer health benefits by acting as nutraceuticals and medicines (Chauhan et al., 2014).

3.0 CONCLUSION

For many years, the food industry has employed edible coatings to store food. These coatings utilize a range of materials which include hydrocolloids, waxes, and proteins. Recently, researchers have developed new edible coatings that are not only safe and environmentally friendly but can also be consumed together with food without any concerns. According to the findings of this review, edible coatings have proven to prolong the lifespan of fresh produce, decrease moisture loss, delay the maturing process, and effectively inhibit microorganism development, particularly in food. A recent innovation in edible coatings is the introduction of herbal edible coatings, which have demonstrated enhanced outcomes and health benefits. Food coated with herbal edible coatings not only retain their nutrients but also exhibit medicinal properties, offering additional advantages.

REFERENCE

Arvanitoyanni, A. & Gorris, L.G.M. (1999) Edible and biodegradable polymeric material for food packaging or coating, In: *Processing food quality optimisation and process assessment*. 357-371, press Boca Raton, Florida.

Baldwin EA, Nesperos-Carriedo MO, Chen X, Hagenmaier RD. Improving storage life of cut apple and potato with edible coating, *Postharvest Biology and Technology*, 9, 151-163

Banker GS (1966) Film coating theory and practice. *Journal of Pharmaceutical Sciences*, 55, 81-89

Chauhan, S., Gupta, K.C & Agrawal, M. (2014). Development of Aloe vera gel to control postharvest decay and longer shelf life of Grapes, *Int. J. Curr. Microbio. App. Sc.*3(3), 632-642.

Dangaran, K., Tomasula, P. M., & Qi, P. (2009). Structure and Function of Protein-Based Edible Films and Coatings. In K. Huber, M. Embuscado (Eds.), Edible Films and Coatings for Food Applications *Springer, New York*, NY. 25-56.

Debeaufort F., & Voilley A. (2009). Lipid-Based Edible Films and Coatings. In K. Huber, M. Embuscado (Eds.), Edible Films and Coatings for Food Applications, *Springer, New York*, NY., 135-168.

Douglas, M., Heys, J., & Smallfield, B. (2005). Herb spice and essential oil: post- harvest operation in developing country, 2, 45-55.

Ghaouth, E., Arul, J., Ponnampalam, R., & Boulet, M. (1991). Chitosan coating effect on stability of fresh Strawberries, *Journal of Food Science,*57,1618-1620.

Espino-Díaz, M., De JesúsOrnelas-Paz, J., Martínez-Téllez, M. A., Santillán, C., Barbosa-Cánovas, G. V., Zamudio-Flores, P. B., & Olivas, G. I. (2010). Development and characterization of edible films based on mucilage of Opuntiaficus-indica (L.). *Journal of Food Science*, 75, 347-352

Garcia, C.C., Caetano, L. C., Silva, K. S., & Mauro, M. A. (2014). Influence of Edible Coating on the Drying and Quality of Papaya (Carica papaya). *Food Bioprocess Technology*, 7, 2828–2839.

Gonzalez-Aguilar, G., Ayala-Zavala, J, Olivas, G., Rosa, L & Alvarez-Parrilla, E. (2010). Preserving quality of fresh-cut products using safe technologies. J. Für Verbraucherschutz und Lebensmittelsicherheit, 5: 65-72. DOI: 10.1007/s00003-009-0315-6

Kader, A.A. (2002). Quality parameters of fresh-cut fruits and vegetables products, 11-28.

Lacroix, M., & Tien, L.C. (2005). Edible films and coatings from non-starch poly- saccharides. In: Han JH (Ed) Innovations in Food Packaging, *Elsevier, Cambridge* (UK), 338-361

Min, S., & Krochta, J. M. (2005). Antimicrobial films and coatings for fresh fruit and vegetables. In: Jongen W (Ed) Improving the Safety of Fresh Fruit and Vegetables, *CRC Press, New York,* 455-492.

Nasution, Z, Wei, J.N. & Hamzah, Y. (2015). Characteristics of fresh-cut Guava coated with Aloe vera gel as affected by different additives. *Kas. J. (Nat. Sc.)*, 49, 111-121.

Olivas, G.I., J.E. Davila-Avina, N.A. Salas-Salazar & Molina, F.J (2008). Use of edible coatings to preserve the quality of fruits and vegetables during storage. Stewart Postharvest Rev., 4: 1-9. DOI 10.2212/spr.2008.3.6

Ouattara, B., Simard, R., Piette, G., Begin, A., & Holley R. A. (2000) Inhibition of surface spoilage bacteria in processed meats by application of antimicrobial films prepared with chitosan. *International Journal of Food Microbiology*, 62, 139-148.

Park, H.J. (1999) Development of advanced edible coating of fruits, Trends of Food Science & Technology., 10, 250-260.

Parreidt, T.S., Schmid, M., & Müller, K. (2018). Effect of Dipping and Vacuum Impregnation Coating Techniques with Alginate Based Coating on Physical Quality Parameters of Cantaloupe Melon. *Journal of Food Science*, 83(4), 929-936.

Prasad, N., & Batra E (2015). Edible coating (the future of packaging): cheapest and alternative source to extend the post-harvest changes: A review, Asian Journal of Biochemistry & Pharmacology Research, (5),2231- 2560.

Rojas-Grau, M.A, Raybaudi, R.M., Solvia-Fortany, R.C., Avena-Bustillos, R.J., McHugh, T.H. & Martin-Bellos, O. (2007) Apple puree alginate edible coating as carrier of antimicrobial agents to prolong shelf life of fresh cut apples, Postharvest Biology and Technology, 45, 254-264.

Rojas-Graü, M.A., Oms-Oliu, G. Soliva-Fortuny, R. and Martin-Belloso, O. (2009). The use of packaging

techniques to maintain freshness in fresh-cut fruits and vegetables: a review. International Journal of Food Science and Technology, 44: 875-889. DOI: 10.1111/j.1365-2621.2009.01911.x

Salleh, N.S. (2013). Development of starch and Soy Protein edible coating and its effect on the postharvest life of Mango (Mangiferaindica) Uni. of Tech. MARA, 40450 Shah Alam Seannager.

Song, J., Wang, X., Li, D., Liu, C., Yang, Q. & Zhang, M. (2018). Effect of starch osmo-coating on carotenoids, colour and microstructure of dehydrated pumpkin slices. Journal of Food Science and Technology, 55(8), 3249–3256.

Song, Z., Li, F., Guan, H. Xu, Y., Fu, Q., & Li, D. (2017). Combination of nisin and ε-polylysine with chitosan coating inhibits the white blush of fresh-cut carrots. Food Control, 74, 34-44.

Suhag, R., Kumar, N., Petkoska, A. T., & Upadhyay, A. (2020). Film formation and deposition methods of edible coating on food products: A review. Food Research International, 136, 109582.

Tufan, E., Borazan, A., & Koçkar, O (2021). A Review on Edible Film and Coating Applications for Fresh and Dried Fruits and Vegetables. BSEU Journal of Science, 8(2), 1073-1085.

Xing Y, Li X, Xu Q, Yun J, Lu Y, Tang Y (2011) Effects of chitosan coating enriched with cinnamon oil on qualitative properties of sweet pepper (Cap- sicum annuum L.). Food Chemistry, 124, 1443-1450.

PAPER 219 – EFFECT OF PROCESS VARIABLES ON THE SYNTHESIS OF ZEOLITE A FROM ALOJI KAOLIN

V. C. Eluwa[1*], A.S. Kovo[1,3], A.S. Abdulkareem[1,3], J.O. Tijani[2,3]

[1] Department of Chemical Engineering, Federal University of Technology, Minna
[2] Department of Chemistry, Federal University of Technology, Minna
[3] Nanotechnology Research Group, African Centre for Excellence on Mycotoxin, Federal University of Technology, Minna.
*Email: Victoria.eluwa@futminna.edu.ng

ABSTRACT

This study investigates the effects of alkalinity (5,6.5,8 M), metakaolinization temperature (600, 725, 850 ˚C), crystallization temperature (80, 115,150 ˚C), and stirring time during aging (1,2,3 h) on zeolite A synthesis from kaolin. The hydrothermal method of synthesizing zeolite A was used in the study, and the synthesized zeolite was characterized for XRD and SEM. The findings showed that, alkalinity of 5M yielded only pure zeolite A crystals. The metakaolinization temperature of 850 ˚C, crystallization temperature 115 ˚C and stirring time of 2h gave the best crystallinity and cubic morphology, a feature that is widely associated with zeolite A. Further, findings reveal that increasing metakaolinization temperature and crystallization temperature increases crystallinity and crystal size while stirring time did not have significant effect on zeolite A synthesis.

KEYWORDS: Zeolite, Metakaolinization, Crystallization, Temperature, Alkalinity, kaolin

1. INTRODUCTION

Zeolites are crystalline, nontoxic microporous aluminosilicate materials formed by a three-dimensional network of $[AlO_4]^{5-}$ and $[SiO_4]^{4-}$ tetrahedral sharing oxygen atoms. This tetrahedral framework consists of a highly ordered system of cavities and pores having molecular dimensions which are occupied by either exchangeable cations or water molecules. (Johnson *et al.,* 2014; Olaremu *et al.,* 2018; Kirdeciler and Akata 2020; Kamyab and Williams 2021). Zeolites, also known as molecular sieves have very unique system of channels and cages in the molecular size range, hus resulting in their high surface area, adjustable porosity, fast diffusion characteristics, and high mechanical strength over amorphous porous silica. (Johnson *et al.,* 2014; Albert *et al.,* 2018). This is the basis for their applications in fields such as catalysis (Krisnandi *et al.,* 2019; Liu *et al.,* 2019), adsorption processes (Salimkhani *et al.,* 2021; Belachaw and Hinsene 2020), bacterial adhesion (Schwanke *et al.,* 2022), water treatment (Rozhkovskaya *et al.,* 2021) and ion exchange (Rengaraj *et al.,*2001)
Zeolite was first discovered by Freiherr Axel Fredrick Cronstedt a Swedish mineralogist in the year 1756. The term zeolite is a greek word coined from two words zeo and lithos meaning “boiling stone. This unique mineral is made up of primary building units $[TO_4]$ that are linked together to form the secondary units and subsequently the zeolite framework. The T is usually Silicon or Aluminuim, but can also be Boron, Phosphorous. The linking of this individual units generates different structures having cages, channels, and cavities of molecular dimensions. (Klunk *et al.,* 2020; Schwanke *et al.,* 2022)

Zeolites exist in two categories, both as natural and synthetic. They are natural occurring when they are mined from the earth and synthetic when they are produced in the laboratory. Natural zeolites are found in sedimentary rocks that are near the earth’s crust. Commonly found natural zeolite include Clinoptilolite, Analcime, chabazite, heulandite, erionite, laumontite, and mordenite (Derbe *et al.,* 2020; Nasief *et al.,* 2021). Natural zeolites are known to contain contaminants like $Fe^{2+,}$ $SO_4^{2-,}$ SiO_2, and sometimes other zeolites, these impurities tend to reduce their pores and channels thereby making them unsuitable for commercial use where purity and uniformity are highly essential. Therefore, in order to eliminate these limitations prompted researches to investigate the synthesis of zeolite. (Yoldi *et al.,* 2019)

The International Zeolite Association (2021) has stated that there are over 250 synthetic zeolite framework that have been reported. Synthetic zeolites are characterized by uniform composition (pore size and shape), high surface area, lack of impurity, larger pore volume and are mostly synthesized to fit a specific purpose. (Kirdeciler and Akata 2020; Khaleque *et al.,* 2020). Some common synthetic zeolites are A, X, Y, ZSM5, P, L, J, N, and W. Conventional synthesis of zeolite involves the mixing of Al and Si sources in an alkaline environment to generate a supersaturated solution that is crystalized at particular temperature and time (Yoldi, et al. 2019).

Zeolite preparation and synthesis are very challenging and the common synthesis methods involves the use of very expensive sources of alumina and silica (synthetic chemicals) which in turn leads to high cost of zeolite and environmental burden due to pollution. (Otieno et al., 2019; Kumar and Jena 2022). In an attempt to reduce the cost of zeolite, several other alternative sources of alumina and silicas have been explored and are still currently

being investigated. This include Halloysite (Meftah *et al.,* 2017), Diatomite (Yao *et al.,* 2018), Basalt powder (Ke *et al.,* 2019), Rice husk (Zhang *et al.,* 2018; Klunk *et al.,* 2020), illite clay (Liu *et al.,* 2019), feldspar (Nyankson *et al.,* 2018), coal fly ash (Joseph *et al.,* 2020; Kumar and Jena 2022) and Bentonite (Abukhadra *et al.,* 2019).

Kaolinite clays mineral is another raw material that is being used in recent times as a starting material for zeolite synthesis due to its purity and high content of alumina and silica. The Si/Al ratio of kaolin is 1, this therefore makes it very suitable for the production of low silica zeolites. Low silica zeolites like zeolite A also LTA are of very special interest due their high adsorption and ion exchange properties. (Arasi *et al.,* 2021; Kirdeciler and Akata 2020; Kamyab and Williams 2021).

Zeolite A as earlier stated are superior adsorbents and have high ion exchange capacities, as such they have very high commercial usage and vast application. It has been used in detergent making (Shehu *et al.,* 2018; Yusriadi *et al.,* 2020). Zeolites are used as fertilizers or stabilizers, when mixed with fertilizers they reduce the leaching of nutrients (Nayak and Mohanty 2019). Zeolites are also very capable of controlling and completely removing offensive odour from organic manure, since they can absorb volatile substances and gases such as H_2S, CO_2, NH_3, N_2, H_2O, SO_2, HCHO and CH_3OH (Mahesh *et al.,* 2018). This work is concerned with synthesizing zeolite A from Aloji kaolin, a low-cost material that is also readily available using hydrothermal synthesis technique. The effects of metakaolinization temperature, crystallization temperature, stirring time during aging and alkalinity were studied.

2. MATERIALS AND METHODS/METHODOLOGY/EXPERIMENTAL PROCEDURE

2.1 Materials

Raw kaolin was obtained from Aloji in Kogi state, Nigeria. The only chemical reagent used was analytical grade sodium hydroxide (NaOH) pellet obtained from Sigma Aldrich. Similarly, the deionized and distilled water used were all obtained within Chemical Engineering Laboratory Federal University of Technology Minna and were used as at when received.

2.2 Synthesis of Zeolite A

Zeolite A was synthesized from Aloji kaolin using the conventional hydrothermal method. Refined kaolin was metakaolinzed at varying temperatures (600,725 and 850 ˚C). The metakaolin obtained were then mixed with different concentration of sodium hydroxide (5M, 6.5M, and 8M) and the resulting mixture was stirred using a magnetic stirrer for varying stirring time (1, 2, and 3h). The homogenous solution was aged and then heated in a Teflon lined stainless steel autoclave at varying temperatures (80, 115, and 150 ˚C) for 3h. The resultant product obtained was continuously washed with deionized water until a pH of 7 was obtained, after which the zeolite sample was dried in an oven at 100 ˚C for 8h and the crystals obtained stored in an air-tight container.

2.3 Zeolite Characterization

2.3.1. X-Ray Diffraction (XRD)

X-ray diffraction (XRD) is an efficient and effective technique that is used to identify crystallographic structure of solids. XRD was used to determine the crystal size of the synthesized zeolites, study the crystal structure of zeolite, and to determine the crystallinity of the synthesized zeolites. The percentage crystallinity was calculated using Equation 2.1

$$Percentage\ crystalinity = \frac{\text{Sum of relative intensities } of\ synthesized\ zeolite}{\text{Sum of relative intensities of standard zeolite}} \times 100 \quad \text{.....2.1}$$

2.3.2. Scanning Electron Microscopy (SEM)

Scanning electron microscope (SEM) is a technique that is used to study the surface of solids materials. The morphology of the zeolite was characterized for SEM using a FEI Quanta 400 instrument. The samples were first treated by gold coating this is aimed at decreasing static charging during their observation under SEM conditions

3.0 RESULT AND DISCUSSION

3.1 XRD ANALYSIS

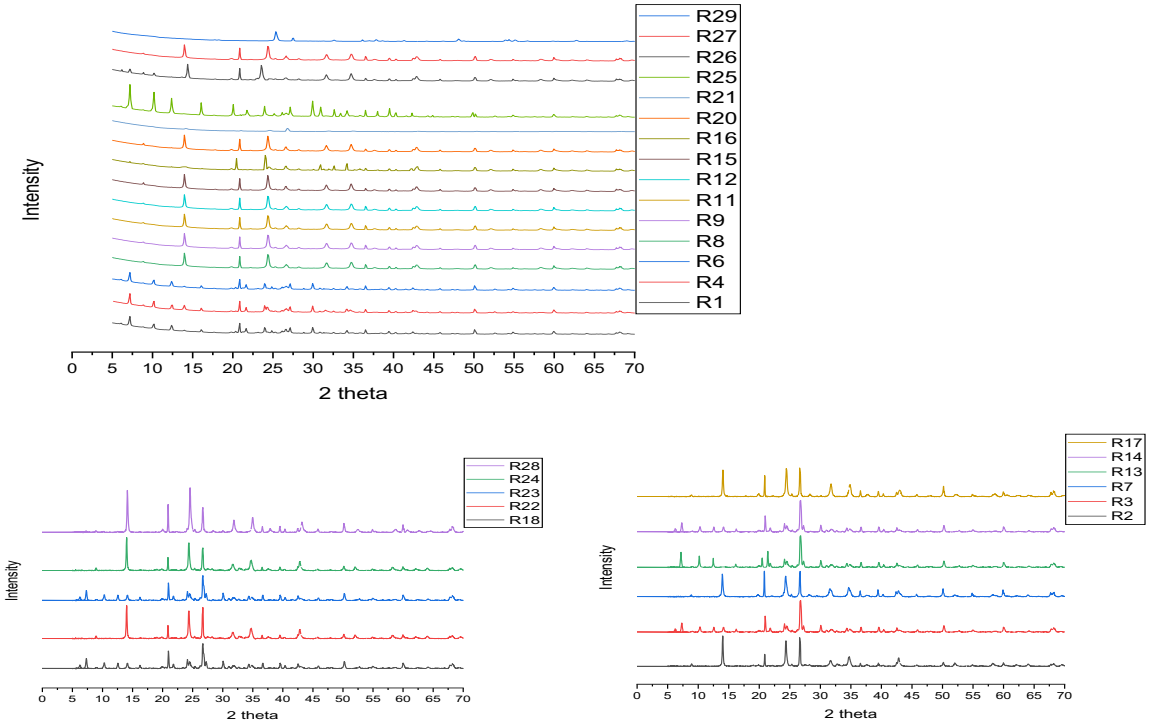

Figure 3.1 XRD patterns for synthesized zeolite

The XRD diffractions for the synthesized zeolites were compared and it was observed that all zeolites synthesized at crystallization temperature of 80 ˚C for 3h had diffractions whose peaks had low intensities and as such were not very pronounced and distinct. This is evident for run 1,4, and 6 in Figure3.1a. However, all zeolite synthesized at crystallization temperature of 115 ˚C and 150 ˚C for 3h all had distinct and pronounced peaks with much higher intensity thus indicating that the most crystalline products were obtained at these temperatures (Binary *et al.,* 2019.)

Most zeolites synthesized in this study at 5M and 6.5M alkaline concentration regardless of the crystallization temperature or metakaolinization temperature contained most of these diffraction peaks. This is in agreement with the work of Maia *et al.* (2019) that reported a synthesis of zeolite A from kaolin calcined at 600 and 700 ˚C using 5M NaOH concentration and at a temperature of 110 ˚C, the authors successfully synthesized zeolite A having peaks similar to those obtained from this work. Similarly, Pereira *et al.,* 2018 synthesized zeolite A at a crystallization temperature of 80 ˚C from kaolin calcined at 600 ˚C with an alkaline concentration of 5M. The authors reported synthesized zeolite A with peaks whose 2 theta values were similar to that obtained from this study. The peaks obtained for zeolite synthesized in this study that had the highest crystallinity had the diffraction peaks at 2Θ values of 7.18, 10.24, 12.49, 16.04, 20.46, 21.71, 24.04, 25.15, 30.01, 30.89, 32.68, 34.21, 36.64, 38.04, 39.62, 40.27, 42.38, 44.20, 44.85, and 49.83. These peaks obtained from this work were somewhat similar to that obtained from the works of Yusriadi *et al.* (2020) and Vegree *et al.* (2020)

However, zeolite synthesized at 6.5M also showed diffraction peaks that is similar to faujasites and this was also very evident in zeolite synthesized at 8M alkaline concentration. The other diffraction peaks observed are at 2Θ values of 6.19, 14.32, 24.75 28.87, 31.31, 32.13, 36.12, 37.81, 41.30, and 44.09. This result is in agreement with Al-Jubouri *et al.* (2019) that reported synthesizing zeolite A to a crystallization temperature as high as 125 ˚C at low alkalinity, but obtained a mixture of faujasite and zeolite A when the alkalinity is increased during the synthesis of zeolite A.

The zeolite synthesized at 150 ˚C had diffraction peaks at 2Θ values 20.83, 24.40, 25.37, 27.41, 31.58, 32.64, 34.75, 36.69, 39.51 and 42.89. These peaks obtained are also similar to those obtained by Nasief *et al.* (2021).

3.2 Effect of Variables on Synthesis of Zeolite A through Hydrothermal Method

3.2.1. Effects of Alkalinity

The alkaline concentration for the zeolite synthesis was varied from 5M, 6.5M and 8M. The XRD diffractogram showed that pure zeolite A was synthesized at 5M NaOH concentration while a mixture of zeolite A and faujesite was synthesized at 6.5M and 8M with 8M NaOH concentration having more faujesite peaks. This implies that increasing the alkaline concentration from 5M to 8M increased the formation of faujesite and this is in consistency with the work of Kwakye-Awuah *et al.* (2018). However, this is slightly different from Vegree *et al.* (2020) that reported the presence of zeolite NaP phases for all zeolite synthesized from kaolin irrespective of the alkaline concentration. In this work zeolites synthesized at 5M concentration were pure A only at higher concentration of 6.5 and 8M did peaks at 2Ɵ values of 13.96, and 14.3 emerge. Similarly, the authors noted the presence of quartz peaks at 26.7 for zeolites synthesized from kaolin, this is in conformity with this work as increasing alkaline concentration did not eliminate the impurity in the synthesized zeolite.

3.2.2. Effects of Metakaolinization temperature

Zeolite synthesis using kaolin calcined at different temperatures of 600,725 and 850 ˚C all yielded zeolite. It was however deduced that the crystallinity of the zeolite synthesized increased with increasing temperature of calcination. Furthermore, the quartz content of the zeolite decreased with increasing calcination temperature, this is evident in the decrease in intensity of peaks at 2Ɵ values of 26.7 as the calcination temperature increased from 600 to 725 and finally 850 ˚C. This finding is in appreciable consistency with the report of Belachaw and Hinsene (2020).

3.2.3. Effects of Crystallization temperature

In zeolite synthesis, crystallization temperature is said to alter the morphology of zeolite. Vegree *et al.* (2020) and Shamkhani *et al.* (2021) reported a change in the morphology when synthesizing zeolite, A as crystallization temperature increased above 80 ˚C. This is completely in contrast with the findings of this work as zeolite A was successfully synthesized at crystallization temperature of 80, 115 and 150 ˚C. These authors used alkaline concentration of 4M and 0.2 M respectively which is much lesser than 5M used for this study but reported a change in morphology and XRD patterns. The reason for the difference in findings may be attributed to the lower crystallization time (3h) used for this work in comparison to their longer time of 20h and 10h respectively. This work is in considerable agreement with the work of Nasief *et al.* (2021) as the authors synthesized zeolite A at 150 ˚C crystallization temperature with XRD patterns and morphology showing that zeolite A was synthesized. Furthermore, in relation to the crystallinity and crystal size of the synthesized zeolite, increasing crystallization temperature results in increase in both crystallinity and crystal size. This is in good agreement with the works of Kovo (2011) and Oyinade *et al.* (2016) that reported increasing crystallinity and crystal size in the synthesis of zeolite A and zeolite Y respectively from kaolin.

3.2.4. Effects of Stirring Time during Aging

The stirring time during aging was studied as a variable that affects zeolite synthesis. In the course of this study, it was observed that with respect to crystallinity and crystal size of the synthesized zeolite, stirring time did not have a much effect during zeolite synthesis, when stirring time was varied from 1, 2, and 3h, it was deduced that zeolite LTA was synthesized in each case and crystallinity increased very slightly with increasing time. This result is in good agreement with the work of Ayele *et al.* (2016) and Kovo (2011) that reported that varying stirring time during aging did not transcend to very high crystallinity of zeolite.

3.3. Sem Analysis

The morphology of the synthesized zeolite A was obtained via SEM. The micrographs shown in Figure 3.2 below depict cubic crystals with well-developed edges that are typical of zeolite A. This shape is in conformity with the findings of Maia *et al.* (2019), Otieno et al., (2019), Kovo (2011) and Salimkhani *et al.* (2021) who reported images having cubic morphology for zeolite A from kaolin as a starting material.

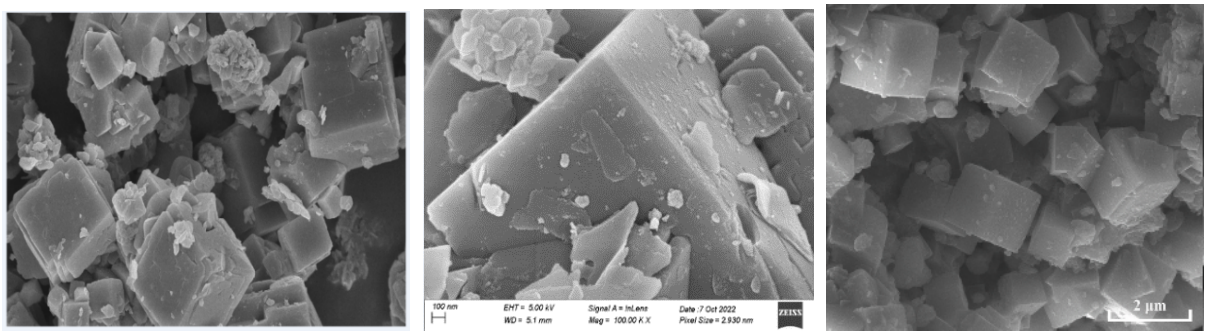

Figure 3.2. SEM images for zeolite A synthesized at 5M, 850 ˚C, 115 ˚C and 2h

4. CONCLUSION

This study found that zeolite A can be synthesized from Aloji kaolin via hydrothermal method. The effect of varying alkalinity, metakaolinization temperature, crystallization temperature, and stirring time during aging was investigated during synthesis. The characterization results of XRD and SEM indicated that, alkalinity of 5M, metakaolinization temperature of 850 ˚C, crystallization temperature 115 ˚C and stirring time of 2h gave only pure zeolite A with the best crystallinity and cubic morphology. In addition, it was found that increasing crystallization temperature and metakaolinization temperature increases crystallinity and crystal size while stirring time did not have significant effect on zeolite A synthesis. Alkalinity is the major parameter that determines the type of zeolite synthesized, thus increasing alkalinity above 5M would yield a combination of zeolites.

ACKNOWLEDGMENT

The research was mostly carried out with funding support from Tertiary Education Trust Fund (TETFund) National Research grant TETFUND/ES/DR/&D-CE/NRF/2020/SETI/116/Vol.1

REFERENCE

Abukhadra, M.R., Ibrahim, S.M., Yakout, S.M., El-Zaidy, M.E., & Abdeltawab, A.A. (2019). Synthesis of Na+ trapped bentonite/zeolite-P composite as a novel catalyst for effective production of biodesiel from palm oil; Effect of ultrasonic irradiation and mechanism. *Energy Conversion and Management,* 196:739-750.

Albert, C. A., Asadu, C.O., & Mark A. Abuh, M.A (2018). Synthesis of Zeolite by Thermal Treatment Using Locally Sourced Ugwaka Clay (Black Clay). *Journal of Materials Science Research and Reviews,* 1(2), pp. 1-12.

Al-Jubouri, M. S., Adil Sabbar, H., Lafta, H. A., and Waisi, B. I. (2019). Effect Of Synthesis Parameters on the Formation 4A Zeolite Crystals: Characterization Analysis and Heavy Metals Uptake Performance Study for Water Treatment. *Desalination and Water Treatment*, 165 290–300.

Arasi, M. A., Salem, A., & Salem, S. (2021). Production of Mesoporous and Thermally Stable Silica Powder from Low Grade Kaolin Based on Eco-Friendly Template free Route via Acidification of Appropriate Zeolite Compound for Removal of Cationic Dye from Wastewater. *Sustainable Chemistry and Pharmacy* 19.

Ayele, L., Perez-Pariente, J., Chebude,Y., & Díaz, I. (2016). Conventional versus alkali fusion synthesis of zeolite A from low grade kaolin. *Applied Clay Science*, 132–133,485–490

Belachew,N., & Hinsene, H. (2021). Preparation of Zeolite 4A for Adsorptive Removal of Methylene Blue: Optimization, Kinetics, Isotherm, and Mechanism Study. *Silicon*

Binay, M.I., Kirdeciler, S.K., & Akata, B. (2019). Development of antibacterial powder coatings using single and binary ion-exchanged zeolite A prepared from local kaolin. *Applied Clay Science,* 182

Derbe, T., Temesgen, S., and Bitew, M. (2021). A Short Review on Synthesis, Characterization, and Applications of Zeolites. *Advances in Materials Science and Engineering.*

He, Y., Tang, S., Yin, S., & Li, S (2021). Research progress on green synthesis of various high-purity zeolites from natural material-kaolin. *Journal of Cleaner Production,* 306 (2021) 127248.

Johnson, E.B.G, Arshad, S.E., & Asik, J (2014). Hydrothermal Synthesis of Zeolite A using Natural Kaolin from KG. Gading Bongawan Sabah. *Journal of Applied Sciences*, 14(23), pp. 3282-3287.

Joseph, I.V., Tosheva, L., & Doyle, A.M. (2020). Simultaneous removal of Cd (II), Co (II), Cu (II), Pb (II), and Zn (II) ions from aqueous solutions via adsorption of FAU-type zeolites prepared from coal fly ash. *Journal of Environmental Chemical Engineering* 8(4), 103895.

Kamyab, S. M., & Williams, C. D. Pure zeolite LTJ synthesis from kaolinite under hydrothermal conditions and its ammonium removal efficiency. *Microporous and Mesoporous Materials*. 318(2021)111006

Ke, G., Shen, H., and Yang, P. (2019). Synthesis of X-Zeolite from Waste Basalt Powder and its Influencing Factors and Synthesis Mechanism. *Materials,* 12, 3895

Khaleque, A., Alam, M.M. Hoque, M., Mondal, S., Haider,J.B., Xu, B., Johir, M.A.H., Karmakar, A.K. Zhou, J.L., Ahmed, M.B., & Moni, M.A. (2020). Zeolite synthesis from low-cost materials and environmental applications: A review. *Environmental Advances 2*, 100019

Kirdeciler, S. K. & Akata, B. One pot fusion route for the synthesis of zeolite 4A using kaolin. *Advanced Powder Technology,* 31 (2020) 4336–4343

Klunk, M. A., Das, M., Dasgupta, S., Impiombato, N. A., Caetano, N. R., Wander, P. R., and Moraes, C. A. M. Comparative study using different external sources of aluminum on the zeolite's synthesis from rice husk ash. *Materials Research Express* 7 (2020)015023.

Kovo, A.S. (2011). Development of Zeolite and Zeolite membrane from Ahoko Nigerian kaolin. PhD Thesis, University of Manchester, United Kingdom.

Krisnandi, Y.K., Saragi, I.R., Sihombing1, R., Ekananda, R., Sari, I.P., Griffith B.E., and Hanna, J.V. (2019). Synthesis and Characterization of Crystalline NaY-Zeolite from Belitung Kaolin as Catalyst for n-Hexadecane Cracking. *Crystals,* 9, 404; doi:10.3390/cryst9080404

Kumar, M.M & Jena, H (2022). Direct single-step synthesis of phase pure zeolite Na–P1, hydroxy sodalite and analcime from coal fly ash and assessment of their Cs+ and Sr2+ removal efficiencies. *Microporous and Mesoporous Materials,* 333 (2022) 111738.

Liu, Y., Han, S., Guan, D., Chen, S., Wu, Y., Yang, Y., & Jiang, N (2019). Rapid green synthesis of ZSM-5 zeolite from leached illite clay. *Microporous and Mesoporous Materials,* 280 (2019) 324–330

Mahesh, M., Thomas, J., Kumar, K.A., Bhople, B.S., Saresh, N.V., Vaid, S.K., & Sahu, S.K (2018). Zeolite Farming: A Sustainable Agricultural Prospective. *International Journal of Current Microbiology and Applied Sciences,* 7(5), pp.2912-2924.

Maia, A. B., Dias, R. N., Rômulo, S. A., and Neves, R.F. (2019). Influence of an aging step on the synthesis of zeolite NaA from Brazilian Amazon kaolin waste. *Journal of Material Research and Technology*; 8(3):2924–2929

Meftah, M., Oueslati, W., Chorfi, N., Abdesslem, B.H (2017). Effect of the raw material type and the reaction time on the synthesis of halloysite based Zeolite Na-P1. *Results in Physics,* 7, pp. 1475–1484.

Nasief, F.M., Shaban, M., Alamry, K.A., Abu Khadra, M.R., Khan,A.A.P., Asiri, A.M., & Abd El-Salam, H.M. Hydrothermal synthesis and mechanically activated zeolite material for utilizing the removal of Ca/Mg from aqueous and raw groundwater. *Journal of Environmental Chemical Engineering,* 9 (2021)105834

Nayak, S.K., & Mohanty, S.R (2019). Zeolite Synthesis from Waste and its Applications: A Retrospective. *International Journal of Innovative Science and Research Technology,* 4(2), pp. 2456-2165.

Nyankson, E., Efavi, J.K., Yaya, A., Manu,G., Kingsford, A., Daafour, J., & Abrokwah, R.Y. (2018). Synthesis and Characterisation of Zeolite-A and Zn Exchange Zeolite-A based on Natural Aluminosilicates and their Potential Applications. *Cogent Engineering*

Olaremu, A.G., Odebunmi, E.O., Nwosu, F.O., Adeola, A.O. & Abayomi, T.G. (2018). Synthesis of Zeolite from Kaolin Clay from Erusu Akoko Southwestern Nigeria. *Journal for Chemical Society of Nigeria,* 43 (3), pp. 381-786

Otieno, S.O., Kengara, F.O., Kemmegne-Mbouguen, J.C., Langmi, H.W., Kowenje, C.B.O., & Mokaya, R. The effects of metakaolinization and fused-metakaolinization on zeolites synthesized from quartz rich natural clays. *Microporous and Mesoporous Materials,* 290 (2019) 109668

Oyinade, A., Kovo, A.S., & Hill, P. (2016). Synthesis, characterization and ion exchange isotherm of zeolite Y using Box–Behnken design. *Advanced Powder Technology*, 27, 750–755

Pereira, P.M., Ferreira, B.F., Oliveira, N.P., Nassar 1, E.J., Ciuffi, K.J., Vicente, M.A., Trujillano, R., Rives, V., Gil, A, Korili, S., & Emerson, H (2018). Synthesis of Zeolite A from Metakaolin and its Application in the Adsorption of Cationic Dyes. Applied Science 2018, 8, 608; doi: 10.3390/app8040608

Rengaraj, S., Yeon, K.-H., & Moon, S.-H. (2001). Removal of chromium from water and wastewater by ion exchange resins. *Journal of Hazard Materials.* 87 (1–3) 273–287.

Rozhkovskaya, A., Rajapakse, J., & Millar, G.J (2021). Synthesis of high-quality zeolite LTA from alum sludge generated in drinking water treatment plants. *Journal of Environmental Chemical Engineering*,9(2021)104751.

Salimkhani, S., Siahcheshm, K., Kadkhodaie, A., & Salimkhani, H (2021). Structural analysis and the effect of the chromium on LTA (Na) zeolite synthesized from kaolin. *Materials Chemistry and Physics*, 271 (2021) 124957.

Schwanke, A.J., Silveira, D.R., Puton, B.M.S., Cansian, R.L., & Bernardo-Gusm˜ao, K (2022). Sustainable conversion of Brazilian Amazon kaolin mining waste to zinc-based Linde Type A zeolites with antibacterial activity. *Journal of Cleaner Production*

Shehu, Kovo A.S., Azeez, S.O., Saka, A.A., & Salako O (2018). Production Of 100 Kg/Day of Zeolite a as a Builder for Powdered Detergent from Nigerian Ahoko Kaolin Using Locally Fabricated Mini Zeolite Plant. IOP Conference Series: Materials Science and Engineering 413 (2018)012064doi:10.1088/1757-899X/413/1/012064

Sivalingam, S., & Sujit, S. (2018). Optimization of Synthesis Parameters and Characterization of Coal Fly Ash Derived Microporous Zeolite X. *Applied Surface Science*

Vegere, K., Kravcevica, R., Krauklis, A.E., & Juhna, T. (2020). Comparative study of hydrothermal synthesis routes of zeolite A. *Materials Today: Proceedings* https://doi.org/10.1016/j.matpr.2020.06.326

Yoldi, M., Fuentes-Ordonez, E.G., Korili, S.A., & Gil, A. (2020). Zeolite synthesis from industrial wastes. *Microporous and Mesoporous Materials*, 287 (2019) 183–-191.
Youcef, L.D., López-Galindo, A., Verdugo-Escamilla, C., & Belaroui, L.S (2020). Synthesis and characterization of zeolite LTA by hydrothermal transformation of a natural Algerian palygorskite. *Applied Clay Science*, 193 (2020) 10569

Yusriadi, Y., Sulastri, E., & Lembang, N.P (2020). Synthesis of Type A Zeolite from Rice Husk Ash and Its Application as a Builder on Effervescent Tablet Form Detergent. *Tenside Surfactant Detergent,* 57 (2020) 3.

Zhang, C., Li, S., & Bao, S. (2019). Sustainable synthesis of ZSM-5 Zeolite from Rice Husk Ash without Addition of Solvents. *Waste and Biomass Valorization* 10; 2825-2835.

PAPER 220 – OPTIMIZATION OF SOME SELECTED PROPERTIES FOR BIOPLASTIC PRODUCTION FROM WASTE CASSAVA AND POTATO PEELS

K. W. Tambari* and Y. Adamu

Department of Chemical Engineering, Ahmadu Bello University, Zaria, Nigeria.
*Email: kaseemwaziry@gmail.com

ABSTRACT

Starch-based bioplastics produced using waste cassava peel and potato peel. Glycerol and white vinegar used as plasticizers, while Kenaf nanofiber used as reinforcement. 3:1 ratio of cassava to potato starch was mixed with different proportions of additives (glycerol, kenaf and white vinegar) at a temperature of 50℃ for 20 minutes. The percentage proportion of the two alpha glucan types (amylose and amylopectin) showed that Potato Peels starch has 27.22% amylose and 72.78 % amylopectin while Cassava Peels starch has 13.13% amylose and 86.87% amylopectin. Optimization was carried out on the waste starch (CP and PP) and was found that the optimal values were gotten at 8. wt% K, 2 ml G, and 2.5 ml WV with a predicted TS and WA values of 2.465 MPa and 7.56 % respectively. Aspergillus Niger was used as a microorganism to monitor weight loss after 10 days for biodegradation. It was found that, run 1 (8% kenaf, 5ml glycerol and 2.5ml white vinegar) has the highest weight loss of 69.66% while the optimized value for the weight loss was 42.05%. Therefore, the optimal sample in terms of tensile strength and water intake can be degraded in 43.90 days.

KEYWORDS: Bioplastic, Cassava-peel, Potato-peel, Optimization, Mechanical Properties

1 INTRODUCTION

In recent decades, interest in developing renewable materials with biodegradable properties has increased in order to contribute to sustainable development and reduce the environmental impact of non-biodegradable petroleum-based plastics (Thakur *et al*., 2018; Moshood *et al*., 2022). To solve this problem, several studies have been reported using biodegradable starch from different sources to create films and coatings with different properties (Kumar *et al*., 2022; Kocira *et al*., 2021; Shivangi *et al*., 2021). Starch is an important polysaccharide polymer used in the design of biodegradable films due to its potential to form continuous matrices. Interest in antimicrobial polymer packaging is growing rapidly today, especially in the medical, healthcare and food industries (Vieira *et al*., 2022; Teixeira-Costa *et al*., 2022; Priyadarshi *et al*., 2022; Saha *et al*., 2020). Antimicrobial polymer wraps are one of the most promising active packaging systems that have been used to protect surfaces from microorganisms such as parasites, bacteria and fungi (Manzoor *et al*., 2023; Jafarzadeh *et al*., 2022; Nizam *et al*., 2021; Suvarna *et al*., 2022).

Plastic waste can harm the environment if left unchecked, and affect living things such as humans, plants and animals (Singh *et al*., 2020; Kilic, 2021; Olufunke 2022). This is because most plastics are made from non-biodegradable petrochemical-based polymers. Economic, environmental, and safety concerns have led scientists to invent biodegradable polymers (bioplastics) as an alternative (Sid *et al*., 2021; Rahman *et al*., 2019). Unfortunately, the development of bioplastics is costly and process-dependent, requiring additives such as fillers, colorants and plasticizers (Adams *et al*., 2022). In Southeast Asia, abundant agricultural waste such as cassava husks is seen as an excellent alternative to replace synthetic plastics. Plasticizers and fillers must be added to improve the properties of bioplastics (Acquavia *et al* 2021; George *et al*., 2021; Bhardwaj *et al*., 2020).

The main aim of this present work is to produce bioplastics from waste biomaterial by optimizing the amount of reinforcement, plasticizers etc.

2 MATERIALS AND METHODS

2.1 Materials

Cassava (Manihot esculenta) peels were sourced from Bomo village Zaria, Kaduna State, *Niger*ia. Potato peels were gotten from Ahmadu bello university Zaria (ABU), Zaria, Kaduna State. While, the Aspergillus *Niger* were obtained from the culture selection unit of the Microbiology ABU Zaria. Glycerol, Distilled water, White vinegar and other chemicals used for this study were of analytical grade and were obtained from chemical shops in Zaria).

2.2 Methods

Figure 1 shows the flow chart for the production of bioplastic from the sourcing of the raw materials down to the final production stage.

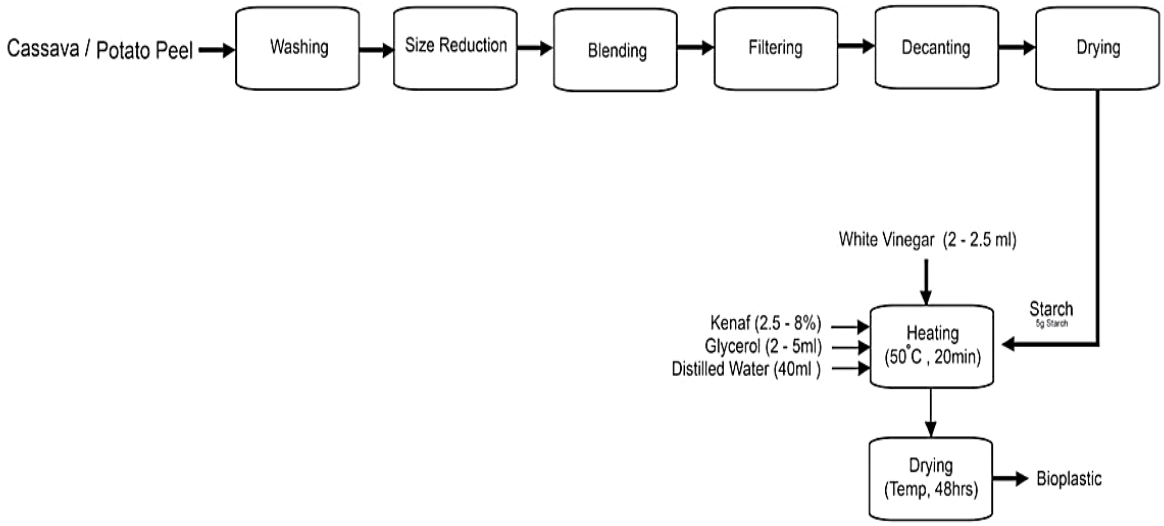

Figure 1: Flow chart for the production of bioplastics

2.2.1 Extraction of starch from cassava and potato peels

The cassava and potato peels were collected, washed, dried and then mashed with a mechanical grater (Figure 1). The grated cassava and potato peels was mixed with water three (3) times the volume of the grated cassava peels. The mixture was sieved and filtered using a coarse sieve and filter cloth respectively. Thereafter, the filtrate was allowed to settle for seven (7) hours. The resulting starch was mixed with water again and allowed to settle for four (4) hours. The starch (wet) was dewatered manually and then open-dried at room temperature for another 4 hours. Figure 2 shows the starch produced after the fourth hour.

Figure 2: Starch produced

2.2.2 Production of bioplastic films

From Figure 1, 17 samples of bioplastic films were produced (design of experiment) using the same quantity of starch, 75% w/w cassava and 25% w/w potato of 5g of starch and different proportion of glycerol, kenaf nano fiber and white vinegar. Different proportion of glycerol, kenef and white vinegar were weighed (glycerol 2ml to 5ml, Kenaf 2.5% to 8.0% and white vinegar 2ml to 2.5ml). Each of the quantity was mixed with 40ml distilled water of glycerol. The mixture was stirred to yield a desired mixture. After which the mixture was heated at 50°C for twenty minutes to produce a biodegradable film as shown in Figure 3, while Figure 4 shows the dried samples of the bioplastics.

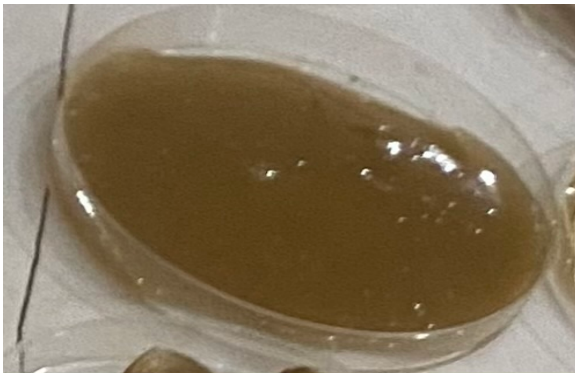

Figure 3 Bioplastics film before drying

Figure 4 Bioplastic films after drying

2.2.3 Biodegradation preparation

Aspergillus Niger was homogenized with 10 mL sterile aquadest using McFARLAND turbidity standard a wire loop to obtain spore suspension as the stock culture. Into 9 mL of sterile aquadest, 1 mL stock culture was added and the mixture was mixed by vortex to get a 10^{-1}culture. Into 9 mL of sterile aquadest, 1 mL of 10^{-1}culture was added and the mixture was mixed by vortex to get a 10^{-2} culture. An amount of 100 µL of 10^{-2} culture was added into a sterile petri dish. Each dish was added with 20 mL of SA media (44°C - 47°C). Petri dish was then stirred to make the mixture homogenous and the mixture was left for about 2 hours until it became solid. After 2 hours, samples of bioplastic, synthetic plastic were each placed onto solid Potato Dextrose Agar (PDA) media surface. One-hundred µl of 10^{-2}culture was spread equally onto bioplastic samples. Bioplastic samples and controls were incubated at 30°C for 10 days as shown in Figures 5 – 7.

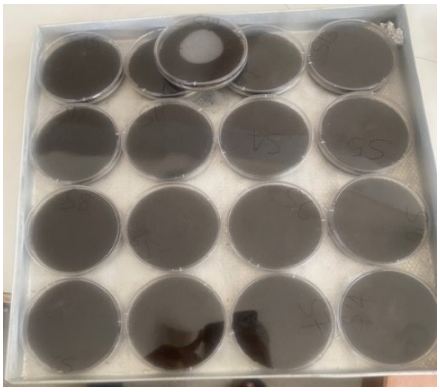

Figure 5 *A. niger* culturing

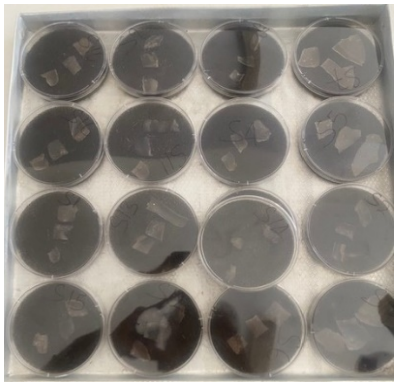

Figure 6 Samples preparation

Figure 7 Samples after 10 days

3.0 RESULTS AND DISCUSSION

3.1 Determination of Amylose and Amylopectin Contents

After the extraction of starch from cassava and potato peels, two types of alpha-glucans (Amylose and Amylopectin) test were carried out (Table 1). It showed that 27.22% amylose and 72.78% amylopectin where present in the potato starch peel, while cassava peels starch contained 13.13% amylose and 86.87% amylopectin.

Table 1: Amylose and amylopectin analysis of cassava and potato peel starch

S/No	Samples	Amylose Contents (mg/ml)		Percentage (%)			
				Amylose		Amylopectin	
1	Potato peel starch	12.47	14.75	24.94	29.50	75.06	70.50
2	Cassava peel starch	7.11	6.01	12.02	14.23	85.77	87.98

Figures 8 – 10 shows the tensile strength, modulus and water absorption analysis of the bioplastic films. The bioplastic films of varying plasticizer (glycerol), reinforcement (Kenaf) and white vinegar were produced as shown in Figure 4. The tensile strength of the samples was tested using a tensile strength testing machine (TM210T-7) at a crosshead of 2 mm/min and the result was captured in Figure 8. A water intake test was carried out for 24 hours to monitor the amount of water intake after 24 hours (Figure 10).

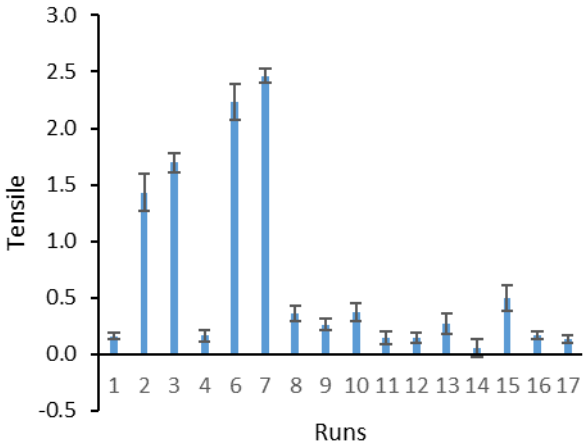

Figure 8: Tensile strength test

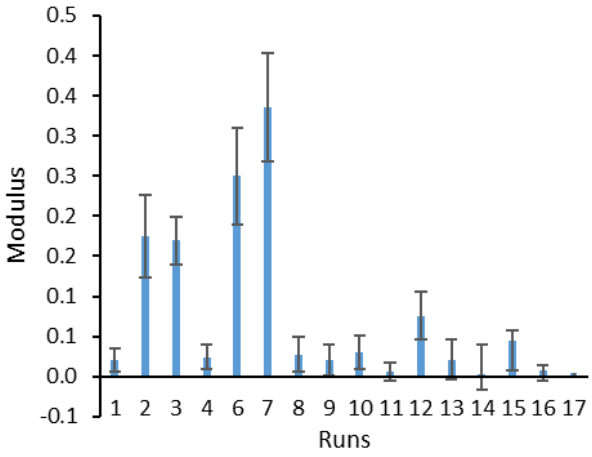

Figure 9: Modulus of elasticity

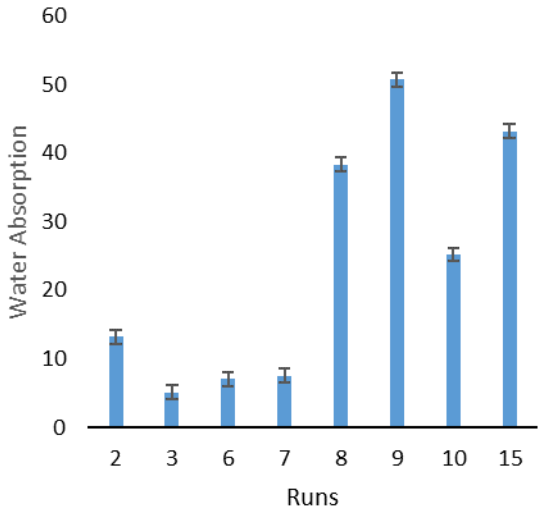

Figure 10: Water absorption

From Figure 8 it was showed that run 7(8% kenaf, 2ml glycerol and 2.5ml white vinegar) gives the highest tensile strength due to the high percentage of kenaf that served as reinforcement and the minimum amount of glycerol and white vinegar to reduces the brittleness of the material while run 14 (5.25% kenaf, 6ml glycerol and 2.25ml white vinegar) gives the lowest tensile strength due to the high amount of glycerol which make the material high hydrophilic in nature and at the same time reduces the strength**.** Figure 9 showed that the higher the strength the higher the modulus of elasticity. While, Figure 10 showed that run 9(0.6% kenaf, 3.5ml glycerol and 2.25ml white vinegar) absorbed much water due to insignificant amount of reinforcement and also high amount of glycerol.

3.3 Biodegradability Test Result

Qualitative biodegradability tests were carried out by using a modified ASTM G21-70. This method commonly uses fungi (*A. Niger*) was used as the decomposing agent. *A. Niger* is easy to identified as contaminant fungi widely spread in the air.

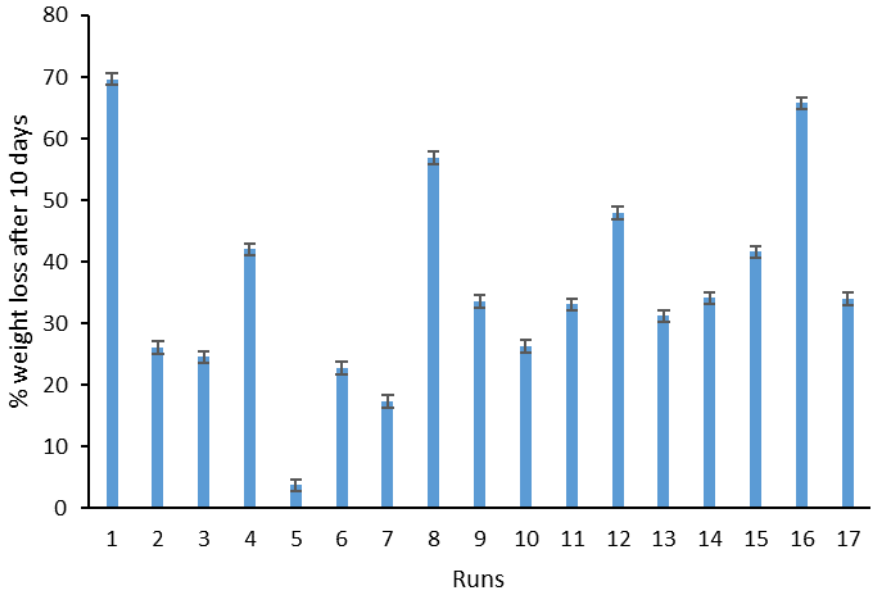

Figure 11 Biodegradation test results

Figure 11 shows the biodegradation using *Aspergillus niger* after 10 days with run 1 (8% kenaf, 5ml glycerol and 2.5ml white vinegar) having the highest weight loss of 69.66%, while the optimized value for the weight loss was 42.05%.

4. CONCLUSION

i. Design expert software was used to obtain the optimum number of runs to perform in the laboratory using response surface (RS) design and Box-Behnken (by varying three parameters glycerol, kenaf and white vinegar at center point of three). A minimum of 17 runs was obtained.

ii. Starch extracted from cassava and potato peels has two types of alpha glucan (amylose and amylopectin). potato peel starch has 27.22% amylose and 72.78% amylopectin while cassava starch contained 13.13% amylose and 86.87% amylopectin.

iii. A material is defined as bioplastics if it is either biobased, biodegradable or features both properties. The bioplastics produced are starch based and biodegradable.

iv. Converting waste that could have been wasted and pollute the environment due to their toxin smell into useful product indeed added value to the waste.

v. Optimization was carried out on the waste starch (CP and PP) and was found that the optimal values were gotten at 8. wt% K, 2 ml G, and 2.5 ml WV with a predicted TS and WA values of 2.465 MPa and 7.56 % respectively. The experimental values gotten are 2.515 MPa and 6.12 % for tensile strength and water absorption with an error of 2 % and 24 % respectively.

ACKNOWLEDGEMENT

I will like to acknowledgement Ahmadu Bello University, Zaria for giving me the platform to carry out this research work. Also, my special gratitude goes to my parents Alhaji Tambari Waziri and Hajiya sa'adatu umar kigo and also my cousin Engr. Jamil Abubakar Marafa for their encouragement, moral upbringing and tireless support.

REFERENCES

Acquavia, M. A., Pascale, R., Martelli, G., Bondoni, M., & Bianco, G. (2021). Natural polymeric materials: A solution to plastic pollution from the agro-food sector. *Polymers*, *13*(1), 158.

Adams, T., Schoch Jr, K. F., Pelczar, E., Xia, H., Hu, X., Reynaud, S., & Sauerbrunn, S. (2022). Abstracts of the 2022 48th Annual NATAS Conference.

Bhardwaj, A., Alam, T., Sharma, V., Alam, M. S., Hamid, H., & Deshwal, G. K. (2020). Lignocellulosic agricultural biomass as a biodegradable and eco-friendly alternative for polymer-based food packaging. *Journal of Packaging Technology and Research*, *4*, 205-216.

George, N., Debroy, A., Bhat, S., Bindal, S., & Singh, S. (2021). Biowaste to bioplastics: An ecofriendly approach for a sustainable future. *Journal of Applied Biotechnology Reports*, *8*(3), 221-233.

Jafarzadeh, S., Hadidi, M., Forough, M., Nafchi, A. M., & Mousavi Khaneghah, A. (2022). The control of fungi and mycotoxins by food active packaging: A review. *Critical Reviews in Food Science and Nutrition*, 1-19.

Kilic, Z. (2021). Water pollution: causes, negative effects and prevention methods. *İstanbul Sabahattin Zaim Üniversitesi Fen Bilimleri Enstitüsü Dergisi*, *3*(2), 129-132.

Kocira, A., Kozłowicz, K., Panasiewicz, K., Staniak, M., Szpunar-Krok, E., & Hortyńska, P. (2021). Polysaccharides as edible films and coatings: Characteristics and influence on fruit and vegetable quality—A review. *Agronomy*, *11*(5), 813.

Kumar, L., Ramakanth, D., Akhila, K., & Gaikwad, K. K. (2022). Edible films and coatings for food packaging applications: A review. *Environmental Chemistry Letters*, 1-26.

Manzoor, A., Khan, S., Dar, A. H., Pandey, V. K., Shams, R., Ahmad, S., ... & Pandiselvam, R. (2023). Recent insights into green antimicrobial packaging towards food safety reinforcement: A review. *Journal of Food Safety*, e13046.

Moshood, T. D., Nawanir, G., & Mahmud, F. (2022). Sustainability of biodegradable plastics: a review on social, economic, and environmental factors. *Critical Reviews in Biotechnology*, *42*(6), 892-912.

Nizam, N. H. M., Rawi, N. F. M., Ramle, S. F. M., Abd Aziz, A., Abdullah, C. K., Rashedi, A., & Kassim, M. H. M. (2021). Physical, thermal, mechanical, antimicrobial and physicochemical properties of starch based film containing aloe vera: A review. *Journal of Materials Research and Technology*, *15*, 1572-1589.

Olufunke, K. A. (2022). Water Pollution in *Niger*ia and Its Effect on Agriculture: A Case Study of *Niger* Delta. *Res. & Sci. Today*, *23*, 21.

Priyadarshi, R., Roy, S., Ghosh, T., Biswas, D., & Rhim, J. W. (2022). Antimicrobial nanofillers reinforced biopolymer composite films for active food packaging applications-a review. *Sustainable Materials and Technologies*, *32*, e00353.

Rahman, R., Sood, M., Gupta, N., Bandral, J. D., Hameed, F., & Ashraf, S. (2019). Bioplastics for food packaging: a review. *Int. J. Curr. Microbiol. Appl. Sci*, *8*(3), 2311-2321.

Saha, T., Hoque, M. E., & Mahbub, T. (2020). Biopolymers for sustainable packaging in food, cosmetics, and pharmaceuticals. In *Advanced Processing, Properties, and Applications of Starch and Other Bio-Based Polymers* (pp. 197-214). Elsevier.

Shivangi, S., Dorairaj, D., Negi, P. S., & Shetty, N. P. (2021). Development and characterisation of a pectin-based edible film that contains mulberry leaf extract and its bio-active components. *Food Hydrocolloids*, *121*, 107046.

Sid, S., Mor, R. S., Kishore, A., & Sharanagat, V. S. (2021). Bio-sourced polymers as alternatives to conventional food packaging materials: A review. *Trends in Food Science & Technology*, *115*, 87-104.

Singh, J., Yadav, P., Pal, A. K., & Mishra, V. (2020). Water pollutants: Origin and status. *Sensors in water pollutants monitoring: Role of material*, 5-20.

Suvarna, V., Nair, A., Mallya, R., Khan, T., & Omri, A. (2022). Antimicrobial nanomaterials for food packaging. *Antibiotics*, *11*(6), 729.

Teixeira-Costa, B. E., & Andrade, C. T. (2022). Natural polymers used in edible food packaging—History, function and application trends as a sustainable alternative to synthetic plastic. *Polysaccharides*, *3*(1), 32-58.

Thakur, S., Chaudhary, J., Sharma, B., Verma, A., Tamulevicius, S., & Thakur, V. K. (2018). Sustainability of bioplastics: Opportunities and challenges. *Current opinion in Green and Sustainable chemistry*, *13*, 68-75.

Vieira, I. R. S., de Carvalho, A. P. A. D., & Conte-Junior, C. A. (2022). Recent advances in biobased and biodegradable polymer nanocomposites, nanoparticles, and natural antioxidants for antibacterial and antioxidant food packaging applications. *Comprehensive Reviews in Food Science and Food Safety*, *21*(4), 3673-3716.

PAPER 221 – BIODIESEL PRODUCTION FROM WASTE COOKING OIL: THE INFLUENCE OF HIERARCHICAL AND CONVENTIONAL BETA ZEOLITE ON YIELD AND QUALITIES

A. Babashehu[1*], E.A. Afolabi[1], R.S. Safiyanu[1], A.S. Kovo[1], F.O. Bello[1]

[1]Department of Chemical Engineering, Federal University of Technology, Minna, Nigeria.
Email: aisha2018shettima@gmail.com

ABSTRACT

This study reports biodiesel production from waste cooking oil: the influence of hierarchical and conventional beta zeolite catalyst on yield and qualities. Both commercial zeolite beta (CZB) and hierarchical zeolite beta (HZB) synthesized from Ahoko kaolin were characterized using X-Ray diffraction (XRD), Scanning electron microscopy (SEM), and Energy Dispersive X-ray (EDX) analysis. The XRD of CZB shows a series of characteristic diffraction peaks assigned to the zeolite beta type as its fingerprint. It can be seen that zeolites beta had strong characteristic peaks at position 2θ of 7.8°, 21.6°, 22.6°, 25.3°, 27.0°, and 29.6° while the SEM/EDX determined the crystal size and the morphology, the sample maintains the same surface structure of beta zeolite even after it was protonated. From the EDX, the CZB Si/Al ratio was calculated to be 1.59. HZB gave a biodiesel yield of 91.67 % at a methanol-to-oil ratio of 9:1, while CZB gave a yield of 84.0 % at the same condition. The reusability test carried out showed that at repeated 6th runs, biodiesel yield using the same HZB catalyst dropped to 75 % which was still much more active compared to the commercial zeolite Y (CZY) catalyst.

KEYWORDS: Biodiesel, Hierarchical zeolite beta, Commercial zeolite beta, Transesterification.

1. INTRODUCTION

In recent times, fossil-based fuels have been used to meet the global energy demand. These energy resources are non-renewable, and over usage of these fuels will lead to an energy crisis in the coming years (Meena *et al*., 2019, Sidhu et *al*., 2016). Hence, a need to research alternative sources of energy that are renewable to meet the ever-increasing energy demand (Parthiba *et al*., 2018, Patel *et al*., 2019, Toor et *al*., 2020). Biodiesel has received global attention in the energy sector due to its production from renewable materials (Anto *et al*., 2020, Bhatia *et al*., 2019, Nguyen *et al*., 2020). This is also because of it biodegradability, low Sulphur content, and its application in power engines with or without modification (Ma *et al*., 2018). Biodiesel mainly contains fatty acid alkyl esters obtained from the transesterification of oils with alcohol (Bhatia *et al*., 2017). Generally, living organisms contain oil present in the form of triacylglycerol. Biodiesel can be obtained from different edible (castor oil, sunflower oil, mustard oil, vegetable oil) and non-edible oils (Jatropha, jojoba oil, pogamia oil) (Bhatia *et al*., 2018, Thushari and Babel, 2018). The food security issues would restrict the use of edible oils for biodiesel production and the need for extra land for non-edible oil crops would also affect the production of biodiesel on a large scale. Hence, there is a need for alternative feedstock for biodiesel production.

Waste cooking oil (WCO) is the oil remaining after the deep-frying process (Bhatia *et al*., 2020). This oil is an alternative for the production of biodiesel. It was reported that approximately 16.5 million tons of WCO are produced annually (Loizides *et al.,* 2019). The Management of WCO is also an issue as its disposal in open spaces affects flora and fauna due to its lower solubility in water. The collection of WCO and its conversion into biodiesel may help to solve its disposal problem and will contribute to the energy sector.

Biodiesel is produced through transesterification reactions and requires alkaline, acidic or enzymatic catalysts. Alkali catalysts have a saponification problem and result in difficulty in product separation. Concentrated sulfuric acid is able to catalyze esterification and transesterification reactions simultaneously but cause corrosion of equipment and generates a lot of wastewaters (Li *et al*., 2014). Hierarchical Zeolite beta is an intergrowth hybrid of two distinct structures and has a stacking order and disorder co-existing. This structure makes zeolite beta hydrophobic and thermally stable even at high temperatures. Hierarchical Zeolite beta has many advantages due to the improved mass transport and tunable active sites and hence can be used for the catalytic conversion of waste vegetable oils to biodiesel (Tian *et al*., 2016).

In this work, Biodiesel was produced from waste cooking oils using the Hierarchical and conventional Beta Zeolite catalyst. The influence of the two catalysts on the quality and yield of the biodiesel was also further investigated to understand the optimum condition of production.

2. MATERIALS AND METHODS

2.1 MATERIALS

Waste cooking oil (WCO) was collected from Esther Restaurant Minna, Niger State, and pre-treatment processes were carried out to remove impurities. The major pre-treatment processes conducted were filtration and dehydration. The commercial beta zeolites that were used in this study as catalysts were provided by Zeolite International, China.

2.2 PROTONATION PROCESS AND CHARACTERIZATION

The commercial beta zeolite sample was crushed and then brought into a protonic form whereby 0.1 M of NH_4NO_3 was prepared and then mixed with a certain amount of beta sample. The heat was applied to the mixture under reflux at 90 °C for 2 h, and afterward, filters and oven dried at 80 °C then calcined in static air at 550 °C for 3 h. The raw beta zeolite produced from Ahoko kaolin was also undergone a protonation process and then calcined at 550 °C for 3 h in order to compare the two-catalyst effectiveness on biodiesel production. Both samples obtained were characterized using X-ray diffraction (XRD), Scanning Electronic Microscopy (SEM), and Brunnauer, Emmett, and Teller (BET) analyses.

2.3 CHARACTERIZATION OF SYNTHESIZED BETA ZEOLITE

2.3.1 X-RAY DIFFRACTION (XRD)

First, 2 g of beta zeolite sample was pressed in stainless steel holder and then identification of the crystalline phase was conducted by X-ray Diffractometer system named (EMPYREAN) using Cu as an anode material whereby Kα radiation operated at 45 kV, 40 mA with 0.026° 2θ step size and then scan speed continuously. High-quality diffraction data of the sample was obtaining via this method.

2.3.2 SCANNING ELECTRON MICROSCOPE (SEM) ANALYSIS

The physical surface morphology of the catalyst sample obtained was examined using LEO S-440 Scanning Electron Microscope. Little among of beta zeolite catalyst sample was raised on an aluminum holder by a double-sided tape. To avoid poor image resolution and discharge of electrostatics, the catalyst sample was coated with gold (Au) to a thickness of 1.5 to 3 nm. The test was conducted at different magnifications and data generated was recorded.

2.3.3 BRUNAUER, EMMEITT AND TELLER (BET) ANALYSIS

The BET apparatus analyzed the N_2 adsorption–desorption isotherms at liquid nitrogen temperature. Outgassing at 77.100 K with an equilibration interval of 10 seconds before each measurement ensured accurate results on all the samples. T-plot methods and Brunauer–Emmett–Teller (BET) were used to analyze the specific surface area, microporous area and microporous volume, and pore-size distribution.

3. RESULTS AND DISCUSSION

3.1 RESULTS OF PROTONATED AND CHARACTERIZATION OF BETA ZEOLITE

Figure 3.1 show the XRD pattern of protonated commercial zeolite beta (CZB) Sample to determine the crystalline phase.

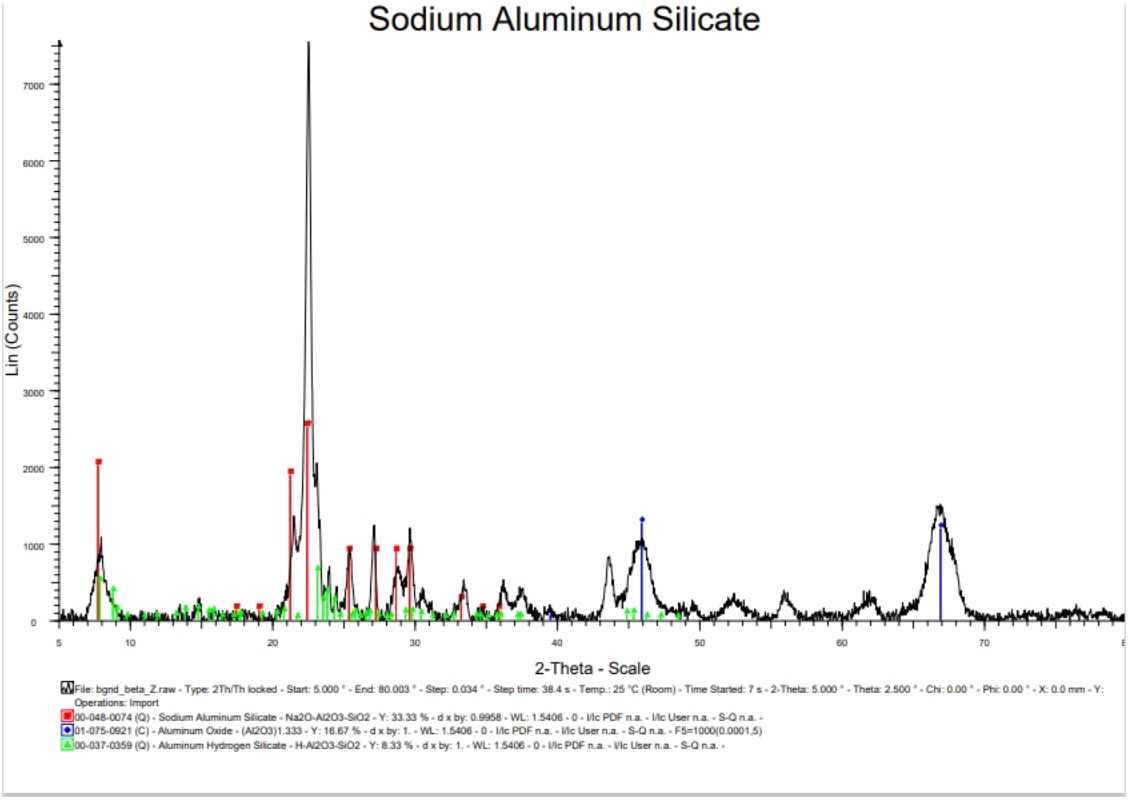

Figure 3.1: XRD pattern of commercial zeolite beta (CZB) sample

XRD patterns were taken to study the crystallinity of the zeolite beta sample. The XRD patterns of the zeolite samples can be found in Figure 3.1, the well-defined characteristic peaks of zeolite beta can be seen in Figure 3.1. These shows a series of characteristic diffraction peak assigned to the zeolite beta type as its finger print. It can be seen that zeolites beta had strong characteristic peak whereby the peaks occur at position 2θ of 7.8°, 21.6°, 22.6°, 25.3°, 27.0° and 29.6° (Qiang *et al,* 2010). It was also be observed that minor noise and background interferences were detected in patterns. The broad peaks observed are an indication of this structure's disordered nature.

3.2 SCANNING ELECTRON MICROSCOPY (SEM) ANALYSIS

SEM images were collected in order to study the shape and size of the particles, whereas EDX measurements were taken to determine the elemental composition of the zeolite samples. The following sets of images illustrate the SEM images collected, in varying magnifications, shown in Figure 1.

The SEM images in Figure 1a: showed the morphology of (CZB) catalyst. The sample maintains the same surface structure of beta zeolite even after it was protonated (1b). The SEM image (1c) of this sample indicated that this sample is crystalline.

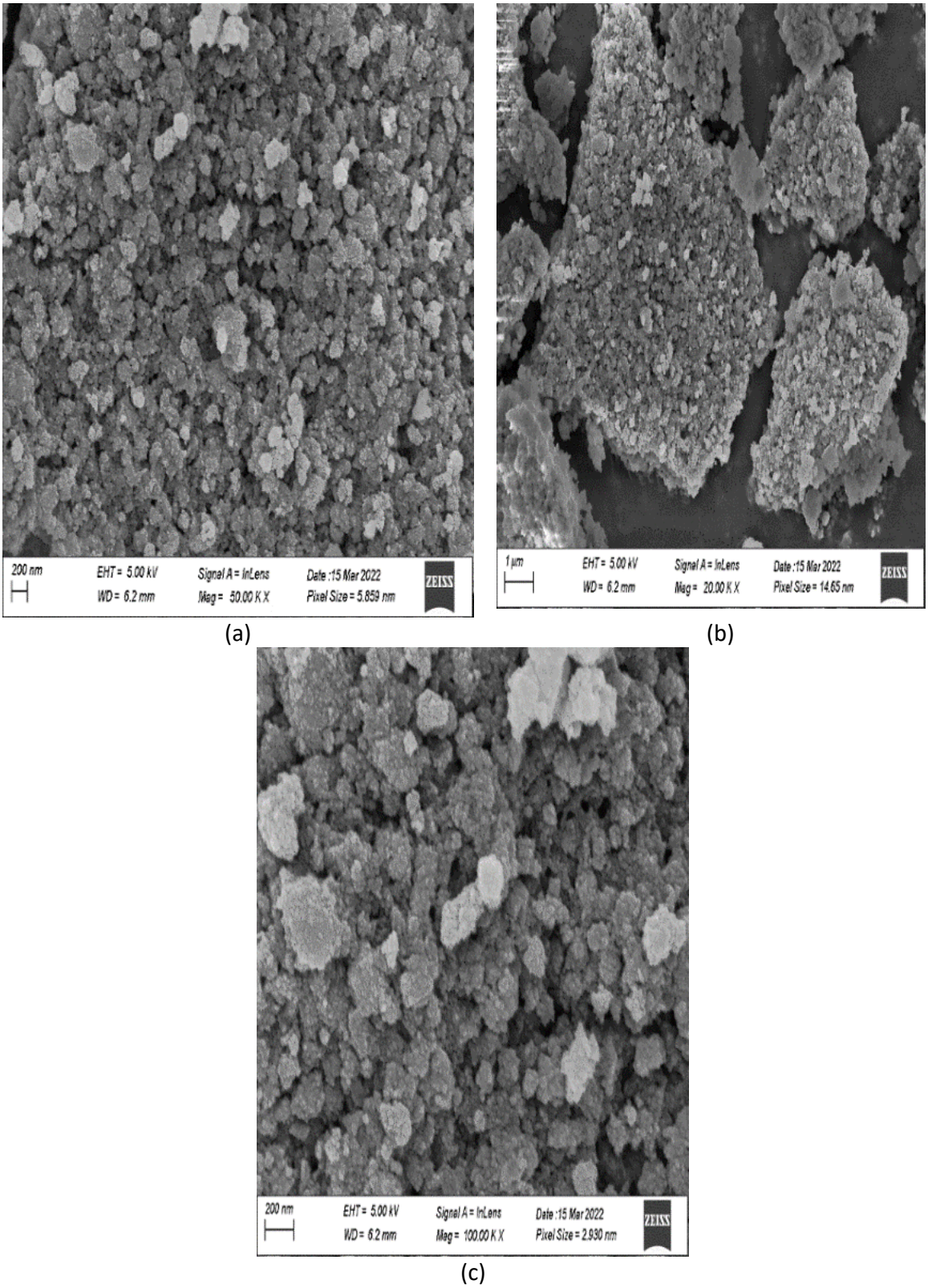

Figure 1: SEM micrograph of commercial zeolite beta (CZB) catalyst at different magnifications

3.3 OPTIMIZATION OF BIODIESEL PRODUCTION FROM WASTE COOKING OIL

Optimization of the transesterification process from Waste Cooking Oil) was conducted for both commercial zeolite beta catalyst and hierarchical zeolite beta catalyst produced. The parameters considered include methanol to oil ratio (A), reaction time (B), and catalyst dosage (C), and both results obtained were presented in Table 1.

Table 1: Result of optimization of biodiesel produced from WCO for both CZB and HZB catalyst

Run No.	A (v/v)	B (g)	C (mins)	Biodiesel Yield of CZB catalyst Value (%)	Biodiesel Yield of HZB catalyst Value (%)
1	6	1.4	120	66.00	74.0
2	9	1.8	90	65.33	79.33
3	6	0.2	60	72.00	70.15
4	3.9	0.8	90	66.67	69.33
5	14	0.8	90	72.0	77.79
6	12	0.2	120	66.67	80.07
7	9	0.0	90	47.67	48.00
8	9	0.8	90	70.99	82.01
9	6	0.2	120	67.00	74.99
10	9	0.8	90	84.00	92.00
11	12	1.4	60	62.50	83.00
12	9	1.0	90	70.93	86.50
13	9	0.8	40	58.87	77.98
14	9	0.8	90	68.33	83.00
15	12	1.4	120	66.67	80.06
16	6	1.4	60	66.67	77.99
17	14	0.8	90	75.33	81.77
18	9	0.8	120	67.48	83.00
19	12	0.2	60	66.67	69.94
20	9	0.8	140	77.33	87.00

The optimization study was carried out following the parameters investigated that is, methanol/oil molar ratio, catalyst dosage, and reaction time which were shown in Table 3.3 It was observed that at methanol/oil molar ratio of 9:1, 0.8 wt% catalysts, and 90-minute reaction time at a constant temperature of 55 °C, CZB catalyst gave the optimum biodiesel yield of 84.00 % while HZB catalyst gave the optimum biodiesel yield of 92 % at the same condition.

3.4 CHARACTERIZATION OF PRODUCED BIODIESEL FROM WCO FOR BOTH CZB AND HZB

The biodiesel produced from both catalysts (CZB and HZB) was characterized through laboratory analysis in order to determine the properties of the biodiesel, such properties carried out are shown in Table 2.

Table 2: Properties of biodiesel produced by both CZB and HZB catalyst

S/N	Property	Unit	Result Obtained for CZB Catalyst	Result Obtained for HZB Catalyst	ASTM D6751
1.	Density 40 ° C	g/cm^3	0.928	0.922	-
2.	Flash Point	° C	128	125	130
3.	Kinematic Viscosity at 40 ° C	mm^2/s	4.5	5.1	1.9 – 6.0
4.	Cetane Index		56	51	47
5.	P^H Value		7.1	6.9	-
6.	Color		Amber Yellow	Amber Yellow	-
7.	Pour Point	° C	9	11	18 max
8.	Cloud point	° C	10	9	-
9.	Iodine Value	mgI/100g	57.4	60.7	120 max
10.	Ester Value	wt. %	111.3	100.5	96.5
11.	Acid value	mgKOH/g	0.836	0.72	0.8 max
12.	FFA	wt %	0.118	0.08	-

4. CONCLUSION

Conclusively, quality biodiesel was produced using waste cooking oil and using both hierarchical zeolite beta and commercial zeolite beta as catalysts via the transesterification process. The prepared catalyst was characterized using X-Ray diffraction (XRD) and Scanning Electron Microscopy (SEM/EDX) analyses and response surfaces

methodology was successfully applied for transesterification of methanol for both CZB and HZB. The process parameters considered for the optimization study of the transesterification reaction for CZB catalyst resulted in an optimum biodiesel yield of 84% at operating conditions of catalyst dosage of 0.8 g, methanol to oil ratio of 9:1 and a reaction time of 90 minutes while that of the transesterification reaction for HZB catalyst resulted in an optimum biodiesel yield of 92 at the same conditions. Therefore, HZB proved to be a better catalyst for the production of biodiesel in terms of yield and quality than CZB.

ACKNOWLEDGEMENT

The authors wished to thank the staff of the Chemical Engineering Department, the Federal University of Technology, Minna for their support towards the completion of the research work, the effort of Mr Friday Ohiani, Mr Bulus of the Fishery Department, Federal University of Technology Minna, is also appreciated during the laboratory procedure. We would also wish to extend our gratitude to Dr. Tijjani of the Chemistry Department, Federal University of Technology Minna for assisting with the analysis.

REFERENCES

Achanai, B., Nattawut, C., Vorrada, L., Phatsakon, W. & Sarinthip T. (2013). Calcium oxide derived from shells of mussel, cockle, and scallop as heterogeneous catalyst for biodiesel production. *The scientific World Journal, 13,* 1-7. doi:10.1155/2013/460-923.

Alalwan, H. A., Alminshid, A. H., & Aljaafari, H. A. (2019). Promising evolution of biofuel generations. Subject review. *Renewable Energy Focus*, *28*, 127-139.

Allori, V., Goldstein, S., Tumulka, R., & Zanghì, N. (2020). On the common structure of Bohmian mechanics and the Ghirardi–Rimini–Weber theory. *The British Journal for the Philosophy of Science*.

Alsultan, A. G., Asikin-Mijan, N., Ibrahim, Z., Yunus, R., Razali, S. Z., Mansir, N., & Taufiq-Yap, Y. H. (2021). A Short Review on Catalyst, Feedstock, Modernised Process, Current State and Challenges on Biodiesel Production. *Catalysts*, *11*(11), 1261.

Anto, S., Mukherjee, S.S., Muthappa, R., Mathimani, T., Deviram, G., Kumar, S.S., Verma, T.N. & Pugazhendhi, A., 2020. Algae as green energy reserve: *technological outlook on biofuel production. Chemosphere* 242, 125079

Arun, N., & Dalai, A. K. (2020). Environmental and socioeconomic impact assessment of biofuels from lignocellulosic biomass. In *Lignocellulosic Biomass to Liquid Biofuels* (pp. 283-299). Academic Press.

Atabani, A. E., Silitonga, A. S., Badruddin, I. A., Mahlia, T. M. I., Masjuki, H., & Mekhilef, S. (2012). A comprehensive review on biodiesel as an alternative energy resource and its characteristics. *Renewable and sustainable energy reviews*, *16*(4), 2070-2093.

Baloch, H. A., Nizamuddin, S., Siddiqui, M. T. H., Riaz, S., Jatoi, A. S., Dumbre, D. K., & Griffin, G. J. (2018). Recent advances in production and upgrading of bio-oil from biomass: A critical overview. *Journal of environmental chemical engineering*, *6*(4), 5101-5118.

Baskar, G., Ebenezer Selvakumari, I.A. & Aiswarya, R., 2018. Biodiesel production from castor oil using heterogeneous Ni doped ZnO nanocatalyst. *Bioresource. Technol*. 250, 793–798.

Bharathi, D. & Rajalakshmi, G. (2019). Microbial lipases: An overview of screening, production and purification. *Biocatalysis and Agricultural Biotechnology*, *22*, 101368.

Bhatia, S.K., Bhatia, R.K., Yang, Y. H., 2017. An overview of microdiesel a sustainable future source of renewable energy. *Renew. Sustain Energy. Rev*. 79, 1078–1090.

PAPER 222 – SYNTHESIS AND CHARACTERIZATION OF HIERARCHICAL BETA ZEOLITE CATALYST FROM AHOKO KAOLIN

R. S. Safiyanu[1*], E. A. Afolabi[1], A. Babashehu[1], A. S. Kovo[1], A. Shehu[1]

[1]Department of Chemical Engineering, Federal University of Technology, Minna, Nigeria.
Email:safiyanurashida@gmail.com

ABSTRACT

Ahoko kaolin clay has been employed as the unique source of silica and alumina in the synthesis of hierarchical beta zeolite using a simple hydrothermal method, first by transforming the kaolin into metakaolin. Zeolization of the beta crystals was performed at optimized conditions using the top-down and bottom-up approach. In the top-down approach, dealumination was carried using 8 M HCl at 90 °C for 3 h under reflux. The hierarchical form of the beta zeolite was obtained by desilicating (bottom-up) the synthesized beta with 10 wt% urea solution. Different analytical analysis such as XRD, XRF, SEM, BET and EDX were used to determine the structure and crystallinity of the synthesized beta, elemental composition, morphology, pore volume and surface area. The characterization results shows that hierarchical beta zeolite synthesized from Ahoko kaolin is a high silica zeolite (about 77 % silica content) that possess good crystallinity and bimodal pore structure. The morphology of the synthesized hierarchical beta zeolite also gives the spheroid shape of beta crystal with a hexagonal structure. Urea also proves to be a mild desilicating agent in the generation of mesopores.

KEYWORDS: Zeolite, Beta zeolite, Hierarchical Beta zeolite, Kaolin, Metakaolin.

1. INTRODUCTION

Zeolites are microporous, crystalline, aluminosilicate minerals composed of 3-dimensional framework of silica (SiO_4) and alumina (AlO_4) tetrahydrally linked together by shared of oxygen atoms (Kovo, 2012). The framework of zeolite is an open cage structure where cations could locate within the material pores, these cations neutralizes the negative charge on the lattice of the framework (Breck, 1974). The movement of these cations gives the zeolite its unique ion-exchange, adsorption and catalytic properties. There are about 250 zeolites structures identified by the international zeolite association, about 40 of these structures exist in natural forms while the vast majority are synthesized commercially in autoclaves in the laboratory (Rissheng *et al.,* 2019). Although only about 13 structures of these synthetic zeolites have been utilized in commercial catalysis, only 5 (Ferrierite, Mordenite, ZSM-5, Faujasite, and Beta) are produced in commercial quantity for catalytic application (Fernandez *et al.,* 2020).

Zeolite Beta is a high-silica zeolite with three dimensional (3D) 12-membered ring channels structure. As one of the most predominantly used zeolite materials (Vogt *et al.,* 2015), zeolite beta was first discovered in the laboratory by Mobil Research and Development Corporation via a basic hydrothermal reaction of tetraethylammonium ions with sodium, silicon and aluminum oxides (Wadlinger et al, 1967). It was discovered to possess three mutually intersecting channels with a 12-membered ring pores. The structure has a large micropores of about 0.55 x 0.55 nm and 0.76 x 0.64 nm (Fernandez *et al.,* 2020), high thermal and hydrothermal stability, high SiO_2 / Al_2O_3 ratio and outstanding catalytic properties (Tran *et al.,* 2018).

Even though, zeolite beta exhibit high performance superiority in diverse acid-catalyzed reactions, its practical application is greatly hindered due to its high production cost (Shen *et al.,* 2008,) and limited by mass transfer diffusion when used as a microporous material (Yue *et al.,* 2019).

Therefore, much effort has been made by researchers to reduce its production cost (Duan *et al.,* 2011) either by decreasing or eliminating the use of organic template which is expensive and causes environmental pollution or substituting the synthetic organic chemical sources of silicon and aluminum with inexpensive, naturally occurring sources of silica and alumina such as Kaolinite, Rectorite and Diatomite (Duan *et al.,* 2011, Kovo *et al.,* 2012, Kerstens *et al.,* 2020,). The use of these low-cost natural sources of aluminosilicate minerals with abundant reserves worldwide have been investigated by different researchers such as Shen *et al.,* 2009, Kovo *et al.,* 2012, Yue *et al.,* 2019, Frink *et al.,* 2020.

In addition to the high cost of zeolite synthesis, the diffusion limitation imposed by the sole presence of microporous channel system in zeolite is another challenge hindering the catalytic performance of zeolite beta (Duan *et al*., 20011). Therefore, to overcome this challenge, significant effort has been made by many researchers towards fabrication of hierarchical zeolite beta. In 2006, Junliang *et al*., successfully synthesize hierarchical zeolite beta via the steam-assisted technique and obtained a good result, but only few literatures are available on synthesis of hierarchical zeolite beta, from lowcost material such as kaolin via a particular synthesis method.

Hierarchical beta zeolite is a type of zeolite that integrate bimodal pore systems of micro/mesopores structures that have been developed to enhanced the diffusion of bulkier molecules in the zeolite structure, hence addressed the issue of mass transfer limitations (Yu *et al.,* 2019).

Kaolinite [$(Al_2SiO_5(OH)_4$] materials are abundant worldwide and have a Si/Al ratio to that of zeolites. Kaolin generally can be converted into zeolites by hydrothermal action (Kovo, 2012). This was achieved by the thermal treatment of kaolin to obtain a more reactive phase metakaolin and hydrothermal treatment of the metakaolin with an aqueous alkali medium to form the zeolite structure (Fernandez *et al.,* 2020). Hence the main purpose of this study is to synthesized and characterized hierarchical beta zeolite using a cheap and natural source of silica and alumina (kaolin) using a simple hydrothermal technique that utilizes top-down and bottom-up approach without the use of organic template. This will reduce the synthetic cost and also enhance the utilization of the catalyst.

2. MATERIALS AND METHODS

2.1 MATERIALS

Ahoko kaolin was gotten from Ahoko site in Kogi state, Nigeria, Sodium hydroxide pellet (NaOH) (>99 Sidmach Aldrich), Sodium silicate nonahydrate ($Na_2SiO_3.9H_2O$) (>99 Sidmach Aldrich, Hydrochloric Acid (HCl) (>99 Sidmach Aldrich, Urea powder (Dona Hills Chemical), Deionized Water. All reagent were of analytical grade and used as purchased.

2.2 METHODOLOGY

About 1 kg of the Ahoko kaolin clay collected was grinded for pretreatment. The pretreatment was carried out via sedimentation process by soaking the grinded kaolin clay in water. The soaked kaolin clay was then stirred thoroughly and allowed to settle down for 3 h. 3 layers were observed. The filtrate layer, middle layer and the bottom layer. The filtrate consists of water which was decanted out, the middle layer was the kaolin which was collected separately, the bottom layer was basically made up of quartz and other impurities this was discarded. The sedimentation process was repeated thrice (3X) until white kaolin was obtained. The white kaolin collected was then placed in crucibles and dried in an oven at 100 oC overnight. The refined kaolin clay was grinded into powder form with the aid of a mortar and pestle and stored in clean plastic container. 500 g of the refined kaolin was placed in a crucible and calcined at 700 oC for 1 h to obtain metakaolin. The metakaolin was used as silica and alumina source and dealuminated using 8 M HCl for 3 h under reflux condition. Zeolization of the beta crystals was performed with a mixture containing 2.76 g of acid-treated metakaolin added to 2.0 g of an aqueous solution of NaOH under stirring for 10 mins, 0.93 g of zeolite beta seed was also added under stirring into the above suspension and stirred for further 10 mins to form a homogenous mixture. The final mixture obtained had the molar composition of: 30 SiO2 :1 Al 2 O3 : 1.5 NaO : 600 H2O (Yue et al., 2020).

The obtained mixture was then stirred for 4 h before transferring into a 100 ml Teflon-lined autoclave and crystallized at 170 ^{o}C for 14 h under static conditions and autogeneous pressure. The solid product obtained after crystallization was filtered, washed until neutral pH and dried in an oven at 80 ^{o}C overnight.

The hierarchical form of the zeolite beta was obtained by desilication method using 10 wt% urea solution at 80 ^{o}C for 5 h. The solid obtained was filtered, washed until neutral pH and calcined at 550 ^{o}C for 3 h (Tian *et al.,* 2016) to obtain a template free hierarchical Beta (h-beta) zeolite.

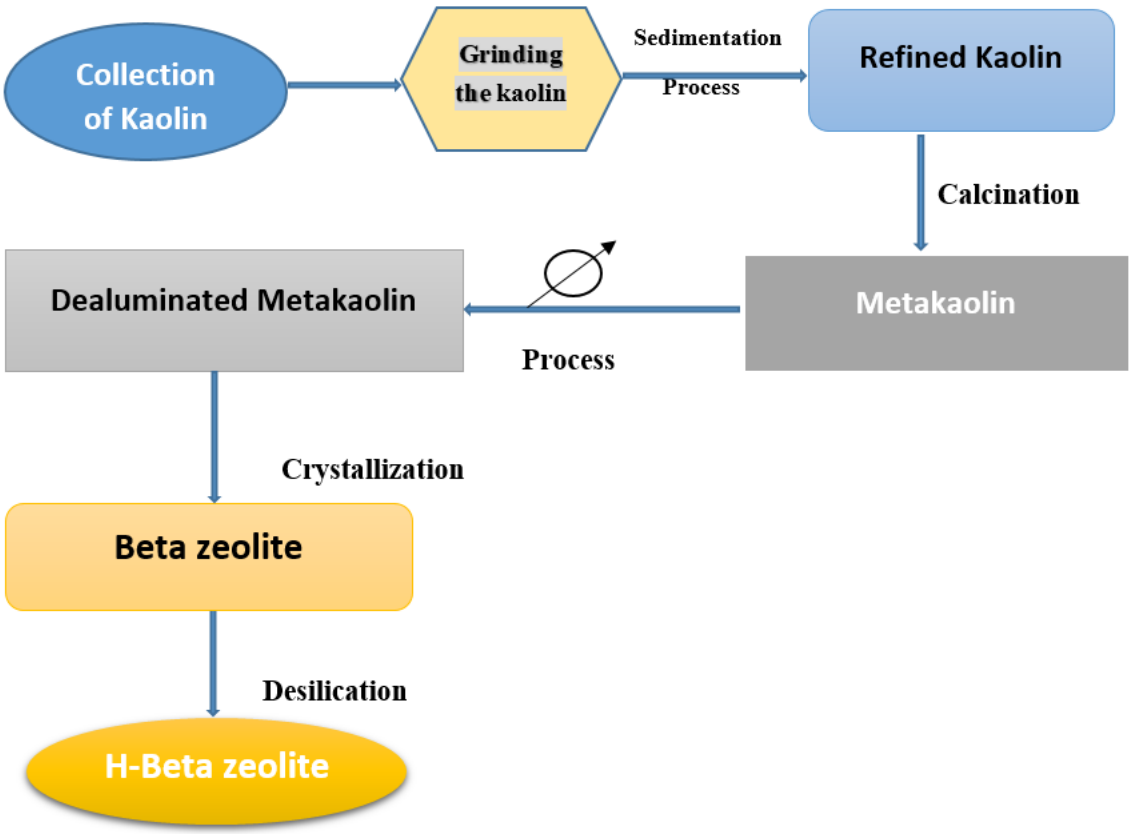

Figure 2 : Process flow diagram for synthesis of H-beta zeolite from Ahoko Kaolin

2.2 CHARACTERIZATION OF SYNTHESIZED BETA ZEOLITE

Crystallinity and the phase purity of the zeolite beta samples were identified from their X-ray diffraction patterns. The X-ray diffraction pattern (XRD) of all the samples were obtained using a BRUKER-binary V4 (RAW), Gonio, using a monochromic Cu-Kα radiation. The chemical composition of the zeolites beta samples were analyzed using by X-ray Fluorescence (XRF) conducted on a Bruker S4 explorer instrument, The morphologies and crystal sizes of the synthesized samples were observed byMira3 TESCAN 435VP (Variable Pressure Scanning)Scanning Electron Microscopy (SEM). The micrographs of SEM were taken in the magnification range of 3000 to 5000 times.Brunauer-Emmett-Teller(BET) analysis was used to calcite the specific surface area (S_{BET}), the micropore specific surface area (S_{micro}), and the pore volume (V_{pore}) were obtained using *t*-plot.

3.0 RESULTS AND DISCUSSION

The XRD pattern of Ahoko kaolin in Figure 3.0 indicated two intense diffraction peaks at 2Θ = 12.5° and 25.3° (d = 7.2 Å), a sharp and narrow peak with basal reflection which shows the crystallinity of Ahoko kaolin, these peaks are similar to the once obtained by Kovo *et al.,* 2012. It was also observed that Ahoko kaolin contain high level of quartz and other trace elements such as illite and mica while the peak of metakaolin in Figure 3.1 reflect a complete loss of crystallization water due to heating. The peak indicated that Ahoko metakaolin is a non-crystalline (amorphous) material containing free silica and alumina.

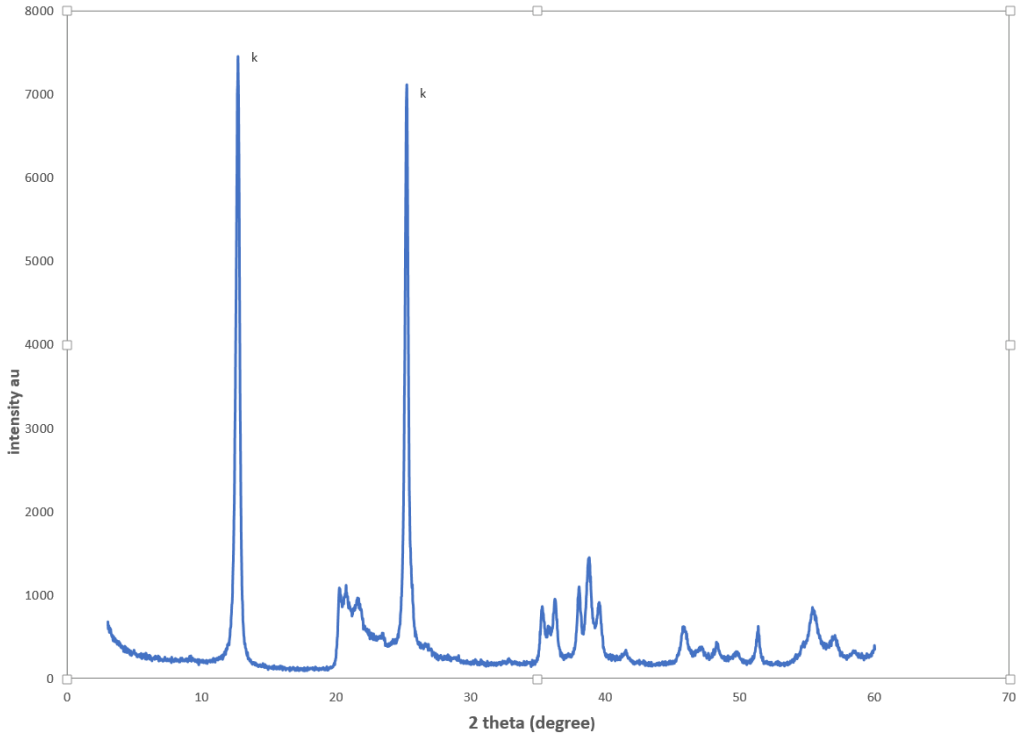

Figure 3: XRD pattern of Ahoko kaolin at 2Θ

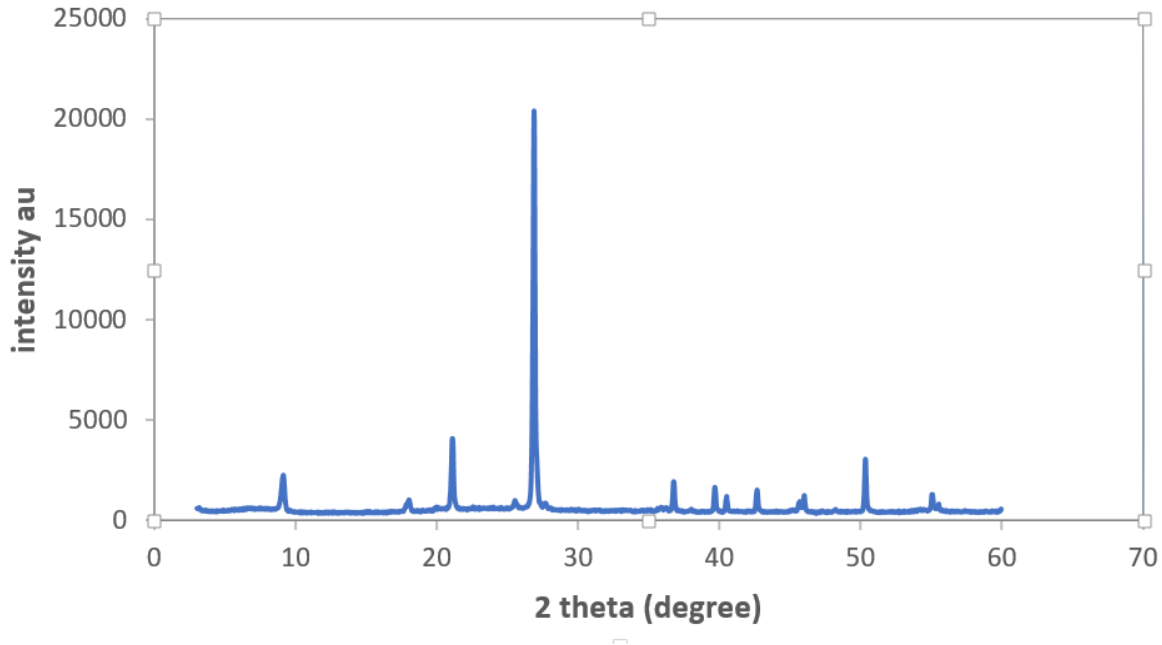

Figure 3.1: XRD pattern of metakaolin at 2Θ

Figure 3.2 shows the XRD pattern of the conventional beta zeolite which comprises of both sharp and broad features due to highly faulty structures in BEA framework as shown by Treacy. The intense reflections at 2Θ = 7.8°, and 22.6° and weaker once at 21.2°, 25.3° and 29.8° conforms well to the typical features of zeolite Beta topology (Baerlocher *et al*., 2007). XRD pattern of the synthesized Beta zeolite in Figure 3.3 was compared with that of conventional Beta (Figure 3.2). The characteristics peak of Beta zeolite synthesized from acid leached metakaolin indicate high silica beta zeolite closely related to the peaks of the conventional Beta zeolite (Yue *et al.,* 2020).

Table 3.0: XRF analysis of synthesized beta zeolite using acid treated metakaolin

S/N	**Composition**	**Weight (%)**
1	SiO_2	77.16
2	Al_2O_3	12.7
3	Fe_2O_3	0.18
4	MgO	0.07
5	CaO	0.19
6	Na_2O	7.56
7	K_2O	0.02
8	TiO_2	0.76
9	P_2O_5	0.02
10	LOI	1.43
	Total	**100.09**

Table 3.0 above shows the XRF analysis of synthesized beta zeolite using acid leached metakaolin as the unique source of silica and alumina. The analysis was carried out to determine the elemental oxide and there percentage weight composition of the synthesized beta zeolite. It was also used to determine the Si/Al of the H-Beta. The result obtained shown that synthesized beta zeolite from Ahoko kaolin clay contains high level of silicon oxide of about (77.16 %) weight percent as a major component follow by aluminium oxide of about of (12.7 %) weight percent. Also present in varying proportions are Fe_2O_3, MgO, CaO, Na_2O, K_2O, TiO_2 and P_2O_5. The Si/Al ratio of Beta zeolite usually ranges between the values of 4 – 6 (Li *et al., 2022*), the Si/Al ratio was calculated to be 6.07 this high value is due to the process of dealumination. This value also have great influence on the crystallinity of the H-beta zeolite.

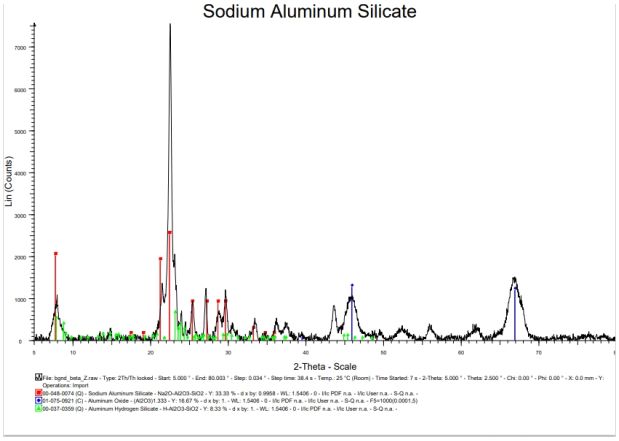

Figure 3.2: XRD pattern of conventional beta zeolite

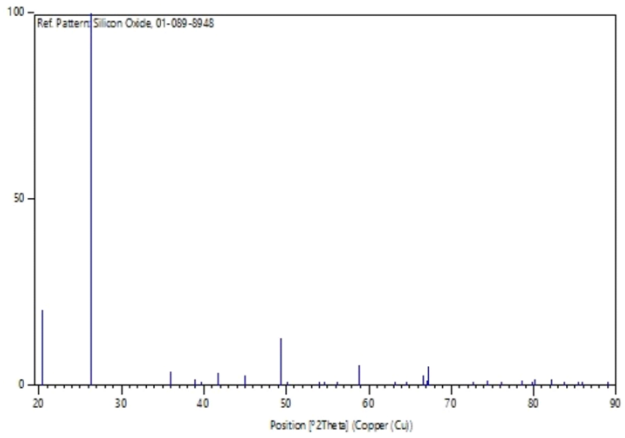

Figure 3.3: XRD Pattern of synthesized Beta Zeolite

SEM was used to analyze the morphology, size and shape of the synthesized hierarchical beta zeolite. The SEM has the ability to observe the solid-state topography with a resolution and depth of field far exceeding the corresponding parameters of optical microscopes. The micrographs are shown in Figure 3.4 below.

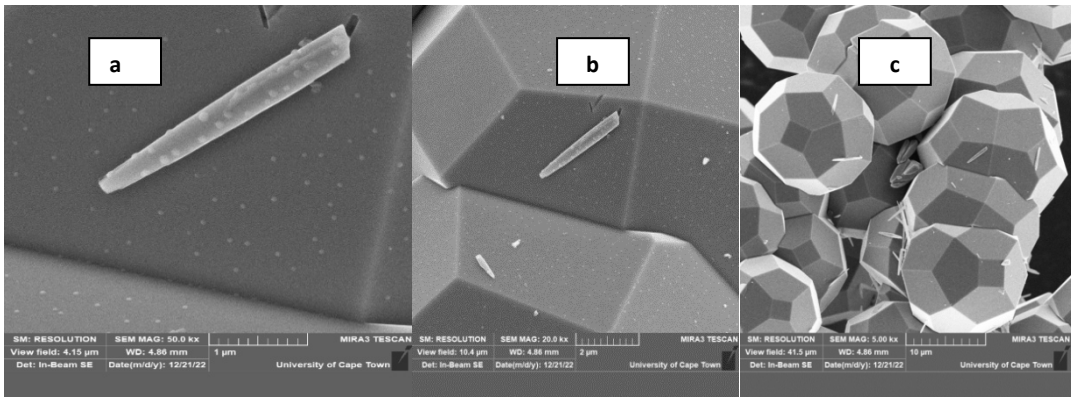

Figure 3.4 (a): micrographs at 1 µm (b) micrographs at 2 µm (c) micrographs at 10 µm

The micrographs indicated in figure 3.4 above shows the formation of Beta crystals. The morphology indicates the micro/mesoporous nature of H-beta zeolite. The micrographs at 1 µm (a) shows micropores attached to the surface of the Beta crystals. From the micrographs at 2 µm (b) the tetragonal structure of the Beta crystals became visible, these also indicates some degree of micro/mesopores. The micrographs at 10 µm (c) gives the proper morphology on comparison with the one synthesized by Yue *et al.,* 2019, Tamer, 2006, and Zhang *et al.,* 2016. Spheroid shapes of Beta were observed in addition to a hexagonal structure as seen in figure 3.4c.

In addition to SEM, Energy dispersive X-ray micro spectroscopy (EDX) was used to also determine the elemental composition of the synthesized hierarchical Beta (H-beta). From the elemental composition of the EDX results it can be seen that the synthesized H-beta zeolite is a highly siliceous material with a silica content of about 80 wt% and alumina content of 22.4 wt%

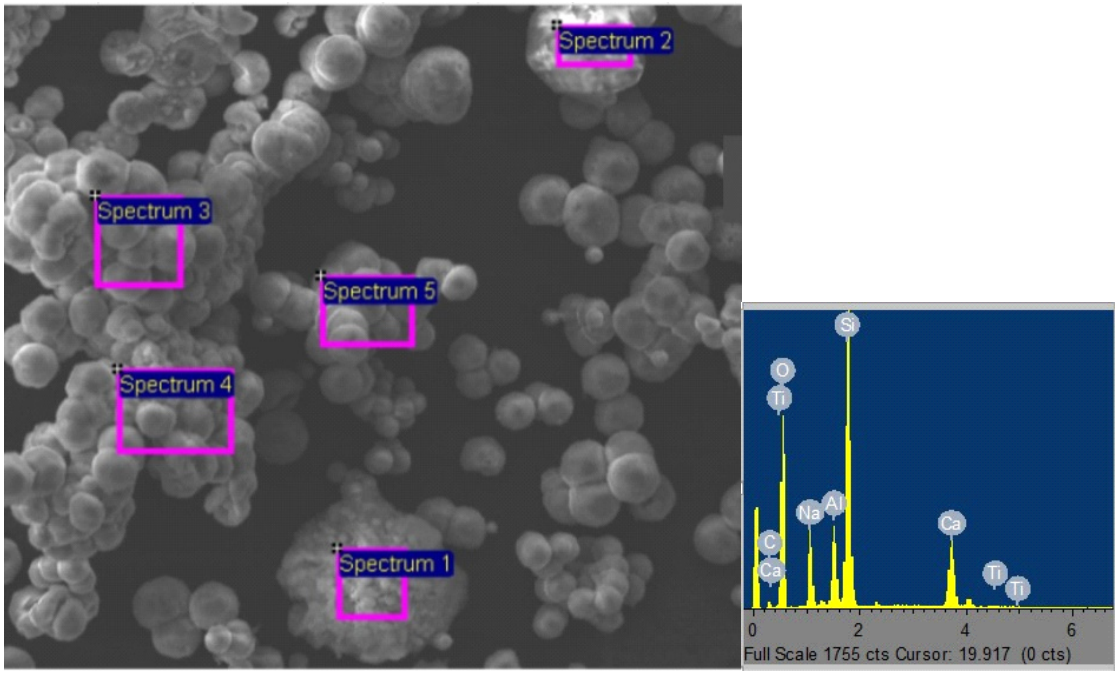

Figure 4: EDX of synthesized H-beta

The surface area was evaluated using Brunauer-Emmett-Teller (BET) analysis and it was found to be 488.1 m^2/g. and of 0.16 cm^3/g. This results indicates a continuous uptake of N_2 at from literature, Tian *et al.,* 2016 obtained 481 m^2/g as the total surface area and 0.10 as the pore volume. Also in another study Yue *et al.,* 2019 obtained 542 m^2/g and a pore volume of 0.17 respectively. Comparing these literature values and the $S_{(BET)}$ value obtained, it can be deduced that the surface area of the synthesized beta zeolites falls within the acceptable range. Therefore, on the basis of N_2 physiosorption isotherm shows a continuous uptake of N_2 at 0.7 from P/P_0 due to the additional porosity generated by urea, it can be concluded that synthesized H-beta zeolite possess high level of micro/mesoporosity.

4.0 CONCLUSION

Hierarchical beta zeolite has been successfully synthesized from Ahoko kaolin clay as a unique source of silica and alumina. The synthesis was done mainly to substitute the chemical sources of silica and alumina with Ahoko kaolin. The synthesis of beta zeolite was achieved by crystallization of a mixture of dealuminated metakaolin in alkaline medium under optimized hydrothermal conditions. The H-beta zeolite was achieved via hydrolysis of the synthesized beta zeolite with urea solution. Urea was chosen because it provides a stable, mild, and homogenous alkaline medium for desilication. The synthesized hierarchical beta zeolites was characterized using various techniques such as XRD, XRF, BET and SEM. The synthesis with dealuminated metakaolin gives beta crystals with spheroid hexagonal shape. The synthesized H-beta was found to possess good crystallinity, intra and intercrystals and large surface area. The synthesis method used would provide a low-cost and environmentally friendly approach for the synthesis of H-Beta zeolite which could serve as a sustainable platform for large-scale production of H-beta.

ACKNOWLEDGEMENT

The authors wished to thank the staff of Chemical Engineering Department, Federal University of Technology, Minna for their support towards the completion of the research work, the effort of Shehu Ahmed is also appreciated during the laboratory procedure. We would also wish to extend our gratitude to Dr. Tijjani of Chemistry Department, Federal University of Technology Minna for assisting with analysis.

REFERENCES

Baerlocher, C., Mccusker, L.B., Olsom, D.H. (2007). Atlas of Zeolite Framework Types, Elsevier, Amsterdam, 6th Edition.

Breck, D.W. (1974). Zeolite Molecular Sieves: structure, chemistry and use. New York, john Wiley and sons.

Duan, A., Wan, G., Zhang, Y., Zhao, Z., Jiang, G., & Liu, J. (2011). Optimal synthesis of micro/mesoporous beta zeolite from kaolin clay and catalytic performance for hydrodesulfurization of diesel. Catalysis Today, 175(1), 485–493. https://doi.org/10.1016/j.cattod.2011.03.044

Fernandez, S., Ostraat, M. L., & Zhang, K. (2020). Toward rational design of hierarchical beta zeolites: An overview and beyond. Aiche Journal, 66(9). https://doi.org/10.1002/aic.16943

Fink, A., Gierlich, C. H., Delidovich, I., & Palkovits, R. (2020). Systematic Catalyst Screening of Zeolites with Various Frameworks and Si/Al Ratios to Identify Optimum Acid Strength in OME Synthesis. Chemcatchem, 12(22), 5710–5719. https://doi.org/10.1002/cctc.202000972

Kerstens, D., Smeyers, B., Van Waeyenberg, J., Zhang, Q., Yu, J., & Sels, B. F. (2020). State of the Art and Perspectives of Hierarchical Zeolites: Practical Overview of Synthesis Methods and Use in Catalysis. *Advanced Materials*, *32*(44), 2004690. https://doi.org/10.1002/adma.202004690

Kovo, A. S. (2012). Effect of Temperature on the Synthesis of Zeolite X From Ahoko Nigerian Kaolin using Novel Metakaolinization Technique. *Chemical Engineering Communications*, *199*(6), 786–797. https://doi.org/10.1080/00986445.2011.625065

Shen, B., Wang, P., Yi, Z., Zhang, W., Tong, X., Liu, Y., Guo, Q., Gao, J., & Xu, C. (2009). Synthesis of Zeolite β from Kaolin and Its Catalytic Performance for FCC Naphtha Aromatization. Energy & Fuels, 23(1), 60 – 64. https://doi.org/10.1021/ef800681e

Tran, H. T., Pham, V. V., & Chao, H. (2018). Surfactant modified zeolite as amphiphilic and dual-electronic adsorbent for removal of cationic and oxyanionic metal ions and organic compounds. Ecotoxicology and Environmental Safety, 147, 55–63. https://doi.org/10.1016/j.ecoenv.2017.08.027

Yue, Y., Guo, X., Liu, T., Liu, H., Tinghai, W., Yuan, P., Haibo, Z., Bai, Z., & Bao, X. (2020). Template free synthesis of hierarchical porous zeolite Beta with natural kaolin clay as alumina source. Microporous and Mesoporous Materials, 293, 109772. https://doi.org/10.1016/j.micromeso.2019.109772

Wadlinger R.L., Kerr, G.T., Rosinski, E.J. (1967). A crystalline zeolite with improved adsorption and catalytic properties. United *States patent* 3,308,069.

PAPER 224 – HIGH-CAPACITY DATA-HIDING USING RLE COMPRESSION AND LSB STEGANOGRAPHY ALGORITHM

H. A. Gbigbadua[1*], A. F. Danfack Kana[2], A. O. Yusuf[3]

[1,2]Department of Cyber Security, African Centre of Excellence on Technology Enhanced Learning (ACETEL), National Open University of Nigeria.
[3]Department of Electrical and Electronics Engineering, Faculty of Engineering and Technology, University of Ilorin, Ilorin, Nigeria.
[*]Email: hamedkarle@gmail.com

ABSTRACT
The exponential growth of computer networks and people sharing highly confidential information has driven data security into high alert around the globe, several algorithms and models have been developed to conceal secret information during communication over unsecured channels without suspicion. Different techniques such as steganography and cryptography (i.e. encryption and hiding of secret messages in a cover file) have been adopted to secure classified messages. However, the more the secret message the larger the file size of the message making it suspicious and can be subjected to brutal attacks to access the information. The work proposed an improved run-length encoding (RLE) compression algorithm to compress the cover image before applying the Least Significant Bit (LSB) steganography technique to hide the secret message in the cover image to obtain the stego-image. The lena.jpg with the file size of 36.9KB was used as a sample cover file to hide the secret messages of 5.08KB, 113KB and 655KB stego-image was obtained when the compressed cover file was used and uncompressed cover file was used respectively. Hence the file size of the stego-image when the uncompressed cover file was used is larger compared to the stego-file when the compressed cover file was used which gives room for more messages. The Mean Squared Error (MSE) and Peak signal-to-noise ratio (PSNR) result was 0.03% and 63.64dB respectively when comparing the cover file and the stego-file when the compressed cover file was used. This signifies the proposed algorithm result is less distorted, effective, efficient, and less suspicious when applied to secure secret messages during communication over unsecured channels.

KEYWORDS: Steganography, Secret Message, Cover Image, Visual C#, Image Compression Algorithm, MATLAB

1. INTRODUCTION

Steganography is the art of concealing the fact that communication is taking place by hiding secret information within other information such as image files, text, audio files etc. The secret message or information may be a text, image, audio, or video file that is required to be securely conveyed from the transmitter to the receiver over an unsecured channel without suspicion, thus the information must be highly secured to avoid being revealed when a vigorous attack is launched on the carrier which is also referred to as the cover file (Pramanik, Bandyopadhyay, & Ghosh, 2020; Pramanik et al., 2021; Rakhra, Kumar, & Walia, 2021). The cover file is the carrier or the container where the secret message or information is securely encrypted to. The cover file can be a text, image, audio, or video file which is irrelevant or entails insignificant messages. The secret message is encrypted into the cover file using the user-defined password to have a stego-file which can be used to secretly communicate between two or more acknowledge parties. The secret message is embedded with high-level security algorithms such as cryptography to avoid intruders from having access to the secret message (Basuki & Anugrah, 2019; Gladwin & Gowthami, 2020; Matted, Shankar, & Jain, 2021; Rasras, AlQadi, Sara, & Research, 2019).

Steganography and cryptography are parallel data security techniques which are mostly adopted in concealing secrets, digital copyrights management, protection information, data confidentiality and digital forensics investigation. As Steganography becomes a commonly used technique in secret communication between two or more acknowledge parties, the size of the secret message represents a significant challenge for steganography since the size of cover files mostly restricts the steganographic capacity. Hence there is a need to enhance and increase the amount of data we can hide within a cover image (Bansal & Ratan, 2022; Hammad et al., 2022; Varghese & Sasikala, 2023). There are three commonly used algorithms for the steganography process which are Advanced Encryption Standard (AES) algorithm, Rivest, Shamir and Adleman (RSA) algorithm, and Least Significant Bits (LSB). The two major methods used to secure data transmission over an open channel are steganography and cryptography (Pramanik, Samanta, et al., 2020; Wahab, Khalaf, Hussein, & Hamed, 2021). Hybrid data security techniques are always applied together to ensure robust data security during the data transmission, cryptography is used for the secret message encryption and steganography is used for concealing the secret message (Chavali, Kandavalli, Sugash, & Prakash, 2023; Khari et al., 2019).

The cover file compression entails the process of compressing the cover file, the cover file retrieved from the user is in image format i.e Joint Photographic Experts Group (JPEG), Portable Network Graphics (PNG) etc., the image compression technique is the process of reducing or minimizing the file size or quality of an image, the compressed image tends to occupy less storage space or lower cost during transmission. Image compression is classified into two categories which are lossless compression technique and lossy compression technique. The lossless compression technique is the process of compressing images by using statistical/decomposition techniques to eliminate/minimize redundancy by applying entropy coding. It involves no loss of information, and no noise is added to the original image, thus it is referred to as the noiseless compression technique. The original image can be perfectly retrieved from the compressed image, and it is used for a few applications such as medical imaging because of its special requirements in the algorithm application. The various algorithms used to achieve lossless compression techniques are Run length encoding, Huffman encoding, LZW encoding and Area coding. Saravanan & Priya, (2019) and Subramanian, *et. al.* (2021) proposed a novel model for hiding image information by converting the information into another format to reduce its computational complexity. The work encodes the input image into an audio file at the transmitter end to obtain a stego-file, the process is reversed at the receiver end to extract the image from the stego-file. Patnaik *et. al.* (2021) also presents the use of high-level security data method in cloud computing by applying both symmetric key cryptography algorithm and steganography. The developed algorithm uses Block-wise data security for the cryptography method extracted from the AES, blowfish, RC6 and BRA algorithms where their key size is 128 bits (Hemeida, Alexan, & Mamdouh, 2019).

Forgáč *et. al* (2021) present a novel model for image authentication, the model uses a neural network, symmetric encryption, and cryptographic hash functions to achieve steganography. The most important feature used in the developed software module is the Optimized Pulse-Coupled Neural Network Model (OM-PCNN). The matrices position was generated by the neural network to embed authentication data into the cover image with emphasis on the image entropy. However, the network weights are initialized using a steganographic key to increase the security of the applied model. Mandal *et al. (*2020) and Li *et al.* (2021) present a scheme for implanting secret messages using a skillful model of the number system. The receiver only knows the secret message, the technique to hide the secret message and the method to extract the secret information from the cover file. The transmitter is also aware of the encoding technique and method that is used to apply the secret message inside the text.

Data/information security is evolving every day thus the attack and intrusion algorithms are also becoming more sophisticated, (Bhat *et al*., 2017) proposed a data embedding approach by combining steganography and cryptography techniques to improve data transmission security over unsecured channels. However, an increase in the size of the secret information increases the size of the position array used and the embedded process involves the use of the position array, thus little pieces of secret information can be embedded in the cover file. Hence, this study enhances the steganographic capacity of the cover file for more secret information to be hidden in it. The developed approach will enable users to encrypt more secret information inside the cover file using an improved RLE compression technique without compromising the content and integrity of the hidden data/information. However, the developed technique will enable users to transfer bulky secret messages over an unsecured channel with less or no suspicion.

METHODOLOGY

The developed technique was achieved by compressing the cover file to accommodate more secret information and to make the file size of the cover file to be relatively small to prevent it from being suspicious to unauthorized users which can prompt brutal attacks to be carried out on the cover file. The secret information will be embedded in the compressed cover file using the LSB steganography approach, the stego-file can then be transmitted over the unsecured channel to the receiver for description and retrieval of the secret information. The steganography process involves the encryption and decryption procedure as shown in Figure 1.

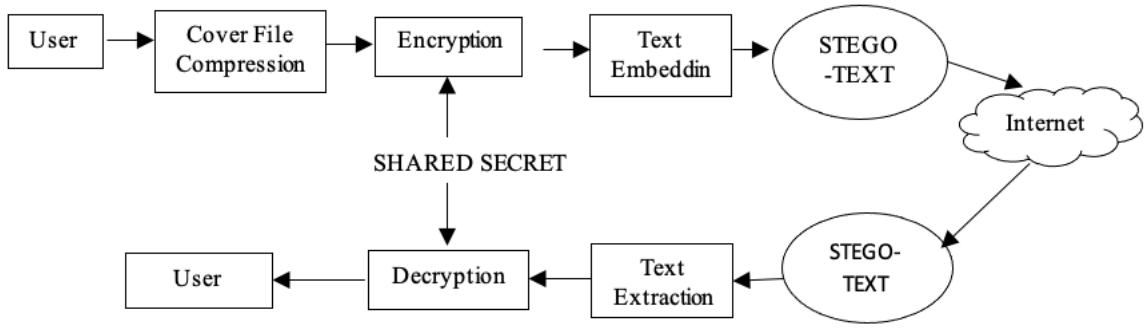

Figure 1. Block diagram of the steganography encryption and decryption system

The data encryption module entails the data collection unit which is to collect the cover file, secret information and password, the image compression unit compresses the cover file and has more space for storing secret information while the steganography unit encrypts the secret information with the user password into the compressed cover file to have a stego-file. The stego-file is output for user transmission and communication, the process of the steganography for the data encryption is described in the block diagram shown in Figure 2.

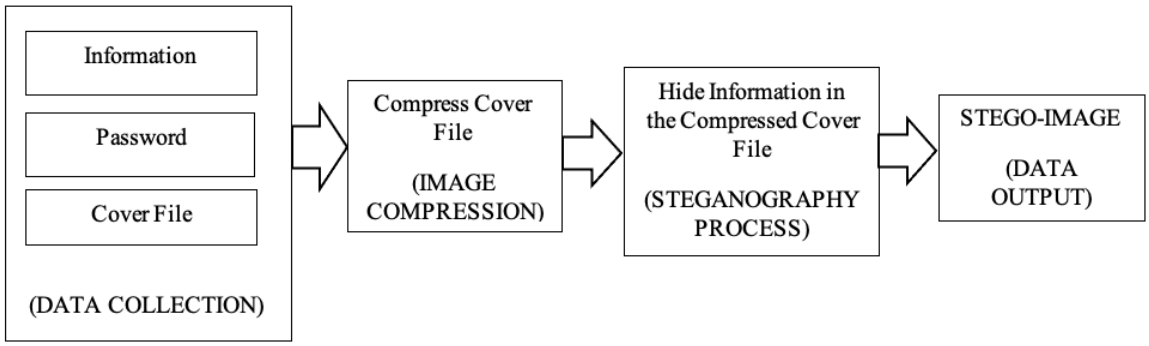

Figure 2: Block of the Data Encryption and Image Compression

The developed technique collects the cover file, secret information and the password from the input unit, the cover image file inserted by the user will be passed to the next stage for file size compression without decreasing the quality to increase the capacity of the secret information to be encrypted in it, then steganography algorithm will be applied to encrypt the secret information in the compressed cover file with the inserted password. The secret information is encrypted in the compressed cover file using the LSB steganography approach, hence there is a need to compress the cover file and make it unsusceptible when transmitting secret information over an unsecured channel. The cover file is in image format such as JPEG, JPG and PNG, hence image compression algorithm can be applied to compress the image by reducing the file size without degrading its quality. Reducing the file size enable more secret information to be embedded in it without suspicion during transmission since the file size is at the average value. Furthermore, the cover file is in image format that requires less bandwidth when being transmitted over the internet or downloaded from a webpage, reducing network congestion, and speeding up content delivery.

There are different algorithms used for the lossy compression technique which are transformation coding, vector quantization, fractal coding, block truncation coding and sub-band coding. The lossless compression technique is used for the study because no noise will be added to the original image and the original image can be easily retrieved from the compressed image thus the entire process can be easily reversed with no loss of information. The application of the lossless compression technique will ease the process of decrypting the compressed file to have the original image without loss of information which is very important in data security. The lossless image compression decreases the size of the cover image without losing its quality by removing irrelevant metadata from the cover file. The application of a lossless compression algorithm enables the quality and integrity of the cover file to be intact, thus making it less suspicious to intruders during transmission over an unsecured channel. The algorithms used for lossy compression include the discrete wavelet transform, fractal compression, and transform encryption while the lossless compression algorithm includes Huffman coding, arithmetic encoding, and run-length encoding. The run-length encoding was adopted to compress the cover file without losing its image quality. Run length encoding (RLE) is a commonly used compression algorithm technique applied for the compression of digital objects such as texts, images and so on. RLE compression algorithms are lossless and work by searching for runs of bits, bytes, or pixels of the same value, and encoding the length and value of the run. Hence, RLE achieves the best results with images containing large areas of contiguous colour, most especially if it is adopted in monochrome images. There are several RLE variants commonly applied which are experienced in the Tag Image File Format (TIFF), PiCture eXchange (PCX), JPG and bitmap graphics formats (BMP). Run-length encoding represents a string by replacing each subsequence of consecutive identical characters with (char; length). The string 555511111223333311144 would have representation of (5; 4) (1; 5) (2; 2) (3; 5) (1; 4) (4; 2). Then compress each (char; length) as a unit using Human coding. However, this technique works best when the characters often repeat such as is in fax transmission, which contains alternating long sequences of 1's and 0's. The distribution of code words is taken over many documents to compute the optimal Human code. The digital object which is the colour image consists of the basic three colours (R, G, B), the RLE algorithm represented the image consisting of N pixels as shown in Table 1.

Table 1. Representation of image data (MxN Image pixel)

Red (R)	Green (G)	Blue (B)	Number of pixels (C)
$\boldsymbol{r_1}$	g_1	b_1	c_1

.....	.....	.....	.....
r_{n-1}	g_{n-1}	b_{n-1}	c_{n-1}
r_n	g_n	b_n	c_n

The proposed algorithm computes the differences between the adjacent pixels for each colour, the threshold set for the proposed algorithm is 50 which is an arbitrary value selected to have optimum compression ratio. If the difference between r_1 and r_2 is less than or equal to the threshold value (i.e. th<=50) and if the difference between g_1 and g_2 less than or equal to a threshold value (i.e. th<=50) and also if the difference between b_1 and b_2 is less than or equal to a threshold value (th<=50), we add 1 to c_1 and if the difference is greater than 50 (i.e th>50), we set c_1 to 0. The operation was carried out between next adjacent pixels to the last pixel in the image.

The step-by-step instruction programmed to implement the proposed improved RLE algorithm is as follows:

1. READ the Image file
2. GET the width M and the height N for the Image file
3. GENERATE an Array to have R(M,N), each element of the array should consists of the three fields which are R, G, B
4. CONVERT the Image file to the R array; R(M,N)
5. LET Y=R(0,0); R(0,0) is the first element in the array
6. LET th = 50; where th is the threshold
7. FOR i=0 to N-1
    7.1. FOR j=0 to M-1
        7.1.1. IF Y - R(i,j) <= th THEN
            7.1.1.1. k = k + 1
        7.1.2. ELSE
            7.1.2.1. Y=R(i,j) and k = 0
8. END

The proposed RLE algorithm was implemented to compress the cover image before the steganography process. The LSB steganography technique involves the encryption of the text in the compressed cover image, the compressed image was further processed to encrypt the secret message with the user password.

A simple illustration is a grid for 3 pixels of a 24- bit image:

(00101101 00011100 01011110) (10100110 11100100 00001100) (11011010 10101101 01101011)

When the number 200, whose binary representation is 11001000, is embedded into the LSB of this part of the image, the resulting grid is as follows:

(00101101 0001110**0** 01011110) (10100110 1110010**0** 00001100) (11011010 1010110**1** 01101011)

Although the number was embedded into the first 8 bits of the grid, only the underlines bits (3) needed to be changed according to the message. On average, only some of the bits in an image will need to be modified to hide a secret message using the maximum cover size.

The LSB concept exploits the fact that the level of precision in many image formats is far greater than that perceivable by average human vision. Therefore, an altered image with slight variations in its colors will be indistinguishable from the original image by human, the LSB algorithm is used for the steganography process to hide the secret in the compressed image. The embedding algorithm used for the Least Significant Bit (LSB) based on steganography is defined in equation (1).

$$y_i = 2\left|\frac{x_i}{2}\right| + m_i \quad (1)$$

Where m_i, x_i and y_i are the *i*-th message bit, and the *i*-th selected pixel value before and after embedding, respectively.

Let $P_m(x=0), P(x=1)$ represent the distribution of the least significant bits of the cover image, and $P_m(m=0), P(m=1)$ also represent the distribution of the secret binary message bits.

The secret message is to be compressed or encrypted before being embedded just to protect its secrecy, based on this, the distribution of the secret message may be presumed to be equal to an averaged distribution such that $P_m(m=0) \approx P(m=1) \approx \frac{1}{2}$.

However, the cover image and the secret message can be assumed to be independent. Hence, noise introduced into the image is as shown in the model equation shown in equation 2.

$$P_{+1} = \frac{P}{2} P_x(x=0) \quad (2)$$

Where *P* is the embedding rate, measured in bits per pixel (bpp).

The steganography encryption process involves the hiding of the text in the cover image, the developed system has an interface to retrieve the cover file (i.e image file) and the secret message to be hidden which is in text

format, the cover file and secret message will be both processed using the steganography algorithm to produce the stego-image using the stego-key which is the password to access the encrypted secret message, the steganography encryption interface is illustrated in Figure 3.

The software interface for embedding secret messages in the cover file was successfully developed using Visual C#. Visual C# is an Integrated Development Environment (i.e. IDE) which is a multi-paradigm programming language encompassing strong typing, imperative, declarative, functional, generic, object-oriented (class-based), and component-oriented programming disciplines. It is a programming language designed for the common language infrastructure. The first step in steganography is to embed and hide information inside the encoder, one or several protocols will be implemented to embed the secret message into the cover file. An encrypted key is needed in the embedding process using the stego-key reduces the chance of third-party attackers getting hold of the stego-object and it is also required to decode the stego-image to have access to the secret information.

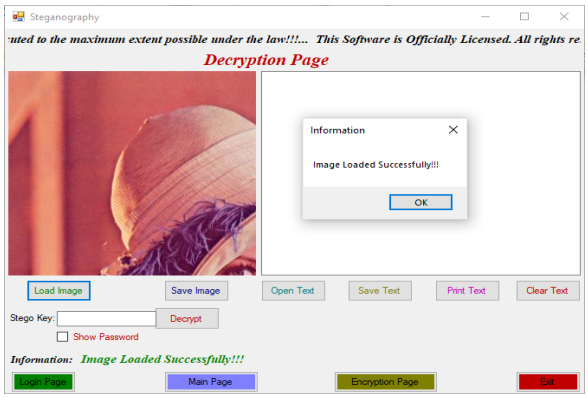

Figure 3. Steganography encryption Interface

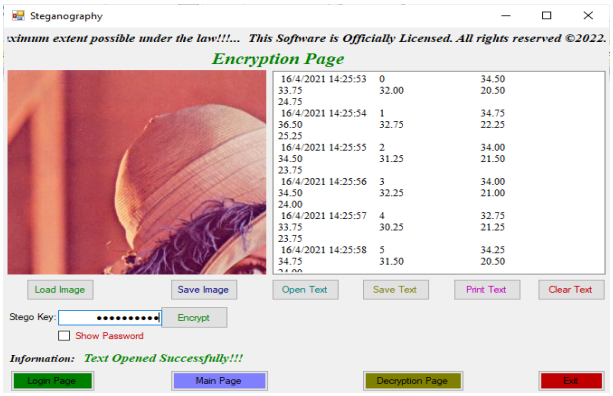

Figure 4. Steganography decryption Interface

2. RESULTS AND DISCUSSION

The developed algorithm was implemented using Visual C# programming language to develop the customized software. Different samples of cover images were used to hide secret messages before being transmitted over an unsecured channel. The lena.jpg shown in Figure 5 was used as the cover file, the file size of the sample text message is 5.08KB with 676 characters, and the cover file size (i.e. lena.jpg) is 36.9KB as shown in Figure 6. The secret message was hidden in the cover file with the user password without compressing the cover file, the obtained stego-image file size was 768KB as shown in Figure 7.

Hence, the cover file was compressed to 18KB using the improved RLE compression technique with an arbitrary threshold value of 50. The secret message was hidden in the compressed cover file with the user-defined password to obtain stego-file with file size of 113KB as shown in Figure 8. Furthermore, the stego-file when the cover file was not compressed is 768KB, hence the stego-image file size when the cover file is not compressed is large compared to the stego-image when the cover file is compressed which makes it suspicious when transmitting over an unsecured channel and can be brutally attacked to extract the secret message from it. The obtained result is tabulated in Table 2 when lena.jpg was used as the cover image.

Figure 5. Cover Image (lena.jpg)

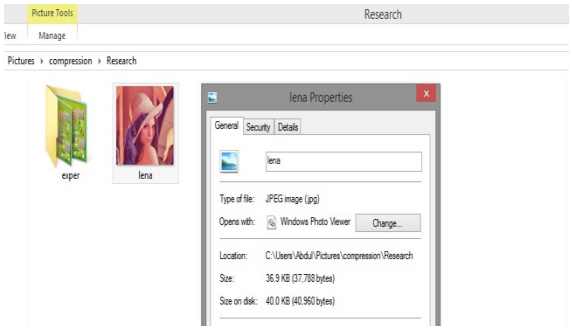

Figure 6. Cover Image File Size

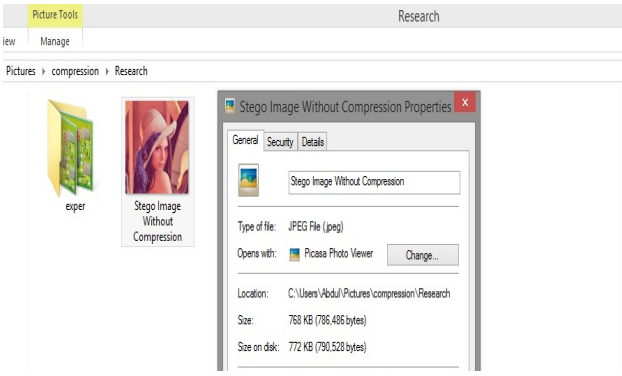

Figure 7. Stego-image using uncompressed cover image

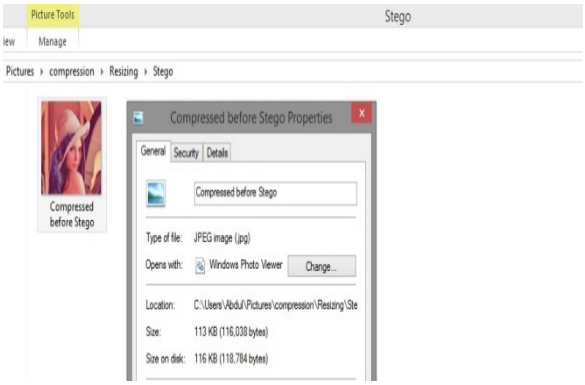

Figure 8. Stego-image using compressed cover image

The same secret message and user-defined password were hidden in the Circuit Diagram.jpeg and the result is also tabulated in Table 2. It can be deduced that stego-image that has its cover file compressed before hiding the secret message is smaller in file size compared to the stego-image that has its cover file not compressed. Hence, the stego-image that has its cover file compressed is less suspicious and has more storage capacity due to its file size and can be less attacked during transmission over an unsecured channel compared to the large file size of stego-image with its cover file not compressed making it suspicious and can be brutally attacked to retrieve the secret message during transmission over an unsecured channel.

Table 2. Result from the compression and steganography algorithm

S/No.	Cover File	Cover File Size (KB)	Secret Message File Size (KB)	Compressed Cover File Size (KB)	Stego-image using Compressed Cover File (KB)	Stego-image using Compressed Cover File (KB)
1	lena.jpg	36.9	5.08	18	655	113
2	Circuit Diagram.jpeg	231	5.08	116	1080	621

The MSE and PSNR as expressed in equations 3 and 4 were used to evaluate the embedded texture image by comparing the stego-image when the compressed cover file was used to the original image, this validates that the cover file is not distorted to avoid suspicion during transmission. The MSE measures the difference between the original image and the stego-image (processed image) from the compressed cover file (i.e the lower the MSE result the less the distortion of the cover file). The PSNR is inversely proportional to the MSE, if the PSNR result falls below 30dB it indicates the stego-image is distorted which signifies low quality but when the PSNR result is 40dB and above, it signifies high-quality stego-image (Carvajal-Gamez, Gallegos-Funes & Lopez-Bonilla (2009); Laskar & Hemachandran, (2012); Ulutas, Ulutas & Nabiyev (2011)).

$$MSE = \frac{1}{m \times n} \sum_{i=0}^{m-1} \sum_{j=0}^{n-1} [I(i,j) - K(i,j)]^2 \quad (3)$$

$$PSNR = 20 \cdot \log_{10}(MAX_I) - 10 \cdot \log_{10}(MSE) \quad (4)$$

The result obtained from the lena.jpg for the MSE when comparing the original Image to the stego-image that has its cover file compressed is 0.03% while the PSNR is 63.64dB which illustrates very low distortion (i.e. 0.03) as shown in Table 3, the MSE and PSNR were computed for Circuit Diagram.jpeg file. The PSNR result for the stego-image that has its cover file compressed is above 40dB which signifies the compression and embedding process introduces lower perceptual distortion.

Table 3. The PSNR and MSE result for the stego-image when the cover file was compressed

S/N	Original Image	Cover File Size (KB)	Secret Message (KB)	Compressed Cover File Size (KB)	Stego File with Compressed Cover File (KB)	MSE (%)	PSNR (dB)
1	lena.jpeg	36.9	5.08	18	113	0.03	63.64
2	Circuit Diagram.jpeg	231	5.08	116	621	0.00	71.48

The PSNR result affirms that the quality degradations could hardly be perceived by the human eye after the compression and embedding process. Thus, the stego-image file size has been reduced by compressing the cover file using the RLE compression technique before using the LSB steganography technique to hide the secret message without degrading the quality of the image which is suitable for communication over an unsecured channel without suspicion compared to using steganography technique without compressing the cover file to hide the secret message. Hence, the developed technique is efficient and effective to hide secret messages in a compressed cover file and transmit the stego-image over an unsecured channel without suspicion.

5.0 CONCLUSION

The proposed algorithm was implemented to compress the cover file and hide secret messages in the compressed cover file to have more storage without compromising the integrity of the information. The lena.jpg file size of 36.9KB was used as a cover image to hide the secret message of 5.08KB including the user password, the stego-image was 768KB by hiding the secret message in the cover file without compressing the cover file. However, the stego-image was 113KB when the same secret message with the user password was hidden in the compressed cover file of lena.jpg. The stego-image file size using a compressed cover file is smaller compared to stego-image when using the uncompressed cover file. The MSE and PSNR result is 0.03 and 63.64dB respectively for the sample file of lena.jpg when compressed which signifies that there is less noise and distortion when the cover file is compressed and used to hide secret messages. The stego-image when using a compressed cover file is less suspicious because of the file size when transmitted over an unsecured channel. Hence, the proposed algorithm is efficient and effective and can be deployed to secure classified information inside a compressed cover file with a user-defined password, the stego-file can be transmitted over unsecured channel without compromising the integrity of the message.

REFERENCES

Bhat, D., Krithi, V., Manjunath, K. N., Prabhu, S., & Renuka, A. (2017, September). Information hiding through dynamic text steganography and cryptography: computing and informatics. In *2017 international conference on advances in computing, communications and informatics (ICACCI)* (pp. 1826-1831). IEEE.

Bansal, M., & Ratan, R. (2022). Comprising Survey of Steganography & Cryptography: Evaluations, Techniques and Trends in Future Research. Paper presented at the 2022 8th International Conference on Signal Processing and Communication (ICSC).

Basuki, S., & Anugrah, R. J. (2019). Transaction Document Security Protection In The Form Of Image File, Jpg Or Tif Interbank Transfer Using Steganography And Cryptography. 1(1), 42-48.

Carvajal-Gamez , B.E., Gallegos-Funes, F. J. & Lopez-Bonilla,J. L. (2009). Scaling Factor for RGB Images to Steganography Applications. Journal of Vectorial Relativity, 4(3), 55-65.

Chavali, S. T., Kandavalli, C. T., Sugash, T., & Prakash, G. (2023). Comparative Study of Image Encryption and Image Steganography Using Cryptographic Algorithms and Image Evaluation Metrics. In Semantic Intelligence: Select Proceedings of ISIC 2022 (pp. 297-311): Springer.

Forgáč, R., Očkay, M., & Javurek, M. (2021, October). Steganography Based Approach to Image Authentication. In *2021 Communication and Information Technologies (KIT)* (pp. 1-6). IEEE.

Gladwin, S. J., & Gowthami, P. L. (2020). Combined cryptography and steganography for enhanced security in suboptimal images. Paper presented at the 2020 International Conference on Artificial Intelligence and Signal Processing (AISP).

Hammad, R., Latif, K. A., Amrullah, A. Z., Subki, A., Irfan, P., Zulfikri, M., Marzuki, K. (2022). Implementation of combined steganography and cryptography vigenere cipher, caesar cipher and converting periodic tables for securing secret message. Paper presented at the Journal of Physics: Conference Series.

Hemeida, F., Alexan, W., & Mamdouh, S. (2019). Blowfish–secured audio steganography. Paper presented at the 2019 Novel Intelligent and Leading Emerging Sciences Conference (NILES).

Khari, M., Garg, A. K., Gandomi, A. H., Gupta, R., Patan, R., Balusamy, B. J. (2019). Securing data in Internet of Things (IoT) using cryptography and steganography techniques. 50(1), 73-80.

Laskar, S. A., & Hemachandran, K. (2012). High Capacity data hiding using LSB Steganography and Encryption. International Journal of Database Management Systems, 4(6), 57.

Li, Y. H., Chang, C. C., Su, G. D., Yang, K. L., Aslam, M. S., & Liu, Y. (2021). Coverless Image Steganography Using Morphed Face Recognition based on Convolutional Neural Network.

Mandal, K. K., Chatterjee, S., Chakraborty, A., Mondal, S., & Samanta, S. (2020). Applying Encryption Algorithm on Text Steganography Based on Number System. In *Computational Advancement in Communication Circuits and Systems* (pp. 255-266). Springer, Singapore.

Matted, S., Shankar, G., & Jain, B. B. (2021). Enhanced image security using stenography and cryptography. Paper presented at the Computer Networks and Inventive Communication Technologies: Proceedings of Third ICCNCT 2020.

Patnaik, S., A.Sunil & Reddy, R. (2021). HYBRID CRYPTOGRAPHY ALGORITHM FOR SECURE FILE STORAGE IN THE CLOUD. Journal of Composition Theory, 14(10), 25-29.

Pramanik, S., Bandyopadhyay, S. K., & Ghosh, R. (2020). Signature image hiding in color image using steganography and cryptography based on digital signature concepts. Paper presented at the 2020 2nd International Conference on Innovative Mechanisms for Industry Applications (ICIMIA).

Pramanik, S., Ghosh, R., Pandey, D., Samanta, D., Dutta, S., & Dutta, S. (2021). Techniques of Steganography and Cryptography in Digital Transformation. In Emerging Challenges, Solutions, and Best Practices for Digital Enterprise Transformation (pp. 24-44): IGI Global.

Pramanik, S., Samanta, D., Dutta, S., Ghosh, R., Ghonge, M., & Pandey, D. (2020). Steganography using improved LSB approach and asymmetric cryptography. Paper presented at the 2020 IEEE international conference on advent trends in multidisciplinary research and innovation (ICATMRI).

Rakhra, M., Kumar, R., & Walia, H. (2021). A Review on Data hiding using Steganography and Cryptography. Paper presented at the 2021 9th International Conference on Reliability, Infocom Technologies and Optimization (Trends and Future Directions) (ICRITO).

Rasras, R. J., AlQadi, Z. A., Sara, M. R. (2019). A methodology based on steganography and cryptography to protect highly secure messages. 9(1), 3681-3684.

Saravanan, M., & Priya, A. (2019). An algorithm for security enhancement in image transmission using steganography. Journal of the Institute of Electronics and Computer, 1(1), 1-8.

Subramanian, N., & Al-Maadeed, S. (2021). A secure cloud system for maintaining COVID-19 patient's data using image steganography. *Journal of Emergency Medicine, Trauma and Acute Care*, *2021*(2-Qatar Health 2021 Conference abstracts), 37.

Subramaniyan, V., Sivakumar, V., Vagheesan, A. K., Sakthivelan, S., Kumar, K. J., & Nagarajan, K. K. (2021). GANash--A GAN approach to steganography. *arXiv preprint arXiv:2110.13650*.

Ulutas, G., Ulutas, M. & Nabiyev,V. (2011). Distortion free geometry based secret image sharing. Elsevier Inc, Procedia Computer Science 3. 721–726.

Varghese, F., & Sasikala, P. J. (2023). A Detailed Review Based on Secure Data Transmission Using Cryptography and Steganography. 1-28.

Wahab, O. F., Khalaf, A. A., Hussein, A. I., & Hamed, H. F. (2021). Hiding data using efficient combination of RSA cryptography, and compression steganography techniques. 9, 31805-31815.

PAPER 225 – CHEMICAL MODIFICATION OF LOCUST BEAN POD HUSK FIBRE AS A REINFORCING COMPONENT FOR POLYMER COMPOSITE APPLICATION

J.A. Olowokere[1]*, U.G. Akpan[2], J.O. Okafor[2], S.M. Auta[3]
[1]Department of Chemical Engineering, Federal University Wukari, Taraba State, Nigeria.
[2]Department of Chemical Engineering, School of Infrastructure, Process Engineering and Technology, Federal University of Technology Minna, Niger State, Nigeria.
[3]Department of Civil Engineering, School of Infrastructure, Process Engineering and Technology, Federal University of Technology Minna, Niger State, Nigeria.

*Email: olowojo@yahoo.com

ABSTRACT
This paper focuses on the chemical modification of raw locust bean pod husk (LBPH) fibre using sodium hydroxide. The LBPH fibres were cleaned and reduced to a particle size range of (250-150µm). Sequential extraction method of biomass analysis was used to determine the chemical composition of the LBPH fibre. Analysis shows that the chemical composition consists of cellulose (59.3%), hemicellulose (20.2%), lignin (10.2%), extractive (9.1%) and ash (1.2%). 100 g of raw LBPH was mercerized at varying treatment concentration and contact time using NaOH to optimally improve the cellulose content, reduce the hydrophilic property of the LBPH fibre and improve the interfacial adhesion capacity of the LBPH fibre for polymer composite. Upon mercerization, a high optimum cellulose content of 80% was achieved using 1.5% NaOH at a contact time of 3 h. This indicates that the alkaline treatment process has a positive effect on the raw LBPH fibre. This is further confirmed by the FTIR spectrum of the treated LBPH fibre, recording minimal OH groups and aromatic lignin peaks. High NaOH treatment concentration weakens and denature the LBPH fibre. The LBPH treated fibre with the optimum cellulose content was preserved as a reinforcing material for polymer composite production.

***KEYWORDS*:** Chemical Treatment, Locust Bean Pod Husk, Cellulose, Mercerization and Polymer Composite.

1. INTRODUCTION

The availability of abundant and cheap natural fibre alongside its ease of processing, for use as reinforcing materials in polymer composite, is currently of great interest to researchers. However, a major challenge with polymer reinforced composites with natural fibre is their incompatibility leading to weak interphase and uneven dispersion within the polymer composite. Polymer is hydrophobic in nature while natural fibres are hydrophilic. This difference in character can be narrowed by chemical or physical modification of the fibre or polymer, thereby improving their compactibility. The surface of natural sourced fibres can be chemically modified through processes like coupling agents, chemical treatment, and graft co-polymerization, with the essence of improving the mechanical properties of polymer composites (Kumar *et al*., 2018).
According to Malkapuram *et al.* (2008), these processes reduce the hydrophilic property of the natural fibre. Alkali treatment is a suitable and cheap chemical treatment method of modifying natural fibre. The usage of alkaline, increases the surface roughness of fibre and also help to eliminate the network structure of the hydrogen bonding present within the natural fibre (Lee *et al.,* 2009). This chemical treatment assists in removing the extractives (oils and wax) and lignin that form a coating around the cell wall of the fibre to a reasonable degree. Exposition of the short length crystallites and depolymerization of the native structure of the cellulose is also observed (Li *et al.,* 2009). The reaction which takes place between natural fibre (NF) such as locust bean pod husk and sodium hydroxide for the chemical treatment process is shown in Equation 1.1.

$$Fibre - OH + NaOH \rightarrow Fibre - O^{-}Na^{+} + H_2O \quad \ldots\ldots\ldots\ldots\ldots\ldots\ldots\ldots\ldots\ldots\ldots\ldots 1.1$$

Locust bean pod husk (LBPH) is dark brown in colour with a density of l0.97kg/m^3 and pH of 6, indicating its weak level of organic acidity. The chemical composition shows that it has a tannin content of 27- 44%. LBP concentrated extract are known to strengthen the water resistance of walls, ceramic pots and floors. Ash obtained from burnt LBP husk has been used for dying and tanning of indigo clothes and for soap making (Aguwa and Okafor, 2012). Ndububa and Uloko (2015) ascertained the water absorption capacity and compressive strength of the production of concrete mortar, using LBPH ash as a partial replacement of cement in the concrete mix. Adama and Jimoh (2011) reported that LBPH ash can be used as a pozzolan- which is a cementitious stabilizing additive in weak laterite for road construction. This paper explores the alkaline treatment of locust bean pod husk (LBPH) fibre as a reinforcing material for polymer composite production.

2. Materials and Method

2.1 Materials
Locust bean pod husk (LBPH) fibre, Soduum hydroxide and distill water of analytical grade were used for this research.

2.2 Sample Collection and Preparation of Locust Bean Pod Husk
Locust bean pod husk (LBPH) fibre was collected from the heap of agricultural waste of farmers involved in the processing of locust bean condiment in Bosso, Minna, Niger State. The husks were cleaned, dried in the sun and reduced into a particle size range of 60 -100 mesh (250-150µm). It was further dried in an oven at a temperature of 80^{o}C for 24 h to further reduce the moisture content. This was stored for chemical treatment (Muhammad *et al.,* 2011).

2.3 Chemical Composition and Treatment of Locust Bean Pod Husk
The sequential extraction method of biomass analysis according to Sridevi *et al*., (2015) was used to determine the chemical composition of the raw and treated LBPH fibre. The prepared LBPH fibre was dried in an oven for 24 h at 80^{o}C to a constant weight. 100 g of LBPH each was taken and treated with sodium hydroxide based on the experimental design input factors. The treated LBPH was washed with enough distilled water until the pH of the solution attains neutrality to modify the LBPH particles in order to enhance better bonding and interaction with the polymer matrix. Thirteen (13) runs were carried out for the treatment process. The run that was observed to have the highest optimum response of cellulose content was noted. This was stored and preserved as a reinforcing filler for polymer composite production (Olowokere *et al*., 2022).

Table 2.1 shows the design of experiment using central composite design (CCD) that was used in carrying out the chemical treatment process. This was carried out at varying treatment concentrations and contact time. Thirteen (13) runs were generated in all as captured in Table 3.2.

Table 2.1: Experimental Design Using Central Composite Design

Input Factors	**-**	**-1**	**0**	**+1**	**+**
Treatment Concentration (%)	0.88	1.5	3	4.5	5.12
Contact Time (hours)	0.59	1	2	3	3.41

2.4 Fourier Transform Infrared (FTIR) Spectroscopy
The observations and changes in the functional group present in the raw and treated reinforcing fibre was determined and captured by Fourier Transform Infrared (FTIR) spectroscopy machine of model NICOLET 155 thermo scientific Nicolet corporation, madison USA. The FTIR spectra of the samples were analyzed in the range of 4000 cm^{-1} to 500 cm^{-1}.

3.0 RESULTS AND DISCUSSION
The chemical compositions of locust bean pod husk (LBPH) for the untreated sample are presented in Table 3.1.

Table 3.1: Chemical Composition of untreated Locust Bean Pod Husk (LBPH) Fibre

Sample	**Cellulose %**	**Hemi-cellulose %**	**Lignin %**	**Extractive %**	**Ash %**
Untreated LBPH	59.3	20.2	10.2	9.1	1.2

3.1 Untreated of Locust Bean Pod Husk (LBPH)
The chemical composition of the raw LBPH fibre, as shown in Table 3.1 is made up of cellulose, hemicellulose, lignin, extractives and ash. The extractives may include wax and oils. The cellulose content (59.3%) of the untreated LBPH is the highest among other components and the lowest is ash with 1.2%. This result is similar to that obtained by Pereira *et al.,* (2013) on several species of *Eucalyptus globulus* sawdust (EGS) wood for charcoal yield, and for untreated sugar palm fibre by Iiyas *et al*., (2017). In most cases, plant and fruit fibre have higher cellulose content than wood fibre (Olowokere *et al.* 2022; Khairiah and Khairul, 2006).

The results of the treated LBPH are presented in Tables 3.2.

Table 3.2: Chemical Composition of Treated Locust Bean Pod Husk at Different Treatment Concentration and Contact Time

Std Run	**Factor 1**	**Factor 2**	**Responses**				
	Treatment concentration (%)	**Contact Time (h)**	**Cellulose %**	**Hemi-cellulose %**	**Lignin %**	**Extractives %**	**Ash %**
1	1.50	1.00	74.20	9.00	7.00	8.80	1.00
2	4.50	1.00	55.70	15.50	20.10	8.20	0.50
3	1.50	3.00	80.00	6.10	5.00	8.00	0.90
4	4.50	3.00	53.80	14.40	23.50	7.70	0.60
5	0.88	2.00	60.20	13.00	23.10	2.60	1.10
6	5.12	2.00	51.20	18.00	25.20	5.10	0.50
7	3.00	0.59	67.40	10.70	9.60	11.50	0.80
8	3.00	3.41	61.10	12.30	22.10	3.40	1.10
9	3.00	2.00	60.1	16.1	13.1	9.5	1.2
10	3.00	2.00	60.0	16.1	13.2	9.6	1.1
11	3.00	2.00	59.9	16.2	13.5	9.4	1.0
12	3.00	2.00	60.2	16.0	13.0	9.6	1.2
13	3.00	2.00	60.0	16.0	13.3	9.7	1.0

3.2 Alkaline Treatment of Locust Bean Pod Husk (LBPH)

The results on Table 3.2 for LBPH alkaline treatment shows that as the treatment concentration and contact time continue to increase from 0.87% to 1.5% for 1 – 2 h, the cellulose content increases, while other components like hemicellulose, lignin extractives and ash content continues to decrease. Iiyas *et al*., (2017) recorded a similar observation with the exception of the ash content for sugar treated palm fibre. However, beyond 1.5% treatment concentration, the cellulose content begins to decrease progressively at 3, 4.5 and 5.12%. In this case, the highest cellulose content obtained for LBPH was 80% at experimental design conditions of 1.5% alkaline treatment concentration and contact time of 3 hours. It is evident that excessive alkaline treatment beyond 1.5% has adverse effects on LBPH fibre. This is an indication that LBPH fibre requires mild treatment process to achieve high cellulose content. In this case, LBPH fibre treatment concentration has a stronger effect on the fibre content than contact time. This is also observed by Jabar (2017). Comparing the chemical composition of treated LBPH fibre and *Eucalyptus globulus* sawdust fibre, it is clear that the LBPH has higher cellulose content for both raw and treated fibre. This is an indication that sources of fibres from fruit husk are higher in cellulose content than in bast fibres such as wood sawdust (Olowokere *et al*. 2022; Khairiah and Khairul, 2006).

In most cases, natural fibres such as LBPH are subjected to chemical modification inorder to minimize their hydrophilic character. This is because, water-loving reinforcing materials poses a threat to the mechanical property and durability of polymer composites. This mercerization process assists in breaking the hydrogen bonds which exist between cellulose and other components such as lignin and hemicellulose. Similarly, free hydroxyl groups in the LBPH fibres capable of bonding with moisture are eliminated (Dittenber and GangaRao, 2012). The LBPH treated fibre with the optimum cellulose content was reserved as a reinforcing material for polymer composite production.

The FTIR Spectra of the raw and treated Locust Bean Pod Husk is presented in Figure 3.1 and Figure 3.2.

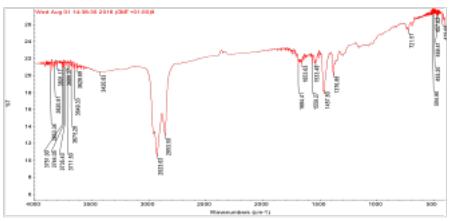

Figure 3.1: FTIR Spectrum for Raw Locust Bean Pod Husk

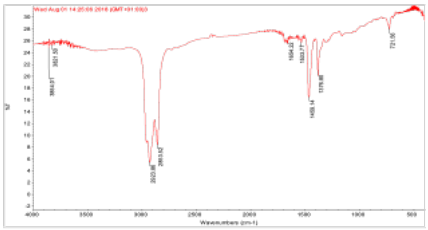

Figure 3.2: FTIR Spectrum for Treated Locust Bean Pod Husk

3.3 FTIR Analysis for Raw and Treated Locust Bean Pod Husk

Figure 3.1 presents the FTIR spectrum of raw locust bean pod husk (LBPH) fibre. The absorbance region is within the wavelength range of 500 cm^{-1} - 4000cm^{-1}. This extends from the fingerprint skeletal vibration region to single bond stretch region. The FTIR spectrum shows the three (3) basic chemical constituents found in natural fibre. These include cellulose, lignin and hemicellulose at their designated functional group and wavelength peaks. Starting from the single bond stretch region, multiple hydroxyl (OH) groups of not less than 12 peaks in the range of 3751.00 –3628.69cm^{-1} were observed. Functional groups within this range of peaks are commonly found in most natural fibres having hemicellulose and cellulose as part of their chemical compositions. This report is similar to (Jabar 2017 and Hyas *et al.,* 2017). The presence of these OH groups is a confirmation of the hydrophilic property of raw natural fibres, linked to the hemicellulose and cellulose component of the raw LBPH. These OH groups are held and bonded together by hydrogen bond. However, the hydrophilic nature of raw LBPH fibre can be a limiting factor for it to be suitable for use as a reinforcing material in polymer composite application. This is because of its incompatibility with the hydrophobic character of polymer matrix (Jabar, 2017; Olowokere *et al*., 2022). Furthermore, Figure 3.1 presents the alkane C-H peaks observed at 2923.63 and 2863.50 cm^{-1}. This is also an indicative presence of hydrocarbons in raw LBPH fibre, which also reported by Khalil *et al.,* (2001). Further observations reveals that variable C=C aromatic rings and C=C double bond stretch groups are present in the spectrum. These are indicative of the presence of lignin components, having the attributes of aromatic as observed at (1684.41 – 1653.63 cm^{-1}) and (1559.27 – 1533.49 cm^{-1}) respectively. Similarly, C –Cl stretch peak for aliphatic chloro compound is captured at a wavelength of 721.57 cm^{-1}. This is similar to the results obtained by Olowokere *et al*. (2022).

The subjection of raw fibre to chemical treatment is of great importance, if it must serve as valuable reinforcing materials in polymer composite application. The FTIR spectrum in Figure 3.2 presents the treated LBPH fibre with the optimum cellulose content yield at 1.5% NaOH for 3 h. Observation from the FTIR spectrum shows there are minimal peaks associated with the OH hydroxyl group at 3854.01 – 3821.50 cm^{-1}. This reduction in OH group peaks is a manifestation of the effect of the alkaline treatment process, which has shifted and transformed the hydrophilic character of the raw LBPH fibre to a hydrophobic one, for ease of compatibility with any available polymer matrix. This transformation is possible through the breaking of the hydrogen bond network within the LBPH fibre by the NaOH, thereby exposing more crystalline cellulose components with active surface site for good interfacial bonding. Similarly, there are minimal aromatic lignin peaks at 1654.22 and 1533.77 cm^{-1}. In this case, the chemical treatment is able to initiate and promote the depletion of some of the amorphous aromatic lignin components, which also poses a setback to good interfacial bonding within a polymer composite.

3.4 Statistical Analysis of the Optimization Treatment Process

The analysis of variance (ANOVA), model summary, model equation and optimum parameters of the LBPH treatment process, is presented in this section.
The statistical analysis of variance (ANOVA) for LBPH cellulose response is presented in Table 3.3.

Table 3.3: ANOVA for LBPH Cellulose Response Surface Quadratic Model

source	Sum of Squares	df	Mean square	F value	p- value prob>F	
Model	415.38	2	207.69	6.23	0.0175	significant
A- treat conc	412.25	1	412.25	12.38	0.0056	
B-contact time	3.14	1	3.14	0.094	0.7652	
Residual	333.12	10	33.31			
Lack of fit	333.07	6	55.51	4270.17	<0.0001	significant
Pure error	0.052	4	0.013			
Cor.Total	748.51	12				

In Table 3.3, the model F- value of 6.23 signifies that the model is significant. There is only a 1.75% chance that a "model F-value" of this magnitude could probably occur as a result of noise. Values of "prob >F" that are less than 0.05 indicate a significance in their model terms. In this case, treatment concentration (A) is a significant model term since the "prob>F" value is less than 0.05 as shown in Table 3.3. While values greater than 0.1 indicate the model terms are not significant. In this case, B which is 0.7652 is not a significant model term in relation to "prob>F".

The lack of fit F-value of 4270.17 is significant and this actually influences the fitness of a model.

The model summary of the statistical analysis of LBPH cellulose response is presented in Table 3.4.

Table 3.4: Model Summary for LBPH Cellulose Response

Std. Deviation	Mean	C.V (%)	PRESS	R-squared	Adj. R-squared	Pred. R-squared	Adeq. precision
5.77	61.83	9.33	718.69	0.7549	0.6659	0.0398	7.323

The information on Table 3.4 shows that the "Pred R-Squared" of 0.0398 is not as close to the "Adj R-Squared" of 0.6659 as one might normally expect. This may indicate a large block effect or a possible problem with the model and/or data. Things to consider are model reduction, response tranformation, outliers. "Adeq Precision" measures the signal to noise ratio. A ratio greater than 4 is desirable. This ratio of 7.323 indicates an adequate signal. This model can be used to navigate the design space.

The final model equation that describes the LBPH treatment process in terms of coded factors is expressed in Equation 3.1.

Given that A = Treatment Concentration and B = Contact Time

Cellulose = 61.83 -7.18A – 0.63B ----------3.1

Equation 3.1 is valid within the range of 1.5 to 4.5% treatment concentration and contact time of 1 to 3 h.

The predicted optimum cellulose response contour plot and the overlay plot for LBPH are presented in Figure 3.3 and 3.4 respectively.

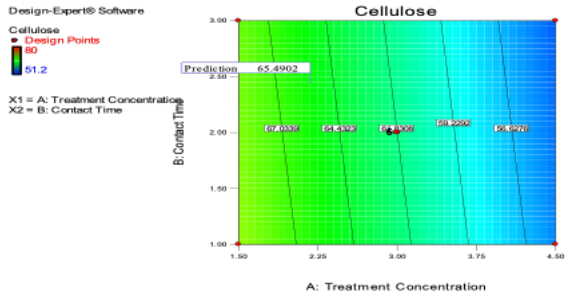

Figure 3.3: Predicted Optimum Cellulose Response Contour Plot for LBPH

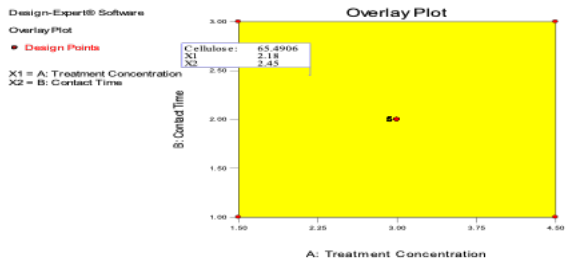

Figure 3.4: Overlay Plot for Optimum Cellulose Response Parameter for LBPH

Figures 3.3 and 3.4 present the optimum treatment conditions that give the optimum composition of cellulose and other non-cellulosic chemical composition of the treated LBPH fibre. The predicted optimum alkaline treatment concentration is 2.18% at a contact time of 2.45 h, to give a cellulose composition of 65.4906%. This value is less than the actual experimental value obtained upon confirmation. In the actual experimental analysis of the optimum treated LBPH fibre, a high cellulose content of 80% was achieved using 1.5% NaOH at a contact time of 3 h.

4. CONCLUSION

Natural fibres such as locust bean pod husk are promising reinforcing materials for polymer composite production. However, these fibres need to be chemically modified to better suit this purpose through mercerization. This will assist in optimally improving the cellulose content, reduce the hydrophilic property and ultimately improve the interfacial adhesion bonding capacity of the natural fibre with the polymer matrix in a composite. Using sequential

extraction method of biomass analysis, the chemical composition of raw locust bean pod husk fibre was characterized. It was found to be composed of cellulose, hemicellulose, lignin, extractives and ash. Out of these 5 components, the cellulose content recorded the highest composition of 59.3%. This value increased to 80% upon exposure to alkaline treatment at a NaOH concentration of 1.5% for 3 h. Furthermore, the alkaline treatment is able to improve the crystallinity nature of the LBPH fibre, while reducing its hydrophilic character for better interfacial bonding for polymer composite application. This is confirmed by the FTIR result. All of these observations are confirmation of the positive effect of the alkaline treatment process of the LBPH fibre.

ACKNOWLEDGEMENT

The authors in this work acknowledge the financial support of petroleum technology development fund (PTDF), as well as the support of the school of infrastructure, process engineering and technology, Federal University of Technology MINNA, the engineering staff of Nile University and African University of Science and Technology (AUST).

REFERENCES

Aguwa, J.I., and Okafor, J.O. (2012). Preliminary Investigation in the use of Locust Bean Pod as Binder for Production of Laterite Blocks for Building. International Journal of Environmental Science, Management and Engineering Research, 1 (2), 57-67.

Adama, A.Y and Jimoh, Y.A. (2011). Production and Classification of Locust Beans Pod Ash (LBPA) as a Pozzalan. Project Report. Engineering Civil.com.

Dittenber, D.B; GangaRao, H.V.S. (2012). Critical Review of Recent Publications on use of Natural Composites in Infrastructure. Compos A Appl Sci Manuf;43: 1419–29.

Iiyas, R.A; Sapuan, S.M; Ishak, M.R; and Zainudin, E.S. (2017). Effect of Delignification on the Physical, Thermal, Chemical and Structural Properties of Sugar Palm Fibre. Bioresources. Com. 12(4), 8734 – 8754.

Jabar, J.M. (2017). The Effect of Surface Modification on Chemical Composition of the Oil Palm and Coir Fibres. International Journal of Advanced Research in Chemical Sciences (IJARSC), Vol. 4, Issue 1, PP 13- 21.

Khairiah, B; and Khairul, A.M.A. (2006). Biocomposites from Oil Palm Resources. *Journal of Oil Palm Research*. (Special Issue-April): 103-113.

Kumar, R.,UI-Haq, M.I., Raina, A., and Anand, A. (2018). Industrial Applications of Natural Fibre- Reinforced Polymer Composites – Challenges and Opportunities. International Journal of Sustainable Engineering. Vol 12 (3), 212-220.

Khalil, H.P.S.A., Ismail, B., Rozman, H.D., and Ahmad, M.N. (2001). The Effect of Acetylation on Interfacial Shear Strength between Plant Fibres and various Matrices. Eur Poly J 37:1037–1045.

Lee, B.H; Kim, H.J; and Yu, W.R. (2009). Fabrication of Long and Discontinuous Natural Fibre Reinforced Polypropylene Biocomposites and their Mechanical Properties, Fiber and Polymers. Vol. 10, pp. 83-90.

Li, X., Panigrahi, S., and Tabil, L.G. (2009). A Study on Flax Fiber-Reinforced Polyethylene Biocomposites, Applied Engineering in Agriculture, Vol. 25, pp. 525-531.

Malkapuram, R., Kumar, V., and Yuvraj, S. N. (2008). Recent Development in Natural Fibre Reinforced Polypropylene Composites. Journal of Reinforced Plastics and Composites. Vol. 28, pp. 1169-1189.

Muhammad, A.M.M; Sinin, H; Muhammad, R.R. (2011). Treated Tropical Wood Sawdust- Polypropylene Polymer Composite: Mechanical and Morphological Study. Journal of Biomaterials and Nanobiotechnology, 2, 435-444. doi:10.4236/jbnb.2011.24053, (http://www.SciRP.org/journal/jbnb).

Ndububa, E.E and Uloko, J.O (2015). Locust Bean Pod Ash (LBPA) as a Pozzolanic Material in Concrete. Proceedings of the International Academic Conference for Sub-Sahara African Transformation & Development Vol. 3 No.4.

Olowokere, J.A; Akpan, U.G; Okafor, J.O; and Auta, S.M. (2022). Production and Characterization of Polymer Composite from Recycled Low Density Polyethylene and Modified *Eucalyptus globulus* Sawdust Fibre. FUW Trend and Technology Journal, www.ftstjournal.com. Vo 7 (3), 243-252.

Pereira, B.L.C; Carneiro, A.C.O; Carvalho, A.M.L; Colodette, J.C; Olivera, A.C; and Fonts, M.P.F. (2013). Influence of Chemical Composition of Eucalyptus Wood on Gravimetric Yield and Charcoal Properties. Bioresources ,8(3) 4574 – 4592.

Sridevi, A., Narasimha, G., Ramanjaneyulu, G., Dileepkumar, K., Rajasekhar-Reddy B., and Suvarnalatha-Devi, P. (2015).Saccharification of pretreated sawdust by *Aspergillus niger* cellulase. 3 Biotech. 2015 Dec; 5(6): 883–892.

PAPER 226 – STUDY OF THE PYROLYTIC CONVERSION OF PALM KERNEL SHELLS BIOMASS TO FUEL

O. R. Ayadju[1], I. Bori[2*]

[1]Department of Mechanical Engineering, Federal University of Technology, Minna, Nigeria.
[*]Email: chat2obus@yahoo.com

ABSTRACT
The overdependence on the use of fossil fuels, environmental problems caused by conventional energy sources and deforestation caused by the excessive use of wood for energy has brought the need for alternative energy sources. Agricultural residue such as palm kernel shells have shown great promise in solving this energy problem. The biomass material used (palm kernel shell) was obtained from Suleja, Niger state. The palm kernel shell was washed and sun dried to reduce the level of moisture present in the feedstock. A pyrolyzer was designed, fabricated and was used for the pyrolysis of palm kernel shell. The process of pyrolysis was carried out at pyrolyzing temperature range of 300°C – 700°C and at a pyrolysis duration of 20 minutes. The result showed that palm kernel shell at 300°C yielded 71.34% char, 20.69% tar and 7.92% gas; 400°C yielded 44.04% char, 26.12% tar and 18.1% gas; 500°C yielded 42.10% char, 37.29% tar and 20.61% gas; 600°C yield 33.71% char, 40.14% tar and 26.14% gas; 700°C yielded 29.88% char, 33.04% tar and 37.08% gas. From the above result, it can be concluded that as the pyrolyzing temperature increases, both tar and gas increases rapidly while the char production reduces and vice-versa.

KEYWORDS: Biomass, energy, pyrolysis, tar, char, fabricated, design.

1. INTRODUCTION

The surging worldwide clamour and the unfavourable effects of non-renewable fossil fuels on the environment had inspired substantial research attention in a wide range of engineering application of renewable resources such as biomass (Oyedepo et al., 2019).Biomass is clean, they can renew or replenish themselves. Its initial energy comes from the sun, and can regrow in a relatively short amount of time. Its sources are consistently available and can be managed sustainably. Hence the heightening energy demand must be progressively contended by varied energy resources, including sustainable and renewable sources like biomass (Ciubota-Rosie et al., 2008).We use four types of biomass today- wood and agricultural products, solid waste, landfill gas and biogas, and alcohol fuels (like ethanol or biodiesel) (National Energy Education Development, 2008). The main benefits of biomass are biomass is a renewable energy source, biomass helps climatic changes by reducing greenhouse gas emissions, cleaner environment and widely available source of energy.

The problems with biomass energy is that it takes a lot of land area and water to grow plants, and it can setup a potential food versus fuel feedstock as food crops like cassava, maize, sweet potato are used as biomass feedstocks and could increase deforestation due to the use of wood biomass, which can in turn affect the environment. The major components of biomass are cellulose, hemicellulose and lignin, each of which is different in their decomposition behaviour (Vigouroux, 2001). Moreover, decomposition of each component depends on heating rate, temperature and the presence of contaminants due to different molecular structures (Jahirul et al., 2012). Biomass can be converted into useful forms of energy using a number of different processes. Factors that influence the choice of conversion process are the type and quantity of biomass feedstock, the desired form of the energy, environmental standards, economic conditions, and project specific factors. The methods of converting biomass to energy: Conversion of biomass to energy is undertaken using two main process technologies: The conversion of biomass to energy is undertaken using biochemical/biological method or thermochemical methods. The biochemical conversion is the process by which biomass is converted into gas (CO_2/CH_4), waste (compost or fertilizer) and water (water or C_2H_5OH) by using microorganisms (Ciubota-Rosie et al., 2008).

1.1 Thermochemical methods

Solid fuels, such as biomass and coal, undergo thermal conversion to provide various forms of energy and other products. The three thermochemical processes by which solid fuels are converted are: Direct combustion, Gasification, Liquefaction, Torrefaction, and Pyrolysis (Mafu, 2018). Pyrolysis is defined as the thermal destruction of organic materials in the absence of oxygen, or partially combusted in a limited oxygen supply, to produce a hydrocarbon rich gas mixture, an oil-like liquid and a carbon rich solid residue. Pyrolysis converts biomass at temperatures around 5000 C, in the absence of oxygen, to liquid (bio-oil), gaseous and solid (charcoal)

fractions (Ciubota-Rosie et al., 2008). The advantages of pyrolysis are but not limited to the production of few air emissions due to limited use of oxygen, carbon sequestration, high energy efficiency, versatility, and energy independence.

2. THEORETICAL ANALYSIS

2.1 Moisture content is the weight of water contain in the sample. It was determined by measuring the difference between the weights of the samples before and after the drying process, and it is mathematically determined with the relation:

$$\text{M.C.} = \frac{\text{Wo}-\text{WI}}{W1} \times 100 \quad (2.1)$$

The same analysis is carried out on the sample three times and the average of the three results is calculated using the relation:

$$\text{M.C.}_T = \frac{\text{M.C.1}+\text{M.C.2}+\text{M.C.3}}{3} \quad (2.2)$$

$MC_1 + MC_2 + MC_3$ are the moisture content of the first, second, and third trial of the moisture content determination.

2.2 **Weight determination**

Weight determination is very important in the analysis, because it gives the amount of products (char, tar, and gas) at different temperature. It also helps in determining the efficiency of the process and that of the equipment.

$$W_{pks} = w_{ppks} - w_p \quad (2.3)$$

$$W_{char} = w_{pchar} - w_p \quad (2.4)$$

Weight of measuring pan is denoted as w_p, and the weight of measuring pan together with the sample is denoted as $w_{ppks,}$ weight of char produced is $W_{char} = w_{pchar} - w_p$

Weight of Tar produced

The condensate receiver containing the tar was weighed and the weight of the tar was determined by subtracting the weight of the condensate receiver from the weight obtained. If the weight of the condensate receiver is represented as $W_{Crtar,}$ then the weight of the tar W_{tar} produced was determined using the relation:

$$W_{tar} = W_{Crtar} - W_{CR} \quad (2.5)$$

The project work was based on the assumption that there was no loss or any leakage, therefore, since the weight of char and weight of char and weight of tar is gotten as given in the expression above. Then weight of gas can be determined according to the relation:

$$W_{pks} = W_{char} + W_{tar} + W_{gas} \quad (2.6)$$

$$W_{gas} = W_{pks} + W_{char} - W_{tar} \quad (2.7)$$

2.3 Product yield

Product yield is the ratio of the weight of product to the sample in percentage. It was determined for each product by weighing each product of the pyrolysis, and the sample.

Char yield

Having determined the weight of char, W_{char} and the weight of the sample W_{pks} according with the relations given above. Then char yield Y_{char} was determined according to relation:

Char yield, $Y_{char} = \frac{W_{char}}{W_{pks}} \times 100$ (2.8)

Tar yield, $Y_{char} = \frac{W_{tar}}{W_{pks}} \times 100$ (2.9)

Gas yield

Gas yield Y_{gas} was determined with the known weight of the gas, W_{gas}, and weight of the sample, $W_{pks.}$ And it is given in the relation as:

Gas yield, $Y_{gas} = \frac{W_{gas}}{W_{pks}} \times 100$ (2.10)

Energy content in the sample before pyrolysis

The energy content is the product of the sample weight and the heating value of the sample. The energy content in the sample before pyrolysis is the input energy of the processes, while the energy content to the products (which includes the energy of the processes, while the energy content to the products (which includes the energy content in the char, tar and that of the gas) is the output energy of process, also the energy produced by the furnace is the input energy of the equipment.

Energy content in the sample before pyrolysis

The energy content is the product of the sample weight and the heating value of the sample. The weight of the sample (palm kernel shells), W_{pks} was determined as given above and the heating value of palm kernel shell H_{pks} was given as 21.10MJ/kg by Ojolo, and Ismail, (2012). Therefore, the energy content in the sample is given in the relation:

$$\epsilon pks = W_{pks} \times H_{pks} \quad (3.11)$$

However, a constant weight of 500g was used throughout the experiment and since the heating value of palm kernel shells has been known to be 21.1 MJ/kg.

Hence, the energy content in the shell is

$$\epsilon pks = \frac{500g}{1000} \times 21.1 \text{ MJ/kg} = 10.55 \text{ MJ} \quad (3.12)$$

3. MATERIALS AND METHODS

This section should include apparatus and equipment setup, work materials, design, experimental methods, problem formulation, etc, as applicable.

3.1 **Cost Estimation of Constructing the Electric Furnace and its accessories**

The cost for the design and fabrication of the electrical furnace and its accessories are shown in the table 1.

Table 1: Bill of engineering measurement and evaluation.

S/N	Component	Unit Price	Quantity	Price (₦)
1.	Cabinet with lagging materials	₦60,000	-	₦60,000
2.	Retort with double pipe	₦15,000	2	₦15,000
3.	Temperature control (range 0^{o}c-1300^{o}c)	₦15,000	1	₦15,000
4.	Heating element	₦25,000	1	₦25,000

5.	Thermocouple	₦3,000	1	₦3,000
6.	Wire, switch, connector	₦3,000	-	₦3000
7.	Contactor (40amps)	₦5000	1	₦5000
			Grand total	₦126,000

3.2 The Pyrolyzer

A pyrolyzer is a device used in converting biomass into useful fuels in the absence of oxygen. The components of the Pyrolyzer are: electrically operated furnace, heater band, clay, retort, pyrometer, contactor, galvanized iron pipe, rubber hose, rubber gasket, clips, thermostat, heating element, bolts and nuts, lagging.

Plate I: Pyrolysis furnace

4. RESULTS AND DISCUSSION

a. Pyrolysis of palm kernel shells

The result of the pyrolysis of palm kernel shells at a temperature range of 300 °C to 700 °C for 20 minutes is presented in table 2 below

Table 2: Result of the pyrolysis of palm kernel shells.

Temperature (°C)	Initial Weight (g)	Char Weight (g)	Tar Weight (g)	Gas Weight (g)
300	500	356.95	103.47	39.58
400	500	220.22	130.61	149.17
500	500	210.55	186.47	103.03
600	500	168.58	250.73	130.69
700	500	149.40	165.20	185.40

The result presented in the Table 2 above shows that a temperature of 300°C, there was a mixture of char and unpyrolysed shells, some amount of tar and very little gas, because it is still very low to generate more gas but as the temperature increased, there was increase in tar production and gas weight while the weight of char reduced. This means that the sample gets more pyrolyzed as the temperature increases for a constant time consideration.

5. CONCLUSION

The following conclusions are drawn from the research work

i. the pyrolysis set up using electrically operated metal furnace is considered to be efficient.
ii. pyrolysis of palm kernel shell gives three types of fuels, the solid (char), the liquid(tar), and the gaseous fuel.
iii. pyrolysis should be done at a lower temperature if more of char is needed and at higher temperature if tar and gas are needed.

iv. the completion of pyrolysis process at different temperature is affected by time.

The following recommendation are made;

(i) cement should not be used in the casting of the clay lagging material used for the furnace.

(ii) the gas cylinder should be placed at a lower datum level to be the gas collection unit so as to increase the pressure in the cylinder.

(iii) the gas collection unit should be increased in order to retain a large volume.

ACKNOWLEDGEMENT

My sincere gratitude goes to my project supervisor Engr. Dr. I. Bori, for his support and continuous guidance all through this project work. Also my profound gratitude goes to the Renewable energy laboratory, LAUTECH, Ogbomoso for giving me the opportunity of fabricating the electric furnace (pyrolyser) within its centre.

REFERENCES

Ciubota-Rosie, C., Gavrilescu, M., & Macoveanu, M. (2008). Biomass - An important renewable source of energy in Romania. *Environmental Engineering and Management Journal*, *7*(5), 559–568. https://doi.org/10.30638/eemj.2008.079

Jahirul, M. I., Rasul, M. G., Chowdhury, A. A., & Ashwath, N. (2012). Biofuels production through biomass pyrolysis- A technological review. *Energies*, *5*(12), 4952–5001. https://doi.org/10.3390/en5124952

Jain, S., & Ph, D. (2015). *ENVIRONMENT IMPACTS OF ENERGY SECTOR (NON-RENEWABLE) Non-renewable energy sources*.

Kamimoto, M. (2006). The significance of liquid fuel production from woody biomass. *AIST Today (International Edition)*, *21*, 2–3.

Mafu, L. D. (2018). *Chemical and structural changes of biomass during pyrolysis and the influence on gasification reactivity in coal -biomass blends*. *October*, 11–46.

National Energy Education Development. (2008). Biomass Biomass at a Glance 2008. *The NEED Project*, 12–15.

Ojolo, S. J, Ismail, S.O, (2012). "Mathematical modelling of plastic waste pyrolysis kinematics"

Mechanical Engineering Department, University of Lagos, Lagos, Nigeria.

Okoroigwe, E. C., Enibe, S. O., & Onyegegbu, S. O. (2016). Determination of oxidation characteristics and decomposition kinetics of some Nigerian biomass. In *Journal of Energy in Southern Africa* • (Vol. 27, Issue 3).

Osueke, C., & Ezugwu, C. (2011). Study of Nigeria Energy resources and its consumption. *International Journal of Scientific & Engineering Research*, *2*(12), 121–130.

Oyedepo, S. O., Dunmade, I. S., Adekeye, T., Attabo, A. A., Olawole, O. C., Babalola, P. O., Oyebanji, J. A., Udo, M. O., Kilanko, O., & Leramo, R. O. (2019). Bioenergy technology development in Nigeria – Pathway to sustainable energy development. *International Journal of Environment and Sustainable Development*, *18*(2), 175–205. https://doi.org/10.1504/IJESD.2019.099513

Philander, S. G., & Winograd, C. (2012). International Energy Agency. In *Encyclopedia of Global Warming & Climate Change*. https://doi.org/10.4135/9781452218564.n379

Vigouroux, R. Z. (2001). *PYROLYSIS OF BIOMASS • Rapid Pyrolysis at High Temperature • Slow Pyrolysis for Active Carbon Preparation*. 113.

PAPER 227 – PERFORMANCE EVALUATION OF FURFURAL PRODUCTION FROM RICE STRAW USING DIFFERENT SOLVENTS AS PROMOTERS

V.T. Effiong[1*], H. Uthman[1], A.S Kovo[1] and J. E. Oguche[2]

[1] Chemical Engineering Department, FUT. MINNA
[2]Department of Chemical Engineering, A.B.U., Zaria
[*] Email: victoreffiong24@gmail.com:

ABSTRACT
This paper reports a study on the production of furfural from rice straw biomass using different and specifically investigate the effects of solvents as promoters on furfural Yield from rice straw by carrying performance evaluation on various KCr_2O_7, H_2O/THF and H_2O/Toluene at constant reaction temperature (180 ^{0}C), reaction time of 30 min and acid concentration of 0.5M H_2SO_4. Furfural production was carried out by hydrolysis of Pentosans to Pentoses where Pentosans in hemicelluloses is hydrolyzed with dilute mineral acids and various solvents as a promoter at relatively temperature to pentoses and subsequent dehydration of pentoses to furfural in a single stage process. The results showed that potasium dichromate salt gave a better yeild of 84.7% using 0.5M H_2SO_4 of the three salt employed in the experiment followed by H_2O/THF with yield of 78.3% at 0.5M H_2SO_4 and H_2O/toulene with a yield of 68.9% at 0.5M H_2SO_4 respectively. Furfural produced was successfully characterized and compared to that of commercial grade. Its molecular weight is 96.03 g/mol, boiling point of 160.48 °C, and its chemical formula is $C_5H_4O_2$ with a bitter almond odor. FTIR Resultconfirms the presence of carbonyl and aldehyde functional groups at wave length of 1666.27cm^{-1} and 2844.18cm^{-1} . The FTIR of furfural produced was compared with that of commercial furfural both followed a similar pattern.

KEYWORDS: Rice straw, Furfural, Solvent, Performance and Yield.

1. INTRODUCTION

Rice straw is the vegetative part of rice plant which is considered as waste after harvesting the rice grain. After wheat and corn, rice is believed to be the third most important grain crop in the world (Binod *et al*., 2010). Global rice production in 2016 was estimated to be 751.9 million tonnes by Food and Agriculture Organization (FAO) of United Nations. In 2016 (FAO, 2017). The quality of rice varies from one region to other, as the quality depends on rainfall, quality of soil and local climate. In recent years, rice straw is seen as potential source for producing furfural. Hemicellulose from rice straw mostly consists of xylose which on dehydration using sulphuric acid gives furfural (Machado *et al.,* 2016). At present, China is leading in furfural production followed by South Africa and Dominican Republic. Furfural is widely used as an important chemical raw material for pesticides, pharmaceuticals, food additives, and so on. It can also be used as a raw material for refined petroleum, oil, and solvents for various industrial applications (Yan *et al.,* 2014). Understanding the way to convert these molecules into high-value and high-quality add chemicals is important as they can substitute their fossil-based equivalents. These bio-based chemicals and materials are synthesized from feedstocks rich in carbohydrates and starch. (Sweygers *et al.,* 2020). The increasing demand of new .materials is on the rise due to continuous search for innovation and new technology so as to improve the previous ones. Also, interest in developing and advancing more efficient solvents has been the focus of researcher lately due to rise in applications of green chemistry (Duan et al., 2020). Solvents is central to development of new chemicals, compounds and systems hence, there is continuous search for new solvents is on the rise due to growing demand from other end user sectors such in chemical industries such as biotechnology, medicine, pharmaceutical, cosmetics, personal care goods, food and drinks as well as the increasing adoption for eco-friendly environment and packaging materials. Numerous challenges and limitations have been identified during production and recovery of furfural using the conventional solvents such as acids or bases thus, to increase yield, purity and achieve eco- friendly environment, green solvents such as potassium dichromate, water/toluene and water /tetrahydrofuran as substitutes for traditional organic solvents (acid and base) should be sought for which has minimal or no generation of hazardous by-products have to be developed to assure effective production of products and achieve sustainable environment.(Chen et al., 2019).These solvents are easily recyclable and does increase yield. Hence, the aim of this current work is to carry out performance evaluation of four solvents (potassium dichromate, water/toluene and water /tetrahydrofuran) on furfural production from rice straw. For the manufacture of furfural, homogeneous catalysts, mineral acids, and metal chlorides have been studied. The two mineral acids that are most frequently utilized as catalysts in the industrial manufacture of furfural are sulfuric acid and hydrochloric acid. In order to increase the yield and conversion of furfural, Yadav *et al*., 2017) researched and analyzed the catalytic activity of various acids,

including sulfuric acid, nitric acid, phosphoric acid, hydrochloric acid, acetic acid, and formic acid (Zhang *et al*., 2014) found that xylan produced 84.8% of the furfural yield using $AlCl_3$ and 65% of the furfural from xylose using hydrochloric acid. Studies generally reveal that a high yield of furfural was produced by mineral acids. However, mineral acids are highly harsh on machinery, recovering catalysts from reaction mixtures is challenging, and we are unable to recycle the catalysts (Ameh *et al*., 2016). Researchers have made a number of initiatives to reduce the chemical pollution brought on by the usage of acid homogeneous solvents. Hence, to address the issues with the use of homogeneous solvents such as minerals acids, heterogeneous solvents such as potassium dichromate, water/toluene and water /tetrahydrofuran as substitutes for traditional organic solvents (acid and base) for furfural production were evaluated in this work.

2. MATERIALS AND METHODS

2.1: Material

Some of the materials and equipment used during the experiment are listed as followed; Dried rice straw biomass, distilled water, funnels, H_2SO_4, toluene, tetrahydrofuran, potassium dichromate, chloroform, digital weighing balance, heating mantle, GCMS machine, 3-Neck Round bottom flask, retort stand, FTIR Machine, water bath, separating funnels, quick fit thermometer, condenser, beaker and vacuum pump.

From a field in Nigeria's Nasarawa state, rice straw was harvested. To get rid of weeds and other contaminants, the straw bail was sifted. The grinder was used to chop the straw. Standard test sieves were used to size the straw, and any flax straws with particle sizes smaller than 0.6 mm mesh size were collected and placed in a Ziploc bag. In order to get particle sizes within the range of the maximum particle size (1000µm), this particle size was chosen (Vidal *et al.,* 2011). At this particle size, the further reduction has no effect on the yield of furfural. The sample was stored at room temperature in a firmly closed container.

2.2 Methods:

The methodology for this research was splitted into four phases. The first phases of the experiment focused on feedstock (rice straw).The rice straw was collected from Nasarawa state then it was washed to remove impurity after which it was dried at room temperature until weight was obtained. The rice straw finely grounded and sieved to 1000 µm mesh size. The prepared rice straw samples were analyzed for dried moisture content, ash contents, lignin, oil content, and cellulose and hemicellulose contents after the oven drying at Institute for Agricultural Research (IAR/ABU), Zaria. Furfural production was carried out using a batch reactor and a distillation system, while the acid hydrolysis of the microalgae samples took place in the batch reactor. Aqueous Sulphuric acid (various amounts) of 0.5M Concentration, Uniform quantity 10 g of potassium dichromate, water/toluene and water tetrahydrofuran at a ratio of 1:2 and 10 g of rice straw sample respectively, were introduced into a 500 mL 3-necked round bottom flask, fixed to a Vigreux column and a Condenser and the reaction mixture was heated. The effluent from the batch reactor experienced rapid distillation at 105 °C, then the aqueous distillate mixture was collected over 40 mL chloroform in a separating funnel and two distinct layers were formed which are, the furfural-chloroform layer as well as the aqueous layer (Ameh *et al.,* 2016). After 2 h of distillation (after which there was no increase in the furfural-chloroform layer), the furfural-chloroform layer was decanted, then poured into a conical flask. The decanted furfural-chloroform mixture was subjected to a rotary evaporation at a temperature of 65 °C for 10 min where all the chloroform was observed to be evaporated leaving the furfural as the products. This procedure was repeated for various reaction temperatures, concentration and reaction time.

$$\underset{\text{Pentosans}}{(C_5H_8O_4)n} + nH_2O \rightarrow \underset{\text{Pentoses}}{(C_5H_{10}O_5)n}$$

$$\underset{\text{Pentoses}}{(C_5H_{10}O_5)n} \rightarrow \underset{\text{Furfural}}{(C_5H_4O_2)n} + 3H_2O$$

Scheme 1: Reaction for the Production of furfural

Furfural Yield is calculated using this equation

$$\textbf{Furfural Yield (\%)} = \frac{\text{mass of furfural produced (g)}}{\text{mass of straw rice biomass used (g)}} \times 100 \ldots\ldots\ldots (1)$$

The experimental set up during the research is shown in Plate 1

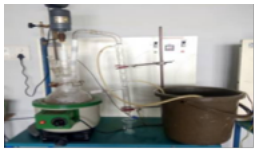

Plate 1: Experimental set up for production of furfural from rice straw

3.0 RESULTS AND DISCUSSION

Proximate analysis was carried out to determine % moisture content, % Ash content, % volatile matter content and % fixed carbon content of the rice straw biomass. The result is presented in Table 3 while Furfural yield using different solvents are presented in Table 4.

Table 3: Proximate analysis of rice straw

Parameters	Values
Moisture Content	7.53 %
Ash Content	9.92 %
Volatile Matter	61.23 %
Fixed Carbon	21.32 %
Cellulose	25 %
Hemicellulose	20.23 %
Lignin	15 %

Table 4: Furfural yield using different solvents

		FURFURAL YIELD (%) Solvents used		
S/NO	ACIDCONC.USED	KCr_2O_7	H_2O/THF	H_2O/Toluene
1	0.5M H_2SO_4	81.6	78.3	68.9
2	0.5M H_2SO_4	84.7	74.8	67.6
2	0.5M H_2SO_4	83.2	71.7	61.4
4	0.5M H_2SO_4	78.9	62.4	55.8

The furfaral yield for various solvent are presented in Table 4.8 above, as seen potasium dichromate salt gave a better yeild of 84.7% using 1.5M H_2SO_4 of the three salt employed in the experiment followed by H_2O/THF with yield of 78.3% at 0.5M H_2SO_4 .and H_2O/toulene with a yield of 68.9 at 0.5M H_2SO_4 this shows that the yield of fufural using for H_2O/THF and H_2O/toulene system decreases with increase in acid concentration and a non-linear relationship is observed for dichromate salt.

Important characterisation techniques were carried out and the results are presented and discussed as follows. Qualitative Chemical analysis of furfural using Fourier Transform Infrared Spectroscopy (FTIR) was done on furfural produced to determine the functional group present and both the commercial and furfural produced was qualitatively characterized and compared. Figure 1 show the FTIR result, of furfural produced and that of commercial furfural.

The Infrared Spectrum of furfural produced was compared to that of commercial in Figure 1 and both followed a similar peaks trend.

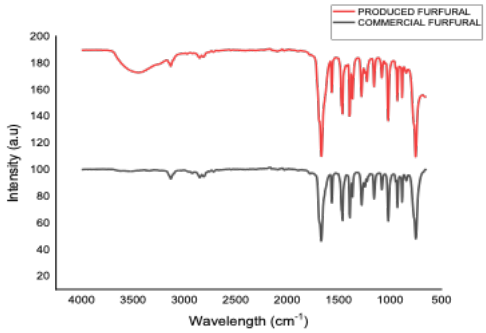

Figure 1: Overlaid FT-IR Spectra of Furfural Produced and commercial furfural.

As shown in Figure 1, the Fourier Transform Infrared Spectrum exhibited a strong absorption at 1669.8 cm^{-1} indicating a significant functional, the presence of conjugated carbonyl C=O group. The presence of an aldehyde was further proven by two peaks attained at 3134.7 cm^{-1} and 2810 cm^{-1}. These absorption shows a moderate intense stretching of aldehydic C=H. The strong peaks indicated from 1566.25 cm^{-1} to 1388.79 cm^{-1} are inactive stretching of C=C from aromatic ring while the aromatic bending out of plane peaks was observed from 964.44 cm^{-1} to 849.5 cm^{-1}. Peaks at 3134.7, 2810, 1669.8, 1565.5, 1461.1, 1394, 1274.7, and 1017.6 cm^{-1} in the spectra could clearly be seen. Additionally, no broad peaks were seen in the hydroxyl (OH) region between 3400 and 2400 cm^{-1}. This

demonstrates that a carboxylic acid group is not present. At 1714.46 cm^{-1}, the spectra revealed a very significant absorption. This absorption points to a carbonyl with a double bond (C=O). Because conjugated unsaturated aldehydes have internal hydrogen bonding, the absorption wave number is a little lower than typical. However, this peak can also be seen for chemical substances including ketone, ester, and aldehyde groups, as well as carboxylic acid (COOH). Since there was no peak at 1763.72 cm^{-1}, aldehyde rather than the ketone group is present. Furthermore, the appearance of two peaks at 3019.55 cm^{-1} and 2811.71 cm^{-1} provided further evidence of the aldehyde's presence. Due to the Fermi resonance between the basic aldehydic C-H stretching and the first overtone of the aldehydic C-H bending vibration, these absorptions demonstrate a moderately intense stretching of the aldehydic C-H bond. The spectral position is 1367.41 cm^{-1}. For the aldehyde group, these bands can be seen often. But the stretching of C=C from the aromatic ring is visible as strong peaks at 1521.45 cm^{-1} and 1421 cm^{-1}. From 928.72 cm^{-1} to 849.53 cm^{-1}, aromatic =C-H peak bending out of plane was found. Indicating the C-O stretching vibration were two prominent peaks at 1045.28 cm-1 and 1214.45 cm-1. This is similar to that of Oguche et al., 2017.

Qualitative Chemical analysis of furfural using GC-MS was done on the furfural produced to determine the quantity (percentage composition) furfural present in the sample produces. With an Agilent 6890/5973 GC-MS outfitted with an HP-5MS capillary column, the produced furfural's qualitative analysis is carried out, and Figures 2 depict the corresponding GC/MS spectra for the various alcohols' oxidation products. According to the GC-MS spectra, Furfural is the primary product in the system others include methyl 2-furoate, 2-furoate, and 3 -(furan-2-yl-)-2-methylacryaldehyde

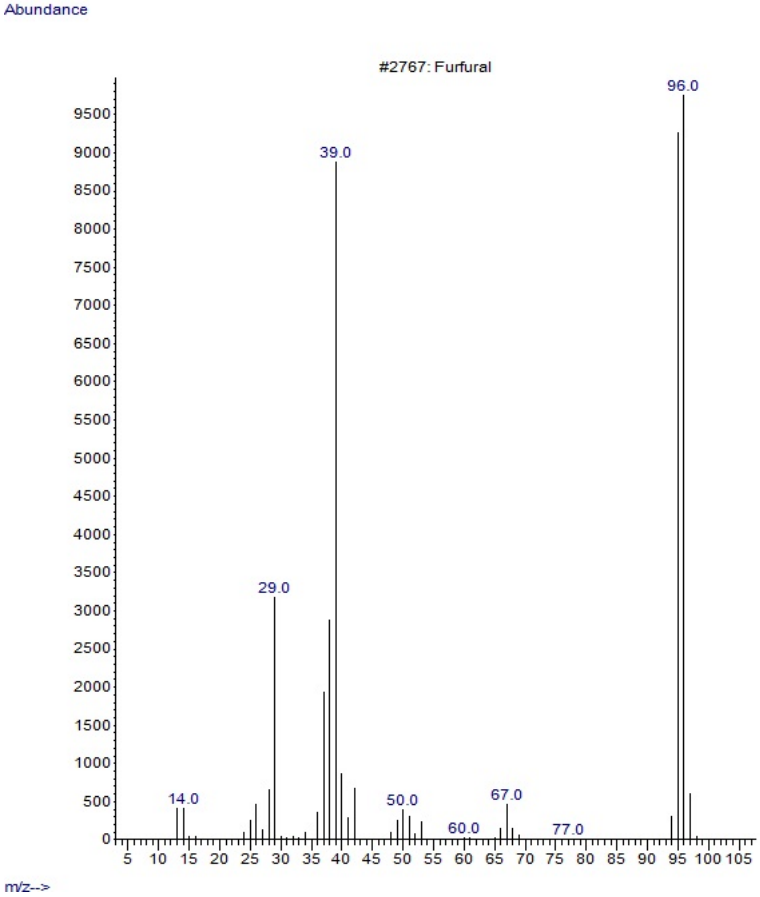

Figure 2: GC-MS of furfural produced from rice straw using 1.5M acid

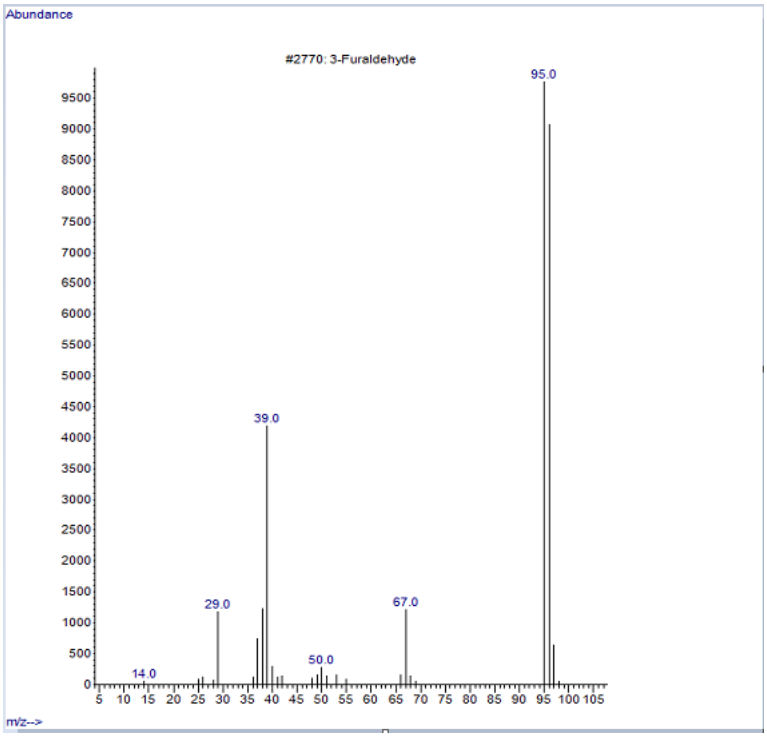

Figure 3: GCMS of Commercial Furfural

Results obtained from Gas Chromatogram (Figure 2 and Figure 3) shows that furfural has a retention time of 6.5466 min with a relatives abundance of 62 %. The Gas Chromatogram Spectrum shows a molecular ions peaks at mass to charge (m/z) ratio of 96 which correlate to a molecular formular of furfural of $C_5H_4O_2$. However a peak at m/z of 95.0 (Figure 4.13) was obtained for furfural produced from rice straw (this work) due to loss of hydrogen to form a carbonium ion. An electron was given away by the aldehyde carbon to hydrogen to form this fragmentation since more stable catio can be formed due to formation of hydrocarbon pattern, peak at m/z of 95 becomes dominant. The Gas Chromatogram of furfural produced was compared with that of commercial furfural in Figure 4.114 and both followed a similar pattern

4.0 CONCLUSION

Proximate analysis of the rice straw showed that the feedstock contained 7.53 % of moisture, 9.92 % of ash content had higher hemicellulose contents (20.23%) hence it is a suitable raw material for production of furfural having dried matter content of 61.23%. The impact of the solvents on furfural production from rice straw was analysed using solvents such as dichromate, THF and toluene. Dichromate produced a higher yield of furfural with 0.5M H_2SO_4 acid concentration used for all, furfural yield decreases from 81.6%,78.3%, 68.9% for KCr_2O_7, H_2O/THF H_2O/Toluene solvents respectively. KCr_2O_7, showed a better yield at 1.5M H_2SO_4 acid concentration compared to other solvents like H_2O/THF H_2O/Toluene. Furfural produced was successfully characterized and compared to that of commercial grade. Its molecular weight is 96.03g/mol, boiling point of 160.48 °C, and its chemical formula is $C_5H_4O_2$ with a bitter almond odor. FTIR Result confirms the presence of carbonyl and aldehyde functional groups at wave length of 1666.27cm^{-1} and 2844.18cm^{-1} . The FTIR of furfural produced was compared with that of commercial furfural both followed a similar pattern.

REFERENCES

Ameh A.O, Ojo A.A and Gaiya.J (2016).preliminary investigation into the synthesis of furfural from sugarcane bagasse, FUW Trends in Science & Technology Journal, www.ftstjournal.com. E-ISSN: 24085162; p-ISSN: 20485170; Vol. 1 No. 2 PP 582 - 586.

Chen Jingnan 1, Yun Li 2, Xiaoping Wang 1 and Wei Liu (2019): Application of Deep Eutectic Solvents in Food Analysis: A Review *Molecules* ***2019****, 24, 4594*

Duan Ming, Mengjuan Luo, Ziyi Yang, Yan Xiong, Peng Shi, Shenwen Fang Shan Qin (2020): Application of Choline-Based Deep Eutectic Solvent for Extraction of Crude Oil Contaminated Soils, Environmental Technology, DOI: 10.1080/09593330.2020.1717643

Food Agricultural Organisation (FAO) (2016), Annual report

Machado, G., Leon, S., Santos, F., Lourega, R., Dullius, J., Mollmann, M.E. and Eichler, P. (2016). Literature Review on Furfural Production from Lignocellulosic Biomass. *Journal of Natural Resources,* (7): 115-129 .http://dx.doi.org/10.4236/nr.2016.73012

Oguche J.E, Ameh A.O, Tanimu Y and Egu S.A (2017).Determination and Optimization of furfural production from Microalgae. *FUW Trends in Science & Technology Journal, www.ftstjournal.com. E-I*SSN: 24085162; p-ISSN: 20485170; October 2017 Vol. 2 No. 2 PP 784 – 789

Sweygers. N, Dewil, R and Appels, L, (2016). Production of Levulinic Acid and Furfural by Microwave-Assisted Hydrolysis from Model Compounds: Effect of Temperature, Acid Concentration and Reaction Time. *Waste Biomass Valor*. DOI 10.1007/s12649-016-9797-5 11:27-35

Yadav, S. P., Ghosh, U. K. & Ray, A. R., 2017. Kinetic studies on Pisum Sativum waste (peapod) hydrolysis to furfural. *Biotechnology Resources,* 12(2), pp. 2326-2338.

Yan. K. W, Lafleur. T. and Jarvis, C. (2014) Production, Properties and Catalytic Hydrogenation of Furfural to Fuel Additives and Value-Added Chemicals. *Renewable and Sustainable Energy Reviews*, 38, 663-676.http://dx.doi.org/10.1016/j.rser.2014.07.003

Zhang LX, Yu H, Yu HB, Chen Z, Yang L (2014) Conversion of xylose and xylan into furfural in biorenewable choline chloride–oxalic acid deep eutectic solvent with the addition of metal chloride. *Chinese Chem Lett* 25(8):1132–1136

PAPER 228 – SPATIAL AND TEMPORAL ANALYSIS OF RAINFALL AND MEAN TEMPERATURE PATTERN UNDER CLIMATE CHANGE IN NIGERIA

D. A. Olasehinde[1*], K. A. Adeniran[2], M. F. Amodu[1], A. T. Ogunrinde[1], M. O. Abioye[1], D. C. Uwaga[1], V. A. Ugochukwu[1]

[1] Department of Agricultural and Bio–Systems Engineering, Landmark University SDG13 (Climate action) research cluster, Omu–Aran, 251103, Nigeria
[2] Department of Agricultural and Bio–Systems Engineering, University of Ilorin, P.M.B. 1515, Ilorin, Kwara State, Nigeria
[*]Email: olasehinde.david@lmu.edu.ng

ABSTRACT
Climate change is expected to cause significant changes in weather patterns, with overreaching effects on agriculture, water supply, amongst other key sectors. Understanding the spatial and temporal characteristics of climate change is important for developing effective adaptation and mitigation strategies against the threat of climate change This study investigates the spatiotemporal characterization of climate change effect in Nigeria under two different Representative Concentration Pathways (RCPs), namely RCP4.5 and RCP8.5. Using the Mann-Kendall test, dynamically downscaled Global Circulation Models (GCMs) obtained from the Coupled Model Intercomparison Project phase 5 (CMIP5) for the period 1950-2100 were evaluated for three temporal scales, the "historical", "near future" and "far future". The results show that Nigeria is experiencing significant spatiotemporal variations in temperature and precipitation trends under the two concentration pathways. The Mann-Kendall test revealed a warming trend across the country, with some regions in the north experiencing up to 667% increase in temperature. Comparing the two RCPs, our results indicate that RCP8.5 has more severe impacts on temperature and precipitation than RCP4.5. The study provides valuable insights into the spatial and temporal patterns of climate change in Nigeria and highlights the potential impacts of different greenhouse gas concentration trajectories.
KEYWORDS: Climate variability, Nigeria, Non-parametric trend test, Climate change, RCP4.5, RCP8.5

1. INTRODUCTION

The effect of the Climate Change (CC) phenomenon is felt globally, and the serial comprehensive assessment reports of the Intergovernmental Panel on Climate Change (IPCC) gives an insight into the causes, potential impacts, and response options to CC (IPCC, 2014). After the latest complete IPCC report in 2014 there has been a shift from a focusing on the greenhouse gas inputs to the concentrations of greenhouse gases in the carbon cycle. Four original Representative Concentration Pathways (RCPs) of greenhouse gas concentration, RCP2.6, RCP4.5, RCP6, and RCP8.5 were developed as a possible range of radiative forcing values by the year 2100 (Vuuren et al., 2011). Furthermore, the additions of RCP1.9, RCP3.4, and RCP7 were consistent with the Shared Socioeconomic Pathways (SSP) indicating the potential futures for human society based on assumptions on population growth, economic development, and technological progress. The RCP 8.5 has been more widely employed by researchers, code named "business as usual" and presents a worst-case scenario of future climate system (Rogelj, *et al.,* 2012). The high emissions scenario of the RCP8.5 has been found more practicable to better separate the signal of a greenhouse gas forcing from the noise of natural variability. The medium emissions scenario of the RCP4.5 code named "stabilization with overshoot scenario" which assumes peak emissions by 2040 and then a decline is also employed in several studies especially for Africa. This scenario is more consistent with many current policies and trends, hence more realistic outcome than the RCP8.5 scenario. Under a high emissions scenario in Nigeria, it has been projected that more people will be affected by flooding in Nigeria due to sea-level rise, impacting on the socio-economic status of the people who are predominantly engaged in rain-fed agriculture, (Tunde, *et al.,* 2013; World Bank, 2015; Ojo, *et al.,* 2011). In the same light, the strategic location of Nigeria off the ocean's shelf extending into the arid hinterlands, presents a uniquely variable climate experience for the country. This variableness may make certain parts of the country experience drought and flooding almost simultaneously, providing a more complicated response to climate for policymakers. Therefore, an up-to-date fact on the historical trends and spatial variability of climate is imperative for future planning and sustainability of the agricultural, water resources and the entire ecosystem in the country (Ogunrinde, *et al*., 2019). Studies such as Attogouinon, *et al.,* (2017); Gbode *et al.,* (2019); and Oguntunde, *et al.,* (2017); have evaluated the modification of the Africa's climate and show increasing temperature trends, rainfall variableness, and frequency of extreme climate events. However, spatial-temporal evaluation for Nigeria's climate under RCP8.5 especially is yet to be carried out. This study investigates to investigate the spatiotemporal characterization of the historical climate

(1981 – 2015), the near future (2020 – 2059) and far future climate (2060-2100) under RCP4.5 and RCP8.5 for Nigeria.

2. MATERIALS AND METHODS

2.1 The Study Area

Nigeria is located in West-Africa between Latitude 4°N and 14°N and Longitudes 2°E and 15°E. It shares land borders with the Republic of Benin in the west and Cameroon to the east, while the Sahelian countries of Niger and Chad lie to its North. Agriculture is the mainstay of the Nigerian economy, accounting for more than 45% of the gross domestic product (GDP) and employing more than half of the workforce (Onah, 2020). Nigeria has a comprehensive climate variation from the south's wet and humid coastal regions to the dry and Sahel North. The south generally gets more annual rainfall, which usually spreads across 8 months (March to October), while the northern part experiences a shorter rainfall period (May to September). Nigeria is a tropical country, with only two seasons (dry and wet). The dry season typically last from November until March and it is characterized by low humidity and higher temperatures than the wet season because of warm winds from the Sahara Desert (Ogungbenro & Morakinyo, 2014).

2.2 Multi-Modal Ensemble Predictions of Monthly Precipitation and Mean Temperature

Regional Climate Models (RCMs) are utilized in CC studies instead of the traditional General Circulation Models (GCMs) to better capture the local effects of topography and land surface characteristics on climate. This study used to seven RCM simulations drive by Coupled Model Intercomparison Phase 5 (CMIP5) GCMs. Detailed information on the GCMs name, resolution, and characteristics are provided in the supplementary material. The Rossby Centre regional atmospheric model (RCA4) of the Swedish Meteorological and Hydrological Institute (SMHI) performed the downscaling. The SMHI-RCA4 model was driven by the seven selected GCMs for historical all-forcings simulations. The outputs covered the years 1951 to 2005 for historical data, and 2006 to 2100 for the future data, RCP4.5 and RCP 8.5 (Dieterich, *et. al.,* 2013). Studies by Demessie, et al., (2023); Gnitou *et al.*, (2019); Gyamfi, *et al.,* (2021); Hernández-Díaz *et al.,* (2013); and Mascaro, *et al.,* (2015) amongst others have assessed the reliability of its outputs and found that the model satisfactorily simulates the seasonal mean and annual cycle, with few exceptions. Multi-model ensembles (MMEs) are used primarily to increase the accuracy of climate models (Jang, 2021). The extracted RCMs was used to compare observed data via the multilayer perceptron of an artificial neural network (ANN). The input of the networks comprised the monthly climate variable of the seven RCMs during the baseline period while the observational data is used as the output

2.3 Mann- Kendall Trend Test

The Mann–Kendall (MK) test, which is often used to test trends in hydro-climatological time series. MK trend test is applicable in cases when the data values (x) of a time series obeys equation 1.

$$\chi = f(t) + \sum t \quad (1)$$

where f(t) is a continuous monotonic increasing or decreasing function of time and the Residual $\sum t$ can be assumed to be from the same distribution with zero mean. The MK test was executed in the R-Studio environment. The MK test statistic S is as given by equation 2. (Salami et al., 2014):

$$S = \sum_{k=1}^{n-1} \sum_{j=k+1}^{n} sign(x_j - x_k) \quad (2)$$

where n is the length of the time series $x_{i....}$ x_n, and sgn (·) is a sign function, x_j and x_k are values in years j and k, respectively. The expected value of S equals zero (E[S] = 0) for series without trend and the variance is computed as given in equation 3:

$$\sigma^2(S) = \frac{1}{18}\left[n(n-1)(2n+5) - \sum_{p=1}^{q} t_p(t_p-1)(2t_p+5)\right] \quad (3)$$

where q is the number of tied groups and t_p is the number of data values in pth group. The test statistic Z is as defined in equation 4:

$$Z = \begin{cases} \frac{s-1}{\sqrt{\sigma^2(s)}} \; if \; S > 0 \\ 0 \; if \; S = 0 \\ \frac{s+1}{\sqrt{\sigma^2(s)}} \; if \; S < 0 \end{cases} \quad (4)$$

As a non-parametric test, no assumptions as to the underlying distribution of the data are necessary. The Z-statistic is then used to test the null hypothesis, H_o that the data is randomly ordered in time, against the alternative hypothesis, H_1 where there is an increasing or decreasing monotonic trend. To estimate the true slope of an existing trend, the Sen's non-parametric method was used.

2.4 Spatial Representation of Meteorological Information

This study employs an ArcGIS package to render maps using spatial data as inputs and applying analytical methods to detect variability. The Inverse Distance Weight (IDW) function in ArcGIS was used with a spatial

interpolation of moderate weighting value (2). The IDW interpolation determines cell values using a weighted combination of a set of sample points. Yang et al., (2015) reports that IDW is superior to other interpolation methods for climate data with fewer relative errors and more computational efficiency.

3. RESULTS AND DISCUSSION

3.1 Summary of Historical Metrological Information

The GCMs and the observational dataset were extracted from forty-one (41) WMO/NiMET locations across the study area for easy reference and bias correction. The GIS locations and elevation of each observation station are provided in the supplementary materials. The observational dataset is used for the validation of the statistically downscaled GCM ensembles. The dataset is then grouped into seven clusters, Sahel Savannah (SAS), the Sudan Savannah (SUS), the Northern Guinea Savannah (NGS), the Southern Guinea Savannah (SGS), the Derived/Coastal Savanna (DRS), the Mid-Altitude (ALT) and the Humid Forest (HMF) agroecological zone patterned after (Mereu et al., 2015). The box and whisker plots are employed as a descriptive statistical tool in identification of outliers and assessment of the normality of the dataset. Representations of the climate variable for each zone are presented in the supplementary material.

The Potiskum, Maiduguri and Nguru stations are situated in the SAS zone with an interquartile range (IQR) for temperature ranging from 25-29.6°C, 26.1-28.4°C and 25.5-30.75°C. Statistically the chance that future temperature will fall to this range is 50%. Lange & Vinke, (2021) reports that Africa's Sahel has a tropical semi-arid climate, typically hot, sunny, and dry in accordance to Koppen climate classification. The small length of IQR in comparison to the whiskers also suggest a middle clustering of the data about the median values of 27.4°C, 28.8°C and 26.9°C. Also, the Maiduguri observational station presents a more reliable dataset in deterministic modelling due to the relative smaller dispersion of its value. The rainfall values in the region are significantly skewed with mean values of 62.76, 43.91 and 54.01mm/month in comparison with low median values of 6.75, 2.7 and 6.9mm/month. Generally, positive skewness suggests a positive deviation from the median and the outlying values are less probable in that direction. Ordinarily, this may imply increase in rainfall values for the region but the employed descriptive tool does not factor in the non-parametric temporal attributes of the dataset. At the SUS zone, the Katsina station dataset has the smallest dispersion for rainfall, between 81.5-0.73mm/month. The large presence of outliers in most of the station in this zone is indicative of the changing pattern of the dataset in the region. Several reports have highlighted the changing pattern of climate in the Sudan agroecological zone (Mertz et al., 2012; Siddig, Stepanyan, Wiebelt, Grethe, & Zhu, 2020). Also. the rainfall values in the region are significantly skewed with low median values of in comparison with higher mean values of for the SAS zone. The IQR of temperature values in the region are 30.1-26.8°C, 30.7-26.8°C, 28.9-24.4°C, 27.5-24.5°C, 30.9-27°C, and 29.3-25.5°C with slight negative skewness is also observable in the temperature pattern at the Yelwa, Sokoto, Kano, Birnin-Kebbi and Gusau station respectively.

At the NGS zone, IQR shows a compact dataset for the region. For the observational stations in Zaria, Yola, Kaduna, and Bauchi, it runs from 27.4-24°C to 29.7-26.4°C to 21.52-24°C to 27.4-24.3°C, respectively. The rainfall values in the region are also skewed similar to the datasets in the SUS, but with a closer median to mean values and higher rainfall values. The median values of 26.25, 50.65, 62.15, 20.15mm/month to mean values of 86.22 and IQR length ranging from 168-0.2, 153.38-0, 191.4-0.6, 161.15-0.2mm/month are recorded for the Zaria Yola, Kaduna and Bauchi stations respectively. The Kaduna station recorded higher rainfall values (mean of 62.15mm/month) and it's known as a commercial hub in the geopolitical region. Blanc & Perez, (2008) work on the correlation between rainfall and human density largely explains the relative increased commercial and agricultural activity in this basin, however, larger population leads to increased production of GHG and water stress. From literature the SGS is reported to have more rainfall and denser vegetation in comparison with the NGS (Adenle, et al., 2020; Ayanlade, 2009). A broad comparison between the box and whisker plots of the NS and SGS zones, demonstrably explains this difference. The temperature of the region is higher in the SGS compared to the NGS but the rainfall values are also higher in the SGS. This may be as a result of the relative incidence of the sun to the two regions. Because the equator is located in the direct plane of the sun, the SGS closer to the equator receives relatively more solar radiation in comparison the NGS. The mean values of rainfall in the two regions are similar but with a more asymmetrical dataset for the SGS, which in meteorological terms, may imply longer rainy season. The temperature presented in the DRS zone is milder in comparison to the other guinea savannas. At the Ilorin station temperature dataset presents an almost ideal dataset with little dispersion and skewness with the relative short tails of the whiskers to the box plot indicative of a bimodal distribution of temperature values. The IQR ranges from 25-26.6°C, a mean of 25.7°C, and a median of 25.5°C. Temperature ranges between 25-35°C has been reported to be optimum for several crops grown in the tropics (Adedapo, 2020; Akpenpuun & Busari, 2018; Ghadirnezhad & Fallah, 2014). The mean DRS rainfall values are also slightly higher than the SGS rainfall values (except for the Shaki and Ibi stations). The Ilorin rainfall also datasets presented a fairly symmetric dataset with IQR range between 145.575-19.25mm/month. At the HMF zone rainfall datasets in

the region are slightly skewed with the median values generally higher than the mean values for many of the stations. The observable long tails of the whiskers and the outliers also indicates a changing pattern of rainfall in the region. The temperature datasets assumed a fairly symmetrical nature with a diverse IQR range amongst the stations, with the Port-Harcourt, Akure and Calabar stations returning much lower IQR range compared to others, the observation stations seem to belong to different climatological zonation. Contrariwise, this study considers agroecological zonation, which according to the FAO not only considers climate but landform, soils, land cover and its potentials for agriculture (Mereu, et. al 2015).

3.2 TRENDS ANALYSIS OF HISTORICAL RAINFALL AND TEMPERATURE

An overview of the Historical dataset evidently shows a changing pattern for climate with temperature on the increase and observable presence of outliers in rainfall data. In a bid to situate the presence and quality of trend at each of the agroecological zone several time-series trend analyses were conducted. Seven representative stations, one in each of the seven agroecological zones were selected for in depth temporal analysis. The monthly trend test for average temperature and precipitation for the time series data for all the locations are presented in the supplementary material. Positive z-values show an upward tendency, whilst negative values show a downward trend. At the Maiduguri observation station, with the exception of January, which saw a slight decline and a negative z-value of 0.8, the trend of mean temperature is significantly on the rise. The Sen's slope estimator, which measures the strength of the trend in the time series, also reveals that April is the month most negatively impacted. Ogunrinde et al., (2020) projected that rising temperature in the Sahel may lead to increase incidences and intensity of drought. The UN climate risk assessment profile has also noted that the Sahel region is one of the most vulnerable to CC with the warming climate to lead to higher reduction in agricultural output in the region in comparison to the reductions of global outputs; a consequence of this will be to further put food security at risk. (Sallaba et al., 2017). Rainfall is not widely varied from the MK trend test. With little or no amount of rainfall recorded in five months, five out of the remaining months returned an upward trend while the months of May and August had decreasing trend though not significant. The Sahel has been reported to be experiencing an increase in summertime rainfall (Bichet & Diedhiou, 2018; Kumi et al., 2021; Pausata et al., 2020). The regional monsoon circulation and the global Hadley cell are both dynamically connected to the Sahel's rainfall. As a result, it is vulnerable to regional land effects like rising temperatures and changes in greenhouse gases brought on by anthropogenic activities as well as local forcings from distant waters. These mechanisms can account for the apparent interannual fluctuations in the region.

The densely populated Sudan Savannah agroecological zone returned a positive z-value of 6.9 for the yearly average mean temperature and a Sen's slope value of 0.024 for the month of April (the largest change), the trend analysis shows that the temperature in the area is significantly rising. From a yearly average temperature of 26°C in the 1950s to approximately 28°C in the 2010s, the temperature has steadily increased. The record high monthly average of 30.40°C for the month of February in the year 2010 eloquently demonstrates this. Rainfed agriculture, aquaculture, natural ecology systems and biodiversity, water resources, and energy are the sectors of the Sudan agroecological zone that are most susceptible to temperature increases, according to Siddig et al., (2020). While August typically received the biggest quantity of rainfall over the time period under review, December and January had no rainfall at all. With July and September showing decrease trends, eight of the remaining 10 months exhibited slightly increased trends in rainfall amount. The effects of prolonged dry spells occurring during vulnerable crop growth stages, which may also have significant effects on overall crop yield, need to be further examined to determine whether the increases have been accompanied by changes in intra-seasonal variability that have relevance for agriculture. In the same light, works in the region have projected varying impact on the different crops. For example, Mereu et al., (2015) projected cassava yield to improve by +20 % in the Sudan while crop yield risk increases are expected for maize for the same period.

The largest agroecological zone in Nigeria is the Guinea Savannah, and produces the bulk of staple food consumed in the country. The reference stations for the northern, southern, and derived guinea savannah are chosen to be the observation from the Kaduna, Bida, and Ilorin stations, respectively. Similar to multiple studies in the area, the MK test shows a rise in mean temperature for all the months (A. Bello et al., 2020; Gbode et al., 2019; Ibitolu & Balogun, 2019; Ogunjo et al., 2019). Sen's slope suggests that the months of November for the northern Guinea savannah and March for both the southern and derived Guinea savannahs recorded the greatest significant shift. Notably, there were significant differences in the inter-seasonal magnitude of change, with the northern Guinea Savannah experiencing a change of 6.5% from January to 67% in November, the southern Guinea Savannah experiencing a change of 15.42% from January to 56.98% in March, and the Derived Guinea Savannah experiencing a change of 25.68% from January to 65.38% in March. Buis, (2020) postulated that the seasonal fluctuations are as a result from variations in solar insolation resulting from the tilt of the Earth's rotation axis. In the Guinea Savanah, rainfall values over time varied as well. Seven of the months at the Kaduna and Ilorin

observation stations and five of the months at the Bida station recorded increasing amounts of rainfall. As more evaporation takes place with temperatures rise, the potential for precipitation also increases. It has been anticipated that precipitation would rise in many places as the temperature warms (Dai, Zhao, & Chen, 2018). Contrariwise, in all agroecological zones, the months of July and March showed a declining tendency. The altitude-modified wet and dry tropical agroecological zones are found in parts of Plateau and Adamawa State It is characterized by a relative increase in precipitation and a reduction in mean temperatures.

3.3 SPATIAL ANALYSIS OF RAINFALL AND MEAN TEMPERATURE FOR HISTORICAL, AND FUTURE SCENARIOS

The Mann-Kendall (M-K) trend test is utilized to measure the changes in climatic variables, whether they are increasing or decreasing, over a span of several years in the time series data. In order to identify areas vulnerable to climate change, spatial interpolation was performed for rainfall and mean temperature. Figure1 & 2 depicts the spatial representation of the magnitude of change in mean temperature and annual rainfall across the country respectively. The areas depicted in red represents areas of high magnitude of change while areas in blue represents the low areas. In general, there was no significant change in annual rainfall throughout the country. The historical period showed a negative trend in annual rainfall (reduction in rainfall), with a slight increase projected for the future under the RCP4.5 and RCP8.5 scenarios. The z-values for rainfall ranged from -4.74 to 0.344, with an average value of -1.425 during the historical period. In the near and far future, under RCP 4.5 and RCP 8.5 respectively, the average z-values increased to 0.123, 0.28, 0.39, and 0.32. Similarly, Oguntunde et al. (2017) found that annual rainfall did not exhibit a significant increasing or decreasing trend, but there was an observed increase in variability, and more extreme weather events. The coastal regions and certain parts of the Sudan area in the north are experiencing the most significant reductions in rainfall. This finding contradicts the assertion made by Akinbile, et al., (2019) which suggested a negative linear correlation between rainfall quantity and latitude, stating that rainfall decreases with increasing latitude away from the Atlantic Ocean due to latitudinal zonality in precipitation. However, it is possible that this discrepancy is a result of limited data used for their spatial analysis. Climate change has the potential to modify global and regional atmospheric circulation patterns, leading to increased variability in rainfall. This can result in more frequent and intense extreme weather events, such as droughts and heavy rainfall events. Coastal areas, due to their proximity to the ocean and potential interactions with changing weather patterns, may be particularly vulnerable to these variations in rainfall. Consequently, this heightened variability can contribute to an overall reduction in the trend of annual rainfall even in the coastal areas. In contrast, for future scenarios under RCP4.5 and RCP8.5, these vulnerable areas show slight increases in annual rainfall amounts

There is a significant increase in mean temperature values in the country for the historical as well as the future case scenarios in agreement with the general axiom of global warming and climate change. The spatial representation historical change in mean temperature does not show a distinction between the pattern in the southern and northern region, however there is observable lowering of the magnitude of change in the future under the RCP4.5 case scenario. Contrariwise, under the RCP8.5 scenario greater areas experiences significant increase in the mean temperature. Quantifying temporal variability of change in mean temperature may be less apparent than rainfall variability as rainfall tends to be more spatially heterogeneous, climate change can also influence temperature variability. As the average temperature may increase, there can also be greater fluctuations in temperature, including more extreme hot and cold events. The z-values for average temperature ranged from 5.11 to 7.52, with an average value of 6.52 during the historical period. In the near and far future, under RCP 4.5 z-values decreases to 4.6570 and 2.604 a testament to the effect of a "stabilization case scenario". While the average z-values remain largely unchanged under the "business-as-usual case scenario" with an average z-value of 6.063 and 5.910 for the near and future temporal time scales respectively. Increasing temperature can have significant implications for agriculture in Nigeria as it may negatively affect crop growth, reduce yields, and impact livestock productivity. Also, the increasing temperature can disrupt the local water availability as higher temperatures increase evaporation rates, leading to greater water loss from surface water bodies and soil moisture

4. CONCLUSION

This study investigates the spatiotemporal characterization of the historical climate (1981 – 2015), the near future (2020 – 2059) and far future climate (2060-2100) under RCP4.5 and RCP8.5 by using Multi-Modal Ensemble Predictions, Mann Kendall test and IDW. The findings of this study indicate that: The analysis of reveals a significantly changing climate pattern. The results of the Mann-Kendall trend test indicate a significant increase in temperature with minimal interannual variability. However, the changes in rainfall were mostly not found to be statistically significant. Furthermore, the spatial interpolation analysis revealed that the coastal regions and Sudan areas exhibited the most substantial decreases in annual rainfall. When examining the historical change in mean

temperature, the spatial representation did not indicate a distinction between the patterns in the southern and northern regions. However, it is noteworthy that there is an observable decrease in the magnitude of change in the future under the RCP4.5 case scenario. These findings highlight the importance of understanding and monitoring climate trends to assess their potential impacts on sectors such as agriculture, water resources, and energy. Further research is needed to explore the specific implications of these changing climate patterns on various crops and ecosystems within each agroecological zone.

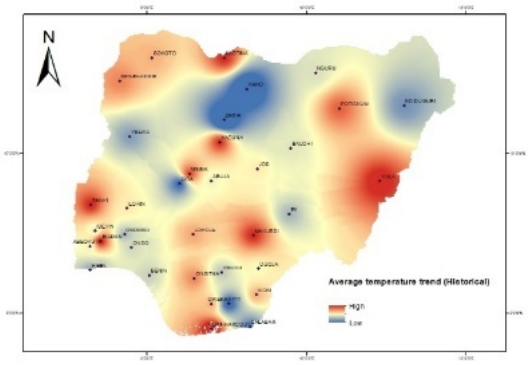

(a) **Trend in mean temperature (historical)**

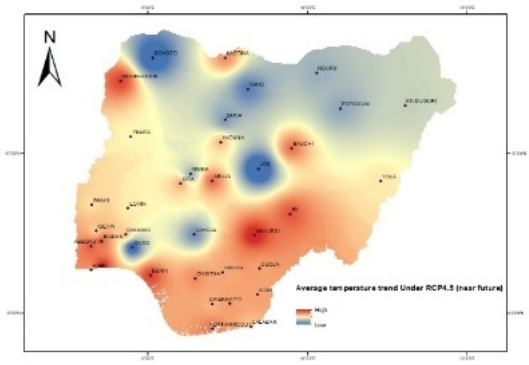

(b) **Trend in mean temperature Under RCP4.5 (near future)**

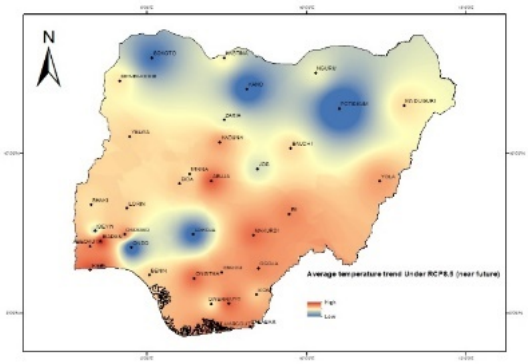

(c) **Trend in mean temperature Under RCP8.5 (near future)**

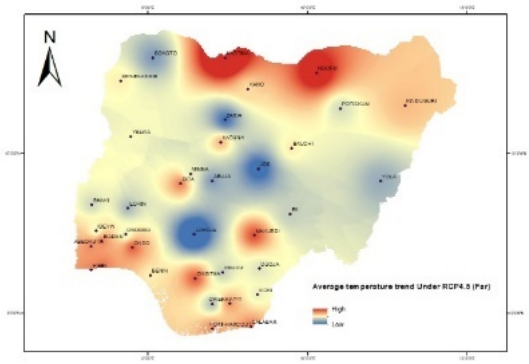

(d) Trend in mean temperature Under RCP4.5 (far future)

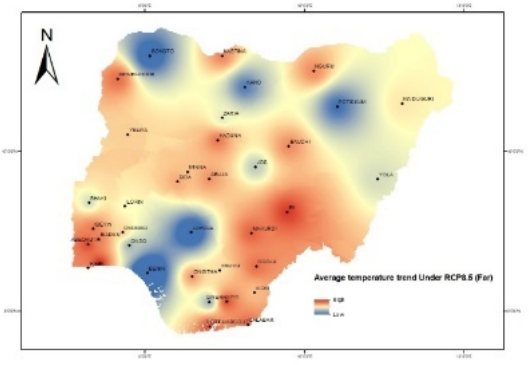

(e) **Trend in mean temperature Under RCP8.5 (far future)**

Figure 1. Changes in Mean Temperature

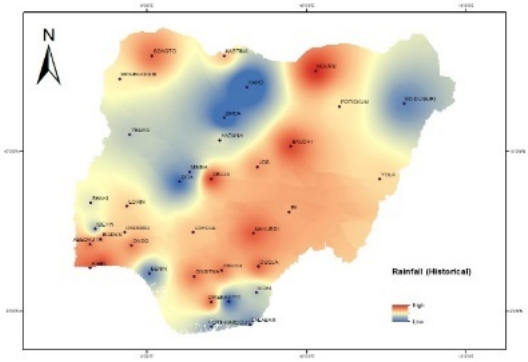

(a) **Trend in Rainfall (historical)**

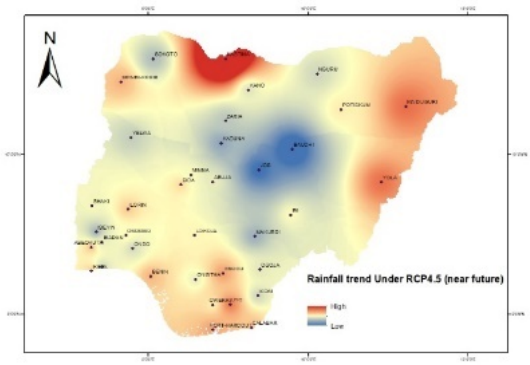

(b) **Trend in Rainfall Under RCP4.5 (near future)**

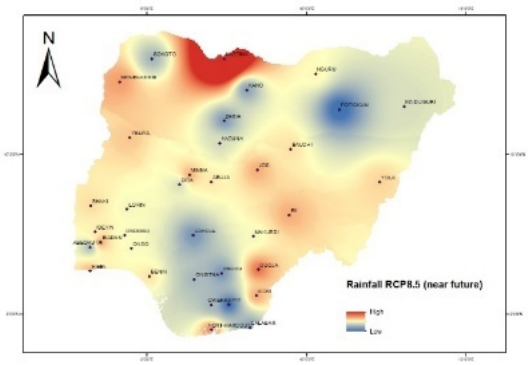

(c) **Trend in Rainfall Under RCP8.5 (near future)**

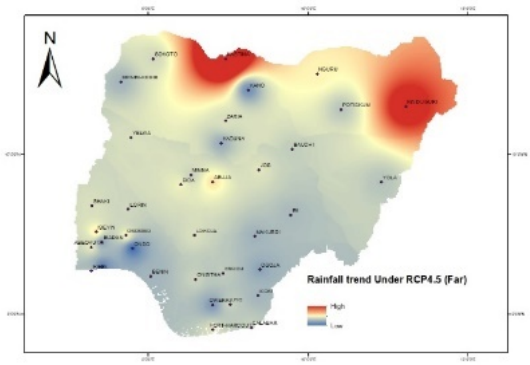

(d) Trend in Rainfall Under RCP4.5 (far future)

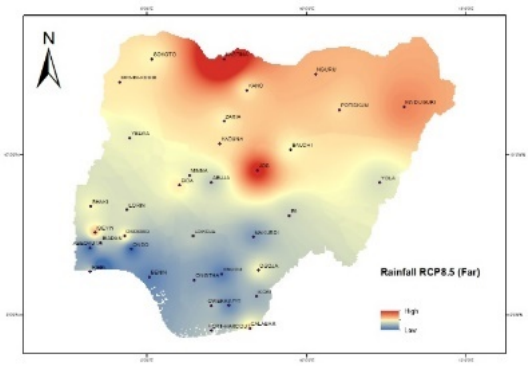

(e) **Trend in Rainfall Under RCP8.5 (far future)**

Figure 2. Changes in Annual Rainfall

REFERENCES

Adedapo, A. (2020). Trend Analysis of Temperature and Humidity in Kwara State, Nigeria. *Journal of Environmental Geography*, 13(3–4). Retrieved from https://doi.org/10.2478/jengeo-2020-0011

Adenle, A., Eckert, S., Ifejika Speranza, C., Oluwatola, A., & Ellison, D. (2020). Human-induced land degradation dominance in the Nigerian Guinea Savannah between 2003 – 2018. *Remote Sensing Applications: Society and Environment*, 19, 100360. Retrieved from https://doi.org/10.1016/j.rsase.2020.100360

Akinbile, C., Ogunmola, O., Abolude, A., & Akande, S. (2019). Trends and spatial analysis of temperature and rainfall patterns on rice yields in Nigeria. *Atmospheric Science Letters*. Retrieved from https://doi.org/10.1002/asl2.944

Akpenpuun, T. D., & Busari, R. A. (2018). Impact of climate on the yield of major tuber crops in Kwara State, Nigeria. *Global Journal of Agricultural Sciences*, 16(1). Retrieved from https://doi.org/10.4314/gjass.v16i1.8

Attogouinon, A., Lawin, A., N'Tcha M'Po, Y., & Houngue, R. (2017). Extreme Precipitation Indices Trend Assessment over the Upper Oueme River Valley-(Benin). *Hydrology*, 4, 36. Retrieved from https://doi.org/10.3390/hydrology4030036

Ayanlade, A. (2009). Seasonal rainfall variability in Guinea Savanna part of Nigeria: A GIS approach. *International Journal of Climate Change Strategies and Management*, 1(3). Retrieved from https://doi.org/10.1108/17568690910977492

Bello, A., Bashir, Bello, Y., Adebayo, A. A., & Abubakar. (2020). *ANALYSIS OF RAINFALL… ANALYSIS OF RAINFALL AND TEMPERATURE CHANGES IN GOMBE STATE, NIGERIA*. *FJS FUDMA Journal of Sciences (FJS* (Vol. 4).

Bello, N. J. (1998). Evidence of climate change based on rainfall records in Nigeria. *Weather*, 53(12). Retrieved from https://doi.org/10.1002/j.1477-8696.1998.tb06358.x

Bichet, A., & Diedhiou, A. (2018). West African Sahel has become wetter during the last 30 years, but dry spells are shorter and more frequent. *Climate Research*, 75(2), 155–162. Retrieved 29 August 2022 from https://doi.org/10.3354/CR01515

Buis, A. (2020). Milankovitch (Orbital) Cycles and Their Role in Earth's Climate – Climate Change: Vital Signs of the Planet. *Nasa Global Cimate Change*.

Dai, A., Zhao, T., & Chen, J. (2018). Climate Change and Drought: a Precipitation and Evaporation Perspective. *Current Climate Change Reports*. Retrieved from https://doi.org/10.1007/s40641-018-0101-6

Demessie, S. F., Dile, Y. T., Bedadi, B., Gashaw, T., & Tefera, G. W. (2023). "Evaluations of regional climate models for simulating precipitation and temperature over the Guder sub-basin of Upper Blue Nile Basin, Ethiopia". *Modelling Earth Systems and Environment*. Retrieved from https://doi.org/10.1007/s40808-023-01751-0

Dieterich, C., Schimanke, S., Wang, S., Väli, G., & Liu, Y. (2013). *Evaluation of the SMHI coupled atmosphere-ice-ocean model RCA4-NEMO*. Retrieved 30 November 2021 from https://www.diva-portal.org/smash/record.jsf?pid=diva2:947918

Gbode, I. E., Adeyeri, O. E., Menang, K. P., Intsiful, J. D. K., Ajayi, V. O., Omotosho, J. A., & Akinsanola, A. A. (2019). Observed changes in climate extremes in Nigeria. *Meteorological Applications*, 26(4). Retrieved from https://doi.org/10.1002/met.1791

Ghadirnezhad, R., & Fallah, A. (2014). Temperature effect on yield and yield components of different rice cultivars in flowering stage. *International Journal of Agronomy*, 2014. Retrieved from https://doi.org/10.1155/2014/846707

Gnitou, G. T., Ma, T., Tan, G., Ayugi, B., Nooni, I. K., Alabdulkarim, A., & Tian, Y. (2019). Evaluation of the rossby centre regional climate model rainfall simulations over west Africa using large-scale spatial and temporal statistical metrics. *Atmosphere*, 10(12). Retrieved from https://doi.org/10.3390/ATMOS10120802

Gyamfi, C., Tindan, J. Z. O., & Kifanyi, G. E. (2021). Evaluation of CORDEX Africa multi-model precipitation simulations over the Pra River Basin, Ghana. *Journal of Hydrology: Regional Studies*, 35, 100815. Retrieved 17 March 2023 from https://doi.org/10.1016/J.EJRH.2021.100815

Hernández-Díaz, L., Laprise, R., Sushama, L., Martynov, A., Winger, K., & Dugas, B. (2013). Climate simulation over CORDEX Africa domain using the fifth-generation Canadian Regional Climate Model (CRCM5). *Climate Dynamics*, 40(5), 1415–1433. Retrieved from https://doi.org/10.1007/s00382-012-1387-z

Ibitolu, H. A., & Balogun, I. (2019). An assessment of drought in Northern Nigeria using spatiotemporal remote sensing data. In *Proceedings of the International Astronautical Congress, IAC* (Vol. 2019-October).

IPCC. (2014). *IPCC's Fifth assessment Report: Impacts, Adaptation, and Vulnerability*. *IPCC WG2*.

Kumi, N., Abiodun -, B. J., Abdi, A. M., Seaquist, J., Tenenbaum, D. E., Porkka, M., … Gordon, L. J. (2021). Is wetter better? Exploring agriculturally-relevant rainfall characteristics over four decades in the Sahel. *Environmental Research Letters*, 16(3), 035002. Retrieved 29 August 2022 from https://doi.org/10.1088/1748-9326/ABDD57

Lange, S., & Vinke, K. (2021). Climate Risk Profile: Sahel * Summary. Retrieved 7 September 2022 from

le Blanc, D., & Perez, R. (2008). The relationship between rainfall and human density and its implications for future water stress in Sub-Saharan Africa. *Ecological Economics*, 66(2–3). Retrieved from https://doi.org/10.1016/j.ecolecon.2007.09.009

Mascaro, G., White, D. D., Westerhoff, P., & Bliss, N. (2015). Performance of the CORDEX-Africa regional climate simulations in representing the hydrological cycle of the Niger River basin. *Journal of Geophysical Research: Atmospheres*, 120(24), 12425–12444. Retrieved from https://doi.org/https://doi.org/10.1002/2015JD023905

Mereu, V., Carboni, G., Gallo, A., Cervigni, R., & Spano, D. (2015). Impact of climate change on staple food crop production in Nigeria. *Climatic Change*, 132(2). Retrieved from https://doi.org/10.1007/s10584-015-1428-9

Mertz, O., D'haen, S., Maiga, A., Moussa, I. B., Barbier, B., Diouf, A., … Dabi, D. (2012). Climate variability and environmental stress in the Sudan-Sahel zone of West Africa. *Ambio*, 41(4). Retrieved from https://doi.org/10.1007/s13280-011-0231-8

Odigwe, M., Efe, S. I., & Atubi, A. O. (2020). A Statistical Discourse of the Climate of the Niger Delta Region of Nigeria. *Journal of Management and Social Science Research*, 1(1/2). Retrieved from https://doi.org/10.47524/jmssr.11.4

Ogungbenro, S. B., & Morakinyo, T. E. (2014). Rainfall distribution and change detection across climatic zones in Nigeria. *Weather and Climate Extremes*, 5(1). Retrieved from https://doi.org/10.1016/j.wace.2014.10.002

Ogunjo, S., Ife-Adediran, O., Owoola, E., & Fuwape, I. (2019). Quantification of historical drought conditions over different climatic zones of Nigeria. *Acta Geophysica*, 67(3). Retrieved from https://doi.org/10.1007/s11600-019-00279-1

Ogunrinde, A. T., Oguntunde, P. G., Akinwumiju, A. S., & Fasinmirin, J. T. (2019). Analysis of recent changes in rainfall and drought indices in Nigeria, 1981–2015. *Hydrological Sciences Journal*. Retrieved from https://doi.org/10.1080/02626667.2019.1673396

Oguntunde, P. G., Abiodun, B. J., & Lischeid, G. (2017). Impacts of climate change on hydro-meteorological drought over the Volta Basin, West Africa. *Global and Planetary Change*. Retrieved from https://doi.org/10.1016/j.gloplacha.2017.07.003

Oguntunde, P. G., Lischeid, G., & Abiodun, B. J. (2017). Impacts of climate variability and change on drought characteristics in the Niger River Basin, West Africa. *Stochastic Environmental Research and Risk Assessment 2017 32:4*, 32(4), 1017–1034. Retrieved 26 July 2021 from https://doi.org/10.1007/S00477-017-1484-Y

Ojo, D., Connaughton, M., Kintomo, A., Olajide-Taiwo, L. O., & Afolayan, S. (2011). Assessment of irrigation systems for dry season vegetable production in urban and peri-urban zones of Ibadan and Lagos, Southwestern Nigeria. *African Journal of Agricultural Research*, 6.

Onah, E. I. (2020). Nigeria: A Country Profile. *Journal of International Studies*. Retrieved from https://doi.org/10.32890/jis.10.2014.7954

Pausata, F. S. R., Gaetani, M., Messori, G., Berg, A., Maia de Souza, D., Sage, R. F., & deMenocal, P. B. (2020). The Greening of the Sahara: Past Changes and Future Implications. *One Earth*, 2(3), 235–250. Retrieved 29 August 2022 from https://doi.org/10.1016/J.ONEEAR.2020.03.002

Rogelj, J., Meinshausen, M., & Knutti, R. (2012). Global warming under old and new scenarios using IPCC climate sensitivity range estimates. *Nature Climate Change*, 2(4), 248–253. Retrieved from https://doi.org/10.1038/nclimate1385

Salami, A. W., Olanlokun, O., Salami, A. W., Mohammed, A. A., Abdulmalik, Z. H., & Olanlokun, O. K. (2014). Trend Analysis of Hydro-meteorological Variables using the Mann-Kendall Trend Test: Application to the Niger River and the Benue Sub-Basins in Nigeria. *International Journal of Technology*, 2, 100–110. Retrieved 30 November 2021 from https://doi.org/10.14716/ijtech.v5i2.406

Sallaba, F., Olin, S., Engström, K., Abdi, A. M., Boke-Olén, N., Lehsten, V., … Seaquist, J. W. (2017). Future supply and demand of net primary production in the Sahel. *Earth System Dynamics*, 8(4). Retrieved from https://doi.org/10.5194/esd-8-1191-2017

Siddig, K., Stepanyan, D., Wiebelt, M., Grethe, H., & Zhu, T. (2020). Climate change and agriculture in the Sudan: Impact pathways beyond changes in mean rainfall and temperature. *Ecological Economics*, 169. Retrieved from https://doi.org/10.1016/j.ecolecon.2019.106566

Tunde, A. M., Adeleke, E. A., & Adeniyi, E. E. (2013). Impact of climate variability on human health in Ilorin, Nigeria. *Environment and Natural Resources Research*. Retrieved from https://doi.org/10.5539/enrr.v3n1p127

van Vuuren, D. P., Edmonds, J., Kainuma, M., Riahi, K., Thomson, A., Hibbard, K., … Rose, S. K. (2011). The representative concentration pathways: An overview. *Climatic Change*. Retrieved from https://doi.org/10.1007/s10584-011-0148-z

World Bank. (2015). *Climate and Health country Profile - 2015 Nigeria*. *World Bank Global Health Expenditure Database United Nations Development Programme Human Development Reports*. Retrieved from http://apps.who.int.ezproxy.lib.gla.ac.uk/iris/bitstream/10665/246140/1/WHO-FWC-PHE-EPE-15.40-eng.pdf

Yang, X., Xie, X., Liu, D. L., Ji, F., & Wang, L. (2015). Spatial Interpolation of Daily Rainfall Data for Local Climate Impact Assessment over Greater Sydney Region. *Advances in Meteorology*, 2015. Retrieved 30 November 2021 from https://doi.org/10.1155/2015/563629

PAPER 230 – EFFECT OF DIFFERENT MULCHING MATERIALS ON GROWTH PARAMETERS AND YIELD OF OKRA (*Abelmoschus esculentus)* PRODUCTION IN MINNA, NIGERIA

I. M. Mohammed*, E. P. Lydia, J. J. Musa

*Department of Agricultural and Bioresources Engineering, Federal University of Technology Minna
Email-Isahmohammed07@yahoo.com

ABSTRACT
An experiment was conducted to investigate the impact of mulching on the growth, yield, and moisture content of Okra at four growth stages (initial, development, mid, and late stage) and at different soil depths (0-30 cm and 30-60 cm). The experiment was carried out in a randomized complete block design with four replications, and the treatments were control (T0), groundnut shells mulch (T1), black polythene mulch (T2), and white polythene mulch (T3). The maximum average Okra fresh pod yield of 23.4t/ha was obtained from the white plastic mulch treatment, while the lowest yield of 22t/ha was obtained from the control treatment. Yield reductions of up to 32% were observed in the control plots compared to the white plastic mulched plots. The quality yield was significantly affected by the application of mulch, with the highest quality observed in the white plastic mulch treatment (26t/ha) and the lowest in the control treatment (24.3t/ha). Groundnut shells mulch also had an effect on moisture conservation, but they did not show any significant difference from the control plots. Therefore, the study suggests that polythene mulch may be the most suitable type to enhance quality on okra production by conserving soil moisture.

1. INTRODUCTION

Agriculture is heavily dependent on the amount and timing of rainfall, which in many areas of the world is highly variable (Singh, 2022). Agriculture is a critical sector in Nigeria as it contributes about 35 percent in terms of the Gross Domestic Product (GDP); provides 70-80 percent of employment; and contributes significantly (up to 30 percent) to foreign exchange earnings (Jafari *et al.,* 2017). Okra (*Abelmoschus esculentus*) is an important vegetable crop cultivated in many parts of Nigeria, including Minna, Niger State. However, the productivity of okra cultivation is often constrained by the inadequate moisture content in the soil, particularly during the dry season. Mulching is a common practice that helps to conserve soil moisture by reducing water loss through evaporation from the soil surface. Several studies have investigated the effect of different mulching materials on soil moisture retention and yield of various crops, including okra. The year-to-year variability of rainfall is a significant constraint to the sustainability of rain-fed farming systems in poorer countries of the tropics in some parts of Nigeria as farming decisions must be made despite production and season quality uncertainty (Zhang *et al*, 2019).

In agriculture, climatic parameters, which includes temperature, relative humidity (RH), and light intensity, is a critical factor in crop growth and productivity. Plant growth and development depend on climatic conditions along with management practices. Soil climatic conditions can be altered through the application of different conservational practices. Conservation Agriculture can be one of the solutions to the challenges faced by rural farmers as it protects the soil and reduces erosion which mulching is one of it. Mulches manipulate the soil heat flux and thereby affecting soil temperature. Mulch cover reduces evaporation from the land surface; soil water content is retained (Olaniyi et al*.,* 2013). Additionally, mulch cover suppresses weed infestation in the crop field. Therefore, various types of mulching material are used to alter the moisture content and improve crop yield (Awasthi *et al.,* 2016).

The high economic value of Okra crops justified the modification to the producers, improved quality and extended the growing season, producers of Okra crops often used different mulching types to suppress weeds or conversation of residual moisture near the crop's root. Okra generally is used as nutritional supplements for vitamin C and A, B complex, iron, calcium etc. (Feng *et al.,* 2021). Dried Okra is sometimes processed into soup. The process involves slicing, drying and grinding. The resulting material is then mixed with other ingredients to make soup (Iqbal *et al*, 2020). The water requirement for okra production in Nigeria can vary depending on factors such as climate, soil type, and cultivation practices (Lorenz & Maynard, 2019). Generally, okra requires a consistent supply of water throughout its growing period to ensure good yields. In Nigeria, the amount of water required for okra production may range from 500-1000 mm per growing season, depending on the location and the prevailing weather conditions (Agrawal *et al*., 2014). Mulches affect not only the soil environment. However, mulches change the plants' environment depending on the properties and the level of the physical contact between the mulch's materials and the soil. The use of sawdust, plastic, and straw mulches for dry season vegetable

production in the research farm, increases the soil temperature, and conserves soil residual moisture, thus, playing a positive role in water conservation.

2. MATERIALS AND METHOD

The study area lies between Latitude 9^0 34'N and 6^0 29'E in Minna, Niger State, Nigeria. The climate of the study area exhibits the characteristics of a tropical wet and dry/ savanna climate (Köppen-Geiger classification: Aw) with a pronounced dry season in the low-sun months, no cold season, the wet season is in the high-sun months: - with an average temperature is 27 degrees Celsius (80.7 degrees Fahrenheit). The total annual Precipitation averages 1209.7 mm (47.6 inches), equivalent to 1209.7 Liters/m^2 (29.67 Gallons/ft^2). The mean annual relative humidity is 80%, On average there are 2672 hours of sunshine per year making about 7.5 h/day and The upland soils under the basement complex formation around Minna are generally deep, weakly to moderately structured sand to sandy clay with gravelly and concretionary layers in the upper or beneath the surface layers (Ojanuga, 2018)

2.1 Experimental Design

The experimental design used in this study was a randomizes complete block design (RCBD) and replicated four times. The total experimental plot was 100m^2 consisting of 16 plots and the experimental units were 1m by 1m, 0.3 m in between the units. The treatment were different mulching materials which are as follows: T0- control (no mulch) T1- groundnut shell mulch, T2- black polythene mulch and T3- white polythene mulch. The experiment was conducted at the research farm of the Federal University of Technology, during raining season between August and October, 2022.The experimental plots were prepared manually using spade and big African hoe. On each plot, 5 seeds were planted, 15 seeds in each replicate, and all, 60 okra seeds were produced. Immediately after planting, mulching of appropriate plots followed. Out of the total 12 plots, 9 plots were mulched and 3 were not mulched No standardised planting distance between and within crops was maintained because the study is purely indigenous. An attempt to standardise the space meant a deviation from the strictly traditional practice this study investigated. The local farmers would not also benefit from the results and recommendations of such standardisation because they refuse to operate the central planting technique seeing it as non-cultural and a waste of time. After planting, the distances between and within the treatments were measured. Because of the ethno-scientific nature of the work, no organic or inorganic fertiliser, nematicide, insecticide, fungicide, or herbicide was applied. All noticeable pests such as termites and spittlebugs was controlled using a traditionally prepared solution from the neem tree as practised by most traditional farmers, owing to the high cost of insecticides, which is far beyond the reach of most farmers. One plant in each treatment was randomly sampled for measurement on four dates corresponding to the four-phase stages. The growth and developmental parameters were monitored from 1 month after planting (MAP) to 8 (MAPS).

3. RESULT AND DISCUSSION

3.1 Growth and Yield Components of Okra

The growth components of okra were measured weekly till 12 weeks after planting (WAP), this includes Plant height which is the distance from the soil surface to the tip of the main stem, the stem diameter which is the thickness of the main stem measured at a specific height above the

Table 3.1: Effect of mulch on the growth parameters

Mulch Type	Number of pods per plant (NP)	Pod length (cm)	Pod dry weight (gm)	Harvest period	Total dry matter
Control (T0)	12.25d	9.04c	0.33c	7.00c	6.63c
Groundnut shells (T1)	14.32bc	10.04b	0.55b	9.00b	9.30b
White plastic (T2)	16.65a	11.00a	0.7675a	12.00a	12.00a
Black plastic (T3)	16.03a	10.70b	0.7625a	14.00a	11.30a
LSD (0.05)	1.68	6.06	0.18	3.03	2.38
CV (%)	7.58	0.94	20.7	18.16	16.07

3.2. Quality yield harvested

A significant variation at $P < 0.001$ was observed in marketable okra yields due to different mulch types. The highest mean for the marketable product (35.28 tonnes/hectare) was observed from plots that were mulched by transparent polythene, while the lowest quality yield (24.39 tonnes/hectare) was recorded at un-mulched plots (control). No significant variation in quality yield was observed between transparent and black polythene mulch. This indicates that mulch helps keep a pod of crops from contacting the ground. This reduces soil rot and helps keep the product clean. From this, we can conclude that inorganic mulch (polythene mulch) effectively improves pod quality.

3.3 Poor Harvested Yield

For this study, the highest poor yield was obtained from un-mulched plots, while the lowest (about 25 % less) was observed from plots that were applied with transparent polythene. This result is similar to what was reported in a study by Feng *et al.* (2021), wherein an investigation on the effect of mulching on the yield and quality of okra in Zimbabwe was conducted. The researchers used three types of mulch: maize stover, cattle manure, and no mulch (control). The results showed that using maize stover and cattle manure mulch significantly reduced the poor yield of okra compared to the control treatment. Specifically, the poor yield was reduced by 36% and 43% with maize stover and cattle manure mulch, respectively. Similarly, a study by Kader *et al.* (2019) evaluated the effect of different mulching materials on the yield and quality of okra in Nigeria. The researchers compared four types of mulch: maize stover, dry grass, sawdust, and no mulch (control). The results showed that using maize stover and dry grass mulch significantly reduced the poor yield of okra compared to the control treatment. Specifically, the poor yield was reduced by 45% and 26% with maize stover and dry grass mulch, respectively. The study also found that mulching improved soil residual moisture and nutrient retention, contributing to increased okra yield and quality.

3.4 Total Yield

For this study, a significant difference ($P < 0.001$) was observed among the different mulch applications for total pod yield. The highest total pod yield (37.53 tonnes/hectare) was recorded from the plots mulched with transparent polythene, followed by the black (35.62 tonnes/hectare), with no significant difference between them. In General, the fine polythene mulch, black polythene mulch, and groundnut shells mulch increased the total fruit yields by 32%, 25%, and 16%, respectively, compared to un-mulched treatments. However, the total fruit yields obtained from the plots mulched with groundnut shells and un-mulched plots did not vary statistically. From this, it can be generalized that inorganic mulch (transparent polythene and black polythene) significantly improves vegetable production. Among the mulches, weed control was best under polythene mulches. This conforms to the report that polythene mulch most effectively controls weeds (Sarolia and Bhardwaj, 2018).

Table 3.2: Mean value of fresh pod weight, Quality harvested yield, Poor harvested yield, and total Yield

Mulch Type	**Fresh pod weight (t/ha)**	**Quality harvested yield (t/ha)**	**Poor harvested yield (t/ha)**	**Total yield (t/ha)**
Control (T0)	0.11d	24.39c	4.20a	28.44d
Groundnut shells (T1)	0.13bc	28.82b	3.23bc	33.00bc
White plastic (T2)	0.15a	35.28a	2.16d	37.53a
Black plastic (T3)	0.14ab	33.49a	2.85cd	35.62ab
LSD (0.05)	1.2	293.5	87.57	299.78
CV (%)	5.89	6.39	17.36	5.89

4. CONCLUSION

The study examined the impact of mulching on residual moisture conservation in okra production. The results showed that inorganic mulch (polythene mulches) had a higher mean compared to organic mulch, and controlled plots in all growing seasons except for the late season. Polythene mulch helped conserve water by varying percentages at different growth stages when compared to the control group. While black polythene mulch consistently had a higher residual moisture content than transparent polythene mulch, the difference was not significant at any soil depth. This could be due to transparent polythene's low absorption of solar radiation,

leading to less evaporation. In contrast, black polythene absorbed more radiation, resulting in higher soil temperatures and more soil residual moisture evaporation.

Groundnut shells also helped conserve residual moisture at different growth stages, but there was no significant difference in residual moisture between groundnut shells mulch and control plots in all growing locations. Yield components measurement showed that okra yield from polythene mulch was higher than control plots, with a total yield increment of 32%. Polythene mulch also had a higher quality yield value than the control group by 37.3%. Overall, mulching had a significant impact on soil residual moisture conservation and agronomic parameters, with polythene mulch proving to be the most effective material for the study area.

REFERENCES

Agrawal, K. K. (2014). Agron 604 advances in crop growth and development. *Erişim adresi http://www. jnkvv. org/PDF/24042020101707234*, *202103*.

Awasthi, O.P., Singh, I.S. and Sharma, B.D. (2016). Effect of mulch on soil hydrothermal regimes, growth and fruit yield of brinjal (*Solanum melongena* L.) under arid conditions. Indian Journal of Horticulture. 63: 192-194.

Das, S. K., & Ghosh, G. K. (2022). Soil hydro-physical properties affected by biomass-derived biochar and organic manure: a low-cost technology for managing acidic mountain sandy soils of northeastern region of India. Biomass Conversion and Biorefinery, 1-15.

Dhakal, M., Pandey, B., & Maharjan, S. (2019). Effects of moisture content on soil physical properties: A review. Journal of Agricultural Sciences, 64(1), 1-13.

Eze, P. C., Odofin, A. J., Onyekwere, I. N., Musa, J. J., & TASDO, P. (2019). Influence of rice husk-mulch on soil water balance components under sorghum and millet crops in Maiduguri, semi-arid northwest Nigeria.

Feng, W., Zhang, Y. S., Shao, Y. W., Huang, T., Zhang, N., Yang, J. H., ... & Wang, Y. (2021). Coaxial electrospun membranes with thermal energy storage and shape memory functions for simultaneous thermal/moisture management in personal cooling textiles. European Polymer Journal, 145, 110245.

Iqbal, R., Raza, M. A. S., Valipour, M., Saleem, M. F., Zaheer, M. S., Ahmad, S., ... & Nazar, M. A. (2020). Potential agricultural and environmental benefits of mulches—a review. *Bulletin of the National Research Centre*, *44*(1), 1-16.

Kader, M. A., Singha, A., Begum, M. A., Jewel, A., Khan, F. H., & Khan, N. I. (2019). Mulching as water-saving technique in dryland agriculture. Bulletin of the National Research Centre, 43(1), 1-6.

Jafari, S., Javadi, T., & Rostami, M. (2017). Effects of sawdust mulch on soil water content, yield, and quality of apple (Malus domestica Borkh) fruit in semi-arid regions. Scientia Horticulturae, 216, 167-174. https://doi.org/10.1016/j.scienta.2017.01.023

Lashari, A., Liu, X., Zhang, L., Imran, M., Mehmood, S., & Li, R. (2020). Effect of soil moisture on soil permeability: A review. Sustainability, 12(5), 1825.

Lopez, R., & Maynard, J. (2019). The effect of mulching on soil moisture and temperature in a warm climate. Soil Science Society of America Journal, 78(3), 744-752.

Mandal, A., Das, A. K., & Patra, A. K. (2020). Effect of soil moisture content on soil properties: A review. Bulletin of Environmental Contamination and Toxicology, 105(2), 161-167. Press.

Olaniyi, A. O., Abdullah, A. M., Ramli, M. F., & Sood, A. M. (2013). Agricultural land use in Malaysia: an historical overview and implications for food security. *Bulgarian Journal of Agricultural Science*, *19*(1), 60-69.

Sarolia, D. K. and Bhardwaj, R. L. (2018). Effect of mulching on crop production under rainfed condition: A review. *Int. J. Res. Chem. Environ., 2*: 8-20.

Singh, A. (2022). Soil salinity: A global threat to sustainable development. *Soil Use and Management*, *38*(1), 39-67.

Zhang, X., You, S., Tian, Y., & Li, J. (2019). Comparison of plastic film, biodegradable paper and bio-based film mulching for summer tomato production: Soil properties, plant growth, fruit yield and fruit quality. *Scientia Horticulturae*, *249*, 38-48.

PAPER 231 – Exploring the Effects of Heat Treatments on Ti6Al4V: A Review

I. M. Oritogun[1*], J. T.Udi[1], P. O. Omoniyi[1,2], A. A. Adeleke[3], P. P. Ikubanni[4], and T.C. Jen[2]

[1] Department of Mechanical Engineering, University of Ilorin, P. M. B. 1515, Ilorin, Nigeria
[2] Department of Mechanical Engineering Science, University of Johannesburg, P. O. Box 524, Johannesburg, South Africa
[3] Department of Mechanical Engineering, Nile University of Nigeria, 900001, Nigeria
[4] Department of Mechanical Engineering, Landmark University, 252201, Nigeria
Email: oritzijesese@gmail.com

ABSTRACT
Ti–6Al–4V is a widely used titanium alloy in various industries due to its strength, toughness, and corrosion resistance. Heat treatment is one of the most critical aspects of its processing, which can significantly affect its microstructure and mechanical properties. This review provides an overview of the heat treatment of Ti–6Al–4V, including its annealing, solution treatment, aging, and stress relief processes, while it also provides the effect of these heat treatment methods on the microstructural properties of Ti6Al4V. Results reviewed show that the solution heat treatment technique improves the material's ductility, making it easy to machine, form, and more wear-resistant, allowing for wide application of the alloy, Ti–6Al–4V.

KEYWORDS: Heat treatment, Annealing, Solution heat treatment, Mechanical properties, Stress relief.

1. INTRODUCTION

Ti6Al4V has its applications in numerous fields of engineering, such as the biomedical, mechanical, chemical, and aerospace industries. Due to its exceptional strength, low density, and corrosion resistance, the titanium alloy Ti-6Al-4V has been thoroughly investigated and employed in various applications. The mechanical qualities of this alloy, such as its ductility, toughness, and fatigue resistance, are frequently enhanced through heat treatment (Rack & Qazi, 2006)**.** Ti-6Al-4V undergoes a heat treatment process that can significantly change its microstructure and mechanical properties (Pederson, 2002). This alloy has three main heat treatment methods which are annealing, solution treatment, and aging. The annealing process softens the alloy and removes any remaining stress, whereas solution treatment and aging can increase the material's strength, hardness, and ductility (Galarraga et al., 2017; Jaber et al., 2022).

Ti-6Al-4V is frequently used in the aerospace and automotive industries due to its excellent strength-to-weight ratio and heat resistance (Boyer, 2010). It is used to manufacture aircraft and automobile components like landing gear, engine components, connecting rods, exhaust systems, and airframe structures (Inagaki et al., 2014; Veiga et al., 2012). It can also be used in the medical sector to produce biomedical devices, including bone support implants, dental implants, and joint replacements, because of its biocompatibility and mechanical properties (Putrantyo et al., 2021). Because Ti-6Al-4V is strong, lightweight, corrosion-resistant, and has a very low risk of patients experiencing an adverse biological reaction, it is a popular choice for medical implants (Bammidi & Prasad, 2020; Din, 2021). The process of heating metal, maintaining it at that temperature, and then allowing it to cool again in order to alter its microstructure and mechanical properties is known as heat treatment (Ingellis & Leone, 2016). The mechanical characteristics of the metal component may change during the procedure, depending on the heating temperature. the microstructure is changed by the high temperature and the mechanical

properties are significantly influenced by its microstructure (Velling, 2020). There are several processes involved in the heat treatment process. The metal is heated to the proper temperature, immersed there for a predetermined period, and then cooled down in different media such as water, air, furnace, etc. The final qualities of the metal are determined by the cooling process, which is equally crucial (Saif, 2022). Different heat treatment methods can alter the microstructure of Ti-6Al-4V and enhance its mechanical properties (Liu et al., 2021). The microstructural and mechanical properties of Ti-6Al-4V also differ depending on the temperature range used in heat treatment. Figure 1 shows the plot of temperature versus percentage of Vanadium in the Ti-6Al-4V. The temperature within the 882-995°C is the β transus temperature, where there is the transformation of the microstructure from the room temperature α + β phase as shown in Figure 2.

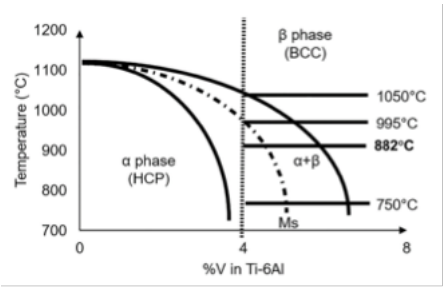

Figure 1. Temperature versus Vanadium percentage in Ti-6Al phase diagram Source: (Omoniyi et al., 2021)

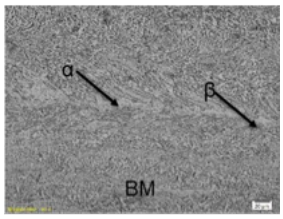

Figure 2. Microstructure of Ti-6Al-4V at room temperature Source: (Omoniyi et al., 2021)

2. THEORETICAL ANALYSIS

2.1 Annealing

Annealing is a heating and cooling procedure that typically softens the metal grains (Ahmed, 2020; Gestwa et al., 2003). The phase can also apply to procedure designed to change the mechanical or physical characteristics of a material or create a specific microstructure (Fadare et al., 2011). The material being annealed determines the operation's temperature and the cooling rate (Thomas Digges, Samuel Rosenberg, 1960). There are two types of annealing, which are full annealing and process annealing. Full annealing is by raising the temperature above its upper critical temperature, or "full anneal," the microstructure is completely altered. High-carbon steels frequently undergo this annealing process, which aims to soften the metal (Mackenzie, 2018). Another method is process annealing, also known as "subcritical" annealing, which entails heating the material to a temperature typically 10–20°C below the lower critical temperature. The material is heated and cooled in still air to room temperature (Çelik et al., 2020).

The annealing process has been used on Ti-6Al-4V and its alloy for stress relieving and improving the material's fracture toughness. Ti-6Al-4V was heated at a temperature of 970°C for about an hour in an induction furnace

and was later cooled in air. The microstructure changed from the fine α' phase with few randomly distributed β particles to a widmanstatten microstructure. This showed increased hardness and had a negative effect on tensile strength (El-Hadad et al., 2018). Figure 3 shows the microstructure of the annealed sample at 970°C, below the transus temperature, and cooled in air. However, heat treating Ti-6Al-4V above the β transus temperature of 995 °C and up to 1030°C in an open hearth furnace for 30 minutes, followed by cooling in air changed the microstructure. Microstructure changes from martensitic α' to a Widmanstätten β microstructure (Dewangan et al., 2021). The phase transformation means the ductility of the sample increased, but the strength was affected. Other microstructures obtained after heat treatment and air cooling are also shown in Figure 3.

Furthermore, when the material is heat treated and cooled in the furnace, the microstructure changes from an equiaxed microstructure to a lamellar α+β microstructure. This resulted in higher ductility but a lower tensile strength (Vrancken et al., 2012). Figure 4 shows the microstructure of Ti6Al4V annealed above the transus temperature and cooled in the furnace.

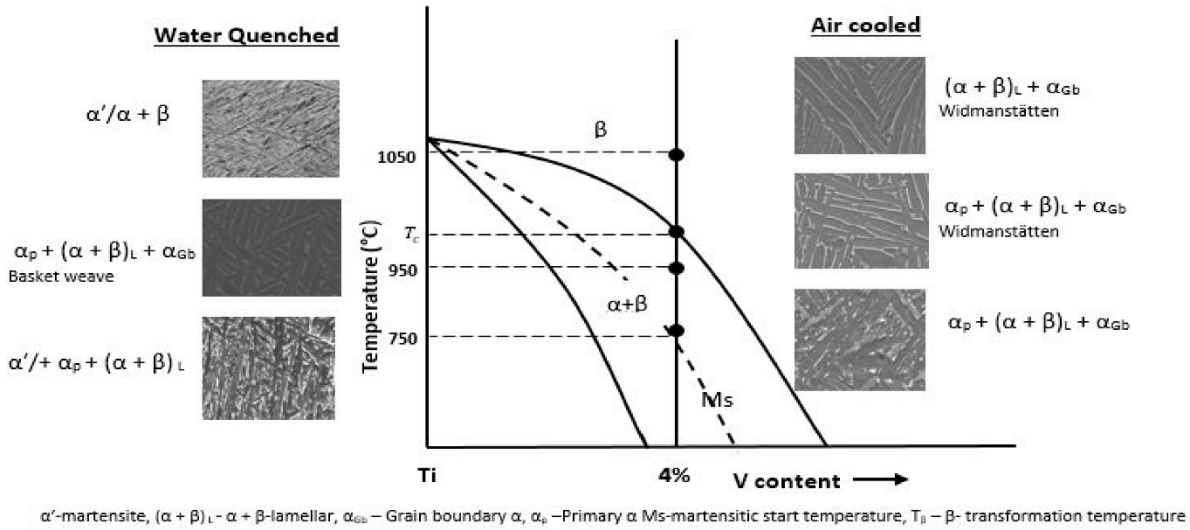

Figure 3. Microstructure of Ti6Al4V under different quenching conditions Source: (Muiruri et al., 2020)

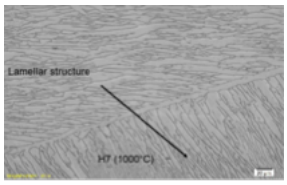

Figure 4. Furnace-cooled Ti6Al4V at heat treatment temperature above the β transus temperature source: (Omoniyi et al., 2021)

2.2 Solution Heat Treatment and Aging

Solution treatment involves heating the material to a particular temperature and holding it at that temperature for about 30 to 45 minutes and then rapidly cooling it to obtain desired properties like hardness, strength, impact resistance, etc. (Madhusha, 2018). On the other hand, aging is a technique used to increase the strength and

ductility of metals by heating it to a lower temperature compared to solution treatment and holding it for a duration of about 2 hours (Sajadifar et al., 2021). An alloy is heated to an appropriate temperature, maintained at that temperature for about 30 to 45 minutes to allow one or more phases to dissolve into a solid solution, and then quickly cooled to maintain the phases in the solution followed by aging (Impro, 2021). The regulated release of these components either naturally (at room temperature) or artificially is made possible by subsequent precipitation and heat treatments at higher temperatures (Bodycote, 2022). Figure 5 shows the solution heat treating procedure and aging process.

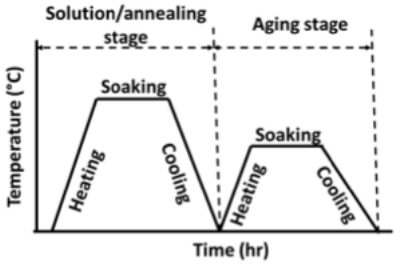

Figure 5. Schematics of the solution heat treating procedure and the aging process Source: (Omoniyi, 2022)

Effect of solution heat treatment and aging was observed on the microstructure of Ti-6Al-4V when it was heated in a furnace at 1050°C for about 30 minutes and then quenched with water leading to formation of basket weave structures with 'α' as reported by Wang et al., (2021). This was followed by aging at 900°C for approximately 2 hours, followed by furnace cooling which led to the transformation from α' to α+β phase. The microstructure of Ti-6Al-4V that was heat treated and aged resulted in basket weave structures with few fine β phases surrounded by equiaxed α phases (Wang et al., 2021). This indicated that the heat-treated Ti-6Al-4V sample has good strength with reasonable ductility. However, there is little martensitic α presence, which could have resulted in a higher hardness increase. Table 1 summarizes the heat treatment technique used in Ti-6Al-4V, the temperature range, and the corresponding phase transformation within the material. Furthermore, the tensile strength and hardness ranges reported in different studies from the literature were presented.

3. RESULTS AND DISCUSSIONS

Table 1. Summary of the works of literature reviewed

Author	Type of heat treatment	Temperature range	Phase changes	Average tensile strength (MPa)	Hardness
Wang et al.	Solution Heat Treatment and aging of Ti-6Al-4V	1050°C and 900°C	From Widmanstatten to basket weave structures with α' to basket weave with fine β and equiaxed α phase	893	-
Zhang et al.	Aging of Ti-6A1-4V	730°C	A phase change from α' phase to α +β lamellar phase	1417.9-1447.3	356 HV

			with residual stresses released		
Dewangan et al.	Annealing of Ti-6al-4v	1030°C	It changed from martensitic α' to Widmanstätten β structure	-	
Jovanović et al.	Solution Heat Treatment of Ti-6Al-4V	1100°C	It showed the formation of martensitic α'	1400	423 HV
El-hadad et al.	Annealing of Ti-6al-4v	970°C	It changed from a fine α' phase with few β particles to a widmanstatten microstructure	644	380 HV- 500 HV
Vrancken et al.	Annealing of Ti-6Al-4V	1020°C	It changed from an equiaxed structure to a lamellar α+β structure	867-813	-
Galarraga et al.	Solution heat treatment of Ti-6Al-4V	1100°C	It changed from an α+β lamellar structure to a martensitic α' phase	1250-1150	447-318

4. CONCLUSION

The microstructure of Ti-6Al-4V samples changed as a result of heat treatment at various temperatures and cooling rates from the journals reviewed. It was observed that fast cooling rates resulted in higher strength and hardness of the material, and slower cooling rates resulted in increased ductility. Temperatures below the beta transus temperatures do not significantly impact the microstructure of Ti-6Al-4V. To increase knowledge and practical use of heat treatment for Ti6Al4V, based on the experiments evaluated about the impact of heat treatment on the microstructure and mechanical properties of Ti-6Al-4V. It should be investigated how the creation of the (alpha) and (beta) phases, among other phase transitions that take place during heat treatment, affects the mechanical properties of the alloy. In addition, it is important to research how varied heating and cooling rates, temperatures, and holding durations affect phase transformation kinetics. Conducting comprehensive mechanical testing, including tensile testing, hardness testing, fatigue testing, and impact testing, to evaluate the effect of heat treatment parameters on the alloy's mechanical properties should be adequately explored. The changes in yield strength, ultimate tensile strength, ductility, fatigue life, and fracture toughness resulting from different heat treatment conditions should be studied. Examining the thermal stability of Ti6Al4V after heat treatment by subjecting the alloy to elevated temperature exposures or thermal cycling and also investigating how the heat-treated microstructure and mechanical properties evolve over extended periods to assess the long-term stability and reliability of the alloy in service conditions should be examined. Exploring optimization techniques for heat treatment parameters to achieve desired microstructures and mechanical properties and utilizing design of experiments (DOE) or numerical simulations to identify the optimal combination of heating/cooling rates, soaking temperatures, and holding times that will result in superior properties and minimize distortion or residual stresses should be studied. Finally, the development of computational models and simulations to predict the microstructure evolution and mechanical behavior of Ti6Al4V during heat treatment should be explored. This can aid in understanding the underlying mechanisms, optimizing heat treatment processes, and predicting the resulting properties.

REFERENCES

Ahmed, Y. M. (2020). The Influence of Annealing and Normalizing Processes on the Mechanical Properties and Chemical Composition of Carbon Steel ASTM A285Gr.C. *International Journal of Recent Technology and Engineering (IJRTE)*, *8*(5), 4928–4933. https://doi.org/10.35940/ijrte.e6020.018520

Bammidi, R., & Prasad, K. S. (2020). *EAS Journal of Dentistry and Oral Medicine Abbreviated Key Title: EAS J Dent Oral Med Ti-6Al-4V as Dental Implant*. *1849*(1), 14–18. https://doi.org/10.36349/easjdom.2020.v02i01.003

Bodycote. (2022). *Solution and age - Heat treatment - Bodycote Plc*.

Boyer, R. R. (2010). Titanium and Its Alloys: Metallurgy, Heat Treatment and Alloy Characteristics. *Encyclopedia of Aerospace Engineering*, *July*. https://doi.org/10.1002/9780470686652.eae198

Dewangan, S., Nagubandi, T. S., Mishra, V., & Chowrasia, M. K. (2021). Discussion and analysis of microstructural variation in welded joint of Ti-alloy after heat treatment. *AIP Conference Proceedings*, *2341*(May). https://doi.org/10.1063/5.0050162

Din, S. H. (2021). Biomedical Applications of Titanium and Its Alloys. *Proceedings on Engineering Sciences*, *3*(1), 41–52. https://doi.org/10.24874/PES03.01.005

El-Hadad, S., Nady, M., Khalifa, W., & Shash, A. (2018). Influence of heat treatment conditions on the mechanical properties of Ti–6Al–4V alloy. *Canadian Metallurgical Quarterly*, *57*(2), 186–193. https://doi.org/10.1080/00084433.2017.1412557

Fadare, D. A., Fadara, T. G., & Akanbi, O. Y. (2011). Effect of Heat Treatment on Mechanical Properties and Microstructure of NST 37-2 Steel. *Journal of Minerals and Materials Characterization and Engineering*, *10*(03), 299–308. https://doi.org/10.4236/jmmce.2011.103020

Galarraga, H., Warren, R. J., Lados, D. A., Deho, R. R., Kirka, M. M., & Nandwana, P. (2017). Effects of heat treatments on microstructure and properties of Ti-6Al-4V ELI alloy fabricated by electron beam melting (EBM). *Material Science and Engineering A*, *685* (March 2016), 417–428. https://doi.org/10.1016/j.msea.2017.01.019

Gestwa, W., Przylecka, M., MacKenzie, D. S., Pye, D., & Totten, G. E. (2003). Heat treatment. In *Smithells Metals Reference Book* (pp. 1–83). Elsevier Ltd. https://doi.org/10.1016/B978-075067509-3/50032-4

Impro. (2021). *Stress Relief Annealing*.

Inagaki, I., Takechi, T., Sharai, Y., & Ariyasu, N. (2014). Application and Features of Titanium for the Aerospace Industry. *Nippon Steel & Sumitomo Metal Technical Report*, *106*, 22–27.

Ingellis, A. G., & Leone, L. (2016). Fomento de la autoeficacia, esperanza hacia el futuro y compromiso con la comunidad: Los efectos de la participación juvenil. *Prisma Social*, *4*(17), 438–463. https://doi.org/10.1361/asmhba000

Jaber, H., Kónya, J., Kulcsár, K., & Kovács, T. (2022). Effects of Annealing and Solution Treatments on the Microstructure and Mechanical Properties of Ti6Al4V Manufactured by Selective Laser Melting. *Materials*, *15*(5). https://doi.org/10.3390/ma15051978

Liu, J., Liu, J., Li, Y., Zhang, R., Zeng, Z., Zhu, Y., Zhang, K., & Huang, A. (2021). Effects of post heat treatments on microstructures and mechanical properties of selective laser melted Ti6AL4V alloy. *Metals*, *11*(10). https://doi.org/10.3390/met11101593

Mackenzie, D. S. (2018). *HOT Understanding different types of heat treatment : Annealing Annealing provides a uniform microstructure*. 20–22.

Madhusha. (2018). *Difference Between Heat Treatment and Annealing | Definition, Process, Types, Differences*.

Muiruri, A., Maringa, M., & Preez, W. (2020). Crystallographic Texture Analysis of As-Built and Heat-Treated Ti6Al4V (ELI) Produced by Direct Metal Laser Sintering. *Crystals*, *10*.

Omoniyi, P. O. (2022). *Joint Integrity Evaluation and Optimization of Additive Manufactured and Laser Welded Ti6Al4V* (Issue April). University of Johannesburg.

Omoniyi, P. O., Mahamood, R. M., Arthur, N., Pityana, S., Akinlabi, S. A., Okamoto, Y., Maina, M. R., & Akinlabi, E. T. (2021). Investigation and optimization of heat treatment process on tensile behaviour of Ti6Al4V alloy. *Materialwiss. Werkstofftech*, *52*, 1057–1063. https://doi.org/10.1002/mawe.202000314

Pederson, R. (2002). Microstructure and phase transformation of Ti-6Al-4V, PhD thesis, Lulea university of technology, Sweden. *PhD Dissertation: Lulea Univeristy of Technology*.

Putrantyo, I., Anilbhai, N., Vanjani, R., & De Vega, B. (2021). Tantalum as a novel biomaterial for bone implant: A literature review. *Journal of Biomimetics, Biomaterials and Biomedical Engineering*, *52*(August), 55–65. https://doi.org/10.4028/www.scientific.net/JBBBE.52.55

Rack, H. J., & Qazi, J. I. (2006). Titanium alloys for biomedical applications. *Materials Science and Engineering C*, *26*(8), 1269–1277. https://doi.org/10.1016/j.msec.2005.08.032

Saif, M. (2022). *What is Heat Treatment Process? Types & Applications*. Theengineerpost.Com.

Sajadifar, S. V., Krooß, P., Fröck, H., Milkereit, B., Kessler, O., & Niendorf, T. (2021). Effects of aging under stress on mechanical properties and microstructure of en aw? 7075 alloy. *Metals*, *11*(7), 1–15. https://doi.org/10.3390/met11071142

Thomas G. Digges, Samuel J. Rosenberg, G. W. G. (1960). *Heat Treatment and Properties of Iron and Steel*. *35*(October 3, 1960), 13.

Veiga, C., Loureiro, A. J. R., & Davim, J. P. (2012). Properties and applications of titanium alloys. *Reviews on Advanced Materials Science*, *32*, s?. 133-148.

Velling, A. (2020). *An Overview of Heat Treatment Methods & Their Benefits*. Fractory.

Vrancken, B., Thijs, L., Kruth, J. P., & Van Humbeeck, J. (2012). Heat treatment of Ti6Al4V produced by Selective Laser Melting: Microstructure and mechanical properties. *Journal of Alloys and Compounds*, *541*, 177–185. https://doi.org/10.1016/j.jallcom.2012.07.022

Wang, L., Ma, H., Fan, Q., Yao, J., Shen, X., Zhang, S., Zhou, Y., Peng, Y., Gao, Y., & Wang, D. (2021). Materials Characterization Simultaneously enhancing strength and ductility of Ti-6Al-4V alloy with the hierarchical structure via a novel thermal annealing treatment. *Materials Characterization*, *176*(February), 111112. https://doi.org/10.1016/j.matchar.2021.111112

PAPER 232 – PERFORMANCE EVALUATION OF DEVELOPED ENGINE POWERED TIGERNUT HARVESTING MACHINE

A.I. Gbatigbi[1*], A.A. Balami[1] and B.O. Atteh[1]

[1]Department of Agricultural and Bioresource Engineering, Federal University of Technology Minna, Niger State, Nigeria.
*Email: engralismaila@gmail.com

ABSTRACT
Tiger-nut (*Cyperus esculentus*) is a valuable crop known for its nutritional and economic significance. Harvesting tiger-nuts manually is labour intensive and time-consuming, leading to a growing interest in mechanized solutions to improve efficiency and productivity. This study is about the performance evaluation of developed engine powered tiger-nut harvesting machine. The Harvesting efficiency, Actual Capacity of the Machine and Cleaning efficiency of the machine were determined with respect to speed rate (15, 20 and 25 rpm) at three levels of digging depth (50mm, 80mm, and 100mm). At digging depth of 50mm the harvesting efficiency, actual capacity and cleaning efficiency increase with increase in speed. At 80mm and 100mm digging depth, the harvesting efficiency decrease with speed while both the actual capacity and cleaning efficiency increased with speed at 80mm and 100mm, respectively.
KEYWORDS: Tiger-nut, Performance evaluation, Harvesting efficiency, Actual capacity and Cleaning efficiency

1. INTRODUCTION

Tiger-nut (*Cyperus esculentus*) is a tuber with high health benefits and nutritive value, found in the tropical and Mediterranean regions (Oguwike *et al.*., 2017). It belongs to the family of sedge crops rich in energy content (starch, fat, sugar, and protein), and essential nutrients like vitamins E, C and minerals such as magnesium, phosphorus, iron, calcium, including unsaturated fats and some enzymes which aid digestion (Sanchez-Zapata *et al.*., 2012; Ogbonna *et al.*., 2013). In Nigeria, tiger-nut is available in fresh, semi-dried and dried form in the markets where it is sold locally and consumed even uncooked.

Tiger-nut is a known plant food that is common to West Africa countries. Its cultivation, processing, distribution, and selling has been reported in Nigeria, Mali, Niger, and Ghana. In Nigeria, the crop is well grown in the middle belt and northern region (Oladele *et al.*., 2009); these states include: Benue, Niger, Kogi, Katsina, Sokoto, Taraba, Kano, Plateau and Kebbi. In Nigeria, tiger-nut is usually sown in April and harvested in November. There are three varieties which include (Black, brown, and yellow). Among these, only two varieties, yellow and brown are readily available in the Nigerian market. The yellow variety is preferred because of its bigger size, attractive colour, fleshier body, milk yield, higher protein content and has less anti-nutritional factors, especially polyphenols (Okafor *et al.*., 2003). The juice extracted from the nut is non-alcoholic and milky in appearance. Tiger-nut is also said to be high in oil content producing high quality oil of about 25.5 % of its total content (Adejuyitan, 2011). It is the best nutritional crops that can be used to augment the diet of humans (Afenu, 2008). The tiger-nut flour is considered as a good additive for the bakery industry and as flavoring agent for ice cream (Al-Shaikh *et al.,*2013). Ogunlade *et al.,* (2015) reported that tiger-nut contains methanol, phenol and a substantial amount of protein, carbohydrate and has significantly high contents of Na, K and Ca which suggest that it is good for formulating diet for hypertensive patients. Its fibre content could cut down the rate of obesity aiding complete digestion thus prevent slow metabolic rate in humans (Owusu, 2016). In Nigeria, the utilization of tiger-nut is highly limited in spite of the fact that tiger-nut is cultivated widely in the Northern part of the country.

There are two methods of harvesting which includes manual and mechanical methods. The manual method is associated with so much drudgery and because of this, the mechanical harvesting method is hereby proposed. Harvesting is a significant operation in the cultivation stages of tiger-nut. The ease of harvesting is essential to the drift from subsistence to commercial production of tiger-nut. Harvesting of tiger-nut is the most important and labour-intensive operations in tiger-nut cultivation as the present practice of manual harvesting consumes huge amount of labour to the magnitude of 84-man hours per hectares. During harvesting periods, high cost of labour result in low yield as the farmers will be compelled to embark on the share crop system whereby the farmer takes two-third of the harvest while the harvesters take a third (Tetteh and Ofori, 1998)

In addition, the migration of agricultural labour force from the rural areas aggravated the problems to the farmers. One of the solutions for increasing the profit and productivity is to mechanize harvesting operations in tiger-nut cultivation. For mechanizing these operations, power operated tiger-nut harvesting machine is hereby developed to reduce the labour requirement and drudgery associated with manual harvesting by the peasant farmers. The aim of this study is to carry out the performance evaluation of developed engine powered tiger-nut harvesting machine.

2. MATERIALS AND METHODS

2.1 Materials

The material of study is tiger-nut *(Cyperus esculentus)*. The following instruments were used to measure the required engineering properties which is critical to the design of the harvester and presented in Table1.

Table 1: Engineering properties of tiger-nut and their measuring instruments

S/No	Instrument / Procedure	Sensitivity	Physical / Engineering properties
1	Digital Vernier Calliper	0.01mm	Geometric mean diameter (GMD) of tiger-nut (mm)
2	Weighing balance	0.001g	Bulk density (kg/mm^3)
3	Weighing balance	0.001g	True density (kg/mm^3)
4	Meter stick and protractor		Coefficient of static friction (°)

Machine construction

The developed tigernut harvester was constructed with readily available angled iron made of carbon steel used for general engineering purpose. The construction was done using arc welding of all metal parts as well as other machine operations such as drilling, facing boring riveting, bending, grinding filleting, chamfering smoothing and painting. Assembly and component installation was done using wire, shaft and cable fixing

2.2 Method

Description of machine

The developed tiger-nut harvester consists of ground drive wheel, digger, separator, conveyor, tuber box and the transmission mechanism. Angled iron which is made of carbon steel has high strength and was used for general engineering purpose (Ani *et al.*, 2016). The frame of the harvester has a rectangular shape 150mm × 900mm. It is a skeletal structure of the harvester on which all other components are mounted. It is constructed from 75mm×75mm angled iron carbon steel of 6mm thickness to give the required strength. Provisions were made for the handlebars for pushing and guiding the machine while in operation. During road transportation and harvesting operation the whole frame is supported by drive wheel. The structure of the developed tiger-nut harvester is shown in figure 2.

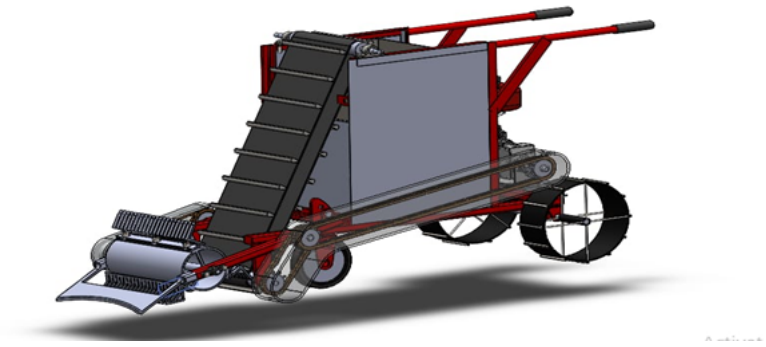

Figure 2: The developed Tiger-nut harvester

Design calculations

Harvesting device

The harvesting or digging mechanism is like a tine tooth in three segments, around a cylindrical drum. The digger's angle of inclination (α) ha is to be as less as possible, to avoid clods, sliding and to reduce draw resistance. On the other hand, the value of this angle associated with the height of rear of the digger (H), and working length (***Ld***) as shown in figure 3.

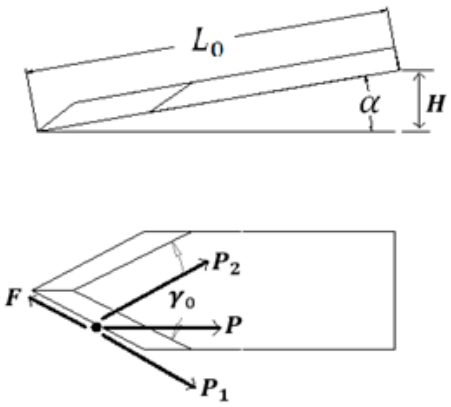

Figure 3: Geometric dimensions of digger blade and force affecting on it.

The angle of inclination is calculated using equation 1

$$\text{Sin}\alpha=((H+\Delta))/Ld \quad (1)$$

Where α is the angle of inclination from the horizontal, H is the height of the rear of the digger (mm), Δ is the clearance (mm), Ld is the working length (mm).

According to experiments, with increasing α, the cleaning operation improve as well.

The smooth sliding of tiger nut and clods on the digger blade depends on α and has to satisfy the sliding condition.

$$\alpha \leq 90-\emptyset \quad (2)$$

Where ∅ is angle of friction between the soil and blade material

To calculate the number of notches using the following expression equation 3.14

$$Bd=ns+nb \quad (3)$$

Where:

Bd is the width of the digger's blade (working width) (mm),

n is the number of notches,

s is the clearance (spacing) between notches (mm),

b is the width of the notch (mm).

Bd is determined from tiger nut requirement such as max depth of nuts deposit and repose angle of tiger nut in the soil.

Speed of separator (*vs*):

The efficiency of separator depends greatly on its speed. Increasing the speed increases the separation and helps to flatten the soil layer over separator area. Nevertheless, shorten the residence time of the soil on separator area and that reduces soil dropping through gaps. The speed of separator is calculated using the equation 4

$$vs \geq V\cos \propto s \quad (4)$$

Where:

V = forward speed of the machine; m/s

Angle of inclination

It depends on separation and elevation requirement. Small values negatively affect machine dimension and reduces the separation performance, and vice versa. However, great values could cause accumulation of soil and nut on separator surface.

- The top part of separator usually fixed at angle (20°- 22°).
- In case of using, a second separator usually fixed at angle (12° - 15 °).
- Angle of inclination of first separator $\boldsymbol{\alpha s}$ depends on coefficient of friction between material of separator and soil $\emptyset I$ i.e.$tan \propto s < tan\emptyset$I

Wheel shaft

Angular speed of wheel shaft is calculated using the equation 5.

$\omega = \frac{2\Pi n}{60}$ rad/s (5)

Where n =14 rpm

$\omega = \frac{2\Pi(14)}{60} = 1.5$rad/s

Since the shaft rotates about two anti-friction bearings, initial torque on the shaft is negligible.

For the purpose of design, maximum load is taken to be the mass of substance i.e carrying capacity 55kg plus the mass of the chassis 35kg). This load turns the shafts about the radius of the wheel (R)

Load on one shaft and sprocket = 45kg + 35kg = 80kg

Wheel speed

To reduce rolling resistance especially in the case of traction wheels, Wheels of larger diameters are used. Outer diameter of wheel d_0 = 600mm, Maximum width = 131 mm

d_0 = 131mm

Loaded radius = 65.5mm

Maximum load = 90.7 kg

Translational speed of harvester = 0.45m/s

Circumference of wheel = πd_0

= π x 131 mm

= 411.602 mm

No. of revolutions of wheel at 0.45 m/s

rpm = $\frac{450}{411.602} \times 6$ = 65rpm

Torque on the shaft

The torque on the shaft is calculated using the equation 6

Ts = Force (F) x radius (R) (6)

Ts = m × a × R

Ts = 45.63 x 9.81 x 0.600 = 268.6Nm

Diameter of the wheel shaft

Diameter of the wheel shaft is calculated using the equation 7.

$D^3 S = \frac{16}{\pi}\sqrt{(ks\ Mb)^2}$ (7)

Where:

S = Shear stress associated with the shaft, S = 5.63Mpa,

ks =Shear constant 1.5 to 3.0 (2.0 was chosen)

Mb = Bending moment (1.35Nm)

D = 0.0135m

The diameter of the wheel shaft is calculated to be 13.5mm

3. RESULTS AND DISCUSSION

Harvesting Efficiency

The discussion based on figure 4 which represents the harvesting efficiency (%) at different speeds (15-25rpm) and three levels of digging height (50mm, 80mm, and 100mm), considering the harvesting efficiency (%) at different speeds (rpm) and three levels of digging depth (50mm, 80mm, and 100mm). At digging depth of 50mm the harvesting efficiency ranges from 64.4% to 64.9%, the highest harvesting efficiency is observed at a speed of 25rpm (64.9%), followed closely by 20rpm (64.8%), and then 15rpm (64.4%), the differences in harvesting efficiency between the speeds are relatively small, with a maximum difference of 0.5%. At digging depth of 80mm the harvesting efficiency ranges from 62.5% to 62.9%. The highest harvesting efficiency is observed at a speed of 15rpm (62.9%), while 20rpm and 25rpm were 62.5%, with both speeds showing very similar efficiency levels while the difference in harvesting efficiency between the highest and lowest speeds is only 0.4%. At a digging height of 100mm, the harvesting efficiency ranges from 59.3% to 61.1%, the highest harvesting efficiency is observed at a speed of 15rpm (61.1%), followed by 20rpm (60.5%), and then 25rpm (59.3%), the difference in harvesting efficiency between the highest and lowest speeds is 1.8%. Generally, the data suggests that the harvesting efficiency of the tiger-nut harvesting machine is influenced by both the speed and the digging height. Lower digging depth generally led to slightly higher harvesting efficiency, while lower speeds tend to be associated with better efficiency across all digging heights. However, it's important to note that the differences in harvesting efficiency between the tested speeds and digging depths are relatively small, ranging from 0.4% to 3.8%.

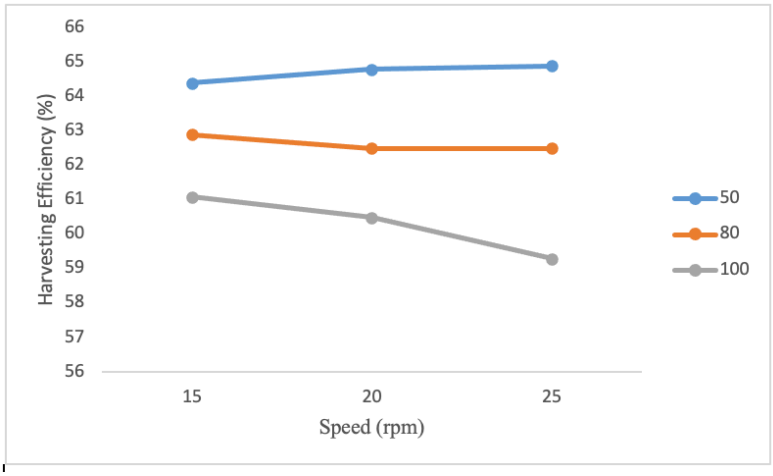

Figure 4: Graph of Speed and the Harvesting Efficiency

3.2 Actual Capacity of the Machine

Figure 5 shows the results of the effect of speed on the actual capacity (kg/hr) of the tiger-nut harvesting machine at three different digging depths, using the provided data. At a digging depth of 50mm, the actual capacity ranges from 44.2 kg/hr to 44.7 kg/hr, the highest actual capacity is observed at a speed of 25rpm (44.7 kg/hr), followed by 20rpm (44.3 kg/hr), and then 15rpm (44.2 kg/hr), the differences in actual capacity between the speeds are relatively small, with a maximum difference of 0.5 kg/hr. At a digging depth of 80mm, the actual capacity ranges from 44.1 kg/hr to 44.2 kg/hr. the actual capacity is consistent across all speeds, with only a 0.1 kg/hr difference observed between the highest and lowest speeds, the differences in actual capacity between the speeds are negligible at this digging height. At a digging depth of 100mm, the actual capacity ranges from 43.2 kg/hr to 43.9 kg/hr, the highest actual capacity is observed at a speed of 20rpm (43.9 kg/hr), followed by 25rpm (43.9 kg/hr), and then 15rpm (43.2 kg/hr), the difference in actual capacity between the highest and lowest speeds is 0.7 kg/hr. Consequently, the data suggests that the actual capacity of the tiger-nut harvesting machine is influenced by speed, but the effect is relatively small. There is no consistent trend of increasing or decreasing actual capacity with increasing speed across all digging heights. At the 50mm digging depth, the actual capacity slightly increases with higher speeds, with a maximum difference of 0.5 kg/hr between the highest and lowest speeds. However, at the 80mm digging depth, the actual capacity remains consistent across all speeds. At the 100mm digging depth, the actual capacity is highest at a speed of 20rpm, followed closely by 25rpm, and then 15rpm. It's worth noting that the differences in actual capacity between the speeds are generally small, ranging from 0.1 kg/hr to 0.7 kg/hr.

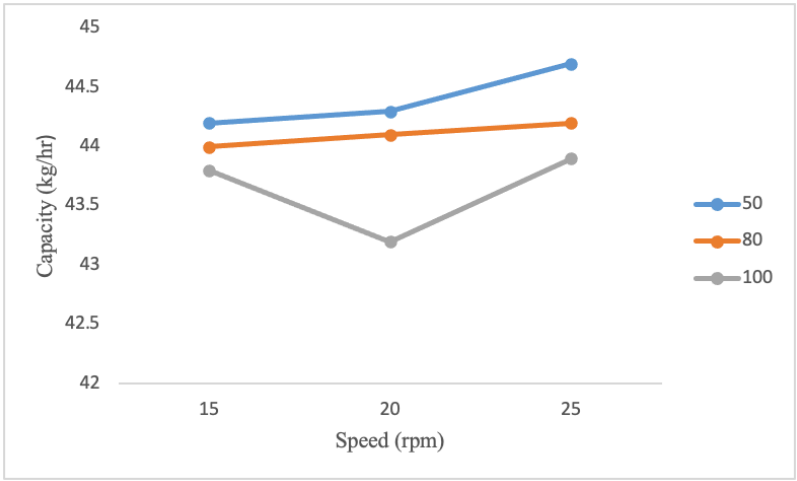

Figure 5: Graph of Speed and Actual Capacity of the Machine

3.3 Cleaning Efficiency

Figure 6 shows the cleaning efficiency (%) of the tiger-nut harvesting machine at different speeds (rpm) and three levels of digging depth (50mm, 80mm, and 100mm). At a digging height of 50mm, the cleaning efficiency ranges from 48.5% to 50.3%. The highest cleaning efficiency is observed at a speed of 25rpm (50.3%), followed

by 20rpm (50.2%), and then 15rpm (48.9%), the differences in cleaning efficiency between the speeds are relatively small, with a maximum difference of 1.4%. At a digging height of 80mm, the cleaning efficiency ranges from 48.7% to 62.2%. The highest cleaning efficiency is observed at a speed of 25rpm (62.2%), followed by 20rpm (50%), and then 15rpm (48.7%). The difference in cleaning efficiency between the highest and lowest speeds is 13.5%. At a digging depth of 100mm, the cleaning efficiency ranges from 48.5% to 50%. The highest cleaning efficiency is observed at a speed of 20rpm (50%), followed by 25rpm (50%), and then 15rpm (48.5%), the difference in cleaning efficiency between the highest and lowest speeds is 1.5%. The effect of speed on cleaning efficiency varies depending on the digging depth. At a digging depth of 50mm and 100mm, the cleaning efficiency remains relatively consistent across the different speeds, with small variations between them. However, at a digging height of 80mm, there is a significant increase in cleaning efficiency as the speed increases from 15rpm to 25rpm.Digging depth and Cleaning Efficiency: The cleaning efficiency varies slightly across the different digging depths. However, the differences in cleaning efficiency between the digging heights are relatively small for each speed. Maximum Cleaning Efficiency: The highest cleaning efficiency is observed at a speed of 25rpm at the 80mm digging depth, with a value of 62.2%.

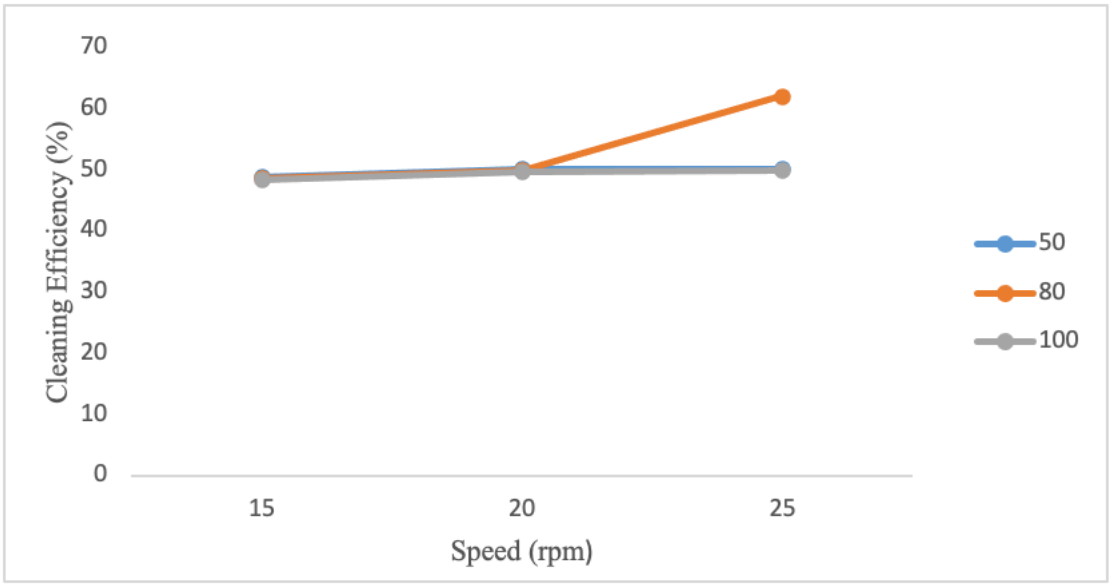

Figure 6: Graph of Speed and Actual Capacity of the Machine

4. CONCLUSION

Based on the result of analysis obtained on the development of tigernut harvesting machine, we can draw the following conclusions:

The speed of the machine has a minimal effect on the harvesting efficiency across all digging heights. The differences observed in harvesting efficiency based on speed are relatively small, indicating that speed alone may not significantly impact the machine's ability to harvest tiger-nuts efficiently. The speed of the machine also has a negligible impact on the actual capacity of the harvesting process. The differences in capacity between different speeds are minimal, suggesting that variations in speed do not significantly affect the machine's ability to handle a certain volume of tiger-nuts per hour. The speed of the machine does not show a clear trend in terms of its impact on cleaning efficiency. The differences observed in cleaning efficiency based on speed are small and inconsistent, indicating that speed alone may not be a critical factor in determining the machine's ability to clean tiger-nuts effectively.

REFERENCE

Adejuyitan, J.A. (2011). Tigernut processing: its food uses and health benefits. American Journal of Food Technology 6(3):197–201.

Afenu, S. (2008) Production of Tigernut Beverage. HND Dissertation, Cape Coast Polytechnic. Cape Coast, Ghana 1:4 - 36.

Al-Shaikh, M.N, Wahab, T.A, Kareem, S.A, & Hamoudi, S.R. (2013). Protective effect of chufa tubers (*Cyperus esculentus*) on induction of sperm abnormalities in mice treated with lead acetate. *Int. J. Drug Dev. Res.* 5: 387-392.

Ani, O., Uzoejinwa, B., & Anochili, F. (2016). Design, construction and evaluation of a vertical plate maize seed planter for gardens and small holder farmers. Nigeria Journal of Technology, 35,3, 647-655

Oladele, A.K., Ibanga, U.I. & Adebesin, O.L. (2009). Effect of substituting maize with tigernut on the quality and acceptability of Dakuwa.In: Proceedings of the 33rd Annual conference and General Meeting of Nigerian Institute of Food Science and Technology, Yola, Nigeria.

Ogbonna, A.C., Abuajah, C.I., & Utuk, R.A. (2013). Tigernut Milk: A Nutritious Under-Utilized Food Ingredient. *Food Biology*, 2(2):14-17.

Ogunlade, I., Adeyemi, B.A, & Aluko, O.G. (2015). Chemical compositions, antioxidant capacity of tigernut (cyperus esculentus) and potential health benefits. *Eur. Sci. J., SPECIAL/ edition*: 217-224.

Oguwike, F., Eluke, B., Eze, R., Asika, C., Nwosu, P., Nwafor, C., & Onumonu, C. (2017). The effects of *Cyperus esculentus* (Tigernut) on Haematological and Biochemical Profile of Male Hypercholesteremic Subjects in Uli, Anambra State Nigeria. *Greener J. Med. Sci.* 7(4): 36-41.

Okafor, J.N., Mordi, J.I., Ozumba, A.U., Solomon, H.M., & Olatunji, O. (2003). Preliminary studies on the characterisation of contaminants in tigernut (yellow variety). In: Proceedings of 27th Annual Conference and General Meeting of Nigerian Institute of Food Science and Technology Kano. Pp.210- 211.

Osagie, A.U., Okoye, W.I., Oluwayose, B.O & Dawodu, O.A (1986).Chemical quality parameters and fatty acid position of oils of underexploited tropical seeds. Nig. J. Appl. Sci.; 4:151-162.

Owusu, N.R, & Owusu, PB (2016). Tigernuts: a healthier pseudo - nut of all nuts in the tropics. *Int. J. Innov. Res. Multi. Field*. 2(12): 307-312.

Sánchez-Zapata, E., Fernández-López, J., & Pérez-Alvarez, J.A. (2012). Tigernut (*Cyperus esculentus*) Commercialization: Health Aspects, Composition, Properties, and Food Applications. *Comp. Rev. Food Sci. Food Safety*, 11: 366-377

Tetteh, J. & Ofori, E. (1998). A baseline survey of tigernut production in the kwahu South District of Ghana. Ghana journal agricultural science, 31, 211-216

PAPER 233 – QUALITY ENHANCEMENT OF STIFF DOUGH (*TUWO*): A REVIEW

E.N, Danjuma[1], B.A Adejumo[1], B.O Atteh[1]

Department of Agricultural and Bioresources Engineering, Federal University of Technology Minna, PMB 65, Niger State, Nigeria
Email: nuyelned@gmail.com

ABSTRACT
In West Africa, specifically in Nigeria, cereals such as corn and sorghum flour are widely consumed. These grains are transformed into a stiff dough called "tuwo" in the local language, Hausa. Tuwo is a semi-solid dough made by cooking cereals flour in a slurry form. To shape and solidify the dough, it is moulded and wrapped in polythene materials or food-grade plastic containers. Tuwo is traditionally enjoyed with various soups, garden egg, and locus beans. Cereals have relatively low protein content but high caloric value. Therefore, it is important to supplement the production and consumption of tuwo with additional nutrients to create a well-balanced meal. To improve the quality of tuwo, it is possible to enhance the chemical properties of the grains by utilizing selected pre-treatment methods. These methods, including blanching, soaking, and malting, can improve the nutritional and functional quality of the cereals while reducing anti-nutritional components. By implementing pre-treatment techniques on cereal grains, the resultant stiff dough, tuwo, can be enhanced to provide a balanced meal, improve overall acceptability, and optimize production.
KEYWORDS: *Cereal, quality, nutritional, functional, anti-nutritional, tuwo.*

1. INTRODUCTION

Stiff dough refers to a semi-solid or solid substance created by combining cereals flour with water and heat energy. This process produces a meal commonly known as "tuwo" in Hausa, Nigeria, specifically in West Africa. The types of cereals used to create stiff dough include corn, sorghum, and rice. The shape and size of tuwo are determined by the container in which it solidifies, and its physical characteristics and colour are influenced by the specific grains or varieties used (Bolade *et al*., 2009). Tuwo is typically consumed alongside various types of soup, such as garden egg and locus beans soup. Since cereals have a low protein content and may lack other essential nutrients, the high carbohydrate content can be enhanced through proper pre-treatment methods or supplemented with necessary nutrients to achieve a well-balanced diet.

1.2 Production of *tuwo*

Tuwo, a traditional Nigerian dish, is made from flour obtained from cereals such as corn, sorghum, millet, or rice. The preparation process, as described by Bolade *et al*. (2002), is depicted in Figure 1. To tuwo, a ratio of 1 part flour to 3.5 parts water (w/v) is used. The first step involves creating a cold slurry by mixing 20% of the desired quantity of flour (1 kg) with 25% of the desired quantity of water (3.5L). Next, 60% of the water is brought to a boil. The previously prepared cold slurry is then added to the boiling water while vigorously stirring with a wooden flat spoon until a porridge-like consistency is achieved. Gradually, the remaining 80% of the flour is added to the boiling mixture, ensuring continuous stirring to prevent the formation of lumps and to ensure a smooth, uniform gel. The remaining 15% of the water is added to the gel, and the mixture is covered without stirring. It is then allowed to cook for approximately 5-7 minutes. After this, vigorous stirring is performed to ensure the smoothness of the gel. The end result is tuwo, a stiff dough ready for consumption.

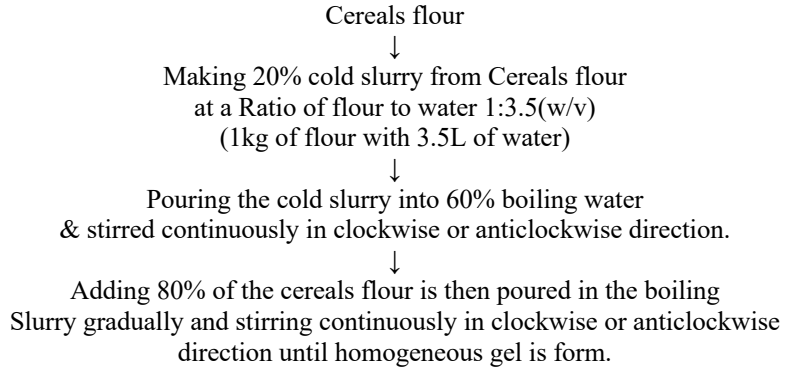

↓
15% of H_2O is finally added and covered
& allow cooking for 5 minutes
↓
Finally, it is stirred vigorously
to ensure smoother gel.
↓
End product
(Tuwo)

Figure 1: Flow chart for the preparation of stiff dough (*tuwo*).
Source: Bolade *et al*, (2002)

2. Common cereal crops used in Tuwo production

Cereals are the grains of cultivated grasses belonging to the Poaceae family (formerly Graminae), and they are known for their affordability and adaptability to various climates (Abebaw, 2018). Cereal grains, such as rice (Oryza sativa L.), corn (Zea Mays L.), wheat (Triticum aestivum L.), oats (Avena sativa L.), and sorghum (Sorghum bicolor (L.) Moench), are widely cultivated in Nigeria and serve as staple foods globally (Abebaw, 2018; Fardet, 2010; Muhammad *et al*., 2013).

Studies indicate that cereals are rich sources of carbohydrates, comprising approximately 72% of their nutritive content. They also contain about 12% protein, 12% water, 2% fat, 1% minerals (such as calcium and iron), and 1% vitamins (B and E) (Kulp and Ponte, 2000). However, cereals are relatively poor sources of protein, which is a significant concern as they contribute to more than 70% of the dietary intake in developing countries (Anigo *et al*., 2010). Additionally, antinutrients like phytic acid can hinder the absorption of essential minerals like calcium, magnesium, zinc, and iron (Lestienne *et al*., 2005; Gupta *et al*., 2015; Sandberg, 2000). One of the challenges faced with the acceptability of stiff dough (tuwo) made from cereals flour is its poor textural quality. This is evident in difficulties with molding, rapid retrogradation, and gel instability after cooling (Bolade *et al*., 2009).

2.1 Corn

Corn, scientifically known as Zea mays L., is a cereal grain and a member of the Poaceae family. It is widely cultivated worldwide and ranks as the third most important crop globally, following rice and wheat (Sandhu *et al*., 2007). Corn holds significant economic and agricultural importance, serving as a staple food in many regions, including Africa (Olakojo *et al*., 2005; Mboya *et al*., 2011). It is grown in all six ecological zones of Nigeria and plays a vital role in providing income for farming households. Corn also serves as a valuable raw material for various agro-based industries (Oluwatayo *et al*., 2008; Babatunde *et al*., 2008).

2.2 Sorghum

Sorghum, scientifically known as Sorghum bicolor L. Moench, has been a staple food in Asia and Africa for centuries. It belongs to the Poaceae family, specifically the tribe Andropogoneae and the subtribe Sorghinae, with all cultivated sorghum falling under Sorghum bicolor subsp. bicolor. Sorghum exhibits variations in its morphology, influenced by different varieties and growing conditions. While traditionally used as livestock feed, sorghum also serves as food and finds applications in various industries (Rooney and Waniska, 2000).

Sorghum is recognized as one of the key grains contributing to approximately 85% of the world's food energy supply, with Africa playing a significant role (Henley *et al*., 2010). It holds promise for increased human consumption due to its abundance of beneficial phytochemical components (Awika and Rooney, 2004; Taylor and Belton, 2002). Sorghum is a resilient crop that can adapt to diverse soil conditions and is consumed in various forms, including pasta, boiled grains, and traditional beverages (Kayodé, 2006). The starch present in sorghum plays a vital role in producing a wide range of sorghum-based food products, such as bread (Schober *et al*., 2005).

2.3 Effect of pre-treatment methods on the qualities of cereal flour

Bolade (2010) conducted a study to evaluate the suitability of commercially available corn grains for the production of 'stiff dough' in Nigeria. The research found that the corn varieties used exhibited different physical characteristics in their kernels, varied physicochemical properties in their flours, and different rheological properties of the resulting corn stiff dough. Additionally, the assessment of organoleptic properties showed variations among the corn varieties.In another study by Bolade and Adeyemi (2012), the quality dynamics of corn 'stiff dough' were investigated, focusing on the influence of steaming corn grits at different resident times. The findings revealed that pre-gelatinization of starch through maize grit steaming enhanced the textural and sensory quality attributes of the corn-based dumplings. Optimal results were obtained with a 30-minute steaming duration, which significantly improved the sensory attributes of the corn stiff dough. The practical application of this research is relevant for both household and commercial production of high-quality corn flour for stiff dough preparation.

Olajide and Nsakpuma (2019) studied the functional properties of corn flour and the stability of its paste (stiff dough) by incorporating baobab pulp and using different processing methods. The research demonstrated that grit soaking operation improved the functional and sensory properties of corn flour intended for stiff dough production. Furthermore, the inclusion of baobab pulp enhanced the properties of corn flour produced through both grit soaking and grit non-soaking methods. The addition of 5% baobab pulp resulted in the best stability of stiff dough produced by grit soaking, while 10% baobab pulp inclusion yielded the best stability for stiff dough produced by grit non-soaking. Storing the stiff dough under refrigerated conditions also improved paste stability compared to ambient storage. This study emphasized the positive impact of baobab pulp inclusion on the quality of corn flour and the stability of stiff dough.

Mella (2011) investigated the effects of malting and fermentation on the composition and functionality of sorghum flour. The research revealed that both malting and fermentation processes can improve the nutritional quality of sorghum flour. These methods resulted in changes in the composition and functionality of sorghum kernel components, which positively impacted the nutritional quality and increased the consumption of sorghum food products. The study recommended further investigations to determine the amounts of reducing sugars, proteins, and amino acids in flour samples, as well as functional property analysis of products made from pre-treated sorghum flours.

Shabir and Sowriappan (2013) studied the effect of soaking temperature on the physical and functional properties of parboiled rice cultivars in India. The research found that higher soaking water temperatures increased the hardness value, leading to increased milling yield of rice. Parboiling significantly decreased the pasting properties of rice samples, with more severe decreases observed at lower temperatures, specifically 80˚C.

Opeyemi *et al* (2016) explored the effect of malted sorghum on the quality characteristics of wheat-sorghum-soybean flour, particularly for potential use in confectionaries. The study revealed that malting sorghum can enhance the nutritional quality of flours used in the production of value-added products like confectionaries.

Kaur (2011) investigated the functional properties and anti-nutritional factors present in cereal bran. The study highlighted that bran is an excellent source of dietary fiber, which improves the nutritional and nutraceutical benefits of whole grains. Cereal brans possess favorable functional properties such as bulk density, water absorption, and fat absorption. Additionally, cereal bran aids in increasing the shelf life of products and facilitates calorie reduction. However, anti-nutritional factors such as phytic acid, polyphenols, tannins, oxalates, saponins, and trypsin inhibitors limit the potential of cereal brans as high-quality feed ingredients.

Fulufhelo *et al* (2018) investigated the effect of germination period on the physicochemical, functional, and sensory properties of finger millet flour and porridge. The study showed that germination positively influenced some physicochemical, functional, and sensory properties of finger millet flour and porridge. Germination resulted in decreased pH and viscosity while increasing the oil and water absorption capacity and solubility of germinated finger millet flour samples. However, the swelling power and bulk density of the flour samples significantly decreased with longer germination periods. The study suggested that germinated finger millet flour could be used as an ingredient in various foods, including baby food, sauces, and cakes, due to its improved functional properties.

Chandra *et al* (2013) assessed the functional properties of different flours, focusing on the trend of utilizing novel sources of protein, fat, vitamins, and minerals in bakery products to reduce the proportion of wheat flour. The addition of green gram flour and potato flour was found to enhance the functional properties and nutritional quality of the value-added products.

Sharma *et al* (2018) worked on the development of functional flour using malted cereals and legumes. The research demonstrated that malting improved the nutritional and physicochemical characteristics of sorghum-based composite flour mixtures. Food products developed using these composite flour mixtures exhibited significant functional properties, including protein content, crude fibre, phytonutrients (particularly phenolic compounds), and minerals, along with potent antioxidant capacity. The study emphasized the importance of popularizing the consumption of sorghum through the commercialization of value-added products to meet the changing lifestyle preferences of people.

Kulamarva *et al* (2019) focused on the nutritional and rheological properties of sorghum. The research highlighted that despite the absence of gluten, which makes sorghum suitable for gluten-intolerant populations, it possesses poor rheological properties. The study suggested that incorporating sorghum into composite flours with other cereals and legumes could effectively enhance the nutritional and rheological properties. Further research on processing techniques and their effects on the nutritional and viscoelastic properties of sorghum could contribute to increasing the utilization of sorghum in human diets.

2.4 Possible Methods of Enhancing the Quality of Tuwo

Germinated grains offer beneficial nutrients to humans, and the germination process also reduces anti-nutritional factors (Tian *et al*., 2010; Hemalatha *et al*., 2007; Dicko *et al*., 2005; Noda *et al*., 2004). Sprouting provides a rich

source of phytochemicals, minerals, vitamins, enzymes, and essential amino acids, which have positive effects on human health (Gan *et al*., 2017).

Pretreatment processes significantly influence the appearance, texture, and nutritional content of cereal flour. Enhancing the nutritional quality and sensory properties (taste, appearance, aroma, and texture) of cereal-based foods can be achieved through genetic improvement, fortification or supplementation of amino acids (Kaukovirta-Norja *et al*., 2004). Processing technologies, such as milling, malting, fermentation, and sprouting, are employed to utilize protein-rich sources in cereals. Increasing the germination rate results in higher soluble sugar content for fermentation (Kouakou *et al*., 2008). Traditional methods of food preparation, including fermentation, cooking, and malting, improve the nutritional quality of food by reducing specific anti-nutrients like phytic acid, polyphenols, and oxalic acid.

Germinated cereal seeds are a good source of ascorbic acid, riboflavin, choline, thiamine, tocopherols, and pantothenic acid (Sangronis and Machado, 2007). Germinated and coarsely ground grains increase the protein content and improve protein digestibility. Furthermore, malting reduces the concentration of anti-nutritional factors like phytates, thus enhancing the nutritional quality of malted grains (Traore *et al*., 2004). The viscosity of foods is also reduced through malting, making them more suitable for frequent consumption (Ikujenlola and Fashakin, 2005).

3. CONCLUSION

Despite the series of work that was carried out on the processing of cereal grains to better cereal flour for quality stiff dough *tuwo* production. The nutritional and functional quality can be improved by adequately varying the blanching, soaking and malting duration/temperature. The present of anti-nutrients in corn and sorghum which depletes most of the vital nutrients can be reduced or removed by proper pre-treatment methods. Optimized cereals flour can be produced and its composite flour for better quality *tuwo* production.

REFERENCES

Abebaw, D. (2018) Cereal Crops Research Achievements and Challenges in Ethiopia. *International Journal of Research Studies in Agricultural Science*. 4, 23-29 ISSN No. (Online).2454–6224.

Adom K. K., & Liu R H. (2002). Antioxidant Activity of Grains. *Journal on Agricultural Food Chemistry*. 9.50(21), 6182-7.

Amaducci S, Amaducci M.T., Benati R & Venturi G. (2000). Crop Yield and Quality Parameters of Four Annual Fibre Crops (hemp, kenaf, maize and sorghum) in the North of Italy. *Journal on Industrial Crops and Products* 11, 179–186.

Awika, J.M. & Rooney, L.W. (2004). Sorghum Phytochemicals and their Potential Impact on Human Health. Phytochemistry. *Journal of Human Health*. 65, 1199-1221.

Anigo, K.M, Ameh, D.A., Ibrahim, S. & Danbauchi, S.S. (2010). Nutrient Composition of Complementary Food Gruels Formulated from malted cereals, soybeans and groundnut for use in North-western Nigeria. *African Journal of Food Science* 4(3), 65-72.

Bolade, M.K, Usman M.A, Rasheed A.A, Benson, E.L, & Salifou, I. (2002). Influence of hydrothermal treatment of maize grains on the quality and acceptability of tuwon masara (traditional maize gel). *Food Chem.,* 79, 479-483.

Bolade, M.K (2009). Effect of flour production methods on the yield, physicochemical properties of maize flour and rheological characteristics of a maize-based non-fermented food dumpling. *Afr J Food Sci,* 3, 288–298.

Bolade, M.K. (2010). Evaluation of suitability of commercially available maize grains for 'tuwo' production in Nigeria. Department of Food Science and Technology, Federal University of Technology, P. M. B. 704, Akure, Ondo State, Nigeria. *African Journal of Food Science.* 4(6), 371-381. matbolade@yahoo.co.uk.

Bolade M.K & Adeyemi I.A. (2012). Quality dynamics of maize 'tuwo' (non-fermented maize-based dumpling) as influenced by steaming of maize grits at different resident time. Association of Food Scientists & Technologists (India). *Journal Food Science Technology*. 51(11),3217–3225. DOI 10.1007/s13197-012-0852-3

Brigid, M. (2004). Nutritional Aspects of Cereals. Nutrition Scientist. *Journal for British Nutrition Foundation*, High Holborn House, 52–54.

Chandra, S. & Samsher (2013). Assessment of Functional Properties of different Flours. Department of Agricultural Engineering and Food Technology, S.V. Patel University of Agriculture and Technology, Modipuram, Meerut (UP) - India. *African Journal of Agricultural Research.* 8(38), 4849-4852. DOI: 10.5897.

Dicko M.H, Gruppen H, Traore A.S, Van Berkel W.J, & Voragen A.G. (2005). Evaluation of the Effect of Germination on Phenolic Compounds and Antioxidant Activities in Sorghum Varieties*. Journal Agriculture for Food Chemistry*. 53(7), 2581-2588.

Dillon, S.L., Shapter, F.M., Henry R.J., Cordeiro, G., Izquierdo, L., & Lee, L.S. (2007). Domestication to Crop Improvement*: Journal of Genetic Resources for Sorghum and Saccharum* 1270.

Dubois, V., Breton S., Linder M., Fanni, J., & Parmentier, M. (2007). Fatty Acid Profiles of 80 Vegetable Oils with regard to their Nutritional Potential. *Europian Journal for Lipid Science Technology* (109), 710 -732

Fardet A (2010) new hypotheses for the health-protective mechanisms of whole-grain cereals: what is beyond fibre? *Nut Res Rev.* 23(1),65–134.

Fulufhelo, E. Nefale, N., & Mpho E.M. (2018). Effect of Germination Period on the Physicochemical, Functional and Sensory Properties of Finger Millet Flour and Porridge. Department of Food Science and Technology, School of Agriculture, University of Venda, Private Bag X5050, Thohoyandou, 0950. South Africa. *Asian Journal of Applied Sciences*. (ISSN: 2321 – 0893), 06.

Gan, R.Y., Lui, W.Y., Wu, K., Chan. C.L., Dai, S.H., Sui Z.Q., & Corke, H.H. (2017). Bioactive compounds and bioactivities of germinated edible seeds and sprouts: an updated review. *Trends Food Sci. Technol.* 59,1–14.

Gupta, R.K., Gangoliya, S.S., & Singh, N.K. (2015). Reduction of phytic acid and enhancement of bioavailable micronutrients in food grains. J Food Sci Technol 52(2), 676–684.

Hemalatha, S., Platel, K., & Srinivasan, K. (2007) Influence of germination and fermentation on bioac cessibility of zinc and iron from food grains. Eur J Clin Nut 61(3), 342.

Henley, E.C., Taylor, J.R.N., & Obukosia, S., (2010). The importance of Dietary Protein in Human Health: Combating Protein Deficiency in Sub-Saharan Africa through transgenic biofortified Sorghum. *Advance in Food and Nutrition Response.* 60, 21-52.

Houssou, P., & Ayemor, G.S. (2002). Appropriate Processing and Food Functional Property of Maize Flour. *African Journal of Science and Technology*.126–131.

Ikujenlola V.A. & Fashakin J.B. (2005). The Physico-Chemical Proiperties of a Complementary diet prepared from vegetable proteins. *Journal of Food Agriculture and Environment*. 3(3 and 4), 23-26.

Kaur, S., Sharma, S. & Nagi, H. P. S. (2011). Functional properties and anti-nutritional factors in cereal bran. Department of Food Science and Technology, Punjab Agricultural University,

Kouakou, B., Alexis K.K, Adjehi, D., Marcelin D. K. & Dago, G. (2008). Biochemical changes occurring during germination and fermentation of millet and effect of technological process on starch hydrolysis by the crude enzymatic extraction of millet. *Journal of Applied Science Response* 4(11), 1502-1510.

Kulp, K., & Ponte J.G. (2000). Handbook of Cereal Science and Technology, 2nd edn. Marcel Dekker, New York.

Kulamarva, A.G., Venkatesh, R. & Raghavan, G.S. (2009). Nutritional and Rheological Properties of Sorghum', International Journal of Food Properties, 12: 1, 55 — 69 To link to this Article: DOI: 10.1080/10942910802252148 URL: http://dx.doi.org/10.1080/10942910802252148.

Lestienne, I., Rivier, C.M., Verniere, C.I., Rochette, I. & Treche. S. (2005). The Effects of soaking of whole, dehulled and ground millet and soybean seeds on phytate degradation and Phy/Fe and Phy/Zn molar ratios. *International Journal for Food Science Technology.* 40(4), 391-399

Mboya, R, Tongoona, P, Derera, J, Mudhara, M & Langyintuo, A. (2011). The Dietary, Importance of Maize in Katumba ward, Rungwe district, Tanzania and its contribution to household food security. *African Journal of Agricultural Research*. 6(11), 2617-2626.

McCan, J. (2001). Maize and Grace: History, Corn, and Africa's New Landscapes, 1500–1999. Comparative Studies in Society and History 43 pp: 246-272.

Mella N.O. (2011). Effects of Malting and Fermentation on the Composition and Effects of Malting and Fermentation on the Composition and Functionality of Sorghum Flour Functionality of Sorghum Flour. Dissertations, Theses, & Student Research in Food Science and Technology Food Science and Technology Department. Mella University of Nebraska-Lincoln, Onoilula@yahoo.co.uk

Muhammad, H.S., Muhammad, F.S., Muhammad S., Niaz A.Q., & Safia M. (2013). The importance of cereals (Poaceae: Gramineae) nutrition in human health: A Review. 4(3), 32-35. DOI 10.5897/JCO12.023 ISSN 2141-6591.

Noda Canberra, T., Takigawa S., Matsuura-Endo C, Saito K, Takata K, Tabiki T, & Yamauchi H.H. (2004) The physicochemical properties of partially digested starch from sprouted wheat grain. Carbohyd Polymers 56(3):271–277

Olakojo, S.A., Kogbe, J.O, Iken, J.E., & Daramola, A.M. (2005). Yield and Disease Evaluation of Some Improved Maize (Zea mays L) varieties in South Western Nigeria. Trop. Subtrop. Agroecosyst. 5: 51-55.

Opeyemi. O.A., Stephen, A.A. & Oluwatooyin F.O. (2016). Effect of Malted Sorghum on Quality Characteristics of Wheat-Sorghum-Soybean Flour for Potential Use in Confectionaries. Department of Food Science and Technology, Federal University of Technology, Akure, Nigeria. Food and Nutrition Sciences.1241-1252 http://www.scirp.org/journal/fns.

Orhun, G.E. (2011). Maize Oil for Health Importance. 4th Annual International Symposium on Agricultural Research, Atiner

Rooney, L.W., & Waniska, R.D. (2000). Sorghum Food and Industrial Utilization. In: Sorghum: Origin, History, Technology, and Production. 689-750.

Sandberg, A.S. (2000). Bioavailability of minerals in legumes: *Journal of mineral bioavailability*.281-285.

Sandhu, K.S., Singh, N., & Malhi, N.S. (2007). Some properties of corn grains and their flours I: Physicochemical, functional and chapati-making properties of flours. *Journal of Food Chemistry,* 101, 938–946. http://dx.doi.org/10.1016/j.foodchem.2006.02.040

Sangronis, E. & Machado, C. (2007). Influence of Germination on Nutritional Quality of Phaseous vulgaris and Cajanus cajan. *Journal for Science Technology*, 116-120.

Shabir, A.M. & Sowriappan, J.D. (2013). Effect of Soaking Temperature on Physical and Functional Properties of Parboiled Rice Cultivars Grown in Temperate Region of India. Department of Food Science and Technology, Pondicherry University, Puducherry, India. *Journal of Food and Nutrition Sciences,* 2013, 4, 282-288. sjdbosco@yahoo.com.

Sharma, M., Das, M. & Alam, S. (2018). Development of functional flour using malted cereals and legumes. Assam Agricultural University Jorhat, College of Community Science, Student Dept. of Food Science and Nutrition, Assam, India. *International Journals for Home Science.* 4(3), 36-42.

Taylor, J.R., & Belton, P.S. (2002). Sorghum. Pages 26-91 in: *Journal of Pseudocereals and Less Common Cereals.*

Thompson T. (2000). Questionable foods and the gluten-free diet: Survey of current recommendations. *Journal Am. Diet. Association*. 100; 463-465.

Tian, B., Xie, B., Shi, J., Wu J, Cai, Y., Xu, T., & Deng, Q. (2010) Physiochemical changes of oat seeds during germination*. Food Chem* 119(3),1195–1200.

Traore, T., Mouquet, C., Icard-Verniere, C., Traore, A.S. & Treche, S. (2004). Changes in nutrient composition phytate and cyanide contents and amylase activity during cereal malting in small production units in Ouagadougou (Burkina Faso). *Journal of Food Chemistry,* 105-114

Ünay A., Baúal H., & Konak, C. (2004). Inheritance of grain yield in a half-diallel maize population. Turk. *Journal of Agriculture*, 28, 239-244.